GCOE
Institute of Fluid Science
TOHOKU
UNIVERSITY

Eighth International Conference on Flow Dynamics

November 9-11, 2011

Hotel Metropolitan Sendai, Japan

Proceedings

Global COE Program "World Center of Education and Research for Trans-disciplinary Flow Dynamics" Tohoku University

Preface

I would like to express my heartfelt condolences to the victims of the Great East Japan Earthquake. I would also like to express my appreciation for the heartfelt support and speedy assistance received from overseas.

The earthquake happened on 11th March 2011, measuring 9.0 on the Richter scale was one of the largest recorded in our history, and the accompanying tsunami and the accident of Fukushima Daiichi Nuclear Power Plant cased enormous damage. However, our campuses proved secure and happily no injuries were sustained.

Tohoku University is currently putting all its energy into the restoration of our educational and research capabilities.

The people living in the 21st century are facing at big risks as global warming, shortage of food and energy, epidemic diseases, local starvation, poverty, and so on. In the mean time, we are always dreaming and making very best efforts for the progress of civilization by realizing higher quality of life and welfare. For those reasons, people are placing high expectations on the technology development in the frontier fields as state-of-the-art medical sciences, life sciences, IT, space technology, aviation technology, oceanology, and so forth.

"Flow Dynamics" is a comprehensive scientific field which deals with the flow and transport phenomena concerning to quantum wave, air, any fluid, any material, energy and information. Research on "Flow Dynamics" is expected to contribute to the society by challenging such crucial and unexplored tasks as above, and, by producing solutions for people's better life and dreams.

We are pleased to announce that we are strongly motivated to hold "Eighth International Conference on Flow Dynamics", ICFD2011, broadly as originally planned, aiming to explore new science horizon and cutting edge technologies of "Flow Dynamics", and to provide young researchers with unique opportunities of experience and self-development in this very attractive and competitive field of science and technology. We believe that this conference will give us a great opportunity to discuss what we have learned from this disastrous effects, how to fortify our social systems to be durable and safer under these kinds of forces of nature, and, what we can do to transform our society living in harmony with the mother nature, from the viewpoint of flow dynamics.

The Conference is comprised of 1 General Session, 13 Organized Sessions, 4 Planned Sessions and 1 Special Session.

The number of presenters will be over 400. We are glad to see the number of presenters increasing compared to last year. Your continued support will be greatly appreciated. This international conference will be a typical symbol of recovery in Tohoku area in spite of catastrophic damage of earthquake and tsunami.

On behalf of the organizing committee of the Eighth International Conference on Flow Dynamics, I express my best wishes for your very enjoyable participation, successful exchanges of fruitful information and interactions among the participants from all over the world.

Dr. Shigenao Maruyama
Distinguished Professor and Project Leader
Tohoku University Global COE Program
"World Center of Education and Research for Trans-disciplinary Flow Dynamics"

Eighth International Conference on Flow Dynamics

Organized and Sponsored by:

- The Global COE Program, "World Center of Education and Research for Trans-disciplinary Flow Dynamics"
- Institute of Fluid Science, Tohoku University

In cooperation with:

- Cryogenics and Superconductivity Society of Japan
- Combustion Society of Japan
- The Japan Society of Applied Physics
- The Japan Society of Mechanical Engineers
- Atomic Energy Society of Japan Computational Science and Engineering Division
- The International Centre for Heat and Mass Transfer (ICHMT)
- Japan Society of Maintenology, Tohoku/Hokkaido Branch
- Aoba Foundation for the Promotion on Engineering
- Fluid Sciences Foundation

SCOPE:

It was a disaster the earthquake and tsunami hit the north-eastern part of Japan on March 11, 2011. This unprecedented tragedy also left the Fukushima Dai-ichi Nuclear Power Plant crippled, on which we are continuing to put lots of efforts to stabilize in safe. During this course of the time, we have received innumerous calls, letters and e-mails from our friend worldwide expressing condolences, sympathies and support offers onto us. We, in Japan, felt comforted, encouraged and empowered tremendously by such kind of warm and heartfelt messages and offers. On behalf of all the people of Tohoku and Japan, we thank you very much for the support of you. Yes, we are all right and we shall come back soon to the ordinary course of our family life, education, research and industrial works. Here in Sendai, recovery works are proceeding fairly smoothly and we have a firm confidence in that Tohoku University shall contribute to the creation of revitalized Tohoku District and Japan. Under the circumstances, we have decided to have the annual conference ICFD2011 in November, in Sendai as ordinarily, and we like to encourage you all to join in it to contribute for the development of methodologies and practical measures for our harmonious co-existence and symbiosis with the earth and all the lives living on the planet.

The Eighth International Conference on Flow Dynamics, in the annual series, which is fully supported by Tohoku University Global COE Program "World Center of Education and Research for Trans-disciplinary Flow Dynamics (ICFD2011)" will be held on November 9th through 11th at Hotel Metropolitan Sendai, Sendai, Japan. We changed the venue from the originally planned Matsushima to Hotel Metropolitan Sendai, Sendai. The objectives of this conference are not only to explore new science horizon and exchange information in cutting edge technologies in "Flow Dynamics", but also to provide young researchers and students with unique opportunities of education and self-development.

Flow dynamics is a comprehensive scientific field which deals with the flow and transport phenomena concerning to any fluid, any material, energy and information. The scope of this conference covers the fluid, thermal, material, molecular and quantum dynamics of the multi-scale flows ranging from nano-scale flows such as behavior of molecules, atoms, ions and electrons, to gigantic scale flows such as solar radiation, air-flow, multi-phase flow, typhoon on earth, oceanic flow and volcanic flow, etc.

We cordially invite you scholars, researchers, engineers, educationists and planners in the related research and development areas of bio-, nano-, material-, energy- and environmental-sciences and technologies, particularly in the academic field of mechanical engineering, aerospace engineering, nuclear engineering, physics, medical science, chemistry, chemical engineering, to join in the conference.

CONFERENCE COMMITTEE:

General Chair:

Shigenao Maruyama (Tohoku University)

Executive Committee Members:

Keisuke Asai (ICFD2011 Chair, Tohoku University)
Kaoru Maruta (AFI/TFI-2011 Chair, Tohoku University)
Toshiyuki Takagi (CEO of ICFD2011, Tohoku University)
Toshiyuki Hayase (IFS Director, Tohoku University)

International Scientific Committee Members:

Chair: Shigenao Maruyama (Tohoku University)

Australia
- Masud Behnia (The University of Sydney)
- Gary Rosengarten (The University of New South Wales)

Canada
- Javad Mostaghimi (University of Toronto)

China
- XinGang Liang (Tsinghua University)
- Xing Zhang (Tsinghua University)

France
- Patrick Bourgin (ECL)
- Jean-Yves Cavaille (INSA de Lyon)
- Philippe Kapsa (ECL)

Germany
- Serge A. Shapiro (Freie University Berlin)

India
- Subhash C. Mishra (Indian Institute of Technology Guwahati)

Italy
- Gian Piero Celata (ENEA)

Japan
- Yu Fukunishi (Tohoku University)
- Masato Furukawa (Kyushu University)
- Nobuhide Kasagi (The University of Tokyo)
- Chisachi Kato (The University of Tokyo)
- Yoichiro Matsumoto (The University of Tokyo)
- Junichiro Mizusaki (Tohoku University)
- Kazuhiro Nakahashi (Tohoku University)
- Masami Nakano (Tohoku University)
- Tomohide Niimi (Nagoya University)
- Hideya Nishiyama (Tohoku University)
- Masaki Sano (The University of Tokyo)
- Akihiro Sasoh (Nagoya University)
- Masaaki Sato (Tohoku University)
- Toshiyuki Takagi (Tohoku University)
- Michio Tokuyama (Tohoku University)
- Takashi Yabe (Tokyo Institute of Technology)
- Satoru Yamamoto (Tohoku University)

Korea
Joon-Hyun Lee (KETEP)
Joon Sik Lee (Seoul National University)
Hyung Jin Sung (Korea Advanced Institute of Science and Technology)
Russia
Mikhail Ivanov (Institute of Theoretical and Applied Mechanics SB RAS)
Oleg P. Solonenko (Insitute of Theoretical and Applied Mechanics SB RAS)
Alexander Vasiliev (Moscow State University)
Sweden
Fredrik Lundell (KTH)
Switzerland
Bastien Chopard (University of Geneve)
Dimos Poulikakos (ETH Zurich)
Taiwan
Wu-Shung Fu (National Chiao Tung University)
UK
Yiannis Ventikos (University of Oxford)
USA
Louis N. Cattafesta III (University of Florida)
Yiguang Ju (Princeton University)
Kozo Saito (Kentucky University)
John P. Sullivan (Purdue University)
Rongia Tao (Temple University)
Satish Udpa (Michigan State University)

Organizing Committee Members:

Chair: Keisuke Asai (Tohoku University)
Hideyuki Aoki, Shinji Ebara, Yu Fukunishi, Hidetoshi Hashizume, Nozomu Hatakeyama, Yuka Iga, Jun Ishimoto, Takatoshi Ito, Tetsuya Kodama, Atsuki Komiya, Kaoru Maruta, Goro Masuya, Hiroyuki Miki, Hideo Miura, Akira Miyamoto, Junichiro Mizusaki, Kazuhiro Nakahashi, Masami Nakano, Hideya Nishiyama, Shigeru Obayashi, Taku Ohara, Katsuhide Ohira, Makoto Ohta, Seiji Samukawa, Mamiko Sasao, Kazuhisa Sato, Takehiko Sato, Keisuke Sawada, Atsuhi Shirai, Yuriko Takeshima, Takashi Tokumasu, Michio Tokuyama, Tetsuya Uchimoto, Yutaka Watanabe, Shigeru Yonemura, Noritaka Yusa

Administrative Staff

Farouq Ahmed, Mehdi Baneshi, Arunabhiram Chutia, Ardian Gojani, Natsuko Hatakeyama, Mizuho Ito, Kaoru Kano, Hiroyuki Kosukegawa, Hisanori Masuda, Tomomi Nagayoshi, Fumio Saito, Yuko Sasaki, Yuko Shimokawara, Ryoko Suzuki, Masashi Takeyama, Naoto Wada, Pengfei Wang

Plenary Lectures

Energy Sustainability: A Combustion Perspective

Suk Ho Chung (King Abdullah University of Science and Technology, Saudi Arabia)
(10:00-10:50, November 9, at SENDAI (EAST))

Transport Phenomena, Fluid Mechanics and Multiscale Modelling Techniques for Clinical Decision Support

Yiannis Ventikos (University of Oxford, UK)
(11:00-11:50, November 9, at SENDAI (EAST))

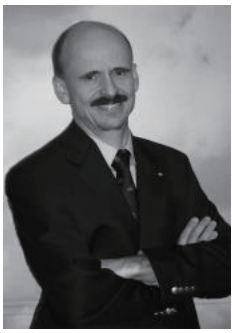

Low-Order Aeromechanical Modeling for Conceptual Design of Fuel-Efficient Aircraft

Mark Drela (MIT, USA)
(8:00-8:50, November 10, at SENDAI (EAST))

Sessions

General Session:

- GS1: General Session

Organized Sessions:

- OS1: Next-Generation CFD
  Organizer: K. Nakahashi, H. Kobayashi, S. Obayashi, S. Yamamoto and K. Yamamoto (Tohoku University)

- OS2: Advanced Control of Smart Fluids and Fluid Flows
  Organizer: M. Nakano, Y. Fukunishi (Tohoku University)

- OS3: Wind Tunnel Experiment on Unsteady Phenomena
  Organizer: S. Izawa, H. Nagai (Tohoku University)

- OS4: Research Frontiers in Green Aviation
  Organizer: S. Obayashi, K. Asai (Tohoku University) and S. Watanabe (JAXA)

- OS5: Research Frontiers in Green Hybrid Rocket Propulsion
  Organizer: T. Shimada (JAXA), K. Sawada (Tohoku University)

- OS6: Aerodynamics for Mars Exploration Aerial Vehicle
  Organizer: H. Nagai(Tohoku University), A. Oyama (JAXA)

- OS7: Thermal-Fluid Flows and Plasma Physics
  Organizer: W. S. Fu, C.Y. Chen (National Chiao Tung University, Taiwan)

- OS8: Flow-induced Degradations in Piping Systems of Nuclear Power Plants
  Organizer: Y. Watanabe, T. Takagi (Tohoku University) and Joël Courbon (INSA-Lyon, France)

- OS9: Fluid-induced Seismicity: Modeling and Application
  Organizer: T. Ito, H. Asanuma (Tohoku University)

- OS10: Biofluid for Medical Application
  Organizer: T. Nakayama, M. Ohta (Tohoku University)

- OS11: Micro Channels and Membrane Proteins
  Organizer: N. Tomita, M. Ohta (Tohoku University)

- OS12: The Seventh International Students/Young Birds Seminar on Multi-Scale Flow
  Organizer: Y. Shimizu, R. Sakai and J. F. Torres (Tohoku University)
  Supervisor: J. Mizusaki, K. Sato, Y. Iga, A. Komiya(Tohoku University)

- OS13: Clean and Efficient Combustion Technology (AFI/TFI-2011)
  Organizer: O. Fujita (Hokkaido University), K. Maruta (Tohoku University)

Planned Sessions:

- PS1: IFS Collaborative Research Forum (AFI/TFI-2011)
  Organizer: K. Maruta (Tohoku University)

- PS2: 5th Functionality DEsign of the COntact Dynamics: (DECO2011)
  Organizer: T. Takagi, H. Miki (Tohoku University) and Julien Fontaine (LTDS, France)

- PS3: Plasma Medicine and Cell Engineering
  Organizer: T. Sato (Tohoku University), T. Ohashi (Hokkaido University) and T. Hirata (Tokyo City University)

  PS4: The 12th Japan-Korea Students' Symposium New Energy Flow for Sustainable Society －Properties and Applications of Energy Materials－
  Organizer: M. Shimizu (Tohoku University), J. Wonhyo (Seoul National University)
  Supervisor: J. Mizusaki (Tohoku University), H. I. Yoo (Seoul National University)

Special Session:

- Memorial Session for the Late Professor Hiroshi Higuchi, Syracuse University, USA
  Organizer: T. Hayase (Tohoku University)

General Information

Registration:
8:00 - , Wednesday, November 9
The conference registration desk is located in the lobby, 4th floor in the morning. It will be moved to 3rd floor in the afternoon.

7:30 - , Thursday, November 10
The conference registration desk is located in the lobby, 3rd floor.

7:50 - , Friday, November 11
The conference registration desk is located in the lobby, 3rd floor.

Opening: (at SENDAI (EAST))
9:30- , Wednesday, November 9

Students/Young Birds Friendship Night: (at SAKURA HALL, Tohoku University)
18:00 – 20:00, Wednesday, November 9
All students and young researchers can attend to Students/Young Birds Friendship Night.

Banquet: (at SENDAI)
18:30 – 21:00, Thursday, November 10

Internet access corner
All conference attendees may use internet for free. Free Ethernet access will be possible during the conference at 3rd floor. Standard wired hubs (with RJ45 sockets) will be provided for networking.

Coffee service:
Coffee is served in the lobby, 3rd floor.

ICFD2011 Secretariat:
COE Building, Institute of Fluid Science, Tohoku University
2-1-1, Katahira, Aoba, Sendai, 980-8577, Japan
Phone&Fax: +81-22-217-5301 E-mail: icfd2011@gcoe.ifs.tohoku.ac.jp

3rd floor (AKEBONO, SEIUN, FUJI)

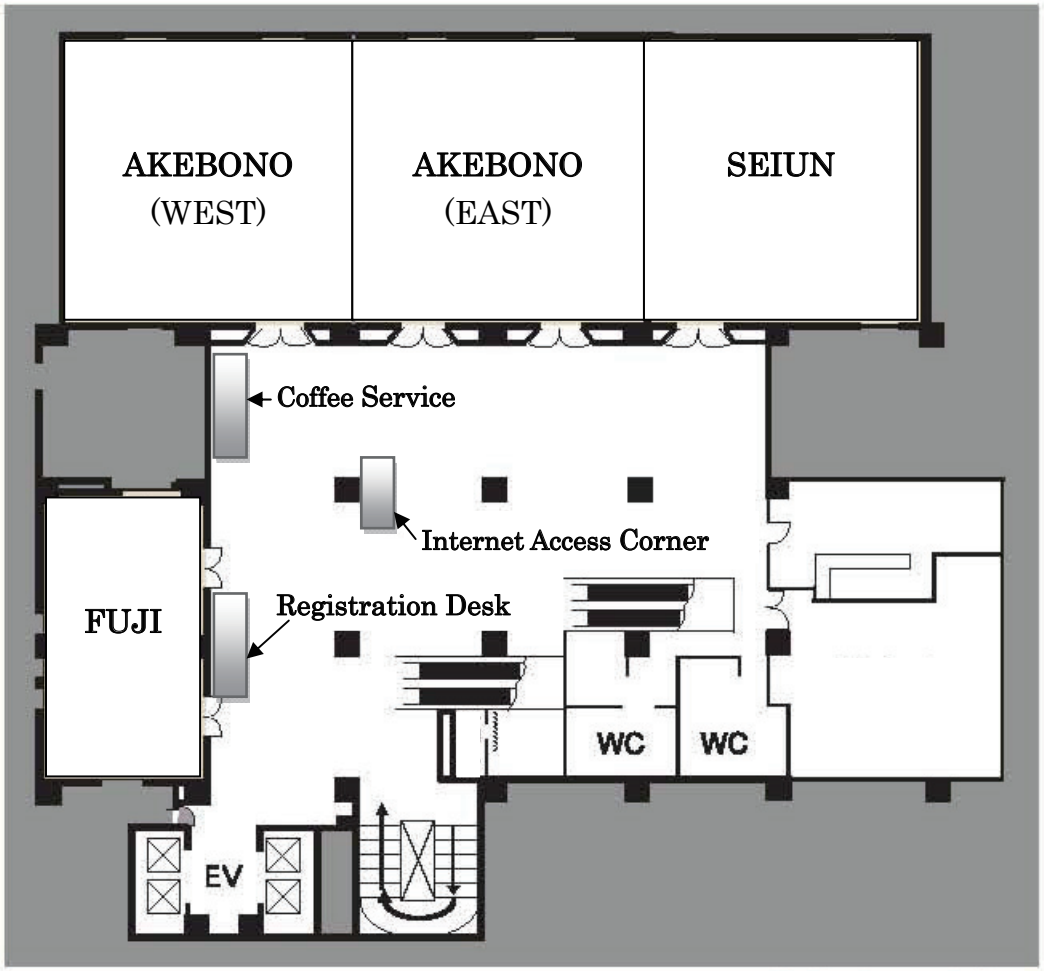

4th floor (SENDAI, FUYOH, HAGI)

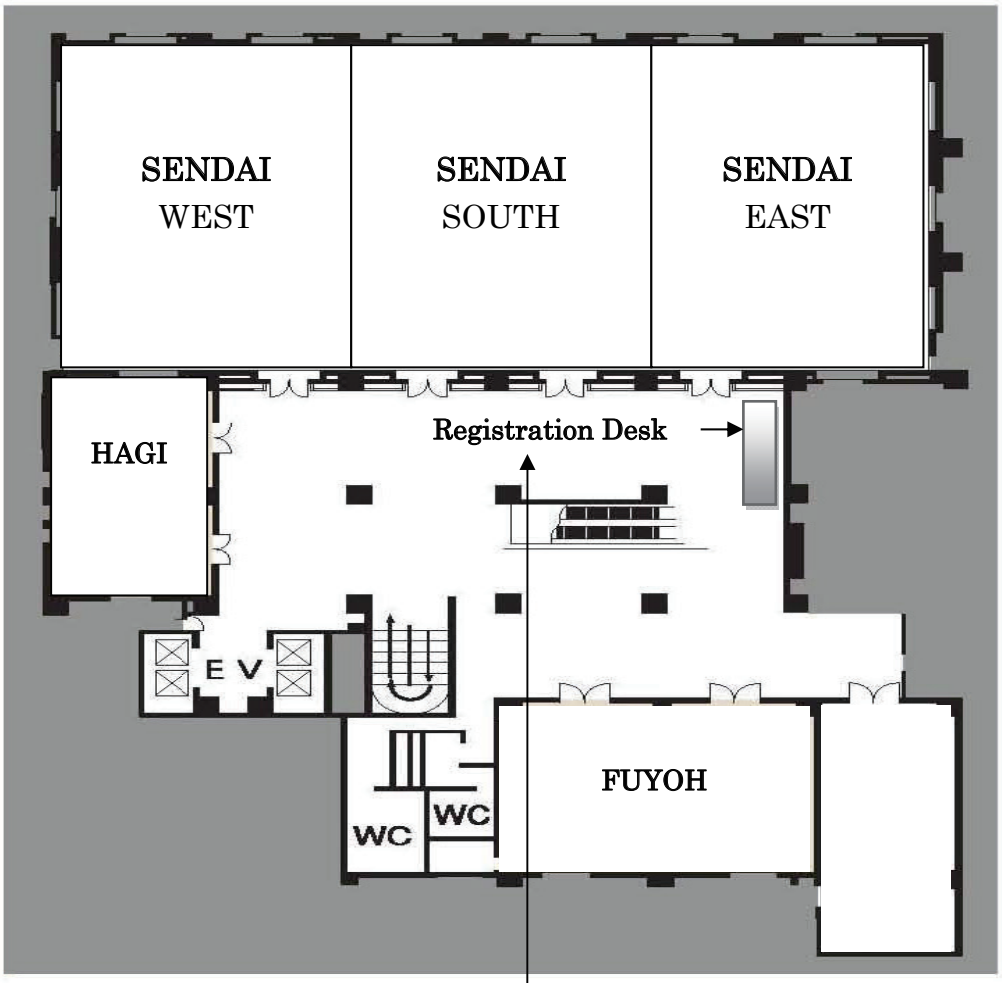

The conference registration desk is located in the lobby, on 4th floor in the morning of November 9.
Then, it will be moved to 3rd floor in the afternoon onwards.

21st floor (La Boaune)

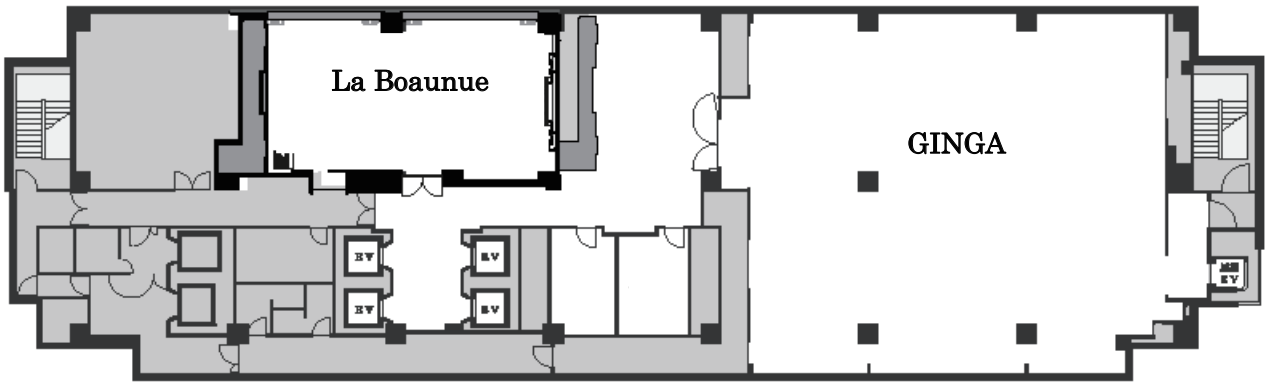

8th ICFD (2011) Time Table

Wednesday, November 9, 2011

ROOM	AKEBONO (WEST)	AKEBONO (EAST)	SEIUN	FUJI	SENDAI (EAST)
Floor	3rd Floor				4th Floor
8:00					
9:00					
10:00	9:30-10:00 **Opening Address** @SENDAI (EAST)				
	10:00-10:50 **Plenary Lecture** @SENDAI (EAST) "Energy Sustainability: A Combustion Perspective" Suk Ho Chung (King Abdullah University of Science and Technology, Saudi Arabia)				
11:00	BREAK				
	11:00-11:50 **Plenary Lecture** @SENDAI (EAST) "Transport Phenomena, Fluid Mechanics and Multiscale Modelling Techniques for Clinical Decision Support" Yiannis Ventikos (University of Oxford, UK)				
12:00					
13:00	13:00-13:05 Opening 13:05-(14:05) OS12-1 - OS12-20 Session 1 -Award Session- *Short Oral Presentation*	13:00-13:35 OS8-1 John M. Pietralik (Invited)		13:00-13:30 OS13-1 Yiguang Ju (Invited)	
		13:35-14:00 OS8-2 Toshiaki Ikohagi (Invited)		13:30-14:00 OS13-2 Vladimir E. Zarko (Invited)	
14:00	(14:05-16:05) OS12-1 - OS12-20 *Poster Presentation*	14:00-14:25 OS8-3 Satish Udpa (Invited)	14:00-14:40 OS5-1 Carmine Carmicino (Invited)	BREAK	
		14:25-14:50 OS8-4 Fumio Kojima (Invited)		14:10-14:30 OS13-3 Hideaki Kobayashi	
		BREAK	14:40-15:00 OS5-2 Shintaro Iwasaki	14:30-14:50 OS13-4 Shenqyang Steven Shy	
15:00		15:00-15:25 OS8-5 Fumio Inada (Invited)	15:00-15:20 OS5-3 Sakashi Hatagaki	14:50-15:10 OS13-5 Ayane Johchi	
		15:25-15:50 OS8-6 Nobuyuki Fujisawa (Invited)	15:20-15:40 OS5-4 Harunori Nagata	15:10-15:30 OS13-6 Makito Katayama	
			BREAK	BREAK	
16:00		15:50-16:15 OS8-7 Jun Ishimoto (Invited)	16:00-16:40 OS5-5 Arif Karabeyoglu (Invited)	15:40-16:00 OS13-7 Mohammad Akram	
		16:15-16:35 OS8-8 Hiroaki Kikkawa		16:00-16:20 OS13-8 Sergey Minaev	
	16:30-17:00 GS1-1 Sung Jin Kim (Invited)	16:35-16:55 OS8-9 Hiroshi Abe		16:20-16:40 OS13-9 Jeongmin Ahn	
17:00		BREAK	16:40-17:00 OS5-6 Koki Kitagawa	16:40-17:00 OS13-10 Takeshi Yokomori	
	17:00-17:20 GS1-2 Makatar Wae-Hayee	17:05-17:30 OS8-10 Gábor Vértesy (Invited)	17:00-17:20 OS5-7 Takafumi Ishiguro	BREAK	
	17:20-17:40 GS1-3 Toshimi Takagi		17:20-17:40 OS5-8 Takakazu Morita	17:10-17:30 OS13-11 Mitsumasa Ikeda	
	BREAK	17:30-17:55 OS8-11 Joël Courbon (Invited)	BREAK	17:30-17:50 OS13-12 Osamu Fujita	
18:00	17:50-18:10 GS1-4 Wakana Iwakami Nakano	17:55-18:20 OS8-12 Zhenmao Chen (Invited)	18:00-18:40 OS5-9 Alberto Guardone (Invited)		
	18:10-18:30 GS1-5 Takeshi Sugimoto	18:20-18:40 OS8-13 Ryoichi Urayama			
	18:30-18:50 GS1-6 Daiki Terakado	18:40-19:00 OS8-14 Shejuan Xie	18:40-19:00 OS5-10 Shigeru Aso		
19:00	18:50-19:10 GS1-7 Hiroaki Konno		BREAK		
			19:20-19:40 OS5-11 Kang Ming Chuang		
			19:40-20:00 OS5-12 Shinya Maruyama		
20:00			20:00-20:20 OS5-13 Keisuke Sotozono		
21:00					

FUYOH	HAGI	La Boaune	SAKURA HALL (Tohoku University)	ROOM
4th Floor		21st Floor	Katahira Campus	Floor
				8:00
				9:00
9:30-10:00 **Opening Address** @SENDAI (EAST)				10:00
10:00-10:50 **Plenary Lecture** @SENDAI (EAST) "Energy Sustainability: A Combustion Perspective" Suk Ho Chung (King Abdullah University of Science and Technology, Saudi Arabia)				
BREAK				11:00
11:00-11:50 **Plenary Lecture** @SENDAI (EAST) "Transport Phenomena, Fluid Mechanics and Multiscale Modelling Techniques for Clinical Decision Support" Yiannis Ventikos (University of Oxford, UK)				
				12:00
13:00-13:40 OS6-1 Kojiro Suzuki (Invited)	13:00-13:10 Opening Remarks			13:00
	13:10-13:50 OS9-1 Françoi Henri Cornet (Invited)			
13:40-14:00 OS6-2 Masaru Koike		13:30-14:00 OS7-1 Subhash C. Mishra (Invited)		
14:00-14:20 OS6-3 Koju Hiraki	13:50-14:30 OS9-2 Michael Fehler (Invited)	14:00-14:20 OS7-2 Ching-Shii Wang		14:00
14:20-14:40 OS6-4 Masahiro Kanazaki		14:20-14:40 OS7-3 Yao-Hsien Liu		
BREAK	BREAK	14:40-15:00 OS7-4 Ramjee Repaka		
15:00-15:20 OS6-5 Shintaro Shigeoka	14:45-15:25 OS9-3 Xinglin Lei (Invited)	15:00-15:20 OS7-5 Ching-Yao Chen		15:00
15:20-15:40 OS6-6 Gaku Sasaki		15:20-15:40 OS7-6 Chi-Chuan Wang		
15:40-16:00 OS6-7 Takahiro Kobayashi	15:25-15:50 OS9-4 Kazuhiko Tezuka	15:40-16:00 OS7-7 Yi-Wei Yang		
16:00-16:20 OS6-8 Ken Nishihara	15:50-16:15 OS9-5 Hiroshi Asanuma			16:00
BREAK	BREAK			
16:40-17:00 OS6-9 Koji Fujita	16:30-16:55 OS9-6 Takatoshi Ito			
17:00-17:20 OS6-10 Takashi Hayashida	16:55-17:20 OS9-7 Tsuyoshi Ishida			17:00
17:20-17:40 OS6-11 Masayuki Anyoji	17:20-17:45 OS9-8 Hiroyuki Shimizu			
17:40-18:00 OS6-12 Hiroki Nagai	17:45-17:55 Closing			18:00
			18:00-20:00 **Students / Young Birds Friendshp Night** @ SAKURA HALL, Katahira, Tohoku University	
				19:00
				20:00
				21:00

Thursday, November 10, 2011

ROOM	AKEBONO (WEST)	AKEBONO (EAST)	SEIUN	FUJI	SENDAI (EAST)
Floor	3rd Floor				4th Floor
8:00	8:00-8:50 **Plenary Lecture @** SENDAI (EAST) "Low-Order Aeromechanical Modeling for Conceptual Design of Fuel-Efficient Aircraft" Mark Drela (MIT, USA)				
9:00	9:00-(9:40) OS12-21 - OS12-32 Session2 *Short Oral Presentation*	8:50-9:10 PS4-1 Yu Inagaki 9:10-9:30 PS4-2 Eui-Chol Shin 9:30-9:50 PS4-3 Li Xinxin	9:00-9:20 OS5-14 Takaya Koda 9:20-9:40 OS5-15 Nobuyuki Tsuboi 9:40-10:00 OS5-16 Daisuke Saito	9:00-9:30 OS11-1 Yoshiyuki Kamio (Invited) 9:30-10:00 OS11-2 Yoshikazu Tanaka (Invited)	
	(9:40-11:40) OS12-21 - OS12-32 *Poster Presentation*	BREAK			
10:00		10:00-10:20 PS4-4 Fang Wang 10:20-10:40 PS4-5 Sung Min Choi 10:40-11:00 PS4-6 H. Kudo	BREAK 10:20-10:40 OS5-17 Tzu Hao Chou 10:40-11:00 OS5-18 Yen-Sen Chen	10:00-10:30 OS11-3 Liviu Movileanu (Invited) BREAK 10:45-11:10 OS11-4 Noriko Tomita (Invited)	
11:00		BREAK 11:10-11:30 PS4-7 Y. Fujimaki 11:30-11:50 PS4-8 Kiyong Ahn	11:00-11:20 OS5-19 Toru Shimada 11:20-12:00 Wrap-up	11:10-11:40 OS11-5 Takuo Yasunaga (Invited) 11:40-12:00 OS11-6 Atsushi Kase	
12:00		11:50-12:10 PS4-9 Taihei Miyasaka 12:10-12:30 PS4-10 Shinji Sukino			
13:00	13:00-(14:00) OS12-33 - OS12-51 Session3 *Short Oral Presentation*		12:40-13:00 OS3-1 Daisuke Aoki 13:00-13:20 OS3-2 Kei Nose 13:20-13:40 OS3-3 Tomoki Hayashi	13:00-13:05 Opening 13:05-13:45 PS3-1 Keynote Lecture Gyoo-Cheon Kim	
14:00	(14:00-16:00) OS12-33 - OS12-51 *Poster Presentation*	13:30-14:15 Tutorial Lecture Kisuk Kang BREAK	13:40-14:00 OS3-4 Shun Tazoe 14:00-14:20 OS3-5 Kounosuke Matsumoto BREAK	13:45-14:25 PS3-2 Keynote Lecture Kerry Manton BREAK	
15:00		14:30-14:50 PS4-11 Keiichi Shirasu 14:50-15:10 PS4-12 Jaeyeon Hwang 15:10-15:30 PS4-13 Syo Onodera	14:30-15:00 OS3-6 Nobumasa Sekishita (Invited) 15:00-15:30 OS3-7 Hitoshi Ishikawa (Invited)	14:45-15:15 PS3-3 Hajime Sakakita (Invited) 15:15-15:45 PS3-4 Takamichi Hirata (Invited)	
16:00		15:30-15:50 PS4-14 Ryusuke Mihara 15:50-16:10 PS4-15 Wonhyo Joo BREAK	15:30-15:50 OS3-8 Shailendra D. Sharma 15:50-16:10 OS3-9 Ryohei Norimatsu 16:10-16:30 OS3-10 Kenta Watanabe	BREAK 16:00-16:30 PS3-5 Yukiko T. Matsunaga (Invited)	
17:00	17:00-17:20 GS1-8 Ardian B. Gojani 17:20-17:40 GS1-9 Kisa Matsushima 17:40-18:00 GS1-10 Jing Wang	16:25-16:45 PS4-16 Y. Kimura 16:45-17:05 PS4-17 Y. Shirai 17:05-17:25 PS4-18 Hannah Cho 17:25-17:45 PS4-19 T. Masumitsu	16:30-16:50 OS3-11 Sharad Trivedi, Viren Menezes 17:00-18:30 Special Session: Memorial Session for the Late Professor Hiroshi Higuchi Presenter: Mark Glauser Yasuaki Kohama Yoshiya Nakamura	16:30-17:00 PS3-6 Taiji Adachi (Invited) BREAK 17:15-17:45 PS3-7 Sunao Katsuki (Invited)	
18:00	18:00-18:20 GS1-11 Wei Liu	17:45-18:05 PS4-20 Hyung-Soon Kwon		17:45-18:15 PS3-8 Oleg P. Solonenko (Invited)	
19:00					
20:00	18:30-21:00 **Banquet** @SENDAI				
21:00					

SENDAI (WEST)	FUYOH	HAGI	La Boaune	ROOM
4th Floor			21st Floor	Floor

8:00-8:50
Plenary Lecture @ SENDAI (EAST)
"Low-Order Aeromechanical Modeling for Conceptual Design of Fuel-Efficient Aircraft"
Mark Drela (MIT, USA)

9:00-10:24 CRF-1 - CRF27 *Short Oral Presentation*	9:00-9:30 OS2-1 Rongjia Tao (Invited)			9:00
	9:30-10:00 OS2-2 Ishwar K. Puri (Invited)	9:30-10:00 OS7-8 J. -S. Wu (Invited)	9:30-10:00 OS1-1 Mikhail S. Ivanov (Invited)	
	10:00-10:30 OS2-3 Jean-Yves Cavaillé (Invited)	10:00-10:20 OS7-9 Biao Shen	10:00-10:30 OS1-2 Fumiya Togashi (Invited)	10:00
		10:20-10:40 OS7-10 Yu-Sheng Huang		
	10:30-11:00 OS2-4 Miklós Zrínyi (Invited)	10:40-11:00 OS7-11 Chi-Chuan Wang	10:30-11:00 OS1-3 Jaw-Yen Yang (Invited)	
10:40-11:30 Progress in Transdisciplinary Collaborative Research Project	11:00-11:20 OS2-5 Shinya Yamanaka	11:00-11:20 OS7-12 Yun Huang	11:00-11:30 OS1-4 JC Chen	11:00
	11:20-11:40 OS2-6 Katsufumi Tanaka	11:20-11:40 OS7-13 Sohey Nozawa		
	11:40-12:00 OS2-7 Roman V. Brizitskii		11:30-12:00 OS1-5 Yuichi Matuo	
12:00-13:00 *Lunch and Poster Session*				12:00
13:00-14:00 CRF-28 - CRF-47 *Short Oral Presentation*	13:00-13:20 OS2-8 Yan Zheng		13:00-13:20 OS1-6 Zhifeng Zuo	13:00
	13:20-13:40 OS2-9 Takeshi Yamaguchi	13:30-13:50 OS7-14 Ching-Yao Chen	13:20-13:40 OS1-7 Mitsuhiro Murayama	
	13:40-14:00 OS2-10 Aphaiwong Junchangpood	13:50-14:10 OS7-15 Ramjee Repaka	13:40-14:00 OS1-8 Taro Imamura	
BREAK	14:00-14:20 OS2-11 Shashank Khurana	14:10-14:30 OS7-16 C. -T. Liu	14:00-14:20 OS1-9 Akihito Deguchi	14:00
14:15-15:21 CRF-48 - CRF-69 *Short Oral Presentation*	BREAK	14:30-14:50 OS7-17 Y. -M. Chiu	14:20-14:40 OS1-10 Yuuma Fukushima	
	14:30-15:00 OS2-12 Louis Cattafesta (Invited)	14:50-15:10 OS7-18 Kuen-Rung Huang	14:40-15:00 OS1-11 Ryotaro Sakai	
	15:00-15:20 OS2-13 Tomoki Kurinami	BREAK	BREAK	15:00
15:30-16:30 *Poster Session*	15:20-15:40 OS2-14 Tetsuji Nagata	15:20-15:40 OS7-19 Ching-Yao Chen	15:20-15:50 OS1-12 Kenji Ono (Invited)	
	15:40-16:00 OS2-15 Kazuo Matsuura	15:40-16:00 OS7-20 Wei-Hsiang Wang	15:50-16:10 OS1-13 Xinrong Su	
	BREAK	16:00-16:20 OS7-21 Ch. Hari Krishna		16:00
	16:10-16:30 OS2-16 Mikael A. Langthjem	16:20-16:40 OS7-22 Yun Huang	16:10-16:30 OS1-14 Yasutaka Nishimura	
	16:30-16:50 OS2-17 Tadatsugu Imura	16:40-17:00 OS7-23 Hidemasa Takana	16:30-16:50 OS1-15 Kazuhiko Komatsu	
	16:50-17:10 OS2-18 Tameo Nakanishi	17:00-17:20 OS7-24 Chieh-Tsan Hung	16:50-17:10 OS1-16 Takashi Furusawa	17:00
	17:10-17:30 OS2-19 Cancelled		17:10-17:30 OS1-17 Shun Takahashi	
			17:30-17:50 OS1-18 Michitaro Hashiba	
			17:50-18:10 OS1-19 Xinrong Su	18:00
				19:00

18:30-21:00
Banquet @SENDAI

20:00

21:00

Friday, November 11, 2011

ROOM	AKEBONO (WEST)	AKEBONO (EAST)	SEIUN	FUJI
Floor	3rd Floor			
8:00			8:00-8:20 GS1-12 Chih-Yung Huang	
			8:20-8:40 GS1-13 Jia-Syuan Li	
			8:40-9:00 GS1-14 WooJae Kim	
9:00	9:00-(9:45) OS12-52 - OS12-65 Session4 *Short Oral Presentation*	8:50-9:10 PS4-21 Hidetaka Watanabe	BREAK	9:00-9:40 PS3-9 Keynote Lecture Tetsuji Shimizu
		9:10-9:30 PS4-22 Euisung Kim	9:10-9:30 GS1-15 Mehdi Baneshi	
		9:30-9:50 PS4-23 R. A. Budiman	9:30-9:50 GS1-16 Hideyuki Tanno	9:40-10:10 PS3-10 Satoshi Hamaguchi (Invited)
10:00	(9:45-11:45) OS12-52 - OS12-65 *Poster Presentation*	BREAK	9:50-10:10 GS1-17 Chayut Nuntadusit	
		10:00-10:20 PS4-24 Y. Kawamura	BREAK	BREAK
		10:20-10:40 PS4-25 Jakyu Chun	10:30-11:00 GS1-18 Bing-Yang Cao (Invited)	10:25-10:55 PS3-11 Masaru Tanaka (Invited)
		10:40-11:00 PS4-26 S. Nakakawaji		
11:00		BREAK	11:00-11:20 GS1-19 Yoshio Masuda	10:55-11:25 PS3-12 Yoshinori Sawae (Invited)
		11:10-11:30 PS4-27 Kiyotaka Konno	11:20-11:40 GS1-20 Yuan Dong	11:25-11:45 PS3-13 Xiaobo Han
		11:30-11:50 PS4-28 D. Hari Prasad	11:40-12:00 GS1-21 Ruo-Yu Dong	
12:00		11:50-12:10 PS4-29 Hiroaki Kobayashi		
		12:10-12:30 PS4-30 Makoto Shimizu		
13:00	13:00-(13:45) OS12-66 - OS12-80 Session5 *Short Oral Presentation*			13:00-13:30 PS3-14 Yukinori Sakiyama (Invited)
		13:30-14:15 Tutorial Lecture Noriko Sata		13:30-14:00 PS3-15 Toshiro Ohashi (Invited)
14:00	(13:45-15:45) OS12-66 - OS12-80 *Poster Presentation*	BREAK		14:00-14:30 PS3-16 Takehiko Sato (Invited)
		14:30-14:50 PS4-31 Yu Cheol Shin		14:30 Closing
15:00		14:50-15:10 PS4-32 Taewon Lee		
		15:10-15:30 PS4-33 Yuta Fujiwara		
		15:30-15:50 PS4-34 Dae-Hee Kim		
16:00		15:50-16:10 PS4-35 Mi-Young Oh		
		BREAK		
		16:25-16:45 PS4-36 Kiho Bae		
17:00		16:45-17:05 PS4-37 Hiroaki Matsuo		
		17:05-17:25 PS4-38 Ji-Hyun Kim		
		17:25-17:45 PS4-39 T. Hori		
18:00		17:45-18:05 PS4-40 Jinsoo Kim		
19:00				
20:00				
21:00				

FUYOH	HAGI	La Boaune	ROOM
4th Floor		21st Floor	Floor
8:00-8:30 GS1-22 Masud Behnia (Invited)			
8:30-8:50 GS1-23 Yukiko Agata			
8:50-9:10 GS1-24 Sivakumar Deivandren	9:00-9:45 OS10-1 Karkenahalli Srinivas (Invited)	9:00-9:30 OS4-1 Akihiro Sasoh (Invited)	9:00
9:10-9:30 GS1-25 Takeshi Kanda			
BREAK		9:30-10:00 OS4-2 Masahisa Honda	
9:40-10:10 GS1-26 Fredrik Lundell (Invited)	9:45-10:30 OS10-2 Teruo Matsuzawa (Invited)		
10:10-10:30 GS1-27 Kiyonobu Ohtani		10:00-11:00 OS4-3 Takeshi Ohnuki (Invited)	10:00
10:30-10:50 GS1-28 Thien Xuan Dinh	10:30-10:45 OS10-3 S. D. Muskawad		
BREAK	10:45-11:00 OS10-4 Kenichi Kono		
11:00-11:20 GS1-29 Thien Xuan Dinh	11:00-11:15 OS10-5 Shusaku Sone	11:00-12:00 OS4-4 Gary A. Dale (Invited)	11:00
11:20-11:40 GS1-30 Masayuki Takashima	11:15-11:30 OS10-6 Toshio Nakayama		
11:40-12:00 GS1-31 Arunabhiram Chutia			
			12:00
	12:30-13:00 PS2-1 Robert W. Carpick (Invited)		
13:00-13:20 GS1-32 Masahiro Hayashi	13:00-13:25 PS2-2 Minoru Goto (Invited)	13:00-14:00 OS4-5 Takashi Misaka (Invited)	13:00
13:20-13:40 GS1-33 Babak Fakhim	13:25-13:50 PS2-3 Hirotaka Ito (Invited)		
13:40-14:00 GS1-34 Takashi Yabuki	BREAK		
14:00-14:20 GS1-35 Hideo Sawada	14:00-14:25 PS2-4 Philippe Kapsa (Invited)	14:00-14:20 OS4-6 Kazuaki Hatanaka	14:00
BREAK	14:25-14:45 PS2-5 Masanori Iwaki	14:20-14:40 OS4-7 Daichi Ono	
14:30-14:50 GS1-36 Masahiro Shiono	14:45-15:05 PS2-6 Takanori Takeno	14:40-15:00 OS4-8 Takahiro Ukai	
14:50-15:10 GS1-37 Kohei Kitadera	BREAK		15:00
15:10-15:30 GS1-38 Masayuki Takahashi	15:15-15:35 PS2-7 Pengfei Wang		
15:30-15:50 GS1-39 Hideaki Ogawa	15:35-16:00 PS2-8 Alexander N. Vasiliev (Invited)		
			16:00
			17:00
			18:00
			19:00
			20:00
			21:00

Eighth International Conference on Flow Dynamics

Program

Plenary Lectures

SENDAI (EAST)
November 9, 2011

Chair: Kaoru Maruta (Tohoku University, Japan)

10:00-10:50 **Energy Sustainability: A Combustion Perspective** 74
Suk Ho Chung (King Abdullah University of Science and Technology, Saudi Arabia)

Chair: Shigenao Maruyama (Tohoku University, Japan)

11:00-11:50 **Transport Phenomena, Fluid Mechanics and Multiscale Modelling Techniques for Clinical Decision Support** 76
Emilie C. Holland, Tom W. Peach, Alisa Selimovic, Brett J. Tully, Paul N. Watton, Yiannis Ventikos (University of Oxford, UK)

SENDAI (EAST)
November 10, 2011

Chair: Keisuke Asai (Tohoku University, Japan)

8:00-8:50 **Low-Order Aeromechanical Modeling for Conceptual Design of Fuel-Efficient Aircraft** 78
Mark Drela (MIT, USA)

GS1: General Session

AKEBONO (WEST)
November 9, 2011

Impinging Jet & Injection

Chair: Seiichiro Izawa (Tohoku University, Japan)

General Fluid Flow (1)

Chair: Wakana Iwakami Nakano (Tohoku University, Japan)

AKEBONO (WEST)
November 10, 2011

Measurement (1)

Chairs: Kenichi Takita (Tohoku University, Japan)

SEIUN
November 11, 2011

Measurement (2)
Chair: Daiju Numata and Toshinori Kouchi (Tohoku University, Japan)

9:00-9:10 BREAK

Heat, Non-Newtonian Flow
Chair: Taku Ohara (Tohoku University, Japan)

FUYOH
November 11, 2011

Gas Turbine, Turbopump
Chair: Yasuhiro Ogami (Tohoku University, Japan)

Micro Scale

Chair: Shigeru Yonemura (Tohoku University, Japan)

General Fluid Flow (2)

Chair: Masud Behnia (The University of Sydney, Australia)

General Fluid Flow (3)

Chair: Koji Shimoyama (Tohoku University, Japan)

OS1: Next-Generation CFD

La Boaune
November 10, 2011

NextGen CFD for Complex Physics
Chair: Satoru Yamamoto (Tohoku University, Japan)

12:00-13:00 LUNCH

NextGen CFD for Aeroacoustics
Chair: Kazuomi Yamamoto (Japan Aerospace Exploration Agency, Japan)

OS2: Advanced Control of Smart Fluids and Fluid Flows

FUYOH
November 10, 2011

Chair: Masami Nakano (Tohoku University, Japan)

Chair: Masaya Shigeta (Tohoku University, Japan)

OS3: Wind Tunnel Experiment on Unsteady Phenomena

SEIUN
November 10, 2011

Chair: Yasufumi Konishi (Tohoku University, Japan)

14:20-14:30 BREAK

Chair: Daiju Numata (Tohoku University, Japan)

OS3-10
16:10-16:30

Disturbance Structures in a Low Reynolds Number Channel Flow 260

Kenta Watanabe (Shinshu University, Japan), Tsutomu Natori (Naganokeiki, Japan) , Syunsuke Akaoka (Shinshu University, Japan), Kvick Mathias (KTH Royal Institute of Technology, Sweden) and Masaharu Matsubara (Shinshu University, Japan)

OS3-11
16:30-16:50

Pressure Measurement On A Hypersonic Lifting Model For The Validation Of An Accelerometer Force Balance 262

Sharad Trivedi, Viren Menezes (Indian Institute of Technology Bombay, India)

OS4: Research Frontiers in Green Aviation

La Boaune
November 11, 2011

Chair: Shigeya Watanabe (Japan Aerospace Exploration Agency, Japan)

Chair: Shigeru Obayashi (Tohoku University, Japan)

OS5: Research Frontiers in Green Hybrid Rocket Propulsion

SEIUN
November 9, 2011

Chair: Toru Shimada (Japan Aerospace Exploration Agency, Japan)

15:40-16:00 BREAK

Chair: Saburo Yuasa (Tokyo Metropolitan University, Japan)

17:40-18:00 BREAK

Chair: Harunori Nagata (Hokkaido University, Japan)

OS5-9 18:00-18:40 **Nozzle Design for Supersonic Flows of N_2O at Supercritical and Close-to-Critical Conditions *(Invited)*** 300
Alberto Guardone (Politecnico di Milano, Italy)

OS5-10 18:40-19:00 **Enhancement of Multi-Section Swirl Injection Method for Increase of Regression Rate and Combustion Efficiency of Hybrid Rockets** 302
Shigeru Aso, Yoshihide Hirata, Yasuhiro Tani, Takahiro Hayashida and Ryuji Nakawatase (Kyushu University, Japan)

19:00-19:20 BREAK

Chair: Shigeru Aso (Kyushu University, Japan)

OS5-11 19:20-19:40 **Numerical Simulations of N_2O Flow Past a Low-Cost Ball Valve** 304
Kang-Ming Chuang, Jong-Shinn Wu (National Chiao Tung University, Taiwan) and Yen-Sen Chen (Hsinchu Science Park, Taiwan)

OS5-12 19:40-20:00 **Study on Mechanical Characteristic of Paraffin-Based Fuel** 306
Shinya Maruyama, Takafumi Ishiguro, Keiji Shinohara and Ichiro Nakagawa (Tokai University, Japan)

OS5-13 20:00-20:20 **Study on Flow Inside the Nozzle of Ejector Jet by Numerical Analysis** 308
Keisuke Sotozono, Y. Higa and Ichiro Nakagawa (Tokai University, Japan)

SEIUN

November 10, 2011

Chair: Keiichi Hori (Japan Aerospace Exploration Agency, Japan)

OS5-14 9:00-9:20 **Effect of Oblique Injection on Swirling Oxidizer Flowfield in Combustion Chamber for Hybrid Rocket Enginge** 310
Takaya Koda, Yousuke Ogino and Keisuke Sawada (Tohoku University, Japan)

OS5-15 9:20-9:40 **Three-Dimensional Numerical Simulation on Unsteady Compressible Flow Using Preconditioning Method: Swirling Injector Flowfield in Hybrid Rocket Engine** 312
Nobuyuki Tsuboi (Kyushu Institute of Technology, Japan), Katsuyoshi Fukiba (Shizuoka University, Japan) and Toru Shimada (Japan Aerospace Exploration Agency, Japan)

OS5-16 9:40-10:00 **Combustion Characteristics of Paraffin-Fueled Swirling-Oxidizer-Flow-Type Hybrid Rocket Engines** 314
Saito Daisuke, Yuasa Saburo, Hirata Kousuke and Sakurai Takashi (Tokyo Metropolitan University, Japan)

10:00-10:20 BREAK

Chair: Keisuke Sawada (Tohoku University, Japan)

OS5-17 10:20-10:40 **3D Simulations of Cold Gas Flow in a Hybrid Single-Port Combustion Chamber with a Mixing Enhancer** 316
TzuHao Chou, Jong-Shinn Wu (National Chiao Tung University, Taiwan) and Yen-Sen Chen (Hsinchu Science Park, Taiwan)

OS5-18 **Three-Dimensional Modeling of Hybrid N2O-HTPB Combustion with Mixing Enhancers** 318
10:40-11:00
Yen-Sen Chen (Hsinchu Science Park, Taiwan), T. H. Chou, B. R. Gu and J. S. Wu (National Chiao Tung University, Taiwan)

OS5-19 **Some Issues on Hybrid Rocket Internal Ballistics Evaluation** 320
11:00-11:20
Toru Shimada and Yuki Funami (Japan Aerospace Exploration Agency, Japan)

Chair: Toru Shimada (Japan Aerospace Exploration Agency, Japan) and Keisuke Sawada (Tohoku University, Japan)

11:20-12:00 **Wrap-up**

OS6: Aerodynamics for Mars Exploration Aerial Vehicle

FUYOH
November 9, 2011

Chair: Hiroki Nagai (Tohoku University, Japan)

14:40-15:00 BREAK

Chair: Kojiro Suzuki (The University of Tokyo, Japan)

OS7: Thermal-Fluid Flows and Plasma Physics

La Boaune
November 9, 2011

Chair: C. C. Wang (National Chiao-Tung University, Taiwan)

HAGI
November 10, 2011

Chair: Subhash C. Mishra (Indian Institute of Technology Guwahati, India)

Chair: Ramjee Repaka (Indian Institute of Technology Ropar, India)

OS8: Flow-induced Degradations in Piping Systems of Nuclear Power Plants

AKEBONO (EAST)
November 9, 2011

Session1
Chair: Yutaka Watanabe (Tohoku University, Japan)

Session2
Chair: Jean-Yves Cavaillé (INSA-Lyon, France)

OS9: Fluid-induced Seismicity: Modeling and Application

HAGI
November 9, 2011

13:00-13:10 **Opening Remarks**
Takatoshi Ito (Tohoku University, Japan)

Chair: Takatoshi Ito (Tohoku University, Japan)

14:30-14:45 BREAK

Chair: Hiroshi Asanuma (Tohoku University, Japan)

16:15-16:30 BREAK

Chair: Takatoshi Ito (Tohoku University, Japan)

17:45-17:55 **Closing**
Hiroshi Asanuma (Tohoku University, Japan)

OS10: Biofluid for Medical Application

HAGI
November 11, 2011

Chair: Makoto Ohta and Toshio Nakayama (Tohoku University, Japan)

OS11: Micro Channels and Membrane Proteins

FUJI
November 10, 2011

Chair: Noriko Tomita (Tohoku University, Japan)

10:30-10:45 BREAK

Chair: Makoto Ohta (Tohoku University, Japan)

OS12: The Seventh International Students/Young Birds Seminar on Multi-Scale Flow

AKEBONO (WEST)
November 9, 2011

13:00-13:05	**Opening**	
Session 1 13:05-(14:05)	**-Award Session -** **Short Oral Presentation** 3 min for Short Oral Presentation without PC preparation	
OS12-1	**X-Ray Computed Tomographic Study of Changes in Packing State of Hydrogen Storage Alloys** Masahiko Okumura, Ayaka Ikado, Yasuhiro Saito, Hideyuki Aoki, Takatoshi Miura (Tohoku University, Japan) and Yoshiaki Kawakami (Takasago Thermal Engineering Co., Ltd. , Japan)	476
OS12-2	**Process of Leading Edge Receptivity to Periodic Disturbances** Yu Nishio, Masaya Shigeta, Seiichiro Izawa and Yu Fukunishi (Tohoku University, Japan)	478
OS12-3	**Comparison of Carbon Black Configurations Formed by Benzene and Acetylene Pyrolysis** Kiminori Ono, Miki Yanaka, Sho Tanaka, Yasuhiro Saito, Masakazu Shoji, Hideyuki Aoki, Takatoshi Miura (Tohoku University, Japan), Okiteru Fukuda, Takayuki Aoki and Togo Yamaguchi (Asahi Carbon Co., Ltd., Japan)	480
OS12-4	**Quantification of Non-adhesion Particle Boundary by Observation of Coke Fracture Cross-section** Tetsuya Kanai, Yoshiaki Yamazaki, Xiaoqing Zhang, Ataru Uchida, Yasuhiro Saito, Masakazu Shoji, Hideyuki Aoki, Takatoshi Miura (Tohoku University, Japan), Seiji Nomura, Yukihiro Kubota and Hideyuki Hayashizaki (Nippon Steel Corporation, Japan)	482
OS12-5	**A Study of 4 Dimensional City Modeling from Car-mounted Omnidirectional Images** Ken Sakurada, Jun Yanagisawa, Daiki Tetsuka, Takayuki Okatani and Koichiro Deguchi (Tohoku University, Japan)	484
OS12-6	**Simulation of Boundary Layer Receptivity to Outer Disturbances** Shuta Noro, Masaya Shigeta, Seiichiro Izawa and Yu Fukunishi (Tohoku University, Japan)	486
OS12-7	**Conceptual Examination of a Small UAV for Mars Exploration Flight** Koji Fujita, Hiroki Nagai and Keisuke Asai (Tohoku University, Japan)	488
OS12-8	**The Effects of Standoff Distance on the Laser-Induced Liquid Jet in a Narrow Channel** Muhd Hilmi Bin Shapien, Mingyu Sun (Tohoku University, Japan)	490

AKEBONO (WEST)
November10, 2011

Session 2
9:00-(9:40) **Short Oral Presentation**
3min for Short Oral Presentation without PC preparation

OS12-47 **High Temperature Steam Oxidation Kinetics and Film Characteristics for Austenitic Stainless Steels** 568
Seung Mo Hong, Yutaka Watanabe and Hiroshi Abe (Tohoku University, Japan)

OS12-48 **Effect of Temperature Compensation for Dual-layer PSP/TSP in Low Speed Flow** 570
Kil-Ju Moon, Yuichiro Ambe, Hiroaki Kawabata and Hideo Mori (Kyushu University, Japan)

OS12-49 **A Study on Turbulent Premixed Combustion for $CO/H_2/CO_2/O_2$ Mixture at High Pressure** 572
Futoshi Matsuno, Jinhua Wang, Yuki Otawara, Yasuhiro Ogami and Hideaki Kobayashi (Tohoku University, Japan)

OS12-50 **Traveling Performance Evaluation of Various Planetary Rover Locomotion Mechanisms** 574
Masataku Sutoh, Keiji Nagatani and Kazuya Yoshida (Tohoku University, Japan)

OS12-51 **Effects of Gas Properties on Molecular Gas-Film Lubrication** 576
Susumu Isono, Shigeru Yonemura, Takanori Takeno, Hiroyuki Miki and Toshiyuki Takagi (Tohoku University, Japan)

(14:00-16:00) **Poster Presentation**

AKEBONO (WEST)

November11, 2011

Session 4

9:00-(9:45) **Short Oral Presentation**
3 min for Short Oral Presentation without PC preparation

OS12-52 **Investigation of Dielectric Barrier Discharge Planar Jets at Atmospheric Pressure** 578
Qing Li (Tohoku University, Japan / Tsinghua University, China), Hidemasa Takana (Tohoku University, Japan), Yi-Kang Pu (Tsinghua University, China) and Hideya Nishiyama (Tohoku University, Japan)

OS12-53 **Incompressible SPH Simulation of a Droplet and a Liquid Column with Marangoni Convection** 580
Masumi Ito, Seiichiro Izawa, Yu Fukunishi and Masaya Shigeta (Tohoku University, Japan)

OS12-54 **Experimental Study of Water Jet Formation by Electric Discharge in Tubes with Various Width** 582
Kentaro Hayashi, Taketoshi Koita and Mingyu Sun (Tohoku University, Japan)

OS12-55 **Simulation of Velocity Fluctuation Generated by Vibrating Actuator** 584
Hajime Okawa, Masaya Shigeta, Seiichiro Izawa and Yu Fukunishi (Tohoku University, Japan)

Session 5
13:00-(13:45) **Short Oral Presentation**
3 min for Short Oral Presentation without PC preparation

OS13: Clean and Efficient Combustion Technology (AFI/TFI-2011)

Please refer to separate proceedings.

FUJI
November 9, 2011

Chair: Kaoru Maruta (Tohoku University, Japan)

OS13-1 13:00-13:30 **Development of A High Pressure Syngas Kinetic Mechanism for Advanced Gas Turbines (*Invited*)**
Jeffrey Santner, Michael. P. Burke, Frederick L. Dryer and Yiguang Ju (Princeton University, USA)

OS13-2 13:30-14:00 **Numerical Simulation of Radiation Driven Transient Combustion of Energetic Materials (*Invited*)**
Vladimir E. Zarko, Lev K. Gusachenko and Alexander D. Rychkov (SB RAS, Russia)

14:00-14:10 BREAK

Chair: Sergey Minaev (ITAM SB RAS, Russia)

OS13-3 14:10-14:30 **Turbulent Combustion of Model Coal-gasification Syngas at High Pressure**
Hideaki Kobayashi, Yasuhiro Ogami (Tohoku University, Japan)

OS13-4 14:30-14:50 **High-Pressure Turbulent Ignition Transition**
Shenqyang Steven Shy, Yao-Wen Shiu, Chien-Chia Liu, Hua-Jung Chung, Ming-Wei Peng (National Central University, Taiwan)

OS13-5 14:50-15:10 **Measurement of Three-Dimensional Flame Structure by Simultaneous Dual-Plane CH PLIF, Single-Plane OH PLIF and Dual-Plane Stereoscopic PIV**
Ayane Johchi, Masayasu Shimura, Mamoru Tanahashi and Toshio Miyauchi (Tokyo Insitute of Technology, Japan)

OS13-6 15:10-15:30 **DNS on Autoignition and Flame Propagation of Methane-Air Mixtures at High Pressure**
Makito Katayama, Naoya Fukushima, Masayasu Shimura, Mamoru Tanahashi and Toshio Miyauchi (Tokyo Institute of Technology, Japan)

15:30-15:40 BREAK

Chair: Osamu Fujita (Hokkaido University, Japan)

OS13-7 15:40-16:00 **Flame Propagation in Diverging Microchannels**
Mohammad Akram (Indian Institute of Technology Bombay, India), Roman Fursenko, Sergey Minaev (ITAM SB RAS, Russia) and Sudarshan Kumar (Indian Institute of Technology Bombay, India)

OS13-8 **Oscillating and Rotating Flame Patterns in Microchannels**
16:00-16:20 Sergey Minaev, Roman Fursenko, Evgeniy Sereschenko (ITAM SB RAS, Russia), Aiwu Fan (Huazhong University of Science Technology, China), Sudarshan Kumar (Indian Institute of Technology Bombay, India) and Kaoru Maruta (Tohoku University, Japan)

OS13-9 **High Performance Flame Fuel Cell Using and Anode Supported SOFC**
16:20-16:40 Kang Wang, Pingying Zeng, James Schwartz and Jeongmin Ahn (Syracuse University, USA)

OS13-10 **Porous Oxide Particles Prepared by Flame Spray Pyrolysis**
16:40-17:00 Takeshi Yokomori, Kazuki Tsukuda and Toshihisa Ueda (Keio University, Japan)

17:00-17:10 BREAK

Chair: Shenqyang Steven Shy (National Central University, Taiwan)

OS13-11 **Combustion Characteristics of Polyethylene in Microgravity**
17:10-17:30 Mitsumasa Ikeda, Yudai Koshiro (Akashi National College of Technology, Japan)

OS13-12 **Transition from Laminar to Turbulent Flame Induced by Laser Irradiation Method in a Propagation Tube**
17:30-17:50 Osamu Fujita, June Sung Park and Yoshikazu Taniyama (Hokkaido University, Japan)

PS1: IFS Collaborative Research Forum (AFI/TFI-2011)

Please refer to separate proceedings.

SENDAI (WEST)
November 10, 2011

Chair: Yasuhiro Ogami (Tohoku University, Japan)
9:00-10:24 **Short Oral Presentation**
(3 min for Short Oral Presentation)

CRF-1 **Pressure Drop and Heat Transfer for Boiling Two-phase Flow of Liquid Nitrogen in a Horizontal Pipe**
Tadashi Nakayama, Takayoshi Nagai, Katsuhide Ohira, Koichi Takahashi (Tohoku University, Japan), Hiroaki Kobayashi, Hideyuki Taguchi, Ttakayuki Kojima and Motoyuki Hongo (Japan Aerospace Exploration Agency, Japan)

CRF-2 **Measurement Coupled Computation of Cooling and Wafer Cleaning Performance Using Micro-Solid Nitrogen**
U Oh, Jun Ishimoto (Tohoku University, Japan) and Kozo Saito (University of Kentucky, USA)

CRF-3 **Quantitative Visualization by using Background-Oriented Schlieren**
Toshiharu Mizukaki (Tokai University, Japan), Ardian Gojani and Shigeru Obayashi (Tohoku University, Japan)

CRF-4 **Direct Numerical Simulation on the Effects of Free-stream Turbulence on a Turbulent Boundary Layer with Heat Transfer**
Yasuhiko Sakai, Kouji Nagata, Hiroki Suzuki (Nagoya University, Japan) and Toshiyuki Hayase (Tohoku University, Japan)

CRF-5 **Aerodynamic Characteristics of a Badminton Shuttlecock at High Reynolds Numbers**
Seigo Kitta, Hiroaki Hasegawa (Akita University, Japan), Masahide Murakami (University of Tsukuba, Japan)and Shigeru Obayashi (Tohoku University, Japan)

CRF-6 **Numerical Simulation of the Aerodynamic Characteristics on a Detailed Motorcycle**
Chenguang Lai (Chongqing University of Technology, China), Shigeru Obayashi (Tohoku University, Japan), Yuting Zhou and Haibin Xing (Chongqing University of Technology, China)

CRF-7 **Analysis and Optimization for Multi-Hull Ship**
Hyunyul Kim (George Mason University, USA) and Shinkyu Jeong (Tohoku University, Japan / George Mason University, USA)

CRF-8 **Development of Efficient Hole Searching Algorithm of Overset Grid System for Helicopter Rotor Analysis and Design Framework**
Seonhyeong Lee, Sanghyun Chae (Pusan National University, Korea), Shinkyu Jeong (Tohoku University, Japan) and Kwanjung Yee (Pusan National University, Korea)

CRF-9 **Improvement of Reality of CG Motion Pictures by Hydrodynamic Effects**
Takashi Ishihara (Nagoya University, Japan), Yuji Hattori (Tohoku University, Japan)

CRF-10 **Investigation of Hypersonic Flows about Leading Edges of Small Bluntness**
Mikhail Ivanov (Khristianovich Institute of Theoretical and Applied Mechanics, Russia), Shigeru Yonemura (Tohoku University, Japan), Yevgeniy Bondar, Dmitry Khotyanovsky, Alexey Kudryavtsev (Khristianovich Institute of Theoretical and Applied Mechanics, Russia)

CRF-11 **Experimental Studies of Sonic Boom Using a Two-stage Light Gas Gun**
Kazuaki Hatanaka, Tsutomu Saito (Muroran Institute of Technology, Japan), Kiyonobu Ohtani, Toshihiro Ogawa, Shigeru Obayashi (Tohoku University, Japan) and Masahide Katayama (Itochu Techno-Solutions Corporation, Japan)

CRF-12 **Effect of Electron Behavior in front of Shock Wave on Thermo-Chemical Process behind the Shock Wave**
Gouji Yamada, Shota Ago, Shingo Otsuta, Takashi Matsuno, Hiromitsu Kawazoe (Tottori University, Japan) and Shigeru Obayashi (Tohoku University, Japan)

CRF-13 **Development of Force Balance for Its Application to a Silent Supersonic Biplane Model in the Low Speed Wind Tunnel**
Hiromitsu Kawazoe, Hiroshi Suemura, Gouji Yamada, Takashi Matsuno (Tottori University, Japan) and Shigeru Obayashi (Tohoku University, Japan)

CRF-14 **Shock Induced Temperature Measurement using Laser-Induced Thermal Acoustics**
Toshiharu Mizukaki (Tokai University, Japan) , Shigeru Obayashi (Tohoku University, Japan)

CRF-15 **Streamer Propagation Mechanism in Water**
Hidemasa Fujita (Tohoku University, Japan), Seiji Kanazawa (Oita University, Japan) and Takehiko Sato (Tohoku University, Japan)

CRF-16 **Advancement of Numerical Method for Cavitating Flow around a Hydrofoil**
Yuka Iga, Naoya Ochiai (Tohoku University, Japan), Wang Guoyu, Zhang Mindi and Huang Biao (Beijing Institute of Technology, China)

CRF-17 **Effect of Neighboring Solid Wall on Generation of Residual Microbubbles after Collapse of Laser-Induced Bubble**
Takehiko Sato (Tohoku University, Japan), Marc Tinguely (Swiss Federal Institute of Technology Lausanne, Switzerland), Masanobu Oizumi (Tohoku University, Japan) and Mohamed Farhat (Swiss Federal Institute of Technology Lausanne, Switzerland)

CRF-18 **Observation of Bubble Formation and Collapse Process by Generating a Plasma**
Takehiko Sato (Tohoku University, Japan), Takashi Miyahara (Shizuoka University, Japan) and Tatsuyuki Nakatani (Toyo Advanced Technologies Company, Ltd., Japan)

CRF-19 **Analysis of Plasma Flow at Gas-Liquid Interface for Biological Interaction**
Naoya Kishimoto (Tohoku University, Japan), Tetsuji Shimizu, Gregor E.Morfill (Max-Planck Institute for Extraterrestrial Physics, Germany) and Takehiko Sato (Tohoku University, Japan)

CRF-20 **Anti-bacterial Effect of a Dielectric Barrier Discharge Plasma against Biofilm-producing Gram Negative Bacilli**
Yoshihisa Nakano, Shigeru Fujimura and Takehiko Sato (Tohoku University, Japan)

CRF-21 **Computational Study on Atmospheric RF Discharge with Kinetic-Fluid Integrated Model**
Zhi-Bin Wang, Pei-Si Le, He-Ping Li, Cheng-Yu Bao (Tsinghua University, China), Hidemasa Takana and Hideya Nishiyama (Tohoku University, Japan)

CRF-22 **Radical Generation During Streamer Propagation in Methane/Air DBD Under High Pressure and High Temperature Conditions**
Hidemasa Takana (Tohoku University, Japan), Yasunori Tanaka (Kanazawa University, Japan) and Hideya Nishiyama (Tohoku University, Japan)

CRF-23 **Investigation of Supersonic Hybrid-Stabilized Argon-Water Arc for Biomass Gasification: The Role of Radiation Transfer Method Used in Computer Simulation**
Jiri Jeništa (Institute of Plasma Physics, Czech Republic), Hidemasa Takana, Hideya Nishiyama (Tohoku University, Japan) and Milan Hrabovskỳ (Institute of Plasma Physics, Czech Republic)

CRF-24 **Instability of High-Temperature Premixed Flames**
Satoshi Kadowaki, Takuya Oshima (Nagaoka University of Technology, Japan) and Hideaki Kobayashi (Tohoku University, Japan)

CRF-25 **Real Time Modeling of Flame Front Evolution by Kinematical Model**
Boris Mazurok, Alex Menschikov, Boris Dolgovesov (Institute of Automation and Electrometry SB RAS, Russia), Roman Fursenko, Sergey Minaev (ITAM SB RAS, Russia) and Kaoru Maruta (Tohoku University, Japan)

CRF-26 **GPU-based Parallel Computations of Low Lewis Number Stretched Premixed Flames**
Roman Fursenko, Sergey Minaev (Khristianovich Institute of Theoretical and Applied Mechanics, SB RAS, Russia), Kaoru Maruta and Hisashi Nakamura (Tohoku University, Japan)

CRF-27 **Numerical Studies of the Reacting Rarefied Flows in Tubes**
Yevgeniy Bondar, Georgy Shoev (Khristianovich Institute of Theoretical and Applied Mechanics, Russia), Kaoru Maruta (Tohoku University, Japan) and Mikhail Ivanov (Khristianovich Institute of Theoretical and Applied Mechanics, Russia)

Chair: Kaoru Maruta (Tohoku University, Japan)
10:40-11:30 **Progress in Transdisciplinary Collaborative Research Project**
Presenter: Jun Ishimoto, Kaoru Maruta, Takehiko Sato (Institute of Fluid Science, Tohoku University, Japan)

12:00-13:00 **Lunch and Poster Session**

Chair: Hidemasa Takana (Tohoku University, Japan)

13:00-14:00 **Short Oral Presentation**
(3 min for Short Oral Presentation)

CRF-28 **Rheological Analysis of the Mechanism of Fetal Brain Hemorrhage**
Takuya Ito, Kenichi Funamoto, Kiyoe Funamoto, Kaori Tanabe, Ai Nakamura, Toshiyuki Hayase and Yoshitaka Kimura (Tohoku University, Japan)

CRF-29 **Left Atrial Vortex**
Muneichi Shibata (Miyagi Cardiovascular and Respiratory Center /Tohoku University, Japan), Tomoyuki Yambe, Kenichi Funamoto and Toshiyuki Hayase (Tohoku University, Japan)

CRF-30 **Computational Simulation of Blood Flow in Intracranial Aneurysms under Patient-Specific Pulsatile Inlet Condition**
Shin-ichiro Sugiyama (Kohnan Hospital, Japan), Kenichi Funamoto, Toshiyuki Hayase (Tohoku University, Japan) and Teiji Tominaga (Tohoku University school of Medicine, Japan)

CRF-31 **Local Blood Flow Instability and Oscillatory Shear in Intracranial Aneurysms**
Shin-ichiro Sugiyama (Kohnan Hospital, Japan), Toshio Nakayama, Makoto Ohta (Tohoku University, Japan) and Teiji Tominaga (Tohoku University School of Medicine, Japan)

CRF-32 **Detection of Microcalcification in Soft Tissue Employing B-Flow "Twinkling" Sign**
Lei Liu (GE Healthcare Japan Corporation, Japan), Kei Ozawa, Kenichi Funamoto, Makoto Ohta, Toshiyuki Hayase (Tohoku University, Japan) and Masafumi Ogasawara (GE Healthcare Japan Corporation, Japan)

CRF-33 **Preliminary Experiments for Investigation on Mechanism of Contra-Coup Injury in Blast-Induced Traumatic Brain Injury**
Atsuhiro Nakagawa, Kinonobu Ohtani (Tohoku University, Japan), Keisuke Goda (University of California, USA), Tatsuhiko Arafune (The University of Tokyo, Japan), Toshikatsu Washio (National Institute of Advanced Industrial Science and Technology, Japan), Toshiyuki Hayase and Teiji Tominaga (Tohoku University, Japan)

CRF-34 **Effect of Initial Conditions of Stent Geometry on Optimized Design of Flow Diverters**
Hitomi Anzai (Tohoku University, Japan), Jean-Luc Falzone, Bastien Chopard (University of Geneva, Switzerland) and Makoto Ohta (Tohoku University, Japan)

CRF-35 **Friction Analysis of Biometal on PVA Biomodel**
Hiroyuki Kosukegawa (Tohoku University, Japan), Vincent Fridrici, Philippe Kapsa, Boyko Stoimenov (Ecole Centrale de Lyon, France), Koshi Adachi and Makoto Ohta (Tohoku University, Japan)

CRF-36 **Study of Magnetic Stimulation for the Peripheral Nerve**
Hitoshi Mori (IFG CO., Ltd., Japan), Toshiyuki Takagi, Shinichi Izumi, Hiroyasu Kanetaka, Eizaburo Suzuki (Tohoku University, Japan) and Toshihiko Abe (IFG CO., Ltd., Japan)

CRF-37 **Springtail Jump on Water Surface**
Toshiya Kainuma, Seiichi Sudo (Akita Prefectural University, Japan), Atsushi Shirai and Toshiyuki Hayase (Tohoku University, Japan)

CRF-38 **Si Single-Electron Transistor with Single-Hole Trap Formed by Photo-Irradiation**
Michito Shinohara, Yuki Kato, Masashi Arita (Hokkaido University, Japan), Akira Fujiwara (NTT Corporation, Japan) and Yasuo Takahashi (Hokkaido University, Japan)

CRF-39 **Optical Properties of Quantum Dot Superlattices**
Takashi Kita, Osamu Kojima and Yuikihiro Harada (Kobe University, Japan)

CRF-40 **Neutral Beam Fabrication Technology for the Double Gate MOSFET**
Kazuhiko Endo (Advanced Industrial Science and Technology, Japan), Akira Wada and Seiji Samukawa (Tohoku University, Japan)

CRF-41 **Low Damage Fabrication of Si Photonic Devices by Neutral Beam Technology**
Jingnan Cai (The University of Tokyo, Japan), Seiji Samukawa (Tohoku University, Japan) and Kazumi Wada (The University of Tokyo, Japan)

CRF-42 **Consolidation of Ti-6Al-4V Powder by a Compression Rotation Shearing Method at Room Temperature**
Sou Kato, Noboru Nakayama (Shinshu University, Japan), Hiroyuki Miki (Tohoku University, Japan) and Hiroyuki Takeishi (Chiba Institute of Technology, Japan)

CRF-43 **Development of Structure-controllable Multi-disk Single-electron Transistors by Ultimate Etching Technique with Bio-templating**
Ichiro Yamashita (Nara Institute of Science and Technology, Japan), Seiji Samukawa (Tohoku University, Japan)

CRF-44 **Development of High Performance Strained-Ge Channel Device Utilizing Neutral-beam Oxidized Film**
Toru Kurebayashi, Yusuke Hoshi, Kentarou Sawano, Yasuhiro Shiraki (Tokyo City University, Japan), Akira Wada and Seiji Samukawa (Tohoku University, Japan)

CRF-45 **Fundamental Study on Spiking Neuron Devices**
Takashi Morie, Haichao Liang, Yilai Sun (Kyushu Institute of Technology, Japan), Makoto Igarashi and Seiji Samukawa (Tohoku University, Japan)

CRF-46 **Numerical Simulation of Electronic States of Regularly Arrayed Si Quantum Dot System**
Nurrul Syafawati Binti Humam, Nobuhiro Tsumori, Motoki Takahashi, Toshiharu Saiki (Keio University, Japan) and Seiji Samukawa (Tohoku University, Japan)

CRF-47 **Development and Flow Evaluation of Electro-Rheological Nano-Suspensions**
Katsufumi Tanaka, Takanobu Hira, Ryuichi Fukui, Haruki Kobayashi, Ryuichi Akiyama (Kyoto Institute of Technology, Japan), Masami Nakano and Shouta Enami (Tohoku University, Japan)

14:00-14:15 BREAK

Chair: Hiroyuki Miki (Tohoku University, Japan)

14:15-15:21 **Short Oral Presentation**
(3 min for Short Oral Presentation)

CRF-48 **Study of Contact Alignment for the Slider Specimen of Tribometer**
Minoru Goto (Ube National College of Technology, Japan), Kosuke Ito (Nihon University, Japan), Hiroyuki Miki and Takanori Takeno (Tohoku University, Japan)

CRF-49 **Tribological Behavior and Electrical Contact Resistance of Metal-containing DLC Coating for Electrically-Conductive Tribo-elements**
Julien Fontaine, Michel Belin, Sandrine Bec, Thierry Le Mogne (Ecole Centrale de Lyon, France), Toshiyuki Takagi, Takanori Takeno, Koshi Adachi and Hiroyuki Miki (Tohoku University, Japan)

CRF-50 **Optimization of Ink Viscosity of a Continuous Inkjet by Experiment and Numerical Simulation**
Masami Nakano (Tohoku University, Japan), Tameo Nakanishi and Hinoki Tsunokake (Yamagata University, Japan)

CRF-51 **Impact of Liquid Drops on Heated Grooved Surfaces**
Sivakumar Deivandren (Indian Institute of Science, India), Kazunari Katagiri, Tomoki Nakajima, Hidemasa Takana and Hideya Nishiyama (Tohoku University, Japan)

CRF-52 **Transport Phenomena at Nano-Structured Interfaces**
Masahiko Shibahara (Osaka University, Japan), Taku Ohara and Gota Kikugawa (Tohoku University, Japan)

CRF-53 **A Classical Molecular Dynamics Study on Thermodynamic Properties of Cryogenic Hydrogen/Oxygen System**
Shin-ichi Tsuda (Shinshu University, Japan), Masato Tomi, Nobuyuki Tsuboi (Kyushu Institute of Technology, Japan), Hiroki Nagashima, Takashi Tokumasu (Tohoku University, Japan) and Mitsuo Koshi (The University of Tokyo, Japan)

CRF-54 **A Molecular Dynamics Study of Momentum Transport in a Nanoscale Liquid Bridge**
Takashi Tokumasu (Tohoku University, Japan), Marie-Hélène Meurisse, Nicolas Fillot and Philippe Vergne (INSA-Lyon, France)

CRF-55 **Proton Transport in Hydrogen Bond Network of Confined Water**
Nobuya Miyoshi, Ikuya Kinefuchi (The University of Tokyo, Japan), Takashi Tokumasu (Tohoku University, Japan), Shu Takagi and Yoichiro Matsumoto (The University of Tokyo, Japan)

CRF-56 **Oscillation Characteristics of Levitated Magnet-Magnetic Fluid System**
Michihiro Shinozaki, Seiichi Sudo (Akita Prefectural University, Japan), Hidemasa Takana and Hideya Nishiyama (Tohoku University, Japan)

CRF-57 **New Exact Solutions for Vortex Rings with Swirl and Magnetic Field**
Yuji Hattori (Tohoku University, Japan), Stefan G. Llewellyn Smith (UCSD, USA)

CRF-58 **A Numerical Study of the Effect of Large Deformations of a Trailing Vortex on Its Breakdown**
Naoya Takahashi (Tokyo Denki University, Japan), Takeshi Miyazaki (The University of Electro-Communications, Japan), Nozomu Hatakeyama, Yuji Hattori (Tohoku Univeresity, Japan)

CRF-59 **The Instability of a Helical Vortex Tube with Axial Flow**
Yasuhide Fukumoto (Kyushu University, Japan), Yuji Hattori (Tohoku University, Japan)

CRF-60 **Numerical and Experimental Research on Active Control of the Hole-Tone Feedback Problem**
Mikael A. Langthjem (Yamagata University, Japan), Masami Nakano (Tohoku University, Japan)

CRF-61 **Entropy Flow in Magnetically Ordered Heusler Alloys under Influence of Temperature or Magnetic Field**
Vladimir Khovaylo, Ekaterina Avilova (National University of Science and Technology, Russia), Hiroyuki Miki, Toshiyuki Takagi, Makoto Ohtsuka (Tohoku University, Japan), Vasiliy Buchelnikov (Chelyabinsk State University, Russia), Konstantin Skokov (Tver State University, Russia / Leibniz Institute for Solid State and Materials Research, Germany) and Oliver Gutfleisch (Leibniz Institute for Solid State and Materials Research, Germany)

CRF-62 **Simulation Analysis on the Change of B-H Curve Pattern for Sensitized Alloy 600**
Katsuhiko Yamaguchi, Kenji Suzuki (Fukushima University, Japan), Tetsuya Uchimoto and Toshiyuki Takagi (Tohoku University, Japan)

CRF-63 **Nondestructive Evaluation of Austenitic Stainless Steel Residual Strain with EMAT**
Liqiang Zhong (Tsinghua University, China), Tetsuya Uchimoto, Toshiyuki Takagi (Tohoku University, Japan), Naoki Chigusa (Kansai Electric Power Company, Inc., Japan) and Luming Li (Tsinghua University, China)

CRF-64 **Reconstruction of Wall Thinning from Pulse Eddy Current Signals**
Zhenmao Chen (Xi'an Jiaotong University, China), Shejuan Xie (Tohoku University, Japan), Xiaowei Wang, Yong Li (Xi'an Jiaotong University, China), Tetsuya Uchimoto and Toshiyuki Takagi (Tohoku University, Japan)

CRF-65 **Energy Transfer Simulation and Analysis on Mega-scale Environment**
Noboru Yamada (Nagaoka University of Technology, Japan), Atsushi Sakurai (Niigata University, Japan), Atsuki Komiya and Shigenao Maruyama (Tohoku University, Japan)

CRF-66 **Heat Transfer Analysis in a Biological Tissue Exposed to Laser Irradiation**
Atsushi Sakurai (Niigata University, Japan), Yoshiyuki Sato, Shigenao Maruyama, Junnosuke Okajima and Atsuki Komiya (Tohoku University, Japan)

CRF-67 **Usage of the Lattice Boltzmann Method Applied to the Analysis of Radiative Transfer in a Participating Medium Subjected to Collimated Loading**
Subhash C. Mishra, Rohan Ranganath Vernekar (Indian Institute of Technology Guwahati, Indai)

CRF-68 **Detection Accuracy Analysis of Several Eddy Current Probes on the Impact Damage of Carbon-Fibre Plastic Composite**
Jun Cheng, Jinhao Qiu (Nanjing University of Aeronautics & Astronautics, China), Toshiyuki Takagi, Tetsuya Uchimoto (Tohoku University, Japan), Fuqiang Wu (Nanjing University of Aeronautics & Astronautics, China) and Ning Hu (Chiba University, Japan)

CRF-69 **Evaluation of Thin Coating Layers using Non-Specular Reflection of Rayleigh Waves**
Hak-Joon Kim, Sung-Jin Song (Sungkyunkwan University, Korea), Sung-Duk Kwon (Andong National University, Korea), Toshiyuki Takagi, Hiroyuki Miki and Tetsuya Uchimoto (Tohoku University, Japan)

15:30-16:30 **Poster Session**

PS2: 5th Functionality DEsign of the COntact Dynamics:(DECO2011)

HAGI
November 11, 2011

Chair: Julien Fontaine (Ecole Centrale de Lyon, France)

13:50-14:00 BREAK

Chair: Hiroyuki Miki (Tohoku University, Japan)

15:05-15:15 BREAK

Chair: Toshiyuki Takagi (Tohoku University, Japan)

PS3: Plasma Medicine and Cell Engineering

FUJI
November 10, 2011

13:00-13:05 **Opening**
Takehiko Sato (Tohoku University, Japan)

Chair: Takehiko Sato (Tohoku University, Japan)

PS3-1 13:05-13:45 **Nonthermal Plasma-mediated Cancer Cell Death; Targeted Cancer Treatment (*Keynote Lecture*)** 660
Byul-Bo Ra Choi, Uk-Kyu Kim, Hae-Jun Lee (Pusan National University, Korea), Jae-Koo Lee (Pohang University of Science and Technology, Korea) and Gyoo-Cheon Kim (Pusan National University, Korea)

Chair: Toshiro Ohashi (Hokkaido University, Japan)

PS3-2 13:45-14:25 **Enhancing Skin Repair through a 3D In-Vitro Human Skin Equivalent Model (*Keynote Lecture*)** 662
Kerry Manton, Rebecca Dawson, Yan Xie, Derek Van Lonkhuyzen, David Leavesley and Zee Upton (Queensland University of Technology, Australia)

14:25-14:45 BREAK

Chair: Takehiko Sato (Tohoku University, Japan)

PS3-3 14:45-15:15 **Experimental Studies of Plasma Medicine on Prevention for the Adhesion (*Invited*)** 664
Hajime Sakakita, Yuzuru Ikehara (National Institute of Advanced Industrial Science and Technology (AIST), Japan)

PS3-4 15:15-15:45 **Regenerative Medicine Using Novel Biomedical Plasma Techniques (*Invited*)** 666
Takamichi Hirata, Chihiro Tsutsui and Akira Mori (Tokyo City University, Japan)

15:45-16:00 BREAK

Chair: Toshiro Ohashi (Hokkaido University, Japan)

PS3-5 16:00-16:30 **Engineering Tissues From the Bottom up: Designing Microarchitectural Features of Tissues (*Invited*)** 668
Yukiko T. Matsunaga (The University of Tokyo / Japan Science and Technology Agency, Japan)

PS3-6 16:30-17:00 **Biomechanical Regulation of Actin Cytoskeleton Dynamics in Migrating Cells (*Invited*)** 670
Taiji Adachi, Kennedy O. Okeyo (Kyoto University, Japan)

17:00-17:15 BREAK

Chair: Takehiko Sato (Tohoku University, Japan)

PS3-7 17:15-17:45 **Biological and Medical Applications of Pulsed Power (*Invited*)** 672
Sunao Katsuki, Masahiko Yano, Kazunori Mitsutake, Keisuke Abe and Hidenori Akiyama (Kumamoto University, Japan)

PS3-8 17:45-18:15 **Advantages of Cascade Plasma Torches for APS and SPS of Bioactive Hydroxyapatite Coatings (*Invited*)** 674
Oleg P. Solonenko, Andrey V. Smirnov, Igor P. Gulyaev, Marina V., Chaikina, Andrey V. Pefiliev (Shiberian Branch of RAS, Russia)

FUJI
November 11, 2011

Chair: Takamichi Hirata (Tokyo City University, Japan)

PS3-9 9:00-9:40 **Atmospheric Plasma for Wound Treatment: Lab to Clinical Study (*Keynote Lecture*)** 676
Tetsuji Shimizu, Julia L Zimmermann, Gregor E Morfill (Max-Planck Institute for extraterrestrial physics, Germany), Georg Isbary and Wilhelm Stolz (Hospital Munich Schwabing, Germany)

PS3-10 9:40-10:10 **Plasma Surface Treatment of Artificial Bones and its Application to Regenerative Medicine (*Invited*)** 678
Satoshi Hamaguchi, Dae-Sung Lee, Kazuto Masuda, Yu Moriguchi, Akira Myoui and Hideki Yoshikawa (Osaka University, Japan)

10:10-10:25 BREAK

Chair: Toshiro Ohashi (Hokkaido University, Japan)

PS3-11 10:25-10:55 **Control of Cell Adhesion and Functions Using 2D and 3D Biocompatible Surfaces (*Invited*)** 680
Masaru Tanaka (Yamagata University, Japan)

PS3-12 10:55-11:25 **Effect of Mechanical Loading on Chondrocyte Biosynthesis of Extracellular Matrix in Agarose Construct (*Invited*)** 682
Yoshinori Sawae (Kyushu University, Japan)

PS3-13 11:25-11:45 **Involvement of ERK in Morphological Response of Endothelial Cells to Spatial Gradient of Shear Stress** 684
Xiaobo Han, Naoya Sakamoto, Naoki Saito, Masaaki Sato, Makoto Ohta (Tohoku University, Japan)

11:45-13:00 LUNCH

Chair: Takamichi Hirata (Tokyo City University, Japan)

PS3-14 13:00-13:30 **Modeling and Simulation of Gas Plasma-assisted Wound Healing (*Invited*)** 686
Yukinori Sakiyama, Marat Orazov, David Graves (University of California at Berkeley, USA) and Gregor Morfill (Max Planck Institute for Extraterrestrial Physics, Germany)

PS3-15 13:30-14:00 **Traction Force Measurement During Cell Migration By Using Micropillar-Integrated Device (*Invited*)** 688
Toshiro Ohashi, Akito Sugawara (Hokkaido University, Japan), Justin J. Cooper-White (The University of Queensland, Australia) and Eijiro Maeda (Hokkaido University, Japan)

PS3-16
14:00-14:30

Effect of Chemical Species Generated by a Plasma Flow on Inactivation of HeLa Cell Viability (*Invited*) 690

Takehiko Sato, Mayo Yokoyama (Tohoku University, Japan) and Kohei Johkura (Shinshu University, Japan)

14:30

Closing

Toshiro Ohashi (Hokkaido University, Japan)

PS4: The 12th Japan-Korea Students' Symposium
New Energy Flow for Sustainable Society
-Properties and Applications of Energy Materials-

AKEBONO (EAST)
November 10, 2011

Session1
Chairs: Hyung-Soon Kwon and Riyan Achmad Budiman

PS4-1 8:50-9:10 — **Low-temperature Operating Micro–SOFC with Perovskite–type Proton Conductive Electrolytes** — 694
Yu Inagaki, Kensuke Kubota, Fumitada Iguchi, Syuji Tanaka, Noriko Sata, Masayoshi Esashi and Hiroo Yugami (Tohoku University, Japan)

PS4-2 9:10-9:30 — **Electrical Characterization of Ni-YSZ Supported Thin Film YSZ Electrolyte with GDC Top Buffer Layer** — 696
Eui-Chol Shin, Jung-Mo Jo (Chonnam National University, Korea), Pyung-An Ahn, Ho-Sung Noh, Ji-Won Sohn, Jong-Ho Lee (Korea Institute of Science and Technology, Korea) and Jong-Sook Lee (Chonnam National University, Korea)

PS4-3 9:30-9:50 — **Investigation on Oxygen Reduction Reaction on an $La_{1-x}Sr_xCo_{1-y}Fe_yO_{3-\delta}$ Thin Film Electrode** — 698
Li Xinxin, Atsushi Unemoto, Shin-Ichi Hashimoto, Koji Amezawa and Tatsuya Kawada (Tohoku University, Japan)

9:50-10:00 BREAK

Session2
Chairs: Jakyu Chun and Yusuke Kawamura

PS4-4 10:00-10:20 — **Effect of Nb Doping on the Properties of $SrCoO_{3-\delta}$ Based Cathode for Intermediate Temperature Solid Oxide Fuel Cells** — 702
Fang Wang, Keiji Yashiro, Kazuhisa Sato and Junichiro Mizusaki (Tohoku University, Japan)

PS4-5 10:20-10:40 — **Fabrication of Anode-Supported Type Protonic Ceramic Fuel Cells (PCFCs)** — 706
Sung Min Choi (Korea Institute of Science and Technology / Korea University, Korea), Jong-Heun Lee (Korea University, Korea), Jong-Ho Lee, Hae-Weon Lee, Ho Il Ji and Byung-Kook Kim (Korea Institute of Science and Technology, Korea)

PS4-6 10:40-11:00 — **Mass Transport in Perovskite Oxides $(La,Sr)(Co,Fe)O_3$** — 708
Honami Kudo, Keiji Yashiro and Junichiro Mizusaki (Tohoku University, Japan)

11:00-11:10 BREAK

Session3
Chairs: Dasari Hari Prasad and Tomohisa Masumitsu

PS4-7 11:10-11:30 — ***In-situ* Evaluation of Oxygen Chemical Potential in an SOFC Cathode** — 710
Yoshinobu Fujimaki, Hidetaka Watanabe, Koji Amezawa, Tatsuya Kawada (Tohoku University, Japan) and Yasuko Terada (JASRI, Japan)

PS4-8 11:30-11:50 — **Study on the Origin and Characteristics of Oxygen Storage Capacity for Pr doped Ceria** — 714
Kiyong Ahn (Korea Institute of Science and Technology / Hanyang University, Korea), Yong-Chae Chung (Hanyang University, Korea), Hae-Weon Lee and Jong-Ho Lee (Korea Institute of Science and Technology, Korea)

PS4-9 11:50-12:10 — **Effects of Redox Cycling on the Mechanical Properties of Ni-YSZ Cermets for SOFC Anodes** — 716
Taihei Miyasaka, Shinji Sukinou, Satoshi Watanabe, Kazuhisa Sato, Tatsuya Kawada, Junichiro Mizusaki and Toshiyuki Hashida (Tohoku University, Japan)

PS4-10 12:10-12:30 — **Thermo-Mechanical Analysis of Cyclic Reduction and Oxidation Behavior of SOFC Ni-YSZ Cermets** — 718
Shinji Sukino, Taihei Miyasaka, Satoshi Watanabe, Kazuhisa Sato Tatsuya Kawada, Junichiro Mizusaki and Toshiyuki Hashida (Tohoku University, Japan)

12:30-13:30 LUNCH

Tutorial1
Chairs: Taewon Lee and Hidetaka Watanabe

13:30-14:15 — **Tutorial Lecture**
Kisuk Kang (Seoul National University, Korea)

14:15-14:30 BREAK

Session4
Chairs: Dae-Hee Kim and Yu Cheol Shin

PS4-11 14:30-14:50 — **Investigation of Fracture Mechanism in Carbon Nanotube Reinforced Alumina Composites and Its Relation with Nanostructure** — 720
Keiichi Shirasu, Go Yamamoto, You Nozaka, Mamoru Omori, Toshiyuki Takagi and Toshiyuki Hashida (Tohoku University, Japan)

PS4-12 14:50-15:10 — **Gradient Structure Modification of LSC Cathode for Performance Improvement of Thin Film SOFCT** — 724
Jaeyeon Hwang (Korea Institute of Science and Technology / Korea University, Korea), Doo-Hwan Myung (Korea Institute of Science and Technology / Yonsei University, Korea), Hae-Weon Lee, Byung-Kook Kim, Jong-Ho Lee and Ji-Won Son (Korea Institute of Science and Technology, Korea)

PS4-13 15:10-15:30 — **Evaluation Method of Stress Conditions in Operated SOFC by In-Situ Raman Scattering Spectroscopy** — 726
Syo Onodera, Masafumi Nagai, Fumitada Iguchi, Noriko Sata, Tatsuya Kawada and Hiroo Yugami (Tohoku University, Japan)

PS4-14 **Study of Alcohol Fueled Single Chamber Solid Oxide Fuel Cells** 730
15:30-15:50 Ryusuke Mihara, Noriko Sata, Kohei Oba, Yuu Sugawara (Tohoku University, Japan), Yuki Nagao (Kyoto University, Japan), Fumitada Iguchi and Hiroo Yugami (Tohoku University, Japan)

PS4-15 **Nonstoichiometry and Thermoelectric Efficiency of β-$Ag_{2+\delta}Te$** 732
15:50-16:10 Wonhyo Joo (Seoul National University, Korea)

16:10-16:25 BREAK

Session5
Chairs: Ji-Hyun Kim and Tetsuya Hori

PS4-16 **Effects of Temperature and Oxygen Partial Pressure on Mechanical Properties of $La_{0.6}Sr_{0.4}Co_{1-y}Fe_yO_{3-\delta}$** 734
16:25-16:45 Yuta Kimura, Takuto Kushi, Shin-Ichi Hashimoto, Satoshi Watanabe, Koji Amezawa, Tatsuya Kawada, Yasuhiro Fukuda, Atsushi Unemoto, Keiji Yashiro, Junichiro Mizusaki, Kazuhisa Sato and Toshiyuki Hashida (Tohoku University, Japan)

PS4-17 **Evaluation of High Temperature Mechanical Properties of $La_{1-x}Sr_xMnO_{3+\delta}$ under Controlled Atmosphere** 738
16:45-17:05 Yoshikazu Shirai, Yuta Kimura, Takuto Kushi, Shin-Ichi Hashimoto, Kazuhisa Sato, Keiji Yashiro, Koji Amezawa, Junichiro Mizusaki and Tatsuya Kawada (Tohoku University, Japan)

PS4-18 **Electrical Conductivity of La-doped $BaTiO_3$ Thin Film via Pulsed Laser Deposition** 742
17:05-17:25 Hannah Cho (Seoul National University, Korea)

PS4-19 **Oxygen Potential Measurement in Oxygen Nonstoichiometric Oxides under the Stress** 744
17:25-17:45 Tomohisa Masumitsu, Satoshi Watanabe, Shin-Ichi Hashimoto, Koji Amezawa and Tatsuya Kawada (Tohoku University, Japan)

PS4-20 **Insulation Resistance Degradation of $BaTiO_3$ under D.C Bias** 746
17:45-18:05 Hyung-Soon Kwon (Seoul National University, Korea)

AKEBONO (EAST)
November 11, 2011

Session6
Chairs: Eui-Chol Shin and Li Xinxin

PS4-21 **Development of Evaluation Techniques of the Electrochemically Active Zone in a Ni-GDC Cermet Anode for SOFC** 748
8:50-9:10 Hidetaka Watanabe, Shin-ichi Hashimoto, Koji Amezawa and Tatsuya Kawada (Tohoku University, Japan)

PS4-22 **A Correct Access to Hydration Phenomenon of the Proton Conductor, Barium Zirconate, and Effects of NiO as a Sintering Aid.** 752
9:10-9:30 Euisung Kim (Seoul National University, Korea)

PS4-23 **Electrochemical Oxygen Reduction Process on $LaNi_{0.6}Fe_{0.4}O_3$ Electrode** 754
9:30-9:50 Riyan Achmad Budiman, Shin-Ichi Hashimoto, Koji Amezawa and Tatsuya Kawada (Tohoku University, Japan)

9:50-10:00 BREAK

Session7
Chairs: Sung Min Choi and Fang Wang

PS4-24 **Stress Effect for Conductivity Characteristics of Functional Ceramics** 758
10:00-10:20 Yusuke Kawamura, Kazuhisa Sato, Keiji Yashiro and Junichiro Mizusaki (Tohoku University, Japan)

PS4-25 **The Effect of Electric Field on Ternary Oxides – Electrotransport and Decomposition in Model System $NiTiO_3$** 762
10:20-10:40 Jakyu Chun (Seoul National University, Korea)

PS4-26 **Conductivity Variation in Mixed Ions Electric Conductor under Uniaxial Stress** 766
10:40-11:00 Shusaku Nakakawaji, Kazuhisa Sato, Keiji Yashiro and Junichiro Mizusaki (Tohoku University, Japan)

11:00-11:10 BREAK

Session8
Chairs: Kiyong Ahn and Shinji Sukino

PS4-27 **Design of Surface Periodic Microstructure on Refractory Metals for Solar Selective Absorbers** 768
11:10-11:30 Kiyotaka Konno, Makoto Shimizu, Hiroaki Kobayashi, Fumitada Iguchi and Hiroo Yugami (Tohoku University, Japan)

PS4-28 **Structural Characterization and CO Oxidation of $Ce_{0.65}Zr_{0.25}RE_{0.1}O_2$ Nano-composite Oxides Synthesized By Glycine-nitrate-process** 770
11:30-11:50 D.Hari Prasad, S.Y.Park, H. Ji, H.-R. Kim, J.-W. Son, B.-K.Kim, H.-W. Lee and J.-H. Lee (Korea Institute of Science and Technology, Korea)

PS4-29 **The Evaluation of Solar Selective Absorbers Using Refractory Metal in Concentrated Solar Power System** 774
11:50-12:10 Hiroaki Kobayashi, Kiyotaka Konno, Makoto Shimizu, Fumitada Iguchi and Hiroo Yugami (Tohoku University, Japan)

PS4-30 **Development of High Temperature Solar Selective Absorber Using Refractory Material with Surface Microstructures** 776
12:10-12:30 Makoto Shimizu, Kiyotaka Konno, Fumitada Iguchi and Hiroo Yugami (Tohoku University, Japan)

12:30-13:30 LUNCH

Tutorial2
Chairs: Wonhyo Joo and Makoto Shimizu

13:30-14:15 **Tutorial Lecture**
Noriko Sata (Tohoku University, Japan)

14:15-14:30 BREAK

Session9
Chairs: Jaeyeon Hwang and Keiichi Shirasu

Session10
Chairs: Hannah Cho and Yuta Kimura

Special Session:
Memorial Session for the Late Professor Hiroshi Higuchi

SEIUN
November 10, 2011

Chair: Toshiyuki Hayase (Tohoku University, Japan)
17:00-18:30
Presenter;

Mark Glauser (Syracuse University, USA)

Yasuaki Kohama (Tohoku University, Japan)

Yoshiya Nakamura (INC Engineering Co., Ltd Japan)

Plenary Lectures

Energy Sustainability: A Combustion Perspective

Suk Ho Chung
Clean Combustion Research Center
King Abdullah University of Science and Technology
Thuwal, Saudi Arabia
sukho.chung@kaust.edu.sa

ABSTRACT

Combustion is one of the key subject areas associated with the energy and environmental issues related to air pollution, global warming, and climate change. Considering the limited reserve of petroleum fuels, various options for energy sustainability will be discussed including the perspectives of alternative and renewable energy sources. Combustion will remain as a critical element for the sustainability in the next several decades and this presentation covers several key combustion research topics.

1. Introduction

Over 80% of world energy is consumed through combustion processes for energy conversion from fossil fuels. About 70% of petroleum is utilized for transportation fuels due to high energy density and easy of handling. Although there is a growing concern on the petroleum depletion issue related to the sustainability, there are plenty of other hydrocarbon fuel sources including heavy oil, tar sand, oil shale, gas to liquid (GTL) and coal to liquid (CTL), which are expected to last about 100 years in the future. Although there is a growing interest in renewable energy sources including biofuels and solar energy, the economical competitiveness of such sources is yet to be required for appreciable usage. Details will be covered in the presentation.

One of the near-term solution for the energy and environment issues is efficiency increase and emission reduction from internal combustion engines. Engine efficiencies have been increases about 2.5 % per year during last 25 years through the advances in control and injection technologies. Recent researches are focused on advanced engines such as low temperature concept engines.

The understanding of combustion science has been advanced significantly during last 30 years. This is based on the development of supercomputing capability and of chemical kinetic mechanisms. Supercomputing power becomes 1000 times faster in every 10 years. Chemical kinetic mechanisms have been developed for the application to realistic fuels such as gasoline, diesel, and aviation fuels up to C20 hydrocarbons. As a result, prediction capability in combustion phenomena has been advanced to cover such fuels. Although, science-based detailed calculations in engine combustion are still limited at this stage, it will be promising in next two decades.

In such development, understanding of autoignition behavior and emission characteristics of soot and NOx of fuels are important. Autoignition is an ignition mode of diesel engines and efficiency limiting factor for gasoline engines. Also it is a controlling factor for advanced concept engines of low temperature concept engines and premixed-charge compression ignition (PCCI) engines. Soot is a source of particulate matter emission in combustion systems and strictly regulated since it is carcinogenic and mutagenic. Research activities on these topics will be introduced in the following.

2. Soot Formation

Soot formation is one of the most complex phenomena, which involves gas-phase kinetics, particle inception, surface growth, aerosol dynamics and oxidation. Fuel pyrolysis generates C2 or C3 species which react to form incipient rings such as benzene. The hydrogen-abstraction-C_2H_2-addition (HACA) process and odd-carbon chemistry lead to polycyclic aromatic carbons (PAHs), from which inception proceeds to form soot particles. Soot is growing its size through HACA, odd carbon chemistry or PAH coagulation, and coalescence. Subsequently, soot can be oxidized by OH or O_2 species. Various chemical species are involved in soot formation process such that fuel constituents are important.

Binary mixtures of n-heptane/toluene and iso-octane/toluene have been investigated in counterflow diffusion flames to test soot behavior of gasoline surrogate fuels [1]. Laser-induced incandescence and laser-induced fluorescence techniques were employed for soot volume fraction and PAH concentrations. Figure 1 shows the maximum LII and LIF signals in the flame zone as a function of toluene ratio in iso-octane/toluene mixture fuels, normalized at the condition of toluene fuel. The PAH concentration represented by the LIF signal shows an interesting non-monotonic behavior in that certain mixture fuels exhibited higher PAH concentrations as compared to toluene. The soot volume fraction does not affected much by toluene addition up to about 40% and then increases reasonably linearly, which implies a tolerance of toluene on soot formation. Note that toluene is used as octane booster in gasoline fuels.

Existing kinetic mechanisms having pyrene (A4) as largest molecule cannot predict such behavior for various diffusion flames tested. Therefore, a new kinetic mechanism has been proposed by adopting the density functional theory (DFT) and the transition state theory (TST) for reaction energetic and kinetics [2]. This consists of 231 species and 2126 reactions covering up to coronene (A7). Figure 2 shows the reaction path diagram from benzene (A1) to coronene. The mechanism can successfully predict PAH formation behavior for various diffusion flames of gasoline

surrogate fuels.

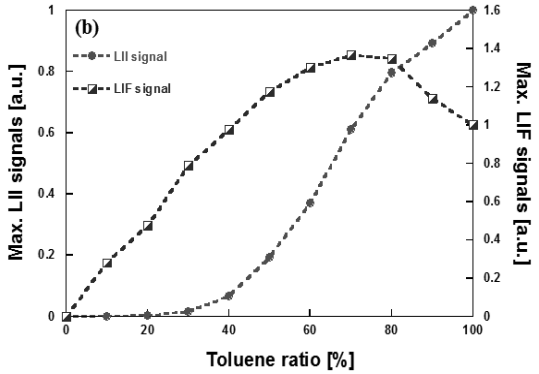

Fig. 1 PAH and soot behavior for iso-octane/toluene mixture fuels.

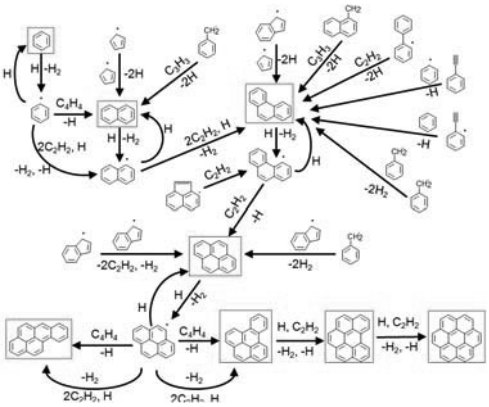

Fig. 2 Reaction path diagram from benzene to coronene.

3. Autoignition behavior in jets

Typical experimental procedure for autoignition study is using a shock tube which utilizes reflected shock to determine ignition delay time of homogeneous mixture of fuel and oxidizer, with available time of O(1-10 ms). There can be two issues in this experiment: one is that for low temperature combustion, the ignition delay time can be much longer than the available time and the other is that autoignition process frequently occurs in inhomogeneous mixtures, typically in jets.

Autoignition behavior of fuel jets has been studied in coflow air at elevated temperature [3,4]. For the temperature higher than a certain ignition temperature, the jet was autoignited and stabilized as a lifted flame. Near the blowout condition, a critical autoignition was observed, having repetitive extinction and reignition. This process can be explained based on the effect of buoyancy.

Near the blowout condition when the system is autoignited, the burnt gas could induce local acceleration in the streamwise velocity due to the buoyancy, leading to blowout (extinction). As the local velocity decelerates by the mitigation in the buoyancy, an autoignition could occur again (reignition). Thus, the extinction and reignition repeats. In such a case, the location of autoignition can be determined experimentally.

A characteristic flow time can be defined from autoignition height divided by jet velocity. It can be conceived that the characteristic flow time balances with ignition delay time. However, heat loss is associated with heat generation, which occurs with the square root of time through transverse diffusion, the characteristic flow time correlated with the square of ignition delay time as exhibited in Fig. 3.

The ignition delay times calculated from various existing kinetic mechanisms are quite different in the temperature range we have tested. The values are differ by O(10). Accurate kinetic mechanism should be developed in the future.

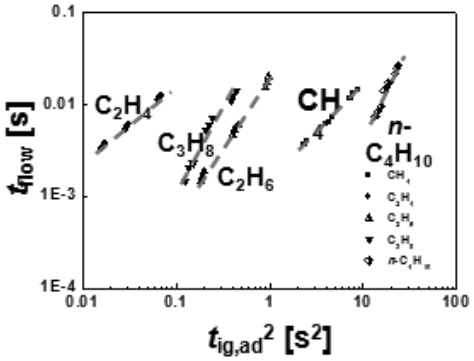

Fig. 3 Correlation of flow time with ignition delay time.

References

[1] BC Choi, SH Chung, Proc. Combust. Inst. 33 (2011), P609.
[2] A Raj, SH Chung, to appear in Combust. Flame (2011).
[3] BC Choi, KN Kim, SH Chung, Combust. Flame, 156 (2009), P396.
[4] BC Choi, SH Chung, Combust. Flame, 157 (2010), P2348.

Eighth International Conference on Flow Dynamics
November 9 - November 11, 2011

Transport Phenomena, Fluid Mechanics and Multiscale Modelling Techniques for Clinical Decision Support

Emilie C. Holland, Tom W. Peach, Alisa Selimovic, Brett J. Tully, Paul N. Watton, Yiannis Ventikos,
Institute of Biomedical Engineering and Department of Engineering Science,
University of Oxford, Parks Road, Oxford OX1 3PJ, UK.
yiannis.ventikos@eng.ox.ac.uk

ABSTRACT

The use of computer models in biomedical engineering has grown very substantially in the last two decades, but it is only very recently that such techniques are finding their way into the clinical setting. In this paper, we present concepts and methodologies, at different stages of maturity, that promise to tackle unmet clinical needs and help diagnosis, treatment planning and prognosis. The cases we shall be concerned with involve both focal diseases of the vascular system such as aneurysms, but also ailments that involve entire organs and cannot therefore be localized, but need to be addressed in an integrative manner, like hydrocephalus.

1. Introduction

Transport phenomena are dominant in the human physiology and pathophysiology, and that is why biological fluid mechanics, or biofluids, have received so much attention in both the engineering and the medical communities [1]. At the same time, cardiovascular diseases – where flow of blood is a dominant process – are responsible, directly or indirectly, for the majority of deaths worldwide, [2] (when compared to other causes, like cancers or accidents), with a percentage that approaches 50% in the western world. This is a staggering demographic that substantiates further the widespread involvement of engineers, applied mathematicians and computer scientists in the effort to enhance our understanding of these conditions through modelling. Diseases like myocardial infarction, aneurysms, dissections, oedemas, hydrocephalus, ischemic strokes, valve deficiencies, and numerous others, are all necessitating intense research, since progress needs to be made in their diagnosis and treatment.

In this paper, we shall focus on three examples that involve recent efforts in addressing unmet clinical needs in transport phenomena-related diseases. Namely, we shall discuss cerebral aneurysms, in two aspects – first, evaluation of rupture risk using growth and remodelling simulation concepts and second, interventional planning via the simulation of implanted flow diverter performance. Finally, we shall discuss a newly developed multicompartmental poroelasticity model, which is used for the evaluation of transport of cerebrospinal fluid (CSF) and blood in the entire brain.

2. Cerebral aneurysms: Growth & Remodelling

Cerebral aneurysms are pouch-like deformations of the cerebral vasculature. They are relatively commonplace in the general population (3.6 % found in autopsies, up to 6.0% discovered angiographically, [3]), but they rarely rupture – between 9-20/100,000, [4]. The ubiquitous availability of diagnostic brain scans today has resulted in an ever-increasing number of incidental detection of asymptomatic aneurysms. The markedly grave consequences of rupture introduce a dilemma for patients and doctors: to intervene, or to follow-up? So far, this decision has been based almost exclusively on statistical measures of the geometric features, an approach that has repeatedly proven inadequate. This need, and the pressure on healthcare systems worldwide for more rational decision making, has led to the development of sophisticated computational frameworks that account for hemodynamic features as aneurysm inception triggers, [5], or for coupled vascular wall biomechanics & hemodynamic platforms that are capable of simulating the remodelling processes of arterial components (elastin and collagen fibres, fibroblasts, smooth muscle cells and endothelium) and capture the evolution of such aneurysms, either towards stabilization or rupture, [6].

Such techniques bring together high specificity CFD computations of blood flow (which often feature patient-specific flow boundary conditions and image-based reconstructions of the computational domains), high accuracy computation of deformations of the vascular wall under fluid forces, and sophisticated remodelling concepts that account for fibre deposition, degradation and crosslinking – thus allowing for the development of evolving constitutive relationships for the vascular wall. Figure 1 demonstrates the results obtained for an aneurysm from such a computation.

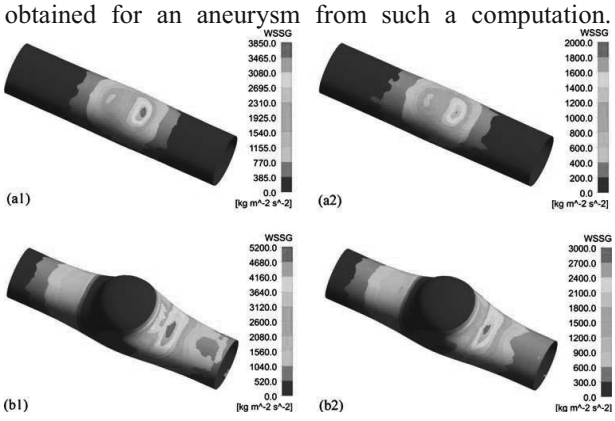

Fig 1 Wall Shear Stress Gradient (WSSG, the spatial gradient of WSS): First row, *a1* corresponds to a steady computation and *a2* to a pulsatile flow one. Both images depict an early stage of aneurysm development. In the second row, *b1* corresponds to a steady computation and *b2* to a pulsatile one, for the later stages of aneurysm development, [6].

3. Cerebral aneurysms: Intervention planning

Large scale clinical studies have shown that minimally invasive interventions for cerebral aneurysms have measurably better long-term patient outcome, [7].

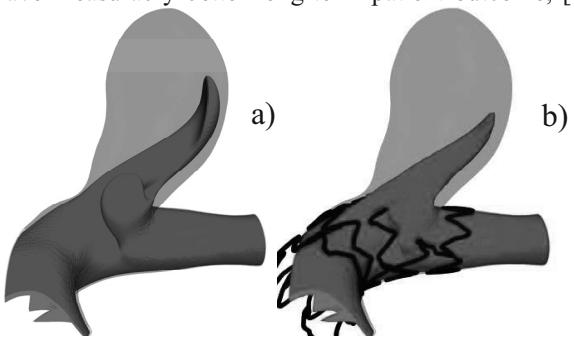

Fig 2 Isosurface of velocity magnitude (v = 0.1m/s) for an unstented (a) and a stented (b) aneurysm.

The prevailing technique for such interventions has been the implantation of thin platinum wires in the aneurysm sac (Guglielmi Detachable Coils). These coils increase the flow resistance, induce blood stagnation, trigger thrombosis and thus obliterate the aneurysm through the formation of a stable clot, [8].

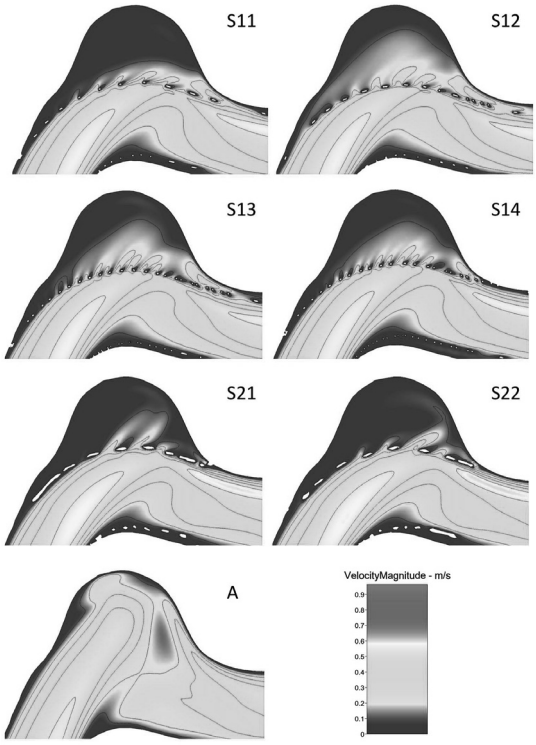

Fig 3 Velocity magnitude contours on an aneurysm midplane. Two different flow diverters (S1 and S2) and different deployment positions for these diverters (4 positions for S1 and 2 for S2). The unstentend aneurysm flow is shown in A.

Recently, coils are being replaced by open stents, or *flow diverters*, devices that are placed in the parent vessel and induce a similar increase in resistance, since they result in the placement of a *grid* across the aneurysm neck, Figure 2. It is becoming clear nowadays that the specifics of the implant (and also its positioning, Figure 3) must match the particular aneurysm that is to be treated. Computational simulation is currently the only viable way to help interventionists decide on the appropriate flow diverter for each individual aneurysm, and how it should be positioned. The spatial scale discrepancy (aneurysm scale $O(10^{-2}m)$, wire scale $O(10^{-4}m)$) results in very substantial requirements regarding resolution (often tens of millions of elements for grid independent solutions), and appropriate grid generation techniques become important, [9].

4. Hydrocephalus: MPET

There are numerous, often very serious, conditions of the brain that involve the transport of all fluids in that environment; blood and CSF (or, to put it differently, the transport of water within the cranial cavity). Oedemas, hydrocephalus, vasospasms etc. often engage responses of the cerebral system as a whole and thus do not allow the isolation of elements or sections for investigation.

A recently developed approach that allows for such integrative modelling is the Multicompartmental Poroelasticity framework or MPET, [10]. This technique is based upon the idea that the brain is an elastic matrix permeated by a number of networks, with pores of different size (but distinct within each network) that may or may not communicate with each other. This technique, applied for a paradoxical brain ailment called Normal Pressure Hydrocephalus (a disease resulting in substantial ventricle dilatation and hydrocephalus-like clinical symptoms, but without any radiographically significant aqueduct occlusion to explain the ventriculomegaly), showed that such a multiscalar model can account for both macroscopic and microscopic interactions. It is found that combinations of microscopic effects, like stiffening of vessels and increased leakiness of capillaries can indeed result in macroscopic effects, like clinically relevant ventricular enlargement.

5. Concluding remarks

Computational modelling of flow and transport phenomena in biomechanics is finding its place in clinical medicine. Techniques span the range from aiming at basic disease understanding to practical day to day clinical support. As the computational models gain in maturity, we expect to see an ever increasing penetration of such techniques in the clinic.

References

[1] M Siebes, Ann. Biomed. Eng. **38**(2010), 1216.
[2] CJL Murray, Harvard School of Public Health, 1996.
[3] GRF Rinkel, Stroke, **29**(1998), 251.
[4] CEP van Munster, Stroke, **39**(2008), 3166.
[5] Y Shimogonya, J Biomech, **42**(2009), 550.
[6] PN Watton, Biomech Model Mechan, **10**(2011), 109.
[7] ISUIA Investigators, Lancet, **362**(2003)m 103.
[8] NMP Kakalis, IEEE T Med Imaging,**27**(2008), 814.
[9] Y Ventikos, Brit J Radiol, **82**(2009), S62.
[10] BJ Tully, J Fluid Mech, **667**(2011), 188.

Low-Order Aeromechanical Modeling for Conceptual Design of Fuel-Efficient Aircraft

Mark Drela
MIT Aeronautics and Astronautics, Cambridge, USA.
drela@mit.edu.

ABSTRACT

Multidisciplinary optimization of fuel-efficient aircraft requires the use of effective low order models. These provide rapid structural, aerodynamic, and propulsion sizing and analysis, and thus allow global optimization of the aircraft and operating parameters for minimum mission fuel burn. Current modeling approaches are reviewed, and their importance for obtaining the lowest fuel burn designs is demonstrated. Recent transport aircraft concepts developed with such a method will be presented.

1. Background and Motivation

Fuel efficiency is one of the most important design considerations for modern transport aircraft, for reasons of operating cost and low emissions. Because fuel burn depends on many competing drivers, effective conceptual transport aircraft design must address the key features of all the disciplines involved. As a minimum, the airframe structure and weights, the aerodynamic performance, the propulsion performance, and the flight trajectory must all be represented with sufficient fidelity. Many conceptual design formulations have been developed, for example Roskam [1], Torrenbeek [2], Raymer [3], and others. Most of these methods have relied on historical correlations for estimating weight, drag, and engine performance, so that they are reliable only for conventional configurations and engine parameters.

Recently there has been interest in unconventional configurations such as the Strut-Braced Wing (SBW) of Pfenninger [4], the BlendedWing Body (BWB) of Liebeck [5], and the D8 concept of Drela [6]. The traditional correlation-based conceptual design formulations are not reliable for the evaluation and optimization of these configurations. Instead, methods based more on physics rather than correlations are required, such as those by Jayaram [7], Wakayama [1][8], Kroo [9], and that author's TASOPT method [10]. The presentation will outline the modeling techniques and calculation methods used by these physics-based methods, with specific examples drawn from the TASOPT methodology.

2. Physical Modeling

The physical models in TASOPT are sketched in Figure 1, and can be summarized as follows.

- Beam and pressure-vessel theory for primary-structure sizing and weight prediction.
- Variable wing airfoils and viscous/inviscid CFD for all profile drag prediction.
- Full engine flowpath simulation.
- Variable flight trajectory.

These models do not use historical primary-structure weight correlations, wetted-area drag prediction methods, engine lookup tables or correlations, or fixed climb and cruise profiles. Hence they are expected to be reliable for unconventional configurations, or for evaluating the influence of unusual aircraft parameter or technology combinations for which historical data does not exist.

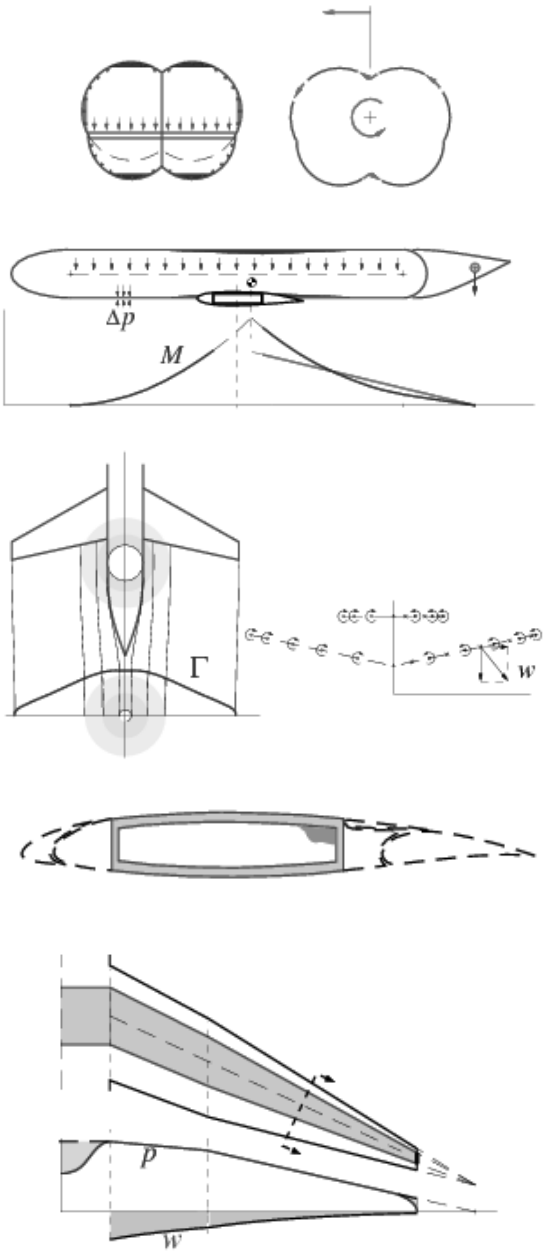

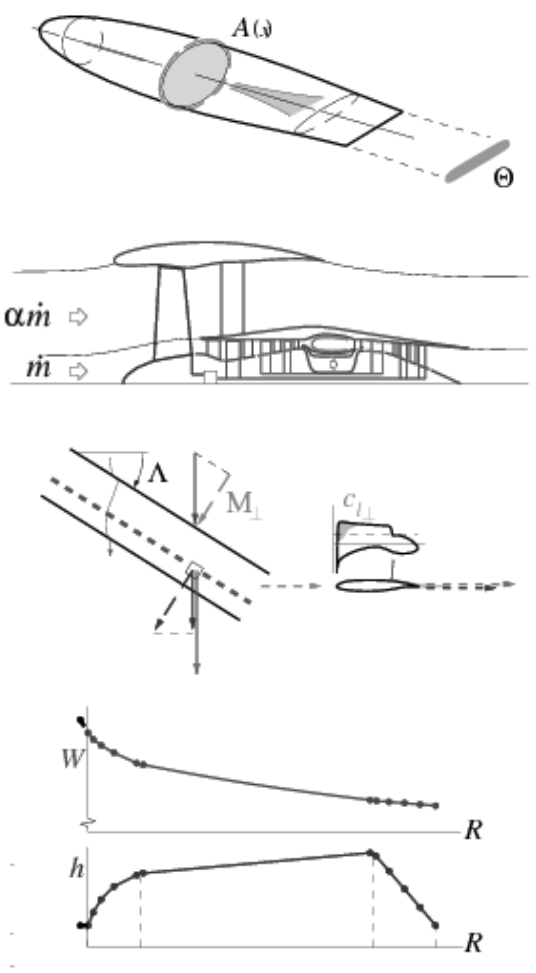

Figure 1: TASOPT structural, weight, aerodynamic, engine, and operation models.

3. Applications

Example applications will show the importance of using sound physical modeling of the component disciplines for obtaining an effective and realistic conceptual design. The examples will also show the importance of using global optimization spanning all the disciplines for obtaining the true minimum-fuel design which meets all operating constraints.

The power of physics-based conceptual design goes beyond obtaining an optimum design. Also shown will be the computed dependence of fuel burn on various technology parameters such as material strength/weight, engine metal temperature and overall pressure ratio, and skin-friction reduction via riblets or laminar flow. Finally, a few novel configurations will also be evaluated, such as the D8 concept developed for the NASA N+3 program [11], and shown in Figure 2.

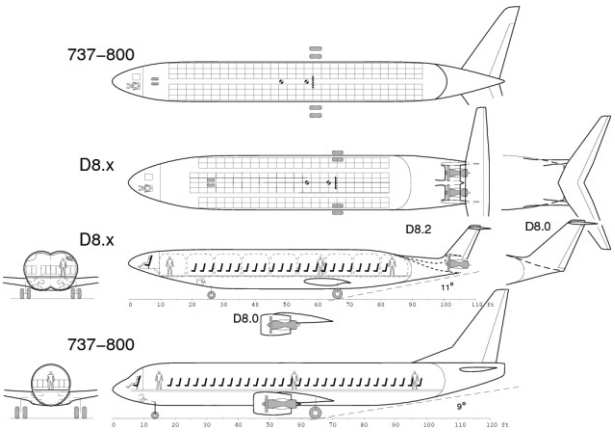

Figure 2: D8 fuselage on the D8.0 and D8.2 variants, compared with a B737-800 fuselage.

References

[1] J. Roskam, *Airplane Design*, DAR Corporation, Lawrence, Kansas (2000).

[2] E. Torrenbeek, *Synthesis of Subsonic Airplane Design*, Delft University Press (1988).

[3] D. P. Raymer, *Aircraft Design: A Conceptual Approach,* AIAA Education Series, AIAA (1992).

[4] W. Pfenninger, Some thoughts on the design of large global range LFC transport airplanes, *In Special Course on Concepts for Drag Reduction*, AGARD (1976).

[5] R. Liebeck, Design of the Blended Wing Body subsonic transport. *Journal of Aircraft*, vol. 41, No.1 (2004) 10.

[6] M. Drela, Development of the D8 Transport Configuration, AIAA Paper 2011-3970 (2011).

[7] S. Jayaram, A. Myklebust, and P. Gelhausen, ACSYNT – A standards-based system for parametric computer aided conceptual design of aircraft, AIAA Paper 92-1268 (1992).

[8] S. Wakayama, *Lifting Surface Design Using Multidisciplinary Optimization,* PhD thesis Stanford (1994).

[9] I. Kroo, PASS: Program for Aircraft Synthesis Studies, Desktop Aeronautics, Palo Alto, CA (2005).

[10] M. Drela, N+3 Aircraft Concept Designs and Trade Studies – Appendix. Technical Report, NASA/CR-2010-216794/VOL2 (2010).

[11] E. G. Greitzer, N+3 Aircraft Concept Designs and Trade Studies. Technical Report, NASA/CR-2010-216794/VOL1 (2010).

GS1: General Session

Eighth International Conference on Flow Dynamics
November 9 - November 11, 2011

Impinging Jets: Fundamentals and Applications

Sung Jin Kim[1], Kyosung Choo[2]
[1]School of Mechanical, Aerospace & Systems Engineering,
Korea Advanced Institute of Science and Technology, Daejeon, 305-701, South Korea
[2]Mechanical Engineering Department, University of Maryland, College Park, MD 20742, United States
sungjinkim@kaist.ac.kr

ABSTRACT

This talk is intended to give an overview of fundamentals of impinging jets together with recent advances achieved at the Applied Heat Transfer Lab of KAIST. Specifically, some interesting results on the hydraulic jump of impinging jets will be presented. Then a simple imaging technique based on hydrodynamics of an impinging jet, the Scanning Flow Impedance Microscope (SFIM), will be followed. The SFIM can be used to image the surface topography of a specimen.

1. Introduction

Major industrial applications of the impinging jet include cooling of turbine blades and electronic components, annealing of metal sheets, drying of textile and paper products, and deicing of aircraft systems.

A hydraulic jump is a hydraulic phenomenon which is frequently observed in rivers and canals, industrial applications, and manufacturing processes, as well as in kitchen sinks. The determination of the hydraulic jump radius is very important since the heat transfer characteristics of impinging jets are drastically changed at the location of the hydraulic jump, as mentioned by previous researchers [1, 2]. Even though much data has been obtained by previous researchers, no systematic study of the effect of nozzle diameter on the hydraulic jump radius has been conducted. In this study, a wide range of nozzle diameters (0.381, 0.506, 1, 2, 3.9, 6.7, 8, 10.5 mm) were considered using water as the test fluid.

The scanning flow-impedance microscope (SFIM [3, 4]) proposed in the present study is a sort of scanning probe microscope based on hydrodynamics. As a probe microscope, the SFIM has some advantages. In the SFIM, specimens can be observed in any gas or liquid under atmospheric pressure and temperature conditions, unlike an electron microscope [5] which requires specimens be in a partial vacuum. The resolution of the SFIM is not limited by the diffraction of light or electrons but by the size of the probe. Applications of the SFIM would include surface fabrication, electronics cooling, or surface coating by means of an impinging jet from the aperture of the probe.

2. Method

2.1 Hydraulic jump

A schematic diagram of the experimental apparatus for impinging water jets is shown in Figure 1. A coriollis flowmeter (Micro motion Inc.) was used to measure liquid flow rates and liquid density, both measured with an accuracy of 0.1%. Eight circular, stainless-steel nozzles were used in the experiment. The nozzles had inner diameters of 0.381, 0.506, 1, 2, 3.9, 6.7, 8, and 10.5 mm. Photographs were used to measure the hydraulic jump radius as shown in Figure 2. Ten measurements of the hydraulic jump radius were obtained from photographs [6].

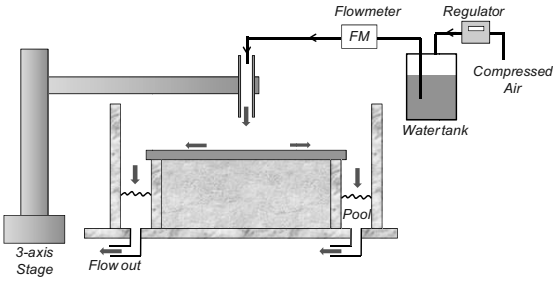

Fig. 1 Schematic diagram of experimental set-up

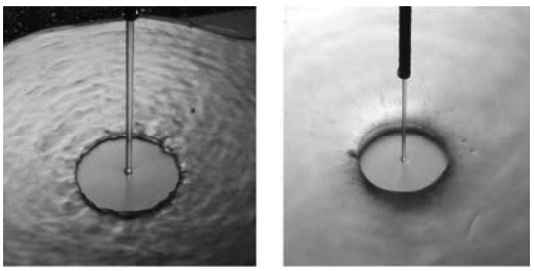

(a) (b)

Fig. 2 Hydraulic jump for an impinging jet: (a) d = 2.0 mm (b) d = 0.506 mm

2.2 Scanning Flow-Impedance Microscope (SFIM)

The operating principle of the SFIM is based on hydrodynamic phenomena. As the name implies, the SFIM can image the surface topography of a specimen by measuring the flow impedance variation that strongly depends on the probe-to-specimen distance. When the fluid flow issuing from the aperture of the probe impinges on the specimen surface, the surface affects the flow stream. As a result, the pressure needed to drive the fluid flow with the fixed average velocity u through the probe also increases. The difference between probe tip pressure and the ambient pressure is given as

$$\frac{\Delta P_l}{\frac{1}{2}\rho u^2} = f\left(\frac{\rho u D_i}{\mu}, \frac{z}{D_i}\right) \quad (1)$$

where ρ, μ, u, and D_i are the density of the fluid, the viscosity of the fluid, the average stream velocity at the probe tip, and the ID of the probe, respectively.

Figure 3 shows the schematic diagram of the experimental setup. A mass flow controller (Brooks Inc.)

was used for precise control of the stream velocity of the air. A micromanometer (FCO510, Furness-Controls Ltd.) measured the difference between the internal pressure of the probe and the ambient pressure.

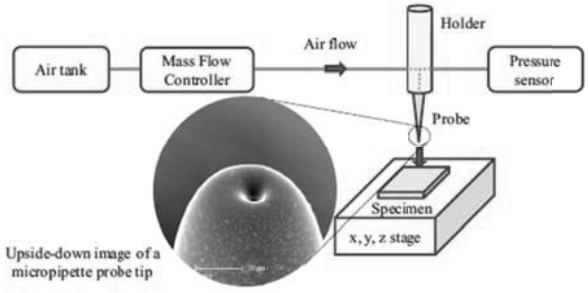

Fig. 3 Schematic diagram of the experimental setup.

3. Results and Discussion

3.1 Hydraulic jump

The variation of dimensionless hydraulic jump radius with the nozzle diameter is shown in Figure 4. The hydraulic jump radius (r_{hj}) is proportional to $d^{3/4}$ at the fixed Reynolds number condition. Based on the experimental results, a new correlation of the dimensionless hydraulic jump radius was obtained as a function of Reynolds number and Froude number.

$$\frac{r_{hj}}{d} = 0.037\left(\frac{\pi}{8}\right)^{1/4}\left(\mathrm{Re}^7\,\mathrm{Fr}^2\right)^{1/12} \tag{2}$$

As shown in Figure 4, the correlation of Stevens and Webb [1] and Bohr et al. [2] using Reynolds number could not predict the flow characteristics of impinging jets, while the developed present correlation of Eq. (2) predicts well the variation of the dimensionless hydraulic jump radius.

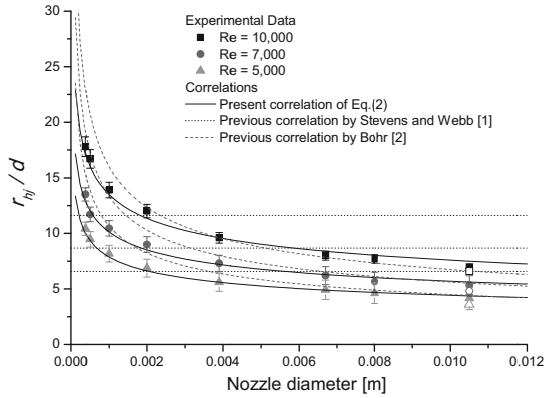

Fig. 4 Variation of the dimensionless hydraulic jump radius

3.2 Scanning Flow-Impedance Microscope (SFIM)

A two-dimensional scan was performed using an aluminum probe with an inner diameter (ID) of 100 μm and an outer diameter (OD) of 1 mm. In the experiment, the topography of the specimen was obtained under the constant height mode for convenience. The test specimen has microscale patterns of various sizes created on a silicon wafer by a dry etching process. The scanned image is a structure that appears as the letter "K" with a minimum feature size of approximately 100 μm. Figure 5(a) is the picture of the pattern obtained using an optical microscope (Olympus TH4–200). The scan result obtained using the SFIM is shown in Fig. 5(b). Comparison of results between the optical microscope and the SFIM shows that the SFIM can discern the pattern. After applying the distance-flow impedance curve to the SFIM result, contour lines of the pattern could be obtained as shown in Fig. 5(c). The contour lines show that the depth of the pattern is approximately 90 μm that is comparable to 110 μm, the result of a surface profiling system (SIS-1200, SNU precision).

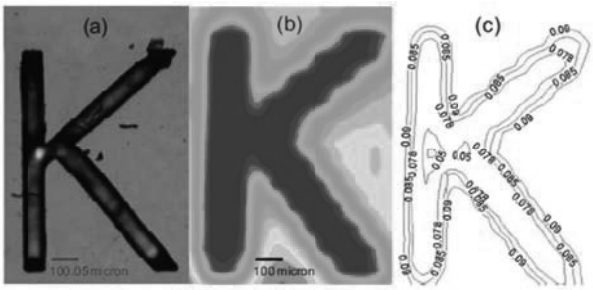

Fig. 5 Two-dimensional scan results obtained using an aluminum probe with an ID of 100 μm and an OD of 1 mm (a) Optical image of the pattern with 100 μm line width. (b) SFIM micrograph. (c) Contour lines (unit: mm)

4. Concluding remarks

In this study, a wide range of nozzle diameters (0.381, 0.506, 1, 2, 3.9, 6.7, 8, 10.5 mm) were considered using water as the test fluid. Based on the experimental results, a new correlation of the dimensionless hydraulic jump radius was obtained as a function of Reynolds number and Froude number.

Using a simple experimental setup including a mass flow controller and a manometer, the operating principle of SFIM is validated under atmospheric pressure and temperature conditions. Experimental results show that the flow impedance strongly depends on the relative distance between a probe and a specimen. SFIM micrographs of microscale patterns with various linewidths are presented.

References

[1] J. Stevens, B.W. Webb, ASME J. Heat Transfer **113** (1991), pp. 71–78.
[2] T. Bohr, P. Dimon, V. Putkaradze, J. Fluid Mech. **254** (1993), pp. 635-648
[3] S.J. Kim, T.Y. Kim, D.-K. Kim, Korean Patent No. 10–2008–0119103 (2008)
[4] T.Y. Kim, D.-K. Kim, S.J. Kim, Rev. Sci. Instruments **80** (2009), 103702.
[5] H. K. Wickramasinghe, Sci. Am. **260** (1989), 98.
[6] K. Choo, S.J. Kim, Int. J. Heat Mass Transfer **53** (2010), pp. 5692-5699.

Eighth International Conference on Flow Dynamics
November 9 - November 11, 2011

Flow and Heat Transfer Characteristics of Non-Circular Impinging Jet in Crossflow

M. Wae-hayee, C. Nuntadusit
Energy Technology Research Center and Department of Mechanical Engineering, Faculty of Engineering,
Prince of Songkla University, Hat Yai, Songkhla 90112, Thailand
chayut@me.psu.ac.th

ABSTRACT

The aim of this research is to enhance the heat transfer rate on surface of impinging jet in crossflow. The round orifice (AR=1) was replaced by elongated round orifices with aspect ratio AR=4 in based on identical exit area. Effect of attacking angle (θ=0°, 45°) and jet to crossflow velocity ratio VR=3 and 7 were studied. The numerical simulation was employed to gain insight into the fluid flow, and thermochromic liquid crystal was used to visualize heat transfer characteristic on a target surface. Results show that the orifice with AR=4 and θ=45° can increase the heat transfer rate at stagnation region under the low crossflow velocity (VR=7).

1. Introduction

A jet impingement is a high performance technique for heating, cooling or drying process. When high and uniform heat transfer rate on surface are required over a large area, multiple of impinging jets are applied. An important factor that influences on the multiple jet impingements in a confined space is crossflow. The crossflow is produced by accumulating spent jets from upstream to downstream of the confined space. The crossflow has been found to significantly reduce the heat transfer of impinging jet [1].

The aim of this research is to enhance the heat transfer rate on the impinged surface with crossflow. The conventional round orifice was replaced by elongated round orifices with identical exit area. The effect of velocity ratio and attacking angle were also studied.

2. Model and parameters

The model is the jet discharging from orifice and impinging normal to opposite surface in rectangular duct as shown in Fig. 1. The crossflow is generated by introducing air through the rectangular duct, flow normal perpendicular to the impinging jet. An origin of coordinate is located on the impinged surface as shows in Fig.1. The X-, Y- and Z-axes are along the crossflow streamwise, normal to the streamwise, and along the spanwise directions, respectively.

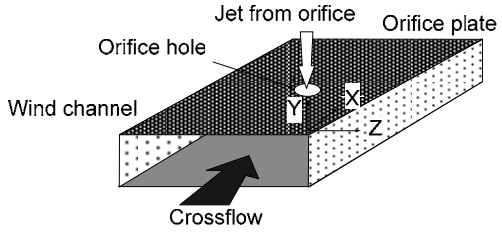

Fig. 1. The model of the impinging jet in the crossflow

The investigation was conducted for orifice aspect ratios (ratio of orifice length to orifice width) AR=4 (Fig.2) for compare the results with the round orifice (AR=1). The comparisons of flow and heat transfer characteristics are based on the constant jet velocity and varied crossflow velocity according to the velocity ration (jet to crossflow velocity) VR=3 and 7. The orifice diameter of round jet was D=13.2 mm, and jet-to-plate distance was H=2D. The attacking angle of major axis of elongated round orifice to the crossflow direction (θ=45°) also studied. During the elongated round orifice test run, the jet mass flow rate was set based on the exit area identical with the conventional round orifice for the required Reynolds number (Re_E=13,400).

Fig. 2. Orifice geometry with identical area cross-section (AR is length over width of orifice)

3. Method

The flow characteristic was illustrated by using 3-D numerical simulation (ANSYS ver.12.0). The standard k-ε turbulent model with general wall-function mode was used for solving numerical simulation problems. A non-uniform grid was finely generated in orifice hole and impingement regions. A solution method is based on SIMPLE algorithm with second order upwind for all spatial discretization. The experimental investigation was carried out the heat transfer characteristic by using thermochromic liquid crystal (TLC) sheet, and Nusselt number distribution was evaluated by using image processing method. The details of both numerical and experimental method were explained in ref. [2].

4. Results and Discussion

The velocity vectors and contours of Y-component velocity (direction from orifice plate to target surface is positive velocity) in XZ-plane at 1.0-mm-height from the targer surface were shown in Fig. 3. The area of highest Y-component velocity represent the region of stagnation point. Due to high crossflow velocity, the stagnation point of VR=3 is shifted to downstream of crossflow (X/D>0) when compare with each identical experimental condition for VR=7.

The area of high Y-component velocity expands in –Z-axis (pressure side) slighly larger than in +Z-axis (suction side) in the case of θ=45° under low crossflow velocity (Fig. 3 (e)). Moreover, due to the high velocity crossflow, the area of high Y-velocity expands in +Z-axis and contracts in –Z-axis (Fig. 3 (f)). The expansion area of high Y-velocity in +Z-axis can be

explained that the wall jet flows in same direction with crossflow. In contrast to the contraction area of high Y-velocity in -Z-axis, the wall jet collide with the counter direction of crossflow, and wall jet in -Z-axis rapidly turn to downstream direction of crossflow.

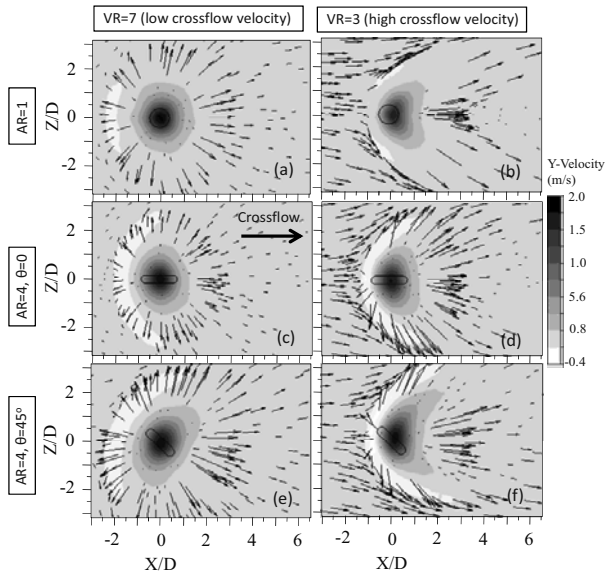

Fig.3. Velocity vectors and Y-velocity contours in XZ-plane at 1.0-mm-height from the targer surface

Vectors and contours of velocity in YZ-plane for the case of AR=4, θ=45° and VR=7 is shown in Fig. 4. The circulation flow was appeared in +Z-axis, and the size of circulation flow become larger at far X/D to downstream. The circulation flow in +Z-axis turn to the jet flow; consequencetly, the jet is more entrain in +Z-axis than in –Z-axis.

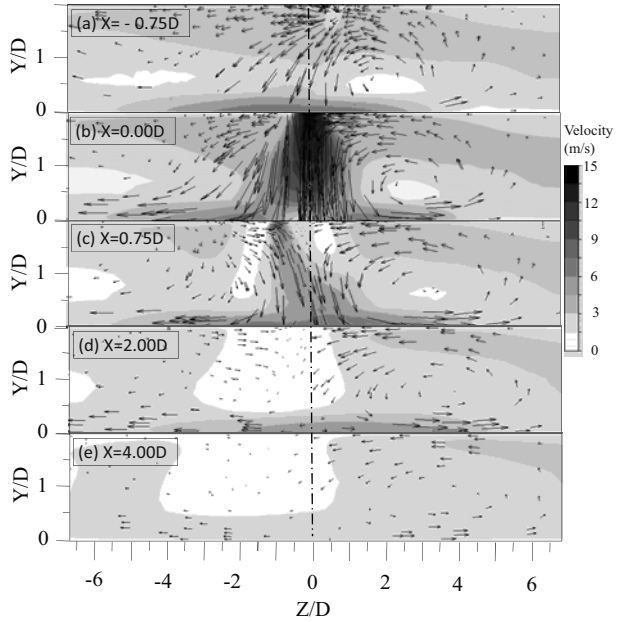

Fig.4 Vector and contour of velocity in YZ-plane for AR=4, θ=45° and VR=7 at different X/D

The distributions of Nusselt number on target surface are shown in Fig. 5. The results show that the area of high Nusselt number (Nu>180) appears in stagnation region for the case of low crossflow velocity. In the case of high crossflow velocity, the areas of high Nusselt number are shifted to downstream of crossflow due to the higher crossflow velocity. The location of high Nusselt number coincide the locations of high Y-component velocity that illustrated in Fig.3.

The peak of Nusselt number is highest for AR=4, θ=0 with VR=3 (Fig.5(d)), because the jet can penertrate into the crossflow and strongly impinges on target surface despite high crossflow velocity. In the case of AR=4, θ=45° with VR=7 (Fig.5(e)), the area of high Nusselt number expand in +Z-axis and contracts in –Z-axis coincide with the results illustrated in Fig. 3(e). Moerover, the area of high Nusselt number in -Z-axis is smaller when crossflow velocity increases (Fig.5(f)). Finally, the area of high Nusselt number is largest in the case of AR=4, θ=45° and VR=7 (Fig.5(e)) corresponding to largest area of high Y-velocity as shown in Fig. 3(e).

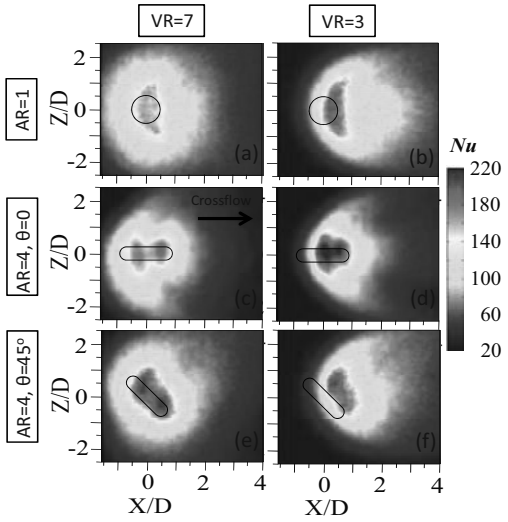

Fig.5. The Nusselt number distribution (experimental results) on the impinged surface

5. Concluding remarks

The jet from orifice with AR=4 can increases heat transfer on stagnation region when compare with the AR=1. In the case of AR=4 with θ=45° under low crossflow velocity (VR=7), the area of high Nusselt number is largest corresponding to the large area of high velocity that impinges on target surface, and the areas of high Nusselt number expands in +Z-axis and contracts in –Z-axis when crossflow velocity increases to VR=3.

Acknowledgements

This research was supported by grants from Thailand Energy Policy and Planning Office, Ministry of Energy, the Graduate School and Faculty of Engineering, Prince of Songkla University.

References

[1] R. J. Goldstein, Int. J. Heat Mass Transfer, **25** (1982), pp. 1377-1382.

[2] M. Wae-hayee, ICET5th Int. Conf., **MME-P77,** (2011). pp. 783-788.

Analysis of Influences on the Initial Process of Liquid Injection

Toshimi Takagi*, Kikuo Narumiya** and Hiroshi Hattori***
*(Emeritus) Osaka University, 2-1, Yamada-Oka, Suita, Osaka, 565-0871, Japan
Osaka Sangyo University, * (Emeritus) Osaka Sangyo University,
3-1-1, Nakagaito, Daito, Higashiosaka, Osaka, 574-0013, Japan
ttakagi@tcn.zaq.ne.jp

The analysis of liquid injection into gas is practiced by applying the MARS method for simulating free surface of two phase flow. The characteristic features of the initial liquid injection shape and break-up are investigated to understand the effects on surrounding pressure, initial velocity, initial liquid level and the throttling effect due to the nozzle configuration. Focus is the pressure irregularity near the nozzle wall which causes initial perturbation on liquid column at the exit of the nozzle. It induces large eddies at the surface of the liquid column and promotes the disintegration of the liquid film.

1. Introduction

A lot of investigations of transient injection flows of the liquid into gas were made concerning the processes of self-ignition engines, for example [1]. Observations of the injection flows with both continuous shooting and single shot, have been made focusing on the magnification technique of the initial shape of injection flows [2] ,[3]. Various surrounding pressures were used for understanding the initial shape of the injection [4].

The MARS method [5] for simulating free surfaces is applied and the initial shape of the injection flow is analyzed to get various influences paying attention to the flow in the nozzle.

2. Fundamental Equations and Boundary Conditions

Fundamental equations are the equations of continuity and motion for both gas and liquid. The MARS (multi-interface advection and reconstruction solver) method is applied to the free boundary between the liquid and gas. Two types of computation domain are used as shown in Figs. 1 (a) and (b).The domain in Fig. 1 (a) consists of a cylindrical chamber with lengths of 3-6 mm in the axial direction and 1 mm in the radial direction. At the center of the chamber bottom, a circular nozzle with 0.3 mm diameter and 2 mm length is installed, and liquid is injected upward through the nozzle. Figure 1 (b) shows another computation domain. The diameters of the chamber and nozzle are the same as before but the axial length of the nozzle is 0.75 mm. This nozzle can induce the throttling effect. The left and bottom boundaries of the domain in Fig. 1 (a) are no-slip walls. The boundaries forming the throttle in Fig.1 (b) are also no-slip walls. The right boundary of each domain is a symmetrical axis. The upper boundary of each domain is the outlet, where the natural in-out boundary condition is defined. The lower boundary in Fig.1 (a) is the inlet of the nozzle and the initial flow velocity v_{inj} is uniform. In the domain in Fig.1 (b), the liquid flows uniformly at the boundary, and the average velocity is set to be the initial flow velocity v_{inj} at the nozzle. The initial liquid surface is set to be flat.

3. Computation Conditions

The surrounding gas is air and the injected liquid is light oil. The initial liquid velocity v_{inj} is 50 and 170 m/s. At the beginning of liquid injection, the gas in the chamber and nozzle is stagnant. No turbulence or cavitation is assumed to be formed. The flow is axisymmetric and the fluids are assumed to be incompressible.

The temperature is 20℃ for both the gas and liquid. The surrounding pressure is selected to be 0.1-3.0 MPa. The liquid is assumed to have a density of 840 kg/m^3, a viscosity of 2.0×10^{-3} Pa.s and a surface tension of 20×10^{-3} N/m. The viscosity of air is assumed to be 17.98×10^{-6} Pa.s. The density of air is predicted from the ideal gas law. The effect of gravity is neglected.

The computations are transient ones with a time step of 1.0×10^{-9} s when initial liquid velocity is 170 m/s. However, when it is 50 m/s, the time step is increased depending on the inverse of the initial velocity. The mesh size is almost 2 μm in the radial and axial directions. Computations are performed using STREAM for Windows V8 [6].

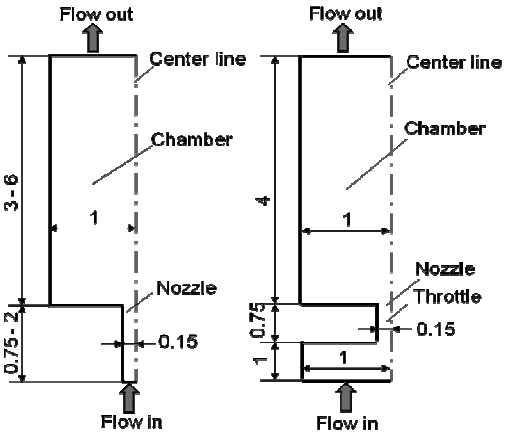

Fig.1 Computation domain (unit:mm)

4. Results

Figure 2 shows the computed liquid contours and pressure in a color distribution based on the surrounding pressure P_a = 0.1 MPa, initial liquid velocity v_{inj} = 170 m/s and nozzle length L = 2 mm at the computation domain Fig.1(a). The tip of the liquid extends along with the flow in the nozzle and it collides

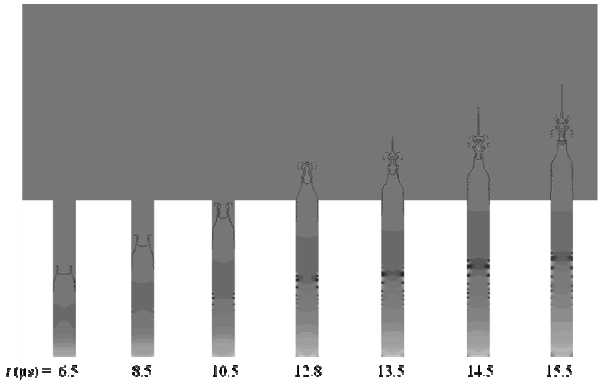

Fig.2 Liquid contours and pressure profiles (P_a = 0.1 MPa, v_{inj}= 170m/s, L=2 mm)

at the center line to form a thin string. This phenomenon was observed in experiments[2],[4]. The pressure nonuniformity is observed near the nozzle wall. But, it does not yet go through the nozzle exit and then it would not influence on the initial shape. When the initial velocity is lowered to be 50 m/s, fundamental features of the initial shape is similar.

Figure 3 shows the computed liquid contours and pressure in a color distribution based on the surrounding pressure P_a =3.0 MPa, initial liquid velocity v_{inj} = 170 m/s and nozzle length L = 2 mm at the computation domain Fig.1(a). The tip of the liquid does not extend and is almost flat under the surrounding pressure of 3 MPa. The pressure nonuniformity is observed near the nozzle wall. It goes downstream along with the flow. When the low pressure part goes out of the nozzle, the pressure drop becomes large and the shape of the interface between the liquid and gas tends to make a small depression. After the depression goes out of the nozzle, it grows to form a large eddy and then large disturbances at the interface. The low pressure parts go out of the nozzle successively and the formation of the injection flow is determined.

When initial velocity v_{inj} = 50 m/s, the pressure nonuniformity in the nozzle is not formed. Instead, the ripples are formed which may be induced by the shear stress between the liquid and air. There may be no

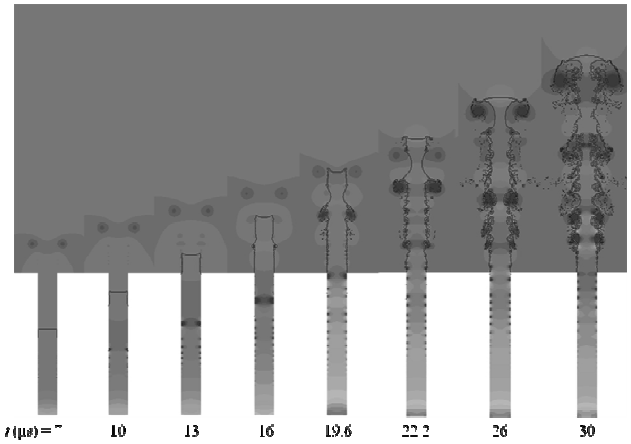

Fig.3 Liquid contours and Pressure profiles (P_a = 3.0 MPa, v_{inj} =170 m/s, L = 2 mm)

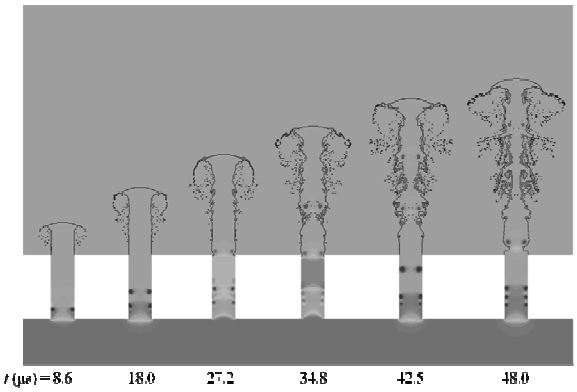

Fig.4 Liquid contours and pressure profiles (P_a = 3.0 MPa, v_{inj}= 50m/s, L=0.75 mm, Throttling effect, Liquid initial surface is the outlet of the nozzle.)

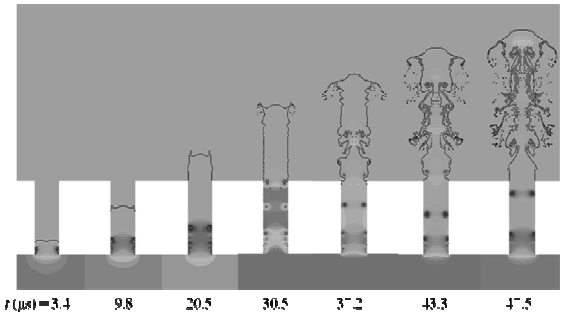

Fig.5 Liquid contours and pressure profiles (P_a = 3.0 MPa, v_{inj}= 50m/s, L=0.75 mm, Throttling effect, Liquid initial surface is the intlet of the nozzle.)

interference between the nozzle flow and the flow in the chamber.

Figure 4 is a case with throttling effect. Liquid initial surface is the outlet of the nozzle. Even though the initial injection velocity v_{inj} is 50 m/s, the pressure nonuniformity in the nozzle is observed. Separation due to the throttling effect may be the reason for the nonuniformity. It goes downstream along with the flow. When the low pressure part goes out of the nozzle, a small depression is made at the interface between the liquid and gas. After the depression goes out of the nozzle, the story is the same as Fig.3.

Figure 5 is a case as Fig.4, but the liquid initial surface is the inlet of the nozzle. The liquid involves the air bubbles. That has the same effect as the low pressure part of Fig.3 and Fig.4.

References

[1] T. Takagi, et al, Combust. Sci. Tech. 75(1991), 1-12.
[2] K. Narumiya, H. Hattori, et al, 8th Symp. on Atom. (1999), 59 -264.
[3] H.Hattori, K. Narumiya., et al, SAE World Congress, 2004-01-0528 (2004).
[4] T. Takagi, K. Narumiya., et al, JSME Journal of Fluid Science and Technology, 6-5 (2011).
[5] Kunugi,Trans. JSME B, 63 (1997), 576-1584.
[6] Software Cradle, STREAM for Windows V8 (2009).

Eighth International Conference on Flow Dynamics
November 9 - November 11, 2011

Error Reduction for the Volume Penalization Method

Wakana Iwakami Nakano[1], Nozomu Hatakeyama[2], Yuji Hattori[1]
[1]Institute of Fluid Science, Tohoku University,
[2]Department of applied chemistry, Tohoku University
wakana@dragon.ifs.tohoku.ac.jp

ABSTRACT

The volume penalization method can be used for numerical simulations of a flow around moving intricately shaped bodies. It can be easily implemented to a conventional hydrodynamics code. In the method, solid bodies are regarded as porous media with small permeability η. We intend to reduce an error caused by the penalization term depending on η and the mask function $\chi(x)$. In this study, we show that displacement of $\chi(x)$ makes the penalization error decrease with increasing spatial resolution.

1. Introduction

Many kinds of flows around solid bodies have been investigated by means of numerical simulations for both engineering and academic significances. A method of imposing boundary conditions on surfaces of bodies with a boundary-fitted computational grid has been normally used in hydrodynamic simulations. However, a numerical procedure with a boundary-fitted computational grid can become very complicated one if bodies are movable, deformable, and shaped intricately. The volume penalization method (VPM), which is a kind of the immersed boundary methods (IBMs)[1], is one of the simplest ways to calculate a flow around intricately shaped bodies which deform and move. Furthermore, VPM can be implemented to a numerical code with a high accuracy space discretization scheme such as the spectral method[2].

In the previous study, we used VPM for solving the one-dimensional Burgers' equation discretized with a high-resolution finite difference method, the compact scheme[3]. We confirmed that the total error converges to a constant which depends on η with decreasing grid spacing, where the penalization error dominates[4]. In this study, we show one way to reduce the penalization error.

2. Numerical Method

In VPM, solid bodies are approximated by porous media having permeability η. Existence of the solid bodies is represented by adding a damping force term, called a penalization term, to the equations of motion. In this paper, we solve the one-dimensional Burgers equation with a penalization term

$$\frac{\partial u}{\partial t} + u\frac{\partial u}{\partial x} = \nu\frac{\partial^2 u}{\partial x^2} - \frac{\chi(x)}{\eta}u, \qquad (1)$$

where t, x, u, ν, η and $\chi(x)$ denote time, spatial coordinate, velocity, kinetic viscosity coefficient, permeability, and mask function, respectively. Solutions of the diffusion equation with a penalization term converge to those of the original diffusion equation when η is close to zero. The penalization error from the original diffusion equation is $O((\nu\eta)^{0.5})$[5]. As for the Navier-Stokes equations, the penalization error is $O(\eta^{0.5})$[6]. This means that the penalization error can be less than the discretization error for a sufficiently small η. However, if we use an explicit time integration scheme, η must be larger than the time step Δt because of numerical stability. The asymptotic behaviors described above have been proved for the case of

$$\chi(x) = \begin{cases} 0 & \text{in } \Omega_s \\ 1 & \text{in } \Omega_f \end{cases}, \qquad (2)$$

where Ω_s denotes solid regions, and Ω_f fluid regions.

In this study, Ω_f is set to be for $0 \le |x| < L_{VP}$, and Ω_s for $L_{VP} \le |x| \le L_b$. The size of the computational region L_b is about 2π. The absolute value of the wall locations L_w is fixed to π, and that of the penalization boundaries L_{VP}, satisfying $\chi(\pm L_{VP})=0.5$, is changed adequately. The whole region $|x| \le L_b$ is equally divided into N. Each node point is termed as i=0, 1,$\cdots$, N in order. Arbitrary physical quantities at i are expressed as f_i. The terms of spatial derivative in Eq.(1) are evaluated by the 4th-order Padé type compact finite difference scheme[3]. The 4th-order compact scheme for the first derivative at i=1, 2, $\cdots$, N-1 is given by

$$\alpha_1 f'_{i-1} + f'_i + \alpha_1 f'_{i+1} = a_1\frac{f_{i+1} - f_{i-1}}{2\Delta x}, \qquad (3)$$

where α_1=1/4, a_1=3/2. At i=0 and N, we use

$$f'_i + \alpha_{1b} f'_{i+1} = \frac{a_{1b} f_i + b_{1b} f_{i+1} + c_{1b} f_{i+2} + d_{1b} f_{i+3}}{\Delta x}, \qquad (4)$$

where α_{1b}=3, a_{1b}=-17/6, b_{1b}=3/2, c_{1b}=3/2, d_{1b}=-1/6. The 4th-order compact scheme for a second derivative at i=1, 2, $\cdots$, N-1 is given by

$$\alpha_2 f''_{i-1} + f''_i + \alpha_2 f''_{i+1} = a_2\frac{f_{i+1} - 2f_i + f_{i-1}}{\Delta x^2}, \qquad (5)$$

where α_2=1/10, a_2=6/5. At i=0 and N, we use

$$f''_i + \alpha_{2b} f''_{i+1} = \frac{a_{2b} f_i + b_{2b} f_{i+1} + c_{2b} f_{i+2} + d_{2b} f_{i+3} + e_{2b} f_{i+4}}{\Delta x^2}, \qquad (6)$$

where α_{2b}=10, a_{2b}=-145/12, b_{2b}=-76/3, c_{2b}=29/2,d_{2b}=-4/3, e_{2b}=1/12.

The initial values are

$$u(0,x) = \begin{cases} 0 & \text{in } \Omega_s \\ -\sin x & \text{in } \Omega_f \end{cases}. \qquad (7)$$

The 4th-order Runge-Kutta method is used for time development of Eq. (1) with $\Delta t=10^{-5}$. The permeability η is set to meet the stability condition $\eta \ge \Delta t$.

The actual distributions of $\chi(x)$ are shown in Fig.1. Here we consider two types of mask functions. One is the normal type: penalization boundaries located at the middle of two adjacent grid points are set to $x = \pm L_{VP} = \pm L_w$ (Fig. 1(a)). The other is the modified type: penalization boundaries located in the same way are set to $x = \pm L_{VP} = \pm[L_w - (\eta\nu)^{1/2}]$ (Fig. 1(b)).

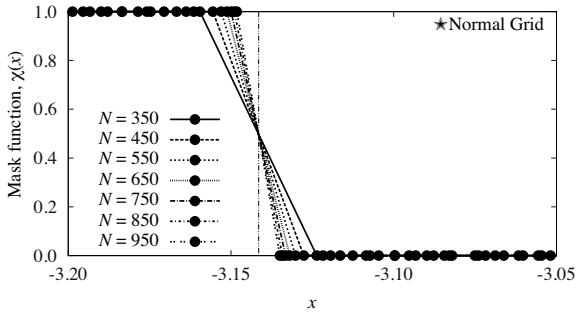

(a) Normal type

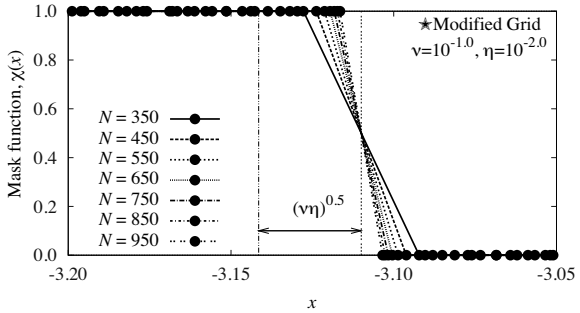

(b) Modified type

Fig. 1 The mask functions on (a) the normal type grid and (b) the modified type one.

3. Results and Discussion

We show the dependence of the total error on the grid number in Fig.2. When the grid number N is large enough for the penalization error to be larger than the space discretization error, the total errors converge to constants which depends on η for the normal-type mask function (Fig.2 (a)). The smaller the permeavility η, the smaller constant values they have. This is why the penalization error is proportional to $\eta^{0.5}$. On the other hand, for the modified type mask function (Fig.2 (b)), the total error decreases continuously with increasing N. Moreover, the errors for the modified type mask function are lower than those for the normal type one when η is comparatively large. The penalization term with smaller η less affects numerical solutions than a discretization of the basic equation. Thus the effect of changing the mask function would appear for larger N.

4. Concluding remarks

We found a way to reduce the penalization error for the one-dimensional Burgers equation. If the penalization boundaries between the flow and solid regions are displaced $(\nu\eta)^{0.5}$ toward the flow regions, the total error continuously decreases with increasing grid number.

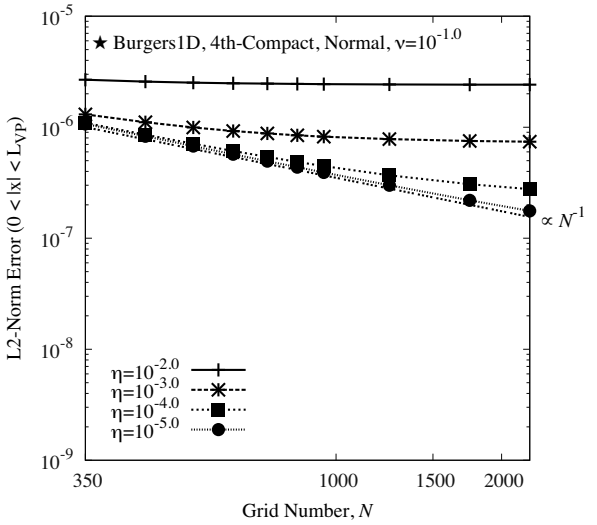

(a) Normal type

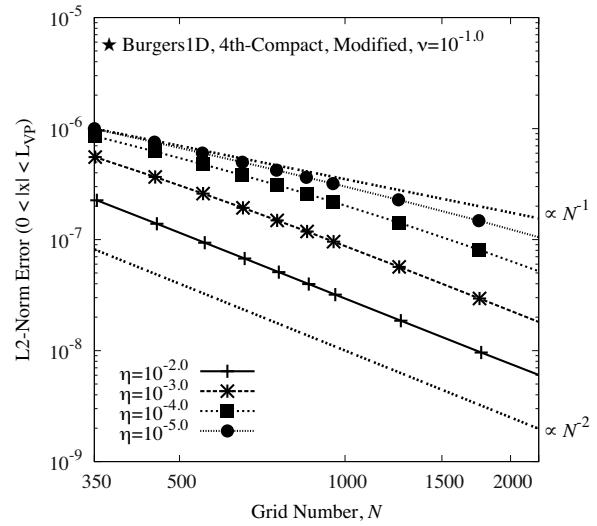

(b) Modified type

Fig. 2 The L2-norm error averaged in the range of $0<|x|<L_{VP}$ for (a) the normal type mask function and (b) the modified type one.

References

[1] A. Mittal and G. Iaccarino, Annu. Rev. Fluid Mech., **1** (2005), pp. 239 - 261.

[2] K. Schneider and M. Farge, J. Fluids Struct., **20** (2005), pp. 555 - 566.

[3] S. K. Lele, J. Comp. Phys., **103** (1992), pp. 16-42.

[4] W. I. Nakano, N. Hatakeyama, and Y. Hattori, Proceedings of Seventh International Conference on Flow Dynamics, (2010), pp. 138-139.

[5] N. K.-R. Kevlahan and J.-M. Ghidagria, Euro. J. Mech. B-Fluids, **20** (2001), pp. 333-350.

[6] G. Carbou and P. Fabrie, Adv. Differ. Equat., 8 (2003), pp. 1453-1486.

Eighth International Conference on Flow Dynamics
November 9 - November 11, 2011

Formation of the Rotating Stellar Structures

Takeshi Sugimoto
Kanagawa University, 3-27-1 Rokkakubashi, Kanagawa Ward, Yokohama 221-8686 Japan
sugimt01@kanagawa-u.ac.jp

ABSTRACT

It is very common that derivative stellar masses, *i.e.*, satellites and stellar rings, discretely distributes around a large star. Aihara's work on account of formation of Saturn's rings is revisited. Based on Chandrasekhar's formalism mathematically rigorous treatments, *i.e.*, generation of a general solution to the first-order PDE and use of similarity solution, lead to an analytic closed-form solution consisting of a couple of special functions. The solution shows the existence of many potential wells in the equatorial plane around the stellar core. This theory gives a clue to explanations for the Titius-Bode relation and formation of Saturn's rings.

1. Introduction

Chandrasekhar[1] paved the way to construct a basis for physics of stellar structures by use of fluid dynamics, gas dynamics and the gravitation potential. Aihara[2] made use of Chandrasekhar's formalism to annotate Saturn's rings. We revisit Aihara's work and show we can get the analytic closed-form solution.

2. Theory

The framework of this theory is within the classical celestial physics[1]: we assume that stellar materials are the perfect gas that changes in a polytropic manner; we also treat stellar materials as to obey compressible fluid dynamics; the entire system is governed by law of the gravitation.

Figure 1 shows the coordinate systems to be used in our study. In Cartesian system Zenith is located at (0, 0, ∞), whilst Nadir is at (0, 0, -∞). We fix the origin to the centre of our stellar structures, and hence in the equatorial plane z is equal to naught. Another independent variable is the time t.

The basic equations consiste of the Euler's equations, the equation of state in polytropic gas and the equation of the gravitational potential, respectively given by

$$\frac{\partial \rho}{\partial t} + \operatorname{div} \rho \mathbf{u} = 0, \tag{1}$$

$$\frac{\mathrm{D}}{\mathrm{D}\,t} \rho \mathbf{u} = -\operatorname{grad} p - \rho \operatorname{grad} \Omega, \tag{2}$$

$$p = K\rho^{\gamma'}, \tag{3}$$

and

$$\nabla^2 \Omega = 4\pi G\rho, \tag{4}$$

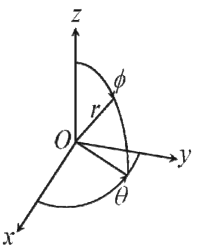

Fig. 1 Cartesian and spherical coordinates; the polar angle θ and the azimuth angle ϕ.

where the variables ρ, $\mathbf{u}$, p and Ω respectively designate the mass density, the velocity vector, the pressure and the gravitational potential, whilst the parameters K, γ' and G respectively designate a product of the gas constant and the polytropic temperature, the polytropic specific-heat ratio and the gravitation constant.

3. Theoretical Results and Discussion

We shall consider the steady-state stellar structure with rotation about z-axis: we neglect $\partial/\partial t$ terms in equations (1) and (2); we make use of the spherical coordinate and assume the velocity vector has only one non-zero component in θ-direction, *i.e.*, u_θ.

Introducing one-component assumption upon $\mathbf{u}$ in equation (1), we find ρu_θ is independent of θ.

Using this information as well as one-component assumption upon $\mathbf{u}$, θ-direction equation in (2) leads us to the fact that p and Ω are also independent of θ. Eliminating p, by use of (3), from r- and ϕ-direction equations in (2), we obtain a set of simultaneous PDEs upon ρ and Ω. This set has a general solution:

$$K\frac{\gamma'}{\gamma'-1}\rho^{\gamma'-1} + \Omega = \Psi(\xi), \tag{5}$$

where $\xi = r\sin\phi$; there is a boundary condition for Ψ:

$$\frac{\mathrm{d}\Psi}{\mathrm{d}\xi} = \frac{{u_\theta}^2}{r}. \tag{6}$$

That is the centrifugal acceleration that must be in equilibrium with the centripetal gravitation. The argument above shows that ρ and Ω have similarity solutions with respect to ξ.

Using (5), we can eliminate ρ from (4); introducing the compound variable ξ into the Laplacian in (4), we obtain an ODE for the gravitation potential.

$$\frac{1}{\xi}\frac{\mathrm{d}}{\mathrm{d}\xi}\left(\xi\frac{\mathrm{d}}{\mathrm{d}\xi}\right)\Omega = (\Psi - \Omega)^{1/\gamma'-1}. \tag{7}$$

The equation above is already made legible by introducing the scaling parameter defined by

$$\lambda = \sqrt{\frac{4\pi G}{(K\gamma'/\gamma'-1)^{1/\gamma'-1}}}.$$

The equation (7) is an extension of the Lane-Emden equation, and hence we need to have recourse to numerical integration to get the solutions for general

values of γ'. We can, however, get a mathematically rigorous and analytic solution of (7) in case of $\gamma' = 2$, which is a plausible value for our solar system. So let us solve (7) for this case.

We shall use the solution to the classical Lane-Emden equation for formation of the central stellar core. This is given by the spherical Bessel function of the first kind of degree zero, *i.e.*, $-j_0(\xi)$. It is shown in Fig.2. The solution is valid within the radius π. Although there exist both positive and negative regions for $\xi > \pi$, it is not feasible to generate spherical shell layers containing vacuum gaps among themselves. Therefore there is one core sphere only.

To close our problem we need to give a physical explanation to the arbitrary function Ψ: rigid rotation in the stellar core and inverse-square law for outer space. After some computation we get the following form:

$$\Psi(\xi) = \begin{cases} -\dfrac{\kappa}{\xi} & \text{for } \xi > \pi, \\ \dfrac{\kappa}{2\pi^3}\xi^2 - \dfrac{3\kappa}{2\pi} & \text{for } \xi \in [0, \pi], \end{cases} \tag{8}$$

where κ is a gravitation-related constant; the rotation is continual at the surface of the stellar core. Substitution of (8) for Ψ in (7) leads us to the equation for the gravitational potential with rotation.

Assuming a quadratic function of ξ within the stellar core, we get the particular solution as follows.

$$\Phi(\xi) = \frac{1}{\pi^4}\xi^2 - \frac{4}{\pi^4} - \frac{3}{\pi^2}, \tag{9}$$

where $\Phi = 2\Omega/\pi\kappa$. The stellar core is spherical but the above potential is cylindrical.

In the outer space the centrifugal force due to the stellar core *in the equatorial plane only*. We shall rewrite the equation in a following form:

$$\left(\frac{\mathrm{d}^2}{\mathrm{d}\xi^2} + \frac{1}{\xi}\frac{\mathrm{d}}{\mathrm{d}\xi} + 1\right)(-\Phi) = \frac{2}{\pi\xi}.$$

This is a Struve's differential equation of degree zero, and hence the solution is given by

$$\Phi(\xi) = -\mathbf{H}_0(\xi) + \left\{\mathbf{H}_0(\pi) - \frac{4}{\pi^4} - \frac{2}{\pi^2}\right\}\frac{\mathrm{Y}_0(\xi)}{\mathrm{Y}_0(\pi)}, \tag{10}$$

where $\mathbf{H}_0$ and Y_0 denote the Struve function of degree zero and Bessel function of the second kind of degree zero, respectively. The homogeneous solution is added to assure the continuity of the potential at the surface of the stellar core. Its graphical representation is given in Fig.3. We notice there are many potential wells that accommodate dense mass distributions.

In case of the cylindrical potential (10) in the equatorial plane it is possible to allow the existence of vacuum gaps between stellar material distributions, which may become spherical structures or ring structures. If we presume the existence of orbiting spherical structures smaller than the stellar core, this toy model corresponds to the Titius-Bode relation. If we assume the existence of orbiting ring structures, that toy model corresponds to Saturn's rings.

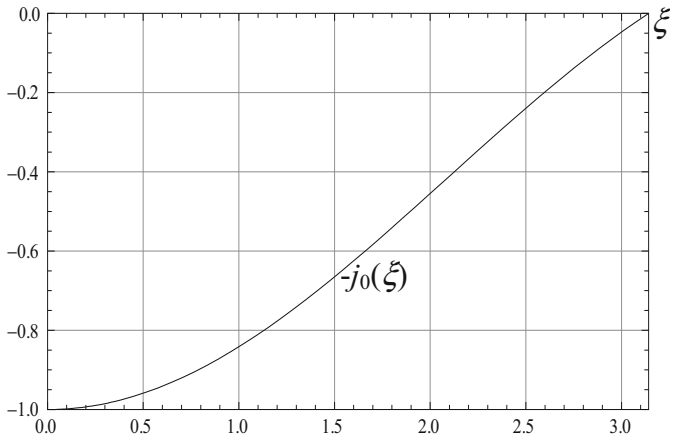

Fig. 2 The normalised spherical potential $-j_0(\xi)$ plotted against the normalised distance ξ from the centre of the stellar core.

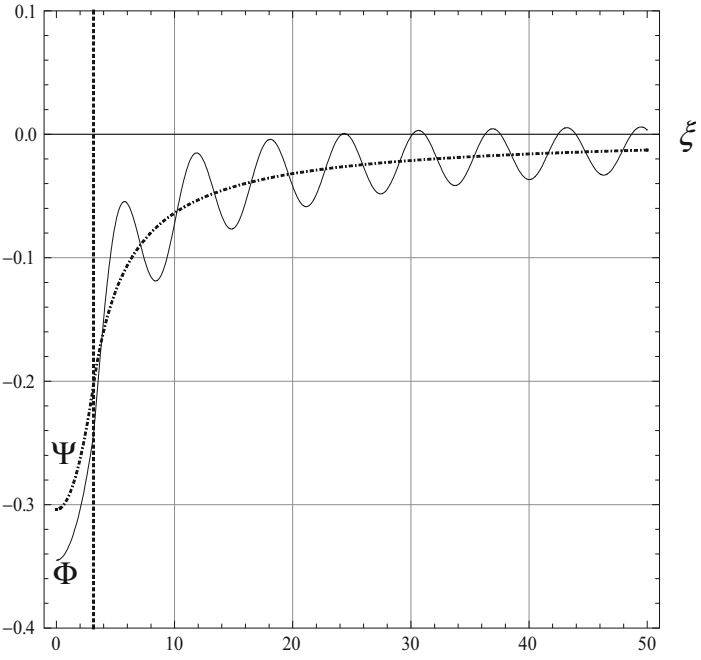

Fig. 3 The normalised cylindrical potentialΦ (solid line) with centrifugal acceleration Ψ (dash-dot line) plotted against the normalised distance ξ from the centre of the core stellar; the broken line shows the boundary of the stellar core.

4. Concluding remarks

We revisit Aihara's work on formation of Saturn's rings and reformulate it in a mathematically rigorous way. This leads us to the analytic closed-form solution that gives us a clue to explanations to the Titius-Bode relation or formation of Saturn's rings.

References

[1] S. Chandrasekhar, An Introduction to the Study of Stellar Structure, (1958), Dover Pub., pp.507.
[2] Y. Aihara, Acta Astronaut., **11**(1984), pp.313-317.

Eighth International Conference on Flow Dynamics
November 9 - November 11, 2011

Initial Condition Dependency in Two-Dimensional Decaying Compressible Turbulence

D. Terakado[1], Y. Hattori[2]
[1]Department of Applied Information Sciences, Graduate school of Information Sciences, Tohoku University
daiki@dragon.ifs.tohoku.ac.jp
[2]Institute of Fluid Science, Tohoku University
hattori@fmail.ifs.tohoku.ac.jp

ABSTRACT

It is known that some of the statistical properties of turbulence depend sensitively on the initial conditions. However, the details of the dependence have not been explored for compressible turbulence yet. In this study we carry out direct numerical simulations (DNS) of isotropic homogenous two-dimensional decaying compressible turbulence. We consider eight types of initial conditions (two types of energy spectrum and four types of pressure and density distributions). It is found that the initial energy spectrum affects the exponent of the direct cascade. Moreover, tangential discontinuity is seen to form for some initial pressure and density distributions.

1. Introduction

Compressible turbulent flows appear in a lot of engineering problems. However, because of the limitation of the computational capacity, it is difficult to carry out DNS of these flows. Therefore, we need to use turbulence model which reduces the degrees of freedom. Until today, various turbulence models have been proposed, but their validity is verified only in limited situations.

To improve the turbulence models, we should know the statistical properties of turbulence. Our goal is to understand the statistical properties of compressible turbulence and thereby propose a new turbulence model which is applicable for various types of turbulent flow. As a first step, we study the statistical properties of the compressible turbulence by direct numerical simulation. We concentrate on the two-dimensional weakly compressible turbulence since it is possible to simulate turbulence at sufficiently high Reynolds number in two dimensions and to study the compressibility effects in details.

There are several well-known statistical properties of two-dimensional turbulence. For isotropic homogenous forced two-dimensional incompressible turbulence, Kraichnan[1] predicted theoretically the double cascade scenario; when the turbulence is sustained by an external forcing acting on a typical scale l_f, an inverse cascade of kinetic energy $E=1/2<u^2>$ to large scales ($l>>l_f$) and a direct cascade of enstrophy $Z=1/2<\omega^2>$ to smalls scales ($l<<l_f$) develop. It also predicts the kinetic energy spectrum $E(k)\sim k^{-5/3}$ for the inverse cascade and $E(k)\sim k^{-3}$ for the direct cascade. Recently, Boffeta et al.[2] carried out DNS with high resolution and showed the double cascades clearly. However, in compressible turbulence, whether Kraichnan's theory applies or not has not been known yet.

In addition the statistical properties of turbulence depend on the initial conditions, particularly on those of density and pressure distributions. Samtaney et al.[3] carried out DNS of three-dimensional compressible turbulence and found that the initial conditions affect the development of shocklet statistics.

In this paper, we consider eight types of initial conditions and study how the properties of the isotropic homogenous decaying two-dimensional weakly compressible turbulence depend on the initial conditions by DNS.

2. Method

2-1. Equation

The compressible Navier-Stokes equations in the following form is used

$$\frac{\partial \rho}{\partial t} + \nabla \cdot \mathbf{m} = \mathbf{0} \tag{1}$$

$$\frac{\partial \mathbf{m}}{\partial t} + \frac{1}{2}\frac{\partial m_i u_j}{\partial x_j} + \frac{1}{2}(\mathbf{m}\cdot\nabla)\mathbf{u} + \frac{1}{2}(\nabla\cdot\mathbf{m})\mathbf{u} = -\nabla p + \frac{\partial \tau_{ij}}{\partial x_j} \tag{2}$$

$$\frac{\partial p}{\partial t} + \mathbf{u}\cdot\nabla p + \gamma p \nabla\cdot\mathbf{u} = (\gamma-1)\nabla\cdot(\kappa\nabla T) + (\gamma-1)\phi \tag{3}$$

where ρ is density, $\boldsymbol{m}$ is momentum, $\boldsymbol{u}$ is velocity, p is pressure, τ_{ij} is viscosity stress tensor, γ is ratio of specific heat, κ is thermal conductivity, T is temperature and ϕ is viscosity dissipation.

2-2. Numerical Method

We integrate eqs. (1)-(3) by spectral method (Fourier collocation) on a doubly periodic square domain of side $L_x=L_y=2\pi$ with spatial resolution $N=1024^2$. For time integration, we use 4th-order Runge-Kutta method. We normalize the variables by the initial speed of sound, the length 2π, and the initial density.

2-3. Initial Condition

The initial velocity field is solenoidal

$$\nabla\cdot\mathbf{u} = 0 \tag{4}$$

with mean Mach number M = 0.1. We consider two types of initial kinetic energy spectrum below

$$\text{Run A:}\quad E(k) = \lambda_1 k^{-2} \tag{5}$$

$$\text{Run B:}\quad E(k) = \lambda_2 k \exp(-k^2/k_0^2) \tag{6}$$

where k is wave number, k_0 is the wave number at which the spectrum peaks, and λ_1, λ_2 are constants chosen to obtain a specified value of initial kinetic energy.

We also consider four different types IC1-IC4 of initial density and pressure fields which are determined by the following equations:

IC1: Constant total energy, constant entropy

$$\frac{1}{2}\rho|\mathbf{u}|^2+\frac{p}{\gamma-1}=\frac{1}{\gamma-1},\quad \frac{p}{\rho^\gamma}=\frac{1}{\gamma} \tag{7}$$

IC2: Poisson equation, constant density

$$\nabla^2 p=-\rho_0\frac{\partial u_i}{\partial x_j}\frac{\partial u_j}{\partial x_i},\quad \rho_0=1 \tag{8}$$

IC3: Poisson equation, constant entropy [3]

$$\nabla^2\left(\frac{p}{\rho}\right)=-\frac{\gamma-1}{\gamma}\frac{\partial u_i}{\partial x_j}\frac{\partial u_j}{\partial x_i},\quad \frac{p}{\rho^\gamma}=\frac{1}{\gamma} \tag{9}$$

IC4: Constant density, constant pressure

$$\rho=1,\ p=p_0 \tag{10}$$

In all simulations, we set the viscosity $\mu=2.5\times10^{-5}$.

3. Results and Discussion

The Reynolds number for the direct cascade or enstrophy cascade and the dissipative scale are given by $R_\lambda=Z^{3/2}/\eta_\nu$ and $l_\nu=\nu^{1/2}/\eta_\nu^{1/6}$, respectively, where Z is the enstrophy and ν is the kinematic viscosity. In Run A, $R_\lambda\simeq11$ and $l_\nu\simeq0.0139$, while in Run B, $R_\lambda\simeq50$ and $l_\nu\simeq0.0205$.

We show the energy spectrum in Fig.1. We see that the energy spectrum depends on the initial spectrum.

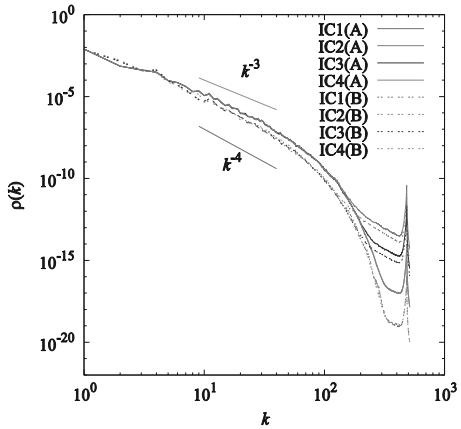

Fig.1 Energy spectrum at t=70.

The solid lines show Run A and the dotted lines show Run B. In the inertial range, the spectra of Run A are $E(k)\sim k^{-3}$, while for Run B they are close to $E(k)\sim k^{-4}$. In contrast, there are little differences between the four types of the initial density and pressure distributions. Comparing the exponent for IC1(A) and IC1(B), they are -3.78 and -4.11 each.

However, there are remarkable differences in the density fields between the four types of density and pressure initial conditions IC1-IC4. Figure 2 shows the density and pressure fields for IC2(A) at t=40. In the density field, discontinuities emerge, but they do not appear in the pressure field. Therefore, we confirm these discontinuities are not shocklets but tangential discontinuities. They are found for IC2 and IC3. The other features are independent of the initial conditions.

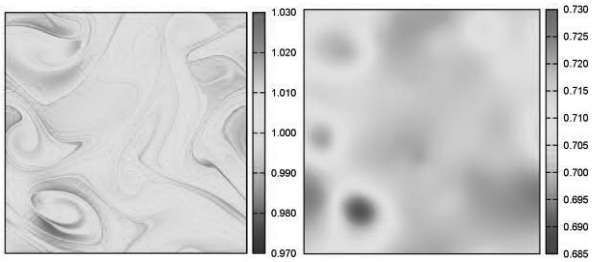

(a) (b)

Fig.2 (a) Density field, (b) pressure field for IC2(A) at t=40.

Figure 3 shows the density spectrum at t=40. The remarkable point is that IC2 and IC3 have larger components at high wave numbers than IC1 and IC4 which reflects the presence of tangential discontinuities. It should be noted that the Poisson equations are solved to obtain density and pressure in IC2 and IC3.

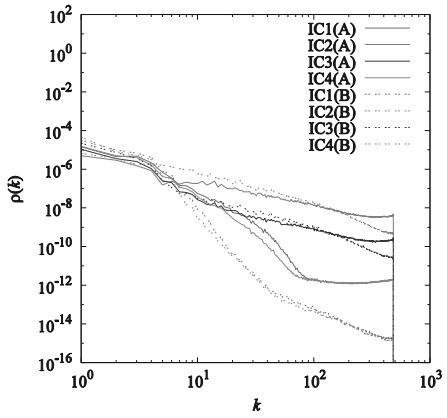

Fig.3 Density spectrum at t=40.

4. Concluding remarks

We carried out DNS of isotropic homogenous two-dimensional decaying compressible turbulence with eight different types of initial conditions. We found that the exponent in the inertial range of the energy spectrum depends on the initial spectrum. Furthermore, for the initial conditions which involve the Poisson equation there emerge tangential discontinuities.

References

[1] R. H. Kraichnan, J. Atmos. Sci, **33** (1976), pp. 1521 - 1536.

[2] G. Boffeta and S. Musacchio, Phys. Rev. E **82** (2010), 016307.

[3] R. Samtaney, D. I. Pullin, and B. Kosovic, Phys. Fluids **13** (2001), pp.1415-1430.

Eighth International Conference on Flow Dynamics
November 9 - November 11, 2011

Pressure Fluctuation Characteristics of Complex Turbulent Flow in a Dual Elbow with Small Curvature Radius in a Three-dimensional Layout

Hiroaki KONNO[1], Shinji EBARA[1], Hidetoshi HASHIZUME[1], Hidemasa YAMANO[2], Kosuke AIZAWA[2]
[1] Tohoku University, 6-6-01-2, Aramaki-aza aoba, Aoba-ku Sendai, Miyagi, Japan
[2] Japan Atomic Energy Agency, 4002 Narita, O-arai, Ibaraki, Japan
hkon@karma.qse.tohoku.ac.jp

ABSTRACT

To clarify the pressure fluctuation characteristics of the coolant in the cold-leg piping of JSFR, a pressure measurement test for a dual elbow piping was conducted. From the results, a prominent peak appeared in a profile of pressure fluctuation PSD obtained in and downstream of first elbow of a dual elbow, which also appeared in a single elbow experiment. However, another peak with smaller frequency appeared in and downstream of the second elbow. This peak could be inferred to be generated by an interaction of separation vortices shed from the intrados of the first elbow.

1. Introduction

A two-loop cooling system is adopted for the conceptual design of the Japan Sodium-cooled Fast Reactor (JSFR) [1] in order to reduce plant construction costs substantially. For a compact layout of the system, triple-short-elbow piping is designed for its cold-legs, and therefore, the flow in the piping can be assumed to be very complicated. It is essential from the viewpoint of integrity evaluation of the piping to evaluate flow-induced vibration which is triggered by pressure fluctuation. For this purpose, therefore, it is very important to elucidate the characteristics of pressure fluctuation in the piping.

In this study, an experiment for pressure fluctuation measurement is conducted by using a 1/7-scale model with high Reynolds number region up to one million referred to as a postcritical corresponding to [2], the JSFR operating flow condition. In our previous [3], studies the pressure measurement test for a single elbow piping has been already performed to analyze the pressure fluctuation characteristics. A prominent peak in the power spectrum density of the pressure fluctuation appeared especially in the downstream of the elbow, and the profiles of pressure fluctuation characteristics did not depend on Reynolds number. In this paper, a pressure measurement test for a dual elbow piping is carried out to evaluate and analyzed, and then differences between results from the single and dual elbow piping, i.e., an effect of multiple elbows, and flow structure in the dual elbow piping.

2. Experimental Method

The test section used in the study is a three-dimensionally connected dual-elbow piping, as shown in Fig. 1, made of SS304 with a diameter, D, of 126.6 mm. The curvature ratio of the elbows is 1.0, and the elbows are connected with a straight pipe of 0.57 D in length away. Tap water heated up to 45 °C is used in the experiment, and Reynolds number is varied from 320,000 to 1,000,000. An entrance region of 27 D in length is set upstream of the test section, and the water flow becomes almost fully developed turbulence before entering into the dual-elbow. Figure 2 shows installation locations of pressure sensors in the circumferential direction on the test section. The degree of 0° is set right at the each intrados side of the first and second elbow. Sensors for pressure measurement are installed as shown in Figs. 2 and 3. Near the intrados of the first elbow where the separation vortices are assumed to affect largely to pressure fluctuations, many sensors are installed in the circumferential direction. The sampling frequency of the pressure data is set at 500 Hz and a time-series of 65,536 data points are obtained from each sensor every measurement.

The time series of the pressure data is analyzed in terms of PSD (power spectrum density) obtained by FFT. Results obtained from different Reynolds number are discussed by using dimensionless frequency, St, and dimensionless PSD, P which are frequency f [Hz] divided by u/D and pressure fluctuation PSD [kPa^{2}s] divided by $\{(\rho u^2/2)^2 \cdot \mathrm{D}/u\}$, respectively, where u and ρ correspond to mean fluid velocity and fluid density, respectively.

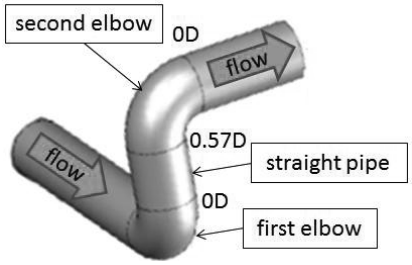

Fig. 1 Schematic view of the dual elbow piping

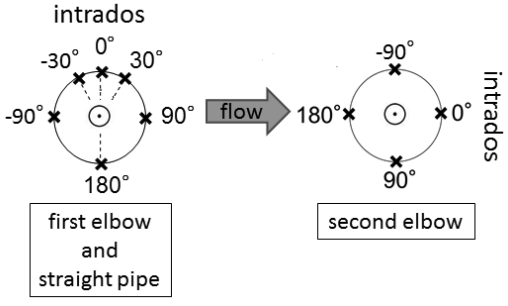

(a) On the first elbow (b) On the second elbow

Fig. 2 Installation locations of sensors in the circumferential direction

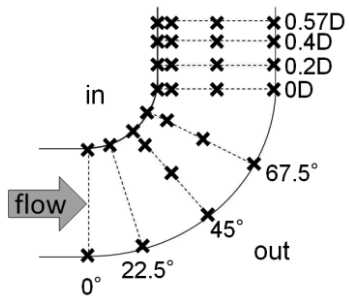

(a) On the first elbow and the downstream

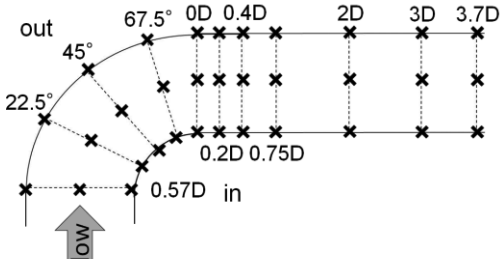

(b) On the second elbow and the downstream

Fig. 3 Installation locations of sensors

3. Results and Discussion

It is found from the frequency analysis that near the first elbow, there are remarkable peak in the PSD profiles at *St* of about 0.5 obtained at ±30° in the circumferential direction in the downstream of the first elbow. This is quite similar to the single elbow result [3], and can be considered that the peak is attributed to separation vortices generated in the intrados of the first elbow. However, PSD profiles 0.4D and more downstream of the first elbow become different from those of the single elbow; peaks appearing in the PSD profiles become smaller than those of the single elbow and the circumferential positions where the peaks appear are different from the single elbow. These differences can be inferred because the separated vortices are drawn to the intrados of the second elbow and their paths are changed.

Figures 4 show pressure fluctuation PSD profiles obtained at 0D downstream of the second elbow. There are remarkable peaks at *St* of about 0.5 in the all profiles, and the same results are observed in the PSD profiles obtained 0D and more downstream of the second elbow. The reason can be considered that two kinds of separation vortices from ±30° in the first elbow one passing through the second elbow with swirling motion, and therefore, all sensors installed in the circumferential direction detect the pressure fluctuation by the separation vortices. From these results, the effect of multiple elbows can be expressed that the flow downstream of the first elbow is bent toward the second elbow inlet and swirling motions are added to it. From the above-mentioned, the paths of the two kinds of separation vortices can be illustrated as shown in Fig. 5.

On the other hand, there appears another peak at $St = 0.2 - 0.3$ at the location of 180° and -90° in the circumferential direction, as shown in Figs. 3. It has not been clarified yet what this peak means and what generates this peak. However, there seems to be a possibility of the interaction of the two kinds of separation vortices by the swirling motions as the effect of multiple elbows.

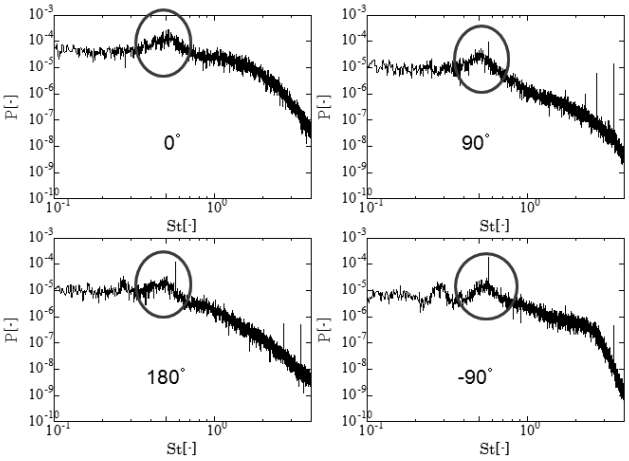

Fig. 4 Pressure fluctuation PSD at 0D downstream of the second elbow

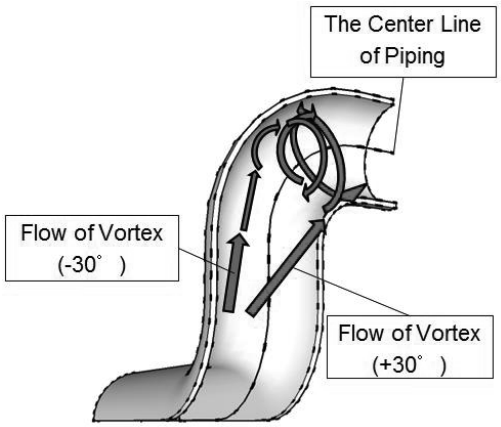

Fig. 5 Expected flow of separation vortices

4. Concluding Remarks

The experiment was conducted by using a 1/7-scale model of a dual elbow piping to evaluate the characteristics of pressure fluctuations. As a result, it was clarified that the characteristics of the dual elbow flow is very similar to that of the single elbow flow in and near the first elbow. Large characteristics differences in the single and dual elbow flow appeared 0.4D and more downstream of the first elbow. In this region, it could be considered that the influence of the second elbow became large and the flow in the dual elbow changed drastically compared with that in the single elbow. Moreover, another peak in the PSD profile at $St = 0.2 - 0.3$ appeared in the second elbow flow. This could be inferred to be caused by an interaction of the separation vortices shed from the first elbow, and this has to be elucidated in future.

References

[1] S. Kotake, et al., Nuclear Tech. **170** (2010), 133-147.
[2] I.E. Idelchik, Handbook of Hydraulic Resistance (1986), Hemisphere, Washington
[3] S. Ebara, et al., J. Fluids Engng. **132** (2010), 111102.

Development of Background Oriented Schlieren for Supersonic Flow Over Inclined Plane

Ardian B. Gojani [1], Toshiharu Mizukaki [2], Toshihiro Ogawa [1], Kiyonobu Ohtani [1],
Takamasa Kikuchi [1], Takuya Yoneyama [1] and Shigeru Obayashi [1]
[1] Institute of Fluid Science, Tohoku University, 2-1-1 Katahira, Aoba, Sendai 980-8577, Japan
[2] School of Engineering, Tokai University, 1117 Kitakaname, Hiratsuka, Kanagawa 259-1292, Japan
gojani@edge.ifs.tohoku.ac.jp

ABSTRACT

The principles behind background oriented schlieren as a possible quantitative technique for density field measurements are outlined, with emphasis to shock tube measurements. Ultimately, the developed technique will be used for 3D density field measurement in and around Busemann's biplane. At this stage, BOS is applied to a steady temperature field and to shock reflection/diffraction from an inclined plane. Potential of using regular distribution of background dots for a single shot and ray tracing evaluation is discussed.

1. Introduction

The visualization technique Background Oriented Schlieren (BOS) [1-2] is being developed for 3D density field measurements in and around the Busemann type supersonic biplane. Computational studies show that some particular two wing configurations can lead to the decrease of sonic boom intensity on the ground by wave cancellation and reduction [3-4].

The principle of BOS lays in the difference between two focused images of the same pattern imaged through a test fluid: a reference image is taken without and a measurement image with a disturbance in the fluid that is to be evaluated. The disturbance, e. g. a shock wave, causes local changes of density, resulting in changes of the refractive index. Hence, an imaging light beam passing through the disturbance will deflect and the angle of deflection is encoded in the difference between the measurement and the reference image. This angle, and subsequently the refractive index, can be extracted, for example, by cross-correlation or ray tracing algorithms, enabling the deduction of the fluid's density from the relationship between the density and the refractive index. This relationship is given by the Gladstone-Dale relation

$$n-1=K\rho, \tag{1}$$

where K is a constant of the medium, $n=n(\mathbf{r})$ is the refractive index, and $\rho=\rho(\mathbf{r})$ is the density.

BOS is a line-of-sight integrating technique that gives the 2D projection of the density field. Its spatial and temporal resolutions depend on the optical setup and instruments used, while its sensitivity and accuracy depend - in addition to the above, - on the density gradients in the flow that is being imaged. It is the ultimate goal of this study to design a BOS system that can be applied for the construction of 3D density field of the Busemman's biplane, by recording data of a model of the biplane in flight in a ballistic range. Since the aim is to detect the cancellation of the sonic boom, the sensitivity of the measurement technique is of paramount importance. A set of tests of BOS is done by investigating temperature fields achieved from a linear tube heater, and later a shock tube experiment was designed and conducted in order to apply BOS to a planar shock reflection and diffraction from an inclined plane.

2. Measurement principles

A BOS measurement consists of two stages: image recording and image evaluation. Image recording constitutes the choice of the background pattern, the recording system, i. e. cameras and lightning, and their arrangement, a side view of which is shown in Fig. 1. Here B is the background, T is the test section with refractive index gradient in the y direction $\partial n/\partial y$, ε is the angle of deflection proportional to this gradient, L is the objective lens, I is the image plane; a, w, d, s_o and s_i are respective distances, and dy_o and dy_i are the dot shifts in the background and in the image plane. The background is characterized by two numbers: dot size and dot density, which are determined based on the pixel size and pixel count of the camera sensor. For good S/N ratios a single background dot covers about 2-4 camera sensor pixels, and overall about 15-35% of the background area is covered with dots. The sensitivity of the setup increases by using longer focal length lenses on cameras with large pixel count, as well as by setting the test section closer to the lens [5]. In paraxial approximation, with $s_o >> w$, the detected deflection angle is expressed as

$$\varepsilon=\frac{dy_i}{f}\left(1+\frac{a}{d}\right), \tag{2}$$

where $f \approx s_i << s_o$ is the focal length of the lens. Since the lens is focused on the background, d is limited by the blur, which, on the other hand, gains some extent from the image evaluation. This later stage involves comparison of interrogation subimage areas between reference and measurement images through cross-correlation procedures. Usually, interrogation areas are smaller than 1/10th of the overall image size.

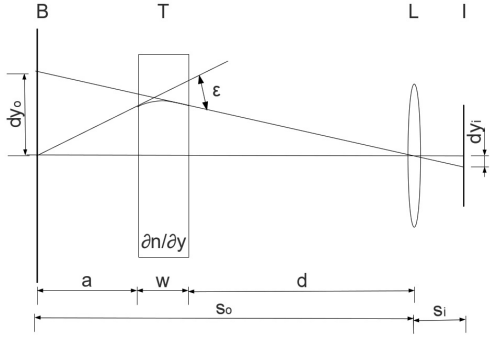

Fig. 1. A side view of BOS setup.

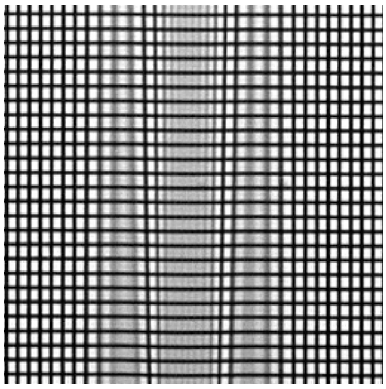

Fig. 2. A BOS measurement image of a background with regular distribution of dots.

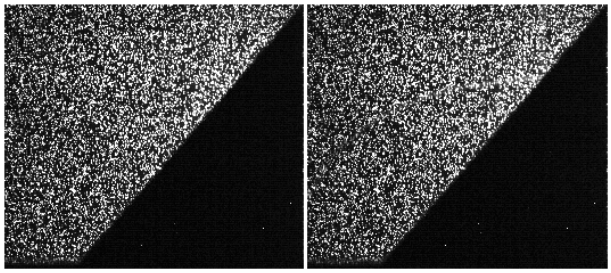

Fig. 3. BOS reference and measurement image of shock reflection from an inclined plan.

Presented experiments were done using two types of cameras: steady temperature field was investigated by using DSLR camera (Nikon D80) with 3900 x 2600 px count and ~ 6 μm linear size of a pixel. For shock tube experiments, high speed camera (HSV-1 Shimadzu) with 1 μs time resolution was used. Pixel count and linear size were 312 x 260 and 5 μm, respectively.

3. Results and Discussion

Figure 2 is a BOS measurement image showing the deformation of the imaged background with regular distribution of dot pattern, in which a white rectangle has dimensions of 1.5 mm x 2 mm, and black line is 0.8 mm thick. Here, the change of the refractive index was caused by the temperature field of a linear radiative heater placed perpendicularly to the background. The image is a test of the sensitivity of the setup, with the gradient along vertical (~0.1 deg/mm) not being strong enough to deform the image, compared to the gradient along the horizontal (~1 deg/mm). The regular features of the background can be used to quantify line deformations without a reference image. This type of image can be used for mapping the refractive index by using ray tracing, although this has not been attempted.

A typical result of BOS images from the shock tube experiment is shown in Fig. 3, and its evaluated pixel shift map is given in the lower image of Fig. 4. The upper part of Fig. 4 shows the pixel shift map at the moment when the shock wave reached the plane with inclination of 49°. In all experiments, incident Mach number of the shock wave was 1.3 and the maximal shift, denoted by black color, was smaller than 2 px. The evaluated field of view, that is the rotated rectangle over

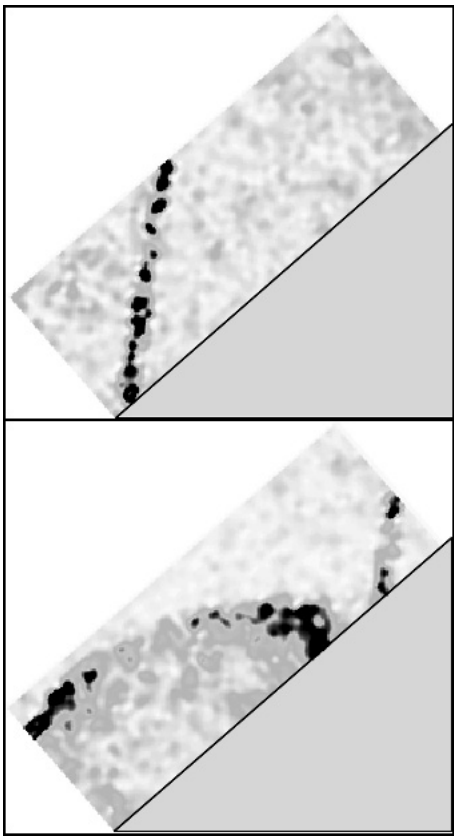

Fig. 4. Two magnitude map images of the pixel shift, interframe is 216 μs.

the wedge, has dimensions of 300 mm x 120 mm. Image evaluation was done with interrogation widows of 8 px x 8 px, with one pixel corresponding to a field of view of 1 mm. Planar shock wave is visualized, albeit there are many artifacts in the line depicting the shock front. Diffracted shock is also captured, with a higher value of pixel shift, while the reflected shock connecting reflection point and triple point is not observed. Although the poor spatial resolution does not allow for minute investigations, it can be noticed that this is a case of transitioned regular reflection.

4. Concluding remarks

Preliminary results of BOS application to flow visualization are presented. The outline of technique's parameters that determine its sensitivity show that there is room for improvement, which mainly is required in enhancing spatial resolution.

References

[1] H. Richard and M. Raffel, Meas. Sci. Technol., **12** (2001), pp. 1576-1585.
[2] G. E. A. Meier, Exp. Fluids, **33** (2002), pp. 181-187.
[3] K. Kusunose, K. Matsushima and D. Maruyama, Prog. Aerosp. Sci., **47** (2011), pp. 53-87.
[4] A. Toyoda, M. Okubo, S. Obayashi, K. Shimizu, A. Matsuda, and A. Sasoh, 48th AIAA Meeting (2010), paper AIAA-2010-0873.
[5] E. Goldhahn and J. Seume, Exp. Fluids, **43** (2007), pp. 241-249.

Eighth International Conference on Flow Dynamics
November 9 - November 11, 2011

Inverse Aerodynamic Analysis of Vehicle Wakes using PIV and CFD

Kisa Matsushima [1], Masahito Yonezawa [2] and Atsushi Ogawa [2]
[1] University of Toyama, 3190 Toyama, 930-8555, Japan.
[2] Honda R&D Co. Ltd.. Hagamachi, Tochigi, 321-3393, Japan.
kisam@eng.u-toyama.ac.jp

ABSTRACT

A pressure estimation system using velocity data measured by PIV experiment has been developed and validated. It could be regarded as an inverse problem, which recovers three dimensional flow patterns from limited data on a two dimensional plane. Two formulations of 2D and 2.5D models are prepared. They are examined to estimate pressure in the wakes of an automobile and a wing. Through the examination, it has been found that 2.5Dmodel works excellently.

1. Introduction

The purpose of this paper is to examine a method for pressure estimation using velocity data by stereo PIV. The stereo PIV has advantages as an experimental tool [1, 2]. However, it does not measure pressure that is needed to develop aerodynamic shape of vehicles. Thus, we have developed a pressure estimation method using velocity data as well as a drag calculation tool using properties on a PIV plane in vehicles and airplane wake.

2. Pressure Estimation Method – Formulation -

Formulation is based on 3D incompressible Navier-Stokes (N-S) equations. First, we take the divergence of three momentum balance equations letting time dependent terms zero, then we obtain 3D Poisson equation for pressure. Next, we assume the *x* gradient of flow variables were zero, the 3D Poisson equation yields to the 2D Poisson equation for pressure, *Eqs. 1 and 2*. The estimation using them is called 2D model.

$$\frac{\partial^2 p}{\partial y^2}+\frac{\partial^2 p}{\partial z^2}=-\left\{\left(\frac{\partial v}{\partial y}\right)^2+\left(\frac{\partial w}{\partial z}\right)^2+2\frac{\partial w}{\partial y}\frac{\partial v}{\partial z}+v\frac{\partial D}{\partial y}+w\frac{\partial D}{\partial z}\right\}+\frac{1}{\mathrm{Re}}\left(\frac{\partial^2 D}{\partial y^2}+\frac{\partial^2 D}{\partial z^2}\right) \quad ---Eq.(1)$$

$$where \quad D=\frac{\partial v}{\partial y}+\frac{\partial w}{\partial z} \quad ---Eq.(2)$$

If the flow has three-dimensionality, additional terms should be needed to account three-dimensional effect. Thus, we derive *Eqs. 3 and 4* with some considerations [3]. In this article, the estimation by them is called 2.5D model.

$$\frac{\partial^2 p}{\partial y^2}+\frac{\partial^2 p}{\partial z^2}=-\left\{\begin{array}{c}\left(\frac{\partial v}{\partial y}\right)^2+\left(\frac{\partial w}{\partial z}\right)^2+\\ \frac{\partial v}{\partial x}\frac{\partial u}{\partial y}+2\frac{\partial w}{\partial y}\frac{\partial v}{\partial z}+\frac{\partial u}{\partial z}\frac{\partial w}{\partial x}\\ +u\frac{\partial D}{\partial x}+v\frac{\partial D}{\partial y}+w\frac{\partial D}{\partial z}\end{array}\right\}+\frac{1}{\mathrm{Re}}\left(\frac{\partial^2 D}{\partial y^2}+\frac{\partial^2 D}{\partial z^2}\right) \quad --- Eq.(3)$$

$$where \quad D=\frac{\partial v}{\partial y}+\frac{\partial w}{\partial z} \quad --- Eq.(4)$$

3. Results and Discussion

In this research, everything has been done by computational fluid dynamics (CFD) to examine the pressure & drag estimation method, which is the first stage of the construction of an aerodynamic design system using PIV measurement. At first, instead of PIV experiment, three-dimensional CFD simulation was conducted about a realistic car as well as a rectangular wing and we obtained velocity data on several wake planes (see Figs. 1 and 2). The data on wake planes are called pseudo PIV data. Then, pressure estimation was computationally conducted by solving Poisson equation of the 2D and 2.5D models. As input data, the pseudo velocity data on one two-dimensional plane were used for the 2D model, while the data of three planes were used for 2.5D one.

Figures 3 and 4 show the estimated Cp distributions using pseudo PIV data. Figure 3 is of a car. Figure 4 is of a wing. The area indicated by thick white broken lines corresponds to the car (Fig. 3(c)) or wing (Fig. 4(c)) location in the *Y-Z* plane.

Figure 3(a)1 is the result of the three-dimensional CFD simulation which serves as correct Cp for the present examination. The wake plane location in stream wise (*X*) direction is at 0.1**L** behind the car body end. **L** means the total length of the car. Figures 3(b) and 3(c) are estimated Cp contours by the 2.5D and 2D model, respectively. Because the flow field on the wake plane of 0.1L still varies along *X* direction, the estimation result in Fig. 3-3 using a single plane PIV data is poor. The estimated result can be much improved when the pseudo PIV data on three planes are used as shown in Fig. 3(b). As for estimation pressure by the 2.5D model, the error rate to the correct value is 0.5% in average and 5% at most.

In the same way, Figure 4(a) is the correct Cp distribution to evaluate estimated results on wing wake planes. The wake plane location is at 0.2**C** behind the wing trailing edge. **C** means the chord length. Making a comparison of Figs. 4(b) and 4(c), referencing Fig. 4(a), the 2.5D model gives almost identical Cps to the correct ones, while the 2D model can estimate trailing vortices, but does not do the wake region of wings. The error rate of Fig. 4(b) (2.5D model) to Fig 4(a) is less than 0.065%.

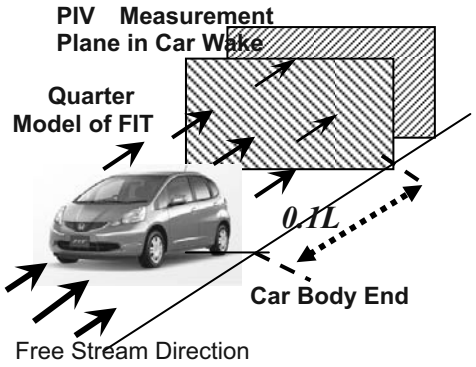

Fig. 1 CFD simulation serving as PIV for Honda Fit wake [4].

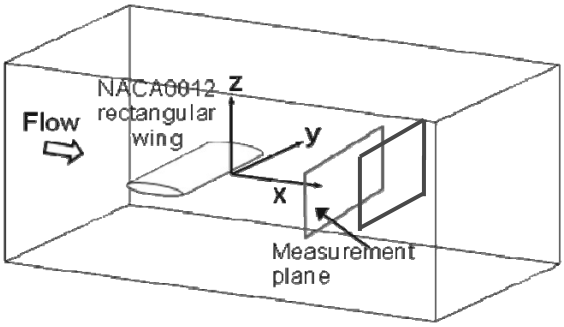

Fig. 2 CFD simulation serving as PIV for wing wake.

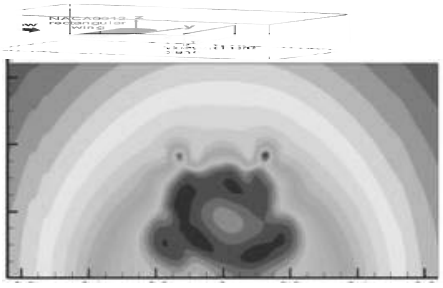

(a) 3D CFD (Correct Phenomena).

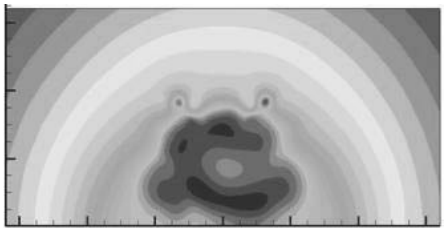

(b) 2.5D model（Three Planes).

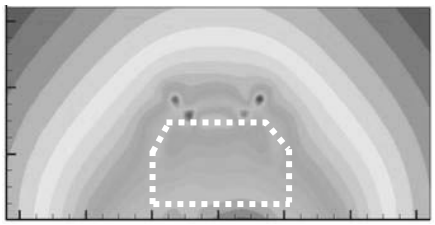

(c) 2D model（Single Plane).

Fig. 3 Cp distributions of a car wake plane.

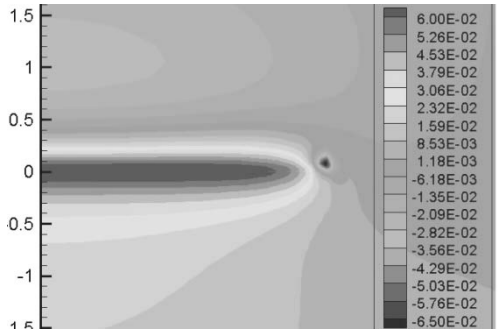

(a) 3D CFD (Correct Phenomena).

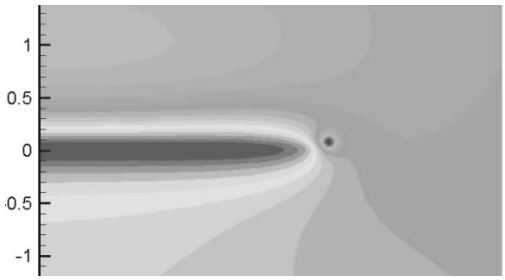

(b) 2.5D model（Three Planes).

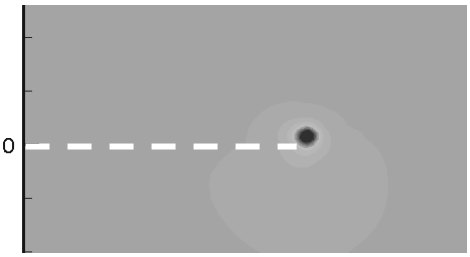

(c) 2D model（Single Plane)

Fig. 4 Cp distributions of a wing wake plane.

4. Concluding remarks

A computational method was proposed and validated to estimate pressures for the PIV measurement in the automobile and wing wake planes. We established the basic equation of the 2.5D model which included proper gradient terms in the free stream direction because the wake had three-dimensionality. The pressure estimation using the 2.5D model gave excellent results, while that using 2D one did poor results in wake planes which is cross section of free stream direction. Consequently, for pressure estimation there, the gradient of flow properties in free stream direction should be accounted.

References

[1] Passmore, M. A., Spencer, A., Wood, D., Jowsey, L., Newnham, P. S., *SAE Paper*, No.2010-01-0120, 2010. .

[2] AIAA, “Aerodynamic Measurement Technology”, *Aerospace America*, pp. 15-16, Dec. 2009.

[3] Matsushima, K, Yonezawa, M., Ogawa, A., Motohara, H., CD proceeding of the Asian Symposium on Visualization, ASV 11-08-09, 2011.

[4] http://www.honda.co.jp/Fit/

Eighth International Conference on Flow Dynamics
November 9 - November 11, 2011

Investigation of Application of Remote Field Eddy Current Testing for Inspecting Flaws in Large Diameter Tubes from Outside

Jing Wang[1,2], Noritaka Yusa[1], Hongliang Pan[2], Hidetoshi Hashizume[1]
[1]Department of Quantum Science and Energy Engineering, Graduate School of Engineering, Tohoku University.
6-6-01-2, Aramaki Aza Aoba, Aoba-Ku, Sendai, Miyagi, Japan
[2]School of Mechanical and Power Engineering, East China University of Science and Technology
200237, Meilong, Xuhui, Shanghai, China
jwang@karma.qse.tohoku.ac.jp.

ABSTRACT

This paper discusses the difference between remote field eddy current testing and conventional low-frequency eddy current testing from the viewpoint of inspecting flaws in large diameter tubes from outside through finite element numerical simulations. The discussions are carried out on the basis of the dependency of the amplitude of signals on the depth of a flaw. The results show that the conventional low-frequency eddy current testing is comparable to remote field eddy current testing when exciting frequency is sufficiently low.

1. Introduction

Remote field eddy current testing (RFECT) has been used for the inspection of tubes[1,2] because it can detect inner and outer flaws with almost the same sensitivity. Whereas conventional remote field eddy current testing aims at the inspection from inside for a tube, the inner surface of a tube is not always accessible and thus several studies have proposed the application of RFECT from outside for a tube, using a probe encircling the tube[3,4].

When the diameter of a tube is large, however, it is difficult to handle a probe encircling the tube and thus a probe facing the outer surface of the tube is preferable. Since a tube with a large diameter can be regarded as a flat plate, reports on the application of RFECT to the inspection of flat plates indicate that it is possible to inspect a tube with a large diameter from outside the tube using a probe facing the surface. The RFECT technique firstly was extended to the inspection of metallic plates by Y. S. Sun et al. 1996[5]. N. Kasai et al. used the RFECT for the evaluation of back-side flaws of the bottom plates of an oil-storage[6]. H. Wang et al. utilized the new remote field eddy current transducer for testing flat conductive plate by the corresponding simulations and experiments[7]. However, the advantage of RFECT over low-frequency eddy current testing (LECT) has not been fully evaluated yet. Actually recent reports have implied that remote field eddy current phenomena are not always necessary to inspect back-side flaws appearing in a thick metallic plate[6].

In the present study, we evaluate the difference between RFECT and LECT using finite element simulations. Signals due to inner and outer flaws are evaluated by the numerical simulations, in order to discuss the sensitivities of the RFECT and LECT against the flaws.

2. Materials and methods

Figure 1 illustrates a finite element model used in this study. A long flaw situated at a ferromagnetic plate is inspected. The size of plate is 300 mm in length, 300 mm in width and 10 mm in thickness. Flaws with the same width (2 mm) but different depth (2 mm, 4 mm, 6 mm, 8 mm) shown by character of d in Figure 1 are considered. A shield to attenuate direct flux and realize remote field effect is a U-type one with 300 mm in length, 34 mm in width, 24 mm in height and 10 mm in thickness. There is no air gap between the shield and the plate. The axes of exciter and detector are both 7 mm far from the surface of plate. Material characteristics of model and parameters of coils are shown in Table 1. The frequencies are 20 Hz and 200 Hz, which provides skin depths of 17.8 mm and 5.6 mm, respectively. The distance between the exciter and the detector is decided on the basis of preliminary simulations to evaluate the effect of the shields.

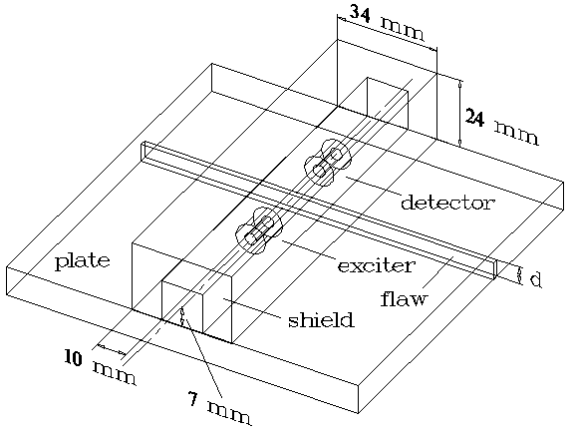

Fig. 1 geometric model of simulation

The simulations were carried out using the AC/DC module of commercial software Comsol multiphysics 4.2. The magnetic flux density is small ($B \approx 4e\text{-}3\ T$) in these simulations, so the governing equation is

$$(j\omega\sigma - \omega^2\varepsilon)A + \mu^{-1}\nabla \times \nabla \times A = J_e \quad (1)$$

where ω is the angular frequency, σ is the conductivity, ε is the permittivity, A is the magnetic vector potential, μ is the permeability, J_e is the current density of exciter. The model was discretized using edge elements. The size of computational domain is 800 mm×800 mm×800

mm; boundary condition was imposed so that the tangential component of magnetic vector potential is zero. The total number of elements of the model is 340,881.

Table 1. Material characteristics of model and parameters of coils

Item	Value
Conductivity of plate and shield	4×10^6 S/m
Relative permeability of plate and shield	10
Inner radius of exciter and detector	2 mm
Outer radius of exciter and detector	5 mm
Length of exciter and detector	10 mm
Current density of exciter	1.25×10^6 A/m^2
The number of detector coil turns	120

3. Results and Discussion

Figure 2 shows the effect of the distance between the exciter and the detector on induced voltage when there is no flaw. The figure indicates that indirect flux is dominant if the detector is situated more than about 50 mm away from the exciter for the two frequencies. Then 60 mm coil distance is utilized.

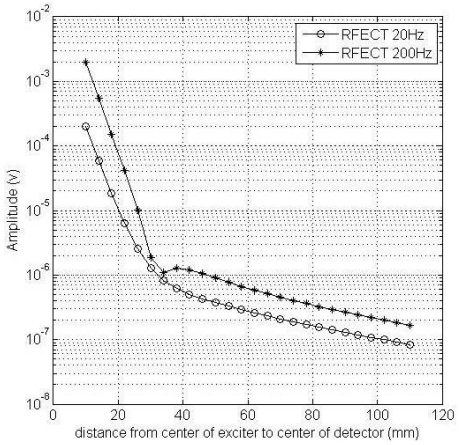

Fig. 2 The effect of coil interval on the amplitude of induced voltage

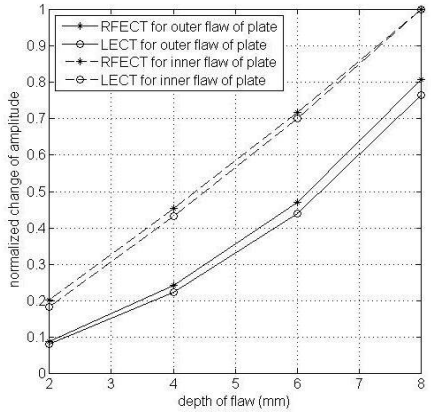

Fig. 3 normalized change of amplitude as a function of flaw depth with frequency of 20Hz.

Figures 3 and 4 present the maximum signals obtained using RFECT and LECT. The distance between the exciter and the detector was set to 60 mm. The signals are normalized with respect to the signals obtained due to the deepest inner flaw. Figure 3 indicates that the sensitivity of LECT is similar to that of RFECT from the viewpoint of their sensitivity to outer flaws. In contrast, there is clear difference between RFECT and LECT when frequency is higher.

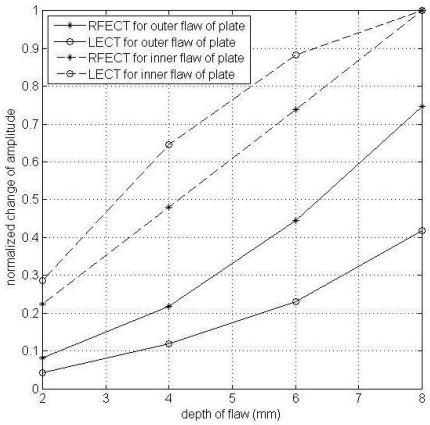

Fig. 4 normalized change of amplitude as a function of flaw depth with frequency of 200 Hz.

4. Concluding remarks

The study evaluated the application of remote field eddy current testing for inspecting flaws in large diameter tubes from outside. The results revealed that when sufficiently low frequency is adopted, the sensitivity of LECT is comparable to that of RFECT.

References

[1] M. Isobe, R. Iwata, M. Nishikawa, High sensitive remote field eddy current testing by using dual exciting coils, Nondestructive Testing of Materials (1995), pp.145-152.

[2] H. Fukutomi, T. Takagi, M. Nishikawa, Remote field eddy current technique applied to non-magnetic steam generator tubes, NDT&E Int., **34** (2001), pp.17-23.

[3] L. Janousek, T. Marek, D. Gombarska, K. Capova, Eddy current non-destructive testing of magnetic tubes, Journal of Electrical Engineering, **57** (2006), pp.126-129.

[4] Young-Kil Shin, et al., Design of Encircling Remote Field Eddy-Current Probe, IEEE Transactions on Magnetics, **38(2)** (2002), pp.1273-1276.

[5] Y.S. Sun, et al., A remote field eddy current NDT probe for the inspection of metallic plates, Materials Evaluation, **54(4)** (1996), pp.510-512.

[6] N. Kasai, et al., Evaluation of back-side flaws of the bottom plates of an oil-storage tank by the RFECT, NDT&E Int., **41** (2008), pp.525-529.

[7] H. Wang, et al., Simulation and experimental study of remote eddy current testing on flat conductive plate, Int. J. Appli. Electromag. Mech., **33** (2012), pp.1261-1266.

Eighth International Conference on Flow Dynamics
November 9 - November 11, 2011

Evaluation of Thermal Stress Distribution With Elasticoluminescent Materials

Wei Liu[1], Taku Nagatake[1], Kazuyuki Takase[1]
Chuan-Xing Wu[2,3], Daisuke Ono[2], Hiroshi Yamada[2], Chao-Nan Xu[2,4]
*1 Nuclear Science and Engineering Directorate, Japan Atomic Energy Agency, Tokai, Ibaraki, Japan
liu.wei@jaea.go.jp
*2 National Institute of Advanced Industrial Science and Technology (AIST), Kyushu, Saga 841-0052, Japan
*3 Interdisciplinary Graduate School of Engineering Science, Kyushu University, Fukuoka 816-8580, Japan
*4 Japan Science and Technology Agency (JST) CREST, Saitama 322-0012, Japan

ABSTRACT

Elasticoluminescent materials, so far, has been used in visualization of stress distribution of constructions, such as a bridge or a building, under normal temperature condition. In this paper, it is used under high temperature condition to seek the possibility of the visualization of the distribution of thermal stress. Test section was designed to be able to generate thermal stress. Luminescence data from the elasticoluminescent materials, strain data and temperature distribution data were derived. The comparison between the luminescence data and the strain data show the elasticoluminescent material can measure the distribution of thermal stress qualitative.

1. Introduction

Today, more than fifties Boiling Water Reactors are in operation in Japan and those constructed in earlier days have been operated more than 30 years. For these reactors, aging degradation is a problem needs more researching. Damage due to thermal stress that caused by thermal fluid is considered being one reason for the aging degradation. It is therefore necessary to monitor the stress and its distributions for a reactor structure.

Stress strain gauge can be used for the measurement of the thermal stress. By setting the gauge on the structure surface, we can get the stress of the point accurately. In other words, the gauge has the advantage to give out the reading of stress to a certain point but is difficult to indicate where the point that has the maximum stress is.

Recently, a new elasticoluminescent material, which is a kind of mechanoluminescence, has been developed by National Institute of Advanced Industrial Science and Technology (AIST) [1][2][3]. The material has the characteristic that can produce luminescence repeatedly even at very small elastic deformation. By coated to the surface of a structure, the material can visualize the distribution of stress and can make a diagnosis to the soundness of the structure. So far, this has been carried out for building, bridge, etc, under normal temperature condition. Because this material has a characteristic that luminescence not only with the change of stress, but also with the change of the temperature and even the temperature changing rate, it is considered being difficult to be used under high temperature condition.

In this paper, we tried to use the elasticoluminescent material under high temperature condition to seek the possibility of the visualization of the distribution of thermal stress.

2. Experiment

Test section for the experiment is shown in Fig.1.The test section is made of copper. It consists of two rectangular flow channels. One is for high temperature water and the other is for low temperature water. The test section is silver brazed into the flanges made of sus. The test section is fixed by fixing the upper and the lower flanges with bolts.

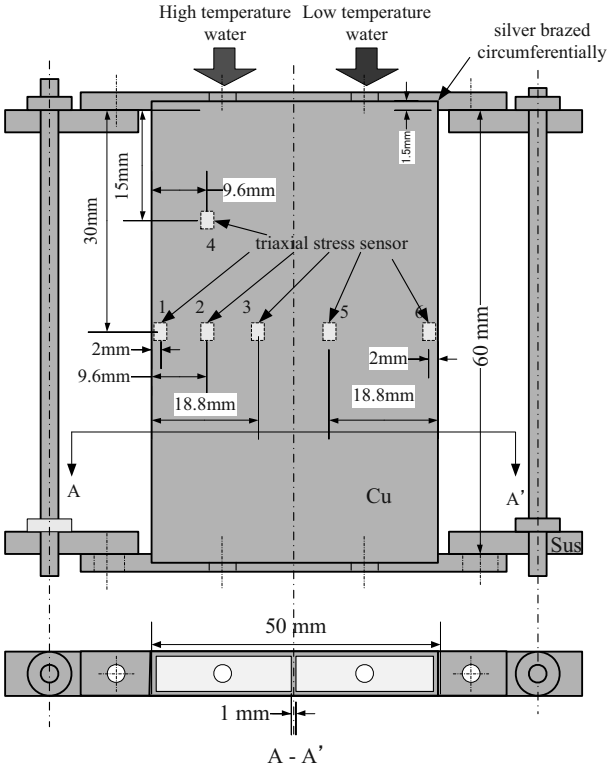

Fig.1 Test section used for the experiment.

In the experiments, we measured: (1) the stress distributions from 6 triaxial strain sensors, whose setting positions are shown in Fig.1. (2) Surface temperature of the test section with a thermograph and (3) luminescence data from elasticoluminescent material.

To measure the surface temperature with a thermograph, we painted one surface of the test section with blackbody painting. To measure the illumination information, we coated the other surface of the test section with the elasticoluminescent material.

The experiment condition is summarized in Table1. In the experiments, we firstly flow the two flow

channels with low temperature water. After a steady state is reached, high temperature water is flowed into the high temperature water channel at the desired flow rate whilst the low temperature channel is kept flowing the low temperature water. Thermal stress is generated in this heating process. After the steady state is reached, low temperature water is flowed again into the high temperature channel to decrease the temperature of the test section. Measurements were performed for the heating process.

Table 1 Experiment conditions

	High temperature water	Low temperature water
Temperature	120 °C	25 °C
Flow rate	2.1-11.5 L/min	12 L/min

3 Experiment Results

Experiment results for the case that flow rate for high temperature water is 2.1 L/min is reported below. Fig.2 shows the von Mises stress of each point calculated from the measured triaxial strain data. Time 0 corresponds to the time the high temperature water is flooded into the high temperature water channel. We found the point 2 has the highest Mises stress at the initial stage of the heating process.

Fig.3 shows luminescence image at t = 1.6s. In the figure 3, there are 2 abnormal luminescence points. They are points 1 and 2. Point 1 is an abnormal over luminescence point due to the over flow of coating glue, which has an effect to enhances the luminescence. Point 2 is an abnormal under luminescence point because the elasticoluminescent material is failed to be glued on the point. As the result, we found that the most luminescence point in fig.3 is point 3, which matches the highest von Mises stress in fig.2.

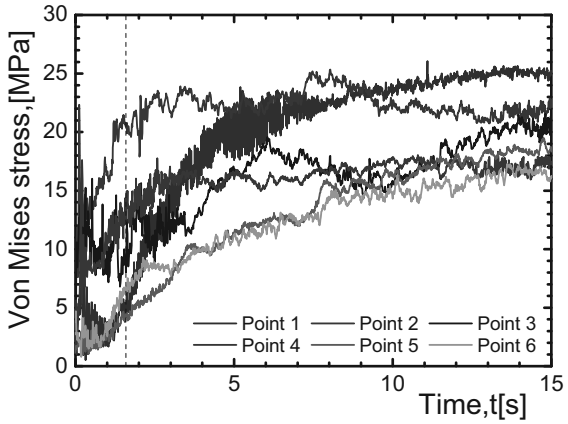

Fig.2 The von Mises stress in the heating process.

4. Analysis Results

The change of thermal stress in the experiment is tried to be analyzed. The analyzation is performed in two steps. Firstly, the temperature distribution in the test section is calculated by ACE-3D code, which is a thermal fluid code developed by JAEA. With using the calculated structure temperature, ABAQUS code is run to get the thermal stress distribution. In the calculation, the up and the down sides of the test section are set being fixed entirety. The calculation result is shown in Fig.4. Compared to the fig.3, fig.4 gives the highest thermal stress at four corners. This is reasonable for this complete fixing assumption, which, however, is some different from the experimental fixing condition. Fig.4 shows a high thermal stress region A at the left center of the test piece, which matches the point 3 in fig.3 qualitatively.

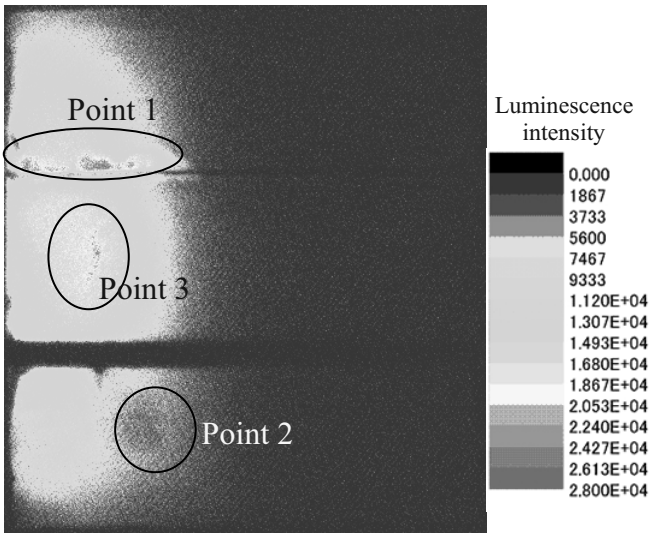

Fig.3 Experimental result of luminescence of elasticoluminescent material in a heating process.

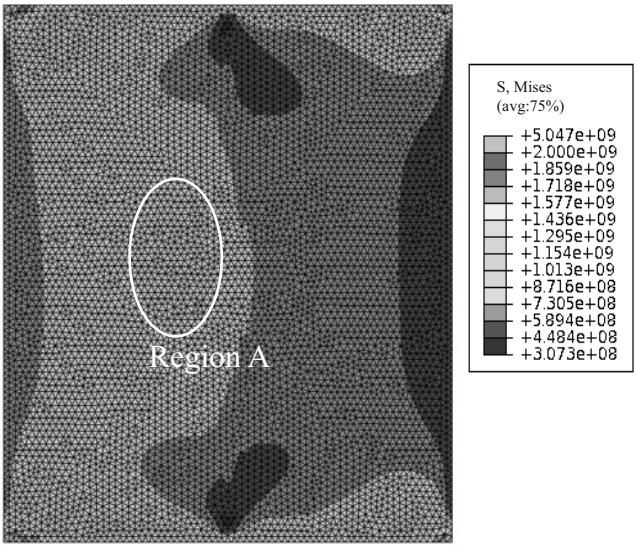

Fig.4 Distribution of thermal stress by ABAQUS code

5. Concluding remarks

The elasticoluminescent material is used under high temperature condition. It is confirmed being able to measure the distribution of thermal stress qualitative.

References

[1] C.N.Xu, et al., Appl. Phys. Lett., **74**(1999), 1236-8
[2] C.N.Xu, et al., Appl. Phys. Lett., **74**(1999), 2414-6.
[3] C.N.Xu, et al., Mat. Res. Bull., **34**(1999), 1491-1500.

Pressure Measurement with Molecule Based Pressure Sensor in Constricted PDMS Microchannels

Chih-Yung Huang[1], Chih-Min Lai[1], Hsiang-Yu Wang[2]
[1]Department of Power Mechanical Engineering, National Tsing Hua University, Hsinchu, Taiwan.
[2]Department of Chemical Engineering, National Cheng Kung University, Tainan, Taiwan
cyhuang@pme.nthu.edu.tw

ABSTRACT

In this work, the molecule-based pressure sensor technique was applied in the microscale pressure measurements to investigate the flow fields inside straight and constricted PDMS microchannels. The pressure distributions inside these microchannels were acquired at Reynolds number ranging from 9 to 78 and Knudsen number changing from 0.0001 to 0.021. The experimental results acquired in the straight microchannel showed good agreement with the analytical solution. The results acquired in the constricted microchannel showed the pressure drop near the constricted area which indicated the flow recirculation.

1. Introduction

The physics in the micro scale has drawn great attention due to the extensively applications of the micro devices [1]. Not only the researchers are interested in studying the physical phenomena at the micro scale but also the industry is eager to know the flow fields in order to improve the performance of these micro devices. However, most of the studies are focused on theoretical analyses and simulations due to the difficulty of sensor implantation inside the micro devices. Micro-sized mechanical sensors for pressure and temperature measurements have been fabricated using standard lithography processes, but they require complicated procedures to fabricate. Additionally, these sensors have sizes around several hundred micrometers and consequently, they are mostly deployed outside the micro devices to acquire the pressure and temperature at the inlet and the exit. Even if the mechanical sensors were embedded inside micro devices, only discrete points can be obtained due to the size effect [2, 3]. The complexity of fabrication and the limitation of data points have limited the resolution of mechanical sensors and therefore encumber the understandings of the micro scale flow fields. Around a decade ago, a new experimental method which was originally applied to macro scale experiments in aerospace engineering and mechanical engineering has been adapted to micro scale measurement [4]. This pressure sensitive technique has the advantages of straightforward application and non-intrusive measurement, providing an alternative method for pressure measurements. It uses pressure sensitive luminescence molecules and translates the luminescence signal to pressure data. It can acquire global pressure profiles with great spatial resolution as fine as just a few micrometers. Promising results have been acquired in varies micro devices such as microchannels, micronozzles, microturbines, and microjets [5, 6]. The results have also been validated by the numerical data [7]. In this study, the pressure profiles inside straight and constricted PDMS microchannels have been obtained using the molecule-based pressure sensor and more than thousands of data points have been acquired for the whole channel with spatial resolution as fine as a few micrometer apart.

2. Method

To study the pressure profiles inside the microchannels with different geometries, the molecule-based pressure sensor, Pt(II)meso-tetrakis-(pentafluorophenyl)Porphine (PtTFPP), mixed with the Polydimethylsiloxane (PDMS) has been selected as the pressure probe for the experiments. The binder, PDMS, is selected due to its comparability to microchannel devices. These microchannel devices were fabricated using the standard soft-lithography technique with PDMS as the material. In the experiments, straight microchannel devices with geometry of 1 cm long, 100 μm wide and 67 μm deep was constructed with two reservoirs positioned at the channel entrance and exit. The constricted microchannel devices have the same design as the straight channel, except for a pair of small square ribs at the center inside the channel to provide the channel constriction ratio of 1:2. The experimental arrangement of microchannel measurements with molecule-based pressure sensor is shown in Figure 1.

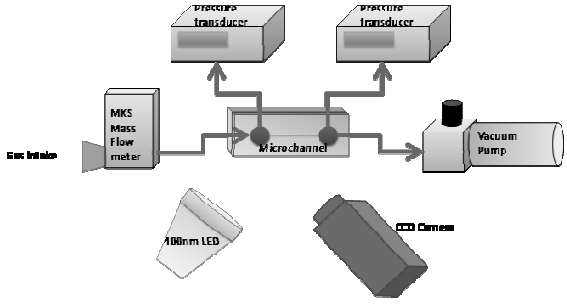

Fig. 1 The experimental setup of molecule-based pressure sensor measurements for microchannel devices

3. Results and Discussion

Due to the large ratio between the channel length and width, the pressure measurement inside the straight microchannel was divided into three parts without sacrificed the spatial resolution in the cross-section direction. Combining the three measurements taken inside the microchannel, more than 3000 data points from the channel inlet to exit have been obtained and the results provided detailed pressure distribution inside the channel. The experimental data acquired with the

molecule-based pressure sensor have been compared with the analytical solution and plotted in Fig. 2. The analytical solution is obtained using Navier-Stokes equations with the 1st order slip boundary condition [8]. The experimental results show good agreement with analytical solutions in all the test conditions. Some experimental data points near the inlet have been removed due to the entrance effect or the reflection from the inlet reservoir. These phenomena require further investigations which are not included in this study. To avoid confusion, the excluded results have been replaced with the extrapolated values from the pressure 10% downstream from the inlet. The results acquired with molecule-based pressure sensor have superior spatial resolution up to 3 μm and more than 3000 data points were acquired inside the channel, which was much better than the conventional pressure measurements. In the pressure measurements inside constricted microchannel devices, in-situ calibration and pixel-by-pixel calibration method were applied to correct the non-uniform illumination due to the single UV LED array for excitation. The pressure map acquired with the molecule-based pressure sensor is shown in Fig. 3. Fig. 4 shows the pressure distributions along the center line inside the constricted microchannel device. The pressure dropped while flow passing through the constricted region, indicating the increasing of speed while flowing around the ribs.

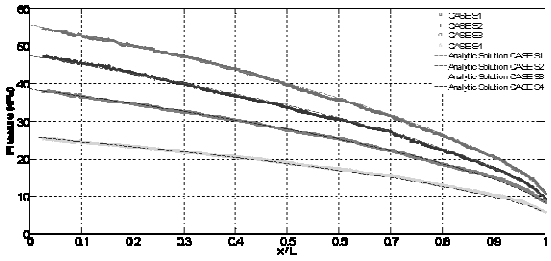

Fig. 2 The pressure distribution inside straight microchannel acquired with molecule based pressure sensor and compared with analytical solution

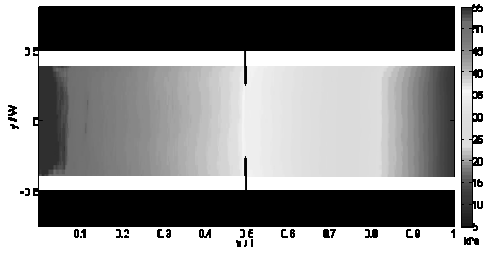

Fig. 3 The pressure map of constricted microchannel acquired with molecule-based pressure sensor at the Reynolds number of 78

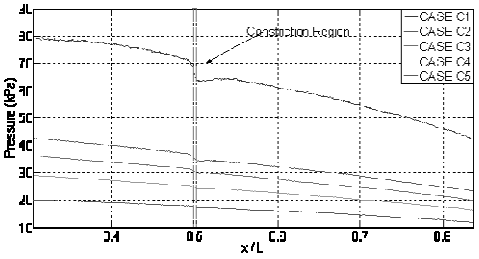

Fig. 4 The pressure distributions near constriction region inside the constricted microchannel

4. Concluding remarks

The flow fields inside straight and constricted PDMS microchannel have been studied with experimental approach utilizing molecule-based pressure sensor technique. The PtTFPP/PDMS pressure sensor has been applied to acquire detailed pressure distribution in the microchannel devices with fine spatial resolution. The pressure distribution acquired with the molecule based pressure sensor show good agreement with the theoretical analysis calculated with 2D Navier-Stokes equations with the 1st order slip boundary condition. The pressure drop around the constriction area inside the microchannel has also been investigated with the molecule-based pressure sensor. The pressure drops identified the recirculation region generated from the constricted structure.

Acknowledgements

The authors would like to thank Prof. T.-M. Liou from Department of Power Mechanical Engineering in the National Tsing Hua University at Taiwan for valuable discussions and suggestions. This work is funded by the National Science Council of Taiwan via NSC100-2221-E-007-107 and NSC99-2628-E-007-027.

References

[1] C.-M. Ho, and Y.-C. Tai, Annu. Rev. Fluid Mech., **30** (1998), pp. 579-612

[2] W. Lee, M. Wong, and Y. Zohar, Journal of MEMS, **11** (2002), pp. 236-244

[3] S.S. Hsieh, H.H. Tsai, C.Y. Lin, C.F. Huang, C.M. Chien, Int. J. Heat Mass Transfer **47** (2004), pp. 3877–3887.

[4] C.Y. Huang, H. Sakaue, J.W. Gregory, J.P. Sullivan, 40th Aerospace Sciences Meeting & Exhibit, AIAA-2002-0256 (2002)

[5] C.Y. Huang, J.W. Gregory, and J.P. Sullivan, Journal of Visualization, **10** (2007), pp. 281-288

[6] C.Y. Huang, J.W. Gregory, and J.P. Sullivan, Journal of MEMS, **16** (2007), pp. 777 - 785

[7] H. Nagai, R. Naraoka, K. Sawada, and K. Asai, AIAA Journal **46** (2008), pp. 215–22

[8] E. B. Arkilic, K. S. Breuer, M. A. Schmit, J. of MEMS, 6 (1997), pp. 167-168

Calibration Method of Molecule Based Pressure Sensor Technique in Microfluidic Measurements

Chih-Yung Huang, Chih-Min Lai, Jia-Syuan Li
Department of Power Mechanical Engineering, National Tsing Hua University, Hsinchu, Taiwan.
cyhuang@pme.nthu.edu.tw

ABSTRACT

This paper presents comprehensive discussion of a calibration method while applying molecule-based pressure sensor at micro scale measurements. The calibration method utilized every pixel on the photo detector as an individual pressure sensor to correct the deviation caused by non-uniform irradiation and shadow due to the geometrical effect, which is apparent at micro scale. The pixel-by-pixel calibration method has been demonstrated in the pressure measurements inside PDMS microchannels.

1. Introduction

Molecule-based pressure sensor technique, also known as pressure-sensitive paint (PSP), was developed for macro scale measurements in aerospace and mechanical engineering applications in the early 80's. Promising results including global pressure profiles as well as detailed pressure distributions have been acquired either in wind tunnel experiments or even during flight tests [1]. This technique uses photo-chemical reaction of luminescence molecules to reveal the pressure data through optical arrangements. Molecule-based pressure sensor technique provides a simple and fast way to conduct non-intrusive experiments and it had been further extended to the micro scale measurements in 2002 [2]. Before molecule-based pressure sensor technique was introduced in the micro scale experiments, the studies of micro scale flow fields are mostly limited in the theoretical analysis and simulations due to the difficulty of embedding sensors inside micro devices. There are not many reports for the experimental approaches, especially for the inner flow fields; and most of the experimental results can only provide discrete data points from the measurements [3-5]. With the introduction of molecule-based pressure sensor technique, several studies at micro scale have been performed and detailed pressure maps have been successfully acquired with resolution as fine as several micrometers in various micro devices such as micronozzles [6] and microchannels [7]. The detailed pressure maps provide valuable information for investigations of the physical phenomena in the flow fields at micro scale. This technique has been proven as one of the powerful tools for experimental investigation and compared with numerical simulations in the MEMS research [8]

2. Method

For micro scale measurements, PDMS microchannel devices are selected to examine the single point and pix-by-pixel calibrations using intensity data acquired inside the devices. The microchannel device is made with PDMS using soft lithography, and the microchannel is 10 mm long, 100 μm wide and 67 μm deep with a rectangular cross section. The measurement region is focused at the area near the channel exit where will experience the most effect from background noise due to light feeding and reflection from connected reservoir and tubing. The detailed experimental setup is shown in Fig. 1.

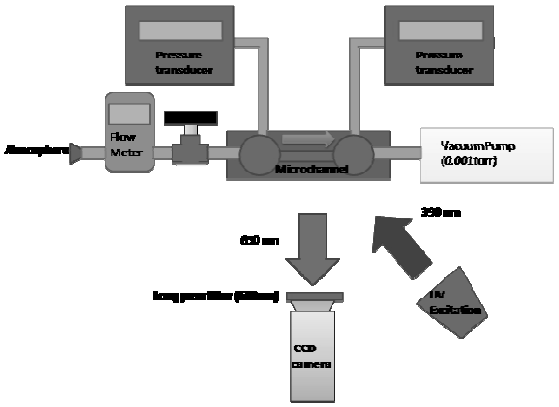

Fig. 1 The experimental setup of molecule-based pressure sensor measurements for microchannel devices

3. Results and Discussion

To examine the pixel-by pixel calibration method, PDMS microchannels were selected as the micro-size environment to perform the pressure measurements with the molecule-based pressure sensor. During the measurement, the single light source, a UV LED array, was used as the excitation light source and positioned at the right. There was one circular reservoir at each end of the inlet and the exit of the microchannel. It has been observed that the luminescence light from the reservoir fed back into the microchannel through the exit during the calibration and measurements. The reflection from the connected tubing also contributed the luminescence as the background noise, and that luminescence intensity did not represent the true physical phenomena in the flow fields. This situation changed the luminescence response of the PSP molecules to pressure at different locations inside the microchannel and the extent of the variation depended on the distance to the reservoir and to the reflection of the tubing. The calibration curves obtained at different locations inside the microchannel in the region from x/L of 0.75 to the exit have been selected and plotted in Fig. 2. It should been noticed that the deviation can be as high as 77% in the pressure data between these calibration curves. Fig. 3 shows the

pressure distribution along the center of the microchannel in the region near the exit. The pressure data were calculated by selecting three calibration equations at x/L equaled to 0.75, 0.87, and 1. Three pressure distributions showed similar trend when calibrated with the single point method but the pressure difference among them was as high as 7 kPa. This phenomenon can cause false information and misinterpretation of the physical behavior during the experiment. To prevent this error, the pixel-by-pixel calibration method was applied to obtain the correct pressure distribution in the microchannel. The pixel-by-pixel corrected pressure distribution is shown in Fig. 3 and the corrected pressure profile is shown in Fig. 4.

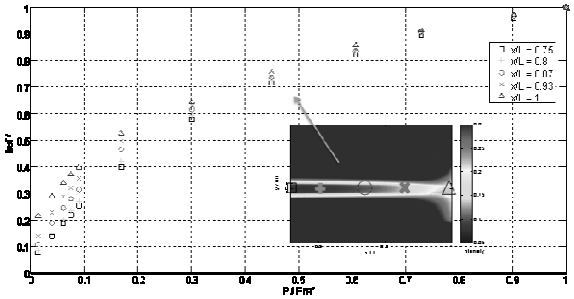

Fig. 2 Calibration curves acquired at different locations x/L from 0.75 to 1 inside the microchannel device

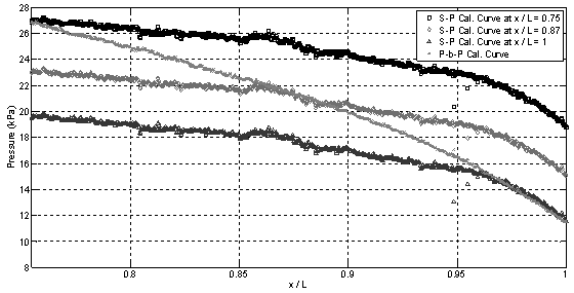

Fig. 3 Pressure distributions inside the microchannel device near exit area with single point calibration and pixel-by-pixel calibration

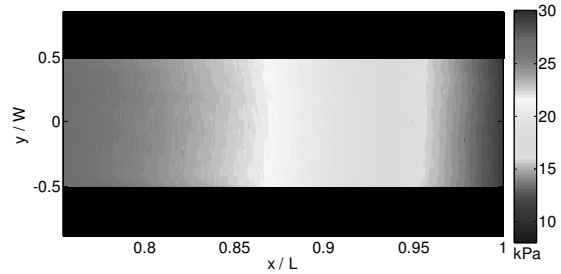

Fig. 4 Pressure profile inside the microchannel near the exit after applying the pixel-by-pixel calibration

4. Concluding remarks

In this work, a new calibration method has been proposed for micro scale measurements using molecule-based pressure sensor. The conventional calibration method with single reference point (equation) can be applied to the macro scale measurements, but not sufficient in correcting the problems arose with the reduced scale in micro scale measurements, such as environment light or shadow from the geometry in a limited space. This situation will greatly change the intensity response in the affected region and the calibration curves at different locations in that area have been observed with great deviation. Up to 77% of the pressure deviation has been observed at the near exit region in the microchannel experiment if the single-point calibration equation is applied. With the help of the pixel-by-pixel calibration, most of the problems aforementioned can be corrected and true pressure distribution near the channel exit can be presented. With the benefit of molecule-based pressure sensors and the pixel-by-pixel calibration method, the pressure profiles inside the micro-sized flow field, and the subsequent physical phenomena, can be acquired with detailed information.

Acknowledgements

The authors would like to thank Prof. T.-M. Liou from the Department of Power Mechanical Engineering in the National Tsing Hua University at Taiwan for valuable discussions and suggestions. This work is funded by the National Science Council of Taiwan via NSC100-2221-E-007-107 and NSC99-2628-E-007-027.

References

[1] T. Liu and J.P. Sullivan, Pressure and Temperature Sensitive Paints, Springer-Verlag (2004).

[2] C.Y. Huang, H. Sakaue, J.W. Gregory, J.P. Sullivan, 40th Aerospace Sciences Meeting & Exhibit, AIAA-2002-0256 (2002)

[3] W. Lee, M. Wong, and Y. Zohar, Journal of Microelectromechanical System, **11** (2002), pp. 236-244

[4] J. Jang and S.T. Wereley, Microfluid Nanofluid **1** (2004) pp. 41–51

[5] S.S. Hsieh, H.H. Tsai, C.Y. Lin, C.F. Huang, C.M. Chien, Int. J. Heat Mass Transfer **47** (2004), pp. 3877–3887.

[6] C.Y. Huang, J.W. Gregory, and J.P. Sullivan, Journal of Visualization, **10** (2007), pp. 281-288

[7] C.Y. Huang, J.W. Gregory, and J.P. Sullivan, Journal of Microelectromechanical Systems, **16** (2007), pp. 777 - 785

[8] H. Nagai, R. Naraoka, K. Sawada, and K. Asai, AIAA Journal **46** (2008), pp. 215–22

Fast Evaluation of An Linear Scale by using A Fizeau Interferometer

WooJae KIM[a], Akihide Kimura[a] , Yuki Shimizu[a] and Wei Gao[a]
A Department of Nanomechanics, Tohoku University, Aramaki Aoba 6-6-01, Aoba-ku, Sendai, Japan, 980-8579
Phone & Fax : +81-22-795-6953, E-mail : wjkim@nano.mech.tohoku.ac.jp

ABSTRACT

A linear scale used in an interferential 2-DOF linear encoder is evaluated by the Fizeau interferometer. Firstly, the Z-directional out-of-flatness e_Z(x,y) of the linear scale is evaluated from the wavefront of the 0th-order diffracted beam reflected from linear scale. The linear scale is then tilted to align the axes of the 1st-order diffracted beams with that of the interferometer so that the X-directional period deviation e_X(x,y)of the linear scale can be evaluated from the wavefronts of the ±1st-order diffracted beams. Finally, the Z-directional out-of-flatness e_Z(x,y) and X-directional period deviation e_X(x,y) were then verified by comparing them with the nonlinear components of the 2-DOF linear encoder using the evaluated linear scale.

1. Introduction

The 2-DOF linear encoder can measure not only displacement along the moving axis (X-axis) but also out-of-straightness. The graduations of the linear scale with a uniform period are read by the optical read so that the actual position of the moving table can be obtained. On the other hand, the measurement accuracies of the 2-DOF linear encoder are mainly determined by the X-directional scale period deviation and the Z-directional out-of-flatness of the linear scale. The period deviation and the out-of-flatness of the linear scale are calibrated from the wavefronts of the 0th-order diffracted beam, the X-directional ±1st-order diffracted beams from the scale, which are measured by a commercial Fizeau interferometer. The evaluation principle and evaluation experiment are reported.

2. Evaluation Method

A Fizeau interferometer is employed to evaluate not only the out-of-flatness but also the period deviations of a linear scale [2]. Let the X-directional period deviations and the Z-directional out-of-flatness of the linear scale be e_X(x,y) and e_Z(x,y), respectively [3]. Fig. 1 shows the evaluation procedure for the Z-directional out-of-flatness e_Z(x,y). The wavefront of the 0th-order diffracted beam from the linear scale is measured by the Fizeau interferometer. The 0th-order phase output I_0(x,y) can be expressed by:

$$I_0(x,y) = 2\pi \cdot \frac{2e_Z(x,y)}{\lambda} \tag{1}$$

where λ represents the wavelength of the light source. The Z-directional out-of-flatness e_Z(x,y) can thus be calculated as follows:

$$e_Z(x,y) = \frac{\lambda}{4\pi} \cdot I_0(x,y) \tag{2}$$

The X-directional period deviation e_X(x,y) of the linear scale causes a phase shift in the wavefront of the X-directional +1st-order diffracted beam as can be seen in fig. 2. Meanwhile, an opposite phase shift is caused in the wavefront of the X-directional -1st-order diffracted beam. The two opposite phase shifts are employed to evaluate e_X(x,y). Fig. 3 shows the measurement of the wavefront in the X-directional +1st-order diffracted beam, which was included not only Z-directional out-of-flatness but also X-directional period deviation in the phase output. As can be seen in the figures, the linear

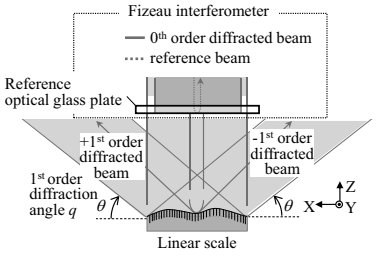

Fig.1 Evaluation of the out-of-flatness.

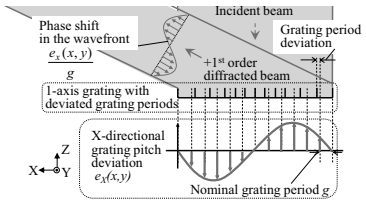

Fig. 2 Influence of the pitch deviation in the wavefront of the 1st-order diffracted beam.

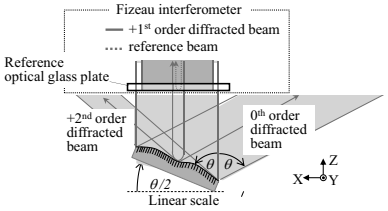

Fig.3 Wavefront of the +1st-order diffracted beam.

scale is inclined to superimpose the X-directional +1st-order diffracted beams on the light beam from the reference optical glass plate of the Fizeau interferometer. The inclination angle is equal to half of the 1st-order diffraction angle. The wavefront of the -1st-order diffracted beam can also be measured by turnning the linear scale on the counter clockwise of $\theta/2$. The X-directional ±1st-order phase outputs from the Fizeau interferometer $I_{X\pm1}$(x,y) can be expressed by:

$$I_{X+1}(x,y) = 2\pi \cdot \frac{e_X(x,y)}{g} + 2\pi \frac{2e_Z(x,y)}{\lambda} \cdot \cos\frac{\theta}{2} \tag{3}$$

$$I_{X-1}(x,y) = -2\pi \cdot \frac{e_X(x,y)}{g} + 2\pi \frac{2e_Z(x,y)}{\lambda} \cdot \cos\frac{\theta}{2} \tag{4}$$

where g and θ represent the nominal pitch of the linear scale and the ±1st-order diffraction angle, respectively. The X-directional period deviation e_X(x,y) can be calculated as:

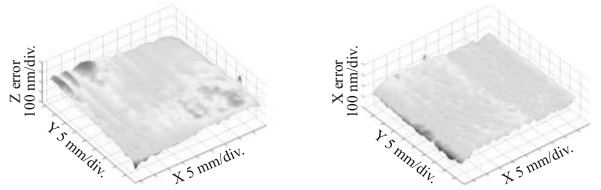

(a) Out-of-flatness (b) Pitch deviation

Fig. 4 Measurement results of the out-of-flatness

$$e_X(x,y)=\frac{g}{4\pi}\left\{I_{X+1}(x,y)-I_{X-1}(x,y)\right\} \quad (5)$$

The influence of the setting error of the inclination angle can be reduced by adjusting the manual tilt stage, on which the grating is mounted, to make the number of the interference fringes of the Fizeau interferometer minimum.

3. Experiments & Results

A Fizeau interferometer using He-Ne laser was used in the experiment. The field of view of the interferometer was 100 mm in diameter. The resolution and accuracy of the Fizeau interferometer in the Z-axis were 0.05 nm and λ/20, respectively. A linear scale, which was fabricated with pitch of 1.67 μm in area of 45 mm x 45 mm, was used as the measurement surface. Fig. 4 shows the measurement result of the out-of-flatness and The period deviation of a linear scale. The peak-to-valley values of the Z-directional out-of-flatness and the X-directional period deviations were 208 nm and 231 nm respectively. The out-of-flatness was mainly determined by that of the grating substrate. The period deviations were mainly caused by the fabrication process of the grating. It took approximately 3 minutes to finish all the measurements.

Fig. 5 shows the experimental setup for evaluation of the measurement errors of the 2-DOF linear encoder, which can measure not only X-directional displacement but also Z-directional out-of-straightness along the X-position of the linear air bearing stage. The laser interferometer (X) and the capacitive sensor (Z) were set to compensate X-directional displacement and Z-directional straightness of the linear air bearing stage with 2-DOF linear encoder. Fig. 6 shows the noise components in the compensated sensor outputs. The corresponding grating errors, which were extracted from the results shown in Fig. 4(a) and Fig. 4(b), are also plotted in the figures for comparison. It can be seen that the grating errors and the encoder errors had high correlations with each other, indicating that the grating errors are the main error sources of the encoder. Other factors influencing the accuracy of the encoder include assembling errors of optical elements in the optical sensor head, tilt error motions of the stage, which caused the differences between the grating errors and encoder errors shown in Fig. 6.

4. Conclusion

The Z-directional out-of-flatness and X-directional period deviation of the linear scale has been analyzed by using Fizeau interferometer in a short evaluation time.

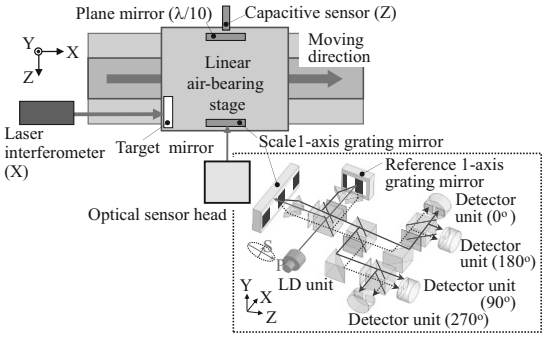

Fig. 5 Experimental setup for evaluation of the measurement errors of the 2-DOF linear encoder.

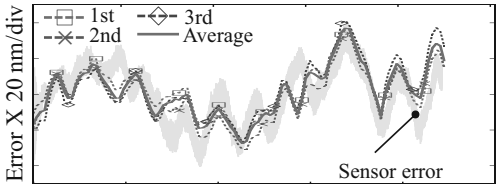

Position X 10 mm/div

(a) Z-axis

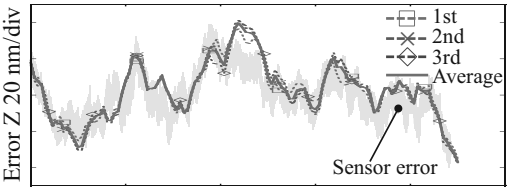

Position X 10 mm/div

(b) X-axis

Fig.6 Comparison of the encoder errors with the grating errors.

The X-and Z-directional error maps of the linear scale with a pitch of 1.67 μm were obtained over an area of 45 mm x 45 mm. The evaluated grating has been employed in the 2-DOF linear encoder. Experimental results have confirmed that the measurement errors of the 2-DOF linear encoder were mainly caused by the corresponding errors of the linear scale.

Acknowledgements

This project was supported by Japan Society for the Promotion and Science (JSPS) and National Natural Science Foundation of China (NSFC) under the Japan-China Scientific Cooperation Program.

References

[1] A. Kimura, W. Gao, Yoshikazu Ari, Zeng Lijiang, Design and construction of a two-degree-of-freedom linear encoder for nanometric measurement of stage position and straightness, Precision Engineering, Vol. 34, No.1(2010), pp.145-155.

[2] Fizeau interferometer Catalogue, Zygo Corporation.

[3] W. GAO, A. Kimura, A fast evaluation method for pitch deviation and out-of-flatness of a planar scale grating, Annals of the CIRP, Vol. 59,No.1(2010), pp.509-508.

Eighth International Conference on Flow Dynamics
November 9 - November 11, 2011

Evaluation of Radiative Properties of Cr_2O_3:Fe_2O_3 Pigment Powder in Solar Spectrum Range using Experimental Diffuse Reflectivity Measurement

Mehdi Baneshi [1], Hiroki Gonome [2], Junnosuke Okajima [1], Shigenao Maruyama [1]

[1] Institute of Fluid Science, Tohoku University, 2-1-1, Katahira, Aoba-ku, Sendai, 980-8577

[2] Dep. of Mech. Systems and Design, Tohoku University, 6-6 Aramaki Aza Aoba, Aoba-ku, Sendai, Miyagi, 980-8579
mehdi.baneshi@pixy.ifs.tohoku.ac.jp

ABSTRACT

A new optimization method in designing pigmented coatings which considers both thermal and aesthetic effects has been introduced by authors in previous works. The spectral radiative properties of pigment powders in solar spectrum range are required to find the optimum design parameters. In this work, an inverse analysis to obtain the spectral scattering and absorption coefficients using experimental reflectivity measurement was conducted. The method was applied to evaluate the radiative properties of Cr_2O_3:Fe_2O_3 black pigment powder. The results show that this pigment powder has good performance for our objective.

1. Introduction

Pigmented coatings with dark visual appearance which can stay cool in sun are desired to paint buildings and cars in warm climates to satisfy simultaneously both aesthetic and thermal demands. To design such these coatings Baneshi et al. [1] proposed a design method by controlling the material, size and concentration of pigment particles in order to control the spectral behavior of paint layer. The share of visible (VIS) and near infrared (NIR) lights in global solar irradiance is about 43% and 52%, respectively. Our proposed pigmented coatings have low visible (VIS) reflectivity to keep the brightness low and have high NIR reflectivity to reduce the unwanted thermal heating. [1].

To find the optimum design, the radiative properties are calculated using Mie theory. However, for some pigment powders the required data for obtaining the radiative properties from Mie theory such as complex index of refraction or size distribution of particles are not available. Thus, the radiative properties cannot be obtained using Mie theory. On the other hand measuring these required data is a time consuming work which needs enough proficiency and special experimental apparatuses. However, what we need to evaluate the spectral behavior of a pigmented coating are reduced scattering coefficient and absorption coefficient. To find these coefficients, an inverse analysis that uses experimental reflectivity measurements has been proposed.

In this work, the Newton-Raphson method usually used for inverse analysis in radiative transfer problems is utilized. For the direct method the radiation element method by ray emission model (REM^2) [2] is used. Finally, the inverse analysis is applied to the experimental reflectivity measurement of chromium-iron oxide (Cr_2O_3:Fe_2O_3) pigmented coatings. Cr_2O_3:Fe_2O_3 pigment powder is a commercial black powder but there is no catalogue data available for the size distribution of particles and the ratio of Cr_2O_3 and Fe_2O_3 in this powder. The spectral absorption and reduced scattering coefficients are obtained for this powder in the solar spectrum range from 0.3 μm to 2.5 μm. The effects of using this powder on VIS and NIR reflectivity are discussed.

2. Experiment

To conduct the inverse calculation in order to obtain the absorption and reduced scattering coefficients two experimental reflectivity measurements are used. Two coating samples with different thicknesses volume fraction of about 5% were made on black and white substrates. The standard black and white papers were introduced by Japan Industrial Standards (JIS). Spiral bar coaters (Elcometer 4360) installed on a motorized film applicator (Elcometer 4330) were used to make the coatings with desired thickness. The spectral reflectance measurement is performed in the wavelength range of 0.3–0.85 μm using UV-VIS spectrometer (Shimadzu UV-2450) and in 0.85–2.5 μm by infrared spectrometer (Shimadzu FTIR-8000).

3. Method of inverse calculation

The unknown parameters required are absorption coefficient (α) and reduced scattering coefficient (σ') defined as follows:

$$\sigma' = \sigma(1-g) \tag{1}$$

where g is asymmetry factor. For the inverse analysis using Newton-Rophson method, the first step is to construct a database for Jacobin matrix which involves the information of how the reflectivity of samples change with control parameters; α and σ'. To make the database the REM^2 code was employed by using a one-dimensional parallel plane model as shown in Fig. 1. The incident angle of direct beam was set according to experimental condition. The specular reflection produced by the difference between the refractive indices at the top boundary is calculated using Fresnel's equation.

The calculation at each wavelength starts with initial guesses for α and σ'. The reflectivities of two samples are calculated using REM^2 code. Then, the calculated and measured reflectivities are compared and the new values of α and σ' for the next iteration are obtained using Newton-Rophson method as follows:

$$\begin{bmatrix}\sigma'\\ \alpha\end{bmatrix}_{n+1}=\begin{bmatrix}\sigma'\\ \alpha\end{bmatrix}_{n}+\begin{bmatrix}\frac{\partial R_1}{\partial \sigma'} & \frac{\partial R_1}{\partial \alpha}\\ \frac{\partial R_2}{\partial \sigma'} & \frac{\partial R_2}{\partial \alpha}\end{bmatrix}^{-1}\begin{bmatrix}\Delta R_1\\ \Delta R_2\end{bmatrix} \quad (2)$$

where R_1 and R_2 are the reflectivities of samples 1 and 2, and Δ shows the difference between calculated and measured reflectivities. This procedure continues until the difference between measure and calculated reflectivities becomes less than desired error.

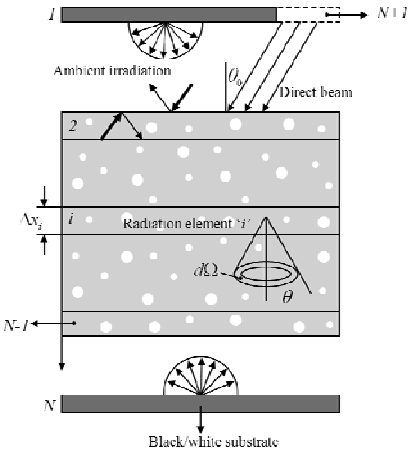

Fig. 1 Analysis model and boundary conditions

4. Results and discussions

Two different coatings with f_v=5% were made on black and white substrates. The measured spectral reflectivities of these two samples and both black and white substrates are shown in Fig. 2. As seen in Fig. 2, the Cr_2O_3:Fe_2O_3 powder can produce a large difference between VIS and NIR reflectivities especially when it is applied on a white substrate. The predicted spectral distribution of reduced scattering and absorption coefficients are shown in Fig. 3. The results have a logical tendency and in agreement with observed behavior in spectral reflectivities. There are two peaks in scattering coefficient at λ=0.7 μm and 1.2 μm. The absorption coefficient is very high at UV region; almost uniform at VIS region and near zero for λ>1.3 μm.

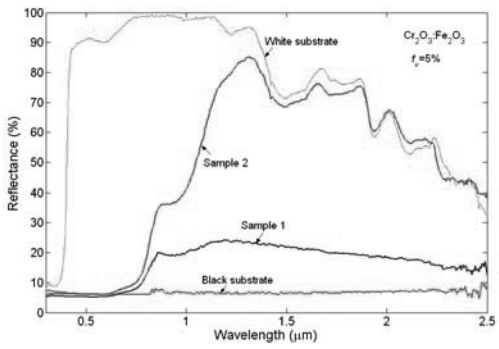

Fig. 2 Spectral reflectivity measurements of two samples and substrates

The properties of two samples are given in Table 1. The sample with black substrate has 19.8% of NIR reflectance and 5.3% of brightness, which shows very dark gray color. For the sample with white substrate the NIR reflectance is about 52.7% and brightness is 6.1% which again represents very dark gray color. It should be noted that this high value of NIR reflectance is due to high NIR reflectance of white substrate in addition to low absorption of Cr_2O_3:Fe_2O_3 pigment powder at this region.

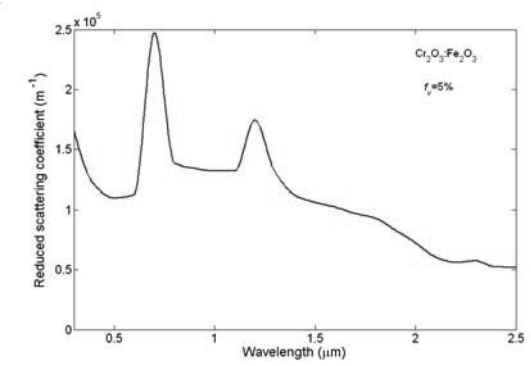

(a) Reduced scattering coefficient

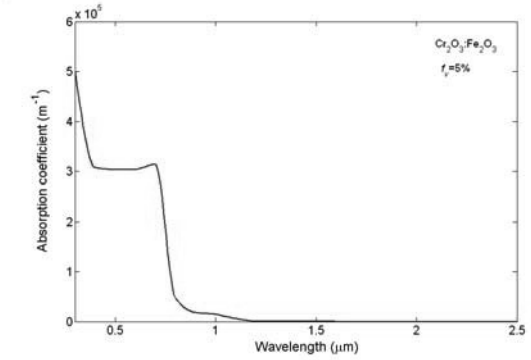

(b) Absorption coefficient

Fig. 3 Results of inverse analysis

Table 1. Properties of two Cr_2O_3:Fe_2O_3 pigmented coating samples with f_v=5%

Subs.	t (μm)	NIR Reflec. (%)	Total Sunlight Reflec. (%)	Brightness Y(%)
Black	8	19.8	12.2	5.3
White	12	52.7	27.5	6.1

5. Concluding remarks

An inverse analysis to find the spectral distribution of scattering and absorption coefficients of a pigmented coating sample was conducted. The Cr_2O_3:Fe_2O_3 powder shows good performance for our objective to have dark coating with high NIR reflectance.

6. References

[1] M. Baneshi, et al., JQSRT, **110** (2009), pp. 192-204.
[2] S. Maruyama, Light energy engineering, (2004), Yokendo , Tokyo.

Eighth International Conference on Flow Dynamics
November 9 - November 11, 2011

Radiation Temperature Measurement of Hayabusa Reentry Capsule from NASA DC-8 Airborne Laboratory

Hideyuki Tanno[1], Akira Yumiyama[2] and Tetsuya Yamada[3]
[1]Japan Aerospace Exploration Agency Kakuda Space Center, Miyagi, JAPAN
[2]Internet Initiative Japan Inc., Tokyo, JAPAN
[3]Japan Aerospace Exploration Agency, Institute of Space and Astronautical Science, Kanagawa, JAPAN
tanno.hideyuki@jaxa.jp

ABSTRACT

This report described about optical measurement campaign of Hayabusa capsule reentry with NASA DC-8 Airborne laboratory. JAXA original 4-wavelength spectroscopy was developed and applied on the spectroscopic measurement when Hayabusa reentry to the atmosphere at super-orbital speed. Although the spectroscopy system has several technical issues, history of radiation temperature of the capsule at reentry was successfully obtained. Analyzing scheme and measurement results were discussed.

1. Introduction

Hayabusa SRC (Sample Return Capsule) was successfully re-entered into atmosphere at 13:51 on June 13, 2010(UT) after the return flight from the asteroid ITOKAWA [1]. The reentry speed of SRC was approximately 12km/s at an altitude of 200 km and its estimated peak heat flux was 14MW/m^2. In order to observe Hayabusa super-orbital reentry, a flight observation campaign was conducted with the NASA DC-8 flight observatory. The campaign was international cooperation including the U.S., Germany, the Netherland, Australia and Japan. In this airborne measurement campaign, JAXA tried to measure radiation temperature of the SRC surface or its shock layer with a flight-onboard spectroscopy system, which can measure radiation intensity of four-different wavelength. Since the measurement data obtained in real flight was quite rare, it is important to verify and to validate numerical codes for the prediction of surface condition. In addition, to provide knowledge to possible future missions which will adopt similar TPS material, the real flight data is also quite important.

2. JAXA 4-camera spectroscope

A general view and a schematic diagram of the JAXA 4-wavelength spectroscopy system are shown in Fig. 1. To reduce manufacturing time and cost, the system had a quite simple configuration with the following components; (1) Telephoto lens (BORG 45ED f=300mm) and reducer lens (Celestron f/6.3), (2) Band path filter (Semrock laser line filter - MaxLine), (3) High sensitivity CCD video camera (Watec WAT-120N+) and (4) Video recorder (SONY GV-D800). Since the system was designed to measure intensity of four different wavelengths, the system had four-channels of above configuration for each wavelength.

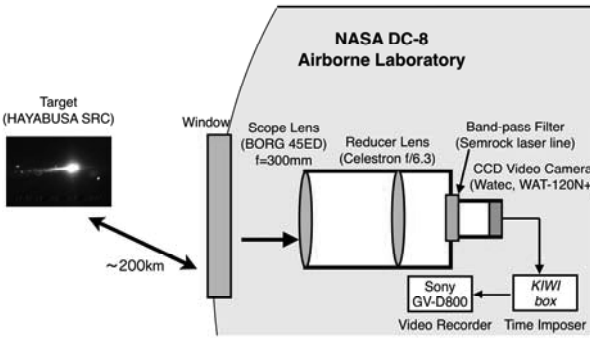

Fig.1 Top: the four-camera spectroscope installed on the flight observatory NASA-DC8. Bottom: The block diagram of observation system (one channel)

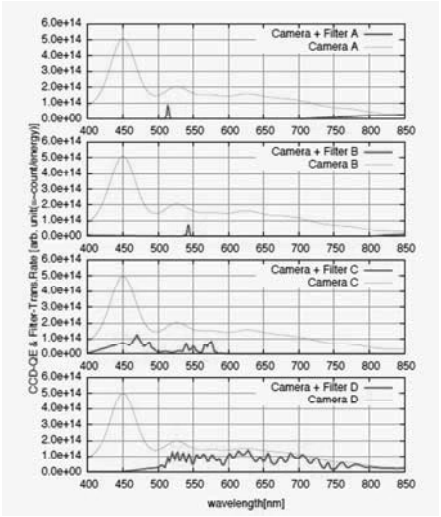

Fig.2 Wavelength characteristics of the 4-wavelength spectroscopy (A: 514nm, B:543nm, C:785nm and D:1064nm). Red thick lines showed the characteristics of the whole system. Green thin lines showed the characteristics of the CCD with lens of the system.

When Hayabusa reentry, the predicted distance between SRC and the mother spacecraft was 1.8km. Namely, the view angle of the SRC and the mother spacecraft will be about 1-degree. While the distance between Hayabusa and the airborne observatory was predicted to be approximately 200km. Hence high-power lens will be required for high-resolution observation. However, high-magnification may easily receive disturbances caused from back ground mechanical vibration on the airplane. A trade-off study between resolution and the disturbances decided to adopt a telephoto lens of focal-length 300mm and of view-angle 3-degree.

The wavelength of filters was selected from the preflight numerical prediction. In the numerical

prediction, we assumed that the radiation from the capsule was similar to the black body radiation. Since the estimated surface temperature was at most 4000K, we selected wavelength 514, 543, 785, and 1064 nm. The band path filters were laser-line band path filters, which filters have quite narrow-bandwidth of FWHM 2-4 nm. As shown in the Fig.2 the whole wavelength characteristics of each filter with CCD camera became worse as the filtering wavelength increase, these characteristics were incorporated in the data reduction procedure.

3. Analysis of observed Results

With the four-wavelength spectroscopy, each of four video images was recorded on four sets of videotapes. The images of Hayabusa reentry were recorded for 50sec (about 1500 frames), which images were converted to BMP format on PC. The recorded GPS time stamps provided through KIWI box were used as the reference time for time correction of each video tape images. Since these images were recorded at different exposure timing, time-gap compensation between each image was necessary.

For the data reduction procedure, we build a model of the optical characteristics for the spectroscopy system. The relation with the output $N(i,j)$ of intensity I_λ of the light which enters into an observation system, and CCD of a certain pixel (i, j)

$$N_k(i,j) = K \int I_\lambda(i,j)\tau(\lambda)f_k(\lambda)q(\lambda)d\lambda \qquad (1)$$

I_λ[J .s^{-1} .m^{-2} .sr^{-1} .nm^{-1}]:Intensity
$\tau(\lambda)$: Transmittance of lens
$f_k(\lambda)$: Transmittance of optical filter k
q(λ)[count .J^{-1}]: quantum efficiency of CCD

where, K [s .m^2 .sr^1] is a coefficient of cameras A-D, and it will be theoretically cancelled-out because the coefficient should be same for each camera. If we assume the spectrum of radiation is a function of temperature (assumed to be black body radiation), intensity of radiation G(T) recorded with the camera k at temperature T is shown as follows.

$$G_k(T) = \int I(T,\lambda)\tau(\lambda)f_k(\lambda)q(\lambda)d\lambda \qquad (2)$$

where, I(T,λ) is the normalized function and it shows relative intensity of radiation with T and λ.

Fig.3 showed intensities of each camera A-D, which intensities were calculated with Eq.(2) from T=1000 to 8000K. It should be noted that the equation cannot be solved because radiation model I(T,λ) is normalized function. Radiation temperature will be obtained by the inverse function of Eq.(2)

$$T_k = g_k(\alpha H_k) \qquad (3)$$

If intensity H_k and arbitrary coefficient α are given, radiation temperature T_A, T_B, T_C and T_D will be calculated. The radiation temperature will be determined when standard deviation of each temperature became minimum value. In the Fig.3, examples of radiation temperature determination procedure were plotted. For instance, when intensity of each camera and α are given like the value shown in the figure, the mean temperature can be determined to 4800K with standard deviation (σ) of 162. If α was varied from 10^{-6} to 100,

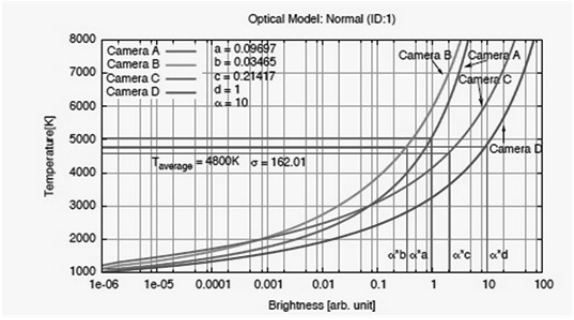

Fig.3 Relationship of radiation temperature and intensity of each four camera .

σ became minimum (σ=0) at α=3.6, and radiation temperature was determined to 4000K.

In the Fig.4, measured temperature of the Hayabusa reentry was shown as crosses and the smoothed curve was shown as green thick line. In addition, a result of the flight environment computation was also overlapped (radiation equilibrium temperature) as a thick line, which peak was 4ms advanced than the measurement. It should be noted that the measured results reasonably agreed with the computation although it was approximately 10% less than the computation. In our arc-tunnel experiments, radiation temperature was approximately 10% lower than those of radiation equilibrium temperature. The Fig.4 may show same tendency in the real-flight measurement.

4. Summary

Radiation temperature measurement of Hayabusa reentry capsule was performed with the JAXA 4-wavelentgh spectroscopy system. The measurement was one of the Hayabusa reentry observation campaign

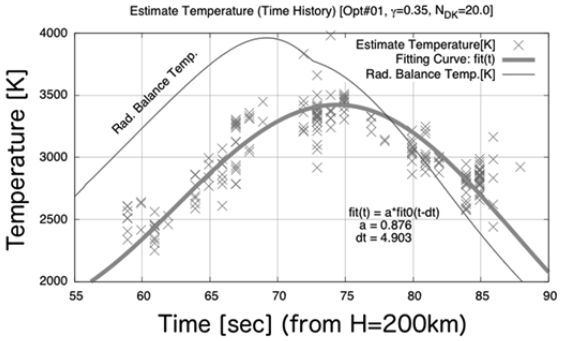

Fig.4 Radiation temperature extracted from the recorded image.

from the NASA flight observatory DC-8. Radiation temperature history was successfully obtained, which history agreed reasonably with the computation. Although the peak temperature was 10% lower than those of the computations, the tendency was similar to the preflight arc-tunnel test.

References

[1] T.Yamada, Y.Inatani, N.Ishii, K.Hirai, S.Morita, AIAA Paper No.2011-3322, 2011

Eighth International Conference on Flow Dynamics
November 9 - November 11, 2011

Development of Temperature Measurement Sensor using Thermographic Phosphor Coating

Chayut Nuntadusit, Makatar Wae-hayee
Energy Technology Research Center and Department of Mechanical Engineering, Faculty of Engineering,
Prince of Songkla University, Hat Yai, Songkhla 90112, Thailand
chayut@me.psu.ac.th

ABSTRACT

The temperature-dependent characteristics of thermographic phosphor YVO_4:Eu, ZnS:Ag and La_2O_2S:Eu were investigated for developing temperature coating sensor. The phosphor film was continuously excited by ultraviolet lamp. The emitting fluorescence from phosphor film was introduced through bandwidth filter and lens to monochromic CCD camera for measuring intensity distribution. By repeating the temperature calibrations, the empirical relationships for temperature prediction for each phosphor film were developed. The phosphor film ZnS:Ag was applied to measure temperature distribution on surface impinged by a hot air jet.

1. Introduction

Various temperature measurement methods have been developed: the contact measuring method by a thermocouple, the non-contact measuring method by an infrared radiation thermometer and so on. However, these methods are easily affected by the conditions of the measuring parts and surrounding environment. Especially, it is difficult to measure surface temperature on a rotating part like turbine blade in hostile environment. Thermographic phosphor (TP) method has been studied and developed as an indirect and non-contacting measuring method [1, 2]. This method is optical technique of measurement by using the temperature-dependence of fluorescence emitted from excited phosphors. It has many advantages over conventional methods. Unlike thermocouple, it is absence of lead wires and allows to measure at high spatial and temporal resolution at fast response time. In addition, it is not easily affected by radiation variation on measurement surface and surrounding environment like as infrared radiation thermometer. Moreover, the measurement principle is relatively simple, and it is easy to apply. However, the temperature-dependent characteristics of phosphor should be evaluated before using for temperature measurement.

2. Experimental Apparatus and Method

In this study, commercial phosphor powder YVO_4:Eu, ZnS:Ag and La_2O_2S:Eu (Phosphor Technology Co.) were used. The phosphor films were prepared by mixing phosphor powder with Cerama-bind No.643-1 (Aremco Co.), and it were painted by spaying on a surface using airbrush. We selected this method because it was practical and easy for preparing uniform coating on a large surface. In this study, the phosphor film was coated on the test piece which made of stainless with 2 mm in thickness.

To investigate the emission spectrum from phosphor film, the phosphor film was excited by UV lamp which has a maximum peak at 254 nm. The fluorescence emission was measured at arbitrary point on phosphor film with CCD based spectrometer USB4000 (Ocean Optics Co.) through a fiber optic.

Fig. 1 shows the schematic diagram of experimental apparatus. The test piece with phosphor film coating is attached on the temperature controllable ceramic heater plate. In this experiment, the phosphor film was continuously excited by two of 10W ultraviolet lamps which have a maximum emission peak at 254 nm. The emission fluorescence from phosphor film was then passed through bandwidth filter to cut unnecessary emissive wavelength and then condensed with a lens to monochromic CCD camera. The CCD camera was very sensitive to light (>0.2 lux) with resolution of 768x494 pixels. The signal from the camera was transmitted through RS-170 video output and then was digitized to 8 bits digital image using a commercial image grabber board. To evaluate the temperature-dependent characteristics of phosphor films, the fluorescence intensity variation was investigated with increasing the temperature on the test piece. For calibration measurement, the thermocouples type K was attached on the surface of test piece, and the temperature was monitored using programmable data acquisition system.

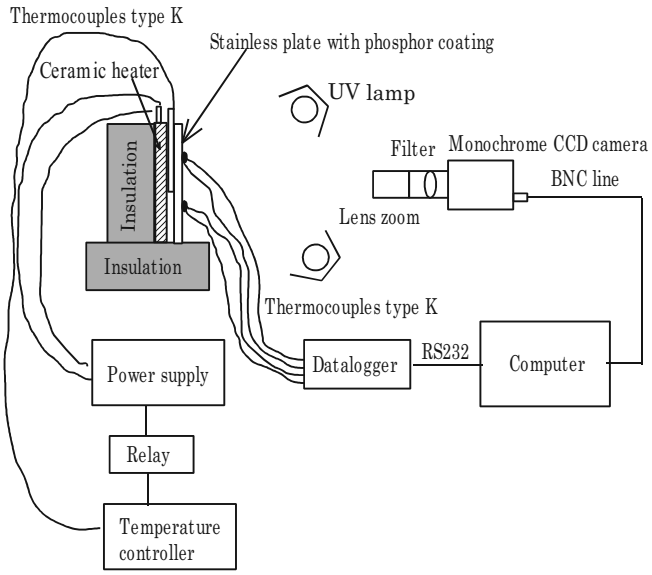

Fig. 1 Schematic of experimental apparatus

3. Results and Discussion

The red emission spectrum has maximum intensity, and its wavelength of sharp peak was about 624 nm and 619 nm for phosphor film La2O2S:Eu and YVO4:Eu,

respectively. For phosphor film ZnS:Ag, the maximum intensity is obtained around the wavelength of 450 nm (blue emission). Table 1 shows the characteristics of bandpass filter used in temperature calibration and measurement for each phosphor film.

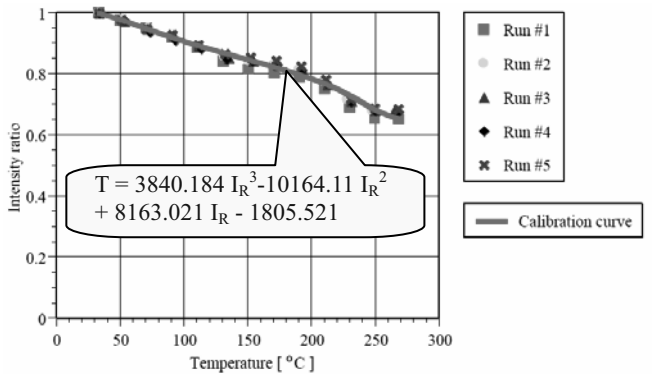

(a) For phosphor film La_2O_2S:Eu

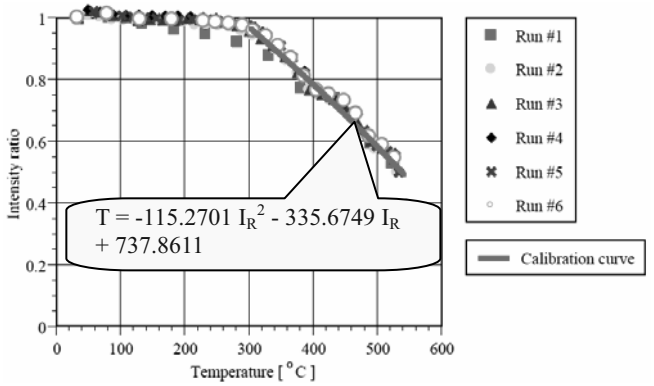

(b) For phosphor film YVO_4:Eu

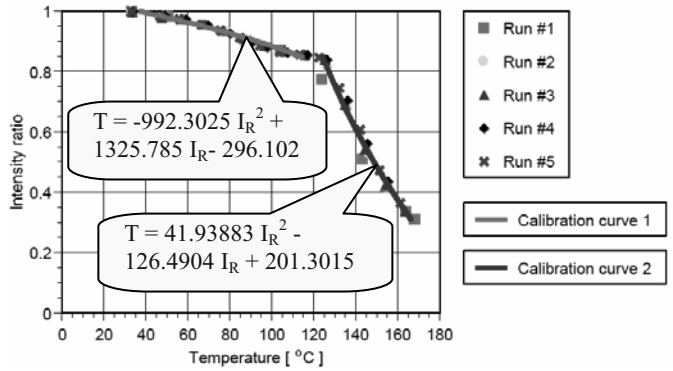

(c) For phosphor film ZnS:Ag

Fig. 2 Variation of relative fluorescence intensity at different temperature

Table 1. Characteristics of bandpass filter

Bandwidth filter for phosphor	Central Wavelength (CWL)	Full Width-Half Maximum (FWHM)
La_2O_2S:Eu	600 nm	80 nm
YVO_4:Eu	620 nm	10 nm
ZnS:Ag	450 nm	10 nm

Fig. 2 shows the variation of relative intensity ratio at different temperature for each phosphor film. The relative ration was calculated by that the intensity of each temperature dividing by referent intensity at 33°C (room temperature). In order to ensure the repeatability, the experiment was repeated at least 5 times. The intensity for each point of temperature was an average intensity of 100x100 pixels selected from the central region of test piece. Employing the regression analysis, the variations of temperature-dependent relative intensity were fitted to empirical relationships as indicated in each graph in Fig. 3. The solid lines which appear in each graph are plots of segmented empirical relationships. The maximum percentage errors between temperature measurement with thermocouples and the temperature calculated using the obtained empirical equation were approximately within 10% for all phosphor films.

Fig. 3 shows the example of temperature measurement on the surface with hot air jet impingement. The phosphor film ZnS:Ag was coated on the rear side of jet impingement surface.

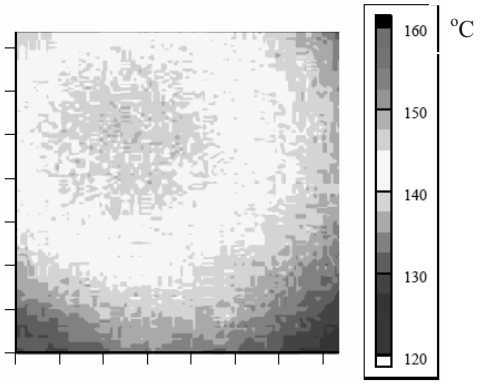

Fig. 3 Temperature distribution on rear side of surface with hot air jet impingement using phosphor film ZnS:Ag (T_j=240°C)

4. Concluding remarks

In this study, the temperature-dependent characteristics of some thermoghaphic phosphors were investigated, and the empirical relationships between relative intensity and temperature were developed for temperature measurement on hot air jet impinged surface. However, this study is still in early stages. It needs more experiments to verify the accuracy of this technique.

Acknowledgements

This study was supported by the fund of National Research Council of Thailand.

References

[1] S.W. Alison and G.T. Gilles, Rev. Sci. Instrum., **68** (1997), pp. 2615-2647.

[2] D.M. Cunningham, S.W. Alison and D.B. Smith, Proceeding of the 39th International Instrumentation Symposium, Albuquerque, USA, (1993), pp.561-567.

Eighth International Conference on Flow Dynamics
November 9 - November 11, 2011

Insight into Heat Conduction from the Thermomass Dynamics

Bing-Yang Cao, Yuan Dong, Zeng-Yuan Guo
Key Laboratory for Thermal Science and Power Engineering of Ministry of Education,
Department of Engineering Mechanics, Tsinghua University, Beijing 100084, P. R. China
caoby@tsinghua.edu.cn

ABSTRACT

We show that diffusive heat conduction in media can be characterized by the thermomass, equivalent mass of thermal energy defined by the Einstein's mass-energy relation, dynamics through the first principle. A general heat conduction law, including driving force, inertia and resistance, is derived from both the macroscopic conservation equations and the microscopic Boltzmann transport equation. It shows that the physical essence of Fourier's law of heat conduction is a balance between the driving force and the resistance, and that the non-Fourier heat conductions are caused by the inertia effects in space or in time.

1. Introduction

Heat conduction in media is generally characterized by the famous Fourier's law, which was proposed by Fourier at as early as 1822. Though Fourier's law of heat conduction is just an empirical relationship, it has been verified in numerous engineering designs and has been widely applied. However for transient heat conduction, Fourier's law leads to the nonphysical conclusion that the heat propagation speed is infinite since the heat conduction equation based on Fourier's law is parabolic. This physical drawback has attracted many attempts to improve Fourier's model. Cattaneo[1] and Vernotte[2] developed a new heat conduction model, often called the CV equation, to replace Fourier's law. The CV equation is hyperbolic due to the additional term including the derivative of the heat flux with respect to time, which makes the heat propagation speed finite. Later, more general heat conduction equations, similar to the CV equation, were also developed.

In recent years, the applicability of Fourier's heat conduction law has been questioned even for steady state conditions. Lepri et al. (Lepri et al., 1997) numerically studied the heat transport in a nonlinear one-dimensional harmonic-vibrator chain and found that its thermal conductivity is approximately proportional to the square root of the particle number (chain length), which indicates the breakdown of Fourier's law. Such non-Fourier phenomena were attributed to the effect of low dimension of the materials by Livi and Lepri. [3,4] In the stead state cases, the obtained thermal conductivity was based on Fourier's law, that is, equal to the ratio of the heat flux to the temperature gradient. Hence, this method to estimate the thermal conductivity is inappropriate when Fourier's law breaks down.

Recently, Prof. Guo et al. [Refs. 5-8] proposed the thermomass theory to characterize heat conductions. The basic concept introduced in the thermomass theory is called thermomass, which is defined as the equivalent mass of thermal energy according to the Einstein's mass-energy relation. A general heat conduction law has been proposed based on the thermomass concept. Heat conduction mechanisms are discussed based on the thermomass dynamics in this paper.

2. Thermomass theory

In the thermomass theory, the thermal energy in media has an equivalent mass defined by the Einstein's mass-energy equivalence relation

$$M_h = \frac{E_D}{c^2}. \tag{1}$$

The thermal vibration energy is assumed to be E_D, c is the speed of light in vacuum. The density of the thermomass contained in the media is $\rho C_v T/c^2$. The thermomass density has a unit of kg·m^{-3}. The drift velocity of the thermomass u_h is defined as

$$\boldsymbol{u}_h = \frac{\boldsymbol{q}}{\rho C_V T}. \tag{2}$$

q is the heat flux. The thermomass pressure is related to the energy by the state equation of a phonon gas as

$$p_h = \gamma \rho_h C_V T = \frac{\gamma \rho \left(C_V T\right)^2}{c^2}. \tag{3}$$

In the thermomass theory, Einstein's mass-energy relation is just used to determine the equivalent mass of a phonon gas, while Newton/fluid mechanics is used to investigate the motion of the phonon gas, since the drift velocity of a phonon gas is normally much less than the speed of light. We have

$$\mathbf{F} = \frac{d\mathbf{p}_h}{dt} = m_h \frac{d}{dt}(u_h). \tag{4}$$

3. Thermomass dynamics and general heat conduction law

(1) Conservation equations for thermomass

For heat transport in a solid without an internal heat source, the equivalent mass of the phonon gas remains constant during the motion of the phonon gas. The continuity equation is

$$\frac{\partial \rho_h}{\partial t} + div\left(\rho_h U_h\right) = 0, \tag{5}$$

The driving force for heat transport is the pressure gradient. The momentum variation in the phonon gas results in a change of the inertia. In addition, a resistance must exist because of the non-linearity of the lattice vibrations and defects in the solid. The resistance is assumed to be linearly related to the velocity

$$\boldsymbol{f}_{\mathrm{h}} = -\beta \boldsymbol{u}_{\mathrm{h}} = -\frac{2\gamma C_V \left(\rho C_V T\right)^2}{\kappa c^2} \boldsymbol{u}_{\mathrm{h}}, \quad (6)$$

Thus, the momentum conservation equation of motion for the phonon gas can be written as in fluid mechanics

$$\rho_h \frac{dU_h}{dt} + \nabla P_h + f_h = 0, \quad (7)$$

Since the motion equation of the thermomass is based on the first principle, it is just a general heat conduction equation. Substituting Eqs. (5) into Eq. (6), we can get the equation for one-dimensional heat conduction in dielectrics as follows:

$$\tau_{\mathrm{TM}} \frac{\partial q}{\partial t} - l\rho C \frac{\partial T}{\partial t} + l \frac{\partial q}{\partial x} - bk \frac{\partial T}{\partial x} + k \frac{\partial T}{\partial x} + q = 0, \quad (8)$$

Here $\tau_{\mathrm{TM}} = k / 2\gamma\rho C^2 T$, $l = qk / 2\gamma C\left(\rho C T\right)^2 = u_{\mathrm{h}} \tau_{\mathrm{TM}}$, and $b = q^2 / 2\gamma\rho^2 C^3 T^3$.

(2) Boltzmann transport equation for thermomass

The phonon Boltzmann equation focuses on the distribution function of phonons to describe its deviation by operators as

$$\left(\frac{\partial}{\partial t} + \boldsymbol{v}^s \cdot \nabla\right) f_D^s = \frac{f_E^s - f_D^s}{\tau_R}, \quad (9)$$

where s is the index of phonon branches, f_{E} is the Planck distribution, f_{D} is the displaced Planck distribution, τ_{R} and is the relaxation time.

In the transport theory for gases, multiplying the Boltzmann equation by the momentum of molecules mv gives the momentum conservation equation. Multiplying Eq. (9) by $\hbar\omega$ and $\hbar\omega v_{\mathrm{i}}$ respectively and integrating it in k space yields

$$\frac{\partial \int_k f_D^s \hbar\omega}{\partial t} + \int_k \boldsymbol{v}^s \cdot \nabla f_D^s \hbar\omega = \frac{\int_k \left(f_E^s - f_D^s\right)\hbar\omega}{\tau_R}, \quad (10a)$$

$$\frac{\partial \int_k f_D^s \hbar\omega v_i}{\partial t} + \int_k \boldsymbol{v}^s \cdot \nabla f_D^s \hbar\omega v_i = \frac{\int_k \left(f_E^s - f_D^s\right)\hbar\omega v_i}{\tau_R}, \quad (10b)$$

With a Taylor expansion of f_{D} around equilibrium up to second order, we can get the governing equation of heat conduction from the Boltzmann equation as

$$\frac{\partial q_i}{\partial t} + \frac{15}{16}\nabla_j \frac{q_i q_j}{E} + \frac{1}{3}\nabla_j \int_k f_E^s \hbar\omega \left(v^s\right)^2 = -\frac{q_i}{\tau_R}, \quad (11)$$

The transport equation could be compared with the general heat conduction obtained by the conservation equations.

(3) General heat conduction law

I. Fourier's law: If the first four terms on the left-hand side of Eq. (8) are neglected, the general heat conduction law will degenerate to Fourier's law. When the inertial force is negligible, the resistant force is proportional to the velocity of the phonon gas. Therefore, the physical essence of Fourier's law of heat conduction is the motion of a phonon gas when its driving force (or pressure gradient) is in equilibrium with its resistant force. When any of the four inertial terms are taken into account, the heat transport will deviate from Fourier's law, say non-Fourier heat conduction takes place. Essentially, the non-Fourier heat conduction arises from the inertial effects of the thermomass.

II. Thermal wave model: If the second to fourth inertial terms on the left-hand side of Eq. (8) have been neglected, we get

$$\tau_{\mathrm{TM}} \frac{\partial q}{\partial t} + k \frac{\partial T}{\partial x} + q = 0, \quad (12)$$

which possesses a similar appearance to the CV model. It is worth noting that the physical meanings of their characteristic times are intrinsically different. The characteristic time τ_{CV} in the CV model is the relaxation time as the energy carriers approaching the thermodynamic equilibrium. The characteristic time τ_{TM} in the thermomass model, on the other hand, describes a lagging response, in time, between the heat flux (the drift velocity of the phonon gas) and the temperature gradient (the driving force of the phonon gas). Hence, their values and predicted wave propagation velocities are different.

4. Concluding remarks

Based on the thermomass theory, diffusive heat conduction in media can be characterized by the thermomass dynamics through the first principle. From both the macroscopic conservation equations and the microscopic Boltzmann transport equation, we can derive a general heat conduction law, including driving force, inertia and resistance. It shows that the physical essence of Fourier's law of heat conduction is a balance between the driving force and the resistance, and that the non-Fourier heat conductions are caused by the inertia effects in space or in time.

Acknowledgement

This work is financially supported by National Natural Science Foundation of China (No. 51076080, 51136001) and Tsinghua University Initiative Scientific Research Program.

References

[1] C. Cattaneo, Atti. Sem. Mat. Fis. Univ. Modena, **3**(1948), pp. 3.
[2] P. Vernotte, C. R. Hebd. Seances Acad. Sci., **246**(1958), pp. 3154.
[3] S. Lepri, R. Livi and A. Politi, Phys. Rev. Lett., **78**(1997), pp. 1896.
[4] R. Livi and S. Lepri, Nature, **421**(2001), pp. 327.
[5] Z.Y. Guo, B.Y. Cao, H.Y. Zhu, and Q.G. Zhang, Acta Physica Sinica, **56**(2007), pp. 3306.
[6] Z.Y. Guo, X.G. Liang and B.Y. Cao, Proceedings of 13th International Heat Transfer Conference, Sydney, Australia, 2006.
[7] B.Y. Cao and Z.Y. Guo. J. Appl. Phys. **102**(2007), pp. 053503.
[8] Y. Dong, B.Y. Cao and Z.Y. Guo, J. Appl. Phys. (DOI: 10.1063/1.3634113).

Eighth International Conference on Flow Dynamics
November 9 - November 11, 2011

Heat and Fluid Flow in Solvothermal Autoclave for Single-Crystal Growth Process

Yoshio Masuda[1], Akira Suzuki[1], Tohru Ishiguro[2] and Chiaki Yokoyama[2]
[1]AIST, 4-2-1, Nigatake, Miyagino-ku, Sendai, 983-8551, Japan
[2] IMRAM, Tohoku Univ., 2-1-1, Kataira, Aoba-ku, Sendai, 980-8577, Japan
y-masuda@aist.go.jp

ABSTRACT

We report and discuss the experiment and numerical simulation of heat transfer by natural convection inside the autoclave for the solvothermal growth of GaN bulk crystal. The inner diameter and height of the autoclave are ϕ 20 and 335 mm, receptivity. When the bottom heater is removed and the space between upper and lower heaters becomes wider, the growth rate is increased. From the axisymmetric numerical simulation, a rising flow from the center hole of the baffle cause such fast grow rate because the rising fluid is GaN-rich and it reaches the GaN seed crystal soon.

1. Introduction

The GaN bulk single crystal is expected to be suitable for application as a substrate in high-quantum-efficiency light-emitting diodes and high-frequency/high-power electronic devices. The solvothermal crystal growth process is one of the methods used for growing GaN single crystals. In this method, the autoclave is filled with supercritical ammonia. A baffle is used to divide the inner autoclave into two zones—an upper zone and a lower zone. The two zones are heated independently, and the heater is controlled to maintain the lower zone at a higher temperature than the upper zone. In view of the variation in the solubility, the raw material (polycrystal) is dissolved in the lower zone and the GaN crystal is grown on a seed crystal in the upper zone. In this paper, we report and discuss the experiment and numerical simulation of heat transfer by natural convection inside the autoclave for the epitaxial growth of GaN bulk crystal.

2. Experimental Results

The experimental autoclave and the heater are shown in Fig.1. The inner diameter is ϕ 20 mm and inner height is 335 mm. The upper and the lower parts are divided by a baffle. The upper zone is a crystal growth zone and the lower zone is a raw material zone. The pressure of ammonia sets 140 MPa. We have employed NH_4Cl as an acidic mineralizer. For further details, refer to Ref. [1]. We have to make the bottom-heater temperature higher than the top-heater one because the solution of raw material efficiently moves toward the crystal growth zone in order to generate a strong natural convection.

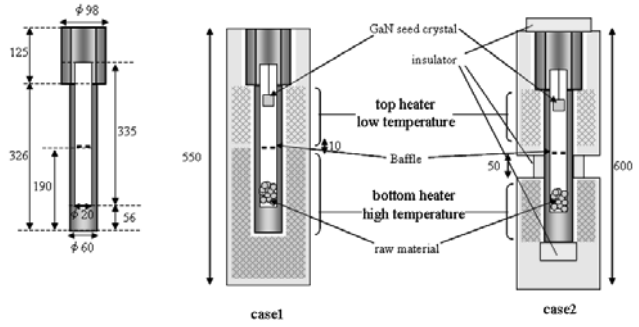

Fig.1 Experimental autoclave and two cases of heater arrangement

Thus we set up the top temperature and bottom one are 450 °C and 550 °C, receptivity.

Two cases of heater arrangement are employed to growth GaN crystal. In case1, the autoclave is inserted to the sealed heater. Since the gap of the upper heater and the lower heater is only 10 mm, a sudden temperature change is observed by the height direction near a baffle plate. In case2, the bottom heater is removed and the space between upper and lower heaters becomes wider. In order to reduce heat loss, heat insulators are installed at the top, bottom and the space between the heaters.

The grown GaN crystal and the growth time and growth rate are shown in Table 1. In both cases, epitaxial growth on the GaN seed crystal is possible in the autoclave and the heater in Fig.1. However, we observed the difference of the GaN growth rate between two cases. The growth rate in case1 and case2 are 0.29 and 0.50 μm/day, receptivity. Furthermore, it is found that a long time growth is possible in case2. We measured the inner temperature in the autoclave and found that the temperature difference of case2 between the raw material zone and crystal growth zone become smaller than the difference of case1. In general, we can consider that the growth rate is larger when the difference of temperature (solubility) is large. However, the experimental result does not agree. Therefore, it is necessary to calculate heat and fluid flow in the autoclave.

Table 1 Cross-sectional SEM images and the GaN growth time and growth rate

	case1	case2
SEM	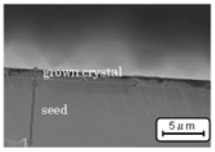	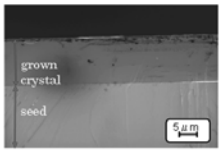
growth time	96 h	720 h
growth rate	0.29 μm/day	0.50 μm/day

3. Numerical Simulation

Fig. 2 shows the schematic diagram of an autoclave for solvothermal crystal growth and the physical model

of numerical simulation. In the present simulation, the system is assumed to be axisymmetric, and the raw material and seed crystal are neglected. The boundary conditions of case1 and case2 are shown in Fig.2. The autoclave and baffle are assumed to be made of Inconel and platinum, respectively. The temperature and pressure of ammonia are assumed to be 450 C° and 140 MPa, respectively. The thermal properties of ammonia are obtained from VMGThermo as the thermophysical property calculator. According to our empirical knowledge, a small interspace is required between the baffle and the surrounding (Inconel) wall. The interspace is 2 mm and the hole of the baffle center is ϕ 4 mm. The open-space ratio of the baffle is approximately 40%. SC/Tetra produced by SOFTWARE CRADLE Co., Ltd. is used as computational fluid dynamics software. We solve mass conservation equations, momentum conservation equations, energy conservation equations, and equations of turbulent energy and turbulent dissipation rate (MP k-ε equations). For further details, refer to Ref. [2-4].

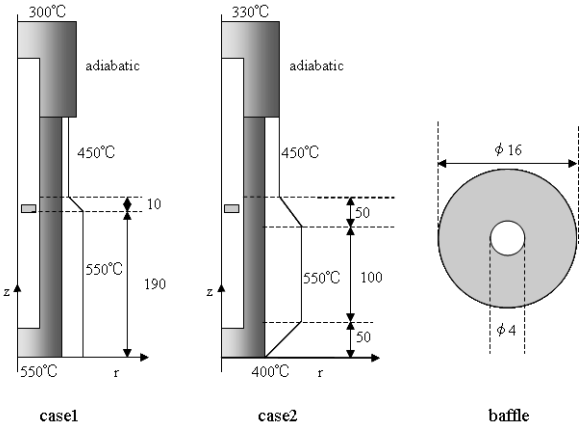

Fig.2 Schematic diagram of a solvothermal autoclave and baffle in the present calculation

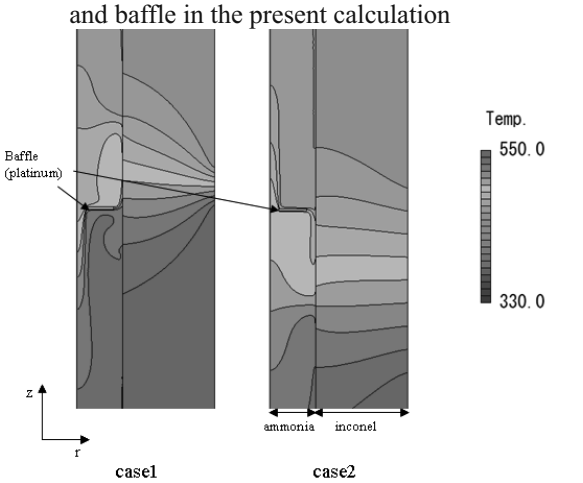

Fig.3 Temperature fields near baffle in case 1 and 2

Fig. 3 shows the temperature distributions that include the part of a surrounding wall and the baffle in both cases. From our further researches [2-4], we obtain a stable solution for the case wherein a rising flow exists in the space between the baffle and the surrounding wall. In case1, such flow pattern can be observed. On the contrary, a strong rising flow exists in the center hole in case2. In solvothermal GaN single crystal growth process, small and micro GaN crystal can be observed at the surrounding wall and such microcrystal is wasted for GaN bulk single crystal growth on the seed. In case 2, the fluid goes directly from raw material zone to crystal growth zone. We can consider that the fluid is GaN-rich and it reaches the GaN seed crystal soon. Thus it is easy to grow GaN crystal on the seed.

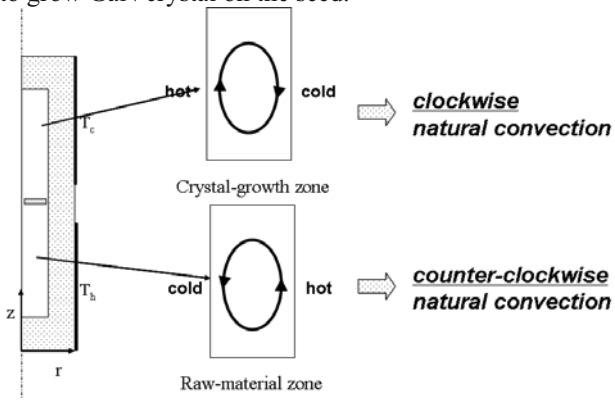

Fig.4 Main flow direction of natural convection in a raw material zone and a crystal growth zone

We discuss why such natural convection pattern is obtained. Fig. 4 shows the main flow direction of natural convection in the raw material zone and crystal growth zone. The temperature in the fluid comparatively becomes constant easily because of the natural convection. Therefore, counterclockwise natural convection is dominant in the raw material zone; on the other hand, clockwise flow is dominant in the crystal growth zone. In case1, counter-clockwise natural convection is dominated slightly up to the baffle because the hottest region on the inconel outer wall is slightly upper than the height of the baffle and natural convection in the raw material zone is dominated. On the other hand, the coldest wall is near the baffle in case2. Therefore, clockwise natural convection is dominated slightly under the baffle. We can change the natural convection pattern by arrangement of the heaters.

4. Conclusions

A solvothermal GaN bulk single crystal growth process has been studied experimentally and numerically. When the bottom heater is removed and the space between upper and lower heaters becomes wider, the growth rate of GaN bulk single crystal can be increased. A rising flow from the center hole of the baffle cause such fast grow rate.

References

[1] Y. Kagamitani et al., Jpn.J.Appl.Phys., **45** (2006), pp.4018-4020.
[2] Y. Masuda et al., JTST., **3** (2008), pp.540-551.
[3] Y. Masuda et al., J. Cry. Growth, **311**(2009), pp.675-679.
[4] Y. Masuda et al., Int. J. Heat Mass Trans., **53** (2010), pp.940-943.

Theoretical Study On The Non-Newtonian Behavior Of Simple Fluids

Yuan Dong, Zeng-Yuan Guo
Key Laboratory for Thermal Science and Power Engineering of Ministry of Education,
Department of Engineering Mechanics, Tsinghua University, Beijing 100084, China
dony327@yahoo.com.cn

ABSTRACT

In tranditional opinions, the non-Newtonian behaviors of fluids generally come from the microscopic structrues of the material. However, such behavior can also be observed in simple fluids, e.g. monatomic gases and liquids of spherical particles. Here we present a new method to analyze the constitution equation of these simple fluids based on the concept of kineto-mass. The various behavior of flow are attributed to the magnitude of the inertia effects of momentum transport processes.

1. Introduction

The non-Newtonian flow, or the rheology phenomenon, is a hot topic in both theories and applications. There are many models describing these flow behaviors. In the linear viscoelasticity region, the behaviors of materials are generally modelled by the Maxwell and Kelvin model, with relaxation relations of strain and stress [1-3]. For practical solutions, suspensions or melts, the nonlinear viscoelasticity constitution equations and empirical relations are appliable. In polymeric liquids, rheological behavior such as shear thinning and rheopectic can be understood as a result of the change of molecular structure. However, for simple fluids, i.e. monatomic gases and liquids of spherical particles, the rheology behavior can also be observed at extreme conditions such as high shear rate of high frequency disturbance [4-6], which can hardly be attributed to internal structures of fluids.

The Newton's viscous law is the linear constitution relation of the momentum transport processes, which are parallel to the heat transport and mass fraction transport processes. These linear relations have a common defect that they neglect the acceleration stage of paticles, so the predicted propagation speeds of disturbance are unphysically infinite. Introducing a relaxation term in linear relations can reduce the propagation speed to the sound speed and is preferable in high frequency conditions, yet lacks of explicit physical sence. In this paper, we introduce the concept of kineto-mass to describe the momentum transport process. This analysis can combine different constitution equations with novel physical meanings, and is especially applicable for simple fluids..

2. Kineto-mass

According to the Einstein's mass-energy equivalence relation, when the total momentum is zero, the sum of kinetic energy of particles divided by the square of light speed, is the "proper mass" of the system [7-8]. Consider the simpliest situation of flow, i.e. the couette flow as Fig. 1, wherein the kinetic energy of particles can be seperated into the internal energy and kinetic energy while the total momentum is zero. Therefore the density of kineto-mass can be defined as

$$\rho_k = \frac{1}{2}\frac{\rho u_x^2}{c^2} \tag{1}$$

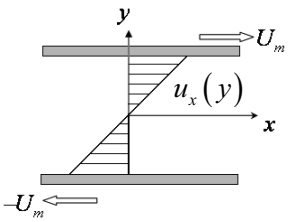

Fig. 1 The model of couette flow

where ρ is the density of fluid, u_x is the velocity in Fig. 1. Note that the coodinate is not arbitrarily chosen, it should guarantee the vanishment of total momentum. The internal energy corresponds to the thermomass and leads to the theory for heat transfer in media [9]. The momentum flux is the shear stress τ, as indicated in tranditional theory of transport processes. In this way, the flux of the kineto-mass is obtained as

$$q_{ky} = \frac{\tau u_x}{c^2}. \tag{2}$$

The conservation equation is

$$\frac{\partial \rho_k}{\partial t} + \frac{\partial}{\partial y} q_{ky} = \frac{\tau}{c^2}\frac{\partial}{\partial y} u_x, \tag{3}$$

where the right hand side term expresses the conversion rate of kinetic energy into internal energy. Equation (3) reduces to the mechanical relation when Eqs. (1) and (2) are inserted

$$\frac{\partial \tau}{\partial y} + \rho \frac{\partial u_x}{\partial t} = 0. \tag{4}$$

Then the transport process can be described by the momentum equation of kineto-mass as in the hydro-dynamics

$$\frac{\mathscr{D}\boldsymbol{q}_k}{\mathscr{D}t} + \nabla p_k + \boldsymbol{f}_k = 0. \tag{5}$$

where $\mathscr{D}$ is the derivative operator and corrsponds to the Oldroyd or Zaremba-Jaumann derivatives. The pressure or state equation of the kineto-mass can be determined by comparison with the kinetic theory of gases, which is

$$p = \frac{1}{3}\rho v_{\text{ave}}^2. \tag{6}$$

where, p is the gas pressure, v_{ave} is the average particle velocity. The pressure of kineto-mass can be similary defined as proportional to the density and square of shear wave speed, which is

$$p = \rho_k v_{wave}^2 . \tag{7}$$

The coefficent 1/3 vanishes in Eq. (7) because of the difference between wave speed and average particle speed in 3-D isotropic media. In liquids and solids the shear wave speed is generally expressed as

$$v_{wave}^2 = G/\rho , \tag{8}$$

where G is the elastic modulus. For liquids the modulus is defined as

$$G = \mu/\lambda , \tag{9}$$

where μ is the viscosity and λ is the relaxation time. This definition is widely applied in oscillatory problems. Some properties of simple fluids are listed in Table 1.

Table 1. The rheology property of some simple fluids at room temperature [6]

Liquid	$10^{12}\lambda$ (s)	$10^4\mu$ (Ns/m^2)	v_{wave}(m/s)*
CCl_4	2.46	9.69	481
CS_2	1.38	3.63	570
Benzene	1.67	6.52	665
Toluene	1.60	5.90	635
Acetone	2.19	3.20	587

* Refer to the shear wave speed, generally half of the longitudinal wave speed

3 From Hookean to Newtonian

The rheology behavior is recognized as between the solids and liquids. The transport equation (5) can illustrate this concept. If there is no friction, i.e, f_k is negligible, then it becomes

$$\frac{\mathscr{D}\tau}{\mathscr{D}t} + G\frac{\partial u_x}{\partial y} = \frac{\mathscr{D}\tau}{\mathscr{D}t} - G\dot{\varepsilon} = 0 , \tag{10}$$

the integration of which gives the Hook's law for elastic solids. In this sence, the elasticity characterizes the non-dissipative transport process of the kineto-mass. When the inertia term in Eq. (5) is negligible, and the friction term is assumed to be proportional to the flux $\boldsymbol{q}_k$, we get

$$\boldsymbol{f}_k = -\nabla p_k = -\frac{1}{\lambda}\frac{\boldsymbol{q}_k}{c^2} , \tag{11}$$

$$\tau = -\mu\,\partial u_x/\partial y , \tag{12}$$

which is the Newton's viscosity law. It shows that the transport in ordinary liquids is pure diffusive, and the friction is proportional to the flux, similar to the Darcy's law in porous hydrodynamics.

If the friction term is comparable with the inertia term, then the flow behavior is visco-elastic. According to the supposition of Eq. (11), Eq. (5) transfers to

$$\lambda\frac{\mathscr{D}\tau}{\mathscr{D}t} + \tau = -\mu\frac{\partial u_x}{\partial y} , \tag{13}$$

if the operator $\mathscr{D}$ is the partial derivatives, Eq. (13) reduces to the classical Maxwell model, which can be applied under the condition $\lambda\dot{\varepsilon} \approx 1$[11]. However, for simple fluids, the relaxation time is rather small, so the rheological behavior should appear until the shear rate raise up to 10^{12} s^{-1}, which can be observed in molecular simulation methods or experimental methods such as inelastic neutron scattering (INS) and inelastic x-ray scattering (IXS) [4]. When $\mathscr{D}$ is chosen to be the Oldroyd or Zaremba-Jaumann derivative, Eq. (13) turns to the White–Metzner model or the DeWitt model respectively [1-3].

4. Concluding remarks

In the above derivation, the non-Newtonian behavior of simple fluids is attributed to the inertia effect of momentum (or kineto-mass) transport processes. The kineto-mass analysis is mechanical and does not require the inner structure of moleculars. However, the non-Newtonian behavior of simple fluids at high strain rate of high frequency oscillation may comes from the anisotropic distrbution in the coodinate or velocity spaces, which is different from the equilibrium state. This opinion is also carried out by some thermodynamic theories, which focus on the elastic and dissipative part of the kinetic energy (e.g GENERIC) [12] or the modificated definition of state variables in non-equilibrium states (e.g. Extended Irreversible Thermodynamics) [6]. However, the kineto-mass analysis postulate an "impact and action" profile of transport processes and characterize them with the Newton's mechanical law. The connection between these methods can be further analyzed by the microscopic interpretation.

References

[1]Q.Y. Wu, J.A. Wu. Polymer Rheology, Beijing: Higher Education Press, (2002).

[2]H.A. Barnes, J.F. Hutton, K. Walters. An Introduction to Rheology. New York: Elsevier, (1989).

[3]S. Zahorski, Mechanics of viscoelastic fluids. London: Martinus Nijhoff Publishers, (1982).

[4]G. Monaco, A. Cunsolo. Phys. Rev. E, **60** (1999), pp. 5505-5521.

[5]D.J. Evans, Phys. Rev. A, **23** (1981), pp. 1988-1997.

[6]D. Jou, J. Casas-Vazquez, G. Lebon, Extended Irreversible Thermodynamics, 4th ed. Berlin: Springer, (2010)

[7]E. F. Taylor, J. A. Wheeler Spacetime Physics, New York: W.H. Freeman and Company (1966), pp. 135.

[8]C. Moller. The Theory of Relativity 2nd ed, Oxford: Clarendon Press (1972), pp. 69-80.

[9]B. Y. Cao, Z. Y. Guo J. Appl. Phys. **1**02 (2007), pp. 53503-53506.

[11]H. Rehage, H. Hoofmann. J. Phys. Chem. **92** (1988), pp. 4712-4719.

[12]H.C. Ottinger, Beyond Equilibrium Thermo-dynamics, Hoboken: Wiley (2005).

Eighth International Conference on Flow Dynamics
November 9 - November 11, 2011

Molecular Dynamics Simulation on the Non-Newtonian Behavior of Simple Fluids

Ruo-Yu Dong, Bing-Yang Cao, Zeng-Yuan Guo
Key Laboratory for Thermal Science and Power Engineering of Ministry of Education,
Department of Engineering Mechanics, Tsinghua University, Beijing 100084, P. R. China
caoby@tsinghua.edu.cn

ABSTRACT

We use molecular dynamics simulations to study the rheological behavior of Lennard-Jones fluid. Shear thinning and normal stress differences are observed in the Couette flow simulations. We find that the radial distribution function is different and the potential energy increases with the increase of strain rates. By applying an oscillatory shear flow, several findings like the phase difference between shear stress and shear rate indicate the appearance of viscoelasticity at high frequency.

1. Introduction

Complex liquids like colloidal solutions and polymer melts can exhibit distinct non-Newtonian behavior, namely the changing of viscosities and other physical properties with shear rate [1]. This is the common sense for the rheological properties can be observed, measured and explained in the laboratory. In the meantime, with the widely application of computer simulations, we are realizing at high enough shear rates, simple fluids like argon can also shear thin, shear thicken or display viscoelasticity. Usually, the Weissenberg number (Wi) which is the product of structural relaxation time and shear rate can be used to compare rheological behavior between simple and complex liquids. It's believed that under the same Wi fluids show the same flow behavior and for the complex liquids in industry or labs the value is of order unity [1]. Considering the relaxation times of simple fluids are of order picoseconds, the very much high shear rates of THz are unrealizable experimentally for the macroscopic turbulence prevents the attachment of high enough shear rates [2]. That's why people are still not totally accepting the standpoint that all fluids can be expected to be non-Newtonian.

Lots of work has already been done to generalize the rheological laws of simple fluids under various conditions with molecular dynamics (MD) simulations. Erpenbeck [3] observed the alignment of particles along the flow direction known as the "string phase" using a hard-sphere model. Evans [2, 4-5] did a series of work concerning the Lennard-Jones (LJ) fluids under steady and oscillatory shear flow and obtained some remarkable results agreeing well with ''hard-sphere" like colloidal suspensions in experiments.

Now, we also use MD simulations to explore the flow behavior and underlying mechanisms of LJ fluid.

2. Simulation method and details

Our simulation is carried out on atomic fluids governed by the LJ potential at the state point of T^*=0.722 and ρ^*=0.8442 in reduced units. The systems all consist of N=4000 particles and are divided into N slabs (labeled from 1 to N) along the z direction. The Nose-Hoover thermostat is applied only in two directions (y, z) except the flow direction (x). Every time step, we choose the atoms in Slab 1 to give them an additional positive velocity v_x, while the atoms in Slab N/2+1 are with a negative velocity $-v_x$. By using periodic boundary conditions, Couette flow can be established at both halves of the system. The numbers of the atoms involved in this process of the two slabs are chosen to be the same. Then after time t, the momentum flux, i.e. shear stress, can be expressed as

$$\tau = \frac{\sum_t \sum_i v_x}{2L_x L_y t}, \qquad (1)$$

where i denotes the atoms in Slab 1 applied with v_x. Besides the common steady flow, we are also concerned with oscillatory shear flow and the imposed velocity is in the form of $v_x = v_{x0}\cos(\omega t)$.

3. Results and Discussion

3.1 Steady flow

First, we plot the shear viscosity as a function of the strain rate in Fig. 1. A comparison is made between our results and the famous Carreau model [6]. We can easily see a Newtonian plateau before γ^*=0.01 where the viscosity is independent of strain rate. From around γ^*=0.1, shear viscosity decreases markedly with the increasing of strain rate which indicates the appearance of shear thinning.

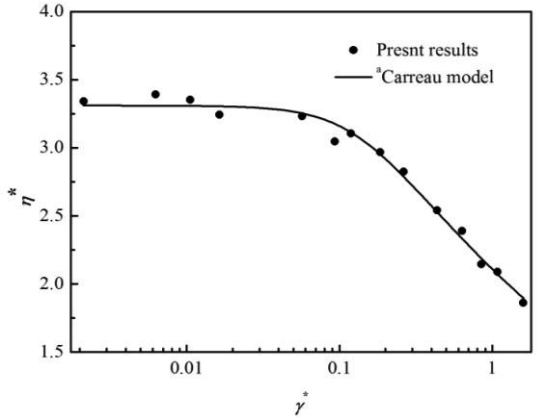

Fig. 1 Dependence of the shear viscosity on the strain rate, [a] Carreau model

For the viscoelastic fluids three variables are needed to describe the flow characteristics which are shear stress τ and the normal stress differences $N_1=\sigma_{xx}-\sigma_{zz}$ and $N_2=\sigma_{zz}-\sigma_{yy}$. Figure 2 shows the dependences of the normal stress differences on strain rate. At low shear rates, N_1 and N_2 are both close to zero, while with the

increasing shear rate, N_1 increases greatly and N_2 has a slight decrease.

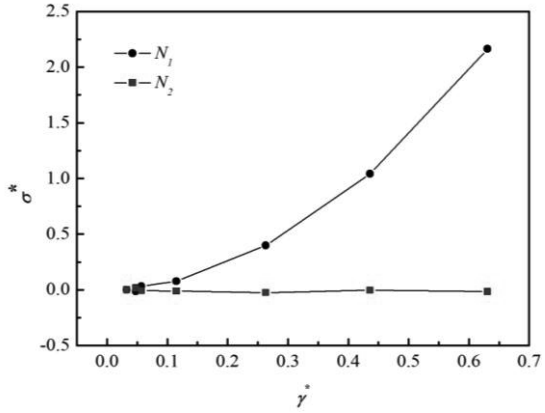

Fig. 2 Dependences of the normal stress differences on the strain rate

To explain the Non-Newtonian behavior under steady shear, we use the pair radial distribution function $g(r)$ as the monitor of the shear induced structural changes. It gives the probability of finding a pair of atoms a distance r apart, relative to the probability of a random distribution at the same density [7]. Figure 3 shows $g(r)$ in two strain rates. When r/σ<1.0, we find $g(r)$ is larger for a stronger shear flow at the same r/σ and an opposite rule exists for the slope just past the first peak. These may suggest that for a larger strain rate the repulsion is more powerful while the attraction is weaker. Through the calculation of the repulsive and attractive part of the potential energy, we confirm this conjecture. Moreover, we think the shear thinning is due to that the applied energy is not all dissipated but with some conserved as the potential energy, which is

$$E_p = \mu(\frac{du}{dy})^2 - \mu'(\frac{du}{dy})^2 \qquad (2)$$

where μ is the Newtonian viscosity and μ' is the value when shear thinning occurs. Our simulations point out the potential energy increases monotonically with strain rates and the results also agree with Eq. (2).

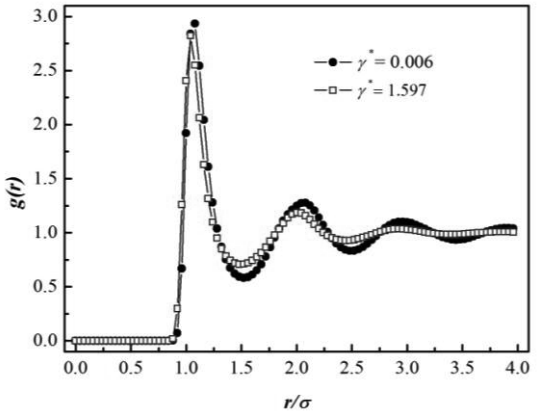

Fig. 3 Pair radial distribution function for two strain rates

3.2 Oscillatory shear flow

We choose a fixed value of the velocity amplitude v_{x0} and by controlling the number of atoms applied with $\pm v_x$ from Slab 1 and N/2+1, the stress amplitude is also fixed. We gather the statistics from Slab 1 under different angular frequencies. First, we note the shear stress τ and strain rate $\dot{\gamma}$ are both sinusoidal functions of time. The phase difference between τ and $-\dot{\gamma}$ increases with the increasing of frequency which is shown in Fig. 4. Second, we also find out the real and imaginary part of viscosity tend to decrease and increase with frequency, respectively. Third, the elastic modulus can also be derived and have a monotonic increase with frequency. These three findings all illustrate the same point that under oscillatory shear the LJ fluid does exhibit viscoelasticity.

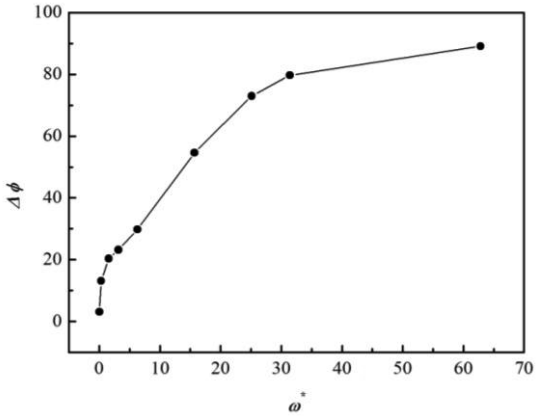

Fig. 4 Dependence of phase difference on the angular frequency

4. Concluding remarks

In this paper, we study the non-Newtonian behavior of simple fluids by using steady and oscillatory shear flow. At high strain rates, the fluids exhibit obvious shear thinning behavior and normal stress differences. We think these phenomena suggest that some applied kinetic energy is transformed to potential energy, which is confirmed in the simulations. By studying the oscillatory shear flow, we further conclude that viscoelasticity occurs at relatively high frequency.

From our simulations, it can be summarized that simple fluids do have some similar rheological behavior to complex fluids and we are expecting a unified theory to be developed to underpin rheology.

References

[1] D. M. Heyes, J. Non-Newtonian Fluid Mech. **21** (1986), pp.137-155.
[2] D. J. Evans, Phys. Rev. A, **23** (4) (1981), pp.1988-1997.
[3] J. J. Erpenbeck, Phys. Rev. Lett. **52** (15) (1984), pp.1333-1335.
[4] J. Delhommelle, J. Petravic, D. J. Evans, Phys. Rev. E, **68** (2003), 031201(6).
[5] J. Delhommelle, J. Petravic, D. J. Evans, J. Chem. Phys. **120** (13) (2004), pp.6117-6123.
[6] P. J. Carreau, PhD thesis, University of Wisconsin (1968).
[7] D. J. Evans, G. P. Morriss, Statistical Mechanics of Nonequilibrium Liquids (Academic, London, 1990).

Optimization of Prime Movers in Trigeneration Systems

Mehdi Aghaei Meybodi, Antony Tiranon Straubhaar, Masud Behnia
School of Aerospace, Mechanical and Mechatronic Engineering, The University of Sydney, NSW 2006, Australia
m.meybodi@sydney.edu.au

ABSTRACT

Optimum selection of nominal power for prime movers in combined heating, cooling, and power (CHCP) systems is of crucial importance due to the fact that inappropriate choices considerably reduce the benefits of CHCP systems. In this paper, a thermo-economic method for selecting the optimum nominal power and planning the operational strategy of gas turbines and internal combustion engines as the prime movers of a medium scale (500 kW-5000 kW) CHCP system is presented. Emissions trading under the Greenhouse Gas Reduction Scheme of New South Wales is considered.

1. Introduction

The addition of absorption chillers to a combined heat and power (CHP) system provides it with cooling capability and thus potentially raises overall system efficiency up to 90% [1]. This system is known as trigeneration or combined heating, cooling, and power (CHCP).

In this study, a thermo-economic approach is developed to determine the optimum nominal power of gas turbines, gas engines, and diesel engines. Their operational strategy is planned with two operational modes while considering the NSW Greenhouse Gas Abatement Scheme (GGAS) Generation and Demand Side Abatement Rules [2]. Two-way connection (TWC) mode allows buying electricity from the grid and selling back the excess electricity. One-way connection (OWC) mode only allows buying electricity from the grid.

2. Annual cash flow (ACF) analysis

In this method, the objective is to convert money (all costs and benefits) to equivalent uniform annual cost (EUAC) and equivalent uniform annual benefit (EUAB). The method is used to compare different options and the one that has the minimum difference of EUAC and EUAB (EUAC-EUAB) is the most economical choice [3]. Based on the ACF method, the proposed objective function (Net Annual Cost (NAC) $/year) is defined as:

$$\mathrm{NAC} = \left[\sum_{j=1}^{k}\left(CC_j - SV_j\left(\frac{1}{(1+i)^{LT}}\right)\right)\right]\left(\frac{i(1+i)^{LT}}{i(1+i)^{LT}-1}\right) + \mathrm{NGAC} + \sum_{m=1}^{N}\left[\sum_{j=1}^{k}(MC_j + COF_j) + P_b \times C_{el,b} + P_{CHCP,r} \times C_{el} - \dot{H}_{CHCP,r} \times C_h - \dot{C}_{CHCP,r} \times C_c - P_{CHCP,s} \times C_{el,s}\right] \times \tau_m \quad (1)$$

3. Selection and planning of the operational strategy

The following procedure is applied to determine the optimum nominal power and the operational strategy considering specific electricity and heat demand profile:

- For nominal powers from 500 kW to 5000 kW and for each time interval of demand profile (τ_m) changing partial load from 20% to 100%.
- Calculating NAC for a given partial load (NAC_m) and choosing the minimum NAC_m values ($NAC_{m,min}$) with its associated partial load.
- Calculating NAC by summing $NAC_{m,min}$ values for all time intervals and choosing the nominal power that results in the minimum NAC as the prime mover's nominal power of CHCP system.
- For the selected nominal power and for each time interval the partial load at which the $NAC_{m,min}$ is obtained is the operational strategy of CHP system.

4. Results and Discussion

To demonstrate the proposed method, it has been used for a case study. Fig. 1 shows the monthly average electricity, heating, and cooling demand profile of an industrial building located in New South Wales, which cannot be named for confidentiality purposes.

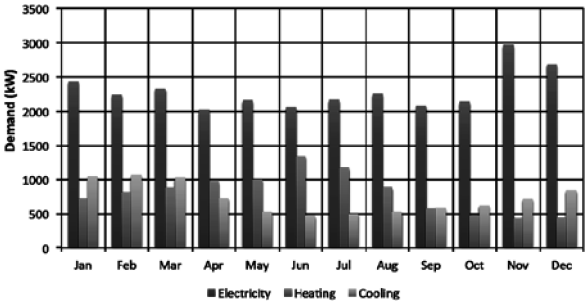

Fig. 1 Demand profile for the case study

The variation of Net Annual Cost versus nominal power of prime movers for both modes of operation has been shown in Figs. 2-4. As figures show, minimum NAC values correspond to gas turbines of 2.9 MW (TWC mode) and 2.5 MW (OWC mode). These values for a diesel engine correspond to 3.3 MW (TWC) and 3.2 MW (OWC) and for a gas engine, at 2.8 MW (TWC) and 2.6 MW (OWC).

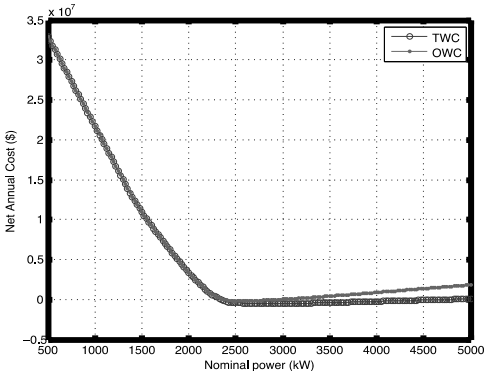

Fig. 2 Gas turbine NAC versus nominal power in TWC and OWC mode

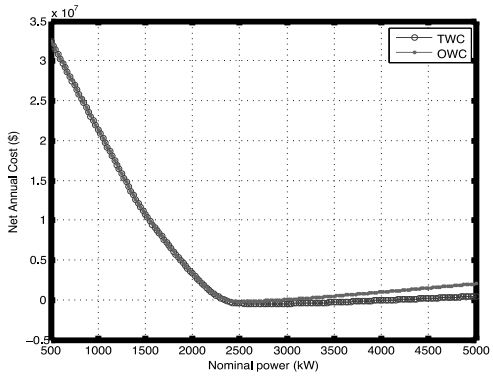

Fig. 3 Gas engine NAC versus nominal power in TWC and OWC mode

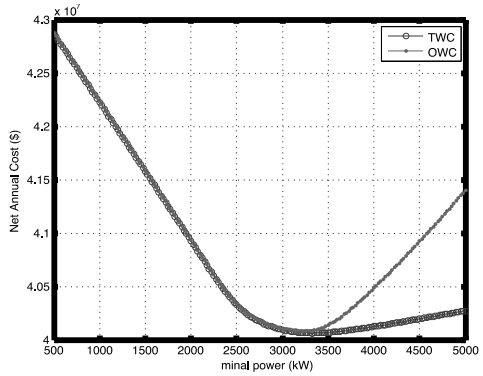

Fig. 4 Diesel engine NAC versus nominal power in TWC and OWC mode

Figs. 5-7 illustrate the operational strategy of prime movers in both operational modes. As figures show, in TWC mode the gas turbine and gas engine work at full load all year. In OWC mode the prime movers produce the required electricity, but the diesel engine operates the same in TWC mode as well as it is uneconomical.

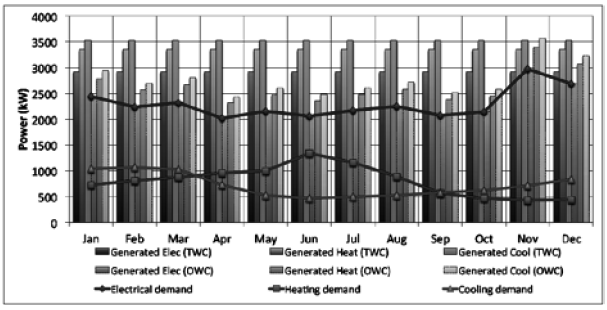

Fig. 5 The operational strategy in TWC and OWC mode for a gas turbine

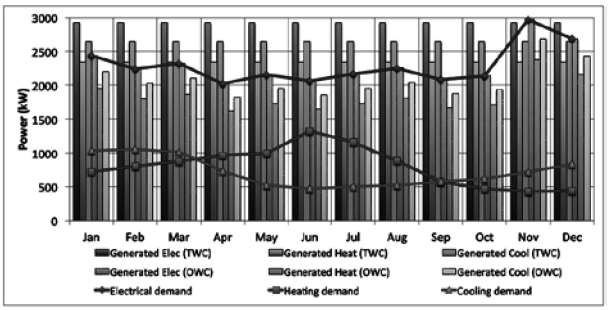

Fig. 6 The operational strategy in TWC and OWC mode for a gas engine

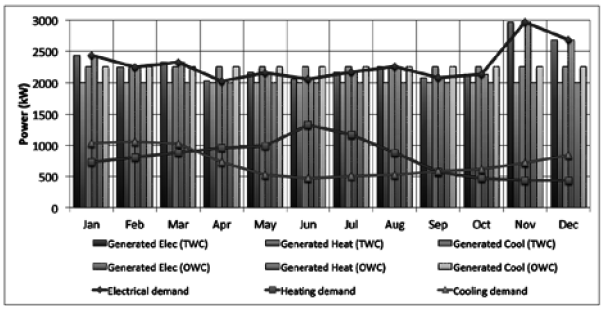

Fig. 7 The operational strategy in TWC and OWC mode for a diesel engine

4. Concluding remarks

In this paper, a thermo-economic approach to selecting the optimum nominal power and planning the operational strategy of gas turbines and internal combustion engines in a medium scale combined heating, cooling and power system is presented to demonstrate the Net Annual Cost (NAC) criterion. Minimum NAC values corresponded to gas turbine sizes of 2.9 MW (TWC) and 2.5 MW (OWC). These values for a diesel engine correspond to 3.3 MW (TWC) and 3.2 MW (OWC) and for a gas engine, at 2.8 MW (TWC) and 2.6 MW (OWC). The operational strategy of the three prime movers in both operational modes was studied and the results have been presented.

Nomenclature

P= electric power (kW)
Ḣ= heat rate (kW)
Ċ= cool rate (kW)
CC= capital cost ($/year)
NAC= Net Annual Cost ($/year)
k= number of equipment
SV= salvage value ($)
i= interest rate (%)
LT= lifetime (year)
NGAC= emissions tradable certificate
N= number of time intervals of demand profile
MC= maintenance cost per hour ($/hr)
COF= cost of fuel per hour ($/hr)
C= cost ($/kWh)

Subscripts

CHCP= combined heating, cooling and power
f= fuel
b= buying electricity
s= selling electricity
el= electricity
h= heat
r= required

References

[1] D.W. Wu, R.Z. Wang, 2006, Combined Cooling, Heating and Power: A Review, Prog. Energ. Combust, **32**, pp. 459–495.
[2] NSW Greenhouse Gas Reduction Scheme. http://www.greenhousegas.nsw.gov.au/
[3] D. G. Newnan, T. G. Eschenbach, J. P. Lavelle, 2004, Engineering Economic Analysis, 9th ed., Oxford University Press, New York, USA.

Eighth International Conference on Flow Dynamics
November 9 - November 11, 2011

Power Output Increase of Gas Turbine by Utilizing Mist Atomization

Yukiko Agata, Shinya Ishikawa, Shinichi Akabayashi
Tohoku Electric Power Co., Inc, Tohoku Electric Power Co., Inc, Niigata University, Japan
agata@criepi.denken.or.jp

ABSTRACT

Power outputs of gas turbines decrease due to ambient temperature increases in summer. For the recovering of lost output, mist atomization system using efficient spray nozzles was focused on. The system was installed in an inlet air flow path of a gas turbine at Higashi-Niigata thermal power station No.4 train, a commercial plant. The nozzles can efficiently decrease inlet air temperature of gas turbines because of their minute particle size and highly-efficient evaporation properties. After activating the atomization system, inlet temperature decreased by up to about 7.5 degrees Celsius and power output increased by up to 6% in the gas turbine.

1. Introduction

It is generally known that gas turbine power output decreases due to ambient temperature increases [1]. It is because that inlet mass flow rate decreases due to ambient temperature increase and decreases in inlet air density.

The aim of this study was power output increase of gas turbine. In order to improving gas turbine inlet air cooling, mist atomization technology which can efficiently cool air because of minute mist particle size and highly-efficient evaporation properties was tried to be utilized. The atomization system was to be introduced to a gas turbine inlet at the Higashi Niigata thermal power station. A flow path which was in the upstream of the gas turbine inlet filter and unique to the power plant was used for mist evaporation by the system. In this case, erosion risk of air compressor blades and vanes could be reduced. In this study, experiment and numerical simulation were first conducted as basic considerations to confirm the system's effectiveness and to set up the system. And then, the system was successfully installed in the commercial plant, and the performance, effects, and influence of the system were carefully investigated. After activating the system, the power output increase effect which was almost the same to prediction was able to be achieved without any problem. [2]

2. Model experiments

Model experiments were conducted in order to evaluate effectiveness of the mist atomization system.

As a first step, the most effective nozzle type with the largest amount of atomization and small particle diameter was selected from among some commercially available varieties. Because the mist particles with small diameters evaporate easily, the air cooling ability of them are high.

Figure 1 shows model experimental apparatus which simulated the atomization system. The selected nozzle was set in the duct. The air with varied temperature and humidity was led into the duct. Then, the change of temperature and humidity between upstream and downstream portion of the nozzle were measured. Figure 2 shows the amount of temperature decrease between upstream and downstream portions of the nozzle under 30% humidity. In this figure, the black line signifies the limits of temperature decrease between upstream and downstream portions of the nozzle where downstream temperature was decreased to wet-bulb temperature of upstream air. At all temperature range, air temperatures could be almost decreased near the limits. Furthermore, air temperature could be decreased to the limits under other humidity conditions as well as the 30% humidity condition [3]. From these results, we could confirm the effectiveness of mist atomization.

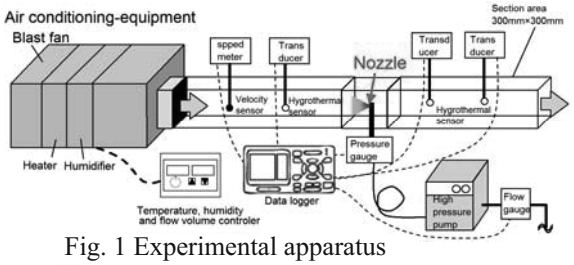

Fig. 1 Experimental apparatus

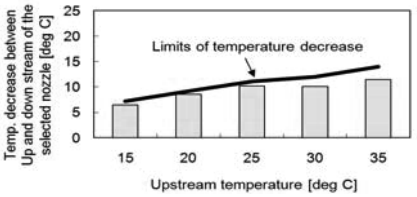

Fig. 2 Temperature decrease by the selected nozzle

3. Numerical simulation

The gas turbines inlets at Higashi-Niigata thermal power station are the unique structures for preventing direct snowfall. This unique inlet structure makes an inlet air path (see figure 3). Atmospheric air is sucked in from air inlet tower atop the roof, then flows down to air inlet filter rooms. In the last portion of the rooms, air is cleaned by inlet filters, and flows into air compressor through an inlet duct. This unique path was intended to be utilized for the mist evaporations.

The advantage of the mist atomization technology is that a minute particle with high evaporation efficiency gives a larger effect of the temperature decrease. It was thus most important to make more atomization mist evaporate in the space upstream of the inlet filter to achieve the maximum effect, and the positioning of mist nozzles was also very important. So the flow field in this path was analyzed in order to investigate an actual flow field and to reduce mist turning into useless drainage due to collision with other particles or obstacles.

Figure 5 shows the CFD analysis result of half of the inlet flow path. This analysis was conducted using a

commercially available software, STREAM, and standard k-ε model as a turbulence model. From the result, it was clarified that flow velocity is high at the air inlet tower, but flow rapidly stabilized after passing down to the inlet filter room. From the clarified flow field condition, need of keeping distance between nozzles and filter to obtain a residence time for evaporation, and considering the workability of installation or maintenance, the position of the bottom of the air inlet tower where velocity begins to weaken was determined as the optimal nozzle position.

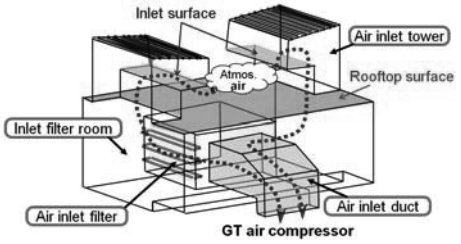

Fig. 4 Flow path of inlet air

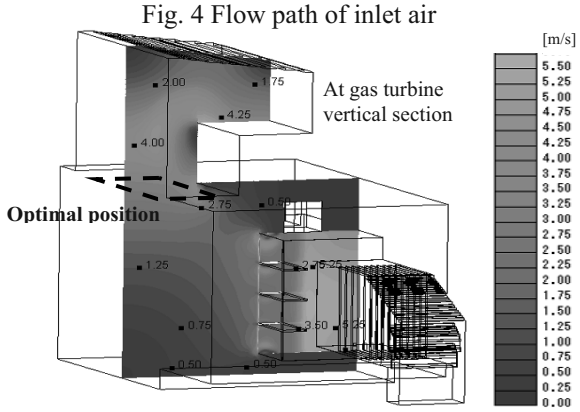

Fig. 5 Contour figures of velocity distribution

4. Influences of the system on GT equipment

There had been no prior experiences involving atomization of such minute water particles in upstream portions of gas turbine's inlet filter, so, there were some serious concerns about the possible effects it might have on gas turbine equipment.

One main concern was erosion on compressor blades due to super-saturation of inlet air humidity. In this system, the risk of erosion was reduced significantly by atomizing mist into the upstream portions of the inlet filter. But in the case of supersaturation, the erosion concern was caused by the minute mist particles passing through filters. For this concern, mist atomization was stopped when humidity rose by up to the determined limit. This way, super- saturation was kept off.

Another concern was overshooting of turbine inlet temperature or exhaust gas temperature caused by inlet air temperatures soaring after mist stoppages. When the mist supply is stopped all together, inlet air temperature soars in an instant. Therefore those temperatures caused concern about overshooting and exceeding their limit values. For this, field tests of all mist supply stoppage were performed and it was confirmed that atomization stoppage influences were not significant.

After activating of the atomization system, three years have passed and we have never had trouble.

5. Effects of power output increase

Because no significant problems due to the operation of the system were detected, operation of the system continued throughout the period until atmospheric temperature decreased (2008.09-2008.11). Figure 6 shows increased outputs in the case where inlet humidity after atomization was about 95% and the stabilized gas turbine state were extracted from mentioned term operating data. This figure demonstrates that in the cases of the higher temperature and the lower humidity, this system could give the more amount of output increase. In the maximum case, output increased by about up to 6% compared with before atomization. Additionally, an output increase can be obtained at a comparatively lower ambient temperature around fifteen degrees Celsius, so the increase effect can be confirmed to be obtained not only in summer as a high temperature season, but over long periods.

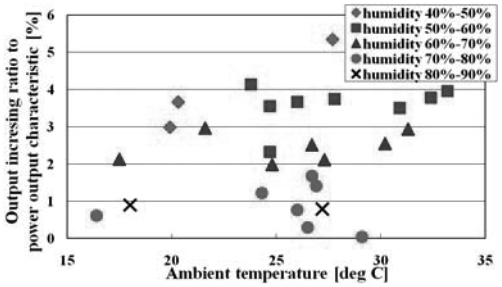

Fig. 6 Output increase at a broad range of temperature

6. Conclusions

Mist atomization system which has a high ability of air cooling due to minute mist particles with high evaporation efficiency was successfully introduced into an inlet air flow path of a gas turbine at Higashi-Niigata thermal power station No.4 train, a commercial plant. The system's effectiveness was confirmed by conducting basic experiments, and effective composition of the system was investigated by the numerical analysis. Furthermore, following installation, the safety and effectiveness of the system were confirmed by conducting field tests. By the introduction of the system, we got power output increase by about up to 6% in the maximum case. This system has continued stabilized operating, and distributed to supply electric power in this summer.

Acknowledgements

The authors acknowledge the Visualization laboratory in Niigata University for their support of this research, and also greatly appreciate MHI, Ltd. for assistance in introducing the system.

References

[1] K. Kishimoto, et. al., MHI, Ltd. Tech. Rev., **34**-3 (1997), pp. 91-95.

[2] T. Minami, et al., Proc. Thermal and Nuclear Power Generation Convention (2009), pp. 228-232.

[3] S. Akabayashi, et. al., Summary of technical papers of Annual Meeting Architectural Institute of Japan (2008), pp. 557-558.

Pulsating Spray from Gas-Centered Swirl Coaxial Atomizers

Sivakumar Deivandren,[1] Satish Babu Umesh,[1] Vikram Rout,[2] and Thomas John Tharakan[3]
[1]Department of Aerospace Engineering Indian Institute of Science, Bangalore 560012, India
[2]Department of Mechanical Engineering, National Institute of Technology, Surathkal 575025, India
[3]Liquid Propulsion Systems Center, Valiamala, Thiruvananthapuram 695547, India
E-mail of corresponding author: dskumar@aero.iisc.ernet.in

ABSTRACT

The study investigates the self-pulsating dynamics of sprays discharging from a gas-centered swirl coaxial atomizer. The atomizer discharges an annular swirling liquid jet and a central gaseous jet from its outer and inner orifices respectively. The spray pulsation is characterized by employing a high speed video imaging system. Two different bursts are dominantly seen in the spray: big bursts and regular bursts. For a given liquid sheet condition, the frequency of spray pulsation (bursts) increases with increasing gas jet velocity. The frequency of big bursts is one order magnitude smaller than the regular bursts.

1. Introduction

Gas-centered swirl coaxial injection system has been employed in liquid propellant rocket engines which operate under a staged combustion cycle with an oxygen rich preburner [1,2]. The central gas jet is analogous to the gaseous oxygen (GOX) and the annular swirling liquid sheet to the liquid kerosene (RP-1). The spray formation occurs by means of an interaction process between the swirling liquid sheet and the gas jet. A recent study by Kulkarni et al. [3] revealed that the sheet breakup region is marked by features such as ejection of ligaments from the sheet surface, droplet clusters, increased surface corrugations on the liquid sheet, and cellular structures on the liquid sheet. An extended analysis [4] showed that the spray exhibits a periodic ejection of liquid masses at certain combinations of liquid and gas flow conditions. The spray pulsation in gas-centered swirl coaxial atomizers is believed to be the result from the interaction of the liquid and gas at the end of the separating lip [5]. Canino et al. [6] carried out numerical works of the gas flow over splitter plate to understand vortex shedding in recessed-post coaxial injectors. It was showed that the Strouhal number increases with the jet momentum ratio. The vortex shedding frequency was in the range 7–25 kHz. Recently Starasser [7] studied sprays from a three stream coaxial airblast injector. The spray exhibits self-pulsations with frequencies in the range 75 – 600 Hz. This study analyzes the pulsation behavior of sprays discharging from a gas-centered swirl coaxial atomizer.

2. Method

A schematic of the injector assembly is given in Fig. 1. It consists of an inner atomizer with orifice diameter, D_i = 3 mm and an outer atomizer with orifice diameter, D_o = 5.2 mm to discharge air and water respectively. The swirling motion was imparted to the liquid by passing the experimental liquid through a helical swirler with six starts placed upstream of the converging section of the outer atomizer. The experiments were conducted with water and air as simulants. A spray test facility was used to carry out experiments. The temporal features of spray pulsations were characterized by taking high speed motion pictures of the sheet breakup. For this purpose, a high speed camera system (Redlake Y4L)

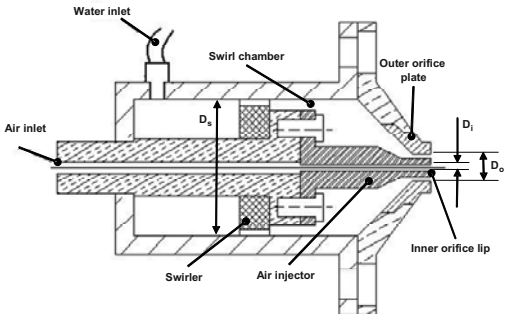

Fig. 1. A schematic sketch of the gas-centered swirl coaxial atomizer.

along with a backlighting source was operated with different combinations of camera frame speed and image resolution. For majority of experimental runs, the camera was operation in the range of frame speed 5000 frames per second. The experimental methods adopted for the estimation of axial velocity of liquid sheet, U_l and the central air jet velocity, U_g were described in Ref. [4].

3. Results and discussion

It is observed from the experimental data that for a given U_l, the spray discharging from the gas-centered swirl coaxial atomizer exhibits self-pulsation behavior for higher values of U_g. The interaction and mixing processes between the liquid sheet and the central air jet results in a self-periodic ejection of liquid masses in the

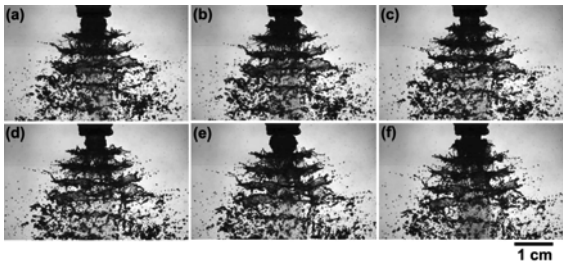

Fig. 2. A high speed camera image sequence showing the burst formation in pulsating spray discharging from the gas-swirl coaxial atomizer. U_l = 6.93 m/s and U_g = 244 m/s. Images are separated by a time interval of 0.2 ms.

very near region of the orifice exit. Figure 2 shows a typical high speed image sequence illustrating self-periodic ejection of liquid masses/ligaments during the spray formation under this flow regime of the gas centered swirl coaxial atomizer. Such ejection process occurs continuously without any external assistance. Figure 2 also highlights the development of bursts in the pulsating spray. At the beginning of burst formation, a bulb like portion (like a closed liquid sheet) appears in the near region of the orifice exit as seen in the images (a) and (e) of Fig. 2. With time, the bulb collapses and subsequently results in the ejection of liquid masses. The ejected liquid masses stretch along the radial direction as they flow in the downstream and break up further into drops as seen in the images (b), (c), and (d) of Fig. 2. The burst formation causes a sudden decrease in the jet width ('necking') in the near region of the orifice exit (images (b) and (f) of Fig. 2).

The analysis further reveals that the burst phenomenon in the pulsating spray is not 100% periodic. It also highlights different bursting structures. Two types of bursting are dominantly seen in a typical pulsating spray discharging from gas-centered swirl coaxial atomizers: big bursts and regular bursts. Figure 3 shows typical

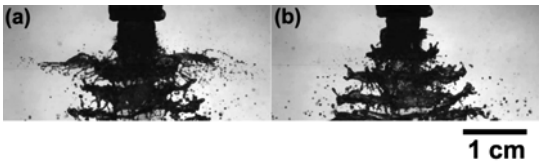

Fig. 3. (a) Big burst, and (b) regular bursts seen in pulsating sprays from the gas-centered swirl coaxial atomizer. U_l = 6.93 m/s and U_g = 244 m/s.

images of big burst and regular bursts in a pulsating spray condition. As seen in Fig. 3(a), the big burst is marked by a rapid radial spreading of liquid masses along with a cloud of micron-sized ligaments/droplets. The regular bursts are marked with a radial spreading liquid mass without any dominant presence of micron-sized ligaments/droplets clouds as seen in Fig. 3(b). Analysis shows that the frequency of big bursts is much smaller compared to that of the regular bursts.

The high speed image recordings were used to deduce the distance between two spray pulses, λ and the velocity of spray pulse, C. It is observed from the experimental measurements that, for a given liquid sheet condition (U_l), the variation of λ decreases with increasing U_g whereas the variation of C is almost constant with U_g. The trends suggest that the central air jet accelerates the formation of spray pulses in the spray. The frequency of spray pulsation, f_p was determined from the measurements λ and C as $f_p = C/\lambda$. Figure 4 shows the variation of f_p (regular bursts) with U_g for pulsating sprays discharging from the gas-centered swirl coaxial atomizer. The frequency of spray pulsation (regular bursts) increases with increasing U_g as seen in Fig. 4. Attempts were also made to extract the details on the characteristics of big bursts seen with the pulsating

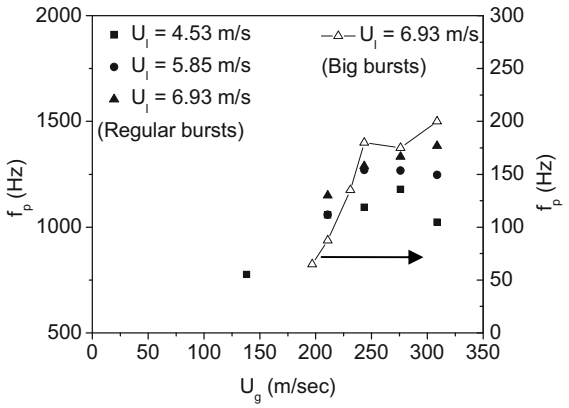

Fig. 4. The variation of f_p with U_g for the pulsating sprays discharging from the gas-centered swirl coaxial atomizer.

sprays. The values of f_p for the big bursts were estimated from the manual count of big bursts seen in a continuous tracking of sprays for a time interval of 0.2 to 0.4 seconds. The open symbols in Fig. 4 corresponds the variation of f_p of big bursts. As observed in the case of regular bursts, the frequency of big bursts in the pulsating sprays also increases with increasing U_g for a given liquid sheet condition. However, the estimated value of f_p for the big bursts is one order of magnitude smaller compared to that of the regular bursts.

4. Conclusions

A study was carried out with the aid of a high speed imaging system to understand the pulsation dynamics of sprays discharging from the gas-centered swirl coaxial atomizer. The bursting phenomenon seen in the pulsating spray may be comprised of the following events: necking, bulb formation, bulb collapsing, radial spreading of liquid, and atomization of spreading liquid. The spray pulsation dynamics is influenced significantly by the central air jet flow conditions. Two different bursts are mainly seen in the spray: smaller frequency big bursts and higher frequency regular bursts.

The research work is supported by Space Technology Cell, Indian Institute of Science under the Grant ISTC/MAE/DSK/235.

References

[1] R.K. Cohn, P.A. Strakey, R.W. Bates, D.G. Talley, J.A. Muss, and C.W. Johnson, AIAA 2003-0124 (2003).
[2] S. Soller, R. Wagner, H.-P. Kau, P. Martin, and C. Maeding, AIAA 2005-3750 (2005).
[3] V. Kulkarni, D. Sivakumar, C. Oommen, and T.J. Tharakan, J. Fluids Engg. **132** (2010) 011303.
[4] D. Sivakumar and V. Kulkarni, Exp. Fluids **51** (2011) pp. 587-596.
[5] M.D.A. Lightfoot and S.A. Danczyk, ICLASS 2009, Vail, Colorado, USA, 2009.
[6] J.V. Canino, S.D. Heister, V. Sankaran, and S.I. Zakharov, AIAA 2005-4297 (2005).
[7] W. Strasser, Int. J. Multiphase Flow **37** (2011) pp. 831-844.

Eighth International Conference on Flow Dynamics
November 9 - November 11, 2011

Throttling of Turbopump by Circulation

Takeshi Kanda and Tomoyuki Hashimoto
Japan Aerospace Exploration Agency, Kakuda Space Center
1 Koganesawa, Kimigaya, Kakuda, Miyagi 981-1525, Japan
kanda.takeshi@jaxa.jp

ABSTRACT

Throttling of pump of the liquid rocket engine is examined by use of circulation. The relationships of the flow rates and enthalpies are derived analytically. Operation of a LOX pump of a 100 kN-level rocket engine is calculated with the analytical relationships and a LOX property code. The flow rate of oxygen by the circulation duct was small and the increase of temperature of the confluence flow was small during the throttling. LOX pump could be throttled by the circulation within this increase level of pressure.

1. Introduction

The liquid rocket engine produces thrust by high pressure in the combustion chamber and choking of the combustion gas at the throat. The engine usually operates at a design condition. Its pump also operates at the design condition, that is, discharges propellant to a design pressure at a design rotational speed. If the engine can be throttled, its operation becomes flexible, and another kind of flight or operation will be realized in the space transportation.

In the rocket engine, thrust, F, is proportional to the combustion chamber pressure.

$$F = C_F A_t P_c \tag{1}$$

Here C_F, A_t and P_c are the thrust coefficient, throat cross section and combustion chamber pressure, respectively. Under a specified mixture ratio of propellants, the chamber pressure is proportional to propellant mass flow rates. In the throttling of the rocket engine, both the mass flow rate and the pressure level have to change simultaneously and proportionally.

However, in general, a flow rate of a pump is proportional to rotational speed, while head is to square of the speed at a specified specific speed. To keep the operation of the pump around the specific speed, circulation is often integrated to the pump for the throttled operation.

Herein the relationships of the pump with the circulation are derived analytically with the affinity laws. Operating condition of an imaginary pump is calculated with the relationships, and features with the circulation are discussed.

2. Relationships at circulation

2.1 Circulation flow rate

According to the affinity laws, the pump has following relationships.

$$\frac{\dot{Q}}{\dot{Q}_0} = \frac{(\dot{m}/\rho)}{(\dot{m}/\rho)_0} = \frac{\dot{m}}{\dot{m}_0} = \frac{N}{N_0} \tag{2}$$

$$\frac{\Delta H}{\Delta H_0} = \frac{(\Delta P/\rho)}{(\Delta P/\rho)_0} = \frac{\Delta P}{\Delta P_0} = \left(\frac{N}{N_0}\right)^2 \tag{3}$$

$\dot{Q}$, H, $\dot{m}$, ρ, N, and P are volume flow rate, head, mass flow rate, density, rotational speed, and pressure, respectively. Subscript 0 indicates a design condition. In this paper, operation under these relations is examined.

In the rocket engine, throttled level of thrust is proportional to the combustion chamber pressure, and the pressure is proportional to the mass flow rate discharged from the pumps. To make proportional relationship between the flow rate and the pressure, circulation is herein adopted. Figure 1 shows a schematic of the pump with the circulation. The relationship between the mass flow rates with the circulation is

$$\begin{aligned} \dot{m}_4 &= \dot{m}_1 = r \cdot \dot{m}_0 \\ &= \dot{m}_2 - \dot{m}_3 \end{aligned} \tag{4}$$

r is the throttled level of thrust. In the pump system of Fig. 1, the discharged mass flow rate of $\dot{m}_4$, that is, the oxidizer or fuel mass flow rate of the combustion chamber, is proportional to the throttled thrust at the throttled condition, whereas the mass flow rate of the pump of $\dot{m}_2$ is not proportional to the thrust in the throttled condition.

From the pump characteristic of Eq. (3),

$$r = \frac{F}{F_0} \approx \frac{\Delta P}{\Delta P_0} = \left(\frac{N}{N_0}\right)^2 \tag{5}$$

Eq. (5) is rewritten as

$$N = N_0 \sqrt{\frac{\Delta P}{\Delta P_0}} \approx N_0 \sqrt{r} \tag{6}$$

With this relationship, Eq. (2) is rewritten as

$$\dot{m}_2 \approx \dot{m}_0 \sqrt{r} \tag{7}$$

The mass flow rate of the circulation valve is

$$\dot{m}_3 = A_r \cdot \sqrt{2\rho_3 \cdot \Delta P} \tag{8}$$

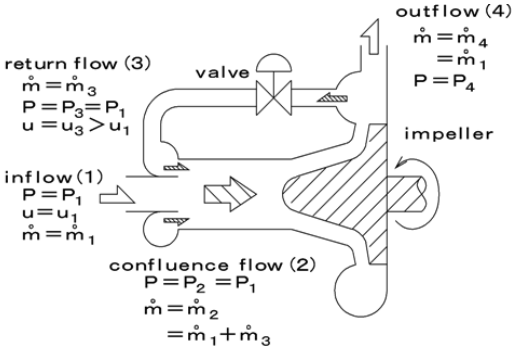

Fig. 1 Pump with circulation.

A_r is cross section of the valve and is a function of the throttled level of thrust, r. With Eqs. (7) and (8), Eq. (4) is rewritten as

$$\dot{m}_4 \approx \dot{m}_0 \cdot \sqrt{r} - A_r \sqrt{2\rho_3 \cdot r \cdot \Delta P_0} \approx r \cdot \dot{m}_0 \tag{9}$$

The cross section of the circulation valve is

$$A_r \approx \frac{\dot{m}_0\left(1-\sqrt{r}\right)}{\sqrt{2\rho_3 \cdot \Delta P_0}} \tag{10}$$

The circulated mass flow rate is

$$\dot{m}_3 = \dot{m}_2 - \dot{m}_4 \approx \dot{m}_0\left(\sqrt{r} - r\right) \tag{11}$$

Differentiation of Eq. (11) shows the largest circulation flow rate is at $r = (1/4)$.

2.2 Enthalpy and temperature at pump entrance

Temperature at the pump entrance increases by the circulation. Enthalpy of the confluence flow is

$$h_{t2} = \frac{\dot{m}_1 \cdot h_{t1} + \dot{m}_3 \cdot h_{t3}}{\dot{m}_1 + \dot{m}_3} \approx \sqrt{r} \cdot h_{t1} + \left(1-\sqrt{r}\right) \cdot h_{t3} \tag{12}$$

h_t is total enthalpy. The power required to the pump is

$$W_p = \dot{m}_2\left(h_{t4} - h_{t2}\right) = \frac{1}{\eta_p}\dot{Q} \cdot \Delta P \tag{13}$$

Eq. (13) is rewritten as

$$h_{t4} = h_{t3} \approx \frac{1}{\eta_p}\frac{r \cdot \Delta P_0}{\rho_2} + h_{t2} \tag{14}$$

Eq. (14) is put into Eq. (12), then

$$h_{t2} \approx h_{t1} + \left(\sqrt{r} - r\right)\frac{1}{\eta_p}\frac{\Delta P_0}{\rho_2} \tag{15}$$

Temperature of the confluence flow is calculated with Eq. (15).

3. Results and discussion

Operating condition of the throttled LOX pump is calculated with the relationships for an imaginary 100 kN-level LOX/LH_2 rocket engine. Its operating conditions at the design point are listed in Table 1. Properties of oxygen are calculated with a code.[1)] Total pressure of the confluence flow, Pt_2, is presumed to be equal to Pt_1.

Figure 2 shows an area ratio of the circulation valve, A_r, to that at the entrance of LOX pump, A_1. Fig. 2 also shows total temperature of the confluence flows. Figure 3 shows the Net Positive Suction Heads (NPSH) and the cavitation parameter, CP. Herein their definitions are

$$\mathrm{NPSH} = \frac{P_{t2} - P_s}{\rho_2 \cdot g} \tag{16}$$

$$CP = \frac{P_2 - P_s}{(1/2)\rho_2 \cdot u^2} \tag{17}$$

Here u is tip speed of the pump inducer. P_s is saturation pressure at T_{t2}. In the figures, r = 1 indicates the operation at the design point.

Table 1. Specifications of LOX pump at design point.

Inflow temperature, T_{t1}, K	90
Inflow pressure, P_{t1}, MPa	0.2
Flow rate, kg·s^{-1}	20
Efficiency	0.80
ΔP_0, MPa	4.8
Entrance diameter., m	0.07
Rotational speed, rpm	16000
Specific speed, m, m^3/m, rpm	174

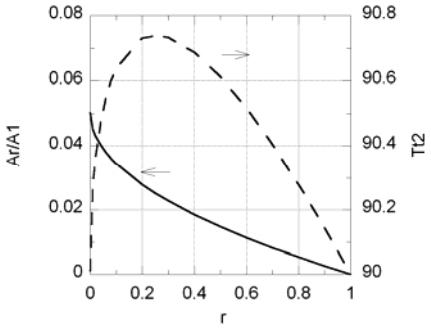

Fig. 2 Circulation area ratio and temperature of confluence flow.

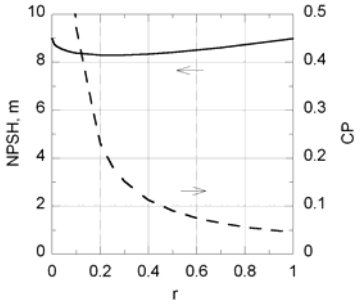

Fig. 3 NPSH and cavitation parameter.

The circulation valve cross section was much smaller than the original entrance cross section. Temperature of the confluence flow did not greatly increase by the throttling. It was caused by large density of oxygen and small increase of its enthalpy by the pump work during the throttling, as shown in Eq. (15).

The NPSH did not change greatly due to the small change of temperature of the confluence flow. The cavitation parameter became large in the deep throttled condition, since the rotational speed and u of the pump decreases with the throttling as shown in Eq. (6).

4. Concluding remarks

The throttled operation of the pump of the liquid rocket engine by the circulation is examined analytically. The pump operating conditions are calculated for a LOX pump of an imaginary 100 kN-level rocket engine with the analytical relationships. The calculated results show the applicability of the circulation to the pump.

References

[1] Y. Wakamatsu, T. Kanda and A. Kanmuri, NAL TM-564, (1987).

Non-Spherical Particles and Their Rotation: An Upcoming Issue in Particulate Flows

Fredrik Lundell
Linné FLOW Centre, KTH Mechanics, Royal Institute of Technology, S-100 44 Stockholm, Sweden
fredrik@mech.kth.se

ABSTRACT

In order to model flows with non-spherical particles, it is necessary to predict the rotational motion of the particles. Here, motions of ellipsoids with non-negligible particle inertia in linear shear flow is studied under Stokes flow conditions. This constitutes a fundamental system that is used as a basis for simulations and analysis of flows with heavy non-spherical particles. Particle inertia induces a drift towards rotation around the shortest axis for all ellipsoids studied. As this motion is approached certain parameter combinations (light slender particles) end up in a chaotic motion whereas other end up in a well defined periodic motion.

1. Introduction

Nonspherical particles occur in many engineering situations. The correct understanding of the rotation of such particles is necessary for proper modeling of flows with such particles.

In this paper, a study on the motion of such particles in flow is reported. The flow case studied is shown in Fig. 1, where a triaxial ellipsoid in shear flow is depicted. The axes of the particle are 2, $2k_b$ and $2k_c$ from the longest to the shortest axis.

The study is made in order to gain fundamental knowledge of particle motion in simplified flow situations. This serves as a starting point when analysing more complex flow situations, particle interactions, etc.

2. Method

The physical model is described in detail in [4]. In short, the torques on the particle in creeping flow are given analytically by [2] and are coupled to the equations of motion for rotation of a 3D-body. The motion of the particle is then seen to be governed by the aspect ratios k_b and k_c together with a parameter quantifying the effects of particle inertia, the Stokes number $St=4\rho_p\tau l^2/\rho_f\mu$ where ρ_p and ρ_f are the densities of the particle and fluid, respectively, τ. is the rate of shear, l is half the length of the main axis and μ is the dynamic viscosity of the fluid.

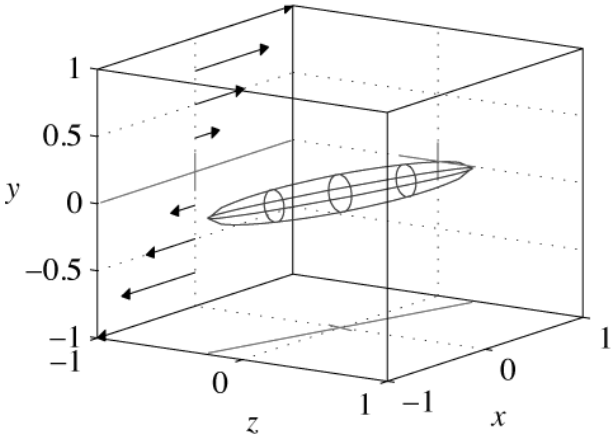

Fig. 1 A triaxial ellipsoid in shear flow. Here, k_b=0.14 k_c=0.1. This is the case (and initial condition) studied in Figs. 2 and 3.

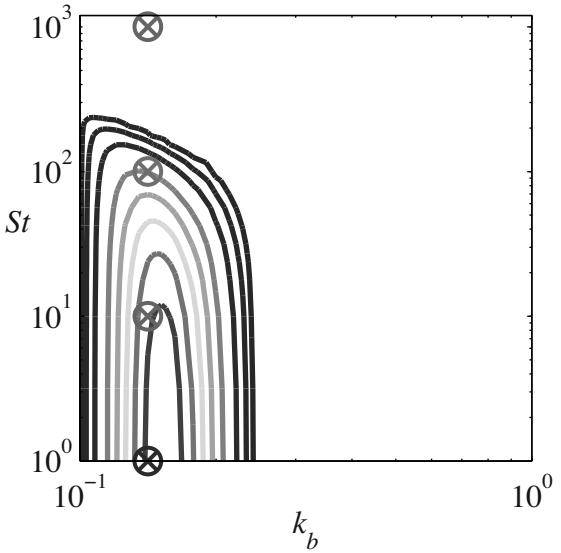

Fig. 2 Result from the Floquet stability analysis of rotation around the smallest axis for triaxial ellipsoids with k_c=0.1. The four markers indicate the cases studied in Fig. 3 (colour coded). The contours show the magnitude of the largest Floquet eigenvalue. The region inside the contours is unstable.

Here, this system is studied in two ways. First through Floquet stability analysis (see [3]) of rotation with one particle axis fixed to the vorticity axis of the flow (the z-axis in Fig. 1). These results are followed with some examples of particle motion.

3. Results and Discussion

The results from the stability analysis are shown in Fig. 2. It is known that light particles (St=0) ae unstable for certain aspect-ratio combinations, [1], and that this instability can lead to chaotic particle motion [5]. For low St, Fig. 2 shows a distinct region of instability for $0.1<k_b<0.23$ when k_c=0.1. For higher St, the instability is stabilized

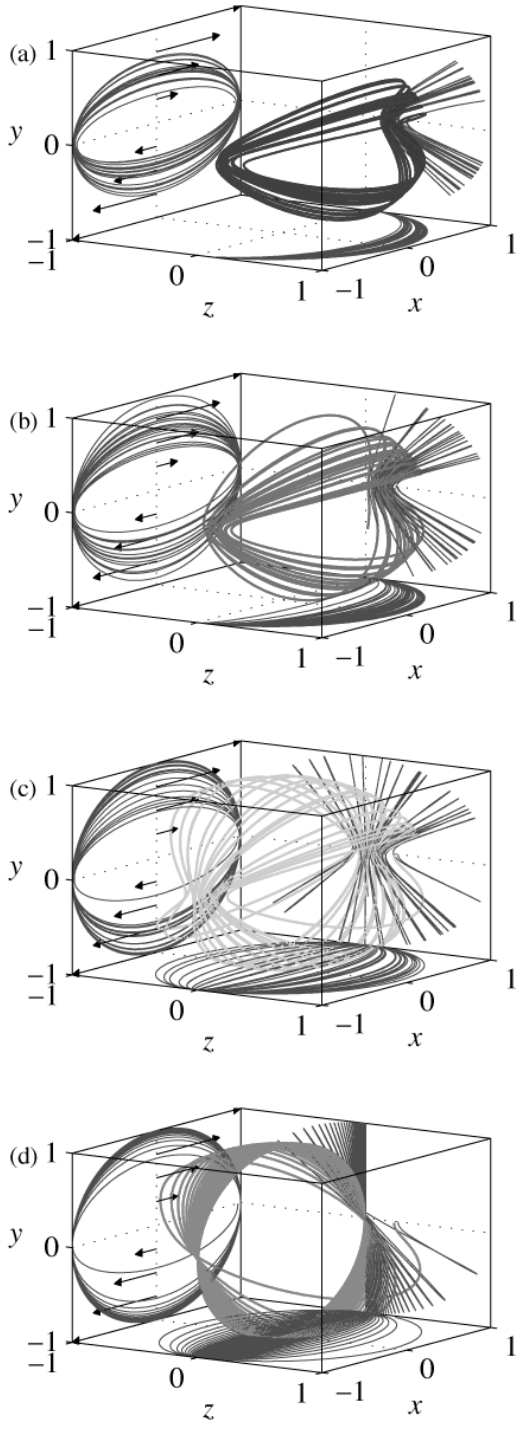

Fig. 3 Orbits of the longest particle axis from the initial condition shown in Fig. 1 for the parameter values indicated in Fig. 2 (colour coded). The Stokes number is 1, 10, 100, 1000 from (a) to (d).

This result extends the results for light particles of [1,5] to the case of particles with inertia and show that particle inertia can stabilize the particle motion. As a result, the particle motions, shown in Fig. 3, are fundamentally different for light (low *St*) as compared to heavy (high *St*). At low *St* (a,b), the particle performs a kayaking motion with increasing amplitude whereas at higher *St* in (c), there is an initial increase in amplitude followed by a chaotic motion, where the particle end point switches intermittently from one side to the other. At very high *St*, the motion is stabilised and the particle approaches rotation around the shortest axis in an ordered manner.

4. Concluding remarks

Stability analysis and integration of the governing equations have been used to investigate the motion of heavy triaxial ellipsoids in creeping shear. The principal effect of particle inertia is to induce a drift towards rotation around the shortest axis. However, if the median axis is not to much longer than the shortest axis, rotation around the latter is unstable for light particles.
Thus, it is concluded that light (albeit not mass free) particles approach a chaotic layer where they perform a kayaking motion but intermittently switches from one side to the other. Heavier particles (heavy enough for the particle inertia to stabilise the flow-induced instability) do not show a chaotic motion but instead end up rotating with the shortest axis aligned with the vorticity axis of the flow. The results show the importance to take inertial effects into account when modeling particulate flows with non-spherical particles.

References

[1] E.J. Hinch & L.G. Leal, J. Fluid Mech. **92** (1979), pp 591-608.
[2] G.B. Jeffery, Proc. Roy. Soc. A, **102** (1922), pp 161-179.
[3] D.D. Joseph, “Stability of Fluid Motion”, Springer, (1976).
[4] F. Lundell & A. Carlsson, Phys. Rev. E, **81** (2010), 011704.
[5] A.L. Yarin, O. Gottlieb, I.V. Roisman, J. Fluid Mech., **340** (1997), pp 83-100.

Eighth International Conference on Flow Dynamics
November 9 - November 11, 2011

Expansion Wave and Bubble Generation by Underwater Micro Explosion

Kiyonobu Ohtani, Toshihiro Ogawa. Shigeru Obayashi.
Institute of Fluid Science, Tohoku University, 2-1-1, Katahira, Aoba, Sendai, JAPAN 980-8577
ohtani@ifs.tohoku.ac.jp

ABSTRACT

This paper reports a preliminary experimental result of the expansion wave and cavitation bubble generation near the water surface. Underwater spherical shock wave generated by detonating of micro explosive of a 10 mg silver azide pellets propagated and reflected from the water surface. The reflected wave is an expansion wave. The process of expansion wave and cavitation bubble generation near the water surface were observed by shadowgraph method and recorded by a high-speed camera. The pressure distribution near the water surface was measured by a PVDF needle hydrophone.

1. Introduction

Underwater shock wave, expansion wave and cavitation bubble generation near the water surface by underwater explosion are large interested in relation to medical and biomedical engineering[1].

Kedrinskii[2][3] investigated numerically the influence of the development of the cavitation bubble zone on the rarefaction wave (expansion wave) in the region of regular reflection of spherical shock wave of an underwater explosion from the free surface. He calculated the expansion wave profile by using a charge of 1 g in weight at different depths, described the cavitation bubble zone development. The numerical results were compared with the experimental results.

In this study, the experiment of the underwater explosion near the water surface was performed. The process of the propagation of expansion wave and cavitation bubble generation was observed by shadowgraph method and recorded by a high-speed camera.

2. Experimental setup

Figure 1 shows a schematic diagram of experimental setup for underwater micro explosion near water surface in a water chamber. A stainless steel chamber of 200 x 200 x 200 mm with 200 x 200 mm observation acrylic windows is used. A spherical underwater shock wave was generated by exploding a silver azide pellet (AgN_3, 99.9 % purely, density of ρ= 3.8 g/cm^3, 10±0.1 mg, Showa Kinzoku Co., Ltd.,). A silver azide pellet is glued at the tip of a 0.6 mm in diameter quartz optical fiber (G.C.600/750, Fujikura Ltd.) and placed at the depth (h_e = 20~70 mm) from the water surface. A pulsed Nd:YAG laser beam (7 ns pulse duration) guided through this optical fiber then ignites the silver azide pellet. We observed the process of the propagation of expansion wave and cavitation bubble generation by shadowgraph method and recorded by using a high-speed camera (Imacon 200, DRS Technologies, Inc., spatial resolution 1280 x 980 pixel per frame, interframe time of 5 ns to 1 ms, exposure time of 5 ns to 2 ms). The pressure profile near the water surface was measured by a PVDF needle hydrophone (Platte Needle Probe, Muller Instruments, detectable pressure range of -10 to 200 MPa, sensitive diameter of 0.5 mm, rise time of 50 ns).

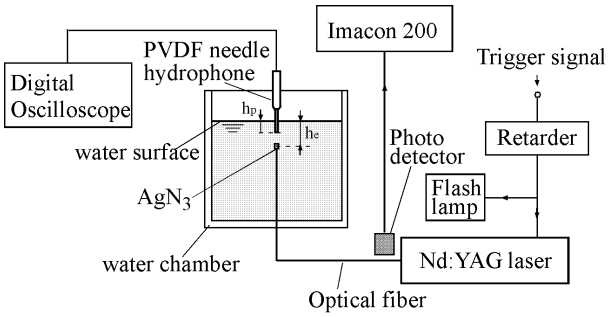

Fig.1 Schematic diagram of experimental setup for underwater explosion near the water surface.

3. Results and Discussion

Time resolved shadowgraph images of the propagation of expansion wave and cavitation bubble generation is shown in Fig 2. The observation was performed at interframe time of 5 μs and exposure time of 20 ns. The silver azide pellet was placed at h_e=40 mm.

The spherical underwater shock wave is generated and propagated and then reflected from the water surface. The propagation speed of the underwater shock wave is estimated about 1588.0 m/s, which Mach number is about 1.06. The reflected wave from the water surface is an expansion wave. The pressure near the water surface is decrease by the propagation of expansion wave and generated cavitation bubbles, and the cavitation bubble zone is extended. A several wave behind the expansion wave was generated by underwater shock wave interaction with water surface and interacted with cavitation bubble.

Figure 3 shows the pressure history at about h_p=10.6 mm from the water surface. The silver azide pellet was placed at about h_e=40 mm. The dash line in Fig. 3 indicates Nd: YAG laser beam pulse signal for the ignition of micro explosive. At about 18.5 μs after ignition, the incident shock wave reached the hydrophone surface and indicated pressure of about 20.9 MPa. The negative peak pressure of expansion wave was observed -4.57 MPa at about 32.1 μs.

Figure 4 shows the pressure distribution near the water surface at different depths of micro explosion (h_e=20~70mm): (a) incident shock wave peak pressure; (b) expansion wave negative peak pressure. The peak

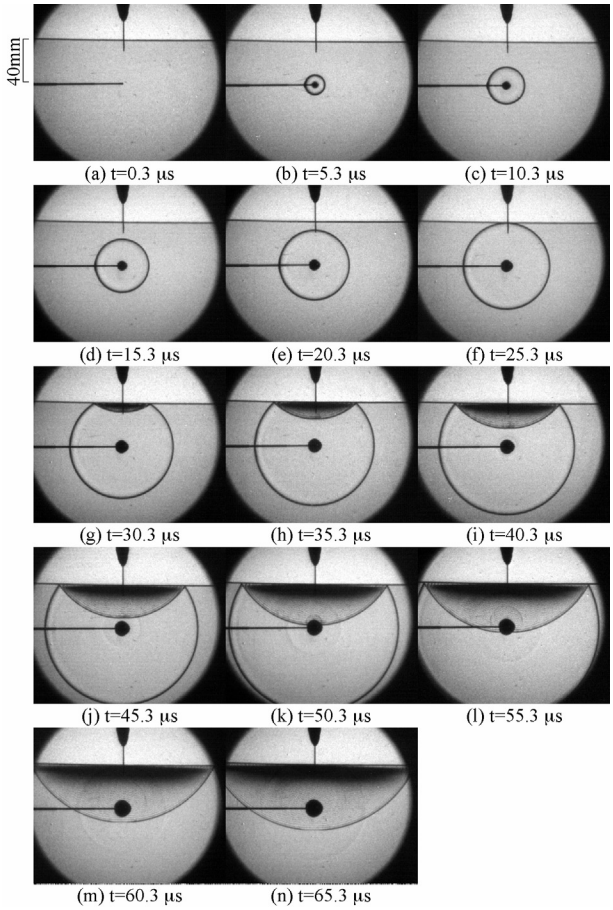

Fig.2 Sequential shadowgraph images of expansion wave and bubble generation near the water surface by underwater micro explosion. (Interframe 5 μs, exposure time 20 ns, h_e=40.7 mm)

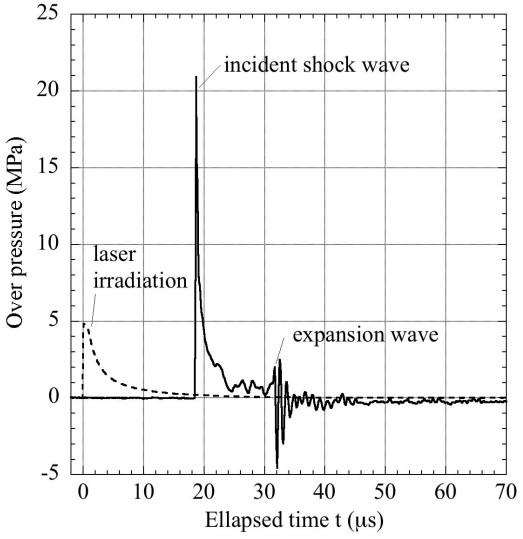

Fig. 3 Pressure history near the water surface. (h_e=40.7 mm, h_p=10.6 mm)

pressure was increased near the hydrophone. The negative peak pressure was increased near the water surface.

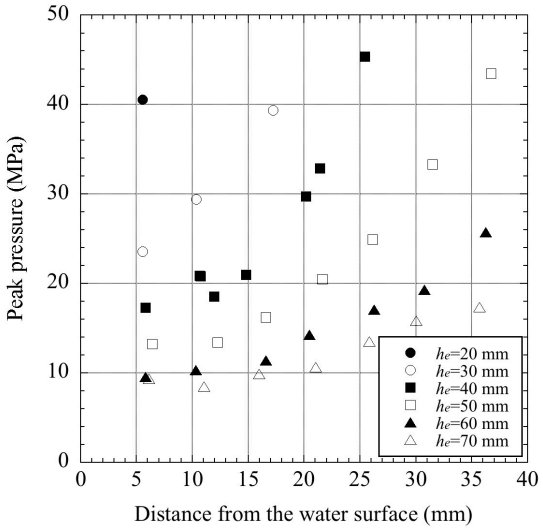

(a) Peak pressure of incident shock wave

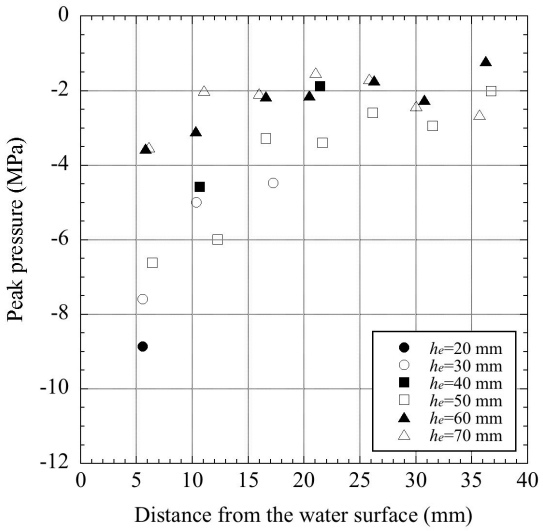

(b) Negative peak pressure of expansion wave

Fig. 4 Pressure distribution near the water surface at different depths of micro explosion. (h_e=20~70mm)

4. Concluding remarks

We performed a preliminary experiment of the expansion wave and cavitation bubble generation near the water surface. The process of expansion wave and cavitation bubble generation was observed by shadowgraph method and recorded by a high-speed camera.

References

[1] K. Ohtani, T. Hashimoto, K. Takayama, Expansion wave propagation and cavitation bubble generation near the water surface. the 27th International Symposium on Shock Waves, (2009), Book of Proceedings, pp. 297.

[2] V.K. Kedrinskii, Dynamic of the cavitation zone during an underwater explosion near a free surface. Journal of Applied Mechanics and Technical Physics, **16**(5) (1975), pp. 724-733.

[3] V.K. Kedrinskii, Negative pressure profile in cavitation near free surface. Acta Astronoutica **3** (1976), pp. 623-632.

A Dynamic Model of Valveless Micropumps with Squeeze Film Effect

N T M Le[1], T X Dinh[2], and Y Ogami[2]
1 Petrovietnam University, 173 Trung Kinh Str., Cau giay, Hanoi, Vietnam
2 Ritsumeikan University, 1-1-1 Nojihigashi, Kusatsu, Shiga 525-8577, Japan
E-mail of corresponding author: thien@cfd.ritsumei.ac.jp.

ABSTRACT

A simple fluid-diaphragm coupling model for studying the dynamic performance of valveless micropumps is presented. The model includes fluid inertia and squeeze film effect by solving the coupling equation simultaneously with Reynolds equation. The model is validated with valveless diffuser micropump actuated by either piezoelectric or electromagnetic diaphragm. The performance of the pump is considered for pumping liquid and air. The resonant frequency and dynamic performance of the micropumps obtained by the model are in good agreement with the experiment data. The model can predict well the damping behavior of the pump.

1. Introduction

The necessity of flow in a Lab-on-a-chip (LOC) –a term reduces macroscale experiments to analysis on a chip– has enabled the opened research on micropumps [1]. Since the flow in displacement micropumps is actuated by the vibratory diaphragm of the micropump, the motions of the diaphragm and the fluid flow are always coupled, which determines the resonant frequency and dynamic performance of the micropump.

In this paper, we develop a fluid-diaphragm coupling scheme considering fluid inertia and squeeze effect, which is different from [2]-[6]. Then the model is applied to investigate the dynamic performance of valveless diffuser pumps which is actuated by either electromagnetic or piezoelectric diaphragm. The performance of the pump is considered for both pumping liquid and air.

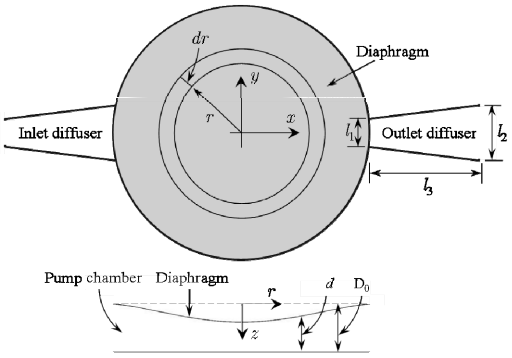

Fig. 1. The schematic design of the considered diffuser micropump.

2. Fluid–Diaphragm Interaction Scheme

Fig. 1 shows the schematic of the considered valveless micropump in this study. The inlet diffuser and outlet diffuser have identical geometrical structure.

For a circular diaphragm used in micropumps, the deflection is often the first axisymmetric mode whose deformation shape can be analytically obtained. Hence, the motion of a position r on the diaphragm is written as $z(r,t) = Z(t)\varphi(r)$ where Z(t) is central displacement of the diaphragm and $\varphi(r)$ is the shape function of the deflection [7]. The central displacement of the diaphragm, Z(t), is modeled as the vibration of a spring-mass system as

$$M\ddot{Z} + C\dot{Z} + KZ = f_e + P \quad (1)$$

where M, C, and K are equivalent mass, damping coefficient, and spring constant, respectively. f_e is the external force. P is the fluid pressure force exerted on the diaphragm, which is obtained by solving the below Reynolds equation

$$\partial\left(d^3\partial p/\partial x\right)/\partial x + \partial\left(d^3\partial p/\partial y\right)/\partial y = -12\mu\dot{Z}\varphi(r) \quad (2)$$

The pressure condition for Eq. (2) at the interfaces between the diffusers and pump chamber are assumed equal and obtained from the empirical pressure loss through a diffuser and the mass conservation.

The equivalent mass M is the sum of the the equivalent masses of diaphragm M_D and fluid M_F as, where K_v the deformed volume rate of the pump chamber due to the deflection of the diaphragm and η is diffuser efficiency.

$$M_D = \int_{A_D} h\varphi^2(r)\rho_D dA \quad (3)$$

$$M_F = \rho\frac{1}{h_1}\frac{l_3}{l_1}\frac{\log\left(l_2/l_1\right)}{l_2/l_1 - 1}\frac{\eta+1}{\left(\sqrt{\eta}+1\right)^2}K_v^2 \quad (4)$$

3. Results and Discussion

3.1. Application of the model to an electromagnetic micropump

In this section, the developed model is applied to investigate the dynamic performance of the electromagnetic micropump proposed by Yahamata [5].

Since Young's modulus of the magnet is much larger than that of PDMS, the deflection of a position $r \le b$ (radius of the magnet) of the diaphragm is constant. In the counterpart of the diaphragm, the deflection is expressed as [8]

$$z(r) = \frac{Fa^2}{8\pi D}[\bar{r}^2(\log\bar{r} - 1) + C_1\bar{r}^2/2 + C_2\log\bar{r} + C_3] \quad (5)$$

where $\bar{r} = r/a$, a is radius of the diaphragm, F is the force applied on the magnet, and $D = Eh^3/\left(12(1-\nu^2)\right)$. E and ν are Young's modulus and Poisson ratio, respectively, of the PDMS material. h is the thickness of the diaphragm. The constants C_1, C_2, and C_3 are determined by using the clamped condition at $r = a$ and built-in condition at $r = b$. Then, and the equivalent spring stiffness is $K = 8\pi D/(k_1 a^2)$, where k_1 is

obtained by substituting $\bar{r} = b/a$ into Eq. (5).

Fig. 2 and 3 show the good agreement between the simulation and experiment flow rate for pumping air and pumping water. The solid-dotted lines represent the simulation data whereas the symbols indicate the experiment counterpart. The results attained by Pan et al. model [4] were also plotted by dashed line. Pan et al. model can reproduce this behavior for pumping air and strongly underestimates for pumping water. A possible explanation might be the importance of losses caused by squeeze film damping in the pump chamber.

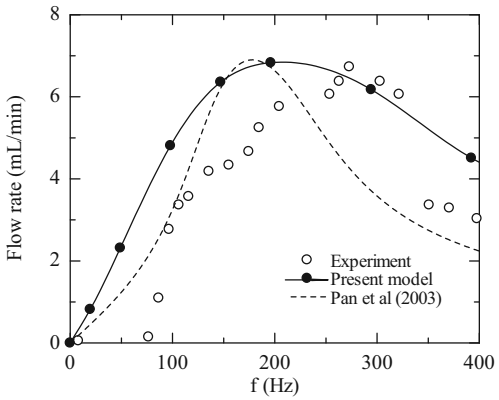

Fig. 2. The variation of the air flow rate of the considered electromagnetic micropump with exciting frequency without backpressure.

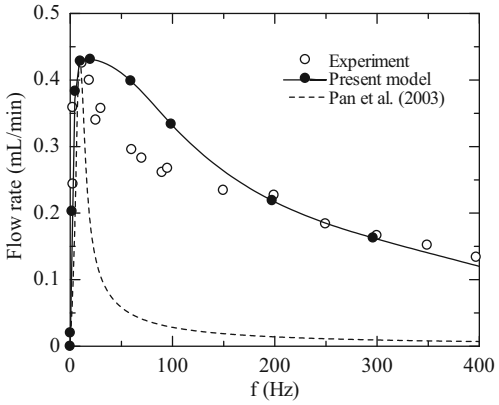

Fig. 3. The variation of the water flow rate of the considered electromagnetic micropump with exciting frequency without backpressure.

3.2. Application the model to a piezoelectric micropump

In this section, the present model is validated with the dynamic performance of a piezoelectric micropump for pumping water [6]. In this micropump, the piezoelectric force is assumed being uniform on the piezoelectric disk with the intensity of q. Therefore, the deflections of the outer ($r \geq b$) and inner ($r \leq b$) portions of the diaphragm, respectively, are [8]

$$z(r) = \frac{F}{4\pi Db^2}\int_0^b z_o(r,r')r'dr'$$
$$z(r) = \frac{F}{4\pi Db^2}\left(\int_0^r z_o(r,r')r'dr' + \int_r^b z_i(r,r')r'dr'\right) \quad (6)$$

where $F = \pi q b^2$. $z_o(r,r')$ and $z_i(r,r')$ are in [8].

The spring constant is determined as $K = 4\pi Db^2/k_1$, where k_1 is the constant computed by substituting $r = 0$ into the second equation of Eq. (6).

Fig. 4 compares the flow rate-frequency relation predicted by the present model with the experiment data and Pan's model. The figure shows that the damping behavior of the pump which is underestimated by Pan et al model is well predicted by the present model.

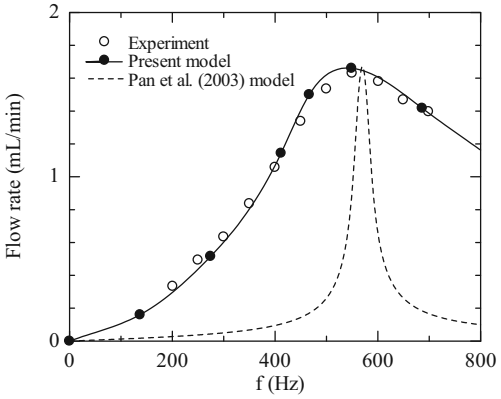

Fig. 4. The variation of the water flow rate of the considered piezoelectric micropump with exciting frequency without backpressure.

4. Conclusion

A simple dynamic model for studying the dynamic performance of valveless micropumps has been developed. The interaction between fluid and diaphragm is reduced to a lump mass-spring motion. Instantaneous fluid pressure acting on the diaphragm is obtained by solving the Reynolds equation. This technique can include the squeeze film losses in the pump chamber to the damping behavior of the pump. The model was applied to study the dynamic performance of valveless diffuser micropumps actuated by either piezoelectric or electromagnetic actuators. The performance of the pump is considered for pumping liquid and air. The analytic resonant frequency of the pump is in good agreement with experiment data. The model predicts well the damping behavior of the pump which is underestimated by the model of Pan et al, particular for pumping liquid.

References

[1] D. J. Laser et al. J. Micromech. Microeng., **14** (2004).
[2] A. Olsson et al., J. Micromech. Microeng., **9** (1999).
[3] L. S. Pan, et al., Sensors Actuators A, **93** (2001).
[4] L. S. Pan et al., J. Micromech. Microeng., **13** (2003).
[5] C. Yamahata et al., J. Microelect. Eng., **78/79** (2005).
[6] A. Ullmann et al., J. Fluid Eng., **123** (2001).
[7] I. I. Anik'ev et al., J. Int. Applied Mecha., **13** (1977).
[8] S. P. Timoshenko et al., Theory of plate and shells, 2nd Ed., McGraw Hill (1959)

Simulation of a Triple-Axis Thermal Bubble Accelerometer

Thien Xuan Dinh, Yoshifumi Ogami
1-1-1 Nojihigashi, Kusatsu, Shiga, 525-8577 Japan.
thien@cfd.ritsumei.ac.jp

ABSTRACT

The paper presents the numerical design and performance of a triple-axis thermal accelerometer. In contrast with conventional design of a dual-axis thermal accelerometer, in our new design, the heater is formed a wide ring and the sensing elements are located both inside and outside of the heater ring with a small elevation from the heater plane. The obtained results show that the sensitivity of the vertical axis measurement attains to the order of the horizontal axes measurements. The cross-sensitivities among three axes are less than 4%.

1. Introduction

The broad market for measurement devices, covering automobile, defense, smart phone, biomedical care, biomimetic robots and the other fields, has led to a large amount of research on inertial sensors using microscope electromechanical structures. Thermal-bubble accelerometers eliminate the drawbacks of vibratory accelerometers because they avoid using solid proof mass. Their operation is based on the displacement of a hot air bubble generated by a heated wire in an enclosed chamber under acceleration. Various gas and liquid media have filled in the chamber [1-4] to improve the sensitivity of this type of accelerometers. Nevertheless, the developed thermal-bubble accelerometers can measure only two components of acceleration. Recently, a principle for a triple-axis accelerometer has been proposed [5]. However, there is no discussion if this principle is efficient or not.

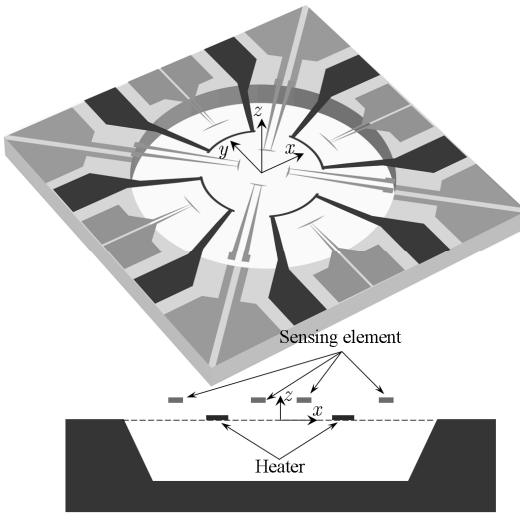

Fig. 1. The configuration of the accelerometer

In this study, we present a thermal-bubble based accelerometer that can measure simultaneously three components of acceleration. First, the temperature distribution in the sensor is investigated by the use of computational fluid dynamics technique. Next, positions of the thermistors are optimized with the minimum cross-sensitivity. Finally, the sensitivity of the sensor is studied for various room temperature conditions, heating power on the resistors.

2. The Accelerometer

In a typical thermal-bubble based accelerometer, a heater is suspended at the center and sensing elements are located around the heater on the opening side of a cavity. Consequently, the sensitivity of the vertical axis measurement is very low in comparison with the horizontal axes measurements and the cross-sensitivity between these measurements is very high. In our new design as shown in Fig. 1, the heater is formed a wide ring and the sensing elements are located both inside and outside of the heater ring with a small elevation from the heater plane. The device is packaged in a sealed chamber containing the working media such as air, helium, and liquid.

3. Results and Discussions

In this discussion, T_0 and T represent temperature at normal state, $a_n = (0, 0, 1g)$, and at applied state, $a = (a_x, a_y, a_z–g)$, respectively. ΔT is $T–T_0$.

As a simple way to determine the positions of the sensing elements, the sensitivities S_x and S_z of the accelerometer are computed for one applied acceleration $a = (1g, 0, 0)$ and $a = (0, 0, 1g)$, respectively. Obviously, the sensing element should be located where the cross-sensitivity $S_{zx} = S_x/S_z \times 100$ and $S_{xz} = S_z/S_x \times 100$ are minimized and sensitivity is maximized as possible. With constrains of $S_{xz} \leq 5\%$, the optimal position of the sensing element for x-measurement is $z = 100$ μm and $x = 500$ μm, and $z = 100$ μm and $x = 40$ μm for z-measurement in the present design.

The temperature differences $2\Delta T$ on the sensing elements for x- and z-measurements under different applied acceleration are depicted in Fig. 2. The figure shows that the accelerometer has good linearity in the range from 0 to 10 g. The temperature change rate $2\Delta T/a$ are about 0.25^0C/g and 0.12^0C/g for x-measurement and z-measurement, respectively. Fig. 3 plots the variation of $2\Delta T/a$ with the heating power of the heater. It is indicated that the temperature change rate of the accelerometer are almost linear with the heating power. Increasing the heating power can increase $2\Delta T/a$.

Fig. 4 shows the temperature change rate versus

ambient temperature for a constant heating power. The temperature dependence $2\Delta T/a$ is not linear. As increasing room temperature, i.e. the wall temperature of the accelerometer, with keeping the heating power constant, the difference of temperature between the heater and wall is reduced. This results in deteriorating the heat convection in the accelerometer. Consequently, the temperature change rate decreases.

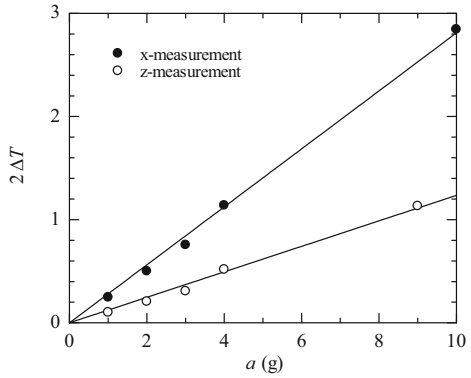

Fig 2. The variation of the temperature change on the sensing element with applied acceleration.

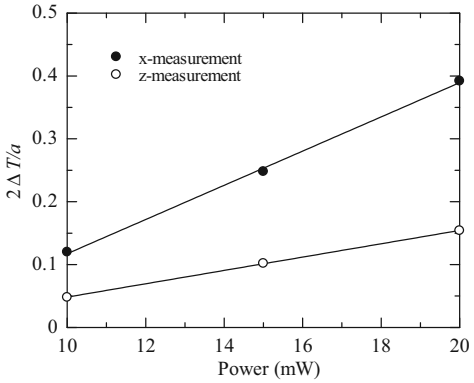

Fig 3. The variation of the temperature change on the sensing element with applied acceleration.

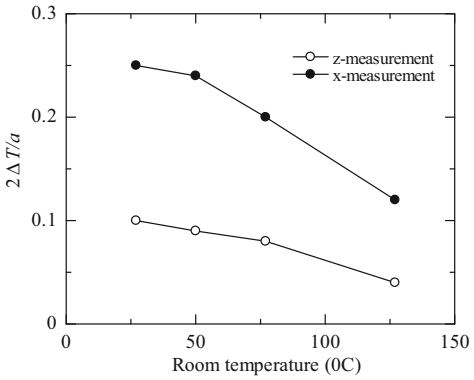

Fig. 4. The variation of the sensitivity with room temperature

We can observe that the temperature change rate for *x*-measurement is about twice of that for *z*-measurement in any considered working condition of the accelerometer. It is noted that the true sensitivity of the accelerometer should be multiplied $\alpha I R_0$ to $2\Delta T/a$. Therefore, we can adjust R_0 to balance the sensitivities between *x* and *z* measurements. Assume that all the sensing elements of the accelerometer are made of the same material with the electrical resistivity of ρ_e. The resistance R_0 can be expressed as $R_0 = \rho_e A l$, where A is the cross section area and l is the length of the sensing elements. Therefore, it suggests that we can fabricate the length of the *z*-sensing elements double of that of the *x*-sensing elements as shown in Fig. 5.

4. Conclusion remarks

A triple-axis thermal accelerometer was proposed and numerically studied. The heater of the accelerometer is formed a wide ring and the sensing elements are located both inside and outside of the heater ring with a small elevation from the heater plane. With this arrangement, the sensitivity of the vertical axis measurement attains to the order of the horizontal axes measurements, which is usually very small in a conventional design. The cross-sensitivities among three axes are less than 4%. For instance, at the supplied power of 15mW to the heating resistor, the sensitivity of the accelerometer is 0.12^0C/g in the vertical axis and 0.25^0C/g in the horizontal axes.

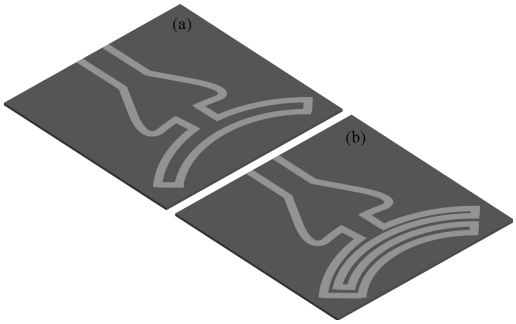

Fig 5. The proposed sensing element shapes for *x*-measurement (a) and for *z*-measurement (b).

5. Acknowledgment

This work is partially supported by Japanese Society for Promotion Science Fellowships for Post Doctoral Research at Ritsumeikan University.

References

[1] V. Milanovic, E. Bowen, N. Tea, J.S. Suehle, B. Payne, M.E. Zaghloul, M. Gaitan, MEMS Symp. IMECE (1998), pp. 627–630.
[2] X.B. Luo, Z.X. Li, Z.Y. Guo, Y.J. Yang, Heat Mass Transfer, **38** (2002), pp.705–712.
[3] S. Billat, H. Glosch, M. Kunze, F. Hedrich, J. Frech, J. Auber, H. Sandmaier, W. Wimmer, W. Lang, Sens. Actuators A **97–98** (2002), pp. 125–130.
[4] K. M. Liao, R. Chen, B.C.S Chou, 2006, Sensor Actuator A, **130-131** (2006), pp. 282-289.
[5] Y. Hua, L. Jiang, Y. Cai, A. Leung, Y. Zhao, US Patent No. 2007/0101813 A1, MEMSIC Inc.

Eighth International Conference on Flow Dynamics
November 9 - November 11, 2011

Effect of Surfactant on Generation of Microbubbles

Masayuki Takashima,[1] Takayasu Kubozono,[1] Yuuki Fujioka,[2] Shuya Yoshioka,[2]
[1]Lion Corporation, 7-2-1 Hirai Edogawa-ku Tokyo, [2]Ritsumeikan University, 1-1-1 Nojihijashi Kusatsu city Shiga
E-mail : masa-t@lion.co.jp

ABSTRACT

Microbubbles have a unique character such as high retentivity in liquid, huge surface area, and surface electricity. We've focused on the microbubble's high retentivity to use gas efficiently. To make microbubble's retentivity better, the bubble diameter should be small and microbubbles coalescence should be prevented. So, we've investigated the effect of the surfactant on the generation of microbubbles. As a result, we clarified that surface tension and surface electricity are important to make bubble the diameter smaller and make the amount of microbubbles higher. The addition of surfactants is effective to make retentive microbubbles due to the low surface tension and electricity.

1. Introduction

Microbubbles have a unique character such as high retentivity in liquid, huge surface area, and surface electricity. Recently, the technique using microbubbles for industrial applications have been focused on[1]. We've focused on the microbubble's high retentivity to use gas efficiently. Because of keeping gas in the liquid more retentively, the effect of gas such as sterilization, decomposition of deleterious materials and growth stimulation etc, is also lasting. To obtain retentive microbubbles, it is important to generate smaller bubbles. According to Storks equation, floatation speed of bubble is corresponding to its diameter. And the bubble diameter is also corresponding to the surface tension[2].

Furthermore, to keep gas in the liquid, it is also important to prevent bubble coalescence. We think that electrical repulsion between microbubbles prevents the coalescence. It is already known that the microbubble's surface prepared by air and water is negatively charged by ζ-potential measurement[3]. However, the details of microbubble's electrical behavior have been unknown. Surfactants cause low surface tension and surface electricity on the generation of the microbubble. So, several effects of surfactants about bubble retentivity were reported[4-11], but the discussions about the surface charge were very few.

At the time of measuring the microbubbles size distribution, Dynamic Light Scattering (DLS) is generally used. But that measurement gives bubble diameter information only. It cannot analyze the amount of bubbles. If we want to evaluate the entire amount of gas of industrial use, we should measure the void fraction. Pycnometer is compact and suitable for the evaluation of void fraction.

2. Method

We used a commercially available microbubble generator. Pycnometer was used at the same temperature to the bubble-in-liquid at the evaluation of void fraction. It measures the amount of before and after microbubbles generated liquid. The difference of the amount can be an approximation of void fraction. Surface tension was measured by SITA online +60 SITA Messtechnik co.

In this work, aqueous solution of some solvents and surfactants were used to investigate the relation between void fraction and interfacial phenomenon. As solution of solvents; ethanol, acetone, diacetin and triacetin were used at 5000ppm concentration. Air was used as the gas. On the other hand, alcohol ethoxylate (AE), alkyl trimethyl ammonium chloride (TAC) and alkyl sulfate (AS) was used as the surfactant solutions with several numbers of carbon chain and ethylene oxide chain.

The aqueous solution of amphoteric surfactant; dodesyl amino propionic acid, was used at 1.0mM concentration with changing pH for evaluation of electrical effect.

3. Results and Discussion

As shown in Fig.1 and Fig.2, void fraction is corresponding to surface tension, both using solvents and surfactants. Especially, using surfactants achieved higher void fraction than solvents in spite of almost the same surface tension value.(Fig.3) We've considered that the hydrophobic interaction of surfactant molecules on the bubble surface keeps the bubbles retentive. Furthermore, non-ionic surfactant AE shows a lower value of surface tension, but void fraction was almost the same value to ionic one(AS, TAC). In other words, ionic surfactant AS and TAC achieved high void fraction in spite of its high surface tension value. As shown in Fig.4, bubble size distribution was monodispersed and mean diameter of microbubbles is about 40 micro meters by generation in SDS 1.0mM aqueous solution. And it's larger than alcohol ethoxylate's 10.(Fig.5) It shows that AS and TAC give large microbubbles but keep the bubbles retentive. Though, SDS microbubbles are smaller than pure water's 120 micro meters.(Fig.6) There is another factor besides bubble diameter. It is considered to be electricity.

Because the surfaces of microbubbles are covered with ionic surfactant molecules, the surface charge is enhanced. Thus, microbubbles are less likely to show the coalescence. So, microbubble size can be maintained and the retentivity of microbubbles becomes enhanced. As shown in Fig.7, void fraction value is lowest at the isoelectric point. It suggests that electricity is an important factor of keeping large amounts of microbubbles in water.

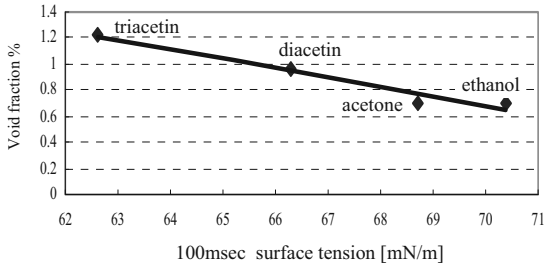

Fig.1 Void faction vs surface tension of solvent aqueous solution.

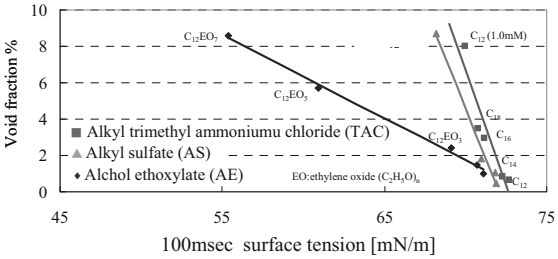

Fig.2 Void fraction vs surface tension of surfactant aqueous solution.

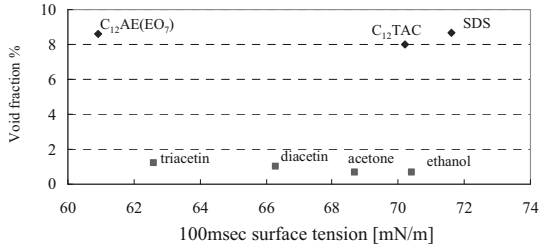

Fig.3 Void fraction comparison of solvents and surfactants.

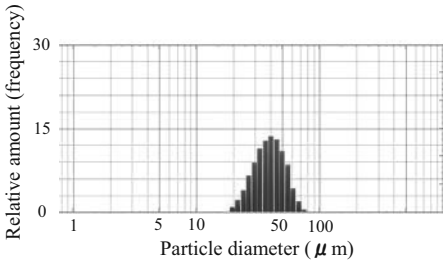

Fig.4 Bubble size distribution in C_{12}AS(SDS) 1.0mM aqueous solution.

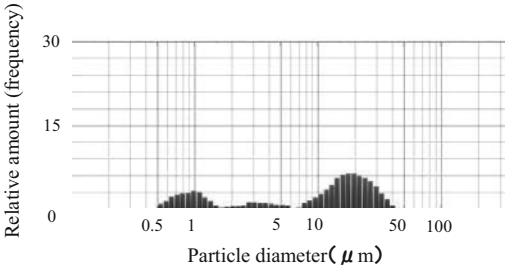

Fig.5 Bubble size distribution in C_{12}AE 1.0mM aqueous solution.

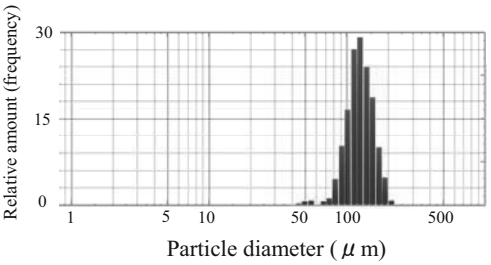

Fig.6 Bubble size distribution in pure water.

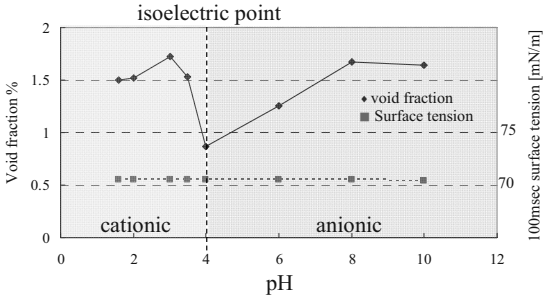

Fig.7 Void fraction vs pH using amphoteric surfactant.

4. Concluding remarks

Surface tension and electricity are important to achieve a high void fraction value. Lower surface tension gives higher void fraction. Especially, surfactants that show high void fraction due to its unique surface behavior such as electricity. But the most suitable way to measure electricity on the microbubble surface has not been established yet. As for future work, we will try measuring the surface electricity and confirm the structure effect of surfactants on the generation of microbubbles.

References

[1] H. Tsuge, "The Latest Technology on Micro bubbles and Nanobubbles II" CMC (2010)
[2] T. Tamura, J. Colloid Interface Sci. **173** (1995) , pp. 493-499.
[3] M. Takahashi, J. Phys. Chem. B. **109** (2005), pp. 21858-21864.
[4] A. Frumkin, and V. Levich, Zhur. Fiz. Khim, **21** (1947) pp. 1183-1204.
[5] J. Magnaudet, and I. Eames, Annual Review of Fluid Mechanics, **32** (2000) pp. 659-708.
[6] B. Cuenot., Magnaudet, J. and Spennato, B., J. Fluid Mech., **339** (1997) pp. 25-53.
[7] Y. Liao and J. B. McLaughlin, J. Colloid Interface Sci., 224 (2000) pp. 297-310.
[8] P. C. Duineveld, J. Fluid Mech., 292 (1995) pp. 325-332.
[9] R. B. Fdhila and P. C. Duineveld, Phys. Fluids, **8** (1996) pp. 310-320.
[10] Y. Zhang, and J. A. Finch, J. Fluid Mech., **429** (2001) pp. 63-66.
[11] S. Takagi, Nagare, **23** (2004) pp. 17-26.

Eighth International Conference on Flow Dynamics
November 9 - November 11, 2011

Water Confined in Carbon Nanotube: A Density Functional Theory Study

Arunabhiram Chutia[1], Ikutaro Hamada[2], Michio Tokuyama[1,2]
[1]IFS, Tohoku University, 2-1-1 Katahira, Aoba-ku, Sendai 980-8577, Japan
[2]WPI-AIMR, Tohoku University, 2-1-1 Katahira, Aoba-ku, Sendai 980-8577, Japan
ac@athena22.ifs.tohoku.ac.jp/achutia@gmail.com

ABSTRACT

An attempt has been made to comprehend the interaction of water molecules inside pristine carbon nanotubes. Density functional theory calculations show the arrangement of water molecules inside carbon nanotube to be dependent on their diameter. In carbon nanotubes with relatively smaller diameter water molecules are arranged as chain like structures while carbon nanotubes with larger diameter shows water clustering. To clearly understand the interaction of water molecule with graphitic wall a simpler model of water and graphene sheet is employed.

1. Introduction

The study of confined water has attracted much attention because of their fascinating properties, which is not observed in bulk water. They exist in our surroundings and even inside our bodies [1]. In recent years many theoretical and experimental efforts have been devoted to study confined water (CW) in carbon nanotubes (CNT). These studies are focused on various aspects such as such as water and proton conduction, formation of ice-nanotubes and water-nanotube etc. in CNTs [1–4]. Even some studies by high-resolution electron microscopy have revealed atomic scale interactions between the entrapped liquid phase and wetted graphite walls of carbon nanotubes [5]. While these investigations have provided insights into the unusual properties, still the picture related to the interaction between water molecules and the walls of carbon nanotube needs to be clarified.

In the current study we attempt to comprehend the interaction between CNT walls and CW. We performed density functional theory (DFT) calculations and study the interaction between water and CNT, hydrogen bonding between water molecules, and the interplay between them. Particular attention is paid to the interaction between water and CNT wall, which is challenging even at the present accuracy of DFT. For the latter purpose, we performed comparative DFT calculations on water monomer on graphene to assess the accuracy of present DFT and inspect the interaction between them.

2. Method

All the calculations are performed employing the DMol3 quantum chemical package [6,7]. We use the DNP (Double Numerical Plus polarization) basis set. DNP basis set is comparable to 6-31G** basis sets. The (7,0) and (10,0) CNT models with five water molecules are optimized at LDA/VWN level of exchange and correlation functional. The number of atoms in (7,0) CNT is 112 atoms (length=17.040Å and diameter=5.430 Å) and in (10,0) 160 atoms (length=16.904Å and diameter=7.740Å) For calculations involving water monomer on graphene we use LDA/VWN and GGA/(PBE, HCTH and BOP) levels of exchange and correlation functionals. The binding energy of water molecules on graphene surface (BE_{H_2O}) is calculated using the following formula:

$$BE_{H_2O} = E_{(graphene+H_2O)} - [E_{(graphene)} + E_{(H_2O)}]$$

Where, $E_{(graphene+H_2O)}$ is the energy of the model system with water molecule and graphene sheet, $E_{(graphene)}$ is the energy of the pristine graphene sheet and $E_{(H_2O)}$ is the energy of isolated water molecule.

3. Results and Discussion

First, we perform geometrical optimization of five water molecules within a pristine (7,0) CNT. As shown in Figure 1 (a and b) in (7,0) CNT we see the formation of water chain like structure. Each of the molecule form H-bonds with the nearest water molecule and at an average distance of 2.169Å from the walls of (7,0) CNT. For comparison of the structure of water molecules another CNT with bigger diameter i.e., (10,0) CNT with 5 H_2O is also optimized. However, in (10,0) CNT we see the formation of a network of H-bonding in water molecules like bulk water instead of chain like structure (See Fig. 1 (c and d)).

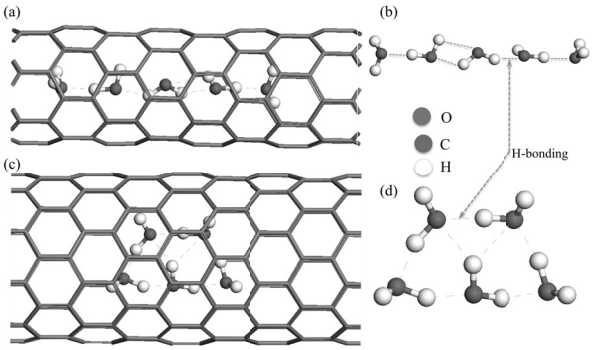

Fig. 1 Optimized structures of (a) 5 H_2O molecule in (10,0) CNT, (b) network of water molecules inside (10,0) CNT, (c) 5 H_2O molecule in (7,0) CNT and (d) water chain inside (7,0) CNT.

The formation of water chain like structure in (7,0) CNT could be attributed to several reasons. For example, this might be due to the smaller radius of (7,0) CNT electrostatic repulsion between lone-pairs of oxygen and puckered p_x orbitals of carbon atoms in CNT come into play. On the other hand due to slightly larger radius of

the (10,0) CNT lone-pair and p_x repulsive interaction is less and this favor accommodation of more water molecule to form water cluster through H-bonding similar to bulk water. Another major reasons could be associated with van der Waals interaction between water molecules and wall of (7,0) CNT.

For comparing the structure of the water cluster formed in (10, 0) CNT we further optimize the five-water molecules in (10,0) CNT within similar computational conditions. In the optimized model water molecules reorient to form more intense H-bonds. This reflects that a detailed study of the interaction of water molecule with the walls of CNT is required.

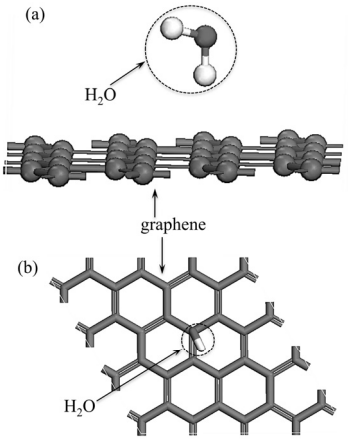

Fig. 2 (a) Side view and (b) top view of water monomer on graphene surface.

Since CNT can be regarded as rolled graphene for this purpose, we consider a simpler model of a water monomer on graphene surface [8]. Fig. 2 displays the geometry of water monomer on graphene. There could be several possibilities of the configuration of water molecule over graphene surface such as (a) on top of carbon atom, (b) on bridge site and (c) on hollow site. Additionally, the water molecule itself could be placed in different orientation such as H or O atoms of H_2O molecule towards the graphene surface.

Here, we present the calculated binding energy as a function of water-graphene distance for the arrangement in which H-atom is on top of carbon atom of graphene surface. The results are shown in Fig. 3. Our binding energies are slightly larger than the values obtained using pseudopotentials and plane-wave basis sets. In addition, equilibrium distances are much smaller than previous theoretical ones [9]. The discrepancy may be attributed to the basis-set superposition error, which is to be corrected using the counter-poise method. Furthermore, our LDA/GGA calculations cannot describe the van der Waals (vdW) interaction accurately, which is important in weakly water-graphene as well as water-water interactions.

In our presentation we will present a detailed analysis of the interaction of water molecule on graphene surface. In the presentation, we will also present the results obtained using the van der Waals (vdW) density functional, which is able to include the vdW interaction within DFT [10].

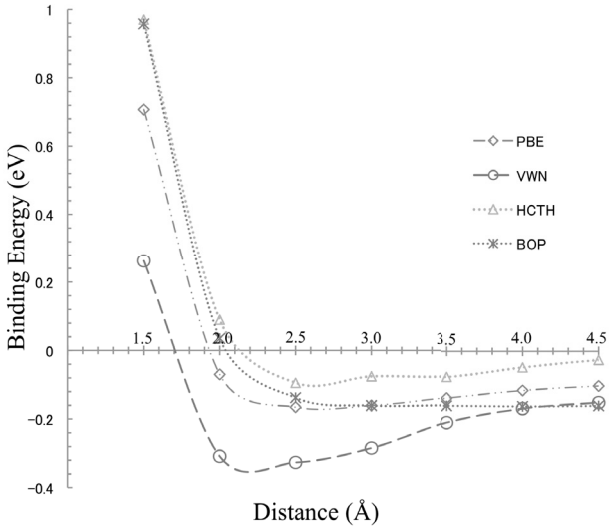

Fig. 3. Binding energy (eV) as a function of water-graphene distance.

4. Concluding remarks

Density functional theory calculations show that water arrangement in CNTs is dependent on their diameter. Water molecules in CNTs with smaller radius tend to arrange as chain like structures while in CNTs with larger arranges as cluster like structure. A detailed study on the interaction of water molecules with the walls of CNTs is strongly desired. This could be done by consideration of various quantum mechanical effects between water molecules and graphitic surface.

5. Acknowledgment

We thank the allocation of computational time on SGI Altix 3700B at the Advanced Fluid Information Research Center, IFS, Tohoku University.

References

[1] Y. Maniwa, H. Kataura, M. Abe, A. Udaka, S. Suzuki, Y. Achiba, H. Kira, K. Matsuda, H. Kadowaki, Y. Okabe, Chem. Phys. Lett. **401** (2005), 534.
[2] G. Hummer, J. C. Rasaiah, J. P. Noworyta, Nature **414** (2001), 188.
[3] Y. Nakamura, T. Ohno, Phys. Chem. Chem. Phys. **13** (2011), 1064.
[4] D. J. Mann, M. D. Halls, Phys. Rev. Lett. **90** (2003), 195503.
[5] Y. Gogotis, J.A. Libera, A.Güvenç-Yazicioglu, C.M. Megaridis Appl. Phys. Lett. **79** (2001), 1021.
[6] B. Delley, J. Chem. Phys. **92** (1990), 508.
[7] B. Delley, J. Chem. Phys. **113** (2000), 7756.
[8] V.R.Coluci, D. S. Galvão, A. Jorio, Nanotechnology, **17** (2006), 617.
[9] A. Ambrosetti, P. L. Silvestrelli J. Phys. Chem. C **115** (2011), 3695.
[10] M. Dion, H. Rydberg, E. Schröder, D. C. Langreth, B. I. Lundqvist, Phys. Rev. Lett. **92** (2004), 246401.

Eighth International Conference on Flow Dynamics
November 9 - November 11, 2011

Numerical Simulation of Sediment Resuspension by Wind-induced Flow

Masahiro Hayashi, Shuya Yoshioka
Ristumeikan University 1-1-1 Nojihigashi, Shiga, Japan
E-mail of corresponding author: shuya@fc.ritsumei.ac.jp

ABSTRACT

At closed shallow water regions, sediment resuspension which influences water environment is mainly caused by the wind-induced flow. However, there is limited number of numerical studies to consider the relationship between natural wind and resuspension. In this study, sediment resuspension is regarded as a combined phenomenon of air-water multiphase flow and mass transport. Numerical results show positive vertical mass flux of sediment is larger in higher wind velocity. This sediment transport may be caused by oscillatory water flow observed in seabed region.

1. Introduction

Sediment influences water environment because of various chemical substances in it. Therefore, it is important to predict sediment transport to evaluate water environment. Sediment resuspension is one of the major phenomena of sediment movement. At the shallow closed water region, sediment resuspension is mainly caused by the natural wind above the water[1,2], i.e., wind raises waves on the water surface; these, in turn, create currents in the water; and then, these currents stir up the sediment. However, there is limited number of studies to simulate such entire phenomena of sediment resuspension. The aim of this study is to reveal the relationship between natural wind and sediment resuspention by simulating wind, water current and sediment transport.

2. Numerical method

Figure 1 shows coordinates system of computational domain and boundary conditions. This 2-dimensional computational domain represents the sloping beach. It has been known that nearshore regions are hydrodynamically active. Hence sediment resuspension in nearshore region is evaluated. Air and water phase are first located in upper and lower region. In the right region a beach is located. Initial free-surface of air-phase and water-phase is located at y=0. Sediment is first located in the bottom of the water region, y<-0.0175. Left boundary is wind inlet and right boundary is free outlet. Top of domain, seabed and beach are expressed by no-slip conditions. Governing equations for two-dimensional, laminar incompressible flow are described with continuous equation and Navier-Stokes equation. To simulate the movement of sediment, convection and diffusion equation of mass is used. Air-water surface is expressed by phase-field method. In this study, uniform wind inlet velocity V(m/s) is treated as a parameter. In table.1 inlet velocities V and corresponding Reynolds number and Froude number are represented. Reynolds number Re is determined by V(m/s) and horizontal length of initial free-surface. Froude number Fr is based on V(m/s) and initial depth of water-phase. Wind duration t(s) is 45 seconds. Above equations are numerically analyzed by COMSOL Multiphysics by finite element method. Number of elements is about 20000.

V (m/s)	Re	Fr
1.0	$4.0*10^5$	0.7
2.0	$9.0*10^5$	1.4
3.0	$1.3*10^6$	2.1
4.0	$1.8*10^6$	2.9
5.0	$2.2*10^6$	3.6
6.0	$2.7*10^6$	4.3

Table 1. Variety of uniform inlet velocity, Reynolds number and Froude number.

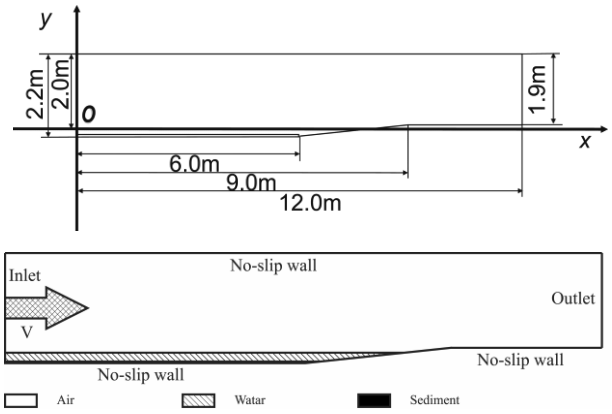

Fig. 1 Coordinates system of computational domain and boundary conditions.

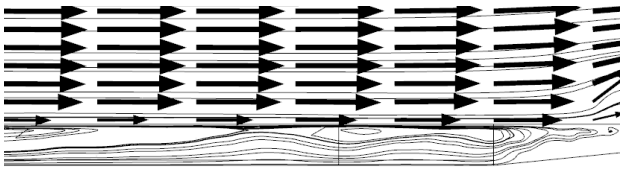

Fig. 2 Streamlines of water flow and velocity vectors of wind near the sloping beach.

3. Results and discussion

Figure 2 represents streamlines of water flow and velocity vectors of wind near the slope. As shown in the figure, airflow from left to right drives water. As a whole there is the current in water-phase. In near the seabed there may be an undertow. In some areas close to the free-surface, small vortical structures are observed. Fig. 3 shows concentration of sediment under V=6.0(m/s) in the water just above the seabed. As time t(s) goes by, distribution of concentration changes and suspends upward. This movement of sediment is evaluated by vertical mass flux of sediment E(kg/m^2/s) at the line of y=-0.0175(m) (initial interface of mass and water). Positive mass flux suggests upward movement of sediment. In Fig. 4 vertical mass flux in various wind velocity at inlet is compared. The higher the wind velocity is the larger the positive mass flux.

Figure 5 expresses time course of horizontal component of water velocity u(m/s) at x=3.0(m), y=-0.0175(m). As shown in the figure, velocity fluctuation is observed in all V cases. This suggests that natural uniform wind may form oscillatory boundary layer in this seabed region. It seems that higher inlet velocity V gives large amplitude oscillation. RMS values of these velocity fluctuation are 0.026, 0.030 and 0.052 respectively. Though fluctuating frequency seems to be increasing in time, it is difficult to evaluate frequency because wind duration is limited to only 45 seconds.

It is said that oscillatory flow reduces critical stress of sediment[3,4]. This observed fluctuating flow may be a primary factor of sediment resuspension.

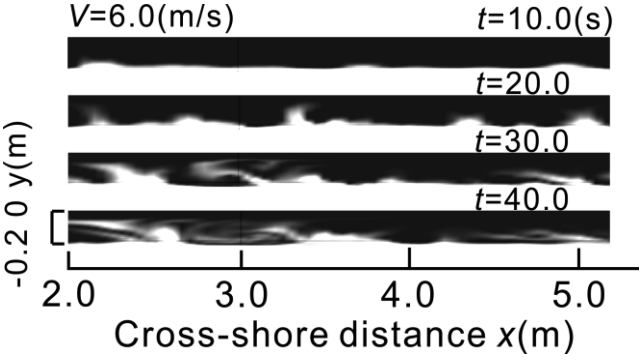

Fig. 3 Concentration of sediment.

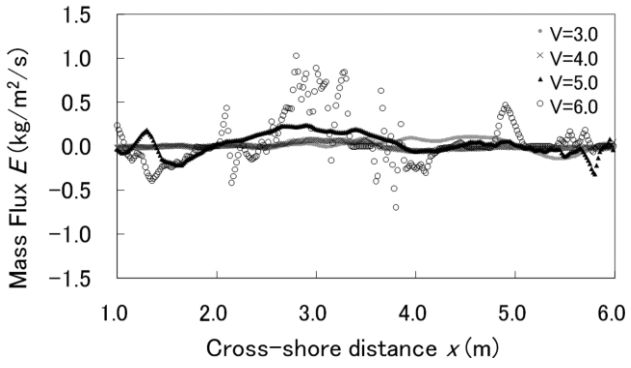

Fig. 4 Vertical mass flux in various wind velocity.

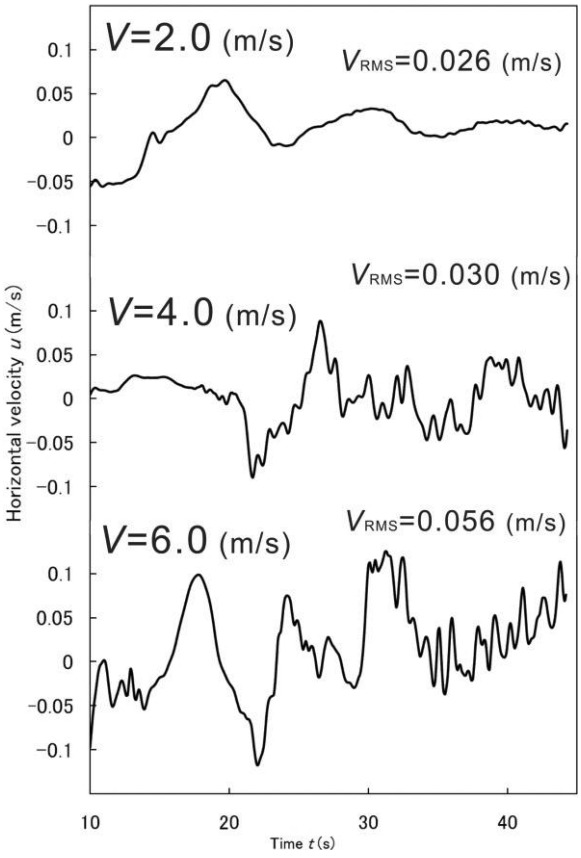

Fig. 5 Time course of horizontal velocity of water.

4. Conclusion

The two-dimentional numerical simulation of sediment resuspension is conducted. In this simulation mass transport in air-water two phase flow is investigated. The result shows higher inlet velocity gives larger vertical mass flux of sediment. At the bottom region of water oscillatory flow is observed. In addition, amplitude of this oscillation is increased when wind velocity increases. This oscillatory flow may cause sediment resuspension.

References

[1] Y. Bettou, M. Umeda. Study on resuspension of sediment in lake Izunuma caused by wind induced current. Tohoku journal of natural disaster science, **47** (2011), p.135-140

[2] J. G. Booth, R. L. Miller, B. A. McKee, R. A. Leathers. Wind-induced bottom sediment resuspension in a microtidal coastal environment. Continental shelf research 20 (2000), p.785-806

[3] W. van. Leussen, J. Dronkers. Physical processes in estuaries (1988), p.13-14

[4] C. A. Pildtch, D. C. Miller. Phytoplankton deposition to permeable sediments under oscillatory flow: Effects of ripple geometry andresuspension, Continental shelf research 26 (2006), p.1806-1825

Eighth International Conference on Flow Dynamics
November 9 - November 11, 2011

The Effect of Room Configuration on Thermal Performance of Data Centres with Detailed Rack Models

Babak Fakhim, Nagarathinam Srinarayana, Martin Naimo, Masud Behnia & Steven W. Armfield
School of Aerospace, Mechanical and Mechatronic Engineering,
The University of Sydney, NSW 2006, Australia
E-mail: m.behnia@usyd.edu.au

ABSTRACT

In this work, a room level study of data centre rooms along with highly detailed model of server racks is conducted. In this regard, a hypothetical data centre room with four rows of racks and four air conditioning units is modelled. The cold air from CRAC units is supplied to the server racks through an under floor plenum. Different configurations of the data centre rooms are also studied, and the results are compared.

1. Introduction

The high density of computing technology in data centres with racks housing thousands of servers produces large heat loads which can lead to system malfunctions and hardware failure. For this reason, ensuring the cooling infrastructure is sufficient has become one of the main concerns in modern data centre operation. A typical data centre consists of three main components: Racks containing servers and IT systems, computer room air conditioning (CRAC) units, and air distribution systems. The cold air from CRAC units is supplied to the server racks through the air distribution system. Then, the hot air exiting the racks returns back to the CRAC units, and this cycle continues to provide optimal environmental conditions in the data centre room. There are considerable publications in the literature regarding thermal management of data centres, using thermal-flow analyses [1-3]. In our previous work[4], different semi-populated rack models regarding server arrangements with void spaces were modelled in a raised floor configuration to investigate the interaction of the various servers inside the rack. In this work, one of the rack models is considered in all simulations, in which a cluster of 21 servers are clumped in the middle of a semi-populated rack. Then, this rack model is applied in all racks of in the data centre and the effect of different configurations of the data centre room on the thermal performance is studied.

2. CFD Modelling

The data centre under consideration is modeled as a 130 m^2 × 3.3 m enclosure as shown in figure 1. There are four CRAC units in the data centre with a nominal cooling load of 75 kW each, which supply cold-air at 15 ^oC at a fixed flow rate of 2.75 m^3/s each. There are 40 perforated tiles in the data centre placed in front of each rack, of 0.6 m× 0.6 m size (producing a cold aisle at front of the racks, and consequently the aisle at the back of the rack which the hot exhaust air enters is called the hot aisle) For simplicity, any obstructions (cable trays, piping), usually present under the floor for a raised-floor configuration, are not taken into account. There are four rack rows (indicated in figure 1 as A, B, C and D) with 10 racks each. Each rack is 42U modelled as a 0.6 m×2 m×1 m cabinet. 21 1U servers are mounted inside the rack, modelled as 262 W heat sources with fixed flow rate of 11.4 L/s each, resulting in a heat load of 5.5 kW per rack. The racks also integrate cabling, which runs from front to back and is approximated by solid cuboids inside the cabinet on either side of the servers. These cables have been approximated as solids due to the fact that tightly packed cabling can block almost all airflow due to its density and coverage. Blanking panels have been installed on all void spaces at the front face of the rack in the simulations undertaken in this work. A schematic of the model utilised in all racks of the data centre is depicted in figure 2(a).

Two different room configuration models are also considered for this data centre along with room return configuration (Model I); ceiling return (Model II) and cold aisle containment (Model III) which are displayed in figures 1 and 3.

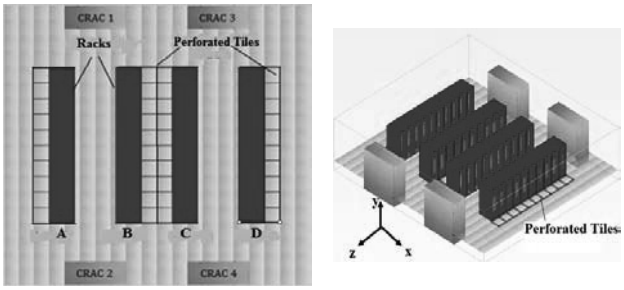

Fig. 1 Schematic of the studied data centre (Model I)

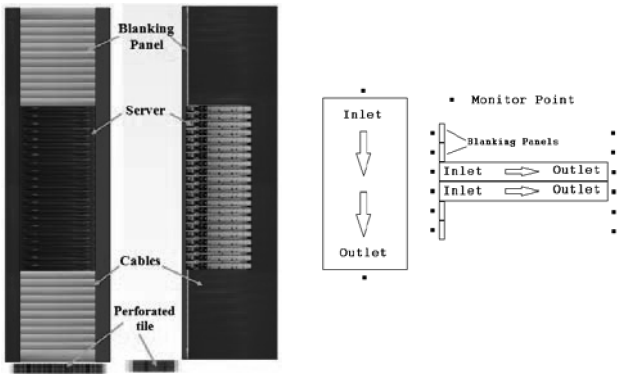

(a) Front view Side view (b) Location of the monitor points

Fig. 2 Schematic of (a) the rack model with the cluster of 21 servers clumped in the middle of the rack (b) monitor points

In model II, angled funnels are installed to lead the air from the rear of the servers to the roof cavity. The

purpose of the funnels is such that the hot air from rack exhaust directly flows through them, with minimal recirculation, into the ceiling void space before returning to the CRACs. In model III, the cold aisles are sealed off so the cold air exiting the perforated tiled is not mixed with the air from the hot aisle.

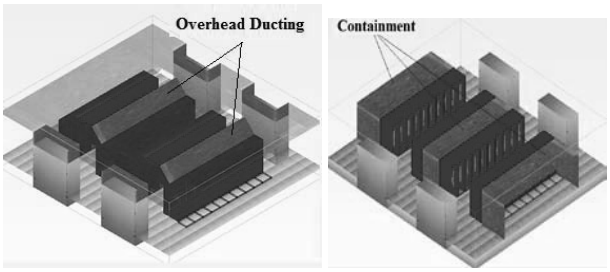

(a) Ceiling return (b) Cold aisle containment

Fig. 3 Configurations for models (a) II and (b) III

FloVENT V8.2 [5] by Mentor Graphics Mechanical Analysis was used for all CFD modelling. A Cartesian grid and the standard k-ε turbulence model were used for all simulations.

3. Results and Discussion

In this work, supply heat index (SHI) introduced by Sharma et al. [6] is used to investigate the data centre performance. SHI is defined as the ratio of enthalpy rise due to the infiltration and total enthalpy rise at the rack exhaust. The lower the SHI, the better the performance of the rack or the room. SHI values for the room were measured using a system of monitor points at the inlet and outlet of each server. Each cabinet has 10 monitor points, 5 are located directly in front of the inlet and 5 directly behind the outlets, as outlined in figure 2(b). The monitor points are dispersed vertically every 4 shelves (from shelves 11 to 31), so as to measure only the areas where servers are operating. A total of 400 monitor points are used in each model to assess the SHI values of the room.

SHI values have been calculated for each model, on the basis of rack rows and the whole of the room, as shown in figure 4. While the SHI values displayed are all fairly low, the difference between the simulations is significant. Model III produced the lowest overall SHI value. This is a logical progression as the models were of growing complexity, in terms of airflow segregation, avoiding mixing of hot air and cold air, from model I through to model III.

To compare the effect of the ceiling ducts on the data centre performance, temperature fields of the models I and II are presented in figure 5. It is observed that the vast area of the data centre room becomes colder which is also witnessed by the lower value of SHI. This is primarily due to a reduction in the overhead recirculation zone. As expected a reduction in overhead recirculation yielded impressive results when converted to SHI values.

Similarly, in model III, by removing any possibility of mixing using cold aisle containment, the cold air is delivered to the server inlets at a considerably lower temperature and in turn a considerably lower SHI is produced.

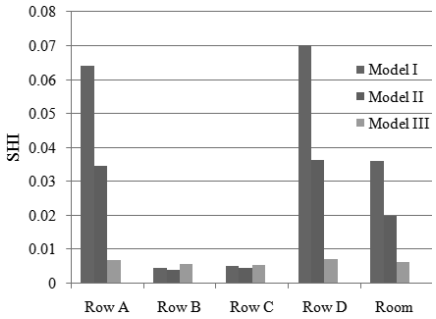

Fig. 4 SHI values of rack rows and the whole of the room for different configuration models

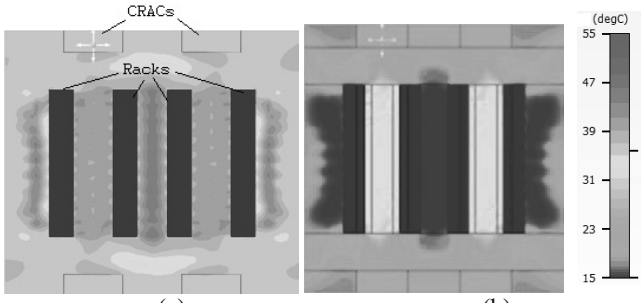

(a) (b)

Fig. 5 Temperature field in vertical direction at height 1 m (a) Model I, (b) Model II

4. Concluding remarks

A room level study of a data centre, along with a highly detailed model of server racks, is conducted. Different configuration designs applied in data centre rooms are also studied. It is shown that by installing ceiling ducts and cold aisle containment, the data centre performance will be improved.

References

[1]Bash, C.E., C.D. Patel & R.K. Sharma, Efficient Thermal Management of Data Centers—Immediate and Long-Term Research Needs. HVAC&R Research, 2003. **9**(2): pp. 137-152.

[2]Fakhim, B., M. Behnia, S.W. Armfield, and N. Srinarayana, Cooling solutions in an operational data centre: A case study. Applied Thermal Engineering, 2011. **31**(14-15): pp. 2279-2291.

[3]Patankar, S.V., Airflow and Cooling in a Data Center. Journal of Heat Transfer, 2010. **132**(7): pp. 073001-17.

[4]Fakhim, B., N. Srinarayana, M. Behnia, and S.W. Armfield. Rack Level Thermal-flow Analysis of Data Centres in 9th Australian heat and mass transfer conference - 9AHMTC. 2011. Melbourne, Australia.

[5]FloVENT v8.2, Mentor Graphics Mechanical Analysis Division

[6]Sharma, R.K., C.E. Bash & R.D. Patel. Dimensionless Parameters For Evaluation Of Thermal Design And Performance Of Large-Scale Data Centers. in 8th ASME/AIAA Joint Thermophysics and Heat Transfer Conference. 2002.

Potential for Ocean Fertilization by Perpetual Salt Fountain: Each Basin Estimation of Upwelling Flow Rate

Takashi Yabuki*, Mikihito Watanabe**, Atsuki Komiya* and Shigenao Maruyama*
*Institute of Fluid Science, Tohoku University, Miyagi 980-8577, Japan
**Graduate School of Engineering, Tohoku University, Miyagi 980-8579, Japan
yabuki@pixy.ifs.tohoku.ac.jp

ABSTRACT

Perpetual salt fountain is a principal leading upwelling of deep seawater. Upwelling flow in the vertical pipe filled with less saline deep seawater results from heating by outside warm water. In order to investigate its impact on ocean fertilization and its dependence on the region, upwelling flow rate is estimated in the global ocean based on the relationship between modified Rayleigh number and dimensionless flow rate. Resulting upwelling flow rate and nutrient supply rate are high in the subtropical region. Accordingly artificial upwelling by perpetual salt fountain is expected to contribute to fertilization of the large part of oligotrophic ocean.

1. Introduction

Perpetual salt fountain, first proposed by Stommel et al. [1], is a principal which allows bringing the deep seawater to the surface. In the ocean characterized by the minimum salinity layer, upwelling flow in the vertical pipe results from heating by outside warm water. Low salinity water is observed at the depths of 300–600 m in the tropical and subtropical region [2,3]. In the tropical and subtropical region, primary production is restricted because of the lack of nutrient such as nitrate (NO_3) and phosphate (PO_4). In contrast, rich nutrient is accumulated in deeper layer than surface mixed layer. If this upwelling system is deployed on a large scale, upwelling provides a great deal of nutrient for surface layer. Accordingly oceanic productivity, and thus fishery resources, is expected to increase.

Since 2001 we have conducted several ocean experiments. Upwelling flow is first observed in the experiment in 2002 [4]. This experiment was conducted in the Mariana Trench region (11.43°N, 142.42°E) and estimated upward flow speed was 15 t/day. Furthermore, Tsubaki et al. [5] estimated an upwelling flow rate of approximately 46 m^3/day on the assumption that the eddy diffusivity was 1.0×10^{-5} m^2/s. In addition, Sato et al. [6] predicted the upwelling flow rate at the Okinotorishima Island Region (20.425°N, 136.070°E) and the Southeast Indian Ocean (19.82°S, 101.48°E). Using these results, they concluded that unified representation of oceanic conditions was achieved by introducing the modified Rayleigh number Ra_R, and the dimensionless flow rate can be evaluated by modified Ra_R.

In order to deploy this system to the real ocean to contribute to fishery industry, the impact of artificial upwelling on oceanic productivity and its dependence on ocean condition should be considered. We estimated the global distribution of upwelling flow rate and nutrient supply based on results of numerical simulation and climatological hydrographic dataset and discussed the effect of upwelling deep seawater on sea surface productivity.

2. Method

In order to obtain upwelling flow rate, the relationship between the modified Ra_R and the dimensionless flow rate [6] was used. The modified Ra_R is as follows:

$$Ra_R{}^* = \frac{g r_w^{\,3}}{\alpha \nu} \cdot \frac{R_\infty - R_i}{R_i} \cdot \frac{r_w}{l}, \tag{1}$$

where g, α, ν, r_w, l are gravitational acceleration, thermal diffusivity, kinematic viscosity, pipe radius and pipe length, respectively. Moreover, R_∞ and R_i are as follows:

$$R_\infty = \int_{x_{in}}^{x_{out}} \rho_\infty dx, \qquad R_i = \int_{x_{in}}^{x_{out}} \rho_i dx, \tag{2}$$

where ρ_∞ ρ_i are density outside and inside the pipe, respectively. x is depth. The dimensionless flow rate is also as follows:

$$G = \frac{Q}{\mu \cdot Gr \cdot r_w}, \tag{3}$$

where Q, μ are upwelling flow rate, and viscosity, respectively. Gr is as follows:

$$Gr = \frac{g r_w^{\,3}}{\nu^2} \cdot \frac{R_\infty - R_i}{R_i}, \tag{4}$$

Because of the relationship between the modified Ra_R and the dimensionless flow rate [6], the following approximation is obtained.

$$G = 10^{-0.33984} Ra_R{}^{*-0.7076}. \tag{5}$$

Then, the upwelling flow rate Q can be estimated. In this study, thermal diffusivity and kinematic viscosity are assumed to be same as the eddy diffusivity, which is estimated to be 1×10^{-5} m^2/s [5]. Pipe radius r_w is adopted to be 0.15 m.

In order to calculate seawater density, the equation of state of seawater [7] is introduced. Temperature, salinity and nutrient concentration from World Ocean Atlas 2005 (WOA05) [8, 9, 10] are used.

3. Results and Discussion

When modified Ra_R is calculated, the minimum salinity between 200 m and 1000 m is used as the salinity inside the pipe. In addition, the pipe outlet is decided to be 50 m bellow the sea surface.

The upwelling flow rate is shown in Fig.1. The highest upwelling flow rate (more than 1000 t/day) is

predicted in the subtropical region of the North Atlantic Ocean. In addition, relatively high flow rate is shown at the subtropical gyre in each basin. Because of the high surface evaporation rate at the subtropical region, the sea surface salinity is high. Thus, it found that the upwelling flow rate strongly depends on the sea surface salinity.

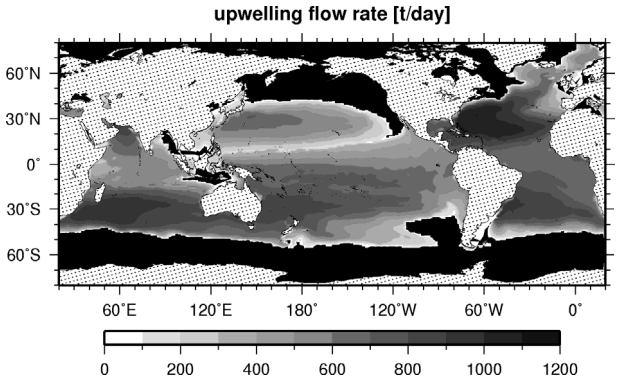

Fig. 1 Global distribution of upwelling flow rate.

Nutrient supply rate is also investigated in order to consider the impact of upwelling deep seawater on the biological productivity. To distinguish between natural nutrient input and artificial input, we subtracted surface nutrient concentration from concentration of upwelling seawater, and then, calculated the nutrient supply rate as the product of residual concentration and upwelling flow rate. Phytoplankton needed mainly nitrate and phosphate as nutrients. However, we discussed here only nitrate because exhaustion of nitrate occurs frequently more than phosphate in most cases. The nitrate supply rate is shown in Fig. 2. The pattern of nitrate supply rate is very similar to one of upwelling flow rate. Namely, high nitrate supply rate is predicted at the oligotrophic subtropical regions in each basin. Compared with upwelling rate, it is found that quite high rate is depicted at not only the North Atlantic Ocean but each basin in the Southern Hemisphere. Thus, the upwelling by perpetual salt fountain is surely effective in fertilization of most oligotrophic regions.

We have conducted several ocean experiments in the Mariana Trench region [4, 5]. This area is adequate to the experiment because minimum salinity layer is shallow (~300 m). However this analysis indicated that upwelling flow rate is quite low in this region and the biological effect is expected to be small. In the future study it should be necessary to conduct ocean experiment in other regions. However, in the region where high upwelling flow rate and nutrient supply rate are expected, the salinity minimum layer is extremely deep (1000 m). Therefore the experimental pipe system should be improved. Moreover, mooring pipe system for purposes of the appropriate management of fishery resources requires large sinker and buoy. When the problem is solved, ocean fertilization by upwelling deep seawater is expected to contribute to management of fishery resources.

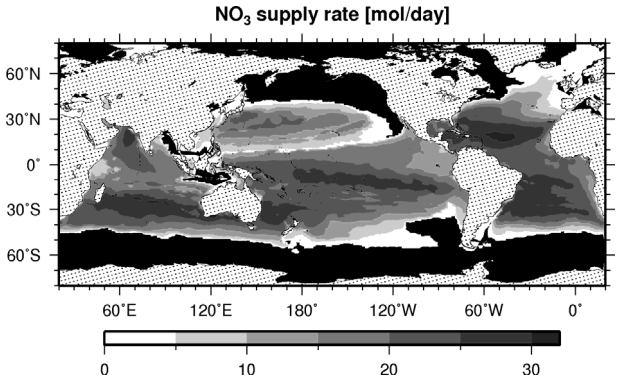

Fig. 2 Global distribution of nitrate supply rate.

4. Concluding remarks

The effect of deep seawater upwelling system by the principal of perpetual is investigated over the global ocean. Upwelling flow rate strongly depends on the sea surface salinity, resulting in the high upwelling rate at the subtropical region, especially the North Atlantic Ocean (more than 1000 t/day). Nitrate supply rate is also characterized by the similar pattern, showing high nitrate supply rate in the subtropical region. Accordingly, upwelling by perpetual salt fountain is expected to contribute to ocean fertilization of oligotrophic subtropical region.

Acknowledgements

We would like to acknowledge the financial support of Tokyo Metropolis and Japan Society for the Promotion of Science, Grant-in-Aid for Scientific Research (B).

References

[1] H. Stommel, A. B. Arons & D. Blanchard, Deep-Sea Res., **3** (1956), pp. 152–153.

[2] J.L. Reid, Johns Hopkins Oceanogr. Stud., **5**, (1965), 96 pp.

[3] L.D. Talley, J. Phys. Oceanogr., **23**, (1993), 517–537.

[4] S. Maruyama, K. Tsubaki & S. Sakai, J. Oceanogr., **60**, (2004), pp. 563–568.

[5] K. Tsubaki, S. Maruyama, A. Komiya & H. Mitsugashira, Deep-Sea Res. I, **54**, (2007), pp. 75–84.

[6] T. Sato, S. Maruyama, A. Komiya & K. Tsubaki, Proc. 16th Australasian Fluid Mech. Conf., (2007), pp. 394–397.

[7] Millero & Poisson, Deep-Sea Res. A, **28** (1981), pp. 625–629.

[8] R.A. Locarnini, A.V. Mishonov, J.I. Antonov, T.P. Boyer & H.E. Garcia, NOAA Atlas NESDIS 61, (2006), 182 pp.

[9] J.I. Antonov, R.A. Locarnini, T.P. Boyer, A.V. Mishonov & H.E. Garcia, NOAA Atlas NESDIS 62, (2006), 182 pp.

[10] H.E. Garcia, R.A. Locarnini, T.P. Boyer & J.I. Antonov, NOAA Atlas NESDIS 64, (2006), 396 pp.

Eighth International Conference on Flow Dynamics
November 9 - November 11, 2011

An Experimental Study about the Blockage Effects on Circular Cylinders Aligned with Uniform Flow

Hideo Sawada[1], **Hiroki Sugiura**[2], **Ryo Konomi**[3]
[1]Institute of Fluid Science, Tohoku University, 2-1-1 Katahira, Aoba-ku, Sendai 980-8577, Japan
[2]Fluid Dynamics Group, JAXA, 7-44-1 Jindaiji Higashi-machi, Chofu-shi, Tokyo
[3]Graduate School of Fundamental Science and Engineering, Waseda University, 3-4-1 Okubo, Shinjuku-ku, Tokyo
sawada@edge.ifs.tohoku.ac.jp

Abstract

We measured the drag coefficient for cylinders with a fineness ratio of 4 aligned with uniform flow under interference-free conditions. In these measurements, 10 models with different diameters were used and corrections according to the methods of Thompson and Maskell were applied. These two methods could not suitably correct the drag coefficient by themselves. Therefore, for three-dimensional bluff bodies, the two corrections must be combined to correct the drag coefficient properly.

1. Introduction

A number of unsolved issues remain when evaluating the aerodynamic characteristics of a bluff body by computational fluid dynamics (CFD) or experimental fluid dynamics. For example, large unsteady wakes prevent accurate evaluation of drag by CFD, and the mechanical support system and wind tunnel walls prevent reliable drag measurement in wind tunnel tests. The interference in wind tunnel testing occurs because the mechanical support system distorts the wake form and the tunnel walls distort the flow field around the body. Wake distortion due to the mechanical support system has been addressed by using a magnetic suspension and balance system (MSBS; Sawada and Suda, 2011). However, the blockage effect of the wall interference has not been adequately resolved for a bluff body. In particular, studies concerning the blockage effect for three-dimensional bluff bodies are limited. The most widely used blockage correction method was proposed by Maskell (1965), but that method is restricted to bluff bodies without significant volume, such as plates. However, many bodies occupy a large volume; flow separation occurs at their front and the majority of the body is in the separated flow region, that is, the wake. As a result, the part will affect the wake structure. Sawada et al. (2004) measured the time-averaged flow field around a cylinder aligned with a uniform flow under support interference-free conditions by using the Japan Aerospace Exploration Agency (JAXA) 60 cm MSBS. The obtained results show that the flow separates at the front of the cylinder and reattaches downstream at a distance of around 1.6 times the cylinder's diameter, and that the flow around the cylinder forms a velocity profile comparable with that of a turbulent boundary layer. However, the wake cross section extended beyond twice the diameter of the cylinder; this wake cross section is large when compared with that of a streamlined body. Consequentially, the wake for a bluff body having volume is different from that of a streamlined body and from that of a bluff body without volume. In this research, we studied the blockage effect on a bluff body having volume by measuring the drag of a cylinder with a fineness ratio of 4 aligned with uniform flow under support interference-free conditions.

2. Analysis of Blockage Effect

Here, ideal solid wind tunnel walls are assumed. Thus, the drag of a bluff body can be estimated by the difference between the summations of the pressure and the momentum flux passing through two inspection planes surrounding the body. We consider one inspection plane, Σ_1, far upstream and the other inspection plane, Σ_2, at a position downstream of the body, as shown in Fig. 1. The displacement thickness boundary in Fig. 1 is defined in a similar manner as the displacement thickness of the boundary layer. The drag coefficient, C_D, is estimated as follows:

$$C_D = \mathrm{m}\left\{2\frac{\Theta}{B}\left(\frac{C}{C-B}\right)^2 - \overline{C_{pB}} - \frac{B}{C-B}\right\} \qquad (1)$$

where C and S are the tunnel cross-sectional area and the representative cross-sectional area of the bluff body, respectively. Furthermore, B, m and $\overline{C_{pB}}$ are defined by

$$\mathrm{m} = \frac{\mathrm{B}}{\mathrm{S}}, \qquad \mathrm{B} = \iint_{\Sigma_2}\left(1-\frac{v}{V_2}\right)d\sigma \qquad (2)$$

$$\overline{C_{pB}} = \frac{1}{B}\iint_B \frac{P-P_\infty}{\frac{1}{2}\rho {V_\infty}^2}d\sigma \qquad (3)$$

where $d\sigma$ is the cross-sectional area element. In Eqns. (2) and (3), v and P are the flow speed and the static pressure, respectively, V_2 is the flow speed at the displacement thickness boundary in Σ_2, and ρ and V_∞ are the density and the uniform flow speed, respectively. Furthermore, Θ, the loss of momentum over Σ_2, is defined as

$$\Theta = \iint_{\Sigma_2}\left(\frac{v}{V_2}\right)\left\{1-\frac{v}{V_2}\right\}d\sigma \qquad (4)$$

In the limit C approaches infinity, the blockage effect becomes negligible. In addition, when Σ_2 is located far downstream, $\overline{C_{pB}} \to 0$. For this case, the drag coefficient without any blockage effect, C_{D_c}, is estimated from

$$C_{Dc} = \frac{2\Theta_c}{S} \qquad (5)$$

where the subscript *c* indicates that the value obtained is for the corrected blockage effect. Eqn. (5) is equivalent to the Betz formula for drag evaluation. Here, we follow the assumption of Maskell (1965):

$$\frac{1-\overline{C_{pB}}}{1-\overline{C_{pB_c}}} = \frac{C_D}{C_{Dc}} \qquad (6).$$

By assuming that m and Θ are invariant as wall constraints, the following ratio between C_D and C_{D_c} is obtained:

$$\frac{C_D}{C_{D_c}} = \frac{1}{(1-mS/C)^2}\left\{1-\frac{m^2S/C}{m-2\Theta/S}\right\} \qquad (7).$$

For the case where $\Theta = 0$, Eqn. (7) corresponds to Maskell's correction. According to this equation, Maskell's correction is the maximum correction that can be obtained from consideration of the existence of a wake.

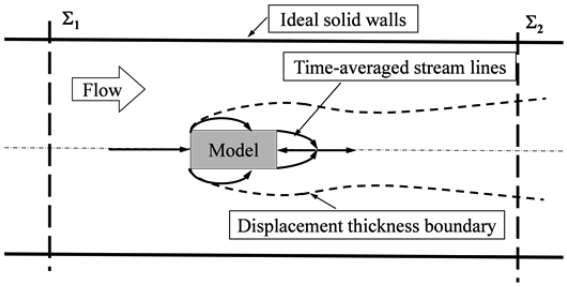

Fig. 1 Time-averaged flow field around bluff body

3. Experimental Apparatus

The wind tunnel contains a closed-type test section with a square cross section of 60 cm in side length and a maximum uniform flow speed of 45 m/s. The models tested were 10 similar cylinders of different diameters, each with a fineness ratio of 4. The cylinders were aligned with the uniform flow and their drag coefficients were measured at a Reynolds number of 0.1 million for their diameter. The cylinders were supported by the JAXA 60 cm MSBS and tests were conducted under support interference-free conditions. For each test, the drag was time-averaged over approximately 8 s. The error in drag coefficient measured by the MSBS is less than 1%.

4. Results and Discussion

Measured values for C_D are plotted against the blockage ratio, *C*/*S*, in Fig. 2. Although, the relation between the coefficient and ratio is slightly nonlinear, we can evaluate C_D at zero blockage ratio to obtain a value of 0.833 ± 0.012. The figure also shows corrections by the Thompson (Pankhurst, 1952) and Maskell methods. However, both of these corrections are too small. Correction of a drag coefficient by Thompson's method is obtained with a wake blockage factor of 0.25 that has been widely used in other studies (Pankhurst, 1952). The correction by Thompson's method is not zero even with zero drag, because it is estimated under a potential flow condition. In contrast, correction by Maskell's method is based on the existence of a wake and accounts for the wake blockage effect. Therefore, the two corrections are as a result of different factors that are independent of each other. The solid squares in Fig. 2 denote the values corrected by Maskell's method after first being corrected by Thompson's method. The resulting drag coefficients are close to the true values under wall interference-free conditions when compared with those coefficients corrected by Thompson's or Maskell's method alone. Thus, the combination of the two corrections gives the greatest accuracy in removing the blockage effects for bluff bodies having volume.

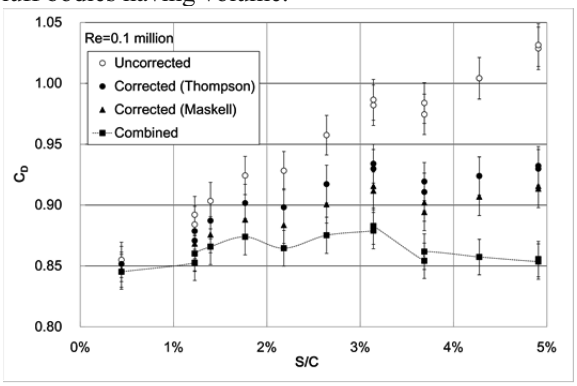

Fig. 2 C_D–blockage ratio plots for 10 cylinders with fineness ratio of 4 aligned with air stream.

5. Concluding Remarks

We have derived a new method for estimating the blockage effect for a bluff body having volume (i.e., a body unlike a flat plate), by using a time-averaged loss of momentum distribution over a cross-sectional area of the body's wake. Using the JAXA 60 cm MSBS, we measured C_D for 10 different cylinders with a fineness ratio of 4 aligned with uniform flow under interference-free conditions. To the measured values of C_D, we applied two corrections according to the Thompson and Maskell methods. We found that these methods are not able to correct the coefficients by themselves and that, for bluff bodies having volume, the combination of the two corrections is necessary for proper correction of C_D.

Acknowledgements

This study was conducted with support from a 2010/2011 Grant-in-Aid for Scientific Research for "A Study about Wind Tunnel Wall Correction on Three-Dimensional Bluff Bodies".

References

[1] E. C. Maskell, ARC R&M 3400, (1965)

[2] C. R. Pankhurst, and W. D. Holder, Pitman, London, (1952), pp. 327–348

[3] H. Sawada, H. Higuchi, T. Kunimasu, and S. Suda, J. of Wind Engineering, JAWE, Vol. 29, No. 4, (2004)

[4] H. Sawada and S. Suda, Exp. Fluids, Vol. 50, (2011), pp. 271–284

Movement of Springtail in Air

M. Shiono, S. Sudo
Akita Prefectural University, Ebinokuchi 84-4, Yurihonjyo 015-0055, Japan
A.Shirai, T. Hayase
Tohoku University, Katahira 2-1-1, Aoba-ku, Sendai 980-8577, Japan
E-mail: sudo@akita-pu.ac.jp

ABSTRACT

This paper describes the analysis of springtail jumping motion. The free jumping analyses were performed using a digital high-speed video camera system. It was found that the jump distance in the air was over a hundred times of body length of springtail. Microscopic observation of garden springtail was also conducted using a laser beam microscope. Detailed shape of the furcula was clarified. A springtail mechanism was produced based on the experimental analysis. The jump performance of the mechanism was compared with the real springtail. The springtail mechanism could jump and rotate like real springtail.

1. Introduction

In the development of biomechanics and biomimetics, the study on various functions of many animals is of fundamental interest and importance with respect to a variety of applications. Recently extensive investigations on insect jump mechanisms have been conducted [1-3]. For example, Christian [4] observed the free jump of springtails with a high-speed shootings (750-1600 frames/s), and analyzed the jump performance theoretically. Brackenbury [5] analyzed jump kinematics and energetics of two kinds of springtails, using a computer model. In spite of many investigations, there still remains a wide unexplored domain on the jump dynamics of springtails in the air.

In this paper, the free jump of springtail, *Bourletiella hortensis* was studied using a high-speed video camera with frame rate 27000 frame/s. Based on the experimental analysis of the springtail, the test springtail mechanism was produced. And it was compared with the jump of springtails. Furthermore, microscopic observation of garden springtail was also conducted using a laser beam microscope to study the morphology for jump motion. Especially the furcula was focused and the detailed surface structure was measured.

2. Garden springtail

Garden springtail, *Bourletiella hortensis* belongs to the Collembola. The body length of the garden springtail used in the experiment is about 1 mm. Garden springtail is comparatively smaller than other springtails. In springtail, the usual way to move is by crawling but jumping is used as a very efficient mechanism to escape from attack or disturbance.

3. Experimental apparatus and procedures

Experiments for the free jump analysis of garden springtails were conducted with the high-speed video camera system. A schematic diagram of the experimental apparatus is shown in Fig.1. The experimental system is composed of a high-speed video camera, a control unit, a video cassette recorder, a video monitor, and a personal computer. In this experiment, the garden springtail with body length 1.0 mm, and mass 0.13 mg were used as test insect. The value of mass was determined by the averaging of the sum of 10 insects. The experiment was performed under the condition of the room temperature at 18-25 ℃.

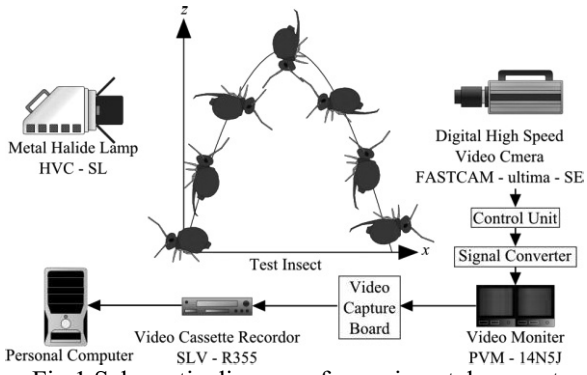

Fig.1 Schematic diagram of experimental apparatus

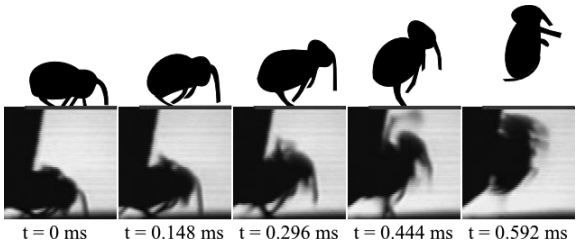

Fig.2 A sequence of photographs showing the jumping motion

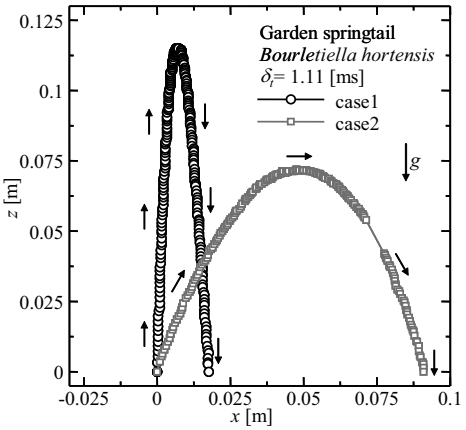

Fig.3 Jumping trajectories of the springtail

The microscopic observation of the furcula structure of garden springtail was performed using the laser microscope (Keyence VK-9700). The laser microscope employs a short waveform violet laser. As well as

enabling 18000x high definition magnification, the laser microscope examines objects based on an ultra depth image technique that focuses over the entire field of the microscope. The obtained data were analyzed using the analysis software (Keyence VK-Analyzer).

4. Experimental results and discussion

4.1 Jumping analysis of garden springtail

Jumping behavior of the garden springtail was examined by the digital high-speed video camera. Figure 2 shows the high speed photographs showing the jump of the garden springtail. It can be seen from Fig.2 that the garden springtail takes off using the furcula and flipping the ground momentarily. After taking off, the garden springtail shows the body rotation with higher angular velocity. Figure 3 shows two kinds of jump trajectories of the garden springtail (case1 and case2). In Fig.3, δ_t is time interval of data plot. It can be seen from Fig.3 that the garden springtail can jump to the height more than one hundred times of body length. The take off speed is about 1.62 m/s, and highest acceleration reached 486 m/s^2. We can obtain the kinetic energy E_k and the potential energy E_p for jump motion of the springtail from Fig.3.

$$E_k = \frac{1}{2}mv^2 = 1.66\times10^{-7}\ \mathrm{J} \quad (1)$$

$$E_p = mgh = 1.47\times10^{-7}\ \mathrm{J} \quad (2)$$

where m is mass of the springtail, g is the gravitational acceleration, and h is the jumping height of springtail. The values of Eq.(1) and Eq.(2) shows $E_k > E_p$. The difference between these two values corresponds to the loss caused by the drag force. Drag force acted on the moving body in fluid, D_f, is described as follows;

$$D_f = \frac{1}{2}\rho v^2 \cdot C_D \cdot S \quad (3)$$

where ρ is density of fluid, v is the velocity of moving body, and S is the projection area of the body.

4.2 Microscopic observation of furcula

The furcula of the garden springtail was observed by a laser scanning microscope. Figure 4 shows the microscopic photograph of the furcula. It can be seen from Fig.6 that the furcula is biforked. The furcula consists of three segments as shown in Fig.4.

4.3 Springtail mechanism

Based on the jump experiment of the springtail, the mechanism was designed and produced. Figure 5 shows dimensions of springtail mechanism. This mechanism composed of electric magnet, wood chip, rubber and spring. Mass of the mechanism was 0.69 g.

Figure 6 shows jumping trajectory of the springtail mechanism. In Fig.6, z is the one dimensional vertical coordinate. The springtail mechanism was almost jumping vertically. It can be seen from Fig.6 that the springtail mechanism can jump and rotate like real springtail.

5. Concluding remarks

The Jumping motions of garden springtail were investigated experimentally. The results obtained are summarized as follows;

(1) The garden springtail can jump to the height more than one hundred times of body length.
(2) The springing organ (furcula) is biforked.
(3) The springtail mechanism can jump and rotate like real springtail.

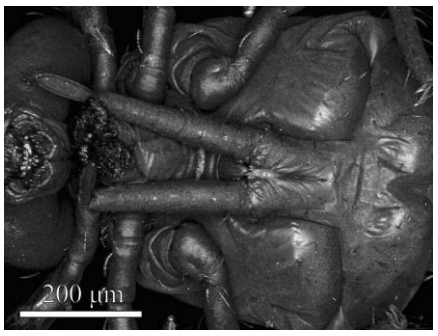

Fig.4 Microscopic photograph of furcula

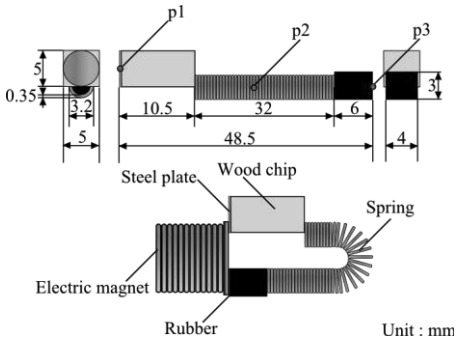

Fig.5 Dimensions of springtail mechanism

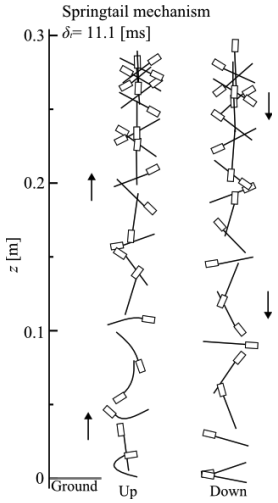

Fig.6 Jumping trajectory of springtail mechanism

References

[1] M.Burrows., Nature., **424**(2003), 509.
[2] M.Burrows., J. Exp. Biol., **211**(2008), 1021.
[3] H.C.Bennet-Clark., et al., J. Exp. Biol., **47**(1967), 59.
[4] E.Christian., Naturwissenschaften., **65**(1987), 495.
[5] J.Brackenbury., et al., J. Zool., Lond., **229**(1993), 217.
[6] H.Y.Elder, and E.R.Trueman, Cambridge University Press., (1980), 1-25.

Observation of Fly Wings and Flight Behavior

Kohei Kitadera[1], Seiichi Sudo[1], Atsushi Shirai[2], and Toshiyuki Hayase[2]
[1]A kita Prefectural University, Ebinokuchi 84-4, Yurihonjyo 015-0055, Japan
[2]Tohoku University, Katahira 2-1-1, Aoba-ku, Sendai 980-8577, Japan
E-mail: sudo@akita-pu.ac.jp

ABSTRACT

The results of experimental study on the fly flight are described. The free and tethered flight analyses of diptera insects were performed using a digital high-speed video camera system. An unusual transverse flight of the fly was observed. The wings of fly showed the elastic bend deflection with anisotropy during flapping cycle. In the experiment of drop impact test with fly wing, the fly wing showed flexibility and high water repellency for the water drop collision. The details of the fly wing surface were revealed by microscopic observation.

1. Introduction

Insects have been developing from the remote past, and their tissue and structure elements have various superior mechanical functions. Flying insects have the ability to fly by flapping. Flight is an effective form of transport because it is fast and direct. The study of the flying function of insects is of fundamental interest and importance with respect to a variety of applications. Extensive investigations on the motion of many insects have been conducted [1]. In our previous papers, the wing structure and the aerodynamic characteristic of an in-flight dragonfly were examined using a scanning electron microscope and small low-turbulence wind tunnel [2]. The surface roughness of some insect wings was measured by a three-dimensional, optical shape measuring system [3]. The measurement of displacement and frequency of extrinsic skeleton vibration produced by wing flapping of wasp were made by an optical displacement detection system [4]. Some functional principles underlying insect wing design were revealed by the measurements of surface roughness and flapping analysis [5]. In spite of many investigations, however, there still remains a wide unexplored domain. Research data on free flights of flies and detailed measurement of the surface shape of fly wings are sparse, and there are many points which must by clarified.

In this study, unusual transverse flight of the fly and flapping behavior of the tethered fly were studied by the high-speed video camera system. The surface of fly wing was observed by the confocal laser scanning microscope.

2. Experimental apparatus and procedures

Experiments on free flight analysis and tethered flapping analysis were conducted with the high-speed video camera system. A schematic diagram of the experimental apparatus system is shown in Fig.1. The experimental system is composed of a high-speed video camera, a control unit, a video cassette recorder, a video monitor, and a personal computer. The free flight behavior of the fly can be gained by using the camera system. A series of frames of free flight of the fly were analyzed by a personal computer. In this study, the tethered flight of the fly was also examined. The drop collision test on the wing of fly was also performed by

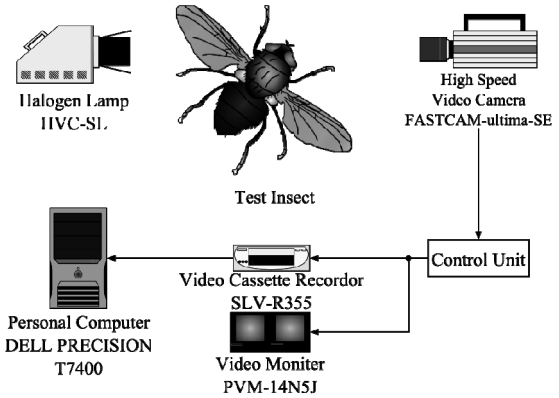

Fig. 1 Block diagram of experimental apparatus.

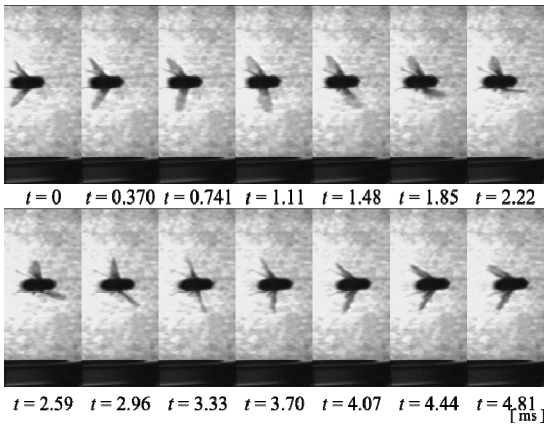

(a) Selected frames from high-speed movie

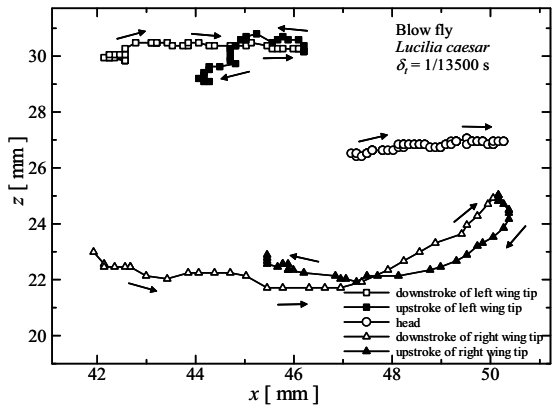

(b) Trajectories of wingtips and head

Fig. 2 Free flight of the fly, *Lucilia Caesar*.

using the high-speed video camera.

The surface of fly wings was observed by the confocal laser scanning microscope. The test wing was severed from the insect body before the measurement. Test insects were collected in the field in Yurihonjo, Japan. The experiments were conducted under the room temperature in summer.

3. Experimental results and Discussion

3.1 Free flight of fly

In general, many species of house flies and blow flies exhibit different kind of flight behavior, depending on circumstances. Schilstra and Van Hateren showed five distinct flight maneuvers that is, the 'banked turn', 'dive', 'zigzag', 'u-turn', and 'reverse' [6]. In this experiment, the unusual fly flight that had not been discovered was observed.

Figure 2 shows the free flight behavior of the blow fly, *Lucilia caesar*. Figure 2 (a) shows a sequence of images taken for a transverse flight in the direction of gravity, and Fig.2 (b) shows the wingtips and head orbits during the transverse flight. This kind of flight is not depending on normal lift generation. Drag generated by the right (under) wing functions as important lift generation in this transverse flight.

3.2 Tethered flapping

The flapping motion of the fly wings was also analyzed in the same manner as before. Figure 3 shows the selected frames from the high-speed movie for the tethered fly flapping. In Fig.3, the test insect is the fly, *Muscina stabulans*. The body length is L = 8.11 mm, and the wing length is l = 7.11 mm. It can be seen that the wings bend at the lowest point of the down stroke (t = 4.00-4.67 ms). This wing bending brings the speedy recovery stroke of wings. Strain energy stored by bending is released when the flapping motion changes into the recovery stroke.

3.3 Microscopic observation of fly wing

Microscopic observations of the fly wings were conducted with the confocal laser scanning microscope. Figure 4 shows the microscopic photographs of the part in leading and trailing edges of the fly wing. A lot of micro hairs are observed along trailing edge of the fly wing. The number of hairs is 59 per 1 mm along trailing edge on the surface of wing. The total number of hair is 118 per 1 mm on the surface and back side. The length of the hair is approximately 41.9 μm. It is considered that these large number of hairs are related to the stability of wing flapping of the fly.

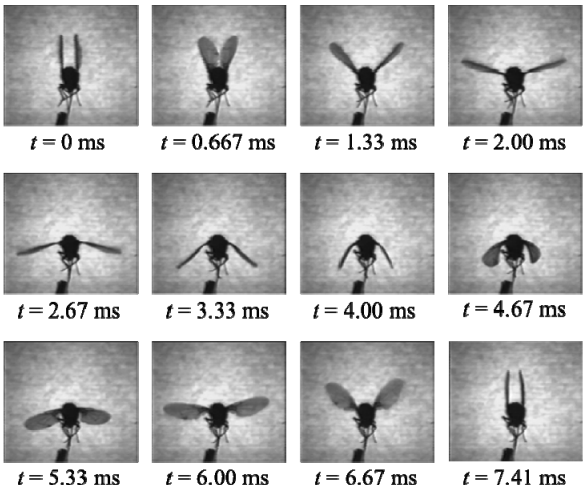

Fig. 3 Selected frames from high-speed movie showing tethered flapping of the fly.

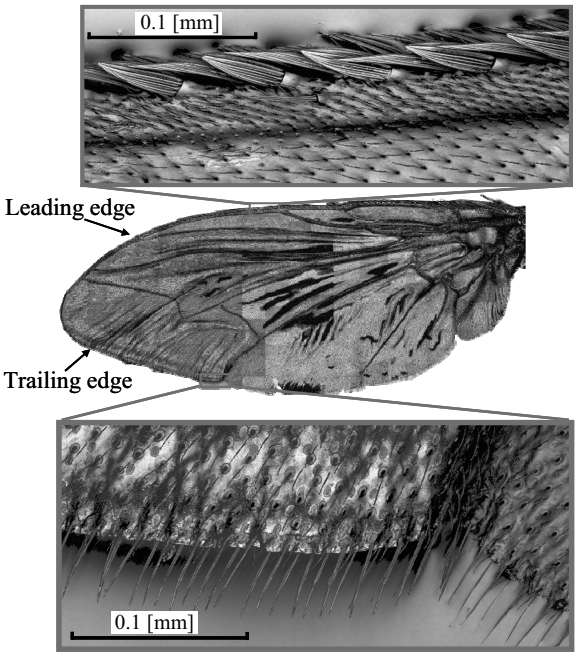

Fig. 4 Microscopic photographs of the fly left wing.

4. Conclusions

The wing characteristics of flies were studied by the free flight and tethered flapping analysis. Furthermore, the microscopic observation of fly wing was performed by the confocal laser scanning microscope. The results obtained are summarized as follows.

1) The fly can fly with transverse flight to gravity direction.
2) The fly wing presents the elastic bend deflection throughout the recovery stroke. There is anisotropy in the wing elasticity.
3) The wing surface of fly is clothed in minute hairs.

References

[1] A. K. Brodsky, The Evolutions of Insect Flight (Oxford Science Publications, Oxford, 1994).
[2] S. Sudo, K. Tsuyuki, T. Ikohagi, F. Ohta, S. Shida and J. Tani, JSME Int. J. , **42** - 3 (1999), pp.721-729.
[3] S. Sudo, K. Tsuyuki and J. Tani, JSME Int. J. , **43** - 4 (2000), pp.895-900.
[4] S. Sudo, K. Tsuyuki, Y. Ito and J. Tani, JSME Int. J. , **44** - 4 (2001), pp.1103-1110.
[5] S. Sudo, K. Tsuyuki and K. Kanno, Exp. Mech. , **45** - 6 (2005), pp.550-555.
[6] C. Schilstra and J. H. VanHeteren, Exp. Biol. , **202** (1999), pp.1481-1490.

Eighth International Conference on Flow Dynamics
November 9 - November 11, 2011

6-DOF Flight Simulation of Beam-Riding Vehicle

Masayuki Takahashi, Naofumi Ohnishi
Depertment of Aerospace Engineering, Tohoku University
6-6-01 Aramaki-Aza-Aoba, Aoba-ku, Sendai 980-8579, Japan
mtakahashi@rhd.mech.tohoku.ac.jp

ABSTRACT

We have developed a three-dimensional hydrodynamics code coupling equation of motion of a rigid body for analyzing posture stability of laser propulsion vehicle through numerical simulations of flowfield interacting with unsteady motion of the vehicle. Lightcraft reveals good centering performance in out simulation, that is, vehicle moves to cancel out an initial offset. However, the Euler angle grows and never returns to zero in a time scale of laser pulse. We examined the tipping performance by varying focal points, and we found that the vehicle can cancel an initial tipping angle examined over the wide angle range.

1. Introduction

Laser propulsion is expected as a new low-cost technique for a launch of small satellites. In an aero-driving-type vehicle, a high-power pulse laser is irradiated to the parabolic mirror equipped on the vehicle from a ground base and is focused by the mirror. As a result, the blast wave is generated at the focal spot (ring), and the vehicle obtains thrust power by interacting with the blast wave.

A good beam riding performance assures the vehicle of continuously receiving thrust. The total performance is assessed by the centering and tipping performances. When a laser is irradiated with a offset respect to the vehicle axis, it is necessary that the vehicle moves to cancel out the offset (centering performance). On the other hand, when the laser is irradiated to the vehicle with some tipping angle, it is necessary that the vehicle obtains restoring moments to parallel the vehicle axis and beam one (tipping performance). If the restoring force does not act enough on the vehicle, the offset and the tipping angle increase rapidly and the vehicle will deviate from a laser beam line.

In previous studies, Kenoyer [1] measured lateral and angular impulse on a type-200 lightcraft for laser offset, and orbital calculation was conducted based on the impulse data by Ballard [2]. However, the centering and the tipping performances have not been examined for laser offset and oblique incidence quantitatively. In particular, discussions about the beam riding performance are not sufficient for oblique incidence.

Objective of this study is assessing the centering and the tipping performances of laser propulsion vehicle to improve its beam riding performance. We calculate lateral and angular forces from a flow solution and solve 6-DOF equation of motion with these forces to estimate the orbit and the posture of the vehicle. The centering and the tipping performances of lightcraft are evaluated for given laser offsets and incident angles with the developed code.

2. Numerical Methods

2.1 Flowfield

Flowfield around the lightcraft-type vehicle is solved to estimate the forces and the moments acting on the vehicle. For the flowfield calculation, three-dimensional Euler equation is numerically solved to reproduce the compressible gas dynamics. Discretization was done by cell-centered finite volume manner. The AUSM-DV method is employed for numerical flux with 2nd-order MUSCL method. In the MUSCL method, we choose characteristic variables as interpolation quantities and use minmod limiter to fulfill the TVD condition. The time integration is performed by the 1st-order explicit Euler method. The velocity and angular velocity of the vehicle are subtracted from the flowfield at every time step to introduce the effect of the motion of the vehicle. The pressure drag which is caused due to the motion of the vehicle is added to the previous step.

2.2 Orbital Calculation

An flight orbit of the vehicle can be determined by 6-DOF equation of motion with aerodynamic forces and moments estimated from a flowfield solution. According to the orbital calculation, we obtain time evolutions of laser offset and tipping angle as the position of center of gravity and the Euler angles.

In an orbital calculation, the aerodynamic forces and moments are estimated by integrating surface pressure distribution given by the flowlield solution in the body-fixed coordinate system. In addition, as the external forces acting on the vehicle by gravity, we introduce the gravity force and the gravity gradient torque in the body-fixed coordinate system.

We calculate the velocity and the angular velocity of the vehicle by time integration of 6-DOF equation of motion with 4th-order Runge-Kutta method. In the flowfield computation these velocities are subtracted from the flowfield of the previous time step for introducing a motion of the vehicle.

2.3 Energy Deposition Model

In order to introduce the off-axis and/or inclined laser incidence, it is necessary to estimate the spot position where the reflected laser is focused and the amount of energy at the focal spot. We perform ray-tracing for determining the initial energy deposition. If the laser is irradiated even with offset, the focal spot is not changed from analytical one, but the energy distribution cannot be estimated without the ray-tracing. Also, in the case of oblique laser incidence, the ray-tracing is needed for estimations of the focal spot and the distribution of the deposited energy. A 420-J Gaussian laser is divided into about 10,000 rays and is irradiated with the variable intensity obeying the spatial distribution of 2.3-cm FWHM. The efficiency of laser energy absorption by plasma is assumed to be 40 % according to the past studies [3].

3. Results

First, we examined the centering and tipping performances with 5-mm laser offset. Since the laser offset decreases from the initial value with time. The vehicle has a good centering performance. Ideally the tipping angle should be 0 degree, but the computed angle increases with time. So, the tipping performance should be improved.

In order to improve the tipping performance, we prepared three types of vehicle with different focal point at a distance of 20 mm, 25 mm and 30 mm. Figure 1 shows time evolution of the tipping angle when the laser is irradiated to each vehicle with the initial offset of 5 mm. If we set the focal point far from the connection arm, we can reduce the tipping angle. It is noted that the centering performance is comparable among them.

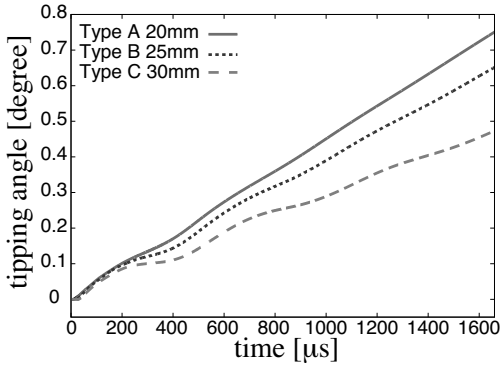

Fig.1 Time evolution of tipping angle for different focal points.

The tipping performance was examined when the laser is irradiated to the vehicle with initial tipping angles 5, 10 and 15 degree. According to the results of ray tracing, the laser is not focused at the expected point in all the cases. In particular, the laser is focused on the outside of the cowl for the cases of 10 and 15 degrees (Fig. 2). We measured the tipping angle α formed by the laser axis and the vehicle axis (Fig. 3). When the initial angle is 5 degree, the tipping angle decreases because the focal point is within the cowl, and the pressure of the lower side is higher than that of the upper side. On the other hand, the tipping angle does not decrease for 10 degree because the pressure of the upper side which leads to α increasing is high compared with the lower side. For the case of 15 degree, the tipping angle decreases because the pressure of the upper side is not so high while the focal point is out of the cowl as well as the case of 10 degree. The strong blast wave makes the tipping angle smaller as it propagates on the lower side.

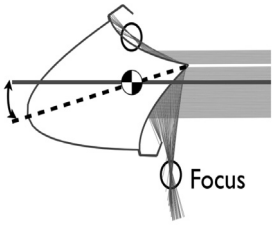

Fig. 2 Result of ray-tracing for initial angle of 15 degree.

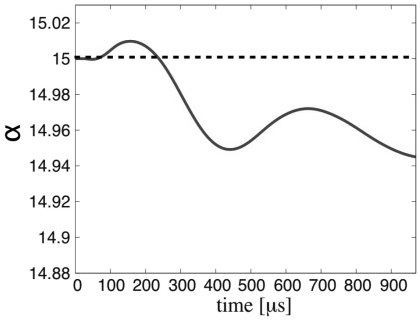

Fig. 3 Time evolution of tipping angle for laser oblique incident for the case of 15 degree. Initial tipping angle is 15 degree.

4. Conclusion

We have developed a three-dimensional hydrodynamics code coupling with 6-DOF equation of motion. Computed results show the lightcraft is excel in the centering performance. Setting the focal point away from the connection arm or eliminating it can improve the tipping performance for the initial laser offset. The vehicle can obtain a restoring force for the oblique laser incidence over the wide angle range. It is necessary that the beam riding performance will be assessed for a longer flight with multiple laser pulse in order to find the laser propulsion vehicle which has better beam riding performance.

5. References

[1] D. A. Kenoyer et al., Beamed Energy Propulsion, A. V. Pakhomov (2008), pp. 325–337.

[2] C. G. Ballard et al., Journal of Computational and Nonlinear Dynamics, 4 (2009), pp. 041005-1–041005-8.

[3] T. S. Wang et al., AIAA Paper 2001-0648 (2001).

Numerical Investigation of Baseflow Effects on Flow Separation in Axisymmetric Scramjet Nozzles

Hideaki Ogawa and Russell R. Boyce
Centre for Hypersonics, School of Mechanical and Mining Engineering
The University of Queensland, St. Lucia, Brisbane, QLD 4072, Australia
h.ogawa@uq.edu.au

ABSTRACT

Nozzle flowfields play a crucial role in hypersonic scramjet propulsion for flexible and economical access-to-space. Overexpansion of the nozzle flow in off-design operation at higher ambient pressure can critically deteriorate thrust production and vehicle stability due to boundary layer separation and resultant side loads. This paper numerically investigates the influence of baseflow on the nozzle flowfield of an axisymmetric scramjet. The results indicate effectiveness of thick baseflow in delaying separation and remarkable similarity in pressure distributions between flow separations caused by baseflow and ramp compression.

1. Introduction

Hypersonic airbreathing propulsion, in particular, scramjet engines, offers a great potential for reliable and economical access to space and high-speed atmospheric cruise. The SCRAMSPACE project [1] is now underway to explore innovative concepts such as inlet fuel injection and radical-farming shock-induced separation in internal compression axisymmetric scramjet engines, led by The University of Queensland (UQ).

Scramjet engines typically consist of an inlet, combustor and nozzle, where compression of captured airflow, fuel injection / mixing, ignition, combustion, and expansion of reacted gas take place in a sequential manner. Nozzle design optimisation studies have been performed extensively at UQ [2,3] due to the crucial role played by the nozzle section in thrust production and vehicle stability. In off-design scramjet operation, boundary-layer separation and unfavourable side loads can be caused by overexpansion of the nozzle flow, which can lead to significant deterioration of the vehicle performance in thrust generation and stability [4].

This paper presents the results of a numerical study conducted to investigate the effects of the baseflow on boundary layer separation in an axisymmetric scramjet nozzle by varying the base height and external pressure, in comparison with separation due to ramp compression.

2. Methods

1. Nozzle configuration and flow conditions

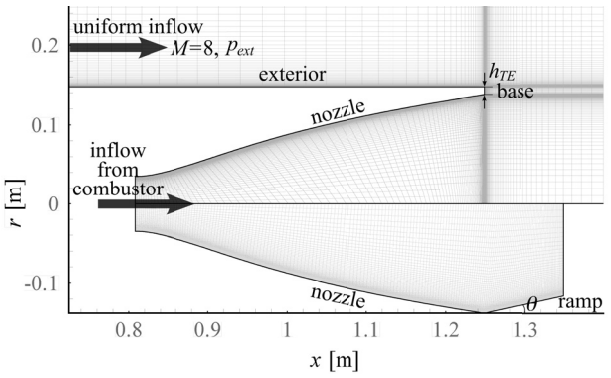

Fig. 1 Nozzle configurations and computational meshes for baseflow and ramp setups

The configuration considered in the present study comprises a nozzle, base, and external wall at the rear part of an axisymmetric scramjet, as shown in Fig. 1. Used for the nozzle is the optimal contour obtained in a previous design optimisation study performed to maximise the nozzle thrust at Mach 8 at an altitude of 27 km in the presence of fuel (H_2) injection on the 2nd inlet ramp with a fuel/air equivalence ratio 0.5 [3]. All walls are assumed to be adiabatic in this study. The base height h_{TE} is varied between 0.5 and 10 mm.

The pressure distribution of the inflow profile imposed at the nozzle entrance is scaled down from that used in [3] by a factor of 10 in order to amplify the baseflow effects by enhancing the sensitivity of the boundary layer to adverse pressure gradient. Uniform inflow of Mach 8 and static temperature 224 K is assumed for the external flow, with the static pressure p_{ext} varied between 1 and 10 kPa. Supersonic outflow is assumed at the downstream end of flowfields.

Also presented Fig. 1 is a configuration with a ramp employed in order to investigate flow separation induced by ramp compression. The ramp angle θ is varied between -7° (no flow deflection) and 20°.

2. Computational fluid dynamics and meshes

Nozzle flowfields are computed by utilising a commercial high-fidelity code CFD++, which solves the Navier-Stokes equations implicitly with second order spatial accuracy. Finite-rate chemical reactions and gas composition are represented by Evans & Schexnayder's model, which consists of 25 elementary reactions among 12 species. An advanced wall-function technique is used for near-wall treatment and turbulence is modelled by the two-equation SST k-ω RANS model.

Two-dimensional structured meshes are generated by utilising a commercial grid generator Pointwise, as superimposed in Fig. 1. The computational domains comprise 35,850 and 17,226 cells for flowfields with a base and ramp, respectively, with the minimum cell width of 10^{-5} m ($y^+ = 0.32$). This mesh resolution has been chosen in a preliminary mesh sensitivity study in order to strike balance between computational cost and simulation fidelity, with care taken on the surface pressure and separation (results are not included here).

3. Results

The separation length computed for various sets of base height and external pressure is plotted Fig. 2, along

with contours generated from surface fitting[1]. A distinct trend is evident for the separation length l_{sep}, indicating the occurrence of larger separation with higher external pressure p_{ext} rises and smaller base height h_{TE}[2].

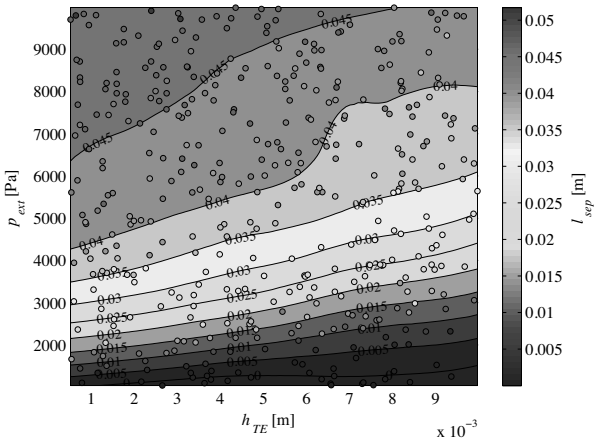

Fig. 2 Contour plot of separation length l_{sep} with base height h_{TE} and external pressure p_{ext} variation

The correlation between flow deflection and the separation length l_{sep} has been obtained in a parametric study by varying the ramp angle θ, where l_{sep} has been found to increase monotonically with θ once the boundary layer separates at $\theta = 2.9°$. Compared in Fig. 3 are the Mach number distributions between the flowfield with a baseflow and that with a ramp, both of which are characterised by the same separation length l_{sep} of 43mm. Nearly identical flowfields can be seen inside the nozzle, while the downstream regions exhibit different shock angles due presumably to different flow displacements.

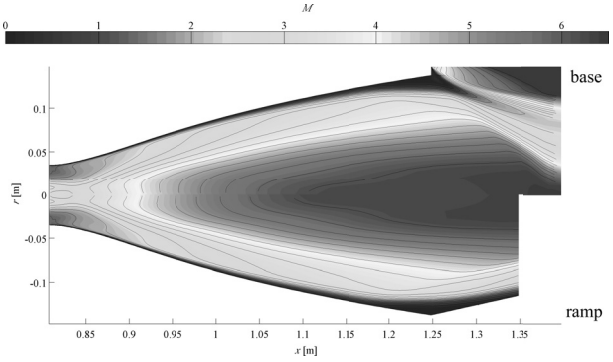

Fig. 3 Comparison of Mach number distributions between base ($h_{TE} = 9.7$mm) and ramp ($\theta = 12.5°$) flows with the same separation length ($l_{sep} = 43$ mm)

The inner surface pressure distributions in the vicinity of the trailing edge are compared in Fig. 4 for nozzle flowfields with baseflow and equivalent ramps associated with various separation lengths, i.e. $l_{sep} = 3$, 23, and 43 mm. It is noteworthy that separated flows in the presence of ramps yield remarkably similar pressure distributions to those with base flows. Also compared in Fig. 4 are the surface pressure distributions with various combinations of the base height h_{TE} and external pressure p_{ext} that produce the same separation length l_{sep} = 43 mm. Essentially the same surface pressure distributions can be found in the three cases, except at the trailing edge, where the exit flow undergoes rapid expansion with a thinner base ($h_{TE} = 0.5$ mm) and further compression with a thicker base ($h_{TE} = 9.7$ mm).

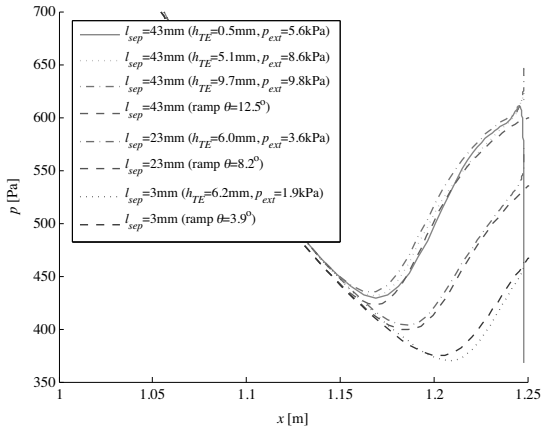

Fig. 4 Comparison of the inner surface pressure p near the trailing edge between base and equivalent ramp flows with various separation lengths

4. Concluding remarks

The effects of the baseflow on flow separation have been investigated numerically for an axisymmetric scramjet nozzle with various base heights and ambient pressures. Respectable delay of separation onset has been observed over the entire pressure range, suggesting effectiveness of base thickening in separation control.

An additional study has been performed for flow separation induced by ramps in order to compare the flowfields in the presence of baseflow and ramp compression. Considerable similarity has been found in the static pressure distributions on the inner nozzle surface between flowfields with baseflow and ramps characterised by the same separation lengths.

References

[1] Boyce, R. R., Tirtey, S. C., Brown, L., Creagh, M., and Ogawa, H., "SCRAMSPACE : Scramjet-based Access-to-Space Systems," AIAA Paper 2011-2297, 17th AIAA International Space Planes and Hypersonic Systems and Technologies Conference, San Francisco, CA, Apr 2011.

[2] Ogawa, H., and Boyce, R. R., "Physical Insight into Nozzle Flow Behaviour of Axisymmetric Scramjets for Access-to-Space via Design Optimisation," 10th Australian Space Science Conference, Brisbane, Australia, Sep 2010.

[3] Ogawa, H, Brown, L, Boyce, R. R., and Ray, T., "Multi-Objective Design Optimisation of Axisymmetric Scramjet Nozzle and External Components Considering Static Stability by Using Surrogate-Assisted Evolutionary Algorithms," ISABE-2011-1513, 20th International Society for Airbreathing Engines (ISABE) Conference, Göteborg, Sweden, Sep 2011.

[4] Östlund, J., Damgaard, T., and Frey, M., "Side-Load Phenomena in Highly Overexpanded Rocket Nozzles," AIAA Paper 2001-3684, 37th AIAA/ASME/SAE/ASEE Joint Proplusion Conference and Exhibit, Salt Lake City, UT, Jul 2001.

[1] Separation onset is detected by the surface shear stress τ_w.

[2] The apparent distortion of the contour of $l_{sep} = 40$ mm may be attributed to insufficient convergence of CFD solutions.

OS1: Next-Generation CFD

Eighth International Conference on Flow Dynamics
November 9 - November 11, 2011

Software System SMILE++ for Modeling of High-Altitude Aerothermodynamic Problems

M. Ivanov, A. Kashkovsky, P. Vashenkov, A. Shevyrin, Ye. Bondar
Khristianovich Institute of Theoretical and Applied Mechanics, 4/1 Institutskaya str., Novosibirsk 630090, Russia
ivanov@itam.nsc.ru

ABSTRACT

The paper presents a new effective software system SMILE++ for comprehensive studying of rarefied gas flows by the DSMC method. The system design is based on the principles of Object-Oriented Programming, which makes it readily modifiable in order to add new capabilities.

1. Introduction

A wide range of problems in both science and industry, starting from micronozzle flows and extending to high-altitude aerothermodynamics of spacecraft and complex fundamental investigations of rarefied flows, have been solved using the Direct Simulation Monte Carlo (DSMC) method [1]. Thus, the ever-growing need for a robust, reliable, easy-to-use, and well-validated code for DSMC computations is clearly seen. Such a code should be well-documented and suitable for users without specialized training in DSMC techniques.

There exist a number of both freeware and commercial packages that address these needs for numerically and ergonomically efficient DSMC systems. These codes include DS2V/3V [2] developed and maintained by G.A.Bird, MONACO [3] developed by Iain D. Boyd et al., and DAC [4] developed in Johnson Space Center. The development of a powerful software system based on the DSMC method was started at the Laboratory of Computational Aerodynamics (ITAM, Novosibirsk, Russia) at the end of the 1980s. This research resulted in the creation of the SMILE system (Statistical Modeling In Low-Density Environment) [5] based Majorant Frequency Scheme [6] of the DSMC method and capable of solving a very wide range of basic and applied problems of rarefied gas dynamics.

Our experience during the development of the SMILE software system clearly demonstrates the fact that the greater the capabilities of the DSMC system are, the harder it is to modify the system by implementation of new models, methods and algorithms. The necessity for the creation of a DSMC software system based on the new-generation Object-oriented programming (OOP) approach became evident to us several years ago. The main goal of the present talk is to describe the basic ideology and demonstrate example applications of the SMILE++ parallel software system developed at ITAM. The SMILE++ is based on the OOP approach and is completely written in C++. SMILE++ is the descendant of SMILE system and incorporates most of its capabilities. At the same time, it has new capabilities and significant advantages offered by OOP.

2. Object-oriented approach in DSMC

Specific features of high-altitude aerothermodynamics of space vehicles impose specific requirements on software applications used in this field: the need for generating and using complicated three-dimensional geometric models and grids; possibility of using various collisional models of physicochemical processes and various gas/surface interaction models; availability of a database of chemical elements, their molecular properties and parameters determining their collisional interaction with other chemical elements; possibility of automation of the parallelization process while retaining high efficiency of parallelization; possibility of using a multizone approach and boundary conditions of various types. The necessity to satisfy all these requirements makes computational systems extremely cumbersome and sophisticated. On the other hand, the DSMC software system should be readily modified for new capabilities. Simultaneously, it is important to retain all already available capabilities of the system. Object-oriented programming (OOP) is a key mechanism in this task.

OOP implies that the code is a model of a real process as a set of interacting objects. The object is described by a number of parameters whose values determine the state of the object and the set of operations (actions) that can be performed by the object. It is important that there can be several replaceable objects performing identical (or similar) operations, but by different methods. If each object is responsible for a certain model of physical phenomena (e.g., different types of chemical reactions), then one can configure the code from properly chosen objects (molecular models) for a particular problem, like a bricklayer makes a wall from bricks.

As the objects are rather closed structural units of the code, it is more convenient to use OOP in large-scale codes developed by a team of programmers. As the interactions between the objects (actions) are limited (the number of actions usually does not exceed 20) and are specified at an early stage of code design, the code for each object is created independently of other codes. This approach substantially simplifies the code development and prevents erroneous usage of data stored for other purposes.

The OOP advantages are not visible for the final user. For developers of the DSMC software, however, it is much simpler to add new models and methods, because all changes are concentrated only in two or three places of the source code.

2. Parallelization

An important specific feature of the DSMC method is a rapid growth of its computational cost with increasing free-stream density. Moreover, it is possible to state now that the possibilities for further improvement of numerical efficiency of the DSMC method by modification of its numerical schemes have been exhausted. Therefore, the only realistic way to increase the efficiency of the method for aerothermodynamic applications is its parallelization. In particular, it should be noted that modeling of real three-dimensional flows around space vehicles at flight altitudes of about 80 km (in the near-continuum regime) is impossible without using multiprocessor computers.

The SMILE++ code parallelization is based on the domain decomposition concept where each processor operates only with some part of the cells of the computational domain and with particles located in these cells. If a particle after moving falls into a cell that belongs to another processor, the particle should be transferred to this processor. Domain decomposition can involve a dynamic algorithm, which periodically re-distributes the cells between the processors, based on accumulated statistical information.

4. Example of SMILE++ application: Clipper spacecraft aerothermodynamics.

A specific feature of the Clipper spacecraft is its configuration: it has a lifting body shape, and its wings have tip fins to increase the lift force and control spacecraft motion in terms of the yawing angle. Computations were performed to determine the aerothermodynamic characteristics of this spacecraft at altitudes from free-molecular flight to 95 km. As a symmetric geometry with a zero rolling angle was studied, the computations were performed only for one half of the body to reduce the computation time. The computations were performed on supercomputers of the Joint Supercomputer Center (Moscow) and of the Siberian Supercomputer Center (Novosibirsk). Low-altitude computations required approximately 10^8 particles and 2×10^7 collision cells. The most expensive computations took about 300 processor-hours. Up to 128 processors were used. The efficiency of parallel computations was about 0.85.

Zones of extreme heating on the spacecraft surface were obtained in these computations. The bow shock wave at low altitudes (below 100 km) was found to be rather thin; when the bow shock wave is incident onto the spacecraft wing, it induces significant local heating. Figure 1 shows the Mach number field and also the surface distribution of the heat-transfer coefficient at an altitude of 95 km. Zones of extreme heating at the tip of the wing and at the area of incidence of the bow shock wave are clearly visible.

4. Concluding remarks

A powerful software system SMILE++ for studying rarefied gas flows by the DSMC method is presented. The system design is based on the principles of Object-Oriented Programming, which makes it readily modifiable in order to add new capabilities. The multiprocessing functionality of SMILE++ is realized through an MPI interface and is capable of running on multiprocessor SMP machines with shared memory and HPC clusters with distributed memory. The dynamic load balancing algorithms realized inside the computation code allow one to achieve high speedups and efficiency even on a large number of processors (up to 1000 and more).

The SMILE++ system provides a complete lifecycle of computations starting from a geometry model, pre-processing, going through the computation proper, and finishing with post-processing and presentation of results. All SMILE++ subsystems have a Graphic User Interface, which makes them user-friendly and easy to use. Results of application of the system demonstrate its capabilities for computing various problems of rarefied gas dynamics.

References

[1] G.A. Bird. *Molecular Gas Dynamics and the Direct Simulation of Gas Flows*. Clarendon Press, Oxford, 1994.

[2] G.A.Bird. Rarefied Gas Dynamics: 24th Int. Symp., Porto Giardino, Italy, July 10-16, 2004, (Ed. M.Capitelli), AIP Conference proceedings, **762** (2005), 541-546.

[3] Dietrich, S. and Boyd, I. D. *Journal of Computational Physics,* **126** (1996), 328-342.

[4] G.J.LeBeau "A User Guide for the DSMC Analysis Code (DAC) Software for Simulating Rarefied Gas Dynamic Environments," Revision DAC97-G, Jan. 2002.

[5] M.S. Ivanov, G.N. Markelov, S.F. Gimelshein, AIAA Paper 98-2669, Albuquerque, June 1998.

[6] M. S. Ivanov and S. V. Rogasinsky, *Sov. J. Numer. Anal. Math. Model.* **3** (1998), 453-465.

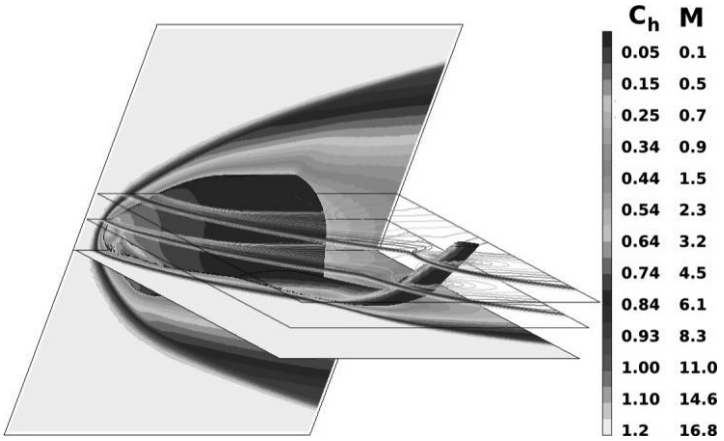

Fig. 1. Mach number flowfield around the Clipper spacecraft. Heat transfer coefficient distribution. Altitude 95 km.

Numerical Simulation of Blast Wave in Confined Room

Fumiya Togashi[1], Joseph D. Baum[1], Orlando A. Soto[1], and Rainald Löhner[2]
1. SAIC, 1710 SAIC Dr., McLean, VA 22102, USA
2. George Mason University, 4400 University Dr., Fairfax, VA 22030, USA
fumiya.togashi@saic.com

ABSTRACT

A coupled fluid-structure dynamics methodology was applied to the modeling of interior wall response subject to an internal blast in a building. The test facility modeled included non-reinforced CMU walls which separated the blast room and adjacent bays. The HE used for this test is a bare charge, detonated very close to the first wall. The JWL EOS and the Miller afterburning model with Cheetah for the afterburning energy estimation were used for the detonation modeling.

1. Introduction

Understanding blast effects is critical to protect buildings, personnel, and equipment because HE remains the most frequently used form of terror attack. Several engineering models to predict the response to blast loading have been recently developed. In addition, there are various fast-running codes that predict airblast loading on structures and the structural response to such loading. Never the less, most of them are modeled only in external blast effects. Engineering models for modeling internal blast effect have been relatively unexplored. Blast propagation inside a building is far more complicated than open-air blast because of the multiple shock reflections from the adjacent walls and blast propagation through collapsed walls. Afterburning effects should be modeled as this is a confined facility. To better understand and model these processes, the Defense Thread Reduction Agency launched a program to investigate internal blast propagation and the response of common construction interior walls.

This paper describes the numerical modeling of one test of this program, in which we modeled CMU wall response to blast loading. The computed results are compared with experimental data.

2. Method

Figure 1 shows the test facility layout. There are four rooms separated by 6" full-weight concrete masonry units (CMU) wall. The CMU conformed to ASTM C-90 specifications for grade "N" units with f'm = 1500 psi. Exterior walls are non-responding walls and the west and east wall have an openings at center of the wall. Bay 1 is the next to the detonation room and Bay3 is the furthest from the detonation room (Fig. 1). An HE bare charged is placed in the detonation room at a height of 3ft above the floor.

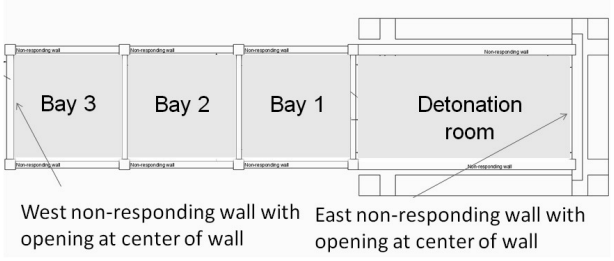

Fig. 1 Test facility layout

The flow solver employed is FEFLO that has had a long history of relevant applications [1, 2] and has been ported to both shared memory [3, 4] and distributed memory [1, 5] machines. The general principles of the code are as follows; 1) Use of unstructured mesh, 2)Finite element discretization of space, 3) Separate flow modules for compressible and incompressible flows, 4) ALE formulation for body fitted moving grids, 5) Embedded formulation for complex/dirty geometries, 6) Automatic mesh adaptation, 7) Various EOS including air, water , and explosives, 8) Optimal data structures for different supercomputer architectures, 9) Bottom-up coding from the subroutine level to assure an open-ended, expandable architecture, and etc.

The structural dynamics solver is SAICSD [6, 7]. This code solves the continuous mechanics equilibrium equation. The weak formulation (virtual work principle) is written in the spatial configuration (actual configuration) and it is discretized in time using an explicit second-order central difference scheme. In space, the virtual work equation is solved by using stable finite element types. The most used elements are: a full integrated large-deformation Q1/P0 solid element (hexahedra with an 8 nodes interpolation scheme for the cinematic variables and constant pressure) which does not present hourglass modes and it does not lock for incompressible cases. Several 3-node and 4-node large-deformation shell elements (Hughes-Liu shell, Belytschko shells, MITC shells, ASGS stabilized shells) which are formulated using standard objective stress update schemes (Jaumann-Zaremba, co-rotational embedded axis, etc,), are fully integrated to avoid hourglass spurious modes. Finally, some objective truss and beam elements (i.e. Belytschko and Hughes-Liu beams) have also been implemented. Many different material models have been included into the code. The most used are: a plasticity model which relies on a hyper-elastic characterization of the elastic material response for the solid elements, and a standard hypo-elastic plasticity model for the shell, beam and truss elements. The most often used failure criterion is based on the maximum effective plastic strain and the stress tensor inside the element. The fracture may be simulated by element erosion and/or node disconnection.

3. Results and Discussion

Figure 2 shows the computed fluid and structure velocity Gouraud shading contours at 102msec. The HE detonation was modeled with the JWL EOS and the Miller model [8] for the afterburning effect. The HE placed very close to the first wall produced a breach at the center-bottom of the CMU wall. As the wall is breached, a strong jetting into Bay 1 was observed as shown in Fig. 1. As the breach size was relatively small, strong shocks were not expected in Bay 1 or in other Bays.

Figure 3 shows comparison of the measured pressure/impulse time histories (black) with the computed results (red) at blast room. The pressure gauge was located at the ceiling of the blast room. The computed peak pressure value, time of arrival (TOA), blast wave reverberation value and their TOAs, and impulse value agreed very well with experimental data. The detonation model combined with the Miller afterburn model and using Cheetah[9] to estimate the afterburn time-dependent energy releases are shown to successfully model the blast effects in this study.

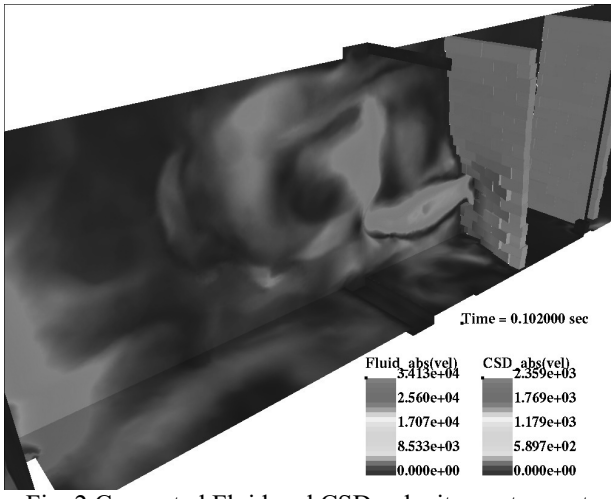

Fig. 2 Computed Fluid and CSD velocity contours at 102 msec

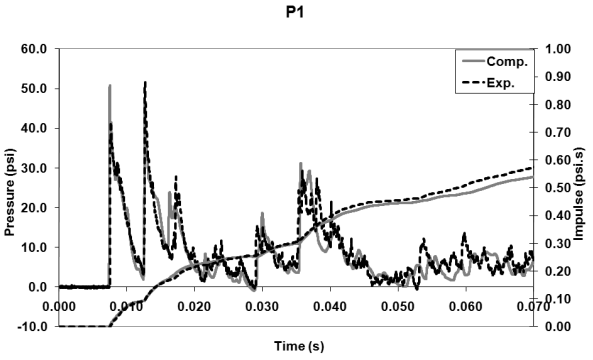

Fig. 3 Comparison of the experimental and computed pressure/impulse histories at detonation room

4. Concluding remarks

A coupled fluid-structure dynamics methodology was applied to the modeling of interior wall response subject to an internal blast in a building.

The test facility modeled included non-reinforced CMU walls which separated the blast room and adjacent bays. The HE used for this test is a bare charge, detonated very close to the first wall.

The JWL EOS and the Miller afterburning model with Cheetah for the afterburning energy estimation were used for the detonation modeling. This approach successfully modeled the HE detonation. The computed pressure and impulse time histories at selected locations agreed well with the experimental data in terms of peak pressure values, time of arrival (TOA), blast wave reverberations values and their TOAs, and impulse values in the blast room. This procedure improved significantly the accuracy of the computed results.

The coupled CFD and CSD methodology, where the structural domain is embedded into the fluid domain, was applied to model the structural response to the blast loading. The simulation successfully demonstrated the creation of the wall breach and the jetting into Bay1. Both the experiment and the computation showed that the wall response is controlled by the exerted quasi-steady pressure.

References

[1] R. Ramamurti and R. Löhner, pp. 1049, 1050 in *Proc.11th AIAA CFD Conf.*, Orlando, FL, July, 1993

[2] J. D. Baum, H. Luo, E. Mestreau, R. Löhner, D. Pelessone, and C. Charman, AIAA-99-0794, 1999

[3] R. Löhner, *Comp. Meth. Appl. Mech. Eng.* 163, pp. 95-109, 1998

[4] D. Sharov, H. Luo, J. D. Baum and R. Löhner, AIAA-00-0927, 2000

[5] R. Ramamurti and R. Löhner, *Computers and Fluids* 5, pp. 119-132, 1996

[6] O. Soto, Baum, J.,D., Löhner, R., Mestreau, E. Luo, H., Fluid Structure Interaction 2005. September 19-21. La Coruna, Spain

[7] O. Soto, Baum, J., Löhner, *Engineering Fracture Mechanics,* 77, pp. 549–564, 2010

[8] P.J. Miller, MRS Sym.Proc., Vol. 418, p. 413, 1996 MRS Society Pub.

[9] L E. Fried, K. R. Glaesemann, W. M. Howard, P. C. Souers, and P. A. Vitello, “Cheetah 4.0 User’s manual,” LLNL, 2004

Eighth International Conference on Flow Dynamics
November 9 - November 11, 2011

Computations of Rarefied Gas Flows of Arbitrary Statistics Using an Accurate Direct Solver for Semiclassical Boltzmann-BGK Equation

Jaw-Yen Yang, Bagus P. Muljadi and Manuel Diaz
Institute of Applied Mechanics, National Taiwan University, Taipei 10764, TAIWAN.
yangjy@iam.ntu.edu

ABSTRACT

An accurate and direct method for solving the semiclassical Boltzmann-BGK equation in phase space is presented for parallel treatment of rarefied gas flows of particles of three statistics. The discrete ordinate method and WENO schemes are combined to advance the solution. The method is developed for 2-Dproblems and implemented on gas particles that obey the Maxwell-Boltzmann, Bose-Einstein and Fermi-Dirac statistics. Computations of unsteady shock diffraction by a finite body covering wide range of Knudsen numbers are presented.

1. Introduction

In recent years, due to the rapid advancements of microtechnology and nanotechnology, the device or structure characteristic length scales become comparable to the mean free path and the wavelength of energy and information carriers (mainly electrons, photons, phonons, and molecules), some of the classical continuum transport laws are no longer applicable. It is generally believed that the microscopic description of Boltzmann equation (classical and semiclassical) is adequate to treat transport phenomena in the mesoscale range. Besides, due to the different types of carriers may involve simultaneously in a single problem, it is desirable to have a method that can allow one to treat them in a unified and parallel manner. Indeed, this is the view advocated in micro- and nano-scale energy transport by Chen [1]. With the semiclassical Boltzmann equation [2], it is possible to describe adequately the mesoscale transport of particles of arbitrary statistics. In this work, we aim at developing an accurate direct solver for the semiclassical Boltzmann equation with relaxation time approximation [3] in phase space that can treat particles of three statistics on equal foot and in a parallel manner. Such a method will allow one to examine the same physical flow problems but with different gas of particles.

2. Method

The semiclassical Boltzmann-BGK equation can be written as

$$\frac{\partial f}{\partial t} + \vec{\xi}\cdot\nabla f + \vec{a}\cdot\nabla_{\vec{\xi}} f = -\frac{f - f^{eq}}{\tau} \quad (1)$$

$$f^{eq} = \{\exp[\frac{(\vec{p} - m\vec{u})^2}{2mk_B T} - \frac{\mu}{k_B T}] - \eta\}^{-1} \quad (2)$$

Here, $f(\vec{x},\vec{p},t)$ is the distribution function, $\vec{p}$ is the momentum, τ is the relaxation time, $\vec{u}$ is the mean velocity, T is the temperature, k_B the Boltzmann constant and μ is the chemical potential. Here, one has the Bose-Einstein statistics for $\eta = +1$ and Fermi-Dirac statistics for $\eta = -1$. In this work, a direct solver in phase space for solving Eq. (1) is constructed. Taking the first few moments of Eq. (1), one obtains the conservation laws of semiclassical hydrodynamics as follows:

$$\frac{\partial n}{\partial t} + \nabla_{\vec{x}}\cdot(n\vec{u}) = 0$$

$$n(\frac{\partial}{\partial t} + \vec{u}\cdot\nabla_{\vec{x}})u_\alpha + \frac{\partial P_{\alpha\beta}}{\partial x_\beta} = 0$$

$$\frac{\partial \varepsilon}{\partial t} + \nabla_{\vec{x}}\cdot(\varepsilon\vec{u}) + \nabla_{\vec{x}}\cdot\vec{Q} + D_{\alpha\beta}P_{\alpha\beta} = 0 \quad (3)$$

Here, P_{ij} is the pressure tensor, P the pressure and Q_i is the heat flux vector. Applying the discrete ordinate method to Eq. (1), one renders a set of hyperbolic conservation equations with source terms.

$$\frac{\partial f_{\sigma,\delta}}{\partial t} + v_\sigma\frac{\partial f_{\sigma,\delta}}{\partial x} + v_\delta\frac{\partial f_{\sigma,\delta}}{\partial y} = \frac{(f_{\sigma,\delta}^{(0)} - f_{\sigma,\delta})}{\tau}. \quad (4)$$

We discretize the space (x,y) and time t into a number of cells centered at (i,j) at time n, hence we approximate $f_{\sigma,\delta}$ by $f_{\sigma,\delta}{}^n_{i,j}$ in terms of numerical fluxes, the evolution from n^{th} time level to $(n+1)^{th}$ time level is expressed by

$$f_{\sigma,\delta}{}^{n+1}_{i,j} = f_{\sigma,\delta}{}^n_{i,j} - \frac{\Delta t}{\Delta x}\left(F^N_{i+\frac{1}{2},j} - F^N_{i-\frac{1}{2},j}\right) - \frac{\Delta t}{\Delta y}\left(G^N_{i+\frac{1}{2},j} - G^N_{i-\frac{1}{2},j}\right) + \frac{\Delta t}{\tau}\left(f^{eq}{}_{\sigma,\delta}{}^n_{i,j} - f_{\sigma,\delta}{}^n_{i,j}\right) \quad (5)$$

where the time step Δt is chosen to be less than the local relaxation time, τ. Then high resolution TVD and WENO schemes are applied to Eq. (5) to advance the solution in time. The details can be found in [4,5]. Once one has solved $f_{\sigma,\delta}(x,y,t)$, then the macroscopic flow properties, such as the number density and number flux in the x-direction, can be computed by the quadrature formulas,

$$n(x,y,t) = \sum_{\sigma=1}^{N_1}\sum_{\delta=1}^{N_2} W_\sigma W_\delta e^{v_\sigma{}^2} e^{v_\delta{}^2} f_{\sigma,\delta}$$

$$j_x(x,y,t) = \sum_{\sigma=1}^{N_1}\sum_{\delta=1}^{N_2} v_\sigma W_\sigma W_\delta e^{v_\sigma{}^2} e^{v_\delta{}^2} f_{\sigma,\delta} \quad (6)$$

3. Results and Discussion

The unsteady shock wave diffraction by a finite body and 2-D Riemann problems present two good examples to illustrate the gas dynamical flows as the main flow features are covered [6,7]. We illustrate the present method by simulating the unsteady shock wave diffraction by a square cylinder in a degenerate gas. In this example, we set Ms =2.0 and the initial conditions for the Fermi-Dirac gas at rest ahead of shock are set as (n1, ux1, uy1, P1)= (0.1497, 0, 0, 0.038) which correspond to z1 =0.1 and T1 =0.5 whereas the conditions before the shock are set as (n2, ux2, uy2, P2)= (0.2994,0.7125, 0, 0.192) which correspond to z_2=0.078. The relaxation time is set at 0.0005. In Fig. 1, the density contours of the three particle statistics obtained using TVD scheme and Van-Leer's limiter with CFL =0.9 and 20 X 20 discrete velocity points are shown. The primary incident shocks, reflected bow shocks, Mach shocks, contact discontinuities, triple points and vortices can be clearly identified and the complicated nonlinear wave interaction can be well represented. The difference between the three particle statistics can be identified through detailed quantitative comparison as well as different flow patterns due to different viscosity. More computational examples such as 2-D Riemann problems as studied in [7] will be presented in the full paper.

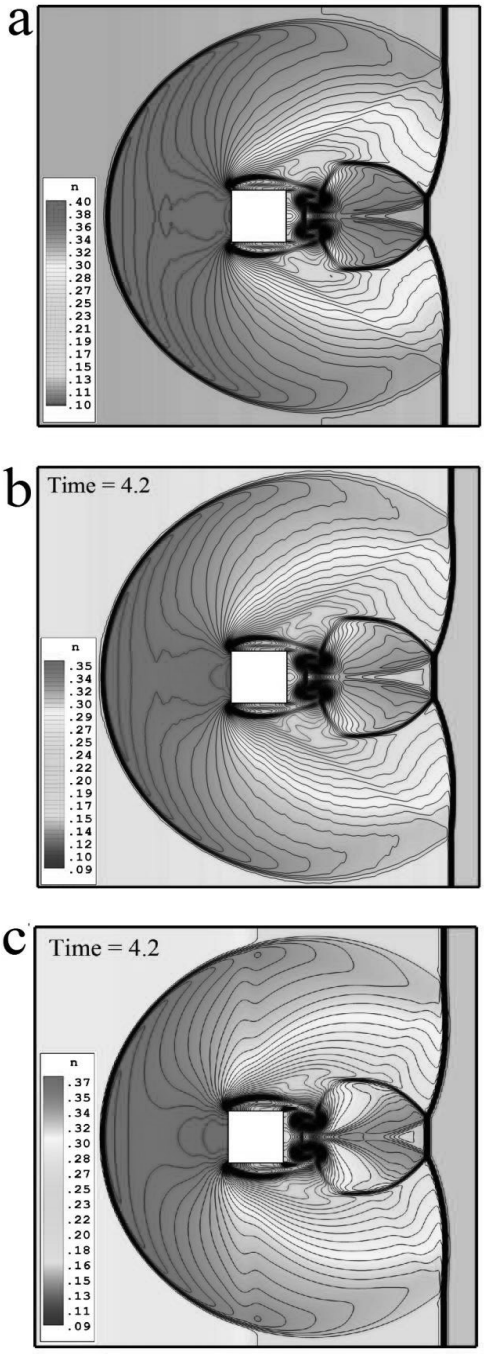

Fig. 1. Uunsteady shock wave diffraction by a square cylinder with τ=0.0005 and Ms = 2.0. Density contours of (a) Bose-Einstein gas (b) Fermi-Dirac gas (c) Maxwell-Boltzmann gas.

4. Concluding remarks

An accurate algorithm using discrete ordinate method and TVD and WENO schemes for solving semiclassical Boltzmann-BGK transport equation in phase space is presented. The results see the method applied to 1-D shock tube problems and 2-D Riemann problems for quantum gases. Unsteady shock wave diffraction by a finite body is simulated for three statistics. Different aspects of the present algorithm are tested including ranges of constant relaxation time values, various Knudsen numbers and physical relaxation times. All the expected flow profiles comprising shock, rarefaction wave and contact discontinuities can be seen with considerably good detail. The feasibility of this algorithm and its capability in describing the quantum gas flows in various flow regimes have been illustrated.

Acknowledgement – This work was supported by National Science Council, Taiwan through grant NSC97-2221-E-002-063-MY3 and by CASTS/ NTU.

References

[1] G. Chen, Nanoscale Energy Transport and Conversion. Oxford University Press, USA (2005) .
[2] E. A. Uehling and G. E. Uhlenbeck, Phys. Rev. **43**, 552, (1933).
[3] P. L. Bhatnagar, E. P. Gross, M. Krook, Phys. Rev. **94,** 511 (1954).
[4] J. Y. Yang, and J. C. Huang, J. Comput. Phys., **120**, 323 (1995)
[5] J. Y. Yang and Y. H. Shi, Proc. Roy. Soc. A **462**, 1553 (2006).
[6] M. Sun and K. Takayama, J. Fluid Mech., **478**, 237 (2003).
[7] P. D. Lax and X. D. Liu, SIAM J. Sci. Comput., **19**, 319 (1995).

Eighth International Conference on Flow Dynamics
November 9 - November 11, 2011

Non-Uniform Grids in Numerical Simulations of Boundary Layer Turbulence Transition

JC Chen* and Chen Weijia
Block N1 Nanyang Avenue Singapore 639798
*E-mail of corresponding author: jimchen@ntu.edu.sg

ABSTRACT

Numerical simulations of turbulence transition meet with the challenge of astronomical computational demands needed to visualize the underlying physical phenomena. Reprieve from the onerous computational load avails when considering that boundary layer turbulent flow structures intermittently concentrate near the wall. Astute implementation of non-uniform grids with microscopically precise resolution near the wall boundary that tapers off away from the wall offers potential for vast computational efficiency. The numerical method with non-uniform grid further strengthens the numerical stability of the boundary condition schemes.

1. Introduction

The wave interaction dynamics underlying the transition to turbulence presents a view of the process from the perspective of periodic oscillations of the disturbance velocities in wave form. A concomitant perspective views the process in terms of the evolution of physical flow structures during transition. Some of the commonly observed flow structures include the Λ-vortex, Ω-vortex, high shear layer, and turbulent streaks [1]. An important physical flow structure of note is the formation of turbulent eddies strewn intermittently throughout the flow. The intermittent turbulent eddies also experience progeneration where first generation eddies beget second and third generations in cascading fashion [2]. The posterior eddies will sequentially decrease in length and time scales, imposing taxing demands on the computational power required to visualize them. Chen, 2009 [2] and Chen and Chen, 2011 [3] offer excellent expositions on turbulent eddy progeneration. The numerical simulation must have the computational capacity to reach the necessary level of computational resolution.

Since the numerical realization of turbulence transition exerts impractically onerous computational demands, one would do well to preserve computational resources during the simulation as much as possible. One method of conservation uses non-uniform grids that concentrate the computational resolution in regions of interest and relax to coarse resolutions in regions of less relevance. For the case of boundary layer turbulence transition, this entails using very fine grids near the wall where the transition process occurs and gradually coarsening the grid with increasing distance away from the wall. In so doing, the precious resource of computational capacity would be allocated with maximum utility.

Furthermore, microscopic-scaled wave interactions occurring during turbulence transition can be easily distorted by numerical errors. So, high-order numerical methods would seem to be a logical remedy to control the errors. However, the use of high-order numerical methods presents an additional issue of concern at the wall boundary. To properly close a high-order numerical method, the appropriate boundary scheme would generally be at least one order lower than the original numerical scheme in the interior domain, in order to prevent numerical instability [4]. The difference in orders between the interior and boundary schemes widens with increasing order of the numerical method [4]. So, even when using a high-order numerical method, the overall order of the numerical method would be diluted by the need for lower-order boundary schemes and hence poses a threat to the numerical stability [4]. One means to preserve numerical stability of high-order methods at the boundary and combat the dilutive effects of lowering the order of the boundary scheme implements non-uniform grids that concentrate fine grid spacing near the wall. The solution would first generate a non-uniform grid and then derive a numerical method bespoke to the non-uniform grid [4]. The numerical method would be compatible with the non-uniform grid because the coefficients of the former are derived using the latter.

2. Non-Uniform Grid Generation

The non-uniform grid is generated in the wall-normal y-direction using a piecewise function:

$$y = y_c\left(1+\frac{\operatorname{asin}\left(-\alpha_g\cos\left(\frac{\pi i}{2c}\right)\right)}{\operatorname{asin}\left(-\alpha_g\right)}\right) \quad for \quad 0 \le i \le c \tag{1}$$

$$y = y_c + (y_c - y_{c-1})\left(\frac{\beta_g^{(i-c)}-1}{\beta_g-1}\right) \quad for \; c+1 \le i \le n \tag{2}$$

where α_g and β_g are the grid stretching parameters and c is the index for a designated node point where the two piecewise functions will meet.

3. Numerical Scheme Bespoke to Non-Uniform Grid

The numerical scheme would be derived bespoke to the non-uniform grid. High-order combined compact difference (CCD) schemes provide the dual advantages of accuracy of simulations and control of numerical errors. The CCD scheme combines the discretization for the function, f, its first derivative, F, and second derivative, S, with a, b, and c as the coefficients of the numerical scheme and h as the grid size:

$$h\sum_{j=j_1}^{j_2} a_{1,j}F_{i+j} + h^2\sum_{j=j_1}^{j_2} b_{1,j}S_{i+j} + \sum_{j=j_1}^{j_2} c_{1,j}f_{j+j} = 0 \tag{3}$$

$$h\sum_{j=j_1}^{j_2} a_{2,j}F_{i+j} + h^2\sum_{j=j_1}^{j_2} b_{2,k}S_{i+j} + \sum_{j=j_1}^{j_2} c_{2,j}f_{i+j} = 0. \tag{4}$$

The coefficients of the CCD scheme are derived using Lagrange polynomial interpolation. The Lagrange polynomial interpolation of a function $y(x)$ is [4]:

$$y(x) = \sum_{i=1}^{n} l_i(x) f(x_i) \quad (5)$$

where $l_i(x)$'s are Lagrange basis polynomials [4]:

$$l_i(x) = \prod_{j=1, j\neq i}^{n} \frac{(x-x_j)}{(x_i-x_j)} \quad (6)$$

The Lagrange polynomial interpolation can be extended to include higher-order derivatives [4]:

$$y(x) = \sum_{d=0}^{D} \sum_{i\in I_n} \rho_{d,i}(x) f^{(d)}(x_i) + \sum_{i\in I_m} r_i(x) f(x_i) \quad (7)$$

where $f^{(d)}(x_i)$ denotes the D^{th}-order derivative of the function $f(x_i)$, I_n is the set of points defining $f^{(d)}(x_i)$ up to D^{th}-order derivative, I_m is the set of points defining only the function values of $f(x_i)$, and $\rho_{d,i}(x)$ and $r_i(x)$ are additional interpolation polynomials. The numerical schemes can be derived by differentiating Eq. (7) D times to obtain the expressions for $y^{(p)}(x)$ as [4]:

$$y^{(p)}(x) = \sum_{d=0}^{D} \sum_{i\in I_n} \rho_{d,i}^{(p)}(x) f^{(d)}(x_i) + \sum_{i\in I_m} r_i^{(p)}(x) f(x_i) \quad (8)$$

for p =1, 2, …, D. The coefficients of the numerical scheme are derived from Eq. (8). In this study, the numerical scheme derived by this method is a 12$^{\text{th}}$-order 5-point non-uniform CCD scheme. The concomitant boundary schemes are 10$^{\text{th}}$ and 11$^{\text{th}}$-order. The discretization of the temporal derivative uses a 4$^{\text{th}}$-order 5-6 alternating stages Runge-Kutta (RK) scheme.

4. Stability of Numerical Scheme

With the objective of customizing the numerical method to a non-uniform grid for strengthening numerical stability, a logical evaluation of the numerical method would consider its range of stability. The stability of a numerical method entails two facets, the temporal and spatial discretizations. Both aspects must be numerically stable. Mathematical theory decrees that the properties of the eigenvalues of a spatial discretization define its range of numerical stability. The eigenvalue analysis begins with applying the numerical method, in this case, a 12$^{\text{th}}$-order 5-point non-uniform CCD scheme with concomitant 10$^{\text{th}}$ and 11$^{\text{th}}$-order boundary schemes, to a reference governing equation, the classical one-dimensional convective diffusion equation. The theory mandates that the real part of the eigenvalue of the numerical discretization must be less than zero to ensure stability.

For the temporal discretization, the theory examines its amplification factor. A temporal discretization will be stable if the absolute value of the amplification factor is less than one. Since the temporal discretization integrates the spatial discretization over time, the amplification factor is a function of the eigenvalue. This linkage allows for concurrent examination of the stabilities of both discretizations. The overall stability condition would require first that the real part of the eigenvalue be less than zero. Next, of these eigenvalues, those that would limit the amplification factor to less than one would be further selected.

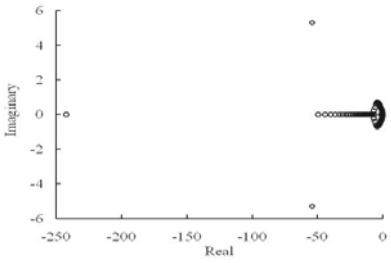

Fig. 1 Stability range of eigenvalues.

Applying this two-step analysis to the one-dimensional convective diffusion equation indeed yields a set of eigenvalues for which the numerical method will remain stable, as depicted in Fig. 1. The stability of the numerical method when applied to this reference case provides indications as to how it will fare on the actual flow problem.

5. Numerical Visualization of Turbulent Transition

Consider turbulence transition in boundary layer flow with adverse pressure gradient. The computational model uses a three-dimensional rectangular simulation box. A blowing and suction strip at the base of the flow near the entrance introduces disturbance waves. The background flow conditions match those of experiments by Borodulin, et al., 2002 [5], which provides validation for the simulations. The computational visualization does indeed realize the development of the classical turbulent flow structures, shown in Fig. 2. Finally, the amplification behavior of disturbance waves agrees with that of Borodulin, et al., 2002 [5].

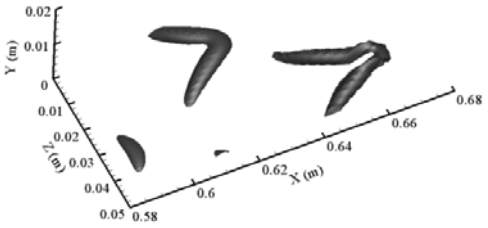

Fig. 2 Computational visualizations of flow structures.

6. Conclusion

Derivation of numerical schemes bespoke to a non-uniform grid offers computational efficiency and stability. Numerical visualization of boundary layer flow reveals the classical turbulent flow structures.

References

[1] J. Chen and W. Chen, Intl J Emerg Multidiscip Fluid Sci, **2** (2010), 183 - 203.
[2] J. Chen, Intl J Emerg Multidiscipl Fluid Sci, **1** (2009), 165 - 179.
[3] W. Chen and J. Chen, Intl J Numer Methods Fluid, (2011), in press.
[4] X. Zhong and M. Tatineni, J Comput Phys, **190** (2003), 419 - 458.
[5] V. I. Borodulin, V. R. Gaponenko, Y. S. Kachanov, D. G. W. Meyer, U. Rist, Q. X. Lian, and C. B. Lee, Theoret Comput Fluid Dynamics, **15** (2002), 317 - 337.

Eighth International Conference on Flow Dynamics
November 9 - November 11, 2011

A Parallel Structured Adaptive Mesh Refinement Approach for Complex Turbulent Shear Flows

Yuichi Matsuo[*1], Takuhito Kuwabara[*2], and Ichiro Nakamori[*2]
*1 Japan Aerospace Exploration Agency, 7-44-1, Jindaijihigashi, Chofu, Tokyo, Japan, matsuo.yuichi@jaxa.jp
*2 Advancesoft cooperation, 1-9-20, Akasaka, Minato-ku, Tokyo, Japan

ABSTRACT

In numerical fluid dynamic simulations, adaptive mesh refinement (AMR) approaches are becoming popular these days, particularly when the target flow field includes complex turbulent shear flows like jets, mixing layers, and shear layers in separated regions as well as the ones originated from shock discontinuities. In this AMR approach, for numerical simplicity and practical use, we adopt a block-based method where in each block, a structured mesh, a body-fitted coordinate and a conventional finite volume method are used, and numerical issues like memory reduction, load balance are considered.

1. Introduction

Adaptive mesh refinement (AMR) approaches are becoming popular these days in numerical fluid dynamic simulations, particularly when the target flow field includes complex turbulent shear flows like jets, mixing layers, and shear layers in separated regions as well as the ones originated from shock discontinuities. On AMR, many researches have been done since the Berger-Oliger historical paper [1], and several production codes have already been developed [2,3]. In this AMR approach, for numerical simplicity and practical use, we adopt a block-based method where in each block, a structured mesh, a body-fitted coordinate and a conventional finite volume method are used, and numerical issues like memory reduction, load balance are considered.

In this paper, our structured AMR approach for turbulent shear flows is briefly described first, next some example results with the AMR code are shown, and pros and cons of the AMR method are discussed.

2. Approach

AMR is efficient and effective in treating problems with multiple spatial and temporal scales. The basic idea of AMR is as follows. It represents computational domain as hierarchal refinement levels and increases points per wavelength only in areas of interest. A given spatial error tolerance is achieved by recursively refining meshes. Subsequently a localized mesh of high grid resolution is distributed within an otherwise coarse mesh. The computational efficiency is improved by reducing the required number of computational cells. The operation of refinement could be made either for each single cell, i.e. cell-based AMR, or for each single block and called block-based AMR. For the block-based AMR method, a computational domain consists of blocks with a predefined number of cells, e.g. 32x32x32 cells in each block. If any cell in one block requires refinement, the whole block is refined. As a result, the data structure is only maintained for blocks. It is well accepted that block-based AMR requires less programming efforts and is computationally more effective than cell-based AMR with respect to communication costs and memory requirements.

In this study, we extend our earlier effort where a block-based AMR code was constructed and tested against some simple benchmark problems as shown in Fig. 2. In order to solve aerodynamic problems of practical significance in aerospace including turbulent shear flows, the original AMR code is improved so as to support body-fitted meshes with multi-block topology initially constructed, and to work on parallel machines using message passing interface (MPI) library with less memory requirement and better load balance. The AMR code is written by Fortran 90 in modules as shown in Table 1 and the work flow is illustrated in Fig. 1.

Table 1 Modules of the parallel SAMR code.

Modules	Function
parallel.f90	Define parallel computation variables
params.f90	Define flow parameters
comarry.f90	Define common arrays
comindx.f90	Define common variables
func.f90	Collections of functions
derefine.f90	Derefine blocks
refine.f90	Refine blocks
mblock.f90	Manipulate multi-blocks
transfer.f90	Manipulate guard-cell filling
transfer2.f90	Interpolate data from children to parents
bnd.f90	Set boundary conditions
io.f90	File I/O
restart.f90	Manipulate computation restart
rewind.f90	Error control

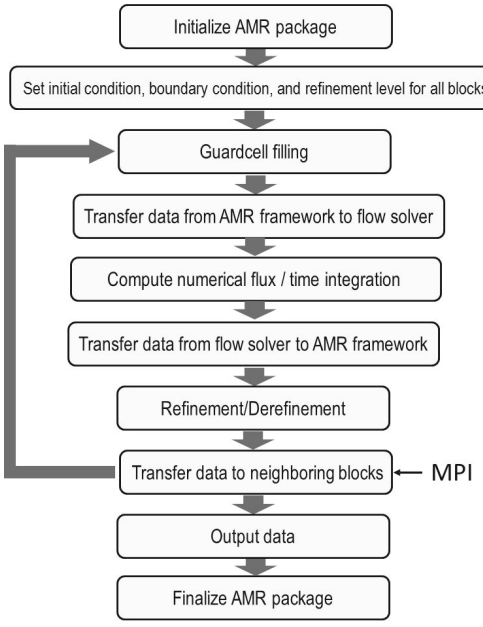

Fig. 1 Flow chart of the parallel SAMR code.

3. Results and Discussion

In order to demonstrate the capability of the present AMR approach, some numerical examples are shown below.

The first example is a 3D supersonic jet. In this case, a multi-block mesh with 32 blocks, each has 32x8x20 points, is presumably refined into 2-level AMR blocks (752 blocks) as in Fig. 3(a). Consequently, the flow field is obtained as shown in the instantaneous density distribution of Fig. 3(b) where very fine structures of flow mixing can be resolved.

The second example is a flow around an atmospheric reentry vehicle at transonic regime where oscillatory wake occurs. In this case, an ORION CM model configuration is solved and a 2-level refinement is set at the beginning in Fig. 4(a). A snapshot of the velocity magnitude distribution is shown in Fig. 4(b), and a complicated wake structure can be seen.

With AMR, fine flow structures can be obtained with less mesh points so that the approach would be effective for the simulations like LES where the mesh size in important. However, the computational load is so large that the software development conscious of computer science is strongly required.

4. Concluding remarks

In this paper, a parallel structured AMR approach for complex turbulent shear flows with which we often encounter in practical aerodynamic problems is shown, and some numerical examples are illustrated and the features of the method are discussed.

References

[1] Berger, M. J., and J. Oliger, 1984, J. Comput. Phys. **53**(3), 484.

[2] Hornung, R. D., and S. R. Kohn, SAMRAI: Structured Adaptive Mesh Refinement Application Infrastructure, `https://computation.llnl.gov/casc/SAMRAI/index.html`.

[3] Deiterding, R., AMROC: Block structured adaptive mesh refinement in object-oriented C++, `http://amroc.sourceforge.net/index.htm`.

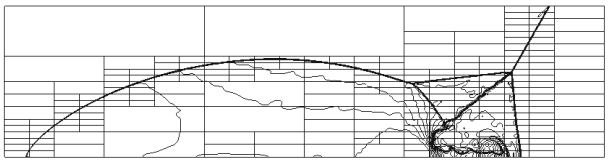

(a) Double Mach reflection.

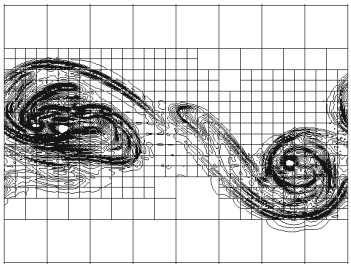

(b) Mixing layer.

Fig. 2 Snapshots of density contours obtained by the baseline AMR code for 2D benchmark problems.

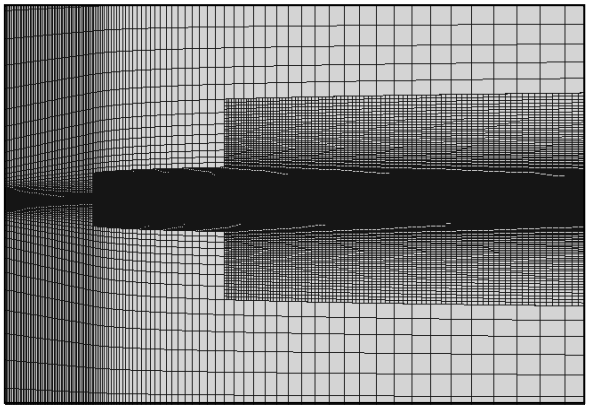

(a) Structured AMR grid

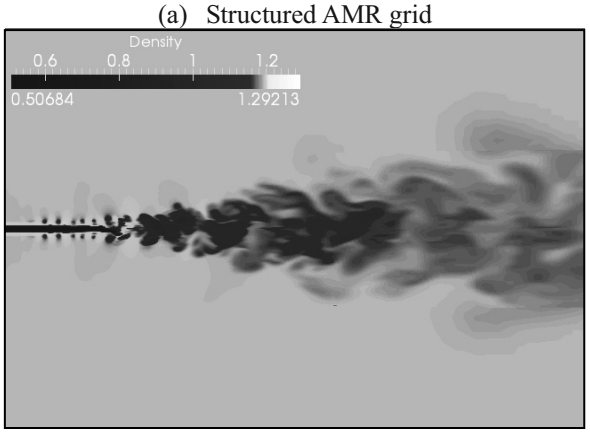

(b) A snapshot of density distribution

Fig. 3 3D supersonic jet.

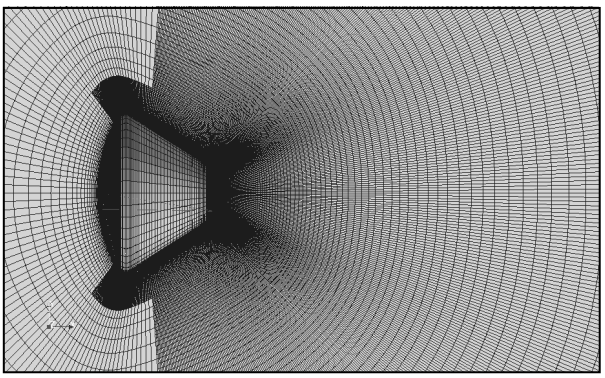

(a) Structured AMR grid

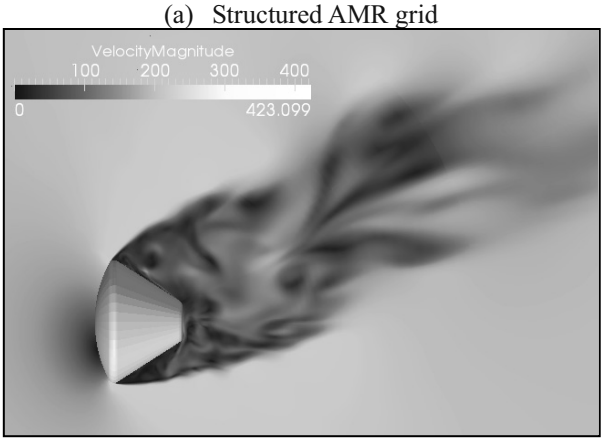

(b) A snapshot of velocity magnitude distribution

Fig. 4 Transonic flow through an ORION CM model.

Computational Aeroacoustics by the Near Wall Vortex-Shock Interaction Using WCNS

Zhifeng Zuo, Hiroshi Maekawa
Department of Mechanical and Control Engineering, University of Electro-Communications
1-5-1 Chofugaoka, Chofu-shi, Tokyo 182-8585
zuozhifeng@maekawa.mce.uec.ac.jp, maekawa@mce.uec.ac.jp

ABSTRACT

The simulation shows the production of acoustic waves develops in a two-stage process. At the early times, a precursor having a quadrupolar nature is produced and expands radially, then is deformed to be tripolar by colliding with the wall. With the shock passes the vortex, a Mach structure is generated. One of reflected shocks (MR2) propagates downward and is reflected from the wall. The reflected MR2 wave causes an additional shock-vortex interaction. By the MR2-precursor interaction, a secondary acoustic wave is apparent and remains its quadrupolar nature. The circumferential variation of the two sound pressures is opposite in sign.

1. Introduction

In the last few decades, several high-resolution non-linear schemes, such as Weighted Compact Non-linear Scheme (WCNS) [1], are developed to capture discount-inuities. According to our previous work [2], WCNS is a good choice for computational aeroacoustic problems.

As one of the major sources of noise, the interaction between shock waves and vortices has been given much attention. However, the study of the interaction between a shock and near wall vortex is very few. In this paper, two-dimensional, unsteady, compressible flow field produced by the interactions of a shock wave and near wall vortex is simulated numerically using WCNS.

2. Numerical Method And Initial Conditions

2.1 Governing Equations

The two-dimensional, compressible Navier-Stokes equations are solved in this study.

$$\frac{\partial U}{dt}+\frac{\partial E_j}{\partial x_j}=\frac{\partial E_{vj}}{\partial x_j} \qquad (1)$$

where the vectors $\boldsymbol{U}$, $\boldsymbol{E}_j$ and $\boldsymbol{E}_{vj}$ are dependent variables, convective flux and viscous flux in the jth spatial direction respectively (j=1,2).

2.2 Initial Conditions

We consider an initially planar shock interacting with a near wall vortex rotating in the clockwise direction. The shock propagates from left to right, and interacts with the vortex.

The computational domain is rectangular (4.0×3.0), and the vortex is located at (2.4, 0.4). The core radius of vortex is set to 0.2. A schematic diagram of initial flow is presented in Fig.1. The Mach number of the shock wave (M_s), Reynolds number (Re) and Mach number of the vortex (M_v) are listed in Tab.1.

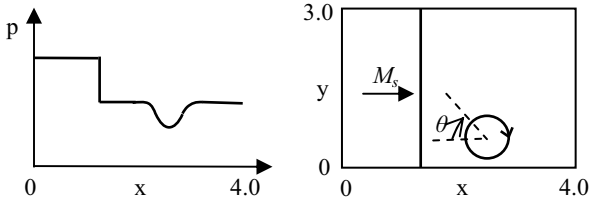

Fig.1 Schematic diagram of initial flow

The computational domain consists of an 800×600 uniform grid. We adopt fifth-order explicit WCNS with FVS method to calculate convective flux. For viscous flux computation and time integration, sixth-order compact scheme and fourth-order Runge-Kutta scheme are employed respectively. Adiabatic no-slip wall boundary conditions (NSCBC, Poinsot-Lele 1992) are used at y=0 and 3.0.

Tab.1. Parameters used for the simulation

M_s	M_v	Re
1.28	0.39	3000

3. The Effect of The Near-Wall Vortex on a Planar Shock

The time development of pressure contour is shown in Fig.2. At the early times, a compression region and a rarefaction region appear downstream of the shock wave [Fig.2(a)]. The compression region expands radially along the $\theta=-45^\circ$ direction, then is deformed by colliding with the wall. As the shock emerges from the vortex flow field, a Mach structure is formed [Fig.2(b)]. The MR2 wave expands radially, and is strongly reflected from the wall [Fig.2(c)]. The reflected MR2 propagates toward the vortex, then an additional shock-vortex interaction is generated [Fig.2(d)].

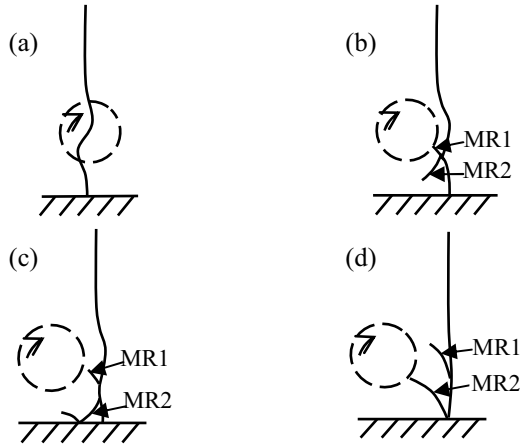

Fig.2 Schematic diagram of time development of pressure contour. Time increases from (a) to (d)

4. Production of Acoustic Waves

Now we discuss the production of acoustic waves. The normalized pressure variation $\Delta p=(p-p_s)/p_s$, where p_s is the pressure behind the shock, is presented in Fig.3. At the early times, the interaction of the shock with the vortex flow field changes the pressure variation along the shock front. The pressure field behind the

shock consists of a weak expansion in the region, where the vortex velocity aids the shock propagation and a weak compression, where the velocity opposes the shock propagation, i.e. a precursor appears first [Fig.3(a)]. As the shock interacts with the core of the vortex, a large pressure peak develops; then a new rarefaction region appears outside the compression region, and a new compression region appears outside the rarefaction region [Fig.3(b)]. This series of events shows the generation of the precursor and its quadrupolar nature consisting of alternating compressions and expansions. The compression region (downside one) expands radially along the $\theta = -45^\circ$ direction. By colliding with wall, the compression region is deformed, and the precursor turns into having a tripolar nature [Fig.3(d) - 3(h)].

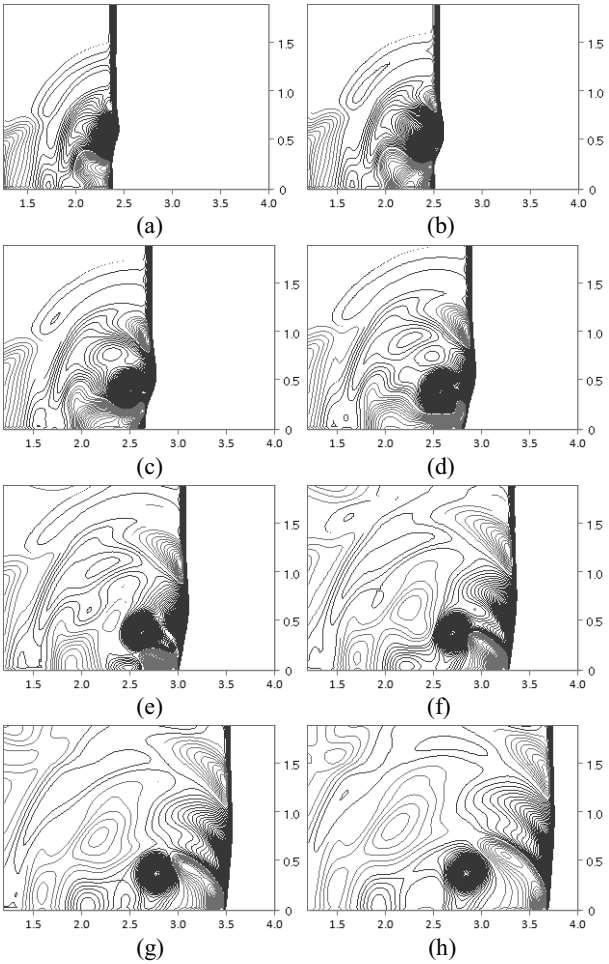

Fig.3 Time development of the pressure variation Δp
The contour levels are from -0.2 to 0.2 with an increment of 0.002. (— :△p>0, — :△p< 0). t= a:0.0859, b:0.0988, c:0.1160, d:0.1332, e:0.1503, f:0.1761, g:0.1954, h:0.2148.

With the shock emerges from the vortex flow field, the two reflected waves (MR1 and MR2) are generated and propagate upward and downward respectively [Fig.3(c)]. The MR2 wave expands radially, and is strongly reflected from the wall. The reflected MR2 wave propagates toward the vortex, so an additional shock-vortex interaction is caused. By the interaction of the reflected MR2 wave with the precursor wave, a secondary acoustic wave is apparent. As shown in Fig.3(f)-3(h), the secondary sound has a quadrupolar nature.

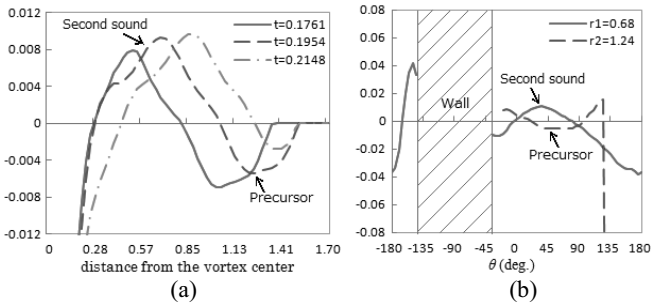

Fig.4 Radial and circumferential distribution of the sound variation Δp
(a) Radial distribution at t=0.1761, 0.1954 and 0.2148 ($\theta = 45^\circ$)
(b) Circumferential distribution at t=0.1954.

In Fig.4(a), distributions of the sound pressure are plotted against the distance from the vortex center for a fixed value of $\theta = 45^\circ$ (Fig.1 shows the definition of θ) at t=0.1761, 0.1954 and 0.2148. It can be seen that both the precursor and the second sound propagate radially. The Δp peak value of the precursor decays with the radial distance, but the one of the second sound wave is strengthened with the reflected MR2 wave passes the vortex. From this figure, we can determine r1=0.65 where the peak amplitude of the secondary acoustic wave is maximum, and r2=1.24 where the peak amplitude of the precursor is maximum at t=0.1954. Thus we plot the circumferential variation of the second sound (solid line) and the sound pressure of the precursor (dashed line) in Fig.4(b). The secondary sound has a quadrupolar nature, but the precursor turns into being tripolar. The circumferential variation of the sound pressure of the second sound is opposite in sign to that of the precursor.

5. Concluding remarks

The flow field produced by the near wall vortex-shock interaction is simulated numerically using WCNS.

The simulation shows the production of acoustic waves develops in a two-stage process. At the early times of interaction, a precursor is produced and expands radially, then is deformed by colliding with the wall. With the shock wave emerges from the vortex flow field, a Mach structure is generated. The stronger one of reflected shocks (MR2) propagates downward, and is reflected from wall. A secondary acoustic wave is generated by the interaction of the reflected MR2 wave with the precursor wave. Both sounds propagate radially. The precursor turns into a tripolar nature from its initial quadrupolar one, but the secondary sound remains its quadrupolar nature. The circumferential variation of the two sound pressures is opposite in sign due to the finite area of the vortex motion.

References

[1] X. G. Deng and H. Zhang, J. Comput. Phys. **165** (2000), pp.22-44.
[2] Z. F. Zuo and H. Maekawa, Proc. of AJK-2011 (2011), in press.

Eighth International Conference on Flow Dynamics
November 9 - November 11, 2011

Noise Prediction Study from Two-Wheel Main Landing Gear Using Lattice Boltzmann Method

Mitsuhiro Murayama[1], Kazuomi Yamamoto[1], Yuzuru Yokokawa[1] and Tohru Hirai[2]
[1]Japan Aerospace Exploration Agency, 7-44-1 Jindaiji-Higashi, Chofu, Tokyo 182-8522, Japan
[2]Ryoyu Systems. Co., Ltd. 2-19-13 Takanawa, Minato-ku, Tokyo 108-0074, Japan
murayama.mitsuhiro@jaxa.jp

ABSTRACT

In this paper, a Lattice Boltzmann Method Code on a Cartesian mesh system with an extended turbulent wall model is evaluated for aeroacoustic computations of a landing gear. It is shown that the present computations can give reasonable agreement with wind tunnel test results even for highly complicated flows around landing gears and the approach is useful to simulate unsteady flow around landing gears with much less demanding near wall resolution requirements.

1. Introduction

The noise from landing gears is known to be one of the major sources of the airframe noise besides the noise from high-lift devices. The landing gear mainly consists of an assembly of a number of bluff components. Flowfield around landing gear is complicated with the bluff components and complicated detail parts such as torque link, brake-caliper, and wheel cap with cooling holes around tires. The noise from landing gears mainly consists of broadband noise by turbulent vortex shedding from the structures, interaction of turbulent wake among components, and broadband noise by interaction of shear layer from gear bay [1]. To reduce the noise effectively, clarification of the unsteady flow structure with complex turbulent flow interactions and the contributions to the noise level on the detailed configuration is useful.

To investigate the aeroacoustic characteristics, accurate unsteady computations with less dissipation and phase error are important. Higher-order LES computations using multi-block structured mesh can give promising results in the point of view of accuracy [2], while the mesh generation for complicated landing gear geometries is quite difficult. Several computations using unstructured meshes have showed good results for landing gears [3], while the mesh generation for landing gear is still not trivial even for unstructured mesh.

Cartesian-type mesh CFD has several advantages of mesh generation, spatial accuracy and efficiency of flow solver. Computations using a block-structured Cartesian mesh employing equally-spaced Cartesian mesh in each block, Buliding-Cube Method, have showed good results for landing gears [4] even for using a simple stair-case representation of curved wall surfaces.

Recently, a Lattice Boltzmann Method (LBM) solved on a Cartesian mesh system with an extended turbulent wall model to simulate wall boundary layer with much less demanding near wall resolution requirements also has shown good results for landing gears [5]. The inherent low numerical dissipation scheme of LBM is preferable for low-speed aeroacoustics applications. In this study, the LBM with an extended turbulent wall model is evaluated for aeroacoustic computations of landing gear.

2. JAXA's Landing Gear Research Model, LEG

A two-wheel main landing gear model of JAXA's Landing gear noise Evaluation Geometry (LEG), was used in this study, which was designed based on the two-wheel landing gears design for modern 100-PAX class regional jets with wing-mounted engines by a landing gear manufacturer in Japan [6]. The wind tunnel testing model was fabricated as 40% scale size. The height and tire-diameter are 1.2m and 0.42m.. The model can include all details of landing gear components such as electrical wirings and hydraulic tubes to reproduce detailed flowfields and resultant noise from actual landing gear. The model can change its configuration from a simple to fully-dressed geometry by removing and attaching components to assess the contribution of each component to noise level.

3. Computational Method

As CFD code based on a LBM, PowerFLOW was used [5]. The system of equations is solved on a Cartesian mesh using a renormalization group-based VLES two-equation turbulence model with an extended turbulent wall model, which allows easy grid generation for highly complex geometries without simplification of the detail parts of the model to simulate wall boundary layer with much less grid resolution near wall. The wall boundary conditions are generalized for arbitrarily oriented surface elements, which are called "Surfel" that occur where the surface of a body intersects the fluid, within the Cartesian volume elements (Voxel). The far field results are obtained with the Ffowcs Williams and Hawkings (FW-H) method.

Computations were conducted at freestream velocity of 54.4m/s. Re is 1.83×10^6 based on tire diameter.

4. Results and Discussion

Figure 1 shows the computational domain and grid for partially-dressed configuration without wirings, tubes and gear bay. The computational grid consists of a total of 8 levels of variable resolution (VR) with the finest level of 0.48mm. The total number of voxel is about 160 million. The computational Δt was set to 8×10^{-7}[sec]. The total number of time step was about 350,000, which corresponds to computations for 0.28[sec]. The total CPU time for the computation was approximately 20,000 CPU hours using 92 cores in a Xeon E5450 PC-cluster system.

Figure 2 compares spectra of sound pressure level (SPL) at a microphone location right above the model between the computational result and experimental

result of fully-dressed configuration. Although there are several differences in the configuration such as wirings and gear bay, the computational result agrees reasonably with experimental results below 3kHz at model-scale. The difference around 100Hz is due to omitting of gear bay in the computation. Figure 3 shows contribution ratio of model componnets to SPL roughly estimated in a wind tunnel test by removing and attaching model components [6]. “Cylinder+Axle+Tire” shows the largest contribution for most frequency range. “Sidebrace” shows the second largest contribution and “Door” is also the dominant noise source. Figure 4 shows the bandpass-filtered pressure fluctuation level in dB for the frequency range of 353-707Hz. By the computational results, possible noise sources on each component can be identified.

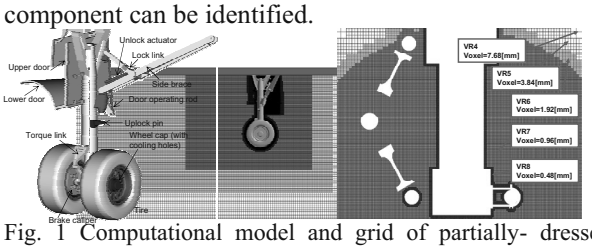

Fig. 1 Computational model and grid of partially- dressed configuration

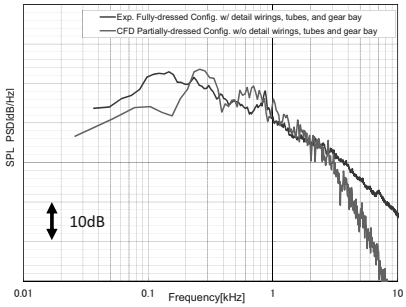

Fig. 2 Comparison of spectrum of SPL

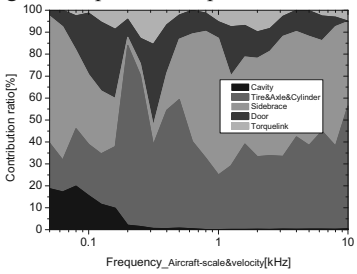

Fig. 3 Rough estimation of contribution ratio of model components to SPL

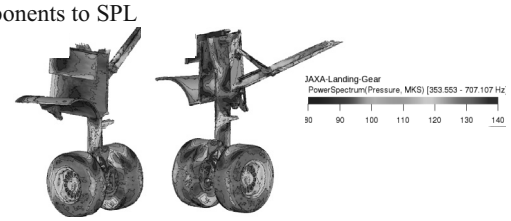

Fig. 4 Bandpass-filtered pressure fluctuation level in dB (353-707Hz at model-scale)

Tire-axle region was the largest contributor to the noise generation. Next, influences of toque-link between tires on the flowfield around tire-axle region and far-field noise are evaluated.

Figure 5 compares difference of SPL in the case with and without backward torque-link. Experimental result for the no-torque-link shows 0.5 to 1.0dB reduction from the baseline configuration over a wide frequency range. Although some over- and under-estimations are observed in the computational result, the computational result captures similar trend for such small differences.

Figure 6 compares the bandpass-filtered pressure fluctuation level in dB for the frequency range of 353-707Hz. Remarkable pressure fluctuations can be observed on back side of the tire. These regions exist near separation points of boundary layer on the tire or downstream of strong shear-flow by torque-link. The backward torque link itself has high level regions widely. The pressure fluctuation generated around the junction of the center cylindrical strut, the piston, and the backward torque link increases pressure fluctuation around the backward torque link and back side of the tire. The no-torque-link configuration has less pressure fluctuation than the baseline configuration.

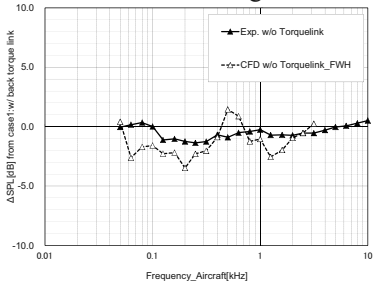

Fig. 5 ΔSPL from the baseline configuration at microphone location right above the model.

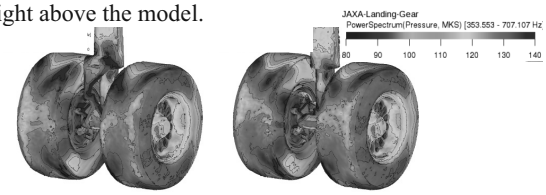

(a) Backward torque-link (b) No torque-link

Fig. 6 Bandpass-filtered pressure fluctuation level in dB (353-707Hz at model-scale)

4. Concluding remarks

In this study, a LBM code on a Cartesian mesh system with an extended turbulent wall model has been evaluated for aeroacoustic computations of landing gear. It was shown that the present computations using LBM on Cartesian grid with an extended turbulent wall model can give reasonable agreement with wind tunnel test results even for highly complicated flows around landing gears and this kind of numerical approach on Cartesian grid will be useful to simulate unsteady flow around landing gears with much less demanding near wall resolution requirements.

References

[1] W. Dobrzynski, *J. of Aircraft*, **47** (2010), No. 2.
[2] T. Imamura, T. Hirai, S. Enomoto and K. Yamamoto, AIAA 2011-2943 (2011).
[3] V. Vatsa, D. Lockard and M. Khorrami, AIAA 2011-2820 (2011).
[4] D. Sasaki, H. Onda, A. Deguchi, K. Nakahashi, M. Murayama, K. Yamamoto and Y. Yokokawa, *Proc. of inter-noise 2011* (2011).
[5] S. Noelting, G. Bres and P. Dethioux, AIAA 2010-3976(2010).
[6] Y. Yokokawa, T. Imamura, H. Ura, H. Kobayashi, H. Uchida and K. Yamamoto, AIAA 2010-3973 (2010).

Eighth International Conference on Flow Dynamics
November 9 - November 11, 2011

Hybrid LES/RANS Computations for Airframe Noise Problems

Taro Imamura, Mitsuhiro Murayama, and Kazuomi Yamamoto
Japan Aerospace Exploration Agency, 7-44-1, Jindaiji-higashi, Chofu, Tokyo, 182-8522
imamura@chofu.jaxa.jp

ABSTRACT

This paper summarizes the numerical simulations related to the prediction and reduction of airframe noise which becomes dominant during the landing phase of an aircraft. The noise source locations are flap-edge, slat, and landing gears and each of those are investigated independently. Each noise source simulation requires extensive computational resources since unsteady flow simulation is necessary. The numerical results were validated through experimental results. This paper will summarize the current status of our hybrid LES/RANS computations and clarify the points that we need to modify in our future code.

1. Introduction

Due to the increase in air travel, noise problem around airports is urgent and crucial concern. Therefore, noise prediction and reduction during takeoff and landing is one of the key technologies for the future aircraft development. In earlier days, the dominant noise source was the engine. Various noise reduction technologies are applied to date, and still further improvements are in progress. Due to the decrease in engine noise, airframe noise during the approach phase became relatively important for the overall noise level [1]. High-lift-devices (HLD) and landing gears are known to be the locations of the major airframe noise.

Therefore, airframe noise research is ongoing at Aviation Program Group of JAXA from 2003. The research focuses on the prediction of airframe noise, further understanding of noise generation mechanism, and noise reduction technology. All of the researches are performed using numerical and experimental approaches to complement each other. This paper will focus on the numerical works that are done previously, and those are wing-tip flow [3], slat cove flow [4], landing gear flow[5], and tandem cylinder flow[6] simulations. This paper will focus on what we have learned through these computational cases and summarize the issues that need to be modified in our future CFD code.

2. Numerical Methods

Numerical methods are briefly described. In this study, we use a flow solver called UPACS-LES [2]. This flow solver is developed based on the UPACS code, which is a structured-based multi-block CFD solver for aerodynamic simulations. The governing equations are the compressible Navier-Stokes equations. The flow solver of the current version is based on a cell-centered finite-volume method on multi-block structured grids. The code is parallelized by a flexible domain decomposition concept and MPI. To capture vortices or acoustic wave with small number of grid points, 6th-order compact scheme developed by Kobayashi [7] is implemented in the code. The viscous terms are discretized using 2nd-order central scheme. Hybrid LES/RANS method is used in all of the studies as a turbulence model. In our code, Standard Smagorinsky model [8] is used in the LES region and Spalart-Allmaras one equation model [9] is used in the RANS region.

Based on the near-field unsteady flow simulations, Ffowcs Williams and Hawkings (FW-H) solver is used to obtain the far-field sound pressure.

3. Discussions on Airframe Noise Simulations

We have performed wing-tip flow [3], slat cove flow [4], landing gear flow [5], and tandem cylinder flow [6] simulations using UPACS-LES code. The following list summarizes the finding from the unsteady flow simulations for airframe noise.

1) Hybrid LES/RANS method is promising for analyzing high-Reynolds number unsteady flows that appear in airframe noise simulations. Combination with FW-H solver reduces the computational time required to obtain the pressure signal at a far-field point. Tonal and broadband components of the far-field spectrum can be predicted qualitatively.
2) Comparison with experimental data is crucial, because the results from the flow simulations involve many open questions, such as grid dependency, turbulence modeling etc. Comparisons of various physical quantities, such as mean/root-mean-square of pressure, velocity etc., at different locations are preferable in order to avoid a coincidental match. Through this process, the credibility of the computational results will increase and sometime, this will motivate additional experiment to clarify the reason for the difference (Sometimes, simulations might be correct).
3) Visualization of three-dimensional vortical flow gives us a big picture of the unsteady flow field, which is significantly different from that of steady-state flow. For visualization purpose, using fine scale grid with the use of high-order method improves the resolution of the vortices. The animation of the flow field also helps the experimental people to understand the flow, and the information, although intuitive, will be helpful to plan as well as to design low noise devices.

4. Discussions on Unsteady Flow Simulations

The computational grid sizes are on the order of 5 to 70 millions, and each case requires several days to weeks of computational times on a cluster system using

50-150 cores. Before we start this research, most of the experience was based on steady state simulations. There are significant differences between steady and unsteady simulations. Following is some examples.

1) In the case of steady RANS computations, most of gridding efforts are made to resolve the geometry and associated boundary layer. However, separated flow simulations require grid resolution off the surface of the body. This will add additional constraint when generating the grid. The grid size in the LES region is often related to the size of large scale vortices that need to be resolved. When block-structured type grid is used, this will increase the difficulty of gridding. Additionally, if high order scheme for aeroacoustics simulations is used, extra smooth grid is necessary.
2) Before executing flow simulations, attentions need to be paid to the time step size and number of time steps in order to capture the time dependent phenomenon. This is often restricted by the computational resource available. The order of lowest and highest frequency resolved in a single simulation is around 100, thus it is very important to know unsteady flow feature which needs to be simulate.
3) Output data from unsteady flow simulations becomes significantly larger than those of steady simulation if data of every time step are saved. Therefore, it is important to select the data to be saved on a disk. Reducing the size of spatial data has a large impact. At minimum, final step data and time-averaged data is necessary. For the purpose of making an animation file, several hundreds of spatial data will be necessary. If disk size does not allow you to save those files, figures could be drawn along with the simulation by defining the parameters for the visualization in advance of the simulation. The size of surface and point data is smaller than spatial data. Although, more data can be saved in time series, the locations needs to be define before the calculation in anticipation of the post processing. The surface data is used as an input to calculate the sound pressure history at selected far-field point by FW-H solver. The surface location need to be defined depending on the flow field. Most of the time series data from the experiment is point data (velocity from hot-wire measurement, surface unsteady pressure etc). Therefore, the same location need to be defined in the calculations to output those data.

4. Summary and Future works

We have been learning from unsteady flow simulations targeting prediction and reduction of airframe noise. In all cases, simulations were performed parallel to the experiment and this was crucial for improving the accuracy of the computations. By current LES/RANS hybrid approach, each noise source could be investigated and reasonable comparisons are obtained for all cases.

We came to a certain level where simulations could be used parallel to the experiment. However, items listed below needs to be considered in future flow simulations for better understanding the airframe noise source.

1) Ability to handle complex geometry like real landing gear configuration.
2) Turbulence modeling and transition prediction needs to be modified, especially for high-lift noise prediction.
3) Ability to capture the low frequency component. Longer computational time is required and this means that we need to be able to use large number of cores. For real aircraft simulations, frequency range from 50 to 20000Hz (400 times difference) needs to be calculated for certification purpose.
4) Post processing methods to clarify the noise source mechanism needs to be developed. This information will be valuable for sophisticated designing purpose.
5) Current FW-H method assumes uniform flow during propagation, but non-linear propagation effect (effect of atmosphere) needs to be considered.
6) Current simulations correspond to the wind tunnel case where the model and far-field point are fixed in airflow. However, primary interest is to predict the pressure signal on the ground under real flight condition. Conversion methodology needs to be established.
7) In real flight situation, interactions of two different components could be also a large contributor to the overall noise, such as landing gear and flap interaction.

References

[1] J. Astley, UK-Japan Bilateral Workshop (Aircraft Emissions and Noise), Tokyo, (2006).

[2] T. Yamane, K. Yamamoto, H. Yamazaki, R. Takaki, T. Iwamiya, Parallel Computational Fluid Dynamics - Proceedings of the Parallel CFD 2000 Conference, , Elsevier Science B. V., (2001), 257-264.

[3] T. Imamura, Y. Yokokawa, S. Enomoto, K. Yamamoto, AIAA Journal **46(5)** (2008) 1045-1053

[4] T. Imamura, S. Enomoto, K. Yamamoto, 25th Congress of the International Council of the Aeronautical Sciences (ICAS) Hamburg Germany, 3 Sep. 2006

[5] T. Imamura, T.Hirai, K. Amemiya, Y, Yokokawa, S. Enomoto, K. Yamamoto, IUTAM Symposium on Computational Aero-Acoustics for Aircraft Noise Prediction (2010)

[6] T. Imamura, T.Hirai, S. Enomoto, K. Yamamoto Benchmark Problems for Airframe Noise Computation (BANC-I) (2010)

[7] M. H. Kobayashi, Journal of Computational Physics, **156(1)** (1999) 137-180.

[8] J. Smagorinsky, Mon. Weath. Rev., **91(3)** (1963) 99-164

[9] P. R. Spalart, S. R. Allmaras, AIAA Paper 92-0439, (1992)

Eighth International Conference on Flow Dynamics
November 9 - November 11, 2011

Aeroacoustic Simulation of JAXA Landing Gear by Building-Cube Method

Akihito Deguchi, Daisuke Sasaki, Kazuhiro Nakahashi
Department of Aerospace Engineering, Tohoku University, Aoba 6-6-01, Sendai 980-8579, Japan
E-mail: deguchi@ad.mech.tohoku.ac.jp

ABSTRACT

Landing gear noise analysis is becoming more important because noise issue around the airport becomes more prominent. In this research, flow around JAXA landing gear is simulated using Building-Cube Method (BCM), and the aeroacousic noise is estimated by non-compact Curle's equation. BCM emploiesy Cartesian mesh and solves the incompressible Navier-Stokes equation. The difference of aeroacostic noise by changing torque link location and wheel cap shape, and assessment method of aeroacoustic noise are investigated.

1. Introduction

Due to the continuous increase in air travel, much attention has to be paid to the environment around an airport, and thus noise reduction is one of the key topics for aircraft development. In this study, we will focus on landing gear noise prediction.

There are many studies devoted to landing gear noise problem. Japan Aerospace Exploration Agency (JAXA) is actively engaged in aeroacoustic experiment and numerical analysis of landing gears. They designed a Landing gear noise Evaluation Geometry (LEG) for experimental and numerical study of landing gear noise [1].

In our previous study [2], the aeroacoustic noise of the landing gear was calculated by block-structured Cartesian mesh incompressible flow solver with compact Curle's equation. However the characteristic wave length of the landing gear noise is not compact against the characteristic length of the landing gear in reality. In addition, Curle's equation calculates as the aeroacoustic noise propagates in the motionless fluid, but the aeroacoustic noise of the experiment for comparison is measured in the uniform flow. Therefore, the non-compact assumption and the effect of the uniform flow have to be introduced to estimate the aroacoustic noise of landing gear more accurately.

In this study, landing gear noise of simplified LEG model (Fig.1) which is constructed with detail components is investigated using block-structured Cartesian mesh solver, Building-Cube Method (BCM), non-compact Curle's equation with Doppler effect. Cartesian mesh helps to generate the mesh easily and to construct the high order scheme required to solve flowfield around complicated LEG model. Incompressible Navier-Stokes solver is used to compute flow fields around the simplified LEG model. The non-compact Curle's equation enables to consider the size of the landing gear (the non-compact assumption) and the uniform flow effect is introduced as Doppler-effect.

2. Method

3.1 Curle's equation

Curle's equation transformed Lighthill equation to form an exact integral equation, but this equation is too difficult to solve because it requires the computation of the volume integration and the space derivative. Curle's equation can be simplified by introducing the low Mach flow and converting space derivative to temporal differentiation as in Eq.3.1.

$$p = \frac{1}{4\pi}\int \frac{x_i - y_i}{r^2}\left(\frac{1}{c_0}\left[\frac{\partial P_i}{\partial t}\right] + \frac{[P_i]}{r}\right)dS \qquad (3.1)$$

This equation is so-called non-compact Curle's equation. In this study, the landing gear noise is investigated by this equation.

3. Analysis of simplified LEG

In this study, the differences of aeroacoustic noise due to the changes of the torque link location and the wheel cap shape are investigated. There are 3 locations of torque link (back toward the flow [B], front [F], removed [N]), and there are 2 shapes of wheel cap (seal [S], tear porosity [T]), thus there are six configurations of simplified LEG. The six models are calculated and compared with the experimental result. The characteristics of the six pattern LEGs are summarized in Table 1.

3.1 Spectrum

The SPL spectrums of the two computational and experimental results are plotted in Figs.2 and 3. The spectrums are converted from narrow band to 1/3 octave band. All results of analysis are well matched with the experiment between 200[Hz] and 3000[Hz] frequency range. In the experiment, SPL spectrum of FT (Front torque link and cap with Tear porosity) is lower than that of BT spectrum over a wide range. In the computational analysis, FT is lower than BT, but the result is overrated than the experiment. BCM and non-compact Curle's equation can qualitatively estimate the difference of spectrum of the different configurations.

3.2 Overall SPL

The experimental and the computational results of overall SPL (OASPL) are indicated in Figs.4 and 5. In the experimental result, torque link which is located at back toward the flow shows larger OASPL, especially BS is the noisiest configuration. The noise tendency of the six configurations is matched with the experimental result. From the above result, the aeroacoustic sound from LEG is expected to be influenced a great deal by the location of torque link.

3.3 Comparison of flow

The time averaging velocity distribution of the mainstream at cross-section surface of the wheel and sound pressure fluctuation on surface (*SPrms*) are

indicated in Figs 6 and 7. From these figures, the value of *SPrms* becomes high around the burble point (at the circle) on the wheel, and the velocity gradient around burble of FT is more gradual velocity gradient than BT.

4. Conclusion

In this study, flow around LEG was simulated by BCM, and the aeroacoustic noise was estimated by non-compact Curle's equation. In LEG, the differences of aeroacoustic noise by changing torque link location and wheel cap shape were investigated. The computational result of spectrum was well matched with the experimental result between 200[Hz] and 3000[Hz] frequency range, and the noise tendency of LEG was also matched with the experimental result because non-compact Curle's equation with Doppler effect was considered to treat the size of LEG and the uniform flow unlike compact Curle's equation of the previous study [2]. The comparison of the spectrum and OASPL were shown that the aeroacoustic noise were significantly influenced by the torque link position. From the sound pressure fluctuation on the LEG surface and of the velocity distribution, the torque link were found to be attributed to reduction of the velocity gradient at the burble point by dividing the flow that through into between the wheels.

Acknowledgments

The computations in the study ware conducted by NEC SX-9 at Cyber Science Center, Tohoku University. This study was supported by JSPS KAKENHI 21226018.

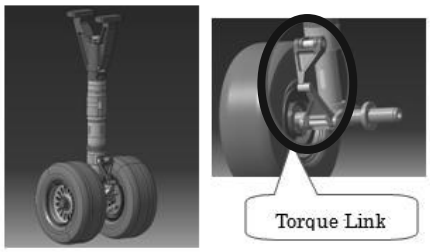

Figure 1 Simplified LEG

Table 1 Abberviation of simplifed LEG

Abberviation	Torque link location	Wheel cap shape
BS	Back	Seal
BT	Back	Tear
FS	Front	Seal
FT	Front	Tear
NS	Removed (No Torque link)	Seal
NT	Removed (No Torque link)	Tear

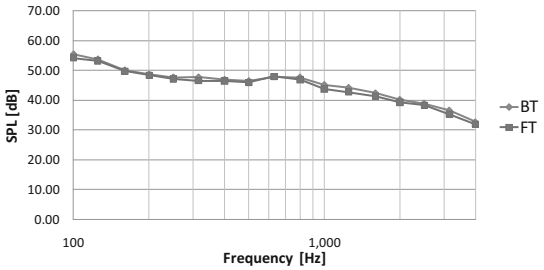

Figure 2 BT and FT are compared (Experiment)

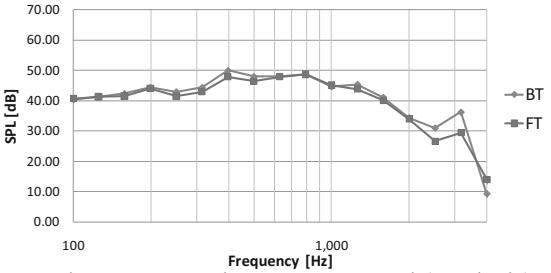

Figure 3 BT and FT are compared (Analysis)

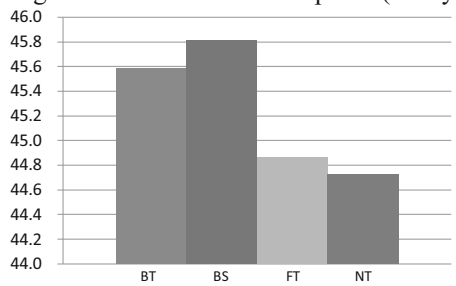

Figure 4 OASPL of experiment

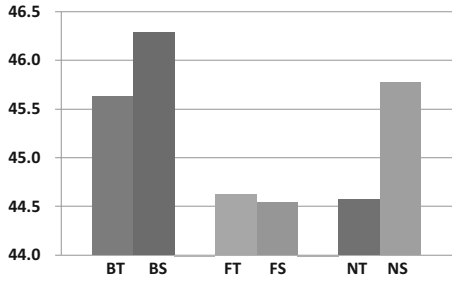

Figure 5 OASPL of analysis

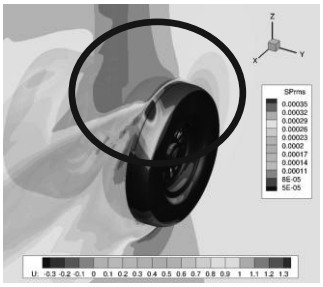

Figure 6 Velocity distribution and SPrms (BT)

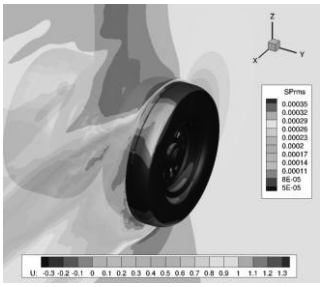

Figure 7 Velocity distribution and SPrms (FT)

References

[1] Imamura. T, Hirai. T, Amemiya. K, Yokokawa.T, Enomoto. S, Yamamoto, K, "Aerodynamic and Aero acoustic Simulation of a Two-wheel Landing Gaer", Procedia IUTAM, Vol. 1, pp. 293-302, 2010.

[2] Onda. H, Sakai. R, Sasaki. D, Nakahashi. K, "Unsteady Flow Aerodynamic Noise Analysis around JAXA Landing Gear Model by Building-Cube Method", AIAA paper 2011-1081, Jan, 2011.

Linearized Euler Equation on Block-Structured Cartesian Mesh for Noise Propagation from 2D Nacelle Configuration

Yuuma Fukushima, Sasaki Daisuke, Kazuhiro Nakahashi
Department of Aerospace Engineering, Tohoku University, 6-6-01, Aramaki-Aza-Aoba, Sendai, 980-8579, Japan
fuku@ad.mech.tohoku.ac.jp

ABSTRACT

Recently, acoustic analysis using the Linearized Euler Equation (LEE) on multi-block structured or unstructured mesh is focused. However, mesh generation around complicated geometries takes time on structured mesh and cost of high order calculation gets larger on unstructured mesh. In this research, a LEE code for aeroacoustic analysis is developed on block-structured Cartesian mesh, Building-Cube Method. As a target, the noise shielding effects of over-the-wing mounted nacelle (OWN) configuration is investigated. The results show the qualitative shielding effect of OWN configuration for engine noise.

1. Introduction

Noise of airplane is getting lower due to the improvement of each component. However, regulations of airport noise are just the same getting harder, thus the attention is currently focused on noise analysis for the further noise reduction. To achieve reduction of engine noise, several concepts have been proposed. One of them is to install engine nacelles over the aft fuselage. Another configuration is to install engine nacelles over the main wing[1]. These concepts intend to shield the engine noise toward ground by wing or fuselage. In this study, the latter case called the Over-the-Wing Nacelle (OWN) configuration is focused.

The purpose of this study is to develop an estimation code of noise propagation to investigate the noise shielding effect due to the nacelle location.

2. Computational methods

The governing equation of noise propagation is the Linearized Euler Equation given by the followings:

$$\frac{\partial Q'}{\partial t}+\frac{\partial E}{\partial x}+\frac{\partial F}{\partial y}+H=S \tag{1}$$

$$Q'=\begin{bmatrix}\rho'\\ u'\\ v'\\ p'\end{bmatrix}, E=\begin{bmatrix}\rho_0 u'+\rho' u_0\\ u_0 u'+\dfrac{p'}{\rho_0}\\ u_0 v'\\ u_0 p'+\gamma p_0 u'\end{bmatrix}, F=\begin{bmatrix}\rho_0 v'+\rho' v_0\\ v_0 u'\\ v_0 v'+\dfrac{p'}{\rho_0}\\ v_0 p'+\gamma p_0 v'\end{bmatrix} \tag{2}$$

$$H=\begin{bmatrix}0\\ u'\left(\dfrac{\partial u_0}{\partial x}-\nabla\vec{v}_0\right)+\dfrac{1}{(\rho_0)^2}\left(\rho'\dfrac{\partial p_0}{\partial x}+p'\dfrac{\partial \rho_0}{\partial x}\right)\\ v'\left(\dfrac{\partial v_0}{\partial y}-\nabla\vec{v}_0\right)+\dfrac{1}{(\rho_0)^2}\left(\rho'\dfrac{\partial p_0}{\partial y}+p'\dfrac{\partial \rho_0}{\partial y}\right)\\ (\gamma-1)\left[p'\nabla\vec{v}_0-\vec{v}'\nabla p_0\right]\end{bmatrix} \tag{3}$$

The spatial derivation is calculated by fourth-order Dispersion Relation Preserving (DRP) scheme. Time integration is calculated by 6-stage fourth-order Low Dissipation and Dispersion Runge-Kutta (LDDRK) scheme. For high order calculation, Immersed Boundary Method (IBM) using Ghost Cell and Image Point is employed at the wall boundary and third-order Lagrange interpolation is employed for data exchange at the Cube boundary. At outer boundary, unsplit variables Perfectly Matched Layer (PML) is implemented[2].

As the computational approach, block-structured Cartesian mesh method called Building-Cube Method (BCM)[3] is employed in this study. BCM has several advantages over structured or unstructured mesh: (1) quick mesh generation for complicated geometries, (2) easy application of high order scheme, (3) high efficiency in calculation, (4) easy parallelization of process. Computational grid of BCM is generated in the following procedures. Firstly, computational domain is divided into aggregation of square area named “Cube” as the left side in Fig. 1. Next, each Cube is divided by equi-spaced Cartesian mesh named “Cell” as the right side of Fig. 1. Calculation is performed in each Cube and all Cubes are parallelized using OpenMP. One Cube has three Ghost Cells (Fig. 1) overlapped with adjacent Cubes for data exchange.

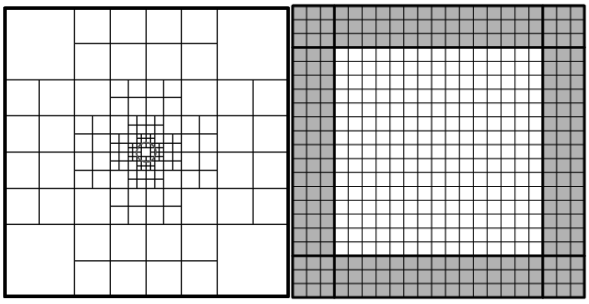

Figure 1. Computational mesh of BCM
Left: Computational domain
Right: Component of one Cube (15×15, 3Ghost Cell)

3. Calculational condition and results

In this study, sound propagations around three nacelle-wing configurations are calculated to investigate the shielding effect of OWN configuration in 2D. Base configurations are the cross-section shape of CFM-56 engine nacelle and the DLR-F6[4] wing at 35% semispan location. In this calculation, the effect of pylon is not considered. As noise source, fan noise is focused. The real length of the nacelle is about 4.9[m] and monopole sound source as a model of fan noise is located at the fan plane. It is about 1.1[m] from the inlet of the nacelle. When the reference length D is taken as the nacelle length, 4.9[m], and the reference sound speed is 340[m/s], the nondimensionalized frequency 4 gives the real frequency of 277 [Hz]. Input condition is in Eq. (4) with parameters of Eq. (5).

$$S = A\exp\left[-\ln 2\left(\frac{(x-x_s)^2+(y-y_s)^2}{b^2}\right)\right]\sin\omega t \quad \omega=8\pi \tag{4}$$

$$(x_s, y_s) = (0,0), A = 1.0\times10^{-4}, b = 0.02 \tag{5}$$

Three configurations are examined; nacelle-only, under-the-wing nacelle (UWN) and OWN configurations. Location of the leading edge in UWN and OWN configurations is (0.544*c*,-0.913*h*) and (-1.00*c*,-6.00*h*), respectively, where *c* is the chord length and *h* is the diameter of inlet. In all the calculations, computational domain is 20*D*×20*D*, number of Cells in each Cube is 4096 (64×64), minimum grid spacing equals to 0.048*D* and the minimum Point Per Wavelength (PPW) is 12.8.

Figure 2 shows the pressure distribution around each configulation. In case of nacelle-only configulation, it is clear that noise from sound source is diffracted at the inlet and outlet, and then propagates to upper and lower. Especially, the diffracted wave at the inlet is dominant. The result of UWN configulation shows that diffracted wave is reflected to downward by the wing. In the result of OWN configulation, major diffracted wave near the inlet is shielded by the wing and is then reflected widely to upside.

Figure 3 shows Sound Pressure Level (SPL) at the sampling points. Reference pressure is 2.0×10^{-5}[Pa]. Sampling points are counterclockwise rotation at radius *r=5D* from the origin of 0[deg.] location of (-5*D*, 0) to 180[deg.] location of (5*D*, 0). In the figure, SPL from 50 to 90[deg.] of OWN configulation is lower than that of the others by about 5[dB]. The result prove the shielding effect of OWN configulation qualitatively.

4. Conclusion

In this study, an estimation code of noise propagation based on linearized Euler equations was developed. BCM based on Cartesian mesh enables to calculate sound pressure with sufficient mesh resolution for specific wavelength, and IBM at the wall boundary and Lagrange interpolation at the Cube boundary achieve the high order simulation. To validate the noise shielding effect of OWN, noise propagations around three nacelle-wing configurations were computed. The comparison of pressure distribution and SPL at the sampling points shows the potential of noise shielding effect of OWN configuration.

Acknowledgement

This work was supported by JSPS KAKENHI (21226018). The calculation in this research was conducted by AltixUV1000 of Institute of Fluid Science, Tohoku University.

References

[1] D. Sasaki and K. Nakahashi, "Aerodynamic Optimization of an Over-the-Wing-Nacelle-Mount Configuration," *Modeling and Simulation in Engineering*, vol. 2011, Article ID 293078, 13 pages, 2011. doi:10.1155/2011/293078

[2] Y. Fukushima, *et al.* "Code Development of Linearized Euler Equation on Block-Structured Cartesian Mesh Combined with Immersed Boundary Method," 43th Fluid Dynamics Conference / Aerospace Numerical Simulation Symposium 2011, Jul. 2011. (in Japanese)

[3] H. Onda, *et al.* "Unsteady Flow and Aerodynamic Noise Analysis around JAXA landing Gear Model by Building-Cube Method," 49th AIAA Aerospace Sciences Meeting, AIAA Paper 2011-1081, Jan. 2011.

[4] K. Laflin, *et al.* "Data Summary from the Second AIAA Computational Fluid Dynamics Drag Prediction Workshop," *Journal of Aircraft*, vol. 42, No. 5, 2005, pp. 1165-1178.

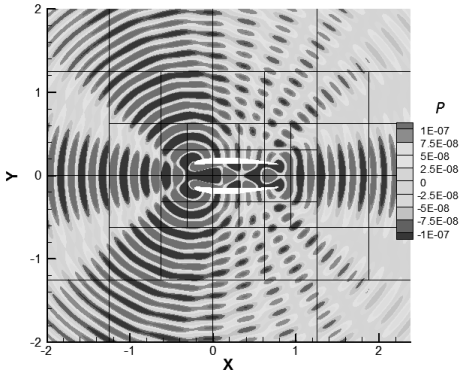

(a) Nacelle only

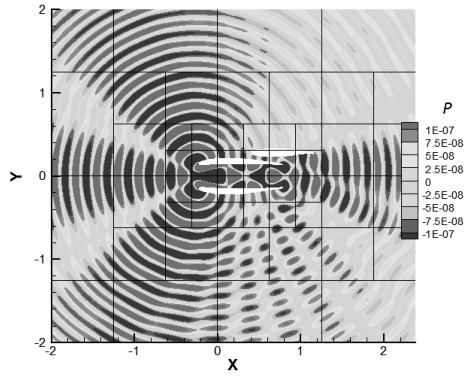

(b) Under-the-wing Nacelle

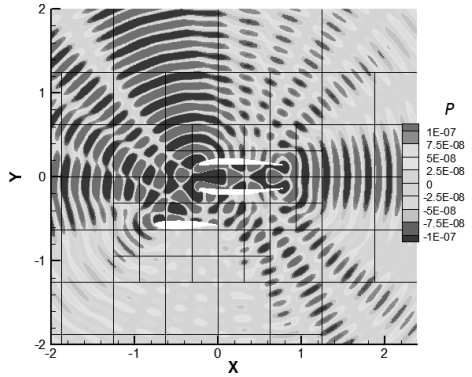

(c) Over-the-wing Nacelle

Figure 2. Pressure distribution

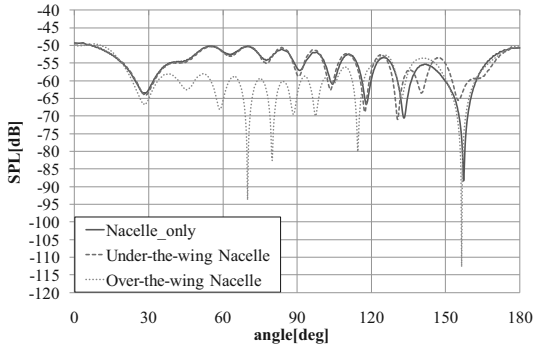

Figure 3. SPL at the sampling points

Large-Scale Unsteady Flow Data Compression for Buildng-Cube Method

Ryotaro Sakai, Akihito Deguchi, Daisuke Sasaki, Kazuhiro Nakahashi
Department of Aerospace Engineering, Tohoku University
6-6-01 Aramaki-Aza-Aoba, Aoba-ku, Sendai, Miyagi, Japan, 980-8579
sakai@ad.mech.tohoku.ac.jp

ABSTRACT

A data compression method was developed for large-scale, unsteady flow simulation data. The method includes three steps of discrete wavelet transform, quantization and entropy encoding. Data compression was implemented to unsteady flow simulation data obtained by a block-structured Cartesian mesh method named Building-Cube method. It was demonstrated that the present compression method gave high compression ratio with good quality of compressed data in terms of velocity distributions and aeroacoustic analysis.

1. Introduction

Performance of supercomputers has continued to grow and Computational Fluid Dynamics will be able to treat more complex problem in larger scale than ever. Under expectation of this progress, Building-Cube Method (BCM) is proposed [1]. Numerical computation is implemented with high efficiency as demonstrated in [2]. However, the huge amount of output data causes various difficulties in visualization, data transfer, and data storage. Data size problem is inevitable in large-scale computation, especially in unsteady flow computation.

The objective of this study is to develop a data compression method for large-scale, unsteady flow data. Here discrete wavelet transform (DWT), quantization, and entropy encoding are employed to compress data. DWT extracts important features in the flow field, and high quantization bit rate is assigned to only the important region extracted by DWT. Present method was applied to unsteady flow simulation data with $O(10^7)$ mesh points, and the usefulness of the proposed method towards large-scale data compression is discussed.

2. Building-Cube Method

BCM is based on block-structured Cartesian mesh. A flow field is divided into many blocks of cuboids, named 'Cube', as shown in Fig. 1 (a). Each cube is a sub-domain of the original computational domain, and has an equally-spaced Cartesian mesh named 'Cell' in itself, as shown in Fig. 1 (b). Although the geometrical size of cube becomes large as the cube gets away from the object, all cubes have completely the same number of cells regardless the cube size. This means computational resolution is determined by the size of each cube, and computational cost is ideally the same among all cubes. This approach enables (1) quick and robust mesh generation around complex geometries, (2) easy introduction of a higher-order scheme in numerical computation, (3) easy introduction of adaptive mesh refinement by changing size of cube, (4) efficient parallelization of computation procedure based on cube, and (5) easy treatment of data in the post-processing.

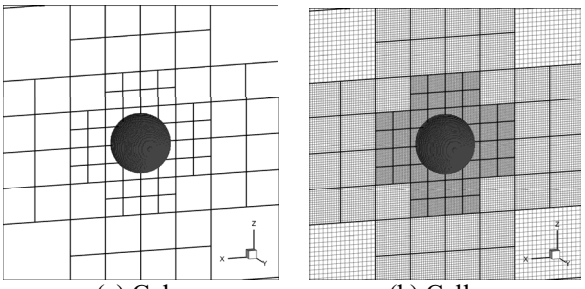

(a) Cube (b) Cell

Fig. 1 Dividing scheme of Building-Cube Method

3. Data Compression Process

Data compression process is composed of three steps: At first, DWT is applied to original flow simulation data. Using Cohen-Daubechies-Feauveau 9/7 wavelet [3], the transform is applied to instantaneous data at each time step, and then applied to time-series data by cube separately. After the transform, the data are divided into approximation part as important part, and detail part as negligible part. Next, quantization is applied to the transformed data. To obtain both high data quality and high compression ratio, quantization bit rate is changed according to the importance of the part. High quantization bit rate is assigned to approximation part to keep important information of flow field. By contrast, low quantization bit rate is assigned to detail part to obtain high compression ratio. In addtion, quantization bit rate is also subject to the importance of flow field. Quantization bit rates in small cubes are generally higher than that in large cubes because small cubes are closer to the object. Finally entropy encoding is applied to each part to reduce the size, using range encoding [4].

4. Data Compression Results

Flow data around a three-dimensional cylinder were compressed. Reynolds number in flow computation is 10^4 based on uniform flow velocity and the cylinder diameter. In the computational domain, there are 260 cubes and 64^3 cells in one cube. Total number of cells in the computational domain is about 68 million, the original data size is about 1.09 GB per time step, and time-series data include total 256 time steps.

Figure 2 shows instantaneous streamwise velocity distribution at z=0 cross section. The compressed data reproduces the original velocity distribution, including vortex shedding from the side of the cylinder and periodic wake flow behind the cylinder. Figure 3 shows RMS value of u-velocity fluctuation at z=0 cross section. The fluctuation is reconstructed well from the compressed data, keeping characteristic generation and development from the side of the cylinder as flow separation point. Figure 4 shows sound pressure level obtained from both original and compressed data as application to aeroacoustic analysis. The peak value of the sound pressure level is clearly captured from the compressed data. These results indicate that compressed data can capture unsteady flow characteristics of the original data.

Table 1 describes RMSE, maximum error, and total compression ratio. Both the same order from the beginning to the end of the time step. Compression ratio is 15.5:1. After compression the data size becomes about 18 GB, which is much smaller compared to the size of the original data.

5. Concluding remarks

A data compression method based on discrete wavelet transform, quantization, and entropy encoding was developed for large-scale, unsteady flow simulations. The present method was proved to be very effective to compress large-scale unsteady flow field data obtained by BCM, which amounted to about 279 GB, for the purpose of unsteady flow analisis such as aeroacoustic analysis.

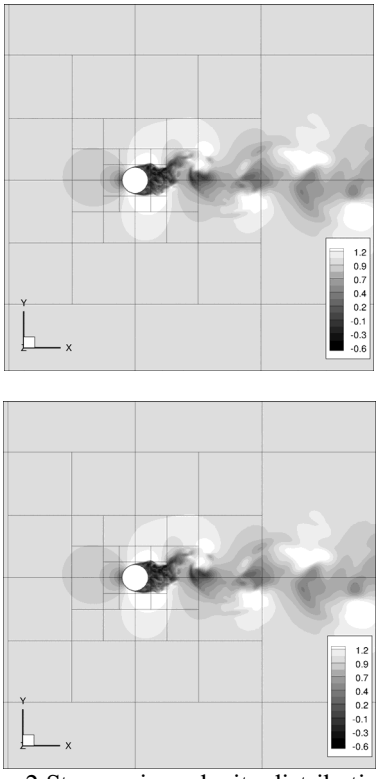

Fig. 2 Streamwise velocity distributions
in cross section z=0 (upper: original, lower: compressed)

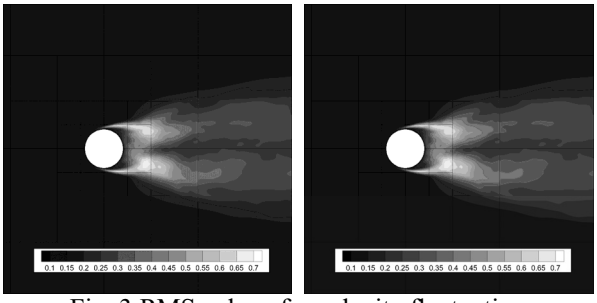

Fig. 3 RMS value of u-velocity fluctuation
in cross section z=0 (left: original, right: compressed)

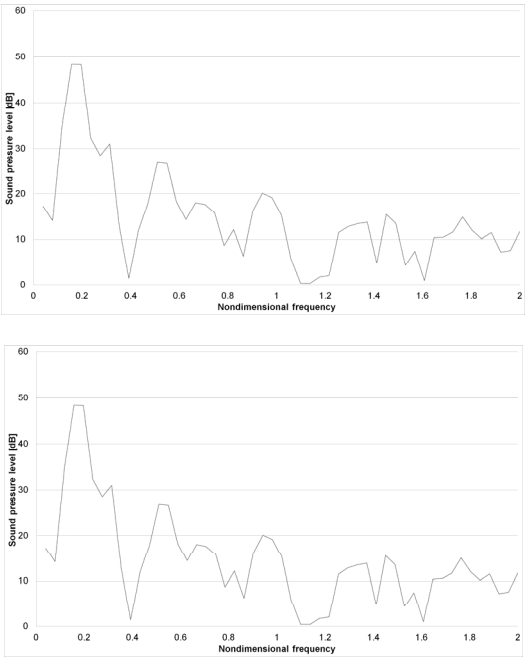

Fig. 4 Sound pressure level spectrum
(upper: original, lower: compressed)

Table 1. Error evaluation and total compression ratio

	RMSE	Max. error	Total comp. ratio
1st step	3.29E-04	8.70E-03	15.5:1 (279 GB / 18.0 GB)
128th step	1.94E-04	6.31E-03	
256th step	3.41E-04	9.27E-03	

Acknowledgements

This work is supported by JSPS KAKENHI 21226018. Computations in this paper were conducted using NEC parallel computers at Cyber Science Center in Tohoku University.

References

[1] K. Nakahashi, AIAA Paper 2005-4876, 2005.
[2] S. Takahashi, AIAA Paper 2009-0563, 2009.
[3] A. Cohen, Comm. Pure Appl. Math., **45** (1992), 485-560.
[4] G.N.N. Martin, *Video and Data Recording Conference*, 1979.

Eighth International Conference on Flow Dynamics
November 9 - November 11, 2011

Towards Large-Scale Practical CFD in Industry

Kenji Ono and Chisachi Kato
Institute of Industrial Science, The University of Tokyo
keno@iis.u-tokyo.ac.jp

ABSTRACT

A coming supercomputer that has peta-scale ability enables us to compute very large problem of which results provide useful information for a product design. The large-scale CFD, however, brings many difficulties such as a grid generation, visualization and calculation, which are inherent barrier of the distributed parallel computation. From a standpoint of the engineering, these issues must be tackled so as to enhance the utilization of the large-scale parallel CFD to engineer's daily work. In this paper, the authors clarify the issues to be resolved and propose a foundational framework to drive a practical large-scale parallel CFD in industry field.

1. Introduction

The PFLOPS computation is becoming down to earth with the progress of the development of K-computer [1] that will be available at the end of 2012. Skilled manufacturing (mono-tsukuri) field is one of the important application fields of the computer simulation. Several simulation codes, which are designed to large-scale parallel computation, have been developed in national projects. The developments of those codes, however, were focused on the physical simulator itself and didn't include peripheral technologies, e.g., pre-processing and post-processing. From here on, in order to meet the need of industry field with taking advantage of huge computational resources, it will be required an integrated environment that is not only generating a large-scale grid and visualizing the generated results but also organizing the all stuff related to the simulation to enhance the utilization of the simulation. In this paper, the authors would like to clarify the issues to be resolved and to propose a foundational framework to organize the execution of large-scale parallel CFD.

2. Issues and Strategy for Practical Large-Scale Parallel CFD

Issues related to the large-scale parallel CFD are classified into several items as follows.

2.1. Grid Generation

Our CFD approach needs to generate a grid system from well-defined geometry data. However, the geometry data has defects such as overlapping, holes, and non-manifold in many cases. We introduce a hierarchical Cartesian grid system as depicted in Fig. 1 since its grid generation process can be automated and be alleviated the issue described above. Besides, this method can keep the size of generated file and memory footprint used small so that the engineer can make the grid on a modest PC with interactive operation. The generated grid is converted to other formats for unstructured solvers.

2.2. Visualization and Post-Processing

Computed results on the parallel computer are written in a large number of files and the files cannot be moved any more because the limitation of disk space and the operation time of the data operation. Thus, it is required that the visualization system has the ability to handle many files at the same time and to visualize the data in distributed parallel environment. In visualization and analysis process, users have their own way to analyze the data, and the visualization environment is depending on user's platform. We use the large-scale visualization system (LSV [3]) developed at RIKEN. LSV is designed to cover operator's various scenarios. For data analysis, we have a plan to take advantage of the open-source software in combination with a program to supply the extracted data from the raw dataset. The map reduce framework [4] can be effectively used as the data supply program.

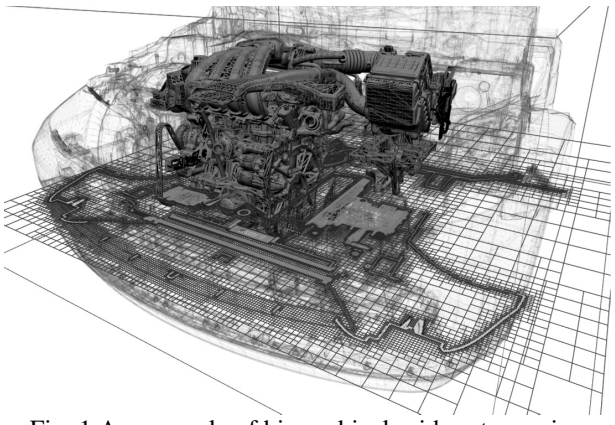

Fig. 1 An example of hierarchical grid system using Octree data structure for an engine bay configuration[2].

2.3. File Handling

In parallel computation, each core reads and writes a file at the same time, which degrades file I/O performance. Therefore, the most important and critical issue is a mechanism of file handling in terms of performance of the proposed system. MPI-I/O is one of the candidates to improve the performance by its parallel file accessing, but the distributed file I/O is beyond the scope of one. Besides, it is difficult to put together the file formats used in simulators because each format is optimized to a specific simulator. Our approach is to introduce a mechanism to treat a lot of files as it looks one file instead to employ a unified I/O library. To do so, an index of file is defined and utilized. This index plays a role of managing raw files and supplying the information in entire system.

2.4. Project Management

Parallel computation uses and generates many files,

e.g., grid files, parameter files, result files, analyzed files, and so on. Since many files are found in a directory of file system, we need to organize the files.

In our approach, all files needed to a specific simulation are managed by an asset list that describes necessary files. The asset list represents the smallest unit of simulation, which is defined as a case. We often need to manage a number of cases in the parametric study that is performed in practical simulation. In consequence, multiple cased forms a project defined as one group that has parameters associated each other.

2.5. Workflow

In practical simulation cases, the engineer repeats predetermined routine tasks to obtain the information to be needed in the design or for the optimization. The conventional shell script is assumed to describe the workflow scripts because the workflow is required to run on various machine including special hardware like K-computer.

2.6. High-Performance Simulators

In the heart of this HPC/PF system, various physical simulators will be available. Those simulators are developed in the national project up to now, e.g., FFB [5], FFR, FISTR, Adventure, UPACS [6], VCAD [7], and so on. Program tuning is now performing to achieve high-performance on massively parallel computers.

2.7. Reliability and Guideline

The reliability of simulators is very important for the use of applications in the design process. In order to authenticate, the verification and validation process should be emphasize. To do so, we include a database system. Computed results with experimented data are stored away in the database and are used to browse it. Accumulated validation data tells us the guideline of the utilization of the simulator.

3. Concept of HPC/PF

To enhance the utilization of large-scale parallel CFD to the product design, the peripheral technologies are essential not only the development of simulators. Figure 2 represents a concept of an integrated problem-solving environment so that the engineer will be able to concentrate on their thinking work. In the proposed HPC/PF (High-Performance Computing Platform) system, one of the several subsystems divert from well-established open-source software to quickly set up the whole system.

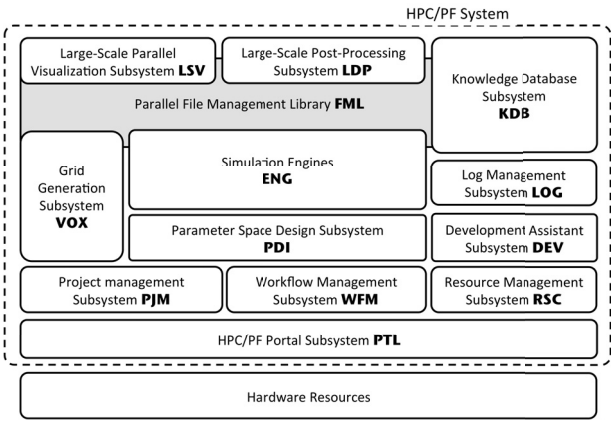

Fig. 2 Conceptual design of HPC/PF, which consists of several subsystems.

4. Concluding remarks

We have been outlined the issues on large-scale parallel computation and the basic concept of an infrastructure to provide useful functions. The important point is that the proposed approach is based on the combination of computer science and computational science. The developed HPC/PF system will be branched out to a purpose-build design system like a thermal design system for automobile.

Acknowledgement

A portion of this research was supported by the grant for "Strategic Program on HPCI" Field No. 4: Industrial Innovations from the Ministry of Education, Culture, Sports, Science, and Technology (MEXT)'s "Development and Use of Advanced, High-Performance, General-Purpose Supercomputers Project," and carried out in partnership with the University of Tokyo. We express our thanks to all parties involved.

References

[1] http://www.aics.riken.jp/index_e.html.
[2] Tawara, T., Ono, K., 10th ISGG Conference on Numerical Grid Generation (2007).
[3] http://www.csrp.riken.jp/application_h_e.html.
[4] Pike, R., Dorward, S., Griesemer, R., Quinlan, S., Scientific Programming Journal, Vol.13, No.4(2005) 227-298.
[5] http://www.ciss.iis.u-tokyo.ac.jp/rss21/en/
[6] Takaki, R., Yamamoto, K., Yamane, T., Enomoto, S., Mukai, J., High Performance Computing, Lecture Notes in Computer Science, Vol.2858(2003) 307-319.
[7] http://vcad-hpsv.riken.jp/en/

Eighth International Conference on Flow Dynamics
November 9 - November 11, 2011

Developments of a Directional Ghost Cell Method and the Multigrid Acceleration for the Building Cube Method

Xinrong Su, Daisuke Sasaki, Kazuhiro Nakahashi
Department of Aerospace Engineering, Tohoku University, Aoba 6-6-01, Sendai, Japan
su@ad.mech.tohoku.ac.jp

ABSTRACT

In this paper we explore a ghost cell based method for the wall treatment of the Building Cube Method. This method employs the ghost cell technique to impose the boundary conditions. The original ghost cell method suffers from the problem of degenerate ghost cells near the trailing edge and also thin bodies. In the current work, by introducing multiple and directional ghost values at given position, the current method can handle these cases successfully. The current method is further accelerated by a multigrid method and favorable speed-up has been demonstrated.

1. Introduction

Computational Fluid Dynamics (CFD) offers the ability to perform high fidelity predictions at relative low cost. While the accurate and fast-turnaround simulation for complex geometry still demands new strategies. The Building Cube Method developed by Nakahashi uses block structured Cartesian mesh to discrete the computational domain. With this method the large scale mesh for complex geometries can be generated with extremely low cost and fast speed. While the solid walls need special treatments as the mesh lines are in general not aligned with the solid bodies.

The ghost cell based Immersed Boundary method [1] can be used to impose the boundary conditions. The values at the ghost cell are determined by the boundary conditions. This method is simple and works well in most cases. While in some cases this method is degenerated and there may be no ghost cell or may be more than one candidate image points. One solution is introducing complex steps to deal with such cases [2]. Kirshnan and Liu, also Luo et al. use the least-square method to treat the near wall cells for Cartesian mesh.

These problems always take place in the domain with sharp geometries. In this paper a directional ghost cell method is developed. With this method, at given position multiple values of ghost cells are allowed and for every direction, the ghost cell value with best quality is selected and thus the degeneration can be avoided. In this paper the BCM method with ghost cell is further accelerated with a carefully designed multigrid strategy.

2. Method

As shown in Fig. 1, near the trailing of airfoil, for the cell inside the solid region, there are two candidate image points, one is inside the lower part and the other is located in the upper part of the fluid region. In the original ghost cell method this leads to the confusion of how to define the value at the ghost cell. Simply using either image point would be not correct in some cases.

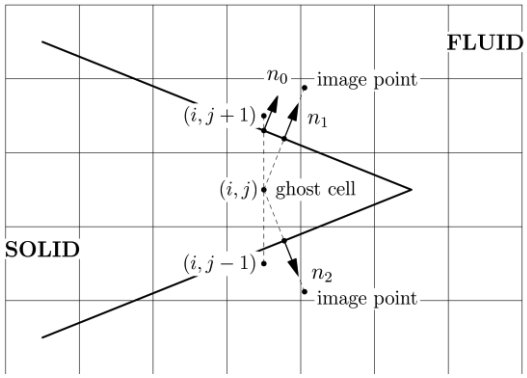

Fig. 1 Degenerated case that have multiple candidate image points near the trailing edge.

As shown in Fig. 1, in the calculation of the residual at cell (i,j+1), the geometry information of the upper solid wall, n_1 should be used. And for cell (i,j-1), n_2 should be used to correctly reflect the effects of solid wall. Thus the key of the current method is to use suitable wall information in the definition of image points.

For example, in the definition of ghost cell for cell (i,j+1), there are two choices of the image points, according to the analysis in the above part, the one with the wall normal n_1 is the best choice. In the current method we have to calculate the intersection point of the vertical mesh line with the solid wall and denoting n_0 be the local wall normal at the intersection point, as demonstrated in Fig. 1, selecting the image point which maximize the dot-product of n_0 and n_i would yield the correct image point. In the same manner for cell (i,j-1) selecting the image point maximizing the dot-product of n_0 and n_i would automatically select the image point in the lower part of the fluid region. In this case there would be two values of ghost cells have to be stored at cell (i,j) and corresponding value has be used for cell (i,j-1) and cell (i,j+1), respectively.

In the above the definition of ghost cell and image point in the vertical direction is discussed and for the horizontal direction the same method applies and at given position inside the solid region, in two dimensions there maybe at most four values of the ghost cells have to be stored at given position and these values should be used in the corresponding directions. As a result, the definition of the solid cell, fluid cell and the transient cell is a bit different from that in the original ghost cell method. In the current method, the pre-processing stage can be described in the following steps:

1. The cell is denoted as solid cell if its center is inside the solid walls. Then if the lines connecting its four neighboring cell centers with itself have no intersections with the solid walls, this cell is denoted as fluid cell. The rest cells are denoted as transient cells.
2. For the transient cells, calculate the intersection points of the lines defined in the first step with the solid walls and calculate the wall normals at the intersections.
3. Use the wall normal to select the best candidate of

image point direction by direction. In general only a small part of ghost cells need the method developed in this paper. Compared to the approaches in Mittal et al. [2] and the hybrid least-square method in Kirshnan and Liu [3], Luo et al. [4], the current method is simple and the original ghost cell method needs little modifications.

In the current method bilinear interpolation is used to calculate the physical variables of the image point, for inviscid flow the value at the ghost point is defined by

$$\begin{cases} \dfrac{\partial p}{\partial \mathbf{n}} = \rho \dfrac{u_t^2}{R} \\ \mathbf{u}_{n,g} + \mathbf{u}_{n,i} = 0 \\ s_g = s_i \end{cases}$$

In the above equation the simplified momentum equation is used to calculate pressure. Numerical results indicate that by introducing curvature the numerical dissipation in the near wall region can be obviously reduced.

Currently the spatial residual is computed with third order WENO scheme with HLLC Riemann solver and a five-stages Runge-Kutta method is used to integrate the governing equation towards convergence. In order to accelerate the convergence, multigrid method is used. For the current Building Cube Method, as the mesh lines are not aligned with the solid bodies, thus on the coarser meshes, the ghost cells and image points are more irregular. In the multigrid method the high frequency disturbances are damped on the coarser mesh, while in the current method the use of non-aligned mesh would introduce high frequency disturbances on the coarser mesh and it is contrary to the multigrid method and may harm the acceleration ratio. In the current paper this effect is observed in cases with irregularly positioned image points. In the current work two strategies are used to augment the multigrid method:

1. On the coarser mesh, the spatial accuracy is reduced from third order to only first order.
2. The coarse grid corrections are smoothed before transferred to the fine grid.

3. Results and Discussion

A series of test cases from subsonic to transonic flow regime are used to validate the accuracy and efficiency of the current method and of which the results of the NACA 0012 case will be given in this paper.

For the NACA 0012 case with freestream Mach number of 0.3 and zero angle of attack, both the current ghost cell method and the original ghost cell method are used. Also a structured code with more refined grid of about 1M mesh points is used for the same case and the result is used as reference. The comparison of the surface pressure coefficient near the trailing edge is given in Fig. 2. As shown in Fig. 2, with the original ghost cell method, as near the trailing edge there are degenerated cases of multiple candidates of image points, the surface Cp is discontinuous near the tailing edge. While in the current method, with the use of directional ghost cell, the calculated distribution of Cp is smooth and is in better agreement with the result of structured mesh.

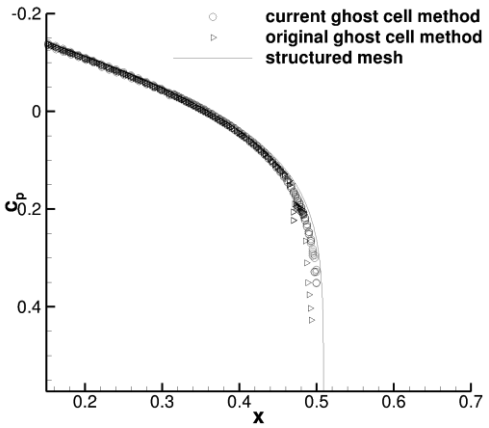

Fig. 2 Comparison of the surface Cp for the current and the original ghost cell methods near the trailing edge.

The convergence histories for the current ghost cell method are given in Fig. 3 and the convergence speed has been obviously improved.

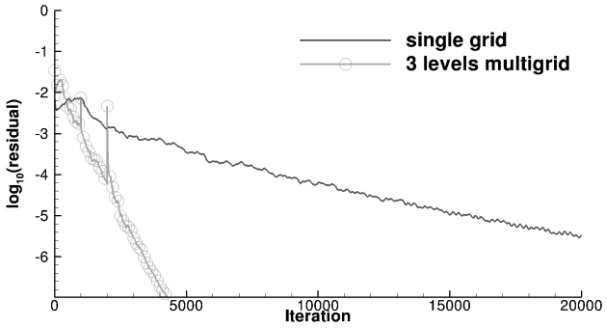

Fig. 3 Convergence histories of the current method

More results will be given in the presentation.

4. Concluding remarks

In the current paper a directional ghost cell based Immersed Boundary method is developed for the wall treatment of the Building Cube Method. Compared to the original ghost cell method, in the current method multiple values of ghost cells are allowed at given position. Thus for different directions, the ghost cell value which best suits the local geometrical information is automatically selected. The current method can be used in the case with sharp trailing edge and thin body. The current method is accelerated by multigrid method with special treatments. Numerical results demonstrate the accuracy and the efficiency of the current method.

Acknowledgement

This work was supported by JSPS KAKENHI (21226018).

References

[1] R. Mittal, G. Iaccarino, Annu. Rev. Fluid Mech., **37** (2005), 239-261.

[2] R. Mittal, H. Dong, M. Bozkurttas, et al, J. Comput. Phys, **227** (2008), 4825-4852.

[3] Kirshnan, D. J., Liu, F., J. Comput. Phys, **201** (2004), 119-147.

[4] Hong Luo, J. D. Baum, R. Lohner, J. Comput. Phys, **214** (2006), 618-632.

Eighth International Conference on Flow Dynamics
November 9 - November 11, 2011

Aeroelastic Analysis using BCM Euler Compressible Solver

Yasutaka Nishimura, Daisuke Sasaki, Kazuhiro Nakahashi
Department of Aerospace Engineering, Tohoku University, Japan
yasutaka@ad.mech.tohoku.ac.jp

ABSTRACT

The objective of this study is to establish a practical, efficient flutter simulation tool based on IBM-based Cartesian mesh solver , which achieves low computational costs and high accuracy to simulate the wing flutter phenomenon. Building Cube Method(BCM) is firstly validated by computing inviscid flows around ONERA M6 wing. The code is then extended for flutter simulation by integrating and structural analysis. Flutter simulation results of AGARD 445.6 weakened model and more complex model will be presented.

1. Introduction

In recent years, the aerodynamic analysis using computational fluid dynamics (CFD) has been widely used in the actual aircraft design. Unstructured mesh is widely used now, because it can treat complex objects. However, there are several difficulties in the CFD using the unstructured mesh solver.

For an example, the unstructured mesh solver is not efficient for moving body problems, because the unstructured volume mesh movement is time-consuming and not reliable. To overcome these issues, the Building Cube Method (BCM) has been proposed. The BCM basically employs an equi-spaced Cartesian mesh, and the body boundaries are immersed in the mesh so that it can treat moving bodies without deforming the volume mesh. This simplifies the algorithm and reduces the computational time as compared with the unstructured mesh approach.

The final objective of this study is to establish a practical and, efficient flutter simulation tool based on BCM-based Cartesian mesh solver. To achieve low computational costs and high accuracy to simulate the wing flutter phenomenon by Cartesian mesh, an efficient immersed boundary method (IBM) for compressible inviscid flow simulations is one of the key points..

2. Numerical Scheme

2.1 Compressible Building Cube Method

The governing equation in the BCM is the compressible Euler equation. It is discretized using the cell centered finite volume method. The HLLEW(Harten-Lax-van Leer-Einfeldt) scheme, a type of the approximate Riemann solver is implemented to solve the inviscid flux, and 3rd order MUSCL is used to construct the high order scheme satisfied TVD condition. For the time integration, LU-SGS (Lower-Upper Symmetric Gauss-Seidel) implicit method is employed. In this study, three points backward difference scheme is adopted to achieve 2nd order time accuracy for unsteady calculations.

2.2 Wall boundary Conditions Using the IBM

In this study, an immersed boundary method [1] using the ghost cell (GC) and the image point (IP) is used, for the wall boundaries treatment. The process of the IBM is as follows:

(1) The wall cell adjacent to a fluid cell is defined as "ghost cell".
(2) "Image point" is defined at the point of a distance (1.5 for 2D, 1.75 for 3D), which is larger than the diagonal distance of the cell from GC to the surface normal direction.
(3) Physical values at IP is obtained by the inverse distance weighted interpolation [3] from fluid cells around IP .
(4) Physical values at GC are determined using the values at IP. The slip conditions and the zero-gradient of pressure are imposed at the wall boundary. The density is calculated from the total enthalpy. The velocities are modified for moving wall.
(5) To calculate thin objects, multiple-valued GC is defined and 1st order numerical fluxes are constructed using GC values at the cell interface near the wall boundary.

3. Results and Discussion

Inviscid flow around the ONERA M6 wing was computed by the present method to evaluate the computational accuracy and efficiency. The number of cubes is 5,212 with Cartesian mesh(cell) of 16^3 in each cube. The total number of cells are 21,348,352. The minimum grid spacing is 1.8×10^{-3}. Multi core cluster (Xeon, 2.93[GHz]x8, 64GB memory) is used for the computation with OpenMP parallelization. Computed Cp distribution is compared with the result obtained by unstructured mesh solver (TAS-code).

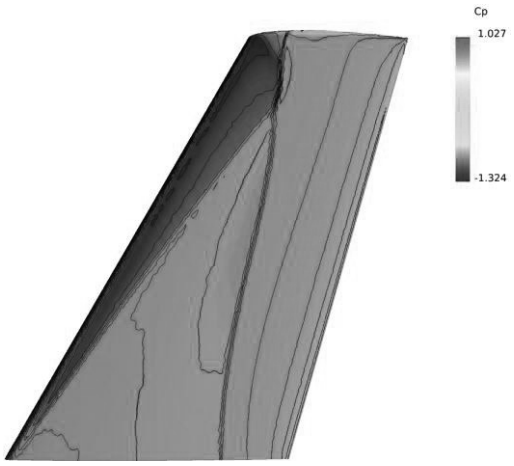

Fig.1 Cp distribution on the upper surface of M6

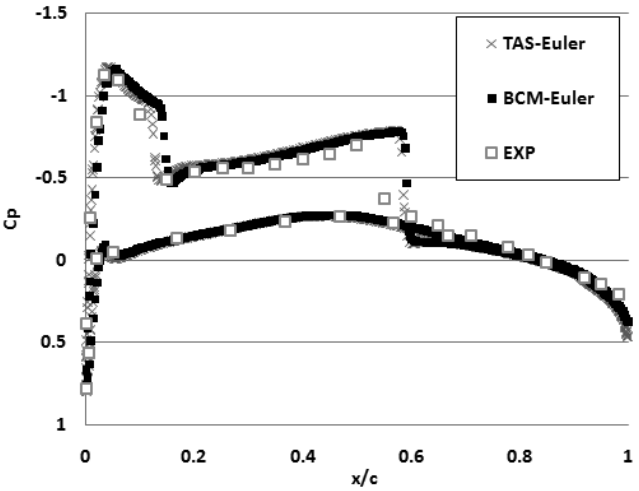

Fig.2 Cp distribution around ONERA M6
(44% semi span)

Figure 1 shows Cp contours on the wing upper surface, and Lambda shock wave is clearly observed. Figures 2 shows comparisons of sectional Cp distributions among BCM, unstructured mesh (TAS-code), and experimental data at 44%, semi span. The result of BCM reasonably agrees with the one of TAS-code, except for the location of the first shock wave. This is because mesh resolution at leading edge is still insufficient, therefore mesh at the leading edge must be finer than this case. Both Cp distributions of BCM and TAS are not agreed with the experimental data, because of the computations neglect the viscosity.

4. Unsteady Flutter Simulation with Direct Method

4.1 Approach

In this study, nonlinear aeroelastic simulations will be carried out by direct coupling of the CFD and the structural equations. A flow chart of this aeroelastic simulation tool is shown in Fig. 3. Each CFD time step, pressure distributions at the CFD mesh is projected onto the FEM mesh for structural analysis. Modal FEM analysis is used for calculating the deformation and deformation velocity under the surface pressure load. After the structural analysis, the parameters of the immersed boundary method in the Cartesian mesh is recomputed for CFD analysis for next time step.

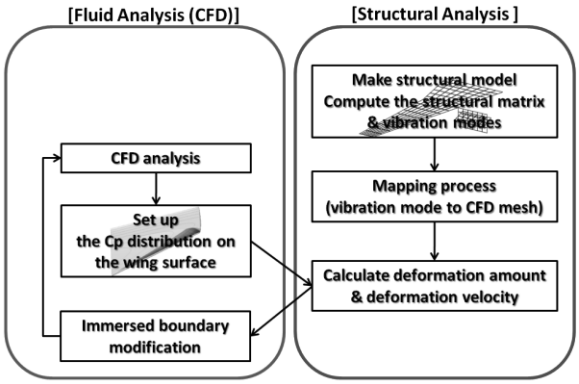

Fig.3 Flow chart of the aeroelastic simulation tool

4.2 Structural Analysis

The governing equation for structural analysis can be written as follows:

$$[\boldsymbol{M}]\{\ddot{\boldsymbol{d}}\}+[\boldsymbol{K}]\{\boldsymbol{d}\}=\{\boldsymbol{F}\} \qquad (1)$$

where $[\boldsymbol{M}]$ and $[\boldsymbol{K}]$ are the mass and stiffness matrix, $\{\boldsymbol{d}\}$ and $\{\boldsymbol{F}\}$ are the displacement vectors and aerodynamic load, respectively. To solve eq.(1), the Rayleigh-Ritz method is employed. The characteristic mode shapes and frequencies can be calculating by the finite-element method. When the first N modes are considered, the displacement vector can be given as follows:

$$\{\boldsymbol{d}\}=[\Phi]\{\boldsymbol{q}\} \qquad (2)$$

where $[\Phi]$ is the model matrix and $\{\boldsymbol{q}\}$ is the generalized displacement vector. As the characteristic modes are orthogonal with the respect to the mass and stiffness matrices, eq.(2) can be transformed as follows:

$$\dot{\boldsymbol{S}}+\boldsymbol{A}_i\boldsymbol{S}_i=\boldsymbol{f}_i \qquad (3)$$

$$\text{where } \boldsymbol{S}_i=\begin{bmatrix}\boldsymbol{q}_i & \dot{\boldsymbol{q}}_i\end{bmatrix}^T \quad \boldsymbol{A}_i=\begin{bmatrix}0 & -1\\ \omega_i^2 & 0\end{bmatrix}$$

$$\boldsymbol{f}_i=\begin{bmatrix}0\\ [\Phi]_i^T\boldsymbol{F}/\boldsymbol{M}_i\end{bmatrix} \quad \omega_i^2=[\Phi]_i^T[\boldsymbol{K}][\Phi]_i$$

$$\boldsymbol{M}_i=[\Phi]_i^T[\boldsymbol{M}][\Phi]_i$$

Equation (3) is discretized with the 3 point backward difference scheme to achieve 2nd order time accuracy. It can be written as follows,

$$\Delta\boldsymbol{S}_i^m=\left[\boldsymbol{I}+\frac{2}{3}\Delta t\boldsymbol{A}_i\right]^{-1}\frac{2}{3}\Delta t\left[-\left(\frac{3\boldsymbol{S}_i^{m-1}-4\boldsymbol{S}_i^n+\boldsymbol{S}_i^{n-1}}{2\Delta t}\right)-\left(\boldsymbol{A}_i\boldsymbol{S}_i^{m-1}-\boldsymbol{f}_i^{m-1}\right)\right] \qquad (4)$$

The index m represents sub-iteration times, and Δt represents count by time steps, respectively.

5. Concluding Remarks

The Euler computational result of ONERA M6 using BCM with IBM agrees reasonably with unstructured mesh solver. In the conference, computational flutter results of AGARD 445.6 weakened model [4] will be presented. The reduction of computational time including mesh deformation and accurate flutter prediction are expected due to the Cartesian mesh solver with high spatial accuracy. In addition, the benefit of the present approach over the existing unstructured mesh method will be also discussed.

Acknowledgement

This work is supported by JSPS KAKENHI 21226018.

References

[1] R. Mittal et al. , *Journal of Computational.Physics*. 227(2008)4827-4825

[2] M. Murayama, K. Nakahashi, K. Matsushima, *Transaction of the Japan Society for Aeronautical and Space Sciences*, 46 (152), 104-112, 2003.

[3] R. Franke, *Math. Comptational*. 38(1082) 181-200

[4] E. Yates, Carson, Jr., NASA TM-100492, 1987.

Eighth International Conference on Flow Dynamics
November 9 - November 11, 2011

Performance of Building Cube Method on Various Platforms

Kazuhiko Komatsu*, Takashi Soga*╬, Ryusuke Egawa*╪, Hiroyuki Takizawa*╪, Hiroaki Kobayashi*╪,
Shun Takahashi┼, Daisuke Sasaki*, Kazuhiro Nakahashi*
*Tohoku University, Sendai 980-8578, Japan
╬NEC System Technologies, Ltd., Osaka 540-8551, Japan
┼Tokyo University Agriculture and Technology, Koganei 184-8588, Japan
╪Japan Science and Technology Agency, Core Research for Evolutional Science and Technology, Japan
komatsu@sc.isc.tohoku.ac.jp

ABSTRACT

The Building-Cube Method (BCM) has been proposed as a next generation CFD method for an efficient 3D flow simulation on large scale supercomputers. As a flow domain is divided into equally-partitioned cells, the flow computations can be divided to partial computations of the same computational cost. To clarify the behavior of BCM on various platforms, this paper compares the performance of BCM on NEC SX-9, an Intel Nehalem-EP cluster, an Intel Nehalem-EX cluster, Fujitsu FX-1, and a GPU cluster. The performance evaluations show that memory capabilities effects the performance of BCM rather than computational potentials.

1. Introduction

The *Building-Cube Method* (BCM) has been proposed for 3D large-scale flow computations around practical geometries using high-density grids. The basic idea of BCM is to decompose a whole flow domain into sub-domains called *cubes*, and further decompose each cube into equally-spaced Cartesian meshes called *cells*.

One of the advantages of BCM is its huge parallelism. The calculations of cubes can easily be decomposed into many data parallel tasks of the same size because the calculations are independent from each other. Moreover, each cube has the same computational cost and the same data size for the calculations.

This paper describes the implementations of BCM on NEC SX-9, an Intel Nehalem-EP cluster, an Intel Nehalem-EX cluster, Fujitsu FX-1, and a GPU cluster to evaluate the sustained performance of those systems for BCM. From experimental results, this paper analyses the performances and scalabilities.

2. Implementation of BCM on Various Systems

To evaluate the performance characteristics of various systems shown in Table 1, BCM is implemented and optimized for each system. This section briefly describes the overview of each platform and explains the implementation and optimizations of BCM.

2. 1 Implementation on a Vector System

SX-9 is a vector parallel supercomputer with 102.4 Gflop/s vector processors. SX-9 provides a large Symmetric Multi-Processing (SMP) node of 16 processors. SX-9 has an on-chip 256KB software-controllable cache named Assignable Data Buffer (ADB). Once data for ADB specified by programmers are accessed, these data are stored in ADB and used in the next accesses. An effective use of ADB becomes an important factor for memory-intensive applications such as BCM. In this implementation, ON_ADB directives are used for data to be used in the next iteration. Thus, multiple data can be simultaneously transferred from both the main memory and ADB.

The Red-Black SOR method using mask tables is used in the implementation on SX-9. The Red-Black method can avoid indirect memory accesses and exploit the data parallelism among cells. As parallelizing the SOR method generally shorten the length of loop, the mask tables can avoid accessing unnecessary data without shortening the length of a loop. Thus, the loop remains long enough to utilize all of the vector units of SX-9.

2. 2 Implementation on Scalar Systems

The Nehalem-EP cluster, the Nehalem-EX cluster, and FX-1 are scalar parallel supercomputers that equip Nehalem-EP, Nehalem-EX, and SPARC64VII processors, respectively. As shown in Table 1, these scalar processors also have on-chip cache memories. On-chip L2 and/or L3 caches should be used for data with high locality to avoid redundant memory accesses. For Nehalem processors, uses of SIMD instructions are essential to efficiently process multiple data.

Although the Red-Black method can eliminate the data dependency, the stride memory accesses are required, resulting in performance degradation. Even though dividing an array into two arrays, unit stride accesses are required. Thus, in the implementation on the scalar systems, the naïve SOR method is adopted to avoid degrading the performance by the stride memory accesses.

2. 3 Implementation on a GPU System

A GPU cluster has GPUs and CPUs. Each GPU consists of hundreds of stream processors (SPs). In CUDA (Compute Unified Device Architecture), which is the programming framework for GPU computing, SPs are grouped into stream multiprocessors (SMs).

In the implementation of BCM on a GPU cluster system, cubes are hierarchically assigned to nodes and then to SMs of GPUs. The calculations for the cells in cubes are assigned into threads, which are executed on SPs. As the computational cost of each cell is also the same, efficient parallel processing using SPs can be performed. To effectively use the on-chip memory in a GPU, a ring buffer allocated on the on-chip memory is utilized in the implementation. By storing data with high locality on the ring buffer, it can reduce the number of off-chip memory accesses requiring long access latency.

Table 1. System specifications.

System	Peak flop/s	Nodes	PEs/node	Cores/PE	Mem. BW	On-chip Memory	Network	B/F
NEC SX-9	26.2 Tflop/s	16	16	1	256 GB/s	256 KB ADB	2x 128 GB/s IXS	2.5
Nehalem EP	0.75 Tflop/s	8	2	4	25.6 GB/s	256 KB L2 / core 8 MB shared L3	40 Gb/s Infiniband	0.55
Nehalem EX	1.74 Tflop/s	6	4	8	34.1 GB/s	256 KB L2 / core 24 MB shared L3	20 Gb/s Infiniband	0.47
Fujitsu FX-1	5.16 Tflop/s	128	1	4	40.0 GB/s	6 MB shared L2	20 Gb/s Infiniband	1.0
Tesla S1070	1.248 Tflop/s	16	1	1	102 GB/s	16 KB / SM	10 Gb/s Infiniband	1.3

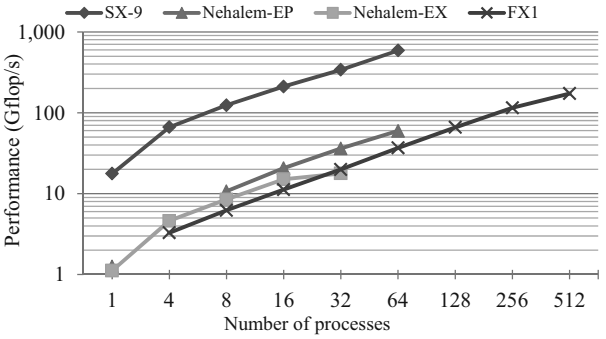

Fig. 1 Performance of BCM on the F1 model.

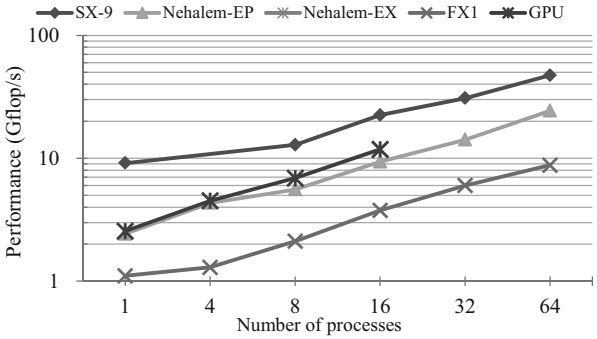

Fig. 2 Performance of BCM on the Sphere model.

3. Performance Evaluation and Discussions

The flow simulations using BCM around 3D test models are performed on the supercomputers shown in Table 1. As a large model, F1 of 200 million cells is used. Sphere of 5 million cells is used as a small model.

Fig. 1 shows the sustained performance of BCM achieved for the F1 model. The results show that SX-9 achieves higher performance than the others. As BCM is a memory intensive application, the sustained memory bandwidth has a great impact on the performance. In addition to the essential high memory bandwidth, the effective use of ADB further improves the bytes/flop ratio, resulting in the high performance.

Even though the peak memory bandwidth of FX-1 outperforms those of Nehalem EP and EX, its sustained performance is lower. This is because the sustained memory bandwidth of Nehalem is higher than that of SPARC64VII. In the STREAM benchmark, FX1 achieves 10.0 GB/s while Nehalem EP and EX achieve 17.0 and 17.6 GB/s, respectively.

Fig. 2 shows the sustained performance of BCM on the Sphere model, which includes the results of the GPU system. This results shows that a GPU cluster system achieves comparable and/or better performance than the scalar cluster systems although SX-9 achieves higher performance than the GPU cluster. This is because GPUs can accelerate the data parallel calculations of BCM using a number of SPs and high memory bandwidth. Effective use of SPs and on-chip memory contributes to the good sustained performance larger than the other scalar systems. However, even if the calculations using the GPUs are fast, data transfers between a GPU and a CPU in a node and between GPUs in different nodes are slow and cannot be negligible. As a result, the data transfer dominates the most of time in the simulation. To further accelerate BCM using the GPU system, the time of data transfers should be shortened and be hidden by transferring data during the calculations.

The efficiency of the sustained performance to the peak performance on a SX-9 vector processor is about 17%, while those of the other systems are about 1.5~3.2%. This is because the vector units in a vector processor are efficiently utilized for the calculations.

Taking a look at the scalability, all of the systems achieve high scalability in the F1 model due to a large number of parallel tasks and sufficient network bandwidth. The scalabilities in the Sphere model are not high compared with those of the F1 model. The low scalability of the GPU system comes from the overhead of data transfers. The lower scalabilities of the other systems come from the lack of parallel tasks due to a small number of cubes in the Sphere model.

4. Concluding remarks

In this paper, the performances of SX-9, a Nehalem-EP cluster, a Nehalem-EX cluster, FX-1, and a GPU cluster are evaluated based on fluid simulations with BCM. From the experimental results, it is clarified that memory bandwidth greatly effects the performance of BCM except in the GPU cluster. For the GPU cluster, data transfers easily become a bottleneck. To further improve the performance of BCM, the development of a memory-friendly and network-friendly implementation is desired in aspect of software. In hardware side, the wider bandwidth and higher-speed network has a possibility to accelerate BCM.

5. Acknowledgements

This research was partially supported by Grant-in-Aid for Scientific Research (S) #21226018; Grant-in-Aid for Young Scientists (B) #21700049; Core Research of Evolutional Science and Technology of Japan Science and Technology Agency (JST CREST).

Eighth International Conference on Flow Dynamics
November 9 - November 11, 2011

Supercritical-fluids Simulator (SFS) coupled with Building Cube (BC) :SFS+BC

Takashi Furusawa, Kotaro Makino, Ryo Anan, Satoru Yamamoto.
Graduate School of Information Sciences, Tohoku University
Aramaki Aza Aoba 6-6-01, Aoba-ku, Sendai 980-8579, Japan
furusawa@caero.mech.tohoku.ac.jp

ABSTRACT

The supercritical-fluids simulator (SFS) developed by our group is coupled with Building Cube (BC) method for the computation of complex geometry. We call this method SFS+BC. First, forced convection around the cylinder is calculated and the length of the vortex behind the cylinder is compared with existing result. Next, H_2O and CO_2 flows around a cylinder are calculated and compared with each other. The calculated values of the case across the critical point were far different from other ordinary cases. SFS+BC enables us to calculate thermophysical flows over a complex geometry.

1. Introduction

A number of substances such as water, carbon dioxide and nitrogen exist in practical flow environments. Each substance has own thermophysical properties, boiling point, critical point and so on. Figure 1 shows the density change of water at each pressure. Almost all existing CFD methods are constructed for ideal gas or incompressible fluids and ignoring these thermophysical changes of substance.

We have proposed a numerical method for simulating supercritical-fluid flows across critical point [1]. In this method, the preconditioning method is coupled with a program package for thermo-physical properties of fluids (PROPATH) [2]. In PROPATH, mathematical models based on a polynomial equation approximating thermophysical properties are defined in wide range of temperature and pressure. This program package enables to evaluate the accurate thermophysical properties of gas, liquid and also supercritical fluids. This method is called supercritical fluid simulator(SFS) and has already extended to supercritical-fluid, gas and liquid flows of arbitrary substance. Especially, supercritical-fluid flows across the critical point are quite varied by changing the substance, temperature condition and pressure condition.

For the practical use of SFS, the computation of flows over a complex geometry is required. However, SFS employs the structured grid system and the pre-processing of grid generation is restricted. Building-Cube (BC) method has been proposed by Nakahashi et al [3] for the complex geometry computation. In BC method, the computational domain is divided into a number of sub-domains called cubes which has equally-spaced Cartesian mesh.

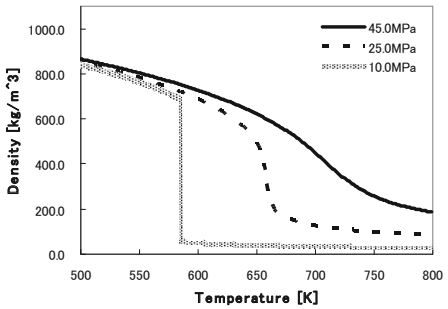

Fig. 1 Density change in temperature.

In this study, SFS is successfully coupled with BC. We call this method SFS+BC. First, we calculate forced convection of H_2O vapor and the length of the vortex behind a cylinder is compared with existing result. Next, we calculate H_2O and CO_2 flows around a cylinder with different temperature and pressure conditions and compared with each other.

2. Numerical method

The fundamental equations are based on two-dimensional compressible Navier-Stokes equations in general curvilinear coordinates and modified by the preconditioning method. The set of equations is written in vector form as

$$\Gamma\frac{\partial\hat{Q}}{\partial t}+\frac{\partial F_i}{\partial\xi_i}+\frac{\partial F_{vi}}{\partial\xi_i}+H=0\ \ (i=1,2) \tag{1}$$

where

$$\Gamma=\begin{bmatrix}\theta & 0 & 0 & \rho_T\\ \theta u_1 & \rho & 0 & \rho_T u_1\\ \theta u_2 & 0 & \rho & \rho_T u_2\\ \theta h-(1-\rho h_p) & \rho u_1 & \rho u_2 & \rho_T h+\rho h_T\end{bmatrix},$$

$$\hat{Q}=J\begin{bmatrix}p\\ u_1\\ u_2\\ T\end{bmatrix},\ F_i=J\begin{bmatrix}\rho U_i\\ \rho u_1 U_i+\dfrac{\partial\xi_i}{\partial x_1}p\\ \rho u_2 U_i+\dfrac{\partial\xi_i}{\partial x_2}p\\ (e+p)U_i\end{bmatrix},$$

$$F_{vi}=-J\frac{\partial\xi_i}{\partial x_j}\begin{bmatrix}0\\ \tau_{j1}\\ \tau_{j2}\\ \tau_{jk}u_k+\kappa\dfrac{\partial T}{\partial x_i}\end{bmatrix}.$$

Eq. (1) is solved by the numerical method based on the preconditioned flux-vector splitting scheme and the preconditioned LU-SGS scheme [4].

Thermophysical properties are calculated from PROPATH. It contains thermophysical properties for 48 substances such as water, carbon dioxide, oxygen, nitrogen and so on, in wide-range pressure and temperature conditions. The properties of gas, liquid and supercritical fluid are defined as a polynomial function of pressure and temperature. For example, the equation

of state (EOS) for carbon dioxide was standardized by International Union of Pure and Applied Chemistry (IUPAC).

BC method is used as the grid system. Computational domain is divided into a number of sub-domains called cubes. Each cube has equally-spaced Cartesian mesh. By using the same number of grid point in all cubes, it is simple to keep load balance among all cubes in the use of large scale computers with massively parallel processors

3. Numerical results

First, forced convection around a cylinder is calculated. The computational cube is shown in Fig. 2. The total number of cubes is 320 and each cube has 16x16 grids. H_2O vapor is assumed and the Reynolds number is 40. The temperature and pressure condition are 650 K and 0.1013 MPa, respectively. The stream lines near the cylinder are shown in Fig.3 The vortex separation behind the cylinder is observed. The length of vortex separation is 2.17 which is similar to 2.27 by Ye et al. [5].

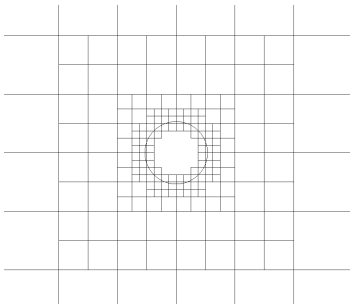

Fig. 2 Computational cube near the cylinder.

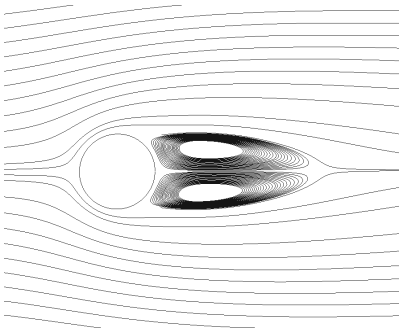

Fig. 3 Stream lines at Re=40.

Next we calculated forced convection of H_2O and CO_2. The computational condition is shown in Table 1. T_{fluid} is the fluid temperature and T_{wall} is the cylinder temperature. The Reynolds number is 40. The critical point of H_2O is 22.06 MPa and 647 K. Case 2 is that across the critical point. The temperature contours and the density contours are shown in Fig. 4. In case 2, large difference of density is observed near the cylinder as compared with those of Case 1. The density contour of Case 3 is slightly different from Case 1.

4. Conclusions

We coupled SFS with BC method. We call this method SFS+BC. First, we calculated the forced convection of H_2O vapor and the length of the vortex behind the cylinder was compared with existing result. Next, we calculated H_2O and CO_2 flows around a cylinder and compared with each other.

SFS+BC enables us to calculate thermophysical flows over a complex geometry.

Table 1 Computational conditions

	Case 1	Case 2	Case 3
Pressure [MPa]	0.1013	30.0	0.1013
T_{fluid} [K]	650		350
T_{wall} [K]	700		400
Substance	H_2O		CO_2

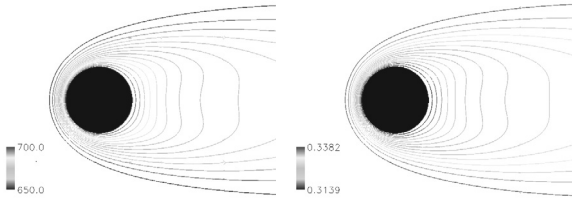

Temperature contours Density contours

(a) Case 1

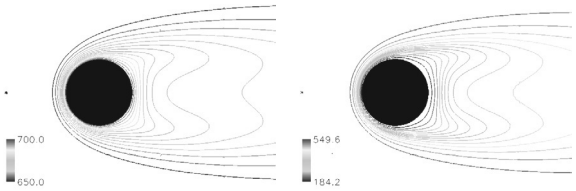

Temperature contours Density contours

(b) Case 2

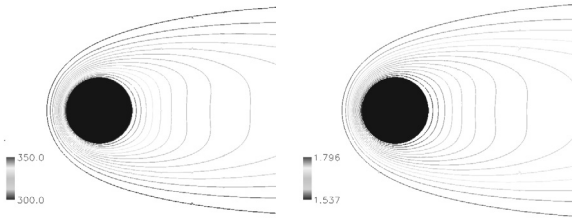

Temperature contours Density contours

(c) Case 3

Fig. 4 The Calculated results.

References

[1] S.Yamamoto and T.Furusawa, and R.Matsuzawa, Int. J. Heat and Mass Transfer, **54-4**(2011), 774-782.

[2] A PROGRAM PACKAGE FOR THERMO-PHYSICAL PROPERTIES OF FLUIDS by PROPATH group.

[3] K. Nakahashi, Proc. of 2nd Int. Conf. on Computational Fluid Dynamics, (2002), Springer.

[4] S.Yamamoto, J. Comp. Phys., **207-1** (2005), 240-260.

[5] T.Ye, R. Mittal, H.S. Udaykumar and W. Shyy, J. Comp. Phys., **156-1** (1999), 209-240.

Eighth International Conference on Flow Dynamics
November 9 - November 11, 2011

Overset Grid Approach for Moving Boundary Problem based on Cartesian Grid Method

Shun Takahashi, Norio Arai
Tokyo University of Agriculture and Technology, 2-24-16, Naca-cho, Koganei, Tokyo, 184-8588
takahass@cc.tuat.ac.jp

ABSTRACT

It is difficult to solve flowfields including multiple objects with relative motion. Overset grid method is most effective way to treat the flowfield especially when the object performs large displacement. In the present study, overset grid method for moving body problem is proposed based on Cartesian grid as background grid and body fitted coordinate mesh around objects. The Cartesian mesh is Building-Cube Method (BCM) developed as one of next generation CFD tools. One of the objectives of the present method is to reduce the computational cost for the overset grid method by exploiting the characteristics of BCM.

1. Introduction

Today, numerical analysis by CFD is widely used for flowfields around not only complicated geometries but also moving objects. For instance, single object like a turbine wing can be analyzed by using Arbitrary Lagrangian and Eulerian (ALE) method with moving mesh. However, flowfields around multiple objects including static and moving objects like a full-model of helicopter cannot be solved easily by using the moving mesh method. For moving mesh algorithm, dynamic mesh method is well-known because of the high applicability to various flowfields with low computational cost. But large mesh displacement is not applicable to the method since the mesh distortion is occurred. In this situation, overset mesh method has been used generally by various computational meshes. This method is effective to solve the flowfields involving some objects with relative motion. Moreover, the degree of freedoms of the mesh motion is almost nothing since a computational mesh is constructed around each object. However, the computational cost to define the intersectional region between meshes becomes large. One of the biggest tasks of this method is reduction of the additional computational cost.

Building-Cube Method (BCM) proposed as one of the next-generation CFD methods based on the advantages of equally-spaced Cartesian mesh has been developed until now. Characteristics of BCM are algorithm simplicity and adaptively refined Cartesian mesh to utilize a number of mesh points efficiently by next-generation supercomputers. Flowfields around engineering products are mainly focused in this analysis. Therefore, many practical applications are discussed by BCM until now. As a result, it is suggested that one of biggest issues of BCM is representation of the object surface. This problem is discussed not only for BCM but also for common Cartesian mesh all the time. The applicability of Immersed Boundary Method (IBM) and gridless method was demonstrated with BCM as same as general Cartesian mesh method. Additionally, the applicability of the staircase surface representation with pretty minimal mesh was also discussed as well. As results, resolving the boundary layer must be necessary to estimate the fluid force accurately and tremendous mesh points are still needed to capture flowfields around practical engineering products in the relatively high Reynolds number flows even though adaptively refined Cartesian mesh is used with today's supercomputers.

From these backgrounds, overset mesh method based on BCM and body fitted coordinate (BFC) mesh is proposed in the previous study [1]. In the present study, three-dimensional analysis is discussed from the point of the advantage and applicability.

2. Numerical Method

2.1. Computational Grid

In this study, BCM mesh takes a role of background mesh based on low numerical error as one of advantages of equally-spaced Cartesian mesh. The background mesh is important to capture overall flowfield and flow structure. Moreover, the intersection region must be constructed in the overset mesh method between BCM and BFC meshes. The intersection region is dynamically changed with the object motion in moving boundary problem. The mesh location of BCM is easily obtained by using the characteristic of the Cartesian mesh. It is beneficial for the overset mesh method since the intersection information can be constructed directly.

Meanwhile, BFC mesh is located around the object to capture boundary layer accurately. Numerical method to make the intersection region between these meshes is discussed later.

2.2. Governing Equation and Numerical Scheme

The governing equations are three-dimensional incompressible Navier-Stokes equations. However, the formulation is slightly different between BCM and BFC mesh. In BCM mesh, conservative formed incompressible NS equation is solved by finite volume method with fractional step method on collocated mesh arrangement. The convective term is treated as fully conservative second order central scheme. However, first order upwind scheme is blended at connecting boundary between different sized cubes. The approximate formulation of diffusive terms and Poisson equation of pressure term becomes same as second order central difference scheme accordingly. Discretization of time for convection and diffusion terms is not applied in the present scheme. Furthermore, standard Smagorinsky model is implemented for LES.

In BFC mesh, ALE incompressible Navier-Stokes equations are solved by finite difference method on the regular mesh arrangement. The metrics of the computational mesh is estimated by conservative formulation to decrease numerical error. Convective terms are discretized by fourth order skew symmetric

finite difference scheme. Other derivatives are approximated by second order scheme. Time marching is performed by fractional step method with second order Adams-Bashforth method and Crank-Nicolson method as same as conventional scheme. On the object surface, acceleration of the object should be taken as the boundary condition of the pressure. This treatment is going to be implemented if it is required.

2.3. Overset Grid Method

In the case of an overset grid around static object, the intersection region should be constructed once at the beginning of the simulation. However, in the case of the moving object, the region should be constructed with following the motion of the object, repeatedly. Therefore, the computational cost becomes one of the biggest issues of overset mesh method.

The present intersection region is determined between donor-cell and accept-node. Figure 1 shows the relationship between BCM and BFC meshes as donor-cell and accept-node. In this relationship, an accept-node is surrounded by a donor-cell, certainly. But a donor-cell can involve several accept-nodes. In this study, equally-spaced Cartesian mesh is distributed with BCM mesh to determine the relationship quickly. By using the equally-spaced Cartesian mesh, a BCM donor-cell for a BFC accept-node can be determined easily. It is one of the advantages to use BCM as background mesh in the present overset method.

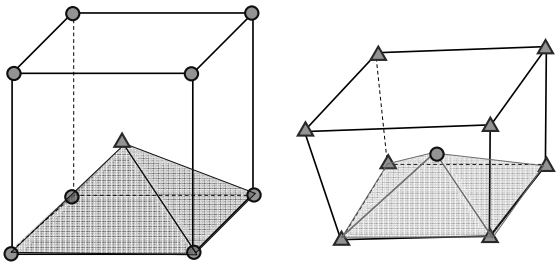

Fig. 1 Donor cell and accept node
(Right: BCM donor cell and BFC accept node)
(Left: BFC donor cell and BCM accept node)

However, a BFC donor-cell for a BCM accept-node can not be determined, directly. Therefore, the relationship is determined by using bounding-box and several numerical techniques to reduce the computational cost. This methodology should be investigated to achieve quick searching.

An accept-node receives primitive variables from eight vertices of a donor-cell by trilinear interpolation. This interpolation is implemented with the weight based on the volume of the pyramids formed by the accept-node and vertices of the donor-cell like Fig. 1. The accept-node forms six pyramids in a donor-cell. It is very simple and robust algorithm.

3. Numerical Result

As a first validation, moving body problem with single BFC mesh is solved in static flowfield. The geometry of the object is circular cylinder with rounded corner. The object performs alternative translational motion represented by trigonometric function as Eq. (1).

$$x = A\cos(\omega t) \tag{1}$$

The diameter of the cylinder, the amplitude of the translation and the angular velocity are 0.10 [m], 0.10 [m] and 5.0 [rad/sec], respectively. Maximum translational velocity is 0.50 [m/sec] so that Reynolds number based on the velocity is 3.3×10^3 in standard atmospheric condition.

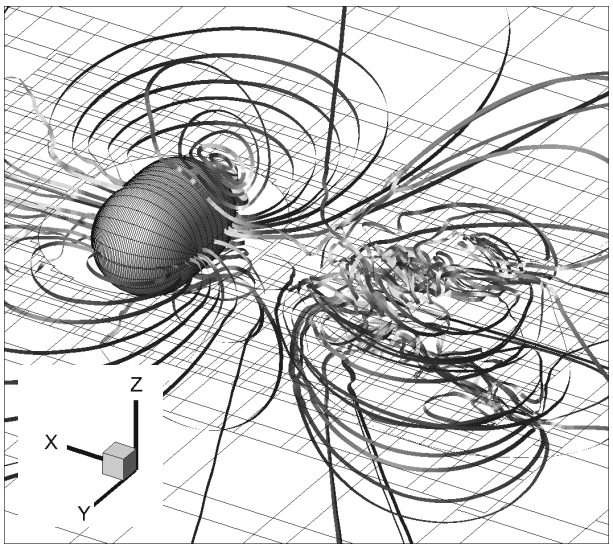

Fig. 2 Instantaneous streamline around moving cylinder

Figure 2 show the flowfield around moving cylinder by instantaneous streamline distribution. At this moment, the cylinder moves toward positive direction along with x-axis. There is a complicated wake as shown like a complicated streamlines. In contrast, smooth doublet shaped streamlines are observed around the cylinder. From now, the flow is clarified quantitatively to investigate the fluid force generated by flapping wing to develop an Unmanned Aerial Vehicle.

Acknowledgement

The present study is supported by Institute of Fluid Science, Tohoku University “Multidisciplinary Coupled Analysis to Develop Maneuverable VTOL Aircraft as an Exploring Vehicle for Disaster Area”.

References

[1] Takahashi, S. and Arai, N., “Multidisciplinary Investigation by Fluid-Structure-Motion Integrated Simulation,” Proc. of IV International Conference on Computational Methods for Coupled Problems in Science and Engineering, 2011.

Eighth International Conference on Flow Dynamics
November 9 - November 11, 2011

Development of Cartesian-Mesh Based CFD Solver combined with Unstructured-Mesh

Michitaro Hashiba, Daisuke Sasaki, Kazuhiro Nakahashi
Department of Aerospace Engineering, Tohoku University, Aoba 6-6-01, Sendai 980-8579, Japan.
E-mail of corresponding author: hashiba@ad.mech.tohoku.ac.jp

ABSTRACT

The new Cartesian-mesh based CFD solver combined with unstructured mesh has been developed so that the calculation of flow around a complicated body can be conducted accurately in a short time. The objective of this study is to compare the CFD solver with the existing unstructured grid CFD solver, TAS-code, and to make clear the usefulness and problems. The validation was conducted with JMRTS helicopter fuselage and ONERA M6 wing. Both results show good agreement.

1. Introduction

The Cartesian mesh has several advantages compared to other meshes such as the simple and quick mesh generation, easy implementation of the higher-order scheme, and so on. The Building-Cube Method (BCM) [1], which is based on Cartesian mesh has been proposed with the expectation of the progress of high performance computers. However, since Cartesian mesh does not conform to the curved surface, it is very critical for aeronautical applications where very high accuracy is usually required for surface pressure and skin friction distributions. Although staircase representation of Cartesian mesh is attractive because of its simplicity and flexibility, the required large number of computational points is formidable even for the current supercomputers.

In the present study, unstructured mesh is employed near the body surfaces in order to compute flows with Cartesian mesh CFD solver in a practical time. This enables to reduce the total number of computational points while computation accuracy at surface is maintained.

The objective of this study is to develop a coupling CFD solver and to compare the result with the existing unstructured mesh CFD solver, TAS-code [2]. The validations are conducted with helicopter fuselage model of JMRTS (Jaxa Multi-purpose Rotor Test System) [3] and ONERA M6 wing [4].

2. Method

BCM is a computational flow simulation method which is based on a multi-block structure of equally-spaced Cartesian meshes. In BCM, a flow-field is divided into various sizes of cuboids called “Cube”, and the cubes are subdivided into equally-spaced Cartesian meshes called “Cell”. Because each cube has the same number of cells, it is expected to achieve the uniform computational load at each cube and the high parallel performance.

The base of the present coupling CFD solver is the Cartesian mesh solver (BCM), which covers almost the entire computational domain. The unstructured mesh is adopted only near the wall region to represent the body surface efficiently as shown in Fig. 1. The figure shows the computational domains for JMRTS model, where the unstructured mesh is generated by MEGG3D (Mixed-Element Grid Generator in 3 Dimensions) [5]. In BCM domain, compressible Euler equation is solved, while compressible Euler/NS equation is solved by TAS solver in unstructured mesh region. Each mesh solves its own computational domain independently and exchanges flow variables at every time step. Linear interpolation is conducted between the two meshes. The detailed procedure of the present coupling CFD solver for steady inviscid/viscous flow computations is shown in Fig. 2.

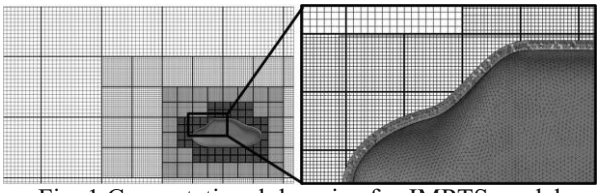

Fig. 1 Computational domains for JMRTS model

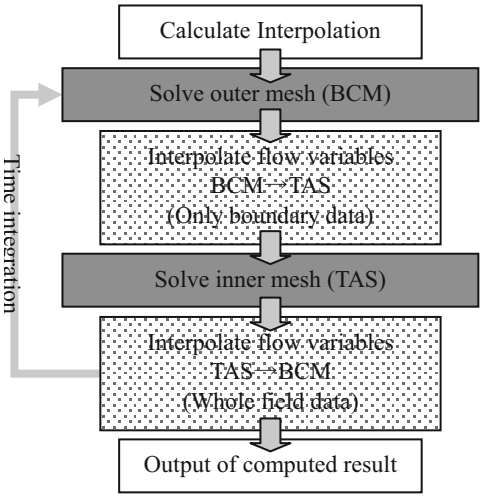

Fig. 2 The procedure of the present coupling CFD solver

3. Results and Discussion

JMRTS model and ONERA M6 wing are selected for the validation of the present coupling solver. JMRTS model is an experimental helicopter fuselage designed by JAXA. The results obtained with the present coupling solver are compared with the experimental data and computational results by TAS-code.

3.1 JMRTS

The overlapping meshes for the calculation are shown in Fig. 1. There are in total 72,699 nodes in the unstructured mesh and it is constructed with tetrahedral elements. Calculation condition is shown in Table 1. The calculated pressure distributions are compared in Figs. 3 and 4. As shown in Figs. 3 and 4, good agreement

between the Coupling and TAS-code is obtained. On the other hand, two calculations are different from experimental measurement on the aft body of the fuselage. There are several possible reasons. First reason is that the two calculations are based on Euler equations, so that flow separations on the aft body cannot be predicted. Since the drive shaft and hub are rotated at the experiment, the flow field is expected to be highly influenced by the wake of the shaft and hub.

Table 1 Calculation condition of JMRTS (Euler)

	TAS-code	Coupling
Mach	0.175	
A.o.A	-2.0[deg.]	
number of points	0.42 M	BCM:4.4 M ＋TAS:0.07M
computation time	2h (SX-9, Single)	2h (SX-9, 4parallel)

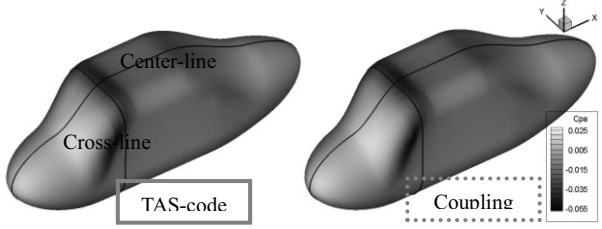

Fig. 3 Comparison of surface pressure distribution on the JMRTS model

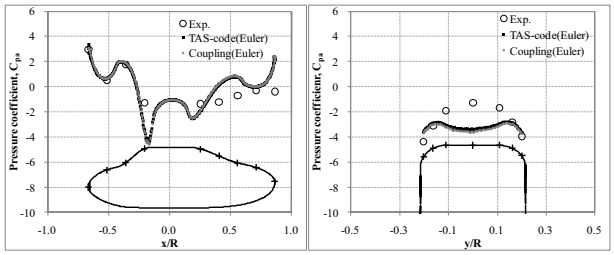

Fig. 4 Comparison of pressure distribution at Center-line and Cross-line

3.2 ONERA M6 wing

The overlapping meshes for the calculation are shown in Fig. 5. There are in total 177,133 nodes in the unstructured mesh and it is constructed with tetrahedral elements. Calculation condition is shown in Table 2. The calculated pressure distributions are compared in Figs. 6 and 7. As shown in Figs. 6 and 7, good agreement between the coupling and TAS-code is obtained. However, at the 80% semi span location, the forward shock predicted by the coupling solver is not as sharp as that of TAS-code. The reason may be that the distribution of nodes in unstructured mesh of the coupling solver is not completely the same as that of TAS-code. The mesh density in unstructured mesh region may be coarser than the other, thus the forward shock is not sharp.

Table 2 Calculation condition of ONERA M6 (Euler)

	TAS-code	Coupling
Mach	0.8395	
A.o.A	3.06[deg.]	
number of points	0.37 M	BCM:7.4 M ＋TAS:0.18 M
computation time	2h (SX-9, Single)	2.5h (SX-9, 16parallel)

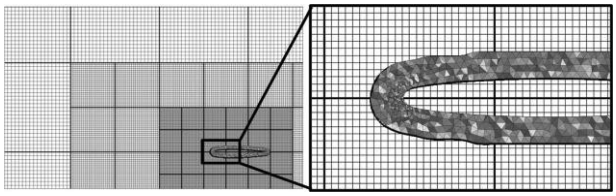

Fig. 5 Computational domains for ONERA M6 Wing

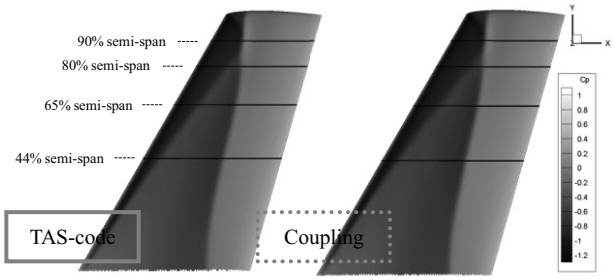

Fig. 6 Comparison of surface pressure distribution on the ONERA M6 wing

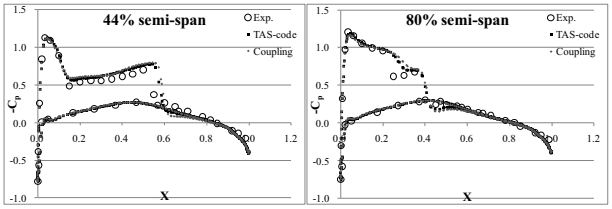

Fig. 7 Comparison of pressure distribution at 44% and 80% semi-span

4. Concluding Remarks

The new Cartesian-mesh based CFD solver combined with unstructured-mesh was developed. JMRTS model and ONERA M6 wing were used for the validation. In both cases, good agreement was obtained between the present coupling solver and TAS-code. In this study, it is proved that the calculation accuracy of the present coupling solver is identical as the existing unstructured mesh solver.

Acknowledgements

This study was supported by research grants from the JAXA, and JSPS KAKENHI (21226018). Computations in this paper were conducted by NEC SX-9 at Cyber Science Center, Tohoku University and JSS, JAXA.

References

[1] Nakahashi, K., and Kim, L. S., AIAA Paper 2004-0423, 2004.

[2] Nakahashi, K., Ito, Y., and Togashi, F., Int. J. for Numerical Methods in Fluids, **43**, pp.769-783, 2003.

[3] Tanabe, Y., Saito, S., Kobiki, N., Murota, K., Sugawara, H., Hayashi K., and Hiraoka, K., 35th European Rotorcraft Forum, Hamburg, Germany, 2009.

[4] Schmitt, V. and F. Charpin, Report of the Fluid Dynamics Panel Working Group 04, AGARD AR 138, May 1979.

[5] Ito, Y. and Nakahashi, K., *International Journal for Numerical Methods in Fluids*, **45**, Issue 1, pp. 79-108, May 2004.

Eighth International Conference on Flow Dynamics
November 9 - November 11, 2011

A Hybrid Scheme for the Near Wall Treatment of Building Cube Method

Xinrong Su, Daisuke Sasaki, Kazuhiro Nakahashi
Department of Aerospace Engineering, Tohoku University, Aoba 6-6-01, Sendai, Japan
su@ad.mech.tohoku.ac.jp

ABSTRACT

In this paper we explore a new hybrid scheme for the near wall treatment of viscous computation with Building Cube Method. Cloud of points are generated to resolve the boundary layer and most of the points are distributed on the one-dimensional lines along the wall normal direction, thus enabling the usage of high order scheme for the wall-normal direction. In the streamwise direction second order least-square method is used. The current method offers opportunity for high order in the normal direction and relives the burden of body-fitted near-wall mesh generation. The current approach is tested with several high Reynolds number cases.

1. Introduction

Computational Fluid Dynamics (CFD) offers the ability to perform high fidelity predictions at relative low cost. While the accurate and fast-turnaround simulation for complex geometry still demands new strategies. The Building Cube Method developed by Nakahashi uses block structured Cartesian mesh to discrete the computational domain. Within this method the large scale mesh for complex geometries can be generated with extremely low cost and fast speed. While the solid walls need special treatments as the mesh lines are in general not aligned with the solid bodies.

For flows with low and moderate Reynolds number, the Immersed Boundary method can be used to impose boundary conditions for the BCM method. While at high Reynolds number, the boundary layer is much thinner and anisotropic, thus the adaption of mesh size to the local boundary layer length scale would results in huge amount of mesh points. Thus with the current limited computation resources, some kind of body-fitted method is needed for the viscous computation. Meakin et al.[1] proposed the concepts of "strand grids" in which the near-wall mesh is generated in a one-dimension fashion and second order finite-volume method is used in the this part. While because of the complex geometry the near-wall mesh is of low quality and may include negative-volume cell. Ishida et al. [2] proposed to use the second order least-square for the near wall treatment.

In the current work, a hybrid method is proposed. For the near wall points located on the one-dimensional lines, high order finite difference type method is used in the wall-normal direction; in the other direction second order least-square is used. In the current method, the degenerated cell problem in the Meakin's method is avoided and also high accuracy can be available at least in the wall-normal direction.

2. Method

First the meshless least-square method will be introduced. As shown in Fig. 1, clouds of supporting points are used to calculate the flow derivative in the governing equation. Take 2D case as example, at point indexed 0, solving the linear least-square problem for any variable f yields the approximation of ∇f

$$\nabla f = \sum_{i=1}^{n} (f_i - f_0)[a_i \quad b_i]^T \tag{1}$$

and in the above equation, coefficients a_i and b_i are only related to the positions of the least-square supporting nodes.

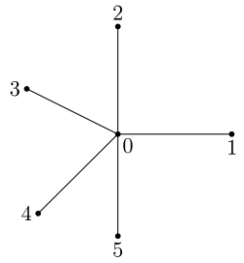

Fig. 1 Cloud of least-square supporting points.

For 2D case the governing equation can be expressed in the form of

$$\frac{\partial U}{\partial t} + \frac{\partial F}{\partial x} + \frac{\partial G}{\partial y} = 0 \tag{2}$$

, with Eq.(1), the spatial residual has the form of

$$\sum_{i=1}^{n} [F_i \quad G_i] \begin{bmatrix} a_i \\ b_i \end{bmatrix} - [F_0 \quad G_0] \sum_{i=1}^{n} \begin{bmatrix} a_i \\ b_i \end{bmatrix} \tag{3}$$

The above least-square method is second order in space. In theory arbitrary order least-square can be used, while higher than second order least-square method is always ill-conditioned and the above equation is hard to be extended to high order accuracy. Suppose a cloud of points are generated to resolve the boundary layer and some points are located on the lines along the wall normal direction, as demonstrated in Fig. 2. Thus we can setup a local coordinate system (n,s) in which the axis n is the unit direction to generate the points and is approximately perpendicular to the solid surface. The remaining axis is along the streamwise direction. With

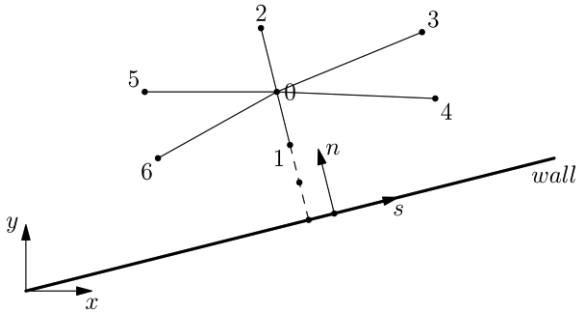

Fig. 2 Cloud of supporting points for the hybrid method.

coordinate transformation, the governing equation in Eq.(2) can be transformed into the local system (n,s) in the form of

$$\frac{\partial U}{\partial t}+\frac{\partial\left(Fn_x+Gn_y\right)}{\partial n}+\frac{\partial\left(Fs_x+Gs_y\right)}{\partial s}=0 \qquad (4)$$

For high Reynolds number flow, the flow near the solid wall is highly anisotropic and there are large gradients in the wall-normal direction. The current idea is to use high accuracy scheme to resolve the wall-normal direction. As a result the wall-normal direction falls into a purely one-dimensional problem and numbers of highly accurate algorithms are available. Currently third order and fifth order accurate WENO scheme are available to calculate $\partial/\partial n$ term in Eq. (4). In the streamwise direction second order least-square method is used to discrete the $\partial/\partial s$ term in Eq. (4).

Now we have to introduce how the near-wall points are generated. Points along the one-dimensional lines perpendicular to the solid wall are used to cover the near wall region. The information needed to generate these points are the local wall normal and the 1D spacing function that fits the requirement of accurate boundary layer capturing. For cases with convex and concave structures, scattered points are used to resolve the local geometry instead of 1D lines. In the current work the advancing front method proposed by Löhner and Onate [3] is used to generate these meshless points. Thus the current method relives the burden of near wall mesh generation and also provides the opportunity of high order accuracy, at least in the wall-normal direction.

In the off-body part the flow region is resolved by block structured Cartesian mesh. Both the near-wall part and the off-wall part are solved with the implicit LU-SGS solver. Currently the Spalart-Allmaras one-equation turbulence model is used.

3. Results and Discussion

A series of test cases are used to validate the current method and two of them will be given in the manuscript.

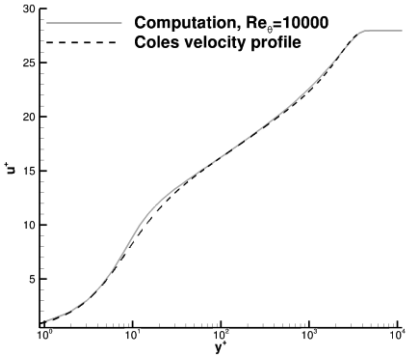

Fig. 3 Comparison of the computed velocity profile with the Coles' mean velocity profile.

The first test case is the turbulent flat plate with Reynolds number of 5M. One dimensional positioned points are used to resolve the boundary layer. The distribution of these points will be omitted here and will be given in the presentation. To assess the accuracy of the current method, the dimensionless velocity profile at the position with momentum thickness based Reynolds number of 10000 are compared with the Coles' mean velocity profile, as given in Fig. 3. The current result agrees well with the Coles' velocity profile throughout the boundary layer and is proven to be accurate.

The second test case is the 30P-30N three elements airfoil. In this case the one dimensional points are used to resolve the boundary layer and the method developed by Löhner and Onate is needed to generate points to fill in the concave and concave regions, as shown in Fig. 4.

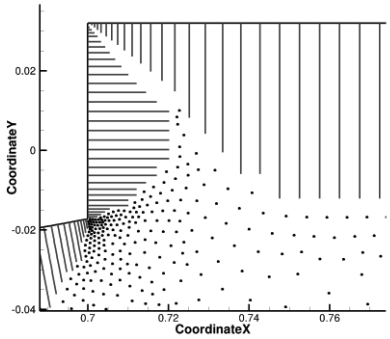

Fig. 4 Near wall points for the 30P-30N case.

The computed Mach number distribution is given in Fig. 5 and more results will be given in the presentation.

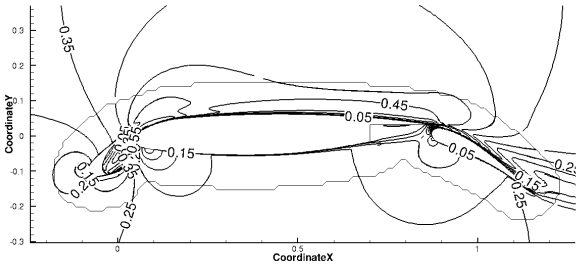

Fig. 5 Computed Mach number distribution.

4. Concluding remarks

In the current work a hybrid method is developed for the near-wall treatment of the BCM applied to high Reynolds number flow. 1D spaced points are used to resolve the boundary layer and high accuracy scheme can be used in one dimensional fashion to resolve the wall-normal direction. For the streamwise direction second order least-square is used. Compared with the body-fitted mesh method, in the current approach points instead of mesh cells has to be generated, thus the burden of near-wall mesh generation has been relived. Also in the wall-normal direction the current method offers the opportunity of using high accuracy scheme. Several test cases are used to test the current method and the results are discussed.

Acknowledgement

This work was supported by JSPS KAKENHI (21226018).

References

[1] R. L. Meakin, A. M. Wissink, W. M. Chan, et al., AIAA Paper 2007-3834, 2007

[2] T. Ishida, S. Kawai, K. Nakahashi, AIAA Paper 2011-1296, 2011.

[3] R. Löhner, E. Onate, Commun. Numer. Meth. Enging, **14** (1998), 1097-1108.

OS2: Advanced Control of Smart Fluids and Fluid Flows

Eighth International Conference on Flow Dynamics
November 9 - November 11, 2011

Controlling The Viscosity Of Liquid Suspensions By Electromagnetic Fields

Rongjia Tao
Department of Physics, Temple University, Philadelphia, PA 19122, USA
rtao@temple.edu

ABSTRACT

Controlling the viscosity of liquid suspensions is important in science and technology. Currently changing temperature is the leading method to control the fluid's viscosity, inefficient, slow and taking too much energy. Here we show that the viscosity of liquid suspensions can be controlled by either electric or magnetic field, which forces the particles to form many chains along the field direction. When the field is parallel to the flow direction, the viscosity is reduced. When the field is perpendicular to the flow direction and along the shearing direction, the viscosity is increased. The technology will have many important applications.

1. Introduction

Viscosity of liquid suspensions is of great importance in all areas of science and engineering. Controlling their viscosity is vital. In some cases, such as clutches and vibration dampers, we need to increase the working fluid's viscosity to make the device more efficient.. Electrorheological (ER) and magentorheological (MR) fluids are such suspensions, where we use, electric or magnetic field to increase the viscosity [1]. In many other cases, we need to lower the viscosity. For example, reducing blood viscosity improves circulation and prevents cardiovascular events [2]. Lowering the viscosity of crude oil is the key to transporting offshore oil via undersea pipelines [3,4].

Currently, changing temperature is the leading method to control the fluid's viscosity. Especially we often raise the fluid's temperature to reduce its viscosity. For example, to transport crude oil from Alaska to California, every ten miles there is one heating station, which raises the temperature of crude oil inside the pipeline. The purpose is to reduce the viscosity of crude oil, so that the flow rate of crude oil inside the pipeline will not be reduced. Also in some other cases, we lower the temperature to increase the fluid's viscosity.

However, changing temperature to control fluid's viscosity is not efficient. It takes much energy and is quite slow. Especially, in many occasions, such as blood inside a body, we cannot change the temperature to control its viscosity. Therefore, a more effective method to control the fluid's viscosity is needed.

Here we present a theory and experimental results showing that we can control viscosity of liquid suspension by breaking the symmetry with suitable electric or magnetic field.

2. Method

Einstein first studied a dilute liquid suspension of non-interacting uniform spheres in a base liquid of viscosity η_0 [5].The apparent viscosity η was found,

$$\eta = \eta_0(1+2.5\phi), \qquad (1)$$

for the volume fraction of the spheres $\phi < 0.01$. For high ϕ, we must consider the maximum volume fraction, ϕ_m, available for adding particles. A face-centered cubic (fcc) lattice and a close packed hexagonal lattice of uniform spheres provides the ideal maximum packing 0.74. For liquid suspensions, ϕ_m is about 0.64, smaller than 0.74, since it is a random packing. Following the idea of Mooney [6], let us consider adding $d\phi$ volume fraction of spheres to a liquid suspension of volume fraction ϕ. Since the net available volume fraction to add spheres is only $1-\phi/\phi_m$, the increase of viscosity would be

$$d\eta/\eta = 2.5d\phi/(1-\phi/\phi_m). \qquad (2)$$

Integrating the above equation gives us an expression to estimate the viscosity at high ϕ

$$\eta/\eta_0 = (1-\phi/\phi_m)^{-2.5\phi_m} \qquad (3)$$

Krieger-Dougherty [7] introduced the intrinsic viscosity, $[\eta]$,

$$\eta/\eta_0 = (1-\phi/\phi_m)^{-[\eta]\phi_m}, \qquad (4)$$

which enables us to estimate the viscosity for particles of any shape by choosing a suitable $[\eta]$

When ϕ and temperature are unchanged, the effective way to change the viscosity is through changing of $[\eta]$. When $[\eta]$ is increased, the viscosity will be significantly enhanced. When $[\eta]$ is decreased, the viscosity will be substantially reduced.

We can achieve such goal with electric field or magnetic field [2-4]. Here we discuss the magnetic field, but the same physics applies to the case of electric field. We assume that the magnetic permeability μ_p of the particles is different from μ_f of the base liquid. In a magnetic field, the particles are polarized along the field direction. If the particles are uniform spheres of radius *a,* the dipole moment is given by

$$\vec{m} = \vec{H}a^3(\mu_p - \mu_f)/(\mu_p + 2\mu_f), \qquad (5)$$

where $\vec{H}$ is the magnetic field acting on the sphere. The interaction between two induced magnetic dipoles takes

$$U = \mu_f m^2(1-3\cos^2\theta)/r^3, \qquad (6)$$

where *r* is their distance and θ is the angle between the field and the line joining the two dipoles. If this

interaction is strong enough to overcome the Brownian motion, the particles aggregate and align in the field direction.

Once the particles form chains along the field direction, the symmetry is breaking. Under such a condition, similar to flow of nematic liquid crystal with its molecule alignment in one direction, the viscosity is no longer isotropic.

As shown in Figures.1-3, the flow velocity is along the x-direction, but varies along the y-direction. If the applied magnetic field is also along the x-direction, then the induced chains is parallel to the flow direction, the viscosity is reduced, becoming the lowest (Fig.1).

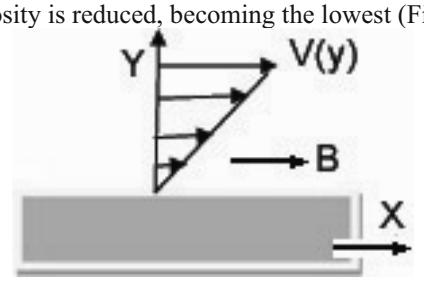

Fig.1. When the fluid flow direction is the same as the field direction, the viscosity is reduced, becoming the lowest.

If the magnetic field is along the y-direction, the induced chains are perpendicular to the flow direction, the viscosity will be increased, becoming the largest (Fig.2).

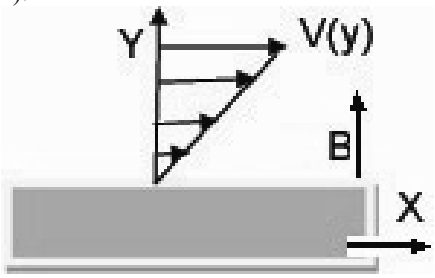

Fig.2 When the field is along the y-direction, the viscosity will be increased, becoming the largest.

If the magnetic field is along the z direction, the viscosity will be higher than the situation in Fig.1, but lower than the situation in Fig.2.

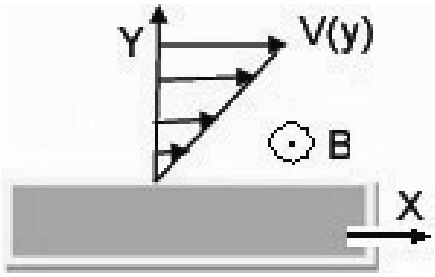

Fig.3. When the applied field is along the z-direction, the viscosity will be intermediate.

Based on the above physical mechanism, we can control the viscosity of liquid suspensions, either reducing it or increasing it with application of electric or magnetic field.

3. Results and Discussion

To increase the viscosity, we need to produce chains perpendicular to the flow direction, but along the shearing direction. In this way, the chains are blocking the flow, as shown in Figure 4. This is a well-known phenomenon in ER and MR fluids.

Fig. 4. The induced chains block the flow and make the apparent viscosity increased.

We can control the chain size by selecting the field strength and application duration. In most applications of ER and MR fluids, the applied field should be very strong and keep on ,so that the fluids become solid. When we do not need such high viscosity, we can apply weak field and keep the field for a short duration. Then the viscosity will be increased, but not as strong as a solid.

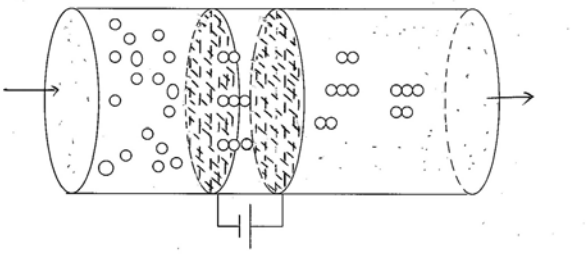

Fig.5 As the flow passes a strong local electric field, the suspended particles aggregate along the field direction, and the viscosity is reduced.

As shown in Fig.5, the suspension flows from left to right. Initially at the left, the viscosity is high. When the fuel passes a strong local field, the suspended particles are polarized and the induced dipolar interaction forces the particles to aggregate into short chains. The viscosity is significantly reduced.

The technology developed is expected to have many important applications.

References

[1].T. Murakami & M. Nakano, J. of Intelligent Materials Systems and Structure, **22** (2011), 327

[2] R. Tao & K. Huang, Physical Review E, **84** (2011), 011905.

[3] R. Tao R. and X. Xu, Energy & Fuels, **20** (2006), 2046.

[4] R. Tao, J. of Intelligent Material Systems and Structure (in press).

[5] A. Einstein, Ann. Physik **17** (1905), 549; **19** (1906) 289; **19** (1909) 371.

[6]. M. Mooney, J. of Colloid Sci., 6 (1951), 162.

[7] I. M. Krieger & T. J. Dougherty, *Tans. Soc. Rheol*. **3** (1959), 137.

Eighth International Conference on Flow Dynamics
November 9 - November 11, 2011

Transport of Magnetic Nanoparticles: Fundamentals and Applications

Ishwar K. Puri
Department of Engineering Science and Mechanics, Virginia Tech, Blacksburg VA 24060, USA
ikpuri@vt.edi

ABSTRACT

Single domain nanoparticles of iron oxides ranging 5-15 nm in diameter can be coated with a surfactant layer and suspended in a nonmagnetic liquid carrier. The suspension, a ferrofluid, exhibits magnetic behavior when an external magnetic field is imposed. The nanoparticles can be embedded within solid materials, e.g., inside 1-2 μm size polystyrene microspheres. The transport of both ferrofluids and magnetic microspheres can be controlled using suitable guiding magnetic fields. A combination of (bio)chemical functionalization and "action-at-a-distance" using a magnetic field has considerable potential for MEMS and NEMS devices

1. Introduction

Single domain nanoparticles of iron oxides ranging 5-15 nm in diameter behave as superparamagnetic materials. These particles can be coated with an adsorbed surfactant layer and be stably suspended in a nonmagnetic liquid carrier. The resulting suspension, called a ferrofluid, exhibits magnetic behavior when an external magnetic field is imposed, which aligns the thermally disoriented magnetic moments of these particles. The nanoparticles can also be embedded within solid materials, e.g., inside 1-2 μ m size polystyrene microspheres, so that the beads respond to magnetic fields. The transport of both ferrofluids and magnetic microspheres (containing superparamagnetic nanoparticles) can be controlled using suitable guiding magnetic fields. The nanoparticles or microspheres can be functionalized with chemical substances and bioconjugates to accomplish specific tasks. This combination of the (bio)chemical functionalization and the "action-at-a-distance" using the magnetic field has considerable potential for applications of superparamagnetic nanoparticles in MEMS and NEMS devices (Ganguly and Puri, 2010).

Flowfields established with ferrofluids can be altered by applying external magnetic fields to realize enhanced heat transfer, controlled mass transfer or field-assisted self organizations and assemblies that form three dimensional structures, from the nano- to the mesoscale. Magnetic microspheres can be advantageously used as "mobile substrates" for microscale bio-assays or in vivo applications. This talk provides an insight into the magnetic behavior of the nanoparticles and the transport phenomena associated with ferrofluids and magnetic microspheres.

The controlled transport of fluids and fluid-borne solids in microfluidic environments is generally produced using many imposed influences, e.g., inertial, viscous, surface tension, electrostatic, magnetic, chemical, or molecular interactions. Magnetic particles overcome a major challenge for lab-on-a-chip devices since these can be influenced by "action at a distance". The ability to manipulate these particles from a distance frees space on microfluidic platforms for other purposes.

The magnetic force that such particles experience is generally insensitive to the biochemical environment and other physical forces that are otherwise important at the microscale, e.g., electrostatic, surface tension, Brownian or van der Waals forces.

2. Method

Magnetic fields are produced due to free $\mathbf{J_f}$ and bound $\mathbf{J_b}$ electric currents. A static magnetic field obeys the Maxwell's equations of magnetostatics (Griffiths 2004),

$$\nabla \times \mathbf{H} = \mathbf{J_f}, \nabla \times \mathbf{M} = \mathbf{J_b}, \nabla \times \mathbf{B} = (1/\mu_0)\,\mathbf{J}, \text{ and}$$
$$\nabla \cdot \mathbf{B} = 0, \qquad (1)$$

where $\mathbf{H}$ is produced due to a free current, $\mathbf{M}$ represents the magnetization of the material, and $\mathbf{J} = \mathbf{J_f} + \mathbf{J_b}$. The magnetization is a property of the material and also a function of the imposed $\mathbf{H}$. Materials for magnetic particles used in microfluidics are usually ferrimagnetic and ferromagnetic that have large magnetization and hysteresis (Spaldin 2006). A magnetic material placed in a nonuniform magnetic field experiences a volumetric Kelvin body force (KBF) (Zahn 1979),

$$\mathbf{f} = \mu_0(\mathbf{M}\cdot\nabla)\mathbf{H} + \nabla(\tfrac{1}{2}\,\mu_0\,\mathbf{M}\cdot\mathbf{M}). \qquad (2)$$

Hence, the bulk of a magnetic material is attracted towards the region with a stronger magnetic field. The total force on a finite size magnetizable body is the volumetric integral of the KBF,

$$\mathbf{F} = \iiint \left[\mu_0 \left(\mathbf{M}\cdot\nabla\right)\mathbf{H} + \nabla\left(\tfrac{1}{2}\mu_0\mathbf{M}\cdot\mathbf{M}\right)\right] \mathrm{d}\vartheta, \qquad (3)$$

where $\mathrm{d}\vartheta$ is a differential volume element. Using the corollary of the Gauss divergence theorem, $\iiint \nabla\left(\tfrac{1}{2}\mu_0\mathbf{M}\cdot\mathbf{M}\right)d\vartheta = \tfrac{1}{2}\mu_0 \oiint \left(\mathbf{M}\cdot\mathbf{M}\right)\hat{\mathrm{n}}ds$, where $\hat{\mathrm{n}}\mathrm{d}s$ is a differential area vector on the control surface. This vanishes for a finite magnetic body immersed in a nonmagnetic medium and,

$$\mathbf{F} = \mu_0 \iiint \left(\mathbf{M}\cdot\nabla\right)\mathbf{H}\mathrm{d}\vartheta. \qquad (4)$$

3. Results and Discussion

In a microfluidic medium, a stable colloidal ferrofluid can be treated as a continuum fluid (Cowley and Rosensweig 1967, Ganguly et al. 2004a,b), a self-assembled aggregate (Ganguly et al. 2005), or can be dispersed as a suspension of finely divided droplets in a background liquid (Banerjee et al. 1999). Such a ferrofluid suspension can also be mathematically treated through a continuum approach since the size of the dispersed nanoparticles is comparable to the molecular

mean free path of the carrier liquid.

The hydrodynamic equations describing the mass, momentum, and species equations for the ferrofluid in another medium are, respectively (Ganguly and Puri, 2010),

$$\partial\rho/\partial t + \partial(\rho v_j)/\partial x_j = 0, \quad (5)$$

$$\partial(\rho v_i)/\partial t + \partial(\rho v_j v_i)/\partial x_j = -\partial p/\partial x_i + \partial \tau_{ij}/\partial x_j + f_i, \text{ and} \quad (6)$$

$$\partial(\rho Y_f)/\partial t + \partial[\rho v_j Y_f - \rho D \cdot \partial Y_f/\partial x_j + 1/(6\pi\eta a_{np}) \cdot \rho Y_f f_j]/\partial x_j = 0, \quad (7)$$

Here, ρ denotes fluid density, v_i the velocity, p the pressure, D the ferrofluid diffusivity, and Y_f the ferrofluid mass fraction. The viscous stress tensor τ_{ij} in the momentum equation is expressed in terms of the fluid viscosity η and velocity gradient, i.e.,

$$\tau_{ij} = \eta(\partial v_i/\partial x_j + \partial v_j/\partial x_i) - (2/3)\ \eta\delta_{ij}(\partial v_k/\partial x_k), \quad (8)$$

where δ_{ij} denotes the Kronecker delta. The last term in the momentum equation contains the KBF expressed per unit volume $f_i = M_j(\partial B_j/\partial x_i)$ as explained in Eq. (4). The mass fraction Y_f of nanoparticles in the host fluid and the particle volume fraction φ are related through the relation $\varphi = \rho^{-1} Y_f/[\rho^p - (\rho^p - \rho^{-1})Y_f]$, where ρ^p and ρ^{-1} denote the densities of the particles and the host liquid respectively, and the local fluid density ρ is related to the local volumetric fraction of the nanoparticles through the expression $\rho = (\rho^p - \rho^{-1})\varphi + \rho^{-1})$. For a dilute ferrofluid, the diffusivity D of the magnetic nanoparticles of radius a_n is obtained from the Stokes-Einstein equation, $D = k_B T/6\pi\eta a_n$. The last term in the species equation (Eq. 7) represents magnetophoretic motion, which arises from the Stokesian migration of superparamagnetic nanoparticles under the magnetic force $f_j = \mu_0 m^p{}_k \partial H_j/\partial x_k$. Here, $m^p{}_k$ denotes the component of the particle magnetic moment vector along x_k axis.

The dynamic interactions of the gravity, surface tension and viscous forces with the KBF in ferrofluids give rise to several interesting hydrodynamic actuations and field-induced self-assembly behaviors, which can be used for a range of novel microfluidic applications.

For larger particles, An isolated magnetic microsphere suspended in a nonmagnetic fluid under an imposed magnetic field gradient experiences a magnetic force $\mathbf{F}_m$, a drag force $\mathbf{F}_d = K_{wall} 6\pi a\eta\left(\mathbf{V} - \mathbf{V}_p\right)$ that is exerted by the fluid since the particle tends to move with a finite slip velocity relative to the fluid, a gravitational force (including the effect of buoyancy) $\mathbf{F}_g = \left(\frac{4}{3}\pi a^3\right)\left(\rho_p - \rho_l\right)\mathbf{g}$, and a Brownian force $\mathbf{F_B}$. Here, ρ_p and ρ_l denote the densities of the particle and the carrier fluid, g the acceleration due to gravity, and $\mathbf{V}_p$ and $\mathbf{V}_l$ the absolute velocities of the particle and the carrier fluid, respectively. The motion of a particle under these forces is described by applying Newton's second law of motion, i.e.,

$$\left(\frac{4}{3}\pi a^3 \rho_p\right) d\mathbf{V}_p \Big/ dt = \left[\mathbf{F}_m + \mathbf{F}_d + \mathbf{F}_g + \mathbf{F}_B\right]. \quad (9)$$

4. Concluding remarks

Several challenges must be overcome to integrate magnetic nano- and microparticles in microfluidic devices, such as particle agglomeration that alters magnetophoretic mobility and induces gravitational settling. Agglomeration also diminishes the binding sites available on particles, impeding surface (bio)chemical reactions. Clogging of microfluidic channels is another challenge. Colloidal stability of ferrofluids is another issue. Surfactants improve particle stability but induce creeping along a microchannel making it dirty. The use of magnetic particles is at a proof-of-concept stage due to these practical challenges. Future research should better characterize particle transport in microfluidic environments, improve material properties and surface functionalization, and particle response to the environment (Ganguly and Puri, 2010).

References

Banerjee, S., M. Fasnacht, S. Garoff, and M. Widom. 1999. Elongation of confined ferrofluid droplets under applied fields. *Phys. Rev. E* 60: 4272-4279.

Cowley, M.D., and R.E. Rosensweig. 1967. The interfacial stability of a ferromagnetic fluid. J. Fluid Mech. 30(4):671−688.

Ganguly, R., S. Sen, and I.K. Puri. 2004a. Heat transfer augmentation in a channel with a magnetic fluid under the influence of a line-dipole. *J. Magn. Magn. Mater.* 271:63−73.

Ganguly, R., S. Sen, and I.K. Puri. 2004b. Thermomagnetic convection in a square enclosure using a line dipole. *Phys .Fluids*. 16:2228−2236.

Ganguly, R., A.P. Gaind, and I.K. Puri. 2005. A strategy for the assembly of 3-d mesoscopic structures using a ferrofluid. *Phys. Fluids* 17: 057103.

Ganguly, R. and I. K. Puri. 2010. Microfluidic Transport in Magnetic MEMS and BioMEMS. *WIREs Nanomedicine & Nanobiotechnology*, 2:382-399.

Spaldin, N.A. 2006. *Magnetic Materials: Fundamentals and device applications*. Cambridge: Cambridge University Press.

Zahn, M. 1979. Introduction to Electromagnetic Field Theory: a Problem Solving Approach, New York, John Willey and Sons, Inc. Chapter 5, p. 369.

Physical Modeling of the Electromechanical Behavior of unfilled Polymers

Jean-Yves Cavaillé
MATEIS, INSA-Lyon, UMR CNRS 5510
ELyT lab, Lyon-Tohoku joint laboratory
Villeurbanne, 69100, France
jean-yves.cavaille@insa-lyon.fr

ABSTRACT

Some polymers exhibit very high electromechanical activity, and there is a lack of physical understanding of the mechanisms at the origin of this behavior. In this work, it is believed that both heterogeneities of local stiffness and dielectric constants allowed by a phase separation at the scale of few nanometers are responsible for this unexpected behavior in heterogeneous polymers such as polyurethanes.

1. Introduction

Polymers are more and more used to design actuators based on electromechanical coupling. Most of devices are in fact capacitors consisting in 2 electrodes separated by a soft polymer (elastomer). Basically, 3 main mechanisms are considered, namely (i) electrostatic compressive stress due to the applied voltage on the electrodes, (2) intrinsic deformation of the polymer induced by the electric field and (3) forces due the interaction of the applied electric field on free electrical charges inside the polymer.

The first one is known as the Maxwell effect [1], and the strain S is a quadratic function of the electric field, E, such as :

$$S_M = M_M E^2, \text{ avec } M_M = \frac{\varepsilon_0 \varepsilon}{Y} \qquad 1$$

where ε_0 refers as to the vacuum permittivity, ε, to the average dielectric constant of the material, Y its average Young modulus. M_M is the Maxwell electromechanical coefficient.

The forces due to the free electrical charges is proportional to their density and to E. It can be neglected in pure non ionic polymers. Finally, the intrinsic mechanism, which will be called here after "electrostriction" is often described by an empirical relationship linear with E^2 [2]. This effect can be much stronger, i.e. by 2 to 3 orders of magnitude that the Maxwell effect, especially in polar heterogeneous polymers. It is always reported as a compressive effect. Up to now, no physical description of this effect has been proposed in the literature.

2. Physical Mechanisms Involving Dipole – Electric Field Interaction

In recent work devoted to magneto-mechanical coupling [3], it was shown that magnetic particles randomly dispersed within a soft polymeric matrix were responsible for the extension of the composite material along the applied magnetic field H. In this study, the iron particles were magnetically polarized by the applied field, and the strain S was shown to varies with H^2. This situation should be similar to a homogeneous (i.e. amorphous) polar polymer, in which dipoles are randomly dispersed. This effect has been evaluated for a polyurethane (PU) and was shown to lead to an extension of the material, but with a very weak efficiency [4].

In fact, in heterogeneous materials like some polyurethanes which are block copolymers, the phase separation (enhanced by the very weak entropy of mixing polymers) leads to the formation of rigid domains with a high dielectric constant dispersed within an almost non polar matrix with a low stiffness, at room temperature, as shown in Fig.1:

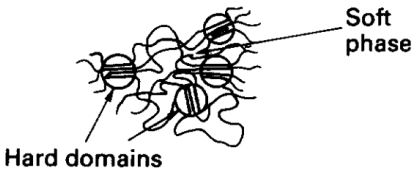

Fig.1: schematic representation of block-copolymers microstructure after phase separation (from [5])

As it is well known, a dipole $\vec{p}$ in a homogeneous electric field $\vec{E}$ is submitted to a torque but to zero force. In a field gradient, the force can be written as:

$$f = \vec{p} \cdot \frac{d\vec{E}}{dz} \qquad 2$$

where z is a direction chosen here parallel to $\vec{E}$.

On the other hand, the polarization of dipoles $\vec{p}$, or their orientation parallel to the field leads to a macroscopic electric displacement $\vec{D}$ such as:

$$\vec{D} = \varepsilon_0 \vec{E} + \vec{P} = \varepsilon_0 (1 - \chi)\vec{E} = \varepsilon_0 \varepsilon \vec{E} \qquad 3$$

where P is the polarization density and χ the susceptibility of the material, so that, along z :

$$P = \varepsilon_0 (\varepsilon - 1) E = \alpha E \qquad 4$$

If we consider a lamellar material (see Fig.2) perpendicular to $\vec{E}$, with 2 different dielectric constants, ε_1 and ε_2, the field gradient leads to internal stresses.

As a rough approximation, it comes that:

$$\varepsilon_1 E_1 = \varepsilon_2 E_2 \qquad 5$$

and:

$$\left| \overrightarrow{grad} E \right|_z = \frac{dE}{dz} \approx \frac{E_1 - E_2}{a/2} = \frac{2\Delta E}{a} \qquad 6$$

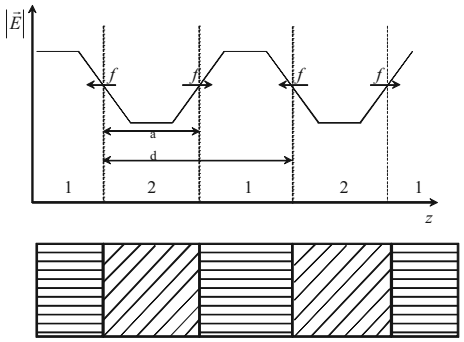

Fig.1: Schematic representation of a lamellar material made of domains with different dielectric constants. The curve represents the electric field variation and *f,* the resulting forces applied on the inside the material. *d* is the long period of the lamellar material, and *a* the thickness of type (2) lamellas.

Near the interface between two domains (i.e. over a distance of about *a*/2), the total force *F* applied per surface unit, can be written as (for $\varepsilon_2 \gg \varepsilon_1$):

$$F = \sum f = \varepsilon_0 \varepsilon_2 E \frac{a}{2} \frac{dE}{dz} \approx \varepsilon_0 \varepsilon_2 E \Delta E \qquad 7$$

As it is shown, forces are compression in the domains with low ε (i.e., of type (1)) and are tension in domains of type (2). The macroscopic strain *S* is thus:

$$S = F\left(\frac{1-\delta}{Y_1} - \frac{\delta}{Y_2}\right) = \varepsilon_0 \varepsilon_2 E \Delta E \left(\frac{1-\delta}{Y_1} - \frac{\delta}{Y_2}\right) \qquad 8$$

where δ is the volume fraction of the stiff PU segments (δ=*a*/*d* in Fig.2)

For polymers like PUs, it is easy to fill in the following two conditions, $\varepsilon_2 \gg \varepsilon_1$ (which in turn leads to $E_1 \gg E_2$ and $\Delta E \approx E_1 \approx E$) and $Y_2 \gg Y_1$. Thus:

$$S = \frac{\varepsilon_0 \varepsilon_2 (1-\delta)}{Y_1} E^2 \qquad 9$$

and the electrostriction coefficient is:

$$M_E = \frac{\varepsilon_0 \varepsilon_2 (1-\delta)}{Y_1} \qquad 10$$

In fact, such polymers are normally not lamellar but more often consist in soft matrix with dispersed stiff polar domains, as it is schematically recalled in Fig.1.

On the other hand, field lines are "concentrated"[6] within the polar spherical particles, and at their surface, E_1 becomes φE_1 with $\varphi \approx 3$ (and may be even higher for ellipsoids for instance).

Thus the total electromechanical coupling effect is described by:

$$M_{cal} = M_E + M_M = \frac{\varepsilon_0 \varepsilon}{Y} + \varphi \frac{\varepsilon_0 \varepsilon_2 (1-\delta)}{Y_1} \qquad 11$$

3. Results and Discussion

At this point, it is of importance to compare the 2 terms of eq.11, as they look rather similar. The difficult point is the evaluation of the soft domains stiffness. In fact, the macroscopic Young modulus of such polymers results from two main effects, namely (i) the reinforcement of the soft matrix by dispersed stiff domains, and (ii) the crosslinking of chains by the stiff domains, if temperature in use is higher than the glass transition temperature T_g of soft domains and lower than T_g of stiff domains.

However, with the following data, considering a classical commercial PU [2] (Estane 58888 NAT 021, purchased from Lubrizol Corporation): Y_1=1 MPa ; Y=30 MPa ; ε_2=40 [7] ; ε=5 ; δ=0,5 ; φ=3, it comes:

$$\frac{M_E}{M_M} = \varphi \frac{\varepsilon_2}{\varepsilon} \frac{Y}{Y_1} (1-\delta) \approx 400 \qquad 12$$

with $M_M = 1.6\ 10^{-18}$ and $M_E = 6\ 10^{-16}$.

It appears clearly that for this kind of polymers, the main driving force at the origin of the electromechanical activity of dielectric actuators plays a negligible role in heterogeneous polar polymers.

However, the predicted value for M_E appears to be too small, compared to experimental data (found [2] at 3.10^{-15} m^2V^{-2}). As discussed above, this may come from the overestimated value for the soft phase stiffness. As the average distance between stiff domains is in the order of 10 nm [8], it means that the average distance between stiff domain surfaces is about 2 nm for δ=0.5. At this scale, soft segments may present an apparent Young modulus much lower than 1MPa (in fact the rubber modulus of polymers lays from 0.1 MPa to 10 MPa depending on their chemistry [9]).

4. Concluding remarks

This very simple model helps to understand the high electromechanical coupling activity exhibited by heterogeneous polar polymers like some polyurethanes. It is clear that heterogeneities of both mechanical stiffness and dielectric constants are the key points of this activity. More details will be given soon [10].

References

[1] R. Pelvine and R. Kornbluh in "Dielectric Elastomers as Electromechanical Transducers", ed. by F. Carpi, D. de Rossi, R. Kornbluh, R. Pelrine, P. Sommer-Larsen Elseviers, New York, 2008.
[2] K. Wongtimnoi, B. Guiffard, A. Bogner-Van de Moortele, L. Seveyrat, C. Gauthier, J.Y. Cavaillé, *Comp Sci Tech* **71**(2011) 885-892
[3] G. Diguet E. Beaugnon.; J.Y. Cavaille, *J. Magnet Magnet Mat*, **321**(2009) 396-401
[4] T. Le Gall, master thesis (2011) INSA-Lyon, France
[5] Z. S. Petrovic and J. Ferguson, *Prog. Polym. Sci*., **16** (1991) 695-836
[6] J. A. Stratton, "Electromagnetic theory", Wiley-IEEE, 2007
[7] https://dow-answer.custhelp.com/app/answers/detail/a_id/5142/kw/Dielectric%20constant%20MDI
[8] K. Wongtimnoi, PhD thesis (2011), INSA-Lyon, France
[9] John D. Ferry, Viscoelastic Properties of Polymers 3rd ed. (1980), John Wiley & Sons Inc
[10] J.Y. Cavaillé, to be published

Eighth International Conference on Flow Dynamics
November 9 - November 11, 2011

Electrorotation of Novel Electroactive Polymers in Uniform DC and AC Electric Field

Miklós ZRÍNYI[1], Masami NAKANO[2] and Teppei TSUJITA[2]
[1]Semmelweis University, Department of Biophysics and Radiation Biology
H-1089 Budapest, Nagyvarad ter 4, HUNGARY,

[2]Intelligent Fluid Control Laboratory
Institute of Fluid Science
Tohoku University
2-1-1 Katahira, Aoba-ku, Sendai, 980-8577, JAPAN

mikloszrinyi@gmail.com

ABSTRACT

Small non-conducting objects dispersed in liquid dielectrics and subjected to homogeneous DC electric field exceeding some threshold value exhibit spontaneous rotation, called Quincke rotation. We have studied the angular motion of polymer disks around to an axis that perpendicular to the direction of applied electric field and have concluded that dynamics of the polymer rotor is very complex. It was found that angular deformation can also be induced by low frequency AC fields. Controllable rotation of small rotors is of relevance for a range of practical applications, for example in micro-motors or in microfluidics.

1. Introduction

Recent trend in science and technologies is in direction of micro- and nano dimension due to their extraordinary properties. In order to construct a novel type of micro-motors, we have intended to exploit Quincke rotation phenomenon. In 1896 G. Quincke observed that some solid particles can spontaneously rotate in certain media if a large uniform electric field is applied [1-7]. The rotational axis is always perpendicular to the electrostatic field. The phenomenon exhibits a threshold value of the electric field and occurs only if certain conditions concerning to the conductivity and permittivity of the particles and of the liquid are satisfied [1-7]. Due to these special criteria of material characteristics, it is not easy to observe the phenomenon. Only a limited number of experimental studies are available. If a semi-insulating sphere is immersed in a dielectric liquid and a uniform electrostatic field is applied, the appearance of a non-zero electric torque tends to accelerate any initial rotation. There is threshold electric field strength E_{cr} at which the solid particles begin to rotate. E_{cr} is independent of the size of the dispersed particle and depends on the electric properties of particles and the medium. The angular velocity, ω as a function of the applied field, E can be expressed as [1,8]:

$$\omega(E) = \pm \frac{1}{\tau_{MW}} \sqrt{\frac{E^2}{E_{cr}^2} - 1} \qquad E > E_{cr} \qquad (1)$$

where τ_{MW} is the Maxwell-Wagner interfacial polarization relaxation time.

In Eq.1 the $\pm$ sign takes into account the two possible directions of rotation. Since τ_{MW} does not depend on the particle size, Eq.1 predicts that the angular velocity of rotating particles is independent of the particle dimension.

2. Methods

We have studied the electrorotation of orthorhombic FeO(OH) particles as well as polymer disks loaded by these particles. The angular frequency, ω as a function of particle size as well as electric field intensity was measured. We have found that despite the theoretical prediction, the angular velocity strongly depends on the particle size. The rotation speed is higher for smaller particles than for larger particles.

3. Results and discussion

With increasing electric field intensity, the angular frequency of rotation increases. We have studied the angular motion of our composite disks and have concluded that dynamics of the rotor is very complex. If the strength of static DC field is accounted for, three regimes have been observed:

- Below a threshold value, E_{cr} of the electric field, the disk does not show any motion.
- At the threshold value and slightly above, the disk begin to rotate, but the angular displacement is less than 2π .
- At DC field intensities much higher than the threshold value, continuous rotation was observed. The angular frequency was found to be dependent on the square of $(E - E_{cr})$

The observed angular displacement was found to be either in clockwise or counter-clockwise direction. We have found that electrorotaion of polymer disk occur in AC field if the frequency is very low (f<1.5 Hz).

We have studied the effect the nature of polymers, filler particles as well as the dielectric liquids on the electro-rotation. We were able to achieve Quincke rotation by using pure epoxy based polymer, fabricated by photochemical method. The rotating disk acts like micro sized motors with tunable angular frequency.

Conclusion

We have presented the first experimental demonstration of the development of novel electroactive polymer and polymer composites which perform rotation in uniform DC and AC electric field. Controllable rotation of small rotors is of relevance for a range of practical applications, for example in micro-motors or in microfluidics.

Acknowledgements

This research was performed under the Collaborative Research Project of Institute of Fluid Science, Tohoku University and in the frame of Cooperation Agreement between Japan and Hungary (Jp-23/09). This work was also supported by the National Development Agency Grant TAMOP-4.2.1.B-09/1/KMR-2010-0001.

References

[1] Quincke G., Ann. Phys. Chem.,**59**, (1896), pp. 417-486
[2] LampaA.S., Sitzungberichted Akademie der Wissenschaften, **115**, 1(1906) 659
[3] JonesT.B.,Electromechanics of Particles (Cambridge University Press, New York) 1995.
[4] Jones T.B., Kallio.G, J.Electrostatic 6, **207** (1979)
[5] Pannacci L., Lobry L., Lemaire L., PRL 094503 (2007)
[6] Turcu I. J., Phys. A: Math. Gen., **20**, (1987) pp. 3301-3307
[7] Antal M, Filipcsei G, Zrínyi M., Composites Science and Technology, **67**, (2007), pp. 2884-2885.
[8] M.Zrinyi, M.Nakano, T.Tsujita: Development of Micro-motor for MEMS utilizing Novel Smart Polymers Sixth International Conference on Flow Dynamics,Nov. 4-6 2009, Sendai, Japan, Proceedings pp. 114-115.
[9] M.Zrinyi, M.Gadhvi, M.Nakano, T.Tsujita: Study on Micro-motor utilizing Quincke Rotation of Novel Smart Polymers, Proceedings of the Tenth International symposium on Advanced Fluid Information and Transdisciplinary Fluid Integration, CRF-49, pp. 132-133, Nov. 1-3 2010, Sendai, Japan
[10] M.Zrinyi, M.Gadhvi, M.Nakano, T.Tsujita: Development of Micro-motor forMEMS utilizing Novel Smart Polymers II
From single particle rotaton to Rotating Polymer Disk
Proceedings of Seventh International Conference on Flow Dynamics, OS3-27 pp. 284-285 Nov. 1-3 2010 Sendai, Japan
[11] M.Zrinyi: Colloidal particles that make smart polymer composites deform and rotate, Colloids and Surfaces A: Physicochemical and Engineering Aspects, **382**, issue 1-3, (2011), pp.192-197

Effect of Fatty Acid Coating on Dynamic Magnetorheology of Iron Particles in Mineral Oil

Shinya Yamanaka[1], Toshiyuki Fujimoto[1], Yoshikazu Kuga[1], Hiroya Abe[2], Makio Naito[2]
[1] Department of Applied Sciences, Muroran Institute of Technology, Mizumoto-cho 27-1, Muroran, Hokkaido, Japan
[2] Joining and Welding Research Institute, Osaka University, 11-1 Mihogaoka, Ibaraki, Osaka, Japan
E-mail of corresponding author: syama@mmm.muroran-it.ac.jp

ABSTRACT

The iron nanoparticles were dispersed in silicone oil for preparing colloidal magnetorheological (MR) fluids. The solid loading of the nanoparticles was 15 vol%, and a fatty acid (oleic acid) was used as surfactant. It was found that the amount of the fatty acid added significantly influenced the dynamic rheological behaviors in both the absence and the presence of the external magnetic field. The results indicated that the control of colloidal stability is quite important for preparing colloidal MR fluids.

1. Introduction

Magnetorheological (MR) fluids are suspensions of non-colloidal magnetic particles dispersed in lubricant oils. The rheological behavior of MR fluids can be rapidly and reversibly changed according to magnitude of applied magnetic field (MR effect).

However, the conventional MR fluids have drawbacks for being adopted in designing MR devices. One problem is gravitational settling of the micron-sized particles which may affect the operation of MR devices as well as the redispersion. Several methodologies including addition of additives (polymers, thixotropic agent, fillers) have been investigated to prevent this deficiency [1, 2]. Another problem is unwanted abrasion, as MR fluids are used for polishing medium as well.

Replacing the micron-sized particles by nanoparticles may solve the problems associated with the micron-sized particles [3]. Yet, enhancing colloidal stability of the iron nanoparticles in non-polar oil phase, which enables to increase the solid concentration without significant increase of suspension viscosity, represents a challenge. In such uncharged system, sterically functionalized nanoparticles resulting from adsorbing surfactants or polymers may be potentially useful. In our previous research, we have investigated the influences of oleic acid as surfactant on the dispersibility into oil phase and MR response [4]. The suspension of the iron nanoparticles (approximately 100 nm in diameter) exhibited a clear MR effect and a good stability against sedimentation [4]. Herein, we report the influence of oleic acid coating on dynamic magnetorheology for high concentrated suspensions of the iron nanoparticles.

2. Method

The iron nanoparticles were fabricated by the arc-plasma method [5]. They were of spherical on the TEM observation as shown in **Fig. 1**. The specific surface area of the iron nanoparticles was 7.2 m^2/g determined by nitrogen gas adsorption based on BET multipoint method. The equivalent diameter is calculated to be 106 nm. A silicone oil (KF96-50cs, Shin-Etsu Chemical, Japan) was used as the carrier liquid and oleic acid (Kanto Chemical, Japan) as the surfactant.

The MR fluids were prepared as following. The iron nanoparticles were coated with oleic acid using planetary centrifugal mixer (AR-100, THINKY, Japan) during 10 min. Next, the modified iron particles mixed with mineral oil by means of the planetary centrifugal mixer during 10 min. The solid concentration of MR fluids was set to 15 vol%. Additive amount of oleic acid was 1.4 and 7.1 mass% of the total mass of the iron nanoparticles in order to evaluate the effect of the oleic acid coating on dynamic magnetorheology of the suspension. Actually, 1.4 mass% was an optimal amount of the oleic acid to obtain the low viscosity suspension.

MR responses of the prepared fluids were measured at 293 K using a parallel-plate rheometer (RheoStress600, HAAKE, Germany) attached with the electro-magnetic system (MR-100N, EKO Instruments, Japan). The diameter of the plates was 20 mm and the gap distance was fixed at 0.5 mm. Magnetic flux from 0 to 0.1 T was applied perpendicular to the direction of the shear flow. In the dynamic measurements, an oscillatory shear stress was applied with amplitude in the range 10^{-1}–10^{4} Pa at a constant frequency of 1 Hz. The storage modulus (G') and the loss modulus (G'') was evaluated.

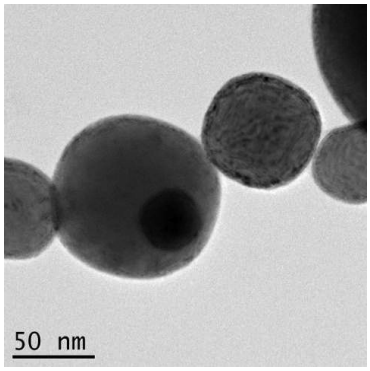

Fig. 1 TEM image of iron nanoparticles

3. Results and Discussion

In our previous research, apparent viscosity of the suspension at shear rate of 1 s^{-1} under no external magnetic field has been measured [4]. Briefly, the relatively low apparent viscosity of 12.4±2.4 Pa·s was observed when 1.4 mass% of the fatty acid was added. The viscosity increased (25.8±3.2 Pa·s) for the excess addition of 7.1 mass%, indicating the suspension was more unstable.

The interparticle potential energies between the suspended nanoparticles are currently being studied in order to discuss colloidal stability of the present suspensions.

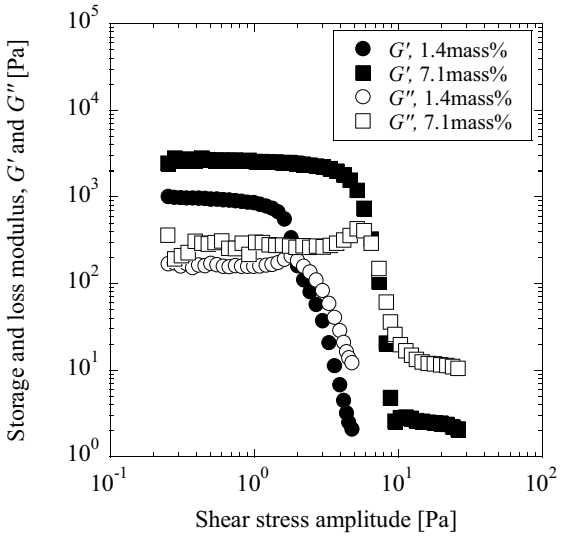

Fig. 2 Storage and loss modulus as a function of the shear stress amplitude for suspensions.

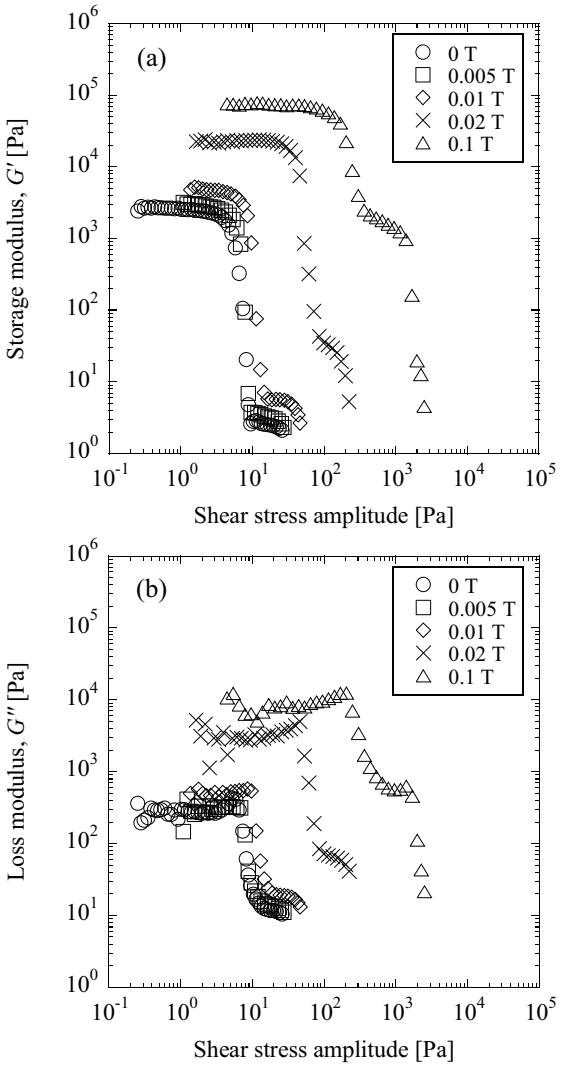

Fig. 3 (a); Storage and (b); Loss modulus of the suspension containing 7.1 mass% oleic acid as a function of the shear stress amplitude. The values of the internal magnetic field strength are indicated.

Further experiments on dynamic magnetorheology were performed for the stabilized suspension with 1.4 and 7.1 mass% amount of the fatty acid. The storage modulus *G'* and loss modulus *G"* was measured for the two suspension. **Figure 2** shows the *G'* and *G"* as a function of the amplitude of shear stress in the absence of applied magnetic flux density. As observed in Fig. 2, a viscoelastic linear region appears in *G'* and *G"* at low shear stresses. In this region, the internal structure of the suspension is not disordered. At larger shear stresses than a critical point, the viscoelastic moduli decrease drastically, indicating a nonlinear viscoelastic response. It is noted that *G'* (elastic modulus) and *G"* (viscous modulus) of 7.1 mass% suspension was larger than that of 1.4 mass% suspension, indicating the lager addition of oleic acid clearly gave more flocculated states.

Figure 3 shows the viscoelastic moduli of the suspension containing 7.1 mass% oleic acid under various field strengths. The viscoelastic moduli as a function of the amplitude of shear stress are shown in Fig. 3(a) (for *G'*) and Fig. 3(b) (for *G"*). The *G'* is considerably stronger than *G"* for any field applied. The *G'* and *G"* was increased depending on the strength of applied magnetic flux density. These results indicate that robust chain-like structures of the iron nanoparticles can be formed in the suspension under the magnetic field applied.

4. Concluding remarks

Concentrated colloidal suspensions of the magnetic nanoparticles have been prepared for an iron-based colloidal MR fluid. The flocculated structure of the nanoparticles in the absence of magnetic field could be controlled by amount of the oleic acid added. The dynamic measurements were performed for the stabilized suspension with 1.4 and 7.1 mass% amount of the fatty acid. It was indicated that the two suspensions were different in the flocculated structure of the nanoparticles in the absence of magnetic field. For the excess addition of oleic acid, the suspension was more unstable. Upon the magnetic field, the robust chain-like structures of the iron nanoparticles could be formed in both suspensions.

Acknowledgment

We are grateful to Kurimoto Ltd. for their important contributions to the experiments.

References

[1] S. T. Lim et al., J. Magn. Magn. Mater. **282** (2004) 170
[2] I. B. Jang et al., J. Appl. Phys. **97** (2005) 10Q912J
[3] M. T. López-López et al., J. Phys.: Condens. Matter **22** (2010) 324106
[4] S. Yamanaka et al., Proc. of the Visual-JW2010, (2010) 256
[5] J. Noma et al., J. Magn. Magn. Mater., **322** (2010) 1868.

Eighth International Conference on Flow Dynamics
November 9 - November 11, 2011

Electro-Rheological Effect of Nano-Suspensions based on Titanium Dioxide Nano-Particles

Katsufumi Tanaka[*1], Ryuichi Akiyama[*1], and Masami Nakano[*2]
[*1]Department of Macromolecular Science and Engineering,
Kyoto Institute of Technology, Matsugasaki, Kyoto 606-8585, Japan
[*2]Institute of Fluid Science,
Tohoku University, Katahira, Sendai 980-8577, Japan
E-mail of corresponding author: ktanaka@kit.ac.jp

ABSTRACT

Suspensions based on nano-particles of titanium dioxide (TiO_2) with particle diameter around 300 nm and particle volume fractions of 8.8 and 12 vol% were prepared. The flow behavior and micro-structure were evaluated. The electro-rheological effect was also investigated for the nano-suspensions. The ER effect was discussed in comparison to the effect previously reported for the nano-suspension based on TiO_2 with particle diameter around 15 nm.

1. Introduction

The electro-rheological (ER) effect is the reversible rheological responses of fluids only by application and removal of an external electric field. A suspension composed of micro-particles and insulating oil is known to show the ER effect [1]. The flow of the ER micro-suspension under no electric fields is generally assumed to be the Newtonian flow. Under an electric field, the flow is well assumed to be the Bingham flow. Because a characteristic response time of the ER micro-suspension is on the order of milliseconds [2, 3], there are substantial expectations for applications [4], such as dampers, clutches, valves, robotics, force display devices, and so on.

For practical applications, however, there are still demands for the ER fluid to be improved. Although a much higher yield stress has been a major demand, stability in the ER effect would also be a demand. Recently, a suspension based on rutile titanium dioxide (TiO_2) nano-particles has been reported [5-7]. The suspended particles were remarkably stable against sedimentation and electrical breakdown. The nano-suspension also showed a good fluidity with a gap of 50 μm.

At a given particle volume fraction of ϕ, it is expected that secondary particles based on the larger particles are smaller than those based on the smaller particles of the same chemical nature, crystal structure, and so on. In such a nano-suspension, a lower apparent yield stress can be observed.

In the present paper, flow behavior and microstructure will be discussed for electro-rheological nano-suspensions based on TiO_2 nano-particles with particle diameter around 300 nm and ϕ = 8.8 and 12 vol%. The effect of shearing time on the ER responses will also be reported.

2. Experimental

Nano-particles of anatase TiO_2 with diameter of the primary particles ($2a$) around 300 nm were suspended in a silicone oil with the viscosity η_c of 5×10^{-2} Pa·s [8]. The volume fractions of the particles were 8.8 and 12 vol%. In the present paper, a nano-suspension will be coded for convenience based on a typical particle diameter of $2a$ and/or particle volume fraction of ϕ. The rheological measurements were performed at room temperature using rotational rheometers with fixtures of parallel plates. Particle behavior was observed using an optical microscope equipped with a CCD camera. Furthermore, the effect of shearing time on the ER responses was also investigated. The flow behavior was also observed simultaneously [9, 10].

3. Results and Discussion

Under no electric fields, the nano-suspension of 300 nm and 8.8 vol% showed a plateau stress around 5 Pa at the lower shear rates. At the higher shear rates, the stress of the sample of 300 nm gradually approached that of 15 nm and 8.8 vol% [5]. Similarly, the nano-suspension of 300 nm and 12 vol% showed a plateau stress at lower shear rates, but the plateau stress was higher than that of the nano-suspension of 300 nm and 8.8 vol%.

Figure 1 shows responses of shear stress to the dc electric field measured at a shear rate of 1.88 s^{-1} for the nano-suspension of 300 nm and 12 vol%. The data for the nano-suspension of 300 nm and 8.8 vol% are also plotted for comparison in the figure.

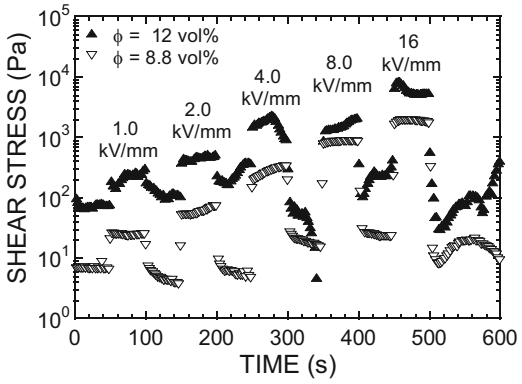

Fig. 1 Responses of shear stress to the dc electric field for the nano- suspension of 300 nm and 12 vol%. The data for the nano- suspension of 300 nm and 8.8 vol% are also plotted. The strength of the applied dc electric field is shown in the figure. The gap between the electrodes was 50 μm, and the shear rate was 1.88 s^{-1}.

The dc electric field, the strength of which is shown in the figure, was applied and then removed. Correspondingly, the increase and recovery of the stress is seen in the figure. The ER responses were observed even at 1 kV/mm, the results of which suggest that the polarization forces were slightly predominant over the Brownian agitation. Although the flow behavior of the sample of 12 vol% was not stable very much, the ER responses were effectively induced by the strengths of the electric field of 1 and 2 kV/mm. Furthermore, the induced stress around 6 kPa was observed at 16 kV/mm.

The stability of the micro-gap flow under the dc electric field was further evaluated for the sample of 300 nm and 8.8 vol% [8]. Figure 2 shows the shear stress under the electric field plotted against time. The shear rate was 100 s^{-1}. The gap h was set to be 50 μm for (a), and 100 μm for (b).

For h = 50 μm, the flow was stable during the period on the order of 10^2 s at lower strengths of the electric field. However, a gradual increase, or a very slow mode of the ER response at 5 kV/mm is seen in the figure. For the flow of h =100 μm, a more stable flow than that of h = 50 μm is found in Fig.2. Especially, the stability of the flow of h = 100 μm was fairly well even at 5 kV/mm.

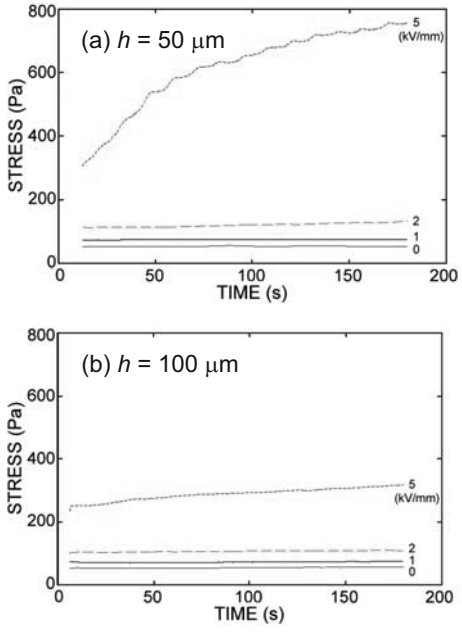

Fig. 2 The effect of shearing time on the ER responses for the sample of 300 nm and 8.8 vol% within micro-gaps (h) between electrodes, h = 50 μm for (a), and 100 μm for (b). The shear rate was 100 s^{-1}.

It should be pointed out that a very slow mode in the ER response was also found for the sample of 15 nm and 8.8 vol%, but the very slow mode was found even within a micro-gap of 200 μm [9, 10]. Therefore, the flow within a micro-gap of 100 μm for the sample of 300 nm was more stable than that of the sample of 15 nm.

In a micro-suspension, a chain-like microstructure along the electric field is induced, the ground state of which was found to be a body-centered tetragonal (bct) lattice [11]. A columnar microstructure or further developed ring-like microstructure was observed under shear and electric fields [12].

The development and gradual changes in a ring-like microstructure were also observed simultaneously for the flow of the sample of 15 nm and 8.8 vol% with the very slow mode [9, 10], suggesting the close relation between the very slow mode and the development of the ring-like microstructure. In the present study, the ring-like microstructure has not been observed for such a flow, but a similar very slow mode was observed. Further study is now in progress to evaluate the micro-gap flow behavior and microstructure of the ER nano-suspension.

4. Conclusions

The nano-suspension of 300 nm and 12 vol% showed the induced stress around 6 kPa. The stability of the micro-gap flow under the dc electric field was also found to be fairly well for the sample of 8.8 vol%.

Acknowledgement

This work was partially supported by the Cooperative Research Program of the Institute of Fluid Science, Tohoku University.

References

[1] W. M. Winslow, J. Appl. Phys., **20** (1949), 1137.

[2] A. Hosseini-Sianaki, W. A. Bullough, R. Firoozian, J. Makin, and R. C. Tozer, Int. J. Mod. Phys. B, **6** (1992), 2667.

[3] K. Tanaka, A. Sahashi, R. Akiyama, and K. Koyama, Phys. Rev. E, **52** (1995), R3325.

[4] M. Nakano, and K. Koyama (eds.), Proc. of 6th Int. Conf. on ER Fluids, MR Suspensions and Their Applications (World Scientific, Singapore, 1998).

[5] K. Tanaka, T. Wakayasu, A. Kubono, and R. Akiyama, Sensors and Actuators A, **112** (2004), 376.

[6] K. Tanaka, H. Nakahori, K. Katayama, and R. Akiyama, Colloid Polym. Sci., **285** (2007), 1201.

[7] K. Tanaka, N. Sezaki, H. Nakahori, and R. Akiyama, Nihon Reoroji Gakkaishi (J. Soc. Rheol., Jpn.), **37** (2009), 17.

[8] K. Tanaka, T. Hira, R. Fukui, N. Nakagawa, R. Akiyama, M. Nakano, K. Yoshida, and T. Tsujita, Colloid Polym. Sci., **289** (2011), 855.

[9] M. Nakano, S. Yamamura, R. Keta, K. Tanaka, Proc. of Mechanical Engineering Congress, Japan, vol. 2, (2006), pp.25.

[10] M. Nakano, Jpn. J. Multiphase Flow, **23** (2009), 135.

[11] R. Tao, and J. M. Sun, Phys. Rev. Lett., **67** (1991), 398.

[12] S. Henley, and F. E. Filisko, J. Rheol., **43** (1999), 1323.

Control and inverse problems for the models of magnetic hydrodynamics

Roman Brizitskii
Institute of Applied Mathematics FEB RAS, 7, Radio St., Vladivostok, 690041, Russia
mlnwizard@mail.ru

ABSTRACT

Control problems for the stationary equations of the magnetic hydrodynamics considered under Dirichlet boundary conditions for the velocity and mixed boundary conditions for the electromagnetic field are formulated. Necessary conditions of an extremum and estimates of local stability of solutions of concrete extreme problems concerning certain perturbations as cost functional and one of the set functions, velocity making sense a vector on boundary are deduced.

1. Introduction

In recent years, much attention has been given to optimal control problems for flows of viscous electrically conducting fluids. The study of these problems was motivated by the necessity of the most effective control mechanisms for hydrodynamic processes in such fluids. A rigorous theoretical study of control problems in hydrodynamic and magnetic hydrodynamics can be found, for example, in [1-13].

Along with optimal control problems, an important role is played by identification problems for MHD models. In the latter problems, the unknown coefficients involved in the differential equations or in the boundary conditions for the model in question are determined from additional data on the solution. Note that identification problems can be reduced to optimization problems with a suitable choice of the minimized cost functional. In [13] this approach was used to analyze the solvability, uniqueness and stability of solutions to identification problems for models of magnetic hydrodynamics of viscous incompressible fluid.

In this paper control problems for the stationary magnetic hydrodynamics (MHD) model governing a flow of a viscous electrically-conducting fluid are stated and analyzed. This model consists of the Navier-Stokes equations, the generalized Ohm law, and the stationary Maxwell equations without displacement currents, considered under Dirichlet boundary condition for the velocity and mixed boundary conditions for the electromagnetic field. The solvability of the problem is proved, an optimality system is derived, and sufficient conditions on the initial data are established that ensure the uniqueness and stability of the solution.

Detail in this paper will be formulated and studied control problems for stationary equations of magnetic hydrodynamics of a viscous incompressible fluid

$$-\nu\,\Delta\mathbf{u}+(\mathbf{u}\cdot\nabla)\mathbf{u}+\nabla p-\kappa\,\mathrm{rot}\,\mathbf{H}\times\mathbf{H}=\mathbf{f},\ \ \mathrm{div}\,\mathbf{u}=0, \quad (1)$$

$$\nu_1\,\mathrm{rot}\,\mathbf{H}-\rho_0^{-1}\,\mathbf{E}+\kappa\,\mathbf{H}\times\mathbf{u}=\upsilon_1\mathbf{J}_0,\ \mathrm{div}\,\mathbf{H}=0,\ \mathrm{rot}\,\mathbf{H}=\mathbf{0}, \quad (2)$$

considering in domain Ω under following inhomogeneous boundary conditions:

$$\mathbf{u}=\mathbf{g},\ \ \mathbf{H}\cdot\mathbf{n}=q\ \ \text{and}\ \ \mathbf{E}\times\mathbf{n}=\mathbf{k}\ \ \text{on}\ \ \Gamma. \quad (3)$$

Here $\Omega\in\mathbf{R}^3$ is a bounded domain with boundaryΓ, **u**, **H** **E** are vectors of velocity and intensity of magnetic and electric fields, $p=P/\rho_0$ where P is the pressure, ρ_0=const is a density, $\mathbf{J}_0$ is a vector of density of external currents, **g**, q and **k** are given functions on Γ. We shall refer to problem (1)-(3) as Problem 1.

For model (1), (2) papers [3,7-9] are devoted theoretical research of extremum problems. In these articles solvability of considered extreme problems is proved, the systems of an optimality describing necessary conditions of an extremum are deduced and analyzed. In essentially smaller degree questions of uniqueness and stability of solutions of extreme problems are studied. In this plan we won'te only works [7] in which questions of uniqueness of solutions of extreme problems are studied for model of magnetic hydrodynamics viscous heat conducting fluids. Taking into account it the basic attention will be more low given construction of the theory of research of uniqueness and stability of decisions of extreme problems for model (1), (2). The developed theory is based on the new a priori estimates of solutions of a boundary problem (1)–(3) and the auxiliary theorem about properties of a difference of solutions of the initial control problem the perturbed control problem of received by certain perturbation initial cost functional. The obtained estimates of stability have a bulky appearance. However with use of specially introduced dimensionless parameters which are analogs of Reynolds, Gartman and Prandtl numbers widely known in hydrodynamics they will be written down in enough compact and evident kind.

2. Optimal Control Problems

Our goal is the theoretical analysis of the boundary control problems for the models under consideration. This problem consists in minimization of certain cost functional depending on the state and controls. In order to formulate control problem for the model (1)-(3) we split the set of all data of Problem 1 into two groups: the group of controls containing the one function $q\in\widetilde{H}^{1/2}(\Gamma)$ and the group of fixed data comprising the invariable functions **g, f, k** and $\mathbf{J}_0$. We assume that the control q can change in some closed convex set $K\subset\widetilde{H}^{1/2}(\Gamma)$. The mathematical statement of the optimal control problem is as follows: find a pair (**x**, q), where $\mathbf{x}=(\mathbf{u},\mathrm{H},p)\in X$, and $\mathrm{q}\in K$ such that

$$J(\mathbf{x},u)=I_i(\mathbf{u},T)+\frac{\mu_1}{2}\|q\|^2_{1/2,\Gamma}\to\inf,$$

$$F(\mathbf{x},q)=0,\ \ \mathbf{x}\in X, q\in K \quad (4)$$

Here $F(\mathbf{x},\mathrm{q})=0$ is the operators form of the weak formulation of Problem 1; μ_1 is nonnegative parameter,

$I_i(\mathbf{u},p)$ is a cost functional. The possible cost functionals are usually defined as

$$I_1(\mathbf{v}) = \|\mathbf{v} - \mathbf{v_d}\|_Q^1, \quad I_2(\mathbf{v}) = \|\mathbf{v} - \mathbf{v_d}\|_{1,Q}^1$$
$$I_3(\mathbf{v}) = \|\mathrm{rot}\ \mathbf{v} - \eta_\mathbf{d}\|_Q^1, \quad I_4(p) = \|p - p_\mathbf{d}\|_Q^1 \qquad (5)$$

Here Q is a some subset of domain Ω, $\mathbf{v}_d \in \mathbf{L}^2(Q)$ (or $\mathbf{v}_d \in \mathbf{H}^1(Q)$) is function, which simulates a given distribution of the velocity field in Q. Functions $\eta_d \in \mathbf{L}^2(Q)$ and $q_d \in \mathbf{L}^2(Q)$ have a similar sense.

The existence of an optimal solution is based on the a priori estimates and standard techniques (see [3]). Optimality systems describing first-order necessary optimality conditions were obtained, and, by analysis of their properties, conditions ensuring the uniqueness and stability of the solution were established.

3. Uniqueness and Stability of the Extremum Problem

Sufficient conditions on the initial data providing local uniqueness and stability of solutions of concrete extremum problems and stability estimates are main results of this paper.

Let us consider the extremum problem

$$J(\mathbf{v},\tilde{q}) \equiv \frac{\mu_0}{2}\|\mathbf{v} - \mathbf{v_d}\|_Q^2 + \frac{\mu_1}{2}\|\tilde{q}\|_{1/2,\Gamma}^2 \to \inf,$$
$$F(\mathbf{x},\tilde{q},\tilde{\mathbf{g}}) = 0,\ \mathbf{x} \in X, \tilde{q} \in K, \qquad (6)$$

corresponding cost functional $I_1(\mathbf{v})$. Let us assume below, that the boundary function $\tilde{\mathbf{g}}$ in (6), can change in some bounded set $G \subset \mathbf{H}_\mathbf{T}^{1/2}(\Gamma)$. Denote by $(\mathbf{x}_1,q_1) \equiv (\mathbf{u}_1,\mathbf{H}_1,p_1,q_1)$ the solution of a problem (6) corresponding to functions $\mathbf{v}_d \equiv \mathbf{u}_d^{(1)} \in \mathbf{L}^2(Q)$ and $\tilde{\mathbf{g}} = \mathbf{g}_1 \in G$. By $(\mathbf{x}_2,q_2) \equiv (\mathbf{u}_2,\mathbf{H}_2,p_2,q_2)$ we denote the solution of a problem (6) corresponding to perturbed functions $\mathbf{v}_d \equiv \mathbf{u}_d^{(2)} \in \mathbf{L}^2(Q)$ and $\tilde{\mathbf{g}} = \mathbf{g}_2 \in G$.

Let us put

$$\Delta \equiv \left\|\mathbf{u}_d^{(1)} - \mathbf{u}_d^{(2)}\right\|_Q + \|\mathbf{g}_1 - \mathbf{g}_2\|_{1/2,\Gamma}.$$

Simple enough stability estimates of the solution the problems (6) which are looking like are received

$$\|\mathbf{u}_1 - \mathbf{u}_2\|_{\mathbf{H}^1(\Omega)} \le M_\mathbf{u}\Delta, \ \|\mathbf{H}_1 - \mathbf{H}_2\|_{\mathbf{H}^1(\Omega)} \le M_\mathbf{H}\Delta,$$
$$\|p_1 - p_2\| \le M_p\Delta, \ \|q_1 - q_2\|_{1/2,\Gamma} \le M_q\Delta,$$

where $M_\mathbf{u}$, $M_\mathbf{H}$, M_p and M_q are not decreasing functions of norms of the initial data.

Acknowledgments

The work was supported by the Council about grants of the President of the Russian Federation for the state support of Young Russian scientists - candidates of science (MK-3311.2011.1), Russian Foundation for Basic Research (project no. 10-01-00219-a) and the Far East Branch of the Russian Academy of Sciences (projects no. 09-I-P29-01 and 09-I-OMN-03).

References

[1] M. Gunzburger, L. Hou, T. Svobodny, Analysis and finite element approximation of optimal control problems for the stationary Navier–Stokes equations with Dirichlet conditions // Math. Mod. Numer. Anal., **25** (1991), 711-748.

[2] G.V. Alekseev, V.V. Malikin, Numerical analysis of optimal boundary control problems for Navier-Stokes equations // Comp. Fluid Dynamics J., **3** (1994), 1-26.

[3] L.S. Hou, A.J. Meir, Boundary optimal control of MHD flows // Appl. Math. Optim. **32** (1995), 3-162

[4] A.V. Fursikov, Stabilization for the 3D Navier-Stokes system by feedback boundary control // Discrete Continuous Dynamical Syst., **46** (2004), 289-314.

[5] G.V. Alekseev, Solvability of the control problems for the stationary magnetohydrodynamic equations of viscous fluid // Sib. Math. J. **45** (2004), 243-262.

[6] A.V. Fursikov, M.D. Gunzburger, L.S. Hou, Optimal boundary control for the evolutionary Navier-Stokes system: The three-dimensional case // SIAM J. Contr. Optim., **46** (2005), 2191-2232.

[7] G.V. Alekseev, R.V. Brizitskii, Control problems for stationary magnetohydrodynamic equations of viscous heat-conducting fluid under mixed boundary conditions // J. Comp. Math. and Math. Physics. **45** (2005), 2049-2065

[8] M. Gunzburger, C. Trenchea, Analysis of an optimal control problem for the three-dimensional coupled modified Navier-Stokes and Maxwell equations // J. Math. Anal. Appl., **333** (2007), 295-310.

[9] M. Gunzburger, J. Peterson, C. Trenchea, The velocity tracking problem for MHD flows with distributed magnetic field controls // Int. J. Pure Appl. Math. **42** (2008), 289-296.

[10] G.V. Alekseev, D.A. Tereshko, Analysis and Optimization in Viscous Fluid Hydrodynamics. Dalnaulka. 2008.

[11] G.V. Alekseev, R.V. Brizitskii, On uniqueness and stability of solutions of extremal problems for the stationary of Navier–Stokes equations // Differential equations, **46 (**2010**)**, 70–82.

[12] R.V. Brizitskii, A study of a class of control problems for the stationary Navier–Stokes equations with mixed boundary conditions // J. Appl. Indust. Math., **4**. (2010), 309-317.

[13] G.V. Alekseev, Optimization in Stationary Problems of Heat and Mass Transfer and Magnetic Hydrodynamics. Moscow. Nauchny Mir. 2010.

Eighth International Conference on Flow Dynamics
November 9 - November 11, 2011

Wavelet Analysis of Particle Fluctuation Velocity near the Minimum Conveying Velocity in a Horizontal Pneumatic Conveying

Yan Zheng, Akira Rinoshika and Fei Yan
Department of Mechanical Systems Engineering
Graduate School of Science and Engineering
Yamagata University
4-3-16 Jonan, Yonezawa-shi, Yamagata 992-8510, Japan
zy30003333@163.com

ABSTRACT

The high-speed particle image velocimetry (PIV) is first used to measure fluctuating particle velocity at low air velocity in a horizontal pneumatic conveying. Then orthogonal wavelet multi-resolution technique is employed to analyze the fluctuating particle velocity. It is revealed that the axial fluctuating energy of particle velocity is mainly contributed from the wavelet components of low frequency in bottom part of pipe. High spatial correlation is found in the low frequency range by using multi-scale two-point correlation method.

1. Introduction

Pneumatic conveying of solid particles in pipeline is frequently used in a significant number of industrial processes. To get lower energy consumption and lower pipe erosion, pneumatic conveying is usually conducted at the low velocity [1]-[2]. To realize the purpose, it is necessary to reveal the mechanism of gas-solid two-phase flows, especially the dynamics of solid particles in the range of low air velocity.

In recent years, the experimental measurements of particle velocity in dilute gas-solid two-phase flows have been attracted considerable interest. Tsuji and Morikawa [3] measured air and particle velocities in a dilute phase gas-particle suspension flow of a horizontal pipe by use of LDV. Yan and Rinoshika [4] analyzed the particle velocity and concentration characteristics in a horizontal pneumatic conveying with dune model using High-speed PIV.

Over the past decades wavelet transform has emerged as a major time-frequency decomposition tool for extracting new information on the turbulence structures of various scales [5].

This study aims at revealing the velocity fluctuation of solid particles using wavelet analysis. The distributions of particle fluctuation velocity are measured by the high-speed PIV at low air velocity. Particle fluctuation velocity is decomposed into different scales using wavelet multi-resolution technique. The particle fluctuation velocities of different scales are analyzed in terms of the mean-squared particle fluctuation velocity, and two-point correlation.

2. Experimental Setup

The experimental facility of the positive pressure conveying system, as shown in Fig.1, is used. Air from a blower flows through the orifice meter, and picks up the solid materials fed by gravity from the feed tank at the inlet of the conveying pipeline. Then, the gas-particle mixture enters the test pipeline and at the pipeline exit the particles are separated by the separator. The conveying pipeline consists of a horizontal smooth acrylic tube with an inside diameter of D = 80 mm and total length of about 5 m. The airflow rate and the solids mass flow rate are respectively measured by the orifice meter and load cell. The gauge pressures along the pipeline are measured by pressure transducers.

A high-speed camera is used to capture the successive digital particle images at a frame rate of 1000fps with a resolution of 1024×576 pixels. A thin light sheet of thickness=5mm produced by a high-intensity continuous light source, is used to illuminate the objective particulate flow on the center plane. The measurement is carried out at a location of x=3.5 m (x/D=44, location C) from the particle inlet.

3. Results and Discussion

3.1 Profile of particle velocity

To study behaviors of particles, the distributions of the time-averaged particle velocity $\overline{u_p}/U_a$ versus y/D (y is the ordinate from bottom to top of pipe) measured by PIV at the air velocity of 14.13m/s, and is shown in Fig.2.

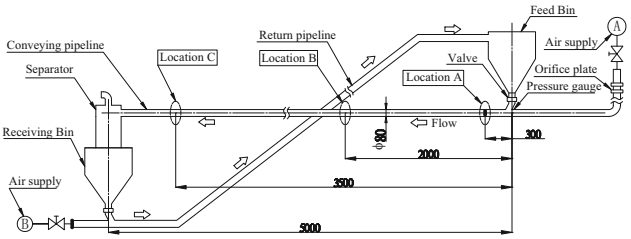

Fig.1. Schematic diagram of the experimental apparatus

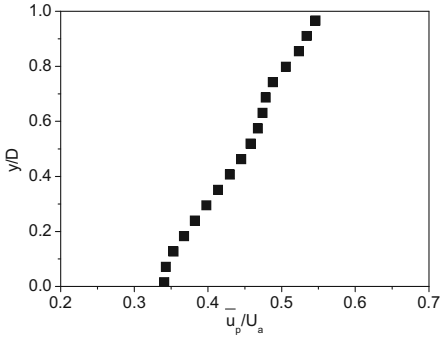

Fig.2 Profiles of time-averaged particle velocity

It is evident that the particle velocity in the upper part of pipe is higher than that in the bottom of pipe. It is because particles exhibit suspensions and sliding strands along the bottom of the pipe and the particle concentration is low in the upper part of pipe.

3.2. Orthogonal wavelet decomposition of mean-squared particle fluctuation velocity

In order to get the intensities of particle fluctuation velocity at various frequencies, Daubechies orthogonal wavelet basis with order 10 is used to decompose particle fluctuation velocity into 8 levels. Fig.3 shows the profiles of $\overline{u'^2_{pi}}/\overline{u'^2_p}$ in various frequencies (3Hz - 400Hz). Here $\overline{u'^2_{pi}}$ represents the horizontal fluctuation energy of *i*th wavelet level, and it is normalized by the measured fluctuation energy of $\overline{u'^2_p}$. $\overline{u'^2_{pi}}/\overline{u'^2_p}$ provides a measure of the contribution from each wavelet component to the intensity of particle fluctuation velocity.

In Fig.3(a), the wavelet components of 3-25Hz accounts for about 84% in the bottom of pipe, in the range of 50-400 Hz (Fig.3b), the largest contribution accounts for about 78% near the top of pipe. These imply that, particle fluctuation has a close relationship with low frequency components in the bottom of pipe, and the component of high frequency makes comparable contribution to horizontal particle fluctuating energy in the upper part of pipe as the effect of suspension flow.

4.6 Two-point velocity correlation of various frequencies

To evaluate the two-point correlation of the particle velocity at different frequency, the two-point correlation coefficient of the wavelet component, $Ru_{p0i}u_{pi}$, in the measurement plane is defined as:

$$Ru_{p0i}u_{pi} = \frac{\overline{u_{p0i}u_{pi}}}{\left(\overline{u^2_{p0i}}\,\overline{u^2_{pi}}\right)^{1/2}} \qquad (1)$$

where u_{p0} is the reference particle velocity selected at $y/D \approx 0.5$, the subscript i denotes the wavelet component.

As shown in Fig.4, larger particle velocity correlation appears in the wavelet components of lower than 50Hz in the lower part of pipe. The wavelet component of 6Hz exhibits the largest space correlation. It indicates that the large particle velocity correlation results from the low frequency components, which corresponds to the sliding strands of high particle concentration flow.

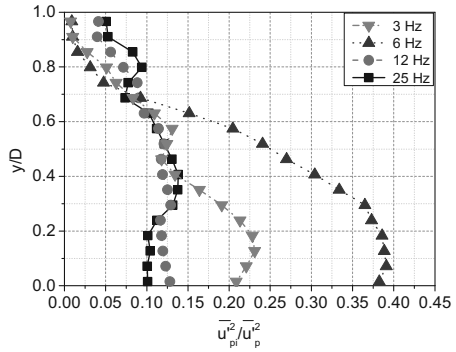

(a) 3 -25 Hz

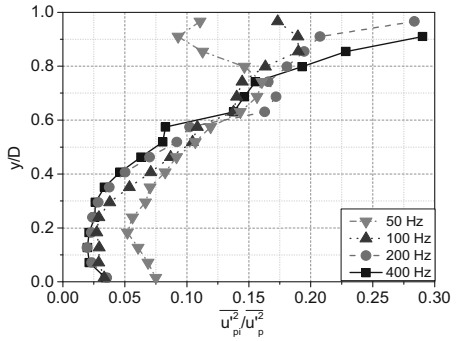

(b) 50 – 400 Hz

Fig.3. $\overline{u'^2_{pi}}/\overline{u'^2_p}$ of wavelet components at various frequencies

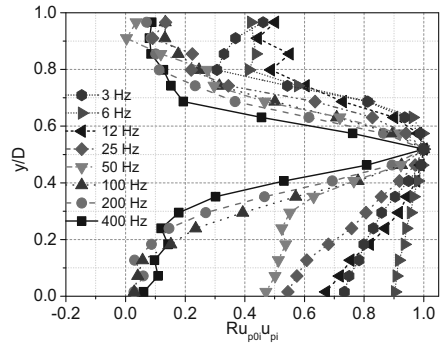

Fig.4 Two-point correlation coefficients of wavelet components at various frequencies

4. Concluding remarks

(1) In lower part of pipe, the fluctuating energy of horizontal particle velocity is mainly contributed from the wavelet components of low frequency, accounting for about 84%.

(2) The wavelet components of high frequency make comparable contribution, accounting for about 78%, to the fluctuating energy of horizontal particle velocity in upper part of pipe.

(3) The low frequency components (less than 50Hz) exhibit large space correlation in the lower part of pipe, and this space correlation increases with the decrease of frequency.

References

[1] C. Herbreteau & R. Bouard, Powder Technology, **112** (2000), 213–220.

[2] S. P. Goy, J. W. Chew & K. Hadinoto, Powder Technology, **208** (2010), 166–174.

[3] Y. Tsuji & Y. Morikawa, J. Fluid Mech., **120** (1982), 385-409.

[4] F. Yan & A. Rinoshika, Powder Technology, **208** (2011), 158–165.

[5] A. Rinoshika & Y. Zhou, J. Fluid Mech., **524** (2005), 229-248.

Transient Flow field Analysis Around a Lockup Clutch

Takeshi Yamaguchi[1], Shogo Ikeda[2], Kazuhiro Tanaka[2]
1. Engineering Division, Aisin AW Co., Ltd. 10 Takane Fujii-cho Anjyo Aichi, 444-1192, Japan
2. Dept. of Mechanical Information Science and Technology, Kyushu Institute of Technology,
680-4 Kawazu Iizuka, Fukuoka, 820-8502, Japan
i23962_yamaguchi@aisin-aw.co.jp

ABSTRACT

The purpose of this paper is to study flow field of a lockup clutch inside a torque converter. The performance of a torque converter has been one of the most important areas of improvement for an automatic transmission equipped automobile. Improving the torque converter's performance and efficiency is key to saving fuel consumption, which is an important consideration with recent environmental awareness. Moreover, the locking up operation or slipping control of an automatic transmission is another good opportunity for improving fuel economy.

1. Introduction

The torque converter is a major component of an automatic transmission that transfers power from the engine to the transmission gearing system. Moreover, there are two important roles for the torque converter. One is the reducing vibration or noise from the engine by means of an automatic transmission fluid. The other is the multiplication of engine toque. A typical automotive torque converter cross-section is shown in Fig. 1.

In order to improve the efficiency of automatic transmission, it is often desired to engage the torque converter lockup clutch as soon as possible to conserve the power flow from the engine. Understanding of the flow field around lockup clutch is of great importance from the fluid dynamics point of view.

There are many researches carried out about the torque converter performance [1-7] and a few papers are focused on a flow field of the lockup clutch by using CFD [8-9]. However, these simulations were only performed by steady-state conditions. In this research, transient calculation is carried out and mainly the lockup engagement time is studied.

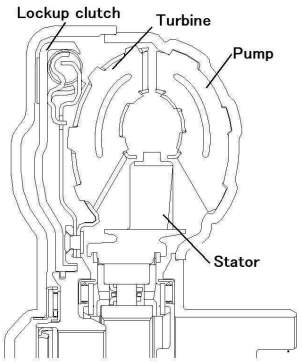

Fig. 1 A typical torque converter cross-section

2. Description of the model and CFD method

ANSYS CFX Ver.12.1 has been used for CFD solver. And the lockup clutch CFD model is shown in Fig. 2. Since this is axis-symmetric and reducing computational time only seventy-seconds of the lockup clutch is modeled with periodical boundary condition. In this study, it is assumed that the flow field around the lockup clutch is independent of the flow field inside a torus (pump, turbine, stator blade area), a torus was not included this model. Boundary conditions are varied as follows; Inlet , Outlet pressure: 0kPa to 200kPa, Pump rotational Speed: 1000rpm, Speed ratio:0.6 to 0.9. Speed ratio is defined as the turbine rotational speed divided by the pump rotational speed.

In this simulation, the lockup motion is not known a priori, and will be calculated using the forces that acting on the lockup clutch. According to Newton's Second Law, the time rate of change in the lockup clutch's linear momentum is proportional to the net force acting on the lockup clutch. The equation to be solved for the motion of the lockup clutch is re-assembled and translated to CFX CEL (CFX Expression Language). Then, Navier–Stokes equations can be solved and specified explicitly by using this CEL.

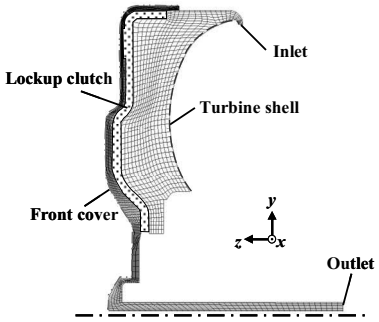

Fig.2 Computational grid of the lockup clutch

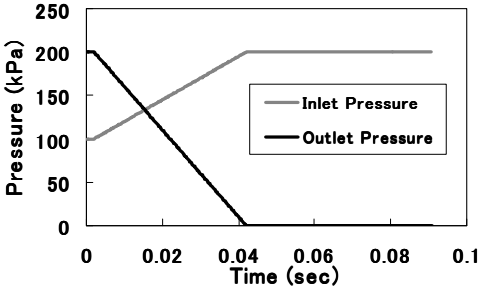

Fig.3 Inlet and outlet pressure distribution

3. Results and Discussion

The lockup engagement time is shown with various speed ratios in Fig. 4. The turbine slipping speed is varied to achieve different speed ratio. The higher speed ratio, the shorter engagement time is shown. Due to the fact the slipping speed (rotational speed difference between the pump and the turbine) is higher at the lower speed ratio, more shear flow or more energy is created into the working fluid. So even extra pressure is needed for this low speed ratio, boundary condition limits inlet pressure as shown in Fig.3, as the result, it takes longer time for the engagement time at the lower speed ratio.

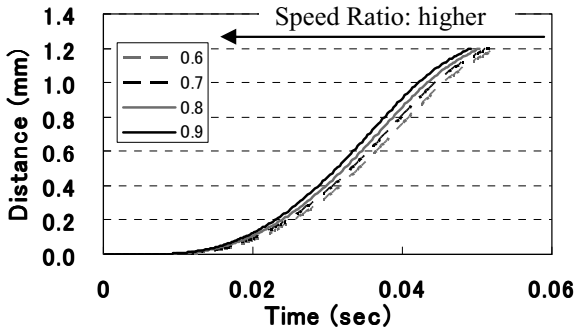

Fig.4 Lockup time with various speed ratios

Fig.5 shows the friction paper with groove. One of the reasons that the lockup clutch is slowed down before reaching the engagement point shown in Fig.4 is the increase of the pressure between the lockup clutch and the front cover. This groove plays an important role in relief this pressure. Lockup time with or without groove at speed ratio 0.9 is shown in Fig.6. The engagement time is almost 20% faster with groove friction surface model.

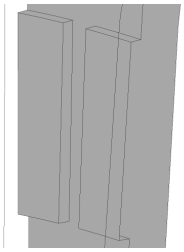

Fig.5 groove on the friction paper

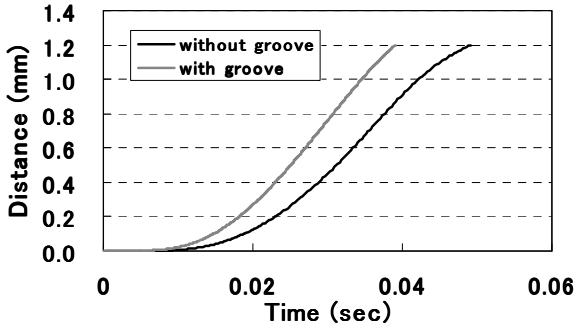

Fig.6 Lockup time with and without groove on the friction paper (at speed ratio = 0.9)

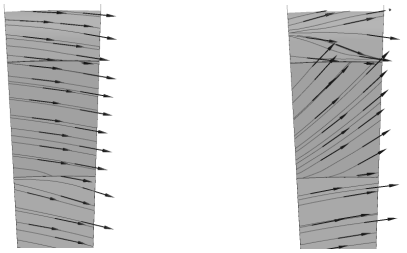

(a) steady solution (b) transient solution

Fig.7 Limiting streamlines on the lockup clutch

The limiting streamlines on the lockup clutch solved by steady state and transient solution are compared and discussed. Fig. 7 (a) shows, velocity vector on the friction surface calculated by steady state solution and Fig. 7 (b) is from transient solution. There is clear difference the flow over the friction paper between steady state solution and transient solution. For steady state case, the flow tends to move downward, however for transient case, the flow is moving upward.

The volume change due to the movement of the lockup clutch is one of the reasons. The volume of the region between the lockup clutch and the turbine shell is increased. On the other hand, the volume between the lockup clutch and the front cover is decreased. As the result, the fluid between the lockup clutch and the front cover is squeezed and moved up to the region where the volume is increased.

4. Conclusion

The flow around the lockup clutch has been simulated with a commercial CFD code. It has been found the motion of the lockup clutch is not moving linearly, and small gap between the front cover and the friction paper has enormous effect of the lockup engagement time and flow fields. Moreover, the groove on the friction paper affects reduction of lockup engagement time.

The flow field of transient flow analysis is quite different from that of steady state analyses. In addition, flow field is so complex enough to do extra research is needed.

References

[1] Kim B S., et al., International Journal of Automotive Technology, Vol. 9, No. 2, (2008), pp.141-148.

[2] Watanabe H., Toyota Central Labs R&D Review, Vol. 34 , No. 1, (1999), pp.57-66.

[3] Yamaguchi T., The 9th ISROMAC

[4] Abe et al., SAE No.910800

[5] Brun et al.,ASME paper 95-GT-293

[6] By et al., J.Fluids Eng., Vol.117, pp.109-115

[7] Cigarini et al., SAE No.950673

[8] Ejiri E., JSME International Journal, Series B 49(1), (2006), pp.131-141.

[9] Abe H. et. al., HONDA R&D Technical Review, Vol.11 No2, (1999).

Vortex Structure around Ideal Elastic Deformation of Flapping Wing Due to Some Ribs

Aphaiwong Junchangpood, Masaki Fuchiwaki[*1], Kazuhiro Tanaka[*2]
Department of Mechanical Information Science and Technology, Faculty of Computer Science and Systems Engineering, Kyushu Institute of Technology, Fukuoka, Japan 820-8502
Tel: +81 948 29 7783, Fax: +81 948 29 7751,
E-mail: apaiwong@vortex.mse.kyutech.ac.jp

ABSTRACT

In this paper, we present the changing of vortex structure around ideal elastic deformation of flapping wing due to some ribs . We designed small flying robot to use as an observation system in hazardous environments, and it could be stable flying in experiment. However, the wing elasticity is important, but elastic details are affected to flow field and aerodynamic forces have not clarified. We have proposed an ideal elastic deformation of flapping wing due to some ribs. In the structural analysis, the simulation results demonstrate, that some ribs attached with the main spar on the wing structures could control the wing deformation influentially. To clarify the structural deformation affected to a flow field, we investigate the vortex flow structure around flapping elastic wings of small flapping robot by fluid-structure interaction (FSI) simulation (ANSYS EF 13. and ANSYS-CFX 13.)

1. Introduction

Many creatures, such as flying insects, birds, or aquatic animals, fly and swim skillful by controlling a flow field around their body using their wings or tail flukes of complex shape and their elastic deformations. Since, the flying insects have been evolved and perfected their flight for their size today. Hence, many researchers attempt to mimic these characteristics of the insect flight, and construct a small flapping robot or MAVs for performing the special missions[1]. However, the flow field around the moving elastic body is treated as a coupled problems of fluids and structures (Fluid Structure Interaction (FSI) problem)[2,3]. In addition, there are a variety of the phenomena with applications in many areas. The flying robot is only one of the application on the fluid-structure combination working. For solving FSI problems, 3-D structural deformations largely and complexly have not been solved fully yet. In our previous works, we have performed about the elastic deformations of the flapping wing with structural analysis by finite element method(FEM) as shown in Fig.1. However, the elastic deformations, affected to a vortex flow structure around the flapping wing, had not been solved yet. Furthermore, it is shown, that some ribs attached with main spars of wing structures dominate over the elastic deformation on membrane strongly.

In this work, the vortex structure around the wing structure included some rib effects are clarified.

2. Method

The elastic wing structure attached with some ribs was used in the simulation. The wing structures are defined two parts as the main spar and membrane parts as shown in Fig.2. The main spar and membrane are a carbon rod and special paper material, respectively. The linear elastic behavior as isotropic elasticity was defined with both the carbon rod and special paper. The material properties and the structural and fluid analysis conditions are defined as shown in Table 1 and 2.

For solving this fluid-structure coupling problem, the numerical analysis divided between computational fluid dynamic(CFD) and computational solid dynamic(CSD) are described. The phenomena of the flow over the flapping elastic wing are assumed as an unsteady flow, three-dimensional incompressible, and turbulent flow. Hence, the governing equations of the fluid dynamic part are the continuity, and Navier-Stokes equation given by Eqs. (1) and (2). Due to the flow behaviors over the flapping wing is the turbulent flows, Shear-Stress transport(SST) k-ω mode is considered[3].

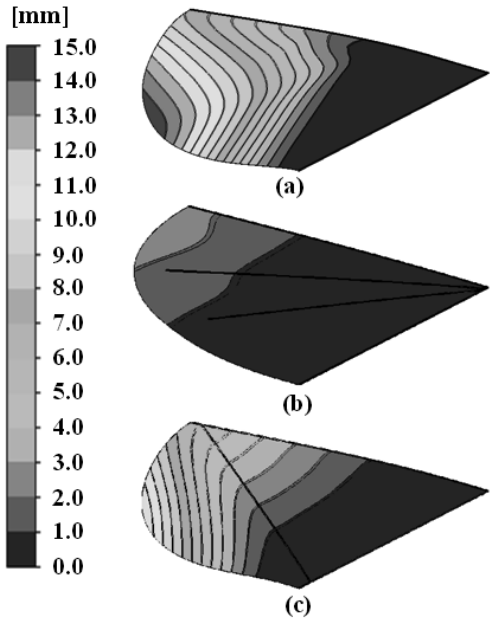

Fig. 1 The elastic deformation of flapping wing due to some ribs, (a) A-Type wing, (b) B-Type wing, (c) C-Type wing

In continuum mechanics, the equation of motion, that govern the structural dynamics of the flapping elastic wing can be given as Eq. (4). For the kinematics equation of flapping motion, a time-varying flapping angle as setting with the supports is defined by Eq. (3) referred with the paper[5]. In structural analysis, the nodal displacement data are calculated and send to fluid solver for solving the coupling phenomena.

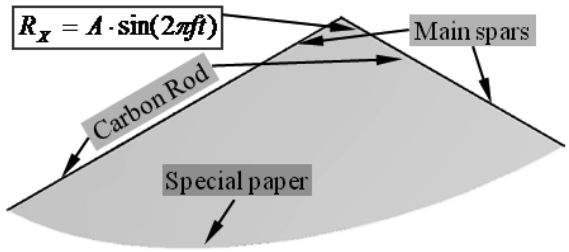

Fig. 2 The wing structure for Structural modeling

Table 1. Fluid simulation condition

Fluid	Air	Inlet	1.5 [m/s]
Mesh	Hexa &Tetra	Outlet	0 [Pa]
Element number	3.e+06	Wall	Symmetry
Turbulence	SST k-w	Time step	2.5.e-04 [s]
Re	8215	Flap. cycle	≈ 1.
Iteration	20	Cal. Time	Two months

Table 2. Structural simulation conditions

Structure	E [MPa]	Density [kg/m^3]	Poison's ratio
Carbon rod	133	1400	0.28
Special Paper	1.	300	0.3
Model	Linear elastic	Node number	1.e+04

$$\nabla \bullet (\rho U) = 0 \tag{1}$$

$$\frac{\partial(\rho U)}{\partial t} + \nabla \bullet (\rho U \otimes U) = \nabla \bullet \left(p\delta + \mu\rho\left(\nabla U + (\nabla U)^T\right)\right) \tag{2}$$

$$\theta(t) = [A]\sin(2\pi f(t + t_0) + \varphi) + \theta_0 \tag{3}$$

$$[M]\{\ddot{q}(t)\} + [C]\{\dot{q}(t)\} + [K]\{q(t)\} = \{R(t)\} \tag{4}$$

In the coupling method, we used the decoupled solver with the governing equations of the structural and fluid region independently. We perform a coupling simulation transferring on the fluid structure interaction by using ANSYS 13.0 and ANSYS-CFX 13.0. For a boundary surface of the wing structure, the interface transmitting pressure and displacement data is defined for the wing surfaces. The phenomena on the fluid, structural, and their interface region adequately are needed to keep convergence using iterative calculation because of strong interaction between the fluid and structural region.

3. Results and Discussion

We captured the flow field around the flapping wing at first flapping clycle. The vortex structure varying with flapping wing positions were explained by the vorticity contours as shown in Fig. 3. This is the iso-surface vorticity of 160 [1/s] at the top-dead point, and moving down after top point as shown in Figs. 2(a) and 2(b), respectively. We found, that the high velocities occur at the tip-wing and trailing edge, because these positions have the high momentum transferred from the wing's edge to the vortex structure around the wing. However, the vorticity are largest behind trailing edge and near tip-wing, because velocity gradient in X and Y axis have been large. The discontinuous vorticity at the trailing edge is also occurred by deforming membrane as shown in Fig. 3(a). The vortices behind the wing is generated by both flapping motion and elastic deformation.

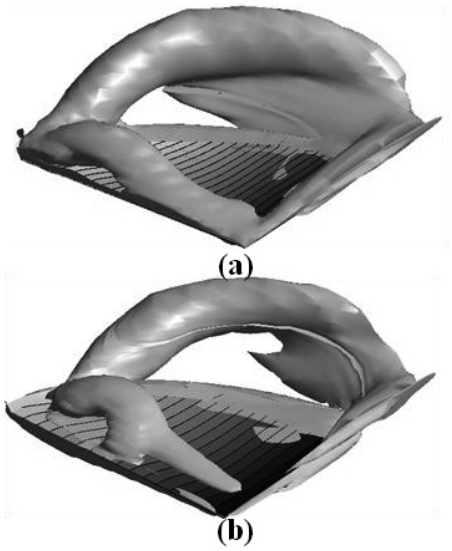

Fig. 3 Vorticity around flapping elastic wing varying the wing positions, (a) top-dead point, (b) moving down after top point.

4. Concluding remarks

In this paper, we have proposed a new idea how to control the wing's deformations by some ribs attached with the main spar of wing structure. We have simulated the vortex flow structure around the flapping elastic wing attached with some ribs. The simulation results are illustrated, that the vorticity around the wing is varied with, that the flapping wing position varied as flapping angle are stronger than the order of wing deformations. Moreover, the high vortices occur at the near center of trailing edge, these positions have thigh momentum transfer from the trailing edge due to an high total acceleration also.

In future work, we will consider the results at third and forth flapping cycle due to these results are only first cycle. It is just simple data. We expect, that the results from third cycle are significant for considering the deformation affected to the flow phenomena.

References

[1] T. Fujikawa, K. Hirakawa, S. Okuma, T. Udagawa, S. Nakano, K. Kikuchi, Mechanical Systems and Signal Processing, Vol. 22(2008), pp.1304-1315.

[2] K. Sugiyama, Y. Sumoto, Journal of Coputational Physics. Vol. 230(2011), pp.596-627.

[3] J.-M. Miao, M.-H. Ho., Journal of Fluids and Structers, Vol. 22(2006), pp.401-419.

[4] K. A. Hoffmann, and S. T. Chiang, Computational Fluid Dynamic III.(2000) 4th ed., Engineering Education System, Wichita Kan.

[5] A. Junchangpood, M. Fuchiwaki, K. Tanaka, (2010), The 10th Global Congress on Manufacturing and Management(GCMM2010).

Water-channel Visualization of Flow around a Spiked Body

Shashank Khurana[1], Kojiro Suzuki[2], Yasumasa Watanabe[3] and Ethirajan Rathakrishnan[4]
[1,2]Department of Advanced Energy, University of Tokyo, 5-1-5 Kashiwanoha, Chiba 277-8561
[3]Department of Aeronautics and Astronautics, University of Tokyo, Bunkyo-ku, Tokyo 113-8654
[4]Department of Aerospace Engineering, IIT-Kanpur, India 208016
shashank@daedalus.k.u-tokyo.ac.jp

ABSTRACT

Flow field around a cylindrical body with hemispherical nose, with and without a spike was visualized in a water flow channel using water color dyes. Attention was focused on the formation of vortices near the stagnation area of the forebody, and the effect of spike on the zone of influence. The effect of spike-nose configuration on the zone of influence and the base region was also studied. Two vortices of opposite family were observed on either side of the spike, as well as at the base of the forebody. The size of these vortices was quantified with respect to the forebody diameter.

1. Introduction

For simultaneous reduction of drag and aerodynamic heating at high-speeds, a forward facing spike attached to the nose of the body, as a passive control device, had been investigated in detail in the past, using numerous experiments and numerical analysis [1]. The flow physics around a spiked body accompanying recirculation region (comprising of vortices), as shown in Fig. 1, have been discussed, but the literature fails to report any information about the mechanism of formation of the vortices, its quantitative measurement and the zone of influence around the spiked body. Hence, an attempt has been made to understand the flow physics of vortex formation near the stagnation zone and the shedding of vortices at the base, using a low-cost device. The present work mainly deals with the influence of the flow field around the spike at a predetermined Reynolds number and the effect of spike-nose configuration on the same.

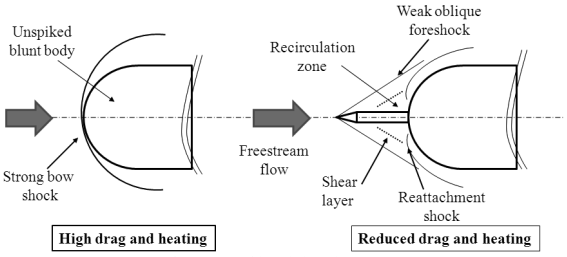

Fig. 1 Spiked-body concept

2. Experimental facility and method

In the present study, the flow around a spiked body, comprising of vortices near the stagnation area, was visualized using a rectangular water flow channel [2-3], manufactured in-house in the Suzuki K. Laboratory, University of Tokyo. Schematic diagram and a pictorial view of the channel are shown in Fig. 2(a) and Fig. 2(b), respectively. Water from the chamber, spills over the inclined plate and is conditioned using an array of wire-meshes, before reaching the downstream of the test-section. The flow quality is found to be fairly uniform in the test-section. The velocity of the flow is measured using the floating-particle method technique, over the length of the test-section. The average of a set of measured velocities is taken as the representative velocity of the flow.

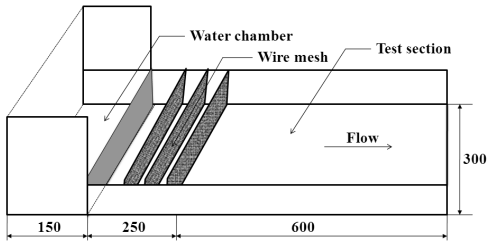

(a)

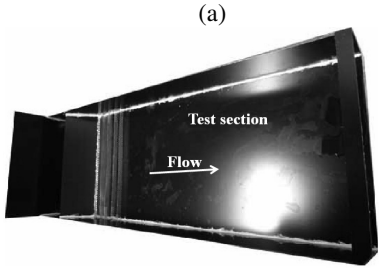

(b)

Fig. 2 (a) Schematic diagram of experimental set-up (dimensions in mm), (b) pictorial view of the set-up

The schematic diagrams of the test models and spike geometries, manufactured from ABS material using PC-controlled Modela MDX-504A (Roland DG Corporation) Rapid-prototyping machine available onsite in the laboratory, are shown in Fig. 3. The axis of the model was aligned parallel to the flow direction at the middle of test-section for every test. The model consists of a hemisphere-cylindrical forebody with various spike-nose configurations (hemispherical, conical, flat and a specific case of square cross-section with side or equivalent diameter equal to $(\pi/4)^{0.5}$ d, d being the spike root diameter). All the tests of the present study were carried out at Reynolds number 3070 based on the main body diameter. After the proper alignment has been ensured, sometime is given for the flow to develop properly. The flow field in the test-section was ensured to be parallel and uniform by observing parallel streak lines of dye injected upstream of the empty test-section. Then the model was placed in the test-section and the flow field was recorded on a video camera (PANASONIC, Model DMC-ZX3) at 30 frames per second. The videos recorded clearly exhibit the zone of influence (Z), head (H) and the vortices (V) at the base, as illustrated in Fig. 4.

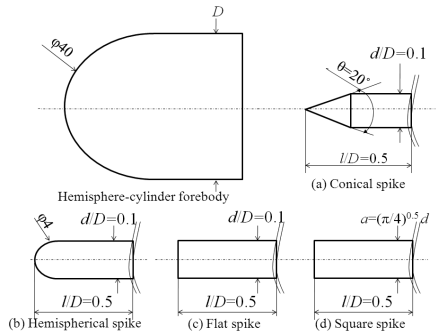

Fig. 3 Test geometry with spike configurations

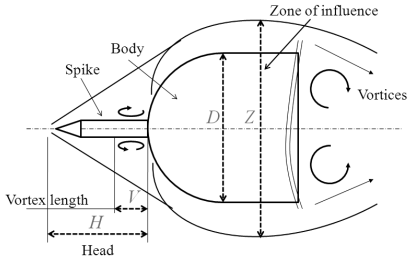

Fig. 4 Flow field nomenclature

3. Results and Discussion

Some representative visualization pictures, around the base body without and with spikes of different shapes at Reynolds number 3070 are shown in Fig. 5. The zone of influence, the head and the vortex length were measured from the video clippings. The measured values are given in Table 1. For all the cases visualized, two vortices were positioned at the base of the model as seen in Fig. 5. The measured values of *H*, *Z* and *V* were non-dimensionalized with *D*. The *H*/*D* magnitudes for the base body and with different spike configurations are shown in Fig. 6. It is interesting to see that with the introduction of spike, the head increases significantly for all the spike configurations. However, the increase is the maximum for the spike with conical nose. For this case, the *H*/*D* increase is from 0.3 to 0.68. Furthermore, for the square face spike with cylindrical and square shoulders the increase in the head zone is almost identical. The change in the influence zone with all the spikes is substantial as seen in Fig. 7. It is seen that accepting the conical nose for which the influence zone increases from 70.3 mm to 72.6 mm, for all other spikes the influence zone comes down significantly. For the hemispherical spike, the influence zone is the minimum in the present study. The vortex length variation for different spikes is compared in Fig. 8. It is seen that the longest vortex is for the spike with hemispherical nose. For the flat nosed cylindrical and square spikes the vortex size is almost the same. It is well known that the reduction of positive pressure at the nose of the model can give rise to drag reduction. From these results, it can be inferred that, the reduced expanse of the influence zone and longer vortex at the nose of the basic body can be taken as an indication of reduced positive pressure at the nose of the body. With this inference it may be summarized that among the spikes studied, the spike with hemispherical nose is the potential candidate for reducing the drag of the basic body.

Table 1. Measured values of *H*, *Z* and *V* (mm)

Spike	*H*	*Z*	*V*
No spike (NS)	12.1	70.3	0.0
Conical (CN)	27.0	72.6	4.8
Hemispherical (HM)	24.0	63.8	14.1
Flat (FL)	25.9	66.0	8.2
Square (SQ)	25.3	68.6	8.6

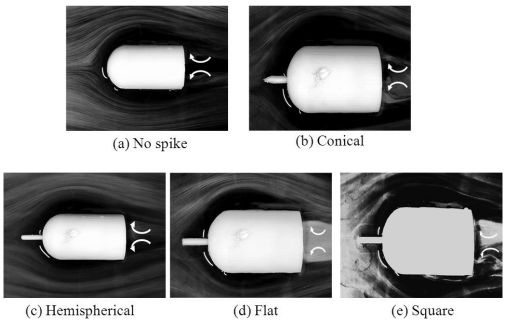

Fig. 5 Flow field for the test cases

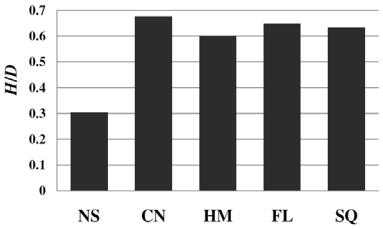

Fig. 6 Head variation for various spikes

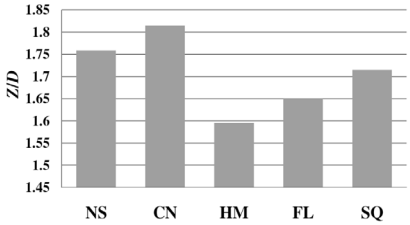

Fig. 7 Zone of influence variation for various spikes

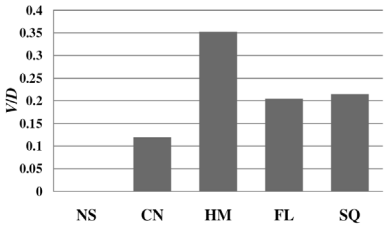

Fig. 8 Vortex length variation for various spikes

References

[1] M.Y.M. Ahmed and N. Qin, Prog. in Aerosp. Sciences (2011).

[2] H. Sharma, A. Vashishtha and E. Rathakrishnan, Proc. IMechE Vol. 22 Part J.Aerosp. Engg. (2008).

[3] Y. Takama, K. Suzuki and E. Rathakrishnan, Int. Rev. Aerosp. Engg., **1** (2008).

Eighth International Conference on Flow Dynamics
November 9 - November 11, 2011

Transfer Matrix Modeling for Synthetic Jet Actuators

Sam Yang, Fei Liu, Matias Oyarzun, Louis Cattafesta
Department of Mechanical and Aerospace Engineering, University of Florida, Gainesville, FL 32611-6250
Florida Center for Advanced Aero-Propulsion (FCAAP)
cattafes@ufl.edu

ABSTRACT

A transfer matrix (TM) model is developed in this paper for a synthetic jet or zero-net mass-flux actuator used in flow control applications. The analysis and design of a synthetic jet actuator is greatly simplified by the use of the transfer matrix method, which treats the synthetic jet actuator as a two-port network with input and output ports. The TM method is a more powerful alternative to lumped-element modeling. The model is summarized, and the resulting predictions match previously published results.

1. Introduction

A synthetic jet or zero-net mass-flux (ZNMF) actuator has numerous flow control applications [1-3]. The typical ZNMF actuator discussed in this paper, shown in Fig. 1, drives a piezoelectric diaphragm to alternately expel/ingest flow from/to a cavity through an orifice or slot. Its first-order modeling for design purposes is traditionally accomplished using quasi-static lumped element modeling (LEM), which has some fundamental limitations [2,4].

The transfer matrix method is introduced in this paper to model a synthetic jet actuator with the ultimate goal of circumventing some LEM limitations. A transfer matrix is traditionally employed in electrical and mechanical vibration anlysis [5]. Complex electromechanical devices can be simply modeled as a "two-port network" with input and output ports, as shown in Fig. 2. Matrix algebra can then be applied for analysis of such networks. The interconnection of parallel, series-parallel, and parallel-series network combinations can thus be handled by simple linear addition or multiplication of the transfer matrices. The TM approach is outlined for a prototypical actuator and compared to both LEM and experiments.

2. TM for the Synthetic Jet Actuator

For a two-port network, as shown in Fig. 2, the TM representation is given by

$$\begin{bmatrix} e_2 \\ f_2 \end{bmatrix}_{\text{output}} = \begin{bmatrix} T_{11} & T_{12} \\ T_{21} & T_{22} \end{bmatrix} \begin{bmatrix} e_1 \\ f_1 \end{bmatrix}_{\text{input}} \tag{1}$$

where e and f denote generalized effort and flow variables at the input and output ports in various energy domains. For instance, in the acoustic domain, the effort variable is the acoustic perturbation pressure, p', while the flow variable is the acoustic volume velocity, Q' (used in this paper), or perturbation velocity, u'.

In order to develop the TM for a synthetic jet actuator with a side-mounted PZT disk, the device is divided into several sub-systems as shown in Fig. 1: PZT disk, Duct A, Duct B, and the orifice/slot. The TM of each sub-system is then derived, and the TM for the actuator is obtained by multiplication or addition of the TM of the sub-systems [6].

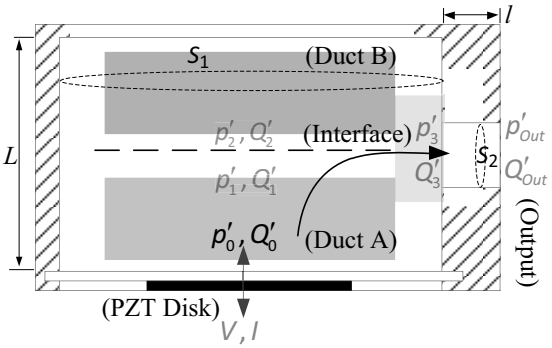

Fig. 1. Schematic of a side-mounted ZNMF jet actuator.

Fig. 2. A two-port network.

The TM for a PZT disk is derived using the terminology and lumped-element approach outlined in [4], as shown in Fig. 3

$$\begin{bmatrix} p_0' \\ Q_0' \end{bmatrix} = \begin{bmatrix} \dfrac{\phi^2 + j\omega C_{eB} Z_{aD}}{\phi} & -\dfrac{Z_{aD}}{\phi} \\ -\dfrac{j\omega C_{eB}}{\phi} & \dfrac{1}{\phi} \end{bmatrix} \begin{bmatrix} V \\ I \end{bmatrix}, \tag{2}$$

where ϕ is the turns ratio, C_{eB} is the is the blocked electrical capacitance of the piezoelectric diaphragm, and Z_{aD} is the short-circuit acoustic impedance of the piezoelectric diaphragm, and V and I are the input voltage and current, respectively.

As shown in Fig. 1, at the interface, one has

$$p_1' = p_2' = p_3', \tag{3}$$

and

$$Q_1' = Q_2' + Q_3'. \tag{4}$$

Furthermore, the perturbation pressure p_2' is related to the acoustic volume velocity Q_2' via

$$\frac{p_2'}{Q_2'} = -\frac{j\rho_0 c_0 \cot(kL/2)}{S_1}, \tag{5}$$

where ρ_0 and c_0 are the density of the air and the speed of sound, respectively, and $k = \omega / c_0$ is the

wavenumber. Eqs. (3)-(5) thus lead to

$$\begin{bmatrix} p_3' \\ Q_3' \end{bmatrix} = \begin{bmatrix} 1 & 0 \\ -1/\left(\dfrac{\rho_0 c_0}{j\tan(kL/2)\cdot S_1} \right) & 1 \end{bmatrix} \begin{bmatrix} p_1' \\ Q_1' \end{bmatrix}, \quad (6)$$

where (p_1', Q_1') is related to (p_0', Q_0') via a TM of a duct with cross sectional area S_1 [5]:

$$\begin{bmatrix} p_1' \\ Q_1' \end{bmatrix} = \begin{bmatrix} \cos\left(\dfrac{kL}{2}\right) & -\dfrac{j\rho_0 c_0}{S_1}\sin\left(\dfrac{kL}{2}\right) \\ -\dfrac{jS_1}{\rho_0 c_0}\sin\left(\dfrac{kL}{2}\right) & \cos\left(\dfrac{kL}{2}\right) \end{bmatrix} \begin{bmatrix} p_0' \\ Q_0' \end{bmatrix}. \quad (7)$$

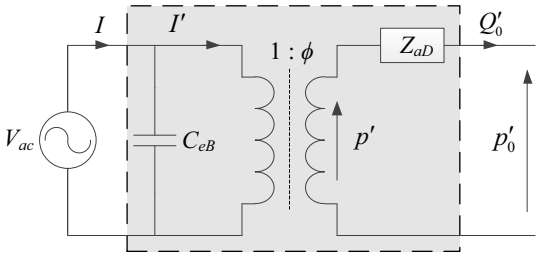

Fig. 3. PZT disk electrical representation.

The nonlinear resistance of an orifice or slot is significant for large output velocity. Its unsteady nonlinear dynamics can be described by direct multiplication of two TMs: the pressure loss TM due to nonlinear behavior and the acoustic TM for small perturbations that propagate through the orifice

$$\begin{bmatrix} p_{out}' \\ Q_{out}' \end{bmatrix} = \begin{bmatrix} 1 & \dfrac{\frac{1}{2}K_D\rho_0|Q_{out}'|}{S_2^2} \\ 0 & 1 \end{bmatrix} \times \begin{bmatrix} \cos\left(\dfrac{k\ell}{2}\right) & -\dfrac{j\rho_0 c_0}{S_2}\sin\left(\dfrac{k\ell}{2}\right) \\ -\dfrac{jS_2}{\rho_0 c_0}\sin\left(\dfrac{k\ell}{2}\right) & \cos\left(\dfrac{k\ell}{2}\right) \end{bmatrix} \begin{bmatrix} p_3' \\ Q_3' \end{bmatrix}, \quad (8)$$

where K_D is a nondimensional loss coefficient, which is a function of geometry, Reynolds number and Strouhal number [4, 7].

With all TM sub-systems determined, the TM for the actuator shown in Fig. 1 can be obtained by sequential multiplication of TMs from Eqs. (2), (7), (6) and (8)

$$\begin{bmatrix} p_{Out}' \\ Q_{Out}' \end{bmatrix} = \begin{bmatrix} T_{11} & T_{12} \\ T_{21} & T_{22} \end{bmatrix} \begin{bmatrix} V \\ I \end{bmatrix}. \quad (9)$$

3. Results and Discussion

For the synthetic jet actuator shown in Fig. 1 issuing into a quiescent medium, the output perturbation pressure and volume velocity satisfy a radiation impedance boundary condition

$$\frac{p_{Out}'}{Q_{Out}'} = R_{rad} + j\omega M_{rad}, \quad (10)$$

where R_{rad} and M_{rad} are the radiation resistance and mass of the orifice, respectively [8]. Thus, the volume velocity Q_{out}' (as well as particle velocity through the orifice) can be computed from Eqs. (9) and (10) once the input voltage V or current I is provided. However, because the volume velocity $|Q_{out}'|$ is included in the TM of the synthetic jet actuator (see Eq.(8)), an iterative solution is required.

Fig. 4 shows a comparison between the TM predictions, the lumped element model, and the experimental data for a synthetic jet actuator with dimensions listed in Tables 1 and 3 of reference [4]. Both TM and LEM predictions match the experimental data very well, thus validating the TM approach. Good agreement is expected because Eq. (2) is based on LEM.

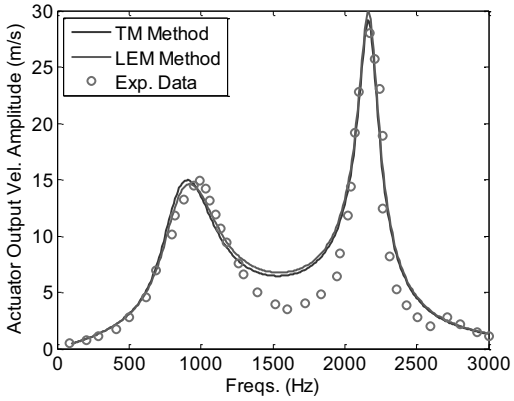

Fig. 4. Comparison of TM, LEM and experimental data.

4. Concluding remarks

The transfer matrix (TM) representation for a typical synthetic jet actuator is developed in this paper. The analysis and design of the synthetic jet actuator is greatly simplified by the use of the transfer matrix method. The TM predictions closely match the LEM predictions and provide good agreement with experimental data. However, the TM of the PZT disk used in this paper is derived based on a quasi-static lumped-element model. This model is limited to frequencies between dc and just beyond the fundamental frequency of the diaphragm. In future work, a TM will be derived that uses a dynamic diaphragm model so that the frequency range of predictions can be extended. The resulting model will then be compared with additional experiments.

References

[1] A. Glezer and M. Amitay, Annu. Rev. Fluid Mech., **34** (2002).

[2] L. Cattafesta and M. Sheplak, Annu. Rev. Fluid Mech., **43** (2011).

[3] M. Oyarzun, and L. Cattafesta, AIAA-2010-4414, 5th AIAA Flow Control Conference (2010).

[4] Q. Gallas, et al., AIAA Journal, **41**(2) (2003).

[5] M. Lampton , Acustica, **39** (1978).

[6]. M.L. Munjal , Acoustics of Ducts and Mufflers, John Wiley & Sons (1987).

[7] F. White, Fluid Mechanics, McGraw-Hill (1998).

[8] D. Blackstock, Fundamentals of Physical Acoustics, Wiley Interscience (2000).

Eighth International Conference on Flow Dynamics
November 9 - November 11, 2011

The Variation of Growth Process of Vortex in the Vicinity of a Wall by Elastic Deformation

Tomoki Kurinami, Masaki Fuchiwaki and Kazuhiro Tanaka
Department of Mechanical Information Science and Technology, Kyushu Institute of Technology
680-4, Kawazu, Iizuka-city, Fukuoka, 820-8502
E-mail : kurinami@vortex.mse.kyutech.ac.jp

ABSTRACT

The authors performed PIV measurement for vortex flow generated in the vicinity of a wall of rigid NACA0010 and elastic NACA0010 to clarify the growth process of vortices which change by elastic deformation, quantitatively. We evaluated the vortex flow by vorticity and the positive value of second invariant of velocity gradient tensor and clarified vortices which the rotate dominates deformation are generated only in the vicinity of a wall of elastic NACA0010. Therefore, the generation of vortices which the rotate dominates deformation depends on the elastic deformation.

1. Introduction

The authors have studied on a flow field around an unsteady airfoil by an experimental way and a numerical way over the years. In particular, a number of studies on wake structures and the characteristics of dynamic thrusts of an unsteady airfoil have been reported [1] [2]. However, behaviors of vortices that form wake structures and processes from generation to development have not been clarified yet.

Meanwhile, animals fly and swim within a narrow range of Strouhal number ($0.2<St<0.4$) [3] by skillfully controlling vorticies generated around their bodies. The elastic airfoil that enables elastic deformation in order to fly and swim with low energy has recently attracted a great deal of attention, and industrial applications of this elastic airfoil are expected [4]-[6]. Therefore, it is important to clarify the growth process of vortex in the vicinity of a wall of elastic moving airfoil.

We also clarified the relationship between the characteristics of dynamic thrust acting on a heaving elastic airfoil and its wake structure [7]. We clarified that thrust producing vortex streets are formed in the wake of both rigid and elastic airfoils, but that the vorticity and the interval of the vortices formed in each wake are different. However, the effects of elastic deformation on the process of generation, growth, and development of vortices in the vicinity of a wall have not been clarified.

In this study, we clarify the variation of the growth process of vortices in the vicinity of a wall by elastic deformation, quantitatively. We evaluate the vortex flow in the vicinity of a wall with vorticity and the positive value of second invariant of velocity gradient tensor to clarify the effect of elastic deformation on the growth process of vortices.

2. Method

PIV measurement system consists of water tunnel, test airfoil, water cooled Ar-ion laser, plane mirror and high speed camera. The chord length and span length of rigid NACA0010 and elastic NACA0010 are c=0.06 [m] and l=0.20[m], respectively. Elastic NACA0010 consists of rigid part and elastic part and this proportion is 1:1

The objective of this study is to clarify the variation of growth process of vortex in the vicinity of a wall by elastic deformation. Therefore, we need high density vectors in the vicinity of wall. However, tracer particles

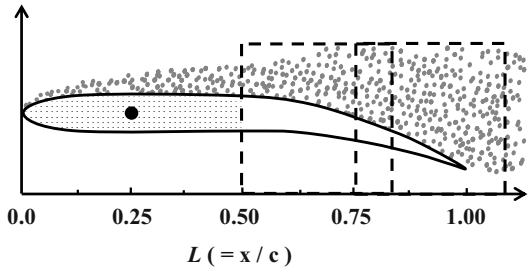

Fig. 1 Injection of tracer particle with pinholes and shooting domains for PIV measurement

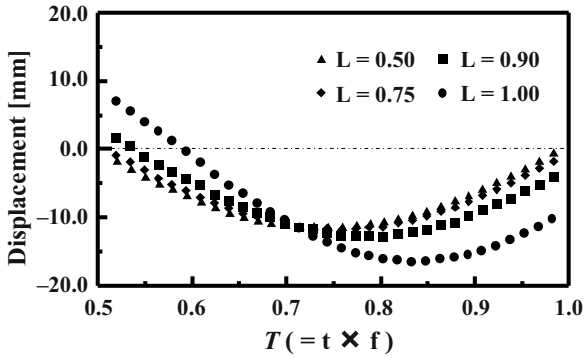

(a) Displacement

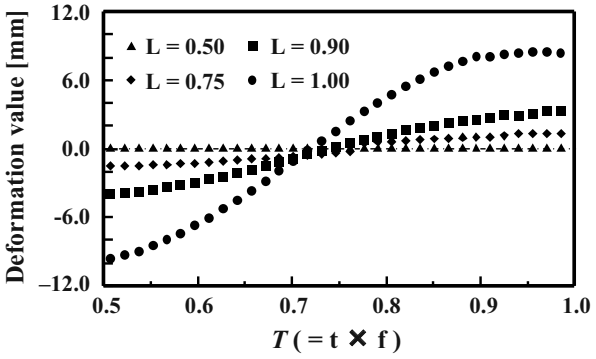

(b) Elastic deformation value

Fig. 2 The time variation of elastic deformation of heaving elastic NACA0010

decrease in the vicinity of a wall because of the development of boundary layer. We use the test airfoil with some pinholes (ϕ = 1.0 [mm]) and injected the tracer particle (ϕ = 10 [μm]) directly into the vicinity of a wall as shown in Fig. 1. Two regions shown in Fig.1 indicate the shooting domains for PIV measurement and

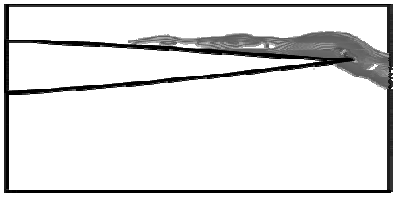

(a) Rigid NACA0010

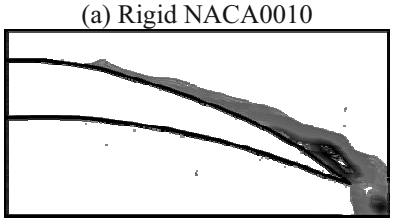

(b) Elastic NACA0010

Fig.3 The vorticity contours obtained from the vicinity of a wall of heaving NACA0010 at $T = 0.90$

we confirmed the density of tracer particle is sufficiently to perform the PIV measurement.

Figure 2 shows the detail of time variation of elastic deformation of heaving elastic NACA0010 at $St = 0.64$. Figures (a) and (b) indicates the displacement and elastic deformation value. The symbols ▲, ◆, ■ and ● indicate each location (L=0.50, 0.75, 0.90 and 1.0), respectively.

As shown in Fig.2(a), we can confirm the elastic part of elastic NACA0010 deforms sufficiently. In addition, the maximum amplitude becomes 1.35 times larger than heaving amplitude (L=0.50) at $L = 1.0$ and $T = 0.83$. Elastic deformation tends to become larger toward the trailing edge as shown in Fig.2(b). In this study, we focused on $T = 0.90$ when the elastic deformation becomes maximum.

3. Results and Discussion

Figure 3 shows the vorticity contours obtained in the vicinity of a wall of heaving NACA0010 at $T = 0.90$. Figs.(a) and (b) show the rigid and elastic NACA0010.

The vorticity is generated in the vicinity of a wall of rigid and elastic NACA0010 but vortices in the vicinity of rigid NACA0010 is formed small region and its vorticity are weak, compared with elastic NACA0010.

We evaluate the vortex flow in the vicinity of a wall with the second invariant of velocity gradient tensor (Q) shown in Eq.(1) to clarify the difference of property of vortex generated in the vicinity of a wall of rigid and elastic NACA0010. The positive value of Q indicates that the vortex which the rotation dominates deformation is generated.

$$Q = \frac{1}{2}\left(W_{ij}W_{ij} - S_{ij}S_{ij}\right) \qquad (1)$$

Figures 4 and 5 shows the contour of the positive value of Q at T =0.75 and 0.90. Figures (a) and (b) show the rigid and elastic NACA0010, respectively.

At $T = 0.75$ (Fig. 4 (a) and (b)), the positive value of Q does not generate in the vicinity of wall of rigid NACA0010 and elastic NACA0010. This is because the elastic deformation is very small.

As shown in Fig. 5 (a), the positive value of Q does not generate in the vicinity of wall of rigid NACA0010. Therefore, rigid NACA0010 cannot generate the vortex which the rotation dominates deformation in the vicinity of a wall.

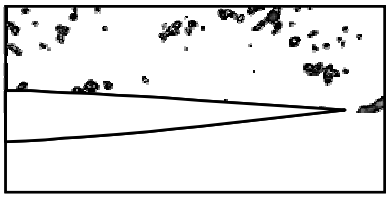

(a) Rigid NACA0010

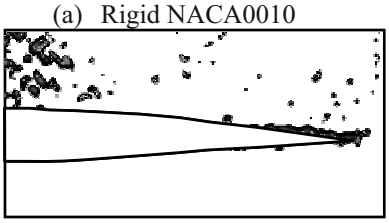

(b) Elastic NACA0010

Fig.4 The contour of the positive value of second invariant of vector gradient tensor at $T = 0.75$

(b) Rigid NACA0010

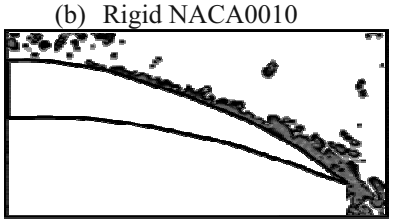

(b) Elastic NACA0010

Fig.5 The contour of the positive value of second invariant of vector gradient tensor at $T = 0.90$

Meanwhile, as shown in Fig.5(b), We can confirm that the positive value of Q is generated large region in the vicinity of a wall of elastic NACA0010. From the point of view of the result of T=0.75(Fig.4), the generation of vortex which rotation dominates deformation depends on the elastic deformation.

4. Concluding remarks

The elastic deformation increases the scale and the magnitude of vorticity generated in the vicinity of a wall. In addition, elastic deformation can generate the vortex which rotation dominates deformation in the vicinity of a wall.

References

[1] Jones,K.D., et al. AIAA J., Vol. 36, No.7 (1998)
[2] Lai,J.C.S. et al., AIAA J., Vol.37, No.12 (1999)
[3] Taylor G.K. et al., Nature 425 (2003)
[4] Heathcote, S., et al., AIAA Journal, Vol. 42, (2005)
[5] Heathcote S., et al., AIAA Journal, Vol. 45, (2007)
[6] Young Y.L., J. of Fluid and Structure,Vol.24, (2008)
[7] Fuchiwaki M., et al., J. of F. S. & Tech., Vol.4,(2009)

Eighth International Conference on Flow Dynamics
November 9 - November 11, 2011

Vorticity Components of Vortices Rolled up from an Elastic Moving Thin Film

Tetsushi Nagata, Masaki Fuchiwaki and Kazuhiro Tanaka
Graduate School of Computer Science and Systems Engineering, Kyushu Institute of Technology, 680-4 Kawazu, Iizuka-city, Fukuoka, 820-8502, Japan
nagata@vortex.mse.kyutech.ac.jp

ABSTRACT

Flow fields around a moving thin body is treated as Fluid-Structure Interaction (FSI), and these phenomena have been continued a series of moving, elastic deformation of the body, vortex generation, growing and development. Thin film materials deform easily and it is not easy to treat surrounding vortex structures. In this paper, we simulate the fluid structure interaction simulation of flow field around an elastic thin film using ANSYS 12.1/ANSYS CFX 12.1. The purpose of this study is to clarify the elastic advantage to the vortex growth and development around thin films and focus on a strain and a rotational component in fluid.

1. Introduction

The flow field around a moving body is treated as a fluid-structure interaction(FSI), which is a series of phenomena ranging from the elastic deformation of a body to vortex generation/growing/development. In particular, thin films easily deform by their small motion and the fluid pressure around the body.

Flow fields around thin materials have attracted a great deal of attention due to their importance in the development of MAVs and understanding a mechanism of a paper jam in the printing press and so on. However, their flow fields and dynamic forces have been not clarified sufficiently because the vortex structures induced by the elastic deformation are dependent on the stiffness and the motion condition of the thin film. Therefore, it is difficult to obtain the actual phenomena.

Flow fields that exhibit elastic deformation have primarily been clarified using numerical methods[1][2][3]. However, actual phenomena are not reproduced under considering the governing equation and transferring the data passing in the fluid and the structural fields, so few researches have been reported through such method as bi-directional coupling simulation. In other words, analyses under the assumption that the structural deformation is small and elastic deformation expressed by functions have been performed. However, these analyses cannot consider the effects of the fluid pressure to the structural deformation. Therefore, it has been not clarified in the details of the flow fields with fluid structure interaction. In particular, it is complicated problems in the case of the discussion about the characteristics of fluid deformations of the axisymmetric expansion-contraction, shear and rotation. Therefore, the extractions of the component in fluid using numerical methods come in more useful.

In the present paper, we simulate the fluid structure interaction of a flow field around elastic heaving thin film using ANSYS 12.1/ ANSYS-CFX 12.1. The goal of the present study is to clarify a development of vortex structure induced by the elastic deformation. In particular, we clarify vortex structures formed around the elastic heaving thin film used by a micro flapping robot. More specifically, we focus on components of a strain and a rotational deformation in fluid and clarify an elastic advantage to the flow fields.

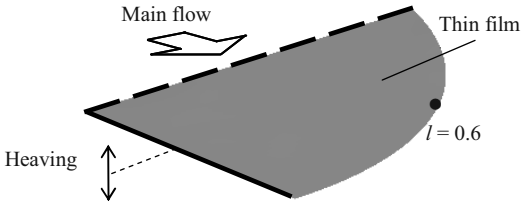

Fig.1 Thin film configuration

Table 1 Material properties

	Frame	Thin film
EI [Pa・m^4]	7.2×10^{-4}	8.6×10^{-7}
ν	0.3	0.3
ρ [kg/m^3]	1530	1000

Table 2 Simulation conditions

Fluid		Structure	
Number of nodes	6×10^5	Number of elements	1×10^4
Mesh	Hexa	Mesh	Hexa
Method	FVM	Method	FEM
Turbulence	k-ω	Motion	Heaving
Re	2.5×10^3		$y=A\sin(2\pi ft)$
St	0.25		

2. Method

The shape of the elastic thin film is given by the wing model in Fig. 1, which is used in a micro-flapping robot in the simulation. The chord c, span length l, and thickness h are 80, 120, and 0.035 [mm], respectively. The chord and span directions are fixed with frame. Non-deformation condition and the heaving motion are applied to the part of chord. The amplitude A and frequency f are 12 [mm] and 5.0 [Hz], respectively and the frame of span that is leading edge is passively-deformed due to the heaving motion. Tables 1 and 2 show the material properties and the simulation conditions, respectively. The structural governing equation is constitutive equations applied Newton-Raphson method. The fluid governing equations are the equations of continuity and the Navier-Stokes equation. For the boundary surface of the thin film, an interface that transmits pressure and displacement data is defined for the thin film surface and the data passing are treated with relaxation of load implicitly.

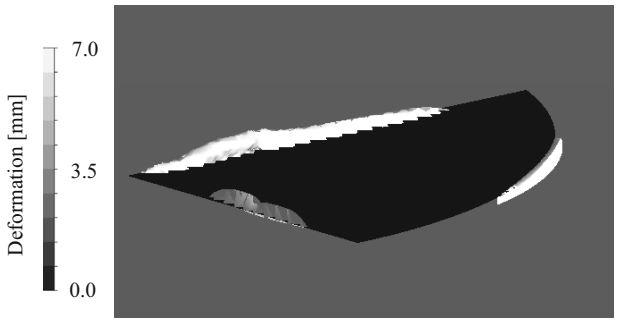

(a) Thin plate

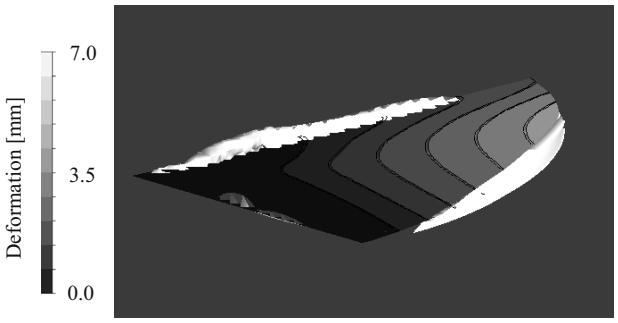

(b) Thin film

Fig.2 Isosurfaces of second invariants of velocity gradient tensor Q around the thin plate and thin film at t/T=0.35

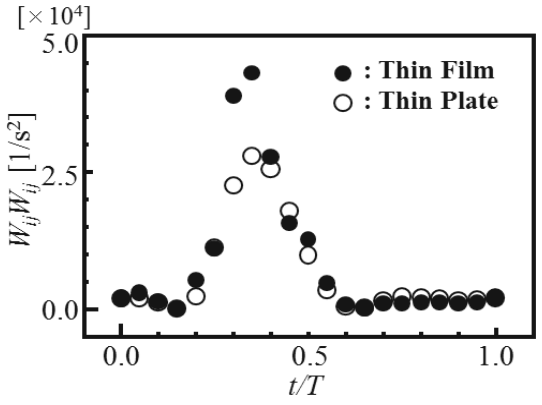

(a) $W_{ij}W_{ij}$

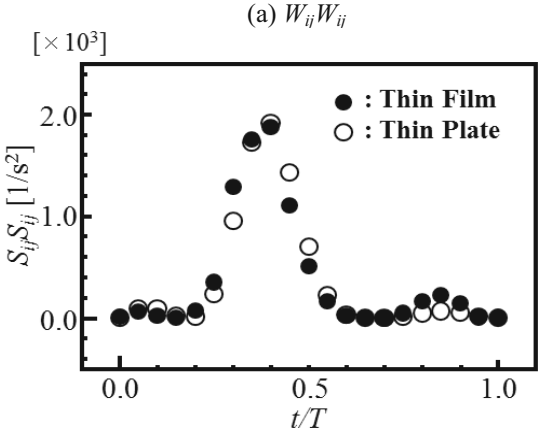

(b) $S_{ij}S_{ij}$

Fig.3 Rate of rotational and rate of strain tensors of the thin film and thin plate at l = 0.6 in the trailing edge

3. Results and Discussion

3.1 Flow field around the heaving thin film and plate

Figures 2(a) and 2(b) show the isosurfaces of the second invariant Q (=0.4[1/s^2]) of the velocity gradient tensor of the thin plate and the thin film at t/T=0.35, respectively. Q is defined by Eq. (1), and S_{ij} and W_{ij} indicate the rate of strain and the rate of rotation tensors, respectively. In the positive of Q, the vorticity dominates the strain. The contour indicates the elastic deformation.

$$Q = \frac{1}{2}\left(W_{ij}W_{ij} - S_{ij}S_{ij}\right) \qquad (1)$$

As shown in Fig. 2(a), the vortices are rolled up from the leading edge of the thin plate by heaving motion, and it also can be seen that they are rolled up near the mid-span in the narrow range of the trailing edge. On the other hand, as shown in Fig. 2(b), the thin film deforms, and it produces rate of rotation of velocity gradient in the trailing edge as well as in the leading edge. Therefore, the elastic deformation can change the flow direction such as to produce the rate of rotation.

3.2 Vorticity tensor and rate of strain tensor

Figures 3(a) and 3(b) show the square of the rate of rotational tensor(vorticity tensor) and the rate of strain tensor at the l=0.6 in the Fig.1, respectively. In other words, these mean the proportional to the total enstrophy and the kinetic energy dissipation rate. The horizontal axis indicates the cycle t/T, and the vertical axis in the Figs. 3(a) and 3(b) indicate the $W_{ij}W_{ij}$ and $S_{ij}S_{ij}$, respectively. The ● and ▲ symbols indicate the results for the thin film and the thin plate, respectively.

As shown in Fig. 3(a), the differences of rate of rotation between the thin film and the thin plate become pronounced in 0.25<t/T<0.5 when the elastic deformation becomes large. In particular, the rate of rotation tensor of the thin film is 1.5 times stronger than that of the thin plate at t/T=0.35. Therefore, the rate of rotation tensor becomes large with increasing of the elastic deformation. In other words, in order to obtain the vorticity, it is need to greatly change the flow direction by the elastic deformation such as Fig. 2(b).

However, as shown in Fig. 3(b), the rates of strain tensor are almost similar behavior between the thin film and the thin plate in one cycle. Moreover, these values are less than one-tenth of the values of the rate of rotation in the Fig.3(a). Therefore, the elastic deformation has a very small effect to the rate of strain. This means that the rate of strain tensor is dependent on the heaving motion, and not deformation.

4. Concluding remarks

In the trailing edge of the heaving thin film, the velocity gradient in the flow fields becomes large by the elastic deformation, and the large rotation rate is produced. On the other hand, the rate of strain tensor has small impact from the elastic deformation. Therefore, the elastic deformation can dominantly produce the rate of rotation in the flow fields.

References

[1] Maio J.-M.,et al,J. Fluids and Structures, **22**(2006), 401.
[2] Stanford B.,et al, Prog. Aero. Scie., **44**(2008), 258.
[3] Dominic D.J. et al. AIAA Journal, **46** (2008), 429.

Direct Computation of the Passive Control of a Hole-Tone Phenomenon

Kazuo Matsuura[1], Masami Nakano[2]
[1]International Advanced Research and Education Organization, Tohoku University
6-3 Aoba, Aramakiaza, Aoba-ku, Sendai, Miyagi, 980-8578, Japan
[2]Institute of Fluid Science, Tohoku University
2-1-1 Katahira, Aoba-ku, Sendai, Miyagi, 980-8577, Japan
E-mail: matsuura@alba.ifs.tohoku.ac.jp

ABSTRACT

Direct computations and experiments for the passive control of a hole-tone phenomenon are conducted. The mean velocities of air-jets are 10 m/s in both the computations and experiments. The diameters of a nozzle and an end plate hole are both 51 mm, and an impingement length between the nozzle and the end plate is 50 mm. The hole-tones are successfully suppressed by an obstacle on the end plate, and the mechanism is well reproduced by the present computations.

1. Introduction

The sound produced when a jet, issued from a circular nozzle or hole in a plate, goes through a second plate with a hole of the same diameter as the jet is referred to as a hole-tone. We encounter the tone in many practical situations such as solid propellant rocket motors, automobile intake- & exhaust-systems, ventilation systems, gas distribution systems, whistling kettle, etc. The mechanism of the tone is considered that the sound is maintained by a feedback mechanism in which pressure fluctuations generated at the second hole cause pulsations in the jet flow rate that excite axisymmetric instabilities of the jet [1]. Despite the long history of the hole-tone problem, a comprehensive analytical/numerical solution including methods to minimize the tone has not yet been given [2]. So far, the authors have conducted direct computations to investigate the details of the hole-tone [3].

In this paper, the passive control of the hole-tone phenomenon is investigated by direct computations as well as experiments.

2. Numerical Method

The governing equations are the unsteady three-dimensional compressible Favre-filtered Navier-Stokes equations. To close the system the perfect gas law is assumed. The equations are solved by the finite-difference method. Spatial derivatives that appear in metrics, convective and viscous terms are basically evaluated by the 6th-order tridiagonal compact scheme [4]. Time-accurate solutions to the governing equations are obtained by the 3rd-order Runge-Kutta scheme. In addition to the above-mentioned spatial discretization and time integration, a 10th-order implicit filtering [5] is introduced to suppress instabilities of the computations. The parameter that appears in the left-hand side of the filtering formulation is set to be 0.492 in interior grid points. The details of the present numerical method are shown in [6].

3. Computational and Experimental Systems

Figs. 1 and 2 show the computational overview of the present problem, and an experimental system with an obstacle for the passive control of the hole-tone phenomenon, respectively. The diameters of the nozzle and the end plate hole are d_0=51 mm. In the numerical model, the outer diameter of the end plate is taken to be 250 mm. The impingement length between the nozzle and the end plate L_{im} is 50 mm. The thickness of the end plate is 10 mm. The mean velocities u_0 of the air-jets are

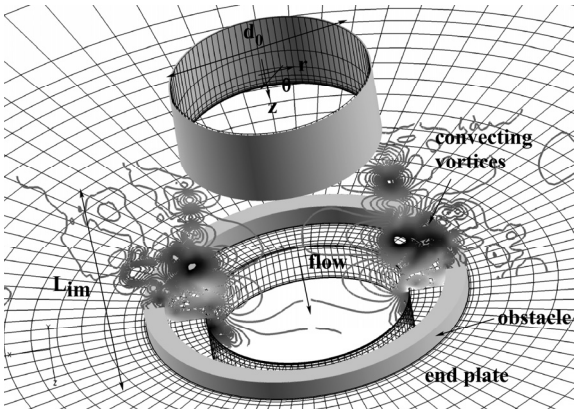

Fig. 1 Hole-tone system
(Contours: instantaneous pressure by CFD)

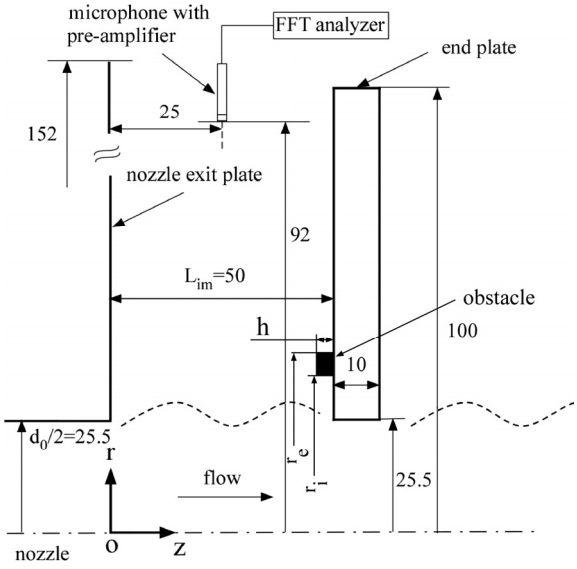

Fig. 2 Experimental system with an obstacle

Table 1. The geometries of the obstacles used in the computations and experiments

	r_i	r_e	h
exp	35.5	40.5	0, 2, 3, 5
cfd	35.5	40.5	5

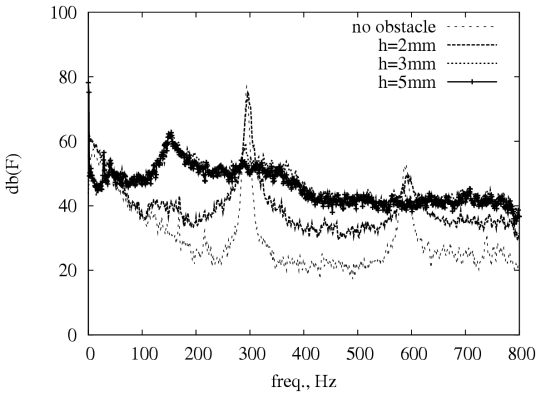

Fig. 3 Measured sound pressure levels for h=0, 2, 3, 5 mm

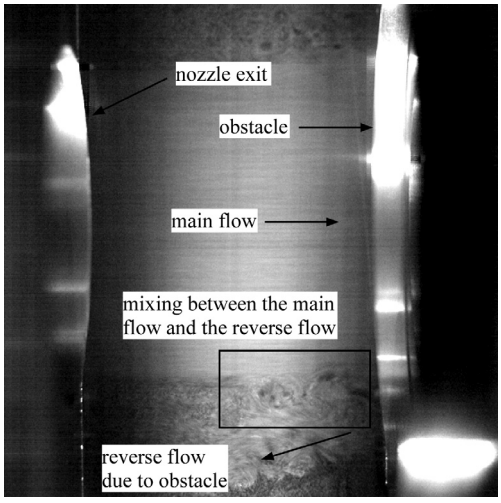

Fig. 4 Experimental visualization of the flow field when h=5 mm by a laser-smoke method

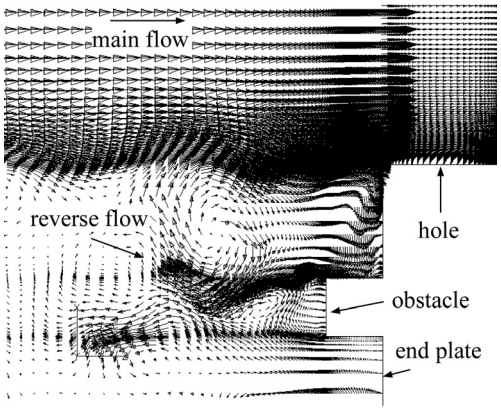

Fig. 5 Computational visualization of the flow field around the obstacle when h=5 mm

10 m/s. At 15°C, this corresponds to a Reynolds number $Re=u_0d_0/\nu\approx3.42\times10^4$. The overall computational domain consists of 7 zones, and cylindrical-coordinate grids of the O-type topology are generated in each zone. The total number of grid points is 9.21×10^6 points. Table 1 shows the geometries of the obstacles used in the computations and experiments.

4. Results and Discussion

Fig. 3 shows measured sound pressure levels for h=0(no obstacle), 2, 3, 5 mm. Peaks observed around 300 Hz for h=0 and 2 mm disappear when h=3 and 5 mm, which means that the present obstacle is effective in suppressing the hole-tone. Fig. 4 shows an instantaneous jet shear layer visualized by a laser-smoke method. By reverse flows due to the obstacle, organized vorticies in shear layers which are important for the hole-tone [3] are broken. Fig. 5 shows a computational visualization of the flow field around the obstacle when h=5 mm. The hole-tone suppression mechanism mentioned above is successfully reproduced in the computations.

5. Concluding Remarks

Direct computations and experiments for the passive control of the hole-tone phenomenon are conducted. The mean velocities of the air-jets are 10 m/s in both the computations and experiments. The diameters of the nozzle and the end plate hole are both 51 mm, and the impingement length between the nozzle and the end plate is 50 mm. The hole-tones are successfully suppressed by the present obstacle, and the mechanism is well reproduced by the present computations.

Acknowledgements

This research was supported by the Global COE Program "World Center for Education and Research for Transdisciplinary Flow Dynamics," of Tohoku University. Computational resources are provided by Advanced Fluid Information Research Center of Institute of Fluid Science, Tohoku University. The experiment is conducted with cooperation of Mr. Atsushi Totsuka, a technical staff at Institute of Fluid Science.

References

[1] M. S. Howe, Acoustics of Fluid-Structure Interactions, (1998), Cambridge Univ. Press.
[2] M. A. Langthjem, M. Nakano, J. Sound and Vibration, **28** (2005), p. 133.
[3] K. Matsuura, M. Nakano, J. Fluid Sci. Tech., **6**(4) (2011), p. 548.
[4] S. K. Lele, J. Compt Phys., **103**(1) (1992), p. 16.
[5] D. V. Gaitonde, M. R. Visbal, AIAA J., **38**(11) (2000), p. 2103.
[6] K. Matsuura, C. Kato, AIAA J., **45**(2) (2007), p. 442.

Eighth International Conference on Flow Dynamics
November 9 - November 11, 2011

Self-sustained flow oscillations and sound generation in a simple axisymmetric silencer model

Mikael A. Langthjem[1], Masami Nakano[2]
[1]Graduate School of Science and Engineering, Yamagata University
[2]Institute of Fluid Science, Tohoku University
E-mail of corresponding author: mikael@yz.yamagata-u.ac.jp

Abstract

This paper is concerned with a mathematical model of a simple axisymmetric silencer model consisting of an expansion chamber followed by a tailpipe. The unstable shear layer is modeled via a discrete vortex approach, based on axisymmetric vortex rings. The aeroacoustic model, which is described in the present short paper, is based on the Powell-Howe theory of vortex sound. The boundary integrals, which represent the scattering by the cavity and the tailpipe, are discretized via the boundary element method.

1. Introduction

Expansion chambers are often used in connection with silencers in engine exhaust systems, with the aim of attenuating the energy flow. The flow through the chamber may however generate self-excited oscillations, thus becoming a sound generator rather than a sound attenuator. Similar geometries (and problems) may be found in, for example, solid propellant rocket motors and heat exchangers.

A related problem is that of flow past a rectangular cavity. This, too, has connections to a number of practical applications, such as the sunroof in an automobile, weapon and landing gear bays of aircraft, and musical instruments. Analytically, the two-dimensionality makes the problem attractive; accordingly is has been extensively studied and a large number of articles are available [1].

The aim of the present work is to contribute to the understanding of the interaction between oscillations of the flow field and the acoustic field.

By oscillations of the flow field we mean the self-sustained oscillations of the jet shear layer. It is unstable and rolls up into a large, coherent vortex ('smoke-ring') which is convected downstream with the flow. It cannot pass through the hole in the downstream plate but hits the edge of the hole, where it creates a pressure disturbance. The disturbance is thrown back (with the speed of sound) to the upstream plate, where it disturbs the shear layer. This initiates the roll-up of a new coherent vortex. In this way an acoustic feedback loop is formed, making up one type of flow-acoustic interaction.

These so-called hole-tone feedback oscillations may interact with the acoustic axial and radial eigenoscillations of the cavity and the tailpipe. It is these interactions that we seek to understand in the present work.

We study a configuration as that shown in Fig. 1. The unstable shear layer is modeled via a discrete vortex approach, based on axisymmetric vortex rings. The aeroacoustic model is based on the Powell-Howe theory of vortex sound [1, 2]. The boundary integrals, which represent the scattering by the cavity and the tailpipe, are discretized via the boundary element method.

The present short paper gives an outline the aeroacoustic analysis. The geometry of the problem facilitates the use of cylindrical polar coordinates (r, θ, z), with the fluid flowing in the positive z-direction. Although it is possible that non-axisymmetric modes may be excited, the present work will, at this stage, consider only the axisymmetric modes (r, z).

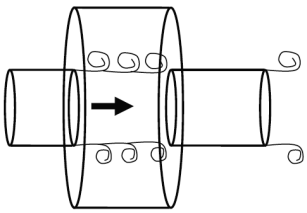

Fig. 1. The silencer model with a closed cavity and a tailpipe. The arrow indicates the direction of the flow.

2. Aeroacoustic model

The starting point is taken in Howe's equation for vortex sound at low Mach numbers [1, 2]. Let $\mathbf{u}$ denote the flow velocity, $\boldsymbol{\omega} = \nabla \times \mathbf{u}$ the vorticity, c_0 the speed of sound, and ρ the the fluid density. The sound pressure $p(\mathbf{x}, t)$ at the position $\mathbf{x} = (r, z)$ and time t is related to the vortex force (Lamb vector) $\mathfrak{L}(\mathbf{x}, t) = \boldsymbol{\omega}(\mathbf{x}, t) \times \mathbf{u}(\mathbf{x}, t)$ via the non-homogeneous wave equation

$$\left(\frac{1}{c_0^2} \frac{\partial^2}{\partial t^2} - \nabla^2 \right) p = \rho \nabla \cdot \mathfrak{L}, \tag{1}$$

with boundary conditions ($\mathbf{n}$ = normal vector)

$$\frac{\partial p}{\partial n} = \nabla p \cdot \mathbf{n} = 0 \ \text{ on the surfaces}, \qquad p \to 0 \ \text{ for } \ |\mathbf{x}| \to \infty. \tag{2}$$

To solve (1) and (2) in an axisymmetric setting, use is made of the time-domain axisymmetric Green's func-

tion $G(t,\tau;r,z;r_*,z_*)$ which is a solution to

$$-\frac{1}{c_0^2}\frac{\partial^2 G}{\partial t^2}+\frac{\partial^2 G}{\partial r^2}+\frac{1}{r}\frac{\partial G}{\partial r}+\frac{\partial^2 G}{\partial z^2} \quad (3)$$
$$=-\frac{\delta(r-r_*)}{r}\delta(z-z_*)\delta(t-\tau),$$

where the δ's are Dirac delta functions. It can be shown that the solution is given by

$$G(t,\tau;r,z;r_*,z_*)=\frac{c_0}{\pi}\frac{H(f_n^+)H(f_n^-)}{\sqrt{f_d^+}\sqrt{f_d^-}}, \quad (4)$$

where

$$f_n^+ = r+r_*-\sqrt{c_0^2(t-\tau)^2-(z-z_*^2)}, \quad (5)$$
$$f_n^- = \sqrt{c_0^2(t-\tau)^2-(z-z_*^2)}-|r-r_*|,$$
$$f_d^+ = (r+r_*)^2+(z-z_*)^2-c_0^2(t-\tau)^2,$$
$$f_d^- = c_0^2(t-\tau)^2-(z-z_*)^2-(r-r_*)^2,$$

and $H(f)$ is the Heaviside unit function which takes the value 1 when $f>0$ and the value 0 when $f<0$.

By making use of the Green's function the pressure $p(\mathbf{x},t)$ at any point $\mathbf{x}=(r,z)$ can be determined as

$$p(t,r,z)=-\rho\int_\tau\left\{\int_{z_*}\int_{r_*}\nabla_{\mathbf{y}}G\cdot\mathfrak{L}r_*dr_*dz_* \quad (6)\right.$$
$$\left.-\int_{z_{*1}}^{z_{*2}}p_*\frac{\partial G}{\partial r_*}2\pi r_*dz_*-\int_{r_{*1}}^{r_{*2}}p_*\frac{\partial G}{\partial z_*}2\pi r_*dr_*\right\}d\tau,$$

where, in the first term, $\nabla_{\mathbf{y}}=(\partial/\partial r_*,\partial/\partial z_*)$. This term represents the 'source' contribution p_s from the vortex rings. The vorticity related to a single ring is given by $\boldsymbol{\omega}_j=\Gamma_j\delta(r_*-r_j)\delta(z_*-z_j)\mathbf{i}_\theta$, where $\mathbf{i}_\theta$ is a unit vector in the azimuthal direction of the cylindrical polar coordinate system (r,θ,z). Then, by making use of (4, 5), the first term in (6) takes the form

$$p_s=\frac{c_0}{\pi}\rho\sum_j\left\{\mathrm{sgn}(r,r_j)\frac{\partial}{\partial r}\int_{t-d_j^+/c_0}^{t-d_j^-/c_0}\frac{\Gamma_j(\tau)v_{zj}(\tau)\,r_j}{\sqrt{f_d^+}\sqrt{f_d^-}}d\tau \quad (7)\right.$$
$$\left.-\frac{\partial}{\partial z}\int_{t-d_j^+/c_0}^{t-d_j^-/c_0}\frac{\Gamma_j(\tau)v_{rj}(\tau)\,r_j}{\sqrt{f_d^+}\sqrt{f_d^-}}d\tau\right\}.$$

Note that differentiation with respect to the source variables r_j and z_j have been converted into differentiation with respect to r and z. Here care should be taken with the signs related to r_j and r; see (5). This is taken care of by the function $\mathrm{sgn}(r,r_j)$.

The main contributions to the τ-integrations will be at the end point singularities. Hence the functions f_d^+ and f_d^- can be approximated as follows

$$f_d^+ \approx 2c_0d_j^+\left\{\tau-(t-d_j^+/c_0)\right\}, \quad (8)$$
$$f_d^- \approx 2c_0d_j^-\left\{(t-d_j^-/c_0)-\tau\right\},$$

where

$$d_j^+=\{(r+r_j)^2+(z-z_j)^2\}^{\frac{1}{2}}, \quad (9)$$
$$d_j^-=\{(r-r_j)^2+(z-z_j)^2\}^{\frac{1}{2}}.$$

Another approximation that will be made is that the vortex strengths $\Gamma_j(\tau)$ and the corresponding velocities $v_{rj}(\tau,r_j,z_j), v_{zj}(\tau,r_j,z_j)$ are approximately constant within the boundaries of the integration over τ, and equal to their values at the mean retarded time $\bar{t}=t-(d_j^++d_j^-))/2c_0$.

By applying these approximations (7) reduces to

$$p_s=\frac{\rho}{2}\sum_j\Gamma_j(\bar{t})\left\{v_{zj}(\bar{t})\frac{\partial}{\partial r}\frac{r_j}{\sqrt{d_j^+d_j^-}}\mathrm{sgn}(r,r_j) \quad (10)\right.$$
$$\left.-v_{rj}(\bar{t})\frac{\partial}{\partial z}\frac{r_j}{\sqrt{d_j^+d_j^-}}\right\}.$$

The second and the third term of (6) make up the scattering contribution p_{sc}, due to the solid surfaces. p_* refers to the surface pressure. The second term is for the horizontal sections (integration along the z axis) while the third term is for the vertical surfaces (integration along the r axis). By making use of the same kind of approximations as applied to the vortex source term p_s these terms can be evaluated as

$$p_{sc}=\pi\sum_e p_e(\bar{t})\left\{\frac{\partial}{\partial r}\int_{z_{e1}}^{z_{e2}}\frac{r_e}{\sqrt{d_e^+d_e^-}}dz_e\,\mathrm{sgn}(r,r_e) \quad (11)\right.$$
$$\left.+\frac{\partial}{\partial z}\int_{r_{e1}}^{r_{e2}}\frac{r_e}{\sqrt{d_e^+d_e^-}}dr_e\right\}.$$

Here the index e indicates discretization via boundary elements and $\sum_e$ 'summation' over all elements. The integrals in (11) are evaluated numerically, using Gauss quadrature.

3. Concluding remarks

We have derived an aeroacoustic model, based on the theory of vortex sound, to evaluate the sound generation from an expansion chamber-type silencer model. The final acoustic pressure expressions are simple and easy to implement numerically.

The coupled flow-acoustic analysis (computer program) includes a model of acoustic feedback. The acoustic particle velocity is coupled with the acoustic pressure through the (linearized) momentum equation. The acoustic velocity field is evaluated by integrating this equation. This velocity is then added to the 'hydrodynamic' velocity of the vortex rings, making up the acoustic feedback.

Acknowledgements. This work is supported by a Collaborative Research Project Grant from the Institute of Fluid Science, Tohoku University.

References

[1] M. S. Howe, Acoustics of Fluid-Structure Interactions, Cambridge University Press, Cambridge, 1998.

[2] M. S. Howe, Theory of Vortex Sound, Cambridge University Press, Cambridge, 2003.

Eighth International Conference on Flow Dynamics
November 9 - November 11, 2011

Flight velocity control of small flapping robot by flapping frequency

Tadatsugu Imura[1], Masaki Fuchiwaki[2] and Kazuhiro Tanaka[2]
[1] Graduate School of Computer Science and Systems Engineering Kyushu Institute of Technology
680-4 Kawazu, Iizuka-city, Fukuoka 820-8502, Japan
[2] Department of Mechanical Information Science and Technology Kyushu Institute of Technology
680-4 Kawazu, Iizuka-city,Fukuoka 820-8502, Japan
imura@vortex.mse.kyutech.ac.jp

ABSTRACT

This paper shows the flight characteristics of small flying robot which do not have tail wings as flapping frequency changes. The flight velocity and body angle increase as flapping frequency increases. The flapping frequency can be important element for the control of flight altitude because the flight altitude depends on flight velocity. In fact, the flight altitude can be controlled by flapping frequency changing on a flight.

1. Introduction

In the 1990s, Defense Advanced Research Projects Agency (DARPA) provided huge grants for developing small airplane called Micro air vehicles (MAVs). MAVs are expected to many applications, such as routine maintenance check of structures, surveillance and rescue operation assists at a remote disaster area and at the other planets. As rapid advance in various technologies, many researchers have developed many MAVs of fixed wing, rotation wing and flapping wing [1].

Recently, flapping robots which do not have tail wing have been reported [2]. However, research which is put emphasis on flight control is few, it is not clarified sufficiently how mechanism to fly. In previous our study, it is clarified that the proper wing deformation is one of necessary element to realize the flight. However, the effect of wing motion for the flight is not clarified. The purpose of this paper is clarifying the effect of wing motion (flapping frequency) for the flight of small flying robot without tail wing. Specifically, we measured the body angle and flight velocity of flying small flying robot with different flapping frequency.

2. Method

Figure 1(a) shows a small flying robot developed by this study. The wing span length l, wing chord length c and weight m of this small flying robot are 240[mm], 80[mm] and 1.97[g], respectively. The wing loading W / S indicating loading per unit area is 1.5[N/m^2], This small flying robot does not have tail wing, therefore it realize a flight actuating the only one pair of wings. The power source is motor and battery. The flapping frequency can be changed by voltage of the battery. The small flying robot can fly in a whirl for 20 [min] which was the battery's duration.

The small flying robot flight is evaluated by measurement its body angle and flight velocity. We make its flight to start with initial velocity 0 [m/s]. The author shot the motion of robot with high speed camera (500 [fps]) at the horizontal location of 2 [m]. We measure coordinate points on the nose and end of body of small flying robot with the high speed camera movies(Fig. 1(b)).

3. Flights by different flapping frequencies

Fig. 2 shows mean values of the body angle of flying small flying robot on a flapping period for different flapping frequencies. The horizontal axis and vertical axis respectively indicate flapping frequency f and body angle θ_b, respectively. In addition, ● and ■ indicate decreasing and increasing flight altitudes, respectively. The line indicates linear approximation.

Increasing flapping frequency from 7.8 [Hz] to 10.5 [Hz], the body angle increases linearly from approximately 5 [deg.] to 25 [deg.]. The rate of increase is approximately 6 [deg./Hz]. In addition,

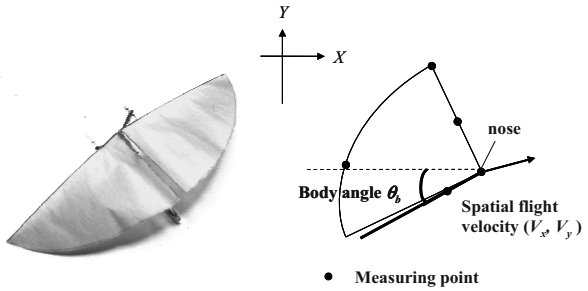

(a) Small flying robot (b) Coordinate system

Fig.1 Experimental set up

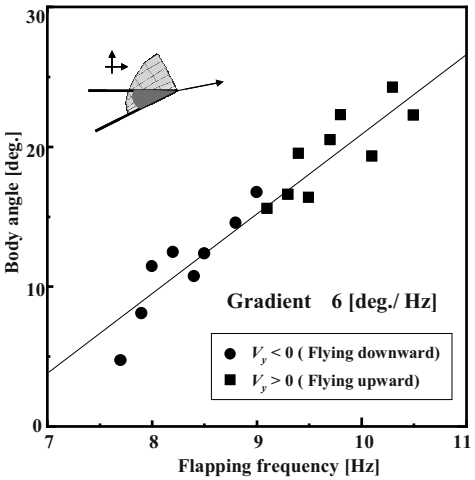

Fig.2 Body angles of small flying robot with different flapping frequencies

flying micro-robot tends to fly upward for larger body angles. In the other words, the flight altitude tends to increase due to the increased flapping frequency associated with the increased body angle. Based on these results, body angle is believed to affect flight velocity.

Fig. 3 (a), (b) and (c) show mean values of the spatial horizontal velocity, the vertical velocity and the resultant flight velocity on a flapping period, respectively, in stable flight for various flapping frequencies. The horizontal axes of Fig 3 (a) show flapping frequency f, and the vertical axes of Figs. 3 (a), (b) and (c) show the spatial horizontal velocity V_x, the vertical velocity V_y , and the resultant flight velocity V ,respectively. The line indicates linear approximation.

The horizontal velocity increases linearly from 1.6 [m/s] to 2.1 [m/s] with flapping frequency in the range from 7.8 [Hz] to 10.5 [Hz] (Fig. 3 (a)). The gradent is approximately 0.04 [m/s*Hz]. The vertical velocity also increases linearly from -0.3 [m/s] to 0.3 [m/s] with 10.5 [Hz], and the gradient of that is 0.20 [m/s*Hz] (Fig. 3 (b)). The vertical velocity changes primarily by flapping frequency because the gradient of vertical velocity is approximately five times as large as that of horizontal velocity (Fig. 3 (a) and (b)). The resultant flight velocity which is obtained by combining horizontal and vertical components (Fig. 3 (c)) has similar distribution to horizontal velocity because of small absolute values of vertical velocity (Fig. 3 (a) and (c)). The resultant flight velocity also increases linearly with flapping frequency.

The aerodynamic forces on a small flying robot appear to increase with flapping frequency because flight velocity increases in proportion to flapping frequency. Based on this fact, the resultant synthesis flight velocity appears to increase because significant forces on the wings generated by the increase in flapping frequency.

Based on these results, it seems to consider that the body angle and flight velocity can be control. Moreover, the flight altitude can be control because flight altitude depends on flight velocity. To try to find out, the author tried to change the flight altitude with remote controlling device which can control the flapping frequency. As the result, small flying robot changes flight altitude, and high (low) flapping frequency made it increase (decrease).

4. Concluding remarks

The body angle and flight velocity of small flying robot is measured on flights. By the flapping frequency, these increase linearly and flight altitude can be controlled on an actual flight. Based on these result, it is clarified that flapping frequency is one of important factor for controlling flight of flapping robot which do not have tail-plane.

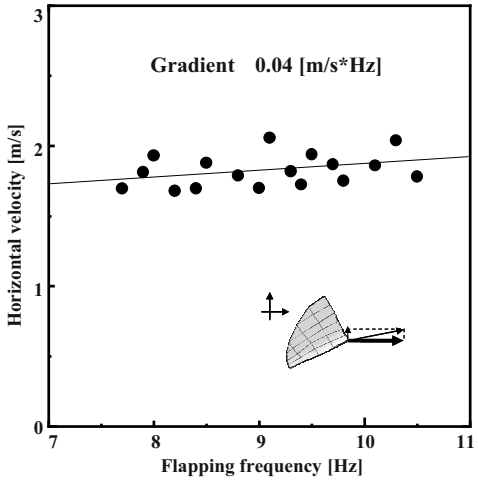

(a) Horizontal velocities

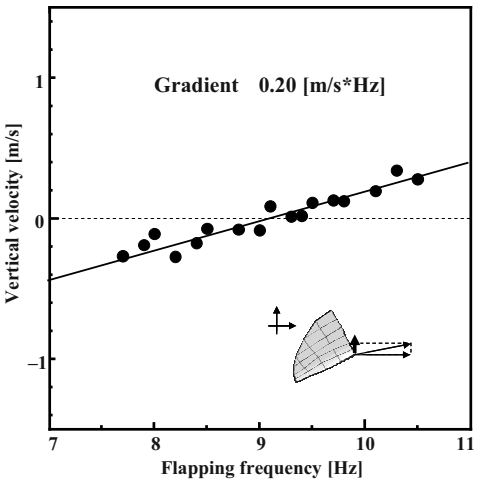

(b) Vertical velocities

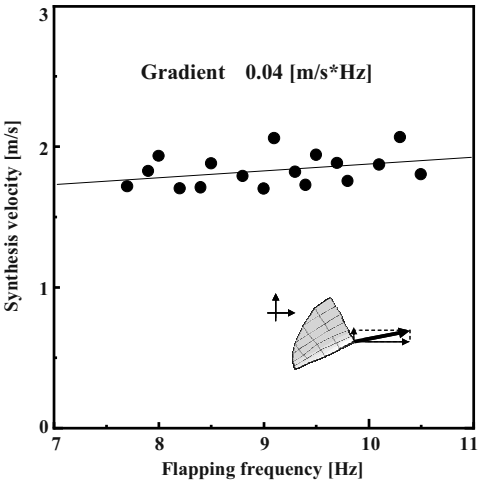

(c) Synthesis velocities

Fig. 3 Flight velocities of small flying robot with different flapping frequencies

References

[1] Yongsheng L et al., Prog. in Aerospace Sci., **39** (2003)
[2] H. Tanaka et al., Proc. of IEEE / RSJ Int. Conf. on Intelligent Robots and Systems 2008

Droplet Formation of a Continuous Inkjet with Different Viscosities: A Comparison of Experiment and Numerical Simulation

Tameo Nakanishi[1], Masami Nakano[2], and Hinoki Tunokake[1]
[1] Graduate School of Science and Engineering, Yamagata Univ., 4-3-16, Jonan Yonezawa, 992-8510, Japan
[2] Institute of Fluid Science, Tohoku Univ., 2-1-1, Katahira Aoba-ku, Sendai, 980-8577, Japan
tameo@yz.yamagata-u.ac.jp

ABSTRACT

The droplet formation from a nozzle of a continuous inkjet printer with different viscosities was investigated by both of the experiment and numerical simulation. Similar patterns were obtained in each approach. The calculated breakup length increases as to decreasing viscosity. The reason is considered due to the velocity distribution from the nozzle exit. More investigations should be made to further clarify the phenomenon.

1. Introduction

In an industrial continuous inkjet printer, pressurized ink subject to piezoelectric vibration is continuously ejected from the nozzle. Ink droplets are formed beyond the breakup length (L_b) due to Plateau-Rayleigh instability. The droplet patterns formed from a continuous inkjet may be classified into satellite-free uniform droplets and main droplets along with various types of satellites. The dimensionless breakup length and the droplet formation constant are defined by ratios of the breakup length (L_b) and the perturbation wave length (λ) to the initial jet diameter (d_n). The dimensionless breakup length (L_b / d_n) and the droplet patterns depend on the Weber number ($We = \rho U^2 d_n / \sigma$), the Reynolds number ($\mathrm{Re} = \rho U d_n / \mu$), the droplet formation constant (λ / d_n), the dimensionless amplitude of the piezoelectric vibration, and the initial dimensionless velocity distribution. Here, U is the mean velocity at the nozzle exit, ρ, μ and σ are density, viscosity, and surface tension of the ink, respectively.

According to Weber's small disturbance theory [1], the most unstable wavelength and the corresponding breakup length from a liquid jet of uniform velocity are calculated by:

$$\lambda_w / d_n = \pi\sqrt{2(1+3Z)}, \quad L / d_n = \left(\ln\frac{d_n}{2\varepsilon}\right)\cdot(1+3Z)\sqrt{We} \quad (1)$$

Here, ε is the perturbation amplitude of the initial inkjet radius, and $Z = \sqrt{We}/\mathrm{Re}$ is the Ohnesorge number.

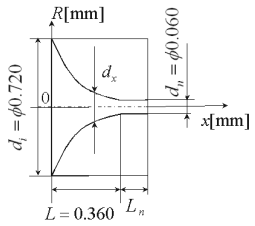

$$d_x = d_i - (d_i - d_n)\sin\left(\frac{\pi}{2}\frac{x}{L}\right)$$

Fig.1 Dimensions of the nozzle

Given the nozzle shown in Fig.1 with a straight length of $L_n = 0.04$[mm], the objective of the present study is to determine the breakup length and the droplet patterns for inks with different viscosities. Both the experiment and the numerical simulation were conducted and the results were compared.

2. Experiment and Simulation Methods [2-5]

The piezoelectric vibrator is operated at 64 kHz. The inkjet velocity is adjusted by the ink tank pressure. The vibration amplitude is managed by changing the applied voltage to the piezoelectric vibrator. The details of experiment method can be found in Ref [2, 3].

The density, viscosity, and surface tension of the original ink are 900 [kg/m^3], 4.0×10^{-3} [Pa·s] , and 2.6×10^{-2} [N/m]. The ink viscosity is adjusted by adding solvent into the ink. The density and the surface tension remain unchanged. As of the first step to investigate the influence of the ink viscosity, measurements are made for $\lambda / d_n = 4.5$, i.e., a initial mean velocity of U=17[m/s], and $\mathrm{Re}_l = 233$, $We = 620$. Assuming a 10% disturbance in initial mean velocity (5% disturbance in initial radius) and ignoring the effect of the Ohnesorge number, the dimensionless breakup length is estimated to be 74.

In numerical simulation, the axisymmetric model of the VOF method [4, 5] using curvilinear meshes was employed. The precise shape of the nozzle was reproduced in the computation. Dimensionless velocity at the inlet of the nozzle is given by

$$U_i(t) = \left(\frac{d_n}{d_i}\right)^2\left(1 + A\cos\left(\frac{2\pi t}{T}\right)\right) \quad (2)$$

where A is the dimensionless velocity perturbation amplitude, and $T = 4.5$ is the dimensionless period.

Computations were conducted for (a) half, (b) one, and (c) twice of the original ink viscosity.

3. Results and Discussion

Figures 2 compares droplet patterns of experiment and numerical simulation of the original ink. Similar pattern was obtained. However, the satellites were not reproduced in the simulation, and the oscillation patterns of the main droplet are quite different. We are still on the way to improve the accuracy of the numerical simulation. Figure 3 shows computed droplet formation patterns of a liquid jet from the nozzle for three different viscosities. Be contrary to our consideration, the breakup length increase as to decreasing viscosity.

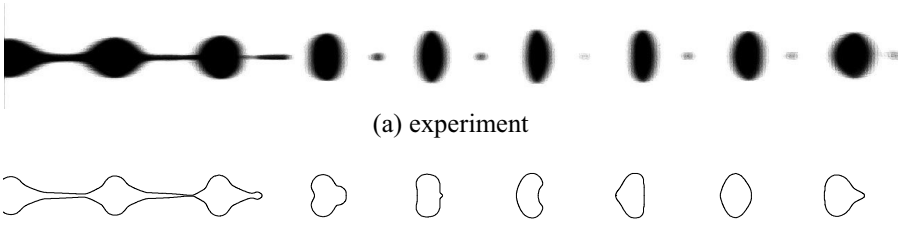

(a) experiment

(b) numerical simulation

Fig.2 Comparison of droplet patterns of experiment and numerical simulation (Viscous factor=1.0)

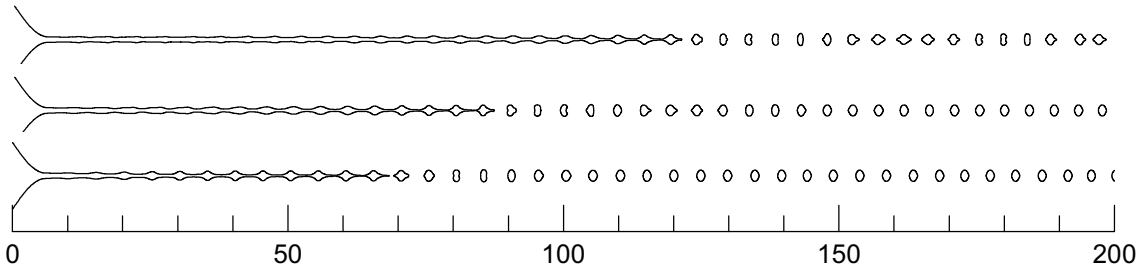

Fig.3 Droplet formation patterns of liquid jet from the nozzle of Ln=0.04.
The viscosity factor is 0.5, 1.0, and 2.0 from top to bottom.

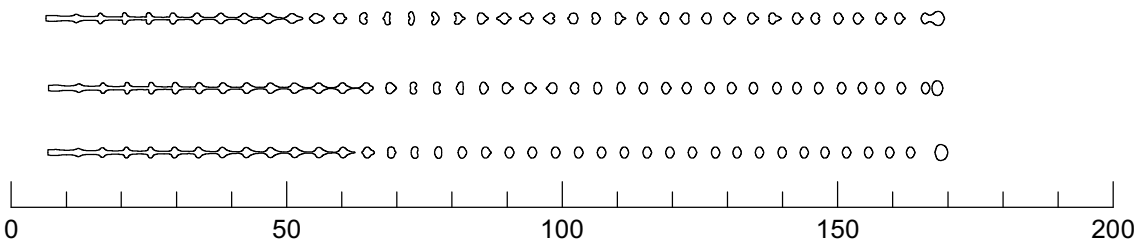

Fig.4 Droplet formation patterns of a liquid jet from a uniform stream
The viscosity factor is 0.5, 1.0, and 2.0 from top to bottom.

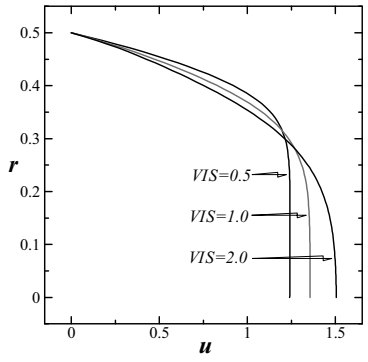

Fig.5 Velocity distributions at nozzle exit.

To clarify the reason we computed the liquid jet from a uniform velocity distribution. The results are shown in Fig.4. Without the effect of the nozzle on the velocity distribution, the breakup length decreases as to decreasing viscosity, which qualitatively agrees with Eq.(1). Figure 5 shows time averaged velocity distributions at the nozzle exit. Greater maximum velocity is seen for larger viscosity case. More investigation should be made to determine the influence of the velocity distribution on the breakup length.

4. Concluding Remarks

Concluding remarks has been provided in the abstract and is therefore omitted here.

References

[1] C. Weber, Z. angew. Math. Mech., 11(1931), 136.

[2] T. Nakanishi, M. Nakano and H. Tunokake: *Proceedings of the Seventh International Conference on Flow Dynamics*, Sendai, (2010), 274.

[3] M. Nakano, T. Nakanishi and M. Yokoyama, *Proceedings of the Ninth International Symposium on Advanced Fluid Information and Transdisciplinary Fluid Integration,* Sendai, (2009), 94.

[4] J. U. Brackbill, et al., C., J. Comput. Phys., 100 (1992), 335.

[5] K.Yokoi, J Sci Comput., 35 (2008), 272.

Cancelled

Cancelled

OS3: Wind Tunnel Experiment on Unsteady Phenomena

Eighth International Conference on Flow Dynamics
November 9 - November 11, 2011

The Effect of Surrounding Air Flow Profile to Breakdown Process of a Plane Liquid Sheet

D. Aoki, M. Senchi and M. Matsubara
Department of Mechanical Systems Engineering, Shinshu University,
4-17-1 Wakasato, Nagano, 380-8553, Japan
10ta101b@shinshu-u.ac.jp

ABSTRACT

Instability of a plane liquid sheet has been studied experimentally and theoretically. The present study focuses on the effect of the surrounding air. A plane liquid sheet is oscillated by the effect of the surrounding air. The growing rate value of the oscillation is a little larger than a present stability analysis regardless of surrounding air flow. The velocity distribution of surrounding air flow is measured and compared with the theoretical distribution. The experimental data has a smaller boundary layer thickness than theoretical distribution like for the Blasius boundary layer.

1. Introduction

When plane liquid sheet is ejected into air, the sheet begin oscillating normal direction, and the oscillation is developing as it goes downstream, at last, the sheet breaks down into droplets. In regard the emphasis, the stability of a plane liquid sheet has been studied experimentally and theoretically. Söderberg performed a linear stability analysis of the problem including viscosity and velocity profiles of the surrounding air as well[1]. In addition, Tammisola *et al.* performed a linear stability analysis of the problem when surrounding air is uniform stream and the oscillating growth rate fits in the stability analysis[2]. However, the growing rate value is a little larger than the stability analysis regardless of surrounding air flow. About this cause, the surrounding air flow distribution is defined theoretical distribution like for the Blasius boundary layer, but it may be different.

In this study, we focus on the profile of surrounding air flow, and compare with the distribution of the theory.

2. Experimental apparatus and method

The experimental facility consists of a nozzle unit ejecting a liquid sheet vertically into a water basin. Coordinate systems are x, y and z for streamwise, sheet-normal and spanwise directions, respectively. The origin is defined at the centre of a central nozzle outlet for the water. The nozzle unit consists of three nozzles: one central nozzle for the water and two side nozzles for the co-flowing air. All nozzles have contractions near the outlet in order to generate as flat velocity profiles as possible. The width of the nozzle exits in the z-direction is 400 mm and the thickness in the y-direction is 1 mm for the water nozzle and 50 mm for each air nozzle. The water is pumped in a closed loop by a centrifugal pump and the air is taken from the room and pressurized with a fan before entering the nozzles via dampers and flow regulators. The nominal velocities of air and water are the mean velocities over the cross sections. The sheet can be forced to oscillate at a given frequency by speakers mounted at the counter ends of the flow regulators. To avoid inclination of the air free stream velocity, suction is applied at the walls near the outlet. Further, the air flow is surrounded by walls of length 600 mm at a sheet-normal distance of 50 mm from the centreline, to create a constant and parallel air free stream velocity.

The flow visualization was made using a digital single-lens reflex camera. The velocity distribution of surrounding air flow measuring was made using Laser Doppler Velocimeter(LDV). When measuring, alcohol mist inserts in the air flow as a tracer particle.

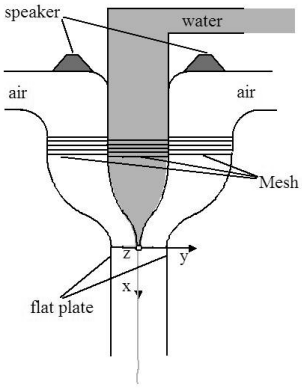

Figure 1: Experimental setup for two dimensional water film.

3. Results

Figure 2 shows flow visualization of the plane liquid sheet without being forced to oscillate at a given frequency by speakers. The photography was taken in the range of $x = 650\sim1800$ mm as 1/400 shutter speed. The sheet velocity at the nozzle outlet is 6 m/s. The sheet at upper stream begin oscillation, and the oscillation is developing as it goes downstream, at last, the sheet breaks down into droplets. The break point is moved downstream when air flow velocity at the nozzle outlet changes into $Ua = 3$ m/s from $Ua = 0$ m/s. Further, when the surrounding air velocity reaches the sheet velocity, the oscillation amplitude is extremely small no collapse is observed until $x = 1800$ mm. The oscillation becomes small so that surrounding air velocity gets at a liquid sheet velocity, and the same result as the experiment of

Tammisola *et al.*[2] was checked. Distribution of the streamwise velocity in the air flow without the liquid sheet is measured by hot wire. The distribution is shown Figure 3. The air flow velocity at the nozzle outlet is 3 m/s. The air velocity is constant and fairly parallel to the sheet. Near the walls surrounding the air flow, there are clear boundary layers development and therefore a velocity decrease at $x = 500$ mm. However, this boundary layer is far enough from the sheet so that the free stream velocity near the sheet remains unaffected in the measurement region.

Tammisola *et al.*[2] showed that the emphasis is related to the surrounding air flow. So the velocity distribution of surrounding air flow is measured by LDV. The distribution is shown Figure 4. The sheet velocity at the nozzle outlet is 6 m/s. The velocity is 6 m/s at $y = 0$ mm, it is the liquid sheet velocity. The shear layers apparent at $y = 0 \sim 4$ mm. And there is free stream beyond. Figure 5 is the nondimensionalization result by length scale of boundary layer equation. Boundary layer thickness of the experimental data is thinner than that of the theory. Therefore, it suggests that the disturbance growth rate may be larger than that Tammisola suggested in the stability.

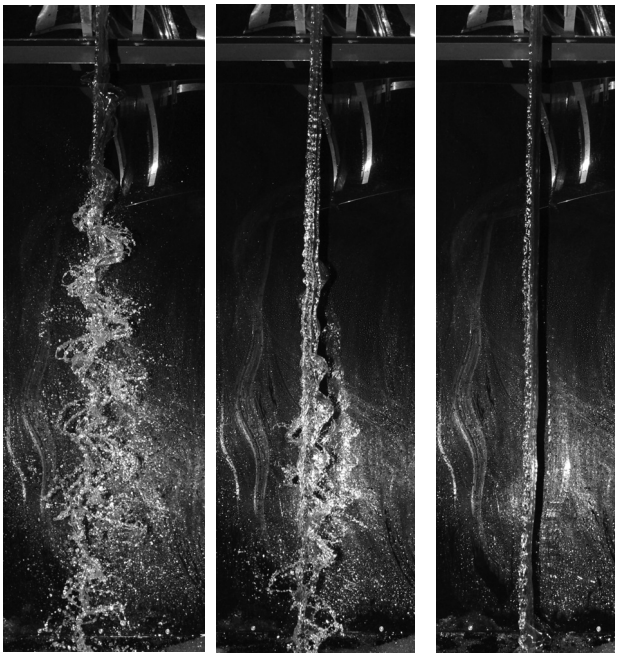

(a) (b) (c)

Figure 2: Flow visualization.
(a) $Ua = 0$ m/s (b) $Ua = 3$ m/s (c) $Ua = 6$ m/s

4. Summary

We investigate the velocity distribution of surrounding air flow. As a result, the experimental data has a smaller boundary layer thickness than theoretical distribution like for the Blasius boundary layer.

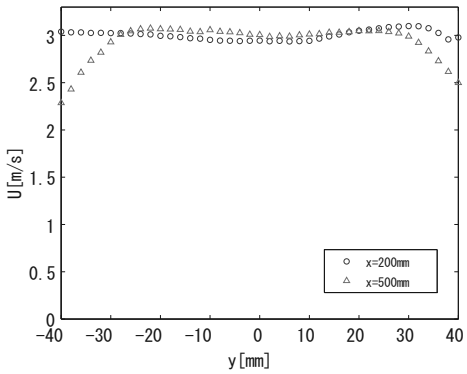

Figure 3: The verocity profles of the surrounding air.

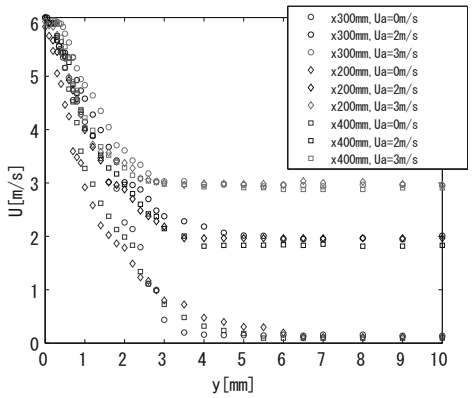

Figure 4: The velocity profiles of the surrounding air around water film.

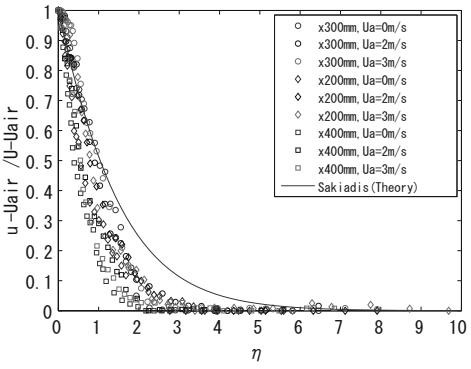

Figure 5: Nondimensionalization for velocity profiles of the surrounding air around water film.

References

[1] Daniel.Söderberg, Absolute and Convective Instability of a Relaxational Plane Liqulid Jet, J. Fluid Mech. Vol.493(2003), pp. 89–119.

[2] Outi Tammisola, Atsushi Sasaki,Akihiko Mori,Fredrik Lundell, Masaharu Matsubara, Daniel.Söderberg , Stability of a plane liquid sheet surrounded by air, J. Fluid Mech.

Eighth International Conference on Flow Dynamics
November 9 - November 11, 2011

Unsteady Aerodynamic Experiment of NACA0012 Airfoil at Low Reynolds Number

Kei Nose[*1], Nobuaki Sakai[*1], Daiju Numata[*1], Hiroki Nagai[*1], Keisuke Asai[*1], Tomoaki Ikeda[*2], Takashi Atobe[*2]
*1 Dept. of Aerospace Engineering, Tohoku University,
6-6-01, Aramaki-Aza-Aoba, Aoba-ku, Sendai, Miyagi 980-8579, JAPAN
*2 Fluid Dynamics Group, Japan Aerospace Exploration Agency,
7-44-1, Jindaiji Higashi-machi, Chofu, Tokyo182-8522, JAPAN
nose.kei@aero.mech.tohoku.ac.jp

ABSTRACT

In this study, we measured pressure fluctuations near the trailing edge of a NACA0012 airfoil at low Reynolds number. Experiments were conducted in low-pressure environment of the Mars Wind Tunnel at Tohoku University. Mach number was 0.2 and Reynolds number was $1.1\text{x}10^4$ and $4.7\text{x}10^4$. The pressure fluctuation with the peak frequency of 2.9 kHz appeared on the both surfaces for α = 3 to 6 deg (at Re = $1.1\text{x}10^4$) and 0.5 to 1.5 deg (at Re = $4.7\text{x}10^4$). This frequency is fixed over the ranges of angle of attack, suggesting the possibility of an acoustic feedback loop formed around the airfoil.

1. Introduction

In recent years, an airplane that flies at low Reynolds number (Re = $O(10^4$ - $10^5)$), such as Mars exploration airplane and Unmanned Air Vehicle (UAV), has attracted much attention in aerospace community. For conventional airfoils, laminarized boundary layer may easily induce massive separation at low Reynolds number, which significantly reduces the maximum lift-to-drag ratio [1].

Additionally, recent studies show that the unsteady flow behavior is non-negligible at low Reynolds number in considering aerodynamic characteristics of an airfoil. According to the computational study conducted by Atobe, et al. [2], pressure fluctuation on the airfoil can be increased drastically due to an acoustic feedback loop between boundary-layer instability on the suction side of the airfoil and acoustic disturbance scattered from the trailing edge. However, the experimental data on this unsteady phenomenon at low Reynolds number are very limited.

In this study, we focused on the amplification effect of an acoustic feedback loop and measured pressure fluctuations near the trailing edge of a NACA0012 airfoil at low Reynolds number. Experiments were conducted by utilizing the low-Reynolds number ability of the Mars Wind Tunnel (MWT) at Tohoku University.

2. Experimental method

2.1 Mars Wind Tunnel

The MWT is composed of a vacuum chamber, an induction-type wind tunnel and a buffer tank. The induction-type wind tunnel is located inside the vacuum chamber where the pressure condition of Martian atmosphere can be simulated. This wind tunnel is driven by multiple-nozzle supersonic ejector located downstream the test section. Ejection of high pressure gas from the ejector induces the flow in the test section. The total pressure in the wind tunnel is kept constant by exhausting the gas inside the vacuum chamber to the buffer tank.

2.2 Test Model

The test model is a NACA0012 airfoil. The chord length of the model is 50 mm and the span length is 100 mm. A high-frequency pressure transducer (kulite LQ-062-5A) was installed at x/c = 0.9 on both upper and lower sides of the model.

2.3 Experimental condition

Mach number (M) was fixed at 0.2. Reynolds number (Re) was set at $1.1\text{x}10^4$ and $4.7\text{x}10^4$, that correspond to the total pressure of the free stream at 5 and 22 kPa, respectively. The angle of attack (α) was changed from 0 to 15 deg.

3. Results and Discussion

Figure 1 shows pressure fluctuations on each surface of the model. ΔC_p represents the root-mean-square (rms) value of the pressure fluctuation on the model surface normalized by the free-stream dynamic pressure. For Re = $1.1\text{x}10^4$ and α = 0 to 2 deg, the pressure fluctuation is almost zero. At α = 3 deg, the pressure fluctuation starts to increase on both surfaces. The pressure fluctuation reaches the maximum value at α = 4 deg (on the upper surface) and 3 deg (on the lower surface). For higher angles, pressure fluctuation decreases with an increasing angle of attack. At Re = $4.7\text{x}10^4$, the pressure fluctuation appears on both surfaces even at α = 0 deg and it increases suddenly and reaches the maximum value at α = 1.5 deg (on the upper surface) and 0.5 deg (on the lower surface). After these angles of attack, the pressure fluctuation starts to decrease and becomes almost zero at α = 5 deg. The pressure fluctuation appears again at α = 11 deg.

Figures 2 and 3 show the power spectrum of pressure fluctuation. At Re = $1.1\text{x}10^4$, the peak appears at the frequency of 2.9 kHz on both surfaces for α = 3 to 6 deg. For α = 6 to 15 deg, the broadband peak with low frequencies up to about 2 kHz appears on the upper surface. This broadband peak does not appear in the lower surface. At Re = $4.7\text{x}10^4$, the peak fluctuation appears at the frequency of 5.5 kHz on both surfaces at α = 0 deg. For α = 0.5 to 1.5 deg, the peaks appear at 2.9 kHz and its harmonic frequency (5.8 kHz). Then, the peak frequency is changed to 4.5 kHz (at α = 2 and 2.5 deg) and 5.3 kHz (at α = 2.5 and 3 deg). For α = 11 to 15 deg, the broadband peak at low frequencies up to

about 2 kHz appears on the upper surface.

4. Concluding remarks and future work

The pressure fluctuations near the trailing edge of a NACA0012 airfoil were measured at low Reynolds number. Pressure fluctuation with the peak frequency of 2.9 kHz appears on both surfaces for α = 3 to 6 deg (at Re = 1.1x10^4) and 0.5 to 1.5 deg (at Re = 4.7x10^4). This frequency is fixed over the ranges of angle of attack, suggesting the possibility of an acoustic feedback loop formed around the airfoil. For the future, we will measure pressure fluctuations for higher Mach number conditions to investigate the effects of the sound speed on the acoustic feedback.

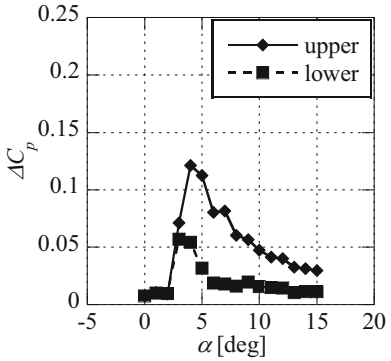

(a) Re = 1.1x10^4, M=0.2

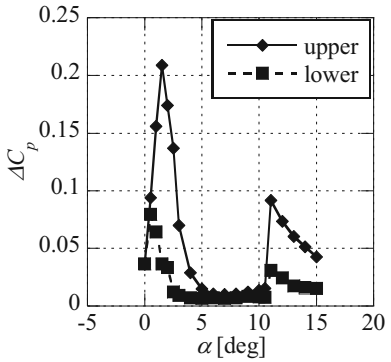

(b) Re = 4.7x10^4, M=0.2

Fig. 1 pressure fluctuation on each surface of the model

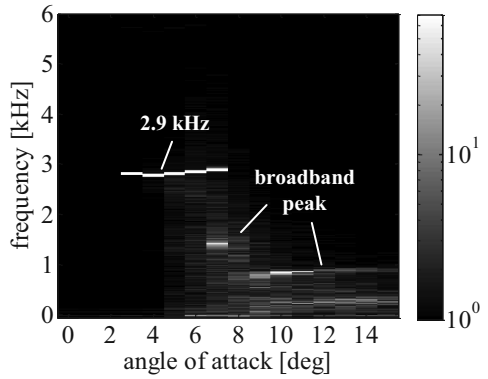

(a) Upper surface

Fig. 2 Power spectrum of pressure fluctuation (Re = 1.1x10^4, M=0.2)

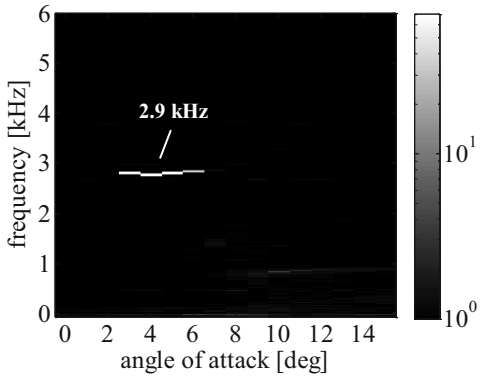

(b) Lower surface

Fig. 2 Continued

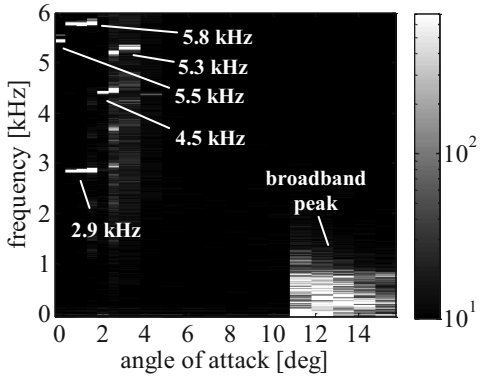

(a) Upper surface

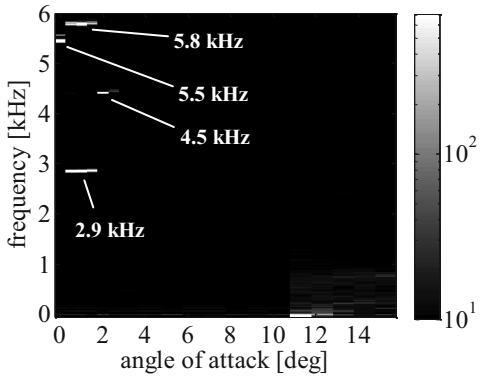

(b) Lower surface

Fig. 3 Power spectrum of pressure fluctuation (Re = 4.7x10^4, M=0.2)

References

[1] M. Anyoji, et al, AIAA 2010-4627, 40th Fluid Dynamics Conference and Exhibit, Chicago, Illinois, 28 June - 1 July, 2010.

[2] T. Atobe, et al, ICAS 2010-3.9.4, 27th Congress of International Council of the Aeronautical Sciences, Nice, France, 19 - 24 September, 2010.

Eighth International Conference on Flow Dynamics
November 9 - November 11, 2011

Flow Control of Unsteadily Separating Flow

Tomoki Hayashi, Hiromasa Oe, Masaya Shigeta, Seiichiro Izawa and Yu Fukunishi
Depart. of Mechanical Systems and Design, Tohoku University, 6-6-01 Aramaki-Aoba, Aoba-ku, Sendai, Miyagi, Japan
tomoki@fluid.mech.tohoku.ac.jp

ABSTRACT

Passive control was attempted against an unsteadily separating flow generated on a flat plate surface. The unsteadily separating flow was generated by periodically changing the opening angle of the ceiling. The device used for separation control consisted of two flaps linked together. Measurements using a direction-sensitive probe revealed that the device was effective in decreasing the size of the separating region whose size and location changed with the movement of the ceiling.

1. Introduction

Flow separation very often has an unfavorable effect on the performance and stability of fluid machineries such as turbines and airplanes. Hence, separation control is one of the key technological issues. Vortex generators or plasma actuators are the typical control devices which are effective in separation suppression. However, the effectiveness of these devices against strongly unsteady flows, where separation point moves widely in the streamwise direction, is unknown.

The purpose of this study is to develop a control device that can suppress the separation in such strong unsteady flows. Oe et al. [1] proposed a simple passive control device, which consists of two parallel slots, normal to the streamwise direction, that are connected to each other under the flat plate surface. Their device had a certain effect on the separation. However, the control effect became smaller against large separations. Thus, in this study, a new device using a reverse flow inside the separation bubble is tested. The control effects are discussed on the basis of the flow measurement using a direction-sensitive probe as well as the previous study [1], [2].

2. Method

2.1 Experimental setup

Figure 1 shows the schematic view of the experimental setup. The experiment was carried out using a blowing-type wind tunnel with a two-dimensional nozzle which contracted the flow in the vertical direction. The nozzle had a rectangle cross-section of 170 mm in height and 588 mm in width at the outlet. A flat plate with 5 mm thickness was set horizontally at the 50 mm in height from the bottom wall of the closed test section which was 1000 mm long. The origin of the coordinate system was located at the center of the leading edge, where the axes of x, y and z denote the streamwise, wall-normal and spanwise directions. The test section was followed by an asymmetric diffuser in order to generate an adverse pressure gradient, as shown in Fig. 1. In the region of x = 150 through 750 mm, the ceiling shape had the moderate curve of the parabolic function. The ceiling was oscillated up and down at 1.7 Hz using a motor. The ceiling's opening angle α changed from 10 to 12 degrees, so that separation point moved back and forth on the flat plate surface. To prevent the flow separation at the ceiling, suction was carried out at the ceiling side

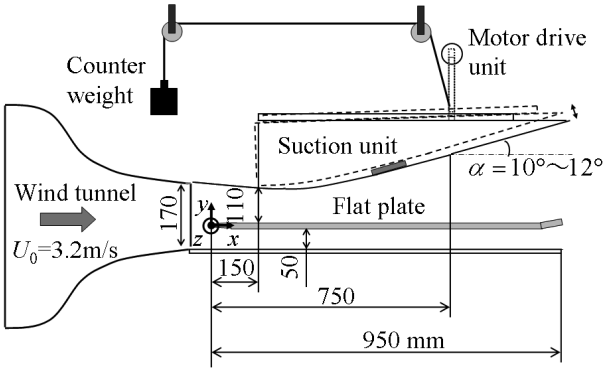

Fig. 1 Schematic view of experimental setup

surface. The main flow velocity U_0 was 3.2 m/s, where free-stream turbulence intensity was less than 0.5%.

2.2 Detection of separation region

A direction-sensitive probe proposed by Wei et al. [3] was used to measure the separating flow. It consisted of a hot-wire anemometer and two cold-wire thermometers. The hot wire and cold wires were made of tungsten wires whose diameter was 5 μm. The horizontal (z-wise) wire at the center, about 1.4 mm long, was a single hot wire. Two vertical (y-wise) wires, about 2 mm long, were temperature-sensitive cold wires. They were fixed 0.7 mm away from the central hot wire, upstream-side and downstream-side. The heated wake from the central hot wire was picked up by either of the two cold wires, depending on the flow direction. The flow direction can be determined by monitoring the voltage changes of both upstream-side and downstream-side cold wires. Each cold wire signal was converted to the signal of 0 or 1 using an appropriate threshold, where each threshold was chosen to be an optimum value from output signals. The time averaged value of the difference between binary signals given by downstream-side and upstream-side cold wires is called the forward flow coefficient C_f, in this study. The region where C_f is negative is defined as the flow separation region.

2.3 Separation control device

Figure 2 shows the concept of the passive control device. The device consisted of the two flaps (10×0.3×300mm), whose ends were mutually connected under the flat plate surface. The trailing edges of the

upstream and downstream flaps were located at x = 450 mm and 500 mm, respectively, where the downstream flap location was expected to be inside the separation bubble.

These flaps are designed to be parallel to the flat plate surface when there is no separation. Once the separation occurs, the downstream flap will be lifted up by the reverse flow near the wall inside the separation bubble. At the same time, the upstream flap will also be lifted up because it is connected by the link mechanism. If the system works as planned, the boundary layer transition triggered by the upstream flap movement should suppress the separation.

3. Results and Discussion

Figure 3 shows the contour maps of the ensemble-averaged value of the forward flow coefficient C_f in x-y plane at z = 0 mm. The region x = 490 mm to 510 mm in these figures could not be measured owing to the presence of the control device. Figure 3(a) shows the results without control when the flaps were fixed, and Figure 3(b) shows the results with control when the flaps were free to move. The phase when the ceiling angle α is 10 degrees is defined as t = 0 and normalized by oscillation period of the ceiling T. The time when the ceiling is opening from α = 10 to 12 degrees corresponds to t/T = 0 to 0.5, while the time when the ceiling is closing from α = 12 to 10 degrees corresponds to t/T = 0.5 to 1.0. The separating flow region where C_f is negative moves upstream and downstream accompanying the movement of the ceiling. No separated region is observed at t/T = (i) 0 and (ii) 0.3 in both cases, while it is clearly observed at t/T = (iii) 0.5 and (iv) 0.7 in the case with no control. In the figures, it can be found that the separation bubble becomes much smaller when the flaps are working.

4. Concluding remarks

Passive control was attempted for an unsteadily separating flow whose separation point oscillates largely in the streamwise direction. The control device consisted of two parallel flaps driven by the reverse flow inside a separation bubble. It was found that the separation region could be suppressed by employing the flaps.

References

[1] H. Oe, S. Teramoto, M. Shigeta, S. Izawa, and Y. Fukunishi, Proc. Seventh International Conference on Flow Dynamics, Sendai, Japan (2010-11), (2010), 254-255.

[2] S. Teramoto, M. Shigeta, S. Izawa, and Y. Fukunishi, Trans. Japan Society of Mechanical Engineers, **09-8** (2009), 71-72 (in Japanese).

[3] Qing-Ding Wei and Hiroshi Sato, J. Fluid Mech., **143** (1984), 153-172.

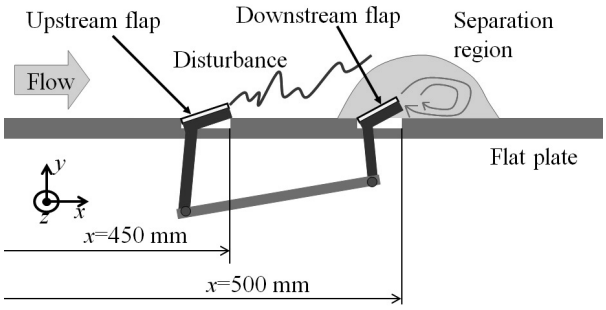

Fig. 2 Concept of the separation control device

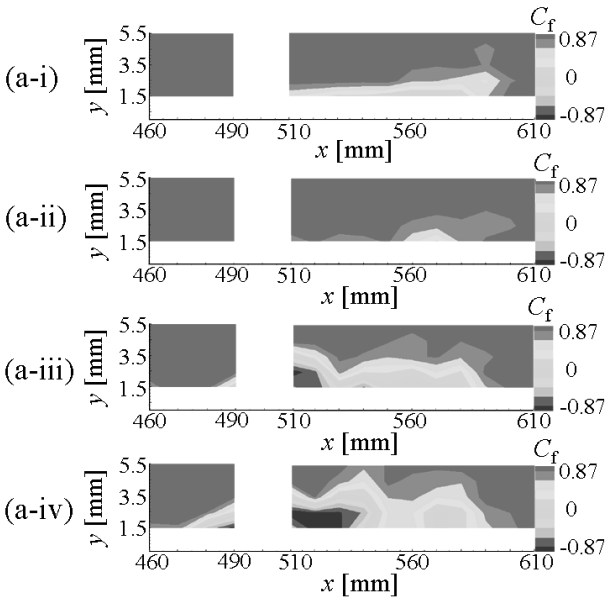

(a) Without control (when flaps are fixed)

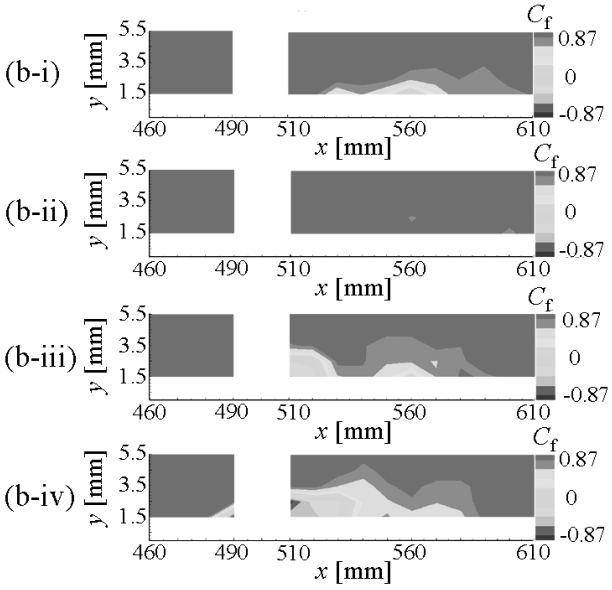

(b) With control (when flaps are free to move)

Fig. 3 Contour maps of the forward flow coefficient at z = 0 mm in x-y plane at t/T = (i) 0, (ii) 0.3, (iii) 0.5 and (iv) 0.7

Eighth International Conference on Flow Dynamics
November 9 - November 11, 2011

Experimental and theoretical analyses of linear disturbance in a two dimensional turbulent jet

S. Tazoe, S. Aruga and M. Matsubara
Department of Mechanical Systems Engineering, Shinshu University,
4-17-1 Wakasato, Nagano, 380-8553, Japan
mmatsu@shinshu-u.ac.jp

ABSTRACT

In a two-dimensional turbulent jet, there exists a lateral vibration of the jet core. In the present experiment, a periodic initial disturbance is introduced into a fully developed turbulent jet in order to extract this vibration mode. The streamwise and lateral velocity fluctuations are measured with an anemometer with an X-type probe, and are filtered using a phase ensemble average technique based on the periodic initial disturbance. The experimental result shows that the extracted disturbance amplitude is directly proportional to the intensity of the initial disturbance. A linear stability theory with parallel flow assumption well captures futures of tis experimental mode.

1. Introduction

It is a known fact that there exists a large-scale disturbance with periodic vertical motion in a two-dimensional jet emitting from a orifice or a nozzle, so called 'flapping' [1], [2].Though the periodic disturbance is not clearly observed when the exit of emitting a jet is a fully developed turbulence, the disturbance of the similar structure to flapping can be excited by introducing an artificial initial disturbance. Even if disturbance is infinitesimal, this disturbance can be extracted from other turbulent disturbances using an ensemble average technique. In the present study, The extracted disturbance is experimentally investigated and compared with the linear stability theory.

2. Three-component decomposition

Employing the periodicity of the disturbance, an instantaneous quantity q can be decomposed into a time average $\overline{q}$, periodic component $\tilde{q}$ and random component $\hat{q}$. The periodic component $\tilde{q}$ is obteined by $\langle q \rangle - \overline{q}$ and the random component $\hat{q}$ is obteined by $q - \langle q \rangle$. Applying this decomposition to the Navier-Stokes equation, and the periodical average gives the equation for the periodic component,

$$\frac{\partial \tilde{u}_i}{\partial t} + \overline{u_l}\frac{\partial \tilde{u}_i}{\partial x_l} = -\frac{1}{\rho}\frac{\partial \tilde{p}}{\partial x_i} + \nu\frac{\partial^2 \tilde{u}_i}{\partial x_l^2} - \tilde{u}_l\frac{\partial \overline{u_i}}{\partial x_l} - \frac{\partial \widetilde{\tilde{u}_i\tilde{u}_l}}{\partial x_l} - \frac{\partial \widetilde{\hat{u}_i\hat{u}_l}}{\partial x_l} \quad (1)$$

All terms in Eq. (1) except the last two terms in the right hand side are linear terms to $\tilde{q}$. If the periodic disturbance is infinitesimal, the fourth term in the right hand side can be neglected. If the last term $\partial\widetilde{\hat{u}_i\hat{u}_l}/\partial x_l$ is proportional to the periodic fluctuations, Eq. (1) is linear for the infinitesimal periodic disturbance.

3. Experimental setup

The experimental setup is shown in Fig. 1. The experiment was performed in a absorbing room. The air outside of the room sucked into a settling chamber through a filter. The channel has a width of $d = 10$ mm, a length of 1000 mm and the aspect ratio of 30. The coordinates are x for the streamwise direction, y for the wall-normal direction, z for the spanwise direction. For exciting the initial disturbance, two slot devices were fitted on the channel. The slot devices have a chamber connected to a loudspeaker via a plastic tube. Input voltage signals to the two loud speakers are out of phase to excite an antisymmetric initial disturbance. A MEMS microphone monitors pressure fluctuation in the slot chamber whose rms value p_0 is adopted as a indicater of the initial disturbance amplitude. The streamwise and lateral velocity components u, v are measured by a hot wire anemometer with X-type probe of 2.5 μm diameter platinum wires. The intersection angles of the wires is about 90°.

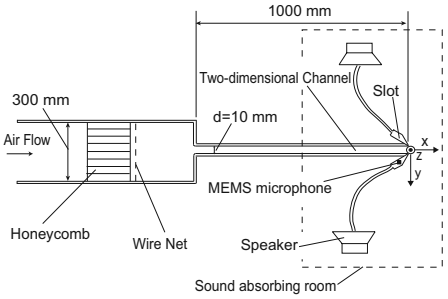

Figure 1: Experimental setup of the two-dimensional turbulent jet

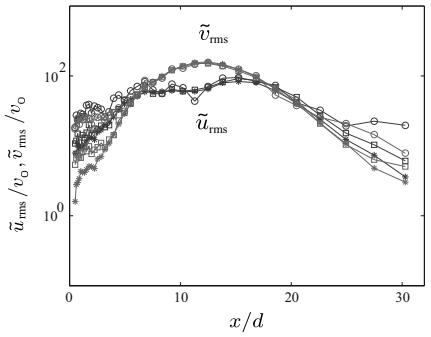

Figure 2: Distributions of $\tilde{u}_{rms}$, $\tilde{v}_{rms}$. ○: $p_0 = 0.20$ Pa, □: $p_0 = 0.60$ Pa , ∗: $p_0 = 2.0$ Pa.

4. Experimental result

In the measurements, the mean velocity at the center of the duct exit, U_0 is 22 m/s, and the initial disturbance frequency f is 165 Hz, then Reynolds number $Re = 14500$ and Strouhal number $St = 0.075$. The initial disturbance amplitudes are $p_0 = 0.20, 0.63, 2.0$ Pa. The rms values of $\tilde{u}$, $\tilde{v}$ and $\widetilde{\hat{u}\hat{u}}$, $\widetilde{\hat{v}\hat{v}}$, $\widetilde{\hat{u}\hat{v}}$ at $y = \delta$, where δ is the integrate jet width defined as $\delta = \frac{1}{U_c}\int_0^\infty \overline{u}dy$ are show in Fig. 2 and Fig. 3. Each values are normalized by $v_0 = p_0/\rho a$, where

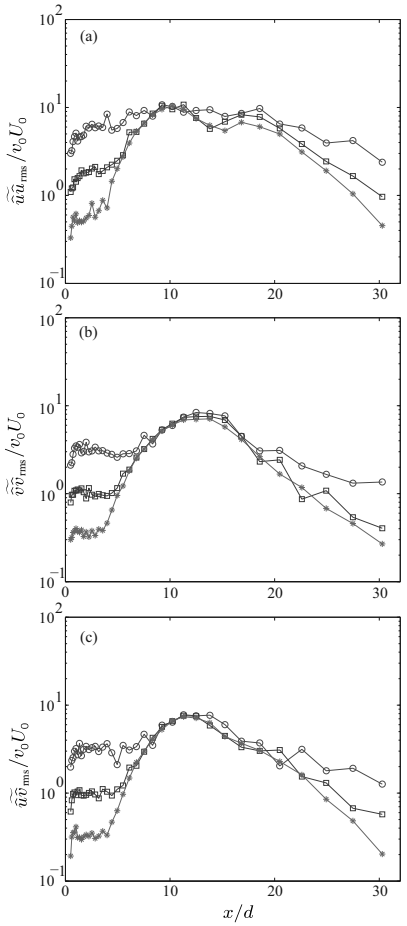

Figure 3: Distribution of $\widetilde{\hat{u}\hat{u}}_{rms}$, $\widetilde{\hat{v}\hat{v}}_{rms}$ and $\widetilde{\hat{u}\hat{v}}_{rms}$. ∘: p_0 = 0.20 Pa, □: p_0 = 0.60 Pa , ∗: p_0 = 2.0 Pa.

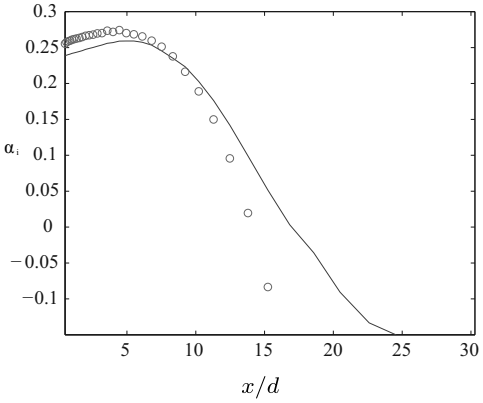

Figure 4: Growth rate of disturbance. ∘: Experimental result, —: Linear stability theory.

ρ is the density of air and a is the speed of sound, v_0 correspond to the fluctuation velocity of the initial disturbance. $\tilde{v}$ distributions are constant and well proportional to p_0 except in the region close to the duct exit and downstream in p_0 = 0.2 Pa case. The deviations are due to insufficient ensemble average time. $\tilde{u}$ also have linearity with p_0. The second order terms $\widetilde{\hat{u}\hat{u}}$, $\widetilde{\hat{v}\hat{v}}$ and $\widetilde{\hat{u}\hat{v}}$ shown in Fig. 3 are found to be linear such as $\tilde{u}$ and $\tilde{v}$, These linearities suggest that the Eq. (1) are linear and the extracted disturbance follows this equation.

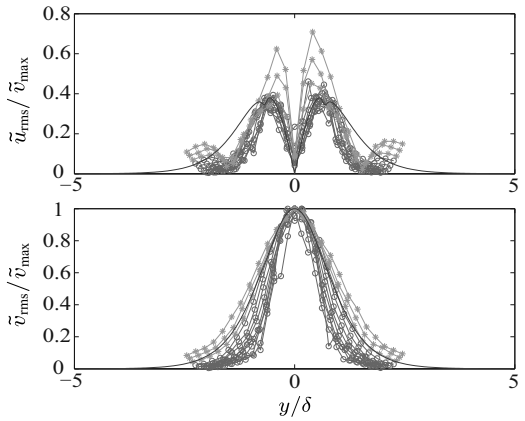

Figure 5: Profiles of $\tilde{u}_{rms}$, $\tilde{v}_{rms}$, ∗: x = 102, 113, 125 mm, ∘: x = 138, 152, 168, 186, 205, 226, 249, 275, 303 mm, —: Linear stability theory

.

5. Comparison with linear theory

Fig. 4 shows comparison of the growth rate between $\tilde{v}$ amplitude and the theoretical curve. Theoretical curve are obtained by the linear theory with the parallel flow assumption. Both experimental and theoretical growth rates are relatively high in the near region and reach the peak at x/d = 5 in the experiment and at x/d = 6 in the theory. They are in good agreement in x/d < 10 though the experimental growth rate is slightly lower in the downstream region. Fig. 5 shows comparison between profiles of $\tilde{u}_{rms}$, $\tilde{v}_{rms}$ and the theory. They are normalized by the maximum lateral fluctuation, $\tilde{v}_{max}$ at each x position. The experimental ratio between the peak values of $\tilde{u}_{rms}$ and $\tilde{v}_{rms}$ correspond with the theoretical one in x/d > 13, though the experimental profiles are narrower than the theory. The theory is not considered the last term in in Eq. (1) and using the parallel flow assumption. It is expected that reasons of difference between theory and experimental is due to the parallel flow assumption.

6. Conclusion

The periodic ensemble technique with the weak initial disturbance demonstrated extraction of a coherent mode from time signals of the velocity components in the two-dimensional turbulent jet. It is notable that the extracted result indicates the existence of the linear mode and the linear stability theory captures its features substantially, suggesting possibility of physical description of the mode with linear stability theory. If the linear modes are ubiquitous in turbulent shear flow, this idea would be a key to comprehension of turbulence.

References

[1] Thomas, F.O. and Goldschmidt, V.W., Structural characteristics of a developing turbulent planar jet, J. Fluid Mech., **163**, pp. 227-256, (1986).

[2] Makita, H., Hasegawa, T. and Sekishita, N., Turbulence Production and energy transfer mechanism in the transition process of a two-dimensional jet, Transactions of the japan society of mechanical engineers. B, **70**(698), pp. 2507-2514, (2004).

Eighth International Conference on Flow Dynamics
November 9 - November 11, 2011

Linear disturbance excited by a finite initial disturbance in a turbulent boundary layer

K. Matsumoto, Y.sendai, T.mishiba, and M. Matsubara
Department of Mechanical Systems Engineering, Shinshu University,
4-17-1 Wakasato, Nagano, 380-8553, Japan
mmatsu@shinshu-u.ac.jp

ABSTRACT

In general, disturbances in turbulence are cause and effect of strong interactions between themselves so that turbulence is non-linear phenomenon and difficult to be treated mathematically. In recent years, it was surprisingly discovered that a linear disturbance excited by a periodic vibration disturbance exists in a planar turbulent jet. In this study, artificial pulse jet disturbance from to a wall surface was introduced to a flat-plate turbulent boundary layer and development of the disturbance was investigated using hot wire anemometry. The ensemble-average enables extraction of the periodical component from velocity signals. The extracted disturbance has apparent linearity to the initial disturbance intensity indicating that the linear disturbance also exists in a wall-bounded turbulent shear flow.

1. Introduction

Turbulence is a collection of structural disturbances, near the walls are known to be present to some extent form the tissue structures of various sizes, such as streaks and hairpin vortices. Disrupters have become a complex phenomenon and it appears that turbulence for the nonlinear interactions with each other. Therefore, to observe the structural disturbance is difficult to experimentally. Disturbance structure has been studied, such as direct numerical simulation and visualization. But I can hardly say enough any cases are caught their time-development.

On the other hand, flow field is different; if very weak initial disturbance gives vent, Disturbance changed linearly in proportion to the intensity giving an initial disturbance was found to exist in the experiment about the two-dimensional turbulent jet. Then in this study, The exited disturbance was investigated growth and linearity. Focus on the weak initial disturbance range likely that the presence of linearity was evaluated.

2. Experimental set-up

In this experiment, using a wind tunnel type of ocean currents.The air sent out from blower is rectified by a honeycomb and mesh. Further the air compressed by three dimensions nozzle of 9 contraction ratio entered the test section. A test section that is 400 mm wide, 600 mm high and 4 m .

The leading edge is located 1600 mm downstream from the exit of the nozzle.he coordinate system is denoted by streamwise x, wall-normal y and spanwise z with the origin at the center of the leading edge. To further to turburent, five rows of plastic tapes embossed with letter 'V's located between x = 315 and 415 mm. To insert initial disturbance, The speaker located at x = 1530 mm was used. The speaker buried test plate was linked the surface through a pipe of 2.5mmdiameter,6.0mmlength. Eventually jet was insert a hole 1.0mmdiameter,1.0mmlength. This speaker was caused the intermittent jet by applying periodic 10Hz stepped-voltage. The free stream velocity U_∞ is 15.5 m/s. Voltage amplitude applied to the speaker E is $0.022, 0.026, 0.03$V. In this experiment,as the voltage amplitude was prpotional to the initial disturbance intensity, used as the basis for disrubance strength.Measurement point is measured at intervals of 1mm 0 $\sim$ 7mm downstream from the disturbance hole.

3. Result

Mean velocity end turbulent intensity was shown in fig1 with no insert initial disturbance. Notice that the mean velocity distribution of the no initial disturbance shows that the distribution of a typical turbulent boundary layer; near the wall there is a sudden change in velocity, which is a mild variation with distance from the wall. Insert the initial disturbance, even if the velocity distribution does not change very much. the turbulence intensity distribution is also same shape. For this reason, Indicate that the initial disturbance was no significant impact on the characteristics of turbulent.

Employing the periodicity of the disturbance, an instantaneous quantity q can be decomposed into a time average $\overline{u}$, periodic component $\tilde{u}$ and random component $\hat{u}$. The periodic component $\tilde{u}$ is obteined by $\langle u\rangle - \overline{u}$ and the random component $\hat{u}$ is obteined by $u - \langle u\rangle$.

$$\langle u(\phi)\rangle \equiv \frac{1}{N}\sum_{i=1}^{N} u(\phi + iT) \tag{1}$$

in Eq.(1), T is cycle of disturbance. N is sampling number in this experiment N = 1800. ϕ is phase of disturbance.

Using above periodic component $\tilde{u}$, Fig. 2, and Fig. 3 were shown x-y cross section of typical phase contour map of $\tilde{u}/EU_\infty$ [1/V]. The upthrust low-velocity component by initial disturbance near the wall about ϕ=0.4 msec in fig.2 have sprawled to about 6mm at ϕ=2.75 msec in fig.3. In any phase, contour map shows very similar distribution regardless of the strength of the initial disturbance.

Fig.4 is distribution of The wall normal direction of periodic component in $x = 0 \sim 4$mm. At first periodic component was decrease with distance from the wall. Turns to increase over y = 4 mm. This peak using wall units was $y^+ = u_\tau y/\nu \approx 16$ and coincided with turbulent intensity peak. Then asymptotically go to zero slowly. The vertical axis in this figure use value divided by each voltage amplitude. The distribution has exactly the same properties with each other. If voltage amplitude is proportional to the intensity of the initial disturbance, this result show that occurred disturbance have linearity to initial disturbance.

X-axis is variation of periodic fluctuation component and y-axis is voltage amplitude of initial disturbance in fig.5. This value is integral value of the range to streamwise $x = 0 \sim 7$ mm from above disturbance hole and $y = 0.13 \sim 0.7$ mm. This figure showed that the extracted disturbance component is linearly changed in proportion

to strength of initial disturbance. It is revealed that disturbances have the property of linearity exist.

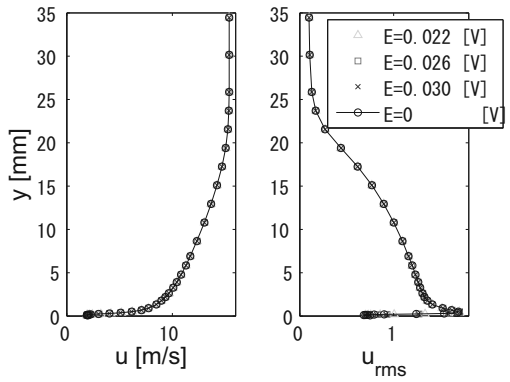

Figure 1: Mean velocity plofiles and turburent intencity

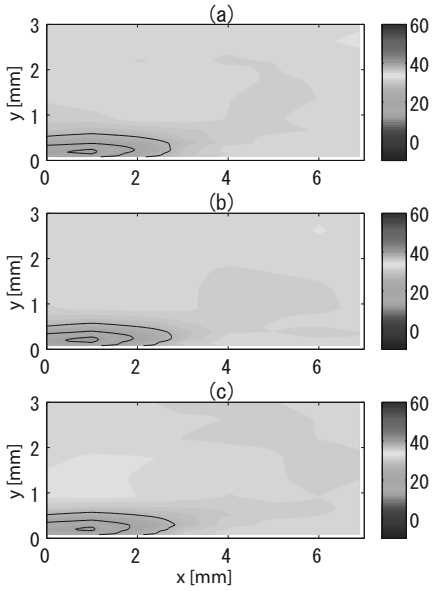

Figure 2: Contour maps of the ensemble-averaged streamwise velocity at ϕ=0.45 ms, (a) E=0.022V, (b) E=0.026V, (c) E=0.03V.

4. Conclusion

To investigate the growth of structure of disturbance ,jet was inserted from the wall in the turbulent boundary layer. At the time little effect on the mean velocity profiles and turbulent intensity. it was showed disturbance component excited the speaker was grown in streamwise and has linearity to the initial disturbance intensity.

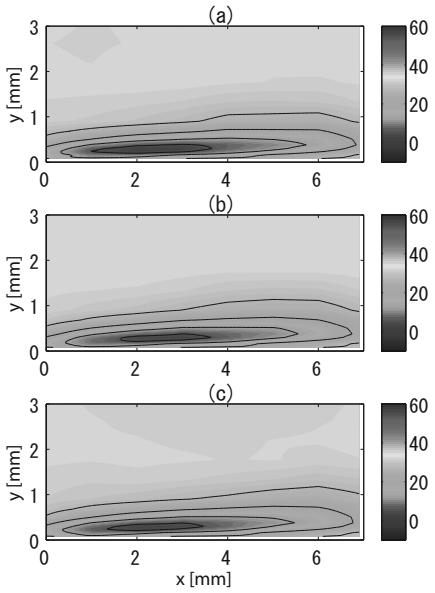

Figure 3: Contour maps of the ensemble-averaged streamwise velocity at ϕ=2.75 ms, (a) E=0.022V, (b) E=0.026V, (c) E=0.03V.

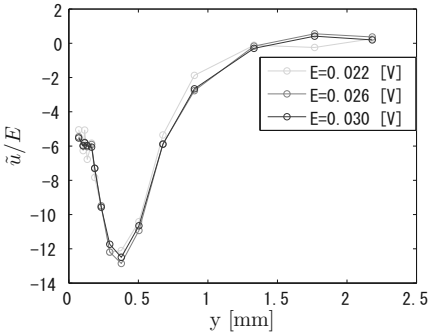

Figure 4: Wall-nomal distributions of $\tilde{u}$

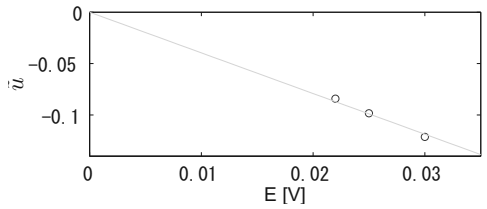

Figure 5: Relation between the initial disturbunce intensity and the periodical components $\tilde{u}$

References

[1] Ronald J. Adrian, ”Hairpin vortex organization in wall turbulence,” Physics of Fluid (2007), vol. 19, 041301.

[2] Yamauchi, T.,Matsubara, M.,”Linear disturbance growth in a two-dimentional turbulent jet”, Proceedings of 2009 Annual Meeting, Japan Society of Fluid Mechanics, p. 171,(2009)

Eighth International Conference on Flow Dynamics
November 9 - November 11, 2011

Unsteady Smoke Dispersion from a Point Source in a Wind Tunnel (Investigation of Basic Characteristics)

Nobumasa Sekishita, Arie Sukma Jaya, Wataru Isebaba
Toyohashi Univ. of Tech., Tenpaku 1-1, Hibarigaoka, Toyohashi, Aichi 441-8580, JAPAN
seki@me.tut.ac.jp

ABSTRACT

The behavior of smoke ejected with vertical jet in a cross flow was experimentally investigated in a small wind tunnel with an active turbulence grid or conventional turbulence grid. The smoke diffusion was observed by a high speed video camera and a YVO4 laser. The structures of the smoke with heated jet or unheated jet were compared for the mean velocity of the cross flow U_0=0.4-2m/s and the mean velocity of the vertical jet U_j=0.2-2m/s. These smoke structures were divided into three modes: structure with two vortex tubes (mode I), horse-shoe-type (mode II) structure and turbulence-type structure (mode III).

1. Introduction and Purpose

The investigation and the assessment of not only global atmospheric phenomena (green house gas problem, climate change, etc.) but also local turbulent phenomena (smoke diffusion from forest fires, particle dispersion from a volcano, etc.) are important for environmental and disaster prevention. The wind tunnel experiment data with high accuracy and reliability for a smoke dispersion in a cross flow with high Reynolds number is necessary for them. On the other hand, serious forest fires often occur in the world such like Indonesia, Australia, Russia, etc. The prediction of atmospheric diffusion of smoke from these forest fires is important for evacuation and human health.

Our final target is to construct database for the environmental assessment and estimate of atmospheric smoke diffusion by using a turbulent shear flow generator developed by H. Makita[1].

The present paper aims to investigate smoke diffusion in a cross wind generated by an active turbulence gird or a traditional turbulence grid by using flow visualization technique.

2. Experimental Equipment and Method

A blown-type small wind tunnel was employed and it has a test section of 200x200mm^2 in cross sectional area and 1000mm in long. A jet nozzle of D=4mm in inside diameter was placed on the floor of this test section as shown in Fig. 1. The system of pipe connection until jet nozzle was composed of a compress, an air dryer, an air regulator, a flow meter, a smoke generator and a surge tank for the smoke, a heater. The jet velocity at the jet exit controls by the compress and the air regulator. The origin of a coordinate system was the center of the jet nozzle on the floor of the test section. The main stream direction was x, the vertical direction was y, and the span-wise direction is z.

A high speed video camera (500 frame/s) and a YVO4 laser were employed for flow visualization experiments. The experiments were conducted in the case of the temperature difference between the cross wind and the jet at the jet exit was $\Delta\theta$=0, 60K, the mean velocity of the cross wind in the large-scale turbulence or the grid turbulence was 0.4, 0.6, 0.8, 1.0, 1.5, 2.0m/s and the vertical jet velocity at the jet exit was 0.2, 0.4, 0.6, 0.8, 1.0, 1.5, 2.0m/s.

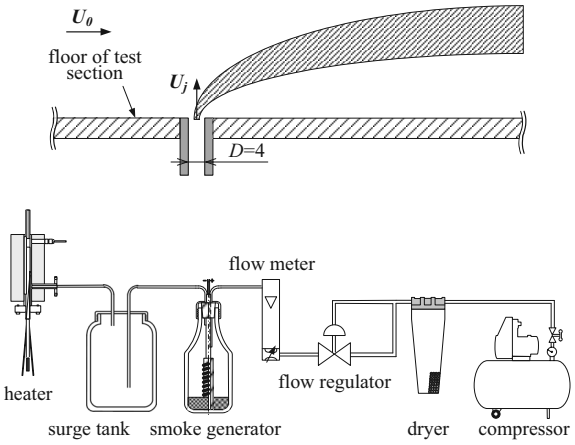

Fig. 1 Experimental setup. unit: mm

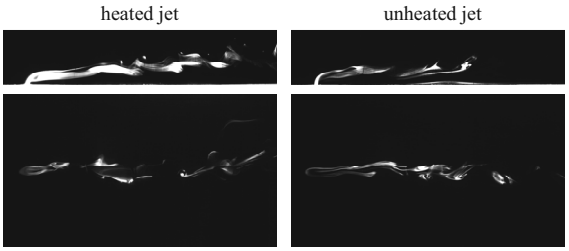

Fig. 2 Typical smoke structure (mode II) in large-scale turbulence for U_0=0.4m/s and U_j=0.2m/s.
upper: vertical cross section
lower: horizontal cross section

3. Results and Discussion

Fig. 2 shows typical smoke structure. The jet ejected from the nozzle is curved by the cross wind. The cross wind flows along the curved jet and vortices occurs and develop due to velocity shear. In the far region from the jet exit, hairpin-type vortices connected each other or vortex or vortex tube-type vortices are generated. Meandering structure was observed in the horizontal cross section of Fig. 2. Compared between the heated jet and the unheated jet, the smoke of the heated jet rises higher in the vertical cross sectional view by the effect of buoyancy and is more meandering in the horizontal cross sectional view due to unstableness.

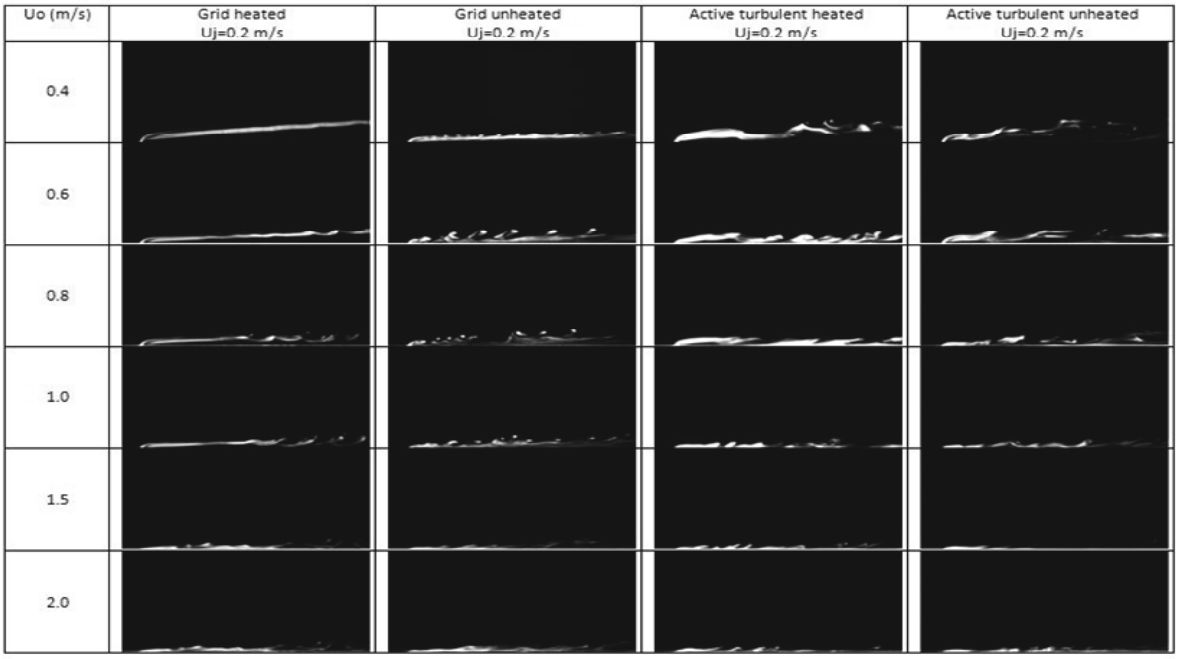

Fig. 3 Typical smoke structure (mode II) in large-scale turbulence.

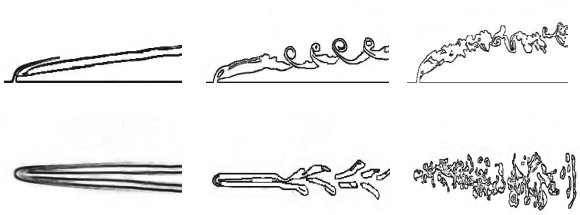

mode I mode II mode III

Fig. 4 Smoke structure.

Fig. 3 shows various smoke behavior in large-scale and grid turbulence fields for U_0=0.4-2.0m/s and U_j=0.2m/s. The height of smoke ejected from jet exit is higher and the smoke is more stable for slower U_0.

For U_0=0.4-0.8m/s and U_j=0.2m/s in the large-scale turbulence, the smoke of heated jet rises higher than the smoke of unheated jet due to buoyancy effects. The smoke of heated jet risen in the sky from jet exit attaches on the ground for U_0=0.4-0.8m/s and U_j=0.2m/s in the large-scale turbulence. This would be because of strong turbulence intensity and large-scale eddy. On the other hand, the smoke almost reaching on the ground goes downstream for U_0=1.0-2.0m/s.

Since vortices occur and develop due to velocity shear, the vortices can clearly observed in the region where is far from the jet exit. Especially in the smoke with unheated jet for U_0=0.6m/s and U_j=0.2m/s in the grid turbulence, typical vortices effected by Kelvin-Helmholtz instability are generated. Compared with smoke of heated and unheated jet for same condition, the vortices in the unheated jet can be observed more upstream due to more stable.

Although there is no picture of vertical cross section of Fig. 3, the smoke structure of heated jet is more meandering than of unheated jet both in the large-scale turbulence and in the grid turbulence. And, the smoke in the large-scale turbulence is more meandering than in the grid turbulence. This fact shows the effect of large-scale turbulence eddy and strong turbulence intensity.

The smoke structures shown in Fig. 3 were divided into three modes. Mode I is structure with two vortex tubes, mode II is horse-shoe-type, and mode III is structure and turbulence-type structure in Fig. 4. The mode I occurred for low speed U_0 and U_j only in the grid turbulence. The mode III was generated for higher U_0 and U_j in the large-scale turbulence and the grid turbulence. The mode II was situation transited from the mode I to the mode III.

4. Concluding remarks

Smoke dispersion was investigated by using a wind tunnel equipped with an active grid. There were three modes: structure with two vortex tubes (mode I), horse-shoe-type (mode II) structure and turbulence-type structure (mode III).

Acknowledgment

This study was partly supported by a grant from SATREPS Project (Principal investigator: Prof. Mitsuru Osaki, Hokkaido University) by JST.

References

[1] H. Makita, Fluid Dynamics Research, **8** (1991), p53-64.

Eighth International Conference on Flow Dynamics
November 9 - November 11, 2011

Unsteady Vortex Structures in the Wake behind Bluff Bodies

Hitoshi ISHIKAWA
Department of Mechanical Engineering, Tokyo University of Science
ishi@rs.tus.ac.jp

ABSTRACT

Unsteady vortex structure in the wake behind bluff body was experimentally investigated by wind tunnel experiment. A flexible rectangular plate, which was made of a soft polyurethane block, shows the sway motion and flow-induced vibration caused by fluid force. Phase averaged vortex structure behind the plate were measured by Particle Image Velocimetry (PIV). The size of recirculation region and upwash flow in the wake were influenced by unsteady motion of the rectangular plate.

1. Introduction

Unsteady vortex structure which separated from a flexible rectangular plate with sway motion and flow-induced vibration was experimentally investigated by wind tunnel experiment. Vortex shedding from bluff bodies such as a rectangular plate or a circular cylinder shows "time-dependent" unsteady motion by the movement of separation point. The flexible rectangular plate, which was made of soft material (polyurethane block), was cantilevered on a flat ground plate. The top free end of the plate showed a sway motion when the plate bent itself for the downstream direction by fluid force. Then increasing sway angle, the top free end showed the flow-induced in-line vibration which has a small amplitude. This is a typical phenomena on fluid-structure interaction problem. Vortex structures behind a surface-mounted bluff body have been researched by many researchers [1-2]. Most of these studies reported about not a flexible body but a solid body. However more experimental research for unsteady vortex structure organized by the motion and the flow-induced vibration of flexible body which is expected to be used more for engineering applications in the future is required. In this paper, phase averaged vortex structures which was defined by the phase of the vibration were measured by Particle Image Velocimetry (PIV). We focused on phase averaged vortex structure when the vibration amplitude was at the top and bottom position of the vibration.

2. Method

PIV experiment was conducted in a circuit-loop type wind tunnel with working section 400 mm height, 200 mm wide and 900 mm long. The measurement was conducted at mean flow velocity, U_0 of 2.0 m/s. The turbulent intensity in the main flow is 1.5%. The corresponding Reynolds number Re, based on the plate width b, main flow velocity and kinetic viscosity is 11,000. Figure 1 shows schematic diagram of the experimental setup, coordinate system and a flexible rectangular plate. The flexible rectangular plate, which was used as a test piece, has a height h of 200mm, width b of 80mm and depth d of 20 mm respectively. The plate was cantilevered on a flat ground plate with airfoil leading edge. The x axis is in the direction of the main flow, the y axis is the plate's height direction and the z axis is the width direction. The velocity components u, v and w defined respectively x, y and z axial velocity. The measurement regions were located in xy plane at z/b = 0, 0.125, 0.250, 0.375 and 0.500.

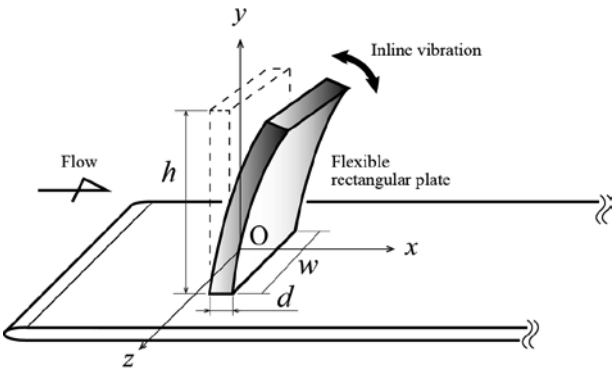

Fig.1 Experimental setup and flexible rectangular plate

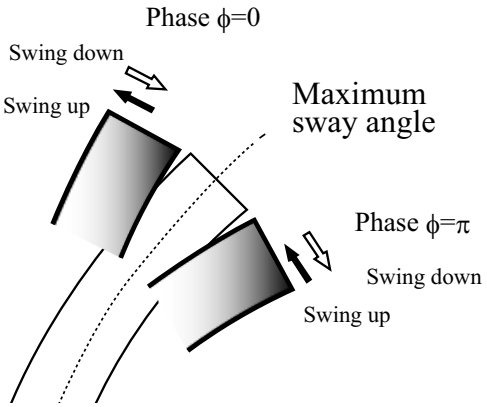

Fig.2 Phase definitions of plate's position caused by flow-induced vibration

In the flow field, this flexible rectangular plate was swayed in the downstream direction, and involves a flow-induced vibration after reaching the maximum sway angle. The definition of phase of the plate vibration is defined in Fig. 2. The "swing up state" when the top free end is located at top dead position of the vibration is defined as phase ϕ=0. The "swing down state" when the top free end is located at bottom

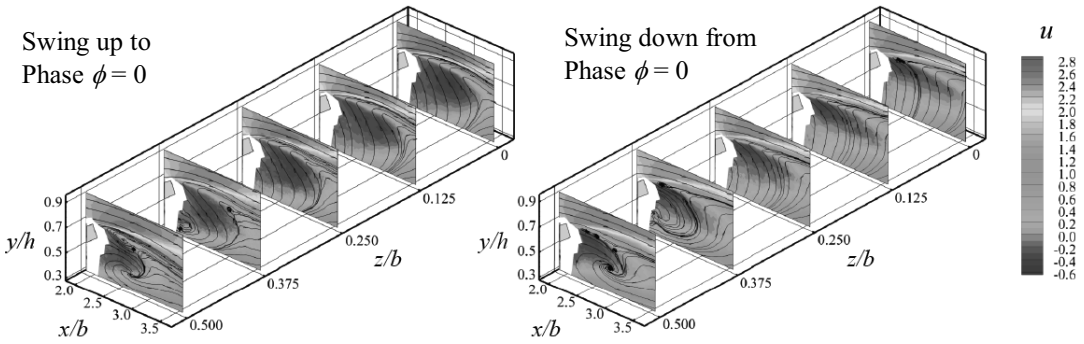

Fig.3 Contours of mean streamwise velocity u and flow pattern (Phase $\phi = 0$)

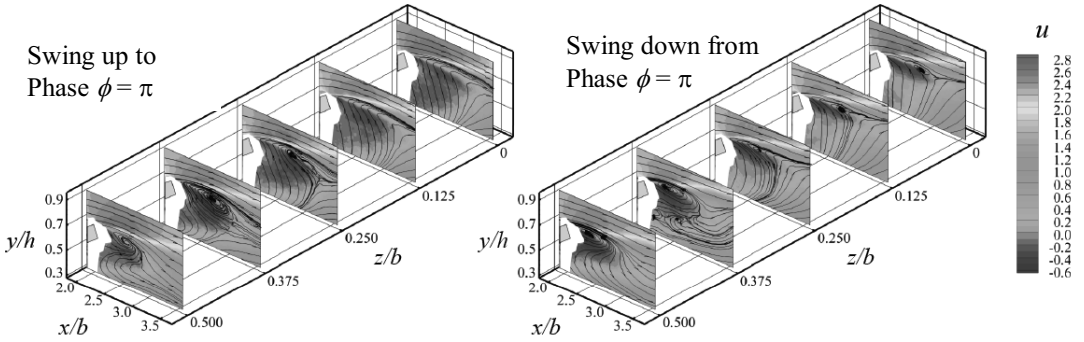

Fig.4 Contours of mean streamwise velocity u and flow pattern (Phase $\phi = \pi$)

dead position is defined as phase ϕ=π. In order to detect the position of the plate's end, two light sensors which measure the change of the light intensity when the plate motion intercepts the beams, were synchronized with PIV system. By using these two light sensors to distinguish between the phase ϕ=0 or ϕ=π and the "swing up state" or "swing down state", it makes possible to capture four pattern PIV images at each phase.

PIV images are recorded with a 1392 × 1024 pixel CCD camera. Light sheet that is created by the double pulsed Nd:Yag laser(120mJ/pulse). The flow was seeded with 5 μm dioctyl sebacate (DOS) particles. Each pair of synthetic PIV images is analyzed by computing the image cross-correlation in 4 mm × 4 mm (32×32 pixel) sub-images with a 50% overlap between adjacent interrogation regions. The size of PIV measurement region is 174 × 128mm.

3. Results and Discussion

Figure 3 shows contours of mean streamwise velocity and flow patterns. First, a general flow pattern in the wake behind our flexible rectangular plate is described as follows. Approaching flow stagnated in the front of the flexible plate. Then flow moved up and separated from top free end of the plate. Fluid force acts on the pressure side and swayed the plate in the upstream and downstream direction. Large recirculation region was formed just behind the plate.

In the case of swing up to the phase $\phi = 0$, flow approached the stagnation point in the pressure side. Then the flow moved to the top free end and both side ends of the flexible plate. An upwash flow from the surface of the ground plate was generated. While the case of the swing down from phase $\phi = 0$, the upwash flow is enlarged. The size of recirculation region became further small due to the enlarged upwash flow. Separated shear layer was moved upward because of the enhanced upwash flow.

Figure 4 shows flow pattern at the phase $\phi = \pi$. A focus point is formed close to the top free end. Especially the size of recirculation region is small when flexible plate swings down to the phase $\phi = \pi$. It was found that thickness of shear layer from top free end was unsteadily changed with the phase.

4. Concluding remarks

In this study, unsteady vortex structure in the wake behind flexible rectangular plate with sway motion and flow-induced vibration was measured by PIV experiment. Phase averaged vortex structure was educed by our technique using two light sensor. The swing down motion of the plate's vibration enhanced the upwash flow in wake region of the plate.

References

[1] A.Okajima, T. Kosugi and A. Nakamura, *JSME International Journal*, Vol.44(2004), 695.

[2] H.F. Wang, Y. Zhou, C.K. Chan, W. O. Wong and K.S. Lam, K.S., *Proceedings of 15th Australasian Fluid Mechanics Conference* (2004)

Measurements in Flow past Yawed Circular Cylinder

BalabhadraV. Venkata Rao and Shailendra D. Sharma
Aerospace Engineering Department, IIT Bombay
Powai, Mumbai 400076, India.
sd.sharma@iitb.ac.in

ABSTRACT

Salient features of flow over a yawed circular cylinder, captured through wind tunnel measurements at subcritical Reynolds number, are presented here. Surface pressure distribution, vortex shedding frequency, mean and fluctuating velocity profiles in the near wake region, obtained along the model span, showed strong effects of increasing yaw angle. Reduction in sectional coefficient of drag along span toward downstream end, complete suppression of vortex shedding, reduction in both the wake defect velocity and wake turbulence energy were observed as the yaw angle was increased.

1. Introduction

Power transmission line, cable stayed bridge, missile, mid-air refueling boom, etc. are some of the engineering applications of yawed circular cylinder facing the wind. The flow over slant surface and in the near wake is quite complex with strong three dimensionality depending on the yaw angle. The present investigation of flow over a circular cylinder is focused on measurement of surface pressure distribution, vortex shedding, mean velocity and turbulence profiles in the near wake for yaw angles of 0°, 12.5°, 31° and 45°.

2. Experimental Method

The test model was turned out of teak wood with 44 mm diameter and 680 mm length. The model surface was polished to a smooth finish. It was provided with a pair of pressures taps in two diametrically opposite rows along span at every 35 mm. The model spanned floor and ceiling in the middle of a close circuit wind tunnel having square test section of 500 mm side as shown schematically in Figure 1.

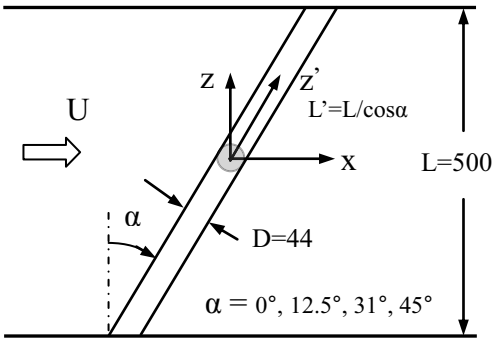

Fig. 1 Definition sketch of model mounting.

Experiments were carried out at the Reynolds number of 2.75×10^4 based on the free-stream velocity of 10 m/s and the model diameter. ALNOR digital micro-manometer, model AXD 560, was used in conjunction with Furness Controls Pressure Scanner Box, model FCS 421, for measurement of pressures. The model was rotated about its axis in steps of 5° to obtain the surface pressure distribution. To measure mean and fluctuating velocities, Dantec Dynamics mini CTA (model 54T30), 5 micron hot wire was used.

3. Results and Discussion

Figure 2 shows that the surface pressure distribution is nearly invariant along the span when the yaw angle is zero. The plot suggests flow separation around θ=85 and 275 degrees and shows symmetry about the horizontal

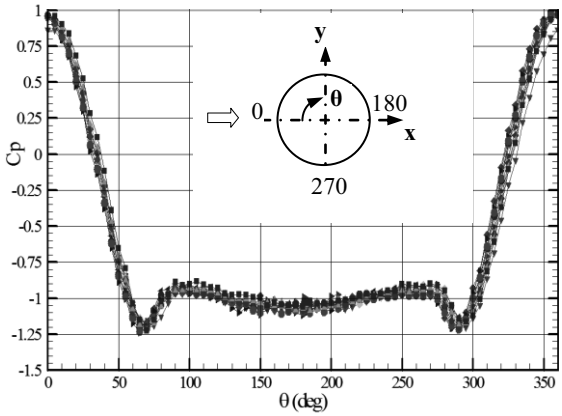

Fig. 2 Pressure distribution for zero yaw (α=0°) along the span from z/L= -0.33 to z/L=0.44.

axis with mean base pressure coefficient (C_{pB}) of about -1.05. With increase in the yaw angle, generation of the spanwise flow evidently affected the surface pressure as C_p registered overall decrease on the front and increase on the rear of the cylinder. Fig. 3 shows pressure plots for one of the yaw angles, α = 31°. It is noted that the yaw has greater influence on C_p variation on the base as

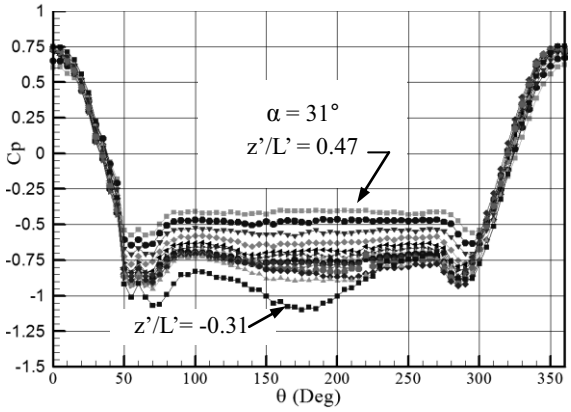

Fig. 3 Pressure distribution for α=31° along the span from z/L= -0.31 to z/L=0.47.

it is seen to vary from -1.1 to -0.4 along the span in the direction of the cross flow from z'/L' = -0.31 to 0.47. On the front (θ = 0°), pressures do not seem to vary along span despite cross flow as C_{po} is found to be about 0.7. Similarly, C_{pB} was seen to vary from -1.05 to -0.85 and from -0.85 to -0.35 for α =12.5° and 45°, respectively, and the corresponding C_{po} was found to be about 0.9 and 0.5, respectively.

Differential pressure, $\delta C_p = C_{po} - C_{pB}$, is indicative of drag and that is seen not only to reduce with the yaw but also reduce along the span in the direction of cross flow as shown in Figure 4.

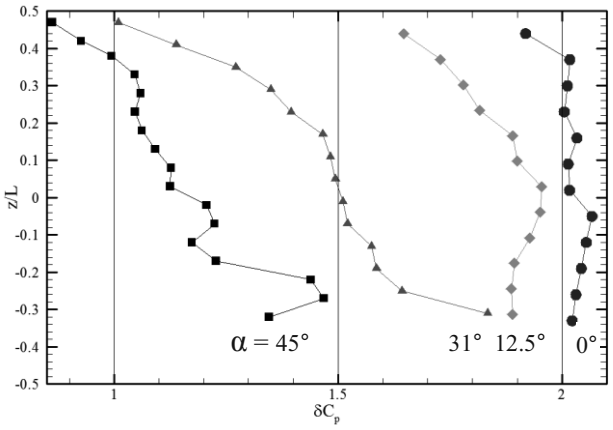

Fig. 4 Effect of yaw on drag.

Hot wire probe was positioned near the wake edge behind the model at three spanwise locations (x/D=3 and z/L=0.25, 0, -0.25) to capture the vortex shedding. Frequency spectrum of the velocity fluctuations clearly indicated occurrence of periodic vortex shedding if there appeared a spectral peak. With increasing yaw angle, the spectral peak progressively diminished with somewhat lowering of frequency and eventually at α=45° it was difficult to distinguish it. Further, due to spanwise flow the spectrum was affected on either side of the mid-span.

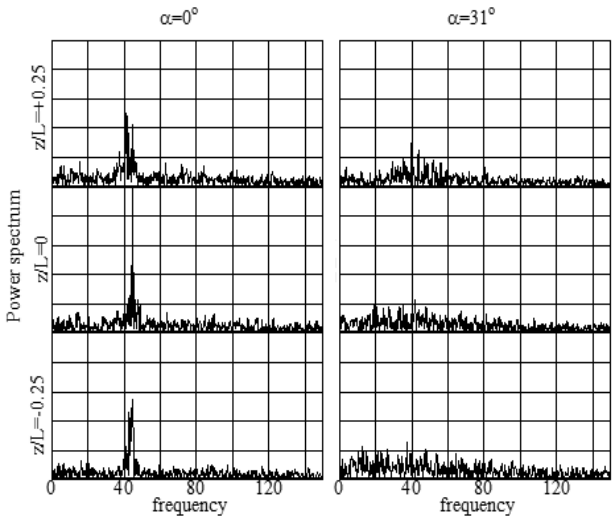

Fig. 5 Frequency spectra for two different yaw angles.

Figure 5 shows frequency spectra for α=0° and 31° at three different spanwise locations. For zero yaw, all three spectra exhibit distinct peak having maximum amplitude in the middle of span at 44.6 Hz which gives the Strouhal number of 0.196. With the yaw, attenuated spectral peak shifts to 40 Hz at z/L=0.25 and becomes indiscernible at other spanwise locations.

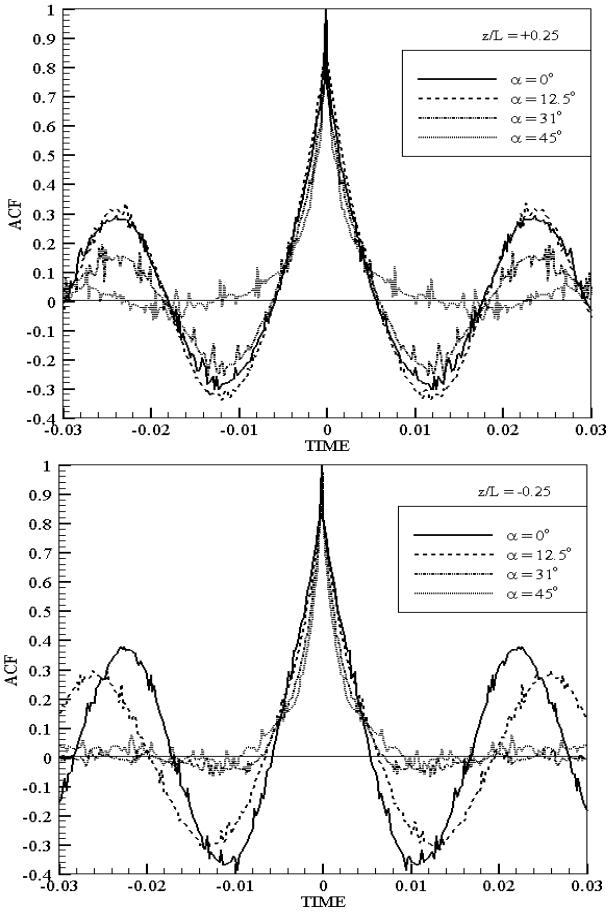

Fig. 6 Auto-correlation of hot wire signal.

Auto-correlation can detect periodic signal buried in noise. Figure 6 shows that with increasing yaw, negative peak of the wave is decreased with marginal increase in the time period. This signifies suppression of periodicity with reduced frequency. Thus, it is clear that there is no vortex shedding for α=45°; however, for α=31° it exists around z/L= + 0.25 but not around z/L= - 0.25. Flow visualization results by Ramberg [1] have shown similar pattern. Further, the wake defect velocity and wake turbulence energy, both appeared to reduce as the yaw angle was increased.

4. Concluding remarks

The cross flow due to yaw has significant influence on flow over circular cylinder – spanwise variation of base pressure, drag reduction and suppression of vortex shedding being the prime observations.

References

[1] S.E. Ramberg, J Fluid Mech, **128** (1983), 81.

Eighth International Conference on Flow Dynamics
November 9 - November 11, 2011

Experimental investigation of boundary layer transition in wide range of free stream turbulence intensity

R. Noirmatsu, S. takai, Y. Iwatani and M. Matsubara
Department of Mechanical Systems Engineering, Shinshu University,
4-17-1 Wakasato, Nagano, 380-8553, Japan
mmatsu@shinshu-u.ac.jp

ABSTRACT

Experiments and DNS of flat plate boundary transition due to free stream turbulence of modalate intensity have revealed that the transition is caused by the non-modal growth that results the streamwise fluctuation energy peak at the middle of boundary layer and disturbance growth proportional to the streamwise distance. In this study transition process caused by variety of the free stream turbulence including anisotropic turbulence are scrutinized grids and their relation to the disturbance growth in the boundary layer is investigated. The visualization results in both the wind tunnel and the towing tank facilities indicate that streaky structures appear in the transition boundary layer in wide range of turbulence intensity of free stream.

1. Introduction

A flat plate boundary layer subjected to free stream turbulence of a few % turbulence intensity, streamwisely elongated streaks grow in the boundary layer, and at the certain level of their amplitude they break down to turbulence after wavy motions [1][2] as the secondary instability. The experimental results showed that the profile of the streamwise velocity fluctuation has a peak at the middle of boundary layer and that the disturbance energy increases in proportion to the streamwise distance from the leading edge. These results are sufficiently consistent with the non-modal theory [3][4]. The streaks were also observed in a numerical simulation [5], though trigger of breakdown to transition was due to a backward jet from the outside of the boundary layer. In spite of these progress of research on the transitional process in the boundary layer subjected to free stream turbulence, prediction method for the transition is far from completion because of lack of quantitative data in various cases of free stream turbulence. The present investigation was performed by smoke flow visualization and a hot-wire measurement in wide range of free stream turbulence with focusing on the non-modal transition. Especially the spanwise scale of the free stream turbulence and its relation to the streak growth are investigated.

2. Experimental set-up

The experimental set-up of wind tunnel is shown in Fig. 1. The quantitative measurements were carried out in a circuit wind tunnel that has a length of 10.2 m, height of 4.1 m and width of 1.2 m. The tunnel includes a test section that is 400 mm in width, 600 mm in height and 4 m in length and a setting chamber with five sheets of wires netting and a honeycomb followed by a three dimensional nozzle of 9 contraction ratio. A duralumin test plate is 2.1 m in length, 580 mm in width and 10 mm in thickness and mounts at 100 mm apart from a side of test section. The plate has a 10 : 1 elliptic leading edge of a 20 mm minor axis and the leading edge is located at 1600 mm downstream from the exit of the nozzle. The coordinate system is denoted by the streamwise x, wall-normal y and spanwise z directions with the origin at the center of the leading edge. For control of free-stream turbulence intensity and scale, four turbulence grids and a screen are used. Grid A, B, D and Screen are inserted downstream the nozzle, while grid C is inserted upstream the nozzle. Grid C consists of 13 mm pipes that have 2 mm diameter holes at a middle point between grid intersections for jet injection. Total number of the holes is 275. Adjustment of pressure inside the pipes enables turbulence intensity control.

Flow visualization has partly been conducted in a towing tank facility shown in Fig. 2. The towing tank has a length of 9 m, depth of 0.7 m, width of 0.8 m. Test plate towing track has 5 rollers and run along railway by two trucks towing a test plate and a turbulent grid each timing belt drive with a brushless DC motor. The test plate has a length of 1750 mm, width of 500 mm, thickness of 12 mm and made of aluminium. Its leading edge has the same shape of that in the wind tunnel and is jointed smoothly to the downstream section of test plate. It is located horizontally 300 mm from the bottom of the tank. Furthermore, a ship mounted on the test plate towing truck has a window for visualization. Test plate upper surface is touch on the water surface that is 200 mm above the test plate surface. Grid B is used for the towing tank experiments.

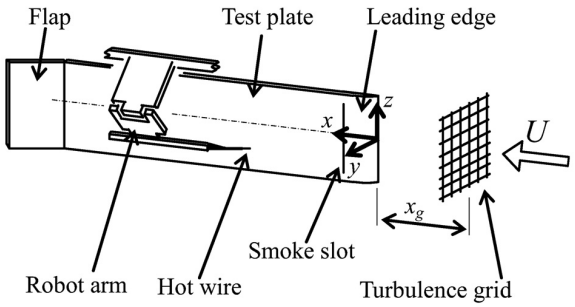

Figure 1: Wind Tunnel.

3. Results and Discussion

The test cases are listed in Tab.1. Fig. 3 shows flow visualization in a transitional boundary layer in Case 2. The flow direction is from left to right and the streamwise area of the picture is $0.83 \times 10^5 \leq Re_x \leq 2.75 \times 10^5$. The streaky structures elongated in the streamwise direction are seen in the upstream region. There exists a turbulent spot at the center. From the video observation, the streaks break down with the spanwise wavy motion and a turbulent spot is generated.

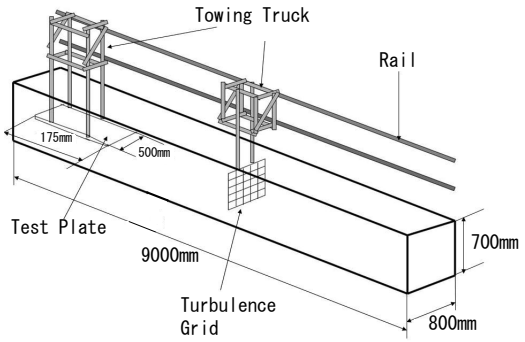

Figure 2: Towing Tank.

Table 1: Experimental condition(Wind Tunnel).

Case	Grid	u_∞	ΔP	Tu_u	Tu_v
1	A	5 m/s	-	2.36 %	2.39 %
2	B	5 m/s	-	2.13 %	1.93 %
3	B+Screen	7 m/s	-	1.29 %	1.48 %
4	C	6 m/s	3.00 kPa	1.65 %	1.26 %
5	C	12 m/s	3.00 kPa	0.63 %	0.86 %
6	C	14 m/s	0 kPa	0.22 %	0.43 %
7	C	12 m/s	0.35 kPa	0.29 %	0.36 %
8	D	10 m/s	-	0.45 %	0.28 %

Fig. 4 shows flow visualization in the towing tank in Case 2. The flow direction is from left to right and the streamwise area of the picture is $0.83 \times 10^5 \leq Re_x \leq 2.75 \times 10^5$. The streaky structure that look alike wind tunnel can observed. But lighting was uneven and small in area. Making a comparison between Fig. 3 and Fig. 4, the streaky structure in case 2 is shorter than in towing tank visualization. It is considered that the difference of tracer, alcohol mists in the wind tunnel and flakes in the towing tank, effect results the visualization.

Fig. 5 shows a relation between velocity fluctuation energy and Reynolds number based on the streamwise position. The cases on Tu_v is over 1 % have sharp slope and the other cases increase slowly. On the observation of visualization, the streamwise position where the fluctuation energy reaches to a peak is roughly correspond to the middle of the transition area. Previous studies[6][7] mentioned that the linear energy growth was explained by the non-modal theory. It is concluded that streaky structures grow in wide range of free stream turbulence intensity.

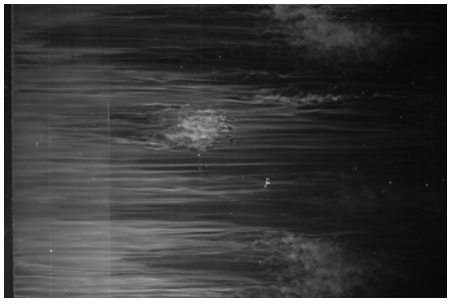

Figure 3: Flow Visualization in Case 2

4. Concluding remarks

As a result, streaky structures were observed in both the wind tunnel and the towing tank. In addition, the turbulence intensity in the boundary layer is proportional to the distance of streamwise direction. These results suggests strongly that as resultant of the non-modal growth, streaky structure is a dominant disturbance in the transitional boundary layer subjected to free stream turbulence in wide ranges of its intensity.

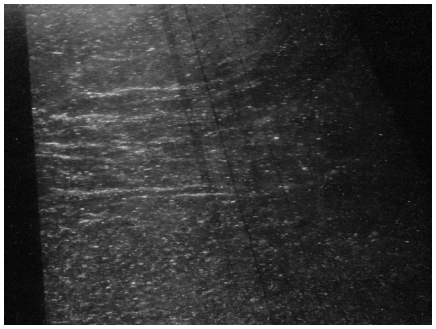

Figure 4: Flow Visualization in Towing tank

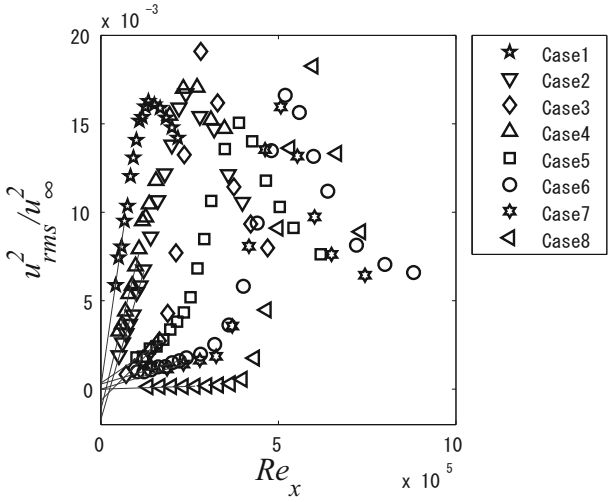

Figure 5: Energy growth.

5. Reference

[1] Matsubara, M., Alfredsson, P. H., 2001. "Disturbance growth in boundary layers subjected to free-stream turbulence", *J. Fluid Mech*, **430**, pp. 149–168.

[2] Fransson, J.H.M., Matsubara, M., Alfredsson, P.H., 2005. "Transition induced by free-stream turbulence", *J. Fluid Mech*, **527**, pp. 1–25.

[3] Andersson, P., Berggren, M, Henningson, D.S., 1999. " Optimal disturbances and bypass transition in boundary layers", *Phys. Fluids*, **11(1)**, pp. 134–150.

[4] Luchini, P., 2000. "Reynolds-number-independent instability of the boundary layer over a flat surface: optimal perturbations", *J. Fluid Mech*, **404**, pp. 289–309.

[5] Jacobs, R.G., Durbin, P.A., 2001. "Simulations of bypass transition", *J. Fluid Mech*, **428**, pp. 185–212.

[6] Matsubara, M. and Alfredsson, P.H., 2001. *J. Fluid Mech*, **430** , pp. 149-168.

[7] Fransson, J.H.M., Matsubara, M. and Alfredsson, P.H., 2005 *J. Fluid Mech*, **527** , pp. 1-25.

Eighth International Conference on Flow Dynamics
November 9 - November 11, 2011

Disturbance structures in a low Reynolds number channel flow

Kenta Watanabe, Tsutomu Natori, Syunsuke Akaoka,Kvick Mathias and Masaharu. Matsubara
Department of Mechanical Systems Engineering, Shinshu University,
4-17-1 Wakasato, Nagano, 380-8553, Japan
11ta144k@shinshu-u.ac.jp

ABSTRACT

A two-dimensional channel flow becomes intermittent and large-scale disturbances appear streak structures above but close to the minimum transitional Reynolds number.Intermittent factor gradually increases with increase of Reynolds number.The streamwise scale of streak structures is twice longer than the turbulent disturbance scale.The phase velocity of disturbances has tendency of acceleration with Reynolds number increase.These results show that the streak disturbances in the intermittent flow have apparently different properties from those of the turbulent disturbance.

1. Introduction

In the two dimensional channel flow, the flow become turbulence at under the critical Reynolds number when initial disturbance is strong. However decreasing Reynolds number from this turbulent state, the flow inversely transit to laminar flow at a certain Reynolds number. This Reynolds number is defined minimal Reynolds number in this study.

In the experiment [1] , when Reynolds number are very higher than minimal Reynolds number, flow is accounted turbulent disturbance. But streak structure is observed that have shape and scale different from turbulent disturbance in the around minimal Reynolds number. It is confirmed that rate of between turbulent disturbance and streak structure gradually change as against Reynolds number.
Flow field of relaminarizing flow is studied already, but quantify of streak structure, turbulent disturbance scale, disturbance phase velocity are not enough at over a wide range Reynolds number.

In this study, we survey disturbance structures in the relaminarizing channel flow in flow visualization. And we quantify disturbance scales and phase velocity.

2. Experimental apparatus and method

Experimental apparatus is circuit water cistern. Water pressurized by pump run through orifice flowmeter and contracted by nozzle are flow in inlet region. The flow just downstream of the nozzle are disturbed by tripping wire, at a downstream of inlet region, flow become fully development turbulent. At a expansion section, flow broadened spanwise direction decrease 0.61 times of Reynolds number and flow in test section. Get out water are pressurized by pump again and recirculation upstream. The streamwise length of inlet region, expansion section and test section are 2000mm,400mm,4550mm. The spanwise length of inlet region, test section are 360mm, 580mm. Coordinate origin is center of wall of entrance of test section. Coordinate systems are x, y, z for streamwise, wall-normal and spanwise directions. Channel width d is 7.1mm. The flow visualization was made using a 6.0 megapixel video camera at 10fps and 1/1000 shutter speed. Pearl flakes were used as tracer particles that have a specific gravity of 3.1and size of $7 \sim 8\mu$m. These flakes have tendency to align along the shear plane, and were illuminated by three halogen lamps. Visualization experiment was run at a position of $x/d = 600$.

The Reynolds number is defined as $Re = U_m \mathrm{d}/\nu$, where U_m is bulk mean velocity and $\nu$is the kinematic viscosity. For mean velocity adjustment of the water channel, pressure drop at an orifice inserted in the return pipe to the pump was monitored.

3. Results

Intermittency rate and disturbance scale are quantified from visualization results. Image procession that brightness value from original picture minus average of 1000 pictures the value executes in order to remove blot of glass and unevenness of illumination. Moreover, when intermittency rate is deriving, moving average is used to smooth picture and bandpass filter is used to remove high frequency components. After that, original picture is compared to root-mean-square deviation picture. Using decided threshold value, separate laminar and turbulence. Intermittency rate is derived that turbulent areas divide all area.

Figure.1 shows intermittency rate. Intermittency γ is time occupation ratio of turbulence so that it is 0 for laminar flow and 1 for fully turbulent flow. This figure compared to Hot-wire measurement in air relaminarizing field.[2] In the visualization results, at under the $Re = 1400$, γ have a almost constant value under 0.1, and gradually increases up to $Re = 2400$. And over the $Re = 2400$,γ have a almost constant value over 0.9. In this result, flow is almost turbulent at over the $Re = 2400$, and flow is almost laminar at under 1400. There is a little difference when compared with Hot-wire measurement. The reason of difference guess that We cannot separate turbulent and laminar perfectly by light, and threshold value is insufficiency. However both results has a similar inclinable, this two results are almost good. At the $Re = 1900$, γ is 0.5.For this reason, flow have a high rate of turbulent at over the $Re = 1900$, and have a high rate of laminar at under the $Re = 1900$. Transition region is between $Re = 1400 \sim 2400$.

Figure.2 shows spanwise and streamwise scales of disturbance derive from correlation of pictures

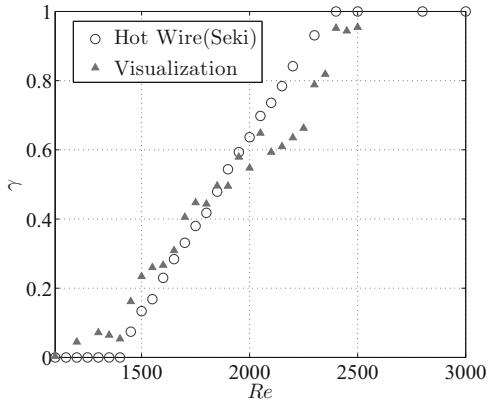

Fig 1: Intermittency Rate

brightness value. Spanwise scale is defined equation (1). Δz_{min} is the distance to minimum value of correlation. d is channel width.

$$\lambda = \frac{2\Delta z_{min}}{d} \tag{1}$$

Disturbance have constant scale at over $Re = 1900$. Spanwise scale is about 0.7 as against channel width. The scales become big when Reynolds numbers decrease. Spanwise scale have about $1 \sim 1.3$ at under $Re = 1800$. Streamwise scale is defined equation (2). This equation is integral scale.

$$\Lambda = \frac{1}{d}\int_0^\infty R_x dx \tag{2}$$

Disturbance have constant scale at over $Re = 2400$. Streamwise scale is about 0.7 as against channel width. The scales become big when Reynolds numbers decrease too. Streamwise scale have about $2 \sim 2.2$ at under $Re = 1800$. Figure.2 and visualization result,flow is almost turbulence at over $Re = 2400$. So turbulent disturbance have 0.7 in spanwise and streamwise scale as against channel width. Similarly, flow is derived from laminar and streak structure at under $Re = 1800$. In this result, streak structure have $1 \sim 1.3$ spanwise scale, and $2 \sim 2.2$ streamwise scale.

Figure.3 is normalized phase velocity of disturbances obtained from temporal-spatial correlation. U_p is phase velocity, and U_m is mean velocity. Phase velocity become fast with the decreasing Reynolds number. This phase velocity is mixing streak and turbulent phase velocity. So these results have dispersion. In this result, streak structure faster than turbulent disturbance. Streak structures phase velocities are almost same as mean velocity. Turbulence disturbances phase velocity are 0.7 as against channel width.

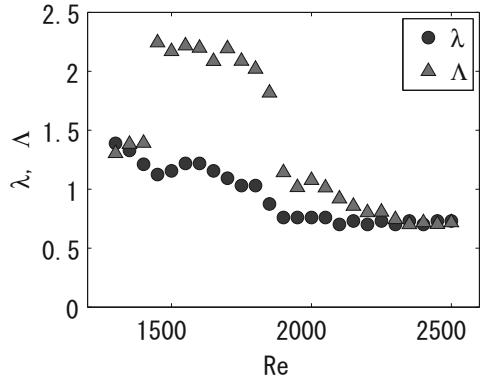

Fig 2: Disturbance Scale

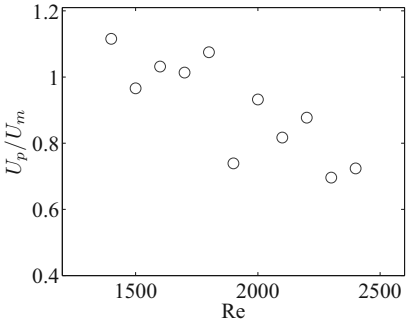

Fig 3: Phase Velocity

4. Summary

In visualization result, flow field was observed that variety disturbance mixing. In intermittency rate, we found that disturbance rate change almost constant rate as against Reynolds number. In quantify disturbance scale, streak structure have $1.5 \sim 2$ times scale as against turbulent disturbance, and streak structures scale change as against Reynolds number. Streamwise and spanwise scales big change at $Re = 1900 \sim 1800$. But big change is not seen in intermittency rate. In this result, we guess that flow dominant structure change turbulent disturbance to streak structure at this Reynolds number.

References

[1] Numano,T.,Matsubara,M, Proceedings of 2008 Annual Meeting,Japan Society of Fluid Mechanics,(2008),pp.29

[2] Seki,D.,Matsubara,M, Proceedings of 2010 Annual Meeting,Japan Society of Fluid Mechanics,(2010)pp.24.

Pressure Measurement On A Hypersonic Lifting Model For The Validation Of An Accelerometer Force Balance

Sharad Trivedi and Viren Menezes
Department of Aerospace Engineering, Indian Institute of Technology Bombay, Powai, Mumbai 400076, India.
E-mail: sharad@aero.iitb.ac.in

ABSTRACT

Drag, lift and rolling moment on a hypersonic lifting model were measured in a shock tunnel using a pressure measurement technique, where high frequency pressure sensors were used on the surface of the model to sense the local pressure. The measured values of aerodynamic forces and a moment were used to validate an accelerometer force balance technique developed in-house. The force and moment coefficients obtained through pressure measurements compared well with the coefficients obtained through the force balance technique. The force and moment coefficients for the model were also deduced using an analytical method called Newtonian theory. A good comparison was observed among the three sets of data.

1. Introduction

A measurement technique developed for ultra-short duration hypersonic test facilities generally requires a validation of its performance, as the technique operates on models with complicated flow-fields within the stringent constraints of the short duration test facilities. Well-established theoretical models and robust CFD codes can provide an insight into the experimental measurements, provided the theory and the codes are pre-validated against well-controlled experiments. Hence, the best validation methodology for a new experimental technique is to validate against a known or an established experimental technique.

We developed a six-component accelerometer balance to measure all the forces and moments on a flapped, triangular lifting model in a hypersonic shock tunnel [1, 2]. The balance, after development and testing, required a secondary validation as the theoretically estimated data had some discrepancy with the measurements. The theory considered/available (Newtonian theory) for such test models [3] did not take into account some of the complex, viscous flow phenomena on the model, and the discrepancy/deviation observed in the data was attributed to this drawback in the theory.

The pressure measurements carried out in the present study aimed at validating the six-component force balance, out of which the data for 3 components viz. drag, lift and rolling moment are presented in this article.

2. Method

The aerodynamic forces and moments on a flapped, triangular, lifting model, as shown in Fig. 1, were measured in the IIT Bombay Shock Tunnel (IITB-ST) [1], at a hypersonic Mach number of 8. The tunnel was driven by a 50 mm diameter (inner) shock tube that operated in a reflected mode. An aluminum diaphragm of 1.2 mm thickness was ruptured by pressurization of the driver gas in the shock tube to start it. A converging-diverging nozzle was attached to the end of the shock tube to expand the shocked test gas (air) to a freestream of Mach 8 in a test section of dimensions 300X300X450 mm. The freestream conditions for the present set of experiments are listed in table 1.

Table1. Freestream conditions for the tests in the tunnel.

Test gas	P (Pa)	T (K)	Mach No.	Total enthalpy (MJ/kg)	Reynolds No. (/m)
Air (γ=1.4)	61 ± 8.5%	58 ± 5.4%	8 ± 0.2%	0.812 ± 5.4%	$1.14X10^6$ ± 3.1%

High frequency pressure sensors (MEAS-France, model:EPIH-373-1.5B-/V5/L3M/M)were flush-mounted on the surfaces of the model to sense the magnitude of pressure. The model was rigidly fastened through a sting in the tunnel test section during the tests. The pressure transducers with a sensitivity range of 14.5 to 17 mV/kPa were embedded in the surfaces of the model with a good spatial resolution and an emphasis on the likely locations of complex flow features. The model was tested at different angles of attack (AOA) of 0, 5, 10 and 15 degrees with the freestream.

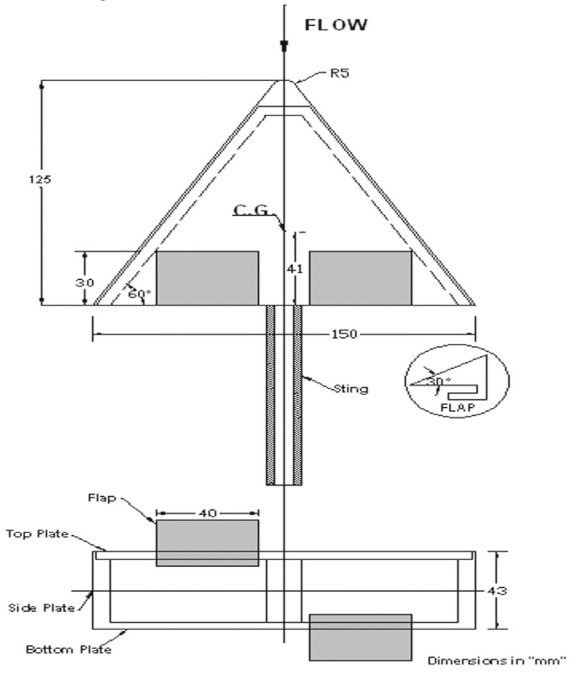

Fig.1 Schematic of the test model.

The measured surface pressure was resolved in the appropriate directions and was multiplied by the area of

the domain of influence to obtain the local aerodynamic forces. Summation of the local forces along the freestream and normal to the freestream gave the drag and the lift on the model, respectively. The rectangular flaps located at the trailing edge of the model were the major source of rolling. The net rolling moment on the model was obtained by the summation of the moments of all the contributing individual forces about the longitudinal axis of the model. Equations 1-3 give the expressions for the drag, lift and rolling moment on the model. The force and moment coefficients are expressed by eqns. 4-6.

$$D(t)=\sum_{i=1}^{n} P_i A_i \sin\theta_i \quad (1) \qquad L(t)=\sum_{i=1}^{n} P_i A_i \cos\theta_i \quad (2)$$

$$R(t)=\sum_{i=1}^{n} P_i A_i l_i \cos\theta_i \quad (3) \qquad C_D=\frac{D(t)}{q_\infty A_{ref}} \quad (4)$$

$$C_L=\frac{L(t)}{q_\infty A_{ref}} \quad (5) \qquad C_R=\frac{R(t)}{q_\infty A_{ref} L_{ref}} \quad (6)$$

where, $D(t)$, $L(t)$, $R(t)$ are the drag, lift and rolling moment, respectively; P_i is the measured local pressure at any point i on the model surface, A_i is the area of action of P_i, θ_i is the effective angle of resolution at any point i with respect to the freestream, l_i is the arm for the local moment at any point i, C_D, C_L, C_R are the coefficients of drag, lift and rolling moment, respectively; q_∞ is the freestream dynamic pressure, A_{ref} and L_{ref} are the model base area and base length, respectively.

3. Results and Discussion

Figure 2 presents the representative signals from the pressure transducers in the shock tube reservoir and a location in the model surface, respectively. The reservoir pressure (P_5) is presented to indicate the steady time available for the test.

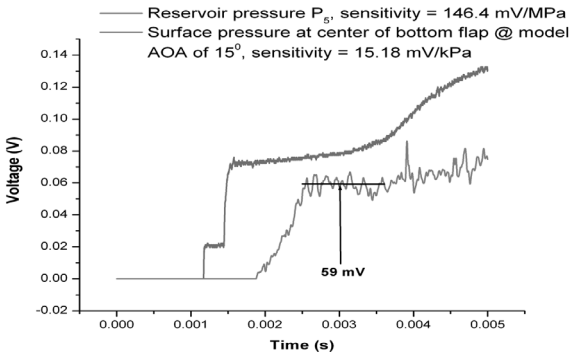

Fig. 2 Typical pressure traces obtained during a test in the shock tunnel.

Figure 3 presents the variation of the coefficients of drag, lift and rolling moment on the model with its Angle of Attack (AOA). These coefficients were also estimated using the Newtonian theory, which is a well-established analytical method for the estimation of force coefficients on hypersonic bodies. A close agreement was observed between the two sets of experimental data, which in fact validated the accelerometer force balance technique developed in-house. The Newtonian theory considered in this case is inviscid and hence, could not predict the viscous and strong shock effects of the flow field over the model, to which the difference between the theoretical and the experimental results could be attributed.

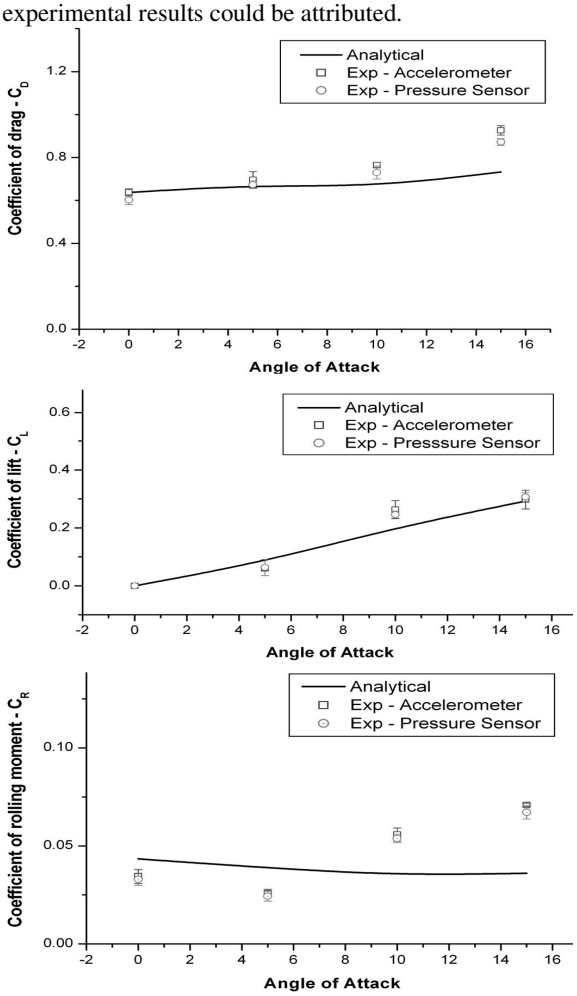

Fig.3 Variation of coefficients of drag, lift and rolling moment with the model AOA.

4. Concluding remarks

Drag, lift and rolling moment on a flapped, triangular, hypersonic, lifting model were measured in a shock tunnel using a pressure measurement technique. The investigations were aimed at validating an accelerometer force balance developed in-house. Theoretically estimated force and moment coefficients are also presented for a comparison. A good agreement has been found between the experimental data. The theoretical data exhibited some deviation from the experiments, which is explicable.

References

[1] V. Menezes, Meas. Sci. Technol., **22** (2011) 067003-1.

[2] S. Trivedi, In Proc. W. C. E. London, **3** (2011) 2184.

[3] R.W. Truitt, Hypersonic Aerodynamics, New York, Ronald (1959), pp. 318–330.

OS4: Research Frontiers in Green Aviation

Eighth International Conference on Flow Dynamics
November 9 - November 11, 2011

Laboratory Simulation of Quiet Supersonic Flight

Akihiro Sasoh, Kakuei Suzuki, Takahiro Imaizumi and Atsushi Toyoda
Department of Aerospace Engineering, Nagoya University, Furo-cho, Chikusa-ku, Nagoya 464-8603, Japan
sasoh@nuae.nagoya-u.ac.jp

ABSTRACT

Experimental and numerical simulations related to aircraft sonic boom are being conducted. Using a square-bore ballistic range, three-dimensional flight models are launched to a supersonic speed, and near-field overpressure measurement and flow visualization are conducted. The attention is focused on to the effect of the rear shape on the rear shock wave.

1. Introduction

In order to develop a scheme to experimentally study sonic boom problems, a square-bore ballistic range system has been developed. The primary function of the square bore is to prevent rolling motion of the test model. This paper reports results of our investigation on sonic boom caused by supersonic models.

2. Apparatus

Figure 1 shows the schematic illustration of the ballistic range used in this study[1,2]. The range has two distinct and unique features. One is its square bore, see Fig. 2. In order to launch a three-dimensional model(s) the square cross-section is useful for suppressing the rolling motion of a projectile. Another one is the in-tube, aerodynamic sabot separation [1]. After experiencing an acceleration driven by the driver gas (He), the sabot experiences a large pressure unbalance, and thereby being decelerated, while a projectile keeps its entry speed.

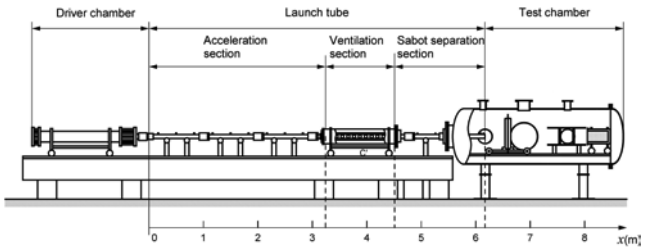

Fig. 1 Square-bore ballistic range.

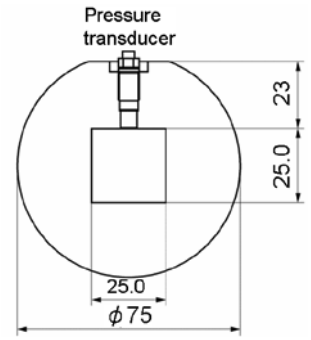

Fig. 2 Cross-section of square-bore.

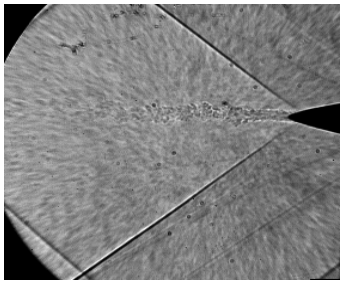

(a) Tail symmetrical to frontal

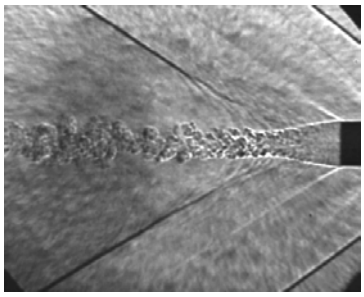

(b) Bluff model

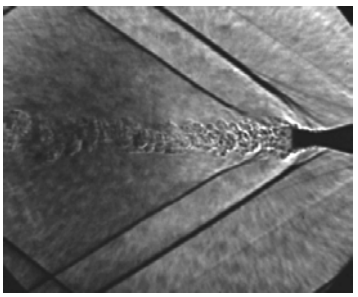

(c) one-stage trucation model

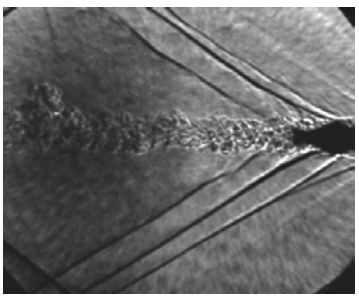

(d) Two-stage truction model

Fig. 3 Schlieren images with various rear shapes.

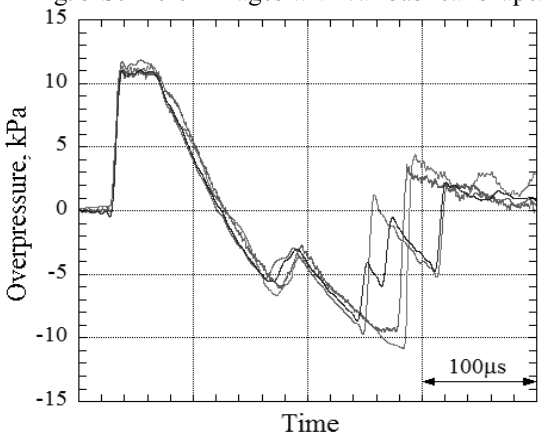

Fig. 4 Overpressure histories with four rear shape models, red; (a), green; (b), blue; (c) and black; (4) in Fig. 3.

3. Results and Discussion

Figures 3 and 4 shows examples of the experimental results obtained using four different projectile tail shapes with their frontal shape being kept unchanged. With the two stage truncation, the pressure jump in the rear boom is dispersed into two jumps, thereby alleviating a sonic boom.

4. Concluding remarks

This system using the square-bore ballistic range is useful for simulating supersonic flight in a laboratory.

Acknowledgment

The authors would like to express our gratitude to all of our lab. members and Technical Division of Nagoya University, for their valuable technical assistances. This research was supported by Japan Aerospace Exploration Agency as a project Nos. 27-J-J6710 and 27-J-J6711 and as Grant-in-Aid for Scientific Research (S) 22226014 from Japan Society for the Promotion of Science.

References

[1] A. Sasoh and S. Oshiba, Rev. Sci. Instrum., **77** (2006), 105106.

[2] A. Sasoh, K. Kikuchi, K. Shimizu and A. Matsuda, Intl. J. Aerospace Innovations, **2** (2010), pp. 147-156.

Flight Results of D-SEND#1 Drop Test using Stratospheric Balloon

Masahisa Honda
JAXA(Japan Aerospace Exploration Agency),
6-13-1 Osawa, Mitaka-shi, Tokyo 181-0015, Japan
honda.masahisa@jaxa.jp

ABSTRACT

As part of silent supersonic research, JAXA launched the two phased D-SEND project to verify its low sonic boom design concept in 2010. In the first phase called D-SEND#1, two different axisymmetric bodies were dropped from a stratospheric balloon at ESRANGE space center in Sweden on May 7 and 16, 2011. The conventional N-type and shaped sonic boom signatures were successfully measured as expected in the air and the ground. In this paper, the configurations of the drop bodies, the aerial sonic boom measurement system and the sequence of the balloon drop test are described. The flight results are discussed as well.

1. Introduction

Japan Aerospace Exploration Agency (JAXA) has been promoting a supersonic technology research program since 1997. This program contains not only various kinds of basic researches but also some flight demonstrations. In 2010, JAXA launched a new project called "D-SEND (Drop test for Simplified Evaluation of Non-symmetrically Distributed sonic boom)" as one of the flight demonstrations. The project aims at verifying JAXA's aerial sonic boom measurement system and original low sonic boom design concept.

In the D-SEND project[1], there are two phases, D-SEND#1 and D-SEND#2 drop tests. The test sequences of these drop tests are shown in Fig.1. In the D-SEND#1, two different axisymmetric bodies are successively dropped from a stratospheric balloon. In the D-SEND#2, a new unmanned supersonic experimental airplane designed by JAXA's original concept is dropped. In this paper, the configurations of the drop bodies, the aerial sonic boom measurement system, the sequences of the balloon drop test of the D-SEND#1 and the flight results are discussed.

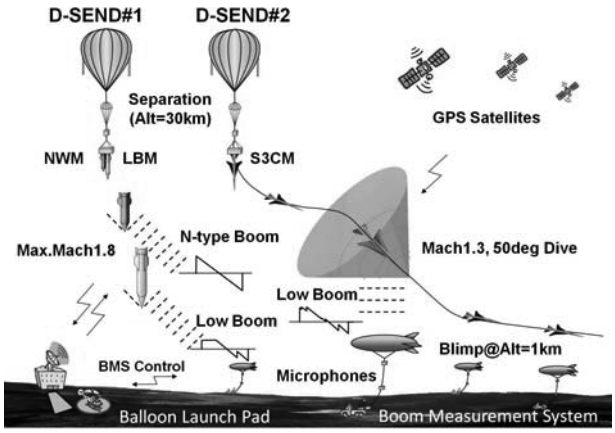

Fig. 1 D-SEND#1&#2 drop tests sequences

2. D-SEND#1 Drop Test

The objectives of the D-SEND#1 are (1) to establish the aerial sonic boom measurement technology with axisymmetric bodies, (2) to confirm the feasibility of the measurement of the low level sonic boom, (3) to perform preliminary testing for the next phase, D-SEND#2. In the D-SEND#1, two different axisymmetric bodies are newly designed. One (NWM: N-wave Model) has a body shape which generates a conventional N-type sonic boom signature like Concorde. The other one (LBM: Low Boom Model) has that of a shaped low sonic boom signature. The configurations are shown in Fig.2.

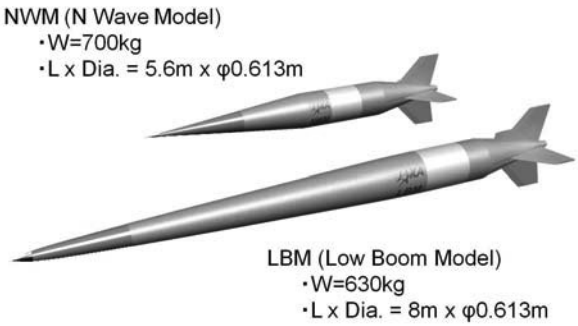

Fig. 2 Drop bodies (NWM & LBM)

They are successively dropped from the stratospheric balloon at an altitude of 30km. Both bodies trace almost the same Mach number history and generate sonic booms forward and perpendicular to the Mach cone angle. Information such as accelerations, velocities, positions and angular rates are transmitted to the ground by onboard telemetry system. The sonic booms are measured by a boom measurement system (Fig.3).

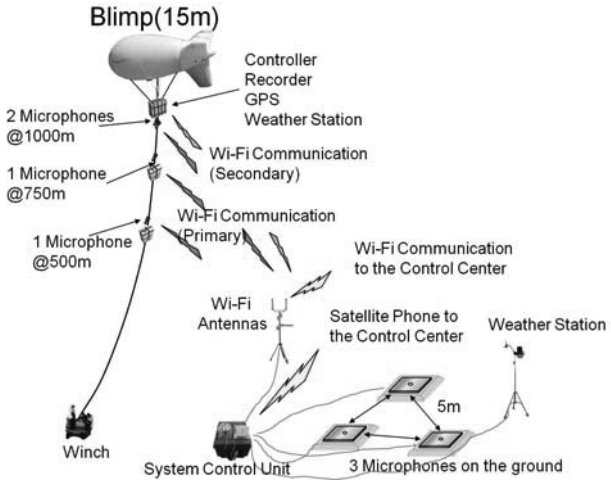

Fig. 3 Boom measurement system (BMS)

In order to measure the effect of atmospheric turbulence to the sonic boom signature, the blimp(15m) is held at an altitude of 1km. Low frequency microphones are installed along the tether line (500m, 750m, 1000m). The sonic booms are also recorded on the ground(3points). The GPS time clock is used for the time synchronization on the drop bodies and the BMS.

In the drop zone(100kmx70km), four BMSs are laid out to cover the possible release points of the balloon trajectories as shown in Fig.4. Each BMS site has a limited circle area(r=10km), which means a measureable area of sonic boom when the body is released. They are controlled from the control center through Wi-Fi or satellite phones(back up) network.

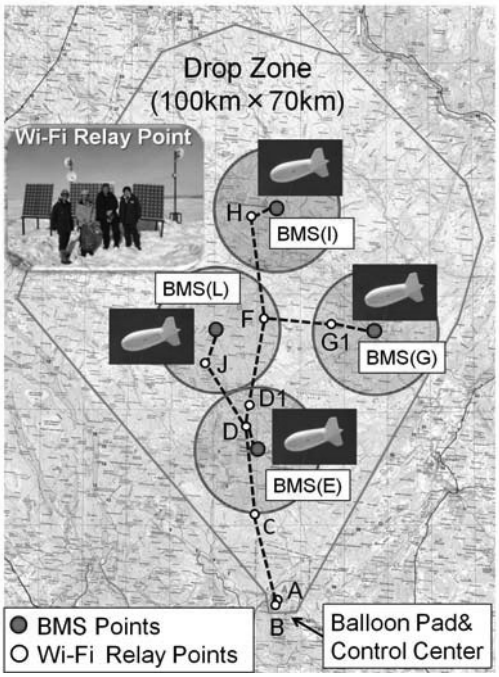

Fig. 4 BMS layout in the drop zone

3. Flight Results and Discussion

The D-SEND#1 drop test was conducted twice on May 7th and 16th of 2011 at ESRANGE space center(Fig.5). In the both drop tests, the BMSs functioned well as planned. The N-type and shaped sonic boom signatures were successfully obtained in high resolution on the ground and along the tether line. The measured typical sonic boom signature of NWM and LBM ,compared with the calculation, are shown in Fig.6. The N-type sonic boom signature was clearly measured by the NWM. Meanwhile, the LBM was validated that its sonic boom could be reduced by half compared with that of the NWM. Moreover it is confirmed that the calculations of both bodies by JAXA's design tools agree with the measure data very well. Through these tests, JAXA has successfully demonstrated its low sonic boom axisymmetric design concept technology that reduced the sonic boom by half.

The sonic boom signatures on the ground are also shown in Fig.7. The top and rear parts of the both signatures are clearly deformed compared with those of Fig.6. This characteristics indicates that there exist some effects of atmospheric turbulence near the ground.

Fig. 5 D-SEND#1 preparation

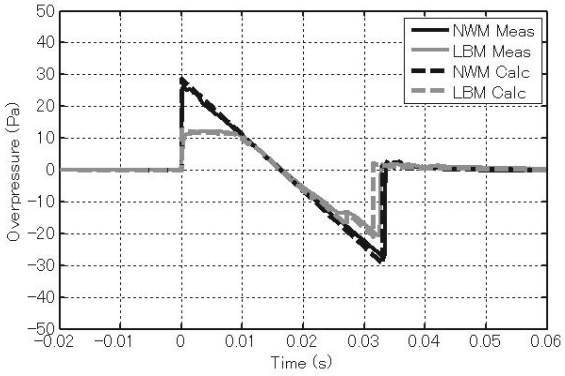

Fig. 6 Sonic booms at alt=500m (1st test)[2]

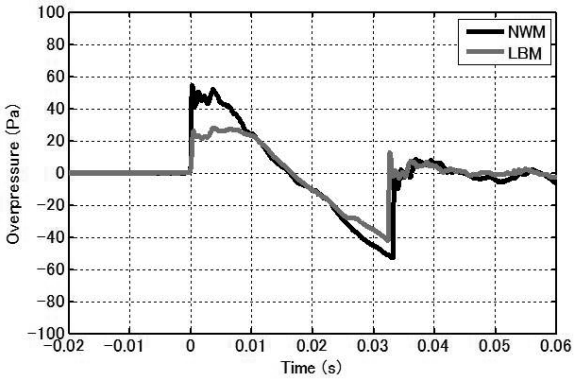

Fig. 7 Sonic booms on the ground (1st test) [2]

4. Conclusion

A new sonic boom measurement technique by a stratospheric balloon drop test is demonstrated. Furthermore, the feasibility of measuring the low level sonic booms is confirmed. Now JAXA has advanced forward the next step, D-SEND#2. A new supersonic experimental airplane is under detailed design phase. The D-SEND#2 drop tests will also be conducted in the summer of 2013 at ESRANGE space center.

References

[1]M. Honda et al., Balloon Drop Test Results Overview of D-SEND#1, 49th JSASS Aircraft Symposium, October 2011

[2]Y. Naka et al., Results of Sonic Boom Measurement in D-SEND#1 Flight Test, 49th JSASS Aircraft Symposium, October, 2011

Eighth International Conference on Flow Dynamics
November 9 - November 11, 2011

JAXA's Environment Conscious Aircraft Technology Program Initiative

Takeshi Ohnuki
Japan Aerospace Exploration Agency, JAXA
6-13-1, Osawa, Mitaka-City, Tokyo, 181-0015, JAPAN
E-mail: ohnuki.takeshi@jaxa.jp

ABSTRACT

JAXA has set up a working group in order to conduct study on program plan of aviation technology research and development (R&D) program aiming at mitigating environmental impacts. Element researches on environmental technologies JAXA has been conducted so far are strategically integrated into this program. This program is supposed to be launched in 2013 coincidentally with commencement of the 3rd JAXA's Mid-Term R&D Period 2013-2017. The paper introduces "JAXA's' Environment Conscious Aircraft Technology (E-CAT) Program Initiative".

1. Introduction

Both Airbus and Boeing predict that passenger traffic alone will grow more than 2 times (based on revenue passenger kilometer) in the next 20 years[1,2]. Reducing greenhouse gas is one of aviation's biggest challenges today along with safety and security. This paper introduces JAXA's research and development challenge of environmental conscious aircraft technologies.

2. E-CAT Program Initiative

JAXA's' Environment Conscious Aircraft Technology (E-CAT) Program Initiative is composed of three research and development (R&D) projects, one research initiative, and one concept research/technology evaluation as shown in Figure 1. Element researches on environmental technologies JAXA has been conducted so far are strategically integrated into this program

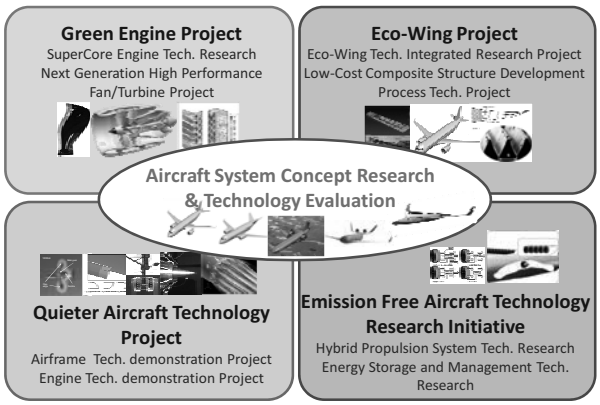

Fig. 1 Framework of E-CAT Program Initiative

Green Engine Project

Technologies for the next generation high performance fan/turbine engines with drastic reduction of fuel burn CO_2 emission will be verified in this project. This includes application of composite materials to the fan blades and low pressure turbine blades and/or the case. Also, R&D of elemental technologies such as cooling technology for super-high pressure turbine, high load compressor technology, and low NOx combustor technology will be conducted.

Eco-Wing Project

The purpose of this project is to improve airframe fuel efficiency by increasing aerodynamic efficiency and reducing airframe weight. To increase airframe efficiency, the boundary layer control technologies and morphing technologies will be demonstrated. Also, research on improving type certificate process with development of highly reliable structure design technology and database of composite materials will be conducted in order to decrease airframe weigh without cost penalty.

Quieter Aircraft Technology Project

Noise reducing technologies for both airframe noise and engine noise will be demonstrated in this project.

Emission Free Aircraft Technology Research Initiative

This includes evaluation of the power management system technologies aiming at improvement of aircraft system efficiency by fuel-cell and bio-fuel technologies, etc.

Aircraft System Concept Research & Technology Evaluation

This is to clarify the position of above projects/initiative in an airplane system and to pursue creation of innovative airplane concepts. Also, fundamental technology R&D such as MDO will be conducted.

3. Technology Target

In this program, the technology targets for environmental impact mitigation are provisionally set in year 2022 and 2035 (See Table 1) .

Fuel Burn (CO_2 Emission) Reduction

This target in 2022 (-30% relative to similar existing type of aircraft) is settled in consideration of competitive advantage over other aircrafts. It is required 7% improvement of lift-to-drag ratio, 15% reduction of SFC, and 20% airframe weigh reduction in order to reach this target.

Table 1. Technology Target for Future Subsonic Aircraft (Provisional)

	Year 2022 100-150pax.	Year 2035 150-200pax.
Fuel burn[A] (CO_2 Emission)	-30%[B]	-50~-100%[C]
Airport Noise[D]	-20dB	-30~-75dB
NOx Emission[E]	-70%	-70~-100%

A: Relative to similar existing types of aircraft, B: Excluding Bio fuel, C: Including Bio fuel, D: Relative to ICAO Stage 4, E: Relative to CAEP/6

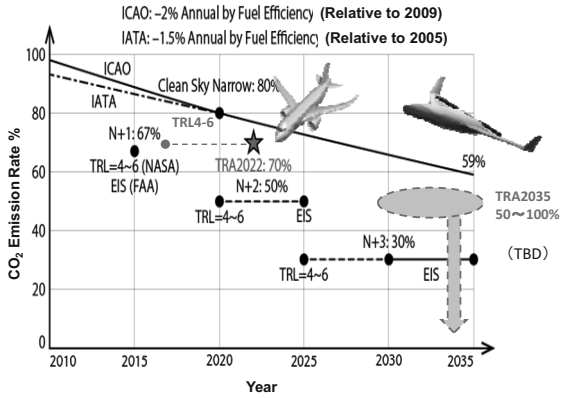

Fig. 2 Fuel Burn (CO_2 Emission) Reduction Target

Noise Reduction

Taking into account discussions in ICAO, it seems that more than 20dB cumulative below current Chapt.4 would be necessary in 2022. Technologies such as ultra high bypass engine technologies and airframe noise reduction technology are required.

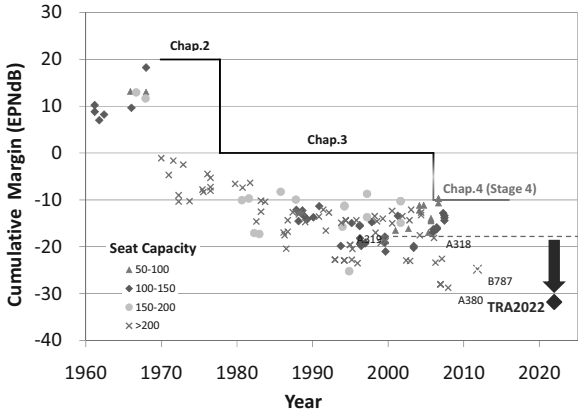

Fig. 3 Noise Reduction Target

NOx Emission Reduction

This target in 2022 (-70% relative to CAEP/6) is determined by reference to reduction target 2026 of NOx emissions by CAEP. Technological results from JAXA's "TechCLEAN Project" will be applied.

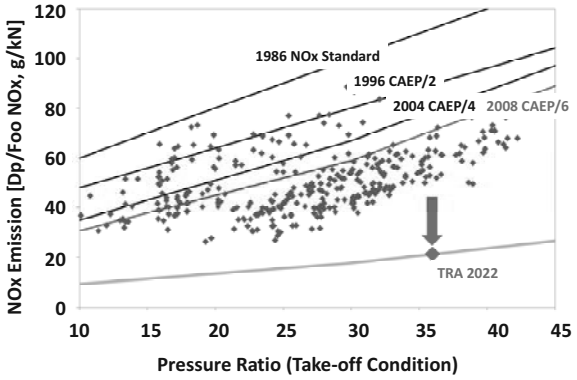

Fig. 4 NOx Emission Reduction Target

4. Technology Reference Aircraft

Technology Reference Aircraft (TRA) 2022 and TRA 2035 are defined as aircrafts to be entry in service in 2022 and 2035, respectively. They are defined with technological goals expected in 2022 and 2035. Figure 5 shows the image of TRA 2022 with technical goals of 30% reduction of CO_2 emission relative to the same sized in-production aircrafts, 20dB reduction in airport noise relative to ICAO Chapter 4 regulation, and 70% reduction of NOx emission relative to CAEP/6 regulation. Required technologies to the goal are also shown in the figure.

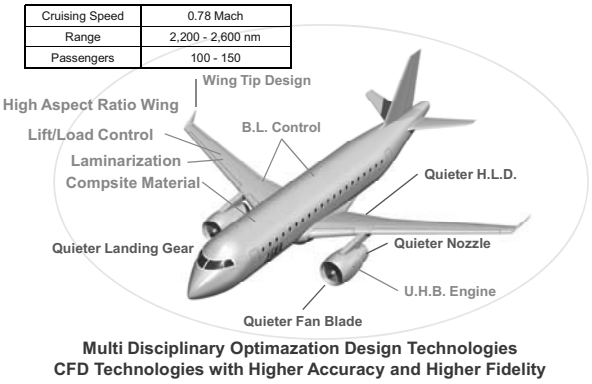

Fig. 5 Technology Reference Aircraft 2022

5. Concluding remarks

This program is supposed to be launched in 2013 coincidentally with commencement of the 3rd JAXA's Mid-Term R&D Period 2013-2017, though all of above mentioned projects could not be launched at the same time. Detailed planning is required for all of the projects.

References

[1] Airbus, "Global Market Forecast 2010-2029", http://www.airbus.com/company/market/gmf2010/
[2] Boeing, "Current Market Outlook 2011-2030", http://www.boeing.com/commercial/cmo/

Green Aviation: Aircraft Concepts and Enabling Technologies

Gary A. Dale, Energy Efficient Airframe Technology Lead, Ryan Plumley, Aerospace Engineer
AFRL Air Vehicles Directorate (AFRL/RBAL), Wright Patterson Air Force Base, Ohio, USA 45433
gary.dale@wpafb.af.mil

ABSTRACT

The U.S. Air Force (USAF) is the single largest energy user in the U.S. Government with jet fuel as the predominant form of energy consumed. Since energy is a mission critical capability the USAF has put in place energy policy and plans to "Reduce Demand, Increase Supply and Change the Culture". This paper focuses on airframe technology programs being pursued by the USAF Air Force Research Laboratory (AFRL) to enable the USAF to reduce demand for both current and future aircraft.

1. Introduction

The United States Air Force (USAF) uses over 2 billion gallons of jet fuel every year creating one of its largest operational expenses, approaching $10B/year. In fact, the Air Force is the single largest energy user in the U.S. Government with jet fuel as the predominant form of energy consumed (Figure 1.).

Fig 1 USAF Energy Usage

Since energy is a mission critical capability the USAF has put in place policy[1] and plans to Reduce Demand, Increase Supply and Change the Culture; the directives from the 2010 USAF Energy Plan[2].

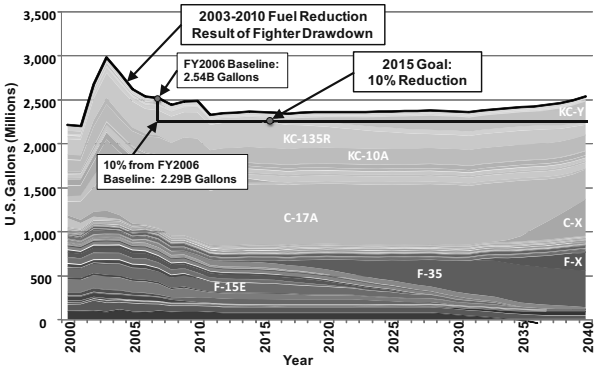

Fig 2 USAF Fuel Consumption and Savings Goal

As shown in Figure 2 the U.S. Air Force has an energy goal to reduce fuel burn by 10% by 2015 from a 2006 baseline. Operational improvements and reduction in flying hours are projected to achieve about one-half of the goal. However, new technology developments will also be required. The technology approach is structured around two primary strategies:

• Reducing fuel burn and greenhouse gas emissions in legacy systems via engine and airframe upgrades

• Advanced Research and Development (R&D) to develop the technologies to reduce fuel demand, increase fuel supply, and reduce greenhouse gas emissions in legacy and future systems.

2. Method

The Air Vehicles Directorate of AFRL has approached the USAF goal of reducing demand for aviation fuel by initiating S&T programs directed towards airframe improvements. These programs can be categorized in 3 areas; Change How the USAF Flies, Improve What the USAF Currently Flies and Energy Efficient Aircraft for the Future. Most, but not all, of these S&T programs are directed towards air mobility, the largest single user of fuel in the US. These programs provide a robust set of solutions for the USAF to implement.

3. Results and Discussion

Change How the USAF Flies. AFRL's current aerodynamic S&T program is focused on formation flight of the large USAF transport which consumes approximately ¼ of USAF fuel annually. CFD modeling and flight tests show modifications to the station keeping software will enable a trailing aircraft to achieve a projected 10% fuel burn reduction by automatically positioning itself a safe distance aft and outboard of the wingtip of the leading transport. It is projected that if the trailing aircraft was able to sense the exact position of the vortices of the lead aircraft the fuel burn reduction could be doubled.

AFRL is planning future S&T programs which focus on formation flight of an arbitrary number and dissimilar types of aircraft in formation to include mixes of strategic transports, tactical transports, aerial refueling tankers, and fighter aircraft.

Improving What the USAF Currently Flies. A common feature of both strategic and tactical transports is an upswept aft fuselage to accommodate cargo doors. However this feature is a source of drag; in some cases more than 10% of the total aircraft drag. AFRL has 2 flight test programs to evaluate flow control devices to reduce aft fuselage drag on a tactical transport. One flight test program, using "finlet" flow control devices, demonstrated 6% drag reduction. The other flight test program used smaller, "microvane", flow control devices demonstrated more than 3% drag reduction.

AFRL is assessing other airframe improvements for the legacy mobility fleet. Industry and AFRL studies

Cleared for public release: Case number - 88ABW-2011-5065

show that the fuel burn of current large transport aircraft could be reduced by up to 7% by straightforward modifications such as winglets and drag clean-up. The latter encompasses a large variety of modifications such as replacement of control surface seals, aerodynamic fairings and fillets and conformal antennas.

Energy Efficient Aircraft for the Future. The AFRL Air Vehicles Directorate has completed Phase I of the Revolutionary Configurations for Energy Efficiency (RCEE) program which examined the anticipated USAF mobility mission (theater lift, strategic lift, and tankers) for the 2040 timeframe. The ultimate program goal of RCEE Phase I was to identify the configurations and enabling technologies towards a 90% energy reduction for the entire 2040 mobility mission[3]. Two-thirds of this goal is assigned to technology developments in aerodynamics, structures and materials, and propulsion. The remaining 1/3 of this goal is assumed to be met by future operational changes such as using optimal routing and payload combinations. The mission planners at the USAF Air Mobility Command are currently working towards these efficiencies. As these solutions lie outside of AFRL's S&T responsibilities they are not addressed here.

Achieving 60% energy efficiency would seem to be wildly unrealistic compared to the usual short term technology projections of 3, 5, or 10% improvements. However, by utilizing a multi-dimensioned approach, the hope is to create "virtuous spirals" in which new technologies can evolve together and break down perceived barriers for efficient aircraft.

Fig 3 Energy Efficient Mobility Configurations

Several very efficient aircraft configurations for the 2040 mobility mission were identified in RCEE Phase I. As shown in Figure 3 the configurations ranged from rather conventional looking tube and wing designs - some with strut-braced wings, to box wing and integrated wing body aircraft.

Once the configurations were identified initial structural layouts and mass properties were determined. The configurations were then lofted and further refined using CFD. Efficient propulsion systems and concepts were considered; open rotor, very high by-pass turbofans, geared turbofans, and distributed propulsion. Alternative energy sources than crude oil products were considered, but the majority of technologies investigated were compatible.

The final step of RCEE Phase I was to assess a wide range of technologies to further improve the efficiency of the configurations. An example of a technology ranking from RCEE Phase I is shown in Figure 4.

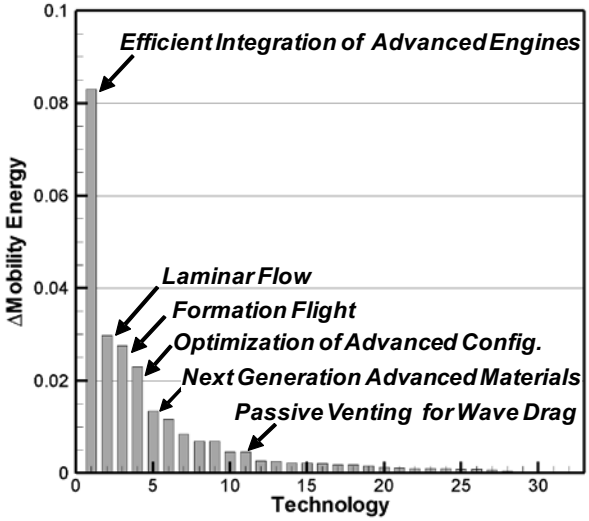

Fig 4 Technology Impacts on Fuel Burn Reduction

In general the airframe technologies having the biggest impact on reducing fuel burn were:

- High effective aerodynamic span (hybrid wing body, strut braced wing, box wing, active aeroelastics, winglets and raked wing tips)
- Airframe-propulsion integration of efficient engines
- Parasite drag reduction (reduced empennage size, laminar flow, reduced turbulent viscous drag-riblets)
- Unconventional propulsion (distributed propulsion, boundary layer ingestion, hybrid electric)
- Formation flight

Phase II of RCEE, which will run through 2015, will further develop the key technologies and configurations identified in Phase I.

4. Concluding remarks

The AFRL Air Vehicles Directorate is making investments in airframe technologies which will help the USAF meet its fuel burn reduction goals. These technology programs can be categorized in 3 areas; Change How the USAF Flies, Improve What the USAF Currently Flies and Energy Efficient Aircraft for the Future.

References

[1] U.S. Air Force Energy Program Policy Memorandum, United State Air Force (2008)
[2] U.S Air Force Energy Plan (2010)
[3] R. Plumley, D. Multhopp, Energy Efficient Air Mobility: How far can we go?, AIAA 2009-4314, (2009)

Eighth International Conference on Flow Dynamics
November 9 - November 11, 2011

Large-Eddy Simulation of Spatially Developing Aircraft Wake

Takashi Misaka, Frank Holzäpfel, Thomas Gerz
Deutsches Zentrum für Luft- und Raumfahrt (DLR), Institut für Physik der Atmosphäre
E-mail: Takashi.Misaka@dlr.de

ABSTRACT

Development of aircraft's wake vortex from the roll-up until vortex decay is studied. An aircraft model and a surrounding flow field obtained from high-fidelity Reynolds Averaged Navier-Stokes simulation are swept through a ground fixed computational domain to initialize the wake. After the initialization, large-eddy simulation of the vortical wake is performed until vortex decay, i.e., 2-3 minutes after the passage of aircraft. Here, the methodology and some results from the simulations using the DLR-F6 wing-body model are presented.

1. Introduction

Wake vortices generated by a flying aircraft pose a potential risk for following aircraft due to the strong and coherent vortical flow structure[1]. In addition, it is pointed out that condensation trails (contrails) originated from the interaction of jet exhaust, wake vortices and the environmental atmosphere may trigger the formation of cirrus clouds (contrail cirrus), which is suspected to have influence on the climate change[2]. The evolution of aircraft's wake can be divided into several phases, for example, (1) roll-up phase, (2) vortex phase, and (3) diffusion phase. Because of the broad spatiotemporal scale of the problem, the use of numerical simulation is usually limited to each of those phases. The roll-up phase is simulated by high-fidelity Reynolds Averaged Navier-Stokes (RANS) simulations because detailed aircraft geometries of fuselage, flaps, etc. affect the roll-up process and the resulting wake vortices. Dynamics of wake vortices in the vortex phases is studied mainly by large-eddy simulation (LES) or direct Navier-Stokes (DNS) simulation[3]. The third diffusion phase is related to meteorological simulations where microphysical processes of contrails are of primary interest.

The present study aims to develop a methodology which enables to simulate wake vortex evolution from the generation until the decay, i.e., from the roll-up phase to the vortex phase mentioned above. The vortex decay occurs 2-3 minutes after the passage of aircraft in a typical cruise condition, i.e., 28-43 km behind a flying aircraft. The study bridging the gap between the roll-up and the vortex phases would provide understandings toward properties of realistic aircraft wake such as vortex core radius and circulation evolutions, as well as roll-up and entrainment of jet exhaust by considering tracer materials, which might be useful for detailed contrail modeling studies.

2. Method

An aircraft model and the surrounding flow field obtained from high-fidelity RANS simulation are swept through a ground fixed LES domain to initialize the aircraft's wake[4]. The RANS flow field is provided as a forcing term of Navier-Stokes equations in the LES. Similar approach might be referred to as the fortified solution algorithm (FSA)[5], or a nudging technique used in data assimilation[6]. The resulting velocity vector of the flow field is represented by the weighting sum of LES velocity field $\mathbf{V}_{\mathrm{LES}}$ and RANS velocity field $\mathbf{V}_{\mathrm{RANS}}$,

$$\mathbf{V} = f\,\mathbf{V}_{\mathrm{LES}} + (1-f)\mathbf{V}_{\mathrm{RANS}}. \tag{1}$$

The weighting function f could be a smooth function of the wall-distance y, or of other physical quantities such as velocity magnitude. Here, we employ the following function of wall-distance to realize smooth transition between the solutions,

$$f(y) = \frac{1}{2}\left[\tanh\left[\alpha\left(\frac{y}{\beta} - \frac{\beta}{y}\right)\right] + 1.0\right], \tag{2}$$

where the constants α and β represent the slope of the transition and the wall-distance where solutions of RANS and LES are equality weighted, respectively. These constants can be determined by try and error basis, as well as by optimization techniques.

In this study, the RANS flow field around the DLR-F6 wing-body model is employed to initialize the wake. The RANS solution is obtained by the DLR TAU-code with hybrid unstructured mesh, where the number of mesh points is approximately 8.5 million[7]. The flow conditions of Mach number M=0.75 and Reynolds number Re=5.0×10^6 are considered.

There are several reasons to employ the ground fixed LES domain. Decay of a fully rolled-up vortex pair strongly depends on environmental conditions such as ambient turbulence, temperature stratification and wind shear. Therefore, the control of these conditions is crucially important to assess the influence of ambient conditions on vortex decay. Unlike the consideration of realistic inflow conditions, the generation of controlled turbulence fields in the ground fixed LES domain is straightforward. The other reason is that the present approach can reduce a domain length in the flight direction compared to an aircraft fixed computational domain. Therefore, computational resources can be used to increase spatial resolution.

Because of the large difference of RANS and LES mesh sizes near body surfaces, the connection of detailed flow and turbulence quantities cannot be hoped.

Here, we rather attempt to connect flow quantities related to wake vortex evolution, e.g., the strength of wing-tip vortex, downwash along wings and span-wise load distributions obtained from a high fidelity RANS flow field.

In this study, the incompressible Navier-Stokes code MGLET is employed for LES[8,9]. An equation for potential temperature is solved to take into account buoyancy effects employing Boussinesq approximation. The equations are discretized by a finite-volume approach with the fourth-order finite-volume compact scheme. Lagrangian dynamic model is employed for a turbulence closure. The third-order Runge-Kutta method is used for time integration.

3. Results and Discussion

Figure 1 shows vorticity distributions on several downstream planes where the results from different mesh resolutions of 0.5 and 1.0 m are compared. The origin of the coordinate in the flight direction is set to trailing edge of wing-tip and the downstream distance x is normalized by the wing-span b. Boundary layer around the fuselage appears in the region with high vorticity magnitude in both mesh resolutions. The boundary layer of 0.5 m mesh case shows a sharp vorticity distribution compared to that of 1.0 m at x/b=0.0, however, the thickness of boundary layer does not reflect that in the RANS simulation even with the 0.5m mesh. It is simply due to the less resolution of the LES mesh compared to RANS mesh near body surfaces. At x/b=1.0, peaks of vorticity magnitude from wing-tip and fuselage are kept high in the 0.5 m mesh case. Then, the roll-up of wing-tip vortices proceeds at x/b=3.0. The overall vorticity distribution is similar in both cases during the roll-up phase, however, the underestimated vorticity peak might affect the time evolution of wake vortex at a later time.

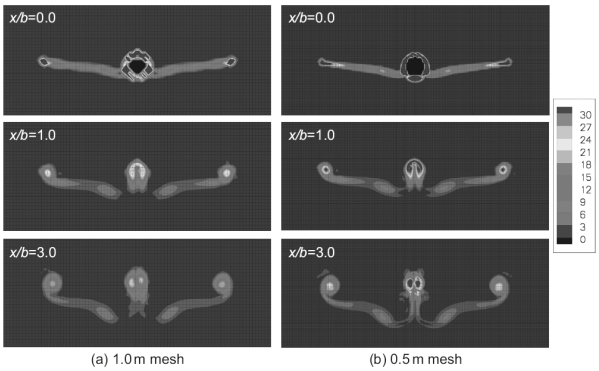

Fig. 1 Vorticity distribution on several downstream planes with mesh resolutions of 0.5 and 1.0 m.

Figure 2 shows the time evolution of vorticity distribution on a ground fixed vertical plane from T=2 until 39 s, which corresponds to the distance of 450 to 8,800 m (x/b=7 to 146) from the aircraft model. The vorticity from fuselage decays quickly as shown in Fig. 2(c), on the other hand, the vorticity distribution from wing-tips preserve their peak values. The vorticity from inboard wing rotates around the wing-tip vortex, which realizes the wake's roll-up establishing a well-known counter-rotating vortex pair. In Fig. 2(f), the flow field is reorganized to a fully rolled-up vortex pair. The roll-up process takes approximately one vortex time unit, i.e., the time a vortex pair descends one vortex separation.

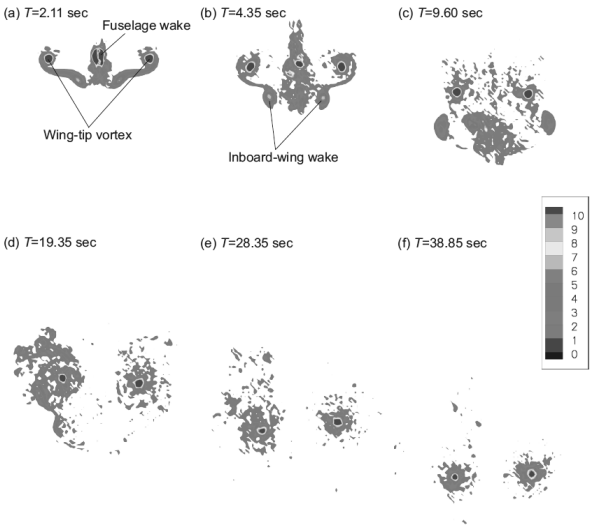

Fig. 2 Time evolution of vorticity distribution during the roll-up of DLR-F6 model's wake.

4. Concluding remarks

LES of wake vortex evolution from its generation to vortex decay is performed by combining flow fields from RANS and LES computations. The RANS flow field is employed in the LES computation as a forcing term sweeping through the ground-fixed LES domain.

Finer mesh resolution in the LES domain realizes higher peaks of vorticity distribution in the aircraft wake, however, the global vorticity structure of the wake is not sensitive to the mesh resolution. The roll-up process is simulated by the present approach, which realizes a counter-rotating vortex pair after one vortex time unit. It is confirmed that the consideration of spanwise load distribution is important to study realistic aircraft wake.

Acknowledgements

Computer time provided by Leibniz-Rechenzentrum (LRZ) is greatly acknowledged. The current work is conducted within the DLR project Wetter & Fliegen (Weather & Flying).

References

[1] T. Gerz *et al.*, Prog. Aerosp. Sci., **38** (2002), 181.
[2] P. Minnis *et al.*, Geophys. Res. Lett., **25**(1998), 1157.
[3] F. Holzäpfel *et al.*, Aerosp. Sci. Tech., **7**(2003), 263.
[4] T. Misaka, *et al.*, AIAA Paper 2010-1003 (2010).
[5] K. Fujii, J. Comput. Phys., **118** (1995), 92.
[6] E. Kalnay, Cambridge University Press, 2003.
[7] O. Brodersen, *et al.*, J. Aircr., **45** (2008), 823.
[8] M. Manhart, Comput. Fluids, **33** (2004), 435.
[9] A. Hokpunna, *et al.*, J. Comput. Phys., **229** (2010), 7545.

Eighth International Conference on Flow Dynamics
November 9 - November 11, 2011

Numerical analysis of weak shock attenuation resulting from molecular vibrational relaxation

K. Hatanaka[1], T.Saito[1]
[1] Muroran Institute of Technology, 27-1, Mizumoto-cho Muroran Hokkaido, Japan
S1822207@mmm.muroran-it.ac.jp

ABSTRACT

The attenuation of a weak shock wave generated by the explosion of a unit mass of TNT was numerically analyzed. The effects of viscous and thermal conduction losses and of the molecular vibrational relaxation of oxygen and nitrogen molecules were considered. The effect of each diffusion term on wave attenuation and waveform change was investigated in detail. In addition, the characteristics of each attenuation effect were examined by frequency analysis.

1. Introduction

The shock wave that forms in the near field of an aircraft flying at supersonic speed weakens due to attenuation while propagating in the atmosphere. The explosive sound of the shock wave, commonly known as a sonic boom, is also called an N-wave because its pressure history is shaped like the letter N. Although the shock front segment for an N-wave located near the aircraft is discontinuous and several times that of the mean free path, its duration increases due to relaxation and reaches finite value during propagation in the air. The rise time, which is the time required for the N-wave to go from atmospheric pressure to its peak overpressure, is often used for evaluating the shock front.

The actual rise time of the sonic boom measured near the ground is significantly longer and often several orders of magnitude greater than that expected from the mechanisms of viscous and heat conduction losses alone [1]. The effect of relaxation due to the molecular vibrational excitation of oxygen and nitrogen in the atmosphere has been suggested as the reason for this anomaly [2, 3].

The degree of the annoyance from a sonic boom depends on the rise time and the peak overpressure of the shock front. Since next-generation quiet supersonic aircraft have been studied more intensively in recent years, accurately predicting the extent of weak shock wave attenuation has become increasingly important.

The objective of this work is to investigate the attenuation and dispersion of the N-wave by taking into account molecular vibrational relaxation of oxygen and nitrogen molecules and viscosity. The characteristics of each attenuation effect are examined by frequency analysis. An explosion of a unit mass of TNT was simulated numerically as the source of the N-wave.

2. Numerical Analysis with the Random Choice Method (RCM)

Numerical simulation is carried out with the numerical procedure according to Honma et al. [4]. The effects of viscous and heat conduction losses and of the vibrational relaxation of oxygen and nitrogen are added to the one-dimensional, spherically symmetric Euler equation. The harmonic vibration is assumed for molecular vibration. In the first step, the Euler equation is solved using the Random Choice Method (RCM). Corrections are then made with operator splitting by introducing the spherical, viscous, and vibrational relaxation terms sequentially. In operator splitting, the fourth-order Runge-Kutta method is used for time integration.

As an initial condition at the explosion center, it is assumed that 1kg of spherical TNT was converted into the reaction product at time 0. Considering the physical properties of TNT, the radius of the sphere is calculated to be 5.30×10^{2} m, the initial condition at the explosion center is assumed to ideal gas of 2000K, 7.94×10^{8} Pa, 1.6×10^{3} kg/m^3. The specific heat of both the reaction product gas and atmospheric air is assumed to be $\gamma = 1.4$. The speed of sound a in the ambient atmosphere is 346m/s. While the effect of molecular vibrational relaxation is influenced by the relative humidity of the air, the analysis in the present study is conducted for a fixed relative humidity of 10%.

In this work, we deal with a very weak shock wave whose strength is several tens of pascals. Since the temperature changes with such shock waves are very small, the change in the viscosity and thermal conductivity coefficients are negligible. Thus, viscosity μ and heat conductivity λ are assumed to be constant. The TNT explosion is used to create the weak N-wave used as the initial condition of the current study. The real gas effects

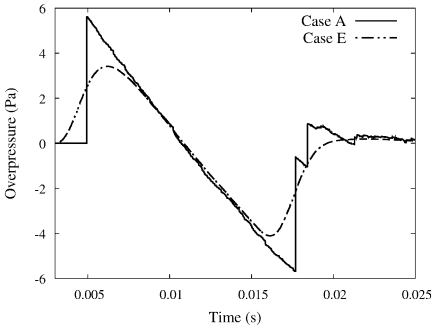

(a) N-wave profile

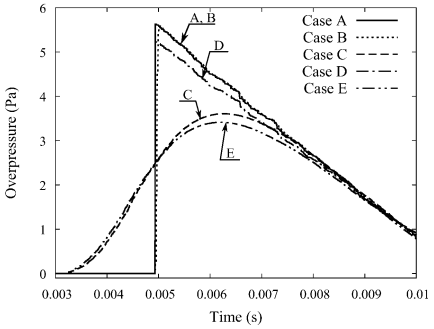

(b) A close-up to the positive phase of Fig.1a.

Fig. 1 Overpressure histories at 5000m.

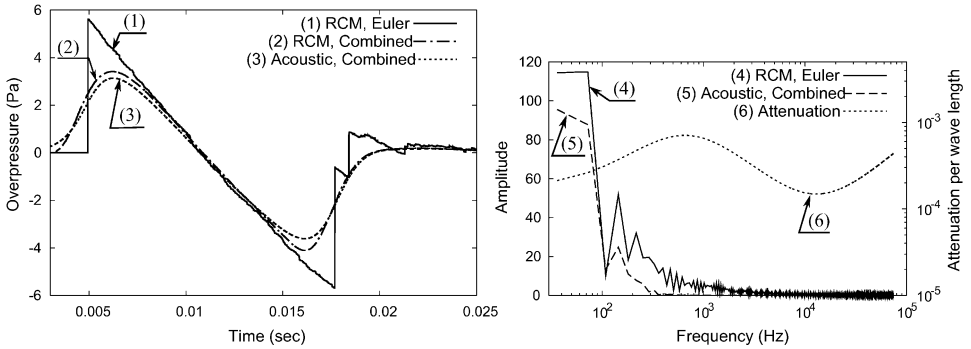

Fig. 2 The attenuation including all attenuation effects.

in the vicinity of the explosion center are not considered here. The pressure history obtained at 500m from the explosion center by solving the Euler equation is taken as the initial waveform. Propagation of the wave from 500 to 5000m is simulated and the solutions of following different cases are obtained. The results were then compared and discussed.

A. The solution that uses only the Euler equation, and addresses the spherical geometric effect.
B. The solution that addresses the relaxation effects by viscosity and heat conduction.
C. The solution that addresses the vibrational relaxation effect of oxygen.
D. The solution that addresses the vibrational relaxation effect of nitrogen.
E. The solution that addresses all of the effects of cases A through D.

The pressure history sampled at 5000m is presented in Fig. 1a for cases A and E. The expanded plots of positive phases are shown in Fig. 1b for all cases. The "peak overpressure" is defined as the maximum pressure of the positive phase, and the "rise time" is defined as the time required for the pressure to change from 10% to 90% of the peak overpressure. Because the time required for the N-wave to reach 5000m is different in each case, the position of each waveform is adjusted to facilitate comparison. Figure 1 clearly indicates that attenuation occurs due to molecular vibrational relaxation, and that the major part of the attenuation is due to the vibrational relaxation of oxygen. Although the nitrogen molecule somewhat attenuates the peak overpressure of the N-wave, it contributes very little to the increase in rise time.

3. Frequency Analysis

In the acoustics, the attenuation of monotone sound waves in the atmosphere and the effects of molecular vibrational relaxation have been investigated. Attenuation has been measured experimentally in a wide bandwidth. One can predict the attenuated waveform by decomposing an N-wave into its Fourier components and applying the frequency-dependent attenuation to each of them. Frequency analysis is performed according to Bass et al [5].

4. Results and Discussion

Figure 2 plots the pressure history and the amplitude spectrum distribution of the N-wave in order to compare the results of the RCM with those of frequency analysis at 10% relative humidity. The six plots represent: the waveform obtained after solving the Euler equation with the RCM (Line 1); the amplitude spectrum distribution of the waveform in Line 1 (Line 4); the solution of case E described in Sect. 2 with the RCM (Line 2); the attenuated amplitude spectrum distribution obtained by applying attenuation in Line 6 (Line 5); the attenuated waveform obtained from the inverse FFT of the distribution in Line 5 (Line 3); and the attenuation due to the viscosity and the molecular vibrational effects of oxygen and nitrogen effects. (Line 6).

Figure 2 indicate good agreement between the results obtained with the case E of the RCM (Sect. 2) and the results obtained by frequency analysis. When the attenuation of viscous and molecular vibrational effects are considered together, analysis indicates that since the attenuation occurs in a wide frequency band, the overall waveform is smoothened. When each relaxation effect is considered separately, results obtained by the frequency analysis showed good agreement with case B–D.

5. Conclusions

Numerical calculations for the N-wave caused by the explosion of a unit mass of TNT were carried out. The attenuation due to molecular vibrational relaxation was examined by the Random Choice Method (RCM) and frequency analysis. The results were compared and indicated good agreement between them.

The dependence of the attenuation effect on differing molecular species, which was difficult to explain by use of the RCM alone, was clarified through the use of frequency analysis, and the effectiveness of frequency analysis in predicting attenuation of the N-wave was demonstrated.

References

[1] A. D. Pierce et al., J. Acoust. Soc. Am. **51**, 3 (1972) pp 702-721
[2] H. E. Bass et al., J. Acoust. Soc. Am. **64**, 4 (1978) pp 1208-1210
[3] J. P. Hodgson, J. Fluid Mech. **58**, 1 (1973), pp 187-196
[4] H. Honma et al., UTIAS Report 253 (1983)
[5] H. E. Bass et al., J. Acoust. Soc. Am. **111**, 1 (2002) pp 481-486

Sonic Boom Analysis Considering Multiple Atmospheric Uncertainties Using a Polynomial Chaos Method

Daichi Ono[1], Atsushi Hashimoto[2], Koji Shimoyama[1], Shinkyu Jeong[1], and Shigeru Obayashi[1]
[1]Institute of Fluid Science, Tohoku University, Sendai, Miyagi, 980-8577, Japan
[2]Japan Aerospace Exploration Agency, Chofu, Tokyo, 182-8522, Japan
ono@edge.ifs.tohoku.ac.jp

ABSTRACT

This study performed the sonic boom analysis considering atmospheric uncertainties at low computational costs. Non-Intrusive Polynomial Chaos (NIPC) method, which approximates statistical behavior under uncertainties, was applied to the sonic boom analysis method solving an augmented Burgers equation. Compared to Monte Carlo (MC) method, NIPC offered equivalent accuracy for the present sonic boom analysis even with smaller sample size. In addition, the present simulation results revealed that humidity uncertainty and temperature uncertainty have significant impact on sonic boom, while wind uncertainty has no impact.

1. Introduction

In the design of low-boom supersonic aircraft, the waveform parameter method [1] is commonly used to estimate the strength of sonic boom. However this method cannot consider the rise time of sonic boom, which may psychologically impact on human beings. Instead, the sonic boom analysis solving an augmented Burgers equation [2] is proposed. Unlike the waveform parameter method, this approach can consider the rise time of sonic boom because the augmented Burgers equation accounts for thermal viscosity and relaxation effects.

Furthermore, in order to evaluate sonic boom characteristics under more realistic conditions, atmospheric "uncertainties" should also be considered. In general, atmospheric temperature, wind velocity, wind direction, etc. are always fluctuating in a real-world situation where aircrafts are operated. Thus, if a low-boom aircraft is designed at an ideal flight condition without any uncertainties, its performance in actual flights may be lower than expected. Therefore, it is necessary to make the design more robust in an uncertain environment based on the analysis considering possible uncertainties. A simple approach for robust design is to sample performance at a lot of conditions with different environments, and then evaluate the statistics (mean value and standard deviation) of performance. However, the computational time is too enormous to be allowed for practical use.

In this study, Non-Intrusive Polynomial Chaos (NIPC) method [3] was applied to the sonic boom propagation analysis solving an augmented Burgers equation for efficient evaluation of sonic boom characteristics against atmospheric uncertainties. First, NIPC accuracy was checked by comparing the statistics obtained from NIPC and Monte Carlo (MC) method. Then, sonic boom characteristics against atmospheric temperature, wind, and humidity uncertainties were compared and discussed.

2. Numerical Methods

2.1 NIPC

NIPC is a kind of probabilistic method, which approximates the behavior of an output against input uncertainties as a superposition of orthogonal polynomials. This method considers an output variable α^* as a function of independent deterministic variables x and t, and a random variable ξ representing input uncertainties. Then, it decomposes α^* into deterministic and stochastic components as follows:

$$\alpha^*(\vec{x},t,\vec{\xi}) \approx \sum_{j=0}^{P} \alpha_j(\vec{x},t)\Psi_j(\vec{\xi}) \tag{1}$$

where α_j and Ψ_j are the coefficient and orthogonal polynomial corresponding to the deterministic and stochastic components, respectively, for j-th mode. A choice of Ψ is determined by a choice of the probability distribution of ξ. For example, the Hermite polynomial is used as Ψ, when input uncertainties are normally distributed. P is the number of samples. The mean value μ and standard deviation σ are calculated as follows:

$$E[\alpha^*(\vec{x},t,\vec{\xi})] = \mu = \alpha_0(\vec{x},t) \tag{2}$$

$$Var[\alpha^*(\vec{x},t,\vec{\xi})] = \sigma^2 = \sum_{j=0}^{P} [\alpha_j^2(\vec{x},t)\left\langle \Psi_j^2 \right\rangle] \tag{3}.$$

After obtaining α_j from the system of Eq. 1 given at all samples, μ and σ can be promptly obtained by substituting α_j into Eqs. 2 and 3, respectively. Therefore, NIPC can estimate statistics even with a smaller sample size than the methods, which calculate statistics directly from a lot of samples, such as MC.

2.2 Sonic Boom Analysis Method

The present sonic boom analysis solved the augmented Burgers equation formulated as follows:

$$\frac{\partial p}{\partial x} = \frac{\beta}{2\rho_0 {c_0}^3}\frac{\partial p^2}{\partial t'} - \frac{1}{2A}\frac{\partial A}{\partial x}p + \frac{1}{2\rho_0 c_0}\frac{\partial(\rho_0 c_0)}{\partial x}p + l_{old}(t')p + l_{relax}(t')p \tag{4}$$

where p is the sound pressure, x is the ray path distance, A is the ray tube area, c_0 is the small-signal sound velocity, ρ_0 is the ambient density, β is the coefficient of nonlinearity, and t' is the retarded time. The first, second, and third terms in the right-hand side of Eq. 4 consider nonlinear effect, geometric damping effect, and stratification effect (atmospheric conditions change according to altitude), respectively. In addition, l_{old} and l_{relax} used in the fourth and fifth terms are the operators, which model thermal viscosity attenuation and relaxation attenuation, respectively.

3. Numerical Settings

The near-field pressure wave created by the D-SEND#2 model (S3CM: S-cube Concept Model) produced in the JAXA D-SEND project was used to analyze sonic boom propagation. The flight altitude, Mach number, and flight path angle were set to be 8000 [m], 1.3, and -50 [deg], respectively, and the near-field pressure wave was obtained at the location twice length of the model away from the model axis. The present analysis considered the uncertainties included in atmospheric temperature, wind (speed and direction), and humidity in August from 2000 to 2009 at the Esrange Space Center. Atmospheric temperature and wind were distributed in 17 atmospheric layers corresponding to different altitudes from 100 to 30000 [m], and atmospheric humidity was distributed in 8 layers. The mean value μ and standard deviation σ of atmospheric properties were given in each layer separately, and the uncertain behaviors of these properties were represented as $\mu + \xi \sigma$, where ξ is a normally-distributed random variable with its mean value and standard deviation of 0 and 1, respectively. Here the present study applied a common value of ξ to all layers.

4. Result and Discussion

Convergence histories of the mean value and standard deviation of sonic boom strength at t = 0.033 [ms] against atmospheric temperature uncertainty are shown in Fig. 1. The dotted lines represent the histories obtained by NIPC with different sample size, and the solid lines denote the statistics obtained by MC with 10000 sample points. The NIPC statistics with more than 11 sample points agree with the MC statistics. This result indicates that 11 sample points are enough for NIPC to accurately analyze sonic boom under atmospheric uncertainties.

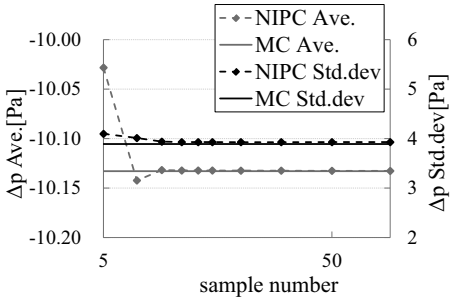

Fig.1 Convergence histories of the statistics of sonic boom strength

Sonic boom waveforms considering atmospheric temperature uncertainty, wind uncertainty, and humidity uncertainty, which were obtained by NIPC with 11 sample points, are shown in Figs. 2, 3, and 4, respectively. The lines represent the mean values and the error bars represent the standard deviations of sonic boom waveforms. It was confirmed that the humidity uncertainty has a largest impact on sonic boom. This is because atmospheric humidity significantly affects an atmospheric absorption coefficient. Next, the temperature uncertainty has an impact on the peak pressure. This is because atmospheric temperature affects thermal viscosity and relaxation attenuation, which have effects on pressure gradient. Finally, the atmospheric wind uncertainty has no effect on sonic boom. This is because the present study assumes that the wind direction is constant at all atmospheric layers. Therefore, if the wind direction is allowed to change according to the atmospheric layers, the atmospheric wind uncertainty may have a certain effect on sonic boom.

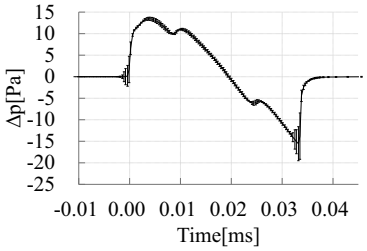

Fig. 2 Sonic boom waveform considering atmospheric temperature uncertainty

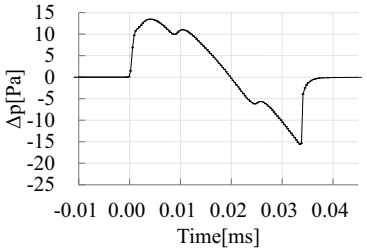

Fig. 3 Sonic boom waveform considering atmospheric wind uncertainty

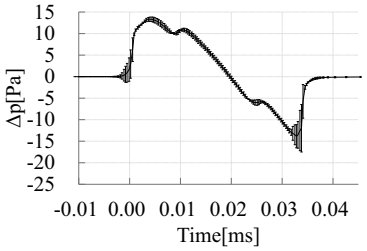

Fig. 4 Sonic boom waveform considering atmospheric humidity uncertainty

5. Concluding Remarks

In this study, Non-Intrusive Polynomial Chaos (NIPC) which can consider uncertainties at low computational cost was applied to the sonic boom analysis solving an augmented Burgers equation. It was demonstrated that, compared to Monte Carlo (MC) method, NIPC could estimate the statistics of sonic boom strength with equivalent accuracy and smaller sample size. In addition, the present simulation results revealed that atmospheric humidity uncertainty and temperature uncertainty have significant impacts on sonic boom, while wind uncertainty has no impact.

Acknowledgement

The authors would like to thank the supersonic transport team in JAXA for providing the experimental data in D-SEND project.

References

[1]C. L. Thomas, NASA TN D-6832 (1972).
[2]R. O. Cleveland, and D. T. Blackstock, NASA CP-3335 (1996).
[3]S. Hosder, and R. W. Walters, AIAA-2010-129

Eighth International Conference on Flow Dynamics
November 9 - November 11, 2011

Development of Measuring Technique on Near-Field Pressure for Supersonic Projectiles Using Ballistic Range

Takahiro Ukai, Kiyonobu Ohtani, Takamasa Kikuchi and Shigeru Obayashi
Institute of Fluid Science, Tohoku University, Sendai, Miyagi, 980-8577, Japan
ukai@edge.ifs.tohoku.ac.jp

ABSTRACT

A simultaneous measurement of a flight attitude, a shock wave visualization and a near-field pressure have been carried out for a supersonic projectile of the spherical model flown in a ballistic range at Institute of Fluid Science, Tohoku University. The broadening of the near-field pressure waveform obtained in detail by measuring multi-point pressure.

1. Introduction

The number of air passengers seeking rapid transport is continuously increasing. The Super-Sonic Transport (SST), although at the present not operational, has potential to meet this demand in the future. One of the reasons for the absence of SST service is noise pollution in the form of sonic booms. The propagation of shock waves and expansion waves from the aircraft in supersonic flight to the ground generates huge noises, similar to explosions. Therefore, a SST with low-boom property is actively sought [1], [2].

In order to develop a low-boom SST, an airframe configuration that makes the waveform of pressure generated from the airframe into the low-boom waveform is devised. Initially, the near-field pressure waveform is calculated by Computational Fluid Dynamics (CFD), and later the boom on the ground is estimated by the numerical simulation of the propagation of the resulting waveform. The validation of CFD simulations necessitates experimental measurements of a pressure waveform near the airframe.

These measurements have been generally performed in a wind tunnel, in which case the installed aircraft model is supported by a sting. But, since the disturbances generated from the sting affect pressure waves generated from the tail of the model, it is difficult to precisely measure the near-field pressure along the entire region of the model.

The main advantage of the experiment performed in a ballistic range the removal of sting's influence to the measurement because the model is launched into free flight. However, the experiment in a ballistic range has a demerit in the flight attitude of the projectile, which means that the flight of the model may become irregular.

Therefore, for accurate measurements of the near-field pressure waveform, the flight attitude should be observed in addition to the optical visualization of flow field and the measurement of the near-field pressure waveform.

To measure the near-field pressure of a low-boom SST in a ballistic range, this research aims to conduct a simultaneous shadowgraph visualization of the flow field around a spherical projectile launched by the ballistic range, the observation of a flight attitude by using a diffused light and the measurement of the near-field pressure waveform. This paper summarizes the experimental method and presents the results on the near-field pressure for supersonic projectile flight from a ballistic range.

2. Method (experimental setup)

This experiment was performed in the ballistic range at the Institute of Fluid Science, Tohoku University run in the gas gun mode. The schematic diagram of the experimental setup is shown in Fig. 1, where the test section (recovery chamber) has diameter of 1.66 m and is 12 m long. Figure 2 shows the pressure instrument and the projectile with the sabot. The pressure instrument has six pressure transducers (model 603B, Kistler Corp.) arranged to measure the pressure distribution and a flight path of the projectile from the pressure history. The pressure instrument was located at approximately 8 m from the end of the accelerating tube, and 254 mm under the flight path.

We simultaneously measured flight attitude and the detached shock from the projectile. The projectile is made of polyamide resin, weights 16 g, and is of spherical shape with diameter of 30 mm. It is accommodated in a four-piece cylindrical polycarbonate sabot with diameter of 51 mm and length of 60 mm, weighting 110 g. Projectile was separated from the sabot by aerodynamic sabot separation at the test section pressure of 51 kPa. Projectile surface has dot and line markings, which are used for determination of

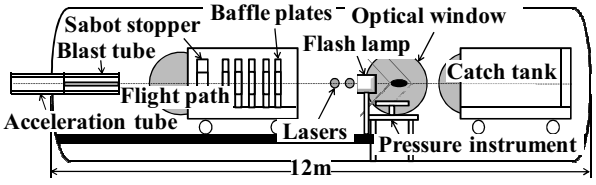

Fig. 1 Schematic diagram of the test section.

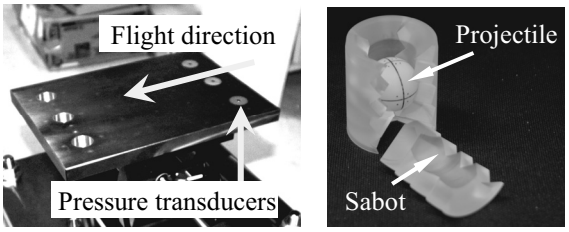

Fig. 2 Pressure instrument (left) and projectile with sabot (right).

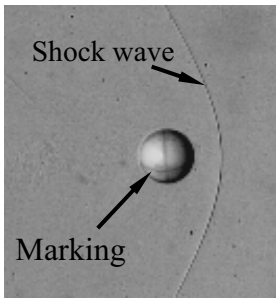

Fig. 3 Simultaneous visualization image, showing the shock wave and the markings of the projectile (M_s=1.28, interframe 16 μs, exposure time 2 μs).

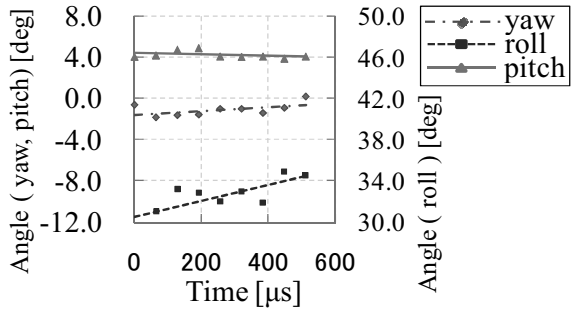

Fig. 4 Flight attitude for spherical projectile (M_s=1.28).

projectile's flight attitude through direct visualization with a flash lamp. In order to visualize the detached shock wave, we used the optical arrangement of the shadowgraph method with a pair of schlieren mirror of 5 m focal length and a continuous light source (metal halide lamp MME-250, Moritex Corp., 250 W). Sequential recording of the direct visualization images and shadowgraph images was done by a high-speed video camera (HPV-1, Shimadzu Corp., 104 frames at 312 × 260 pixel count, maximal framing rate 1,000,000 frame/sec).

3. Results and Discussion

Figure 3 shows the simultaneous visualization image of model surface and the detached shock wave over the spherical projectile. This image clearly shows the markings on the model surface and the detached shock wave over the spherical projectile.

Figure 4 shows a flight attitude measurement for spherical projectile, in which case a flight with a roll is noted. Near-field pressure measurements are shown in Fig. 5, with part (a) and (b) showing pressure histories obtained from the three pressure transducers at the upstream and the downstream side, respectively. It can be noticed that the compression wave reached first pressure transducers (b) and (e), while pressure transducers (a) and (c), as well as (d) and (f) detected the expansion wave simultaneously. The trajectory of the spherical projectile was directly above the pressure transducers (b) and (e).

Table 1 shows characteristics of the near-field pressure waveform obtained from the pressure histories of pressure transducers PT (a), (b) and (c). ΔT indicates the rise-time of the compression wave, $\Delta T_{p\text{-}p}$ indicates

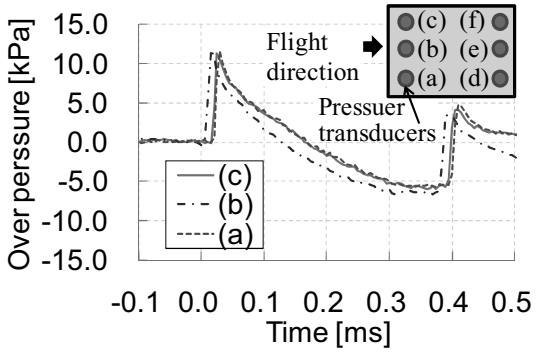

(a) Upstream side.

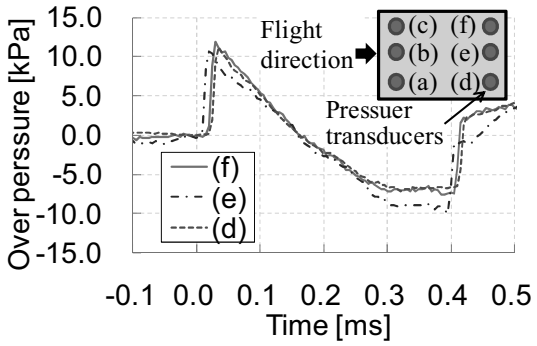

(b) Downstream side.

Fig. 5 Pressure distribution (M_s=1.28).

Table 1 Characteristics of the near-field pressure waveform.

PT	ΔT [μs]	$\Delta T_{p\text{-}p}$ [μs]	ΔP_1 [kPa]	ΔP_2 [kPa]
(a)	10.0	360.0	11.6	-5.4
(b)	10.0	360.0	11.9	-6.4
(c)	10.0	360.0	11.4	-5.7

the peak-to-peak time, which is the time from the compression wave to the expansion wave, ΔP_1 indicates the pressure difference from zero (atmospheric pressure) to the maximum value of the first compression wave, and ΔP_2 indicates the pressure difference from zero to the minimum value of expansion wave. ΔP_2 of the pressure transducer (b) is larger than the pressure transducers (a) and (c), hence it shows the broadening of the expansion wave.

4. Concluding remarks

The final target of near-field pressure experiment is to measure the detailed pressure histories of a low-boom SST models. In this paper, the spherical projectile was flown supersonically using ballistic range. The results indicate that the simultaneous measurements of the near-field pressure, the shock wave visualization and the flight attitude was achieved. The broadening of the near-field pressure waveform was obtained in detail by measuring pressure at several points.

References

[1] J. M. Morgenstern et al, AIAA 2010-5114, 28th AIAA (2010).
[2] A. Bugeau et al, AIAA 2008-7181, 26th AIAA (2008).

OS5: Research Frontiers in Green Hybrid Rocket Propulsion

Eighth International Conference on Flow Dynamics
November 9 - November 11, 2011

The European Research Activity on Hybrid Rocket Propulsion

Carmine Carmicino, Annamaria Russo Sorge
Department of Aerospace Engineering, University of Naples "Federico II", P.le Tecchio, 80, Naples, 80131, Italy.
carmicin@unina.it.

ABSTRACT

This paper presents the structure and the main purpose of the Operative Research Project on Hybrid Engine in Europe, along with some preliminary experimental results. New fuel formulations are analyzed to raise the regression rate required in some typical propulsion applications envisaged for a hybrid rocket system. A series of static firing tests have been carried out on a lab-scale hybrid engine. Gaseous oxygen and two different fuel compositions have been tested to assess the improvement in the regression rate deriving from HTPB fuels with additives.

1. Introduction

The main objective of the Operative Research Project on Hybrid Engine in Europe (ORPHEE) is to improve the technological maturity level of hybrids with a special focus on the development of optimized formulations of solid fuels which would allow for a significant increase of regression rate. Three space platforms may take advantage of hybrid propulsion[1], that are: a generic exploration mission (due to the inherent safety of hybrid propulsion, throttlability and stop/restart capability); upper stage, thanks to the large thrust provided; low cost launcher, mainly thanks to the potential cost reduction. In the framework of this program two demonstrators, representative of the selected missions, are being developed: a booster-stage demonstrator and a lunar-lander demonstrator, which allow assessing complementary key requirements such as high specific impulse, multiple ignition and wide throttling capability together with a high regression rate. The latter, as shown in a dedicated system analysis, should be in the range of 0.5-4 mm/s for the lander application and even larger for engines requiring higher thrusts (booster stage). To tackle this challenge, a dedicated work package is included in ORPHEE with the aim of investigating advanced fuels. A trade-off study has been carried out to select potential interesting fuel formulations for the identified space applications. Attention has been drawn both to HTPB with the addition of either metallic particles (nano-sized aluminum powder) or metal hydrides (AlH3 or MgH2) and to paraffin-based fuels. Owing to the high specific surface area of nano-scale aluminum particles, shorter ignition delay and faster burn times can be expected compared to micro-scale aluminum, leading to an improvement of rocket performance. Additives are employed to increase the specific impulse. The main results of this selection process can be summarized as follows. For a Moon soft landing, the best result is achieved by using LOx as oxidizer. Performance is improved with a loading of 15% in mass of nano-sized aluminum powder. The effect of this additive is to increase the regression rate as long as to raise the fuel density, even if the theoretical specific impulse is not significantly increased compared to pure HTPB. For the upper-stage and booster applications, the same tendency as for Moon lander is observed. The combination of high performance and large density is obtained with the LOx/HTPB nano-sized aluminum propellants couple. Note that, based on the considered criteria, the poorer rating of the paraffin fuel is essentially a consequence of its weak mechanical properties.

A preliminary assessment of the selected fuels regression rate is performed at SPLab in Milan on a small-scale set-up, while only some fuel formulations are planned to be evaluated at a larger scale at the University of Naples. With this purpose, a set of firings has been defined, which allows analyzing the effects of gaseous oxidizer mass flux, and port diameter upon the regression rate with a given fuel. Several firing times, mass flow rates, fuel compositions are defined, for a total number of 24 firing conditions.

2. Lab-scale motor testing

The firing tests conducted on the lab-scale hybrid engine of the University of Naples represent a step in scaling up between the small-scale results of SPlab and the ones which will be achieved on the demonstrator engines. The fuel grains burned in this test campaign have been produced at "Le Bouchet Research Center". Three formulations have been developed using different ingredients: 1) no additives (pure HTPB); 2) magnesium hydride additive; 3) Nano-sized aluminium powder additive (Alex type). Pure HTPB has been formulated as a reference in terms of mechanical properties and fuel performance. For an exhaustive account on the experimental set-up see Refs. 2,3, and 4. The lab-scale motor has an axisymmetric combustion chamber, with a 720-mm length and a 133-mm inner case diameter. Upstream and downstream of the fuel grain a dump plenum and an aft-mixing chamber are set up respectively. A water cooled converging-diverging nozzle with 16-mm throat diameter, 82-mm length and 2.44-area-ratio, made of copper alloy, ensures long duration firings without throat erosion, which allows one to obtain a more accurate measurement of the combustion efficiency. A spark plug is arranged in the prechamber where methane is injected for 3 s together with oxygen to ignite the motor.

3. Results and Discussion

A first subset of the firings planned in the program test matrix has been performed at the current stage. The average parameters measured over the firings are reported in Table 1. Most of the tests involved pure

HTPB grains; two out of three tests have been performed using HTPB with nano-aluminum, and two with magnesium hydrides.

Table 1. Firing tests results

Fuel	M_{ox} [kg/s]	G_{ox} [kg/m^{2}s]	O/F	G [kg/m^{2}s]	P_{aft-ch} [atm]	regression rate [mm/s]	average port D [mm]	etaC*
HTPB	0.0256	39.7	0.948	81.5	3.73	0.556	27.92	0.972
HTPB	0.0718	55.0	1.576	89.8	10.05	0.659	40.03	0.984
HTPB	0.1367	59.8	1.897	91.3	18.51	0.773	50.15	1.010
HTPB	0.0869	128.9	1.892	197.0	10.94	0.923	28.54	0.944
HTPB	0.1442	145.4	2.094	214.8	17.62	1.134	33.03	0.950
HTPB	0.1150	210.6	2.126	309.7	13.78	1.190	25.60	0.941
HTPB	0.1848	219.1	2.345	312.5	22.19	1.393	30.46	0.977
HTPB/Al	0.0701	53.5	1.288	95.1	10.12	0.700	37.96	0.935
HTPB/Al	0.1444	145.4	1.871	223.2	20.14	1.140	33.04	1.053
HTPB/MgH2	0.0698	86.1	1.388	148.1	-	0.913	29.85	0.925
HTPB/MgH2	0.1010	47.1	1.248	84.9	13.92	0.904	24.45	0.918

In this paper only regression rate is discussed. The average regression rate is plotted versus the oxidizer mass flux in Figure 1a; here, for comparison, the regression rates measured in the framework of ESA TRP (Ref. 5) are superimposed along with some classical data retrieved from the literature[6]. The latter have been obtained from the combustion of pure HTPB and gaseous oxygen in a laboratory-scale hybrid rocket.

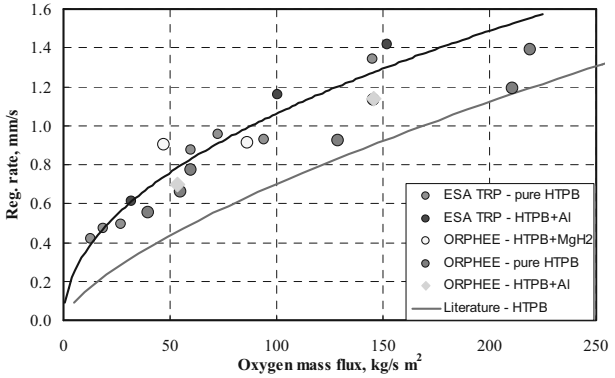

a)

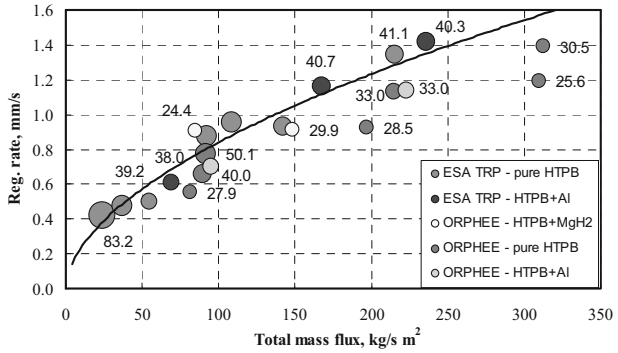

b)

Fig. 1 Regression rate as a function of: oxygen mass flux a); total mass flux and average port diameter b).

In contrast to the data from the literature (the red curve in Figure 1a), regression rates with pure HTPB in the current program are higher; the regression-rate increase ranges between 20% and 50%, being larger at low mass fluxes. This was well expected and it is a consequence of the fluid dynamics of the gaseous oxygen jet inside the fuel port. At large oxygen fluxes, however, the current regression-rates are lower than the ones obtained in the ESA TRP program. The four tests with HTPB and additives (two with nano-Al and two with magnesium hydride) do not display any significant increase in regression rate. In particular, regression rates measured in the tests with nano-Al are exactly the same as the ones with pure HTPB at the same oxygen mass flux (green points in Figure 1). The clusters of values at around 50, 140 and 225 kg/m^{2}s seem to be scattered; this is a consequence of the port diameter effect. This feature is clarified in Figure 1b, where regression rate is reported versus the total mass flux. Here points have been traced with an area proportional to the average port diameter. Smaller points fall on a lower level than larger points with almost the same mass flux. For example, the regression rate of the three points at around 100 kg/m^{2}s increase from 0.556 mm/s to 0.773 mm/s passing from 27.9-mm port diameter to 50.1 mm. The same observation applies to all the data deriving from pure HTPB combustion. Note that, in this diagram, the points relevant to HTPB and nano-Al are shifted to higher mass flux with respect to the ones obtained with pure HTPB at the same oxygen flux, because, even if the regression rate is the same, the fuel mass flow rate is higher due to the larger density of fuel with additives.

4. Concluding remarks

A number of tests on a lab-scale hybrid engine have been carried out in the ORPHEE project with pure HTPB and gaseous oxygen axially injected in single port cylindrical grains, to establish a baseline performance and to ascertain the effect of port diameter upon the regression rate with a given mass flux. HTPB with nano-scale aluminum powder and HTPB with magnesium hydride have been burned as well. Results achieved at this stage of the program confirms a significant effect of the port diameter on the regression rate and show that regression rate is not significantly improved by additives.

Acknowledgments

The research leading to these results has received funding from the European Community's Seventh Framework Programme (FP7/2007-2013) under grant agreement n°218830.

References

[1] Martin, F., Chapelle, A., Orlandi, O., Yvart, P., AIAA paper 2010-6633, Jul. 2010, Nashville, TN

[2] Carmicino, C., and Russo Sorge, A.,, Journal of Propulsion and Power, Vol. 22, No. 5, 2006, pp. 984-995

[3] Carmicino, C., Journal of Propulsion and Power, Vol. 25, No. 6, 2009, pp. 1322-1335

[4] Carmicino, C., and Russo Sorge, A., Aerospace Science and Technology, Vol. 11, 2007, pp. 61-67

[5] Carmicino, C., Orlandi, O., Russo Sorge, A., Dauch, F., De Amicis, R., De Rosa, M., AIAA paper 2009-4937, Aug. 2009, Denver, CO

[6] Sutton, G. P., and Biblarz, O., Rocket Propulsion Elements, 7th Ed., 2001, pp. 585-593

Eighth International Conference on Flow Dynamics
November 9 - November 11, 2011

Ultrasonic Study on Hybrid Rocket Motor

Shintaro Iwasaki[1],Keiich Hori[2],Katsuya Hasegawa[2], Tsuyoshi Yagishita[2], Yutaka Wada[3], Hideki Sato[4]
[1] *Tokyo University, Tokyo, Japan* [2] *ISAS/JAXA, Kanagawa, Japan* [3]*Akita University, Akita, Japan*
[4]*Tokai University, Kanagawa, Japan*
E-mail : iwasaki.shintaro@ac.jaxa.jp

ABSTRACT
Ultrasonic measurement is employed to evaluate the instantaneous surface regression rate. Ultrasonic technique was employed and special sensor was developed and trial was conducted to measure the regression rate of PEG(Poly ethylene glycol) as solid fuels in a traditional hybrid rocket system using gaseous oxygen as an oxidizer. The time history of the traverse time of ultrasonic signal from the regressing surface was successfully measured and instantaneous regression rate was obtained.

1. Introduction

Surface regression rates are generally mean value for designing hybrid rocket motor and there are many studies in the past[1-2]. However, every experimental parameter changes gradually in traditional hybrid motors as the combustion proceeds, thus, the measurement of the instantaneous regression rates is essentially necessary for the detailed discussions.

Ultrasonic measurement was employed to evaluate the instantaneous surface regression rates. The combustor and ultrasonic sensors are specially designed for this purpose, and ultrasonic sensors can be excited up to 100V which enables signal acquisition from regressing fuel surface easier. Experiment started with PEG sample and the minimum excitement voltage of the ultrasonic sensor from the safety consideration, and several information was obtained.

2. Experimental

A. Fuel sample

PEG needs a crosslinking agent for cureing. Trimethylolpropane (TMP) is used as a crosslinking agent, and Hexamethylenediisocyanate (HMDI) and Dibutyltindilaurate (DBTDL) are used as a curing agent and the catalyst for the curing reaction, respectively.

B. Hybrid rocket testing

The samples were loaded directly in the chamber.
A schematic of the experimental setup is shown in Fig.1. A special combustor was prepared for this purpose. Its inner diameter and length are 90mm and 1300mm, respectively, and the chamber is equipped with three ultrasonic measurement ports and three temperature measurement ports. Oxygen gases are introduced to the combustion chamber from four ports, then forced to flow along the wall of pre-combustion section, and finally converged into the bore of the grain. Igniter is common with that used in the firing tests of solid motors, and composed of an initiater and non-metallized solid propellant grain, and the oxygen flow was started one second before the ignition. Typically, ten to thirty seconds burning tests were conducted, and the mean values of surface regression rate, burning pressure, oxygen mass flux (*Gox*), and O/F were evaluated.

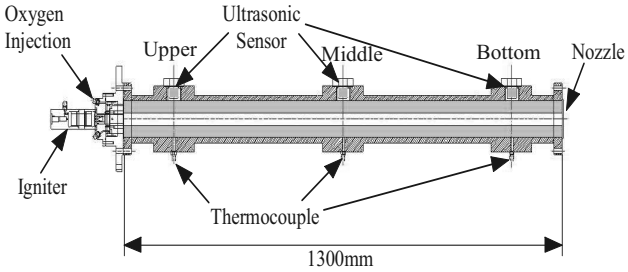

Fig.1 Hybrid rocket motor for ultrasonic measurement

C. Ultrasonic measurement

Ultrasonic sensor was also specially designed and manufactured by Honda Electronics Co., LTD. Sensor diameter is 20mm and the sensor is composed of a set of a pulser and a receiver. The wave frequency was set at 1MHz because this frequency ultrasonic wave penetrates rubber materials well and is suitable for this measurement. 100V was adopted as the excitement voltage of the sensor and made the signal from the surface strong and clear.

3. Results and Discussion

Ten seconds burning test was conducted successfully. The chamber pressure is 3MPa and Fig.2 shows the firing test of PEG.

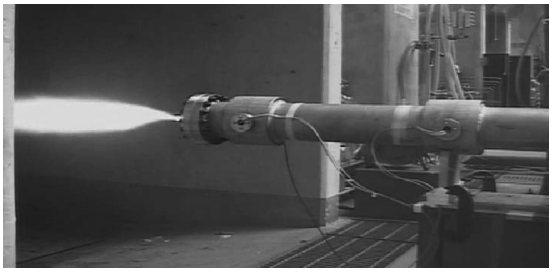
Fig.2 Firing test of PEG100

Strong multi-reflection within the stainless steel holder plate and the signal through the peripheral part of the combustor hampers the ultrasonic measurement, however, a specially developed software makes it possible to pick up the signal from the regressing surface at an acceptable accuracy. Fig.3 shows the result of the thickness trace of burnt PEG fuel which is obtained from traverse time of the ultrasonic signal and sonic speed of the PEG as functions of pressure and initial temperature of the grain.

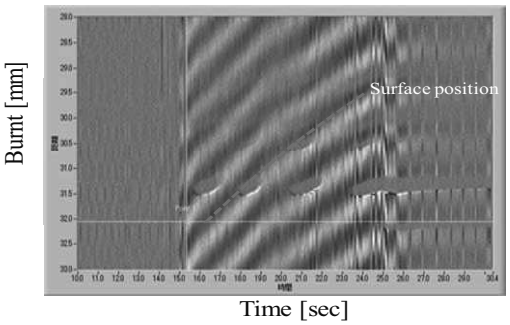

Fig.3 The thickness trace of burnt PEG fuel

Fig.4(a) shows the pressure pattern of hybrid test and ultrasonic sensor data (upper position) of instantaneous surface regression rate is obtained as is shown in Fig.4(b). About result of ten second test, regression rate at 2.0 second is reduced at 0.46mm/s, and 0.28mm/s at 8.0 second, which shows regression rate is higher at the initial stage because of smaller bore area and the result was suggested that fuel regression rate is not constant in the case of large chamber.

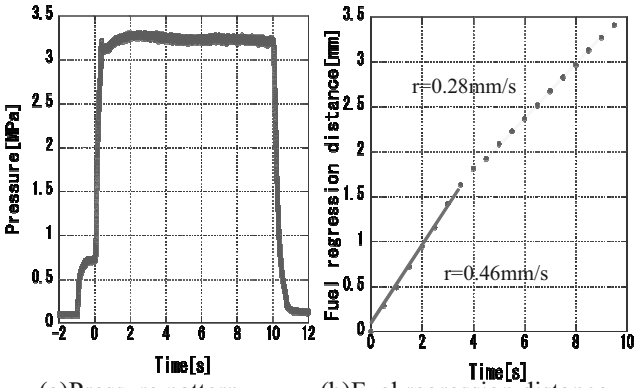

(a)Pressure pattern (b)Fuel regression distance

Fig.4 Result of 10 seconds firing test

The firing test which changes combustion pressure to three steps for each 10 seconds was conducted and result was shown in the Fig.5 and Fig.6. Total burning time is 30 second, and chamber pressure changes three steps; 0-10 second is 0.6MPa, 10-20 second is 1.0MPa and 20-30 second is 1.5MPa (Fig.5). When the burning test finished, it seems that the combustion pressure remains slightly. It is the pressure of the nitrogen purge for fire extinguishing. Fig.6 shows result of fuel regression distance from ultrasonic sensor data of 3 positions. The fuel regression distance is the same almost by all the positions during first 10 seconds. It is observed to burn at the speed in which a middle position and the bottom position are almost the same after during 20sec. In middle position, a lot of mass flow from fuel surface was generated and total mass flux was increased compared to the upper position. Therefore fuel regression distance was also increase. In the bottom position, although the mass flux is increasing further, however oxygen concentration is low. Accordingly, it seems that regression distance becomes as same as the middle position. It is well shown that the ultrasonic technique can provide the instantaneous regression rate, and such data is useful to discuss the effects of experimental parameters on the regression rate correctly, thus, indispensable for the establishment for the combustion mechanism of hybrid rocket motor.

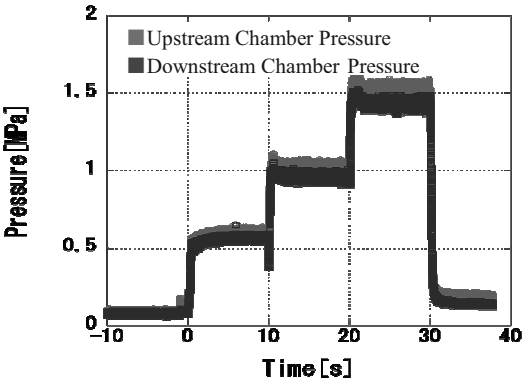

Fig.5 Pressure pattern

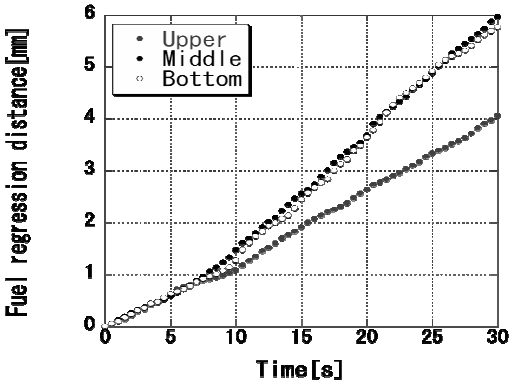

Fig.6 Instantaneous regression distance

4. Summary

Ultrasonic technique was employed in the hybrid motor, and special sensor was developed for this purpose and trial was conducted to measure the regression rate of PEG fuel. The time history of the traverse time of ultrasonic signal from the regressing surface was successfully measured and instantaneous regression rate was obtained using the calibration data of ultrasonic speed of PEG as functions of pressure and temperature. The three position sensor data was also obtained successfully, and the result was suggested that fuel regression rate is not constant in the case of large chamber and it is important data for the design of a large hybrid rocket. This measurement will be a strong help to establish the comprehensive combustion model of hybrid rocket motor.

References

[1] Hori K., “Application of Glycidyl Azide Polymer to Hybrid Rocket Motor”, AIAA Paper, (2009), 2009-5348
[2]Hori K.et al , “Combustion Characteristics of Hybrid Rocket Motor using GAP as a Solid Fuel”, AIAA-2010-702946th AIAA/ASME/SAE/ASEE Joint Propulsion Conference, Nashville (2010).

Effectiveness of Concave-convex Surface Grain for Hybrid Rocket Combustion

Hatagaki Sakashi, Yuasa Saburo, Hirata Kousuke, Sakurai Takashi
Tokyo Metropolitan University, Hino City, Tokyo 191-0065, JAPAN
syuasa@sd.tmu.ac.jp

ABSTRACT

In order to increase the fuel regression rate of hybrid rocket engine, the concave-convex surface grain was adopted for the swirling-oxidizer-flow-type hybrid rocket engine. The concave-convex surface grain was burned under the swirling and non-swirling oxygen flow conditions. The fuel regression rate of concave-convex surface grains with swirl and without swirl increased up to about 1.4 and 2.0 times of the rates of cylindrical grains at the same oxygen mass flux conditions, respectively. Especially, the upstream side of the convex part increased the fuel regression rate. However, combustion oscillations by the Helmholtz resonance occurred.

1. Introduction

In hybrid rocket engines, a major drawback is low fuel regression rates. We found the swirling oxidizer injection at the head of the fuel grain increased the fuel regression rates of polymethylmethacrylate (PMMA) up to about 3 times in comparison with the oxidizer injection without swirling[1]. The swirling effect varied with fuel type. However, the fuel regression rate is still low compared with those of the solid rocket engines. We used the concave-convex surface grain to increase the fuel regression rate. The concave-convex surface grain was expected to increase in surface area and the intensity of turbulence in the flow field over the surface, which enhances the turbulent transport properties such as the turbulent thermal conductivity.

This paper examines the effects of concave-convex surface grain and the best size of concave and convex parts.

2. Experimental Apparatus

Figure 1 shows a schematic of the hybrid rocket engine used in this study. The engine consisted of a swirling-oxidizer-flow-type injector, a fuel grain and a graphite nozzle. The oxidizer was gaseous oxygen (GOX). In this study, we used two types of oxygen injector with and without swirl. Each of the injectors had eight oxygen injection slits. The slits with swirl were turned to the tangential direction to make a swirling flow (Sg=19.4, where Sg is the geometrical swirl number[2]), and the slits without swirl were turned radially (Sg=0). In this experiment, the oxygen mass flow rate $\dot{m}_o$ was about 43g/s.

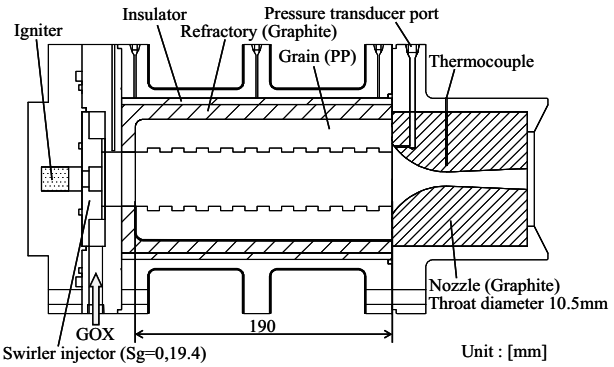

Fig. 1 Swirling-oxidizer-flow-type hybrid rocket engine with concave-convex surface grain.

Figure 2 shows the concave-convex surface grain used in this study. The grain made of PP was used, and had a single port with an inner diameter of 40 mm and a length of 190 mm. Burning experiments were carried out by changing the convex width, a, from 9 to 18mm and the concave width, b, from 4.5 to 18mm. The concave depth, c, was 3mm.

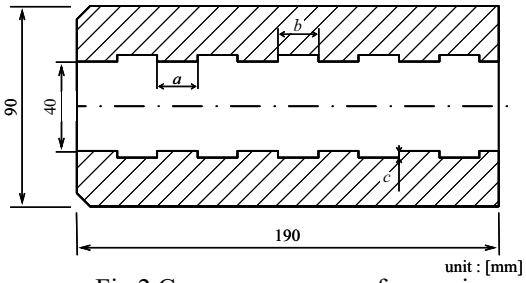

Fig.2 Concave-convex surface grain.

3. Results and Discussion

3.1 Time-averaged Overall Fuel Regression Rate

Table 1 shows the experimental conditions and results. The relationships between $\dot{r}_{over}$ and G_{oitm} for the experiments using the concave-convex surface grain and the cylindrical grain are shown in Fig. 3. Here, the lines in Fig. 3 are the experimental formulas of the cylindrical grains obtained in our laboratory. Figure 3 shows the concave-convex surface grains with swirl and without swirl increased the overall fuel regression rates up to about 1.4 and 2.0 times in comparison with the cylindrical grains, respectively. Therefore, the concave-convex surface grain is effective in increasing the fuel regression rate.

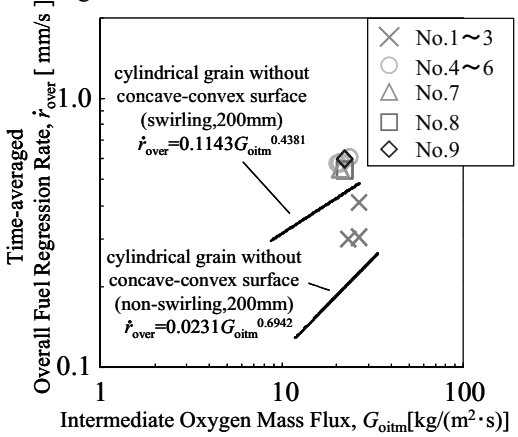

Fig. 3 Relation between time-averaged overall fuel regression rate and intermediate oxygen mass flux.

3.2 Time-averaged Local Fuel Regression Rate and Configuration Change of Fuel Grain

Figure 4 shows the measurement points of the time-averaged local fuel regression rate, $\dot{r}_{loc}$. The interval of the measurement points were 2.25 mm. Figure 5 shows the time-averaged local fuel regression rates measured after combustion at each measurement point for the experiments of No. 4, 5, 7 and 9. For all the experiments, $\dot{r}_{loc}$ of the convex parts were higher than those of the concave parts. $\dot{r}_{loc}$ of the convex parts decreased with burning time. They decreased as going to the downstream and lowered more than $\dot{r}_{over}$ (about 0.6mm/s) in the downstream from 7.75mm(*C*). However, $\dot{r}_{loc}$ of the corner in the convex part was higher than $\dot{r}_{over}$. On the other hand, $\dot{r}_{loc}$ of the concave parts were almost constant with time. $\dot{r}_{loc}$ of the concave parts increase as going to the downstream by 11.25mm(*E'*), and decreases in the downstream from 11.25mm(*E'*). As a result, $\dot{r}_{loc}$ of the concave parts didn't exceed $\dot{r}_{over}$.

Table 1 shows that when the width of the concave parts and convex parts were enlarged (No.7, 8), $\dot{r}_{over}$ decreased than that of $\dot{r}_{over}$ (No.5) though the burning time was long. This is due to a decrease of the surface area. When the width of the concave parts was reduced (No.9), $\dot{r}_{over}$ increased slightly than No.5. However, there was no substantial difference in $\dot{r}_{over}$, because the concave depth was small and then the concave-convex surface became smooth soon. Therefore, in order to increase fuel regression rate, it is necessary to decrease both the concave and convex widths. In order to decide the best size of concave and convex parts, it is necessary to conduct experiments for various concave depths.

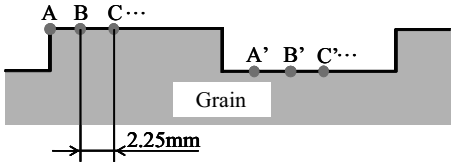

Fig. 4 Measurement points for time-averaged local fuel regression rate

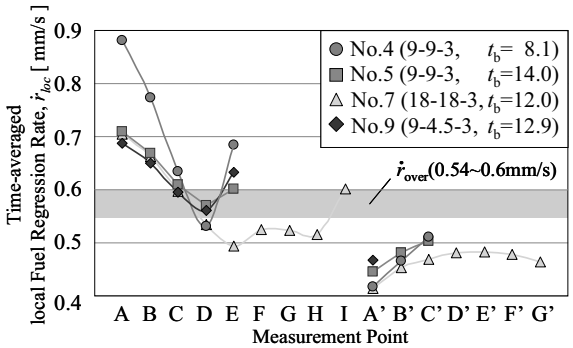

Fig. 5 Relation between time-averaged local fuel regression rate and measurement point

3.3 Engine Performance

Figure 6 shows the typical traces of the combustion chamber pressure, P_c, and thrust, F, for the experiment No.6. Using swirling-oxidizer-flow-type hybrid rocket engine with the cylindrical grain, P_c and F tended to increase slightly with burning time. However, the experiments with the concave-convex surface grain showed that P_c, and F decreased with time. A possible explanation is that fuel regression rate decreased, because the concave-convex surface becomes smooth and then the intensity of turbulence in the flow field over the surface decreases with burning time.

Combustion oscillations occurred for all the experiments. Vibration frequency of P_c was about 140 Hz and that of F was about 30 and 140 Hz. Here, 30Hz was characteristic frequency of the engine trestle. 140Hz was almost corresponding to the vibration frequency of the Helmholtz resonance occurring between combustion chamber and nozzle throat.

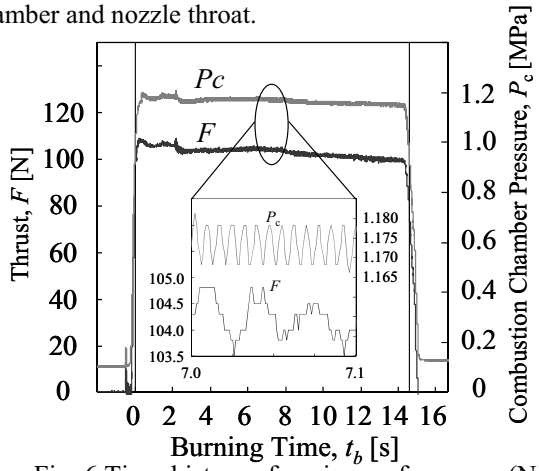

Fig. 6 Time-history of engine performance (No.6)

4. Concluding remarks

・Using the concave-convex surface grains with swirl and without swirl, the overall fuel regression rates up to about 1.4 and 2.0 times in comparison with the cylindrical grains, respectively.

・The time-averaged local fuel regression rates of the convex parts were higher than those of the concave parts.

・In the both cases of swirling and non-swirling flows, combustion oscillations by the Helmholtz resonance occurred.

Table 1. Experimental conditions and results

Exp.No	a-b-c	Surface area [cm²]	O_2 flow	t_b[s]	G_{oitm} [kg/(m2·s]	P_c[MPa]	F[N]	$\dot{r}_{over}$ [mm/s]	η_{c^*}
1	9-9-3	335	Non-swirling	3.1	23.2	0.72	55	0.30	0.92
2	9-9-3	335	Non-swirling	4.9	26.7	0.94	65	0.41	0.94
3	9-9-3	335	Non-swirling	8.2	26.6	0.80	57	0.30	0.88
4	9-9-3	335	Swirling	8.1	23.5	1.16	92	0.60	0.97
5	9-9-3	335	Swirling	14.0	21.1	1.18	97	0.58	0.97
6	9-9-3	335	Swirling	14.6	20.2	1.16	103	0.57	0.97
7	18-18-3	294	Swirling	12.0	22.3	1.15	90	0.54	0.99
8	18-9-3	296	Swirling	15.1	21.1	1.14	86	0.55	0.98
9	9-4.5-3	353	Swirling	13.5	22.1	1.16	105	0.60	0.96
10	cylinder	237	Swirling	10.1	22.7	0.91	87	0.42	1.00

References

[1] YUASA Saburo, SHIMADA Osamu, IMAMURA Tohru, TAMURA Takashi,and YAMAMOTO Kengo,AIAA Paper 99-2322, (1999).

[2] J. Beer, N. Chigier., Combustion Aerodynamics, Applied Science Pub., London, (1972), p.109.

Eighth International Conference on Flow Dynamics
November 9 - November 11, 2011

Effect of Reynolds Number on Regression Characteristics around Jet Stagnation Region

H. Nagata[1], S. Hagiwara[2], M. Nohara[2], M. Wakita[1], T. Totani[1]
[1] Division of Mechanical and Space Engineering, Hokkaido Univ., Sapporo 060-8628, Japan.
[2] Graduate School of Engineering, Hokkaido Univ., Sapporo 060-8628, Japan.
nagata@eng.hokudai.ac.jp

ABSTRACT

Regression formulas for solid fuels in CAMUI type hybrid rockets were developed. The empirical values of the mass flow density exponent for upstream end faces obtained by two motors with similarity shape and different scaling did not agree with each other. The different *Re* range caused this disagreement. By decreasing mass flow rate in the larger motor to equalize *Re* range, the empirical exponent approaches the value of the smaller motor case.

1. Introduction

The authors have developed CAMUI type hybrid rockets as a non-toxic propellant sounding rocket system. A main purpose is to drastically downsize the cost and scale of rocket experiments and attract potential users in various research fields. Figure 1 shows the key idea[1], a distinctive fuel grain design to accelerate gasification rates of solid fuels. The grain design, designated as CAMUI as an abbreviation of "cascaded multistage impinging-jet", makes the combustion gas collide repeatedly with fuel surfaces, resulting in intense heat transfer to the fuel.

As Fig. 2 shows, a CAMUI type fuel block has three burning surfaces; an upstream end face, inner wall of ports, and a downstream end face. To design initial fuel shape appropriately, regression formula for each burning surface is necessary. Previous studies by the authors provided the following regression formulas:

Upstream end face: $$\dot{L}_f = a\, G_p^m \left(\frac{H}{D}\right)^n \quad (1)$$

Inner wall of ports: $$\dot{r} = a\, G_p^m \quad (2)$$

Downstream end face: $$\dot{L}_b = a\, G_p^m H^n \quad (3)$$

where G_p , H, and D are mass flow density in ports, impingement distance, and port diameter, respectively, and a, m, and n are empirical constants. Because the dependence of regression rates on G_p comes from the dependence of Nusselt number *Nu* on Reynolds number *Re*, the empirical value *m* is the same of the exponent of *Re* in a function giving *Nu*.

The first series of firing tests[2] to develop regression formulas employed EM-S motor, giving the empirical value *m* of 0.55. Another series with 250FM motor gave different value of 0.75[3]. Figure 3 shows dimensions of fuel blocks in 250FM (left) and EM-S (right) motors. Flow channel geometries are different with each other; 250 FM motor has smaller *L*/*D* ports, where *L* is axial length of a fuel block. Different *Re* exponents between these two motor cases mean that the flow fields are not similar with each other, may be due to the different flow channel geometries. However, a following series of tests with 90FM motor, having a similar geometry to 250FM motor with 3/5 scaling, gave the empirical value *m* of 0.61, being even closer to the EM-S motor case than the 250FM motor case.

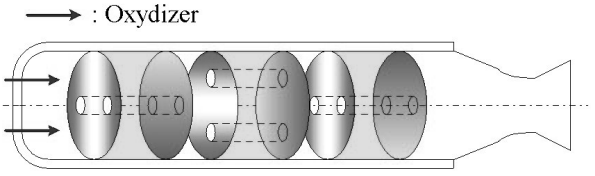

Fig. 1. Basic concept of CAMUI type hybrid motor.

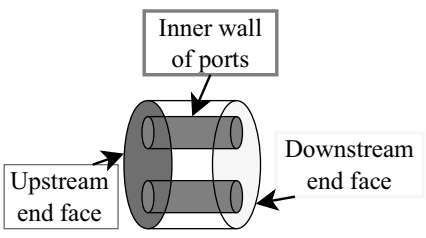

Fig. 2. Burning surfaces on a CAMUI type block.

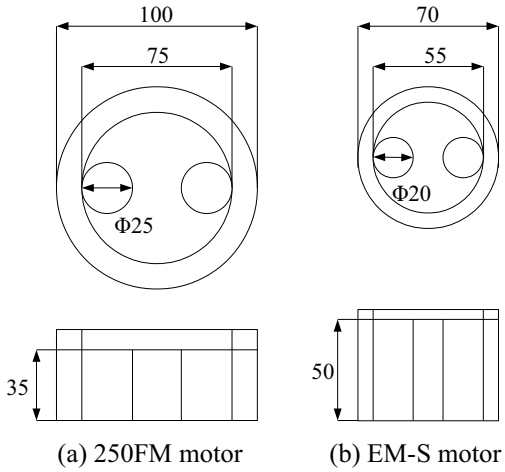

Fig. 3. Dimensions of fuel blocks.

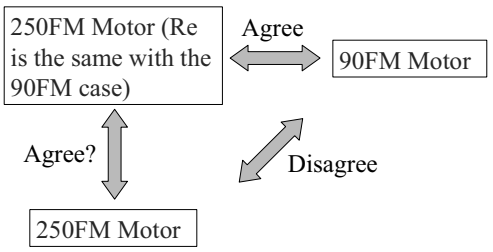

Fig. 4. Agree/Disagree map between motors.

A previous research revealed that a similarity rule based on convective heat transfer mechanism is valid when *Re* is common between different scaling[4]. This means that the *Re* exponent can vary by changing the *Re* range, as Fig. 4 shows. The purpose of this paper is to investigate the effect of *Re* range on the *Re* exponent.

2. Method

Figure 5 shows a schematic of 250FM motor. It uses liquid oxygen (LOX) and polyethylene as propellants. LOX flow rate at the design point of this motor is about 600 g/s, and the corresponding *Re* is 150,000 to 180,000 depending on the stage of fuel blocks. The design point *Re* of 90FM motor is 50,000 to 80,000. To cover this *Re* range by 250 FM motor, LOX flow rate was decreased to 400 g/s or 200 g/s. Figure 6 shows *Re* range (vertical axis) for the three flow rate conditions. The horizontal axis is mass flow density in ports. For mass flow density calculation, mass flow rate includes fuel flow rate adding to LOX flow rate. As the result, *Re* varies with stages.

3. Results and Discussion

Figure 7 shows regression rates of forward end faces at reference O/F of 3[?] as functions of mass flow density in ports. The empirical values of *Re* exponents with larger *Re* range was around 0.8, being close to the previous value by this motor of 0.75. With a smaller *Re* range, on the other hand, the value was 0.64, being close to the value with 90FM motor of 0.61. Based on a simplified analysis[5], *Nu* is proportional to *Re* to the 0.5th power in stagnation region and 0.8th power in wall jet region. Considering that *Nu* in wall jet region increases more rapidly than that in stagnation region with increasing *Re*, it is likely that the heat transfer in the wall jet region becomes dominant due to the increase of *Re*, resulting in the change of *Re* exponent from 0.5 in stagnation region to 0.8 in wall jet region.

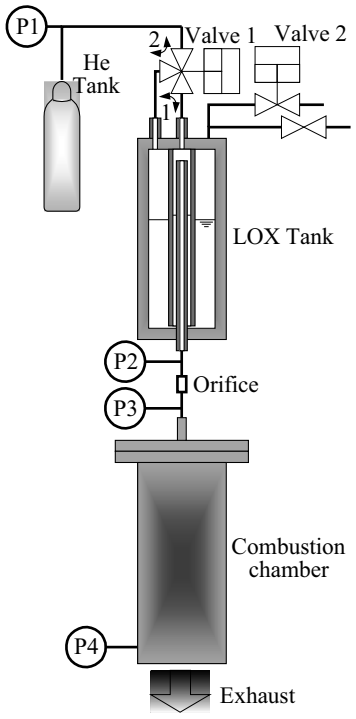

Fig. 5. Schematic view of 250FM motor.

4. Concluding remarks

The empirical values of *Re* exponents in the function giving *Nu* obtained by two motors with similarity shape and different scaling did not agree with each other. The different *Re* range caused this disagreement. By decreasing mass flow rate in the larger motor to equalize *Re* range, the *Re* exponent approaches the value of the smaller motor case.

Acknowledgment

This research was partially supported by the Ministry of Education, Science, Sports and Culture, Grant-in-Aid for Scientific Research (B), 21360410, 2009.

This research is supported by the Hybrid Rocket Research Working Group (HRrWG) of Institute of Space and Astronautical Science, Japan Aerospace Exploration Agency. The authors thank members of HRrWG for their helpful discussion.

References

[1] H. Nagata, et al., 49th IAC, IAF-98-S.3.09, 1998.
[2] M. Ito, et al., J. of JSASS (2007), **55**, 337.
[3] H. Nagata, et al., 46th JPC, AIAA 2010-7117, 2010.
[4] H. Nagata, et al., 47th JPC, AIAA 2011-6105, 2010.
[5] C. Donaldson, et al., J. of Fl. Mech., **45** (1971), 477.

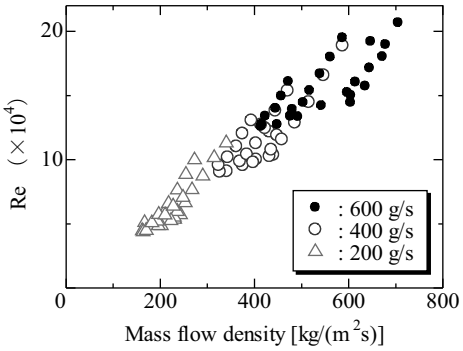

Fig. 6. *Re* range of each LOX flow rate condition.

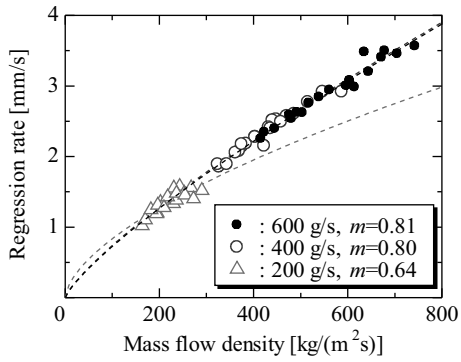

Fig. 7. Regression rate vs. mass flow density.

Feed System Coupled Instabilities in Hybrid Rockets

Arif Karabeyoglu
Space Propulsion Group Inc.
Sunnyvale, CA
arif@spg-corp.com

Abstract

In this paper, the transient combustion theory has been extended to hybrid rockets using liquid oxidizers with feed systems characterized by finite response times. Models for generic hybrid feed systems have been developed and these have been coupled to the combustion chamber dynamics with lag times introduced to model the delays associated with oxidizer vaporization and fuel gasification processes.

1. Introduction

A good understanding of the transient combustion characteristics of a hybrid rocket is critical to determine the system response during the ignition, throttling and thrust termination events and even more importantly to predict the stability behavior of the propulsion system. In fact, the motor stability is one of the most frequently encountered problem areas in the development and testing of hybrid propulsion systems. The low frequency instabilities frequently observed in hybrids can be broadly categorized into two groups 1) pressure oscillations inherent to the turbulent boundary layer combustion and other fluid dynamic behavior in the chamber and 2) feed system coupled instabilities.

In this paper the concentration is on feed coupled instabilities with emphasis on liquid fed systems. Even though feed coupled instabilities are commonly observed in hybrids using liquid oxidizers, no comprehensive theory to predict the influence of the feed system dynamics on the instabilities exists in the open literature. Our purpose in this development effort is to address this important aspect of transient modeling with the following specific objectives:

- Methods to distinguish feed coupled instabilities from other kinds of low frequency instabilities that are common in hybrids will be established.
- A transient model for the hybrid rocket that includes the feed system response will be developed.
- The modeling results will be used to devise practical methods to eliminate or minimize the low frequency instabilities.

The following approach has been taken to accomplish the stated objectives:

- Physics based models for the system components will be developed.
- The component models will be integrated to establish the overall system response.
- The formalism of transfer functions will be used such that the feed system response can easily be integrated into the other transient models to establish the dynamics of the overall rocket system[1].

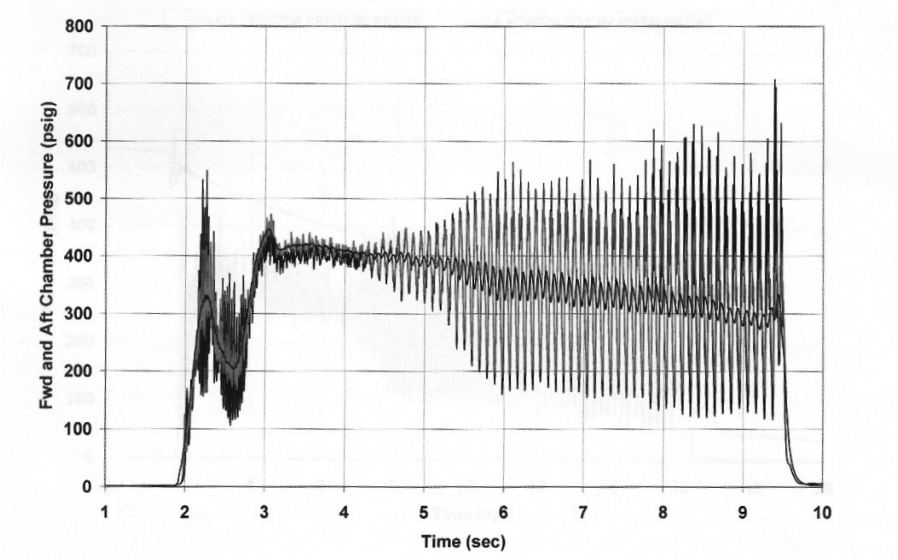

Fig. 1 Pressure time history for a 10 inch OD HTPB/LOX hybrid (Data from Ref. 1)

2. Conclusions

The important results and conclusions of our investigations on the feed coupled instabilities can be summarized as follows:

- Feed system instabilities are commonly observed in liquid fed hybrid rockets. Unlike the intrinsic instability of the hybrid combustion system, feed coupled instabilities are generally easier to model and control.
- A transient model has been developed for the generic liquid feed system of a hybrid rocket motor. This model is composed of the following key components
- Injector elements.
- Pipe system that also includes other minor elements such as valves.
- A simplified model for the combustion chamber that has the delays for that oxidizer and fuel gasification processes that take place in the chamber.
- The system of ODE's obtained from component models have been linearized and non-dimensionalized. Transfer functions between the combustion chamber pressure and the input variable (tank pressure or flow rate at the exit of the flow control element) has been developed for systems with and without flow isolation devices.
- The model predicts that instabilities are possible for systems with or without flow isolation elements. Specifically, the finite compressibility of the fluid in the feed lines can lead to combustion chamber oscillations for systems even with flow isolation elements. However systems with isolation elements are much more resilient to feed system related instabilities.
- The only adjustable parameter in the developed model is the delay time for the oxidizer vaporization process. The value of this parameter can be estimated from the spectral information on the measured combustion chamber pressure. The vaporization delay time can be used to evaluate different injectors and pre-combustion chamber configurations for hybrid motors.

References

[1] Knowles T., Kearney D. and Roberts R., "Overview of 10 inch Diameter HTPB Hybrid Motor Testing with Liquid Oxygen at Stennis Space Center", AIAA Paper 2005-4092, 41th AIAA/ASME/SAE/ASEE Joint Propulsion Conference and Exhibit, Tucson, Arizona, July 2003.

Eighth International Conference on Flow Dynamics
November 9 - November 11, 2011

Novel Fuels Based on Chemically-Modified Polymers with Si for Hybrid Rocket Propulsion

Koki Kitagawa[1], Paul Joseph[2], Vasily Novozhilov[2] and Toru Shimada[1]
[1]Japan Aerospace Exploration Agency, Sagamihara, Kanagawa, 252-5210, Japan
[2]School of the Built Environment, University of Ulster, Newtownabbey, County Antrim, BT37 0QB, UK
kitagawa.koki@jaxa.jp

ABSTRACT

With a view to investigating the effect of Si on the fuel regression rates, polymethyl methacrylate (PMMA) and polypropylene (PP) containing Si were made, and the relevant thermal data regarding the fuel regression rates were obtained. It was found that the presence of oxygen substantially influences the degradation profiles of the PP-based polymers, however only to a minimum extent in the case of PMMA polymers. The results showed that by incorporating Si into homopolymers has the potential for increasing fuel regression rates of both PMMA and PP.

1. Introduction

Hybrid rocket engines have a number of very attractive features over solid and liquid propulsion engines, and a lot of research has been conducted in this area for more than 80 years. However, hybrid rocket engines have not used widely due to its inherent problems. One of the most serious problems of a hybrid rocket engine is its low fuel regression rate. To address these problems, physical techniques like swirling flow or impinging flow, and chemical technique like energetic additives or advanced fuel have been tried.

To increase the fuel regression rates, we have focused on chemically-modified polymers with silicone (Si)-containing monomer as the rocket fuel, because silicon-containing groups make decomposition easy[1]. As the first step in our study, in order to investigate the effect of Si on the fuel regression rate, novel polymers containing Si were made, and the heats of combustion and other thermal decomposition data relevant to the fuel regression rate were obtained.

2. Experimental

2.1 Materials and reaction procedure[2]

Polymethyl methacrylate (MMA) and polypropylene (PP) that are conventional fuel for the hybrid rocket were used as the base materials. The Si-containing monomers used in this work where 3-(trimethoxysilyl)-propylmethacrylate (TSPM) and 3-[tris(trimethylsily-loxy)silyl]-propylmethacrylate (TTSSPM).

Copolymerization reactions of MMA and the Si-containing monomers were carried out in toluene solutions using 2,2'-azoisobutyronitrile (AIBN) as the initiator. In the case of PP, the post-modification grafting was achieved by employing di-tert-butylhydro-peroxide initiator in o-dichlorobenzene, as the solvent, at an elevated temperature. Hexane was used as non-solvent for the polymers based on MMA and acetone was used as the non-solvent for PP-based systems. The recovered polymers were dried at about 50 ^{o}C for several hours before examinations.

2.2 Characterization of copolymers

^{1}H NMR (400 MHz) spectra of the polymers based on MMA were recorded in $CDCl_3$ at ambient temperature. Thermograbimetric analyses (TGA) were carried out on about 3-8 mg samples, in different oxidative atmospheres, by employing mixtures of nitrogen/air/oxygen. A heating rate of 10 ^{o}C/min was employed up from 30 to 800 ^{o}C. The heats of combustion (gross calorific value) of the samples were measured using an oxygen bomb calorimeter.

3. Results and discussion

PMMA and PP containing the Si-groupings were successfully made by radical copolymerization, or by grafting, reactions. The compositions of the copolymers based on MMA were deduced from ^{1}H NMR spectra, by comparing the integral areas of appropriately assigned signals (MMA/TSPM contained 2.78% and MMA/TTSSPM contained 11.2% by weight of Si respectively). The wt.% of Si in the case of PP polymers needs to be determined by micro-elemental analysis. However, evidence for the presence of grafts was observed in the FT-IR spectra of the modified polymers.

The heat of combustion of MMA/TSPM was almost the same as that of PMMA whereas that of MMA/TTSSPM was about 6.5% greater than that of PMMA (Table 1). The heat of combustion of the re-precipitated PP was almost same as that of the virgin PP. The values for PP/TSPM and PP/TTSSPM decreased slightly as compared to that of the re-precipitated PP.

As an example, TGA results for MMA based polymer in nitrogen mixture is shown in Fig.1. The thermal decomposition features of all MMA based polymers are also shown in Table 1. Fig.1 shows that the decomposition temperatures of MMA/TSPM and MMA/ TTSSPM are lower than that of PMMA, particularly, it was lower in the case of MMA/TSPM. Compared to results obtained in nitrogen and in nitrogen/oxygen atmospheres, decomposition temperatures of all samples were higher in the latter case due to stabilizing effect of oxygen on PMMA degradation[3]. In nitrogen/oxygen, temperature at 5 wt.% decomposition of MMA/ TTSSPM is almost same as PMMA. However, the corresponding temperature for MMA/TSPM is significantly lower than in the other cases. It seems that at a high concentration of oxygen, MMA/TSPM decomposes to a greater extent. Furthermore, MMA /TSPM also left 6 wt.% as residue.

As an example, the TGA result for PP based polymer

in nitrogen is shown in Fig. 2. The thermal decomposition properties of all PP based polymers are also shown in Table 1. The result for the re-precipitated PP is different from that of PP. This might be due to fractionation and the accompanying re-distribution of molecular weights of the re-precipitated PP. The decomposition temperatures of PP/TSPM and PP/ TTSSPM are lower than that of the re-precipitated PP, in nitrogen. Compared to the results obtained in nitrogen and in nitrogen/oxygen, the decomposition temperatures of all samples were much lower in nitrogen/oxygen. It can be also noted that the decompositions of the PP based polymers are significantly affected by the presence of oxygen. In nitrogen/ oxygen, temperature at 5% decomposition of PP/TTSSPM is almost the same as re-precipitated PP, but the slope of TGA plot of PP/TTSSPM is found to be sharper than that of the re-precipitated PP (This plot is not shown in this paper). Temperature at 5 wt.% weight loss of PP/TSPM is also slightly lower than the others. It seems that at high concentration of oxygen, PP/TSPM copolymer decomposes better. In addition, the PP/TSPM was found to leave about 6 wt.% as the residue.

In a hybrid rocket engine, if the heat transferred by gas-phase radiation is negligible, then the heat balance at the surface of a solid fuel grain can be expressed by the following equation,

$$\lambda_g \left(\frac{\partial T}{\partial y}\right)_{y=+0} = \lambda_s \left(\frac{\partial T}{\partial y}\right)_{y=-0} + \rho_s \dot{r} h_v \qquad (1)$$

where λ_g is thermal conductivity of gas, λ_s is thermal conductivity of fuel grain, T is temperature, y is vertical distance from the surface of grain, ρ_s is density of fuel, $\dot{r}$ is fuel regression rate and h_v is effective heat of gasification of the fuel. Assuming that only temperature of thermal decomposition is lower, or in other words, the temperature on the surface of fuel grain decreased, the term on the left-hand side increases, and the first term on the right-side decreases. As a result, fuel regression rate tend to increase.

These results show that, in the term of heat of combustion and degradation temperature, by incorporating Si into PMMA or PP has the potential to increase the fuel regression rate.

4. Concluding remarks

PMMA and PP containing the Si-groups were successfully made by appropriate synthetic routes. Heat of combustion and thermal decomposition data of these samples were also obtained.

It was shown that the presence of oxygen substantially influences the degradation profiles of the PP-based polymers, but only to a minimum extent in the case of PMMA polymers. The value of the heats of combustion of MMA/TTSSPM was slightly higher than that of PMMA. The decomposition temperatures of Si-containing polymers are lower than that of the homopolymers. These results show incorporating Si to homopolymers has the potential for increasing fuel regression rates.

References

[1] G. Camino, et al., Polymer, 43, 2002, pp.2011-2015.
[2] J. R. Ebdon, et al., Polymer Degradation and Stability 83, 2004, pp.181-185.
[3] J. D. Peterson et al., J. Phys. Chem. B, 103, 1999, pp.8087-8092

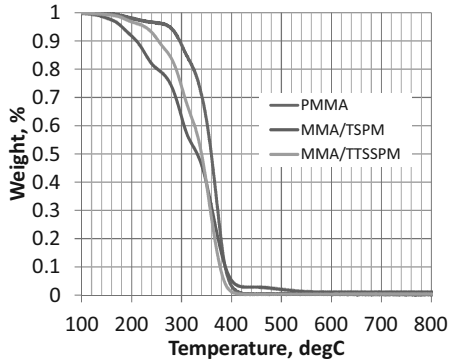

Fig. 1 TGA data (PMMA-based copolymers in nitrogen)

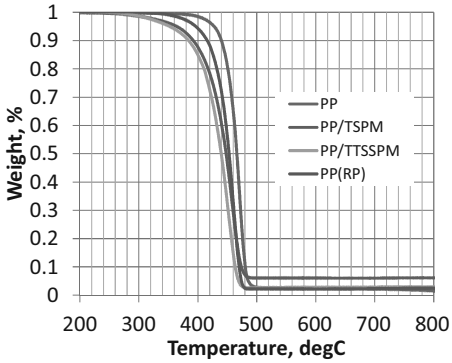

Fig. 2 TGA data (PP-based copolymers in nitrogen)

Table 1 Heat of combustion and TGA data

	Heat of combustion (MJ/kg)	Decomposition start temp.,	Temp. at 5% loss,	Residue (500)	Residue (800)	Decomposition start temp.,	Temp. at 5% loss,	Residue (500)	Residue (800)
PMMA	26.6	133	277	0.3%	0.2%	172	269	0.2%	0.0%
MMA/ TSPM	26.2	91	181	2.0%	1.1%	106	226	7.4%	6.1%
MMA/ TTSSPM	28.3	105	227	0.3%	0.4%	106	260	2.4%	2.2%
PP	46.4	369	428	2.8%	1.6%	239	270	0.5%	0.1%
PP(RP)	46.3	289	397	2.2%	2.5%	208	241	0.9%	0.2%
PP/ TSPM	45.2	232	364	6.1%	6.1%	207	228	4.0%	2.7%
PP/ TTSSPM	45.6	239	352	2.6%	2.9%	210	238	2.3%	0.2%
		In nitrogen atmosphere				In nitrogen/oxygen atmosphere			

A Study to Improve Combustion Efficiency of Paraffin-baced Hybrid Rockets

Takafumi Ishiguro, Kai Izima, Keizi Sinohara, Kazuki Sakio, Ichiro Nakagawa
Tokai University, Kitakaname 411, Hiratuka, Kanagawa, Japan, 259-1207
0bmjm004@mail.tokai-u.jp

ABSTRACT

Hybrid rocket has some technical problems. Those are low regression rate, low combustion efficiency and so on. Especially, low regression rete is key problem. Paraffin-based fuel burns 3 to 5 times faster than that of HTPB. The reason why paraffin-based fuel has high regression rate is that this regression proceeds almost without vapourization. Therefore, liquid fuel is supplied to frame zone. This phenomenon makes combustion efficiency of paraffin-based hybrid rockets low level. We consider that it is effective to set up baffle plate inside combustion chamber and post combustion chamber behind baffle plate for atomization of the liquid fuel.

1. Introduction

Paraffin-based fuel burns 3 to 5 faster than conventional fuel such as HTPB. The reason why paraffin-based fuel has high regression rate property is related to low melting point and low viscosity characteristic of paraffin-based fuel. The reason why paraffin-based fuel has high regression rate is that regression proceeds almost without vapourization. Therefore, liquid fuel is supplied to frame zone. This phenomenon makes combustion efficiency of paraffin-based hybrid rockets low level. We consider that it is necessary to vaporize liquid fuel and mix it with oxidizer rapidly. So we set up a baffle plate inside combustion chamber and post combustion chamber behind baffle plate for atomization of liquid fuel. In this paper, we show the relationship between combustion efficiency and capacity of post combustion chamber.

2. Effect of Post Combustion Chamber

A. Experimental Setup

We installed a laboratory-scale hybrid rocket engine. (Overview is shown Fig. 1.) The pressure transducers were placed at the upstream of the orifice to calculate Go¥OX mass flux, the upstream of the injector and the nozzle inlet to measure chamber pressure. A thermocouple was placed upstream of the orifice to calculate density of oxidizer.

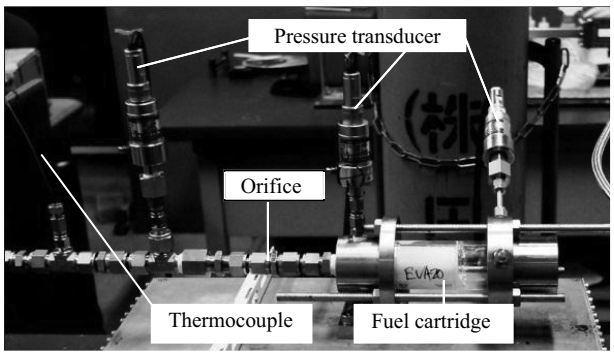

Fig. 1 Overview of the laboratory scale hybrid engine

The configuration of engine is shown Fig. 2. We adopted the fuel cartridge so that it could be used under different length of post combustion chamber. The acrylic resin pipe is from 90mm to 150mm in length, 50mm in diameter, and 5mm in thickness. And the fuel is 80mm in length, 10mm in thickness, and the initial inner port is 20mm. In order to flow GOX smoothly, we made a 45 degree cut at the front of the fuel.

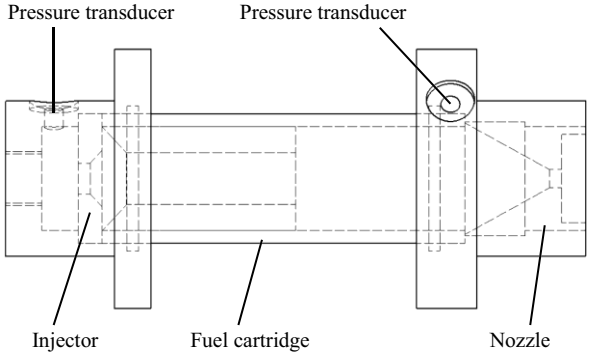

Fig. 2. The configuration of engine

B. Results and Discussion

On this study, η_{C^*} is adopted to an index of combustion efficiency. From the experiment all result, the theoretical C^* is calculated with NASA's CA400 reference. The relationship between the combustion efficiency and characteristics length of the combustion chamber is shown as Figure 3. The η_{C^*} is improved by extending L^* until approximately 2.4 m, and the η_{C^*} is almost same over 2.4 m L^*.

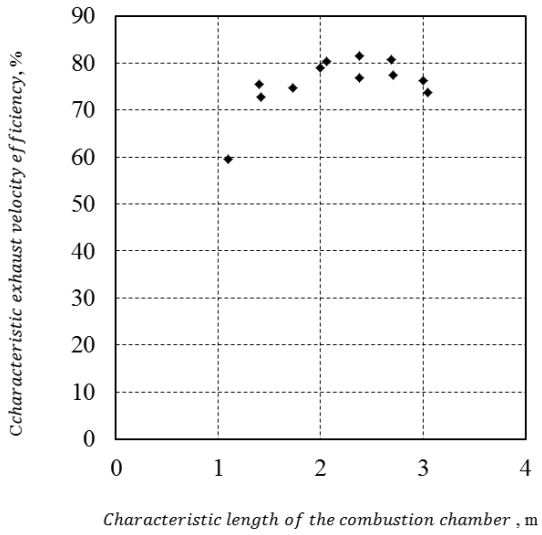

Fig. 3. The L^* vs. The η_{C^*}

3. Baffle Plate Effect

A. Experimental Setup

We built an adaptor of baffle plate and some baffle plates to conduct experiments. The fundamental set-up is same as the experimental's before mentioned. We worried pressure drop through the baffle, so a pressure transducer was set up ahead of baffle plate. The position and shape of baffle plate are shown in Fig. 4 and Fig. 5

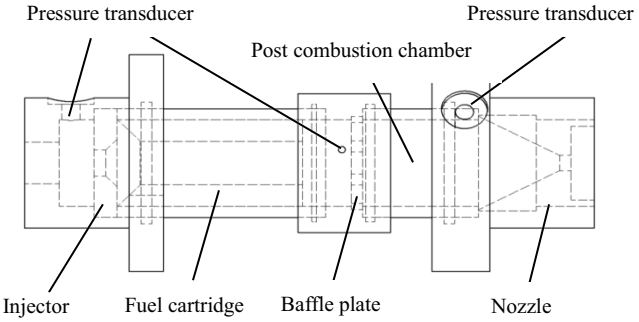

Fig. 4. The Assembly of baffle plate engine

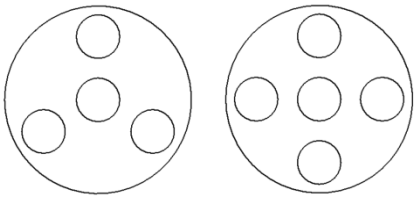

Fig. 5. The shape of baffle plate

B. Results and Discussion

Fig. 6 and Table 1 show these experimental results. We confirmed that η_{C^*} is improved about 20 % with baffle plate. In Fig. 6, × shows experimental results of baffle plate and ◆ shows results without baffle plate.

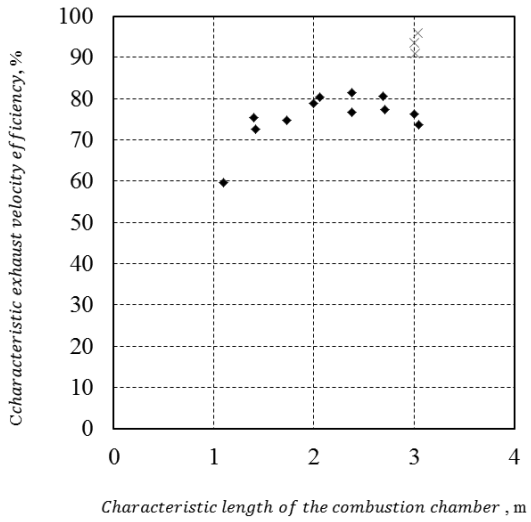

Fig.6. The L^* vs. The η_{C^*}

Table 1. Experimental Results

Number of Holes	Baffle Holes Total Area [mm^2]	Chamber Pressure [MPa]	C^*efficency [%]	Pressure Drop [%]
4	314	0.289	91.0	0.52
5	393	0.304	96.0	0.56
		0.302	93.6	1.27
without baffle plate	0	0.226	76.3	
		0.222	73.7	

4. Conclusion

In this study, effects of post combustion chamber and baffle plate on combustion efficiency using a laboratory-scale hybrid rocket engine are obtained. From the results of our experiments, the following points were revealed about paraffin fuel

1) Combustion efficiency is improved $L^*$is extended, and it is confirmed that proper L^* of this engine is approximately 2.4 m in this laboratory-scale engine.

2) The improve the combustion efficiency is achieved by setting up baffle plate in the chamber.

3) The pressure drop through the baffle plate is negligible small.

Acknowledgments

This research is supported by the Hybrid Rocket Research Working Group (HRrWG) of the Institute of Space and Astronautical Science, Japan Aerospace Exploration Agency. The authors would like to thank members of the
HRrWG for their helpful discussions.

References

[1]Karabeyoglu M. A., Cantwell B. J., and Altman D., "DEVELOPMENT AND TESTING OF PARAFFINE-BASED HYBRID ROCKET FUELS," AIAA 2001-4503, 2001.

[2]Michael A. Dornheim, "Ideal Hybrid Fuel Is … Wax?," AVIATION WEEK & SPACE TECHNOLOGY, February 3. 2003.

[3]Satosi Hikone, Shinya Maruyama, Takahumi Ishiguro, Ichiro Nakagawa, "Regression Rate Characteristics and Burning Mechanism of Some Hybrid Rocket Fuels" AIAA-2010-7030

[4]Ichiro Nakagawa, Satoshi Hikone, and Takao Suzuki, "A Study on the Regression Rate of Paraffin-based Hybrid Rocket Fuels," AIAA 2009-4935, 2009.

Eighth International Conference on Flow Dynamics
November 9 - November 11, 2011

Solid Fuel Regression Rate for Standard-Flow Hybrid Rocket Motors

Takakazu Morita[1], Saburo Yuasa[2], Shigeru Yamaguchi[3] and Toru Shimada[4]
[1]Department of Aeronautics and Astronautics, Tokai University, Kanagawa, Japan
[2]Department of Aerospace Engineering, Tokyo Metropolitan University, Tokyo, Japan
[3]Department of Physics, Tokai University, Kanagawa, Japan
[4]Institute of Space and Astronautical Science, Sagamihara, Japan
E-mail: morita@tokai-u.jp

ABSTRACT

In this study, we obtained a semi-empirical correlation between the Stanton number and the skin-friction coefficient in a turbulent boundary layer. This is applicable to hybrid rocket combustion and also includes effects of the Prandtl number variation. Using this correlation, we obtained a fuel regression rate equation for standard-flow hybrid rocket motors and examined its characteristics.

1. Introduction

According to Marxman's diffusion-limited analysis, the mass flux exponent of hybrid rocket propellants is 0.8[1,2]. In this analysis, the laminar and turbulent Prandtl number is assumed to be 1, respectively. However, from many experiments, the mass flux exponents are not equal to 0.8. These differences are caused by the following factors: swirling flow, flow impingement, radiant heating, slow chemical reactions in gas phase, etc. These factors were not considered in this study. We treated only the diffusion-limited boundary layer combustion under standard-flow condition. From many experimental results, Yuasa et al. suggested that diffusion-limited combustion is dominant on the gas-phase reactions of polymethylmethacrylate (PMMA) with gaseous oxygen in laboratory-scale hybrid rocket engines[3]. In this case, the mass flux exponent is slightly smaller than 0.8[4,5]. Although various factors are considered as this cause, in particular, we investigated effects on the Prandtl numbers[6].

2. Analytical method

In a turbulent boundary layer, the total shear stress and the total heat flux are represented by the following equations.

$$\tau = \rho\ (\nu + \varepsilon_M)\frac{\partial u}{\partial y} \tag{1}$$

$$\dot{q} = \rho c_p(\alpha + \varepsilon_H)\frac{\partial T}{\partial y} \tag{2}$$

The following assumption is usually used for analogies between heat and momentum transfer in a turbulent boundary layer.

$$\dot{q}/\dot{q}_s = \tau/\tau_s \tag{3}$$

Substituting Eqs.(1) and (2) into Eq.(3), we can obtain the following equation.

$$\frac{\partial T}{\partial y} = \frac{\dot{q}_s}{\tau_s c_p}\cdot\frac{\nu+\varepsilon_M}{\nu/\mathrm{Pr}+\varepsilon_M/\mathrm{Pr}_t}\frac{\partial u}{\partial y} \tag{4}$$

Integrating the above equation from a fuel surface to the flame edge, the result shows

$$T_f - T_s = (\dot{q}_s/\tau_s c_p)\cdot u_e I_H \tag{5}$$

where

$$I_H = \int_0^{\delta_f/\delta}\frac{\nu+\varepsilon_M}{\nu/\mathrm{Pr}+\varepsilon_M/\mathrm{Pr}_t}\frac{d}{d\eta}\left(\frac{u}{u_e}\right)d\eta. \tag{6}$$

The local Stanton number can be written in terms of the heat flux to the fuel surface as

$$St = \left\{\dot{q}_s/(T_f - T_s)\right\}/(\rho_f u_f c_p). \tag{7}$$

Using the local skin friction coefficient, the shear stress at the fuel surface can be expressed by

$$\tau_s = (c_f/2)\rho_e u_e^2. \tag{8}$$

Substituting Eqs.(7) and (8) into Eq.(5), we can obtain the relation between the local Stanton number and the local skin friction coefficient.

$$St = (c_f/2)\cdot(\rho_e u_e/\rho_f u_f)/I_H \tag{9}$$

In particular, if both the laminar and turbulent Prandtl numbers are equal to one, I_H becomes u_f/u_e. In this case, the above equation can be simplified as shown below.

$$St = (c_f/2)\cdot(\rho_e u_e^2/\rho_f u_f^2) \tag{10}$$

This expression is the same as the result obtained by Marxman et al. Lenglle proposed the velocity distribution in a turbulent boundary layer with blowing as shown below[7].

$$\phi = \eta^{\ell} \tag{11}$$

Here, $\ell = \ell_0(1+B_a)\ln(1+B_a)/B_a$, $\ell_0 = 1/7$. (12)

As the blowing becomes stronger, the accuracy of this equation becomes higher than that obtained by Marxman et al[8]. We therefore used this velocity distribution in order to obtain a theoretical regression rate of hybrid rocket combustion. Equation (6) can be integrated approximately. The result shows

$$I_H = \phi_f F_R, \tag{13}$$

where $F_R = \mathrm{Pr}_t + (\mathrm{Pr}-\mathrm{Pr}_t)\left\{C_1 + \frac{C_2}{(1-\ell')c_H^{\ell'}\phi_f}\right\}$, (14)

$$C_1 = \left(1 + c_H\phi_f^{1/\ell'}\right)^{-1}, \tag{15}$$

$$C_2 = -C_1^{1-\ell'} + \left(\frac{\beta_0}{1+\beta_0}\right)^{1-\ell'} + \frac{1-\ell'}{1+\ell'}\cdot\frac{C_3}{\beta_0^{\ell'}}, \tag{16}$$

$$C_3 = (1+\beta_0)^{-(1+\ell')}. \tag{17}$$

When B_t is defined as Eq.(18), the energy balance on the fuel surface is expressed by Eq.(19).

$$B_t = \left(u_e / u_f\right)\left(\Delta h / \Delta H\right) / F_R \quad (18)$$

$$B_a = B_t \quad (19)$$

Solving Eq.(19) yields a fuel regression rate equation as shown below.

$$\rho_c \dot{r} = 0.03 c_b \, G\left(Gx/\mu\right)^{-0.2} B^{1-b} \quad (20)$$

Using an analogy between mass and momentum transfer, the ratio of the velocity at the flame edge to the velocity at the boundary-layer edge is written in

$$\phi_f = \frac{1}{2}\left(-Sc_t K_D + \sqrt{\left(Sc_t K_D\right)^2 + 4Sc_t K_D}\right), \quad (21)$$

where

$$K_D = \frac{0.03\, c_b (O/F)(T_f/T_e)}{\kappa^2 Y_{OX,e}} \left(\frac{x}{\mu}\right)^{-0.2} G^{-0.2} \frac{B_a^{1-b}}{\ell^2}. \quad (22)$$

3. Calculation results

Figure 1 shows the non-dimensional regression rate vs. non-dimensional total mass flux plot.

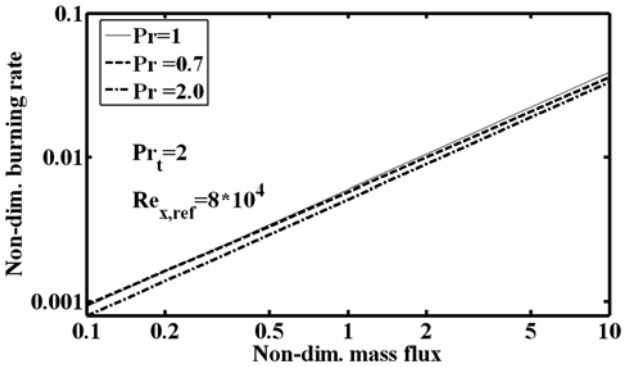

Fig. 1 A log-log plot of the fuel regression rate vs. total mass flux.

4. Concluding remarks

A semi-empirical correlation between the local Stanton number and the local skin friction coefficient in a turbulent boundary layer with blowing was obtained. This is consistent with the conventional hybrid combustion models and allows for effects of the Prandtl number variation. A fuel regression rate equation of standard-flow hybrid rocket motors was derived using it. In addition, the fuel regression rate characteristics was examined.

Nomenclature

b : blowing exponent

B_a : aerodynamic blowing parameter

B_t : thermal blowing parameter

c_f : skin-friction coefficient

c_H : $c_H = (\mathrm{Pr}/\mathrm{Pr}_t)\,\mathrm{Re}_x(\delta/x)\kappa^2\ell$

c_p : constant-pressure specific heat

G : local, bulk mass flux

ℓ' : $\ell' = \ell/(1+\ell)$

O/F : oxidizer-to-fuel mass ratio

Pr : Prandtl number

Pr_t : turbulent Prandtl number

Re_x : Reynolds number based on length

Sc_t : turbulent Schmidt number

St : Stanton number

u : velocity

x : axial location

Y_{OX} : mass fraction of oxidizer

β_0 : constant of integration, $\beta_0 = 2$

ΔH : total heat for pyrolyzing solid fuel from its initial temperature

Δh : enthalpy difference between flame sheet and fuel surface

δ : velocity boundary-layer thickness

δ_f : flame standoff distance

ε_D : eddy diffusivity

ε_H : thermal eddy diffusivity

ε_M : momentum eddy diffusivity

κ : von Karman mixing-length constant

μ : viscous coefficient

ν : kinematic viscosity

ρ : density

τ : shear stress

ϕ : $\phi = u/u_e$

Subscripts

c: condensed phase

e: boundary-layer edge

f: flame

s: fuel surface

Acknowledgments

This research is supported by the Hybrid Rocket Research Working Group (HRrWG) of Institute of Space and Astronautical Science, Japan Aerospace Exploration Agency. The authors thank members of HRrWG for helpful discussions.

References

[1] G. A. Marxman, C. E. Wooldrige, and R. J. Muzzy, Progress in Astronautics and Aeronautics, **15** (1964), 485-521.

[2] G. A. Marxman, Tenth Symposium on Combustion (1965), 1337-1349.

[3] S. Yuasa, T. Ide, M. Masugi, T.Sakurai, N. Shiraishi, and T. Shimada, Journal of Thermal Science and Technology, **6**(2) (2011), 268-277.

[4] T. Tamura, S. Yuasa, and K. Yamamoto, AIAA Paper 99-2323 (1999).

[5] S. Yuasa, O. Shimada, T. Imamura, T. Tamura, and K. Yamamoto, AIAA Paper 99-2322 (1999).

[6] T. Morita, Proceedings of 54th Space Sciences and Technology Conference, JSASS-2009-4227(in Japanese), (2009).

[7] G. Lengelle, AIAA Journal, **13**(3) (Mar.1975), 315-322.

[8] M.A. Karabeyoglu, Ph.D.Dissertation, Stanford Univ. (1998).

Nozzle Design for Supersonic Flows of N_2O at Supercritical and Close-to-Critical Conditions

Alberto Guardone
Dipartimento di Ingegneria Aerospaziale, Politecnico di Milano
Via La Masa 34, 20156, Italy
alberto.guardone@polimi.it

ABSTRACT

A nozzle design tool for real gases is used for investigating the gasdynamics of nozzles operating with supercritical or close to critical N_2O. Differently from the well-known ideal-gas results, the nozzle shape depends on the reservoir or total flow conditions and therefore different designs are obtained for a given exit Mach number depending on the relative location of the initial state in the volume-pressure thermodynamic plane with respect to the liquid-vapor saturation curve. For the considered cases, the nozzle length and height are larger than the corresponding ideal gas designs.

1. Introduction

It was recently suggested to use oxidizer N_2O to cool the surface of the nozzle to reduce ablation and nozzle performances degradation in hybrid rocket motors. In these applications, it is preferable to operate in the vicinity of the liquid-vapor saturation curve, so that the latent heat of vaporization can contribute to increase the heat transfer rates and the fluid temperature and pressure are relatively constant during the vaporization [1].

Unfortunately, the design of injectors and nozzles operating in the vicinity of the liquid-vapor saturation curve is limited by the availability of suitable analysis and design tools and to the limited knowledge on the gasdynamics of real-gas flows. Indeed, if on the one side Computational Fluid Dynamics (CFD) codes allow for a detailed investigation of the flow field, on the other side the computational burden due to the non-ideal thermodynamic model is usually too high to allow for the use of these tools in the design phase [2,3,4].

The present paper reports on preliminary results obtained from a standard design procedure based on the Method of Characteristics applied to the design of the divergent section of subsonic-supersonic nozzles operated with N_2O in the vapor phase and close to the liquid-vapor saturation curve.

2. Method

Two-dimensional nozzles of convergent-divergent type are considered. Nozzles discharge from a reservoir of infinite capacity into an ambient at constant pressure, which is lower or equal to the adapted-flow exit pressure; therefore, the Mach number in the divergent section and at the exit of the nozzle is supersonic. It is assumed here that both the viscous and thermal boundary layer thicknesses are negligible with respect to the nozzle diameter. The effect of the viscosity and of thermal conductivity are therefore neglected in the present study. Under the above assumptions, the flow is steady and can be described by the well-known potential equation for irrotational compressible flows. To account to real gas effects, the flow equation is completed by the polytropic van der Waals thermodynamic model of the fluid, in which the specific heat at constant volume is assumed to be a constant in the dilute gas limit. For N_2O, the constant value of the isochoric specific heat reads $c_v / R = 3.5$.

The design procedure of the divergent section of the nozzle moves from the determination of the transonic flow at the nozzle throat. The transonic flow region is solved by means of the approximate solution procedure of Sauer [5]. The transonic flow solution provides the initial data curve for the Method of Characteristics, which has been implemented in the present work according to the textbook of Zucrow and Hoffman [6]. The expansion in the divergent section to the desired design Mach number M_D is achieved via an initial circular profile followed by the so-called turning region, in which the nozzle upper wall geometry is determined by imposing the conservation of the mass flow at each section. The resulting flow at the nozzle exit is with uniform Mach number M_D and parallel to the x axis. Further details on the design procedure can be found in [6,7].

2. Method

Four expansion conditions are examined. In all cases, the exit Mach number is $M_d = 3$. In Figure 1, the thermodynamic states within the divergent section are plotted in the density-pressure plane for all cases. Reduced variables, made dimensionless by their critical value, are shown; for nitrous oxide, one has $T_c = 309.6$ K, $P_c = 7.238$ MPa, $\rho_c = 453.3$ kg/m^3. Study cases are chosen so to investigate real-gas effects in the single-phase vapor region and are labeled as case I for ideal and R_1, R_2, R_3, with increasing real-gas effects. Reservoir conditions are listed for all cases in Table 1, where the reservoir temperature, pressure, density, fundamental derivative and compressibility are listed. The reservoir temperature is 405.6 K, or $T_r / T_c = 1.31$, for all cases and reservoir states are all in the vapor phase. The local value of the fundamental derivative of gasdynamics $\Gamma = 1 + \rho/c\ (\partial\rho/\partial c)_s$ and the compressibility factor $Z = P/(RT\rho)$ is reported to assess departure from ideal gas conditions, $\Gamma_{\text{ideal}} = 1.143$ and $Z_{\text{ideal}} = 1$. In case I, the expansion process is sufficiently far from saturation to be considered as ideal, a result confirmed by the value of Γ and Z in the reservoir, at sonic condition and at the exit of the nozzle. In cases R_1, Γ and Z slightly depart from ideal gas values; in case R_2

and R_3 the expansion process ends very close to the liquid-vapor saturation curve and real gas effects are more evident.

Table 1 Reservoir thermodynamic conditions for the ideal and real gas study cases.

Case	T_r [K]	P_r [MPa]	ρ_r [kg/m³]	Γ_r	Z_r
I	405.6	0.10	1.29	1.142	0.998
R_1	405.6	0.98	13.13	1.140	0.980
R_2	405.6	4.90	72.04	1.143	0.893
R_3	405.6	9.81	166.56	1.261	0.772

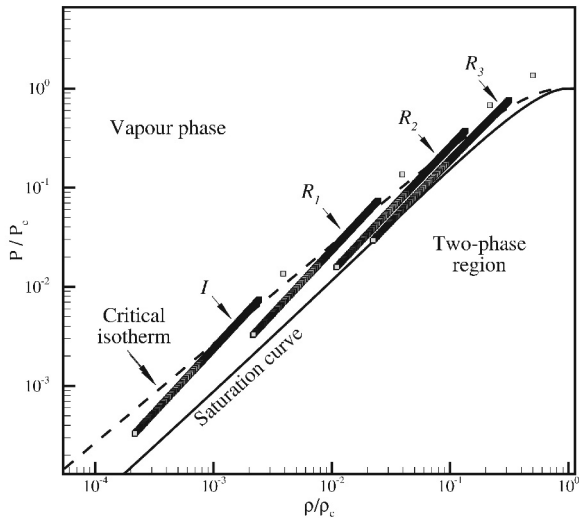

Fig. 1 Thermodynamic states for the ideal and real gas study cases in the reduced ρ-P thermodynamic plane. Flow states are plotted as square symbols.

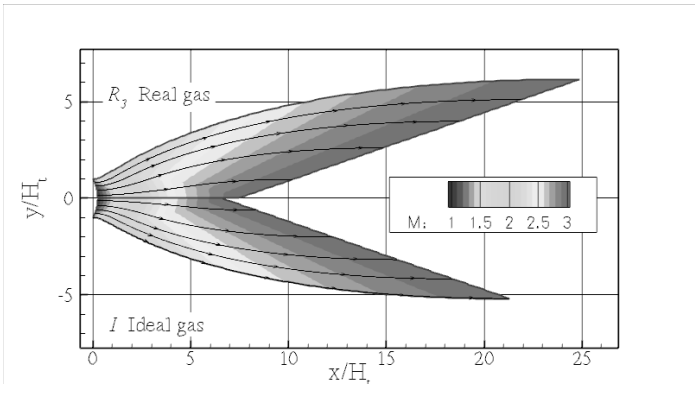

Fig. 2 Nozzle geometry for the real gas case R_3.(top) and the ideal gas case I, with the Mach number distribution and selected streamlines.

In Figure 2, the nozzle geometry obtained by the design procedure are plotted for cases I and R_3. For expansion processes that occur close to the saturation curve, the nozzle length L and height H are larger than the corresponding ideal gas cases. Moreover, nozzle dimensions monotonically increase with the reservoir pressure, that is, with the degree of gas non-ideality.

Table 2 Nozzle dimensions for $M_d = 3$.

Case	L_d / H_t	H_d / H_t	$\Delta L_{IR}/H_t$	$\Delta H_{IR}/H_t$
I	21.31	5.21	-	-
R_1	21.52	5.27	1.0%	1.1%
R_2	22.66	5.57	6.0%	6.9%
R_3	24.90	6.17	17.0%	18.4%

Nozzle geometries are reported in Table 2, where the nozzle length, height and the mass flow per unit length are reported. The reference length is the nozzle height at the throat section H_t. For comparison, relative differences with respect to the ideal gas are also shown with $\Delta L_{IR} = (L_{d,\,real} - L_{d,\,ideal}) / L_{d,\,ideal}$, $\Delta H_{IR} = (H_{d,\,real} - H_{d,\,ideal}) / H_{d,\,ideal}$. The design procedure in the real gas case R_3 gives a nozzle that is 17% longer and 18.4% higher than the corresponding ideal gas design at the exit section.

4. Conclusions

A standard nozzle design procedure was applied to the design of the divergent section of two-dimensional convergent-divergent nozzles operating in adapted-flow conditions and close to the liquid-vapor saturation curve.

The nozzle geometry was found to be significantly influenced by real-gas effects. In particular, for flow states close to the liquid-vapor saturation curve and critical point, the nozzle length and height are larger than the corresponding ideal gas designs. Differences are as large as 17% for the divergent length and 18.4% for the nozzle height.

Current research activities are devoted to the study of additional state points in the real gas thermodynamic region and of the behavior of different types of fluids.

References

[1] P. Lemieux, Prog. Aerosp. Sci. **46**:1-2 (2009).

[2] J. Hoffren, T. Talonpoika, J. Larjola, T. Siikonen, ASME J. Eng. Gas Turbines Power, **124** (2002).

[3] P. Cinnella, P. M. Congedo, J. Fluid Mech. **580** (2007).

[4] P. Colonna, J. Harinck, S. Rebay, A. Guardone, J. Propul. Power **24**:2 (2008).

[5] R. Sauer, NACA TM 1147 (1947)

[6] M.H. Zucrow, J. D. Hoffman, Gas dynamics: multidimensional flow, vol. 2. Wiley, John & Son (1977).

[7] Guardone, A. HEFAT 2010 Conference (2010).

Eighth International Conference on Flow Dynamics
November 9 - November 11, 2011

Enhancement of Multi-Section Swirl Injection Method for Increase of Regression Rate and Combustion Efficiency of Hybrid Rockets

Shigeru Aso, Yoshihide Hirata, Yasuhiro Tani, Takahiro Hayashida, Ryuji Nakawatase
Department of Aeronautics and Astronautics, Kyushu University
744 Motooka, Nishi-Ku, Fukuoka 819-0395, Japan
aso@aero.kyushu-u.ac.jp

ABSTRACT

In order to improve fuel regression rate of hybrid rockets, a new method with multi-section swirl injection is proposed. The new method is to introduce swirling flow through multi-section swirl injector ports, which are placed at several locations along the fuel grain. The method is applied for high density polyethylene fuel and paraffin fuel (FT-0070) with pressurized gaseous oxygen. The results show the average regression rate of the proposed method is about 2 or 3 times with high density polyethylene fuel and 10 times with paraffin fuel compared with that of the conventional no-swirl injection method.

1. Introduction

Recently, hybrid rocket engine becomes one of the promising space propulsion systems. The advantages of hybrid rocket engines are 1) safety, 2) low cost, 3) throttling of thrust, 4) re-ignition, 5) nontoxic and nonhazardous propellant. However, hybrid rocket engines have low fuel regression rate and low combustion efficiency. In order to overcome those disadvantages, there are several research activities.[1]-[3]

In the present study the new method that can improve the fuel regression rate more than that of conventional methods is proposed. The method is multi-section swirl injection method.

2. Method

Figures 1 and 2 show the schematic diagram of multi-section swirl injection method and the combustion chamber. The injection of the oxidizer through a number of injector ports that are set in the fuel grain causes swirling flow. In addition, swirling flow in multi-section enables without weaken over the entire length of the fuel grain.

High density polyethylene fuel and paraffin fuel (FT-0070) are used for the present study. Three different grain length of fuel grain with inside diameter of 35 mm are tested in high density polyethylene fuel and paraffin fuel. Diameter of the injector ports, which inject the oxidizer, are 1 mm. In the present study four injector ports are located at four cross-sections along the axis of the fuel grain.

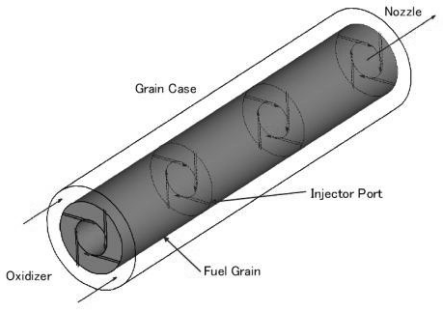

Fig. 1 Schematic diagram of multi-section swirl injection method.

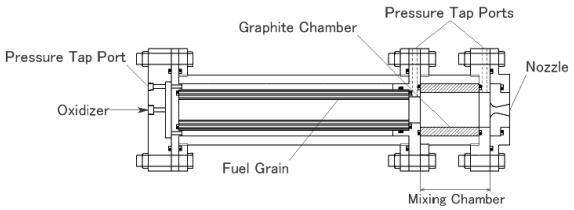

Fig. 2 Schematic diagram of the combustion chamber.

3. Results and Discussion

3.1 High Density Polyethylene Fuel Cases

In the tests of shorter grain (grain length of 200 mm or 80 mm) the average regression rate is improved. In the multi-section swirl injection method the groove is formed on the surface of the fuel grain after combustion. The ratio of the groove to the grain length is higher in the tests of shorter grain compared with the tests of longer grain (grain length of 400 mm). Therefore, the effect of the groove on the average regression rate is more significant in the tests of shorter grain compared with the tests of longer grain. In addition to that, average O/F is improved in the tests of shorter grain. The picture during combustion and the time histories of combustion pressure and thrust are shown in Figs. 3 and 4.

The comparison of the average regression rate obtained from the present study with the conventional method is shown in Fig. 5. The regression rate law of HTPB fuel[4] and paraffin fuel[5] are also plotted. In the tests of high density polyethylene fuel the average regression rate is about 2 or 3 times that of the conventional method with HTPB fuel.

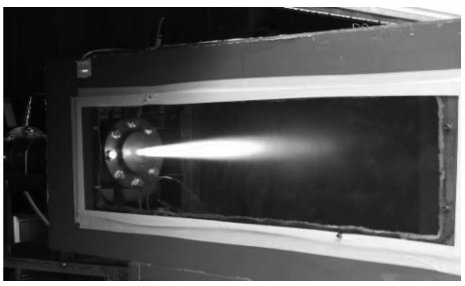

Fig. 3 Picture during combustion in high density polyethylene fuel.

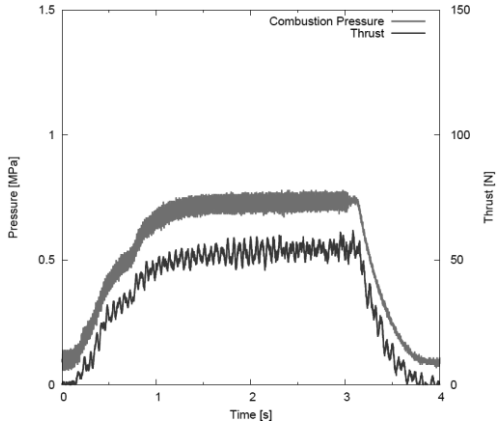

Fig. 4 Time histories of combustion pressure and thrust in high density polyethylene fuel.

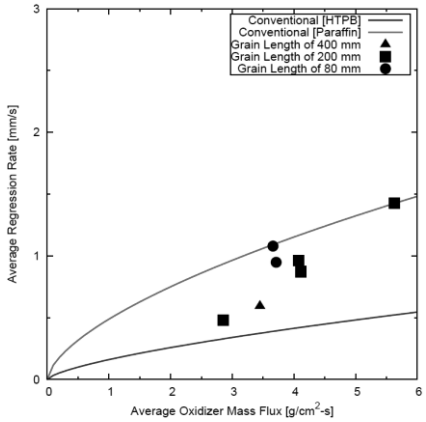

Fig. 5 Comparison of the average regression rate in high density polyethylene fuel.

3.2 Paraffin Fuel Cases

Same as the tests of high density polyethylene fuel, in the tests of shorter grain (grain length of 80 mm or 40 mm) significant increase of the average regression rate is realized in the tests of paraffin fuel. In addition, c^* efficiency and I_{sp} efficiency are also improved. However, it is necessary to improve O/F so that the theoretical value of the characteristic velocity and the specific impulse reaches the maximum.

The picture during combustion and the time histories of combustion pressure and thrust are shown in Figs. 6 and 7.

The comparison of the average regression rate obtained from the present study with the conventional method is shown in Fig. 8. In the case of grain length of 40 mm the average regression rate is about 10 times that of the conventional method with paraffin fuel.


Fig. 6 Picture during combustion in paraffin fuel.

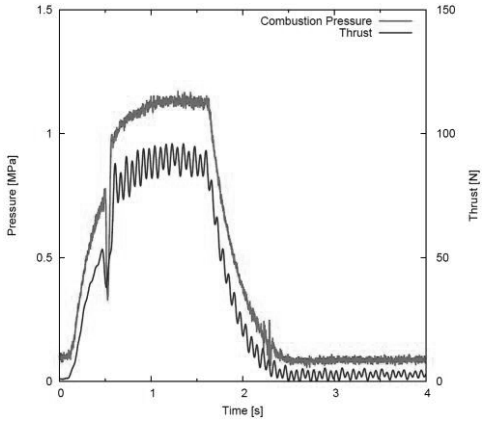

Fig. 7 Time histories of combustion pressure and thrust in paraffin fuel.

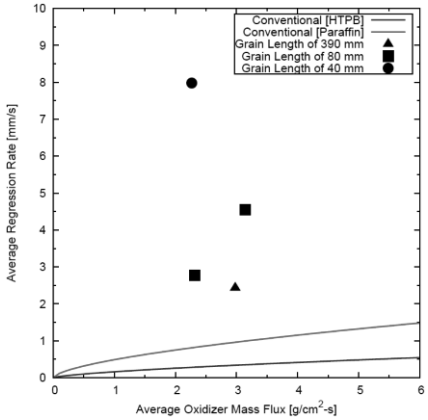

Fig. 8 Comparison of the average regression rate in paraffin fuel.

4. Conclusions

1) The new method with multi-section swirl injection is proposed in order to improve fuel regression rate of hybrid rockets.
2) By using multi-section swirl injection method average regression rate is about 2 or 3 times with high density polyethylene fuel and 10 times with paraffin fuel compared with that of the conventional no-swirl injection method.
3) A lot of data are required to obtain new correlation in multi-section swirl injection method.

References

[1] Nagata H., Ito M., Maeda T., Watanabe M., Uematsu T., Totani T., Kudo I., Acta Astronautica, Vol.59, Issues.1-5, 2006.
[2] Tamura T., Yuasa S., Yamamoto K., AIAA paper, AIAA 99-2323, 1999.
[3] William H. Knuth, Martin J. Chiaverini, Daniel J. Gramer, J. Arthur Sauer, AIAA paper, AIAA 99-2318, 1999.
[4] Sutton G. P., Rocket Propulsion Elements, John Willey & Sons, New York, 6th Edition, 1992.
[5] Arif Karabeyoglu, Greg Zilliac, Brian J. Cantwell, Shane DeZilwa, Paul Castellucci, Journal of Propulsion and Power, Vol.20, No. 6, 2004.

Numerical Simulations of N_2O Flow Past a Low-cost Ball Valve

Kang-Ming Chuang[1], Jong-Shinn Wu[1]* and Yen-Sen Chen[2]
[1]Department of Mechanical Engineering, National Chiao Tung University, Hsinchu, Taiwan
[2]National Space Organization, Hsinchu Science Park, Hsinchu, Taiwan
(*e-mail: chongsin@faculty.nctu.edu.tw)

ABSTRACT

In this paper, a parallel Navier-Stokes equation solver is used for investigating complex flow phenomena of nitrous oxide fluid flow through a low cost industrial ball valve. We can control mass flow rate by changing the angle of the ball vale and upstream pressure. Results show that mass flow rate decreases with increasing angle of valve nonlinearly at constant upstream pressure. In addition, mass flow rate increases with increasing upstream pressure at constant angle of valve. In the investigated range of test conditions, mass flow rate ranges from 1 to 10 kg/s, which is expected to provide 300 to 3,000 kgf of thrust, if hybrid N2O and HTPB is used.

1. Introduction

Hybrid propulsion has attracted much attention recently. Major advantages of the hybrid propulsion include good ISP (specific impulse), simplicity of system, high safety of operation and throttling capability, as compared to the technologically matured solid and liquid propulsions [KK Kuo's book]. Hybrid propulsion system generally employs solid fuel and liquid oxidizer, in which the throttling capacity of liquid oxidizer can be used for thrust profiling to further improve the rocket propulsion performance. To reduce the cost of operation of hybrid rocket, the use of a low-cost ball valve becomes necessary. However, the flow past a ball vale is complex and thus requires detailed numerical investigation..

There had been few numerical and experimental studies [2, 3] focusing on water passing a ball valve under normal pressure. However, in a hybrid propulsion using N_2O the working pressure is in the range of 60-70 atm and the real-fluid properties of N_2O is critical, unlike water.

In this paper, we have employed a parallel 3D Navier-Stokes equation solver with real-fluid model of N2O to study the complex flow phenomena past a ball valve. Mass flow rates under various upstream pressures and angles of valve are predicted.

2. Numerical Method

In this paper, the UNIC-UNS code, a general-purpose Navier-Stokes equation solver was used to study the nitrous oxide liquid flow phenomena numerically by considering the real-fluid properties. This code solves a set of governing equations describing the continuity equation, momentum equations (Navier-Stokes equations), energy equation, species continuity equations and turbulence related equations [4]. It employs the cell-centered finite-volume, pressure-based method with a hybrid 2D/3D unstructured-grid topology, which can be used to deal with all-speed gas flows. Second-order linear reconstruction upwind scheme is used for the treatment of convection flux. Details of various numerical and physical modules employed in this solver can found in [5, 6] and are not repeated here. In addition, HBMS [7] real-fluid model was used in this study.

3. Results and Discussion

Figure 1 shows the sketch of a typical industrial ball valve we have used in our previous propulsion experiments [8]. The inner diameter of the pipe is 10 mm, angle of valve is defined as the angle relative to the axial flow direction along the pipe and can be adjusted from 0-90 degrees. In current study, we consider a control ball valve set between high-pressure oxidizer tank and combustion chamber. Thus, inlet of the valve is set as higher pressure in the range of 50~80 atm, based on a pressurized helium tank and regulator settings. Exit is set as 45 atm as measured in the combustion chamber.

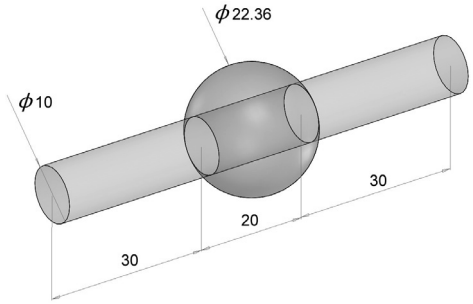

Fig. 1. Geometry (unit: mm) of a typical industrial ball valve used in the simulations.

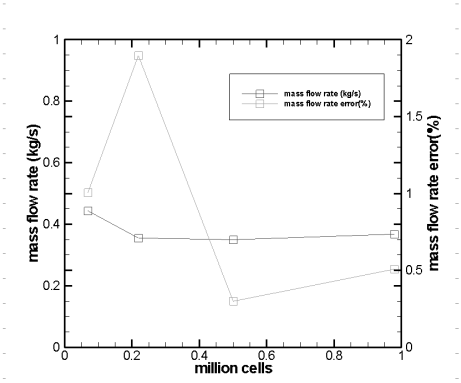

Fig. 2. Mass flow conservation errors (%) using different numbers of cell (0.07, 0.22, 0.5, 0.98 million) with angle of valve of 30°.

Figure 2 shows the grid convergence was studied using four sets of grid size (70k, 220k 500k and 980k) with angle of valve of 30°. Results show that use of 220k cells is good enough for a converged solution. Thus, 220k cells are used throughout the study, unless

otherwise specified.

Figure 3 shows the cross-section distributions of axial velocity with different inlet pressures in the range of 50-80 atm with exit pressure of 45 atm and angle of valve of 30°. Results show that N2O passes through the tube-like passage and accelerate at the exit of the passage. Strong circulations are found in the upper and lower parts of the valve and pipe. In generally, the flow rates are found to be proportional to the pressure difference between upstream and downstream. Figure 4 shows the predicted flow rates as a function a pressure difference between upstream and downstream. Results show that the mass flow rate almost linear to the pressure difference as mentioned earlier. This is beneficial for the implementation of a practical thrust control mechanism.

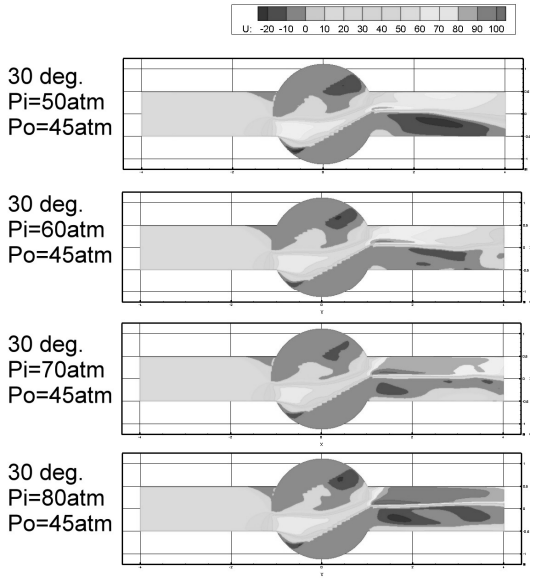

Fig. 3. Distribution of axial velocity with different inlet pressures with 30 deg opening.

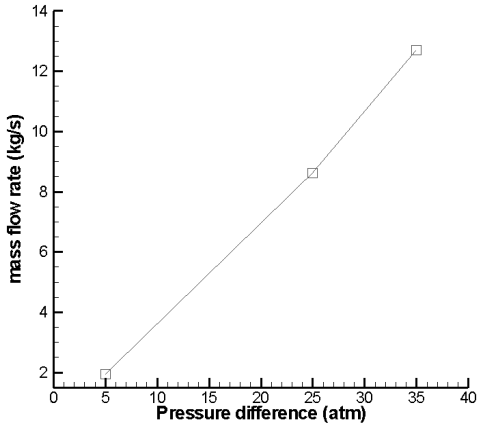

Fig. 4. Predicted mass flow rates as function of pressure difference of upstream and downstream sides with angle of valve of 0°.

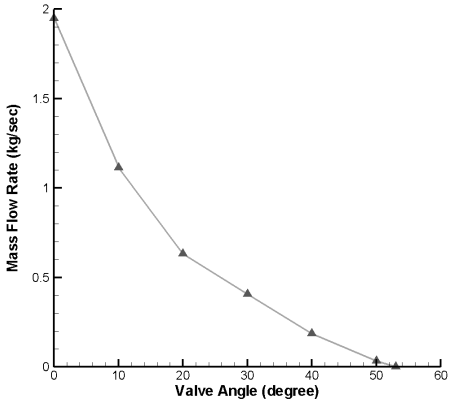

Fig. 5 Predicted mass flow rates as a function of angle of valve with upstream and downstream pressure of 50 and 45 atm respectively.

Figure 5 shows the predicted mass flow rates as a function of angles of valve. Results show that the flow rate decreases with increasing angle of valve and becomes zero at angle of 52.5°. As expected the flow rate is not linearly proportional to the angle of valve. It shows a dramatic decrease of flow rate before 20° (from 1.95 to 0.65 kg/s) and a slow decrease afterwards. This means that it is highly sensitive to control the thrust if it is at high thrust level of the motor. This needs to be considered when implementing the thrust control mechanism.

4. Conclusions

In this study, we have performed a numerical study of high pressure nitrous oxide fluid flow through an industrial ball valve. Results show that a dramatic decrease of flow rate before 20° and a slow decrease afterwards at constant pressure difference between upstream and downstream sides. In addition, non-linear flow rate as a function of angles of valve is also found. Experimental validations of these findings are currently in progress and will be reported in the future elsewhere.

References

[1] M. J. Chiaverini, K. K. Kuo, ***Fundamentals of Hybric Rocket Combustion and Propulsion***, AIAA (2007).
[2]S. F. Moujaes, et al., Journal of Energy Eengineering © ASCE (2008) 26-28
[3]The 7th National Computational Fluid Dynamics Conference , Tainain, Taiwan
[4] B. J. Wendt, AIAA-95-1797 (1995).
[5] B. J. Wendt, AIAA-2004-2185 (2004).
[6] Shang HM, et al., AIAA-97-3183 (1997).
[7] Richard C. Farmer, et al., ***Computational Transport Phenomena for Engineering Analyses***, (2009)
[8] Y. S. Chen, et al., 7th International Conference on Flow Dynamics, Sendai, Japan (2010) 174-175.

Study on Mechanical Characteristic of Paraffin-Based Fuel

Shinya Maruyama, Takafumi Ishiguro, Keiji Shinohara and Ichiro Nakagawa
Tokai University, Kitakaname 4-1-1, Hiratuka, Kanagawa, Japan, 259-1292
0bmjm024@mail.tokai-u.jp

ABSTRACT

The paraffin-based fuel has high fuel regression rate of 3 to 4 times in comparison with a conventional hybrid rocket fuel. However, the paraffin-based fuel has the problem in manufacturing because of their low tensile strength etc. To increase tensile strength, we tried to mix the EVA with paraffin-based fuel. In addition, the change in the characteristic of the wax fuel when EVA is mixed is observed. The maximum strength rises up to about 1.6 times and maximum strain increases up to 2.2 times when the content of EVA is 20% as a result of the experiment. However, the regression rate decreases about 35% when the EVA content is 20%.

1. Introduction

In general, a hybrid rocket engine is a rocket engine which uses liquid oxidizer and solid fuel. A hybrid rocket has the advantages of high safety, a thrust adjustment, a re-ignition, low-cost, and a low negative environmental impact, etc. However, a hybrid rocket has technical problems of low fuel regression rate, low combustion efficiency, and low volume efficiency, etc. Therefore, there is little practical use example now. Many studies are conducted to overcome especially on low regression rate. Karabeyoglu et.al in Stanford University studied the paraffin-based fuel for hybrid rockets. In Japan, the study of the Cascaded Multi Impinging- jet is conducted in Hokkaido University. Oxidizer swirling flow is conducted in Tokyo Metropolitan University. We also study the paraffin-based fuel.

From previous research, the paraffin-based fuel regression rate is 3 to 4 times than that of conventional fuels such as HTPB. However, the paraffin-based fuel has a mechanical problem. It is frangible. In this study, we try to improve mechanical characteristics. As the improvement method, we mix ethylene vinyl acetate copolymer (EVA) which has good compatibility with paraffin and is mass product for industrial use.

2. WAX

The etymology of the wax originally comes from so-called beeswax to secrete when a bee forms one's nest. Wax came to be produced in large quantities and at a low price by the development of the oil industry in the latter half of the 19th century. It means the oil wax if it is called wax now. And it may be called merely paraffin because the ingredient of the oil wax is a paraffin system hydrocarbon. The oil wax is divided roughly into the paraffin wax and microcrystalline wax. And the hydrocarbon-based wax which is newer than oil wax is called synthetic wax. The hydrocarbon-based synthetic wax is the hydrocarbon-based synthetic wax is classified roughly into polyethylene wax and Fischer-tropsch wax. In this study, FT-0070 that was synthetic wax was used.

Table 1. The characteristic of FT-0070

	The number of carbon	Melting point [℃]	Flash point [℃]	Density [g/cm^3]
FT-0070	35	72	258	0.76

(Density is defined at 120 ℃)

3. Ethylene-Vinyl Acetate copolymer (EVA)

It is the thermoplastic resin which copolymerized ethylene and vinyl acetate and is called EVA. The one up to about 40% of the content of the vinyl acetate is used usually. The one with few contents of the vinyl acetate possesses a character near the low-density polyethylene, and shows strength. Flexibility is increased as the content of the vinyl acetate increases, and it comes to show characteristics of rubber. It is widely used by these characteristics as a flexible seat, wrapping, and a hot-melt adhesive. In addition, EVA is mixed with paraffin wax well.

In this study, EV210ETR made of Du Pont-Mitsui Polychemicals Ltd. was used. The specification of EV210ETR is shown in Table 2.

Table 2. The specification of EV210ETR

	Content of vinyl acetate [%]	Density [kg/m^3]	Tensile fracture stress [MPa]	Flash point [℃]
EV210ETR	28	950	6	72

4. Mechanical characteristics

Fuel strength of the praffin-based fuel is measured. The shape of the test piece is made in accordance with the standard of JANAF. The shape of the test piece is shown in Figure 1 . The EVA content mixes from 0 to 20% at intervals of 10%, and produces the test piece.

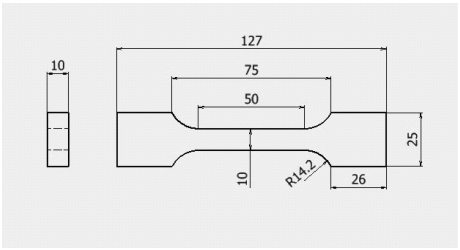

Fig. 1 Shape of the test piece (unit : mm)

The tensile tests were conducted three times per each

EVA content samples. The relation between the maximum stress and the content of EVA is shown in Figure 2. And the relation between the maximum strain and the content of EVA is shown in Figure 3.

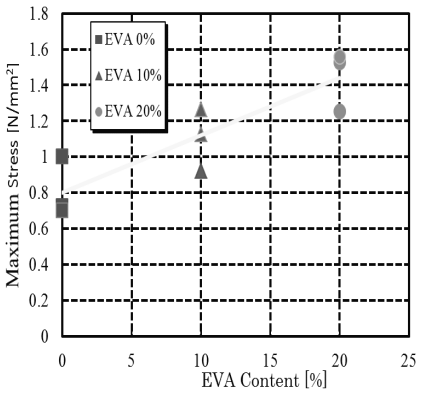

Fig. 2 The content of EVA and the graph of the maximum stress

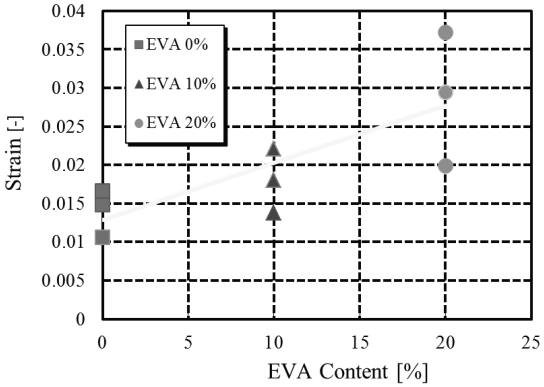

Fig. 3 The content EVA and the graph of the strain

The maximum stress of EVA 20% content fuel is a 1.6 times compared with that of 100% paraffin fuel. And the maximum strain of EVA 20% content fuel is approximately 2.3 times compared with that of 100% paraffin fuel.

5. Viscosity of melted fuel

The viscosity was measured when the EVA content was changed from 0 to 20%. Figure 4 shows the graph of the EVA content and the viscosity.

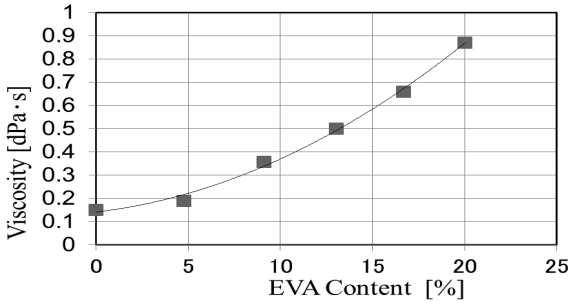

Fig. 4 EVA content and viscosity

The viscosity increases as EVA content increases. The viscosity of 20% EVA content fuel is approximately six times of 0% EVA content fuel.

6. Regression rate characteristics

We measure regression rate of 0, 10, 20% EVA content paraffin-based fuel with the 2-Dimensional visualized chamber.

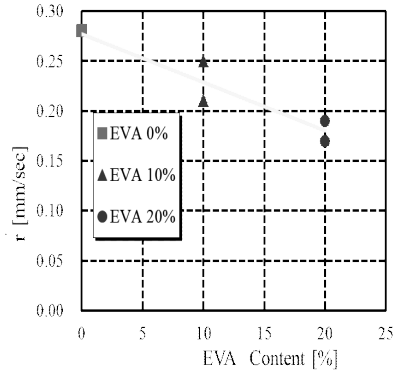

Fig. 5 EVA content and the regression rate
(P = 0.1 [MPa], G_dot = 11 [kg/(m^3*sec)])

Figure 5 shows the results of the experiment. The regression rate decreases as EVA content increases. The regression rate decreases approximately 35% when the EVA content is 20% compared with EVA 0% content.

7. Conclusion

We obtained some effects on paraffin-based fuels by mixing EVA.

1) The maximum tensile stress increases as the EVA content increases.
2) The maximum strain increases also as the EVA content increases.
3) The viscosity of melted fuel increases as the EVA content increases.
4) The regression rate decreases as the EVA content increases.

Acknowledgements

This research is supported by the Hybrid Rocket Research Working Group (HRrWG) of Institute of Space and Astronautical Science, Japan Aerospace Exploration Agency. The authors thank members of HRrWG for their helpful discussion.

References

[1] M. A. Karabeyoglu, B. J. Cantwell and D. Altman, “DEVELOPMENT AND TESTING OF PARAFFINE-BASED HYBRID ROCKET FUELS,” AIAA 2001-4503, 2001.

[2] S. Hikone, “Regression Rate Characteristics and Burning Mechanism of Some Hybrid Rocket Fuels”, *Proceedings of 46th AIAA/ASME/SAE/ASEE JPC(2010)*, AIAA-2010-7030.

[3] J. D. DeSain, B. B. Brady, K. M. Metzler, T.J.Curtiss, , and Thomas, V., “Tensile Tests of Paraffin Wax for Hybrid Rocket Fuel Grains”, *Proceedings of 45th AIAA/ASME/SAE/ASEE JPC(2009)*, AIAA -2009-5115.

Study on Flow inside the Nozzle of Ejector Jet by Numerical Analysis

Keisuke Sotozono, Y. Higa and I. Nakagawa
Tokai University, Department of Aeronautics and Astronautics school of Engineering
411 Kitakaname, Hiratsuka, Kanagawa, 259-1207, Japan
0bmjm014@mail.tokai-u.jp

ABSTRACT

In recent years, the combined cycle engine for the horizontal-takeoff-space plane has been researched all over the world. This kind of space plane is hoped to realize for the space travel, re-use type space transportation system, and so on. Therefore we can achieve takeoff, space flight, and landing by switching flight modes using only one combined cycle engine. In this study, we carried out the numerical simulation about internal flow of Ejector jet nozzle. This result will be used for the experimental study of ejector jet engine.

1. Introduction

Present space transportation is done by a rocket. Rockets are disposable transport systems which load a large amount of oxidants and fuels to produce thrust. The operational cost is high, and the specific impulse is low on the performance side. Hence, the space plane has been researched as the next generation space transportation system that takes the place of the rocket. Space plane is a reusable horizontal-take off spacecraft with wings. The basis of the system design of the space plane is flexibility of operation, cost reduction, improvement of safety and reliability of system, and positive use of air. It is necessary to establish the engine system to achieve these. There is a combined cycle engine that combines a rocket motor and an air breathing type engine among a large variety of engine systems which have been proposed. This engine is called RBCC(Rocket Based Combined Cycle), and changes the operation mode as the flight Mach number increases. RBCC can accelerate from the takeoff to outer space by doing so. The combined cycle engine was proposed since it is difficult to make ram jet and scram jet operates at low speed. The operation mode is changed in order of Ejector jet mode, ram jet mode, scram jet mode, rocket mode, and re-entry mode. The ejector jet mode is used from takeoff to in the area of a comparatively low Mach number. Ejector jet mode that operates in a low-speed area inhales air by using ejector effect of the exhaust of rocket that is set up in the engine. Ejector effect is inhaled by the pressure difference and by effect of viscosity. To improve engine performance, the air inhalation performance is important.

2. Ejector Jet Engine

The feature of hybrid rocket is high safety. Therefore, achievement in the space travel is expected. In this laboratory, studies TSTO (Two-Stage-to-Orbit) system. In first stage, accelerates to Mach 2 by Ejector rocket that uses Hybrid rocket. Afterwards, switch to Ram jet and accelerates Mach 6 and in second step uses Hybrid Rocket too. Fig.1 is overview of Ejector Hybrid Rocket. And Fig.2 is shown simple Ejector Jet Engine outline.

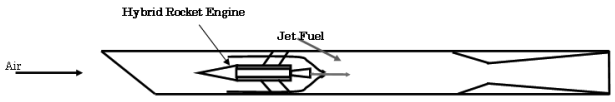

Fig.1 Ejector Hybrid Rocket

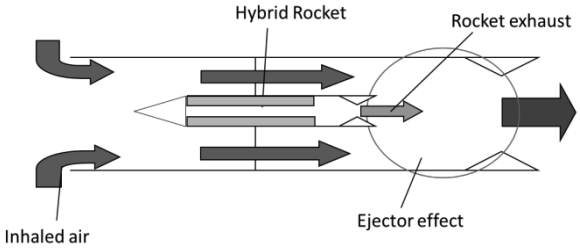

Fig.2 Simple outline

The purpose of this engine is to build up thrust by inhaling air. It is necessary to build up thrust to aim at practical use. And it is necessary to inhale more air to build up thrust. In this study, the inhalation performance of air by the nozzle shape is examined. Therefore, the best nozzle shape is calculated by the experiment and numerical analysis.

3. Cold Flow Test

To examine the best nozzle shape, in this laboratory experimented Cold Flow test. 10 kinds of nozzles were made and it experimented.

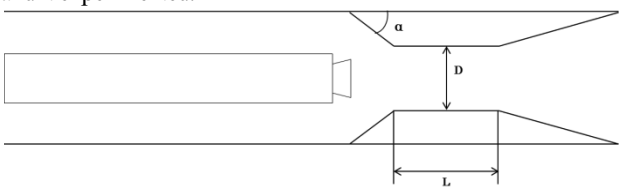

Fig.3 Scale of Ejector Jet Engine

Table 1. Size of Nozzle

Nozzle	α[°]	L[mm]	D[mm]	Nozzle	α[°]	L[mm]	D[mm]
EJN01	30	60	40	EJN06	25	60	40
EJN02	30	70	40	EJN07	35	70	40
EJN03	40	60	30	EJN08	40	80	40
EJN04	40	60	40	EJN09	45	80	40
EJN05	45	70	30	EJN10	40	100	50

In this time, Oxygen was jetted instead of Rocket exhaust. Oxygen jetted it by the pressure of 0.3[MPa] and 0.5[MPa]. Experimental results (Air mass flow vs nozzle Numbers) are shown in Fig.4. And thrust results (thrust vs nozzle number) are shown in Fig.5.

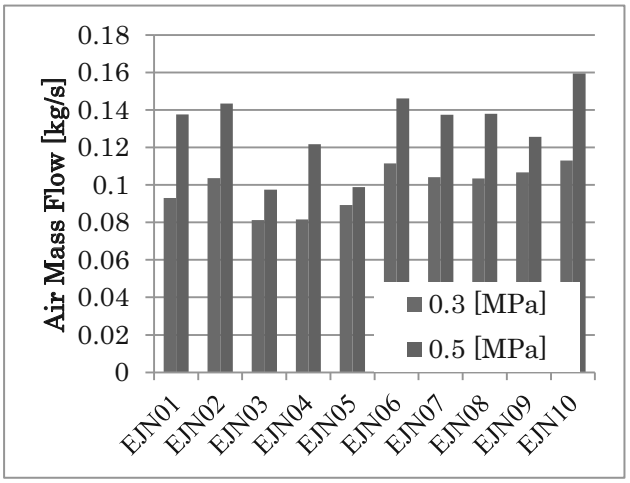

Fig.4 Air mass flow results

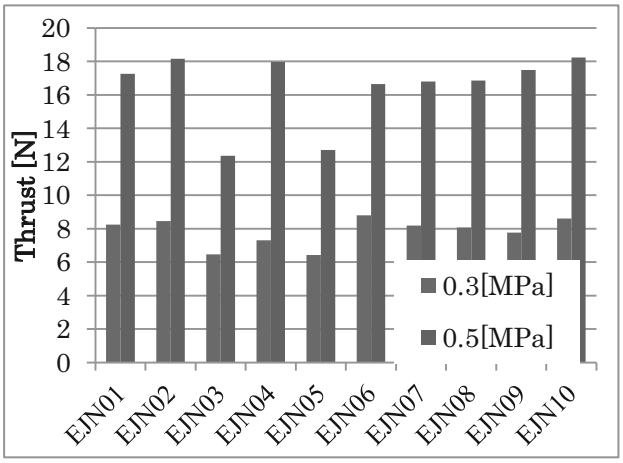

Fig. 5 Thrust results

Attention air mass flow, best inhalation performance is EJN10, and worst performance is EJN03. Similarly, about Thrust we got same results. Therefore, we decided best nozzle shape is EJN10 and bad shape is EJN03 in cold flow test. In this study, about EJN03 and EJN10 are numerical calculated.

4. Numerical Analysis

In this calculation, FLUENT is used. All wall conditions are No-slip adiabatic wall. In order to achieve higher order accuracy for space, second order upwind method is used. The evaluation of flux used Roe-FDS. Turbulence model is κ-ε model used.

5. Boundary Conditions

Rocket exhaust : temperature is 300 [K], inlet pressure is 0.3 [MPa]. Inhalation area and outflow area are atmospheric pressure.

6. Results and Discussion

In this numerical results are shown Fig. 5 and 6. Fig.5 nozzle shape is EJN03, Fig.6 is EJN10. There are displayed velocity distribution.

EJN10 inhalation velocity is about 45[m/s] higher than EJN03. And inhalation pressure is 46[KPa]. On other hand, EJN03 inhalation velocity is low, and inhalation pressure is 38[KPa]. Therefore, reason why thrust of EJN10 is better than EJN03 is balance of pressure and kinetic term in thrust formula.

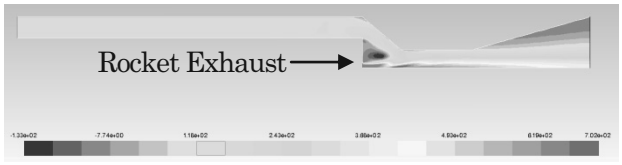

Fig.5 EJN03 Velocity distribution

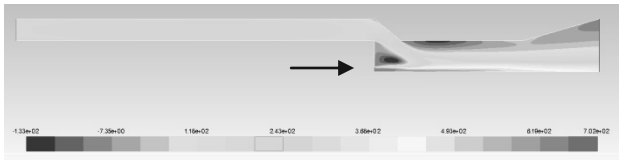

Fig.6 EJN10 Velocity distribution

Acknowledgement

This research is supported by the Hybrid Rocket Research Working Group (HRrWG) of Institute of Space and Astronautical Science, Japan Aerospace Exploration Agency. The authors thank members of HRrWG for their helpful discussion.

References

1) Kitamura, E., Tomioka, S., Sakuranaka, N., Watanabe, S., Masuya, G.: Dominant Parameter for Pressure Recovery Performance of Constant-Area Mixing Tube of Ejector Jets, *JSASS.*, Vol. 57, No.660, pp.1-8, 2009.

2) Okai, K., Taguchi, H., Nimura, H.: A Study on Ejector Ramjet, *JSASS.*,1A11, 71-74, 2002.

Eighth International Conference on Flow Dynamics
November 9 - November 11, 2011

Effect of Oblique Injection on Swirling Oxidizer Flowfield in Combustion Chamber for Hybrid Rocket Enginge

Takaya Koda, Yousuke Ogino, and Keisuke Sawada
Department of Aerospace Engineering, Tohoku University, Sendai 980-0579, Japan
koda@cfd.mech.tohoku.ac.jp

Abstract

Effect of oblique injection on swirling flowfield is examined using equilibrium gas NS solver. The mass conservation equations for oxidizer and fuel gas are included and the equilibrium composition, thermodynamic properties, and transport coefficients are interpolated from a lookup table. A preliminary calculation is conducted for two geometries which is injected 90° and 60° toward central axis. Computed results show that oblique injection suppresses reverse flow region.

1. Introduction

Swirling injection of gaseous oxidizer enhances the regression rate of solid fuel in the combustion chamber of hybrid rocket [1, 2]. In the experimental studies of Yuasa et al., a higher regression rate was indeed demonstrated when oxidizer was injected tangentially at the upstream side of the combustion chamber [2]. Swirling flowfield is believed to enhance heat transfer to the fuel surface because of thinner boundary layer along the surface due to centrifugal force. However, detailed mechanism of the enhanced regression rate is yet unknown.

By the Hybrid Rocket Research Working Group (HRrWG), a practical design of a hybrid rocket that can insert a small satellite into the sun synchronous orbit is now underway. In order to obtain a higher regression rate and then achieve a high performance, a swirling oxidizer injection is assumed to be employed in that design. For such design to be successful, detaild study of swirling oxidizer flowfield needs to be accomplished both experimentally and numerically.

Past numerical studies for the similar swirling flowfield of Yuasa et al. showed formation of a reverse flow region in the combustion chamber [3]. The reverse flow region is believed to be formed due to an adverse pressure gradient along the central axis toward the nozzle exit. However, the mechanism of formation of reverse flow region and influence on the performance of the hybrid rocket is yet unknown also.

In this study, we attempt to compute the swirling flowfield in the combustion chamber using chemical equilibrium NS gas solver. As a preliminary study, swirling flowfield for two geometries are calculated whose injection angle is 90° and 60°.

2. Numerical Methods

The governing equations are the Navier-Stokes equations that have two mass conservation equations without mass generation term. Mass conservation for fuel and oxidizer gas, and momentum and energy conservation for gas mixture are considered.

We assume 1,3-butadiene (C_4H_6) as fuel and gaseous oxygen as oxidizer, and then obtain an equliblium state for a gas mixture consisting of 9 chemical species such as CO, CO_2, H, H_2, H_2O, O, O_2, OH and C_4H_6. Equilibrium composition and thermodynamic properties of gas mixture are determined by utilizing NASA CEA [4]. As input variables of CEA, we choose density and temperature for easier curve fitting. Hence, total density and temperature of gas mixture and weight fraction of fuel gas are required in order to obtain the properties of gas mixture. We consider the total density range of 0.1 to 100kg/m^3 divided into 25 data points equally spaced in logarithmic space. On the other hand, the weight fraction of fuel is considered from 0 to 100% divided into 21 data points equally spaced. We fit thermochemical properties of gas mixture in terms of temperature with assigned total density and weight fraction of fuel gas. The fitted curve is described as

$$f(T) = c_1 T^{-1} + c_2 + c_3 \ln T + c_4 T + c_5 T^2, \qquad (1)$$

where coefficients are determined by least square fitting.

The governing equations are discretized by the discontinuous Galerkin finite element method [5]. The current version is second order accurate in space with the BR2 formulation for the viscous and diffusion terms. The time integration is made by the cellwise relaxation implicit scheme developed by Yasue et al. [6].

3. Computed cases

We consider the flowfield in the combustion chamber named HTE 5-1 hybrid rocket engine which is a technology demonstrator and is in preliminary design phase studied by HRrWG. The inner diameter of the fuel grain is 0.08m and its length is 0.15m. The chamber pressure is designed to be 3MPa.

This combustion chamber has 8 oxidizer injector ports at the upstream end of the chamber. We consider two injection angles, 90° and 60°, toward the central axis. Table 1 shows oxidizer injection conditions for the two cases. In order to match tangential velocity component, the injector diameter and the axial velocity component are different, respectively.

The fuel gas is injected with a total mass flow rate of 0.122kg/s. The temperature of injected fuel gas is assumed to be 603K and the pressure is assumed to be the same as that in the boundary layer. The injection velocity at the fuel surface is about 0.1m/s and the direction is normal to the fuel surface.

Table 1 Oxidizer injection conditions

injection angle	90°	60°
diameter [mm]	5.00	4.65
mass flow rate [kg/s]	0.26	0.26
density [kg/m^3]	40.18	40.18
pressure [Pa]	3.0	3.0
temperature [K]	293	293
tagential velocity [m/s]	41.20	41.20
axial velocity [m/s]	0	23.8

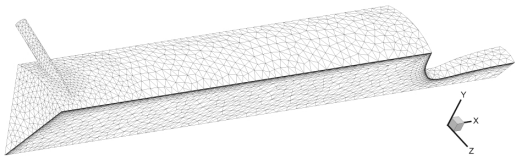

(a)

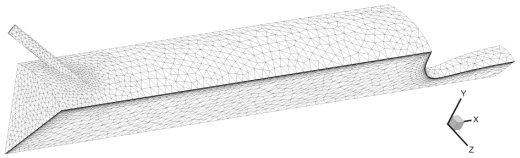

(b)

Fig. 1 Computational meshes: (a) 90° injection for Case A and (b) 60° injection for Case B.

The computational meshes are shown in Fig. 1. In order to reduce the computing time, we assume 1/8 symmetry in the present calculation. Therefore, a periodic boundary condition is employed at the cut surface where velocity vectors are rotate for 45°. The number of tetrahedral cells is 132,569 for Case A and 151,017 for Case B.

4. Results and Discussion

Figure 2 (a) and (b) show the resulting pressure contours for each case. In both cases, the pressure at the chamber surface is higher and that at the central axis is lower, since the radial pressure gradient balances with centrifugal force by swirling flowfield. The pressure in the combustion chamber is up to 1.9MPa for each case which is 2/3 of the designed value. Because present calculation doesn't take account of turbulence transport, the mixing of fuel and oxidizer gas isn't enough. Hence, it seemed that the lower pressure is caused by less significant combustion.

Figure 3 (a) and (b) show the resulting contours of axial velocity component for each case, respectively. In these figures, the maximum value of the contour is set to be zero, only reverse flow region is shaded. In Case A, large reverse flow region at the upstream end is formed by vortices induced by oxidizer injection, but not in Case B. This is because the oxidizer injection with axial velocity forces axial flow in the inner chamber. Thus, the oblique injection has an effect on the reverse-flow suppression in the combustion chamber.

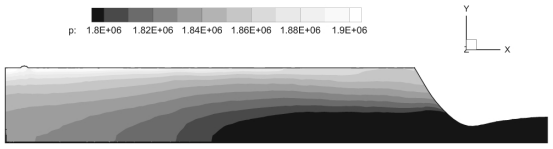

(a)

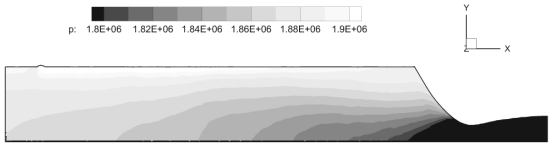

(b)

Fig. 2 Computed results of pressure: (a) Case A and (b) Case B.

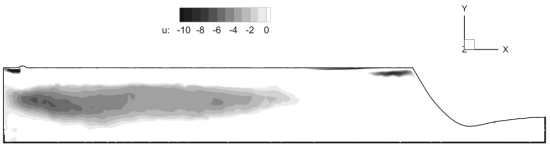

(a)

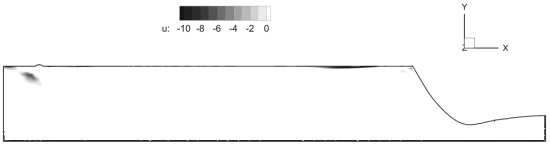

(b)

Fig. 3 Computed results of axial velocity: (a) Case A and (b) Case B.

5. Conclusoin

In order to examine the effects of oblique injection on the swirling oxidizer flowfield, we employed chemical equilibrium NS gas solver. Two chamber geometries were considered whose injection angle toward central axis is 90° and 60°. The computed results show that oblique injection suppresses reverse flow in the combustion chamber. Detailed computational results will also be shown in the conference presentation.

References

[1] W. H. Knuth et al., AIAA paper 98-3348, 1998.
[2] S. Yuasa et al., AIAA paper 99-2322, 1999.
[3] K. Yoshimura and K. Sawada, AIAA paper 2010-905, 2010.
[4] S. Gordon and B. J. McBride, NASA RP-1311, 1996.
[5] B. Cockburn and C-W. Shu, *J. Comput. Phys.*, **141**(1989), 199-244.
[6] K. Yasue et al., *CiCP*, **7**(2010), 510-533.

Eighth International Conference on Flow Dynamics
November 9 - November 11, 2011

Three-dimensional Numerical Simulation on Unsteady Compressible Flow Using Preconditioning Method: Swirling Injector Flowfield in Hybrid Rocket Engine

Nobuyuki Tsuboi, Kyushu Institute of Technology, 1-1 Sensui-chou, Tobata-ku, Kitakyushu, Fukuoka, Japan
Katsuyoshi Fukiba, Shizuoka University, 3-5-1 Johoku, Naka-ku, Hamamatsu, Shizuoka, Japan
Toru Shimada, Japan Aerospace Exploration Agency, 3-1-1 Yoshinodai, Chuo-ku, Sagamihara, Japan
tsuboi@mech.kyutech.ac.jp.

Abstract

The swirling flow in the hybrid rocket motor with high *Re* number and low speed is simulated by using the time-dependent preconditioned compressible Navier-Stokes solver. The numerical flux is calculated by the preconditioned AUSMDV schemes and the time integration adopts the preconditioning LU-SGS method. The stable swirling flow in the chamber is observed except the region near the injection ports and converging section of the nozzle. The swirling flow in the chamber affects the nozzle flow in the diverging section as well as in the converging section.

1. Introduction

The hybrid rocket engine uses a solid fuel and gas oxidizer to become more safety and less expensive than the solid rocket engine because the fuel and oxidizer are separated and solid fuel is typically made of polymer materials. Therefore the hybrid rocket is a candidate for the transportation of the manned space mission. An oxidizer is injected axially through the core of the solid fuel in the conventional hybrid rockets. After the ignition, the combustion of the oxidizer and fuel provides the heat release required to vaporize the solid fuel. The combustion process is strongly coupled with the flowfield in the hybrid rocket engine. The engine requires high combustion efficiency and large regression rate to obtain enough thrust performance. Its thrust performance can be increased by the tangential or impingement injection of oxidizer than the axial injection[1, 2]. The tangential injection generates complex flowfield in the combustion chamber and exhaust nozzle. Therefore the flow structure should be understood by using the numerical simulations as well as the experiments.

Although the numerical simulations are necessary for the design of the hybrid rocket motor, common compressible flow solvers are " density-based " schemes, which are impossible to solve incompressible flow lower than free-stream Mach number of 0.1 due to small time step and slow converging rate. This causes a stiffness problem in which the ratio of maximum eigen value to minimum one in inviscid flux is of the order of 100. This stiffness problem also arises in the simulations with chemical reaction. The preconditioned Euler or Navier-Stokes equations [3] , which is control the eigenvalues without stiffness, can be solved for such the low speed as well as high Mach number.

We have recently developed the time-dependent preconditioning Navier-Stokes code to solve such the high *Re* number and low speed flow in order to understand flow mechanism in the hybrid rocket combustion chamber. In this paper, we discuss the flowfield in the hybrid rocket motor by using the unsteady preconditioning compressible Navier-Stokes solver.

2. Numerical Method

The three-dimensional compressible Navier-Stokes equations are shown as follows:

$$\frac{\partial \boldsymbol{Q}}{\partial t}+\frac{\partial \boldsymbol{E}}{\partial x}+\frac{\partial \boldsymbol{F}}{\partial y}+\frac{\partial \boldsymbol{G}}{\partial z}=\frac{\partial \boldsymbol{E}_v}{\partial x}+\frac{\partial \boldsymbol{F}_v}{\partial y}+\frac{\partial \boldsymbol{G}_v}{\partial z}, \quad (1)$$

where $\boldsymbol{Q}=[\rho u, \rho u, \rho v, \rho w, e]^T$ is conservative variables, $\boldsymbol{E}, \boldsymbol{F}, \boldsymbol{G}$ are invisced fluxes, $\boldsymbol{E}_v, \boldsymbol{F}_v, \boldsymbol{G}_v$ are viscous fluxes, respectively. The governing equations are transformed by using the preconditioning method proposed by Weiss and Smith[3]. The dependent variables change from conservative variables $\boldsymbol{Q}$ to primitive variables $\boldsymbol{W}=[p, u, v, w, T]^T$, and the preconditioning matrix Γ is introduced in the governing equations, then

$$\Gamma\frac{\partial \boldsymbol{W}}{\partial t}+\frac{\partial \boldsymbol{E}}{\partial x}+\frac{\partial \boldsymbol{F}}{\partial y}+\frac{\partial \boldsymbol{G}}{\partial z}=\frac{\partial \boldsymbol{E}_v}{\partial x}+\frac{\partial \boldsymbol{F}_v}{\partial y}+\frac{\partial \boldsymbol{G}_v}{\partial z}. \quad (2)$$

The inviscid fluxes are linearlized by $\boldsymbol{W}$ instead of $\boldsymbol{Q}$ as follows:

$$\Gamma\frac{\partial \boldsymbol{W}}{\partial t}+\Gamma A_\Gamma\frac{\partial \boldsymbol{W}}{\partial x}+\Gamma B_\Gamma\frac{\partial \boldsymbol{W}}{\partial y}+\Gamma C_\Gamma\frac{\partial \boldsymbol{W}}{\partial z} = \frac{\partial \boldsymbol{E}_v}{\partial x}+\frac{\partial \boldsymbol{F}_v}{\partial y}+\frac{\partial \boldsymbol{G}_v}{\partial z}, \quad (3)$$

where $A_\Gamma=\Gamma^{-1}\partial\boldsymbol{E}/\partial\boldsymbol{W}$, $B_\Gamma=\Gamma^{-1}\partial\boldsymbol{F}/\partial\boldsymbol{W}$, and $C_\Gamma=\Gamma^{-1}\partial\boldsymbol{G}/\partial\boldsymbol{W}$. The eigenvalues of $A_\Gamma, B_\Gamma, C_\Gamma$ are $(u, u, u, u'+a', u'-a')$, $(v, v, v, v'+a', v'-a')$, and $(w, w, w, w'+a', w'-a')$, respectively.

In high speed flows, the eigenvalues of the preconditioned system become their traditional form, $u'\pm a'\rightarrow u\pm a$. At low speed, however, $u'\pm a'\rightarrow u/2\pm\sqrt{u^2/4+(\varepsilon a)^2}$. The eivenvalues for y and z directions are similar to those for x direction. In this study, ε is equal to 0.25 based on Weiss and Smith method though ε is arbitrary control parameter. Therefore stiffness in the inviscid flux is improved by using these eigenvalues. The reference Mach number sets 3.0 in these simulations.

The inviscid flux adopts the preconditioned AUSMDV proposed by Edwards and Liou[4]. The second-order MUSCL with van Albada limiter is used and time

integration uses preconditioned LU-SGS scheme[5]. The turbulent model adopts Baldwin-Lomax model. In this simulation, the number of sub-iterations in the pseudo-time-derivative is thirty to preserve time-accuracy. The viscous terms are second-order central difference without preconditioned scheme. The detail of the present procedures is presented in Ref. 6.

3. Computational Grids and Simulation Conditions

The computational grid in the cylindrical chamber is shown in Fig.1. The tangential inflow conditions employed the experiments conducted by Yuasa et al[7, 8]. The number of grid points is 146 x 93 x 51. The number of injection ports are eight near the closed end wall in the chamber. The injection pressure, temperature, and specific heat ratio are 1.37 MPa, 300 K, and 1.21, respectively. Therefore Re number is 3.9×10^8/m. The injection mass flux equals 136 g/s. The wall boundary conditions are non-slip and adiabatic wall. The non-dimensional computational time step uses 1×10^{-4} and the corresponding CFL number becomes approximately 100.

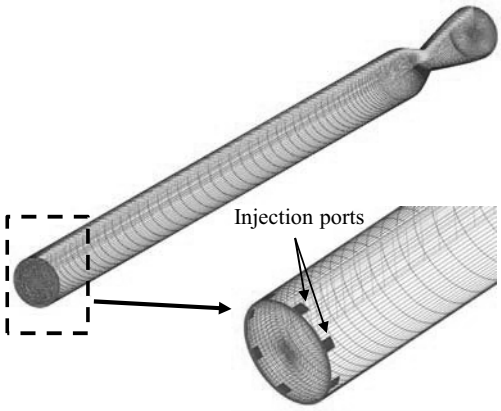

Fig. 1 Computational grid in the hybrid rocket engine.

4. Results and Discussion

Figure 2(a) shows the instantaneous Mach number contours in the chamber. The streamlines near the injection ports and nozzle exits are also presented in Fig. 2 (b) and (c). The stable swirling flow exists in the chamber and in the nozzle though an unsteady inverse flow near the injection ports in Fig. 2 (b) and near the converging section are observed. The detail of the swirling flow structure and the effects of the preconditioning method will be presented in the conference.

5. Conclusions

The swirling flow in the hybrid rocket motor with high Re number and low speed is simulated by using the time-dependent preconditioned compressible Navier-Stokes solver. The stable swirling flow in the chamber is observed except the region near the injection ports and converging section of the nozzle. The swirling flow in the chamber affects the nozzle flow. We should estimate the swirling flow effects in the nozzle flow field as well as in the chamber.

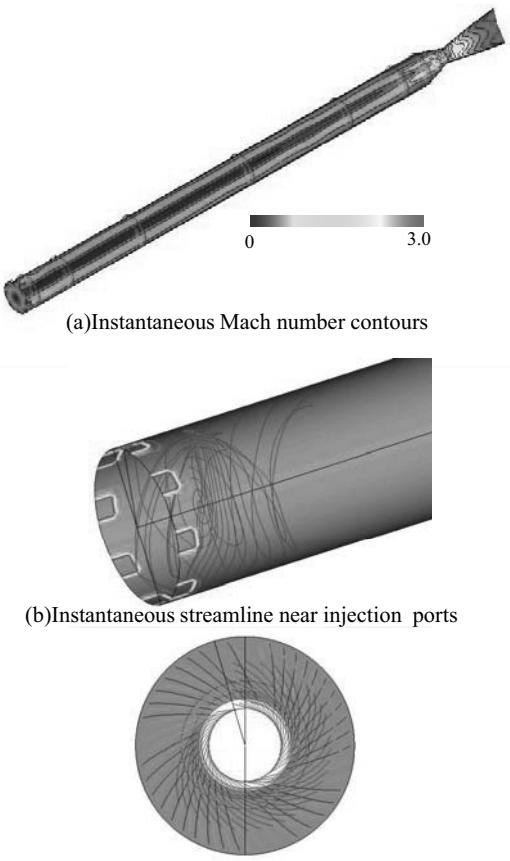

(a)Instantaneous Mach number contours

(b)Instantaneous streamline near injection ports

(c)Instantaneous streamline viewed from nozzle exit

Fig. 2 Computational results in the hybrid rocket engine.

Acknowledgements

This research is conducted as a contribution to the Hybrid Rocket Research Working Group (HRrWG) with the approval of the Space Engineering Steering Committee of Institute of Space and Astronautical Science, Japan Aerospace Exploration Agency.

This research has also been supported by the Ministry of Education, Science, Sports and Culture, Grant-in-Aid for Scientific Research (B) (No.23360380). The present numerical simulations are collaborated with Cybermedia Center in Osaka University and V system in JAXA supercomputer system.

References

1. T. Tamura, S. Yuasa, and K. Yamamoto, AIAA paper 99-2323 (1999).
2. H. Nagata, M. Ito, V. Maeda, M. Watanabe, T. Uematsu, T. Totani, and I. Kudo, Acta Astro., **59**, (2006), 253.
3. J.M. Weiss and W.A. Smith, AIAA J., **33**, **11**, (1995), 2050.
4. J.R. Edwards and M.-S. Liou, AIAA J., **36**, **9**, (1998), 1610.
5. S. Yamamoto, J. Comp. Phys., **207**, (2005), 240.
6. N.Tsuboi, K. Fukiba and T. Shimada, AJCPP2010-088, AJCPP (2010).
7. K. Kitagawa, T. Sakurazawa, and S. Yuasa, JSASS, **6**, (2007), 47.
8. R. Itakura, K. Okamoto, S.Teramoto, T.Nagashima, AJCPP2010-079, AJCPP (2010).

Combustion Characteristics of Paraffin-Fueled Swirling-Oxidizer-Flow-Type Hybrid Rocket Engines

Saito Daisuke, Yuasa Saburo, Hirata Kousuke, Sakurai Takashi
Tokyo Metropolitan University, Hino City, Tokyo 191-0065, JAPAN
syuasa@sd.tmu.ac.jp

ABSTRACT

In order to increase fuel regression rates, we carried out combustion experiments with the swirling-oxidizer-flow-type hybrid rocket engine using paraffin fuels. The fuel regression rates of paraffin fuels were obtained to be about 7 times higher than those of polypropylene fuels in swirling oxygen condition. However there were two problems that the equivalence ratio became too large and the combustion efficiency was too low. To solve these problems, an improved hybrid rocket engine with a short grain length and an aft combustion chamber was fabricated. The improved engine reduced the equivalence ratio and increased the combustion efficiency.

1. Introduction

A hybrid rocket has been considered to be a new hopeful rocket engine but it has some problems. Especially, low fuel regression rate is the key problem. We proposed a unique technique, a swirling oxidizer injection at fuel grain head and it was shown increase the regression rate up to about 3 times than that without swirling[1]. We aim to obtain further high regression rate using paraffin fuels in swirling flow field. However, it is known that paraffin fuels are difficult to burn completely and to handle because they are brittle. The purpose of this paper is to burn paraffin fuels completely by installing the aft combustion chamber.

2. Characteristics of paraffin fuels

The property of FT0070 paraffin fuels (Nippon Seiro rroduct) is shown in Table1[2]. h_T is total energy required to heat a unit mass of the solid fuel from initial temperature to the surface temperature and then to vaporize it[3]. h_T and the melting point of paraffin are lower than those of PP. Thus, paraffin fuels may have high regression rate.

The theoretical hybrid rocket performances with PP and paraffin fuels were calculated by CEA400[4]. Table1 shows calculated results by the maximum *Isp* when the chamber pressure, *Pc*, is 1 MPa. There is no big difference in theoretical performance between paraffin and PP fuels.

Table 1. properties of PP and Paraffin

Fuel	Density [kg/m³]	Melting Point [K]	Heart Value h_T [kJ/kg]	Theoretical Performances at *Pc* of 1 MPa	
				Maximum *Isp* [s]	φ [-]
PP	910	444	1129	233	1.50
Paraffin (FT-0070)	760 (at 393 [K])	345	314	235	1.57

3. Experimental Apparatus

In this study, 2 types of hybrid rocket engines with a swirling-oxidizer-flow-type injector were used. The oxidizer was GOX. The paraffin fuel grain was a single port grain with the inner diameter of 40mm and was produced using a centrifugal casting process. Figure.1 shows the schematic of the conventional swirling-oxidizer-flow-type hybrid rocket engine which was used in the burning tests of PP and PMMA fuels. The engine has the grain with a diameter of 60mm, and a length, *l*, of 200mm. Figure.2 shows the schematic of the improved engine with an aft combustion chamber for paraffin fuels. The improved engine has a shorter *l* to reduced φ and has a grain diameter of 100mm to make burning time longer. *l* is able to vary 27 to 63mm. The aft combustion chamber has the aperture section at the inlet because of promoting mixing between the oxidizer and the unburned fuels by forming reverse flow region due to the swirling flow.

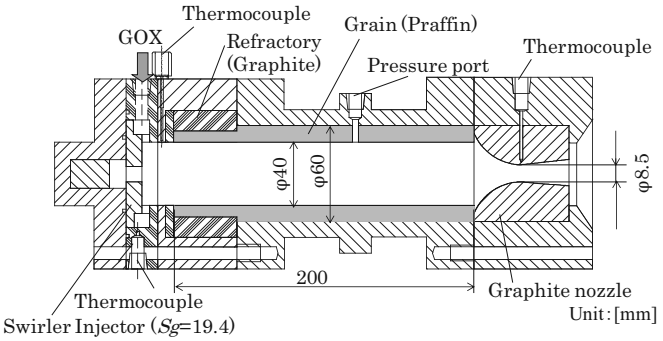

Fig.1 Conventional swirling-oxidizer-flow-type hybrid rocket engine without aft combustion chamber

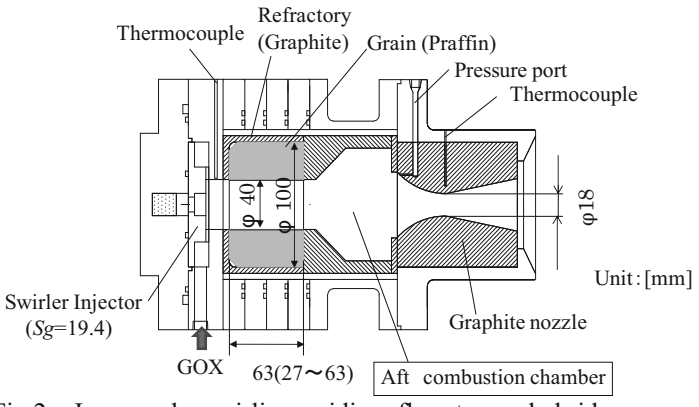

Fig.2 Improved swirling-oxidizer-flow-type hybrid rocket engine with aft combustion chamber

4. Results and Discussion

4.1 Increase of fuel regression rate

The experimental results of paraffin and that of PP using conventional engine are listed in Table2. The time-averaged overall fuel regression rate, $\dot{r}_{over}$, of paraffin is much higher than PP. The regression mechanism of paraffin is probably considered as follows[5]. The melting point of paraffin is low and solid

fuel melts quickly. There is melted fuel flow layer on the solid fuel surface. Some part of melted fuel vaporized from the melted layer like PP and PMMA fuels, but the main part of melted fuel is entrained in the gas stream without vaporized from the melted layer. Thus, $\dot{r}_{over}$ of paraffin may be higher than that of other fuels.

Figure.3 shows the $\dot{r}_{over}$ and intermediate oxygen mass flux ,$G_{oitm,}$ for PP, PMMA and Paraffin. Paraffin fuels have much higher regression rates than PP and PMMA fuels for all the tests at the same G_{oitm}. The $\dot{r}_{over}$ of paraffin using the conventional engine were about 7 times higher than that of PP with swirl and 16 times higher than that of PP without swirl. The $\dot{r}_{over}$ using the improved engine were higher than the $\dot{r}_{over}$ using the conventional engine due to higher time-averaged local fuel regression rate at the leading edge.

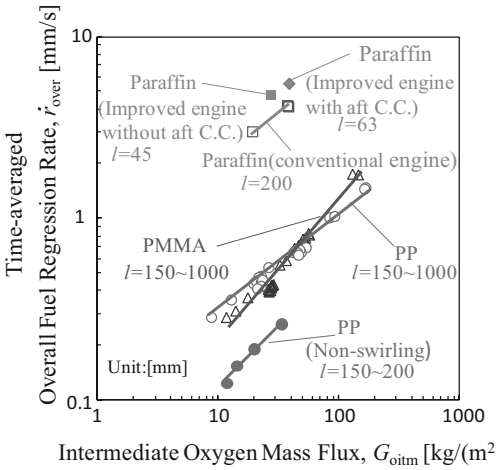

Fig.3 Relation between time-averaged overall fuel regression rate and intermediate oxygen mass flux

4.2 Effect of combustion chamber length

In comparison with the results of the PP and #1 tests using the conventional engine, table2 shows that φ of paraffin was higher than that of PP due to higher fuel regression rate. The theoretical φ at the maximum *Isp* of paraffin is 1.57 as shown in Table1, but φ of the #1 test was 5.32. The paraffin did not accomplish the suitable φ. To reduce φ, the l was shortened. The result the using improved engine of Fig.2 with a short grain length is shown in the #3 test. The φ was substantially reduced and approached the suitable φ.

4.3 Effect of aft combustion chamber

Paraffin fuels have a serious problem of low combustion efficiency and thus the C^* efficiency. Table2 shows that the C^* efficiencies of paraffin without the aft combustion chamber (#1~#3) were only 0.73 to 0.83. Our experiments showed that the C^* efficiencies for PP and PMMA fuels were 0.87 to 0.97 and 0.95 to 1.0, respectively. This means that a large amount of fuel which regressed from the paraffin surface was exhausted from the combustion chamber without burning completely. The #3 test of Fig.4 shows that the unburned fuel exhausted from the nozzle was mixed with air and burned behind the nozzle. This is due to that paraffin fuels did not have an insufficient reaction time to burn completely.

Installing an aft combustion chamber to make a space in which fuel burn completely is a possible approach in order to increase the C^* efficiency. The #4 test shows that the C^* efficiency was increased to 0.96 by installing aft combustion chamber. The #4 test of Fig.4 shows that the flame of unburned fuel was not observed behind the nozzle. These results mean that the paraffin fuel burned almost completely. The aft combustion chamber was effective in our experiments.

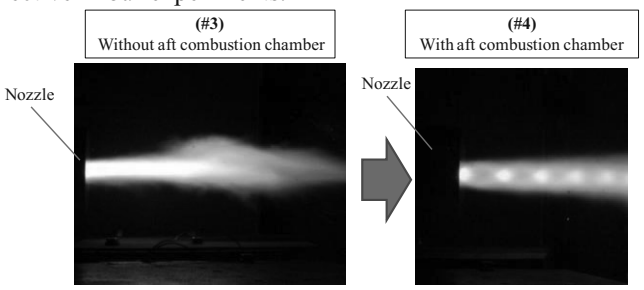

Fig.4 Appearance of exhausted flames from the nozzle in #3 and #4 tests

5. Concluding remarks

- Paraffin fuels have about 7 times of the regression rate in swirling flow than PP fuels.
- The improved engine with a short grain length reduced equivalence ratio .
- Installing an aft combustion chamber increased the C^* efficiency.

Table 2.Paraffin and PP fuels Experimental results

Fuel	Engine Type	Burning Time [s]	Pc [MPa]	$\dot{r}_{over}$ [mm/s]	G_{oitm} [kg/(m^2・s)]	φ [-]	l [mm]	C^*efficiency [-]
PP	Conventional engine (without Aft C.C.)	7.1	0.94	0.46	23.7	1.12	200	0.95
Paraffin #1	Conventional engine (without Aft C.C.)	3.0	1.04	3.00	19.2	5.32	200	0.73
Paraffin #2	Conventional engine (without Aft C.C.)	2.1	2.03	4.16	37.4	3.80	200	0.83
Paraffin #3	Improved engine (without Aft C.C.)	2.1	0.51	4.77	27.1	1.48	45	0.76
Paraffin #4	Improved engine (with Aft C.C)	1.9	0.89	5.51	39.0	2.08	63	0.96

References

[1] S. Yuasa, et al, 37thJPC, AIAA Paper 2001, 3537.

[2]Nippon Seiro, Co.,Ltd. (2011).

[3] S. Yuasa, K. Hirata, N.shiraishi, T. Sakurai, 28th International Symposium on Space Technology and Science, 2011-o-1-08v.

[4]Gordon, S. and McBride, B, J. NASA RP-1311, 1994

[5] I. Nakagawa, S. Hikone, T. Suzuki, 45thJPC, AIAA Paper 2009, 4935.

Eighth International Conference on Flow Dynamics
November 9 - November 11, 2011

3D Simulations of Cold Gas Flow in a Hybrid Single-port Combustion Chamber with a Mixing Enhancer

T.-H. Chou[1], J.-S. Wu[1]* and Y.-S. Chen[2]
[1]Department of Mechanical Engineer, National Chiao Tung University, Hsinchu, Taiwan
[2]National Space Organization, Hsinchu Science Park, Hsinchu, Taiwan
(*e-mail: chongsin@faculty.nctu.edu.tw)

ABSTRACT

In this paper, cold gas flow phenomena within a single-port hybrid combustion chamber with a novel mixing enhancer are investigated using a parallel Navier-Stokes equation solver. The mixing enhancer consists of 4-8 planar blades with different angles of attack with respect to the axial flow in the port. Results show that addition of the mixing enhancer increases greatly the vorticity in the port as compared to the same chamber without mixing enhancer. In addition, increase of angles of attack of the blades is found to be more effective than increase of the span.

1. Introduction

Hybrid propulsion has attracted much attention recently. Major advantages of the hybrid propulsion include good ISP (specific impulse), simplicity of system, high safety of operation and throttling capability, as compared to the technologically matured solid and liquid propulsions [1]. Hybrid propulsion system generally employs solid fuel and liquid oxidizer, in which combustion takes place in a form of diffusion flame. However, combustion efficiency of diffusion flame is generally low because of poor mixing between fuel and oxidizer. Thus, how to efficiently improve the mixing between fuel and oxidizer while keeping the simplicity of the system is one of the major research topics in hybrid propulsion.

To overcome the low combustion efficiency in hybrid propulsion system, the most commonly used approach is to design a combustion chamber with multiple ports in the fuel grain to increase the mixing surface area [e.g., 2]. However, this not only complicates the fabrication process and structural integrity of the grain but also increasing the unburned weight/volume of the grain. In addition, multiple cavities were used to generate recirculation that enhances mixing, named as CAMUI [3], which also increases the complexity of the grain design and fabrication, and non-uniform chamber pressure distribution. In the past, there had been several studies focusing on the vane-type vortex generators used in duct under atmospheric-pressure condition [e.g., 4, 5], in which the design is simple but very effective in increasing the mixing of flow. In this paper, we intend to study the mixing enhancement using a similar device in a typical single-port hybrid combustor.

In this paper, as a first step we investigate numerically the high-pressure (30 bar) cold nitrogen gas flow field in a single-port combustion chamber with a novel mixing enhancer made of multiple blades. Several parametric studies such as the number of blades, chord length, span and angle of attack of the blades were conducted to understand their influence on the vorticity generated behind the mixing enhancer.

2. Numerical Method

In this paper, the UNIC-UNS code, a general-purpose Navier-Stokes equation solver was used to study the cold gas flow phenomena numerically. This code solves a set of governing equations describing the continuity equation, momentum equations (Navier-Stokes equations), energy equation, species continuity equations and turbulence related equations [6]. It employs the cell-centered finite-volume, pressure-based method with a hybrid 2D/3D unstructured-grid topology, which can be used to deal with all-speed gas flows. Second-order linear reconstruction upwind scheme is used for the treatment of convection flux. Details of various numerical and physical modules employed in this solver can found in [7, 8] and are not repeated here.

There are two integral parameters: “area-averaged axial vorticity” and “transverse-to-streamwise kinetic energy ratio”, which are often used to represent degree of mixing in the literature. In this study, these two parameters are calculated at different downstream positions behind the mixing enhancer.

3. Results and Discussion

Figure 1 shows the sketch of the hybrid combustion chamber we have used in our previous combustion experiments [9]. In the current study, we consider a uniform cold gas flow flows from the inlet through the central port of fuel grain, then flows through the post combustion chamber and nozzle. Inlet and initial chamber gas pressures are both set as 30 atm based on earlier measurements. Exit pressure is set as 1 atm. A mixing enhancer is.installed in the early portion of the flow. This mixing enhancer is made of 4-8 blades with different spans and chord lengths at various angles of attack. Note α is angle of attack, *c* is chord length, and *h* is airfoil span hereafter.

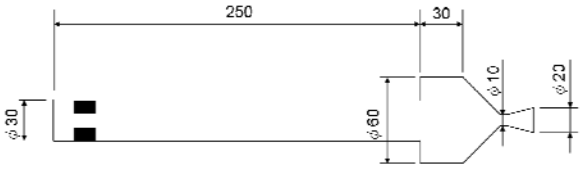

Fig 1. Combustor geometry (unit: mm) for simulation with mixing enhancers install in inlet location.

To save computational time, we have only used one quarter of the real chamber. This is justified by the same solution obtained using either one quarter or full

chamber. In addition, we have found that the vorticity increase is largest when 8 blades are used as compared to 4 and 6 blades. Thus, in the following we only present those cases with 8 blades.

Figure 2 shows the comparison of sliced distributions of Mach number with and without a mixing enhancer installed in the early portion of the port. Results show that the velocity behind the mixing enhancer increases dramatically because of blockage effect caused by the mixing enhancer.

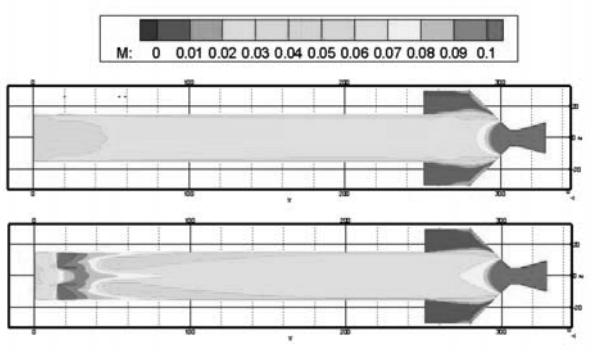

Fig 2. Distributions of Mach number without (top) and with (bottom) a mixing enhancer.

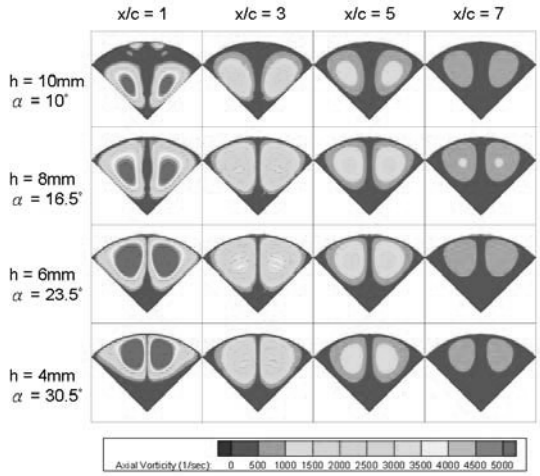

Fig 3. Distributions of absolute axial vorticity at different downstream positions with different combinations of span and angle of attack.

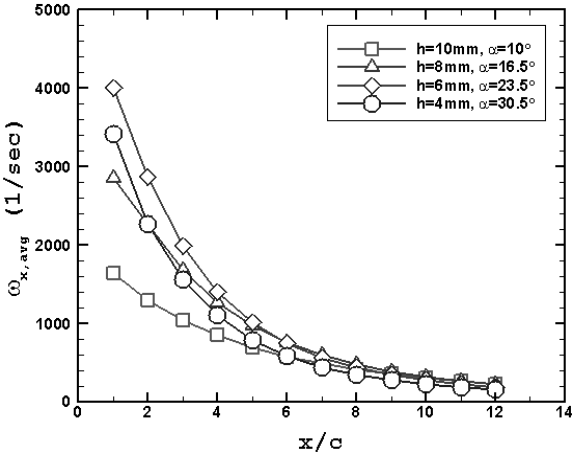

Fig 4. Average axial vorticity at different downstream positions of span and angle of attack.

Figure 3 shows several typical cross-section distributions of absolute axial vorticity with different combinations of span and angle of attack. We have found that the vorticity behind the mixing enhancer is greatest at all downstream positions at the condition of h=6mm and α=23.5°. Figure 4 shows this observation more clearly at different locations behind the mixing enhancer. Figure 5 shows the similar trend in transverse-to-streamwise kinetic energy ratio.

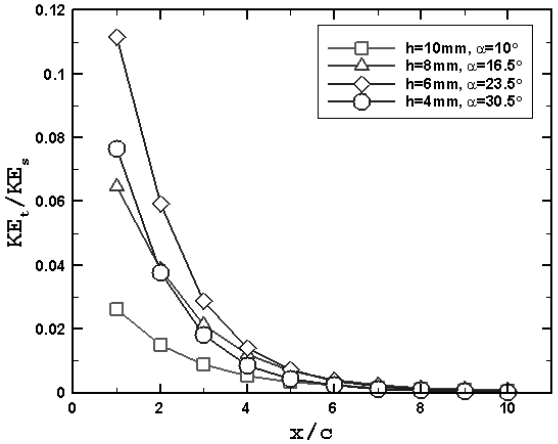

Fig 5. Kinetic energy ratios at different downstream positions with different combinations of span and angle of attack.

4. Conclusions

In this study, we have performed a numerical study of cold gas flow within a hybrid combustion chamber with a mixing enhancer installed in the early portion of the port. Results show that, with proper selection of span 6 mm) and angle of attack (23.5°) of the blades, maximal vorticities and transverse-to-streamwise kinetic energy ratios at various downstream positions behind the mixing enhancer can be achieved, which is desired to enhance the mixing of gas flow in the port. To further improve the mixing enhancement, another one to two mixing enhancer will be placed at some distance behind the first one. Results will be reported elsewhere in the near future.

References

[1] M. J. Chiaverini, K. K. Kuo, *Fundamentals of Hybrid Rocket Combustion and Propulsion*, AIAA (2007).
[2] M. A. Karabeyogl, et al., AIAA-2003-6475 (2003).
[3] H. Nagata, et al., Acta Astronautica, **59** (2006), 253-258
[4] B. J. Wendt, AIAA-95-1797 (1995).
[5] B. J. Wendt, AIAA, **42** (2004), 2185-2195.
[6] Wang & Chen, *J. of Prop. & Power*, **9**:5 (1993)
[7] H. M. Shang, et al., AIAA-95-2781 (1995).
[8] H. M. Shang, et al., AIAA-97-3183 (1997).
[9].Y. S. Chen, et al., *Proceedings of the 7th International Conference on Flow Dynamics* (2010), 174-175.

Three-dimensional Modeling of Hybrid N2O-HTPB Combustion with Mixing Enhancers

Yen-Sen Chen[1], T. H. Chou[2], B. R. Gu[2], J. S. Wu[2]
[1]National Space Organization, Hsinchu Science Park, Hsinchu, Taiwan
(e-mail: yenchen@nspo.narl.org.tw)
[2]Department of Mechnical Engineering, National Chiao Tung University, Hsinchu, Taiwan
(e-mail: chongsin@faculty.nctu.edu.tw)

ABSTRACT

Recently, the hybrid rocket propulsion has become attractive to the research community and has developed the trend to become an alternative to the conventional liquid and solid rockets. Unfortunately, even until now, research in developing hybrid N_2O-HTPB propulsion system still strongly depends on trials-and-errors, which are time-consuming and expensive. A comprehensive numerical model with real-fluid properties and finite-rate chemistry is developed in this research to predict the combustion flowfield inside a N_2O-HTPB hybrid rocket system. Good data comparisons are presented.

1. Introduction

In searching for payload mass fraction performance enhancement of human's access to space technical capabilities, ramjet and scramjet (supersonic combustion ramjet) studies have been a long-term research effort in the aerospace community since the 1960's. Since the 1980s, computational modeling approaches have been gradually adopted in the aerospace community in the development of combustion devices and space launch systems. Numerical models using computational fluid dynamics (CFD) methods have been applied to liquid and solid rocket combustion systems with successful supports to the technical programs[1-6].

In the recent development of space launch systems, hybrid rocket propulsion has drawn a lot of attention, especially in the civilian space tourism community, and has been demonstrated to become a viable alternative to the liquid and solid rockets. The hybrid rocket is a combination of both the solid and liquid systems with half of the plumbing of the liquid rockets but retaining the flexibility of operation and avoiding the explosive nature of the solid rockets [7].

There are many types of hybrid combustion systems, in which fuel is classically a solid and the oxidizer is a liquid or gas. Typical examples of combination of fuel and oxidizer with optimum O/F, Isp (184 to 326 sec) and characteristic velocity (1224 to 2118 m/sec) are discussed in [7]. The maximum vacuum Isp of the N_2O-HTPB propulsion system is only fair around 250 seconds Very few [8,9] have attempted to model complicated reactive flow phenomena of a realistic hybrid propulsion system, they employ an energy-balanced surface decomposition model.

The modeling efforts have reached success to some extent based on fitting of experiments and numerical simulations. However, the real-fluid effects were not considered in their models. This can affect the overall flow structure in the combustion chamber, especially near the injectors, and affect the combustion processes and heat transfer characteristics, which is the key to the regression rates of the solid grain. Thus, a comprehensive numerical model is developed in this research to include the real-fluid property, finite-rate chemistry and radiative heat transfer effects in the simulation of N_2O-HTPB hybrid rocket systems.

2. Method of Approach

The present numerical method solves a set of governing equations describe the conservation of mass, momentum (Navier-Stokes equations), energy, species concentration and turbulence quantities [10].

For complete description of the thermal environment in the combustion chamber, a radiative heat transfer model with discrete-ordinate solution method [11,12] is employed in the present model. For transient flow computations, an efficient second-order time-marching scheme, which has been validated for vortex shedding and transient start-up nozzle flows [6], is employed in the present study. The turbulence fields are predicted with an extended two-equation model [13,14]. An efficient method for comprehensive real-fluid equations of state and fluid properties is also tested for liquid propellant combustion flows.

In order to make analyses of phase change phenomena, liquid sprays or cryogenic fluid flows, real-fluid thermal and caloric equations of state (EOS) were developed for use with the present CFD code. The HBMS equations of state [15-17] were chosen for this purpose. Thermal and caloric equations of state, vapor pressure, heat of vaporization, surface tension, and transport properties are modeled with the equations of state proposed by Hirshfelder, et al. [18,20] (we term these the HBMS equations of state) and with conventional correlations [18], for the other properties.

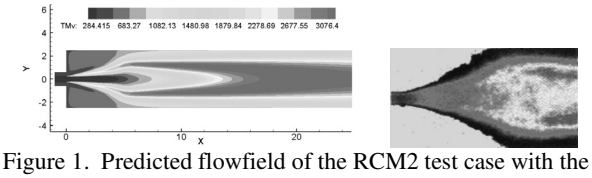

Figure 1. Predicted flowfield of the RCM2 test case with the current real-fluid-table combustion model with the flame Abel-transformed emission image of the experiment on the right.

A benchmark LOX/GH2 single-injector combustor test case of DLR, Lampoldshausen, Germany (RCM2), is simulated to validate the current real-fluid table lookup model. This is one of the benchmark cases presented in the 2nd International Workshop on Rocket Combustion Modeling [21].

Figure 1 shows the flowfield solutions of the RCM2 test case. The predicted shape of the flame zone is in close resemblance with the flame Abel-transformed

emission image of the experiment, which is the same result as the original real-fluid model [21].

3. Hybrid Rocket Combustion Modeling with Mixing Enhancer

The present hybrid rocket combustion model include a 580 mm combustion chamber with the design of forward-end and aft-end mixing chambers. A simple convergent-divergent conical nozzle is attached to the end of the combustion chamber. A single-port simple solid grain of HTPB is cast in two sections and assembled into a single segment through bonding. To boost the mixing efficiency, a mixing enhancer (patent pending) is also installed near the forward corner of the solid grain. A pintle-type injector made of stainless steal is employed for steady injection of the N_2O oxidizer. Due to the properties of the oxidizer and the absence of thermal control for the oxidizer tank and without using a presurant tank upstream, the injection flow rates of this pressure-fed injection system depend directly on the temperature of the environment. A small pyro grain is attached to the forward face of the solid grain, which is ignited at engine start-up to melt the HTPB solid and start the combustion process after the N_2O control valve is commanded to open.

Typically, a hot-fire test of this experiment runs between 15 to 20 seconds. During the test, motor thrust, chamber pressures and HTPB port temperatures are measured. The oxidizer flow rates and the regression rates of the solid grain are obtained through post-processing after the hot-fire tests. Overall, the experimental data show that the averaged solid regression rate is around 1.2 mm/sec for the current design, which is slightly lower than the correlation burning rate equation of Lohner et al.[22] The measured specific impulse, sea-level Isp, of the motor with the mixing enhancer is around 213 sec (or vacuum Isp of 222.18 sec). From test cases without the mixing enhancer, the measured sea-level Isp is around 178 sec (or vacuum Isp of 187.18 sec) for the same motor geometry.

During the test, the tank pressure and temperature are reduced rapidly due to high flow rate and the expansion effects. Therefore, in the present model, we compare the numerical predictions to the test data when the oxidizer injection stays in the liquid phase, i.e. between 2 to 7 seconds after ignition.

Overall, the experimental data show that the solid regression rate is around 1 mm/sec for the current design. The measured specific impulse, sea-level Isp, of the motor with the mixing enhancer is around 213 sec (or vacuum Isp of 222.18 sec). For cases without the mixing enhancer, the measured sea-level Isp was around 178 sec. The predicted averaged sea-level Isp of an axisymmetric model is 181.2 sec, which is lower than the measured data as expected since the mixing enhancer is not present in such approach. The numerical solutions of 3D models show an averaged vacuum Isp of 223.77 sec and 190.82 sec for the cases with and without the mixing enhancer, respectively. Notice that the predicted Isp for the case without mixing enhancer is close to that predicted by the axisymmetric model. This shows the modeling consistency between 2D and 3D approaches (Fig. 2).

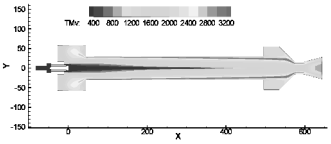

(a) Axisymmetric Model (Time Averaged)

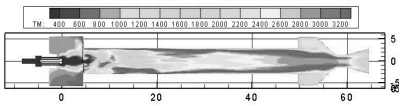

(b) 3-D Model (Instantaneous)

Figure 2. Predicted temperature distributions in a N_2O-HTPB hybrid rocket motor.

4. Conclusions

In this study, we have developed a comprehensive numerical model for predicting the combustion flowfield of a hybrid rocket motor. A real-fluid property model has been employed for accurate description of the fluid dynamics of the N_2O-HTPB hybrid rocket combustion system.

The experimental investigation of the N_2O-HTPB hybrid rocket combustion system has demonstrated the effective, reliable and low-cost setup of the present design. The present numerical solutions and test data have shown enhanced combustion efficiency for the hybrid motor with mixing enhancer.

Acknowledgements

This work is supported by the Sounding Rocket Program of the National Space Organization of the National Applied Research Laboratory of Taiwan. The computational resources and services are provided by the National Center for High-performance Computing of the National Applied Research Laboratory.

References

[1] Y.S. Chen, et al., NAS8-00002 (2001), ESI.
[2] P. Liaw, et al., AIAA-94-2780 (1994).
[3] Y.S. Chen, et al., H-34345D (2002), ESI.
[4] T.S. Wang, et al., *J.Prop. & Power* (2002) **18**:6.
[5] T.S. Wang, *J.Prop. & Power*, (2005) **22**:1.
[6] T.S. Wang, AIAA-2005-3942 (2005).
[7] M. Chiaverini, K. Kuo, Prog. Astro. & Aero, (2007)**218**.
[8] R.C. Farmer, et al., JANNAF 35th (1998).
[9] R.C. Farmer, et al., JANNAF Propul. (1996).
[10] T.S. Wang, Y.S. Chen, *J. of Prop. & Power*, (1993) **9**:5.
[11] J. Liu, Y.S. Chen, *Num. Heat Trans.*, (1999) B, **36**,
[12] J. Liu, Y.S. Chen, *J.Quant.Spec.Radi.Transfer*, (2000) **22**.
[13] Y.M. Kim, et al., AIAA-92-3763 (1992).
[14] Y.S. Chen, et al., AIAA-92-3602 (1992).
[15] O.A. Uyehara, et al., National Petro. News (1944).
[16] J.B. Maxwell, Data Book on Hydrocarbons, (1950).
[17] R.C. Farmer, et al., SECA-FR-02-02 (2002).
[18] R.B. Dooley, Sept. (1997) Release, IAPWS web.
[19] Anon., ASME Press, NY, NY, (1998).
[20] L.E. Dean, L.A. Shurley, TCR-70, (1957).
[21] G. Cheng, et al., RCM-2 Workshop (2001).
[22] K. Lohner, et al., AIAA 2006-4671 (2006).

Eighth International Conference on Flow Dynamics
November 9 - November 11, 2011

Some Issues on Hybrid Rocket Internal Ballistics Evaluation

Toru Shimada and Yuki Funami
Institute of Space and Astronautical Sciences, Japan Aerospace Exploration Agency
3-5-1 Yoshinodai, Chuo-ku, Sagamihara, 252-5210, Japan
shimada.toru@jaxa.jp

ABSTRACT

Discussions are made on challenges in evaluation of the internal ballistics of hybrid rocket, especially on simple models for design use. The issues are averaging effect in the quasi-1D formulation, calculating proper numerical flux quantities according to chemical reaction models, a proper boundary condition at the fuel web external surface, proper evaluation of the enthalpy and the velocity ratio at the flame, practical efficient methodology dealing with the chemical equilibrium solution, and need for chemical kinetics modeling, etc.

1. Introduction

The concept of hybrid propulsion has been generating increasing interest in application to both spacecraft propulsion and space transportation. Inherent safety makes this technology very attractive for application in space tourism industry.

In designing a hybrid rocket, it is a fundamental need to evaluate the pressure and its temporal changes of the combusting gas in the engine chamber because they are related to various phenomena such as ignition and extinction, shape change of a fuel grain due to the combustion, instability due to vortices, acoustics, and injectors, and so on. Characteristics of the chamber pressure are sometimes called “internal ballistics” of a rocket. In this paper, challenges in evaluating internal ballistics of hybrid rockets will be described.

In this line of researches, there are several previous works about prediction of fuel regression rate [1, 2] and about combustion stability analyses [3]. In spite of these efforts, it seems that there still have rooms to be improved.

2. Issues in quasi-1D modeling

In general, fluid dynamic and combustion phenomena inside a hybrid-rocket combustion chamber are so complex that it is very difficult to use rigorous models in order to simulate them over a whole burning period that is usually of 1-2 minutes. Hence, simple models are required for such purposes and we have been developing a quasi-1D model for evaluation of the internal ballistics of hybrid rockets [4] shown in Fig.1.

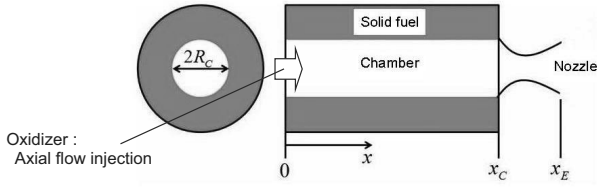

Fig. 1 Schematic of hybrid rocket model

In the model, the following assumptions are made. Fuel type is represented by parameters in Arhrenius function for mass generation rate. Single gas species is generated from fuel surface. Oxidizer is injected in gas phase (oxygen). Quasi-steady evolution of inner port geometry (no coupling) is assumed. Characteristic times are such that gas-phase chemical reaction is very fast, fluid dynamics is fast, thermal decomposition and surface gasification of fuel are very fast, thermal conduction in fuel is slow, and gas-phase fuel and oxidizer mixing in a cross-section perpendicular to the axis is very fast (Q1D restriction). Diffusion-controlled situation on fuel regression rate (neither radiation nor pressure effect) is also assumed.

Based on such assumptions, it is appropriate to treat fluid dynamics of mainstream and thermal conduction in the solid fuel as time-dependent phenomena whilst the others are time-fixed or quasi-steady phenomena. The fluid dynamics is described in quasi-1D framework along with the axis, on the other hand, the thermal conduction in the fuel is described at each axial location in local 1D framework perpendicular to the fuel surface. The equations are coupled and simultaneously solved with the energy balance equation at the solid fuel surface.

The governing equations for gas dynamics and mixture fraction transportation are written as follows.

$$\frac{\partial A\mathbf{Q}}{\partial t}+\frac{\partial A\mathbf{F}}{\partial x}=\mathbf{S}_{Q1D}+\mathbf{S}_{Mass}, \tag{1}$$

$$\mathbf{Q}=\begin{pmatrix}\rho\\ \rho u\\ \rho e_t\\ \rho\xi\end{pmatrix},\quad \mathbf{F}=\begin{pmatrix}\rho u\\ \rho u^2+p\\ (\rho e_t+p)u\\ \rho\xi u\end{pmatrix},$$

$$\mathbf{S}_{Q1D}=\begin{pmatrix}0\\ p\frac{dA}{dx}\\ 0\\ 0\end{pmatrix},\quad \mathbf{S}_{Mass}=\begin{pmatrix}l_p\dot{m}_F\\ 0\\ l_p\dot{m}_F h_w\\ l_p\dot{m}_F\end{pmatrix}.$$

The mass generation flux from the fuel surface, $\dot{m}_F$, is defined by the product of fuel density ρ_s and the regression rate $\dot{r}$. The fuel mixture ratio ξ is defined by

$$\xi \equiv \frac{b_C - b_C^{(injector)}}{b_C^{(fuel)} - b_C^{(injector)}}, \tag{2}$$

where b_C is kg-mole number of Carbon atom per unit mass. The first issue in the quasi-1D formulation is that the mixture fraction is averaged within a cross-section perpendicular to the *x*-axis. This constraint changes the flow field characteristics significantly. Since mass fractions of chemical species are evaluated by the value of the mixture fraction, this constraint affects the combustion reaction, or flame, characteristics. It is important to manage to use or not to use such improper information in the simulations.

There is an issue of calculating the flux Jacobian $\partial \mathbf{F}/\partial \mathbf{Q}$ and also numerical flux, the speed of sound, etc. according to chemical reaction models.

The governing equation for the in-fuel thermal conduction is written at any *x* as follows.

$$\frac{\partial T}{\partial t} + \dot{r}\frac{\partial T}{\partial y} - \alpha_s \frac{\partial^2 T}{\partial y^2} = 0 \tag{2}$$

The thermal conduction equation, Eq. (2) is currently solved in semi-infinite space and this is only good when the fuel web thickness is sufficiently larger than the thermal penetration length, e.g., $\kappa/\dot{r}$, where κ is the thermal diffusivity. The equation is written on the framework moving with the regressing fuel surface. It is a small issue to treat this equation with a proper boundary condition at the fuel web external surface.

The fluid dynamics and the in-fuel thermal conduction should be solved simultaneously with satisfying the following energy balance at the interface, fuel surface, at any *x*.

$$\lambda_s \left(\frac{\partial T}{\partial y}\right)_{y=-0} = \lambda_g \left(\frac{\partial T}{\partial y}\right)_{y=+0} - \rho_s \dot{r} h_v \tag{3}$$

This enables us to estimate fuel regression rate by modeling the heat-feedback term in the left-hand side. We use Karabeyoglu's model[5] dependent on total mass flux.

$$\lambda_g \left.\frac{\partial T}{\partial y}\right|_{y=+0} = \left(\frac{0.03q}{\mu^{-0.2}}\right)^{1/(1-k)} \frac{B_t h_v}{\rho_s^{k/(1-k)}} x^{-0.2/(1-k)} G^{0.8/(1-k)} \dot{r}^{-k/(1-k)} \tag{4}$$

The parameter B_t is a thermo-chemical blowing parameter defined by

$$B_t \equiv \frac{u_e}{u_b}\frac{h_b - h_w}{h_v}. \tag{5}$$

It is important to evaluate h_b, the enthalpy at flame, and u_e/u_b, the velocity ratio, so that they are corresponding to the situation of mainstream and boundary-layer combustion at any axial location.

Chemical reaction is assumed to be very fast. If one employs only 4 chemical species, e.g., fuel gas C_2H_4, oxidizer O_2, products CO_2, H_2O, then the mass fractions of each species are uniquely determined for the value of ξ only by the element conservation constraint. In this case, no thermal decomposition is considered and the temperature of the flame becomes unrealistically high. On the other hand, if one employs 9 chemical species (C_2H_4, O_2, CO_2, H_2O, CO, H_2, OH, H, O), mass fractions are not determined only by the elemental conservation. It becomes necessary to introduce additional principle, such as local chemical equilibrium, or introducing other reactions. We have successfully tested chemical equilibrium concept in which the composition is determined by a free-energy minimization method. The practical methodology dealing with the chemical equilibrium solution efficiently shall be improved.

Such very fast reaction constraint precludes simulations of phenomena like ignition, flame spreading, and extinction. In such sense, chemical kinetics modeling is also to be pursued.

3. Summary

Several issues in evaluating the internal ballistics of hybrid rocket are discussed.

References

[1] A. Antoniou and K. Akyuzlu, AIAA Paper 2005-3541 (2005).
[2] Y. Yang, C. Hu, T. Cai and D. Sun, AIAA Paper 2007-5350 (2007).
[3] M. Stoia-Djeska and F. Mingireanu, AIAA Paper 2010-3909 (2010).
[4] Y. Funami, 2011-a-33s, 28th ISTS (2011).
[5] A. Karabeyoglu, *Fundamentals of Hybrid Rocket Combustion and Propulsion*, AIAA (2007), 351-411.

OS6: Aerodynamics for Mars Exploration Aerial Vehicle

Eighth International Conference on Flow Dynamics
November 9 - November 11, 2011

On Planetary Exploration by Deployable Membrane Aeroshell Probes Realizing Scattered Landing Points

Kojiro Suzuki
Department of Advanced Energy, Graduate School of Frontier Sciences, The University of Tokyo
5-1-5 Kashiwanoha, Kashiwa, Chiba 277-8561, Japan
kjsuzuki@k.u-tokyo.ac.jp

ABSTRACT

To understand the complicated planetary system, it is necessary to make observation and measurement simultaneously at various points covering a wide area of its surface. Based on the three-dimensional atmospheric entry trajectory analysis for the Mars exploration, we propose the variable geometry membrane aeroshell vehicle that enables the high-drag-force low-ballistic-coefficient flight at the early stage of the entry and the high-L/D turning flight afterwards. A large downrange of a high L/D vehicle results in a long time visibility from its mother spacecraft (orbiter) and ensures a sufficient time for the data transmission.

1. Introduction

A planet is a system of high complexity. It is almost impossible to recognize all the features at once by the exploration using a single landing probe, even though it is big and has high capability of observation. On the other hand, the exploration using a group of small landing probes may be more suitable for the recognition of complexity than that by such a single "pin-point" landing probe. In this paper, we propose a novel concept of the landing probe called "FS Landers"[1], which stands for "a Flock of Scattered Landers". Though the observation capability of each small lander will be quite limited, the synthesis of the observation data simultaneously transmitted from the landers scattered over the planetary surface to their mother spacecraft (orbiter) is expected to bring us a fruitful understanding of the whole planetary system.

Figure 1 shows the mission concept of FS Landers. Many small landing probes with the total mass in the order of 1 kg are released at once from their mother spacecraft on the planetary orbit and land at scattered points by taking different atmospheric entry trajectories, depending on the difference in their aerodynamic characteristics. Due to the strictly tight mass budget, the vehicle must be composed of the minimum required items, that is, the scientific instrument (for example, cameras), the data transmission, the battery, the body structure and the aeroshell. Namely, such vehicle will look like a "cellular phone wearing aeroshell".

The design requirements for FS Landers are: 1) To realize a small total mass, 2) To be stored compactly in the mother spacecraft before release, 3) To survive under severe aerodynamic heating during the entry flight, 4) To provide a wide coverage of the planetary surface available for landing, and 5) To ensure sufficient time for the data transmission from each lander to the mother spacecraft. As a solution to the above requirements, we propose the variable geometry vehicle made from flexible membrane materials with the Shape Memory Alloy (SMA) frame, realizing the transition from the high-drag low-ballistic-coefficient mode to the high-L/D mode, as shown in Fig. 1. Apparently, the membrane aeroshell is suitable for the requirements 1) and 2). The transition is initiated by the temperature rise of the SMA frame receiving the aerodynamic heating. By choosing the SMA and thermal insulation materials appropriately, the timing of the transition can be controlled. The low-ballistic-coefficient enables a probe to decelerate at high altitudes and reduces the peak aerodynamic heating. To move the landing point in the cross-range direction, the turning flight is necessary using the lift force and the bank angle modulation. The cross-range increases with the maximum available L/D of the flying vehicle.

In the present study, we consider the case of the Mars exploration. The important design parameters are specified and determined by the trajectory analysis. Some design concepts and their experimental results at the hypersonic wind tunnel are presented.

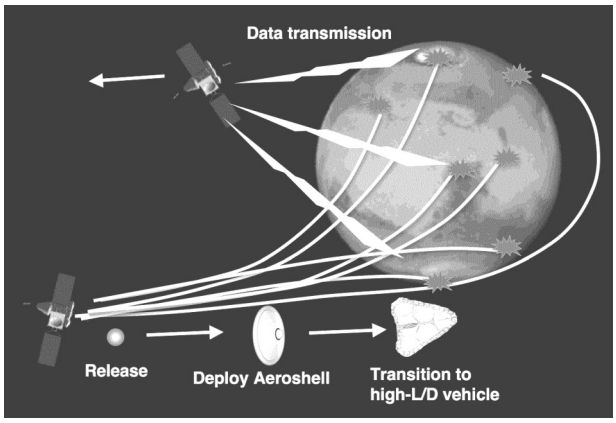

Fig. 1 The mission concept of FS Landers

2. Trajectory Analysis

We numerically solve the equations of motion of a point mass on the spherical coordinates. The detail of the analysis is given in [1]. We assume that the constant bank angle is available during the entry flight by setting the center of mass of the vehicle at an appropriate location out of the symmetry plane. The mother spacecraft carrying the landing probes is on an elliptic orbit at 0 degree inclination. The probes are separated at the apoapsis. Based on the study of the JAXA's Mars exploration mission called "MELOS"[2], the apoapsis and periapsis distances from the center of the planet are set as 27,000 km and 3,700 km, respectively. The outer boundary of the atmosphere is set at 130 km altitude. We evaluate the aerodynamic heating in terms of the reference temperature calculated under the assumption

of the stagnation-point convective heating for the nose radius of 1 m and the radiation equilibrium of the black body.

We consider a lander with the mass of 1kg and the aeroshell area of 1 m^2. At the mode transition, the drag coefficient and L/D change from 1.0 to 0.02 and from 0 to 3.0, respectively. The lander is released from the mother spacecraft at the apoapsis with the delta-V of 20 m/s. The transition temperature is set as 770 K. For the stability in the atmospheric flight, we assume slow and smooth transition taking 200 s for its completion.

As a typical case, the results at the constant bank angle of 20 degrees are shown in Figs. 2 and 3. Figure 2 shows the time history of the velocity and altitude. Due to the lift force, the probe repeats the descent and ascent flight many times. The peak heating occurs at the bottom of the first dip in the trajectory. The maximum reference temperature is 887 K, which is lower than the maximum service temperature of the existing material (923K for Zylon® cloth). The velocity is largely reduced from 5 km/s down to 3 km/s in the low-ballistic-coefficient mode. Due to the turning flight with high L/D, the probe lands at 35 degrees latitude and performs high cross-range capability. The trajectories of the lander and the orbiter viewed from the north pole are shown in Fig. 3. Though the entry occurs on the periapsis side, the probe lands on the other side because of a large down range of the high L/D flight. Consequently, the probe is visible from the orbiter for a long time. A long time visibility ensures the sufficient time (more than 10 hours in this case) for the data transmission from the lander to the orbiter. In the case of non-lifting entry, the orbiter will have gone beyond the horizon before or soon after landing.

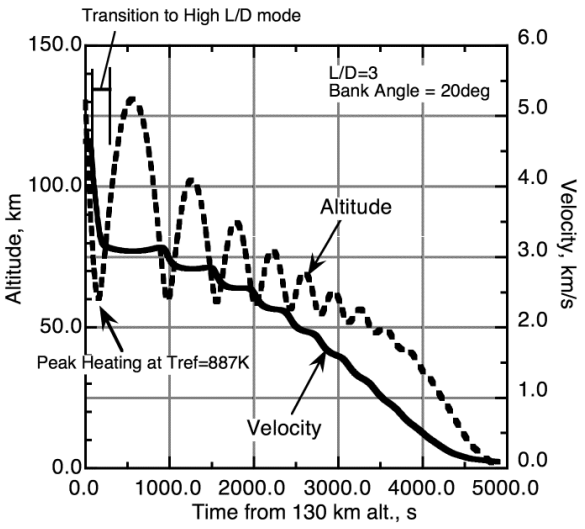

Fig. 2 Time history of altitude and velocity

3. Aerodynamic Design by Wind Tunnel Experiment

We have been conducting a series of the wind tunnel experiments at the Mach 7 hypersonic wind tunnel in Kashiwa campus, the university of Tokyo in quest of the appropriate design of the membrane aeroshell for high L/D [1]. The results are summarized in Fig. 4. To invent a lightweight structure to endure the bending moment caused by the aerodynamic lift force is the key issue.

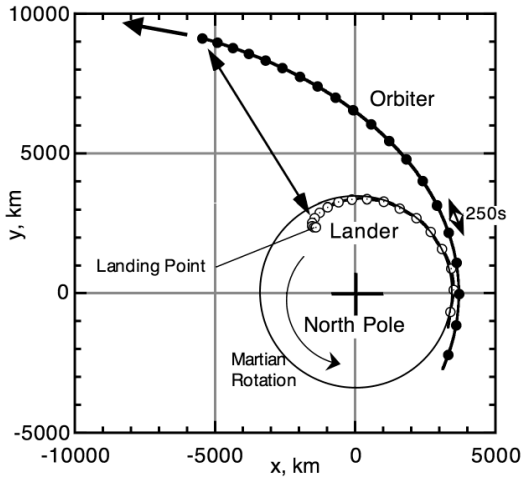

Fig. 3 Trajectories of lander and orbiter

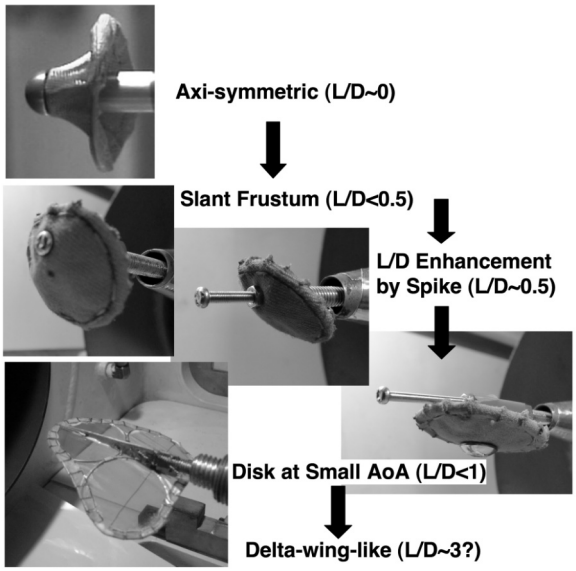

Fig. 4 Quest of high L/D membrane aeroshell design

4. Concluding Remarks

To understand the complexity of the planetary system, a concept of the "FS Lander", in which many small landing probes land at different points to cover a wide area of the planetary surface, is proposed. The three-dimensional trajectory analysis for the Mars entry shows that the membrane aeroshell with the shape memory alloy frame that enables the transformation from the high-drag mode for a low-ballistic-coefficient flight at the early stage of the entry to the high-L/D mode for the turning flight at the later stage is promising, because it can reduce the aerodynamic heating and provide high cross-range capability. The results of the hypersonic wind tunnel experiments of some candidates for the aeroshell design are presented.

References

[1] K. Suzuki, 28th ISTS-2011-e-48, 2011.
[2] N. Ogawa, et al., 27th ISTS-2009-k-23, 2009.

Comparison of Aerodynamic Data of a Wing Tested in 4 Wind Tunnels at Low Reynolds Numbers

Masaru Koike[1)], Hiroki Nagai[2)], Kouichi Yonemoto[3)], Keisuke Asai[2)]
[1)]Department of Mechanical Engineering, Osaka Institute of Technology, [2)] Department of Aerospace Engineering, Tohoku University, [3)] Department of Mechanical and Control Engineering, Kyushu Institute of Technology.
mkoike@med.oit.ac.jp, nagai.hiroki@aero.mech.tohoku.ac.jp, yonemoto@mech.kyutech.ac.jp, asai@aero.mech.tohoku.ac.jp

ABSTRACT

For Mars exploration by unmanned aircraft development of airfoils that have high aerodynamic performance at low Reynolds numbers is needed. At low Reynolds numbers, below 10^5, it is known that aerodynamic data of some wings measured in a wind tunnel are different from the data of the same wing in another wind tunnel[1]. In this paper aerodynamic data of "Ishii airfoil", which has high performance at low Reynolds numbers, measured in 4 wind tunnels are compared, and considered on it.

1. Introduction

At low Reynolds numbers, aerodynamic data of a wing changes depending on wind tunnels. For example Fig.1 shows polar diagrams of E205 measured in three wind tunnels at Reynolds number 200,000, these data are almost agree together. In other hand Fig.2 is the polar diagrams of the same wing but at lower Reynolds numbers, 60,000, these data are apparently different together.

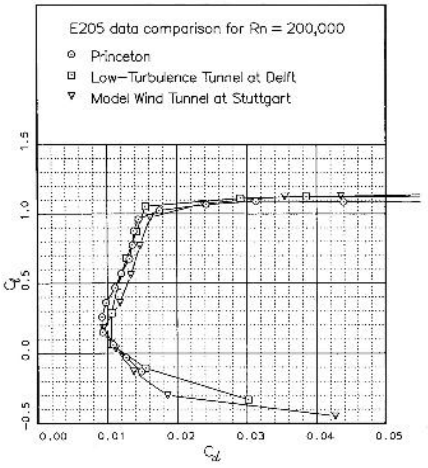

Fig. 1 E205 Re=200,000[1]

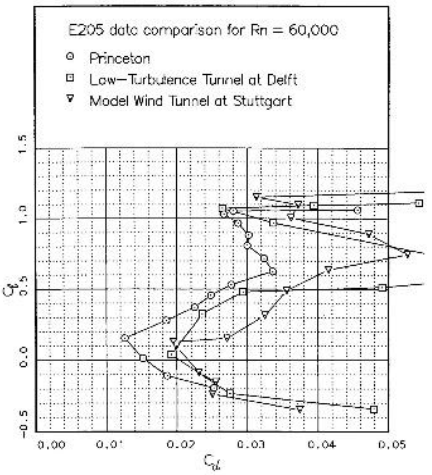

Fig. 2 E205 Re=60,000[1]

Fig. 3 E205

Cause of the differences in data are estimated turbulence of the wind tunnels, but it is not proved precisely.

This "Low Reynodls number problem" is thought to be exist in our project "Mars Airplane", so we compared the aerodynamic data of "Ishii airfoil", in 4 wind tunnels in Japan.

2. Method

Fig.4 shows the 4 wind tunnels we tested. In these figures "(a) Akashi" is the wind tunnel of Akashi National College of Technology[2], "(b) Tohoku" is the "Mars wind tunnel" of Tohoku University, "(c) Kyushu"

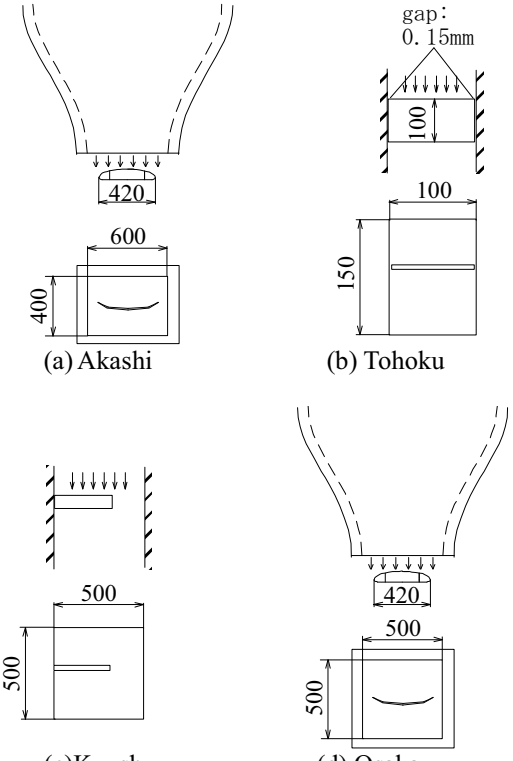

(a) Akashi (b) Tohoku

(c)Kyushu (d) Osaka

Fig. 4 Test section of each wind tunnel

is the wind tunnel of Kyushu Institute of Technology, and "(d) Osaka" is the wind tunnel of Osaka Institute of Technology. (a) and (d) have open test section and tested wing is 3-dimensional ellipse and has dihedrals. (b) has 2-dimensional test condition. (c) has half cut model of 3-dimensional rectangular wing.

Airfoil of the tested wings in the above wind tunnels is "Ishii airfoil"[2], that has 7.1% thickness and 2.3% camber as shown in Fig.5. Ishii Airfoil has high performance at low Reynolds numbers around 20,000, and used for the indoor hand launch model airplane that has world record[3].

Fig. 5 "Ishii Airfoil"

3. Results and Discussion

Fig.6 shows Cl-α characteristics measured in the wind tunnels. Data of "Akashi" and "Osaka" are corrected the error caused by wing surface change by dihedrals. Also data of "Akashi", "Kyushu" and "Osaka" are translated from 3-dimensional to 2-dimensional characteristics using following equation.

$$\alpha_2 = \alpha_3 - \frac{C_L}{\pi A} \qquad (1)$$

$$C_{D2} = C_{D3} - \frac{C_L^2}{\pi e A} \qquad (2)$$

Where α_2 and α_3 are attack angle of 2-dimensional and 3 dimensional wing respectively, C_L is lift coefficient, A is aspect ratio, C_{D2} and C_{D3} are drag coefficient of 2-dimensional and 3-dimensional wing respectively, e is span efficiency[4]. Value of the e is 0.96-0.99 for rectangular wing[4], so we approximate e=1 in the following study.

CL-α curves are considerably different together as shown in Fig.6. The order is "Akashi" ≒ "Osaka" > Tohoku > Kyushu. CD's of "Kyushu" are smaller than others as shown in Fig.7.

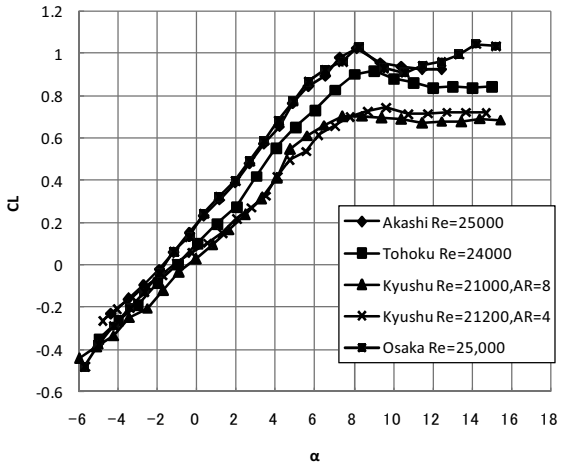

Fig. 6 CL-α characteristics

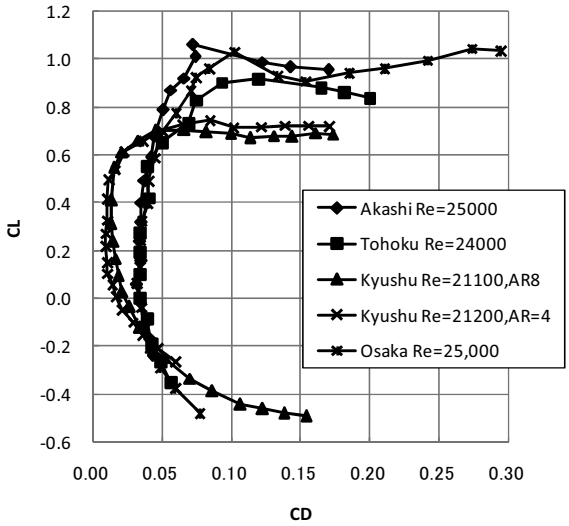

Fig. 7 Polar diagram

One of the cause of the differences in wind tunnel data may be turbulence level of the flow of wind tunnels. Turbulence levels are 0.2% in "Akashi" and "Osaka", and 0.3% in "Kyushu". Turbulence of "Tohoku" has not measured yet. Another causes are applicability of the equation (1) and (2) to such a low Reynolds numbers, and side wall boundary layer influence on the data of "Tohoku". From these study we don't conclude which data is right.

4. Concluding remarks

In order to develop Mars airplane we are studying "Ishii Airfoil" that has high performance at low Reynolds numbers. Using the same airfoil aerodynamic characteristics of wings are measured in 4 wind tunnels, as a results data are different together. We are going to study the problems.

References

[1] M. S. Selig, J. F. Donovan, D. B. Fraser, Airfoils at Low Speeds, H. A. Stokely, publisher (1989).
[2] M. Koike, M. Ishii, "Aerodynamic Performance of Hand Launch Glider", J. of the Japan Society for Aeronautical and Space Sciences, Vol.57, No.663, 2009
[3] http://www.aero.or.jp/record/rec-modelsF1N.htm
[4] R.F. Anderson, Determination of the characteristics of tapered wings, NACA report No.572, 1936

Eighth International Conference on Flow Dynamics
November 9 - November 11, 2011

Aerodynamic Advantages of Compulsively-Inflated Paraglider for Mas Exploration

Koju Hiraki[1], Yasutomo Hidaka[1], Takashi Abe[2], Kazuhiko Yamada[2] and Shin'Ichiro Higashino[3]
[1] Kyushu Institute of Technology, 1-1 Sensuicho Tobataku, Kitakyushu, Fukuoka 804-8550
[2] Japan Aerospace Exploration Agency, 3-1-1 Yoshinodai, Chuoku, Sagamihara, Kanagawa 252-5210
[3] Kyushu University, 744 Motooka, Nishiku, Fukuoka, Fukuoka 819-0395
hiraki@mech.kyutech.ac.jp

ABSTRACT

An aerial vehicle employing a paraglider is a favorable way to explore Mars for its slower flight speed than a fixed-wing vehicle. Due to the low density of Mars atmosphere a hermetically-sealed paraglider was proposed. In order to investigate the effect of the modification of the inlet on the lift-to-drag ratio the wind-tunnel tests were carried out. It was found that the elimination of the inlet not only decreased the drag but also increased the lift. In the preliminary design of a propeller it should have a diameter of 1m and be a deployable type to generate the required thrust. The one-forth scale model was fabricated to show its self-deployment capability.

1. Introduction

In the past years a number of spacecrafts were sent to Mars: The Mars orbiters mapped the whole surface of the planet and obtained the images in good resolution, and the ground rovers were also successful to carry out the in-situ scientific analyses in detail. These rovers can move to the desired area by itself, however, the travelling speed is quite low. In order to enlarge the field of the investigation with limited resources it is advantageous to employ an aerial vehicle.

Since the atmospheric density is low on Mars, the flight speed of such vehicle should be high enough to sustain its weight with a limited wing area. A high-speed flight should raise undesired effect on the scientific measurement. In order to avoid this problem the aerial vehicle using a paraglider is proposed. This aerial vehicle has two big advantages. First, the flight speed could be drastically reduced because of its deployable large wing area. Secondly, it can be controlled by a simple mechanism and can land softly on a desired place on the Martian surface.

Since the density of Martian atmosphere is only about one hundredth of that of Earth atmosphere, the ram pressure might be insufficient to withstand the wing loading on the canopy due to the low flight speed. Therefore, it is beneficial to seal the inlet of the paraglider and to inflate it compulsively by the gas supplied from an on-boarded bottle. Such hermetically-sealed paraglider is expected to have a better gliding performance since the aerodynamic drag is not generated at the air intake. In the present study, the validation of the improvement of the gliding performance was conducted in the low-speed wind tunnel test. Then, the preliminary design of the propeller was also conducted.

2. Concept of Compulsively-Inflated Paraglider

In Fig.1 the required power of an aerial vehicle is shown as a function of the wing loading. A higher wing loading means a higher flight velocity. To achieve a higher flight speed, higher power is required to maintain the flight. In the figure, two cases were considered, a flight on the surface and that at the altitude of 10km. Since the atmospheric density is thicker on the surface, the required power should increase. In the figure the lift-to-drag ratio of the vehicle was set to 4. For the comparison, the higher-gliding-ratio case (L/D=10) was also presented. As is readily known, the higher lift-to-drag ratio drastically decreases the required power. In the present calculation the upper limit of the required power was assumed 500W. Under such condition the maximum wing loading should be 2N/m^2 when L/D is 4, and 10N/m^2 when L/D is 10.

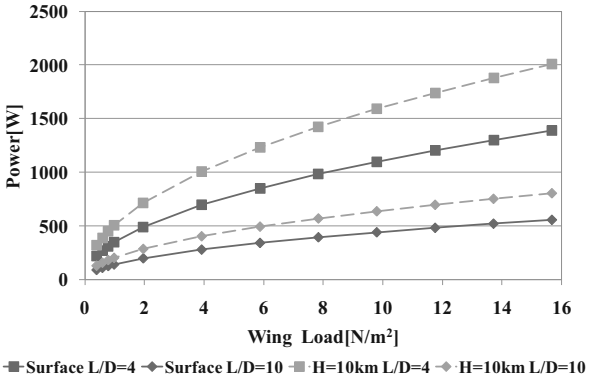

Fig.1 Required power at Mars surface and 10km in altitude as a function of wing loading

The lower wing loading results in the lower ram pressure. For the wing loading of 2~3N/m^2 the corresponding ram pressure was 6Pa. This low ram-air pressure might be insufficient to withstand the wing loading of the canopy. Then, the hermetically-sealed paraglider was proposed. The difference is the elimination of the air inlet. The inflation of the canopy was not achieved by the ram pressure of the Martian atmosphere but by the supplied gas from the on-boarded bottle. The merits of such sealed paraglider are the reliable wing formation due to the inflator and the better gliding performance. Since the air intake generates the aerodynamic drag, the elimination of the intake should contribute to the improvement of the lift-to-drag ratio. For comparison, three kinds of paragliders were considered, conventional ones with the aspect ratio of 3 and 6, and the hermetically-sealed one with the aspect ratio of 3. In Table 1, the comparisons of the configurations and aerodynamic characteristics were made for the three canopies.

Table 1 Comparison of configurations and aerodynamic characteristics of paragliders.

	With Inlet AR=3	No Inlet AR=3	With Inlet AR=6
Aspect ratio	3	3	6
h/c	0.08	0	0.08
Inlet C_D	0.04	0	0.04
Induced drag C_D (C_L=0.3)	0.014	0.014	0.007
Airfoil drag	0.015	0.015	0.015
Surface Irregularities and Fabric Roughness	0.004	0.004	0.004
Line drag C_D	0.014	0.014	0.020
Total drag C_D	0.087	0.047	0.086
L/D	3.46	6.40	3.50
Power [W]	545	307	539

Noting the lift-to-drag ratio, it was found that the increment of the aspect ratio did not contribute to the improvement of the lift-to-drag ratio. Since the increment of the aspect ratio requires the increment of line number, the increment of the line drag cancels the advantage of the decrement of the induced drag. It should be noted that the lift-to-drag ratio of the hermetically-sealed paraglider was estimated 6.40 even with the aspect ratio of 3. The elimination of the inlet decreases 40% of the total drag of the canopy and serves in 44% decrease of the required power.

3. Validation of Lift-to-Drag Ratio in Wind Tunnel

In order to investigate the effect of the elimination of the inlet on the lift-to-drag ratio, the wind-tunnel tests were carried out. This experiment was conducted in Eiffel-type low-speed wind tunnel. A wing model with a span of 300mm and a chord of 600mm was inserted in the test section. The sectional airfoil was Clark-YM15. Three different wing models were prepared in the present tests: a model with open inlet, one with closed inlet, and one without inlet. The leading edge and the ribs of the models were made of styrene form and the film covered the rest of the surface. The free-stream velocity was set 15m/s. The angles of attack of the wing were varied from 0 to 15 degrees.

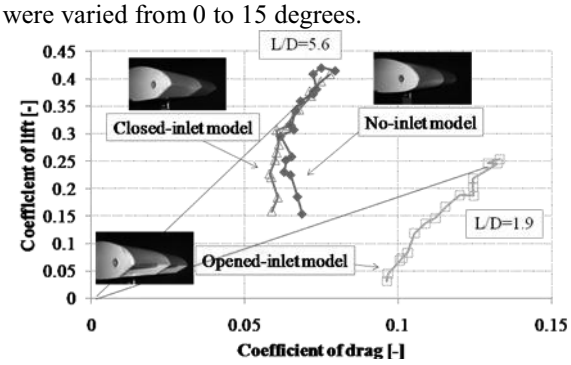

Fig.2 Estimated polar curves of three models

Fig.2 compared the polar curves of the three models. Since the aspect ratio of the wing models was 0.5, the obtained polar curves in the tests were converted to those for an aspect ratio of 2.2. The open-inlet model a) showed the worst lift-to-drag ratio and the other models showed the similar curves. As was known, the best lift-to-drag ratio was 5.6. Through the measurement in the wind tunnel the drastic improvement of the lift-to-drag ratio was confirmed. This improvement of the lift-to-drag ratio is quite advantageous in the Mars exploration, because the tremendous reduction of the require thrust should be achieved.

4. Preliminary Design of Deployable Propeller

Next, the preliminary design of the propeller for the Mars paraglider was conducted. In this analysis the necessary thrust was set 7.88N and the upper limit of input power was set 500W.

The preliminary design of the propeller blade was made using the formula presented by Adkins and Liebeck. In Fig.3 the obtained propeller shape was presented in the span-wise direction. The diameter of the propeller was 1.0m. Since the acceptable envelope in the spacecraft is expected to be around 0.5m, therefore, some deploying mechanism is needed.

Fig 4 shows the pictures taken during the self-deployment sequence of the one-fourth scaled model of the propeller, and it demonstrated successfully its self-deployment capability.

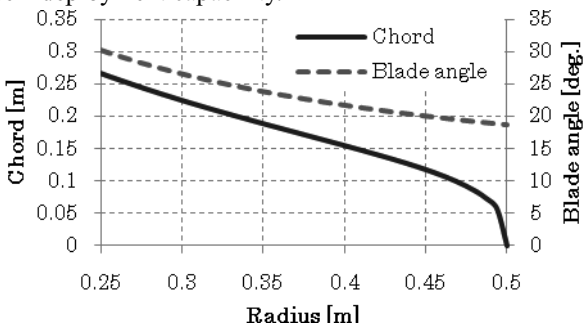

Fig.3 Designed propeller shape in spanwise direction.

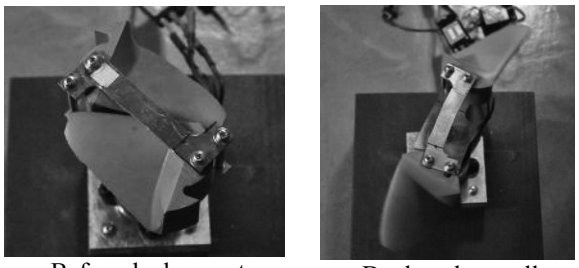

Before deployment Deployed propeller

Fig.4 Deployment test of one-fourth scaled propeller

5. Concluding remarks

A compulsively inflated paraglider was proposed in the present study. The elimination of the inlet was expected to decrease the aerodynamic drag. In order to investigate the effect of the modification of the inlet on the lift-to-drag ratio the wind-tunnel tests were performed. It was found that the elimination of the inlet not only decreased the drag but also increased the lift. The preliminary design of a propeller to generate the required thrust was also conducted. It was found that the propeller should have a diameter of 1m and should be a deployable type to be stored in a spacecraft. The one-forth scale model was fabricated for the feasibility purpose, and it successfully demonstrated its self-deployment capability.

Eighth International Conference on Flow Dynamics
November 9 - November 11, 2011

Airfoil Design for Mars Aircraft Using Modified PARSEC Geometry Representation

Masahiro Kanazaki *, Tomoyoshi Yotsuya *, and Kisa Matsushima **
*Tokyo Metropolitan University, 6-6 Asahigaoka Hino-shi Tokyo, Japan.
** University of Toyama, Gofuku 3190, Toyama-shi, Toyama 930-8555, Japan.
kana@sd.tmu.ac.jp

ABSTRACT

Designers can easily understand which parameters are important in the PARSEC (PARametric SECtion) representation, because each parameter is determined based on the flow physics. To solve various airfoil design problems with a number of design variables, a modified PARSEC representation was proposed. In this study, the proposed representation is used along with multi-objective genetic algorithms to solve the airfoil design problem in the Martian atmosphere for several target lift coefficient. MOGA results show set of airfoils which has possibility to be employed for Martian airplane.

1. Introduction

The PARSEC (PARametric SECtion) airfoil representation [1] and its modifications [2] are generic methods for designing airfoils. Previously, a modification of the original PARSEC representation was proposed, which represented supersonic/transonic airfoils and low-Reynolds-number airfoils very well [2, 3].

In the present study, this modified representation is employed for designing an airfoil to be used in a low Reynolds number flow, such as the Martian atmosphere [4]. A design exploration process based on a multi-objective genetic algorithm (MOGA) is applied to this airfoil design problem.

2. Design Method

2. 1. Airfoil Representation

To improve the design performance around the leading edge, the airfoil's thickness and camber should be separately defined. This idea is based on the common theory of a wing section, shown in Fig. 1. The thickness distribution (z_t) and the camber (z_c) are defined by Eqs. (1) and (2), respectively. z_c is defined by a quintic equation, to which a square root term is added to obtain better performance. By weighting this term, the camber of the leading edge can be varied independently. The present modification is expected to represent an airfoil with a drooping leading edge.

$$z_t = \sum_{n=1}^{6} a_n \times x^{\frac{2n-1}{2}} \tag{1}$$

$$z_c = b_0 \times \sqrt{x} + \sum_{n=1}^{5} b_n \times x^n \tag{2}$$

In Eqs. (1) and (2), a_n and b_n are determined from the design variables shown in Fig. 1.

2. 2. Design Problem

In this study, airfoils design problem was solved using a MOGA [3, 4] and considering the objective functions as

maximize: airfoil thickness (t)
minimize: drag coefficient (C_d)
subject to: lift coefficient (C_l) = target C_l.

The designed airfoil is supposed to be used for 60m/s flight in the Martian atmosphere. On the basis of this condition, CFD calculation is carried out with Reynolds number as 208235.3 and Mach number as 0.233. Flowfield is solved structured mesh based Reynolds-averaged Navier-Stokes solver. In this study, the design problem is solved assuming three values of target C_l: 0.8, 1.0, and 1.2.

2. 3. Computational Fluid Dynamics

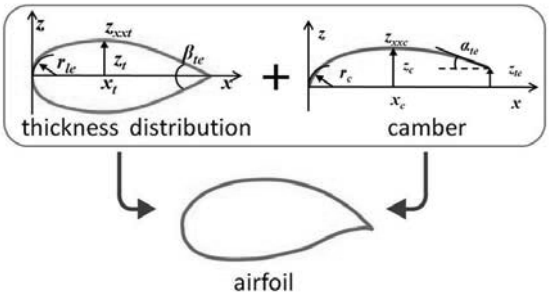

Figure 1 Modified PARSEC representation and design parameters.

3. Results and Discussion

Each non-dominated solution is shown in Fig. 2. Many non-dominated solutions could be obtained, and it was found that in each case, there is a trade-off between two objective functions. It was also found that the design result for C_l = 1.2 showed the most severe trade-off, as is evident by comparing Fig. 2(a)-(c).

The non-dominated solutions that have about 7%c thickness are selected from Fig. 2(a)-(c) to observe their geometries and pressure distributions; these are shown in Fig. 3(a)-(c), respectively. According to Fig. 3, each design has a large camber and small leading edge radius. Remarkably, all solutions have a drooped camber around the leading edge and a smooth surface with a large camber. Because of this, the flow on the upper surface of each design is gradually accelerating. Comparing Fig. 3(a)-(c), it can be seen that the design in Fig. 3(c) has the largest camber without an extreme suction peak; this is because the camber around the leading edge is designed properly. Figure 4 shows the comparison of drag polar among the selected solutions. According to this figure, if an airfoil that achieves higher C_l without increasing C_d is required, the design problem should be solved under the higher target C_l.

Detailed data mining results and the characteristics of the thicker airfoil will appear in the final presentation.

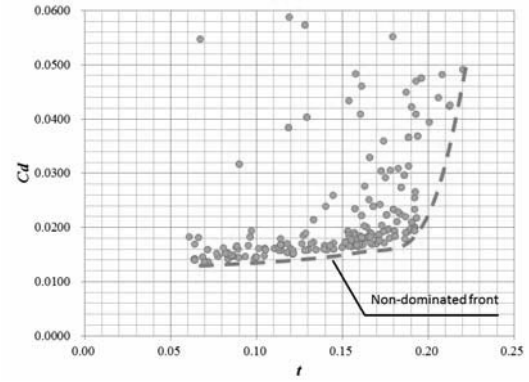

(a)

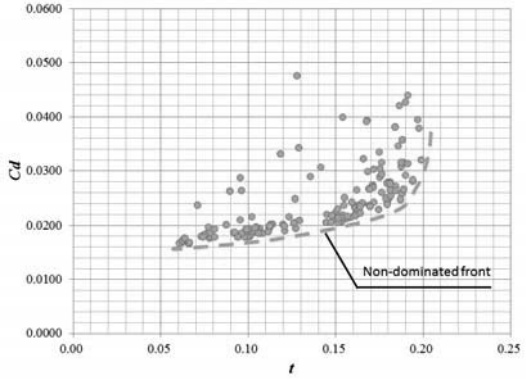

(b)

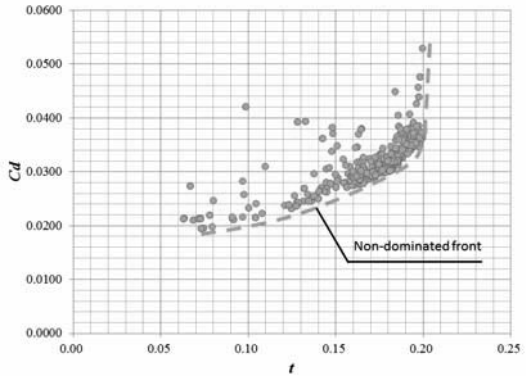

(c)

Figure 2 MOGA results. (a) C_l = 0.8, (b) C_l = 1.0, and (c) C_l = 1.2.

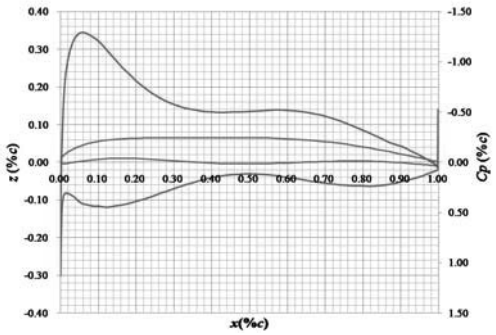

(a)

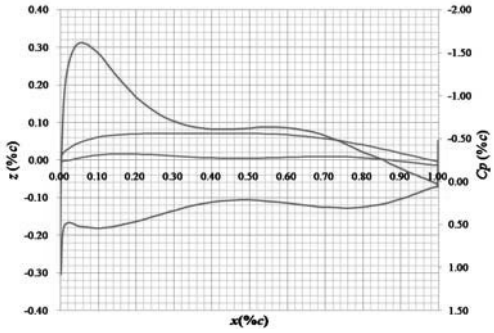

(b)

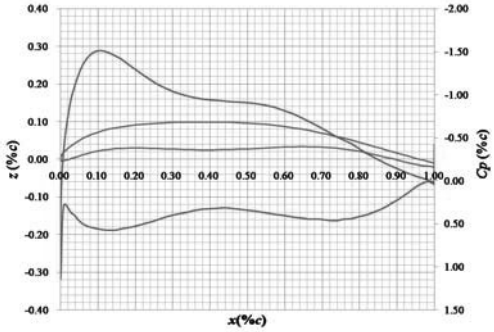

Figure 3 Selected designs (t/c is about 7%*c*) and their pressure distributions. (a) C_l = 0.8 (angle of attack = 2.85°), (b) C_l = 1.0 (angle of attack = 3.65°), and (c) C_l = 1.0 (angle of attack = 3.09°).

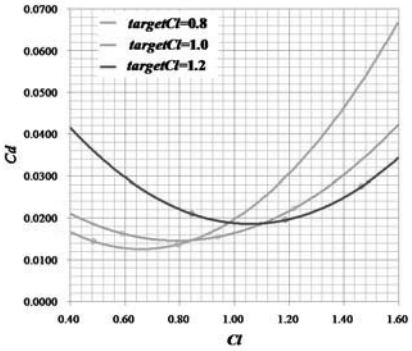

Figure 4 Comparison of drag polar among selected solutions.

References

[1]H., Sobieczky, *Notes on Numerical Fluid Mechanics*, (1998), pp. 71-88.
[2]K.,Matsushima, et al., *Proc ECCOMS2008*, (2008).
[3]T.,Yotsuya, et al., Proc EUROGEN2011, (2011).
[4]A.,Oyama, et al, AIAA-2006-1484, (2006).

Eighth International Conference on Flow Dynamics
November 9 - November 11, 2011

Variable-pressure Wind Tunnel Test on Low Reynolds Number Aerodynamic Characteristics of Three-dimensional Wings

Shintaro SHIGEOKA, Hiroshi OCHI, Koichi YONEMOTO, Takahiro KOBAYASHI,
Eiji KATO, Tomohiro NARUMI, Takaaki MATSUMOTO
E-mail: yonemoto@mech.kyutech.ac.jp

ABSTRACT

In order to achieve flight in Mars atmosphere, which is characterized by low Reynolds number, knowledge about aerodynamic characteristics of wing in low Reynolds number flow is necessary. The purpose of this study is to investigate wing geometric effects on aerodynamic characteristics of three-dimensional wing by using a variable-pressure wind tunnel. Aerodynamic characteristics of nine wings, which differ in airfoil shape (NACA0012, flat plate and Ishii airfoil) and aspect ratio (4, 6 and 8) are investigated. The results show that Ishii airfoil has higher stall angle, and linear lift curve slope compared with those of NACA0012 and flat plate.

1. Introduction

Mars exploration airplane is now under research in Japan. Authors are researching aerodynamic characteristics of wing in low Reynolds number flow as a member of the working group for Mars exploration aircraft[1].

Since the Mars exploration airplane must fly with low-speed at higher angle of attack, the flight Reynolds number in Mars atmosphere is very small. Airfoil shape and aspect ratio affect aerodynamic performance significantly in the low Reynolds number. Yonemoto et al. have studied the strong nonlinearity of aerodynamic characteristic in low Reynolds number range[2-3].

In this paper, the characteristics of three-dimensional wings at low Reynolds number is investigated. Wind tunnel tests of nine wings that differ in aspect ratio and airfoil shape are conducted in the range of Reynolds number from 5.0×10^3 to 1.0×10^5.

2. Experimental setup

2-1 Wind tunnel

In order to generate low Reynolds number condition, a variable-pressure wind tunnel that belongs to Nishinippon Institute of Technology is utilized (Fig. 1). Experimental conditions are as follows; Reynolds number varies from 5.0×10^3 to 1.0×10^5, by changing the total pressure from 10 [kPa] to 101.3 [kPa].

Fig.1 Variable-pressure wind tunnel.

2-2 Force balances

Since the test Reynolds number range is very wide, two kinds of tri-axial force balance that have different load capacities are used in order to measure aerodynamic characteristic accurately (Fig. 2).

The force balance is mounted to a turn table on the ceiling of wind tunnel. The test wing is fixed under the force balance. The angle of attack is changed from -10 to 30[°] every 1 [°] by the turn table.

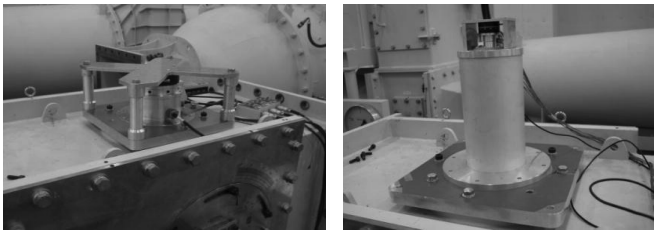

(Load capacity 5N) (Load capacity 0.5N)

Fig. 2 Force balances

2-3 Test wings

Nine wings, which have NACA0012, flat plate (thickness is 6 mm) and Ishii airfoil cross section with three aspect ratios of 4, 6 and 8, are tested (Fig.3 and 4).

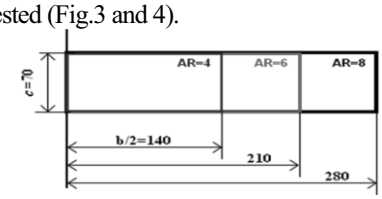

Fig.3 Plan views of tested wings.

(NACA0012) (Flat plate)

(Ishii airfoil)

Fig.4 Wing cross-sections

3. Test Results

Wind tunnel test are conducted to obtain aerodynamic coefficients, C_L, C_D and $C_{Mc/4}$ by measuring aerodynamic forces. Fig. 5~7 show lift characteristics of each airfoils; for the Reynolds number of 3×10^4.

The lift curve slopes of NACA0012 are completely nonlinear, and depend on aspect ratio for the whole angle of attack region. However, the maximum lift coefficient increases in proportion to aspect ratio. On the other hand, the stall angle decreases as aspect ratio increases. The lift curve slope and stall angle of flat

plate and Ishii airfoil are less affected by the aspect ratios than NACA0012. The lift curve slope of flat plate and Ishii airfoil are linear up to stall angle. The lift coefficients are almost constant when the angle of attack exceeds stall angle.

The stall angle of flat plate is almost the same as NACA0012, but Ishii airfoil has larger stall angle. Ishii airfoil yields high lift coefficient in higher angle of attack in comparison with other wings. The maximum lift coefficient of Ishii airfoil is 1.5 times larger than that of NACA0012 and flat plate.

The lift characteristics of Ishii airfoil under different Reynolds numbers from 7.85×10^3 to 1.05×10^5 are compared as shown in Fig.8. The maximum lift and stall angle increase as the Reynolds number get larger for $10^4<Re<10^5$. However, the lift curve slopes for $Re<10^4$ are relatively moderate. The smaller the Reynolds number, the gentler the lift curve slope becomes. The lift coefficients far beyond the stall angle become constant and independent of aspect ratio.

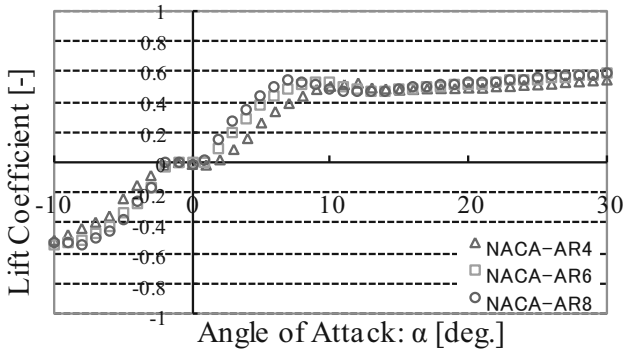

Fig. 5 Lift coefficient of NACA0012 (Reynolds number: 3×10^4).

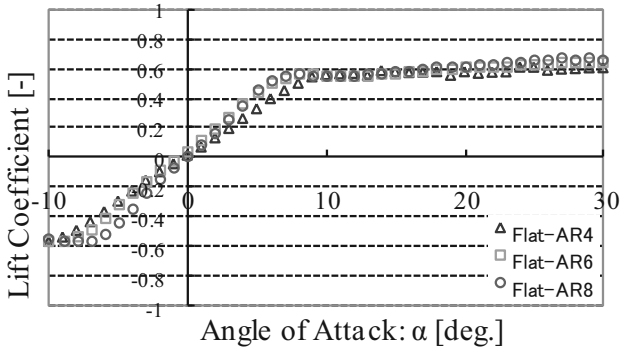

Fig. 6 Lift coefficient of flat plate (Reynolds number: 3×10^4).

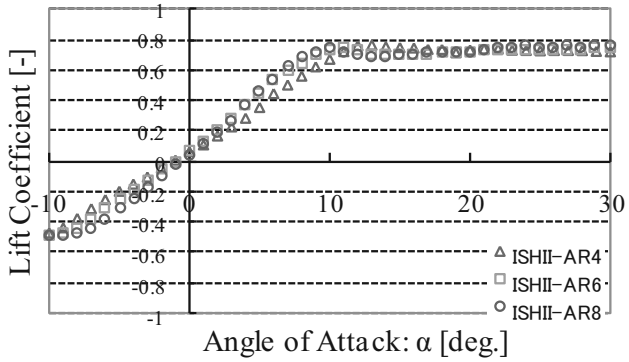

Fig. 7 Lift coeffient of Ishii airfoil (Reynolds number: 3×10^4).

4. Conclusions

Using variable-pressure wind tunnel, three dimensional aerodynamic characteristic measurement of NACA0012, flat plate and Ishii airfoil of aspect ratio of 4, 6 and 8, are conducted for the Reynolds number from 5×10^3 to 1×10^5. The findings are following:

- The lift coefficient characteristics of flat plate and Ishii airfoil are linear and less affected by aspect ratio. However, NACA0012 has strong nonlinearity.
- The stall angle of attacks of all tested wings get smaller as the aspect ratio becomes larger.
- The maximum lift coefficient and the stall angle of Ishii airfoil are affected by Reynolds number for $Re>10^4$, and the lift curve slope for $Re<10^4$ respectively.
- Ishii airfoil has the highest lift coefficient and stall angle among the three airfoils.

References

[1] A. Oyama, "Conceptual Design of Mars Airplane for MELOS1," 54th Symposium on Space Science and Technology Conf., (2010) 3F01.

[2] K. Yonemoto, T. Sato, H. Ochi, and K. Takato, "Aerodynamic Characteristics of Wings at Low Reynolds Number Using Variable-Pressure Wind Tunnel," Proceedings of the 2007 JSASS- KSAS Joint International Symposium on Aerospace Engineering, (2007), pp. 172-175.

[3] T. Otake, Y. Nakae, T. Motohashi, "Nonlinearity of the Aerodynamic Characteristics of NACA0012 Aerofoil at Low Reynolds Numbers," Journal of the Japan Society for Aeronautical and Space Sciences. Vol. 55, No. 644, (2007), pp. 439-445.

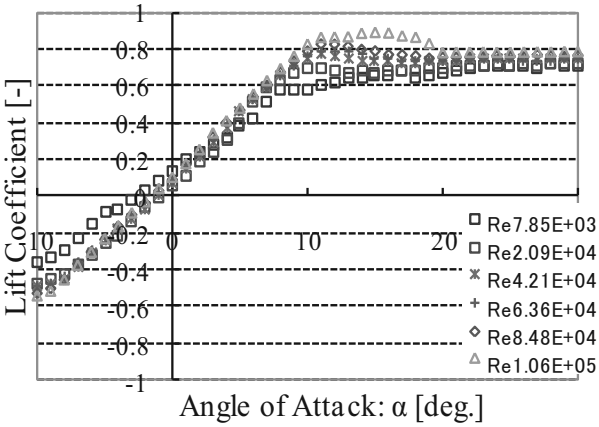

Fig. 8 Lift coeffient change of Ishii airfoil (aspect ratio: 6).

Eighth International Conference on Flow Dynamics
November 9 - November 11, 2011

PIV Flow Visualization around Three-dimensional Wings in a Variable-pressure Wind Tunnel

Gaku Sasaki[1], Kyoshiro Itakura[1], Eiji Kato[1], Hiroshi Ochi[2], Koich Yonemoto[1],
Tomohiro Narumi[1] and Takaaki Matsumoto[1]
[1] Department of Mechanical and Control Engineering, Kyushu Institute of Technology
[2] Department of Mechanical System Engineering, Nishinippon Institute of Technology
yonemoto@mech.kyutech.ac.jp

ABSTRACT

Mars exploration aircraft is currently under research in Japan for a planetary exploring mission in near future. Aerodynamic characteristics on Mars are extremely different from that of Earth because and the atmospheric density is approximately 1/100 and the range of Reynolds number is from 10^4 to 10^5. The purpose of this study is to investigate the flow field around the three-dimensional wings in terms of three different kinds of airfoil in low Reynolds number flows using PIV (Particle Image Velocimetry) method. The visualization results show that the laminar separations can be classified into three types.

1. Introduction

Mars exploration airplane for widespread and detailed reconnaissance is researched as a future mission. Authors are studying aerodynamic characteristics of fixed-wing aircraft in Mars atmosphere as a member of the working group for Mars exploration aircraft [1].

The flight Reynolds number on Mars is 10^4~10^5 because the atmospheric density is approximately 1/100 of that of the earth. Therefore the aerodynamic characteristics in Mars atmosphere are different from that of our planet, where complex laminar separation is likely to occur. Thus the knowledge on low Reynolds number flow around three-dimensional wings is necessary and important for developing Mars airplane.

In this paper, wind tunnel test results of Particle Image Velocimetry (PIV) measurements are discussed, which were conducted for observing flow filed around 3 types of wing models in a variable-pressure wind tunnel at the flight Reynolds numbers of Mars airplane.

2. Method

The wind tunnel test is conducted in the variable-pressure wind tunnel at Nishinippon Institute of Technology using a PIV system consists of laser, high-speed camera and synchronizer (Fig. 1). The total pressure in the wind tunnel can be reduced to 10 kPa, and the Reynolds number can be changed to the order of 10^4 without changing flow velocity.

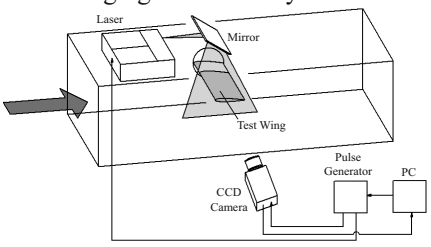

Fig. 1 Experimental setup of PIV measurement.

All the wind tunnel test models are rectangular semi-span wings with the chord length of 70mm and the aspect ratio of 6. They have three different airfoil cross sections (Fig. 2). NACA0012 airfoil has a lot of wind tunnel test data as a typical reference shape. Ishii airfoil has been invented for hand launch gliders to perform good flight capability under low Reynords number.

Small tracer particles in a cross-sectional area around the test model, which are shed in the wind tunnel by spraying aqueous solution of glycerin using a nebulizer, is illuminated by laser light sheet irradiated from a ceiling window of the measurement section. Then the photos of scattered light from the tracer particles are taken from the side wall of the measurement section. The laser photographing and irradiation are synchronized by a pulse generator, and the interval time between a couple of images is 20-50 micro seconds. Up to 15 image pairs can be stored per second.

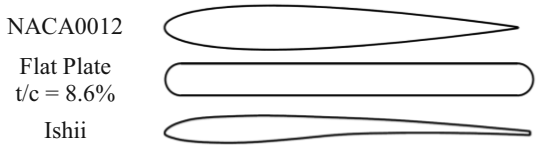

Fig. 2 Airfoil cross sections.

It is possible to obtain velocity vector distributions from 95 sets of image pairs per one wind tunnel test using an image analysis software. The inspection area is 32×32 pixels.

Overlap rate is 50 percent. The lower surface of airfoil, where the laser does not illuminate, is masked. The wind tunnel tests are conducted for four different Reynolds number conditions; 1.0×10^4, 2.0×10^4, 3.0×10^4 and 4.0×10^4. Angle of attack is changed every 2° from 0° to 14°. In case of photographing over all airfoil, the captured area is 100 × 100 mm^2, whereas in case of zooming in forward edge or trailing edge, the area is 45 × 45 mm^2.

3. Results and Discussion

Fig. 3 shows velocity vector distributions near the trailing edge of the three different wind tunnel test models for Re=2.0×10^4 at α=2°, 6°. The flow separation from airfoil surface generates unsteady vortices sheds downstream on the surface of airfoil, except for the trailing edge flow separation of NACA0012 and Ishii wings at low angles of attack. Nonlinear lift characteristic in low Reynolds number flow, which is

influenced by its size and presence or absence of separation bubble, is caused by reattaching flow behind the laminar separation. However it is difficult to identify the reattachment in the unsteady flow condition. Therefore, we employ time-averaged flow fields to evaluate the flow characteristics.

Fig. 4 shows the averaged flow fields produced by averaging 95 sets of image pairs. The flow fields can be divided into three groups: 1) Separation covers around trailing edge under low angle of attack. 2) Separation bubble is produced by reattaching flow after the separation. 3) Stalled flow generated by flow separation from the leading edge to trailing edge.

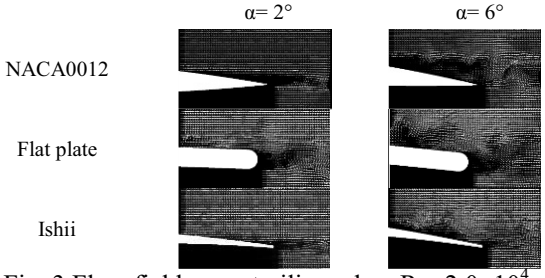

Fig. 3 Flow fields near trailing edge: Re=2.0×10^4.

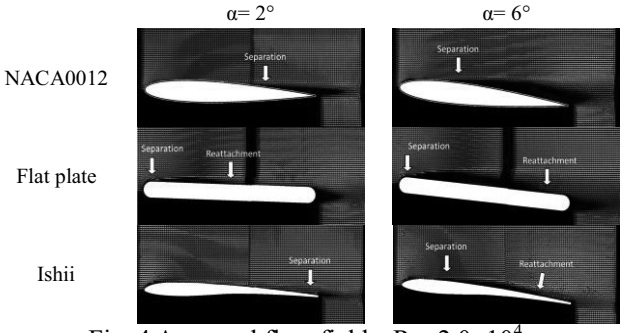

Fig. 4 Averaged flow fields: Re=2.0×10^4.

Fig. 5 shows the force balance test results[4] measured in the same condition of the present PIV tests. Ishii wing has a lift curve slope becomes slightly steep nearα=6°, where separation bubble starts to generate. Flat plate wing shows linear lift curve slope, where separation bubbles always exist near the leading edge for the whole angles of attack. The average upper surface flow for the three wings is classified into four groups as shown in Table 1.

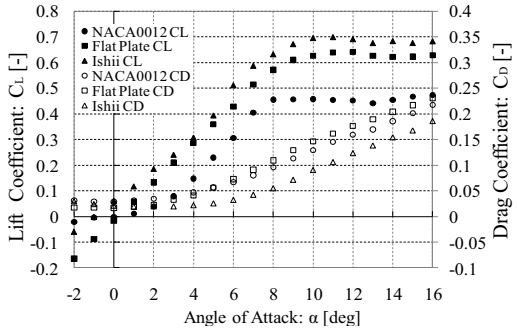

Fig. 5 Lift and drag characteristics by force balance measurement (Re=2.0×10^4).

Table 1. Classification of flow pattern characteristics of upper surface airfoil (Re=2.0×10^4).

where NS: No Separation, STE: Separation at Trailing Edge, SB: Separation Bubble, SLE: Separation at Leading Edge, TS: Transition between STE and SLE.

Airfoil	Re (×10^4)	angle of attack (°) 0	2	4	6	8	10	12
NACA 0012	1.0	STE			TS		SLE	
	2.0	STE			TS		SLE	
	3.0	STE			SB		SLE	
	4.0	STE			SB			SLE
Flat Plate	1.0	NS	SB				SLE	
	2.0	SB					SLE	
	3.0	SB					SLE	
	4.0	SB					SLE	
Ishii	1.0	STE			TS		SLE	
	2.0	STE			SB		SLE	
	3.0	NS		STE		SB		SLE
	4.0	NS				SB		SLE

4. Conclusions

PIV measurements for the flow around three types of airfoil are conducted at four different Reynolds numbers. As the result, the following findings are obtained;

1) Most of the separation flows are accompanied by unsteady vortices. However, the separation size and presence of separation bubble can be inferred by observing averaged flow field.

2) Averaged flow field can be classified into four groups that relate to the aerodynamic force characteristics of each airfoil as follows:

- Flat plate wing has always reattached flow before the stall, and the size of separation bubble at the leading edge becomes larger as the angle of attack increases. It results in the linear lift curve slope, which is less affected by the Reynolds number.
- Ishii wing has also three flow separation patterns as well as NACA0012. However, the nonlinearity of lift is small due to the small flow separation. The drag is the smallest among the three wings.

3) At Reynolds number of 1.0×10^4~4.0×10^4, the smaller the Reynolds number, the flow separation at trailing edge more likely to occur. On the other hand, the larger the Reynolds number, the separation bubble with reattachment more likely to occur, the size of which get smaller as the Reynolds number increases.

References

[1] A. Oyama, "Conceptual design of Mars airplane for MELOS," *54th Space Science Technology Conf.*, 2010, 3F01.

[2] Y. Jimba et al., "Study of the low Reynolds number aerodynamic characteristics for Mars airplane," *54th Space Science Technology Conf.*, 2010, 3F05.

[3] K. Yonemoto et al., "Non-linear Aerodynamic Characteristics of Three Dimensional Wing at Large Range of Reynolds Number," *40th Fluid Dynamics Conf. / Aerospace Numerical Simulation Symp.*, 2008, pp.323-326.

[4] S. Shigeoka et al., "Variable-pressure Wind Tunnel Test on Low Reynolds Number Aerodynamic Characteristics of Three-dimensional Wings," *8th Int. Conf. on Flow Dynamics*, 2011. (to appear)

Eighth International Conference on Flow Dynamics
November 9 - November 11, 2011

Profile and Induced Drag Decomposition of Low Reynolds Number Flow around Three-dimensional Wing by Wake Survey

Takahiro Kobayashi, Koichi Yonemoto, Tomohiro Narumi, Takaaki Matsumoto
Department of Mechanical and Control Engineering, Kyushu Institute of Technology
E-mail : yonemoto@mech.kyutech.ac.jp

ABSTRACT

This paper addresses lift and drag distributions along wing span in low Reynolds number flow. The wakes of three-dimensional wings with NACA0012, flat plate and Ishii airfoil cross sections are surveyed in a low speed wind tunnel using a wake integration method (WIM), which can decompose the total drag into the profile and induced drags. The results of wake survey agree well with those obtained by the force balance test, and show that not only the induced drag but also the profile drag increases remarkably with increase of angle of attack.

1. Introduction

An aircraft is expected as a new exploration method on Mars. Kyushu Institute of Technology is conducting researches on the aerodynamics of Mars aircraft as a member of the working group organized by JAXA (Japan Aerospace Exploration Agency). The flight Reynolds number in Mars atmosphere is low (10^4 to 10^5), because the atmospheric density of Mars is about 1/100 of the earth. The aerodynamic characteristic differs significantly from that on the earth[1].

Force balance test is commonly used as an aerodynamic measurement in wind tunnel. However, authors use a wake integration method (WIM) instead, which enables spatial analysis of lift and drag distribution along wing span, and decomposition of the drag into profile and induced drags[2]. These measurement capabilities are important to clarify the aerodynamic characteristic of three dimensional wings in low Reynolds number flow.

In this paper, the lift and drag distributions of three dimensional wings with NACA0012, flat plate and Ishii airfoil cross sections are measured. In addition to, the relationship between the profile and induced drag is investigated quantitatively.

2. Experimental setup

Wind tunnel tests were carried out in a low speed wind tunnel facility at Kyushu Institute of Technology. The test section size is 0.45m(H)×0.45m(W)×1.35m(L). The velocity turbulence level is 0.1% or less. The measurement Reynolds number are 30000 and 100000. The Range of angles of attack was from 0 to 14° at the interval of 2°. Three wings, that have NACA0012, flat plate (t/c=8.6%) and Ishii airfoil cross sections[3] were tested. The wing dimensions are shown in Table 1 and the wing cross section are shown in Fig.1. Static and total pressure, pitch and yaw angles of wake region are measured by 5-holes pitot tube of which tip diameter is 1.8mm and shape is 30° conical.

Table 1 Wing dimensions

Airfoil Cross Section	Aspect ratio (AR)	Span[mm]	Chord[mm]
NACA0012	4	140	70
Ishii airfoil	6	210	70
Flat plate(t/c=8.6%)	8	280	70

Fig. 1 Wing cross-sections.

3. Wake integration method

The force acting on wing is calculated by momentum difference between the upstream and downstream[2]. The momentum conservation law gives the lift as in Eq.(1), where subscript ∞ refers to the upstream.

$$\begin{aligned} L &= -\iint_S \rho w(\vec{u}\cdot\vec{n})ds - \iint_S (P-P_\infty)n_z ds \\ &= \rho_\infty U_\infty \iint_{WA} y\xi ds - \rho_\infty {U_\infty}^2 \iint_{WA} \frac{w}{U_\infty}\frac{\Delta u}{U_\infty} ds + O(\Delta^3) \end{aligned} \tag{1}$$

The drag is decomposed as follows:

$$\begin{aligned} D = \iint_{W_A} P_\infty \frac{\Delta s}{R} dydz + \frac{\rho_\infty}{2}\iint_{W_A}\left(v^2+w^2\right)dydz \\ - \iint_{W_A}\frac{P_\infty}{2}\left(\frac{\Delta s}{R}\right)^2 + O(\Delta^3) \end{aligned} \tag{2}$$

where the variation of entropy Δs is given by the total pressure loss ratio $P_{T\infty}/P_T$ as follows:

$$\Delta s = R\ln\frac{P_{T_\infty}}{P_T} \tag{3}$$

The first term of right hand side of Eq. (2) is the profile drag, and the second term is the induced drag. Other terms are negligible small so that Eq. (2) is approximately reduced to the following equation:

$$D \approx D_p + D_i \tag{4}$$

where,

$$D_p = \iint_{W_A} P_\infty \frac{\Delta s}{R} dydz = qSC_{D_P} \tag{5}$$

$$D_i = \frac{\rho_\infty}{2}\iint_{W_A}\left(v^2+w^2\right)dydz = qSC_{D_i} \tag{6}$$

where q is the dynamic pressure, S is the wing reference area.

4. Results

4.1 Comparison with force balance test

In order to evaluate the accuracy of WIM, the measurement result was compared with that of force balance test conducted in a Variable Pressure Wind Tunnel at Nishinippon institute of technology . The lift

and drag characteristics of Ishii wing (AR=6) for Re=1×10^5) are shown in Fig.2 with fairly good agreement with the force balance test.

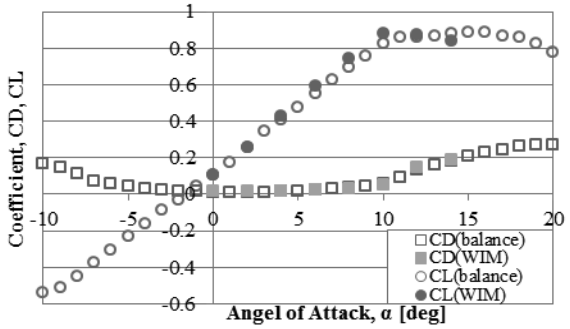

Fig. 2 Lift and drag of Ishii wing (AR=6) in comparison with force balance test (Re=1×10^5).

4.2 Spanwise lift and drag distribution

The span wise lift distribution of Ishii wing (AR=6) for Re=1×10^5 is shown in Fig.3. The lift is almost constant along the wing span from the root to middle, and decreases gradually toward wing tip at lower angle of attack. However, when the angle of attack exceeds the stall angle at around α=12°, the lift distribution slightly decreases at the inboard span.

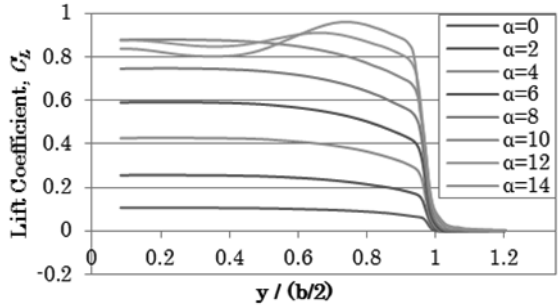

Fig. 3 Span wise lift distribution of Ishii wing (AR=6) for Re=1×10^5.

The spanwise profile and induced drag distributions of Ishii wing (AR=6) for Re=1×10^5 are shown in Fig.4 and Fig. 5 respectively. The profile drag along the wing span except in wing tip is almost constant regardless of the angle of attack. When the angle of attack exceeds stall angle, it increases rapidly as the angle of attack increases due to the large upper-surface flow separation from the wing leading edge. In contrast, the profile drag at the wing tip increases with the increment of angle of attack due to the pressure loss caused by wing tip vortices.

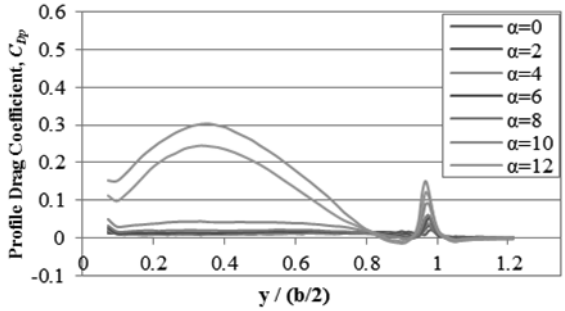

Fig.4 Span wise profile drag distribution of Ishii wing (AR=6) for Re=1×10^5

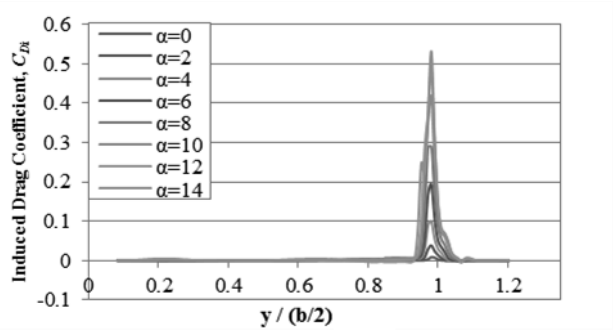

Fig. 5 Span wise induced drag distribution of Ishii wing (AR=6) for Re=1×10^5

4.3 Profile and induced drag

The profile and induced drag coefficients of Ishii wing at Re=1×10^5 is shown in Fig.6. The induced drag coefficient increases with increasing the angle of attack. The profile drag coefficient is almost constant until α=8°, but then increases rapidly. Most of the total drag is occupied by the profile drag at the higher angle of attack.

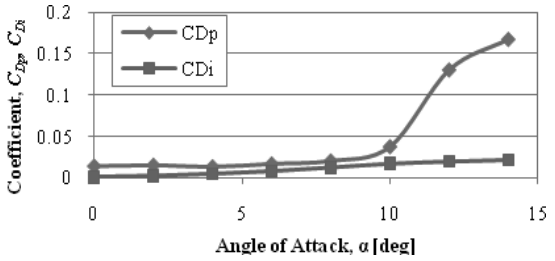

Fig. 6 Profile and induced drag (AR=6) for Re=1×10^5.

5. Conclusion

In order to investigate the aerodynamic characteristics of three dimensional wings in low Reynolds number flow, WIM was applied to the wind tunnel wake measurement. The WIM shows fairly good agreement with that of force balance test. The profile drag is almost constant at lower angle of attack, but increases rapidly when large flow separation occurs. Most of the total drag is occupied by the profile drag rather than the induced drag at higher angle of attack.

References

[1] Yonemoto, K. "Research Issues on Mars Exploring Micro Plane Using Energy Transmission," 25th International Symposium on Space Technology and Science, ISTS 2006-k-14, Kanagawa, Japan, June 4-11, (2006).

[2] Kusunose, K. "A Wake Integration Method for Airplane Drag Prediction," The 21st Century COE of Flow Dynamics Lecture Series Volume 3, Tohoku University Press, (2005).

[3] Koike, M. and Ishii, M., "Aerodynamic Performance of Hand Launch Glider," Journal of the japan society for aeronautical and space sciences, Vol.57, No.663, (2009), pp. 166-174.

Eighth International Conference on Flow Dynamics
November 9 - November 11, 2011

Numerical Study on Aerodynamic Characteristics of Two-dimensional Airfoil for Mars Exploration UAV

Ken Nishihara[1], Keiichiro Takato[2], Kouki Ishibashi[1], Koichi Yonemoto[1],
Tomohiro Narumi[1], Takaaki Matsumoto[1]
[1]Department of Mechanical and Control Engineering, Kyushu Institute of Technology
[2]Department of Mechanical System Engineering, Nishinippon Institute of Technology
yonemoto@mech.kyutech.ac.jp

ABSTRACT

The aerodynamic characteristic of wing in low Reynolds number flow is greatly different from that of higher Reynolds number for ordinary aircrafts. This paper addresses airfoil shape effects on the low Reynolds number aerodynamic characteristics. Three different airfoils, that have NACA0012, Ishii and flat-plate cross sections, are investigated using numerical analysis. The results show that Ishii airfoil has the best lift-to-drag ratio among the three airfoils and linear lift curve slope. A comparison between the numerical analysis and wind tunnel test on Ishii airfoil indicates both results are almost identical but minimum drag coefficients are different.

1. Introduction

The Mars exploration by a small airplane in 2020 is planned by JAXA (Japan Aerospace Exploration Agency) in collaboration with Japanese Universities[1]. The authors conduct aerodynamic research of the wing design as a member of the working group[2].

The flight Reynolds number of on the small Mars exploration airplane will be the order of 10^4~10^5, since the atmospheric density of Mars is about 1/100 of that of the earth. Yonemoto et al. studied the strong nonlinearity of wing aerodynamic characteristic in such the low Reynolds number flow[3]. They concluded that the laminar separation near the upper surface trailing edge is the main cause.

In this paper, the three dimensional NS (Navier -Stokes) equation of incompressibility flow is solved under the condition of low Reynolds number that represents Mars flight. The aerodynamic characteristics of NACA0012, Ishii airfoil[4] and flat-plate airfoil are studied numerically.

2. Calculation Method

A direct numerical simulation (DNS) for the NS equation of three-dimensional incompressibility flow is conducted. The NS equations are solved by the MAC (Marker and Cells) scheme. The Kawamura-Kuwahara's scheme is applied to solve the convection terms. A central-difference scheme of second-order accuracy is used to represent other space differences. The discretization of Poisson's equation is also done by the central-difference scheme of second-order accuracy.

The computational grid has 352 points around wing, 150 points for the vertical direction, and 51 points for the span wise direction (Fig. 1). Calculations are conducted for the Reynolds number of 1.0×10^4, 3.0×10^4, 5.0×10^4, 7.0×10^4 and 1.0×10^5. The range of angle of attack is from −4° to 10°.

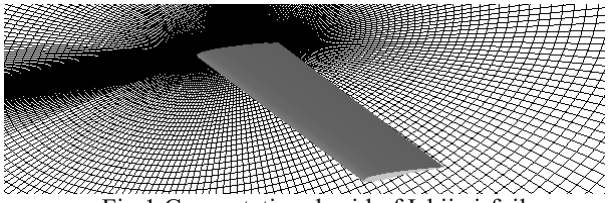

Fig.1 Computational grid of Ishii airfoil.

3. Performance Comparisons of Ishii Airfoil, NACA0012 and Flat-plate

The lift coefficient and the lift-to-drag ratio for Re=3.0×10^4 and 5.0×10^4 are compared in Fig. 2 and Fig. 3 respectively.

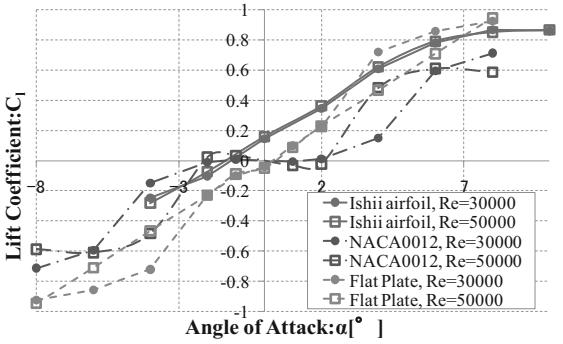

Fig. 2 Lift characteristics.

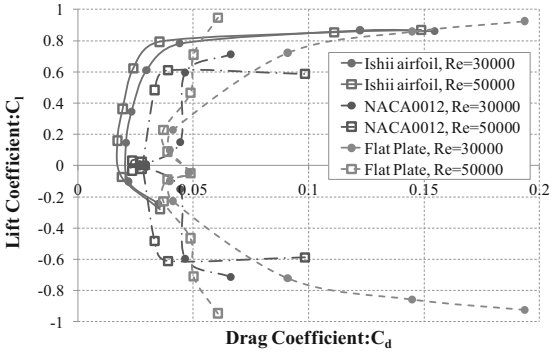

Fig. 3 Lift-to-drag ratio characteristics.

Ishii airfoil: The airfoil has lift at lower angle of attack due to the camber effect. There is little difference between the lift curve slopes of both the Reynolds numbers, and the maximum lift-to-drag ratio is the largest among the three airfoils.

NACA0012: The lift curve slope is completely nonlinear for both the Reynolds numbers. The velocity vectors of flowfield (Re=3.0×10^4, α=2°, 4° and 6°) are shown in Fig. 4. Laminar separation of upper surface flow is found at α=2°, and moves upstream at α=4°. The laminar separation reduces lift because the flow has small negative pressure. However, the lift increases rapidly at α=6° when a separation bubble is generated near the leading edge and the laminar separation moves down stream. Therefore, the lift curve slope at α=6°

becomes very large in comparison with those at α=2° and 4°. The lift-to-drag ratios of NACA0012 airfoil for both the Reynolds number are lower than Ishii airfoil.

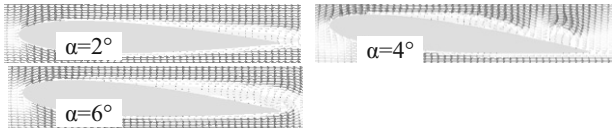

Fig. 4 Velocity vector of NACA0012 (Re=3.0×10^4).

Flat plate: The lift of Re=3.0×10^4 at α=4° and 6° is slightly larger than that of Re=5.0×10^4. But the drag of Re=3.0×10^4 above α=4° increases rapidly compared with that of Re=5.0×10^4, where the upper surface flow of which separates from the leading edge as shown in Fig. 5.

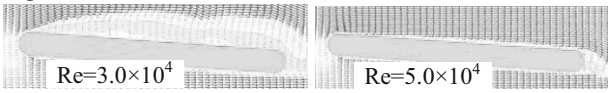

Fig. 5 Velocity vector of flat plate (α=4°).

As a conclusion, Ishii airfoil shows linear lift curve slope and an excellent lift-to-drag ratio in the low Reynolds number flow similar to the Mars atmospheric flight.

4. Comparison Between Numerical Simulation and Wind Tunnel Experiment of Ishii Airfoil

The numerical aerodynamic characteristic of Ishii airfoil is compared with the Mars wind tunnel test result conducted by Tohoku University[5].

Fig. 6 shows the lift characteristic. The numerical calculation shows good agreement with the wind tunnel test result.

Fig. 7 shows the lift-to-drag ratio characteristic. The minimum drag coefficient of numerical calculation is about half of the wind tunnel test result, but is close to the theoretical analysis of friction drag[6]. The lift-to-drag ratios of both the numerical calculation and wind tunnel test results increase as the Reynolds number becomes larger.

Fig. 8 shows the upper surface pressure distribution at α=4°, in which the maximum lift-to-drag ratio appears. The pressure distributions of both Re=3.0×10^4 and 5.0×10^4 by numerical calculation are almost identical except near the trailing edge. However, the pressure distribution of wind tunnel test result differs between Re=2.4×10^4 and 4.8×10^4. There is a region where negative pressure jump is observed at about the 40 percent of airfoil chord for Re=4.8×10^4. This probably indicates that a large separation bubble is generated at the mid-chord of airfoil.

5. Conclusions

Numerical flow analysis on Ishii airfoil, NACA0012 and flat plate are conducted. The lift and lift-to-drag ratio characteristic are investigated. The results show that Ishii airfoil has the best lift-to-drag ratio among the three airfoils and linear lift curve slope. A comparison between the numerical analysis and wind tunnel test on Ishii airfoil is conducted. The lift characteristics by numerical calculation and wind tunnel result are almost identical. However, the minimum drag coefficient by numerical calculation is about half of the wind tunnel test result, but is closer to the theoretical analysis.

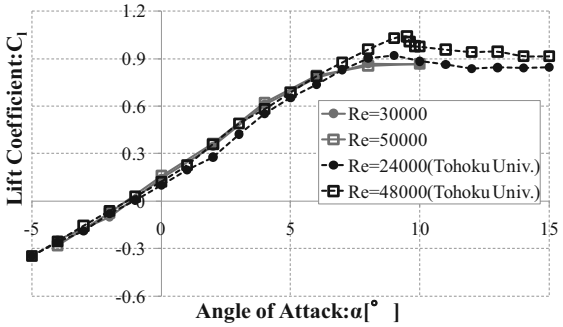

Fig. 6 Lift characteristics of Ishii airfoil.

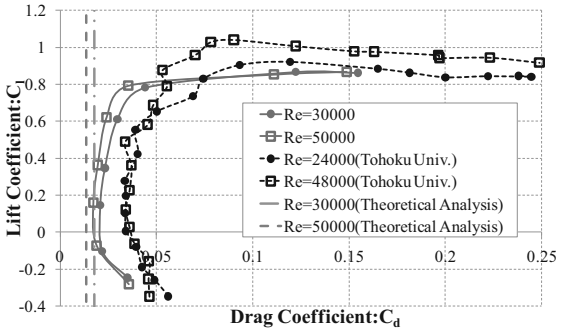

Fig. 7 Lift-to-drag ratio characteristic of Ishii airfoil.

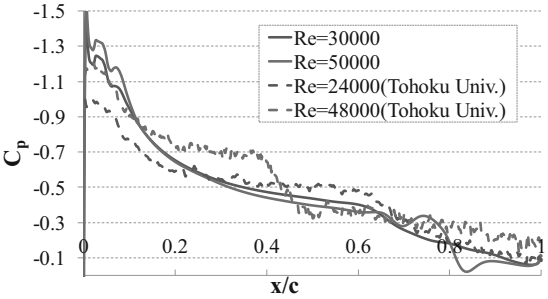

Fig. 8 Pressure distribution of Ishii airfoil (α=4°).

References

[1] A. Oyama, "Conceptual Design of Mars Airplane for MELOS1," *54th Symposium on Space Science and Technology Conf.*, 2010, 3F01.

[2] K. Yonemoto et al., "Non-linear Aerodynamic Characteristics of Three Dimensional Wing at Large Range of Reynolds Number," *40th Fluid Dynamics Conf. /Aerospace Numerical Simulation Symp.*, 2008, pp.323-326.

[3] Y. Jimba et al., "Study of the low Reynolds number aerodynamic characteristics for Mars airplane," *54th Space Science Technology Conf.*, 2010, 3F05.

[4] M. Koike et al., Aerodynamic Performance of Hand Launch Glider," *Journal of the Japan Society for Aeronautical and Space Science*, 2009, pp.166-174.

[5] K. Asai et al., "Low Reynolds Number Airfoil Testing in a Mars Wind Tunnel," *54th Space Science Technology Conf.*, 2010, 3F06.

[6] "Aerospace Engineering Handbook," Japan Society for Aeronautical and Space Sciences, 2005.

Eighth International Conference on Flow Dynamics
November 9 - November 11, 2011

Aerial Deployment Test of a Small UAV for Mars Exploration Flight

K. Fujita[1], H. Nagai[1], K. Asai[1] and H. Tokutake[2]
[1] Dept. of Aerospace Engineering, Tohoku University,
6-6-01, Aramaki-Aza-Aoba, Aoba-ku, Sendai, 980-8579, JAPAN
[2] Faculty of Mechanical Engineering, Kanazawa University,
Kakuma-machi, Kanazawa, 920-1192, JAPAN
fujita.koji@aero.mech.tohoku.ac.jp

ABSTRACT

Aerial deployment technique is required for next-generation airplanes. In this technique, dynamic behavior of an airplane during the deployment motion is one of the big problems. In order to evaluate this, a drop test via a balloon was performed for a small unmanned aerial vehicle (UAV) which has a foldable wing and flight data was analyzed.

1. Introduction

As aviation technologies advance, higher level of mechanisms for airplane is required. Deployable wing is one of them. It attracts attention as a technology for next-generation airplanes. In past, the deployable wing was mainly applied to get well storing property in parking. Therefore the wing was deployed on the ground. But recently, certain types of airplanes are using aerial deployment motion as shown in ARES[1].

However, airplanes may become unstable during such deployment motion. It is mainly caused because of two reasons. One is the difference of lift on the right and the left wing. And another is the reaction force of the deployment motion. Impacts of them change by speed and symmetry of the deployment motion.

In order to evaluate dynamic behavior during the deployment motion, a drop test was conducted. In this test, an airplane was ascended via a balloon in folded state. Then the airplane was dropped and started a deployment motion. Finally, the airplane has reached a steady straight gliding. During this phase, flight data was logged using a flight control module.

2. Experimental Procedures

Dynamic behavior during a deployment motion was evaluated through drop test. In this test, an airplane was ascended to the altitude of some dozen meters via a balloon in folded state. Then the airplane was dropped and started a deployment motion. Finally, the airplane has reached to steady straight gliding. From about 1 second before the airplane starts dropping, flight data such as altitude, azimuth angle, 2D position coordinate and angular rates of each axis were logged using a flight control module. And flights were shot by several video cameras on the ground.

Flight data was obtained using commercially-available ultra light flight control module 'MAVC1' manufactured by Y's Lab INC.[2]. It is shown in Fig. 1(a). This module can measure altitude, azimuth angle, 2D position coordinate and angular rates of each axis. Altitude is measured by atmospheric pressure. Azimuth angle is measured by orthogonally placed two magnetometers. 2D position coordinate is obtained by GPS. Angular rates of each axis are measured by micro electro mechanical system (MEMS) rate gyro. Measurement time and sampling rate were set to 15s and 20Hz, respectively.

Several different deployment methods such as a folding method and an inflatable method have been known[3]. The folding method using hinges was adopted as the deployment mechanism, since it was adopted in many other previous studies[1, 4] and offers high reliability due to its simple structure. An experimental plane has two hinge lines on its main wing along the chord direction. The wing is divided into three sections.

A commercially available and disposable rubber balloon was used to ascend the experimental plane. It was inflated to about 1.4m in diameter by helium gas as shown is Fig. 1(b). Figure 1(c) shows an airplane suspender frame. It was made by carbon rod to save weight. The balloon, a mooring rope and a drop device were tied at each end of the airplane suspender frame. Figure 1(d) shows the drop device. It consists of a main frame, a pin, a servomotor and a receiver. The experimental plane was suspended using the pin and the loophole attached to the empennage. It can start dropping anytime by pulling the pin using the servomotor.

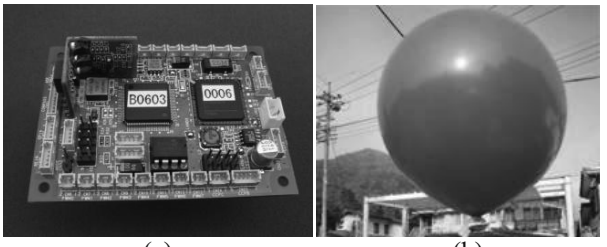

(a) (b)

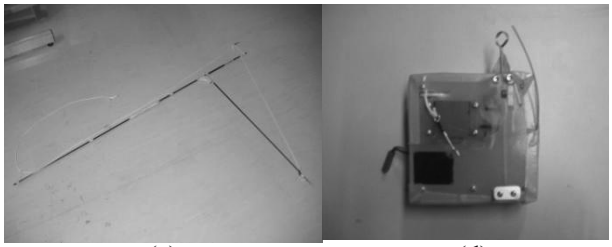

(c) (d)

Fig. 1 Equipment. (a) Flight control module. (b) Balloon. (c) Airplane suspender frame. (d) Drop device.

3. Experiment

The drop test using a normal airplane which doesn't have deployment mechanism was performed in first. Figure 2(a) shows the airframe and inside of the experimental plane. It is a radio control glider. Only the elevator and the rudder can be used for steering. The total mass is about 0.5kg and the span is 1m. The main material is expanded polypropylene (EPP).

Figure 2(b) shows the ascended experimental plane at an altitude of about 30m. As shown, the experimental airplane was suspended, with its head facing the ground. It was dropped and flown to leeward side.

(a) (b)

Fig. 2 Pretest. (a) The airframe and inside. (b) The ascended experimental plane.

Figure 3 shows altitude-time history. As shown in Fig. 3, the experimental plane could glide smoothly without an up-and-down motion. Figure 4 shows angular rates of each axis at same flight. The pitch rate Q quickly rose up to nearly 0.8rad/s and then gradually decreased. These results mean that the experimental plane can pull up its nose and reach to steady gliding smoothly.

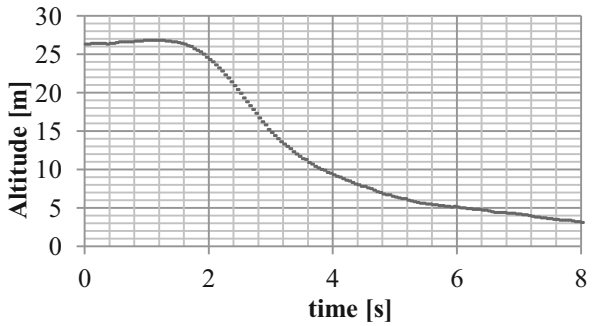

Fig. 3 Altitude-time history.

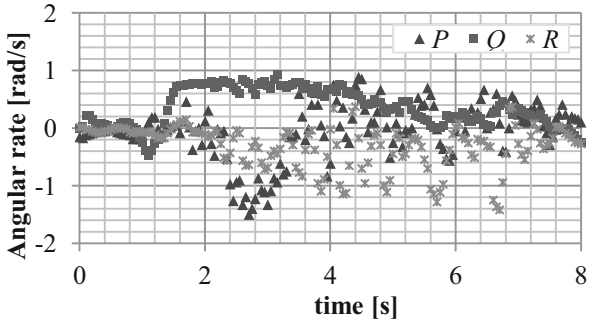

Fig. 4 Angular rate-time history.

4. Conclusion and future work

The drop test was performed in order to evaluate dynamic behavior during the deployment motion. The normal airplane which doesn't have deployment mechanism was tested at first. Flight data such as altitude and angular rates of each axis were logged using a flight control module. Results indicated that the experimental plane can pull up its nose and reach to steady gliding smoothly.

Future work will focus on the drop test using the airplane which has deployment mechanism. Effects of deployment speed, deployment timing of the right and left wings will be brought out.

References

[1] M. D. Guynn, M. A. Croom, S. C. Smith, R. W. Parks, and P. A. Gelhausen: "Evolution of a Mars Airplane Concept for the ARES Mars Scout Mission," 2nd AIAA Unmanned Unlimited Systems, Technologies, and Operations, AIAA paper 2003-6578.

[2] Y's Lab INC., Products, MAVCx Series, MAVC1, URL: http://www.yslab.co.jp/products/mavcx/mavc1.php [cited 26 July 2011]

[3] J. D. Jacob, S. W. Smith: "Design Limitations of Deployable Wings for Small Low Altitude UAVs," 47th AIAA Aerospace Sciences Meeting Including The New Horizons Forum and Aerospace Exposition, AIAA 2009-1291, Orlando, Florida, 2009.

[4] D. W. Hall, R.W. Parks, and S. Morris: "Airplane for Mars Exploration", Tech. rep., NASA Ames Research Center, Moffett Federal Airfield, California, 1997.

Eighth International Conference on Flow Dynamics
November 9 - November 11, 2011

Design of A Propeller of An Airplane on Mars

Takashi Hayashida[1], Shigeru Sunada[1], Ryohei Ishida[1], Ken-ichi Kaneko[1],
Testuya Suwa[2], Hiroki Nagai[2], Keisuke Asai[2]
Yudai Goto[3], Koichi Yonezawa[3] and Yoshinobu Tsujimoto[3]
[1]Osaka Prefecture University, 1-1 Gakuenmachi, Nakaku, Sakai, Osaka, 599-8531, Japan
[2]Tohoku University, 6-6-01, Aramaki-Aza-Aoba, Aoba-ku, Sendai 980-8579, Japan
[3]Osaka University, 1-3, Machikaneyama, Toyonaka, Osaka, 560-8531, Japan
10_hayashida_takashi@aero.osakafu-u.ac.jp

ABSTRACT

Activity of our group designing a propeller of a Mars airplane till now is introduced. Some tools for designing a propeller form viewpoints of aerodynamics and structural mechanics have been prepared. More research from other viewpoints will be required to complete a propeller on Mars.

1. Introduction

An airplane flying on Mars is being developed by the working group in ISAS. A developed airplane possibly has a propeller to generate thrust. The propeller on Mars has the following characteristics.

(1) Reynolds number and Mach number on Mars are lower and higher than those on Earth, respectively. These are caused by the differences of gravitational acceleration and physical values of atmosphere between Mars and Earth.
(2) A ratio of an inertial force to an aerodynamic force on Mars is larger than that on earth. This is caused by the difference of atmosphere density between Mars and Earth.
(3) An airplane with propellers will be stored in a capsule when it is transported to Mars. Then, the size and the mass should be reduced as much as possible.

In this paper, it will be stated how we have designed a propeller on Mars considering these characteristics.

2. Research up to now

We have made a fundamental research to prepare tools for designing the airplane propeller with its span length of about 1m. Here, the propeller which has the diameter of 0.18m and generates 0.36N on Mars is considered as an example. And the propeller is made by a carbon plate with the thickness of 0.6mm. This carbon plate is composed of three carbon sheets with the thickness of 0.2mm. Carbon fibers are arranged by [0・90deg] in one sheet and by [45/-45deg] in the other 2 sheets. These angles are measured from the blade span.

(1) Aerodynamics

(1-1) It can be expected that Reynolds number and Mach number of the airplane propeller are 10^3-10^4 and about 0.5, respectively. The airfoil[1] shown in Fig.1 was selected because Okamoto et al. reported that the airfoil had a high lift-drag ratio at the Reynolds number stated above.

(1-2) A Mach number effect on the aerodynamic characteristics was investigated by Asai et al. at Mars Wind Tunnel at Tohoku Univ. Figure 2 shows an example of the results. The Mach number effect on the present airfoil is smaller than that estimated by Prandtl-Glauert rule.

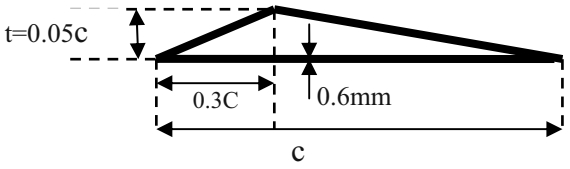

Fig. 1 Airfoil

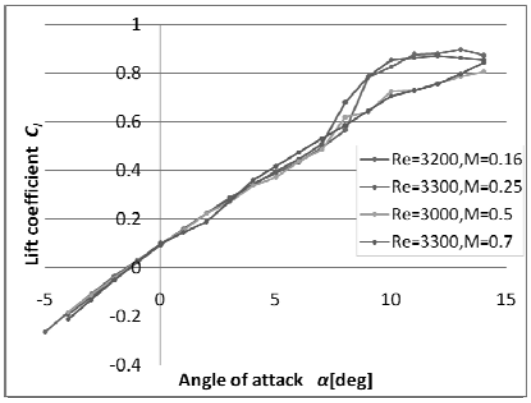

Fig.2 $C_l - \alpha$ around Re=3000

(1-3) A Three-dimensional shape of the propeller blade was determined by Adkins and Liebeck's method[2], using the airfoil characteristics obtained at Tohoku Univ. In this calculation, the resultant angle of attack at any blade elements is required to be equal to 6.5deg, where the lift-drag ratio of the airfoil is the highest at Re=10^3-10^4 and M=0.3-0.5 according to the experimental results. The distributions of the chord length and the twsit angle of the propeller are shown in Fig.3. The mid chord-wise points at any cross sections are on one line connecting the rotational axis and the blade tip. This is because the torsional deformation by a moment due to the centrifugal force is decreased as much as possible as stated later.

(1-4) In the method by Adkins and Liebeck for designing a propeller, steady airfoil characteristics are used. However, the three-dimensional flow around a propeller might be different form that assumed in this method. For example, a strong leading edge vortex, which is not observed around a (two-dimensional)

airfoil in a steady flow, might exist around a propeller[3]. Then, the performance of the propeller obtained by Adkins and Liebeck's method should be estimated by a wind tunnel test or CFD. However, it is difficult in a wind tunnel filled with air to make a measurement under the Reynolds number and Mach number on Mars. Though Mars Wind Tunnel at Tohoku Univ., where the airfoil characteristics were obtained by Asai et al., can be filled with CO_2, it is too small for a test of the propeller. Therefore, CFD is indispensable for estimating the performance of the propeller.

Yonezawa's group at Osaka Univ. is making CFD analysis on the characteristics of the designed propeller. At the present stage, they are using ANSYS CFX. It has been confirmed that the thrust and torque acting on the propeller predicted by the CFD are close to those by Adkins and Liebeck's method. They will make the same analysis by using ANSYS FLUENT.

(a)

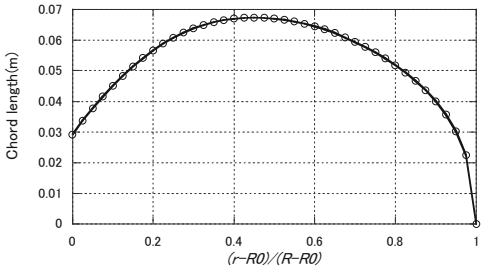

(b)

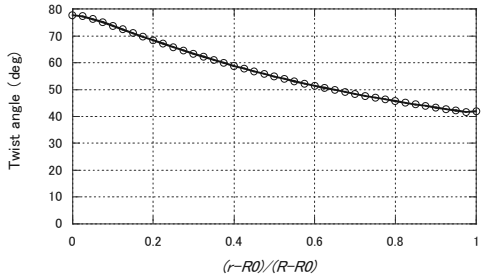

Fig.3 Three-dimensional shape of the propeller. (a)chord length, (b)twsit angle.

(2) Structural mechanics

The propeller is deformed by aerodynamic and inertial forces. The torsional deformation should be estimated carefully, because it affects an angle of attack, that affects the propeller performance. As stated above, the torsional deformation of the propeller on Mars is mainly caused by a moment due to centrifugal force acting on it. Then, the torsional deformation of the rotating propeller was measured in the chamber where the density was reduced to 15% of standard atmosphere on Earth. Symbols in Fig.4 show the variation of torsional angle at 61% span-wise position. The rotational speed Ω of the propeller in a flight on Mars is about 80rps. However, the maximum rotational velocity in the measurement was about 40rps, because the power of the motor used in the present measurement is not sufficient. Measurements where the rotational speed exceeds 80 rps will be made using a motor with higher power. The line shows the analytical results. In the analysis, the value of $G = 2 \times 10^{10}$ [N/m^2] was assumed and the variation of torsional angle at wing elements was integrated from the blade root to the 61% span-wise position. Fig. 4 shows a good agreement between the experimental results and analytical ones. This implies the availability of the present analysis.

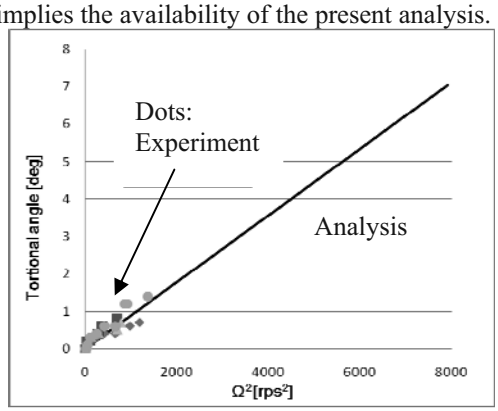

Fig.4 Variation of torsional angle at 61% span-wise position of the propeller.

3. Conclusions

Some tools introduced here will be improved in order to estimate the propeller performance with the higher accuracy. Requirements on the propeller such as the generated thrust and the maximum mass will be changed in near future. The tools designing a propeller introduced here will be utilized for developing a new propeller which satisfies new requirements. Furthermore, it will be an important subject in the development how the propeller is stored in the capsule.

References

[1] A.Azuma, The biokinetics of flying and swimming. Second Edition,AIAA,Reston,Va.(2006),pp.223-226.

[2] C.N. Adkins and R.H. Liebeck. Design of optimum propellers. Journal of propulsion and power. Vol.10,No 5(1994), pp.676-682.

[3]D. Lentink, W.B. Dickson, J.L. van Leeuwen and M.H. Dickinson, Leading-edge vortices elevate lift of autorotating plant seeds, Science, Vol. 324(2009), pp. 1438-1440.

Appendix

The value of $G = 2 \times 10^{10}$ [N/m^2] was assumed by the following test using a triangular pole having the cross section with c=5cm shown in Fig.1. The height of the triangular pole is 5cm. The torsional angle θ, which is defined by a torsion between both the sides of the pole, was measured when a moment Q was applied. The value of G was obtained as $G = Q/(J\, d\theta/dx)$. Here, the torsional constant J is 3.1×10^{-11} [m^4] and x axis corresponds to the direction of the height of the pole. Similarly to the propeller blade, the pole was made by a carbon plate. This carbon plate is composed of three carbon sheets with the thickness of 0.2mm. Unlike the propeller blade, carbon fibers are arranged by [0/90deg] in all the sheets.

Eighth International Conference on Flow Dynamics
November 9 - November 11, 2011

Aerodynamic Characteristics of Ishii Airfoil at Low Reynolds Numbers

Masayuki Anyoji[1], Taku Nonomura[1], Akira Oyama[1], Kozo Fujii[1],
Kei Nose[2], Daiju Numata[2], Hiroki Nagai[2], Keisuke Asai[2]
[1]Japan Aerospace Exploration Agency, 3-1-1 Yoshinodai, Chuo-ku, Sagamihara, Kanagawa, 252-5210, Japan
[2]Tohoku University Graduate School, 6-6-1 Aramaki-Aza-Aoba, Aoba-ku, Sendai, Miyagi, 980-8579, Japan
anyoji@flab.isas.jaxa.jp

ABSTRACT

Flow fields and aerodynamic characteristics of Ishii airfoil at Reynolds number 23,000 are evaluated by large-eddy simulation. The results show that the flow over the airfoil has trailing edge separation at low angles of attack. The flow separates, transit and reattaches, resulting in generation of a laminar separation bubble at angle of attack of 4 to 8 degree. Although these flow characteristic are almost same as that of NACA0012, the airfoil characteristics of Ishii airfoil are much better than those of NACA0012. This is because of enhancement in lift by the pressure-side camber.

1. Introduction

Aircraft-type Mars explores called “Mars airplanes” have been considered as a feasible system for exploring the Mars, and the researches for establishing their mission have been conducted by several groups in Japan [1]. A flight condition for the Mars airplane becomes the low Reynolds number one (Re=10^3-10^5). Under the low Reynolds number condition, it is difficult to gain a high lift coefficient (C_L) because the boundary layer often separates. In addition, at medium angle of attack in which the flow can transit to turbulent after laminar separation, the separated flow may reattach on a wing and then a separation bubble is formed. In the past studies, it was found that the separation bubble causes a nonlinear lift-curve [2]. Because of these unusual flow characteristics, a conventional aerodynamic-design approach cannot be applied to the design of the Mars airplane. For the airfoil design of Mars airplanes, it is indispensable to understand the aerodynamic and flow characteristics.

Several characteristics of airfoils in a low Reynolds number region have been clarified: a sharp leading edge fixes the separation point at the edge and can improve its Reynolds number dependency on the aerodynamic performance; a flat upper surface reduces the separation region; a cambered airfoil gains a higher lift than a symmetric airfoil. The airfoil named “Ishii airfoil” is one of the airfoils having above shapes and a good aerodynamic performance at the low Reynolds number condition. In the past experimental studies [3], it has been clarified that Ishii airfoil has a high lift/drag (L/D). However, the detailed reasons such as the association between the flow field and the lift and drag characteristics has not been well understood.

In this research, to evaluate the flow field around Ishii airfoil at low Reynolds number, three-dimensional LES computations were conducted. Based on the unsteady flow data, the reason why Ishii airfoil has a higher aerodynamic performance compared to the other airfoils such as NACA 0012 are discussed.

2. Computational Set up

2.1. Computational Model

The shape of Ishii airfoil is shown in Fig. 1. As reference, those of NACA0012 and NACA002 are also shown in Fig. 1. Mach number (M) was set to 0.2 at which compressibility can be ignored and computational efficiency is improved. Reynolds number (Re) was set to 23,000. The angle of attack was changed from 0 to 9. Ideal flow with no turbulence level was assumed.

Fig.1 Shape of Ishii airfoil
(dashed line: Ishii airfoil, short-dashed line: NACA0012, solid line: NACA0002)

2.2 Computational Methods

In the present study, LANS3D [4] developed in ISAS/JAXA was adopted and three-dimensional implicit LES were conducted. Three-dimensional compressible Navier-Stokes equations were employed as the governing equations. The spatial derivatives of convective terms were evaluated by the sixth-order compact difference scheme. For span direction, 20% chord length is computed. The grid spacings are evaluated by wall unit after the computation. The computational meshes satisfy the following inequalities;

$$\Delta\xi^+<25,\quad \Delta\eta^+<3,\quad \Delta\zeta^+<15$$

where $\Delta\xi$ is stream-wise grid spacing, $\Delta\eta$ is wall-normal minimum grid spacing and $\Delta\zeta$ is span-wise grid spacing. Here, the superscript plus denotes the normalized value based on wall unit. In these criteria, the turbulent analysis including near wall structure is well resolved with the present computational methods.

3. Results and Discussion

3.1 Averaged flow fields

Temporal and spanwise averaging are conducted for results of LES. Figure 2 shows time averaged velocity distributions and the streamlines. Figure 3 shows pressure profiles compared to NACA0012 and NACA0002. Separation points and reattachment point were judged from friction coefficients (Cf) obtained by averaged results of LES.

Attached flow is observed at α=0 degree, but the flow separates near the trailing edge in the range from α=1 degree to α=3 degree. The separation point moves

to the leading edge with increasing angle of attack. The separated flow reattaches on the surface in the range from α=4 degree to α=8 degree and then the separation bubble is formed. At α=9 degree, a reattachment point pass over the trailing edge and the flow does not reattach on the surface. These flow field characteristics in the suction side are extremely similar to the results of NACA0012 [5]. In Fig. 3, the suction peak is observed and the pressure in the suction side gradually recovers. However, the pressure distribution in the pressure side is different from that of NACA0012 and NACA0002, especially at the pressure-side camber near the trailing edge. At all angle of attack of Ishii airfoil, the positive pressure at the pressure-side camber is higher.

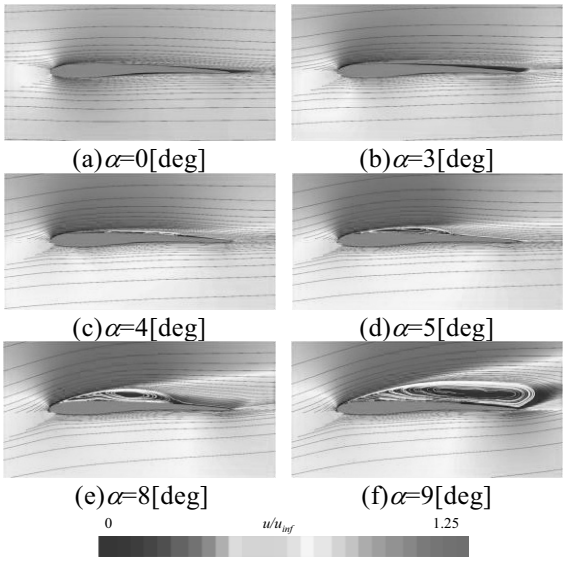

(a) α=0[deg] (b) α=3[deg]

(c) α=4[deg] (d) α=5[deg]

(e) α=8[deg] (f) α=9[deg]

Fig. 2 Time averaged flow field

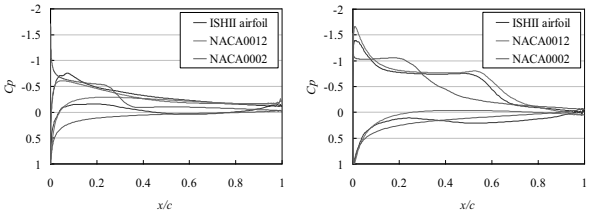

(a) $\Delta\alpha$=3[deg] (b) $\Delta\alpha$=6[deg]

Fig. 3 C_p distribution

3.2 Aerodynamic performance

Figure 4 shows the aerodynamic performance. The lift curve is almost linear, but a low nonlinearity of the lift curve is observed around α=4 degree in which the flow filed in the suction side changes. This nonlinearity of the lift curve is attributed to the presence of the separation bubble. Moreover, the lift curve is much higher than that of NACA0012 and NACA0002 at over α=4 degree. This is because that Ishii airfoil gains the higher positive pressure in the pressure side camber while the flow field in the suction side is similar to the other airfoils. On the other hand, the drag increases with approximately the square of angle of attack. Thus the drag characteristics are similar to that of conventional airfoils. The maximum *L/D* is about 18 at α=4 degree. Compared to NACA0012 and NACA0002, the value is considerably high. In addition, Ishii airfoil has the maximum *L/D* at higher angle of attack than conventional high-Reynolds number airfoils. This is due to that the contribution of the higher lift to the *L/D* is larger than the increase of the pressure drag at high angle of attack.

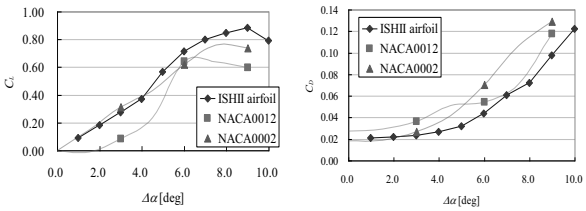

(a) Lift curve (b) Drag curve

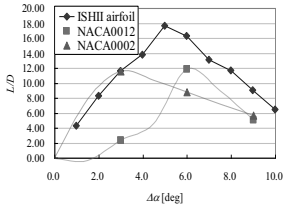

(c) Lift/Drag

Fig. 4 Aerodynamic characteristics

4. Concluding remarks

Three-dimensional LES simulations of flow around Ishii airfoil at the low Reynolds number condition were conducted. It was found that the reason why Ishii airfoil has high aerodynamic performance at low Reynolds number condition is that Ishii airfoil gains the higher positive pressure in the pressure side camber while the flow field in the suction side is similar to the other airfoils. This result indicates that the shape of the pressure side strongly affects the aerodynamic performance and it is important factor for the design of the Mars airplane wing.

References

[1] A. Oyama, K. Fuji, "A Study on Airfoil Design for Future Mars Airplane", AIAA-2006-1484, 44th AIAA Aerospace Sciences Meeting and Exhibit, Reno, Nevada, January 9-12 (2006).

[2] M. Okamoto, "An experimental study in aerodynamic characteristics of steady and unsteady airfoils at low Reynolds number", Ph.D thesis, Nihon University (2005).

[3] K. Asai et al, "Low Reynolds-Number Airfoil Testing in a Mars Wind Tunnel", 54th Symposium on Space Science and Technology, Sizuoka, November 17-19, 3F06 (2010).

[4] K. Fujii and S. Obayashi, "High-resolution upwind scheme for vortical-flow simulations". *Journal of Aircraft,* ***26***(12) (1989), pp. 1123–1129.

[5] R. Kojima et al, "Computational Study of Flow Characteristics of Thick and Thin Airfoil with Implicit Large-Eddy Simulation at Low Reynolds Number", ASME-JSME-KSME Joint Fluids Engineering Conference 2011, July 24-29, Shizuoka, AJK2011-15026 (2011)

Eighth International Conference on Flow Dynamics
November 9 - November 11, 2011

Experimental Study of Low-Reynolds-Number Aerodynamic Characteristics of Thin Airfoils in a Mars Wind Tunnel

Hiroki Nagai, Shingo Ida, Kei Nose, Masayuki Anyoji, Daiju Numata and Keisuke Asai
Department of Aerospace Engineering, Tohoku University,
6-6-01, Aramaki-Aza-Aoba, Aoba-ku, Sendai, 980-8579, JAPAN
nagai.hiroki@aero.mech.tohoku.ac.jp

ABSTRACT

In this study, we investigated the aerodynamic performance of thin airfoils in a Mars Wind Tunnel at Tohoku University at low Reynolds number (Re=1.1×10^4) and Mach number about 0.2. To measure lift and drag, we developed a two-component balance system. This system has enough sensitivity and linearity to measure small force acting in low-density conditions. In this test, it is found that a very thin airfoils having a camber between 3% and 6% are suitable for a Mars airplane.

1. Introduction

Airplanes have been seriously considered as a new method of exploring Mars. However, the Martian surface pressure is much lower than the earth atmosphere. This leads to that a Mars airplane has to fly at low Reynolds number. In the range of Reynolds number of 10^4 to 10^5, it is known that the maximum lift-to-drag ratio (L/D) of smooth airfoils significantly deteriorates[1]. On the other hand, thin airfoils that are close to insect wings can provide better performance in $(C_l/C_d)_{max}$ than smooth airfoils at low Reynolds number. The result of numerical optimization of Mars Airplane's airfoil at Re = 10^5 and M = 0.47 also indicates that thin airfoils can provide good performance at low Reynolds number. However, the reasons why thin airfoils are superior to thick airfoils at low Reynolds number remain unexplained.

The objective of this research is to clarify the reasons why thin airfoils can provide better performance than thick airfoils at low Reynolds number, by conducting airfoil tests in a Mars Wind Tunnel (MWT) at Tohoku University. Five airfoils (NACA0012-34, 5% flat plate, 1% flat plate, 3% circular arc, 6% circular arc) are used in the present tests. To measure aerodynamic forces, a two-component balance system has been developed and used. Also, Pressure-Sensitive Paint technique (PSP) was used to measure pressure distributions around the airfoils.

2. Experimental Setup

2.1 Mars Wind Tunnel (MWT)[2]

The MWT has been developed by Tohoku University in 2007 (Fig. 1). An induction-type wind tunnel is placed inside the vacuum chamber where the condition of Martian atmosphere can be simulated. It can simulated that the Reynolds number is ranged from 2.6×10^3 to 1.3×10^5 with the Mach number range up to 0.84 at the maximum.

Fig. 1 The Mars Wind Tunnel at Tohoku University

2.2 Test Model and Test conditions

Five airfoils (NACA0012-34, 5% flat plate, 1% flat plate, 3% circular arc, 6% circular arc) used in the present tests were shown in Figure 2. All models were two-dimensional airfoil that had the chord length of 50 mm and the span length of 100 mm. One thermocouple and one pressure tap were provided in the centerline of the model.

Mach number was fixed at about M=0.21 and Reynolds number (Re) was set at about 1.1×10^4. The corresponding total pressure of the flow was 5.0kPa. The angle of attack (α) was changed from -5 to 15 deg.

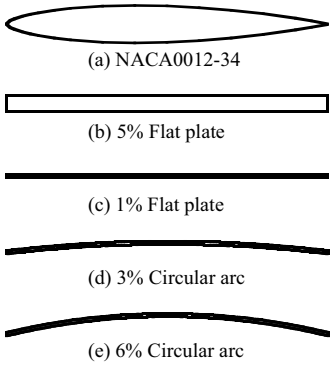

Fig.2 Test models

2.3 Balance Systems

The two-component balance system consists of two load cells and a stepping motor for changing the angle of attack. The range of load cells for lift measurement (A&D AC4101 –K006) and drag measurement (A&D AC4101-G600) is 60N and 6N respectively. The accuracy of load cells is 0.015 % of the full-scale output. The angle resolution of the motor is 1.44×10^{-2} deg and the accuracy is 3.4×10^{-2} deg. The angle of attack can be changed remotely from outside of the vacuum chamber. The output signal from the load cells are amplified by a DC strain amplifier (NISSHO-ELECTRIC-WORKS, DSA-100A) and then measured by PC.

2.4 Optical Systems

In this experiment, we used PdTFPP as the luminescent molecule and poly(TMSP) as the binder. This PSP is known to have high sensitivity at low

pressure conditions. The absorption peak of PdTFPP is 407*nm* and the emission peak is 670*nm*.

The optical setup for PSP measurement is shown in Fig. 3. The optical equipment was placed on the optical window located on the top of the vacuum chamber. The excitation light source was UV-emitting LED units with a peak wavelength of 395*nm*. The luminescence of PSP was captured by a 12-bit CCD camera with an optical band-pass filter (transmission wavelength 670±20*nm*).

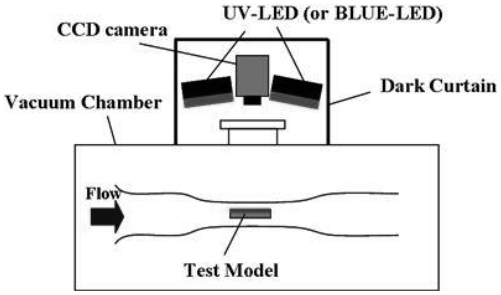

Fig.3 Optical setup

3. Results and Discussion

Figure 4 shows the lift curve and the drag polar of various airfoils obtained by the balance system.

The C_l curves of the NACA0012-34 and the 6% circular arc are nonlinear and $C_{l\alpha}$ becomes larger than 2π at certain angle of attack range. On the other hand, the $C_{l\alpha}$ of the 5% flat plate equals to 2π, while the $C_{l\alpha}$ of the 1% flat plate and the 3% circular arc is smaller than 2π. The circular arc airfoils have a minimum C_d value when there is no separation bubble on the lower surface of the airfoils. The C_{dmin} becomes large for the airfoils of which surface curvature is large, because a separation occurs near the trailing edge at low angle of attack. The maximum lift to drag ratio of the 3% circular arc is the largest among the airfoils tested in this study.

Figure 5 shows the C_p profiles around airfoil measured by PSP. It is found from Fig. 4(a) and Fig.5 show that the lift slope becomes large where a bubble with relatively short length appears on the airfoil surface. A comparison between the two flat plates results indicates that the thicker airfoil has longer separation bubble than the thin airfoil at the same angle of attack. This makes it narrower the range of angles of attack where the reattaching point exists. Therefore, the stall angle of the thick airfoil becomes smaller. The effect of the camber is to increase circulation around the airfoil, as shown by the potential theory. For the airfoil surface having large curvature, the range of angles of attack where the separation bubble exists becomes narrow because the appearance of a separation bubble by an increase of angle of attack is delayed. The small leading edge radius reduces the angle of attack at which a separation bubble appears because the separation point is fixed at the leading edge over the wide range of angles of attack. Concerning the stall characteristics, we found even thick airfoil cause what is called “thin-airfoil stall.” at low Reynolds number.

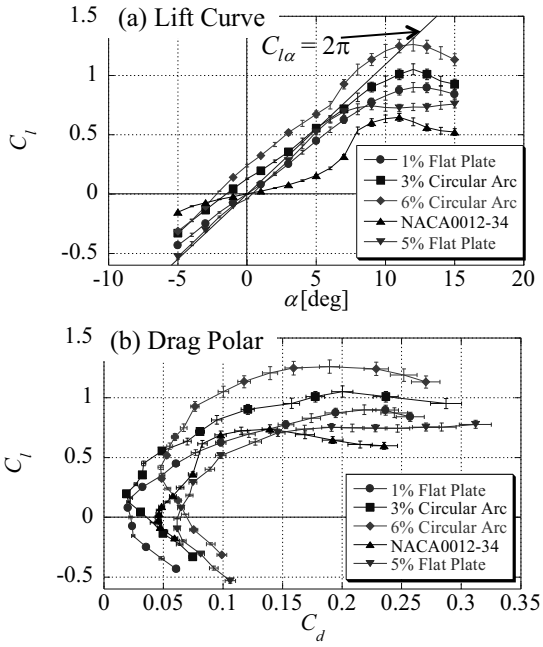

Fig.4 Aerodynamic performance of airfoils

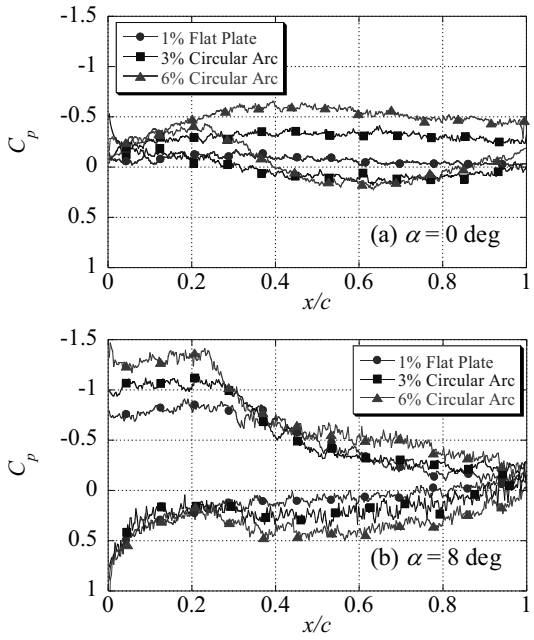

Fig.5 Lift-to-Drag ratio

4. Concluding remarks

A criterion to select an airfoil for the Mars airplane has been suggested. The recommendation is to use very thin airfoils having a camber between 3% and 6%.

References

[1] T. J. Mueller (Editor), Low Reynolds Number Aerodynamics, Lecture Notes in Engineering 54, Springer Verlag, 1989.

[2] Masayuki Anyoji et al, "Low Reynolds Number Airfoil Testing in a Mars Wind Tunnel", The 40th AIAA Fluid Dynamics Conference, June 28- July 1, 2010.

OS7: Thermal-Fluid Flows and Plasma Physics

Thermal Analysis of a Biological Tissue - Estimation of Its Thermophysical Properties

Subhash C. Mishra, Koushik Das and Rupesh Singh
Dept. of Mechanical Engineering, Indian Institute of Technology Guwahati, India - 781039
Corresponding author: scm_iit@yahoo.com

ABSTRACT

A simplified one dimensional tissue geometry is considered and bioheat transfer equation is solved using lattice Boltzmann method. An inverse heat transfer analysis is performed for estimating thermo-physical properties such as blood perfusion rate and metabolic heat generation rate, in which optimization is done using the genetic algorithm.

1. Introduction

Thermo-physical and optical properties of healthy and malignant tissues are not the same. And, with change in properties, thermal response of the tissue will vary according to its malignancy. With thermal response known, knowledge of these variations could be an important tool in characterizing the shape, size, location, grade, etc., of the malignancy.

Manifestation of a cancer is nothing but a malignancy in the healthy tissue. With cancer spreading like an epidemic, the human race is facing a new challenge. Any step in containing the spread of the cancer is, thus a welcome one.

In checking or curing any kind of abnormalities, the first step is to know its various attributes – its kind, location, size, shape and its stage. Yes, there are various ways, for example, MRI, to know the above mentioned attributes, but thermal means can also be an effective one. This paper explores the latter one.

Heat transfer in biological tissue is governed by Pennes bioheat equation, and subject to given initial and boundary conditions, its solution will depend on the thermophysical and optical properties, viz., thermal conductivity, blood perfusion rate, metabolic heat generation rate, etc., of the tissue. In a step towards diagnosis of a cancer, with known temperature field, this work explores feasibility of estimating the thermophysical properties of the tissue. In both direct and inverse method, the lattice Boltzmann method (LBM) is used to formulate and solve the Pennes bioheat equation, and in the inverse method, the objective function is minimized using the genetic algorithm. Methodology is demonstrated for a 1-D planar geometry (Fig. 1).

1. Formulation

With core body temperature $T(L) = T_L$ and convective boundary conditions, for the geometry shown in Fig. 1, the governing Pennes bioheat equation is [1]

$$\rho C_p \frac{\partial T}{\partial t} = k \frac{\partial^2 T}{\partial x^2} + \eta_b \rho_b C_{pb} (T_a - T) + Q_m + Q_s \qquad (1)$$

where $t, T, k, \rho, c_p, \rho_b, c_{pb}, \eta_b, Q_m, Q_s$ and T_a are time, temperature, thermal conductivity, density, specific heat of the tissue, density of blood, specific heat of the blood, blood perfusion, metabolic heat generation of the tissue, distributed volumetric heat source due to spatial heating and temperature of the artery, respectively.

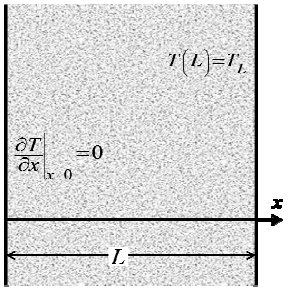

Fig.1: Schematic of the 1-D planar tissue.

Heat generation rate Q and the effective local heat source temperature T_e as defined below [1]

$$Q = \eta_b \rho_b C_{pb} (T_e - T), \; T_e = T_a + \frac{Q_m + Q_s}{\eta_b \rho_b C_{pb}} \qquad (2)$$

Eq. (1) is written as:

$$\rho C_p \frac{\partial T}{\partial t} = k \frac{\partial^2 T}{\partial x^2} + Q \qquad (3)$$

In the LBM formulation, the Pennes' bioheat equation takes the form:

$$f_i(x + e_i \Delta t, t + \Delta t) - f_i(x,t) = -\frac{1}{\tau}\left[f_i(x,t) - f_i^{eq}(x,t) \right] + w_i \Delta t \frac{Q}{\rho C_p} \left(\frac{\tau - 0.5}{\tau} \right) \qquad (4)$$

where $f_i, i = 1 \text{and} 2$ are the particle distribution functions in the D1Q2 lattice, $e_i = \Delta x / \Delta t$ is the velocity, $w_1 = w_2 = 0.5$ are the weights, $f_i^{eq} = w_i T$ is the equilibrium particle distribution function and $\tau = \frac{\alpha}{e_i^2} + \frac{\Delta t}{2}$ is the relaxation. Following the procedures in [1], temperature is written as

$$T = \sum_i f_i + \frac{\Delta t}{2} \frac{Q}{\rho C_p} \qquad (5)$$

In Eq. (5), the heat generation rate is function of temperature, and it can be written as

$$T = \frac{\sum_i f_i + \eta' T_e}{1 + \eta'} \tag{6}$$

where the dimensionless perfusion η' is defined as [1]

$$\eta' = \frac{\Delta t}{2} \frac{\rho_b c_{pb}}{\rho c_p} \eta_b \tag{7}$$

The solution methodology for obtainment of temperature T has been adopted as per Zhang [1]

Temperature distribution T_n at discrete points n known, next an inverse problem is solved to estimate the unknown properties. In this work, we estimate blood perfusion rate and metabolic heat generation rate, and for this the objective function has to minimize using the genetic algorithm.

$$J = \sum_{n=1}^{N} \left(T_n - T_{n,ref} \right)^2 \tag{8}$$

2. Results and discussion

With $T_a = 37\ ^0C$, in the present study, the properties $k = 0.5\ W \cdot m^{-1} \cdot K^{-1}, \rho = \rho_b = 1052\, kg \cdot m^{-3}$, $c_p = c_{p,b} = 3800\ J \cdot kg^{-1} \cdot K^{-1}, \eta_b = 1.0 \times 10^{-4}\, s^{-1}$ k, $Q_m = 400 W \cdot m^{-3}$, in the direct method, temperature distributions at different times including the steady-state are compared in Fig. 2, with that against Zhang [1]. Results are found to compare well.

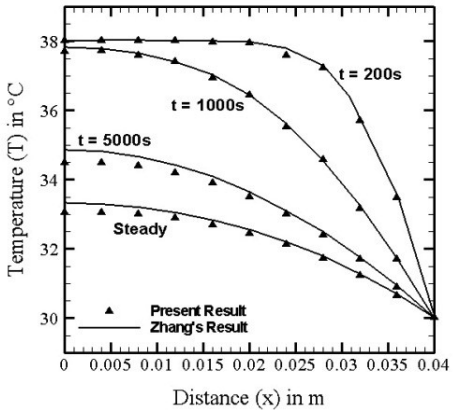

Fig. 2 At different times, comparison of temperature distributions with Zhang [1].

In the inverse analysis, in the GA, for a population size 100, although runs were taken for 100 generations, as shown in Figs. 3a and b, in both the cases considered, the convergence was achieved much before. Single point crossover was adopted with constrained dependent mutation. As seen from Table 1, the errors in the estimated values of η_b and Q_m are 9.99% and 0.5%, respectively.

Table 1: Estimated thermo physical parameters

Design Variable	Exact value	Found value	Error (%)
η_b (s^{-1})	1×10^{-4}	1.0999×10^{-4}	9.99
Q_m (Wm^{-3})	400	402	0.5

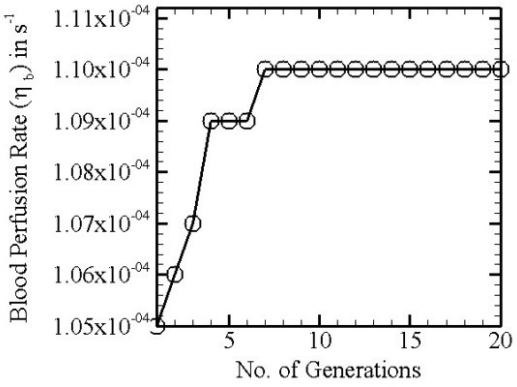

(a)

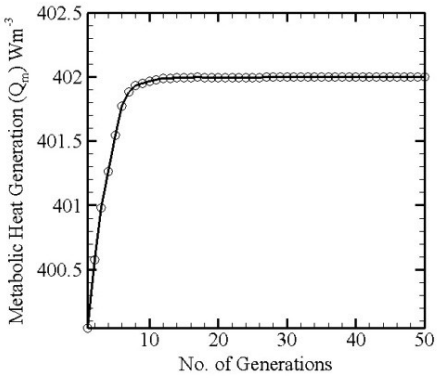

(b)

Fig. 3 Effects of number of generations on (a) blood perfusion rate and (b) metabolic heat generation.

3. Conclusions

Blood perfusion rate and metabolic heat generation rate were estimated for a 1-D biological tissue. Errors in the estimated values were found to be 9.99% and 0.5%, respectively. The LBM was used to solve the bioheat transfer and in the inverse method, GA was used for the optimization of the objective function.

Reference

[1] Zhang H., Phys. Med. Biol. **53** (2008) N15-N22.

Eighth International Conference on Flow Dynamics
November 9 - November 11, 2011

High Rotation Number Effect on Heat Transfer in a Triangular Channel with Discrete V-shaped Ribs

Ching-Shii Wang, Yu-Shun Lin, Yao-Hsien Liu
Department of Mechanical Engineering, National Chiao-Tung University, Hsinchu, Taiwan, 30010
Email: yhliu@mail.nctu.edu.tw

ABSTRACT

Effects of rotation on heat transfer distributions in a triangular-shaped cooling channel with discrete V-shaped ribs are investigated in this study. The rib spacing-to-height ratio (P/e) is 9 and rib height-to-hydraulic diameter ratio (e/D_h) is 0.085. The channel orientation is 135º with respect to the direction of rotation. The range of rotation number is form 0.0 to 0.62 and the Reynolds numbers (Re) are 15000 and 25000. The results show that the average Nusselt number on the leading and trailing surfaces gradually increases with the rotation number.

1. Introduction

The gas turbine inlet temperature keeps increasing to reach the greater efficiency for power generation. This extremely high temperature may destroy the gas turbine blades and cooling of the engine components is necessary. Turbulence promoters usually arrange in the cooling passages of turbine blades in order to enhance heat transfer. Han et al. [1] investigated heat transfer enhancement of V-shaped ribs in cooling channels. They summarized that V-shaped angled ribs perform better than angled ribs. Fu et al. [2] obtained heat transfer data in a rectangular channel with various rib configurations. Results showed that the V-shaped ribs and discrete V-shaped ribs have higher heat transfer enhancement than others for both rotating and nonrotating cases. When turbine blades rotate, Coriolis force and rotating buoyancy force influence the heat transfer distribution in the cooling passages. Wagner et al. [3] studied heat transfer in a rotating square channel. Heat transfer is increased on the trailing surface and decreased on the leading surface for the radially-outward flow case. Recently, high rotation number effect has been investigated in various channels with ribs by many scholars because it's close to real turbine conditions [4-5]. Triangular shaped cooling channel can be applied to the leading edge of the gas turbine blade [6-8], and the objective of the current study is to investigate the heat transfer variation due to discrete V-shaped ribs in this channel under high rotation numbers.

Method

The facility and the detailed components for rotating heat transfer research are shown in Fig. 1. The equilateral triangular cooling channel with the hydraulic diameter (D_h) of 29.4mm is sealed in a pressure vessel. Coolant air entering into the heated test section is supplied by a compressor. The length of the heated region is 190 mm. Twenty-one copper plates are installed on each side of the channel with the thermocouples on each copper plate for temperature measurement. Each copper plate has a dimension of 15mm x 25mm x 0.5mm and electric resistant heaters are used for supplying heat. A motor and a frequency controller adjust the rotational speed (Ω) freely from 0 to 330 rpm. The air pressure is pressurized to 4 kg/cm^2 to achieve the maximum rotation number of 0.62. The flow rate is measured by a Tokyo KEISO thermal mass flow meter. A slip-Ring, serving as an interface between stationary and rotating components, is used to transfer thermocouple signals and heater currents.

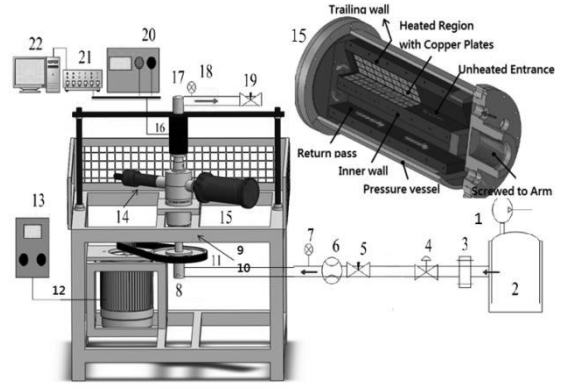

Fig. 1 Rotating facility and test section

Fig. 2 shows the discrete-V rib configuration in the triangular channel with 135º channel orientation. The square ribs are made of brass with a cross-section of 2.5mm x 2.5mm. They are put on the leading and trailing surfaces with the angle of attack of 45° and the distance between ribs (P) is 22.5mm.

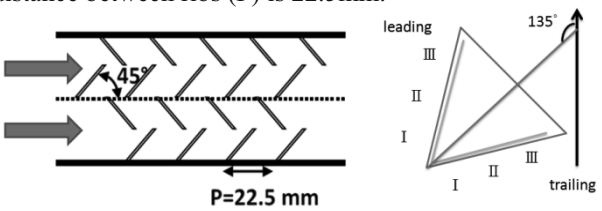

Fig. 2 Discrete-V rib configurations

The heat transfer coefficient (h) is calculated using the net heat transferred from the heated copper plates (Q_{net}), the surface area of each copper plate (A), the regionally averaged temperature of the plate ($T_{w,x}$), and the local bulk mean temperature of the air flow in the channel ($T_{b,x}$). The regionally averaged heat transfer coefficient can be determined:

$$h = Q_{net} / A\left(T_{w,x} - T_{b,x}\right) \tag{1}$$

The net heat transfer is by subtracting heat loss from the heat input. Heat input is based on the voltage and current measured by the multimeter. The Nusselt number (Nu) is presented based on the heat transfer coefficient obtained from the measurement. The Dittus–Boelter/McAdams correlation for turbulent flow in the smooth tube (Nu_o) is chosen as the reference:

$$\frac{Nu}{Nu_0} = \frac{hD_h / k}{0.023\,\mathrm{Re}^{0.8}\,\mathrm{Pr}^{0.4}} \tag{2}$$

k is thermal conductivity of the coolant and Pr is Prandtl number of the coolant. In order to determine the effect of rotation on heat transfer inside cooling channels, Rotation number (Ro) is considered based on the bulk flow velocity (V) and the rotational speed (Ω)as shown below:

$$Ro = \Omega D_h / V \tag{3}$$

3. Results and Discussion

Fig. 3 shows the Nusselt number ratios (Nu/Nu_o) along the streamwise directions under stationary and rotating condition at a Reynolds number of 25000. The rib-induced secondary flow moves along rib orientation from region I and III towards region II. Heat transfer in region I and III is higher than region II, and the region III has the highest Nusselt number under stationary condition. Region III on the trailing surface and region I have the highest Nusselt number ratios due to the combined effects from ribs and rotation. It also shows region III has larger difference in Nu ratios between leading and trailing surfaces.

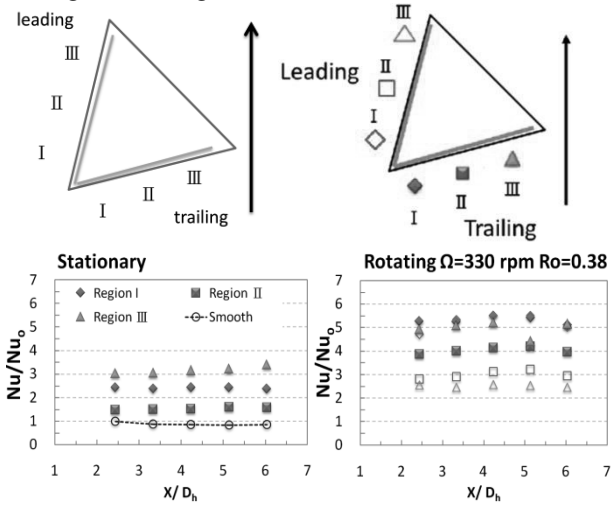

Fig. 3 Nusselt number ratio distribution at Re=25000

Fig. 4 shows the the ratio of rotating Nusselt number to the stationary Nusselt number (Nu/Nu_s) at Reynolds numbers of 15000 and 25000. The Nu ratio increases as the rotation number increases on region I and II. The rotational effect is more obvious at the lower Reynolds number of 15000.

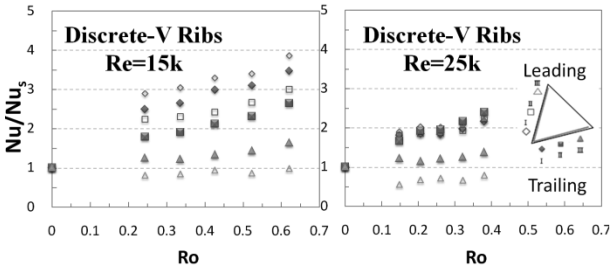

Fig. 4 Effect of rotation number on Nu ratio distribution

Average Nusselt number ratios on the leading and trailing surfaces are demonstrated in Fig. 5. The result shows that Nusselt number ratio gradually increases with the rotating number on both surfaces. Heat transfer enhancement due to rotation is about 2.6 times at the highest rotation number of 0.62. The difference between the leading and trailing surfaces is smaller than the case of 90°channel orientation.

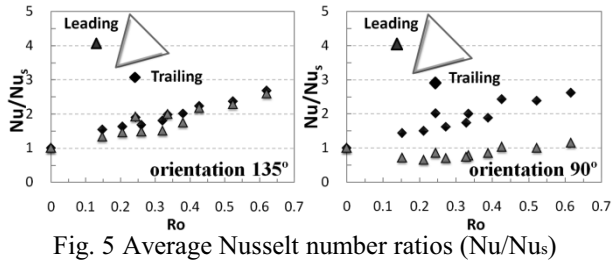

Fig. 5 Average Nusselt number ratios (Nu/Nu_s)

4. Concluding remarks

Heat transfer variation due to discrete V-shaped ribs in a triangular channel is investigated under high rotation numbers for gas turbine application. Heat transfer distribution is affected by the channel orientation and rotation number. The highest heat transfer enhancement due to rotation is about 2.6 times.

5. Acknowledgements

This research has been funded through National Science Council in Taiwan (NSC-98-2218-E-009-016).

References

[1] Han, J.C., and Zhang, Y.M., International Journal of Heat and Mass Transfer, 35(1992), 513-523.

[2] Fu, W. L., Wright, L. M., and Han, J. C., AIAA Journal of Thermophysics and Heat Transfer, 20 (2006), 569-582.

[3] Wagner, J. H., Johnson, B. V., and Hajek, T.J., ASME Journal of Turbomachinery, 113 (1991), 42-51.

[4] Liou, T.M., Chang, S.W., Hung, J.H., and Chiou, S.F., International Journal of Heat and Mass Transfer, 50 (2007), 4063-4078.

[5] Liu, Y. H., Huh, M., Han, J.C., Moon, H. K., ASME Journal of Heat Transfer, 132 (2010), 071702(1-10).

[6] Metzger, D. E. and Vedula, R. P., Experimental Heat Transfer, 1 (1987), 31-44.

[7] Lee, D. H., Rhee, D. H., and Cho, H. H., ASME GT 2006-90973 (2006).

[8] Amro, M., Weigand, B., Poser, R., and Schnieder, M., International Journal of Thermal Sciences, 46 (2007), 491-500.

Eighth International Conference on Flow Dynamics
November 9 - November 11, 2011

Heat Transfer Characteristics of Jet Impingement on a Target Surface with Grooves

Yuan-Hsiang Lo, Siao-Jhe Song, and Yao-Hsien Liu
Department of Mechanical Engineering, National Chiao-Tung University, Hsinchu, Taiwan, 30010
E-mail: yhliu@mail.nctu.edu.tw

ABSTRACT

Jet impingement heat transfer is experimentally measured on a half-smooth, half-rough target surface by transient liquid crystal thermography. The half-rough surface with rectangular grooves is placed either upstream or downstream in the impingement channel. Inline jet arrays are studied with the jet-to-jet spacing of 4. The jet-to-target plate spacing is 3 and the average jet Reynolds numbers are from 2500 to 7700. Higher heat transfer can be achieved with the half-smooth, half-rough surface compared to the fully smooth surface at higher Reynolds numbers.

1. Introduction

Jet impingement cooling has broad engineering applications such as cooling of the gas turbine blade, power electronics, and industrial drying process. Single or multiple jets can be utilized based on the actual conditions. When multiple jet arrays are used, the development of crossflow from spent air pushes the impinging jets away from the jet holes [1-2]. Experimental measurement of jet impingement heat transfer by liquid crystal thermography can provide detailed surface distribution and it has been applied to impingement on the smooth surface with different exit flow direction [3] and impingement surface with film cooling extraction [4]. Numerous research works have been performed to seek further enhance of jet impingement heat transfer by the roughened target surface. The roughened surface can be ribs [5-7], pin-fins [8-9], dimples [10], or grooves [11]. Besides, the surface may become non-smooth due to corrosion or contamination. It is found that the presence of the surface roughness could increase or decrease heat transfer. The presence of the surface roughness could potentially destroy the impingement core and the heat transfer under the directly striking region is reduced. However, heat transfer is enhanced near downstream due to stronger crossflow over the rough surface. In the current study, the target surface is a half-smooth, half-rough design. Detailed heat transfer distribution is measured by transient liquid crystal technique.

2. Method

The schematic of experimental setup is shown in Fig 1. It consists of a blower unit, a pipe heater, a three-way ball valve, a test section, and a 32-bit CCD camera. The liquid crystal (Hallcrest R30C5W) and black paint is coated on the target surface. An orifice plate, with an array of 4 by 12 rows of circular holes, sets between the pressure chamber and impingement channel of the transparent acrylic test section. The diameter of the jet hole is 0.5 cm and the jet-to-jet spacing(S) is 2cm. The cross sectional area of the inlet pressure chamber and the impingement chamber is 2cm x 8 cm and 1.5cm x 8cm, respectively. The target plate has the surface area of 24cm by 8cm. The heights of the pressure chamber and impingement channel are 2 cm and 1.5 cm, respectively. The mainstream temperature during the transient test is measured by the thermocouples installed at the inlet of the pressure chamber.

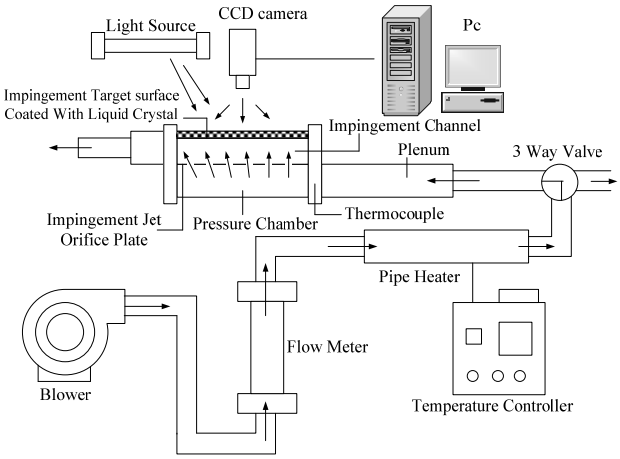

Fig. 1 Schematics of the experimental setup

The half of the target surface is roughened with grooves which are designed orthogonal to the exit flow direction. These grooves are aligned with the jet holes. The grooves have the width of 0.5cm and the depth (e) of 0.25cm, and the pitch between the grooves is 2 cm. The grooved portion is configured either upstream or downstream of the impingement channel as demonstrated in Fig. 2.

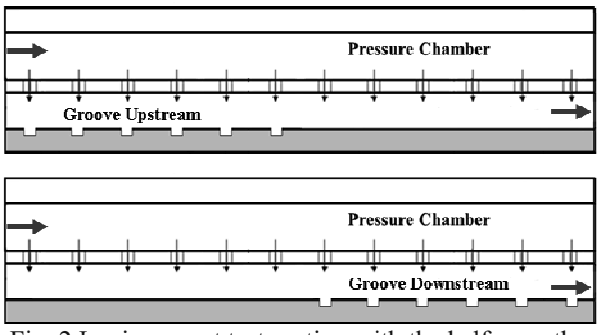

Fig. 2 Impingement test section with the half smooth, half-rough target surface

The one-dimensional transient heat conduction equation for semi-infinite solid is used to model the heat

transfer phenomena on the tested surface. Since the mainstream temperature changes with time, the equation is modified by Duhamel's superposition theorem:

$$T_w - T_i = \sum_{j=1}^{N} \left\{ 1 - \exp\left(\frac{h^2 \alpha (t - \tau_j)}{k^2} \right) erfc\left(\frac{h\sqrt{\alpha (t - \tau_j)}}{k} \right) \right\} [\Delta T_m]$$

where ΔTm and τj are the change of the mainstream temperature and the time-step. The surface temperature is obtained from the liquid crystal and the initial temperature is measured by the thermocouples. The Nusselt number is based on the measured convective heat transfer coefficient (h):

$$Nu = \frac{hd}{k_a}$$

where k_a is the thermal conductivity of air. A calibration process is performed to obtain the relationship of the color of the liquid crystal with respect to the corresponding temperature. The uncertainty of the measured convective heat transfer coefficient (h) is 10.5% based on [12].

3. Results and Discussion

When the impinging jet strikes on the rough surface, the impingement core is altered due to non-smooth surface. When the grooves are configured downstream in Fig. 3(a), higher Nusselt number occurs upstream where the impinging jet is directing on the smooth surface. Heat transfer is enhanced due to flow mixing near grooves downstream. It should be noticed that the spent jet pushes the jets downstream. It can be seen that the effect of crossflow pushes the impinging jet away from the center of the jet holes. When the grooves are designed upstream of the impingement channel in Fig. 3(b), higher Nusselt number can be observed upstream where the jets directly impinge on the grooves. Effect of crossflow increases downstream and the impingement heat transfer on the smooth surface is significantly reduced. The half-smooth surface downstream gives the lowest Nusselt number. Detailed Nusselt number distributions are altered due to grooves. As the Reynolds number increases, the Nusselt number also increases for both cases.

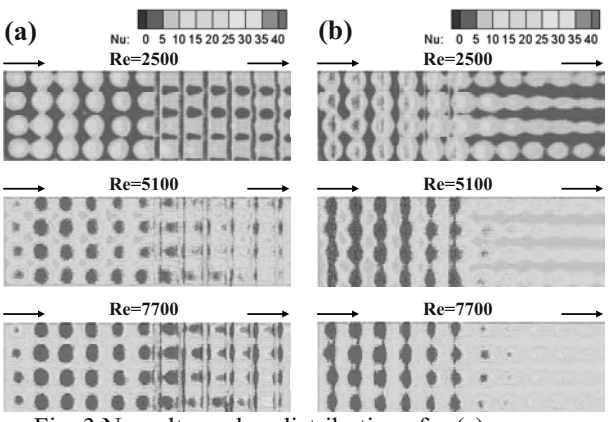

Fig. 3 Nusselt number distributions for (a) groove downstream and (b) groove upstream

The overall-averaged Nusselt numbers on the target surface are plotted in Fig. 4. Results show that this half-smooth, half-rough configuration performs better than the smooth surface at higher Reynolds numbers. At the lowest Reynolds number of 2500, the Nusselt numbers for all the cases are comparable.

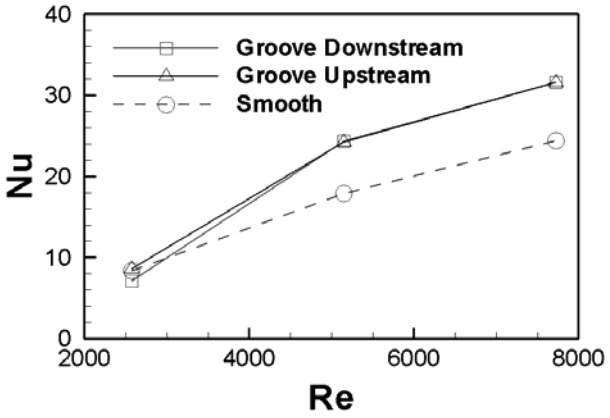

Fig. 4 Overall-averaged Nusselt numbers

4. Concluding remarks

Detailed impingement heat transfer distribution on a half-smooth, half-rough target surface is measured by the transient liquid crystal technique. The impingement heat transfer on the half-smooth, half-rough surface is higher than the fully smooth surface at higher Reynolds numbers.

5. Acknowledgements

This research has been funded through National Science Council in Taiwan (NSC-98-2218-E-009-016)

References

[1] R.J. Goldstein, and A.I. Behbahani, Int. J. of Heat and Mass Trans., **25** (1982), 1377-1382
[2] L.W. Florschuetz, D.E. Metzger, and C.C. Su, ASME J. of Heat Transfer, **106** (1984), 34-41
[3] Y. Huang, S.V. Ekkad, and J.C. Han, AIAA J. of Thermo. and Heat Trans., **12** (1998), 73-79
[4] S.V. Ekkad, Y. Huang, and J.C. Han, AIAA J. of Thermo. and Heat Transfer, **13** (1999), 522-528
[5] C. Gau, and C.C. Lee, Int. J. of Heat and Mass Trans., **35** (1992), 3009-3020
[6] D.H. Rhee, Y.W. Nam, and H.H. Cho, 2004, ASME J. of Turbomach., **126** (2004), 615-626
[7] W.M. Yan, H.C. Liu, C.Y. Soong, and W.J. Yang, Int. J. of Heat and Mass Trans., **48** (2005), 2420-2428
[8] G.S. Azad, Y. Huang, and J.C. Han, Int. J. of Rotating Machinery, **8** (2002), 161-173
[9] S.K. Hong, D.H. Rhee, and H.H. Cho, AIAA J. of Thermo. and Heat Transfer, **20** (2006), 728-737
[10] S.V. Ekkad, and D. Kontrovitz, Int. J. of Heat and Fluid Flow, **23** (2002), 22-28
[11] B. Sagot, G. Antonini, and F. Buron, Int. J. of Thermal Sciences, **49** (2010), 1026-1030
[12] R.J. Moffat, Experimental Thermal and Fluid Science, **1** (1988), 3-17

Eighth International Conference on Flow Dynamics
November 9 - November 11, 2011

Diagnosis of Malignances in Human Tissues: A Review of Non-Invasive Thermal Techniques

Arka Bhowmik[1], Ramjee Repaka[1], Subhash C. Mishra[2*]
[1]Department of Mechanical Engineering, Indian Institute of Technology Ropar, Punjab, India
[2]Department of Mechanical Engineering, Indian Institute of Technology Guwahati, Guwahati, India
[*] E-mail of corresponding author: scm_iit@yahoo.com

ABSTRACT

Optical and thermophysical properties of human tissues are function of abnormalities such as increase in metabolic activities and cellular growth, which also vary with time. The radiative outputs with and without transillumination from tissues, conveys details of in-vivo changes in properties indicating normal and abnormal conditions, which can be a means to detect underlying cancers. Present review discusses on these in-vivo changes of properties and its dependence on other factors. It also highlights various progresses made in non-invasive thermal techniques for cancer detection, and the associated problems and the developments in this area.

1. Introduction

Recent 'Cancer Facts and Figures 2010' from American Society of Cancer suggested 1529560 new cases in America alone, and some earlier trends suggested 10 million people worldwide are diagnosed with cancer which is expected to reach 7.5 billion of world population by 2020 [1]. Despite the huge amount of developments, cancer still remains an elusive disease. This is due to various inherited genetic defects, improper lifestyle, environmental causes and various unknown factors. Many treatments are there but complete cure is still not guaranteed. Additional screening and diagnosis techniques do assist doctors to identify and treat cancer well ahead. Present invasive techniques and biopsy for diagnosis are quiet accurate, but are incapable of identifying early signs of cancer and dynamic prognostic features which are possible using non-invasive techniques. Current non-invasive conventional techniques, viz., X-rays, CT scans, etc. are cheaper. But these are rated low for detection and prognosis of cancer, and are inept to generate better images of sparse tissues and to define detailed functional changes. However, non-invasive thermal techniques, viz., IR and short pulse laser, etc. are more reliable and are efficient to identify both dense and sparse cancerous tissues along with various prognostic details.

Human body is capable of generating heat invariably due to various biochemical reactions at cells, and is able to regulate temperature by various heat transfer phenomena. In the malignant tissue the metabolic heat generation is more and which acts as a heat generation source. The metabolic heat from tissue is either transferred to other location or dumped to environment by combination of several heat transfer mechanisms to obtain thermal equilibrium. Cancerous regions suffer thermal imbalance due to incomplete heat exchange, since rate of heat generation and dissipation are uneven, causing local temperature rise. Consequent increase in local temperature of tissues exhibits thermal contrasts and patterns in thermogram, compared to surrounding normal tissues. Although infra-red imaging with and without transillumination exhibits high sensitivity for detection of cancerous regions near outer skin, it loses its ability in case of deep body cancerous regions due to multiple scattering of signals from thick participating bio-media. On contrary, transilluminated time resolved radiative outputs using short pulse laser from tissues convey information about various optical and thermal changes of received signals and the corresponding changes in thermophysical and optical properties of tissues. These are the different means to identify underlying abnormalities in the tissues. Apart from this, there are numerous other optical techniques to identify the presence of cancer and they are beyond the scope of the present article.

The article discusses various non-invasive thermal techniques for cancer diagnosis and in-vivo changes in thermophysical and optical properties.

2. Available Non-Invasive Thermal Techniques

Earlier use of thermal imaging for medical diagnosis gained exceptional interest in breast cancer diagnosis, followed by various military applications of infra-red imaging techniques [2]. Initial investigations revealed that the local temperature of cancer affected tissues is few degrees higher compared to surrounding normal tissues, and similar healthy tissues, which are marked as hot spots assisted by asymmetrical vascular proliferation in thermogram [3]. Further infra-red findings [4] affirmed that vascular proliferation enhances metabolic rate followed by convection heat transfer due to increased vascular flow, along with capability to identify hypervascularity and hyperthermia [5] in breast cancers. Moreover, infra-red findings are successfully correlated with various prognostic features based upon dynamic analysis [6], and at times provide useful information that remains unwrapped in pathological tests. In addition, infra-red thermography has unique ability to detect early signs of cancer [7] such as angiogenesis process [8] about 8 to 10 years ahead before any mass accumulation is observed in the breast. Another technique [9, 10], i.e., thermal recovery from cold stress, is also available to obtain better infra-red images. It was observed [11] that, vascular pattern disappears under cold stress and reappears gradually on removal of cold stress, which can discern benign from malignant tumors, and can even identify small tumors by dynamic breast thermography.

Infra-red imaging for breast cancer detection exhibits high sensitivity [12] of 80-95% close to outer skin, but is unreliable because of significant cases of

false positive and false negative results due to heavy scattering of emanating signals from complex bio-media. Few other attempts to identify breast cancer are based on noticeable absorption patterns of affected tissues, when transilluminated with visible and near infra-red lights [13]. But the scattering issue remains unresolved since infra-red wavelengths of visible spectrum exhibit heavy scattering and low absorption in participating bio-media [14]. To mitigate the scattering issues, time resolved techniques are utilized where tissues are transilluminated using short pulse laser of the order of few picoseconds and time-resolved transmitted outputs [15] are detected. Common observations revealed that initial transmitted signals from illuminated tissues remains straight and un-scattered through participating media, compared to delayed scattered signals. These transmitted initial signals carry prominent information about tissue properties indicating abnormal and normal conditions.

The radiative outputs with and without transillumination using any form of light source depends on the in-vivo optical and thermophysical properties of considered tissue. Thus various thermal and optical changes of received signals can be a means to identify in-vivo changes in properties and patho-physiological conditions.

3. Associated Alteration of Tissue Properties

Various in-vivo thermophysical and optical properties of tissue depends on associated normal and abnormal physiological conditions, and are also function of degree of abnormalities that vary with time.

Thermophysical properties of living substances which are of interest are specific heat, density, thermal conductivity, thermal diffusivity and volumetric perfusion rate, which are functions of temperature, pressure, physiological and patho-physiological conditions. Available data obtained from measurement of tissue thermophysical properties are based on few factors because of complex nature of biological systems, and are detailed in bio-heat transfer literature. Especially, thermal properties of biological systems show significant changes due to temperature, and play an important role in understanding normal and abnormal phenomena.

Similarly, optical properties of tissue vary with associated patho-physiological activities, growth of abnormalities and time. Generally, emissivity is a function of local energy contents of tissue and is different for tissues with and without abnormalities. Further, absorptivity of tissues depends on intensity of incident radiation and medium density, and indirectly depends on the wavelength of incident radiation. Scattering is due to localized non-homogeneity in the medium and can either augment or attenuate the emitted intensity. Scattering due to fluctuation of refractive index at interface and deep inside tissue can be wavelength dependent. The distinctive radiative outputs from abnormal tissues due to changes in optical properties can be identified by various optical diagnostic techniques. Moreover, optical properties are obtained by converting radiative outputs into useful data that characterizes light tissue interaction. Various optical properties and their influence on radiative outputs are detailed in literature of tissue-optics [16].

4. Conclusions

Compared to conventional tools for medical diagnosis, non-invasive thermal techniques are competent for identification of various in-vivo functional and dynamic changes. Due to which it continues to be a research interest since two decades and added substantial improvements in the diagnosis of cancer. Despite this progress, thermal diagnosis of cancer is not yet considered reliable since multiple scattering of radiative outputs in terms of transmittance and reflectance from participating media reduces the spatial resolution and at times can be ambiguous. Hence is the requirement for further investigation to optimize scattering of transmitted and reflected signals. Also it warrants further investigations to identify various changes in thermophysical and optical properties of cancerous tissues. These issues can be substantially resolved by interdisciplinary study.

References

[1] F. Brayand, B. Moller, Nat. Rev. Cancer, **25** (2006), 63.

[2] J.F. Head, R.L. Elliott, IEEE Eng. Med. Biol. Mag, **21** (2003), 80.

[3] K.L. Williams, F.L. Williams, R.S. Handley, The Lancet, **278** (1961), 1378.

[4] R.N. Lawson, M.S. Chughati, Can. Med. Assoc. J, **88** (1963), 68.

[5] M. Anbar, IEEE Eng. Med. Biol. Mag, **17** (1998), 25.

[6] J.F. Head, F.Wang, R.L. Elliot, Ann. N Y Acad. Sci, **698** (1993), 153.

[7] J. Keyserlingk, P. Ahlgren, E. Yu and N. Belliveau, Breast J., **4** (1998), 245.

[8] A.J. Guidi, S.J. Schnitt, Breast J., **2** (1996), 364.

[9] A. Nagasawa, H. Okada, Thermal recovery In: Medical Thermography, Uni. Tokyo Press, (1973), 151.

[10] J. Steketee, M.J. Van der Hoek, Phys. Med. Biol., **24** (1979), 583.

[11] Y. Ohashi, I. Uchida, IEEE Eng. Med. Biol. Mag, **19** (2000), 42.

[12] J. Gershon-Cohen, J.A. Haberman-Brueschke, E.E. Brueschke, Radiol. Clin. North Am., **3** (1965), 403.

[13] E.N. Carlsen, Diag. Imag., **3** (1982), 28.

[14] D.T. Delpy, M. Cope, P. Van der Zee, S. Arridge, S. Wray, J. Wyatt, Phys. Med. Biol., **33** (1988), 1433.

[15] C. Das, A. Trivedi, K. Mitra, T. Vo-Dinh, J. Phys. D: Appl. Phys., **36** (2003), 1714.

[16] S.A. Prahl, W.F. Cheong, A.J. Welch, IEEE J. Quantum Electron, **26** (1990), 2166.

Eighth International Conference on Flow Dynamics
November 9 - November 11, 2011

Numerical Simulations on Miscible Radial Hele-Shaw Flows with a Non-Monotonic Viscosity Profile

Li-Chieh Wang, C. W. Huang, Ching-Yao Chen
Department of Mechanical Engineering, National Chiao Tung University Hsinchu, Taiwan, Republic of China.
chingyao@mail.nctu.edu.tw.

ABSTRACT

Injection-driven miscible flow in a Hele-Shaw cell results in a highly ramified pattern if the viscosity profile is nonmonotonic. We perform highly accurate simulations to investigate the vigorous fingering phenomena. Various parameters, such as the overall viscosity contrast, local maximum viscosity contrast and position of local maximum viscosity, are analyzed systematically. In general, the nonmonotonic feature enhances the prominence of interfacial instability. Formation of dual vortex pairs and reverse fingers are observed, which are not present in the situations with a monotonic viscosity distribution.

1. Introduction

Viscosity fingering (VF) is a hydrodynamic instability occurring where a high viscous fluid is displaced by a less viscous one in porous media. The related studied can be classified into two categories depending on whether viscosity profiles are monotonic or nonmonotonic. For convenience, Tan and Homsy [1] defined a particular case in which viscosity varies exponentially with concentration, as well as monotonic viscosity profiles. However, some driving fluid used to petroleum secondary recovery techniques such as a mixture of alcohols and water need not to be monotonic. It is found a nonmonotonic viscosity profile for the viscosity concentration data of alcohols to approximate nature fluid behavior. They have carried out a parameter study to understand the effects of nonmonotonicity on the stability of the flow.

Although researchers agreed the viscosity profiles effects the stability of fluid. Detail discusses, especially the fluids are close to stability turn to instability, have not found before. We are therefore interested in developing a fundamental understanding of miscible radial flow with nonmonotonic viscosity profile.

2. Method

Consider a Hele-Shaw cell of constant gap thickness d containing two miscible, incompressible, viscous fluid (Fig. 1). Denote the injecting fluid of viscosity μ_1 displaces the displaced fluid of viscosity μ_2 at a given injection rate Q, equal to the area cover per unit time. Further, we assume two fluids mix in all proportions and inertialess. The concentration of the injecting fluid is represented by c. Assume the permeability and the physical dispersion to be homogeneous and isotropic. Solve the unstable, time-dependent, incompressible flow generated by a miscible displacement process under Darcy's law are expressed as:

$$\nabla \cdot u = \frac{\partial u}{\partial x} + \frac{\partial u}{\partial y} = 0 \tag{1}$$

$$\nabla p = \frac{\partial p}{\partial x} = -\frac{\mu}{k} u \tag{2}$$

$$\frac{\partial c}{\partial t} + u \cdot \nabla c = \frac{\partial c}{\partial t} + u \frac{\partial c}{\partial x} + v \frac{\partial c}{\partial y} = D \nabla^2 c \tag{3}$$

D is the constant diffusion coefficient, and c is the concentration of the injecting fluid, μ is supposed to be a function of the injecting fluid concentration.

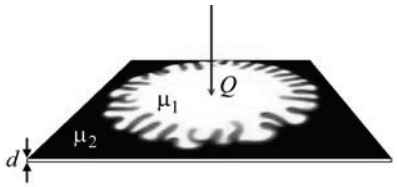

Fig. 1 Schematic setup for the injection-driven radial Hele-Shaw flow with miscible fluids.

The nonlinear evolution of viscous fingering instabilities in miscible displacement flows with nonmonotonic viscosity-concentration profile have been investigated first by Manickam and Homsy [2]. It can be observed that nonmonotonic viscosity profiles are characterized by the interplay of the maximum viscosity μ_m, the location of the maximum occurs at $c = c_m$, and the end-point viscosities α.

3. Results and Discussion

We use the largest value μ_m for which our numerical code remains stable for μ_m=14 (α=3 and c_m=0.1) with a locally unfavorable viscosity profile and μ_m= 9 (α=0.2 and c_m=0.2), respectively. By analyzing Fig. 2 and Fig. 3 which depicts the concentration images, we obtained for increasingly μ_m, the length of fingers will increase with both end-point viscosities contrast, respectively, corresponding to the findings for the radial source flow displacement by Pankiewitz and Meiburg [3].

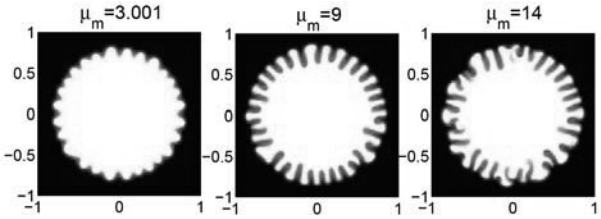

Fig. 2 Concentration images for Pe=400, α=3, c_m=0.1, and μ_m=3.001, 9, and 14 at t=0.30.

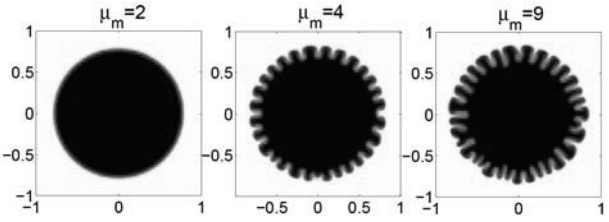

Fig. 3. Concentration images for Pe=400, α=0.2, c_m=0.2, and μ_m=2, 4, and 9 at t=0.30.

We begin analyzing the unfavorable (α=3) and favorable (α=0.7) end-point viscosities contrasts viscosity profiles set shown in Fig. 4 (a) and (b), respectively. Peculiar feature of these miscible structures is the shape of fingers. Adapt the original code (Chen and Meiburg [4]) employed for monotonic case to the present nonmonotonic case.

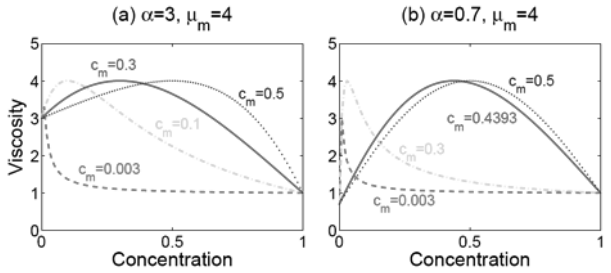

Fig. 4. Viscosity profiles for (a) unfavorable cases with α=3, μ_m=4 and c_m=0.003, 0.1, 0.3, and 0.5. The critical position of c_{mc}=0.3027, (b) favorable cases with α=0.7 μ_m=4 and c_m=0.003, 0.3, 0.4393, and 0.5. The critical position of c_{mc}=0.4393.

The results show a strong relationship to the distance between the viscosity profiles to the tangent emanating from the maximum viscosity μ_m to the end point (1, 1) which can be solved by the second derivative of viscosity profile is essential. For random α and μ_m, a critical position c_{mc} for the second derivative of viscosity equal to zero can be identified. The critical position for α=3 and μ_m=4 is c_{mc}=0.3027. For Pe=400 as illustrate in Fig. 5(a), there are some example not follow the rule (c_m =0.1 is the most unstable case and c_m=0.5 is more stable than c_m=0.03). In contrast, for the same viscosity profile set, and decrease Pe=200 as illustrate in Fig. 5 (b), is follow this rule.

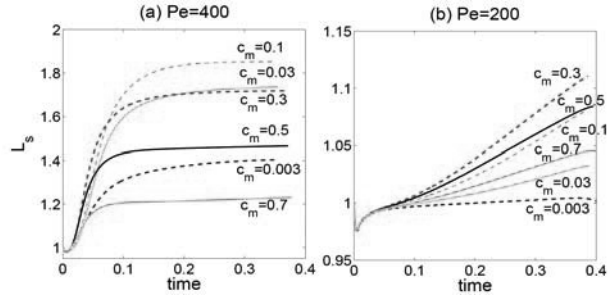

Fig. 5 Time evolution of the interfacial length with viscosity profile α=3, μ_m=4 and c_{mc}=0.3027 for (a) Pe=400, (b) Pe=200.

We found that higher difference between end-point viscosities α and maximum viscosity μ_m create richer phenomenology, such as tip splitting observed in Fig. 6(a). A schematic of these profiles with the parameters that characterize them is shown in Fig. 7(a). There are almost overlap between four lines, but in the inset the detail viscosity profiles for the four sets is clearly observable far away from the tangent line to the graph of viscosity profile at the point (1, 1) in turn from 1 to 0.2. It is almost superposition of the stability of the fluid is illustrated in Fig. 7(b).

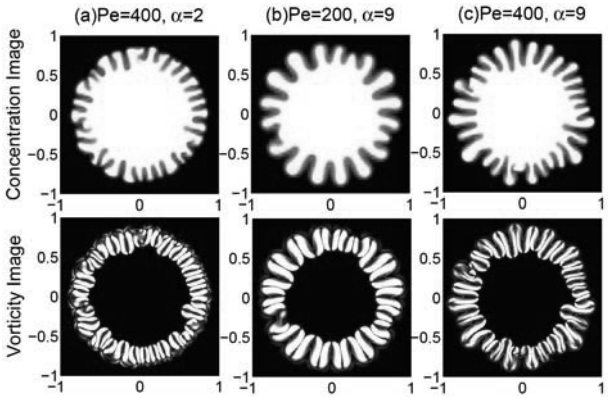

Fig. 6 Concentration images (top row) and Vorticity images (bottom row) for viscosity profile set with μ_m=13 and c_m=0.1 for (a) Pe=400 and α=2. (b) Pe=200 and α=9. (c) Pe=400 and α=9 at t=0.30. The outer fluid is more viscous ($\eta_1 > \eta_2$).

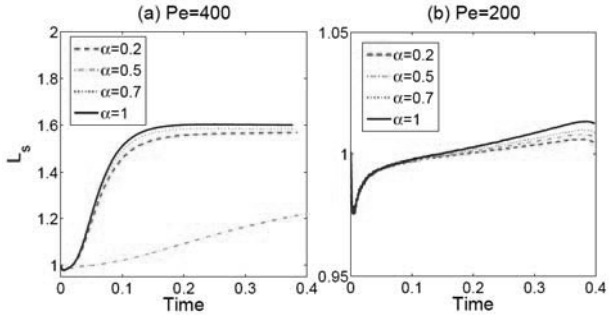

Fig. 7 Time evolution of the interfacial length with μ_m=4, c_m=0.1, α=0.2, 0.5, 0.7, and 1 for (a) Pe=400, (b) Pe=200. In the inset the detail viscosity profiles for the four parameters sets.

4. Concluding remarks

Usual miscible flows in radial Hele-Shaw geometry with nonmonotonic viscosity profiles lead to the formation of complex morphological structures. In this work, we have presented highly accurate numerical simulations for an injection-driven radial Hele-Shaw flow with miscible fluids. Our analysis explicitly indicates how the relevant parameters of the system influence the morphology of the interfacial patterns.

In conclusion, we have suggested a relation between viscosity profile and fluid stability, and observed a damping effect in normalized interfacial length. An open relation is whether these relations have an underlying physical interpretation, we hope experimentalist will feel motivated to check, and hopefully validate the ideas put forward in this work.

References

[1]C. T. Tan and G. M. Homsy, Phys. Fluids 30 (5) (1987), pp 1239-1245.
[2]O. Manikcam and G. M. Homsy, Phys. Fluids 6 (1) (1993) , pp 96-107.
[3]C. Pankiewitz and E. Meiburg, J. Fluid Mech. (1999), vol. 388, pp.171-195.
[4]C. Y. Chen and E. Meiburg, J. Fluid Mech. (1998), vol. 371, pp.233-268.

Performance of Tube in Tube Heat Exchanger with Supercritical CO_2 Fluid

Kai-Hsiang Lin[1], Chi-Chuan Wang[1], Steven Yu[2]
[1]Department of Mechanical Engineering, National Chiao Tung Ubiversity, Hsinchu 300, Taiwan.
ccwang@mail.nctu.edu.tw
[2]Green Energy Research Laboratories, Industrial Technology Research Institute

ABSTRACT

The study developed a tube-in-tube heat exchanger for supercritical fluid CO_2 and water. The calculations are in line with existing measurements. It is found that the CO_2 shows a different trend as compared to typical sub-critical fluids. The local heat transfer rate does not monotonically decrease with the tube length. In fact, a plateau occurs somewhere inside the heat exchanger. Moreover, a second maximum is seen when the inlet pressure is below 10 MPa, yet a significant of recovering of local heat transfer rate is seen for an inlet pressure of 8 MPa.

1. Introduction

The use of natural refrigerants for HVAC&R application has attracted much attention recently. Among the possible candidates, carbon dioxide (CO_2) is regarded as the most promising one because it is environmentally benign, non-toxic, and is equipped with comparatively good thermodynamic properties. Carbon dioxide is also comparable to that of HCFC refrigerants and outperforms conventional refrigerants when it is being used in hot water heaters and automobile air conditioners [1–3]. In CO_2 air-conditioning and heat pump systems, CO_2 rejects heat at a pressure above the critical pressure (7.38 MPa) in the gas cooler without no phase change. When the CO_2 is at super-critical pressures, some small fluid temperature and pressure variations may produce large changes in the thermophysical properties, resulting in significant deviations in both heat transfer and fluid flow behaviors. There were some studies concerning the heat transfer characteristics of CO_2 in supercritical state and recent studies suggested that the Fang [4] correlation gives fair overall predictivity. Despite considerable efforts were devoted to the heat transfer performance of CO_2 above critical points. It seems that none of the existing studies were associated the performance of tube-in-tube heat exchangers. Note that the heat transfer performance changes appreciably alongside the heat exchanger, hence it would be expected some difference should occur. In this sense, it is the objective of this study to investigate and to analyze the heat transfer behavior of CO_2 subject to inlet conditions.

2. Method

The heat exchanger is a tube-in-tube type, and the water flows counter-currently against the coolant (carbon dioxide) during the heat exchanging process. Fig. 1 is a schematic of the heat exchanger.

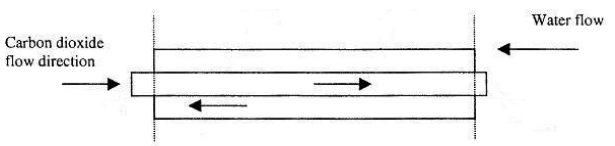

Fig.1 Schematic of the tube-in-tube heat exchanger.

Due to considerable change of physical properties, especially near pseudo-critical temperature, the heat exchanger must be subdivided into many small segments. Hence the heat balance amid water and coolant in each segment can be written in the following equations:

$$Q_1 = \dot{m}_c c_{p,c}\left(T_{a1} - T_{a2}\right) = \dot{m}_w c_{p,w}\left(T_{b1} - T_{b2}\right) \quad (1)$$

$$Q_1 = \left(UA\right)_1 \times \left(LMTD\right)_1 \quad (2)$$

$$P_{a2} - P_{a1} = \frac{4L}{d} f \frac{G_c^2}{2\rho_c} \quad (3)$$

3. Results and Discussion

For validating the proposed model, calculation is compared with the measurements of Pitla et al. [5]. Pitla had conducted CO_2 tube-in-tube heat exchanger with an ID of 0.00472 m and OD of 0.00635m for the inner tube. The ID for the outer tube is 0.01575 m. Their test conditions are tabulated in Table 1. Using the inlet conditions of their raw data, the calculated cooling capacity against their measurements are depicted in Fig. 2. As seen, the calculations are in line with the experimental measurement, suggesting the applicability of the present modeling.

Table 1 Test conditions of Pitla et al. [5]

	$T_{CO2,in}$ (°C)	$P_{CO2,in}$ (MPa)	$T_{water,\ in}$ (°C)	Mc (kg/s)	Mw (kg/s)
Run1	121.2	9.44	20.8	0.01963	0.04011
Run2	126	11.19	24.2	0.0274	0.040497
Run3	73.3	13.33	36.12	0.02043	0.12914
Run4	123.5	10.8	27.21	0.02862	0.084087
Run5	107.2	8.11	24.2	0.0198	0.0455
Run6	123.4	8.98	22.3	0.02996	0.067864
Run7	118.3	7.79	21.2	0.02123	0.066434
Run8	115.8	8.60	18.9	0.03436	0.084087
Run9	114.9	8.76	18.9	0.03638	0.065091
Run10	113.4	9.50	15.9	0.03825	0.109052

For further examining the special characteristics of the CO_2 tube-in-tube heat exchanger, with an ID = 0.020 m and an OD = 0.025 m for inner tube and an ID = 0.050 m for outer tube, calculations are further made

with inlet pressures of 12, 10, and 8 MPa, respectively. The variation of the local heat transfer rate subject to change of dimensionless tube length is shown in Fig. 3. For typical tube-in-tube heat exchanger, the local heat transfer rate decreases asymptotically from the inlet (CO_2 inlet) toward the outlet. This is because the largest temperature occurs at the inlet and the feature of counter-current arrangement.

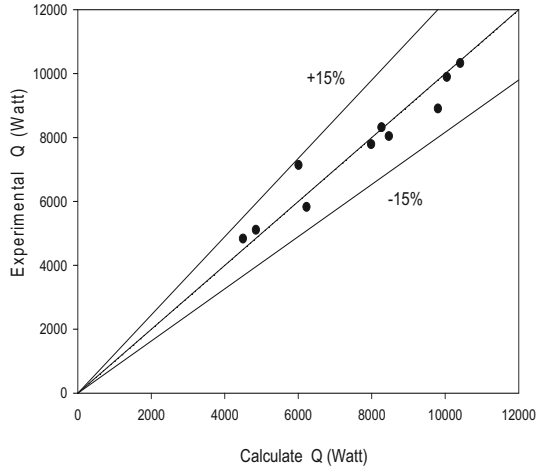

Fig. 2 Comparison of local heat transfer rate amid calculations and Pitla et al.'s data [5].

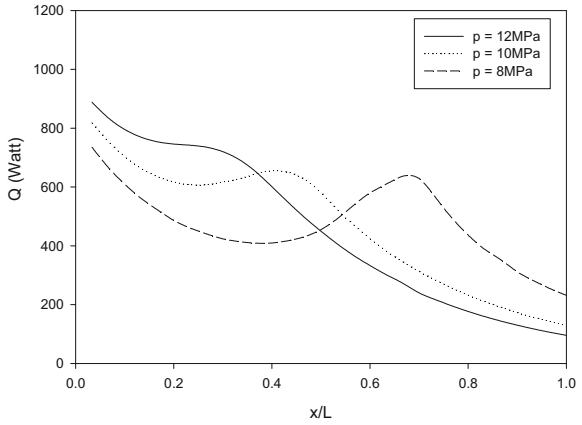

Fig. 2 Variation of local heat transfer rate vs. dimensionless tube length subject to change of inlet pressure.

However, as clearly shown in this figure, the CO_2 shows a different trend as compared to typical sub-critical fluids. The local heat transfer rate does not monotonically decrease with the tube length. In fact, a plateau occurs somewhere inside the heat exchanger. Moreover, a second maximum is seen when p is below 10 MPa, yet a significant recovering of local heat transfer rate is encountered for p = 8 MPa despite the maximum temperature difference still occurs at the CO_2 inlet. To explain the phenomenon, one must understand the variation of specific heat capacity of CO_2 above critical point as shown in Fig. 4. For a given super-critical pressure, a maximum of c_p is seen at certain temperature which is called pseudo-critical temperature. Apparently, cooling of the very hot CO_2 gas may inevitably pass through this temperature. In this sense, a momentous raise of c_p is seen nearby this temperature, leading to a considerable raise of heat transfer coefficient. This phenomenon becomes more and more pronounced when the pressure is decreased since a tremendous jump of c_p occurring adjacent to the pseudo temperature. As a result, a significant recovering of local heat transfer rate and a second maximum occurs in the tube-in-tube heat exchanger. From Figs. 3 and 4, one can see that the plateau of local heat transfer rate is actually in phase of specific heat.

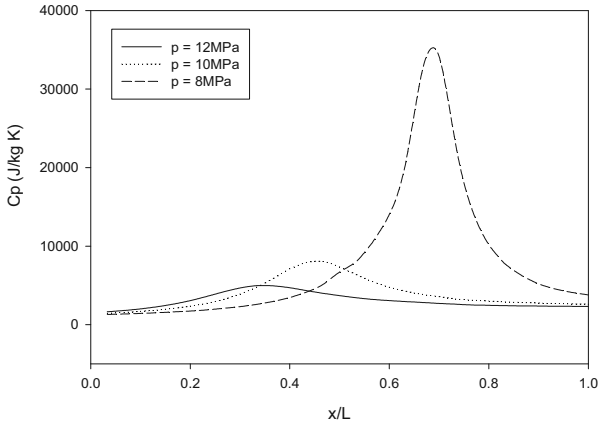

Fig. 2 Variation of c_p vs. dimensionless tube length subject to change of inlet pressure.

4. Concluding remarks

The study developed a tube-in-tube heat exchanger model applicable for supercritical fluid CO_2 and water. The developed model is validated with some existing measurements. And a further calculation is made to examine the influence of inlet pressure of CO_2. Unlike conventional working fluid which normally shows a monotonically decrease of local heat transfer rate along the tube length, the CO_2 shows a different trend as compared to typical sub-critical fluids. The local heat transfer rate does not monotonically decrease with the tube length. In fact, a plateau occurs somewhere inside the heat exchanger. Moreover, a second maximum is seen when p is below 10 MPa, yet a significant recovering of local heat transfer rate is encountered for p = 8 MPa despite the maximum temperature difference still occurs at the CO_2 inlet. The phenomenon is attributed to the significant rise of specific heat of CO_2 near pseudo critical temperature.

References

[1] G. Lorentzen, J. Pettersen, Int. J. Refrig., **16** (1993), 4–12.
[2] G. Lorentzen, Int. J. Refrig., **17** (1994), 292–301.
[3] G. Lorentzen, Int. J Refrig., **18** (1995), 190–7.
[4] X.D. Fang, ACRC CR-16. Department of Mechanical and Industrial Engineering, University of Illinois at Urbana- Champaign, USA, 1999.
[5] S.S Pitla, D.M. Robinson, A. Zingerli, E.A. Groll, S. Ramadhyani, ASHRAE research project report #3613-1.

Eighth International Conference on Flow Dynamics
November 9 - November 11, 2011

Improvement of Cell Attachment and Proliferation of Polylactide Surface Using a Two-Step Atmospheric-Pressure Plasma Jet Treatment Procedure

Yi-Wei Yang[1], Chi-Liang Kuo[1], Chun-Chieh Wen[2], Jane-Yii Wu[2], Hao-Yuan Huang[1], Ming-Hung Chiang[1] and Jong-Shinn Wu*
[1]Department of Mechanical Engineering, National Chiao Tung University, 1001 Ta-Hsueh Road, Hsinchu, Taiwan
[2]Department of Bioindustry Technology, Da Yeh University, Changhua, Taiwan
E-mail: chongsin@faculty.nctu.edu.tw

ABSTRACT

In this paper, we report the development of fast incorporation of amino functional group into polylactide (PLA) surface using an atmospheric-pressure nitrogen-based dielectric barrier discharge (DBD) in post-discharge region. Plasma treatments were carried out in two steps, which include: 1) nitrogen with 0.1% oxygen and 2) nitrogen with 5% ammonia. Analyses show that N1s concentration, contact angle and roughness of the treated PLA surface can reach ~3%, 30 degrees and 72 nm respectively. The proposed two-step plasma treatment can produce a PLA surface with two times OD as compared to pure PLA in cell activity tests for C_2C_{12} cells.

1. Introduction

Recently, rapid progress in the development of novel approaches of surface modification for biomaterials has been made [1-4 and references cited therein]. Among these, plasma related technologies (gas discharges) have been considered as one of the promising approaches to improve surface biocompatibility (cell attachment and proliferation). Gas discharges include plasma enhanced chemical vapor deposition, corona discharge, plasma surface treatment and ion implantation, among others, which are often operated in a low-pressure environment. This induces several disadvantages, which include inconvenience in dealing with living objects, higher cost because of maintaining the vacuum condition throughout the test, and difficulties in in-line processing. Thus, operation of plasma under atmospheric-pressure condition for modification of surfaces is one of the important research topics in recent years [5-7].

In our previous study [9], we have demonstrated surface characteristics such as contact angle measurements, XPS analysis, IR analysis and biological test results of PLA with and without two-step plasma treatment. However, we did not measure surface roughness of the PLA surface which is crucial for incorporation of functional groups and cell activities [8].

Owing to the above, in this study we focus on applying the AP plasmas to improve the bio-compatibility of poly-lactic acid (PLA) surface that has been considered as one of the potential biomaterials. We measure surface roughness and morphology with and without plasma treatments. Furthermore, we try to propose the correlation of contact angle, functional groups incorporation, cell activities and surface roughness with two-step plasma treatment procedure.

2. Experimental Methods

The PLA films were treated in the post-discharge jet region of an atmospheric, nitrogen-based, parallel-plate (5x5 cm), dielectric barrier discharge (DBD). The DBD plasma system was operated in Townsend-like discharge mode, which was driven by a 20-60 kHz quasi-pulsed power supply (EN Technologies Inc. model Genius 2). Both the thicknesses of dielectric material (quartz) and the gap distance between quartz plates are 1mm.

In our experiment, the plasma treatments were carried out in two steps: 1) to pretreat the surface using the N_2 DBD jet with 0.1% addition of O_2; and 2) to incorporate amino functional groups using the same N_2 DBD jet but with addition of 5% NH_3. In addition, a single axis moving plate was placed under the DBD to provide different residence time of treatment by controlling the number of passes, the plate moving velocity ranges from 1cm/s to 9cm/s.

For cell experiment, we chose the C_2C_{12} as the test cells. Detailed procedures in preparing the test cells and measurements of contact angle, cell culture, photomicrography observation and MTT assay were described in our previous study [9] and were not repeated here for brevity. In addition, AFM analysis was used to analyze surface morphology and roughness.

3. Results and Discussion

Fig. 1 illustrates the measured contact angle as a function of number of passes of APPJ treatment. The contact angle obtained by two-step treatment is the lowest (~30°) after 40 passes as compared to the other two processes. This shows that the two-step plasma treatment exhibits the best process for potentially increasing the surface energy and may provide the best incorporation of amino functional group.

Fig. 2 shows the results of AFM analysis. The surface roughness (rms) of original PLA is about 0.88 nm. After applying pretreatment, ammonia plasma treatment and two-step plasma treatment, the roughnesses (rms) are 50.16 nm, 1.50 nm and 73.22 nm respectively. We can find that pretreatment contributes to roughness increase most effectively. Surprisingly and interestingly, surface roughness can be increased to 73.22 nm by the two-step plasma treatment, although the second step alone (ammonia plasma) shows essentially no influence at all on the contact angle. The results of XPS analysis (N1s) in Table 1 shows a similar trend, which are described next.

XPS measurements were used to analyze the surface modifications done by the plasma treatment. Table 1 summarizes the atomic concentration of untreated and treated PLA surfaces. The O/C ratio of pretreatment sample increases as compared to pure PLA which means that oxygen related functional groups is incorporated on PLA surface. They can act as attractive sites to produce

an aminated surface more easily by the followed ammonia plasma treatment. In addition, the rougher surface by pretreatment provides larger area for incorporation of amino functional groups.

These two effects (large roughness and O/C ratio) probably leads to high concentration of N1s (~ 3%) and the lowest (~30°) contact angle which are both beneficial to the cell attachment and cell growth as described next.

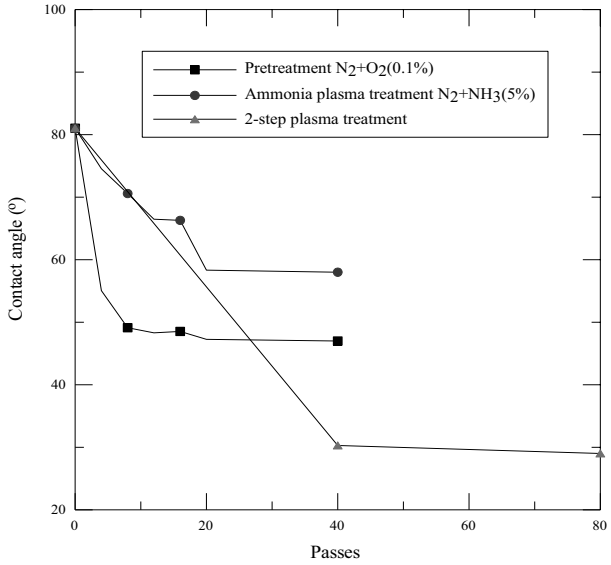

Fig. 1 Measured contact angles for different plasma treatment procedures.

Table 1 Atomic concentration of pure and plasma treated PLA films using XPS analysis

Conditions	O1s (%)	N1s (%)	C1s (%)	O/C	N/C
Pure PLA	36.43	0.00	63.57	0.57	0.00
Pretreatment	37.60	0.51	61.89	0.61	0.01
Ammonia plasma treatment	36.06	0.07	63.87	0.56	0.001
2-step plasma treatment	37.03	2.97	60.00	0.62	0.05

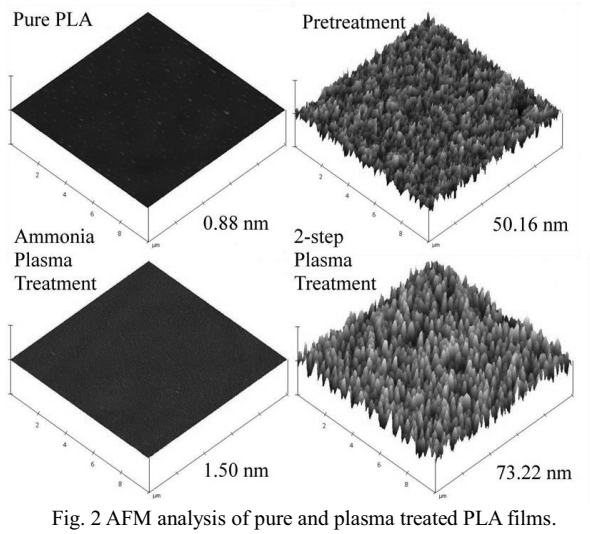

Fig. 2 AFM analysis of pure and plasma treated PLA films.

In the aspect of cell morphology, the C_2C_{12} cells stretched very well, attached tightly and appeared in spindle shape on the PLA surface by using the two-step plasma treatment (not shown here). In contrast, cell morphology using pure PLA was found to be much worse than using two-step plasma treatment during the three-day test period.

Fig. 3 shows the measured optical density (OD) with different test periods for the cases of pure PLA and two-step plasma treated PLA. The cell attachment test shows that OD using the two-step procedure is two times larger as compared to the pure PLA sample, at the 24th hour after cell mass culturing. In the cell proliferation test, after three days OD using the two-step procedure is always much greater than that using the pure PLA. This shows that the PLA surface has become more biocompatible in terms of cell attachment and proliferation after the proposed two-step plasma treatment.

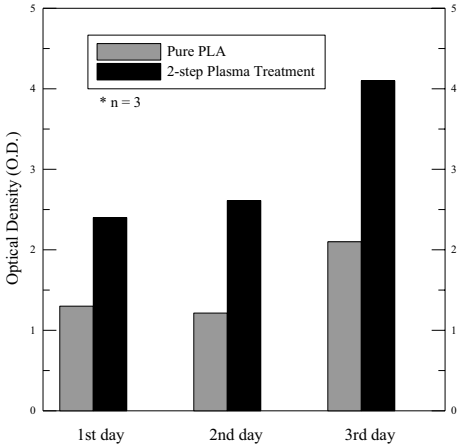

Fig. 3 Optical density of cell culturing on pure and two-step plasma treated treated PLA films for a three-day test period.

4. Concluding remarks

In this paper, a two-step plasma treatment procedure using the post-discharge jet region of a parallel-plate, nitrogen-based DBD is proposed. By using the two-step plasma procedure, we can incorporate amino functional groups very efficiently. Results show that on the PLA surface N1s and roughness can reach ~3% and 73 nm, respectively. It was verified to be very effective in improving the hydrophilic property, cell attachment and cell proliferation on PLA surface for muscle cells.

References

[1] J.M. Goddard, J.H. Hotchkiss, Prog. Polym. Sci., **32** (2007), 698–725

[2] B. Johansson, A. Larsson, Ocklind A., J. Appl. Polym. Sci., **86** (2002), 2618–2625

[3] G. Altankov, V. Thom, Th. Groth, J. Biomed. Mater. Res., **52** (2000), 219–230

[4] P.A. Ramires, L. Mirenghi, A.R. Romano, F. Palumbo, G. Nicolardi, J. Biomed. Mater. Res., **51** (2000), 535–539

[5] A. Schütze, J.Y. Jeong, S.E. Babayan, J. Park, G.S. Selwyn, R.F. Hicks, IEEE Trans. Plasma. Sci., **26** (1998) 1685

[6] K. Chaudhary, K. Inomata, M. Yoshimoto, H. Koinuma, Mater. Lett., **57** (2003), 3046

[7] M. Laroussi, T. Akan, Plasma Proc. Polym., **4** (2007), 777

[8] A. Vesel, I. Junkar, U. Cvelbar, J. Kovac, M. Mozetic, Surf. Interface Anal., **40** (2008), 1444-1453

[9] Y.W. Yang, C.L. Kuo, C.C. Wen, J.Y. Wu, H.Y. Huang, M.H. Chiang, J.S. Wu, The 7th ICFD, (2010)

Eighth International Conference on Flow Dynamics
November 9 - November 11, 2011

Development of a Parallel 2-D Hybrid Gas Flow and Plasma Fluid Modeling Algorithm and Its Application in Atmospheric-Pressure Plasma Jets

K.-M. Lin[1], M.-H. Hu[1**], C.-T. Hung[1] and J.-S.Wu[1,2*]
[1]National Chiao Tung University, Hsinchu, Taiwan.
[2]National Center for High-Performance Computing, Hsinchu, Taiwan.
[*]E-mail: chongsin@faculty.nctu.edu.tw

ABSTRACT

In this paper, a parallel weakly coupled algorithm hybridizing 2-D gas flow simulation and plasma fluid modeling is presented. Both the compressible Navier-Stokes equations and fluid modeling equations are discretized by the cell-centered finite-volume method. The former were solved by an all-speed extended SIMPLE scheme, while the latter were solved by a semi-implicit numerical scheme. Both solvers are parallelized using domain decomposition method. At the end, several challenging and realistic atmospheric-pressure plasma jet problems are demonstrated.

1. Introduction

Atmospheric-pressure plasma jets have found wide applications in several important disciplines in recent years because they are operated in atmospheric-pressure condition and potentially inexpensive. These applications may include surface modification, surface cleaning, thin-film deposition, sterilization, and tooth breaching, among others [1-5]. Optimal design of these plasma devices relies heavily on trial-and-error approach, which is often very time-consuming and costly. Understanding of these complex plasma physics and chemistry through experimental method could be limited, time-consuming and difficult, if not impossible. Thus, numerical simulation becomes an inevitable tool in fully appreciating the complex physics in a gas discharge.

Fluid modeling equations, which are the velocity moments of Boltzmann equation, are often employed to model gas discharges when continuum assumption is valid. Continuum assumption breaks down when the pressure is very low in the range of tens of mtorr such as sputtering plasma [6]. For low-pressure gas discharges, fluid modeling without considering the fluid dynamics is often considered to be valid. However, as the pressure rises, fluid dynamics becomes important in affecting the gas discharges. Thus, understanding of the gas discharges requires proper modeling of gas flow and gas discharge simultaneously. However, there have been very few studies in the literature which have focused on this regard [7-9]. Moreover, it often takes from weeks up to months of runtime in coupling the gas flow simulation and plasma fluid modeling because of large disparity of characteristic time scales between fluid dynamics and plasma. Parallel implementation using MPI can shorten the runtime tremendously. Unfortunately, there has been nearly no report on parallel computing of plasma fluid modeling previously, except Wu *et al.* [10-11].

In this paper, we report our recent progress in developing a parallel hybrid gas flow and fluid modeling algorithm and its applications in atmospheric-pressure plasma jets driven by several power sources with a frequency in the range of kHz-MHz, which is often seen in practical applications.

2. Numerical Methods

In this study, the modeling equations are classified into two folds. The first is the compressible conservation equations for modeling the fluid dynamics in a gas discharge. The second is the fluid modeling equations which describe the behavior of charged and neutral species in a gas discharge. They are described in the following in turn.

Gas Flow Simulation

For the neutral gas flow simulation, a complete set of 2D compressible Cartesian-grid conservation equations, including continuity equation, momentum equations (Navier-Stokes), energy equation, species continuity equations and equation of state for ideal gas, are solved using a cell-centered finite-volume method, named extended SIMPLE (Semi-Implicit Method for Pressure Linked Equations) scheme [12]. A second-order upwind scheme with linear reconstruction is used to evaluate the inviscid flux across the cell interface. A flux limiter is used to prevent from local extrema introduced by the data reconstruction. Pressure smoothing is used to avoid the pressure oscillations on a collocation grid. The solver is parallelized using domain decomposition approach. In general, this solver can deal with gas flows at all speeds and can consider conjugate heat transfer involving convection in the gas and conduction in the solid. In addition, velocity slip and temperature jump at solid boundaries can be also considered if rarefaction is important. Details of the implementation can be seen in [12] and are skipped here for brevity.

Plasma Fluid Modeling

For modeling the gas discharge, the fluid modeling is used. The modeling equations include the continuity equations with drift-diffusion approximation for all charged species, the continuity equations for neutral species, the electron energy density equation, and the electrostatic Poisson's equation. The transport coefficients (drift and diffusion) and the rate constants related to electrons are functions of the electron temperature, which are obtained by integrating either the experimental collision cross section, or the EEDF from the solution of the simplified Boltzmann equation solver [13]. All model equations are discretized by using the backward Euler's method on the temporal domain and cell-centered finite volume with the Scharfetter-Gummel scheme for the mass fluxes on the spatial domain. To

ensure stability when larger time steps are used, linearization in time and electron energy density is applied for the source term of Poisson's equation and electron energy density equation, respectively. All discretized fluid modeling equations are solved by using the libraries in PETSc package [14], in which MPI (message passing interface) is employed for parallel communication. Details of implementation are presented elsewhere [15].

Hybrid Flow-Plasma Simulation

It is well known that there exists a large disparity of time scales between neutral gas flow (10^{-4}~10^{-6} s) and gas discharge (10^{-9}~10^{-11} s). Thus, strongly coupling at each time step of discharge would be impossible and unnecessary. Figure 1 illustrates the proposed weakly coupled algorithm hybridizing 2-D gas flow simulation and plasma fluid modeling. The modeling starts at neutral gas flow simulation and, after reaching a steady state, then passes simulation data such as velocities, temperature and number densities of background species to the fluid modeling. Then, the fluid modeling starts to run based on these data and, after reaching a quasi-steady state, collects numerical data such as momentum force and gas heating (Joule heating of ions and electron-neutral elastic collision heating) induced by charged particles. These data are then passed back to the gas flow simulation module to update the flow and thermal fields. Generally, 2-3 cycles of coupling are enough to have a converged solution.

3. Results and Discussion

A planar DBD-APPJ with a substrate near the exit of the jet is used for demonstration of the developed hybrid algorithm. Gap distance is 1 mm with each electrode covered with a flat dielectric layer (alumina, ε=11.63, 1 mm). 30 slm of helium with 100 ppm of N_2 flows into the discharge gap from the left and exits from the right into a nitrogen environment and impinges on the substrate at the right. In addition, both electrodes are covered by thick Teflon (ε=2.0) for preventing from generating arching with the air. Nearly sinusoidal voltages with $V_{p\text{-}p}$= 6 kV and f= 25 kHz are applied to the electrodes. A set of plasma chemistry consists of 10 species (e, He^+, He_2^+, He_m, He_{ex}, He_2^*, N^+, N_2^+, N_4^+, N) and 43 reaction channels were employed for the simulation using a grid of 1001x620 cells. It takes about 48 hours for 5 AC cycles using 128 processors on a IBM-1350 cluster at National Center for High-Performance Computing of Taiwan.

Figure 2 shows the temperature distribution. Gas heating due to ion Joule heating and electron-helium elastic collision is very obvious, which causes the gas heated up to 330 K as compared to 300 K at the inlet. Prediction of temperature distribution is important for several applications, especially in bio-medical field.

Figure 3 shows the cycle averaged distribution of electron density near the discharge exit. The electron density reaches 9×10^{16} m^{-3} in the bulk and 2×10^{16} m^{-3} in the sheath region. The density distribution near the discharge exit is important since it is directly related to the applications in the afterglow region.

4. Concluding remarks

A parallel weakly coupled algorithm hybridizing 2-D gas flow simulation and plasma fluid modeling is presented. A planar DBD-APPJ with a substrate near the exit of the jet is used for demonstration of the developed hybrid algorithm with spatial distribution of temperature and electron density. Detailed results will be presented in the conference.

References

[1] Y. Qiu et al, J. Adhes. Sci. Technol. 16 (2002), 449.
[2] U. Kogelschatz, Plasma Chem. and Plasma Process. 23, 1 (2003)
[3] C. H. Yi et al, Surf. Coat. Technol. 171 (2003), 237.
[4] Y. F. Hong et al, Lett. Appl. Microbiol. 48 (2009), 33.
[5] H. W. Lee et al, Plasma Processes and Polymers, 7 (2010), 274
[6] A. Bogaerts et al, Journal of Physics D: Applied Physics, 42 (2009), 194918
[7] Y. Sakiyama et al, Plasma Sources Sci. Technol., 18 (2009), 025022
[8] J. van Dijk et al, J. Phys. D: Appl. Phys., 42 (2009), 194012
[9] M. J. Kushner, J. Phys. D: Appl. Phys., 42 (2009), 194013
[10] C. T. Hung et al, Comput. Phys. Commun., 177 (2007), 138
[11] C. T. Hung et al, Comput. Phys. Commun., 182 (2011), 161
[12] M. H. Hu et al, Computers and Fluids, 45 (2011), 241
[13] G. J. M. Hagelaar, Plasma Sources Sci. Technol., 14 (2005), 722
[14] S. Balay *et al*, "PETSc home page", 2001, http://www.mcs.anl.gov/petsc.
[15] K. M. Lin et al, Comput. Phys. Commun., submitted, 2011

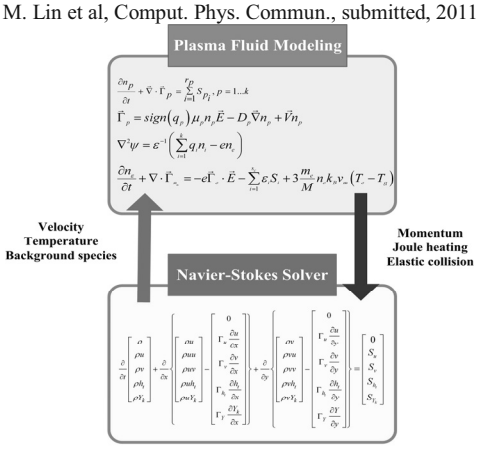

Figure 1. Proposed weakly coupled algorithm hybridizing gas flow simulation and plasma fluid modeling.

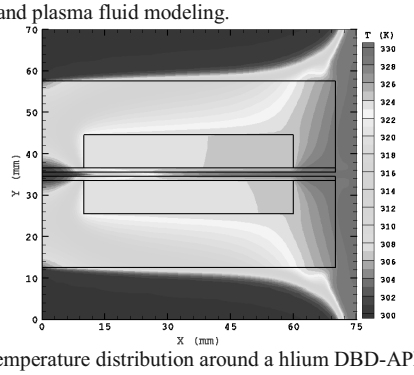

Figure 2. Temperature distribution around a hlium DBD-APPJ impinging on a substrate.

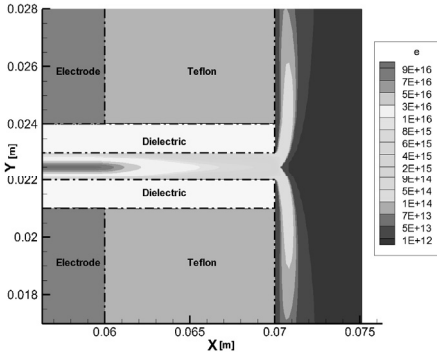

Figure 3. Number density of electron near the exit

Numerical Study of Rayleigh–Bénard Convection Near the Critical Point

Biao Shen, Peng Zhang
Institute of Refrigeration and Cryogenics, Shanghai Jiao Tong University
800 Dongchuan Road, Shanghai 200240, P.R.China
zhangp@sjtu.edu.cn

ABSTRACT

We study the thermogravitational convection of supercritical nitrogen along its isochore in a two-dimensional Rayleigh-Bénard cell. By means of numerical simulation, different convective patterns are obtained dependent on the initial distance to the critical point, ranging from turbulent thermal plumes to large-scale rolls. On the other hand, the characteristic time observed in the time evolution of the temperature drop across the fluid layer is found to follow a simple scaling relation with the Rayleigh number.

1. Introduction

Near the liquid-gas critical point (CP), various thermodynamic properties exhibit striking abnormalities. Notably the thermal diffusivity goes to zero, and the isobaric expansion coefficient strongly diverges. A thermomechanically-based heat transfer mechanism called "the piston effect" (PE) was unveiled to explain the surprisingly fast and homogeneous thermalization of near-critical fluids [1]. Under terrestrial conditions, the potential of achieving extremely high Rayleigh number has incited enormous interest over the past decade. Kogan et al.'s landmark experiment of supercritical ^{3}He [2] and the following theoretical and numerical works [3-4] revealed that, on approaching the critical point, the onset of Rayleigh-Bénard (RB) convection experiences a transition from the Rayleigh criterion to the Schwarzschild criterion, under which the contribution to the hydrodynamic stability by the fluid compressibility needs to be taken into account.

The aim of this paper is to present the two-dimensional (2D) numerical simulation of the RB convection along the critical isochore of nitrogen. Our results show that, dependent on the criticality [denoted by the reduced temperature $\varepsilon = (T-T_c)/T_c$, where T_c = 126.192 K is the critical temperature], the thermogravitational flow structure varies significantly.

2. Methodology

We consider a rectangular RB cell with an aspect ratio (vertical height/horizontal length) of A = 4, filled with near-critical nitrogen. Initially, on account of the shallow configuration with the height L = 2.5 mm, the fluid is assumed to be free of stratification ($\rho_i = \rho_c$ = 313.3 kg/m^3, where ρ_c is the critical density). For times $t > 0$, a constant heat flux q = 1 W/m^2 is applied at the bottom boundary, while the top plate remains at the initial temperature. No-slip condition is imposed at all boundaries, including the two adiabatic lateral walls.

The exact Navier-Stokes description for a Newtonian, compressible, viscous, and heat conducting fluid is employed to capture the dynamics of the system. To reduce the computational time, we use a low-Mach number approximation to remove unnecessary alternating motion of sound from the equations [5]. The resulting equations are then solved numerically by the SIMPLE algorithm [6]. Very close to the CP, as we will see later, the RB flow is characterized by the chaotic release of thermal plumes. In general, the shedding of thermal plumes cannot be predicted a priori. For this reason, a uniform and dense mesh of 201×101 is used in the simulation, along with a matching timestep of 5×10^{-3} s. By varying the distance to the CP, we investigate the evolution of the RB convection pattern.

3. Results and discussion

In Fig. 1, we plot the profiles of the spatially-averaged temperature difference ΔT(t) across the fluid layer at different initial temperatures ε. Note that for each curve, the vertical axis in the figure has been scaled by the peak value ΔT_p, and accordingly the horizontal axis by the occurring time t_p. Two signature features of near-critical fluids, as established by the experimental findings [2], are evident: the temperature overshoot and the ensuing damped oscillations before reaching the steady state. Quantitatively, more severe temperature decrease after peaking is predicted further away from the CP. Also, as ε rises, the route to the final steady state appears increasingly less oscillatory.

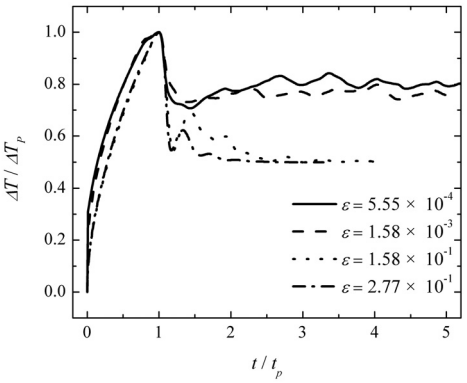

Fig. 1 The vertical temperature drop $\Delta T/\Delta T_p$ as a function of t/t_p, under different values of ε.

The time of the first peak t_p is one of the characteristic times that indicate substantial development of convection. Figure 2 shows the scaling of t_p/τ_{diff} obtained for different ε with the corresponding reduced Rayleigh number Ra^* (steady state). Here $\tau_{diff} = L^2/(4D_T)$ is the diffusion time, where D_T denotes the thermal diffusivity. Close to the CP, Ra^* is defined as

$$Ra^* = \left(Ra^{corr} - Ra_c\right)/Ra_c = \frac{\alpha_P g L^3 \theta}{\nu D_T Ra_c} - 1, \qquad (1)$$

where α_P is the isobaric expansion coefficient, g the acceleration of gravity, ν the kinematic viscosity, and

Ra_c = 1810 the critical Raleigh number with A = 4 and no-slip horizontal boundaries [7]. In Eq. (1), $\theta = \Delta T - LgT\alpha_P/C_p$ is the potential temperature difference, where C_p is the isobaric specific heat. The second right-hand-side term represents the contribution of the adiabatic temperature gradient (ATG) under the Schwarzschild regime. It is noteworthy that the data points collapse onto a single curve. Over nearly five decades of Ra^*, t_p/τ_{diff} is found to follow a power law with a scaling exponent of -0.67.

Figure 3 depicts the evolution of the flow pattern at different ε, from the initiation of convection to the steady state. In proximity of the CP, the RB convection is dominated by the violent outbursts of thermal plumes from the thermal boundary layers, while the fluid remains stagnant at the core [Fig. 3(a)]. Note that, due to the PE, the boundary layer exists near the top plate as well despite weak penetration by thermal diffusion, which makes the situation akin to being concurrently heated from below and cooled from top. The flow structure at later stage seems particularly chaotic, as a result of the interaction between large-scale circulations in the bulk and the random merging and separation of periodically detached thermal plumes [Fig. 3(b)]. In the intermediate range of ε, the rising thermal plumes turn thick [Fig. 3(c)], whereas no falling thermal plumes are detectable due to the diminished PE. In Fig. 3(d), a stable and symmetric pattern of four-cellular structure ultimately emerges in the bulk. Far from the CP, the increased thermal diffusivity prevents thermal plumes from being generated. The instability starts off in the form of the large vortices and wavy isotherms at the center [Fig. 3(e)], which later evolves into the sustained rising warm current and sinking cold current [Fig. 3(f)]. Interestingly the steady flow pattern consists of six rolls [cf. Fig 3(d)].

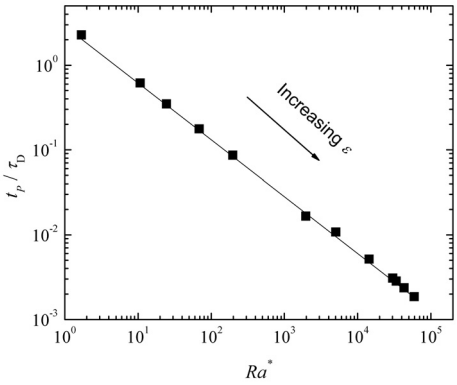

Fig. 2 The peaking time t_p, scaled by the diffusion time τ_{diff}, versus reduced Rayleigh number Ra^*.

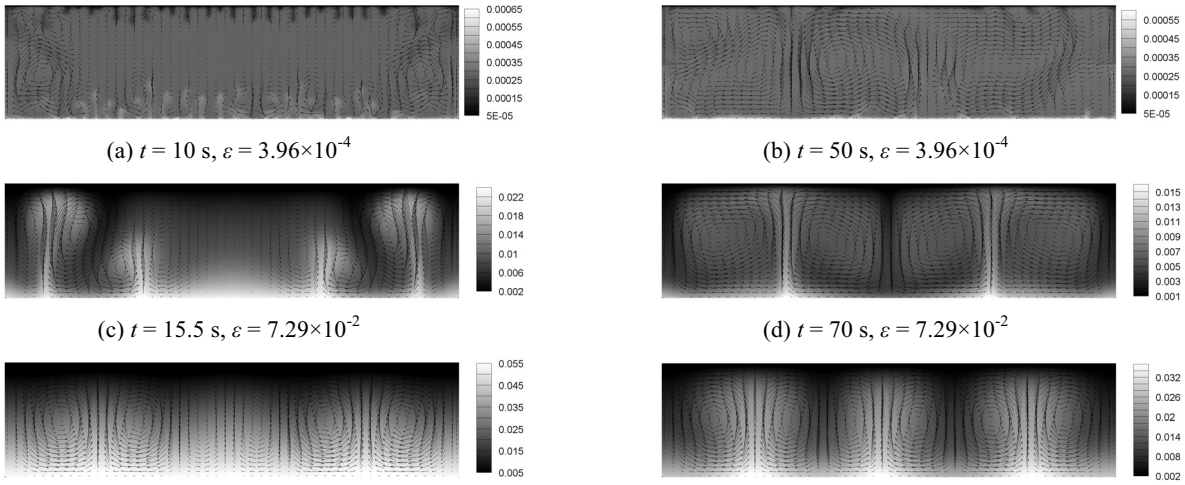

(a) t = 10 s, $\varepsilon = 3.96\times10^{-4}$ (b) t = 50 s, $\varepsilon = 3.96\times10^{-4}$

(c) t = 15.5 s, $\varepsilon = 7.29\times10^{-2}$ (d) t = 70 s, $\varepsilon = 7.29\times10^{-2}$

(e) t = 43 s, $\varepsilon = 7.29\times10^{-1}$ (f) t = 87.8 s, $\varepsilon = 7.29\times10^{-1}$

Fig. 3 Convective pattern (temperature contour and velocity vector map) at different t and ε.

4. Conclusions

We have numerically solved the RB problem of supercritical nitrogen along its critical isochore. Over a wide range of Rayleigh numbers, the convection shows fundamentally different patterns, the characteristic time of which is found to form a simple scaling relation.

Acknowledgements

This research is supported by the National Natural Science Foundation of China under Contract No. 50976068. B. Shen acknowledges financial support of the Scholarship Award for Excellent Doctoral Student granted by Ministry of Education.

References

[1] B. Shen and P. Zhang, Phys. Rev. E **83** (2011), 011115.

[2] A. B. Kogan and H. Meyer, Phys. Rev. E **63** (2001), 056310.

[3] A. Furukawa and A. Onuki, Phys. Rev. E **66** (2002), 016302.

[4] S. Amiroudine and B. Zappoli, Phys. Rev. Lett. **90** (2003), 105303.

[5] S. Paolucci, Tech. Rep. 82-8257 Sandia National Laboratories. (1982).

[6] S. V. Patankar, *Numerical Heat Transfer and Fluid Flow*, Hemisphere, New York (1980).

[7] M. Lappa, *Thermal convection: patterns, evolution and stability*, Wiley, Chichester (2010).

Eighth International Conference on Flow Dynamics
November 9 - November 11, 2011

Numerical Simulations on Immiscible Rotating Hele-Shaw Flows: A Phase-Field Approach

Yu-Sheng Huang, Ching-Yao Chen
Department of Mechanical Engineering National Chiao Tung University, Hsinchu Taiwan, 30010 Republic of China
Email: chingyao@mail.nctu.edu.tw.

ABSTRACT

We present numerical simulations based on a diffuse interface model for this particular two-phase displacement that capture a variety of pattern forming behaviors. This is implemented by employing a Boussinesq Hele-Shaw-Cahn-Hilliard approach, considering the whole range of possible values for the viscosity contrast, and by including inertial effects due to the Coriolis force. The role played by these two physical contributions on the development of interface singularities is illustrated and discussed.

1. Introduction

Rotating Hele-Shaw flows have been the object of considerable interest during the last two decades. This particular type of confined flow offers a variation to the traditional viscosity-driven Saffman-Taylor problem [1]. It occurs when a fluid, surrounded by another of lower density, is located in a Hele-Shaw cell which rotates about a perpendicular axis.

In this work, we consider a diffuse interface approach which is based on a simplified version of the Navier-Stokes-Cahn-Hilliard model [2-3], originally applied to two phase fluid flow in motionless (non-rotating) Hele-Shaw cells [4-5]. We extend the results obtained to the rotating Hele-Shaw setup, and used intensive numerical simulations to analyze the fully nonlinear behavior of the evolving inter- facial patterns. It is also worth mentioning that our analysis is done by spanning the whole range of values of the viscosity contrast A, and by taking Coriolis force effects into account.

2. Physical Problem and Governing Equation

We investigate the interfacial instability between two immiscible fluids in a rotating Hele-Shaw cell (Fig. 1). The cell has gap spacing h and turns around an axis perpendicular to the plane of the flow with constant angular velocity Ω. Inside the cell an initially circular drop (radius R_0) of fluid 2 is surrounded by an outer fluid 1. The densities and viscosities of the fluids are denoted by ρ_j and η_j, respectively (j = 1, 2). We focus on the centrifugally-induced motion where $\rho_2 > \rho_1$, but allow the inner fluid to be either more or less viscous than the outer fluid.

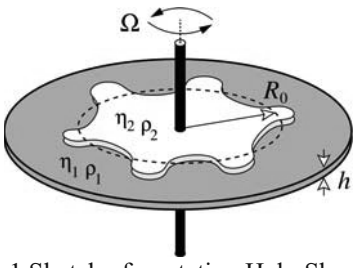

Fig. 1 Sketch of a rotating Hele-Shaw cell

The governing equations of such a diffuse interface problem are based on a model proposed by Cahn and Hilliard [2]. In the context of a rotating Hele-Shaw cell system the dimensionless equations can be written as

$$\nabla \cdot \mathbf{u} = 0, \tag{1}$$

$$\nabla p = -\eta \mathbf{u} - (c + \frac{\rho_2}{\Delta\rho})\left[\mathbf{r} + 2\,\mathrm{Re}(\mathbf{e}_z \times \mathbf{u})\right] - \frac{C}{Ga}\nabla \cdot \left[(\nabla c)(\nabla c)^T\right] \tag{2}$$

$$\frac{\partial c}{\partial t} + \mathbf{u} \cdot \nabla c = \frac{1}{Pe}\nabla^2 \mu,\ \mu = \frac{\partial f_0}{\partial c} - C\nabla^2 c \tag{3}$$

$$f_0 = c^2(1-c)^2 \tag{4}$$

Here, **u** denotes the fluid velocity vector, p the pressure, η the viscosity, and ρ the density of the binary fluid system. The phase-field variable is represented by c, so that c = 1 in the bulk of fluid 1 (phase 1), and c = 0 in the bulk of fluid 2 (phase 2). The chemical potential is denoted by μ, and f_0 is a free energy. **r** is the radial position vector, and e_z represents the unit vector along the rotation axis (z-axis). Equations (1)-(5) define the so-called Hele -Shaw- Cahn -Hilliard model [4-5]

Correlations of viscosity (η) and density (ρ) with the phase-field variable c are required by the present app roach and are taken as

$$\eta(c) = \eta_1 e^{[R(1-c)]}, R = \ln(\eta_2/\eta_1) \tag{5}$$

$$\rho(c) = \rho_1 c + \rho_2(1-c) \tag{6}$$

Dimensionless parameters, such as the Peclet number Pe, the viscosity contrast A, the Cahn number C, the rotationally modified Galileo number Ga, and the (Coriolis force related) Reynolds number Re are defined as

$$A = \frac{e^R - 1}{e^R + 1},\ Pe = \frac{\rho_b \Delta\rho \Omega^2 h^2 R_0^{\,2}}{12\eta_1 \alpha f^*},\ Ga = \frac{\Delta\rho\Omega^2 R_0^{\,2}}{\rho_b f^*},$$

$$C = \frac{\varepsilon}{R_0^{\,2} f_0},\ Re = \frac{\Delta\rho\Omega h^2}{12\eta_1}$$

A dimensionless rotational Bond number, can be used to evaluate the ratio between the capillary and centrifugal forces, It's defined as

$$Bo_e = \sqrt{C/2}\,/3Ga \tag{7}$$

To reproduce the fine fingering structures, a highly

accurate pseudospectral method is employed to solve the streamfunction equation. Time integration is fully explicit by a third order Runge-Kutta procedure.

3. Results and Discussion

(A) Fingering dynamics without the Coriolis force

In this section we introduce numerical results for rotating Hele-Shaw flows which neglect Coriolis force effects. Numerical simulations illustrating the effect of the viscosity contrast on the mechanisms of finger competition and pinch-off are depicted in Fig. 2 for three different values. First, we focus on the left panel of Fig. 2 which shows characteristic pattern morphologies before the occurrence of complicated pinch-off events.

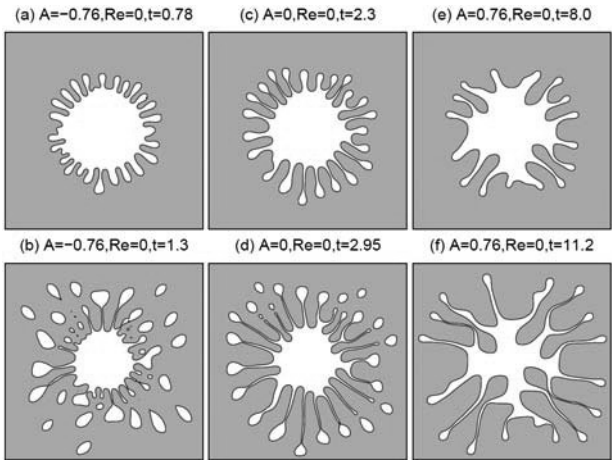

Fig. 2 Typical fingering patterns for A =−0.76 [(a) and (b)], A = 0 [(c) and (d)], and A = 0.76 [(e) and (f)]. The remaining parameters are: Pe = 9×10^3, Ga = 0.4 and C = 10^{-5} [$Bo_e = 1.86 \times 10^{-3}$]. The top (bottom) panel shows patterns before (after) the occurrence of pinch-off.

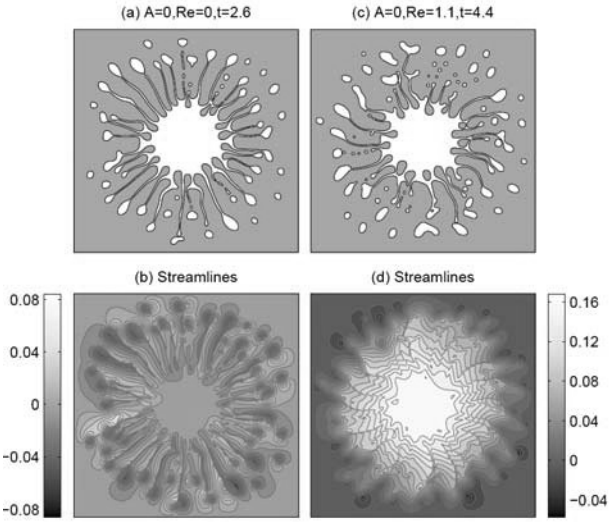

Fig 3. Fingering patterns and streamlines for Pe = 9×10^3, Ga = 1 and C = 10^{-5} [$Bo_e = 7.45 \times 10^{-4}$] for A = 0 and Re = 0 [(a) and (b)]; A = 0 and Re = 1.1 [(c) and (d)].

(B) Influence of the Coriolis force

We initiate our analysis of the Coriolis effects by examing Fig. 3. It plots fingering patterns and their corresponding streamlines when Coriolis force is neglected [Fig. 3 (a) and (b)], and when it is taken into account [Fig. 3 (c) and (d)]. In Fig. 3 (a) and (b) A = 0 and Re = 0, while in Fig. 3 (c) and (d) A = 0 and Re = 1.1.

We conclude by presenting Fig. 4 which provides complementary information about the role played by the Coriolis effects. It plots the pattern's interfacial lengths as a function of time, for different values of A and Re. In agreement with our previous observations we see that the inclusion of the Coriolis force leads to interfacial stabilization, resulting in shorter lengths.

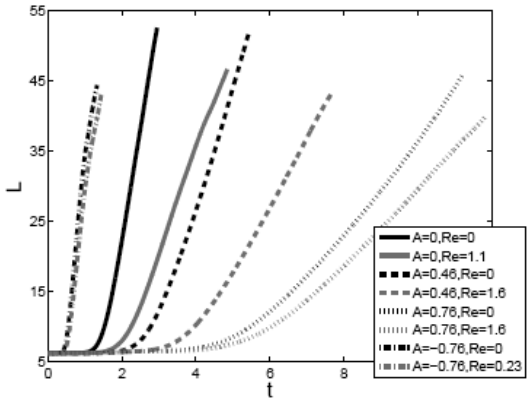

Fig. 4 Time evolution of the interfacial length L for various viscosity contrasts and Reynolds numbers. Here Pe = 9×10^3, Ga = 0.4 and C = 10^{-5} [$Bo_e = 1.86 \times 10^{-3}$].

4. Concluding remarks

We have presented a diffuse interface numerical study for the rotating Hele-Shaw problem, which has been implemented by utilizing a Boussinesq Hele-Shaw-Cahn-Hilliard (BHSCH) approach. When Coriolis force contributions are taken into account our numerical experiments clearly reveal three basic behaviors: a stabilized radial growth, existence of pattern phase drift, and development of finger bending. All these features are in line with what has been obtained by previous simulating investigations of the problem, which employed distinct numerical techniques. Furthermore, we have also verified that important topological changes related to finger pinch-off and emission of satellite droplets are significantly favored by the action of the Coriolis force.

References

[1] P. G. Saffman and G. I. Taylor, Proc. R. Soc. London Ser. A **245** (1958), 312.
[2] J. W. Cahn and J. E. Hilliard, J. Chem. Phys. **28** (1958), 258.
[3] D. Jacqmin, J. Comput. Phys. **155** (1999), 96.
[4] H.-G. Lee, J. Lowengrub, and J. Goodman, Phys. Fluids **14** (2002), 492.
[5] H.-G. Lee, J. Lowengrub, and J. Goodman, Phys. Fluids **14** (2002), 514.

Eighth International Conference on Flow Dynamics
November 9 - November 11, 2011

Trajectory of Table Tennis Ball - A Visual Study

Feng-Yun Yu[1], Po-Lung Tien[2], Hsien-Kuo Chang[3], Sien Chi[4], Huai-Po Lo[5], and Chi-Chuan Wang[5,*]
[1]Office of Physical Education, [2]Department of Electrical Engineering, [3]Department of Civil Engineering, [4]Department of Photonics Engineering, [5]Department of Mechanical Engineering , National Chiao Tung University
E-mail: ccwang@mail.nctu.edu.tw.

ABSTRACT

The present study conducts a visual observation of trajectory of topspin table tennis ball subject to initial velocity using high speed cameras. Trajectory, velocity, acceleration, angular velocity, and relevant parameters are reduced from the recorded image file. The trajectory shows a significant departure to the frictionless, irrotational ball. And the initial velocity casts an appreciable influence on V_x whereas the effect on V_y is quite small. A significant velocity surge is found right just impact. This is applicable for either V_x or V_y. Yet a significant reduction of angular velocity is observed after impact, this is applicable for either low or high initial velocity.

1. Introduction

Table tennis is a popular sport around the globe. One of the features of the table tennis sport is its wide spanning of ages, gender, and type of build. Regardless its easy playing, fast speed, spinning, diversity, instantaneous reactions, and relevant interactions makes table tennis competition a very devastating sport to handle. Topspin by forehand is one of the most aggressive shots in table tennis especially against backspin balls. Some world-class players can put up to 9000 rpm of topspin on table tennis balls.

Aerodynamics plays an essential role in every sport ball either being struck or thrown in the air. There had been some many studies concerning this subject, and some intensive reviews were made by Mehta [1] and Mehta [2]. Sports ball interacts with aerodynamics had been studied during the past, including tennis ball [3], Soccer ball [4], Volleyball [5] , Golf ball [6], Baseball [1] and Cricket ball [7]. Irrespective of the popularity of table tennis, relevant studies on this subject were quite limited. Notice that the table tennis ball is quite different from other sport ball at least from three aspects. Firstly, the ball is rather small and light weight and its interactions with air flow may be comparatively pronounced. Secondly, the speed of table tennis is quite high and the significant spinning is often incorporated with the high speed ball, thereby resulting in erratic ball trajectory. Thirdly, the table tennis ball will bounce from the table to and fro during completion which makes even more complicated interactions amid ball, table, and flow field. Unfortunately, the existing literatures associated with table tennis sport were mainly on other subjects such as timing and attacking [8], analysis of coordination dynamics [9], and kinematics of the table tennis [10]. In practice, the aerodynamics cast a tremendous impact on the table tennis game. In this regard, it is the objective of this study to examine its influence qualitatively and quantitatively. The present study focus on the topspin of table tennis ball using a service machine. The trajectory of the table tennis is recorded by some high speed camera, followed by some analysis of the measured trajectories.

2. Method

The experiment is conducted via direct visualization of the trajectory of the topspin table tennis ball using three Casio EX-F1 video cameras. Schematic showing the location of video camera and the service machine is shown in Fig. 1. The recoding speed of the video camera can at 600 pictures/s. For easier keeping track of the trajectory, the background of the table is covered with black fabric material with white net as the XY position map as shown in Figure 2. The edge of the right hand side of table is regarded as the datum of the coordinate system with upward and rightward as the positive direction. The service machine is placed 35 cm above and 27 cm right to the datum point, and it provides low and high speed topspin ball. The test balls are official 3-star ball from Nittaku. Three independent experiments were conducted with each experiment testing ten balls for recording trajectory for each speed, followed by averaging the measuring results. Paint marker is placed around the periphery of the test ball, and detailed revolutions of the test ball can be examined from the recorded image file. The recorded image file is analyzed using NI Vision Development Module software.

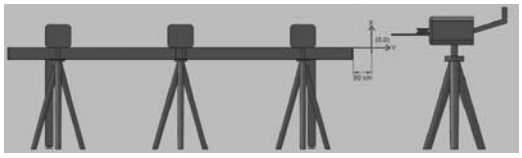

Fig. 1 Schematic showing the location of video camera and service machine.

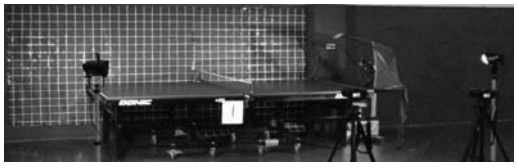

Fig. 2 Photo of the test equipment, including X/Y position net, table, service machine, and lighting.

3. Results and Discussion

Figure 3 denotes the trajectory of the top spin ball subject to low and high initial velocities. The angle of incidence of the service machine relative to horizontal direction is fixed at 6 degrees with respective mean inlet velocity being (I) 11.6 m/s (low speed) and (II) 15.8 m/s (high speed). The trajectory is also compared with the trajectory of a frictionless and irrotational ball having the same initial velocity, incident angle, and mass. It

appears that the travel distance of the spin ball is much shorter than that of the frictionless and irrotational ball. The departure amid these two trajectories increases with the rise of initial velocity, and the explanations are as follows. Firstly, the drag force is imposed on the moving ball which apparently reduces the traveling distance. Secondly, as clearly shown in the trajectory that the top spinning ball hits the table much quicker than the trajectory of the non-spin one, the results implicate a higher descending acceleration of the spinning ball. In general, sidespin causes a ball to swerve; topspin gives rise to dip, and backspin lift the ball upwards. For the present topspin ball, it is clear that Magnus effect causes the ball to arrive at the table much earlier. Table 1 depicts the descending acceleration and the angular velocity of the flying ball in this study. Initially, the descending acceleration is about 22.5 m/s^2 and remains almost the same before impact, yet a tremendous change of this acceleration right after the impact, but soon recovers almost back to its original value.

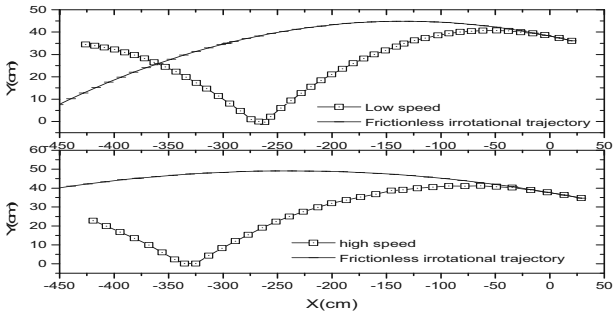

Fig. 3 Trajectory of the topspin ball subject to initial velocity and their comparisons against frictionless and irrotational ball.

Table 1. Descending acceleration and the angular velocity of the flying subject to initial velocity

	a_y (m/s^2)		
	Initial	On Net	Leaving table
Low Speed V_i = 11.5 m/s	-22.6	-21.86	-22.29
High Speed V_i = 15.7 m/s	-24.6	-22.13	-23.89
	ω (r/s)		
	Initial	On Net	Leaving table
Low Speed V_i = 11.5 m/s	68.33	56.67	29.61
High Speed V_i = 15.7 m/s	87.03	85.5	59.44

Cross [11] measured the grip-slip behavior of bouncing balls, including baseball, basketball, superball, tennis ball, and golf ball. His results indicated a sharp rise of reaction force in the normal direction after impact [11]. This consequently leads to a surge of V_y after impact. Also shown in the preceding discussion, the general trend of V_x and V_y vs. flight direction is roughly the same, and the variation of angular velocity before impact is small. For example, at a low initial velocity, the drop of angular velocity is about 13% whereas it is only 1.8% for the higher initial velocity. However, as clearly seen in Table 1, a sharp decline of angular velocity is observed after impact. In fact, for a lower initial velocity, the angular velocity is reduced to only 44% of its original angular velocity after impact. Yet, the angular velocity is reduced to 68.3% of its original angular velocity after impact at a higher initial velocity. Again the results are in line with the nature of a topspin ball. As aforementioned previously that a topspin ball featuring a counterclockwise rotation and when it dropped on to horizontal table will bounce to the left. A higher initial velocity will assist the ball to bounce left further, thereby retaining more angular velocity after impact. The results had been also seen for a tennis ball [12].

4. Concluding remarks

This study performs a visual observation of trajectory of topspin table tennis ball subject to initial velocity. Based on the foregoing discussions, the following results are concluded:

1. The observed trajectory shows significant departures to the frictionless, irrotational ball due to Magnus force and imposed drag.

2. The initial velocity casts an influence of V_x whereas the effect on V_y is quite small.

3. A significant velocity surge appears right just impact for either V_x or V_y, the formal surge phenomenon appears due to the nature of topspin ball where the latter is subject to significant reaction force. The surge phenomenon becomes more pronounced with the rise of initial velocity.

4. Normally the angular velocity decreases slightly along the flight line, the deterioration is more severe when the initial velocity is low. However, a significant reduction of angular velocity is observed after impact.

5. Acknowledgements

The authors would like acknowledge supporting fund from the diamond project of the National Chiao Tung University.

References

[1] R.D. Mehta, Fluid Mech. Rev., **17**(1985), 151-189.
[2] R.D. Mehta, Springer Wien New York, (2008), 229-331.
[3] S.R. Goodwill, J. of Wind Eng and industrial aerodynamics, **92**, (2004), 935-958.
[4] S. Barber., Springer-Verlag Berlin Heidelberg, (2009), 83-102.
[5] Q. Wei, Fluid D S, **3**(1988), 231-237.
[6] J.M.. Davies, J of applied phys., **20** (1949), 821-828.
[7] R.D. Mehta., Sports Eng., **8** (2005), 181-192.
[8] R.J. Bootsma., J of Exp Psy, **16** (1990), 21-29.
[9] V. Sørensen, Biological Cybernetics, **85** (2001), 27-38
[10] Y.Iino, J. Sports S., **27** (2009), 1311-1321.
[11] R. Cross, J. Phy., **70** (2002), 1093-1102.
[12] J.M. Davies, J. applied phys., **20**(1949), 821-828.

Eighth International Conference on Flow Dynamics
November 9 - November 11, 2011

Special characteristics of mixed convection in a three dimensional vertical channel

Wu-Shung Fu, Yun Huang, Kuan-Lan Liu
EE306, Department of Mechanical Engineering, 1001 Ta Hsueh Road, Hsinchu, Taiwan
wsfu@mail.nctu.edu.tw

ABSTRACT

Mixed convection and natural convection of air in a vertical 3-D channel of finite length are investigated numerically. A quantity of information on the effects of flow reversal and instability phenomenon are carried out. Results obtained the heat transfer rate for buoyancy-assisted flow in a vertical rectangular channel with heat wall for various Richardson number and Reynolds numbers in the range about $1< Ri <95$ and $100< \mathrm{Re} <950$.

1. Introduction

With the advancement in technology, the minimized electronic products with high-power density and the cloud computing market grow rapidly. For this reason, cooling of electronic equipment has been playing an important role on electronic system design. In general, air is used as a cooling fluid to remove the waste heat produced by electronic components. Among the cooling techniques which use air as a cooling fluid, the mixed or natural convection heat transfer techniques can provide suitable temperature conditions for many cases.

A vast amount of literature about vertical channels in different situations is available [1] ~ [4], and studies with buoyancy-assisted flow showed that the occurrence of the instable phenomenon and turbulent at low Reynolds numbers and high Richardson numbers. Therefore, the topic of this study investigates variation of the mass flow rate accompanying with the constant velocities at the inlet, and analyses if the heat transfer efficiency is enhanced by the variant mass flow rate and instable phenomenon in a vertical channel.

2. Physical Model

A three-dimensional finite length channel is investigated in this study and shown in Fig. 1. The gravity g is downward and the high temperature of the heat surfaces is T_h. Cooling fluids which possess uniform velocity u_0 and temperature T_0 flow into the channel. The boundary condition at the outlet of the channel is non-reflecting for saving the usage of computational grids.

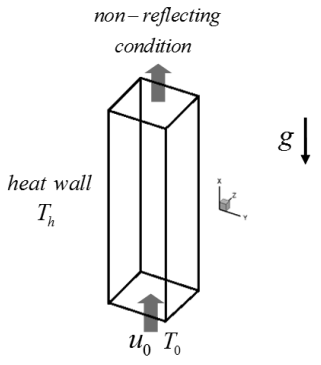

Fig. 1 physical model

3. Numerical Method

The Navier–Stokes equation is indicated as follows.

$$\Gamma\frac{\partial U_p}{\partial \tau}+\frac{\partial U}{\partial t}+\frac{\partial F_1}{\partial x}+\frac{\partial F_2}{\partial y}+\frac{\partial F_3}{\partial z}=S \quad (1)$$

where Γ is the preconditioning matrix derived by Weiss and Smith [5] and the right hand side is the gravity term regarded as a source term in the governing equation.

For the condition of the heat transfer with high temperature difference, the variations of the compressibility and density of the fluid are considered without Boussinesq assumption.

3-D Navier–Stokes equations are divided into two parts, which are inviscid and viscous term. Roe scheme [6] with MUSCL (Monotonic Upstream-Centered Scheme for Conservation Laws) method is used to compute inviscid term, and added dual-time stepping to resolve transient states of a low Mach number flow. Viscous terms are solved by the second order central difference. Finally, the temporal advancements are computed by the LUSGS [7] (Lower-Upper Symmetric Gauss Seidel).

4. Results and Discussion

The distributions of the mass flow rate changing over time at the inlet of the channel are plotted in Fig. 2. In the case of natural convection, the cooling fluids from the surrounding are induced from entrance into the channel by the buoyancy force. However, the mass flow rate at the inlet of the channel in the cases of mixed convection is fixed with the constant inlet velocities.

The mass flow rate is defined as follows,

$$Q=\rho u d^2 \quad (2)$$

To investigate the heat transfer in the cases of different ratios of buoyancy force to inertia force, the Richardson number is represented by

$$Ri=Gr/\mathrm{Re}^2 \quad (3)$$

The results of the streamline for various Reynolds numbers are as shown in Fig. 3. In the situation of natural convection and Re = 950, the mass flow rate from the inlet is almost the same and enough for the ascending fluid accelerated directly to the outlet of the channel driven by the buoyancy force. Furthermore, the fluids flowing from the inlet in the other cases are not enough, and cooling fluids in the surroundings are sucked into the channel through the outlet for the lack of

mass flow rate.

Fig. 4 is the variations of mass flow rate in yz-cross section along x-direction. Results obtained show that the larger magnitude of Ri, and the more cooling fluids flow from the outlet into the channel. Accordingly, the mass flow rate increases in the downstream region.

The distributions of average Nusselt number and velocities in the channel are obtained in Table 1. Results of the study show that the heat transfer rate in the case of natural convection is better than the other cases. Since there is an abundance of the cooling fluids flowing through the exit into the channel at Re =100 and Re = 200, the average Nusselt numbers at Re =100 and Re = 200 are larger than Re = 400.

5. Concluding remarks

Several conclusions are summarized as follows.

1. Results of this study show that the heat transfer rate in the case of natural convection is superior to the other cases.
2. Due to an abundance of cooling fluids from the outlet, the average Nusselt number increase at Re = 200.
3. The occurrence of the instable phenomenon exists as the ratio of maximum velocity to inlet velocity greater than 5.25.

References

[1] A. Behzadmehr, N. Galanis and A. Laneville, Int. J. Heat Mass Transfer **46** (2003) 4823-4833.

[2] L. Martinez-Suastegui and C. Trevino, Int. J.Heat Mass Transfer **51** (2008) 5991-6005,

[3] G. Desrayaud and G. Lauriat, Int. J. Thermal Sciences 48 (2009) 2036-2045.

[4] M. Zghal, N. Galanis and C. T. Nguyen, Int. J. Thermal Sciences 40 (2001) 816-824

[5] J. M. Weiss and W. A. Smith, AIAA. **33** (1995) 2050-2056

[6] P.L. Roe, J. Compu. Phys. 43(1981) 357–372.

[7] S. Yoon, A. Jameson, AIAA. **26** (1988) 1025-1026.

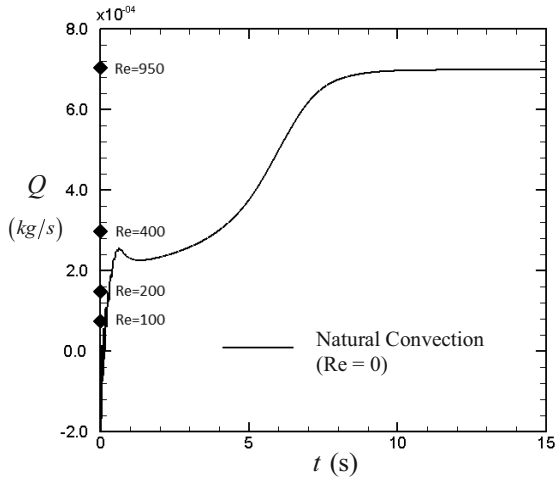

Fig. 2 the time-varying mass flow rate at the inlet of various cases

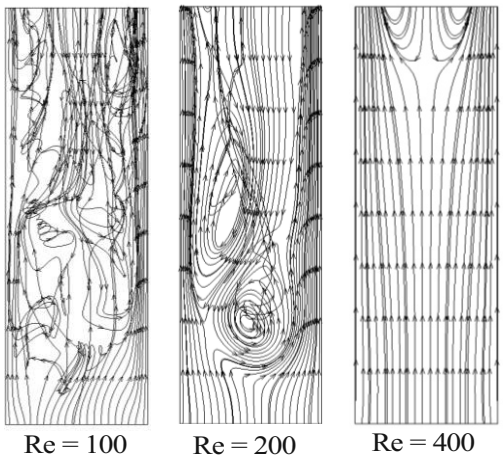

Fig. 3 the streamlines in different situations

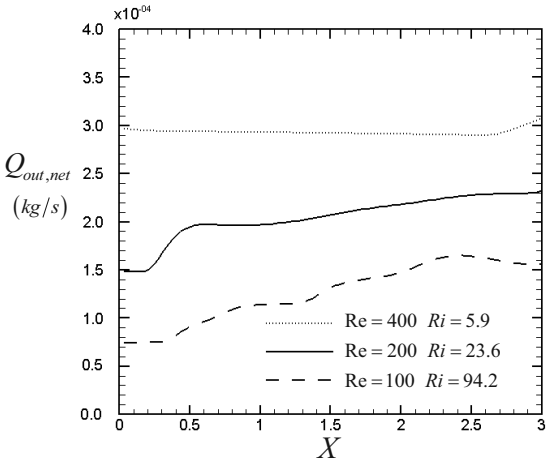

Fig. 4 the variations of mass flow rate in yz-cross section along x-direction in different situations

Table 1 average Nusselt numbers and magnitudes of velocities in various cases

Flow	Ri	Re	V-inlet(m/s)	V-max(m/s)	$\overline{\mathrm{Nu}}$
Natural		0	0.37	0.53	9.46
Mixed	1.0	950	0.37	0.54	8.87
Mixed	5.9	400	0.17	0.47	7.16
Mixed	23.6	200	0.08	0.42	7.71
Mixed	94.2	100	0.04	0.35	7.64

Eighth International Conference on Flow Dynamics
November 9 - November 11, 2011

Outflow Boundary Condition in Finite Volume Method for Unsteady-state, Variable Density, Incompressible Fluid Flow Calculation in Unstructured Grid

Sohey Nozawa[1], Yohsuke Matsushita[1], Hiroaki Tominaga[2], Masayasu Mouri[2]
[1] Research and Education Center of Carbon Resources, Kyushu University
6-1 Kasuga-koen, Kasuga, Fukuoka 816-8580 Japan
[2] DELIGHT Co., Ltd., 1-2-3-2F Manpukuji, Asou-ku, Kawasaki, Kanagawa 215-0004 Japan
nozawa@cm.kyushu-u.ac.jp

ABSTRACT

This paper presents the application of the outflow boundary condition for unsteady-state, variable density, and incompressible fluid flow computations as a part of SIMPLE calculation procedure in Finite Volume Method, FVM, to the unstructured grid. The concept is to satisfy the mass flow rate between the inflow and the outflow boundary conditions and the summation of the transient terms in the whole of the computational domain. When the outflow boundary condition is applied to the thermal fluid flow calculation, the stable, robust and high accuracy in the mass conservation are obtained.

1. Introduction

The boundary conditions such as the wall, inflow, and outflow boundary conditions are important in the fluid flow computations since they sometimes determine the numerical results. When we consider the mass conservation, the inflow and outflow boundary conditions should be prescribed carefully. The outflow boundary condition is especially important, and the error or the residual of the continuity equation should be decreased to sufficiently small value when we treat the minor chemical species with low concentration such as the NO_X prediction. Therefore, Matsushita *et al*. propose the outflow boundary condition in Finite Volume Method, FVM, for steady-state, variable density, incompressible fluid flow, which ensures the mass conservation exactly between inflow and outflow boundaries[1]. The concept of the outflow boundary condition is to apply the Neumann condition not to the velocity or the momentum but to the mass flux as a part of Semi-Implicit Method for Pressure-Linked Equations, SIMPLE, algorithm [2]. Then, it is extended to the unsteady-state, variable density, incompressible fluid flow computation [3]. In previous studies, the accuracy of the mass conservation and the stability of calculation using aforementioned outflow boundary conditions for the structured grid (Staggered grid [3], Co-located grid [4]) are presented. In this study, the outflow boundary conditions are applied to the unstructured grid, and the accuracy of the mass conservation and the stability of the calculation are discussed.

2. The outflow boundary condition

For the steady-state situations, the velocities on the outflow boundary u_O should be corrected to satisfy the mass flow rate as:

$$u_O = \acute{u}_O + \frac{F_I - F_O}{\sum \rho A|_O} \tag{1}$$

where $\acute{u}_O$ is the velocity on the outflow boundary obtained by solving the momentum equation, F_I and F_O are the mass flow rates though the inflow and the outflow boundary, respectively. The second term corrects the mass imbalance between the mass flow rate through the inflow and the outflow boundary, and becomes sufficient small when the convergence is obtained. For the unsteady-state situations, the mass flow rate through the outflow boundary is not always equal to the one through the inflow boundary due to the transient term in the continuity equation. Therefore, Eq. (1) is modified by adding the summation of the transient terms over the whole of the computational domain as:

$$u_O = \acute{u}_O + \frac{F_I - F_O - \sum \frac{\rho_P^{n+1} - \rho_P^n}{\Delta t} \Delta V_P}{\sum \rho A|_O} \tag{2}$$

This outflow boundary condition ensures the mass balance of the mass flow rate through the inflow and the outflow boundary condition and all of the transient terms in the computational domain corresponding to the continuity equation used in SIMPLE algorithm. By applying the outflow boundary condition as a part of SIMPLE calculation procedure, the stable, robust, and high accuracy in the mass conservation using structured grid has already presented in previous studies. In this study, the outflow boundary conditions are applied to the unstructured grid.

3. Models, numerical schemes and solutions

To demonstrate the validity of the outflow boundary condition, the simple duct with the quadrilateral cylinders as heat source is considered. The layout and geometry are shown in Fig. 1. Standard k-ε two-equation model is employed to describe the turbulence flow. Wall function and Pee function are used with the turbulence model to estimate the share stress and the convective heat transfer coefficient on the wall boundary. The governing equations for mass, momentum, enthalpy, kinetic energy of turbulence and its dissipation rate are discretized by Finite Volume Method, FVM, with the unstructured grid. Fluid density is estimated by the ideal gas equation with respect to temperature. Hybrid method and Euler implicit method are used as the discretization scheme for the space, convection and the diffusion term and for the time, transient term, respectively. Semi-Implicit Method for Pressure-Linked Equations, SIMPLE, is chosen for the pressure and the velocity field calculation procedure. The discretized equations are iteratively solved by Bi-Conjugate Gradient Stabilized method, BiCGStab, with the polynomial precondition until the convergence is obtained for every time steps.

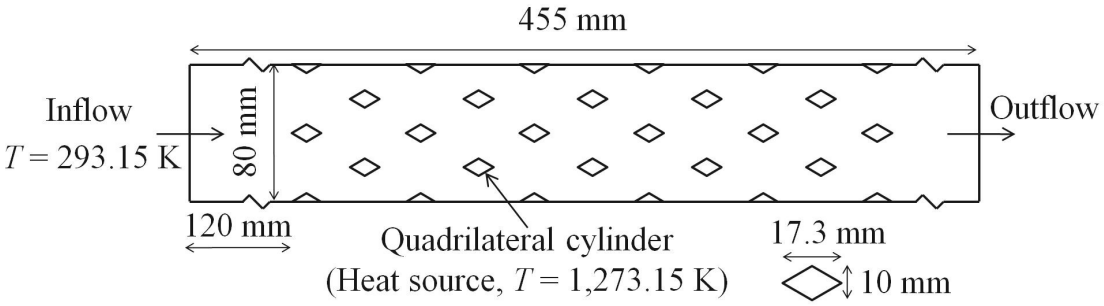

Fig. 1 Layout and geometry of the computational domain

4. Results and discussion

As one of the typical results, the residual histories of the continuity equation for the first step ($t = \Delta t$) with the outflow boundary conditions given by Eq. (1) and (2) are shown in Fig. 2, respectively. The residual with Eq. (2) rapidly decrease whereas the one with Eq. (1) not. Similar with the results of the structured grid, the outflow boundary condition expanded to the unsteady-state flow calculation is found to satisfy the continuity equation with high accuracy in the calculation using the unstructured grid. For the following time steps, the same accuracy is achieved (not shown here).

In the initial conditions of present calculation, the fluid flow is stationary state. The evolution of the unsteady-state flow field from a stationary state cannot be reproduced with the outflow boundary condition for the steady-state calculations even if under-relaxation factors are changed. On the other hand, the evolution of the unsteady-state flow field from a stationary state is reproduced with the expanded outflow boundary condition for the unsteady-state calculation (not shown here), due to the residuals decreases rapidly and the convergence solution with high accuracy is obtained. The outflow boundary condition is considered to be widely applicable to the practical situations such as combustion calculations.

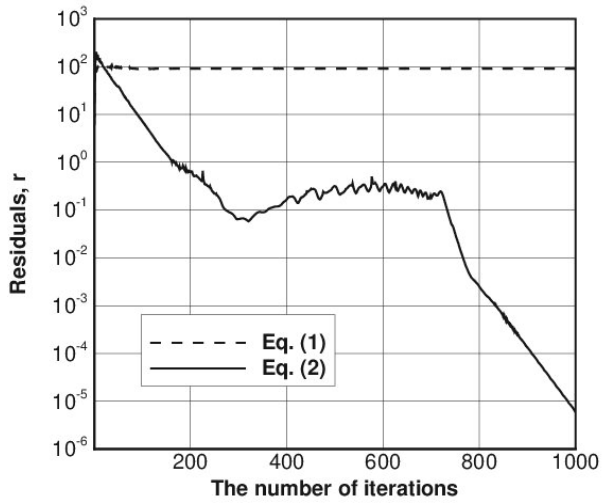

Fig. 2 Residual history for the iterations

5. Concluding remarks

In this study, the outflow boundary condition for unsteady-state, variable density and incompressible fluid flow computations as a part of SIMPLE calculation procedure in Finite Volume Method, FVM, is applied to the unstructured grid. When the outflow boundary condition is applied to the thermal fluid flow calculation, the stable, robust and high accuracy in the continuity equation is obtained. Therefore, the outflow boundary condition is considered to be widely applicable to the practical situations such as combustion calculations.

Nomenclature

A	cell face area	[m^2]
F	mass flow rate	[kg/s]
u	velocity component	[m/s]
x	coordinate	[m]
	Greek symbols	
ρ	fluid density	[kg/m^3]
Δt	time step	[s]
ΔV	cell volume	[m^3]
	Subscripts	
I	inflow boundary	
O	outflow boundary	
P	present cell	
	Superscript	
n	time level	

References

[1] Y. Matsushita *et al.*, The 42th National Heat Transfer Symposium, (2005), H224.
[2] S. V. Patankar and D. B. Spalding, Int. J. Heat Mass Trans., **15**, (1972), 1787.
[3] Y. Matsushita, The 7th International Conference on Flow Dynamics, (2010), OS6-15.
[4] S. Nozawa *et al*, SCEJ 43rd Autumn meeting, (2011), G115.

Eighth International Conference on Flow Dynamics
November 9 - November 11, 2011

Manipulations of Magnetic Particle Chains in a Vibrating Field

Yan-Hom Li,. Shih-Tsung Shen, Jay-Min Pai, Ching-Yao Chen
Department of Mechanical Engineering, National Chiao Tung University
Hsinchu, Taiwan, Republic of China

ABSTRACT

This article outlines and illustrates the manipulations and mechanisms of micro magnetic particles by experimental analysis. A reversible micro chain consisting of several particles whose diameters are about 4.5 micro-meters is formed under a uniform directional field and manipulated by an additional vibrating field. The manipulability of micro chain can be potentially applied in MEMS system. We demonstrate the chains appear different behaviors, from rigid body vibrations, bending distortions to breaking failures by increasing amplitude of the vibrating field.

1. Introduction

The dynamics of Magnetorheological (MR) suspensions under rotating magnetic field has been studied extensively in recent years. It has been shown that the field induced magnetic particle chains rotate synchronously with the field but lag behind by a constant phase lag [1][2]. The dependence of the cross-over frequency on the viscosity of the carrier fluid was analyzed by applying a rotating field of constant amplitude on suspensions [3][4]. Some research have revealed simulation results of the break up type of the chains under rotating field with varied Mason number, a dimensionless ratio of viscous forces to the dipolar forces [5].

In this paper, we analyze the manipulations of the magnetic particle chains under vibrating field. We have studied the vibrating and breaking types of the chains with different length, amplitude but constant frequency. We have found that the vibration of the chain can be separated into two types, rigid and distortion. Besides, depending on the vibrating phase, the rupture position of the chain can occur at either middle or two outer parts.

2. Experimental Procedure

The magnetorheological suspensions used in our experiment are water suspensions of polystyrene (PS) microspheres coated with iron oxide grains. The aqueous suspensions (Dynabeads M-450 Epoxy) possessing superparamagnetic behavior with no hysteresis or magnetic remanence was purchased from Invitrogen Life Technologies. The particle properties are listed in Table 1.

A schematic diagram of the relative equipment is shown in figure 1. For aggregating magnetic particles to form a chain, we applied an unidirectional magnetic field which was generated by a pair of coils connecting with a DC power supply. Then turn on the power to create a steady unidirectional magnetic field. Due to the superparamagnetic behavior, the particles will aggregate to form chains under the unidirectional field.

For creating a vibrating field, we set another pair of coils perpendicular to the former pair as shown in figure 2. Connecting the perpendicular coils with the AC power supply which can generate sinusoidal electric signals to apply a vibrating field to the chain. For analyzing the dynamics of the particle chains under different vibrating field, we enhanced the strength of the vibrating field by increasing the amplitude with constant frequency until the chains breakup.

Table 1. Properties of Magnetic Particles

Category	M-450
Diameter	4.5 μ m
Density	1.5 g/cm3
Susceptibility	1.6

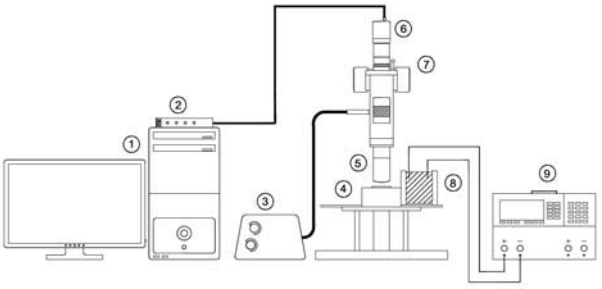

Fig 1. Experimental setup, ① computer ② image recorder ③ light generator ④ movable platform ⑤ metallurgical microscope ⑥ colorful CCD ⑦ coarse and fine adjustment ⑧coils ⑨DC power supply

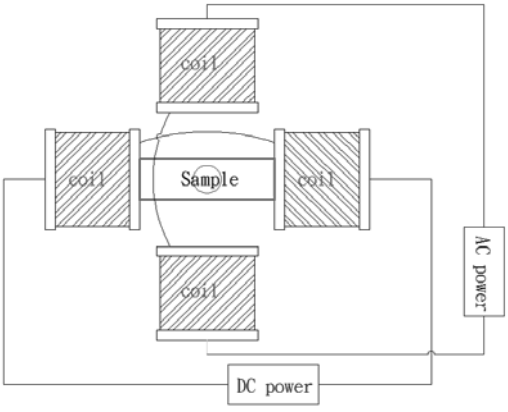

Fig.2 Schematic diagram of generating vibrating magnetic field.

3. Results and Discussion

3.1 Vibration

Fig. 3 shows the sequential images of the chain of 8 particles vibrating with the vibrating field of amplitude 48.02 Oe within one period. The chains were formed by

a uniform directional magnetic field of 17 Oe. We found that the chain vibrated as rigid body and synchronously with the magnetic field but lag behind by a slight changeable phase lag. The maximum lag angle is about -3.04. For studying the chain deformation, we used the chain of 15 particles to demonstrate the bending distortion behavior under vibrating field of amplitude 48.02 Oe within one period. Fig. 4 depicts the sequence of the distorting process of the chain vibrating with the field. Due to the longer length of the 15-particles chain, the total drags acted on it are greater than the 8-particles one, which resulted in the lag angle of the 15-particles chain with respect to the field is larger than 8-particle one.

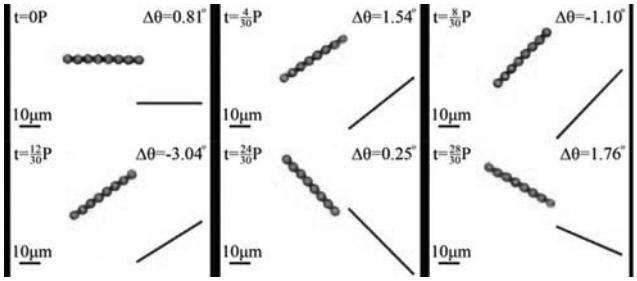

Fig. 3 Sequential images of a vibrating chain of 8 particles under a vibrating field of amplitude 48.02 Oe and frequency of f=1Hz.. The blue solid line indicates the direction and magnitude of the magnetic field.

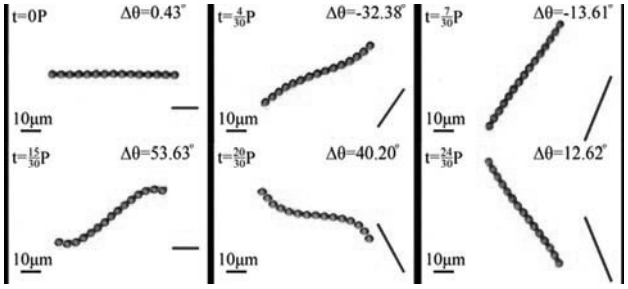

Fig 4. Sequential images of a vibrating chain of 15 particles under a vibrating field of amplitude 48.02 Oe and frequency of f=1Hz.

3. 2 Rupture

In order to study the rupture type of the chains, we increased the amplitude of the vibrating field until the breaking failure occurred. Based on our experimental results, the breaking can be classified into two categories by the rupture position, one is breaking at middle of the chain, the other is at two outer parts.

Fig. 5 indicates the middle breaking type of the chain. The rupture occurred at the time of t =4/30P just after the initial moment. The reason is the dipolar force was weakest due to there in no radial component of induced dipolar force generated by the vibrating field apply on the chain at the moment. If the total radial dipolar force could not stand the shear stress caused by hydrodymanics drag, the rupture will occur at the middle just at moment of start to vibrate.

Fig. 6 shows the sequential images of vibrating chains of 15 particles from bending distortion to breaking failures at two outer parts. In fig. 6, at the time of t=16/36P, the chain broke into three smaller chains, the three chains might vibrate with the field but lag behind by different phase angles which depend on the length of the chain.

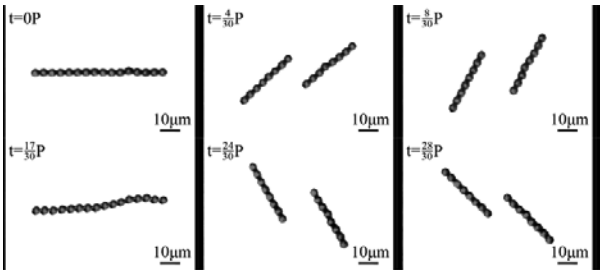

Fig.5 Sequential images of a vibrating chain of 20 particles from bending distortion to breaking at middle.

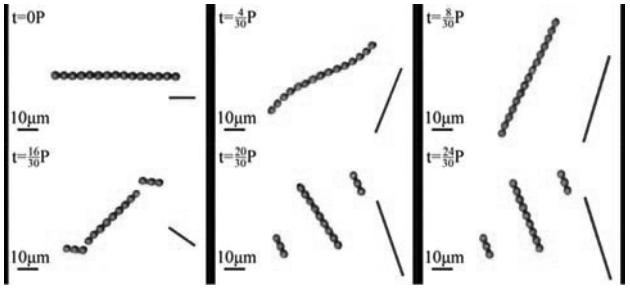

Fig.6 Sequential images of a vibrating chain of 15 particles from bending distortion to breaking failures at two outer parts under a vibrating field of amplitude 56.25 Oe and frequency of f=1Hz.

4. Concluding remarks

In this work, we carried out fundamental study on the manipulations of the magnetic particle chains under vibrating magnetic fields. We found two different behaviors for the vibrations and ruptures as well. The two kinds of vibrations were rigid body and distortion. For ruptures, the behaviors can be classified into two categories by the rupture position, one is breaking at the middle of the chain, the other is at two outer sides. The experimental results show that the middle ruptures occur at the moment just after vibrating start, but the outer ruptures occur at the moment just after P/4.

References

[1] S. Melle, G. G. Fuller and M. A. Rubio, Phys. Rev. E 61, 4111(2000).

[2] S. Melle, J. E. Martin, Journal of Chemical Physics: Vol. 118, no. 21 June(2003).

[3] S. Melle, O. G Calderon, G. G. Fuller and M. A. Rubio, Journal of Colloid and Interface Science, (2001).

[4] S. Melle, G. G. Fuller and M. A. Rubio, XIIIth International Congress on Rheology, Cambridge, UK, Vol. 3 pag. 81 (2000).

[5] T. G. Kang, M. A. Hulsen, P. D. Anderson, J. M. J. den Toonder, and H. E. H. Meijer, Phys. Rev. E 76, 066303(2007).

Laminar Forced Convection in the Thermally Developing Region of a Parallel Plate Channel with Viscous Dissipation: Wall Heat transfer and Energy Gain by the Fluid

Ramjee Repaka[1], V.V. Satyamurty[2]
[1]Assistant Professor, Mech. Engg. Deptt., Indian Institute of Technology Ropar, Rupnagar, India
[2]Professor, Mech. Engg. Deptt., Indian Institute of Technology Kharagpur, Kharagpur, India
Corresponding author: ramjee.repaka@iitrpr.ac.in

ABSTRACT

Effect of viscous dissipation on steady, laminar forced convection in hydrodynamically developed and thermally developing flow between parallel plates kept at equal, uniform wall temperatures is described. It has been shown that, in spite of the presence of unbounded swing in the local Nusselt number at certain axial locations, the wall heat transfer and the energy gain by the fluid continuously vary with the axial distance. The wall heat transfer differs from the energy gain by the fluid when viscous dissipation is included, unlike the cases when viscous dissipation is neglected.

1. Introduction

Viscous dissipation effects are important in convection heat transfer when the Prandtl number of the fluid is high. Several studies appeared on the subject in the literature. The earliest studies on forced convective heat transfer through channels including viscous dissipation have been reported by Hwang, Knieper and Fan [1], El-Ariny and Aziz [2] and Cheng and Wu [3]. Later, Barletta [4] considered viscous dissipation assuming the flow and temperature profiles as fully developed. Aydin and Avci [5] studied the problem including viscous dissipation in the thermally developing region of parallel plate channel. Sheela-Francisca and Tso [6] studied viscous dissipation effects on flow through parallel plates with constant heat flux conditions. No results on average Nusselt number or a method of calculating heat transferred up to a desired axial distance and the energy gain by the fluid have been reported for duct flows when viscous dissipation is included.

2. Mathematical Formulation

The problem has been studied assuming laminar, steady flow of a Newtonian fluid. The physical model is a parallel plate channel of spacing L. The fluid enters with a temperature of T_i and the channel walls are kept at and T_w. Non-dimensional governing equation for hydrodynamically developed and thermally developing flow field including viscous dissipation is given by,

$$U\left(\frac{\partial\theta}{\partial X^*}\right)=\frac{\partial^2\theta}{\partial Y^2}+Br\left(\frac{dU}{dY}\right)^2 \qquad (1)$$

where X^* {$= X/Pe = x/(Pe\ D_h)$} and Y ($=y/D_h$) are the non-dimensional axial (modified) and normal coordinates, U ($= u/u_{avg}$) is the non-dimensional fully developed velocity. u_{avg}, is the average velocity through the channel. θ {$= (T–T_w)/(T_i–T_w)$} the non-dimensional temperature. D_h ($=2L$) is the hydraulic diameter. Pe the Peclet number is the product of Reynolds number and the Prandtl number, $\{(\rho\ u_{avg}\ D_h)/\mu\}\{\mu\ C_p)/k\}$. Br, the Brinkman number is defined by $\mu\, u_{avg}^2/\{k\ (T_i - T_w)\}$. μ and k are the dynamic viscosity and thermal conductivity of the fluid.

Equation (1) is subjected to the boundary conditions,

$$\left.\begin{array}{l}\theta = 1 \text{ at } X^* = 0 \text{ for } \quad -1/4 \le Y \le +1/4\\ \theta = 0 \text{ at } Y = -1/4 \text{ for all } X^* > 0\\ \theta = 0 \text{ at } Y = 1/4 \text{ for all } X^* > 0\end{array}\right\} \qquad (2)$$

Numerical results to Eq. (1) for the conservation of thermal energy have been obtained for $-2 \le Br \le 2$ and for $A = 1$, i.e., symmetric boundary condition by employing the Successive Accelerated Replacement (S A R) scheme which has been described in Satyamurty [7], and used in Marpu and Satyamurty [8]. Recently this scheme has been employed for the present class of problems by Repaka and Satyamurty [9]. $T_w < T_i$ shall be referred to as fluid getting cooled ($Br > 0$) and $T_w > T_i$ shall be referred to as fluid getting heated ($Br < 0$).

3. Results and Discussion

Complete depiction of variation of the local Nusselt number, Nu_x ($= (1/\theta^*)\ (\partial\theta/\partial Y)\big|_{Y=-1/4}$ from entry, thermally developing region, to the limiting condition is given in the detailed paper for $-2 \le Br \le 2$. The limiting Nusselt number value of 17.48 has been obtained for all $Br \neq 0$ which is close to the analytical value of 17.5 as reported in Barletta [4]. Nu_x displays an unbounded swing for $Br < 0$ at some value of X^* before attaining the limiting value. This is not due to heat transfer becoming unbounded, but due to the bulk mean temperature $T_b \rightarrow T_w$ This feature can be better understood by considering the wall heat transfer.

Heat transferred from the walls to the fluid up to x in non-dimensional form, $\bar{Q}_{xw}$ can be expressed as {Repaka and Satyamurty [9]},

$$\bar{Q}_{xw} = 4\int_0^{X^*}(\partial\theta/\partial Y)\big|_{Y=-1/4}\,dX^* \ \textbf{or}\ -4\int_0^{X^*}(\partial\theta/\partial Y)\big|_{Y=1/4}\,dX^* \qquad (3)$$

Plots of $\bar{Q}_{xw}$ vs. X^* are shown in Fig. 1(a) and (b) for $Br > 0$ and $Br < 0$ respectively. It is clear from Fig. 1, that $\bar{Q}_{xw}$ at a given X^* does vary continuously with X^* for both $Br > 0$ and $Br < 0$, there by establishing continuity in the wall heat transfer, even though the Nusselt number displays an unbounded swing for $Br < 0$. When $Br < 0$, $\bar{Q}_{xw}$ reaches a maximum and decreases as X^* further increases. The X^* at which this maximum

in $\bar{Q}_{xw}$ occurs corresponds to $T_b \rightarrow T_w$, beyond which the heat transfer direction reverses. Further, this X^* decreases as Br decreases.

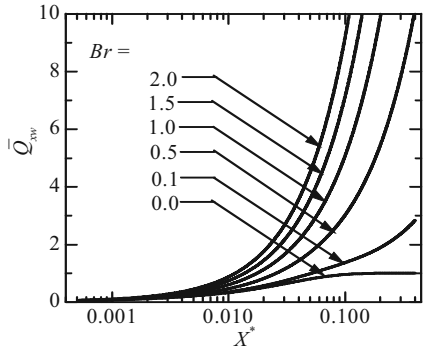

(a) $Br > 0$

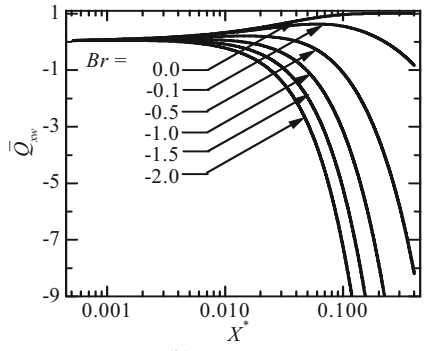

(b) $Br < 0$

Fig. 1 Variation of $\bar{Q}_{xw}$ with X^*

Non-dimensional heat gained (or lost) by the fluid $\bar{Q}_{xf}$, can be written as,

$$\bar{Q}_{xf} = (1 - \theta^*) \tag{4}$$

where, θ^* is the non-dimensional bulk mean temperature defined as $(T_b - T_w)/(T_i - T_w)$.

Plots of $\bar{Q}_{xf}$ vs. X^* are shown in Figs. 2(a) and (b) for $Br > 0$ and $Br < 0$ respectively. At a given X^*, $\bar{Q}_{xf}$ does vary monotonically with Br. $\bar{Q}_{xf}$ approaches a constant value of less than unity for $Br > 0$ and a value greater than unity for $Br < 0$ for large X^*.

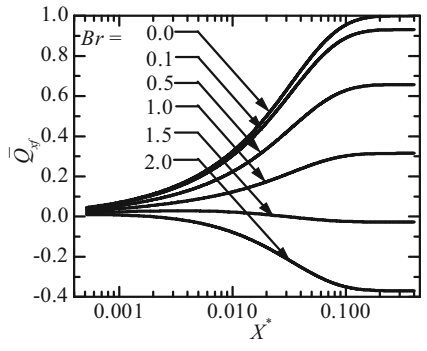

(a) $Br > 0$

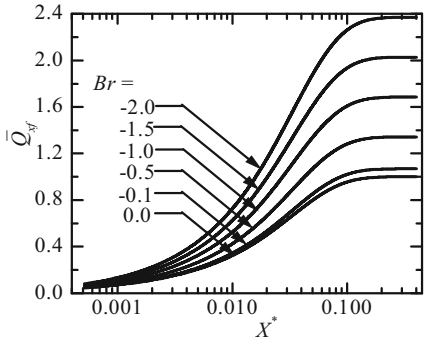

(b) $Br < 0$

Fig. 2 Variation of $\bar{Q}_{xf}$ with X^*

Further, it can be observed from Figs. 1 and 2 that $\bar{Q}_{xw}$ and $\bar{Q}_{xf}$ are not equal unlike when $Br = 0$, the case when viscous dissipation is neglected. In the detailed article, it has been shown that the wall heat transfer and energy gain by the fluid are related by,

$$\bar{Q}_{xw} = \bar{Q}_{xf} + 48\, Br\, X^* \tag{5}$$

4. Conclusions

It has been shown that the heat transferred from the wall varies continuously with axial distance as well as with the Brinkman number even though the Nusselt number displays unbounded swing. Further, it has been established that heat transferred from the wall (fluid) to the fluid (wall) $\bar{Q}_{xw}$ is not equal to the heat gain (or loss) by the fluid $\bar{Q}_{xf}$ when $Br \neq 0$. For this case, relation between $\bar{Q}_{xw}$ and $\bar{Q}_{xf}$ has been obtained.

References

[1] C.L. Hwang, P.J. Knieper, L.T. Fan, ZAMP, **16** (1965), 599.

[2] A.S. El-Ariny, A. Aziz, ASME J. Heat Transfer, **98** (1976), 427

[3] K.C. Cheng, R.S. Wu, Appl. Sci. Res., **32** (1976), 327.

[4] A. Barletta, Int. J. Heat Mass Transfer, **41** (1998), 3501.

[5] O. Aydin, M. Avci, Appl. Energy, **83** (2006), 495.

[6] J. Sheela-Francisca, C.P. Tso, Int. Commun. Heat Mass Transfer, **36** (2009), 249.

[7] V.V. Satyamurty, Proceedings of the ASME Winter Annual Meeting, Paper no. 85-WA/HT-37, 1984.

[8] D.R. Marpu, V.V. Satyamurty, ASME J. Ener. Res. Techn., **111**, **(**1989**)**, 214.

[9] R. Repaka, V.V. Satyamurty, Int. J. Heat Mass Transfer, **53**(9-10) (2010), 1654.

Eighth International Conference on Flow Dynamics
November 9 - November 11, 2011

Experimental Characterization of a Helium Round Atmospheric-Pressure Plasma Jet with a Convergent Nozzle

Chih-Ting Liu[1], Yi-Wei Yang[1], Zhi-Hua Lin[2], Po-Tsun Shen[1],
Ching-Jung Wu[1], Jhih-Ren Lin[1], Kuo-Chi Liao[2] and Jing-Shinn Wu[1]*
[1]Department of Mechanical Engineering, National Chiao Tung University, Hsinchu, Taiwan
[2]Department of Bio-industrial Mechatronics Engineering, National Taiwan University, Taipei, Taiwan
*E-mail: chongsin@faculty.nctu.edu.tw

ABSTRACT

This paper presents experimental characterization of a helium round atmospheric-pressure plasma jet (APPJ). This APPJ is driven by a distorted sinusoidal power source having a frequency of 20 kHz. By applying 60 W of power, the jet plume is about 30 mm in length. Electrical properties and optical emission spectra were measured. Results show that atomic oxygen, hydroxyl radical and NO were found in both the discharge and jet plume regions, which is important for practical bio-medical applications such as tooth bleaching and sterilization.

1. Introduction

In recent years, atmospheric pressure plasma has attracted much attention for applications such as surface modification, tissue engineering, sterilization and tooth bleaching [1], among others. Among these applications, tooth bleaching and sterilization of root canal by atmospheric pressure plasma jet (APPJ) have found increasingly interested because of its geometrical characteristics and its efficient sterilization ability [2]. Plasma can easily fill up an enclosed space rather than treating a point; and it can kill Streptococcus mutans in a few seconds [3]. Due to these important features, round APPJ is very suitable for the sterilization treatment of root canal and possibly tooth breaching if radicals such as atomic oxygen and hydroxyl radical can be generated, respectively, in the plume of APPJ [4].

Most round APPJ devices apply a co-axial type with powered electrode inside the tube and grounded electrode covered outside the tube [7]. However, since the electric field is directed in the direction perpendicular to the flow direction, the jet length is generally short. There are some alternative designs to improve the length of the jet plume or for safety reason by placing the both the powered and grounded electrodes outside the flowing tube [1, 8] or powered electrode inside and grounded electrode outside the flow tubes [9].

In this study, we report a new helium round APPJ with a convergent nozzle that can generate abundant hydroxyl radicals and atomic oxygen in the discharge and post-discharge regions with extended jet plume length under some operating conditions

2. Experimental Methods

The schematic diagram of the experiment setup and the plasma plume image is shown in Fig. 1. The plasma device consists of five major parts: a silicon tube, a stainless steel tube, an aluminum tube, an aluminum ring and a glass nozzle. A silicon tube (6 mm outer diameter and 3 mm inner diameter) acts as the dielectric barrier layer. Powered electrode, including a stainless steel tube and aluminum tube, is placed into the silicon tube tightly with inner diameter of 1.5 mm and 0.5 mm respectively. An aluminum ring with 3 mm thickness is installed outside and at end of the silicon tube as the grounded electrode. The distance between the aluminum tube and the aluminum ring is kept as 2 mm. There is a glass nozzle added at the end of the silicon tube which can accelerate the gas flow rate to enhance the length of the plasma jet plume. The powered electrode was driven by a 20 kHz distorted sinusoidal power supply (EN Technologies Inc. model Genius 2).

We used helium (99.99%) as the working gas at a gas flow rate of 4 slm throughout the study, unless otherwise specified. Corresponding Reynolds number based on the averaged speed and inside diameter of the tube is 1392, which is a typical laminar jet flow. Jet length could be longer than the turbulent jet length because of less ambient entrainment [5]. The discharge sustains at maximum voltage about 7.6 kV with maximum current about 400-600 mA. Under these operating conditions, a visible plasma jet of ~30 mm is generated.

The voltage and current waveforms across the electrodes of the discharge were measured by a high-voltage probe (Tektronix P6015A) and a Rogowski coil (IPC CM-100-MG, Ion Physics Corporation Inc.) through a digital oscilloscope (Tektronix TDS1012B). The optical emission spectroscopy (OES) analysis of the plasma jet is measured by a monochromator (PI Acton SP 2500) with a Photomultiplier tube (Hamamatsu R928), which was mounted on a mobile 3-D table. The OES in the discharge region is measured with a lense covered by a quartz plate, and the distance between the plate and the plasma outlet is 0.1 mm. The OES in the post-discharge region was measured as with the arrangement similar to that shown in Fig. 1.

3. Results and Discussion

Fig. 2 shows the result of input voltage and discharge current waveforms under the condition of 4 slm and 60 W (the output power of power supply). Pulsed width is about 25 ms. Results show that the discharge current increases dramatically as the voltage rises and drops rapidly, and becomes nearly zero (extinguished) otherwise. The measured peak current for helium is about 400-600 mA and the peak voltage is about 7.6 kV.

Fig. 3 shows the measured OES in the range of 180-900 nm in the discharge and post-discharge regions. We can clearly see that the excited species such as N2,

N2+, OH, O and He are generated in the discharge region and are carried downstream by the flowing helium, although the intensities are generally much reduced for the latter. This tremendous reduction is caused by the disappearance of the electric field and entrainment of ambient air in the plume region. It is well known that these species especially O atom and OH are very chemically reactive; they play an important role in tooth bleaching and sterilization. In the discharge region, the H_α line (656 nm) might come from the collision between H_2O (impurity of helium tank) and electrons [6],

$$H_2O + e \rightarrow OH + H + e.$$

Details of the plasma physics and chemistry involved can be further studied by a detailed fluid modeling, which is currently in progress and will be reported elsewhere in the near future..

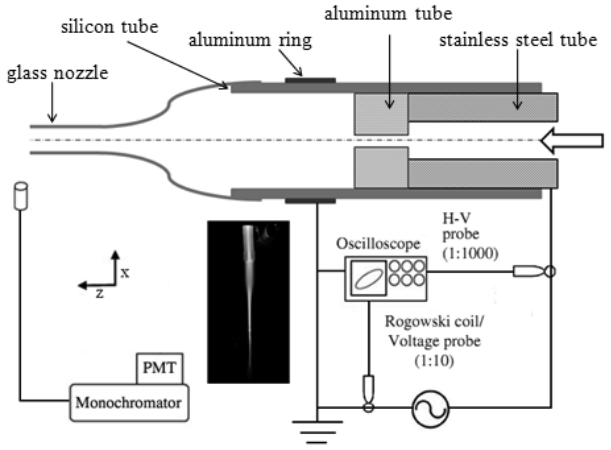

Fig. 1 Sketch of the APPJ system

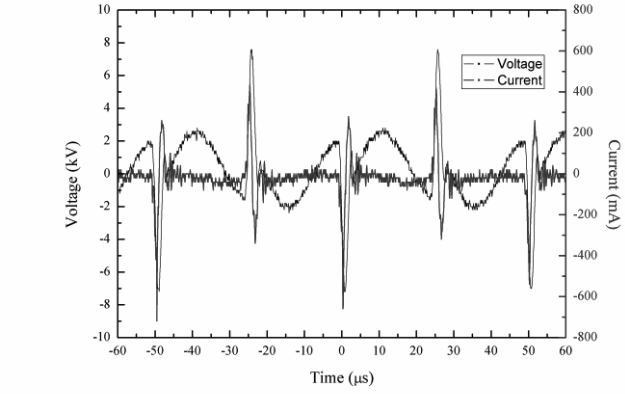

Fig. 2 Typical current and voltage waveforms for He discharge.

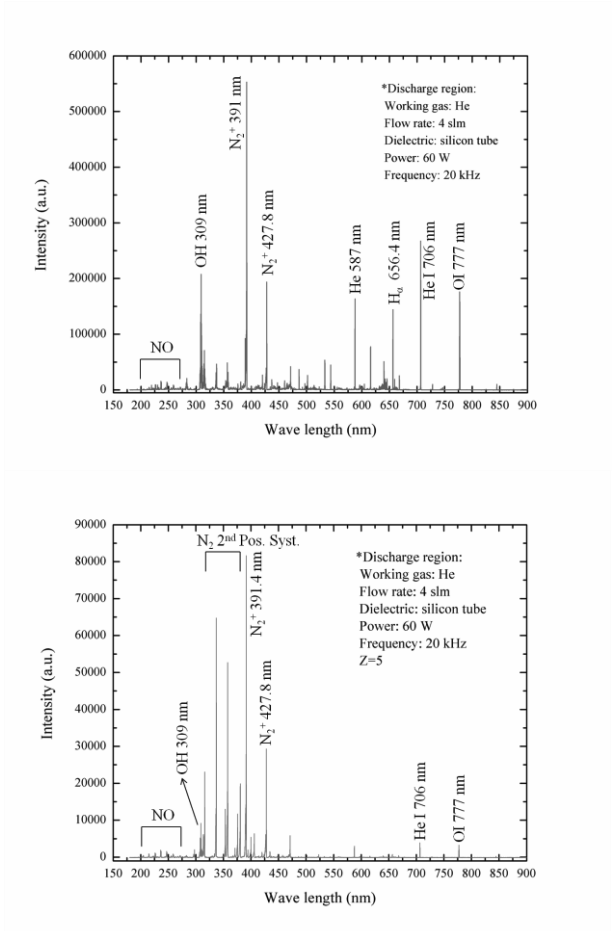

Fig. 3 OES distributions (180–900 nm) for discharge region (upper) and post-discharge region (lower).

4. Concluding remarks

In this paper, characteristics of a round helium atmospheric pressure plasma jet have been examined experimentally. This plasma device can generate many chemically reactive radicals and atoms such as OH radical and O atom, which are potentially very important for the applications in in tooth bleaching and sterilization.

References

[1] H. W. Lee, S. H. Nam, A.-A. H. Mohamed, G. C. Kim, J. K. Lee, Plasma Process. Polym., **7** (2010), 274–280

[2] R. Bussiahn, R. Brandenburg, T. Gerling, E. Kindel, H. Lange, N. Lembke, K.-D. Weltmann, Th. von Woedtke, T. Kocher APPLIED PHYSICS LETTERS, **96** (2010), 143701

[3] S. Rupf, A. Lehmann, M. Hannig, B. Schafer, A. Schubert, U. Feldmann, A. Schindler, Journal of Medical Microbiology, **59** (2010), 206–212

[4] H. W. Lee, G. J. Kim, J. M. Kim, J. K. Park, J. K. Lee, G. C. Kim, JOE, **35** (2009)

[5] J. F. Kolb, A.-A H. Mohamed, R. O. Price, R. J. Swanson, A. Bowman, R. L. Chiavarini, M. Stacey, K. H. Schoenbach, APPLIED PHYSICS LETTERS, **92** (2008), 241501

[6] N. Georgescu, A. R. Lupu, IEEE TRANSACTIONS ON PLASMA SCIENCE, **38** (2010), 8

[7] A. Gulec, L.Oksuz, N. Hershkowitz, Physics Letters A **375** (2011) 1733–1736

[8] S. K. Kang, M. Y. Choi, G. Koo, P. Y. Kim, Y. Kim, G. J. Kim, A-A. H. Mohamed, G. J. Collins, J. K. Lee1, APPLIED PHYSICS LETTERS **98** (2011), 143702

[9] H. Akamatsu, K. Ichikawa, Surf. Coat. Technol. (2011), doi:10.1016/j.surfcoat.2011.04.050

Eighth International Conference on Flow Dynamics
November 9 - November 11, 2011

Development of Parallel Fluid Modeling for Low-temperature Inductively Coupled Plasma Source in Etching or Deposition Process

Yuan-Ming Chiu[1], Chieh-Tsan Hung[1], Jong-Shinn Wu[1]*, Feng-Nan Hwang[2]
[1]Department of Mechanical Engineering, National Chiao Tung University, Hsinchu, Taiwan
[2]Department of Mathematics, National Central University, Chungli, Taiwan
E-mail: chongsin@faculty.nctu.edu.tw

ABSTRACT

A parallel fluid modeling for simulating silane (SiH_4) and gas discharge in an inductively couple plasma (ICP) source is reported. we consider 34 species and 58 reaction processes in the model to predict the temporal and spatial distributions of plasma properties. The results indicate that SiH_2^- and SiH_3^+ ions are the most abundant negative and positive charge species respectively. In addition, the most abundant neutral species are found to be H_2 and Si_2H_6, and the most abundant radicals are H and SiH_3. All the above are consistent with the experimental observation wherever are available

1. Introduction

In recent yests, inductively couple plasma source (ICPs) has become increasingly important for semiconductor etching and nano-material deposition because of its advantages such as operation at low pressure, controllable energetic ions, and potential of generating chemically active radical species. Measurements of plasma properties in an ICP chamber are generally difficult and expensive, while a plasma modeling can be a valuable tool for understanding plasma physics and chemistry. The latter can possibly contribute greatly to the development of plasma reactors or devices with improved performance at lower development cost. Therefore, in this study, a parallel fluid modeling is developed for simulating silane (SiH_4) and fluorocarbon (CF_4) gas discharges in an ICP source.

2. Numerial Method

We have employed a fluid modeling which includes the continuity and momentum equations for all species, and the electromagnetic, Maxwell's equations and surface kinetic equations. In the case of negative plasma, the thin sheath near the walls was not considered in the simulation since the sheath thicknesses are typically only hundreds of micronmeter in the high density negative plasma for a typical ICP condition. Therefore, we assume that the negative plasma is ambipolar and quasineutral, and this method had been adopt by Hsu et al. [1], Ramamurthi et al. [2], and Fukumoto et al. [3]. Figure 1 shows the architecture of our simulation model that consists of many key modules. These modules include Chemistry Module, Geometry Module, Electric Field Module, Electron Module, Ion Module, Neutral Module, Maxwell's Equation Module and Surface Kinetic Module. This simulation tool is capable of modeling complex reactor geometries and wide variety of operating conditions for a wide range of gas and surface chemistries. The electromagnetic field in plasma due to the antenna coil is obtained by solving the Maxwell's equations. Only the Maxwell equation is described in the following here since others are the same as our earlier work [4] :

$$\nabla^2 E_\varphi = \mu_0\left(\frac{\partial}{\partial t}\sigma_p E_\varphi + \frac{\partial}{\partial t}J_f + \varepsilon_0(1+\varepsilon_r)\frac{\partial^2}{\partial t^2}E_\varphi\right) + \frac{1}{c^2}\frac{\partial^2}{\partial t^2}E_\varphi \quad (1)$$

where E_φ is the time varying electric field in the azimuth direction. Note the first, second and third terms in the parenthesis represent the rate of change of current density related to plasma, coil and displacement in the quartz. ε_r is relative permittivity of quartz. The power dissipation in the plasma is given as

$$P_{abs} = \bar{J}(t)\cdot\bar{E}(t) = \frac{1}{2}\int \mathrm{Re}\left\{J^*(t)\cdot E(t)\right\}dt \quad (2)$$

Previously, we have developed a parallel 2D/2D-axisymmetric fluid modeling code for gas discharge simulations without the inclusion of Maxwell equation solver [4]. In this paper, we have modified the code to include the Maxwell equation solver. In our model, the flow convection effects have been ignored in very low pressure condition, and the drift and diffusion coefficients and rate constants related to electrons are functions of electron temperature. Such functional relations, obtained by a publicly available Boltzmann equation solver, BOLSIG+ [5], were prepared as a lookup table prior to the computer simulation. For the numerical scheme, the set of nonlinear coupled partial differential equations for the Maxwell's equation, the electron energy density equation and species transport equation were spatially discretized and linearized using a finite difference method to form a system of Ax=b where A denotes the matrix representation of a linear operator, b is the right-hand-side vector, and x is the solution vector. We employ the combination of a preconditioner and the iterative Krylov subspace method to solve this system of discretized equations. In this study, we have employed LU as a preconditioner and GMRES for the solution of preconditioned matrix equation. The numerical procedure is iterated until a steady-state solution is obtained.

3. Results and Discussion

We have employed our validated fluid model to study SiH_4 and CF_4 plasma in gaseous electronics conference (GEC) reference cell with a planar coil, which is shown as Fig. 2. For SiH_4 gas discharge, we consider 34 species and 58 reaction processes in the model to predict the temporal and spatial distributions of plasma properties. The results of spatial averages of charges shown as Fig. 3 indicate that SiH_3^- and SiH_3^+ are

the most abundant negative and positive charge species respectively. Fig. 4 shows that most abundant neutral species are found to be H_2 and Si_2H_6. In addition, the most abundant radicals are H and SiH_3. All the above results are consistent with the experiments wherever are available. For the CF_4 discharge under the similar condition, we consider 10 species and 23 reaction channels in the model to predict the temporal and spatial distributions of plasma properties (Fig. 5-a ~ Fig. 5-f). Results show that F atom (Fig. 5-f) is the dominant neutral species and CF_3^+ is the dominant charged species in CF_4 discharge respectively.

4. Concluding remarks

A parallel two-dimensional fluid model using domain decomposition method through MPI has been developed to investigate the complicated SiH_4 and CF_4 inductively coupled plasma. This code has been used to predict the distributions of plasma properties of SiH_4 and CF_4 ICPs in a GEC respectively. Results show that simulations are consistent with experimental findings wherever are available.

References

[1] C. C. Hsu, and D. B. Graves, J. Phys. D: Appl. Phys., **39** (2006), 3272.

[2] B. Ramamurthi and D. J. Economou, J. Vac. Sci. Technol. A, **20** (2002), 467.

[3] H. Fukumoto, I. Fujikake, Y. Takao, K. Eriguchi and K. Ono, Plasma Source Sci. Technol., **18** (2009), 045027.

[4] C.-T. Hung, Y.-M. Chiu, F.-N. Hwang, J.-S. Wu, Comput. Phys. Comm., **182** (2011), 161.

[5] http://www.laplace.univ-tlse.fr

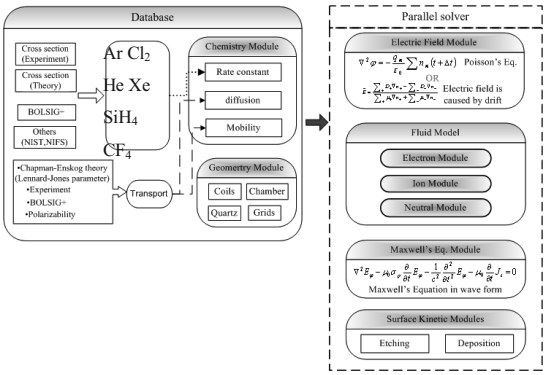

Fig. 1 Architecture of the current simulation model

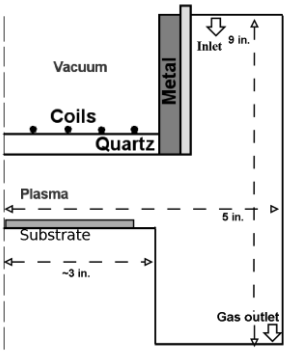

Fig. 2 Configuration of cylindrical ICP-GEC chamber

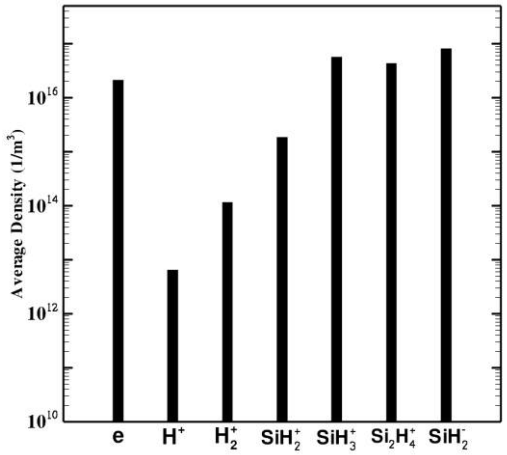

Fig. 3 Spatial averages of charges in SiH_4 discharge

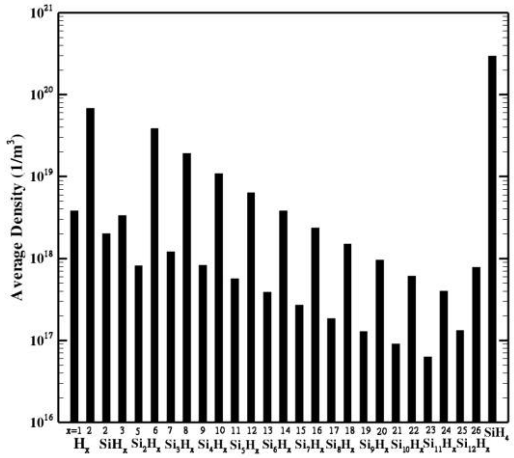

Fig. 4. Spatial averages of neutral species in SiH_4 discharge.

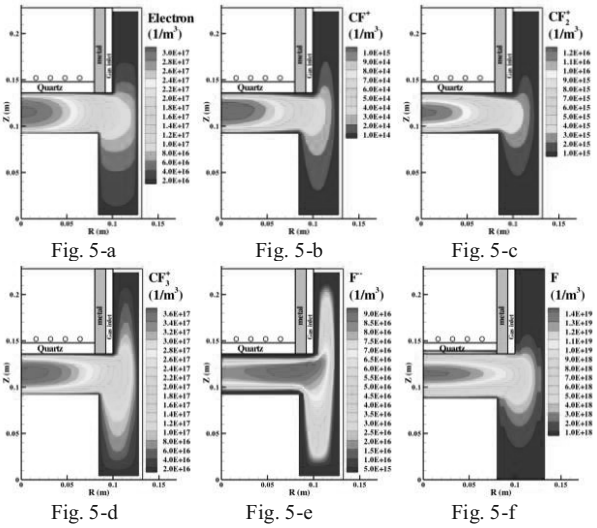

Fig. 5-a Fig. 5-b Fig. 5-c

Fig. 5-d Fig. 5-e Fig. 5-f

Fig. 5 Profiles of (a) electron, (b) CF^+, (c) CF_2^+, (d) CF_3^+, (e) F^-, and (f) F atom in CF_4 discharge.

Natural convection flow in a three dimensional vertical wavy channel with uniform surface temperature

Kuen-Rung Huang, Wu-Shung Fu
(National Chiao Tung University, Taiwan) 1001 Ta Hsueh Road, Hsinchu, Taiwan
gibu.me95@nctu.edu.tw, wsfu@mail.nctu.edu.tw

ABSTRACT

Pure natural convection in a three dimensional wavy channel is studied numerically. The mass and energy flow rate are restricted by the temperature and geometry. By using different channel geometry, the mass and energy flow rate come to change and so is the Nusselt number.

1. Introduction

Natural convection has more energy conservation then force convection. There are many researches of natural convection about the flat plate flow, and some special geometry has the remarkable effect. The phenomenon at opened-ended finite length channel is a very important issue in both academic and industrial researches. Although using the Bossinesq assumption to solve the natural convection problem is easy and fast in the low temperature difference condition, it is not unsuitable in the high temperature difference condition. A compressible fluid flow is taken into consideration instead of renunciation of the Boussinesq assumption.

2. Method

Compressible natural convection flow in a three dimensional waved channel is investigated and the model is shown in Fig. 1.

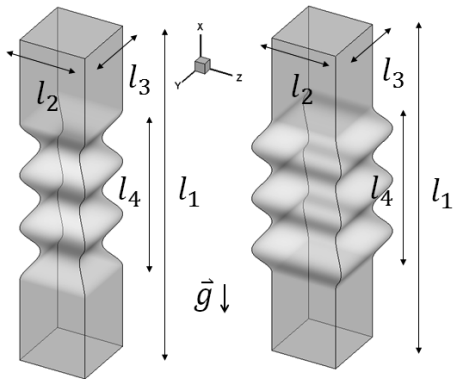

Fig. 1 convex and concave channel model

The initial temperature in the channel is the normal atmospheric temperature $T_i = 25\ ^oC$ and the constant temperature zone $T_h = 100\ ^oC$ is located at four walls. The length, width, and height of the channel are l_2, l_3, and l_1, respectively.

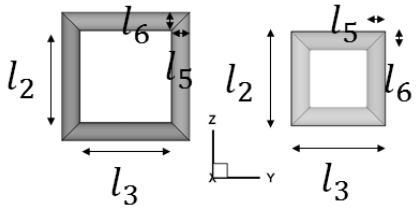

Fig. 2 Top view of the convex and the concave channel model

The boundaries of the inlet and outlet are non-reflection condition. In Fig. 2 the length, y-surface amplitude, and z-surface amplitude of the waved zone are l_4, l_5, and l_6, respectively. Fig.3 shown that the z-directional waved wall function is $z(x) = \pm\frac{l_6}{2}(1-\cos 6\pi x)$ and y-directional is also same.

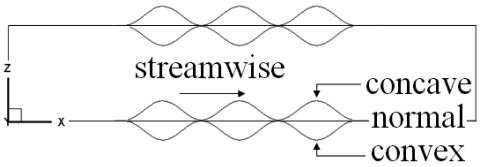

Fig. 3 Three types of channel boundary geometry

The gravity is downward and the temperature and pressure of the surroundings are 298K and 101300Pa, respectively.

The governing equations in which the parameters of viscosity and compressibility of the fluid and gravity are considered simultaneously are shown in the following equations.

$$\frac{\partial U}{\partial t}+\frac{\partial F}{\partial x}+\frac{\partial G}{\partial y}+\frac{\partial H}{\partial z}=S \tag{1}$$

$$P=\rho RT \tag{2}$$

3. Numerical model

In truly natural convection flow, its fluid speed slower than sound wave so use the Roe scheme matching preconditioning [1] method and coordinate transformation [2] are adapted to resolving Eq. (1) and transformed into the following equation Eq. (3).

$$\Gamma\frac{\partial U_p}{\partial \tau}+\frac{\partial \tilde{U}}{\partial t}+\frac{\partial \tilde{F}}{\partial x}+\frac{\partial \tilde{G}}{\partial y}+\frac{\partial \tilde{H}}{\partial z}=S' \tag{3}$$

Then use 3th order MUSCL proposed by Abalakin et al. [3] to compute the inviscid terms. Other derivative terms are solved by the second order central difference. Finally, use the LUSGS [4] to suitable for preconditioning in solving temporal advancements.

4. Results and discussion

In order to compare different geometry model, three models has been used, there are convex, normal, and concave, respectively.

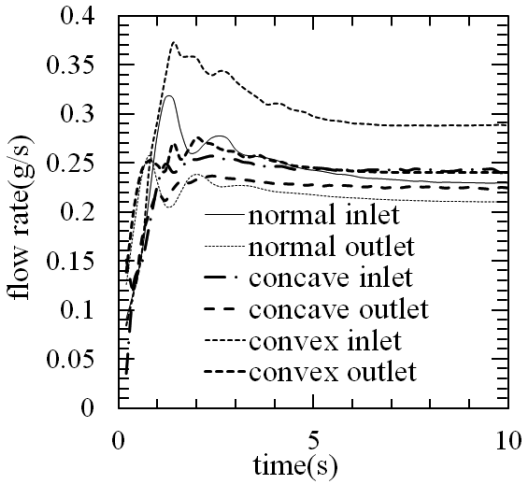

Fig. 4 The mass flow rate of the inlet and the outlet

The conservations of mass are shown in Fig.4. The mass flow rate of the inlet and the outlet come to steady after 7 seconds, the difference of the mass conservation are both less than 8%. Although the width of the concave channel is narrower than normal, the mass flow rate of deformed channel is still larger than normal. It is due to that the curved wall has the larger heating zone than normal, and the contact time between the fluid and the heating wall will be longer.

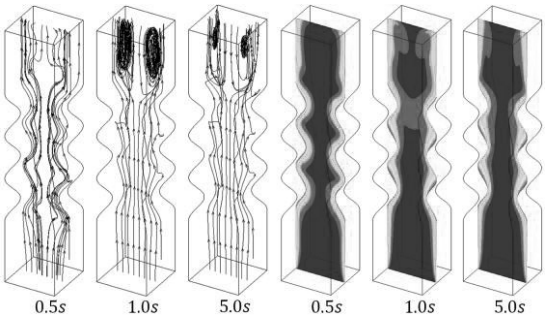

Fig. 5 Temperature distribution and streamlines in the concave channel at the time equal to 0.5s, 1.0s, and 5.0, respectively

The phenomenon of backflow at the opened-ended long channel in the transient process of natural convection is common. Fig.5 shows that some of fluid was been sucked from the top, and the speed of the most of fluid are accelerated gradually along the wall.

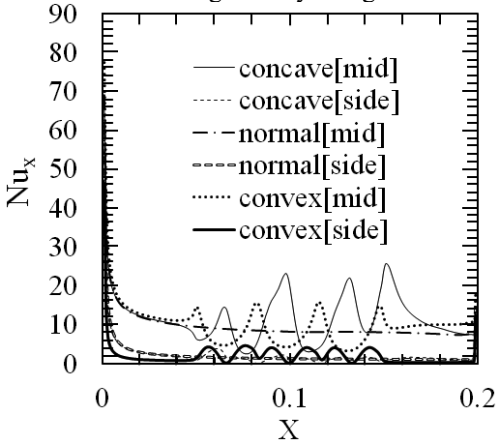

Fig. 6 Nusselt numbers profile along the z-direction heating wall

The mass affected by the fast flow to satisfy the continuous equation bringing about the backflow is expected. In Fig. 5, the streamline distribution at t=5s shows that the backflow separates main flow to the sides, this phenomenon also induced some cool fluid backward to the channel. The temperature distribution of the top of the channel at t=1.0 and t=5.0 shows the heat exchange is stronger than vicinity. In Fig. 6, the deformed channel has larger Nusselt number than normal at some positions which located at the curve peak inside the channel.

Table 1. The average Nusselt number and total mass flow rate at different types

Type	convex	normal	concave
Amplitude(m)	0.004	0	-0.004
Average Nu#	9.89	10.15	9.32
Energy flow rate(W)	5.28	5.07	4.49

The average Nusselt number and energy flow rate was shown in the following equation Eq. (4) and (5) ,respectively.

$$\overline{Nu} = \frac{1}{t}\int \frac{1}{A}\iint_A Nu(x,y)dxdydt \tag{4}$$

$$\dot{q} = \bar{h}A(T_\infty - T_{wall}) = \frac{\overline{Nu}k}{l}A(T_\infty - T_{wall}) \tag{5}$$

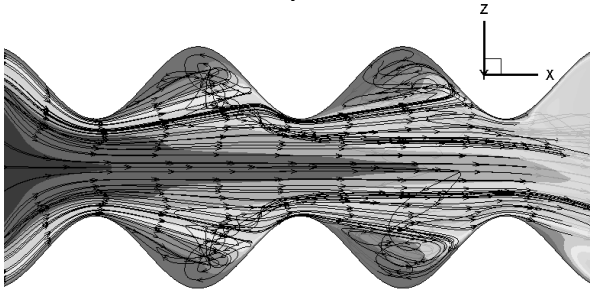

Fig. 7 the eddy and temperature contour of highly deformed channel

5. Concluding remarks

1. Deformed channel mass flow rate is larger than normal.
2. Although concaved channel has more mass flow rate than normal, the Nusselt number is lower.
3. Waved channel provide the extra area for heat exchange but the eddies will appear in the concave zone inside the channel when the amplitude (l_5,l_6) up to ±0.01m, that will reduce the Nusselt number.

References

[1]J. M. Weiss and W. A. Simth, AIAA. 33 (1995) 2050-2056.
[2]Upender K. Kaul *NASA Ames Research Center, M/S 258-5, Moffett Field, CA 94035, United States
[3] I. Abalakin, A. Dervieux, T. Kozubskaya, INRIA (2002) No4459.
[4] S. Yoon, A. Jameson, AIAA. 26 (1988) 1025-1026

Eighth International Conference on Flow Dynamics
November 9 - November 11, 2011

Effects of Surface Tension on Ferrofluids in a Radial Field

Yan-Hom Li, Y-S Yang, W-L Wu, Ching-Yao Chen
Department of Mechanical Engineering, National Chiao Tung University, Taiwan R.O.C.
E-mail of corresponding author: chingyao@mail.nctu.edu.tw.

ABSTRACT

Pattern formation in both a miscible and an immiscible ferrofluid system are experimentally investigated. The experiment is performed by immersing a thin ferrofluid droplet in a cylindrical container, overfilling it with a nonmagnetic miscible/immiscible fluid, and applying an in-plane radial magnetic field. Visually striking patterns are obtained whose morphologies change from circular at a zero field to complex starburst-like structures at finite field. Proper rescaling of the experimental data indicates that the time evolution of the droplets' area increments obeys a universal 4/3 (1) power law behavior for a miscible /immiscible drop.

1. Introduction and Experimental Setup

An interesting aspect is the close connection between the radial magnetic body force and centrifugal forces [1,2]. This offers the promise of a magnetic analogue for spin coating processes[3,4], in which the actual rotation of the system is not required. The phenomenon of spin coating, the flow of a thin liquid film spreading on a rotating horizontal surface, is a topic of considerable scientific and practical importance. In this context, it is of fundamental importance to find ways to predict and control the shape of emergent patterns. In this study, we investigate a system consisting of an immiscible or a miscible thin ferrofluid drop subjected to a radial magnetic field. The focus of our study is to identify the influences of surface tension to the pattern selection mechanism by comparing the results between a miscible interface and its immiscible counterpart.

We examine the time evolution of its effectively 2D interface of a ferrofluid droplet subjected to a radial magnetic field, as the experimental setup shown in Fig. 1. An initially circular ferrofluid droplet is placed on the bottom of a flat, horizontal cavity. A radial field H_r is generated by a pair of coils in an anti-Helmholtz configuration. The time evolution of the interface is directly recorded from above by a charge-coupled device (CCD) camera, providing an upper view of the situation.

2. Results and Discussion

For a miscible droplet, as shown in Fig. 2, the magnetic effects work to activate the rising of the tiny initial peaks at the diffusing interface. On top of magnetic and diffusive effects, the variations of viscosity and magnetic force lead to a locally varying convective motion of the fluids, leading to the rising of numerous long, thin spikes. As to an immiscible droplet with the effects of surface tension, our experimental results suggest a great resemblance to regular spin coating for thin ferrolfuid film spreading [3,4], where centrifugal force is replaced by a radial magnetic body force, as shown in Fig. 3. They also demonstrate the feasibility of a novel magnetically tuneable pattern selection mechanism by first applying a field perpendicularly and then a radial field, as shown in Fig. 4, which provides a predicable way to obtain symmetric shapes with a specific number of fingers. The thicknesses of expanding fluid layers, represented by the grayscale intensity, without/with the presences of surface tensions are demonstrated in Figs. 5 and 6, respectively, and show apparent distinctions. The ferrofluids are preserved mainly at the central region under a miscible condition (Fig. 5). On the contrast, the surface tension existing between an immiscible interface provides a barrier, and leads to mass accumulation at the rim (Fig. 6). A interesting behavior can be found if we consider the time evolution of the area increment ΔA, defined as the difference between the time-dependent area A, and its value at t = 0. Fig. 7 plots the evolutions of dimensional area as well as the dimensionless area increment $\Delta A'$. We can see that the memory of initial conditions is lost for larger times, and that the evolution of $\Delta A'$ is universal defining a regime where both larger and smaller droplets follow a common power law behavior $\Delta A' \sim t'^{\alpha}$, where $\alpha=4/3$. Similar asymptotic behaviors are found in immiscible conditions as shown in Fig. 8. Nevertheless, the power scale of decreases to $\alpha=1$ due to the constraints of surface tension.

3. Concluding remarks

In this work we have described the behavior of a thin ferrofluid droplet experiences a radial magnetic field and therefore spreads, forming starlike patterns. The rapid outward growth is driven by magnetic forces, which act against the stabilizing viscous contribution. Within this scenario a universal 4/3 power law behavior is found for the long time evolution of the droplets' area increments. As to an immiscible system, in which the ferrofluids are exposed under air, the interface appears much more stable because of the constraint of surface tension and the power law scale is reduced to 1.

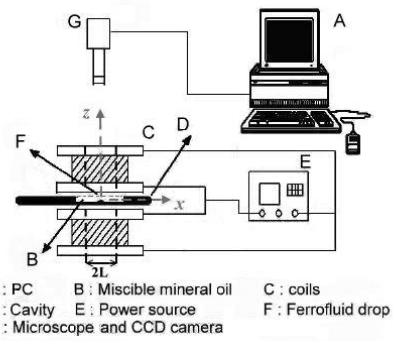

FIG. 1: Scheme of the experimental setup.

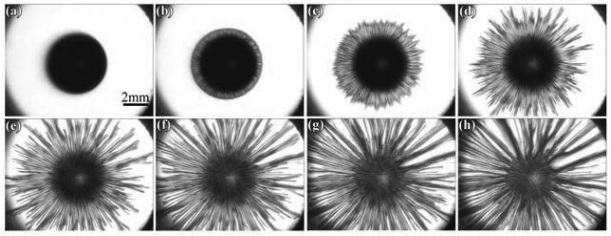

FIG.. 2: Snapshots of top views for a miscible droplet with a diameter of d=5.12 mm and H_0=147 Oe.

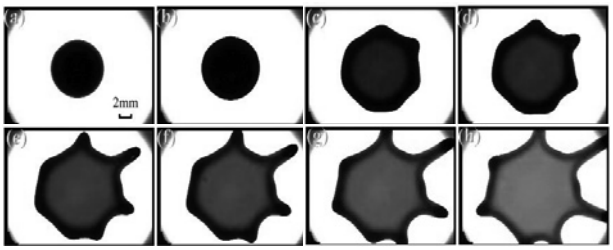

FIG. 3: Time evolution of ferrofluid drops subjected to a purely radial magnetic field (d=7.70mm and H_0=288 Oe).

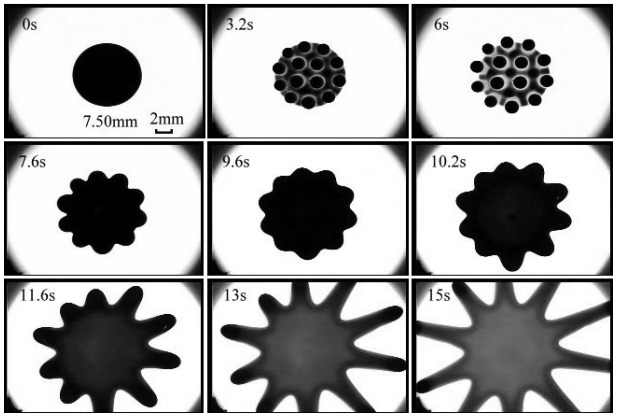

FIG. 4: Time evolution of a ferrofluid drop subjected first to a perpendicular magnetic field, and then to a purely radial field (d=7.5 mm and H_0=211 Oe).

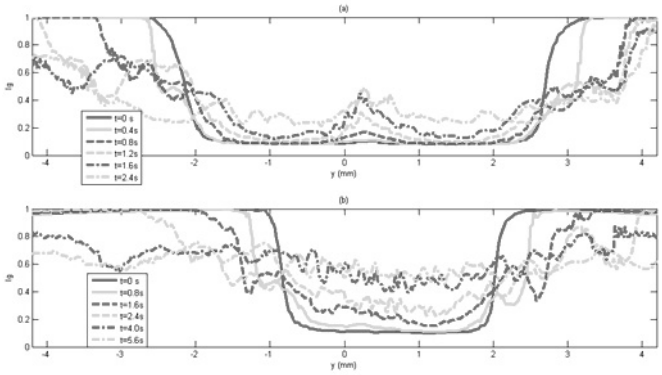

FIG. 5: Distribution of the grayscale intensity Ig (thickness of fluid layer) along the y-axis for miscible conditions of (a) d=5.12 mm, and (b) 3.27 mm.

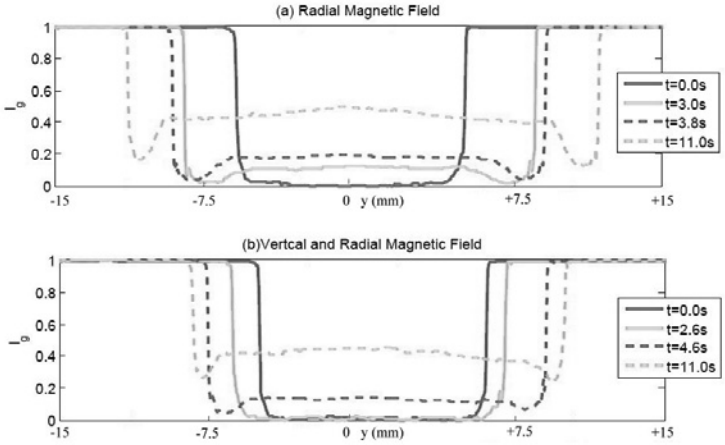

FIG. 6: Distribution of the grayscale intensity Ig for immiscible conditions in (a) a pure radial field, and (b) perpendicular then radial fields.

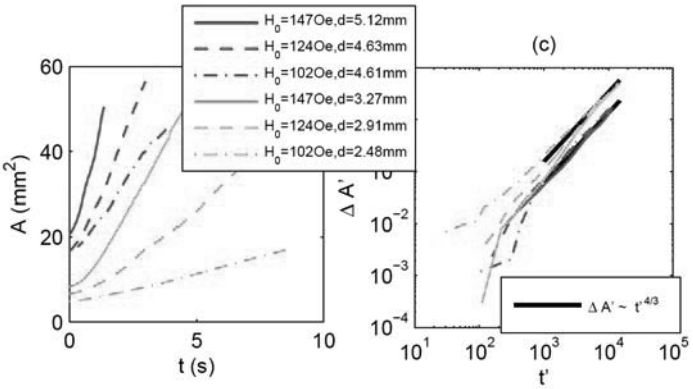

FIG. 7: Expanding area of miscible drops in dimensional form (left) and the dimensionless area increment (right).

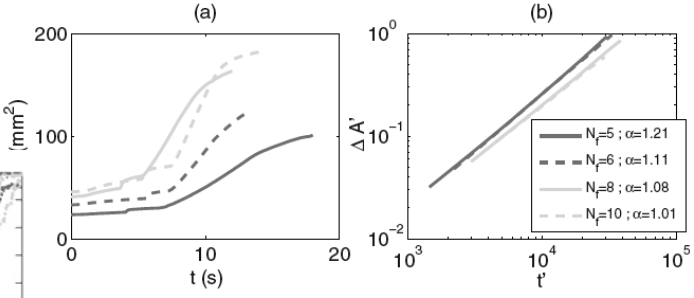

FIG. 8: Dimensional expanding areas of immiscible drops (a), and dimensionless area increment (b).

References

[1] C.-Y. Chen, Y.-S. Yang, and J. A. Miranda, Phys. Rev. E **80**, 016314 (2009).

[2] C.-Y. Chen, W.-L. Yang, and J. A. Miranda, Phys. Rev. E **82**, 056321 (2010).

[3] F. Melo, J. F. Joanny, and S. Fauve, Phys. Rev. Lett. **63**, 1958 (1989).

[4] K. E. Holloway, P. Habdas, N. Semsarillar, K. Burfitt, and J. R. de Bruyn, Phys. Rev. E 75, 046308 (2007).

Eighth International Conference on Flow Dynamics
November 9 - November 11, 2011

The Fundamental Research of jet Acoustic Noise

Wu-Shung Fu, Wei-Hsiang Wang, Kuei-Yi Lin, Chiou-Jong Chen, Chih-Yong Chen, Cheng-Ping Chang

EE306, Department of Mechanical Engineering, No.1001, Daxue Rd., East Dist., Hsinchu City 300, Taiwan (R.O.C.)
flyman.me98g@nctu.edu.tw;wsfu@mail.nctu.edu.tw

ABSTRACT

With the improvement of the life quality, the noise induced by aeroacoustic becomes one of the most important and complicated problems of the noise control. This study will develop simulation method to analyze and reduce noise problems. Firstly, this study will use CFD software to construct the simulation way of jet field and acoustic field under three different velocities. Secondly, it will simulate transient flow field and spectrum. Finally, it will optimize and analyze the caliber and velocity of secondary jet of Dual-Stream Jet which is the most common way to reduce jet noise in industry.

1. Introduction

The discipline of acoustics, which is a study of pressure waves in fluids, is intimately related to fluid dynamics. Many sounds those are technologically important in industrial applications are generated by and propagated in fluid flows.

Generally, acoustic problems can be divided into structure-born acoustic and air-bone aeroacoustic. For solving the above problems, Lighthill[1] proposed a brilliant method named Lighthill analogy to resolve the aeroacoustics. The content of Lighthill analogy is that the acoustic source is calculated by CFD and substituted it to the Lighthill equation to compute the acoustic propagation. The Ffowcs Williams and Hawkings(FW-H) equation by Williams et al.[2] adopts the most general form of Lighthill's acoustic analogy, and is capable of predicting sound generated by equivalent acoustic sources.

In order to solve the jet acoustic noise control problem, an asymmetric parallel secondary stream is used and exactly reduced the overall sound pressure level of jet acoustic.

2. Physical model and Numerical method

A three dimensional jet model shown in Fig. 1 is used to simulate the steady and transient flow field and acoustic field. By adopting k-ε and LES turbulence model and FW-H acoustic model, the results of acoustic quantities as the overall sound pressure level (SPL) and power spectra are solved.

The FW-H equation cab be written as:

$$\frac{1}{a_0^2}\frac{\partial^2 p'}{\partial t^2}-\nabla^2 p'=\frac{\partial^2}{\partial x_i \partial x_j}\{T_{ij}H(f)\}-\frac{\partial}{\partial x_i}\{[P_{ii}n_j+\rho u_i(u_n-\upsilon_n)]\delta(f)\}+\frac{\partial}{\partial t}\{[\rho_0\upsilon_n+\rho(u_n-\upsilon_n)]\delta(f)\} \quad (1)$$

where

u_i = fluid velocity component in the x direction

u_n = fluid velocity component normal to the surface

v_i = surface velocity components in the x direction

v_n = surface velocity component normal to the surface

$\delta(f)$ = Dirac delta function

$H(f)$ = Heaviside function

The inlet boundary condition for jet flow velocities are 10m/s, 30m/s and 50m/s, and outlet boundary condition is pressure boundary where $P = P_{atm}$. The timestep size is set to $2.5\text{x}10^{-5}$s.

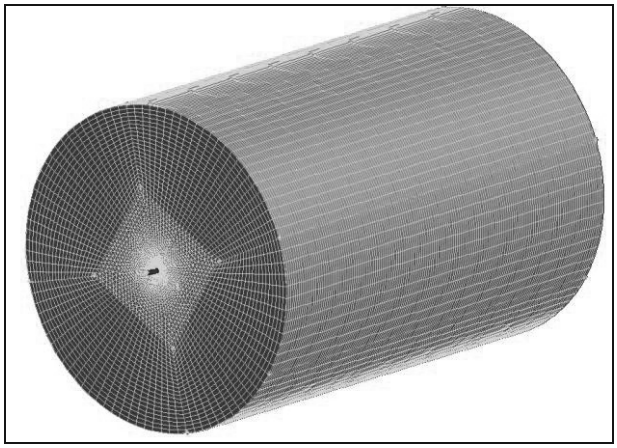

Fig. 1 Physical model of jet flow

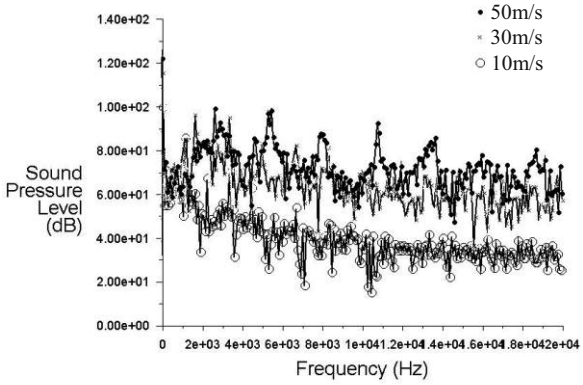

Fig. 2 The sound pressure spectral of jet flow

3. Results and Discussion

By using LES turbulence model with 10% turbulence intensity for different Reynolds number (1300, 3900 and 6500 for inlet velocity 10m/s, 30m/s and 50m/s), the results of sound pressure spectral are shown in Fig.2.

We can see for aerodynamically generated noise, it does not have any distinct tones, and the sound energy is continuously distributed over a broad range of frequencies. With the increasing of the Reynolds number, the overall sound pressure level increases for 74.4dB, 90.8dB and 100.9dB.

To reduce the jet acoustic noise, an asymmetric parallel secondary stream is used to reduce the velocity and pressure gradient between the jet flow and the static fluid.

With different diameter ratio of primary and secondary streams and different velocities of secondary stream, the highest sound pressure level of the flow field is changed.

Fig. 3 indicated the sound pressure level of primary jet velocity 10m/s. As a result, in some situations the sound pressure level decrease compared to the original model. However, for some cases, the sound pressure level slightly increased.

We can see also in Fig. 4 and Fig. 5, the sound pressure level changed and decreased. To summarize, there is an optimized situation for reducing the jet acoustic noise by adopting the velocity of secondary stream for half of the primary stream, and it will reduce almost 20% of the acoustic noise.

4. Concluding remarks

1. By increasing the velocity of jet flow, the acoustic noise is increased, and the jet acoustic noise is a broadband noise source.
2. The acoustic noise is generated by the velocity and pressure gradient of the fluid field.
3. To reduce the jet acoustic noise, an asymmetric parallel secondary stream is used.

References

[1] M. J. Lighthill, Proceedings of the Royal Society of London. Series A, Mathematical and Physical Sciences, 211(1952), 564-587.

[2] J. E. Ffowcs Williams and D. L. Hawkings, Philosophical Transactions of the Royal Society of London. Series A, Mathematical and physical Sciences, 264(1969), 321-342.

[3] E. Z. William, Computational Aeroacoustics Berlin: Springer-Verlag(1992), 41-49.

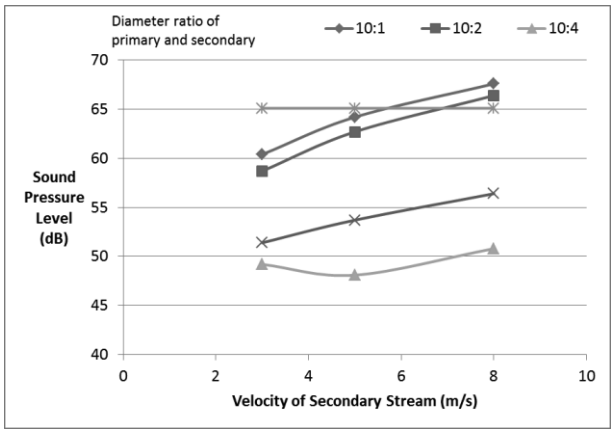

Fig. 3 The sound pressure level of dual-stream jet for primary jet velocity 10m/s

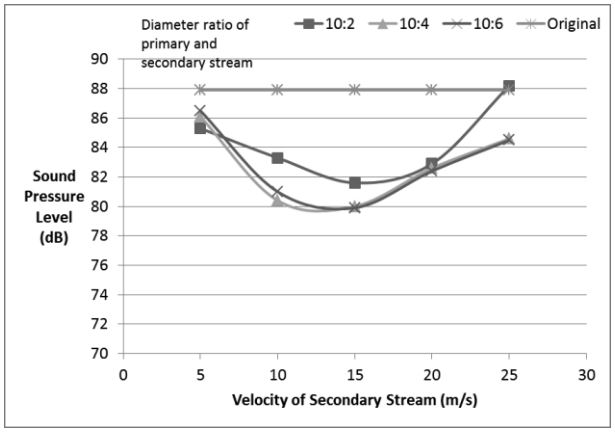

Fig. 4 The sound pressure level of dual-stream jet for primary jet velocity 30m/s

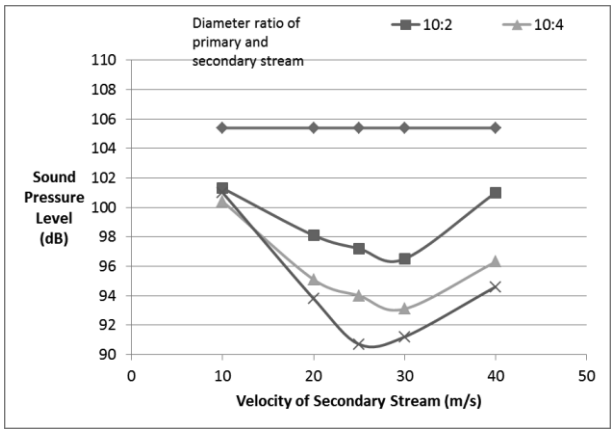

Fig. 5 The sound pressure level of dual-stream jet for primary jet velocity 50m/s

Analysis of Radiative Transport in a Cylindrical Participating Medium with Collimated Radiative Loading

Subhash C. Mishra[1,*], Praveen Agarwal[2] and Ch. Hari Krishna[3]
[1,2]Dept. of Mechanical Engineering, Indian Institute of Technology Guwahati, India - 781039
[3]Institute of Fluid Science, Tohoku University, 2-1-1 Katahira, Aoba-ku, Sendai, 980-8577, Japan
[*] Corresponding author: scm_iit@yahoo.com

ABSTRACT

The present work deals with the application of the finite volume method (FVM) to solve a radiative transport problem in a 2-D finite cylindrical enclosure containing an absorbing, emitting and scattering medium with its top boundary subjected to collimated radiation. Heat flux and temperature distributions are computed for the effects of various values of the extinction coefficient, the scattering albedo and the radius ratio. Results are compared with those available in the literature. A good agreement has been found.

1. Introduction

Radiative transport in a participating medium is a volumetric phenomenon. Owing to its dependence on polar and azimuthal angles, the governing radiative transport equation turns out to be an integro-differential one. Compared to the other two modes of heat transfer, viz., conduction and convection, the analysis of radiative heat transfer in a cylindrical geometry is difficult. Analysis of thermal radiation in cylindrical geometry has plenty of applications in science and engineering. Depending upon the applications, the boundary of the participating medium can be subjected to diffuse radiation filed, in which case, the emitted radiation from the concerned boundary is direction blind, or it can have collimated loading in which the incident radiation enters the medium at a particular angle. As the collimated radiation source travels through the medium, it attenuates and the attenuated component manifests in the form of the diffuse radiation. Thus, with collimated radiative loading, the radiation in the medium consists of both collimated and diffuse components, and the governing radiative transfer equation has to account for the both. Further, the radiative loading at the boundary can be a continuous one or short-lived as in the case of pulse radiation transport. But whatever be the case, the analysis of the collimated radiation transport forms the basis of all and is the most general one. FVM [1,2] is a widely used numerical radiative transfer method, however, its application to radiation transport in a 2-D cylindrical enclosure subjected to collimated radiation source is scarce. The objective of the present work is, therefore, to extend the usage of FVM [1, 2] to analyze radiative heat transfer in 2-D cylindrical enclosure subjected to collimated radiation.

2. Formulation

Let us consider a cylinder containing participating medium as shown in Fig. 1(a). Its top boundary is subjected to collimated radiation of intensity I_0. The radiative heat transfer in cylindrical medium is governed by

$$\frac{1}{r}\frac{\partial}{\partial r}\left[\mu r I_d\right]+\frac{\partial}{\partial z}\left[\zeta I_d\right]-\frac{1}{r}\frac{\partial}{\partial \phi}\left[\eta I_d\right]=-\beta I_d+S_t \quad (1)$$

where $\mu=\sin\theta\cos\phi$, $\eta=\sin\theta\sin\phi$ and $\zeta=\cos\theta$ are direction cosines in the r, φ and z directions, respectively. Here the total source composed of two parts

$$S_t=S_c+S_d \quad (2)$$

For isotropic scattering, source terms S_c and S_d are given by

$$S_c=\frac{\sigma_s}{4\pi}G_c \qquad S_d=\kappa_a\left(\frac{\sigma T^4}{\pi}\right)+\frac{\sigma_s}{4\pi}G_d \quad (3)$$

Integration of Eq. (1) over the control volume and the control solid angle as shown in Fig. 1(b) results

$$\begin{aligned}&D_n^m\left(\Delta A_n I_{d,n}^m-\Delta A_s I_{d,s}^m\right)+D_t^m\left(\Delta A_t I_{d,t}^m-\Delta A_b I_{d,b}^m\right)\\&+\left(\Delta A_e D_e^m I_{d,e}^m-\Delta A_w D_w^m I_{d,w}^m\right)\\&=-\beta I_{d,p}^m\Delta V\Delta\Omega^m+S_{t,p}^m\Delta V\Delta\Omega^m\end{aligned} \quad (4)$$

To relate the facial intensities and the angular edge intensities to the nodal intensities, we use step scheme.

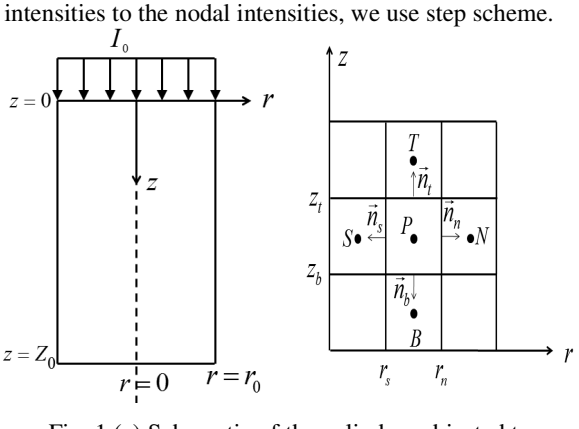

Fig. 1 (a) Schematic of the cylinder subjected to collimated radiation (b) 2-D control volume in front view.

2: Currently: Electronics India Pvt. Ltd., Plot No-51, Udyog Vihar, Surajpur, Kasna Road, Greater Noida, India.
2, 3: contributed to the work while they were MTech students in the Dept. of Mechanical Engineering at IIT Guwahati.

Using step scheme, for first quadrant, the nodal intensity can be calculated as follows

$$I_{d,p}^{m} = \frac{\begin{array}{r} D_n^m \Delta A_s I_{d,s}^m + D_t^m \Delta A_b I_{d,s}^m - \Delta A_w D_w^m I_{d,w}^m \\ + \Delta V \Delta\Omega^m S_{t,P}^m \end{array}}{D_n^m \Delta A_n + D_t^m \Delta A_t - \Delta A_e D_e^m + \beta \Delta V \Delta\Omega^m} \quad (5)$$

After calculating the intensity distribution in entire computational space, the collimated and the diffused incident radiations are calculated as follows

$$G_c = I_c(\theta_c) \qquad G_d = 2\sum_{l=1}^{N_\theta}\sum_{k=1}^{N_\phi} I_d^m \Delta\Omega^m \quad (6)$$

where N_θ and N_ϕ are the number of divisions in angular and azimuthal space. Collimated radiative flux and the axial diffusive radiative flux are calculated as follows:

$$q_c = I_c(\theta_c)\cos\theta_c \qquad q_d^z = 2\sum_{l=1}^{N_\theta}\sum_{k=1}^{N_\phi} I_d^m D_t^m \quad (7)$$

3. **Results and Discussion**

In this paper, all results are presented in non-dimensional form and for grid and ray independent situations.

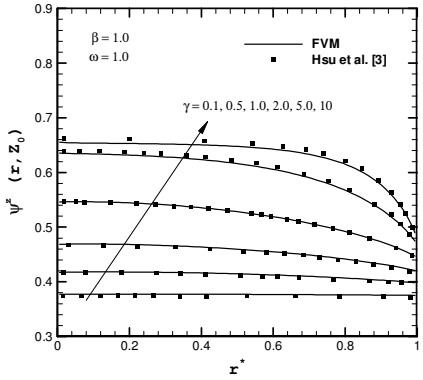

Fig. 2 Effect of the aspect ratio on axial heat flux.

To validate our result**,** we consider the problem, in which the top boundary of the cylinder is subjected to collimated radiation (Fig. 1(a)) and for extinction coefficient $\beta = 1.0$ the medium is fully scattering. Axial heat flux at the bottom of the cylinder has been compared with [3] for different aspect ratios $\gamma = {}^{2r_0}\!/_{Z_0}$.

For extinction coefficient $\beta = 1.0,$ and aspect ratio $\gamma = {}^{2r_0}\!/_{Z_0} = 1.0,$ effect of scattering albedo on the incident radiation at the outer surface of the cylinder is given in Fig. 3.

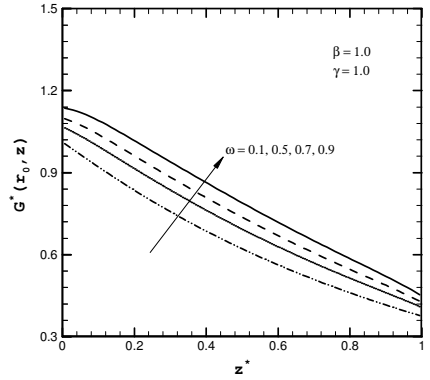

Fig. 3 Effect of scattering albedo on incident radiation.

Effect of extinction coefficient on incident radiation at just one node before the center of cylinder has been studied for aspect ratio $\gamma = 1.0$ and scattering albedo $\omega = 1.0$ in Fig.4.

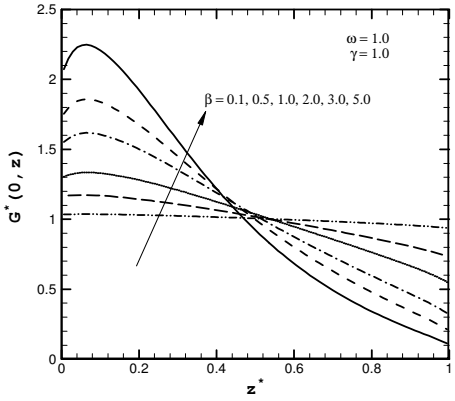

Fig. 4 Effect of extinction coefficient on incident radiation.

4. Conclusions

Radiative heat transfer in a two-dimensional cylindrical medium subjected to collimated radiation was studied using the FVM. Distributions of heat flux and incident radiation were studied for the effects of extinction coefficient, the scattering albedo and the aspect ratio. FVM was found to provide good results for analysis of radiative heat transfer dealing with collimated radiation

References

[1] M.Y. Kim, Int. J. Heat Mass Transfer, **51**(2008), R5144.

[2] R. Singh and S.C. Mishra, Numer. Heat Transfer. A, **52**(2007), R481.

[3] P. F. Hsu, Z. M. Tan, S. H. Wu and C.Y. Wu, Numer. Heat Transfer. A, **35**(1999), R655.

Eighth International Conference on Flow Dynamics
November 9 - November 11, 2011

An investigation of natural convection in a three dimensional tapered chimney

Yun Huang, Wu-Shung Fu
EE306, Department of Mechanical Engineering, 1001 Ta Hsueh Road, Hsinchu, Taiwan
yunhuang.neko@gmail.com; wsfu@mail.nctu.edu.tw

ABSTRACT

Compressible natural convection in a three dimensional tapered chimney with the heating wall is investigated numerically. A chimney is composed of three main parts, a large pedestal, a convergent duct and a small extending duct. In general, the increasement of the average Nusselt number accompanies with the decreasement of the cross section area. The present study is concerned with the velocities and the heat transfer rate affected by the variant geometries in the chimney and the effects of buoyancy forces on the flow pattern.

1. Introduction

It is well-known that the structure of the chimney is indispensably used in the high temperature systems of combustion, pollution control, ventilation, etc. That the importance of practical application of the chimney is indisputable is the main reason for the study of heat transfer mechanisms of the chimney still received lots of attentions.

Lots of papers [1] ~ [3] had already adopted a two dimensional models to investigate the subject of thermal and flow mechanisms in the convergent duct and obtained available results. Regretfully, the effect of neighboring convergent walls on the thermal and flow mechanisms is hard to be taken into consideration in the two dimensional model. A previous study [4] had studied the forced convection in a three dimensional tapered chimney and revealed the unique characteristic of the effect of the neighboring convergent walls on the thermal and flow mechanism in the chimney. However, the characteristic is hardly investigated in the situation of the natural convection in the three dimensional tapered chimney. The aim of the study is investigating thermal and flow phenomena of natural convection in a three dimensional tapered chimney.

2. Physical Model

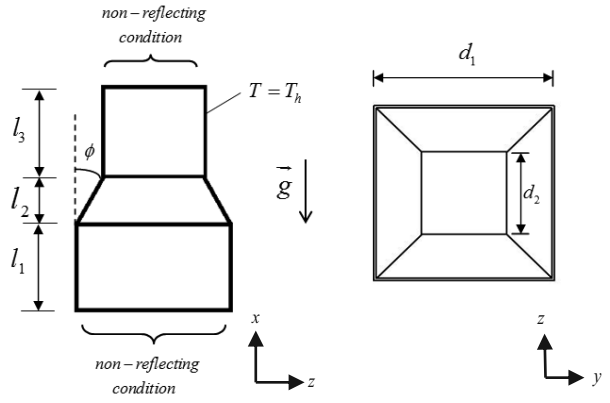

Figure 1 Physical Model

A three dimensional tapered chimney regarded as a physical model is shown in Fig.1. Lengths of the pedestal, tapered duct and extending duct are l_1, l_2 and l_3, respectively. Widths of the pedestal and extending duct are d_1 and d_2, respectively. The tapered angle is ϕ and the cross section of the chimney is square.

The gravity g is downward, and the temperature and pressure of surroundings are 298K and 101,300Pa, respectively. The temperature of the heat surfaces is constant and equal to T_h. The boundary condition at the inlet and outlet of chimney is non-reflecting for saving the usage of computational grids. From a point view of application, two different tapered angles of 30 and 45 degrees are selected.

3. Method

Schemes of Roe, preconditioning[5] for resolving compressible flow under a low Mach number situation, dual time stepping and MUSCL (Monotonic Upstream-Centered Scheme for Conservation Laws) coordinating LUSGS[6] (Lower-Upper Symmetric Gauss Seidel) are adopted to resolve 3-D Navier–Stokes equations. Methods of algebraic grid generation and a non-reflecting boundary condition are used to execute coordinates transformation and decrease the computational domain, respectively. Furthermore, Boussinesq assumption is no longer used and the compressibility of fluid is considered instead.

4. Results and Discussion

In Fig. 2, the distributions of velocity U on the different cross sections. At the inlet $\overline{AB}$, fluids are sucked from the outside and it causes the velocities of fluids in the central region are faster than those near the wall region decelerated by the wall. At the cross section of $\overline{CD}$, since the effect of buoyancy force on the velocity of fluid begins to appear, the velocities of fluids in the region between the central and near wall regions are faster than those in the two neighboring regions. At the cross section of $\overline{EF}$, the cross section area is just contracted that naturally caused the velocities of fluids at this location to be accelerated. The smaller cross section area leads the corner region to be more easily affected by the heat walls. As a result the velocities of fluids in the corner region are slightly faster than those in the other regions. At the outlet of $\overline{GH}$, the high velocities of fluids apparently gather in the near wall region because of buoyancy effect that causes the thickness of velocity boundary layer in the corner region to be thinner than that in the other regions. This phenomenon is advantageous to the heat transfer

mechanism.

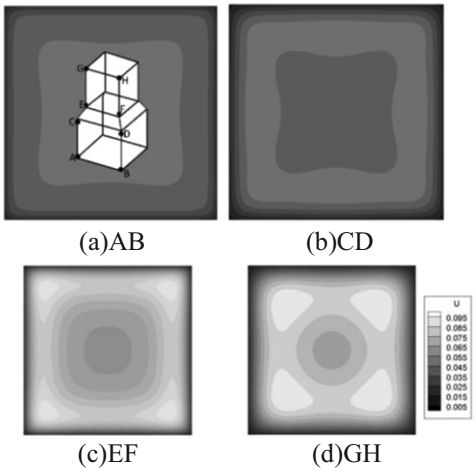

Figure 2 Distributions of velocity U on different cross sections. ($Ra = 6.04\times10^4$, $\phi = \pi/6$)

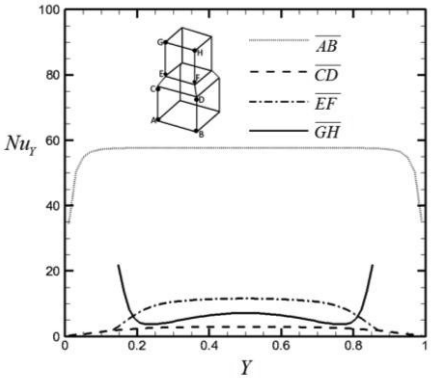

Figure 3 Distributions of local Nusselt number on the different lines. ($Ra = 6.04\times10^4$, $\phi = \pi/6$)

In Fig. 3, the definition of Nu_Y is shown as follows.

$$Nu_Y = \frac{d_1}{k_0(T_h - T_0)}\left[k(T)\frac{\partial T}{\partial n}\right] \tag{1}$$

Generally, local Nusselt numbers distributed on the inlet line have the larger magnitude than those on the other location. Meanwhile the influence of buoyancy is not apparent yet, in the corner region the drag resistance caused by neighboring walls is larger than that in the central region. Then the local Nusselt number Nu_Y becomes small in the corner region. Since the line $\overline{EF}$ is located at the end of tapered duct, the cross section area is contracted and the flow velocity is accelerated at this location. This phenomenon causes local Nusselt numbers distributed on this location to be enhanced relative to thosed distributed on the line $\overline{CD}$. At the outlet $\overline{GH}$, the cross section area is constant in the extending duct and local Nusselt numbers distributed in the central region are decreased and smaller than those distributed on the line $\overline{EF}$. However, close to the corner region the influence of the increment of the buoyancy force induced by neighboring heat walls is more effective than that of the increment of drag resistance likewise induced by neighboring heat walls on the acceleration of fluid flow. As a result, local Nusselt numbers close to the corner region are larger than those of the central region.

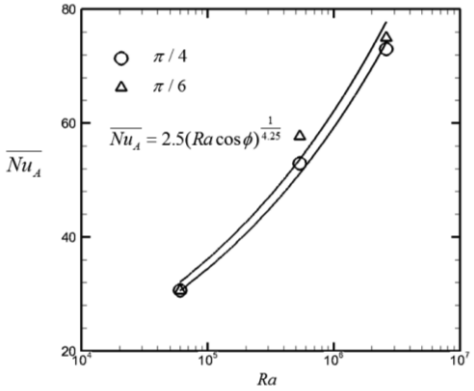

Figure 4 Distributions of average Nusselt number in the various cases

Fig.4 is the comparisons of average Nusselt numbers in different situations and the numerical correlation of average Nusselt number. The definition of average Nusselt number of the whole heat surface expressed as follows.

$$\overline{Nu}_A = \frac{1}{A}\int_{L_x}\int_{L_y} Nu_y dydx \tag{2}$$

The trends of distributions of average Nusselt number in the situation of the same Raleigh number are similar, but the magnitudes of average Nusselt numbers of the tapered angle of $\pi/6$ are slightly larger than in the tapered angle of $\pi/4$.

4. Concluding remarks

The main points may be concluded as follows.

1. In this study, the optimal situation for heat transfer rate is the condition of $\phi = \pi/6$.
2. Due to the buoyancy effect, the fluids flow accelerated near the wall region causes the thickness of velocity boundary larger in the corner region. The heat transfer mechanism is enhanced by this phenomenon.

References

[1] E.M. Sparrow and R. Ruiz, Int. J. Heat Mass Transfer **31** (1988) 2197-2205.
[2] S.A.M. Said, Int. J. Energy Research **20** (1996) 559-567.
[3] N. Bianco, O. Manca, and S. Nardini, Int. J. Heat Mass Transfer **50** (2007) 2772-2786.
[4] W. S. Fu, W. H. Wang, Y. Huang, C. G. Li, Int. J. Heat Mass Transfer **54** (2011) 3420-3430.
[5] J. M. Weiss and W. A. Smith, AIAA. **33** (1995) 2050-2056
[6] S. Yoon, A. Jameson, AIAA. **26** (1988) 1025-1026.

Eighth International Conference on Flow Dynamics
November 9 - November 11, 2011

Streamer Dynamics in Methane/Air DBD Under High Pressure and High Temperature Conditions

H. Takana[1], Y. Tanaka[2] and H. Nishiyama[1]
[1] Institute of Fluid Science, Tohoku University, 2-1-1 Katahira, Aoba-ku, Sendai 980-8577, JAPAN
[2] Dep. of Electrical and Electronic Eng., Kanazawa University, Kakuma, Kanazawa 920-1192, JAPAN
takana@paris.ifs.tohoku.ac.jp

ABSTRACT

Computational simulation of methane-air dielectric barrier discharge at high pressure and temperature is conducted for plasma assisted combustion. The effect of ambient pressure on streamer dynamics is successfully simulated with considering photo ionization. Furthermore, generation characteristic of chemically reactive species under different pressure and temperature was shown.

1. Introduction

The plasma assisted combustion has been especially paid attention in aerospace and automobile engineering. Most of the experimental studies and analyses are typically carried out at pressures close to 1 atm. For the practical application of the plasma assisted combustion, it is essential to understand the radical generating process with streamer propagation and also to clarify the chemical kinetics under high pressure, especially for the application to internal engines.

In this study, a computational simulation of methane-air dielectric barrier discharge is conducted to clarify the effect of ambient pressure and temperature on streamer dynamics and chemical kinetics in methane-air DBD.

2. Governing Equations and Computational Conditions

Following continuity equations for electrons and ions with drift-diffusion approximation are solved coupled with Poisson's equation:

$$\frac{\partial n_k}{\partial t} + \nabla \cdot \boldsymbol{\Gamma}_k = S_k, \tag{1}$$

$$\boldsymbol{\Gamma}_k = \mathrm{sgn}(q_k)\mu_k \boldsymbol{E} n_k - D_k \nabla n_k, \tag{2}$$

$$\nabla \cdot (\varepsilon \nabla \phi) = -\sum_k q_k n_k, \tag{3}$$

where n_k, $\boldsymbol{\Gamma}_k$, S_k, q_k, μ_k, D_k, are the number density, flux, source term, charge, mobility and diffusion coefficient for species k, respectively. E, ε and ϕ are electric field, permittivity and electric potential, respectively. Charged particle fluxes are given by the Scharfetter-Gummel formulation. The electron transport properties and rate coefficients are given as a function of reduced electric field and they are obtained by solving Boltzmann's equation for the electron energy distribution.

The rate of photoionization in a gas volume is included in the source term in equation (1). In this study, two-exponential Helmholtz model was employed for photoionization of oxygen. The photoionization processes in O_2 are caused by the radiation in the wave range 98 – 102.5 nm. The radiation in this range is produced by the radiative transitions from three singlets of N_2 ($b^1\Pi_u$, $b'^1\Sigma_u^+$ and $c'^1_4\Sigma_u^+$) to the ground state ($X^1\Sigma_g^+$).

The self-biased potential on the dielectric surface is calculated by Gauss's law, assuming a constant electric filed in the dielectric. The secondary electron emission probability by ion impact on a surface is given as 0.01.

The composition ratio of methane-air mixture is $N_2 : O_2 : CH_4 = 15 : 4 : 1$. The chemical kinetics of methane-air mixture studied in this work includes processes with participation of species of N_2, $N_2(A^3\Sigma_u^-)$, $N_2(B^3\Pi_g)$, $N_2(C^3\Pi_u)$, $N_2(a'^1\Sigma_u^-)$, N_2 ($b^1\Pi_u$, $b'^1\Sigma_u^+$ and $c'^1_4\Sigma_u^+$), N_2^+, O_2, $O_2(a^1\Delta_g)$, $O_2(b^1\Sigma_g^+)$, O, O_2^+, $O_2(c^1\Sigma_u^-, C^3\Delta_u,$ and $A^3\Sigma_u^+)$, O_3, CH_4 CH_3, CH_2, CH_4^+, CH_3^+, CH_2^+, H_2, H, H_2O, OH, HO_2, CH_2O, CH_3O and electron.

The chemical kinetics of methane-air mixture studied in this work is based on that developed in the model described in except for the reactions associated with argon. Moreover, the O atom decay processes through recombination with oxygen resulting in ozone formation, $O + O_2 + M \rightarrow O_3 + M$ and also through recombination with ozone, $O + O_3 \rightarrow O_2 + O_2$ are incorporated. It was shown from the sensitivity analysis that the increased atomic oxygen loss rate in methane-air occurs primarily due to reactions of H atoms and CH_3 radicals, in particular $H + O_2 + M \rightarrow HO_2 + M$, $O + HO_2 \rightarrow OH + O_2$, $OH + CH_4 \rightarrow CH_3 + H_2O$, and $O + CH_3 \rightarrow H + CH_2O$. These reactions are also taken into account. In addition to that, the following reactions of OH production and decay are also considered; $OH + HO_2 \rightarrow O_2 + H_2O$, $HO_2 + CH_3 \rightarrow OH + CH_3O$, $CH_3O + O_2 \rightarrow HO_2 + CH_2O$, and $H + O_2 \rightarrow O + OH$.

Figure 1 shows the computational domain and initial electron distribution. Only the grounded electrode is covered with quartz glass ($\varepsilon/\varepsilon_0 = 3$) with the thickness of 0.8 mm. The flat powered electrode (cathode) and grounded electrode (anode) are separated by 2.05 mm. The voltage on the powered electrode has a stepwise change to -8.0 kV for 1 atm and -18.0 kV for 3 atm. For the initiation of electron avalanche, local

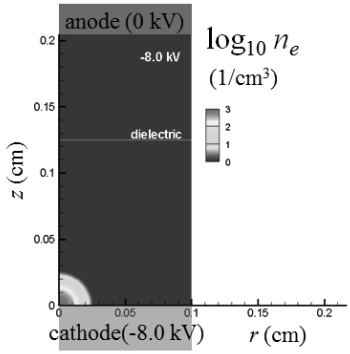

Fig. 1 Computational domain and initial condition.

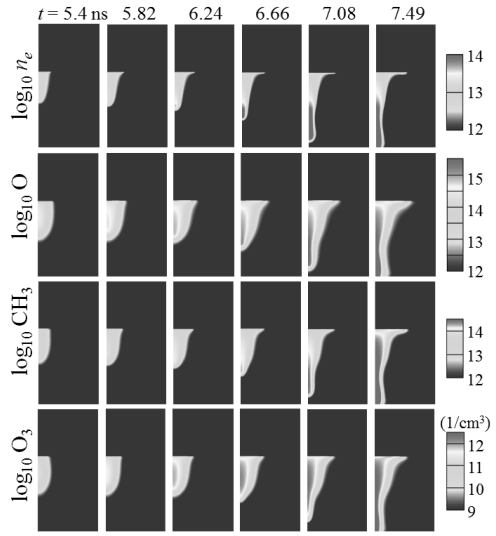

Fig. 2 Radical generation process during positive streamer propagation at 3 atm and 300 K with applied voltage of -18.0 kV.

seed charges consist of electron and N_2^+ were given by a Gaussian distribution only in the vicinity of powdered electrode. The peek number density of initial seed charges are 1.0×10^3 $1/cm^3$ at the powered electrode on the symmetric axis.

3. Results and Discussion

Figure 2 shows the distribution of electron, oxygen radical, CH_3 radical and ozone during positive streamer propagation at 3 atm and 300 K with stepwise applied voltage of -18.0 kV. These chemical species play an important role in plasma assisted combustion. The propagation of streamer accelerates toward the cathode due to high electrical filed around the streamer head induced by locally high concentration of positive charge. This locally high concentration of positive charge is caused by the difference in the mobility and drift direction between positive ions and electron. Oxygen radical and CH_3 radical are rapidly produced at the streamer head mainly due to high energy electron impact dissociation by induced high electrical field. Then, they gradually increase behind the streamer head with quenching of electronically excited N_2 by O_2 and CH_4. On the other hand, ozone is produced only behind the

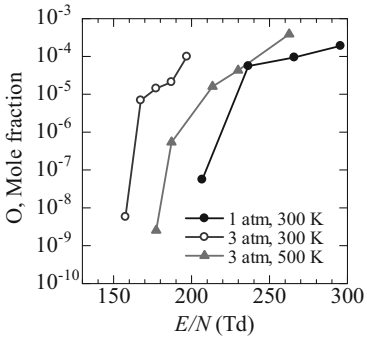

(a)

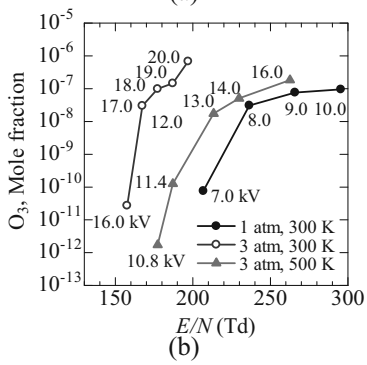

(b)

Fig. 3 Generation characteristics of (a) oxygen radical and (b) ozone.

streamer head by the three body reaction; $O + O_2 + M \rightarrow O_3 + M$ as can be found at t = 7.08 ns.

Figure 3 shows the volume averaged mole fraction of oxygen radical and ozone in computational domain at t = 20 ns. The initial gas number density is the highest at 3 atm, 300 K and it is 3 times higher than that at 1 atm, 300 K. In the case of 3 atm, 500 K, the initial gas number density is 1.8 times higher than that at 1 atm, 300 K. The operation range of initial reduced electric field strength (*E/N*) shifts lower values for higher gas number density, although the required applied voltage increases for high enough *E/N*. For a given *E/N* of ~200 Td, generated oxygen radical and ozone increases with initial gas number density. This is because the higher initial gas number density is, the more electron impact ionization occurs under high enough *E/N*. High frequency electron impact ionization creates highly concentrated electric field around the streamer head. Therefore, radicals are efficiently produced there through electron impact reaction even at lower initial *E/N*.

4. Concluding remarks

Computational simulations of CH_4/air dielectric barrier discharge with photo ionization at high pressure and temperature conditions were successfully conducted for plasma assisted combustion. Streamer dynamics and radical generation process during positive streamer propagation were clarified in detail.

References

[1] N. L. Aleksandrov, et al., Plasma Physics Reports, **35** (2009), 867-882.

Eighth International Conference on Flow Dynamics
November 9 - November 11, 2011

Parallel Fluid Modeling of Large-Area Plasma Enhanced Chemical Vapor Deposition of Amorphous Silicon Thin Film

Chieh-Tsan Hung[1], Kun-Mo Lin[1], Jong-Shinn Wu[12*] and Jen-Perng Yu[3]
[1]National Chiao Tung University, Hsinchu, Taiwan.
[2]National Center for High-Performance Computing, Hsinchu, Taiwan.
[3]Ming Chuan University, Taipei, Taiwan
*E-mail: chongsin@faculty.nctu.edu.tw

ABSTRACT

In this study, simulation of gas discharges in a plasma-enhanced chemical vapor deposition (PECVD) chamber using silane/hydrogen as precursors for a-Si:H thin film deposition is presented. A 2D finite volume fluid modeling code was developed for solving the densities of all species and electron energy density, in which the electrostatic and electromagnetic filed was obtained by Poisson's equation and Maxwell's equation respectively.

1. Introduction

In the pass decade, amorphous silicon thin film has found wide applications in transistors, liquid crystal displays, light emitting diodes, thin film solar cell, among others. Especially, the solar module is one of the fastest growing markets in the world since it is one of the feasible alternative energy sources to the oil crisis and nuclear energy. Because of the cost reduction requirements in the fabrication process, the use of large-area plasma source, such as Plasma Enhanced Chemical Vapor Deposition (PECVD), becomes popular than others source (e.g., ICP and ECR), in which the plasma uniformity is strongly related to local current and magnetic source. PECVD process has been demonstrated as an effective fabrication tool in thin film deposition. There are, however, several challenges for large-area PECVD process, which include: 1) the nonlinear plasma system could not easily scale up based on the knowledge from the small area plasma chamber; 2) the difficulties of measurement inside a plasma led to the inefficient chamber design process; 3) the role of species and their complex chemistry reactions occurred in gas discharges were unclear; 4) the standing wave in the chamber, caused by the high-frequency RF power source, leads to highly non-uniform film deposition. The above issues could be addressed more easily using large-scale simulation owing to the recent rapid development of high-performance computer technology and numerical schemes.

Kushner [1] studied the chemical kinetics in a PECVD using $Ar/SiH_4/H_2$, which included the important species observed from experiments. The electron impact reaction rate coefficients and electron distribution function (EEDF) were obtained by a time-dependent Monte Carlo calculation. Gallagher [2] purposed a simplified homogeneous plasma chemistry model where particles primarily grow from SiH_3^- anions and SiH_m radicals. Bhandarkar *et al.* [3] developed a zero-dimensional chemical kinetic nucleation model in which linear and cyclic silicon hydride species containing up to ten silicon atoms were considered. The ion density was assumed as a constant proportional to the RF power. A 1D fluid model for describing a silane/hydrogen discharge was developed by Nienhuis *et al.* [4], in which a 1D fluid model was used by incorporating silicon hydrides Si_nH_m containing up to 12 silicon atoms. A set of plasma chemistry, including 24 species and 37 reactions, were considered. In brief summary, 1D or 2D simulations help understand the temporal and spatial plasma properties. However, plasma chemistry and problem size has to be reduced if simulation needs to be controlled in an acceptable runtime.

Many studies had shown that the standing waves take place when the chamber size is compatible to or larger than wavelength of applied power source [e.g, 8]. Generation of standing waves in a PECVD chamber leads to non-uniform thin film deposition, which is one of the serious problems in the related industry.

In recent years, the advancement of high-performance parallel computing and numerical scheme has opened a window of opportunity to overcome the challenges mentioned above and understand the plasma discharge though large-scale simulations.

In this study, we demonstrate a parallel 2-D fluid modeling for silane/hydrogen gas discharge considering the solution of the Maxwell's equation. A Maxwell's equation solver using cell-centered finite volume method is proposed and implemented, which is still in progress. More results will be presented in the meeting.

2. Numerical Method

The governing equations considered in fluid modeling include the continuity equations with drift-diffusion approximation for all charged species, the continuity equations for neutral species, the electron energy density equation, in which the electric field induced by applied power source and spatial charged is determined by the Poisson's equation and the Maxwell's equation solvers. The initial background gas densities and flow convection effects are obtained by a neutral Navier-Stokes solver developed by Hu *et al.* [9]. The drift and diffusion coefficients and the rate constants related to electrons are functions of the electron temperature, which are obtained by integrating either the experimental collision cross section, or the EEDF from the solution of the Boltzmann equation solver such as the BOLSIG+ [10]. All model equations are discretized by using backward Euler's method on the temporal

domain and cell-centered finite volume with the Scharfetter-Gummel scheme for the mass fluxes on the spatial domain. To ensure stability when larger time steps are used, linearization in time is applied for the source term of Poisson's equation and linearization in electron energy density and transport coefficients for the source terms of electron energy density equation. All discretized fluid modeling equations are solved by PETSc package [11], which is portable through MPI, a standard in message passing interface. Details of fluid modeling including its parallel performance will be presented in ICFD 2011 conference [12].

The electric field, which results from a liner superposition by applied power source, current densities and spatial charges, is calculated by the Poisson's equation and Maxwell's equation solvers. The electric filed induced by time independent static spatial charge is calculated by the Poisson's equation. The electric field driven by power source and spatial current densities is obtained by solving Faraday's and Ampere's laws, which are discretized by using 4^{th} order Runge-Kutta method in time and cell-centered finite volume scheme in space. The sum of the electric field from the the Poisson's equation and Maxwell's equation self-consistently coupled with fluid modeling equation by space charges and current densities throughout the simulation.

We had employed a set of silane/hydrogen plasma chemistry consisting 15 species and 28 reaction channels. The plasma chemistry includes: electron impact dissociative ionization, electron impact vibrational excitation, electron impact dissociation, electron attachment, electron impact ionization, as well as the reactions with Si_nH_m (n=1~4). The electron impact reaction rate coefficients were, as mentioned above, obtained by BOSIG+, while the gas phase reaction rate coefficients were from the first principle quantum chemistry calculation.

In this study, simulation conditions included: 1) a chamber pressure of 600 mtorr; 2) a square glass plate with a size of 20x20 cm; 3) a substrate temperature of 250°C; 4) a gap distance between showerhead and substrate of 10 mm and 5) an inflow rate ratio of silane to hydrogen as 80:50 sccm. Note the plasma is powered by a 27 MHz radio-frequency power supply.

3. Results and Discussion

Figure 1 shows the cycle averaged radical species SiH_2 and SiH_3, which are most important radical species for a-Si:H deposition without considering the standing wave effect. The fluxes of radical into the substrate are uniform except at the edge of substrate, where the stronger electric field slightly increases plasma density and induces higher flux of radicals. We know the deposition rate strongly correlated to the radical fluxes into the substrate, and most of the researches using fluid modeling treat the surface reaction by fitting the sticking coefficient with experimental results. However, the mechanism of deposition also can be understood by *ab intio* quantum chemistry calculation, which is currently in progress.

Figure 2 shows the preliminary result of the Maxwell's equation solver in solving the EM wave caused by a standing wave in a square cavity made of a perfect conductor at various phases of a cycle. The simulation conditions are 1) cubic cavities with length 5 m surround by perfect conductor. 2) the initial wave was at frequency 60 MHz, wave length 5 m, and electric field amplitude 1 V/m in y-direction. The non-reflection boundary condition for wave propagation is currently implemented and will be applied to simulate a real PECVD in the near future. More results will discuss in ICFD2011 conference.

4. Concluding remarks

We have demonstrated a 2D chamber-scale simulation of a realistic silane/hydrogen PECVD chamber using the developed parallel fluid modeling. The simulation shows that uniformity of film deposition can still be obtained with a power source having a frequency of 27 MHz. However, standing wave problem will arise with increasing frequency of power source and destroy the uniformity of the film deposition. Addition of a time-dependent Maxwell's equation solver into the fluid modeling is currently in progress to understand this important effect when large-area PECVD process is employed for thin-film deposition.

References

[1] M.Kushner, Journal of Applied Physics, 63, pp 2532.
[2] A. Gallagher, Physical Review E 62, 2:(2000) 2690.
[3] U. V. Bhandarkar *et al*, Journal of Physics D: Applied Physics 33, 21: (2000) 2731.
[4] G. J. Nienhuis Ph.D. thesis, Utrecht University, Nieuwegein, The Netherlands, 1998.
[5] P. Raghunath *et al*, The Journal of Physical Chemistry A, 114, 13353-13361.
[6] D.-H. Varma *et al*, The Journal of Physical Chemistry A, 114, 3642-3648.
[7] S.-Y. Wu *et al*, The Journal of Physical Chemistry A, 114, 633-639.
[8] Y. Yang *et al*, Plasma Source Science and Technology, 2010.
[9] M. H. Hu *et al*, ICFD 2011, Japan.
[10] G. Hagelaar, Gerjan. "BOLSIG+ : user-friendly solver for electron Boltzmann equation.", 2009.
[11] S. Balay *et al*, "PETSc home page.", 2001. http://www.mcs.anl.gov/petsc.
[12] K. M. Lin *et al*, ICFD 2011, Japan.

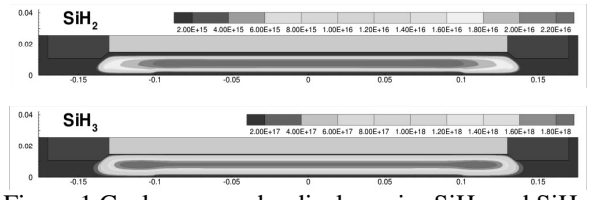

Figure 1 Cycle averaged radical species SiH_2 and SiH_3.

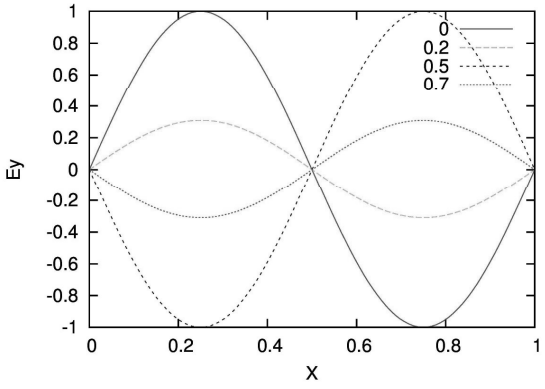

Figure 2 Standing wave in a perfect conductor cavity at 0, 0.2, 0.5 and 0.7 of cycle.

OS8: Flow-induced Degradations in Piping Systems of Nuclear Power Plants

Eighth International Conference on Flow Dynamics
November 9 - November 11, 2011

The Role of Flow in Flow-Accelerated Corrosion under Nuclear Power Plant Conditions

John M. Pietralik
Component Life Technology, Atomic Energy of Canada Ltd., Plant Road, Chalk River, K0J 1P0, Ontario, Canada
mpietral@magma.ca

ABSTRACT

In a mechanistic model of flow-accelerated corrosion (FAC), one of the steps affecting the FAC rate is the mass transfer of ferrous ions from the oxide-water interface to the bulk of the flowing water. This step is dominant under alkaline conditions and high temperature, an environment frequently occurring in nuclear power plants. The intensity of this step is described by mass transfer coefficient, which, in turn, predominantly depends on local flow characteristics. Therefore, those flow characteristics play a dominant role in the local FAC rate distribution. An example of an FAC rate distribution is presented.

1. Introduction

Flow-accelerated corrosion (FAC) causes wall thinning in carbon steel piping and equipment under water flowing conditions. Although the secondary side of nuclear power plants is more affected, piping and equipment on the primary side are also susceptible to FAC.

Mechanistic models of FAC assume that ferrous ions form at the metal-oxide interface, diffuse through the oxide layer, and are transported to the bulk water by convective mass transfer. Convective mass transfer explains the role of flow in FAC and is the focus of this paper.

2. Transport Phenomena in FAC

2.1 Mechanistic Models

Mechanistic models of FAC presume that there are three consecutive steps involved [1] in the transport of ferrous ions and, generally, any of them can control the FAC rate, see Fig. 1:

(a) The electrochemical oxidation of metal atoms to form ferrous ions at the metal surface.
(b) The diffusion of ferrous ions in the water through the porous oxide layer and precipitation of the ferrous ions in the inner sublayer as well as dissolution in the outer sublayer of the oxide layer.
(c) The convective mass transfer of ferrous ions from the oxide-water interface to the bulk of water.

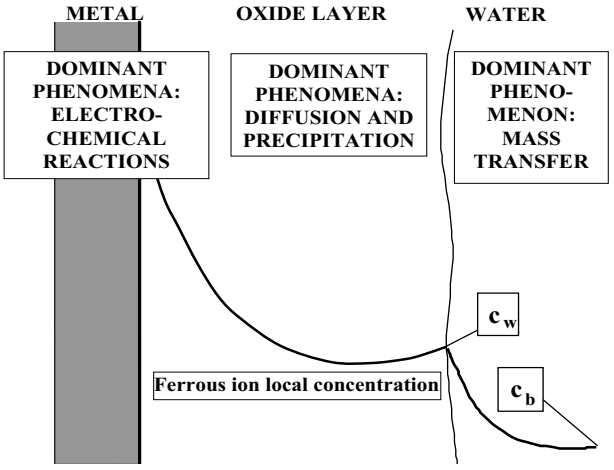

Fig. 1 Basic steps and a ferrous ion concentration distribution in a mechanistic FAC model.

Because the solubility of magnetite changes through the oxide layer as a function of crystal size, ferrous ions precipitate into magnetite crystals in the pores where crystals are small (the inner sublayer) and magnetite crystals dissolve in the outer sublayer where crystals are large.

Diffusional mass transfer of ferrous ions occurs through the pores in the oxide layer and the pore size is of the order of a small fraction of a micrometer. The mass transfer resistance of this step depends on the size of the pores, flow path, and the thickness of the layer. The available information on this mass transfer rate is limited. However, it is expected that this mass transfer resistance is not rate limiting for small oxide layer thicknesses. Convective mass transfer of the ferrous ions in the water depends mostly on the local flow characteristics and is discussed below.

2.2 Mass Transfer of Ferrous Ions

The mass flux of ferrous ions transported from the oxide-water interface to the bulk water is written as

$$N_{Fe}=MTC*(c_w-c_b) \qquad (1)$$

where N_{Fe} is the mass flux of ferrous ions (kg/m^2s), MTC is the mass transfer coefficient for ferrous ions (kg/m^2s), c_w is the concentration of ferrous ions at the water-oxide interface (kg of ferrous ions/kg of water) and c_b is the concentration of ferrous ions in the bulk water (kg of ferrous ions/kg of water).

The MTC depends predominantly on the hydrodynamics near the oxide-water interface. In two-phase flows (steam-water), mass transfer occurs only in the liquid because steam does not dissolve ferrous ions. Therefore, the part of the interface that is occupied by steam is void for mass transfer. However, the presence of steam affects the hydrodynamics near the interface and increases the MTC. The net effect is typically an increase in mass transfer rate, especially for low and intermediate steam qualities.

The mass flux of ferrous ions could be calculated from the above equation if the concentration difference were known. This difference, however, is a function of the transport phenomena in the oxide layer and it is impossible to predict from first principles. Therefore, Equation (1) cannot be used directly for FAC rate predictions in a general case.

2.3 Mass Transfer Coefficient

The MTC depends predominantly on flow characteristics and weakly on the properties of the water and the diffusing species. Among flow characteristics are velocity, steam quality (or void fraction) in two-phase flows, upstream turbulence level, local geometry, upstream component, and surface roughness of the inside surface. Steel properties, especially chromium content, affect the mass flux of ferrous ions by changing the concentration of ferrous ions at the water-oxide interface.

The best known dependence of FAC rate based on plant artefacts is that on flow velocity and the velocity exponent is 1.0. Literature MTC correlations for a rough wall indicate that the velocity exponent varies between 0.8 for low Reynolds numbers and 1.0 for very high Reynolds numbers. Because over time, an initially smooth surface becomes rough as a result of FAC, a correlation for rough wall should be used for power plant applications.

In power plant applications, flows measured by Reynolds numbers are very high and reach tens of millions. Almost all literature correlations of MTC are valid for much smaller ranges, e.g., typically below 100,000 and rarely exceed 500,000. Expanding the range of an MTC correlation beyond its tested range can lead to significant errors.

The MTC is also affected by the local turbulence intensity, which in turn, is affected by the upstream turbulence level and the geometry; see [2] for an example of increased turbulence downstream of a turn.

Despite some claims that shear stress at the wall plays a role in FAC rate, this hypothesis has not been proven. The apparent success in predicting the FAC rates results from an analogy between the momentum transfer (represented by the wall shear stress) and mass transfer (represented by the mass flux) [3].

2.4 FAC Rate Under Power Plant Conditions

Although theoretical models help understand the degradation mechanism and predict FAC rate, it is not possible to rely on predictions only. Under power plant conditions, components experience changes due to operational cycles and other abnormal conditions, e.g., start-up and shutdown, power maneuvering, partial power, and system aging. The FAC rate measured for artefacts is a sum of all these changes. In complex geometries, the flow pattern is not known, especially under two-phase flow conditions and in many others, even the flow rate is not known enough, e.g., in vent lines. Also, flow patterns and MTC correlations are not well known for large piping. Correlations for MTC derived for small Reynolds numbers and applied for power plant conditions can have an error measured by a factor of two or three for single-phase flows and even larger for two-phase flows.

3. Example of FAC Rate in a Bend

An example of local distribution of FAC rate measured on a 2.5-inch bend after 12.5 effective full power years in service under alkaline conditions together with a numerically predicted distribution of MTC is shown in Figures 2 and 3. More details for the bend and its environment are elsewhere [4]. The agreement of the distributions is very good.

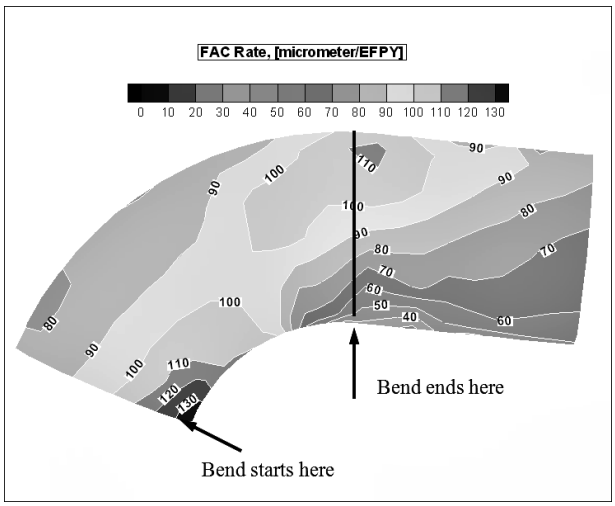

Fig. 2 Measured FAC rate

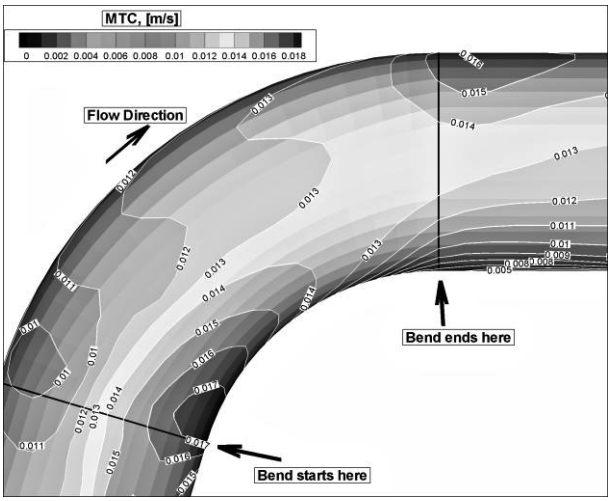

Fig. 3 Predicted MTC distribution

4. Concluding Remarks

Under nuclear power plant conditions (alkaline water and high temperature), the local flow characteristics, expressed by the mass transfer coefficient, determine the distribution of the local FAC rate.

References

[1] J.M. Pietralik, Proceedings of the 8th CNS International Conference on CANDU Maintenance Toronto, Ontario, Canada, November 16-18, 2008.

[2] J.M. Pietralik and B.A.W. Smith, Proceedings of the 14th International Conference on Nuclear Engineering, ICONE-14, Miami, FL, July 17-20, 2006.

[3] B. Poulson, Corrosion Sci., 23(4), 1983, 391.

[4] J.M. Pietralik and C.S. Schefski, J Eng. Gas Turbines and Power, 133, 1, 012902, 2011.

Eighth International Conference on Flow Dynamics
November 9 - November 11, 2011

On Evaluation of LDI Erosion Rate based on Fluid/Solid Coupled Simulation

Toshiaki Ikohagi
Institute of Fluid Science, Tohoku University, 2-1-1 Katahira Aoba-ku Sendai, 980-8577, Japan
E-mail: ikohagi@ifs.tohoku.ac.jp

ABSTRACT

A prediction equation for Liquid Droplet Impingement (LDI) erosion rate is proposed using numerical result of fluid/solid coupled simulation and a simple dimensional analysis of primary factors of flow and material. The prediction equation contains dependencies of droplet impact velocity, droplet diameter, acoustic impedance, and damping effect of liquid film etc..

1. Introduction

It is important for the safety of piping systems in nuclear power plant to evaluate accurately Liquid Droplet Impingement (LDI) erosion caused on the inner pipe wall. In this study, a prediction equation for LDI erosion rate is proposed by means of fluid/solid coupled simulation and a simple dimensional analysis of primary flow and material factors, and the validity is discussed comparing with previous works [1,2].

2. Fluid/Solid Coupled Simulation Method

In order to simulate high speed phenomena of a liquid droplet impact on flat surface, the governing equations based on the compressible gas-liquid two-phase medium for flow and homogeneous isotropic elastic medium for material are simultaneously solved. The details of governing equation and numerical scheme used have been described elsewhere [3,4]. The boundary condition on the flat surface between fluid and solid is imposed by acoustic impedance matching. Figure 1 shows an outline of initial condition with and without liquid film. Liquid and gas phases consist of water and vapor, and carbon steel is used as elastic solid phase. Present 3D calculation is performed only in the 1/4 plane symmetric region.

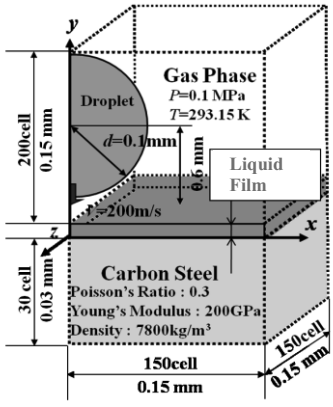

Fig. 1 Outline of initial condition

.

3. Results and Discussion

Figure 2 shows maximum pressures at cental impact point and on contact edge for droplet diameter d =0.1mm. These maximum pressures are almost proportional to droplet impact velocity, though the gradient for contact edge is about 1.5 times larger than that of central impact point. The gradient for 2D culcula-

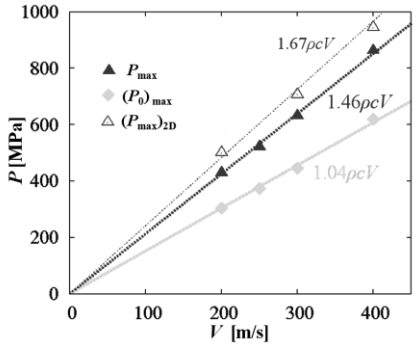

Fig. 2 Maximum pressures at cental impact point and on contact edge (d = 0.1 mm)

-tion is somewhat overestimated.

Damping effect of liquid film is shown in Fig. 3 for various droplet impact Mach number M and ratio of liquid film thickness h to d. Maximum pressures at central impact point are exponentially decreased with increase in h/d and decrease in M.

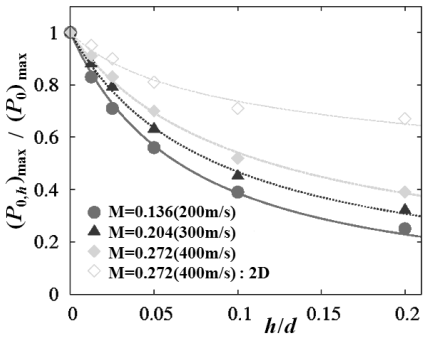

Fig. 3 Damping effect of liquid film thickness

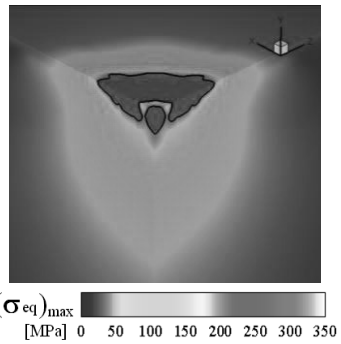

Fig. 4 Definition of impulsive elastic volume

Next, we focus on the elastic volume deformed

impulsively after droplet impact. Figure 4 shows the impulsive elastic volume v_e in which the maximum equivalent stress $(\sigma_{eq})_{max}$ is beyond the yield stress σ_Y = 205MPa. The elastic volume inside the black line is found in and around the impact point. In Fig. 5, the maximum equivalent stress larger than σ_Y clearly appears though $(\sigma_{eq})_{max}$ decreases with increase in h/d.

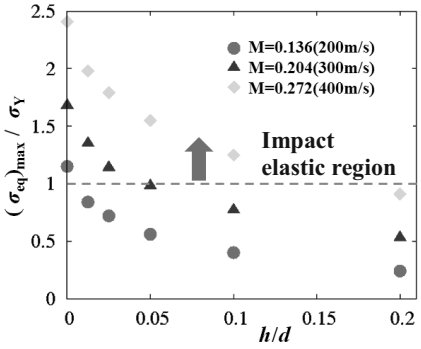

Fig. 5 Damping effect on maximum equivalent stress

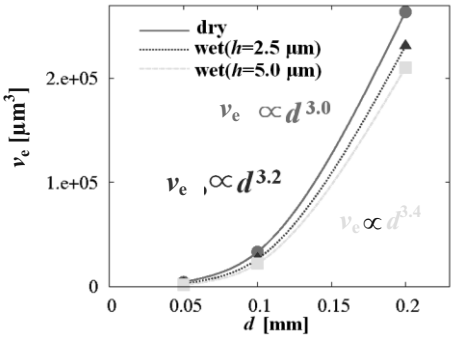

Fig. 6 Relation of impulsive elastic volume and droplet diameter (V=400m/s)

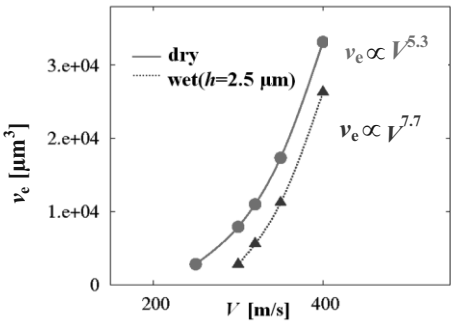

Fig. 7 Relation of impulsive elastic volume and droplet impact velocity (d=0.1mm)

In Figs. 6 and 7, the impulsive elastic volume v_e with and without liquid film is indicated against droplet diameter and impact velocity. Dependency of d and V on v_e is indicated that their indexes tend to increase with h.

Here, consider LDI erosion rate $\dot{m}$ by a dimensional analysis of primary flow and material factors.

$$\dot{m} = vN_i \tag{1}$$

$$\frac{v}{d^3} = f_1(E_R, \frac{h}{d}, \mathrm{M}, \mathrm{Re}, \mathrm{We}) \approx (E_R)^{n_1} \cdot F_s(\frac{h}{d}, \mathrm{M}) \tag{2}$$

where, $E_R = \rho c V^2 / \varepsilon_c \sigma_B c_s$, and assume $\sigma_B \propto p$.

For n_1=2 and F_s=1, $\quad v \approx (\rho c)^2 d^3 V^4 / (\varepsilon_c p c_s)^2$ (3)

For n_1=2.5 and F_s=1, $\quad v \approx (\rho c)^{2.5} d^3 V^{5.0} / (\varepsilon_c p c_s)^{2.5}$ (4)

For n_1=2.8 and F_s=1, $\quad v \approx (\rho c)^{2.8} d^3 V^{5.6} / (\varepsilon_c p c_s)^{2.8}$ (5)

In the case of dry surface, three equations (3), (4) and (5) for v respectively correspond to those of Sanchez[2] for impact velocity dependency, Heymann[1] for material hardness dependency, and Wilson[5] for acoustic impedance dependency. Then, the droplet diameter dependency on v is still held d^3. In the case of wet surface with liquid film thickness h, a following formula for F_s is suggested, assuming that v can be evaluated through impulsive elastic volume v_e which is obtained by the present numerical simulation, as

$$F_s = \exp\left\{-a\left(\frac{h}{d}\right)^{n_2}(\mathrm{M}-\mathrm{M}_{th})^{n_3}\right\} \tag{6}$$

However, a constant a , indexes n_2 and n_3 should be validated using laboratory experimental results and/or practical wall thinning data. Further, if liquid film thickness changes due to successive droplet impact, h/d can be considered to depend on Re and We.

$$\frac{h}{d} = f_2(\mathrm{Re}, \mathrm{We}) \tag{7}$$

Table 1. Notation of physical properties

$\dot{m}$	Erosion rate [m/s]
v	Erosion volume per one droplet [m^3]
N_i	Droplet impact frequency per unit area [$m^{-2}s^{-1}$]
ρ	Droplet density [kg/m^3]
d	Droplet diameter [m]
V	Impact velocity [m/s]
c	Sound velocity of liquid [m/s]
μ	Liquid viscosity [Pa s]
h	Liquid film thickness [m]
p	Hardness of material [-]
ε_c	Critical strain [-]
c_s	Sound velocity of material [m/s]
σ	Surface tension coefficient [N/m]
σ_B	Tensile strength [Pa]
E_R	Energy ratio of droplet impact to strain [-]
M	Droplet impact Mach number [-]
M_{th}	Threshold velocity Mach number [-]
Re	Droplet Reynolds number [-]
We	Droplet Weber number [-]
F_s	Function of liquid film damping [-]

Acknowledgement

This work was partially funded by NISA Project on Enhancement of Ageing Management and Maintenance of Nuclear Power Plants, METI, Japan.

References

[1] F. J. Heymann, ASTM STP474 (1970), pp. 212-248.
[2] L. E. Sanchez-Caldera, Doctor Thesis, MIT (1984).
[3]Y. Aoki et al., Proc. of AFI/TFI (2008), pp. 82-83.
[4]H. Sasaki et al., Proc. SNA+MC, No.10189 (2010).
[5]R. W. Wilson and R. Graham, Conf. Lubrication and Wear, IME (1957), pp. 707-712.

Detection and Characterization of Vibration Induced Flaws in Nuclear Steam Generator Tubes

Tariq Khan, Amin Tayebi, Lalita Udpa and Satish Udpa
Department of Electrical and Computer Engineering
Michigan State University, East Lansing, MI 48224-1226, U.S.A.
udpa@egr.msu.edu

ABSTRACT

The principal heat exchanger in a nuclear power plant is called a steam generator. Heat exchanger tubes transfer heat from the primary loop to the secondary loop to produce steam. Eddy current inspection techniques are used routinely for detecting and characterizing steam generator tube degradation. Multifrequency eddy current (EC) systems are used for detection and diagnosis of all degradation types. This paper presents a system for automated analysis of multi-frequency array probe EC data for the detection of vibration induced u-bend wear (fretting) in power plants.

1. Introduction

Heat exchanger tubes are used in a variety of industries, including power stations, petrochemical plants and oil refineries, for transferring heat to fluid circulating outside the tube. The principal heat exchanger in a nuclear power plant is called a steam generator as shown in Figure 1. Tubes within the steam generator serve to transfer heat from the primary loop to the secondary loop to produce steam. The steam is then employed to operate the turbines. The tubes are typically made of Inconel Alloy 600 or Alloy 690.

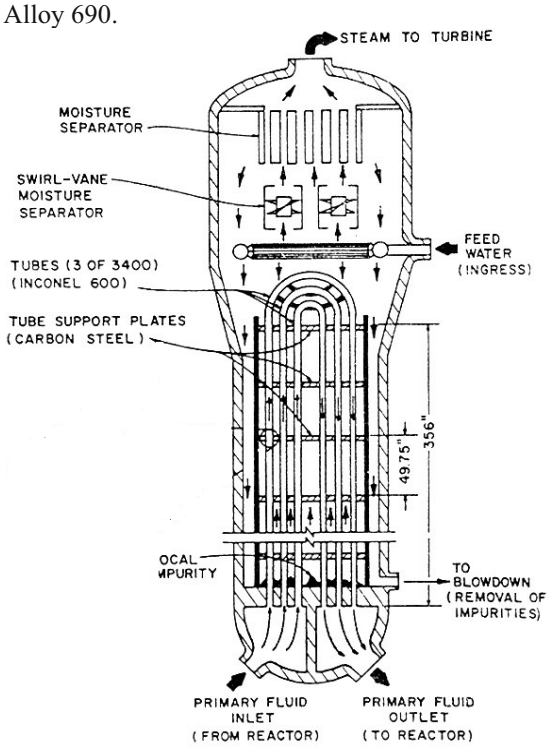

Figure 1. Steam Generator of a nuclear reactor

The tube bundle is supported by support structures, distributed along the length of the tubes.

The steam generator tubes are exposed to harsh environmental conditions such as high temperatures, high pressures and high fluid flow rates. Chemical reactions, mechanical vibrations and material transformations under these harsh conditions result in various types of tube degradation [1]. These include mechanical fretting and wear between tube and tube supports (caused by flow induced vibrations), outer diameter stress corrosion cracking (ODSCC), pitting, volumetric degradation, primary water stress corrosion cracking (PWSCC), and inter granular attack (IGA).

2. Eddy current inspection techniques

Eddy current inspection techniques are used routinely for detecting and characterizing steam generator tube degradation. Multifrequency eddy current systems, employing a variety of probe designs, are capable of acquiring the necessary data to allow detection and diagnosis of all degradation types [2]. Not surprisingly, the interpretation of SG tube eddy current inspection data can be challenging. Conventional eddy current data analysis is carried out by human data analysts. Analysts utilize their vast experience in reviewing the impedance plane trajectory, amplitude and phase of the signal, and other factors in each channel to make a decision. The sheer volume of data and the desire to minimize plant downtime, however, makes automated data analysis schemes very attractive. The application of consistent and reliable automated analysis techniques to achieve improved detection, classification, and characterization results is increasingly becoming the norm in the nuclear power industry [3].

3. Automated analysis of eddy current data

This paper presents a system for automated analysis of multi-frequency array probe eddy current (EC) data for the detection of vibration induced u-bend wear (fretting) in actual power plants. The data is first calibrated and then processed using appropriate mixing algorithms to suppress signal components generated by support structures. A moving average filter followed by a median based threshold filter is applied to eliminate any artifacts and noise in the mixed data. Regions of interest (ROIs) are then detected using a combination of adaptive thresholding and morphological processing schemes. Features such as amplitude, phase and correlation coefficient (flaw length) are then extracted from each of ROI and classified as "defect" or "no defect" using a simple rule-base. The presentation will describe the details of various steps involved in automated processing and analysis of the data. Results obtained by processing real field data from power plants will be presented. Initial detection results are tabulated in Table 1. Effort is currently underway to reduce the number of false calls. Classification results obtained as a result will be presented at the conference.

Table 1. Detection results of vibration induced U-bend fretting in actual power plant

No.	Number of Tubes	Total Flaws	Detected	False Calls
1	33	8	8	9
2	19	11	11	6

References

[1] S. Chuang, Eddy current automatic flaw detection system for heat exchange tubes in steam generators, PhD Thesis, Iowa State University, 1997

[2] S. S. Udpa, L. Udpa, "Eddy Current Nondestructive Evaluation", Wiley Encyclopedia of Electrical and Electronics Engineering, edited by John G. Webster, Vol. 6, pp. 149-163, 1999

[3] S. Majumdar, S. Ramakrishnan, P. Ramuhalli, L. Udpa and S. Udpa, J. Benson, R. Williams and T. U. Bipes, Automated Data Analysis System for Steam Generator Tube Inspection, Materials Evaluation, Volume 69, No. 2, February 2011.

Eighth International Conference on Flow Dynamics
November 9 - November 11, 2011

Pipe Wall Thickness Management for Flow Accelerated Corrosion using EMAT Monitoring System

Fumio Kojima, Daigo Kosaka, Kosuke Umetani
Organization of Advanced Science and Technology, Kobe University
1-1, Rokkodai-cho, Nada-ku, Kobe 657-8501 Japan
kojima@koala.kobe-u.ac.jp

ABSTRACT

This paper is concerned with a monitoring system for pipe wall thinning using electro-magnetic acoustic transducer (EMAT). The precise measurements using electro-magnetic acoustic resonance method (EMAR) are verified both for calibration test specimens of carbon steels (SS400) and for test pipes fabricated to simulate a growth of wall thinning. The experimental results showed good agreement with detection results of ultrasonic testing (UT). The several critical issues are discussed for the practical implementations of on-line monitoring system.

1. Introduction

Recent progress on condition monitoring (CM) has attracted attention in improving system reliability and decreasing human error influences. CM plays in essential roles in developing extensive instrumentation of measurement equipments and together with better performance for analyzing condition data. In this paper, a CM system for pipe wall thinning using electromagnetic acoustic transducer (EMAT) is considered. The proposed system provides no contact, highly resolvable measurements, and remote capability of inspection procedures [1]. First, the precise measurements using electromagnetic acoustic resonance method (EMAR) [2] are verified both for calibration test specimens of carbon steels (SS400) and for test pipes fabricated to simulate flow accelerated corrosions (FAC). In the final part, the several critical issues are shown for practical implementation of on-line monitoring.

2. Measurement Method

Our experimental apparatus is composed of an EMAT, a pulser-receiver, an A/D converter and a computer as shown in Fig. 1. The sensor consists of two permanent magnets with 10 mm width each and single coil with 10 mm diameter with 80 turns. Thickness measurements by EMAR method can be evaluated by sound velocity and a peak interval (Δf) with respect to the frequency

$$T = \frac{v}{2\Delta f} \tag{1}$$

From Eq. (1), it ca be recognized that EMAR allows high accurate thickness sizing since the thickness T is inversely proportional to the peak interval Δf. Throughout our experiments, the burst waveform of the excitation voltage of 800Vpp is added to EMAT by pulsar. Exciting time is taken as 100μs, and the range of sweeping frequencies is set as 1MHz to 3MHz. In Fig. 2, we admit the detecting accuracy was up to 0.1 [mm] for SS400 [3].

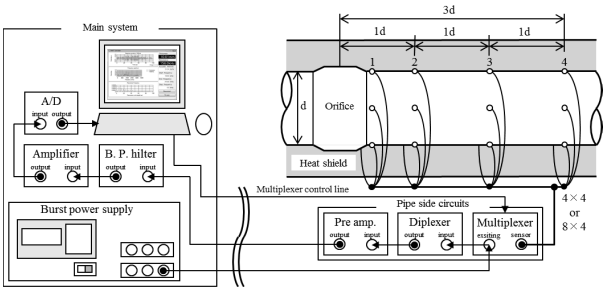

Fig. 1 Experimental setup

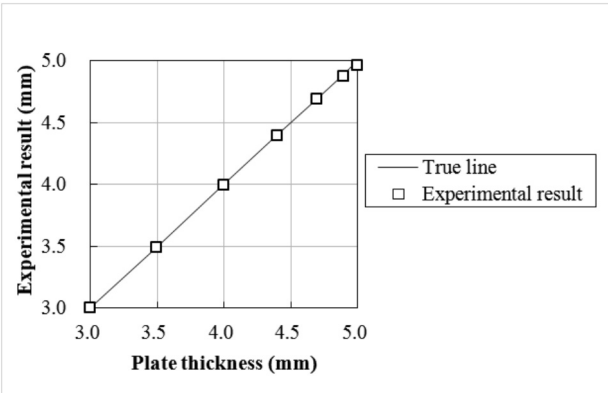

Fig. 2 Thickness resolution by EMAR

3. Detection of Graduated FAC Level

In our research, we made numerous test pipes that were fabricated to simulate the axial growth of wall thinning. As shown in Fig. 3, six 2B-sch80-STP370 pipes were tested for this purpose. The extents of axis were taken as 'a' = 30, 60 and 120 mm with the maximum thinning depth 'b' = 0.5 and 1.0mm. Figure 4 shows estimating sizing results of the sample specimens by EMAT. It can be verified that the sizing accuracy of thickness measurements was within 0.3 [mm]. The extent and location of corrosion can be accurately detected. These results showed good agreement with detection results of UT.

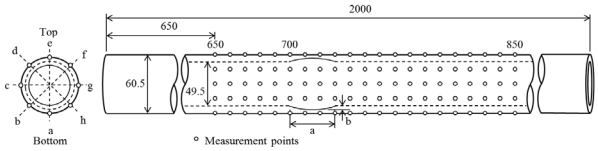

Fig. 3 Test pipes with graduated level of FAC

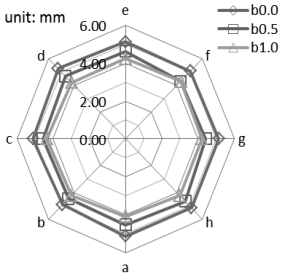

(a) Thickness

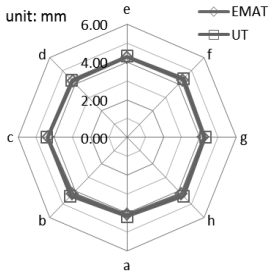

(b) EMAT and UT

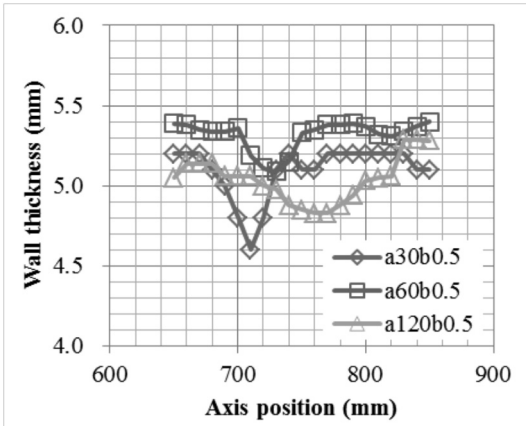

(c) Extent and location

Fig. 4 Detection of graduated level of FAC

4. Characterization of Locally Thinning Profiles

A 2B-sch80-STP370 pipe was tested and the corrosion shape was fabricated to simulate FAC with a locally thinning profile. The extent of FAC was taken as 'a' = 120 mm with the maximum thinning depth 'b' = 1.0mm. Figure 6 depicts sizing results for the sample specimen. The region of wall thinning could be accurately detected by EMAT. For the purpose of the comparative discussions, the conventional UT techniques were also performed. These detection results showed good agreement with detection results of UT.

5. Critical Issues

There are many critical issues for the practical use of the proposed method. The feature of real FAC is the locally distributed and the surface of FAC is characterized by scaly profile. This is considerable problem for thickness sizing. Experimental tests were examined for the sensitivity analysis [4].

In the real plant, temperature inside the pipe might be extremely varied day and night. This is one of the considerable problems for on-line monitoring. From (1), the thickness sizing by EMAR affects the sound velocity. The surface temperature must be measured at the grid point of thickness measurements.

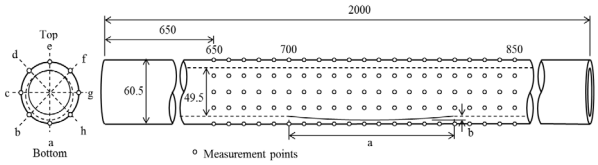

Fig. 5 Test pipes with locally thinning profile

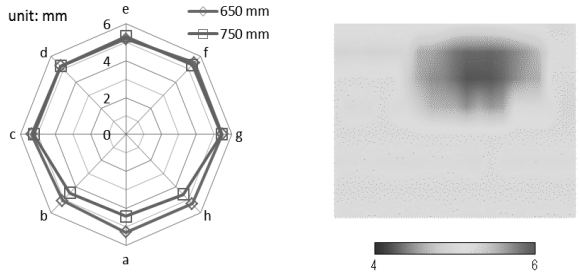

(a) Measurements by EMAT

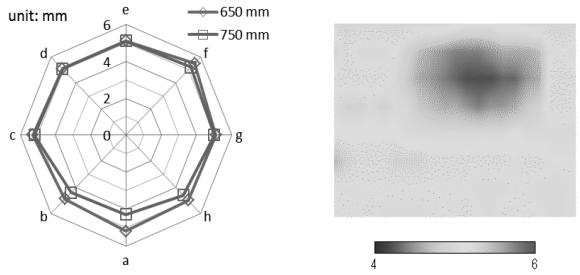

(b) Measurements by UT

Fig. 6 Characterization of local profiles

6. Conclusions

Effectiveness and feasibility of monitoring system for pipe wall thinning using EMAT were reported. Verification tests were implemented based on thickness measurements at grid points on the outer surface of pipe. Test pipes with mock FAC were provided for our laboratory experiments. These experimental results showed good agreement with detection results of UT.

Acknowledgement

This work has been performed as a part of the National Research Project for Enhancement of Measures against the Ageing of Nuclear Power Plants sponsored by the Nuclear and Industrial Safety Agency (NISA).

References

[1] R.B. Thompson, Physical Acoustics, Vol.19, Academic Press, New York, (1990), pp. 157-200.

[2] K. Kawashima, Proc IEEE Ultrasonic Symposium, **2** (1994)**,** pp.1111-1119.

[3] D. Kosaka, F. Kojima, H. Yamaguchi, and K. Umetani, E-Journal of Advanced Maintenance, **2**-1 (2010), pp.34-42.

[4] D. Kosaka, F. Kojima, and K. Umetani, Studies in Applied Electromagnetics and Mechanics, to appear

Eighth International Conference on Flow Dynamics
November 9 - November 11, 2011

A Consideration of Effects of Hydrodynamics on Pipe-Wall-Thinning Phenomena

Fumio Inada, Kimitoshi Yoneda, Ryo Morita, Masaaki Satake, and Kazutoshi Fujiwara
Central Research Institute of Electric Power Industry (CRIEPI)
2-11-1. Iwado-kita, Komae-shi, Tokyo 201-8511 Japan
E-mail: inada @ criepi.denken.or.jp

ABSTRACT

Turbulent mass transfer is one of the key factors on the evaluation of flow accelerated corrosion (FAC), and the mass transfer in the straight pipe can be obtained using the analogy with the turbulent heat transfer. In this research, we proposed a method to evaluate the mass transfer at the turbulent region such as elbow and the downstream of orifice when the effective friction velocity is used, in which the turbulent velocity near wall surface is taken into account. STAR CCM+ code is used to evaluate the velocity profile in the viscose sublayer of turbulent region, and geometry factor correlations were evaluated for turbulent region.

1. Introduction

Pipe-wall thinning is important for plant safety, and it can be also important for maintenance management because the management of pipe-wall thinning can affect the periodic inspection schedule.

The major causes of pipe-wall thinning are Flow Accelerated Corrosion (FAC) and Liquid Droplet Impingement Erosion (LDI). FAC occurs. FAC is the phenomenon in which the corrosion becomes extremely fast due to turbulent mass transfer of fluid flow at the locations where turbulence is strong such as elbows, T-junctions, the downstream of an orifice or valve, and reducers. It can occur when the pipe material is the carbon steel. Erosion occurs when the high speed droplet attacks the pipe wall, or when very high impact pressure is produced due to the bubble collapse of the cavitation.

Turbulent mass transfer, which is one of major factor of FAC, is almost clarified for the simple flow such as the developed flow in the circular pipe. It can be obtained using Chilton-Colburn's analogy of mass transfer and heat transfer. On the other hand, the turbulent mass transfer at the turbulent region such as elbows and the downstream of an orifice is not clarified.

In this report, we proposed a method to evaluate the mass transfer at the turbulent region.

2. Modeling of Mass Transfer at the Turbulent Region

2.1 Modeling of Mass Transfer of the developed flow in the circular tube

In general, it is said that there is an analogy between the heat transfer and the mass transfer from the wall surface. There are some models to show the analogy. It is said that Chilton-Colburn's analogy[1] is simple and agrees well to experimental results.

Chilton-Colburn[1] showed from the experimental data of heat and mass transfer as follows:

$$f/2 = N_u \Big/ \left(\mathrm{Re}\bullet P_r^{1/3}\right) = S_h\left(1-\omega_s\right) \Big/ \left(\mathrm{Re}\bullet S_c^{\,1/3}\right) \qquad (1)$$

where Nu is Nusselt number ($= \dfrac{hd}{\lambda} = \dfrac{|q_w|d}{\lambda\left(T_s - T_\infty\right)}$), Pr is Prandtl number, ωs is the concentration at the interface, Re and Sc is Reynolds number and Schmidt number expressed as:

$$\mathrm{Re} = dU_m/\nu, \quad S_c = \nu/D \qquad (2)$$

Blasius's friction factor expressed as:

$$f/2 = 0.0395\,\mathrm{Re}^{-1/4} \qquad (3)$$

is applied to eq.(1), then

$$N_u = 0.0395\,\mathrm{Re}^{0.75}\,P_r^{\,1/3}, \quad S_h = 0.0395\,\mathrm{Re}^{0.75}\,S_c^{\,1/3} \qquad (4)$$

On the other hand, the following Dittus-Boelter's empirical formula is used as heat and mass transfer evaluation of xperimental:

$$S_h = kd/D = 0.023\,\mathrm{Re}^{0.8}\,S_c^{1/3} \qquad (5)$$

The equation is quite similar form with eq.(4).

The above relation can be shown theoretically to some degree[2]. From the friction loss formula, the following equation can be derived:

$$\frac{f}{2} = \frac{|\tau_w|}{\rho U_m^2} = \frac{1}{\mathrm{Re}}\left(\frac{d\left(\overline{u}/U_m\right)}{d\eta}\right)_{wall}\left(\frac{d}{\delta}\right) \qquad (6)$$

where d is the diameter of the pipe, Um is the averaged flow velocity, $\eta = y/\delta$ the nondimensional location, and d is the thickness of viscose sub-layer.

Sherwood number is defined by:

$$Sh\left(1-\omega_s\right) = \left(\frac{d\theta_c}{d\eta}\right)_{wall}\left(\frac{d}{\delta}\right) \qquad (7)$$

where $\theta_c = \left(\omega_s - \overline{\omega}\right)/\left(\omega_s - \overline{\omega}_{av}\right)$ is the nondimensional concentration.

From eqs.(6) and (7), we can obtain the following equation:

$$\frac{f}{2} = \frac{Sh\left(1-\omega_s\right)}{\mathrm{Re}}\frac{\left(\dfrac{d\left(\overline{u}/U_m\right)}{d\eta}\right)_{wall}}{\left(\dfrac{d\theta_c}{d\eta}\right)_{wall}} \approx \frac{Sh\left(1-\omega_s\right)}{\mathrm{Re}}\left(\frac{\delta_c}{\delta}\right) \qquad (8)$$

where the boundary layer thickness can be expressed as:

$$\frac{\delta_c}{\delta} = Sc^{-1/3} \qquad (9)$$

From the above analysis, the part of the latter half of eq.(1) can be obtained. The part of the former half of eq.(1) can be also obtained from the similar analysis for turbulent heat transfer.

Equations (1) and (6) shows that the mass transfer is proportional to the wall shear stress. Though it is a rough discussion, when we assume the isotropic turbulence, then

$$\tau_w \approx \tau_{turb} = \rho\overline{u'v'} \approx \rho\overline{u'^2} \qquad (10)$$

It shows that the mass transfer can be proportional to the turbulence energy.

2.2 Modeling of the turbulent region

In the above discussion, mass transfer of the straight tube is obtained, but when we consider the pipe wall thinning, we need to evaluate the mass transfer of the turbulent region such as the elbow and the downstream of the orifice. Yoneda et al.[3] takes the turbulent velocity profile near wall surface, in

which the slope is higher than the general 1/n power low, into account, and they defined the following effective friction velocity:

$$U_{\tau e} = \sqrt{\nu \left. \frac{d\{\overline{u} + c_1(\overline{u'} - c_2\overline{u})\}}{dy} \right|_{wall}} \qquad (11)$$

The mass transfer coefficient of the straight tube is expressed as follows:

$$k = \gamma \, \mathrm{Re}^{\alpha} \, Sc^{\beta} \frac{D}{d} \qquad (12)$$

The mass transger coefficient at the turbulent region, ke, is obtained from:

$$k_e = k \left(\frac{U_{\tau e}}{U_{\tau}} \right)^{\frac{\alpha(n+1)}{n}} \qquad (13)$$

To develop the prediction code of FAC, it can be convenient to obtain the ratio of the thinning rate of the turbulent region to the straight tube beforehand by using eq.(13).

To analyze the mass transfer at the turbulent region, STAR-CCM+ ver.4.04 is used. If the wall function is used, we cannot obtain the mass transfer at the turbulent region. So, realizable k-ε two layer model is used as a turbulent model, and the first mesh from the wall is set in the viscous sub-layer.

3. Flow Field and Mass Transfer

The valu of α and c1 are assumed to be 0.88 and 0.4, respectively.

Figure 1 shows the averaged flow velocity and the mass transfer coefficient. In the case of elbow, the mass transfer of the ventral side is higher, which coincides with the tendency of the FAC.

When the geometry factor is obtained from eq.(13), it becomes less than 2. Geometry factor was obtained by Keller, and one of the downstream of orifice was obtained by Nakamura et al.[4] experimentally, and the value obtained by them is higher than the analytical results of eq.(13).

We looked at the several experimental data, and found the region where FAC hardly occurred in the low mass transfer condition. So, we assumed the threshold mass transfer coefficient, below which FAC hardly occurred. Figure 2 shows the concept. As a first step, the ratio of threshold mass transfer coefficient to the mass transfer coefficient of straight tube was assumed to be 0.7 so that the geometry factor can be close to six when the ratio of orifice diameter to the internal diameter of the pipe is 0.5.

The geometry factor of the elbow is shown in Fig.3(a) as a function of the ratio of the bending diameter of the elbow to the internal diameter of it. It shows that the geometry factor is

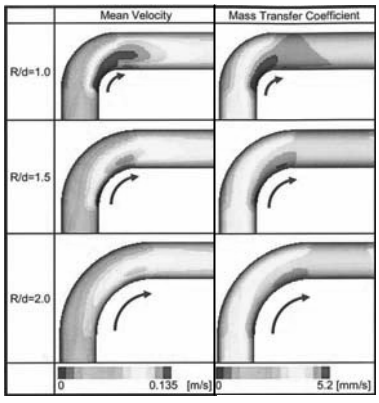

Fig.1 Contours of flow features and mass transfer coefficient near wall surface around the elbow[3]

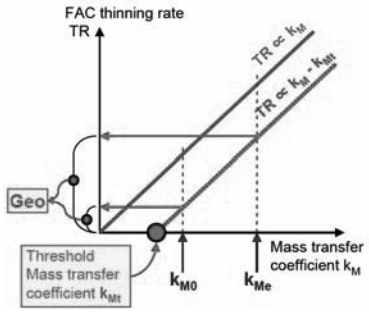

Fig.2 Concept of threshold mass transfer coefficient[3].

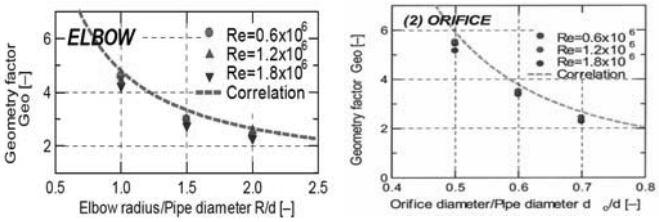

(a) Elbow. (b) Downstrema of orifice.

Fig.3 Examples of Geometry factors[3].

Table 1 Correlation of geometry factor for piping elements[3].

	Correlation for Geo	a_1	a_2	a_3	a_4	Sample values
Elbow	$a_1/(A^{a2}+a_3)+a_4$	3.8	1.2	0.0	1.0	Geo=5.0 (R/d=1.0)
Orifice	$a_1/(A^{a2}+a_3)+a_4$	0.7	2.9	0.0	0.7	Geo=6.0 (do/d=0.5)
T-union*	$a_1/(A^{a2}+a_3)+a_4B$	-10	4.0	-3.0	2.0	Geo=5.8 (d_2/d=0.8 & V_2/V_1=1.0)
T-sepa.*	$(a_1+B)/(A^{a2}+a_3)+a_4B$	1.0	1.0	0.0	2.5	Geo=6.0 (d_2/d=0.8 & V_2/V_1=1.0)

*evaluation for main pipe

decreasing with the ratio of the bending diameter of the elbow to the internal diameter of it, and the effect of Reynolds number can be small. Figure 3(b) shows the result of the orifice.

Table 1 shows the correlation equations of geometry factors of several turbulent equipments including elbow from eq.(13).

4. Concluding remarks

We proposed a method to evaluate the mass transfer at the turbulent region such as elbow and the downstream of orifice when the effective friction velocity is used, in which the turbulent velocity near wall surface is taken into account. STAR CCM+ code is used to evaluate the velocity profile in the viscose sublayer of turbulent region, and geometry factor correlations were evaluated for turbulent region. The validity of the correlation equations will be confirmed based on the experiment and the plant data in the future.

References

[1] Chilton, T.H. & Colburn, A.P., Industrial and Engineering Chemistry, Vol.26(1934)1183-1187.

[2] K. Asano, “Base and application of mass transfer, from the Fick's law to the distillation of multi-component,” Maruzen (2004) in Japanese.

[3] K. Yoneda, R. Morita, K. Fujiwara, CRIEPI Report No.09006 (2010) in Japanese.

[4] A. Nakamura, M.Murase, INSS Journal, Vol.15 (2008)p.78 in Japanese.

Eighth International Conference on Flow Dynamics
November 9 - November 11, 2011

Occurrence of Asymmetric Pipe-wall Thinning behind an Orifice by Combined Effect of Swirling Flow and Orifice Bias

Nobuyuki Fujisawa, Takayuki Yamagata, Akihiro Ito, Syo Kanno, Tsuyoshi Takano
Visualization Research Center, Niigata University, 8050 Ikarashi-2, Nishi, Niigata, Japan, 950-2181.
fujisawa@eng.niigata-u.ac.jp

ABSTRACT

In this paper, the mechanism of asymmetric pipe-wall thinning behind an orifice in a circular pipe is studied by PIV measurement for the velocity field and naphthalene sublimation method for the mass transfer coefficient. An attention is placed on the variations of velocity and mass flux under the combined effect of swirling flow and orifice bias. The present measurement indicates that the flow field becomes asymmetric about the pipe axis due to the influence of swirling flow and orifice bias, which contributes to the asymmetric distribution in the mass transfer coefficient behind the orifice.

1. Introduction

Pipe wall thinning in actual pipeline of nuclear power plant is an important topic of interest for safety management and maintenance of aged power plants. The flow accelerated corrosion (FAC) is known as one of the causes of the wall thinning in the prototype pipelines of nuclear power plants. This phenomenon often occurs in the flow behind an orifice [1], which is due to the acceleration of the mass transfer of the wall material by the flow turbulence, though the mechanism is still not clear.

The pipeline accident in the Mihama nuclear power plant in 2004 was known to be caused by FAC. Most interesting point is the asymmetric thinning in one of the pipelines behind an orifice. In order to understand the physical mechanism of asymmetric pipe-wall thinning in the pipeline, various studies have been carried out in literature [2-4], but the mechanism has not been fully clarified yet.

One of the causes of the asymmetric pipe-wall thinning can be caused by the appearance of asymmetric flow, which can be induced by the influence of the orifice bias. The velocity measurement in a square pipe behind an orifice shows that the asymmetric flow occurs even if a small bias of 0.8% of the side length exists in a square pipe [3]. According to the standard of the steel pipe, the maximum allowable eccentricity of the pipeline is known to be 0.8% of the pipe diameter. Therefore, the flow asymmetry behind the biased orifice may trigger the development of the asymmetric flow behind the orifice, which results in the asymmetric pipe-wall thinning in the prototype pipeline. On the contrary, the prototype pipeline in a nuclear power plant is composed of many curved sections, so that another topic of interest is the influence of the swirling flow caused by the secondary flows through the three-dimensional pipe loop. Therefore, the combined effect of the swirling flow and the orifice bias on the asymmetry of the flow behind an orifice has to be studied to discuss the causes of the asymmetric pipe-wall thinning in the prototype pipeline [4].

The purpose of this paper is to study experimentally the velocity field and mass flux in a circular pipe behind an orifice under the combined effect of swirling flow and orifice bias.

2. Experimental Method

The velocity measurement behind an orifice in a circular pipe under the influence of swirling flow and orifice bias is carried out in a water tunnel. The diameter of the circular pipe is 56mm and the diameter ratio of the orifice to pipe diameter is 0.6. The velocity measurement is carried out by using a standard PIV system, which consists of a CCD camera with frame straddling function (1018 × 1008 pixels with 8 bits in gray level), double pulsed Nd:YAG lasers and a pulse controller. The illumination for flow visualization was made by a laser-light sheet having 1 mm in thickness.

The mass transfer measurement behind an orifice was measured quantitatively by naphthalene sublimation method [5], which allows the evaluation of mass flux behind the orifice. Note that the mass flux is closely related to the pipe-wall thinning rate by FAC, since the FAC is considered as the diffusion of wall material into the fluid. The experimental test section behind the orifice in a wind tunnel is made by two semi-circular sections of aluminum material with groove, where the melted naphthalene at 353 K is supplied for mass transfer measurement. Then, the surface was polished by emery paper to be smooth enough from the point of hydraulics. The diameter of the pipe was 56mm and the orifice diameter ratio was 0.6. The measurement of surface roughness before and after the experiment was made by a laser displacement sensor with an accuracy of 1 μm. It should be mentioned that both experiments in water and in air are carried out at the same Reynolds number Re (= Ud/ν) =21000 for the purpose of comparison, where U is bulk velocity through the pipe and ν is the kinematic viscosity of fluid.

3. Results and Discussion

3.1 Variation of flow field behind an orifice

Figure 1 shows the streamwise mean velocity fields behind an orifice in a circular pipe, which are measured by PIV. The mean velocities are normalized by the bulk velocity U and the distance from the orifice is made dimensionless by the pipe diameter d. Each figure shows the variations of mean velocity due to the influence of swirl flow at fixed orifice bias 0.8%. The result shows mean velocity without swirl (swirl intensity S=0, Fig.1(a)), with weak swirling flow (S=0.09, Fig.1(b)) and with strong swirling flow (S=0.25, Fig.1(c)). These velocity fields are under the influence of upward bias of the orifice, that is, the shorter orifice height in the top

and longer orifice height in the bottom. The mean velocity at small orifice bias 0.8% without swirl in Fig.1(a) shows the flow acceleration along the centerline and the flow separation near the wall behind the orifice, which are typical features of the flow behind an orifice in a circular pipe. Therefore, the influence of the orifice bias is not clearly observed in the mean velocity field behind an orifice without swirl.

In the case of weak swirling-flow (Fig.1(b)), the length of the high velocity region behind the orifice is reduced, so that the reattachment point moves slightly upstream in comparison with the standard circular pipe flow without swirl. This indicates the suppression of the separation region behind the orifice due to the presence of swirling flow.

In the case of strong swirling-flow (Fig.1(c)), the mean velocity field behind the orifice changes greatly due to the combined effect of swirling flow and orifice bias. The length of the accelerating flow region is greatly reduced in comparison with that of the weak swirling-flow behind the orifice. In the strong swirling-flow, the flow asymmetry is clearly observed behind the orifice. The flow reattaches on the wall in the shorter orifice height behind the orifice, so that it leaves from the other side of the wall on the longer orifice. Therefore, the reattachment point on the upper wall moves upstream and that on the lower wall moves downstream. These results indicate that the occurrence of asymmetric flow behind the orifice due to the combined effect of strong swirling-flow and the orifice bias in the pipe flow.

3.2 Variation of mass flux behind an orifice

Figure 2 shows the Sherwood number distributions behind a biased orifice at various swirl intensities. The Sherwood number distribution without swirl shows the maximum value 400 at x/d = 1.5 behind the orifice. It should be mentioned that the Sherwood number distribution increases slightly on the shorter orifice height in comparison with that without swirl and with orifice bias. The Sherwood number distribution on the longer orifice stays almost the same level as that without swirl and with orifice bias.

When the swirling flow intensity increases to S = 0.25, the influence of the orifice bias becomes evident. The Sherwood number on the shorter orifice increases more clearly and the position of the maximum Sherwood number moves upstream (x/d = 1.0). While, the Sherwood number distribution on the longer orifice stays almost the same level as that without swirl. These results indicate that the mass transfer on the shorter orifice is enhanced, and it stays at the same level on the longer orifice. Therefore, the asymmetric pipe-wall thinning occurs behind the orifice with a certain combinations of swirling intensity and the allowable orifice bias. These results qualitatively agree with the observation of velocity field measured by PIV. Therefore, it is concluded that the allowable orifice bias can generate an asymmetric pipe-wall thinning behind

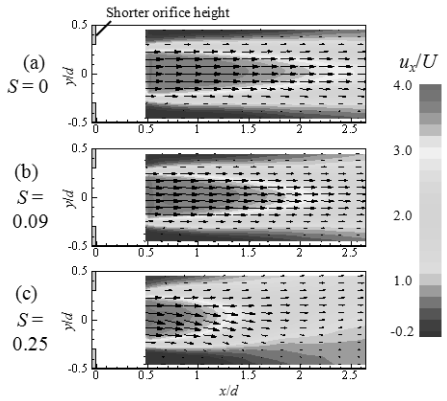

Fig.1 Streamwise mean velocity field behind an orifice

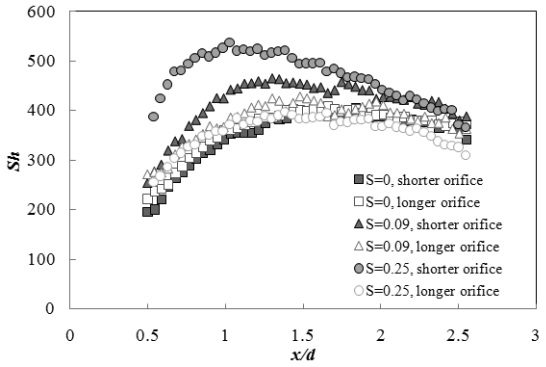

Fig.2 Sherwood number distributions behind an orifice

the orifice combined with the large swirling-flow intensity.

4. Conclusions

In order to understand the mechanism of asymmetric pipe-wall thinning in a pipe behind an orifice, the velocity measurement by PIV and the mass transfer measurement by naphthalene sublimation method are carried out under the combined effect of swirling flow and orifice bias at the same Reynolds number. The results indicate that the asymmetric velocity field can be generated behind the orifice due to the combined effect of allowable orifice bias and relatively large swirling-flow intensity 0.25. The mass flux is enhanced on the shorter orifice and suppressed on the longer orifice, which results in the occurrence of asymmetric mass flux behind the orifice.

References

[1] JSME, JSME S CA1-2005, (2005), pp. 13-47.
[2] Ministry of Economy, Trade and Industry, http://www.meti.go.jp/committee/materials/g40906aj.html.
[3] N. Fujisawa and H. Yamamoto, *Journal of Visualization*, Vol. 12, (2009), pp. 93-94.
[4] M. Ohkubo et al., *Journal of Visualization*, Vol. 14, (2011), pp. 15-17.
[5] R.J. Goldstein and H.H. Cho, *Experimental Thermal and Fluid Science*, Vol. 10, (1995), pp. 416-434.

Eighth International Conference on Flow Dynamics
November 9 - November 11, 2011

Computational Study of Liquid Droplet Impingement Erosion in Nuclear Power Plant

Jun ISHIMOTO[1],*, Shinji AKIBA[2],
Kazuhiro TANJI[2] and Kazuo MATSUURA[3]
[1]Institute of Fluid Science, Tohoku University, 2-1-1, Katahira, Aoba-ku, Sendai 980-8577, Japan
[2]Tohoku Electric Power Co., Inc., 1-7-1 Honcho, Aoba-ku, Sendai, Miyagi 980-8550, Japan
[3]International Advanced Research and Education Organization, Tohoku University, Sendai 980-8578, Japan
E-mail: ishimotojun@ieee.org

ABSTRACT

3-D structure of the high-speed liquid droplet-vapor two-phase pipe flow characteristics and LDI erosion behavior in a nuclear power plant is numerically predicted by integrated parallel CFD analysis. Governing equations of two-phase flow taking into account the condensed liquid-droplet generation, vapor-liquid phase change in conjunction with the coupled Euler-Lagrange dispersed two-fluid model were developed. Furthermore, data on such factors as the droplet impingement pressure, droplet diameter, and pipe thinning rate (erosion rate) by LDI which are difficult to confirm by experiment, were acquired.

1. Introduction

3-D structure of the high-speed liquid droplet-vapor two-phase pipe flow characteristics and LDI erosion behavior in a power plant [1] is numerically predicted by integrated parallel CFD analysis. The most important point in this study is that the liquid-droplet generation by condensation from steam vapor-phase is precisely taken into account, and the growth of the droplet diameter accompanying with the surrounding high speed vapor flow is successfully computed by phase change model.

Governing equations of two-phase flow taking into ac-count the vapor-liquid phase change in conjunction with the coupled Euler-Lagrange dispersed two-fluid model were developed. Furthermore, data on such factors as the droplet impingement pressure, droplet diameter, and pipe thinning rate by LDI which are difficult to confirm by experiment, were acquired.

2. Governing Equations

Governing equations of two-phase flow taking into account the vapor-liquid phase change in conjunction with the coupled Euler-Lagrange dispersed two-fluid model were derived as follow.

2.1 Equations of Continuum Phase (Vapor Phase)

Mass conservation equation:

$$\frac{\partial \rho}{\partial t}+\nabla\cdot\left(\rho U\right)=S_m \tag{1}$$

Momentum equation:

$$\frac{\partial\left(\rho U\right)}{\partial t}+\nabla\cdot\left(\rho UU\right)-\nabla\cdot\left[\mu\left(\nabla U+\left(\nabla U\right)^T\right)\right]=-\nabla\left(P+\frac{2}{3}\mu\nabla\cdot U\right)+S_U \tag{2}$$

Energy equation:

$$\frac{\partial \rho h}{\partial t}+\nabla\cdot\left(\rho hU\right)-\nabla\cdot\left(\alpha\nabla h\right)=\frac{Dp}{Dt}+S_h \tag{3}$$

Equation of state:

$$\rho=\rho\left(P,T\right) \tag{4}$$

where the source terms in Eqs. (1)–(3) include the effect of mass, momentum and energy transfer between droplet-phase and surrounding vapor phase. The constitutive equations of source term are derived as following equation:

$$S_m=-\left\{\sum_m^{mp}\sum_n^{nt}\left[\left(\dot{m}_p\right)_{mn}^{t+\Delta t}-\left(\dot{m}_p\right)_{mn}^{t}\right]\right\}/V_{CV}$$

$$S_U=-\left\{\sum_m^{mp}\sum_n^{nt}\left[\left(\dot{m}_pU_p\right)_{mn}^{t+\Delta t}-\left(\dot{m}_pU_p\right)_{mn}^{t}\right]\right\}/V_{CV}$$

$$S_h=-\left\{\sum_m^{mp}\sum_n^{nt}\left[\left(\dot{m}_ph_p\right)_{mn}^{t+\Delta t}-\left(\dot{m}_ph_p\right)_{mn}^{t}\right]\right\}/V_{CV} \tag{5}$$

where m_p is the droplet-phase mass generation density, U_p is the droplet-phase velocity.

$$h_p=h_b+\frac{3\left(\sigma_p-T_p\frac{d\sigma}{dT}\right)}{\rho_p r}+\frac{u_p^2}{2} \tag{6}$$

where the terms of r.h.s is the enthalpy, surface enthalpy and momentum energy.

2.2 Equations for Dispersed Phase (Droplet Phase)

Momentum equation:

$$\frac{d\left(m_du_d\right)}{dt}=-\frac{\pi D^2}{8}\rho C_D\left|u_d-u\right|\left(u_d-u\right)+m_dg \tag{7}$$

$$C_D=\begin{cases}\dfrac{24}{Re_d}\left(1+\dfrac{1}{6}Re_d^{2/3}\right) & Re<1000\\ 0.424 & Re>1000\end{cases} \tag{8}$$

$$Re_d=\frac{\rho\left|u_d-u\right|D}{\mu} \tag{9}$$

To evaluate the initially nucleated condensed droplet radius, the classical nucleation theory for water droplets from subcooled vapor to the bulk liquid is employed.

By introducing the formulation of the growth process for condensed droplets, we assume that the growth rate of a droplet is controlled by the rate at which the enthalpy of condensation can be conducted away from the droplets to the bulk liquid.[4)]
Under that assumption, the equation of the growth process for a condensed droplet is derived as following equations.

$$\frac{\partial r}{\partial t} = \frac{k_v \Delta T \left(1 - r_* / r\right)}{\rho_l h_{vl} \left(r + 1.89\left(1 - v\right)\lambda_v / Pr_v\right)} \tag{10}$$

$$\lambda_v = \frac{1.5\mu_v \sqrt{RT_v}}{p} \tag{11}$$

$$v = \frac{RT_s\left(p\right)}{h_{vl}}\left[\beta - 0.5 - \frac{2 - q_c}{q_c}\frac{\gamma + 1}{2\left(\gamma - 1\right)}\frac{RT_s\left(p\right)}{h_{vl}}\right] \tag{12}$$

Discrete Droplet Model; DDM and TAB model used in KIVA-II are applied to consider the breakup and deformation of droplet. The unsteady change of droplet radius is calculated by Eq. (10) in consideration with the vaporization and condensation rate caused by energy exchange of different phase.

2.3 Evaluation of LDI Erosion Rate

The erosion rate is evaluated as following equation.

$$E = K_m m_p f\left(\theta\right) V_p^n \tag{13}$$

where E is the erosion rate (kg/s), m_p the particle flux (kg/s), Km the material constant (m/s), θ the droplet impact angle, $f\left(\theta\right)$ the function of impact angle, V_p the particle impact velocity and superscript n the velocity exponent, normally between 2.5 and 3.0.

3. Results and Discussion

Figure 1 shows the numerical result of LDI erosion rate E and actual image of LDI erosion phenomena. The magnitude of erosion rate extensively increases around the elbow central of bent portion and actual large pipe system used in nuclear plant (A-system). The large size particle (about 2.0 mm) causes the LDI erosion by high-speed impact pressure of its inertia force. The erosion is also caused by the rebounded liquid-droplets flow around the bent section. Furthermore, erosion rate increases just downstream region of the orifice throat. It is considered that the erosion is caused by the liquid-droplets impinging which follow to the counterflow of the steam flow downstream the orifice.

The photograph in Fig. 1 (b) shows actual LDI erosion which it occurs in the elbow bent portion which is used at the nuclear power plant. By comparing the actual phenomenon with numerical result, it is found that the aspect of LDI erosion reasonably agree with both the numerical results and the actual fact.

4. Conclusion

By comparing the actual phenomenon in nuclear power plant with numerical result, it is found that the aspect of LDI erosion reasonably agree with both the numerical results and the experimental results. Therefore, the developed numerical code can be possible to predict the location of erosion occurrence and erosion rate qualitatively.

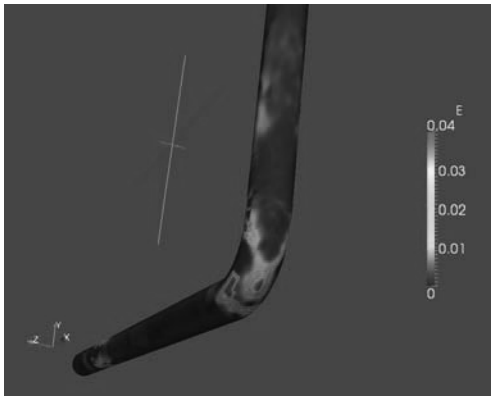

(a) Numerical result (Elbow type pipe)

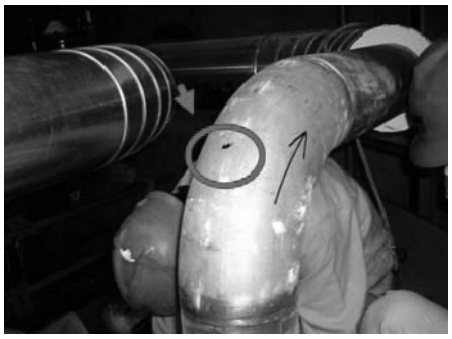

(b) Actual image of LDI erosion phenomena

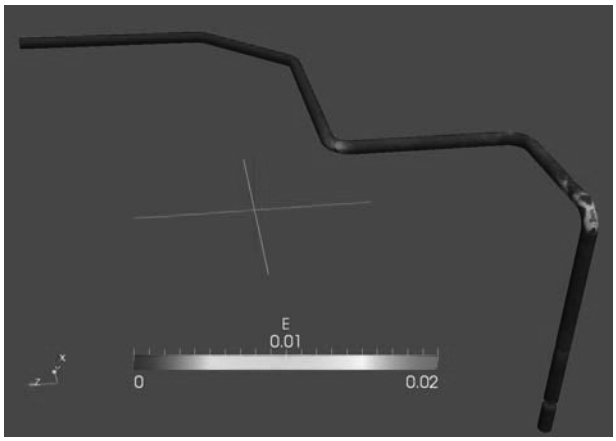

(c) Numerical result (Actual large pipe system used in nuclear plant (A-system))

Fig.1 Numerical result of LDI erosion rate and actual image of LDI erosion phenomena.

References

[1] R. Morita, F. Inada, K. Yoneda, "Development of Evaluation System for Liquid Droplet Impingement Erosion (LDI)," *ASME Conf. Proc. 2009*, 881 (2009), DOI: 10.1115/PVP2009-77557.

Eighth International Conference on Flow Dynamics
November 9 - November 11, 2011

Overview of Pipe Wall Thickness Management at Tohoku Electric Power

Hiroaki Kikkawa, Kunihiro Sato, Akira Sato
Tohoku Electric Power Co., Inc.
1-7-1 Honcho, Aoba-ku, Sendai, Miyagi 980-8550 JAPAN
kikkawa.hiroaki.zt@tohoku-epco.co.jp

ABSTRACT

At Onagawa NPS unit2, a through-hole due to droplet-impact erosion was found in the vent piping of No.2 high-pressure feedwater heater (B). Reflecting on this incident, the management system of piping wall thickness was revised, and a new support system was introduced in order to manage it surely. The same system was introduced at Higashidori NPS unit1 and demonstrated its effectiveness.

1. Introduction

Pipe wall thinning is one of the aging degradation mechanisms, which might give a significant impact on power plant safe and stable operation, and its appropriate management is a common issue for electric power companies.

In 2006, at Onagawa NPS unit 2, a through-hole due to droplet-impact erosion was found in the vent piping of No.2 high-pressure feedwater heater (B). Since then, Tohoku Electric Power Co., Inc. (Tohoku) has made efforts to improve the effectiveness of the pipe wall thickness management such as extensive revisions of the existent program and introduction of computer system.

This report addresses Tohoku's challenges on this matter.

2. Outline of pipe wall thinning in feedwater heater vent system

In May 2006, a through-hole was found in the vent piping of No.2 high-pressure feedwater heater (B) at Onagawa NPS unit2 (See Fig.1). Then this part of piping made of stainless steel was replaced with a new one. As the result of investigation, it was presumed that the through-hole was caused through pipe wall thinning mechanism due to droplet-impact erosion. Therefore, it was considered as a normal aging deterioration incident.

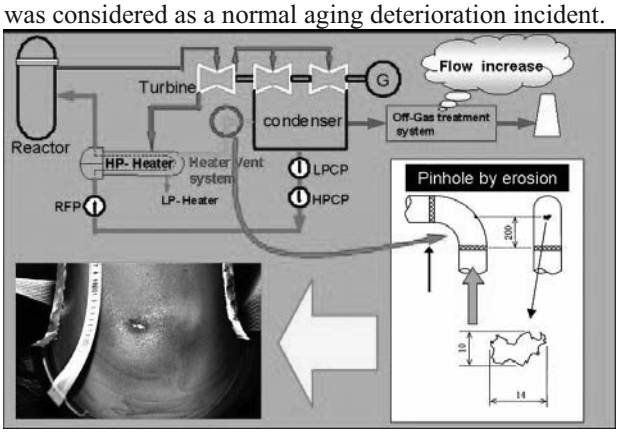

Fig.1 Schematic Diagram

Next year (2007), however, another through-hole was found at the same location of the replaced new piping. Since it was unexpected incident that the through-hole occurred in the new piping within one operational cycle, the piping inside was investigated in detail, and the incident was reconfirmed through a mock-up test. Based on those, the inferred scenario of the incident is as follows;

- There is a structural uniqueness of the heater at Onagawa NPS unit2 that the condensed water generated in the heater easily flows into the "Internal vent pipe" through "Center vent hole".
- Scales gradually accumulate on the surface of the internals, then the discharge flow of the condensed water near the vent hole is obstructed (See Fig.2).
- Water level rises, and the vent hole becomes under the level. As a result, the amount of condensed water flowing into the vent pipe increases.
- The condensed water in the vent pipe is entrained in the fast flow of steam when it went through the orifice. Then the numbers of the fast-speed droplets which collide with the piping wall increase and cause the through-hole at the elbow (See Fig.3).

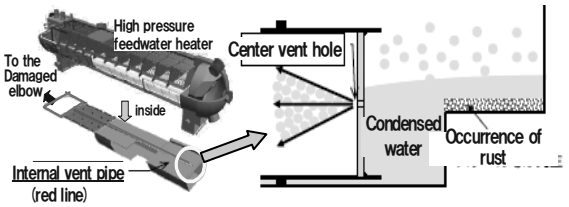

Fig.2 Center Vent Hole

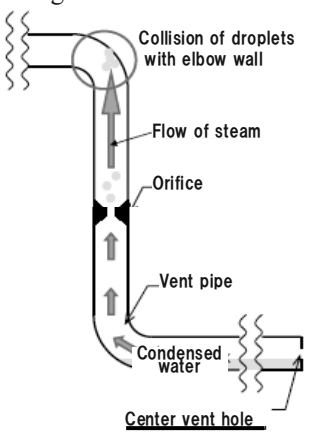

Fig.3 Collision of Droplets

As the countermeasures, the vent hole was closed to prevent the condensed water from flowing into the vent pipe, and the orifice was move to the location inside the main condenser to reduce the fluid velocity in the vent piping.

Before the initial through-hole occurred at the heater

(B), the wall thickness of the same location of the heater (A) had been already measured and shown enough thickness. This fact made the timing to measure that of heater (B) postpone though there was a difference of the piping layout which caused a different velocity.

NISA ordered Tohoku to reconfirm and improve the pipe wall thickness management and review company's quality assurance system comprehensively. The local governments also gave the same kind of request.

Although there was no outflow from the pipe because the pressure of the pipe was negative, and the through-hole itself was caused by normal erosion, the fact that a hole occurred in a pipe of NPP leaded the local society to negative response.

3. Revisions of pipe wall thickness management

Tohoku reviewed the existent procedure about pipe wall thickness management and revised the way of selecting locations to measure from sampling to all where pipe wall thinning possibly occurs. Specificaly, the locations where significant thinning is expected based on operational, structural, or material conditions are to be measured at least every 5 years, and those where thinning might occur but the potential is low are to be measured within about 15 years after the start of plant operation (See Fig.4).

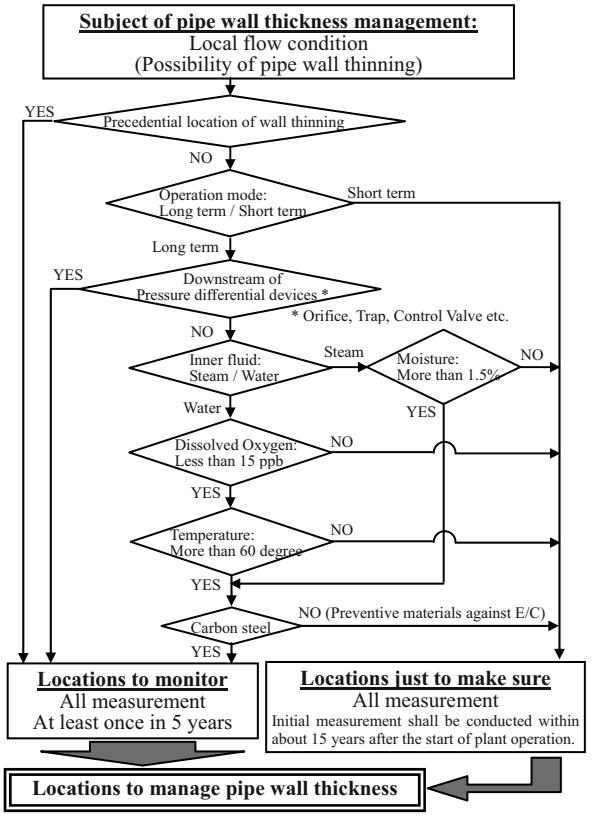

Fig.4 Flow chart for pipe wall thickness management

Consequently, though the revised management system could exclude a risk caused by sampling of measurement location, the number of locations to measure during each outage considerably increases (See Table.1).

Table.1 Number of Locations to Measure

NPS Unit	Number of Locations Total (Monitor/Make sure)	Outage (Year)	Approx. Number to Measure
Onagawa Unit 1	6,000 (800 / 5,200)	18th (2008)	2,700
		19th (2010)	600
Onagawa Unit 2	6,600 (900 / 5,700)	9th (2007-2008)	2,400
		10th (2009)	3,200
Onagawa Unit 3	7,200 (800 / 6,400)	4th (2007)	2,600
		5th (2008-2009)	1,800
		6th (2010)	700
Higashidori Unit 1	7,000 (1,300 / 5,700)	2nd (2008)	1,700
		3rd (2009-2010)	1,300

4. Activities to improve management efficiency

In order for Tohoku to ensure the revised management system and to avoid human error in dealing with enormous data, additional human resources and a computer system were introduced.

(1) Strengthening partnership with a group company

TEPEC, a group company of Tohoku, set up a special plant maintenance section in its Onagawa branch office with the cooperation of Tohoku. Tohoku sent its personnel to the section.

Both companies address issues related to plant maintenance with a close partnership and intended to improve technical skills in the entire group, namely, some part of pipe wall thickness management work was assigned to TEPEC, which had been carried out by a plant manufacturer before.

(2) Introduction of a computer system

A computer system for the pipe wall thickness management was newly introduced, which makes it possible to input on-site data directly to its server database.

Tohoku actually used this system in 4th outage at Higashidori unit1, Tohoku's another NPS. Then the followings are demonstrated;

- It can eliminate human errors, such as input or writing error, because sequential data processing from measurement to residual life evaluation is implemented without human support.
- It can balance workload during outage since it greatly reduces the time for evaluation.
- It can manage records and plans with residual life evaluation. In addition, it has a function to link the measurement point to registered engineering documents. It would be possible to use it more practically utilizing the database of the piping layout and its circumstances in future.

Continuous improvement of the system will be made for more extensive and practical use.

5. Concluding remarks

Extensive revisions were made to the pipe wall thickness management reflecting on the experience of the through-hole incident in the feedwater heater vent piping at Onagawa NPS unit 2.

Extensive revisions of the management system increased the number of measurement points during each outage and lead to the introduction of the computer system. The effectiveness was demonstrated through the actual use at Higashidori NPS unit 1. also.

Tohoku will continuously challenge to improve the effectiveness of the management system.

Eighth International Conference on Flow Dynamics
November 9 - November 11, 2011

Mechanistic Study of Combined Effect of Cr Content and Water Chemistry on FAC Rate of Carbon Steels

Hiroshi Abe and Yutaka Watanabe
Graduate School of Engineering, Tohoku University
6-6-01-2 Aoba, Aramaki, Aoba-ku, Sendai, 980-8579 Japan
hiroshi.abe@qse.tohoku.ac.jp

ABSTRACT

Combined effects of Cr content and pH on flow accelerated corrosion (FAC) rate of carbon steels have been formulated based on the results of FAC experiments. The role of Cr on FAC suppression has been discussed from the oxide layer characteristics points of view. It has been possible that the solubility of Fe_3O_4 was enhanced locally by the high H_2 partial pressure which results from the high corrosion rate. Cr concentration is highest at top surface of inner oxide layer, and that decrease inward toward the oxide / metal interface gradually. It has been suggested that Cr enrichment stabilize oxide layer (decrease solubility of oxide layer), and suppress the increase of FAC rate.

1. Introduction

Flow accelerated corrosion (FAC) of pipes made of carbon steels are understood to be chemical or electrochemical dissolution of metal under very fast mass transportation between pipe wall and bulk water, where a number of influencing parameters are involved in chemical, material, and flow dynamics aspects [1, 2]. FAC rate strongly depend on Cr content in steels, and even an impurity level of Cr in steels suppress FAC under the conditions where magnetite forms. Authors reported that combined effects of Cr content and environmental factors, i.e., pH, dissolved oxygen concentration, and flow rate on FAC rate of carbon steels have been examined by experiments and their relation to oxide scale characteristics have been discussed [3, 4]. While a number of FAC model have been proposed [1, 5], understanding the role of Cr content on FAC suppression is not well known.

In this study, combined effects of Cr content and pH on FAC rate of carbon steels have been formulated based on the results of FAC experiments. The role of Cr on FAC suppression has been discussed from the oxide layer characteristics points of view.

2. Experimentals

The carbon steels used in this study were manufactured with tailored Cr content at six levels from 0.003% to 1.01%. The rest of compositions are based on carbon steel JIS G3455 STS “carbon steel pipes for high temperature service”. The chemical compositions are summarized in Table 1. The steels were machined into small plates as big as 9.5mm x 15mm x 2mm. FAC tests were performed in low-dissolved oxygen concentration (<1ppb) water at 150 ^{o}C under 1.5MPa pressure. The experimental variables were (1) flow rate (quasi-static, or 3.0m/s), (2) pH (neutral to 10.4 at ambient temperature), and (3) test duration (325h or 1100h). FAC rate was evaluated by the weight loss of the specimens. The nanometer-scale oxide properties, e.g. thickness, defect structure, and compositional profile were investigated using transmission electron microscope (TEM) with X-ray analyzer. The thin foils for TEM observation were prepared with focused ion beam technique.

Table 1 Chemical compositions of carbon steels, wt%.

	Fe	C	Si	Mn	P	S	Cr
CS0	Bal.	0.16	0.23	0.7	0.024	0.017	0.003
CS01	Bal.	0.15	0.23	0.69	0.024	0.017	0.014
CS04	Bal.	0.15	0.23	0.69	0.023	0.017	0.043
CS1	Bal.	0.15	0.24	0.69	0.023	0.017	0.10
CS4	Bal.	0.15	0.23	0.68	0.024	0.017	0.42
CS10	Bal.	0.15	0.23	0.7	0.023	0.016	1.01

3. Results and Discussion

Combined effects of Cr content and pH on FAC rate has been evaluated by the results of FAC experiments. These results were plotted in double logarithmic chart (Fig. 1). Linear approximation of each data in Fig. 1 has been represented by the following equation;

$$\text{Log (Relative FAC rate)} = X_{Cr} \cdot \log (\text{Relative Cr content}) + \log (X_{pH}) \quad (1)$$

where, X_{Cr}: material coefficient (Cr effect), X_{pH}: environment coefficient (pH effect).

Linear approximation has been done about FAC rate of below 0.42 wt % Cr content steels (except 1.01 wt % Cr content steel), because there are slight difference in trend of Cr effect on FAC rate between below and above 0.42 wt % Cr content. Therefore, for above 0.42 wt % Cr content steels, predicted FAC rate using these coefficients might be conservative. Cr effect and pH effect plotted as a function of pH at ambient temperature in Fig. 2 suggests that X_{Cr} increase (Cr content effect on FAC mitigation decrease) continuously as pH is increased from neutral to 10.4 and pH effect on FAC mitigation increase significantly from pH 9.1 to 9.4.

Results of TEM observation and compositional analysis of cross-sectional view of oxide film on the 1.01 and 0.003 wt % Cr content specimens which examined under quasi-static water, neutral pH are shown in Fig. 3. While significant FAC did not occur in the both specimens, clear differences in oxide characteristics between the both specimens were observed. Oxides on the high Cr content specimen has duplex structure; porous outer and dense inner layer. Cr enrichment might be due to the preferential dissolution of iron oxide was observed in the inner oxide layer, and

Cr concentration is highest at top surface of inner oxide layer. On the other hand, only porous oxide layer was formed and non-uniform inward corrosion occurred on the low Cr content specimen. These characteristics indicate that corrosion resistance of oxide vary depending on the Cr content (0.003 to 1.01 wt %) even in the quasi-static water environment. Results of TEM investigation on the 1.01 and 0.003 wt % Cr content specimens which examined under flow (3.0m/s), neutral pH are shown in Fig. 4. Oxide characteristics are same as the quasi-static water environment, from the Cr enrichment and porosity in the oxide layer point of view. It is notable that porosity in the oxide / metal interface of 0.003 wt % Cr content specimens which examined under flow (high FAC rate) is significantly higher than that of the 1.01 wt % Cr content specimens. It is possible that the solubility of Fe_3O_4 was enhanced locally by the high H_2 partial pressure which results from the high corrosion rate [5]. It has also been suggested that Cr enrichment stabilize oxide layer (decrease solubility of oxide layer), and suppress the increase of FAC rate.

4. Conclusions

Combined effects of Cr content and pH on FAC rate of carbon steels have been formulated. The role of Cr on FAC suppression has been discussed from the oxide layer characteristics points of view. It is possible that the solubility of Fe_3O_4 was enhanced locally by the high H_2 partial pressure which results from the high corrosion rate. Compact inner oxide layer suppress the diffusion of oxidizer (H_2O) and Fe ion via pores. Cr enrichment stabilize oxide layer (decrease solubility of oxide layer), and suppress the increase of FAC rate.

Acknowledgement

This work was performed in the Tohoku-Hokkaido Cluster as part of the National Research Project on Ageing Management and Maintenance of Nuclear Power Plant from FY2006 to FY2009 sponsored by Nuclear and Industrial Safety Agency (NISA).

References

[1] Sanchez-Caldera, L.E., Transactions of the ASME, Journal of Engineering for Gas Turbines and Power, 110 (1988), 180-184.

[2] Cragnolino, C., Proc. 3rd Int. Symp. on Environmental Degradation of Materials in Nuclear Power Systems – Water Reactors, TMS/ASM, (1987), 397-406.

[3] Y. Watanabe, K. Sue, H. Abe, Proc. 2009 ASME Pressure Vessel and Piping Division Conference, No.78126, (2009)

[4] Y. Watanabe, H. Abe, T. Miyazaki, Proc. 2010 ASME Pressure Vessel and Piping Division / K-PVP Conference, No. 25584, (2010)

[5] G.J. Bignold, K. Garbett, R. Garnsey and I.S. Woolsey, Proc. Second Meeting on Water Chemistry of Nuclear Reactors, British Nuclear Engineering Society, London, pp.5-18, (1980).

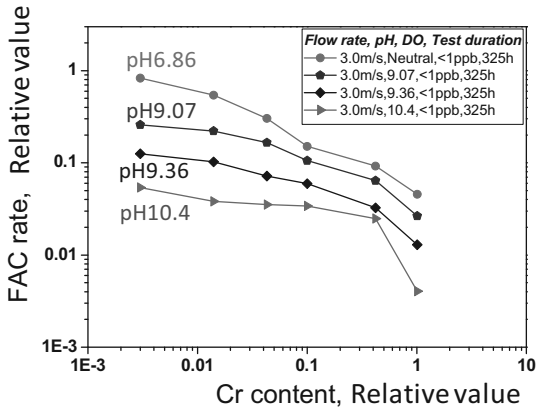

Fig.1 FAC rate plotted as a function of Cr content of carbon steels. Gradient and intercept of the linear approximation corresponding to Cr effect and pH effect, respectively.

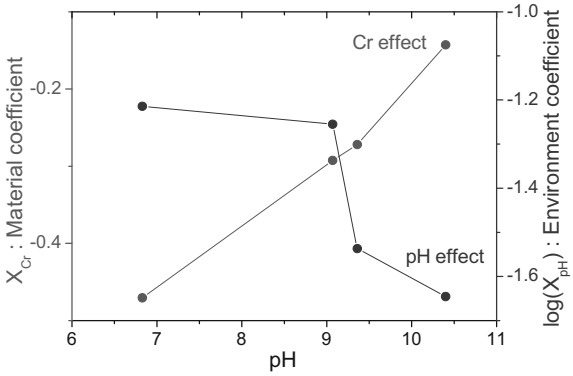

Fig.2 Cr effect and pH effect plotted as a function of pH at ambient temperature.

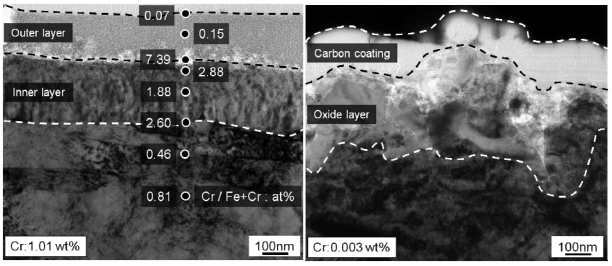

Fig.3 Results of TEM observation and compositional analysis of cross-sectional view of oxide film on the specimens which examined under quasi-static water, neutral pH.

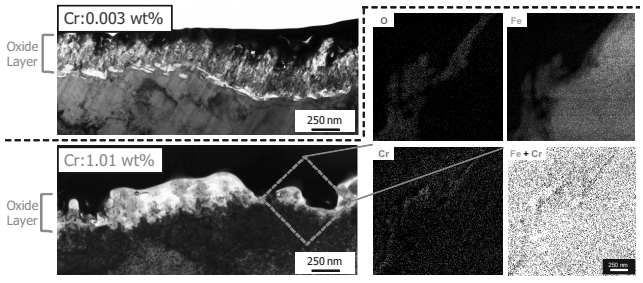

Fig.4 Results of TEM observation and EDX-mapping of cross-sectional view of oxide film on FAC specimens. (3.0m/s, neutral pH, 325h)

Eighth International Conference on Flow Dynamics
November 9 - November 11, 2011

Nondestructive Investigation of Wall Thinning in Doubled Layer Tube by Magnetic Adaptive Testing

Gábor Vértesy[1], Ivan Tomáš[2], Tetsuya Uchimoto[3], Toshiyuki Takagi[3]
[1]Research Institute for Technical Physics and Materials Science, Budapest, Hungary
[2]Institute of Physics, Praha, Czech Republic
[3]Institute of Fluid Science, Tohoku University, Sendai, Japan
E-mail of corresponding author: vertesyg@mfa.kfki.hu

ABSTRACT

A recently developed nondestructive method, called Magnetic Adaptive Testing, which is based on systematic measurement of minor magnetic hysteresis loops was applied for detection of local wall thinning in ferromagnetic tubes. It was shown that an artificially made slot can be detected with good signal/noise ratio from the other side of the specimen even through the support plate.

1. Introduction

Wall thinning is one of the most serious defects for pipes used in industry. Local wall thinning on the inner surface of a pipe in a nuclear power plant may occur due to the stream of coolant flowing inside the pipe. In Japan there is a special concern on the local wall thinning at locations under an enforcement shield that covers outside of the pipe, where a branch pipe is connected to the main one. Detection and evaluation of the thickness reduction of pipes are very important issues for the prediction of lifetime of the pipes in order to avoid severe accidents. However, because the enforcement shield and the pipe wall form two layers of metal, it is difficult to inspect inside of the pipe under the enforcement shield. None of the presently existing inspection methods gives satisfactory result in detection of local wall thinning in the case of ferromagnetic carbon steels, especially if the steel is thick or if it is layered, as in the above mentioned case.

The purpose of the present work is to apply a novel method (Magnetic Adaptive Testing, MAT) for inspection of wall thinning in layered tubes made of ferromagnetic materials. This technique is based on systematic measurement of magnetic minor hysteresis loops [1]. MAT introduces a large number of magnetic descriptors to diverse variations in non-magnetic properties of ferromagnetic materials, from which those, optimally adapted to the just investigated property and material, can be picked up.

2. Sample

Experiments were performed on a layered T-shape carbon steel tube, where the bottom tube contained an artificial slot. The measurement was performed on the tube, shown in Fig. 1.

The diameter of the larger tube is 500 mm, the smaller, perpendicular tube's diameter is 400 mm. The wall of the big tube is 20 mm thick, the cover plate is 10 mm thick. An artifial slot was fabricated in the inner side of the big tube (not seen on the picture, but it is located moreorless under the magnetizing yoke). Its area is 40x20 mm^2, and it is 10 mm deep.

3. Measurement

The tube was measured by the MAT method [1]. A specially designed Permeameter [2] with a magnetizing yoke was applied for measurement of families of minor loops of the magnetic circuit differential permeability. The magnetizing yoke was placed outside, as it is seen in Fig. 1. The yoke was C-shaped laminated Fe-Si transformer core. The legs of the yoke are 40x30 mm^2, the gap between legs is 45 mm. A magnetizing coil and a pick-up coil are wound on the legs of the core. The yoke was moved step by step along the tube's surface, perpendicular to the axis of the large tube, as indicated in Fig. 1 by the arrow, and measurements were performed at each position.

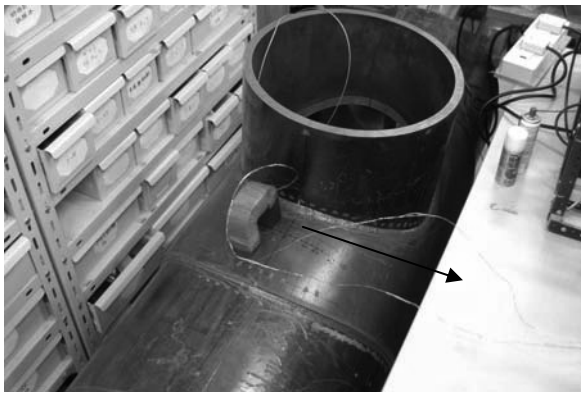

Fig. 1 Photograph of the T-shape tube with the magnetizing yoke placed on the top tube. The arrow shows the direction of movement of the magnetizing yoke (x direction).

The sample was periodically magnetized with step-wise increasing amplitudes. The experimental raw data were processed by an evaluation program, which interpolated the data into a regular square grid of elements, $\mu_{ij} \equiv \mu(h_{ai}, h_{bj})$, of a μ (permeability) matrix with a pre-selected field-step. Each μ_{ij}-element represents one MAT- degradation function of the investigated material structure variation. The consecutive series of the μ-matrices, each taken for one position of the yoke, describes the magnetic reflection of the wall thickness difference. The series of matrices are normalized by a chosen reference matrix, and arranges all the mutually corresponding elements μ_{ij} of all the evaluated μ-matrices into a table of $\mu_{ij}(x)$-degradation functions, where x is the position of the yoke along the line where it is moved.

4. Influence of the sample thickness on the measured MAT signal

Preliminary experiments were performed on flat steel plates to study what modifications of the measured signal can be expected if the compared samples have different thickness.

(a) Generally it can be expected that thick or large samples, if magnetized by a single yoke attached from one side, are magnetized less uniformly than thin or small samples. As a consequence of this, the induced signal can be expected more "blurred" ("lower and wider") on thick and large samples than on thin and small ones, where it can be expected sharp and narrow. Signal on samples of large dimensions can be understood as integrated from all the large body of the sample, where the magnetic conditions are not very uniform.

(b) However, also generally, it can be probably expected, that signal of thick and large samples will be larger than signal measured by the same magnetizing head on thin and small samples. The reason for this statement is that the cross-section of the thick and large samples is larger, i.e. their magnetic resistance is smaller. Evidently, the tendencies (a) and (b) do not work exactly in the same direction, actually they can work to some extent against each other and some work on optimization of the yoke dimensions with respect to different samples will be needed.

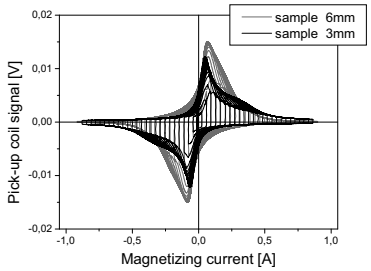

Fig.2 Sample thickness effect on MAT signal, measured on two flat plates having different thicknesses.

For checking validity of the above considerations and to see the influence of sample thickness on the measured signal, two flat samples with different thicknesses (3 and 6 mm) and the same lateral dimensions (100 mm x 100 mm) were measured by MAT. Fig. 2 shows comparison of the two samples, where the primarily measured MAT signal is shown for the two differently thick plates. As clearly seen, the signal of thicker samples is wider and larger than signal of the thinner samples. Both (a) and (b) rules hold.

These preliminary experiments verified that different signal – and different MAT degradation functions – are expected if the thickness of the measured sample slab is locally modified. These considerations mean the theoretical background of measurements, performed of the above shown tube.

5. Results

The measurement on the above described tube was performed by moving the yoke along the line indicated in Fig. 1. MAT degradation functions were evaluated as functions of the yoke position. The center of the slot is at x = 0 mm. Each MAT degradation function is normalized by the corresponding one, which belongs to the x = -60 mm position. The results is shown in Fig. 3. Significant difference was found, compared with the no-slot case if the measurement was performed above the slot. The measurement was repeated several times with identical results, demonstrating reliability and reproducibility of the technique.

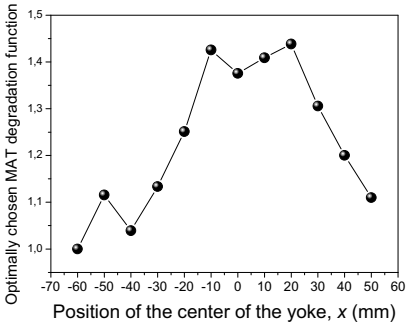

Fig. 3 Optimal MAT degradation functions vs. position of the yoke above the slot in the bottom tube.

In principle – as the worst case – it can happen that edge of the cover plate and/or existence of the perpendicular tube (which is rather close to the area of measurement) can perturb the measured permeability as a function of the yoke position. To be sure that really the existence of the inner slot was detected, the same measurement was also done on the other, symmetrical side of the perpendicular tube, where no artificial slot on the inner wall existed. In this case no difference of any MAT degradation function vs. the yoke position was detected. This was a direct and evident proof that the measurement really detected the slot.

6. Conclusions

The above outlined result illustrates that Magnetic Adaptive Testing is a suitable technique for inspection of wall thinning in thick, layered carbon steel tubes.

Acknowledgements

This study was performed as a part of "Project on enhancement of aging management and maintenance of NPPs" supported by nuclear and industrial safety agency, METI, JAPAN. The work was also supported by Hungarian Scientific Research Fund (project A08 CK 80173), by project No.101/09/1323 of the Grant Agency of the Czech Republic and by the Hungarian-Czech Bilateral Intergovernmental S&T Cooperation project.

References

[1] I. Tomáš, J.Magn.Magn.Mat., **268** (2004), 178.

[2] I. Tomáš and O. Perevertov, *JSAEM* Studies *in Applied Electromagnetics and Mechanics 9*, ed. T.Takagi and M.Ueasaka, IOS Press, Amsterdam, p.5., 2001.

Eighth International Conference on Flow Dynamics
November 9 - November 11, 2011

Can Acoustic Emission Help Monitor Damage of Pipes or Just Understand Damage Mechanisms?

Nathalie Godin, Marion Fregonese and Joël Courbon,
INSA-Lyon, MATEIS lab UMR CNRS 5510, 7 avenue Jean Capelle, 69621 Villeurbanne cedex, France
E-mail of corresponding author: joel.courbon@insa-lyon.fr

ABSTRACT

Acoustic emission is a useful tool for in situ detection of mechanical or electrochemical damage… provided there are detectable energy release events in the monitored material. Thus the energy release of some damage events is recalled and the experience on plant transfer contemplated. The feasability depends on the actual mechanisms at stake.

1. Introduction

Acoustic Emission (AE), the recording of ultrasonic waves generated inside materials undergoing damage by many types of sudden movements, has proven since the 1970s a powerful tool to survey bridges [1]. In such devices, AE was used as a yes / no alarm for cable fracture events releasing an energy far larger than the level of noise due to traffic and environment. Furthermore, the use of many sensors enabled to localise the event and help focus the safety inspection.

At lab scale, less powerful signals, by far more numerous, have been studied on materials undergoing mechanical strain and / or corrosion testing. Indeed, resonant piezoelectric sensors and an amplification / treatment chain enable to deal with very weak signals (order of magnitude : attojoule) [2]. The purpose of this paper is to summarize the main achievements and discuss transfer to industrial plant survey, including those of Mateis lab, notably in the case of pipe damage under flow.

2. Emissive mechanisms

Among the powerful sources events for AE are crack growth and desorption of an hydrogen bubble produced by corrosion [3] and its friction on the material surface. Among weaker ones: fracture of an inclusion inside a strained material [4], buildup or fracture of a surface corrosion layer, collective dislocation movements… Dissolution of matter as well as decohesion between inclusion and metal, being very smooth and progressive, appear to be silent.

Micromechanics enables to provide estimates for the energy released by source events. Among the powerful events, the desorption energy of an hydrogen bubble was estimated around 100 µJ [3]. Among weaker ones, the elastic energy release around a fractured inclusion in aluminium is around 1 µJ [4]. Only a tiny fraction of this energy release is captured by the ultrasonic sensor, but the ratio between the released and the detected energy seems to be constant in given test conditions. Comparison with a three-dimensional material investigation technique as X-ray tomography ensured that AE captured and localized well all inclusion fracture events [5].

3. Classification

Multiconstituent materials seldom damage by a single mode: many concurrent mechanisms may be at work, whether in mechanical damage (matrix voiding, fibre decohesion, fibre fracture…) or in corrosion (localised or generalised corrosion…). The collection of many events and their analysis by statistical classification methods enable to sort out classes of signals that can be assigned with reasonable probability to one mechanism [6]. Then the chronology of the trial enables to determine which type of damage is active at first and how it switches to another. Empirical links between the time at minimal AE activity and the time at fracture have been found for certain specimens. Also statistical physics approaches can be contemplated (percolation theory for instance) in order to try and determine the time at fracture before it happens [7, 8].

4. Transfer to plants

Many difficulties exist: the plant size (what is the limit distance to the sensor for the detection of an AE event?), the possible limitations on the location of sensors, the noxious influence of reactives, temperature ans vibrations on sensor integrity, and most of all the level of noise, far larger than in a laboratory trial. Thus transfer is not straightforward, and a pilot at intermediate scale may be helpful to adapt to the type of information that is actually collected in such an environment.

Nevertheless, successful transfers were reported in the case of thermal fatigue of hot furnace refractories [9], a difficult case indeed due to the noise generated by the cooling system. In the case of corrosion, the tricky case of general corrosion under flow in acid media was also successful: hydrogen bubble emission and friction on the pipe walls could be heard, and the AE activity was correlated to general corrosion at rates as low as 1 mm thickness reduction per year [10]. However, the same authors reported they failed to detect anything significant in a flow at neutral pH.

5. The case of pipe thinning

Flow-accelerated corrosion has many different aspects, one being dissolution and removal of corrosion layers by flow (which should be fairly silent), the other one involving erosion by particles in the flow. The former case matches the one studied at Mateis [10] and may provide AE signals in acid flows where hydrogen bubbles are emitted, and probably not in neutral flows.

The latter has also been studied and induces a specific AE activity proportional to flow velocity, distinct from the AE activity of hydrogen bubbles [11]. Thus there are good hopes that it can be traced.

Finally it must be underlined that so far just discontinous acoustic emission (ultrasonic bursts) has been considered. Continuous acoustic emission also exist, for instance through the flow of liquid inside the pipe, and modifications of boundary conditions due to corrosion may affect this flow and perhaps the continous emission. A recent paper claims that a time / frequency analysis of the continously recorded signal may discriminate between a condition of flow-accelerated corrosion and a sane condition [12]. So why not try AE monitoring, at least on a pilot scale, all the more as the ultrasonic detectors can occasionally be used as emitter - receiver so as to monitor damage by alterations of the transmitted signal?

References

[1] J.L. Robert, M. Brachet-Rolland, Proc. Symp. of the International Association of Bridges and Structural Engineering (IABSE), IABSE report n°39, Zürich (CH), 1982.
[2] S. Yuyama, T. Kishi, J. Acoust. Emission (2009), 71-93.
[3] Y. P. Kim, M. Fregonese, H. Mazille, D. Feron, G. Santarini, Corrosion Science, 48 (2006), 3945-.
[4] V. Carmona, PhD thesis, INSA (2009).
[5] E. Maire, V. Carmona, J. Courbon, W. Ludwig, Acta Materialia, 55 (2007), 6806-.
[6] N. Godin, S. Huguet, R. Gaertner, L. Salmon, NDT&E Internat., 37 (2004), 253-264.
[7] S. Momon, M. Moevus , N. Godin, M. R'Mili, P. Reynaud, G. Fantozzi, G. Fayolle, Composites Part A : Appl. Sci. Manuf., 41 (2010), 913-918.
[8] J.-C. Anifrani, C. Le Floc'h, D. Sornette, B. Souillard, J. Physique, 5 (1995) 631-638.
[9] F. Thummen, PhD thesis, INSA Lyon (2004).
[10] L. Jaubert, M. Fregonese, D. Caron, F. Ferrer, C. Franck, E. Gravy, P. Labeeuw, H. Mazille, L. Renaud, Insight, 47 (2005), 465-471.
[11] F. Ferrer, H. Idrissi, H. Mazille, P. Fleischmann, P. Labeeuw, Wear, 231 (1999), 108-115.
[12] M. Koula, M. Drab, M. Havavka, PowerPlant Chemistry, 6 (2010).

Reconstruction of Stress Corrosion Crack with Multi-frequency ECT Signals

Zhenmao Chen[1*], Shejuan Xie[2], Li Wang[1], Tetsuya Uchimoto[2] and Toshiyuki Takagi[2]
[1]State Key Laboratory for Strength and Vibration of Mechanical Structures, Xi'an Jiaotong University, 28 West Xianning Road, Xi'an, 710049, China
[2]Institute of Fluid Science, Tohoku University, Katahira 2-1-1, Aoba-ku, Sendai, 980-8577, Japan
*Corresponding Author, Tel/Fax: 86-29-82668736; E-mail: chenzm@mail.xjtu.edu.cn

ABSTRACT

In this paper, the signal of Pulsed Eddy Current Testing (PECT) is applied to the reconstruction of deep Stress Corrosion Cracks (SCC) based on the multilayer reconstruction strategy in order to improve the sizing accuracy of SCC. The shape profiles and conductivity of the crack at different depth are reconstructed step by step by using harmonic components of different order of the PECT signals. The profiles of several cracks are reconstructed from simulated signals of conductive notches of an artificial SCC. It is demonstrated that the PECT signals are applicable for the reconstruction of SCC.

1. Introduction

In regular Nondestructive Testing (NDT) for a key structural component of Nuclear Power Plants (NPP), it is necessary to quantitatively evaluate the crack profile especially the depth in order to select a proper maintenance strategy. Recently, Eddy Current Testing (ECT) shows a possibility for crack sizing. Traditional ECT technique is of single frequency excitation. Sizing of natural cracks using ECT often gives under prediction in crack depth especially for Stress Corrosion Cracks (SCC) because of their complicated microstructures.

To improve the sizing precision, a multilayer inversion strategy has been proposed to reconstruct the deep SCC by using multiple frequency ECT signals [1]. To measure ECT signals of multiple frequencies, however, times of ECT inspections have to be performed and sometime the probe also needs to be changed. As it is difficult to keep testing conditions just the same for different inspection, the reconstruction accuracy may be affected by this problem.

Pulsed Eddy Current Testing (PECT) technique [2] is a relative new NDT tool. As its excitation current is in form of a pulse, PECT signals have rich frequency information and can catch information from relative deep position of inspection target. Recently, it is proved by authors that the PECT signal from a local defect is just a superposition of multiple frequency ECT signals [3]. In other words, multiple frequency signals can be obtained from the PECT signal by using spectrum analysis. As the signals of different frequency can be obtained in the same time, the testing conditions problem just mentioned above can be avoided.

In this paper, a scheme is described for sizing deep SCCs based on the multilayer reconstruction strategy by using the PECT signals. Numerical implementation and validations are also presented.

2. Simulation method for PECT Signals

To calculate PECT signal, a code of the time domain integration method based on the Ar formulation is developed. The constant time step Crank-Nicholson method is adopted to solve this transient eddy current problem. Through Galerkin FEM discretization, the governing equations of electromagnetic field of the Ar formulation can be expressed as,

$$[\mathbf{K}]\{\mathbf{A}\}+[\mathbf{C}]\left\{\frac{\partial \mathbf{A}}{\partial t}\right\}=\{\mathbf{M}\}\,\mathrm{I}(t), \tag{1}$$

where I*(t)* is the time variation function of excitation current, [**K**], [**C**] are the global FEM coefficient matrices. For transient problem, the derivative term $\partial \mathbf{A}/\partial t$ can be replaced by using time difference $(\boldsymbol{A}^k-\boldsymbol{A}^{k-1})/\ t$ with $\boldsymbol{A}^k=\boldsymbol{A}(t_0+k\ t)$, k the *k-th* time step, t the time step length, and t_0 is the initial time. In order to improve the integration stability, the Crank-Nicholson direct integration method replaces the vector $\boldsymbol{A}$ by

$$\mathbf{A}=\theta\mathbf{A}^{k-1}+(1-\theta)\mathbf{A}^{k}, \tag{2}$$

where $(0\leq\ \leq 1)$ is a coefficient constant to control the stability of the integration. By substituting equation (2) into equation (1), the vector potential $\boldsymbol{A}$ at present time step (k step) can be calculated through

$$\begin{aligned}&\left[[\mathbf{K}](1-\theta)\Delta t+[\mathbf{C}]\right]\{\mathbf{A}^k\}\\&=\Delta t\{\mathbf{M}\}I(t_0+k\Delta t)+\left[[\mathbf{C}]-[\mathbf{K}]\theta\Delta t\right]\{\mathbf{A}^{k-1}\}.\end{aligned} \tag{3}$$

Following the formulae described above, a numerical code has been developed based on an edge element code of Ar formulation to calculate the PECT signals. The validity of the PECT code has been verified by calculating conventional ECT signals whose excitation current was set as sinusoidal wave. Both the amplitude and phase of the signals can be properly calculated.

3. Correlation of ECT and PECT signals

As well known, a square-wave can be represented by a summation of a series of sinusoidal waves approximately. Therefore, PECT signal can be considered as a summation of pickup signals due to the excitation of single sinusoidal waves of different frequencies as the electromagnetic field in the material is in the linear range for normal PECT problem. On the other hand, to know the signal due to a single frequency excitation, one only needs to get the signal of the corresponding harmonic component from the PECT signal. Supposing that the probe excitation current I*(t)* is of a square wave with $1/f_0$ period, 50% duty, and A_0

amplitude, the excitation current can be represented by a series of sinusoidal waves as

$$I(t) = A_0 / 2 + \sum_{n=1,3,5,\cdots} 2A_0 \sin(2n\pi f_0 t) / n\pi, \quad (4)$$

with n being the order of harmonic component. If denoting the response PECT signal due to current $I(t)$ as $P(t)$, it can be expressed as the following series,

$$P(t) = \sum_{n=1,3,5,\cdots} \left[P_a^n \sin(2n\pi f_0 t) + P_b^n \cos(2n\pi f_0 t) \right], \quad (5)$$

where the coefficient P_a^n, P_b^n can be obtained from the PECT signal through Discrete Fourier Transformation (DFT). Comparing equation (4) and (5), the real and imaginary part R_n, I_n of ECT signal due to unit excitation current of the *n-th* harmonic frequency, i.e., the ECT signal of frequency nf_0, can be obtained as

$$R_n = n\pi P_a^n / 2A_0, \quad I_n = n\pi P_b^n / 2A_0. \quad (6)$$

Following the procedure above, a numerical program is developed based on the Ar code to calculate multi-frequency ECT signals from PECT response. To show the validity of the proposed method and corresponding code, ECT signals of frequency from 19 kHz to 399 kHz due to a surface crack of 14 mm length, 4 mm depth and 0.2 mm width in a SUS304 plate are calculated by using the PECT approach. In Fig.1, the pickup signal of the ECT was selected as the magnetic flux density field at the bottom center of the excitation coil. Comparing with the ECT signals obtained with the conventional single frequency ECT code (FEM-BEM hybrid code), good agreements can be observed that proves the feasibility of the proposed approach.

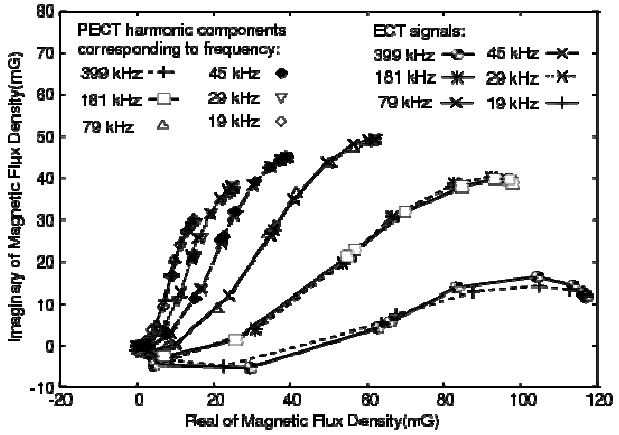

Fig. 1 Comparison of harmonic components of PECT signals and ECT signals of corresponding frequency

4. Multilayer Inversion Scheme for Deep SCC

If we subdivide the inspection target plate into many layers of same thickness, the crack signal of high excitation frequency mainly depends on crack profile at the near surface layers due to the skin effect. Therefore, if the crack profile at the surface layers has been obtained properly by using signals of high frequency, a signal of smaller frequency is more suitable for the reconstruction of the crack profile at deeper layers. In this way, the sizing accuracy is possibly to be improved by using signals of multiple frequencies.

In practice, the depth of multiple layers is set as a constant value referring to the skin depth of the highest selected excitation frequency, while the crack conductivity and length can be different in different layers. Though both the crack width and the crack conductivity affect the crack signal, the crack width can be taken as a constant for all crack segments if we consider the crack conductivity as an equivalent parameter to be determined [4].

In the layering analysis method, the crack profile of the top layer is predicted by adopting ECT signals of high frequency and the conventional ECT inversion scheme developed by authors [1]. By utilizing information reconstructed at top layers, the crack profiles of deeper layers can be evaluated by using signals of lower frequency step by step.

Based on the proposed inversion strategy, profiles of SCC models are reconstructed by using the components of simulated PECT signals. 10% of white noise is added to the signals to consider the applicability for practical problem. Figure 2 shows a numerical result for a conductive crack of complicated shape. Comparing with the conventional method, the sizing precision is improved. In addition with other results that can not be shown here due to page limitation, the proposed strategy is proved applicable for SCC sizing and can improve sizing precision.

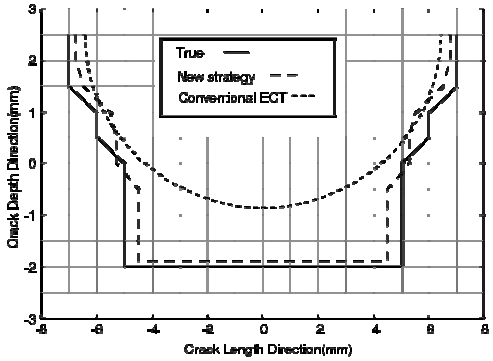

Fig. 2. A results of multilayer strategy for deep crack reconstruction

5. Conclusions

In this paper, a spectrum analysis technique and layering scheme are proposed for the reconstruction of deep SCC from PECT signals. The validity of the proposed scheme is proved through reconstruction of several conductive notch cracks and an artificial SCC.

Acknowledgements:

This work is supported in part by the NSFC (No. 50977070, 11021202), the National 973 Program of China (No.2007CB707702, No.2011CB610303) and the National Magnetic Confinement Fusion Science Program of China (No. 2009GB104002).

References

[1] L. Wang, Z. Chen, Int. J. Appl. Electromagn. Mech., Vol.33, 1017-1023, 2010.
[2] A. Sophian and et al., NDT&E Int., Vol.36, 37-41, 2003.
[3] S. Xie, Z. Chen, T. Takagi, T.Uchimoto, IEEE Trans. Mag., 2011, (in press)
[4] N. Yusa, Z. Chen and K. Miya, NDT&E Int., Vol.20, 103-114, 2005.

Eighth International Conference on Flow Dynamics
November 9 - November 11, 2011

Online Monitoring of Pipe Wall Thinning using Electromagnetic Acoustic Resonance

Ryoichi URAYAMA *[1], Tetsuya UCHIMOTO *[1], Toshiyuki TAKAGI *[1] and Shigeru KANEMOTO *[2]
*[1] Institute of Fluid Science, Tohoku University, 2-1-1Katahira, Aoba-ku, Sendai 980-8577, Japan
*[2] School of Computer Science and Engineering, The University of Aizu, Japan
E-mail: takagi@wert.ifs.tohoku.ac.jp

ABSTRACT

In this study, the electromagnetic acoustic resonance (EMAR) method and the superposition of the nth compression (SNC) for data processing are applied to online monitoring of pipe wall thinning. Furthermore, the accuracy and stability of the measurements are evaluated through field tests using a large-scale corrosion test loop at high temperature. To measure the thickness of pipes with complicated wall thinning, the SNC extracts thickness information from the spectral responses of the EMAR. Results from two months of monitoring show that EMAR with SNC can evaluate pipe wall thinning with an accuracy of a few μm at 165°C.

1. Introduction

The management of nuclear and thermal power plants has generally been achieved through time-based maintenance for pipe wall thinning which occurs as a result of aging. However, recently, to ensure the safety and reliability of the plant's maintenance actions, in addition to shutdown inspections, condition-based maintenance using online monitoring is required, which can identify operational trends in pipe wall thinning.

The electromagnetic acoustic transducer (EMAT) method, which is one of ultrasonic measurement techniques, provides non-contact measurements, since ultrasonic waves are transmitted and received electromagnetically [1]. Because of this advantage, the method is often applied to measurements in a high temperature environment [2, 3]. The electromagnetic acoustic resonance (EMAR) method, which is based on the phenomenon of resonance in the ultrasonic waves propagating in the material, can evaluate the thickness from the resonant frequency intervals. However, it is sometimes difficult to evaluate the thickness of thinning pipe walls. Because the ultrasonic waves are scattered by the incline of the bottom, the amplitudes of the resonance spectrum reduce and peaks of multiple resonant frequencies appear. Consequently, the authors propose the use of the superposition of nth compression (SNC), for evaluating the thickness of a curved bottom surface at room temperature [4].

In this study, EMAR with SNC for the data processing method is applied to online monitoring of pipe wall thinning, and the accuracy and stability of measurement is discussed through field tests using a large-scale corrosion test loop at high temperature.

2. Method

The transducer usually consists of magnets and transmitter and receiver coils. When the coil is driven by a current at the desired ultrasonic frequency, eddy currents are induced in the near surface of the target of the electrically-conducting material. Since a static magnetic field is provided by the magnet, these currents experience Lorentz forces, and a shear wave propagates in the target. Reception of the round-trip waves can be made in a reverse process to that described above.

The principle of using EMAR is based on the through-thickness resonances of the bulk waves [5]. When a transducer is placed on the surface of a plate of thickness d, and transmits a burst of ultrasonic waves with wavelength λ, propagated normal to the surface, the waves reflect repeatedly from both surfaces and are received by the transducer for each burst. Resonance is then observed when the wavelength satisfies $n\lambda = 2d$. The resonance frequency of the nth order is given by

$$f_n = n v / 2 d \tag{1}$$

where v is the sound velocity. Resonance frequencies are identified by sweeping the ultrasonic frequency.

In an ideal spectrum, the resonance peaks appear at every resonance frequency which is equal to the integral multiple of the fundamental resonance frequency. If the frequency axis of the original spectrum is compressed into the nth order resonance frequency, the nth peak moves to the fundamental resonance frequency. Summing up the spectra of the nth compression, the largest peak should appear around the fundamental resonance frequency. Finally, the thickness is evaluated as

$$d = \frac{v}{2 f_1}$$

$$f_1 = \arg\max_f \left\{ \sum_n x\left(\frac{f}{n}\right) \right\} \tag{2}$$

However, the fundamental resonant frequency varies with thickness and sound velocity. Hence, the degree of the resonance frequencies appearing in the test frequency range varies with the thickness and sound velocity. The sound velocity varies with a temperature environment and a test material. If the material under test has a wall thickness of 5.0 mm and the sound velocity is 3240 m/s, the resonant frequency is 324 kHz. Thus the degrees of resonance frequencies range from 5 to 10 in the test frequency range of 1.5 – 3.5 MHz. In addition, it is possible to evaluate the thickness to about a 4 μm resolution for a 5.0 mm thickness using SNC.

3. Experiment and Results

A pulser/receiver (RITEC RPR-4000), a wide range

decade filter (NF Corporation FV-628B) as the filter in the detection frequency, an oscilloscope (TEKTRONIX DPO4104), and a PC for data collection were used in the measurements. The transducer was driven by burst signals with a period of 100 μs. The driving frequency was swept from 1.5 to 3.5 MHz at intervals of 10 kHz. The signal amplitude of each frequency was computed using super heterodyne processing at intervals of 1 kHz.

The test pipe was carbon steel piping (JIS STPT370) of 50A Sch80, with a 60.5 mm outer diameter, a 5.5 mm nominal thickness and 1350 mm long. Fluid flows from the bottom to the top of the test pipe, which has an orifice and an elbow in the upstream position and a U-shaped pipe in the downstream position. Thus, it is possible to accelerate the pipe wall thinning due turbulent flow in the test pipe.

The experiment was carried out over two months at a temperature of 165°C. One probe was attached about 700 mm from the edge of the orifice.

Figure 1 shows the relationship between the elapsed time and wall thickness at high temperatures during operation, using the corrosion test loop for the first test. The results show that there is a clear correlation between the elapsed time and the thinning trend. The wall thinning was evaluated to be 0.18 mm, which was obtained from the difference between the initial thickness of 5.42 mm and final thickness of 5.24 mm.

The final thickness, which was measured by cutting a cross section of the actual test pipe after the test and using a microscope, was 5.18 mm. The difference in the final thickness was 0.06 mm, which is within an acceptable range compared with the error range of ±0.1 mm for the ultrasonic thickness meter.

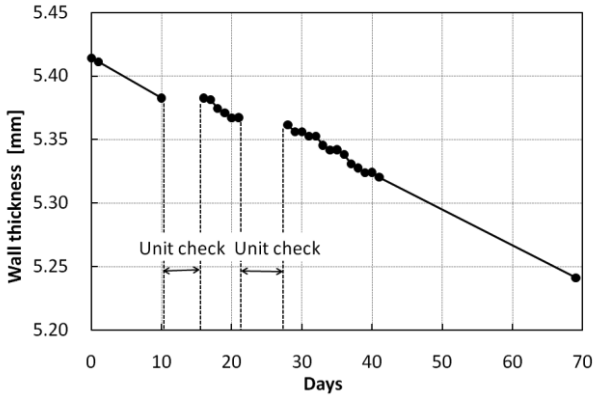

Fig. 1 Measurement result.

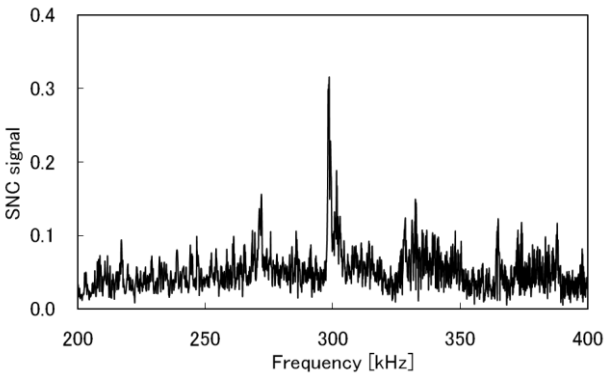

Fig. 2 Signal of the SNC at the 68th day.

Figure 2 shows the signal of the SNC on the 68th day. A fundamental resonance frequency peak emerges sharply around 300 kHz. This peak indicates that there is no inclination in the determination area, since a closely adjacent group of resonance peaks emerge sharply around 300 kHz if this was not the case.

4. Concluding remarks

In this study, EMAR and SNC were applied to online monitoring of pipe wall thinning. In addition the accuracy and stability of measurement was evaluated through field tests using a large-scale corrosion test loop at a high temperature of 165°C.

The results show that it is possible to assess wall thinning inclination over time during the measurement period. Moreover, the difference between the measured thickness and real thickness was 0.06 mm at end of the test. EMAR with SNC, which is able to assess accuracy to a few μm thickness, can accurately evaluate the rate of wall thinning.

Furthermore, by measuring over a long period, EMAR can contribute to elucidating the mechanism of wall thinning.

Acknowledgements

This study was performed as part of the "Project on the management and maintenance of the aging of NPPs" supported by the Nuclear and Industrial Safety Agency, METI, Japan. The study was also supported by the Tohoku University Global COE Program, "World Center of Education and Research for Trans-disciplinary Flow Dynamics". The corrosion test loop was provided by the Tokyo Electric Power Company.

References

[1] R. B. Thompson, Physical principles of measurements with EMAT Transducer, Physical Acoustics Vol.XIX, Academic Press Inc., (1990), 157-200.

[2] N. Yamagata, M. Takahashi and N. Ahiko: Thickness Measuring Technology for Pipes of Thermal Power Plants, Toshiba Review (in Japanese), 63 (4), (2008), 46-49.

[3] R. Urayama, T. Uchimoto, T. Takagi, Application of EMAT/EC Dual Probe to Monitoring of Wall Thinning in High Temperature Environment, International Journal of Applied Electromagnetics and Mechanics, Vol.33, (2010), 1317-1327.

[4] R. Urayama, T. Uchimoto, T. Takagi, S. Kanemoto, Quantitative Evaluation of Pipe Wall Thinning by Electromagnetic Acoustic Resonance, E-Journal of Advanced Maintenance Vol.2, (2010/2011) , 25-33.

[5] M. Hirao and M. Ogi, EMATS for Science and Industry: Non-contacting Ultrasonic Measurements, Kluwer Academic Publishers, (2003).

Eighth International Conference on Flow Dynamics
November 9 - November 11, 2011

Three Dimensional Wall Thinning Defect Reconstruction from Pulsed Eddy Current Testing Signals

Shejuan XIE[1], Zhenmao CHEN[2], Xiaowei WANG[2], Li WANG[2, 3], Toshiyuki TAKAGI[1] and Tetsuya UCHIMOTO[1]
[1]Institute of Fluid Science, Tohoku University, 2-1-1 Katahira, Aoba-ku, Sendai 980-8577, Japan
[2]State Key Lab. for Strength and Vibration, Xi'an Jiaotong University, Xi'an 710049, China
[3]College of Science, Xi'an Posts and Telecommunications Institute, Xi'an 710121, China
Corresponding author: Toshiyuki TAKAGI, takagi@ifs.tohoku.ac.jp

ABSTRACT

In this paper, an inversion algorithm has been proposed and validated, based on a fast simulator of pulsed eddy current testing (PECT) signals and a deterministic optimization strategy, for the profile reconstruction of wall thinning in pipes of nuclear power plants. Local wall thinning is modelled as a group of planar defects with different length and depth, reconstructed from two-dimensional PECT signals. Through inverse analysis of simulated signals, the efficiency of the proposed algorithm has been demonstrated.

1. Introduction

In nuclear power plants (NPPs), local wall thinning is one type of pipe defect caused by flow accelerated corrosion and/or liquid droplet impingement on the inner side of the coolant pipes. Although there is sufficient thickness margin in the initial design of the pipe thickness, when wall thinning becomes serious, it may lead to very dangerous consequences, such as leakage. Therefore, to guarantee the integrity of NPPs, periodic non-destructive testing (NDT) is mandated to evaluate wall thinning. Another important issue is to check whether the wall thinning exceeds the safe tolerance range. This can not only guarantee safety but also save on unnecessary renewal of pipes. This requires a so called quantitative NDT (QNDT) method. However, the defect profile characterization of pipe wall thinning in NPPs has so far not been studied.

Recently, the pulsed eddy current testing (PECT) method has been considered as a promising candidate for the detection of wall thinning. PECT method shows many advantages over conventional ECT method due to its application of large excitation currents and rich frequency components. Also, a high efficiency 3D numerical tool (a fast forward solver) [1] to simulate PECT signals has recently been developed. This 3D tool employs a similar strategy to that developed for the fast simulation of ECT signals, a database strategy and a frequency domain summation scheme. These give a good basis for quantitative wall thinning analysis based on inversion techniques.

Inversion analysis reconstructs the size of a defect from the measured signal, which is the reverse method to forward analysis (that is, get the signal from the known defect shape). Inversion techniques include several methods, such as the deterministic approach, the artificial intelligence approach and the stochastic approach.

In this paper, an inverse analysis scheme is proposed and validated for the sizing of pipe wall thinning in NPPs, based on a deterministic optimization strategy and the fast PECT signal simulator developed by the authors [1].

The contents of this paper are arranged as follows: first, the fast forward simulator for prediction of PECT signals is briefly demonstrated. Second, the model of wall thinning and the principle of the inversion algorithm are explained. Finally, one reconstructed example, using simulated data, is given to show the validity of the inversion algorithm.

2. Fast simulator for PECT signals

In PECT, the transient response signal due to the pulsed excitation can be obtained through a summation of response signals due to excitations of a series of single harmonic frequency with corresponding coefficients by using Eq.(1).

$$\boldsymbol{B}(\boldsymbol{r},t)=\sum_{n=1}^{N}F_n\boldsymbol{B}_n(\boldsymbol{r})e^{\mathrm{j}\omega_n t}\ , \tag{1}$$

where $\boldsymbol{B}(\boldsymbol{r}, t)$ is the transient pulsed response signal at position r, $\boldsymbol{B}_n(\boldsymbol{r})$ is the response signal due to excitation of harmonic frequency ω_n at position $\boldsymbol{r}$ and F_n is the Fourier transformation coefficient of the pulsed excitation signal.

To simulate PECT signal based on Eq.(1), $\boldsymbol{B}_n(\boldsymbol{r})$, the response signal due to single frequency excitation, has to be obtained in advance. In this work, the database approach for fast simulation of ECT signals has been imported for the simulation of the single frequency signals. To deal with wall thinning of 3D (3 dimension) geometry, the conventional fast simulator for 2D defect has been upgraded with help of an interpolation strategy. Through comparing with the numerical results of the full FEM analysis, it was demonstrated that the proposed fast simulation scheme is of high accuracy and over 100 times faster.

3. Principle of inversion algorithm and results

In this study, sizing of wall thinning is conducted based on the inverse analysis strategy, which converts the sizing process to an optimization problem of minimizing the objective function,

$$\varepsilon(\boldsymbol{c}^k)=\sum_{l=1}^{L}\sum_{m=1}^{M}\left|P_{l,m}(\boldsymbol{c}^k)-P_{l,m}^{obs}\right|^2\ , \tag{2}$$

where k means the iteration step, l and m represent the position of 2D scanning point, $\boldsymbol{c}^k$ the shape parameter vector of wall thinning after k-th iteration, $\varepsilon(\boldsymbol{c}^k)$ the objective function (residual error), $P_{l,m}(\boldsymbol{c}^k)$ the feature parameter (this study, peak value is employed) extracted from the PECT signal $\boldsymbol{B}(t)$ at (l, m) scanning point for defect shape $\boldsymbol{c}^k$, and $P_{l,m}^{obs}$ is the corresponding measured signal.

As shown in Fig. 1, the local wall thinning was modelled as a group of planar slit defects (rows) of given width but with different length (for example, in the w-th row, length of wall thinning equals bw-aw) and depth (in the w-th row, depth of wall thinning to total thickness of specimen is dw (%)), which are selected as the defect shape parameters to be reconstructed. As these parameters have to be reconstructed at the same time, 2D PECT signals (Probe scans along the length and width direction in Fig. 1) scanned over the wall thinning in the far side are used for the reconstruction. In cases where the defect length and depth are close to 0 in some rows after reconstruction, then these rows will be treated as unflawed region. In this way, the width information of the wall thinning can also be properly reconstructed.

The conjugate gradient based reconstruction scheme [2] is employed to predict the lengths and depths of each row. In this study, Eq. (3) is adopted for the direct calculation of gradient vector from the calculated electric fields for the TR type PECT probe [3].

$$\frac{\partial B(\boldsymbol{r},t)}{\partial c_{w,i}} = -\sigma_0 \times \sum_{n=1}^{N} F_n \left(\alpha \int_S \boldsymbol{E}_p^u \cdot (\boldsymbol{E}_e^u + \boldsymbol{E}_e^f) \frac{\partial s_w(\boldsymbol{c},\boldsymbol{r})}{\partial c_{w,i}} ds \right) e^{j\omega_n t}, \quad (3)$$

where, σ_0 is the conductivity of specimen in unflawed region, $\boldsymbol{E}_p^u$ is the unflawed electric field generated by unit current in the pickup coil, $\boldsymbol{E}_e^u + \boldsymbol{E}_e^f$ is the flawed electric field generated by excitation coil (including unflawed and perturbed field), α is a coefficient to correspond the output of pickup coil and the PECT signal, $c_{w,i}$ is the i-th wall thinning shape parameter at the w-th planar row in width direction and $s_w(\boldsymbol{c},\boldsymbol{r}) = 0$ is the equation of the defect boundary surface in w-th row.

According to above theory, a reconstruction program has been developed. Figure 2 shows an example of the reconstructed result of wall thinning with 3 rows in width direction after reconstruction of 40 steps iteration. In this case, the initial crack shape parameter is (a1: -1, b1: 2, d1: 10%; a2: -1, b2: 2, d2: 10%; a3: -1, b3: 2, d3: 10%). We can see that the size of the wall thinning was properly reconsctructed.

4. Concluding remarks

An inversion algorithm is proposed based on a fast simulator of pulsed ECT signals and a deterministic optimization strategy. Numerical results show that the profile of the wall thinning can be properly reconstructed by using this inversion scheme.

Acknowledgments

This work was supported by the Grant-in-Aid for the Global COE Program, from the Ministry of Education, Culture, Sports, Science and Technology (MEXT) of Japan.

References

[1] S. Xie, Z. Chen, T. Takagi and T. Uchimoto, Efficient numerical solver for simulation of pulsed eddy current testing signals, IEEE Transactions on Magnetics, 2011 (in press).

[2] Z. Chen, K. Aoto, and K. Miya, Reconstruction of cracks with physical closure from signals of eddy current testing, IEEE Transactions on Magnetics, vol. 36, pp. 1018-1022, 2000.

[3] Stephen J. Norton and John R. Bowler, Theory of eddy current inversion, J. Appl. Phys. 73(2), pp. 501-512, 1993.

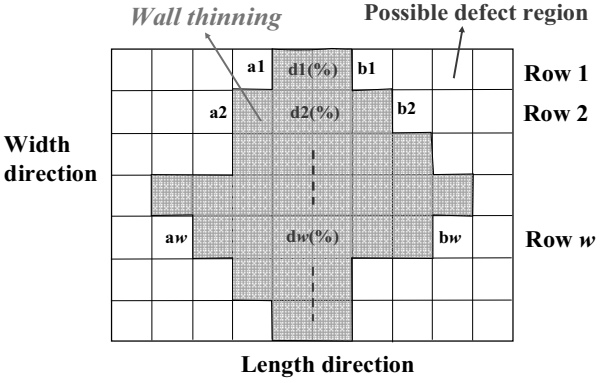

Fig. 1 Reconstruction strategy schematic for 3D profile of wall thinning

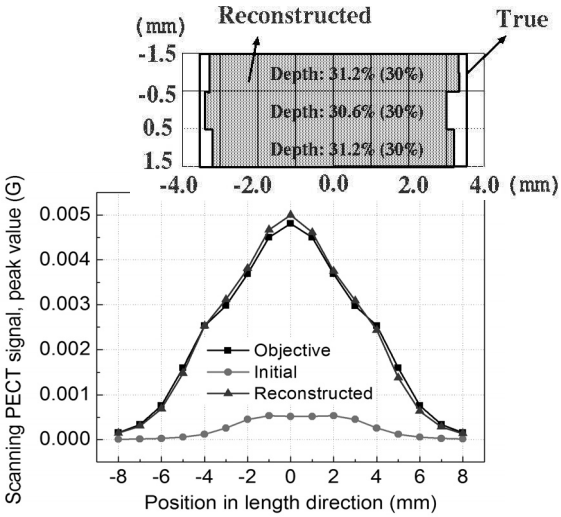

Fig. 2 Reconstruction results of PECT signal and wall thinning shape. Here 31.2% (30%) means reconstructed depth is 31.2%, true depth is 30%

OS9: Fluid-induced Seismicity: Modeling and Application

Eighth International Conference on Flow Dynamics
November 9 - November 11, 2011

Seismic and Aseismic Fluid Induced Motions

François Henri Cornet
Institut de Physique du Globe de Strasbourg; Univ. de Strasbourg, 5 rue René Descartes
67084 Strasbourg cedex ; France
francois.cornet@unistra.fr.

ABSTRACT

The injection of fluid in a rock mass results in variations of effective stresses that generate induced seismicity The effective stress field variations depend on the diffusion process, which depends in turn on the magnitude of the pore pressure variation relative to the total stress. Four diffusion mechanisms are distinguished: diffusion through a poroelastic rock mass, diffusion in preferential directions controlled either by slip along preexisting fractures, or by hydraulic fracturing, or by the development of fresh shear zones. Most importantly, this diffusion process generates also non seismic motion that influences in turn the seismic activity.

1. Introduction

The expression "Fluid Induced motion" is understood here as the rock motion generated by the forced flow of fluid in a geological formation, whether the forcing agent is man made or natural. This concept of fluid induced motion is different from that of fluid triggered motion which refers to a rock motion that would have occurred independently of the fluid flow but that has been accelerated because of it.

In order to force the flow of fluid in a rock mass, the fluid pressure must be increased within a given volume and attention has turned, up to now, to the microseismic activity generated by this pressure increase. An abundant literature addresses this topic some elements of which are recalled shortly here after.

But much less known are the aseismic motions generated by forced fluid flow, i.e. motions that occur at a velocity slow enough for not generating detectable dynamic signals in the rock. We present examples where such aseismic motions have been detected and discuss briefly consequences for the development of seismicity.

2. Sources of Seismic events generated by fluid injections

It has long been known that an increase in pore pressure may induce some microseismic activity (Healy et al., 1968; Gupta et al., 1969; Pearson, 1981). The source mechanism associated with these pressure increases are generally considered to be pure shear events. These shear events are simply explained by a Coulomb failure mechanism in which the increase in pore pressure reduces the effective normal stress acting on preexisting weakness planes, leading to slip on the planes properly oriented with respect to the principal stress directions.

But recently it has been shown that, when the injection pressure is large enough to generate hydraulic fracturing, many events contain non-shear components (Nolen-Hoeksema and Ruff, 2001; Sileny et al., 2009). Consequently, when the sismic monitoring system is properly designed, attention turns today to complete moment tensor analysis in order to identify the pure double couple component, the isotropic component and the Compensated Linear Vector Dipoles (Julian et al., 1998).

3. Mechanisms controlling the growth of the seismic cloud

Four different mechanisms have been proposed for explaining the growth of seismic clouds associated with fluid flow. They correspond to different level of fluid pressure with respect to the minimum principal stress magnitude that acts in the rock mass.

Hydraulic diffusivity in an elastic porous medium

When pressure is raised in the open-hole section of a borehole, the fluid percolates through the formation according to the rock mass diffusivity (Wang, 2000). This results in an increase in pore pressure that varies with time, which in turn results in a variation in effective stresses in the rock mass. As a consequence, the ratio between the maximum differential stress and the effective minimum stress increases with time depending on the distance with respect to the location of the fluid source.

It is well known that when the axial load acting on a rock sample under constant confining pressure increases, some acoustic emissions are generated, even though the rock remains within its elastic domain. This is known as the Kaiser effect (Holcomb, 1993).

Because the pore pressure variation in the formation depends on the rock mass diffusivity, many authors have proposed to interpret the rate of growth of the seismic cloud in terms of rock mass diffusivity (Talwani et al., 1984, Shapiro et al., 1997). However, Cornet et al. (2007) have shown that this proposition is valid only as long as the rock remains within its elastic domain. For larger pore pressure variations, large scale macroscopic failure mechanisms are generated, the rate of growth of which controls that of the seismic cloud.

Slip along large scale preexisting fractures

When the pore pressure gets large enough so that the effective Coulomb stress acting on properly oriented large scale preexisting planes is not satisfied, slip occurs. The difference with the previous mechanism is the dimension of the slipping surface which in the present case dominates the extension process and therefore both the geometry and the rate of growth of the seismic cloud. Fehler et al. (1987) proposed the so called three-point methods to identify such fault zones in otherwise cloudy seismic structures.

Hydraulic fracturing

When the pore pressure gets equal to the minimum principal stress, a so called hydraulic fracture is generated perpendicular to the minimum principal stress direction and the growth of seismic cloud is controlled by both the rate of growth of the hydraulic fracture and the fluid percolation through the walls of the fracture. With such a mechanism, tensile stresses exist only at the tip of the fracture and shear events are observed in the walls of the fracture.

But interestingly, Sileny et al. (2009) have detected the existence of repeated tensile dipole sources, away from the front of the seismic cloud. This led them to propose that some hydraulic fractures are constituted by a network of mode I (pure tension) fractures (fig. 1.), somewhat similar to the "Hill" crack model for volcanic dykes (Hill, 1977).

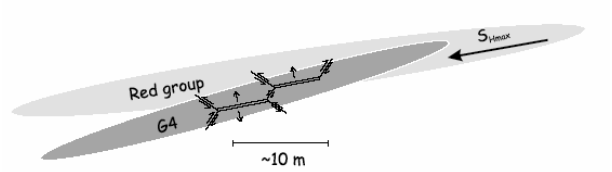

Figure 1. A "Hill" crack model for hydraulic fractures. The "Red" seismic Group fits the minimum principal stress direction but the G4 seismic group (with dipole multiplets) is slightly inclined to it (Sileny et al., 2009).

Development of a fresh shear zone

Numerous large scale hydraulic stimulations have been undertaken on the experimental geothermal site at Soultz-sous-forêts in North Eastern France, at various depths ranging from 2000 m to 4500 m. While in a few instances, hydraulic fractures have been created, for most of the stimulations the seismic cloud is inclined to the maximum principal stress direction in the formation. But this inclination is remarkably steady (22°). This led Cornet et al. (2007) to propose that these zones are not pre-existing fractures but fresh shear zones the geometry of which depends on the regional stress field. This has been confirmed by detailed analysis of the rate of growth of the seismic clouds during the various stimulations at Soultz (Calo et al., 2011).

4. Aseismic motions associated with fluid injections

At Le Mayet de Montagne (central France) where various methods have been tested for developing geothermal reservoirs in Hot Dry Rocks, detailed stress measurements were conducted in boreholes in the vicinity of zones where fluids had penetrated the rock mass (Cornet and Yin, 1995). The stress profiles suggested that slip had occurred aseismically along these zones during fluid injections (Scotti and Cornet, 1994). Observation of aseismic slip induced by large scale water injections was also reported at Soultz sous Forêts, when direct measurements of slip were conducted in the injection well after the first large scale hydraulic stimulation had been completed (Cornet et al., 1997).

The far field extent of such aseismic motions was imaged later by P wave tomography that were undertaken by Calo et al. (2011) for the stimulations conducted around 4 500 m in the various wells of the site. Rapid changes in seismic velocity that happened synchronously with changes in injection flow rate and therefore injection pressure have led to the conclusion that volumes in the order of one cubic kilometer have supported changes in mean stresses of the order of a few MegaPascals because of aseismic slip. These aseismic slip are considered to be partly the cause for the large magnitude seismic events (close to 3) that have been observed after injection stopped.

5. Concluding remarks

Large scale fluid injections induce both, seismic and aseismic motions. Experience has shown that, often, the largest magnitudes are observed after injection has stopped. We propose that when aseismic slip occurs during injection and some temporary equilibrium is reached according to the pore pressure distribution in the rock mass, this equilibrium is destroyed by the drop in pressure associated with the end of injection. This proposition remains to be validated by modeling. Such modeling will require proper understanding of the influence of normal stress and temperature on the velocity dependence of the friction coefficient.

References

[1] M. Calo, C. Dorbath, F.H. Cornet and N. Cuenot; Geophys. J. Int. **186,** 1295-1314 [2011]
[2] F.H. Cornet. and J. Yin; Pageoph, **145,** 677-700 [1995]
[3] F.H. Cornet., J. Helm, H. Poitrenaud and A. Etchecopar, PAGEOPH ,**150**, 563-583 [1997]
[4] F.H. Cornet, Th. Berard and S. Bourouis; Int. J. Rock Mech. Min.Sc. **44**, 47-66 [2007].
[5] M. Fehler, L. House and H. Kaieda, *J. Geophys. Res*., 92, 9407-9414 [1987]
[6] H.K. Gupta, H. Narim, B.K. Rastogi, I. Moham, *Bull. Seism. Soc. Am.*, **59** 1149-1162 [1969]
[7] J.H. Healy W.W. Rubey, D.T. Griggs and C.B. Raleigh, *Science*, **161**, 1301-1310.[1968]
[8] D.P. Hill, , *J. Geophys. Res*. **82**, 1347-1352. [1977]
[9] D.J. Holcomb, ,Int. J. Rock Mech. Min. Sc.& mech. Abs., **30**, 929-935 (1993).
[10] B.R. Julian,A.D. Miller and G.R. Foulger, Rev. Geophys.**36** 525-549 (1998)
[11]R.C.Nolen-Hoeksema, and L.J.Ruff, *Tectonophysics*, **336**, 163-181.[2001]
[12] C.Pearson, J. *Geophys. Res*., **86** , 7855-7864.[1981]
[13] O. Scotti. and F.H. Cornet; Int. Jou. Rock Mech. Min. **31**., 347-358. [1994]
[14] S.A Shapiro., E. Huenges and G. Borm. *Geophys. J. Int.,* **131**, F15-F18 [1997]
[15] J. Sileny, D.P. Hill, L. Eisner and F.H. Cornet, J.Geophys. res. **114** B08307 [2009]
[16] P. Talwani and S. Acree,; *Pageoph*, **122**, 947-965 [1984]
[17] H. Wang, Theory of Linear Poroelasticity, Princeton Univ. Press 2000

Eighth International Conference on Flow Dynamics
November 9 - November 11, 2011

Seismicity and Geomechanics Associated with the Stimulation of a Tight Well on the Boundary of a Producing Geothermal Energy System

Michael Fehler, Alison Malcolm, and Maria Silva
Earth Resources Laboratory; Massachusetts Institute of Technology; Cambridge, MA 02139 USA
fehler@mit.edu

ABSTRACT

We present results of the analysis of seismicity accompanying the stimulation of a tight well on the boundary of an existing producing geothermal energy system. Several methods have been used to analyze the data including tomography using earthquakes as sources, joint hypocenter collapsing of the microearthquake location catalog that results from the tomography inversion, and a new method that uses interferometry to obtain constraints on the distance separating pairs of microearthquakes within the zone of induced events.

1. Introduction

Microseismicity accompanying hydraulic fracturing of tight rock for the development of Enhanced Geothermal Energy (EGS) or Hot Dry Rock (HDR) Systems has long been monitored. The analysis of such data provides information about the probable locations of existing and newly created fractures within the EGS reservoir that are stimulated by the hydraulic fracturing. More recently, there is increased interest in developing geomechanical models of the injection process. Information obtained from the analysis of microseismicity can place important constraints on geomechanical models. Recent advances in analysis methods have provided improved locations of the microearthquakes and, in particular, in the relative locations of the events. We present results of the analysis of seismicity accompanying the stimulation of a tight well on the boundary of an existing producing geothermal energy system. Several methods have been used to analyze the data including tomography using earthquakes as sources, joint hypocenter determination/collapsing of the microearthquake location catalog that results from the tomography inversion, and a new method that uses interferometry to obtain constraints on the distance separating pairs of microearthquakes within the zone of induced events. With improved locations and information about the velocity model, we can determine moment tensors of the larger events, which can be used to place constraints on the stress field. The pattern of the microseismic event location distribution, the temporal change in the pattern in time and the moment tensors can be combined with a geomechanical model to evaluate the overall geomechanical development of the reservoir during the stimulation.

2. Methods

We use several methods to analyze our data. One of the main problems with induced seismic data is the limited availability of observation stations. It is best if observation stations can be located downhole and thus closer to the injection so that frequency content of recorded signals is improved compared to those obtained from near-surface observations. Placing sensors downhole is expensive so near-surface observations are often used exclusively or to complement downhole observations. The limited availability of monitoring stations can reduce the quality of results obtained from analysis of recorded data.

We begin with the use of tomography using the microearthquakes as sources to obtain constraints on the velocity structure and to refine the location catalog that was obtained from conventional single-event location schemes. We conduct a post-tomography analysis of the resulting microearthquake location catalog using a joint hypocenter determination method that includes a collapsing constraint that shifts locations of event towards those of nearby events provided that the shifted location does not result in a significantly larger misfit of arrival time data than does the original location. The use of the collapsing results in a more clustered catalog with the microseismic events located near but below the injection wells.

Given the suboptimal array geometry of the microseismic observation network, the resolution of the velocity structure is somewhat limited. To help mitigate this, we are developing an improvement to the tomography approach that involves the use of event-pair cross-correlations to determine the traveltime between event pairs. This allows the placement of virtual receivers within the microearthquake source region and has the potential to provide improved relative locations of the event pairs and to place additional constraints on the tomography inversion. The relative travel times are determined using cross-correlation of the waveforms recorded at recording stations from the event pairs. The method has been validated using both simulated data and by picking event pairs for which the vector joining them passes through one station, which allows direct arrivals to be used to determine interevent traveltimes. Further details can be found in [1].

Since one goal of our work is to develop a geomechanical model of the reservoir stimulation, we are in the process of determining moment tensor solutions for selected events using the method described in [2].

3. Results and Discussion

Figure 1 shows cross-sections of the locations of events within the stimulated region. The locations of stations are also shown. The event pair that is connected by a near-vertical line that passes through one of the near-surface stations is an event pair that was used to test the reliability of the interferometry method for

determining traveltimes between events. For an event pair having event locations that are joined by a line that passes through a recording station, the result of the interferometry analysis should yield a traveltime that is consistent with that determined from the difference in arrival time of the first arrivals measured at the station. By finding such event pairs, we can obtain a preliminary evaluation of the reliability of the use of interferometry-determined traveltimes between events that make up the event pair.

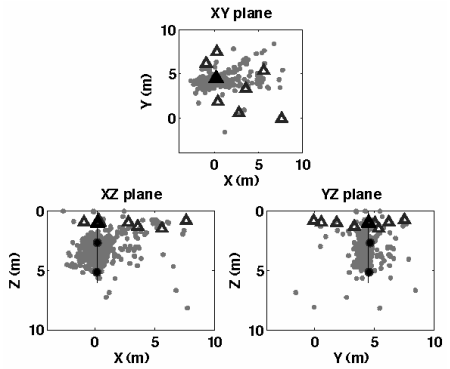

Figure 1. Two-dimensional projections of microearthquake (dots) and receiver (triangles) locations. The two events joined by a line that passes through a receiver were used for testing the interferometry-based method for determination of traveltimes between event pairs.

Figure 2 shows a comparison of the interferometry-determined traveltimes between event pairs with those determined by raytracing between the locations of the events determined by the traveltime tomography. Raytracing was done using the tomography-determined velocity structure. The comparison is rather good, which leads us to conclude that the locations, velocity structure, and interferometry-determined traveltimes are in reasonable agreement. Our next step is to use the interferometry-determined arrival times as constraints in the tomography analysis. Our hope is that this will provide improvements to the results obtained in the tomography.

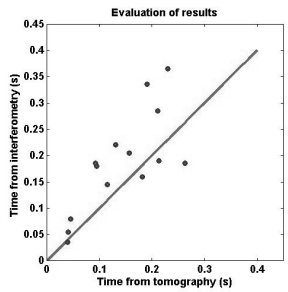

Figure 2. Comparison of traveltimes determined from the interferometry method with those determined from the locations and velocity structure obtained from arrival time tomography.

4. Concluding remarks

When monitoring microearthquakes induced by hydraulic fracturing, limitations on the number of seismic stations and the ability to site the locations within the subsurface mean that observations are never as good as one might hope for. By using a suite of analysis tools to evaluate recorded data, we can place important constraints on the seismicity parameters and velocity structure that will help in constraining the geomechanical model of the reservoir evolution.

References

[1] Melo, G., and A. Malcolm, The Leading Edge **30**(5) (2011)

[2] Li, J., H. Zhang, S. Kuleli, and M. Toksoz, SEG Expanded Abstracts (2009).

Eighth International Conference on Flow Dynamics
November 9 - November 11, 2011

Seismological Aspects about Fluid Induced Seismicity: Insights Gained from Recent Studies at Core, Reservoir, and Regional scales

Xinglin Lei
Geological Survey of Japan, AIST, Japan
xinglin-lei@aist.go.jp

ABSTRACT

In order to explore seismological aspects associated with fluid induced seismicity, statistical behaviors and governing physics of fluid-induced or fluid driven seismicity were investigated for 3 typical cases of different scales. In general, fluid induced seismicity demonstrated following common features: 1) More swarm-like characters as indicated by the epidemic-type aftershock sequence models (more random component and less magnitude dependence in self-triggering); 2) Relatively small b-value; 3) Sensitive to extern stress disturbances caused by such as the earth tides and passing seismic waves.

1. Introduction

Failures within either intact rocks or pre-existing faults generally obey the Mohr–Coulomb failure criteria, in which failure occurs on a plane when the Coulomb failure stress (CFS) exceeds a specific value

$$CFS = \tau_\beta - \mu(\sigma_\beta - P) \quad (1)$$

where τ_β and σ_β are the shear stress and normal stress on the failure plane, respectively, μ is the friction coefficient and P pore pressure. It is well known that changes in CFS caused by any kind of deformation elsewhere or pore pressure increase can trigger seismicity even large earthquakes. Human activities such as fluid injection into a deep well and impoundment of a water reservoir may fasten the occurrence of potential earthquakes along nearby faults stressed critically. Considering the slow process of tectonic loading, small stress changes due to human activities may equal to a few to hundreds of years' worth of natural stress buildup [1]. Thus, fluid induced seismicity is an important issue in risk assessments in applications in which fluid migration or pore pressure diffusion is expected to play a role, such as hydrocarbon reservoirs, enhanced geothermal systems, and geological storage of CO_2.

In cases of fluid-driven seismicity, earthquakes triggered by fluid themselves produce changes in the local stress field. Thus, fluid triggering is always accompanied by stress triggering and it is important to find indicators or signs of fluid from seismic data [2]. Because any given fault system shows fractal or hierarchical complexity at all scales, statistical approaches have received increasing attention.

Faulting at different scales, from acoustic emission (AE) events in stressed rock samples to earthquakes in the earth, show similarities in a wide range of aspects involved in a number of power-laws [3]. This paper has a focus in several power laws, which are widely observed in both laboratory and field. I take much attention to the epidemic-type aftershock sequence (ETAS) model which incorporates the Omori law (power law between aftershock rate of large earthquake and time from the main shock) by assuming that each earthquake has a magnitude-dependent ability to trigger its own aftershocks. The total occurrence rate is described as the sum of the aftershock rate related to all preceding earthquakes and a constant rate p_0 that represents the stable Poisson process, or, in other words, the random background activity:

$$\lambda(t) = p_0 + \sum_{\{i:t_i<t\}} K_0 e^{\alpha(M_i - M_c)} (t - t_i + c)^{-p} \quad (2)$$

where M_c is the low-end magnitude cut-off of the catalog, and α is a constant that specifies the degree of magnitude dependence.

This paper briefly summarize some common features of fluid-induced seismicity through case studies at three typical scales: 1) fracture of porous rock in laboratory; 2) earthquake sequence induced by deep well injection in a gas reservoir; 3) fluid-driven seismicity in a geothermal active area.

2. Role of Drainage Condition on Rock Fracture

Berea sandstone, which has a porosity of ~20%, was used to investigate the role of drainage conditions in deformation and fracture behaviors of porous rocks under compression [4]. Experimental results indicate that the well-established dilatancy-hardening effect can be relaxed more or less by dilatancy-driven fluid flowing into the dilatancy region from surrounding regions. Under drained conditions, fast relaxation of pore pressure leads to 1) a significant reduction in rock strength and dynamic stress drop; 2) stabilization of the dynamic rupture process; 3) enlargement of the nucleation process and thus resulting in relatively larger nucleation zones and precursory slips.

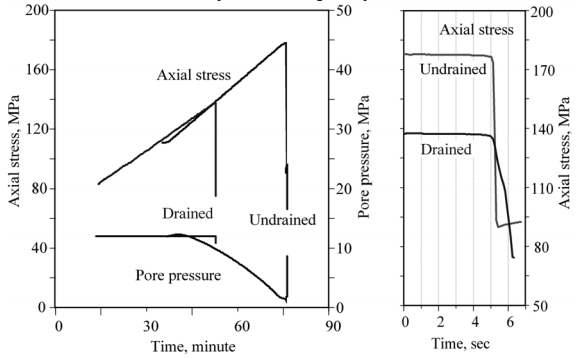

Fig. 1 Axial stress and pore pressure during the fracturing tests of Berea sandstone under drained and undrained conditions (from [4]).

3. An Example of Injection Induced Seismicity

The Rongchang gas field at the south-east border of the Sichuan basin, China, associated with an anticlinal structure overlying a basement fault. Several reverse faults and transverse faults have been identified in the sediments associated with the anticline structure. The reservoir has a thickness about 100–200 m at a depth from ~1700 to ~3000 m beneath the surface. Historically, the gas field and surrounding regions have exhibited low levels of naturally occurring seismicity.

Unwanted water has been injected intermittently at a pumping pressure of 2.1–2.9 MPa to 2.6–2.9 km depth, since July 1988. Until the end of 2006, the injected water reached 1,000,000 m^3. The injections have induced more than 32,000 surface-recorded earthquakes, including 2 of M~5, 14 of M~4, and more than 100 of M~3 [2]. Changes in CFS on pre-existing faults from pore-pressure diffusion are considered as the major inducing the Rongchang earthquake sequence [2]. As see from (1), it is clear that increase on pore pressure by ΔP results in a positive ΔCFS of a value equal to $\mu\Delta P$ on every fault. A pressure increase of 2.1–2.9 MPa at the injection well and corresponding outward diffusion are more than sufficient to induce failure within the fault system surrounding the injection wells. Some injection wells, located in the outside of the fault zone, did not induce significant seismicity. This study with other cases supports following two important facts, which are 1) the existence of a local threshold value of ΔCFS above which changes in seismicity occur, 2) induced or triggered seismicity occurred along pre-existing faults, and 3) the maximum creditable magnitude attributable to a fluid-injection depends on the scale of the nearby faults and the regional tectonic background conditions.

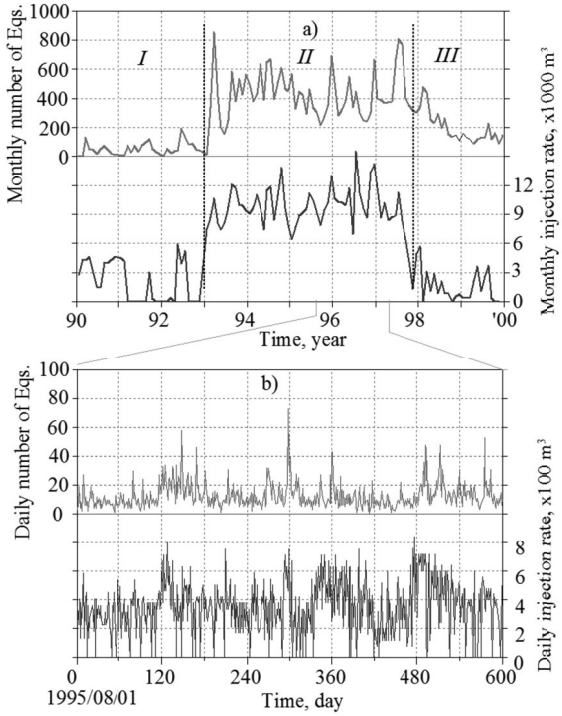

Fig. 2 Monthly/daily number of earthquakes and monthly/daily injected volume at the major well within the Rongchang gas field (from [2]).

4. Fluid-driven Seismicity in Yunnan, China

Multi sources of evidence suggest that the seismicity in north-western Yunnan, located within the Tibet geothermal belt, is governed by somewhat magma/mantle generated CO_2-rich fluids through a fault-valve model. Following the 2004 Mw9.3 Sumatra earthquake, ~2,500 km away, seismicity increased sharply over a wide area. Raised seismicity lasts for approximately 14 days. During this period, more than 800 events having a magnitude of ≥1.5 were observed, including at least 7 M4 class events and a M5.1 event. Major events were clustered at several sites that exhibit complex fault geometries and flowing channels, such as step-overs and junctures [5].

Both rapid-onset dynamic triggering (events embedded in the surface waves from the Sumatra earthquake) and delayed response (clusters shows significant delays in the onset of seismicity, with the dominant energy releasing a few hours to a few days after the surface wave passed) were well established. Triggered seismicity as well as background seismicity can be well represented by ETAS models having great p_0 (>30%) and small α (<1.5).

5. Discussion and Conclusion Remarks

The dilatancy-hardening effect during faulting nucleation can be greatly relaxed by fluid flow into the dilatancy region from nearby fluid sources and thus leads to a significant reduction in failure strength and stress-drop. At the same time, some weakening mechanisms may stabilize the dynamic rupture process and evenly cause aseismic slip. Integrated studies on multi-scale problems may shed some light on predicting and controlling fluid-induced seismicity. As indicated by the induced seismicity in Rongchang, pore pressure increase and diffusion in an area with faults can induce significant seismicity even destructive earthquakes.

High fluid pressure in branched fault zones weakened the faults, making them sensitive to external disturbances due to such as the earth tides and seismic waves. The remote triggering in north-western Yunnan indicates that the stress threshold of stress for unstable rupture of fault, with a stress level close to the critical point or self-organized-critical point, is on the order of few tens of KPa.

Fluid induced activities generally show more earthquake swarm-like characteristics as indicated by the ETAS modeling results (large percentage of random components and less magnitude dependence in Omori law type self-triggering). The statistical results on all cases indicate that ETAS model combined other statistical approaches is a promising method in terms of identifying fluid signals in seismicity patterns.

References

[1] X. Lei, J. Asia Earth Sci., **40** (2011).
[2] X. Lei, et al., J. Geophys. Res., **113** (2008), B10310.
[3] X. Lei, Eur. Phys. J. B, Submitted.
[4] X. Lei, et al., Int. J. Greenh. Gas Con., Submitted.
[5] X. Lei, et al., J. Geophys. Res., **116** (2011), B08303.

Coupled Hydraulic and Microseismic Analysis for Reservoir Stimulation

Kazuhiko Tezuka[1], Yusuke Kumano[1], Tetsuya Tamagawa[1] and Kimio Watanabe[2]
1: Japan Petroleum Exploration Co., Ltd. (JAPEX)
2: Renergies
kazuhiko.tezuka@japex.co.jp

ABSTRACT

The numerical simulator "SHIFT" calculates shearing and/or opening of fractures and related permeability changes along pre-existing fractures by coupling fluid flow and geomechanical analysis. The shearing of fractures can be interpreted as microseismic occurrences. Through the case study using the field data from the hydraulic injection experiment in Yufutsu oil/gas field, the performance of SHIFT was evaluated and verified. SHIFT can be used to design an injection strategy for reservoir stimulation and to predict the effects of the stimulation and the microseismic activities.

1. Introduction

Microseismic monitoring has been getting popular in this decade for imaging hydraulic fracture growth in oil/gas and geothermal fields. Especially, it is recognized as one of the key technologies for development of North American shale gas resources. Recent studies concerning to shale gas developments revealed that the geometries of the fracture growth were not simple but complex and were heavily affected by pre-existing natural fracture system. The microseismic images in the Barnet Shale fields indicate that the stimulations are intersecting pre-existing fracture networks and generating a wide fracture zone appears to be a critical factor in the well performance (Maxwell, 2002). This means that the success of fracture stimulation requires enhancing the flow properties of pre-existing fractures. This in turn depends on the ability of the elevated fluid pressures generated by injection and associated stress changes to cause shear slip and/or opening, and the conditions necessary to do that depend on the stress magnitudes and orientations and the orientations and strengths of the fractures (e.g., Tezuka et al., 2005; Moos and Barton, 2008, Ito and Hayashi, 2003). This paper introduces a numerical simulator "SHIFT", which can simulate shear slip and/or opening, resulting microseismic events (Tezuka et al., 2005), and show some results of case studies from the fractured basement gas reservoir in northern Japan.

2. A numerical simulator "SHIFT"

SHIFT simulates shearing and/or opening of fractures and related permeability changes along pre-existing fractures in a dynamic process by coupling fluid flow and geomechanical analysis as shown in Fig.1. Then the shearing of fracture is interpreted as microseismic occurrence. An initial discrete fracture network (DFN) model is converted to an equivalent continuum mesh model, in which pressure distribution and water/gas saturations are calculated. A geomechanical analysis calculates stress condition acting to each discrete fracture using given stress profiles and updated pressure distribution. According to the calculated stress condition, a possibility of shear slip at each fracture is evaluated on the basis of Mohr-Coulomb criterion and the resulting aperture is assigned to the fracture referring to the type curves presented in Figure 2. The DFN with updated fracture apertures are converted to mesh model again and this cyclic process continues following the given injection schedule. Outputs include a time history of injection pressure and microseismic occurrence, and distributions of pressure, permeability, water saturation and microseismic locations.

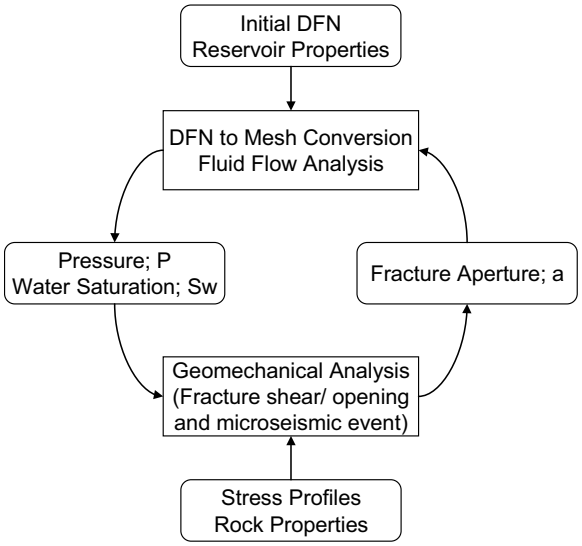

Fig. 1 Schematic flow of coupled hydraulic and microseismic analysis with SHIFT.

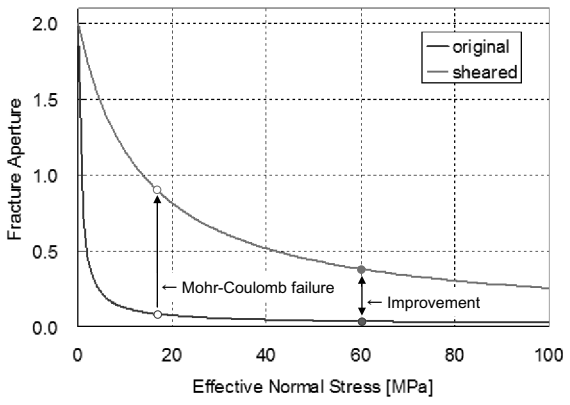

Fig. 2 Fracture aperture as a function of effective normal stress (example).

3. Case Study in Yufutsu oil/gas field

A massive hydraulic injection and microseismic monitoring operation was conducted in 2005 at Yufutsu oil/gas field in Hokkaido, Japan. The objective of this operation is to delineate the spatial distribution of the fractures and to improve the productivity of the well by stimulating pre-existing fractures. The injection schedule and anticipated areas of the stimulation were thoroughly designed and predicted by using the SHIFT. The initial DFN model was created on the basis of fracture information obtained from borehole images. The injection of more than 5,600m^3 of slick water, without any additives, effectively induced microseismic activities and accordingly improved the productivity of the well.

Fig. 3(a) and (b) show the predicted microseismic event locations using the initial DFN and the observed event locations, respectively. Although a preferential direction of the observed microseismic distribution showed a good consistency with the prediction, an aspect ratio (proportion of a longitudinal direction to the others) of the microseismic cloud was slightly different. Additionally, significant mismatches in the pressure responses were observed (Figure 4(a)). These facts lead new understandings of the fracture system and were fed back to the DFN model to modify. Major modifications include a reduction of smaller fractures from the model and a tuning of the parameters which control the compliance of the sheared fractures.

Fig. 4(b) shows a comparison of pressure responses between the observation and the simulations after modifications. The modified model provides better agreement in pressure response. The microseismic distribution is also improved as shown in Fig. 3(c).

4. Conclusions

The performance of SHIFT was evaluated and verified through the case study using the field data from the hydraulic injection experiment in Yufutsu oil/gas field. SHIFT can be used to design an injection strategy for reservoir stimulation and to predict the effects of the stimulation and microseismic activity, taking into account the impact and the contribution of the pre-existing natural fracture system. SHIFT can be also used for evaluations of an initial fracture network models and stress conditions; those are inputs to SHIFT, by comparing the simulated results and the field observations.

Acknowledgments

A massive hydraulic injection and microseismic monitoring operation in 2005 was done as a part of the collaborative project between Japan Oil, Gas and Metals National Corporation (JOGMEC) and Japan Petroleum Exploration Co., Ltd. (JAPEX).

References

[1] T. Ito and K. Hayashi, Pure and Applied Geophy, 160, (2003), 1103-1124.

[2] S. Maxwell, T. Urbancic, N. Steinsberger, R. Zinno, SPE77440 (2002).

[3] D. Moos and C. Barton, ARMA 08-312 (2008), 42nd US Rock Mechanics Symposium and 2nd U.S.-Canada Rock Mechanics Symposium.

[4] K. Tezuka, T. Tamagawa and K. Watanabe, World Geothermal Congress (2005), Antalya, Turkey

[5] K. Tezuka, R. Kamitsuji and T. Tamagawa, IPTC12391, International Petroleum Technology Conference in Kuala Lumpur, Malaysia, 2008.

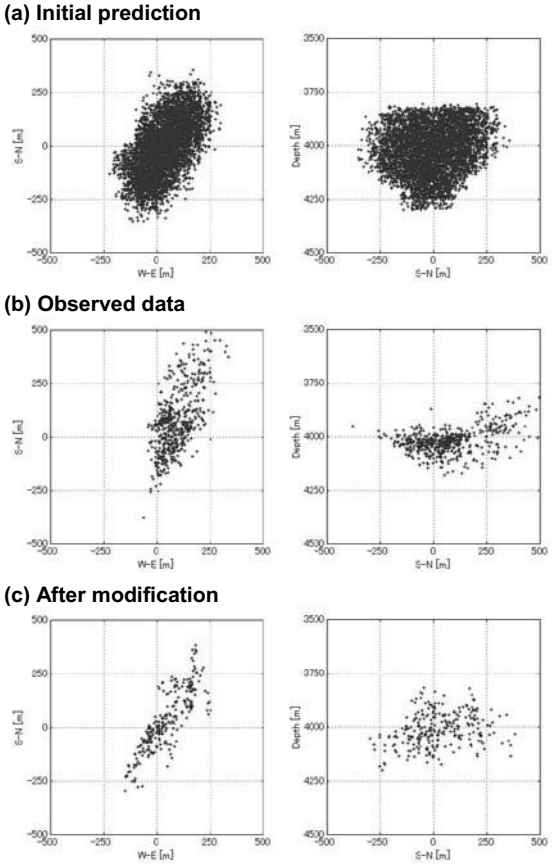

Fig. 3. Comparison of the microseismic distributions showing the initial prediction (a), observation (b) and the simulated result with the modified DFN model (c).

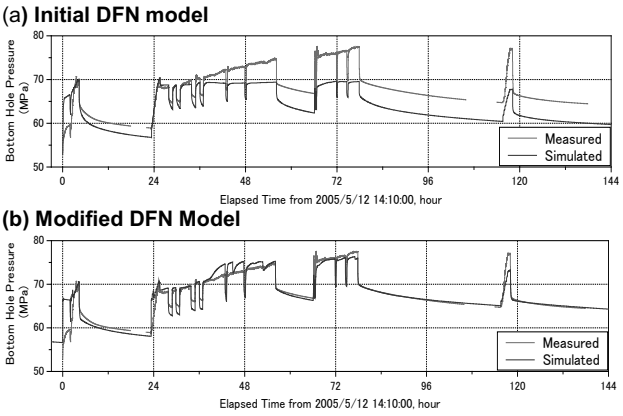

Fig. 4 Comparison of the measured and simulated pressure responses of injection well by using the initial DFN model (a) and the modified DFN model (b).

Eighth International Conference on Flow Dynamics
November 9 - November 11, 2011

Characteristics of Earthquakes Observed at Geothermal Fields

Hiroshi Asanuma, Yusuke Mukuhira, Doone Wyborn, Markus Häring, Masaho Adachi, Hiroaki Niitsuma
Graduate School of Environmental Studies, Tohoku University, 6-6-20 Aramaki-aza-aoba, Sendai, 980-8579, Japan.
asanuma@ni2.kankyo.tohoku.ac.jp.

ABSTRACT

Seismic activity in geothermal area is one of the most critical environmental risks associated with development of geothermal resources. Many of the natural hydrothermal systems are found inside/around naturally fractured zones with seismic activity and triggered/induced seismic activity is commonly observed. Meanwhile, hydraulic stimulation/injection to improve permeability of the reservoir also induces small earthquakes. Some of the earthquakes from the geothermal reservoirs have large magnitude as to be felt on ground surface as presented in this abstract.

1. Introduction

It has been widely accepted that distribution of geothermal resources is highly correlated to activity of natural earthquakes from global point of view. There are a number of geothermal power plants, which were constructed on hydrothermal reservoirs with natural microearthquakes, and activity and hypocentral locations have been successfully used to monitor behavior of reservoirs to production and injection [1]. Meanwhile, microearthquakes are commonly observed during the hydraulic stimulation of EGS/HDR geothermal reservoirs.

One of the recently appeared risks associated with geothermal reservoir creation and power generation is occurrence of earthquakes with unexpectedly high magnitude [2]. Such earthquakes from geothermal reservoir typically have magnitude less than 5 and hypocentral depth of 2-5 km, and some degree of damages to buildings and infrastructure especially in urbanized area have been reported. In many cases, the occurrence of earthquakes from hydrothermal reservoir is not directly correlated to human operation to the reservoir which can be considered to increase pore pressure, and can be interpreted as a part of the pre-existing natural earthquake activity. However, it is of importance to understand physics behind large earthquake from hydrothermal/EGS reservoirs and quantitatively evaluate risk of earthquake to obtain consensus for geothermal power generation from local community. The understanding of large earthquake from the reservoir is also of beneficial for developers because the effect of the earthquake to productivity can be revealed.

In this paper, the authors show microearthquake activity and its characteristics observed at Cooper Basin, Australia, Basel, Switzerland, and Yanaizu-Nishiyama, Japan.

2. Cooper Basin, Australia

A private developer, Geodynamics Limited drilled the first injection well (Habanero 1) into a granitic basement to a depth of 4,421m (754m into granite) in 2003. Several sub-horizontal over pressured fractures were found in the granitic section of the well. The orientation of these existing fractures was consistent with the maximum tectonic stress being horizontal in the central part of Australia as indicated in the global stress field.

The main stimulation of Habanero-1 took place after several tests to initiate fractures. The total amount of liquid injected was 20,000m^3 with a highest pumping rate of 48L/s. All the openhole section was pressurized in the first and main stimulation.

The microseismic network at this site consisted of one deep (depth: 1,794m) high temperature instrument and four near surface instruments (depth: 88-114m). The authors recorded 32,000 triggers with 11,724 of these located in 3D space and time on site during the stimulations [3].

During the hydraulic tests and the main injection, we observed several events with large magnitude. The largest event had a moment magnitude Mw=3.0 which was estimated by Geoscience Australia. The origin time of the large events were also widely distributed in the hydraulic tests and little correlation was observed between the magnitude of the microseismic events and wellhead pressure. In fact, 11 of 30 large events occurred after shut-in. The locations of the large events were widely distributed in the seismic cloud. There is no clear seismic structure of the large events that was able to correlate to existing geological structure. The polarization pattern at each monitoring station is similar to that of the smaller events, suggesting that the source mechanism is common. Spatio-temporal observation of the hypocenter and source radii showed that the seismic cloud subsequently extended beyond the large events which occurred at the edge of the seismic cloud, and a number of seismic events with small magnitude occurred after the large events within the source radius of the large events. Observations suggest that some kind of hydraulic barrier was broken by the large events at Cooper Basin.

3. Basel, Switzerland

An operating company of the Basel Project, GEL, has drilled a deep borehole (Basel-1), penetrating into granitic basement, and made the first stimulation in December 2006. A total amount of 11,500m^3 of fresh water was injected over six days of stimulation operation [4] to openhole section. The maximum wellhead pressure was around 30MPa at a flow rate of 50L/s [5].

The microseismic monitoring network, which consisted of 6 permanent and 1 temporary seismometers

in boreholes, detected more than 13,000 triggers during and after the stimulation (period until Feb. 2008) and 2,900 of them were located. The distribution of the hypocenters showed sub-vertical planar structure with an azimuth of approximately NNW-SSE, which was consistent with the horizontal maximum stress around Basel. Dominant source mechanisms estimated by Swiss Seismological Service (SED) for some of the larger events were strike-slip of sub-vertical fracture with N-S azimuth [6].

The largest earthquake observed at Basel had Mw=2.9, and we defined large event as any event with a moment magnitude larger than Mw = 2.0. As a result, 9 events were identified as large events at Basel. It is seen that 7 large events that occurred during and just after the pumping (on 8 December, 2006) had hypocenters in the bottom and middle of the main body of the seismic cloud. Later, two large events occurred around the shallow edge of the seismic cloud 50 days after the end of pumping, and their hypocenters were estimated approximately 100-200m apart from the main seismic cloud. The large events occurred at the bottom of the seismic cloud, and it can be seen that the source radii of the foreshocks overlapped each other. Coherence of the large events to neighboring smaller events was relatively high for the deep large events and low for that of shallow events, suggesting that hypocentral location is apart from the main seismic body or source mechanism is unique for the shallow large events. Most of the critical pore pressure for shear slip, which was estimated from FPS and stress state at Basel using Coulomb Failure Criterion, was relatively lower to those for the neighboring events with smaller magnitude.

Observations suggest that the shallow large events were triggered at outside of the seismically activated zone and diffusion of pressurized zone is one of the most possible triggers. The deep large events at Basel occurred inside the previously stimulated zone and either re-distribution of stress or change in the friction coefficient might trigger the events.

4. Yanaizu-Nishiyama, Japan

A 65,000kW geothermal power plant is under operation at Yanaizu-Nishiyama, Fukushima, Japan since 1995 by Tohoku Electric Power Co. Ltd., and steam producer Okuaizu Geothermal Co. Ltd. (OAG). The site is located at outside of western edge of Aizu Basin and caldera-related fracture system composes a steam-dominant reservoir at a depth around 2 km. It has been interpreted from production record from wells that the sub-vertical fracture system has higher permeability around the production zone. Western part of the Aizu Basin historically has some degree of natural earthquake activities, and microearthquake activity around the area of Yanaizu-Nishiyama was observed in the exploration phase of the power plant. Therefore, OAG deployed microearthquake monitoring network in 1988, and continuously monitored microearthquakes.

Several relatively large earthquakes in Yanaizu-Nishiyama have been detected by the network of JMA. The largest one occurred on October 12, 2009 and its JMA magnitude has been estimated to be 4.9. Considerable damage was brought to power plant and houses of the residents. The authors have estimated that the hypocenter of a large earthquake had a hypocenter in the center of the cloud of hypocenter of the microearthquakes. No clear correlation between the operation of production/injection and the occurrence of the large events was observed. We have found that the "b-value", which is considered to be correlated to possible largest events in the area of natural seismicity, has spatial and temporal variation in Yanaizu-Nishiyama. Generally evaluating the histogram of the magnitude, the possible largest earthquake in this site is ML=4.1. The fault plane solution (FPS) for 4 large earthquakes from the site has been estimated by JMA. Three of the four events showed FPSs of normal fault which has a strike of NW-SE and dip of around 45°. The last one can be interpreted by the same FPS considering some error in polarity identification for some of the stations. These FPSs are in consistent with the composite focal mechanism solution from the signals detected by the network of OAG. The distribution of the orientation of the seismic multiplet structure suggests that there are three trends in the orientation of the structures; namely, they had azimuths of NW-SE (slip to NE) and NE-SW (NW or SE slip), suggesting that they are correlating to the orientation of the fracture system inside the active seismic zone.

Because of uncertainties in the information, which include stress state and orientation of fractures, interpretation of the large events in Yanaizu-Nishiyama is of difficulty.

5. Conclusions

The physics behind the occurrence of the large earthquake is field dependent as shown in this abstract. It has been also found that simple interpretation of the induced earthquake that increase in pore pressure is the most dominant trigger may not suitable in many cases where events after shut-in or bleeding-off were observed.

Most of the characteristics of the large events from the three geothermal sites have been clarified throughout the studies by the authors. Rock-mechanical modeling will be followed for further understanding of the large events and development of technologies to seismically softly develop geothermal reservoirs.

References

[1] P. D. Roger, and G. B. Charles, BSSA, 72, 1317-1327 (1982).
[2] E. Majer, et al., Geothermics, 36, 185-222, (2007).
[3] H. Asanuma, et al., Trans. GRC, 29, 87-91, (2005).
[4] M. O. Häring, Geothermics, 37, 469-495 (2008).
[5] S. Ulrich, Proc. 5th Swiss Geoscience Mtg., genova2007, (2007).
[6] N. Deichmann, Swiss Journal of Geosciences, (in-press).

Eighth International Conference on Flow Dynamics
November 9 - November 11, 2011

Pressure and Flow Structure Estimation from Microseismic Monitoring

Takatoshi Ito[1], Hiroyuki Maki[2] and Hideshi Kaieda[3]
[1, 2] Institute of Fluid Science, Tohoku Univerisity
[3] Central Research Institute of Electric Power Industry
[1] ito@ifs.tohoku.ac.jp

ABSTRACT

By analyzing data of microseismic events caused by a hydraulic stimulation, we can estimate pore pressure at the location and the occurrence time of each event assuming the Mohr-Coulomb criterion for fracture sliding. The estimated values of pore pressure are sorted to give spatial distribution of pore pressure and its variation with time during hydraulic stimulation. Furthermore, flow pathway structure can be estimated as it gives a good explanation of the pressure distribution estimated from microseismicities.

1. Introduction

Most geothermal reservoirs consist of fractured rock, and productivity of steam / hot water is dominated by water flow through the fracture network in the reservoir. Geothermal energy development depends upon how well the water flow is understood. However, the conventional approaches could bring limited information about the water flow. It is generally considered that each fracture composed of the network is spread over a relatively large area of several hundreds square meters, but its aperture is limited to several millimeters at maximum. There is no way to detect directly such a thin structure nor the fluid flow in it from ground surface through a huge rock mass with few thousands meters in thickness. On the other hand, hydraulic stimulation is carried out to improve fracture permeability and connectivity frequently especially for creating the Enhanced Geothermal System (EGS). Then massive fluid is injected into subsurface rock through drilled wells, the fluid is forced to flow through a fracture network, and a number of microseismic (MS) events are commonly observed during hydraulic stimulation. It is believed that the MS events are induced by the increase in pore pressure at inside of fractures, which is caused by hydraulic stimulation. Based upon our further consideration on the sequence in which hydraulic stimulation leads to the MS events, we have proposed a method to integrate the data of MS events for estimating pressure propagation. Furthermore, the estimated pressure propagation allows us to estimate both of flow-pathway structure and the distribution of hydraulic conductivity.

2. Procedure to Estimate Pressure Propagation and Flow-pathway Structure

Friction between fracture planes decreases with increasing pore pressure in the fracture, P_p, until it reaches the critical pore pressure P_c at which the friction decreases to be balanced with the shear stress of fracture, τ, and then shear sliding occurs on the fracture. Such a critical condition is called as the Coulomb criterion, and is given by

$$\tau = \mu(S_n - P_p) \tag{1}$$

where μ is the coefficient of friction along the fracture plane, S_n is the normal stress of fracture. The stress components of S_n and τ are given as functions of the fracture orientation and the regional state of stress. The detailed analysis of MS events allows us to detect not only the seismic location but also the dip and strike of the fracture on which shear sliding occurs to cause the MS events. Therefore, when the regional state of stress

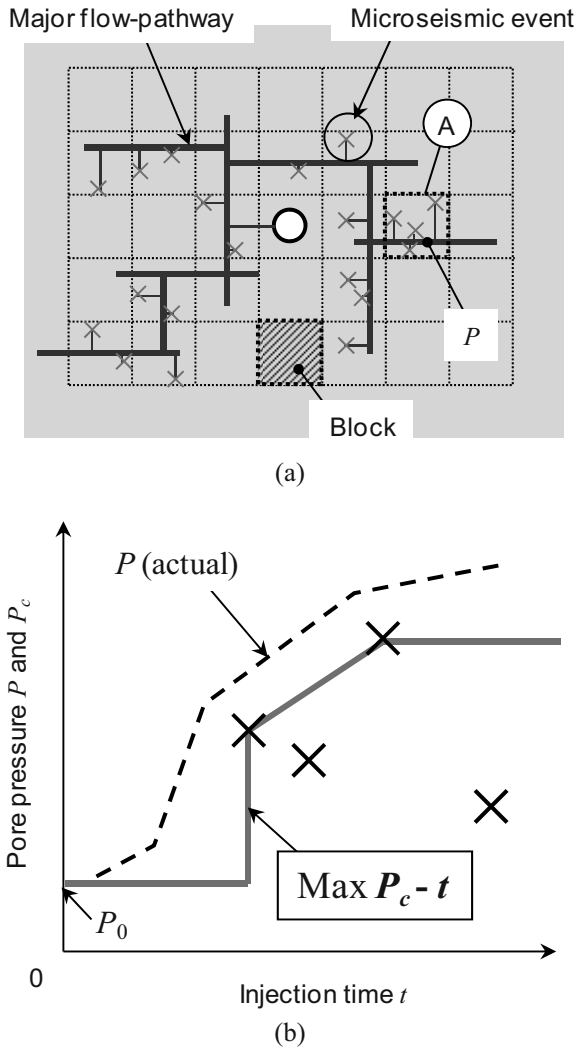

Fig. 1 (a) Concept of "block", (b) the relationship between the pore pressure P in the flow pathway and the critical pore pressure P_c estimated for each of MS events involved in the block "A", and (c) the 2D model of flow-pathway structure.

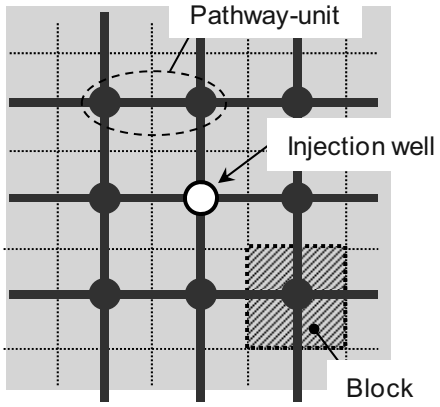

(c)

Fig. 1 (cont'd)

is given in another way, we can estimate the value of P_c so as to satisfy Eq. (1) assuming an appropriate value of μ, e.g. μ, = 0.8. Then we integrate the estimated value of P_c for each MS event into the distribution of pore pressure induced by hydraulic stimulation. To do this, assuming 2D case, we divide the region of interest into blocks with the same size as schematically shown in Fig. 1a. When the estimated values of P_c of the MS events involved in a block are plotted on the pressure - time diagram, the results are to be as illustrated by cross marks in Fig. 1b. We collect the maximum value of P_c in the past at each time, and assume that its variation with time such as the solid line in Fig. 1b represents approximately the variation of pore pressure at inside of the flow pathways at the location of the block. By compiling those results, the regional pressure distribution could be estimated finally. Next, we assume an appropriate model of flow-pathway structure and adjust it as the pore pressure distribution computed by the model agrees well with that estimated from micro-seismicity. Fig. 1c illustrates an example of the 2D model of flow-pathway structure. Again we divide the region in concern into blocks as they are consistent with the blocks used for the estimation of pore pressure distribution from micro-seismicity (see Fig. 1a). We assume hydraulic conductivity between the adjacent blocks, and the conductivity is modeled by a slit-like flow-pathway which is referred to the pathway-unit. The pathway-unit is assumed to be located connecting each center of the adjacent blocks, and it has a constant width everywhere but its height varies one by one according to the degree of local hydraulic conductivity. We applied this method to analyze the MS events obtained by the Australian HDR project. Figure 2a and b show the pressure distribution estimated from micro-seismicity and the distribution of fluid flow simulated using the flow-pathway structure estimated from the pressure distribution, respectively.

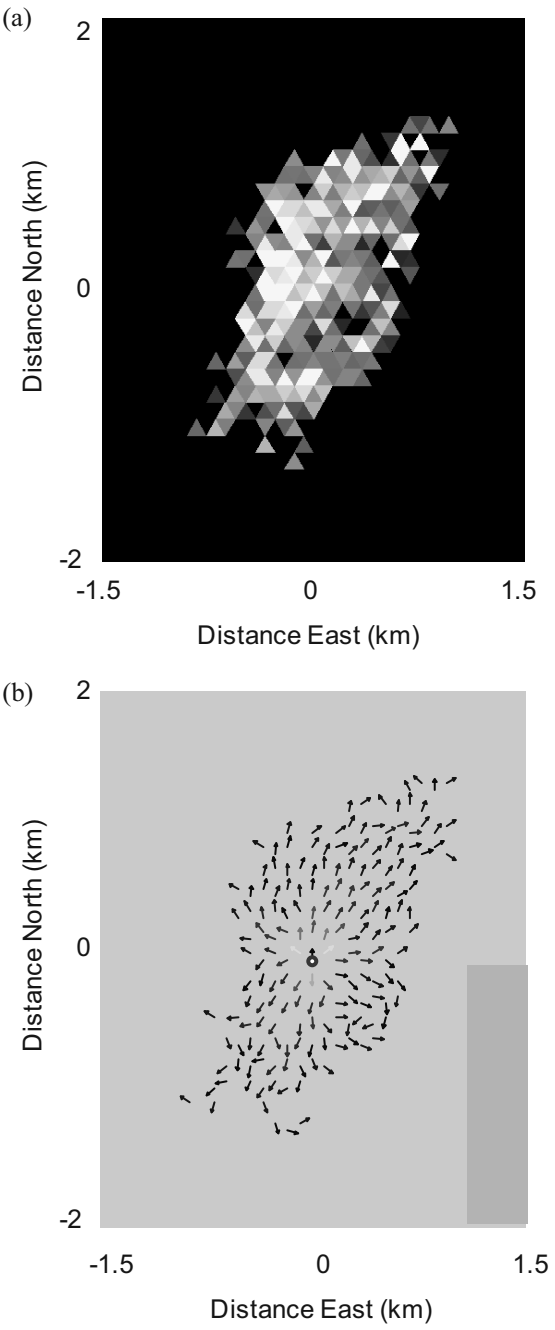

Fig. 2 (a) Pore pressure distribution and (b) distribution of fluid flow simulated using the flow-pathway structure estimated from the pressure distribution.

Eighth International Conference on Flow Dynamics
November 9 - November 11, 2011

Fault-Plane Solution of Acoustic Emission Induced by Pore Pressure Increase in a Tri-axial Experiment of Berea Sandstone

Tsuyoshi Ishida, Daisuke Fukahori, Motoi Ishida, Ryousuke Sato and Sumihiko Murata,
Kyoto University, Kyoto 615-8540, Japan
Shigenobu Onozuka, Kazuhito Oseto and Koji Yamamoto.
Japan Oil, Gas and Metals National Corporation, Chiba 261-0025, Japan
E-mail of corresponding author: ishida.tsuyoshi.2a@kyoto-u.ac.jp

ABSTRACT

We monitored AE events accompanied with a failure of Berea sandstone specimen induced by pore pressure increase in a tri-axial experiment. We obtained fault-plane solutions of AE events and compared them with a loading condition in the experiment. The comparison indicates that the fault plane solutions can provide stress condition inducing rock fracturing, as well as those for usual seismic events. The results suggest that AE monitoring is a useful tool to detect behavior of petroleum reservoirs with fluid injection for operation of enhanced oil recovery and others.

1. Introduction

AE (Acoustic Emission) monitoring has been recently often applied to detect behavior of petroleum reservoirs. For example, at oil fields in Ekofisk and Valhall in North Sea and in Clinton County, Kentucky in U.S., AE events have been monitored with operation of EOR (enhanced oil recovery) [1]. EOR is the technology to recover oil and gas from depleted reservoirs by injecting fluid such as water, natural gas, and carbon dioxide. Since AE events are most likely caused with increase of pore pressure by the injected fluid, the AE monitoring helps to understand how the injected fluid penetrates and permeates.

We monitored AE events accompanied with a failure of Berea sandstone specimen induced by pore pressure increase in a tri-axial experiment. We obtained the fault-plane solutions of the AE events and compared them with a loading condition in the experiment.

2. Specimen and Experimental Method

We used a cylindrical specimen of Berea sandstone as shown in Fig. 1. On the surface of the specimen, twelve cylindrical piezoelectric elements having resonance frequency of 300 kHz (5 mm dia. and 6.7 mm thick) and two cross strain gauges (5 mm long) were glued. The specimen was covered by silicon rubber with pedestals and set in a pressure cell.

3. Results and Discussion

3.1. Procedure of Loading

Fig. 2 shows change of axial pressure (σ_1), confining pressure (σ_3), pore pressure (P), and strains (ε_1, ε_3 and ε_{vol}) along the elapsed time in the experiment.

In the first step from the beginning to the point (1) in Fig. 2, after the axial pressure was applied slightly, under controlling the axial displacement kept to be zero, the confining pressure (σ_3) was applied and kept at 9.64 MPa, and increased again up to the predetermined magnitude, 36.2 MPa. As the result of the control, the axial pressure (σ_1) increased up to 36.8 MPa, keeping condition of hydrostatic pressure on the specimen. During this operation, water was injected from bottom of the specimen, and pore pressure (P) was increased up to the predetermined initial pore pressure (P_0), 23.8MPa.

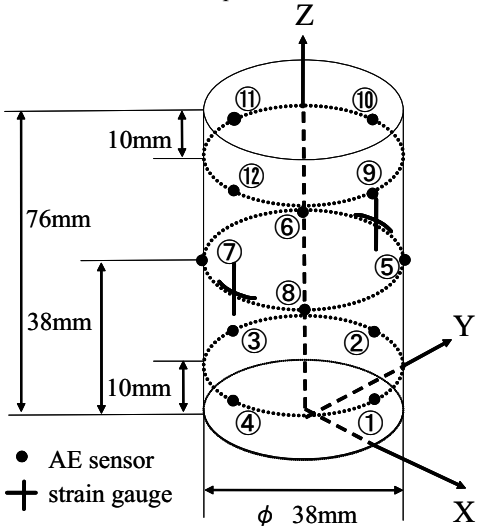

Fig. 1 Specimen and positions of AE sensors.

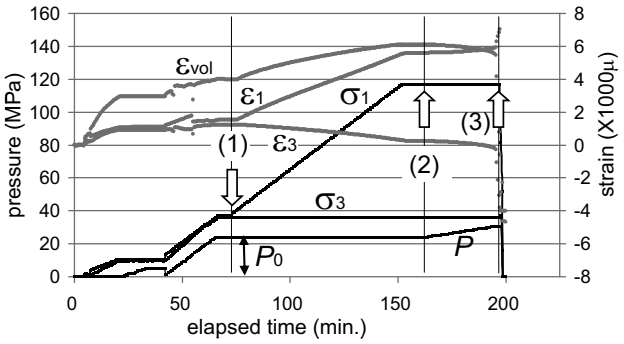

Fig. 2 Stress and strain along the elapsed time.

The pore pressure measured at the top of the specimen became equal to that at the bottom within seconds, due to the large permeability 92.1md measured before the experiment. The predetermined magnitudes of the confining pressure and the initial pore pressure are referred to those at a real oil field in Middle East where seismic monitoring with EOR is planned.

In the second step from the points (1) to (2) in Fig. 2, only the axial pressure was increased up to 116.9 MPa, which was determined so as to make 'stress severity' equal to 0.85, and the stress condition was kept for about 10 minutes. Here, the 'stress severity' is defined as a ratio of a current stress condition to a stress

condition which would have been required to cause failure of the specimen, following the definition by Fairhurst [2]. At the final step from the points (2) to (3) in Fig. 2, when only the pore pressure was increased up to 30.8MPa, the specimen was failed.

3.2. Comparison between AE Sources and X-Ray CT Images

AE sources were obtained from differences of P-wave arrival times at the respective AE sensors. Among them only seven AE events were located within an error less than about 5 mm.

Fig. 3 shows comparison between the located AE sources and the X-ray CT images in the center of the specimen (Y=0) obtained after the experiment. The numbers in Fig. 3 show an order of AE events occurrences along the elapsed time. Actual time along which the AE events from No.1 to No.7 occurred is for only 50.4 seconds just before the specimen failure. In Fig. 3, black parts show low density areas. We can see that the located sources are almost along the macroscopic crack indicated by the thick black line. The fact demonstrates that pore pressure increase induces the failure accompanying AE events that have energy large enough to be located. The fact also suggests that AE monitoring is useful to detect failure of reservoir rock induced by fluid injection in operation of EOR for depleted reservoirs.

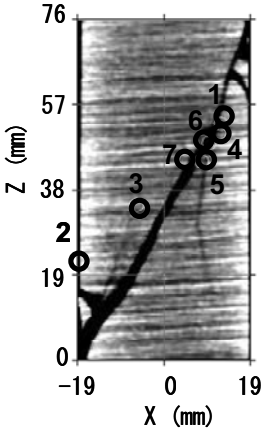

Fig. 3 Comparison between a CT image of the XZ-plane that Y=0mm (the central section of the specimen) and all located AE sources projected onto the plane.

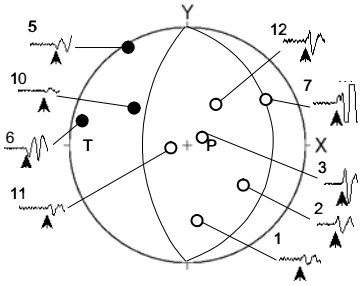

Fig. 4 Fault plane solution of No. 3 AE event.

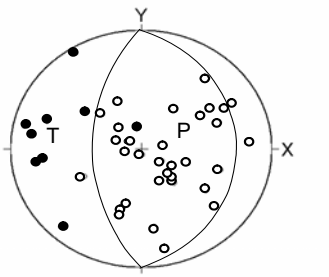

Fig. 5 Fault plane solution obtained by superimposing those of Nos. 2, 3, 5, 6 and 7 AE events.

3.3. Fault-Plane Solution of AE Events

Fig. 4 shows the fault plane solution of No.3 AE event, as an example. In this figure, an open and a closed circles indicate dilatation and compression of P-wave initial motion respectively, which are projected on the lower hemisphere of a Schmidt net. The directions of P- and T-axes, which are the direction of the largest and the smallest principal stresses causing the AE event, are obtained in the almost vertical and horizontal respectively. The directions agree with those of the loading condition in the experiment.

Out of the seven AE events shown in Fig. 3, the directions of P- and T-axes of the solutions for No. 1 and No. 4 do not agree with those of the loading condition, while those of No. 2, 3, 5, 6 and 7 shows good agreement. Fig. 5 shows a solution obtained by superimposing the solutions of No. 2, 3, 5, 6 and 7, on the assumption that the five events are caused by the same fracturing mechanism, in other words, the directions of the fault planes and P- and T-axes are the same. The P- and T-axes agree with the loading condition, excepting the inconsistency that one closed circle exists in the area where open circles should exist. This suggests that the fault plane solutions of AE events induced with pore pressure increase by fluid injection for EOR can provide stress condition inducing rock fracturing, as well as those for usual seismic events. In addition to this, comparison between stress path in the experiment and fracture criterion determined for the Berea sandstone by a series of tri-axial tests demonstrated that the failure can be explained and predicted by a conventional Mohr-Coulomb's fracture criterion and the effective stress theory, which is reported in the other by the authors [3].

4. Concluding remarks

To investigate AE events induced with EOR, we conducted a tri-axial experiment of Berea sandstone specimen with pressurizing pore pressure. Obtained results are summarized as follows.

(1) The seven AE sources were located exactly on or close to the macroscopic crack. The fact demonstrates that pore pressure increase induces the failure accompanying AE events that have energy large enough to be located.

(2) Fault plane solutions for most of the located AE events are consistent with the loading condition in the experiment. This indicates that the fault plane solutions of AE events induced with pore pressure increase by fluid injection for EOR can provide stress condition inducing rock fracturing, as well as those for usual seismic events.

(3) The results suggest that AE monitoring is a useful tool to detect behavior of petroleum reservoirs with fluid injection for operation of EOR and others.

References

[1] A. Jupe et al., Proc. of 2000 SPE (2000), SPE63131.
[2] C. Fairhurst, Int. J. Rock Mech. Min. Sci., **1**(1964), 535-546.
[3] T. Niwa et al., Proc. of 6th Asian Rock Mechanics Symposium (2010), Paper No. 53(CD-Rom).

Eighth International Conference on Flow Dynamics
November 9 - November 11, 2011

Distinct Element Modeling of Acoustic Emission Induced by Hydraulic Fracturing in Laboratory

Hiroyuki Shimizu [a], Sumihiko Murata [b], Takatoshi Ito [a] and Tsuyoshi Ishida [b]
[a] Institute of Fluid Science, Tohoku University, Japan
[b] Dept. of Civil and Earth Resources Engineering, Kyoto University, Japan
E-mail of corresponding author: shimizu@geo.ifs.tohoku.ac.jp

ABSTRACT

The hydraulic fracturing process and the effect of fluid infiltration on the fracturing behavior of rock can be successfully reproduced and discussed in detail by the flow-coupled DEM simulations. The simulation results show good agreement with the actual experimental results including the AE measurement data. The findings obtained from this study are summarized as follows. When the fluid pressure acting on the fracture tip increases sufficiently, the hydraulic fracture has tortuous paths according to the boundary of the mineral grain, and shear cracks that emit significantly large energy are generated to connect pre-existing cracks.

1. Introduction

Most of rock engineering projects are all closely related to fluid flow in fractured rock mass. Especially in the oil production industry and geothermal industry, hydraulic fracturing is often used for improving the productivity of oil/gas and hot water/steam respectively. To use the hydraulic fracturing effectively and control the fracture geometry, it is necessary to clarify the mechanism of the hydraulic fracturing. However, the actual design and operation of an effective hydraulic fracturing is difficult. It is difficult to directly observe the infiltration behavior of fluid and change of stress distribution in surrounding rock mass during the fluid injection. Therefore, even at present, it is still a challenging task to investigate the hydraulic fracturing mechanisms.

On the contrary, the numerical simulation using the Distinct element method (DEM) [1,2] can directly represent grain-scale microstructural features of rock, such as pre-existing flaws, pores, microcracks and grain boundaries by considering each grain as a DEM particle without complicated constitutive laws. The hydraulic fracturing process and the effect of fluid infiltration on the fracturing behavior of rock can be successfully reproduced and discussed in detail by the coupled fluid flow and the DEM.

In this paper, numerical simulations using the flow-coupled DEM code for hydraulic fracturing in rock specimen are presented [3], and the mechanisms of the fracture generation and propagation during hydraulic fracturing is investigated.

2. Flow-coupled DEM

The fluid flow algorithm is introduced into the original DEM code to simulate the hydraulic fracturing [3,4]. In the fluid flow algorithm, the aperture of the adjoining particles is assumed as a flow channel, and a series of enclosed domain is created by connecting the centers of adjoining particles to calculate the change of fluid pressure. The fluid flow in the channel is assumed as laminar flow in the two parallel plates with certain aperture, which can be expressed by the Poiseuille equation. The fluid pressure calculated in each domain was updated during fluid flow calculations and applied to the surface of surrounding particles.

3. Rock specimen model and simulation condition

Fig.1 illustrates the rock model and loading condition for the DEM simulation of hydraulic fracturing. The rock model is expressed by the assembly of particles bonded with each other. The number of particles is 18,505. The particle radius was uniformly distributed between maximum radius (1.0mm) and minimum radius (0.5mm) by using uniform random numbers. A borehole for fluid injection was created at the center of the model. The rock model is surrounded by the four confining walls. The right and upper walls can move to keep the confining pressure constant. Two confining pressures, 10MPa in the *x*-direction and 5MPa in the *y*-direction, were applied to the rock model.

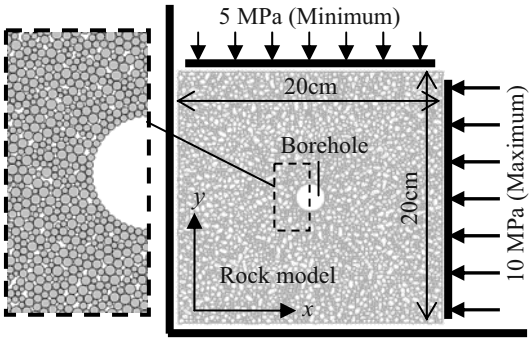

Fig. 1 Rock specimen model and loading condition for the simulation of hydraulic fracturing.

Table 1. Rock model properties and input parameters.

Number of particles:	18,505
Maximum particle radius:	1.0 mm
Minimum particle radius:	0.5 mm
Shear strength of bonding:	249 MPa
Tensile strength of bonding:	21 MPa
Compressive strength of rock model:	199.9 MPa
Tensile strength of rock model:	10.2 MPa
Young's modulus of rock model:	70.2 GPa
Poisson's Ratio of rock model:	0.248
Permeability of rock model:	1.0×10^{-17} m^2

The microscopic mechanical parameters used in this simulation were calibrated by preliminary simulations of uniaxial compression test, permeability test and Brazilian tests. In this study, macroscopic mechanical properties of Kurokamijima granite were used to calibrate the microscopic parameters. The microscopic mechanical parameters used in this simulation and the calibration results are summarized in Table 1. The high viscosity fluid ($100\,\mathrm{mPa \cdot s}$) was used as a fracturing fluid. Fracturing fluid was injected into the borehole at constant pressurizing rate.

4. Results and Discussion

Fig.2 shows the spatial distribution of microcracks generated during the hydraulic fracturing simulation. The closed circle indicates a location of tensile crack and the open circle indicates that of shear crack. The diameter of the circle corresponds to the strain energy released with the crack generation. Since the magnitude of Acoustic emission (AE) event would strongly relate to the released strain energy, the strain energy is assumed to be the energy corresponding to the magnitude of the AE event. As shown in Fig.2, the generated fracture propagated in parallel with the direction of maximum confining stress, and the tensile cracks were dominant. However, a few shear cracks emitting significantly large energy were generated.

Fig.3 shows the fracture propagation and fluid infiltration behavior around the fracture at the time before and after such shear crack generation. The solid lines indicate the generated cracks and the shade of each domain indicates the fluid pressure. The fracturing fluid infiltrates into the fracture after the fracture generation and propagation. The shear cracks that emit significantly large energy were generated when the fluid infiltrated into the fracture after the fracture development.

Since the rock model is expressed by the assembly of particles, the hydraulic fracture is microscopically tortuous due to the particle arrangement. When the fracture is tortuous and there exists the region where fracture width is narrowed locally, fluid infiltration is obstructed. The higher fluid pressure is required in order that a fracturing fluid go through such a narrow region. As a result, when the fluid pressure acting on the fracture tip sufficiently increases, shear cracks emitting significantly large energy are formed to connect pre-existing cracks. This fracturing process is similar to the Hill's model [5] which is originally proposed for volcanic earth quake swarms. Similar phenomena were also observed in actual field scale AE measurement as reported [6]. To validate this phenomenon, more detailed analysis, such as field scale simulation, would be required.

5. Concluding remarks

In this research, simulations for hydraulic fracturing in rock specimen were performed using the flow-coupled DEM code to investigate the mechanisms of the fracture generation and propagation during hydraulic fracturing. When the fluid pressure acting on the fracture tip increases sufficiently, the hydraulic fracture has tortuous paths according to the boundary of the mineral grain, and shear cracks that emit significantly large energy are generated to connect pre-existing cracks. For further discussion on the actual field scale hydraulic fracturing, more detailed analysis including field scale DEM simulation should be done. This is our future work.

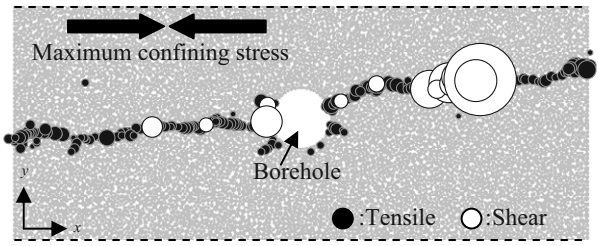

Fig. 2 Crack types and magnitude of energy emitted from the cracks.

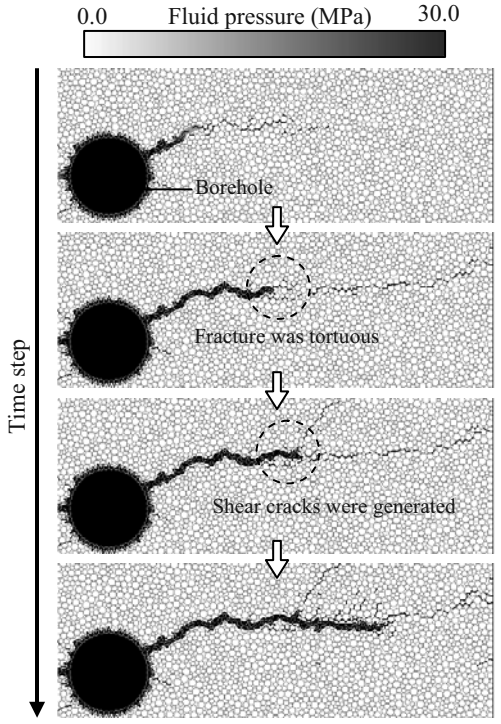

Fig. 3 Fracture propagation and fluid infiltration behavior.

References

[1] P.A.Cundall and O.D.L.Strack: Geotechnique, **29**(1979), pp.47-65.
[2] D.O.Potyondy and P.A.Cundall: Int. J. Rock Mech. Min. Sci., **41**(2004), pp.1329-1364.
[3] H.Shimizu, S.Murata and T.Ishida: Int. J. Rock Mech. Min. Sci., **48**(2011), pp.712-727.
[4] Al-Busaidi, J.F.Hazzard and P.P.Young: J. Geophys. Res., **110**(2005), B06302.
[5] D.Hill: J. Geophys. Res., **82**(1977), pp.1347-1352.
[6] X.Lei, G.Yu, S.Ma, X.Wen, and Q.Wang: J. Geophys. Res., **113**(2008), B10310.

OS10: Biofluid for Medical Application

Eighth International Conference on Flow Dynamics
November 9 - November 11, 2011

Optimisation of Stents for Cerebral Aneurysm Application

Karkenahalli Srinivas and Chang-Joon Lee
School of Aerospace, Mechanical and Mechatronic Engineering
University of Sydney, NSW 2006, AUSTRALIA
Email: karkenahalli.srinivas@sydney.edu.au

ABSTRACT

The study attempts to optimize stents used to cure aneurysms by causing flow diversion in the cavity. The well established technique of Exploration of Design Space is utilized. The objective functions chosen are the reduction of velocity and vorticity in the aneurysm. A sample space of forty to sixty candidates is selected based on the Latin Hypercube technique. Software Fluent is used to compute the objective functions. By standard methods such as Kriging, optimum candidates are evolved. The study focuses both on two and three dimensional flows. Many interesting results are discussed.

1. Introduction

Aneurysms are caused by pathological dilation of the arterial wall. Their excessive growth may result in rupture and cause internal haemorrhage, leading to stroke or death [1]. To avoid rupture, stents are used to cause a flow diversion in the aneurysm cavity. A number of detailed studies on a two-dimensional simplified model of stented aneurysms such as ones carried out by Hirabayahsi et. al. [2] showed that the position of gaps and struts, and their size has a considerable effect on the flow diversion caused. Other studies also revealed the possibility of optimizing stent design to produce preferable flow patterns in the aneurysm dome and maximize the flow reduction [3-7].

In order to optimize the stent design for an effective flow diversion, a number of idealized stent models with variable strut sizes, spacing and porosity were studied using CFD methods and Exploration of Design Space. This is similar to the work reported by Srinivas et. al. [8], which considered optimization of stents for coronary arteries. The details for optimization can be found in Refs [9-10]. Only variable pore density/strut size case will be presented and discussed in this paper.

2. Method

An idealized aneurysm model was used for purpose of simplification. A straight pipe was used to represent the parent blood vessel, and a sphere to represent the aneurysm sac. The diameter of the parent blood vessel is 4 mm, its length 50 mm, while the spherical aneurysm is 10 mm in radius and is 10 mm wide at the neck. For the construction of the blood vessel and aneurysm, Gambit 2.3 preprocessor was used.

An idealized CAD model of a typical stent was generated using Pro Engineer Wildfire 2.0. Stents with variable cross-section size and pore density (the number of pores in the stent per unit area) were considered. The size of the struts was kept between 30 and 150 μm while the pore density varied between 10 and 150 pores/mm^2 (30-99% porosity). A case with unconstrained porosity was first considered and constrained porosity (between 65% and 90%) was studied afterwards. A total of 60 individual samples were modeled using Pro Engineer.

The CAD models were then imported to GAMBIT 2.3, and meshed using tetrahedral scheme and sizing functions. The number of cells ranged from 1.5 million to 3.9 million cells. The blood flow was simplified as isothermal, incompressible, laminar Newtonian flow with a density of 1060 kg/m3 and a viscosity of 0.0035 Pas. The flow velocity at the entry is 0.3 m/s and the Reynolds Number based on entry conditions is 363. The boundary conditions of the inlet, outlet, vessel, aneurysm wall, and stent are time-independent. A constant pressure was set on the outlet, and no-slip condition was employed on the vessel, aneurysm, and stent. The velocity condition at the flow entry is set to constant. The basic equations of continuity and the Navier-Stokes equation were solved to determine the flow field. The calculation using the finite volume method was performed by FLUENT 6.3.26. Computations were performed exclusively on personal computers at the University of Sydney, and the CPU time required varied from three to seven hours depending upon the case.

Once the computations were complete, design optimization was then performed using Kriging method to obtain a set of optimum solutions. The objective functions were velocity and vorticity reduction within the cavity, and these functions were to be maximized.

3. Results and Discussion

Two different conditions were applied while obtaining the optimized solution. At first, the optimization was carried out without applying any constraints. Then a geometrical constraint was applied during Kriging process to keep the nondominated solutions within the range of 60 – 95 % porosity.

The compromise solution for unconstrained case has a cross section of 150 um, a porosity of 37 % and a pore density of 135 pores/mm^2. The constraints were then applied in the second optimization. The cross section of the new compromise solution is now reduced to 138 um, and has a porosity of 60 % and a pore density of 93 pores/mm^2. The recalculated objective functions were in close agreement with the prediction by Kriging. Figure 1 shows a comparison of vorticity contours of no-stent case and optimized solution with geometrical constraints applied. The CAD model for optimized stent design with geometrical constraint is shown in Figure 2.

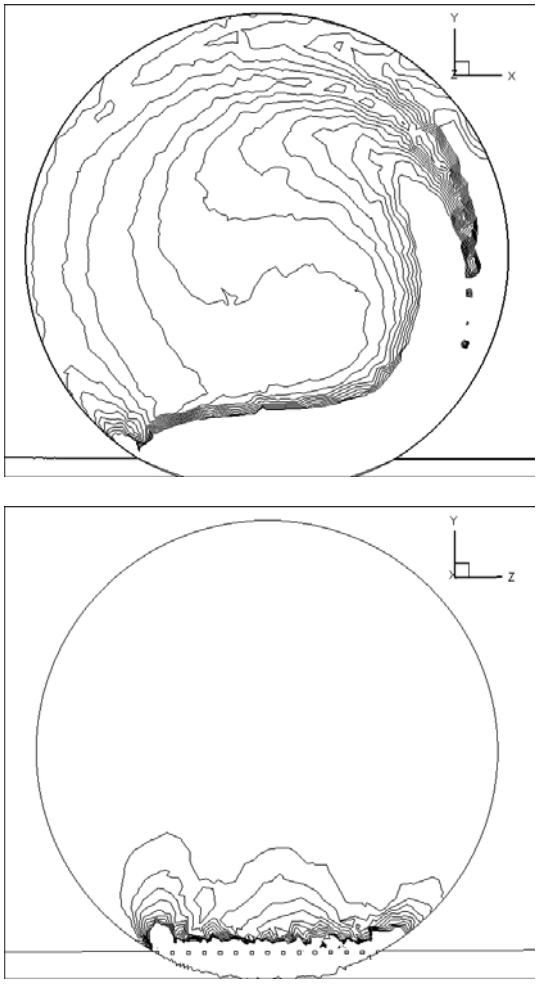

Fig. 1 Vorticity contour for no-stent case (top) and optimized stent (bottom).

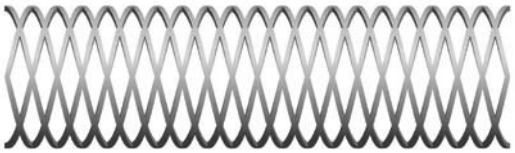

Fig. 2 CAD illustration of optimized stent model.

The results from both unconstrained and constrained cases indicate that both large strut size and high pore density are required for maximum flow reduction.

4. Concluding remarks

Idealized three-dimensional stents for aneurysms have been investigated for observing the relationship between stent design parameters and flow activity within the aneurysm cavity. Optimization was also carried out based on exploration of design space principles, with velocity and vorticity reduction in the aneurysm dome as the objective functions. It was also found that maximum flow reduction occurs for low porosity ratio and large strut size combination. This work has also identified pore density as an important design parameter for an effective flow diversion. The results from this study regarding flow reduction were almost identical to previous two-dimensional study by the authors.

For more practical stent design and optimization, one must clearly understand the cause of rupture mechanism. Hence, it is recommended to investigate aneurysm rupture in more detail, especially the effect of stenting on temporal and spatial WSS distribution in aneurysms. This will allow us to properly consider WSS as part of objective functions in future optimization projects.

References

[1]. D.M. Sforza, C.M. Putman,J.R. Cebral, Hemodynamics of Cerebral Aneurysms. Ann. Rev. Fluid Mech., **41**, pp. 91-107 (2009)

[2]. M. Hirabayashi, M. Ohta, K. Barath, D.A. Rufenacht, B. Chopard, Numerical Analysis of the Flow Pattern in Stented Aneurysms and its Relation to Velocity Reduction and Stent Efficiency. Math. Comput. Simulat., **72**, pp. 128-133 (2006)

[3]. J.C. Lasheras, 2007, "The Biomechanics of Arterial Aneurysms," Annu. Rev. Fluid Mech., **39**, pp. 293-319.

[4]. M. Kim, D.B. Taulbee, M. Tremmel, and H. Meng, , "Comparison of two stents in modifying cerebral aneurysm hemodynamics," Ann. Biomed. Eng., **36**(5), pp. 726-741, (2008) .

[5]. M. Hirabayashi, M. Ohta, D.A. Rufenacht, and B. Chopard, 2003, "Characterization of Flow Reduction Properties in an Aneurysm Due to a Stent," Phys. Rev. E, **68**, pp. 021918

[6]. T. Nakayama, M. Ohta, D.A. Rufenacht, and A. Takahashi, "The Effect of Stenting With Difference Positions on Hemodynamics in a Cerebral Aneurysm," *The Ninth International Symposium on Future Medical Engineering Based on Bionanotechnology* (Tohoku University 21st Century COE Programme), Sendai International Center, Sendai, Janpan, Jan. 7-9, pp. 106-107, (2007).

[7]. M. Ohta, N. Fujimura, L. Augsburger, S. Wetzel, H. Yilmaz, G. Abdo, Karl-Oloflovblod, K. Barath, and D.A. Rufenacht, "Impact of Stent on Blood Flow in a Model of Cerebral Aneurysm," Proceedings of 2005 Annual Meeting, Japan Society of Fluid Mechanics, Paper No. AM05-17-008, (2005).

[8]. K. Srinivas, M. Ohta, T. Nakayama, S. Obayashi, T. Yamaguchi, Studies on Design Optimization of Coronary Stents. J Medical Devices, **2**, pp. 011004-1-011004-7 (2008)

[9]. S. Jeong, S.Obayahsi, Multi-Objective Optimization using Kriging Model and Data Mining. KSAS International Journal, **7**, pp. 1-12 (2006)

[10]. R.H. Myers, D.C. Montgomery, Response Surface Methodology: Process and Product Optimization Using Designed Experiments, Wiley, New York, pp. 1-84 (1995)

Eighth International Conference on Flow Dynamics
November 9 - November 11, 2011

Computational Fluid Dynamics using Medical Images on Biomechanics

Teruo Matsuzawa*, Futoshi Mori**, Kiyoshi Kumahata***, Sho Hanida**
*Research Center for Advanced Computing Infrastructure, Japan Advanced Institute of Science and Technology (JAIST). 1-1 Asahidai, Nomi, Ishikawa, 923-1292, JAPAN
**Information for Science and Technology, JAIST. 1-1 Asahidai, Nomi, Ishikawa, 923-1292, JAPAN
***Fujitsu Nagano Systems Engineering, Ltd, 1415 Turuga Midori-cyo, Nagano, Nagano, 380-0813, JAPAN
matuzawa@jaist.ac.jp

ABSTRACT

We have continued to study for the Computational Fluid Dynamics (CFD) and HPC. Especially, biomechanics flow is major subject. In this paper, we are described four subjects that are Air-Flow Simulation in Nasal Cavity, Blood Flow Simulation in Thrombosed Aortic Dissection, Blood Flow Simulation in Cerebral Aneurysm with stent and Heart Simulation using Medical Images Voxel Based Fluid-Structure-Cell Interaction Analysis.

1. Introduction

There are significant flows, blood flow and airflow in human body. The blood flow impacts mechanically blood vessel wall. This mechanical stress is regarded as one of the cause of circulatory disease e.g. arteriosclerosis, aneurysm, etc. We are investigating mechanical interaction between blood flow and blood vessel wall using realistic blood vessel shape that reconstructed from the medical images such as magnetic resonance imaging (MRI) and computed tomography (CT). In this paper, we are described four subjects that are Air-Flow Simulation in Nasal Cavity, Blood Flow Simulation in Thrombosed Aortic Dissection, Blood Flow Simulation in Cerebral Aneurysm with stent and Heart Simulation using Medical Images Voxel Based Fluid-Structure-Cell Interaction Analysis.

2. Air Flow Simulation in Nasal Cavity

The nasal cavity has complex anatomy, and the flow in nasal cavity is complex. The nasal cavity has functions that are breathing, smelling, humidification, warming and cleaning of the inhaled air. By these functions, humans can adapt to harsh environments. Moreover, physiological functions of maximally sinus have not understood sufficiently. To clarify a function of nasal cavity, we calculate airflow of nasal cavity with maximally sinus using heat and humidity model.

The nasal cavity wall is composed of mucous membranes, blood vessel, and etc. The temperature and humidity of the inhaled air are adjusted by function of the mucous membranes. In this work, we focus on heat and humidity transfer from the organ side via membranes. Therefore, heat and humidity models constructed. Fig.1 shows the reconstruction shape using CT, and airflow in nasal cavity is visualized by streamline. The high velocity area is middle meatus. And, superior meatus and inferior nasal meatus is low velocity area. In the maxillary sinus, airflow is quite slow in comparison with main flow of nasal cavity. And, flow patterns of left and right maxillary sinus are different. In addition, large swirling flow is seen in the each of maxillary sinus. The temperature and humidity function are adjusted in front of nasal cavity.

We examine the flow of nasal cavity include maxillary sinus. Temperature and Humidity of inhaled air are adapted to suitable condition by function of nasal cavity. In the maxillary sinus, temperature and humidity are maintained high and velocity of airflow is low. In addition vortex flow was seen in the each of maxillary sinus.

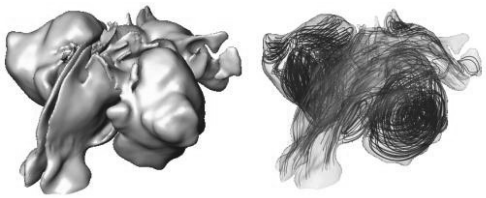

Fig.1 (left) Reconstructed Nasal Cavity Shape (right) Airflow of Nasal Cavity using stream line: The color mens the velocity speed. Red indicates high speed velocity, and Blue indicates low speed velocity.

3. Blood Flow Simulation in Thrombosed Aortic Dissection

The pathogenesis of aortic dissection is an intimal tear or damage to the aortic wall. The aortic dissections can be classified on basis of blood flow in false lumen. The mortality rate for the thrombosed type is higher than that for the patent type. In the thrombosed type, it has been reported that although the false lumen is completely occluded by the thrombosis, blood flow may be preserved, and the aneurysm may form. There is Ulcer-Like Projection (ULP) as a process to the aneurysm of the thrombosed type.

The purpose of this study is clarified the hemodynamics predictive factor. A dynamics stress as risk factor was related for progress of aneurysm due to the thrombosed dissected thoracic aorta.

The realistic shape is reconstructed from the time-series of medical images that developed ULP, and progress the ULP that means before immediately rupture. These shape defined case1-A and case1-B, respectively. The time span is about three month, which rapidly progressing.

Fig.2 shows the velocity in ULP using vector. The flow pattern into ULP is similar. The outline of vortex center is agreed with case1-A and case1-B. At before immediately rupture, the two vortexes is seen into ULP.

Moreover, the pressure distribution of below and both side in ULP is larger than that of upper in ULP. In part of high pressure distribution, the ULP has been progressed. And WSS distribution is almost changeless.

We examined the prediction of hemodynamic factor in the thrombosed aortic dissection. This investigation has indicated that a developing aneurysm occurs in region with high pressure distributions and low WSS region at entry part. This time-dependent of change is important the movement of center of the vortex in ULP for develop.

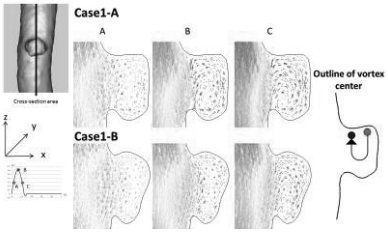

Fig.2 the flow using vector at unsteady analysis: The upper indicate case1-A, and the below indicate case1-B. Right indicate the outline of vortex center that founded by LIC method.

4. Blood Flow Simulation in Cerebral Aneurysm with stent

Endovascular treatment is a low invasive therapy. The clinical experience with stent implantation flow diversion has been reported. Moreover, the effect of only stent on the flow reduction in cerebral aneurysm has been reported in CFD and experiment. In stent treatment, the diameter of stent is larger than that of blood vessel place to prevent the departure of stent by clinical definition. To clarify the effect to aneurysm in non-curvature model that considered the blood vessel expansion by stent placement.

Fig.3(left) shows the inflow to aneurysm and outflow from aneurysm velocity profiles using contour at each expansion rate. The maximum of inflow velocity has decreased by increasing expansion rate. When we assumed inflow at non-expansion to be 100%, the inflow at 3% expansion decreased 10.5%, the inflow at 6% expansion decreased 21.8%. Fig.3(right) shows the WSS on aneurysm using contour at each expansion rate. The WSS distribution is decreased by stent placement. When we assumed mean WSS on aneurysm wall at non-expansion to be 100%, the WSS at 3% expansion decreased 13%, the WSS at 6% expansion decreased 23.9%.

We examined the effect to aneurysm by stent expansion. The inflow to aneurysm and WSS on aneurysm wall has decreased by considering blood vessel expansion by stent placement.

5. Heart Simulation using Medical Images Vovel Based Fluid-Structure-Cell Interaction Analysis

To assist diagnosis and treatment in daily medical scene, our final goal is to make circulatory system simulation for whole human body easily. Blood flow is driven by heart wall deformation,

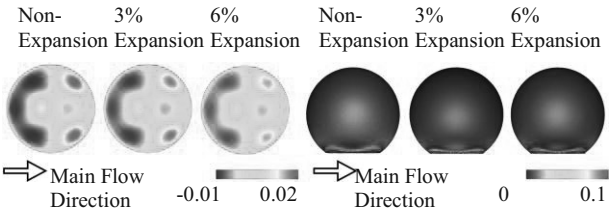

Fig.3 (left) Inflow to aneurysm and outflow from aneurysm using contoru (right) Wall shear stress on aneurysm wall using contour.

the deformation occurred by cardiomyocyte behavior, and cardiomyocyte behavior is under influences of heart shape changing in each time. Therefore it is necessary to consider fluid-structure-cell interaction. It is convenient to calculate the deformation in Eulerian grid because the heart shape is obtained as voxel data by medical imaging devices such as CT. To simulate heart motion in voxel data, we develop the code in Eulerian frame interacting with cardiomyocyte simulator. In our model, both fluid and elastic solid are considered as incompressible continuum. By this assumption, motion of both materials is described by same type momentum equation. Momentum equations of both are combined into a mixture of fluid and solid by formulation that relates deformation velocity and solid stress, and VOF method. And conventional fluid flow analysis method calculates mixture motion. In addition, the force driving heart motion computed by the cell simulator “simBio” and cardiomyocyte model "Kyoto Model" is assigned internal stress of solid as active contractile stress.

Using this method, we simulated self-contraction of elastic solid in a fluid as a simply model of heart motion and blood flow driving. By assigning the contractile stress for the solid, we obtained the result that the solid began to contractile and its magnitude was corresponding to the active contractile stress and the elastic modulus of solid. And Fig.4 shows that using this code, we performed simple heart model shape behavior, and we obtained the result that the fluid flow resembling the blood flow is driven by the solid deformation resembling the heart wall due to cardiomyocyte contractile.

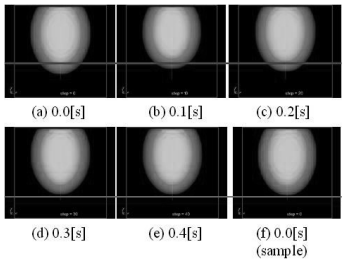

Fig.4 Shape at Typical Time.

6. Summary

We have paid lot attention about CFD. In this paper, we showed some our studies for biomechanics flow. We hope that computational biomechanics simulation will be a useful tool to improve medical and quality of life for everyone.

Eighth International Conference on Flow Dynamics
November 9 - November 11, 2011

Visualization of Flow Characteristics of Prosthetic Mono-leaflet Heart Valve

Sanjeev D. Muskawad and Shailendra D. Sharma
Aerospace Engineering Department, Indian Institute of Technology (Bombay)
Powai, Mumbai. 400076
dmsanjeev@msn.com

ABSTRACT

Orientation of prosthetic heart valve is extremely important during surgical implantation. In mock circulation a pulsatile flow across the Medtronic-Hall and Bjork-Shiley valve was visualized using laser sheet illuminating naphthalene particles suspended in glycerin mixed water. Flow reversal, formation of eddies in the disc wake region, accelerating and decelerating flows curling up into vortices are some of the striking flow features that were observed particularly during closing and opening phases of valve. The flow through Bjork-Shiley valve exhibited considerable regurgitation in the region around the disc rim when the valve was seen in closed position.

1. Introduction

Since the first success in surgical implant of mechanical heart valve prostheses to replace the diseased natural heart valves, the evolution of mechanical heart valves for over last five decades has witnessed a variety of improved physical designs with superior materials. In India the TTK Chitra heart valve which is a single tilting disc valve is in clinical use. In vitro flow visualization studies of various types of cardiac prosthetic valves have revealed evidences of formation of vortices [1, 2, 3, 4, 5, 6], wake [2], cavitaion bubbles [3, 6, 7, 8], and high shear regions [2, 5, 9, 10].

The present experimental work is a simple engineering approach to produce pulsating flow and capture the flow patterns emerging in the vicinity of two different types of mono-leaflet mechanical heart valves, Medtronic-Hall valve and Bjork-Shiley valve, both operating cyclically inside two parallel tubes simulating the aortic tracts. The flow field in the diametrical plane was illuminated using a laser sheet to enable video recording of the flow structures that were evolving periodically. The frame by frame analysis of the flow visualization images elucidates the complex kinematics of the flow through a monoleaflet mechanical heart valve placed in the aortic position

2. Method

The components of mock circulation included two transparent Perspex tubes of 20 mm. At the centre of these tubes a Medtronic-Hall valve and Bjork–Shiley valve denuded from sewing ring were fixed. Proximal ends of these tubes were connected through Y connector to a manually driven periodic flow generator. The distal ends of these tubes were connected through another Y connector to a reservoir cum compliance chamber. The opening direction of valves was opposite to each other, helping to create recirculating flow. The blood viscosity matching fluid used for simulation was mixture of 30% glycerin and 70% of water. The appropriate small amount of fine powder of naphthalene as tracer particles (flow marker) was mixed into this glycerin water mixture. A 5 W power argon-ion laser was used as the light source. The laser beam was passed through a clear glass rod of about 3 mm diameter that served as a cylindrical lens and produced a light sheet which was used to illuminate the flow field.

3. Results and Discussion

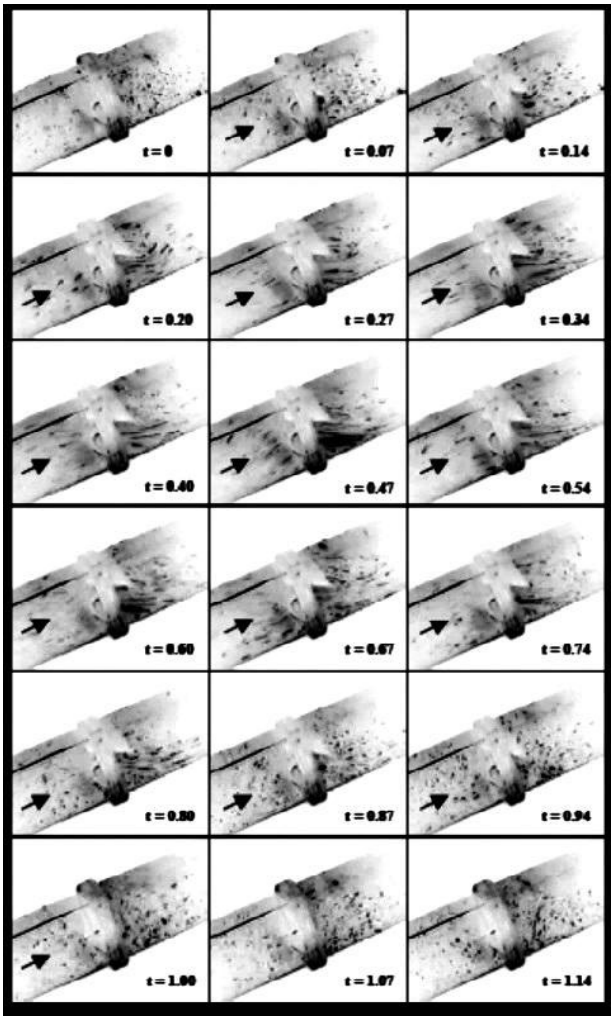

Figure 1. Flow through Medtronic-Hall valve during a complete systole period from opening to fully closed position. Arrows indicate the flow direction and the time shown in each frame is at the interval of 0.07 second.

The Figure 1 shows images of flow through prosthetic Medtronic-Hall valve with its disc in various positions

over a complete opening-closing cycle. The valve begins to open from fully closed position at t = 0, attaining the fully open position with the disc tilting to its maximum design angle of 75° leading to the peak flow rate, and then finally closing to the fully shut position at t =1.
The time shown on each frame is the time lapse in second from the start of the event. It must be pointed out that all through the tests the valves were producing clearly audible sound of disc clapping with the valve seat while closing. Generation of such noise from implanted mechanical heart valves in patients is reported to be of serious concern due to complaints of discomfort and annoyance.

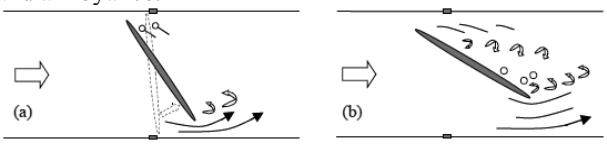

Figure 2. Schematic of flow pattern in the plane of symmetry around the major and the minor orifices during opening of Medtronic-Hall valve. (a) The valve is just opening and (b) during the acceleration phase before reaching the peak flow rate.

When the disc tilts to open the orifices of the valve, the leading edge of the disc pushes the fluid in opposite direction in the region of the minor orifice, whereas the trailing edge of the disc moves in the same direction of the flow allowing acceleration of the flow through the major orifice(Fig. 2). Thus, the flow through both the orifices does not start simultaneously in the same direction and with the same velocity, although the pressure gradient across the valve is the same. From the figure, it appears that the disc reached its maximum opening by t =0.2. However, the flow seems to attain its peak velocity, displayed by the tracer particles in the form of lines, during t =0.34 and t =0.6 and thereafter the phase of deceleration begins. What is surprising to note is that even during the phases of the peak flow, not much activities are seen in the minor orifice region.
Similar observations are reported by Mouret et al. [4]. During the opening phase, when the disc is at steep angles, the wake is formed behind the disc causing locally low pressures that induce the major orifice flow curl around the disc trailing edge as is evident in the frames from t =0.14 to t =0.34.

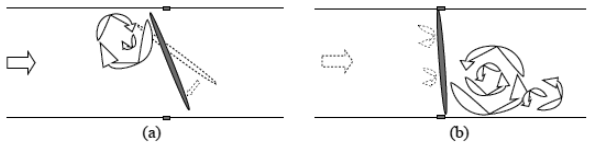

Figure 3. Schematic of flow structures in the plane of symmetry during closure of Medtronic-Hall valve. (a) Valve is about to close, and (b) valve is fully closed.

The deceleration phase is seen to start from t =0.67. As the flow velocity decreases, the major orifice region on both sides of the valve is seen riddled with eddies (t =0.80 to t =0.94). Just after the valve closure, the region downstream of the valve is seen to be dominated by a cluster of vortices (t =1.0 to t =1.14) (Fig. 3).

4. Concluding remarks

Pulsating flow through Medtronic-Hall mechanical heart valve and Bjork-Shiley mechanical heart valve, both with mono-leaflet design, has been investigated in the simulated aortic tubes using the laser sheet flow visualization technique From the observation of resultant flow patterns during the simulated cardiac cycle, following main conclusions are arrived at.
1. During the peak of systolic period, despite the valve being in fully open position, there is hardly any flow seen from the minor orifice of the Medtronic-Hall valve.
2. In the acceleration phase of the systolic period, wake formation accompanied with eddies is noticed behind the disc.
3. Vortices are seen to form during transient phases between systolic and diastolic periods. The vortex downstream of the valve seems to gain strength soon after closure of the valve.
4. Bjork-Shiley valve is seen to suffer from occurrence of very prominent regurgitant flow which was not noticeable for Medtronic-Hall valve, even if it existed.
5. Formation of vortices and resultant generation of turbulence and shear stress seem to be inherent flow features of functioning of a tilting disc.
6. It is demonstrated that crucial information about the complex flow behavior can be elicited from a simple, indigenous and inexpensive test setup.

References

[1] V. Kini, C. Bachmann, A. Fontaine, S. Deutsch and J.M. Tarbell, Annals of Biomedical Engineering, 2000, 28, 431–441.
[2] D. Bluestein, E. Rambod, and M. Gharib, J Biomech Eng., 2000, 122 (2), 125-34.
[3] S. Milo, E. Rambod, C. Gutfinger, and M. Gharib, European Journal of Cardio-thoracic Surgery, 2003, 24, 364–370.
[4] F. Mouret, L. Kadem, E. Bertrand, J.G. Dumesnil, P. Pibarot and R. Rieu, Cardiovascular Engineering: An International Journal, 2005, 5 (1), 13-20.
[5] K.B. Manning, L.H. Herbertson, A.A. Fontaine and S. Deutsch, Journal of Biomechanical Engineering, Transactions of the ASME, 2008, 130 (4), 041001.
[6] W.L. Lim, Y.T. Chew, K.B. Chandran, H.T. Low and K.Y. Seng, J Artificial Organs, 2000, 3, 162-165.
[7] P. Johansen, Expert Rev. Medical Devices, 2004, 1 (1), 95-104.
[8] C. Wu, S.M. Retta, R.A. Robinson, B.A. Herman, and L.W. Grossman, ASAIO Journal: Biomedical Engineering, 2009, 55 (5), 445-451.
[9] Sun Yong-da, Chin. Phys. Letter, 1997, 14 (1), 28-31.
[10] P. Zhang, J.H. Yeo, P. Qian and N.H.C. Hwang, *ASAIO Journal: Biomedical Engineering ,* 2007, 53 (5), 530-536.

Eighth International Conference on Flow Dynamics
November 9 - November 11, 2011

Stent Effects on Aneurysms by Changes in Vascular Architecture

Kenichi Kono, Yuko Tanaka, Ryo Yoshimura, Takeshi Fujimoto, Hideo Okada, Aki Shintani, and Tomoaki Terada
Department of Neurological Surgery, Wakayama Rosai Hospital, Wakayama, Japan
E-mail of corresponding author: Kenichi Kono, vyr01450@gmail.com

ABSTRACT

Intracranial stents are used for treatment of aneurysms. Stents are useful because they can prevent coil protrusion into a parental artery and have some flow diversion effects. Stents also have some effects to change vascular architectures. We have addressed the effects of changes in vascular architectures. We analyzed four clinical cases, which showed change in angles of parental arteries. Computational fluid dynamics simulations were performed for bifurcation type of vascular models with various angles. The results showed that, in most cases, changes of vascular architectures by stent placement may reduce risk of recanalization.

1. Introduction

Intracranial stents are used for treatment of aneurysms. Stents are useful because they can prevent coil protrusion into a parental artery and have some flow diversion effects, which may reduce recanalization. Stents also have some effects to change vascular architectures. However, there are few studies which focused on the effects. Here, we analyzed the effects by using both clinical cases and vascular models. Computational fluid dynamics (CFD) simulations were performed using the vascular models.

2. Method

(a) Clinical cases

There are four cases of bifurcation type of aneurysms treated by stent-assisted coil embolization with Y-stent. We measured changes in angles of parental arteries by stent placements. Using 3-matic software (Materialise NV, Leuven, Belgium), bend angles of parental arteries are measured (Fig. 1). The two 3D vascular structures before and after stent placements were compared.

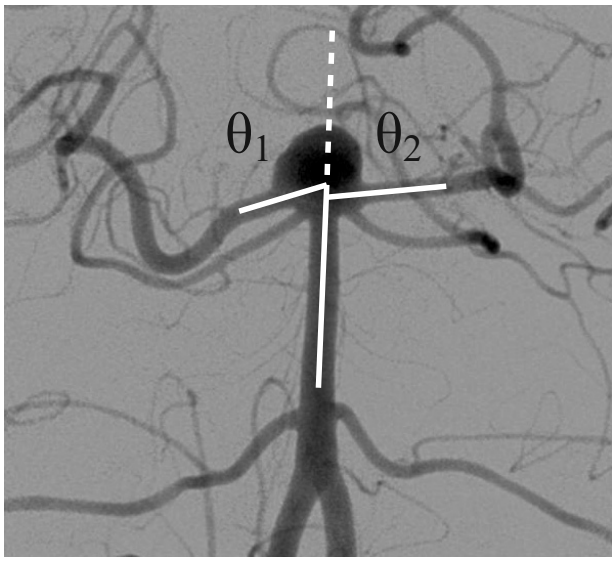

Figure 1. Definition of vascular angles

(b) CFD simulations using vascular models

Using 3-matic software, symmetric bifurcation vascular models (Y-shape) with various angles were made. The bend angles are from 50 degrees to 130 degrees. Figure 2 shows an example of vascular models, which have 50 degrees. The diameters of vascular were 3mm. The top surfaces at the tip of bifurcation were determined for measurements of wall shear stress (WSS), pressure, and other parameters. CFD simulations were performed with the following conditions using ANSYS ICEM CFD and ANSYS CFX (Ansys Inc., Canonsburg, PA, USA).

1. Mesh: Tetrahedral mesh with prism layers on wall surfaces
2. Inlet: 0.3 m/sec, steady flow
3. Outlets: 0 Pascal
4. Blood: density 1053 kg m^{-3}
   viscosity 0.0035 kg m^{-1} s^{-1}
   Newtonian-fluid laminar model

We measured area-averaged WSS and pressure at a top surface of each model.

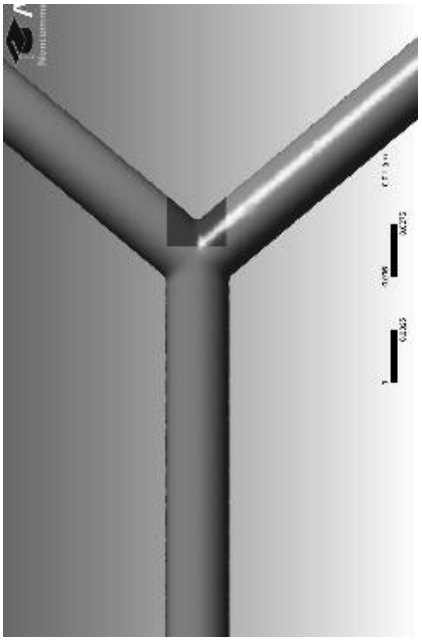

Figure 2. An example of vascular models
(θ_1=θ_2=50 degrees)

3. Results

(a) Clinical cases

There are 8 sets of angles in 4 cases. In all cases, stent placements decreased bend angles with 10.7 degrees in average. Statistical analysis of t-test showed significance at $p = 0.00073$.

(b) CFD simulations using vascular models

Area-averaged WSS at a top surface and vascular angles were calculated. This didn't show any trends between Area-averaged WSS and bend angles.

Area-averaged pressure at a top surface and vascular angles were also calculated. Below 100 degrees, there was a positive relationship between Area-averaged pressure and bend angles. Above 105 degrees, the values of pressure seemed to be almost constant. Between 100 and 105 degrees, there existed a drop of pressure.

4. Discussion

Few reports have yet shown effects of change in vascular architectures by stent placements. First, this study showed vascular angles have actually changed with around 10 degrees by stent placements. Second, CFD simulations showed characteristic feature of change in pressure at a top of surface. Supposed that a low pressure at a top of surface will decrease risk of recanalization after coil embolization for aneurysms (which has yet been proven), the characteristic relationship between Area-averaged pressure and bend angles suggests that in most of cases, vascular change by stent placements will decrease risk of recanalization.

Since these models did not have aneurysms on a top of a bifurcation, it is necessary to figure out better vascular models to elucidate effects on aneurysm by vascular changes.

4. Concluding remarks

We have shown that stents placements changed vascular architecture in clinical cases. CFD simulations showed that the changes may have effects on reducing recanalization after coil embolization for intracranial aneurysms. In addition, this idea can apply for new stent design.

5. Disclosure

Kenichi Kono has received a financial support from Japan Labour Health and Welfare Organization as research funds to promote the hospital functions.

Eighth International Conference on Flow Dynamics
November 9 - November 11, 2011

Comparison between Ultrasonic-Measurement-Integrated Simulation and Ordinary Simulation with Measured Upstream Velocity Condition

Shusaku SONE[1], Takaumi KATO[1], Kenichi FUNAMOTO[2], Toshiyuki HAYASE[2], Masafumi OGASAWARA[3], Takao JIBIKI[3], Hiroshi HASHIMOTO[3], Kouji MIYAMA[3]
1 Graduate School of Biomedical Engineering, Tohoku University, 6-6-4 Aramaki Aza Aoba, Aoba-ku, Sendai 980-8579, JAPAN
2 Institute of Fluid Science, Tohoku University, 2-1-1 Katahira, Aoba-ku, Sendai 980-8577, JAPAN
3 GE Healthcare Japan, 4-7-127 Asahigaoka, Hino 191-8503, JAPAN
sone@reynolds.ifs.tohoku.ac.jp

ABSTRACT

In this study, UMI simulation and ordinary simulation with several upstream velocity boundary conditions were performed for blood flow in a carotid artery. The error of the UMI simulation was found to be almost half that of the ordinary simulation with measured upstream velocity condition, showing better accuracy in reproducing the blood flow.

1. Introduction

Development and progression of cardiovascular diseases is closely related to hemodynamics. As a novel technique to reproduce a blood flow field for advanced diagnosis, the authors have proposed and developed ultrasonic-measurement-integrated (UMI) simulation [1]. This method employs unsteady computation with feed-back of errors in Doppler velocities, which are velocity components in the ultrasound beam direction of the blood flow, between ultrasonic measurement and computation to make the numerical result converge to the actual blood flow field, even if the accurate velocity profile at the upstream boundary is unknown. To date, we have constructed a two-dimensional UMI simulation system (Fig. 1) and shown the relationships between hemodynamic parameters based on the wall shear stress and pathology by investigating a number of clinical data of the carotid artery [2].

However, in the previous study, the accuracy between the UMI simulation and the ordinary simulation with a measured upstream velocity boundary condition was not compared. Thus, in the present study, we performed UMI simulation and ordinary simulation with several upstream velocity boundary conditions for a blood flow in a carotid artery to compare the accuracy of the results.

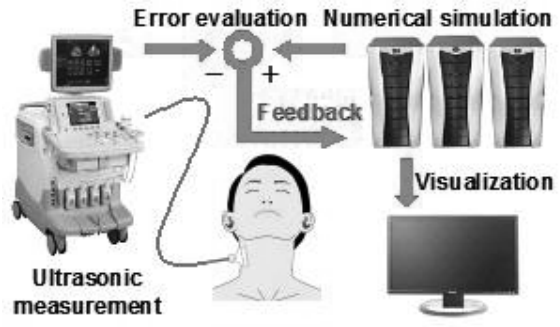

Fig. 1 Ultrasonic-Measurement-Integrated Simulation System

2. Method

The governing equations of UMI simulation are the Navier-Stokes equation (Eq. (1)) and the pressure equation (Eq. (2)) for incompressible and viscous fluid flow,

$$\rho\left(\frac{\partial \mathbf{u}}{\partial t}+(\mathbf{u}\cdot\nabla)\mathbf{u}\right)=\mu\Delta\mathbf{u}-\nabla p+\mathbf{f} \tag{1}$$

$$\Delta p=-\rho\nabla\cdot(\mathbf{u}\cdot\nabla)\mathbf{u}+\nabla\cdot\mathbf{f}, \tag{2}$$

where $\mathbf{u}$ is the velocity vector, p is the pressure, t is time, ρ is the density, μ is the dynamic viscosity, and $\mathbf{f}$ is the feedback signal. It is defined as an artificial body force proportional to the difference of Doppler velocities, V, between ultrasonic measurement and numerical simulation as follows:

$$\mathbf{f}=-K_v^*\frac{V_c-V_m}{U}\left(\frac{\rho U^2}{L}\right), \tag{3}$$

where K_v^* is the feedback gain (non-dimensional), U is the characteristic velocity, L is the characteristic length, and subscripts m and c represent the ultrasonic measure-ment and UMI simulation, respectively. The special case with K_v^* = 0 is the ordinary numerical simulation without feedback. The above governing equations were discretized by means of the finite volume method and were solved with the algorithm similar to the SIMPLER method.

The shape of the carotid artery was extracted by binarizing both time averaged color Doppler images and time averaged B mode images. The shape was then rotated so that the main direction of the blood flow would agree with the x-directional axis, and the computational grid was generated. The size of the computational grid is the same as the resolution of ultrasonic measurement, as Δx=280[μm] and Δy=170[μm], respectively. The objective was a blood flow in a carotid artery of an informed 76-years-old female patient. Ultrasound color Doppler images of 5 heart beats acquired with ultrasound diagnostic imaging equipment (LOGIQ7, GE Healthcare, JAPAN) with an

ultrasonic linear probe was used for analysis. The main frequency and repeated frequency were 5 MHz and 4.4 kHz, respectively. Feedback domain was set from 1/8 to 7/8 of the computational domain from the upstream. Feedback signals were added at each computational grid point in the feedback domain. The ordinary simulation was performed for the following upstream velocity boundary conditions:

(A) velocity profile with the measured Doppler velocity,
(B) velocity profile with the measured Doppler velocity scaled by flow rate estimation,
(C) parabolic velocity profile with flow rate estimation,
(D) uniform velocity profile with flow rate estimation.

UMI simulation was also performed with the same boundary conditions. The feedback gain was set to 100. The downstream boundary condition of all cases was free flow, and the no-slip condition was set on the wall. The blood flow rate was estimated to minimize the summation of the absolute value of the error between the measured and computed Doppler velocities in the feedback domain by means of the golden section method. The accuracy of the calculation was evaluated by the error norm defined as follows:

$$\mathrm{e} = \frac{1}{N}\sum_n |V_c - V_m| \,/V_{\mathrm{type}}, \qquad (4)$$

where V_{type} is typical Doppler velocity at the carotid artery.

3. Results and Discussion

Figure 2 shows a comparison between the ordinary simulation and the UMI simulation for Case (B). In the result for the ordinary simulation in Fig. 2(a), the velocity profile converges to a parabolic distribution in the downstream direction. On the other hand, the result of the UMI simulation in Fig. 2(b) shows downstream drift.

Next, the accuracy of the ordinary simulation and that of the UMI simulation were compared using the error norm of Eq. (4). In Fig. 3(a) for the ordinary simulation, the error norm of Case A was larger than those of the other cases. This implies that ultrasonic measurement in one cross section has some error in evaluating the flow rate. Comparing Cases B, C and D, the error norm of Case B is smallest. Also, for the UMI simulation in Fig. 3(b), the error norm in Case A was the largest, showing that applying the correct flow rate is important. The error norms for Cases B, C, and D are almost the same, implying that the UMI simulation is insensitive to the upstream boundary velocity profile. Comparison of Figs. 3 (a) and (b) shows that the error of the UMI simulation is almost half that of the ordinary simulation, revealing that the UMI simulation has a better accuracy than that of the ordinary simulation with measured upstream velocity condition.

4. Concluding remarks

In this study, UMI simulation and ordinary simulation with several upstream velocity boundary conditions were performed for a blood flow in a carotid artery. The error of the UMI simulation was found to be almost half that of the ordinary simulation with measured upstream velocity condition, showing a better accuracy in reproducing the blood flow.

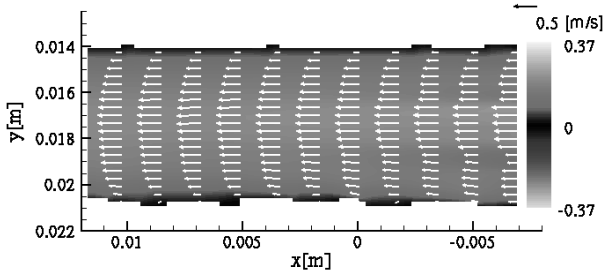

(a) Ordinary simulation.

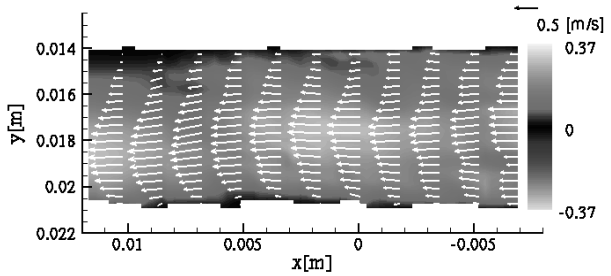

(b) UMI simulation

Fig. 2 Comparison of velocity fields for Case (B)

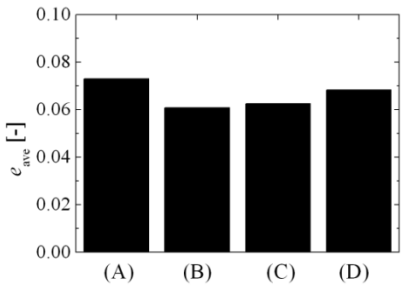

(a) Ordinary simulation.

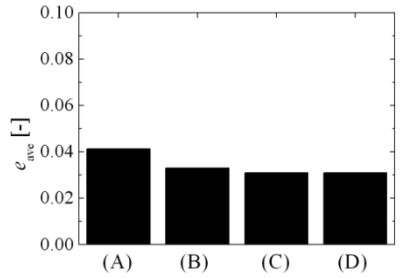

(b) UMI simulation

Fig. 3 Comparison of error norm

References

[1] Funamoto K, et al. Fundamental Study of Ultrasonic -Measurement-Integrated Simulation of Real Blood Flow in the Aorta. *Ann Biomed Eng* **33**, 415-428, (2005).

[2] Kato T, et al. Evaluation of Wall Shear Stress on Carotid Artery with Ultrasonic-Measurement-Integrated Simulation. *Seventh International Conference on Flow Dynamics*, 542-543,(2010).

Eighth International Conference on Flow Dynamics
November 9 - November 11, 2011

Effect of Aspect Ratio of Cerebral Aneurysm on flow reduction with stent

Toshio Nakayama, Makoto Ohta
Graduate School of Biomedical Engineering, Tohoku University, 2-1 Seiryo-Machi Aoba-ku Sendai Miyagi, 980-8575, JAPAN
Institute of Fluid Science, Tohoku University 2-1-1 Katahira Aoba-ku Sendai Miyagi, 980-8577, JAPAN
nakayama@biofluid.ifs.tohoku.ac.jp

ABSTRACT

The effect of stent strut in aneurysm neck was analyzed by computational fluid dynamics (CFD), and the design method of stent strut pattern using optimization has been reported. In this report, the effect of stent strut pattern for classified cerebral aneurysm was analyzed by CFD, the flow pattern in cerebral aneurysm and the wall shear stress on cerebral aneurysm validated the evidence. From the results, the mean wall shear stress was reduced all case, however the maximum wall shear stress was not reduced all case. We think that the select of stent in stenting treatment should be made very careful.

1. Introduction

In the medical field, stent implantation (stenting) in intracranial artery is called as endovascular treatment. The number of this case has been increasing in the world wide, because the surgical damages of endovascular treatment seem to be less than other treatments. The role of stenting for cerebral aneurysm is thought as decreasing the blood flow in cerebral aneurysm. We developed the computational fluid dynamics (CFD) using a realistic stent and aneurysm for the evaluation of stenting[1, 2]. From these results, the stent strut pattern and stenting position are very effect on the blood flow reduction in cerebral aneurysm. Then we have thought that development of searching method for stent strut pattern and the stenting position may be necessary. We performed an optimization way to design stent strut pattern with three-dimensional techniques[3]. The results say that several optimized designs can be proposed.

In this study, the effect of stent on many kinds of cerebral aneurysm is spotlighted. We investigated the effect of stent for cerebral aneurysm using CFD.

2. Material and Method

2.1. Cerebral Aneurysm

An idealized shape was used in this calculation for simplification. The idealized shape was shown in Figure 1. The shape was the parent artery with a straight pipe, and the aneurysm with a straight pipe and a half sphere. The diameter of parent artery was 4 [mm], and the length was 50 [mm]. The aspect ratio (AR) was changed from 0.5 to 2.0, therefore, the diameter of aneurysm was changed from 2 to 10[mm]. The construction of these shapes was performed with Rapid Prototyping software (MagicsRP 13.1 (Materialise, Belgium)).

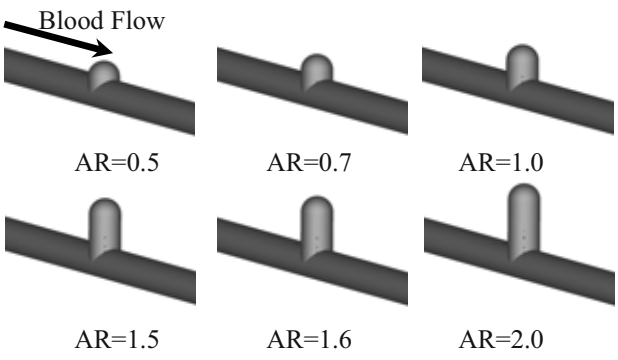

Fig. 1 The cerebral aneurysm shape

2.2. Intracranial Stent

The stent was constructed by CAD system, not realistic one reported previously. The shape was z-type stent geometry, the length and width of strut was fixed, the porosity was kept 80%, and stent strut height was constant at 150 [μm]. The shape of z-type stent on neck was shown in Figure 2.

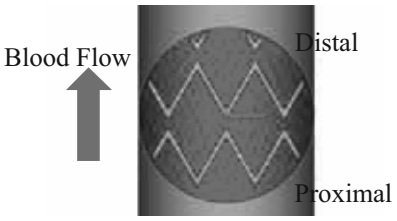

Fig. 2 The stent strut pattern on cerebral aneurysm neck

The stent was implanted at 1.9mm position from the center of parent artery.

2.3. Numerical Simulation

The constructed shape data were transferred to a personal computer and a tetrahedron numerical mesh was generated (ICEM CFD 11.0, Ansys Inc., PA, USA). The number of mesh was from 2,400,000 to 2,600,000 in all cases. To improve analytical accuracy, the mesh refinement was used at near stent strut. Then, the size of mesh near stent strut was finer than other parts. The constructed mesh data were transferred to a supercomputer of Institute of Fluid Science (Silicone Graphics Altix SGI Japan, Ltd, Japan).

The blood flow was simplified as an incompressible, laminar, and Newtonian flow with the density of 1050 [kg/m3] and the viscosity of 0.0035 [Pa s].

The boundary conditions were set as follows. Velocity boundary condition at 0.200[m/s] was set on the inlet. Pressure boundary condition was set on the outlet. No-slip condition was employed on the vessel, aneurysm, and stent.

The equations of continuity and the Navier-Stokes equation were solved to determine the flow field. The calculation using finite volume method was performed by a commercial solver (Fluent 6.3, Ansys Inc. PA,

USA) on the supercomputer (Silicone Graphics Altix, SGI Japan, Ltd, Japan).

3. Results and Discussion

Figure 3 shows the blood velocity vector at the center of blood vessel and aneurysm. The color means the blood flow speed and the direction of arrow means the direction of blood flow at the center plane. By the stenting, the inflow zone is changed from distal to proximal with all case. Therefore, the blood flow pattern in cerebral aneurysm has two patterns that one is a flow on the stent caused by the parent vessel flow, another is a rotational flow caused by that flow in cerebral aneurysm. In this time, the maximum blood flow speed is not reduced by stenting, the maximum blood flow speed becomes higher in AR=0.5 and 0.7 case.

Figure 4 shows the maximum wall shear stress before/after stenting. X-axis means the aspect ratio of cerebral aneurysm and Y-axis means the maximum wall shear stress. In this figure, the blue bar (left bar) means the maximum wall shear stress before stenting, and the red bar (right bar) means the maximum wall shear stress after stenting. In maximum wall shear stress at each AR, the maximum wall shear stress in AR=0.5 and 0.7 case is raised after stenting, the maximum wall shear stress in other cases is reduced after stenting.

Figure 5 shows the mean maximum wall shear stress before/after stenting. X-axis means the aspect ratio of cerebral aneurysm and Y-axis means the mean wall shear stress. The mean wall shear stress on whole cerebral aneurysm is reduced after the stenting.

Ujie et. al. [3] proposed the relationship between rupture of aneurysm and aspect ratio, the appearance of two rotational flow in aneurysm has been the high risk of rupture. If the blood flow pattern regardless aspect ratio has one rotational flow after stenting, the risk of rupture will have been reduced.

After the stenting, the wall shear stress distribution on whole of cerebral aneurysm is reduced, and the mean wall shear stress on the cerebral aneurysm is also reduced. Then, the role of stent reduced the whole wall shear stress is played. However, the maximum wall shear stress of aspect ratio 0.5 and 0.7 cases rises after the stenting. The wall shear stress in local has the possibility of rising by the stenting position and the stent strut pattern. The high wall shear stress is the one of factor affecting the growth aneurysm.

Although the stenting treatment is effective for the treatment of wide neck aneurysm, the wide neck aneurysm is often the low aspect ratio aneurysm, then it is thought that a careful stent selection is necessary.

As a future work, the development of stent that reduces wall shear stress for low aspect ratio aneurysm will be necessary. Then, we will perform the optimization of stent for low aspect ratio aneurysm, and develop the new stent.

4. Concluding remarks

In this study, we connected the effect of classified cerebral aneurysm on the flow with stent. After the stenting, the maximum wall shear stress in low aspect ratio aneurysm increases locally. A careful stent selection is important and necessary.

References

[1]T. Nakayama et al, Proceedings of the 6th International Symposium on Advanced Fluid Information., (2006), 47-48.

[2]T. Nakayama et al, Proceedings ASME. (2010) FEDSM / ICNMM 2010, 30592

[3] H. Ujiie et al, Neurosurgery. 45(1) (1999), 119-29

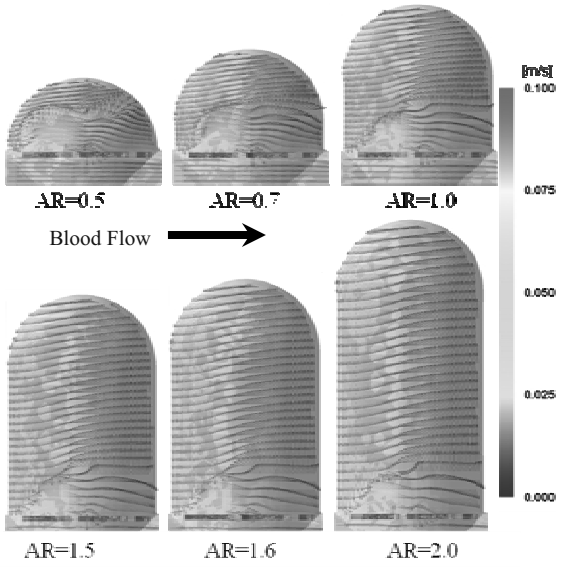

Fig. 3 The velocity vector (center of blood vessel and cerebral aneurysm)

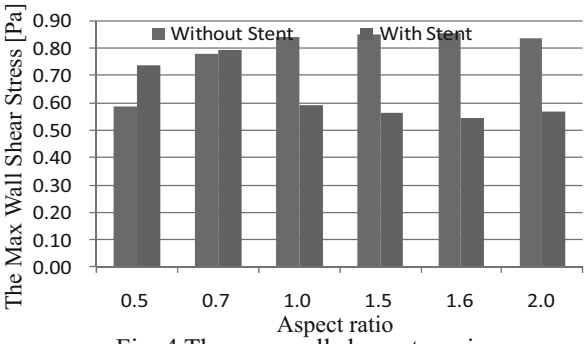

Fig. 4 The max wall shear stress in cerebral aneurysm

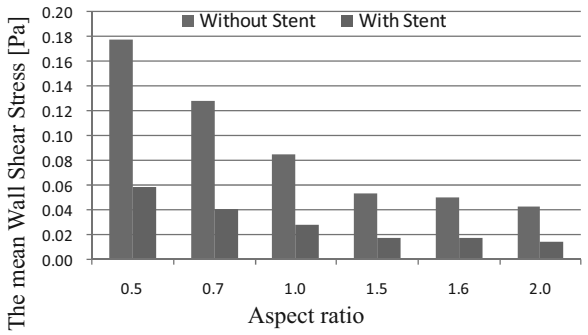

Fig. 5 The mean wall shear stress in cerebral anuerysm

OS11: Micro Channels and Membrane Proteins

Eighth International Conference on Flow Dynamics
November 9 - November 11, 2011

Bacterial Two-component and Hetero-oligomeric Pore-forming Cytolytic Toxins: Structures, Pore-forming Mechanism, and the Organization of the Genes

Yoshiyuki KAMIO
Department of Biochemical Engineering, Graduate School of Science and Engineering, Yamagata University,
4-3-16 Yonezawa, Yamagata 992-8510, Japan
E-mail: yoshikamio@yz.yamagata-u.ac.jp

ABSTRACT

Staphlococcal γ-hemolysin (Hlg), leukocidin (Luk), and Panton-Valentine leukocidin (PVL) are two-component and hetero-oligomeric pore-forming cytolytic toxins (or cytolysin), that are first identified in bacteria. In the present lecture, I will firstly depict molecular basis of the membrane pore-forming nature of Hlg, Luk, and PVL. Next, I will refer to an assembly mechanism of LukF and Hlg2 on the human erythrocytes, which has been first clarified by our study using a single-molecular fluorescence imaging technique. Finally, I will refer to the genetic analyses of the Hlg, Luk, and PVL genes.

Staphylococcus aureus secretes six cytolytic toxins, α-hemolysin (Hla), β-hemolysin, γ-hemolysin (Hlg), δ-hemolysin, leukocidin (Luk), and Panton-Valentine leukocidin (PVL), in which Hlg, Luk, and PVL have a unique characteristic of being composed of two separate and water-soluble proteins. Hlg (Hlg1 of 34 kDa/Hlg2 of 32 kDa) effectively lyses erythrocytes from human and other mammalian species. Luk (LukF [34 kDa] and LukS [33 kDa]) is cytolytic toward human and rabbit polymorphonuclear leukocytes and rabbit erythrocytes (but not hemolytic toward human erythrocytes), and PVL (LukF-PV [34 kDa] and LukS-PV [33 kDa]) reveals cytolytic activity with a high cell specificity to leukocytes (see review, reference [1]). The studies by us and other groups showed that Hlg1 is identical to LukF and that the cell specificities of the cytolysins are determined by Hlg2 and LukS [2-5]. Hence, Hlg1 is hereafter referred to as LukF in the presentation. Based on the primary and 3-dimensional (3-D) structures of the toxin components, Hlg, Luk, and PVL are thought to form a family of proteins. Class F proteins (LukF and LukF-PV) and class S proteins (Hlg2, LukS, and LukS-PV) are approximately 70% identical to each other, whereas between classes the identity is approximately 30%. Interestingly, class F and class S components of Hlg and Luk have 20 to 30% identities with the single-component staphylococcal Hla, which has been intensively studied as a prototype of pore-forming cytolysin. These two-component cytolytic toxins as well as Hla have also been proven to be pore-forming cytolysins [6-8]. Furthermore, the water-soluble LukF and LukF-PV components of Luk and PVL, respectively, have been solved from the X-ray analyses of their crystals [9, 10]. It was also found that the phosphorylation of LukS and LukS-PV of Luk and PVL, respectively, by protein kinase besides their pore formations on the leukocytes is required for the Luk- and PVL-specific leukocytolytic activities [11, 12].

In the first chapter of lecture, I will depict molecular basis of the membrane pore formation of Hlg, Luk, and PVL. I will also refer to the phosphorylation of LukS and LukS-PV and its correlation with the leukocytolytic activity in Luk and PVL.

In the second chapter of lecture, I will refer to the assembly mechanism of LukF and Hlg2 on the human erythrocytes as well as the roles of membranes of the target cells in pore formation by Hlg for understanding their pore-forming nature. Assembly of large macromolecular complexes such as membrane pores is essential for cell function. A crucial problem of protein complex assembly is to understand mechanism of assembly processes by elucidating information on the beginning, intermediate, and final stages involved. Heterogeneous populations of intermediate states, however, are not able to be readily analyzed using ensemble-averaged data. By contrast, single-molecule imaging methods provide direct information about individual intermediate states [13-15]. Recently, individual protein-protein interactions at very low concentrations have been observed in vitro under total internal reflection fluorescence microscope (TIRF-microscope) [16, 17]. At high concentrations of proteins, however, dimers can not be distinguished from crowded monomers using these techniques. Fluorescence resonance energy transfer (FRET) between single pairs of acceptor and donor fluorophores (single-FRET) has allowed observation of the dimerization even at high concentrations because the acceptor only emits fluorescence if located within several nanometers of the donor [18, 19]. Oligomers consisting of more than two molecules are also of great interest in protein assembly although they have not been analyzed yet using single-molecule imaging. Pore-forming cytolysins of bacteria are excellent models for studying the nature of assembly for oligomeric molecules on membranes because of the high stability of recombinant monomeric subunits in solution [9]. In 2003, the assembly mechanism of the LukF and Hlg2 monomers into pore-forming hetero-oligomers of Hlg on the human erythrocyte membranes has been first clarified by our study using a single-molecular fluorescence imaging technique. We estimated 11 sequential equilibrium constants for the assembly pathway which includes beginning with membrane binding of monomers, proceeding through single pore oligomerization, and culminating in the formation of cluster of the pores [20]. Our single molecule observation technique used offered the ability to distinguish intermediates under physiologically relevant conditions. The FRET measurement for single and multiple molecules is effective in distinguishing

oligomers from crowded monomers. Moreover, we developed a novel method to deduce the number of LukF (donor) and Hlg2 (acceptor) molecules in small oligomers, such as trimers and tetramers, by measuring the stepwise photobleaching of FRET and acceptor signals, respectively [20].

In the third chapter of lecture, I will refer to the genetic analyses of the Hlg, Luk, and PVL genes. The LukF, LukS, and Hlg2 proteins are derived from the Hlg gene locus (*hlg*), and have been found in 306 of 309 *S. aureus* clinical isolates [21]. In contrast, LukF-PV and LukS-PV are derived from PVL gene locus (*pvl*) which is distinct from *hlg* locus, and only few % of clinically isolated *S. aureus* strains carried *pvl* [21]. We found the presence of *pvl* on the genome of lysogenic bacteriophages, ϕPVL [22, 23]. We demonstrated the phage conversion of *S. aureus* leading to the production of PVL by discovery of a PVL-carrying temperate phage, ϕSLT from a clinical isolate of *S. aureus* [24]. In this chapter, we also refer to the current status of knowledge of the genetic organization of the PVL-converting phages for understanding their molecular evolution.

The works cited in this lecture after 1977 were reviewed (see reference 25).

Acknowledgements

The works cited in this lecture have been mainly done during my professorship at Tohoku University. I am grateful to all of my co-workers, past and present, for their experimental as well as conceptual contributions. I am also grateful to all the people supporting us to recover and continue the research activity from the crisis occurred on 11th March, 2011. I would like to sincerely express my heartfelt concern for the people still suffering from the disaster, and wish them early and full recovery in fondest regards.

Our works cited in this lecture were supported in part by Grant-in-Aid for Scientific Research from Japan Society for the Promotion of Science (05304028, 06670280, 07660089, 08307004, 08660086, 09460042, 11694191, 11460034, 13460034, and 15380054), The Naito Foundation, Yamada Science Foundation, Takeda Science Foundation, Uehara Memorial Foundation, Intelligent Cosmos Academic Foundation, and Japanisch-Deutsches Kulturinstitute Foundation.

References

[1] T. Tomita and Y. Kamio, Biosci. Biotechnol. Biochem., 61, 565-572 (1997).
[2] J. Cooney, Z. Kienle, T. J. Foster, and P. W. O'Toole, Infect. Immun., 61, 768-771 (1993).
[3] G. Supersac, G. Prevost, and Y. Piemont, Infect. Immun., 61, 580-587 (1993).
[4] Y. Kamio, A. Rahman, H. Nariya, T. Ozawa, and K. Izaki, FEBS Lett., 321, 15-18 (1993).
[5] A. Rahman, K. Izaki, and Y. Kamio, Biosci. Biotechnol. Biochem., 57, 1234-1236 (1993).
[6] N. Sugawara, T. Tomita, and Y. Kamio, FEBS Lett., 410, 333-337 (1997) .
[7] N. Sugawara, T. Tomita, T. Sato, and Y. Kamio, Biosci. Biotechnol. Biochem.,63, 884-891 (1999).
[8] N. Sugawara-Tomita, T. Tomita, and Y. Kamio, J. Bacteriol. 184, 4747-4756 (2002).
[9] R. Olson, H. Nariya, K. Yokota, Y. Kamio, and E. Gouaux, Nature Struct. Biol., 6, 134-140 (1999).
[10] J. D. Pedelacq, L. Maveyraud, G. Prevost, L. Baba-Moussa, A. Gonzalez, E. Courcelle, W. Shepard. , H. Monteil, J. P. Samama, and L. Mourey, Structure, 7, 277-287 (1999).
[11] H. Nariya, A. Nishiyama, and Y. Kamio, FEBS Lett., 415, 96-100 (1997).
[12] A. Nishiyama, H. Nariya, and Y. Kamio, Biosci. Biotech. Biochem., 62, 1824-1838 (1998).
[13] T. Funatsu, Y. Harada, M. Tokunaga, K. Saito, and T. Yanagida, 374, 555-559 (1995) .
[14] A. Ishijima, H. Kojima, T. Funatsu, M. Tokunaga, H. Higuchi, H. Tanaka, and T. Yanagida, Cell, 23,161-171 (1998).
[15] GT. Schütz, G. Kada, VP. Pastushenko, and H. Schindler, EMBO J., 19, 892-901(2000) .
[16] AR. Mendelsohn, and R. Brent, Science, 284, 1948-1950 (1999) .
[17] H. Taguchi, T. Ueno, H. Tadakuma, M. Yoshida, and T. Funatsu, Nature Biotechnol., 19, 861-865 (2001).
[18] T. Ha, T. Enderle, DF. Ogletree, DS. Chemla, PR. Selvin, and S. Weiss, Proc. Natl. Acad. Sci., 93, 6264-6268 (1996) .
[19] Y. Sako, S. Minoghchi, and T. Yanagida, Nature Cell Biol., 2, 168-172 (2000) .
[20] V. T. Nguyen, Y. Kamio, and H. Higuchi, EMBO J., 22, 4968-79 (2003).
[21] G. Prévost, P. Couppié, P. Prevost, S. Gayet, P. Petiau, B. Cribier, H. Monteil, and Y. Piémont, J. Med. Microbiol., 42, 237-245 (1995).
[22] J. Kaneko, T. Kimura, Y. Kawakami, T. Tomita, and Y. Kamio, Biosci. Biotechnol. Biochem., 61, 1960-1962 (1997).
[23] J. Kaneko, T. Kimura, S. Narita, T. Tomita, and Y. Kamio, 215, 57-67 (1998).
[24] S. Narita, J. Kaneko, Y. Chiba, Y. Piemont, S. Jarraud, J. Etienne, and Y. Kamio, Gene, 268, 195-206 (2001).
[25] J. Kaneko and Y. Kamio, Biotechnol. Biochem., 68, 981-1003 (2004).

Eighth International Conference on Flow Dynamics
November 9 - November 11, 2011

Crystal Structure of the Octameric Pore of Staphylococcal γ-hemolysin

Yoshikazu Tanaka[1], Keitaro Yamashita[1], Yuka Kawai[1], Nagisa Hirano[1], Jun Kaneko[2], Noriko Tomita[3], Makoto Ohta[3], Yoshiyuki Kamio[4], Min Yao[1], and Isao Tanaka[1]
1 Graduate School of Life Science, Hokkaido University, Sapporo, 060-0810, Japan,
2 Graduate School of Agricultural Science, Tohoku University, Sendai 981-8555, Japan,
3 Institute of Fluid Science, Tohoku University, 2-1-1 Aoba-ku, Sendai, 980-8577, Japan,
4 Graduate School of Science and Engineering, Yamagata University, Yonezawa, 992-8510, Japan
tanaka@cris.hokudai.ac.jp

ABSTRACT

Staphylococcal γ-hemolysin is a bi-component pore-forming toxin composed of LukF and Hlg2. These proteins are expressed as water-soluble monomers and then assemble into the oligomeric pore form on the target cell. Here, we report the crystal structure of the octameric pore form of γ-hemolysin at 2.5 Å resolution. The octameric assembly consists of four molecules of LukF and Hlg2 located alternately in a circular pattern. The structure demonstrates the elaborate molecular machinery involved in pore formation by two different molecules, in which inter-protomer electrostatic interactions using loops connecting β2 and β3 play pivotal roles.

1. Introduction

Pathogenic bacteria secrete various virulence factors to attack host cells. The pore-forming toxins (PFTs) are among the most sophisticated virulence factors, and are expressed as water-soluble monomeric proteins that assemble on the membranes of the target cells to form bilayer-spanning pores. With the appearance of the pore on the membrane, the cells are killed through leakage.

Staphylococcus aureus, a ubiquitous and pernicious human pathogen, secretes several PFTs including αHL, γ-hemolysin (γHL), leukocidin (LUK), and Panton-Valentine leukocidin (PVL). αHL consists of a single polypeptide, whereas the others are bi-component PFTs that require the synergistic association of a class F component and a class S component. γHL, LUK, and PVL are composed of LukF and Hlg2, LukF and LukS, and LukF-PV and LukS-PV, as class F and S components, respectively. Extensive experiments have been carried out for more than two decades, and the crystal structures of the monomeric forms of bi-component PFTs, i.e., LukF, LukF-PV, and LukS-PV, have been determined. However, the structures of the pore forms have not been reported at atomic resolution, which has hindered detailed discussion of the complicated molecular mechanism of action of bi-component pore-forming toxins.

In the present study, we determined the crystal structure of the pore form of bi-component PFT, γHL. This is the first report of the crystal structure of a heterocomponent β-barrel- type transmembrane protein. This is also the first bi-component β-PFT of which both monomer- and pore-form structures have been determined by X-ray crystallography, which allowed us to discuss the pore formation mechanism based on their real structures at atomic resolution. Based on the structural differences between pore and monomer forms in combination with biological data accumulated over the past two decades, we propose a mechanism of pore formation by PFTs.

2. Method

LukF and Hlg2 were overexpressed in the pET *E. coli* expression system, and purified as a monomeric protein from the soluble fraction by passage through a Ni sepharose 6 Fast Flow column (GE Healthcare Biosciences AB, Uppsala, Sweden) and HiLoad 26/60 Superdex 200-pg column (GE Healthcare Biosciences AB).

The 1:1 mixtures of LukF and Hlg2 monomers were concentrated to 4 mg mL^{-1}. Crystals suitable for further experiments were grown by the sitting-drop vapor diffusion method from a solution containing 0.1 M sodium acetate (pH 4.6), 0.5 M ammonium acetate, and 50% (v/v) MPD. X-ray diffraction experiments were performed on the beamline BL41XU at SPring-8 (Harima, Japan).

The structure of γ-hemolysin was determined by the molecular replacement method with the program Phaser using the structures of monomeric LukF, Hlg2, and the stem region of α-hemolysin protomer as search probes. After several cycles of manual model fitting and building with Coot and refinement with REFMAC5, individual atomic coordinate refinement and individual ADP refinement were performed with phenix.refine. Finally, R-work and R-free values converged to 20.68% and 23.64%, respectively.

3. Results and Discussion

Molecular architecture of γHL pore—The revealed structure was an octameric pore form consisting of 4 molecules of each of LukF and Hlg2 (Fig. 1). Each component was located alternately in a circular pattern along a non-crystallographic fourfold axis. The protomer was composed of cap, rim, and stem domains. The cap domain interacts with those of adjacent protomers, and the rim domain is located beneath the cap domain. The protruding stem domains formed a transmembrane β-barrel, composed of 16 antiparallel β-strands from 8 protomers (four protomers from each of LukF and LukS). MPD molecules were bound at the base of the rim domain of four LukF protomers, and recognized by Trp177 and Arg198. In contrast, no significant electron density was observed at the same region of Hlg2. An aromatic residue layer, which is

commonly observed in transmembrane β-barrel proteins near the lipid/solvent interface, was formed by Tyr117, Phe119, and Phe139 of LukF and Tyr111, Phe129, and Tyr131 of Hlg2. MPD molecules were located close to the aromatic layer, which defines the position of the surface of membrane bound to the toxin pore.

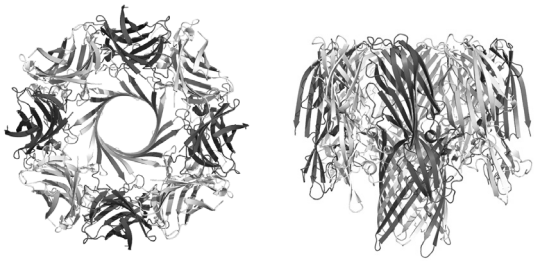

Fig. 1 Crystal structure of the octameric pore of γ-hemolysin. Black; LukF, White; Hlg2

Inter-protomer interactions—There are two types of interface between protomers in the γHL octamer (Fig. 1), i.e., the interface between the left side of LukF and the right side of Hlg2 (hereafter, interface 1), and that between the right side of LukF and the left side of Hlg2 (interface 2). The buried surface areas at interfaces 1 and 2 were calculated as approximately 1148 $Å^2$ and 963 $Å^2$, respectively. Interactions between the cap domains made predominant contributions in both interfaces, in which more than 160 atoms from each protomer were involved. In interface 1, an inter-protomer electrostatic interaction cluster, was observed between a loop connecting β2 and β3 of LukF (loop A) and β1 of Hlg2. In a similar region of interface 2, loop A of Hlg2 formed an electrostatic interaction with β1 of LukF, suggesting that the electrostatic interaction using loop A is conserved in both interfaces. The stem region was composed of an inter-protomer antiparallel β-barrel, in which 34 inter-protomer hydrogen bonds were formed.

Structure comparison of protomers in pore-form with monomeric components—In both LukF and Hlg2, the stem domain, which was folded into a 3-stranded antiparallel β-sheet in the monomer, protruded outward to form a transmembrane β-barrel in the octamer. Through this process, all 12 hydrogen bonds formed in the monomer were disrupted, and instead 18 and 34 new hydrogen bonds were formed within and between protomers, respectively. These observations suggested that the secondary structure of the stem region is transiently completely disrupted, and reoriented as a β-barrel with formation of inter-protomer interactions.

The core of the cap and rim domains was well superposed between monomer and protomer (r.m.s.d. 1.13 Å and 1.18 Å for LukF (220 Cα atoms) and Hlg2 (243 Cα atoms), respectively), suggesting that these two domains are rigid and that their relative orientation does not change upon octamer assembly.

Assembly mechanism—Pore formation is initiated by the binding of LukF onto the cell surface, followed by heterodimer formation [1]. Our previous study indicated that a heterodimer with shorter distance between Ser45 (LukF) and Lys222 (Hlg2) acts as a structural unit for oligomerization [2]. The distance between these residues through interface 1 was approximately 21 Å, whereas that with interface 2 was 43 Å, indicating that the heterodimer interacting with interface 1 must be formed first, followed by assembly into an octamer.

Based on these observations, the following processes were proposed to occur at the initial step of pore formation: (i) LukF first binds at the cell surface with exposure of interface 1; (ii) LukF is bound by Hlg2 through the exposed interface 1; followed by (iii) assembling into tetramer, hexamer, and octamer (Fig. 2).

Function of the N-terminal region and loop A in inter-protomer interaction—The residues reported to be essential for the hemolytic activity coincided with those that formed interactions with loop A [3, 4]. In both LukF and Hlg2, loop A was located alongside the essential N-terminal region of the adjacent protomer, and made electrostatic interactions. These observations indicated a pivotal role of loop A in the inter-protomer interaction. In the monomeric state, loop A made interactions with the pre-stem region, whereas it interacted with the adjacent protomer in the pore structure. These observations indicated that two events, i.e., release of the pre-stem and formation of the interaction with the adjacent protomer, occur on loop A upon oligomerization. Loop A would act as a clamp for the folded pre-stem in the monomer, but act as an adhesive material between protomers after releasing the pre-stem.

4. Concluding remarks

In the present study, we determined crystal structure crystal structure of the octameric pore form of γ-hemolysin at 2.5 Å resolution. The structure revealed that (i) heterodimer interacting with interface 1 acts as a structural unit for oligomerization, (ii) the secondary structure of the stem region is transiently completely disrupted through assembly, and (iii) loopA acts as two different roles in monomer and pore structures.

References

[1] T. Ozawa, J. Kaneko, and Y. Kamio, Biosci. Biotechnol. Biochem., **59** (1995), 1181-1183.
[2] VT. Nguyen, Y. Kamio, and H. Higuchi, EMBO J., **22** (2003), 4968-4979.
[3] N. Monma, VT. Nguyen, J. Kaneko, H. Higuchi, and Y. Kamio, J. Biochem., **136** (2004), 427-431.
[4] G Miles, L. Jayasinghe, and H. Bayley, J. Biol. Chem., **281** (2006), 2205-2214.

Three-state Discrete Kinetics of the OpdK Protein Pore

Belete R. Cheneke[1], Bert Van den Berg[2] and Liviu Movileanu[1,3]
[1]Department of Physics, Syracuse University, 201 Physics Bldg., Syracuse, New York 13244-1130, USA,
and [2]Program in Molecular Medicine, Worchester, Massachusetts 01605, USA
[3]E-mail: lmovilea@physics.syr.edu

Abstract

In this paper, we discuss ion selectivity of a single beta-barrel protein pore. OpdK protein is an 8 Å-wide diameter, kidney-shaped pore located in the outer membrane of *Pseudomonas Aeruginosa*. We were able to record single-channel current fluctuations of this protein when reconstituted into a planar lipid bilayer. We observed that the OpdK protein pore obeys to a three-state, discrete kinetics model, whose current fluctuations among the three sub-states featured different rate constants.

1. Introduction

A single protein pore in a planar lipid bilayer membrane nanopore may act as a flcutuating bionanostructure (1). OpdK is an OprD family member of *Pseudomonas Aeruginosa* (2;3). Recently, vand den Berg and Movileanu groups reported the X-ray crystal structure of the OpdK, which reveals a monomeric, 18-stranded β-barrel with a kidney-shaped transmembrane pore (**Fig. 1**) (4).

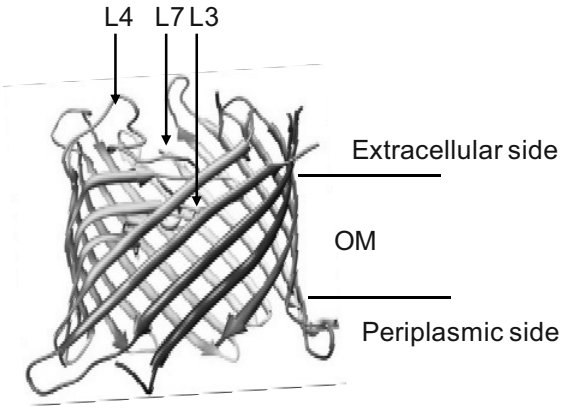

Fig. 1 Crystal structure of the OpdK protein. The figure indicates the most bulky extracellular loops L3, L4 and L7 as well as the portion of the membrane supposed to be inserted into a lipid bilayer (OM).

In this paper, we show a detail analysis of the ion selectivity of the OpdK protein. A weak anion selectivity of the OpdK protein indicates that its substrate should be a negatively charged small molecule, which is consistent with prior hypothesis that vanillate is taken into the cell via this transmembrane protein porin (4).

2. Methods

Cloning, overexpression, and purification of OpdK. The OpdK gene lacking the part coding for the signal sequence was amplified from genomic DNA of *P. aeruginosa* and was then cloned into the pB22 vector (5) with the *E. coli YtfM* signal sequence at the N-terminus. The protein was expressed in C43 (DE3) *E. coli* cells. We used standard protein chemistry techniques for protein expression and purification.

Single-channel current recordings on planar lipid bilayers. Single-channel current measurements were carried out with planar lipid membranes (6;7). Briefly, both chambers (1.5 ml each) of the bilayer apparatus were separated by a 25 μm thick teflon septum (Goodfellow Corporation, Malvern, PA). An aperture in the septum of ~60 μm diameter was pretreated with hexadecane (Aldrich Chemical Co., Milwaukee, WI) dissolved in highly purified n-pentane (Burdick & Jackson, Allied Signal Inc., Muskegon, MI) at a concentration of 10% (v/v). The standard electrolyte in both chambers was 1000 mM KCl, 10 mM potassium phosphate, pH 8.0, unless otherwise stated. The bilayer was formed with 1,2-diphytanoyl-*sn*-glycerophosphocholine (Avanti Polar Lipids Inc., Alabaster, AL, USA). OpdK was added to the *cis* chamber, which was at ground. Current flow is shown as positive and it represents a positive charge moving from the *trans* to *cis* chamber. Currents were recorded by using an Axopatch 200B patch-clamp amplifier (Axon Instruments, Foster City, CA) connected to the chambers by Ag/AgCl electrodes. An Optiplex Desktop Computer (Dell, Austin, TX) equipped with a Digitdata 1440 A/D converter (Axon) was used for data acquisition. The output from this amplifier was also filtered by an 8-pole low-pass Bessel filter (Model 900, Frequency Devices, Haverhill, MA) at a frequency of 10 kHz and sampled at 50 kHz. Acquisition and analysis of data was performed using pClamp 10.2 software (Axon).

3. Results and Discussion

Permanent charges on the internal loops and pore walls are expected to impact the electrostatics of the pore lumen. We performed single-channel electrical recordings under asymmetric KCl concentration. The permeability ratio P_K /P_{Cl} was calculated from the reversal potential (V_r) by applying the Goldman-Hodgkin-Katz (GHK) equation:

$$\frac{P_K}{P_{Cl}} = \frac{[a_{Cl^-}]_t - [a_{Cl^-}]_c e^{VrF/RT}}{[a_{K^+}]_t e^{VrF/RT} - [a_{K^+}]_c}$$

where variable *a* represents the activity of either potassium or chloride in either the *cis* (subscript "*c*") or *trans* (subscript "*t*") chamber. Here, F, R and *T* are the Faraday constant, the gas constant and the absolute temperature, respectively. The current-voltage curves were determined under asymmetric ionic concentrations.

In Fig. 2, we present the current-voltage relationship of the wild-type OpdK protein, revealing reversal potential (V_r). This parameters was later used to determine permeability ratio (P_K/P_{Cl}). In all asymmetric conditions, the OpdK protein exhibited a weak anion selectivity. For the conditions employed in this work, P_K/P_{Cl} was in the range 0.35 – 0.79. We did not find statistically significant alterations of the permeability ratios at pH 6.0 and 8.0, respectively.

The permeability ratios were greater when the KCl concentration was higher in the *cis* side than in the *trans* side. The reversal potentials were positive when the KCl concentration was higher in the *trans* side than in the *cis* side. For c_{cis} = 0.2 M KCl and c_{trans} = 1 M KCl, the reversal potentials at pH 6.0 and 8.0 were 13 ± 4 mV and 15.9 ± 1. 3 mV (n=3), respectively.

On the other hand, for c_{cis} = 1 M KCl and c_{trans} = 0.2 M KCl, the reversal potentials at pH 6.0 and 8.0 were -3.2 ± 0.4 mV and -6.4 ± 3.2 mV (n=3), respectively. The weak anion selectivity of the OpdK protein pore is a result of the basic arginine ladder on the pore walls (3). This observation is also in accord with the anionic nature of the vanillate substrate.

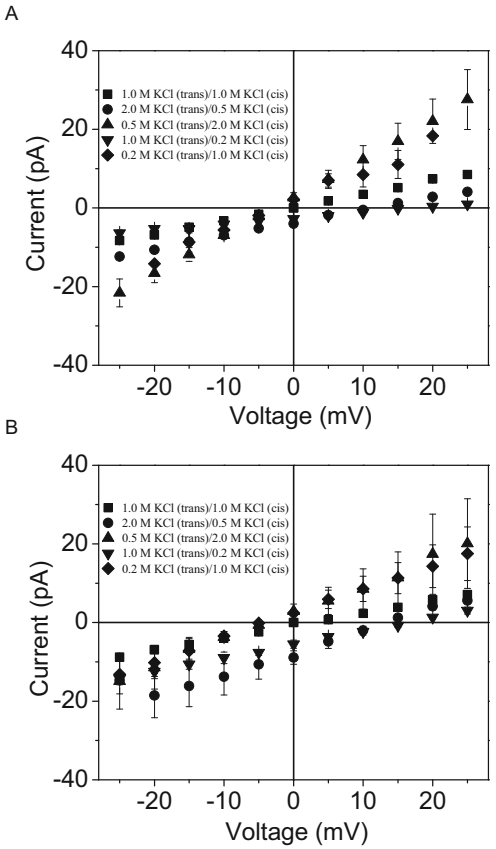

Fig. 2. The current-voltage profile of the OpdK protein under asymmetric ion concentration conditions.

4. Acknowledgments

This work is funded in part by grants from the US National Science Foundation (DMR-1006332) and the National Institutes of Health (R01 GM088403) to L.M.

Reference List

1. L. Movileanu, Trends Biotechnol. **27 (**2009) 333.
2. R.E. Hancock RE and F.S. Brinkman FS. Annu. Rev. Microbiol. **56 (**2002) 17.
3. R.E.W. Hancock, S. Tamber. In: *Bacterial and Eukaryotic Porins: Structure, Function, Mechanism* (ed. Benz R). Wiley-VCH: Weinheim, 2004; 61-77.
4. S. Biswas, M.M. Mohammad, L. Movileanu, B. van den Berg B. *Structure* **16** (2008) 1027.
5. L.M. Guzman, D. Belin D, M.J. Carson, J. Beckwith, J. Bacteriol. **177** (1995) 4121.
6. L. Movileanu, I. Neagoe, M.L. Flonta. Int. J. Pharm. **205 (**2000) 135.
7. S. Howorka, L. Movileanu, X.F. Lu, M. Magnon, S. Cheley, O. Braha, H. Bayley, J. Am. Chem. Soc. **122** (2000) 2411.

Eighth International Conference on Flow Dynamics
November 9 - November 11, 2011

Characterization and image analysis of heteroheptameric structure on staphylococcal γ -hemolysin transmembarne pore

Noriko Tomita[1], Kazuyo Abe[1], Jun Kaneko[2], Yoshiyuki Kamio[3] and Makoto Ohta[1]
1. Institute of Fluid Science, Tohoku University, 2-1-1 Katahira, Aoba-ku, Sendai, Japan
2. Graduate School of Agricultural Science, Tohoku University, 1-1 Amamiya-machi, Tustsumidori, Aoba-ku, Sendai, Japan
3. Graduate School of Science and Engineering, Yamagata University 4-3-16 Jyonan, Yonezawa, Yamagata, Japan
tomita@biofluid.ifs.tohoku.ac.jp

ABSTRACT

Staphylococcal γ-hemolysin (Hlg) is a two-component cytolysin which consists of LukF (Hlg1) and Hlg2. We have studied the pore-forming nature and assembly mechanism of and revealed that Hlg forms heterooligomeric transmembrane pores with a functional diameter of 2 nm on mammalian erythrocyte. Here we show our comprehensive research progresses of the Hlg pore, especially on subunit mismatch arrangement, cluster formation and membrane-damaging activities against several phospholipid membranes. These results suggest the Hlg pores have several novel and unique properties not shared by other pore-forming toxins.

1. Pore-forming nature of γ -hemolysin

Bacterial pore-forming toxins (PFTs) are produced by various bacteria and may play an important role in pathogenesis. Staphylococcal γ-hemolysin (Hlg), leukocidin (Luk), and Pantone-Valentine leukocidin (Luk-PV) are two-component PFTs secreted by *Staphylococcus aureus* (staphylococcal two-component PFT, STPFT), a common pathogen in hospitals [1,2]. Hlg (Hlg1 of 34kDa/ Hlg2 of 32kDa) effectively lyses erythrocytes of human and other mammalian species. Luk (LukF of 34kDa/ LukS of 33kDa) is cytolytic toward human and rabbit polymorph nuclear leukocytes and rabbit erythrocytes (but not hemolytic toward human erythrocytes), and LukF-PV (LukF-PV of 34 kDa/ LukS-PV of 33 kDa) reveals cytolytic activity with high cell specificity to leukocytes [3]. Previous studies by us and other groups have shown that Hlg shares one component with Luk (i.e., Hlg1 is identical to LukF) and that the cell specificities of the cytolysins are determined by the other components, Hlg2 and LukS [4, 5]. Hence, Hlg1 is referred to as LukF.

Because Hlg and Luk cause leakage of intracellular potassium ions from human and rabbit erythrocytes and swelling of the cells before hemolysis, we have studied the assembly and pore-forming nature of these toxins and revealed that Hlg and Luk form a ring-shaped structure with an inner/outer diameter of 3/9 nm on their target membrane, and that they act as a transmembrane pore with a functional diameter of ca. 2 nm [6,7]. Furthermore, high-resolution transmission electron microscopy (TEM) observation revealed that the Hlg transmembrane pores form heteroheptameric structure and chemical cross-linking study has suggested that an Hlg transmembrane pore forms a heteroheptameric structure with alternative arrangement of LukF and Hlg2 at molar ratios of 3:4 and 4:3 [8].

2. Structure analysis by image processing of heptameric structure

Recently, we performed quantitative 2-D image analysis of subunit arrangement in the Hlg pores based on TEM image and revealed mismatch subunit arrangements are in the pore [9,10]. The image analysis was done by using the top TEM views with seven subunits because our previous study showed that the majority number of subunits in the Hlg pore formed on human erythrocyte is seven [8].

Two different methods were used for the analysis. First, the longest distance between two adjacent subunits was numbered as D1 and the others were identified counterclockwise as D2 to D7 [9]. In this way, D1 is significantly larger than the others and that the real mismatch length of D1 against the regular heptagon is approximately 1 nm. In the heteroheptameric structure, the pore is composed of six linkages based on differential subunits lying next to each other (i.e. LukF-Hlg2) and one linkage based on identical subunits placed side by side (i.e. LukF-LukF or Hlg2-Hlg2). Nguyen *et al.* reported the formation of a LukF-Hlg2 heterodimer preceded assembly of the pore during oligomerization [11]. These results suggest that although the linkage between identical subunits could be occurred, this formation is less efficient than that between different subunits. If both linkage patterns exist in a pore, the differences of binding force between identical and different subunits have a potential to induce mismatched arrangement of subunits. Then, D1 that is deformed more easily than the others is estimated to be the site where identical subunits placed side by side.

In the second way, the longest distance between two adjacent subunits was numbered as D1 and others were numbered according to the size, and how each distance was arranged in the pore was investigated [10]. As a result, the following results were clarified: (1) Not all distances between two adjacent subunits are even. This indicates that a mismatch arrangement exists at not only one site but also at other sites. (2) There is a high probability that several patterns of mismatch arrangement could occur. These mismatch patterns tend to be polarized into a region in which the distance between subunits is great and a region in which such distance is small.

The biological significance of the mismatch arrangement is still unknown. We counted the number of subunits in 259 high-resolution pore images. As a result, 184 (71.0%) pores revealed a heptameric structure, whereas 51 (19.7%) and 24 (9.3%) pores appeared to have hexameric and octameric structures,

respectively. Also, Pedelacq *et al*. proposed that Luk–PV assembled into a hexameric pore [12] and Miles *et al*. showed the octameric structure of the Luk pore [13]. Furthermore, crystallization of the Hlg pore was succeeded on 2-methyl-2,4-pentanediol (MPD), and it was revealed that Hlg form octameric structure on the MPD [14]. These results indicate that there is a possibility that hexamer, octamer and mixtures of these oligomers including heptamer can be formed on the erythrocytes membrane.

The existence of larger and smaller distances between two adjacent subunits found by the image analysis could make it possible to insert and remove a subunit with relative ease. This assumed character can lead to cytolytic proteins with flexibility and extensity and will contribute to enhancement of the expression of their cytolytic activities.

3. Cluster forming property of γ -hemolysin

Here, we suggest a novel and unique property of the Hlg pore. TEM observation of Hlg-treated human erythrocyte membrane revealed firstly that Hlg pores gather and form aggregates termed clusters on the membrane. Although aggregation of pores with alignment on the lipid vesicle have been reported in several pore-forming toxins such as α-hemolysin from *Staphylococcus aureus*, a cluster-like structure aggregated by Hlg pores with random accumulation and localization on the erythrocyte membrane have not been found. The membranes around the clusters disappear and large holes with diameters of a few hundred nanometers are formed. As described above, the diameter of Hlg pores is ca. 2nm being smaller than that of hemoglobin. However, hemoglobin seems to easily pass through the large hole around the cluster. Quantitative analysis using transmission electron microscopy and image processing revealed that the formation of single pores and clusters is related to the release of potassium ions and of hemoglobin from erythrocytes, respectively. The number of clusters per cell increases with time and it has positive correlation with the hemolytic activity. This study shows significant results that Hlg has a different cytolytic mechanism from staphylococcal α-hemolysin, which has been intensively studied as a prototype of pore-forming toxin and shown to be a major virulence factor in animal models of infection [15]. In case of Hlg, the effective cytolytic activity by cluster formation has potential to facilitate infection of *S. aureus* to animals.

4. Pore-forming property of Hlg on various lipid membranes

In this section, membrane-damaging activities by γ-hemolysin were investigated by using several kinds of carboxyfluoresceine (CF)-loading phospholipid liposomes. In the previous study, it was reported that LukF component has a binding pocket to phosphatidylcholine (PC) [16]. Our results indicate that Hlg shows the pore-forming activity on the human and rabbit RBC total lipid liposome as well as PC, phosphatidylserine (PS) and cardiolipin (CL) liposomes with toxin concentration-dependent manner. CL is not included in erythrocyte membrane, but in membranes such as cytoplasmic membrane of bacteria and in inner mitochondrial membrane of mammal cell. These novel findings that Hlg can bind and show membrane-damaging activities to various kinds of phospholipid will contribute to elucidate mutual actions between cytotoxicity peptide and phospholipids, and eventually to develop a treatment of staphylococcal infection.

Acknowledgement

This work was partially supported by a Grant-in-Aid for JSPS Fellows (RPD) and by a Global COE Program Grant of the World Center of Education and Research for Trans-disciplinary Flow Dynamics from Tohoku University.

N. Tomita is a recipient of the postdoctoral fellowship from JSPS.

References

[1] Guyonnet, F. and Plommet, M., Annales de Institut Pasteur (Paris), **118** (1970)**,** 19-33.

[2] T. Tomita, and Y. Kamio, Biosci. Biotechnol. Biochem., **61**(1997), 565-572.

[3] H. Nariya, A. Shimatani, T. Tomita, and Y. Kamio, Biosci. Biotechnol. Biochem., **61**(1997), 2095-2099.

[4] Y. Kamio, A. Rahman, H. Nariya, T. Ozawa, and K. Izaki, FEBS Lett., **321(**1993)**,** 15-18.

[5] G. Supersac, G. Prevost, and Y. Piemont, Infect. Immun., **61(**1993), 580-587.

[6] N. Sugawara, T. Tomita, and Y. Kamio, FEBS Lett., **410(**1997), 333-337.

[7] N. Sugawara, T. Tomita, T. Sato, and Y. Kamio, Biosci. Biotechnol. Biochem., **63(**1999), 884-891.

[8] N. Sugawara-Tomita, T. Tomita, and Y. Kamio, J. Bacteriol., **184(**2002)**,** 4747-4756.

[9] N. Tomita, K. Abe, and M. Ohta, Proceedings of ASME 2011 International Mechanical Engineering Congress & Exposition, IMECE2011-63645 (2011), accepted.

[10] N. Tomita, K. Abe, and M. Ohta, Journal of Biomechanical Science and Engineering, (2011), accepted.

[11] V.T. Nguyen, Y. Kamio, and H. Higuchi, EMBO J. **22** (2003), 4968-4979.

[12] J.D. Pedelacq, L. Maveyraud, G. Prevost, L. Baba-Moussa, A. Gonzalez, E. Courcelle, W. Shepard, H. Monteil, J.P. Samama, and L., Mourey, Structure, **7(**1999)**,** 277-287.

[13] G., Miles, L. Movileanu, and H. Bayley, Protein Sci. **11(**2002), 894-902.

[14] K. Yamashita, Y. Kawai, Y. Tanaka, N. Hirano, J. Kaneko, N.,Tomita, M. Ohta, Y. Kamio, M. Yao, and I. Tanaka, Proc. Natl. Acad. Sci. USA (2011), accepted.

[15] L., Song, M.R. Hobaugh, C. Shustak, S. Cheley, H. Bayley, and J.E. Gouaux, Science, **274**(1996), 1859-1866.

[16] R. Olson, H. Nariya, K. Yokota, Y. Kamio, and J.E. Gouaux, Nat. Struct. Biol., **6** (1999), 134-140.

Eighth International Conference on Flow Dynamics
November 9 - November 11, 2011

The Title: Structural analysis of protein complexes by electron microscopy and image analysis

Authors names: Takuo Yasunaga[1], Yoshihiro Tsukada[1], Jin Mingyue[1], Keita Watanabe[1], Kaori Ogawa[1], Hiroko Takazaki[1], Risa Yamashita[1],Takeyuki Wakabayashi[2]
Affiliation and address: 1.Department of Bioscience and Bioinformatics, School of Computer Science and Systems Engineering, Kyushu Institute of Technology; 2. Teikyo University
E-mail of corresponding author: yasunaga@bio.kyutech.ac.jp

ABSTRACT

Electron microscopy is one of the most powerful techniques to elucidate the structure and/or architecture of proteins, ultrastructure, and cells of organisms at the molecular level. Recently, an advanced technique, electron cryo-microscopy, has been supplying us the images of hydrated specimens. Furthermore, combining image analysis supply us their good averaged images and three-dimensional structure. We have also observed protein complexes such as actin filaments/myosin to elucidate their three-dimensional structure at the sub-nanometer resolutions. We will here introduce our results as some examples and show the possibilities and limitations.

1. Introduction

Electron microscopy is one of the most powerful techniques to elucidate the molecular structure and/or architecture of proteins, ultrastructure, and cells of organisms. Recently, a cutting-edge technique, electron cryo-microscopy, has been developed to give us images of hydrated specimens quickly frozen, whereas the specimens used to be dried and stained by heavy metals before. Furthermore, image analysis of their electron micrographs supplys us their images with good signal-to-noise ratios after clustering and averaging and three-dimensional (3D) structure reconstructed many two-dimensional (2D) images. We have also observed protein complexes such as actin filaments to elucidate their 3D structure at the sub-nanometer resolutions [1], and significant images of myosin, dynein, and axonemes [2, 3]. We would here like to introduce our results as some examples of advantages of electron cryo-microscopy and image analysis (3D electron microscopy) and show its possibilities and limitations.

2. Materials and Method

The axonemes were isolated from Chlamydomonas and the axonemal dyneins were purified. Actin was purified from rabbit skeletal back muscle and myosin was isolated from chicken breast muscle for subfragment-1 of myosin to be purified. Pepsin and pepsinogen were purchased from SIGMA Co.

The specimens were quickly frozen using liquid ethane and stored in liquid nitrogen.

Electron micrographs were taken with electron microscopes (EM) (EF-2000, Hitachi; Tecnai Spirit, FEI; JEM-2100, JEOL) using CCD devices we developed [4]. The EM conditions: the accelerating voltage was 200 kV, the defocusing values were 0.5 um to 10 um for making contrast, and the direct magnifications are 50k to 140k.

Almost all the image analysis was performed under the Eos package we have developed [5], the image analysis environment for electron micrographs. The taken raw images were corrected in contrast transfer functions (CTFs) and the regions of interest (ROIs) were boxed out. Then, the images were classified and averaged to get the images with good signal-to-noise ratios.

Then the projection angles of 2D images were determined by using references and/or common lines to reconstruct each of 3D map using back projection methods and/or simultaneous iterative reconstruction techniques. The 3D images were displayed by 3D imaging tools, such as ‘molvie’, an Eos tool, ‘VMD’, and/or ‘chimera’.

3. Results and Discussion

We could successfully observe single particles of pepsin and pepsinogen using an electron cryo-microscope (EF-2000), which implements the energy filtering device and cold field emission gun. The former device can remove inelastic scattered electrons, which induce blurring as noise, and reduce noises. The latter can get coherent electron beams and give us high signal, resultantly high contrast, of images to be largely defocused. These combinations showed good images with high signal-to-noise ratios.

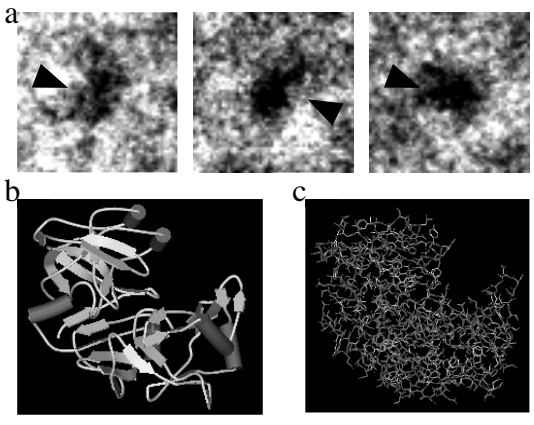

Fig. 1. Pepsin structure (a) Frozen-hydrated pepsin structure observed by electron cryo-microscopy. Black triangles are shown in the active site of pepsin. (b, c) The atomic model of pepsin proposed by X-ray crystallography.

Then we successfully reconstructed 3D maps of pepsin and pepsinogen from each atomic models proposed by X-ray crystallography. Their difference was clear in the region of the prosegment of pepsinogen, which is a lid of pepsin for an active site and block the protease activity. Some cylindrical densities presumably corresponding to alpha-helices were found out in the 3D map. Thus we conclude electron cryo-microscopy is useful for elucidating 3D structural analysis at the sub-nanometer levels.

Next, we reconstructed the 3D map of actin filament at the spatial resolution of approximately 0.5 nm [1]. The map showed some alpha-helices and bulky side-chain of amino acids sequences. Especially we could identify phosphate ions and magnesium ions to the extra mass. One of the phosphate ions is nearby the active site, which binds adenosine di-phosphate (ADP). We postulated the ion is the phosphate released from the ADP. We thus proposed ATP hydrolysis mechanism of filamentous actin.

In constructing the atomic models of actin filaments, we used a flexible fitting tool, 'SRMD (spatially-restricted molecular dynamics)', which we have developed [6]. The sub-nanometer level of 3D structure was not good enough for us to determine the atomic model directly. Our developed tool was proved to be a strong support tool for constructing the atomic model and useful in this case, as well.

We also examined the rigor complexes of actin and myosin by electron cryo-microscopy at the sub-nanometer resolutions. The active site of myosin was opened and has low density in the EM map. In atomic modeling using SRMD, The DNase-I loop in the subdomain-2 of actin lied down to the subdomain-1. Meanings of these conformational changes were not still clear. We have to process structural analysis of myosin more to improve the EM-map and the proposed atomic model.

Last, we observed the axonemes, synthetic axonemes and the purified axonemal dyneins. We could identify the ring structure of dynein and proposed the molecular architecture of dynein hetero heads using mutant domain *in vivo* [2]. Especially, the study of the synthetic axonemes gave us a new proposal of dynein-motility mechanism. The isolated dynein structure was also clearly observed in the solutions [2]. Recently other groups have reported the atomic models of dynein. Our dynein images were similar to them well. As describing below, our electron micrographs showed the precise structure and we here conclude EM is a powerful technique for elucidating *in vitro* structure of proteins and their complexes as well as *in vivo*.

However, we could not identify the subunits of dyneins, such as LC1, LC2, and so on, because the spatial resolution is not enough to be identified. If so, we need some labeling technique using heavy atoms, such as cadmium. Our collaborators have been developing such labels, metallothionein [7]. This label is useful for electron microscopy. Now, we are also examining the validity of the labeling.

4. Concluding remarks

Electron microscopy has been progressing for structural biology, from *in vitro* observation to *in vivo*, and from the cell-level structure, molecular level to the atomic level. These advances will give us the fine molecular mechanism of the relationship between structures and functions.

References

[1] K. Murakami, T. Yasunaga, T.Q.P. Noguchi, Y. Gomibuchi, K.X. Ngo, T.Q.P. Uyeda, and T. Wakabayashi: Structural basis for actin assembly, activation of ATP hydrolysis, and delayed phosphate release, *Cell*, **143**:2, 275-287 (2010)

[2] H. Takazaki, Z. Liu, M. Jin, R. Kamiya, and T. Yasunaga: Three Outer Arm Dynein Heavy Chains of Chlamydomonas reinhardtii Operate in a Coordinated Fashion Both *In Vitro and In Vivo*, *Cytoskeleton*, **67**:7 466-476 (2010)

[3] H. Ueno, T. Yasunaga, C. Shigyoji, and K. Hirose: Dynein pulls microtubules without rotating its stalk, *ProNAS*, **105**, 19702-19707 (2008)

[4] T. Yasunaga, T. Wakabayashi: Evaluation of a 2k CCD camera with an epitaxially-grown CsI scintillator for recording energy-filtered electron cryo-micrographs., *Journal of Electron Microscopy*, **57**(3), 101-112 (2008)

[5] T. Yasunaga, and T. Wakabayashi: Extensible and object-oriented system Eos supplies a new environment for image analysis of electron micrographs of macromolecules., J Struct. Biol. **116**(1):155-60. (1996)

[6] K. Noda, M. Nakamura, R. Nishida, Y. Yoneda, Y. Yamaguchi, Y. Tamura, H. Nakuamura, and T. Yasunaga, Atomic model construction of protein complexes from electron micrographs and visualization of their 3D structure using VR system, *J. Plasma Physics*, **72**(06) 1037-1040 (2006).

[7] Y. Nishino, T. Yasunaga, and A. Miyazawa, A genetically encoded metallothionein tag enabling efficient protein detection by electron microscopy, *Journal of Electron Microscopy*, **56**(3), 93-101 (2007)

Eighth International Conference on Flow Dynamics
November 9 - November 11, 2011

Two-dimensional Numerical Simulation of the Behavior and Deformation of Erythrocyte Passing through a Microchannel

Atsushi Kase*, Kiyoshi Bando**, Kenkichi Ohba**
* Graduate School of Science and Engineering, Kansai University
3-3-35 Yamate-cho, Suita-shi, Osaka, 564-8680, Japan
** Faculty of Engineering Science, Kansai University
E-mail: k040698@kansai-u.ac.jp

ABSTRACT

To quantitatively evaluate the erythrocyte deformability, we performed two-dimensional numerical simulations of the passage of some erythrocytes through a microchannel (MC) under different mechanical conditions. When the viscosity of the inner solution of the erythrocyte was increased, both the MC transit time and the shape-recovery time constant increased. On the other hand, when the stiffness of the membrane was increased, the MC transit time increased but the shape-recovery time constant decreased. Therefore, both the MC transit time and the shape-recovery time constant can be used to determine the mechanical conditions of the erythrocyte.

1. Introduction

It is well known that a healthy erythrocyte is very deformable. However, "erythrocyte deformability" is not a precisely defined physical parameter. We have previously suggested that "erythrocyte shape-recovery time constant [1]" be used as a quantitative evaluation index of "erythrocyte deformability." The time constant can be determined by measuring the time change of strain on an erythrocyte during the recovery of the erythrocyte's normal shape from a deformed state. The time constant is measured in vitro using a microchannel (MC).

The experiment for the observation of the erythrocyte has some limitations, namely, the difficulty in conditioning the blood sample, the measurement limits of instruments, and so on. The numerical simulation may help in understanding the phenomena occurring in the experiment. The in silico simulations represent the erythrocyte deformation behavior passing through an MC. From these simulations, the effects of the change in the viscosity of the erythrocyte's inner solution and the stiffness of the erythrocyte membrane on the shape-recovery time constant and MC transit time [2] were examined.

2. Method

The Stokes equation (Eq. 1) and the equation of continuity (Eq. 2) were used to calculate blood flow. The external force term $\boldsymbol{f}$ in Eq. 1 denotes the reaction force generated by erythrocyte deformation, calculated using the immersed boundary method [3].

$$\rho \frac{\partial \boldsymbol{u}}{\partial t} = -\nabla p + \nabla \cdot \left[\mu \left(\nabla \boldsymbol{u} + (\nabla \boldsymbol{u})^T \right) \right] + \boldsymbol{f} \tag{1}$$

$$\nabla \cdot \boldsymbol{u} = 0 \tag{2}$$

The calculating area was divided into a uniform fixed grid; therefore, the coordinates of node $\boldsymbol{X}$ on the erythrocyte membrane did not generally coincide with the coordinates of node $\boldsymbol{x}$ on the grids for the flow field. Therefore, by applying the adhesion condition to the nodes on the erythrocyte membrane, the current velocity $\boldsymbol{U}$ on the erythrocyte membrane was interpolated from the surrounding flow $\boldsymbol{u}$, as shown in Eq. 3. The force $\boldsymbol{F}$ on the membrane was calculated from the displacement of the nodes on the erythrocyte membrane and was distributed to the nodes on the surrounding flow, as shown in Eq. 4.

$$\boldsymbol{U}(\boldsymbol{X}_i) = \sum_{j=1}^{n} \boldsymbol{u}(\boldsymbol{x}_j) \delta_h(x_j - X_i) \delta_h(y_j - Y_i) h^2 \tag{3}$$

$$\boldsymbol{f}(\boldsymbol{x}_j) = \sum_{i=1}^{m} \boldsymbol{F}(\boldsymbol{X}_i) \delta_h(x_j - X_i) \delta_h(y_j - Y_i) \tag{4}$$

Here, h is the uniform grid interval of the flow calculation area, while the suffixes i and j are the node numbers on the erythrocyte membrane (1 to m) and fluid elements (1 to n), respectively. δ_h denotes the approximate delta function and is expressed by Eq. 5.

$$\delta_h(r) = \begin{cases} \dfrac{1}{4h}\left(1 + \cos\dfrac{\pi r}{2h}\right) & (|r| \le 2h) \\ 0 & (|r| > 2h) \end{cases} \tag{5}$$

The 2D erythrocyte model is as follows. The initial shape of the erythrocyte was modeled by the nodes located on a circle with diameter $d_0 = 8$ μm. Adjacent nodes were connected by a linear spring expressed by Eq. 6.

$$\boldsymbol{F} = K \frac{l - l_0}{l_0} \boldsymbol{e} \tag{6}$$

Here, l is the node-to-node length and l_0 is the initial value. $\boldsymbol{e}$ is the unit vector parallel to the erythrocyte membrane, and the linear spring proportionality constant K is defined by Eq. 7.

$$K = EH \tag{7}$$

Here, E is the Young's modulus of the erythrocyte membrane, and H is the membrane thickness.

The calculation conditions are described below, and a schematic of the calculation conditions is given in Fig. 1. Consider a rectangular calculation area that includes the MC and the MC wall. Conditions of uniform velocity (u = 0.16 mm/s, v = 0 mm/s) were imposed on the left and right boundaries of the rectangular area. Symmetry conditions were imposed on the upper and lower boundaries of the rectangular area. The condition of zero velocity at all times is imposed on elements corresponding to the MC wall, thereby creating a pseudo

MC whose width w is 5 μm. The density ρ and viscosity μ_{out} of the fluid were given as 1030 kg/m^3 and 1.2 cP, respectively, which are similar to those of blood plasma. However, the viscosity of the inner fluid of the erythrocyte, μ_{in}, was replaced by that of the Hb solution. Therefore, in the calculation, the value of μ_{in} was changed from 1.2 to 24 cP, and the value of E was changed from 0.1 to 0.3 MPa. In the simulation, the condition of E = 0.1 MPa [4] and μ_{in}= 6 cP is considered as the healthy condition and the condition of μ_{in} = 1.2 cP corresponds to the erythrocyte ghost condition.

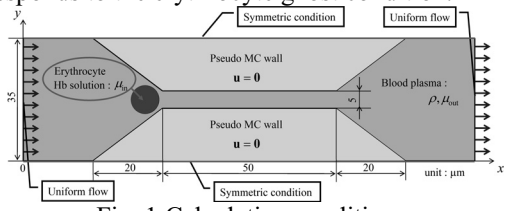

Fig. 1 Calculation conditions.

3. Results and Discussion

The simulation results for an erythrocyte in a healthy condition (μ_{in} = 6 cP, E = 0.1 MPa) are shown in Figs. 2 and 3. Fig. 2 shows the change in the shape of an erythrocyte as it passes through an MC. The variables ε_x and ε_y shown in Fig. 3 are defined in Eq. 8. Here, d_x and d_y are the maximum erythrocyte lengths in x- and y-directions, respectively, at time t.

$$\varepsilon_x = \frac{d_x - d_0}{d_0}, \varepsilon_y = \frac{d_y - d_0}{d_0} \tag{8}$$

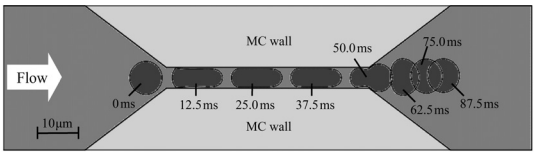

Fig. 2 Deformation behavior of erythrocyte.
(μ_{in} = 6 cP, E = 0.1 MPa)

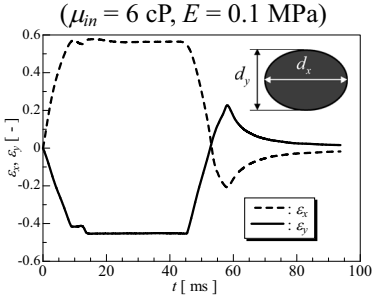

Fig. 3 Time change of strain in each direction.
(μ_{in} = 6 cP, E = 0.1 MPa)

From Figs. 2 and 3, the erythrocyte deformation behavior can be described as follows. The erythrocyte is compressed in the y-direction and enters the MC. When the erythrocyte is completely inside the MC, it deforms into a rounded rectangle-like shape that is stretched along the x-direction, and the deformation almost converges. When the erythrocyte is completely inside the MC, ε_y is less than -0.375; d_y is less than w. Hence the lubrication layers between the erythrocyte and the MC wall exist. When the erythrocyte exits the MC, it recovers its original shape after overshoot of ε_y. This deformation behavior remains qualitatively the same under other conditions.

The erythrocyte shape-recovery time constant τ_σ is defined as the time required from the overshoot peak to the point of reaching below 36.8% of the peak overshoot value. Additionally, the erythrocyte MC transit time t_{past} is defined as the period from the time at which the erythrocyte's head reaches the entrance of the MC to the time when the erythrocyte end completely exits the MC. The calculation results of τ_σ when μ_{in} or E is changed are shown in Figs. 4 and 5, respectively. As seen in Fig. 4, both τ_σ and t_{past} increase with an increase in μ_{in}. However, Fig. 5 shows that when E is increased, τ_σ is decreased while t_{past} is increased. Hence, any change in the erythrocyte's mechanical conditions can be detected by measuring both t_{past} and τ_σ.

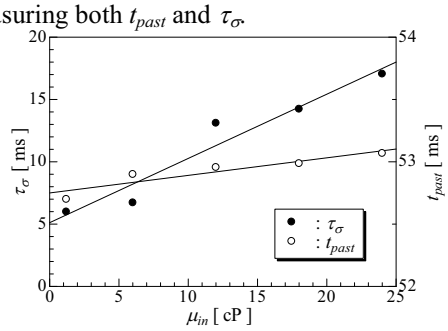

Fig. 4 Change in τ_σ and t_{past} against μ_{in}.

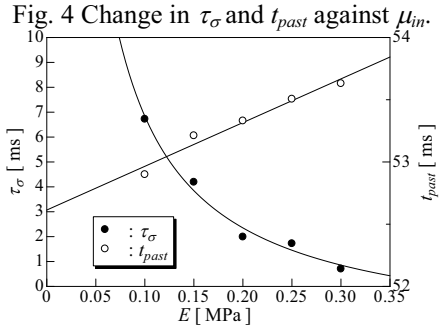

Fig. 5 Change in τ_σ and t_{past} against E.

4. Concluding remarks

The deformation behavior of an erythrocyte passing through a microchannel (MC) was represented by two-dimensional numerical simulation. Additionally, the MC transit time and shape-recovery time constant were evaluated. When the viscosity of the inner solution of the erythrocyte was increased, both the MC transit time and shape-recovery time constant increased. When the Young's modulus of the erythrocyte membrane was increased, the MC transit time increased and the shape-recovery time constant decreased.

References

[1] F. Muranishi, M. Kubota, T. Tajikawa, K. Ohba, Proc. 34th annu. conf. Jap. Soc. Biorheology, (2011), p. 77.
[2] Y. Hirose, R. Iitsuka, T. Shioiri, Y. Yamanishi, F. Arai, T. Arai, M. Higashimori, K. Tadakuma, M. Kaneko, Proc. 10th system integration div. conf., (2009), pp. 1655–1658.
[3] C. S. Peskin, Acta Numerica, **11**(2002), pp. 479–517.
[4] H. Minamitani, T. Kawamura, K. Tsukada, A. Iijima, E. Sekizuka, C. Oshio, Tran. Ins. Elec. Eng. Jap., **122**-C, 9(2002), pp. 1664–1671.

OS12: The Seventh International Students/Young Birds Seminar on Multi-Scale Flow

Eighth International Conference on Flow Dynamics
November 9 - November 11, 2011

X-Ray Computed Tomographic Study of Changes in Packing State of Hydrogen Storage Alloys

Masahiko Okumura[1], Ayaka Ikado[1], Yasuhiro Saito[1], Hideyuki Aoki[1], Takatoshi Miura[1] and Yoshiaki Kawakami[2]
[1] Department of Chemical Engineering, Graduate School of Engineering, Tohoku University,
6-6-07, Aoba, Aramaki, Aoba-ku, Sendai, Miyagi 980-8579, Japan
[2] Research and Development Center, Takasago Thermal Engineering Co. , Ltd. ,
3150, Iiyama, Atsugi, Kanagawa 243-0213, Japan
E-mail: aoki@tranpo.che.tohoku.ac.jp

ABSTRACT

The micro-scale packing structure of hydrogen storage alloys are observed by using a micro X-ray CT system in order to investigate the behavior of packing structure with hydrogen absorption-desorption. As a result, Bulk particles are severally hydrogenated and pulverized and these pulverized particles should fall from the upper region to the bottom and fill the void space in the bottom region.

1. Introduction

Hydrogen storage alloys are functional materials which store hydrogen by forming hydrides. The alloys have the large capacity to store hydrogen, and the hydrogenation occurs under relatively mild conditions (at ordinary temperatures and pressures). For these reasons, hydrogen storage alloys have great potential as hydrogen storage media.

With the progress of hydrogenation, the alloy is swelled and pulverized, and then stress occurs in the vessel. It is well known that the stress often damages the vessel [1]. Hence, the stress has to be assessed quantitatively.

It is known that stress which caused at the surface of a vessel changes depending on a measurement point [2]. In our previous work, we suggest that the concentration of pulverized alloys with hydrogen absorption-desorption causes non-uniform stress [3]. Although the concentration occurs at the alloy particle level, there is no study that focused on the behavior of this packing structure changes with the level.

In this study, we attempt to observe the micro-scale packing structure by using a micro X-ray CT system in order to investigate the behavior of packing structure changes.

2. Experimental

Figure 1 shows a schematic diagram of the experimental apparatus. Pure hydrogen gas (99.99999% purity) is supplied through valve I from the high-pressure vessel. The needle valve is used with both pressure supplied and released in order to prevent influences of the inner pressure changing on the packing structure. The filter is set between valve IV and the vessel because of the need for preventing contamination of pulverized alloys.

Figure 2 shows a schematic diagram of the pencil-type reaction vessel which is used in this study. The vessel is made of aluminum with the inner diameter of 1 mm and the wall thickness of 1 mm because of an increase of X-ray transmission.

The AB_5-type alloy ($MmNi_{4.12}Co_{0.60}Mn_{0.23}Al_{0.05}$) is used as the most typical and reasonable alloy. The pretreatment of our experiment as the alloy activation was conducted by the following process: First, the alloy was packed to the height of 51 mm of the vessel and the vessel was heated up to 500 K. The vessel was evacuated for 2 hours, and then the process, applying pure hydrogen and evacuating, was repeated 3 times after the evacuation.

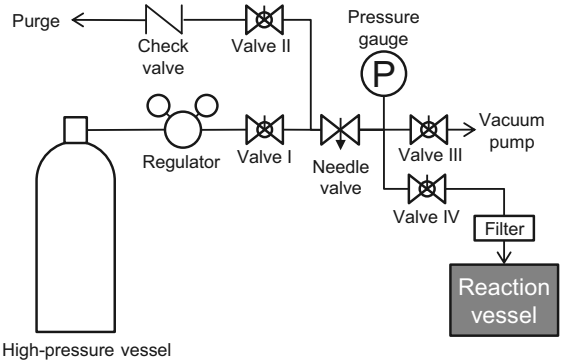

Fig. 1 A schematic diagram of the experimental apparatus.

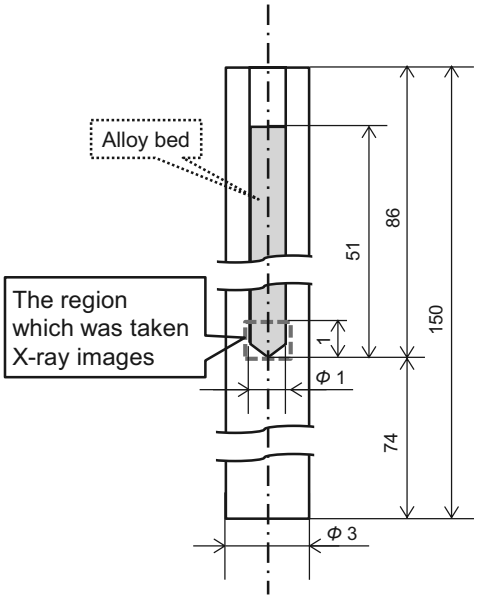

Fig. 2 A schematic diagram of the pencil-type reaction vessel.

After the pretreatment, the hydrogen pressure of 1.3 MPa is supplied to the vessel for 12 hours or more. It is

confirmed that hydrogenation of the alloy occurred from a decrease of the hydrogen pressure. In order to activate the alloy, the purge and supply of the hydrogen gas are repeated four times.

We use SMX-160CTS micro-focus X-ray CT system (SHIMADZU Co. , Ltd. , Japan) to take three-dimensional X-ray images. The packing structural image in the region shown in Fig. 2 is taken at three conditions: before activation, after first hydrogen absorption, and after fifth hydrogen absorption.

Cross-sectional images, which are parallel to the central axis, are acquired by using the software of Volume Graphics Studio MAX 2.1.

3. Results and Discussion

Figure 3 shows the cross-sectional image at the bottom of the vessel. In this figure, the conical shape of the bottom with the burr caused by metal working is shown.

A bulk particle which is placed on the left side in Fig. 3a is not found in Fig. 3b, and many fine particles are observed at that area in Fig. 3b. This result shows that the bulk particle is hydrogenated and pulverized. Other large particles in Fig. 3a can be found in Fig. 3b and the void space which is observed in Fig. 3a filled with fine particles. So it is considered that these fine particles which are hydrogenated and pulverized in the upper region of the vessel, and then fall to the bottom region. Although the large particles have many cracks, they almost keep the shape from Fig. 3a to 3b. Thus, they are hydrogenated after the space is filled with fine particles. These results also suggest that bulk particles does not hydrogenate all at once.

The void space slightly decreases and the packing structure does not change from Fig. 3b to 3c. These results suggest that the most of the packing structure changes in a small numbers of hydrogen absorption-desorption from the activation.

To summarize these results, it is suggested that the change of the packing structure occurs by the following process: Bulk particles are severally hydrogenated and pulverized. These pulverized particles fall from the upper region to the bottom and fill the void space in the bottom region.

4. Concluding remarks

In this study, we attempt to observe the micro-scale packing structure of the alloy by using the micro X-ray CT system in order to investigate the behavior of packing structure.

We succeed in observing of the packing structure at the particle level and discuss the transient change of the packing structure.

Acknowledgement

The authors would like to thank Shimadzu Corporation for their cooperation in conducting these experiments.

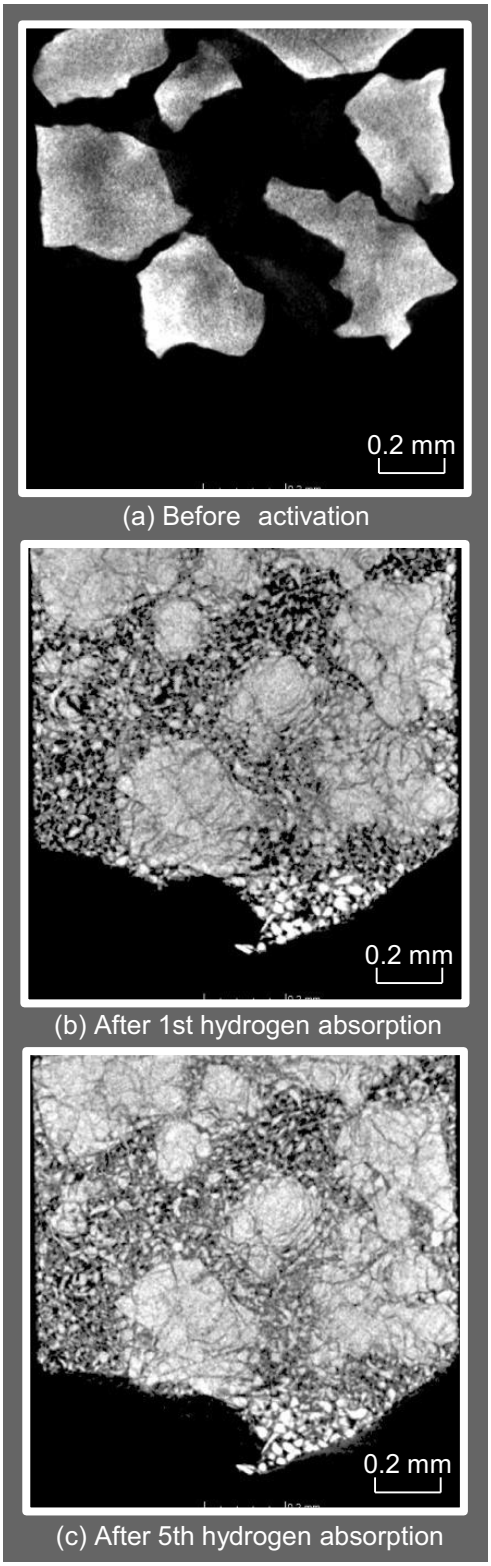

Fig. 3 Cross-sectional images of the packed bed. (black: voids/vessels, white: alloys)

References

[1] F. E. Lynch, J. Less-Common Met. , **74**(2) (1980), 411-8.

[2] E. G. Estochen and J. E. Klein, Fusion Sci. Technol. , **48**(1) (2005), 79-82.

[3] M. Okumura *et al.*, Proc. of the 76th Annual Meeting of SCEJ, (2011), Q315.

Eighth International Conference on Flow Dynamics
November 9 - November 11, 2011

Process of Leading Edge Receptivity to Periodic Disturbances

Yu Nishio, Masaya Shigeta, Seiichiro Izawa, Yu Fukunishi.
Department of Mechanical Systems and Design, Graduate School of Engineering, Tohoku University,
6-6-01 Aramaki-Aoba, Aoba-ku, Sendai, 980-8579, Japan.
nishio@fluid.mech.tohoku.ac.jp

ABSTRACT

Experimental study was carried out to investigate the leading edge receptivity to vortical disturbances in the freestream. The results showed that the disturbances added in the freestream generated velocity fluctuations inside the boundary layer. It was found that numerical simulation was necessary for better understanding of the phenomenon, and our method and preliminary results were presented.

1. Introduction

The receptivity process of a boundary layer has attracted a number of researchers for several decades. The concept of receptivity was originally proposed by Morkovin[1] as a key problem in the boundary layer transition process. Boundary layer transition starts from the spatial amplification of a finite disturbance received from the freestream. When the freestream turbulence level is low, the leading edge receptivity becomes dominant. For example, Nishioka et al.[2] discussed it focusing on the local pressure gradient. However, the reason why the pressure gradient changes the receptivity level still has not been made clear. Recently, Lars-Uve Schrader et al.[3] discussed the receptivity of a flat plate with an elliptic leading edge using a numerical simulation. One of their results tells that the stretching and tilting of vertical or axial vortices at the leading edge are the important factors in the receptivity process.

Since the boundary layer is a layer of vorticity, investigating the changes in the vorticity patterns should give us valuable information to understand receptivity. From this point of view, experimental and numerical studies were conducted to investigate the relation between the freestream disturbance and leading edge receptivity.

2. Experimental Study

2.1 Experimental Apparatus and Method

The experiment was performed in the low turbulent wind tunnel at the Institute of Fluid Science, Tohoku University. The wind tunnel was a closed-loop type with an open jet type test section. The contraction nozzle had an octagonal cross section with 1010 mm distance between the opposite sides. The length of the test section was 2070 mm. A schematic view of the experimental apparatus is shown in Fig. 1. The freestream velocity was set to be 5.0 m/s and the freestream disturbance without an oscillation wing was 0.3 % of the freestream velocity.

The leading edge of the plate had a 5:1 elliptic shape, whose major radius was 60 mm, and minor radius was 12 mm. The flat plate was 24 mm in thickness, 1100 mm in length and 900 mm in width. The Reynolds number based on the flat plate thickness was 8.0×10^3.

The origin of the coordinate system was set at the center of the leading edge of the plate, as shown in Fig. 1, where x, y and z axes denoted the streamwise direction, direction normal to the plate and the spanwise direction, respectively.

An NACA 0012 wing was used to generate velocity fluctuation. The chord length of the wing was 75 mm and its span was 900 mm. A pitching motion was given to the wing at a constant frequency of 64 Hz in order to add a periodic two-dimensional disturbance into the freestream. The pitching angle was between −1.44 and +1.44 degrees. The rotating center was located on the camber line at the 25 percent chord. The pitching wind was set so that its trailing edge was at x = –200mm, and y = –20mm when the angle of attack of the wing was at zero degree.

The flow velocities on the upper side were measured by a hot wire anemometer at the sampling frequency of 10 kHz. While the wing was in oscillation, both the velocity signal and the driving signal of the motor were recorded at the same time. The driving signal of the motor was used as the reference signal for the ensemble averaging. The ensemble averaging was carried out using data of 300 cycles.

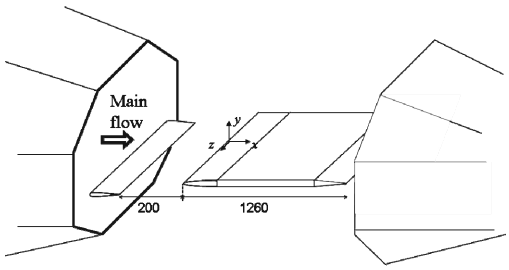

Fig.1 A schematic view of the experimental apparatus.

2.2 Experimental Results and Discussion

Figure 2 shows the mean velocities u and velocity fluctuation intensity u'_{rms} in the wake of the oscillating wing. Measurement locations are y-z cross section 50 mm upstream of the leading edge of the plate. Since the wing is pitching symmetrically around y = –20 mm, the data are obtained only in the upper part from this location. The strong velocity fluctuation deriving from the pitching motion of the wing is observed at y = –20 mm ~ +20 mm. Figure 3 shows the profile of the averaged phase speed c in the boundary layer near the leading edge (x = 10 ~ 30 mm). The phase speed depends on the height from the surface. This implies that the velocity fluctuation inside the boundary layer is not

merely a reflection of the outer disturbance, but are actual deriving from a vorticity fluctuation generated inside the boundary layer. However, it is quite difficult to measure the vorticity within the thin boundary layer. Therefore numerical simulation becomes necessary understand the details.

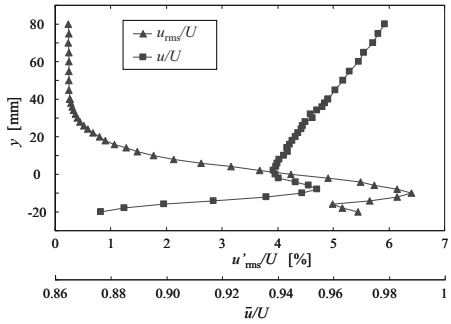

Fig. 2 Profile of u and u' at $x = -50$ mm, and $z = 0$ mm.

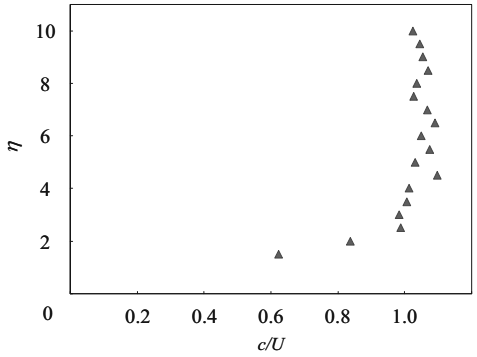

Fig. 3 Profile of the averaged phase speed of u' at $x = 10 \sim 30$mm.

3. Numerical Study

3.1 Numerical Method

Three-dimensional unsteady incompressible Navier-Stokes equations were solved using the SMAC method together with a collocated grid system. Figure 4 shows the computational grid used in the simulation. The governing equations were solved in the generalized curvilinear coordinate system (ξ–η–ζ). The convection term written in divergence form was discretized by the forth-order central finite difference method. For the other terms, the second-order central finite difference method was used. The second-order Adams-Bashforth explicit scheme was used for the time integration in the convection term. In the viscosity term, the Crank-Nicolson implicit scheme was used for time integration. The origin of the Cartesian coordinate system was set at the center of the leading edge of the plate, where x, y and z axes denoted the streamwise, vertical and the spanwise directions, respectively. The numbers of grids were 301 points in ξ direction, 100 points in η direction, and 17 points in ζ direction. The shape of the leading edge was an elliptic with major radius 1 and its aspect ratio was 5:1. The flat plate length was five times larger than the length of the leading edge. Reynolds number was set at 8.0×10^3 for the comparison with the experimental data.

As for the velocity boundary conditions, a non-slip condition was applied to the wall, the Neumann condition to the outlet boundary and the Dirichlet condition to the outer elliptic boundary as an inlet. As for the pressure boundary conditions, the Neumann condition was applied to the outlet boundary and the wall, and the Dirichlet condition to the inlet boundary. Periodic boundary condition was used in the spanwise direction for both the velocity and pressure.

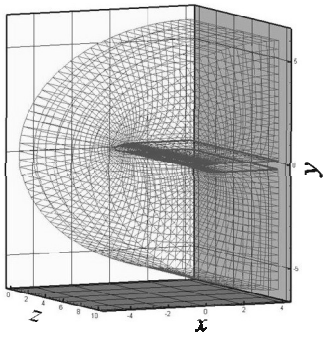

Fig. 4 Grid system for computation.

3.2. Numerical Results and Discussion

Figure 5 shows the instantaneous pressure distribution near the leading edge at the non-dimensional time $t = 2.0\times10^{-5}$. High pressure around the stagnation point and the growth of the boundary layer was observed in the preliminary computations. However, meaningful results are yet to come.

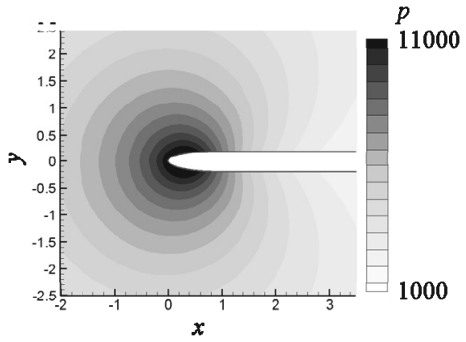

Fig. 5 Pressure distribution near the leading edge.

4. Summary

Experimental study was conducted to investigate the leading edge receptivity. It was observed that the transverse vortical disturbances added in the freestream were taken into the boundary layer and produced a velocity fluctuation inside the boundary layer. The necessity to carry out numerical simulations to observe the details of the fluctuation inside the boundary layer near the leading edge was recognized. Method for the numerical investigation was presented.

References

[1] M.V. Morkovin, Air Force Flight Dyn. Lab. Rep., AFFDL-TR-**68-149** (1969).

[2] M. Nishioka and M.V. Morkovin, J. Fluid Mechanics, **171** (1986), 219-261.

[3] L.-U. Schrader, L. Brandt, C. Mavriplis, and D.S. Henningson, J. Fluid Mechanics, **653** (2010), 245-271.

Eighth International Conference on Flow Dynamics
November 9 - November 11, 2011

Comparison of Carbon Black Configurations Formed by Benzene and Acetylene Pyrolysis

Kiminori Ono[1], Miki Yanaka[1], Sho Tanaka[1], Yasuhiro Saito[1], Masakazu Shoji[1], Hideyuki Aoki[1], Takatoshi Miura[1], Okiteru Fukuda[2], Takayuki Aoki[2] and Togo Yamaguchi[2]
[1]Department of Chemical Engineering, Graduate School of Engineering, Tohoku University, 6-6-07 Aoba, Aramaki, Aoba-ku, Sendai, Miyagi 980-8579 Japan, [2]ASAHI CARBON CO., LTD., 2 Kamomejima-cho, Higashi-ku, Niigata, 950-0883 Japan
E-mail aoki@tranpo.che.tohoku.ac.jp

ABSTRACT

Carbon black configurations formed by benzene and acetylene pyrolysis on the same furnace temperature were compared with each other. Aggregate shapes of carbon black produced by acetylene pyrolysis were complicated compared with that of benzene pyrolysis because nucleation was progressed and the number of particles increased. These results led us to the conclusion that aggregate shapes of carbon black produced by different feedstock are different due to difference of start temperature of reaction.

1. Introduction

Carbon black is an aggregate of nanoparticles and is used for composite materials such as tires. The configurations for a primary particle diameter and the aggregate shape of carbon black are factors affecting properties of those materials. Currently, since there is a technique for controlling the aggregation of particles of carbon black by trial and error, a theoretical breakthrough is therefore required to control the aggregate shape precisely. In order to solve the problem, we have developed a controlling method of carbon black configurations based on formation mechanism using the experimental and numerical method [1].

The formation mechanism is considered as follows [2]: (1) pyrolysis of hydrocarbons, (2) formation of nuclei, (3) coagulation of primary particles, (4) growth of the primary particle by surface growth, (5) growth of the crystallite size, and (6) growth of an aggregate by fusion among primary particles. Since our previous research [3] suggests that the number of nuclei affects carbon black configurations, controlling technique of (1) pyrolysis of hydrocarbons and (2) the formation of nuclei is required. Although polycyclic aromatic hydrocarbons (PAHs) which are thought to be precursors are produced by the reaction of H-abstraction-acetylene-addition [4], little is known about aggregate shape produced by different hydrocarbon on the same condition.

In this study, benzene and acetylene pyrolysis were carried out in an alumina tube heated by an electric furnace. We intended to report comparison of a mean primary particle diameter and aggregate shape formed by benzene and acetylene pyrolysis using a transmission electron microscopy (TEM) and an image analysis.

2. Experimental

Feedstock gas was prepared by aerating primary nitrogen to benzene or acetylene gas and attenuating the saturated gas with secondary nitrogen. The concentration of the feedstock is 1.0 vol. % benzene or 3.0 vol. %. These concentrations were set to the same carbon source. The flow rate of the feedstock gas was 3.0 L/min and the gas was supplied to an alumina tube heated by a pre-heater (length 800 mm) at 873 K and an electric furnace (length 1000 mm). The inner diameter of the tube was 16 mm, and the length was 1970 mm. Furnace temperature was set to 1473K. The produced carbon black was trapped by a glass fiber filter attached to the end of the tube.

Carbon black produced in each feedstock and furnace temperature was micrographed using a TEM (Tecnai G^2 20 ST, FEI Co.), and a maximum length, a width, a projected area, a perimeter, and a covered area of the image were measured by an image analysis. Then an aggregate shape was classified into four categories (spheroidal, ellipsoidal, linear, and branched) according to the classification category criterion [1, 5]. Branched and linear shapes are more complicated shapes than spheroidal and ellipsoidal shapes. A mean primary particle diameter was calculated using the projected area and perimeter according to ASTM–D3849-07 [6].

In order to evaluate the number of nuclei and coagulation, the number flow rate of carbon black (Q) was calculated based on Tesner *et al*. [7] as shown in Eq. (1);

$$Q = \frac{q}{\gamma} \cdot \frac{n_{\mathrm{t}}}{\sum_{i=1}^{1000} V_{\mathrm{p}i} n_i}. \tag{1}$$

3. Results and Discussion

TEM images of carbon black produced by benzene and acetylene pyrolysis are shown in Fig. 1(a) and (b). In the case of acetylene feedstock as shown in Fig. 1(b), the number of primary particle of an aggregate increased and aggregate shapes were complicated compared with the case of benzene feedstock as shown in Fig. 1(a).

Table 1 shows results of the number flow rate, Q, and the mean primary particle diameter d of carbon black produced at 1473 K (relatively low temperature). In the case of acetylene feedstock the number flow rate increased compared with the case of benzene feedstock. At relatively low temperature, since the rate constant for acetylene is large [8], the formation of PAHs may start in heating up period. Thus, increase in number flow rate

is due to progress of nucleation. The mean primary particle diameter produced by benzene pyrolysis was as same as that of acetylene pyrolysis. Since the reaction for benzene starts slower than the reaction for benzene and acetylene [8], the formation of small PAHs which contribute an increase in the primary particle diameter as surface growth may be inhibited in the feedstock of benzene. Thus, the result implies that ratio of amount of carbon which contributes nucleation and surface growth is the same between benzene and acetylene because the number flow rate and the formation of small PAHs are small in the case in which the feedstock is benzene.

The result of aggregate shape classification of carbon black produced at 1473 K is shown in Fig. 2. In the case feedstock is acetylene, aggregate shapes are complicated compared with the case in which feedstock is benzene. This is because a collision rate increases due to an increase in the number of particles.

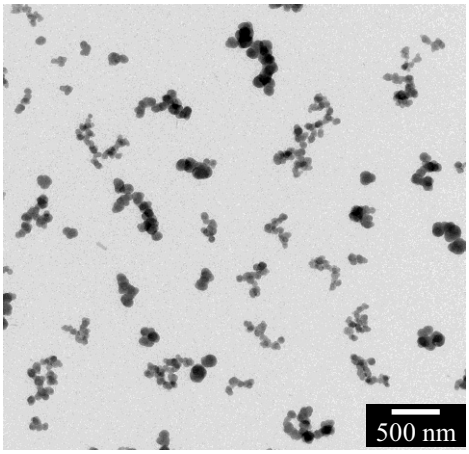

(a) Benzene pyrolysis

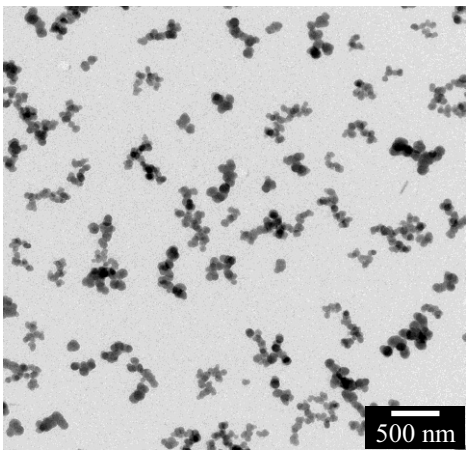

(b) acetylene pyrolysis

Fig. 1 TEM images of carbon black,

Table 1 Number flow rate of carbon black particles and mean primary particle diameter produced

Feedstock	Benzene	Acetylene
Q [10^3 particles/s]	0.916	1.07
d [nm]	42	43

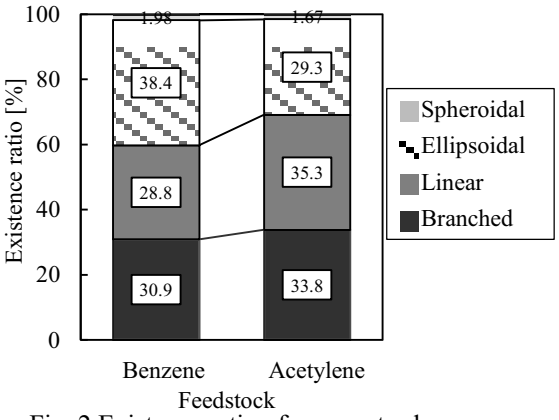

Fig. 2 Existence ratio of aggregate shapes

4. Concluding remarks

In the present work, in order to investigate aggregate shape produced by different hydrocarbon on the same condition, benzene and acetylene pyrolysis were carried out in an alumina tube heated by an electric furnace. Results are summarized as follows.

In TEM images, we identified that aggregate shapes of carbon black by acetylene pyrolysis were complicated compared with by benzene pyrolysis. From results of an image analysis, the aggregate shapes of carbon black produced by acetylene pyrolysis were complicated compared with that of benzene pyrolysis because nucleation was progressed and the number of particles increased.

Therefore, these observations lead us to the conclusion that aggregate shapes of carbon black produced by different feedstock are different due to difference of start temperature of reaction.

Nomenclature

d: mean primary particle diameter [nm], n_i: the number of particle of an aggregate [-], n_t : the total number of particle [-], Q: number flow rate of carbon black particles [10^3 particles/s], q: carbon black yield which is an increase in weight of the filter and of the carbon black in the reaction tube divided by total time [g/s], V_p: mean volume of an aggregate [m^3/particle], γ: density of carbon black (= 1.8×10^6 g/m^3).

References

[1] F. Shishido *et al*., *KAGAKU KOUGAKU RONBUNSHU*, **33** (2007), 306-314. [2] J. B. Donnet, R. C. Bansal and M. J. Wang, Carbon Black, New York, Marcel Dekker (1993). [3] K. Ono *et al*., *Proc. of Carbon*, Shanghai (2011), 806. [4] M. Frenklach *et al*. *Proc. Combust. Inst*., **20**, (1984), 887-901. [5] C. R. Herd, G. C. McDonald and W. M. Hess, *Rubber Chem. Technol.*, **65**, (1992), 107-129. [6] ASTM D 3849-07. Standard test method for carbon black – morphological characterization of carbon black using electron microscopy. [7] P. A. Tesner and S. V. Shurupov, *Combust. Sci. Technol*., **92**, (1993), 61-67. [8] H. Wang and M. Frenkrach, *Combustion and Flame,* **110**, (1997), 173-221.

Eighth International Conference on Flow Dynamics
November 9 - November 11, 2011

Quantification of Non-adhesion Particle Boundary by Observation of Coke Fracture Cross-section

Tetsuya Kanai[1], Yoshiaki Yamazaki[1], Xiaoqing Zhang[1], Ataru Uchida[1], Yasuhiro Saito[1], Masakazu Shoji[1], Hideyuki Aoki[1], Takatoshi Miura[1],Seiji Nomura[2], Yukihiro Kubota[2] and Hideyuki Hayashizaki[2]
[1]Department of Chemical Engineering, Graduate School of Engineering, Tohoku University, 6-6-07 Aoba, Aramaki, Aoba-ku, Sendai, Miyagi 980-8579 Japan,[2] Environment & Process Technology Center, Nippon Steel Corp., 20-1, Shintomi, Futtsu, 293-8511 Japan
E-mail aoki@tranpo.che.tohoku.ac.jp

ABSTRACT

"Non-adhesion particle boundary" is formed when low rank coal does not adhere each other because of dilation failure. In order to clarify the effects of non-adhesion particle boundary on coke strength, a diametral-compression test was carried out on cokes consist of caking coal and low rank coal. Non-adhesion particle boundary was quantified by observation of coke fracture cross-section using SEM. As a results, Non-adhesion particle boundary increased with an increase in blending ratio of low rank coal and coke strength decreased with increasing non-adhesion particle boundary.

1. Introduction

Caking coals for blast-furnace coke are moving to the depletion stage because of recent growth consumption. We should use low rank coal such as non or slightly caking coal as raw materials for blast-furnace coke from a standpoint of effective use of coal resources. Coke must be strong because coke sustains flow passes of liquid metal and reducing gas in a blast furnace. So coke which made from much low rank coal and is tough in a blast furnace is required. Shishido *et al.*[1] reported that the strength of coke made from much low rank coal increases by the addition of the binder, which is extracted from coal and has strong caking property.

However, mechanisms of coke strength improvement have been unclear. In order to improve the techniques of high-volume use of low rank coal, mechanisms of coke strength reduction should be clarified quantitatively.

Arima[2] reported that coke may be fractured from non-adhesion particle boundary which is formed when low rank coal does not adhere to one another because of dilation failure. Fig. 1 shows non-adhesion particle boundary. Non-adhesion particle boundary has not evaluated quantitatively despite a fact that non-adhesion particle boundary may be cause the coke strength reduction. This is because many researchers have observed polished surface of coke using optical microscope. Non-adhesion particle boundary was observed as pore or could not be observed in polished surface of coke because this part was a boundary between low rank coals.

In this study, we quantifid the non-adhesion particle boundary by observation of coke fracture cross-section using SEM. Moreover in order to clarify the effects of non-adhesion particle boundary on coke strength, a diametral-compression test was carried out.

2. Experimental

2.1 Specimen making

Table 1 shows characterization of the coal used and Table 2 shows manufacturing conditions. The coal was charged in a both sides heating oven, the size of which was 40 mm × 60 mm × 60mm, and heated 3K/min to 1273K and kept 30 min. Coke taken out from the oven was drilled and sliced off to the discs, the size of which was 10 mm in diameter and length.

Table 1 Characterization of the coal used

	Elemental analysis results (daf.%)					
	C	H	O	Ro [%]	MF [ddpm]	TD [%]
Caking coal	90.3	5.1	2.1	1.20	3.08	86
Low rank coal	84.6	5.9	7.3	0.78	1.38	0

Table 2 Manufacturing conditions

	Caking coal [mass%]	Low rank coal [mass%]	Coal size [mm]	Bulk density [dry.g/cm^3]
Coke A	100	-	<1 (100%)	0.8
Coke B	75	25	<1 (100%)	0.8
Coke C	50	50	<1 (100%)	0.8
Coke D	25	75	<1 (100%)	0.8
Coke E	-	100	<1 (100%)	0.8

2.2 Diametral-compression test

Tensile strength of coke was measured with a diametral-compression test using universal testing machine (Shimadzu Co., Autograph AG – 150 kN). The loading rate was 2 mm /min. Tensile strength was calculated from following Eq(1) :

$$\sigma = \frac{2P}{\pi dl}, \qquad (1)$$

where, d and l are a diameter and a length of specimen respectively and P is the maximum load when coke fractures. In order to evaluate tensile strength statistically, tensile strength was evaluated with Weibull plot. Weibull plot is widely applied for statistical data analysis of brittle material. A Weibull distribution function is represented as Eq. (2) :

$$\ln\ln\frac{1}{1-P_f(\sigma_t)} = m\ln\sigma_t - m\ln\xi, \qquad (2)$$

where, P_f, is cumulative failure probability, m is the Weibull slope, ξ is scale parameter, and σ_t is tensile strength. Scale parameter means the tensile strength when cumulative failure probability reaches 63 %. Cumulative failure probability was calculated from median rank method[3].

2.3 Quantification of non-adhesion particle boundary

Scanning electron micrographs(1280 × 960 pixels, 0.96 μm special resolution) on coke fracture cross-section were captured using SEM(KEYENCE Co., VE8800). Accelerating voltage was set to 1.7kV.

Fig. 2 shows micrographs of coke fracture cross-sections consists of pore, pore wall, fractured coke

matrix and non-adhesion particle boundary. Pore is black colored part and pore wall has level surface because this part has melted and resolidified once. Fractured coke matrix links with matrix and has fracture traces. Non-adhesion particle boundary has rough surface because coal particle dose not adhere to one another and keep particle shape. Moreover non-adhesion particle boundary dose not have fracture traces because this part has not fractured. We selected the non-adhesion particle boundary by visual judgment and mark it with white color (Intensity value = 255) using a image processing software. The area of non-adhesion particle boundary was measured by counting the number of pixel which has 255 intensity value. The area ratio of non-adhesion particle boundary is the percentage of non-adhesion particle boundary area in the micrographs.

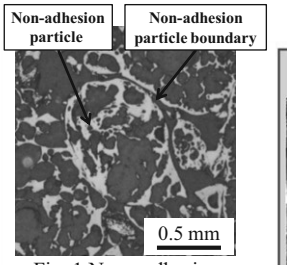

Fig. 1 Noon-adhesion particle boundary

Fig. 2 Micrographs of each coke fracture cross-sections

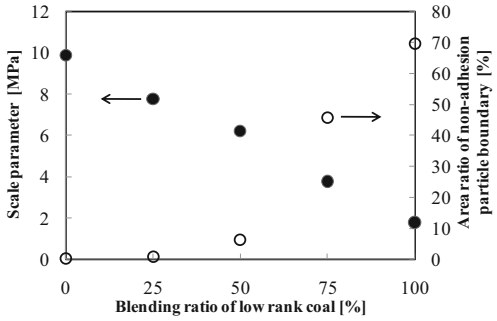

Fig. 3 Relationship of scale parameter and area ratio of non-adhesion particle boundary to blending ratio of low rank coal

3. Results and Discussion

Fig. 3 shows the relationship of scale parameter and area ratio of non-adhesion particle boundary to blending ratio of low rank coal. Scale parameter decreased with an increase in blending ratio of low rank coal. Non-adhesion particle boundary increased with an increase in blending ratio of low rank coal. Area ratio of Non-adhesion particle boundary is little under 50 % of blending ratio of low rank coal. However, area ratio of non-adhesion particle boundary increased rapidly over 50 % of low rank coal. This indicates that caking coal exist between low rank coals and adhere to low rank coals until blending ratio is 50 : 50. Over 50 %, non-adhesion particle boundary forms between low rank coals where caking coal dose not exist.

Fig. 4 shows the relationship between scale parameter and area ratio of non-adhesion particle boundary. Coke strength decreased with increasing non-adhesion particle boundary. This indicates that non-adhesion particle boundary is a factor related to coke strength reduction. Coke strength decreased rapidly until around 10 % of non-adhesion particle boundary and decreased gently over 10 %. This is because coke is brittle material and fractures from the weakest defects as weakest link theory. Until around 10 % of non-adhesion particle boundary, Coke strength decreases because of increase the probability that non-adhesion particle boundary exists at stress concentration area. Over 10 %, coke strength dose not decrease so much unless defects become large size because non-adhesion particle boundary exists at stress concentration area plenty.

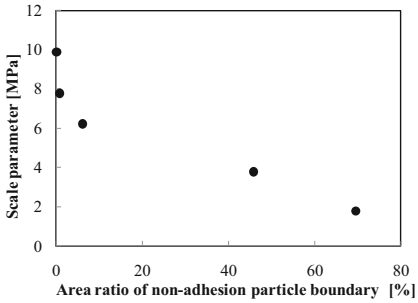

Fig. 4 Relationship between area ratio of non-adhesion particle boundary and scale parameter

4. Concluding remarks

In this study, the effect of non-adhesion particle boundary on coke strength was investigated by the diametral-compression test and the quantification of non-adhesion particle boundary. As a results, non-adhesion particle boundary increases with blending ratio of low rank coal and the coke strength decreases when there is non-adhesion particle boundary even a little.

Nomenclature

d: diameter of specimen [m], l: length of specimen [m], m: Weibull slope [-], P: Load [N], P_f : cumulative failure probability, σ: tensile stress [MPa], σ_t: tensile strength [MPa], ξ : scale parameter [MPa]

References

[1] T. Shishido, T. Takanohashi and I. Saito : Sekitan Kagaku Happyo Ronbunshu, **43** (2006), 125
[2] T. Arima: *Tetsu-to-Hagané*, **87** (2001), 274
[3] D. J. NEVILLE : *Engineering Fracture Mechanics*, **27** (1987), 143

Eighth International Conference on Flow Dynamics
November 9 - November 11, 2011

A Study of 4 Dimensional City Modeling from Car-mounted Omnidirectional Images

Ken Sakurada, Jun Yanagisawa, Daiki Tetsuka, Takayuki Okatani, Koichiro Deguchi
{sakurada, yanagisawa, tetsuka, okatani, kodeg}@fractal.is.tohoku.ac.jp
Graduate School of Information Sciences Tohoku University 6-6-01 Aza Aoba, Aramaki, Aoba-ku, Sendai, Japan

ABSTRACT

Recently, there have been many studies that build 3D models from large unstructured collections of images downloaded from the Internet or the image sequences captured by cameras mounted on a moving car. These studies basically assume static scenes and cannot be applied to dynamic scenes. This study aims at making it possible to create four-dimensional models (i.e., the shape and its temporal changes) of a city from its images. This paper describes the current progress of this study and preliminary results of establishing geometric correspondences among environments that vary with time.

1. Introduction

The purpose of this study is to consider how to create a model of a city which changes its shape with time from its images. The problem we consider includes not only modeling the three-dimensional shape of the city but modeling its changes with time. Thus, we call the problem the 4D city modeling.

Recently, several methods for accurately modeling large scale environments from images have been established. These include the study [1] that builds 3D models from large unstructured collections of images downloaded from the Internet, the study [2] that builds 3D models from image sequences captured by cameras mounted on a moving car in the city street, and many others of visual SLAM/SFM [3].These studies demonstrate that the image-based 3D modeling is as accurate as laser range sensors while maintaining the advantage of passive sensors that they have high degrees of freedom in their operations; e.g.., cameras can capture data of a wide area at once.

However, these studies cannot be directly applied to dynamic environments that vary with time. The key techniques of these studies are geometric optimization method (i.e., bundle adjustment [5]) and accurate methods of matching images using feature point extractor (e.g., SIFT (Scale Invariant Feature Transform) [6]).These techniques basically assume static environments. Recently, there have been a few studies that infer variations of environments with time, e.g., appearance-based localization [7] and the estimation of the time when pictures of a city are taken. However, these studies do not target dynamic environments.

To perform 4D city modeling, we need to match not only images captured at different places but those captured at different times. As target cities, we choose the disaster sites of the tsunami caused by the earthquake in Japan occurred on 11/3/2011.In these areas, we drove a car on which an omnidirectional camera (Point Grey Research, Ladybug3) and a GPS sensor (Hemisphere, R100) are mounted. Our motivation is to model and visualize the recovery process of the disaster sites from the aftermath of the disaster. We have continued recording the scenery of the disaster sites since about one month after the earthquake until now. We intend to perform this recording activity periodically (e.g., every two months) for more than three years.

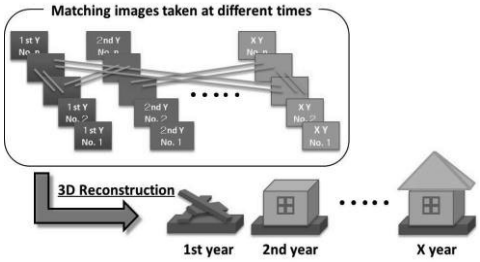

Fig.1 Abstract of 4 dimensional city modeling

Fig.2 Recording Car

2. Related Works

In this study, we realize an optimization method for 3D reconstruction that can deal with the variations of the environment with time. In the research area of visual SLAM/SFM, the standard method for optimization of positions of cameras and feature points is local bundle adjustment that uses only key frames [5].If the target environments are static, it is not necessary to use all the captured images because of the redundancy of the observations. However, the dynamic environment which this study targets does not have the observation redundancy, and therefore a new optimization method is necessary. We employ a filter-based approach [4] that iterates approximation and optimization recursively for all images and realize a new method for solving the problem of optimization with all images.

Furthermore, in this study, we realize a new method which can match feature points in the environment varying significantly and irreversibly. There are studies which infer the temporal variation of environments [7,8].However, the two studies deal with matching different time images and 3D reconstruction in a separate manner. The purpose of the study [7] is the recognition of the reversible variation of environments caused by moving objects, such as humans and cars. The study [8] assumes that the temporal variation of the environments is slow and thus it is easy to match the images. Because of these, the two studies cannot be applied to our problem. This study deals with matching images and 3D reconstruction in a connected manner and realizes the method which can deal with the significant and irreversible environment variations.

3 Experiments of matching point clouds in the spatiotemporal domain

We performed an experiment in which we first reconstruct the shape of a street from its two image sequences that are captured at different times, and then try to match the two reconstructions of the street. The reconstructions are represented as point clouds. Each point of the point clouds is given an image descriptor that is extracted from the original image. Using this image descriptor, we match each point in the point clouds to estimate the geometric transformation between the two reconstructions.

3.1 Method of generating 3D point clouds with each image descriptor

The method is summarized as follows:(1) Feature points are extracted with Speed Up Robust Feature (SURF) [9] and tentative matching is obtained for two consecutive images using the descriptors of those feature points.(2) Essential matrices are calculated with five point algorithm [10].At that time, mismatches of feature points are rejected using Random Sample Consensus (RANSAC)[11].(3) Camera poses and positions of feature points are calculated using those essential matrices.(4) Camera poses and position of 3D points are optimized to minimize reprojection errors of feature points.3D point cloud of which each point has an image descriptor is generated through (1)-(4) processes.
3D point clouds with image descriptors are generated.

3.2 Experimental results

In the experiment, we tested the feasibility of matching two 3D point clouds generated from images captured at different times using local image descriptors.Fig.3 shows two snapshots of the target scene. Let A and B be 3D point clouds generated from images taken at different times; a_i and b_j be points of A and B, each of which has the 3D position (x y z) and 64 dimensional descriptor **dv** ($\{a_i : i = 1, 2, \ldots, N_A\} \in$ A, $\{b_j : j = 1, 2, \ldots, N_B\} \in$ B).$m_k = (a_k, b_k)$ ($k = 1, 2, \ldots, M$) is a candidate match. Outliers in m_k are eliminated by RANSAC, in which the scale s, the rotation marix **R**, and the translational vector **T** satisfying the following equations are computed:

$$\mathbf{x}(b_k) = s\mathbf{R}\mathbf{x}(a_k) + \mathbf{T}$$

Let c_i be points of C, each of which is obtained by transforming a point a_i with s, **R**, **T** ($\{c_i : i = 1, 2, \ldots, N_A\} \in$ C, $\mathbf{x}(c_i) = s\mathbf{R}\mathbf{x}(a_i) + \mathbf{T}$).

Fig.4 shows the result. The A(left) and the B(center) points are a_i and b_j the points reconstructed from the images captured at different times (A: April 26, B: June 13)**.** The C(right) points are the points transformed by the estimated transformation. Number of a_i, b_j are N_A =86099, N_B =80254. If A and B correspond accurately, the scale and orientation of C match with those of B. However, in Fig.4, the scale of C is smaller than that of B and the orientations of B and C are different. Thus, this result shows that the method of this experiment can match two

Fig.3 Panoramic Images taken in Kamaishi

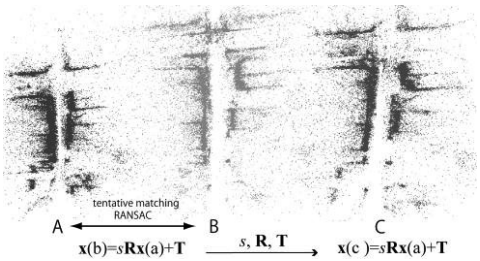

Fig.4 Result of tentative matching and RANSAC (top view)

3D point clouds roughly generated from images taken at different times. However, to recognize the two reconstructions of the street as the reconstruction of the same place, it is necessary to improve the accuracy of matching the two reconstruction of the street.

4. Conclusions

We have described the problem, motivation and method of creating a four-dimensional model of a city from its images that can deal with its temporal variations. We are studying a new approach to the problem, in which we try to solve it by performing matching the images taken at different times and reconstructing the 3D shape of the target scene in an integrated manner.

References

[1] S. Agarwal et al., “Building rome in a day,” ICCV,2009.
[2] M. Pollefeyset al., “Detailed real-time urban 3d reconstruction from video,” Int. J. Comput. Vision,2008.
[3]Davison,A.j. et al. “MonoSLAM: Real-Time Single Camera SLAM”,IEEE Trans. Pattern Analysis and Machine Inteligence, Vol.29, No.6, pp.1052-1067(2007)
[4] Sebastian Thrun,Wolfram Burgard,D. F. (2005). Probabilistic Robotics. The MIT Press.
[5] B. Triggs. P. McLauchlan,R. Hartley and A. Filtzgibbon :Bundle Adjustment – A Modern Synthesis, Vision Algorithm: Theory & Practice, Springer-Verlag LNCS 1883 (2000)
[6] Lowe,David G. (1999). "Object recognition from local scale-invariant features". Proceedings of the International Conference on Computer Vision. 2. pp. 1150–1157. doi:10.1109/ICCV.1999.790410
[7] M. Cummins et al. "Accelerated FAB-MAP With Concentration Inequalities". IEEE TRANS. ON ROBOTICS,VOL.26, No.6, 2010.
[8] G. Schindler et al. "Probabilistic temporal inference on reconstructed 3D scenes",CVPR, 2010
[9] H.Bay,T.Tuytelaars,and L.V.Gool,”SURF:SpeedUp Robust Features”, Proc. of Int. Conf. of ECCV, (2006)
[10] H.Li and R.Hartley, Five-Point Motion Estimation Made Easy, IEEE-ICPR-2006.
[11]Martin A. Fischler et al. "Random Sample Consensus: A Paradigm for Model Fitting with Applications to Image Analysis and Automated Cartography"(1981). *Comm. of the ACM* **24**: 381–395

Eighth International Conference on Flow Dynamics
November 9 - November 11, 2011

Simulation of Boundary Layer Receptivity to Outer Disturbances

Shuta Noro[*1], Masaya Shigeta[*1], Seiichiro Izawa[*1] and Yu Fukunishi[*1]
[*1] Department of Mechanical Systems and Design, Tohoku University, Japan
noro@fluid.mech.tohoku.ac.jp

ABSTRACT

The effect of outer disturbances on the laminar boundary layer was investigated by a numerical simulation. The disturbances were introduced by the combination of a rectangular bar and a jet ejection. The results confirmed the experimental findings that the velocity fluctuations jumped near the wall before the outer disturbances reached the boundary layer. However, these velocity fluctuations that jumped in to the wall do not lead to transition.

1. Introduction

The boundary layer transition has been widely studied through theoretical, experimental and numerical approaches. The transition process starts from a receptivity process in which a boundary layer captures environmental disturbances in the form of instability waves. Most of the studies on the boundary layer receptivity focus on the relation between the freestream disturbances and the leading edge receptivity, because the receptivity is very high around the leading edge where the boundary layer originates. A detailed review was provided by Saric et al. [1].

When the freestream disturbances increase and exceed a certain threshold, the transition occurs rapidly bypassing the linear growth of the instability waves. This rapid transition is known as bypass transition. Even in bypass transition, the disturbances intrude the boundary layer through the leading edge receptivity. However, if the intense disturbances in the freestream are localized in space and intermittent in time, they might directly affect the laminar boundary layer and the transition might occur in different form. These direct effects of outer localized disturbances are not well known. Thus, the present study focuses on the direct receptivity of Blasius boundary layer to these outer disturbances. In our previous study, Shigeta et al. [2] experimentally investigated the effect of the outer disturbances. The disturbances were introduced by two different methods; a conventional turbulence grid and a turbulence-generating bar that was a circular pipe with some holes to eject jets. They reported that the low frequency velocity fluctuations appear first inside the boundary layer before the outer disturbances reaches the outer edge of the boundary layer. In this study, three-dimensional numerical simulations are carried out to investigate the growth of boundary layer under these distinctive environmental disturbances. The results are discussed by comparing with the Shigeta et al.'s experiment [2].

2. Computational Method

Three-dimensional incompressible Navier-Stokes equations are directly solved by the finite-difference method. The third-order upwind method is used in the convection term and the second-order central difference method is used for the others. The Crank-Nicolson implicit scheme is used for the time advancement. Besides, the multi-grid system is adopted to solve the Poisson equation quickly and accurately.

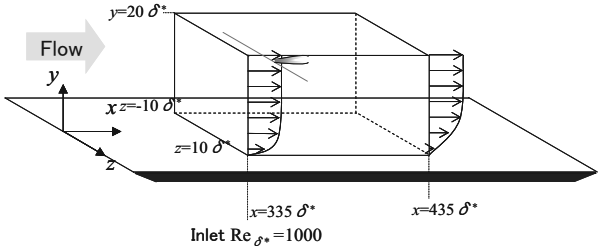

Fig. 1 Computational region.

The computational domain is shown in Fig. 1. The origin of coordinate system is set at the center of leading edge of the plate. The axes x, y and z are the streamwise, wall-normal and spanwise directions, respectively. The size of the domain is $100\delta^* \times 20\delta^* \times 20\delta^*$, where δ^* is the displacement thickness at the inlet of Blasius boundary layer. The domain covers $1{,}010<x<1{,}310$mm, $0<y<60$mm, $-30<z<30$mm at freestream velocity $U = 5$ m/s, which is the experiment's condition [2]. The inflow Reynolds number based on δ^* is 1,000. The number of mesh points is 193×65×65, where their widths are uniform in the x and z directions while they concentrate near the wall in the y direction.

Non-slip and slip boundary conditions are applied to the plate surface and the upper boundary, respectively. The Neumann condition is used as the pressure boundary condition. The periodical condition is given in the spanwise direction, and the Sommerfeld radiation condition is used at the outflow condition.

Rectangular cylinder is located at $335\delta^*<x<337\delta^*$, $8.8\delta^*<y<9.8\delta^*$ and $-10\delta^*<z<10\delta^*$. Jet ejects at $357\delta^*<x<359\delta^*$, $8.8\delta^*<y<9.8\delta^*$ and $-0.6\delta^*<z<0.6\delta^*$. Its velocity is $2.0\times U$.

3. Results and Discussion

Figures 2 and 3 show the contour maps of the RMS values of the streamwise velocity fluctuation, u'_{rms}, in x-y plane where the jet is ejected. Similar fluctuation patterns can be observed in both figures. It should be noted that the disturbances start to grow inside the boundary layer before the outer artificial disturbances reach the outer edge of the boundary layer. The growths of disturbances are also found in the mid-plane of the jet ejections, though they are weaker than those in the jet-ejecting plane. This "disturbance jumping" was a

characteristic phenomenon observed in the experiment.

Figure 4 shows the contour maps of the spanwise vorticity fluctuation, ω_z', in both planes. In the jet-ejecting plane (z=0), regions of positive and negative elongated vorticity fluctuations are observed behind the bar owing to the jet ejection. On the other hand, the Karman vortex street appears in the mid-plane and it soon begins to interact with the vorticity fluctuations inside the boundary layer at around x=380δ^*. Figure 5 shows the three-dimensional vortical structures visualized by the isosurface of Q. The Karman vortex street can be observed except for the region near where the jet is ejected.

In Fig.3, It should be noted that the velocity fluctuation that jumped into the boundary layer does not just gradually grow. The location where the velocity fluctuation suddenly grow corresponds to the x location where in other x-y planes the Karman vortex street starts to interact with the boundary layer (see Fig.4(b)).

4. Conclusions

The effect of outer disturbances on the growth of lower laminar boundary layer was investigated by a three-dimensional numerical simulation. As a result, the experimental finding that the outer disturbances jump into the boundary layer before it reaches the boundary layer was confirmed. In addition, it was also found that the transition was caused not by the growth of these disturbances that jumped in, but by the outer disturbances that penetrated in other spanwise locations.

References

[1]Saric, W. S., *et al.*, *Annu. Rev. Fluid Mech.*, **34**, pp. 291-319, 2002.

[2]Shigeta, M., *et al.*, *12th ACFM*, p. 42, 2008.

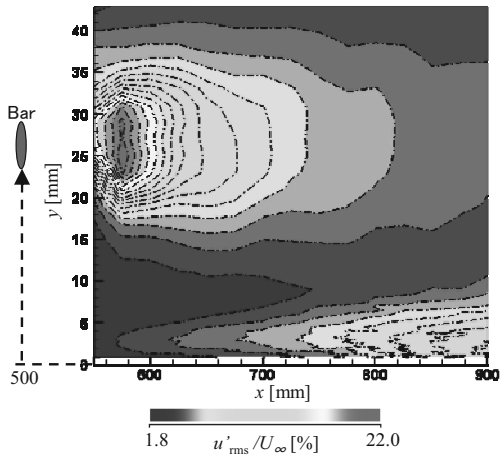

Fig. 2 Contour maps of u'_{rms}/U in x-y plane where the jet is ejecting (Exp. [2]).

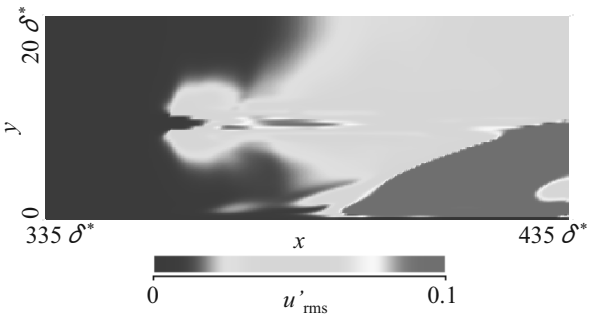

Fig. 3 Contour map of u'_{rms}/U in x-y plane at z=0.

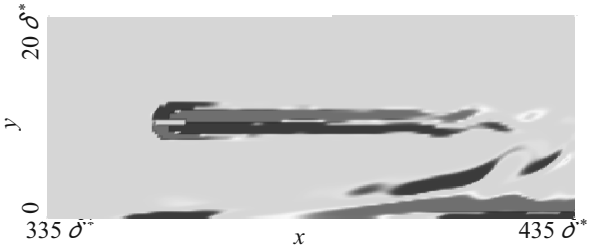

(a) jet-ejecting plane (z=0)

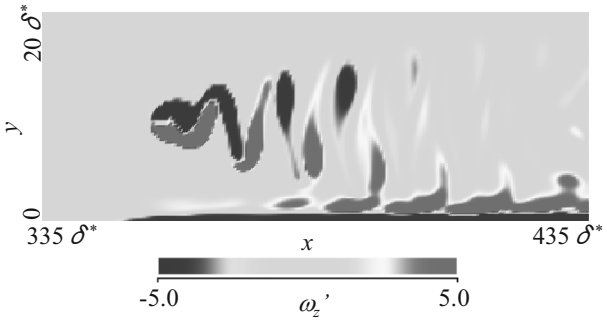

(b) mid-plane (z=10δ^*)

Fig. 4 Contour map of ω_z' in x-y plane.

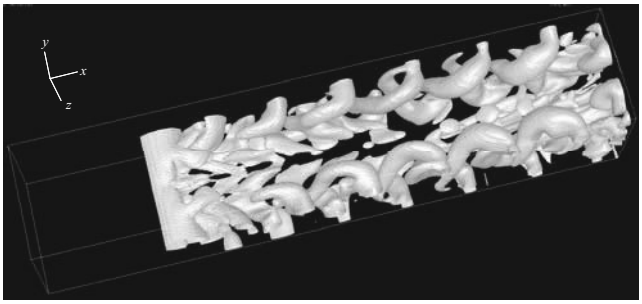

Fig. 5 Isosurface of Q=0.5.

Conceptual Examination of a Small UAV for Mars Exploration Flight

Koji Fujita[*1], Hiroki Nagai[*1] and Keisuke Asai[*1]
*1 Dept. of Aerospace Engineering, Tohoku University,
6-6-01, Aramaki-Aza-Aoba, Aoba-ku, Sendai 980-8579, JAPAN
fujita.koji@aero.mech.tohoku.ac.jp

ABSTRACT

A reconnaissance airplane for Mars exploration offers the possibility to obtain high resolution data on a regional scale of several hundreds to thousands of kilometers, which cannot be achieved with rovers or satellites. This paper discusses the design rationale undertaken to develop a conceptual examination of a 3.5kg fixed-wing, propeller-driven, deployable airplane for the Mars exploration, following a predetermined set of requirements and constraints tailored for a small scale scientific mission to Mars.

1. Introduction

Airplanes have been seriously considered as a new method of exploring Mars at NASA[1]. It offers the possibility to obtain high resolution data on a regional scale of several hundreds of kilometers, which cannot be achieved with rovers or satellites.

Aerodynamic characteristics on Martian atmosphere are quite different from that on the Earth due to low Reynolds number flow caused by low atmospheric density. In addition, it is difficult to get enough lift, as wing area is inversely proportional to the density. In order to reduce required lift, thorough weight saving is needed. However, a Mars Airplane must be small and compact to transport to Mars. As a way to solve this conflicting problem, the Mars Airplane needs some deployment mechanisms.

The purpose of this study is to indicate a feasibility of the Mars Airplane. This paper presents the conceptual examination of a fixed-wing, miniature, and propeller-driven airplane for Mars. And the design rationale following the constraints set by the Martian environment is explained. Based on this design method, trade-off studies were performed. Especially, it was shown that increase of the cruise velocity is significantly effective to save weight of the Mars Airplane.

2. Conceptual examination process

A conceptual examination process followed "*Aircraft Design: A Conceptual Approach*"[2] by Raymer. First, define design requirements and constraints. Then make first guess sizing from a sketch. Estimate specifications, revise the design and make sizing again. Through iterating this cycle, the design is optimized and detailed. In consideration of the low Reynolds number flow, this research uses results of aerodynamic characteristic experiments at low Reynolds number[3,4].

3. Current Mission Scenario

Figure 1 shows a conceptual diagram of the current mission scenario. The Mars Airplane will be transported to Mars with it packed in an aeroshell. At Mars, the aeroshell will entry and descend its atmosphere. When the aeroshell comes at the predefined position, the Mars Airplane will be released. Then it will deploy, control its attitude, and start horizontal flight. It will observe a Martian magnetic field and take pictures of a Martian surface closely in vast area.

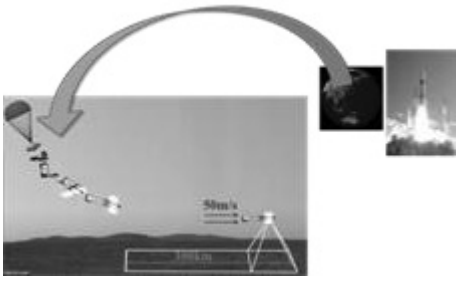

Fig. 1 The conceptual diagram of the current mission scenario (Images: Courtesy of NASA and JAXA).

4. Requirements and Constraints

Table 1 shows requirements and constraints assumed on the basis of the mission scenario. These were used in following estimation as inputs.

Table 1 Requirements and constraints.

Item	Value	Unit
Maximum Total Mass	3.5	kg
Cruise Velocity	50	m/s
Range	300	km
Altitude	0	m
Density	0.015	kg/m^3
Length of Aeroshell	0.60	m
Diameter of Aeroshell	1.0	m
Item	**Comment**	
Configuration	fixed wing	
Propulsion	Propeller / DC Motor	
Payloads	Magnetometer High Resolution Camera	

5. Specifications estimation method

The specifications of the Mars Airplane were estimated and optimized through iterations. This method was made up of three sections: aerodynamic performance estimation, propulsion performance estimation, and mass build-up.

In order to reduce the energy consumption for the propulsion system, the Mars Airplane was designed to maximize the lift-drag ratio during non-accelerated level flight while satisfying requirements and constraints. The main wing area S_{ref} was given by eq. (1). At first, the

total mass M_{total} was assumed to 3.5kg as an initial value. The acceleration due to gravity g was set to 3.71m/s^2. The density ρ and the cruise velocity V were given from requirements and constraints. The lift coefficient of the main wing C_L was given by experiment[3]. Then drag was estimated. The drag coefficient of the main wing was also given by experiment[3]. That of the tail wing was assumed as a zero lift drag coefficient and converted to other form using the main wing area. The drag coefficient of the fuselage C_{Df} was represented as eq. (2)[2], where Re_l is Reynolds number by fuselage length, f is a fuselage taper ratio, and $S_{f\,wet}$ is wetted area of the fuselage. The total drag coefficient was obtained as the sum of those drag coefficients.

A propulsion performance was estimated by the blade element theory. The diameter of the propeller was set to 0.60m from the standpoint of packing in the aeroshell. First, the rate of rotation was assumed. The aerodynamic characteristics of an airfoil for the propeller were given by experiment[4]. Obtained total thrust was compared to the drag and even out by adjusting the rate of rotation. The required shaft power was obtained using load torque and rate of rotation.

The total mass was estimated as the sum of mass of each section. As a battery, the lightest Li-ion battery was selected[5]. Its energy density is 118Wh/kg. The mass of the battery M_{bat} was estimated by eq. (3). Here, P_{total} is the total input power, E is endurance, and ρ_{energy} is energy density of the battery. The input power for the motor was obtained from the propulsion performance calculation described above.

By reentering obtained total mass to Eq. (1), these calculations were iterated until values were converged, with changing input parameters.

$$S_{ref} = \frac{2M_{total}g}{\rho V^2 C_L} \tag{1}$$

$$C_{Df} = \frac{1.328}{\sqrt{Re_l}}\left(1 + \frac{60}{f^3} + \frac{f}{400}\right)\frac{S_{f\,wet}}{S_{ref}} \tag{2}$$

$$M_{bat} = \frac{P_{total}E}{\rho_{energy}} \tag{3}$$

6. Results

Obtained specifications satisfied requirements and constraints. A basic layout of the Mars Airplane was drawn as shown in Fig. 2 based on these results. All parameters were fully following the obtained results.

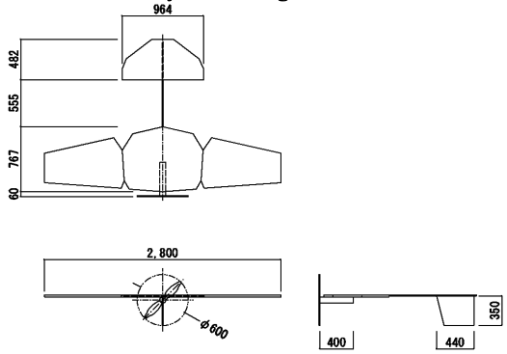

Fig. 2 The basic layout of the Mars Airplane.

Trade-off studies for the total mass to each input parameter were performed. Figure 3 shows a sensitivity of the total mass to the cruise velocity. Only 4m/s increase of the cruise velocity yielded nearly 0.6kg decrease of the total mass. Figure 4 shows a mechanism of this total mass decrease. These processes yielded the big decrease of the total mass although these two configurations have same payloads and range.

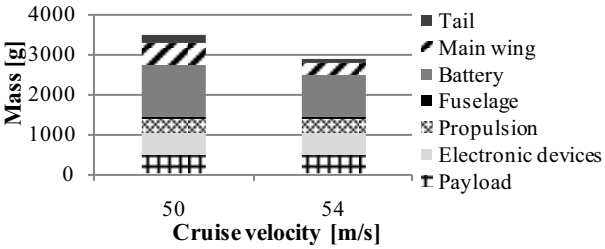

Fig. 3 A sensitivity of the total mass to the cruise velocity.

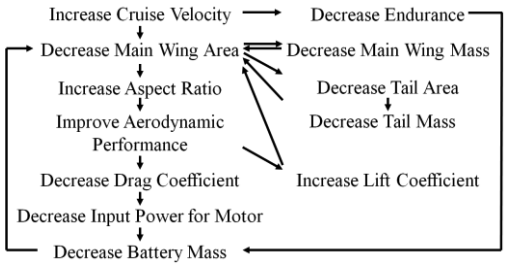

Fig. 4 A mechanism of the total mass decrease due to the increase of the cruise velocity.

7. Conclusion

The conceptual examination and its specifications estimation method were presented to indicate the feasibility of the Mars Airplane. A trade-off study for the total mass to the cruise velocity was presented. It was shown that an increase of the cruise velocity created virtuous cycle of decreasing the mass of the main wing, the tail wing, and the battery.

References

[1] Guynn, M. D., et al., "Evolution of a Mars Airplane Concept for the ARES Mars Scout Mission," AIAA paper 2003-6578, San Diego, CA, 2003.

[2] Raymer, D. P., "Aircraft Design: A Conceptual Approach," AIAA Education Series.

[3] Shigehara, S., et al., "Variable-pressure Wind Tunnel Study of Aspect Ratio Effects on Three-Dimensional Wing at Low Reynolds Number Flow," Proc. of the 64th Kyushu Branch Regular Meeting of the Japan Society of Mechanical Engineers, C42, Kyushu University, Fukuoka, 2011.

[4] Suwa, T., et al., "Aerodynamic Characteristics of a Triangular Airfoil at Low Reynolds Number and High-Subsonic Mach Number," Proc. of the 43rd Fluid Dynamics Conf. / Aerospace Numerical Simulation Symposium 2011, 1D09, Tokyo, 2011

[5] Toyota, H., et al., "Conceptual Design of Power System for Mars Airplane," Proc. of the Space Sciences and Technology Conf., JSASS-2010-4479.

Eighth International Conference on Flow Dynamics
November 9 - November 11, 2011

The Effects of Standoff Distance on the Laser-Induced Liquid Jet in a Narrow Channel

Muhd Hilmi Bin Shapien[1] and Mingyu Sun[2]
[1]Graduate School of engineering, Tohoku University, Aramaki aza aoba 6-3, Aoba, Sendai, 980-8577 JAPAN
[2]Center for Interdisciplinary Research, Tohoku University, Aramaki aza aoba 6-3, Aoba, Sendai, 980-8577 JAPAN
hilmi@iswi.cir.tohoku.ac.jp

ABSTRACT

A high-speed liquid jet can be generated by irradiating a pulsed laser in a tube filled with water. In order to clarify the mechanism of jet and bubble formation, and to investigate the influence of tube geometry, numerical techniques have been developed to analyze the phenomenon. Previous studies have focused on gas-liquid two phase flows without modeling phase changes. In this study, a cavitation model that takes into account phase changes has been considered, and the effects of standoff distance on the jet velocity has been investigated. It is found that the jet velocity reduces with increasing standoff distance.

1. Introduction

It is possible to cut soft tissues without damaging the blood vessel by using the Laser-Induced Liquid Jet(LILJ) [1]. Fig.1 shows a sketch of the LILJ. In LILJ, a small portion of water is evaporated by irradiating the laser in the narrow tube filled with water. Water is pushed out at a high speed by the expansion of this gas and the propagation of the pressure waves. LILJ is excellent in the point that it does not have an electromagnetic influence on surrounding medical equipment. And also it creates a pulsed water jump compared with a past pump type. The area of use of LILJ is expanding now.

In numerical simulation, the flow phenomena associated with the LILJ have both compressible feature because of the bubble expansion and incompressible feature because of low jet velocity compared with the sound speed. A numerical technique should be able to deal with both compressible and incompressible properties simultaneously. In addition, a sinusoidal standing wave was found in the tube[2], and the pressure of this standing wave may run below the vapor pressure. Small cavitation bubbles are expected in this region. In our previous studies, a cavitation model assuming a constant vapor pressure under room temperature was used[3]. However, the room temperature assumption is invalid in the laser-induced bubble, the temperature dependence of the vapor pressure should be taken into account. The amplitude of the standing waves may vary with the strength of the initial energy condition and the distance between the tip of fiber and the tube exit, which is the standoff distance. In this study, we investigate the influence of the standoff distance on the jet velocity using a cavitation model with temperature dependant vapor pressure.

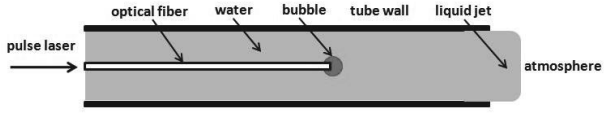

Fig. 1 Laser-induced liquid jet

2. Method

The present simulation is based on a two-velocity two-pressure two fluid model. A semi-implicit Lagrange-Remap method is used to deal with all-speed interfacial flows. It solves pressure and velocities in the Lagrangian frame implicitly, and the linear sparse matrix is solved by the ILU+GMRES method, which is the GMRES iterative method coupled with the ILU preconditioner. The updated conservative quantities in the Lagrangian frame is then remapped back to the Euler frame using formula, formally the same as the finite volume method. Subgrid modeling is included to approximate the interactions at the level of subgrid scale[4]. The traditional solution-adaptive grid technique is used to enhance the computational efficiency.

For the cavitation model, Merkle's cavitation model developed for one-fluid model is adapted to the two-fluid model[5]. In this present study, the Tetens equation[6],

$$P(T) = 6.11\times10^{\left(2+\frac{7.5T}{237.3+T}\right)}[Pa], \qquad (1)$$

was used to approximate the temperature dependence of the saturated vapor pressure. Here, T [˚C] is the temperature of a cell.

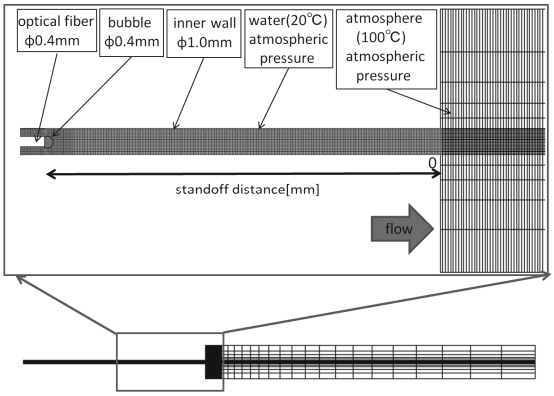

Fig. 2 Initial condition and initial grid

Fig.2 shows an initial grid, and the initial fluid distribution. The figure above shows a close view of fiber point in the nozzle and the figure below shows the overall view of the initial grid. The x-axis is along the axis of the narrow channel and the tube exit was set to $x = 0$. The initial grid interval inside LILJ internal and its neighborhood was set to be 0.1mm. The inside diameter of the tube is 1mm, which is almost the same as that used in the experiment[7]. The fiber for the laser irradiation of 0.4mm in the outside diameter was distributed in the tube. A large domain outside is adopted so that the reflection of the pressure waves by

the outside boundary become negligible.

The bubble in the narrow tube is filled with vapor, and the ambient atmosphere is assumed to be the steam of 100˚C at atmospheric pressure. The boundary condition of the fiber and the narrow tube set to be solid wall, and free boundary conditions for others. It was assumed that a semicircle area on the tip of the fiber is evaporated instantaneously in the present study. The temperature and the pressure of the semicircle bubble were set by adding a certain portion of the laser energy subtracting latent heats. The velocity measurement was made at the leading tip of the water jet.

Three input energies are tested for 170, 190, 210mJ/mm, and the standoff distance is changed at 5mm from 5mm to 50mm. The relation between a standoff distance and jet velocity relation was examined.

3. Results and Discussion

Fig.3 and Fig.4 show the volume fraction α and the velocity u of LILJ in narrow channel for standoff distance from 5mm to 20mm for input energy of 170mJ/mm. It is clearly seen that the bubble expands and drives the liquid jet. It is also confirmed that the phase change occurred in narrow tube.

Fig.5 shows the maximum jet velocity of LILJ against standoff distance for input energy of 170, 190, 210mJ/mm. It is seen that for all condition of input energy, the jet velocity is in inverse proportion to the standoff distance within the range and reaches the maximum velocity of 73m/s at input energy of 210mJ/mm.

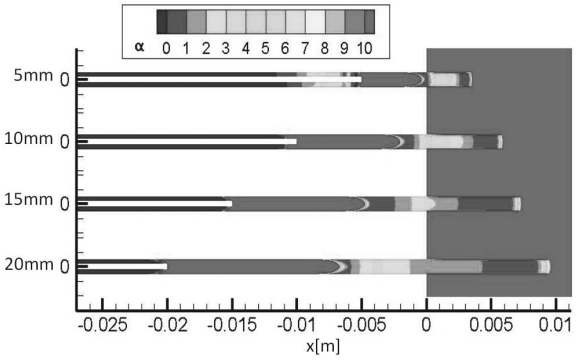

Fig. 3 Volume fraction α, of LILJ for standoff distance of 5 to 20mm for input energy of 170mJ/mm

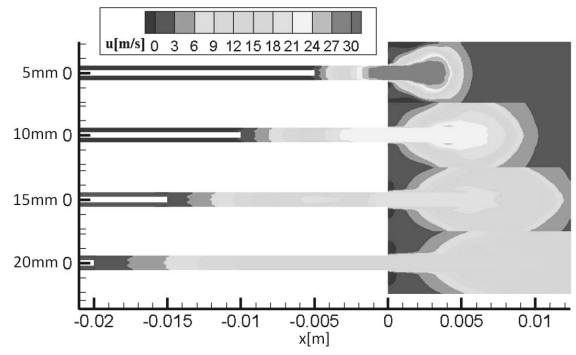

Fig. 4 Velocity u of LILJ for standoff distance of 5 to 20mm for input energy of 170mJ/mm

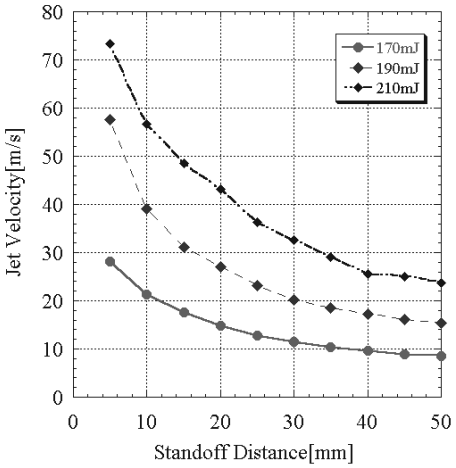

Fig. 5 Maximum jet velocity against standoff distance of 5 to 50mm at input energy of 170,190,210mJ/mm

4. Conclusion

It is found that jet velocity reduces monotonely with the standoff distance, the trend is almost same from that observed in a wider channel as reported[8]. The surface tension and the viscosity in narrow channel are supposed to influence the liquid jet, which are however not considered in the present simulation yet. Hence, we plan to do numerical simulation considering the viscosity and surface tension in the near future study.

References

[1] Nakagawa A., Kumabe T., Ogawa Y., Hirano T., Kanamori M., Saito R., Watanabe M., Hashimoto T, Nakano T., Kamei T., Uenohara H., Takayama K., Tominaga T.: Development of princple to clinical application of pulsed Ho:YAG laser –induced liquid jet: Translational research at Tohoku University, JJSLSM(2009), Vol.30, No.2.

[2] Fujita K.: Numerical simulation of laser-induced liquid jet, Tohoku University(2010), Bachelor thesis.

[3] Muhd Hilmi BS., Sun M.: Numerical simulation of laser-induced liquid jet with phase change, Symposium on Shock Wave in Japan(2011), 16-P-15.

[4] Sun M.: Direct simulation of gas-liquid two-phase flows with subgrid particles, Symposium on Computational Fluid Dynamics(2010), A8-2.

[5] Zhu Y., Sun M.: Numerical simulation of cavitation with two-fluid method, International Conference on Fluid Dynamics(2010), Sendai, Japan.

[6] Saito Y.: A Study on coefficient of vapor pressure equation (Tetens's Eq.), Architectural Institute of Japan(1984), 4392.

[7] Hirano T., Nakagawa A., Uenohara H., Ohyama H., Jokura H., Takayama K., Shirane R.: Pulsed liquid jet dissector using Holmium:YAG laser - a novel neurosurgical device for brain incision without impairing vessels, Acta Neurochirurgica(2003), 145, 401-406.

[8] Hayashi K., Koita T., Sun M.: Experimental study of water jet formation by electric discharge in tubes with various width, International Conference on Fluid Dynamics(2011), Sendai, Japan.

Study on a Micromixing Device Utilizing Surface Tension Effect on Gas-Liquid Free Interface

Takashi Yamada, Naoki Kato, Kazuki Takeda and Naoki Ono
Department of Engineering Science and Mechanics, Shibaura Institute of Technology
3-7-5 Toyosu Koto-ku, Tokyo 135-8548, Japan
naokiono@sic.shibaura-it.ac.jp

ABSTRACT

In this study, as a part of development on rapid mixing by making the convective effect in micro space, we planned a new micromixing device utilizing Marangoni effect. In this study, we made two types of test channel based on T-type mixer with a gas-liquid free interface in the junction point, and did experiments with two fluids having different surface tension. We also conducted CFD simulation which was constructed on a blief model. As a result, a vortex flow was observed and simulated on the interface by Marangoni convection in both experiments and CFD, and we confirmed that it has a possibility to achieve rapid mixing.

1. Introduction

In micro scale, mixing acceleration has been mainly dependent on molecular diffusion because it has large number of surface-to-volume ratio in the area. Therefore, the primary mixing improvement has been generally realized by small diffusive distance for both passive and active mixers. However, it has much smaller products per a device and higher pressure loss into the mixer. Therefore, it is rather difficult to reduce the overall size of micromixing device. We believe that development of a new mechanism for mixing will be necessary in order to further miniaturize the micromixing structure in future. Hessel et al. suggested that convective diffusion should be used to accelerate mixing efficiency in micromixing[1]. The most effective method is to build the technique of making vortex in micro space. Since quite early stage of the development of micromixing, many ideas have been studied, for example, utilizing electro-magnetic fluid, chaos mixing, and sound wave and so on.

In this paper, we studied the micro streaming utilizing Marangoni convection which is the typical phenomenon on gas-liquid free interface. We conducted the experiments to give rise to Marangoni convection by constructing an interface between the two liquids having different value of surface tension on a gas-liquid free interface, which was formed in the junction point of T-type micro channel. We observed the vortex flow involving the two liquids and calculated the situation used by single-phase CFD model as basic study of developing the new mixing process.

2. Estimation for the Flow Velocity

To estimate the maximum velocity just on a gas-liquid free interface by Marangoni effect in micro space, we constructed a simple model between Marangoni force and shear force as illustrated in Figure 1. The model assumes the situation at the moment of the contact between the two liquids on the gas-liquid interface. The circumstances of the model are given as follows; viscosity in liquid 1 and 2 has same value, flow velocity is zero at $y = h$ in x-y plane and at both ends in z-x plane as boundary condition and initial flow velocity and pressure difference between the two liquids are also zero. Then, it could get Eq. (1) for the relation between Marangoni force and shear force at boundary condition.

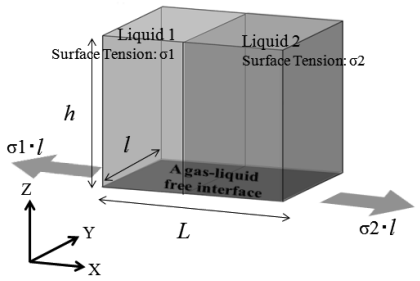

Fig. 1 A simple model to estimate the velocity on a gas-liquid free interface caused by Marangoni force

$$u_{\max} = \frac{(\sigma_1 - \sigma_2)\cdot hl^2}{\mu L\left(l^2 + 4h^2\right)} \quad [\mathrm{m/s}] \quad (1)$$

where, μ: viscosity[Pa・s]. We adopted the values in Eq. (1) as bellow,

$$l \approx L \approx h = 1.0\times10^{-4}[\mathrm{m}], \sigma_1 - \sigma_2 \approx 1.0[\mathrm{mN/m}] = 1.0\times10^{-3}[\mathrm{N/m}]$$
$$\mu \approx 1.0[\mathrm{mPa\cdot s}] = 1.0\times10^{-3}[\mathrm{Pa\cdot s}]$$

The order of the maximum velocity by Eq. (1) becomes,

$$u_{\max} \approx 0.01[\mathrm{m/s}]$$

We think that the velocity at the interface could have the ability to drive vortex flow in the micro space.

3. Method

We made two channels named by Type1 and 2, respectively, which formed gas-liquid free interface at the junction point based on T-type channel. Photo-resist method was used as making the channels [2].

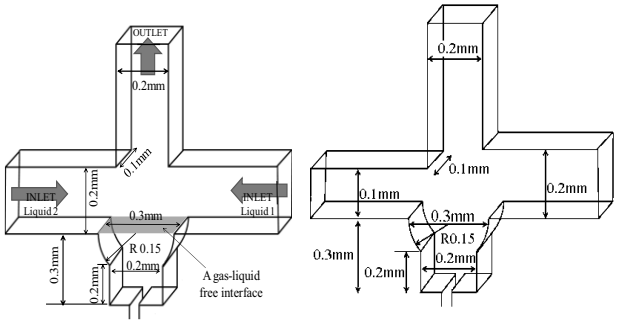

(a) (b)

Fig. 2 Design of junction point including bubble holding section into the micro channel; (a): Type-A, (b): Type-B

Adopted test fluids for the experiments were the following two solutions, 30wt% of acetic acid aqueous solution at inlet 1 and pure water with 1.4wt% of blue dye containing the mixture of Brilliant Blue FCF (8%) and Dextrin (92%) at inlet 2. Physical properties of the two solutions are shown in Table1. Experimental setup was same as previous studies in our laboratory [3].

Table 1 Physical property of the two fluids in the experiments

Test fluids	Surface tension	Viscosity
Pure water with blue dye 1.4wt%	69.0 (mN/m)	0.96 (mPa・s)
Acetic acid solution 30wt%	44.6 (mN/m)	1.54 (mPa・s)

The effect for the Marangoni force in the experiments was simulated by unsteady calculation of single-phase CFD simulation in finite-volume method which solved simultaneous equations with N-S and mass transport equations at each cells. We set the value of time step: Δt=0.05[s] and iterative number of calculation was 10000 at each time step.

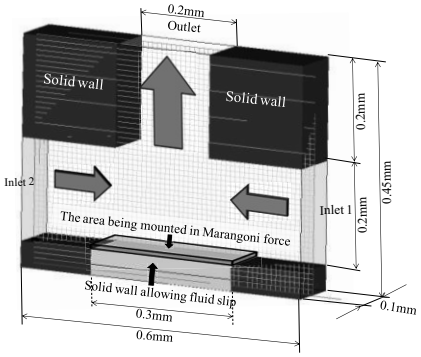

Fig.3 Overall geometry of the CFD model

In actual calculations, we built the two dimensional analysis model by using commercial CFD software "PHOENICS" as shown in Fig. 3, which set physical properties of domain fluid as pure water at 293.15K and 1.24×10^{-9}[m^2/s] of diffusive coefficient by the value of literature, and we put the cells, which have extra value of shear stress by Marangoni force depending on diffusive distribution, in caged area in Fig. 3.

4. Results and Discussion

Photos of flow experiment and CFD results of concentration distributions caused by Marangoni convection in the experiments on Type A and B channels are illustrated in Fig. 4 and 5, respectively.

In Type-A mixer taking 1.5[μl/min] of volume flow rate at each inlet, as shown in Fig.4, we confirmed that vortex flow was caused by Marangoni force when the two liquids contacted on the gas-liquid free interface, but it could keep only 0.5[s], and we obtained same result by CFD simulation because of the saturation in the concentration distribution at the interface in short time.

In Type-B mixer taking 2.0[μl/min] of volume flow rate at inlet1 and 1.0[μl/min] of volume flow rate at inlet 2, we confirmed that, under the condition, quite large vortex flow occurred and could keep over 2.0[s] on the interface, and the flow velocity at the outer edge was about 2mm/s by the images in the experiments. The result of the CFD simulation suggested that it could keep the vortex flow because of being able to hold the concentration distribution relatively long time.

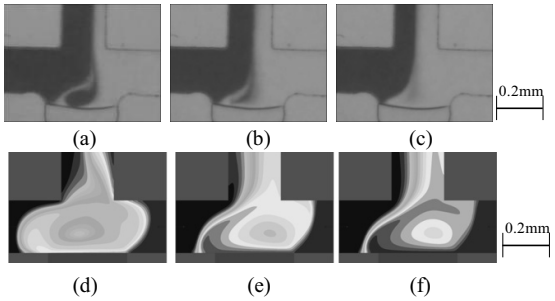

Fig. 4 A series of photos in flow experiments using Type-A channel every 0.1[s] from (a) to (c) and the CFD results of concentration distribution every 0.25[s] from (d) to (f); volume flow rate: 1.5[μl/min] in each inlet.

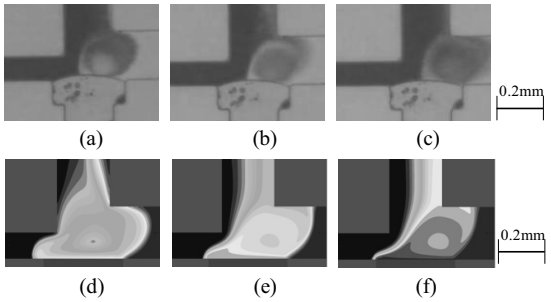

Fig. 5 A series of photos in flow experiments using Type-B channel every 0.1[s] from (a) to (c) and the CFD results of concentration distribution every 0.5[s] from (d) to (f); volume flow rate: 1.0[μl/min] in inlet 1 and 2.0[μl/min] in inlet 2.

4. Concluding Remarks

In this paper, we observed vortex flow caused by Marangoni force on a gas liquid free interface at the junction point of the test channels based on T-type capillary channel and calculated the concentration distribution and the flow property at those experiments by CFD. As a result, it was confirmed that it required keeping concentration gradient on the interface at all time to use Marangoni effect for rapid mixing. We think that the situation as shown in Fig. 5 was one of the suitable condition to keep that distribution. In the future, we will investigate the condition to keep the gradient as long as possible using new channels based on Type-B mixer and the CFD simulations.

References

[1] V. Hessel, et.al, Micromixers - a review on passive and active mixing principles, Chemical Engineering Science 60 (2005), 2494-2501.

[2] Kazawa, E., Ueno, T. and Shinoda, T., High-aspect-ratio lithography for micro module fabrication, Bulletin of Tokyo metropolitan industrial technology research institute No. 5 (2002).

[3] T.Yamada, et.al, Experimental and Numerical Study on Micromixing utilizing Movement of Gas – Liquid Free Interface Journal of Fluid Science and Technology, Vol. 6 (2011), No. 2, pp.128-138

Eighth International Conference on Flow Dynamics
November 9 - November 11, 2011

Effect of Oscillation Frequency on High Pressure Pulse Spray

Ryuichi Sagawa, Yoshinori Kojima, Yasuhiro Saito, Masakazu Shoji, Hideyuki Aoki and Takatoshi Miura
Department of Chemical Engineering, Graduate School of Engineering, Tohoku University,
6-6-07 Aoba, Aramaki, Aoba-ku, Sendai 980-8579, Japan
aoki@tranpo.che.tohoku.ac.jp

ABSTRACT

The effect of the oscillation frequency on rich-lean spray which is formed by pulse sprays is investigated. Spray images are obtained using a high-speed camera. Brightness on the spray image is obtained by image processing. In the case of small oscillation frequency, sprays of the large difference between high and low number density area of droplets are formed at 200 mm downstream from the nozzle tip. In the case of large oscillation frequency, pulse sprays are evenly dispersed. We indicate that the spatiotemporal change of sprays can be considered by using brightness.

1. Introduction

A stationary combustor is widely used in industry. The common rail injection system used in an internal-combustion engine can control a high pressure injection of fuel and injection timing. If the injection system is applied to the combustor, it is expected to become an environmentally-friendly combustion. The previous studies of the injection system have been aimed at small space and only a spray, because the engine space is small [1-3]. Since the stationary combustor space is large scale and sprays affect each other, it is necessary to consider pulse sprays at free space.

The effect of rich-lean spray on combustion has been investigated in previous studies [4, 5]. It is important to consider spatiotemporal changes of sprays, because pulse sprays alternately form high or low number density area of droplets.

In this study, high pressure pulse sprays images at the free space are taken with a high-speed camera and the images are transformed brightness distributions by image processing. We investigate the effect of oscillation frequency on the high pressure pulse sprays.

2. Experimental

2.1 Experimental apparatus and conditions

Fig. 1 shows schematic diagram of experimental apparatus. In the experiments, high pressure pulse sprays images at the free space are obtained using a high-speed camera. Light sources are set up as shown in Fig. 1. Table 1 shows experimental conditions. In the case of the oscillation frequency at 200 Hz, the spray is injected 200 times per second. The fuel flow rate is constant with each oscillation frequency. As the oscillation frequency is larger, injection quantity per one spray becomes lower.

2.1 Evaluation of rich-lean spray using the brightness

Fig. 2 shows measuring points of brightness. At 5, 100 and 200 mm downstream from the nozzle tip, the brightness is measured by image analysis. Fig. 3 shows an example of transient images on the brightness and also shows one cycle of injection, an amplitude and the peak which are defined. The peak is a maximum value of brightness during the 1 cycle of injection. The first rising of the peak shows that the spray has arrived at the measuring point of brightness. If the peak shows large value, the spray of high number density have arrived at measuring points of brightness. Furthermore, a large amplitude shows the large difference between high and low number density area of droplets.

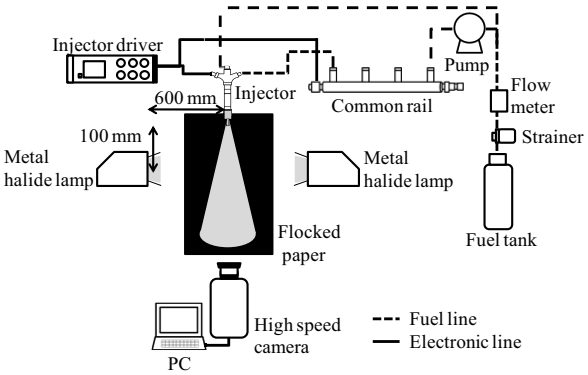

Fig. 1 Schematic diagram of experimental apparatus

Table 1. Experimental conditions

Fuel			Diesel	
Fuel flow rate	[l/min]		0.1	
Injection pressure	[MPa]		40	
Nozzle diameter	[mm]		0.2	
Oscillation frequency	[Hz]	200	300	400
Injection time	[ms]	1.34	0.90	0.68

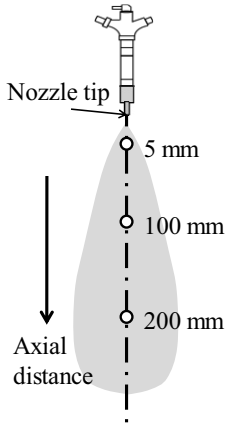

Fig. 2 Measuring points of brightness

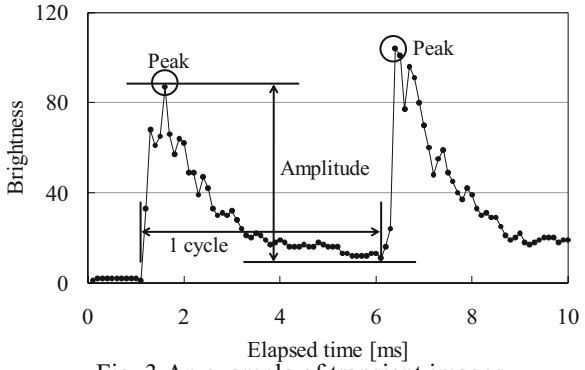

Fig. 3 An example of transient images on the brightness

3. Results and Discussion

Fig. 4 shows the change of the brightness on each of measuring points at 200 Hz. At the measuring point located near the nozzle, a value of brightness increase and decrease at a constant cycle. This cycle is equal to injection interval. At the measuring points of 5 and 100 mm downstream from nozzle tip, the brightness is large value because spray of high number density has arrived at the measuring point of brightness. On the other hand, at the measuring point of 200 mm, the peak has decreased compared with measuring points of 5 and 100 mm because sprays are dispersed with time. It is difficult to evaluate the rich-lean spray at 5, 100 mm downstream from nozzle tip because the maximum value of brightness is 255. Thus, we focus on the rich-lean spray at 200 mm downstream from nozzle tip because the brightness does not approach 255.

Fig. 5 shows the change of the brightness for different oscillation frequency at 200 mm. Table 2 shows the characteristics of the brightness at 200 mm. The maximum value of the average of peak is 200 Hz, followed by 300 Hz and 400 Hz. This means that the injection quantity per one spray of 200 Hz is bigger than that of other oscillation frequencies. Also, there is little difference in 300 Hz and 200 Hz about the average of peak. Injection interval of 300 Hz is shorter than one of 200 Hz. Thus, the spray arrives at residual sprays.

The maximum value of the average of amplitude is 200 Hz, followed by 300 Hz and 400 Hz in Table 2. The injection quantity per one spray and the injection interval of 200 Hz are respectively bigger and longer than others. Although the case of 200 Hz form sprays of the large difference between high and low number density area of droplets. In the case of 400 Hz, the average of amplitude is so small that sprays are evenly dispersed.

4. Conclusions

In this study, observation about transient spray images on brightness and the effect of oscillation frequency on high pressure pulse sprays are investigated. The following results are obtained.

- In the case of small oscillation frequency, sprays of a large difference between high and low number density area of droplets are formed
- In the case of large oscillation frequency, pulse sprays are evenly dispersed.

As a result, we indicate that the spatiotemporal change of sprays can be considered by using brightness.

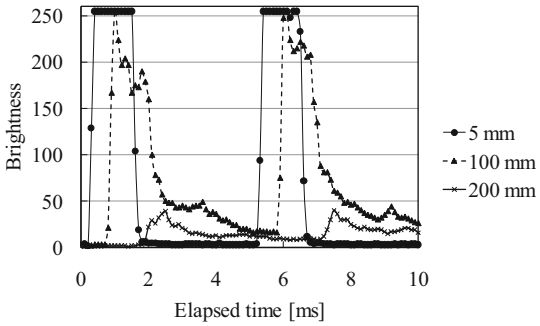

Fig. 4 Change of brightness on each of measuring points at 200 Hz

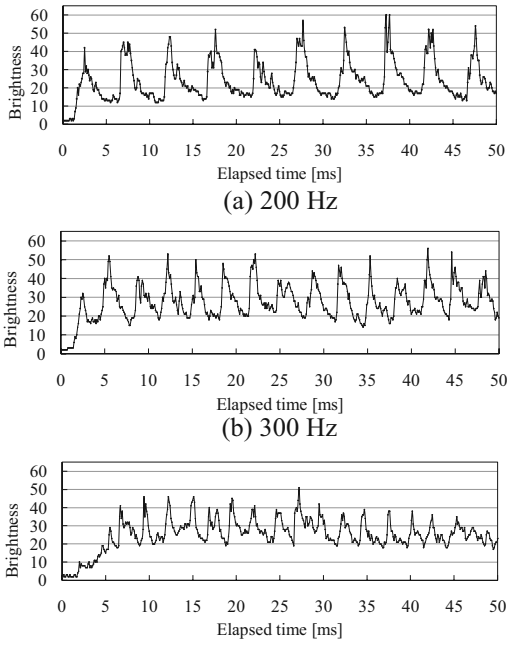

(a) 200 Hz

(b) 300 Hz

(c) 400 Hz

Fig. 5 Change of brightness for different oscillation frequency at 200 mm

Table 2. Characteristics of brightness at 200 mm

Oscillation frequency [Hz]	Average of peak	Average of amplitude
200	50	36
300	47	29
400	38	19

Acknowledgements

This work is supported by KAKENHI（22360318）.

References

[1] C. S. Lee *et al.*, Fuel, **81** (2002), 2417.
[2] H. K. Suh *et al.*, Fuel, **86** (2007), 2833.
[3] Z. Wu *et al.*, Fuel, **85** (2006), 1458.
[4] J. Hayashi *et al*, Transactions of the Japan Society of Mechanical Engineers, Series B, **74**, (2008), 175.
[5] F. Bachmaier *et al.*, Combust. Sci. Tech., **7** (1973), 77.

Quasi-one-dimensional Modeling of Supersonic Combustors

Junji Noda*, Sadatake Tomioka**, and Goro Masuya*
* Dept. of Aerospace Engineering, Tohoku Univ., 6-6-01, Aramaki-aza-Aoba, Aoba-ku, Sendai, Miyagi, Japan
** Japan Aerospace Exploration Agency, Kakuda Space Center, 1 Koganezawa, Kimigaya, Kakuda-shi, Miyagi, Japan
* noda@scrj.mech.tohoku.ac.jp

ABSTRACT

Supersonic combustion tests were carried out in previously. In the previous study, a linear relation between the increase in cross sectional area and pressure rise was fined out in the diverging combustor. The relation was believed very practical in engineering sense. However, the reason, why the relation was gotten linear, was not mentioned. In this study, quasi-one-dimensional calculation was carried out to figure the reason out. The previous test results and the calculation analysis method are stated in this paper.

1. Introduction

The dual-mode scramjet engine has attractive advantages for supersonic and/or hypersonic flight vehicles. The concept of this engines is able to attain both subsonic and supersonic combustion only by controlling fuel equivalence ratio. This enables the vehicle to save its weight.

To generate practical thrust at subsonic combustion, diverging shape is desired to the combustor. In addition, shorter length of the combustor is ideal for stand points of the engine weight and the wall friction force. On the other hand, one previous study showed that the pressure rise in rapid diverging combustor was not enough [1]. Thus, to establish the criteria, which enough pressure rise is attained in diverging combustor, is necessary.

Masumoto [2, 3] et al. and Tomioka et al. [4] carried out dual-mode combustion tests under Mach 2.5, at several total temperature inflow conditions. In the study, the equivalence ratios of gaseous hydrogen fuel was taken at several value. After the combustion tests, some quasi-one-dimensional calculation and analytical consideration were carried out. Finally, they made an engineering model which is able to estimate required condition for enough pressure rise in diverging combustor[5].

Aside from the engineering model, they discovered an interesting relationship in the diverging combustor, i.e., there were the linear relationships between the combustor area increment and the pressure increment, and the slope angles were depend on the combustor diverging angle and the inflow conditions. This relationship is very practical to predict pressure distribution in diverging combustor. However, they did not show why the relationship become linear.

The objective of this study is to figure the reason of the linear relationships out. This paper begins with the description of the previous combustion test methods and the test results. These contents are referenced from some previous studies [2-4]. Following this, quasi-one-dimensional calculation method is noted.

2. Method

As a previous work, Masumoto et al. [5] carried out dual-mode combustion tests. The inflow total pressure and total temperature were 1.0±0.05 MPaA and 1500±50 K, respectively. The total temperature was attained by a lean combustion type air heater. Gaseous hydrogen was used for lean combustion and gaseous oxygen was added to keep oxygen mole ratio at 21% at after the lean combustion. The configuration of the combustor is shown in Fig. 1. The supersonic combustor was directly connected to the Mach 2.5 supersonic nozzle. In the tests, each of three diverging combustors was connected to the constant area combustor. Their first-stage diverging half-angles (θ_{div1}) was 1.55, 3.1 or 6.2 degree. Following the first diverging area combustor, the second

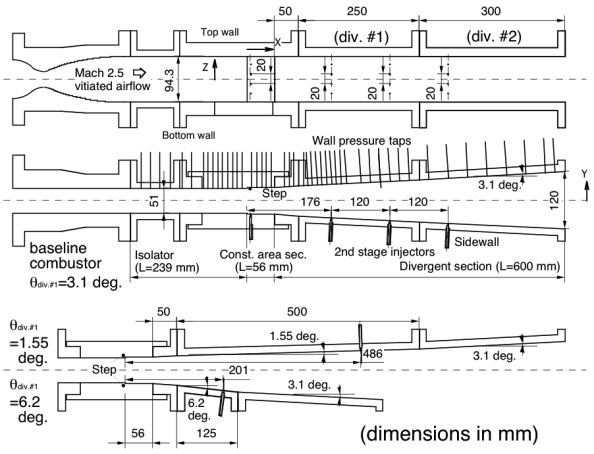

Fig. 1 Configuration of test combustor from Ref. 4

Table 1 Fuel injection position from Ref. 5

configuration	θ_{div1}	Injector		Comb. length
		X_{inj}, mm	A_{inj}/A_i	L_{comb}, mm
N1	1.55	246	1.33	660
N2	1.55	486	1.59	420
N3	1.55	666	1.84	240
N1	3.1	176	1.33	480
N2	3.1	296	1.59	360
N3	3.1	416	1.84	240
N1	6.2	141	1.33	390
N2	6.2	201	1.59	330
N3	6.2	291	1.84	240

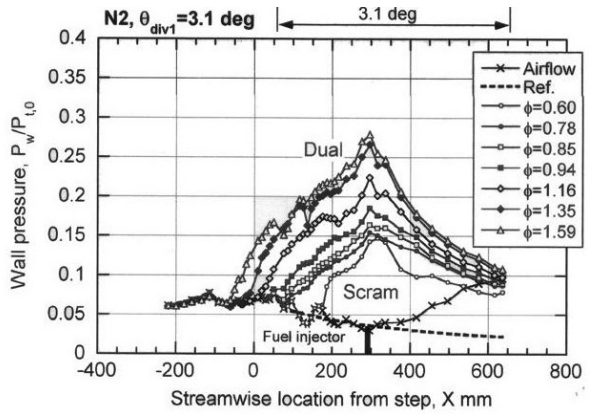

Fig. 2 Wall pressure distributions from Ref. 5 (θ_{div1} = 3.1 deg, N3 injection)

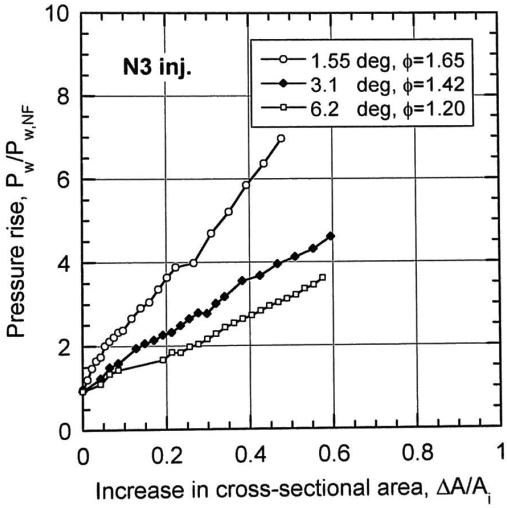

Fig. 3 Relation between the Increase in cross-sectional area and the pressure rise (N3 injection) from Ref. 5

diverging combustor, which angle (θ_{div2}) was 3.1 degree, was connected. Three fuel injection sections, named N1, N2 and N3, was installed in diverging combustor. The positions are also shown in Fig.1. there were four 2.5mm fuel injection ports at each fuel injection sections. Gaseous hydrogen was vertically injected at sonic speed to the main flow via the injection section as fuel at various equivalence ratios. The fuel total temperature was ambient temperature. The coordinate origin of the test section was located at the 2mm back-step which was stood between the Isolator and the constant area combustor. In the study, injector distances from the origin, cross-sectional area at the fuel injected position and the combustor length were different in each condition. This is because the diverging angle and the injected position were variable. Table 1 shows the fuel injection configuration. Supersonic combustion tests were conducted under these configurations.

Figure 2 shows one result of the wall pressure distributions of the combustion test results [2-4]. The figure shows the relation between the streamwise location from the step and the wall pressure. At the low equivalence ratios, supersonic combustion was attained. Then, as to increase fuel equivalence ratio, the wall pressure rising points (flow separation points) went back to the upstream, and then the combustion mode changed to dual-mode, i.e., the flow speed in the combustor was subsonic. Although only one conbustion test result from one combustor configuration is shown in this paper, the other test results had the same tendency. In this study, we focused on the flow state at the dual-mode to find the pressure rise relation in the diverging combustor out.

3. Results and Discussion

Figure 3 shows the relation between the increase in cross-sectional area and the pressure rise at dual-mode[5]. In this figure, ΔA, A_i and $P_{w,NF}$ mean the cross-sectional area increase, the cross-sectional area before the flow separation and the wall pressure at the separation point, respectively. The fuel was injected from N3 point at the condition shown in Fig. 3. We analysis these data. This is because it is easy for the long shock train length to analyze the test results.

In this study, a simple quasi-one-dimensional calculation was carried out. The calculation was based on three fundamental conservation equations. They were about mass, momentum and enthalpy. Additionally, an in-house chemical equilibrium calculation was adopted [6]. Thirteen species (Ar, H, HO_2, H_2, H_2O, H_2O_2, N, N_2, NO, NO_2, O, O_2, OH) were considered in the equilibrium calculation and these thermochemical data were based on JANAF database. In this code, Van Driest formula [7] and Reynolds analogy [8] were also considered to take into account the wall friction and thermal conductivity, respectively. Using the calculation tool, we carry out additional analysis about previous results as shown in Fig. 2. Finally, The reason, why the relation between the pressure rise and the increase in cross-sectional area got linear, is going to be shown at the presentation of 8th ICFD.

References

[1] S. Tomioka, K. Kobayashi, K. Kudo, A. Murakami, and T. Kanda, J. Prop & Power, 22, (1), pp111
[2] R. Masumoto, S. Tomioka, K. Kudo, A. Murakami, K. Kato, and H. Yamasaki, J. Prop & Power, 27, (2), pp346
[3] R. Masumoto, S. Tomioka, and H. Yamasaki, AIAA paper 2009-7364
[4] S. Tomioka, K. Kobayashi, K. Kudo, A. Murakami, and T. Kanda, AIAA paper 2003-4740
[5] R. Masumoto, Ph.D. thesis, 2011
[6] S. Tomioka, A. Murakami, K. Kudo, and T. Mitani, J. Prop & Power, 17, (2), pp293
[7] E.R. Van Driest, J. Aeronautical Science, 18, (3), pp145
[8] F.M. White, Viscous Fluid Flow, Chap. 7, 1974

Eighth International Conference on Flow Dynamics
November 9 - November 11, 2011

Quantitative Evaluation of Relationship between Coke Strength and Microstructure of Ferro-coke with HPC Addition

Ataru Uchida[1], Tetsuya Kanai[1], Yoshiaki Yamazaki[1], Kenichi Hiraki[1], Zhang Xiaoqing[1],
Yasuhiro Saito[1], Hideyuki Aoki[1], Takatoshi Miura[1],
Noriyuki Okuyama[2], Nobuyuki Komatsu[2] and Maki Hamaguchi[2],
[1]Department of Chemical Engineering, Graduate School of Engineering, Tohoku University,
6-6-07 Aoba, Aramaki, Aoba-ku, Sendai 980-8579, Japan
[2]Coal & Energy Technology Department Technical Development Group KOBE STEEL, LTD.
2-3-1, Shinhama, Arai-cho, Takasago, Hyogo, 676-8670 Japan
E-mail aoki@tranpo.che.tohoku.ac.jp

ABSTRACT

The effect of HPC addition on strength of ferro coke is investigated. The tensile strength of the ferro coke is measured. Image analyses of coke microstructure is performed. The tensile strength is increased with HPC addition. On the other hand, the area ratio of pore roundness less than 0.05 decreased. It indicates that the coal particle adhesion is improved by HPC addition. As a result coke strength increases.

1. Introduction

In the blast furnace operation, coke with high strength and high reactivity is required to improve productivity and to decrease in the reducing agent rate. Ferro-coke which contains iron as a catalyst is investigated in order to make high reactivity coke. Hiper-caol (HPC) which improves coal particle adhesion is utilized as binder for improvement of the strength, because strength of ferro-coke is not enough. Shishido *et al.* investigated the effect of improvement of coke strength using HPC[1)]. However, there have been few studies about mechanism of coke strength development with iron and HPC addition.

In this study, we measure the tensile strength of the ferro coke with HPC addition and estimate relationship between coke strength and microstructure of ferro-coke.

2. Experimental

Table 1 shows particle size of materials used in this study. Slightly caking coal and HPC are used. Minerações Brasileiras Reunidas (MBR) is used as a catalyst source. Table 2 shows blending ratio of samples. Samples were compressed at 297 MPa, and were carbonized until 1273 K on the heating rate of 5 K/min. The samples are cut off discs of about 23 mm in diameter and about 5 mm in thickness. Diametral-compression test is performed in order to measure coke strength. Tensile stress is calculated from following Eq. (1):

$$\sigma = \frac{2P}{\pi dl}, \tag{1}$$

where P is load and d is diameter and l is thickness of coke specimen. Tensile strength σ_t is calculated by substituting maximum load P into Eq. (1). Then, scale parameter which is index of strength can be calculated from Weibull analysis. In order to evaluate microstructure of ferro-coke, digital micrographs of coke grinded surface are acquired by optical microscope. The size of the micrograph is 3.11 mm ×2.33 mm, and we combine the micrographs to make a photograph. The site of the photograph is 10 mm ×10 mm and the resolution is 2.43 μm/pixel. In this study, iron particles are considered as pore[2)]. Acquired photographs are binarised by image analysis software(Win roof ver. 6.1.0). Then, absolute maximum pore length and pore roundness are measured. Where absolute maximum length is defined as maximum length of two point on pore counter. Roundness is represented as Eq. (2):

$$Roundness = \frac{4\pi S}{L^2}, \tag{2}$$

where S is pore area and L is boundary length of pore.

Table 1 Particle size of materials

	Donaldson coal	HPC	MBR
Particle size [mm]	< 1	< 0.15	< 0.25

Table 2Blending ratio of samples

Sample	Donaldson [mass%]	HPC [mass%]	MBR [mass%]
A	70	0	30
B	69	1	
C	67	3	
D	65	5	
E	60	10	
F	55	15	

3. Results and Discussion

Fig. 1 shows scale parameter calculated from Weibull analysis on each samples. The larger scale parameter means high strength coke. Coke strength shows different values on each HPC ratio. It implies that coke strength is effected by HPC addition.

Fig. 2 shows area ratio of pores in each absolute maximum length to total area of a photograph. Pores over 1000 μm is the factor related to coke strength reduction[3)]. Sample D is the lowest area ratio of pore over 1000 μm. It suggests that pores over 1000 μm decreases with HPC. However, In sample E and sample F, coke strength decreases with HPC addition and area ratio of pores over 1000 μm increases. It suggests that pores derived from HPC increases with HPC addition.

In spite of increasing pore over 1000 μm with HPC addition, coke strength of sample F is higher than that of sample A.

Fig. 3 shows area ratio of pores in each pore roundness to total area of a photograph. Pores roundness of which is less than 0.2 indicate an origin of fracture[4]. In this study, pores roundness of which is less than 0.2 is divided into more small range to find coal particle void, derived from insufficient coal particle adhesion. In Fig. 3, the area ratio of pore roundness of which is less than 0.05 decreases with HPC addition. It suggests that coal particle adhesion increases by HPC addition and an origin of fracture decreases.

Coke strength increases by coal particle adhesion with optimal blending ratio of HPC and is decreased by pore over 1000 μm with excessive blending ratio of HPC.

We will discuss low roundness pores on ternary images. Figures 4 and 5 show ternary image of sample A and F, respectively. Pores roundness of which is less than 0.05 are gray, other pores are black and coke matrix is white. In Fig. 4, pores roundness of which is less than 0.05 existed between coal particles. It indicates that coal particle adhesion is insufficient without HPC. In Fig. 5, it indicates that low roundness pores decreases and coal particle adhesion is improved by HPC addition.

4. Concluding remarks

The conclusions are summarized as follows:

1) There is optimal blending ratio of making high strength coke with HPC addition.
2) Coal particle adhesion is estimated with pore roundness of which is less than 0.05.

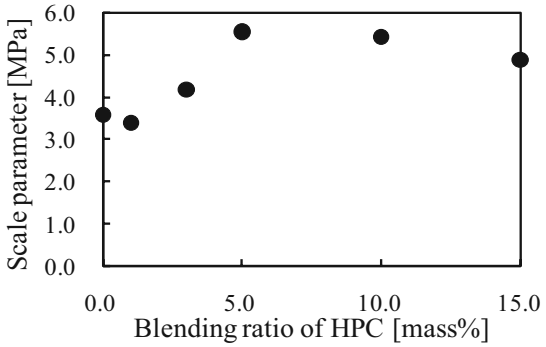

Fig. 1 Relationship between blending ratio of HPC and scale parameter

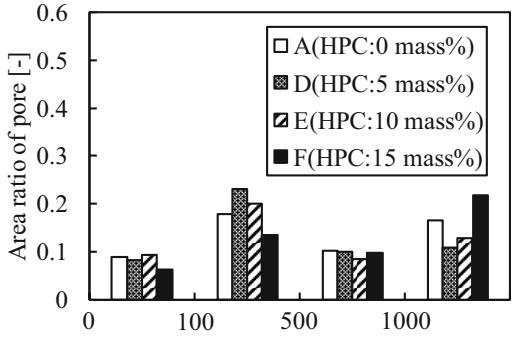

Fig. 2 Relationship between blending ratio of HPC and scale parameter

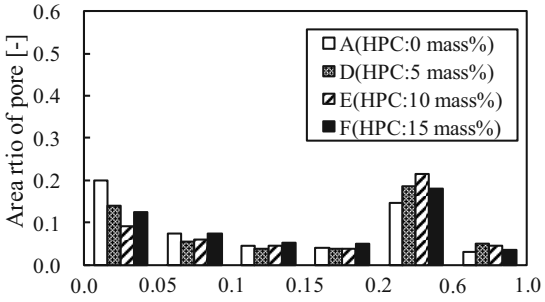

Fig. 3 Relationship between roundness and area of pore.

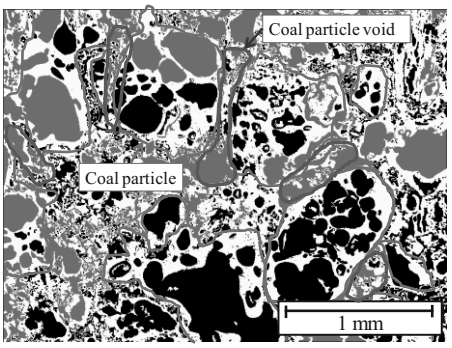

Fig. 4 Ternary image (Sample A)

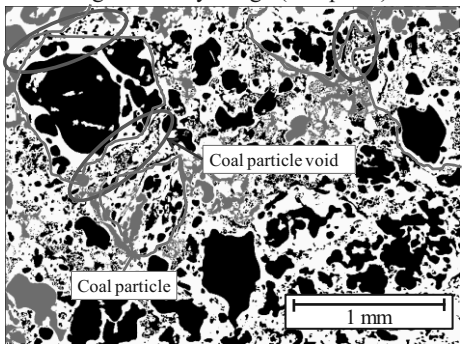

Fig. 5 Ternary image (Sample F)

Acknowledgements

This study was conducted as a part of the research activities “Fundamental Studies on Next Innovative Iron Making Process for Utilization Technology of Finite Resources”. The financial support from New Energy and Industrial Technology Development Organization (NEDO) is gratefully acknowledged.

Nomenclatures

d :diametrical of sample [m], L : boundary length of pore [m], l : length of sample [m], P : load [N], S : pore area [m^2], σ : tensile stress [Pa], σ_t : tensile strength [Pa]

References

[1] Shishido *et al., Sekitan Kagaku Kaigi Happyo Ronbunshu*, **44**, (2001) 130-131

[2] Y. Yamazaki *et al*., *Tetsu-to-Hagene*, **96**, (2010) 536-544

[3] T. Kanai *et al*., *Proceeding of 27th Annual International Pittsburgh Coal Conference*, (2010) 48-2

[4] Y. Kubota *et al*., *Tetsu-to-Hagane*, **96**, (2010) 328-336

Eighth International Conference on Flow Dynamics
November 9 - November 11, 2011

Secondary Cavitation Induced by Underwater Electric Discharge in a Tube

Taketoshi Koita[1], Kentaro Hayashi[1], and Mingyu Sun[2]
[1] Graduate School of Engineering, Tohoku University, 6-3 Aoba, Aramaki aza, Aoba-ku, Sendai 980-8578, Japan
[2] Center of Interdisciplinary Research, Tohoku University, 6-3 Aoba, Aramaki aza, Aoba-ku, Sendai 980-8578, Japan
koita@iswi.cir.tohoku.ac.jp

ABSTRACT

Secondary cavitation induced by high voltage underwater electric discharge in a tube was studied experimentally and numerically. The volume fraction of cavitation region was measured by analyzing visualized photos. Numerical analysis was carried out with a modified Merkle's cavitation model. Two numerical models based on different definitions of sound speed for the cavitation region are tested. One is the classic homogeneous sound speed, and the other introduces a modification, in which the liquid sound speed is adopted if the vapor volume fraction is below certain threshold value. These numerical results are compared with experimental result.

1. Introduction

Secondary cavitations are observed in experimental study of the bubble generation and water jet formation induced by the underwater explosion in the rectangular tube [1, 2] which has been used in medicine as a jet knife [3]. The similar phenomena are seen in laboratory experiment of modeling explosive volcano eruptions [4]. These secondary cavitations may cause the erosion at tube walls and may have an impact on the flow development in the tube. In order to simulate the flow behavior of the tube induced by the underwater explosion accurately, it is necessary to clarify the behavior of secondary cavitation, and to model it properly by considering the phase change. Therefore, we quantitatively measure the volume fraction of secondary cavitation formed in a narrow tube. The cavitation model is based on that developed for simulating the cavitation flow over a hydrofoil, Zhu and Sun [5] reported that the cavitation flow varies dramatically with the relaxation time in the temporal scale of the sound speed propagation in the subgrid scale. We conjecture that this behavior is related to the definition of the sound speed for the two-phase media. Therefore, we further investigate the effect of the two-phase sound speed on the development of the cavitation flow, and compare with measured experimental data.

2. Method

2.1 Experimental method

The underwater explosion is created with high-voltage electric discharge in the rectangular tube which thickness D = 5 mm and width W = 15 mm. The discharge of the voltage power V = 4.5 kV and energy E_e = 2.25 J is used. The explosion depth H is varied at every 5 mm from 5 mm to 50 mm underneath the water surface. Phenomena are photographed by a high speed video camera. The volume fraction of secondary cavitations is obtained by analyzing recorded photos, and is measured in every interval of 10 mm from -20 mm to -80 mm under the wire position, y = 0 mm, in Fig.1(a). The details of this experiments have been reported elsewhere [1][2].

2.2 Numerical method

The secondary cavitation is calculated with the 2-pressure 2-velocity two-fluid model. The discretization is employed with the finite volume method. An semi-implicit Lagrange-Remap method is used. The interaction of the gas-liquid two-phase flow in the cell at the level of subgrid scale is calculated by the subgrid modeling [6]. The traditional solution-adaptive grid technique [7] is employed and the refinement level 4 is used. The EOS of gas phase and liquid phase are the equation of ideal gas and of Tait EOS respectively. The modified Merkle's cavitation model developed for the two-fluid model [5] is employed.

We introduce a modification to the classic homogeneous two-phase sound speed. When the vapor volume fraction is very small, say, below the order of 0.1 %, the large portion of the tube is actually occupied by pure water. The pressure wave more possibly propagates at the speed of water sound speed (a_{water}) instead of the homogeneous two-phase sound speed ($a_{homogeneous}$). Therefore, in this study, we introduce a new two-phase sound speed (a^*),

$$a^* = \begin{cases} a_{\text{homogeneous}} & (\sigma > \varepsilon) \\ a_{water} & (\sigma \le \varepsilon) \end{cases}$$

where σ is the vapor volume fraction, and ε is a threshold value under which the water sound speed is adopted. When ε is zero, the formula becomes the homogeneous two-phase sound speed. The threshold value ε is varied from 0.0 % to 0.2 %. Fig.1 shows the initial grid after analysis is started. The bubble is employed as the vapor and is set at (x, y) = (0, 0). The region of -140 mm < y < 15 mm is water and that of 15mm < y < 140mm is vapor. Initial bubble conditions, bubble radial r_b = 0.05 mm, inside pressure p = 5421.2 MPa, temperature T = 11756 K, calculated with energy conservation of bubble generation at the energy conversion coefficient α = 0.3 [8] are tested.

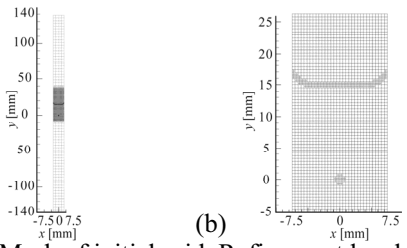

Fig.1 Mesh of initial grid, Refinement level = 4
(a) Overall initial grid, (b) Initial grid zoomed view of near the bubble and water surface

3. Results and Discussion

Phenomena of the tube at H = 15 mm are especially discussed in this paper. Sequential photos are shown in Fig.2. When the copper wire explodes, a blast wave is generated and propagates in the water. This wave reflects at the bottom wall and creates a low pressure region between the bubble and the wall. In Fig.2, second cavitations are observed under the bubble in the water from the time of 0.8 ms to 4.0 ms because of the low pressure. The volume fraction of secondary cavitations at different depths for times obtained from photos is plotted in Fig.3. From Fig.3, it is observed that the volume fraction of y is -20 mm to -40 mm is decreased with time, but that of y is less than -40 mm is increased. The generation of secondary cavitations is small and maximum volume fraction reaches 2.2 % as seen in Fig.3. Fig.4(a) and 4(b) show respectively the numerical result of time histories of difference maximum volume fraction obtained by numerical model with sound speed definition ε and maximum volume fraction for ε. From Fig.4(a) and 4(b), it is clearly found that the volume fraction is depended on ε and it increases as ε becomes to the large value. When the homogeneous two-phase sound speed, ε = 0.0 %, is employed, the volume fraction is much larger than experimental data. The maximum volume fraction obtained by numerical model with ε = 0.1 % is roughly similar with the experimental volume fraction. The numerical model defined by the present sound speed with a properly defined ε is clearly more accurate than that by the homogeneous sound speed.

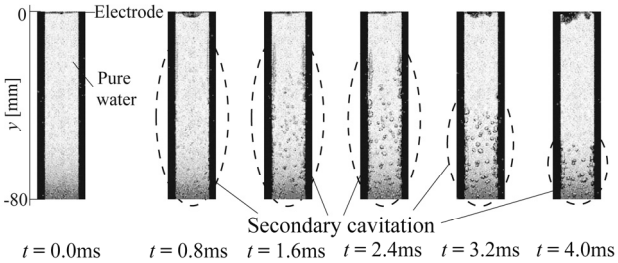

Fig.2 Sequential photos for H = 15 mm at V = 4.5 kV

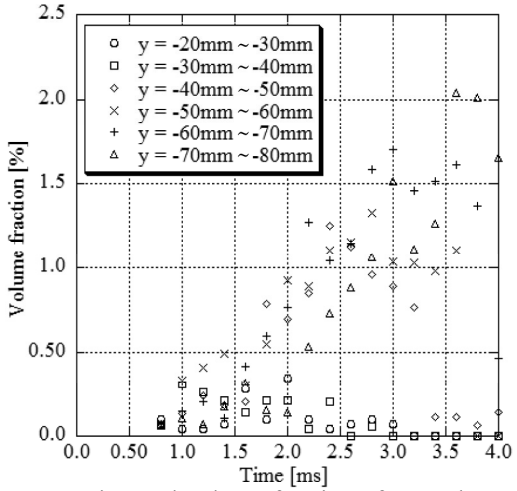

Fig.3 Experimental volume fraction of secondary cavitation at different depths for H = 15 mm at V = 4.5 kV

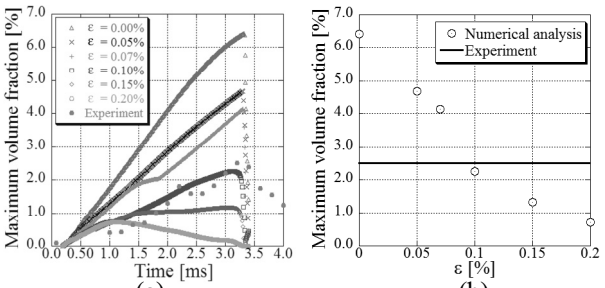

Fig.4 (a) Histories of difference maximum volume fraction obtained by numerical model with sound speed definition(ε), (b) Dependence of maximum volume fraction on sound speed definition(ε)

4. Concluding remarks

Secondary cavitation induced by underwater explosion with a high voltage electric discharge in a rectangular tube was investigated. This cavitation is occurred because of low pressure generated by reflection of the blast wave at the bottom wall. The experimental maximum volume fraction of secondary cavitation in this study case was small. Numerical analysis is carried out with modified Merkle's cavitation model. The numerical solution based on the homogeneous two-phase sound speed over-estimates the experiment data more than two times. It was found that numerical solution depends on the definition of the two-phase sound speed. A new sound speed with a minor modification does give a much better agreement.

References

[1] T. Koita, Y. Zhu, M. Sun, : Investigation of bubble collapse and water jet induced by underwater explosion in a rectangular tube, 28th International Symposium on Shock Waves, (2011).

[2] T. Koita, Y. Zhu, M. Sun, : The Behavior of Bubble and Water Jet Induced by Underwater Explosion in a Rectangular Tube, 49th AIAA Aerospace Sciences Meeting, (2011).

[3] T. Tominaga, A. Nakagawa, T. Hirano, et al., : Application of underwater shock wave and laser-induced liquid jet to neurosurgery, J. Shock Waves, **15** (2006), 55-67.

[3] H. Yamamoto, K. Takayama, K. Ishikawa, : Model experiment on magma fragmentation in explosive volcanic eruption, Journal of Mineralogical and Petrological Sciences, **103** ,No.3,(2008), 192-203.

[5] Y. Zhu, M. Sun,: Numerical Simulation of Cavitation with Two-FluidMethod,AFI/TFI-2010,(2010)

[6] M. Sun, : Direct simulation of gas-liquid two-phase flowswith subgrid particles, 24th Computational Fluid Dynamics, (2010), A8-2.

[7] M. Sun, K. Takayama,: Conservative smoothingon an adaptive ouaelrilateral grid, J. Com. Phys, **150** (1999), 143-180.

[8] T. Koita, M. Sun, : Setup of initial conditions for the simulation of bubble phenomenon induced by underwater point explosion, Symposium of Shock Waves in Japan, (2011), 191-194.

Eighth International Conference on Flow Dynamics
November 9 - November 11, 2011

A Study on Micromixer Utilizing Thin Liquid Film

Kazuki Takeda, Naoki Kato, Takashi Yamada and Naoki Ono
Shibaura Institute of Technology, 3-7-5 Toyosu, Koto-ku, Tokyo 135-8548, Japan
naokiono@sic.shibaura-it.ac.jp

ABSTRACT

As a new idea of micromixing process, we have studied a micromixer using gas-liquid free interfaces of the two bubbles. As the result, we found that, in addition to reducing thickness of liquid film between the bubbles, changing the direction of the flow between the bubbles could influence mixing efficiency. Therefore, we here focused on the change of the flow direction and analyzed the flow with computational fluid dynamics. We studied the influence of the flow direction from the view point of raising mixing efficiency.

1. Introduction

In recent years, there exits intense interest in μ-Tas technology in the fields of chemical and biological engineering. μ -Tas is collected chemical analysis system that combines micro-scaled fluid devices like a pump, mixer, separator and so on. A micromixer is a specific device for mixing and chemical reaction in such systems. The reason why micromixer is required is that it enables much higher reaction rate due to its large area of liquid-liquid contact per volume. Here we study micromixer technology because new methods and ideas for higher mixing are still expected.

In this study, we utilized gas-liquid free interface that was liquid film about 10 μm in thickness between the two bubbles. As the result, relative concentration difference (indicator of mixing ability in our study) went up to 20 %, also we found that indispensable factors to promote the mixing were the thickness of liquid film and the change of the flow direction (here we call "flow angle" as shown in Fig.1) from our previous studies. In particular, the influence of changing the flow direction was investigated in detail with computational fluid dynamics (CFD).

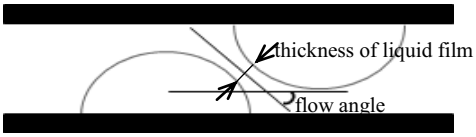

Fig. 1 Definition of flow angle.

2. Method

The experiment was conducted by using a micromixer made by photoresist method [1]. We used pure water that was colored by food dye in the same manner as our previous study [2]. Inflow conditions were 0.5 μl/min in both inlets, and the corresponding Reynolds number was 0.17. Bubbles were formed about 3.0 mm from the junction point of two fluids. Mixing property was measured from values of RGB data from digital photos taken into PC.

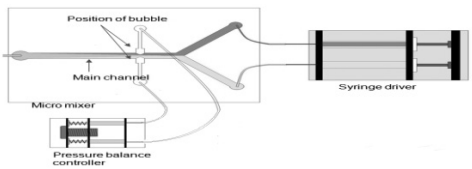

Fig. 2 Experimental apparatus.

We used CFD software package "PHOENICS" to analyze the effect of the flow angle for mixing efficiency. Diffusion coefficient which we used was 3.0×10^{-10} (m^2/s). When we analyzed the contribution of convective mixing, we calculated by setting diffusion coefficient to be zero.

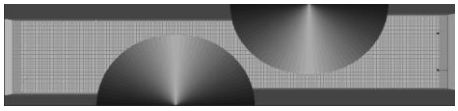

Fig. 3 CFD modeling.

Important parameters to represent the geometry of the micromixers are A, B, C, D as shown in Fig.2. In this study, the flow channel width of parameter A was fixed to be 150 μm, and we analyzed the flow by changing other parameters B, C, D.

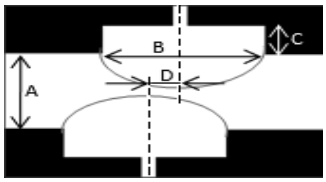

A: channel width
B: chamber width
C: chamber depth
D: bubble distance

Fig. 4 Factors in determining the micromixer.

3. Results and Discussion

At first, we did experiment with chamber width 300 μm, depth of hole 90 μm, bubble distance 0, 260, 300, 340 μm. The experimental results and photos are shown in Fig.5 and 6, respectively. The horizontal axis in Fig.5 is the distance from the junction point of two fluids.

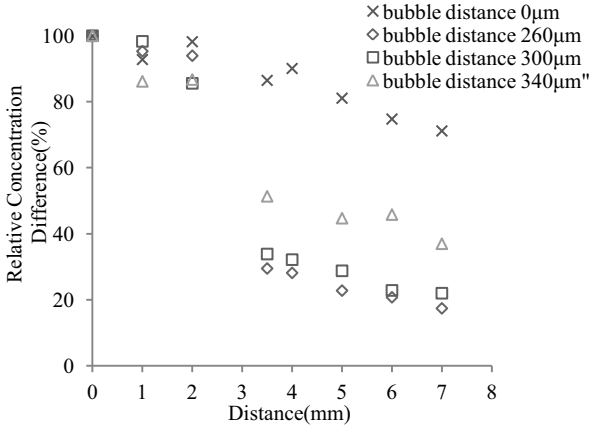

Fig. 5 Experiments of slit width 300 μm.

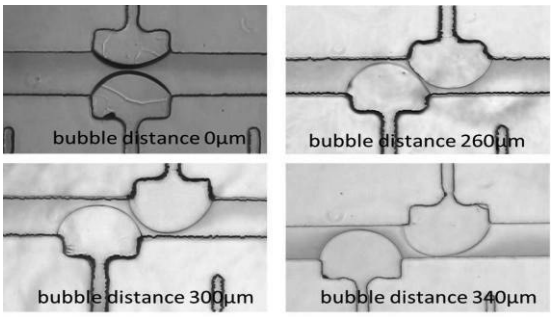

Fig. 6 photos at 3 mm from junction point with chamber width 300 μm.

Micromixer of bubble distance 0 μm hardly promoted mixing, because there was no effect for mixing efficiency of convective diffusion (flow angle = 0°), and bubbles formed liquid film only one point. Hence, there was no time to diffuse the two fluids enough. Accordingly, bubble distance 260 μm was the most effective micromixer for mixing of all cases. Flow angles with bubble distance of 260, 300, and 340 μm were 46.8°, 51.6°, and 53.4°, respectively. From our previous studies, we found that the larger flow angle at the liquid film, the better mixing efficiency. However, from Fig.5, small flow angle was better than large flow angle. We think it was because the thickness of the liquid film was not the same with each other. Incidentally, the thickness with bubble distance of 260, 300, and 340 μm were 6.5, 12.0, and 43.8 μm, respectively. Therefore, we think that not only large flow angle but also thin liquid film was necessary for high mixing efficiency.

Besides, it seems obvious that thick liquid film is inefficient compared to thin liquid film by Fick's laws of diffusion. However, the optimum value of flow angle is unknown. We investigated the effect of the flow angle by using CFD. The results are shown in Fig.7.

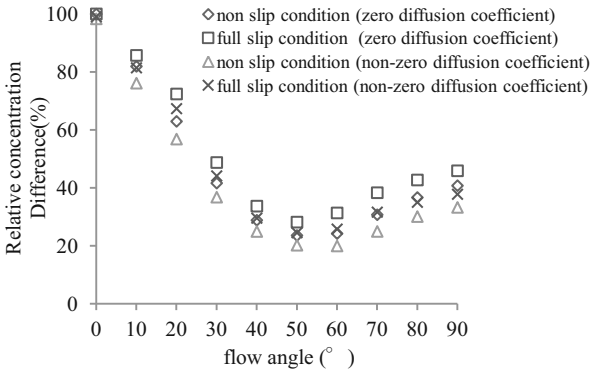

Fig. 7 Relation between Relative Concentration Difference and flow angle by CFD.

The thickness of the liquid film was fixed to be 30 μm in all the cases, and we computed four conditions. First, non slip condition (zero diffusion coefficient), second, full slip condition (zero diffusion coefficient), third, non slip condition (non-zero diffusion coefficient, here D is 3.0×10^{-10} (m^2/s)) and forth, full slip condition (non-zero diffusion coefficient). Flow angle between 50° and 60° tended to give better mixing, as shown in Fig.7, and the mixing efficiency drastically deteriorated when the flow angle was 40°. Hence, it was found that the effect of changing the flow angle was remarkable. There was difference of only a few percent between the two non slip conditions. On the other hand, there was up to 80 percent difference between flow angle 50° and 0° in slip condition (zero diffusion coefficient) of Fig.7. Therefore, the effect of mixing by convection was bigger than the effect of mixing by molecular diffusion.

$$\frac{\partial \omega}{\partial t} + u_x \frac{\partial \omega}{\partial x} + u_y \frac{\partial \omega}{\partial y} = D\left(\frac{\partial^2 \omega}{\partial x^2} + \frac{\partial^2 \omega}{\partial y^2}\right) \qquad (1)$$

Equation (1) shows two-dimensional conservation equation of substance diffusion. First term at left hand side is unsteady term, second and third terms are convection terms, and right hand side is diffusion term. Here we ignored the depth direction. We had thought that the most effective term was diffusion term at right hand side until now. However, under the current conditions in our micromixer, convection terms at third term can be thought to be the most effective, because the change caused by zero/non-zero of diffusion coefficient was smaller than the change caused by flow angle variation, as shown in Fig.7. Non slip condition was better for mixing efficiency comparing with full slip condition in using the same diffusion coefficient, because non slip condition caused shear force, thus generating velocity difference at the liquid film, which could promote mixing. Experimental values of Fig.5 were compared with CFD results, then it was found that the CFD results were relevant because the experimental data of higher mixing efficiency with bubble distance 260 μm and 300 μm, corresponded to the case in which that flow angle was 50°.

4. Concluding remarks

The following conclusions were confirmed from this study.

1. In obtaining high mixing efficiency under the given experimental conditions, there was optimum value about the flow angle, and it was 50°~60°.
2. Convection term seemed to significantly affect the mixing efficiency in the experiment, although the thickness of liquid film could not be negligible.

In future we need to analyze the effect of flow angle and its mechanism by not only simulation but also flow experiment.

References

[1] Kazawa, E., Ueno, T. and Shinoda, T., High-aspect-ratio lithography for micro module fabrication, *Bulletin of Tokyo metropolitan industrial technology research institute* No. 5 (2002).

[2] Ono, N. and Suzumura, T., A Study on Micromixing Process Utilizing Gas-Liquid Free Interface, *Transactions of the Japan Society of Mechanical Engineers, series B,* **74** (2008), pp. 1700-1706.

Analysis of Fluid Flow and Concentration Distribution in a Cylindrical Micromixer

Ryota Suzuki, Ken Yamazaki, Takeshi Hosoya and Naoki Ono
Shibaura Institute of Technology,3-7-5 Toyosu,Koto-ku,Tokyo,135-8548,Japan.
naokiono@sic.shibaura-it.ac.jp

ABSTRACT

A micromixer is a special equipment for chemical reactions which has been used as high value-added chemical production technology. In this study, we streamed liquid into a cylindrical micromixer in spirals to promote the mixing efficiency by increasing the contact interface. We focused on the spiral flow and analyzed fluid flow and concentration distribution in the mixing process in the cylindrical micromixer. The results obtained from observed spiral flow, measurement of concentration distribution and CFD(Computational Fluid Dynamics) were compared and discussed.

1. Introduction

In recent years, micro fluidic systems have been widely used in micro-electromechanical systems to meet the needs of miniaturization in the fields of chemistry and biology. A micromixer, which mixes fluids in a small domain, is a typical microfluidic device. This device has been developed in the chemical engineering field and is also expected to be applied in the medical manufacturing industry[1].

We realized spiral flow of the two liquid in the micromixer to increase the contact area and to promote better mixing[2]. The purpose of this study is an analysis of the spiral flow and mixing process inside a cylindrical micromixer. Fig. 1 shows the process of mixing in a micromixer.

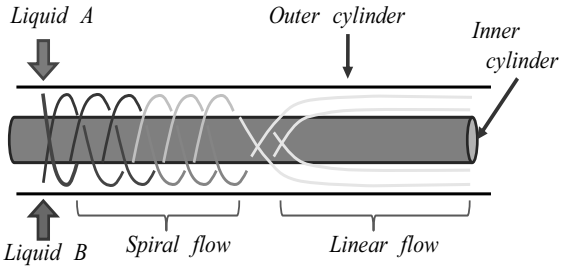

Fig. 1 Mixing process of a cylindrical micromixer

2. Method

To analyze the patterns of streamlines and the concentration distribution, we conducted two experiments, and compared the results with CFD simulation results.

First, to observe the spiral flow, pure water and benzyl alcohol were injected separately in a mixer from the two syringe pumps. A high-speed camera having a shutter speed of 1/500 s recorded the process of mixing in the micromixer. We used benzyl alcohol because it made easy to observe the spiral flow formed with pure water due to its hydrophobic property and because the density of benzyl alcohol (1.042 g/cm^3) is closer to that of pure water.

Next, to measure the concentration distribution by extracting the liquid, pure water and NaCl aqueous solution were injected separately from the two syringe pumps. The NaCl concentration was almost 1.00 wt%. The NaCl aqueous solution was injected to the flow with pure water and extracted from the mixed liquid in the micromixer.

Fig. 2 shows the location of extraction points. The extraction hole was 0.5 mm in diameter, and there were three each for left and right circular cross-section of the mixer (see Fig. 2-a). There were nine cross-section of A to I, which were spaced 4 mm between each other (see Fig. 2-b). These holes were usually plugged and closed, and only the hole for extracting liquid was opened and linked to the extracting tube. Using a salt concentration meter, we measured the concentration of the liquid extracted from 54 extraction points. Extraction was performed three times for each point, and we calculated the averaged value. The concentration of salt in pure water is zero percent, so that 0.50 wt% can be regarded as the state of perfect mixing.

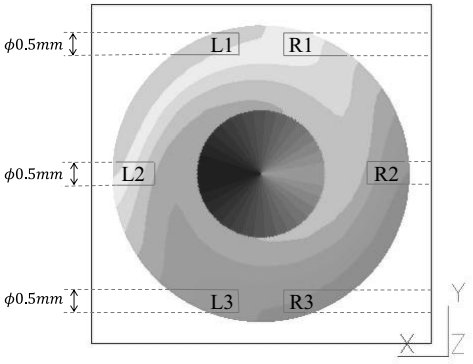

(a) Front view

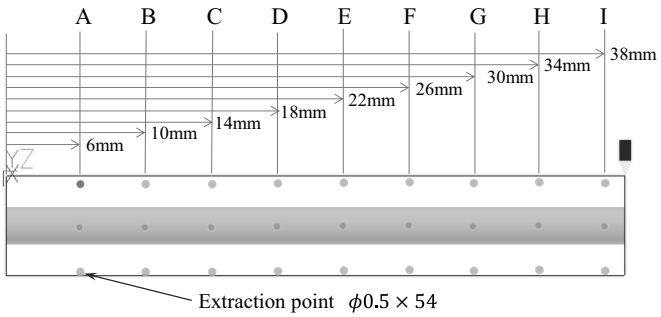

(b) Side view

Fig. 2 Location of extraction points

3. Results and Discussion

Fig. 3 shows an example of photographs of spiral flow. Flow rate of pure water at this experiment was 100ml/min, also streamed the same flow rate of benzyl alcohol. Therefore, the total flow rate was 200ml/min. Fig. 4 shows a simulated stream lines in the same condition as above. This stream line can be regarded as the traces of the particles flowing from the inlet for flow visualization.

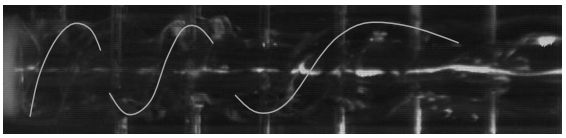

Fig. 3 Spiral flow pattern (Experiment)

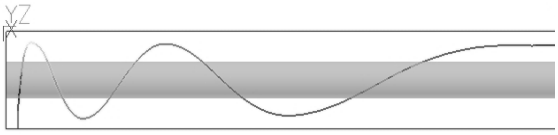

Fig. 4 Spiral flow pattern (Simulation)

Comparing Figs. 3 and 4, it is clear that the experiment and simulation represented the similar results. Table 1 shows the number of spiral flow revolution. We varied the flow rate to compare the results of experiments and CFD. According to Table 1, when the flow rate was small, the number of spiral flow revolution of simulation was more than that of the experiment. In contrast, when flow rate was high, the result was the opposite.

Table 1. Number of spiral flow revolution

Flow rate (ml/min)	35	50	75	100	125
Experimental	0.8	1.4	1.7	2.4	2.5
Simulation	1.1	1.5	1.7	2.1	2.2

Figs. 5 and 6 show the concentration distribution of flow rate 100ml/min. Fig. 5 is a plot of data at the section of 6 mm in the Z axis from the inlet. Fig. 6 is a plot of data at the section of 10mm. There were nine cross-sections, but we gave examples of two sections A and B that were located near the inlet because they indicated significant difference in concentration.

We could detect waving pattern of concentration distribution at extraction holes of each section. When we compare the experiment and simulation, the same trend was found as the wave distribution. We think this indicated how the mixing gradually proceeded by spiral flow. However, there were differences in the concentration values. Possible causes are the contribution of the diffusion coefficient. In the simulation, we used a literature value of diffusion coefficient of NaCl aqueous solution($1.330\times10^{-9}m^2/s$). The diffusion rate in the simulation was found to be higher than that in the experiment. Therefore, mixing in the simulation was more rapid than in the experiment. This tendency was similar in the other flow rate.

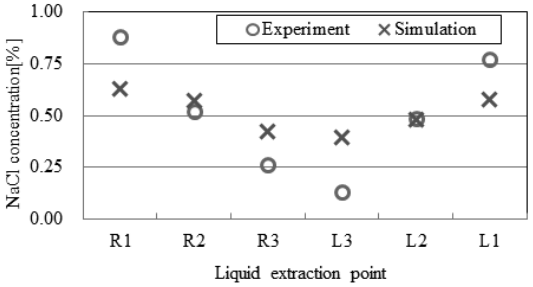

Fig. 5 Concentration distribution (section-A)

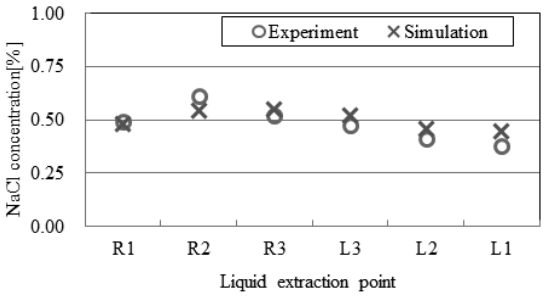

Fig. 6 Concentration distribution (section-B)

4. Concluding remarks

The patterns of streamlines and the concentration distribution obtained by CFD (Computational Fluid Dynamics) simulations agreed well with those obtained experimentally by flow observation and concentration measurements. In particular, the streamlines were able to simulate fairly closely the state of the experiment. From this study, we could well understand the mixing process and the validity of our cylindrical micromixer.

To improve the accuracy of the analysis of the concentration distribution, we need to clarify the mixing factors and to reproduce the rate of diffusion.

In the future, we will make more detailed study of viscosity, density, interfacial tension, which we think are important factors for better mixing.

References

[1]Hessel, V, Löwe, H, and Schönfeld, F, “Micromixers-a review on passive and active mixing principles”, Chemical Engineering Science, 60, (2005), pp.2479-2501.

[2]Y.Mitsuhashi, K.Yamazaki, E.Kobayashi, A.Yoneya and N.Ono, “Fluid-Flow Analysis for a Novel Cylindrical Micromixer”, Journal of Fluid Science and Technology (JSME), Vol.6(2011), No.2, p230-241.

Eighth International Conference on Flow Dynamics
November 9 - November 11, 2011

Dryout of Boiling with Impinging Flow in T-shaped Mini Channel with High-carbon Alcohol Aqueous Solutions

Yuki Kumagai, Minoru Otsuka, Keigo Yonemura and Naoki Ono
Shibaura Institute of Technology, 3-7-5 Toyosu, Koto-ku, Tokyo 135-8548, Japan
naokiono@sic.shibaura-it.ac.jp

ABSTRACT

We investigated combination of impinging flow and high-carbon alcohol aqueous solutions in mini channel. We used three types of the glass tubes. Two of them were square cross sections whose side length were 2.0mm and 5.4mm, and the other one was a circular glass tube of 5.4mm in diameter. We compared heat transfer characteristics including dryout point with varying concentration levels of butanol aqueous solutions. It was found from the experiments that the liquid film of the butanol aqueous solutions extended in the direction toward high-temperature region and that the butanol aqueous solution of 3.00wt% gave highest dryout heat flux.

1. Introduction

In recent years, a variety of electronic control equipment has been widely used for computers, automotive and industrial machineries. CPU used for the control equipment emits larger amount of heat than before due to the needs of rapid performance gain and drastic miniaturization. Therefore, to prevent from heat damage or performance degradation, it is necessary to remove heat and to cool the CPU. However, it is to be concerned that cooling technologies may not keep up well enough with the increase of heat in future.

In this experiment, we have used high-carbon alcohol aqueous solutions as working fluid. In our method, the fluid was impinging against the heated surface to promote heat transfer and to suppress the onset of the dryout. This study would offer basic knowledge to realize compact cooling device with high efficiency.

2. Method

Figure 1 shows the flow loop used in the experiment. This was mainly for the overall observation of boiling bubble and fluid motion. Figure 2(i) to (iv) show the test section (each glass tube A, B, C, and D). After filling the tank with the test fluid, the fluid was fed into the test section by using a pump. Fluid passing through the test section will be then pumped to a disposal tank without circulation. Quartz glass tubes used in the test section were, (i) glass tube A, (ii) glass tube B, (iii) glass tube C and (iv) glass tube D, respectively. The flow rate to the test section was 8.48ml/min when using glass tubes A and B. On the other hand, when using glass tubes C and D, the flow rate was 15.44ml/min. Glass tubes A,B and C were of square cross section, the side length of those tubes were 2.0mm, 2.0mm and 5.4mm in ID, respectively, and the diameter of glass tube D of circular cross section was 5.4mm in ID. Each length was 150mm. At the top center portion of the test section, the copper block was plugged into the holes of the glass tube. After inserting the cartridge heater inside the copper block, we applied direct current to the heater for joule heating. The values of the three K-type thermocouples which were inserted into the copper block at each location (3mm, 7mm and 11mm from the heat transfer surface) were measured. Then the temperature data were used to calculate the temperature gradient, and the heat flux at the heated surface by using Fourier's law. We also observed the boiling bubbles and the liquid film flow with a video camera. Table 1 and Table 2 show the experimental conditions.

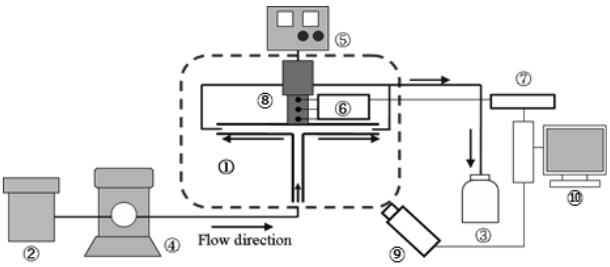

①Test section ②③Tank ④Metering pump ⑤DC power supply ⑥Thermocouple ⑦Thermocouple logger ⑧Copper block ⑨Video camera ⑩PC

Fig. 1 Experimental apparatus

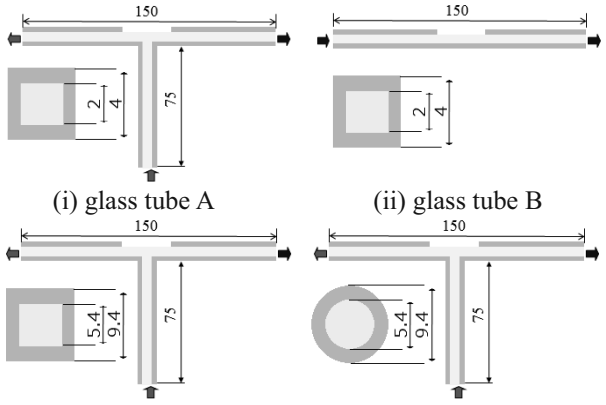

Fig. 2 Test section

Table 1. Experimental conditions (glass tube A and B)

Flow rate [ml/min]	Flow velocity[m/s]	Reynolds number	Subcooling [℃]
8.48	3.53×10^{-2}	79.1	75

Table 2. Experimental conditions (glass tube C and D)

Flow rate [ml/min]	Flow velocity[m/s]	Reynolds number	Subcooling [℃]
15.44	8.83×10^{-3}	53.37	75

3. Results and Discussion

In this experiment, we used butanol aqueous solutions (3.00wt%, 7.15wt%) and pure water which was degassed sufficiently, as working fluids.

(i) Heat transfer characteristics

Figure 3 and Fig. 4 show boiling curves which compare the pure water and the butanol aqueous solutions when using glass tubes A and B, respectively. Note that CHF in the figures for each of the working fluid shows the dryout point.

From these results, in the case of butanol aqueous solution of 7.15wt%, the heat transfer characteristics was lower than in the case of pure water in both T-junction and straight tube. This is because butanol aqueous solution is a two-component aqueous solution and the degradation of heat transfer took place. However, when the butanol aqueous solution of 3.00wt% was applied, the boiling curb indicated a sudden increase in heat flux near CHF point, in both T-junction and straight tube. It was found that the CHF point of 3.00wt% increased about 27% in the T-junction channel and 9% in the straight channel with butanol aqueous solution of 3.00wt%, compared with CHF of pure water. The authors are of the view that 3.00wt% solution could have restrained the degradation of heat transfer, compared with 7.15wt% solution. Moreover, well-balanced work of thermal Marangoni effect and solutal Marangoni effect would be another reason. From the observation, we found that in the case of pure water, the bubble was detached from the heated surface when the size grew to the size of the tube. However, in the case of butanol aqueous solution of 3.00wt%, the bubble tended to become smaller than in the case of pure water, and many small bubbles appeared on the heated surface.

(ii) Observation of boiling bubble

We obtained a better observation using a larger diameter glass tubes C and D. Using glass tubes A and B was not suitable for the observation of precise bubble behavior. The photos of the observed behavior of the boiling bubble are shown in Fig. 5(i) and (ii). In the impinging flow with pure water, the boiling bubble tended to stay around the cross position of the T-junction tube, as shown in Fig. 5(i). The staying bubble sometimes made the heated surface perfectly dry for a while, then worsened the heat transfer. Even when the bubbles coalesced and became a large bubble, liquid layer with boiling on the heated surface could have been observed through the large bubble. The liquid seemingly tended to wet the heated surface, which we think could restrain the onset of dryout in the case of butanol aqueous solution of 3.00wt%.

With the help of the larger glass tube's size (glass tube C and D), we could see the difference between the butanol aqueous solution and pure water in terms of bubble behaviors, more clearly. After comparing the results of the glass tubes C and D, we found that the bubble behavior was significantly different due to the difference of cross-sectional shape. The reasons and its mechanism are currently under investigation.

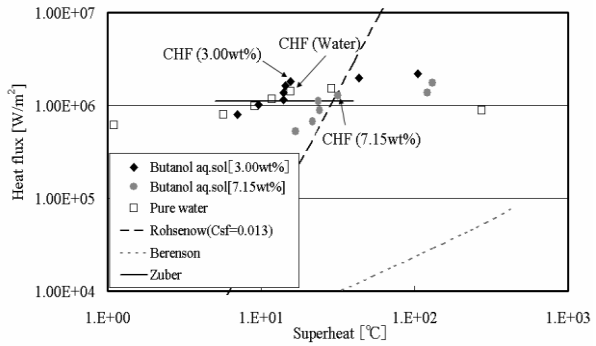

Fig. 3 Boiling curve (T-junction channel, glass tube A)

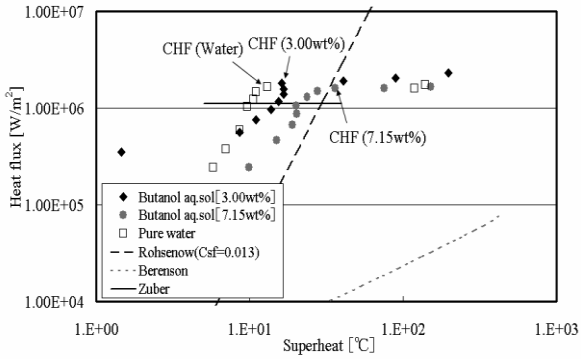

Fig. 4 Boiling curve (Straight channel, glass tube B)

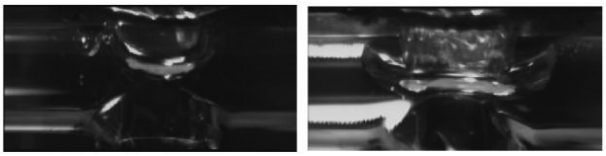

(i) Pure water (ii) Butanol aq. sol(3.00wt%)

Fig.5 Observed boiling bubble motion (glass tube D)

4. Concluding remarks

It was found from this experiment that in using the butanol aqueous solution, the boiling bubbles became much smaller and detached from the heated surface more smoothly than in using pure water. In addition, the heat flux of the dryout point increased by 27% in the T-junction channel and by 9% in the straight channel with butanol aqueous solution of 3.00wt%, compared with pure water. From these results, we think that the impinging flow with butanol aqueous solution of 3.00wt% in mini channel would be one of the suitable conditions for the flow boiling.

References

[1] R.Vochten and G.Petre, J.Colloidal Science, 42-2(1973), pp. 320-327.

[2] Naoki Ono, Takahiro Yoshida, Takahiro Kaneko, Syotaro Nishiguchi and Masahiro Shoji, Thermal Science & Engineering.Vol.16, No3(2008), pp. 79-85.

[3] Naoki Ono, Takahiro Yoshida, Takahiro Kaneko, Syotaro Nishiguchi and Masahiro Shoji, Proc 46th Japan Heat Transfer Symposium(2009), pp. 367-368.

[4] Minoru Otsuka, Atsushi Hamaoka, Yuki Kumagai, Kazushi Kunimatsu and Naoki Ono, Proc 48th Japan Heat Transfer Symposium(2011), pp. 277-278.

Eighth International Conference on Flow Dynamics
November 9 - November 11, 2011

The Effect of Dispersed State to Control of Radiative Properties of Coatings Pigmented with Nanoparticles

Hiroki Gonome[1], Mehdi Baneshi[2], Junnosuke Okajima[2], Atsuki Komiya[2], Shigenao Maruyama[2].
[1] Graduate School of Engineering, Tohoku University, 6-6 Aoba, Aramaki-aza, Aoba-ku, Sendai, Miyagi 980-8579, Japan
[2]Institute of Fluid Science, Tohoku University, 2-1-1 Katahira, Aoba-ku, Sendai, Miyagi 980-8577, Japan
E-mail of corresponding author: hiroki1006@pixy.ifs.tohoku.ac.jp

ABSTRACT

This study describes nanoparticles pigmented coatings used in controlling the radiative properties of surfaces exposed to sunlight. The effect of particle dispersed state to reflectance of the coating is discussed. From Raman spectral intensity of the coating, the dispersed state of particles was confirmed. Comparison between experimental and numerical results shows that the control of dispersed state affects the radiative properties of pigmented coatings.

1. Introduction

Products such as cars and buildings are usually exposed to a great deal of sunlight. In many cases, dark color coatings are used on these products to give them an appealing appearance; however, these dark coatings have large absorption of solar irradiation in the visible (VIS) and near infrared (NIR) regions. Therefore, the interior temperature becomes high and a large cooling load is required [1]. On the other hand, white color coatings, which strongly reflect sunlight, are used to reduce the cooling load. A drawback of this approach is that the high reflectance of visible light produces a high glare that can hurt the eye.

To overcome this problem, a cool pigmented coating using controlled size nanoparticles was proposed. Our desired coating reflects NIR radiation, which accounts for 52% of sunlight energy, and decreases reflectance of VIS radiation. Figure 1 is a concept of a pigmented coating, called a functional film, used as the thermal barrier coating. Baneshi et al. [2] developed the theoretical design method.

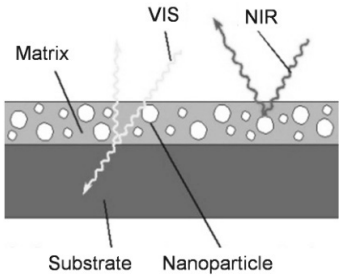

Fig. 1 Concept of a functional film

In this study, the effect of particle dispersed state to reflectance of the coating is discussed. At first Raman spectral intensity of the coating was measured experimentally in order to check the dispersed state of particles. Next, the spectral reflectance was measured by spectroscopy. Furthermore, the effect of particle dispersed state was evaluated by comparing with calculation result.

2. Experiment

The two functional films were made using TiO_2 and Fe_2O_3 as the dispersed particles, clear acrylic synthetic resin as the matrix, and the standard black paper as the substrate. The properties of the particles are shown in Table 1. The paints were made by mixing the pigment powder, acrylic resin and thinner. Then, an ultrasonic apparatus (BRANSONIC5510, BRANSON) was used for the dispersing of the nano particles in the paint. The paint was coated over the substrate using a bar coater machine. The substrate was standard black paper standardized by Japan Industrial Standards (JIS). The thickness of the coatings was measured by a digital micrometer.

Table 1. Specification of pigmented particles

Particles	Mean diameter of particles [μm]	Chemical company
TiO_2	0.175	Tayca Corporation
Fe_2O_3	1.0	Kojundo chemical laboratory co., Ltd

To check the dispersed state of particles, Raman spectral intensity was measured by Raman spectroscopy. The material in the coating was identified from Raman Spectra Database of Minerals and Inorganic Materials (RASMIN) [3].

The diffuse reflectivity of each sample was measured in VIS to NIR region. UV-VIS-NIR spectrophotometer (Lambda 900, Perkin Elmer) equipped with an integrating sphere coated by Spectralon was used for measurements. Spectralon has a reflectivity of nearly 100% in the UV-VIS-NIR region and was used as the reference.

3. Numerical Calculation

Baneshi et al. developed the calculation model to evaluate the performance of the coatings. This calculation model was used in this study [2]. To estimate the effect of the dispersed state of particles on the reflectivity of the coating, the reflectivity of the coating is analyzed theoretically. In this calculation, the dispersed state is assumed to be monodispersed. Radiation Element Method by Ray Emission Model (REM^2) [4] is used for calculating the pigmented coating system using a one-dimensional parallel plane model. From the comparison between measured and calculated reflectances, the effect of dispersed state can be observed.

4. Results and Discussion

Figures 2 and 3 show Raman spectral intensity of TiO_2 and Fe_2O_3 coatings, respectively. As shown in Fig. 2, there are only TiO_2 particles in the surface of coating when the volume fraction is 0.05. On the other hand, as shown in Fig. 3, there are Fe_2O_3 particles and acrylic resin in the surface of coating when the volume fraction is 0.01. These results suggest that particles are dispersed schematically shown as Fig. 4.

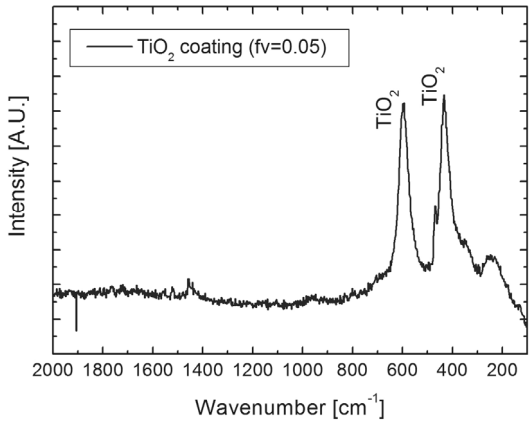

Fig. 2 Raman spectral intensity of TiO_2 coating

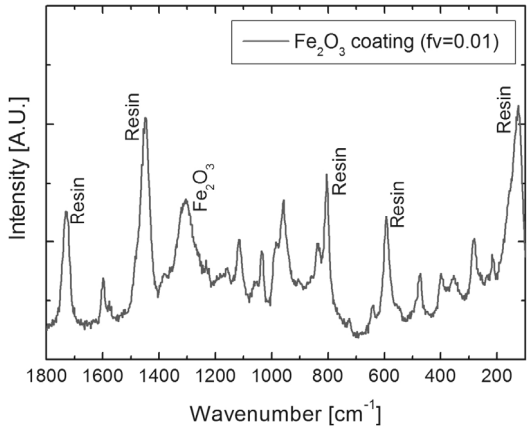

Fig. 3 Raman spectral intensity of Fe_2O_3 coating

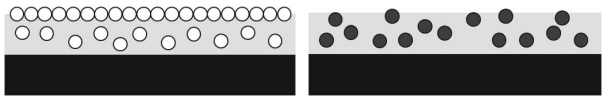

(a) f_v=0.05 (b) f_v=0.01

Fig. 4 Schematic of a pigmented coating

Figure 5 shows the comparison between the measured and calculated reflectance of TiO_2 and Fe_2O_3 coatings, respectively. As shown in Fig. 5, the difference between the measured and calculated reflectance increases as the volume fraction increases. About TiO_2 coating, the maximum absolute error of reflectance is about 10%. In contrast, about Fe_2O_3 coating, the maximum difference of reflectance is about 5%. This behavior suggests that the pigment aggregation like Fig.4(a) might have occurred when the volume fraction is 0.05. In this calculation, the dispersed state is assumed to be homogeneous. When the pigment aggregation occurred, the difference between the measured and calculated reflectance might increase. If the volume fraction is high, the pigment aggregation occurs easily. It is important for the control of reflectance to control the dispersed state of particles and optimum volume fraction.

These differences were caused not only by the dispersed state. In this calculation, using the spectral complex index of refraction [5, 6], the radiative properties of a single Fe_2O_3 particle were calculated in each particle size. For more accurate calculation, the spectral complex index of refraction should be more discussed.

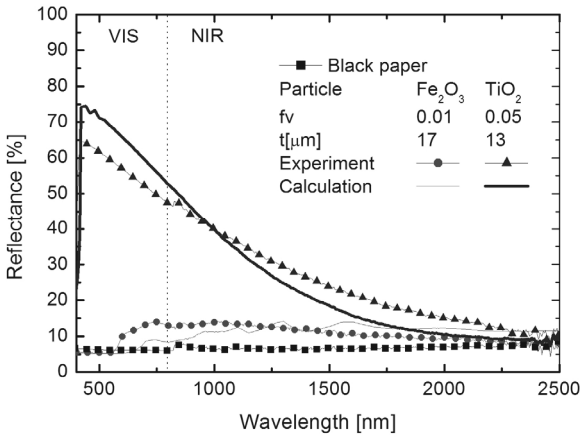

Fig. 5 Comparison between measured and calculated reflectances for the functional coatings

5. Concluding remarks

In this study, the effect of particle dispersed state to reflectance of the coating is discussed. The performance of cool pigmented coatings was studied both numerically and experimentally. To check the dispersed state of particles, Raman spectral intensity is measured.

1. Raman spectral intensity measurement shows the particle concentration on the top of coating when the volume fraction is 0.05.
2. Comparison between measured and calculated reflectances shows the pigment aggregation might occur when the volume fraction is 0.05.
3. For controlling reflectance, it is important to control dispersed state of particles and optimum volume fraction.

References

[1] Y. Kondou, *Gekkan reform*, **10** (2008), 13-17.
[2] M. Baneshi et al., *JQSRT*, **110** (2008), 192-204.
[3] RASMIN Web: http://riodb.ibase.aist.go.jp/rasmin/ (National Institute of Advanced Industrial Science and Technology, 2010/12/24)
[4] S. Maruyama, *Int. J. Heat Mass Tran*, **41** (1998), 2847-2856.
[5] G. Smith, et al., *Sol Energ Mat Sol* C, **79** (2003), 163–177.
[6] G. F. Bohren, et al., *Absorption and Scattering of Light by Small Particles*, A Wiley-Interscience Publication, John Wiley & Sons, Inc., U.S.A. (1986)

Eighth International Conference on Flow Dynamics
November 9 - November 11, 2011

Water Purification Using Activated Mist Flow with Plasma

Tomohiro Shibata[1], Hideya Nishiyama[2].
[1]Graduate School of Engineering, Tohoku University, 2-1-1 Katahira Aoba-ku, Sendai 980-8577, Japan
[2]Institute of Fluid Science, Tohoku University, 2-1-1 Katahira Aoba-ku, Sendai 980-8577, Japan
shibata@paris.ifs.tohoku.ac.jp

ABSTRACT

There are serious problems of water pollution in the world. Recently, the conventional chemical treatment has been replaced by the water treatment system using plasma. In this study, a method for decomposing organic compounds by spraying solution as mist into reactive plasma directly is investigated using DBD plasma tube. Using the plasma tube, the organic compounds are decomposed by ozone, free radicals and ultraviolet rays. Furthermore, the chemical reaction between droplet and plasma is enhanced because the micro droplet has large specific surface area.

1. Introduction

Water pollution is serious problem not only for human but also for all of the ecological system. Recently, the conventional chemical treatment has been replaced by the water treatment system using plasma because the plasma treatment is environmentally friendly. In a plasma treatment, organic compounds are generally decomposed by ozone. Although various kinds of radicals are also generated by reactive plasma, the radicals cannot be used for water purification due to their short life time. Using the high performance power source, plasma treatment using underwater, water surface and gas-liquid multiphase discharge is developed. The decomposition performance is enhanced because radicals and ultraviolet ray can be used for decomposition of organic compounds in this method. It is reported that the method spraying waste water into reactive plasma shows the highest relative energy efficiency [1].

In this study, the characteristics of reactive plasma multiphase flow using mist and DBD plasma tube is experimentally clarified. And liquid decomposition performance is clarified through decomposition of methylene blue. Using this plasma tube, the organic compounds are decomposed by ozone, free radicals and ultraviolet rays. Furthermore, the chemical reaction between droplet and plasma is enhanced because the micro droplet has large specific surface area.

2. Experimental apparatus and measurement procedure

Figure 1 shows a schematic illustration of experimental setup. The experimental setup mainly consists of electric power supply, ultrasonic atomizer unit, DBD plasma tube, mist separator and air pump. The applied sinusoidal voltage range is 5~12 kV and the frequency range is 500~1500 Hz. The carrier gas is air of 9.0 *l*/min. The oscillating frequency of ultrasonic atomizer unit is 2.4 MHz and the electric power consumption is 30 W. The atomization rate is 250 m*l*/h. The mean diameter of mist is several μm. DBD plasma tube made of Teflon with 0.5 mm in thickness. DBD plasma tube has inner mesh electrode made of stainless and outer grounded electrode made of copper. The inner diameter of this tube is 32 mm and length of discharge area is 10 cm. The sinusoidal voltage is applied to inner

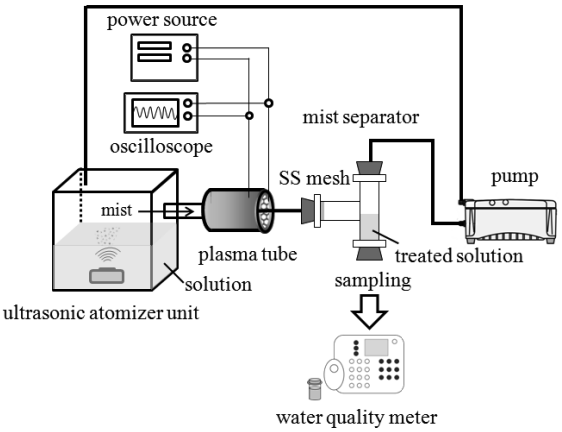

Fig. 1 Schematic illustration of experimental setup.

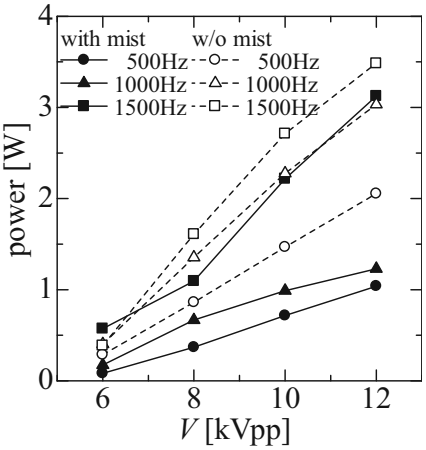

Fig. 2 Electric power as a function of various applied voltage.

mesh electrode. Mist separator is pipe in the shape of T with stainless mesh at inlet port. The mist is separated from gas by collision with stainless mesh. The separated gas is returned to the tank in which mist is generated because the gas includes active species like ozone.

Electric power, ozone generation amount and ozone production efficiency are measured as characteristics of DBD plasma tube. The electric power consumption is evaluated by the Lissajous figures method. Dissolved amount of ozone, hydrogen peroxide (H_2O_2) and reactive oxygen species (ROS) are measured as liquid property. In addition, decomposition efficiency is

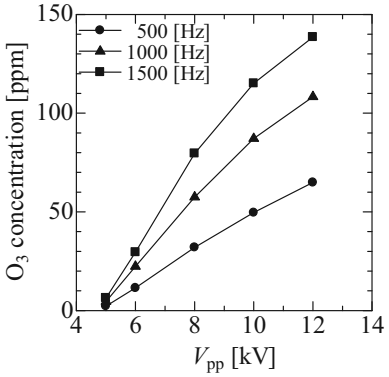

Fig. 3 Ozone concentration as a function of various applied voltage.

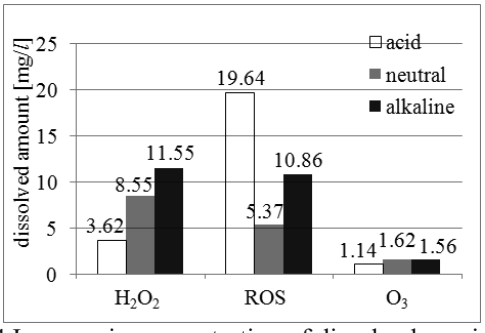

Fig. 4 Increase in concentration of dissolved species for various solution pH.

evaluated by absorptiomatry using methylene blue solution.

3. Experimental results and discussion

Figure 2 shows the power as a function of various applied voltage and frequency with and without mist flow. The power of this reactor is several watts and increases linearly as applied voltage increase. Since the discharge in a DBD plasma tube is not easy with mist flow, the power is lower than that without mist discharge.

Figure 3 shows the ozone concentration as a function of various applied voltage and frequency. The ozone concentration is measured at center and near inner wall of tube exit respectively and averaged. The ozone concentration increases linearly as applied voltage increase. In this study, the highest concentration of ozone, about 140 ppm, is found for 12 kV applied voltage and 1500 Hz applied frequency.

Figure 4 shows the concentration of dissolved species for acid solution, neutral solution, alkaline solution with 10 kV applied voltage and 1000 Hz applied frequency after one pass. Solution is purified water and the solution pH is adjusted by HCl and NaOH. The amount of dissolved H_2O_2 increases as pH increases. This is because the H_2O_2 generation is strongly influenced by OH^- ion. The ROS concentration is increase in any solution especially in acid solution. The dissolved ozone concentration is almost the same in any pH.

Figure 5 shows the decomposition rate of 5mg/*l* methylene blue solution measured by absorptiometry

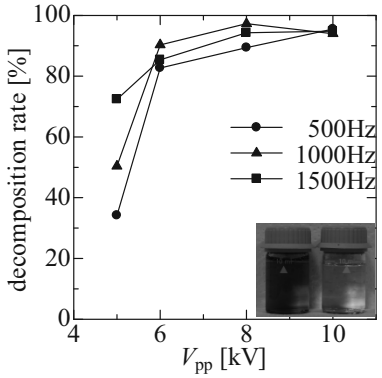

Fig. 5 Decomposition rate of methylene blue solution as a function of various applied voltage.

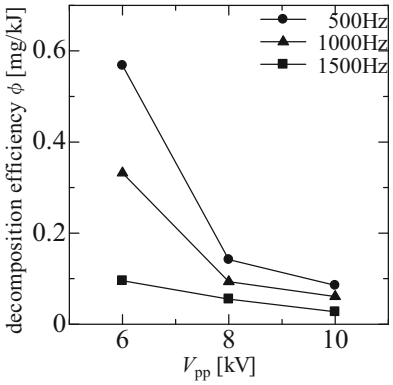

Fig. 6 Decomposition efficiency as a function of various applied voltage.

and the picture of solution before and after treatment. Methylene blue is decolorized completely after one pass for over 6 kV applied voltage in any frequency because the micro droplet has large specific surface area and chemical reaction is enhanced. The decomposition rates of methylene blue solution for 5 kV applied voltage are low because the discharge in a DBD plasma tube is not easy.

Figure 6 shows the decomposition efficiency of methylene blue solution calculated by Fig. 2 and Fig. 5. The decomposition efficiency increases as the applied voltage and frequency decrease.

4. Conclusion

The obtained results can be summarized as follows:

(1) DBD plasma tube for water treatment was produced and its characteristics such as electric power, ozone generation amount and ozone production efficiency are clarified in detail.

(2) Reactive species are dissolved in mist effectively. The effect of solution pH on the amount of dissolved species is clarified.

(3) The decomposition efficiency is clarified through methylene blue decolorizing experiment and DBD plasma tube is effective for water purification.

References

[1] M. A. Malik, Plasma Chem. Plasma Process, No. 30 (2010), pp. 21-31.

Eighth International Conference on Flow Dynamics
November 9 - November 11, 2011

Fibre Orientation and Fibre Streaks in Turbulent Half Channel Flow

Karl Håkansson[†], Mathias Kvick[†], Fredrik Lundell[†*], Lisa Prahl-Wittberg[†*], L. Daniel Söderberg[†‡].
[†]Wallenberg Wood Science Center, KTH Mechanics, Royal Institute of Technology, SE-100 44 Stockholm, Sweden
[*]Linné FLOW Centre, KTH Mechanics, Royal Institute of Technology, SE-100 44 Stockholm, Sweden
[‡]Innventia AB, Box 5604, SE-114 86 Stockholm, Sweden
karlh@mech.kth.se, kvick@mech.kth.se, fredrik@mech.kth.se

ABSTRACT

A fibre suspension in a turbulent half channel flow is studied experimentally. A camera is used to take images of the rigid fibres in the suspension, from the images the positions and orientations of the individual fibres in the wall parallel plane are found. Fibres with different aspect ratios are shown to behave differently, the longer fibres align in the flow direction and shorter align perpendicular to the flow. Particle streaks are observed and the streak widths are seen to scale in the same manner as low velocity streaks in a viscous sublayer. The streakiness is found to have a maximum with respect to the friction Reynolds number.

1. Introduction

In a paper-making machine, pulp is fed into a headbox, where a pipe flow is converted into an elongated flow in a contraction. The pulp is jetted out of the headbox onto a forming wire, where the pulp is pressed and dried into paper sheets. The final properties of the paper are dependent on the flow in the headbox, which is, besides elongated, also turbulent. In this experimental study, a fibre suspension in a turbulent half channel flow is used to study the effects of walls in *e.g.* a headbox.

Boundary conditions are necessary in simulations and this study could give some pointers on the orientations and distributions of fibres close to a wall.

2. Method

An experimental study of a fibre suspension in a turbulent half channel flow is carried out. The experimental setup consists of the KTH water-table, a fibre suspension and a camera. A pump is used to circulate the fibre suspension from a downstream reservoir to an upstream reservoir on the water-table. The suspension is allowed to flow down an inclined glass channel from the upstream reservoir to the downstream reservoir. A camera is mounted underneath the glass channel at a position more than 100 water layer heights downstream of the inlet. Images of the fibres in the flow are acquired, and the fibres positions and orientations are detected with a post processing image analysis algorithm. The flow is driven by gravity alone and the wall shear stress, τ_w, is calculated using eq. 1.

$$\tau_w = \rho g h \sin\alpha \tag{1}$$

In eq. 1, ρ is the density of the fluid, g is the gravitational acceleration, h is the height of the water layer and α is the inclination angle of the glass channel. The frictional Reynolds number is defined in eq. 2:

$$\mathrm{Re}_\tau = \frac{h u_\tau}{\nu} = \frac{h\sqrt{gh\sin\alpha}}{\nu}, \tag{2}$$

and the particle Reynolds number in eq. 3:

$$\mathrm{Re}_p = \dot{\gamma}\frac{l^2}{\nu} = \frac{\tau_w}{\rho\nu}\frac{l^2}{\nu} = \frac{l^2 gh\sin\alpha}{\nu^2}, \tag{3}$$

where u_τ is the friction velocity, ν is the dynamic viscosity, $\dot{\gamma}$ is the shear rate and l is the fibre length. The friction Reynolds number is varied between 50 and 210 and the particle Reynolds number between 10 and 1100. In each experiment 150 images are analysed. The time between two images is longer than the time it takes for the slowest fibre to flow through the field of view of the camera.

The dilute suspension consists of 120 litres of water and rigid cellulose acetate fibres with concentrations of 0.00042 − 0.0033% by weight, corresponding to a number density of nl^3 = 0.0008 − 0.0066. The fibres have density ρ_f = 1300 kg/m^3, diameter d = 70 μm and lengths l = 0.5, 1 and 2 mm, resulting in aspect ratios, r_p = 7, 14 and 28. Most fibres are located very close to the wall due to sedimentation.

Laser Doppler Velocimetry (LDV) measurements were performed and compared with DNS results of a full channel [1]. From this comparison the flow was confirmed to be turbulent and fully developed at the acquisition point.

The fibres positions and orientations in the wall parallel plane are detected using a steerable filter described in [2]. The streak width and a streakiness measure are extracted from a correlation-based method, where the fibre concentration dependence is carefully accounted for.

3. Results and Discussion

The fibre aspect ratio is found to have a large effect on the orientation distribution, see Fig. 1. In Fig. 1 zero is in the flow direction and, 270 and 90 is perpendicular to the flow direction. Short fibres (r_p = 7) are seen to be mostly aligned perpendicular to the flow, while longer fibres (r_p = 28) are aligned in the flow direction. The intermediate fibres (r_p = 14) are more homogenously distributed. The three distributions are all measured at $\mathrm{Re}_\tau \approx 130$. The friction Reynolds number is shown to have a small effect on the orientation distribution and the main effect is identified to be fibre aspect ratio.

It is well known that high- and low speed streaks are present in the viscous sublayer. The low speed streaks have empirically been examined and the mean streak width has been determined to be in the order of $50l^+$ [3],

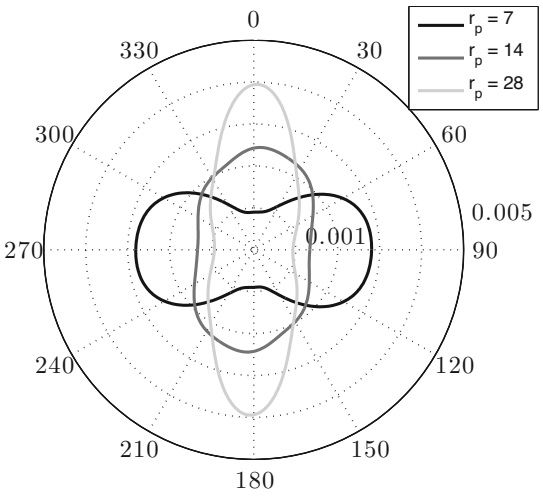

Fig. 1 Fibre orientation distributions for three different aspect ratios, r_p, at $\mathrm{Re}_\tau \approx 130$. Zero is in the flow direction and 90 perpendicular to the flow.

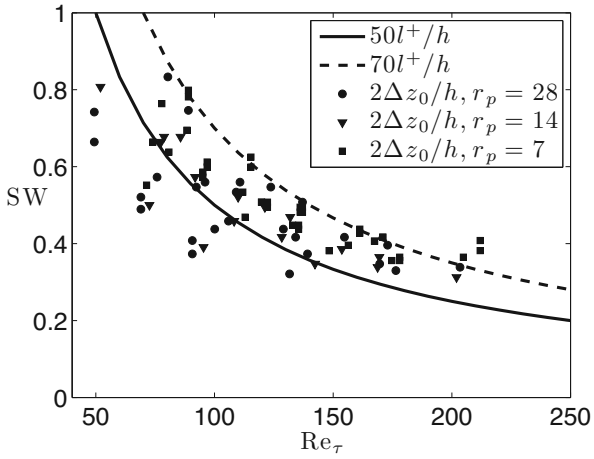

Fig. 2 Streak width (SW) versus Re_τ, where $50l^+$ is an empirically found value for low velocity streaks in the viscous sublayer.

where l^+ is the viscous length scale defined as:

$$l^+ = \frac{\nu}{u_\tau} = \frac{\nu}{\sqrt{gh\sin\alpha}}. \quad (4)$$

In Fig. 2 the streak widths (SW) from all measurements are shown and so are $50l^+$ and $70l^+$. The fibre streaks are seen to be wider than $50l^+$, which also has been observed in simulations with spherical particles [4].

In order for a measure of the streak width to be relevant, streaks must exist. The streakiness, Ξ, is a measure of how strong the streaky structures are. Fig. 3 shows that there is a peak in streakiness at $\mathrm{Re}_\tau \approx 110$. Due to insufficient or excessive amounts of fibres in the images, the streakiness could not be evaluated for all measurements.

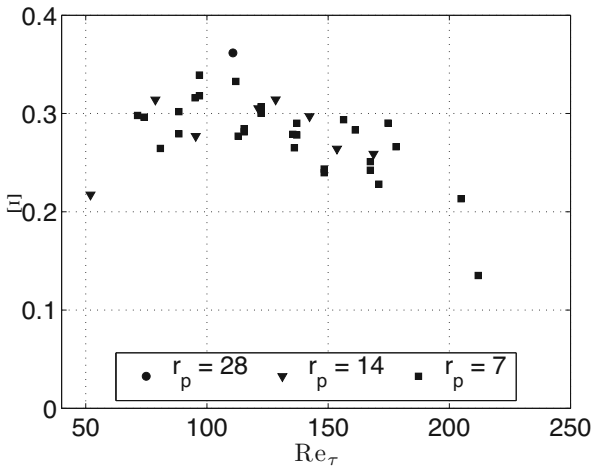

Fig. 3 Streakiness, Ξ, versus Re_τ for different aspect ratios r_p.

4. Concluding remarks

Fibre orientation and fibre streaks in a turbulent half channel flow have been studied experimentally. The fibre aspect ratio was observed to have a large effect on the fibre orientation distribution. The long fibres (r_p = 28) aligned in the flow direction, while the short fibres (r_p = 7) aligned perpendicular to the flow. The particle streak widths were seen to scale in the same manner as the low velocity streaks in the viscous sublayer. Fibre streaks were found in the whole parameter region $50 \leq \mathrm{Re}_\tau \leq 210$, but most pronounced at $\mathrm{Re}_\tau \approx 110$.

References

[1] Tsukahara T, Seki Y, Kawamura H, Tochio D, (2005), Proc. of the Fourth Int. Symp. on Turbulence and Shear Flow Phenomena, pp 935–940

[2] Carlsson A, Håkansson K, Kvick M, Lundell F, Söderberg LD, (2011), Experiments in Fluids, pp 1–10

[3] Zacksenhouse M, Abramovich G, Hetsroni G, (2001), Experiments in Fluids 31(2):229–239

[4] Zhao LH, Andersson HI, Gillissen JJJ, (2010), Physics of Fluids 22(8):081,702

Eighth International Conference on Flow Dynamics
November 9 - November 11, 2011

Irregular Reflection of Weak Shock Waves in Steady Flows

Georgy Shoev, Yevgeniy Bondar, Alexey Kudryavtsev, Dmitry Khotyanovsky and Mikhail Ivanov.
Khristianovich Institute of Theoretical and Applied Mechanics,
Institutskaya str. 4/1, Novosibirsk, 630090, Russia.
shoev@itam.nsc.ru.

ABSTRACT

Irregular reflection of weak shock waves in steady flow is considered under von Neumann paradox conditions. Crucial role of viscosity effects in the shock intersection region are demonstrated. Euler computations based on shock capturing solver show Guderley flow pattern (Prandtl-Meyer expansion fan centered at triple point with supersonic patch behind it) only at high space refinement. Numerical solution of Navier-Stokes equations predicts flow pattern close to Guderley one only at extremely high Reynolds number.

1. Introduction

Guderley theoretical model [1, 2] for weak shock wave reflection is a well-known way to overcome von Neumann paradox within the gas dynamic framework. Recent Euler calculations [3] confirmed conceptual issues of Guderley theory for steady shock reflection. An expansion fan and a local supersonic patch were found behind the triple point. A numerical simulation based on the shock fitting technique was used in that study. Ivanov et al. [4], however, did not reveal any supersonic patches in Euler computations based on both the shock-fitting and shock-capturing techniques. Tesdall et al. [5] discovered a sequence of supersonic patches and triple points along the Mach stem for unsteady shock reflection. The results of numerical simulation showed a sequence of triple points and tiny supersonic patches behind the leading triple point. Another interesting result was also obtained in [6] within the framework of depth-averaged two-dimensional inviscid shallow water flow model. The nested-block grid refinement technique was used in that study to achieve high resolution of the computational mesh. A supercritical patch was discovered. Thus, at the present time, the question about the supersonic patch structure is still open.

Another way to overcome von Neumann paradox is to take into account the effects of viscosity [7, 8]. According to Sternberg model [7], instead of the triple point, there must be a transition zone in a viscous flow, where the Rankine-Hugoniot (RH) relations cannot be applied. Recent viscous computations [9] at low Reynolds numbers confirmed the validity of this viscous model and did not reveal any supersonic patches. Moreover, similarity of the flowfields at different Reynolds numbers was found in the vicinity of shock intersection. However, it is still unclear whether the viscous flow structure at $Re_w \to \infty$ can continuously transform into the flow pattern predicted by the inviscid Guderley model. This question became curious, since the size of the supersonic patch obtained in inviscid computations is commensurable in order of magnitude with the shock wave thickness at moderate Reynolds numbers $Re_w=10^4-10^6$. The computations at extremely high Reynolds ($Re_w=10^9$) numbers are required to completely clarify the behavior of the viscous solution.

2. Problem formulation and numerical technique

In this study we investigate irregular reflection (Fig. 1) of weak shock waves in a steady supersonic flow of monatomic gas ($\gamma=5/3$) with a Mach number $M_\infty=1.7$ between two symmetrical wedges with identical angles $\theta_w=13.5$. The reflection of the incident shock (IS) occurs on the plane of symmetry half-way between the wedges. A reflected shock wave, RS, and a Mach stem, MS, are formed at the intersection triple point.

The computations are conducted with the Euler, Navier-Stokes (NS) equations. The Euler/NS code is a time explicit shock capturing code based on 3rd and 5th order WENO reconstruction of convective fluxes and central 4th order approximation of dissipation terms. The 2nd order Runge-Kutta scheme was used for time iteration.

The NS computations are performed at various Reynolds/Knudsen numbers with full resolution of the internal structure of all shock waves.

Numerical simulations in the entire domain (Fig. 1) between wedges become computationally expensive as the grid resolution increases. Therefore, we also used the nested-block grid refinement technique [6], which has the following features. The computational domain size is reduced, but the number of grid nodes remains constant. The nested-block domains are shown in Fig. 1. The numerical solution obtained in the entire computational domain is interpolated to the sub-domain (block 2). After that, the computations are continued in the sub-domain. This procedure is repeated until necessary grid resolution is achieved.

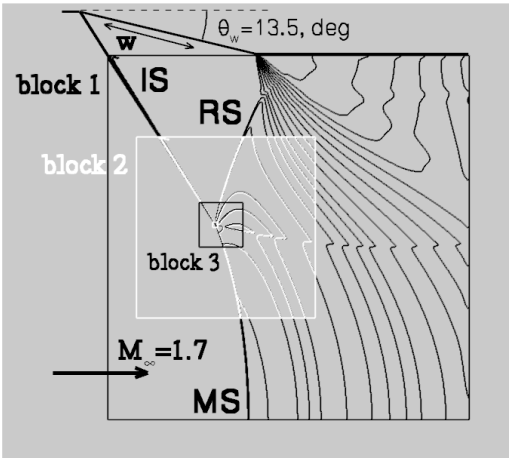

Fig. 1 Euler computations with the use of the nested-block grids

3. Results and Discussion

The results of NS computation obtained by the nested-block grid refinement technique are presented in Fig. 2. This computational method allows considering flowfields near shock interaction in a large range of Reynolds numbers. Numerical simulations predict subsonic flowfields in the vicinity of shock intersections at $Re_w<8\cdot10^8$. At the same time flowfields near the shock intersection are distinct from each other. It is possible to distinguish two main types of a flow near shock intersection. First one is a smooth transition zone between Mach stem and reflected shock without any patches, like in Fig. 2a and 2b. Second one is the flow with sub- or super- sonic patches, like in Fig. 2e, 2f and 3a. It is worth to note that there is transition regime between first and second type. The flow patterns of transition regime are shown in Fig. 2c and 2d. The results of the computations are also illustrated by diagram (θ, p) in Fig. 2g. Numerical data become closer to curve, corresponding to expansion fan centered at the triple point, as the Reynolds number increases.

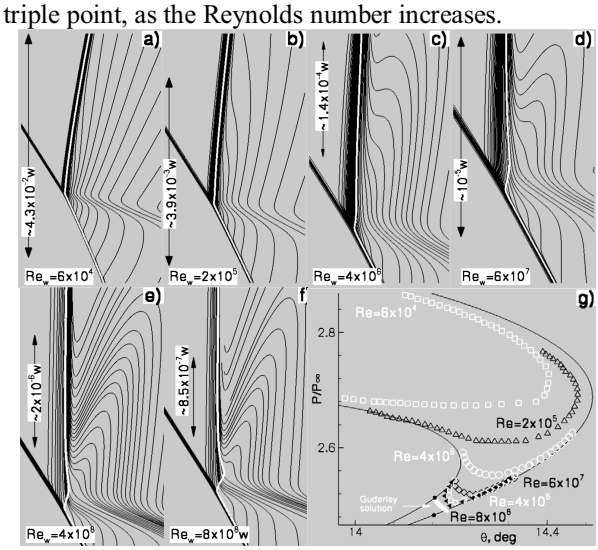

Fig. 2 Results of NS computations at different Reynolds numbers. a)-f) Density contours. The white isolines show sonic lines. g) plane (θ, p).

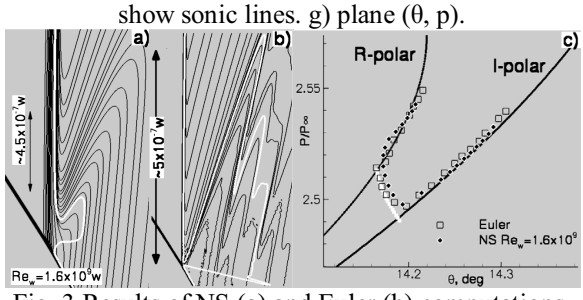

Fig. 3 Results of NS (a) and Euler (b) computations. a)-b) Pressure contours. The white isolines show sonic lines. c) plane (θ, p)

Figure 3 shows comparison between Euler computation and NS computation at $Re_w=1.6\cdot10^9$. Both computations predict supersonic patches behind shock intersection, but structure and size of these patches are quite different. Comparison of numerical data in plane (θ, p) is given in Fig. 3c. It is clearly seen that numerical data of both computations are close to Guderley solution.

4. Conclusions

A steady flow around symmetric wedges with Mach number $M_\infty=1.7$ was numerically studied under von Neumann paradox conditions. Euler computations based on shock-capturing solver and the nested-block grid refinement method predict supersonic patches behind the triple point, which confirm conceptual issues of Guderley model.

In the range of Reynolds numbers $Re_w=10^3-10^9$ results of NS computations did not reveal evidence of supersonic patches. Instead of supersonic patches, in viscous flow there is a smooth three shock transition zone, where R-H relations are not valid.

The first indication of supersonic patch formation near the triple point can only be observed at $Re_w>10^9$.

Acknowledgements

This work was supported by the Russian Foundation for Basic Research (grant No. 10-08-01203-a), Government contract N16.740.11.0303, Board of the Russian Academy of Sciences (Fundamental Research Program 11), Russian-Taiwanese joint project SB RAS - NSC 2010.

The computations were performed at the Siberian Supercomputer Center, Novosibirsk, supercomputer center of Novosibirsk State University and at the Joint Supercomputer Center, Moscow.

References

[1] Guderley K. (1947) Considerations on the Structure of mixed subsonicsupersonic flow patterns, HQ AirMateriel Command,Wright Field, Dayton, Ohio, Technical Report F-TR-2168-ND.

[2] Guderley K.G. (1962) The theory of transonic flow, Translated from the German by J.R. Moszynski. Oxford, New York, Pergamon Press, p. 344.

[3] Vasilev E., Olhovskiy M. (2009) The complex structure of supersonic patches in the steady Mach reflection of the weak shock waves, Abstracts of the 26th international symposium on shock waves, p. 322.

[4] Ivanov M., Paciorri R., Bonfiglioli A. (2010) Numerical simulations of von Neumann reflections, AIAA 40th Fluid Dynamics Conference and Exhibit, 28 June - 1 July 2010, Chicago, Illinois, 4859.

[5] A. M. Tesdall, R. Sanders, B. L. Keyfitz (2008) Self-similar solutions for the triple point paradox in gasdynamics, SIAM J. Appl. Math., 68, pp. 1360-1377

[6] Defina A., Viero D. P., Susin F. M. (2008) Numerical simulation of the Vasilev reflection, Shock Waves, vol. 18. p. 235-242.

[7] Sternberg J. (1959) Triple-Shock-Wave Intersections, Physics of Fluids, vol. 2. no. 2. p. 179206.

[8] Sakurai A. (1964) On the problem of weak Mach reflection, Phys Soc Japan, vol. 19, p. 144-050.

[9] Ivanov M., Bondar Ye., Khotyanovsky D., Kudryavtsev A., Shoev G. (2010) Viscosity Effects on Weak Irregular Reflection of Shock Waves in Steady Flow, Progress in Aerospace Sciences, vol. 46, p. 89-105.

Eighth International Conference on Flow Dynamics
November 9 - November 11, 2011

A molecular Dynamics study on the Thermodynamic Estimation of Cryogenic Hydrogen

Hiroki Nagashima, Takashi Tokumasu, Tohoku University, 2-1-1, Katahira, Aoba-ku, Sendai, Miyagi, Japan
Shin-ichi Tsuda, Shinshu University, 4-17-1, Wakasato, Nagano, Nagano, Japan
Nobuyuki Tsuboi, Kyushu Institute of Technology, 1-1, Sensui-chou, Tobata-ku, Kitakyushu, Fukuoka, Japan
Mitsuo Koshi, University of Tokyo, 2-11-16, Yayoi, Bunkyo-ku, Tokyo, Japan
A. Koichi Hayashi, Aoyama Gakuin University, 5-10-1, Chuo-ku, Fuchinobe, Sagamihara Kanagawa, Japan
E-mail of corresponding author: nagashima@nanoint.ifs.tohoku.ac.jp

ABSTRACT

In this paper, we conducted estimation of thermodynamic and transport properties of cryogenic hydrogen using classical Molecular Dynamics (MD) method. We applied three empirical potential models and one *ab initio* potential. We performed *NVE* constant MD simulation across a wide density-temperature condition to obtain Equation Of State and transport coefficients. Simulation results were compared with experimental data. As a result, it was confirmed that all potential models cannot reproduce the experimental data at the high density region. This distinction is considered to arise from the quantum nature of actual liquid hydrogen.

1. Introduction

Recently, the demand of liquid hydrogen is increasing due to the environmental affair and energy problem. Therefore it is important to understand its thermal and transport properties accurately for efficient and safety use. However liquid hydrogen has unusual thermodynamic properties because of its quantum nature. Therefore, non-classical method in which the quantum nature is considered is needed to analysis of liquid hydrogen and to understand the effect of its quantum nature and mechanism using the molecular simulation. However, non-classical methods such as Path Integral Centroid Molecular Dynamics (PICMD) [1] are difficult to be applied to the thermal flow analysis due to the complexity and the computational cost. Moreover, the current non-classical method cannot reproduce the molecular rotational motion. Therefore, there are some doubts about its accuracy. For this reason, numerical reproducibility of quantum nature of cryogenic hydrogen has not been investigated. Hence, the effect of intermolecular interaction and quantum nature on the numerical reproducibility has not been clarified. From this background, we have investigated the effect of intermolecular interaction on the thermodynamic and transport properties of cryogenic hydrogen and the effect of quantum nature on the Equation Of State (EOS) using classical Molecular Dynamics (MD) method. Through this analysis, the purpose of this study is to clarify the important factor on the numerical reproducibility of quantum nature of cryogenic hydrogen and to determine the limits of classical methods on the analysis of the thermodynamic properties of cryogenic hydrogen clearly.

2. Numerical Method

In this study, we estimated thermal properties using MD with four potential models which are Lennard-Jones (LJ), 2-Center Lennard-Jones (2CLJ) [2], modified Buckingham (exp-6) [3] and *ab initio* potential [4]. This *ab initio* potential is described by equation (1). This potential was constructed based on the Molecular Orbital (MO) calculation results, and the function consists of spherical harmonic expansion. The potential

$$
\begin{aligned}
V(\boldsymbol{r},\theta_a,\theta_b,\phi) &= V^{000} + \sqrt{5}[V^{202}P_2^0(\cos\theta_a) + V^{022}P_2^0(\cos\theta_b)] \\
&+ \frac{\sqrt{5}}{12}\left[V^{220} + 2\sqrt{\frac{5}{14}}V^{222} + \sqrt{\frac{1}{14}}V^{224}\right]P_2^2(\cos\theta_a)P_2^2(\cos\theta_b)\cos 2\phi \\
&+ \frac{\sqrt{5}}{3}\left[V^{220} - \sqrt{\frac{5}{14}}V^{222} - 4\sqrt{\frac{1}{14}}V^{224}\right]P_2^1(\cos\theta_a)P_2^1(\cos\theta_b)\cos\phi \\
&+ \sqrt{5}\left[V^{220} - 2\sqrt{\frac{5}{14}}V^{222} + 6\sqrt{\frac{1}{14}}V^{224}\right]P_2^0(\cos\theta_a)P_2^0(\cos\theta_b),
\end{aligned}
\tag{1}
$$

$$V^{l_a l_b l}(r) = C_1\exp\left(-C_2 r - C_3 r^2\right) - C_4 r^{-6} - C_5 r^{-8} - C_6 r^{-10}.$$

has four variables; intermolecular distance r, and three orientation angles of θ_a, θ_b, and ϕ. $P_2^0(\cos\theta_a)$ denotes associated Legendre polynomials, and C_1, to C_6 are the fitted coefficients to reproduce the MO results. V^{000} to V^{224} are the five even quantum number modes as the function of intermolecular distance r.

EOS was determined by Kataoka's method[5]. In this method, the EOS is expressed by the excess Helmholtz free energy from an ideal gas A^e as the sum of the product of density ρ and temperature T,

$$\frac{\beta A^e}{N} = \sum_{n=1}^{5}\sum_{m=-1}^{5} A_{mn}\left(\frac{\rho}{\rho_0}\right)^n\left(\frac{\beta}{\beta_0}\right)^m \tag{2}$$

where $\beta = 1/(k_B T)$, and N is the number of molecules. The 35 A_{mn} coefficients were determined by a least square fitting of the simulated potential energies and pressures which were derived by MD simulation. In this study, we performed *NVE* constant MD simulation. The temperature range was from 14 to 50 K, and the density range was from 0.01 to 105 kg/m^3, the total number of condition was 304. The cubic cell used in the simulations contained 2048 molecules. For the initial conditions, the velocity vector $\boldsymbol{\upsilon}_i$ and the rotational energy e_{ri} were given according to the Boltzmann distribution at temperature T. Time integration was performed by Velocity Verlet algorithm and the time step was set at 1fs. The molecular rotational motion was calculated using quaternions.

Transport coefficients were calculated using Green-Kubo method [6]. In this method, a transport coefficients K are expressed by equation (3).

$$K = \int_0^\infty \left\langle \dot{A}(t)\cdot\dot{A}(0)\right\rangle dt, \tag{3}$$

where $\dot{A}(t)$ is the flux of a physical quantity $A(t)$. Here

we show only the viscosity coefficient case. In the case of viscosity coefficient, $K = 6Vk_B T\mu$ and $\dot{A}(t)$ is

$$\dot{A}(t) = \frac{1}{m}\sum_{i=1}^{N} \boldsymbol{p}_i \boldsymbol{p}_i + \frac{1}{2}\sum_{i=1}^{N}\sum_{j\neq i} \boldsymbol{r}_{ij} \cdot \boldsymbol{F}_{ij}, \quad (4)$$

where $\boldsymbol{p}$ is a momentum, $\boldsymbol{r}$ is an intermolecular distance, $\boldsymbol{F}$ is an intermolecular force. Simulation condition of transport coefficients were saturation points in liquid phase at temperature T = 17, 20, 25, 30 K.

3. Results and Discussions

Here only the results of reduced saturation line obtained by LJ and *ab initio* potential are shown in Fig. 2. As shown in Fig. 2, calculation results of *ab initio* potential show same tendency with LJ potential results and we confirmed 2CLJ potential results also indicate similar tendency. Thus, we think that qualitative effect of molecular orientation is small. On the other hand, in the case of exp-6 potential, we confirmed EOS clearly depends on the potential parameter. However, in the high density region, exp-6 potential results also show same tendency with other potential results and could not reproduce the experimental data. From these results, it is clarified that even if a high accuracy potential is employed, the classical method is difficult to reproduce the thermodynamic properties of cryogenic hydrogen. Moreover, the reduced experimental data of saturation lines of He, O_2, N_2, and Ar are also shown in Fig. 2 to discuss the reason of the disagreement and the effect of quantum nature on the thermodynamic properties. As shown in Fig. 2, the saturation lines of He and of H_2 are not consistent with those of the other fluids, and the widths of their saturation regions are narrower. It means that the larger the influence of the quantum nature is, the smaller the density at the same temperature and pressure is. The thermal de Broglie wavelength of a light mass molecule becomes the same order as molecular diameter. Therefore, the repulsion region broadens and pressure increases and the density is smaller if a constant pressure is assumed. From this discussion, we conclude that the reason of the disagreement is quantum nature.

In addition, the results of viscosity coefficient are shown in Fig. 3 to investigate the effect of potential model on the transport property. As a comparison, simulation results of Yonetani [1] which were performed same simulation using PICMD are also shown in Fig. 3. As shown in Fig. 3, LJ and *ab initio* potential results show same tendency. The lower the temperature of simulation condition is, the larger the disagreements are. This is as same tendency as saturation line results. From these results, the effect of the intermolecular potentials is also small and classical method could not reproduce the experimental data in the high density region. On the other hand, the results of PICMD agree well with experimental data in whole temperature region. Moreover, some studies in which second virial coefficient is calculated using non-classical method with similar *ab initio* potential [8] show good agreement with experimental data. Therefore, we conclude that the reason why thermodynamic properties of cryogenic hydrogen could not be reproduced is classical method.

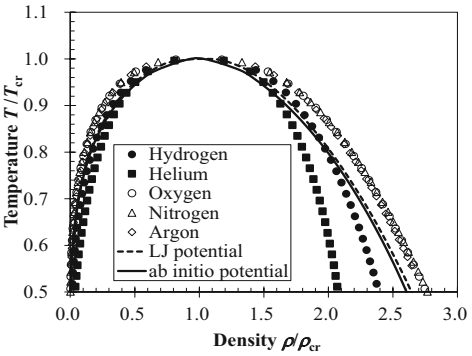

Fig. 2 Comparison of the reduced experimental data [7] and the reduced calculation results. (The subscript "cr" means critical point.)

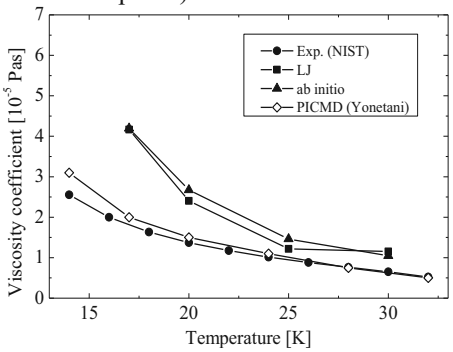

Fig. 3 Comparison of the experimental data [7] and the calculation results of viscosity coefficient.

4. Concluding Remarks

In this study, we clarified the qualitative effect of potential on the thermodynamic and transport properties of cryogenic hydrogen using classical MD method. As a result, even if a high accuracy potential is employed, the classical method is difficult to reproduce the thermodynamic and transport properties of cryogenic hydrogen in the high density region. From the consideration using saturation lines, we think that the reason of the disagreement is its quantum nature and a non-classical method including the quantum nature must be applied for the analysis of thermodynamic and transport properties of liquid hydrogen.

Acknowledgements

This study has been supported by the Ministry of Education, Science, Sports and Culture, Grant-in-Aid for Scientific Research (B) (No. 23360380) and the Collaborative Research Project of the Institute of Fluid Science, Tohoku University.

References

[1] Y. Yonetani and K. Kinugawa, J. Chem. Phys. **120** (2004), 10624.
[2] K. Singer et al., Mole. Phys. **33** (1977), 1757.
[3] Y. Kataoka, Bull. Chem. Jpn. **65** (1992), 2093.
[4] M. Koshi et al., Mol. Sim., in press.
[5] Y. Kataoka, *J. Chem. Phys*. **87**, (1987), 589.
[6] M. P. Allen and D. J. Tildesley, Oxford, (1986).
[7] http://webbook.nist.gov/chemistry/ (2011. 9.1).
[8] K. Patkowski et al., J. Chem. Phys. **129** (2008) 094304-1.

Eighth International Conference on Flow Dynamics
November 9 - November 11, 2011

Influence of Plaque Movement on Blood Flow and Blood Vessel around Stenosis Area

Yasutomo Shimizu*, Shuya Shida*, Makoto Ohta**
*Graduate School of Biomedical Engineering, Tohoku University, 6-6-01, Aobayama, Sendai, 980-8579, Japan
**Institute of Fluid Science, Tohoku University, 2-1-1, Katahira, Aoba, Sendai, 980-8577, Japan
E-mail: shimizu@biofluid.ifs.tohoku.ac.jp

ABSTRACT

Plaque in stenosis parts has various stiffness values depending on disease condition, and may affect the change of blood flow or vessel condition. The purpose of this study is to find out the influence of stenosis stiffness on the blood flow using PVA-H stenosis models with several stiffness values under PIV measurement. The diameter of blood vessel, plaque shape, and blood flow patterns of downstream of plaque are changed with depending on the plaque stiffness. We could lead the conclusion describing that plaque stiffness plays a role in the blood flow.

1. Introduction

Endovascular disease, such as vascular stenosis, is the one of the most common causes of death, and may remain serious sequelae. Blood flow dynamics has an important role for atherosclerosis initiation, progression, plaque rupture, and thrombosis [1], because plaque is always exposed to blood flow. It is well known that stiffness of plaque is different depending on the disease condition [2]. And then, the blood flow pattern depends on the geometry of stenosis and the geometry of stenosis will be also changed by the flow. The mechanical properties (especially stiffness) are one of the important factors of changing the ratio of deformation. However, although the relationship between the change of plaque geometry by blood flow and the stiffness of plaque are important, almost all previous studies about flow dynamics with stenosis model have used rigid tubes, for example [1]. Then, it will be necessary to observe the flow pattern in a biomodel with mechanical properties mimicking the disease. Jie et al., [3] used Poly Vinyl Alcohol – Hydrogel (PVA-H) stenosis models with several plaque stiffness and measured the geometrical change depending on the pressure, however, it is still unclear about the influence of flow on the change of stenosis geometry. Therefore, the purpose of this study is to find out the relationship between plaque stiffness and blood flow using Particle Image Velocimetry (PIV) measurement.

2. Method

2-1. PVA-H model

Three kinds of plaque parts (5, 12, 15 wt% of PVA powder, respectively) and a box part (12wt%) of PVA-H stenosis model were prepared using the previous developed method [4]. Each model had 4mm in diameter and 70% in severity of NASCET like equation(1). *St* means stenosis severity, *Ds* means diameter of narrowest part, *D* means diameter of blood vessel in the model, respectively.

$$St = (1 - \frac{Ds}{D}) \times 100 \ [\%] \qquad (1)$$

2-2. Working fluid & flow condition

Working fluid consisted of mixed solvent of 35wt% glycerol/distilled water solution and 65wt% sodium iodide/water solution, which is including acrylic particles covered with gold and nickel (Bright 6GNR30-MX, Nippon chemical industry Co., Ltd., Japan) as tracer. Glycerol/water solution consisted of 89wt% glycerin and 11wt% distilled water, and sodium iodide/water solution consisted of 53.4wt% sodium iodide and 46.6wt% distilled water, respectively. It has relative index of 1.453, density of 1.465, and kinematic viscosity of 3.919 mm^2s^{-1}, respectively at 25.0°C.

For flow condition, Flow rate was 200ml/min and pressure of upstream was 65mmHg, respectively.

2-3. PIV circuit

The circuit is shown in Fig.1. A screw pump (NBL30PU, R'Tech Co. Ltd., Japan) made a steady flow. A bifurcation flow channel and a valve were used for adjusting the flow rate to the PVA stenosis model. The height of water column in the reservoir loaded a hydrostatic pressure to the circuit. Flow rate and pressures of upstream and downstream of stenosis were measured by Coriolis flowmeter (FD-SS2, Keyence Co. Ltd., Japan) and by pressure meters (PW-100KPA Tokyo Sokki Kenkyujo Co. Ltd., Japan), respectively. For PIV measurement, a Nd:YAG solid laser system (BWN-532-100E, B&W TEK INC.) was used to provide a nominal 1mm-thick continuous laser sheet through the center plane of the channel with a power of 100mW and a wavelength of 532nm. Photo images were captured by a high speed camera (Fastcam SA3, Photron Limited Co. Ltd., Japan) with a telescopic micro lens which had 105mm of focal length and 2.8 of F ratio (Micro-Nikkor, Nikon Co. Ltd., Japan).

3. Results and Discussion

Figure 2, 3, and 4 show the diameter of each model from lateral view and anterior view, plaque geometries of each model in flow and no flow, and the vector velocity field in lower of the plaque, respectively. In fig.2, 5wt% 12wt%, 15wt% plaque models are expanded to 4.84mm, 4.84mm, and 4.59mm in vertical direction of flow, respectively. On the other hand, 5wt% 12wt%, 15wt% plaque models are expanded to 4.99mm, 4.95mm, and 5.04mm in horizontal direction of flow, respectively. The results indicate the vessels are deformed from a cylinder to an elliptical tube and 15wt% plaque model has biggest eccentricity. This various deformation between the directions may be due

to localization of plaque. And then, it is also considered that the degree can be determined by the plaque stiffness. In these results and discussions, it is revealed that plaque stiffness influences on the vessel expansion. In addition, 5wt% plaque model was larger deformed compared with other models in fig.3. Then, the flow patterns are observed and the flow patterns of all models are different. Therefore, the plaque stiffness and the geometry may affect the blood flow.

The reattachment point may be one of the important observation points for diagnosis because the place around the point has various wall shear stresses. The reattachment lengths, which mean the distance between the narrowest part of blood vessel and reattachment point, in each model were 5.71mm in 5wt% plaque model, 8.99mm in 12wt% plaque model, and 21.2mm in 15wt% plaque model, respectively. Despite similar NASCET values of all models, the models have different flow patterns, respectively.

Summarizing these results, it is suggested that plaque stiffness can change the geometries of the plaques and blood vessels, and these deformations affect the blood flow conditions.

4. Concluding remarks

PIV measurements in PVA-H stenosis models with several plaque stiffness values were performed. As the results, plaque geometry and blood vessel size are changed depending on the plaque stiffness. Blood flow patterns are also changed. These results suggest that the flow patterns are affected by the plaque geometry with various stiffness values and then the plaque progression may be also affected by the flow pattern mutually.

Acknowledgement

This study was supported by Tohoku University Global COE Program on World Center of Education and Research for Trans-disciplinary Flow Dynamics.

References

[1]Brunette et al.,J.Med.Eng.&Phys.,30,1193-1200,2008
[2]Yamagishi et al., J.Athe.Throm.,16(5),662-673,2009
[3]Jie et al., J.Biom. Sci. Eng., 6(2),79-88,2011
[4]Shimizu et al., ICFD proceeding, 2010

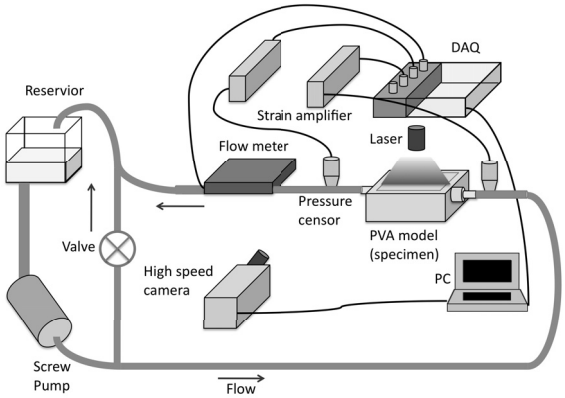

Fig.1 Image of PIV circuit

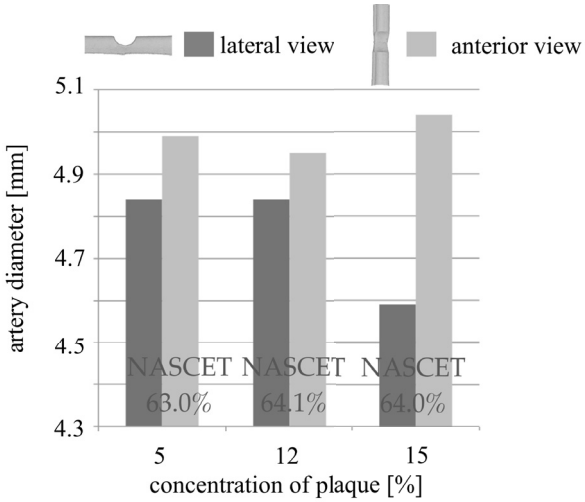

Fig.2 upstream diameters of each model

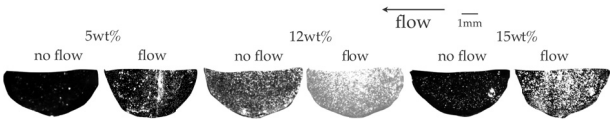

Fig.3 Plaque geometries in flow and no flow

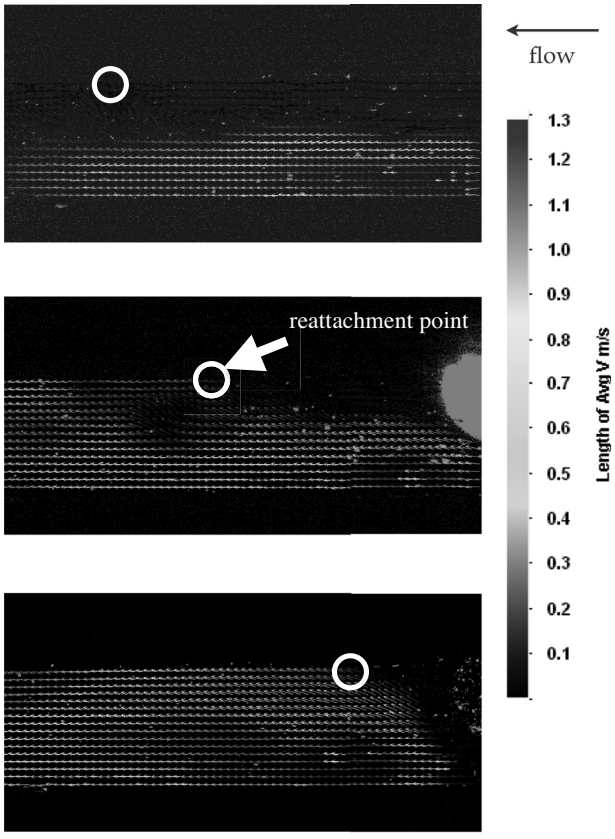

Fig.4 The downstream flow of plaque
Upper: 15mm lower of 15wt% plaque
Center: 10mm lower of 12wt% plaque
Lower: 10mm lower of 5wt% plaque

Eighth International Conference on Flow Dynamics
November 9 - November 11, 2011

Verification of Blunt Dissection Simulation for Brain Surgery

Masano Nakayama, Xin Jiang, Satoko Abiko, Atsushi Konno, Masaru Uchiyama.
Dept. of Aerospace Engineering in Tohoku University. 6-6-01 Aoba-yama, Sendai 980-8579, Japan.
{masano, abiko, jiangxin, konno, uchiyama} @space.mech.tohoku.ca.jp

ABSTRACT

Blunt dissection is a surgical technique to expose structures or to separate tissues without cutting. For blunt dissection simulation, it is important to display accurate reaction force to operator. In this paper, blunt dissection simulation is verified by comparing force measured in experiments with that calculated in simulation.

1. Introduction

The demand for surgery simulators has been increased, because such simulators serves training opportunities for surgeons and enable to make preoperative planning from the results of trial and error in the simulators. Therefore, a lot of surgery simulators have been developed so far [1, 2, 3].

Blunt dissection is one of the most important surgical techniques to extirpate lesion area. Blunt dissection fractures boundary tissues between a lesion area and surrounding normal area by applying a stress to the tissues. Surgeons control the fracture using information from vision and haptic sense. The blunt dissection simulation was verified by comparing shape of fracture in the simulation with shape of actual fracture in an agar plate. However, accuracy of reaction force displayed by haptic interfaces is also important for the blunt dissection simulation. This paper verifies the blunt dissection simulation by comparing result force of actual experiment with that of simulation.

2. Material and Shape of Target Object

Two blocks made of agar are used as specimens to fracture (Fig. 1). Agar is regarded as almost linear elastic body. Though living tissues like a brain are known as a nonlinear viscoelastic body, there are too many parameters to identify to calculate deformation of such object in simulation, and it is very difficult to make homogeneous specimens from living tissue. Therefore the target objects are made of agar to simply verify the proposed blunt dissection simulation in terms of fracture morphology.

The shape of specimen A is square pillar 16 [mm] high, 16 [mm] long and 45 [mm] wide. 10.5 [mm] from the both end of the specimen is glued to fixtures. The shape of specimen B is square pillar 16 [mm] high, 16 [mm] long and 50 [mm] wide. 13 [mm] from the both end of the specimen is glued to fixtures. Both specimens have two notches stopping 5.5 [mm] from top and bottom edge at the center of each specimen, which are shown as black lines in Fig. 1.

Specimen A and Specimen B have different stiffness. Specimen A is stiffer than Specimen B. The Young's modulus of them were identified in advance.

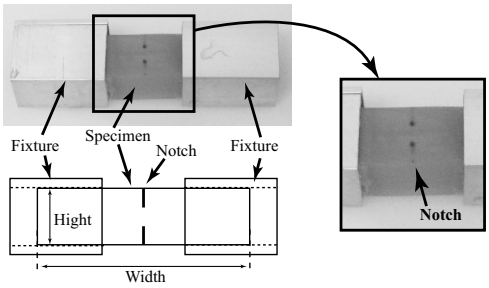

Fig. 1 Target object of fracture used in experiments.

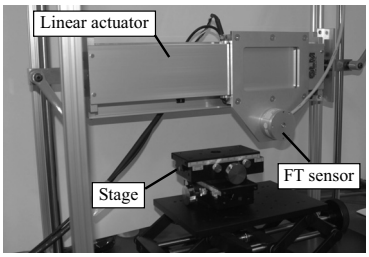

Fig. 2 Experimental equipment tearing specimens.

3. Experimental Setup

Tearing agar experiments are performed to compare a force acting on the specimens with force calculated in the blunt dissection simulation. Fig. 2 shows an experimental equipment to tear the agar specimens. The left end of a specimen is fixed on a stage and the right end is attached on a FT sensor mounted on a linear actuator. The linear actuator moves rightward at 1 [mm/s] and tears specimens at the notches made in advance. Force acting on the fixture attached on the linear actuator was measured by the FT sensor.

4. Blunt Dissection Simulation

To verify the blunt dissection simulation, tearing agar is simulated under the same condition of the experiments described above. In this simulation, deformation of objects is calculated using the Finite Element Method (FEM). Fracture in the objects is expressed by removing tetrahedral elements. Principal stress is set as a fracture criterion. When principal stress of an element becomes larger than 10 % of the Young's modulus, the element is determined to be fractured.

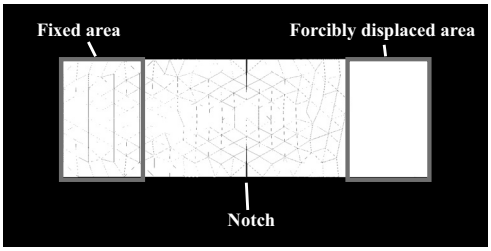

Fig. 3 FEM model of an agar specimen.

Table 1 Simulation parameters of specimen models.

Parameters	Specimen A	Specimen B
Number of nodes	2939	3226
Number of elements	14249	15653
Young's modulus [kPa]	300	39
Poisson ratio	0.44	0.44

It is known that the criterion agrees well with experiment when the target object is a linear elastic body. See [3] for more details of the blunt dissection simulation.

Fig. 3 shows a FEM model of a specimen. The model is divided into tetrahedral elements which is about 2 [mm] on a side. The number of nodes and elements constructing the specimen models and parameters for the blunt dissection simulation are shown in Table 1. Nodes on a surface where was glued to left fixture was set as fixed nodes, and nodes on a surface where was glued to the other fixture was set as forcibly displaced nodes. The forcibly displaced nodes were moved rightward 1 [μm] per loop.

5. Results and Discussion

Fig. 4 and 5 show measured force in the experiments and calculated force in the simulation with respect to time. In the case of simulation A and simulation B1, the fracture criterion was set as 10 % of Young's modulus of each specimen. In the case of simulation B2, the fracture criterion was set as 23 % of Young's modulus. The results of simulation were transfered from force with respect to displacement into force with respect to time on the assumption that forcibly displaced nodes were moved at 1 [mm/s] in the simulation as same as in the experiment.

At the first, the force acting on the specimen A increased linearly in both the experiment and the simulation in the same gradient. After that, the force calculated in the simulation rapidly decreased at 1.2 [s] when the specimen was dramatically fractured, whereas constant force was measured from 1.5 [s] to 4.5 [s] in the experiment before the fracture was occurred. The maximum force acting on the specimen A in the simulation was almost same as that measured in the experiment.

On the other hand, the force acting on the specimen B showed the same trend that the force increased linearly just before the fracture was occurred.

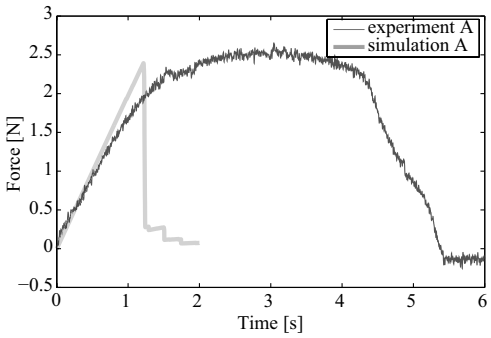

Fig. 4 Results of specimen A.

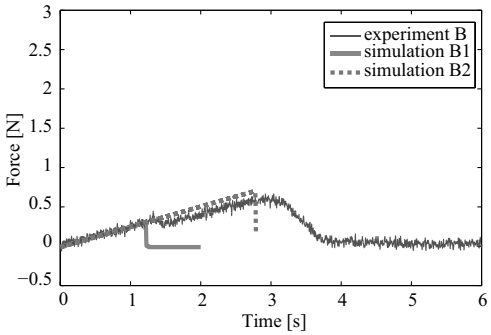

Fig. 5 Results of specimen B.

However, maximum force calculated in the simulation agree well with that measured in the experiment when the criterion of fracture was 23 %, not 10 %, of the Young's modulus. That is because the threshold value, 10 % of the Young's modulus, derived empirically from experiments of hard material such as metals [3]. Therefore, threshold value of the fracture criterion has to be determined for every specimens.

6. Conclusions

In this paper, reaction force measured in tearing experiment and force calculated in the blunt dissection simulation were compared. When a specimen is made of soft agar, calculated external force acting on the fixed area agree well with that measured in experiment. However, the comparison between the experiment and the simulation suggests that the specific threshold value of the fracture criterion has to be determined.

7. Acknowledgement

We would like to acknowledge funding from the Tohoku University Global COE Program on World Center of Education and Research for Trans-disciplinary Flow Dynamics.

References

[1] U. Kühnapfel et al., in *Computers & Graphics*, Vol. 24, no. 5, pp. 671-682, 2000.

[2] D. Sato et al., in *Journal of Robotics and Mechatronics*, pp. 634-642, 2006.

[3] M. Nakayama et al., in *Proceedings of AIM*, pp. 333-338, 2011.

Eighth International Conference on Flow Dynamics
November 9 - November 11, 2011

Observation of Behavior of Injection for Composite Material using Micro-CT

Kei Ozawa[1], Yuji Katakura[2], Yukihiko Shibata[2], Makoto Ohta[3]
1. Graduate School of Biomedical Engineering, Tohoku University, 2-1-1 Katahira, Aoba-ku, Sendai, Japan
2. TECNO CAST
3. Institute of Fluid Science, Tohoku University
E-mail : k-ozawa@biofluid.ifs.tohoku.ac.jp

ABSTRACT

The injection molding is one of the major methods for fabricating specially for composite materials. This method is useful for fabricating complex shape and advanced properties of materials. However, the materials during the molding are hard to be observed because the molding system is, in general, not to be transparent. The X-ray micro tomography (micro-CT) was employed to observe flow behavior with tungsten fibers. The orientation and distribution of fibers shows the flow direction clearly. The micro-CT has a possibility to observe the casting process.

1. Introduction

The injection molding is one of the major process methods for complex geometries. Specially, composite materials used for advanced and complex properties such as bone, recycled plastics or building materials are widely developed [1-4]. The composite materials consist of polymer and another material can show the different properties from original substance [5-7].

A bone biomodeling requires a realistic mechanical properties and the geometry. And the development such as Ozawa et al. is also performed with composite materials with an injection molding [8].

The mechanical properties of bone biomodeling such as elastic modulus, strength or fracture toughness have a strong relation to the compound condition or casting process under the injection molding. The observation of casting process is important to grasp the compound situation and microstructure of each material. The X-ray microtomography can be effective method to observe detail of inner structure and injection flow patterns [9]. The fiber is employed as effective tool for observation of flow direction its orientation and distribution in SEM images [10-12]. However, the flow behavior until full casting has rarely been observed. So, the purpose of present study is to prove the X-ray images enable the injected composite material to visualize the flow condition. Micro-CT scanning of composite material was performed with the metal fibers. It is effective to visualize the flow trace due to high CT number of metals.

2. Material and Methods

2.1 Casting with injection molding for composite model

Acrylic resin and wood sawdust were employed as the basement of composite material for the tissue-mimicking bone. Acrylic had a viscosity for injection. The tungsten fibers (The Nilaco Co.) of ϕ 150 μm diameter were cut 2 mm length were added to composite material as a tracer for capturing of flow behavior. (Acrylic) / (Acrylic + wood sawdust) is defined as ratio of weight. Two samples of 59 % value were prepared to observe flow behaviors at the early condition. The tungsten fibers were included in the samples with the volume ratio of 0.5%. The sample was injected to a gypsum mold with 1500 kgf/cm^2 and the load was kept for 20 min by using (COSMOS EH-23, PLUS ONE Co.,Ltd). The mold size of all samples was 20 × 20 × 30 mm. And the mixture was kept at 100 ˚C for 20 minutes. The sample was solid by heat polymerization. After the polymerization, the sample was cooled 10 min. And then, the gypsum surrounding the sample was removed for scanning the shape.

Two samples were prepared, and the volume of one (Case 1) is smaller than that of the other (Case 2) to check the volume effect to the flow.

2.2 X-ray scanning

Micro-CT (Comscantecno Co., Ltd ScanXmate-E080T) with X-ray emission device was employed to scan the sample modeling. The X-ray tomography can visualize relative position and distribution of each material and fibers. The conditions of X-ray emission of 80 kV, 100 μA, and projection 600 were applied to all samples. In order to perform grading of x-ray absorbance components for confirming the effect of fibers on the observation of flows, a software analysis with TRI/3D-VOL (RATOC SYSTEM ENGINEERING Co., Ltd.) were applied to the image. 3D reconstruction was performed for observing the 3D distribution of fibers.

3. Results and Discussion

Fig. 1 shows 3D constructed X-ray images of composite model in gypsum mold and histogram for grading of the Case 1 sample. The grading distribution could correspond qualitatively with CT number of each component in samples. When the object capturing point (the yellow line on the graph) is placed at the between two peaks, composite materials including acrylic resin, wood sawdust, and inner tungsten fiber can be observed and the surroundings such as air disappear. This means that the left peak can be the surroundings. When the object capturing point moved to right and placed at the right peak, only tungsten can be observed. This result reveals that the left peak includes all composites, however the right side of the peak would express tungsten. Fig. 2 shows original images and transmitted images by X-ray for both cases. The composite material

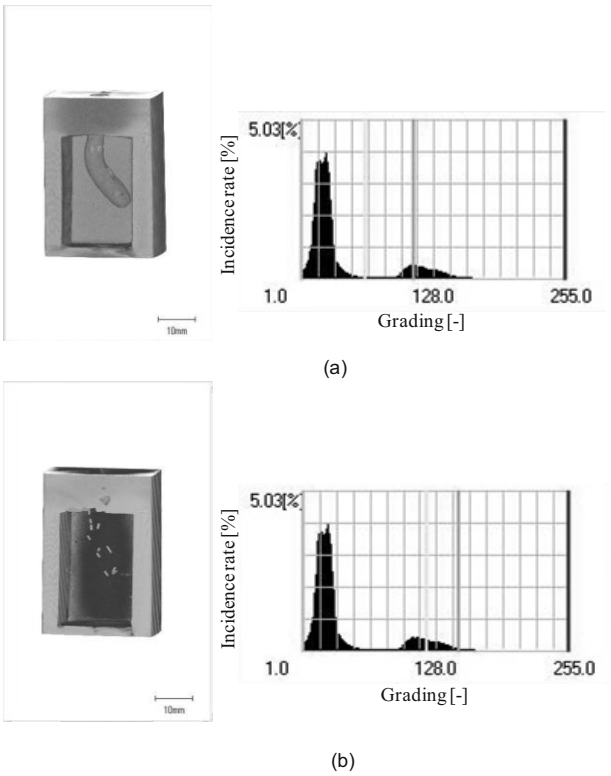

Fig.1 X-ray images with the histogram for grading of composite model. All materials can be observed in case that with the yellow line value in the upper image (a). However, only tungsten can be observed in case that the yellow line in the bottom image (b)

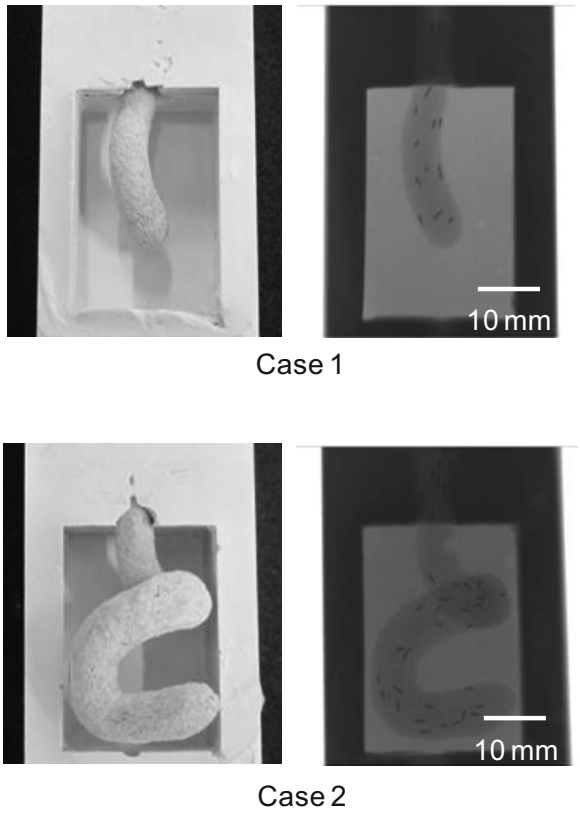

Fig. 2 Scanned composite models by X-ray. Left images shows original figure. Right side shows X-ray transmission images.

was injected into the cavity of mold and a curved shape is progressed. From the observation of curving shape, the material is not injected into the cavity uniformly, and so 3D dimensional observation is useful for analysis of injection. The shape also shows that the mixture material has high viscosity, and a plastic deformation may occur.

The tungsten fibers almost oriented along the progress direction in both cases. Fibers are arranged to the vertical direction against the progress direction at the end of progress. Furthermore, fibers were distributed uniformly in the composite model. This indicates that the fiber method is good for observation of injection molding and the injected composites in this study may have an orientation along the fibers arrangement.

4. Concluding remarks

In this report, composite model with tungsten fiber was injected into a mold and the materials were observed using micro-CT. Orientation of tungsten fibers is observed. Additionally, the distributions of fibers show that components of composite model may be mixed homogeneously. The X-ray scanning of composite materials with metal fibers will be useful method for observation of material behaviors. In order to analyze mechanical properties of composite materials, the filling process should be observed. Furthermore, motion speed of injected material will be measured by using particle tracing and this method will be constructed near future.

References

[1] S.K Najafi et al., *Journal of Applied polymer Science*, **100**, (2006), 3641-3645
[2] R. Bouza et al., *Journal of Applied polymer Science*, **102**, (2006), 6028-6036
[3] N. Sombatsompop et al., *Journal of Applied polymer Science*, **102**, (2006), 1896-1905
[4] P. Turgut, *Building and Environment*, **42**, (2006), 3801-3807
[5] K. Kalaitzidou et al., *POLYMER ENGINERRING AND SCIENCE*, (2007), 1796-1803
[6] N, Karakaya, et al., *POLYMER ENGINERRING AND SCIENCE*, (2010), 677-688
[7] B. Andricic et al., *POLYMER ENGINERRING AND SCIENCE*, (2008), 572-577
[8] K.Ozawa et al., Proceedings of 6th World Congress on Biomechanics, 2010, pp.525
[9] O. Weber et al., *Journal of Material Science*, **46**, (2011), 3568-3573
[10] S. Yun Fu et al., *Journal of Material Science*, **37**, (2002), 3067-3074
[11] H. Yen Ng et al., *POLYMER COMPOSITES*, (2005), 66-73
[12]B. Hausnerova, et al., *Polymer Science Series A*, **48**, (2006), 951-960

Eighth International Conference on Flow Dynamics
November 9 - November 11, 2011

PIV Measurement of Steady Flow in PVA Model with Compliant Wall as Cerebral Aneurysm

Shuya Shida, Hiroyuki Kosukegawa, and Makoto Ohta
Institute of Fluid Science, Tohoku University,
2-1-1 Katahira, Aoba-ku, Sendai, Miyagi, 980-8577, Japan
shida@biofluid.ifs.tohoku.ac.jp

ABSTRACT

The rupture of a cerebral aneurysm is life-threatening. Previous studies have predicted that the hemodynamics in an aneurysm are related to the rupture. In the present research, we focused on Poly (Vinyl Alcohol) hydrogel (PVA-H) as a material for use in aneurismal models and observed the flow in a PVA-H model as a compliant model to compare the flow with that in a silicone model as a rigid model with Particle Image Velocimetry. Steady flow of an intra-aneurysm in the PVA-H model and the silicone model are found to be similar to each other. In future works, pulsatile flow experiment should be carried out to evaluate effect of wall motion.

1. Introduction

The rupture of a cerebral aneurysm, resulting from cerebrovascular disease, can cause a life-threatening pathological condition such as subarachnoidal hemorrhage. The initiation, development, and rupture of cerebral aneurysms are predicted to be caused by hemodynamics such as blood flow and wall shear stress. To investigate the relationships between hemodynamic factors and cerebral aneurysms, previous studies have carried out measurement of intra-aneurysmal blood flow using blood flow simulation by CFD (Computed Fluid Dynamics) [1]-[4]. And, revealing the hemodynamics in an aneurysm is essential to prevention, proper diagnosis and treatment of an aneurysm.

Although various approaches are taken to examine the relationships between hemodynamics and aneurysms, the results of *in vivo* measurements cannot be discussed quantitatively. Thus, Computational Fluid Dynamics (CFD) and *in vitro* measurement are usually focused on. In CFD study, although most research has used a rigid model, in recent years, Fluid-Structure Interaction (FSI) study of wall motion has usually been carried out because FSI can realize *in vivo* vessel compliant behavior [5],[6]. Therefore, the effect of vessel compliance on hemodynamics should be also examined by an *in vitro* measurement to evaluate the results of CFD and *in vivo* measurement.

The model material is one of the important factors for *in vitro* measurement system elements. However, conventional model materials such as silicone are not enough to reproduce an in vivo blood flow with respect to the mechanical properties. To meet this need, Ohta et al. [7] have introduced Poly (vinyl alcohol) hydrogel (PVA-H) used as a material of a biomodel (blood vessel phantom with mechanical properties similar to a human artery). This PVA-H biomodel has good transparency and lower surface friction compared with those of a silicone model [7]. It is indicated that a PVA-H biomodel can mimic the mechanical properties and geometry to a real vessel because the various mechanical properties of PVA-H can be modified by changing its concentration or degree of polymerization. For example, Kosukegawa et al. [8] have shown that PVA gel can have viscoelasticity near to that of a blood vessel, and Yu et al. [9] have developed an *in vitro* system with PVA-H for catheter motion tracking. However, the measurement of hemodynamics with a PVA-H model has not yet been performed because a good working fluid has not been developed. The present authors developed a working fluid for PIV measurement using the PVA-H model [10].

In the present work, we confirm the possibilities of applying PIV to steady flow in PVA-H model as a first step.

2. Method

Models made of PVA-H and silicone, respectively, were placed in the test section (Fig. 1) with sufficient entrance length (> 1 m) to allow smooth connection to the models. The models are shown in Fig. 1: (a) PVA-H straight model; (b) PVA-H aneurysmal model; and (c) silicone model (R'Tech Co., Ltd, Japan). All models were a *box-type*, having an inner flow channel of 4 mm in diameter. The inner flow channel had a sphere 10 mm in diameter that was vertical to the channel wall as an anerurysmal model. Sizes were decided referring to the values of the human intracranial artery [11], and human aneurysms [12].

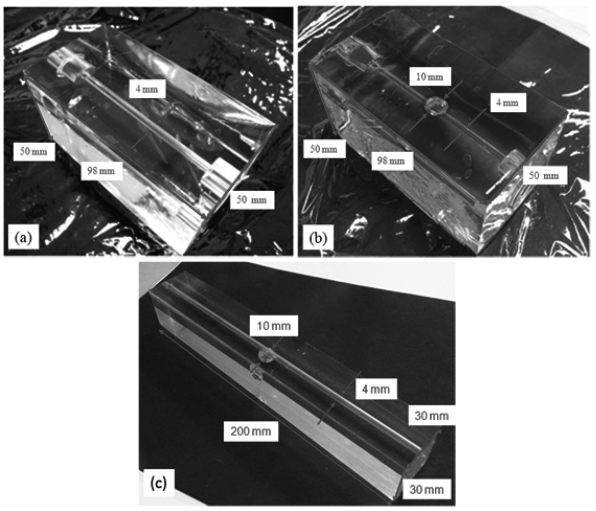

Fig. 1 Models for PIV measurements.
(a: PVA-H straight model, b: PVA-H anurysmal model, c: silicone model)

In the present work, Blood-Mimicking Fluid (BMF) as the working fluid was a mixture of aqueous solution of glycerol (gly. aq.) and aqueous solution of sodium iodide (NaI aq.) based on the method of simultaneous adjustment of refractive index and Kinematic viscosity with a mixture of gly. aq. and NaI aq. in a previous study (Shida et al., 2011). *RI* and *KV* were adjusted to match the *RI* of models and around 4 mm^2 / s, which includes human blood value, respectively.

For PIV measurement, a Nd:YAG solid laser system (BWN - 532 - 100E, B & W TEK INC.) was used to provide a nominal 1 mm-thick continuous laser sheet through the center plane of the channel with a power of 100 mW and a wavelength of 532 nm.

The images of tracer particle scattering were acquired by a high-speed camera (FASTCAM SA3, PHOTRON LIMITED, Japan). Flow rate was measured by using a coriolis flow meter (FD - SS2, KEYENCE CORPORATION, Japan). PIV analysis was carried out by integration software (DaVis version 7.2, LaVision, Inc.). Cross-correlation was performed for displacement of the particles within a 75% overlapping interrogation window with a 64 × 64 pixel size after the masking process.

To compare the theoretical solution with the experimental findings, we measured the flow profile with the PIV method and calculated the flow pattern as a Poisuelle flow. Next, the flow pattern in an aneurysm was measured.

3. Results and Discussion

Figure 2 shows PIV analysis results (left) and graphs comparing those results with the velocity profile of Poiseuille flow (right) under conditions of *Re* = 261.11. The plot of PIV results is on envelope curve. However, velocities lower than the Poiseuille flow profile were measured under the *Re* condition. The velocity result is a value 10 to 20% lower than the theoretical solution. Because this error makes it difficult to discuss the PIV result quantitatively, qualitative analysis should be carried out.

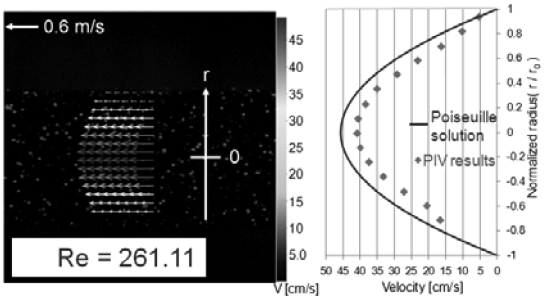

Fig. 2 PIV results for steady flow in a PVA-H straight model (left) and comparison of the results with Poiseuille flow (right).

The velocity distributions in the aneurysm are shown in Fig. 3: (a) PVA-H, (b) silicone. *Re* in the parent vessel each model is about 300. The main flow in the parent artery of both aneurysms enters the aneurysms through the distal side of the neck and both flows in the aneurysms are swirls; then the flows exit the aneurysms. So, it can be seen that the flow behaviors in the aneurysms are very similar to each other under steady flow conditions. Therefore, comparison between flow in PVA-H model and flow in silicone model under pulsatile flow condition would be reasonable for examining the effect of wall motion as next step.

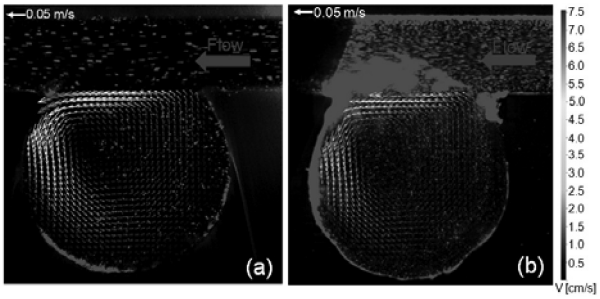

Fig. 3 PIV results for steady flow in an aneurysm model; (a) PVA-H and (b) silicone.

4. Concluding remarks

PIV measurement of steady flow in the PVA-H compliant wall model and the silicone rigid wall model was carried out to examine the possibility of applying the PIV method to flow in the PVA-H model. Although a margin of error was observed in PVA model, qualitative discussion would be possible.

Acknowledgements

This work was supported by Tohoku University Global COE program.

References

[1] D. A. Steinman et al., AJNR Am J Neuroradiol, **24** (2003), pp. 559-566.
[2] M. Shojima et al., Stroke, **35** (2004), pp. 2500-2505.
[3] J. R. Cebral et al., AJNR Am J Neuroradiol, **26** (2005), pp. 2550-2559.
[4] A. Mantha et al., AJNR Am J Neuroradiol, **27** (2006), pp. 1113-1118
[5] E. S. Di Martino et al., Medical Engineering & Physics, **23** (2001), pp. 647-655.
[6] R. Torii et al., Computational Mechanics, **43** (2008), pp. 151-159.
[7] M. Ohta et al., Technol Health Care, **12** (2004), pp. 225-233.
[8] H. Kosukegawa et al., Journal of Fluid Science and Technology, **3** (2008), pp. 533-543.
[9] C. Yu et al., Journal of Biomechanical Science and Engineering, **5** (2009), pp. 11-17.
[10] S. Shida et al., In Proceedings of the ASME 2011 International Mechanical Engineering Congress & Exposition. Denver, Colorado, USA, IMECE2011 - 64388.
[11] N. Hashimoto et al., Journal of Neurosurgery, **67** (1987), pp. 903-905.
[12] H. Nakatani et al., Acta Neurochirurgica, **122** (1993), pp. 244-249.

Eighth International Conference on Flow Dynamics
November 9 - November 11, 2011

A Multi Scale Simulation on the Diffusion and Chemical Reaction of Automotive Exhaust Gas on Metal/Oxide Particles

Sunho Jung[1], Ryo Nagumo[2], Ryuji Miura[1], Ai Suzuki[2], Hideyuki Tsuboi[2], Nozomu Hatakeyama[1], Hiromitsu Takaba[1], Akira Miyamoto[1, 2].
[1]Dept. Chem. Eng., Grad. School Eng., Tohoku Univ., 6-6-10, Aoba, Aramaki, Aoba, Sendai, Miyagi, 980-8579, Japan.
[2]NICHe, Tohoku Univ., 6-6-10, Aoba, Aramaki, Aoba, Sendai, Miyagi, 980-8579, Japan.
E-mail of corresponding author: sunho@aki.che.tohoku.ac.jp

ABSTRACT

We developed a diffusion and chemical reaction simulation and investigated the influence of rare earth element doping on Pt/CeO_2 based oxide catalyst. In atomic scale simulation, we observed that the difference of adsorption energy between the doping and undoping of rare earth element in CeO_2 based oxide. The difference of adsorption energy were reflected in diffusion and reaction simulation and we model the reaction rate in NOx storage process.

1. Introduction

In recent years, extensive studies focus on the emission control of nitrogen oxide (NOx) from the lean-burn or diesel engines. The NOx storage reduction catalyst typically contains platinum (Pt) nano particles on BaO/Al_2O_3 (Pt/Ba/Al) because of the both high catalytic activity and NOx storage capacity as well as high surface area [1]. However, Pt/Ba/Al shows a low sulfur resistance. This leads to the deactivation of the NOx storage on the BaO. Besides, Pt/Ba/Al has a low NOx storage activity under low temperature. It is because the formation of the compound of NOx and BaO needs a certain level of heat.

To overcome those problems above, Pt/CeO_2 based oxide catalyst is examined due to its good performance under low temperature and high sulfur resistance [2]. Especially, extensive experimental studies have discussed the addition of rare earth element (RE) such as, lanthanum (La), praseodymium (Pr), etc. and shown significant influence of RE on the activity. To improve the NOx storage capacity, to understand the nature of its high activity and the modeling of the reaction rate are important.

In this study, we developed a diffusion and reaction simulation method for particle and reactor scale and we suggested a multi scale simulation method by combining the quantum chemistry method in atomic scale.

2. Computational Method

We used density functional theory program "$DMol^3$" for evaluation of the adsorption energy of gas molecule on the oxide surface. GGA-PW91 functional was used for the geometry optimization and energy calculation. The lattice constant of CeO_2 -ZrO_2 models were determined in accordance with the experimental value. The rare earth element (RE = La, Pr) contained models are have one oxygen vacancy with two RE atoms.

The diffusion and reaction simulation follows the material balance which has Fick's second law and reaction rate of gases as shown in (1).

$$\frac{\partial C_i}{\partial t} = -u\frac{\partial C_i}{\partial x} + D\frac{\partial^2 C_i}{\partial x^2} + \sum v_j \cdot r_j \qquad (1)$$

C_i: concentration of element i [mol/m^3] t: time [sec]
x: length of each cell [m]
v_j: stoichiometric coefficient j th reaction
r_j : reaction rate of j th reaction
u: velocity of gas [m/sec]
D: diffusion coefficient [m^2/sec]

We considered adsorption and desorption of NO and O_2 on Pt surface, NO oxidation, adsorption and desorption NO_2 on CeO_2 based oxide.

The time profile of coverage of gas on adsorption site is represented by (2) [3]

$$\frac{\partial \theta_i}{\partial t} = \frac{1}{C_{Pt}}\sum v_j \cdot r_j \qquad (2)$$

C_{Pt}: number of adsorption site on Pt particle per unit volume [mol/m^3]
We followed the diffusion coefficient of gases from Kwon et al. [4].

3. Results and Discussion

Fig. 1 shows the adsorption structure of NO_2 molecule on CeO_2-ZrO_2 (CZ), CeO_2-ZrO_2-Pr_2O_3 (CZP), CeO_2-ZrO_2-La_2O_3 (CZL). Because of the small adsorption energy on the perfect crystal surface (smaller than 5 kcal/mol), we deposited NO_2 molecule on oxygen vacancy (OV) site and optimized the structure. The adsorption energy (AE) of NO_2 on each surface structure and the O-NO distance are shown in Table 1. The AE of NO_2 is in order CZ > CZP > CZL. This order is similar

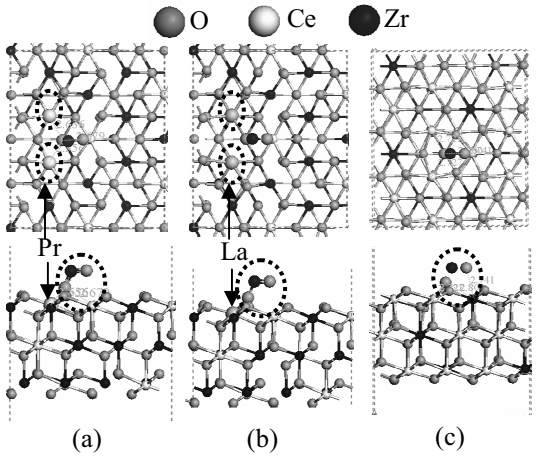

Fig. 1 The adsorbed model of NO_2 on
(a) $Ce_{0.25}Zr_{0.71}Pr_{0.04}O_{1.98}$
(b) $Ce_{0.25}Zr_{0.71}La_{0.04}O_{1.98}$
(c) $Ce_{0.75}Zr_{0.25}O_2$

to the order of valence number of Ce, Pr, La. We found that NO_2 adsorbs on the OV site and the unstable state of oxygen vacancy on CZ leads to the large AE. We predict the distance of O-NO typically becomes longer when the molecule strongly adsorbs on the surface. We could not find any relationship between AE and distance of O-NO.

The result of the order of adsorption energy was used as the kinetic parameter in the diffusion reaction simulation. The U shape tube was assumed as the apparatus model in the simulation as shown in Fig. 2. We adopted the experimental condition of Rohart et al. [5] as shown in Table 2. The dashed line and solid line in Fig. 3 show the experimental and simulated trapped NOx rate values, respectively. The rate increased to the range of about 25 - 50 % at 200 – 300 ^{o}C and decreased to the range of about 50 - 10 % at 300 – 450 ^{o}C. On the other hands, Pt/CZP shows significantly high rate at low temperature. This high rate of Pt/CZP is supposed to be caused by the small AE on Pr site as shown in Table 1. Namely, the comparatively small AE on Pr site make NO_2 easy to diffuse from Pr site to Ce site. We successfully reproduced the trapped NOx rate and the atomic scale information helps to reproduce the experimental values.

4. Concluding remarks

In this manuscript, to model the NOx storage process on Pt/CeO_2 based oxide system, we reflected the difference of AE in diffusion reaction simulation and reasonably simulated the trapped NOx rate. We also observed that RE doping has significantly influence on the NOx storage capacity using a multi scale simulation method.

Table 1. Adsorption energy and bond distance of O-NO in adsorbed NO_2 .

	CeZrPr	CeZrLa	CeZr
Adsorption energy [kca/mol]	- 47.78	- 31.51	- 65.84
ON-O distance of NO_2 (Å)	1.382	1.391	1.340

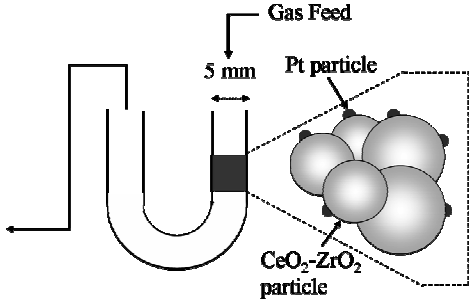

Fig. 2 Simulation model of U-shaped down flow reactor.

Table 2. Conditions for simulation of the trapped NOx [5].

	condition
Amount of Pt	1 wt%
Composition of support	CeO_2/ZrO_2= 7:3 (wt%)
Pt diameter	< 3nm
Gas feed	7.2 L/h
Gas compositon	10% O_2, 5% H_2O, 10% CO_2, 300 ppm NO in N_2

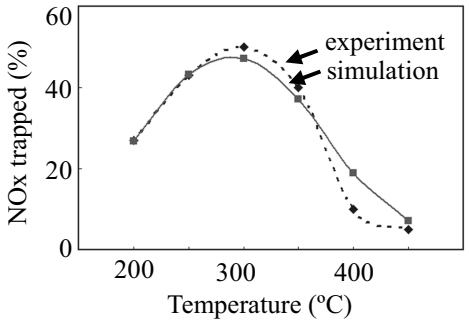

Fig. 3 Ratio of the trapped NOx on Pt/CZ after 1 minute running.

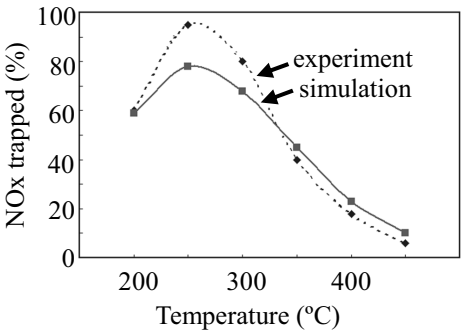

Fig. 4 Ratio of the trapped NOx on Pt/CZP after 1 minute running.

References

[1] N. Takahashi, H. Shinjoh, T. Iijima, T. Suzuki, K. Yamazaki, K. Yokota, H. Suzuki, N. Miyoshi, Catal. Today, **27** (1996), 63.
[2] L. F. Liotta, A. Macaluso, G. E. Arena, M. Livi, G. Centi, G. Deganello, Catal. Today, **75** (2002), 439.
[3] P. Koci, F. Stepanek, M. Kubicek, M. Marek, Chem. Eng. Sci., **61** (2006), 3240.
[4] H. J. Kwon, J. H. Baik, S. B. Kang, I. S. Nam, B. J. Yoon, Ind. Eng. Chem. Res. **49** (2010), 7039.
[5] E. Rohart, V. Belliere-Baca, K. Yokota, V. Harle, C. Pitois., Top. Catal., **42** (2007), 71

Eighth International Conference on Flow Dynamics
November 9 - November 11, 2011

Adaptive Autofocus for Cell Motility

Takeshi Obara[1], Yasunobu Igarashi[2] and Koichi Hashimoto[1]
[1]Graduate School of Information Sciences, Tohoku University
6-6-01 Aramaki aza aoba, Aoba-ku, Sendai City, Miyagi, 980-8579, Japan
[2]Olympus Software Technology Corp. 2951 Ishikawa-cho, Hachioji, Tokyo, 192-8507, Japan
obara@ic.is.tohoku.ac.jp

ABSTRACT

In biological and medical sciences, optical microscopes are widely used. However, moving specimens easily escape from a field of view and a focal plane of it. Therefore, we propose a new microscope that can track and autofocus a moving specimen. A specimen is put back inside of the field of view and on the focal plane by visual feedback controlled microscope stage. The autofocus algorithm is fast (requires only one image) and corrected adaptively. A paramecium was tracked and autofocused during 10 seconds. We believe that the proposed microscope is helpful to research cell motility.

1. Introduction

Many microorganisms sense stimuli from the environment[1-2]. Then they move in order to approach better environment or avoid worse one[3]. This function, motility, is essential for them. However, there is a dilemma to research it. When we observe them in microscopic magnification, they easily escape from a field of view. When in macroscopic magnification, we cannot get detailed and bright images. To solve this dilemma, we propose "Tracking and Autofocus Microscope" that can observe microorganisms in both microscopic magnification and macroscopic area at the same time.

2. Method

2.1 Outline

The proposed microscope was mainly composed of a optical microscope (Bx 51, Olympus), a high-speed camera (CPV3, Camera part, 128 x 128 [pixel], 1 [KHz], Hamamatsu Photonics K. K.), an image processor (CPV3, Processor part, 128 x 128 processing elements, 12.5 [MHz]), a PC (OS: RT-Linux, CPU: Pentium4 1.7[GHz]) and an XYZ stage (special order product, Accuracy: XY 2.5 [μm], Z 1 [μm] HEPHAIST). 20-times objective lens (UApo 20X3/340, Olympus) was used.

A specimen was loaded on the XYZ stage. Its bright field image was captured by the high speed camera. The image was processed by the image processor in order to evaluate position of the specimen. The XYZ stage was controlled by the PC in order to put the specimen back inside of the field of view and on the focal plane. This routine above was continued in 1 [KHz] cycle.

2.2 Z estimation

In order to estimate axial (Z) position, two estimators L and F were used (Fig. 1). L is known as one of the most adaptive estimators against the observation conditions [4]. L is a convex function against Z and has a peak when the specimen exists on the focal plane. However, in order to find the peak, long time is required to compare many images above and below of the specimen. L is adaptive and slow estimator.

F is based on a fringe pattern around the cell boundary as a result of diffraction [5]. F can be approximated as a monotone increasing function near the focal plane. In order to autofocus using F, only one image is required to compare with $F_{Z=0}$. However, $F_{Z=0}$ can be different among individuals (18.0 ± 6.8 in 10 paramecia) because $F_{Z=0}$ depends on specimen's shape, transparency, etc. F is not adaptive and fast estimator.

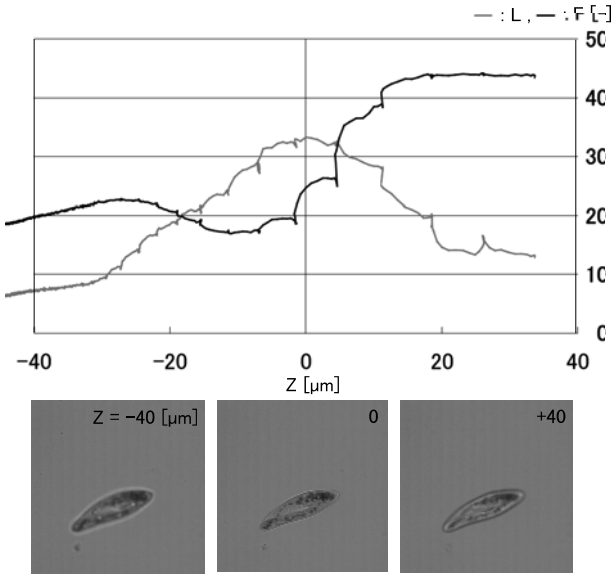

Fig. 1 An immobilized paramecium's images, image features L and F vs Z position. L is averaged Laplacian. F is subtraction value between the averages of brightness outside and inside of the cell membrane. Where Z = 0, the paramecium is on focal plane. The paramecium's thickness is approximately 40 [μm].

Therefore, we propose adaptive and fast autofocus method as shown below; 1) wide-angle scanning to find where L becomes maximum, 2) correcting $F_{Z=0}$ where L becomes maximum, 3) fast autofocus using F and $F_{Z=0}$.

3. Results and Discussion

The proposed autofocus and tracking were performed to a freely moving paramecium (*P. multimicronucleatum*). Its time lapse images are shown in Fig. 2 and its Z trajectory is shown in Fig. 3. When *t = 0 [ms]*, tracking was automatically started because the

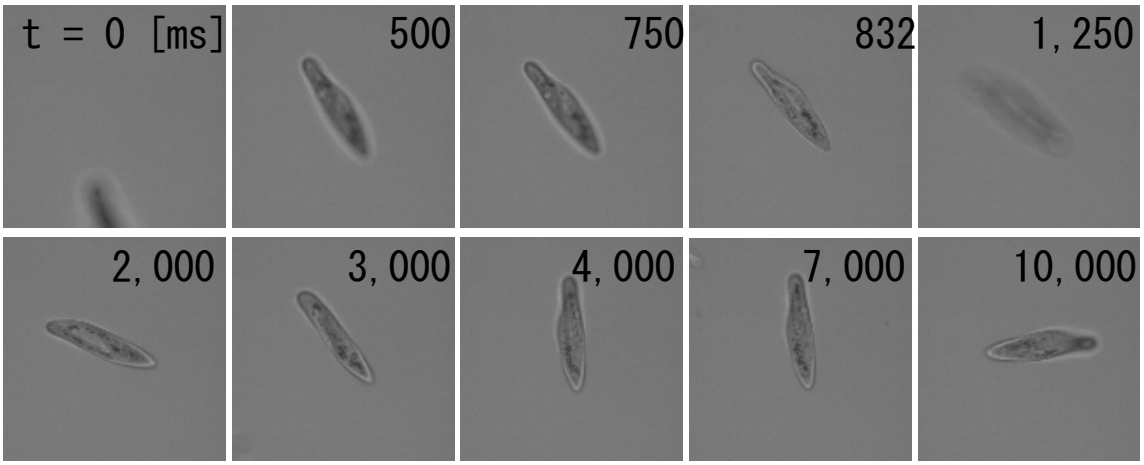

Fig. 2 Time lapse of bright field images of a freely moving paramecium. Time stamps are on upsides of each images.

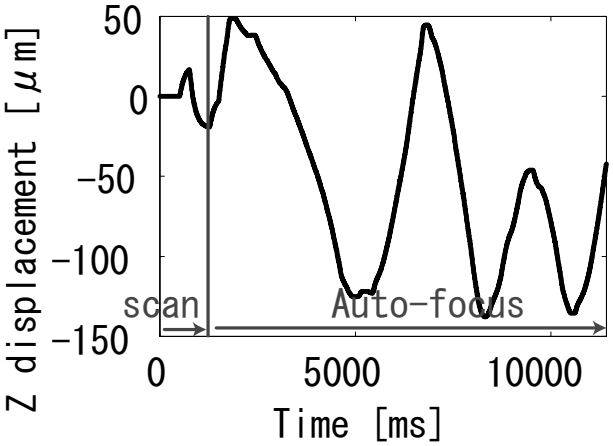

Fig. 3 Reconstructed Z (axial) trajectory of a freely moving paramecium.

paramecium came into the field of view. When t = 500 [ms], wide-angle scanning was started. Scanning range was ± 20 [μm] and its time length was 750 [ms]. When t = 832 [ms], L became maximum and $F_{Z=0}$ was corrected. When t = 1,250 [ms], correcting $F_{Z=0}$ was finished and autofocus was started. When t = 12,000 [ms], observation was stopped because the recording time of the high-speed camera was ran out.

Comparing the images from t =2,000 to 10,000 [ms] with the image when t = 832 [ms] ($F_{Z=0}$ was corrected), focus had kept good. This shows that $F_{Z=0}$ correction and autofocus were done adaptively and successfully.

Paramecia swim very fast as compared with their body size, 5 [diameter/s]. They must go out of the field of the focal plane within 1 [s]. Actually the target paramecium swam in 200 [μm] range in 2 [s]. Its range is much larger than the depth of field (0.5[μm]) of the objective lens and the paramecium's body thickness (approximately 40 [μm]). It is plausible that the paramecium hit the chamber's ceil (where Z = 50 [μm]) and base (where Z = -150 [μm]), and turned quickly.

While the paramecium moved quickly and widely, it had been observed for 10 [s]. Without tracking and autofocusing, it must be unable to observe a freely moving paramecium in both microscopic magnification (20-times) and macroscopic range (200 [μm]). The proposed system can be applied to other microorganisms to research their motility.

4. Concluding remarks

Proposed microscope can track and autofocus a fast moving cell. The autofocus algorithm is fast (requires only one image) and corrected adaptively. We believe it is helpful to research cell motility in both microscopic magnification and macroscopic area.

References

[1] Y. Nakaoka, F. Oosawa, "Temperature-Sensitive Behavior of Paramecium caudatum", J.PROTOZOOL, Vol24, pp. 575-580, 1977

[2] A. Ogura and H. Machemer. "Distribution of mechanoreceptor channels in the Paramecium surface membrane". Journal of Comparative Physiology・A 135, pp.233-242, 1980.

[3] H. S. Jennings. "Behavior of the Lower Organisms", Columbia University Press, 1923.

[4] F. C. A. Groen, I. T. Young, and G. Ligthart, "A comparison of different focus functions for use in autofocus algorithms," Cytometry, pp. 81–91, 1985.

[5] H. Oku, Theodorus, K. Hashimoto, M. Ishikawa, "High-speed Focusing of Cells Using Depth-From-Diffraction Method", 2006 IEEE International Conference on Robotics and Automation / Proceedings, pp.2626-2641, 2006

Eighth International Conference on Flow Dynamics
November 9 - November 11, 2011

Molecular Dynamics Study of Proton and Water Transfer in Polyelectrolyte Membrane

Takuya Mabuchi[a], and Takashi Tokumasu[b]
[a]Graduate School of Engineering, Tohoku University, Sendai, Miyagi 980-8577 Japan
[b]Institute of Fluid Science, Tohoku University, Sendai, Miyagi 980-8577 Japan
mabuchi@nanoint.ifs.tohoku.ac.jp

ABSTRACT

Protons transfer in polyelectrolyte membrane by both Vehicle and Grotthus mechanisms. This study describes the property of proton and water transfer in perfluorosulfonic acid (PFSA) membrane using molecular dynamics (MD) simulation in view of both Vehicle and Grotthus mechanisms. To treat Grotthus mechanism, Empirical Valence Bond (EVB) method was introduced to MD simulation. From this analysis, some perception of the structure of water cluster and the diffusivity of water and proton in PFSA membrane was derived.

1. Introduction

Polymer electrolyte fuel cells (PEFC) are one of the most promising systems for next-generation power supplies. They can be a reliable method to produce efficient and environmentally friendly energy for many uses. A polymer electrolyte membrane (PEM) where protons transfer from anode to cathode is used in PEFC. Power generating efficiency depends on proton transferring efficiency in PEM, and proton transferring property is related to nanoscale structure of water and PFSA. In recent years, attention is focused on analysis of the fundamental process of proton transfer in these membranes at microscopic level. In PEMs, it is considered that protons transfer with two mechanisms. One is that protons transfer normally as H_3O^+, called Vehicle mechanism, and the other is that protons transfer by hopping along hydrogen bond network formed by water molecules, called Grotthus mechanism which increases the ability of proton diffusion considerably.

In this study, we analyzed proton and water transferring mechanism in PFSA by MD simulation to understand a phenomenon of proton and water transferring in PFSA at molecular-scale (only the result of proton transferring was described in this paper because of the paper limitation). We treat not only Vehicle mechanism which has been broadly analyzed, but also Grotthus mechanism by adopting Empirical Valence Bond (EVB) method [1] as proton transferring mechanisms. Without using the existing model [1], we analyzed the simulation with a more reliable model; the potential energy barrier of proton hopping in EVB method was adjusted to the computational result of Density Functional Theory (DFT) to replicate the experimental value of diffusion coefficient of oxonium ions in water. In analysis of PFSA, by changing water content as a parameter, structures and transferring properties of water molecules and oxonium ions were researched.

2. Simulation Method

The PFSA was used as PEMs, which chemical structure simulated in the present work is shown in Fig.1. It was assumed that all sulfo groups SO_3H were ionized to H^+ and SO_3^- in water. PFSA consists of hydrophilic SO_3^- -terminated pendants spaced evenly by five nonpolar $–CF_2$-CF_2- monomers (N) that form a hydrophobic backbone. We generated PFSA by linking the polar monomeric unit (P) to the end of the nonpolar monomeric unit N_5, repeating the procedure five times to obtain $(N_6P)_5$, in the notation of Jang et al.[2], and terminating the two ends with F. The potential model for PFSA was based on the Dreiding force field as referred to previous studies by other authors [3] [4] [5]. F3C water model, which diffusion coefficient was adjusted to the experimental values, was used for water molecules and oxonium ions except for charging parameters [6].

In the initial situation, 25 PFSA molecules were added randomly in the simulation box which is configured to $x \times y \times z = 100 \times 100 \times 100$ Å^3.

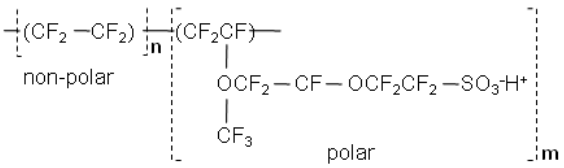

Fig.1 Chemical structure of PFSA

After PFSA was arranged, oxonium ions and water molecules were added at random position. To ensure charge neutrality, a total of 125 oxonium ions were added in this simulation and the membrane is solvated by adding water molecules corresponding to a given λ. The parameter λ indicates the ratio of the number of water molecules to that of SO_3^- ($N_{H2O,\ H3O+}/N_{SO3-}$), and is changed to λ=3, 5, 7, 9, and 11 respectively.

Before the annealing, the simulation box was shrunk gradually to get the experimental density. This density reported here for membrane equivalent weight of 1148 amu is based on a fit to experiment by Morris and Sun [7]. The annealing procedure to establish equilibrium state was carried out composed of five steps as follows [8] : 1. *NPT* MD simulation for 15 ps at 350 K (velocity scaling for constant temperature and changing box-shape for constant pressure are used[9]); 2. *NVT* MD simulation

for 15 ps while the temperature was gradually increased from 350K to 650 K; 3. *NVT* MD simulation for 10 ps at 650 K; 4. *NVT* MD simulation for 15 ps while cooling the temperature gradually down to the target temperature which is 350 K; 5. *NPT* MD simulation for 15 ps at 350 K. During this 90 ps annealing procedure, only Vehicle mechanism was treated and the time step was configured to 1fs. After the annealing, we confirmed that the system is in equilibrium state since the absolute pressure and the temperature is stable at 0 MPa and 350K each without using any thermal or barostat. Then, *NVE* MD simulation was performed to record data such as Radial Distribution Function (RDF) and Mean Square Displacement (MSD).

3. Results and Discussion

The transferring properties of oxonium ions and water molecules were analyzed by MSD. Fig.2 (a) and (b) shows the MSD of oxonium ions and water molecules under the condition of different λ, and these results include only Vehicle mechanism. As shown in both Fig.2 (a) and (b), the MSD of each molecule increases as water content λ increases because sulfo groups are covered with more water molecules and oxonium ions and both have weaker interaction with SO_3^-. Experimental analysis also shows that diffusivity increases at higher water content. However, it is hardly known that which mechanism, Vehicle or Grotthus, is contributed for that. In this study, the improvement of the diffusivity is indicated with even only Vehicle mechanism, therefore Vehicle mechanism is a possible factor of the diffusivity increase. Also, the calculated diffusion coefficient at λ=11 from Fig.2 (b) was $D_{H2O}=1.2\times10^{-5}cm^2/s$ and this result implies a good reproducibility of the system comparing with the experimental results $D_{H2O}=1.0\times10^{-5}cm^2/s$ at λ=16 [10].

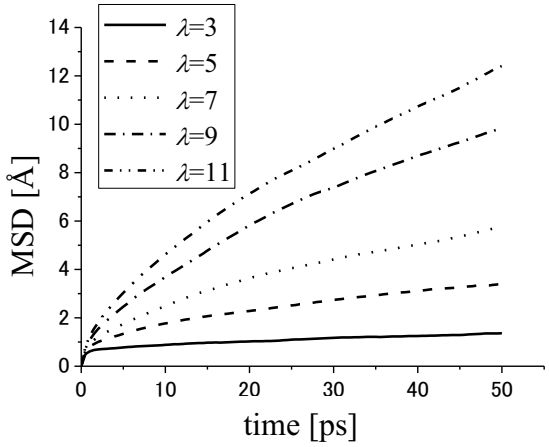

(a) MSD of oxonium ions

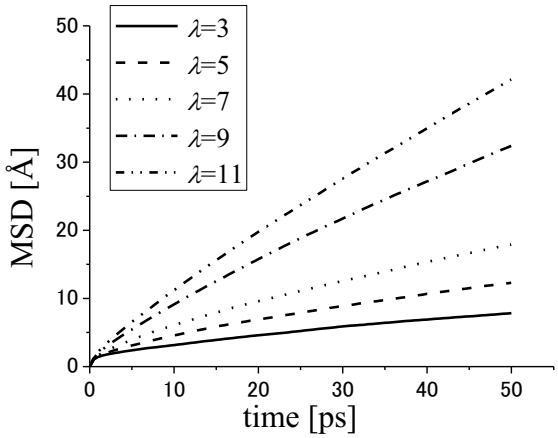

(b) MSD of water molecules

Fig.2 MSD of each λ and molecule

4. Conclusion

In this study, the property of proton and water molecule transfer in PFSA was analyzed by MD simulation including both Grotthus and Vehicle mechanism. To treat Grotthus mechanism, the EVB potential was constructed and the potential energy barrier was fit to the value of DFT.

By the analysis of MSD, it was confirmed that the mobility of oxonium ions and water molecules increased as water content λ increases. This result was attributed to thickness of solvation shells, in other words, more water molecules covered SO_3^- under the condition of higher λ, and as the result, there are more oxonium ions and water molecules that have weaker interaction with SO_3^-.

References

[1] Shengting, C.; Junwu, L.; Myvizhi, E. S.; David, J. K.; Brian, J. E.; William V. S.; *J. Phys. Chem. B*, **111(9)**, 2208 (2007)

[2] Yujie, W.; Hanning, C.; Feng, W.; Francesco, P.; Gregory, A. V.; *J. Chemical Phys.*, **112**, 467 (2008)

[3] S. L. Mayo; B. D. Olafson; W. A. Goddard Ⅲ, *J. Phys Chem.*, **94**, 8897 (1990)

[4] S. S. Jang; V. Molinero; T. Cagin, W. A. Goddard Ⅲ, *J. Phys. Chem. B*, **108**, 3149 (2004)

[5] T. Li; A. Wlaschin, P. B. Balbuena, *Ind. Eng. Chem. Res.*, **40**, 4789 (2001)

[6] M. Levitt, M. Hirshberg, R. Sharon, K. E. Laidig, and V. Daggett, *J. Phys. Chem.*, **101**, 5051-5061 , (1997)

[7] Morris, D. R.; Sun, X.; *j. Appl. Polym. Sci.*; **50**, 1445 (1993)

[8] Iordan, H. H.; Stephen, J. P.; Reginald, P., *J. Phys. Chem. B*, **112(10)**, 2937 (2008)

[9] Allen, M. P.; Tildersley, D. J. *Computer simulations of Liquids*; Oxford University Press; New York, 1989.

[10] R. Paul; S. J. Paddison, *J. Chem. Phys.*, 123, 224704, (2005)

Eighth International Conference on Flow Dynamics
November 9 - November 11, 2011

Molecular Dynamics Study of Oxygen Permeation in the Ionomer on Pt Catalyst

Kiminori Sakai, Takashi Tokumasu,
Tohoku University, Katahira 2-1-1, Sendai, Miyagi
sakai@nanoint.ifs.tohoku.ac.jp

ABSTRACT

In polymer electrolyte membrane fuel cell (PEFC) cathode catalyst layer, PFSA ionomer with which the catalyst is covered is very important on the point of transferring protons to the catalytic surface in the cathode side. On the other hand, an ionomer interferes with oxygen permeation to the catalytic surface. The mechanism of oxygen permeation through an ionomer was not analyzed in detail. In this research, we constructed the system of ionomer on the platinum surface by using molecular dynamics study, and investigated the dependence of water content rate in the ionomer on permeability.

1. Introduction

Fuel cell is expected for a new energy conversion system in place of internal combustion. However, fuel cell is not widespread in general while there is such an advantage. Because an actual power generation efficiency of the system is not high, fuel cell is expensive and durability is low. So, it is necessary to understand the mechanism of PEFC for improving these problems.

PEFC is composed of membrane electrode assemblies (MEAs) that consist of a polymer electrolyte membrane (PEM), catalyst layers (CLs), microporous layers (MPLs), and gas diffusion layers (GDLs). In CLs, Pt catalyst is the particle which diameter is 3~4 nm and it is on a supported carbon. In addition, it is covered with an ionomer because of proton transfer to catalyst surface. The ionomer improves ability of proton transfer but it reduces oxygen permeability to Pt surface and therefore dissociative adsorption reaction becomes slow. The phenomenon is larger when the ionomer is thicker. It is necessary to research the oxygen permeation and proton transfer in such a situation to raise efficiency. However, it is difficult to analyze by experiment because these phenomena occur in the microscopic structure. For this reason, it is necessary to analyze the oxygen permeation and the proton transfer at the microscopic point of view.

In this research, we made the system of the ionomer which consist of PFSA membrane on Pt catalyst surface and distributed oxygen molecules in the space of simulation box. In this system, we analyzed the dependence of water content on oxygen permeability to the ionomer.

2. Method

In this research, we simulated the system of the catalytic layer of the cathode side by molecular dynamics simulation. This system includes Pt wall, PFSA, water, oxonium ion and oxygen molecule as shown in Fig.1. This model was represented the ionomer on Pt surface in the CLs and we didn't consider the existence of carbon and shape of Pt particle.

Pt-Pt interactions were represented by spring mass model considering nearest neighbor atom, the spring constant and equiliburium distance were set at k = 46.8 N/m and r_e = 0.392 nm, respectively. PFSA was represented by the flexible model which interaction was expressed by the DREIDING force field [1]. The rigid SPC/E model was adopted for water, and for the oxonium ion, we selected similar rigid model with four point charges and a Lennard Jones potential imposed at their oxygen. A two centered Lennard Jones model was used for oxygen molecule. The interaction between Pt and water was represented by Spohr and Heinzinger (SH) potential [2] and that between Pt and oxonium ion was represented by the potential that the number of hydrogen atoms changes from two to three. The intermolecular potentials between PFSA and water were represented by the combination of Lennard Jones potential and coulomb interaction. The intermolecular potential between PFSA and oxonium ion was similar to the above. The Ewald method was used for calculating coulomb interaction. The others were connected by LJ potential, calculated using Lorentz-Berthelot mixing rules but the interaction between Pt-O_2 was not considered because we assumed all permeated oxygen dissociated at Pt surface and this reaction speed was faster than oxygen dissolution or diffusion. So, inorderto erase them, we didn't set the interaction.

Fig.1 shows the system of this research. The platinum surface was placed at the bottom of simulation box and ionomer which was composed of hydrated PFSA was place on the surface. In the dotted line box, we adjusted the number of oxygen molecule to be constant in the space between the interface of ionomer and the top of simulation box to keep the pressure of oxygen molecule constant. Also, we transferred the oxygen molecule which permeated through platinum surface to the gas space. By the system, the gradient of concentration of oxygen molecule made up in the ionomer.

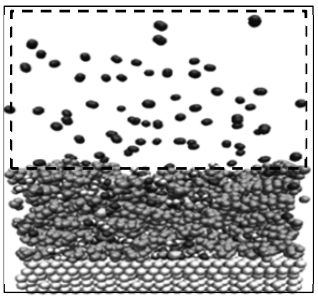

Fig.1 The schematic diagram of this system

3. Results and Discussion

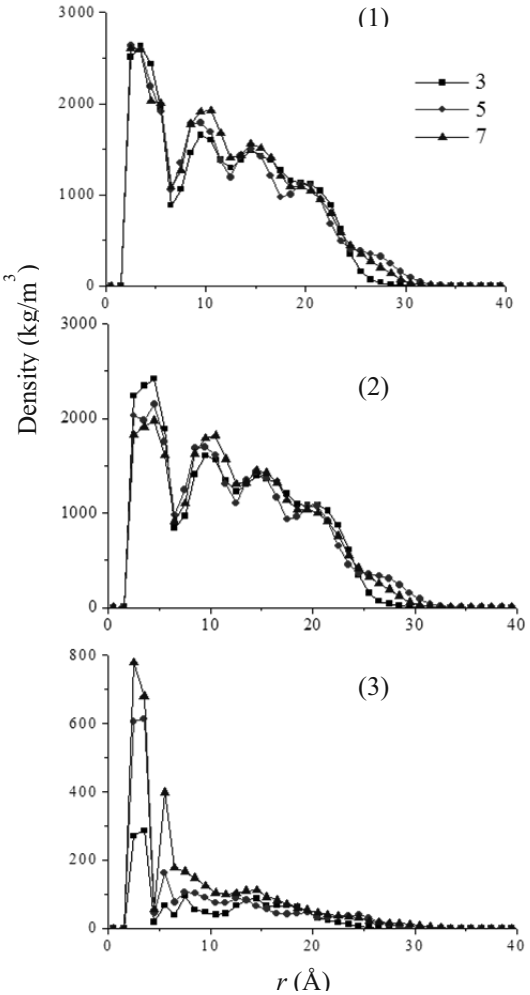

Fig.2 Density distribution of (1)ionomer, (2)PFSA and (3)water. Black line is γ=3, red line is 5 and blue line is 7, respectively

Density distribution of ionomer (PFSA and water), PFSA and water molecules are shown in Fig.2. From upper side, the results of (1)ionomer, (2)PFSA and (3)water molecules distribution in the case of water content rate γ = 3, 5, 7, respectively are shown. Here, x axis is the distance of Pt surface r and y axis is density. From Fig.2 (1), it is said that PFSA membrane gathers toward the catalyst surface. This phenomenon occurs because Pt strongly attracts the other molecules. Also, the thickness of ionomer is about 20~30 Å in all cases and density of ionomer increases as water content rate increases at r = 8~14 Å. However, it is said that the density of PFSA membrane which contain water molecule decreases as water content rate increases and this result is different from this simulation result. In the future, it is necessary to verify whether this reason depends on annealing method or the property of ionomer. From Fig.2 (2) and (3), the density of PFSA on the Pt surface decreases as water content rate increases, which indicates that water molecule adsorbs Pt surface stronger than PFSA atoms. This reason is why the interaction between water and Pt is stronger than that between PFSA and Pt. From this result, it is said that the interaction between PFSA and Pt is very important in this calculation.

Density distribution of oxygen molecule is shown in Fig.2. From this figure, the density rapidly decreases at r = 8Å in all cases. We thought that this reason is why the ionomer gathered on the Pt surface and filled in the void where oxygen molecule went through because in all cases, the densities of ionomer were same but oxygen permeation changed by the change of the density of liquid molecules. In particular, the densities of ionomer are same at r = 3 Å in all cases but oxygen permeated in the case of γ = 3 while it didn't permeate in the case of γ = 5, 7 because at r = 0, the density is approximately zero. Therefore, even if density of ionomer is same, oxygen permeability decreases when density of water is high because mass of water molecule is less than mass of PFSA and many molecules gathered on the Pt catalyst surface. From this result, we think that void distribution in the ionomer influences oxygen permeation.

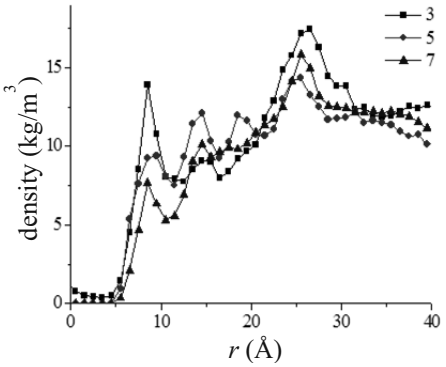

Fig.3 Density distribution of oxygen molecule

4. Conclusion

The oxygen permeability in the ionomer of catalyst surface was examined by using molecular dynamics simulation. In this simulation, PFSA ionomer adsorbed on Pt surface and forms a thin film structure and water adsorbed stronger on the Pt surface, Moreover, It is said that the oxygen permeability decreased as water content rate increased. In the future, we will verify the potentials between oxygen and water, oxygen and PFSA by means of static calculation of solubility and sample the void distribution in the ionomer.

5. Acknowledgment

This research is supported by the super computer system of Institute of Fluid Science, Tohoku University.

References

[1] S. L. Mayo, B. D. Olafson, and W. A. Goddard III, *J. Phys. Chem.*, **94**, 8897-8909 , (1990)

[2] Spohr, E.; *J. Phys. Chem.***93,** 8254(1989)

Analysis of Axisymmetric Radiative Heat Transfer in Biological Tissue using the Radiation Element Method

Shigenao Maruyama[1], Yoshiyuki Sato[2], Atsushi Sakurai[3], Junnosuke Okajima[1], Mehdi Baneshi[1], Atsuki Komiya[1]
[1] Institute of Fluid Science, Tohoku University, 2-1-1, Katahira, Aoba-ku, Sendai, 980-8577, Japan
[2] Graduate School of Engineering, Tohoku University, 6-6 Aoba, Aramaki-aza, Aoba-ku, Sendai, 980-8579, Japan
[3] Dep. of Mechanical & Production Eng., Faculty of Eng., Niigata University, Niigata, 950-2181, Japan
sato.y@pixy.ifs.tohoku.ac.jp

ABSTRACT

The objective of this study is to evaluate the effect of radiative heat transfer on the bioheat transfer in the biological tissue for safe laser therapy. The analysis is important to accurately estimate radiative propagation and heat transfer in the biological tissue. In this study, the radiative heat transfer is solved with the Radiation Element Method by Ray Emission Model (REM^2), and then coupled with axisymmetric bioheat transfer. The radiative propagation and heat transfer effect of laser power and beam radius are evaluated for biological tissue.

1. Introduction

Radiative heat transfer in biological tissue is encountered in applications such as laser therapy for a skin disease. For example, it is used to be such as treatment of cancer and skin disease. However, heat transfer in the biological tissue is difficult to measure experimentally.

The analysis of laser therapy has been conducted for a long time. Guo et al, simulated laser therapy using the ultrafast pulse laser. They used Transient Discrete Ordinate Method (TDOM) to calculate the radiative transfer. In biological tissue, the ultrafast radiative heat transfer of the focused beam is simulated by TDOM and the transient Pennes bioheat equation is solved numerically[(1)]. Moreover, Sakurai et al. calculate radiative heat transfer in laser therapy by Radiation Element Method by Ray Emission Model (REM^2)[(2-3)]. REM^2 employs a deterministic approach so that the computational speed is faster than Monte Carlo method.

However, previous research by using REM^2 is unrealistic because of one-dimensional calculation[(4)]. In order to estimate the exact radiative heat transfer, the consideration of 3-D effect is required. In the case of laser therapy, 3-D transport phenomenon can be approximated by 2-D axisymmetry. In this study, in order to achieve a safer laser therapy, the axisymmetric two-dimensional radiative and bioheat transfer is solved, and to determine the temperature distribution in biological tissue is determined.

2. Computational method

Figure 1 shows the two dimensional axisymmetric model of radiative and bioheat transfer. The bioheat transfer equation for light with internal heat generation duo to laser heating is given by

$$\rho c_p \frac{\partial T}{\partial t} = k\nabla^2 T + q_{met} + \rho_b c_b \omega_b \left(T_b - T\right) - \nabla q_R , \tag{1}$$

where ρ is the density of biological tissue, ρ_b is the density of blood, ω_b is blood perfusion rate, c_p is the specific heat of blood, T is the temperature, T_b is the temperature in blood, q_{met} is metabolic heat generation rate, q_R is the radiative heat flux. Light propagation inside biological tissue is described by the radiative transfer equation,

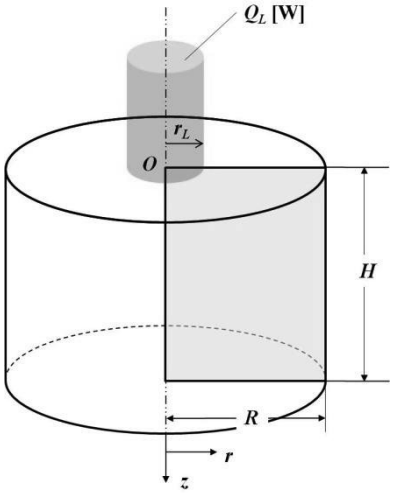

Fig. 1 The axisymmetric radiation and heat transfer model inside a biological tissue

$$\frac{dI_\lambda(\vec{r},\hat{s})}{dS} = \beta\Big[-I_\lambda(\vec{r},\hat{s}) + (1-\omega) I_{b,\lambda}(T) + \frac{\omega}{4\pi}\int_{4\pi} I_\lambda(\vec{r},\hat{s}')\Phi_\lambda(\hat{s}'\to\hat{s})\,d\Omega'\Big], \tag{2}$$

The positional and directional radiation intensity I_λ is obtained by solving eq. (2). The divergence of the radiative heat flux is given by

$$\nabla q_{R,i} = \frac{1}{V_i}\left(A_i^R \varepsilon_i E_{b,i} - \sum_{j=1}^{K} F_{j,i}^A Q_{R,j}\right), \tag{3}$$

where i is number of element, V_i is volume, A_i^R is effective area, ε_i is emissivity, $F_{j,i}^A$ is absorption view factor, $E_{b,i}$ is black body emissive power, $Q_{R,j}$ is radiative energy. The effective area and absorption view factor are defined as follows

$$A_i^R \equiv \frac{1}{\pi}\int_{4\pi} A(\hat{s})\left[1-\exp\left(-\beta_\lambda \bar{S}\right)\right] d\Omega , \tag{4}$$

$$F_{j,i}^A = \frac{\varepsilon_i}{\left(1-\omega_i^S\right)} F_{j,i}^E , \tag{5}$$

Thermal and optical properties are tabulated in Table 1. Laser power Q_L is changed from 0.05 to 2.0 W, and beam spot radius r_L is changed from 1 to 4 mm.

Table 1. Thermal and optical properties of dermis tissue[5-6]

Specific heat, c_p [J/(kg·K)]	3300
Density, ρ [kg/m^3]	1200
Thermal conductivity, k [W/(m·K)]	0.45
Blood perfusion rate, ω_b [1/s]	1.25×10^{-3}
Metabolic rate, q_{met} [W/m^3]	1364
Absorption coefficient, κ [1/m]	16.5
Scattering coefficient, σ_s [1/m]	17100

3. Results and Discussion

To evaluate the effect of laser power on the temperature distribution, beam radius and irradiation time are set at constant. Figure 2 shows the temperature distribution on the center axis of the biological tissue with changing irradiation power. The laser power of 40 J/cm^2 is generally used for laser therapy. As shown in Fig. 2, there is risk of burning that laser of 0.5 W for 10 s is irradiated. Additionally, the heat transfer only a depth of less than 5mm.

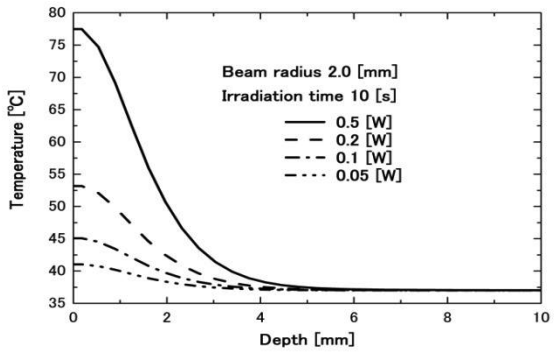

Fig. 2 Temperature distribution on the center axis of the biological tissue with changing irradiation power

To evaluate the effect of beam radius on the time variation, laser power is set at constant. Figure 3 shows the time variation of temperature for four difference beam radii at the center of surface. In addition, the temperature of beam radius of 0.1 mm reached at about 80 ℃, and the temperature converged when time is about 100 s in all cases.

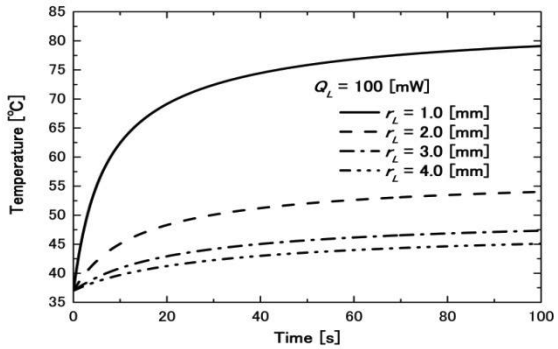

Fig. 3 Time variation of temperature at center with changing the beam radius

Figures 4 show the axisymmetric temperature distribution for different beam radius. Figure 4(a) shows high temperature region is concentrated in the spot of irradiation. Figure 4(b) shows heat transfer in r direction is larger than the case of Fig. 4(a). The temperature distribution can change by changing the beam spot at the same laser power. Moreover, in this case, irradiation time shorter than 100 s is desirable.

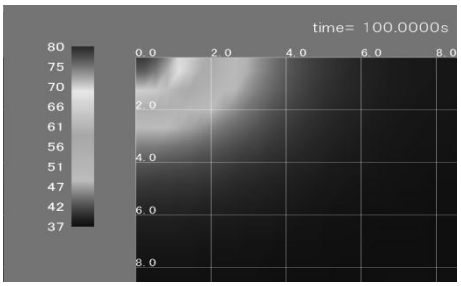

(a) Beam radius is 1 mm

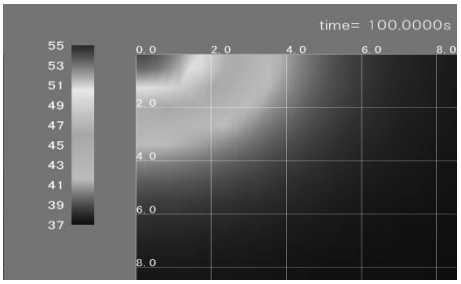

(b) Beam radius is 2 mm

Fig. 4 Comparison of heat transfer between the beam radius is 1 [mm] and 2 [mm]:

4. Conclusion

A thermal analysis combining the radiative heat transfer and bioheat transfer is developed. In this study, the following findings were obtained,

1. In order to describe a heat transfer inside biological tissue, the radiative heat transfer analysis coupled with bioheat transfer axisymmetric analysis.
2. The effect of laser power on the temperature distribution and beam radius on the time variation are evaluated.
3. The maximum temperature was high when the beam spot is small, and the larger beam spot heated up at lower temperature in a wide area.

References

[1] Z. Guo and J. Jiao, Phys. Med. Biol, **54** (2009) 4225-4241.
[2] S. Maruyama, Light Energy Engineering, Yoken-do, Tokyo (2004)(in Japanese)
[3] A. Sakurai et al., Journal of Thermal Science Technology, **4** (2009) 314-323.
[4] S. Maruyama et al., Proceeding of Bioengineering Conference, **23** (2011) 177-178.
[5] D. Fiala et al., Journal of Applied Physiology, **87** (1999) 1957-1972.
[6] A. N. Bashkatov et al., Journal of Physics D : Applied physics, **38** (2005) 2543-2555.

Eighth International Conference on Flow Dynamics
November 9 - November 11, 2011

Multi Scale Simulation on Carrier Multiplication Effect of Si Quantum Dot

Sho Hirose[1], Ryo Nagumo[2], Ryuji Miura[1], Ai Suzuki[2], Hideyuki Tsuboi[2],
Nozomu Hatakeyama[1], Hiromitsu Takaba[1], Akira Miyamoto[2, 1]
[1] Dept. Chem. Eng., Grad. School Eng., Tohoku Univ., 6-6-10 Aoba, Aramaki, Aoba-ku, Sendai 980-8579, Japan
[2] New Industry Creation Hatchery Center, Tohoku Univ., 6-6-10 Aoba, Aramaki, Aoba-ku, Sendai 980-8579, Japan
hirose@aki.che.tohoku.ac.jp

ABSTRACT

In this study, we focused on carrier multiplication effect (CME) of Si quantum dot (QD) as the method for improving the conversion efficiency of Si-QD solar cells. We researched on the suitable structure of QD for CME with computational method. Consequently, we found that the interface structure has big influence on band structure of QDs and CME. Particularly, we found that oxygen around QD have harmful effects on CME. In addition, size of QDs also influenced to them. Therefore, the optimization of QDs structures and surrounding atom is very important for improving the conversion efficiency of Si-QD solar cells.

1. Introduction

Quantum dots (QDs) solar cells have been paid atten-tion to as high-efficiency oriented solar cells. The ideal conversion efficiency of these solar cells is more than 66% [1]. However, the reported efficiencies are at most 10% [2, 3]. Therefore, a further improvement of conversion effi-ciency is needed. One of the approaches to improve the efficiency is use of carrier multiplication effect (CME). Fig. 1 shows the scheme of CME. In this effect, when an electron relaxed, some other electrons are excited by the emitted energy. Therefore, QDs solar cells can use the solar energy more efficiently compared with conventional one.

To use CME effectively, the optimization of band structure of QDs is needed. As a factor of influences to band structure of QDs, dot size and QD/bulk interface structure are suggested [4, 5]. In particular, QD/bulk inter-face structure is important because QDs are buried in other bulk semiconductor.

In this study, we focused on the effect of dot size and interface structure on CME. For the porpose, we construct-ed the Si-QD models with different size and interface structure. We calculated carrier multiplication rate (RCM) by quantum chemical calculation for each model. Then, we compared the difference between these models.

2. Method

Calculation Models

To consider the effect of dot size and interface structure, we constructed 1 nm Si-QD models. Fig. 2 shows the calculation models. In this study, difference of interface structure was considered by changing the passivating atom. Fig. 2(a) is the Si-QD model terminated by Hydrogen (H-model), and Fig. 2(b) is terminated by Hydroxyl (OH-model). We analyzed the electronic structure of each model with quantum chemical calculation. Then, we researched the effect of interface structure on band structure of QDs. Moreover, to investigate the size effect, we constructed 1.5 nm Si-QD models, and we performed the same calculation for 1.0 nm.

Carrier Multiplication Rate

To estimate the influence of change of band structure

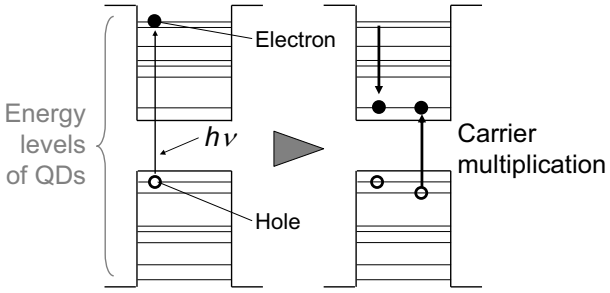

Fig.1 Carrier multiplication effect

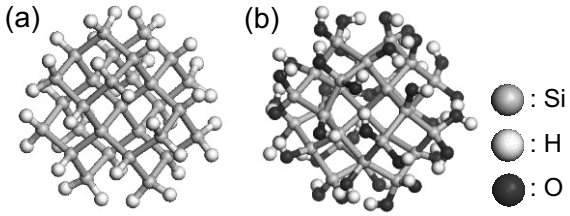

Fig.2 Si-QD model: (a) H-model ($Si_{29}H_{36}$)
(b) OH-model ($Si_{29}(OH)_{36}$)

on CME, we calculated RCM by quantum chemical calcula-tion. Because CME is the inverse Auger process, RCM is ob-tained from Coulomb interaction between

$$R_{CM} = \frac{\Gamma}{\hbar}\sum_{n}\frac{\left|\langle i|\Delta H|f_n\rangle\right|^2}{\left(E_{f_n}-E_i\right)^2+\left(\Gamma/2\right)^2} \qquad (1)$$

where $|i\rangle$ and $\langle f_x|$ are the initial and final electronic states, E_i and E_{fn} are their eigenvalues, and ΔH is the Coulomb interaction. Γ is the parameter including the influence of phonon.

3. Results and Discussion

Electronic Structure

Fig. 3 shows the partial density of states (PDOS) of H-model and OH-model, respectively. In Fig. 3(a), energy levels of Si-QD are discredited and band gap is 3.87 eV. On the other hand, in Fig. 3(b), energy levels are more continuous than those of H-model. Moreover, band gap of OH-model is 1.55 eV, about a half value

than that of H-model. From the comparison of Fig. 3, OH-model mi f ght be more suitable for carrier multiplication than H-model.

Fig. 4 shows the PDOS of 1.5 nm H-model. Comparing Figs. 3(a) and 4, energy levels of 1.5 nm of H-model becomes continuously and band gap is 2.77eV, which is 1.1 eV smaller than 1 nm H-model. On the other hand, about the OH-model, PDOS and band gap were similar for 1 nm and 1.5 nm models. This result suggests that the dot size has big influences on the band structure. In addition, it is suggested that the size effect is influenced by interface structure of QDs.

As a result, it is suggested that the band structure is greatly changed by interface structure and dot size. Then, it is thought that the CME is also influenced by interface structure. Therefore, we performed calculation of R_{CM} and researched the effect of that on CME.

Carrier Multiplication Rate

To research the effect of the difference of band structure on CME, we estimated R_{CM} for each model. Fig. 5 shows the results. In Fig. 5, R_{CM} of H-model are larger than those of OH-model, and the difference increases with increasing in the excess energy for exciting other electron (E_j - E_i - Bg). From the PDOS, OH-model seems to be suitable for carrier multiplication because of the small band gap and continuous energy levels. However, R_{CM} of OH-model is smaller than that of OH-model. This is because the molecular orbital in QDs are biased to the surrounding with OH termination. Therefore, overlap of the molecular orbital weakens and the R_{CM} decreases. As a result, it is suggested that the OH-termination have a bad influence in CME though it is effective for a decrease of band gap. It is suggested that oxygen around QDs decrease the conversion efficiency.

4. Concluding remarks

In this study, we researched on the effect of dot size and interface structure on CME. Consequently, we found that the interface structure has big influence to band structure of QDs and CME. Particularly, oxygen has harmful effect for CME. In addition, the dot size also influenced to them. Therefore, the optimization of QDs structures and surrounding atom is very important. Although we used small models in this case, we learn much knowledge with more large scale calculation.

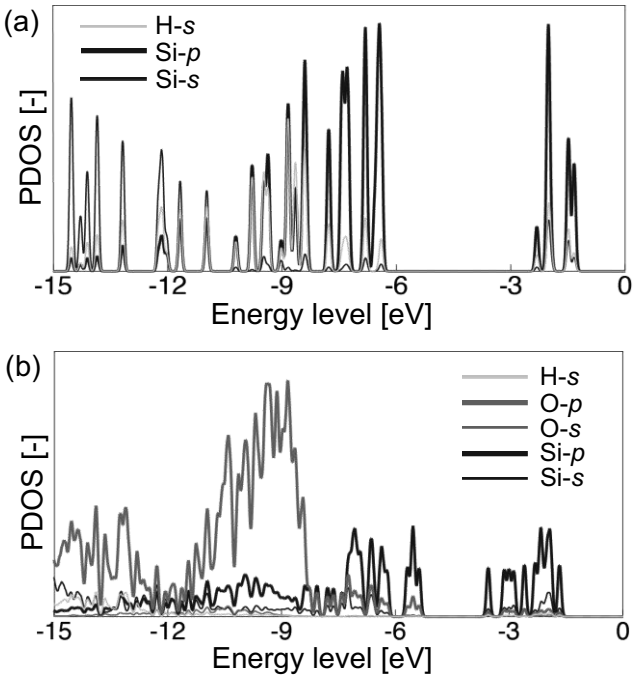

Fig.3 PDOS of 1 nm models:(a) H-model (b) OH-model

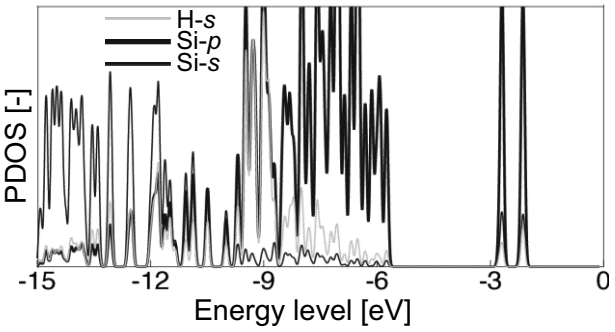

Fig.4 PDOS of 1.5 nm H-model

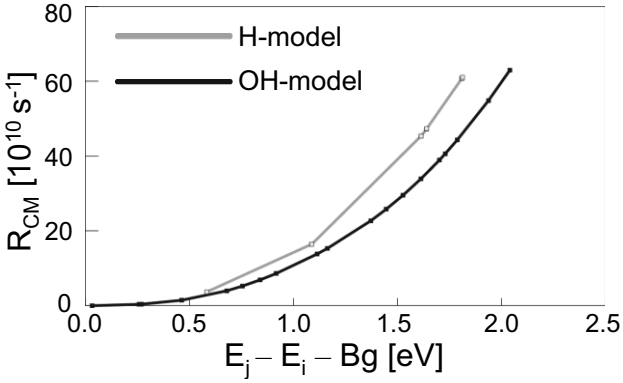

Fig.5 R_{CM} of 1 nm models

References

[1] M. Califano, A. Zunger and A. Franceschetti, Appl. Phys. Lett. 84 (2004) 2409.

[2] N. Zhao, T. P. Osedach, L. Y. Chang, S. M. Geyer, D. Wanger, M. T. Binda, A. C. Arango, M. G. Bawendi and V. Bulovic, ACS Nano 4 (2010) 3743.

[3] J. M. Luther, M. Law, M. C. Beard, Q. Song, M. O. Reese, R. J. Ellingson and A. J. Nozic, Nano Lett. 8 (2008) 3488.

[4] Z. Lin, A. Franceschetti and M. T. Lusk, ACS Nano 5 (2011) 2503.

[5] D. König, J. Rudd, M. A. Green and G. Conibeer, Sol. Energy Mater. Sol. Cells, 93 (2009) 753.

[6] L. W. Wang, M. Califano, A. Zunger and A. Franceschetti, Phys. Rev. Lett. 91 (2003) 056404.

Eighth International Conference on Flow Dynamics
November 9 - November 11, 2011

A Multi Scale Modeling of Anode Reaction in Biofuel Cell

Hiroshi Kobayashi[1], Ryo Nagumo[2], Ryuji Miura[1], Ai Suzuki[2], Hideyuki Tsuboi[2],
Nozomu Hatakeyama[1], Hiromitsu Takaba[1], Akira Miyamoto[2, 1]
[1]Dept. Chem. Eng., Grad. School Eng., Tohoku Univ., 6-6-10, Aoba, Aramaki, Aoba-ku, Sendai 980-8579, Japan
[2]NICHe, Tohoku Univ., 6-6-10 Aoba, Aramaki, Aoba-ku, Sendai 980-8579, Japan
kobayashi@aki.che.tohoku.ac.jp

ABSTRACT

To investigate the effect of diffusion of mediator and electron transfer reaction between mediators on the current density, we have developed a numerical simulation method in biofuel cell anode. The model calculation showed both diffusion coefficient of mediator and rate constant of electron transfer reaction between mediators were found to be significant for an increase of the current density.

1. Introduction

A biofuel cell which uses enzyme as a catalyst is new energy transformation technology to convert chemical energy of fuels to electricity. In biofuel cell electrodes, electron transfer from enzymes to electrodes is an important factor. Mediators are generally used to shuttle electrons from enzymes to electrodes. Because a variety of fuels, such as glucose and ethanol, can be used under moderate conditions, biofuel cell is hoped to work for a portable energy source and an effluent purification device which can generate electricity at the same time [1].

One of the important issues to be addressed in biofuel cell is its low current density. While Tokita *et al.* reported the correlation between mediator and current density, the detailed reason remains unclear [2].

Thus in this study, for the theoretical screening of a high-performance mediator, we performed the model calculation of the biofuel cell anode and analyzed the influence of diffusion of the mediator and the electron transfer reaction between mediators on current density.

2. Method

The schematic illustration of biofuel cell anode is shown in Fig. 1.

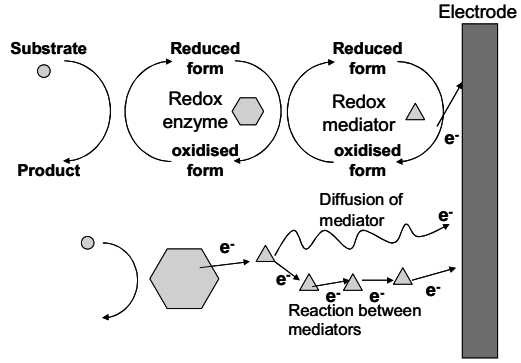

Fig. 1 Schematic illustration of biofuel cell anode

By the model calculation, we modeled the biofuel cell anode as follows.

- Enzyme reaction of the ping-pong mechanism

$$S + E_{ox} \underset{k_{-1}}{\overset{k_1}{\rightleftarrows}} ES \overset{k_2}{\rightarrow} P + E_{red}$$

$$M_{ox} + E_{red} \overset{k_{med}}{\rightarrow} M_{red} + E_{ox}$$

Where E_{ox} and E_{red} are the oxidised and reduced forms of the enzyme, S and P are the substrate and product and M_{ox} and M_{red} are the oxidised and reduced forms of the mediator, respectively.

The rate of enzyme reactions is expressed by

$$v_{Enz} = \frac{k_{cat} C_{Enz}}{1 + K_S / C_S + K_M / C_{MO}}$$

Where C_{Enz}, C_S and C_{MO} are the concentrations of the enzyme, the substrate and the oxidised mediator, respectively, k_{cat} (= k_2) is the turnover rate, and KS [= $(k_{-1} + k_2)/k_1$] and K_M (= k_2/k_{med}) are the Michaelis constants for the substrate and mediator, respectively.

- The electron transfer reaction between mediators

$$M_{ox} + M_{red} \overset{k}{\rightarrow} M_{red} + M_{ox}$$

The electron transfer between mediators was assumed as a reaction mechanism that a proton moved with an electron. The rate of electron transfer reaction is expressed by

$$v_{reaction} = k[M_{ox}][M_{red}]$$

The reaction-diffusion equations of mediator and substrate are

$$\frac{\partial C_{MR}}{\partial t} = D_M \frac{\partial^2 C_{MR}}{\partial x^2} + v_{Enz} + v_{reaction}$$

$$\frac{\partial C_S}{\partial t} = D_S \frac{\partial^2 C_S}{\partial x^2} - v_{Enz}$$

Where C_{MR} is the concentration of the reduced mediator, and D_M and D_S are the diffusion coefficient of the mediator and substrate, respectively.

The current density at the electrode surface(x=0) was calculated by the concentration of reduced form mediator as follows.

$$i = nFAD_M \frac{\partial C_{MR}}{\partial x}\Big|_{x=0}$$

Where A is the surface area of the electrode, F is the Faraday constant, and n is the stoichiometric coefficient for electron transfer.

Fig. 2 shows the calculation model used in our study.

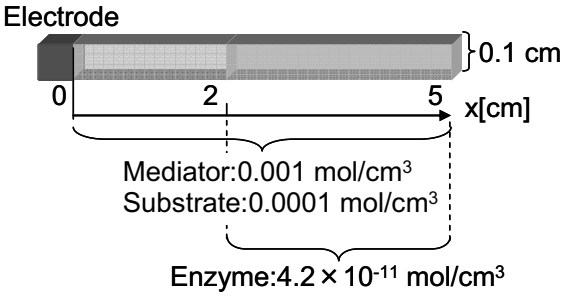

Fig. 2 The calculation model

We adopted the calculation parameters used in Tamaki *et al.* [3]

3. Results and Discussion

Fig. 3 shows the relationship between D_M and maximum current density, as well as D_M and arrival time calculated by the model. The electron transfer reaction between mediators is not considered in this calculation.

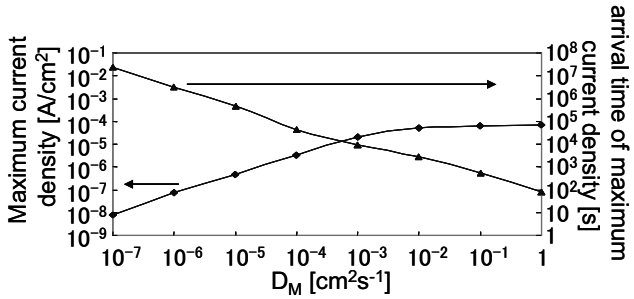

Fig. 3 Relationship between D_M and maximum current density, as well as D_M and arrival time of maximum current density

This figure shows that when the mediator with low D_M, around 10^{-5} cm^2s^{-1}, is used, the apparent electron diffusion of mediator becomes rate-limiting step at the electrode. Thus, to enhance the current density, increase of D_M is shown to be of significant. In addition, it indicates that while the maximum current density reaches the maximum value at higher D_M, arrival time of reaching the maximum current density becomes rapid with increase of D_M.

Fig. 4 shows the relationship between k and maximum current density, as well as k and arrival time of that calculated by the model.

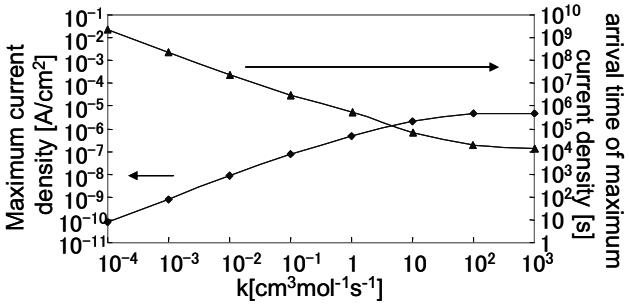

Fig. 4 Relationship between k and maximum current density, as well as k and arrival time of maximum current density

The diffusion of mediator is not considered in this calculation. With increase of D_M, the current density is improved with increase of the rate constant of electron transfer reaction between mediators without considering diffusion. It is suggested that the electron transfer reaction between mediators play an important role as diffusion of mediator.

Because it is thought that both diffusion of mediator and electron transfer reaction between mediators happen at the same time under the realistic condition, it indicates that both D_M and k strongly influence the current density.

Fig. 5 shows the relationship between k_{cat} and maximum current density when D_M and k are 10^{-5} cm^2s^{-1} and 10^{-3} $cm^3mol^{-1}s^{-1}$, respectively.

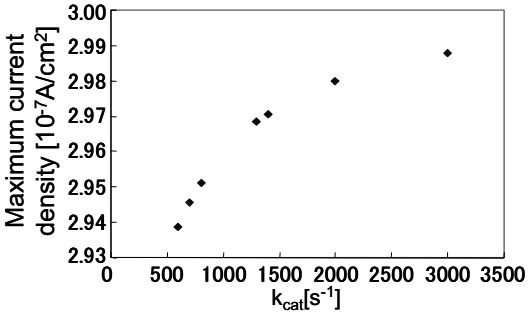

Fig.5 Relationship between k_{cat} and maximum current density. The parameters were D_M and k are set to 10^{-5} cm^2s^{-1} and 10^{-3} $cm^3mol^{-1}s^{-1}$, respectively.

The result shows increase of maximum current density with increase of k_{cat}. The reason why the maximum current density is improved with increase of turnover rate of enzyme is the concentration gradient changes. Thus, compare Fig.5 with Fig.3 or Fig.4, the rate change of the maximum current density is small.

4. Concluding remarks

In this study, for the theoretical screening of a high-performance mediator to enhance the current density, the model calculation of the biofuel cell anode was performed and analyzed the influence of diffusion of the mediator and the electron transfer reaction between mediators on current density.

It was found the electron transfer reaction between mediators played a role as diffusion effect of mediator. Thus, it is indicated that the mediator performance is affected by both the diffusion coefficient of mediator also the rate constant of the electron transfer reaction between mediators.

References

[1] J. Kim et al., *Biotechnology Advances* **24** (2006) 296–308

[2] Y. Tokita, T. Nakagawa, H. Sakai, T. Sugiyama, R. Matsumoto, T. Hatazawa, *ECS Transactions*, **13** (21) 89-97 (2008)

[3] T. Tamaki, T. Ito, T.Yamaguchi, *FUEL CELLS 09*, **1** 37-43 (2009)

Eighth International Conference on Flow Dynamics
November 9 - November 11, 2011

Study on Ignition Characteristics of PRF/Air Mixtures at 1-5 atm in a Micro Flow Reactor with a Controlled Temperature Profile

Mikito Hori*, Akira Yamamoto, Hisashi Nakamura, Takuya Tezuka, Susumu Hasegawa and Kaoru Maruta
Institute of Fluid Science, Tohoku University
2-1-1 Katahira, Aoba-ku, Sendai, Miyagi 980-8577, Japan
hori@edyn.ifs.tohoku.ac.jp

ABSTRACT

Ignition and combustion characteristics of gaseous mixture of major gasoline components (n-heptane, iso-octane, and toluene) were examined using a micro flow reactor with a controlled temperature profile. In the low flow velocity region, multi-stage weak flames which represent fuel ignition characteristics were observed. Distribution of chemiluminescence and flame location were changed when composition of n-heptane / iso-octane was varied. Results of 1-D steady computation reproduced the experimentally observed flame responses. In addition, an effect of toluene addition on ignition process was also examined by observing weak flames.

1. Introduction

In terms of energy savings, improvement of internal combustion systems efficiency is required. Especially for development of compression-ignition engines, the understandings of the ignition process of various fuels would play an important role.

In this study, we employed a micro flow reactor with a controlled temperature profile [1]. Quartz tube with a diameter smaller than the quenching diameter is heated by an external heat source so as to have a stationary temperature gradient. Due to the small inner diameter of the tube, temperature of the gas phase strongly depends on the temperature profile of the inside surface of the tube. In our previous studies, ignition and combustion characteristics of methane/air [2], DME/air [3], and *n*-heptane/air [4] mixtures were examined by the reactor.

This study focused on the ignition and combustion characteristics of major gasoline components, i.e. n-hetpane, iso-octane, toluene, and their blended fuels. Blended fuel of n-heptane and iso-octane is used as PRF (Primary Reference Fuel) which defines octane number, the index of anti-knock property in IC engines. Toluene, which has inhibition effect on ignition, is used as octane booster in IC engine combustion. However, there are less experimental data of ignition of toluene compared to that of PRF, due to its low ignition performance. Thus, its reaction kinetics has not been fully understood.

The first objective of this study is to show the resolution ability of present reactor for octane number change by examining PRF/air flames and confirm the ability of this method to examine combustion and ignition process of practical fuels. In addition, the effect of toluene addition on ignition process is examined.

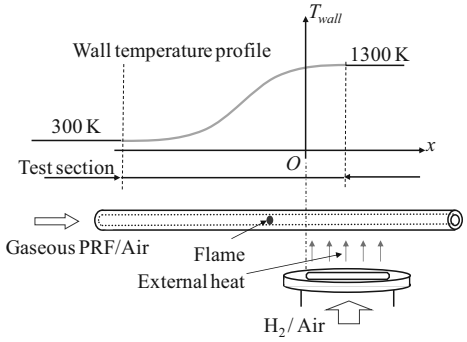

Fig. 1 Experimental setup.

2. Experimental and computational method

Figure 1 shows the schematic of the experimental setup. A quartz tube with an inner diameter of 1 - 2 mm was employed as a reactor and heated by H_2/air premixed burner so as to have a stationary temperature profile (300 - 1300 K). A gaseous fuel/air mixture coming into the quartz tube ignites in the tube and the flame remains at a certain location. This flame image was captured with a digital still camera with a CH filter.

To examine the experimental results for PRF/air, 1-D steady computations were conducted with a code based on PREMIX. Heat convection term between gas phase and wall was added to energy equation. Wall temperature profile was given in the heat convection term. Detailed reaction mechanism of PRF [5] was selected. Flame location was defined as the peak of the heat release rate.

3. Results and discussion

Flame responses to the inlet flow velocity were examined using PRF100 (iso-octane 100%) / air mixture under atmospheric pressure. Stable flat flame (Normal flame) was observed in a high flow velocity region (U > 50 cm/sec). Unstable flames called *flames with repetitive extinction and ignition* (FREI) [1] were observed in an intermediate flow velocity region (U = 8 - 50 cm/s). Stable flames with weak luminescence (Weak flames) were observed in a lower flow velocity region (U < 8 cm/sec).

In the weak flames regime, two luminous zones were observed in the flow direction. Observation of weak flames is expected to be efficient for investigation of the ignition process of the fuel in each temperature region. Thus, special attention will be paid to the weak flame phenomena from the next section.

First, the responses of weak flames to various octane

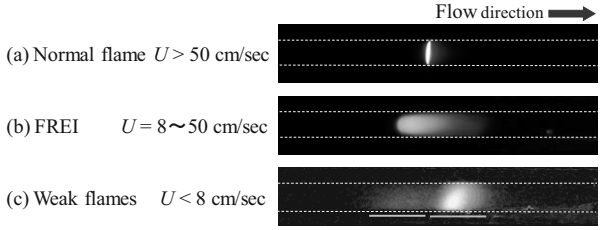

Fig. 2 Flame images captured through optical filter: (a) Normal flame (U = 51 cm/s), (b) FREI (U = 10 cm/s), and (c) Weak flames (U = 1.6 cm/s).

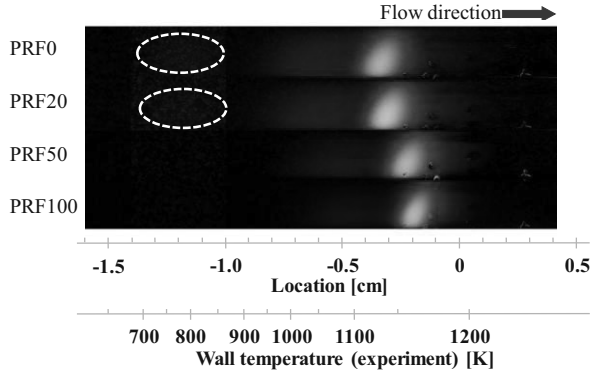

Fig. 3 Weak flame images of fuels with various octane numbers (U = 1.2 cm/sec, P = 1 atm).

numbers were examined using PRF/air. Figure 3 shows the images of weak flames with various octane numbers.

In the case of PRF0 (n-heptane 100%), two luminous zones in the downstream side (high temperature region) and another weak luminous zone in the low temperature region were observed. This three-stage oxidation process of PRF0 was previously observed by Yamamoto et al. [4]. According to their study, the weak luminous zone in the low temperature region is cool flame, and two luminous zones in high temperature region are separated hot flames. Luminosity from cool flame became weaker and the second hot flame position shifted to the higher temperature region as octane number increases.

Figure 4 shows the computational HRR profiles of various PRF. In the case of PRF0, three peaks of the HRR profile were confirmed. By the gas sampling analysis [4], these three reactions were confirmed to correspond to the three luminous zones observed in the experiment. On the other hand, the peak value of cool flame decreased as octane number increases. In addition, the second hot flame position shifted to the higher temperature region as octane number increases. These tendencies well agree with the experimental results. These results indicated the sufficient resolution ability of the present reactor to investigate the general ignition process of practical fuels with various octane numbers.

Secondly, weak flames of PRF0 and blended fuel (PRF0 + Toluene, 70:30) were examined to observe the effect of toluene addition to PRF. In this investigation, pressure was varied from 1 - 5 atm.

Figure 5 shows the comparison of weak flames of PRF0 and the blended fuel. In the case of PRF0,

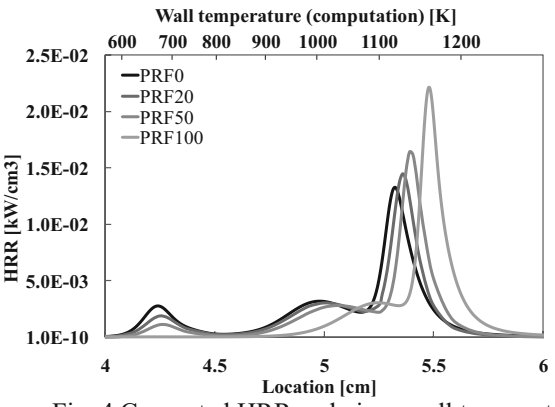

Fig. 4 Computed HRR and given wall temperature profile (U = 1.2 cm/sec, P = 1 atm).

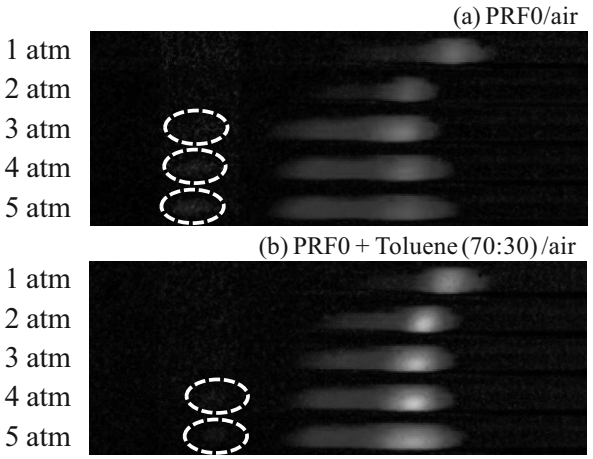

Fig. 5 Weak flame under elevated pressure (U=2.0 cm/sec): (a) PRF0/air, (b) PRF0 + toluene /air.

luminosity of cool and 1st hot flames increased and 2nd hot flame became broader as pressure increases. These tendencies were also observed in the case of blended fuel, however, luminosity of cool and 1st hot flames were weaker than that of PRF0 under every pressre range and luminosity seemed to be more concentrated in the 2nd hot flame. In addition, cool flame was stabilized in higher temperture region compared to the case of pure PRF0. This shift indicates that toluene addition has inhibition effect on the low tempearture reaction.

By examining the weak flames of blended fuel, present method was confirmed to be useful for obtaining experimental data of reaction of toluene.

4. Conclusions

Ignition and combustion characteristics of major gasoline components were investigated using a micro flow reactor with a controlled temperature profile.

- Flame responses to various inlet flow velocities were examined using PRF100 as a fuel. Three different flame regimes were observed; normal propagating flame, FREI, and stable weak flames.
- Weak flame responses to octane number were examined by changing the composition of iso-octane / n-heptane. Sufficient resolution ability of the present reactor for octane number change was confirmed.
- Inhibition effect of toluene addition on ignition was confirmed by observing weak flames at 1 - 5 atm.

References

[1] K. Maruta, T. Kataoka, N.I. Kim, S. Minaev, R. Fursenko, Proc. Combust. Inst. **30** (2005), 2429-2436.

[2] Y. Tsuboi, T. Yokomori, K. Maruta, Proc. Combust. Inst. **32** (2009), 3075-3081.

[3] H. Oshibe, H. Nakamura, T. Tezuka, S. Hasegawa, K. Maruta, Combust. Flame. **157** (8) (2010), 1572-1580.

[4] A. Yamamoto, H. Oshibe, H. Nakamura, T. Tezuka, S. Hasegawa, K. Maruta, Proc. Combust. Inst **33** (2) (2011), 3259-3266.

[5] H.J. Curran, P. Gaffuri, W.J. Pitz and C.K. Westbrook, Combust. Flame. **129** (2002), 253-280.

Eighth International Conference on Flow Dynamics
November 9 - November 11, 2011

Cetane Number and Weak Flames of Diesel PRF in a Micro Flow Reactor with a Controlled Temperature Profile

Satoshi Suzuki*, Mikito Hori, Akira Yamamoto, Hisashi Nakamura, Takuya Tezuka, Susumu Hasegawa , and Kaoru Maruta
Institute of Fluid Science, Tohoku University
2-1-1 Katahira, Aoba-ku, Sendai, Miyagi 980-8577, Japan
suzuki@edyn.ifs.tohoku.ac.jp

ABSTRACT

Gaseous reactions of diesel PRF (n-/iso-cetane) in a micro flow reactor with a controlled temperature profile have been observed. The experimental results showed multiple weak flames which are similar to the observation in our previous work for methane, DME, *n*-heptane and gasoline PRF. Chemiluminescences of weak flames varied depending on cetane number. Results of computation with detailed reaction mechanism showed a qualitative agreement with experimentally observed weak flames.

1. Introduction

Reaction modeling of diesel fuel is an effective method to accelerate further improvement of the efficiency of diesel engine. For development of the modeling capability, it is essential to be validated by experimental measurement of gaseous reactions. However, examining combustion characteristic of diesel fuel by a rapid compression machine or shock tube is not an easy task, because of its high boiling point. This causes insufficiency of experimental results measured by conventional techniques, and new technique is required.

In this study, we employed a micro flow reactor with a controlled temperature profile [1-5]. Quartz tube with a diameter smaller than the quenching diameter is heated by an external heat source so as to have a stationary temperature gradient. Due to the small inner diameter of the tube, temperature of the gas phase in the tube strongly depends on the temperature of the inside surface of the tube. In our previous study, combustion characteristics of methane/air [2], DME/air [3], *n*-heptane/air [4], and gasoline PRF/air [5] mixtures were examined by using the micro flow reactor. These studies clearly indicated the availability of the micro flow reactor as a method to investigate the ignition and combustion process of given fuels.

This study focused on the combustion characteristics of *n*-/iso-cetane as fuel. Blended fuel of *n*-cetane and *iso*-cetane is defined as diesel PRF (Primary Reference Fuel) which represents the combustion characteristics of diesel fuel. Diesel fuel ignition is rated by its cetane number (CN), where fuels with higher values of CN ignite more readily than fuels with lower CN values. *n*-cetane (CN 100) is more reactive than *iso*-cetane (CN 15). The objective of this study is to investigate ignition and combustion characteristic of diesel PRF by using a micro flow reactor with a controlled temperature profile. And the flame responses with the various CN were examined.

2. Experimental and computational method

Figure 1 shows the schematic of the experimental setup. A quartz tube with an inner diameter of 2 mm was employed as a micro flow reactor, and heated by H_2/air premixed burner so as to have a stationary temperature profile (400-1300 K).

A gaseous diesel PRF/air mixture was produced by injecting the PRF with a micro syringe into air which was controlled by mass flow controller. Injection volume of the PRF was controlled by a stepping motor. The mixture coming into the quartz tube ignites in the heated tube and the flame remains at a certain location. This flame was captured with a digital single lens reflex camera with a CH filter. All of the experiments were conducted under the atmospheric pressure.

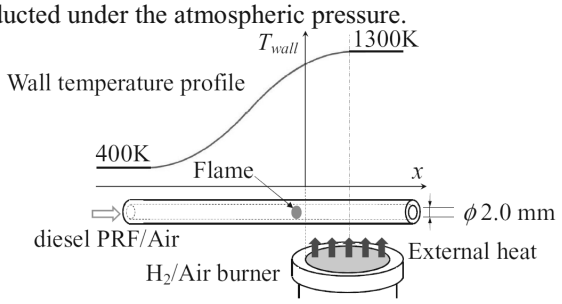

Fig. 1 Schematic of the experimental setup.

Computations were carried out by employing one-dimensional steady code based on PREMIX, and heat convection term between gas phase and wall was added to its energy equation [1], so as to examine the experimental results. The temperature gradient with maximum wall temperature 1300 K, which is the same with the experimental condition, was given as T_w in the heat convection term. Detailed reaction mechanism of *n*-cetane [6] and *iso*-cetane [7] were selected. The transport data was constructed using the data of *n*-heptane and *iso*-octane. For species not appearing in these database, a value of the transport data was estimated based on its molecular weight. Flame location was defined as the peak of the heat release rate.

3. Results and discussion

Flame response of *n*-cetane/air mixture to the various inlet flow velocity was observed. Figure 2 shows the images of the flames captured in the each inlet flow velocity region. Three flame responses were observed by changing inlet flow velocity.

Stable flat flames (Normal flame) were observed in high flow velocity region. Unstable flames called *flames with repetitive extinction and ignition* (FREI) were observed in an intermediate flow velocity region (5 - 35 cm/sec). Stable flames with weak luminescence (Weak

flames) were observed in a lower flow velocity region. This tendency, that is, the existence of three kinds of flame responses observed by changing inlet flow velocity, agrees with the previous experimental results for methane [2], DME [3], *n*-heptane [4], and gasoline PRF [5].

In this study, we focus on the weak flames, which were observed in the lower flow velocity region. The multiple luminous zones were observed in a long exposure image. Reaction zone of high temperature has strong luminosity with weak luminous zone, and that of lowest temperature region has weak luminosity. Those are supposed to have same configuration of weak flames in DME [3] and *n*-heptane [4]. Luminous zones at high temperature region are separated hot flame, and weak luminescence at the lowest temperature region is cool flame.

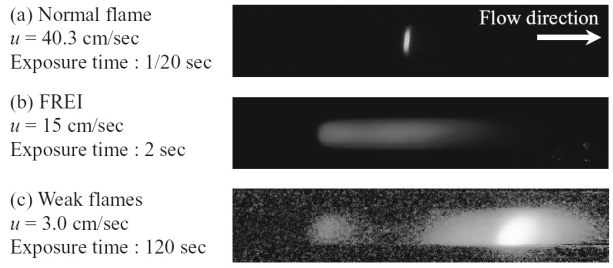

Fig. 2 Three different flames of *n*-cetane in each flow velocity region.

Flame response was observed by changing the mixing ratio of *n*-cetane and *iso*-cetane. Figure 3 shows the images of weak flames with various CN. A cool flame was recognized in the case of pure *n*-cetane (CN 100) and blended fuel (CN 76), but was not recognized in *iso*-cetane (CN 15). The cool flame luminosity of blended fuel (CN 76) was weaker than that of CN 100.

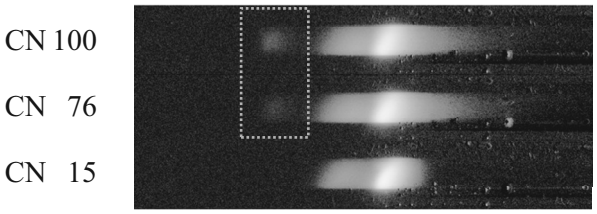

Fig. 3 Weak flame images for CN = 15, 76, and 100. *U*=3.0 cm/sec, Exposure time: 120 sec

Figure 4 shows the computational heat release rate profiles of CN 15 and 100 at the flow velocity of 3.0 cm/sec. At value of CN 100, three peaks of heat release rate were confirmed. It is supposed to correspond to the three luminous zones observed in Fig. 3, according to the study on *n*-heptane [4]. Computed result of CN 15 has small peak at low temperature region, but no luminosity was observed experimentally. Computation for CN 76 is still in progress, but it has a value between 15 and 100 in ignition delay simulation [8].

Computed results show hot flame shifts to the higher temperature region in higher CN, however experimental ones showed no significant difference. The tendency of the heat release rate at the cool flame has a good agreement with experimental results shown in Fig. 3.

Our experimental and computational results show increasing of reactivity at low temperature, as the CN is increased from 15 to 100. This tendency corresponds to results of shock tube or other experimental techniques [8], and the definition of the CN.

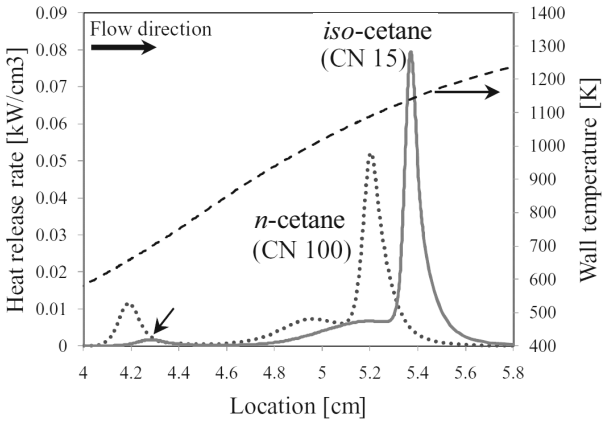

Fig. 4 Heat release rate profiles for CN = 15 and 100.

4. Conclusions

Ignition and combustion characteristics of diesel PRF/air mixture were investigated using a micro flow reactor with a controlled temperature profile.

- Flame responses to various inlet flow velocities were examined using pure *n*-cetane (CN 100) as a fuel. Three different flame regimes were observed; normal propagating flame, FREI, and stable weak flames.
- Responses of weak flames with various cetane numbers were examined by changing the mixing ratio of *n*-cetane and *iso*-cetane. The computational responses agreed with the experimental ones.
- It was indicated that the present reactor has a capability to measure high boiling fuel such as diesel fuel.

References

[1] K. Maruta, T. Kataoka, N.I. Kim, S. Minaev and R. Fursenko, Proc. Combust. Inst. **30** (2005) 2429-2436.
[2] Y. Tsuboi, T. Yokomori, K. Maruta, Proc. Combust. Inst. **32** (2009) 3075-3081.
[3] H. Oshibe, Y. Tsuboi, H. Nakamura, T. Tezuka, S. Hasegawa, K. Maruta, Combust. Flame. **157** (8) (2010) 1572-1580.
[4] A. Yamamoto, H. Oshibe, H. Nakamura, T. Tezuka, S. Hasegawa, K. Maruta, Proc. Combust. Inst. **33** (2) (2011) 3259-3266.
[5] M. Hori, A. Yamamoto, H. Nakamura, T. Tezuka, S. Hasegawa, K. Maruta, **8**th Asia Pacific Conference on Combustion. (2010) pp 1099-1102.
[6] C. K. Westbrook, W. J. Pitz, O. Herbinet, H. J. Curran, Emma J. Silke, Combust. Flame. **156** (2009) 181–199.
[7] M. A. Oehlschlaeger, J. Steinberg, C. K. Westbrook, W. J. Pitz, Combust. Flame. **156** (2009) 2165–2172.
[8] C. K. Westbrook, W. J. Pitz, M. Mehl, H.J. Curran, Proc. Combust. Inst. **33** (2011) 185-192.

Eighth International Conference on Flow Dynamics
November 9 - November 11, 2011

Computational Study on Near-Limit Behavior of Low-Lewis-Number Radiative Counterflow Flame under Microgravity

Koichi Takase, Hisashi Nakamura, Takuya Tezuka, Susumu Hasegawa, Xing Li and Kaoru Maruta
Institute of Fluid Science, Tohoku University, Katahira2-1-1, Aoba, Sendai, Miyagi, Japan
takase@edyn.ifs.tohoku.ac.jp

ABSTRACT

Computational investigation of flammability limit of low-Lewis-number radiative counterflow premixed flames and flame balls were conducted. Flammable region of Xe-diluted counterflow premixed flame was broader than that of Kr-diluted counterflow flame. Lean flammability limit of Xe-diluted counterflow premixed flame was lower than that of flame ball. However, Lean flammability limit of Kr-diluted counterflow flame was higher than that of flame ball. These results were due to diffusive-thermal instability of low-Lewis-number flame.

1. Introduction

For the development of high-efficiency and low-emission combustor, the improvement of lean combustion technology, especially lean flammability limit theory, is required. About seventy years ago, Zeldovich predicted flammability limit mechanism, which is competition between heat release and heat loss mechanisms [1]. His prediction has been revealed by microgravity experiments, especially the observations of steady-state radiative spherical flame in stationary near-limit low-Lewis-number mixture, called 'flame ball' [2] and extinction of counterflow flame induced by radiative heat loss [3]. Near-limit low-Lewis-number flame (fuel Lewis number, Le<1) suffers from diffusive-thermal instability, for example, cellular flame formation occurs [4]. Using lean H_2/air mixture (Le~0.3), the transition from planar propagating flame to flame ball has been observed numerically with the decrease of equivalence ratio, ϕ [5]. Flames suffering from diffusive-thermal instability have been observed experimentally. Counterflow slot-jet H_2/air premixed flames have shown a transition from two nearly planar flames to stationary flame tubes with the decrease of equivalence ratio [6]. Therefore, low-Le counterflow premixed flame and flame ball seems to have some correlations, however, flammability limit theory of planar propagating flame and flame ball were constructed independently. Low-speed counterflow flame method is useful for the construction of near-limit flammability limit theory. For example, theoretical analysis of lean counterflow premixed flame revealed that flammable region became broader with decrease of fuel Lewis number [7]. However, long-duration microgravity condition (over 100 s) was required due to the extremely-low flow speed to compete with the diffusion species of fuel. Recently, our proposal for space experiment was accepted, and it was selected as the candidate theme for International Space Station Japanese Experiment Module. The objective of the present study is to contribute future space experiment by making computations of lean flammability limit of low-Le counterflow premixed flame and flame ball diluted by Xenon (Xe) and Krypton (Kr) for determination of the experimental conditions.

2. Computational Method

PREMIX-based 1-D counterflow flame code [8] and flame ball code were adopted for computations. Optically thin radiation model was used for the computation of radiative heat loss [8]. The computation distance, L is 10 cm. The pressure, the ratio of oxidizer mole fraction to inert mole fraction, Z and initial gas temperature, T_0 were set to 1 atm, 0.141 and 300 K, respectively. Lean $CH_4/O_2/Xe$ (Le~0.5) and $CH_4/O_2/Kr$ (Le~0.7) mixtures were used to decrease Le from lean CH_4/air mixture (Le~1). GRI-Mech 3.0 reaction mechanism without N reactions was adopted and Xe or Kr was included as an inert. Reaction data of Xe and Kr were used from that of Ar in GRI-Mech 3.0. Thermodynamic data of Xe and Kr were extracted from NIST chemistry webbook [9]. Transport data of Xe and Kr were obtained from W.J. Moore's data [10]. Polarizability of Kr was obtained from K. Ohno's data [11]. Thermodynamic and transport data were translated to CHEMKIN format using CHEMKIN3.7 FITDAT program.

3. Results and Discussion

Figures 1 and 2 show the flame ball radii and extinction curves of counterflow premixed flames for Xe-diluted and Kr-diluted mixtures, respectively. C-shaped extinction curve was obtained from the counterflow flame computation. Xe flame had broader flammable region than Kr flame. The upper branch of this curve showed stretch extinction limit and the lower branch showed radiative extinction limit. To investigate the effect of the radiative heat loss quantitatively, the ratio of the radiative heat loss to the heat release at a given stretch rate, called radiation fraction [8], r_f at ϕ=0.50 was computed.

$$r_f = \frac{\int_{-L/2}^{L/2} q_{rad}\,dx}{\int_{-L/2}^{L/2} \sum_{k=1}^{K} \dot{\omega}_k h_k W_k\,dx} \qquad (k=1, 2, \ldots, K) \quad (1)$$

where q_{rad} and K are radiative heat loss per unit volume and the number of species. $\dot{\omega}_k$, h_k and W_k are net chemical production rate, specific enthalpy and molecular weight of the kth species, respectively. Radiation fraction increased with decrease of stretch rate, a, however, radiation fraction decreased with decrease of stretch rate close to the radiative extinction limit. And radiation fraction of Xe-diluted counterflow flame was larger than that of Kr-diluted counterflow flame. These

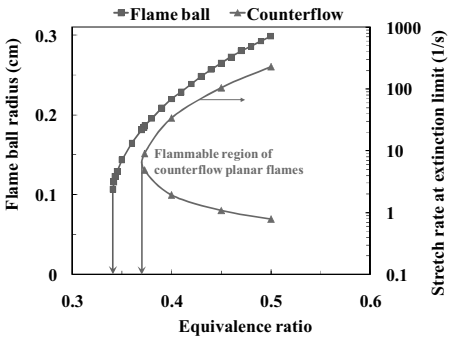

Fig. 1 Computational flame ball radius and extinction curve of counterflow premixed flame. ($CH_4/O_2/Xe$, Z=0.141)

effects are due to lower *Le* of Xe-diluted mixture than that of Kr-diluted mixture. Next, the comparison of lean flammability limits between counterflow premixed flame and flame ball was conducted. Decreasing equivalence ratio, flame ball radius decreased. For Xe-diluted flames, the lean flammability limit of flame ball was ϕ=0.34, lower than that of counterflow flame (ϕ=0.37). For Kr-diluted flames, the lean flammability limit of counterflow flame was ϕ=0.41, lower than that of flame ball (ϕ=0.45). These results were due to lower *Le* of Xe-diluted mixture than that of Kr-diluted mixture. And the maximum temperatures, T_{max}, of counterflow premixed flames at low stretch rate (a=3 s^{-1}) and flame balls were observed. The computed T_{max} of Xe-diluted and Kr-diluted flames were shown in fig. 3 and fig. 4, respectively. Maximum temperatures of flame balls were higher than those of counterflow planar premixed flames for both of the Xe-diluted and Kr-diluted flames. And the difference of maximum temperatures increased with the decrease of equivalence ratio. Therefore, the transition from counterflow planar flame to flame ball at extremely-low stretch rate, lower than 3 s^{-1} is considered to be possible at near-limit region.

4. Concluding remarks

From the numerical simulations of $CH_4/O_2/Xe$ and $CH_4/O_2/Kr$ flames, the conclusions below were obtained.

- C-shaped extinction curves (stretch and radiative extinctions) of both Xe-diluted and Kr-diluted counterflow premixed flames were obtained.

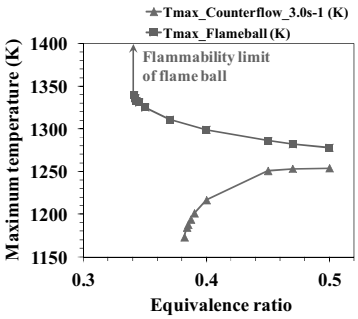

Fig. 3 Computational T_{max} of counterflow premixed flames at a=3.0s^{-1} and flame ball. ($CH_4/O_2/Xe$, Z=0.141)

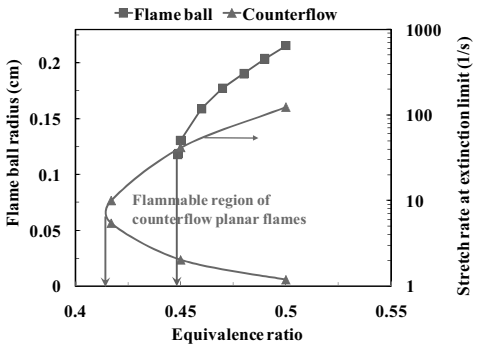

Fig. 2 Computational flame ball radius and extinction curve of counterflow premixed flame. ($CH_4/O_2/Kr$, Z=0.141)

- Xe-diluted counterflow premixed flame had broader flammable region than Kr-diluted counterflow flame, because of lower Lewis number of Xe-diluted mixture.
- For Xe-diluted flames, lean flammability limit of flame ball was lower than that of counterflow premixed flames. However, for Kr-diluted flames, lean flammability limit of counterflow premixed flame was lower than that of flame ball.
- T_{max} of flame balls were higher than those of counterflow premixed flames at a=3.0 s^{-1} and $\phi < 0.5$.

References

[1] Ya. B. Zeldovich, *Zhurn Eksp Teoret Fiz* 11(1940).
[2] P. Ronney, *Combust. Flame* 82 (1990) 1-14.
[3] K. Maruta et al., *Proc. Combust. Inst.* 26 (1996) 1283-1289.
[4] S. Minaev et al., *Combust. Explosion and Shock Waves* 38 (2002) 9-18.
[5] S.Tse et al., *Proc. Combust. Inst*. 28 (2000) 1917-1924.
[6] C. Kaiser et al. *AIAA Aerospace Sciences Meeting* 38 (2000).
[7] Y. Ju et al., *Int. J. Heat and Mass Trans.* 43 (2000) 231-239.
[8] Y. Ju et al., *J. Fluid Mech.* 342 (1997) 315-334.
[9] NIST Chemstry webbook (http://webbook.nist.gov/chemistry)
[10] W. J. Moore, *Physical Chemistry* (1974), Tokyo Kagaku Dojin.
[11] K. Ohno, *Quantum Physical Chemistry* (1989), University of Tokyo Press.

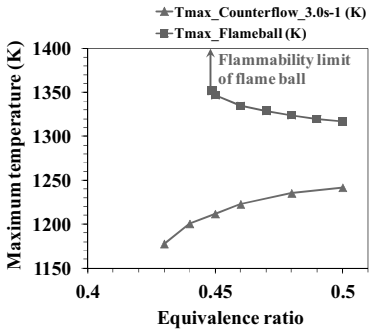

Fig. 4 Computational T_{max} of counterflow premixed flames at a=3.0s^{-1} and flame ball. ($CH_4/O_2/Kr$, Z=0.141)

Eighth International Conference on Flow Dynamics
November 9 - November 11, 2011

Development of Temperature-Sensitive Paint for Cryogenic Cavitation Test

Shota Fujii, Kazuki Niiyama, Hiroki Nagai, Keisuke Asai
6-6-01, Aramaki Aza-aoba, Aobaku, Sendai, Miyagi, 980-8579, JAPAN
Dept. of Aerospace Engineering, Tohoku University
fujii.shota@aero.mech.tohoku.ac.jp

ABSTRACT

In this study, temperature-sensitivity of several Temperature-Sensitive Paints in the cryogenic temperature and endurance of paints under temperature of liquid nitrogen were investigated in order to apply Temperature-Sensitive Paint to cryogenic cavitation tests. Additionally, the temperature distribution of a flat plate surface under cryogenic condition was measured by using a TSP.

1. Introduction

Cryogenic cavitation is one of the major problems in the development of rocket engines [1]. The temperature distribution on the model caused by thermodynamic effect is necessary for the analysis of this phenomenon. Quantitative temperature distribution on the model surface can be measured by using Temperature-Sensitive Paint (TSP). However, there are a few application of TSP to cryogenic condition, for example, boundary layer transition detection in cryogenic wind tunnel [2].

In this study, temperature-sensitivity of several TSPs was investigated by calibration test in order to develop TSP applicable to cryogenic cavitation test. And cryogenic endurance of paints was also studied by dipping TSP samples in LN2. Finally, the measurement of temperature distribution of flat plate under cryogenic condition was demonstrated.

2. Experimental methods and conditions

Four TSPs, cryoTSP, PTMSDPA-TSP, Rhodamin B-TSP, La2O2S: Eu-TSP were made for calibration test, as seen in Table.1. And Fig.1 shows the setup of calibration test. Luminescent intensity of each TSP sample was measured between -190^oC and 10 ^oC. A calibration chamber was used for temperature control. Blue LED and Hg-Xe lamp with optical filter were respectively used as excitation light. And 16bit cooled CCD camera equipped suitable bandpass filter was used as a photo detector.

For cryogenic endurance test, three tests were carried out by changing thickness of TSP, existence of undercoating (Epoxi Primer, White Paint), sample material (aluminum, polycarbonate), cool time, precooling time, crack initiation of TSP after being dipped in LN2 was observed. In the case of the temperature distribution measurement, a polycarbonate sample plate (75 × 25 × t5mm) was used. For comparison, five thermocouples were placed on the sample and connected with data logger. Sequential temperature distribution images were acquired by using TSP when the lower part of the sample was dipped in LN2, at the same time temperature data was acquired by thermocouples. Fig. 2 shows the setup of temperature distribution measurement.

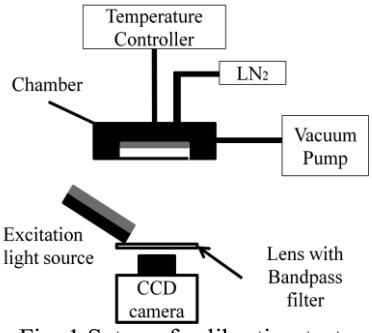

Fig. 1 Setup of calibration test

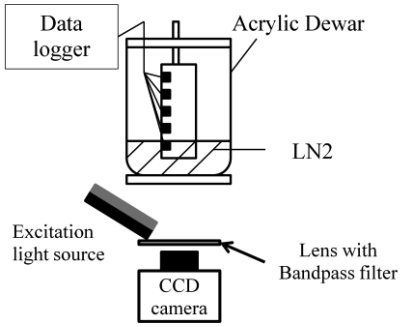

Fig. 2 Setup of temperature distribution measurement

3. Results and Discussion

Fig.3 is the result of calibration test. This shows that cryoTSP has the highest temperature sensitivity under cryogenic temperature, about 0.80%/ ^oC at -190^oC. On the other hand, PTMSDPA has the highest sensitivity between -90^oC and 10 ^oC. CryoTSP was used in the following experiments.

Fig.4 is surface image of some TSP samples in cryogenic endurance test. From this test, paint defect easily occurred when aluminum was used as sample material. This is caused by difference of coefficient of thermal expansion between TSP and sample plate. By spraying Epoxy Primer as undercoating, the endurance can be improved. On the other hand, no need for polycarbonate samples.

Fig.5 shows sequential images of temperature distribution obtained from cryoTSP. This shows that the plate was gradually cooled from the lower part dipped in LN2. Fig.6 is the temperature time history result of comparison with thermocouples data. There are differences between them, especially immediately after

dipping and after enough time passed. This may be mainly caused by heat conduction of thermocouples.

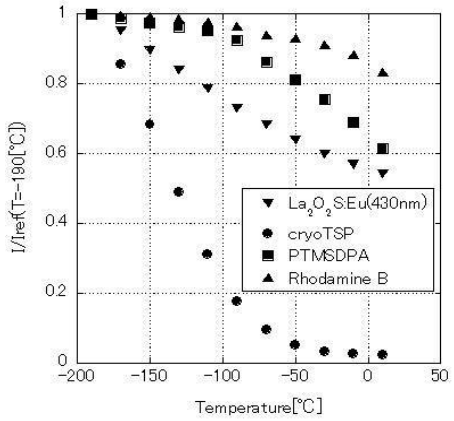

Fig. 3 Temperature sensitivity

Table. 1. Composition of TSPs

Name	Dye	Binder
cryoTSP	$Ru(trpy)_2$	Clearcoat
PTMSDPA-TSP	PTMSDPA(Combined)	
Rhodamin B-TSP	Rhodamin B	Clearcoat
La_2O_2S: Eu-TSP	La_2O_2S: Eu	Clearcoat

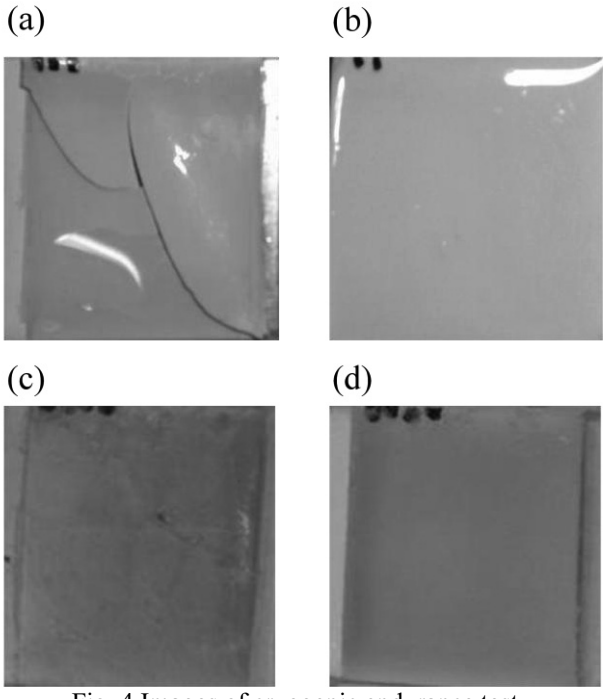

Fig. 4 Images of cryogenic endurance test
(a)Al, cryoTSP 110μm with W.P. (b)Al, cryoTSP 140μm with E.P. and W.P (c)PC, cryoTSP 110μm (d)PC, cryoTSP 140μm with W.P.

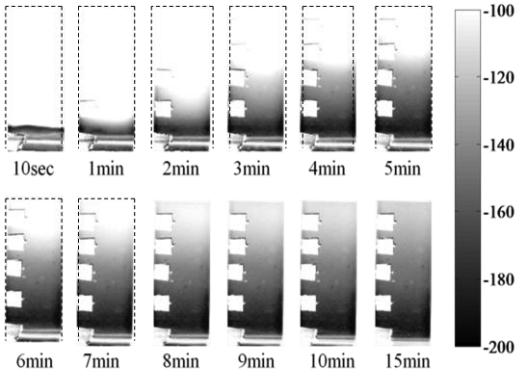

Fig. 5 Time historiyof temperature distribution

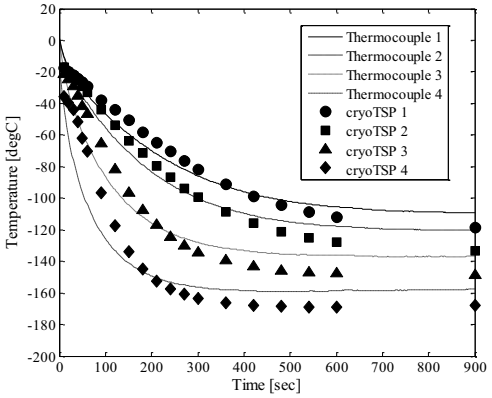

Fig. 6 Comparison of cryoTSP results and thermocouples

4. Conclusion remarks

Four TSPs were made and temperature sensitivity was investigated. As a result, cryoTSP had the highest sensitivity of the four at $-190^{O}C$. The development of higher-sensitive TSP is required in the future to measure the degree of thermodynamic effect with higher temperature resolution.

From the results of cryogenic endurance test, it is revealed Epoxy Primer need spraying as undercoating when aluminum material is used as a model material. On the other hand, no need for polycarbonate material.

Finally, temperature distribution of flat plate under cryogenic condition can be measured by using cryoTSP. Some difference with thermocouples data was observed but they roughly agreed with each other. This may be mainly caused by heat conduction of thermocouple. However, application possibility of TSP to cryogenic cavitation test was indicated.

5. References

[1] C. E. Brennen, “Cavitation and Bubble Dynamics”, Oxford University Press, 1995.

[2] Asai, K.et al,“Boundary-Layer Transition Detection in a Cryogenic Wind Tunnel using Luminescent Paint“, *J. of Aircraft*, Vol 34, 1997, pp 34–42

Eighth International Conference on Flow Dynamics
November 9 - November 11, 2011

Study on Weak Flame Behavior of Lower Alkane Fuels in Micro Flow Reactor with Controlled Temperature Profile

Taiki Kamada, Hisashi Nakamura, Takuya Tezuka, Susumu Hasegawa, Kaoru Maruta.
Institute of Fluid Science, Tohoku University, Japan.
2-1-1 Katahira, Aoba-ku, Sendai, 980-8577, Japan
kamada@edyn.ifs.tohoku.ac.jp

ABSTRACT

Weak flames of methane, propane and n-butane are investigated using a micro flow reactor with a controlled temperature profile. We also conduct one-dimensional computations using detailed reaction scheme. The weak flame of methane located at highest temperature region in these fuels and the n-butane weak flame located at lowest. Computation predicted the flame positions qualitatively, but in methane case, it does not agree with the experimental result. We also found the correlation between weak flame positions and research octane number which is one of the major fuel index of ignition characteristics.

1. Introduction

Since natural gas is advantageous to other fossil fuels in terms of CO_2 and SOx emissions, it is one of the most promising alternative fuels which can be used in gas turbine, boilers, natural gas vehicles and so on. For improving the efficiencies of such combustion devices, knowledge on ignition and combustion characteristics is essential. Hence, we focus on methane, propane, and n-butane in this study which are the main components of natural gas. Although numerous studies on ignition characteristics of these pure fuels based on ignition delay times are conducted using RCM or shock tube, we are going to focus a micro flow reactor with a controlled temperature profile [1] in this study. Using this reactor, ignition temperature of methane [2] was measured and spatially steady multi-stage oxidations of dimethyl ether[3] and gasoline primary reference fuel [4,5] were observed. Observations of those flames provided new knowledge on combustion and ignition characteristics including low temperature oxidation to high temperature oxidation of those fuels.

This work investigates weak flame behaviors of main natural gas components such as methane, propane and n-butane. By focusing the behaviors of weak flame positions of each fuel, and we compare it with Research Octane Number (RON).

2. Experimental and computational methods

Figure 1 shows a schematic of experimental setup. We employed 2 mm inner diameter quartz tube as a reactor and heated it using premixed H_2/air flat flame burner. With this external heating, a steady temperature profile in axial direction with maximum temperature 1300 K was given. The premixed fuel/air mixture, whose temperature is nearly 300 K was introduced into this quartz tube with low flow rate. The mixture was heated by hot wall and ignited at a specific position. We controlled an equivalence ratio at ϕ=1 and mean flow velocity at entrance of tube U=2 cm/s. We used a digital still camera with a band pass filter to observe weak flame in the reactor. We defined maximum brightness point as a weak flame position in experiment. The wall temperature was measured by K-type thermocouple.

One-dimensional steady computations were conducted by PREMIX-based code [6]. We added the term of heat transfer between gas and wall to the gas phase energy equation. In computation, experimental wall temperature profile was given as the wall temperature profile of the channel. We used detailed reaction schemes of Natural gas III [7] and GRI 3.0[8]. Computational condition is the same as experiment; ϕ=1, U=2 cm/s, pressure p=1 atm.

3. Result and discussion

3.1 Experimental weak flame positions

Figure 2 shows the weak flame images of methane, propane and n-butane. We observed only one luminous zone in each fuel. Using these experimental images, we identified wall temperature at the weak flame location. The averaged values are shown in fig. 2. From these results, methane weak flame located at the most downstream side or higher wall temperature position than those of propane and n-butane weak flames. And propane weak flame located at the higher temperature

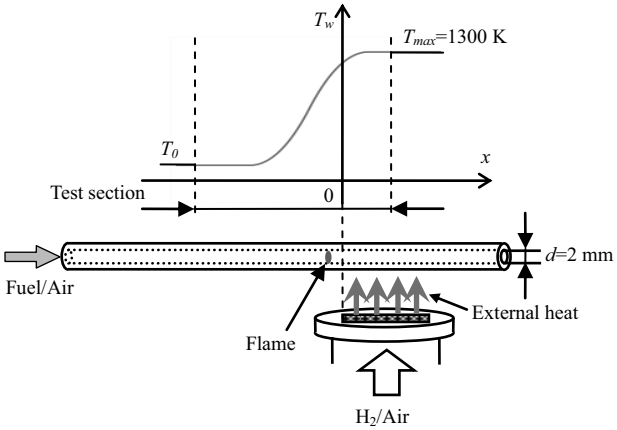

Fig. 1 Schematic of experimental setup.

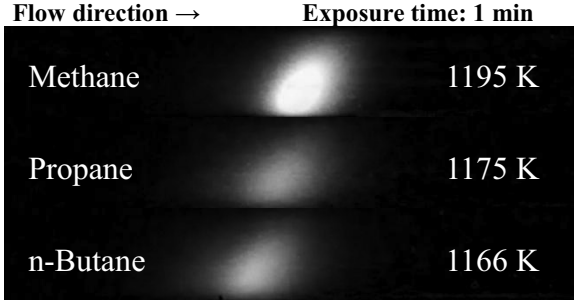

Fig. 2 Weak flame images of each fuel.

than n-butane did. We found a tendency that the weak flame of higher hydrocarbon fuel locates upstream.

3.2 Computational weak flame positions

Figure 3 shows the computational heat release rate (HRR) profiles of each fuel using Natural gas III scheme. Strong correlation between HRR peak and CH peak was confirmed in our past study, and CH peak has strong correlation with chemi-luminescence observed in experiments. Therefore, We defined the maximum HRR position as weak flame position in computation, and compared with experimental weak flame positions. Figure 4 shows the comparison of experimental and computational flame positions of each fuel. Experimental results (□) have a tendency that the weak flames of fuels for larger numbers of carbon atoms locate at the lower temperature region. The computational results (○) using Natural gas III reproduced similar tendency. However prediction for methane case by Natural gas III was not acceptable accuracy. Prediction for methane by GRI3.0 was in satisfactory accuracy with the difference about 6 K. This implies computational weak flame position can be utilized for examining reaction schemes.

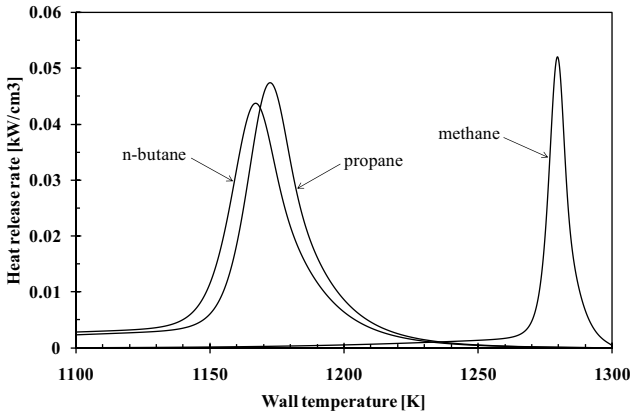

Fig. 3 Computational heat release rate profiles of each fuel.

3.3 Correlation with RON

We investigated the relationship between flame position and ignition characteristics. RON was employed as an index of ignition characteristics. The RONs of each fuel is 120 for methane, 112 for propane, and 94 for n-butane [9]. As extensively known, smaller RON fuel is easier to be ignited. According to RON index, n-butane is the easiest to be ignited, and methane is the hardest.

4. Conclusions

Weak flame positions of methane, propane and n-butane were investigated using a micro flow reactor with a controlled temperature profile. We observed one luminous zone in each fuel experiment and the temperature region of each weak flame was different. Methane weak flame located highest temperature region in three fuels, and n-butane was lowest. This tendency was reproduced by one dimensional computation using Natural gas III reaction scheme. In methane case, GRI3.0 provided better prediction than Natural gas III did. This difference between two reaction schemes indicates a possibility of reaction scheme verification using weak flame positions in the micro flow reactor. We also showed the correlation between weak flame position in micro flow reactor and RON.

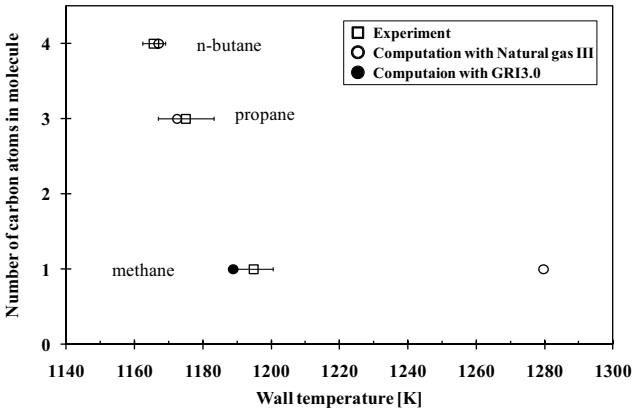

Fig. 4 Experimental and computational flame positions.

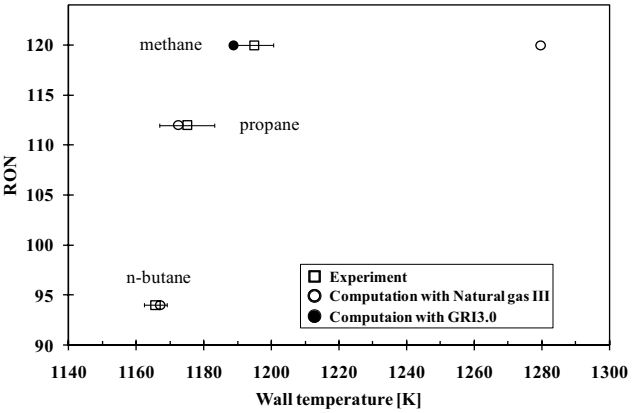

Fig. 5 Correlation between weak flame position and RON.

References

[1] K. Maruta et al., Proc. Combust. Inst. 30 (2005) 2429-2436.

[2] Y. Tsuboi et al., Proc. Combust. Inst. 32 (2) (2009) 3075-3081.

[3] H. Oshibe et al., Combust. Flame 157 (8) (2010) 1572-1580.

[4] A. Yamamoto et al., Proc. Combust. Inst. 33 (3) (2011)3259-3266.

[5] M. Hori et al., 8th ASPACC (2010) 1099-1102.

[6] R. J. Kee et al., Sandia National Laboratories Report (1993) No. SAND85-8240.

[7] Natural gas III, Combustion Chemistry Centre, National University of Ireland, Galway. http://c3.nuigalway.ie/naturalgas3.html.

[8] G. P. Smith et al., http://www.me.berkeley.edu/gri-mech/.

[9] J. Warnatz, U. Maas, R. W. Dibble, Combustion, 3rd edition, Springer, p. 228.

Eighth International Conference on Flow Dynamics
November 9 - November 11, 2011

Numerical Study of Heat Transfer for Cryogenic Slush Flow in a Horizontal Circular Pipe

Takumi Hosono, Katsuhide Ohira
Institute of Fluid Science, Tohoku University, 2-1-1 Katahira, Aoba, Sendai 980-8577, Japan
hosono@luna.ifs.tohoku.ac.jp

ABSTRACT

Cryogenic slush fluids are solid-liquid two phase fluids. Since their density and refrigerant capacity are greater than those of liquid-state fluid alone, there are high expectations for use of slush fluids as functionally thermal fluid in various applications. In this research, 3D thermally non-equilibrium two-fluid model based on Euler-Euler coupling method was applied to clarify the heat transfer characteristic of slush fluids in a horizontal circular pipe. The calculated results were compared with the experimental results. The numerical result was verified to be able to analyze the heat-transfer characteristics of the slush fluid with sufficient accuracy.

1. Introduction

Cryogenic slush fluids, such as slush nitrogen (63 K) and slush hydrogen (14 K), are two-phase single-component fluids containing solid particles in a liquid. The density and refrigerant heat capacity of the slush hydrogen (50 wt%) increase by 16% and 18%, respectively compared with those of liquid hydrogen (20K). Because of its advantages, slush hydrogen allows the efficient transportation and storage of hydrogen energy. The energy system where slush hydrogen is transported as energy and used in superconducting power transmission refrigerant is suggested [1]. In this system, the synergic effect between the transportation of fuel and electrical power at the same time and the storage of those are expected. However, pressure drop reduction and heat transfer deterioration of slush flow are not clarified enough. For such equipments, it is necessary to understand the heat transfer characteristics of slush flow.

The aim of this research is to clarify heat transfer characteristics of slush nitrogen and slush hydrogen in a horizontal pipe with the computational model based on 3D two-phase flow model including the effect of the melting of the solid phase particles.

2. Analysis method

2.1. Computational model

The computational model is solved by a finite volume method. The mesh structure of slush flow in the horizontal pipe is shown in Fig. 1. This mesh structure has total cells of 232,960. And the computational model enables the three-dimensional analysis of flow and heat transfer characteristics of slush flow in a horizontal circular pipe considering the exchange of mass, momentum and energy changes between the solid and liquid phases including the melting of the solid phase by the thermally non-equilibrium two-fluid model.

In this two-fluid model, the solid phase is supposed to be the continuous phase as a dispersed particle system. The collisions among the particles and between the particles and the pipe wall are assumed to be negligible. To reduce the computational load for the numerical calculation, the incompressibility of fluid is assumed.

The standard k-ε is adopted to simulate the turbulence. And the PISO algorithm is utilized for the pressure calculation of the liquid phase.

2.2. Governing equations

Following equations are the modeling equations employed in the Euler-Euler coupling two-fluid model. The continuity equation for the phase φ ($\varphi = l$ for the liquid phase, s for the solid phase) is written as (1).

$$\frac{\partial(\alpha_\varphi \rho_\varphi)}{\partial t} + \nabla \cdot \left(\alpha_\varphi \rho_\varphi \boldsymbol{U}_\varphi\right) = \dot{m}_\varphi \tag{1}$$

The momentum equation is written as (2).

$$\frac{\partial \alpha_\varphi \rho_\varphi \boldsymbol{U}_\varphi}{\partial t} + \nabla \cdot (\alpha_\varphi \rho_\varphi \boldsymbol{U}_\varphi \boldsymbol{U}_\varphi) + \nabla \cdot (\alpha_\varphi \boldsymbol{\tau}_\varphi) + \nabla \cdot (\alpha_\varphi \rho_\varphi \boldsymbol{R}_\varphi) = -\alpha_\varphi \nabla P + \alpha_\varphi \rho_\varphi \boldsymbol{g} + \boldsymbol{M}_\varphi - \dot{m}_\varphi \boldsymbol{U}_\varphi \tag{2}$$

The energy equations are written as (3) and (4).

$$C_{p,l}\rho_l\left(\frac{\partial \alpha_l T_l}{\partial t} + \nabla \cdot \left(\alpha_l \boldsymbol{U}_l T_l\right)\right) = \nabla \cdot \left(\alpha_l \kappa_l^{eff} \nabla T_l\right) + Q_{Ll} + Q_l \tag{3}$$

$$C_{p,s}\rho_s\left(\frac{\partial \alpha_s T_s}{\partial t} + \nabla \cdot \left(\alpha_s \boldsymbol{U}_s T_s\right)\right) = \nabla \cdot \left(\alpha_s \kappa_s \nabla T_s\right) + Q_{Ls} + Q_s \tag{4}$$

The thermal recovery method is introduced to consider the phase transition as (5) and (6).

$$\begin{cases} T_s \le T_{tr}, \quad T_l \ge T_{tr} & \dot{m}_s = 0 \\ T_s > T_{tr}, \quad T_l \ge T_{tr} & \begin{cases} T_s = T_{tr} \\ \dot{m}_s = -\psi(T_s - T_{tr})/h_s \end{cases} \\ T_s \le T_{tr}, \quad T_l < T_{tr} & \begin{cases} T_l = T_{tr} \\ \dot{m}_s = \psi(T_{tr} - T_l)/h_s \end{cases} \\ T_s > T_{tr}, \quad T_l < T_{tr} & \begin{cases} T_s = T_l = T_{tr} \\ \dot{m}_s = -\psi(T_s - T_{tr})/h_s + \psi(T_{tr} - T_l)/h_s \end{cases} \end{cases} \tag{5}$$

$$\psi = nNu\pi d_s \kappa_l \tag{6}$$

2.3. Simulation condition

The inlet condition of each variable is given by a uniform condition. The solid and liquid velocities are assumed to obey the non-slip boundary condition at the wall and the other variables are defined as the Neumann condition.

The physical properties of the slush nitrogen and slush hydrogen are used as the values at the triple point. The solid fraction is set α_s = 13 vol.% and the solid particle diameter is assumed d_s = 1.3 mm. The inlet velocities are set in the ranges of U_{in} = 1.5 - 5.0 m/s. The heat fluxes from the wall are q = 10 and 30 kW/m^2.

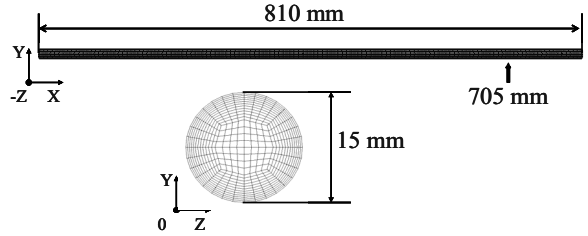

Fig.1 Mesh structure for the circular pipe.

3. Results and Discussions

Fig.2 shows comparisons of the bulk and wall temperatures between the numerical and experimental results for the slush nitrogen. The numerical result is adopted at the position of L = 705 mm which is the same point measured in our experiment [2]. The numerical result agrees well with the experimental result as shown in Fig.2. Thus the validity of the numerical code is ensured. The bulk and wall temperatures decrease with increase in the inlet velocity due to the relative reduction the heat transfer rate from the wall at higher flow rates.

Fig.3 shows the comparisons of the heat transfer coefficient between the numerical and experimental results for the slush nitrogen. The numerical result agrees well with the experimental result in the low velocity. The experimental result of the heat transfer coefficient is lower than numerical result in the high velocity because heat transfer deterioration occurs.

Fig.4 shows heat transfer coefficient increase rate of the slush nitrogen and slush hydrogen compared with the liquid nitrogen and liquid hydrogen. The increase rates of slush nitrogen and slush hydrogen decrease with increase in the inlet velocity. And over the 3 m/s velocity, the increase rates are within only a few percent. In the low velocity, the increase rate of slush nitrogen is higher than that of slush hydrogen. Because of the large viscosity and the high solid-liquid density ratio of nitrogen, the interference between solid and liquid phases for nitrogen increases. Thus the larger turbulence energy of liquid phase for nitrogen promotes the higher heat transfer than slush hydrogen.

4. Concluding remarks

In this research, the 3D thermally non-equilibrium two-fluid model based on Euler-Euler coupling method was applied to clarify the heat transfer characteristic of slush flow.

1) The bulk and wall temperatures of the numerical result agreed well with the experimental result. Thus the validity of the numerical code is ensured.
2) The heat transfer coefficient of the numerical result agreed well with the experimental result in the low velocity. But the numerical result didn't agree with the experimental result in the high velocity because of the heat transfer deterioration.
3) In the low velocity, the heat transfer coefficient increase rate of slush nitrogen was higher than slush hydrogen. Over the 3 m/s velocity, the increase rates were within only a few percent.

References

[1] K. Ohira, Cryogenics (TEION KOGAKU), Vol.41 (2006) 61-72

[2] K. Ohira, K. Nakagomi and N. Takahashi, Cryogenics (TEION KOGAKU), Vol.46 (2011) 148-160

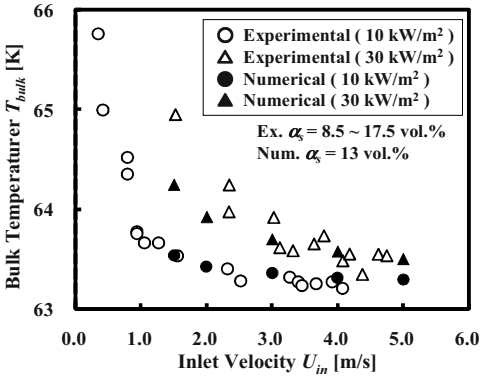

(a) Bulk temperature.

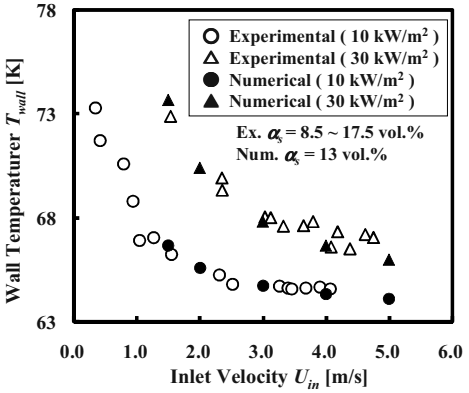

(b) Wall temperature.

Fig.2 Comparison of temperatures for the slush nitrogen.

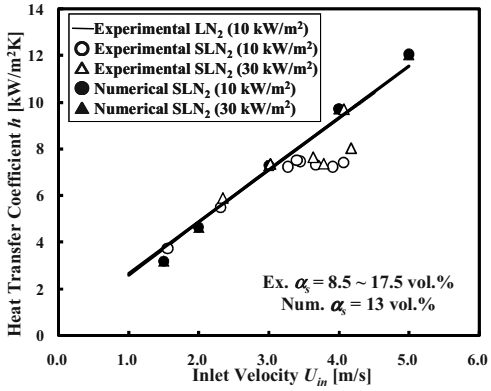

Fig.3 Comparison of heat transfer coefficient for the slush nitrogen.

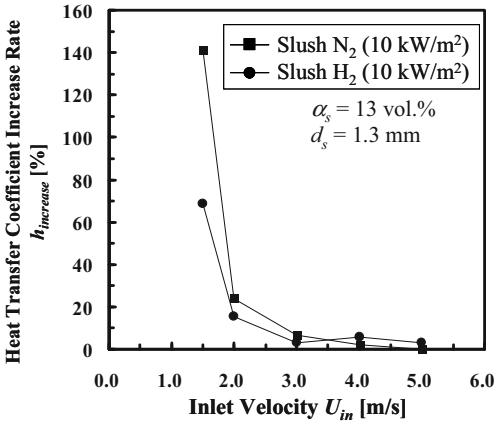

Fig.4 Heat transfer coefficient increase rates of the slush nitrogen and the slush hydrogen.

Eighth International Conference on Flow Dynamics
November 9 - November 11, 2011

High-accuracy Calculation for Aerodynamic Heating Using Temperature-Sensitive Paint

Kazuki Nishigata, Ryosuke Sawamura, Hiroki Nagai and Keisuke Asai
Tohoku University, 6-6-01 Aramaki-Aza-Aoba, Aoba-ku, Sendai, Miyagi, Japan 〒980-8579
nishigata.kazuki@aero.mech.tohoku.ac.jp

ABSTRACT

An existing calculation method to obtain global heatflux maps for temperature sensitive paint (TSP) measurement has applied to a one-dimensional heat conduction model with a semi-infinite model, ignoring its TSP layer and lateral heat conduction. These reduce an accuracy of measuring. In this study, a new calculation method considering these problems has been applied and compared with an existing method. These calculated heatflux have been evaluated with a thermocouple data. As a result, it has been shown that the new calculation method is effective for improving the calculation accuracy of an aerodynamic heating.

1. Introduction

Aerodynamic heating is one of the most important problems in space plane development, and is predicted from wind tunnel experiments. In wind tunnel experiments, various types of method of measuring heatflux have been used, and one of these is TSP (Temperature-Sensitive Paint) measurement. TSP measurement is an optical temperature measurement technique based on photochemical reaction of luminescent molecules, and it can obtain global quantitative heat flux maps of testing models as opposed to local heatflux data obtained from sensors like thermocouple.

An existing heatflux calculation method for TSP measurement has applied to a one-dimensional heat conduction model with a semi-infinite base. This model assumes that a layer of TSP is ignored. Also, it assumes that heat transfer is normal direction to surface of a model, ignoring lateral heat conduction on a three-dimensional body. These assumptions can be sources of error in heatflux measurement if TSP layer is thick or thermal conductivity of base material is high. So, a new calculation method considering TSP layer and lateral heat conduction has been developed by Liu et al.[1,2] and applied to a wind tunnel experiment [2].

In this study, we evaluated an accuracy of heatflux measuring using a new calculation method by directly comparing TSP data to thermocouple data in laser heating experiment.

2. Heatflux Calculation Method

Fig. 1 shows an illustration of one-dimensional heat conduction model with a semi-infinite flat plate. The parameter q is the heatflux at surface of the base or TSP layer, given by the discrete form of the solution of one-dimensional time-dependent heat conduction equation.

In the case of ignoring TSP layer as illustrated in the left side of Fig. 1, the formula for heatflux calculation is

$$q(t_n)=\frac{2\sqrt{\rho_b c_b k_b}}{\sqrt{\pi}}\left[\sum_{i=1}^{n}\frac{T(t_i)-T(t_{i-1})}{\sqrt{t_n-t_i}+\sqrt{t_n-t_{i-1}}}\right] \quad (1)$$

.

The parameter $T(t)$ is the surface temperature given by TSP data, and ρ_b, c_b, k_b is the density, specific heat and thermal conductivity of the base, respectively.

Then, a new calculation method, in the case of TSP layer on the base as illustrated in the right side of Fig. 1, the formula for heatflux calculation is

$$q(t_n)=\frac{k_p(1-\bar{\varepsilon}^2)}{\sqrt{\pi a_p}}\left[\sum_{i=1}^{n}\frac{T(t_i)-T(t_{i-1})}{\sqrt{t_n-t_i}+\sqrt{t_n-t_{i-1}}}\left\{\overline{W}(t_n-t_i)+\overline{W}(t_n-t_{i-1})\right\}\right] \quad (2)$$

,

where

$$a_p=k_p/\rho_p c_p,\ \varepsilon=\sqrt{\rho_p c_p k_p/\rho_b c_b k_b},\ \bar{\varepsilon}=(1-\varepsilon)/(1+\varepsilon)$$

$$\overline{W}(t,\bar{\varepsilon},L)=\frac{2}{\sqrt{\pi}}\int_0^{\infty}\frac{\exp(-\xi^2)d\xi}{1+\bar{\varepsilon}^2-2\bar{\varepsilon}\cos(2L\xi/\sqrt{a_p t})}$$

.

The parameter ρ_p, c_p, k_p is the density, specific heat and thermal conductivity of TSP, respectively, and L is the TSP layer thickness.

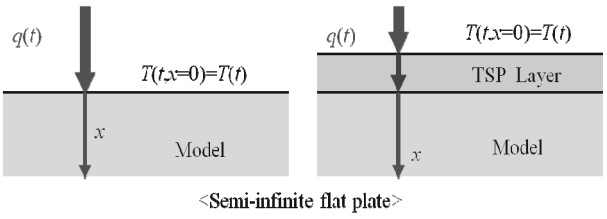

Fig. 1 One-dimensional Heat Conduction Model with Semi-infinite Flat Plate

3. Laser Heating Experiment

3.1. Experimental Setup

TSP measurements using CO_2 laser were conducted. In this experiment, flat plate coated with TSP was heated by 1W power and 3.5mm in diameter laser for 10 seconds. The TSP was PTMSDPA[3], which was coated on ceramic flat plate. Also, a thermocouple was attached in the area of laser heating spot.

Fig. 2 shows a schematic illustration of the measurement, and Table 1 shows thermophysical properties of TSP and ceramic. The TSP thickness was 9.44μm, which was measured by ultra-deep color three-dimensional profile measuring microscope. The frame-rate and exposure time of high-speed camera were 1000fps and 1ms, respectively.

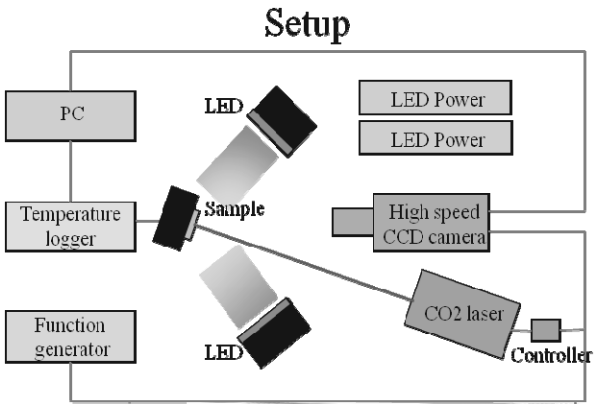

Fig. 2 Schematic Illustration of Laser Heating Measurement

Table 1 Thermophysical Properties

Property	Ceramic	PTMSDPA
Dentity [kg/m^3]	2500	1300
Specific heat [J/(kg×K)]	800	1500
Thermal conductivity [W/(m×K)]	1.4	0.16
Thermal diffusivity [m^2/s]	7.000×10^{-7}	8.205×10^{-8}

3.2. Result and Discussion

Heatflux was calculated by temperature data obtained from TSP images and thermocouple data. The time step of calculation is 0.1s, and t=0 is the start time of laser heating. For quantitative comparison, a relative error is defined as $|\{X_{TSP}(t)-X_{TC}(t)\}/X_{TC}(t)|\times100[\%]$, where X_{TSP} and X_{TC} are the data from TSP and thermocouple, respectively.

An existing method Eq. (1) and a new method Eq. (2) were applied in heatflux calculation. Fig. 3 and Fig. 4 show images of heatflux at t=2s and 8s obtained from an existing method and a new method, respectively. Also, Fig. 5 shows time histories of these heatflux data. In an existing method, a significant error was observed, which was caused by heat conduction in thick TSP layer and differences of thermophysical properties between TSP and Ceramic. Meanwhile, the error has been corrected by applying a new method, especially in its early peak. This is caused by the effect of error function $\overline{W}(t,\bar{\varepsilon},L)$ in Eq. (2). The error was 10% in total average, lower than 50% of existing method. Perhaps, the rest of error was caused by lateral heat conduction in TSP layer and surface roughness of TSP. To correct these effects and increase accuracy of calculation, Gaussian filter will be applied in the future.

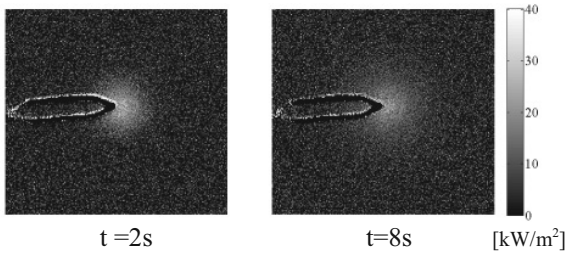

Fig. 3 Heatflux Images by An Existing Method

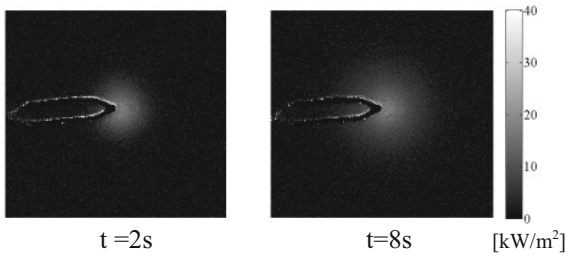

Fig. 4 Heatflux Images by A New Method

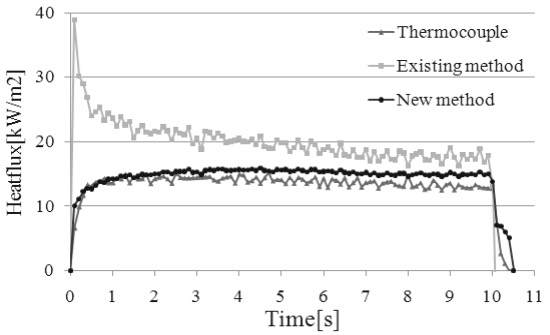

Fig. 5 Time Histories of Heatflux Data

4. Conclusion

TSP measurements using CO_2 laser has been conducted, and a new calculation method considering TSP thickness has been applied and compared with an existing method. These calculated heatflux have been evaluated with a thermocouple data. As a result, it has been shown that the new calculation method is effective for improving the accuracy of the calculation of aerodynamic heating measurement.

References

[1] T. Liu, Z. Cai, J. Lai, J. Rubal and J. P. Sullivan: Analytical Methods for Determination of Heat Transfer Fields from Temperature Sensitive Paint Measurements in Hypersonic Tunnels, AIAA 2009-736, 2009.

[2] T. Liu, B. Wang, J. Rubal and J. P. Sullivan: Correcting lateral heat conduction effect in image-based heat flux measurements as an inverse problem, International Journal of Heat and Mass Transfer 54 1244-1258, 2011.

[3] G. Kwak, S. Fukao, M. Fujiki, T. Sakaguchi and T. Masuda: Temperature-Dependent, Static, and Dynamic Fluorescence Properties of Disubstituted Acetylene Polymer Films, Chem. Mater., Vol.18, 2081-2085, 2006.

Secondary Wick Effect for Performance of Loop Heat Pipes

Kouhei Magome, Hiroki Nagai
Department of Aerospace Engineering, Tohoku University
6-6-01, Aramaki-Aza-Aoba, Aoba-ku, Sendai 980-8579, JAPAN
magome.kohei@aero.mech.tohoku.ac.jp

ABSTRACT

Loop Heat Pipes (LHPs) are thermal transfer devices using vapor-liquid phase change, has been accepted as a thermal control device of the spacecrafts. But, for very complex thermal characteristics, its analysis is not easy. Therefore, lots of experiments had been operated and in those cases, a section called "secondary wick" tends to be ignored for several reasons. In this study, the steady state of the evaporator models was simulated to investigate the secondary wick characteristics. As a result, it found that the thickness of the secondary wick doesn't influence so much for the pressure field in the primary wick at least within the range in this study.

1. Introduction

For the results of becoming miniaturization and high performance of the spacecraft, the thermal requirement has exceeded the limit of traditional thermal control system (TCS) in recent years. Loop Heat Pipe (LHP) is a device that can resolve for this problem, it has highly thermal transfer performance by utilizing vapor-liquid phase change, and has low limitation for its positioning, high robustness.

However, a phenomenon of LHP inside is a two phase flow with vapor-liquid phase shift dominated by complicated thermal fluid dynamics, an analysis of that is not easy. Consequently, some don't want to use this device due to lacking of certainty. To solve this problem, a lot of ground tests, theoretical analysis, and computational simulations have been operated for various situations. In these experiments, characteristics of a section called "secondary wick" tend to be ignored because of its design's trade secret and simplification of numerical method. In a word, the secondary wick is regarded as having infinite liquid transfer abilities and never failing any conditions. But, according to actual test data, it shows that above assumptions are not always proper. Therefore, in this study, steady state evaporator models were simulated numerically to investigate the secondary wick characteristics.

2. Principle

2-1. Operating of Loop Heat Pipes

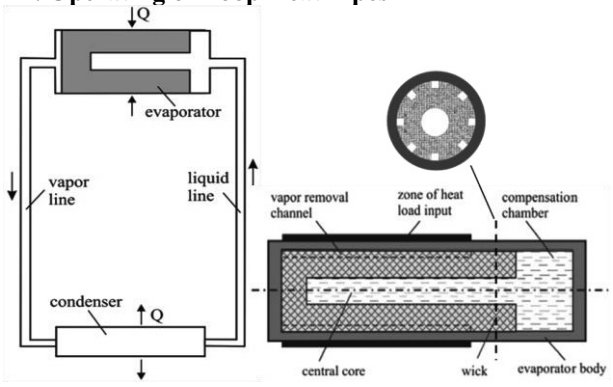

(a) overall loops (b) evaporator

Fig. 1 Schematic of LHP [1]

Fig. 1 (a) is schematic of overall LHP, and (b) is a detailed figure of the evaporator. LHP is composed of main four elements, evaporator, condenser, vapor line, and liquid line. In the evaporator, there is the porous material called wick and the capillary force generated this section is a driving force of a circulation. In the loop, the working fluid is enclosed, it is vaporized by the heat input and flows to the condenser through the vapor line. At the condenser, heat is removed from vapor to ambient, and then vapor condenses, returns into liquid and flows to the reservoir in the evaporator.

2-2. Secondary Wick

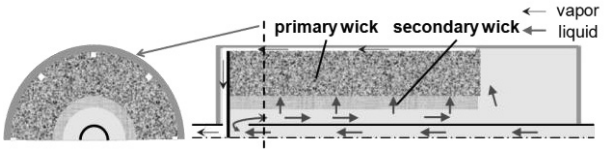

(a) radius (b) along with z axis

Fig. 2 Section of LHP evaporator (upper z axis)

LHP's driving force is a capillary pressure generated at the wick in the evaporator. In operating, this force must exceed total loop pressure drops. Although the capillary pressure increases with reducing the pore radius of the wick, the working fluid becomes difficult to permeate the wick adversely. To solve this conflict, the secondary wick is installed in the location of Fig. 2. The main function of the secondary wick, which is made of the rougher porous material, is a supplying liquid to the primary wick certainly. With the secondary wick, it can transport more smoothly the working fluid from the reservoir to the primary wick.

3. Analysis Method

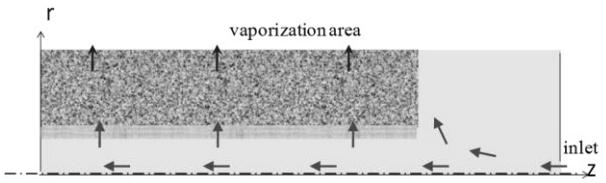

Fig. 3 Simplified Models

The numerical simulation for a steady-state pressure field was conducted for the LHP cylindrical evaporator. A using model is a simplified Fig. 2 in two-dimensional cylinder coordinates as shown in Fig. 3. Boundary conditions are given as no flow crossing boundaries except the vaporization area and the reservoir inlet. The

velocity in the vaporization area v_{out} is given by

$$v_{out} = Q / (2\pi l_v) / (\rho A) \quad (1)$$

where Q is the heat load, l_v is a latent heat of the vaporization, ρ is a density of the working fluid, and A is a surface area of the vaporization section. Under above conditions, the continuity equation and the *N. S.* equations in the cylinder coordinate were solved numerically. In the wick region, a velocity was calculated by using Darcy's law instead of the *N. S.* equations:

$$v = -\frac{K}{\mu}\frac{\partial P}{\partial r} \quad (2)$$

where K is a permeability of wicks, μ is a viscosity of liquid, and P is pressure. The size of the evaporator is 20 mm in diameter and 130 mm in length, and then the primary wick is 91 mm length and 6 mm thickness. The secondary wick length is equal to that of the primary, but its thickness was changed into 3 patterns and for each pattern, the permeability of the primary or secondary wick was changed (Table 1). The working fluid is water and its thermal properties were assumed to be constant independent on the temperature. A HSMAC method was applied for a regular rectangular grid.

Table 1. Permeability of wick

	primary wick	secondary wick
	K[m^2]	K[m^2]
case1	1.42E-14	7.60E-12
case2	1.42E-14	1.22E-10
case3	7.17E-15	7.60E-12
case4	7.17E-15	1.22E-10
case5	1.79E-15	7.60E-12
case6	1.79E-15	1.22E-10
case7	8.10E-16	7.60E-12
case8	8.10E-16	1.22E-10

4. Results and Discussion

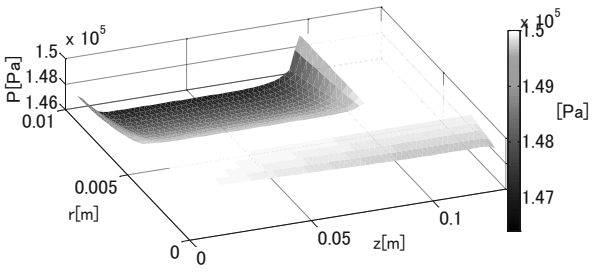

Fig. 4 Pressure field (no secondary wick)

Fig. 4 gives an example of the simulation result of the pressure field in LHP cylindrical evaporator. In the wick, pressure decreases with going from inner to outer of the evaporator. This is because the material of the wick is homogeneous and liquid suffers a uniform capillary pressure according as passing through the wick.

Fig. 5 presents the r direction pressure field in the position z = 0.04. The beginning point of the pressure drop gets closer to the center of the evaporator compared with no secondary wick case. But while the pressure drop in the primary wick all reduces, its whole tendency hardly changes. This result agrees with the analytical solution of the one-dimensional continuity equation. The drop in the saturated vapor pressure promotes the vaporization in the vaporizing region, it is effective for LHP performance due to relaxing the superheating.

However, the effect caused by changing the secondary wick thickness was only in the section close to the central core and this tendency is also seen in the case of changing the secondary wick permeability. In other words, the thickness of the secondary wick doesn't influence so much for the pressure field in the wick at least within the range varied in this study. But, there is possibility that the working fluid becomes difficult to permeate the wick due to a narrow flow path below the wicks by thickening the secondary wick. Therefore, there are the need to restrict the thickness of the secondary wick not to narrow the flow path and a large permeability.

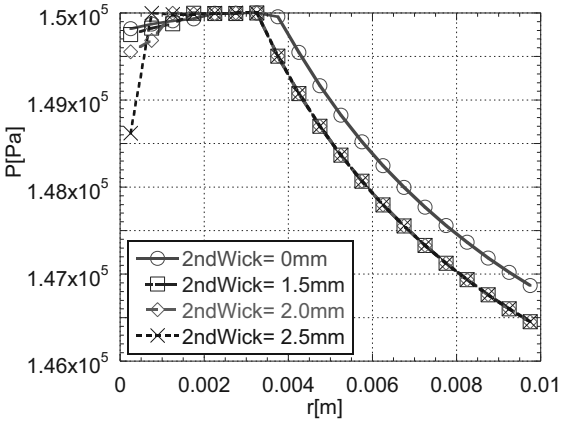

Fig. 5 The r direction pressure field (case1)

5. Concluding remarks

To investigate the secondary wick characteristics, a steady-state pressure field in the LHP cylindrical evaporator was calculated numerically. The thickness of the secondary wick and the permeability of wicks were changed for each case. As a result, it found that the values of pressure in the primary wick dropped compared with no secondary, but a decrease rate on each point in the primary was constant. In the future works, the temperature field in the evaporator will be calculated by using the results of this study.

References

[1] M. A. Chernysheva, Y. F. Maydanik, J. M. Ochterbeck, 'Heat Transfer Investigation in Evaporator of Loop Heat Pipe During Startup', JOURNAL OF THERMOPHYSICS AND HEAT TRANSFER ,Vol. 22, No. 4, October–December 2008

[2] Trim T. Hoang, 'Mathematical Modeling of Loop Heat Pipes Part Ⅱ: Secondary Wick Analysis', 5th IECEC 25-27 June 2007, St. Louis, Missouri

Eighth International Conference on Flow Dynamics
November 9 - November 11, 2011

Heat Transfer Characteristics of Oscillating Heat Pipe by Difference of Surface Characteristic

Takamu. Kanayama[1], Takuro. Daimaru[1], Hiroki. Nagai[1], Hiroyuki. Ogawa[2]
*1 Dept. of Aerospace Engineering, Tohoku University, 6-6-01, Aramaki Aza-aoba, Aoba-ku, Sendai, 980-8579, JAPAN
*2 Thermal System Group, ISAS/JAXA, 3-3-1, Yoshinodai, Chuo-ku, Sagamihara, Kanagawa 252-2510, JAPAN
kanayama.takamu@aero.mech.tohoku.ac.jp

ABSTRACT

Self-Excited Oscillation Heat Pipe is two-phase heat transfer device utilizing pressure oscillation for evaporation and condensation of working fluid. In this study, the change of surface characteristic of OHP's flow path into hydrophobicity resulted in an increase of OHP's thermal resistance and pressure amplitude, when compared to the surface condition with no-hydrophobicity.

1. Introduction

Recently, a new concept of heat pipe differing from traditional concept is attracting attention. This is called "Self-Excited Oscillation Heat Pipe (OHP)". This OHP has higher heat transport and much lighter and thinner than traditional one. In addition, it isn't necessary to have any moving parts. So, OHP has very simple mechanism. Therefore, this is very suitable for heat spreading and for using in radiating surfaces of spacecraft.

But there are several problems in using this technique in spacecrafts. Firstly, there is no data to design the system and data for design method is lacking. Secondly, OHP must have robust ability in microgravity.

In this study, we changed surface characteristic of OHP's flow path. We investigated the difference of surface characteristic on how it affects the heat transfer. We observed the working fluid oscillation, using pressure and temperature sensors.

2. Operating Principle of OHP

OHP operates by using the difference of pressure between the heating and cooling section. Working fluid boils by the heat absorbed at heating section. Vapor bubble is created by nuclear boiling. Working fluid is transported by vapor plug.

Temperature of cooling section is low. So, vapor plug goes to cooling section. Since, this area's saturated pressure is low, the vapor plug at cooling section condenses, and cooling section pressure became low. Therefore, liquid slug moves from heating section to cooling section. For that reason, this round-trip motion arises from a number of flow paths. These round-trip motions cause derived self-excited oscillation.

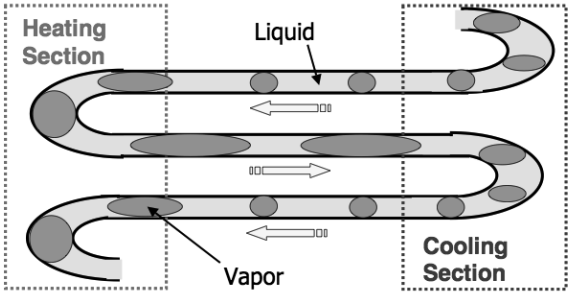

Fig1. Image of self-excited oscillation

3. Experiment

3.1 Design of OHP

An inner diameter of OHP has to be divided into liquid slugs and vapor plugs. The maximum inner diameter can hold a vapor plug. This condition is derived by Bond number. Bond number should be under 4 to start up.

$$D_{\max} = 1.84\sqrt{\frac{\sigma}{g(\rho_l - \rho_v)}} \quad (1)$$

$D_{\max}$ is about 2.8 [mm] for 100% ethanol at 300K. In this study, we selected 98% ethanol. So, we designed OHP's flow path is 2.0[mm].

Table1 Design of OHP's parameters

Type and heat mode of OHP	Looped OHP and Horizontal
Cross section of tubes	Rectangular
Number of parallel tube	15
Length of each tube	240.0[mm]
Inner diameter	2.0 [mm]

3.2 Difference of surface characteristic

This experiment changes surface characteristic of OHP's flow path. We turned surface characteristic into hydrophobicity by using fluorine resin coating. Fig.1 shows comparison of surface characteristic without hydrophobicity and with hydrophobicity.

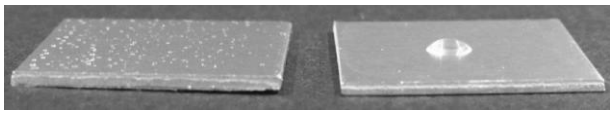

Fig. 2 Difference of surface characteristic
(left : without hydrophobicity,
right : with hydrophobicity)

3.3 Experimental Setup

The experimental setup is shown Fig.3. Thermocouples and pressure sensors are connected to the OHP. Their sampling rates are 100[Hz]. A working fluid oscillation is observed by a high speed camera at 250[fps].

The working fluid oscillation can be observed more easily by using ethanol mixed with perylene. Fig.4 shows perylene is excited by UV laser. In this study, working fluid charge ratio is 75%.

4. Result and Discussion

4.1 Pressure and Temperature

Fig.5 shows pressure oscillations of Base and Hydrophobicity at thermal input of 70W. Base and Hydorophobicity indicate flow path without hydrophobictiy and with hydrophobicity, respectively.

Table2 shows each frequency and amplitude of pressure oscillations at 70W. Compared to Base and Hydrophobicity, frequency is almost same. But, the amplitude of pressure oscillations in Hydrophobicity is larger than that of Base's.

Table2 Frequency and Amplitude

	Frequency [Hz]	Amplitude [kPa]
Base	3.74	6.4
Hydrophobicity	4.01	11.4

4.2 Thermal Resistance

Thermal resistance of Base and Hydorophobicity calculated from Eq. (2).

$$R_{th} = \frac{\Delta T}{W} = \frac{T_{heat} - T_{cool}}{W} \quad (2)$$

And, Fig.7 shows each thermal resistance. Compared to each thermal resistance, Hydrophobicity was slightly larger than Base's.

5. Conclusion and Future Work

In this study, we tried to improve performance of OHP by changing surface characteristics to hydrophobicity. First, flow path was surface changed to hydrophobicity. Then we investigated the change of pressure frequency and amplitude in OHP. In the result, Hydrophobicity's amplitude was larger than Base's. About the performance of OHP, liquid slug distance (amplitude) is related to performance.

For the future, we will investigate relationship of pressure amplitude and liquid slug distance. And, we will investigate difference of thermal resistance. Though, its difference is little. About the difference of surface characteristic effectiveness, we will investigate by changing the condition of thermal input and heat mode.

References

[1] Wook Hyun Lee, Hyun Suck Junk, 「Characteristic of Pressure Oscillation in Self-excited Oscillating Heat Pipe based on Experimental Study」 Proceedings of the 6th International Heat, pp394-407, 2000

[2] Amir Faghri, Yuwen Zhang, 「Thermal Modeling of Unlooped and Looped Pulsating Heat Pipes」 Journal of Heat Transfer, Vol.123, pp1159-1172, 2001

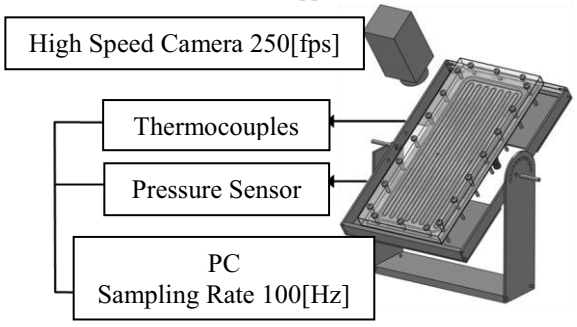

Fig.3. Experimental setup

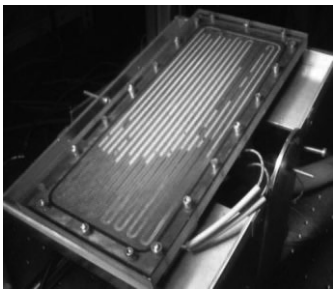

Fig.4. Visualization of working fluid oscillation

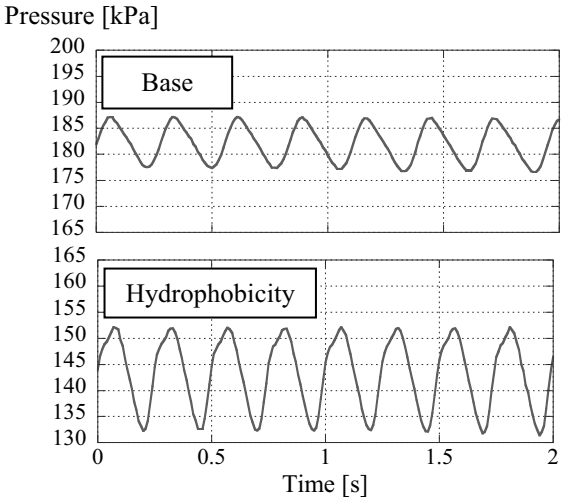

Fig.5 Pressure Oscillation at 70W

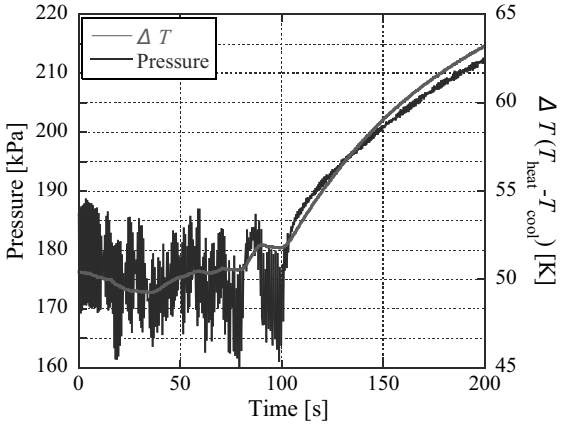

Fig.6 Relation of pressure and temperature

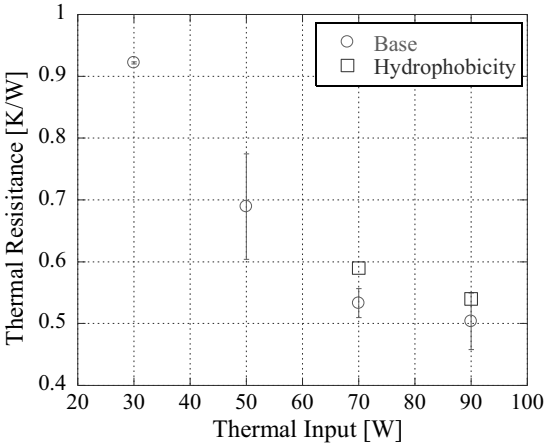

Fig7. Effect of the surface characteristic on thermal resistance

Eighth International Conference on Flow Dynamics
November 9 - November 11, 2011

Development of Temperature-Sensitive Paint for High-Temperature Measurement

Ryosuke Sawamura, Hiroki Nagai, Keisuke Asai
Dept. of Aerospace Engineering, Tohoku University
6-6-01, Aramaki Aza-aoba, Aoba-ku, Sendai, Miyagi, 980-8579, JAPAN

sawamura.ryousuke@aero.mech.tohoku.ac.jp

ABSTRACT

To measure temperature and heat-flux distribution at high temperatures, we have tried to make Temperature-Sensitive Paint composed of thermographic phosphor. In this study, YAG:Tm^{3+}, a kind of phosphor was investigated about its temperature sensitivity and emission spectrum. The luminescence intensity of the phosphor decreases linearly over 1100°C, and has high temperature sensitivity. YAG:Tm^{3+} can be applied as TSP for measuring temperatures over 1100°C.

1. Introduction

Temperature-Sensitive Paint (TSP) is generally used for thermal analysis of model surface. Usual TSP is made of organic compound, but they decompose thermally at temperatures greater than 100°C. So, these days TSP using phosphor has been studied [1]. Phosphor is an inorganic powder, and has high thermal tolerance. Especially the phosphor whose luminescence depends on temperature called "thermographic phosphor".

In this study, we used a kind of thermographic phosphor; YAG:Tm^{3+}. We investigated its temperature sensitivity and spectrum at different temperatures and studied its feasibility of using it as a TSP at high-temperatures.

2. Phosphor

YAG:Tm^{3+} is a phosphor whose peak emission wavelength is 460nm. In the previous study, the lifetime of this phosphor decayed over about 1000°C [2]. In this study, we use YAG:Tm^{3+} made by *Phosphor Technology*, and its doping ratio of Tm^{3+} is 1.5%.

3. Experiment

3.1 Experimental condition

In this experiment, temperature controlled stages; *TS1500* (Linkam scientific instruments) were used for heating the sample. YAG:Tm^{3+} was used as sample, and heated from 20°C to 1300°C by TS1500. A *Hg-Xe* lamp with short pass filter (over 400nm cutoff) was used as excitation light. To measure the spectrum and the emission intensity of phosphor, Photonic Multichannel Analyzer; PMA (HAMAMATSU Photonics) with 460±10nm bandpass filter was used. Fig.1 shows the spectrum of the excitation light, and Fig.2 shows the experimental setup.

The sample stage of *TS1500* was bright at high temperature because of infrared radiation. Thus, the intensity count is equal to the difference between the intensities measured without excitation light and with excitation light.

3.2 Result and Discussion

Fig.3 shows temperature sensitivity of YAG:Tm^{3+}. This figure has count number of the luminescent intensity integrated in the range of 450nm to 470nm measured by PMA. In this figure, luminescence intensity increases from 20°C to 800°C. Fig.4 shows the emission spectrum of YAG:Tm^{3+} in lower temperature range. From this figure, we can see that the shape of the spectrum is not changing with increasing temperature. So, it is proved that this increase of luminescence intensity is not caused by other emission sources. At over 800°C, the luminescence intensity of YAG:Tm^{3+} decreases monotonically. Especially, it has large and linear temperature sensitivity at over 1100°C. This decrease of luminescence intensity is seemed to be brought about by decay of luminescence lifetime [2]. Fig.5 shows the emission spectrum of YAG:Tm^{3+} over 1100°C. From this figure, the shape of its spectrum is proved to be same.

From these results, we can see that YAG:Tm^{3+} can be applied as TSP for measuring temperatures over 1100°C. But, its temperature sensitivity excited by this light source dose not decrease monotonically. Therefore, measurement system, for example excitation light source or measuring method, needs to be improved to use as a dye for TSP.

4. Conclusion remarks

To make TSP for measuring high-temperature, we investigated temperature sensitivity of YAG:Tm^{3+}, a kind of thermographic phosphor. Although luminescence intensity of this phosphor increased under 800°C, it has high temperature sensitivity over 1100°C. So, these results indicate the feasibility of using YAG:Tm^{3+} while the measuring system has to be improved further.

5. Future works

To make TSP using YAG:Tm^{3+}, it is combined with colloidal silica which is a binder having high thermal tolerance. Using this binder, sprayable TSP using phosphor can be made. In addition, the measurement by lifetime method will be done to avoid the effect of infrared radiation for actual temperature distribution measurement

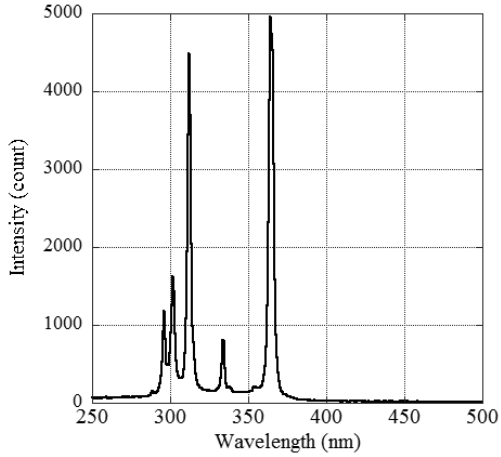

Fig.1 The spectrum of excitation light source

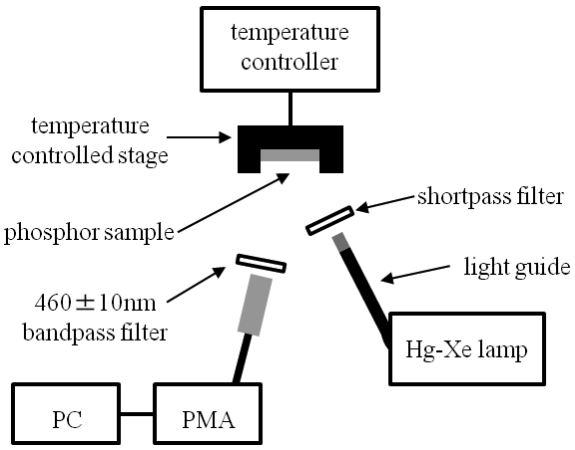

Fig.2 Experimental setup

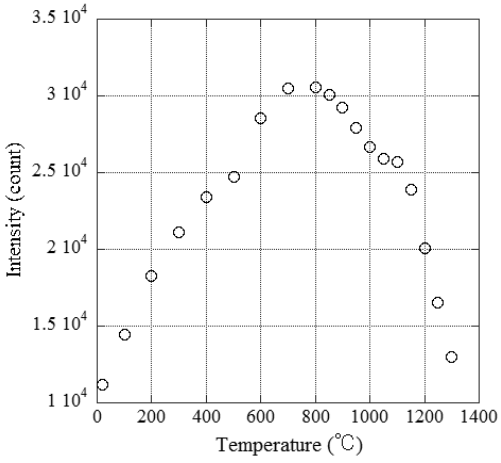

Fig.3 Temperature Sensitivity of YAG:Tm^{3+}

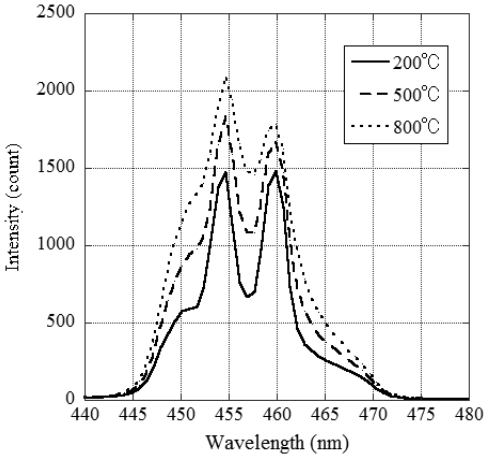

Fig.4 The spectrum of YAG:Tm^{3+} in lower temperature

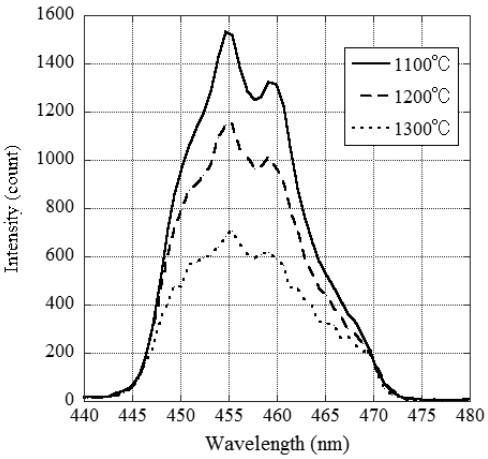

Fig.5 The spectrum of YAG:Tm^{3+} in higher temperature

References

[1]S. W. Allison et al, Rev. Sci. Instrum.,Vol.68, No.7, 1997

[2]M R. Cates, S.W.Allison, S. L. Jaiswal, D.L. Beshears,Oak Ridge National Laboratory, "YAG:Dy and YAG:Tm Fluorescence To 1700C", The 49th International Instrumentation Symposium, Paper # TP03AERO033, 4-8 May 2003

Eighth International Conference on Flow Dynamics
November 9 - November 11, 2011

Gas Phase and Surface Reactions of $H_2/O_2/N_2$ Mixture in a Micro Flow Reactor with a Controlled Temperature Profile

Kenichiro Saruwatari, Hisashi Nakamura, Takuya Tezuka, Susumu Hasegawa, Kaoru Maruta
Institute of Fluid Science, Tohoku University, 2-1-1 Katahira Aoba-ku Sendai Miyagi 980-8577, Japan
saruwatari@edyn.ifs.tohoku.ac.jp

ABSTRACT

Combustion characteristics of $H_2/O_2/N_2$ mixture were investigated by using a micro flow reactor with a controlled temperature profile. Two flame responses were observed experimentally by changing the inlet mixture flow velocity. 2-D computation with detailed chemical mechanisms of gas phase reaction and surface reaction was conducted to examine the effect of radical quenching on the wall surface. By comparing the computation with gas sampling analysis, it was found that the surface reaction mechanism for radical quenching may overestimate the effect of radical quenching on the wall surface.

1. Introduction

With the downsizing and technology advance of mobile devices, the demands on micro power source are increasing. Micro combustion systems are expected to be one of the possible power sources having high energy density. Due to large surface-to-volume ratio, heat loss to the wall is increased in micro combustion and it is difficult to maintain a stable combustion. In addition, the effect of radical quenching on the wall surface is not negligible in micro system and it is important to clarify it. However, there are few experimental and numerical studies on radical quenching [1, 2].

This study focused on a micro flow reactor with a controlled temperature profile [3]. A narrow channel, which diameter is smaller than ordinary quenching diameter, was heated by an external heat source and given a stationary wall temperature gradient. This technique can simulate heat recirculation and enable a stable combustion. In previous studies, combustion characteristics of methane/air [4], DME/air [5] and *n*-heptane/air [6] mixtures were investigated in the micro flow reactor. These studies established the availability of the micro flow reactor with a controlled temperature profile as the method to examine the combustion characteristics of various hydrocarbons.

In this study, we applied H_2 to the micro flow reactor as a fuel which is sensitive to surface radical quenching. The objective of this study is to examine combustion characteristics of H_2 and the effect of radical quenching on the wall surface.

2. Experimental and computational method

Figure 1 shows the schematic of the experimental setup. A quartz glass tube with an inner diameter of 1 mm was used as a micro flow reactor and heated by a H_2/air flat flame burner to obtain a stationary temperature profile from 300 K to 1300 K. A stoichiometric H_2/air/N_2 mixture which was controlled by mass flow controllers was supplied into the tube in atmospheric pressure. In order to decrease the ordinary quenching diameter less than 1 mm, the mole fractions of H_2 and O_2 were diluted with N_2 (X_{H2}:X_{O2}:X_{N2}=2:1:9). Flame images were taken by a high-speed camera with an UV lens to examine flame shapes and flame positions by changing the inlet flow velocity. The exhaust gas was analyzed by a gas chromatograph with a thermal conductivity detector. Argon was used as a carrier gas. Molecular Shieve 5A 60/80 was used.

To investigate the experimental result and the effect of radical quenching, 2-D computation was conduct by FLUENT 6.3 with detailed reaction mechanisms. The conservation equations of mass, momentum, energy and species were solved. Because of cylindrical tube, the computational domain was a half of the tube from central axis (r=0 mm) to the wall (r=0.5 mm). As a boundary condition, the wall surface was assumed as slip wall for simplicity and given a stationary wall temperature profile which is the same as the experimental wall temperature profile. H_2 oxidation mechanism [7] was employed for the gas phase reaction. In order to evaluate the effect of radical quenching on the wall, two surface conditions were assumed; (a) inert wall without any surface reaction, (b) reactive wall with surface reaction mechanism for radical quenching [2].

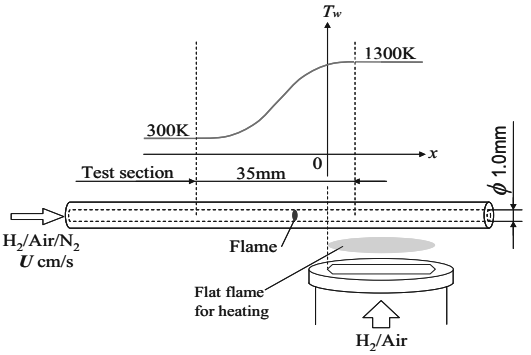

Fig. 1 Schematic of experimental setup and provided wall temperature profile.

3. Results and discussion

3.1. Experimental flame responses

Figure 2 shows the flame images obtained in experiment. *U* is the inlet mean flow velocity of mixture and *t* is the exposure time. Two flame responses were observed by changing the inlet flow velocity.

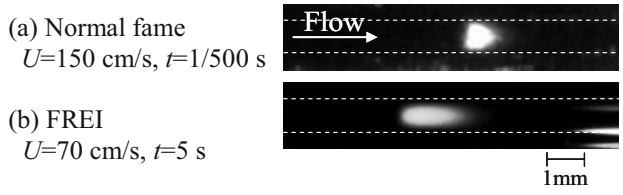

Fig. 2 Flame images.

In high flow velocity condition, $U > 90$ cm/s, stable normal flames (Normal flame) were observed. The mixture flowing into the tube is ignited due to high temperature wall and the flame propagates to upstream. Then it is stabilized at a certain point within the prescribed temperature gradient where local burning velocity and local mixture flow velocity are balanced. The stabilized flame position shifted to upstream with decreasing inlet flow velocity. In the flow velocity condition between 90 and 12 cm/s, unstable flames which are called *flames with repetitive extinction and ignition* (FREI) [3] were observed. The mixture is ignited at ignition point in the downstream. Then the ignition kernel propagates to upstream and it is quenched at extinction point due to increasing heat loss to the wall. After some delay, re-ignition occurs at ignition point. FREI repeats this periodic cycle rapidly. In low flow velocity condition below 12 cm/s, no flames were visually observed. However H_2 was completely consumed and oxidation reactions were recognized by gas sampling analysis. In previous study on various hydrocarbon fuels in the micro flow reactor, stable flames with weak luminescence (Weak flame) were obtained in small flow velocity condition of FREI [4-6].

3.2. Effect of radical quenching

To investigate the effect of radical quenching on the wall, 2-D computation was conducted. Figure 3 shows the computational distributions of H_2, O_2 and H_2O mole fractions, gas phase temperature and wall temperature at inlet mixture flow velocity of 200 cm/s on (a) inert wall and (b) reactive wall. Except for wall temperature profiles, the other distributions are the results on the tube center at r=0 mm. The wall temperature is illustrated the result on the wall surface where r=0.5 mm. In inert wall condition (Fig. 3a), H_2 and O_2 were rapidly consumed and H_2O was produced in a reaction zone. On the other hand, in reactive wall condition (Fig. 3b), a reaction zone was also formed. Even though the gas phase temperature is high enough for hydrogen combustion, 8 % of reactants remained in the downstream of the reaction zone. Figure 4 shows distributions of OH mass fraction and wall temperature. The peaks of it are smaller in the reactive wall condition than in the inert wall condition and shift to downstream in the reactive wall. These differences between inert wall and reactive wall would be attributed to suppression of oxidation reaction because of reduction of radicals by the effect of radical quenching on the wall surface. However, since H_2 was completely consumed in experiment, computations couldn't reproduce the experiment. Thus it was concluded that the radical quenching mechanism may overestimate the effect of radical quenching on the wall surface.

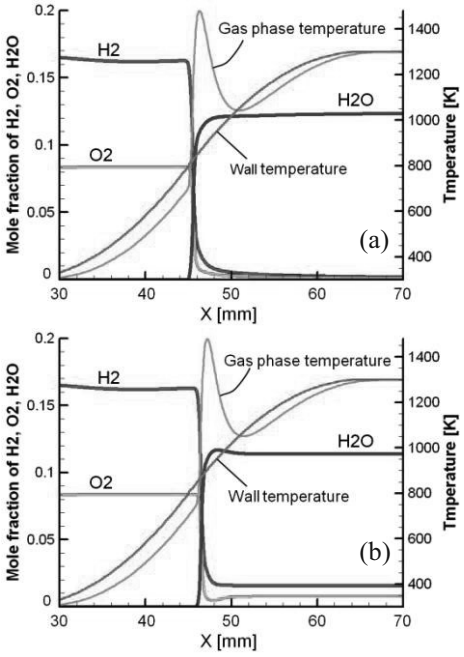

Fig. 3 Distributions of mole fractions (H_2, O_2 and H_2O), gas phase temperature and wall temperature at U=200 cm/s in (a) inert wall and (b) reactive wall.

4. Conclusions

Two flame responses were obtained experimentally by changing the inlet flow velocity of H_2/air/N_2 mixture in a micro flow reactor with a controlled temperature profile. In low flow velocity condition, although no flames were observed, H_2 oxidation was confirmed by gas sampling analysis. The effect of radical quenching was examined by 2-D computation. Comparing the computational results of two types of the wall condition with the result of gas sampling analysis, it was found that radical quenching mechanism may overestimate the effect of radical quenching on the wall surface.

Reference

[1] S. Raimondeau, D. Norton, D. G. Vlachos and R. I. Masel, Proc. Combust. Inst. **29** (2002) 901-907.

[2] P. Aghalayam, P-A. Bui and D. G. Vlachos, Combust. Theory Modeling **2** (1998) 515-530.

[3] K. Maruta, T. Kataoka, N. I. Kim, S. Minaev and R. Fursenko, Proc. Combust. Inst. **30** (2005) 2429-2436.

[4] Y. Tsuboi, T. Yokomori and K. Maruta, Proc. Combust. Inst. **32** (2009) 3075-3081.

[5] H. Oshibe, et al., Combust. Flame **157** (2010) 1572-1580.

[6] A. Yamamoto et al., Proc. Combust. Inst. **33** (2011) 3259-3266.

[7] J. Mantzaras, R. Bombach and R. Schaeren, Proc. Combust. Inst. **32** (2009) 1937-1945.

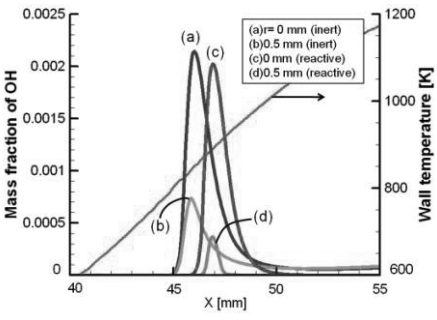

Fig. 4 Distributions of OH mole fraction in gas phase and wall temperature at U=200 cm/s.

Eighth International Conference on Flow Dynamics
November 9 - November 11, 2011

A Study of Thermal Design for the Development of High-efficiency Fluidized Bed Solar Reactor

So Sakuma[1], Atsushi Sakurai[2], Kyohei Ogino[2], Seung-Jae Lee[2], Koji Matsubara[2],
Nobuyuki Gokon[3] and Tatsuya Kodama[4]
[1] Graduate School of Science and Technology, Niigata University, Niigata city 950-2181, Japan
[2] Dep. of Mechanical & Production Engineering, Faculty of Eng., Niigata University, Niigata city 950-2181, Japan
[3] Center for Transdisciplinary Research, Niigata University, Niigata city 950-2181, Japan
[4] Dep. of Chemistry & Chemical Engineering, Faculty of Eng., Niigata University, Niigata city 950-2181, Japan
sakurai@eng.niigata-u.ac.jp

ABSTRACT

Concentrated solar radiation has been received attention due to the application to thermochemical conversion of hydrogen energy. Recently, the solar thermochemical internally circulating fluidized bed reactor has been recognized as a promising technology. Purpose of this study is to develop a radiative heat transfer code, and to develop a high-efficiency fluidized bed reactor model. The spherical harmonics method (hereafter P1 method) is employed in the present study. Consequently, the P1 method showed good performance, the detailed analysis model is based on the P1 method.

1. Introduction

Application of concentrated solar radiation to thermochemical conversion of hydrogen energy and to coal gasification processes is presented in various articles [1, 2]. Recently, the solar thermochemical internally circulating fluidized bed reactor was developed by Kodama and Gokon [3]. Understanding of heat transfer phenomena in this reactor is very important to improve the thermal efficiency.

In this system, radiative heat transfer in dispersed particles plays an important role; however, analysis of radiative heat flux is very difficult due to the complexity. One of the numerical approaches is Monte Carlo Method [4]. This approach is the well-researched method. But, in this method, there is a big problem of that it takes a huge computational time. So, differential methods are adopted. Purpose of this study is to develop a radiative heat transfer code which is more practicable and more reproducible, and to develop a high-efficiency fluidized bed reactor model.

In this study, we take notice of P1 method [4] which is mathematical approximation method. In this way, to develop a faster and more practicable method is expected.

2. Method

In this study, divergence of radiative heat flux is obtained by solving radiative transfer equation, when we use the spherical harmonics method (here after P1 method). In addition, the successive over relaxation method and the second order accurate central difference scheme in space are used.

The P1 method is applied here. Radiative intensity may be expressed in terms of a two-dimensional generalized Fourier series as

$$I(\mathbf{r},\hat{\mathbf{s}}) = \sum_{l=0}^{1}\sum_{m=l}^{l} I_l^m(\mathbf{r}) Y_l^m(\hat{\mathbf{s}}) \qquad (1)$$

where $\mathbf{r}$ is a vector pointing to a location within the medium, $I_l^m(\mathbf{r})$ are position-dependent coefficient and $Y_l^m(\hat{\mathbf{s}})$ are spherical harmonics.

Radiative intensity which be expanded by P1 method is expressed as

$$I(\mathbf{r},\hat{\mathbf{s}}) = \frac{1}{4\pi}\left[G(\mathbf{r}) + 3\mathbf{q}(\mathbf{r})\cdot\hat{\mathbf{s}}\right] \qquad (2)$$

where G is incident radiation, and $\mathbf{q}$ is radiative heat flux. For these equations, divergence of radiative heat flux is shown as

$$\nabla_\tau \cdot \left(\frac{1}{1 - A_1\,\omega/3}\nabla_\tau G\right) = -3(1-\omega)(4\pi I_b - G) \qquad (3)$$

where ω is scattering albedo. Thus, divergence of radiation heat flux given by solving the incident radiation that use the successive over relaxation method and the second order accurate central difference scheme in space.

3. Validation Test

Computational configuration is treated as an axisymmetric plate instead of cylindrical cavity. The cavity wall is assumed to be black body. The cavity is filled with disperse particles. The participating medium is gray. The temperature of walls and disperse particles are shown in Fig 1.

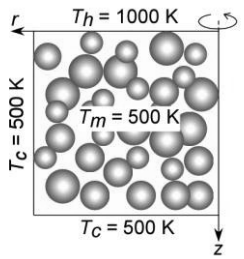

Fig 1. Two-dimensional axisymmetric analytical model

Validity of this model is confirmed by comparing with Monte Carlo method. The optical thickness is set to τ=1.0 and scattering albedo is ω=0.5. Two-dimensional analytical model is shown in Fig 1. Results are shown in Fig 2.

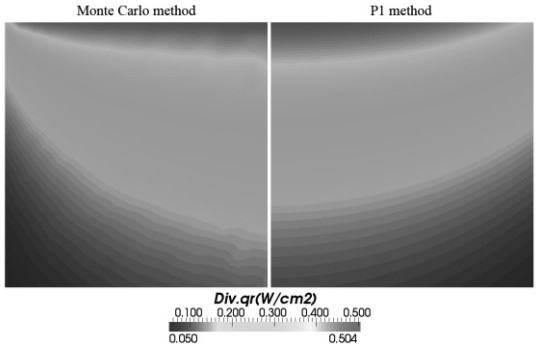

Fig 2. Divergence of radiative heat flux using the Monte Carlo method and P1 method

Comparing numerical results between P1 method and Monte Carlo method, there is a little difference in the extension of distribution of divergence of radiative heat flux. However, as the numerical result by the approximation, it might be enough accuracy. Because value of root mean square of 0.02 is very small. In this case, computational time of P1method and Monte Carlo method are 0.17 sec and 317.75 sec, respectively. Consequently, the computational cost of P1 method can be drastically decreased compared with the Monte Carlo method.

4. Example test

Zirconia and cerium oxide are used as mediums in the substantiative experiment of the solar thermochemical internally circulating fluidized bed reactor by Kodama and Gokon [3]. The numerical analysis by P1 method that uses optical properties of mediums is developed. The analytical model is shown in Fig 3. The cavity wall is assumed to be black body. The cavity is filled with disperse particles. The distribution of concentrating heat flux which is measured by Gokon is given to the top wall (It is shown in Fig 4.). And temperature of the other walls and disperse particles are shown in Fig 3.

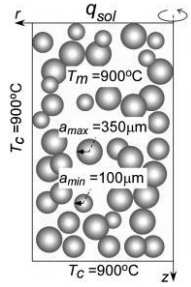

Fig 3. Two-dimensional axisymmetric analytical model of experimental equipment.

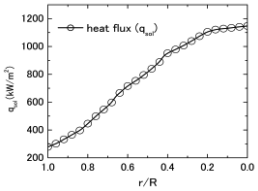

Fig 4. The distribution of concentrating heat flux which is measured by Gokon [5]

The value of the average of visible optical area is used for the absorption coefficient and the scattering coefficient of mediums. The influence by the mediums is investigated. Fig 5 shows the numerical result when the disperse particles are assumed to be zirconia and cerium oxide, respectively. Each value used in the calculation are shown in Table 1.

Table 1. Each value used in the calculation.

	Zirconia	Cerium oxide
Width of the area (r×z)	20×40 (mm^2)	
Weight of the mediums	20 (g)	
Refractive index	2.2	2.2
Absorption coefficient(m^{-1})	2.152	1.668
Scattering coefficient(m^{-1})	0.492	0.381

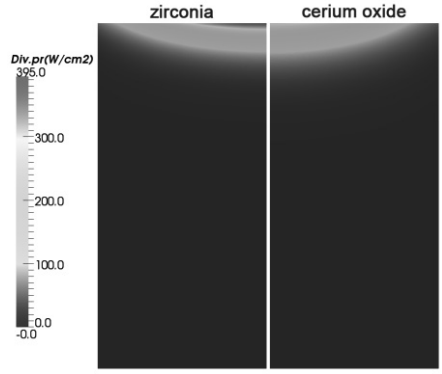

Fig 5. Numerical result when the disperse particles are assumed to be zirconia and cerium oxide.

The influence by the change of the disperse particles is seen in the distribution of divergence of radiative heat flux. The divergence of radiative heat flux in the vicinity of the top wall can be found to be smaller as cerium oxide. This indicates the effect of the particles is very important.

5. Concluding remarks

Conclusions are summarized as;

1. The in-house radiative transfer solver using the spherical harmonics method was validated with the Monte Carlo method.
2. Radiative heat transfer analysis of dispersed particles was performed. It was found that the effect of the particles is very important.

Acknowledgement

This work was supported by the KAKENHI (23760844) and the funding program for next generation world-leading researches by JSPS.

References

[1]A. Steinfeld, R. Palumbo, Encyclopedia of Physical Science & Technology, Vol. 15, (2001), pp 237-256.
[2]D. Hirsch, A. Steinfeld, Chemical Engineering Science, Vol. 59, (2004), pp 5771-5778.
[3]T. Kodama, N. Gokon, Chemical Review, Vol. 107, No. 10, (2007), pp 4048-4077.
[4]M. F. Modest, Academic Press, (2003).
[5]N. Gokon, S. Takahashi, H. Yamamoto, T. Kodama, International Journal of Hydrogen Energy, Vol. 33, (2008), pp 1407-1416.

Eighth International Conference on Flow Dynamics
November 9 - November 11, 2011

Spectral Radiative Properties of Greenhouse Plastic Films Using Inverse Method

A. Al Mahdouri[1], M. Baneshi[2], A. Barthel[3], H. Gonome[1], J. Okajima[2], S. Maruyama[2]

[1] Department of Mechanical System and Design, Graduate School of Engineering, Tohoku University, 6-6 Aramaki Aza Aoba, Aoba-ku, Sendai, Miyagi, Japan, 980-8579

[2] Institute of Fluid Science, Tohoku University, 2-1-1, Katahira, Aoba-ku, Sendai, Japan, 980-8577

[3]Ecole Centrale Lyon, 36 Av. Guy de Collongue, France, 69134

almahdory@pixy.ifs.tohoku.ac.jp

ABSTRACT

Spectral radiative properties of agricultural greenhouse plastic cladding materials such as Polyvinylchloride (PVC) and Polyethylene (PE) were obtained by using a generalized Newton-Raphson inverse analysis. Reflectance (ρ) and transmittance (τ) were measured by using spectrophotometers and the complex refractive index for the spectral region between ultraviolet to far infrared were determined by iterative calculation using REM^2. The results showed variation in n and k values between two materials.

1. Introduction

Agricultural greenhouses are commonly used for providing the optimum environmental conditions for crops and increasing the yield production. Therefore, a good understanding of energy conversion from solar irradiation into inside environment of a greenhouse is important. Cladding material plays a key role in controlling different types of solar radiation and, thus, inside temperature. Glass materials have traditionally been used for covering greenhouses. Nowadays, different plastic films are widely used as cheap cladding materials. Beside the photosynthetically active radiation (0.4-0.7μm), thermal (0.7-300 μm) and ultraviolet (<0.38 μm) radiation also is highly concerned by scientists, manufacturers as well as farmers. However, there is a scarcity of information about precise spectral radiative properties of these plastic materials.

On the other hand, finding the complex index of refraction requires a special experimental apparatus which can be found only in a specialized laboratory. Consequently, the objectives of this study are to find numerically the spectrally-dependent coefficients (n and k values) for two common used plastic materials; Polyvinylchloride (PVC) and Polyethylene (PE), by inverse method and find out the differences between them in term of the reflectance (ρ) and transmittance (τ).

2. Method

According to the flowchart shown in Fig. 1, the generalized algorithm of the method of obtaining the unknown values for each material is summarized. At the beginning, two independent experimental measurements of ρ and τ are obtained for both materials. Measurements have been performed using Shimadzu UV-2450 spectrophotometer which covers the ultraviolet and visible ranges (0.22-0.85μm). The corresponding $BaSO_4$-Covered integrating sphere was used. The longer wavelengths were measured using Shimadzu IR-Prestige spectrophotometer. The corresponding near-infrared (NIR) integrating sphere covered the range 0.85-2.5 μm, whereas the diffuse reflectance attachment allowed us to obtain values of ρ up to 25 μm and direct transmittance at normal incidence was measured from 2.5-25 μm.

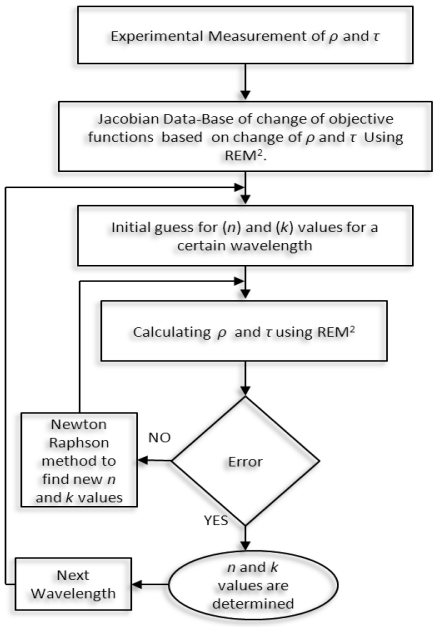

Fig. 1 Inverse Analysis Flowchart.

After that, a data base will be structured for the Jacobian (J) matrix using Radiation Element Method by Ray Emission Model (REM^2), proposed by Maruyama and Aihara[1]. Data-base holds the information of how the ρ and τ change with the change of the control variables, n or k.

REM^2 is a generalized method for calculating radiative heat transfer in absorbing, emitting and scattering media. Figure 2, shows a schematic diagram of a one-dimensional plane-parallel analysis model. The spectral radiative intensity $I_\lambda(\vec{r},\hat{s})$ could be determined by solving Eq. (1) and in the same time ρ and τ values could be predicted.

$$\frac{dI_\lambda(\vec{r},\hat{s})}{ds}=\beta_\lambda\left[-I_\lambda(\vec{r},\hat{s})+(1-\omega_\lambda)I_{b\lambda}(\vec{r})+\frac{\omega_\lambda}{4\pi}\int_{4\pi}I_\lambda(\vec{r},\hat{s}')\Phi_\lambda(\hat{s}'\to\hat{s})d\Omega'\right] \quad (1)$$

where $I_{b\lambda}$,β_λ, ω_λ, Φ_λ are spectral value of blackbody intensity, extinction coefficient, single scattering albedo and radiative heat energy, respectively.

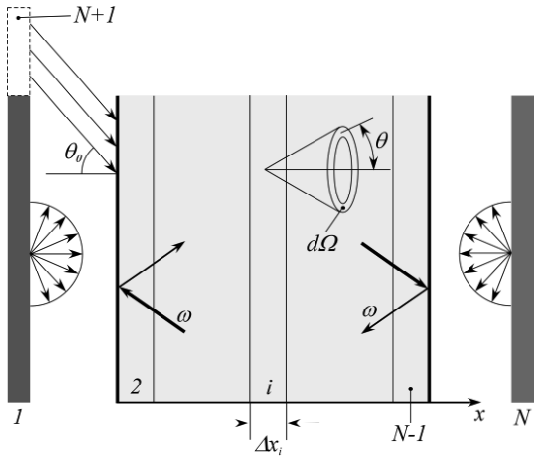

Fig. 2 A schematic diagram of a One-dimensional plane-parallel analysis model.

Diffusely irradiated rays onto the material were discretized using Fiveland's quadrature method [2]. The amount of absorption, extincted and diffusely scattered view factors between two participating elements could be found using the Ray Tracing Method. Generalized Snell's Law and Fresnel's Formulas for absorbing media were used to determine the refraction and reflection of collimated rays at the boundary surfaces.

The best initial guess (n_0,k_0) was performed for first iteration for calculation of ρ and τ using REM^2.Next to that, the error check was executed. Finally, while the error exceeded the limit, the 2-Dimensional Newton-Raphson inverse method, Eq. (2), was applied to find the successful guess of spectrally dependent values of n and k using corresponding ρ and τ measured data [3]. This result in the equation for the iteration step expected to derive the constraint error toward zero.

$$\begin{bmatrix} n \\ k \end{bmatrix}_{i+1} = \begin{bmatrix} n \\ k \end{bmatrix}_{i} + \begin{bmatrix} \frac{\partial A}{\partial n} & \frac{\partial A}{\partial k} \\ \frac{\partial B}{\partial n} & \frac{\partial B}{\partial k} \end{bmatrix}^{-1}_{\substack{n=n_i \\ k=k_i}} \begin{bmatrix} A(n_i,k_i) \\ B(n_i,k_i) \end{bmatrix} \quad (2)$$

where;

$$A(n,k) = \rho_{Measured} - \rho_{Calculated} \quad (3)$$

$$B(n,k) = \tau_{Measured} - \tau_{Calculated} \quad (4)$$

3. Results and Discussion

Due to the fact that there were two different spectrophotometer have been used, the results of ρ and τ have shown some overlapped data between different VIS and NIR and also between NIR and mid-infrared (MIR). An appropriate linear interpolation was carried out. According to full spectral calculation of n and k values of PVC, shown in Fig. 3, at UV and VIS regions the material is highly transparent to the electromagnetic waves. On the other hand, the material has peaks of k value at NIR to MIR range. This means that, absorption behavior at this region has happened. When the wavelength becomes longer, n value isn't change significantly by wavelength and electromagnetic waves were almost steadily absorbed by the material due to the resonant frequency. In Fig. 4, calculated spectral k value is compared between PE and PVC materials at the infrared (thermal) region, the results showed that PVC absorbed higher amount of electromagnetic waves. This difference between two materials could help in deciding material for most optimum environmental conditions inside greenhouses.

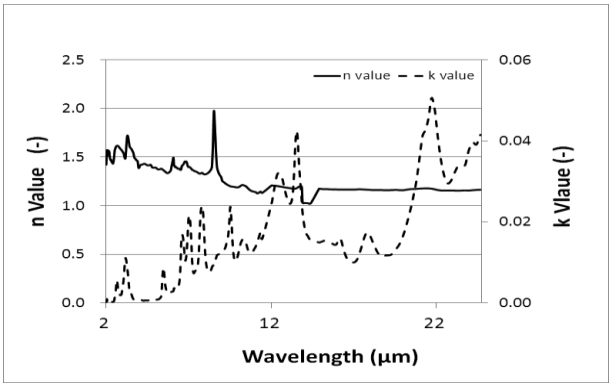

Fig. 3 A full spectrum calculation of complex refractive index for PVC film.

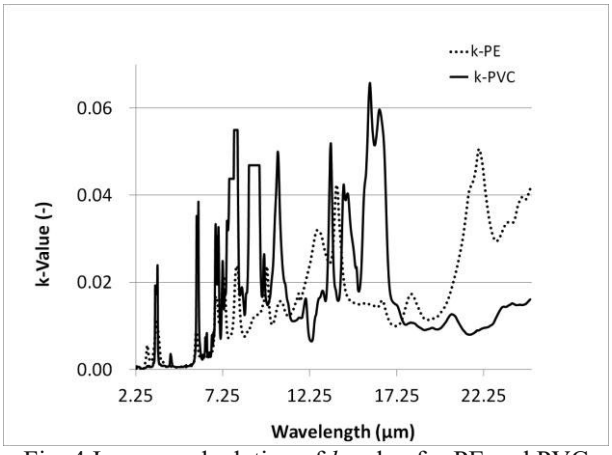

Fig. 4 Inverse calculation of k-value for PE and PVC films at infrared region.

4. Concluding remarks

Inverse analysis using Newton-Raphson method was carried out to find the n and k values of complex refractive index for two different greenhouse plastic materials; Polyethylene (PE) and Polyvinylchloride (PVC). Compared to PE material, PVC absorbs more electromagnetic waves at the region of thermal radiation.

References

[1] S. Maruyama, Light Energy Engineering, (2004), Yokendo , Tokyo

[2] M. Baneshi et al, Quant. Spect. & Radiative Transfer, 110(2009), pp.192–204

[3] J. Stoer, R. Bulirsch, Introduction to Numerical Analysis, (1993), Springer-Verlag, New York

Eighth International Conference on Flow Dynamics
November 9 - November 11, 2011

Experimental Study on $CH_4/O_2/CO_2$ Counterflow Premixed Flame Extinction in Low-Stretch-Rates under Microgravity and Transition from Counterflow Flame to Ball-like Flame

Xing Li[1, 2], Hisashi Nakamura[1], Takuya Tezuka[1], Susumu Hasegawa[1], Koichi Takase[1], Li Jia[2], Kaoru Maruta[1]
1, Institute of Fluid Science, Tohoku University, 2-1-1 Katahira, Aoba-ku, Sendai, 980-8577 Japan
2, School of Mechanical and Electronic Control Engineering, Beijing Jiaotong University, No.3 Shang Yuan Cun, Hai Dian District, Beijing, 100044 China
lixing@edyn.ifs.tohoku.ac.jp

ABSTRACT

Experimental studies on CH_4/Air and $CH_4/O_2/CO_2$ counterflow premixed flame extinction in low-stretch rates were conducted under microgravity by using airplane. Microgravity environment by employing airplane was verified effective by comparison of the drop tower experiment where C-shaped extinction curve was obtained experimentally for the first time under 10^{-4}G microgravity. Transition of $CH_4/O_2/CO_2$ counterflow premixed flame to ball-like flame seems possible in low-stretch-rates with microgravity.

1. Introduction

Flammability limits [1] are very important in both industrial applications and fundamental studies of combustion. Counterflow flame configuration was used to study flammability in 1986 by Law and his colleagues [2]. Stretch extinction occurs when the premixed flames are highly stretched. Another kind of extinction of counterflow flame in low-stretch-rates was found in microgravity experiment by Maruta et al. [3] using lean CH_4/Air mixture which Lewis-number is around 0.97, it is called radiation extinction. There experiment [3] also showed planar flame can be formed in low-stretch-rates under microgravity. Mixtures having high-Lewis-numbers, 1.2, 1.4 and 1.8 were also used for investigations [4], and new phenomena were found. However, experimental study on low-Lewis-number mixtures is scarce to date.

Besides, flame ball in motionless flammable mixture have been predicted by Zeldovich et al. [5]. Nearly 50 years later, microgravity experiments of $H_2/O_2/CF_3Br$ in drop towers by Ronney confirmed flame balls can exist near flammability limits in mixtures with low-Lewis-number [6]. However, limit theory for planar flame and flame ball were constructed independently, the relationship between the limits of planar flame and flame ball was not well discussed.

Hence, the goals of this work are to clarify extinction characteristics of radiative low-Lewis-number mixture in low-stretch-rates under microgravity environment by using counterflow premixed flame. $CH_4/O_2/CO_2$ mixture which Lewis-number is around 0.7 in lean condition was selected for study. Possibility of the transition from planar flame to flame ball at low Lewis number in low-stretch-rates is examined experimentally.

2. Experimental method and system

In this study, 20-sec 10^{-4}G microgravity condition by the parabolic flight at Diamond Air Service Company [8], Nagoya, Japan was utilized. Airplane, MU300 which manufactured by Mitsubishi was employed for flights. Experimental system is illustrated in Fig.1. One pair of 3cm diameter counterflow burner was set in a combustion chamber, the distance between burner lips, L was kept at 3cm. The counterflow burner is made of brazen circular pipe with a porous plate inside. Flat flow profile can be obtained by this arrangement at low velocity condition. In fact, flat twin flames could be established in microgravity environment. Automatic experimental system which consists of PC, digital mass-flow-controllers, AD/DA converter and trigger circuit were designed to conduct experiments. In every experiment the stretch-rates were maintained at a corresponding constant value while the fuel gas concentration of the mixture was gradually decreased until extinction. Several seconds before the start of microgravity, flow velocity at the burner exit which denoted by U, and mixture composition are established. The mixture is then ignited by pilot flame using premixed flame. Just after the commencement of the microgravity experiment, the pilot flame is removed and the fuel concentration is gradually decreased in 20-sec microgravity duration until extinction. The mixture compositions at extinction in different nominal stretch-rates (a=2U/L) were tested by changing experimental conditions. Two video cameras were fixed in horizontal and vertical directions to record flame behaviors. Two thermocouples were mounted in the underside of the burner lips individually to monitor the burner lip temperature.

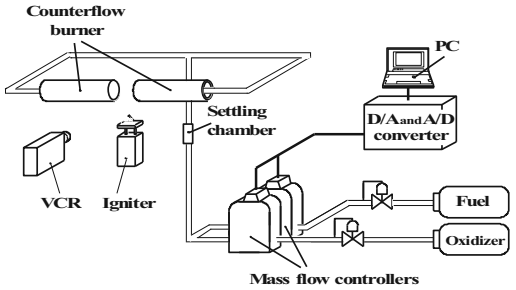

Fig. 1 Schematic of experimental system

3. Results and Discussion

First of all, validation of microgravity condition by airplane should be clarified. Comparison between drop tower result of CH_4/Air premixed counterflow flame by Maruta et al. and airplane experimental results is shown in Fig.2. It is obvious that those experimental results by the different methods agree well with each other. The difference between airplane results and drop tower

results is within 2.5%. Microgravity environment by using airplane is confirmed to be suitable for experimental study on extinction of gaseous flames.

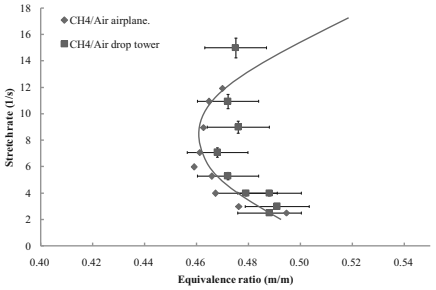

Fig. 2 Comparison of C-shaped extinction curve of CH_4/Air premixed counterflow flame by drop tower and airplane

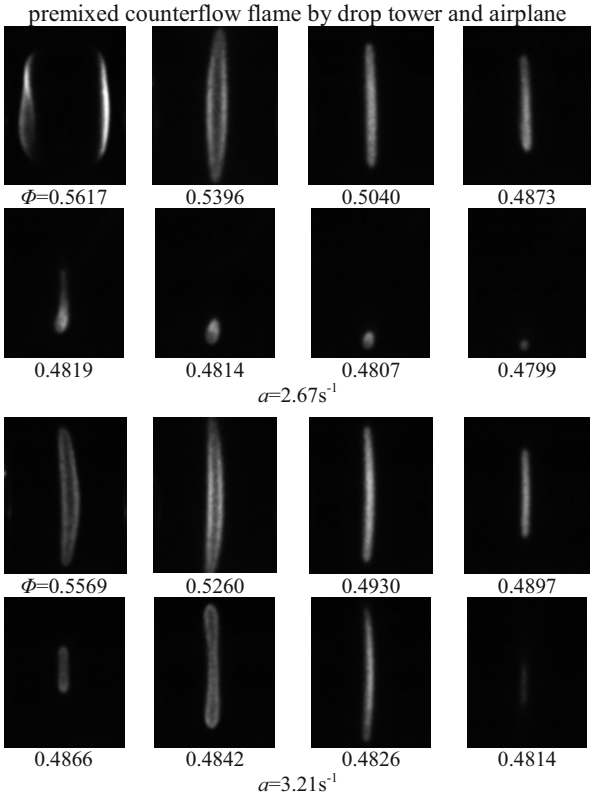

Fig. 3 Premixed counterflow flames of $CH_4/O_2/CO_2$ in low stretch rates under microgravity condition during equivalence ratio variation

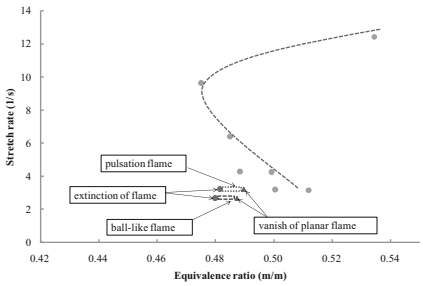

Fig. 4 Extinction characteristics of $CH_4/O_2/CO_2$ premixed counterflow flame in low-stretch-rates under microgravity

Fig.3 shows photographs by CCD camera from vertical direction of premixed counterflow flames of $CH_4/O_2/CO_2$ under microgravity condition at stretch rates equal to 3.21 s^{-1}, during equivalence ratio (Φ) variation. In 2.67 s^{-1} stretch rate case, firstly, twin flames with small curvature were formed at high equivalence ratio about 0.5617. With the decrease of equivalence ratio, the counterflow twin flames become closer and when equivalence decreased to 0.504, the twin flames merged to a single flame. The planar single flame shrunk with decrease of equivalence ratio, 0.4873. After that the flame started transition to ball-like flame. Then finally, it became ball-like flame and extinguished at equivalence ration equals 0.4799. The extinction process at 3.21 s^{-1} stretch rate is similar to that at 2.67 s^{-1}. However, it went back to planar flame and extinguished at last. The behaviors of flames at different equivalence ratios in this two stretch rates shows transition from planar flame to ball-like flame is possible under low stretch rates. Whereas, probably due to the radiation-induced instability of stretched premixed flames [7], it is still hard to judge this transition is due to essential of stretched flame or other mechanism.

Fig. 4 illustrates the extinction characteristics of $CH_4/O_2/CO_2$ (X_{o2}/X_{co2}=0.4) premixed flame under microgravity. The solid circles are extinctions of planar counterflow flames, the solid triangles show the planar flame vanishing. The results show equivalence ratio at extinction decreases with stretch rate when stretch rate larger than around 10 s^{-1}. However, opposite tendency is shown in the stretch range below it. The experiment results generally show C-shaped extinction tendency which consists of stretch extinction and radiation extinction of $CH_4/O_2/CO_2$ (X_{o2}/X_{co2}=0.4) mixture. However, experimental results in low stretch rates also show that the existence of pulsating flame and ball-like flame outside of C-shaped extinction boundary. So the flammable region of $CH_4/O_2/CO_2$ premixed counterflow flame was extended in low stretch rates.

4. Concluding remarks

Microgravity environment by using airplane have been validated to be effective for flame experiment by comparison of CH_4/Air counterflow premixed flame extinction between drop tower and airplane.

Results of $CH_4/O_2/CO_2$ (X_{o2}/X_{co2}=0.4) premixed counterflow flames under microgravity showed C-shaped extinction curve with extended flammability region by pulsating and ball-like flames in low stretch rates.

Transitions from counterflow premixed planar flame to ball-like flame were observed in low equivalence ratios at low stretch rates under microgravity condition by $CH_4/O_2/CO_2$ (X_{o2}/X_{co2}=0.4) mixtures.

Acknowledgements

Mr. Xing Li expresses sincere appreciation to Chinese Scholarship Council and Innovation Fund of Excellent Doctorial Candidate Program of Beijing Jiaotong University (No.141087522) for the scholarship.

References

[1] Y. G. Ju, et al., App. Mech. Rev., 54 (2001), 257-277.
[2] C. K. Law, et al., Sym. (Int.) Combust., 21 (1986), 1419–1426.
[3] K. Maruta, et al., Proc. Combust. Inst., 26 (1996), 1283-1289.
[4] K. Maruta, et al., Proc. Combust. Inst., 27 (1998), 2611-2617.
[5] Y. B. Zeldovich et al., Math. Theo. Combust. Explosion, Plenum Publishing Corporation, New York 1985.
[6] P. D. Ronney, Combust. Flame, 82 (1990), 1–14.
[7] Y. G. Ju, et al., Proc. Combust. Inst., 28 (2000) 1891-1900.
[8] http://www.das.co.jp/

Eighth International Conference on Flow Dynamics
November 9 - November 11, 2011

High Temperature Steam Oxidation Kinetics and Film Characteristics for Austenitic Stainless Steels

Seung Mo Hong, Yutaka Watanabe, Hiroshi Abe
Department of Quantum Science and Energy Engineering, Graduate School of Engineering, Tohoku University,
6-6-01-2 Aoba, Aramaki, Aoba-Ku, Sendai, Miyagi 980-8579 Japan
seungmo.hong@rbm.qse.tohoku.ac.jp

ABSTRACT

A SUS 316L stainless steel, a SUS 310S stainless steel, their cold worked pairs , and 15%Cr-20%Ni austenitic stainless steels have been oxidized in steam with less than 1 ppb and approximately 200 ppb O_2 at 700 ^oC for 1000 hrs. Steam oxidation tests were interrupted at each 30, 100, 250, 500, 1000 hrs and weight changes were measured. After 1000 hrs test, specimen surfaces and cross-sections were observed with optical microscope. From the cross-section observation results of SUS 316L stainless steels and 15%Cr-20%Ni austenitic stainless steels, two oxide layers were observed.

1. Introduction

Austenitic stainless steels have been widely used in power plants because of the increasing temperature and pressure for the thermal efficiency [1]. Oxidation of these steels in steam at high temperatures leads to the development of double layered oxide scales [2]. To study about the oxidation kinetics in high temperature steam condition is very important for the power plant integrity.

In this study, steam oxidation tests at 700 ^oC with some austenitic stainless steels were carried out. These tests can figure out characteristics of the materials for DO level and cold work effect at high temperature steam condition.

2. Steam Oxidation Tests

Tests were carried out with SUS 316L, SUS 310S, their cold worked pair and 15%Cr-20%Ni austenitic stainless steel plates and tubes. All plate specimens were polished up to #2400 emery paper and all tube specimens were used as-received state. Specimens were hanged with Pt wire. Distilled and ion exchanged water was filled in a tank and DO was controlled with inert gas. DO level were controlled with less than 1 ppb and approximately 200 ppb. Each interrupting of steam oxidation tests, specimens were weighed and surface was observed. After 1000 hours test, specimens were cut half after weighing and surface observation. Cut specimens were mounted with epoxy resin. The cross-section was observed with optical micro scope and compared with each others.

3. Results and Discussion

In cases of the SUS 316L series, weight change were larger than that of others. And in case of the 310S, there were few changes in weight gain. (Fig. 1) This oxidation rate tendency was in inverse relation with Cr-Ni contents. From past research [3], the tendency of the oxidation rate at high temperature showed in inverse relation with Cr content. But, in these cases, weight change results of SUS 316L series, 17%Cr-12%Ni, were larger than those of 15%Cr-20%Ni alloys. This can be considered that the oxidation kinetics is affected not only Cr content. The Ni content can be regarded as another affected factor. For more precise interpretation, more analysis method is needed.

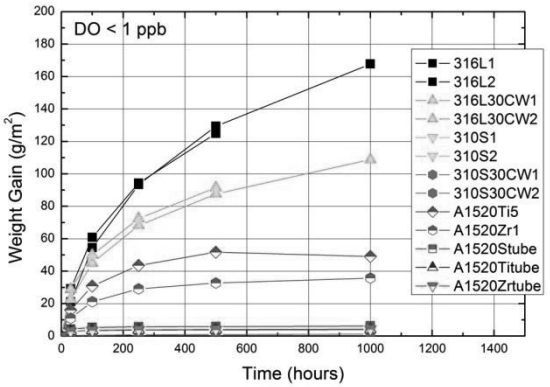

(a) DO < 1 ppb

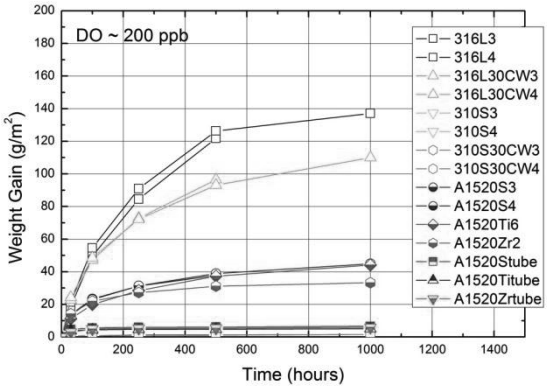

(b)DO ~ 200 ppb

Fig. 1 Oxidation test results plot

In cases of comparison between solution annealed specimens and those cold worked pairs, cold worked specimens showed approximately 30% less weight change than solution annealed specimens. From the past study [4], cold working of steels was considered as causes of the formation of easy diffusion paths for Cr that allow rapid formation of dense protective oxide layer. Firstly, the dislocations introduced by surface working can serve as fast diffusion path, later on the grain boundaries. These will be identified with coming surface analysis method.

For the different DO level condition, it could not be found noticeable differences between two tests results. The reason why noticeable difference did not find could be considered that the steam at high temperature supplied oxygen to specimens.

For the cross-section surface observation, double layered oxide layers were observed for SUS 316L series and 15%Cr-20%Ni austenitic stainless steels. (Fig. 2 and 3) Oxide layers were observed of doublet pattern. If outer oxide layer was thick, the inner oxide layer which was positioned oppositely was thick, too. For 15%Cr-20%Ni alloys, oxide layers were not always connected but doublet patterns were observed most of all surfaces. These patterns can be considered that, in case of outer layer, it can be implied that the outer layer grows by outward cat ion diffusion and inner oxidized zone grows by onward oxygen transport [2]. These patterns can be analyzed with EDAX and EBSD analysis method. In case of SUS 310S series, very thin single layer were observed. To observe the oxide layer, Ni coating was applied. These thin oxide film can explain that the oxidation resistance of SUS 310S is excellent than other two kinds of specimens.

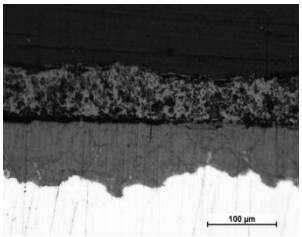

316L

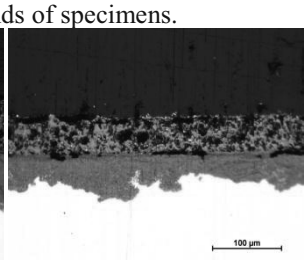

316L cold worked

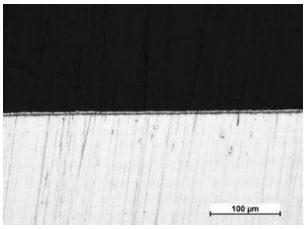

310S

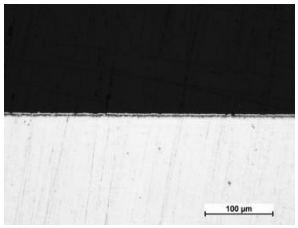

310S cold worked

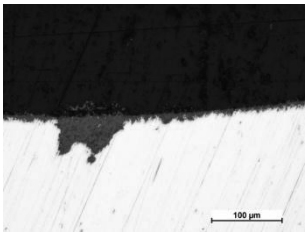

1520Alloy Standard

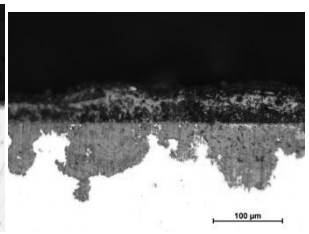

1520Alloy Ti add.

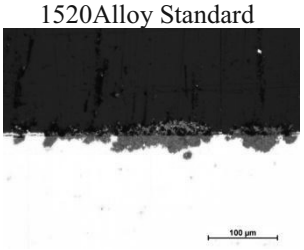

1520Alloy Zr add.

Fig. 2 Cross-section observations – DO < 1 ppb

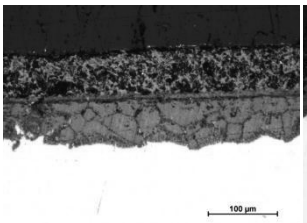

316L

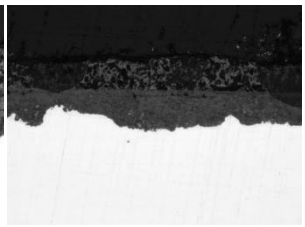

316L cold worked

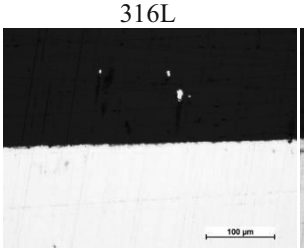

310S

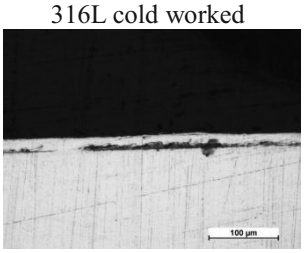

310S cold worked

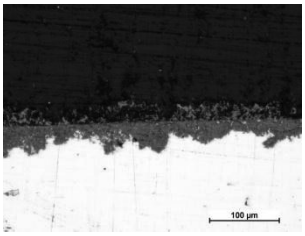

1520Alloy Standard

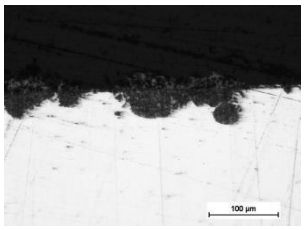

1520Alloy Ti add.

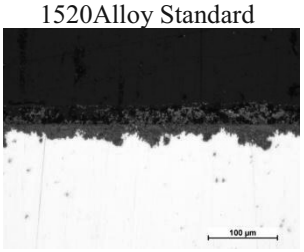

1520Alloy Zr add.

Fig. 3 Cross-section observations – DO ~ 200 ppb

4. Concluding remarks

In high temperature condition, the materials chemical compositions (Cr, Ni) were most dominant factor. In case of DO level, the noticeable difference was not found.

Oxide layers were grown two directions (inward and outward) and this trend was agreed with other research results.

References

[1] P. J. Ennis, W. J. Quadakkers, Int. J. of Pres. V. and P. **84** (2007) 82–87

[2] A. N. Hansson, K. Pantleon, F. B. Grumsen, M. A. J. Somers, Oxid. Met. **73** (2010) 289–309

[3] N. Otsuka, Y. Shida, H. Fujikawa, Oxi. Of Met. **32** (1989) 13-45

[4] H. J. Grabke, E. M. Muller-Lorenz, S. Strauss, E. Pippel, J. Woltersdorf, Oxid. of Met. **50** (1998) 241-254

Eighth International Conference on Flow Dynamics
November 9 - November 11, 2011

Effect Of Temperature Compensation For Dual-layer PSP/TSP In Low Speed Flow

Kil-Ju Moon, Yuichiro Ambe, Hiroaki Kawabata, Hideo Mori
Department of Mechanical Engineering, Kyushu University
819-0395, Motooka 744, Nishi-ku, Fukuoka-shi, Fukuoka-ken, JAPAN
moon@haira.mech.kyushu-u.ac.jp

ABSTRACT

Pressure sensitive paint (PSP) and temperature sensitive paint (TSP) are useful measurement tools in measurement of pressure and temperature distribution on surfaces. However, temperature dependence of PSP will be the factor of an error in pressure measurement, and therefore temperature correction is needed to obtain highly precise pressure distribution. This research shows temperature compensation effect with a low-speed jet flow using Dual-layer PSP/TSP.

1. Introduction

Pressure sensitive paint (PSP)[1]is very powerful method to measure pressure on solid surface, because it is noncontact method using emission of luminescent molecules. Recent days, the range of application of PSP is extended. Mori et al.[2] reported that 0.22kPa of pressure difference can be measured using PSP on a plate with uniform temperature distribution. However, PSP has temperature dependence as well as pressure sensitivity. Therefore, temperature compensation is needed to obtain highly precise pressure distribution in low-speed flow field because the error caused by the temperature dependence of PSP is relatively significant in case of pressure measurement in the condition near atmospheric pressure. Hyakutake et al.[3] reported the simultaneous measurement method of pressure and temperature using multi-layered polymer coating, for the wide oxygen pressure range. In this research we show the feasibility of the dual-layer PSP/TSP for the measurement in low-speed flow fields. Moreover, the paper will discuss effect of temperature compensation using the dual-layer PSP/TSP for jet-impingement experiment with non-uniform temperature distribution on a solid surface in a low speed flow field.

2. Dual-layer PSP/TSP

Figure 1 shows the schematic illustration of the dual-layer PSP/TSP. Dual-layer PSP/TSP is made by stacking up a TSP layer and a PSP layer. Figure 2 shows the chemical structures of the molecules of PSP and TSP luminophore and binder using in this study.

Fig.1 Structure of Dual-layer PSP/TSP

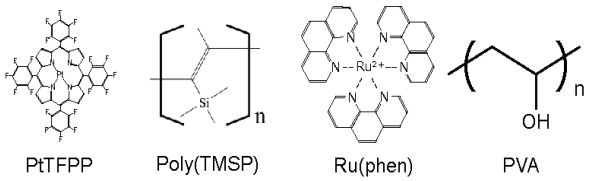

Fig.2 Chemical structures of luminescent molecules and binders

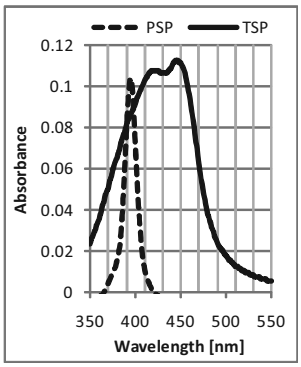

(a) Absorption spectrum

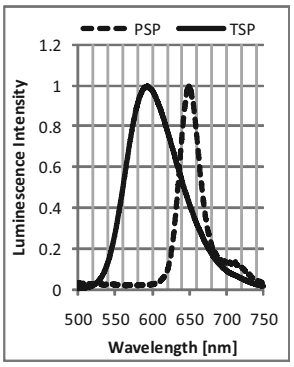

(b) Luminescence spectrum

Fig.3 Absorption and luminescence spectrum PSP and TSP

Dual-layer PSP/TSP system enables combined measurement of pressure and temperature. Temperature distribution obtained by the TSP component can be used for the temperature compensation of the PSP component.

Figure 3(a) and (b) show the spectra of absorption and relative luminescence intensity of both PSP[PtTFPP] and TSP[Ru(phen)]. In this study, LED light source with the center emission wavelength of 395nm is used to excite both PtTFPP and Ru(phen). To separate the emission of the PSP component and that of the TSP component of the dual-layer PSP/TSP, optical filters are used. A high-pass filter with the transmission limit wavelength of 620nm is used to pass the emission of the PSP component, and a band-pass filter with the range of the transmission wavelength of 540nm~600nm is used to pass that of the TSP component.

Usually, pressure distribution is obtained from the luminescence intensity of PSP using Stern-Volmer equation. However, Stern-Volmer coefficients have temperature dependence, because both the quenching probability of luminescent molecules and the oxygen permeability of binder depend on temperature. Hence, In this study, the following equation is used for the calibration of PSP, considering the linear dependence on the pressure and the second-order dependence on the temperature:

$$\frac{I_{ref}}{I} = B_1 + B_2\left(\frac{P}{P_{ref}}\right) + B_3\left(\frac{T}{T_{ref}}\right) + B_4\left(\frac{P}{P_{ref}}\right)\left(\frac{T}{T_{ref}}\right) + B_5\left(\frac{T}{T_{ref}}\right)^2$$

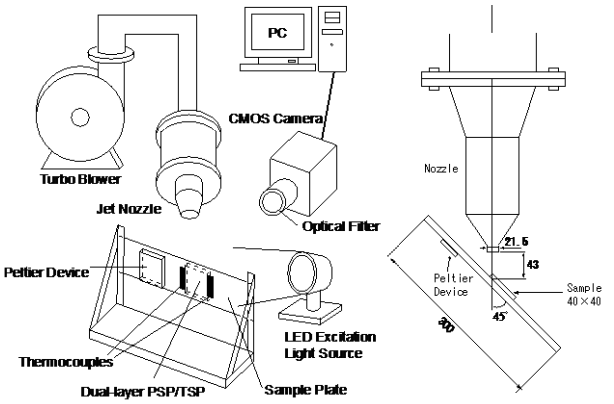

Fig.4 Experimental apparatus for Jet impingement

3. Experiment apparatus

Figure 4 shows the apparatus for measurement of pressure distribution on a sample plate when low-speed jet impinges on the sample plate. In Fig. 4, a jet from a nozzle with a turbo blower makes a pressure distribution on the sample plate. To generate non-uniform temperature distribution on the sample plate, peltier device which has cooling system is attached behind the sample plate. Sample plate angle to the nozzle is 45 degree and jet speed is 60m/s.

4. Results and discussions

Figure 5(L) shows the temperature distribution obtained by TSP component of dual-layer PSP/TSP on the sample plate. Figure 5(R) displays the temperature along the center line shown in Fig. 5(L). Temperature difference of both ends of the center line in Fig. 5(L) is 0.4°C.

Figure 6(L) shows pressure distribution obtained by using the PSP component without the compensation of the temperature effect, and Fig. 6(R) shows the pressure distribution with the compensation of the effect of the non-uniform temperature distribution obtained by TSP component of dual-layer PSP/TSP shown in fig.5(L). Figure 7 shows the measured pressure along the center line in Fig. 6(L) and (R). Moreover, the pressure data measured by pressure tap are also plotted. As shown in Fig.7, both the PSP data without temperature compensation and that with temperature compensation do not match pressure tap data. However, if the pressure data obtained by pressure tap is shifted to the level of that obtained by the dual-layer PSP/TSP with temperature compensation, the two distributions match well. We consider that absolute pressure error comes from the uncertainty of thermocouple used for the calibration. In spite of the shift in the absolute pressure, the coincidence of the differential pressure measured by PSP and pressure taps means temperature compensation of the dual-layer PSP/TSP is very effective. According to these results, we succeeded to measure the pressure difference of 0.8kPa on the sample plate with non-uniform temperature distribution by using the dual-layer PSP/TSP.

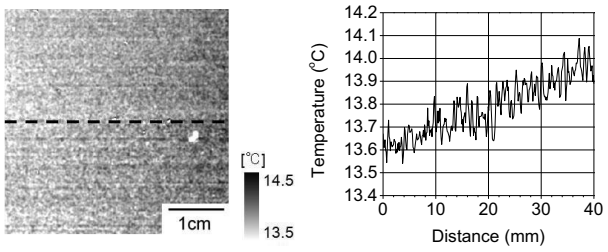

Fig.5 (L) Temperature distribution on sample plate
(R) Temperature along the center line of the sample plate shown in fig.5(L)

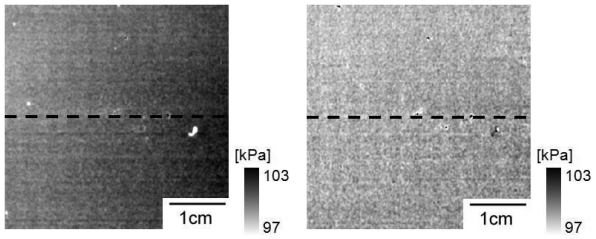

Fig.6 Pressure distribution on sample plate
(L) without temperature compensation
(R) with temperature compensation

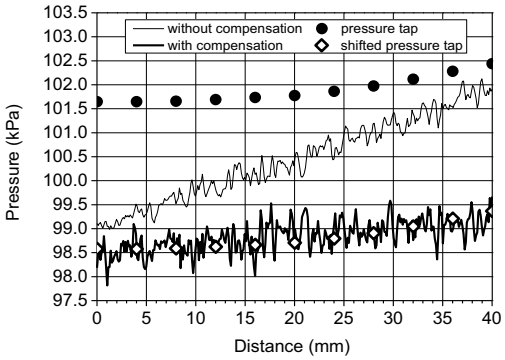

Fig.7 Pressure along the center line of the sample plate shown in fig.6(L) and (R)

5. Concluding remarks

We have visualized the pressure distribution in low-speed jet with non-uniform temperature distribution, by using the dual-layer PSP/TSP. The result shows the feasibility of the temperature compensation in pressure measurement by using the dual-layer PSP/TSP to increase the accuracy of pressure measurement.

References

[1] Liu, T., and Sullivan, J.P., 2005. *Pressure and temperature sensitive paints,* Springer.

[2] Mori, H., Yoshimoto, T., Moon, K.J., and Inoue, Y., 2010. “A priori calibration of pressure sensitive paint for low-speed flows”. 14th International Symposium on Flow Visualization, Paper #148, Daegu, Korea.

[3] Hyakutake, T., Taguchi, H., Kato, J., Nishide, H. and Watanabe, M., 2009. “Luminescent Multi-Layered Polymer Coating for the Simultaneous Detection of Oxygen Pressure and Temperature” *Macromolecular Chemistry and Physics*, **210**, pp. 1230-1234.

Eighth International Conference on Flow Dynamics
November 9 - November 11, 2011

A Study on Turbulent Premixed Combustion for $CO/H_2/CO_2/O_2$ Mixture at High Pressure

Futoshi Matsuno, Jinhua Wang, Yuki Otawara, Yasuhiro Ogami and Hideaki Kobayashi
Institute of Fluid Science, Tohoku University, 2-1-1 Katahira, Aoba-ku, Sendai, Miyagi 980-8577
matsuno@flame.ifs.tohoku.ac.jp

ABSTRACT

An experimental study of turbulent premixed flame for $CO/H_2/CO_2/O_2$ mixture at high pressure was conducted. Result showed that flame structure of $CO/H_2/CO_2/O_2$ flame is more complex than that of CH_4/air turbulent premixed flame. It also showed that bending of S_T/S_L with u'/S_L happened when the smallest scale of flame wrinkles, ε_i, reached the characteristic scale of flame instability, l_i. This would be because the turbulent flame structure of $CO/H_2/CO_2/O_2$ mixture is strongly influenced by the flame instability as well as the conventional CH_4/air flames.

1. Introduction

Integrated Coal Gasification Combined Cycle (IGCC) can achieve higher thermal efficiency than conventional pulverized coal power plants. IGCC is fueled by the coal syngas and main combustible components of syngas are carbon monoxide and hydrogen, whose combustion characteristics when the air was used as the oxidizer were previously clarified by the author's group [1].

When the application of the oxy-fuel combustion to the closed gas turbine is further considered, the burned gas contains high concentration CO_2 and no N_2, making the system fit Carbon Capture and Storage (CCS) technologies [2]. Considering closed gas turbine IGCC system with CCS, it's essential to analyze the fundamental characteristics of oxy-fuel turbulent premixed combustion of the coal gasification syngas at high pressure. In the present study which is the first paper on the experiment used pure O_2 for oxidizer, the combustion characteristics of $CO/H_2/CO_2/O_2$ turbulent premixed flames at high pressure up to 0.5 MPa, i.e., turbulent burning velocities, flame surface densities and flame wrinkle scales, are experimentally discussed.

2. Experimental method

Experiments were conducted using the high pressure combustion test facility at the Institute of Fluid Science, Tohoku University [3]. Burner with an outlet diameter of 20 mm is installed in a high pressure chamber. Perforated plate set in the burner generated the isotropic turbulence.

Table 1 shows characteristics of the mixtures investigated in this study. Mole fractions of CO and H_2 (X_{CO}, X_{H2}, respectively) were X_{CO}/X_{H2} = 65/35. Assuming high caloric syngas and oxy-fuel closed gas turbine, mole fraction of CO_2 in $CO/H_2/CO_2/O_2$ mixture was 0.55 considering the exhaust gas recirculation. Equivalence ratio of the mixture, ϕ was 1.0. The pressure inside the chamber was 0.5 MPa and temperature of unburned mixture was 300 K. Under these experimental conditions, laminar burning velocity of the $CO/H_2/CO_2/O_2$ mixture and that of CH_4/air mixture whose equivalence ratio is 1.0 are almost the same.

In this experiment, OH-PLIF method was used to obtain instantaneous flame cross section images. These images are used to estimate mean progress variable, <c>, turbulent burning velocity, S_T, local flame surface density, Σ, fractal inner cut off, ε_i. <c> is defined as frequency that certain point was included in the burned region during certain time. S_T is estimated by angle method using <c> = 0.1 contour. Σ is defined as flame length in 10 pixels square centered at certain point assuming isotropy in the depth direction. Circle method is used in the fractal analysis.

Table 1 Laminar burning velocity, S_L and adiabatic flame temperature, T_{ad}

Mixtures	ϕ	S_L[cm/s]	T_{ad}[K]
$CO/H_2/CO_2/O_2$	1.0	18.5	2044
CH_4/air	1.0	18.8	2253

Laminar burning velocity, S_L, was estimated by PREMIX [4], CHEMKIN-II [5]. In that, Frassoldati's CO/H_2 detailed reaction mechanism [6] was used for $CO/H_2/CO_2/O_2$ flame and GRI-Mech 3.0 [7] was used for CH_4/air flame. In the following sections, $CO/H_2/CO_2/O_2$ flame is referred to as CO/O_2 flame.

3. Results and Discussion

Figure 1 shows the OH-PLIF images of CO/O_2 and CH_4/air flames. Both of their flame fronts are wrinkled and have many cusps. Turbulent premixed flames at high pressure commonly have complex flame fronts [3]. Compared to flame structure of CH_4/air turbulent flames, the structure of CO/O_2 turbulent flame is much finer and has shallow irregularity.

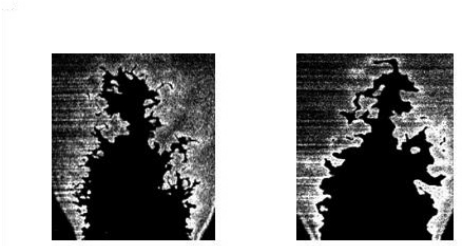

CO/O_2 flame CH_4/air flame

Fig. 1 OH-PLIF image of CO/O_2 and CH_4/air flame (0.5 MPa, 300 K, $u'/S_L \cong 3.0$).

Figure 2 shows the relationship between local flame surface density of CO/O_2 flame and CH_4/air flame and <c>. Flame surface density, Σ, of CO/O_2 flames is

larger than that of CH_4/air flames. This means that the accumulated flame length of CO/O_2 flame surface per unit area is larger than that of CH_4/air flame. This is consistent with the difference in complexity of the flame structure.

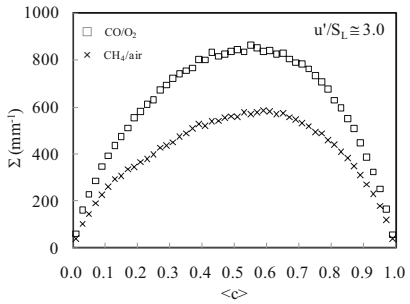

Fig. 2 Flame surface density, Σ, and mean progress variable, <c> (0.5 MPa, 300 K, u'/S_L ≅ 3.0).

Figure 3 shows the relationship between S_T/S_L and u'/S_L where u' is the turbulence intensity. It showed that S_T/S_L increases with the increase of u'/S_L. However, when u'/S_L is greater than 3.5, the increase of S_T/S_L becomes slowly. This trend is called "bending". According to the fractal theory of flame, increase of total area of flame surface caused by wrinkles and complication of flame surface contributes to the increase of S_T. Considering that S_L's of CO/O_2 flame and CH_4/air flame are nearly the same, increase in S_T/S_L is dominated by the complexity of turbulent flame structure of CO/O_2 flame. At u'/S_L > 3.5 formation of fine wrinkles of turbulent flame front with increase of turbulence intensity become slow compared to that at u'/S_L < 3.5, which means the increase of flame front complexity become weak and "bending" occurred. This indicated that the wrinkle of flame front by turbulence has reached a limitation when u'/S_L ≅ 3.5 in this study. It will be discussed based on the comparison of scale of turbulence and flame in the next section.

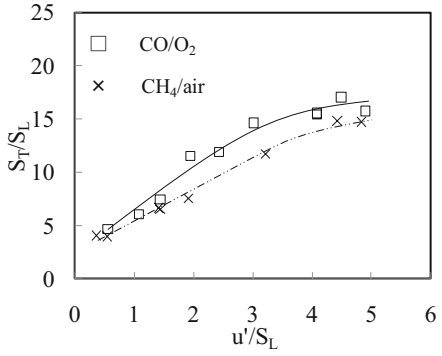

Fig. 3 S_T/S_L and u'/S_L (0.5 MPa, 300 K).

Figure 4 shows relationship between fractal inner cut off, ε_i, ten times of kolmogorov scale, $10\eta_k$, which corresponds to the mean diameter of vortex tubes, the characteristic scale of the flame instability, l_i [8] and turbulent Reynolds number based on Taylor micro scale, R_λ. Fractal inner cut off, ε_i, is regarded as the smallest scale of flame wrinkles. When ε_i reached l_i, decrease of ε_i becomes slow. The value of R_λ, when "bending" occurs for S_T/S_L with u'/S_L is estimated, is almost equal to the value of R_λ when ε_i reaches l_i. This implies that the limit of wrinkle of the turbulent flame structure is affected by the flame instability and "bending" is induced by this limit.

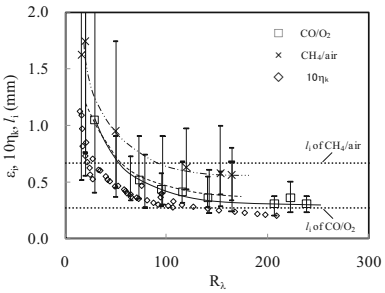

Fig. 4 Characteristic scales of turbulent flame.

4. Concluding remarks

Basic characteristics of $CO/H_2/CO_2/O_2$ turbulent premixed flame at high pressure were experimentally examined, and the following findings were obtained.

1. $CO/H_2/CO_2/O_2$ turbulent flame has finer and more complex flame structure than that of CH_4/air. Accordingly, turbulent burning velocity of $CO/H_2/CO_2/O_2$ turbulent premixed flame is larger than that of CH_4/air turbulent premixed flame while laminar burning velocities of the $CO/H_2/CO_2/O_2$ flame and CH_4/air flame are nearly the same.
2. $CO/H_2/CO_2/O_2$ flame and CH_4/air flame show the same trend that increase of turbulent burning velocity becomes slow for the increase of turbulent intensity. This trend of "bending" implies formation of fine turbulent flame structure become slow due to the smallest scale of flame front wrinkles is limited by the flame instability.

References

[1] Y. Ichikawa, Y. Otawara, H. Kobayashi, et al., Proc. Combust. Inst. **33**: 1543-1550 (2011).
[2] CRIEPI report, CRIEPI, M07003, (2007) 10-22.
[3] H. Kobayashi, T. Nakashima, T. Tamura, K. Maruta, T. Niioka, Combust. Flame 108 (1997) 104-117.
[4] R. J. Kee, et al., *Sandia Rep*., SAND 85 - 8009 (1989).
[5] R. J. Kee, et al., *Sandia Rep*., SAND 85 - 8240 (1983).
[6] A. Frassoldati, T. Faravelli, E. Ranzi, Proc. Combust. Inst. **32**: 3471-3485 (2007).
[7] G. P. Smith, et al, http://www.me.Berkeley.edu/gri-mech/ (1999).
[8] J. Yuan, Y. Ju, C.K. Law, Proc. Combust. Inst. **31**: 1267-1274 (2007).

Eighth International Conference on Flow Dynamics
November 9 - November 11, 2011

Traveling Performance Evaluation of Various Planetary Rover Locomotion Mechanisms

Masataku Sutoh, Keiji Nagatani, and Kazuya Yoshida
Graduate School of Engineering, Tohoku University,
6-6-01 Aoba Aramaki Aoba-ku, Sendai, Miyagi, 980-8579, Japan
sutoh@astro.mech.tohoku.ac.jp

ABSTRACT
Planetary rovers play a significant role in lunar and Martian surface explorations. However, because of slippage, planetary rovers can get stuck in loose soil, causing the exploration mission to fail. To avoid slippage and increase the drawbar pull, planetary rovers typically have parallel fins - called “lugs” (i.e., grousers) - on the surface of their locomotion mechanism. In this study, we conducted experiments using lightweight rovers in a sandbox to provide a quantitative confirmation of the influence of lugs on the traveling performances of planetary rovers.

1. Introduction

Mobile robots, also called rovers, have played a significant role in NASA’s Martian geological investigations. However, the lunar and Martian surfaces are covered with loose soil, and numerous steep slopes are found along their crater rims. In such conditions, rovers can get stuck and even cause mission failure. To avoid such problems, many research groups have studied the traveling performances of rovers on the basis of terramechanics [1, 2].

Traveling performance of large vehicles, such as dump trucks, have been widely studied in terramecanichs. Parallel fins - called “lugs” (i.e., grousers) - on the wheels/tracks of large vehicles have little influence on their traveling performances. On the other hand, it has been reported that lugs substantially influence the traveling performances of lightweight vehicles such as planetary rovers. Therefore, it is important to evaluate the effect of lugs on the traveling performances of planetary rovers.

In this study, the influence of lugs on the traveling performances of wheeled/tracked rover was evaluated by performing traction tests using two-wheeled and mono-tracked rovers with wheels/tracks having different numbers of lugs. In this paper, we introduce the method of evaluating the traveling performance. Then, the above experiments and thier results are reported in greater detail

2. Method for evaluation of traveling performance

To evaluate a traction performance of the locomotion mechanism of a rover, we adopted the slip ratio corresponding to traction load as the indicator. The slip ratio s is defined as [1]

$$s = \frac{r\omega - v_x}{r\omega} = 1 - \frac{v_x}{r\omega} \qquad (1)$$

where v_x denotes the linear speed of the vehicle, r and ω denotes the radius and angular speed of the wheel/track, respectively. In this equation, the slip ratio takes a value between 0 and 1. When a vehicle moves forward without slippage, the slip ratio is 0; when the vehicle does not move forward at all because of slippage, the slip ratio is 1. Therefore, a smaller slip ratio on a given traction load denotes a high traveling performance according to this definition.

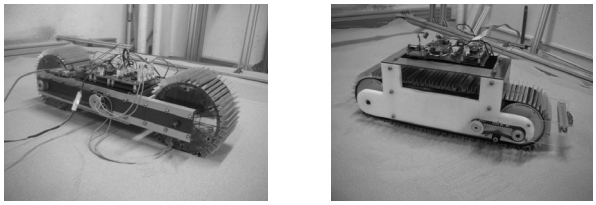

(a) Two-wheeled rover (b) Mono-tracked rover

Fig. 1 Overview of the rovers.

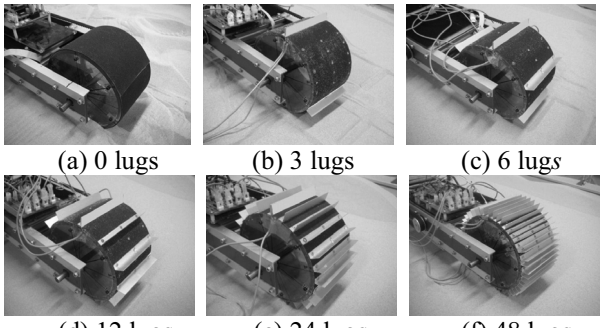

(a) 0 lugs (b) 3 lugs (c) 6 lugs

(d) 12 lugs (e) 24 lugs (f) 48 lugs

Fig. 2 Wheels equipped with different numbers of lugs.

3. Experiments

3.1 Two-wheeled and tracked rovers

In this study, we developed a two-wheeled rover with a wheel mechanism (Fig.1 (a)). The distance between the front and rear wheels of the rover was 400 mm, and each wheel has a diameter of 150 mm and a width of 100 mm. The rover weight was 4.0 kg.

In addition to the two-wheeled rover, we developed a mono-tracked rover with a track mechanism (Fig.1 (b)). As a key feature, the designed rover is almost the same size as the two-wheeled rover. The distance between the front and rear sprockets of the rover is 400 mm, and the track has an outside diameter and width of 115 mm and 100 mm, respectively. The rover weight was 7.0 kg.
Motion measurement systems with optical sensors and laser sources were mounted onto both rovers in order to measure the actual rover's speed without external devices embedded in the target environment. From the rover speed and the angular speed of the wheel/track measured by using an encoder, slip ratio, s, is calculated using Eq.(1).

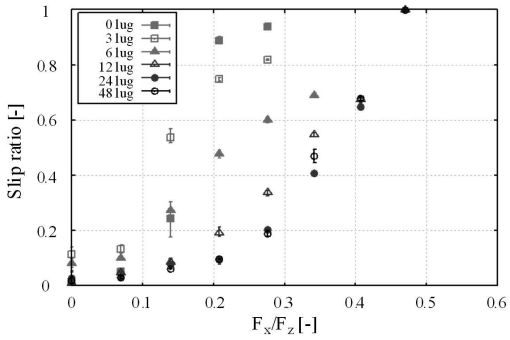

Fig. 3 Traction load vs.slip ratio (wheeled rover).

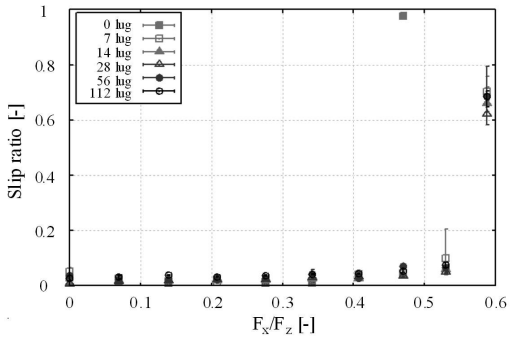

Fig. 4 Traction load vs.slip ratio (tracked rover).

3.2 Experimental overview and conditions

Both the rovers, with six types of tracks/wheels, were used to conduct traction tests with various loads in a sand box. Six track/wheel types have 15mm height lugs and different numbers of lugs. Figure 2 shows the wheels with different numbers of lugs. The lugs on the surface of the tracks are placed at the same spacing as the lugs on the wheels.

The sandbox has a length, width, and depth of 1.5 m, 0.30 m, and 0.15 m, respectively and was filled with Toyoura standard sand (JIS R 5200); this sand has very low viscosity and its particle is almost uniform.

In the traction test, the rover moved forward while pulling an attached weight behind it. To compare the traveling performance of the rovers, which had different weights each other, traction loads were set based on a traction weight (F_x) - to rover's weight (F_z) ratio (i.e., drawbar pull coefficient).

In these experiments, the angular speeds of the wheel and track were fixed at 2.50 rpm and 3.30 rpm, respectively, and we measured the slip ratio after the wheels/track stopped sinking. Each trial was conducted under identical soil conditions, and three trials were conducted for each condition.

3.3 Influence of the number of lugs on the traveling performance of wheeled rover

To evaluate the influence of the number of lugs on the traveling performance of the wheeled rover, the relationship between the traction load (F_x/F_z) and the slip ratio is plotted in the graph shown in Fig 3.

According to the figure, it was found that the slip ratio over a given traction load decrease as the number of lugs increases from 3 to 12. This means that an increase in the number of lugs contributes to the high traveling performance; this is a predictable consequence.

On the other hand, wheels with 12, 24, and 48 lugs show slight differences in the slip ratio values for different numbers of lugs. In these cases, there is little space between lugs. Therefore, the spaces between the lugs would be filled with soil, and shearing would occur across the lug tips. We concluded that this caused an increase in the number of lugs to have little influence on improving the traveling performance.

3.4 Influence of the number of lugs on the traveling performance of tracked rover

To evaluate the influence of the number of lugs on the traveling performance of the tracked rover, the relationship between the traction loads (F_x/F_z) and the slip ratio is plotted in the graph shown in Fig 4.

According to the figure, the tracked rover has a smaller slip ratio over a given traction load compared to the wheeled rover. That is, the tracked rover has a higher traveling performance than the wheeled rover. This is becuase the contact area of a track is much larger than that of a wheel.

Furthermore, it was found that the tracked rovers equipped with lugs had a higher traveling performance than that without lugs. Besides, tracks with lugs showed slight differences in the slip ratio values for different numbers of lugs.

The tracked rover had the high traveling performance even without lugs and showed a very small range within which it can generate a drawbar pull when slippage occurs. Therefore, track does not move forward at all if the drawbar pull increased by lugs is smaller than a given traction load. This is why we were unable to observe any improvement of the traveling performance from an increase in the number of lugs.

4. Concluding remarks

In this study, two-wheeled and mono-tracked rovers experiments were performed. From the results, we concluded that an increase in the number of lugs on wheels contributes to a high traveling performance; however, there is a limitation on the improvement. On the other hand, an increase in the number of lugs does not have much influence on the traveling performance of tracked vehicles.

5. Acknowledgements

This work was partially supported by Tohoku University Global COE Program on World Center of Education and Research for Trans-disciplinary Flow Dynamics.

References

[1] J. Y. Wong, Theory of Ground Vehicles Third edition, Wiley-Interscience, New York (2001).
[2] K. Iagnemma, and S. Dubowsky, Mobile Robots in Rough Terrain, Springer, New York, (2004).

Eighth International Conference on Flow Dynamics
November 9 - November 11, 2011

Effects of Gas Properties on Molecular Gas-Film Lubrication

Susumu Isono[1], Shigeru Yonemura[2], Takanori Takeno[3], Hiroyuki Miki[2], Toshiyuki Takagi[2]
[1]Graduate School of Engineering, Tohoku University, Aramaki Aza Aoba 6-6, Aoba-ku, Sendai, Japan
[2]Institute of Fluid Science, Tohoku University, Katahira 2-1-1, Aoba-ku, Sendai, Japan
[3]Tohoku University International Advanced Research and Education Organization,
Aramaki Aza Aoba 6-6, Aoba-ku, Sendai, Japan
isono@chapman.ifs.tohoku.ac.jp

ABSTRACT

It was found experimentally that the friction between a partly polished diamond coating and a metal surface was drastically reduced to zero in the atomosphere as relative speed increased to a few m/s. It seems that diamond coating took off the counter surface because sliding was noiseless in their experiment. On the other hand, it was also found experimentally that the slider took off the counter surface in the helium gas with atmospheric pressure. In the present study, we investigate the effect of gas properties on molecular gas-film lubrication.

1. Introduction

Nakamori et al. [1] found experimentally that the friction between a diamond coating with partly polished surface and a metal surface is drastically reduced to zero in the atomosphere as relative speed increased. Their results are shown in Fig. 1. The Scanning Electron Microscope (SEM) image of the partly polished diamond coated surface is shown in Fig. 2. This sliding was noiseless during their experiment. This indicates that the slider is lifted by gas flow and the sliding mechanism is gas-film lubrication.

In the previous works [2,3], we performed numerical simulations of micro-/nanoscale gas flow between the two sliding surfaces and successfully reproduced lift force large enough to suspend the slider used in the experiment. On the other hand, Shimono [4] found that the friction reduced to zero as relative speed increased also in the helium gas. In the present study, we investigate the effect of molecular mass and diameter on molecular gas-film lubrication.

2. Numerical method

As mentioned in the introduction, in the case where the spacing between the two sliding surfaces is much larger than the surface roughness, the flow will become Couette flow and high pressure will not appear. Therefore, we consider that the spacing is as large as the surface roughness or smaller. Since the mean free path λ of atmospheric molecules is estimated at 0.065 μm and the surface roughness of the partly polished diamond coating is from 0.28 μm to 0.57 μm, Knudsen number Kn ($=\lambda/L$) will be larger than 0.1, where L is the characteristic length of the flow. This indicates that the gas flow between two sliding surfaces cannot be treated as a continuum. Such kind of gas flow is in nonequilibrium due to lack of intermolecular collisions and is governed by the Boltzmann equation and not by the Navier-Stokes equations. Therefore, we use the direct simulation Monte Carlo (DSMC) method [5], which is the stochastic solution of the Boltzmann equation.

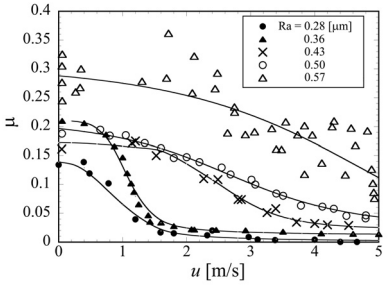

Fig. 1 Experimental results [1] of the friction force as the function of the relative speed of the surface roughness.

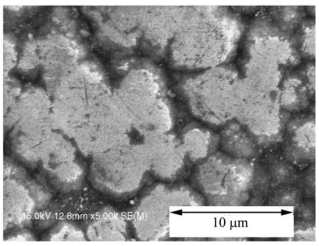

Fig. 2 Partly polished diamond-coated surface.

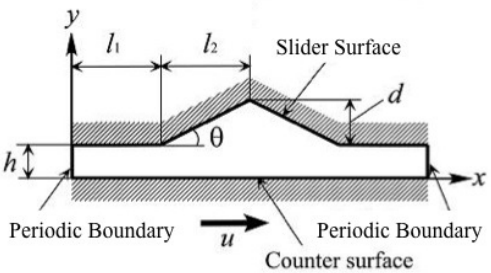

Fig. 3 Computational domain.

The computational domain treated here is shown in Fig. 3. The length of the spacing between two surfaces is h=0.14 μm. The gravity points to the -y direction. The counter surface moves in the x direction with speed u=10m/s. The lengths l_1 and l_2 are set at 11.52 μm. The depth of the concave part is d=1.44 μm. The angle θ is the angle of the oblique part to the horizontal line. The periodic boundary conditions are used for both the left

and right ends of the domain. Some molecules that run out of the domain through the left or right boundary will come into the domain again through the other boundary.

The computational domain is divided into cells. Intermolecular collisions in the same cell are calculated stochastically by using the maximum collision number method [6]. In this work, we perform parametric study about gas properties, therefore, we treat the virtual gas molecules listed in Table 1. At the initial condition, the gas with atmospheric pressure and room temperature, 300K, is put into the computational domain. The wall temperature is also set at the room temperature, 300 K. The hard sphere model is used for collision calculation. The motions and collisions of molecules are traced and hence, time evolution of the flow field is simulated. Simulation molecules represent a huge number of real molecules. Since the mean free time of molecule is $1.4\text{x}10^{-10}$ s, the time step of simulated molecule is set at $1.4\text{x}10^{-11}$ s. The velocities of molecules reflected on the solid wall are determined by using the diffuse reflection model with the wall temperature.

3. Results and Discussion

Table 1 shows computational conditions and obtained lift force. From the comparison of cases a, b and c, we can investigate the effect of the molecular mass. On the other hand, from the comparison of cases a, d and e, we can investigate the effect of the molecular diameter. Figure 4 shows the pressure distribution for cases a, b, and c. The upper curve shows the pressure distribution, and the lower diagram shows the shape of the flow channel. The lift force to suspend the slider is given by the difference between the pressure in the figure and the atmospheric pressure. Along the x-axis, the pressure increases in the concave part, and high gas pressure is maintained in the parallel part. First, we discuss the effect of the molecular mass. Figure 4 shows that the lift force increases with increasing molecular mass. Since the magnitude of the momentum transfer becomes larger for larger molecular mass, heavier molecules receive stronger shear stresses from sliding surfaces, and hence the gas pressure changes more largely.

Next, let us discuss the effect of the molecular diameter. Figure 5 shows that the lift force increases with decreasing diameter. It will be induced by increasing mean free path with decreasing diameter. The viscosity increases with increasing mean free path. The slip velocity increases with increasing mean free path, and hence, flow velocity gradient on the surfaces becomes small. The increasing viscosity increases the shear stress, but the decreasing velocity gradient decreases the stress. The positive effect of viscosity is larger than the negative effect of the velocity gradient. Therefore, the gas pressure changes more largely when smaller molecules are used.

4. Conclusion

In the present study, we investigate the effect of molecular mass and diameter on molecular gas-film lubrication. The lift force increases with increasing molecular mass and decreasing molecular diameter.

Table 1 Computational conditions and lift force.

Case	Molecular mass	Molecular diameter [m]	Lift force [Pa]
a	28.966	3.70×10^{-10}	2048.98
b	10.000	3.70×10^{-10}	749.39
c	4.003	3.70×10^{-10}	298.71
d	28.966	7.40×10^{-10}	707.61
e	28.966	14.80×10^{-10}	271.21

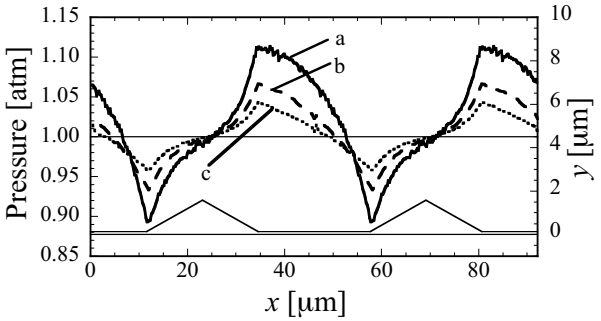

Fig.4 The effect of the molecular mass on pressure distribution.

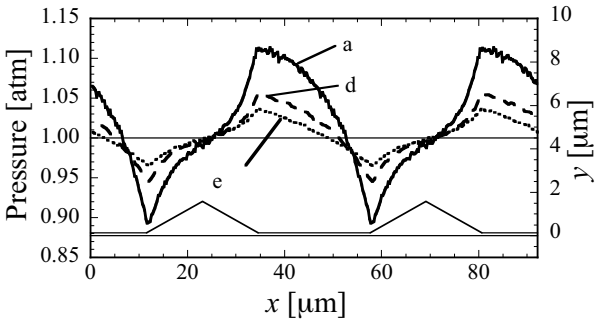

Fig.5 The effect of the molecular diameter on pressure distribution.

References

[1] I. Nakamori *et al.*, *Diamond Relat. Mater.*, **13**, 2122 (2005).

[2] S. Yonemura, M. Yamaguchi, T. Takeno, H. Miki and T. Takagi, *AIP Conference Proceedings,* **1084**, 1153-1157(2011).

[3] S. Isono, M. Yamaguchi, S. Yonemura, T. Takeno, H. Miki and T. Takagi, *AIP Conference Proceedings,* **1333**, 736-741(2011).

[4] H. Shimono, graduation thesis (2004).

[5] G. A. Bird, *Molecular Gas Dynamics and the Direct Simulation of Gas Flows*, (Clarendon Press, Oxford, United Kingdom, 1994).

[6] K. Nanbu, *IEEE Trans. on Plasma Sci.*, **28**, 971 (2000).

Eighth International Conference on Flow Dynamics
November 9 - November 11, 2011

Investigation of Dielectric Barrier Discharge Planar Jets at Atmospheric Pressure

Qing Li[1,2], Hidemasa Takana[1], Yi-Kang Pu[2], and Hideya Nishiyama[1]
[1] Institute of Fluid Science, Tohoku University, 2-1-1, Katahira, Aoba-ku, Sendai, 980-8577, Japan
[2] Department of Engineering Physics, Tsinghua University, Beijing, 100084, China
lqingphysics@gmail.com

ABSTRACT

Atmospheric pressure helium plasma jets, originating from a planar dielectric duct and impinging on a ground dielectric substrate, is investigated by controlling an upstream discharge region. Discharge current directions of plasma jets are the inverse in the two cases of with and without an upstream discharge region. The planar plasma jet with an upstream discharge region has a higher discharge current and has the inverse direction of external electric field in the jet region.

1. Introduction

Atmospheric pressure glow discharge in dielectric barrier discharge (DBD) configuration has been widely studied due to its great potential for applications [1]. Recently, atmospheric pressure plasma jets (APPJs), originating from a dielectric barrier configuration and propagating in the ambient air, have been reported to have characteristics of glow-like discharge, such as quasi-homogeneous in azimuthal direction [2, 3]. This kind APPJ is free of a vacuum system and high species density. However, the small spot size of several mm2 is a disadvantage for a homogeneous treatment of large areas. To generate DBD plasma jets with a large scale, arraying up of many APPJs in parallel [4, 5] and planar plasma jets [6], which could easily scan the substrate placed perpendicularly to the jet, have been designed so far. The physical process of plasma jets is not yet fully revealed, especially the role of an upstream discharge region on the downstream plasma jets.

In this work, we report an investigation of the role of the upstream discharge on the plasma jets impinging on a ground Teflon substrate. An inverse glow-like jet, which shows one negative and one positive glow-like current pulse in the positive and the negative half-cycles of the applied voltage, respectively, is obtained in the downstream region when an upstream discharge is on.

2. Experimental setup

Figure 1(a) shows the schematic of two-parallel plates' configuration with an upstream ground electrode to produce an upstream discharge region. The origin is located at the exit of the rectangular duct on central axis. The helium gas, fixed at 17.0 ± 0.1 L/min, flows through the planar glass duct, 3.1 mm × 50.0 mm × 300 mm (inner) and 6.1 mm × 53.0 mm × 300 mm (outer). Two copper strips of width 5 mm surround the duct at z = -1.0 cm and z = -4.5 cm as a power and a ground electrode, respectively. Two copper planes of 18 cm × 30 cm are both placed perpendicularly to the plasma jet with a separated gap of d. One of them locates at z = -1.0 cm, and connects to the power electrode and the high voltage (H.V.) source. Another downstream one is grounded, covered by a Teflon plane of 2 mm thick, and placed on the pathway of the plasma jet with a moveable location as z_{ground}, which is the z location of the Teflon surface. Thus $d = z_{ground} + 1.0$ cm. To identify the role of

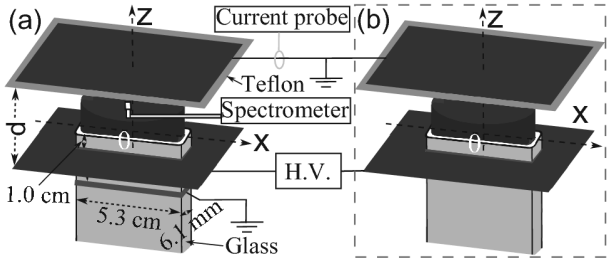

Fig. 1 Schematic of the experimental setups: (a) two-parallel plates' configuration with an upstream discharge region; and (b) two-parallel plate configuration without the upstream ground electrode.

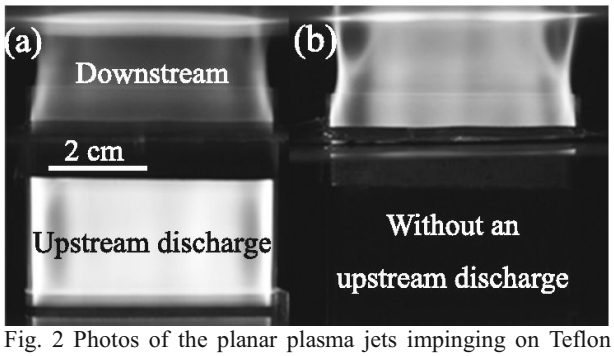

Fig. 2 Photos of the planar plasma jets impinging on Teflon surfaces (a) with and (b) without an upstream discharge region. Discharges both are fixed at the voltage amplitude of 3.1 kV and d = 2.5 cm.

the upstream discharge region, another experimental configuration without the upstream ground electrode was also employed to investigate DBD jet [see Fig. 1(b)]. In experiment, the applied sinusoidal voltage (fixed at 10.0 kHz) and the discharge current were recorded by a digital oscilloscope with a high voltage probe and a current probe, respectively. Discharge photos [see Figs. 2(a) and 2(b)] were taken by a Canon digital camera with the exposure time of 1.0 second.

3. Experimental results and discussion

Figures 2(a) and 2(b) show discharge photos at the voltage amplitude of 3.1 kV and the distance d = 2.5 cm for with and without an upstream discharge region, respectively. Comparing with Fig. 2(b), Fig. 2(a) shows that plasma jet has a lower intensity and higher uniformity emission along the x direction on the substrate surface, especially in the jet core region.

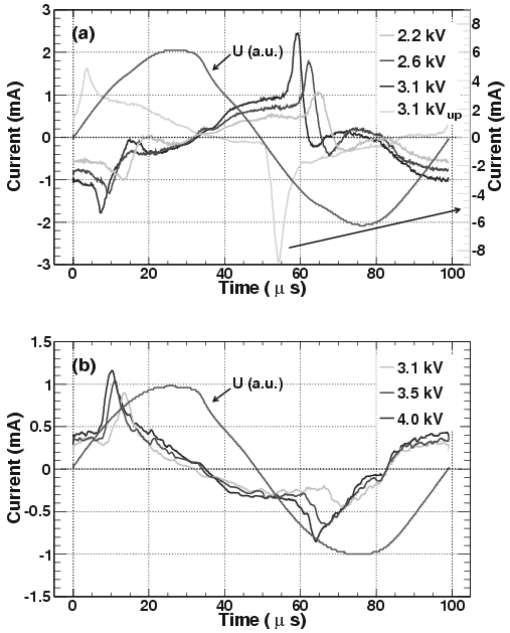

Fig. 3 Discharge currents between the downstream plates with different voltage amplitudes for the cases of (a) with and (b) without an upstream discharge region. The two-plate distance d = 2.5 cm. The aqua curve in (a) corresponds to the discharge current in the upstream discharge region.

Figure 3 shows the dependence of discharge current (displacement current is subtracted) on high voltage amplitude with the two-plate distance fixed at d = 2.5 cm. The voltage increase results in shift of discharge current to early times with respect to the phase of the applied voltage, and results in the increase in discharge current intensity. The current of aqua color in Fig. 3(a), which corresponds to the discharge in the upstream region with the voltage amplitude of 3.1 kV, and these currents in Fig. 3(b) show glow-like DBDs [1]. This typical DBD has a continuous discharge current flowing along the direction of the external electric field in each half-cycle of applied voltages. However, the discharge currents between the downstream plates [blue, red and green curves in Fig. 3(a)] flow along the inverse direction of the external electric field. Furthermore, the discharge has a higher intensity of discharge current, and has an earlier breakdown time and a lower breakdown voltage, due to which the voltages of lower values are selected to be shown in Fig. 3(a).

Figure 4 shows the discharge current with different distances between two parallel plates with the voltage amplitudes of 3.1 kV and 4.0 kV, respectively. Distance decrease results in shift in breakdown to early times with respect to the phase of the applied voltage and results in the increase in discharge current intensity. Comparing with Fig. 4(b), Fig. 4(a) also shows that the discharge has an earlier breakdown time. Another interesting characteristic in the case of with an upstream discharge is that the breakdown time of the downstream discharge decreases with the distance d, whose value is appropriately inversely proportional to the external electric field E_e as $E_e \approx$ V/d, when the applied voltage V is fixed.

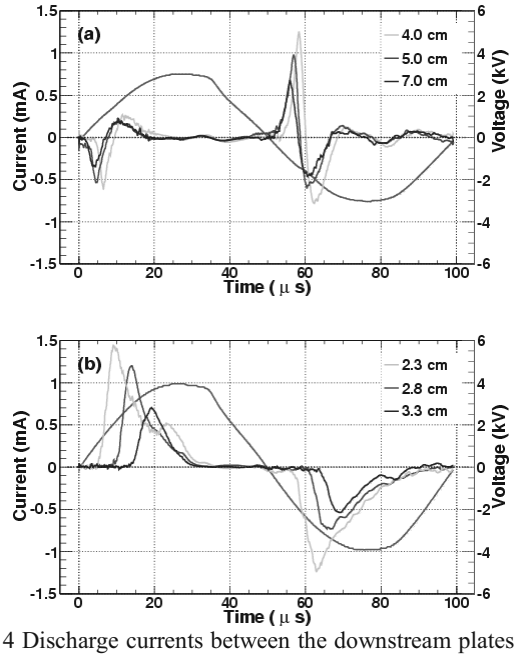

Fig. 4 Discharge currents between the downstream plates with different distance for the cases of (a) with and (b) without an upstream discharge region. Voltage amplitudes are fixed at 3.1 kV and 4.0 kV, respectively.

4. Summary

We have obtained effects of the upstream discharge region on the downstream jet discharge between two plates. According to the above comparison investigation, the main differences in the DBD APPJs with an upstream discharge region are summarized as follows:

(I) The discharge current is in the inverse direction of the external electric field in the jet region.

(II) The breakdown time of the downstream jet discharge decreases with the intensity of the external electric field.

(III) The inverse discharge intensity in the negative half-cycle of the applied voltage is higher than that of the positive one.

This behavior has been supposed to be due to the propagation of the coupling-streamer head from the upstream helium plasma to the region between the two plate electrodes [7].

References

[1] F. Massines, A. Rabehi, P. Decomps, R. B. Gadri, P.Segur, and C. Mayoux, J. Appl. Phys. **83**(1998), 2950.

[2] M. Teschke, J. Kedzierski, E. G. Finantu-Dinu, D. Krozec, and J. Engemann, IEEE Trans. Plasma Sci. **33** (2005), 310.

[3] M. Laroussi, and X. Lu, Appl. Phys. Lett. **87**(2005), 113902.

[4] T. Sakaguchi, O. Sakai, and K. Tachibana, J. Appl. Phys. **101** (2007), 073305.

[5] Z. Cao, J. L. Walsh, and M. G. Kong, Appl. Phys. Lett. **94** (2009), 021501.

[6] Q. Li, H. Takana, Y. K. Pu, and H. Nishiyama, Appl. Phys. Lett. **98** (2011), 241501.

[7] Q. Li, Y. K. Pu, M. A. Lieberman, and D. J. Economou, Phys. Rev. E **83** (2011), 046405.

Eighth International Conference on Flow Dynamics
November 9 - November 11, 2011

Incompressible SPH Simulation of a Droplet and a Liquid Column with Marangoni Convection

Masumi Ito, Seiichiro Izawa, Yu Fukunishi and Masaya Shigeta
Department of Mechanical Systems and Design, Graduate School of Engineering, Tohoku University
6-6-01 Aramaki-Aoba, Aoba-ku, Sendai, Miyagi, Japan
masumi@fluid.mech.tohoku.ac.jp.

ABSTRACT

The Marangoni convection in a droplet and a liquid column were computed by an incompressible SPH method. The Marangoni effect was modeled by adding the tangential accelerations to surface particles which depends on both the gradients of their temperatures and the surface tension coefficient. The simulations showed the reasonable results in which the surface moved according to the surface tension difference generating a convectional flow.

1. Introduction

Smoothed Particle Hydrodynamics (SPH) is a Lagrangian-based method to simulate a fluid motion without a grid. The fluid motion is represented by the behavior of particles that move according to their respective motion equations with interaction. SPH has several advantages over other CFD methods. For example, it is easy to handle deformable boundaries including a free surface of a liquid body.

In a computation of a flow field including a free surface movement, it is important to implement the effect of the surface tension. Generally, when the surface tension is constant, the driving force caused by the surface tension is treated as the pressure difference across the surface, which is called the Laplace pressure. This force works on the surface in its normal direction. On the contrary, the surface tension gradient caused by a difference of temperature or a difference of consistency of the liquid composite generates a tangential movement. This phenomenon is called Marangoni effect. Up until now, the way to treat this tangential force has not been successfully deliberated in SPH. In this study, the effect of Marangoni force is appended to the SPH method, and the thermofluid behavior of the heated droplet and the heated liquid column are simulated using the SPH method.

2. Numerical Method

2.1 Model Description

In the SPH method, the mass distribution of each particle is given as a continuous function of Kernel W, so that the density distribution at the particle position is written as

$$\rho_a = \rho(\boldsymbol{r}_a) = \sum_b m_b W_{ab} = \sum_b m_b W(|\boldsymbol{r}_b - \boldsymbol{r}_a|), \quad (1)$$

where a and b denote the particle indices, $\boldsymbol{r}$ is the position of a particle, and m is the mass of a particle. Then, the momentum equation is written as

$$\frac{\mathrm{d}\boldsymbol{u}_a}{\mathrm{d}t} = -\sum_b \left(\frac{p_a}{{\rho_a}^2} + \frac{p_b}{{\rho_b}^2} \right) m_b \nabla_a W_{ab} + \frac{6\mu}{\lambda_a \rho_a} \sum_b (\boldsymbol{u}_b - \boldsymbol{u}_a) W_{ab} + \frac{\boldsymbol{F}}{m_a}, \quad (2)$$

$$\lambda_a = \sum_b |\boldsymbol{r}_b - \boldsymbol{r}_a|^2 W_{ab}, \quad (3)$$

where $\boldsymbol{u}$ is the velocity, t is the time, p is the pressure, μ is the viscous coefficient, and $\boldsymbol{F}$ is the external driving force. The first and second terms of the right hand side in Eq. (2) represent the forces by the pressure gradient and viscosity, respectively. The detailed model description of the SPH method can be found in Ref. [1].

2.2 Treatment of Surface Tension

In this study, the driving force caused by the surface tension $\boldsymbol{F}_{\mathrm{ST}}$ is expressed as the combination of the normal direction force $\boldsymbol{F}_{\mathrm{Laplace}}$, tangential direction force $\boldsymbol{F}_{\mathrm{tangent}}$, and the attracting force $\boldsymbol{F}_{\mathrm{attract}}$:

$$\boldsymbol{F}_{\mathrm{ST}} = \frac{1}{2}(\boldsymbol{F}_{\mathrm{Laplace}} + \boldsymbol{F}_{\mathrm{tangent}}) + \frac{1}{2}\boldsymbol{F}_{\mathrm{attract}}, \quad (4)$$

$$\boldsymbol{F}_{\mathrm{Laplace}} = -\boldsymbol{n}\gamma d^2 \nabla \cdot \boldsymbol{n}, \quad (5)$$

$$\boldsymbol{F}_{\mathrm{tangent}} = \frac{\mathrm{d}\gamma}{\mathrm{d}T} d\boldsymbol{n} \times \nabla T \times \boldsymbol{n}, \quad (6)$$

and

$$\boldsymbol{F}_{\mathrm{attract}} = \sum_b \gamma d \frac{\boldsymbol{r}_b - \boldsymbol{r}}{|\boldsymbol{r}_b - \boldsymbol{r}|}, \quad (7)$$

where $\boldsymbol{n}$ is the unit normal vector, γ is the surface tension coefficient, d is the particle diameter, and T is the temperature. $\boldsymbol{F}_{\mathrm{Laplace}}$ and $\boldsymbol{F}_{\mathrm{tangent}}$ are given only to the surface particles.

2.3 Computational Condition

The following two cases are simulated.

Case 1 Computation of the droplet on the disk

Figure 1 shows the computational domain representing a droplet attached to a disk with the diameter of 5 mm and the thickness of 0.6 mm. The droplet is discretized by 5,044 particles with the diameter of 0.2 mm. The geometries are set to be similar to the conditions of Ref. [2] for comparison. The disk temperature is increased at the constant rate of 2 K/s. The time step is set to be 0.4 ms.

Case 2 Computation of the liquid column

Figure 2 shows the computational domain representing a liquid body bridging the gap between two disks whose diameter (D) is 50 mm and the thickness is 6 mm. The gap length is H=38 mm, so the aspect ratio Ar=H/D=0.76. The liquid body in the gap is descretized

by about 9,500 particles whose diameter is 2.0 mm. The initial temperature is 300 K and uniform. The temperature of one disk is increased to 320 K. The time step is set to be 1 ms. The heat condition and the geometries are similar to one case of the space experiments called the Marangoni Experiments in Space (MEIS) which were carried out in the International Space Station (ISS) Ref. [3].

In both computations, the material properties of the silicone oil are used. Its surface tension coefficient is $\sigma_T = 6.36\times10^{-2}$ mN/mK, dynamic viscosity $\nu = 5.00\times10^{-6}$ m^2/s. The evaporation of the liquid is neglected. Influence of the ambient gas on the flow field or temperature field is not taken into account.

3. Results and Discussion

Case 1 Computation of the droplet on the disk

Figure 3 shows the flow field in the plane including the center axis. The continuous increase of the disk temperature produced the temperature difference in the droplet. The surface tension difference owing to this temperature difference induced the movement of the droplet surface, which leads to continuous convection with an upward movement of the surface and the downward flow at the center region of the droplet. The flow behavior is similar to the result in Ref. [2].

Case 2 Computation of the liquid column

Figure 4 shows the flow field in the plane including the center axis. The temperature difference between the two disks causes the liquid surface movement. The surface moves from the higher temperature side to the lower temperature side. As a result, the liquid moves to the higher temperature side inside the liquid. This behavior is similar to the result in Ref. [4].

4. Concluding remarks

In this study, SPH method was applied to the simulations of the thermofluid behavior of the heated liquid bodies taking into account the Marangoni effect. The results of the simulations were reasonable, where the surface movement was driven by the surface tension difference, resulting in a convectional flow.

References

[1] M. Shigeta *et al.*: Int. J. Emerging Multidisciplinary Fluid Sci., **1** (2009), pp. 1-18.

[2] R. Savino and S. Fico: Phys. Fluids 16, **3738** (2004)

[3] K. Nisihno *et al.*: Space Utiliz Res, **27** (2011), pp. 80-81, (Japanese)

[4] L.G. Napolitano: Science, 225, **4658** (1948), pp. 197-198

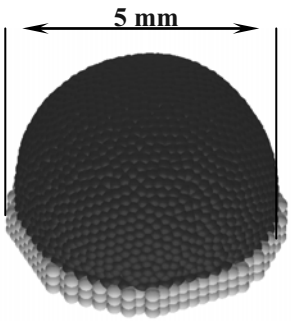

Fig. 1 The droplet and the disk represented by 6496 particles. Black particles denote liquid. Gray particles denote the solid disk.

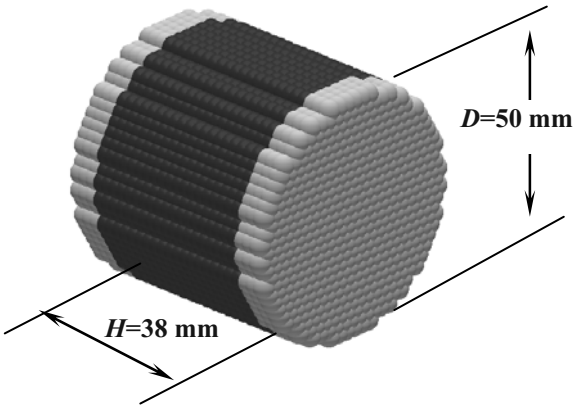

Fig. 2 The liquid column and two disks represented by 12475 particles. Black particles denote liquid. Gray partcles denote solid disks.

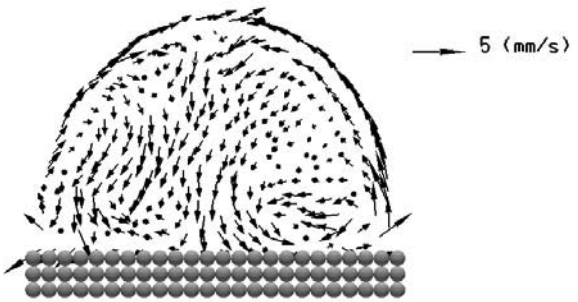

Fig. 3 Instantaneous velocity vectors at particle locations in the center plane of a droplet attaching the disk when t=13.6 s.

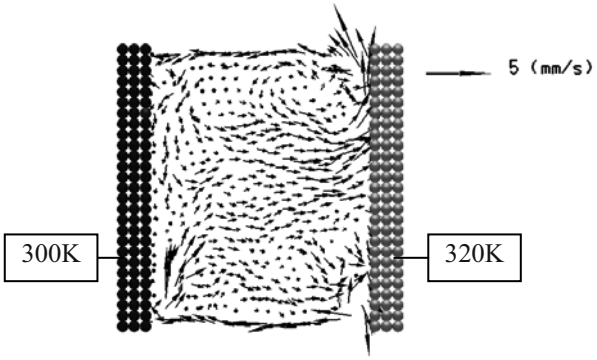

Fig. 4 Instantaneous velocity vectors at particle locations in the center plane of a liquid column when t=80.1 s. Black and gray particles are 300 K disk and 320 K disk.

Eighth International Conference on Flow Dynamics
November 9 - November 11, 2011

Experimental Study of Water Jet Formation by Electric Discharge in Tubes with Various Width

Kentaro Hayashi[1], Taketoshi Koita[1], Mingyu Sun[2]
[1]School of Engineering, Tohoku University, 6-3 Aoba, Aramaki aza, Aoba-ku, Sendai 980-8578, Japan,
[2]Center for Interdisciplinary Research, Tohoku University, 6-3 Aoba, Aramaki aza, Aoba-ku, Sendai 980-8578, Japan
hayashi@iswi.cir.tohoku.ac.jp

ABSTRACT

Experimental study of water jet formation by electric discharge in tubes with various widths is carried out. It is the phenomenon of a bubble interaction with water surface interaction in a closed space. The bubble evolution and the water jet generation are visualized by a high speed camera. The location and the velocity of water jet are also obtained and discussed by analyzing recorded photos.

1. Introduction

The sudden release of high pressure gas bubble in water induced by underwater explosion generates a shock wave outward, resulting in the movement of surrounding water, especially on the side of free surface. When underwater explosion occurs in the straight rectangular tube, the water above the bubble can be accelerated, forming water jet. The mechanism of this jet formation is similar to explosive volcano eruptions that are caused by expanding pressurized soluble gases [1] in volcanic channels. In past few years, the laser-induced liquid jet has been studied in biology and medicine [2]. In this application, the water jet and the bubble is induced in a narrow pipe. In order to generate the water jet with good repeatability, a controllable water jet is preferable. Shallow and deep underwater explosions in free space have been heavily investigated experimentally for decades. However, two side walls may have an significant impact on the water jet formation in the confined space. Therefore, in our previous studies, the water jet velocity and formation in a narrow tube with a rectangular cross-section by underwater explosion is investigated for a few cases. This paper reports our recent experimental results on more explosion depths and widths.

2. Experimental Method

The rectangular tube is used as the test section to investigate the behavior of water jet in closed space. Fig.1(a) shows the test section in this study. The thickness of the rectangular tube , D , is 5mm, and the height is 250mm. The bottom wall and two side walls are made of stainless steel, and other two sides are fixed by two optical windows made of transparent plexigalss. The purefied water is used in this study. Underwater explosion is created with high voltage electric discharge. The experimental equipment in this study is shown in Fig.2(b). The driver circuit in high voltage discharge consists of a high voltage power, a capacitor, a spark trigger and two electrodes (P and N). These electrodes are installed at Y = 140mm and connected with copper wire in water. Capacitor is connected in parallel with voltage power and its capacity C is 0.2 μF. The circuit is triggered manually. When the circuit is triggered, electric discharge is instantly generated and then explosion bubble appears. To investigate the dependence of water jet velocity and its formation on the location of explosion center in the rectangular tube, explosion depth H is changed with 10 patterns, H = 5, 10, 15, 20, 25, 30, 35, 40, 50, 60mm, are tested. The bubble evolution and the water jet formation are directly visualized by a high speed camera at the frame rate of 50 thousands frames per speed. The exposure time is 2μsec per frame. The metal halide white lamp with power of 350w is used as a light source. The location and the velocity of flow structures are also obtained by analyzing recorded photos.

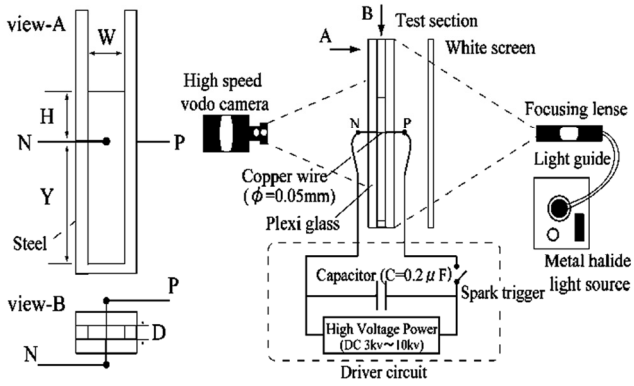

(a)Test section (b)Experimental equipment

Fig.1 Test section and experimental equipment

3. Results and Discussion

3.1 The Behavior of Bubble Evolution and Water Jet Formation

The experiments are conducted at ten depths (H = 5, 10, 15, 20, 25, 30, 35, 40, 50, 60mm). The patterns of the bubble evolution of six depths (H = 5, 10, 15, 20, 25, 30mm) have been reported by [3]. These phenomena observed at W = 15mm are only reported in this paper. Pattern A is observed at the depth of 35mm, and pattern B is seen at the depths of 40mm, 50mm, 60mm. Two typical photos are shown respectively in Fig.2 and Fig.3. At first, the configuration of the bubble is cylindrical. When the electric current passes through the horizontal expansion is affected with two sidewalls and is stopped then the expansion bubble changes to an ellipsoid shape. At the two electrodes, electric energy is released and a blast wave is caused. This blast wave is propagates in the water and it creates the low pressure region in the water behind. In Fig.2 at the time of 1.0*ms*, second cavitation is observed at the pipe wall, in the region between the bubble and the free surface because of the low pressure. When the expansion wave reaches free surface, these cavitation gradually disappears. In all figures, second cavitations are also seen under the bubble in the channel. These cavitation bubbles are formed because of the low pressure in the water generated by expansion waves reflected from the bottom wall. As seen in Fig.2 for H = 35mm, the water above the bubble is accelerated and forms a jet. Two air pockets are generated near pipe wall. The water jet is blunt-sharped at beginning. However, the shape of water jet is changed from a blunt shaped jet to a spike-shaped jet at last. At about t = 1.8ms, it is seen that a micro jet is formed inside the bubble from the bottom of the bubble. This inner jet moves upward. Two air pockets

are generated on both pipe walls at last stages. Another downward inner jet is seen at t = 2.4ms. The bubble is collapsed by the inner jet at last stage. In Fig.3, the shape of water jet is changed from blunt-shaped jet to a spike-shaped jet at t > 4.0ms. It is found that the shape of water jet depends on the explosion depth H. The process of the bubble collapsing is similar to pattern A.

3.2 Location and Velocity of Flow Structures

Fig.4(a) shows the schematic view of typical flow structures. The trajectories of these structures are measured from the photos and are shown in Fig.4(b). Their velocities are evaluated from the displacement and the time interval between two frames. As seen in Fig.4(b), it is found that after upward inner jet and downward inner jet reach same numerical number. The velocities of the top of surface jet at W = 15mm at V = 4.5kv are showed at Fig.5. The velocities are averaged for $t \geqq$ 0.8ms and $H \geqq$ 10mm and plotted in Fig.6. For H = 5mm the average velocity is taken $t \geqq$ 0.2ms. The average velocity dramatically reduces at H < 15mm. The velocity is approximately constant at 15mm < H < 30mm and gradually reduces at 30mm < H < 40mm. The velocity hardly changes for 40mm < H < 60mm.

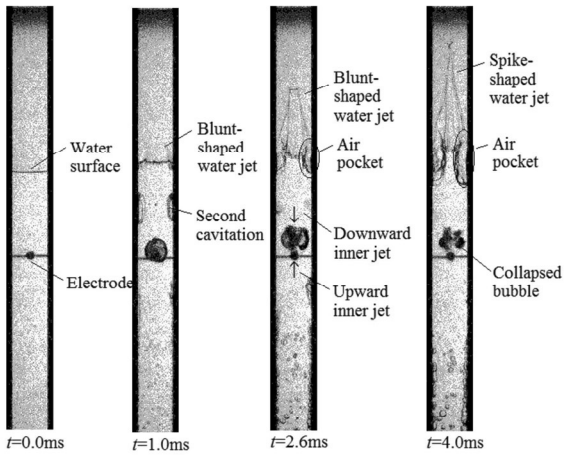

Fig.2 Process of bubble collapse and water jet formation for V=4.5kv at H=35mm

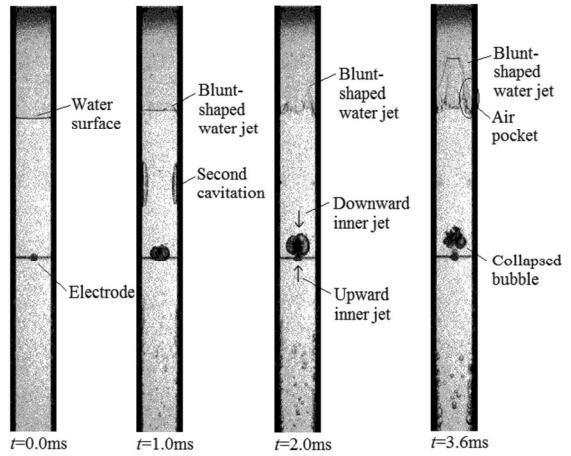

Fig.3 Process of bubble collapse and water jet formation for V=4.5kv at H=60mm

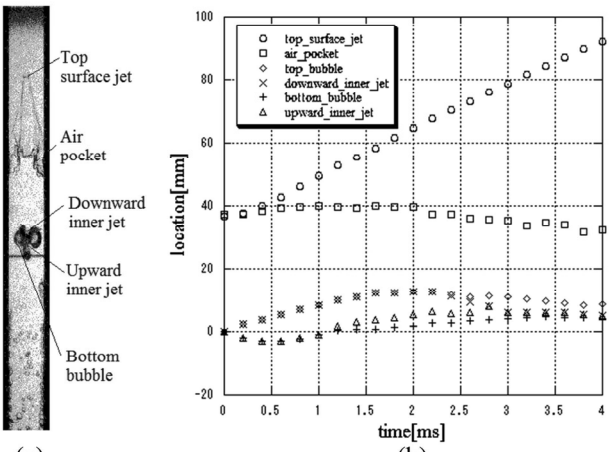

(a) (b)

Fig.4 Trajectories of typical flow characteristics of bubble and jet defined (a), with a width of 15mm for underwater electric discharge located at depth (H): (b) H = 35mm

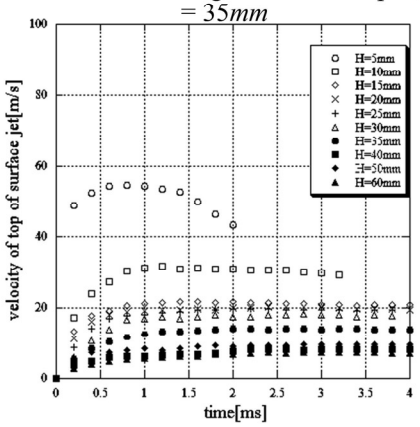

Fig.5 Histories of surface jet velocity at ten explosion depths

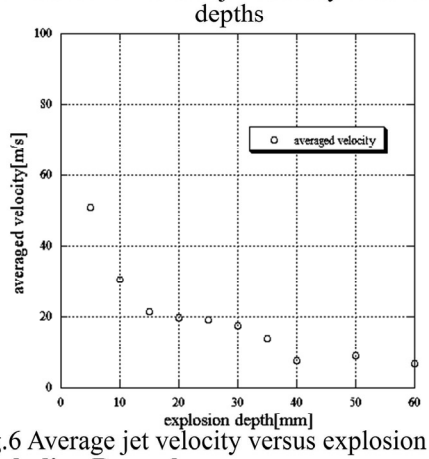

Fig.6 Average jet velocity versus explosion depth

4. Concluding Remarks

The shape and the velocity of water jet depends on the explosion depth H. The jet velocity reduces with the explosion depth, but it hardly changes in the domain 15mm < H < 30mm. We therefore suggest that a jet device should work under this depth domain, to gain a high repeatability of jet velocity.

References

[1]H.Yamamoto, K.Takayama and K.Ishikawa, Journal of Mineralogical and Petrological Sciences (2008), Vol.103, No.3:192-203.

[2]T.Tominaga, A.Nakagawa, Shock Waves (2006), Vol.15:55-67.

[3]T.Koita, Y.Zhu and M.Sun, The 28th International Symposium on Shock Waves, Manchester, UK, (2011).

Eighth International Conference on Flow Dynamics
November 9 - November 11, 2011

Simulation of Velocity Fluctuation Generated by Vibrating Actuator

Hajime Okawa, Masaya Shigeta, Seiichiro Izawa, Yu Fukunishi
Department of Mechanical Systems and Design,
Graduate School of Engineering, Tohoku University
6-6-01 Aramaki-Aoba, Aoba-ku, Sendai, Miyagi, Japan
okawa@fluid.mech.tohoku.ac.jp

ABSTRACT

A two dimensional simulation of velocity fluctuation generation inside a boundary layer by an actuator on the wall was carried out. The results were compared to experiments carried out in the past. Although generation of T-S waves could be observed in the numerical results, the T-S wave pattern decayed quickly and did not grow.

1. Introduction

Tollmien-Schlichting (T-S) waves are typical instability waves observed at the early stage of natural transition of a boundary layer. To delay the turbulence transition, many attempts to control these instability waves have been performed proposing various types of the actuators.[1][2] In the series of our studies, the growth of linear instability waves has been successfully suppressed by the feedforward control system using a combination of an array of upstream sensors and downstream piezo-electric actuators.[3]

In addition, we have focused on methods to use the actuators more efficiently. The effects of using driving signals apart from the sinusoidal signal were examined. It was found out that the types of driving signal have a certain effect on the generated instability waves. However, it is very difficult to measure the flow field in the vicinity of the actuator in the experiment. So, in this study, a numerical simulation of a flat-plate boundary layer is carried out focusing on the velocity fluctuation excited by an activated actuator. The results are compared with the previous experimental results[4] and discussed.

2. Computational method

The target flow is a flat-plate boundary layer with conditions same as the experiment.[4] The computational domain is a rectangular region shown in Fig. 1. The main flow velocity is U_∞=14m/s and the inflow Reynolds number based on the thickness of the boundary layer is 3.5×10^3. The origin of the coordinate system is set at the leading edge of the plate. The axes x and y denote the streamwise and wall-normal directions. Dimensionless height η is defined by

$$\eta = y\sqrt{\frac{U_\infty}{\nu x}} \tag{1}$$

where ν[m^2/s] is kinetic viscosity of the air. The velocity profile of the inlet flow has a Blasius profile.

The governing equations are the two-dimensional incompressible Navier-Stokes equations. These equations are solved by the fractional step method. The convectional term and the viscous term are discretized by the second order central difference scheme. Eulerian method is adopted for time marching.

As for the velocity boundary conditions, the non-slip condition is applied at the wall surface, and the Neumann condition is applied at the top and outlet boundaries. As for the pressure boundary conditions, the Neumann condition is applied to the boundaries, while the pressure at the inlet is fixed. The computational region covers 600mm<x<1200mm and 0mm<y<10mm. A uniform grid system is used and the numbers of grid points are $N_x\times N_y = 400\times100$.

A Piezo actuator expands and shrinks when an alternate voltage is applied. In the experiment, the upstream side of an actuator was glued on the surface, while the downstream side freely moved with a displacement of several micrometers. In the numerical simulation, the movement of the actuator on the plate is expressed by providing finite values for velocity at the actuator surface in the range of 820mm<x<900mm instead of zero. Therefore the thickness of the actuator is neglected in this simulation. Also, the driving frequency is set at 100Hz and the maximum amplitude of velocity fluctuation is 4.4% of the freestream velocity. Although this frequency is slightly different from the experimental condition, it is selected to be within the unstable region predicted by the linear stability theory.

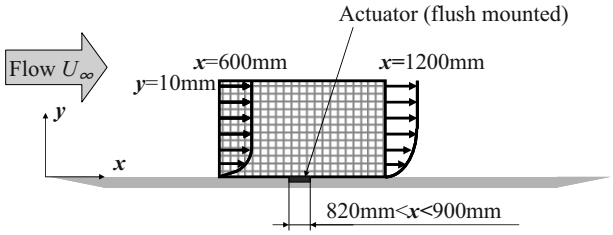

Fig. 1 Computational domain.

3. Results and Discussion

Figure 2 shows the velocity distributions at the different streamwise positions when there is no actuator. All the velocity profiles agree well with the Blasius profile.

Figures 3 and 4 show the vorticity fluctuations when the actuator is activated for the experiment and the simulation, respectively. In the experimental results, the ensemble-averaged velocity gradient $-\partial u'_{ens}/\partial y$ is regarded as the vorticity fluctuation. As shown in Fig. 3, negative and positive fluctuation pattern appears

downstream accompanying the periodic motion of the actuator. Its phase velocity is 5.2m/s, which is 37% of the freestream velocity. This is a typical value for T-S waves. On the other hand, in Fig. 4, although there is a stripe pattern just downstream of the trailing edge of the actuator, it is weak, quickly decays and does not grow.

Figure 5 presents the RMS distribution of the streamwise velocity fluctuations u'_{rms} at x = 915mm, 15mm downstream from the trailing edge of the actuator. The profile has two-humped peaks, which is the characteristic feature of the T-S waves. The result indicates that T-S waves were actually generated in the simulation. The reason why T-S waves' stripe pattern can hardly be found in Fig. 4 is probably due to numerical errors.

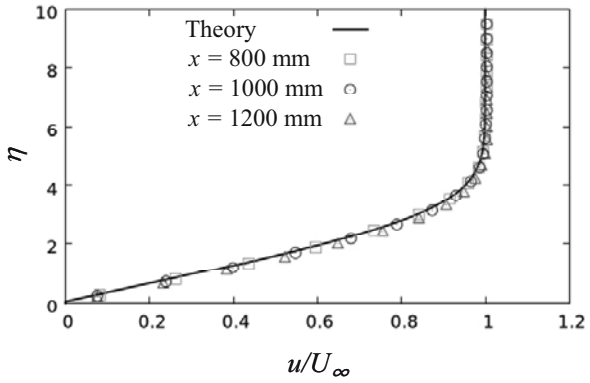

Fig. 2 Velocity of the basic flow at the different streamwise positions, x=800, 1000, 1200mm.

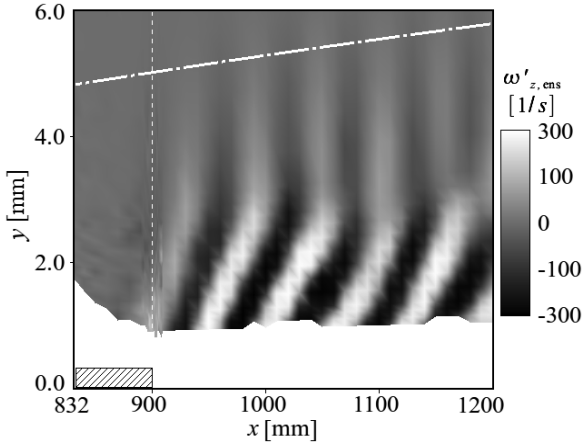

Fig.3 Ensemble averaged local velocity gradient $-\partial u'_{ens}/\partial y$ in x-y plane at z = 0mm.
(Experiment [4])

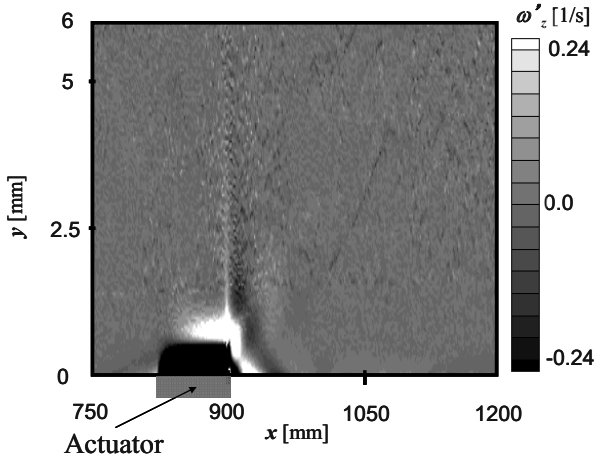

Fig. 4 Vorticity fluctuation in x-y plane in simulation.

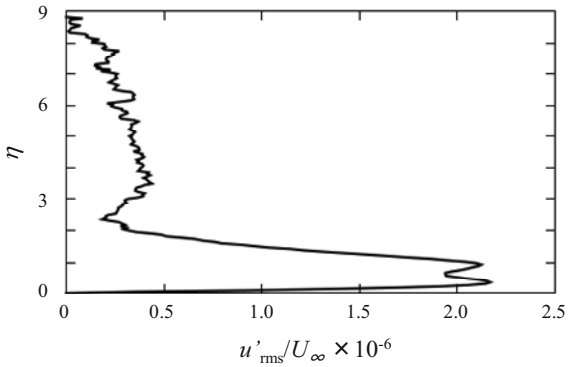

Fig. 5 RMS profile of streamwise velocity fluctuations at x=915mm.
(Simulation)

4. Concluding remarks

An attempt to numerically simulate and reproduce the excitation process of instability waves using the actuator on the wall was carried out. Although T-S waves were generated right behind the actuator, they decayed very quickly and did not grow.

References

[1] M. Baumann, D. Sturzebecher and W. Nitsche, Active Control of TS-Instabilities on an Unswept Wing", *Proc. the IUTAM Symposium*, 2000, pp. 155-160.

[2] S. Grundmann and C. Tropea, Active cancellation of artificially introduced Tollmien-Schlichting waves using plasma actuators, *Experiments in Fluids*, **44**(5), pp. 795-806.

[3] H.Okawa, *et. al.,* Active Feedforward Cancellation of Instability Waves, *Proc. 13th Asian Congress of Fluid Mechanics, Dhaka, Bangladesh*, (17-21 December, 2010), pp.256-258 CD-ROM.

[4] H. Okawa, *et.al.*, Generation of Velocity Fluctuations in a Boundary Layer by a Piezoelectric Actuator, *Proc. AJK2011-FED ASME-JSME-KSME Joint Fluids Engineering Conference 2011, Hamamatsu, Japan*, (24-29 July, 2011), AJK2011-13018 USB Memory.

Eighth International Conference on Flow Dynamics
November 9 - November 11, 2011

A Numerical Study of Bubble Collapsing in Cavitating Flows over A Hydrofoil

Katsuhisa Suzuki[1], Mingyu Sun[2]
[1] School of Engineering, Tohoku University, 6-3 Aoba, Aramaki aza, Aoba-ku, Sendai 980-8577, Japan
[2] Center of Interdisciplinary Research, Tohoku University, 6-3 Aoba, Aramaki aza, Aoba-ku, Sendai 980-8577, Japan
suzuki@iswi.cir.tohoku.ac.jp

ABSTRACT

The behavior of cavitating flows over a hydrofoil Clark-Y is analyzed with numerical method. A semi-implicit method is employed to enhance the computational efficiency of a fully compressible two-fluid model for the low speed liquid flow. In this study, the cycles of cavitation and re-entrant jet are successfully predicted. It is confirmed that the sudden drop of the lift coefficient is due to the high pressure created by the bubble collapsing.

1. Introduction

In liquid flows, cavitation occurs if the liquid is accelerated and pressure of liquid falls below vapor pressure. It is a serious problem that the cavitation deteriorates the performance and cause erosions over propellers. It is a challenging task accurately to predict the cavitation by numerical simulation.

In this study, the solution for dealing with high and low current speeds is developed to analyze the cavitation phenomena over a hydrofoil. Previously work of Liou by using AUSM$^+$-up scheme [1] employed an explicit method. A semi-implicit method is employed to analyze at high speed, and AUSM$^+$-up scheme is employed to deal with low Mach number flows. The cycles of cavitation and high pressure region by collapsing cavitation are observed.

2. Method

In this study, the simulation is conducted with a semi-implicit Lagrange-Remap method. It solves conservative quantities of pressure and velocity in the Lagrangian coordinate. Moreover, to solve discontinuous quantity of state at particle interfaces, the simple acoustic solver [2] is employed as the approximate Riemann solvers. The quantities of pressure p^* and velocity U^* at interface are given as follows:

$$U^* = \frac{\beta_1(p_L - p_R) + I_L U_L + I_R U_R}{I_L + I_R} \quad (1)$$

$$p^* = \frac{\beta_2(U_L - U_R) I_L I_R + I_L p_R + I_R p_L}{I_L + I_R} \quad (2)$$

where I is acoustic impedance, and subscript L and R indicate left and right at interface. β_1 and β_2 are coefficients of numerical viscosity, as introduced in the AUSM$^+$-up scheme to improve the convergence behavior at low Mach numbers, and are given by

$$\beta_1 = \max\left(1, \frac{1}{\beta_2}\right) \quad (3)$$

$$\beta_2 = \min(1, M(2 - M)) \quad (4)$$

with M is the upstream Mach number. The conservative quantity is remapped to the Euler coordinate, and it is used in next step to solve conservative quantity. Subgrid modeling is employed to calculate two-phase interface inside a cell [3]. For the cavitation model, Merkle's cavitation model is adapted to two-fluid model [4].

We calculate Clark-Y hydrofoil at an angle-of-attack of 8°. Fig.1 shows a computational grid structured O-type (160×56). The length of chord is 1[m]. This hydrofoil is located in water. Viscosity is not considered. Computations have been done for various cavitation numbers σ of 0.4-2.0 at every 0.2. The flow Mach number is 0.0065. All cases above are done with the CFL number 0.04 in order to observe the propagation of high pressure waves. The lift and drag coefficients are almost similar for a much higher CFL number of 0.4, but the pressure waves are hardly resolved with the high number.

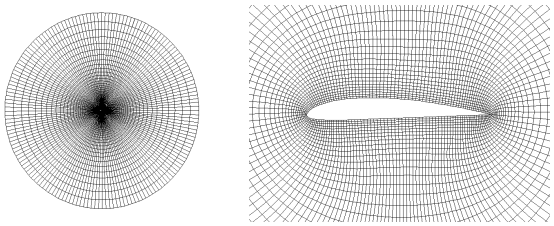

(a)Overall view (b)Magnified view

Fig.1 Computational grid

3. Results and Discussion

The lift and drag coefficients at cavitation number $\sigma = 1.0$ are recorded and shown in Fig.2. The periodic behavior of the cavitation over the hydrofoil is predicted. The volume fraction distributions in a cycle of cavitation are shown in Fig.3. The cavitation is initiated over the hydrofoil, and then forms a cloud cavitation. The re-entrant jet is recognizable at this stage. The re-entrant jet penetrates into the cavitation zone at t = 0.34[s], as shown in Fig.4.

The averaged lift and drag coefficients are shown in Fig.5 again cavitation number σ, together with experimental data by Wang et al. [5] and calculated data by Wu et al. [6]. The data is averaged over a few cycles resolved. These obtained at CFL number 0.4 is also compared. The numerical predicted data agree well with the experiments especially at low cavitation numbers. A discrepancy is seen near the breakdown regime, where a fully three-dimensional effect should be important.

The cloud cavitation reduces its size gradually, and disappears eventually, creating a shock wave and high pressure waves. The pressure distributions, during the collapsing of a cavitation bubble in Fig.3(d), are shown in Fig.6. It is seen that the upper surface is impacted by these high pressure waves, resulting in a sudden drop in

lift coefficient. In Fig.6(a) and (b), the cavitation bubble with the vapor still remains in the high pressure region. This is due to the fact that in the numerical modeling, the cavitation model is performed after updating pressure in integrating Euler equations.

The propagation speed of high pressure waves varies from 1700m/s to 3000m/s, depending on the direction of propagation. The speeds are evaluated from the isobar contours in the figures, which gives only an estimate of the wave speed. Nevertheless, the order of these speeds agrees with the sound speed in water.

4. Concluding remarks

The bubble in cavitating flows over a hydrofoil Clark-Y is analyzed. The periodic cavitation and re-entrant jet are resolved. The calculated data agree with experimental data at low cavitation numbers. Thus it is necessary to improve method at near cavitation number 1.2. A 3D algorithm is under development. It is also confirmed that the sudden drop in lift coefficient is due to the high pressure induced by the bubble collapsing over the upper surface of the hydrofoil.

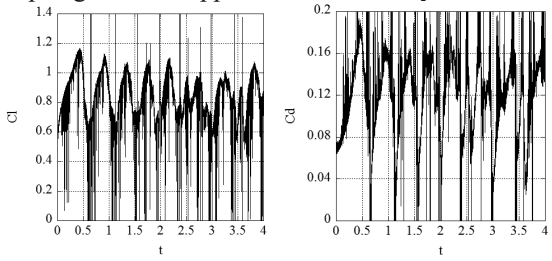

(a) Lift coefficient (b) Drag coefficient

Fig.2 Histories of lift and drag coefficients

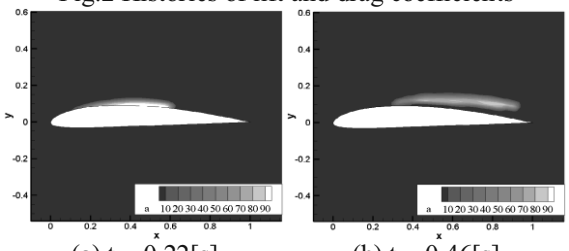

(a) t = 0.22[s] (b) t = 0.46[s]

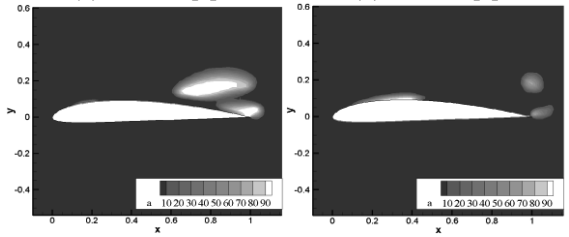

(c) t = 0.57[s] (d) t = 0.64[s]

Fig.3 A cycle of cavitation

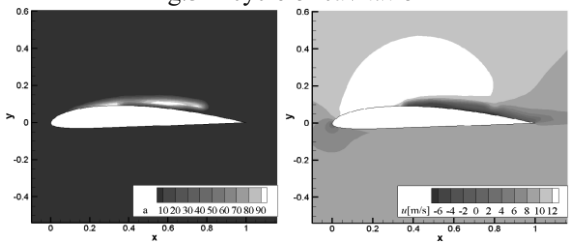

(a) Volume fraction (b) Velocity in direction of x

Fig.4 Re-entrant jet on the upper surface at t = 0.34[s]

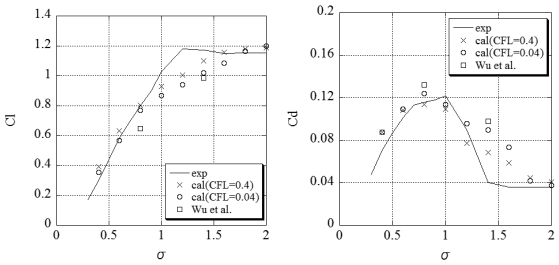

(a) Lift coefficient (b) Drag coefficient

Fig.5 Dependence of lift and drag coefficients of Clark-Y at angle of attack 8° on the cavitation number

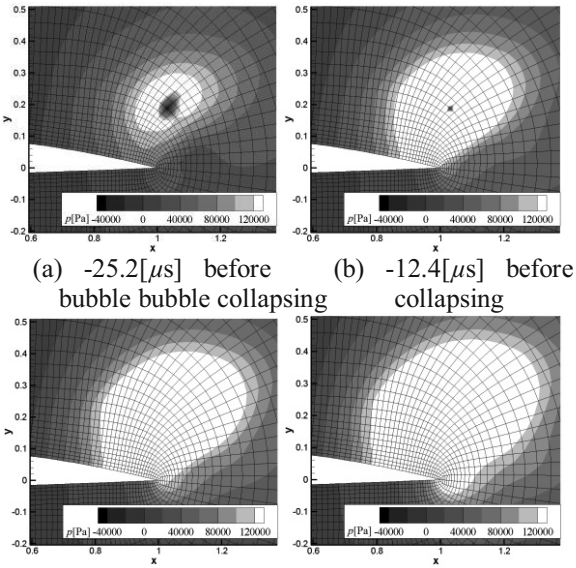

(a) -25.2[μs] before bubble collapsing (b) -12.4[μs] before collapsing

(c) 0[μs] (d) 12.5[μs] after collapsing bubble

Fig.6 Pressure distributions before and after the collapse of a cavitating bubble (The bubble is collapsed at t_0 = 0.6475891[s])

References

[1]M.S.Liou, A sequel to AUSM, Part Ⅱ: AUSM$^+$-up for all speeds, Journal of computational physics 214, (2006), pp.137-170

[2]R.Saurel, F.Peiepas, R.A.Berry, Simple and efficient relaxation methods for interfaces separating compressible fluids, cavitating flows and shocks in multiphase mixtures, Journal of computational physics 228, (2009), pp.1678-1712

[3]M.Sun, Direct simulation of gas-liquid two-phase flows with subgrid particles, Symposium on Computational Fluid Dynamics (2010), A8-2

[4]Y.Zhu, M.Sun, Numerical simulation of cavitation with two-fluid method, International Conference on Fluid Dynamics (2010), Sendai, Japan

[5]G.Wang et al, Dynamics of attached turbulent cavitationg flows, Progress in Aerospace Science 37, (2001), pp.551-581

[6]J.Wu, G.Wang, W.Shyy, Time-dependent turbulent cavitating flow computations with interfacial transport and filter-based models, Journal of numerical methods in fluids 49, (2005), pp.739-761

Eighth International Conference on Flow Dynamics
November 9 - November 11, 2011

Spatial Correlations of Velocity Fluctuation in a Supersonic Flowfield with Transverse Injection

Shohei Uramoto, Toshinori Kouchi, Goro Masuya
Department of Aerospace Engineering, Tohoku University
6-6-01, Aramaki-aza-Aoba, Aoba-ku, Sendai, Miyagi, 980-8579, Japan
uramoto@scrj.mech.tohoku.ac.jp

ABSTRACT

We measured the supersonic flowfield with transverse injection by stereoscopic particle image velocimetry (SPIV) and calculated the single-time two-pint spatial correlations of velocity fluctuations. These correlations showed scale structure of turbulence. Furthermore, the effect of injection species was investigated. The shapes of correlation region changed with the selected velocity component. The bow shock wave was well correlated with a reference point on the 50% averaged concentration track. They were connected by sound wave. The correlation regions for air and helium injection differed each other.

1. Introduction

As a propulsion system of hypersonic flight vehicles, a supersonic combustion ramjet (scramjet) engine has been studied and developed. Flow velocity in a combustor of this engine is supersonic and the time for mixing between air and fuel is very short. Therefore, a fuel injection and mixing were required to be highly efficient.

Transverse injection into a supersonic flow is one of the fuel injection methods. This injection method caused a large loss, but it had a high penetrating in the mainflow and could add a three dimensional disturbance to accelerate mixing.

Takahashi et al. [1] measured this flowfield by planer laser induced fluorescence (PLIF) technique and obtained the turbulent structure of the scalar field. Horikoshi [2] investigated the effect of injection species to the turbulent structures.

In this study, we measured the supersonic flowfield with transverse sonic injection by a stereoscopic particle image velocimetry (SPIV) and calculated the single-time two-pint spatial correlations of the velocity fluctuations, because the velocity fluctuation was regarded as the driving source of turbulent mixing. In addition, the effect of injection species was investigated.

2. Equipment and Method

We used a suction-type supersonic wind tunnel with a two-dimensional Laval nozzle. The mainstream nominal Mach number M_m was 2.0.

The test section had a 30-mm square cross section and was 290 mm long. The walls of this test section were clear acrylic resins. The lower wall used red acrylic resin to reduce the influence of reflection of the laser light sheet. There was a single injection hole of 2.5 mm diameter on the lower wall. This injection hole was located on the center line at 75 mm downstream from the entrance.

The SPIV system used a double-pulse Nd-YAG laser (wave length: 532nm, power: 15mJ/pulse, pulse duration: 5~7 ns, frequency: 15 Hz) as a light source.

The tracer particles were droplets of dioctyl sebacate (density 913.5 kg/m^3 of about 1μm diameter) produced with a Laskin nozzle.

The injectants were air and helium. The jet-to-mainstream momentum flux ratio J was 1.96±0.02 for air and 1.99±0.02 for helium. These parameters referred to Takahashi et al.[1]. The measurement conditions of SPIV are shown in Table 1.

Table 1 Measurement conditions of SPIV

Camera Configuration	Scheinpflug
Camera Angle	27 deg
Lens Tilt Angle	8 deg
Aperture	6.7
Number of Picture pair	1500 pair
Delay Time	500 ns
Thickness of Laser Sheet	1 mm
Correlation Method	Direct Cross-Correlation

3. Results and Discussion

The single-time two-pint spatial correlation $C_{u_iu_j}$ was computed by Eq. (1). Average velocity and root mean square (rms) of velocity fluctuation are computed by the analyzing system (©FtrPIV system). Point (x, y) is a location of the reference point. Δx and Δy are streamwise and transverse distances from the reference point, respectively. We took the reference points on the 50% averaged concentration track that referred to Takahashi et al. [1].

In this study, sample number of picture pairs was 1500. For this number of data, the highly correlation was where the absolute correlation value $|C| \geq 0.1$, as calculated by significance test.

$$
\begin{aligned}
u'_{i,n} &= u_{i,n}(x,y) - \overline{u}_i(x,y), \\
u_{i\_rms}(x,y) &= \sqrt{\frac{1}{N}\sum_{n=1}^{N} u'^2_{i,n}(x,y)}, \\
C_{u_iu_j}(\Delta x,\Delta y) &= \frac{\frac{1}{N}\sum_{n=1}^{N}\left[u'_{i,n}(x,y)\cdot u'_{j,n}(x+\Delta x,y+\Delta y)\right]}{u_{i\_rms}(x,y)\cdot u_{j\_rms}(x+\Delta x,y+\Delta y)} \\
&\qquad (u_i,u_j = u,v,w)
\end{aligned}
\tag{1}
$$

where u, v and w are streamwise, transverse and lateral velocity components, respectively.

Figure 1 showed the nondimensional transverse velocity fluctuation. The dashed-dotted and the two point dashed-dotted lines indicated the 10% and 50% averaged concentration tracks measured by Takahashi et

al. [1], respectively.

The 50% averaged concentration track represented the most intensively concentration fluctuation of jet. However, in this study, this track did not coincide with the track of maximum streamwise velocity gradient shown by dotted line. The highest fluctuation of v appeared near the dotted line.

Figure 2 shows typical examples of the spatial correlation distribution, ones of transverse velocity fluctuation: C_{vv}. The injectant was air for upper of Fig. 2 and helium for lower of Fig. 2.

Both injectant showed a strong correlation region around the reference point at x/d_j = 7 on the 50% averaged concentration track. The shapes of the correlation region were showed vertically elongated ellipses. This shapes changed with the selected velocity components.

The whole bow shock wave correlated with a reference point in the air injection. Furthermore, in this case, a reattach shock wave emanated near the reference point was observed and it was weakly correlated with a reference point, too. On the other hand, in the helium injection case, the bow shock wave was not well correlated with the reference point and the reattachment shock wave was not observed.

Around a point (x/d_j, y/d_j) = (5, 6), the positively and negatively correlated regions existed for both injection. These regions represented sound wave irradiated by the motion of jet plume. Since the injection velocity of helium was faster than that of air, the correlated region for helium injection was larger than that for air injection.

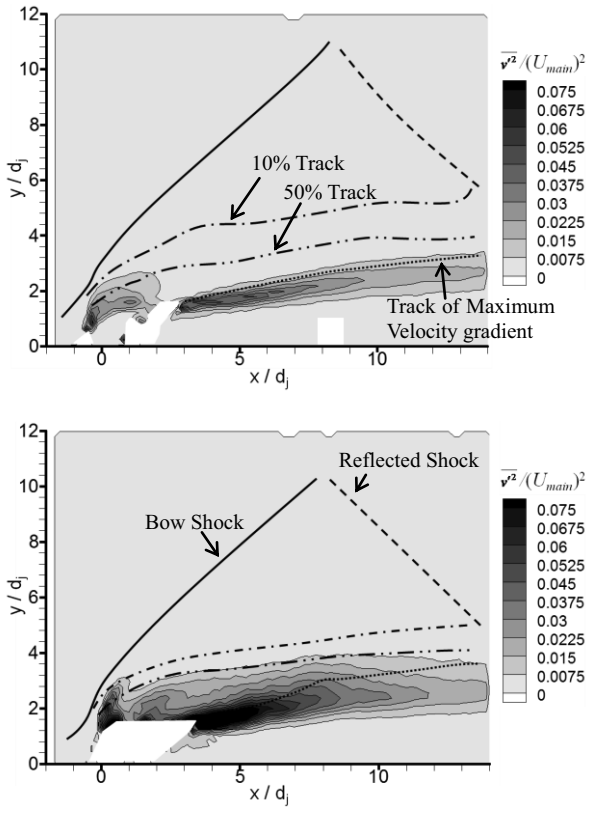

Fig. 1 Velocity fluctuation $\overline{v'^2}$
(Upper: Air, Lower: Helium)

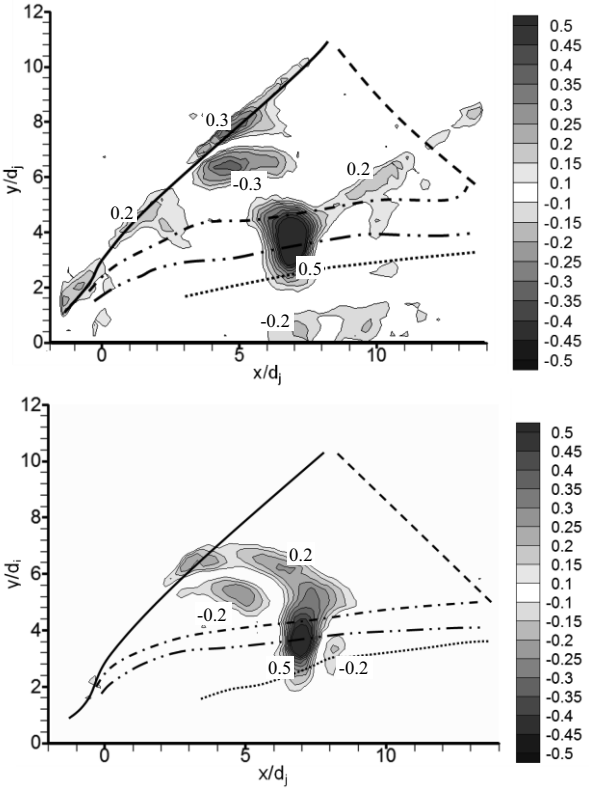

Fig. 2 Spatial correlation distribution of transverse velocity fluctuation: C_{vv} (Upper: Air, Lower: Helium)

4. Concluding remarks

We measured the supersonic flowfield with transverse injection by SPIV and calculated the single-time two-pint spatial correlations of the velocity fluctuations. The following results were obtained.

- The 50% averaged concentration track measured by PLIF was not coincided with the track of maximum streamwise velocity gradient.
- A strong correlation region existed around the reference point and its shapes changed with the selected velocity components in both injection case.
- The whole bow shock wave correlated with a reference point on the 50% averaged concentration track in the air injection case
- Sound wave irradiated by the motion of jet plume was observed between the reference point and the bow shock wave.

Acknowledgments

This work was supported by the MEXT in Japan, Grant-in-Aid (B), 20360081.

References

[1] Takahashi et al., *AIAA Journal*, Val. 48, No. 2, February 2010, pp. 443-452.

[2] Horikoshi, Y., Master thesis, Department of Aerospace Engineering, Tohoku University, 2009

Eighth International Conference on Flow Dynamics
November 9 - November 11, 2011

Numerical Analysis of Cryogenic Solid-Liquid Slush Flow in a Square Pipe

Daisuke Naka, Atsuhito Ota, Katsuhide Ohira
Institute of Fluid Science, Tohoku University, 2-1-1 Katahira, Aoba-ku, Sendai, Miyagi, 980-8577, Japan
naka@luna.ifs.tohoku.ac.jp

ABSTRACT

Cryogenic slush fluids such as slush nitrogen and slush hydrogen are two-phase single-component fluids containing solid particles in a liquid, which have higher density and refrigerant capacity than a shingle-phase liquid. In this study, the three-dimensional thermal non-equilibrium two-phase flow model is developed to clarify flow characteristics of slush fluid in a horizontal square pipe . Flow characteristics of slush nitrogen in a horizontal square pipe became clear by the numerical analysis.

1. Introduction

Cryogenic solid–liquid two-phase slush fluids have superior properties as high-density fluids and refrigerants. The use of slush hydrogen allows more efficient transportation and storage of hydrogen energy, as well as having the superior thermal-fluid properties. However, there has been relatively little research conducted on flow characteristics of slush fluid in horizontal pipe flow.

Therefore, the aim of this research is to clarify flow characteristics of slush fluids in a horizontal pipe based on three dimensional two-phase flow model. In this study, the slush nitrogen is applied and flow characteristic of slush fluid in a horizontal square pipe used widely is analyzed.

2. Numerical method

In this study, the three-dimensional thermally non-equilibrium two-phase flow model is used. As a computational model, two-fluid model is adopted by Euler-Euler coupling approximated the solid-liquid by continuum, assuming incompressible fluid. Therefore, the solid-liquid phase can be treated as a Newtonian fluid. Pressure drop reduction phenomenon and heat transfer deferioration phenomena, which are known as the characteristics of slush fluid, is not considered. Fig. 1 shows the square pipe model used in this numerical analysis. The flow path length L is 600 mm, which is a smooth horizontal square pipe with a side length of 12mm. The calculation result at L=400mm is used to evaluate the characteristics. The governing equations are composed of the continuity equation (1), the momentum conservation equation (2) and the energy conservation equations (3) and (4).

$$\frac{\partial \alpha_\varphi \rho_\varphi}{\partial t} + \nabla \cdot \left(\alpha_\varphi \rho_\varphi \boldsymbol{U}_\varphi \right) = \dot{m}_\varphi \tag{1}$$

$$\frac{\partial \alpha_\varphi \rho_\varphi \boldsymbol{U}_\varphi}{\partial t} + \nabla \cdot (\alpha_\varphi \rho_\varphi \boldsymbol{U}_\varphi \boldsymbol{U}_\varphi) + \nabla \cdot (\alpha_\varphi \boldsymbol{\tau}_\varphi) + \nabla \cdot (\alpha_\varphi \rho_\varphi \boldsymbol{R}_\varphi) = -\alpha_\varphi \nabla P + \alpha_\varphi \rho_\varphi \boldsymbol{g} + \boldsymbol{M}_\varphi - \dot{m}_\varphi \boldsymbol{U}_\varphi \tag{2}$$

$$C_{p,l} \rho_l \left(\frac{\partial \alpha_l T_l}{\partial t} + \nabla \cdot \left(\alpha_l \boldsymbol{U}_l T_l \right) \right) = \nabla \cdot \left(\alpha_l \kappa_l^{eff} \nabla T_l \right) + Q_{Ll} + Q_l \tag{3}$$

$$C_{p,s} \rho_s \left(\frac{\partial \alpha_s T_s}{\partial t} + \nabla \cdot \left(\alpha_s \boldsymbol{U}_s T_s \right) \right) = \nabla \cdot \left(\alpha_s \kappa_s \nabla T_s \right) + Q_{Ls} + Q_s \tag{4}$$

3. Results and Discussion

3.1 The characteristic of flow velocity distribution and the solid phase volume fraction

In order to ensure validity of the simulation for flow characteristic of slush nitrogen, some results of this numerical analysises were compared with the PIV (Particle Image Velocimetry) method using solid particles of slush nitrogen as a tracer (Experimental conditions, Sectional shape is the same shape and numerical models, measured in the low-flow conditions and high-flow conditions). The comparisons of the velocity distribution of the solid phase between the numerical results and the experimental results by the PIV method are presented in Figs. 2(a) and (b). In these figures, the horizontal axis indicates solid phase velocities normalized by the mean velocity of the solid phase, and the vertical axis indicates the position of the cross section of the pipe. By referring to those figures, the numerical results agree well with the experimental results for both low and high velocity conditions. The profiles of the solid phase volume fraction at each inlet velocity along a vertical axis plane are shown in Fig. 3. By referring to Fig. 3, the lower the inlet velocity, the larger the solid phase volume fraction is at the bottom of the flow channel. As the interference between the solid particle, and the liquid increases in the bottom of the tube, the velocity profile becomes asymmetric.

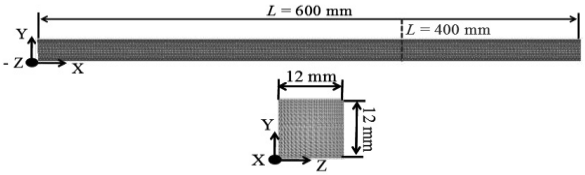

Fig.1 Square pipe model

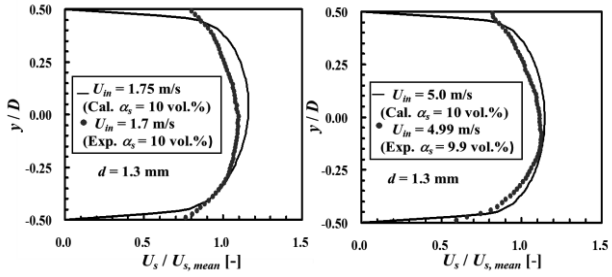

(a) low-flow conditions (b) high-flow conditions

Fig.2 Comparison of the velocity distribution between numerical results and experimental results

3.2 Pressure drop characteristics

The comparison of the pressure drop per length between the numerical result of slush nitrogen and the Blasius equation is shown in Fig. 4. In this figure, horizontal axis indicates the inlet velocity, and the vertical axis indicates the pressure drop per unit length. As shown in Fig. 4, the numerical result of subcooled liquid nitrogen agree well with the Blasius equation. Validity of the simulation method for flow characteristics is also ensured from this results. Moreover, the pressure drop becomes larger with increase in the initial solid phase fraction. This phenomenon can be explained by the relationship between the initial solid fraction and the turbulent energy. Fig.5 shows the relationship between the initial solid fraction and the turbulent energy of liquid phase. From Fig. 5, it is clear that the turbulent energy becomes large with increase in initial solid fraction. This phenomenon is due to the increase in interference between solid and liquid phases with the increase in initial solid fraction. As the result, the pressure drop becomes larger with increase in the initial solid phase fraction.

3.3 Secondary flow characteristics

Secondary flow characteristics of slush nitrogen is presented in Figs. 6(a) and (b). U_{ay} and U_{az} show the velocity distribution for Y and Z directions, respectively. Secondary flow directions expected from U_{ay} and U_{az} are presented in Fig. 6(a) with arrowed lines. This pattern is different from two symmetric vortices in the 1/4 cross section towards the corner measured for the single-phase flow by Brundrett and Gessner [2][3]. This phenomenon is because the effect of gravity becomes stronger by the presence of solid particles. Moreover, in the high flow velocity, the secondary flow velocity becomes smaller than that in the low flow velocity. This is considered, due to the strong inertia force to the mainstream velocity direction in high flow conditions, the secondary flow is reduced.

4. Concluding remarks

・The numerical code was verified to be able to analyze the flow characteristics of slush nitrogen with sufficient accuracy.

・The lower the inlet velocity, the larger the solid phase volume fraction is at the bottom of the flow channel.

・The pressure drop became larger with an increase in the initial solid phase fraction.

・In the high flow velocity, the secondary flow velocity is smaller than that in the low flow velocity.

References

[1] E. Brundrett and W. D. Bines: "The production and diffusion of vorticity in duct flow", J. Fluid Mechanics, vol.19, pp375-394, 1964.

[2] F. B. Gessner and J. B. Jones: "On some aspects of fully-developed turbulent flow in rectangular channels", J. Fluid Mechanics, vol.23, pp689-713, 1965.

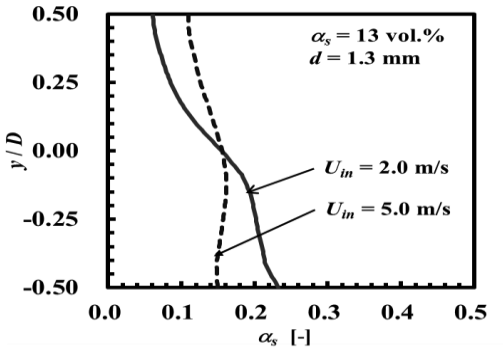

Fig. 3 The solid phase volume fraction

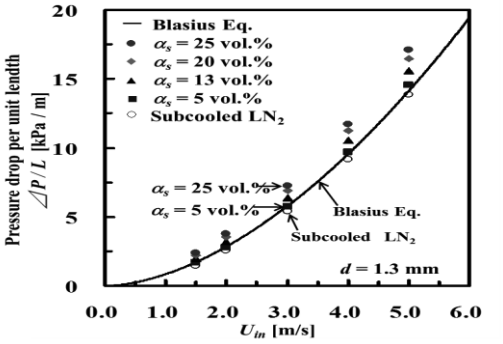

Fig. 4 Inlet velocity and pressure drop per unit length

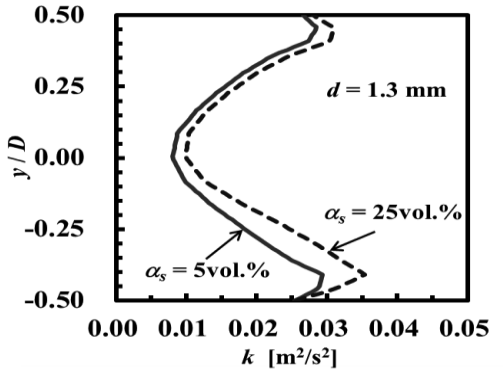

Fig. 5 Solid fraction and turbulent energy

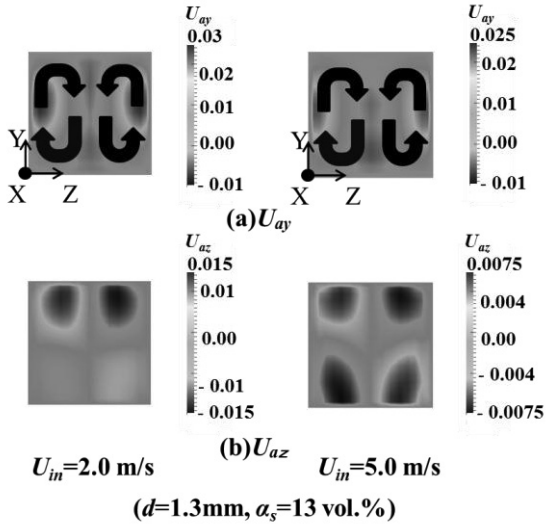

Fig. 6 Secondary flow characteristics of slush nitrogen

Eighth International Conference on Flow Dynamics
November 9 - November 11, 2011

Pressure-Drop Reduction Phenomenon of Cryogenic Solid-Liquid Slush Flow in a Corrugated Pipe

Jun Okuyama, Kei Nakagomi, Katsuhide Ohira, Koichi Takahashi
Institute of Fluid Science, Tohoku University, 2-1-1 Katahira, Aoba-ku, Sendai, Miyagi, 980-8577, Japan
okuyama@luna.ifs.tohoku.ac.jp

ABSTRACT

Cryogenic slush fluids such as slush hydrogen are solid-liquid, two-phase fluids. There are high expectations as a functional thermal fluid. Experimental flow tests were performed using slush nitrogen to elucidate the pressure-drop reduction for two different types of corrugated pipes having inner diameters of 12 and 15 mm, while the behavior of solid particles were observed by using a high-speed video camera and the PIV method to clarify the pressure-drop reduction phenomenon. At a solid fraction of 5~32 wt.% and a flow velocity of 2 m/s or greater, pressure-drop reduction, which was not observed in the case of liquid nitrogen flow, was first confirmed.

1. Introduction

Cryogenic solid-liquid two-phase slush fluids have superior properties as high-density fluids and refrigerants. Our laboratory has proposed a high-efficient hydrogen energy system which is shown in Figure. 1 [1]-[2]. This system can expect synergetic effects using slush hydrogen (14K). For development of this system, flow properties of slush fluids in a corrugated pipe are important because the corrugated pipe is used as both the transport pipe and the refrigerant pipe for superconducting power transmission. In this experiment, by measuring the pressure drop of slush nitrogen (63K) in different two types of corrugated pipes, the pressure-drop reduction phenomenon was shown for the first time. In addition, the behavior of solid particles was observed by using a high-speed video camera and the PIV method to clarify this phenomenon.

2. Experimental apparatus and procedures

Figure. 2 shows the flow test apparatus. This apparatus is composed of a run tank, a transfer pipe, a catch tank and the measurement system. After slush nitrogen is produced in the run tank, it flows into the transfer pipe. Corrugated pipes A and B have inside diameters (d) 12 and 15 mm, outside diameters 17.5 and 19.4 mm, pitch (s) 3.3 and 3.0 mm, height of convex (t) 2.75 and 2.2 mm, and lengths 824 mm (pressure drop measurement section 614 mm), respectively. They are made of stainless steel pipes. The upstream section has a entrance length of 210 mm. In the experiment, liquid nitrogen (63K) was also used for comparison.

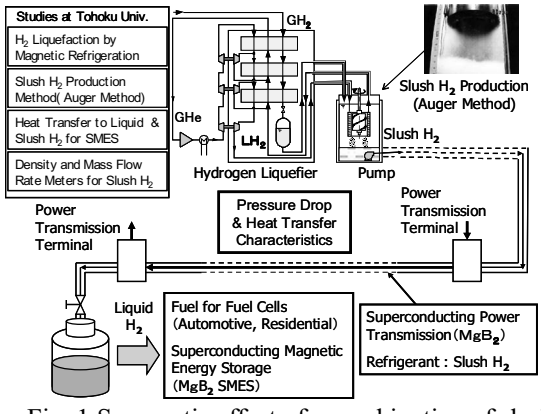

Fig. 1 Synergetic effect of a combination of slush hydrogen and superconducting equipment.

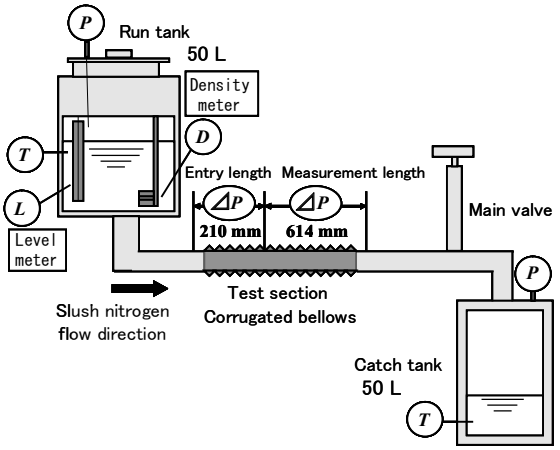

Fig. 2 Experimental apparatus for slush nitrogen flow test.

Experimental conditions are as follows: flow velocity 1.4~4.5 m/s, pressure 0.1~0.2 MPa, solid fraction 5~32 wt.%.

3. Results and Discussion

Figure. 3 shows the result of pressure drop and flow velocity in corrugated pipes A and B. White and black plots show for inside diameters of 12 (A) and 15 mm (B), respectively. In the figure, Prandtl-Karman Eq. (15 mm) and Hawthorne & von Helms Eq. are shown. Prandtl-Karman Eq. shows for the single-phase flow in a smooth circular pipe. Hawthorne & von Helms Eq. shows for the single-phase flow in a corrugated pipe [3].

Pressure drops of the liquid nitrogen for A and B are 5-9 times and 3-6 times larger than that of Prandtl-Karman Eq., respectively. In the range of mean velocity below 2 m/s, pressure drop of slush nitrogen shows equal or slightly greater than that of liquid nitrogen. On the other hand, in the range of over 2 m/s, pressure drop reduction appears and it increases with increase of solid fraction.

Figure. 4 shows results of pipe friction factor λ and Reynolds number (representative length d). Friction factor of liquid nitrogen increases with increase of Reynolds number and approaches Hawthorne, et al. Eq. But, in the area of low Reynolds number, it's different from the trend of Hawthorne, et al. Eq. In the transition range where Reynolds number is about 10^5, friction factor agrees well with experimental value of Daniels & Cleveland [4].

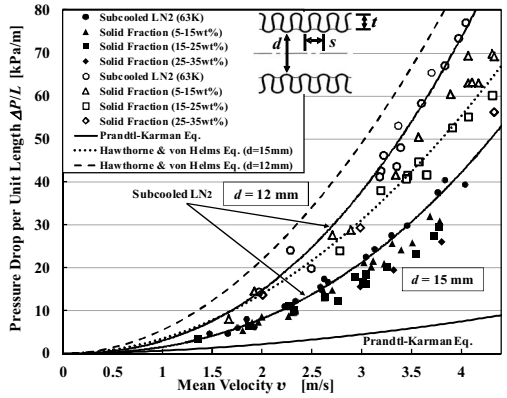

Fig. 3 Pressure drop and mean velocity of slush N_2.

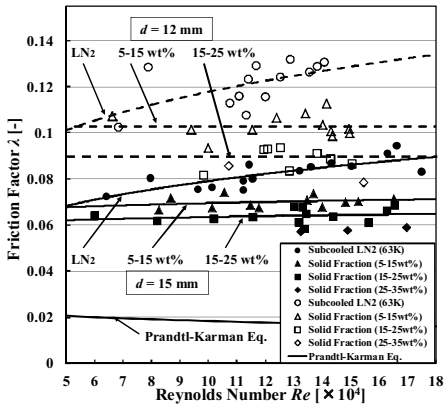

Fig. 4 Friction factor and Reynolds number of slush N_2.

Friction factor of slush nitrogen shows nearly constant value. It decreases with increase of solid fraction.When solid fraction was 30 wt.%, pressure drop reduction was a maximum of about 37 %.

Staggered rectangular pipe for visualization is shown in Figure. 5. The pipe consists of a rectangular pipe (12×12 mm), a staggered rectangular pipe (12×16 mm) and a circular pipe (ID = 15 mm). Pressure drop was measured along the 346 mm length. Only upper and lower surfaces are staggered and the number of convex is 36. Pressure drop ratio r_{dp} is shown in Figure. 6 ($r_{dp}=\Delta P_{sl}/\Delta P_{sub}$). In the case of $r_{dp}<1$, the pressure drop reduction emerges. Pressure drop ratio of slush nitrogen tends to decrease over the mean flow velocity of 2 m/s. However, unlike corrugated bellows, most data is in the range of r_{dp} = 1.1~1.25 and pressure drop reduction didn't clearly emerge. This is probably due to the increased losses since the measurement section contains a rectangular part, an expanded part and a circular part. Figure. 7 (1) and (2) correspond to the high-speed camera images. In Figure. 7 (1), solid particles are caught in vortices in the concave portion and collide with the wall. On the other hand, in the case of Figure. 7 (2), solid particles are hardly caught in the concave portion and relatively tend not to collide with the wall or corner. Consequently, pressure drop ratios are considered to become 1.0 and 1.2, respectively. Also, in the PIV measurement, recirculation streamlines of solid particles were observed in concave potions for high r_{dp} (r_{dp} = 1.2), but in the case of low r_{dp} (r_{dp} = 0.95), such

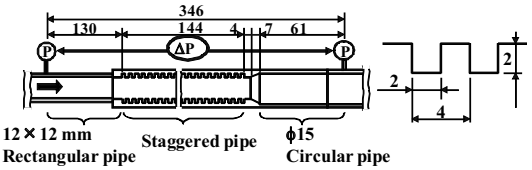

$$\Delta P = \Delta P_{Rectangular} + \Delta P_{Staggered} + \Delta P_{Circular}$$

Fig. 5 Schematic illustration of the staggered pipe.

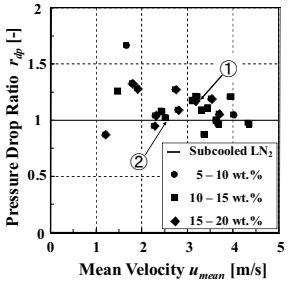

Fig. 6 Pressure drop ratio r_{dp} and mean velocity of slush nitrogen ($r_{dp}=\Delta P_{sl}/\Delta P_{sub}$).

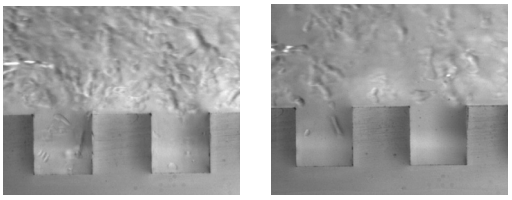

(1) (2)

Fig. 7 Images of solid particles near the bottom of the staggered pipe.
(1) 3.18 m/s, 15.8 wt.%, r_{dP}=1.19
(2) 2.50 m/s, 13.6 wt.%, r_{dP}=1.03

streamlines were not observed. As a result, it's considered solid particles (solid fraction) and the flow velocity are closely related to the pressure drop reduction.

4. Conclusions

When slush nitrogen flows in a corrugated pipe, pressure drop reduction phenomenon that pressure drop reduces compared to the liquid nitrogen flow was shown at the flow velocity 2 m/s or greater. This phenomenon is considered to occur by following reasons:

(1) By the migration of the solid particles to the center of the pipe with increase in the flow velocity, interference between solid particles and the corrugation part is reduced.

(2) Solid particles in the pipe center suppresses turbulence generation of liquid on the pipe wall and inside the corrugation part.

References

[1] Ohira., K., Cryogenics, Vol. 41, 61-72 (2006).
[2] Ohira., K., Jpn. J. Multiphase Flow, Vol. 23, 373-380 (2009).
[3] Hawthorne, R. C. et al, Prod. Eng., Vol. 34, 98-100 (1963).
[4] Daniels, C. M. et al., Machine Design, 187-188 (1965).

Eighth International Conference on Flow Dynamics
November 9 - November 11, 2011

Advancement of Alumina Powder Spheroidization Process in a Low Power DC-RF Hybrid Plasma Flow System by Water Droplets Injection

Juyong Jang[1], Hidemasa Takana[2], Sangkyu Park[3] and Hideya Nishiyama[2]
[1]Graduate School of Engineering, Tohoku University, 2-1-1 Katahira, Aoba-Ku, Sendai 980-8577, Japan
[2]Institute of Fluid Science, Tohoku University, 2-1-1 Katahira, Aoba-Ku, Sendai 980-8577, Japan
[3]Department of Mechanical and Automotive Engineering, Woosuk University, 443 Samnye-ro, Samnye-eup, Wanju-gun, Jeollabuk-do 565-701, South Korea
jang@paris.ifs.tohoku.ac.jp

ABSTRACT

Small amount of water micro droplets is injected into the downstream of plasma flow without disturbing plasma flow directly. The water droplets are vaporized in the tail of thermal plasma flow, and then are dissociated to hydrogen molecules which improve thermofluid characteristics of plasma flow. Therefore, the thermofluid flow characteristics of the plasma flow are enhanced and the powder spheroidization process efficiency is increased with water droplets injection using a DC-RF hybrid plasma flow system under the low electric power.

1. Introduction

Spherical particles achieve more homogenous and stable particle transportation by improving the powder fluidity in the tube. They allow fine control of powder feeding rate without agglomeration problems because of low friction loss between particles and tube surface. Steady powder feeding is the important for achieving high performance thermal spray processes such as dense coating formation and thin film fabrications. Therefore, alumina powder spheroidization processes are needed for high quality sprayed coating processes [1-3].

Argon plasma flow mixed with hydrogen gas improves thermofluid flow characteristics of plasma flow with the concentration of hydrogen gas. Water droplets are dissociated to molecular hydrogen and oxygen molecules in thermal plasma flow, all these species are mixed with the plasma flow and especially improve enthalpy and thermal conductivity of plasma flow [4, 5].

This study aims the improvement of thermofluid flow characteristics of plasma by mixing argon plasma flow with hydrogen molecules. While thermal energy of plasma flow is consumed to vaporize water droplets, mixing effect of plasma flow with hydrogen molecules compensates the energy loss by increasing plasma enthalpy. Therefore, the effects of water droplets injection into the downstream of plasma flow on the thermofluid flow characteristics of plasma flow and the alumina powder spheroidization process are experimentally investigated to achieve the high performance spheroidization process using the low electric power DC-RF hybrid plasma flow system.

2. Experimental setup

Figure 1 shows a schematic illustration of the DC-RF hybrid plasma flow system. The origin point denoted by "O" is located at the exit of the DC plasma torch on the central axis. The operating pressure is 150 torr. The DC power of 1.2 kW and RF power of 6.6 kW are used. The working gas is argon. The flow rates of central gas and swirling sheath gas are 5 and 20 Sl/min, respectively. The central gas flow rate is given as a sum of the DC plasma jet forming gas flow rate of 4.2 Sl/min and the powder carrier gas flow rate of 0.8 Sl/min.

Water droplets are injected by a two-phase atomizer (YS-03, Yaezaki Inc., Japan) at r = 95 mm and z = 195 mm without disturbing plasma flow directly as shown in Fig. 1. The purified water and the atomizing gas of argon are used. The water flow rate (Q_w) is 1 - 15 Sml/min. Atomizing gas flow rate (Q_g) for atomizing water is 4 - 8 Sl/min.

An enthalpy probe is axially installed in the chamber. Sampling gas flow rate of 0.8 Sl/min is decided to satisfy isokinetic conditions under the pure argon plasma flow. The probe sensitivity is 4.57, which represents the ability of the probe to distinguish a change in the measured quantity. Plasma enthalpy is estimated from the energy balance.

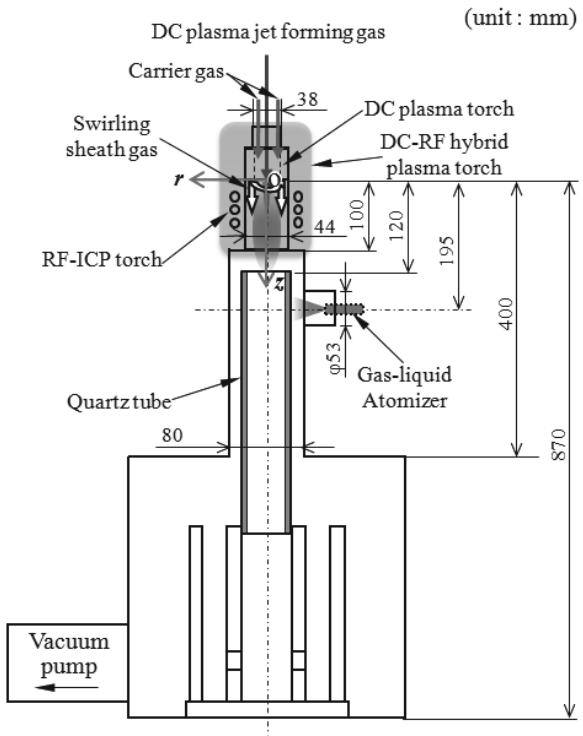

Fig. 1 Schematic illustration of the DC-RF hybrid plasma flow system.

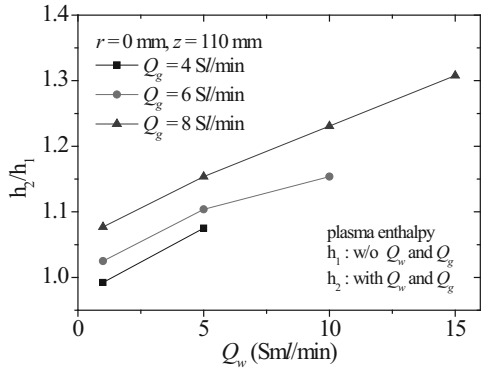

Fig. 2 Effect of water droplets injection on plasma enthalpy increment in the upstream of plasma flow.

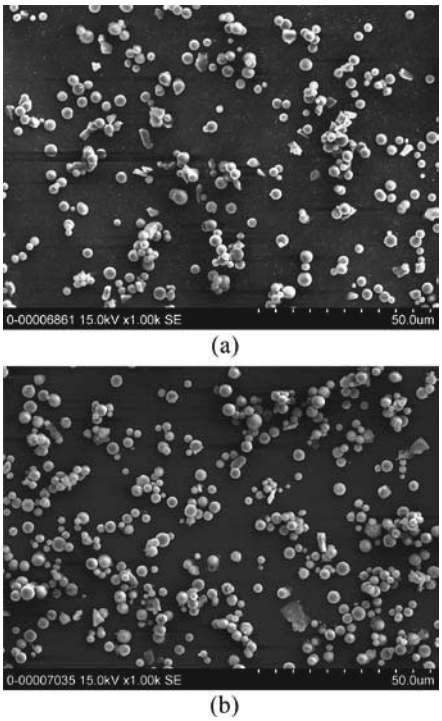

Fig. 3 Effect of water droplets injection on morphology of processed particles in SEM images (a) without and (b) with water droplets injection.

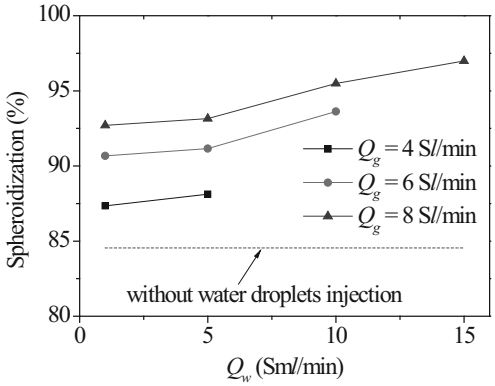

Fig. 4 Effect of water droplets injection on the spheroidization rate.

3. Experimental results and discussion

Figure 2 shows the effect of water droplets injection on plasma enthalpy increment in the upstream of plasma flow. The plasma enthalpy is measured at z = 110 mm. Injected water droplets are sucked to the downstream of the thermal plasma flow and produced to hydrogen molecules. Increasing water flow rate, plasma enthalpy gradually increases because of the mixing effect with hydrogen and plasma flow.

Figure 3 (a) and (b) show the morphology of processed particles in the scanning electron microscope (SEM) images. Without water droplets injection, unprocessed particles still remains as shown in Fig. 3 (a). The spheroidization rate with water droplets injection at water flow rate of 15 Sml/min and atomizing gas flow rate of 8 Sl/min effectively increases as shown in Fig. 3 (b).

Figure 4 shows the effect of water droplets injection on the spheroidization rate. The spheroidization rate is the percentage of the total number of processed particles to the number of processed spherical particles in the SEM images. When the spheroidization process is carried out with water droplets injection, plasma enthalpy is improved by mixing with hydrogen molecules and the spheroidization rate becomes higher compared with the case of without water droplets injection. The spheroidization rate increases from 84.5 % to 97 % under the water droplets injection.

4. Conclusions

The effect of water droplets injection into the downstream of plasma flow on plasma enthalpy and the spheroidization process efficiency has been experimentally clarified using a low power DC-RF hybrid plasma flow system. The results are summarized as follows:

- Water droplets injection increases the plasma enthalpy due to the mixing effect with hydrogen and argon plasma flow.
- Spheroidization rate improves from 84.5 % to 97 % by water droplets injection due to increase of plasma enthalpy by mixing plasma flow with generated hydrogen from water vapor.

Acknowledgements

The present study was partly supported by the Global COE program Grant, “World Center of Education and Research for Trans. Disciplinary Flow Dynamics” in the Japanese Ministry of Education, Culture, Sports, Science, and Technology.

References

[1] H. Nishiyama, et al, J. Therm. Spray Tech., **18** (4), (2009), pp. 593-599.
[2] H. Takana, et al, J. Therm. Spray Tech., **20** (3), (2011), pp. 432-439.
[3] J. Jang, et al, J. Fluid Sci. & Tech., **6** (5), (2011), pp.729-739.
[4] B. Pateyron, et al, Plasma Chem. & Plasma Processing, **12** (4), (1992), pp. 421- 448.
[5] T. Watanabe, et al, Thin Solid Films, **515,** (2007), pp. 4209-4216.

Eighth International Conference on Flow Dynamics
November 9 - November 11, 2011

Numerical Analysis of Aerodynamic Characteristics of JAXA Silent Supersonic Technology Demonstrator including the Effect of Jet Exhaust at Low Speed

Jun Hattori, Daisuke Sasaki and Kazuhiro Nakahashi
Department of Aerospace Engineering, Tohoku University
6-6-01 Aramaki-Aza-Aoba, Aoba-ku, Sendai, Miyagi 980-8579, Japan
hattori@ad.mech.tohoku.ac.jp

ABSTRACT

In this study, flow simulations including the effect of jet exhaust at low speed were performed on 2nd configuration of JAXA's Silent-Super-Sonic Technology Demonstrator. The effect of mesh refinement using unstructured-mesh CFD and computational scheme were investigated in order to improve the accuracy of aerodynamic characteristics prediction of an aircraft including exhaust jet.

1. Introduction

In Japan Aerospace Exploration Agency (JAXA), the Silent-Super-Sonic Technology Demonstration (S3TD) program has been conducted in order to develop the next generation supersonic transport since 2006. As part of the project, low-speed wind tunnel tests on the 2nd configuration of S3TD model were conducted to understand the aerodynamic characteristics with jet from an exhaust nozzle. From the study, it was revealed that the exhaust jet from an engine highly influenced the aerodynamic characteristics of the airframe. Therefore, it is necessary to analyze the effect of the exhaust jet accurately for aerodynamic design.

In the present study, the effects of computational scheme and mesh refinement in the flow simulation using unstructured-mesh CFD are investigated so as to improve the accuracy of aerodynamic characteristics prediction of an aircraft including exhaust jet.

2. Numerical Method

2.1 Target and Meshes

A 12% scale model of the 2nd configuration of S3TD is used as the computational model. The model was used for JAXA low speed wind tunnel tests.

Hybrid unstructured meshes for Navier-Stokes computation are generated by using MEGG3D (Multi-Element Grid Generation, [1]).

It is expected that the flow fields become very complex due to the engine exhaust jets. Therefore, Exhaust-area Fine (E.F) mesh is generated to conduct local mesh refinement behind the nozzle to capture the exhaust jet. The mesh density in the local mesh refinement domain is 2.0×10^{-3} with regard to the reference length of MAC. Figure 1 shows Base mesh without any local mesh refinement, and the locally-refined E.F mesh. The summary of computational meshes is shown in Table 1.

2.2 CFD Solver

In this study, TAS-code (Tohoku university Aerodynamic Simulation code, [2]) is used for CFD simulation. Governing equations are the three-dimensional compressible Navier-Stokes equations. Navier-Stokes equations are solved by using a cell-vertex finite volume method. HLLEW (Harten-Lax-van Leer-Einfeldt-Wada) method and SLAU (Simple Low-dissipative AUSM, [3]) method are used for numerical flux calculations. The effect of SLAU method is investigated so as to improve the accuracy of aerodynamic characteristics prediction at low speed. Venkatakrishnan's limiter, which has good convergence, is used to maintain second-order spatial accuracy. LU-SGS (Lower-Upper Symmetric Gauss-Seidel) implicit method is used for time integration. Modified Spalart-Allmaras (SA) turbulence model [4, 5], which reduces eddy viscosity in the regions of high vorticity is used.

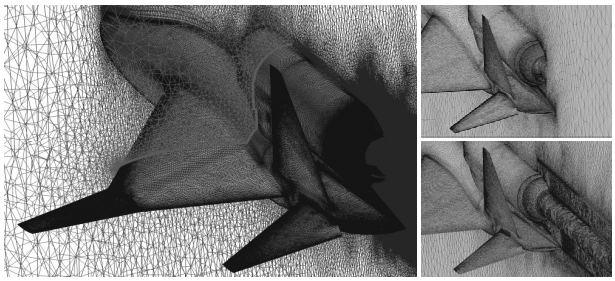

Fig. 1 Unstructured mesh for 2nd config. of S3TD (upper: Base mesh, lower: E.F mesh)

Table 1 Summary of TAS mesh

	Base	E.F
# of Nodes [million]	9.2	13.7
Surf. Nodes [million]	0.29	
Minimum spacing	9×10^{-6}	
# of prismatic layers	30	
Growth rate of prismatic layers	1.25	

2.3 Computational Condition

Computational conditions are shown in Table 2. The jet exhaust effects are simulated by the control of the air mass flow. Nozzle Pressure Ratio (*NPR*) is used to control the exhaust jet condition. The *NPR* is represented as the ratio of total pressure at the nozzle exit to the freestream static pressure as defined below:

$$NPR = \frac{p_{T_{out}}}{p_{S_\infty}} \quad (1)$$

Here, $P_{T_{out}}$: total pressure at the nozzle exit, P_{S_∞}: freestream static pressure. Three *NPR* values are used to compare the aerodynamic characteristics at the different jet conditions (1.00, 1.47 and 2.23). Here, no-exhaust condition corresponds to *NPR* = 1.00.

Table 2 Computational condition

Airflow parameter	
Freestream velocity [m/s]	50.06 (Mach 0.14)
A.o.A [deg]	2.065
Reynolds number	1.4×10^6
Jet parameter	
Gas	Air (Cold gas)
NPR	1.00, 1.47, 2.23

3. Numerical Results

3.1 Effect of Local Mesh Refinement

Flow computations were performed with Base mesh and E.F mesh to evaluate the effect of mesh refinement. HLLEW method was used for numerical flux calculations and modified SA model was used as turbulence model. Figure 2 shows the aerodynamic forces acting on the rear parts of S3TD. In the figure, the result of E.F mesh is compared with that of Base mesh. The result of CFD is relatively good at Jet-Off condition and is qualitatively captured the experimental feature that C_L and C_D nonlinearly increase with the *NPR* from 1.00 to 2.23. However, the large discrepancy is observed compared to the experimental results at Jet-On conditions for both meshes. Even though, it is revealed that the result of E.F mesh is much improved compared to that of Base mesh. It is considered that the diffusion of numerical viscosity was suppressed by setting local mesh refinement at the back of nozzle regions.

3.2 Comparison of Computational Scheme

Flow computations were performed with SLAU and HLLEW to evaluate the computational scheme. Here, E.F mesh was used for computations and modified SA model was used as turbulence model. Figure 3 shows the aerodynamic forces acting on the rear parts of S3TD and compares the result of SLAU to that of HLLEW.

Slight differences were observed between SLAU and HLLEW results. The C_L of SLAU is smaller than that of HLLEW at *NPR*1.00 and *NPR*2.23. However, C_L of SLAU is larger than that of HLLEW at *NPR*1.47. The C_D of SLAU is smaller than that of HLLEW. Figure 4 shows the *Cp* distributions on the surface of S3TD and the Mach number contours at the aft body. There exist differences of the *Cp* distributions between SLAU and HLLEW on the v-tail and under the nozzle exit. It is assumed that the numerical error at low speed was suppressed by using SLAU.

4. Conclusion

In this study, flow simulations including the effect of jet exhaust at low speed were performed for the S3TD configuration using TAS-code. To improve the accuracy of aerodynamic characteristics prediction including the exhaust jets, E.F mesh was used. As a result, it was revealed that local refinement behind the nozzle highly effects on the aerodynamic characteristics. To improve the accuracy at low speed, the flow computations were also performed with SLAU method. As a result, the *Cp* distributions were slightly improved compare to HLLEW. It is assumed that the numerical error at low speed was suppressed by using SLAU. Even though, the effect of computational scheme on the accuracy is smaller than that of mesh refinement.

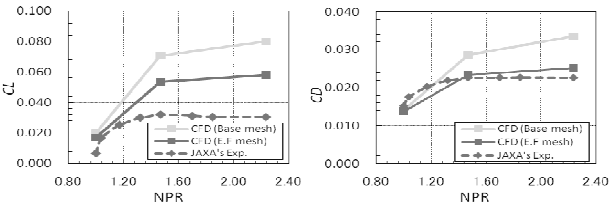

Fig. 2 Comparison of mesh Refinement

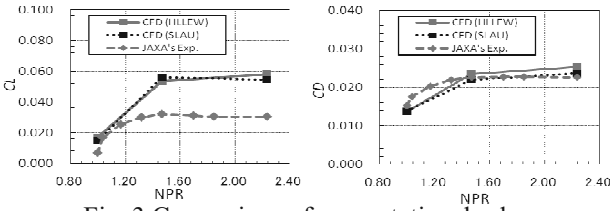

Fig. 3 Comparison of computational scheme

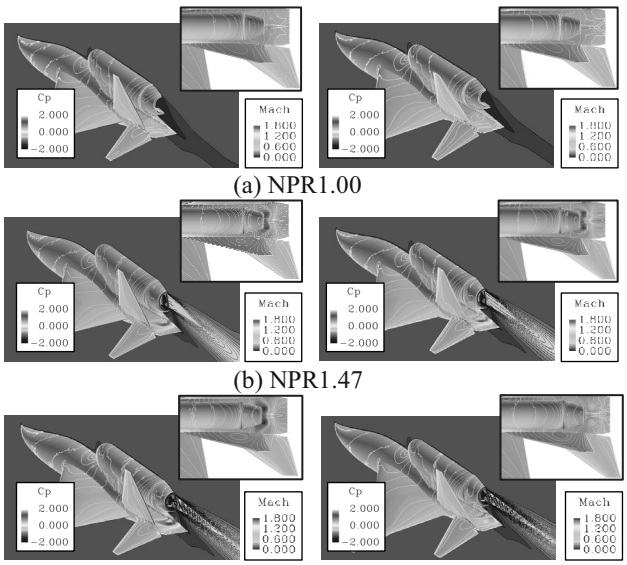

(a) NPR1.00

(b) NPR1.47

(c) NPR2.23

Fig. 4 Comparison of computational scheme
(left : HLLEW, right : SLAU)

Acknowledgements

This study was supported by research grants from JAXA.

In this study, JAXA Supercomputer System (JSS) M-system (Fujitsu FX1) was used for the computations.

References

[1] Y. Ito, K. Nakahashi : Surface Triangulation for Polygonal Models Based on CAD Data, *International Journal for Numerical Method in Fluids* 2002, Vol. 39, pp.75-96, 2002.

[2] K. Nakahashi, Y. Ito, F. Togashi : Some Challenges of Realistic Flow Simulations by Unstructured Grid CFD, *International Journal for Numerical Method in Fluids* 2003, Vol. 43, pp.769-783, 2003.

[3] E. Shima : All Speed Scheme of AUSM Family and Preconditioned Implicit Time Integration Scheme, The 22th CFD Symposium, Tokyo, 2008.

[4] P. R. Spalart, S. R. Allmaras : A one-equation turbulence model for aerodynamic flow, AIAA-Paper 92-0439, 1992.

[5] Lei, Z : Effect of RANS Turbulence Models on computational of Separated Flows over a Wing-Body Configuration, *Transactions of the Japan Society for Aeronautical and space Sciences*, Vol.48, pp.150-160, 2005.

Eighth International Conference on Flow Dynamics
November 9 - November 11, 2011

Reconstruction of Model Movement in Dynamic Wind Tunnel Testing

K. S. N. Abhinav Kumar, Tatsuya Hara, Daiju Numata, Keisuke Asai
6-6-01, Aramaki Aza-aoba, Aoba-ku, Sendai, Miyagi, 980-8579, JAPAN
Dept. of Aerospace Engineering, Tohoku University
abhinav.kumar@aero.mech.tohoku.ac.jp

ABSTRACT

The work presented here is the usage of the Photogrammetric techniques in Dynamic Wind Tunnel testing to determine the position and attitude of a delta wing model. Firstly the cameras used are calibrated using Direct Linear Transformation (DLT) method. Secondly the 3D-coordinates of the registration targets with respect to the wind tunnel are determined by using two different views of the same registration targets. And finally the position and attitude are determined by relating the 3D-coordinates obtained to the 3D-coordinates of the model registrations targets with respect to model coordinate system.

1. Introduction

Image based measurement techniques are being used for a long time to get the forces acting on the body, measuring the position, attitude and deformation of the body. This is because the image based measurement techniques are non-intrusive, accurate and more sensitive. These image based measurement techniques are not being used for dynamic wind tunnel testing as of now. For using the image based measurement techniques in dynamic wind tunnel testing we have to integrate the force measurement techniques, position, and attitude and deformation measurement techniques.

In the present work of reconstructing the model movement the theory discussed below will be used.

2. Theory

In image based measurement techniques the 2D-coordinates of the image (x_n, y_n) are related to the 3D-coordinates of the model (X_n, Y_n, Z_n) by the collinearity equations given below.

$$x_n - x_p + dx = -c\frac{m_{11}(X_n-X_c)+m_{12}(Y_n-Y_c)+m_{13}(Z_n-Z_c)}{m_{31}(X_n-X_c)+m_{32}(Y_n-Y_c)+m_{33}(Z_n-Z_c)} \quad (1)$$

$$y_n - y_p + dy = -c\frac{m_{21}(X_n-X_c)+m_{22}(Y_n-Y_c)+m_{23}(Z_n-Z_c)}{m_{31}(X_n-X_c)+m_{32}(Y_n-Y_c)+m_{33}(Z_n-Z_c)} \quad (2)$$

Here m_{11} to m_{33} are the rotation matrix coefficients and functions of the orientation angles of the camera (ω, ∅, κ).

The collinearity equations include different parameters of the camera. Camera calibration as given by Liu et al [1] is done to determine these different parameters of the camera such as the exterior and interior parameter of the camera. The exterior parameters include the three orientation angles of the camera (ω, ∅, κ) and the perspective center (X_c, Y_c, Z_c). The interior parameters of the camera include the principal distance c and the principal point (x_p, y_p). Also due to lens distortion the image could be shifted by dx and dy. This lens distortion is sum of radial distortion and decentering distortion which can be modeled as K_1, K_2 and P_1, P_2 respectively. Since the collinearity equations are non-linear direct determination of parameters is difficult.

2.1. Camera Calibration

In order to determine the camera parameters, the camera has to be calibrated. Initially for basic results it is assumed that the lens distortion is small and can be neglected. Now the collinearity equations can be given as following (Direct Linear Transformation method)

$$L_1X_n + L_2Y_n + L_3Z_n + L_4 - x_n(L_9X_n + L_{10}Y_n + L_{11}Z_n + 1) = 0 \quad (3)$$

$$L_5X_n + L_6Y_n + L_7Z_n + L_8 - y_n(L_9X_n + L_{10}Y_n + L_{11}Z_n + 1) = 0 \quad (4)$$

The simplified equations are linear and can be solved for different targets to determine the L coefficients. These coefficients are functions of the camera parameters, so solving these coefficients will give us the camera parameters.

This process is carried out for the initial position of the model whose registration targets 3D-coordinates are determined using the coordinate measuring machine. Using these 3D-coordinates and relating them to the corresponding image coordinates we can determine the camera parameters.

2.2. 3D coordinate measurement

Once the camera parameters are determined we can use the same equations to determine the 3D-coordinates of the registration targets. But for a given camera we have only two equations to determine the three unknowns X_n, Y_n, Z_n. To solve this problem a second camera is introduced which is calibrated in the same way as the first camera. Now we have four equations from two cameras to determine the three unknowns [2].

2.3. Position and Attitude measurement

To determine the position and attitude of the model the following theory is proposed. If we consider the model to be rigid and the model deformations to be small, then we can relate the 3D-coordinates of the registration targets with respect to the model coordinate system (X', Y', Z') with zero pitch, roll and yaw angles of the model to the 3D-coordinates obtained by the

imaging process (X, Y, Z) at a given position and attitude by translation and rotation of axes as shown in Fig.1.

This relation can be given by the following equation.

$$X = \Delta X + RX' \quad (5)$$

Where X is the 3D-coordinates of the registration targets with respect to tunnel coordinate system

X' is the 3D-coordinates of the registration targets with respect to model coordinate system

ΔX and R are the translation and rotation of the coordinate systems.

Since we know both X and X' we can determine DX and R for the given position for a given number of registration targets. Here DX and R are the orientation parameters for a given position of the model. If this procedure is applied for all the images covering the model motion one can reconstruct the model movement.

3. Summary

An experiment is conducted by moving the model in predetermined manner using a robotic arm. Fig. 2 shows the delta wing with the robotic arm. The model movement is reconstructed using the procedure given here. Now the model movement induced by the robotic arm and the reconstructed model movement is compared to validate the results.

In summary to reconstruct the movement of a delta wing using imaging techniques in Dynamic Wind Tunnel testing the following procedure is used.

Step-1: Using two cameras the model images are taken

Step-2: 3D-coordinates of the registration targets are determined using the coordinate measuring machine

Step-3: Using the image coordinates and the 3D-coordinates of the registration targets, camera parameters are determined for both the cameras.

Step-4: Using the two cameras the 3D-coordinates of the registration targets are calculated at different positions of the model during Dynamic Wind Tunnel testing.

Step-5: Relating the Model coordinate system and Tunnel coordinate system for each position of the model the corresponding position and attitude are determined for that corresponding position.

Thus the model movement is reconstructed using imaging techniques.

4. Future work

The future work includes determining the lens distortion parameters which are neglected here for increased accuracy. Also this method has to be improved so that it can be applied to flexible model. This can help in understanding the flow phenomenon due to model deformation.

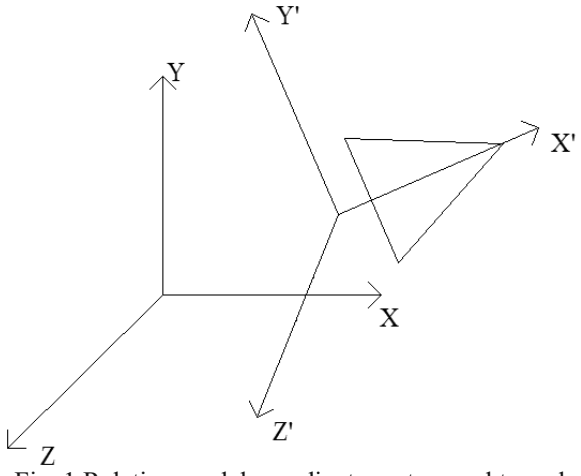

Fig. 1 Relating model coordinate system and tunnel coordinate system.

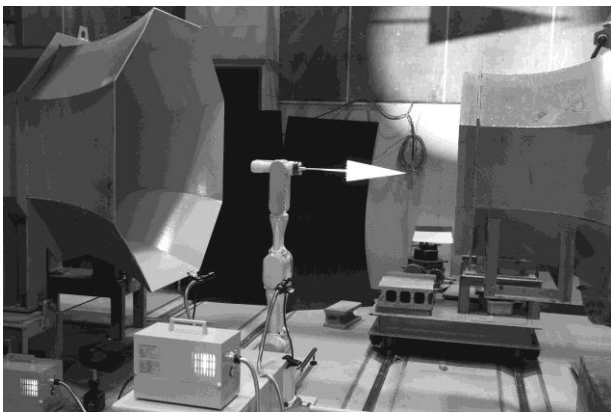
Fig. 2 Robotic arm and the delta wing during Dynamic wind tunnel testing

References

[1] Tianshu Liu, L. N. Cattafesta III, and R. H. Radeztsky, "Photogrammetry Applied to Wind Tunnel Testing,"AIAA Journal, Vol. 38, No. 6, pp. 964-971, June 2000.

[2] W. Ruyten, and M. E. Sellers, "Demonstration of Optical Wing Deformations Measurements at the Arnold Engineering Development Center," AIAA 2009-1520, 47th AIAA Aerospace sciences Meeting Including The New Horizons Form and Aerospace Exposition, 5-8 January 2009, Orlando, Florida.

Eighth International Conference on Flow Dynamics
November 9 - November 11, 2011

Effects of Elevated Ambient Pressure on Atomization Characteristics of Airblast Atomizer

Shinichiro Ishikawa[1], Taku Kudo[1], Hideaki Kobayashi [1], Soichiro Kato[2]
[1]Institute of Fluid Science, Tohoku University, Japan, 2-1-1 Katahira, Aoba-ku, Sendai, Miyagi 980-8577, Japan
[2]IHI Corporation, Japan, 1 Shin-nakahara-cho, Isogo-ku, Yokohama, Kanagawa 235-8501, Japan
ishikawa@flame.ifs.tohoku.ac.jp

ABSTRACT

The atomization characteristics of an airblast atomizer is experimentally investigated, whose atomization mechanism has not been fully understood. In this study, the effect of ambient pressure was resolved using an airblast atomizer operated in a high pressure environment. Also, it was indicated that the equation on droplet diameter which was proposed in the past study could not reproduce the effect of high pressure, and the refinement of the equation is necessary.

1. Introduction

The atomization and spray technology is widely used for gas turbines, internal combustion engines, agriculture, chemistry, food engineering, environmental preservation, and material products[1]. However, the mechanism of atomization has not been fully understood over the wide range of operation condition because it is highly complex and unsteady phenomenon. For example, despite the fact that airblast atomizers of mainly used for gas turbines are operated at high pressure, the pressure effect on atomization properties such as particle size, atomizing angle, velocity of particles are not clarified clearly. These atomizing properties are essential to predict the combustion characteristics and to establish sophisticated numerical simulations. Especially, the pressure dependence of the particle velocity and particle size is important not only for the combustor design but also for elucidating dynamics of the atomization mechanism. In this study, therefore, the effect of ambient pressure on the particle velocity and the particle diameter were investigated using the airblast atomizer operated in a high pressure environment.

2. Experimental method

In this study, Phase Doppler Particle Analyzer, PDPA, was used to measure particle velocity and particle size. Particle velocity is measured from the frequency of the Doppler burst, while the size measurement is based on the comparison of the signals collected by two photo-detectors at different angular positions with respect to the measurement volume: the two signals have a phase difference that is dependent on the particle diameter. For this reason, the high pressure chamber has four windows for optical access. PDPA is designed for the single-point measurement, so an actuator with a stepping motor is attached to the atomizer for multiple-point measurement. In this study, we classified the measurement points into 4 areas, which are inside of the spray cone, IC, along the cone, AC, upper outside of cone, OC-1, and lower outside of cone, OC-2, as shown in Fig. 1. In the present experiment, air and water were introduced to the atomizer as an oxidizer and the fuel, respectively. Air flow velocity, U_A, and Mass Air Fuel Ratio, AFR, were set to 70 m/s and 10, respectively. The ambient pressure in the chamber, Pc, was set to 0.1, 0.3, 0.5, and 0.7 MPa.

3. Results and Discussion

3.1 Effect of pressure on particle diameter

In this study, from measured particle diameter profile, arithmetic mean diameter, D mean, peak diameter from the profile, D peak, and Sauter Mean Diameter, SMD, were calculated. SMD is given by the following equation, where n and d are number of particle and particle diameter, respectively.

$$SMD = \frac{\Sigma_i n_i d_i^3}{\Sigma_i n_i d_i^2} \quad (1)$$

Figure 2 shows relationships between pressure in the chamber and above-mentioned particle diameters in IC region. It was turned out that these diameters are almost constant or become larger with increasing pressure regardless of the measurement point. Figure. 3 shows those in AC region. It can be seen that these diameters are constant or become a little larger with the increasing pressure regardless of the measurement point until 0.5 MPa, while at 0.7 MPa these diameters becomes a little smaller. Figure 4 shows those in OC-1 region. The figure shows that SMD becomes larger with the pressure increases, but the D_{mean} and D_{peak} are approximately constant. Figure 5 shows those in OC-2 region. These four figures show that particle diameters are approximately constant or become larger with pressure increases. It is indicated that the velocity of liquid becomes faster with pressure increase, while the velocity of air does not change because AFR is constant and the velocity difference between gas and liquid becomes small, meaning that the atomization is suppressed under a high pressure condition. Different trend of pressure dependence of SMD was also seen among IC region, AC region, OC-1 region, and OC-2 region. It can be said that the recirculation zone formed inside of the cone

enhanced the collision at the particles and the subsequent merging of them.

3.2 Comparison with the equation proposed by Lefebvre

Lefebvre[2] proposed the following equation to estimate SMD of airblast atomizer.

$$\frac{SMD}{L_C} = \left[A' \left(\frac{\sigma}{\rho_A U_A^2 D_P} \right)^{0.5} + B' \left(\frac{\mu_L}{\sigma \rho_L D_P} \right)^{0.5} \right] \left(1 + \frac{\dot{m}_L}{\dot{m}_A} \right) \qquad (2)$$

In this equation, σ is surface tension, ρ_A is density of air, U_A is the velocity of air, D_P is the radius of outer rip, μ_L is viscosity coefficient of water, $\dot{m}_A$ is mass flow rate of air, A' and B' are constant, respectively. In the present study, the variable in Eq. (2) is only ρ_A, because μ_L, ρ_L and σ are nearly constant with the pressure increase[3]. When pressure increases, ρ_A becomes large, so this equation mean that SMD becomes smaller under the high pressure condition. Symbols "X" in Figs. 2 to 5 means the SMD calculated using Eq. (1) where SMD at 0.1 MPa was normalized by that in our experimental results. Despite the fact mentioned above, SMD did not become smaller in any other region. It can be said that the equation which was proposed by Lefebvre could not reproduce the effect of high pressure, and the refinement of the equation is necessary for the practical combustor design.

4. Concluding remarks

1. Variations of particle diameters with pressure generated by an airblast atomizer depend on the region in spray structure. Also, existance of recirculation flow affects the variations of particle diameter through the increasing residence time. This is due to the difference in speed between air and liquid effected by pressure, and the frequency of particle collision.
2. It was indicated that the equation proposed by Lefebvre in the literature can not reproduce the effect of high pressure found in this study, thus refinement of the equation is necessary.

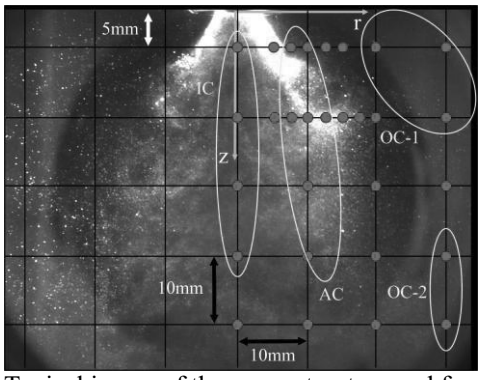

Fig. 1 Typical image of the spray structure and four areas of measurement points.

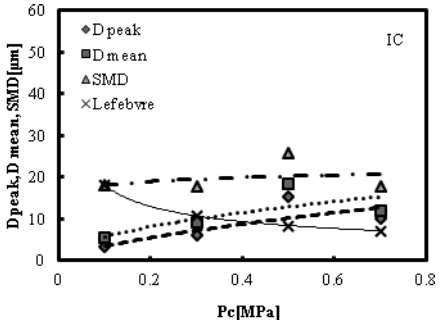

Fig. 2 Pressure dependence on the particle diameter in IC region.

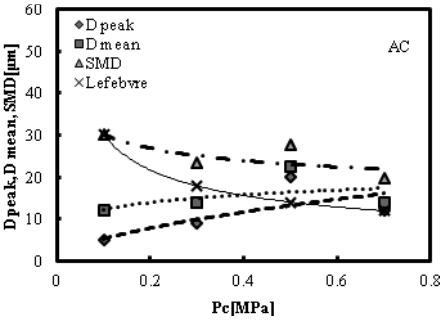

Fig. 3 Pressure dependence on the particle diameter in AC region.

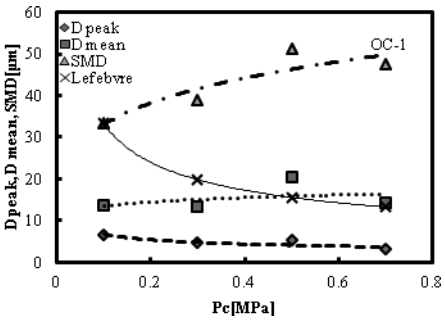

Fig. 4 Pressure dependence on the particle diameter in OC-1 region.

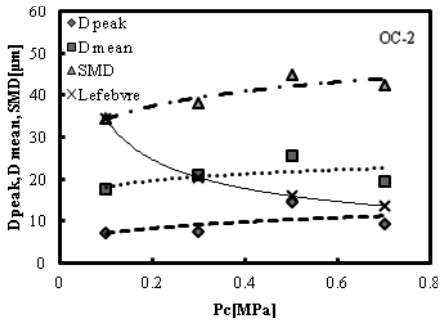

Fig. 5 Pressure dependence on the particle diameter in OC-2 region.

References

[1]Atomization and Technology, Institute for Liquid Atomization and Spray Systems, Morikita shuppan, 2003.

[2]A. H. Lefebvre , Gas Turbine Combustion, Henisphere, 1983.

[3]Physicality Science Encyclopedia, University of Tokyo, The Institute for Solid State Physics, Tokyo shoseki, 1996.

Eighth International Conference on Flow Dynamics
November 9 - November 11, 2011

Evaluation of Aerodynamic Characteristics of a Triangular Airfoil at Low Reynolds Number and High-Subsonic Mach Number

Tetsuya Suwa, Kei Nose, Daiju Numata, Hiroki Nagai and Keisuke Asai
Tohoku University, 6-6-01, Aramaki-Aza-Aoba, Aoba-ku, Sendai 980-8579, JAPAN
suwa.tetsuya@aero.mech.tohoku.ac.jp

ABSTRACT

The objective of this study is to clarify Mach number effect on the characteristics of a propeller blade of a Mars airplane. We measured aerodynamic force and pressure distributions on a thin triangular airfoil at low Reynolds number using a force balance and Pressure Sensitive Paint. The results show that Mach number has an effect to delay a reattachment of shear layer, resulting in a change of aerodynamics characteristics of the airfoil. A comparison between the lift obtained by this test with that estimated using the Prandtl-Glauert (P.G.) rule indicates that, the thrust force of a Mars airplane propeller might be overestimated by the P.G. rule.

1. Introduction

A Mars airplane has been considered as a feasible means of exploring Mars [1, 2]. As shown in Fig. 1, a propeller of the Mars airplane operates at low Reynolds number and high-subsonic number, meaning that it is necessary to consider these factors in designing the propeller. In this study, we select a thin triangular airfoil as propeller section and attempt to obtain its experimental data at Martian atmospheric condition. There are few such experimental data because it is difficult to simulate the flow condition on Mars in a conventional wind tunnel. Thus, the Prandtl-Glauert (P.G.) rule is used to estimate Mach number effect.

The objective of this research is to clarify Mach number effect on the characteristics of a propeller blade of a Mars airplane by conducting airfoil tests in the Mars Wind Tunnel (MWT) at Tohoku University. In this test, a thin triangular airfoil was used as a test model. We measured aerodynamic force and pressure distributions on the model using a force balance and Pressure Sensitive Paint (PSP). Comparing the data obtained by the present tests with those from the P.G. rule, we examined the suitability of applying the P.G. rule for designing a propeller for a Mars airplane.

2. Experimental Devices and Condition

2-1. Mars Wind Tunnel

The MWT is composed of a vacuum chamber, an induction-type wind tunnel and a buffer tank. The induction-type wind tunnel is located inside the vacuum chamber where the pressure condition of Martian atmosphere can be simulated. The test gas is dry air in usual tests, but can be replaced with carbon dioxide. Currently, the MWT is being operated at ambient temperature only.

2-2. Two-component Balance System

A two-component balance system was used to measure aerodynamic force. This balance system is composed of two load cells and has a sufficient sensibility and accuracy to measure lift and drug at reduced pressure.

2-3. Pressure-Sensitive Paint

PSP is a coating type pressure sensor consisting of luminescent molecules and binder. Being illuminated with light at excitation wavelength, the luminescent molecules in PSP are elevated to the excited state. The excited molecules return to the ground state through several photochemical processes; luminescence, thermal deactivation, and oxygen quenching. The principle of PSP is based on oxygen quenching. The rate of quenching depends on local oxygen concentration which is proportional to ambient pressure. Therefore, surface pressure can be calculated from measured luminescent intensity of PSP.

In this experiment, we used PdTFPP as luminescent molecule and poly(TMSP) as binder. This PSP has high pressure sensitivity at low pressure conditions.

2-4. Triangular Airfoil

The triangular airfoil is shown in Figure 2. The maximum thickness of this airfoil is 5% of the chord and is located at x/c=30 % from the leading edge.

2-5. Experimental Condition

The Reynolds number and the Mach number were set to cover the whole operation range of a Mars airplane propeller shown in Fig. 1.

3. Results and Discussion

3-1. Aerodynamic Force

Figure 3 shows the aerodynamic characteristics of the triangular airfoil at Reynolds number of about 3000. As shown in Fig. 3(a), for Mach number of 0.16 and 0.25, the lift slope suddenly increases at 7 deg. On the other hand, for Mach number of 0.5 and 0.7, the lift curve maintains its linearity even above 6 deg. Therefore, it can be said that the compressibility has an effect to enhance the linearity of the lift curve at Reynolds number of about 3000. As shown in Fig. 3(b), however, *L/D* does not change much when the Mach number is changed from 0.16 to 0.7.

Figure 4 shows the aerodynamic characteristics of the triangular airfoil at Reynolds number of about 9000. As shown in Fig. 4(a), there is almost no difference in the lift curves at two different Mach numbers. As shown in Fig. 4(b), however, *L/D* changes with Mach number. For the Mach number of 0.15, *L/D* reaches its maximum value at 6 deg. On the other hand, for Mach number of 0.5, *L/D* reaches the maximum value at 6 deg that is smaller than that for Mach number of 0.15.

3-2. Pressure Distribution

Figure 5 shows pressure distributions at 8 deg for various Reynolds number and Mach number. As shown in Fig. 5, a constant-pressure region near the leading edge expands as Mach number increases. According to Anyoji, et al [4], it is considered that the compressibility has an effect to stabilize a separated share layer and to delay its transition to turbulence. It is suggested that, in the range of Reynolds number from 3000 to 9000, Mach number has an effect to delay a reattachment of the shear layer.

3-3. Evaluation of an Application of Prandtl-Glauert rule

To estimate the lift force of a Mars airplane's propeller blade and at high subsonic Mach number from the incompressible data, we calculated the lift coefficient at Mach number of 0.5 from the data at the Mach number of 0.16 and 0.17 using the Prandtle-Glauert (P.G.) equation.

$$C_l = \frac{C_{l,0}}{\sqrt{1 - M_\infty^2}} \qquad (1)$$

For different Reynolds numbers, the lift coefficient from the P.G. rule is similar to that from the test at angle of attack bellow 3 deg. Above 3 deg, however, the lift from the P.G. rule are higher than that of the test. The P.G. rule is derived from the potential theory. So these results suggest that, on the condition of low Reynolds number and high angle of attack where the viscosity affect is dominate in the flow, it is not safe to employ the P.G. rule for designing a Mars airplane because this rule might overestimate the thrust force of a propeller.

4. Conclusions

To evaluate the Mach number effect on the characteristics of a propeller blade of a Mars airplane, we measured the aerodynamic force and pressure distribution on a triangular airfoil at different Reynolds numbers by using a two-component balance system and PSP.

The results indicate that Mach number has an effect to delay a reattachment of shear layer and to change aerodynamic characteristics of the airfoil. A comparison between the lift obtained by the present test with that estimated from the P.G. rule indicates that it is not appropriate to apply the P.G. rule in the design of a Mars airplane's propeller because its thrust force might be overestimated.

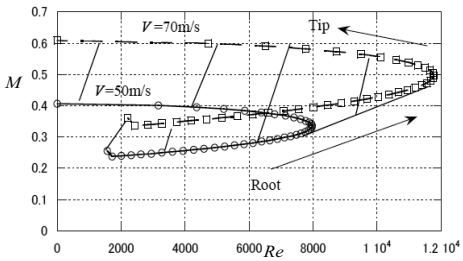

Fig. 1 Operating Range of Mars Airplane Propeller [3]

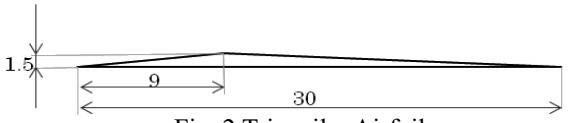

Fig. 2 Triangilar Airfoil

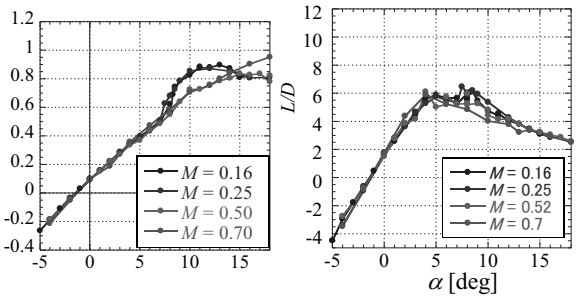

(a) Lift Curve (b) *L/D*

Fig. 3 Results of Balance Measurement for Reynolds Number of 3000

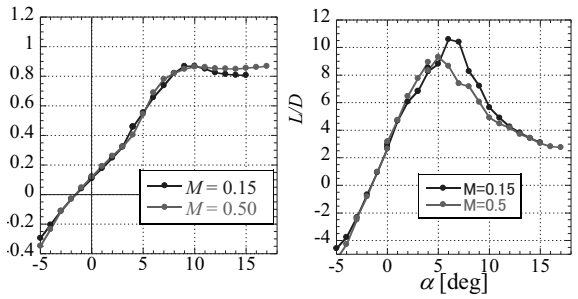

(a) Lift Curve (b) *L/D*

Fig. 4 Results of Balance Measurement for Reynolds Number of 9000

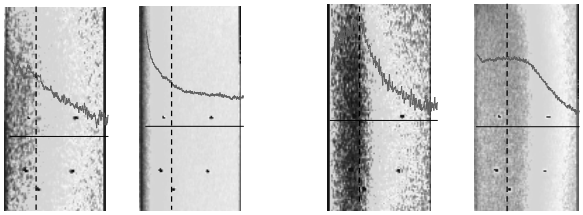
M = 0.16 *M* = 0.50 *M* = 0.15 *M* = 0.50

Re = 3000 *Re* = 9000

Fig. 5 Results of PSP Measurement at 8 deg

References

[1] A. Oyama, K. Fuji, "A Study on Airfoil Design for Future Mars Airplane", AIAA-2006-1484, 44th AIAA Aerospace Sciences Meeting and Exhibit, Reno, Nevada, January 9-12, 2006.

[2] Remi Luong et al. "Mars Airplane Conceptual Deaign", The 54th Proceedings of the Space Sciences and Technology Conference, 3F04, 2010.

[3] S. Sunada, Private Communication.

[4] M. Anyoji, "Development of a Mars Wind Tunnel and Its Applications to Low Reynolds Number and High-Subsonic Airfoil Testing", Ph.D thesis, Tohoku University, 2011.

Gait Analysis of MR-SPCOM KNEE, a Prosthetic Knee Joint with Optional Stance and Swing Control System Utilizing MR Fluid Brake

Takashi Suzuki*, Yuichi Hikichi*, Masami Nakano**
*Graduate School of Engineering, Tohoku University
**Institute of Fluid Science, Tohoku University, 2-1-1, Katahira, Aoba-ku, Sendai, 980-8577, Japan
E-mail of corresponding author: suzuki@ifc.ifs.tohoku.ac.jp

ABSTRACT

In this study, "MR-SPCOM (MR fluid brake-Stance Phase Controlled by Optional Motion knee) KNEE", which is the above-knee prosthesis using MR fluid brake, has been developed. Fast response of MR fluid enables the user to walk naturally. Above-knee prosthesis is required the function of human knee. Therefore, walking states of the user are highly dependent on the performance of the knee joint. In this paper, the performance evaluation of MR-SPCOM knee joint is described by analyzing the motions of walking on flatlands and going up/down stairs and discussing the results.

1. Introduction

Prosthetic legs are classified into several types depending on the cutting position of the leg. We deal with above-knee prosthesis which is used in the case where the above knee is cut and the function of the knee is required. Human walking is the repetitive motion of stance phase and swing phase. To achieve the walking, the knee joint is required the function of locking surely in stance phase and bending naturally in swing phase.

Figure 1 shows the developed "MR-SPCOM" (MR fluid brake-Stance Phase Controlled by Optional Motion) knee joint using MR fluid brake. MR fluid behaves like a Bingham fluid having a yield stress which can be rapidly changed in a reversible manner by applying magnetic field [1]. The MR fluid brake is filled with the MR fluid within the gaps of the brake multi-disks. By applying current to a coil located outside the brake disks, the braking torque acting on the multi-disks rises up due to the increase of the MR fluid yield stress, and the knee joint is capable of locking the knee. So, the MR fluid brake is possible to quickly switch among Lock, Free and Yielding of the knee, to allow flat walking and going up/down the stairs.

In this paper, the gait performances of MR-SPCOM knee joint are described. Specifically, the gait motions of walking on flatland and going up/down stairs are analyzed and discussed. In addition, the time variations of the center of gravity and the center of sole pressure are measured and analyzed. And, the results of non-handicapped person are compared with the results of a prosthetic leg user.

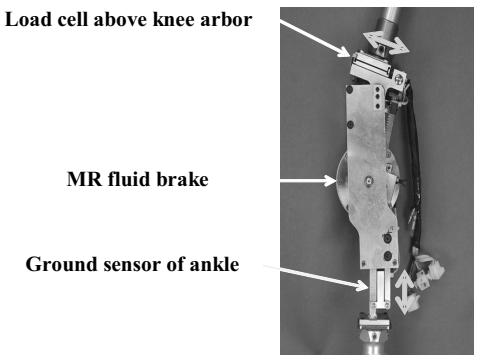

Fig.1 MR-SPCOM knee joint and its sensors

2. Experimental Methods

In the experiments, the some markers are attached to the body of the subject to analyze the gait motion. Each position of the markers is taken on six video cameras and measured by a 3-D video analyzing system. Figure 2 shows the positions of markers attached to the subject and the definition of joint angles [2]. Θ and δ are defined as the angles of the knee and the ankle, respectively. The time variations of Θ and δ are analyzed when walking on flatland and going up/down the stairs. And also, the center of gravity when walking on flatland and the center of sole pressure when going up/down the stairs are measured by using a treadmill with a force distribution platform and a force sensor sheet of F-Scan2, respectively.

3. Results and Discussion

3.1 Gait analysis

Figure 3 shows the time variations of knee angle Θ and ankle angle δ when walking on flatland, indicating

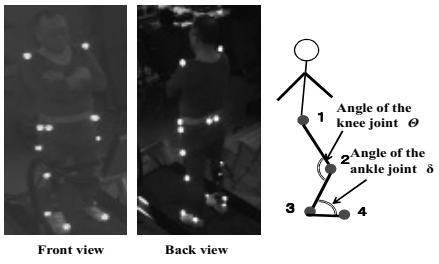

Fig.2 Positions of markers and definition of joint angles

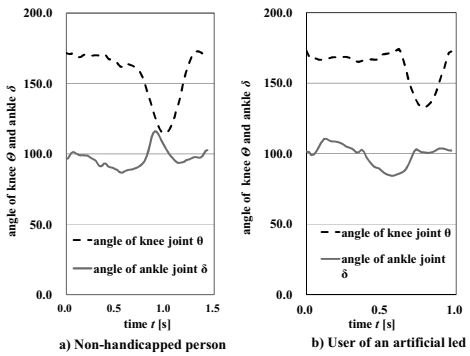

Fig.3 Time variations of knee and ankle angles when walking on flatland

that the developed prosthetic knee joint realizes the function of knee when walking on flat land.

Regarding the walking on stairs, there is a significant difference of gait motion between non-handicapped person and prosthetic leg user when going up the stairs. Figure 4 shows the time variations of knee and ankle angles when a prosthetic leg user going up the stairs, where the green line corresponds to the angle of the MR-SPCOM knee joint. We can see that the MR-SPCOM knee joint keeps the knee angle constant in the swing phase as well as the stance phase, making it possible to going up the stairs with alternative steps by locking the knee angle.

3.2 Time variations of center of gravity

Figure 5 shows the movement of the center of gravity when walking on flatland. For non-handicapped person, the center of gravity moves from heel to toe of each leg, and changes over to the heel of the other leg. However, for the prosthetic leg user, the center of gravity concentrates to the toe in his healthy leg, while moves from heel to toe in his prosthetic leg.

3.3 Time variations of center of sole pressure

Figure 6 shows the time variations of the center of sole pressure when the prosthetic leg user going up/down the stairs. The vertical axis is L_{cp} defined as the distance between the heel and the center of sole pressure as shown in Fig.5.

When going up the stairs, the center of sole pressure of the prosthetic leg moves from heel to toe in the earlier stage than the healthy leg, as seen in Fig.6(a), indicating that the user stands on his heel when the user shifts his

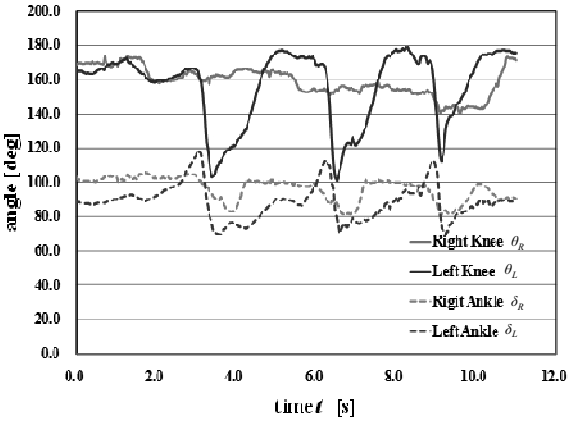

Fig.4 Time variations of knee and ankle angles when going up the stairs (Right: artificial leg)

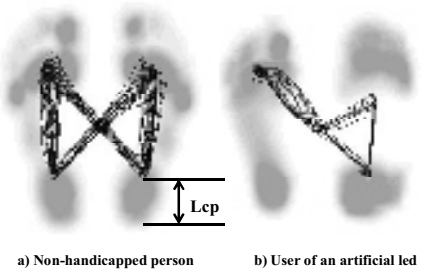

Fig.5 Movement of center of gravity when walking on flatland (Right: artificial leg)

(a) When going up stairs

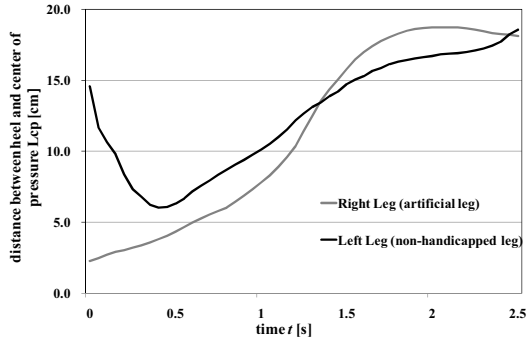

(b) When going down stairs

Fig.6 Time variations of center of sole pressure (Right: artificial leg)

weight to the prosthetic leg. This may be because the mobility of ankle joint of the prosthetic leg is limited.

When going down the stairs, in the same way, the center of sole pressure of the prosthetic leg moves from heel to toe. However, the center of sole pressure of the healthy leg puts on the toe at first, indicating that the user tries to reach his healthy leg on the stair at an early stage to avoid falling. It is a serious problem that the weight support by the prosthetic leg is not easy because the mobility of the prosthetic leg ankle is restricted.

4. Concluding Remarks

In these performance evaluations, the following results are obtained.

(1) The developed MR-SPCOM knee joint makes it possible to walk on flatland and stairs.
(2) When walking on flatland, the center of gravity of a prosthetic leg user concentrates to the toe of his healthy leg.
(3) It is necessary to improve the mobility of the prosthetic leg ankle to reduce a burden of the healthy leg when going up/down stairs.

References

[1] M. Nakano, H. Yamamoto and M.R Jolly, Dynamic Viscoelasticity of a Magnetorheological Fluid in Oscillatory Slit Flow, Int. J. of Modern Physics B, Vol.13-14,15&16, (1999), pp.2068-2076

[2] E. Yosihiko, Hand Book of Clinical Gait Measurements (in Japanese), Ishiyaku Shuppan, (2008), pp.146-150

Eighth International Conference on Flow Dynamics
November 9 - November 11, 2011

Characterization of Carbon Nanotube-Carbon Composite Microstructures

Liang He[1], Masaya Toda[2], Yusuke Kawai[1], Hidetoshi Miyashita[2], Shuai Chen[1], Mamoru Omori[3], Toshiyuki Hashida[3] and Takahito Ono[1]
1. Graduate School of Engineering, Tohoku University, 6-6-01 Aza Aoba, Aoba-ku, Sendai 980-8579
2. Microsystem Integration Center (μSIC), Tohoku University, 519-1176 Aza Aoba, Aoba-ku, Sendai 980-0845
3. Fracture and Reliability Research Institute, Tohoku University, 6-6-11 Aza Aoba, Aoba-ku, Sendai 980-8579
E-mail: hl@nme.mech.tohoku.ac.jp

ABSTRACT

This paper reports high aspect ratio carbon nanotube (CNT)-carbon composite cantilevers fabricated by novel fabrication technique based on the micromolding and pyrolysis of a resist (SU-8) mixed with CNTs. The Young's modulus *E* of CNT-carbon composite is estimated to be 105.8±3.2 GPa, which is higher than pyrolysis carbon, thus Young's modulus was increased by adding CNTs as reinforcing agents to pyrolysis carbon.

1. Introduction

Carbon nanotubes (CNTs) have been appreciated as ideal high toughness fibres for micro/nano composite structures [1], and CNT composites may satisfy various mechanical specifications since the CNTs are ideal candidates for the mechanical reinforcement [2]. The CNTs used as reinforcing agents in composite structures has two advantages, i.e. high modulus and small weight.

The incorporation of CNTs into a bulk material can lead to a large extent promotion of the toughness and strength of the matrix that have been reported. Many researchers have endeavored to fabricate advanced CNT composite materials that exhibit excellent mechanical, thermal, and electrical properties by now. Many methods such as melt blending [3], calendaring [4], ultraviolet radiation initiated polymerization [5] etc. have been utilized to fabricate CNT composites. However, it still remains challenge for the fabrication of composite microstructures with high aspect ratio.

In MEMSs, the critical issues of microactuators, including micro XY stages [6] and optical microscanners, are the difficulty obtaining both large displacement and high frequency response. Si has been often used as an elastic material for actuators, due to its high toughness and no mechanical hysteresis, but even so movable Si portions are broken [6]. For the solution of this problem, another material with better toughness, which should replace Si, is desired as an elastic material, and the CNT composite is one of the candidates.

Various microfabrication methods for carbon micro/nano structures that utilize polymer precursors or photoresists have been proposed by now, and these methods can be divided into two types. Some methods for the fabrication of freestanding carbon structures have been reported, and these microstructures were fabricated by the pyrolysis process of photoresist patterns formed by photolithography [7-9]. Other methods utilize the combination of micromolding and nanotemplating technique, with pyrolysis process [10-12]. In our research, high aspect ratio composite cantilevers are fabricated by a novel technique using the Si micromolding technique and pyrolysis process of a resist mixed with CNTs.

2. Fabrication process and results

In this work, we have fabricated CNT-pyrolysis carbon composite cantilevers with different lengths (400-1000μm) and widths (10-100 μm).

In the fabrication process as shown in Fig. 1, a Si micromold fabricated by photolithography and deep reactive ion etching (deep RIE) was used for CNT/resist filling, and then the CNT/resist was converted to CNT-carbon composite by pyrolysis process.

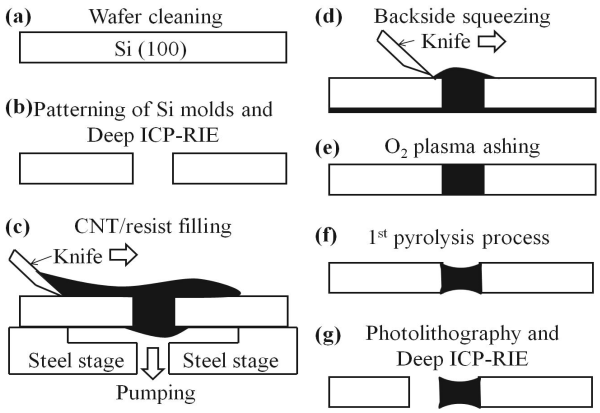

Figure 1. Fabrication process of the CNT-carbon composite microstructures.

At first a 400 μm-thick (100)-oriented Si wafer is cleaned with typical RCA cleaning process. Using deep RIE, a Si micromold was fabricated for filling process. Resist (SU-8 50cp) mixed with MWCNTs (Multi Wall CNTs) with 1 wt% was used as a filling material. Then, the CNT/resist was dropped onto the mold, and the back side of the wafer was evacuated by a pump, thus the CNT/resist was flow and filled into the mold. Then, remained CNT/resist on both sides was removed by squeezing. Additionally, still remained CNT/resist on the surface was removed by O_2 plasma. Then, the CNT/resist in the mold was pyrolyzed at 300 or 400°C in N_2 gas for 1 h. Thus, CNT/resist in the mold was converted to CNT-carbon composite during the 1st

pyrolysis process. In order to fabricate hybrid silicon/composite cantilevers, the photolithography and deep RIE were performed again to release the composite cantilevers. The 2nd pyrolysis at higher temperature of 600°C or 800°C than that of 1st pyrolysis was performed after deep RIE to reduce the shrinkage/depression of the composite microstructures.

SEM images of some released cantilevers after two-step pyrolysis of 400°C (1st, 60 min) and 600°C (2nd, 60 min) were shown in Fig. 2. The height of narrow CNT-carbon composite cantilevers is almost equals to the thickness of the Si mold as shown in Fig. 2. The maximum aspect ratio of 40 can be achieved by this process.

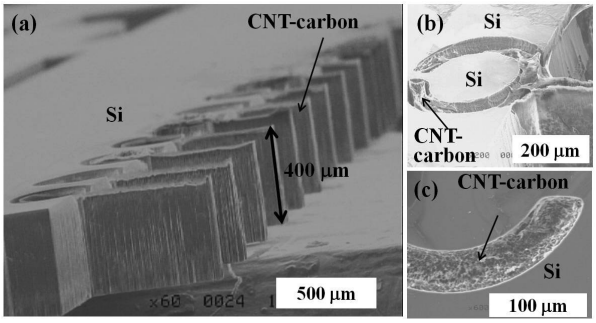

Figure 2. SEM images of the fabricated composite cantilevers: (a) Tilt view of cantilevered microstructures (b) Magnified view of a cantilever (c) Magnified view of the surface of the CNT-carbon cantilever.

3. Characterization results of Young's modulus

For the investigation of the Young's modulus of the composite cantilever, it is estimated from the resonant frequency of the composite cantilevers that was measured by a laser Doppler vibrometer as shown in Fig. 3. For the resonant frequency of a rectangle cantilever, it can be expressed by Equ. (1), where K is the spring constant, and m^* is the effective mass, that can be expressed by Equs. (2) and (3), respectively.

$$f = \frac{\sqrt{K / m^*}}{2\pi} \quad (1)$$

$$K = \frac{Et^3 w}{4l^3} \quad (2)$$

$$m^* = n\rho twl \quad (3)$$

E: Young's modulus; t: Thickness (50 or 100 μm);
ω: Width (~340 μm); l: Length (650-1000 μm);
ρ: Density (2.06±0.06 g/cm^3);
n: Geometrical factor (0.24)

The density of composite microstructures was estimated from the CNT-carbon film fabricated by the same pyrolysis process as the cantilevers. The resonant frequency of one cantilever with a length of 700 μm was shown in Fig. 3. From the resonant frequency f = 237.90 kHz, the Young's modulus E of CNT-carbon composite is estimated to be 105.8±3.2 GPa. The Q factor of the resonance is approximately 30 in ambient atmosphere. The Young's modulus of SU-8 pyrolyzed at 600°C was 32 GPa [9]; thus, the Young's modulus was increased by approximately 230 % by adding 1 wt% of CNTs as reinforcing agents.

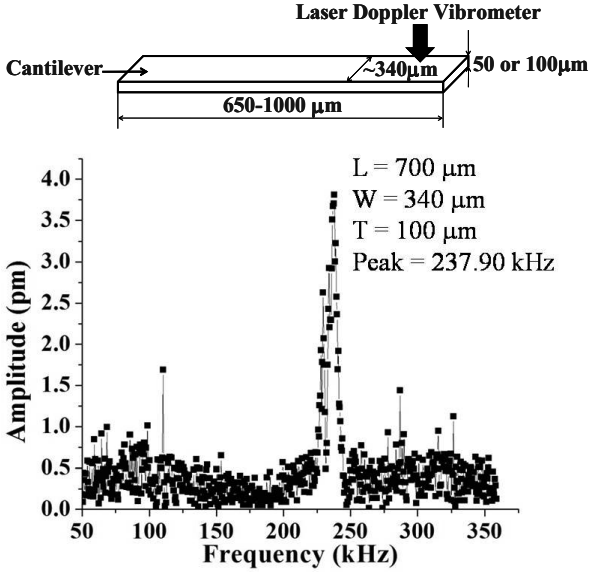

Figure 3. Resonant frequency measurement of CNT-carbon composite cantilever

4. Conclusions

Hybrid microstructures of the CNT-carbon composite and Si with a high aspect ratio of the composite can be fabricated by this novel micromolding and pyrolysis process. Higher Young's modulus was obtained by adding CNTs as reinforcing agents to pyrolysis carbon.

Acknowledgements

This study was partially supported by the Global COE Program, "World Center of Education and Research for Trans-disciplinary Flow Dynamics", Tohoku University, Japan Society for the Promotion of Science.

References

[1] Kim-Tak Lau, David Hui, *Composites Part B*, **33**, pp.263-277 (2002)
[2] J. N. Coleman, U. Khan and Y. K. Gunko, *Adv. Mater*., **18**, pp.689-706 (2006)
[3] P. Potschke, Arup R. Bhattacharyya and A. Janke, *Carbon*, **42**, pp.965-969 (2004)
[4] F. H. Gojny, M. H. G. Wichmann, U. Kopke, B. Fiedler, K.Schulte, *Composites Science and Technology*, **64**, pp.2363-2371 (2004)
[5] L. M. Clayton, A. K. Sikder, A. Kumar et al, *Adv. Func. Mater*.,**17**, pp.101-106 (2005)
[6] M. Faizul Mohd Sabri, T. Ono and M. Esashi, *J. Micromech. Microeng*., **19**, 095004(9pp) (2009)
[7] Chunlei Wang, Guangyao Jia, L. H. Taherabadi and Marc J Madou, *J. Microelectromech. Syst*., **14**, pp.348-357 (2005)
[8] Kartikeya Malladi, Chunlei Wang and Marc Madou, *Carbon*, **44**, pp.2602-2607 (2006)
[9] Jung A Lee, S. W. Lee, K. –C. Lee, S. I. Park and S. S. Lee, *J. Micromech. Microeng*., **18**, 035012(10pp) (2008)
[10] O. J. A. Schueller, S. T. Brittain, C. Marzolin, and G. M. Whitesides, *Chem. Mater*., **9**, pp.1399-1406 (1997)
[11] O. J. A. Schueller, S. T. Brittain, and G. M. Whitesides, *Sens. Actuators A*, **72**, pp.125-139 (1999)
[12] S. Rahman, H. Yang, *Nano.Lett*., **3**, pp.439-442 (2003)

Eighth International Conference on Flow Dynamics
November 9 - November 11, 2011

An Automatic Task Assignment Method for Heterogeneous Computing Systems

Katsuto Sato#, Kazuhiko Komatsu*, Hiroyuki Takizawa#, Hiroaki Kobayashi*
#Graduate School of Information Sciences, Tohoku University, 6-3 Aramaki-aza-aoba, Aoba, Sendai, Miyagi, Japan.
*Cyberscience Center, Tohoku University, 6-3 Aramaki-aza-aoba, Aoba, Sendai Miyagi, Japan.
katuto@sc.isc.tohoku.ac.jp

ABSTRACT

To achieve high performance in heterogeneous computing systems, use of multiple accelerators is a promising approach. Task assignment for good load balance is important to fully exploit the computing potential of the system. However, as the best load balance depends on the combination of available accelerators, it is difficult for a programmer to balance the loads. This paper proposes an automatic task assignment method and shows the performance improvement of load balancing realized by an automatic task assignment method. The proposed method enables programmers to easily use multiple accelerators without considering the load balance.

1. Introduction

Recently, *heterogeneous computing systems* of *general purpose processors (CPUs)* and multiple accelerators such as *Graphics Processing Units (GPUs)* are attractive to achieve high performance and high power efficiency. As many scientific computations such as computational fluid dynamics (CFD) and finite element methods (FEM) involve massive parallelism, heterogeneous computing systems can achieve high performance in various fields[1]. Accelerators such as GPUs have high floating-point operation performance and high memory bandwidth. However, their performance might be degraded if their architectural features are not suitable for the computations. This problem becomes more serious when different accelerators are available in a system.

Suppose that a program contains multiple computations, called *tasks*, which are computationally-expensive parts of the program and offloadable to accelerators. If there are some tasks that can be independently executed, scalable speed-up can be achieved using multiple accelerators with appropriate task assignment.

However, it is difficult to appropriately assign tasks to multiple accelerators because the best accelerator for each task depends on various conditions such as the system configurations, the problem size, and so on. In many cases, as these conditions are determined at runtime, it is difficult even for an expert programmer to properly assume the conditions. Therefore, an automatic task assignment method is required.

This paper proposes an automatic task assignment method and shows the expected performance improvement of load balancing realized by the proposed method. For load balancing among accelerators in a heterogeneous computing system, the proposed method assigns a task to an appropriate accelerator at runtime so as to minimize the execution time of an application program. The proposed method predicts the execution time of a task on each accelerator and analyzes data dependency among tasks to detect independent tasks. Based on the performance prediction and the data dependency analysis, the proposed method selects an appropriate accelerator for a given task.

2. Related work

Unlike CUDA[2] for NVIDIA's GPUs, OpenCL[3] is a non-proprietary standard programming framework released by Khronos Group for heterogeneous computing systems. CUDA and OpenCL assume that programmers explicitly assign every task to an appropriate accelerator. An expert programmer that has enough knowledge of accelerators must decide task assignment considering the configuration of a heterogeneous computing system. However, it complicates programming and performance tuning. Therefore, an automatic task assignment method is required for efficient execution of programs to easily exploit the potential of a heterogeneous computing system.

In addition, OpenCL need neither know nor specify the number of processing elements in an accelerator. However, programmers need the number of accelerators for parallel processing using multiple accelerators and for exploiting the potential of the heterogeneous computing system. The automatic task assignment can allow a programmer to develop a program without considering the number of accelerators, because tasks are assigned at runtime considering the number of available accelerators.

3. Automatic Task Assignment Method

This section proposes an automatic task assignment method consisting of three techniques; execution time prediction, data dependency analysis, and task scheduling.

3.1. Execution Time Prediction

In the predictor proposed in [4], performance profiling is performed to analyze the relations between execution times and execution parameters such as the argument values and the execution granularity.

Execution parameters can be classified into three types according to the effect to execution time; N-type, S-type, and W-type. Parameters of different types are used in different ways to improve prediction accuracy. N-type parameters are not used for prediction because they have no effect on the execution time. S-type parameters are used to build linear prediction models, and W-type parameters are used to select the most appropriate prediction models.

By using multiple linear prediction models, the performance predictor can improve the prediction accuracy. Besides, as this model is built by only profiling data, the performance predictor does not need architectural features of each accelerator and is thus able to predict the performance of any accelerator.

3.2. Data Dependency Analysis

To use multiple accelerators, it is necessary to find the tasks that can be independently executed. The data-dependency analyzer proposed in [5] records the

memory objects, which are passed to tasks, and then analyzes the data dependency among them. As a result, it can determine whether a task reads or writes each memory object.

The data dependency analyzer uses an access history of memory objects recorded at runtime to find independent tasks, among which there are no data dependencies of memory objects. As data dependencies are analyzed by using the access history, the analyzer can find concurrently-executable tasks even if the data dependencies are dynamically changed.

3.3. Task Scheduling

According to the predicted execution time and the data dependencies among tasks, the scheduler in the proposed method decides an accelerator, to which a task is assigned. When the scheduler determines the task assignment, it also has to consider data transfers and their nonnegligible overheads. The proposed method assigns each task to the accelerator that can complete the execution of the task with considering data transfer cost based on the list scheduling method[6].

By scheduling at runtime, a programmer can assign tasks without considering the number of available accelerators, and the tasks are assigned automatically to appropriate accelerators, resulting in the minimization of the execution times.

4. Evaluation

We evaluate the effect of load balancing, which can be realized by the proposed automatic task assignment method. In this evaluation, three accelerators are used; Tesla C1060, GeForce GTX 260, and GeForce GTX 480. We use the MonteCarloAsian benchmark in AMD APP SDK that has many parallel tasks.

Figure 1 shows the execution times of MonteCarloAsian when tasks are assigned to Tesla C1060 and GTX260 while changing the ratio of tasks assigned to each accelerator. Figure 2 also shows the execution times when the program runs using Tesla C1060 and GeForce GTX 480. From these results, it is obvious that load balancing can improve performance and the optimal ratio depends on the combination of accelerators. Hence, programmers must adjust the ratio for the combination of accelerators to achieve optimal load balancing. In these cases, the proposed method can achieve good load balancing by dynamically assigning tasks.

We are currently developing a framework that uses the proposed method to achieve the optimal load balancing automatically for the programs with many parallel tasks.

5. Conclusions

Use of multiple accelerators is a promising approach to achieve higher performance in heterogeneous computing systems that have various accelerators. However, as the optimal task assignment depends on the combination of available accelerators, programmers must adjust the ratio of tasks assigned to each accelerator in order to achieve high performance. An automatic task assignment method can automatically adjust the ratio and allow programmers to avoid tedious performance tuning for individual heterogeneous systems. This paper has shown the overview of the automatic task assignment method and its effects through some evaluation results.

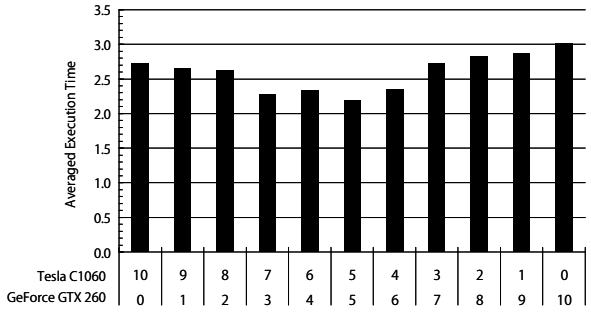

Fig. 1 The effect of load balancing between GeForce GTX 260 and Tesla C1060.

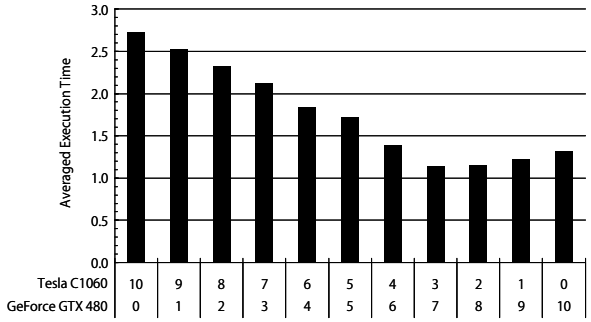

Fig. 2 The effect of load balancing between GeForce GTX 480 and Tesla C1060.

In the future work, we will develop an automatic task assignment framework based on the proposed method, and evaluate the performance gain by appropriate load balancing.

6. Acknowledgements

The authors would like to acknowledge support from the Tohoku University Global COE Program on World Center of Education and Research for Trans-disciplinary Flow Dynamics. This research was partially supported by Grants-in-Aid for Young Scientists(B) #21700049; Excellent Young Researcher Overseas Visit Program of Japan Society for the Promotion of Science (JSPS); and Core Research of Evolutional Science and Technology of Japan Science and Technology agency (JST).

References

[1] GPGPU.org . GPGPU General-Purpose Computation on Graphics Hardware . http://gpgpu.org .

[2] NVIDIA Corporation . NVIDIA CUDA NVIDIA CUDA C Programming Guide Version 4.0 , 2011.

[3] Khronos OpenCL Working Group . The OpenCL Specification version 1.1 . http://www.khronos.org/opencl/ .

[4] Katsuto Sato, Kazuhiko Komatsu, Hiroyuki Takizawa, and Hiroaki Kobayashi. A History-based Performance Prediction Model with Profile Data Classification for Automatic Task Allocation in Heterogeneous Computing Systems. In *The 9th IEEE International Symposium on Parallel and Distributed Processing with Applications*, pages CD–ROM, May 2011.

[5] Katsuto Sato, Kazuhiko Komatsu, Hiroyuki Takizawa, and Hiroaki Kobayashi. A Runtime Dependency Analysis Method for Task Parallelization of OpenCL Programs. In *IPSJ Transactions on Advanced Computing Systems (ACS36)*, 2011.

[6] P. Thambidurai E. Ilavarasan. Low Complexity Performance Effective Task Scheduling Algorithm for Heterogeneous Computing Environments. *Journal of Computer Science*, 3:94–103, 2007.

Friction Properties between Stainless Steel and Partly Polished Polycrystalline Diamond Film with Ti Interlayer

Yosuke Nakayam[1)*], Hiroyuki Miki[2)], Takanori Takeno[3)], and Toshiyuki Takagi[2)]
[1)] Graduate School of Engineering, Tohoku University, Aoba 6-6-04, Aramaki, Aoba-ku, Sendai 980-8579, JAPAN
[2)] Institute of Fluid Science, Tohoku University, Katahira 2-1-1, Aoba-ku, Sendai 980-8577 JAPAN
[3)] Institute for International Advanced Interdisciplinary Research, Tohoku University Advanced Research and Education Organization, Aoba 6-3, Aramaki, Aoba-ku, Sendai 980-8578, JAPAN
E-mail of corresponding author: nakayama@wert.ifs.tohoku.ac.jp

ABSTRACT

To investigate the possibility of party polished polycrystalline diamond films with Ti interlayer as a solid lubricant, friction properties and durability were examined by a reciprocal ball-on disk test. The diamond film was successfully deposited on steel substrates with Ti interlayer that has a thickness of 2 μm, and the film endured the sliding under contact pressure of about 595 MPa and showed steady coefficient of friction (COF) in steady-state regime value of about 0.1 with steel balls under periodic speed changing in the friction test. It can be said that the partly polished polycrystalline diamond film with Ti interlayer is a quite fine solid lubrication film.

1. Introduction

Chemical Vapor Deposition (CVD) diamond films have good properties like high hardness, low coefficient of friction, wear resistance, and chemical inertness and so on. Therefore, CVD diamond films are expected to be applied solid lubrication films. In our past research, it was revealed that the partly polished polycrystalline diamond films deposited on ceramics substrates showed good friction properties against stainless steel [1, 2]. However, it is necessary to deposit diamond films on steel substrates from the viewpoints of resistance to impact and workability for industrial application. To deposit diamond films on steel, the difference of coefficient of thermal expansion between diamond and steel, and graphite synthesized by catalysis of steel are major factors to reduce the adhesion strength of the diamond film to steel. One of answers for these problems is to fabricate interlayer between the diamond film and steel. The difference of coefficient of thermal expansion and the catalytic effect of steel are reduced and avoided by interlayer covering the surface of steel. Based on these backgrounds, the diamond films were deposited on stainless steel with Ti interlayer and its friction properties with stainless steel ball were investigated.

2. Film deposition

Fig.1 shows the schematic of the test piece in this study. We used 20x20x4 mm AISI440C substrate, and its surface roughness was adjusted to Ra = 0.5 μm to improve the adhesion force of the diamond film. Ti interlayer was deposited on the stainless steel substrate by the magnetron sputtering. The sputtering condition is shown in Table 1. We chose Ti for interlayer because of its compatibility of carbon and steel, and flexibility. Thickness of Ti interlayer was changed to 1, 2 and 3 μm. Roughness of the test piece surface was kept after the sputtering.

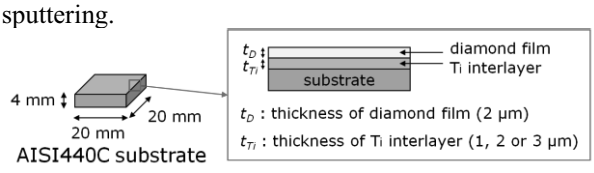

Fig.1 Schematic of the test piece

Table 1 Interlayer sputtering condition

Target	Ti
Ar pressure	1.3 Pa
DC power	100 W
Thickness of the interlayer	1, 2, or 3 μm (Controlled by process time)

Table 2 HF-CVD condition

Particle size of diamond seeds	Less than 0.5 μm
Flow rate of H_2	100 ml/min
Flow rate of CH_4	2.3 ml/min
Gas pressure	11 kPa
Temperature of filaments	2000 K
Thickness of diamond film	2 μm (5hour deposition)

Fig.2 Schematic of polished diamond surface

Polycrystalline diamond films were deposited on the substrate with Ti interlayer used by Hot Filament CVD (HF-CVD). Before the deposition, seeding treatment was done with diamond particle which diameter was less than 0.5μm. The deposition condition is shown in Table 2. After the deposition, the diamond film was polished up to Ra = 0.2 μm used by the same type of the diamond film. By this polishing, surface of the diamond film became the partly flat shape as shown in Fig.2.

A 2 μm-interlayer test piece was successfully polished up to Ra = 0.2 μm, but other test piece was delaminated during polishing. In a 1 μm-interlayer test piece, delamination occurred by the reason that stainless steel surface was not covered completely by Ti interlayer, and graphite synthesized at the spot where surface of the substrate was exposed. In a 3 μm-interlayer test piece, the diamond film was delaminated by buckling caused by excessive compressive stress of the film. Every time we observed delamination of the film, Ti surface appeared which indicates the low interface adhesion strength between Ti interlayer and the diamond film.

From these results, we decided the suitable thickness of Ti interlayer for the diamond film is 2 μm, and this test piece was used for further investigations hereafter.

3. Friction test

We investigated friction properties and durability of the diamond film with Ti interlayer by reciprocal ball-on disk test. Durability of the diamond film and the effect of repeated change in sliding direction were examined in the reciprocal test. The test condition is shown in Table 3. Three patterns of sliding speeds were investigated in this test.

In Hertzian elastic contact theory, the elastic contact radius between two balls is calculated by the following formula.

$$a = \sqrt[3]{\frac{3W}{4}\left(\frac{1-\nu_1^2}{E_1}+\frac{1-\nu_2^2}{E_2}\right)\Big/\left(\frac{1}{R_1}+\frac{1}{R_2}\right)} \qquad (1)$$

According to (1), the mean contact pressure between balls and the diamond films when the radius of the diamond film was assumed to be infinite was about 595 MPa at the beginning of the test.

Fig.3 shows the result of the friction test. The value of the COF at the middle of track (at the point of max sliding speed) was picked up, and smoothed with 10 points moving average. COFs obtained in 0.75 cm/s and 5.0 cm/s had almost same trend. However, the COF of 10 cm/s was scattered and showed the lowest value of the 3 sliding speeds. Fig.4 shows the raw data of COFs in foreword of sliding. COFs of 0.75 cm/s and 5.0cm/s showed almost stable value through the one way sliding. On the other hand, the COF of 10 cm/s was scattered in Fig.4. The reason of the vibration in the COF obtained in 10 cm/s was natural vibration of the tribometer. It is shown that the vibration of the COF in 10 cm/s test was synchronized with natural vibration of the tribometer in Fig.5. From these data, it can be said that the vibration of the COF in 10 cm/s test in Fig.3 was caused by natural vibration of the tribometer.

In each test speed, the wear track on the diamond film was not damaged so much except that the flat areas became slightly larger than before the friction test, and delamination was not occurred. The diameter of wear scar of the ball was about 0.3 mm in each test. In the additional 10,000 cycles test, COFs showed almost same trends and conditions of wear tracks and balls showed no significant changes.

4. Summary

To investigate the possibility of partly polished polycrystalline diamond films with Ti interlayer as a solid lubricant, friction properties and durability of the diamond film with 2 μm Ti interlayer were examined by reciprocal ball-on disk test. The diamond film endured the sliding under contact pressure of about 595 MPa and showed stable COFs value about 0.1 after 4,000 cycles in the friction test of 0.75 cm/s and 5.0 cm/s maximum speed at the reciprocal friction test. The same results were obtained in the additional 10,000 cycles test. From these experimental results, it can be said that the partly polished polycrystalline diamond film with Ti interlayer is a quite fine solid lubrication film under the lightweight conditions. Friction properties between the diamond film and steel balls under bigger load, and more detailed conditions of wear tracks and balls after the friction test will be investigated in near future.

Table 3 Reciprocal friction test condition

Equipment	Standard Tribometer (TRB) (CSM instruments)
Test piece	2 μm-interlayer piece
Max sliding speed A	A = 0.75, 5.0 or 10 cm/s
Sliding speed v	$v = A\sin(\omega t)$, ω: angular velocity
1/2 amplitude	0.75 cm
Load	1 N
Ball	AISI 52100 (ϕ6 mm)
Number of cycles	4000

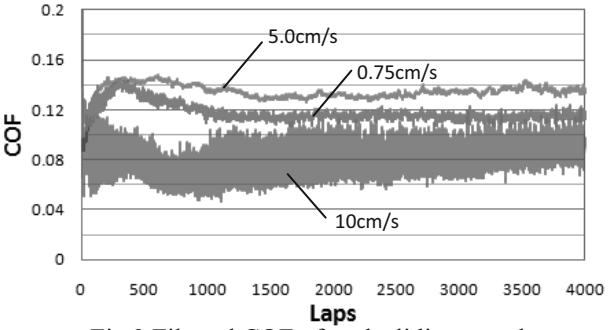

Fig.3 Filtered COF of each sliding speed

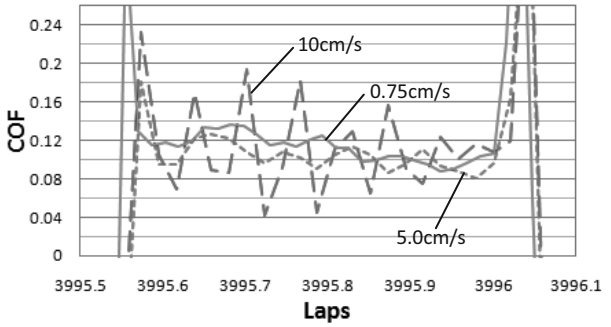

Fig.4 Raw data of COF

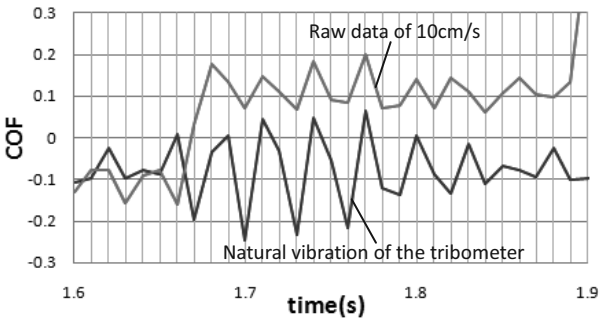

Fig.5 Natural vibration of the tribometer

References

[1] T. Takeno, et al, Diamond and Related Materials, 14 (2005), 2118.
[2] H. Miki, et al, Diamond and Related Materials, 17 (2008), 868-872.

Eighth International Conference on Flow Dynamics
November 9 - November 11, 2011

Continuous Membrane Deformable Mirror for Next-generation Astronomical Observation

Tong Wu, Masayuki Akiyama, Toshiyuki Takagi, and Kazuhiro Hane
Tohoku University, Sendai 980-8579, Japan
wu@hane.mech.tohoku.ac.jp

ABSTRACT

We propose, design and fabricate here a novel electrostatically actuated continuous membrane deformable mirror for the next generation astronomical observation. To get a large stroke, a bimorph spring array is used to generate a large air gap between the mirror membrane and the electrode. A 3.4mm×3.4 mm deformable mirror with a underlying 4×4 electrode array is fabricated by utilizing plasma activated bonding and the subsequent all-dry release process. The fabricated deformable mirror deformed 3.8μm at 130V.

1. Introduction

Deformable mirrors (DMs) have been successfully used in adaptive optics (AO) to correct the optical aberrations. A variety of different DMs based on micro electromechanical system (MEMS) technology have been developed. DMs based on piezo-electric actuation which suffer from hysteresis problem are not preferable for the open-loop control in astronomical application. In comparison, DMs based on electrostatic actuation are free of hysteresis but limited in the stroke [1]. Although a segmented electrostatic DM was demonstrated to possess a large stroke (~10μm) [2], diffraction due to the gaps between segmented elements downgrades the optical performance. In addition, up to 20μm stroke is required for the applicable adaptive optics for the next generation astronomical observation. Therefore, it is of great importance to develop a large stroke continuous membrane deformable mirror.

In this study, we demonstrate a novel structure of continuous membrane electrostatically actuated DM by combining wafer bonding process and bimorph spring array. The design and the fabrication process are first introduced. The static driving experiment is also implemented.

2. Structure Design

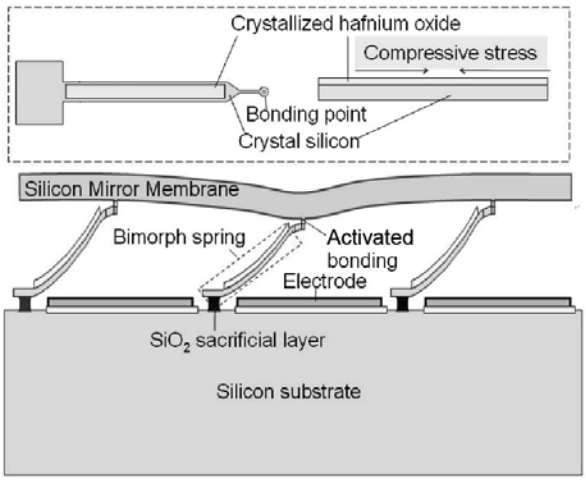

Fig. 1 Schematics of the deformable mirror

As schematically illustrated in Fig. 1, a single-crystal silicon mirror membrane (~2μm) is bonded at the end of the bimorph spring which is comprised of an HfO_2 layer and a silicon layer. The HfO_2 layer is then crystallized to generate a large compressive film stress which bends the bimorph spring out of the electrode plane and elevate the mirror membrane. Other than the fixed micro post array, the soft bimorph spring flexure can enlarge the stroke at low voltage actuation. The electrode array is laid on the silicon substrate to locally actuate the mirror. As shown in Fig.2, a 3.4mm×3.4 mm mirror with a underlying 4×4 electrode array is designed. The electrodes are all 500μm square and the pitch between each one is 100μm for the space of the wiring lines.

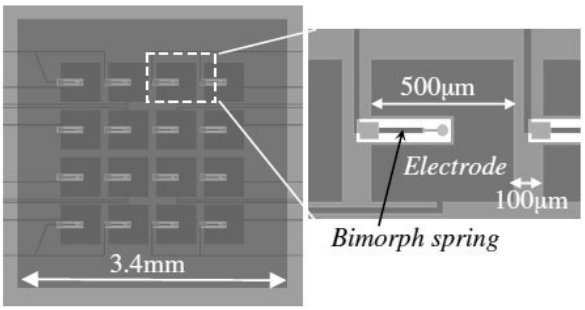

Fig. 2 Main design of the deformable mirror

3. Fabrication Procedure

The proposed DM is fabricated from two parts which are called actuator chip and mirror chip, respectively. Actuator chip loaded with bimorph spring and electrode array is fabricated as shown in Fig.3 (a). The starting SOI wafer includes 10μm device layer which is first patterned and etched ~8μm to from the bonding points. Subsequently, the device layer is patterned and etched to the buried oxide layer to form the silicon layer of bimorph springs and the electrodes. Then, the HfO_2 layer is deposited and patterned by using liftoff technique. Mirror chip fabrication starts from a SOI wafer with 2μm silicon device layer. As illustrated in Fig.3 (b), the device layer is first etched to from the area of mirror membrane. Second, the back side of the wafer is etched to form the alignment marks for the following alignment prior to bonding. As shown in Fig.3 (c), the mirror membrane is bonded with the bonding points of the bimorph spring array on the actuator chip by utilizing Si-Si plasma activated bonding technique. Then, the handle layer of actuator chip is etched to the buried

oxide layer by using silicon deep reactive ion etching (DRIE). Similarly, the handle layer of mirror chip is also removed. To release the mirror membrane and the bimorph spring array, the buried oxide layers of the actuator chip and the mirror chip are removed by using CHF3 plasma dry etching. At last, HfO_2 is crystallized in 800℃ and the mirror is elevated.

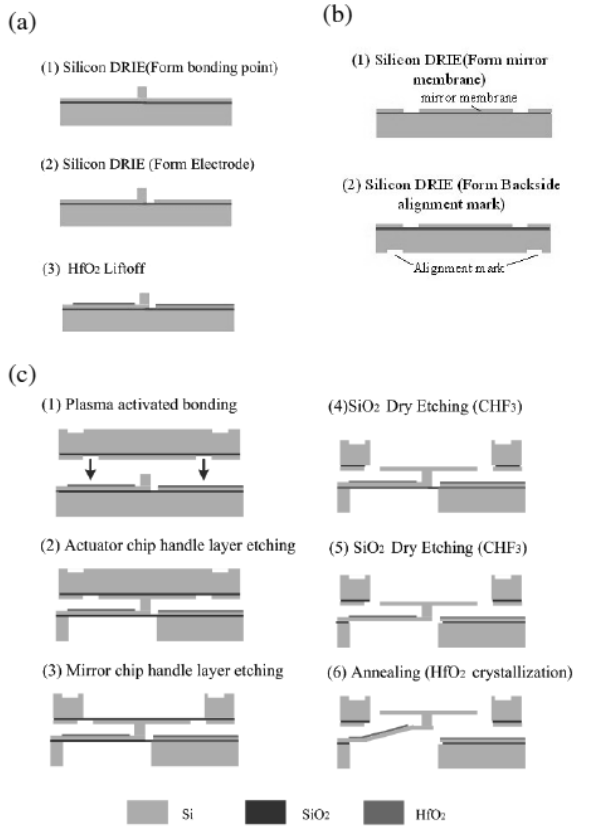

Fig.3 Fabrication process

4. Result and Discussion

The optical micrograph of the fabricated DM is shown in Fig.4. The bimorph spring array under the mirror membrane is shown in Fig.5 (a). As shown in Fig. 5(b), the bimorph spring deflected about 20μm and thus created about 28μm electrode gap with consideration of the 8μm-high bonding points. This value is much lower than the expected 58μm electrode gap. The reason for this mismatch is because the thickness of the silicon layer of the bimorph spring was fabricated larger than the designed thickness in the first prototype. Static deflection of the DM was characterized using a phase-shifting interferometer (Polytec MSA500). The 900μm×670μm mirror surface at the top of the center electrode was measured at different drive voltage. The surface height profiles at 0V and 130V are shown in Fig.6. The mirror initially deflected 160nm upward and deformed 3.8μm at 130V. A symmetrical bimorph deflection structure was also designed and fabricated to suppress the undesirable slope at the bonding point. The design was shown in Fig. 7(a) and the deflection was shown in Fig. 7(b). A flat profile at the bonding point was realized by using the symmetrical structure. The deflection was measured to be 21μm. A larger stroke is expected to achieve by enlarging the deflection of the bimorph spring to create a larger electrode gap.

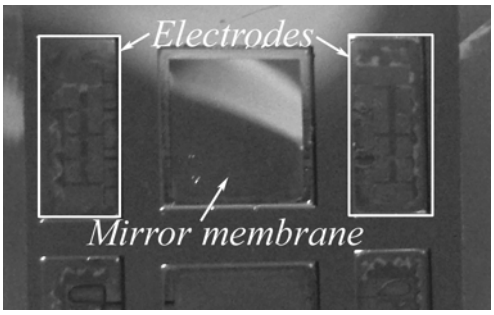

Fig. 4 Fabricated deformable mirror

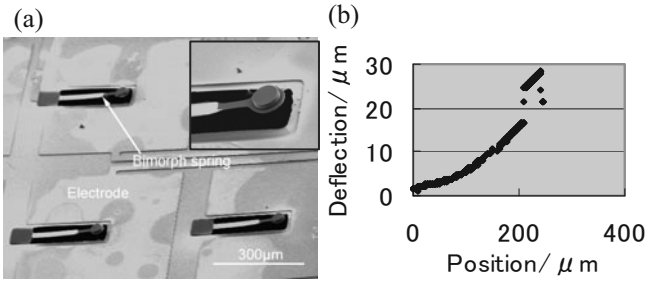

Fig.5 (a) Bimorph springs and electrodes; (b) Deflection of the bimorph spring

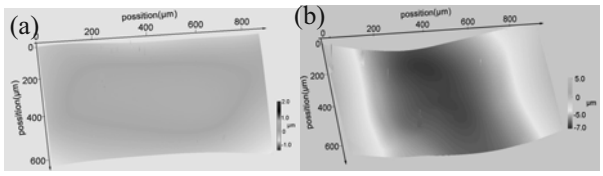

Fig. 6 Mirror profile at (a) 0 V, and (b) 130 V

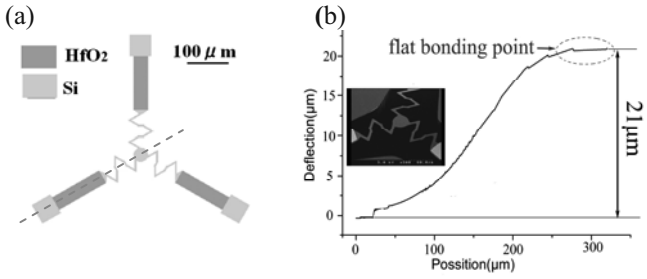

Fig.7 (a)symmetrical bimorph spring structure; (b) deflection of the fabricated spring

References

[1] I. W. Jung, Y.-A. Peter, J.-S. Wang, "Single-Crystal-Silicon Continuous Membrane Deformable Mirror Array for Adaptive Optics in Space-Based Telescopes", IEEE J. Sel. Top. Quantum Electron. , Vol.13 (2), pp.162-167, 2007.

[2] M. A. Helmbrecht, T. Juneau, M. Hart, N. Doble, "Performance of a high-stroke, segmented MEMS deformable-mirror technology", Proc. SPIE, Vol.6113, pp.1-10, 2006.

Eighth International Conference on Flow Dynamics
November 9 - November 11, 2011

Vacuum Package Method Based on Reflowing of Low-Melting Temperature Metal for MEMS

Hoang Manh Chu[1], Jun Mizuno[2], Toshiyuki Takagi[3] and Kazuhiro Hane[1]
Department of Nanomechanics, Tohoku University, 6-6-01 Aza Aoba, Aramaki, Aoba-ku, Sendai 980-8579, Japan[1]
Micro System Integration Center, Tohoku University, 6-6-01 Aza Aoba, Aramaki, Aoba-ku, Sendai 980-8579, Japan[2]
Intelligent Fluid Systems Division, Tohoku University, Katahira 2-1-1, Aoba-ku, Sendai 980-8577, Japan[3]
E-mail: chu@hane.mech.tohoku.ac.jp

ABSTRACT

We present a high effective vacuum seal method, which is based on the reflow of low melting temperature metal combining with anodic bonding. The package method eliminates contaminant caused by package process. A deformable diaphragm structure similar to a capacitive pressure sensor is used to investigate the proposed package method. The yield of the proposed package method is confirmed up to 100% compared to 25% of the novel package method. This vacuum packaging method can be implemented to remove air damping for optimal performance of mechanical resonators.

1. Introduction

Vacuum package is considered to be an effective way which is not only to protect devices but also to decrease the consumption power thanks to the high quality factors of packaged devices. Vacuum package can be carried out using different methods such as anodic bonding, deposition sealing, and glass frit bonding [1, 2]. Anodic bonding has been accepted for not only common MEMS devices but also optical MEMS devices. This is due to the strength of bonding between pyrex glass and silicon, transparence of pyrex glass to light. However, the vacuum packaging based on anodic bonding contains several limits. The bonded contact surface between pyrex glass and silicon wafers is required high flatness for hermetical seal, while evacuation is performed on the interface between glass and silicon wafers without perfect flatness. In addition, to use commercial vacuum packaging machines such as EVG bonder and EVG aligner, all of bonding sample setups are almost followed a fixed process. Therefore, the evacuation for packaging cavity becomes difficult even long evacuating time. The vacuum level in the package is often not uniform for all wafer level packaged devices.

In this paper, we propose a high vacuum package method which is simple and high-yield for commercial package machines.

2. Packaging Method

Figs. 1 (a) and (b) demonstrate conventional and proposed package methods, respectively. The method demonstrated in Fig. 1 (a) is performed, which benefits by non-perfect flatness of bonding interface between the silicon wafer and the pyrex glass wafer for evacuating the hermetically sealed cavity. This method is not easy even long evacuating time. The vacuum in cavities is often not uniform for wafer level package. To solve this problem, the package method based on combining anodic bonding with reflow of low melting tempeature metal is proposed (Fig. 1 (b)). The Au/Sn/Cr layers are designed such as sacrificial poses to form gap for evacuating cavity having defined device before the hermetical seal process is performed by anodic bonding. The trenches prevent contaminant routing into the bonding interface between the pyrex wafer and the silicon wafer and the hermetically sealed cavity.

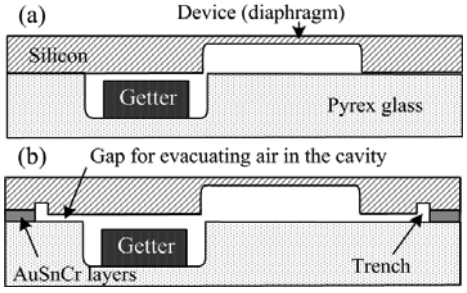

Fig. 1 Schematic of packaging methods: (a) conventional package method, and (b) proposed package method.

3. Design and Fabrication

Device structure for testing package technology is shown in Fig. 2 (a). The package includes two main parts, silicon and pyrex parts. The silicon part is fabricated from a SOI wafer having 10μm thick top device layer, 1μm thick buried oxide (BOX) layer and 200μm thick handle layer. The SOI wafer having cylindrically structured devices is fabricated by an inductive coupled plasma reactive ion etching (ICP-RIE) machine from backside to BOX etching top layer. The cylindrically structured devices with diameters from 250 to 1750μm are designed and fabricated on a 2 x 2 cm^2 SOI wafer for estimating the vacuum level in the package. To form poses for depositing Au/Sn/Cr layers, the poses are also designed and fabricated on the SOI wafer. Moreover, it is easier for the reflow of Au/Sn/Cr layers in package process, the poses are lower than compared with the surface of device layer a height t_s. The thickness of deposited Au/Sn/Cr layers is t_{AuSnCr} (Fig. 2 (d)). To form sacrificial gap for evacuating air in the cavity before packaging, t_{AuSnCr} have to be larger than t_s. To evacuate residual gases generating in anodic bonding process, a non-evaporable getter (NEG) is fixed in the patterned pyrex part.

The pyrex glass wafer having the cavity for fixing the NEG is patterned by liftoff process and wet etching

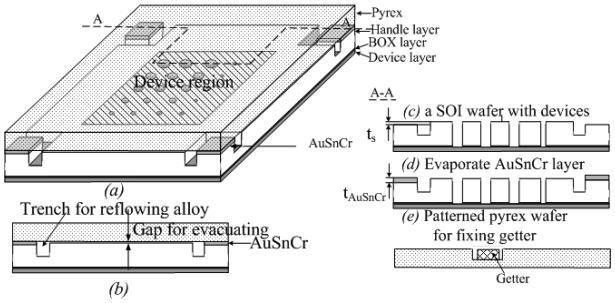

Fig. 2 (a) – (b) schematic of packaging structure and (c) – (e) package process.

with protective mask of Cr/Au in a 49% HF solution. The structures on the SOI wafer are fabricated by ICP-RIE and then sputter deposited Au/Sn/Cr poses using a shadow mask.

4. Vacuum packaging experiment

The package using anodic bonding which usually includes a silicon wafer with fabricated devices and pyrex lid is aligned in an alignment system. After aligned, the silicon wafer is put in intimate contact with

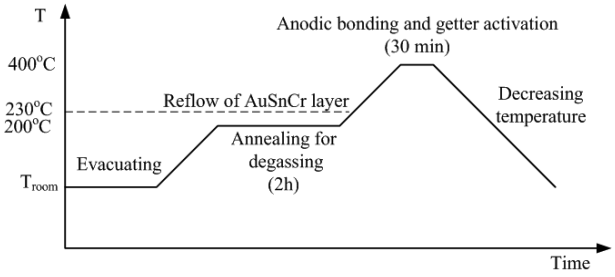

Fig. 3 Temperature process flow for packaging process.

the pyrex lid by flag and force. It is due to the sacrificial air gap formed by sputtered Au/Sn/Cr layers, the SOI wafer and pyrex glass wafer is contacted via the Au/Sn/Cr poses as shown in Fig. 2 (b). Bonding process is described detail in Fig. 3.

5. Results and discussion

Fig. 4 (a) shows a SOI wafer with diaphragms which are fabricated using ICP-RIE. As seen from topography in Fig. 4 (b), the 200μm x 200μm Au/Sn/Cr poses with the height of 2 μm is sputter deposited on the 2000 μm x 2000 μm silicon poses separated from the silicon area having bonding area and diaphragms by trenches.

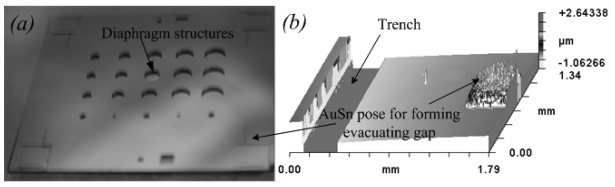

Fig. 4 (a) silicon part with diaphragms of different diameters and (b) topography of an Au/Sn/Cr layer deposited on a silicon pose.

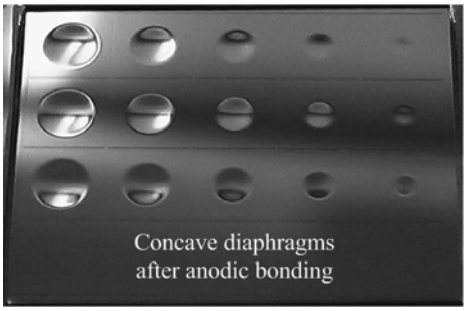

Fig. 5 Optical image showing concave surfaces of diaphragms after packaging.

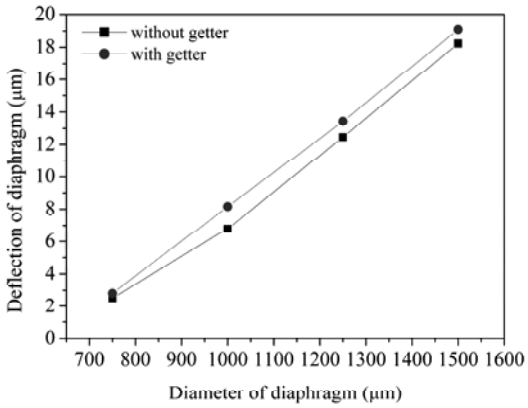

Fig. 6 Center deflection of diaphragm investigated as a function of diameter.

Fig. 5 shows the device after anodic bonding in a vacuum chamber of 0.5 Pa. The surfaces of diaphragms become concave after packaging. The yield of packaging is up to 100%. When we perform packaging process without using sacrificial Au/Sn/Cr layers for pre-evacuating air in the cavity, the package yield is only obtained 25%. Fig. 6 shows the center deflection of diaphragm investigated as a function of diameter sealed with and without getter, respectively. The center deflection of diaphragm in the case of getter sealing is larger than that without getter. Thus, the getter is also effective for absorbing produced gases during bonding process. The vacuum in the package is being investigated, which is based on a capacitive absolute pressure sensor.

6. Conclusions

A high-yield vacuum package method was presented, which was based on combining the low temperature reflow process of metal with anodic bonding. Any metal or alloy having melting temperature lower than the anodic bonding temperature is applicable not only for Sn metal. The method is used for commercial package machines.

References

[1] D. Sparks, S. M. Ansari and N. Najafi, J. Micromech. Microeng. **15** (2005) pp. 1560–1564.
[1] M. Esashi, J. Micromech. Microeng. **18** (2008) 073001 (13pp).

Eighth International Conference on Flow Dynamics
November 9 - November 11, 2011

Stabilization of Hardware in the Loop Simulation

Fumihito Sugai, Xin Jiang, Satoko Abiko, Atsushi Konno and Masaru Uchiyama.
Dept. of Aerospace Engineering in Tohoku University. 6-6-01 Aobayama, Sendai 980-8579, Japan
{sugai, jiangxin, abiko, konno, uchiyama} @space.mech.tohoku.ca.jp

ABSTRACT

In order to develop space robotic technologies, the feasibility and reliability of the systems have to be verified by repetitive tests. Hardware in the loop (HIL) simulation is one of the effective ways to simulate micro-gravity condition on the earth. However, simulating a continuous contact by a HIL simulation, there is a problem that the kinetic energy increases. This paper presents that the energy increase is caused by dead-band processing to force/torque data and suggests a compensation method.

1. Introduction

Hardware in the loop(HIL) simulation is one of the effective methods to test space robotic operations on the ground. The HIL can emulate three dimensional relative motion of a space robot with respect to a certain target in micro gravity environment using numerical dynamic calculation and hardware to which physical interaction occurs (Fig. 1). However, the HIL simulator generally suffers from a problem of energy increase, the coefficient of restitution exceeds one in the collision emulated by the HIL simulator, which does not happen in reality. This problem occurs by mainly two causes, delay time in the loop and dead band in force/torque(F/T) measuring. A number of researches tackled the energy increase problem due to the delay time [1–3]. On the other hand, the influence of the dead band in F/T measuring has not clearly been discussed yet. When the HIL simulator is used to simulate a continuous contact, such as a grasping of a target by an on-orbit space robot, the influence of the dead band becomes more crucial.

This paper proposes two compensation methods to cope with the energy increase due to the dead band in F/T measuring. The effectiveness of the proposed methods are verified by single-axis collision experiments.

2. The HIL simulator and the effect of dead band

As shown in Fig. 1, the HIL simulator consists of a motion table, a numerical simulator and a physical model that is designed as same as a part of the corresponding real target. The physical model is affected by physical interaction or contact. The physical contact is measured by a F/T sensor installed between the motion table and the physical model. The numerical simulator calculates dynamic motion of the entire robotic system due to the contact. Then, the relative motion is demonstrated by the motion table based on calculation result in the numerical simulation. When the environment is modeled with certain stiffness, the total HIL system can be modeled as shown in Fig. 2. In Fig. 2, dead time means a delay due to a lowpass filter and servo delay which is a cause to increase the energy of the system. To compensate the effect of the dead time, the method proposed in [3] is applied, whose advantage is not only to guarantee the stable system but also to enable us to determine any desired value of coefficient of restitution. Besides, in this simulation process, the dead band in F/T measuring is necessary to avoid unexpected motion of the HIL simulator due to the noise and drift data in the F/T sensor. And, the dead band means that when input data is smaller than threshold value, output data is zero (Fig. 2). However, this dead band also causes energy increase in the system. Hereafter, we analyze the effect of the dead band by numerical simulation, in which a floating object collide, with stiff environment. Fig. 3 shows the result of the numerical simulation. In general, energy must be conserved or consumed, and hence integrated power must be zero or negative. However as shown in Fig. 3, the power integrated during a contact becomes positive when a dead band is set to F/T sensing, which shows that the energy is increased. Due to the dead band, a force lower than threshold is regarded as zero, and hence the ignored force causes the energy increase. The total power during a contact is calculated as follows.

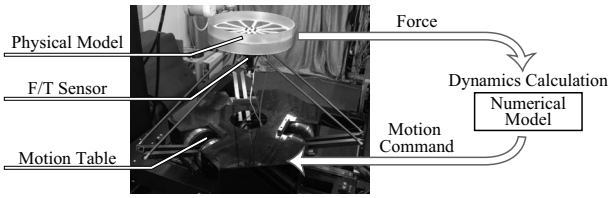

Fig. 1 Concept of HIL.

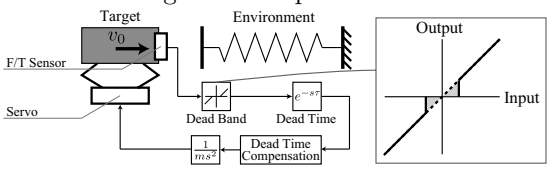

Fig. 2 Numerical simulation model.

$$\int_{\tau+t_{db}}^{\frac{\pi}{\omega_0}+\tau-t_{db}} vf dt = \frac{kv_0^2}{2\omega_0^2}\sin(2\omega_0\tau)\sin(2\omega_0 t_{db}), \quad (1)$$

where v_0 is initial velocity, k is stiffness of the spring, w_0 is natural vibration frequency, τ is the dead time of system. Eq. (1) suggests that the additional energy to the system depends on the v_0. Be-

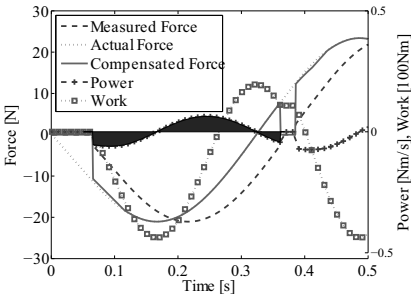

Fig. 3 Numerical simulation with dead band Type A.

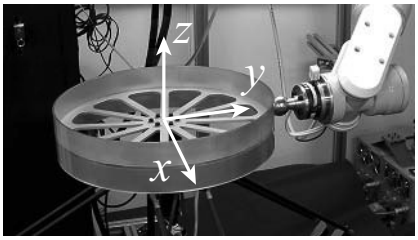

Fig. 4 Experimental setup.

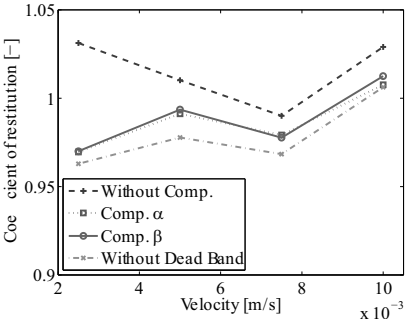

Fig. 5 Result of dead band compensation.

sides, if the duration in the dead band t_{db} equals to zero, it can be easily estimated that the system does not receive any additional energy as the case without the dead band. This analysis gives us the new insight to design the compensation methods presented in the following chapter.

3. Compensation methods for dead band

3.1 Compensation method α

The first proposed method absorbs the increased energy by adding a virtual damping. The coefficient of the virtual damping γ is determined by desired coefficient of restitution by using the following equation.

$$E_a = \frac{mv_0^2}{2}(\varepsilon_{ref}^2 - 1), \tag{2}$$

where ε_{ref} is a desired coefficient of restitution. E_a is work of one contact. On the other hand E_a is a function of γ. And γ is calculated to satisfy Eq. (2). Then the system's damping coefficient is set to γ.

3.2 Compensation method β

The second method compensates the increased energy by supplying the force lost in the dead band. In the HIL simulation, the measured force under the threshold of the dead band is before and after contact. However it is impossible to estimate the duration in the dead band before the contact. Therefore we provide supplementary force for $2t_{db}$ just after contact. The supplementary force F'_{comp} is calculated by the following equation.

$$F'_{comp}(t) = F_{comp}(t_b) + \dot{F}_{comp}(t_b) \cdot (t - t_b), \quad (t_b < t < t_b + 2t_{db}) \tag{3}$$

where F_{comp} is compensated force for delay time shown in [3], t_b is the moment when F_{comp} equals to the threshold of dead band. By virtue of the compensation β, kinetic energy during a contact is expressed as follows:

$$E_b = \int_{\tau+t_{db}}^{\frac{\pi}{\omega}+\tau-t_{db}} p(t)dt + \int_{\frac{\pi}{\omega}+\tau-t_{db}}^{\frac{\pi}{\omega}+\tau+t_{db}} F'_{comp}\dot{x}dt. \tag{4}$$

Without supplying additional force calculated by Eq. (3), the total energy E_b is positive because the second term of Eq. (4) is zero. On the other hand, with proper compensation force, the total energy E_b becomes close to zero.

4. Experimental verification

The experimental verification is carried out. Fig. 4 shows the experimental setup. In the experiment, a rigid body is moved along y axis and collides with environment. The motion of the rigid body before and after the collision is demonstrated. The mass of the rigid body in the numerical model is 350 [kg]. The rigid body moves with four patterns of initial velocity; v ={0.0025, 0.005, 0.0075, 0.01} [m/s]. The threshold of dead band in the F/T measuring is set to be 0.5 [N]. In the experiments, we measured the coefficient of restitution in the case without dead band, with dead band, with dead band and compensation α and with dead band and compensation β. Each case is carried out 5 times.

Fig. 5 shows the experimental result and it shows the average of 5 trials. This figure obviously shows that the coefficient of restitution in the case with dead band is larger than that in the case without the dead band. This means that the dead band induces the energy increase in the system. Especially, it is clearly shown that the coefficient of restitution in the case with dead band, but no compensation becomes more than 1, which does not occur in reality. On the other hand, in the case with compensation α and β, the coefficient of restitution becomes smaller than without compensation even though with the dead band. The experiment demonstrates the effectiveness of the proposed compensation methods.

5. Conclusion

This paper proposed two compensation methods to guarantee the stability and the fidelity of the HIL simulator. The experiment verified the validity of the proposed compensation methods.

References

[1] S. Ananthakrishnan et al. "Role of estimation in real-time contact dynamics enhancement of space station engineering facility," Robotics & Automation Magazine, IEEE, Vol. 3, pp. 20–28, 2002.

[2] M. Inoue et al. "Development of the Docking Dynamics Simulator," Tran. Society of Instrument and Control Engineers, Vol. 28, No. 11, pp. 1306–1313, 1992.

[3] K. Osaki et al. "Delay Time Compensation for a Hybrid Simulator," Advanced Robotics, Vol. 8, No. 9, pp. 1081–1098, 2010.

Eighth International Conference on Flow Dynamics
November 9 - November 11, 2011

Simulation Study of Transport Phenomena in Supercooled Cu-Ti-Zr Liquids

Hiroyuki Fujii[1] and Michio Tokuyama[2, 3].
[1]Graduate School of Engineering, Tohoku University, Sendai 980-8579, Japan
[2]Institute of Fluid Science,
[3]World Premier International Research Center,
Advanced Institute for Materials Research, Tohoku University, Sendai 980-8577, Japan
fujii@athena22.wpi-aimr.tohoku.ac.jp

ABSTRACT

Attempt to extract characteristic temperatures from dynamics is one of significant tasks on glass transition phenomena. In this paper, four characteristic temperatures are obtained from the long-time self-diffusion by comparisons among theoretical works and molecular dynamics simulations on metallic glass formers $Cu_{60}Ti_{40-x}Zr_x$. It is shown that these dynamic temperatures could quantify thermodynamic including a thermal glass transition point and a peak point of the specific heat.

1. Introduction

Understanding of correlations between dynamics and statics is one of fundamental problems on glass transition phenomena. For this purpose, many researchers have proposed characteristic temperatures to specify static and dynamic quantities [1, 2]. In thermal descriptions, a glass transition temperature T_g is defined by the specific volume and heat [3, 4]. Meanwhile, a dynamic T_g is characterized by the self-diffusion coefficient, viscosity, and so on [5]. Despite many efforts, an understanding of how the temperatures specify physical quantities is still incomplete. Thus, in this paper, we try to obtain characteristic temperatures from the long-time self-diffusion coefficient D_S^L by carrying out molecular dynamics simulations on metallic glass formers $Cu_{60}Ti_{40-x}Zr_x$ for different compositions x.

Recently, one of the present authors (M. T) has proposed theoretical curves for D_S^L, which are valid for liquid and supercooled liquid in equilibrium [6]. Then, a separation among simulation results and the curve could represent a dynamical T_g, below which a system is no longer in equilibrium. The above framework is adopted in this paper. Hence, several characteristic temperatures are determined from D_S^L on Cu analyzing by the theories. Moreover, the specific volume and heat are measured to obtain a thermal T_g. We explore correlations between statics and dynamics in terms of the temperatures.

In the next section, we explain current simulation models. We discuss simulation results in section 3 and conclude and summarize in section 4.

2. Simulation Models

In this section, we shall describe details of molecular dynamics (MD) simulation models on metallic glass-forming $Cu_{60}Ti_{40-x}Zr_x$ melts (x=20 and 30). Present models are based on Han and Teichler's works [7]. It has been confirmed that their simulation works quantitatively agree with experiment results by considering not only two-body potentials $U_{\alpha\beta}$ but also the electron gas potential E_{ele}. In [8], we have proposed simple models, where potential parameters are independent of compositions x, give qualitatively consistency with their results within a single-particle dynamics. Present systems are composed of N =10 976 atoms in a cubic at an atmosphere pressure p and constant temperature T under periodic boundary conditions. NpT ensembles are attained by using the Berendsen thermostat and barostat. Particle obeys the Newton equation via $U_{\alpha\beta}$ with the Stillinger-Weber potential [9], where parameter sets of the potential are referred in [7].

In the current paper, reduced units are used for plotting simulation results, which is based on parameters of Cu: energy ε_0 = 0.485 eV, length σ_0 = 2.275Å, and mass $m_0 = 1.054 \times 10^{-25}$ kg. Energy is order of ε_0, length is of σ_0, temperature is of $T_0(= [\varepsilon/k_B])$, and diffusion coefficient is of $\sigma_0 v_0$ with an average velocity $v_0 = \sqrt{(\varepsilon_0/m_0)}$. Mass of Ti and Zr are in units of m_0, that is $m_{Ti}/m_0 = 0.7533$ and $m_{Zr}/m_0 = 1.4356$. For more details of present simulations such as how to obtain equilibrium states, we can refer to Ref. 8.

3. Results and Discussion

In this section, we shall discuss simulation results. Simulation results are taken average over number of particles and ensembles. It is confirmed that thermal properties become stationary and the mean-square displacement on Cu sufficiently approaches a diffusive region in current simulation time.

In order to obtain characteristic temperatures from dynamics, we measure the long-time self-diffusion coefficient D_S^L of Cu. Cu is a main component in current systems and dynamics of Cu has an analogy in that of other components. A definition of D_S^L of component α is given as

$$D_L^S = \lim_{t\to\infty} \frac{1}{N_\alpha} \sum_i \frac{\left\langle \left[\vec{X}_i^\alpha(t) - \vec{X}_i^\alpha(0) \right]^2 \right\rangle}{6t} \quad , \qquad (1)$$

where $\vec{X}_i^\alpha(t)$ denotes a position vector of ith particle at time t, N_α number of particle, and < > ensemble average. Figure 1 shows simulation results for D_S^L on Cu as a function of inverse temperature. The simulation results are analyzed by two theoretical curves mentioned as following. At liquid region, D_S^L is described as a mean-field curve,

$$\frac{D_L^S}{\sigma_0 v_0} = \kappa^{-1} \left(\frac{T}{T_c} \right) \left(1 - \frac{T_c}{T} \right)^2 . \qquad (2)$$

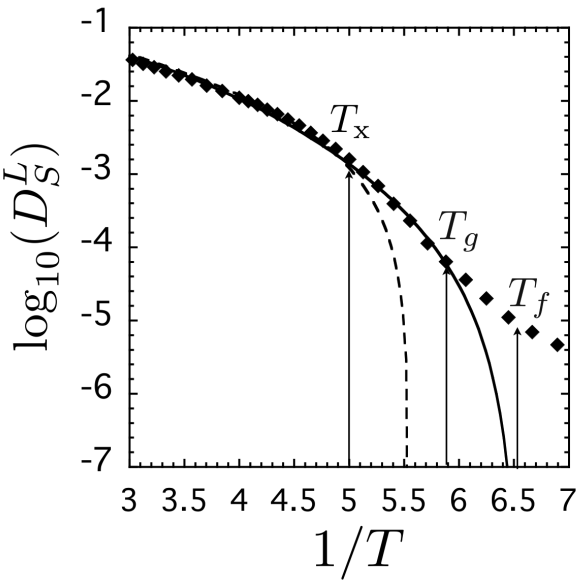

Fig. 1 Logarithm of D_S^L on Cu versus inverse temperature in $Cu_{60}Ti_{20}Zr_{20}$ (x=20). The broken line represents the mean-field curve Eq. (2) and the solid line the master curve Eq. (3). Characteristic temperatures are plotted in.

Here a material constant κ is computed to 9 in Cu, regardless of compositions x. A singular temperature T_c is determined by fitting. The master curve valid for supercooled liquid is given as

$$\frac{D_L^S}{\sigma_0 v_0} = \kappa^{-1}\left(\frac{T}{T_f}\right)\left(1-\frac{T_f}{T}\right)^{10/3}\exp\left[62\left(\frac{T_f}{T}\right)^{13/3}\left(1-\frac{T_f}{T}\right)^{10/3}\right], \quad (3)$$

where T_f is an extended singular temperature. In general, T_c is larger than T_f. As shown in Figure 1, separations among simulation results and theoretical curves appear around T_x and T_g. These points, T_x and T_g, would specify dynamic crossovers, that is, a strong supercooled liquid and glass transition temperatures, respectively. Below T_x, dynamics changes from the two-body to many-body correlation regimes. Dynamic T_g would be interpreted as a crossover point from a metastable to non-equilibrium states because the master curve argues that as long as a system is in equilibrium, the transport coefficient obeys a singular curve.

The above characteristic temperatures should be linked to thermal quantities. In order to confirm it, we measure the specific volume V and heat C_p as shown in Figure 2. In fact, a validity of the suggestion can be checked. Around T_x, C_p has a moderate peak, which implies that a particle can be more activated around T_x. From Figure 2, a good agreement between a thermal T_g and dynamic one is seen. Moreover, at $T_f < T < T_c$, C_p and V largely change. In other words, below T_f, C_p becomes constant. The fact is linked with the Arrhenius behavior of $D_S^L \sim \exp[\Omega/k_B T]$ with a constant activation energy Ω.

Values of the temperatures depend on compositions x. However, the theories indicate if temperature is normalized by T_f, simulation results for D_S^L in different x should be collapsed on a single master curve. In fact,

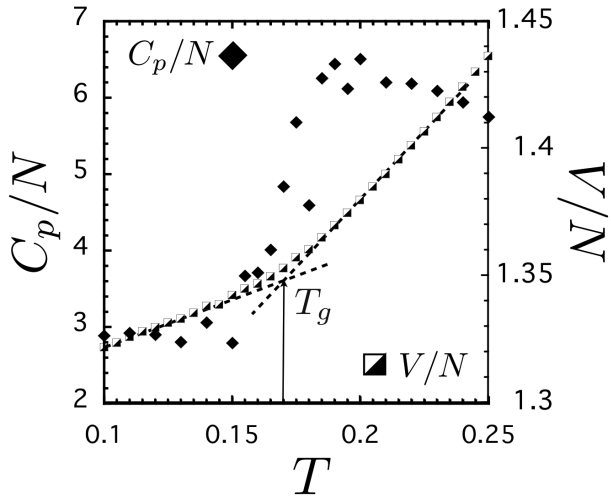

Fig. 2 Temperature dependence of the specific heat C_p/N and volume V/N per atom on $Cu_{60}Ti_{20}Zr_{20}$ x=20 at constant pressure. Broken lines denote linear extrapolations to estimate the thermal glass transition temperature T_g on V/N.

such master curves are seen in not only D_S^L but also C_p.

4. Concluding remarks

In order to explore associations between dynamics and statics, we have performed molecular dynamics simulations on metallic glass formers $Cu_{60}Ti_{20}Zr_{20}$ and $Cu_{60}Ti_{10}Zr_{30}$. We have extracted dynamic temperatures from D_S^L by comparing with the theoretical curves. Then, we have shown the dynamic temperatures are linked with thermal temperatures. The above discussions would be valid for other glass-formers.

Acknowledge

Present simulations were performed on the Advanced Fluid Information Research Center of the Institute of Fluid Science.

References

[1] P. G. Debenedetti and F. H. Stillinger, Nature, **410** (2001), 259.
[2] M. D. Ediger, C. A. Angell, and S. R. Nagel, J. Phys. Chem., **100** (1996) 13200.
[3] G. W. Scherer, *Relaxation in glass and composites* (Wiley, New York, 1986)
[4] A. Mandanici, M. Cutroni, A. Triolo, V. Mora, and M. Ramos, J. Phys. Chem., **125** (2006), 054514.
[5] Y. Zhang, M. Lagi, D. Liu, F. Mallamace, E. Fratini, P. Baglioni, E. Mamontov, M. Hagen, and S-H. Chen, J. Chem. Phys, **130** (2009), 135101.
[6] M. Tokuyama, Phys. Rev. E, **82** (2010), 041501.
[7] X. J. Han and H. Teichler, Phys. Rev. E, **75** (2007), 061501.
[8] H. Fujii and M. Tokuyama, Phys. Rev. E, **83** (2011), 021502.
[9] F. H. Stillinger and T. A. Weber, Phys. Rev. B, **31** (1985), 5262.

Eighth International Conference on Flow Dynamics
November 9 - November 11, 2011

Electromagnetic Non-destructive Evaluation of Creep Damage of Mod. 9Cr-1Mo Steel Focusing on High-frequency Magnetization Process

Kentaro Shibuya [1], Tetsuya Uchimoto [2], Toshiyuki Takagi [2]
*1: Graduate School of Engineering, Tohoku University, 2-1-1 Katahira, Aoba-ku, Sendai 980-8577, Japan
*2: Institute of Fluid Science, Tohoku University, 2-1-1 Katahira, Aoba-ku, Sendai 980-8577, Japan
shibuya@wert.ifs.tohoku.ac.jp

ABSTRACT

In this study, creep damage of mod. 9Cr-1Mo steel is evaluated based on electromagnetic nondestructive evaluation, focusing on high-frequency magnetization process. For this purpose, we employ magneto-optical Kerr effect measurement as well as non-linear eddy current method to identify the complicated structure change by creep damage. These two measuring methods show different correlation for thermal aging specimens and creep specimens, and there is a possibility that details of precipitation are evaluated based on the two different measurements.

1. Introduction

Mod.9Cr-1Mo steel is used for the boiler tubes of high-temperature steam lines in thermal power plants because it has anti-oxidative property and low isothermal expansion. However, they are exposed to severe conditions of 450-600 degrees celsius and 15-100 MPa. Under such conditions, creep damage is dominant as life-limiting mechanism. Therefore, some nondestructive methods are required for detection and evaluation of creep damage in mod. 9Cr-1Mo steel [1].

Magnetic properties have high sensitivity to micro-structures of materials, and they may change with change of precipitations and dislocation density due to creep damage. In a previous study, non-linear eddy current method was applied to evaluation of structure change of mod. 9Cr-1Mo steels, and feasibility was shown [2]. It was found that multi-frequency measurement can evaluate the both precipitation and dislocation change. However, complicated behavior of $M_{23}C_6$, MX and Z phase can not be identified by the method.

In this paper, we employ magneto-optical Kerr effect (MOKE) measurement as well as non-linear eddy current method to obtain the information of magnetization as well as eddy current. Then, the measured data of two different methods are discussed in comparison with structure change of crept mod. 9Cr-1Mo steels.

2. Experimental Setup

Figure 1 shows the experimental setup for MOKE and eddy current measurement. Magnetization can be evaluated by MOKE, measuring the rotation of polarization of light after the reflection [3, 4]. Polarized 3mW He-Ne laser beam is directed to the pole of sample and reflected to be measured by photo-detectors. Plane of polarization light of laser is set to 45° to the vertical direction and divided into two equal intensity beams by a polarizing beam splitter (PBS). They are detected by photo detectors (Si PIN photo diode) and differential signals are amplified. To magnetize the specimen and measure the eddy current, we use B-H loop analyzer (TESLA Corp. 1S-BH-500KS).

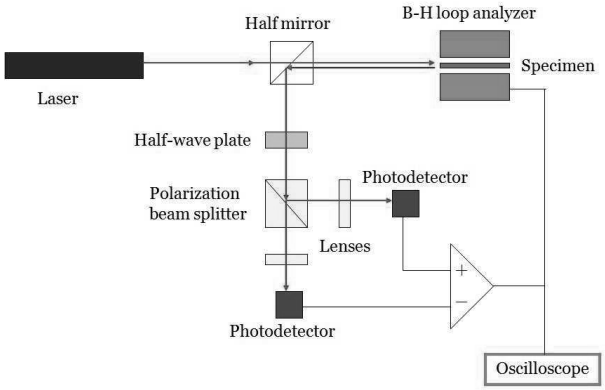

Fig. 1 Schematic drawing of experimental setup for MOKE and eddy current measurements.

Table 1 Chemical composition of Mod. 9Cr-1Mo steel (mass%).

C	Si	Mn	P	S	Cu	Ni
0.1	0.24	0.42	0.006	0.002	0.01	0.07
Cr	Mo	V	Nb	Al	N	Fe
8.68	0.94	0.19	0.08	0.012	0.0599	bal.

3. Specimens

Chemical composition of mod. 9Cr-1Mo steel specimens for this study are shown in Table 1. In this paper, 3 iso-thermal aging specimens and 6 creep specimens are used. Their test conditions are listed in Table 2. All of specimens have cylindrical shape with a diameter of 3mm and height of 30mm. The specimens are magnetized in the axial direction and the bottom

Table 2 Property of specimens.

Number	Temperature, ℃	Time, h	LMP
thermal-1	500	600	17600
thermal-2	550	4000	19400
thermal-3	600	7520	20800
creep-1	550	13.5	17390
creep-2	550	4418	19460
creep-3	600	710	19950
creep-4	600	11341	21000
creep-5	650	260	20690
creep-6	650	3095	21680

surface is polished for MOKE measurement.

4. Experimental Results

Amplitude of applied magnetic field is set to be 19 Oe, and test frequency is 50 kHz. Experimental results are averaged over 512 cycles. MOKE signals and pickup voltages of BH-loop analyzer were plotted as function of applied magnetic field. We use the parameter of "remanence equivalent" which is defined as the distance between two intersection points of vertical axis. For MOKE results, the data were normalized so that peak to peak value becomes the unit.

Figures 2 and 3 show the relationship between remanence equivalent and Larson-Miller Parameter (LMP). LMP is a parametric relation used to extrapolate experimental data on creep and rupture life of engineering materials, and defined as $T(20+\log t)$, where T is the absolute temperature, t is the rupture time. For the thermal aged specimens, results of B-H loop analyzer and MOKE show the same tendency; the signal increase with LMP. On the other hand, results of two measurements show different tendency for crept specimens; results of B-H loop analyzer increase with LMP, though results of MOKE decrease with increase of LMP. Behaviors of MX precipitation are different between thermal aged and crept specimens, though precipitation behaviors of $M_{23}C_6$ are almost same. MOKE may depends on the amount of MX precipitation, and microstructure analysis will be made for the verification.

5. Summary

In this study, creep damage of mod. 9Cr-1Mo steel is evaluated through the two different electromagnetic method: MOKE measurement and non-linear eddy current method to identify the complicated structure change by creep damage. Results of MOKE and eddy current method show that for thermal aging specimens

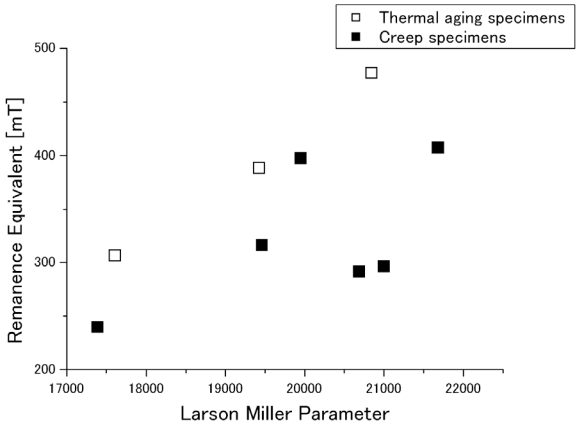

Fig. 2 Measurement results of B-H loop analyzer.

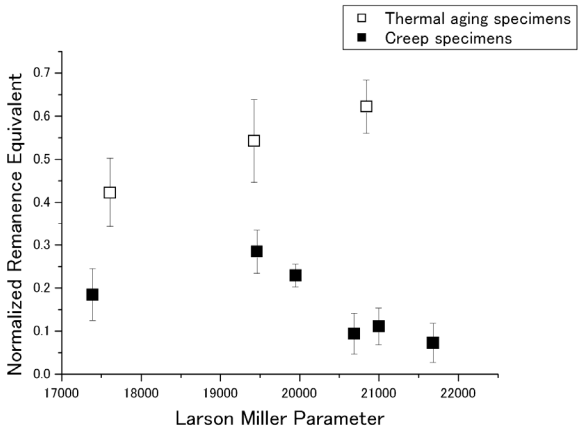

Fig. 3 Measurement results of MOKE.

ECT and MOKE show same tendency, though their results show different tendency for creep specimens. It may due to the different behavior of MX precipitation between thermal aged and crept specimens.

References

[1] F. Abe. Improvement of Creep Strength of Ferritic Steels for Coal-fired Power Plants. Journal of the Japan Welding Society. Vol.70. No.8. pp26-31 (2001)

[2] S. Ueno. Evaluation of Creep Damage of High Chromium Ferritic Steels Based on Non-linear Electromagnetic Response. Master thesis of Tohoku Univ. (2009)

[3] T. Katayama. Some Comments on Magnet-Optical Kerr Effect Measurement in Metallic Ultra-Tin Films. Journal of the Magnetics Society of Japan. Vol.25. No.1. pp.28-36 (2001)

[4] K. Sato. Elementary Course on Magneto-Optics. Journal of the Magnetics Society of Japan. Vol.23. No.4-1. pp.913-919 (1999)

Eighth International Conference on Flow Dynamics
November 9 - November 11, 2011

Slip Characteristics Identification for Biped Walking of a Humanoid Robot on Sand

Shunsuke Komizunai, Atsushi Konno, Satoko Abiko and Masaru Uchiyama.
Graduate School of Engineering, Tohoku University, 6-6-01 Aoba-yama, Sendai 980-8579, Japan.
{shunsuke, konno, abiko, uchiyama} @space.mech.tohoku.ca.jp

ABSTRACT

This paper presents slip-sinkage characteristics of sand as a fundamental research for realization of biped walking of a humanoid robot on sand. Dominant characteristic parameters of sand are identified through slip test using a test plate which is same size of foot of the robot.

1. Introduction

Most of studies for walking of biped robots have assumed stiff ground. Walking of biped robots on loose soil such as sand is a greatly challenging research in the field of humanoid robot. If a robot achieves stable walking on a loose soil, the robot can perform variety of tasks in various activities. To develop such an advanced technology, it is important to acquire proper knowledge of dynamic behavior of a biped robot on sand.

In the case of crawler typed machine, Muro estimated tractive performance of a bulldozer on the basis of a model between crawler and loose soil [1]. However, the study of walking on loose soil by the biped robot has not been investigated yet. The authors identified load-sinkage characteristics of sand to develop static contact model between the robot foot and sand [2]. However, slippage-sinkage characteristics of sand is not identified.

The aim of this paper is to identify slippage-sinkage characteristics of sand.

2. Dominant Parameter Identification

When a humanoid robot walks on loose soil, the soil is deformed by a sole slip as shown in Fig. 1. Therefore, in order for a humanoid robot to walk on loose soil, it is important to analyze the characteristics of slippage and sinkage. Static sinkage s depending on the slip is expressed by the following terramechanic equation [3]:

$$s = c_0 p^{c_1} d^{c_2}, \tag{1}$$

where p is the ground pressure, d is the slippage, c_0, c_1 and c_2 are characteristic values of the soil material. These parameters are required to be experimentally identified.

In order to identify the parameters, multiple linear regression analysis is performed on the experimental data : s, p, d. In logarithmic space, eq. (1) is expressed as follows:

$$\begin{aligned} \log_{10} s &= \log_{10}(c_0 p^{c_1} d^{c_2}) \\ &= c_2 \log_{10} d + c_1 \log_{10} p + \log_{10} c_0. \end{aligned} \tag{2}$$

Eq. (2) can be expressed as a linear function as follows:

$$Y = AX + B, \tag{3}$$

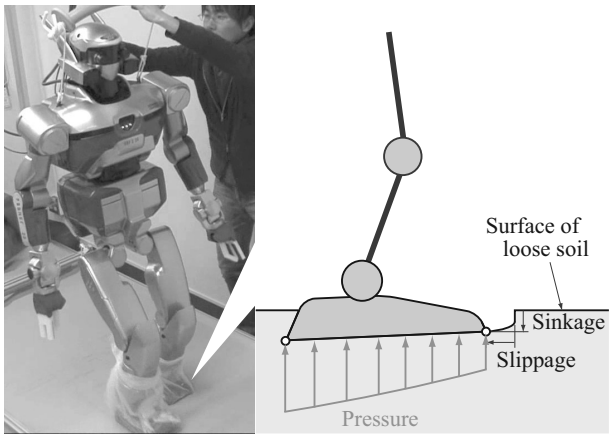

Fig. 1 Slippage and sinkage of foot of a humanoid robot on loose soil

where the symbols are defined as:

$$X = \log_{10} d, \tag{4}$$
$$Y = \log_{10} s, \tag{5}$$
$$A = c_2, \tag{6}$$
$$B = c_1 \log_{10} p + \log_{10} c_0. \tag{7}$$

In the first step, relationship between the slippage $\log_{10} d$ and the sinkage $\log_{10} s$ is analyzed in each pressure. X is expected to be in proportion to Y from eq. (3). Therefore, A and B can be calculated by linear regression analysis on the experimental data. In the second step, the pressure $\log_{10} p$ is expected to be in proportion to B from eq. (7). Therefore, $\log_{10} c_0$ and c_1 can be identified by linear regression analysis on the results of first step. Finally, c_2 is identified by taking an average of c_2 at each pressure.

3. Experimental system

Fig 2 shows an experimental setup to identify the slippage-sinkage characteristics. It consists of a test plate, a loading platform, a sand box and two dial gauges. The setup is fixed on strictly horizontal level. Two pairs of rails on vertical and horizontal frames constrain movement of the loading platform in the vertical and horizontal direction. The loading platform holds weights. The platform and the test

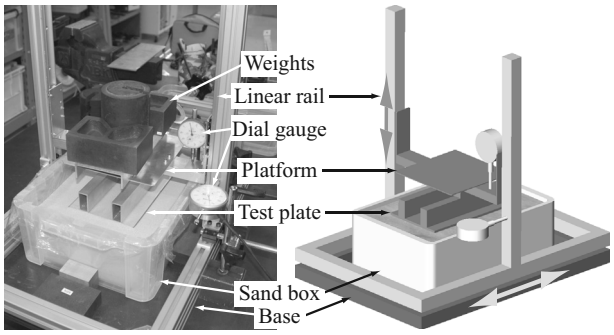

Fig. 2 Overview of developed test machine

plate are connected with common frame. The size of the test plate is equal to the foot of the humanoid robot (0.235×0.135 [m^2]). Therefore, it is not necessary to consider scale effect. Two dial gauges measure the sinkage and the slippage respectively when the loading platform is moved. The gauges can measure in the range between 0 [m] and 0.02 [m] with 1.0×10^{-5} [m] resolution.

The sand box of 0.370 [m] in length and 0.250 [m] in width is filled up to 0.095 [m] with sand. In this experiment, *Toyoura sand* is used that is one of the standard sand in the teramechanics.

To identify the parameters, $5 \sim 45$ [kg] weights are loaded on the weight table. The ground pressure is calculated by using the total load and the area of the test plate.

4. Experimental result

Fig. 3 shows the result of multiple linear regression analysis on measured pressure p, slippage d and sinkage s. The surface in the figure illustrates the relationship of p and d to s ($s = c_0 p^{c_1} d^{c_2}$). In the relationship, s monotonically increases depending on p and d. The mesh depicts the relationship between d and s ($s = 10^B d^{c_2}$) at each pressure. This is a result of the first linear regression analysis. The mesh is well approximated to the surface. From the first linear regression analysis, B and c_2 are estimated at each pressure.

Fig. 4 shows the relationship between $\log_{10} p$ and B. This is a result of the second linear regression analysis. It is observed that there is a positive correlation between $\log_{10} p$ and B. As the result of the linear regression analysis, the following relationship is identified:

$$B = 1.29 \log_{10} p - 7.04 \quad (R = 0.946), \tag{8}$$

where R is the coefficient of correlation. From the relationship, c_0 and c_1 are identified. Finally, c_2 is identified by taking an average at each pressure.

Consequently, c_0, c_1 and c_2 are identified as shown in Table 1.

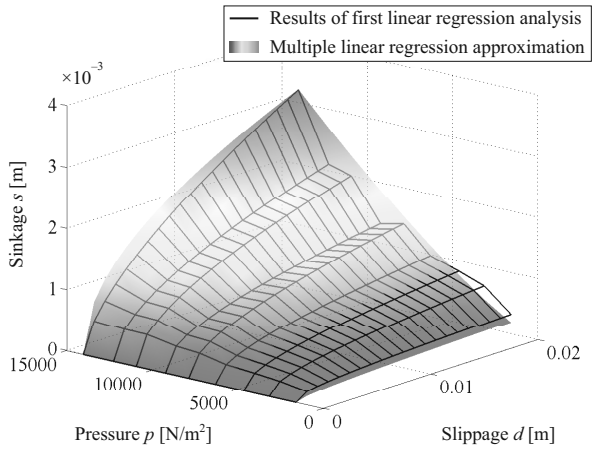

Fig. 3 Relationship of p and d to s

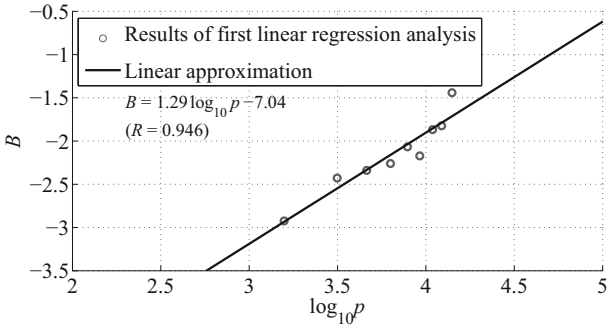

Fig. 4 Relationship between $\log_{10} p$ and B

Table 1. Identified characteristic parameters

	c_0	c_1	c_2
Value	0.904×10^{-9}	1.29	0.459

5. Concluding remarks

This paper presented slippage-sinkage characteristics of a standard sand to develop the static contact model between the robot foot and the loose soil. Static sinkage was measured when the test plate slips on sand. From the experimental data, dominant parameters were identified.

Using these characteristic parameters, the simulation will be performed to predict the walking behavior of the robot on sand.

References

[1] T. Muro: "Tractive performance of a bulldozer running on weak ground," in *Jour. of Terramechanics*, Vol. 26, No. 3, pp. 249–273, 1989.

[2] S. Komizunai, A. Konno, S. Abiko and M. Uchiyama: "Biped walking of a humanoid robot on sand," in *Proc. of the Seventh Int. Conf. on Flow Dynamics*, pp. 608–609, 2010.

[3] T. Muro: "Terramechanics," Gihodo Press, 1993 (in Japanese).

Eighth International Conference on Flow Dynamics
November 9 - November 11, 2011

Thickness Evaluation of Thermal Spraying on Boiler Tubes by Eddy Current Testing

Yohei Takahashi
School of Engineering, Tohoku University, 6-6 Aramaki aza, Aoba, Sendai Miyagi 980-8579, Japan
Ryoichi Urayama, Tetsuya Uchimoto, Toshiyuki Takagi
Institute of Fluid Science, Tohoku University, 2-1-1 Katahira, Aoba, Sendai Miyagi 980-8577, Japan
Hiroshi Naganuma, Kazufumi Sugawara, Tomoaki Sasaki
Technical Research & Development Center, Tohoku Electric Power Engineering & Construction Co. Inc, Shin-nakabori, Iidoi, Rifu, Miyagi-gun, Miyagi 981-0113, Japan
E-mail : takahashi@wert.ifs.tohoku.ac.jp

ABSTRACT

This paper discusses the feasibility of thickness evaluation of Ni-based alloy coating sprayed on type 304 austenitic stainless steels by swept frequency eddy current testing which measures the impedance spectra of coil. Comparing the experimental signals with the numerical ones, the electromagnetic models of coating are made. Using these models, the inverse analyses are conducted. The coating thicknesses are estimated within the maximum error of 22μm.

1. Introduction

Boiler tubes in thermal power plant are used in hot corrosive environment, and thermal spraying is applied on the surface of tubes for mitigation of abrasion[1]. Cracking, delamination, and thinning of thermal spraying can occur due to aging degradation and coating thickness should be non-destructively evaluated for the management of boiler tubes.

Ni-based alloy used for spray coating is conductive materials, and eddy current testing has a capability of evaluating the thickness of Ni-based spray coating. In this problem, factors that affect eddy current signals are many such as lift-off surface roughness and so on.

In this paper, eddy current testing method is applied to the thickness evaluation of thermal spraying and its feasibility is discussed. Impedance spectra are measured by impedance analyzer sweeping the test frequency. Numerical simulation is also carried out to discuss the electromagnetic model of spray coating and shot-peened layer. Finally, thickness of thermal spraying is evaluated through the inverse analysis based on the measured impedance spectra.

2. Experiment and numerical analysis.

2.1 Testpieces

The thermal spraying testpieces were prepared, changing the coating thickness. The type 22 hastelloy was sprayed on the substrate of the type 304 austenitic stainless steel, after the surface of substrate is shot-peened to increase adhesion of coating. The alumina #24 is perpendicularly shot on the substrate for shot-peening.

To discuss the electromagnetic properties of shot-peened layer, testpieces without shot-peening process were also prepared. The thicknesses of coating were measured by micrometer and their thicknesses are in Table 1.

Table 1 Details of testpieces.

ID	shot peening	Thickness of coating[μm]
N1	NA	160
N2	NA	230
N3	NA	310
N4	NA	315
SP1	✓	110
SP2	✓	209
SP3	✓	293
SP4	✓	384

2.2 Experiment

To measure the frequency spectra of coil impedance, impedance analyzer (Agilent 4294A) were used. The probe is a pancake coil and the inner diameter, outer diameter, height, and number of turns are 1.2mm, 3.2mm, 0.8mm, and 140 respectively. The test frequency was swept from 1MHz to 5MHz. The number of sampling points is 801.

2.3 Numerical analysis

2.3.1 Forward analysis for coil impedance

The Dodd-Deeds model is adopted for numerical analysis of coil impedance[2]. This method makes it possible to compute impedance of a pancake coil on multilayer of conductor. In order to take the consideration of wire resistance and stray capacitance of the coil, the equivalent circuit as shown in Fig.1 was considered. The impedance of the equivalent circuit is

$$Z = [(R_0 + \mathrm{Re}(Z_1))/\omega C - j\left\{\left(R_0 + \mathrm{Re}(Z_1)\right)^2 + \mathrm{Im}(Z_1)\left(\mathrm{Im}(Z_1) - \frac{1}{\omega C}\right)\right\}] / \omega C\left\{(R_0 + \mathrm{Re}(Z_1))^2 + (\mathrm{Im}(Z_1) - \frac{1}{\omega C})^2\right\}, \quad (1)$$

where R_0, C and Z are wire resistance, stray capasitance of coil, and probe impedance calculated by Dodd-Deeds model, respectively. Now the R_0 and C are determined so that computed coil impedance agrees with measured one for each test frequency.

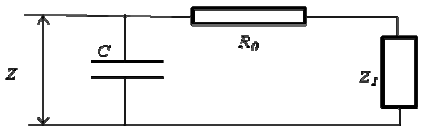

Fig.1 Equivalent circuit.

2.3.2 Inverse analysis

In this study, Newton-Raphson method is applied to evaluate thickness of coating. The objective function is

$$G(t,L)=\sqrt{\frac{\sum_i^n \left(Z_{\exp}(f_i)-Z_{\mathrm{cal}}(f_i)\right)^2}{n}}\ , \qquad (2)$$

where $Z_{exp}(f_i)$ is the measured impedance values as function of frequency f_i. $Z_{cal}(f_i)$ the calculated impedance values as function of frequency f_i. The n is the number of sampling point 801.

3. Experimental and numerical analysis

3.1 Results for the spray coated specimen without shot-peening.

The impedance values were measured for testpieces without shot-peening. The results of swept frequency eddy current testing were shown in the Fig.2. Increasing coating thickness, the peaks of impedance values increase and resonance frequenies reduce. Because the conductivity of coating is smaller than that of substrate, the amount of eddy current decrease. Numerical analysis was conducted to discuss the electromagnetic model of testpieces without shot-peening. Testpieces are modeled with two uniform layer representing the coating and the substrate. Giving conductivity of 1.29×10^6S/m and 0.65×10^5S/m for the substrate and the coating, calculated values agree well with experimental values. In addition, the parameter survey for lift-off noise was conducted. According to the result, high sensitivity to lift-off noise was shown.

3.2 Results for spray coated stainless steels with shot-peening.

The impedance values were measured for shot-peened testpieces. The results of swept frequency eddy current testing were shown in the Fig.3. The impedance peak value change was same tendency to Fig.2. However, resonance frequency is smaller than that for spray coated specimen with shot-peening. Numerical analysis was conducted to discuss the electromagnetic model of shot-peened testpieces. Testpieces are modeled with three uniform layer representing with substrate, coating and shot-peened layer. Giving thickness, conductivity, and relative permeability of 14μm, 1.0×10^5S/m, 8.00 for the shot-peened layer, calculated values agrees well with experimental values.

4. Results of inverse analysis

The inverse analysis was conducted for the specimens with/without shot-peening process. Since lift-off has high sensitivity to signals, thickness as well as lift-off is estimated. The results were shown in the Fig.4. The thicknesses are estimated within the maximum error of 22μm. The root mean square error was 11μm.

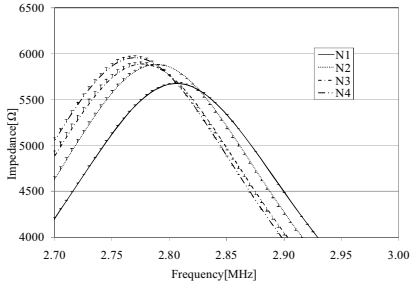

Fig.2 Impedance spectra for specimen without shot-peening.

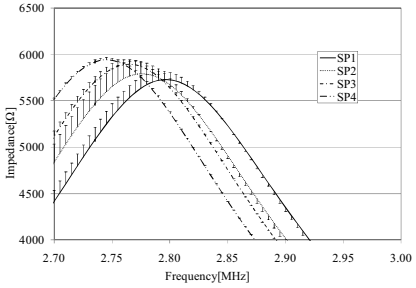

Fig.3 Impedance spectra for specimen for shot-peening.

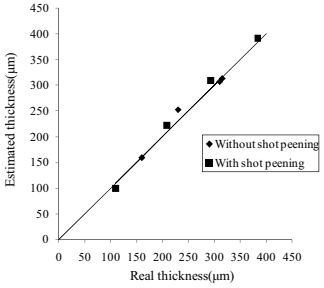

Fig.4 Estimated thickness of coating by inverse analysis.

The lift-off estimated together with coating thickness varies from 0.29 mm to 0.38 mm. Parameter survey shows that this amount of lift-off change gives large impedance change, which means estimation of lift-off is important for accurate estimation of coating. Estimation for shot-peened specimens works well as ones for specimens without shot-peening, and this fact supports for the model of shot-peened layer developed in this study.

5. Conclusion

In this study, thickness of coating was evaluated by a swept frequency eddy current testing. Comparing the numerical analysis and experimental values, we made models of spray coated specimen. In addition, the parameter survey for lift-off noise was conducted, and high sensitivity to lift-off noise was shown. The inverse analysis was conducted. The good agreements of real and estimated thickness were obtained. The maximum error between them was 22μm.

6. References

[1] J. Kawakita, S. Kuroda, T. Fukushima and T. Kodama, Corrosion Resistance of Hastelloy C Coatings Formed by an Improved HVOF Thermal Spraying Process, Materials Transactions, Vol. 44 (2003), pp. 253-258.

[2] C. V. Dodd and W. E. Deeds, Analytical Solutions to Eddy-Current Probe-Coil Problems. Journal of Applied Physics, Vol.39 (1968), pp.2829-2838.

Eighth International Conference on Flow Dynamics
November 9 - November 11, 2011

Development of Wheeled Mobile Robot to Traverse Rough Terrain in Outdoor Fields

Takeshi Ohki, Kiichi Sato, Genki Yamauchi, Keiji Nagatani and Kazuya Yoshida
Department of Aerospace Engineering, Tohoku University
6-6-01 Aramaki Aza Aoba, Aoba-ku, Sendai-shi, Miyagi-ken, Japan
takeshi@astro.mech.tohoku.ac.jp

ABSTRACT

Autonomous mobile robots are useful tool to search outdoor unknown-dangerous environment. To realize such mobile robot, many kinds of technologies such as mobility, localization, sensing, path planning, must be integrated appropriately. For this purpose, we developed a mobile robot platform. In this paper, we introduce our mobile robot designing and implementation and show an example of the autonomous navigation in the real world, to confirm the capability of our mobile robot designing.

1. Introduction

In the case of disasters, remote controlled mobile robots, called "rescue robots" can be of great help when searching inside collapsed buildings, taking the place of the rescue crews. Our research group has been developing rescue robots to explore underground malls in an NBC terrorist attack scenario [1] and the robots of our group were sent to Fukushima 1st power plant to search the unknown inner environment. Not only rescue purpose, mobile robots are used to explore the unknown-danger space mission, such as Moon, asteroid, and Mars. Currently, in practical missions, these types of mobile robots are controlled manually. However, to reduce the workload and solve the problem of time delay, mobile robots should be navigated autonomously.

To realize such autonomous mobile robot, many technologies must be integrated appropriately. Especially, the three technologies; sensing, localization, and mobility are key technologies to realize autonomous navigation. The autonomous robot must recognize the surrounded known environment by its onboard sensors, and also recognize the correct location of the robot itself. And, the robot must be able to traverse rough terrain by the mobility.

In this paper, we introduce our autonomous mobile robot designing and implementations, and show some verification experiments.

2. Hardware Design

We designed a mobile robot platform called "El-Verde" (Fig.1) for large unknown outdoor environment exploration. The length of the robot is 800 mm , the width is 700 mm, the height is 730 mm including onboard sensors. The wheel diameter is 260 mm and total weight is 29 kg.

The robot has four wheels with independent motors and front two wheels can steer by Ackerman linkage driven by the one motor. To traverse rough terrain, the front units with front two wheels are connected to rear unit with rear two wheels by the rocker linkage. On rough terrains, to traverse on rough terrain, all the wheels should contact to the ground. To keep the contacts, the rocker linkage enables to roll the front unit and the rear unit inversely. This is important condition to maintain driving force. The rocker linkage is completely passive. The above linkage enables the robot to get over the obstacle with the half height of the wheel diameter.

El-Verde has several sensors for localization. The rotations of the four wheels are calculated by each wheel encoders. The attitude of the robot is detected by the three gyro sensors and 3 D.O.F acceleration sensor. The robot also has the GPS (Global Positioning System) sensors that detect the location of the robot in world coordinate.

El-Verde also has the sensor for surrounding environment sensing. A 3-Dimensional LIDAR (Light Detection and Ranging) sensor [2] is on the top of the center box of the robot. The sensor can detect the distance to surrounding objects and generate 3D map of point cloud and DEM (Digital Elevation Map).

All the information by these sensors are calculated by an onboard computer. The CPU of the computer is Intel ATOM processor Z530 0.80 GHz (Dual Core). The wireless network is used to communicate the onboard computer with external computers in operators' side. The overview of the control architecture is shown in Fig.2.

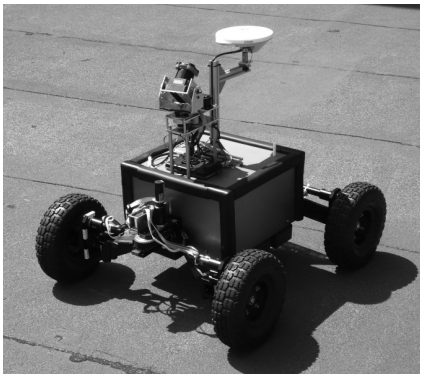

Fig.1 Autonomous mobile robot "El-Verde"

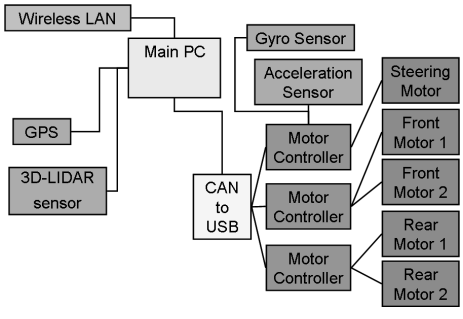

Fig.2 Control architecture

3. System Integration

Fig. 3 shows the system diagram of El-Verde. The gyro based odometory calculated by using the wheel encoders, the gyro sensors and the acceleration sensor. The odometory is memorized in the shared memory successively. Likewise, the location information using GPS and LIDAR sensor information are kept in shared memory. To decrease the accumulated errors of gyro based odometory, the GPS location information and gyro based odometory are integrated by particle filter [3]. A user process can access to the shared memory and also control the robot motion by using the locomotion function. The operator of the robot can observe the state of shared memory via network server process.

To develop the each user programs efficiently, without the process that is related with real devices, we are developing "Field Robot Simulator." Each process can be executed in real and simulated environments by using same source codes. Regardless of the executing environment, the state of the system can be observed by the remote viewer (Fig.4) via TCP/IP network.

4. Autonomous Navigation

To confirm the capability of our robot system, we conducted the autonomous navigation experiment in the real world in Tsukuba City. In this experiment, we used 3D LIDAR sensor for sensing, our navigation algorithm using Distance Time Transform [4] for path planning, and gyro based odometory for localization. In this implementation, the robot repeats the sensing, planning and moving procedure periodically. The interval of the repeating procedure is 1 sec and the 3D LIDAR sensor scanning interval is almost 3 sec.

As the result, the robot traversed 240 m without collision. Fig.5 shows an example scene image of obstacle detection and avoidance. The robot can detect the surrounding obstacles (sky blue bars) by using 3D LIDAR sensor. Then, the robot planed a path (red dots) without collision in the free area (gradation colored area), and followed the path.

5. Conclusion

In this paper, we introduce our mobile robot platform for outdoor environment exploration. In the chaper of hardware designing, the rocker linkage to enable traversing rough terrain was explained. In the next chapter, the shared memory based system integration for the robot and Field Robot Simulator scheme were introduced. The capability of the designed mobile robot was confirmed at the real world autonomous navigation experiments.

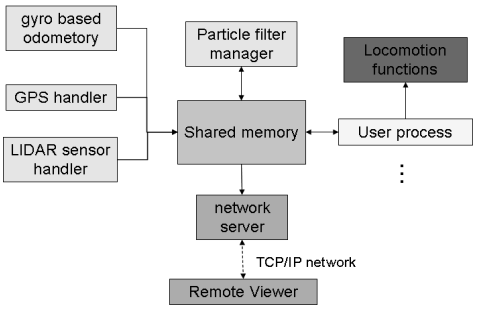

Fig.3 System diagram

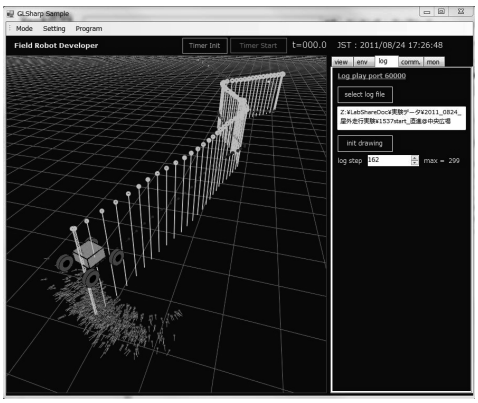

Fig.4 Remote viewer

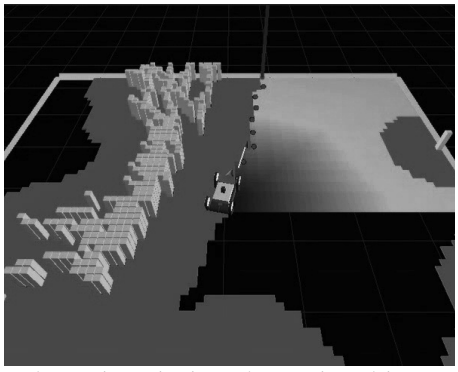

Fig.5 Obstacle detection and avoidance

References

[1] T. Yoshida, K. Nagatani, E. Koyanagi, Y. Hada, K. Ohno, S. Maeyama, H. Akiyama, K. Yoshida, and S. Tadokoro, "Field experiment on multiple mobile robots conducted in an underground mall," In Field and Service Robotics, 2009

[2] K. NAGATANI, T. Matsuzawa, K. Yoshida, "Scan-point Planning and 3-D Map Building for a 3-D Laser Range Scanner in an Outdoor Environment",Preprints of the 7th International Conference on Field and Service Robotics,CDROM (2009-07)

[3] S. Thrun, W. Burgard, D. Fox, "Probabilistic Robotics" (2005)

[4] T. Ohki, K. Nagatani, K. Yoshida, "Collision Avoidance Method for Mobile Robot Considering Motion and Personal Spaces of Evacuees",2010 IEEE/RSJ International Conference on Intelligent Robots and Systems, pp.1819-1824 (2010-10)

Eighth International Conference on Flow Dynamics
November 9 - November 11, 2011

A High Density 2D Array of ϕ6-nm Silicon-Nanodisk Structures and its Optical Characteristics for Solar Cells

Makoto Igarashi, Mohd Fairuz Budiman, Weiguo Hu, and Seiji Samukawa*
Institute of Fluid Science, Tohoku University, Japan; * E-mail: samukawa@ifs.tohoku.ac.jp

ABSTRACT

In this paper, a higher density, smaller sized, and periodic Si-ND structure demonstrated an increase in the optical absorption coefficient and more controllable band gap energy. We successfully fabricated a super-lattice structure with smaller size Si-ND of 6 nm in diameter and a higher Si-ND density of more than 1.2×10^{12} disks/cm^{-2}. By using this 2D Si-ND array, the optical absorption coefficient drastically increased, and more controllable band gap energy could be realized by combining Si-ND diameter and thickness. The new technology is suitable for developing realistic all-Si tandem solar cells.

1. Introduction

An all-Si tandem solar cell comprised of quantum dots (QDs) has attracted much attention for its potential to breakthrough the Shockley-Queisser limit and its compatibility with current Si technology.[1] QDs provide the opportunity to control an energy structure by adjusting the confinement in all three spatial dimensions for various absorption ranges of the solar spectrum through precise control of the size of the QDs. However, not only the uniformity and control of QD size but also high density QDs are essential for improving optical characteristics of QDs such as absorption. In the conventional technique that is widely used to fabricate Si QDs, multiple layers of amorphous silicon-rich oxide (SiO_x, $x < 2$) and stoichiometric silicon dioxide (SiO_2) are alternately deposited by using sputtering or plasma-enhanced chemical vapor deposition followed by annealing at a high temperature (usually 1100ºC).[2] However, the results show poor uniformity of dot size and spacing, which indicates a limited control of quantum confinement. Also, the density of QDs is not high enough.

To overcome these problems, we developed a sub-10-nm-silicon-nanodisk (Si-ND) structure by using a bio-template as a ϕ7-nm etching mask and damage-free neutral beam (NB) etching.[3] The fabricated Si-ND shows distinct quantum effects, such as an electron comfinement and size effect, at room temperature (RT). The Si-ND has two geometrical parameters, thickness and diameter, which can be controlled independently. We previously fabricated a well-ordered arrangement of high density 2D Si-ND arrays by combining a bio-template as a ϕ7-nm etching mask (ferritin) and an etching process with NF3 gas/hydrogen radical treatment (NF3 treatment) and Cl damage-free NB etching. Optical measurements show that the band gap increases from 1.4 to 2.2 eV as the thickness of the Si-ND decreases from 12 to 2 nm.[4]

In this research, a ϕ6-nm, uniform, and high density (1.2×10^{12} disks/cm^{-2}) Si-ND was fabricated by using a newly developed 2D array bio-template (Fe core) as a ϕ4.5-nm etching mask that uses Listeria-Dps ferritin.We expected that the usage of Li-Dps ferritin would achieve a higher nanodisk density due to the smaller diameter of the Li-Dps ferritin iron-core mask (4.5 nm) compared with that of a ferritin iron-core mask (7nm).

In this paper, a higher density, smaller sized, and periodic Si-ND structure demonstrated an increase in the optical absorption coefficient and more controllable band gap energy.

2. Experimental Method

First, we began the fabrication by preparing quartz/poly-Si/SiO2 samples with steps 1 and 2. Bio-template and Cl damage-free NB etching were then used to manufacture a 2D Si-ND array with steps 3 to 6.[3] For step 1, deposition of 6-nm-thick poly-Si thin film on a quartz substrate was performed. In step 2, a 3-nm SiO_2 film was formed on the poly-Si thin film by using our developed neutral beam oxidation (NBO) process at a low temperature of 300ºC (the film is hereafter called "NBO SiO_2"). In step 3, a 2D array of Listeria-Dps ferritin molecules [protein including an iron oxide core (ϕ4.5-nm Fe-core) in the cavity of the ferritin molecule] was placed through directed self-assembly on the surface of the NBO SiO_2. Figure 1(a) contains a structure sketch of Li-Dps ferritin with the ϕ4.5-nm Fe-core. In step 4, ferritin protein shells were removed by heat treatment in oxygen atmosphere to obtain a 2D Fe-core with a hexagonally close-packed array as a template. For step 5, etching was carried out by using NF_3 treatment and Cl damage-free NB etching to remove the NBO SiO_2 and poly-Si, respectively. Finally, in step 6, the 2D Fe-core was removed by using hydrochloric solution to obtain a 2D Si-ND array. For comparison, we also prepared a sample by using ferritin (ϕ7-nm Fe-core) and a control diameter of 2D Si-ND array by changing the NF_3 treatment time. Figure 1(b) shows ferritin with a ϕ7-nm Fe-core.

Optical absorption of the 2D Si-ND array was recorded using a JASCO ultraviolet-visible-near infrared (UV-vis-NIR) spectrophotometer (Model: V-570) with normal incidence light at room temperature.

3. Results and Discussions

Figure 2(a) shows a top view SEM image of the fabricated 2D Si-ND array that used Li-Dps ferritin as the mask, which consisted of a closely packed array of Fe core at a size of ϕ4.5 nm on the surface of the NBO SiO_2. Fifteen-minute NF_3 treatment was performed to remove the NBO SiO_2, and 90 seconds of NB etching was performed to remove the 4-nm poly-Si thin film. As shown in Fig. 2(a), the 2D Si-ND array had a high-density (1.2×10^{12} disks/cm^{-2}) and well-ordered arrangement (diameter: 6.4 nm). Figure 2(b) shows the 2D Si-ND array that uses an etching mask of ferritin ϕ7-nm Fe-core at a density of 7×10^{11} cores/cm^{-2} as a comparison

(diameter: 10.5 nm). By using Li-Dps ferritin, the density of the 2D Si-ND increased to 170% of that using ferritin, while the size of the Si-ND shrunk to 61% of that using ferritin. To confirm regularity in the 2D array of Si-NDs, we measured the center to center distance between adjacent Si-NDs, as shown in Fig. 3(a). Figure 3(b) shows that the absolute value of the center to center distance and its distribution were 8.7 nm and 10.1%, respectively. It was clear that the 2D array of Si-NDs using an etching mask of Li-Dps ferritin with ϕ4.5-nm Fe-core successfully achieved a 2D superlattice structure.

The optical absorption properties of the structure were studied by measuring the transmittance of samples by using an UV-vis-NIR spectrophotometer. The transmittance absorption coefficient is calculated on the basis of the equation[5]

$$ln\,(I_0/I) = \alpha d \qquad (1)$$

where α is the absorption coefficient, d is the total thickness of the Si-ND, and I_0 and I are the intensities of incident and transmitted light, respectively. Figure 4(a) shows the calculated optical absorption coefficient by comparison of the same absorbed area. Figure 4(b) shows the optical absorption coefficient near the E_g region. Figure 4(c) shows the optical absorption coefficient at the E_g edge as a function of Si-ND size in comparison with thin film. We found that a 2D Si-ND array using Li-Dps ferritin has a higher absorption coefficient than a 2D Si-ND array using ferritin and thin film of Si (thickness: 4 nm). This is thought to be due to increasing the Si-ND density and shrinking the Si-ND size, which indicated an advantage in solar cell application. To determine the optical band gap energies, we used the Tauc formula:

(a) (b)

Fig. 1 (a) Li-Dps ferritin with ϕ4.5-nm Fe-core and (b) ferritin with ϕ7-nm Fe-core

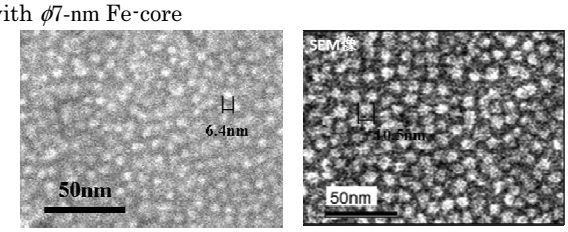

(a) (b)

Fig. 2 (a) 2D Si-NDs array using Li-Dps ferritin. (>12 × 10^{11} cm^{-2}, diameter: 6.4 nm) (b) 2D Si-NDs array using ferritin. (>7 × 10^{11} cm^{-2}, diameter: 10.5 nm)

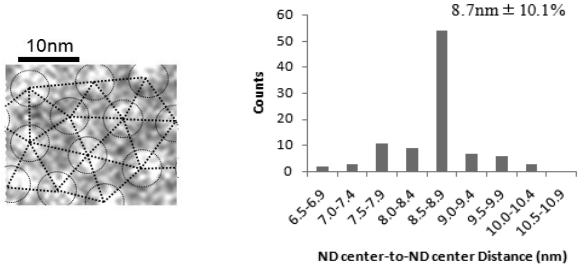

(a) (b)

Fig. 3 (a) SEM image of ND center-to-ND center distance (b) distribution of ND center-to-center distances(8.7nm±10.1%)

$$(\alpha hv)^n = A(hv - E_g) \qquad (2)$$

where A is a constant, h is Planck's constant, v is frequency, E_g is the band gap energy, and n is 1/2 in the case of indirect allowed and forbidden electronic transitions.

The intercept of the linear fitting line at zero absorption in the Tauc plot gives E_g. As shown in Figs. 2(a) and (b), the Si-ND diameter became smaller from 10.5 to 6.4 nm, which resulted in the band gap energy increasing from 1.8 to 2.0 eV. More data about the relationship between the E_g and the function of the Si-ND diameter is shown in Fig. 5. By changing the Si-ND diameter from 12.5 to 6.4 nm, the E_g increased from 1.7 to 2.0 eV, even at a disk thickness of 4 nm. This result indicates that a higher absorption coefficient and more controllable band gap energy can be accomplished at the same time by using a Li-Dps ferritin iron-core mask.

4. Summary

By using a new bio-template ϕ4.5-nm etching mask (Li-Dps ferritin), we successfully fabricated a super-lattice structure with smaller size Si-ND of 6 nm in diameter and a higher Si-ND density of more than 1.2 × 10^{12} cm^{-2}. By using this 2D Si-ND array, the optical absorption coefficient drastically increased, and more controllable band gap energy could be realized by combining Si-ND diameter and thickness. The new technology is suitable for developing realistic all-Si tandem solar cells.

References

[1] M. A. Green et al., 20th EU-PVSEC (2005) 1AP.1.1.

[2] E. C. Cho et al., Nanotechnology 19 (2008) 245201.

[3] S. Samukawa et. al., Appl. Phys. Express 1 (2008) 074002.

[4] C. H. Huang et al., Nanotechnology. 22 (2011)105301.

[5] B. Pejova et al., Mater. Chem. Phys. 90 (2005) 35.

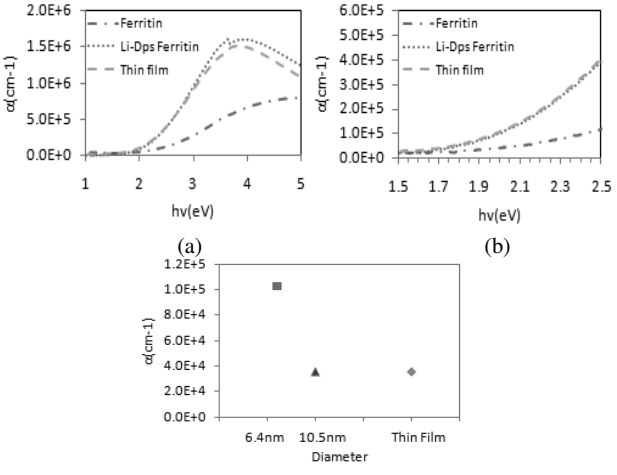

(a) (b)

(c)

Fig. 4 Comparison between 2D Si-NDs array using Li-Dps ferritin, ferritin, Thin film. (a) Absorption coefficient (b)Absorption coefficient at E_g edge (c) E_g edge of Absorption coefficient by the function Si-ND diameter and Si thin film

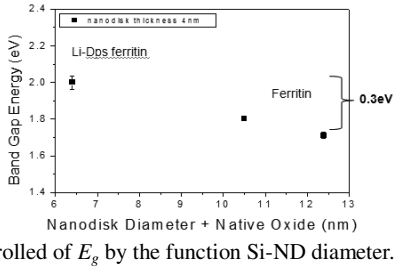

Fig. 5 Controlled of E_g by the function Si-ND diameter.

Eighth International Conference on Flow Dynamics
November 9 - November 11, 2011

Hydrogen Dissociative Adsorption on Pd (111), Pd (100) and Stepped Pd (332) Surfaces: A Comparative Study of Electronic Structures at Different Coverage

Farouq Ahmed[1], Ryo Nagumo[2], Ryuji Miura[1], Suzuki.Ai[2], Hideyuki Tsuboi[2], Nozomu Hatakeyama[1], Hiromitsu Takaba[1], Akira Miyamoto[1, 2]
[1] Department of Applied Chemistry, Graduate School of Engineering, Tohoku University, Japan, [2] New Industry Creation Hatchery Center, Tohoku University, Japan, 6-6-10, Aoba, Aramaki, Aoba, Sendai-980-8579, Miyagi, Japan
E-mail: ahmed@aki.che.tohoku.ac.jp

ABSTRACT

Ultra accelerated quantum chemical molecular dynamics method (UA-QCMD) was used to study the dynamics of dissociative adsorption of hydrogen on Pd (111), (100) and Pd (332) surfaces for better understanding the role of surface hydrogen vacancy for the dissociative adsorption. Here the reaction dynamics, electron transfer, and structural changes were demonstrated. The creation of active sites for H_2 dissociation will thus involve the formation of individual vacancies and their subsequent diffusion. We found for the dissociative adsorption of H_2 on Pd (111), Pd (100) and Pd (332) surfaces, tri-, di- and mono- vacancy of H is required, respectively.

1. Introduction

Surface defects exist extensively on many metal and semiconductor surfaces. Surface defects such as steps, vacancies and kinks play a significant role in surface adsorption [1], epitaxial growth [2-3] and surface diffusion [4-5]. By examining processes such as adsorption, dissociation, and eventually chemical reactions at step, terrace and kink sites of transition metals, for example, information relevant to industrial catalysts may be obtained. Advances in experimental and theoretical techniques, supplemented by enhanced computational power, have made it possible for surface scientists to carry the knowledge gained from studies of homogeneous flat low Miller index surfaces to their heterogeneous stepped high Miller index counterparts.

Dissociative adsorption of the H_2 is a central step in many industrially important catalytic processes. Regardless of persistent investigation, the mechanistic details of the influence of surface H vacancy for the dissociative adsorption of H_2 on Pd (111), Pd (100) and Pd (332) surfaces are still illusive. To explicate the actual mechanism new theoretical work covering the adsorption, dynamics of dissociation of H_2 and comparison of electronic structures are necessary. In this study, we have introduced UA-QCMD as a tool for the qualitative determination of the role of hydrogen vacancy for the dissociative adsorption of hydrogen. The simulation also enables visualization of the electronic and structural changes, as well as the dynamic behavior of this system. The understanding of the influence of surface hydrogen vacancy may help in the design of better catalysts, where one can avoid poisoning by tuning the surface either by doping or introducing different steps, kinks, terraces etc., than originally present.

2. Method

The calculations have been carried out employing a tight-binding quantum chemical approach implemented in our in-house system *New-Colors* [6], which enables the calculation of energies, charges and bond populations for large-scale atomic and molecular systems. The *New-Ryudo* [6] system is used for molecular dynamics simulations under NVT ensemble conditions with a 0.1 fs of integration time at 573 K.

3. Results and Discussion

The influence of the surface hydrogen vacancy for the dissociative adsorption of hydrogen was simulated by applying the UA-QCMD method to Pd (111), Pd (100) and Pd (332) surfaces. A hydrogen molecule was placed in the vacuum region of the unit cell with an initial distance of 6.15 Å from the surface. The initial velocity of hydrogen molecule was fixed to 3350 m/s.

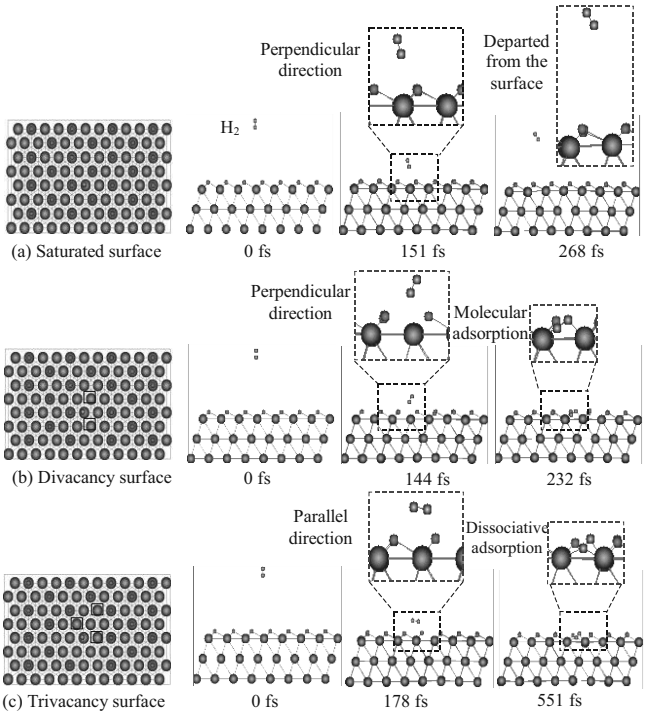

Fig. 1 Snapshots of the dissociative adsorption phenomenon of hydrogen on Pd (111) surface

Here in Fig.1 three different models were prepared on the basis of surface hydrogen vacancy, to investigate the dissociative adsorption of H_2 molecules on a Pd (111) surface. Three different models such as saturated surface, which was fully covered with adsorbed hydrogen. In Fig. 1a, Pd (111) surface was fully saturated with hydrogen and UA-QCMD simulation shows that H_2 molecule without adsorbing departed from the surface at 268 fs. In Fig. 1b in case of di-vacancy, UA-QCMD calculation shows that no

dissociation occurs but hydrogen molecule adsorbed on the surface in molecular form at 232 fs. In case of tri-vacancy, Fig. 1(c) shows that dissociative adsorption of hydrogen molecule occurs at 551 fs.

Similar calculations were performed for Pd (100) surface, where divacancy was found to produce dissociative adsorption of hydrogen whereas at least tri-vacancy is required for Pd (111) surface. In Fig. 2a, snapshot at 270 fs shows that the hydrogen molecule without adsorbing departs from the surface. Here in Fig. 2b, snapshot at 206 fs shows that the hydrogen molecule dissociatively adsorbs on the surface. Finally in Fig. 2c snapshot at 189 fs also shows that the hydrogen molecule dissociatively adsorbs on the surface.

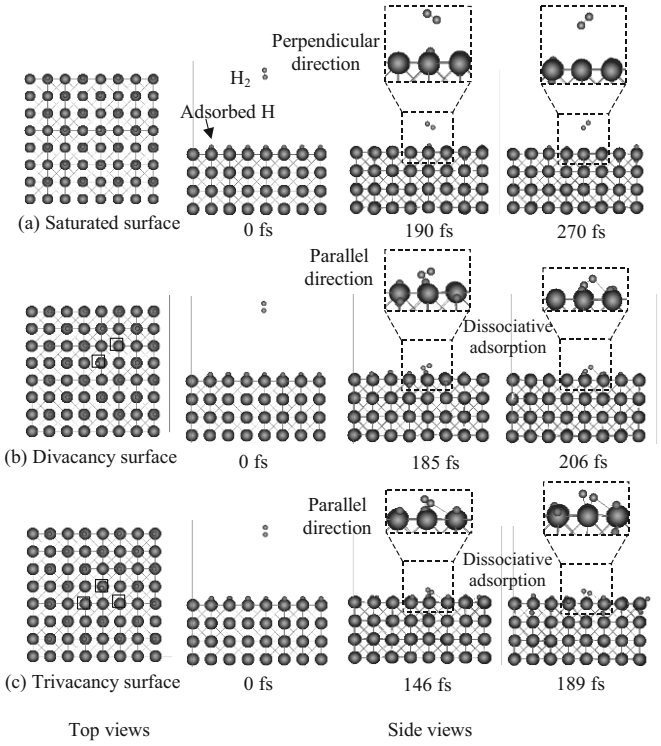

Fig. 2 Snapshots of the dissociative adsorption phenomenon of hydrogen on Pd (100) surface

Simulation of the surface hydrogen vacancy for the dissociative adsorption of hydrogen on Pd (332) surface was carried out on step and terrace sites. From this study it was observed that moderate dissociation of hydrogen occurs at saturated step site (Fig. 3) whereas dissociation occurs at monovacancy step site. It was also observed that hydrogen molecularly adsorbed on fully H covered terrace sites. Saturated terrace sites showed no propensity towards the dissociative adsorption of hydrogen. Comparison of bonding energy, bond length and bond populations between Pd-H at the adsorbed state conclude that stronger interaction occurs in the step site than that of terrace site.

Comparison of the atomic charges and partial density of states (PDOS) also confirms the high reactivity of step surface than that of any other surfaces. The altered adsorption and reaction behavior is often ascribed to the fact that the lower coordination number at a step modifies the electronic structure in its vicinity and that the molecules may adsorb in new geometrical configurations at steps. Finally the adsorption of, and reactions amongst, molecules are often very different at steps than that of the flat or terrace parts. Steps are invariably present on the surface of nanoscale particles commonly used in heterogeneous catalysis. The steps may therefore profoundly influence the catalytic properties of the surface.

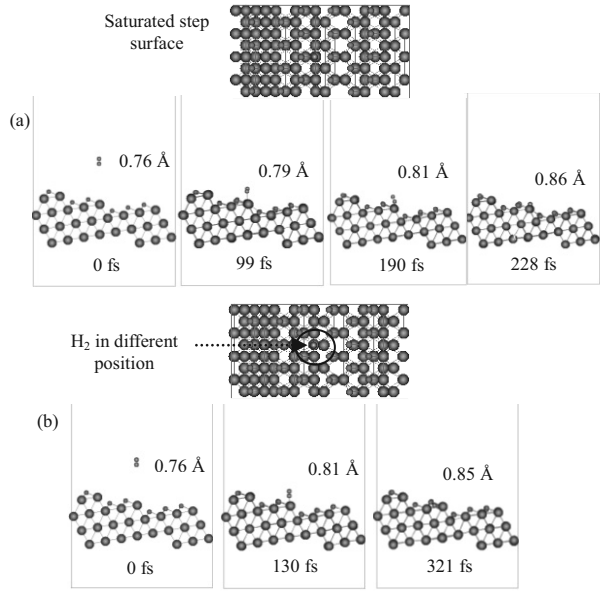

Fig. 3 Snapshots of the dissociative adsorption phenomenon of hydrogen on Pd (332) surface

4. Concluding remarks

We have demonstrated and examined the isolated steps of dissociative adsorption process of hydrogen and the influence of a surface hydrogen vacancy for the dissociative adsorption of hydrogen on Pd (111), Pd (100) and Pd (332) surfaces through UA-QCMD. We have found that H-H dissociation takes place only at the Pd site where metal atoms were not bound to any hydrogen atom. We have also found that the reaction on Pd (111) is strongly coverage dependent. Surface coverage, however, have little effect on the reaction on Pd (100) surface. Stepped Pd (332) monovacancy surface is sufficient for the dissociative adsorption of hydrogen. We have shown that hydrogen molecule still cannot dissociatively adsorb in a hydrogen divacancy sites on almost fully hydrogen-covered palladium surface even using kinetic energy higher than the dissociation barrier.

References

[1] P. Hollins, Surf. Sci. Rep. 16(1992) 51.
[2] Z. Zhang, Phys. Rev. Lett. 72 (1994) 693.
[3] S. Harris, Surf. Sci. 311(1994) L 712.
[4] M. C. Fallis, A. F. Wright, C. Y. Fong, M. S. Daw, Surf. Sci. 311 (1994) L717.
[5] M. Uwaha, Y. Saito, Surf. Sci. 283 (1993) 366.
[6] Ahmed et al. J. Phys. Chem. C 113 (2009) 15676.

Eighth International Conference on Flow Dynamics
November 9 - November 11, 2011

Dynamic Wind-Tunnel Testing of a Rolling Delta-Wing using a Robotic Manipulator

Hiroyuki Abe, Nobuhiro Nakata, Daiju Numata, Xin Jiang, Atsushi Konno, and Keisuke Asai
Tohoku University, 6-6-01, Aramaki-Aza-Aoba, Aoba-ku, Sendai 980-8579, JAPAN
abe.hiroyuki@aero.mech.tohoku.ac.jp

ABSTRACT

The purpose of this study is to measure the unsteady rolling moment acting on a wind-tunnel model using a robotic manipulator. Experiments were conducted with a delta wing of 80 deg sweepback angle. The model was forced to oscillate sinusoidally in roll using a serial-type robot manipulator. The experiments showed characteristic hysteresis-loops of the rolling moment. The break of the rolling moment is delayed, as the non-dimensional frequency increases. It is suggested that these observations were related to the dependency of vortex breakdown on oscillating frequency.

1. Introduction

The airplane is required to fly safety in all-weather as well as to have high mobility. For the flight domains such as high angle of attack (AoA) flight and post-stall maneuver, the stability of the airplane cannot be treated by the linear stability theory based on the traditional perturbation theory. For such flight domains, the nonlinear flight dynamics is necessary, that includes the dependency of stability coefficient on frequency, the treatment of large-amplitude performance and the unsteady aerodynamic force. To establish the nonlinear flight dynamics, it is necessary to conduct the dynamic wind-tunnel testing and measure the unsteady aerodynamic force.

Conventionally, the small-amplitude forced oscillation with one degree of freedom (1-DoF) was common in dynamic wind-tunnel testing. It is known that a hysteresis loop appears in the large-amplitude pitching motion. However, to separate the effects of two terms, the quasi-steady term and the delay term due to downwash, simulation of the 2-DoF motion is necessary in dynamic wind-tunnel testing.

Recently, the studies on multiple-degrees of freedom motion has becoming possible using devices like Kawazoe's link mechanism at Tottori University[1] and Model Positioning Mechanism (MPM) at DLR[2]. These robotic manipulators can cover the wide frequency range.

In this study, we measure the unsteady rolling moment acting on a wind-tunnel model using a serial-type robotic manipulator. Experiments are conducted with a rolling delta wing of 80 deg sweepback angle, which was forced to be oscillated sinusoidally in roll. The effects of non-dimensional frequency and amplitude on the rolling moment are evaluated and their dependency on the breakdown of leading-edge separation vortex is discussed.

2. Experimental method

2-1. Robotic manipulator

In the present study, Mitsubishi Heavy Industries made machinery PA10 (Fig. 1) is used as a robotic manipulator. The PA10 is a multiple multiple-degrees of freedom serial-type robotic manipulator. It has seven motors that cane operated independently, thus can generate 7-DoF motion. In the present study, the roll motion was generated by using end motor.

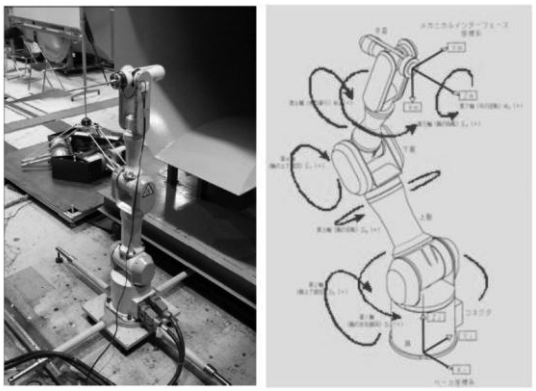

2-2. Wind tunnel

Experiments were conducted in the Low-Turbulence Wind Tunnel at the Institute of Fluid Science, Tohoku University. This wind tunnel is a closed-circuit type. In the present experiment, an open-type test section with an octagonal cross section was used. The width of the test section is 810 mm and the length of the test section is 1420 mm

2-3. Test model and Experimental Condition

The test model was a delta-wing shown in Fig. 2. The sweepback angle is 80 deg and the chord length is 300 mm. The leading-edge is sharp. The model is made of duralumin and its mass is 160 g.

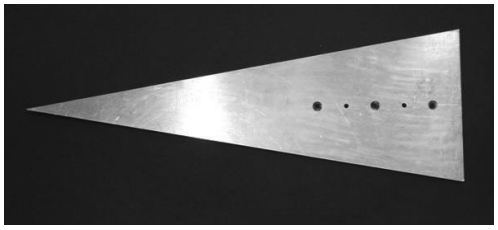

Fig. 2 Test model

To study the effect of angle of attack, AoA was changed from 15 deg to 40 deg. At each angle, the oscillation frequency was changed at 0.1 Hz, 0.5 Hz and 1 Hz to evaluate the effect of non-dimensional frequency.

2-4.Aerodynamic measurement

In the present study, a six component force balance (Nitta IFS-90M31A50-150) was used for rolling moment measurement.

The unsteady rolling moment acting on a delta-wing model was calculated by subtracting the wind-off value from the wind-on value (Fig. 3). To reduce the noise, the same measurement was repeated over 40 times and the obtained data were ensemble averaged and filtered by low-pass filter with 15 Hz cut-off.

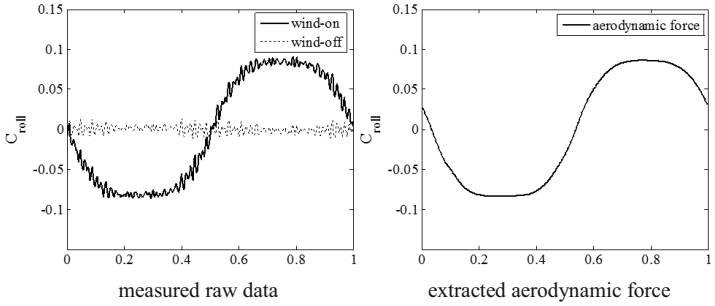

Fig. 3 Data processing Procedure

4. Results and Discussion

Figure 4 shows the rolling moment of the oscillating delta wing. AoA was varied from 15 deg to 40 deg and the non-dimensional frequency (=fL/U) was 0.01. It is shown that the rolling moment depends strongly on AoA. Nonlinearity appears in the rolling moment for AoA larger than 20 deg and the unsteady rolling moment appears for AoA larger than 30 deg. The experiments also show characteristic hysteresis-loops at 30 deg. The results from these forced rolling experiments suggest that energy is supplied from the model to the flow when the roll angle |φ| is lower than 25 deg and the opposite is true when the roll angle |φ| is higher than 25 deg. For higher AoA and higher frequencies, energy is always supplied from the model to the flow.

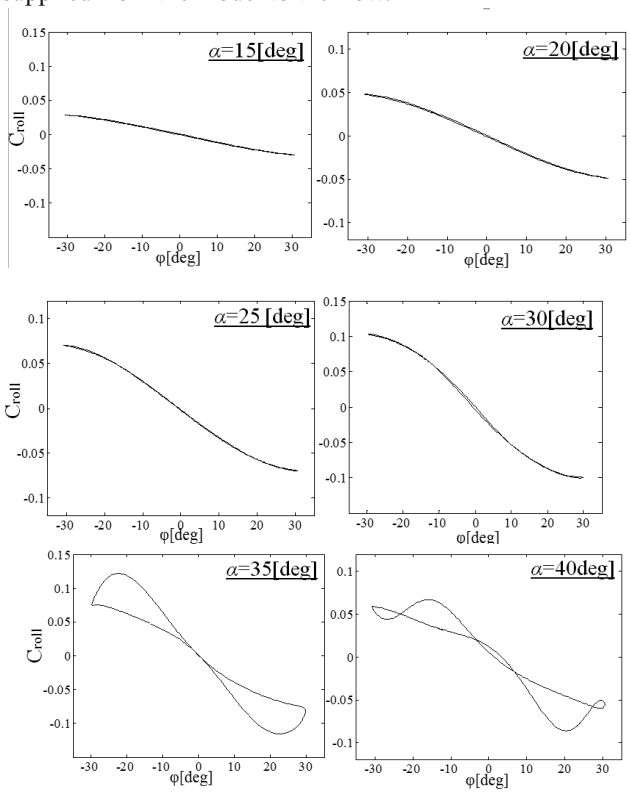

Fig. 4 Effect of AoA for constant oscillation frequency (AoA=15 to 40 deg at 1 Hz)

Figure 5 shows the rolling moment at α=35 deg. The non-dimensional frequency is varied from 0.001 to 0.01. It shows that the rolling moment strongly depends on the non-dimensional frequency. It is also noted that the rolling moment becomes almost constant after it takes an extreme value. The timing of this transition depends on the non-dimensional frequency. From these results, we have concluded that this observation is related to the delay of the breakdown of the leading-edge separation by rolling motion [3]. The beginning of vortex breakdown is delayed with increasing non-dimensional frequency.

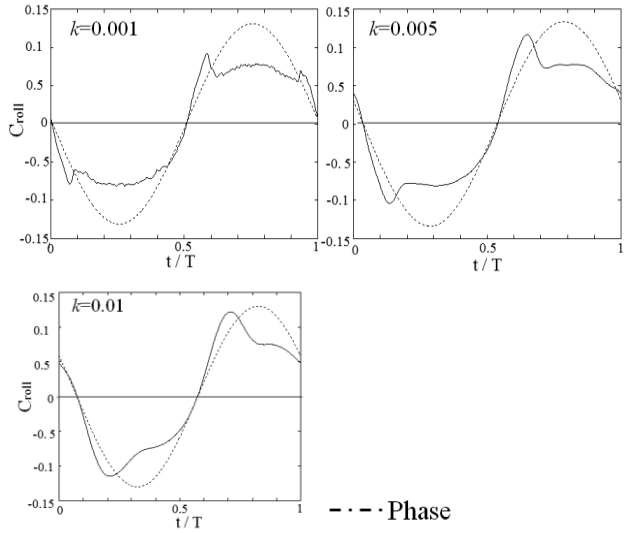

Fig. 5 Effect of frequency for AoA=30 deg

5. Conclusion

We examined the effects of AoA and non-dimensional frequency on the rolling-moment of an 80-deg sweep delta wing using a robotic manipulator. The nonlinearity of the rolling moment became prominent at higher AoA. The nonlinearity of the rolling-moment appeared at higher non-dimensional frequencies. It is suggested that these observations are related to the dependency of vortex breakdown on oscillating frequency. As the next step, we plan to conduct 2-DoF roll-yaw-coupled forced oscillation by using PA10.

References

[1] H. Kawazoe, et al."GROUND EFFECT ON THE DYNAMIC CHARACTERISTICS OF A WING-ROCK DELTA WING", AIAA 2004-2352, 34th AIAA Fluid Dynamics Conference and Exhibit 28 June – 1 July 2004, Portland, Oregon

[2] Andreas Bergmann et al. ," Experimental and numerical research on the aerodynamics of unsteady moving aircraft", Progress in Aerospace Sciences 44 (2008) 121-197

[3] Yuich Shinbo and Junzo Sato. "Unsteady Aerodynamic Forces on Rolling Delta Wings at high Angle of Attack", Journal of JSASS, 37 (1989), pp. 476-484.

Eighth International Conference on Flow Dynamics
November 9 - November 11, 2011

Micro-Motor Utilizing Electric Field-Responsive Polymer Composites

Takayuki Okumura*, Masami Nakano** and Miklos Zrinyi***
*Graduate School of Engineering, Tohoku University, 2-1-1 Katahira, Aoba-ku, Sendai, 980-8577, JAPAN
** Institute of Fluid Science, Tohoku University, 2-1-1 Katahira, Aoba-ku, Sendai, 980-8577, JAPAN
***Semmelweis University, Faculty of Pharmacy, Department of Pharmaceutics,
H-1092 Budapest, Hogyes Endre u.7, HUNGARY
E-mail of corresponding author: okumura@ifc.ifs.tohoku.ac.jp

ABSTRACT

Quincke rotation is the rotation of non-conducting objects immersed in a dielectric liquid and subjected to a strong homogenous DC electric field. The rotation is spontaneous when the field exceeds a threshold value. In this research, for the purpose of developing a micro motor utilizing the Quincke rotation, polymer composites have been developed as materials for a micro motor rotor with micro-fabrication possibilities, and the motor characteristics of disk-shaped polymer composites as a micro motor rotor have been investigated as a function of the electric field intensity and the diameter and thickness of the disk.

1. Introduction

So far, innumerable researches on MEMS have been done. In particular, various micro actuators which are the important parts of MEMS have been much researched. We have proposed a micro motor utilizing the Quincke rotation which is the rotation of non-conducting objects immersed in dielectric liquids and subjected to a strong homogenous DC electric field [1]. The micro motor has several advantages. As only two electrodes are used, the size and weight of the micro motor can be reduced, and the rotational speed of the motor can be simply controlled by only DC electric field applied by DC power supply.

In this research, for the purpose of developing the micro motor utilizing the Quincke rotation, a polymer composite which is contained non-conducting particles in a gelatin has been developed as materials for the micro motor rotor with micro-fabrication possibilities, and the motor characteristics of several disk-shaped polymer composites as a micro motor rotor have been investigated as a function of electric field intensity and the diameter and thickness of the rotor.

2. Experimental Apparatus and Procedure

The disk-shaped rotor of polymer composite is prepared as follows [2]. FeO(OH) particles are dispersed into the gelatin solution at 70℃, and the mass ratio of the filling material to dried polymer is 2.67. The mixture is poured into cylindrical mold made of a brass plate.

In this study, in order to investigate the effects of the diameter d and thickness t of the rotor on motor characteristics, we prepare the polymer rotor disks of 1.00 mm in diameter and 0.20 mm, 0.30 mm and 0.60 mm in thickness and of 0.60 mm in thickness and 0.75 mm, 0.30 mm and 0.60 mm in diameter.

Figure 1 shows an experimental device to apply electric field to the rotor disk. The electric field is supplied by a high voltage DC power supply. The electric field intensity is increased up to 2.0kV/mm. The polymer rotor disk is immersed in the salad oil which is filled up between two parallel electrodes. DC electric field is applied perpendicularly to the axis of the rotor disk. The rotational speed of the rotor disk is determined by recording the spinning motion of the disk using a high speed camera equipped into an optical microscope.

Then, to evaluate the motor characteristics of the polymer disk, the rotational torque of the polymer composite disk is measured. Figure 2 shows an experimental device to measure the torque of polymer composite disk. A shaft of nylon fiber is fixed perpendicular to the center of the rotor of 1.00 mm in diameter and 0.60 mm in thickness. When DC motor rotates the polymer rotor disk immersed in the salad oil between two electrodes under DC electric field, a torsional angle between two nylon fibers (a distance between two fibers is 10mm) adhered perpendicular to the shaft is measured by recording on a high speed camera. The rotor torque is calculated from a relationship between the applied torque and the torsional angle of the nylon shaft.

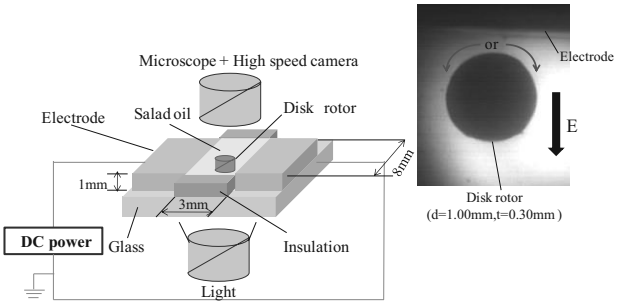

Fig.1 Experimental device to apply electric field to polymer composite disk and measurement of rotational speed of disk rotor

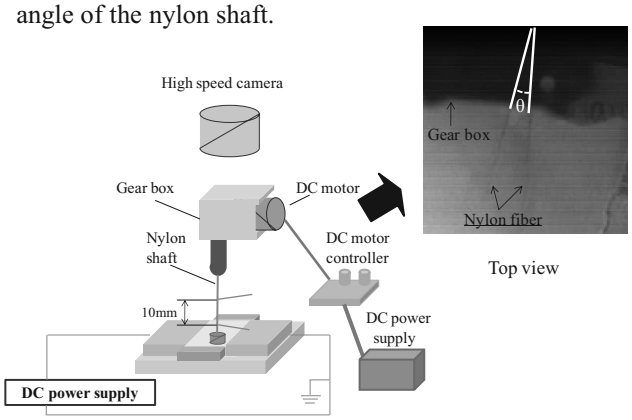

Fig.2 Torque measurement of polymer composite disk rotor

03. Results and Discussion

The polymer disk rotates around itself with an axis pointing in any direction perpendicular to the DC electric field. Above a threshold value of the electric field, the polymer disk rotates. Figure 3 shows experimental relationships between the applied electric field intensity and the rotational speed without load, depending on the diameter and thickness of the disk.

It can be seen in the figure that the rotational speed of the rotor without load increases with increasing the electric intensity not significantly depending on both the diameter and the thickness, and also the threshold value of the electric field is close to 1 kV/mm. The maximum rotational speed of disk rotor is about 1300 rpm at the electric field intensity of 2.00 kV/mm.

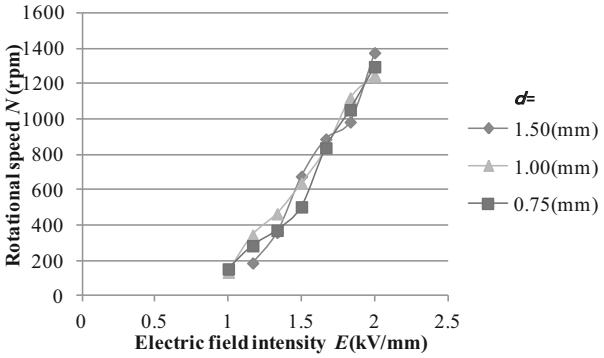

(a) Dependence on disk diameter (t=0.6 mm)

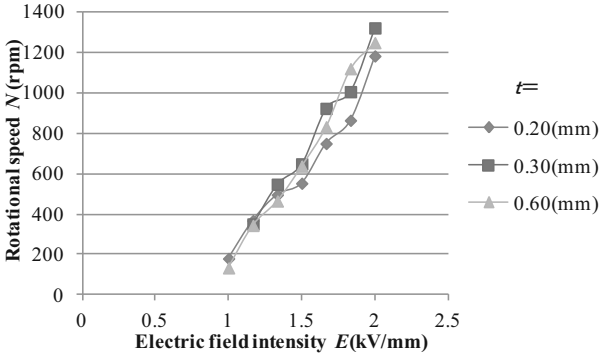

(b) Dependence on disk thickness (d=1.0 mm)

Fig.3 Relationships between electric field intensity and rotational speed under no load

Figure 4 shows a relationship between the applied torque and the torsional angle of the nylon fiber shaft, experimentally obtained to measure the torque of disk rotor. Two nylon fibers (a distance between two fibers is 10mm) are adhered perpendicular to the nylon fiber shaft. And a disk is adhered to the tip of the nylon shaft. After applying the torque by weights which are hung 5mm away from the center of the disk, the torsional angle between the two fibers is measured. Using the approximated linear relation in Fig. 4, the generated torque of the micro motor is calculated from the measured torsional angle of two fibers. And, the motor characteristics of the rotational speed-torque of the micro motor depending on applied electric field intensity are obtained.

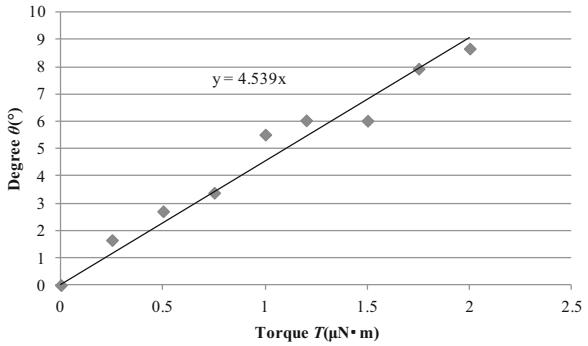

Fig.4 Relationship between applied torque and torsional angle of nylon fiber shaft

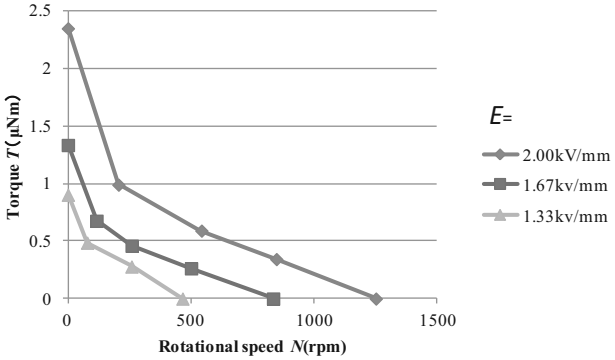

Fig.5 Motor characteristics of rotational speed N – torque T of micro motor depending on applied electric field intensity E

Figure 5 shows experimental results of motor characteristics of rotational speed–torque of the micro motor depending on applied electric field intensity, which is calculated by the linear relationship between the applied torque and the measured torsional angle of the nylon shaft in Fig.4. It can be seen in Fig.5 that the generated torque of the micro motor decreases with increasing the rotational speed and also increases with increasing the applied electric field intensity. The disk rotor generates the maximum torque of 2.4 μNm when the electric field intensity of 2.00 kV/mm is applied .

4. Concluding remarks

The rotational speed of the disk-shaped rotor made of electric field-responsive polymer composites under no load increases with increasing the applied electric field intensity, not significantly depending on both the diameter and the thickness.

The generated torque of the micro motor was measured by utilizing the torsion of the nylon fiber shaft. The measured generated torque of the micro motor decreases with increasing the rotational speed and increases with increasing the electric field intensity.

References

[1]JONES T.B., IEEE Transactions on .Industry Applications., IA-20, pp.845-849, 1984.

[2]Zrinyi M., et al., Composites Science and Technology, Vol.67, pp.2884-2885, 2007.

OS13: Clean and Efficient Combustion Technology (AFI/TFI-2011)

For details, please refer to separate proceedings

PS1: IFS Collaborative Research Forum (AFI/TFI-2011)

For details, please refer to separate proceedings

PS2: 5th Functionality DEsign of the COntact Dynamics:(DECO2011)

Eighth International Conference on Flow Dynamics
November 9 - November 11, 2011

Geometrical Effects in Contact Mechanics: From Atomic Membranes to Evolving Asperities

Robert W. Carpick, Tevis D. B. Jacobs, Xin Z. Liu, Qunyang Li
Dept. of Mechanical Engineering and Applied Mechanics, University of Pennsylvania
220 South 33rd Street, Philadelphia, PA 19104
carpick@seas.upenn.edu

ABSTRACT

In classical contact mechanics, flat surfaces are treated as semi-infinite elastic half-spaces and tip-like bodies are treated as perfect paraboloids. The present experimental results demonstrate how, when the true geometry is accurately accounted for, the stresses in the contact deviate significantly from predictions. Using atomic-scale stick-slip friction measurements on atomically-thin graphene, friction is shown to vary by more than a factor of two depending on the number of layers present. Using *in-situ* TEM experiments, the geometry of a sliding contact is shown to evolve in real time, with the normal contact stress also varying by a factor of two.

1. Introduction

In traditional contact mechanics approaches, flat surfaces are treated as elastic half-spaces and sharp asperities are approximated as paraboloids of revolution [1]. This simplifies the analysis and, in many cases, provides reasonable agreement with experimental results. However, often these simplifying geometrical assumptions mask much more complex behavior, particularly at the nanoscale.

One example of geometrically-induced complexity is in the frictional properties of contacts with graphene. Graphene, meaning single or a few atomic sheets derived from bulk graphite, is a novel material with many extreme properties including high strength [2, 3].

Another example of where simple contact mechanics break down is in the case of a sharp nanoscale asperity sliding over a flat surface, where the asperity shape evolves due to wear. This case is relevant to scanning probe microscopy [4], tip-based nanomanufacturing [5] , and rough macroscale contacts, where a single apparent contact is composed of a large number of nanoscale asperities [6].

2. Method

Friction experiments on graphene were performed in contact-mode by atomic force microscopy (AFM) using a Park Systems XE-100 AFM in ambient conditions (25-50% relative humidity, room temperature), and a RHK UHV350 AFM, where the sample chamber was purged by dry nitrogen gas (1-2% relative humidity, room temperature). Contact-mode silicon AFM probes were used for all the experiments. The number of layers for all sample regions probed was determined based on the topographic AFM images. In several cases, Raman spectroscopy was also used independently for verifying the thicknesses. Adhesion tests were performed in the same RHK AFM system (1-2% relative humidity, room temperature), using the regular force-distance (FD) spectroscopy.

Separate adhesion and sliding experiments were carried out with *in-situ* transmission electron microscopy (TEM) to provide high-resolution characterization of the tip shape. A Hysitron PI-95 nanoindenter was used inside a JEOL 2010 field-emission TEM to bring a sharp silicon AFM tip into contact with a flat diamond substrate. The counter-surfaces were then slid laterally with respect to one another under adhesive loads. The sliding tests were recorded using real-time video, with higher-resolution out-of-contact still TEM images captured periodically over the course of the test. The shape of the evolving tip was characterized with sub-nanometer precision from the periodic still images and the adhesive loads were measured with sub-nanonewton precision by measuring the deflection of the calibrated AFM cantilever.

3. Results and Discussion

In the AFM friction measurements on graphene, we observed that the friction force – starting from one single layer – decreases monotonically with increasing number of layers of graphene. Moreover, the friction force on samples of four layers or more is approximately the same as that on the bulk materials. Those results are shown in Fig. 1. A similar trend has been predicted using finite element modeling (FEM) simulations.

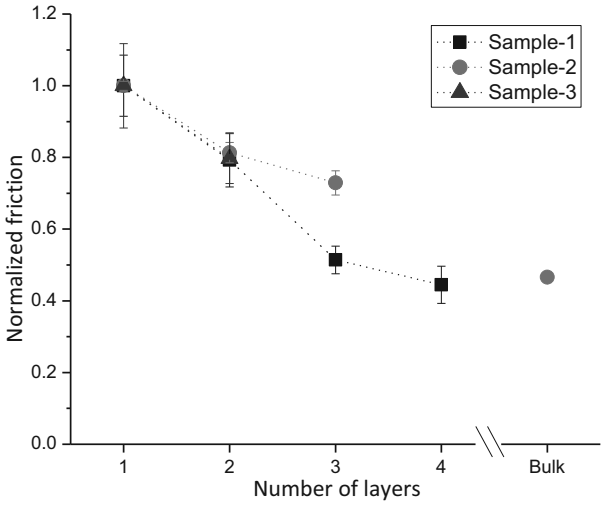

Fig. 1: Normalized friction force on areas with different numbers of layers. Friction forces were normalized to the value obtained on the thinnest layer.

Puckering of the thin sheet around the tip, induced by adhesion and facilitated by the extremely low flexural stiffness of the thin sheet, has been proposed to cause this phenomenon. In this model, thinner sheets are more susceptible to out-of-plane elastic deformation

than thicker sheets, provided they are not strongly bound the substrate, thus leading to larger contact area and higher friction [4, 5].

However, we found that the pull-off force, both in experiments and finite element simulations, has very little dependence on the number of layers. We believe this may be due to the fact that the increased friction requires the puckering and enhanced adhesion which is induced by sliding. Experiments incorporating sliding followed immediately by adhesion measurements are underway, with preliminary results suggesting that indeed sliding can lead to higher adhesion forces.

Now we discuss the *in-situ* measurements. Traditionally, a single asperity would be described using a single parabolic fit, as shown in Fig. 2a. This introduces two sources of error into the mechanics calculations: first, only the geometry of the outermost asperity governs contact; and second, the shape of a nanoscale contact evolves significantly due to wear during sliding – even under zero applied load. Instead, a parabolic fit can be made specifically to the smallest asperity (shown in Fig. 2b), and this shape characterization can be repeated over the course of the test (Fig 2c-d).

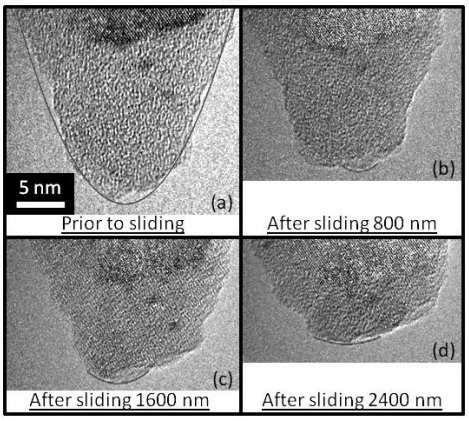

Fig. 2: The silicon asperity wears significantly with sliding. Rather than using a traditional parabolic fit (of the whole probe prior to sliding - shown in a), the contact mechanics is much more accurately described by fitting the smallest contacting asperity (shown in b). Further, the assumption of constant tip shape will introduce further errors, since it is clear that the shape of the contact changes due to wear (c-d).

When the pull-off force and tip shape are characterized periodically over the course of a sliding study, it is shown in Fig. 3 that the average contact stress is reduced by more than a factor of two over the course of the test. Experiments are currently underway to characterize the co-evolution of adhesion and wear, and to investigate the coupling together of the two processes.

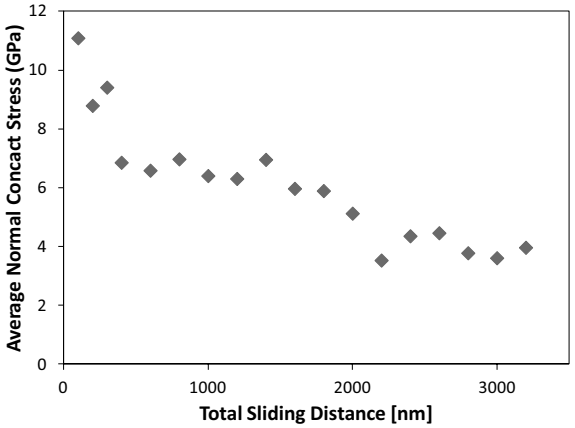

Fig. 3: The evolution of the average normal contact stresses as a single asperity (shown in Fig. 2) is slid over a flat diamond substrate under zero applied load.

4. Concluding remarks

In this paper, we discussed two experiments where geometrical effects led to unexpected behavior and deviations from contact mechanics results. For AFM sliding on graphene sheets, we observed layer-dependent friction. This observation, along with FEM results and our preliminary results from adhesion tests, suggests that sliding of the AFM tip over the thin graphene sheet induces puckering of the sheet around the tip – the thinner the sheet the stronger the puckering effect. Furthermore, this effect in turn will enhance the adhesion and friction force, in which the latter is responsible for the trend of layer-dependent friction.

Separately, using *in-situ* adhesion and sliding experiments, we observed a case where the classic parabolic shape assumption led to significant deviations from the expected contact stresses. Because of nanoscale roughness, the contact geometry was governed by the radius of a sub-asperity on the end of the sharp AFM tip rather than by the radius of the whole tip. Further, even with zero-load adhesion-only sliding, the wear of the AFM tip changed the geometry of the relevant sub-asperity such that the contact stresses dropped by a factor of two in just 3 μm of sliding.

References

[1] K. L. Johnson, Contact Mechanics. 1987: University Press

[2] A. K. Geim, Science, **324**, (2009), 1530

[3] C. Lee, X. Wei, J. Kysar and J. Hone, Science, **321**, (2008), 385

[4] E. Meyer, H. J. Hug and R. Bennewitz, Scanning probe microscopy: the lab on a tip. 2004: Springer Verlag

[5] A. Malshe, K. Rajurkar, K. Virwani, C. Taylor, D. Bourell, G. Levy, M. Sundaram, J. McGeough, V. Kalyanasundaram and A. Samant, CIRP Annals-Manufacturing Technology, **59**, (2010), 628-651

[6] C. M. Mate, Tribology on the small scale. 2008: Oxford University Press New York

Eighth International Conference on Flow Dynamics
November 9 - November 11, 2011

Tribological Properties of Me-DLC Containing Ag and Cu

Minoru GOTO[1)], Julien FONTAINE[2)], Sandrine BEC[2)], Michel BELIN[2)], Thierry LE MOGNE[2)], Kosuke ITO[3)], Takanori TAKENO[4)], and Hiroyuki MIKI[4)]
1) Ube National College of Technology, Japan, 2) Ecole Centrale de Lyon, France, 3) Nihon University, Japan, 4) Tohoku University, Japan
mi-goto@ube-k.ac.jp

ABSTRACT

Cu-DLC showed relatively low and stable friction coefficient independently of both contact pressure and environmental condition. Nanoindentation measurements revealed that relatively soft tribofilm which consist of almost pure copper was formed in the sliding interface. Whereas the friction coefficient of Ag-DLC varied with both shape and morphology of the tribofilm, and the linear dependency of friction coefficient against the inverse of apparent contact pressure was observed. These results indicate that the characteristics of tribofilm play an important role to the tribological properties of Me-DLC.

1. Introduction

Diamond-like carbon (DLC) coatings have been attracting a lot of researchers because of their excellent characteristics as tribo-material [1]. The tribological properties are, however, sensitive to the operation conditions such as contact pressure and operating environment etc. In addition to that, DLC coatings cannot be applicable as lubricant of electric contacts because DLC are lacking in electrical conductivity. Adding metals to DLC coatings is thus considered as a powerful method to improve tribological properties as well as electrical conductivity. In recent years, synthesis and/or characteristics of metal doped DLC (Me-DLC) have been reported [1,2]. Cu is a powerful candidate for the additives because of low electrical resistivity and its cost performance. Silver is also one of the promising metals as dopant because it shows enough lubricity as solid lubricant as well as a good electrical conductivity.

In this study, tribological properties of a copper-diamond-like carbon (Cu-DLC) nanocomposite coating under different initial contact pressures and atmospheric conditions are presented. The tribological properties of silver-diamond-like carbon (Ag-DLC) coatings are also presented together with the measurement of electrical contact resistance.

2. Experimental details

The Cu-DLC and Ag-DLC nanocomposite coatings were deposited on a Si (100) wafer using hybrid deposition process composed of plasma enhanced chemical vapor deposition (PECVD) and DC magnetron co-sputtering of Cu or Ag target [2]. Acetylene was used as a precursor.

The thickness of the Cu-DLC was 1.2 μm, and the Cu concentration in the coating was estimated at 50 at.% by energy dispersive X-ray spectroscopy.

Three kinds of Ag-DLC coatings with different concentrations were prepared for tribological experiments. The Ag concentration in the coatings was measured by energy dispersive X-ray spectroscopy (EDS), and estimated respectively as 63 (for Ag-L), 75 (for Ag-M) and 84 at.% (for Ag-H).

For the tribological experiments of Cu-DLC, two linear reciprocating tribometers were used, one operating in ambient air, the other operating under ultra-high vacuum (UHV, $< 10^{-7}$ Pa). For both tribometers, 52100 bearing steel was used as counterface, with a sliding length of 3 mm and a sliding speed of 2 mm/s. The initial contact pressures were 0.5 and 1.4 GPa. In ambient air, the ball radius was kept constant at 3 mm, and initial contact pressure was controlled by changing the normal load. In UHV, the load was kept constant at 3 N, and the contact pressure was varied by using pins with different tip radii (8 mm and 1.5 mm, respectively). After tribological experiments, the worn surfaces have been investigated with various techniques, including Auger electron spectroscopy and nanoindentation.

The tribological experiments of Ag-DLC were performed under a sliding speed of 2.0 mm/s for a wide range of contact pressure: 0.5 to 1.4 GPa, using pin-on-flat type tribometer in atmospheric condition. Mirror polished bearing steel ball with a diameter of 6 mm was used as slider. The wear tracks on the Ag-DLC surfaces were observed by optical microscope. Tribofilms formed on the ball surfaces were also observed.

3. Results and Discussion

3.1. Tribological properties of Cu-DLC

Cu-DLC showed stable tribological behavior for both initial contact pressures and gaseous environments as shown in Fig. 1. The variations of friction coefficient remained between 0.13 and 0.16 for both initial contact pressures (0.5 and 1.4 GPa) in ambient air. The variations of friction coefficient in UHV were almost the same as in ambient air. It is noteworthy that Cu-DLC provided similar friction coefficient under different contact pressure and different environment. In all cases, non-oxidized copper-rich tribofilm was formed on the steel counterface. Thus, the mechanism of the stable and low friction coefficient in UHV experiments seems to be same as that in ambient air.

The evolution of such tribofilm with sliding cycles was found to depend on contact conditions. At low contact pressure, pure-copper islands evolved thicker and thicker as sliding cycles increase. Whereas, at high contact pressure, the copper flowed out of the contact area.. These results indicate that the copper-rich

tribofilm is relatively soft, thus, the real contact pressure would be kept at similar level.

Nanoindentation measurements performed on the tribofilms showed that the hardness was approximately 2 GPa for both initial contact pressures (0.5 and 1.4 GPa). Since the hardness of copper-rich tribofilm is considerably lower than those of substrate and slider, friction coefficient can be written by the ratio between shear strength and hardness of tribofilm. Thus, Tribofilm keeps friction coefficient constant under various contact pressure, and non-oxidized Cu stabilizes the shear strength at real contact point in ambient air as well as in UHV.

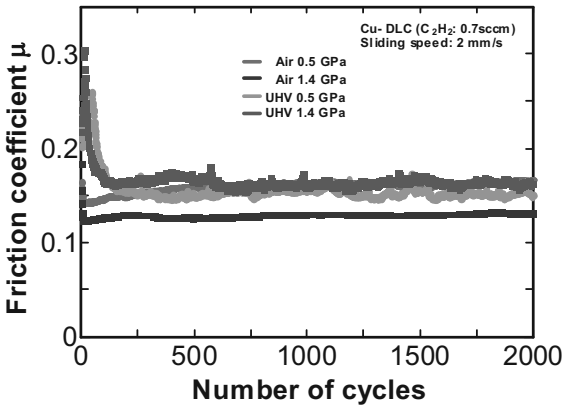

Fig. 1 Friction transition of Cu-DLC as a function of initial Hertz contact pressure and environmental conditions

3.2. Tribological properties of Ag-DLC

Silver concentration in the DLC phase varied proportionally according to the mixture ratio between acetylene and argon gases. As a result, several Ag-DLC coatings with different concentrations were achieved by changing gas mixture ratio of acetylene and argon gases, C_2H_2/Ar, under a fixed DC input. By transmission electron microscopy, we observed that Ag metal clusters with 10-15 nm in diameter are dispersed in an amorphous DLC matrix.

The durability of the coatings was found to increase as the concentration of Ag decreases under a normal load of 0.5 N. The increase of durability of the Ag-DLC is explained by an increase of hardness thanks to the decrease of Ag concentration.

The friction coefficient of the Ag-L coating varied from 0.15 to 0.3 under normal loads ranging from 0.5 to 10 N, and two characteristic tribofilm shapes with three kinds of surface morphologies were observed on the ball. The friction coefficient at the last cycle of the tribological experiments is shown in Fig.2. The linear dependency of friction coefficient against the inverse of apparent contact pressure that was calculated from both applied normal load and apparent area of tribofilm after the experiment was observed. This result indicated that apparent shear strength of tribofilm is proportional to the inverse of apparent contact pressure.

To confirm above consideration, additional experiment was performed with successive decrease of normal loads (2.5 N for 200 cycles, 1.5 N for 100 cycles and 0.5 N for 100 cycles) on the same sliding track. The friction coefficient is found to increase as normal load is decreased. The change in electrical contact resistance was proportional to the change of the friction coefficient, suggesting a change in the apparent contact area.

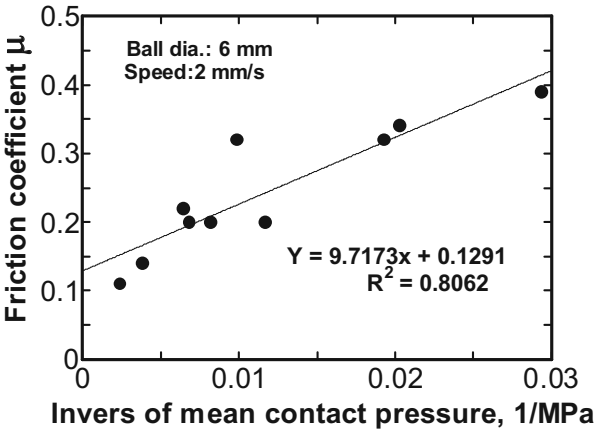

Fig. 2 The friction coefficient at the last cycle

4. Summary

We have demonstrated that the copper-rich tribofilm stabilizes the friction coefficient of Cu-DLC for various initial contact pressure values by means of nanoindentation hardness. Friction coefficient of Cu-DLC is at around 0.15, and is insensitive to both contact pressure and operation environment, when the Cu-rich tribofilm is formed on the slider surface. The evolution process of the tribofilm depends largely upon the Hertz contact pressure, but the contact pressure has little effect to the hardness of the tribofilm. The hardness of tribofilm is about 2 GPa at the most, which is considerably lower than those of both Cu-DLC and slider. Evolution of Cu-rich tribofilm plays an important role to obtain low and stable friction coefficient under various operation condition.

Ag-DLC coatings with different concentrations were achieved by changing gas mixture ratio of acetylene and argon gases, C_2H_2/Ar, under a fixed DC input. Durability of the coatings was found to increase as the concentration of Ag decreases. Apparent shear strength of tribofilm formed on the counterface is proportional to the inverse of apparent contact pressure.

References

[1] C. Donnet and A. Erdemir, “Tribology of diamond-like carbon films – fundamentals and application” 2008 Springer.

[2] T. Takeno, Y. Hoshi, H. Miki, T. Takagi, “Activation energy in metal-containing DLC films with various metals of various concentrations” Diamond and Related Materials Vol.17, 7-10 (2008) 1669-1673.

Eighth International Conference on Flow Dynamics
November 9 - November 11, 2011

Structural and tribological properties of DLC films prepared by Unbalanced Magnetron Sputtering (UBMS)

Hirotaka Ito, Kenji Yamamoto
Materials Research Lab, Kobe Steel Ltd.
1-5-5 Takatsuka-dai, Nishi-ku, Kobe 651-2271 Hyogo, Japan
ito.hirotaka@kobelco.com

ABSTRACT

Hydrogenated and hydrogen-free DLC films were deposited by UBMS system. The maximum indentation hardness was obtained at hydrogen content about 10 at%, and the hardness is strongly correlated with film density instead of sp^2/sp^3 ratio of DLC films. Tribological properties of these films were evaluated by vane on disk type sliding test in oil lubrication with various additives. The additives (GMO and Phosphate) decreased friction coefficient of DLC films with hydrogen content up to 20 or 30 at%

1. Introduction

DLC (Diamond Like Carbon) coatings are commonly used for various sliding parts with an intention to improve durability and to reduce friction coefficient. DLC films have been investigated with various approaches respect to the well-known ternary phase diagram of amorphous carbon in terms of sp^2/sp^3 ratio and hydrogen content [1]. These structures can be controlled by changing the preparing method and parameters for deposition process. Hydrogen-free DLC can be obtained by sputtering or AIP (Arc Ion Plating) method. Kano reported that hydrogen-free DLC showed a very low friction coefficient in oil with Glycerol Mono-Oleate (GMO) additives [2]. This result indicates hydrogen-free DLC exhibits the lowest friction coefficient.

In this study, DLC coatings with various hydrogen contents were prepared by UBMS method and structural properties against hydrogen content was investigated. Tribological tests were conducted at various hydrogen contents, and different oil additives were tested to compare friction coefficient hydrogen-free and hydrogenated DLC films.

2. Method

The DLC coatings were deposited using a multi-cathode UBMS system. The substrate for deposition were polished Si (100) wafers and high speed steel (HRC65) disks. These substrates were loaded in a vacuum chamber and evacuated to pressure of less than 2×10^{-3} Pa. A Cr and Cr-C under-layer was deposited on the substrate to enhance adhesion with the substrate. For DLC deposition, a carbon target was sputtered in an Ar and CH_4 gas mixture at 0.6 Pa pressure. Hydrogen contents were controlled by changing the Ar to CH_4 gas flow ratio. Negative substrate bias of 100 V was applied during the DLC deposition. The total film thickness was about 1500 nm, including the DLC layer thickness of about 600 nm. Coating hardness was measured using a nano-indentation instrument (ENT-1100; Elionix Co. Ltd.) with a Berkovich-type diamond indenter. The hardness was calculated from the load-displacement curve using the method proposed by Sawa et al. [3]. Structural analyses were carried out using Raman scattering spectroscopy (Ar-ion leaser, excitation wavelength: 488 nm) and electron energy loss spectroscopy (EELS) using Auger electron. Hydrogen contents and DLC film density were determined using elastic recoil detection analysis (ERDA) with a He^+ (proton) beam.

Tribological tests were carried out using a Friction & Wear Tester (SHINKO ENGINEERING CO. LTD.). The tribo-test type was a vane-on-disk sliding test with a DLC coated high-speed steel (SKH51) disk rotating against a non-coated SUJ2 vane (Fig.1). The sliding tests were conducted in oil lubricating condition. Additives (GMO, Phosphate) were mixed with PAO (Poly-alfa-olefin) base oil, and the oil temperature was fixed at 80 °C. The rotating speed was changed from 0.02 to 0.18 m/s, and the normal load was 500 N. The wear volume of vane was calculated from the wear width after the sliding test. The wear volume of the DLC coated disk was calculated by measuring the cross-sectional area of the wear track.

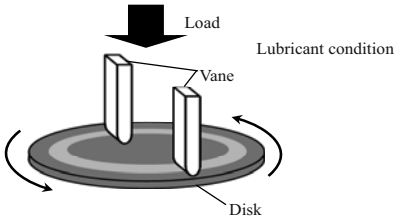

Fig.1 Schematic image of vane-on-disk sliding test

3. Results and Discussion

Fig.2 shows the relations between CH_4 gas ratio during sputtering and hydrogen content of DLC films. Hydrogen content rapidly increases as the CH_4 gas ratio is increased up to 3 vol%. When the CH_4 gas ratio is more than 5 vol%, a gradual increase of hydrogen content is observed.

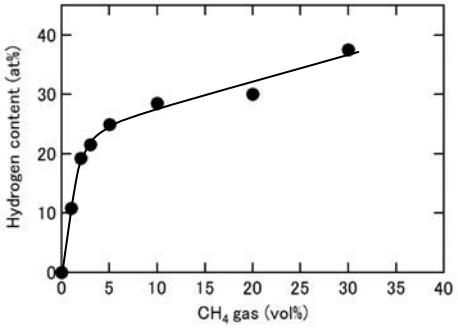

Fig.2 CH_4 gas ratio vs. hydrogen content of DLC films

Fig.3 (a) shows the dependence of nano-indentation hardness on hydrogen content of DLC films. Highest hardness was obtained at the hydrogen content about 10 at%, and the hardness is linearly decreased with hydrogen content above 20 at%. UBMS deposited hydrogen-free DLC had lower hardness than hydrogenated DLC. Fig.3 (b) shows the change of film density with hydrogen content. The film density change curve shows similar trend with indentation hardness.

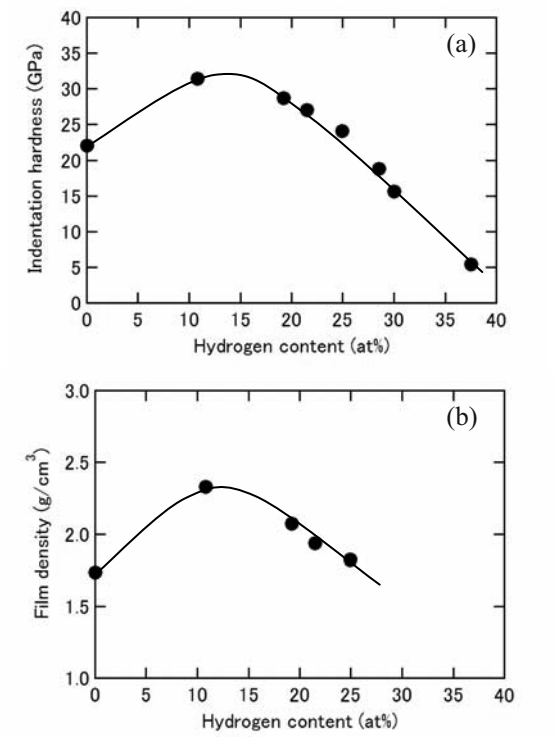

Fig. 3 Hydrogen content vs. Indentation hardness (a), Hydrogen content vs. Film density (b)

EELS measurements show that indentation hardness no relation to sp^2/ sp^3 ratio, but to the film density.

Fig.4 shows the friction coefficient of vane-on-disk sliding tests of sliding speed 0.04 m/s with three types of oil lubricant using various hydrogen content DLC films. In the case of base oil (PAO), friction coefficient increased for DLC films with hydrogen content above 20 at%. But using oil with additives, low friction coefficient is maintained hydrogen content up to 20 or 30 at%. Phosphate additive showed lower friction coefficient than GMO for DLC films with hydrogen content about 30 at%. These results indicate that the hydrogen-free DLC film is not mandatory in order to lower the friction coefficient.

Fig.5 shows the wear volume of non-coated SUJ2 vanes and disks coated with DLC films with 26 at% hydrogen. The lowest vane wear volume is obtained in PAO oil one, but the DLC disk wear volume is the highest. In case of GMO additives, DLC wear volume is smaller than PAO, but the vane wear volume is the highest. In phosphate, vane wear volume is same as PAO case, and DLC disk wear volume is the lowest value. Thus the GMO is effective to the lower the friction coefficient, however the tribofilm generated from GMO additives may deteriorate wear resistance.

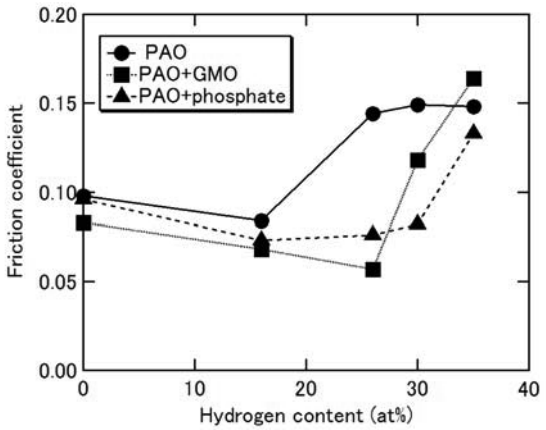

Fig.4 Friction coefficient vs. Hydrogen content in three oil conditions

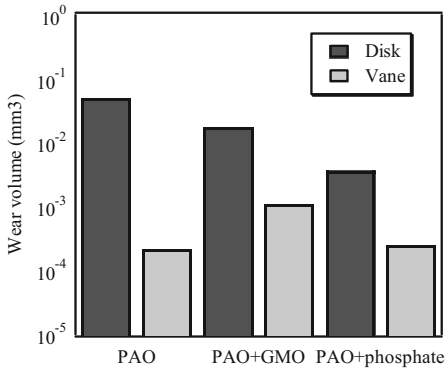

Fig.5 DLC (Hydrogen: 26 at%) disks and SUJ2 vanes wear volume after sliding test in three oil conditions

4. Concluding remarks

DLC films prepared by UBMS were investigated in terms of film properties and tribological properties. The following results were obtained.

· DLC film properties can controlled with hydrogen content.

· Hydrogen content of DLC film is strongly related to film density, and higher film density film shows the higher indentation hardness.

· In oil lubricated sliding test, lower friction coefficient can be achieved hydrogenated DLC. Hydrogen-free DLC is not a mandatory to obtain low friction coefficient.

· GMO is effective to lower the friction coefficient, but the DLC disk and vane wear is increased.

· Phosphate is effective to lower the friction coefficient, and tribofilms may have the protective properties to prevent DLC disk and SUJ2 vane wear.

References

[1] A.C. Ferrari and J. Robertson, Phys. Rev. B **61** (2000) 14095.

[2] M. Kano, Tribology Letters **18** (2005) 245,

[3] T. Sawa, K. Tanaka, J. Mater. Res. **16** (2001) 3084.

Eighth International Conference on Flow Dynamics
November 9 - November 11, 2011

Impact - Sliding of solids: effect of contact conditions.

Philippe KAPSA, Maha MESSAADI, Gaetan BOUVARD, Vincent FRIDRICI
Laboratoire de Tribologie et Dynamique des Systèmes, UMR CNRS 5513 ECL-ENISE, Ecole Centrale de Lyon,
36 avenue Guy de Collongue - 69134 Ecully Cedex, France
Philippe.Kapsa@ec-lyon.fr

ABSTRACT

Damage induced by sliding is already a very widely studied phenomenon. When impact is associated to sliding, the surface phenomena are more complex and less studied... In order to show some important aspects of this problem, we studied the behavior of sintered steels used in industry for various applications. For this, we developed a tester using a ball on flat contact under impact and sliding. Experiments with different impact angles (30°, 45°, 60°, 90°) in dry or lubricated conditions have shown a strong variation of the wear rate in relation to the number of impact-sliding cycles and the contact conditions.

1. Introduction

Sintered steels (manufactured by powder metallurgy, PM) are of increasing interest for various mechanical applications. Thanks to their high wear resistance, nearly 90% of engine manufacturers use PM for valve seat production. The repetitive valve impact on the seat insert is combined with sliding. As a consequence, hybrid damage mechanisms can occur. Moreover, in such systems, the effect of lubrication is not well known.

This study aims to compare the sintered steel wear behavior, in dry and lubricated conditions, under impact-sliding. In addition, the influence of impact angle on the damage mechanisms is investigated.

2. Experimental procedure

A ball-on-flat configuration has been used to determine local wear phenomena of sintered high speed steel compared to cast iron. Hardness of ball (AISI 52100 steel; ∅ 10.5 mm) is 700 HV. The hardness of sintered steel (ref OB1 and M2, 27x14x5 mm^3) is about 500 HV and about 180 HV for the cast iron.

An impact-sliding tribometer has been developed in LTDS (figure 1). A vertical reciprocating ball motion, created by using an electromagnetic shaker, impacts an inclined flat (with an angle of 30°, 45°, 60° or 90°). Micro-sliding occurs during shock due to the deformation of the spring holding the flat samples.

Tests have been carried out under dry and lubricated conditions with two mineral oils. The first is a base oil with a dynamic viscosity of 0.03 Pa.s at 22°C and 1 atm. The second is a fully formulated oil with a viscosity of 0.07 Pa.s (at the same temperature and pressure). Test conditions resulted in boundary lubrication for both oils.

All tests were carried out under controlled impact with an energy of 4 mJ/impact and at a frequency of 16 Hz. The material removal due to wear action was evaluated by optical interferometry.

3. Results

Our experiments have shown an increase in the wear volume with the number of impacts. Figure 2 presents some results obtained with various metals tested (cast iron, OB1 and M2).

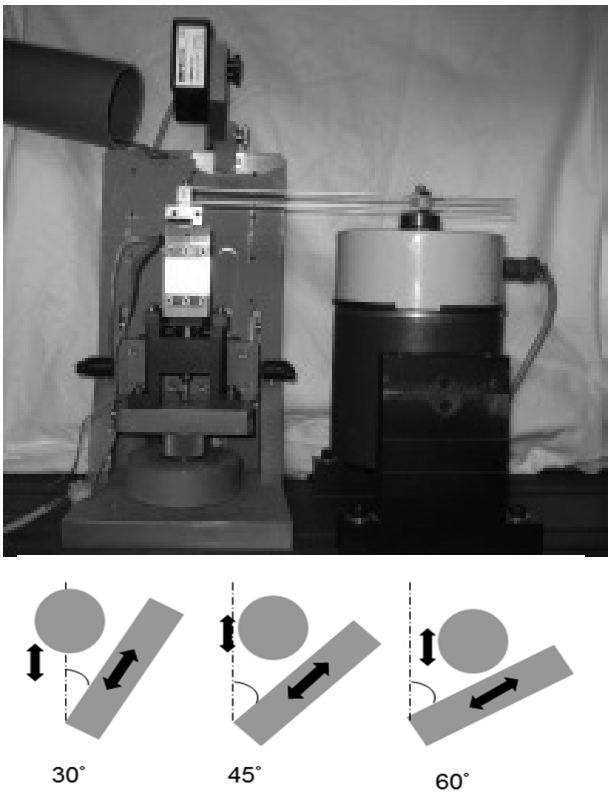

Fig. 1 Impact-Sliding Tribometer

In lubricated conditions, experiments showed that the impact force (measured by piezo sensor) decreases compared to dry conditions. A drop of 55% in the impact force, between dry and lubricated condition, was measured for an impact angle of 30°. Both in dry and lubricated contacts, the impact force increases with the impact angle due to the reduction of sliding distance and increase of stiffness.

The wear volume in dry conditions is higher than in the presence of oil. In lubricated contact, wear is slightly higher for the case of the fully formulated oil compared to the base oil alone.

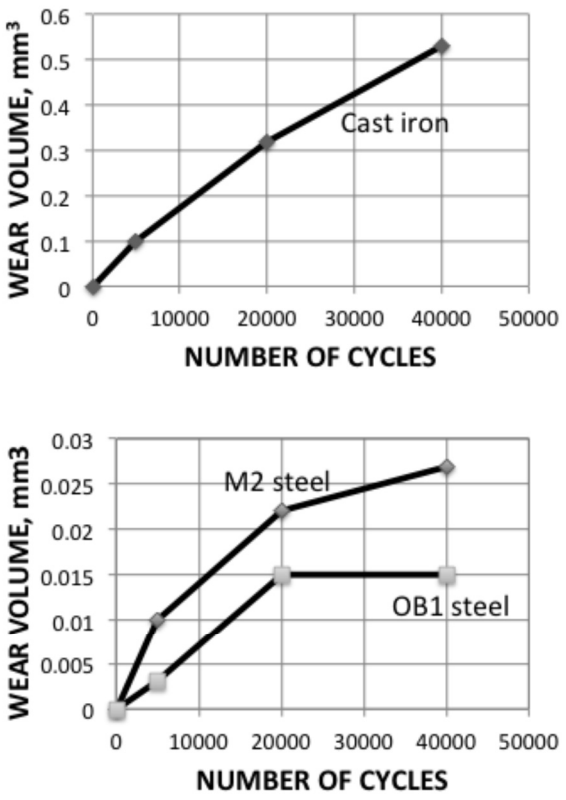

Fig. 2 Wear of cast iron, OB1 and M2 vs the number of impacts at an angle of 45°.

As it can be seen in figure 3, the wear volume increases with the impact angle particularly in dry test conditions. In lubricated contact conditions, wear evolves to a maximum at 60° and then decreases as the impact angle increases.

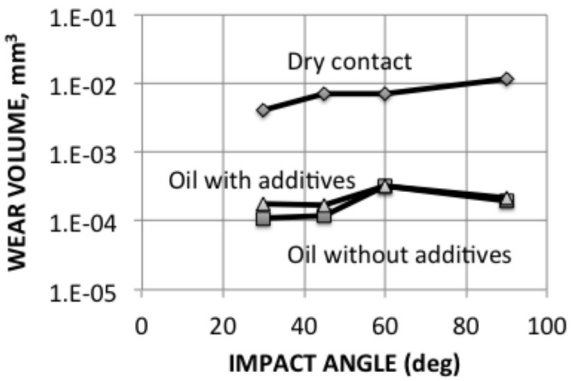

Fig. 3 Variation of wear volume as a function of impact angle (degree).

A transfer film from the flat sintered steel samples to the counter body ball was observed in dry impact (figure 4). This indicates that strong adhesion, combined with abrasion, occurred at the interface. This can explain the increase of the wear volume loss [1].

In the presence of oil, the effect of adhesion is reduced. The surface fatigue becomes the dominant damage mechanism. In fact, we can suppose that the squeeze film pressure forces the lubricant to be trapped in cracks close to the contact area. As the load is imposed over the surface crack, liquid is forced toward tip, causing the regeneration of the crack [2] and propagation of microcracks.

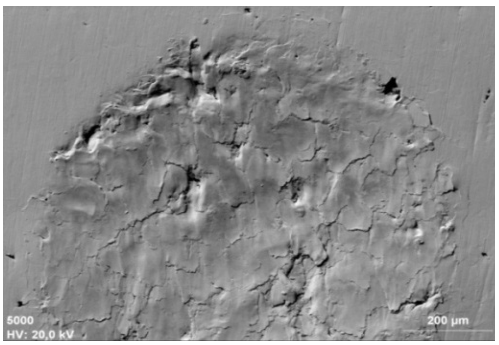

Fig. 4 SEM micrograph of flat sintered steel sample after 40 000 cycles at impact angle of 45°.

4. Conclusion

Damage analysis of sintered steel under different impact-sliding conditions was studied. Two types of damage mechanisms were observed. In dry contact, wear process is governed by adhesion and abrasion mechanisms. In lubricated test conditions, wear is governed by surface crack opening.

References

[1] Chun, K.J and Kim, J.H and Hong, J.S, "A Study of exhaust valve and seat insert wear depending on cycle numbers," Wear, Volume 263, Issue 7-12, 10 September 2007, 1147-1157.

[2] Engel, P. A and Zhao, Z, "Impact of Delrin disc: Lubricated and dry contacts," Wear, Volume 193, Issue 1, April 1996, 114-125.

Eighth International Conference on Flow Dynamics
November 9 - November 11, 2011

Improvement of Vacuum Boundary Lubrication Properties of Multiply Alkylated Cyclopentane Oil by the Concurrent Use with Diamond-like Carbon Coating

Masanori Iwaki[1)2)], Takanori Takeno[1)], Hiroyuki Miki[1)] and Toshiyuki Takagi[1)]
[1)] Institute of Fluid Science, Tohoku University, 2-1-1 Katahira, Aoba-ku, Sendai 980-8577, Japan
[2)] Japan Aerospace Exploration Agency, 2-1-1 Sengen, Tsukuba 305-8505, Japan.
E-mail of corresponding author: iwaki.masanori@jaxa.jp

ABSTRACT

To improve vacuum boundary lubrication properties of multiply alkylated cyclopentane (MAC) oil, diamond-like carbon (DLC) coatings were deposited on the stainless steel disk surfaces. Pin-on-disk vacuum friction tests in boundary lubrication regime were conducted for DLC-coated and non-coated specimens. Extremely low wear rate below 1×10^{-9} mm^3/N·m was obtained for a DLC-coated specimens, as well as lower friction coefficient and longer wear life compared to those of non-coated specimens. It is suggested that high hardness-to-elastic-modulus ratio (H/E ratio) of the DLC coatings contributed this excellent wear resistance.

1. Introduction

Multiply alkylated cyclopentane (MAC) is the most frequently used space liquid lubricant thanks to its excellent tribological properties in vacuum. But it still produces non-negligible wear [1]. Meanwhile, diamond-like carbon (DLC) is already widely applied in industries as wear-resistant coatings. But they have short wear lives in vacuum, caused by strong interaction between carbon atoms [2]. In this research, the combination of MAC and DLC has been tried for vacuum boundary lubrication with the expectation that they mutually compensate their weaknesses.

2. Method

We prepared DLC coatings about 1 μm thick on 440C stainless steel substrates, deposited by physical vapor deposition (PVD) or chemical vapor deposition (CVD). A drop of MAC oil was put on a DLC-coated specimen and uniformly spread over the coating surface to have finally about 1 mg of MAC oil on it. Non-coated 440C disks with MAC oil applied on the surface were also prepared. Rotational friction tests by a pin-on-disk tribometer were conducted under high vacuum at a constant sliding speed until the number of revolutions reached a prescribed value or the friction coefficient exceeded 0.3. Test conditions are described in Table 1. In addition to the "Benchmark" test with typical maximum Hertzian contact pressure (0.88 GPa, corresponding to 3 N load) and sliding speed (20.9 mm/s, corresponding to 50 rpm rotational speed) for a space mechanical component, four other tests with severer test conditions were conducted with lower sliding speed, higher contact pressure or longer test period as shown in Table 2. Surface damage of the specimens was evaluated by optical microscopy and surface profiling after the tests.

Table 1. Conditions of the vacuum friction tests.

Geometry		Pin-on-disk
Counterpart pin	Material	Stainless steel 440C
	Radium	6 mm
Chamber pressure		Below 1×10^{-5} Pa
Load		3 N/24 N/50N
Rotational speed		10 rpm/50 rpm
Number of revolutions		$10^5/10^6$ (stops if $\mu > 0.3$)

Table 2. Test cases.

No.	Name	Load	Speed	No. of revs.
1	Benchmark (BM)	3 N	50 rpm	10^5
2	Low Speed (LS)	3 N	10 rpm	10^5
3	High Pressure 1 (HP1)	24 N	50 rpm	10^5
4	High Pressure 2 (HP2)	50 N	50 rpm	10^5
5	Long Term (LT)	3 N	50 rpm	10^6

3. Results and Discussion

The DLC-coated specimens exhibited lower and more stable friction coefficients than non-coated specimens in all cases (Fig. 1). Also the improvement of load carrying capacity was observed in two "High Pressure" tests: both of the DLC-coated specimens in HP1 test and the CVD-DLC-coated specimen in HP2 test exhibited low friction coefficients until the end of the tests, while non-coated specimens failed during the test. Microscope images and surface profiles revealed that the DLC coatings drastically reduced wear. The wear tracks of non-coated specimens were bumpy and deep, while the DLC-coated specimens were less damaged and sometimes their wear tracks were almost invisible (Fig. 2). Prolongation of wear life was also confirmed in LT test. The PVD-DLC-coated specimen maintained low friction coefficient less than 0.1 until 10^6 revolutions in contrast to the non-coated specimen whose friction coefficient exceed 0.3 at about 5×10^5 revolutions. The wear rates of the disk are summarized in Fig. 3. Decrease in wear rate can be clearly seen when DLC coating is applied on the disk surface. Especially CVD-DLC-coated specimens exhibited extremely low wear rate down to 8.54×10^{-10} mm^3/N·m. According to the mechanical property measurement (Table 3), the difference in hardness is not significant between DLC-coated and non-coated specimens. In contrast, the elastic moduli of the DLC coatings are much smaller than the non-coated specimen, giving much higher hardness-to-elastic-modulus ratio (H/E ratio). It is generally accepted that a material with high H/E ratio has good wear resistance [3] and the result is in a good accordance with this theory as shown in Fig. 4. It is suggested that the CVD-DLC coating had excellent wear resistance thanks to its excellent mechanical properties.

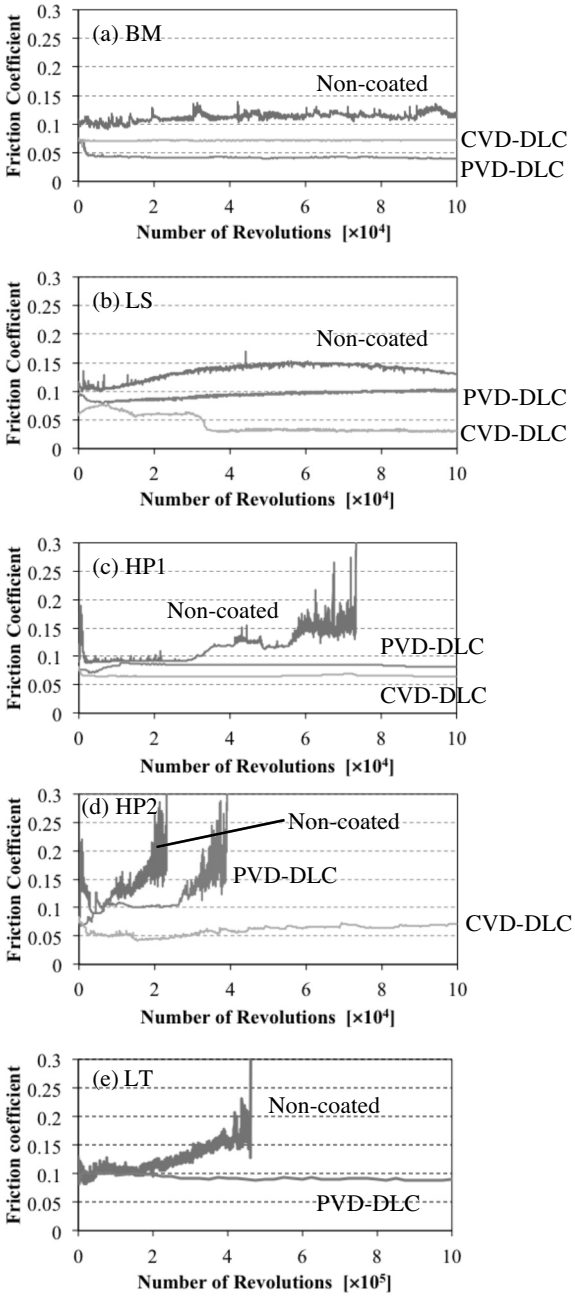

Fig. 1 Friction coefficients of DLC-coated specimens and non-coated specimens lubricated with MAC oil in high vacuum. BM, LS, HP and LT stand for "Benchmark", "Low Speed", "High Pressure" and "Long Term" respectively.

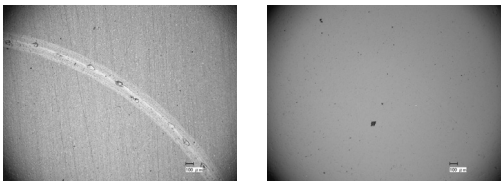

Fig. 2 Wear tracks of non-coated specimen (left) and CVD-DLC-coated specimen (right). Wear track is hardly visible for the CVD-DLC-coated specimen.

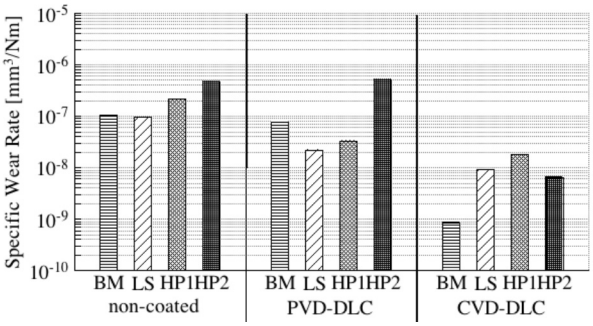

Fig. 3 Wear rates of the specimens. BM, LS and HP stand for "Benchmark", "Low Speed" and "High Pressure" respectively.

Table 3. Mechanical properties of the specimens.

Specimen	Non-coated	PVD-DLC	CVD-DLC
Hardness (H) [GPa]	7.8	8.5	9.8
Elastic modulus (E) [GPa]	199	153	129
H/E ratio	0.039	0.056	0.076
Wear rate [mm^3/N·m]	1.05×10^{-7}	7.78×10^{-8}	8.54×10^{-10}

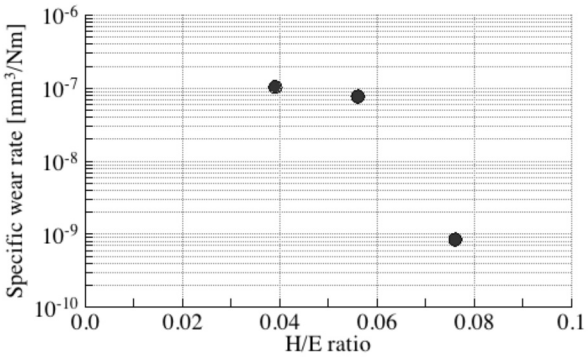

Fig. 4 Specific wear rate as a function of hardness-to-elastic-modulus ratio (H/E ratio).

4. Concluding remarks

Remarkable improvement of the vacuum boundary lubrication properties was achieved using DLC coating together with MAC oil. In the presence of DLC coating, the friction coefficient and the wear rate were drastically decreased and the wear life was prolonged. The CVD-DLC-coated specimen which had the best mechanical properties obtained the best result. Especially it had extremely low wear rate down to below 1×10^{-9} mm^3/N·m.

References

[1] T. Nogi, ASIATRIB 2006 Kanazawa, (2006) 277.
[2] J. Fontaine, Surf. Coat. Tech., **146/147** (2001) 286.
[3] A. Leyland, Wear, **246** (2000) 1.

Eighth International Conference on Flow Dynamics
November 9 - November 11, 2011

Deposition and Tribological Behavior of Amorphous Silicon-Carbon Coatings

Takanori TAKENO[1], Masaki SAWANO[2], Pengfei WANG[3], Hiroyuki MIKI[3], Toshiyuki TAKAGI[3]
1. Tohoku University International Research and Education Organization, Japan
2. School of Engineering, Tohoku University, Japan
3. Institute of Fluid Science, Tohoku University, Japan
E-mail of corresponding author: takeno@wert.ifs.tohoku.ac.jp

ABSTRACT

Amorphous silicon-carbon coatings were prepared by plasma enhanced chemical vapor deposition (PECVD) and DC magnetron co-sputtering of silicon carbide target. Five kinds of specimens were deposited on stainless steel substrate with its surface roughness less than 20 nm in Ra. Microstructure of the coatings was analyzed by Raman spectroscopy and transmission electron microscope. Friction tests were conducted with tribometer with rotational motion. Low friction was obtained for all specimens, and the lowest was ~0.04. Optical images of the counter plate reveal the existence of a tribofilm.

1. Introduction

Since the first discovery of amorphous carbon coatings, intensive researches have been performed. From the tribological point of view, amorphous carbon coatings are very attractive because of their excellent mechanical properties such as low friction, anti-wear and high hardness. However, there are some drawbacks. One of the critical issues is their high residual stress, which results in low wear adhesive strength between coatings and metallic materials.

Recently, doping of other element or addition of material into amorphous carbon coatings has been investigated to overcome the issue. Nitrogen, fluorine and silicon are used as a dopant, and metals as an addition. Among them, many researchers focus on the silicon because silicon-doped amorphous carbon coatings show low friction and low wear of the coating [1].

Deposition techniques for silicon-doped amorphous carbon coatings have been proposed up to now. Almost all depositions have been performed by chemical vapor deposition (CVD) technique with the isolate gas of tetramethylsilane (TMS) or mixture gas of TMS and carbonaceous gases (C_nH_m) [2]. We developed the hybrid deposition technique composed of CVD and physical vapor deposition (PVD). Such deposition apparatus is very unique and silicon-carbon amorphous coatings developed by the technique have not reported, yet.

In this paper, we fabricate silicon-carbon amorphous coatings deposited onto AISI440C stainless steel substrate without any adhesion layer. Friction tests are performed using tribometer.

2. Experiment

The investigated coatings were deposited onto stainless steel substrates and single crystalline silicon, Si(100), substrates. Figure 1 shows the schematic illustration of the deposition apparatus used in this study. DC magnetron sputtering device locates bottom of the deposition chamber, and sputtering target faces up. There is radio frequency cathode upside. The base pressure of the deposition chamber is less than 10^{-3} Pa. Deposition is carried out in 3 steps: 1) cleaning of substrate surface by RF-generated Ar plasma to remove surface contamination, 2) cleaning of target surface, and 3) coating deposition. Silicon carbide (SiC) target with 99 % purity was used. Along the sputtering, methane (CH_4) gas was introduced and RF-plasma was generated. Working pressure and coating thickness were fixed at 1.3 Pa and 500 nm, respectively. In this study, 3 types of the coatings are compared; (1) the Si-C coating deposited with the gas mixture ratio of 10 (= Ar/CH_4), amorphous carbon coating prepared by CH_4 and

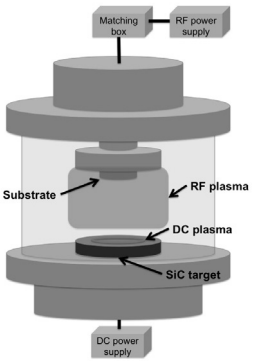

Fig.1 Schematic illustration of the hybrid deposition apparatus used in this study

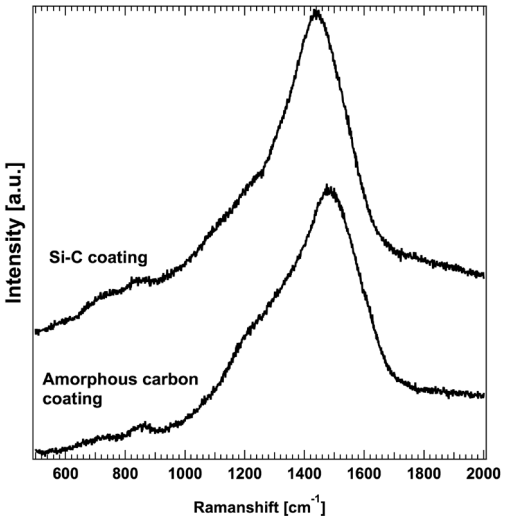

Fig.2 Raman spectra of an amorphous carbon coating and silicon-carbon coating

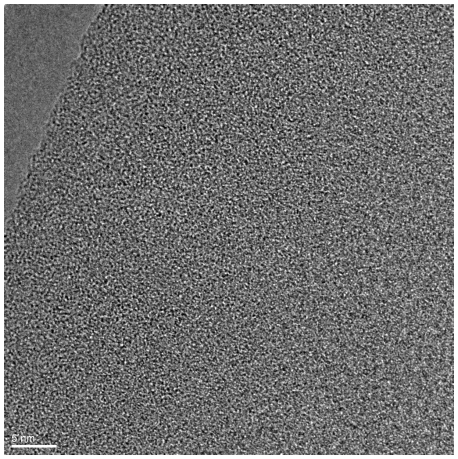

Fig.3 A plan-view TEM image of a silicon-carbon coating

sputtered SiC coating.

Microstructure of the coatings was investigated using Raman spectroscopy and transmission electron microscope. Raman spectrometer employed in this study is JobinYbon LabRam HR-800 with He-Ne (λ = 632.8 nm) laser excitation. Plan-view electron micrographs were acquired by FEI Titan-80 with acceleration voltage of 300 kV.

Friction tests were conducted in ambient air condition by CSM Tribometer. AISI 52100 steel ball was used. Linear speed and load were fixed at 10 cm/s and 1 N, respectively.

3. Results and Discussion

Typical Raman spectra of the Si-C coating and amorphous carbon coatings were shown in fig. 2. These spectra were quite similar to each other. It seems that very similar microstructure was formed in the coating.

A plan-view image of Si-C specimen is shown in fig. 3. One can see very clear amorphous structure of the coating. The composition of the coatings has not yet measured up to now. However, we just confirmed that silicon and carbon atoms are in the coating analyzed by energy dispersive X-ray spectrometer (EDS) in the transmission electron microscope. In addition, certain amount of hydrogen is in the coating because of the introduction of CH_4 as a precursor.

Microstructure of the investigated coatings was completely different from the ones we have studied previously. In metal-containing amorphous carbon coatings (Me-C:H), nano-meter-size metal clusters are embedded into amorphous carbon host matrix [3]. Schiffman et al. have reported that average size of the metallic clusters decreases linearly against the melting temperature of the sputtered metal [4]. Such relation can also be observed in our case, but non-linearly. For example, in W case, Schiffmann's group can achive average size of 1 nm, but our case is around 4 nm. Possibly, plasma density or certain condition of the sputtering device like magnetic field generated by permanent magnet attached backside the sputtering target is different, and we use stronger one, Nd magnet. The deposition apparatus used in this study have also permanent magnet, but magnetic field induced by the

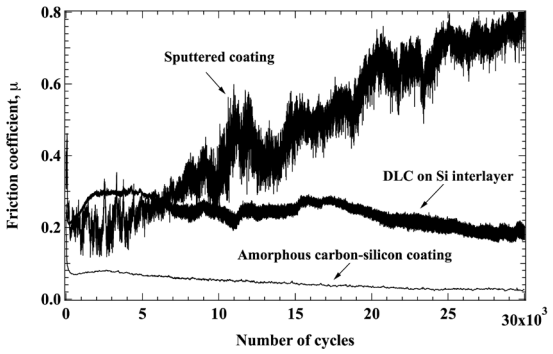

Fig.4 Tribological properties of various coatings investigated in this study

magnet was lower than the one we used previously. Such difference may change the cluster size of the sputtered materials.

Figure 4 shows friction results on various SiC coatings. Friction profile of amorphous carbon coating is also shown in this figure as a reference. The SPT specimen showed the high friction (μ~0.2), then coefficient of friction (COF) increased gradually. For amorphous carbon coating, COF increased up to 0.3 at first and decreased slightly. However, SiC specimen showed very interesting behavior. Although initial COF is rather high, ~ 0.3, but it suddenly decreased and reached 0.08 within 100 friction cycles. The COF then slightly decreased and μ of 0.04 could be achieved at the end of the friction tests. Optical images of the balls and coatings after the friction tests were taken, and these pictures reveal the formation of the tribofilm on the ball and small wear of the coatings.

4. Summary

In this study, we deposited on silicon-carbon coating by CVD and DC magnetron co-sputtering of silicon carbide target. Structural analyses and friction tests were performed.

- The structure of the investigated coatings is amorphous.
- Amorphous carbon phase in the coating could be identified.
- Very low friction coefficient which is less than 0.1 could be achieved in the coating.
- Tribofilm formation on the ball may play important role for low friction.

References

[1] A. Varma, V. Palshin, E.I. Meletis, C. Fountzoulas, Surface Eng, 15 (1999) 301-306.
[2] C. Chouquet, G. Gerbaud, M. Bardet, S. Barrat, A. Billard, F. Sanchette, C. Ducros, Surf Coat Tech, 204 (2010) 1339-1346.
[3] T. Takeno, H. Miki, T. Takagi, H. Onodera, Diamond and Related Materials, 15 (2006) 1902-1905.
[4] K.I. Schiffmann, M. Fryda, G. Goerigk, R. Lauer, P. Hinze, A. Bulack, Thin Solid Films, 347 (1999) 60-71.

Eighth International Conference on Flow Dynamics
November 9 - November 11, 2011

Preparation and Tribological Characterization of Carbon Nitride Coatings in a RF PECVD-DC PVD Hybrid Coating Process

Pengfei Wang[1*], Takanori Takeno[2], Koshi Adachi[3], Hiroyuki Miki[1], and Toshiyuki Takagi[1]
[1] Institute of Fluid Science, Tohoku University, Katahira 2-1-1, Aoba-ku, Sendai 980-8577, JAPAN
[2] Institute for International Advanced Interdisciplinary Research, Tohoku University Advanced Research and Education Organization, Aoba 6-3, Aramaki, Aoba-ku, Sendai 980-8578, JAPAN
[3] Laboratory of Nanointerface Engineering, Division of Mechanical Engineering, Tohoku University, 6-6-01 Aramaki-aza-aoba, Aoba-ku, Sendai 980-8579, JAPAN
* E-mail of corresponding author: wang@wert.ifs.tohoku.ac.jp

ABSTRACT

The CN_x coatings were prepared on Si (100) substrates using a hybrid coating process at different N_2/Ar flow ratios. With the increase of N_2/Ar flow ratio, the deposition rate increased, residual stress decreased, and the surface roughness first decreased and then increased. These results can be explained by the increase of nitrogen gas plasma with increasing N_2/Ar flow ratio. The frictions of CN_x coatings in air and N_2 gas stream were 0.17-0.19 and 0.33-0.42, respectively. The frictions seemed not affected by the N_2/Ar flow ratio. It is suggested that the friction behaviors of CN_x coatings are controlled by the tribo-films formed on the pin surfaces.

1. Introduction

The exceptional performances of carbon nitride (CN_x) coatings, such as low friction and high wear resistance have attracted great interest. However, those behaviors strongly depend on the fabrication method of CN_x coatings. Especially, the CN_x coatings produced by the ion beam assisted deposition method can give super-low frictions (μ<0.01) in inert gases [1]. Recently, a hybrid coating process, combining radio frequency plasma enhanced chemical vapor deposition (RF PECVD) and DC magnetron sputtering has been found to be a powerful technique in preparing the diamond-like carbon (DLC) and related coating materials [2]. The present work gives preliminary results on CN_x coatings prepared by the hybrid coating process at different N_2/Ar flow ratios, and the tribological properties of those new CN_x coatings were investigated.

2. Experimental Procedure

The CN_x coatings (~400 nm) were grown on Si (100) substrates using a unique hybrid coating process with the combination of RF PECVD and DC magnetron co-sputtering of the graphite target (Fig. 1). The coatings were deposited at a pressure of 1.3 Pa using a mixture of nitrogen and argon as a gas source with the N_2/Ar flow ratio varied from 0.05 to 10. Prior to deposition, the silicon substrates were etched by argon plasma for 10 min to remove the native oxide layer. During deposition, the substrate self-bias voltage induced by RF plasma and DC sputtering power were fixed at -400 V and 200 W, respectively.

The thickness of CN_x coatings were measured with a surface profiler. The residual stress of CN_x coatings was calculated by the bending beam method [3]. The surface roughness of CN_x coatings was measured by an atomic force microscope (AFM).

A pin-on-plate reciprocating tribometer was used for friction test. The CN_x coated Si substrates (10×20 mm) were driven to run against AISI 52100 balls (ϕ=6 mm) with a normal load of 1 N, a sliding speed of 3 mm/s, a stroke length of 3 mm, and a sliding period of 5000 cycles. Friction tests were performed in ambient air

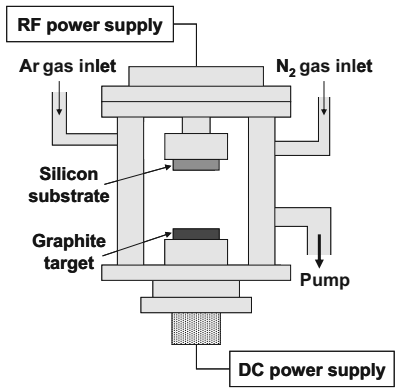

Fig. 1 Schematic illustration of hybrid coating process.

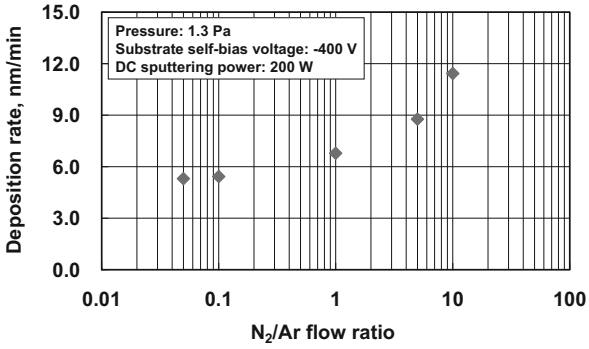

Fig. 2 Deposition rate of CN_x coatings prepared at different N_2/Ar flow ratios.

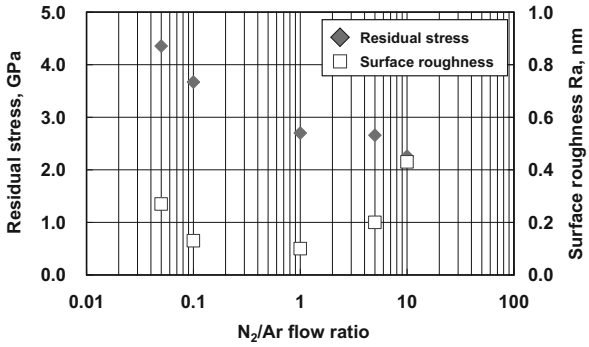

Fig. 3 Residual stress and surface roughness of CN_x coatings prepared at different N_2/Ar flow ratios.

(23-25 °C and 30-40 %RH) and N_2 gas stream (high purity nitrogen gas was supplied to the contact interfaces by a gas nozzle). The worn surfaces on both pin and plate were observed with an optical microscope.

3. Results and Discussion

The deposition rate of CN_x coatings slightly increased from 5.3 to 6.8 nm/min as the N_2/Ar flow ratio increased from 0.05 to 1, and then it increased sharply to 11.4 nm/min when the flow ratio further increased to 10 (Fig. 2). Whereas, the residual stress of CN_x coatings decreased greatly from 4.4 to 2.3 GPa with the increase of N_2/Ar flow ratio from 0.05 to 10 (Fig. 3). The surface roughness (*Ra*) of CN_x coatings decreased at first and then increased with increasing N_2/Ar flow ratio. The minimum value of 0.10 nm was obtained at the N_2/Ar flow ratio of 1 (Fig. 3). These phenomena can be explained by the increase of nitrogen gas plasma with increasing N_2/Ar flow ratio in the deposition chamber. Firstly, it caused higher sputter rate of graphite, thus increased the deposition rate. Secondly, it increased the amount and energy of nitrogen ions for bombardment of the coatings, which caused higher incorporation of nitrogen atoms in the coatings and thus decreased the residual stress of the coatings [4]. Finally, those nitrogen ions caused strong chemical sputtering and resulted in a smooth surface. However, higher energy caused additional etching of the deposited coatings and therefore increased the surface roughness.

Typical friction curves of CN_x coating (N_2/Ar=0.1) sliding against AISI 52100 pin in air and N_2 gas stream are shown in Fig. 4. The friction in air reached steady state after short run-in, the steady value was around 0.20. However, the friction in N_2 gas stream increased continuously without run-in period, and finally a steady value of around 0.30 was obtained. The average friction coefficients of CN_x coatings sliding against AISI 52100 pins in air and N_2 gas stream are summarized in Fig. 5. The frictions in N_2 gas stream (0.33-0.42) were about two times higher than those in air (0.17-0.19). This kind of behavior is similar to that of hydrogen-free DLC coatings [5]. The frictions of CN_x coatings in both conditions seemed not affected by the N_2/Ar flow ratio.

The typical optical images of worn surfaces on the AISI 52100 pins and CN_x coated Si plates after friction tests in air and N_2 gas stream are shown in Fig. 6. The CN_x coatings remained on the silicon substrates after friction tests. Tribo-films were formed on the pin surfaces both in air and N_2 gas stream. It is suggested that the friction behaviors of CN_x coatings are controlled by those tribo-films. Detailed analysis of tribo-films will be conducted for clarifying the friction mechanisms in close future.

4. Concluding remarks

(1) With the increase of N_2/Ar flow ratio, the deposition rate increased, residual stress decreased, and the surface roughness first decreased and then increased.

(2) The frictions in air and N_2 gas stream were 0.17-0.19 and 0.33-0.42, respectively. The frictions seemed not affected by the type of CN_x coatings.

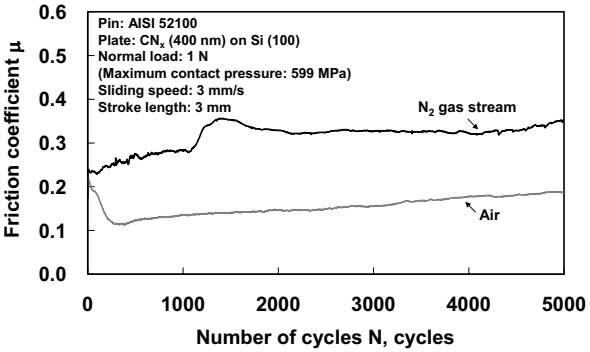

Fig. 4 Friction curves of CN_x coating (N_2/Ar=0.1) sliding against AISI 52100 pin in air and N_2 gas stream.

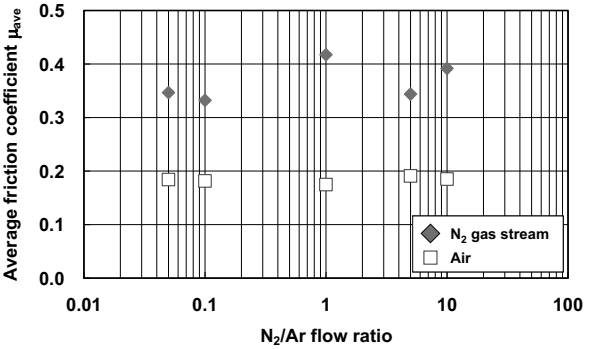

Fig. 5 Average friction coefficients of CN_x coatings sliding against AISI 52100 pins in air and N_2 gas stream.

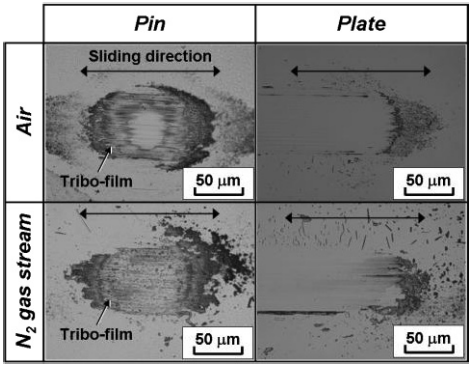

Fig. 6 Optical images of worn surfaces on the AISI 52100 pins and CN_x coated Si plates (N_2/Ar=0.1) after friction tests in air and N_2 gas stream.

Acknowledgement

This research is supported by the Global COE Program, "World Center of Education and Research for Trans-disciplinary Flow Dynamics", by Ministry of Education, Culture, Sport, and Technology in Japan.

References

[1] P. Wang, K. Adachi, *Tribology Online*, 6 (2011) 265-272.

[2] T. Takeno, J. Fontaine, M. Goto, K. Ito, H. Miki, K. Adachi, M. Belin, T. Takagi, *Proc. ICMCTF*, (2011) 5.

[3] G.G. Stoney, *Proc. R. Soc. Lond. A*, 82 (1909) 172-175.

[4] D.F. Franceschini, C.A. Achete, F.L. Freire Jr., *Appl. Phys. Lett.*, 60 (1992) 3229-3231.

[5] Y. Qi, E. Konca, A.T. Alpas, *Surf. Sci.*, 600 (2006) 2955-2965.

Multiple magnetization reversal in $Cr_3(PO_4)_2$

Alexander Vasiliev[1], Olga Volkova[1], Andrea Schmidt[2], Robert Glaum[2], Marius Millot[3], Jean-Marc Broto[3], Jiunn-Yuang Lin[4], Rüdiger Klingeler[5], Mahmoud Abdel-Hafiez[5], Anja Wolter[5], Bernd Buechner[5]
[1]Low Temperature Physics Department, Moscow State University, Moscow 119991, Russia
[2]Institute for Inorganic and Analytical Chemistry, Giessen University, Giessen D-35392, Germany
[3]National Laboratory of High Magnetic Fields, Toulouse University, Toulouse 31400, France
[4]Physics Department, National Chiao-Tung University, Hsinchu 30076, Taiwan
[5]Leibniz Institute for Solid State and Materials Research, Dresden D-01069, Germany
E-mail of corresponding author: vasil@mig.phys.msu.ru

The chromium (II) orthophosphate α-$Cr_3(PO_4)_2$ is a weak ferrimagnet with the Curie temperature T_C = 29 K confirmed by a λ-type peak in specific heat. Dominant antiferromagnetic interactions in this system are characterized by the Weiss temperature Θ = - 95 K, indicating reasonable frustration ratio $\Theta/T_C \sim 3$. In magnetically ordered state, the α-$Cr_3(PO_4)_2$ exhibits remarkable sequence of temperature-induced magnetization reversals sensitive to the protocol of measurements, i.e. either field-cooled (FC) or zero-field-cooled (ZFC) regimes.

1. Introduction

The chromium (II) orthophosphate, α-$Cr_3(PO_4)_2$, belongs to the vast family of anhydrous phosphates of divalent metals $M_3(PO_4)_2$ with M = Mg, Ca, Cr – Zn. The numerous crystal structures met in this multitude differ in the interconnection patterns of the metal-oxide polyhedra being related to those in the naturally occurring minerals farringtonite [1], graftonide [2], and sarcopside [3]. The basic motif in their structures is that of the chains of edge-sharing octahedra similar to olivine structure but with every fourth octahedron missing. This leaves a chain of three octahedra containing two inequivalent cation sites, the central M1 site possessing rather regular symmetry and two distorted M2 sites of the terminal octahedra.

One of the least studied members of this family, the chromium (II) orthophosphate, $Cr_3(PO_4)_2$, can be found it two distinct crystallographic modifications [4,5]. The crystal structure of the high-temperature $P2_1/n$ monoclinic phase β-$Cr_3(PO_4)_2$, stable in the temperature range 1250 – 1350 C, is close to that of farringtonite [1]. It contains interconnected zigzag chains of corner-sharing - edge-sharing elongated octahedra in the Cr2 – Cr1 – Cr1 – Cr2 sequence [5]. This phase experiences the long – range magnetic ordering at T_C = 36 K which is preceded by the short – range correlation maximum at ~ 60 K. The paramagnetic Weiss temperature in β-$Cr_3(PO_4)_2$ is negative, Θ = - 165 K, indicating strong predominance of antiferromagnetic interactions. At variance with "standard" antiferromagnetic behavior, the magnetization in the magnetically ordered state of β-$Cr_3(PO_4)_2$, i.e. at $T < T_C$, rises with lowering temperature. This may indicate either incomplete cancellation of primarily antiparallel sublattice's magnetizations or their canting due to the effects of magnetocrystalline anisotropy or Dzyaloshinskii – Moriya interaction.

2. Method

The present study of α-$Cr_3(PO_4)_2$ includes the sample preparation, the K and $L_{2,3}$ edges X-ray absorption (XAS) spectroscopy, measurements of specific heat in the range 2 – 100 K, magnetic susceptibility measurements in the range 2 – 300 K, and pulsed magnetic field measurements up to 50 T. The chromium (II) orthophosphate α-$Cr_3(PO_4)_2$ has been synthesized as high temperature phase from mixtures of $CrPO_4$ and Cr metal in the ratio 2:1 in evacuated silica ampoules at 1200 C (4 days) and quenched to room temperature [4]. By chemical vapour transport (transport agent I_2, 1200 C → 1100 C, quartz ampoule) deep blue-violet single crystals of α-$Cr_3(PO_4)_2$ with edge-lengths up to tenths of millimeter have been obtained.

The crystal lattice parameters determined at room temperature from X-ray diffraction pattern in the space group $P2_12_12_1$ are Z = 8, *a* = 8.4849(10) A, *b* = 10,3317(10) A, *c* = 14.206(2) A. The arrangement of the structural units in α – $Cr_3(PO_4)_2$ can be rationalized in terms of the close packed tubes (parallel to the crystallographic *b* axis) with Cr^{2+} on their inner surface and PO_4 tetrahedra on the outer surface as well as in the tube centres [4]. The spatial arrangement of Cr^{2+} ions is that of a double helix reminiscent of DNA molecule, as shown in Fig. 1. The atomic arrangement within one tube is related to the one in adjacent tubes by pseudo 3_1-screw axes. The local oxygen coordination of Cr^{2+} ions allows distinguishing five distorted square-planar groups $Cr1O_4$ – $Cr5O_4$ and a slightly distorted square-pyramidal unit $Cr6O_5$. One chain formed by vertex-sharing of alternating PO_4 and CrO_4 units (containing Cr1, Cr2 and Cr3) winds along the pseudo 3_1 axis. By edge-sharing between $Cr2O_4$ and $Cr5O_4$ this one is linked to a second type of chain. The latter consists of "dimers" $Cr4O_4$-$Cr6O_5$, which are linked via $Cr5O_4$ groups and PO_4 tetrahedra by vertex-sharing. This second chain winds around the 2_1 screw axes parallel to the *b* axis at the centre of the "tubes" described above. To avoid irreproducibility of results in different measurements due to the effects of magnetocrystalline anisotropy the necessary amounts of small single crystals were crushed into powder in the agate mortar and pressed into pellets.

3. Results and Discussion

The temperature dependence of the magnetic

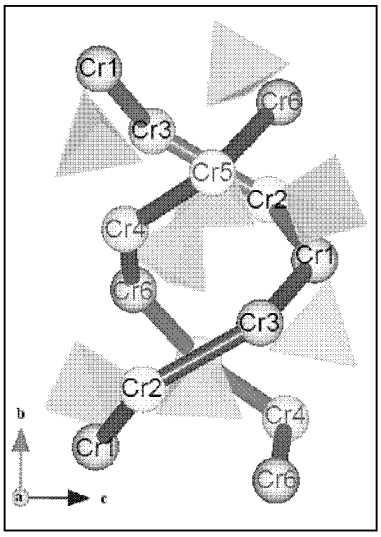

Fig. 1 The spatial arrangement of six inequivalent positions of Cr^{2+} ions in the crystal structure of chromium (II) orthophosphate, α-$Cr_3(PO4)_2$. The metal ions belonging to different chains are shown in red and black denominations. The phosphate groups PO_4 are represented by the grey tetrahedra.

susceptibility χ of α - $Cr_3(PO_4)_2$ taken at B = 0.1 T is shown in Fig. 2. The smooth increase of χ seen at lowering temperature is followed by the abrupt jump of the signal at T_C = 29 K in accordance with the earlier observations [4]. This is what to be expected from the compound whose magnetization in the magnetically ordered state contains the ferromagnetic component. At further lowering temperature, however, the magnetic susceptibility evidences remarkable sequence of temperature-induced magnetization reversals sensitive to the protocol of measurements, i.e. either field-cooled (FC) or zero-field-cooled (ZFC) regimes, as shown in the Inset to Fig. 2. Note, that in FC regime the magnetic susceptibility even shows "diamagnetic" response at lowest temperatures, which rapidly disappears at the increase of external field above 0.1 T.

The temperature dependence of the inverse magnetic susceptibility $\chi^{-1}(T)$, shown in Fig. 6, indicates the predominance of antiferromagnetic interactions in α-$Cr_3(PO_4)_2$. The experimental data in the range 200 – 300 K can be fitted by the Curie – Weiss law with inclusion of the temperature independent term χ_0, i.e.

$$\chi = \chi_0 + \frac{C}{T-\Theta} = \chi_0 + n\frac{N_A g^2 S(S+1)\mu_B^2}{3k_B(T-\Theta)},$$

where C and Θ are the Curie and Weiss constants, N_A, μ_B, and k_B are the Avogadro, Bohr and Boltzmann constants, g is the g-factor. According to this fitting, the paramagnetic χ_0 = 1.6 $\times 10^{-4}$ emu/mol is that of summation of diamagnetic and van Vleck contributions, the Weiss temperature Θ = - 96 K is large and negative, and effective magnetic moment $\mu_{eff} = [ng^2S(S+1)]\mu_B$ = 4.5 μ_B is somewhat smaller as compared with the spin – only value 4.9 μ_B per Cr^{2+} ion. The reduced value of the effective magnetic moment μ_{eff} is hardly to be attributed to the presence of unquenched orbital magnetic moment which can reduce the effective g – factor. While there

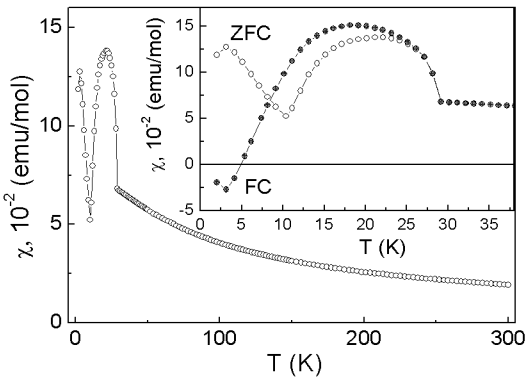

Fig. 2. The temperature dependence of magnetic susceptibility in α-$Cr_3(PO_4)_2$ taken at rising temperature at B = 0.1 T after cooling in zero field. The Inset represents the enlarged portions of χ(T) curves taken with rising temperature after cooling at B = 0 (ZFC regime) and B = 0.1 T (FC regime).

are no either X-band (~ 9 GHz) or Q-band (~35 GHz) electron spin resonance (ESR) studies of "ESR-silent" non-Kramers $3d^4$ Cr^{2+} ions, the measurements at very high frequencies (~ 90 – 440 GHz) provided value of g-factor of Cr^{2+} in frozen aqueous solutions g = 1.98 [6].

At lowering temperature, the $\chi^{-1}(T)$ in α-$Cr_3(PO_4)_2$ deviates from linearity showing presence of ferromagnetic interactions in the system. It is best seen in the temperature dependence of effective Curie constant $C = (\chi - \chi_0)\times(T - \Theta)$. Evidently, the short range magnetic correlations develop in this compound far above the magnetic ordering temperature in correspondence with significant reduction of the jump ΔC_p in specific heat at T_C.

The α-$Cr_3(PO_4)_2$ is a rare case of weak ferrimagnet based on the same transition metal in unique oxidation state Cr^{2+}. The magnetic ordering at the Curie temperature T_C = 29 K is confirmed by a λ-type peak in specific heat. Dominant antiferromagnetic interactions in this system are characterized by the Weiss temperature Θ = - 95 K, indicating a frustration ratio Θ/T_C ~ 3 reasonable for a three-dimensional magnetic entity. Weak ferrimagnetism and multiple magnetization reversal phenomena seen in this compound could be ascribed to incomplete cancellation and distortion of partial spontaneous magnetization functions of Cr^{2+} in its six crystallographically inequivalent positions.

References

[1] A. Nord and T. Eriksson, Am. Mineral., **70** (1985), 624.

[2]E. Kostner and J.R. Rea, Inorg. Chem., **13** (1974), 2876.

[3]P.B. Moore, Am. Mineral., **57** (1972), 24.

[4]R. Glaum and A. Schmidt, Z. anorg. allg. Chem., **623** (1997), 1672.

[5]R. Glaum et al. Z.anorg.allg.Chem., **637** (2011), 1052.

[6] J. Telser et al., Inorg. Chem., **37** (1998), 5769.

PS3: Plasma Medicine and Cell Engineering

Eighth International Conference on Flow Dynamics
November 9 - November 11, 2011

Nonthermal plasma-mediated cancer cell death; Targeted cancer treatment

Byul-Bo Ra Choi, Uk-Kyu Kim[1], Hae-Jun Lee[2], Jae-Koo Lee[3] and Gyoo-Cheon Kim*

Department of Oral Anatomy, [1] Department of Oral & Maxillofacial Surgery, School of Dentistry, [2]Department of Electrical Engineering, Pusan National University, Yangsan 626-870, Korea. [3] Department of Electronic and Electrical Engineering, Pohang University of Science and Technology, Pohang 790-784, Korea

ABSTRACT

Non-thermal air plasma can kill cancer cells. However, there is no selectivity between normal and cancer cells. Therefore, cancer specific antibody conjugated gold nanoparticle (GNP) was pretreated before plasma irradiation. Stimulation of antibody conjugated GNP by plasma treatment resulted in a significant decrease in viability of cancer cells. This technology shows the feasibility of using plasma therapy for killing cancer cells selectively.

1. Introduction

Cancer is a disease that cell grows without controlling. Unfortunately, cancer death rate is increasing all over the world every year, so a lot of therapy is being developed in order to decrease cancer attack rate. Because conventional methods have limitations, a novel therapy is strongly requested. Plasma is known to effect to kill cancer cells without dermal damages [1]. The nonthermal plasma-mediated induction of apoptosis has been clearly demonstrated by a recent paper that investigated cellular signaling related to an apoptotic process [1]. Plasma, however, can't distinguish normal cell from cancer cell. For dealing with this problem, an antibody against overexpressed protein in cancer cells and GNP which is harmless against the human body are used in this therapy [2]. Gold nanoparticles can be used by conjugating with cancer specific antibody to achieve the selectivity in plasma treatment [3-5]. Conjugated nanoparticles can bind selectively to target cells, which are then affected by the plasma. In many cancer cells, some kinds of proteins have known to be over expressed. These proteins are regarded as an attractive target for cancer therapy [6-7]. In this study, we treated plasma with cancer specific antibody conjugated GNP in order to kill cancer cells selectively.

2. Method

Non-thermal air plasma source Fig. 1 shows the schematic diagram of experimental setup. The plasma source was designed to operate in ambient air with 22kHz, few kV sinusoidal voltage source. The plasma source consists of a polytetrafluoroethylene (PTFE) dielectric and Cu electrodes on both sides of the PTFE. The plasma source was a Cu-PTFE-Cu stacked structure of circuit board. The electrode structure was formed by a conventional chemical etching process. The plasma was generated by the fringing field near the front face electrode.

Cell culture Human melanoma G361 cell lines were purchased from the ATCC (Rockville, MD, USA).

Conjugation An aqueous solution of 11-mercaptoundecanoic acid (MUA) (0.1 mg/ml) is added to the colloidal gold suspension and incubated overnight. MUA-modified gold nanoparticles are reacted with a mixture of 1 mM N-hydroxysuccinimide (NHS) and 1 mM N-ethyl-N'-(3-dimethylaminopropyl) carbodiimide (EDC) solution for 20 min. Gold nanoparticles are incubated with 250 μg/ml anti- p-FAK antibodies in PBS buffer (1 mM, pH 7.0) for 6 hr.

Immunofluorescence Cells were treated with the mouse anti-FAK antibody conjugated gold nanoparticle (FAK-GNP), and then fixed in 4% paraformaldehyde. Cells were permeablilzed with 0.2% Triton X-100 in Fluorescent images were observed and analyzed under Zeiss LSM 510 laser-scanning confocal microscope (Goettingen, Germany).

Plasma treatment After 4 x 10^4 G361 cells were incubated on cover slips for 24 hr with the anti-FAK conjugated gold nanoparticle, cover slips without media were placed 2 mm from the plasma source and exposed to a 30 sec plasma treatment.

Live/Dead staining Calcein AM stained the intracellular cytoplasm of live cells, and ethidium homodimer-1 (EthD-1) stained the nucleic acids of dead cells. The cells were washed twice in cold PBS and stained with calcein AM (2 uM), and ehtD-1 (4 uM) for 30 min at 37℃. Fluorescent images were observed under Zeiss LSM 510 laser-scanning confocal microscope (Goettingen, Germany).

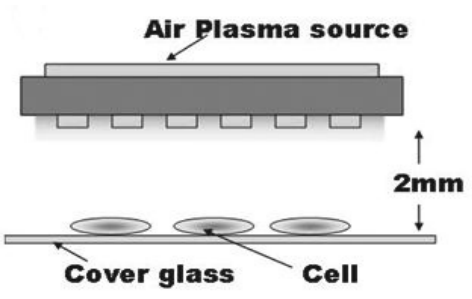

Fig. 1. Schematic diagram of plasma source.

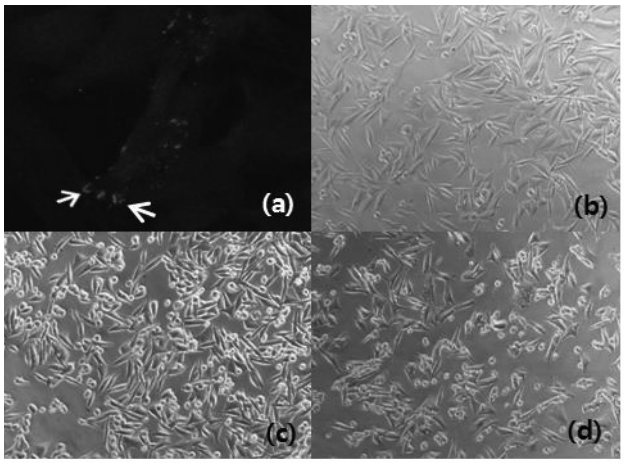

Fig. 2. Immunocytochemistry and plasma treatment on the G361 cells. (a) GNP-FAK uptake in G361 cells. (b) Control (c) Plasma treatment without GNP. (d) Plasma treatment with GNP.

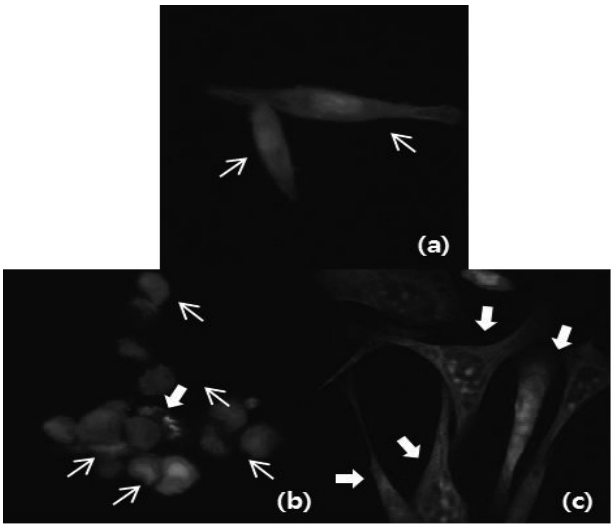

Fig. 3. Calcein AM and ethidium homodimer-1 (EthD-1) stain in the G361 cells. (a) Control (b) Plasma treatment without GNP-FAK. (c) Plasma treatment with GNP-FAK.

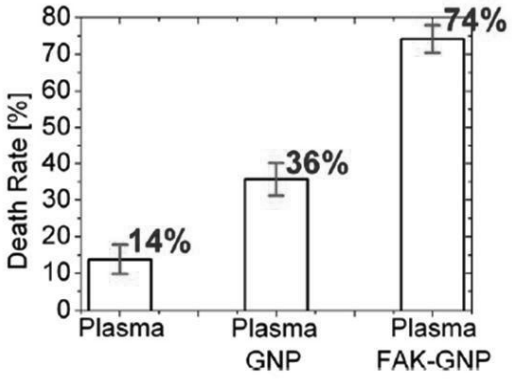

Fig. 4. Contribution of FAK-GNP to dramatic G361 cells death with plasma treatment.

3. Result and Discussion

Fig. 2 (a) shows the uptake of FAK-GNP by G361 melanoma cells. Gold nanoparticles were conjugated with a fluorescein conjugated, affinity purified secondary antibody and the results were examined by confocal laser microscopy. Once FAK-GNPs translocated across the cell membrane, they bound to FAK. As a result nanoparticles appear in the lamellipodial edges and in the outlining areas of the cells. The bright (green) spots in figure 1 represent the gold nanoparticles absorbed by G361 cells over 24 h. To show that plasma can stimulate the GNP inside of the cell, G361 melanoma cancer cells were treated with the plasma for 30 s following 24 h incubation together with colloidal GNP. Fig. 2 shows cells after the plasma treatment without (Fig. 2(b)) and with (Fig. 2(c)) GNP. In the case of treatment with GNP (Fig. 2(c)), the cell morphology was changed to round shape and damage. We confirmed live and death by fluorescence staining calcein AM and Ethd-1 (Fig. 3). In control, only calcein AM (↑) dyed as green. In cells treated with plasma without GNP-FAK, a few cells were stained by Ethd-1 (⬆) and most cells were stained by calcein AM (↑). In cells treated with plasma and GNP-FAK, most cells were stained by only Ethd-1 (⬆) dyed as red, which means that most cells were killed. When the three groups of cells were irradiated by the plasma, the cell death rates were 14%, 36% and 74%, respectively (Fig. 4). After the FAK-GNPs bind to FAK proteins specifically, irradiation of plasma stimulated gold nanoparticles caused deactivation of FAK, thereby drastically increasing the death rate to 74%. Founded on this result, plasma treatment with GNP-FAK can kill cell effectively more than plasma treatment without GNP-FAK. Especially, by using cancer cell specific antibody conjugated GNP, it can kill cancer cell selectively.

4. Concluding Remarks

Nonthermal plasma can stimulate GNP located inside cells to cause cell death even with a low dose plasma treatment. This air plasma is coupled with antibody-GNP, resulting in a significant increase in cancer cell death selectively.

Reference

[1] G. J. Kim, Appl. Phys. Lett, **96** (2010), 021502
[2] G. C. Kim, J. Phys. D: Appl. Phys, **42** (2009), 032005
[3] R.F. Service, Science **310** (2005) 1132
[4] K. Sokolov, Cancer Res. **63** (2003) 1999
[5] R.G. Rayavarapu, Int. J. Biomed. Imag. **2007** (2007) 29817
[6] Daniels TR, Clin Immunol, **121** (2006), 144
[7] Herbst RS, International Journal of Radiation Oncology Biology Physics **59** (2004), S21

Eighth International Conference on Flow Dynamics
November 9 - November 11, 2011

Enhancing Skin Repair Through A 3D *In-Vitro* Human Skin Equivalent Model

Kerry J. Manton[1], Rebecca Dawson[1], Yan Xie[1], Derek Van Lonkhuyzen[1], David Leavesley[1] and Zee Upton[1]
1. Tissue Repair and Regeneration Program, Institute of Health and Biomedical Innovation.
Queensland University of Technology, 60 Musk Avenue, Kelvin Grove, QLD, 4059, Australia.
Corresponding author: kerry.manton@qut.edu.au

ABSTRACT

Chronic wounds are a major healthcare problem whose burden is expected to increase as the world population ages. The current animal models of wound healing are inadequate because they utilise mice and rats which heal through contraction as opposed to re-epithelisation or porcine models which are extremely expensive. We have developed a 3D *in-vitro* model of human skin (DED-HSE) which shows comparable morphology and keratin protein expression to native skin. We are able to examine epidermal and dermal thickness wound healing over 12 days. We can also investigate the effect of novel reagents on wound healing.

1. Introduction

Chronic wounds are defined as wounds that do not heal within three months. They often result from an underlying disease like diabetes or peripheral vascular disease. Chronic wound care is reported to cost around 3% of total health care expenditure in developed countries. Expectations are that this burden will increase due to the aging population. Animal models of wound repair are inadequate due to the different modes of healing in rodents and humans. The current gold standard, porcine models are expensive, thus the need to develop a human skin model in the laboratory which can be utilised to study skin biology and wound repair.

2. Method

Skin Samples: Skin samples were obtained from adult patients undergoing elective surgery which resulted in a surgical discard. The tissue was obtained with patient consent and institutional ethical approval.

Isolation of Primary keratinocytes: Primary keratinocytes were isolated as described previously [1,2]. Briefly, the epidermis was separated from the dermis by incubation in 0.125% trypsin at 4°C overnight. The dermal/epidermal junction was scraped and cells seeded onto irritated murine fibroblast 3T3 cells (ATCC) and cultured in Full Greens medium.

Generation of the DED-HSE model - The DED-HSE model was generated as described previously [1,2]. Sterile stainless-steel rings with an internal diameter of 9mm were placed on the papillary side of each DED piece. Keratinocytes were transferred into the rings and incubated for 2 days. The rings were removed and the DED-HSEs were then lifted to the air:liquid interface using a stainless-steel grid for 9 days to allow for stratification of the epidermal layer (Figure 1).

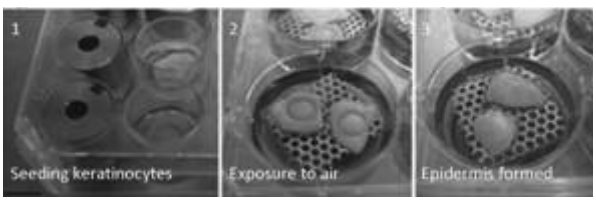

Figure 1. Generation of 3D *in-vitro* DED-HSE

Generation of wounded DED-HSE model

6 mm partial-thickness excisional wounds were created in the DED-HSEs with a 6 mm biopsy punch (Stiefel, Castle Hill, Australia) excising through the epidermis. The epidermis was then peeled away from the DED with forceps and discarded. A full-thickness wound was created in the DED-HSE using a 4mm biopsy punch which cuts through all layers of the DED-HSEs, both epidermal and dermal. This was followed by removal of the 4mm diameter epidermal/dermal core. The DED-HSEs were cultured in Full Greens media at the air:liquid interface for either 0, 3, 7 or 12 days. Samples were then fixed in formalin and paraffin embedded for immunohistochemical analysis.

Immunohistological analysis of DED-HSE

DED-HSE was fixed in formalin, embedded in paraffin and sectioned. These were then either stained with Hemotoxylin and Eosin (H&E) or underwent antibody specific staining with HRP-conjugated antibodies and DAB as the chomogen[2].

3. Results and Discussion

We have generated an *in-vitro* 3D model of human skin which shows comparable morphology and similar expression of the basal cell marker, p63 and epidermal keratin protein k1/10/11 to native skin (Figure 2).

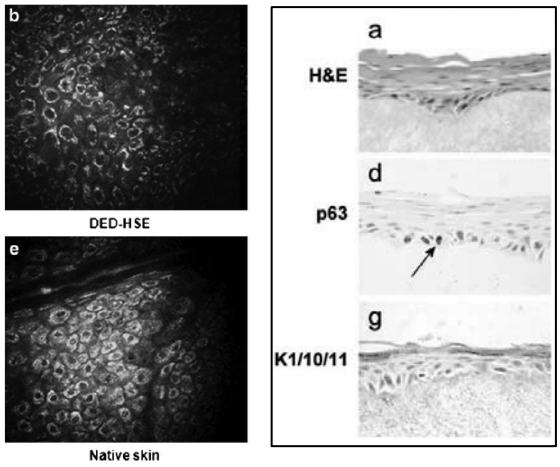

Figure 2. Left panels are multiphoton images of the DED-HSE and native skin. Right panels are H&E and IHC staining of p63 and K1/10/11 in the DED-HSE.

We have been able to create an epidermal thickness wound in the 3D *in-vitro* DED-HSE, monitor and quantitate its healing over a 12 day period (Figure 3).

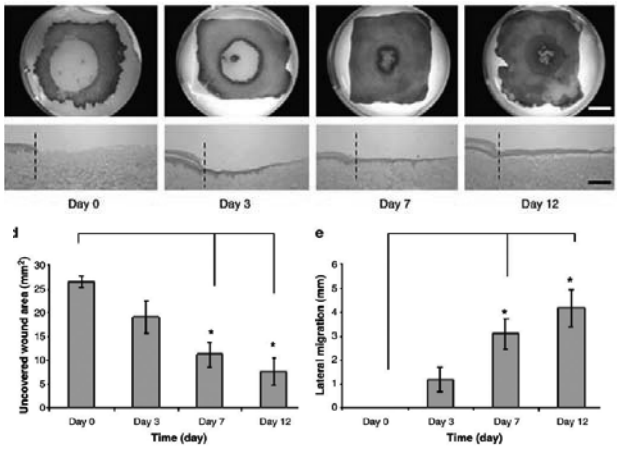

Figure 3. Epidermal wound healing over 12 days in our 3D *in-vitro* DED-HSE model. Top row is MTT staining, purple indicates viable cells. Middle row shows histological staining of paraffin embedded sections. The left graph shows quantitation of the wounded area and the right graph shows epidermal cell migration into the wound.

We have utilised the epidermal wounded 3D *in-vitro* DED-HSE model to examine the effect of a novel wound healing treatment (Figure 4).

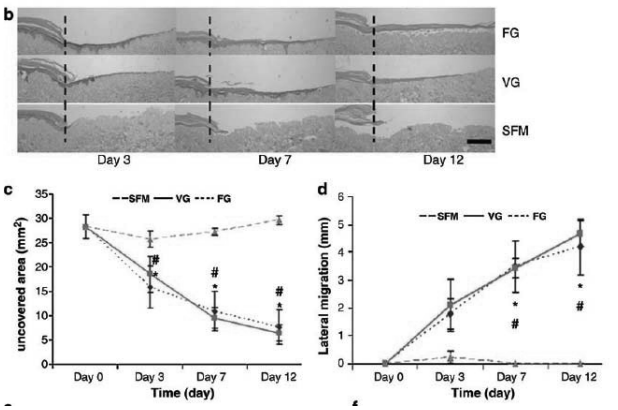

Figure 4. Effect of a novel wound healing treatment VG on epidermal wound healing over 12 days in our 3D *in-vitro* DED-HSE model. Top row shows histological staining of paraffin embedded sections treated with FG (positive control), VG (treatment) and SFM (negative control). The left graph shows quantitation of the wounded area and the right graph shows epidermal cell migration into the wound.

4. Concluding remarks

We have shown that a realistic and practical model of human skin can be engineered *in-vitro.* It can be utilised to study human wound healing and evaluate the effects of various wound healing agents on the process. This model is currently being utilised in our laboratory to test the effects of hyperbaric oxygen treatment, silicones and ultraviolet radiation on human skin.

5. References

1. Xie, Y., Rizzi, S., Dawson, R., Lynam, E., Richards, S., Leavesley, D. & Upton, Z**.** (2010) Development of a 3-dimensional human skin equivalent wound model for investigating novel wound healing therapies. *Tissue Engineering Part C Methods,* 16:1111-1123.

2. Dawson, R.A., Upton, Z**.,** Malda, J. & Harkin, D.G. (2006) IGF-I used in conjunction with IGFBP-5, EGF and vitronectin supports rapid preparation of cultured skin transplants under serum-free conditions. *Transplantation,* 81:1668-1676.

6. Acknowledgements

We wish to acknowledge the contribution of Ms Tara Fernendaz, Ms Emily Lynham, Ms Jessica Heinemann and Ms Jacqui McGovern.

Eighth International Conference on Flow Dynamics
November 9 - November 11, 2011

Experimental Studies of Plasma Medicine on Prevention for the Adhesion

Hajime Sakakita[1] and Yuzuru Ikehara[2]
[1]Innovative Plasma Technologies Group, Energy Technology Research Institute, National Institute of Advanced Industrial Science and Technology (AIST), Tsukuba, Japan
[2]Molecular Medicine Team, Research Center for Medical Glycoscience, National Institute of Advanced Industrial Science and Technology (AIST), Tsukuba, Japan
E-mail of corresponding author: h.sakakita@aist.go.jp

ABSTRACT

This study has been conducted to apply a plasma device which based on the dielectric barrier discharge for the medical use. The plasma jet has been used for the purposes of blood coagulation, wound healing, etc. Usually, high frequency electrical coagulator is used for blood coagulation. In this case, typically, tissues are burned out, and problems associated with scar formation are sometimes occurred after the operation. While, our plasma jets have been treated to the adipose tissues around lower gastric area of mouse. From the histopathological observation, it was found that the tissue damage which induces the adhesion was not observed after two weeks.

1. Introduction

Recently, plasma medical science has been studied, and medical uses of plasma technologies have also been developed [1-4]. An example of the practical use of the atmospheric pressure plasma in medical care is an endoscopic submucosal desection (ESD), which is performed to ablate residual tumors and stop bleeding. This type of plasma is known as an argon plasma coagulator (APC) [5]. However, the treatment with either APC, electrical coagulator and laser coagulator may cause tissue injuries during the intervention, and sometimes cause scaring problems. Therefore, a new type of blood coagulator to reduce tissue damages is strongly desired by physicians.

2. Method

Concerning about reducing risk for perforation and submucosal tissue injury under ESD, instead of the arc plasma, utilizing glow-like plasma is more feasible to prevent accidents. Recently, several techniques to generate the atmospheric pressure plasma have been developed [6,7]. In the present study, plasma jet based on the dielectric barrier discharge is applied [8,9]. Typically, the peak-to-peak voltage $V_{p\text{-}p}$ applied to the electrode is ~7.6 kV, and the frequency is ~67 kHz. The gas flow rate is ~2.0 *l*/min for helium gas, and working gas purity is 99.995 %

3. Results and Discussion

At first, in order to study the effect of tissue damages, the electrical coagulator has been applied to omentum and mesenterium near the stomach of C57BL6 mouse, as shown in Fig. 1(a). After the operation, burned out scars are shown in Fig. 1(b). After the operation in Fig. 1(c), the abdomen is sutured. After two weeks, treated tissue sample were cut out from treated area (Fig. 1(d)). Results from histopathological analysis demonstrated scar that was derived from tissue injury (Fig. 1(e), forming adhesion between small intestines surrounded by a dashed circle).

In order to evaluate the tissue damages, the mild plasma has also been applied to the adipose tissues, as shown in Fig. 2(a). Even after the operation, it is difficult to distinguish the treatment effect, as shown in

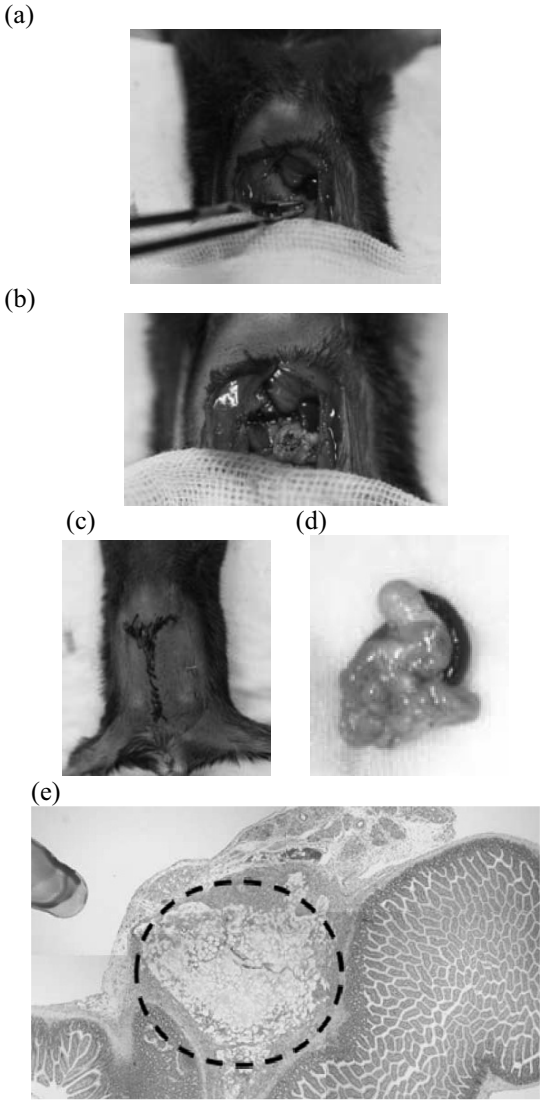

Fig. 1 Photographs in the case of high- frequency electrical coagulator: (a) during the treatment of the coagulator, (b) after the operation, (c) after the suturing, (d) tissues after two weeks, and (e) photomicrograph by histopathological observation.

Fig. 2(b). After the operation in Fig. 2(c), the abdomen is sutured. After two weeks, the abdomen was cut open again, and sample tissues of the treated part shown in Fig. 2(d) were taken. From the histopathological observation shown in Fig. 2(e), the tissue damage which induces the adhesion was not observed.

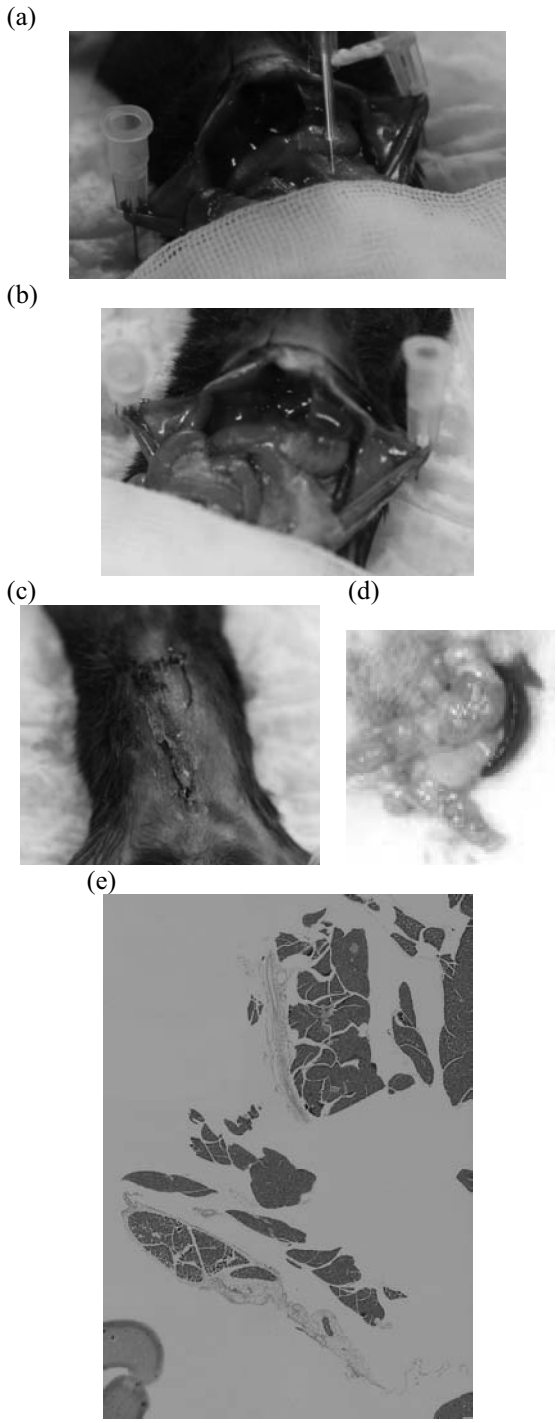

Fig. 2 Photographs in the case of the mild plasma. (a) during the treatment of the plasma, (b) after the operation, (c) after the suturing, (d) sample tissues after two weeks, and (e) photomicrograph by histopathological observation.

4. Concluding remarks

Generally, high-frequency electrical coagulator and APC have been used to coagulate the blood bleeding. However, this type of coagulation method has possibilities to generate scarring problems such as adhesion after the operation, due to the tissue injury. Suppression of the adhesion is one of the important issues in the surgical procedures. In order to study the effect of tissue damages, the mild plasma has been applied to the adipose tissues around lower gastric area of C57BL6 mouse. After two weeks, the abdominal cavity was examined, and prepared sample tissues from the treated area. Histopathological analysis showed that no apparent adhesion and scaring tissue was detected, suggesting that the mild plasma might be effective to reduce the adhesion after the operation.

Acknowledgements

We thank Dr. N. Shimizu and Dr. K. Nozaki at The University of Tokyo Hospital for their fruitful discussions on the clinical uses of the plasma. We thank Dr. S. Kiyama, Ms. S. Tomita, Dr. S. Chang, Dr. K. Nishimura, and Dr. M. Nakanishi at the National Institute of Advanced Industrial Science and Technology (AIST) for their technical supports. We also thank Dr. Y. Hasegawa, Dr. H. Narimatsu, Dr. K. Ueno and Dr. T. Kubota at AIST for their continuous encouragements. This study was financially supported by the AIST Innovation Promoting Project and in part by the Program for the Promotion of Basic Research Activities for Innovative Biosciences (PROBRAIN) and the New Energy and Industrial Technology Development Organization (NEDO) of Japan.

References

[1] Stoffels E *et al* 2006 *Plasma Sources Sci. and Tech.* **15** S169
[2] Fridman G *et al* 2008 *Plasma Process. Polym.* **5** 503
[3] Morfill G E *et al* 2009 *New J. Phys.* **11** 115011
[4] Lloyd G *et al* 2010 *Plasma Process. Polym.* **7** 194
[5] Grund K E *et al* 1994 *Endosope Surgery* **2** 42
[6] Kanazawa S *et al* 1988 *J. Phys. D: Appl. Phys.* **21** 838
[7] Teschke M *et al* 2005 *Proc. 48th Annual Tech. Conf. (Soc. Vac. Coasters)* **505/856-7188** 1
[8] Sakakita H and Ikehara Y 2010 *Plasma and Fusin Res.* **5** S2117-1
[9] Sakakita H *et al* 2010 *Japanese Patent* **2010**-154948

Eighth International Conference on Flow Dynamics
November 9 - November 11, 2011

Regenerative Medicine Using Novel Biomedical Plasma Techniques

Takamichi Hirata[*,**], Chihiro Tsutsui[**], and Akira Mori[*,**]
[*]Department of Biomedical Engineering, [**]Nano Carbon Bio Device Research Center,
Tokyo City University, Tokyo, Japan
e-mail: hirata@bme.tcu.ac.jp

ABSTRACT

We performed experiments involving direct irradiation of tissues and cells using an atmospheric-pressure plasma source for regenerative medicine. Cells irradiated by plasmas exhibited little evidence of cell membrane destruction due to surface interactions such as collisions or ionization of gas molecules. Furthermore, measurements of the nitric oxide (NO) in a medium containing culture cells using a NO sensor revealed that NO is produced by calmodulin that combines with Ca^{2+} ions released from a cell subjected to an external stimulus and combines with nitric oxide synthase (NOS) surface.

1. Introduction

Many studies have been conducted on novel plasmas in the fields of chemistry, solid-state physics, and nanomaterials. Such plasmas have a boundary reaction field in a liquid or a gas–liquid phase. Examples include liquid plasmas, which are plasmas generated in media (e.g., water and ionic solutions) that are denser than gases, and atmospheric-pressure plasmas, which are non-equilibrium plasmas generated under atmospheric pressure or in a gas flow.

Atmospheric-pressure plasmas are indispensable for sterilizing, disinfecting, decomposing hazardous materials, and modifying material surfaces.[1-2] They are also used in new fields of biomedical science. Such plasma technologies include medical sterilization and treatment using floating-electrode dielectric barrier discharge (FE-DBD).[3] These technologies have been attracting considerable attention in recent years as practical applications of plasmas.

Nitric oxide (NO) is produced from arginine and oxygen by various enzymes known as nitric oxide synthase (NOS). Phagocytes such as monocytes, macrophages, and neutrophils, which are part of the immune system, generate NO to kill pathogens that infiltrate cells from the outside. However, generation of excessive NO hinders cell reproduction. NO is unusual in that it is always produced by endodermal cells in blood vessels. When a cell is externally stimulated, the calcium concentration of the cell transiently increases, which promotes NOS activity, resulting in NO being discharged from endodermal cells in blood vessels. Therefore, promoting blood circulation is considered to greatly increase the activation of growth factors in cells.

Against this background, we sought to clarify the relationship between NO and growth factors in cells by directly measuring NO produced from culture cells that are irradiated by an atmospheric-pressure plasma and by visualizing the signal from Ca^{2+} ions, which participate in NO production and NOS activation.

2. Method

As shown in Fig. 1, the plasma source has a coaxial structure consisting of a 1-mm-diameter tungsten wire in a glass capillary (diameter of plasma generation area: 8 mm; tip diameter: 1 mm) with a grounded tubular electrode wrapped around the outside of the capillary. A high-voltage power supply provides a high voltage for plasma generation. The following conditions were used to generate the plasma: applied voltage: 8 kV; frequency: 3 kHz; helium (He) gas flow rate: 1 L/min; plasma irradiation time: 1–300 s.

The experiment was conducted by preparing a culture medium (a serum-free medium) containing mouse fibroblasts (NIH 3T3; cell concentration: 1×10^5 cells/mL) on a 90-mm-diameter polypropylene culture dish. The culture dish was irradiated by the plasma and was then placed in a CO_2 incubator (temperature: 37°C; CO_2 density: 5%). The culture time was 24 h. Several groups have developed electrochemical techniques (i.e., NO sensors) for measuring NO.[4] Direct measurement of NO was performed using a catheter-type NO sensor. Optical observations of the signal from Ca^{2+} ions in the cell were performed by confocal laser microscopy.

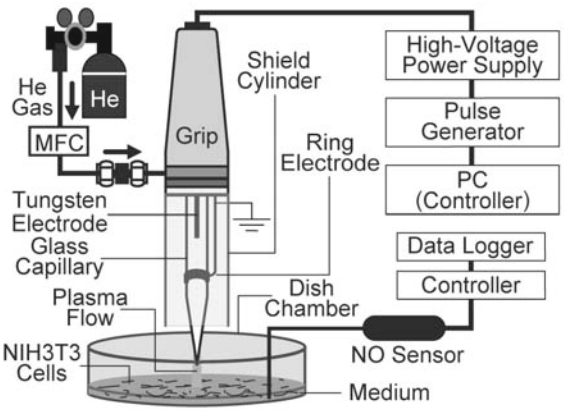

Fig. 1. Schematic view of atmospheric-pressure plasma source.

3. Results and Discussion

Figure 2 shows typical microscope images of NIH 3T3 cells that had been cultured in a serum-free medium for 24 h and dyed with hematoxylin-eosin (HE) after. The black dashed circles in Figs. 2(a) and (b) indicate areas that had been exposed to He gas flow and a plasma, respectively. Cell growth was inhibited when only He gas was flowed through the medium because gas flow promotes cell floatation by agitating the gas in the culture [Fig. 2(a)]. In contrast, cell floatation did not occur and healthy growth was observed for plasma irradiation [Fig. 2(b)].

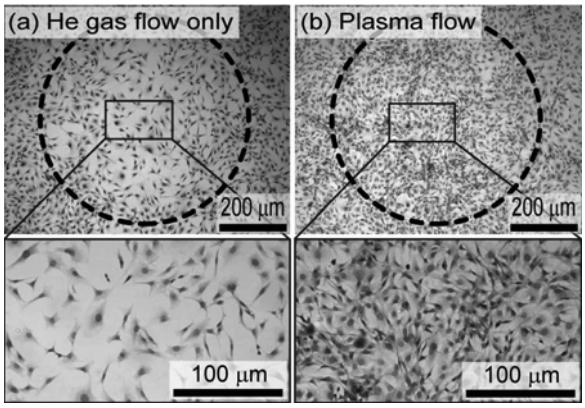

Fig. 2 Typical microscope images of NIH 3T3 cells dyed with hematoxylin eosin (HE).

Figure 3 shows the NO concentration in the medium as a function of time for a plasma flow time of 90 s. No large change in the NO concentration is observed for the medium that did not contain NIH 3T3 cells [Fig. 3(a)]. In contrast, for the medium containing NIH 3T3 cells [Fig. 3(b)], the NO concentration reaches a maximum value at about 40 s and it subsequently decreases gradually. The sharp peak in Fig. 3(b) is thought to be caused by a potential change in the medium due to plasma irradiation. The effect that NO has on growth factors is attracting particular interest. The results of this study are very similar to those obtained by other groups.

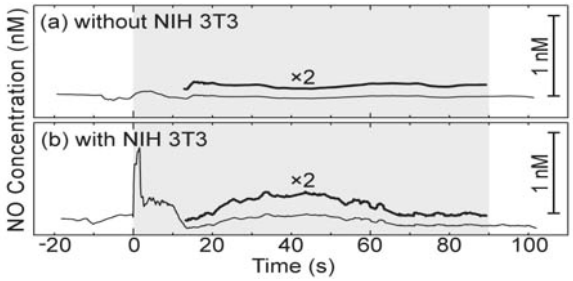

Fig. 3 NO concentration in the medium as a function of plasma flow time.

NOS, which produces NO, is one of the most highly regulated enzymes in biology. It has three known isoforms: a neuronal isoform (nNOS), an endothelial constitutive isoform (eNOS), and an inducible isoform (iNOS). nNOS and eNOS are activated by binding with a calcium-binding protein (calmodulin) at binding sites on the NOS surface. A cell releases calcium ions (Ca^{2+}) when it is subjected to an external stimulus (e.g., heat). NO is produced by calmodulin, which combines with Ca^{2+} ions released from a cell with NOS surface. Figure 4 shows confocal laser microscopy images that indicate the calcium ion distribution. The fluorescence indicator used to measure the Ca^{2+} ion concentration and visualize Ca^{2+} ion signals of cells is Screen Quest™ Fluo-8 NW Calcium Assay Kits. Fluorescence from Ca^{2+} ions was not observed from the control sample [Fig. 4(a)] or the sample that had been exposed to only He gas flow [Fig. 4(b)]. In contrast, fluorescence was observed from samples that had been exposed to plasma flow [Figs. 4(c) and (d)]. Therefore, NO is thought to be produced in the NIH 3T3 cells by calmodulin. Calmodulin combines with Ca^{2+} ions that are released from cells that have been subjected to an external stimulus (especially, electrical stimuli) and combines with the NOS surface. Thus, NO is not produced by the plasma source.

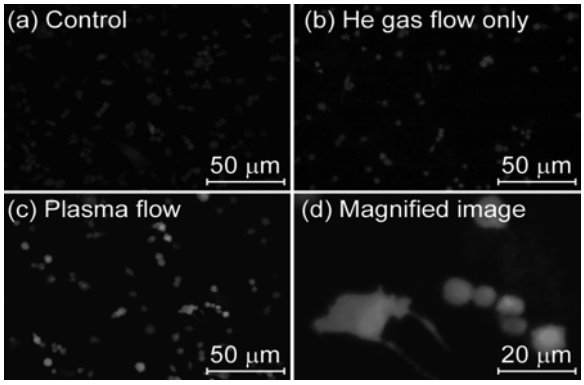

Fig. 4 Typical confocal laser microscopy images of NIH 3T3 cells dyed to visualize Ca^{2+} ions.

4. Conclusions

Experiments have been performed involving directly irradiating body tissues and cells with an atmospheric-pressure plasma for regenerative medicine. When cells were irradiated by a plasma emitted from a glass capillary tip of a plasma source, stromatolysis due to surface interactions such as collisions or ionization of gas molecules was hardly observed in preliminary experiments. Furthermore, direct measurements of nitric oxide (NO) concentration using a NO sensor revealed that NO was generated by plasma irradiation. NO is produced by calmodulin, which combines with Ca^{2+} ions that are released from a cell subjected to an external stimulus and combines with NOS surface.

Acknowledgements

The authors would like to thank Ms. Y. Yokoi, Mr. S. Murata, Mr. T. Kishimoto, and T. Komachi (Plasma Regenerative Medicine Collaboration Team, Department of Biomedical Engineering, Tokyo City University) for assistance with experiments and Prof. T. Yamamoto, Prof. M. Akiya, and Prof. A. Taguchi (Tokyo City University) for experimental advices. This work was supported by the Strategic Research Base Development Program for Private Universities by a matching fund subsidy and a Grant-in-Aid for Scientific Research (B) (No. 21340173) from the Ministry of Education, Culture, Sports, Science and Technology (MEXT), Japan.

References

[1] A. Shashurin, M. Keidar, S. Bronnikov, R. A. Jurjus, and M. A. Stepp, Appl. Phys. Lett., **93** (2008), 181501.
[2] J. Choi, K. Matsuo, H. Yoshida, T. Namihira, S. Katsuki, and H. Akiyama, Jpn. J. Appl. Phys., **48** (2009), 086003.
[3] G. Fridman, G. Friedman, A. Gutsol, A. B. Shekhter, V. N. Vasilets, and A. Fridman, Plasma Process. Polym., **5** (2008), 503.
[4] T. Imanishi, K. Kobayashi, A. Kuroi, S. Mochizuki, M. Goto, K. Yoshida, and T. Akasaka, Hypertension, **48** (2006), 1058.

Eighth International Conference on Flow Dynamics
November 9 - November 11, 2011

Engineering Tissues From the Bottom up: Designing Microarchitectural Features of Tissues

Yukiko T. Matsunaga
1. Institute of Industrial Science, The University of Tokyo, Komaba 4-6-1, Meguro-ku, Tokyo 153-8505, JAPAN
2. PRESTO, Japan Science and Technology Agency, 4-1-8 Honcho Kawaguchi, Saitama 332-0012, JAPAN
mat@iis.u-tokyo.ac.jp

ABSTRACT

Development of macrosocpic tissues mimicking microscopic features of native tissues has been expected in regenerative medicine. We will introduce recent micro-technologies utilized in designing microarchitectural features of tissues from the bottom up. In particular, we will describe our recent progress in MEMS tissue engineering using the cell beads fabricated by microfluidic devices.

1. Introduction

Recent 20 years, researchers succeeded in fabricating tissues mimicking 'macroscopic' features of the desired tissues. However, the obtained tissues prepared by this top-down approaches: seed cells over the molded macroscopic scaffolds, usually do not show physiological functions of native tissues as well as the structures. Therefore, the method to form functional macroscopic tissues has been strongly desired [1].

Tissues are composed of a number of cells (a diameter of approximately 10-μm) with ordered complex structures. Also, extracellular matrices (ECMs) such as collagen, fibronectin, laminin, etc., surround cells, supporting tissue structures and polarities, resulting in development of physiological functions of tissues. To mimic the micro-structure of the native tissues, researchers started to think about handling cells to form 3D tissue as a building tissue unit. Recent progresses in semiconductor field as represented by Micro Electro Mechanical Systems (MEMS) have enabled handling nano- and micro-objects such as protein, DNA, and cells, and succeeded in assembling them into functional units from the bottom up.

In this talk, we introduce overview of bottom-up tissue engineering that builds up tissues from the micro-tissue units. We also describe our recent progress in 3D tissue formation approaches using 'cell beads'.

2. What is important for bottom-up tissue engineering

'Bottom-up' tissue fabrication methods [2] using micro-tissue units as building blocks, including cell sheets [3] and cell aggregates [4, 5], are potentially powerful tools to reconstruct organomimetic and uniformly dense microstructures. However, the existing units still lack an extracellular matrix (ECM) that is essential for the cells to grow and differentiate in a tissue-like environment. A recent approach using cell-laden hydrogel modules provide ECM, [6, 7], and the shape of microtissue units can be easily controlled by using micromold and photomask. On the other hand, a throughput and a rapid fabrication process is necessary for building up numerous cell modules into 3D macroscopic tissues maintaining the tissue geometries and initial conditions of cells (e.g. cell phenotype and cell cycle).

3. Cell-bead based bottom-up tissue engineering

We developed a method for rapid construction of millimeter-thick macroscopic tissues having complex microstructures by stacking massively produced collagen gel-based micro-tissue units [8]. Our tissue fabrication process using monodisperse collagen gel beads covered with cells (here, "cell beads") is shown in Fig. 1.

By exploiting microfluidic technology (Fig. 2A), monodisperse (50–300 μm in diameter) collagen gel beads are prepared and the cell beads are obtained by seeding cells over the collagen gel beads or by encapsulating the cells (Fig. 2B and C).

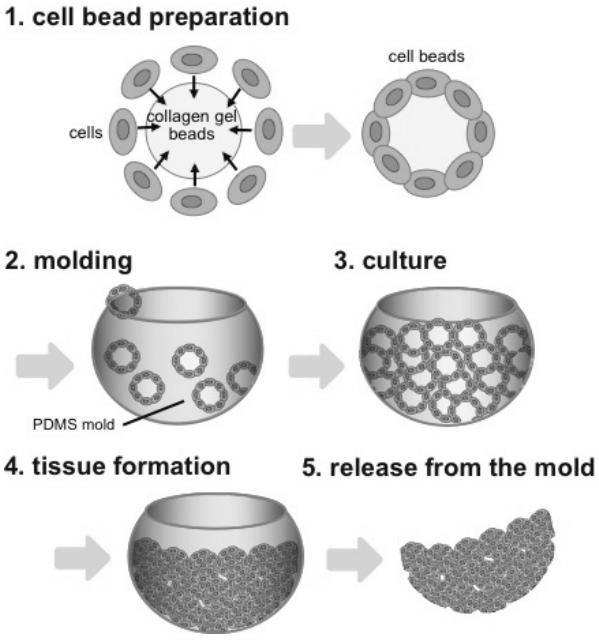

Fig. 1 Conceptual sketch of cell-bead based bottom up tissue engineering. Size controlled collagen gel beads are massively produced by 3D microfluidic device. Any type of cells adhere to collagen gel beads immediately (< 2 hours) to form micro-tissue units. The cell beads are stacked into the designed silicone (PDMS) mold to form millimeter scale 3D tissues. The cells located on the surface of the beads form cell–to–cell connections. Cells migrate and grow within the collagen gel beads and finally form the 3D tissues (< 17 hours after the molding process). The 3D tissues are released from the mold.

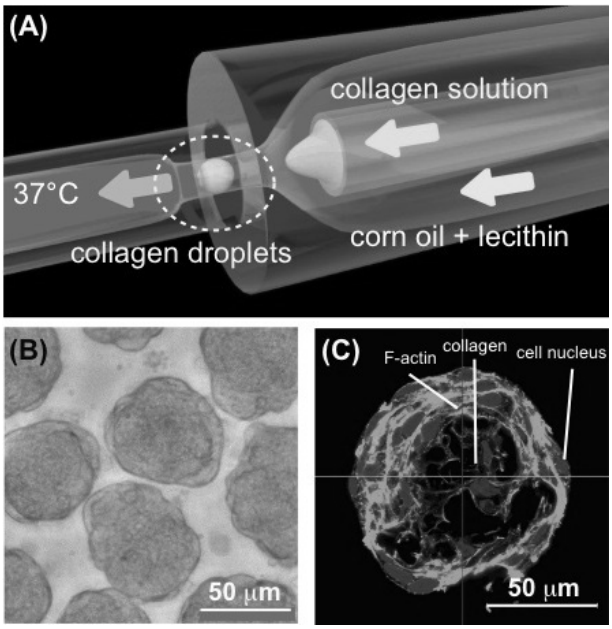

Fig. 2 The cell bead preparation. (A) Schematic diagram of the 3D flow focusing device to produce size-controlled collagen droplets. The device has an axisymmetric flow-focusing channel. Neutralized collagen solution, as an inner fluid, is focused at the narrow orifice and broken into droplets by corn oil containing 2 w/w% lecithin as an outer fluid. (B) Bright-field image of the cell beads prepared by culturing 3T3 cells on the collagen gel beads for 17 hours. (C) Fluorescent confocal microscopy of the cell beads after culture for 17 hours. F-actin was stained with Alexa488-conjugated phalloidin, and cell nuclei were stained with Hoechst 33342.

The cell beads are then molded into the designed silicone chamber to form the macroscopic 3D tissue structures. In the mold, the cell beads can adhere to each other via the cells coated on the collagen gel beads. The cells also migrate and grow into the collagen gel beads, with contraction and decomposition of the collagen, to ultimately form the macroscopic tissues. Finally, the fabricated tissue can be obtained by releasing it from the mold.

By varying a mold shape, the formed 3D tissue with various structures were easily obtained (i.e. ring, bar and string) (Fig.3A and B). The histological analysis showed that: (i) there is no necrosis in the 1.2-mm thick tissues after 30 h reconstruction; (ii) cell densities are uniform even in the various regions at a higher cell density. We also performed the reconstruction of heterogeneous tissues using various macroscopic tissue rings and strings. As the macroscopic tissue rings are ease of handling, they are easily assembled into more complex structures (Fig. 3C and D).

4. Concluding remarks

We have demonstrated the use of massively produced collagen gel beads to assemble uniform and arbitrary shape macroscopic 3D tissues by the molding

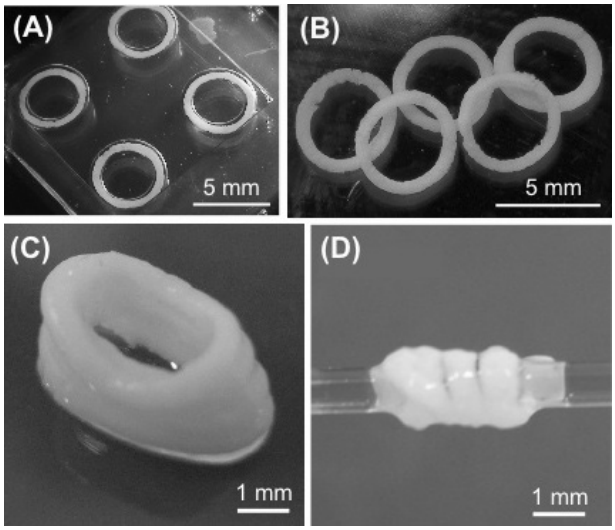

Fig. 3 Formation of macroscopic tissue structures various structures using cell beads. (A) The cell beads are molded into the PDMS chamber and incubated for 17 h. The cell beads connected each other within several hours to form macroscopic 3D tissues. (B) Released tissue rings from the PDMS mold. (C) Hollow structure prepared by layering 5 tissue rings. (D) Tissue string twisted around the glass capillary.

approach. Since the cell beads immediately stick to each other, this method enabled rapid formation of macroscopic cell-dense tissues, without necrosis during tissues. We believe that our method is highly compatible with such a vascularization process since the cell beads can be easily molded with different types of micro-tissue units. Therefore, our method opens a new paradigm for bottom-up macroscopic tissue engineering, realizing functional and spatially structured complex large-scale tissues.

Acknowledgement

The author acknowledges to the Shoji Takeuchi laboratory (The Institute of Industrial Science, The University of Tokyo). Especially, the author thanks Profs. Shoji Takeuchi, H. Onoe, Mr. Y. Morimoto, Ms. H. Aoyagi and Ms. Y. Okubo for their discussion and technical assistances.

References

[1] L. G. Griffith, M. A. Swartz, Nat. Rev. 2006, **7**, 211.
[2] J. W. Nichol, A. Khademhosseini, Soft Matter 2009, **5**, 1312.
[3] J. Yang et al., Adv. Mat. 2009, **21**, 1.
[4] J. Fukuda, K. Nakazawa, Tissue Eng 2005, **11**, 1254.
[5] V. Mironov, R.P. et al., Biomaterials 2009, **30**, 2164.
[6] A.P. McGuigan et al., PNAS 2006, **103**, 11461.
[7] P. Panda et al., Lab on a chip 2008, **8**, 1056.
[8] Y.T. Matsunaga and Y. Morimoto, S. Taketuchi, Adv Mat, 2011, **23**, H90-H94.

Eighth International Conference on Flow Dynamics
November 9 - November 11, 2011

Biomechanical Regulation of Actin Cytoskeleton Dynamics in Migrating Cells

Taiji Adachi[1] and Kennedy O. Okeyo[2]
1: Department of Biomechanics, Institute for Frontier Medical Sciences, Kyoto University
adachi@frontier.kyoto-u.ac.jp
2: Department of Mechanical Engineering and Science, Kyoto University

ABSTRACT

Complex processes involved in cell migration; polymerization, adhesion, and retraction, are mediated by highly orchestrated structure-function interactions that occur within the actin cytoskeletal structure. Thus, understanding how migrating cells regulate the global dynamics of their cytoskeletal components, which result from localized protein-protein interactions, is fundamental to elucidating the mechanisms of cell motility. The purposes of this study were to explore the mechanical regulation of actin network dynamics in migrating cells, and to discuss its regulatory role in cell migration.

1. Introduction

Cell migration is essential to many cellular processes that are fundamental to various biological functions. The events of cell migration are realized by multiscale interactions at different cellular modules, and they need to be carefully orchestrated in both time and space, in order to achieve robust whole-cell movement that is responsive to the biomechanical and biochemical environment of the cell.

Although intensive research over the last few decades has shed light into the molecular players and pathways involved in cell migration, precisely how cells regulate the many molecular and structural dynamics that take place at different cellular modules during cell movement is less understood [1]. Moreover, although it is increasingly becoming clear, that coupling interactions between mechanical and biochemical factors play crucial roles in the regulation of various motility processes, a full understanding of the mechanisms underlying these interactions is yet to be achieved.

This study focuses on the mechanical regulation of the actin cytoskeleton, and explores the roles of mechanical forces involved in the migration process. Specifically, we examine how mechanical factors including network strain and actomyosin tension are generated, and how they contribute to the regulation of actin network dynamics during cell migration.

2. F-actin Network Dynamics in Lamellipodia

A striking feature of the cytoskeletal actin dynamics in adherent cells is that, as filament assembly and elongation continues at the leading edge, the whole network exhibits a net movement from the cell periphery toward the cell center in a process known as “retrograde flow” [2]. The flow was first detected in slow moving cells such as fibroblasts [3], but it remained undetected in fast moving cells like keratocytes [4] until recently when more powerful flow detection and tracking tools such as fluorescent speckle microscopy (FSM) was developed [5]. In fact, using FSM, a number of studies have quantitatively mapped the organization of retrograde flow in various cell types, including keratocytes [6] and epithelial cells [7]. Thus the flow is now known to be ubiquitous, and it is considered as an important property of migrating cells.

We have conducted FSM study [8] that has revealed the organization of actin flow in the lamellipodia of migrating cells. Figure 1A shows a flow map of actin network in the lamellipodia of a migrating keratocyte obtained by a combination of FSM and particle imaging velocimetry (PIV). From the magnified region of the flow field, it can be observed that retrograde flow velocity decreases progressively from the leading edge toward the back of the lamellipodia to reach a minimum at the contractile module. This is also demonstrated by the kymograph in Fig. 1B from where we can observe that the slopes of the speckle streaks decrease from the leading edge (l.e) toward the back (c.b). In similarity with retrograde flow, anterograde flow that emanates from the cell rear also decreases in intensity toward the front of the lamellipodia, as shown in Fig. 1A, and schematically in Fig. 1C. The two flows merge at the middle of the lamellipodia, resulting in regions of markedly reduced flow intensity. Such regions within the contractile module of the lamellipodia are commonly referred to as the convergence zones [8] (marked as CZ in Fig. 1A), and they form an important aspect of F-actin flow organization.

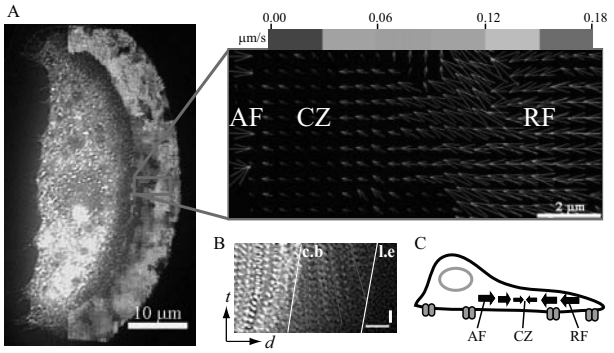

Figure 1: F-actin network flow. A: FSM image overlaid with a flow field with retrograde flow (RF), convergence zone (CZ), and anterograde frow (AF). B: Kymograph showing actin dynamics in the lamellipodium with leading edge (l.e) and cell body boundary (c.b). Time and space axes are indicated by *t* and *d*. Horizontal scale bar is 5 μm, and vertical bar is 8 s. C: Schematic illustration of F-actin flow organization.

The most plausible explanation for this kind of flow organization is that contractile forces generated by myosin II activity produces a gradient of convergent tension on F-actin across the contractile module [9], peaking in the module center. Although little is known about the specific patterns of myosin assembly, it is thought that when coupled with filament polymerization, convergent tension can drive the two F-actin flows by a network contraction mechanism to merge at the convergence zone [8, 9]. While myosin II activity drives flow convergence, FAs may influence the location of the convergence zone such that the zones are localized where F-actin network is strongly coupled to the ECM. Such points of strong coupling are expected to have a dramatic reduction in F-actin flow rate. Whatever the case, F-actin network in the convergence zone is thought to be under increased compressive deformation in the migration direction due to flow convergence [6, 8], and this may promote depolymerization, possibly by a mechanism involving the induction of filament disassembly by negative (compressive) strains [10], as discussed in the next section.

3. Actin Network Strain Induces Filament Depolymerization

As mentioned already, F-actin network is dynamically contracted and realigned by the action of myosin II motors. Concomitantly, the network is further compressively deformed by the convergence of retrograde and anterograde flow at the middle of the lamella. A quantitative study [10] using FSM and PIV-based image cross-correlation determined actin network deformation in the lamellipodia of fish keratocytes, and reported on the existence of negative (compressive) network strains in the actin network. Interestingly, the study found that incremental network strain in the direction parallel to the migration direction (parallel incremental strain) was significantly negative and predominant over the strain component in the normal direction (normal incremental strain). The latter was found to be negligible, consistent with isometric network contraction theory. From this finding, the study suggested that compressive deformation of the actin filament network occurs in the anterior-posterior axis, in agreement with the predictions of dynamic network model [11]. In addition, the study observed that the distributions of parallel incremental strain and actin network density are closely correlated. Based on this correlation, the study proposed a "selective depolymerization model" which is illustrated schematically in Fig. 2.

According to the model [10], negative (compressive) strain may couple with biochemical factors to induce actin filament depolymerization. The model proposes that network contraction by actomyosin-generated mechanical forces may result in compressive network deformation and tension release, which may couple with biomechanical factors such as ADF/cofilin to induce filament depolymerization. Since the direction of the compressive deformation corresponds with the migration direction (Fig. 2), filaments oriented away from the migration direction are likely to escape depolymerization because they bear less negative strain compared to their counterparts oriented in the migration direction (Fig. 2) which are preferentially depolymerized. Filaments that survive are transported back by retrograde flow and eventually form SFs at the back of the lamellipodia to resume the role of contractile force generation. Thus, fascinatingly, the model can account for the observed changes in filament orientation from the leading edge to the back of the lamellipodia. Importantly, it suggests that the cytoskeleton behaves like a self-regulating system which is capable of inducing its own remodeling and reorganization.

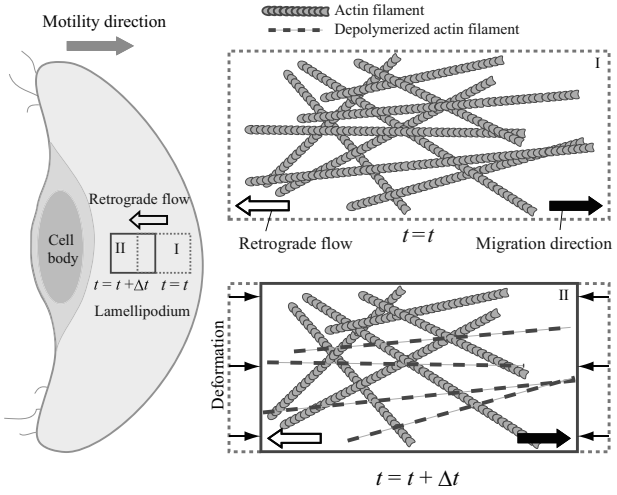

Figure 2: Selective depolymerization model proposed for the involvement of negative strain in the mechanical induction of depolymerization (Modified from [10]). Filaments oriented in the compressed direction preferentially depolymerize after Δt.

4. Concluding Remarks

In this article, we have considered the mechanical regulation of actin network dynamics during cell migration. We have seen that cell migration is a complex process that involves the interplay of numerous components in a manner that is not yet fully understood. We have also looked into how negative mechanical strain resulting from actin network dynamics contributes to the self-regulatory mechanism of the structure. From our discussions, we can conclude that actomyosin tension couple with biochemical factors to determine vital motility processes, including actin network remodeling and FA dynamics.

Mechanochemical coupling elucidated is a fundamental mechanism by which various cell functions are realized and maintained. The physical continuity existing between the cytoskeleton and ECM via integrins at the focal adhesions allows for the mechanotransduction of actin cytoskeleton dynamics and associated forces to the ECM, and vice versa. Therefore, defining specific structures and mechanisms by which forces–both externally and internally generated–are sensed by cells and how this stimulus leads to specific responses is likely to help explain the complex functions of cells and to design better materials for cell and tissue engineering.

It should be noted that work on mechanobiology of cell migration has just began, and a lot still remains to be elucidated. The critical questions remain as to how coupling interactions among mechanical and biochemical factors lead to the spatiotemporal regulation of the molecular and physical processes of cell migration. Therefore, more work is necessary to elucidate the mechanotransduction of mechanical forces generated within and without the cell into relevant biochemical signals to mediate cell functions. To this end, there is hope that emerging powerful tools such FSM, fluorescence recovery after photobleaching (FRAP), and fluorescence resonance energy transfer (FRET), combined with advanced single molecule detection and newly developed tracking techniques will make it possible to probe molecular interactions and highlight force-function interactions within the cell.

Finally, given that cell migration occurs in a physical 3D environment *in vivo*, it is imperative that knowledge gained from 2D *in vitro* investigations be translated into understanding the more complex *in vivo* cell migration. In fact, greater effort should be dedicated to elucidating cell migration in the *in vivo* setting in order to understand the process in the context of clinically relevant phenomena such as metastasis and angiogenesis.

Acknowledgement

This work was partially supported by the Grant-in-Aid for Specially Promoted Research (#20001007) and by the Funding Program for Next Generation World-Leading Researchers (LR-017) from the JSPS.

References

[1] S M Rafelski, *et al*., Annu Rev Biochem, **73** (2004) 209-239.
[2] L P Cramer, Front Biosci: A J & Virtual Lib, **2** (1997) d260-270.
[3] M Abercrombie, *et al*., Exp Cell Res, **73**(2) (1972) 536-539.
[4] J A Theriot, *et al*., Nature, **352**(6331) (1991), 126-131.
[5] C M Waterman-Storer, *et al*., Curr Biol, 8(22) (1998) 1227-1230.
[6] K O Okeyo, *et al*., Biochem & Biophys Res Commu, **390**(3) (2009) 797-802.
[7] A Ponti, *et al*., Science, **305**(5691) (2004) 1782-1786.
[8] K O Okeyo, *et al*., J Biomech, **42**(15) (2009) 2540-2548.
[9] S Schaub, *et al*., Mol Biol Cell, **18**(10) (2007) 3723-3732.
[10] T Adachi, T, *ete al*., J Biomech, **42**(3) (2009) 297-302.
[11] T M Svitkina, *et al*., J Cell Biol, **139**(2) (1997) 397-415.

Eighth International Conference on Flow Dynamics
November 9 - November 11, 2011

Biological and Medical Applications of Pulsed Power

Sunao Katsuki, Masahiko Yano*, Keisuke Abe*, Hidenori Akiyama*
Bioelectrics Research Center, Kumamoto University
*Graduate School of Science and Technology, Kumamoto University,
39-1, Kurokami 2-chome, Kumamoto City, Kumamoto 860-8555, Japan
katsuki@cs.kumamoto-u.ac.jp

ABSTRACT

This paper describes biological effects of intense pulsed electric fields (IPEFs) and typical responses of mammalian cells to IPEF. Physical effects of IPEF including not only a non-thermal electrostatic stress to membrane and biomolecules but also a transient thermal stress induce secondary biological processes as stress responses, which result in apoptosis or in proliferation. These biological responses are being studied to apply for medical treatments, e.g. cancer treatment, wound healing.

1. Introduction

Pulsed-power-driven energetic states, including extremely large electric and magnetic fields, atmospheric pressure plasmas, shock wave, transient heat shock, intense photon flux e.g., can be unique biological stresses, which lead to unique biological responses. These physically induced stresses are attractive for medical, pharmacological and agricultural applications as well as food processing. Research field including basic studies on biological effects of pulsed power and their industrial applications is called "bioelectrics" and is expanding in the last decade. Here, we focus on the biological effects of intense pulsed electric field (IPEF), which we have mainly been working on, and we show their possible medical applications.

2. Primary biological effects of IPEF

2.1 Non-thermal effects

Biological cells are regarded as a complex of various dielectric materials including membranes, huge biomolecules, amino acids, ions and water. Because of their dielectric properties, the IPEF-induced stress to each component is expected to be different and dependent on the applied field. There are basically two non-thermal, physical effects of IPEF on biological cells, which are electrostatic stresses to bio-membrane and/or to bio-molecules. Firstly, bio-membrane, which is regarded as an electrically insulating thin film, significantly affects electric filed distributions. Under an alternating current (AC) electric field, the electric field distribution depends on frequency of the field because of the electrostatic capacity of the cell membrane. At frequencies below 1 MHz, electric field is extremely enhanced at the cell membrane, approximately 1000 times as large as the external field. It is well known that the membrane stress increases the membrane permeability, which is called "electroporation". At the frequencies exceeding 10 MHz on the other hand, the field penetrates into cell. Strength of the intracellular field is the same level as the external field, whereas the field at the membrane is lowered. Fig. 1 shows the typical cell responses to 3 kV/cm burst AC fields for different frequencies [1]. The control indicates cells without applying the pulses. In the case of 0.3 MHz, cell membranes are damaged and intracellular content leaks out of the cell (blebbing). In the case of 10 and 100 MHz, however, the membrane appears to remain intact, whereas the intracellular structure seems to be changed. This intracellular strong field at the frequencies more than 10 MHz directly gives a stress to the intracellular organelles and biomolecules, which may initiate the biological processes.

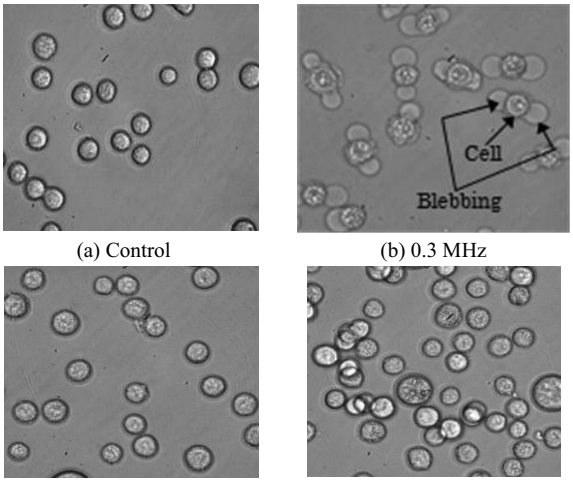

(a) Control (b) 0.3 MHz

(c) 10 MHz (d) 100 MHz

Fig. 1 Microscopic views of HeLa S3 cells subjected to 3 kV/cm burst AC electric fields at different frequencies of 0.3, 10 and 100 MHz. Control indicates cells without pulsing. All photographs were taken 10 minutes after pulsing [1].

2.2 Transient thermal effect

Applications of IPEF to conductive medium raise its temperature more or less, depending on the pulse duration or the pulse repetition rate. Use of repetitive IPEF allows us to raise the medium temperature rapidly and significantly, for instance the rise of 40˚C within 1 s. The deposited heat is quickly released by heat conduction to the surroundings. The biological target is exposed to high thermal stress only for several seconds, which is called the transient thermal shock (TTS) and is likely to be different stress from a conventional heat shock used as hyperthermia. We have demonstrated that the TTS enhances apoptosis activity in HeLa cells induced by the non-thermal IPEF [2].

3. Secondary effects

3.1 Apoptosis

Chemical and physical stresses initiate the secondary biological processes (stress response) leading to cell death or proliferation. Cell responses are determined by balance of these processes. Cells can be selectively led not only to death but also to proliferation by adjusting the stresses.

IPEF is one of the physical stresses to initiate the biological responses. Recent studies have demonstrated that the application of IPEF induces intracellular responses associated with apoptosis in several kinds of cancer cells e.g. eosinophil sparklers, calcium release from endoplasmic reticulum, caspace activation. Histograms in Fig. 2 show degrees of the field-induced apoptotic DNA fragmentation in HeLa S3 cells. Almost all cells were healthy in the control, whereas DNA fragmentation is advanced slowly in the pulsed sample. Fig. 3 shows the expression of apoptosis-related genes and possible chain reactions of proteins (signaling pathway) resulting in apoptosis. Our analysis implies that nanoseconds IPEF directly gives stresses to cell membrane and endoplasmic reticulum as the primary effect, which subsequently initiates the biological process leading to apoptosis [3].

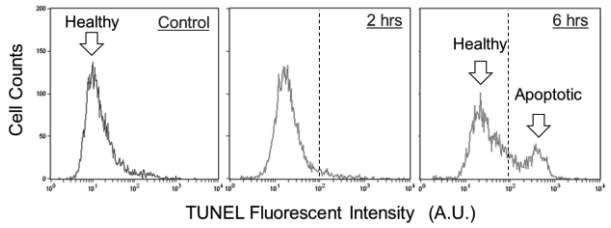

Fig. 2 Apoptotic DNA fragmentation in HeLa S3 cells induced by nanosecond IPEF (12.5 kV/cm, 100 ns, 100 shots), detected by means of TUNEL assay and flowcytometer. From the left, control, samples 2 and 6 hours after pulsing, respectively.

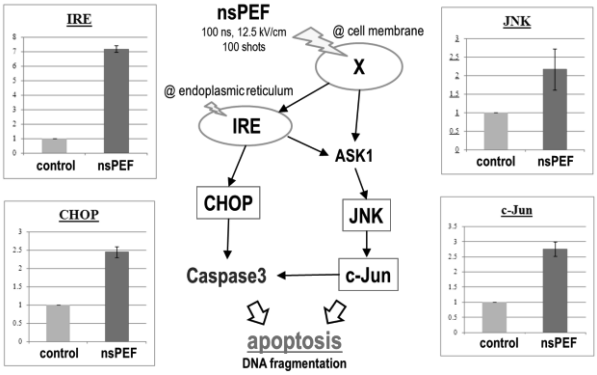

Fig. 3 Expression of apoptosis-related genes and possible signaling pathways of apoptosis induced by IPEF. IRE, CHOP, ASK1, JNK, c-Jun, caspase3, X(unidentified) are proteins associated with apoptosis. Bar graphs show expressions of genes coding the proteins. Left and right bars in each graph indicate in the control and the pulsed samples, respectively.

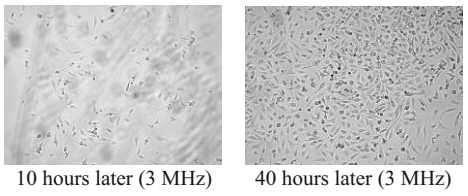

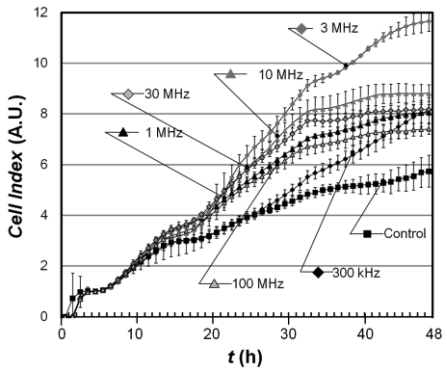

Fig. 4 Proliferation curves of HeLa S3 cells subjected to 3 kV/cm burst AC fields for various frequencies of the field [4]. The cell index is value proportional to number of healthy cells. Upper photographs show snapshots of HeLa cells at different times after pulsing.

3.2 Promotion of proliferation

Also the application of IPEF promotes the proliferation of mammalian cells. Fig. 4 shows proliferation curves of HeLa S3 cells subjected to 300 kV/m, 200 μs-long AC electric fields with a frequency between 300 kHz and 100 MHz. The proliferation activity, which was monitored using an automatic cell counter xCELLigence (Roche Applied Science), depends on the pulse number and the frequency of the AC field. Smaller number of the pulses promoted the proliferation activity, whereas the cells tend to be killed by larger number of the pulses. When the cells were subjected to 30 pulses, the proliferation activity was promoted most at the frequency of 3 MHz. The dependence on the pulse number indicates the biological effects of IPEF are accumulated. The frequency dependence implies the proliferation activity may be associated with electric field strength at cell membrane [4].

4. Concluding remarks

Here, we described the biological effect of IPEF. The effects of IPEF are expected to be used for medical treatments such as cancer treatment based on apoptosis induction and wound healing based on platelet activation. IPEF, which is a novel physical stimulation, will be used not only for medical field but also for all fields associated with organisms.

References

[1] S. Katsuki, et al., J. Electrostatic Jpn., **54** (2009), 106.
[2] S. Katsuki, et al., IEEE Trans. Dielectr. Electr. Insulat., **17** (2010) 678.
[3] K. Morotomi-Yano, et al., Biochem. Biophys. Res. Comm., **408** (2011) 471.
[4] M. Yano, et al., IEEE Trans. Dielectr. Electr. Insulat., (2011) *in print.*

Eighth International Conference on Flow Dynamics
November 9 - November 11, 2011

Advantages of Cascade Plasma Torches for APS and SPS of Bioactive Hydroxyapatite Coatings

Oleg P. Solonenko[1], Andrey V. Smirnov[1], Igor P. Gulyaev[1], Marina V. Chaikina[2], and Andrey V. Perfiliev[1]
[1]Khristianovich Institute of Theoretical and Applied Mechanics, Siberian Branch of RAS, Novosibirsk, Russia
Institute of Solid Chemistry and Mechanochemistry, Siberian Branch of RAS, Novosibirsk, Russia
solo@itam.nsc.ru

ABSTRACT

Potential advantages offered by cascade plasma torches (CPTs) in atmospheric plasma spraying (APS) and suspension plasma spraying (SPS) of bioactive hydroxyapatite (HA) coatings are analyzed. It is shown that the modular design of single-cathode CPTs helps in eliminating many disadvantageous features of conventional plasma torches, including the drift of plasma characteristics, emergence of 1-5 kHz plasma flow pulsations, and intense electrode erosion. The more stable plasma jet discharged from CPT results in a better quality, homogeneity and reproducibility of plasma-sprayed HA coatings.

1. Introduction

Hydroxyapatite (HÀ) coatings deposited by different thermal spraying methods onto titanium and other medical alloys are widely used as biocompatible coatings to coat implants in orthopedics and stomatology [1, 2]. However, the stability problem of such coatings still remains a pressing matter. It involves considerations related to the adhesion and cohesion strength ensured by a particular thermal spraying method, and also to the long-term stability of coatings, defined by the crystalline structure of coating. The crystallinity ensures a low degradation of the coating in biological media and its stability under cyclic loads.

In this connection, different methods for thermal spraying of phosphate coatings, such as HVOF, RF, DC, etc., have been extensively developed and studied during the last two decades. Among such methods, plasma spraying is the most widely used technology due to its technological attractiveness.

In this connection, investigation of different plasma spraying methods intended for deposition of HÀ coatings onto implants and prostheses, and also investigation into the fine structure of plasma-sprayed coatings, presents an important matter for further development of the plasma spray method and for elucidation of possibilities provided by this method in raising the competitive ability of plasma-sprayed coatings in comparison with other coatings.

The following main designs of plasma guns are now commercially available:

- conventional Sulzer Metco guns (9MB, F4,…),
- SG-100 gun (Praxair),
- Mettech 100 kW Axial III gun with axial powder injection,
- water-stabilized plasma (Institute of Plasma Physics, Czech Republic),
- Triplex 50 kW (Sulzer Metco).

The main disadvantageous features of plasma torches with self-adjusted arc length are the following:

1) emergence of low-frequency pulsations of arc voltage that arise due to a short length of the arc and due to anode spot attachment variations, conditioned by the thermal power of discharged plasma jet and by the magneto-hydrodynamic interaction of the radial arm of arc with the cold wall boundary layer [3]. Such pulsations result in a considerable inhomogeneity of the powder-material processing/spraying process, most notably manifested in suspension plasma spraying;

2) absence of axial symmetry in the velocity and temperature fields of discharged plasma jet resulting in non-uniform heating and acceleration of particles over the jet cross-section; the latter leads to the lack of axial symmetry in the distribution of particle parameters within the spraying spot.

A discussion regarding the above-indicated and other disadvantageous features of conventional DC plasma torches can be found in publication [4].

The main purpose of the present article is to illustrate the wide operational window provided by cascade plasma torches [5] in APS and SPS of HA coatings onto titanium substrates under different regimes of plasma jet outflow (laminar, transient, or turbulent). These operation conditions are provided through variation of the working-gas flow rate over a relatively wide range of rate values. As a result, the velocity and temperature of powder particles, their dwell time in plasma jet, and also the phase composition of particles and sprayed coatings can be varied throughout rather broad a range.

2. Advantages offered by cascade plasma torches

A major contribution to the study and development of cascade plasma torches was made by Zhukov et al. [3]. The principal diagram of a cascade plasma torch is shown in Fig. 1.

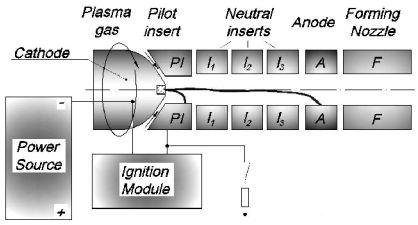

Fig. 1. Schematic of a cascade plasma torch.

In the “cascade” approach, one or several insulated inter-electrode inserts are used to extend the arc length and stabilize the arc over a wide range of gas flows. The inter-electrode inserts, or neutral electrodes, are intermediate electrodes located in between the cathode and anode. A long, high-voltage arc column is stabilized by these neutral inserts rather than by high rate of the

gas flow. As a result, more stable plasma jet with minimized flow pulsations, a higher thermal efficiency and, hence, with a more efficient heating of particles can be obtained. This low-current, high-voltage design also ensures a reduction of cathode and anode erosion, longer hardware life, and minimized contamination of sprayed coating with electrode erosion products. The very low or zero voltage drift thus achieved provides for a better coating quality. Relatively low arc currents (~ 200 A) ensure a low level of electrode erosion, thus diminishing the contamination of sprayed coatings with erosion products (Cu, W, etc.). Cleaner coatings possess a better quality. The "cascade" approach allows easy variation of the flow rate of plasma gases, or the Reynolds number of the jet flow, in a relatively wide range of values without plasma-induced changes of arc current and voltage. Therefore, plasma temperature and velocity also can be varied over a wide range, thus ensuring a wide operational window and the possibility of implementing quasi-laminar and transient plasma jet outflows in the plasma spray process.

3. Results and Discussion

For APS and SPS of HA coatings onto Ti substrates, we used a 50-kW cascade plasma torch [5]. As the working and carrier gases, air was used. In the present study, we used hydroxyapatite mechanochemically synthesized in a planetary activating mill by the reaction

$$3Ca(H_2PO_4)_2 \cdot H_2O + 7CaO = Ca_{10}(PO_4)_6(OH)_2 + 8H_2O \cdot$$

The particle size of the powder material synthesized (see Fig. 2) was mainly 10-50 nm, the specific surface area being ~ 50 m^2/g. This powder was used for SPS of thin coatings, whereas for APS of 200-300 μm thick coatings an agglomerated HA powder obtained by crashing a compact sintered from the initial mechanosynthesized nanopowder was used. The size of agglomerated particles in the latter powder was ~ 100-125 μm. The substrates were 2-mm thick water-cooled Ti plates.

Prior to carrying out experiments on the APS of thick HA coatings, a preliminary study of the influence of jet outflow regime on the morphology and phase composition of the powder subjected to plasma processing and subsequent quenching into water was performed (Fig. 2). In APS tests, samples of HA coatings on Ti substrates were obtained, which have allowed us to establish the relation between the surface morphology of obtained coatings, the microstructure of sprayed layers, and their thickness and phase composition, on the one hand, and the various spraying conditions (flow regime, jet enthalpy, powder injection mode, etc.), on the other hand.

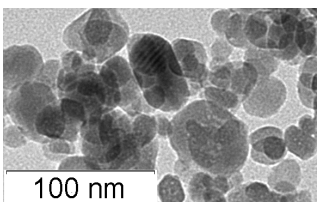

Fig. 2. TEM photo of the nanopowder.

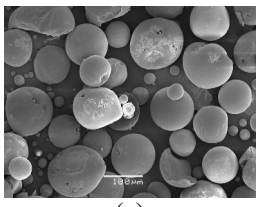

(a)

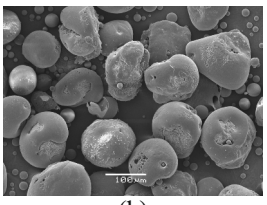

(b)

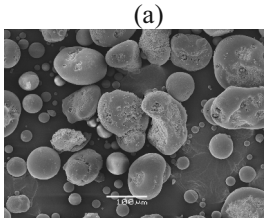

(c)

Fig. 3. HA powder particles treated in plasma and quenched into water at quasi-laminar (a), transient (b) and turbulent (c) jet outflows.

APS of thin coatings ensures rather high adhesion strength; yet, it fails to solve the problem of through-porosity, having a negative effect on the dissolution of the contact zone of implant coating with the base and facilitating diffusion of metal ions out of the implant. To overcome the latter difficulties, experiments on the SPS of thin coatings from the initial HA nanopowder were performed. Samples of obtained coatings were studied, which proved great potential of the used cascade plasma gun for solving this problem.

4. Conclusions

A comparative study of plasma conditions and their influence on the morphology, internal structure, and phase state of HA powders processed in plasma and subsequently quenched into water, as well as coatings sprayed by APS or SPS onto titanium substrates was performed using a cascade plasma torch.

The obtained data prove that the used plasma torch can be successively employed for studying the kinetics of hydroxyapatite thermal decomposition under high temperatures of air flow and controlled residence time of powder particles in plasma jet.

Acknowledgements

This work was supported in part by the Siberian Branch of the Russian Academy of Sciences under Special Integration Project No. 12 (years 2010-2011).

References

[1] Hydroxyapatite Coatings in Orthopedic Surgery, Eds.: Rudolph G.T. Geesink, Michael T. Manley, Raven Press Ltd., New York, 1993, 320 p.

[2] R.Z. LeGros, Calcium Phosphates in Oral Biology and Medicine, Karger, 1991, 201 p.

[3] Thermal Plasma and New Materials Technology. Vol. 1. Investigation and Design of Thermal Plasma Generators, Eds.: O.P. Solonenko and M.F. Zhukov, Cambridge, England: Cambridge Interscience Publishing, 1994, 509 p.

[4] P. Fauchais, R. Etchart-Salas, V. Rat, J.F. Coudert, N. Caron, and K. Wittmann-Te´ne`ze, Journal of Thermal Spray Technology, **17** (2008), 31-59.

[5] O.P. Solonenko, A.P. Alkhimov, V.V. Marusin, et al, High-Energy Processes in Material Treatment, Nauka, Novosibirsk, 2000, 425 p. (in Russian)

Eighth International Conference on Flow Dynamics
November 9 - November 11, 2011

Atmospheric Plasma for Wound Treatment: Lab to Clinical Study

Tetsuji Shimizu[1], Julia L Zimmermann[1], Gregor E Morfill[1], Georg Isbary[2], Wilhelm Stolz[2]
[1]Max-Planck Institute for extraterrestrial physics, Giessenbacstr., 85748 Garching, Germany.
[2]Departments of Dermatology, Allergology and Environmental Medicine, Hospital Munich Schwabing, Kölner Platz, 80804 Munich, Germany
E-mail of corresponding author: tshimizu@mpe.mpg.de

ABSTRACT

Cold atmospheric plasma was used for treatment of chronic infected wounds in patients. We have developed a microwave plasma torch system using argon gas for the purpose. The plasma treatment has a bactericidal property and it was examined that the treatment was safe through a phase I study. A phase II study shows that the plasma treatment could decrease bacterial load in treated wounds with no side-effects. We consider the cold atmospheric plasma treatment as a safe new technique to decrease germ load on chronic wounds.

1. Introduction

Recently, researches in the field of biomedical applications using low temperature atmospheric plasma have received growing attention [1-4]. They can play an important role in different areas of medicine because they have been shown in vitro to kill/inactivate a wide range of pathogenic bacteria without thermal damage. There are several active agents produced by plasma, e.g. reactive species, charged particles, and UV photons. These agents can have an access on rough surfaces down to micrometer scale, therefore, the agents have an effect at the cellular level. By optimizing plasma, it is possible that the plasma has not only a bactericidal property but also a cell regeneration effect [5].

We have developed and tested a plasma device, called MicroPlaSter, as shown in fig. 1. This device contains a microwave plasma torch (see fig. 2) [6]. A plasma discharge is produced in the plasma torch by applying microwave power of ~85 W using argon gas of 2 slm. The plasma torch is placed at the end of flexible arm and can be moved above desired areas. The device allows the treatment of large inhomogeneous areas of about 5 cm in diameter below the threshold of thermal damage using a contact-free and self-sterilizing application. The agents are delivered from the plasma torch to the desired region following the argon flow. It was shown that this plasma had a bactericidal property.

Since 2005, a clinical study was started in a joint effort between the Max-Planck Institute and the Department of Dermatology, Allergology and Environmental Medicine in Hospital Munich Schwabing. Here, we would like to show our current status of our clinical study [7].

2. Phase I study

Bacterial colonization of chronic wounds slows healing and the increase of multiresistance to antibiotics and allergic reactions, the treatment of chronic wounds has become more challenging. The objectives in this study are to examine the safety and efficiency of the cold atmospheric argon plasma produced by MicroPlaSter to decrease bacterial load as a new medical treatment.

Before starting a phase II study (clinical study), a phase I study was carried out. The focus of this study is to show safety parameters and the optimum bactericidal dose for relevant bacteria, satisfying the safety requirements of the medical device directive and the ethics committee. In the phase I study, in addition to the plasma characterization, bactericidal effects on relevant bacteria to chronic wounds were shown. And skin histology showed that there was almost no change by the plasma treatment. This clinical study had the approval of the Bavarian State Association for Medical Issues.

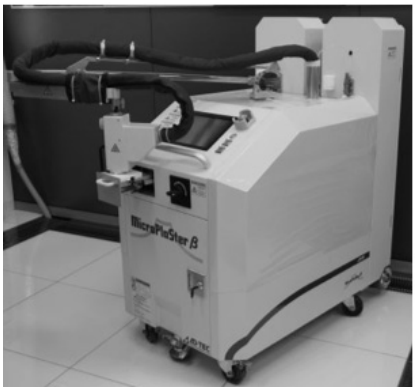

Fig. 1. Clinical device, MicroPlaSter, for wound treatment. This device contains a microwave plasma torch at the end of flexible arm.

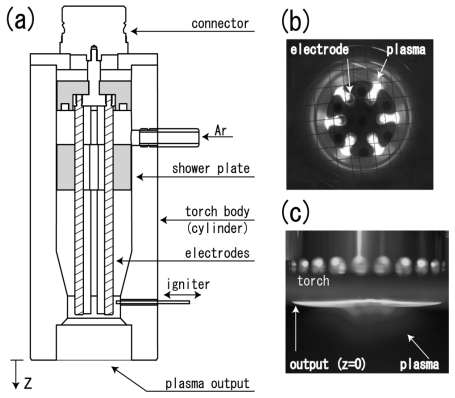

Fig. 2. Plasma torch and plasma. (a) a sectioned view of plasma torch, (b) plasma between the electrodes and the cylinder, (c) plasma below the torch from the side.

3. Phase II study

About 150 patients with chronic infected wounds were treated in a randomized phase II study. In addition to standard wound care, patients received a 5-min cold argon plasma treatment as an add-on therapy. Control wounds remained undressed during the plasma treatments and the same standard wound care was given to both plasma-treated and control areas. Bacterial load was detected using standard bacterial swabs and nitrocellulose filters. The bacterial swabs were used in order to detect the types of bacteria present and the filters were used to see changes in bacterial load. The filters were applied to the wounds with gentle pressure before and after the plasma treatments. These were placed on blood agar plates and incubated for 12 hours. Semiquantitative assessment of the plates was determined by a manual count. This technique can give a spatial profile of bacteria on the wound. Possible side-effects such as pain were specifically asked about and documented according to standardized World Health Organization score from 0 to 10.

In the 36 patients with chronic infected wounds, 24 patients had two separated wounds and 14 patients had one single large ulcer where control and plasma-treated areas could co-exist.

It was found that in an analysis of 291 treatments there was a highly significant (~34 %, $P < 10^{-6}$) reduction in bacterial count in plasma-treated area compared with control (non-treated) area (see fig. 3). The corresponding bootstrap test confirms that the high significance level of the results. No side-effects were reported and the treatment was very well tolerated in almost all cases.

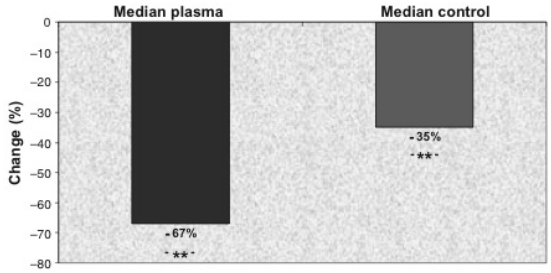

Fig. 3. Change in bacterial load on plasma-treated area and control area.

4. Summary

Due to the produced active agents by plasma, the cold atmospheric plasma treatments can have biological effects. We have developed the cold atmospheric argon plasma device for chronic infected wound treatment. The phase I study showed the bactericidal property of the device and satisfied the safety requirements. In the phase II study, the analysis of treatments showed a highly significant reduction of bacterial load in plasma-treated wounds. The cold atmospheric argon plasma treatment may be a safe and painless new technique to decrease bacterial load of chronic wounds.

References

[1] E. Stoffels, Contrib. Plasma Phys., **47** (2007), 40.
[2] G. Fridman, G. Friedman, A. Gutsol, A. B. Shekhter, V. N. Vasilets, and A. Fridman, Plasma Process. Polym., **5** (2008), 503.
[3] M. Laroussi, IEEE Trans. Plasma Sci., **30** (2002), 1409.
[4] M. Kong, G. Kroesen, G. E. Morfill, T. Nosenko, T. Shimizu, J. van Dijk, and J. L. Zimmermann, New J. Phys., **11** (2009), 115012.
[5] T. Nosenko, T. Shimizu, and G. E. Morfill, New J. Phys., **11** (2009), 115013.
[6] T. Shimizu, B. Steffes, R. Pompl, F. Jamitzky, W. Bunk, K. Ramrath, M. Georgi, W. Stolz, H.-U. Schmidt, T. Urayama, S. Fujii, and G. E. Morfill, Plasma Process. Polym., **5** (2008), 577.
[7] G. Isbary, G. E. Morfill, H.-U. Schmidt, M. Georgi, K. Ramrath, J. Heinlin, S. Karrer, M. Landthaler, T. Shimizu, B. Steffes, W. Bunk, R. Monetti, J. L. Zimmermann, R. Pompl, and W. Stolz, British J. Dermatology, **163** (2010), 78.

Eighth International Conference on Flow Dynamics
November 9 - November 11, 2011

Plasma Surface Treatment of Artificial Bones and its Application to Regenerative Medicine

Satoshi Hamaguchi[1], Dae-Sung Lee[1], Kazuto Masuda[1], Yu Moriguchi[2], Akira Myoui[2], and Hideki Yoshikawa[2]
[1] Center for Atomic and Molecular Technologies, Graduate School of Engineering,
Osaka University, 2-1 Yamadaoka, Suita, Osaka 565-0871, Japan.
[2]Department of Orthopaedics, Graduate School of Medicine,
Osaka University, 2-2 Yamadaoka, Suita, Osaka 565-0871, Japan
hamaguch@ppl.eng.osaka-u.ac.jp

ABSTRACT

Effects of plasma irradiation on artificial bones and living cells have been examined. Plasma treatment of interconnected porous calcium hydroxyapatite (IP-CHA), which is material for artificial bone whose chemical composition is close to that of human bone, is shown to improve its hydrophilicity significantly as well as its osteoconductivity and osteoinductivity. Similar effects were observed whether the IP-CHA was treated by atmospheric-pressure plasmas in air or low-pressure plasmas containing oxygen. It is also shown that a plasma treated medium for cell culture can enhance cell proliferation.

1. Introduction

Various types of hydroxyapatite (HA) have been clinically used as materials for bone substitutes. Among them, interconnected porous calcium hydroxyapatite (IP-CHA) has been proven to be an excellent alternative to autologous bone grafting as its internal pores function as scaffolds for osteogenic cells and facilitate bone tissue regeneration [1-3].

The surface properties of IP-CHA (as well as other artificial bones made of HA), however, may be further improved. For example, the surface of native HA is in general hydrophobic. Our recent study [4] has shown that treatment of HA by plasmas significantly improve its hydrophilicity.

The goal of this work is to demonstrate that IP-CHA treated by either atmospheric-pressure plasmas or low-pressure plasmas containing oxygen exhibits high hydrophilicity of the surfaces of its internal pores. In addition, we will also show that a medium treated by an atmospheric-pressure plasma can enhance cell proliferation if it is used for cell culture.

2. Experiments

Figure 1 shows a schematic diagram and a photograph of an atmospheric-pressure plasma system used in this study. The system is a dielectric barrier discharge (DBD) system and the electrodes are set outside a glass tube in which a He gas flows. The typical applied voltage used in this study was ± 5kV with a sinusoidal wave form at a frequency in the range of 20~30kHz. The plasma extends from the tip of the glass tube with a typical length of about 1cm.

For material processing, we have also used a plasma that operates at a sub-atmospheric pressure. A schematic diagram of the system is shown in Fig. 2 [1]. In this system, typical gas pressure used in this study was 2.2 kPa and the applied voltage was ±1.5kV with a sinusoidal wave form at a frequency of 40 kHz.

The material processed in this study is interconnected porous calcium hydroxyapatite (IP-CHA) with a porosity of 75% in volume, an average pore diameter of 150 μm and an average interpore connection window diameter of 40 μm.

IP-CHA cylindrical tablets with a diameter of 5 mm and a length of 2 mm were placed in the discharge chamber. Figure 3 shows images of IP-CHA tablets obtained from high-resolution X-ray computed tomography (micro-CT) with and without plasma treatment. Here a drop of water with a contrast agent was placed on a surface of each IP-CHA tablet. It is seen that, after 10 min plasma treatment, the dropped water fills almost all pores inside the tablet, which indicates the increase of hydrophilicity of inner pore surfaces.

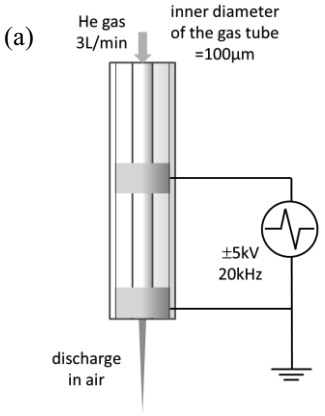

Fig.1 : A schematic diagram of a He-based plasma jet system used in this experiments (a) and a photograph of the plasma (b).

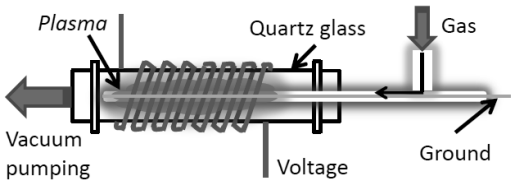

Fig. 2: A schematic diagram of a low-pressure discharge system used in this study [1].

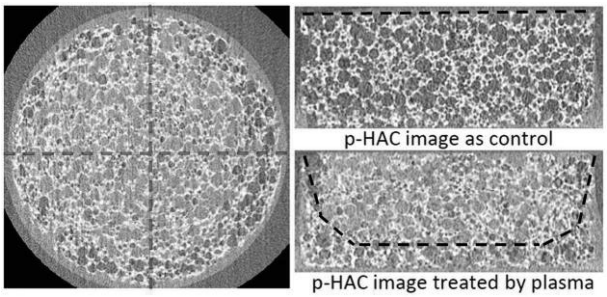

Fig. 3: The micro-CT images of an IP-CHA tablet after 10 min plasma treatment (the horizontal cross section at the mid plane of the tablet: left, and the vertical cross section at the center axis: lower right) and one without treatment (control, the side cross section: upper right). A drop of water containing a contrast agent is placed on the top surface of each tablet. The white color indicates the location of hydroxyapatite (HA), gray the location of water (i.e., water filled pores), and dark the location of empty space (unfilled pores). It is seen that, with plasma treatment, most pores are filled with added water, indicating the increase of hydrophilicity of inner pore surfaces.

We have also examined effects of atmospheric-pressure plasma application to cell proliferation. The rate of enhanced cell proliferation is considered to be associated with the quantity of reactive oxygen/nitrogen species (ROS/RNS) generated in the medium by plasma application. Figure 4 shows the amount of peroxide radicals generated by plasma application obtained from d-ROMs (derivatives of reactive oxygen metabolites) test [5]. In this experiment, we applied atmospheric-pressure plasma jets generated by the system shown in Fig. 1 to 100 μl of DMEM （Dulbecco’s modified Eagle's medium）for the period (i.e., plasma exposure time) indicated by the horizontal axis of Fig. 5. The vertical axis indicates the density of peroxide radicals measured in the units of U. CARR (Carratelli units), where 1 U. CARR means the density of peroxide radicals (R-OOH) equivalent of that of 0.08mg/100ml of H_2O_2. Although the data are not shown here, we have confirmed that the rate of enhanced cell proliferations by application of atmospheric-pressure plasma jets is correlated with the production of peroxide radicals in the medium.

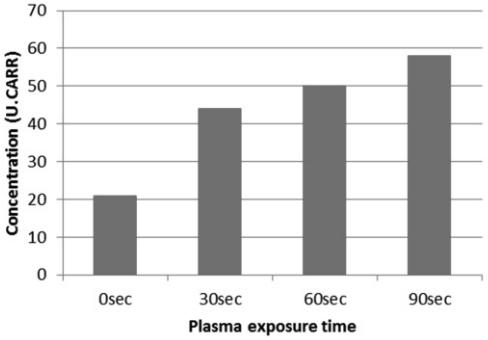

Fig. 4: The amount of peroxide radicals generated in 100μl DMEM by application of atmospheric-pressure plasma jets from the system shown in Fig. 1.

In summary, we have examined effects of plasma irradiation on artificial bones for surface treatment and living cells for cell proliferation. It has been confirmed that either atmospheric-pressure or low-pressure plasma treatment of IP-CHA improves its hydrophilicity significantly. Although the data are not shown here, our preliminary study has indicated that the same treatment of IP-CHA also improves both osteoconduction and osteoinduction. It has been also confirmed that a plasma treated medium for cell culture can enhance cell proliferation.

References

[1] N. Tamai, A. Myoui, T. Tomita, T. Nakase, J. Tanaka, T. Ochi and H. Yoshikawa, J Biomed Mater Res **59**, 110-117 (2002).
[2] H. Yoshikawa and A. Myoui, J. Artif. Organs **8**, 131–136 (2005).
[3] N. Yamasaki, M. Hirao, K. Nanno, K. Sugiyasu, N. Tamai, N. Hashimoto, H. Yoshikawa, A. Myoui, J Biomed Mater Res B **91**, 788-798 (2009).
[4] D.-S. Lee, Y. Moriguchi, K. Okada, A. Myoui, H. Yoshikawa, and S. Hamaguchi, IEEE Trans. Plasma Sci. (2011) *in press*.
[5] A. Alberti, L. Bolognini, D. Macciantelli, and M. Carratelli, Res. Chem. Intermed. **26** (2000) 253.

Eighth International Conference on Flow Dynamics
November 9 - November 11, 2011

Control of Cell Adhesion and Functions Using 2D and 3D Biocompatible Surfaces

Masaru Tanaka

Department of Biochemical Engineering,
Graduate School of Science and Engineering,
Yamagata University, Yonezawa, Japan
tanaka@yz.yamagata-u.ac.jp

ABSTRACT

The design of biocompatible 2D and 3D nano/micro topographies has a variety of potential applications in medical devices. We have reported that biocompatible 2D surface using poly(2-methoxyethyl acrylate) (PMEA) and honeycomb-patterned 3D films with regular interconnected pores that is formed by self-organization. The 3D films exerted a strong influence on cell morphology, proliferation, cytoskeleton, focal adhesion, and ECM production profiles. Growth of cancer cells on 3D films was lesser than that of cells on control flat films. Our results suggest that the topography in contact with cancer cells has a potential anticancer effect.

1. Introduction

The ability of surfaces to control cell adhesion is of crucial importance in biotechnology and biomedical applications. Many attempts to modify surfaces have been made in order to avoid the activation of the body's defense mechanisms through exposure of cells to foreign materials. It has been pointed out that biocompatibility depends on the various physicochemical properties of the material surface, e.g., surface charge, wettability, surface free energy, topography or roughness, stiffness, and the presence of specific chemical groups on the surface [1].

2D and three-dimensional (3D) porous scaffolds fabricated from biodegradable polymers have been widely used as temporary extracellular matrices; these play critical roles in tissue engineering. The 3D scaffolds of appropriate pore sizes and porosities with interconnected pores facilitate cell adhesion, proliferation, differentiationand eventual tissue regeneration in a natural manner.

Inspired by the organization of biological structures, we expected that the self-organization of organic and inorganic components into hierarchical and sophisticated structures would offer an alternative to the conventional nanofabrication and microfabrication techniques. The self-organization technique requires ambient physiological conditions, in contrast to the harsh conditions required by the typical fabrication techniques. This technique can be applied to polymer fabrication for cell culture scaffolds because of its physical generality. We have found that regular structures are formed during the casting of biodegradable and biocompatible polymer solutions on solid surfaces; for example, self-organized honeycomb-patterned films (honeycomb films) with highly regular porous structures can be prepared under humid casting conditions [2]. Here, we examined the growth of human normal and cancer cells cultured on the 3D films.

2. Method

3D honeycomb film from poly(ε-caprolactone) (PCL) was prepared on a glass substrate by employing a previously described method [2]. The flat film was prepared by a spin coater in dry condition. All the cell lines were grown on tissue culture (TC) dishes and PCL films. We performed the WST-8 assay, a colorimetric assay that counts viable cells. DNA synthesis was measured by 5-bromo-2-deoxyuridine (BrdU) incorporation into cellular DNA. As for cancer cells, cell apoptosis was measured by the following two methods. For early-phase apoptosis, caspase-3 and caspase-7 activities were measured by a luminescence assay using the Caspase-Glo 3/7 kit. For late-phaseapoptosis, fragmentation of nuclear DNA was evaluated by terminal deoxynucleotidyl transferase dUTP–biotin nick end labelling.

3. Results and Discussion

Most tissue-derived cells are anchorage dependent and require attachment to a solid surface for viability and growth. Therefore, the initial events that occur when a cell approaches a surface are of fundamental interest. In tissue engineering, cell adhesion to a surface is critical because adhesion precedes other events, such as cell spreading, cell migration, and differentiated cell functions.

We have found that honeycomb-patterned 3D films with regular interconnected pores (Fig. 1) that is formed by self-organization. The highly regular porous structures can be prepared under humid casting conditions. The condensation of water from the air occurred due to evaporation cooling when a water-immiscible solvent was used. The self-packed and monodispersed water droplets formed on the solution surface acted as a temporary template of the pores.

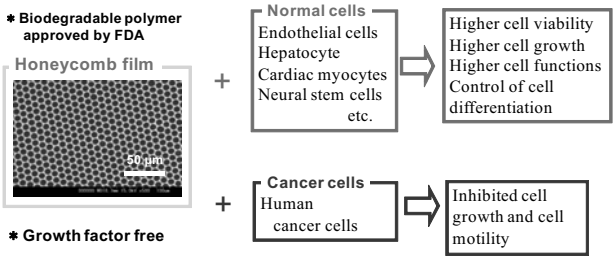

Fig. 1 Cell behavior on the 3D honeycomb films. Cell morphologies and specific functions were greatly influenced by topography of the film.

The tilted and side-view images of the honeycomb film are two hexagonal lattices connected vertically by columns at the vertex of hexagons . By investigating their influence on the cell morphologies, proliferation, and functions, we were able to use them in a range of tissue engineering strategies. The 3D films exerted a strong influence on cell morphology, proliferation, cytoskeleton, focal adhesion, and ECM production profiles (Fig. 2).

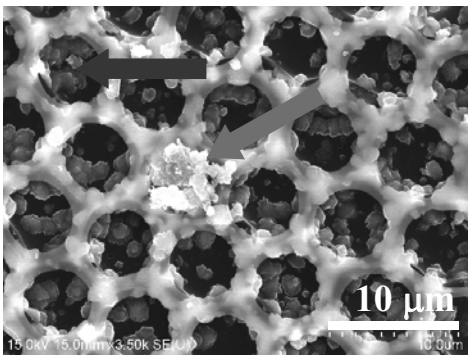

Fig. 2 Enhanced matrix mineralisation by osteoblasts on honeycomb films (Day 28). Quantification of bone formation reveals that the honeycomb films support greater production of matrix compared to flat control.

Growth of cancer cells on honeycomb films was lesser than that of cells on control flat films. In 27 of 58 cell lines, more than 50% inhibition was observed. Cell growth on honeycomb films was not enhanced for any of the cell lines. We attempted to identify the mechanisms underlying the inhibition of cancer cell growth by honeycomb films. One possible mechanism involves the induction of apoptosis by honeycomb films. We first determined the activities of caspase-3 and caspase-7, the essential mediators of early-phase apoptosis. Both A549 and GB-d1 cells exhibited approximately equal levels of caspase-3 and caspase-7 activities on TC plates, flat films and honeycomb films (Fig. 3). Caspase-3/7 activity and TUNEL assays revealed that inhibited growth was not due to apoptosis.

SA-β-galactosidase assay showed that honeycomb films did not induce cell senescence although SEM revealed enlarged and flattened cells, similar to senescent cells, on the honeycomb films. The cells attached to the honeycomb films were relatively resistant to detachment by trypsin treatment as compared to those attached to flat films. Such cells that did not detach easily showed lower expression of cyclin D1 and higher expression of retinoblastoma protein than did the easily detachable ones. Our results suggest that the topography of the honeycomb film in contact with cancer cells has a potential anticancer effect. Although we have no clear evidence to elucidate the reasons for which the cells adhering to the honeycomb films showed lowered growth, we suggest the following possibilities. Some cancer cells infiltrated into the pores of honeycomb films and were trapped, and they may

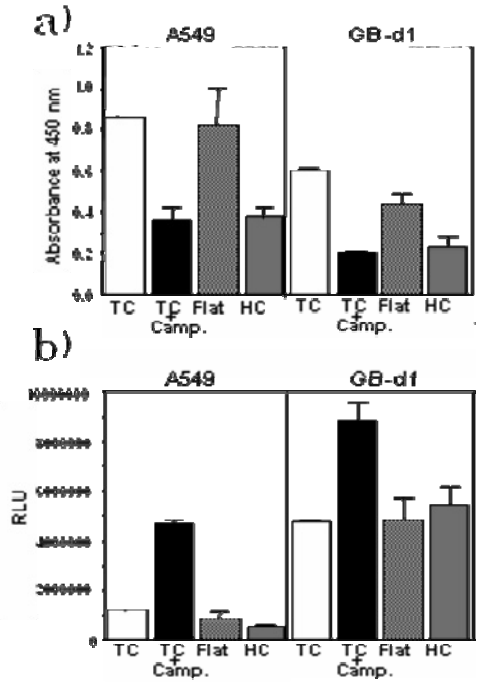

Fig 3. Growth inhibition (a) and Caspase3/7 activity (b) of cancer cells (A549 and GBd-1). TC: Tissue culture plate, Flat: Flat film, HC: Honeycomb-patterned film, Camp: Anti-cancer drug.

have suffered mechanical stress and/or did not have enough space for proliferation. Focal adhesions are known to function as mechanosensors that probe the physical properties of the cell environment. Changes in physical properties such as hardness and contractility are thought to have occurred in parts of the honeycomb films. Out-side-in signal through such abnormal focal contacts may have induced negative regulatory effects on cell proliferation. In our next study, we will attempt to uncover the molecular mechanisms underlying the growth inhibition by honeycomb films, including the above-mentioned possibilities. It should be also noted that adsorbed proteins from serum and water structures [2] may affect cancer cell behaviour. Experiments addressing this possibility are now in progress.

Acknowledgements

This work is supported by Grants-in-Aid and Special Coordination Funds for Promoting Science and Technology of Ministry of Education, Culture, Sports, Science and Technology, Japan.

References

[1] A.E. Nell, Nat. Mater. **8** (2009), 543.
[2] M. Tanaka, Biochim. Biophys. Acta, **1810** (2011), 251.
[3] T. Sato, M. Tanaka, J. Inokuchi, J. Biomat. Sci. Polym. Ed, **21** (2010), 1947.
[4] M. Tanaka, A. Mochizuki, J. Biomat. Sci. Polym. Ed, **21** (2010), 1849.

Eighth International Conference on Flow Dynamics
November 9 - November 11, 2011

Effect of Mechanical Loading on Chondrocyte Biosynthesis of Extracellular Matrix in Agarose Construct

Yoshinori Sawae
Department of Mechanical Engineering, Faculty of Engineering, Kyushu University, 744 Motooka, Nishi-ku, Fukuoka 819-0395, Japan
sawa@mech.kyushu-u.ac.jp

ABSTRACT

Different types of mechanical loadings had been applied to chondrocytes being cultured in agarose constructs and their effects on the cartilaginous tissue formation were examined. Mechanical loadings applied in this study were simple compressive loading, biaxial loading consisting of compression and shear and traction loading on the surface of constructs. All mechanical loadings were applied in a cyclic manner at 1 Hz. Results indicated that all mechanical loadings had certain effects on the biosynthesis of extracellular and enhanced the development of compressive stiffness of the chondrocyte-agarose construct.

1. Introduction

Mechanical stresses and strains exerted in articular cartilage by daily joint movements can stimulate the metabolism of chondrocytes; cells embedded in the cartilage, and play an important role to sustain the health and homeostasis of the cartilage tissue. The upregulative effects of the cyclic compression and the hydrostatic pressure on the chondrocytes biosynthesis of extracellular matrix (ECM) have been studied extensively and utilized in the cartilage tissue engineering. By contrast, the knowledge about the effect of traction loading acting on the cartilage surface is quite limited. During normal activities, articular cartilage of the major load bearing joints is subjected to certain traction force caused by the surface friction and it can exert reciprocating shear strains of approximately 5% in the cartilage tissue. These dynamic shear strains may have some effects on the chondrocytes biosynthesis of ECM molecules.

In this study, three different mechanical loadings, simple uniaxial compressive loading, biaxial loading consisting of compression and shear and traction loading on the tissue surface were applied to chondrocytes being cultured in agarose constructs. Then, the cartilaginous tissue formation in the cultured construct and resultant mechanical stiffness were compared after three weeks culture.

2. Method

The chondrocyte-agarose construct is a well-established three dimensional culture system for isolated chondrocytes and has been employed as an experimental model in the cartilage tissue engineering context [1]. In this study, chondrocytes were isolated from the metacarpal-phalangeal joint of steers using a sequential enzyme digestion process [1]. Subsequently, isolated chondrocytes were seeded in 1% low gelling temperature agarose (Sigma type VII) gel with an initial cell density of 1 x 10^7 cells/ml and cultured in Dulbecco's modified eagle medium (DMEM) supplemented with 20 vol% fetal bovine serum (FBS).

In our first experiment, cylindrically chondrocyte-agarose constructs with a diameter of 4 mm and a height of 2.5 mm were used as test specimens. Uniaxial compressive loading and biaxial loading consisting of compression and shear were applied to specimens, respectively, by using a custom-made biaxial loading system installed in an incubator. A schematic drawing of the loading system is shown in Fig. 1. The system has two PC-controlled liner actuators by which the two dimensional movement of a loading plate was precisely controlled. Both mechanical loadings were applied in cyclic manner at 1 Hz for 6 hours a day. The strain amplitude of compression was varied from 10 to 15 % while the shear strain amplitude was fixed to 5 % of the specimen height.

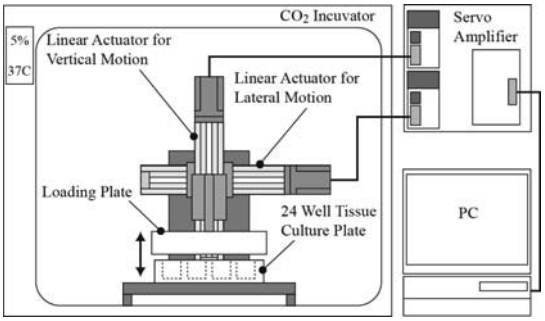

Fig. 1 Schematic drawing of biaxial loading system.

After three weeks culture, the tangent modulus of the cultured constructs was measured by an unconfined compression test. The glycosaminoglycan (GAG) content of cultured constructs and collected culture medium was also evaluated by using dimethylmethylene blue (DMMB) assay to examine the effect of applied mechanical loadings on the biosynthesis of ECM molecules. Finally, elaborated type II collagen and keratin sulfate molecules were stained by immunofluorescent method and the development of cartilaginous tissue structure in constructs was examined by confocal laser scanning microscopy (CLSM).

In the second experiment, the traction loading was applied to the surface of chondrocyte-agarose constructs by plastic rollers in the rolling-sliding loading system. The configuration of the loading system used in this experiment was shown in Fig. 2. After the specimen setup, plastic rollers with silicone rubber surface layer were brought into contact with the upper surface of constructs in culture dishes by a liner actuator. Subsequently the horizontal movement of culture dishes

and the rotation of rollers were exerted by AC-servo system in a coordinated manner to apply rolling-sliding motion with a defined sliding ratio between construct surfaces and plastic rollers.

Culture dishes were reciprocated at 1 Hz for 12 hour during three weeks culture. After that, the construct was sliced perpendicular to the sliding direction and the cross-section was observed by CLSM to examine effects of the reversed traction loading on the morphological characteristics of the elaborated cartilaginous tissue.

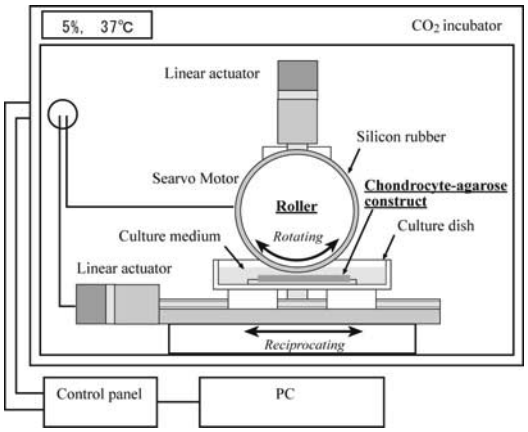

Fig. 2 Configulation of rolling-sliding loading system

3. Results and Discussion

The tangent modulus of chondrocyte-agarose constructs cultured under mechanical loadings is compared with that of control specimens, which were culture under same conditions without mechanical loading, in Fig. 3. The effect of cyclic compressions was depended on the strain amplitude. 15% compression had clear effect to increase tangent modulus of cultured constructs, although effect of 10% compression was quite limited. The effect of biaxial loadings was also strain amplitude dependent. The tangent modulus of loaded constructs became higher than that of control by applying the biaxial loading consisting of 10% compression and 5% shear. In contrast, the above mentioned upregulative effect of 15% compression was countered by the effect of 5% shear strain and the tangent modulus of loaded constructs became almost same as that of control.

The comparison of the total GAG synthesis, which is the total amount of GAG accumulated in the construct and released into culture medium, between the uniaxial loading and biaxial loading is shown in Fig. 4. All values in this figure were normalized with the average GAG synthesis of control specimens. The difference among three groups was not clear and all values became almost 1 at day 22. It means that 5% shear strain combined with 10% compression had little effect on the GAG biosynthesis. However, the enhanced development of collagen fiber network was recognized in constructs cultured with 5% shear and 10% compression by CLSM observation. The biaxial loading with appropriate compressive amplitude might uplegurate the elaboration of collagen fiver network and subsequently improved the compressive stiffness of cultured constructs.

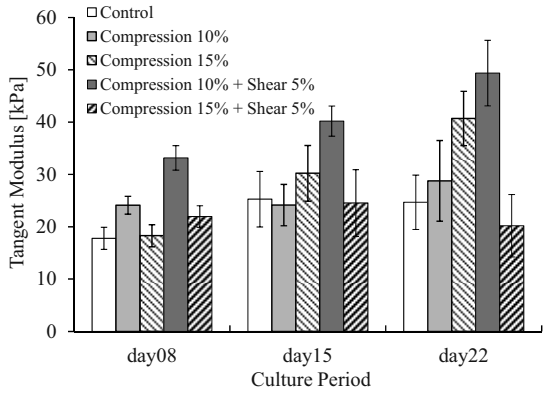

Fig. 3 Comparison of tangent modulus

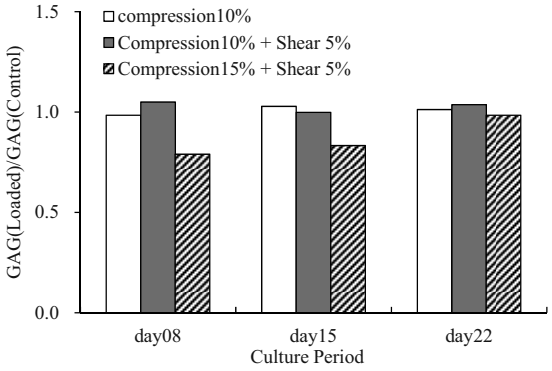

Fig. 4 Comparison of total GAG biosynthesis

Cross-sectional CLSM images of constructs cultured under the traction loading with 50% sliding ratio were shown in Fig. 5. Well-developed collagen fiber network was covered with keratin sulfate rich layer in the upper surface region where the traction loading was applied. Therefore, the traction loading might also stimulate the collagen and GAG biosynthesis. However, the extent of upregulation was limited around the articulating surface and consequently unique anisotropic tissue structure was formed in the construct.

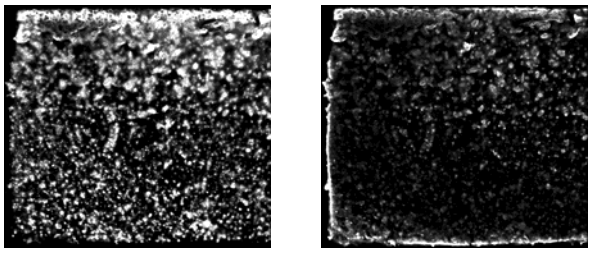

(a) Type II collagen (b) Keratan sulfate

Fig. 5 CLSM image of fluorescently-stained type II collagen and keratin sulfate elaborated in construct.

This study was financially supported by the Grant-in-Aid for Scientific Research of Japan Society for the Promotion of Science.

References

[1] D.A. Lee and D. Bader, J. Orthop. Res., **15** (1997), 181.

Eighth International Conference on Flow Dynamics
November 9 - November 11, 2011

Involvement of ERK in Morphological Response of Endothelial Cells to Spatial Gradient of Shear Stress

Author: Xiaobo Han, Naoya Sakamoto, Naoki Saito, Masaaki Sato, Makoto Ohta
Affiliation: Graduate School of Biomedical Engineering, Tohoku University
Address: 2-1-1, Katahira, Aoba-ku, Sendai, Miyagi, Japan
E-mail: hanxb@biofluid.ifs.tohoku.ac.jp

Abstract

Spatial shear stress gradient (SSG) suppresses the polarity and elongation of endothelial cells (ECs) in response to fluid shear stress (SS). However, the mechanisms about how ECs response to SSG remain to be elucidated. In this study, we explored the relationship between EC morphological changes under SSG and extracellular signal-regulated kinase (ERK). The results showed that ERK-inhibited ECs oriented and elongated under SS with SSG conditions, whereas non-inhibited ECs did not show morphological responses. This suggests that ERK could play a crucial role in EC morphological response to SSG.

1. Introduction

Endothelial cells (ECs) are known to change their morphology and functions to adapt to mechanical environments, such as fluid shear stress (SS) due to blood flow. A lot of research groups have investigated the morphological changes of ECs to SS stimulation. Recently, in addition, a few research groups have explored the relationship between spatial shear stress gradient (SSG) and EC responses [1, 2]. Sakamoto et al. used a novel designed T-shape flow chamber to quantitatively apply a variety of different combinations of SS and SSG to ECs and observed ECs morphological changes [2]. The results showed that after 24 hours of flow-exposure, ECs exposed to SS with SSG did not exhibit favored orientation and elongation unlike ECs exposed to SS without SSG. This result suggested that not only SS but also SSG could affect EC morphological responses to flow conditions. However, it still remains quite unclear about the mechanisms in EC morphological change under SS with SSG.

It was shown that SSG also suppressed the formation of bundles of actin filament stress fibers, which is normally observed in ECs exposed to SS without SSG [2]. Activation of extracellular signal-regulated kinase (ERK) is known to play a crucial role in many cell functions, and is reported to suppress the activation of a Rho family small GTPase RhoA [3, 4], which stimulates stress fiber formation in ECs under SS without SSG [5]. Therefore, to explore the mechanisms of ECs morphological response to SSG, we inhibited the activation of ERK in ECs to examine the role of ERK in EC morphological response to SSG.

2. Methods

2.1 Flow-exposure experiment

Human umbilical vein endothelial cells (HUVECs) were exposed to a defined-steady flow in a flow loop constructed by connecting a pulse damper, flow chambers, a reservoir, and a roller pump with silicone tubes. A T-shape flow chamber, which can create the conditions of SS with SSG, was used in the present experiment (Fig. 1) [2]. Parallel plate flow chambers were also used to create the conditions of SS without SSG. HUVECs were exposed to two conditions, SS of 2 Pa without SSG, and SS of 2 Pa with SSG of 8 Pa/mm, for 24 hours.

2.2 Fluorescence staining

PD98059, a specific inhibitor to ERK activation [6], was used in the flow-exposure experiment to inhibit ERK activity in HUVECs. Immediately after 24 hours of flow-exposure experiment, an intercellular junction molecule, VE-cadherin, was immunostained to evaluate cell morphology. Actin filaments in ECs were also stained to observe the actin filament formation. After staining, fluorescent images of HUVECs were obtained with the confocal fluorescence microscope (Olympus).

2.3 Morphological analysis

The outlines of HUVECs in fluorescent images were manually traced and then fitted to an ellipsoid with ImageJ (National Institutes of Health). The angle between the major axis of the ellipsoid and the direction of flow was defined as the orientation angle of HUVECs. HUVECs with the orientation angle of 0 to 30 degree were defined to orient to the direction of flow.

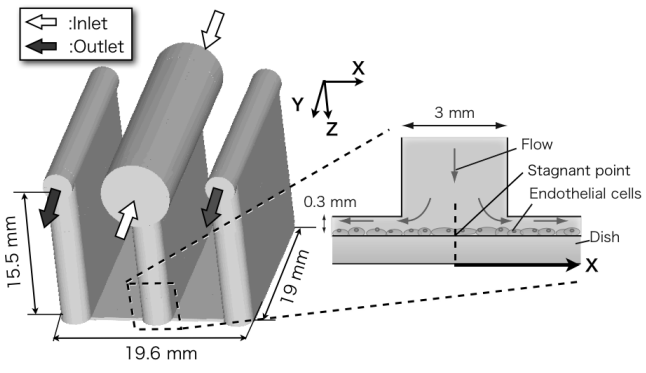

Fig. 1 FEM model of T-shaped flow chamber.

3. Results and discussion

Figure 2 shows the percentage of HUVECs oriented to the direction of flow after flow-exposure experiment. After 24 hours of flow exposure to SS of 2 Pa without SSG, both non-inhibited and ERK-inhibited cells oriented to the direction of flow. However, after 24 hours of flow exposure to SS of 2 Pa with SSG of 8 Pa/mm, ERK-inhibited HUVECs oriented to the direction of flow, while non-inhibited cells did not show favored orientation. This difference suggests that ERK could play an important role in EC morphological changes by SSG.

The formation of actin filaments in ECs was shown in Fig.3. After 24 hours of flow exposure to SS of 2 Pa without SSG, the formation and alignment of actin filaments were both observed in non-inhibited and ERK-inhibited HUVECs. After 24 hours of flow exposure to SS of 2 Pa with SSG of 8 Pa/mm, actin filament formation was suppressed in non-inhibited HUVECs, while the formation and alignment of actin filaments were still observed in ERK-inhibited HUVECs. This result suggests that the activation of ERK decreases the actin filament formation in ECs, and finally suppresses EC morphological changes under conditions of SS with SSG.

To explore whether ERK suppresses actin filament formation in ECs through suppression the activation of RhoA, it is necessary to investigate the activation of RhoA under SSG conditions in the future. The relationship between SSG and ERK activation also remains unknown. It is suggested that SSG causes tensile forces between neighboring cells [7]. Ueki et al. have reported that applying tensile forces to intercellular junctions caused recruitment and activation of Src homology 2-containing tyrosine phosphatase-2 (SHP-2) [8], which is thought to be important for the activation of ERK in ECs [9].

4. Conclusion

In the present study, we inhibited ERK activation in HUVECs and observed morphological response to the conditions of SS with and without SSG. The result suggests that ERK could play a crucial role in EC morphological response to SSG.

References

[1] H. Meng, Z. Wang, Y. Hoi, L. Gao, E. Metaxa, D. Swartz, J. Kolega. Stroke **38** (2008), 1924-1931.

[2] N. Sakamoto, N. Saito, X. Han, T. Ohashi, M. Sato. Biochem Biophys Res Commun **395** (2010), 264-269.

[3] G. Mavria, Y. Vercoulen, M. Yeo, H. Paterson, M. Karasarides, R. Marais, D. Bird, C. Marshall. Cancer Cell **9** (2006), 33-44.

[4] F. Waheed, P. Speight, G. Kawai, Q. Dan, A. Kapu. Am J Physiol Cell Physiol **298** (2010), C1376-87.

[5] S. Li, B. Chen, N. Azuma, Y. Hu, S. Wu, B. Sumpio, J. Shyy, S. Chien. J Clin Invest **103** (1999), 1141-1150.

[6] D. Alessi, A. Cuenda, P. Cohen, D. Dudley, A. Saltiel. J Bio Chem **270** (1995), 27489-27494.

[7] M. Szymanski, E. Metaxa, H. Meng, J. Kolega. Ann Biomed Eng **36** (2008), 1681-1689.

[8] Y. Ueki, N. Sakamoto, T. Ohashi, M. Sato. Exp Mech **49** (2008), 125-134.

[9] M. Osawa, M. Masuda, K. Kusano, K. Fujiwara. J Cell Biol **158** (2003), 773-785.

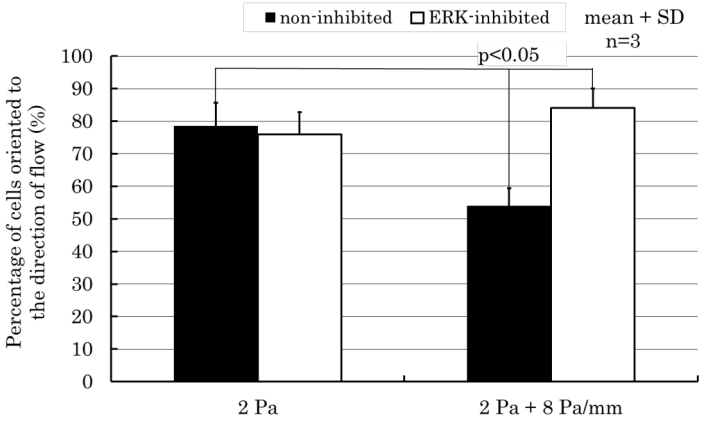

Fig. 2 Percentage of HUVECs oriented to the direction of flow after 24 hours of flow exposure to SS of 2 Pa without SSG, or SS of 2 Pa with SSG of 8 Pa/mm.

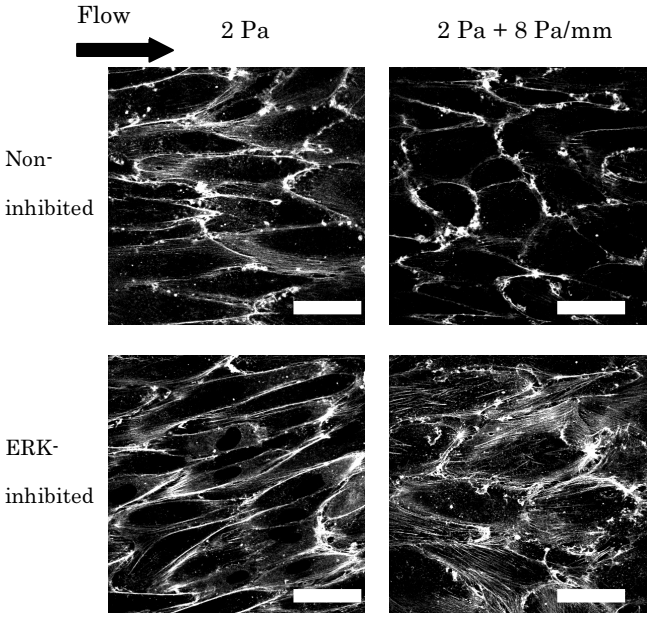

Fig. 3 Representative fluorescent images of actin filaments in HUVECs after 24 hours to flow exposure under SS of 2 Pa without SSG, or SS of 2 Pa with SSG of 8 Pa/mm. Bar = 50 μm.

Eighth International Conference on Flow Dynamics
November 9 - November 11, 2011

Modeling and Simulation of Gas Plasma-assisted Wound Healing

Yukinori Sakiyama[1], Marat Orazov[1], David Graves[1], and Gregor Morfill[2]
[1] University of California at Berkeley, USA
[2] Max Planck Institute for Extraterrestrial Physics, Germany
ysaki@berkeley.edu

ABSTRACT

Ambient gas plasma is a promising technology in various areas of biology medicine. Wound healing is one such application. Recent in vivo study by one of the authors showed that gas plasmas significantly reduce bacterial load in treated wounds. Here, we hypothesize that the reduction of the bacteria is a key factor of plasma-assisted wound healing and develop a numerical model to investigate a possible mechanisms of enhancement of wound healing by gas plasmas.

1. Introduction

Ambient gas plasma is a promising technology in various areas of biology medicine, including infection control, hand hygiene, cavity prevention, and cancer treatment. Chronic wounds represent a substantial public health problem around the world. In the United States alone, $2.8 billion is spent annually to treat an estimated 3 to 5 million chronic wounds. (1) Basically wound healing consists of three different stages: inflammatory phase (~48 hours), proliferative phase (2-10 days), and remodeling phase (~1 year). The inflammatory phase is the initial response of our body to stop bleeding and remove debris from wound site. In the second phase, blood vessels are deposited and collagen is deposited from fibroblast cells. Then tissue is reorganized and rearranged. Apoptosis is an important factor to eliminate/minimize scar on skin in the final stage. However, the fundamental mechanisms in system or cellular level of wound healing are only poorly understood.

Recent reports by other groups showed that ambient gas plasma stimulates apoptosis (2) and proliferation (3) of cells on culture plates *in vitro*. These are encouraging results. Most recently one of our authors have treated ~30 patients using ambient gas plasmas and found a highly significant reduction of bacterial load in treated wounds. (4) Based on the in vivo study, we hypothesize that reduction of bacterial load is a key factor of the plasma-assisted wound healing process. We are developing a numerical model to demonstrate it.

2. Review of numerical model for wound healing

Mechanochemical models of wound healing include the early work by Murray (5), Tranquillo and Murray (6), and Olsen (7). These models consider the connection of cells to the extra cellular matrix (ECM) and are thus relevant for deeper, dermal wounds. They are typically applied to acute (normal) wounds that heals by contraction. In addition to the 1995 paper, Olsen also developed a two-species model of wound healing angiogenesis in one and two dimensions, including endothelial cells and extracellular matrix (8). Schugart (9) developed a model of acute wound healing angiogenesis that accounts for interactions between capillary tips, blood vessels, oxygen, inflammatory cells, chemoattractant, fibroblasts, and ECM during the acute healing process. More recently, Flegg extended the Schugart's model to chronic wound healing. (10) Our model described below is based on Flegg's model and Schugart's model.

3. Model description

The governing equation consists of the following five PDEs.

$$\frac{\partial c}{\partial t} = D_c \frac{\partial^2 c}{\partial x} - \left(k_1 e + k_2 f + \frac{MB}{1+k_3 e} \right) \frac{c}{k_4 + c} + k_5 b (c_0 - c)(1+V) \quad (1)$$

$$\frac{\partial a}{\partial t} = D_a \frac{\partial^2 a}{\partial x^2} - k_6 a b (1+V) - k_7 a + k_8 \frac{H(c-c_L)H(c_H - c)}{e_0 + e} \quad (2)$$

$$\frac{\partial b}{\partial t} = D_b \frac{\partial^2 b}{\partial x^2} + \frac{\partial}{\partial x}\left(\frac{-k_9 e b}{(e_0^2 + e^2)(k_{10} + a)^2} \frac{\partial a}{\partial x} \right) + k_{11} b (k_{12} e + k_{13} f - b) + \frac{k_{14} a}{k_{15} + a} b \quad (3)$$

$$\frac{\partial f}{\partial t} = D_f \frac{\partial^2 f}{\partial x^2} + \frac{\partial}{\partial x}\left(\frac{-k_{16} f}{(k_{17} + a)^2} \frac{\partial a}{\partial x} \right) + k_{18} f \left(\frac{k_{19} c}{(k_{19} + c)^2} - \frac{f}{k_{20}(e + e_0)} \right) \quad (4)$$

$$\frac{\partial e}{\partial t} = D_e \frac{\partial^2 e}{\partial x^2} + k_{21} f \frac{c}{k_{22} + c} \left(1 - \frac{e}{k_{23} c} \right) \quad (5)$$

c is oxygen concentration, a is growth factor for capillary tips and fibroblasts, b is blood vessels, f is fibroblasts, and e is ECM. k_i (i=1-23) represents various coefficients and D_i (i=c, a, b, f, e) is diffusion coefficients.

In our model, we assume that after successive plasma treatment certain amount of bacteria is killed. The reduction of bacteria increases oxygen concentration in cells because bacteria consume a certain amount of oxygen at wound site. The bacterial load of the wound

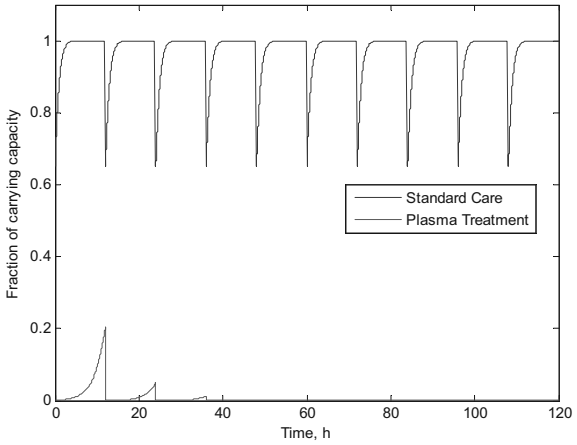

Fig 1 Bacterial load in wound after twice-a-day plasma treatment.

will be a logistic growth function. Each treatment will reduce the current "population" by a certain fraction or to a certain level. After the treatment the bacteria will grow back until they reach the carrying capacity.

Figure 1 shows the load of bacteria in wound after several plasma treatments. A significant reduction of bacterial load was observed in a few days. This will contribute to enhance the healing of wound.

4. Concluding remarks

We are developing mathematical models to investigate the primary roles of gas plasmas in chronic wound healing process. Experimental approach on wound healing often involves in vitro and animal studies. Those are expensive, time-consuming, and technically difficult to obtain statistically significant results. We think numerical model is capable of providing deeper insight into the wound healing process and has potential to develop a powerful tool to predict and optimize the plasma-assisted wound healing. In the presentation, we will show our preliminary simulation results and discuss our hypothesis in detail.

References

(1) T. J. Kindt, Kuby Immunology 6th edition (W. H. Freeman, New York, 2006)
(2) I. E. Kieft, IEEE Trans. Plasma Sci., **34** (2006), 1331-1336.
(3) S. Kalghatgi, Ann Biomed Eng, **38** (2010), 748-757.
(4) G. Isbary, Br. J. Dermatol., **163** (2010), 78-82.
(5) J. D. Murray, J. Math. Biol., **17** (1983), 125-129.
(6) R. T. Tranquillo, J. Theor. Biol., **158** (1992), 135-172.
(7) L. J. Olsen, J. Theor. Biol. **177** (1995), 113-128.
(8) L. Olsen, Math. Med. Biol. **14** (1997), 261-281.
(9) R. C. Schugart, Proc. Natl. Acad. Sci. **105** (2008), 2628-2633.
(10) J. A. Flegg, Bull. Math. Biol., **72** (2010), 18671891.

Eighth International Conference on Flow Dynamics
November 9 - November 11, 2011

Traction Force Measurement During Cell Migration By Using Micropillar-Integrated Device

Toshiro Ohashi[1], Akito Sugawara[1], Justin J. Cooper-White[2], Eijiro Maeda[1]
[1]Graduate School of Engineering, Hokkaido University, Kita 13, Nishi 8, Kita-ku, Sapporo, Hokkaido 0608628, Japan
[2]Australian Institute for Bioengineering and Nanotechnology, The University of Queensland, Old Cooper Road, St. Lucia, 4072, Queensland, Australia
ohashi@eng.hokudai.ac.jp

ABSTRACT

Cell migration plays an important role in many physiological and pathological processes such as morphogenesis, wound healing, and tumor metastasis. Although the majority of such events occur with cells moving as a group, called collective cell migration, the mechanism of collective cell migrations has not been well understood. It is thus important to know how moving cells generate forces at single cell level. The present study performs traction force measurement on migrating mouse NIH 3T3 fibroblasts by using a newly developed migration assay device to clarify the mechanism of collective cell migration.

1. Introduction

Cell migration is known to play an important role in a number of physiological events in living body such as morphogenesis, wound healing, and tumor metastasis. In the majority of such events, cells move as a group, called collective cell migration. Compared to a single cell migration, the mechanism of collective cell migrations has not been understood well and attempts have been made in simple experimental setups exemplified by "wound healing" assay [1, 2]. However, this technique is vulnerable to artefacts associated to the creation of the wound. To overcome such limitations, Doran et al. [3] have proposed a new experimental device using MEMS techniques. A significant advantage of the device was the ability to maintain an intact surface prior to the commencement of the analysis of collective cell migration.

MEMS techniques have also been employed to measure cellular behaviours at micro- and nano-scales and manipulate local cellular environment. One of such application is an array of micropillars [4]. By changing the dimensions of micropillars and/or the coating of the top of pillars, mechanical and biological local cellular environment can be fine-tuned. It is well known that mechanical and biological interactions between cells and their extracellular environment via focal adhesions regulate cell behaviours. For mechanical interaction, stiffness of cell attaching substrate modulates differentiation lineages of stem cells. For biological interaction, types of extracellular matrix protein regulate forces that cells generate to substrates, known as cell traction forces. Thus, the presence of these "outside-in" signaling pathways indicates that our understanding of collective cell migration can be enhanced by appropriate conditionings of extracellular environment both mechanically and biologically in experimental settings.

The purpose of the present study is to clarify the mechanism of collective cell migration at single cell level. To do this, we adopted the micropillar technology and integrated the micropillar arrays into a novel multichannel device [3]. With such novel experimental setup, traction force distribution within a cell collectivity was evaluated, which may reflect positional differences in mechanical roles of individual cells in collective cell migration.

2. Materials and Method

2.1 Specimen

Mouse NIH 3T3 fibroblasts were cultured in DMEM (Gibco, USA) supplemented with 10% of FBS (Gibco) (DMEM + 10%FBS) at 37°C/5% CO2 and used for experiments described below.

2.2 Micropillar-integrated multichannel device

A PDMS-made cell migration device was designed based on a device previously reported [3] and fabricated by standard photolithography and soft-lithography [4]. The current device consists of a reservoir (15.5 mm x 16.8 mm) with a flat surface for establishing a confluent cell monolayer, attached with microchannels for cell migration (Fig. 1). Each set of six microchannels branching off the reservoir converges at a single syringe port. Of six channels, four channels have arrays of micropillars (2 - 3 μm in diameter, 6.5 μm in height) at the bottom surface for the measurement of cell traction forces during migration, whereas the remaining two channels have a flat surface and serve as reference channels.

2.3 Cell migration assay/traction force microscopy

As shown in Fig. 1, a suspension of NIH 3T3 cells at a concentration of 5 x 10^5 cells/mL in DMEM + 10%FBS was loaded to the reservoir from the open top, following the sealing of the top of microchannels with the thin PDMS film. Due to the surface tension at the interface between the reservoir and the microchannels, the medium did not enter the channels. The cells were incubated at 37°C/5% CO_2 until a confluent monolayer was formed within the reservoir.

At the day of experiment, the device containing a confluent cell monolayer was set on a microscope stage. Cell migration was initiated when microchannels were backfilled with the medium from the syringe port. A set of microscopic images of the top of micropillars including cells and the bottom of the same micropillars was obtained every 10 minutes with a x 10 objective lens attached to an inverted microscope (IX81, Olympus, Japan).

To determine traction forces for individual cells in a monolayer that demonstrated a collective migration,

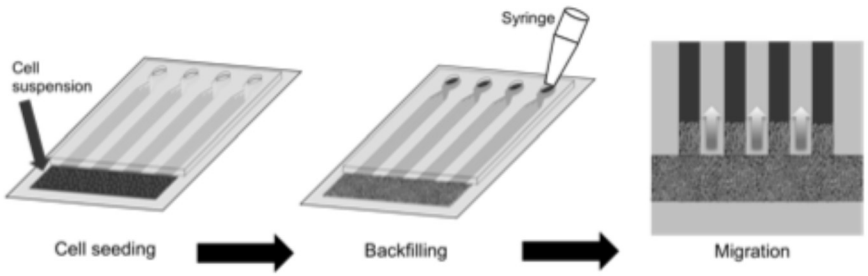

Fig. 1 Experimental procedure. Cells were incubated until confluent within the reservoir. Microchannels were backfilled with culture medium, which initiates the migration of cells from the reservoir into the channels.

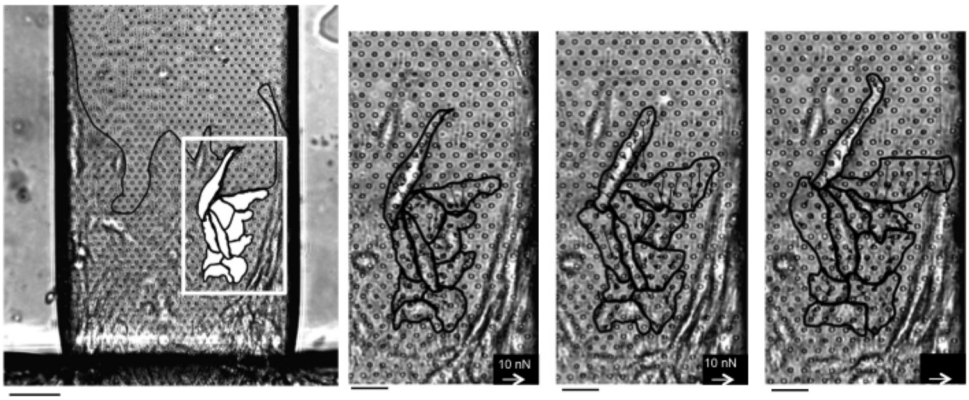

Fig. 2 (a) Micrograph of cells migrating at 24 hours. Bar = 50 mm. (b) Magnified views of the rectangular region in (a), superimposed with traction forces (arrows) at 24, 25 and 26 hours. Bars = 20 mm.

each individual cells was identified from microscopic images. Cellular traction forces were calculated from the deflection of micropillars and the spring constant of micropillars through an image analysis with ImageJ (NIH) using the Hooke's law.

3. Results and Discussion

After the onset of cell migration experiment, the cells migrated into microchannels with both flat surface and micropillar substrates throughout a 26 hours experimental period. Traction force microscopy was performed for the migrating cells (Fig. 2). In the analysis, cells on the moving front (leading cells) and those behind the leading cells (submarginal cells), particularly cells on the second and third rows, were chosen, as it was reported previously that cells within a certain distance from the moving front mainly committed to the forwarding movement of a cell collectivity [1]. It was observed that all the cells analysed generated traction forces but with different degrees. The leading cells generated traction forces over 10 nN at their leading edges, directing the backward of the moving direction. Cells on the second row generated smaller magnitude of traction forces. Most of traction force vectors directed the backward as in the case of the leading cells. Further small magnitude of traction forces was observed in cells on the third row, and the directions of these forces were varied compared to those from the cell on the first and second rows.

The present study demonstrated mechanical behaviour of cells within a moving collectivity at single cell level using a newly fabricated device combining elastic micropillar and microchannel structure. Results obtained demonstrate that cells consisting of collective cell migration generate traction forces with different magnitudes and directions depending on their relative positions, possibly reflecting positional differences in mechanical roles within a moving cell group. In particular, a gradual increase in the magnitude of traction forces towards the moving front may suggest reductions in the degree of cell-cell mechanical connections. Because cells near the moving front need to move forward and tug the rest of the cells within the collectivity, these cells may need to loosen cell-cell interactions and actively migrate like single cells. It remains to study how cells recognize their relative positions to modulate cell-cell and cell-matrix interactions and how mechanical/biochemical signals are transmitted between cells to achieve such coordinated cellular behaviours.

Acknowledgement

The present study was partially supported by JSPS Bilateral Joint Research Project (Japan-Australia).

References

[1] G. Fenteany, et al., Curr. Biol., **10** (2000), 838.
[2] R. Farooqui and G. Fenteany, J. Cell Sci., **118** (2005), 63.
[3] M.R. Doran, et al., Lab Chip, **9** (2009), 2369.
[4] J.L. Tan, et al., Proc. Natl. Acad. Sci., **100** (2003), 1484-1489.

Effect of Chemical Species Generated by a Plasma Flow on Inactivation of HeLa Cell Viability

Takehiko Sato[1*], Mayo Yokoyama[1] and Kohei Johkura[2]
[1]Institute of Fluid Science, Tohoku University, 2-1-1 Katahira, Aoba-ku, Sendai 980-8577, Japan
[2] Department of Histology and Embryology, Shinshu University School of Medicine, 3-1-1 Asahi, Matsumoto 390-8621, Japan
*E-mail of corresponding author: sato@ifs.tohoku.ac.jp

ABSTRACT

We aim at clarifying an effect of chemical species in a culture medium generated by exposure to a plasma flow on HeLa cell viability. When the cells were incubated in the treated culture medium, the cell survival ratio was decreased with the incubation time. The cells showed formation of blebs in their inactivation process and an addition of catalase detoxified plasma-treated culture medium. It was clarified that these effects were due to H_2O_2 generated by exposure to plasma because those trends such as survival ratio, morphological change and effects of catalase addition were close to that of H_2O_2-added culture medium.

1. Introduction

A plasma flow has been recently applied to plasma medicine since it is easily capable of generating chemically reactive species, light, heat, electric field, and shock wave [1,2]. A clinical test for treatment of chronic wounds [3,4], applying to tissue engineering [5,6], plasma inactivation for a low-temperature sterilization [7-8] and preventing nosocomial infection [9] have been reported as the outcome of researches in the plasma medicine field.

Since cells/bacteria are generally covered with water, the plasma-water system is one of the key phenomena for understanding the biological response. Various kinds of chemical species, e.g., NO_2, HNO_3, O_3 and OH, generated in air dissolve and transport in water quickly and decreased pH value [10, 11], and those chemical stimuli cause inactivation of bacteria [12]. However, the mechanism of biological response to plasma flow is still unclear due to its complexity against many stimuli generated.

To identify the specific chemical species which has an inactivation effect on cell viability, we focused on the H_2O_2 among the other species generated by plasma.

2. Method

The HeLa cell (Institute of Development, Aging and Cancer, Tohoku University) was incubated with a regular culture medium which consists of Minimum Essential Medium with addition of 10% Fetal Bovine Serum and Penicillin-Streptomycin (Penicillin 100u/ml; streptomycin 100μg/ml). The procedure to measure the absorbance intensity which indicates the number of cells was shown in Fig. 1. All incubation were performed at 37 ºC with CO_2 5% for 24 hr. The time-lapse images of the HeLa cell were taken by an inverted microscope (Carl Zeiss, Axio Observer D1). The existence of reactive oxygen species (ROS) in the cells was verified

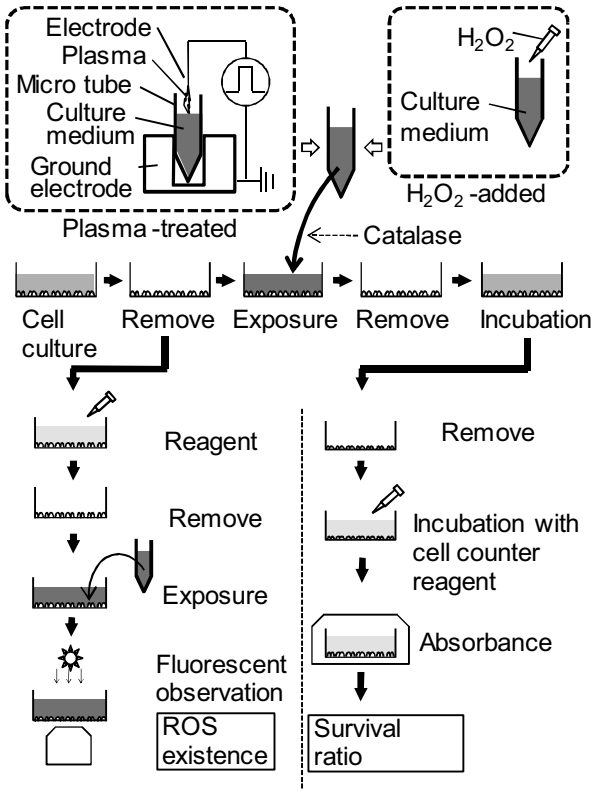

Fig. 1 Experimental procedure

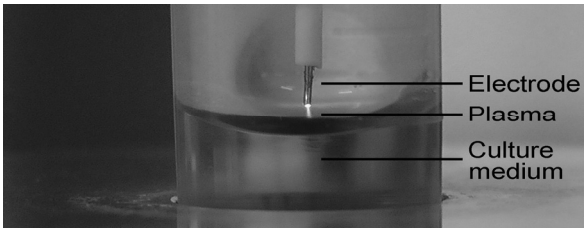

Fig. 2 Photograph of the culture medium exposing to the plasma flow.

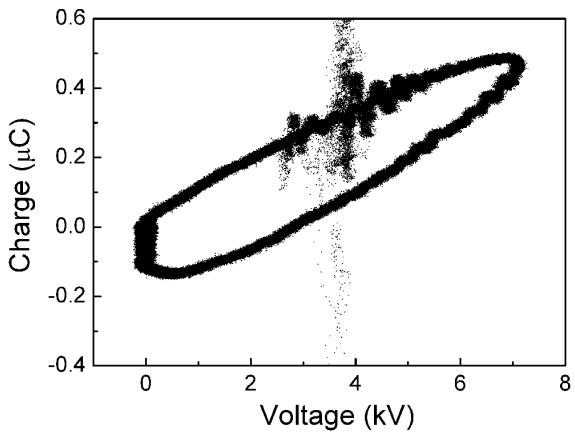

Fig. 3 Lissajous figure

using a fluorescence reagent (CM-H2DCFDA, Invitrogen). This is a cell-permeant indicator for ROS that becomes fluorescent after removal of the acetate groups by intracellular esterases and oxidation within the cell.

Plasma flow was generated between a needle electrode and the surface of culture medium with a gap of 1.5 mm as shown in Figs. 1 and 2. The electrode is made of platinum, 0.3 mm in diameter. The culture medium of 1.0 ml in a microtube of 1.5 ml was set in a ground electrode. The voltage of +7.5 kV_{0p} with frequency of 5 kHz and duty ratio of 4% was applied to the needle electrode for 210 s. The power consumption was 7.1 W calculated by using the Lissajous figure shown in Fig. 3. The H_2O_2 concentration was 304 μM in the plasma-treated culture medium when the exposure time is 210 s.

3. Results and discussion

Figure 4 shows the cell survival ratios in the case of plasma-treated and H_2O_2-added culture media in the presence of catalase of 19.6 unit/ml. After incubation for 48 hr, the survival ratios with plasma-treated and H_2O_2-added media were 95% and 101%, respectively, though the survival ratios without catalase treatment declined to 0% after 120 min of incubation. These results implied that the cell death was prevented by the H_2O_2 reduction due to catalase. This result also implies that the other chemical species such as HNO_2 and HNO_3 in the plasma-treated culture medium have little cytotoxic effect. Thus, H_2O_2 is indicated to play a central role in the cytotoxicity of the plasma-treated culture medium [13].

When the cells were exposed to the regular culture medium, no fluorescence emission was observed as shown in Fig. 5. In the case of exposure to plasma-treated and H_2O_2-added culture media, green fluorescence was observed in most of the cells. In contrast, when catalase (Worthington), an enzyme for H_2O_2 reduction, was added to the culture media at a concentration of 19.6 unit/ml, no fluorescence emission was observed in any condition. These results obviously show that, among ROS, H_2O_2 was the one which permeated into the cells even in the case of plasma-treated medium [13].

4. Conclusions

In this study, we have assessed the survival rate and morphological change of HeLa cells under incubation, and catalase-sensitive H_2O_2 permeation into the cells in plasma-treated and H_2O_2-added culture media. It was clarified that H_2O_2 is the inactivation factor of HeLa cell viability among chemical species generated by exposure to the plasma flow.

This study was partly supported by the Japan Society for the Promotion of Science, Grant-in-Aid for Scientific Research (No. 21246032), and by Collaborative Research Project of the Institute of Fluid Science, Tohoku University. We would like to thank T. Nakajima, Tohoku University for technical support.

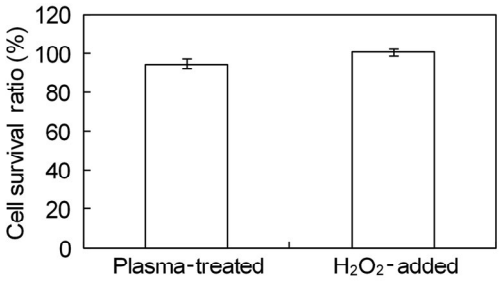

Fig. 4 Cell survival ratios in the cases of plasma-treated and H_2O_2-added culture media with catalase.

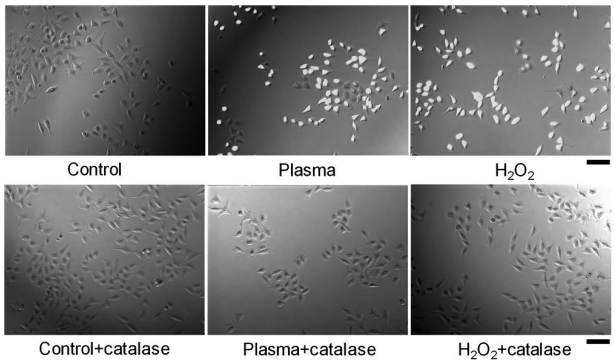

Fig. 5 Fluorescent observation of H_2O_2 permeation into the cells. The reagent is CM-H2DCFDA and the scale bar is 100 μm.

References

[1] G. E. Morfill, M. G. Kong and J. L. Zimmermann, New J. Phys. **11**, 115011 (2009).
[2] G. Fridman, G. Friedman, A. Gutsol, A. B. Shekhter, V. N. Vasilets, A. Fridman, Plasma Process. Polym. **5**, 503 (2008).
[3] J. Heinlin et al., Acad. Dermat. Venere. **25**, 1 (2010).
[4] G. Isbary et al., Brit. J. Dermatol. **163**, 78 (2010).
[5] G. J. Kim, W. Kim, K. T. Kim and J. K. Lee, Appl. Phys. Lett. **96**, 021502 (2010).
[6] A. Shashurin, M. Keidar, S. Bronnikov, R. A. Jurjus, and M. A. Stepp, Appl. Phys. Lett. **93**, 181501 (2008).
[7] T. Sato, T. Miyahara, A. Doi, S. Ochiai, T. Urayama and T. Nakatani, Appl. Phys. Lett., **89**, 073902 (2006).
[8] T. Sato, O. Furuya, K. Ikeda and T. Nakatani, Plasma Process. Polym., **5**, 606. (2008).
[9] M. L. Burts, I. Alexeff, E. T. Meek, and J. A. McCullers, Am. J. Infect. Cont., **37**, 729 (2009).
[10] T. Shimizu, Y. Iwafuchi, G. Morfill and T. Sato, New J. Phys., **13**, 053025 (2011).
[11] T. Shimizu, Y. Iwafuchi, G. Morfill and T. Sato, J. Photopolym. Sci. Tech., **24**, 421 (2011).
[12] S. Ikawa, K. Kitano and S. Hamaguchi, Plasma Process. Polym. **7**, 33 (2010).
[13] T. Sato, M. Yokoyama and K. Johkura, J. Phys. D: Appl. Phys., **44**, 372001 (2011).

PS4:The 12th Japan-Korea Students' Symposium

New Energy Flow for Sustainable Society -Properties and Applications of Energy Materials-

Eighth International Conference on Flow Dynamics
November 9 - November 11, 2011

Low-temperature Operating Micro–SOFC with Perovskite–type Proton Conductive Electrolytes

Yu Inagaki, Kensuke Kubota, Fumitada Iguchi, Syuji Tanaka, Noriko Sata,Masayoshi Esashi and Hiroo Yugami
Graduate School of Engineering, Tohoku University
Aoba 6-6-01, Aramaki, Aobaku, Sendai, 980-8579, Miyagi, Japan
y_inagaki@energy.mech.tohoku.ac.jp

ABSTRACT

This paper reports micro–solid oxide fuel cells (μ–SOFC) using new electrolytes fabricated by silicon MEMS technology. We adopt perovskite–type proton conductors, *i.e.* Y–doped $BaZrO_3$ (BZY) and Sr and Co –doped $LaScO_3$ (LSScCo). These cells were fabricated using a conventional PLD method. The maximam power density of μ–SOFC using BZY was 23mW/cm^2 at 470^{o}C and that using LSScCo was 0.85mW at 490^{o}C. We suceed to operate μ–SOFC with proton conductors. These low values are caused by the large resistance of electrodes. The optimization of electrode materials and structure is essential to improve performance.

1. Introduction

Now, most of energy sources we use are fossil fuels. But there are some problems. First, fossil fuels will be exhausted. Second, global warming is caused by carbon dioxide which is emitted by using fossil fuels. Then, fuel cells attract attention. These are able to change chemical energy to electrical energy in high efficiency. In these fuel cells, especially solid oxide fuel cell (SOFC) has high total changing energy efficiency and diversity. SOFC is used for a large power generation system. This electrolyte is ion conductive ceramics. General materials of SOFC are Yttria stabilized zirconia (YSZ) for electrolyte, $La_{1-x}Sr_xMnO_3$ (LSM) for cathode and Ni and YSZ cermet (Ni-YSZ) for anode.

This paper reports micro–solid oxide fuel cells (μ–SOFC) using new electrolytes fabricated by silicon MEMS technology. Recently, battery which has high power density and long usable time is desired because small-sized electrical machine is offering technical advantage and multiple functions. For new battery, μ–SOFC which has high power density and high energy density attracts attention. μ–SOFC is a small-sized SOFC and able to operate low temperature because of its low resistivity. Previously, some researchers have developed μ–SOFC with YSZ [1]. Instead of YSZ, we adopt perovskite–type proton conductors, *i.e.* Y–doped $BaZrO_3$ (BZY) and Sr and Co –doped $LaScO_3$ (LSScCo), which are promising candidates for electrolytes of SOFC operating in the temperature range of 400^{o}C to 600^{o}C. The adoption of those electrolytes is expected to reduce operating temperature lower than that of μ–SOFC with YSZ.

We fabricated μ–SOFC with these electrolytes and measured electrical characteristics.

2. Method

2.1 Electrolyte materials

We adopt 15mol%Y–doped $BaZrO_3$ (BZY) and 20mol%Sr and 2mol%Co –doped $LaScO_3$ (LSScCo) as an electrolyte.

2.2 Fabricating cells

Figure 1 shows fabrication process flow diagram. Cells were fabricated on (100) oriented Si wafers. At first, thin film electrolyte were deposited on the Si wafer using a conventional PLD method. The thickness is about 500-600nm. To prevent the brittle and buckling fractures of the electrolyte during fabrication and operation, residual stress in the electrolyte is controlled to be a little compressive in the deposition process. Then, the Si wafer was penetrated by wet anisotropic etching as a trapezoid shape to fabricate anode gas chamber. After the penetration, Pt–Pd porous films were deposited on both sides of the electrolyte as electrodes, and thickness of the electrode is about 300nm.

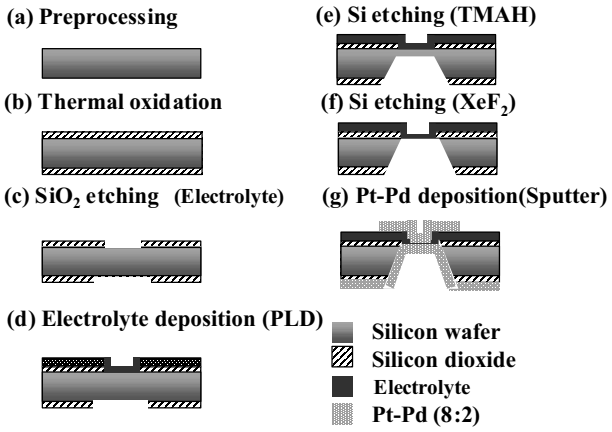

Fig.1 Fabrication process flow diagram

2.3 Power generation test

Power generation test was performed in the temperature range of about 300^{o}C–500^{o}C with humidified H_2 and air as anode and cathode gases, respectively. An external heater was used to heat cells up to testing temperature. We measured I-V characteristics and electrochemical impedance spectra. I-V characteristics were measured using Keithely2400. Electrochemistry characteristics were measured by electrochemical impedance spectroscopy using Sl1260 which is frequency response analyzation equipment and S1196 which is permittivity interface manufactured by solartron. The measurement frequency range was 1Hz-10MHz and the applied voltage was 10mV.

3. Results and Discussion

3.1 Fabricating cells

Almost 100 percent of cells were successfully

fabricated by 2.2 fabricating method. But these electrolytes had debris. These diameters were several μms. Debris are not so bad effect of mechanical stability but harmful effect of electrochemical characteristics and anode and cathode's air sealing.

3.2 Power generation test

3.2.1 I-V characteristics

Figure 2 shows results of I-V characteristics. The observed open circuit voltage of μ–SOFC with BZY and LSScCo is about 1.0V. It is confirmed from the result that anode and cathode were successfully separated by these electrolytes in the same way as conventional SOFC. But these values are slightly lower than theoretical open circuit voltage. This is beacause hole transport namber is high value below 400°C for proton cnductors. The maximam power density of μ–SOFC using BZY was 23mW/cm^2 at 470°C. About μ–SOFC using LSScCo, the maximam power density was 0.85mW/cm^2 at 490°C. When the temperature was downed form 500°C to 392°C the maximam power density was so low value. This shows cells were degradation with time.

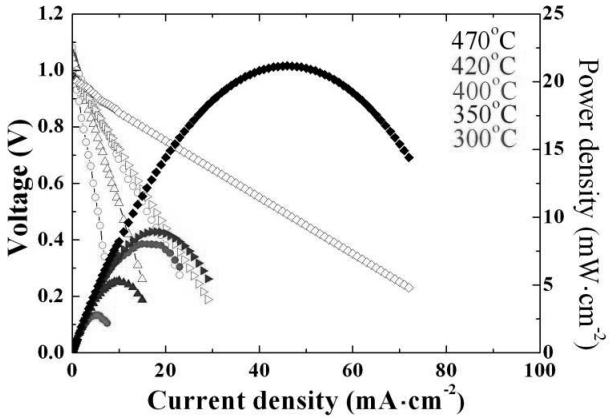

(a)

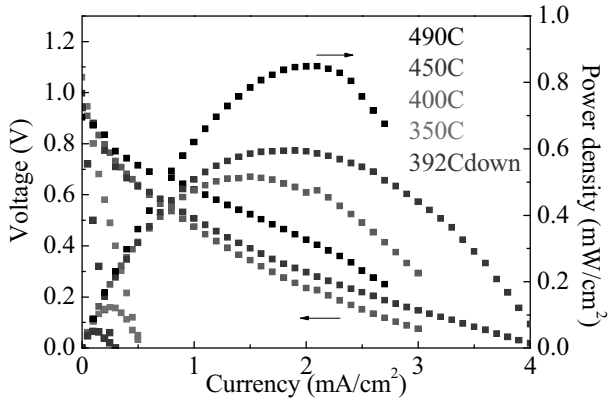

(b)

Fig.2 I-V characteristics (a)BZY, (b)LSScCo

3.2.2 Electrochemical impedance spectroscopy

Figure 3 shows impedance spectra. Both of BZY15 and LSScCo's spectra had three components. First component is high frequency real axis intercept which is electrolyte resistivity including line resistance. Second component is higher frequency arc which is resistivity of electrode reaction. Third component is lower frequency arc which may be resistivity of substance diffusion.

First component was so low values. This shows that electrolyte resistivity is very small. Second and third component were so high values. This shows that electrode resistivity is so big and accounts over 99% of total resistivity. Because of this if electrode resistivity were decreased, cells performance would be increased. To reduce electrode resistivity, triple boundaries of electrolyte, electrode and fuel need to be increased.

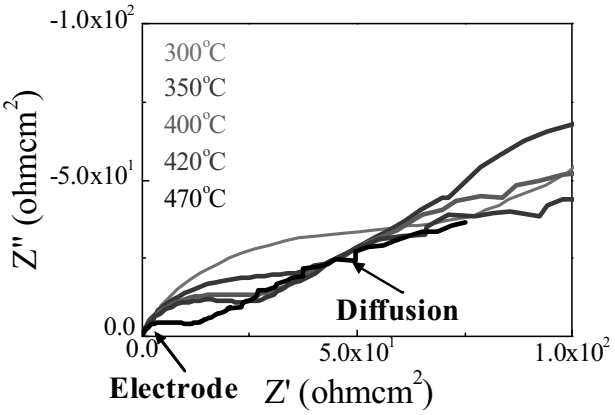

(a)

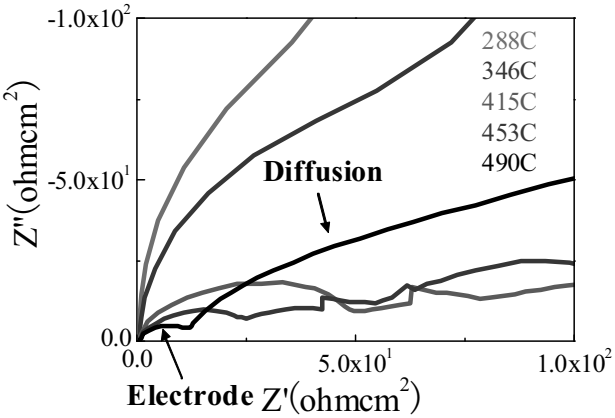

(b)

Fig.3 Impedance spectra (a)BZY, (b)LSScCo

4. Concluding remarks

It was possible to fabricate cells with both BZY and LSScCo as the electrolyte. These cells were observed open circuit voltage which was about 1.0V. It is confirmed from the result of impedance spectra that the electrode resistivity is over 99% of total resistivity. To increase performance of cells, it needs to decrease the electrode resistivity. To reduce electrode resistivity, triple boundaries need to be increased.

References

[1] Anna Evans, Anja Bieberle-Hutter, Jennifer L.M. Rupp, Ludwig J. Gauckler, Journal of Power Sources 194 (2009) 119–129.

Electrical Characterization of Ni-YSZ supported Thin Film YSZ electrolyte with GDC Top Buffer Layer

Eui-Chol Shin[1], Jung-Mo Jo[1], Pyung-An Ahn, Ho-Sung Noh[2], Ji-Won Sohn,[2] Jong-Ho Lee,[2] and Jong-Sook Lee[1,*]
[1]School of Materials Science and Engineering, Chonnam National University, Gwangju 500-757, Korea
[2]Korea Institute of Science and Technology, Seoul 136-701, Korea
*jongsook@jnu.ac.kr

ABSTRACT

The electrical properties of a thin film electrolyte prepared by PLD on a porous Ni-YSZ composite anode substrate were investigated by impedance spectroscopy using sputtered Ti/Au microelectrodes. Three impedance contributions with resistance values were successfully deconvoluted by modulus spectroscopy. The activation energies of the resistances are consistent with the analysis in which high frequency response is attributed to the GDC bulk and the middle frequency response to YSZ bulk response. The low frequency response which corresponds to most of the cell impedance is identified with an electronic transport through the GDC layer.

1. Introduction

Solid oxide fuel cell technology have many advantages to use as the alternative energy much higher energy efficiency with minimal pollutant emission comparing to petroleum. YSZ is well known electrolyte of state-of-the-art SOFCs, however, such as structure changing or mechanical problems arise at high temperature (800-1000℃) operation. The ohmic loss can be decreased by the reduction of thickness of the YSZ electrolyte and/or the used of materials with higher ionic conductivity over YSZ. An intensive investigation has been made on the development of intermediate-temperature range of 500-800℃ SOFCs based on thin film electrolyte of doped ceria. In this work, for the characterization of the electrical properties of thin films, impedance spectroscopy was used. Although it is a standard technique to distinguish the bulk response from other polarizations, the technique is not reliable for estimation of the electrolyte resistance of SOFCs, since the small resistance values and small bulk capacitance values associated are often inflicted by the lead wire resistance and inductance. The strategy is to apply the electrodes of a well-defined small area which would increase the measured electrolyte resistance values for better estimation and also avoid the short circuit by local defects such as pin holes.

2. Experimental

A 2 ㎛ thick NiO–YSZ interlayer, 1 ㎛ thick YSZ electrolyte and 200 ㎚ thick GDC buffer were fabricated by using pulsed laser deposition (PLD) techniques on Ni-YSZ composite anode substrates which was sintered at 1300°C of NiO-YSZ tape-casted anodes (NiO:YSZ = 56:44 wt %). The excellent performance and the microstructural details have been recently reported [1,2]. A gold target and a titanium target were sputtered using a RF-magnetron sputtering system which the rf power during deposition each were 75 W and 200 W and the film thickness were 500 ㎚ and 100 ㎚, respectively in the high purity Ar gases which gas pressure was kept at 10^{-2} torr. The bottom side of the specimen was painted using a conducting silver paste and attached to sapphire plate. Schematics of the microcontact impedance spectroscopy setup are shown in Fig. 1. Impedances are measured by contacting the microelectrodes with tungsten probe tips using micromanipulator arms under an optical microscope. AC impedance measurements were carried out at temperatures ranging from RT to 300°C in air over a frequency range of 1MHz to 0.01Hz by using a frequency response analyzer (Novocontrol, Germany).

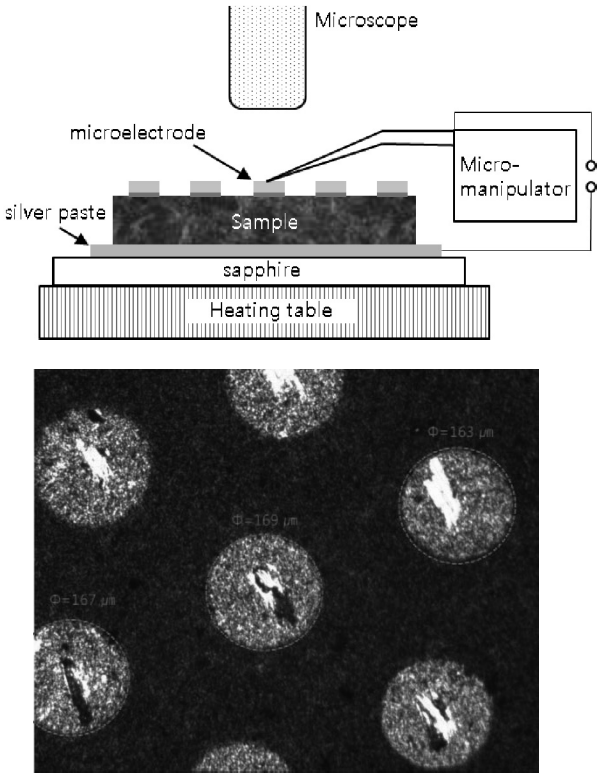

Fig. 1 Schematic setup for microcontact impedance spectroscopy using microelectrodes (up) and the microelectrode array sputtered on GDC/YSZ thin film electrolyte by using a shadow mask. (down)

3. Results and Discussion

Fig. 1 shows the microelectrode arrays were prepared by fixing the shadow mask on top of the GDC/YSZ thin film electrolyte. The electrode size

is different depending on the gap between the mask and sample. Fig. 2 shows the typical impedance spectra of the YSZ thin film at different temperatures. All the spectra were characterized by a big arc covered to a higher degree with increasing temperatures and lowered frequency limit. (The label shows the logarithm of the normalized frequency.) This can be attributed to the impedance elements with similar capacitance values but with much smaller resistance values in series to the major impedance elements.

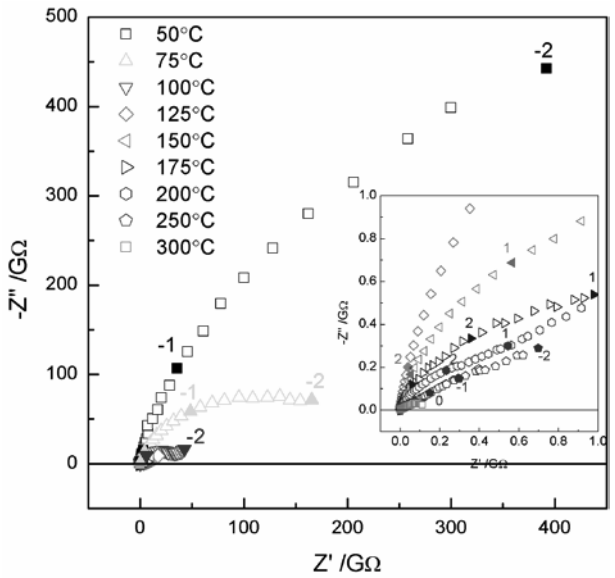

Fig. 2 Impedance spectra at different substrate temperatures of YSZ thin film electrolyte cell.(inset : high temperature spectra)

With both electronically conducting electrodes on both sides the dc resistance of the present cells becomes very large. (Although Ni-YSZ cermet has also ionic path in the fuel cell operation condition, for the measurement temperature range, the ionic resistance is too large from the geometry.)

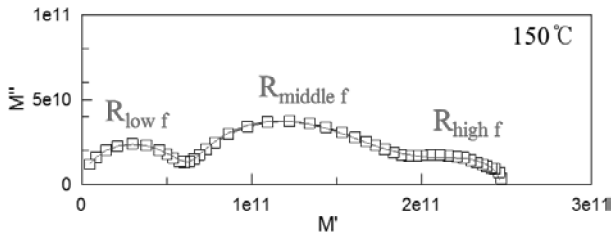

Fig. 3 Modulus spectrum with fitted solid line of the GDC/YSZ bi-layer thin film between microelectrode and the silver paste on heating table.

Modulus spectrum in Fig. 3 can distinguish these elements more clearly. A constant phase element in parallel to the resistance element with arc shape response or so-called Havriliak-Nagami elements[3] which can describe different frequency dispersion at the high and low frequency limit are used to estimate the resistance values and the time constants of three elements. In Fig. 4 the conductivity of GDC [4] and YSZ [5] from the literature is represented. The finite dc resistance would correspond to the electronic resistance of GDC and YSZ. Here again the electronic resistance of GDC is much smaller than that of YSZ. Upon this consideration, three resistance elements exhibit the activation energy consistent with GDC bulk, YSZ bulk and GDC electronic [6] and the shape factors are estimated by the electrode size and the thickness of the electrolytes.

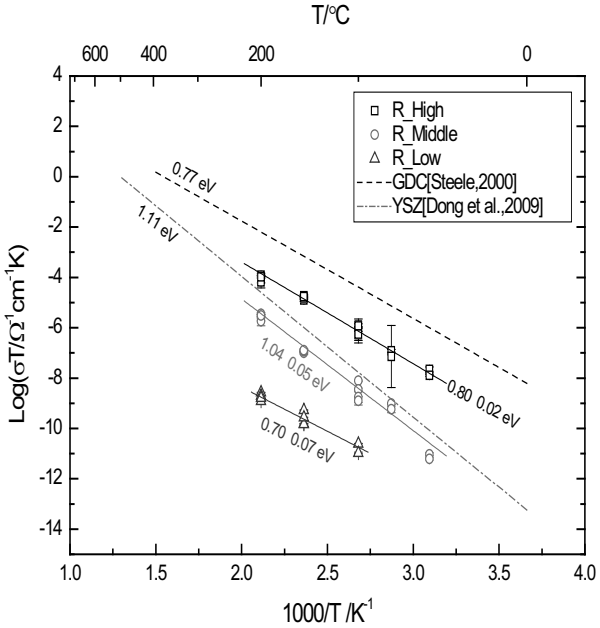

Fig. 4 The conductivities of GDC/YSZ bi-layer thin film electrolyte as a function of temperature plotted in Arrhenius form.

4. Conclusion

The GDC/YSZ bi-layer thin film electrolyte on the porous Ni-YSZ anode supported cell of electrical properties were successfully deconvoluted by using modulus spectroscopy. Each of the activation energy of GDC and YSZ thin layer and GDC electronic are 0.80 eV, 1.04 eV and 0.70 eV, respectively.

References

[1] Noh, J. Electrochem. Soc., 156 (2009) B1484
[2] Noh, Electrochem Solid State Lett., 14 (2011) B26
[3] Havriliak, J. Polymer Sci. C14 (1966) 99
[4] Steele, Solid state ionics, 129 (2000) 95
[5] Dong, Int. J. hydrogen energy. 34 (2009) 7903
[6] Joo, J. Eur. Ceram. Soc., 27 (2007) 4273

Eighth International Conference on Flow Dynamics
November 9 - November 11, 2011

Investigation on Oxygen Reduction Reaction on an $La_{1-x}Sr_xCo_{1-y}Fe_yO_{3-\delta}$ Thin Film Electrode

Li Xinxin, Atsushi Unemoto, Shin-Ichi Hashimoto, Koji Amezawa, Tatsuya Kawada
Graduate School of Environment Studies, Tohoku University
6-6-01 Aoba, Aramaki, Aoba-ku, Sendai, 980-8579, Japan
lixinzsh@ee.mech.tohoku.ac.jp

ABSTRACT

$La_{1-x}Sr_xCo_{1-y}Fe_yO_{3-\delta}$（LSCF）thin films were deposited on $Ce_{0.9}Gd_{0.1}O_{1.95}$ (GDC) electrolytes by pulsed laser deposition. AC impedance and DC bias measurements were carried out at 773～973 K in O_2-Ar gas atmospheres. The obtained impedance spectra consisted of ohmic resistance of the electrolyte and the electrode impedance, which was a parallel circuit of the electrode surface resistance and the chemical capacitance. Rate-determining step of oxygen reduction reaction on the LSCF film electrode was studied by analyzing the chemical capacitances.

1. Introduction

The main goal of current research on solid oxide fuel cells is to improve the performance of solid oxide fuel cells(SOFC) operating at temperatures ranging from 773K to 973K. These IT-SOFCs are expected to increase useful lifespan and reduce operation costs, making them more practical and commercially more attractive. Unfortunately, detrimental phenomena such as electrolyte ohmic losses and cathode polarization increase at lower temperatures[1]. In the SOFC systems, Energy conversion involves a variety of processes in tandem. such as electron transport and gas diffusion, vary little with temperature. Others, such as ion transport and oxidation and reduction reactions, are thermally activated and require significant changes to remain effective as temperature is decreased [6].Ion transport losses in the electrolyte can be reduced by reducing the thickness [1]. So, To solve these problems, one major goal in SOFC research is to understand the rate-determining step of the reaction of SOFC cathode.

In the past studies, Adler et al. brought forth a mechanism for $La_{0.6}Sr_{0.4}Co_{0.2}Fe_{0.8}O_{3-\delta}$(LSCF) electrodes [2]. The authors assumed the charge transfer step at the electrode/electrolyte interface to be facile and oxygen surface exchange as well as solid-state diffusion to be rate-determining. There is still debate around the oxygen reduction mechanism at mixed ionic-electronic electrodes in the literature. The reaction mechanism did not involve any surface pathway. In contrast, Liu pointed out the importance of charge transfer at the electrode/electrolyte interface by measuring the equilibrium impedance of oxygen reduction at porous $La_{0.7}Sr_{0.3}Co_{0.7}Fe_{0.3}O_{3-\delta}$ electrodes with various electrolyte materials [7].

In our research group, $La_{0.6}Sr_{0.4}CoO_{3-\delta}$ (LSC) dense thin film electrodes were used in order to simplify the reaction pathway [3,4]. With the LSC dense electrode, oxygen incorporation/extraction reaction takes place via bulk diffusion of oxide ion in the electrode. The effective oxygen potential in the electrode varies with the applied voltage, which gives rise to variation of oxygen vacancy concentration in the film. In electrochemical impedance measurements, it is detected as a large capacitance[4]. By analyzing the chemical capacitances in a nonstoichiometry thin film electrode, we can understand rate-determining step (rds) reaction and the limiting factor.

So, in this study, $La_{0.6}Sr_{0.4}Co_{0.2}Fe_{0.8}O_{3-\delta}$（LSCF6428）thin films were deposited on $Ce_{0.9}Gd_{0.1}O_{1.95}$ (GDC) electrolytes by pulsed laser deposition (PLD). We will show that detailed information on the oxygen reduction reaction can be obtained from oxygen partial pressure and temperature and dc bias-dependent impedance measurement on LSCF6428 thin film electrode.

2. Theory

From the past studies[4], we knew that when the electrode reaction is controlled by the surface process, oxygen potential in the electrode under small voltage perturbation, δE, would be as the solid line in Fig.3a(case A). On the contrary, if the bulk diffusion or the electrode/electrolyte boundary resistance were not negligible, oxygen potential profile would be as the dotted line(case B) or the dash-dottedline(case C)

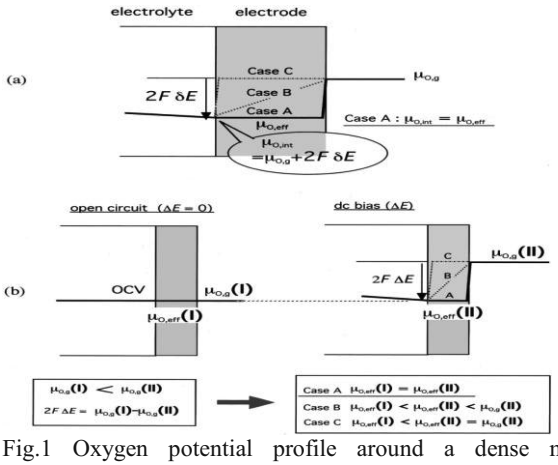

Fig.1 Oxygen potential profile around a dense mixed conductor electrode in three extreme cases of the rds: (case A): surface reaction, (case B): bulk diffusion, (case C): boundary ion transfer. (a) A small voltage perturbation δE is applied to the electrode. (b) Comparison between open circuit and dc biased situations giving the same effective oxygen potential, in case A [4].

Because the change of oxygen nonstoichiometric in the electrode bulk, oxygen ions are incorporated or released,

due to the act to have the electrochemical capacity. So, chemical capacitance in the electrode as follows.

$$C_{chem} = \frac{dQ}{dE} = \frac{d}{dE}\left(\frac{-2FL\delta}{V_m}\right) \qquad (2.1)$$

Where Vm is Molar volume of LSCF, and L is the film thickness of electrode. And E is an overvoltage corresponding to the effective oxygen potential in the electrode, as described as

$$\mu_{O,eff} = \mu_{O,gas} + 2F\Delta E \qquad (2.2)$$

Where $\mu_{O,gas}$ is gas potential, and F is Faraday constant. So, the potential of interface is showed as

$$P(O_2)_{eff} = \exp\left(\frac{2\mu_{O,eff}}{RT}\right) \qquad (2.3)$$

From eqs.(3.1) and (3.2) leads to

$$C_{chem} = 2F\frac{d}{d\mu_{O,eff}}\left(\frac{-2FL\delta}{V_m}\right) \qquad (2.4)$$

The electrode area is not change, so, we use electrode volume V to rewritten L. From eqs.(3.4)and(3.3)leads to

$$C_{chem} = -\frac{8F^2}{RTV_m}\frac{d\delta}{d\ln P(O_2)_{eff}}V_{electr} \qquad (2.5)$$

3. Experimental

3.1 *Electrochemical Cell Preparation*

For evaluation of electrochemical reaction process, an electrochemical cell with an LSCF dense film electrode on a $Ce_{0.9}Gd_{0.1}O_{1.95}$ (GDC) electrolyte substrate was prepared. The GDC substrate was prepared using powers of $Ce_{0.9}Gd_{0.1}O_{1.95}$ (GDC), which were prepared by co-precipitation method. The GDC pellet was calcined at 800℃ for 5 hours, and pressed, sintered at 1550℃ for 5 hours. The obtained the GDC substrate was 16.15 mm in diameter and 1.14 mm in thickness. The relative density was higher than 98%. The sample surface was polished with diamond paste before electrode films were deposited.

The LSCF dense film was formed by pulsed laser deposition (PLD) using Nd-YAG laser. The LSCF target was prepared using commercial $La_{0.6}Sr_{0.4}Co_{0.2}Fe_{0.8}O_{3-\delta}$ powders which were prepared by citric acid method (AGC Seimi chemical Co.Ltd.). The LSCF powers were pressed into a mold and sintered at 1575K for the target preparation. Films were deposited at 1073 K in 1 Pa oxygen. The laser energy and the deposition times of the film were 0.15W for 10 hours. After the PLD process, the samples were annealed in oxygen of 1.01×10^5 Pa oxygen for 30 min in the PLD chamber before cooling.

2.2 *Electrochemical measurement*

Electrochemical properties of the dense electrodes was investigated by the impedance spectroscopy in a single chamber by three-probe method at the temperature of 773K~1073K and oxygen partial pressure 0.001bar ~1bar. The electrode was measured with and without dc bias (-100~50mV). Electrochemical impedance spectra were measured by combination of potentio-galvanostat(2000)/frequency response analyser (FRA 5095) between the working electrode and the reference electrode.

4. Results and Discussion

4.1 *Crystal phase and microstructure of LSCF dens film cathode*

The X-ray diffraction patterns suggested that all the products consisting of single phase. They were showed at Figure 1. The crystal phase of was confirmed by an X-ray diffractmeter (Mac Science M18X, CuKα radiation).The surface and cross section of dense film electrode was observed by a scanning electron microscopy (SEM, JSM – 7001F,JEOL) with EDX (Oxford Instruments). The thickness of film electrode was measured by EDX (SEM, JSM-7001F,JEOL). Figure 2(a) was SEM image of the surface of the LSCF film electrode. It was showed that dense film was successfully prepared on the GDC substrate. Figure 2(b) shows the thickness of film electrode by EDX analysis. The thickness was 700nm.

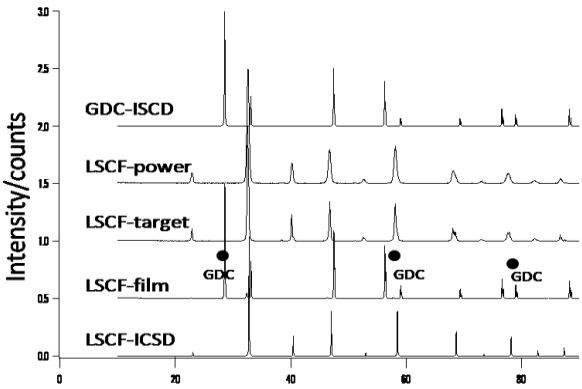

Fig.2 X-ray diffraction pattern of LSCF

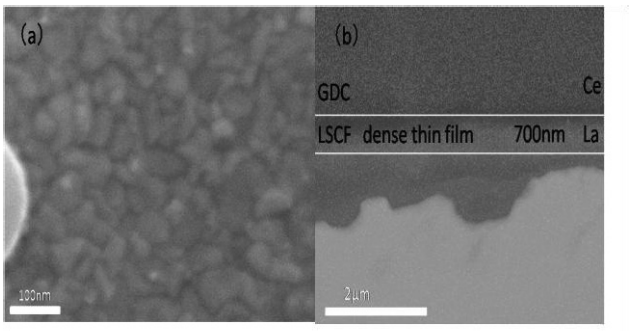

Fig.3 (a) SEM image of the surface of the LSCF film electrode.(b) The thickness of film electrode by EDX analysis.

4.2 Electrochemical property of LSCF dens film cathode and the cathodic reaction mechanism

Fig.4 shows the typical impedance responses observed with a 700nm thick LSCF6428 thin film electrode at 973K (a) under the various $P(O_2)$ conditions and (b) dc bias conditions in 0.001bar. Regardless of the $P(O_2)$ and dc bias, electrochemical impedance response of the electrode consisted of one large semi-circle.

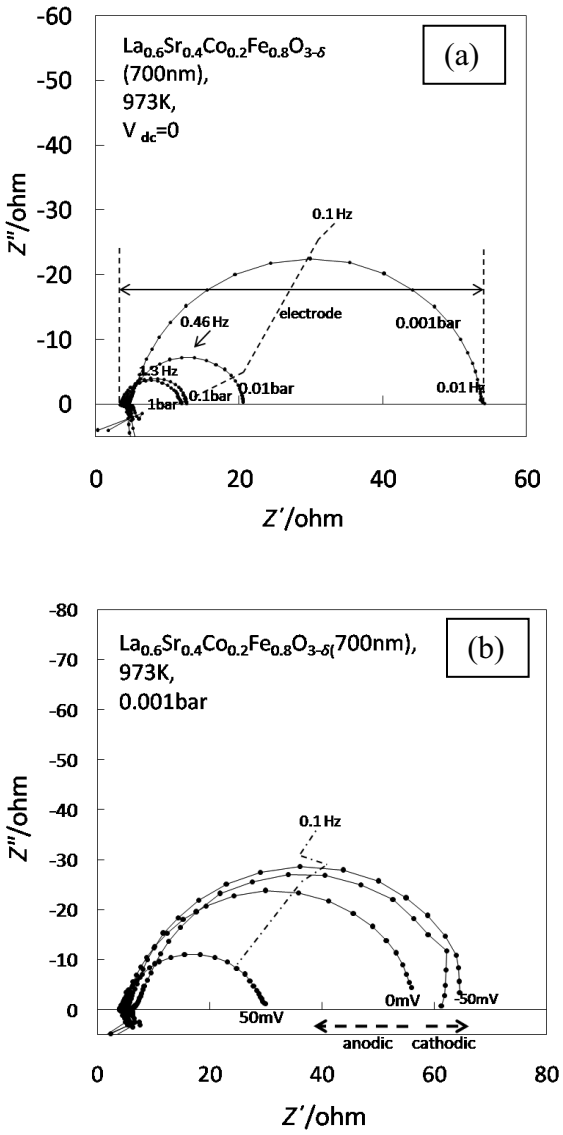

Fig.4 Typical impedance response of $La_{0.6}Sr_{0.4}Co_{0.2}Fe_{0.8}O_{3-\delta}$ dense thin electrode on $Ce_{0.9}Gd_{0.1}O_{1.95}$ electrolyte (a) under various oxygen partial pressure (at 973K, around open circuit voltage) and (b) under dc bias (at 973K, in 0.001bar) .

And with increasing oxygen partial pressure, the semi-circles become smaller as shown in Fig.4(a). Also in Fig.4(b), the semi-circles decreased when the electrode was on the anodic polarization, and increased when the electrode was on the cathodic polarization. According to eq.(2.2), electrochemical overpotential by dc bias can be seen as the effective oxygen potential. Therefore, tendency of change in the semi-circles as a function of $P(O_2)_{eff}$ in Fig.4(a) and (b) is similar each other. Assuming an equivalent circuit consisting of a R-C parallel circuit due to the reaction at the electrode and the Ohmic resistance of electrolyte, made fittings. [3,4] The result was showed at Fig.5.

In Fig.5, the capacitance measured under various oxygen partial pressures and dc biases. The solid symbols represent the capacitance measured in equilibrium with the gas phase, i.e. the overpotential is zero. The other data, which are represented as open symbols, were obtained under positive or negative dc biases. All the data with and without dc bias is aligned on one line. This means the surface reaction is the rate-determining step, just like case A in Fig.3.

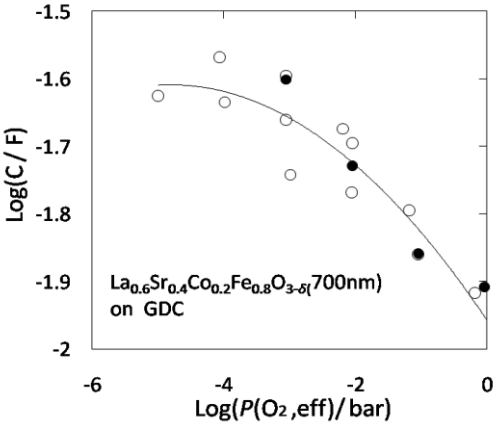

Fig.5 Chemical capacitance of $La_{0.6}Sr_{0.4}Co_{0.2}Fe_{0.8}O_{3-\delta}$ electrode on $Ce_{0.9}Gd_{0.1}O_{1.95}$ electrolyte plotted as a function of the effective oxygen partial pressure.

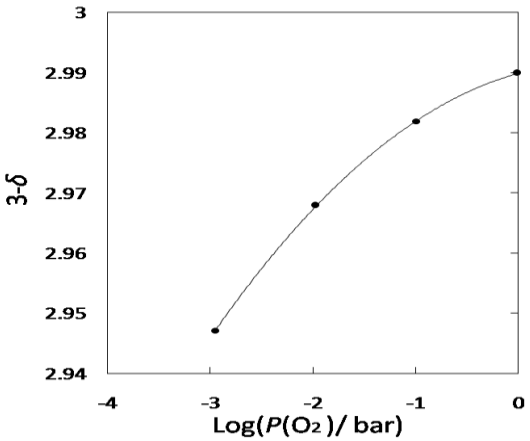

Fig.6 Oxygen nonstoichiometry of $La_{0.6}Sr_{0.4}Co_{0.2}Fe_{0.8}O_{3-\delta}$as a function of the P_{O2} range of 0.001bar~1bar at 973K [5].

On the other hand, the capacitances are decreased with increasing $P(O_2)_{eff}$. Because the oxygen nonstoichiometry δ of LSCF6428 was also decreased with increasing $P(O_2)$.The change of oxygen nonstoichiometry in the electrode bulk, oxygen ions are incorporated or released, due to the act to have the electrochemical capacity. Also from $P(O_2)$ dependence of oxygen nonstoichiometry data for LSCF6428 as shown in Fig.6 [5], chemical capacitance C_{chem} can be estimated according to eq(2.5). Fig.8 shows the comparison of the C_{chem} obtained by electrochemical measurements with the C_{chem} from oxygen nonstoichiometry data.

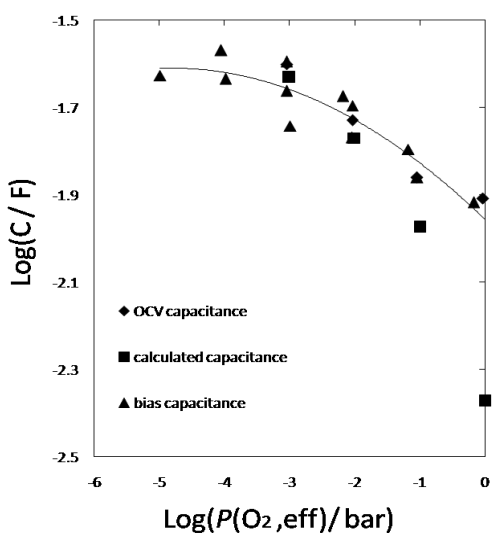

Fig.7 Chemical capacitance of $La_{0.6}Sr_{0.4}Co_{0.2}Fe_{0.8}O_{3-\delta}$ electrode on $Ce_{0.9}Gd_{0.1}O_{1.95}$ electrolyte plotted as a function of the effective oxygen partial pressure and OCV and theoretical.

In Fig.7, Obtained C_{chem} in this experiment is same with C_{chem} from oxygen nonstoichiometry data except high oxygen partial pressure conditions.

It is compared with reported in the literature for the chemical capacitance of $La_{0.6}Sr_{0.4}CoO_{3-\delta}$ dense thin film electrode [4].

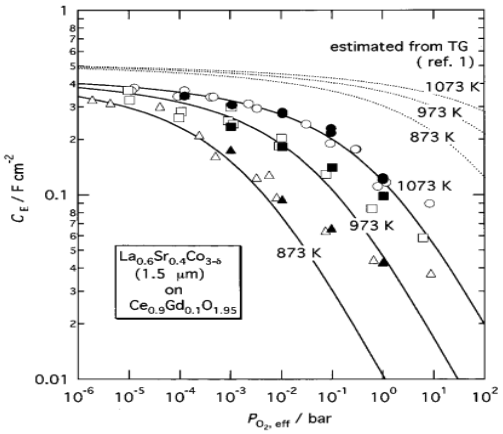

Fig.8 Chemical capacitance of $La_{0.6}Sr_{0.4}CoO_{3-\delta}$ electrode on GDC electrolyte plotted as a function of the effective oxygen partial pressure [4].

Dotted lines in Fig.8 are the calculated value using the oxygen nonstoichiometry data. And solid lines are the experimental results. Both of LSCF and LSC electrode show that the calculated capacitance is in the same order of magnitude with the experimental results. However, in the high oxygen partial pressure, the experimental results and calculated results have large different. In $La_{0.6}Sr_{0.4}CoO_{3-\delta}$ electrode, this might happen if there was significant voltage loss at the interface or inside the electrode. But in $La_{0.6}Sr_{0.4}Co_{0.2}Fe_{0.8}O_{3-\delta}$ electrode, the experimental results are large than calculated ones. The possible reason is the size effect. This means the surface reaction is the rate-determining step, just like in Fig.1b, (ΔE=0).

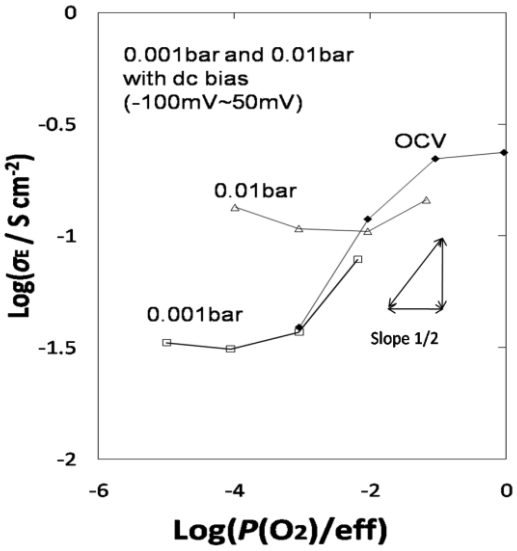

Fig.9 Interface conductivity with $La_{0.6}Sr_{0.4}Co_{0.2}Fe_{0.8}O_{3-\delta}$ dense thin film electrode with and without applying dc bias in various oxygen partial pressure at 973K

Fig.9 shows electrochemical conductivity both at equilibrium with gas phase and under dc polarization. First without dc bias, With increasing oxygen partial pressure, the interface conductivity become smaller. And changes in slope is 1/2. With dc bias, at the same effective oxygen partial pressure, in high equilibrium with gas phase, the interface conductivity is larger. And the capacitance were same as showed at Fig.5. So, it shows that at high oxygen partial pressure, the efficiency of SOFC is high, too.

5. Conclusions

It has been demonstrated that dense thin film microelectrodes of the mixed conducting material LSC on a GDC electrolyte can be employed as a well-defined model system to obtain mechanistic information on the oxygen reduction reaction at SOFC cathodes. An adapted version of an equivalent circuit derived in Ref. [4] has been shown to be an appropriate model for this experimental system. The interpretation of the experimentally observed impedance data according to the equivalent circuit has been validated by additional experimental results. Large capacitance was observed in impedance analysis, attributed to a chemical capacitance due to oxygen nonstoichiometry in the electrode film. The reaction rate is expected what controlled by the surface process about the oxygen reduction reaction of the LSCF6428 thin film electrode.

6. References

[1] S.M. Liu et al., *RARE METAL MATERIALS AND ENGINEERING.,* 2008,37(z2)
[2] S.B Adler *et al. , J.Electrochem.* Soc. , **143** ,3554 – 3564 (1996)
[3] F.S.Baumann *et al.* , *Solid State Ionics. ,* **171**(2006)1071
[4] T.Kawada *et al., J. Electrochem. Soc.*, **149**(7) E252(2009) .
[5] S.Hashimoto *et al*., *Solid State Ionics*. , **181** (2010) 1713.
[6] A.C. Johnson et al. , *J. Power Sources.,* **186**(2009)252–260
[7] M. Liu *et al., Solid State Ionics. ,* **107**,105 (1998).

Eighth International Conference on Flow Dynamics
November 9 - November 11, 2011

Effect of Nb Doping on the Properties of $SrCoO_{3-\delta}$ –Based Cathode for Intermediate Temperature Solid Oxide Fuel Cells

F. Wang[1], K. Yashiro[1], K. Sato[1], J. Mizusaki[1]
[1]Institute of Multidisciplinary Research for Advanced Materials, Tohoku University, Japan
E-mail of corresponding author: f-wang@mail.tagen.tohoku.ac.jp

Abstract

In this paper, a series of Nb doped $SrCoO_{3-\delta}$-based perovskite-type mixed conductor materials were prepared by Pechini method and solid state reaction. The properties of $Ba_{1-x}Sr_xCo_{1-y}Nb_yO_{3-\delta}$ were systemically investigated. The combination of thermal gravimetric analysis, XRD and the high-temperature chemical stability of these materials in different atmosphere were studied. The results show that the $SrCoO_{3-\delta}$-based materials which B-site were partly substituted by a small amount of Nb had better electrochemical performance and better chemical structural stability than $SrCoO_{3-\delta}$ and $Ba_{0.5}Sr_{0.5}Co_{0.8}Fe_{0.2}O_{3-\delta}$.

1. Introduction

Solid oxide fuel cell (SOFC) is the most promising and efficient energy generation technologies that convert chemical energy directly into electrical energy with low or zero pollution. The major requirement for the commercialization of SOFCs is the development of novel low price cathode materials which are capable of providing better performance at lower temperatures (650–850°C). Among the numerous structures that exhibit mixed electronic and oxygen ionic conductivity at high temperature, perovskite has received most attentions due to their high flexibility in component, high mixed electronic–ionic conductivity and good phase stability. $SrCoO_{3-\delta}$ composite is one of these perovskite materials that represent a vital parent compound for the development of many functional materials. The structure of $SrCoO_{3-\delta}$ is transformed from orthorhombic ‘‘O’’ brownmillerite phase to the hexagonal ‘‘H’’ phase when the temperature is 653°C, and then become the cubic perovskite ‘‘C’’ phase above 920°C, which is transformed again, by cooling, into the ‘‘H’’ phase at 774°C.[1] The high-temperature $SrCoO_{3-\delta}$ phases with cubic 3C-like crystal structures are mixed ionic-electronic conductors (MIECs) with very high oxygen permeability values and the highest electronic and oxygen ionic conductivity[2]. However, the $SrCoO_{3-\delta}$ sample with 2H-like hexagonal structures undergoes phase transitions when the sample is heated in air. This phase transition causes abrupt changes in the expansion coefficient that would result in cracking problems during the cell operation [1]. Moreover the $SrCoO_{3-\delta}$ samples with 2H-like hexagonal structures at room temperature have shown to be almost non-oxygen permeable [3]. The stabilization of the $SrCoO_{3-\delta}$ cubic perovskite has been achieved by doping with several elements, up to now, both A-site and B-site doping has been tried [4-10]. Nagai et al. demonstrated that Nb is the most effective dopant among the others (M=Cr, Fe, Al, Ga, Ti, Zr, Sn, V and Nb) in $SrCo_{0.9}M_{0.1}O_{3-\delta}$ for improving its phase stability and also oxygen permeability [9, 11]. The maximum niobium doping concentration in $SrCo_{1-y}Nb_yO_{3-\delta}$ (SCN) at the B-site to form a cubic perovskite phase of the oxide is around 20 mol% [12].

The $SrCo_{0.8}Fe_{0.2}O_{3-\delta}$ [13–15] and $Ba_{1-x}Sr_xCo_{0.8}Fe_{0.2}O_{3-\delta}$ [16–18] which are mixed conductors with high oxygen permeability almost have been found among perovskites containing cobalt, however, have the large drawback of lower phase stability. To keep the high oxygen permeability, the better strategy to develop cathode materials with good performance is to dope Nb to the B-site with the aim to improve their phase stability. The information about the effect of Nb doping on the properties of $SrCoO_{3-\delta}$–based materials is important for optimizing the cathode materials of intermediate temperature solid oxide fuel cells (IT-SOFCs). Therefore, a systematical investigation into the properties, stabilities and the performance of B-site Nb-doped $Ba_{1-x}Sr_xCo_{1-y}Nb_yO_{3-\delta}$ will be presented in this study.

2. Method

2.1. Sample preparation

The $SrCo_{1-y}Nb_yO_{3-\delta}$ (SCN) powder were synthesized by standard solid state methods. Stoichiometric amounts of commercial $SrCO_3$ (99%), Nb_2O_5 (99%) and Co_3O_4 (99%) were mixed fully according to the composition of SCN. The mixture was ground thoroughly using an agate pestle and mortar. The obtained precursors were then pressed into a disk and fired repeatedly at 1000, 1100, and 1200°C for 10 h in air. $Ba_{0.5}Sr_{0.5}Co_{0.8}Fe_{0.2}O_{3-\delta}$ and $Ba_{0.5}Sr_{0.5}Co_{0.9}Nb_{0.1}O_{3-\delta}$ powders were prepared by Pechini method. A mixture of metal ion nitrate solutions of Ba^{2+}, Sr^{2+}, Co^{2+}, Nb^{5+} and Fe^{3+} of known concentration, ethylene glycol and citric acid was heated to 473 K. The obtained polymeric precursor was calcined at 1073 K and sintered at 1273-1373 K to form single-phase perovskite powders. LSGM were used as electrolyte materials in this study. LSGM and NiO powders were synthesized using the glycine-nitrate combustion method [19].

2.2. Characterization

The powder X-ray diffraction (XRD) data were collected using a Rigaku D/Max 2550V/PC X-ray diffractometer with CuKα radiation (λ=1.5418 Å) of 40 KV and 200 mA at room temperature by step scanning in the angle range $20° \leqq 2\theta \leqq 90°$ with increments of 0.02°.

Electrical conductivity of SCN samples were measured in air by the van der Pauw method using a standard DC voltage/current generator (Yokogawa Electric, 2553) and a precision digital multimeter (Yokogawa Electric, 2501A). Ag paste was used for the electrodes in this

measurement.

Thermal expansion coefficient (TEC) was measured using a Netzsch DIL 402C dilatometer, which operated from 30 to 850°C with an air purge flow rate of 60 ml min^{-1} (STP, standard temperature and pressure).

Symmetrical electrochemical cells for the impedance studies were prepared by screen printing an SCN ink sample onto both sides of the LSGM electrolyte pellet. After drying, the samples were sintered at 1000°C for 2 h. Impedance measurements were performed in the temperature range 650−800°C for LSGM electrolytes with 50°C increments for all the samples under open-circuit conditions in the frequency range 0.1-105 Hz. AC impedance spectrometry was carried out using an electrochemical analyzer (CHI604C). The amplitude of the AC signal imposed on the samples was 10 mV.

The thermo gravimetric analysis on BSCF and BSCN samples was carried on a TG-DTA2000s(BRUKER) with a heating rate of 5°C/min and 100ccm total flowing rate to study the weight loss of the samples in 0.1%O_2-99.9%N_2, 5% CO_2+95% N_2 atmospheres from room temperature to 1000°C. 60 mg of $Ba_{0.5}Sr_{0.5}Co_{0.8}Fe_{0.2}O_{3-\delta}$ and $Ba_{0.5}Sr_{0.5}Co_{0.9}Nb_{0.1}O_{3-\delta}$ powder was used for this experiment.

3. Results and Discussion

3.1. Structural characterization

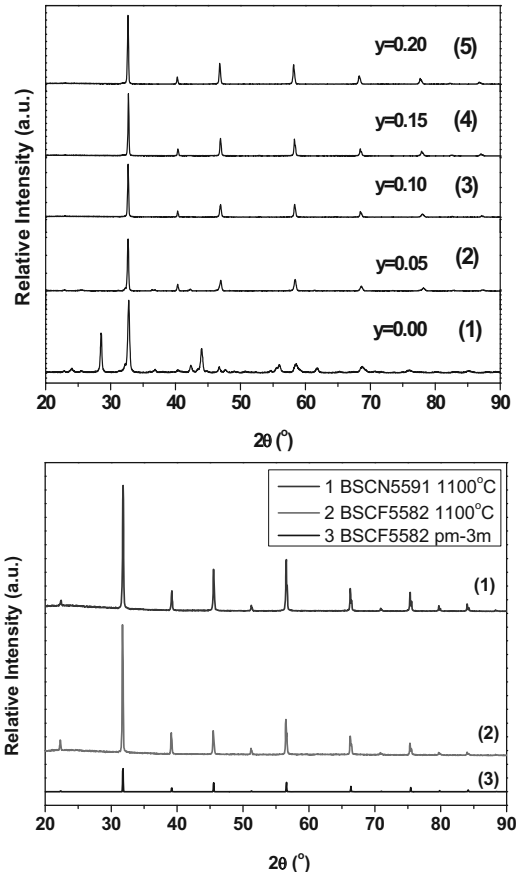

Fig.1.Room-temperature XRD patterns (a) $SrCo_{1-y}Nb_yO_{3-\delta}$ (y=0.0, 0.05, 0.1, 0.15, and 0.2) (b)$Ba_{0.5}Sr_{0.5}Co_{0.8}Fe_{0.2}O_{3-\delta}$ and $Ba_{0.5}Sr_{0.5}Co_{0.9}Nb_{0.1}O_{3-\delta}$ powders

Fig.1 (a) shows the XRD diffraction peaks of SCN samples, which is prepared by standard solid state methods at 1000, 1100 and 1200°C in air for 10h, respectively. Fig.1 (a-1) indicates that the undoped $SrCoO_{3-\delta}$. The pristine oxide $SrCoO_{3-\delta}$ take a distorted 2H BaNiO3-type phase structure, while it was efficiently stabilized into a cubic perovskite phase when the B-site of the oxide is doped with Nb^{5+} at y=0.025-0.2 [12].When the content of Nb is 0.05, the XRD pattern is different of the pristine oxide, the diffraction peaks of $SrCo_{0.95}Nb_{0.05}O_{3-\delta}$ was shown in Fig.1 (a-2). When y ≥0.1, single $SrCo_{1-y}Nb_yO_{3-\delta}$ with perovskite structure are fabricated by standard solid state. Fig.1 (b) shows the single phase $Ba_{0.5}Sr_{0.5}Co_{0.8}Fe_{0.2}O_{3-\delta}$ and $Ba_{0.5}Sr_{0.5}Co_{0.9}Nb_{0.1}O_{3-\delta}$ powders with cubic perovskite structure are fabricated by Pechini method.

3.2. Electrical properties of samples

Electrical conductivity of a cathode electrode for SOFCs was an important performance indicator which larger was better. Fig.2 shows the electrical conductivity behaviors of SCN and $SrCoO_{3-\delta}$ samples versus the temperature. The electrical conductivity of SCN and $SrCoO_{3-\delta}$ gradually decreases with further increasing temperature, which presents metallic-like behavior the versions of temperature from 300 to 850°C. This may be because the localized state electrons start to transfer into collective movement with increasing of temperature. The collective movement of electrons gradually dominated the conductive behavior. The conductivity trends were towards degradation with increasing of temperature. It can be seen from the electrical conductivity of $SrCoO_{3-\delta}$ and SCN attains 2-34Scm^{-1} and 44-461 Scm-1 in the temperature range of 25–800°C. For cathode materials of SOFCs, the general required value for the electrical conductivity is about 100 S cm−1 at the operating temperature. Therefore, the electrical conductivity of SCN as cathode materials is acceptable for application in SOFCs.

This result was close to the value reported by Shao et al [12]. Sample y = 0.05 is metastable phase, is unstable, y is greater than 0.10 was stable. According to the conductivity result, the best sample is $SrCo_{0.9}Nb_{0.1}O_{3-\delta}$.

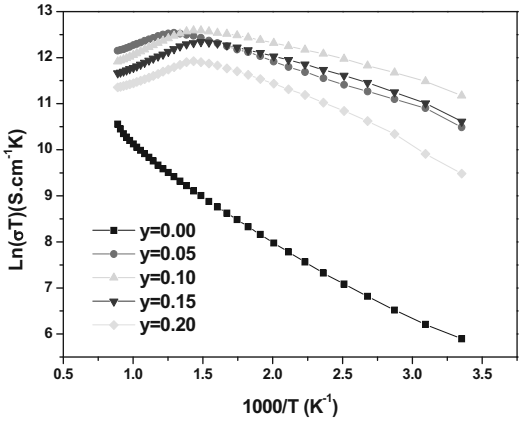

Fig.2. The Arrhenius plots for electrical conductivity of $SrCo_{1-y}Nb_yO_{3-\delta}$ (y=0.0, 0.05, 0.1, 0.15, and 0.2).

3.3. Thermal expansion behaviors of samples

Fig. 3 shows the thermal expansion curves of the samples SCN and $SrCoO_{3-\delta}$ in air. Sample $SrCoO_{3-\delta}$ had special structures, the thermal expansion curves appear the obvious change around 900°C, and it occur a phase transformation at this temperature, as shown in Fig.3 And the phenomenon also appears in the sample of $SrCo_{0.95}Nb_{0.05}O_{3-\delta}$, which is metastable phase, the phase transformation occurs around the same temperature, merely the phase transformation is not more obvious than sample of $SrCoO_{3-\delta}$. The thermal expansion curve of other samples which y =0.1, 0.15, 0.2 did not change obviously at the temperature of 900°C. This result is consistent with the XRD results which had mentioned above.

Therefore, the $SrCo_{0.95}Nb_{0.05}O_{3-\delta}$ is unsuitable for using as a cathode material for SOFCs. It can be seen from the differential curve of thermal expansion for sample SCN in Fig. 3, showing the sample $SrCo_{0.95}Nb_{0.05}O_{3-\delta}$ was unstable above 850°C in air. The other samples (y=0.1, 0.15, 0.2) had inflection point near 400°C.

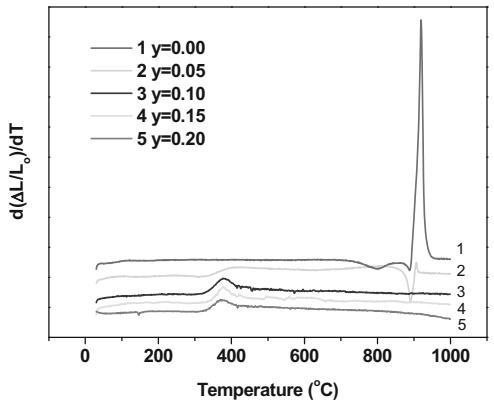

Fig .3 Thermal expansion curves of samples $SrCo_{1-y}Nb_yO_{3-\delta}$.

3.4. Impedance spectroscopy

The impedance spectra of SCN cathodes which the content of Nb was 0.1, 0.15 and 0.2 on LSGM electrolytes measured at the temperature range 650−800°C in air. And the impedance is measured using a symmetrical cell arrangement. For all the samples measured in the investigation, the impedance response for oxygen reduction on the SCN cathode is characterized by both a high-frequency arc and low-frequency arc. The intercept with the real axis at high frequency represents the resistance of the electrolyte and lead wires, whereas the resistance between the two intercepts with the real axis corresponds to the area-specific resistance (ASR, or polarization resistance) of the two interfaces. Consistent with the expected, an increase of the measurement temperature resulted in a significant reduction of the ASR. Table.1 is given the evolution of the ASR in different content with temperature. The ASRs of SCN cathodes on LSGM electrolytes, which were different content of Nb(y=0.1, 0.15, 0.2), are 0.0487Ω cm2, 0.0569Ω cm2 and 0.0648Ω cm2 at 750°C, respectively. The ASR represents the overall cathodic properties related to oxygen reduction, oxygen surface/bulk diffusion and gas-phase oxygen diffusion. It indicated that an SCN cathode has high-electrocatalytic activity for oxygen-reduction reactions at intermediate temperatures. Due to the fact that SCN was a mixed conducting oxide (MIECs) which provides multiple pathways for the oxygen ions to migrate to the electrode/electrolyte interface, the SCN cathodes get better performance. This implies that SCN has high electrocatalytic activity for the oxygen reduction reactions at low to intermediate-temperature.

Table.1.ASR data for $SrCo_{1-y}Nb_yO_{3-\delta}$ cathodes on LSGM electrolytes（with cathode thickness of ~25μm）.

Temperature(°C)	10%Nb (Ω cm2)	15%Nb (Ω cm2)	20%Nb (Ω cm2)
650	0.21	0.2141	0.2264
700	0.0827	0.0991	0.1098
750	0.0487	0.0569	0.0648
800	0.0288	0.0333	0.0400

3.5. TG analysis results

Fig. 4 shows the TG results of BSCF and BSCN in (a) $5\%CO_2$-$95\%N_2$ atmosphere, (b) $0.1\%O_2$-$99.9\%N_2$. BSCF sample's behavior is obviously different from BSCN sample in $5\%CO_2$-N_2 atmosphere. Whereas the TG curve for BSCN is similar as under N_2 atmosphere, a weight loss and weight gain is observed for the BSCF sample, indicating that the BSCN material is much more stable than the BSCF material in $5\%CO_2$-$95\%N_2$ atmosphere.

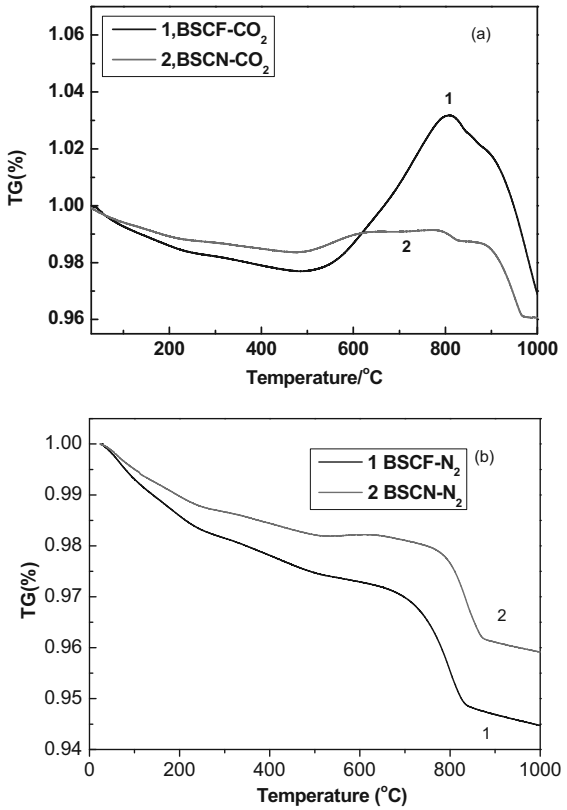

Fig.4. TG results of BCFN and BSCF in (a) $5\%CO_2$-$95\%N_2$ (b) $0.1\%O_2$-$99.9\%N_2$

Specifically, BSCF sample exhibited significant weight gain from 600 to 800°C, corresponding to carbonates formation and lattice oxygen desorption.

According to XRD analysis of BSCF and BSCN after CO_2-TG (Fig. 5), small amounts of $SrCO_3$ and $BaCO_3$ were detected. Further analysis of the TG curve in Fig.4 showed that the stages of weight loss curve corresponded to desorption of adsorbed oxygen (–625°C), the combined effect from carbonate decomposition and desorption of lattice oxygen (625°C–810°C), desorption of lattice oxygen (above 810°C). From the TG curve of BSCN, it can be seen that the weight loss rate of the BSCN sample did not change much comparing to the BSCF sample. However, a small part of BSCN sample's perovskite structure has been destroyed, and a small amount of $BaCO_3$ and $SrCO_3$ was also evidenced by XRD. Therefore, long-term experiment under 5%CO_2-95%N_2 atmosphere should be performed to clearly conclude on the stability of these two materials.

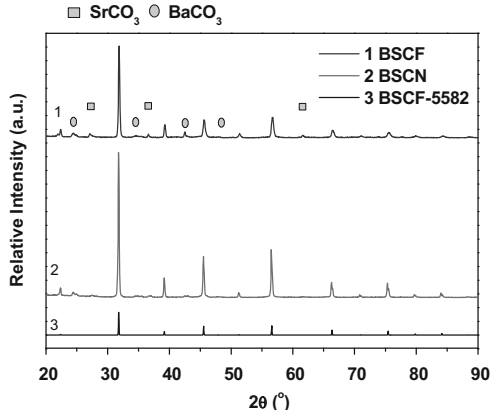

Fig.5. XRD results of BSCN and BSCF after 5%CO_2-N_2 atmosphere TG

4. Concluding remarks

In this study, $Ba_{1-x}Sr_xCo_{1-y}Nb_yO_{3-\delta}$ were successfully synthesized and characterized as novel cathode materials for the intermediate-temperature SOFCs. The SCN has a great increment of the electrical conductivity due to the doping of Nb on B-site. The electrical conductivity increases with the decrease in the content of Nb, obtaining a value as high as 460 S cm^{-1} at 300°C and above 160 S cm^{-1} in the usual range of SOFCs working conditions (650−900°C) for the sample y= 0.1. The Nb-doping $SrCoO_{3-\delta}$ obviously produced an enhancement of the thermal stability and suppressed the presence of reconstructive structural transitions. The polarization resistances for the SCN cathode on LSGM electrolyte was 0.0288Ωcm^2 at 800◦C. The chemical stability of perovskite-type BSCN and BSCF mixed conductor were investigated. The thermo gravimetry study on the thermal stability of BSCF and BSCN materials showed that BSCN has better stability than BSCF. Under 5% CO_2+95% N_2 atmosphere, a gain in weight was observed for BSCF materials which was due to the generation of carbonates, which was followed by a loss of weight as carbonates decomposed; in contrast, not so much change of weight loss rate was observed for BSCN under 5% CO_2+95% N_2 atmosphere. The XRD indicated that, after annealing under 5%CO_2+95%N_2, besides partial original perovskite crystal structure, an amount of strontium and barium carbonates occurred of BSCF which still maintained the primary perovskite crystal structure. In the same conditions, BSCN materials still maintained most of the perovskite crystal structure. These results all indicated that the Nb in B-site plays a positive role in improving the properties and stability of $SrCoO_{3-\delta}$–based perovskite materials as promising cathode for IT-SOFCs.

Acknowledgement

The Japan Society for the Promotion of Science and the Tohoku University Global COE program

References

[1] C. de la Calle, A. Aguadero, J.A. Alonso, M.T. Fernandez-Diaz, Solid State Sci. 10(2008) 1924.
[2] Z.Q.Deng, W.S.Yang, W.Liu, C.S.Chen, J.Solid State Chem. 179 (2006) 362.
[3] B. Lin, S.L. Wang, H.L. Liu, K. Xie, H.P. Ding, M.F. Liu, G.Y. Meng. J. Alloys and Compounds.472 (2009) 556.
[4] C.G. Fan, Y.B. Zuo, J.T. Li, J.Q. Lu, C.S. Chen, D.S. Bae. Sep. Purif. Technol. 55 (2007) 35.
[5] Z.P. Shao, G.X. Xiong, J.H. Tong, H. Dong, W.S. Yang.Sep. Purif. Technol. 25 (2001)419.
[6] P.Y. Zeng, R. Ran, Z.H. Chen, W. Zhou, H.X. Gu, Z.P. Shao, S.M. Liu. J. Alloys Compd. 455 (2008)465.
[7] M. James, D. Cassidy, K.F.Wilson, J. Horvat, R.L. Withers.Solid State Sci. 6 (2004) 655.
[8] X.L. Dong, Z. Xu, X.F. Chang, C. Zhang, W.Q. Jin.J. Am. Ceram. Soc. 90 (2007) 3923.
[9] T. Nagai, W. Ito, T.R. Sakon, Solid State Ionics 177 (2007) 3433.
[10] A. Aguadero, C. de la Calle, J.A. Alonso, M.J.Escudero, M.T. Fernández-Díaz and L. Daza. Chem. Mater. 19(26) (2007) 6437.
[11] W. Ito, T. Nagai, T. Sakon .Solid State Ionics 178 (2007) 809.
[12] K. Zhang, R. Ran, L. Ge, Z.P. Shao, W.Q. Jin, N.P. Xu, Journal of Menbrane Science, 323 (2008) 436-443.
[13] T.H. Lee, Y.L. Yang, A.J. Jacobson, B. Abeles, M. Zhou, Solid State Ionics 100 (1997)
[15] J.F. Vente, W.G. Haije, Z.S. Rak, J. Membr. Sci. 276 (2006) 178.
[16] Z. Shao, G. Xiong, J. Tong, H. Dong, W. Yang, Sep. Purif. Technol. 25 (2001) 419.
[17] H. Wang, C. Tablet, A. Feldhoff, J. Caro, J. Membr. Sci. 262 (2005) 20.
[18] P. Zeng, Z. Chen, W. Zhou, H. Gu, Z. Shao, S. Liu, J. Membr. Sci. 291 (2007) 148.77.
[19] L.G. Cong, T.M. He, Y. Ji, P.F. Guan, Y.L. Huang, W.H. Su, J. Alloys Compd. 348(2003) 325–331.
[20] L. Qiu, T.H. Lee, L.-M. Liu, Y.L. Yang, A.J. Jacobson, Solid State Ionics 76 (1995) 321.
[14] E. Boehm, J.-M. Bassat, M.C. Steil, P. Dordor, F. Mauvy and J.-C. Grenier, Solid State Sci. 5 (2003) 973.
[21] E.P. Murray, S.A. Barnett, Solid State Ionics 143 (2001) 265
[22] S.W. Baek, J.H. Kim, J. Bae, Solid State Ionics 179 (2008) 1570–1574.

Fabrication of Anode-Supported type Protonic Ceramic Fuel Cells (PCFCs)

Sung Min Choi[1,2], Jong-Heun Lee[2], Jong-Ho Lee[1], Hae-Weon Lee[1,] Ho Il Ji[1] and Byung-Kook Kim[1,*]

[1] High-Temperature Energy Materials Center, KIST, Seoul 136-791, KOREA
[2] Department of Materials science & Engineering Korea University, Seoul, Korea
E-mail of corresponding author: bkkim@kist.re.kr.

ABSTRACT

Solid Oxide Fuel Cells (SOFCs) have many advantages such as high energy efficiency, modularity and the high powder density. But they also have various problems such as poor thermo-mechanical and thermo-chemical stability due to their high operation temperature. In order to reduce the operating temperature, many researchers applied proton conducting ceramics with high ionic conductivity at intermediate temperature for the solid electrolyte of fuel cells. In this study, we fabricated Protonic Ceramic Fuel Cells [PCFCs: NiO-$Ba(Zr_{0.84}Y_{0.15}Cu_{0.01})O_{3-\delta}$: NiO-BZYCu / $Ba(Zr_{0.84}Y_{0.15}Cu_{0.01})O_{3-\delta}$: BZYCu / $(La_{0.4}Sr_{0.6}Co_{0.2}Fe_{0.8})O_3$-$Ba(Zr_{0.85}Y_{0.15})O_{3-\delta}$: LSCF-BZY] and evaluate their performance at 650°C

1. Introduction

The Fuel cell is one of the most prosperous alternative energy and renewable energy sources. Among all types of fuel cells, Solid Oxide Fuel Cells (SOFCs) have various advantages such as high efficiency, modularity and the high power density.[1] However SOFC required high operating temperature because yttria stabilized zirconia (YSZ) showed good ionic conductivity only at high temperature. In order to lower the operating temperature, alternative electrolyte was requested. Recently proton conducting oxide has been introduced to replace conventional electrolyte material such as YSZ.[2] Among many proton conductors, perovskite-structured materials such as $BaZrO_3$ and $BaCeO_3$ doped by some rare earth elements have been intensity investigated because of their high proton conductivity.[3, 4] Among the two material systems, $BaCeO_3$ is known to have higher ionic conductivity than $BaZrO_3$ but the chemical stability of $BaCeO_3$ is lower than the $BaZrO_3$.[5] So in this study, we chose $BaZrO_3$ based-ceramics for our test material for PCFC electrolyte.

However the doped $BaZrO_3$ is known to have very refractory nature. So we need at least 1700 °C for the sintering to acquire the sintered density over 95%. In order to practically apply the doped $BaZrO_3$ as electrolyte materials of intermediate temperature SOFCs, one has to overcome this poor sinterability.[6] It was already reported that dense Y-doped $BaZrO_3$ could be obtained at sintering temperature as low as 1500°C by the addition of CuO as sintering aids.[7] Hence, in this study, we fabricated Protonic Ceramic Fuel Cells (PCFCs) based on $Ba(Zr_{0.84}Y_{0.15}Cu_{0.01})O_{3-\delta}$ (BZYCu) electrolyte and characterize their power generating property. :

2. Experimental

$Ba(Zr_{0.84}Y_{0.15}Cu_{0.01})O_{3-\delta}$ (BZYCu) powders were prepared by a conventional solid state reaction. The starting powders, $BaCO_3$(99.9%, CERAC), ZrO_2(99%, Junsei), Y_2O_3(99.9%, High Purity Chemical) and CuO(99.9%, High Purity Chemical) were weighted in the stoichiometric ratio and mixed with ball milling by using zirconia balls. The powder were mixed in ethanol for 24 hours and calcined at 1300°C for 2 hours and then milled again in ethanol for 48 hours. And then the paste was made by using BZYCu powder.

The composite with the nickel oxide and BZYCu (NiO-BZYCu) was prepared by liquid condensation process (LCP). The powder of NiO(Sumimoto, Japan), the BZYCu powder and phenol resin(KNG100, Kolon chemical,Korea) were mixed with ball milling for 20 hours in ethanol. Phenol resin is acting as a binder as well as pore forming agent. The mixed volume ratio of of NiO : BZYCu was 53 : 47. After reduction, Ni : BZYCu volume ratio became 40 : 60. The mixed slurry was poured into the stirred water to make the granule. The granule of NiO-BZYCu mixture were compacted and uniaxially pressed and then pre-sintered at 1100°C in air to remove all organic components from anode substrates. Thin BZYCu film was coated on this pre-sintered NiO-BZYCu plate via screen printing and then sintered at 1500 °C for 3 h in air.

$(La_{0.4}Sr_{0.6}Co_{0.2}Fe_{0.8})O_3$ - $Ba(Zr_{0.85}Y_{0.15})O_{3-\delta}$ (LSCF-BZY) cathode composite was also coated on sintered BZYCu via screen printing and then sintered at 1050°C for 2 h in air. The final configuration of the PCFCs was NiO-$Ba(Zr_{0.84}Y_{0.15}Cu_{0.01})O_{3-\delta}$:NiO-BZYCu/$Ba(Zr_{0.84}Y_{0.15}Cu_{0.01})O_{3-\delta}$:BZYCu/LSCF-$Ba(Zr_{0.85}Y_{0.15})O_{3-\delta}$:LSCF-BZY].

3. Results and Discussion

Fig.1. shows the XRD patterns of the BZYCu powder and granule.

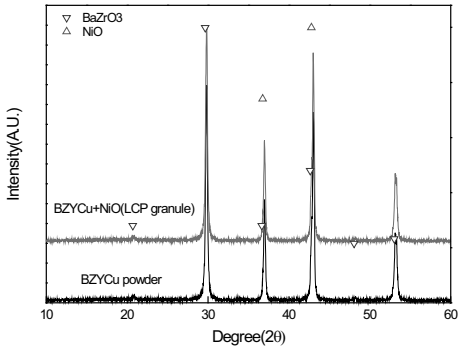

Fig.1. XRD results(powder , granule).

As shown in figure, BZYCu powders with peroviskite structure were successfully synthesized. Also the granules can be found as NiO and BZYCu composite.

Fig.2. shows the shrinkage behavior of the powders of NiO, BZYCu and BZYCu+NiO composite. As shown in figure, anode substrate is shrunk earlier than electrolyte. But the shrinkage rate of electrolyte is faster than anode substrate. From the result of dilatometeric data, co-sintering time of anode-electrolyte had been decided as 1500°C.

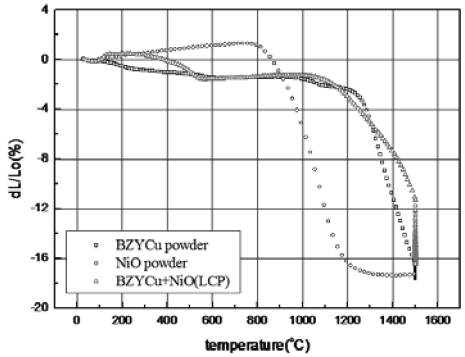

Fig.2. Dilatometric results during sintering of the NiO , BZYCu , NiO-BZYCu.

Fig.3. shows the cross-section view of the single cell after cell testing. It was found that the thickness of BZYCu electrolyte and LSCF-BZY cathode layer were around 10um and 20um, respectively. Moreover the adhesion of the LSCF-BZY cathode to the BZYCu electrolyte was excellent and cathode layer was sufficiently porous.

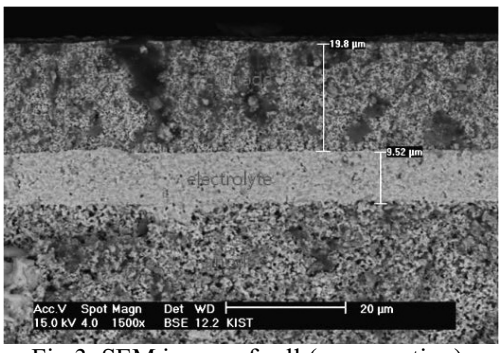

Fig.3. SEM image of cell (cross section).

Fig.4. represents the I–V and I–P characteristics of the cell measuring from 650°C with humidified hydrogen(~3% H2O) or dried hydrogen as a fuel and air as an oxidant. As shown in figure, the maximum power densities of 17 mW cm^{-2} at 650°C while keeping the OCV values of 0.94 V which indicated that the electrolyte membrane is sufficiently dense.

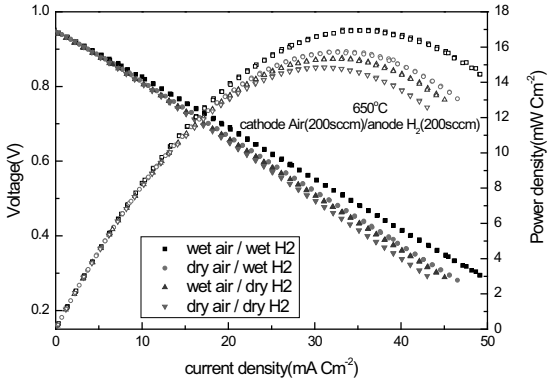

Fig.4. Cell performance of a single cell (LSCF-BZY/BZYCu/NiO-BZYCu) measured at 650°C to change of each electrode's $P(H_2O)$.

4. Concluding remarks

A PCFC was successfully fabricated with layered $(La_{0.4}Sr_{0.6}Co_{0.2}Fe_{0.8})O_3$ - $Ba(Zr_{0.85}Y_{0.15})O_{3-\delta}$ (LSCF-BZY) as a cathode and thin $Ba(Zr_{0.84}Y_{0.15}Cu_{0.01})O_{3-\delta}$ (BZYCu) as an electrolyte. The performance of the 2x2 cm sized unit cell of LSCF-BZY/BZYCu/Ni-BZYCu was tested at 650°C. According to the results, the open-circuit voltage of 0.94V and maximum power density of 17mWcm^{-2} were achieved at 650°C. The power density was changed with respect to water partial pressure which can be attributed to the typical characteristics of proton conducting electrolyte. However the cell performance was extremely low even though the fairly stable open-circuit voltage was kept. Hence further study to improve the performance is now underway.

References

[1] Minh, N.Q., Journal of the American Ceramic Society, **76** (1993): 563.
[2] Iwahara, H., et al., Solid State Ionics, **3-4** (1981), 359.
[3] Kreuer, K.D., et al., Chemical Reviews**, 104** (2004), 4637.
[4] Norby, T., Solid State Ionics **, 125** (1999), 1.
[5] Kreuer, K.D., Annual Review of Materials Research **, 33 (**2003), 333.
[6] Park, J.S., et al., Solid State Ionics **, 181** (2010), 163.
[7] Gao, D.Y. and R.S. Guo, Journal of Alloys and Compounds, **493** (2010), 288.

Eighth International Conference on Flow Dynamics
November 9 - November 11, 2011

Mass Transport in Perovskite Oxides (La,Sr)(Co,Fe)O_3

Honami Kudo, Keiji Yashiro, Junichiro Mizusaki
Institute of Multidisciplinary Research for Advanced Materials, Tohoku University,
2-1-1 Katahira, Aoba-ku, Sendai 980-8577, Japan
h-kudo@mail.tagen.tohoku.ac.jp

ABSTRACT

The isotope abundance ratios of atmosphere and each depth of $La_{0.6}Sr_{0.4}Co_{0.2}Fe_{0.8}O_{3-\delta}$ were measured as a function of P_{O2} and temperature. Their experimental profiles were analyzed to determine the oxygen tracer diffusion coefficients, D^*, and the rate constant of surface exchange reaction, k. D_v were calculated by using D^* and previous nonstoichiometry data. The dependence of D_v on P_{O2} and temperature will be discussed.

1. Introduction

$La_{0.6}Sr_{0.4}Co_{1-y}Fe_yO_{3-\delta}$ (LSCF) shows high mixed ionic-electronic conductivities (MIEC). In this reason, LSCF attracts attention as the cathode materials for intermediate temperature solid oxide fuel cells (SOFCs).

Investigation about bulk diffusion on MIEC oxides is so important for understanding the electrode reaction. Some researchers [1-3] reported that rapid reduction of vacancy diffusion coefficient, D_v, was confirmed at log $P_{O2} \leqq$ -2. These behaviors were contradictory to general hypothesis that D_v is independent of vacancy concentration [4] and against widely observed experimental evidences for many oxides including perovskite-type [4-5].

Nakano et al. confirmed rapid reduction of D_v of LSCF at log $P_{O2} \leqq$ -2 and reported the dependence on δ by analyzing the relaxation process of electrical conductivity shown as Figure 1 [6].

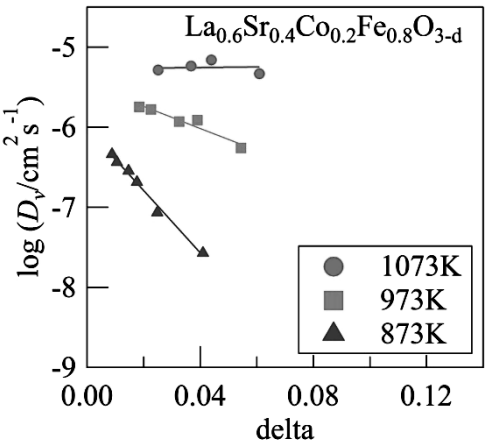

Fig.1 Vacancy diffusion coefficient (D_v) of $La_{0.6}Sr_{0.4}Co_{0.2}Fe_{0.8}O_{3-\delta}$ as a function of δ at 1073-873 K

In this study, the isotope abundance ratios of atmosphere and each depth of $La_{0.6}Sr_{0.4}Co_{0.2}Fe_{0.8}O_{3-\delta}$ (LSCF6428) were measured as a function of P_{O2} and temperature. Their experimental profiles were analyzed to determine the oxygen tracer diffusion coefficients, D^*, and the rate constant of surface exchange reaction, k. D_v were calculated by using nonstoichiometry data [7]. The dependence of D_v on P_{O2} and temperature will be discussed.

2. Experimental

2.1. Sample preparations

Specimens for isotopic exchange were prepared by LSCF6428 powder (Agc seimi chemical co., ltd.). Purity and crystal structures were analyzed by X-ray diffraction (XRD) using Cu Kα radiation. The powder was pressed isostatically at 120 MPa and sintered at 1523 K for 6 h. This procedure gave uniform samples with density above 98 % of the theoretical value. After cut, thicknesses of the samples were 1-2 mm and one-side abrasive finishing.

2.2. Pre-anneals

Before exchange anneals, samples were pre-annealed for 20-24 hours and quenched in an atmosphere which had the same oxygen partial pressure as exchange anneal and natural isotope abundance ratio. The purpose of pre-anneals is to equilibrate the defect concentration with the desired oxygen partial pressure and to eliminate the surface damage formed during cutting and polishing procedures.

2.3. Isotope exchanges

a) Gas phase analysis: Pre-annealed samples were annealed in isotopic oxygen atmosphere with the instrument shown as Figure 2. The decrease in $^{18}O/(^{16}O+^{18}O)$ ratio was monitored by a mass spectrometer, shown as Figure 3.

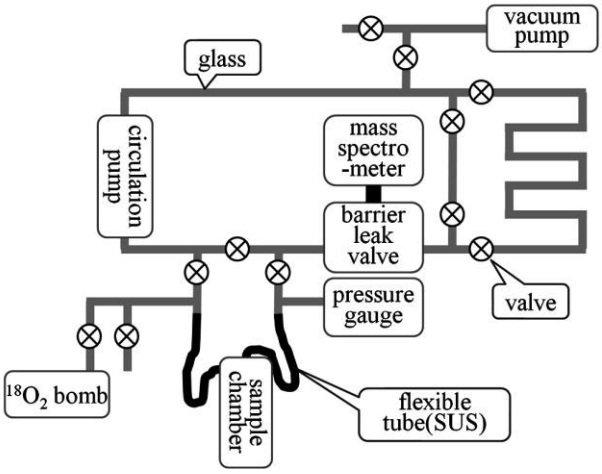

Fig.2 Schematic of the isotopic exchange instrument

b) Depth profile measurement: Isotopic exchanged samples were vertically cut and surfaces of sections were polished. Isotope abundance ratios were obtained by line scan on a secondary ion mass spectrometer (SIMS).

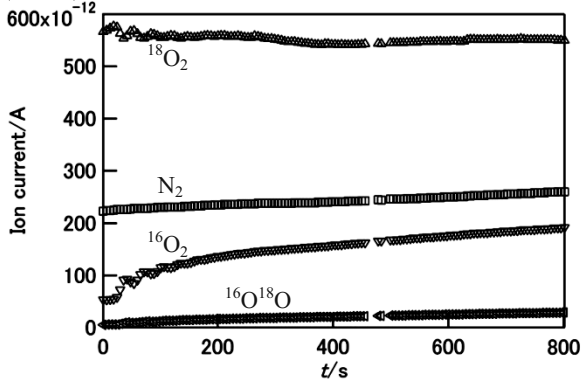

Fig.3 Ion current vs. time of gas phase by a mass spectrometer: T=1073 K, P_{O2}=5×10^{-3} bar

3. Results

3.1. Gas phase analysis

The diffused amounts, M_t/M_∞, of ^{18}O against time were determined, as shown Figure 4, by the ratio of isotopic composition of ^{16}O and ^{18}O in the gas phase from ion current. M_t and M_∞ represent the total ^{18}O amounts diffusing in the solid for a time t and infinite time.

The solution of diffusion equation with the present boundary condition is given by [8],

$$\frac{M_t}{M_\infty} = 1 - \sum_{i=0}^{\infty}\sum_{m=0}^{\infty}\sum_{n=0}^{\infty} \frac{2L_h^2 \exp(-\beta_i^2 D^* t/h^2)}{(\beta_i^2 + L_h^2 + L_h)} \times \frac{2L_w^2 \exp(-\gamma_m^2 D^* t/w^2)}{(\gamma_m^2 + L_w^2 + L_w)} \times \frac{2L_l^2 \exp(-\delta_n^2 D^* t/l^2)}{(\delta_n^2 + L_l^2 + L_l)} \quad (1)$$

where $2h$, $2w$ and $2l$ are height, width and length of a sample, β_is, γ_ms and δ_ns are the positive roots of

$$\beta\tan\beta = L_h$$
$$\gamma\tan\gamma = L_w$$
$$\delta\tan\delta = L_l \quad (2)$$

and

$$L_h = hk/D^*$$
$$L_w = wk/D^*$$
$$L_l = lk/D^* \quad (3)$$

D^* and k were determined by fitting the experimental data to Eq. (1) using a least-square analysis.

3.2. Depth profile measurement

^{18}O concentration, C^*, profiles in the solid phase are determined by SIMS. The one-dimensional solution of diffusion equation in a semi-infinite medium with a boundary of constant atmospheric concentration is given by [8],

$$\frac{C^*(x) - C_0^*}{C_g^* - C_0^*} = \mathrm{erfc}\left(\frac{x}{2\sqrt{D^* t}}\right) - \exp\left(\frac{k}{D^*}x + \frac{k^2}{D^*}t\right) \times \mathrm{erfc}\left(\frac{x}{2\sqrt{D^* t}} + k\sqrt{\frac{t}{D^*}}\right) \quad (4)$$

where C^*_0 and C^*_g are concentrations of isotope abundance ratio at initial state of solid and gas, x is the distance from the surface and t is the time of the isotope exchange. D^* and k were determined by fitting the experimental data to Eq. (1) using a least-square analysis.

The results of depth profile measurement will be shown at the presentation.

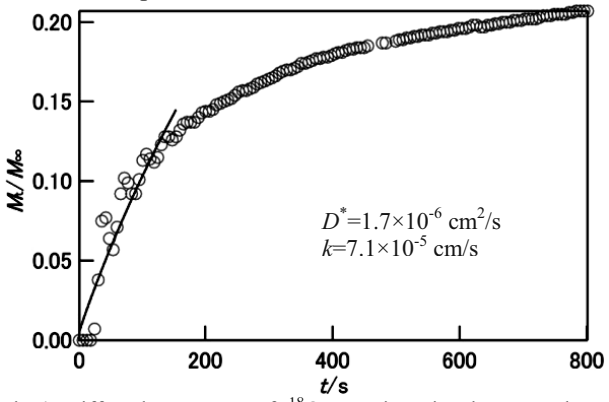

Fig.4 Diffused amounts of ^{18}O vs. time in the gas phase analysis calculated from the data of Fig.3. The solid line represents the fit to Eq. (1). Only initial data with enough $^{18}O_2$ in the gas phase were used in fitting.

3.3. Diffusion coefficient of oxygen ion vacancies

D_v was calculated from the following equation.

$$D_v C_v = D_O C_O \quad (5)$$

where D_O ($\approx D^*$) is oxygen diffusion coefficient and C_v and C_O are concentrations of vacancy and oxygen.

D_v of LSCF6428 was calculated by Eq. (5) using nonstoichiometry data [7].

4. Future Works

It was confirmed that D^* and k can be determined by gas phase analysis and depth profile measurement. The dependence of D_v on P_{O2} and temperature will be discussed with more data.

5. References

[1] Martin Soggard, Peter Vang Hendriksen, Mogens Mogensen, Finn Willy Poulsen, Eivind Skou, *Solid State Ionics*, **177**, (2006), p.3286

[2] Masatoshi Katsuki, Shaorong Wang, Masayuki Dokiya, Takuya Hashimoto, *Solid State Ionics*, **156**, (2003), p.453

[3] H. J. M. Buowmeester, M. W. Den Otter, B. A. Boukamp, *Journal of Solid State Electrochemistry*, **8**, (2004), p.599

[4] Takamasa Ishigaki, Shigeru Yamauchi, Kohji Kishio, Junichiro Mizusaki, Kazuo Fueki, *Journal of Solid State Chemistry*, **73**, (1988), p.179

[5] Junichiro Mizusaki, *Solid State Ionics*, **52**, (1992), p.79

[6] Issei Nakano, Master Thesis, Tohoku Univ., (2011)

[7] Shin-ichi Hashimoto, Yasuhiro Fukuda, Melanie Kuhn, Kazuhisa Sato, Keiji Yashiro, Junichiro Mizusaki, *Solid State Ionics*, **181**, (2010), p.1713

[8] J. Crank, "The Mathematics of Diffusion," 2nd ed., Oxford University Press, (1975)

Eighth International Conference on Flow Dynamics
November 9 - November 11, 2011

In-situ Evaluation of Oxygen Chemical Potential in an SOFC Cathode

Yoshinobu Fujimaki[A,*], Hidetaka Watanabe[A], Koji Amezawa[A], Tatsuya Kawada[A], and Yasuko Terada[B]
[A]Graduate school of Environmental Studies, Tohoku University,
6-6-01 Aoba, Aramaki, Aoba-ku, Sendai 980-8579, Japan
[B]JASRI, 1-1-1, Kouto, Sayo-cho, Sayo-gun, Hyogo 679-5198
*Corresponding author; fujimaki@ee.mech.tohoku.ac.jp

ABSTRACT

The oxygen chemical potential distribution in a porous SOFC cathode of $La_{0.6}Sr_{0.4}Co_{0.2}Fe_{0.8}O_{3-\delta}$ (LSCF6428) under polarization was tried to be evaluated by ac impedance spectroscopy and *in-situ* micro X-ray absorption spectroscopy. In the former technique, the effective reaction zone was estimated from the observed chemical capacitance. In the latter technique, valence changes of Co and Fe ions in LSCF6428 due to the oxygen potential changes were tried to be detected from the absorption edge shifts as a function of the distance from electrode/electrolyte interface. However, no clear absorption edge shifts were observed both in Co and Fe *K*-edge.

1. Introduction

Solid oxide fuel cell (SOFC) is a high efficiency energy conversion system which can directly convert chemical energy of fuels into electrical power. Compared with other types of fuel cells, SOFC has advantages of fuel flexibility and effective utilization of the exhaust heat because of its high operating temperature (873 - 1273 K). However, SOFC has some problems, which have to be solved for its commercialization, arising from its high operating temperature. For example, SOFC needs stability and reliability for the long-term operation, and needs tolerance for the rapid start and stop operation. As a way of meeting these issues, efforts have been devoted to develop intermediate temperature (873 - 1073 K) SOFC. For reducing the operating temperature, degradation of the electrode performance, especially in the cathode, is a critical problem. $La_{1-x}Sr_xCoO_{3-\delta}$, $La_{1-x}Sr_xCo_{1-y}Fe_yO_{3-\delta}$ and other oxides having Perovskite structure are believed to be suitable for the cathode materials working at the intermediate temperatures [1, 2]. This study focuses on $La_{0.6}Sr_{0.4}Co_{0.2}Fe_{0.8}O_{3-\delta}$ (LSCF6428), which is one of the most promising cathodes for intermediate temperature SOFC.

The SOFC electrode reactions, in general, are composed of many elementary reaction processes. Rate limited reaction needs the largest energy loss in the reaction processes. Then the sharp gradient of oxygen potential is observed at the place where the rate limited reaction takes place. Local change in the oxygen chemical potential in the electrode may cause degradations of the material, such as compositional change due to the kinetic demixing/decomposition, the mechanical failures due to the chemical expansion/shrinkage and so on. Thus, it is important to evaluate oxygen chemical potential distribution in an SOFC electrode for ensuring reliability and durability of the system. However, so far, there are no direct experimental techniques to evaluate oxygen potential in SOFC under operation.

This study intended to directly evaluate oxygen chemical potential distribution in a porous cathode of LSCF6428. *In-situ* micro X-ray absorption spectroscopy (XAS) measurement and ac impedance measurement were used for evaluating the potential distribution. By comparing the results from these two measurements, it was tried to reveal the potential distribution in the SOFC cathode under operation.

2. Experiment

2.1 Sample preparation

$Ce_{0.9}Gd_{0.1}CoO_{1.95-\delta}$ (GDC) powder for the electrolyte was synthesized by a co-precipitation method using $Ce(NO_3)_3$ and $Gd(NO_3)_3$ aqueous solutions. Obtained GDC powder was burned at 1023 K for 5 hours and milled for 1 hour. Then it was pressed into a pellet with a uniaxial pressing equipment and sintered at 1823 K for 5 hours. Mirror polishing was performed on both surfaces of the pellet. Composite paste of Pt and LSCF6428 was printed onto another surface as a counter electrode and sintered at 1273 K for 3 hours first. Then paste of $La_{0.6}Sr_{0.4}Co_{0.2}Fe_{0.8}O_{3-\delta}$ (AGC SEIMI CHEMICAL) was painted onto the one surface as a working electrode and sintered at 1223 K for 6 hours. Then the pellet was cut into 2×2×2mm cubes. Finally a porous Pt electrode was set on the side of electrolyte as a reference electrode. Figure 1 shows the schematic illustration of the sample prepared by above procedures.

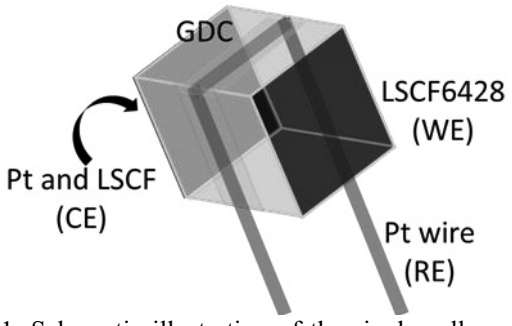

Fig. 1. Schematic illustration of the single cell used in this study.

2.2 Impedance measurement

Electrochemical characteristics of the porous LSCF6428 electrode were investigated by using ac impedance measurements. The effective reaction zone for the SOFC cathodic reaction can be estimated from

the chemical capacitance obtained from ac impedance spectra [3-5]. Measurements were carried at 873, 973 and 1073 K in the oxygen partial pressure range from 10^{-4} to and 1 bar. The impedance analyzer (VersaSTAT 4, Princeton Applied Research) was used for measurements. Impedance spectra were taken in the frequency range from 1 MHz to 0.1 Hz.

2.3 In-situ micro XAS

When the oxygen potential around oxides varies, significant oxygen nonstoichiometry changes are often observed. Such an oxygen nonstoichiometry change in oxides is always accompanied by changes in the average valences of cations in order to keep the electro neutrality condition. LSCF6428 is known to show decrease in the oxygen nonstoichiometrty, accordingly increase in the average valences of Co and Fe, when the oxygen partial pressure is reduced [6, 7]. These mean that the oxygen potential change in LSCF6428 can be detected by measuring the change in the average valences of Co and Fe. Typically changes in the electronic state of a transition-metal sensitively affect the position of the X-ray absorption edge, and higher average valence results in the edge shift to higher energy [8, 9]. In this way, oxygen chemical potential distribution can be principally evaluated by observing the edge shift in XAS. In this study, *in-situ* XAS spectra of the Co *K*-edge and Fe *K*-edge were measured by a fluorescence mode using synchrotron radiation at the beam line BL37XU at SPring-8, JASRI, Japan. XAS measurements were carried out at 973 K under constant polarization with the cathodic voltage of -0.75 V, while the oxygen partial pressure was kept constant at 1 bar. X-ray was focused into 1×1.2μm. Measurement points were changed in the vertical direction from the cathode/electrolyte interface like Fig. 3. The cathode/electrolyte interface was determined by X-ray fluorescence elemental mapping of Co, Fe, and Ce.

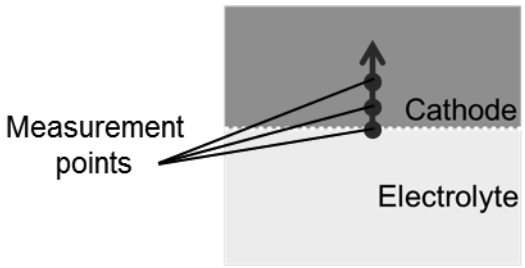

Fig. 2. Schematic illustration of *in-situ* micro XAS measurements. Measurements were carried out at various positions on the cross sectional surface of the single cell.

3. Results and Discussion

3.1 Impedance measurements

Impedance spectra with an LSCF6428 cathode at 973 K in 10^{-2}, 10^{-1} and 1 bar of $P(O_2)$ are shown in Fig. 3. As seen in this figure, two depressed semicircles were observed. It was thought that one semicircle in higher frequency was attributed to the impedance at the electrode/electrolyte interface and the other semicircle in lower frequency to the impedance due to the electrode reaction.

Figure 4 shows the effective length estimated from the chemical capacitance of LSCF6428. The chemical capacitance $C_{measure}$ is expressed by use of the area specific conductivity σ_E.

$$\sigma_E = \frac{1}{AR_E} \quad (1)$$

$$C_{measure} = \frac{\sigma_E}{2\pi f_r} \quad (2)$$

A, R_E and f_r are electrode area, electrode resistance and top frequency of semicircle, respectively.

When the surface reaction is the rate determining step, the capacitance is estimated by the oxygen nonstoichiometry of whole electrode C_{chem},

$$C_{chem} = -\frac{8F^2}{RTV_m}\frac{d\delta}{d\ln P(O_2)}V_{electrode} \quad (3)$$

F, R, T, and δ are the faraday constant, the gas constant, temperature, and the oxygen nonstoichiometry of LSCF6428, respectively. The effective reaction zone E is estimated by the ratio of the capacitance observed in ac impedance spectra $C_{measure}$ and estimated by the oxygen nonstoichiometry of whole electrode C_{chem},

$$E = \frac{C_{measure}}{C_{chem}}h \quad (4)$$

h is the thickness of cathode. This figure shows the effective reaction zone extended from 3 - to 23 μm depending on applied $P(O_2)$ and temperature. The effective reaction zone tended to increase as the oxygen partial pressure decreased. However the average cathode thickness was found to be around 40 μm from the SEM observation of the cross section of the electrode. So, there is contradiction about the effective reaction zone in $P(O_2)$ of 10^{-4} and 10^{-3} bar. One possible explanation for this is that the effect of gas conversion could not sufficiently excluded in the analysis of the chemical capacitance in low $P(O_2)$ range.

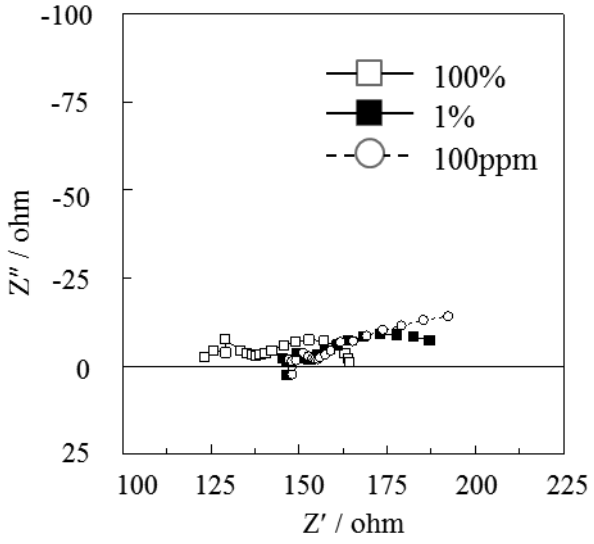

Fig. 3. Impedance spectra for the LSCF6428 cathode at 973 K and in 10^{-2}, 10^{-1} and 1 bar of $P(O_2)$.

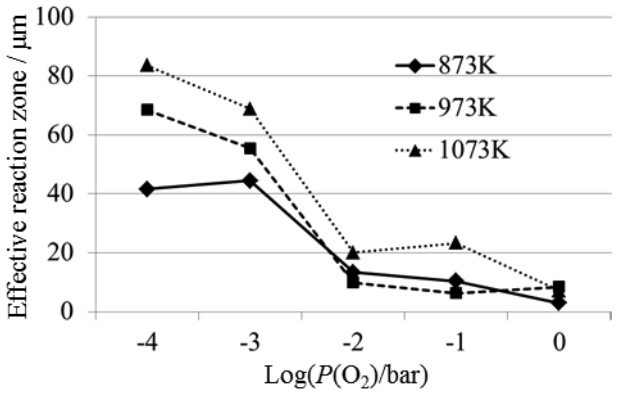

Fig. 4. Effective reaction length of porous LSCF6428, which was evaluated from ac impedance measurement, as a function of oxygen partial pressure.

3.2 In-situ micro XAS measurements

Figures 5 and 7 show *in-situ* XAS spectra for Fe and Co *K*- edge observed at the same position under different oxygen partial pressures. Measurements were performed under OCV at 973K. Figures 6 and 8 are extended views near the absorption edge of Figs. 5 and 7. Both figures showed a similar tendency that the absorption edge shifted to higher energy as oxygen partial pressure increased These results indicated that oxygen potential change can be detected by the absorption edge shift.

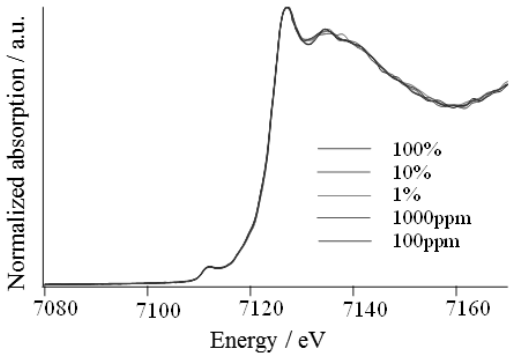

Fig. 5. *In-situ* XAS spectra for Fe *K*-edge of LSCF6428 under OCV at 973K

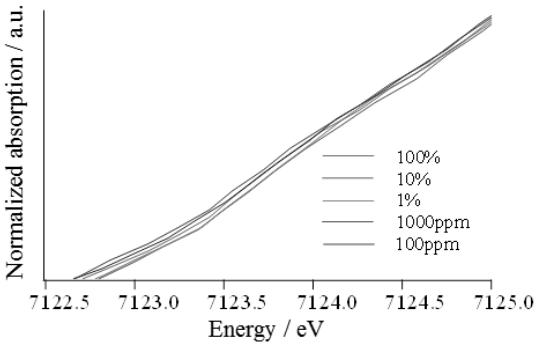

Fig. 6. *In-situ* XAS spectra for Fe *K*-edge absorption edge of LSCF6428 under OCV at 973K

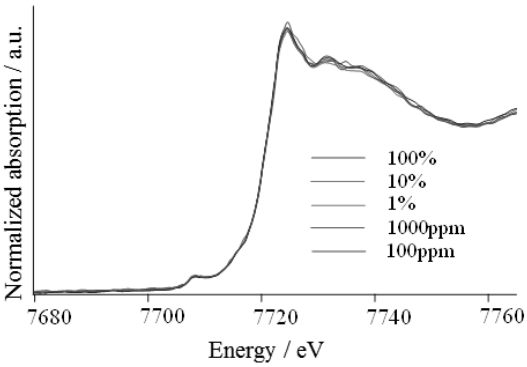

Fig. 7. *In-situ* XAS spectra for Co *K*-edge of LSCF6428 under OCV at 973K

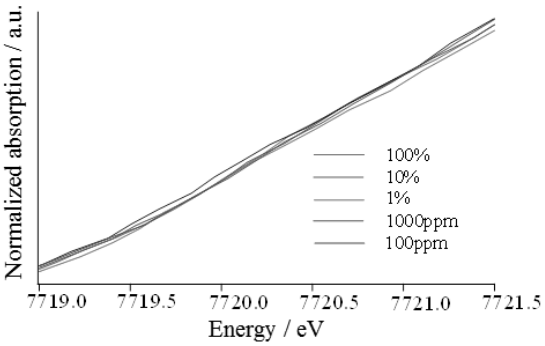

Fig. 8. *In-situ* XAS spectra for Co *K*-edge absorption edge of LSCF6428 under OCV at 973K

Figures 9 and 11 show *in-situ* XAS spectra under cathodic polarization of -0.75V and $P(O_2)$=1 bar at 973K. Figures 10 and 12 are extended views near the absorption edge. However no clear absorption edge shifts were observed. The reason is thought to be due to the low oxygen nonstoichiometry of LSCF6428 in the operated $P(O_2)$.

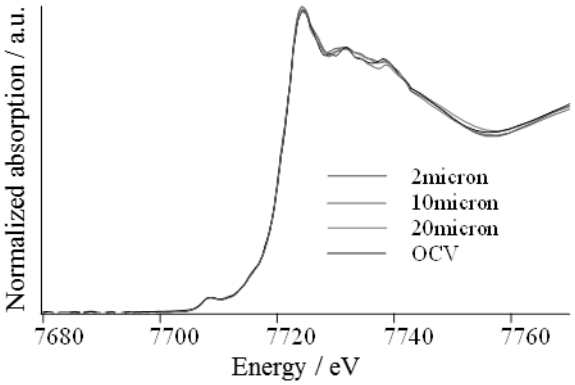

Fig. 9. In-situ XAS spectra for Co *K*-edge of LSCF6428 under conditions of cathodic voltage of -0.75V $P(O_2)$=1bar at 973K.

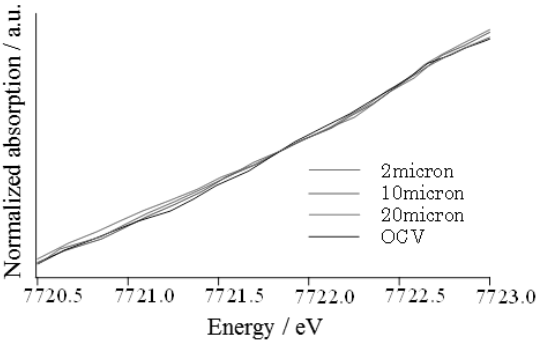

Fig. 10. *In-situ* XAS spectra for Co *K*-edge absorption edge of LSCF6428 under conditions of cathodic voltage of -0.75V and $P(O_2)$=1bar at 973K

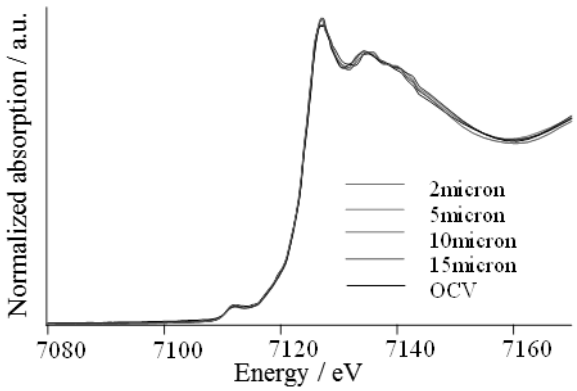

Fig. 11. In-situ XAS spectra for Fe *K*-edge of LSCF6428 under conditions of cathodic voltage of -0.75V $P(O_2)$=1bar at 973K.

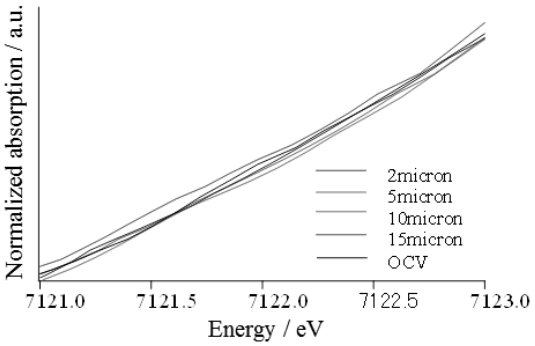

Fig. 12. *In-situ* XAS spectra for Fe *K*-edge absorption edge of LSCF6428 under conditions of cathodic voltage of -0.75V and $P(O_2)$=1bar at 973K

4. Concluding remarks and future works

The effective reaction length in a porous $La_{0.6}Sr_{0.4}Co_{0.2}Fe_{0.8}O_{3-\delta}$ (LSCF6428) cathode for SOFC was roughly estimated as 3 - 23 μm from the electrode/electrolyte interface at 873-1073 K and in 10^{-2} - 1 bar of $P(O_2)$ by using ac impedance spectroscopy. Meanwhile, clear changes in oxygen potential were not observed by using *in-situ* XAS spectroscopy both for Co and Fe *K*-edge. By taking the above result into consideration, the authors will try to evaluate oxygen potential distribution in $La_{0.6}Sr_{0.4}CoO_{3-\delta}$.

References

[1] S. B. Adler, *Chem. Rev.*, **104**, 4791 (2004)
[2] J. W. Stevenson, T. R. Armstrong, R. D. Carneim, L. R. Pederson, W. J. Weber, *J. Electrochem. Soc.*, **143**, 2722 (1996)
[3] T. Kawada, J. Suzuki, M. Sase, A. Kaimai, K. Yashiro, Y. Nigara, J. Mizusaki, K. Kawamura, H. Yugami, *J Electrochem. Soc.*, **149**, E252 (2002)
[4] J. Jamnik and J. Maier, *J Electrochem. Soc.*, **146**, 4183 (1999)
[5] T. Nakamura, K. Yashiro, A. Kaimai, T. Otake, K. Sato, T. Kawada, J. Mizusaki, *J Electrochem. Soc.*, **155**, B1244 (2008)
[6] Y. Fujida, S. Hashimoto, K. Sato, K. Yashiro, J. Mizusaki, *ECS Transactions*, **25**, 2375 (2009)
[7] S. Hashimoto, Y. Fukuda, M. Kuhn, K. Sato, K. Yashiro, J. Mizusaki, *Solid State Ionics*, **181**, 1713 (2010)
[8] T. Shibata, B. A. Bunker, J. F. Mitchell, *Phys. Rev.*, **68**, 024103 (2003)
[9] C. H. Booth, F. Bridges, G. H. Kwei, J. M. Lawrence, A. L. Cornelius, J. J. Neumeier, *Phys. Rev.*, **80**, 853 (1998)

Study on the Origin and Characteristics of Oxygen Storage Capacity for Pr doped Ceria

Kiyong Ahn[1,2], Yong-Chae Chung[2], Hae-Weon Lee[1], and Jong-Ho Lee[1,*]
[1]Korea Institute of Science and Technology, Seoul 136-791, Republic of Korea
[2]Department of Materials Science and Engineering, Hanyang University, Seoul 133-791, Republic of Korea
E-mail address: jongho@kist.re.kr

ABSTRACT

The ever-growing attention in the oxygen storage capacity (OSC) of metal oxides such as fluorite-like structures resides in three-way catalysts (TWCs), and components of SOFCs. Among materials for those applications, ceria has excellent effects for storing and releasing oxygen representing OSC. The effects are intensely linked in the easy formation and diffusion of oxygen vacancies. These properties could be improved by led dopant cations into ceria lattice. In this study, we studied on the different effects of OSC between Pr doped ceria and pure ceria.

1. Introduction

Both pure ceria and doped ceria are of chemical and physical interest because those ceria based materials have oxygen storage capacity (OSC).[1-3] The materials of high OSC which are introduced in oxygen vacancy in the lattice reside in three-way catalyst, and components of SOFCs.[4] In this study, we studied on the differences of oxygen vacancy formation energy between Pr doped ceria and pure ceria with various pressure.[5]

2. Method

$Pr_xCe_{1-x}O_2$ (x = 0, 0.1, 0.2, 0.3, 0.4, and 0.5) powders were prepared via glycine nitrate process (GNP).[6] This process is a self-combustion synthesis technique that can produce fine and homogeneous metal oxide powders. For XAFS experiments at Ce L_{III}- and Pr L_{III} -edges, 10B XRS KIST-PAL beamline of the Pohang Accelerator Laboratory (PAL), operating at 2.5 GeV with a maximum storage current of 200 mA was utilized. This beamline is monochromatized by a double-crystal Si (111) monochromator detuned from 30 to 40%, to suppress higher-order harmonic content from the beam. To confirm exact effect of oxygen storage capacity (OSC), we used DFT method for Pr doped ceria and ceria. In order to create accurate calculation, the electronic structure and physical properties of ceria and Pr doped ceria have been studied from the framework of spin polarized first principles calculation by the all-electron projector-augmented-wave (PAW) method, as implemented VASP (Vienna Ab-initio Simulation Package).[7] The generalized gradient approximation (GGA) with effective U (U_{eff}, U-J) and plane wave set expanded by the cutoff energy of 450 eV (= 33 Ry) has been used to explain the strong on-site Coulomb repulsion among the localized Ce 4f electrons.[8] These results represent that by choosing an appropriate the U_{eff} as 5.3, it is possible to reliably describe structural an electronic properties of CeO_2 and Pr doped CeO_2, which enables modeling of the oxygen reduction reaction processes involving ceria-based materials.

3. Results and Discussion

As EXAFS result shows (Figure 1), Pr ion generates oxygen vacancies more easily than Ce ion and produces more vacancies in accordance with x value. Thus, Pr ion can have larger amount of trivalent state than Ce ion.

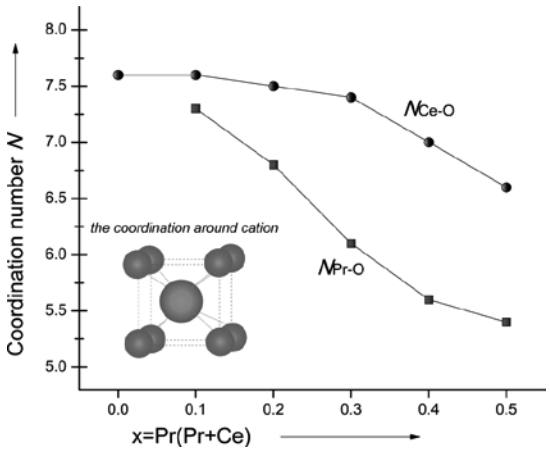

Figure 1. Coordination number of oxygen ions connected with each cation at various concentrations of Pr, *x*=Pr/(Pr+Ce).

The schematics (figure 2) show what Pr state is more favorable with the oxygen vacancy formation. In the result of Figure 2, it necessitates 1.61 eV to create an oxygen vacancy with trivalent Pr ion in the lattice. The vacancy formation energy of the trivalent Pr ion is a lot more stable than that of tetravalent Pr ion as 3.60 eV to create oxygen vacancy.

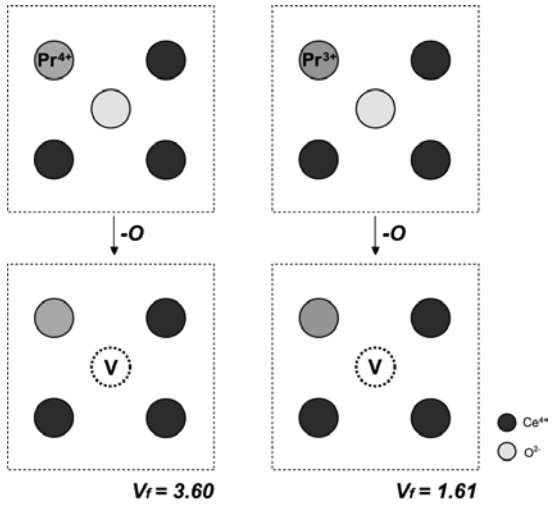

Figure 2. The energetics of oxygen vacancy formation according to the first nearest neighbor cation (Pr^{3+} or Pr^{4+}) fixed from an oxygen atom in the center of a tetrahedron in $Ce_{0.96875}Pr_{0.03125}O_{2-\delta}$.

4. Concluding remarks

We confirmed multivalent Pr ions are primarily transformed from Pr^{4+} to Pr^{3+}. This transformation is augmented with increasing Pr content. The oxygen reduction reaction of the bulk with increasing Pr content is effectively improved as well as that of the surface. Ce ions have transformation from Ce^{4+} to Ce^{3+} though the amount of the reduced ions is comparatively small as compared that of reduced Pr ion. Those results means the fact that Pr doped ceria can create plentiful oxygen vacancies because there are the reducing effects for both of Pr and Ce ions.

References

[1] E. Perry Murray, T. Tsai, and S. A. Barnett, Nature, **400** (1999), 694.
[2] D. H. Prasad, H. -I. Ji, H. -R. Kim, J. -W. Son, B. -K. Kim, H. -W. Lee, and J. -H. Lee, Appl. Catal. B- Eviron., **101** (2011), 531.
[3] A. Bueno-Lòpez, K. Krishna, M. Makkee, and J. A. Moulijn, J. Catal., **230** (2005), 237.
[4] J. Kašpar, P. Fornasiero, and M. Graziani, Catal. Today, **50** (1999), 285.
[5] Z. Song, W. Liu, H. Nishiguchi, A. Takami, K. Nagaoka, and Y. Takita, Appl. Catal. A-Gen., **329** (2007), 86.
[6] L. A. Chick, L. R. Prderson, G. D. Maupin, J. L. Bates, L. E. Thomas and G. J. Exarhos, Mat.Lett., **10** (1990), 6.
[7] G. Kresse and J. Hafner, Phys. Rev. B, **47** (1993), 558.
[8] S. L. Dudarev, G. A. Botton, S. Y. Savrasov, C. J. Humphreys, and A. P. Sutton, Phys. Rev. B, **57** (1998), 1505.

Eighth International Conference on Flow Dynamics
November 9 - November 11, 2011

Effects of Redox Cycling on the Mechanical Properties of Ni-YSZ Cermets for SOFC Anodes

Taihei Miyasaka[a], Shinji Sukinou[a], Satoshi Watanabe[a], Kazuhisa Sato[b], Tatsuya Kawada[a], Junichiro Mizusaki[c] and Toshiyuki Hashida[b]

[a] Graduate School of Environmental Studies, Tohoku University.
6-6-11-709, Aza-Aoba, Aramaki, Aobaku, Sendai 980-8579, Japan
[b] Fracture and Reliability Research Institute, Graduate School of Engineering
Tohoku University, 6-6-11-707 Aoba, Aramaki, Aoba-ku, Sendai, 980-8579, Japan
[c] Institute of Multidisciplinary Research for Advanced Materials, Tohoku University,
2-1-1, Katahira, Aoba-ku, Sendai, 980-8577, Japan
taihei.miyasaka@rift.mech.tohoku.ac.jp

ABSTRACT

Effects of redox cycling on the mechanical properties of the Ni-YSZ cermets were investigated by using a Small Punch (SP) testing method. The porosity range in the Ni-YSZ cermets tested in this study was 25-46%. Experimental results obtained from the in-situ SP tests demonstrated that ductile-like fracture under the reduction environment at 800˚C and damage cause by redox cycling degraded the fracture stress of the NiO-YSZ composites at low porosity. This study revealed that porosity makes a key contribution to the durability of Ni-YSZ cermets by the redox cycling.

1. Introduction

Solid Oxide Fuel Cell (SOFC) can realize very high power generation efficiency to convert the chemical energy of H_2 directly into electrical energy[(1)]. Thus, SOFCs are expected to become a major electric power sources in the future. Typical SOFC anodes are fabricated from a nickel oxide (NiO) / yttria-stabilized zirconia (YSZ) composites. When hydrogen fuel is supplied to the cell first time, NiO-YSZ composites is converted into Ni-YSZ cermets. Under normal operating conditions, fuel is supplied at the anode and Ni is kept in its reduced state. However, the Ni may reoxidize due to factors such as seal leakage, system shutdown or high fuel utilization. Thus, cyclic reduction and oxidation (redox) of the anode may occur commercial during SOFC operations. Many researchers have reported that Ni re-oxidation may cause a degradation or destruction of the cells[(2,3)]. Therefore, it is important to be able to understand the processes occurring during redox cycling of Ni-YSZ cermets.

The object of this work was to investigate on the relationship between mechanical properties of Ni-YSZ cermets and redox cycling, porosity, we evaluated the mechanical properties of the as-sintered NiO-YSZ composites, the reduced Ni-YSZ cermets and the re-oxidized NiO-YSZ by the in-situ small punch (SP) tests.

2. Method

2.1 Sample preparation

In this study, NiO (Sumitomo Metal Mining, Japan) and 8 mol% yttria-stabilized zirconia (YSZ) (Tosoh Co, Japan) and polymethylmethacrylate (PMMA) (Sekisui Plastics Co, Japan) were used as starting materials. The composition of Ni : YSZ : PMMA = 50 :50 : 0 , 40 : 40 : 20, 35 : 35 : 30, 30 : 30 : 40, 25 : 25 : 50, 20 : 20 : 60 (vol. %). The powders were uniaxially pressed at 3 MPa into green compacts. The green bodies were then isostatically cold pressed at 100 MPa. After pressing, the samples were sintered in atmosphere condition at 1400˚C for 3h. The heating rates for the sintering process were 200˚C/h. The as-sintered samples were polished with 3 μm diamond paste and finally size were Φ7.5 mm × 0.5 mm. The as-sintered NiO-YSZ composites were reduced at 800˚C in Ar-1%H_2 environment for 12h. The reduced Ni-YSZ cermets were then re-oxidized at 800˚C in 100%O_2 for 12h. After each treatment, we confirmed that all the samples were fully reduced or re-oxidized from weight measurements. After each step, the density of sample was estimated from the sample dimensions and weight.

2.2Mesurement of mechanical properties

The elastic modulus and fracture stress of the as-sintered NiO-YSZ composites, the reduced Ni-YSZ cermets, and the re-oxidized NiO-YSZ composites were measured by a small punch (SP) testing method[(4)]. The schematic illustration of test apparatus used in this work is shown in Fig.1. The test atmosphere of NiO-YSZ composites was in 100%O_2 (P_{O_2} = 1 atm) at 800˚C and Ni-YSZ cermets was in 100%H_2 (P_{O_2} = 10^{-25} atm) at 800˚C. The SP tests were performed on a universal testing machine (Instron Type 5565,USA) and crosshead speed was 0.5 mm/min.

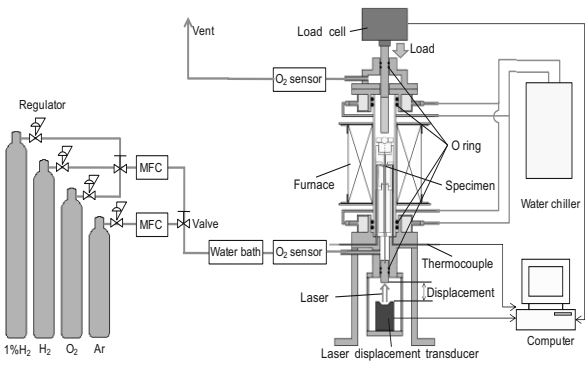

Fig. 1 Schematic of the in-situ material testing equipment used.

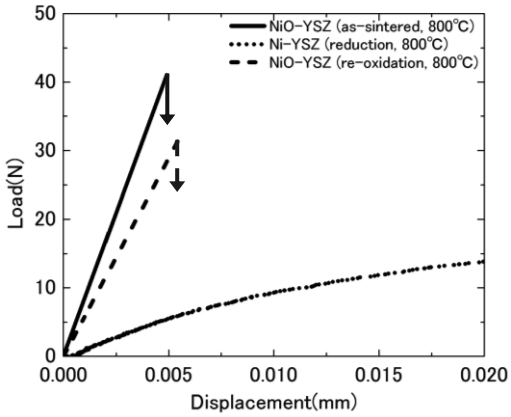

Fig. 2 Load-displacement curve of NiO-YSZ and Ni-YSZ obtained by SP test (PMMA content 30 vol.%).

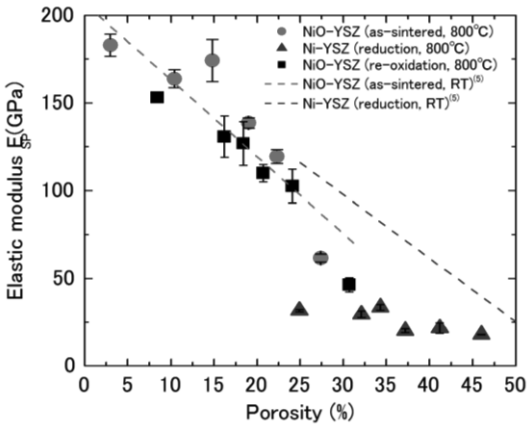

Fig. 3 Elastic modulus E_{SP} of NiO-YSZ and Ni-YSZ as a function of porosity.

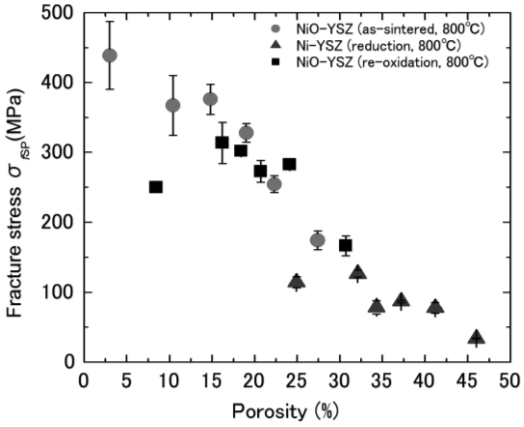

Fig. 4 Fracture stress σ_{fSP} of NiO-YSZ and Ni-YSZ as a function of porosity.

3. Results and Discussion

Examples of the load–displacement curves obtained from the in-situ SP tests are shown in Figure 2. The as-sintered NiO-YSZ composites and the re-oxidized NiO-YSZ composites show a linear elastic brittle fracture in P_{O_2} = 1 atm at 800˚C. In contrast, the Ni-YSZ cermets show a ductile-like fracture in $P_{O_2} = 10^{-25}$ atm at 800˚C.

Figure 3 shows the elastic modulus E_{sp} and Figure 4 shows the fracture stress σ_{fsp} obtained from the in-situ SP tests as a function of the porosity. The elastic modulus of the as-sintered NiO-YSZ composites decreased with increasing porosity. For the dependency of elastic properties on porosity at room temperature have been reported by M.Philatie *et al*[5]. Measured elastic modulus in this work and the reference showed a similar porosity dependency. About the fracture stress, the same tendency as the elastic modulus was shown. The results of the elastic modulus of the reduced Ni-YSZ cermets show only a slight decrease with increasing porosity. In comparison with the reference, the elastic modulus was decreased drastically at 800 ˚C. Hence, Ni-YSZ cermets have the temperature dependence. The fracture stress of the reduced Ni-YSZ cermets decreased with increasing porosity. For the re-oxidized NiO-YSZ composites, the elastic modulus exhibited the same trend with the as-sintered NiO-YSZ. The fracture stress was drastically decreased compared with the as-sintered NiO-YSZ at low porosity. On the other hand the fracture stress remained practically unchanged compared with the as-sintered NiO-YSZ at high porosity. Its reversibility implies that no significant damage occurred within the NiO-YSZ composites structure.

4. Concluding remarks

In this study, the mechanical properties of the as-sintered NiO-YSZ composites, the reduced Ni-YSZ cermets and the re-oxidized NiO-YSZ were measured at 800˚C under different partial pressures (P_{O_2} = 1 atm and $P_{O_2} = 10^{-25}$ atm) by the SP tests. The porosity range in the Ni-YSZ cermets tested in this study was 25-46%. The SP results revealed that the Ni-YSZ cermets show a ductile-like fracture under the reduction environment at 800˚C. Mechanical properties were gradually decreased with increasing porosity. However, degradation of the fracture stress by redox cycling was reduced at higher porosity. It is suggested that porosity makes a key contribution to the durability of Ni-YSZ cermets by the redox cycling.

Acknowledgment

This study was partly supported by "Development of Systems and Elemental Technology on SOFCs," funded by New Energy and Industrial Technology Development Organization (NEDO).

References

[1] A.Atkinson *et al*., Nature. Mater., **3** (2004) 17-27.
[2] D.Sarantaridis *et al*., j. Power Sources., **180** (2008), 704-710.
[3] T.Hatae *et al*., j. Electrochem. Soc., **157 (**5) (2010), B650 – B654.
[4] S.Okuda *et al*., The Japan Society of Mechanical Engineers, **53** (1991), 940-945.
[5] M. Pihlatie *et.al*, J. Eur. Ceram. Soc., **29** (2009), 1657-1664.

Eighth International Conference on Flow Dynamics
November 9 - November 11, 2011

Thermo-Mechanical Analysis of Cyclic Reduction and Oxidation Behavior of SOFC Ni-YSZ Cermets

Shinji Sukino[a], Taihei Miyasaka[a], Satoshi Watanabe[a], Kazuhisa Sato[c]
Tatsuya Kawada[a], Junichiro Mizusaki[b], Toshiyuki Hashida[c]
[a] Graduate School of Environmental Studies, Tohoku University,
6-6-11-707 Aoba, Aramaki, Aobaku, Sendai, 980-8579, Japan
[b] Institute of Multidisciplinary Research for Advanced Materials, Tohoku University, Japan
[c] Fracture and Reliability Research Institute, Tohoku University, Japan
shinji.sukinou@rift.mech.tohoku.ac.jp

ABSTRACT

Effects of Ni/YSZ volume ratio and porosity on the volume expansion of Ni-YSZ cermets during redox cycling,were investigated by thermo-mechanical analysis (TMA). Six samples which have different Ni/YSZ volume ratio and porosity were used in this study. During re-oxidation, we confirmed that the lower porosity was, the larger volume expansion became. And the higher Ni content is, the larger volume expansion becomes. However porosity has more influence on the volume expansion than Ni content. This study revealed the relationship between the microstructure and volume expansion mechanism during re-oxidation of the Ni-YSZ cermet.

1. Introduction

Typical SOFC anodes are fabricated from a nickel oxide/yttria-stabilized zirconia (YSZ) ceramic composite and are reduced in-situ, during operation, to form a Ni/YSZ cermet. However, the nickel component of the anode may re-oxidize in a commercial SOFC system for various reasons, such as the interruption of the fuel supply or too high a fuel utilization at high voltage. In order to use a re-oxidized cell, it must be reduced once more. Thus, cyclic reduction and oxidation (redox) of the anode can occur during SOFC operation. Many researchers have reported that the structure and volume in the anode cannot be restored during redox cycling. The Ni oxidation is associated with a volume expansion of the anode, which may cause a catastrophic failure in the cell [1, 2]. The performance including the resistance to the redox cycling of the anode depends on: Ni content, ratio of NiO and YSZ particle sizes, porosity, sintering temperature, and oxidation environment [3]. Since this redox cycling problem will be present in any commercially viable system, the impact of the microstructure in the cermets on the volume expansion during redox cycling will provide valuable insight into the behavior of SOFC anodes during redox cycling.

In this study, in order to investigate the effects of Ni content and porosity on the volume expansion of Ni-YSZ cermets during redox cycling, thermo-mechanical analysis was conducted.

2. Experimental

2.1. Sample preparation

The cermets tested were manufactured from commercial NiO and 8YSZ powders and polymethylmethacrylate using standard ceramic processing techniques and equipment. The powders were milled in ethanol-based slurries. The green tapes were sintered at 1400˚C. The as-sintered were cut into a number of sibling pieces for use in dilatometry. The final sizes of the dilatometry samples were about 15 mm × 2.3 mm × 0.5 mm. Different modified composites were prepared by varying the Ni/YSZ content and porosity. Table 1 shows the Ni/YSZ volume ratio and total porosite of the Ni-YSZ cermtes. The total porosities were determined by Archimedes method. It should be stressed that there are several parameters affecting the as-sintered microstructure and subsequent redox stability of the composites. In this work, to investigate the effect of Ni and porosity on the volume expansion mechanism during redox cycling, various composites which have different Ni/YSZ volume ratio and porosity were tested.

Table 1. List of samples tested in dilatometry with details on Ni/YSZ volume ratio, and porosity after reduction (sample name represents the Ni/YSZ volume ratio and total poeosity).

Sample neme	$V_{Ni}/(V_{Ni}+V_{YSZ})$ *100(%)	Total *p* (%)
15-p13	15	13
15-p34	15	34
30-p22	30	22
30-p30	30	30
50-p27	50	27
50-p47	50	47

2.2. Thermo mechanical analysis (TMA)

Dimensional behavior during redox cycles were investigated using dilatometer (TD5000S, Bruker AXS). The composites were heated to 800˚C at a heating rate of 5 K/min and a total mass flow of 100 cc/min 99.99% Ar (0.01%O_2) when reduced, and 5%H_2 (95% Ar) when re-oxidized. After 50 minutes at 800˚C, reduction or re-oxidation treatments were carried out as follows: complete reduction of bulk sample with a mass flow of 100 cc/min (5 vol% H_2 in Ar) at least 10000s, purging with Ar, complete re-oxidation of Ni-YSZ cermets with a mass flow of 100 ml/min (100 vol% O_2). This reduction and re-oxidation treatment was kept on until the treatment is completed. Then the sample was cooled down to room temperature as 5K/min.

3. Results and Discussion

Fig. 1a and b show the volume change that occurs upon reduction and re-oxidation of the Ni-YSZ cermets at 800˚C. During reduction, the 15-p13 and 15-p34 NiO-YSZ composites slightly expanded. The 30-p22 and 30-p30 NiO-YSZ composites showed almost no change, and the 50-p27 and 50-p47 NiO-YSZ composites shrank. These different behaviors during reduction indicate that Ni/YSZ volume ratio may influence the reduction behavior. Furthermore compared with the lower porosity NiO-YSZ composite which has the same Ni/YSZ volume ratio, higher porosity NiO-YSZ composite showed the larger volume change.

The volume expansion of the 15-p13 and 30-p22 Ni-YSZ cermets was very large compare with others. This may be because of these lower porosities. On the other hand, the volume change of the 15-p34 was very small, which is because of its lower Ni content. Compared with the lower porosity Ni-YSZ cermet which has the same Ni/YSZ volume ratio, higher porosity Ni-YSZ cermet showed the large volume expansion regardless of Ni/YSZ volume ratio. However the rate of the volume expansion of 50-p47 Ni-YSZ cermet was very slow. The 15-p34, 30-p30, and 50-p27 Ni-YSZ cermets which have almost the same porosity can be compared to study the effect of Ni/YSZ volume ratio on the volume expansion during redox cyclingseems that the higher Ni content is, the larger volume expansion the Ni-YSZ showed when re-oxidized.

The oxidation linear strains of the 15-p34, 30-p30, and 50-p47 Ni-YSZ cermets were relatively small. Moreover the time of fully re-oxidation of Ni-YSZ cermets was relatively short. This is because of the pore plays an important role in the path of oxygen gas. However D. Sarantaridis *et al.* and J. Laurencin *et al.* have remarked that in anode-supported cells electrolyte cracking is expected when the anodic oxidation strain reached 0.1～0.15%[4, 5]. From this view point, the SOFCs using the 15-p34, 30-p30, 50-p47 Ni-YSZ cermets may be susceptible to the redox cycling.

4. Concluding remarks

In this study, in order to investigate the effects of Ni content and porosity on the volume expansion of Ni-YSZ cermets during redox cycling, thermo mechanical analysis was conducted. The volume change behaviors during reduction mainly depend on the Ni/YSZ volume ratio. Moreover the higher porosity may lead to the larger volume change. During re-oxidation, porosity affects the volume change: the lower porosity is, the larger volume expansion becomes. Comparing 15-p35, 30-p30, and 50-p47 Ni-YSZ cermets, it may be said that the higher Ni content is, the larger volume expansion becomes. However compared with 30-p22, the volume expansion of the 50-p27 Ni-YSZ cermets was small. This may indicate that porosity has more influence on the volume expansion than Ni content.

(a)

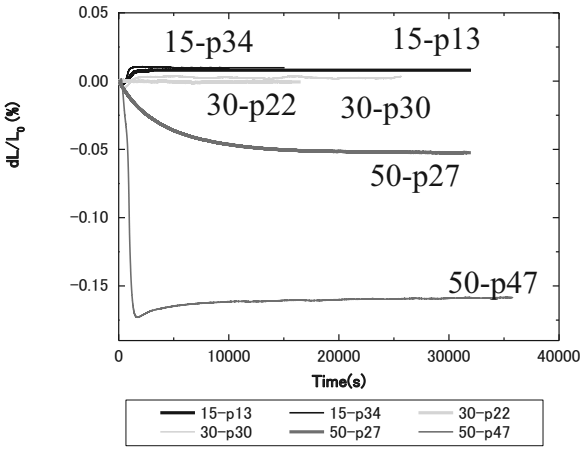

(b)

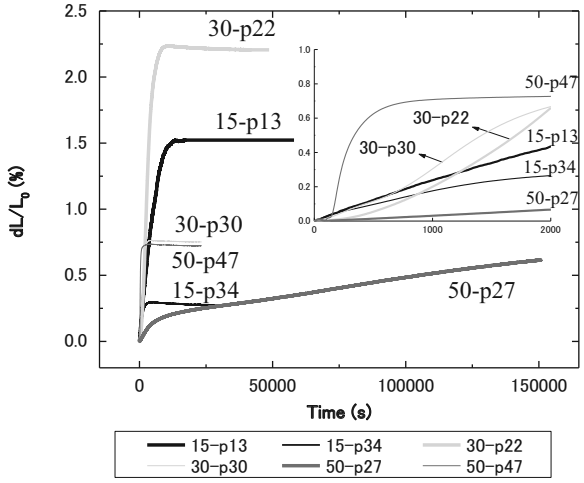

Fig. 1. (a) Reduction TMA of NiO-YSZ composites. (b) Re-oxidation TMA of Ni-YSZ cermets.

Acknowledgments

This study was partly supported by New Energy and Industrial Technology Development Organization (NEDO).

References

[1] M. Ettler et al., J. Power Sources, **195**, 5452 (2010).
[2] T. Hatae et al., J. Electrochem. Soc., **157**, 650 (2010).
[3] D. Sarantaridis and A. Atkinson, Fuel Cells, **7**, 246 (2007).
[4] D. Sarantaridis et al., J. Electrochem. Soc., **155**, B467 (2008) .
[5] J. Laurencin et al., J. Power Sources, **192**,344 (2009).

Eighth International Conference on Flow Dynamics
November 9 - November 11, 2011

Investigation of Fracture Mechanism in Carbon Nanotube Reinforced Alumina Composites and Its Relation with Nanostructure

Keiichi Shirasu[1], Go Yamamoto[2], You Nozaka[3], Mamoru Omori[2], Toshiyuki Takagi[4] and Toshiyuki Hashida[2]
[1]Graduate School of Environmental Studies, Tohoku University 6-6-11, Aramaki Aoba, Aobaku, Sendai, 980-8579 Japan
[2]Fracture and Reliability Research Institute, Tohoku University, Japan
[3]School of Engineering, Tohoku University, Japan
[4]Institute of Fluid Science, Tohoku University, Japan
keiichi.shirasu@rift.mech.tohoku.ac.jp

ABSTRACT

The fracture mechanisms of multi-walled carbon nanotubes (MWCNTs) that were synthesized by a catalytic chemical vapor deposition method followed by high temperature annealing during crack opening in MWCNT/alumina composites were studied. Transmission electron microscope observations revealed that the MWCNTs, rather than pulling out from the matrix, broke in the outer shells, similar to that observed for MWCNTs under tensile loading. These results may provide new insight into the fracture mechanisms and suggest a new design methodology for MWCNT-based ceramic composites, leading to improved fracture toughness.

1. Introduction

Carbon nanotubes (CNTs) have extremely high tensile strength[1] and elastic modulus[2], good flexibility and low density. These superior properties make CNTs attractive for many applications and technologies. In order to take advantage of the intrinsic properties of individual CNTs, various CNTs forms and composites have been demonstrated to overcome the performance limits of conventional materials such as polymers, alloys and ceramics[3][4]. Engineering ceramics have high stiffness, excellent thermostability and relatively low density, but extreme brittle nature restricted them from many structural materials. Incorporating CNTs into a ceramics matrix might be expected to produce tough as well as highly stiff and thermostable ceramic composites.

The strengthening and toughening mechanisms of composites by fibers are now well established[5]; central to an understanding is the concept of interaction between the matrix and reinforcing phase during the fracture of the composite. The fracture properties of such composites are dominated by the fiber bridging force resulting from debonding and sliding resistance, which dictates the major contribution to the strength and toughness. Therefore, a fundamental understanding of the interfacial nature is essential for making decisions on fundamental materials design of composites with CNTs for higher strength and toughness.

In this study, we report the fracture mechanisms of multi-walled carbon nanotubes (MWCNTs) during the crack opening in MWCNT/alumina composites are investigated through transmission electron microscope (TEM) observations. We also show that the relation with mechanical behavior of individual MWCNT by tensile test.

2. Method

The alumina composite made with 0.9 vol.% pristine MWCNTs was prepared by precursor method[6]. The MWCNT material was synthesized by a catalytic chemical vapor deposition (CCVD) method followed by high temperature annealing[7]. The diameters and lengths of the pristine MWCNTs from scanning electron microscope (SEM) and transmission electron microscope (TEM) measurements ranged from 33 to 124 nm (average: 70 nm) and 1.1 to 22.5 μm (average: 8.7 μm), respectively. TEM observations revealed that the MWCNTs have a ‘crystalline’ multi-walled structure with a narrow central channel. The pristine MWCNTs were dispersed in ethanol with aid of ultrasonic agitation. Aluminum hydroxide was added to this solution and ultrasonically agitated. Magnesium hydroxide was added to prevent excessive crystal growth of alumina. The resultant suspension was filtered and dried in an air oven at 60 ºC. Finally, the product obtained in the previous step was put into a half-quartz tube and was dehydrated at 600 ºC for 15 min in argon atmosphere. The composites were prepared by spark plasma sintering in a graphite die with an inner diameter of 30 mm at a temperature of 1500 ºC under a pressure of 20 MPa in vacuum for 10 min. In order to compare the mechanical properties of the composites, a MWCNT-free alumina sample was prepared under similar processing conditions.

The fracture surface and internal structure of the composite, and post-sintering MWCNTs were observed by TEM. The sample of internal structure of the composite for TEM observations were prepared using a grinding and ion-milling routine. The post-sintering MWCNTs were obtained by refluxing the composite in a phosphoric acid at 200 ºC for 1 week, washed thoroughly with distilled water to be acid-free, and then finally filtered.

Tensile test of individual MWCNT and single nanotube pullout experiments were carried out using an in situ SEM method with a nanomanipulator system[8]. In the tensile test of individual MWCNT, an AFM cantilever was mounted at the end of a piezoelectric bender on the X–Y linear motion stage, and a W wire was mounted on an opposing Z linear motion stage. MWCNT powder was dispersed in ethanol with the aid of a magnetic stirrer, and then filtered. The resulting MWCNT paper was torn apart by hand, which caused individual MWCNTs to project from the torn edge. Each MWCNT was extracted from the edge, and then was clamped first onto a cantilever tip and then onto an opposing W wire by electron beam induced deposition

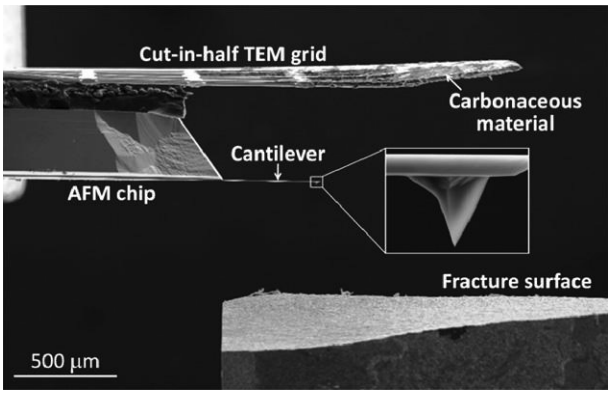

Fig. 1 SEM image showing the experimental setup for pullout tests.

(EBID) of a carbonaceous material[9]. The cantilevers serve as force-sensing elements and the spring constants of each were obtained in situ prior to the tensile test using the resonance method developed by Sader et al[10]. The applied force is calculated from the angle of deflection at the cantilever tip, and the nanotube elongation is determined by counting the numbers of pixels in the acquired SEM images. A crosshead speed – i.e., movement rate of the cantilever – of about 100 nm/s was applied for the each test.

3. Results and Discussion

Results obtained from the tensile test of individual MWCNT revealed that an 11.13 ± 0.03 μm-long section of this MWCNT was attached and then loaded and it fractured in the middle. The resulting fragment attached on the cantilever tip had a length of at least 11.6 μm, whereas the other fragment on the W wire had a length of at least 2.3 μm. Thus, the sum of the fragment length far exceeded the original section length. This apparent discrepancy can be explained as due to a 'sword-in-sheath'-type failure (Fig. 2), similar to that observed in the failure mode of arc-discharge-grown MWCNTs and certain types of carbon fibers. The measured tensile strength of the MWCNTs ranged from ~2 to ~48 GPa (mean 20 GPa). The mean failure strain varied from 2.7%, and the Young's modulus values obtained by a liner fit of each stress-strain curve ranged from ~50 to ~1360 GPa. SEM images of the broken MWCNTs were evaluated to develop an understanding of the fracture mechanism. They are presented as examples of what happens as a result of loading to breaking. Of the 10 pristine MWCNTs tested here, 5 MWCNTs showed no apparent diameter change at the fractured region. As assumed by Yu et al.[8], we assume that the outer shell was carrying the load and the inner shells were not load-bearing. For the remaining 5 MWCNTs, however, the diameter of the broken MWCNTs was smaller at the fractured region; perhaps significant inter-shell load transfer may be facilitated by the unique geometric structure arising from the CCVD synthesis and then high temperature annealing[7]. In particular, TEM images of the MWCNT powder reveal that there can be abrupt structural changes from perfect constant-diameter cylinders, such as pentagon and heptagon insertions and significant gaps between fringes. Similar observations have been made by others for this type of MWCNT[7]. Load transfer between layers is perhaps facilitated in some of these MWCNTs by the different structure and may be correlated to the unevenly spaced lattice fringes on one side of the hollow core.

The mechanical properties of the MWCNT/alumina composite and MWCNT-free alumina sample are shown in Table 1. X-ray diffraction analysis of the sintered body revealed that the aluminum hydroxide has been transformed to α-alumina during SPS at 1500 ºC under 20 MPa. The aluminum hydroxide powder with 0.9 vol.% pristine MWCNTs can be solidified by SPS to near-theoretical density. Measured bending strength and fracture toughness are 543.8 ± 60.9 MPa, 4.74 ± 0.12 MPa·m$^{1/2}$, respectively. From the fracture surface observations, the following features can be noted. First, the fracture surface of the composite exhibits protruding

Table 1 The properties of the alumina composite sample with 0.9 vol.% MWCNTs, and of the MWCNT-free alumina sample.

Sample	Composite	Alumina
Relative density (%)	98.9	98.6
Grain size (mm)	1.43 ± 0.31	1.69 ± 0.35
Bending strength (MPa)	543.8 ± 60.9	502.3 ± 19.4
Fracture toughness (MPa·m$^{1/2}$)	4.74 ± 0.12	4.37 ± 0.07

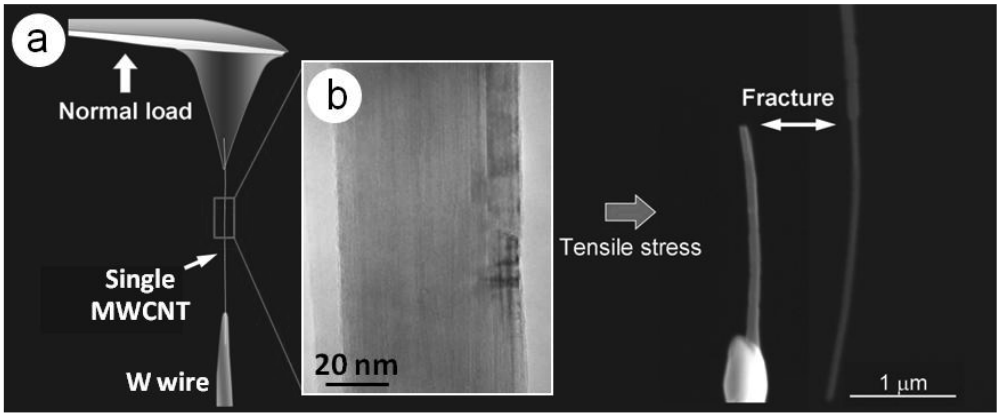

Fig. 2 (a) SEM images showing a MWCNT tensile-loading experiment, before and after the MWCNT was fractured. (b) TEM image of the MWCNT.

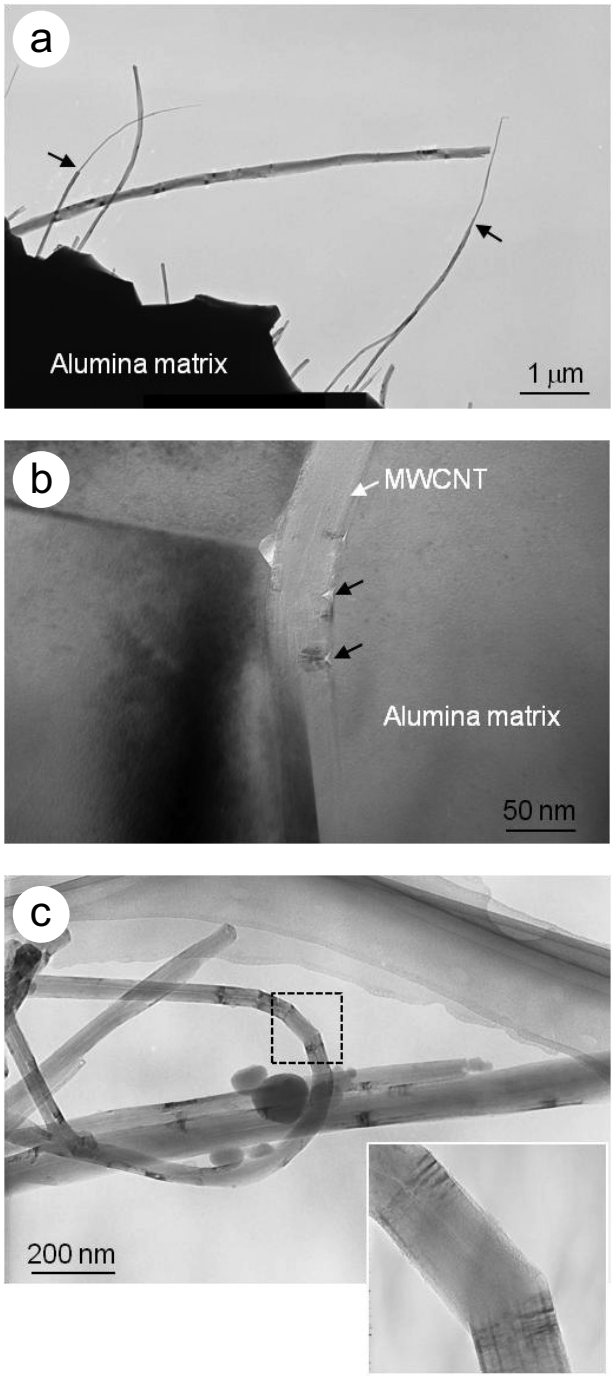

Fig. 3 TEM images of (a) the fracture surface, (b) internal structure of the composite, and (c) post-sintering MWCNTs, respectively.

MWCNTs from the crack flank. Most of MWCNTs are located in the intergranular phase and their lengths are in the range 0–11.8 μm (number average of 160 protruding MWCNTs is 2.8 μm). Second, some MWCNTs are observed to debond from the matrix and leave traces on the fracture surfaces, as exemplified. These MWCNTs are partially exposed to the crack plane, and the exposed area of such MWCNTs lie parallel to the crack plane. Therefore, such MWCNTs are less effective at reinforcing, i.e., they are not load bearing during the failure of the composite, and no significant damage may

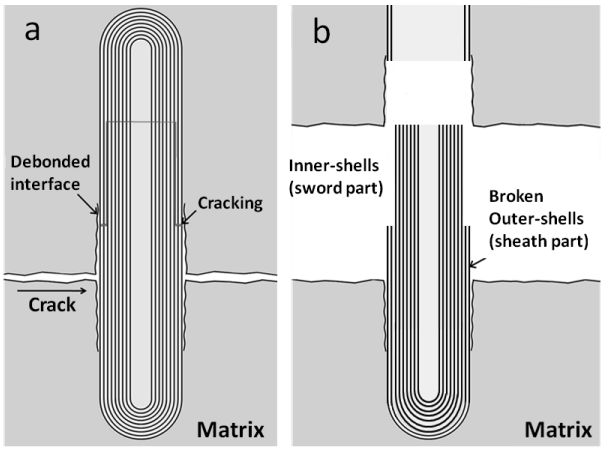

Fig. 4 Schematic description of possible fracture mechanisms of the MWCNT.

be induced in such MWCNTs during crack opening. Third, the morphology of the fracture surface of the matrix shows clearly the edge and corner fractural feature, indicating that intergranular fracturing took place in the matrix. Its microstructure consisted of equiaxed grains structure with a grain size of 1.43 ± 0.31 μm. In addition to the above features, some MWCNTs on the fracture surface show a clean break near the crack plane, and that the diameter of MWCNT drastically slenderized toward their tip. As SEM cannot clearly resolve the thickness of a single MWCNT, TEM was used to determine if the fracture phenomenon of MWCNTs was indeed occurring during crack opening.

TEM observations on the fracture surface demonstrated that a diameter change in the MWCNT structure was evidently observed for a certain percentage of the MWCNTs (Fig. 3a). The high magnification TEM image clearly showed a change in diameter, and this morphology is quite similar to a ‘‘sword-in-sheath’’-type failure as observed in the failure mode of MWCNTs under tensile loading (Fig. 2). The inset showed that outer-walls having approximately 10 shells were observed to break up at location where the MWCNT undergo failure, and that edges of such outer shells were clearly observed to lie perpendicular to the axis of cylinder, demonstrating the sword-in-sheath failure. Since no apparent variation in the diameter of the MWCNTs has been observed along the axis in the as-received MWCNTs, these results imply that some MWCNTs underwent failure in the sword-in-sheath manner prior to pullout from the matrix, and no apparent damage appeared to be induced in some of MWCNTs that were not load bearing. Figure 3b shows a TEM image of internal structure of the composite. MWCNT is observed in the intergranular phase, and bended along the grain boundary. In terms of MWCNT, structural changes and deformations from constant-diameter cylinders, as shown in black arrows. TEM observations on the post-sintering MWCNTs demonstrated that crystallinity change and deformations in the MWCNT structure was observed for some part of MWCNTs. As shown in Fig. 3c, TEM image clearly showed changes in crystalline structure, and were not present in the

as-received MWCNTs. These morphology change may be due to a radial compressive stress of the MWCNT that comes from the difference of coefficient of thermal expansion between MWCNT and ceramics matrix.

On the basis of these results, we schematically describe possible processes and mechanics, explaining the MWCNT failure during crack opening (Fig. 4). As for one example, the initial state of the MWCNT in an ideal case is a completely impregnated and isolated embedded in the matrix. Tensile stresses parallel to the axis of MWCNT length lead to matrix crack formation. Subsequently, interfacial debonding between two phases may occur (Fig. 4a), perhaps over a limited distance (but this is unlikely to make a major contribution to the fracture energy). Since there is variability in MWCNT strength in the debonded region on either side of the crack plane, and it is possible for the MWCNT to break at a certain position, when the stress in the MWCNT reaches a critical value. As displacement increases, the MWCNTs, rather than pulling out from the alumina matrix, undergo failure in the outer shells and the inner core is pulled away, leaving the fragments of the outer shells in the matrix (Fig. 4b).

Creating tough, fracture-resistant ceramics has been a central focus of MWCNT/ceramic composites research. Although there are a few papers that report significant improvement in the fracture toughness[11], the improvements by addition of MWCNTs reported in other studies has been limited[12]. The results reported here suggest that modest improvements in toughness reported previously may be due to the way MWCNT's fail during crack opening in the MWCNT/ceramic composites. The design of tougher composites with MWCNTs as a filler will need to account, or in some way circumvent, the sword-in-sheath failure reported here.

4. Concluding remarks

In conclusion, tensile-loading experiments were performed on MWCNT that was synthesized by a CCVD method following by high temperature annealing. The measured tensile strength ranged from ~2 to ~48 GPa for the MWCNTs, slightly lower than those of arc-discharge-grown MWCNTs. It has been demonstrated from TEM observations of fracture surface, internal structure and post-sintering MWCNTs that the MWCNTs, rather than pulling out from the alumina matrix, broke during the crack opening in a composite, and this morphology is quite similar to a sword-in-sheath-type failure as observed in the failure mode of MWCNTs under tensile loading. In totality, our finding suggests important implications for the design of tougher ceramic composites with MWCNTs. The important factor for such tougher ceramic composites will thus be the use of MWCNT having a much higher load carrying capacity (as well as a good dispersion in the matrix).

References

[1] B. Peng et al., Nat. Nanotechnol, **3** (2008), 626.
[2] J.P. Salvetat et. al., Adv. Mater., **11** (1999), 161.
[3] P.J.F. Harris, Int. Mater. Rev., **49** (2004), 31.
[4] J. Cho et al., J. Mater. Sci., **44** (2009), 1934.
[5] A.G. Evans, J. Am. Ceram. Soc., **73** (1990), 187.
[6] G. Yamamoto et al., Nanotechnology, **19** (2008), 315708.
[7] Y.A. Kim et al., Carbon, **43** (2005), 2243.
[8] M.F. Yu et al., Science, **287** (2000), 637.
[9] W. Ding et al., J. Appl. Phys., **98** (2005), 014905.
[10] J.E. Sader et al., Rev. Sci. Instrum.., **70** (1999), 3967.
[11] G.D. Zhan et al., Nat. Mater., **2** (2002), 38.
[12] J. Cho et al., J. Mater. Sci., **44** (2009), 1934.

Gradient Structure Modification of LSC Cathode for Performance Improvement of Thin Film SOFCT

Jaeyeon Hwang,[a,b] Doo-Hwan Myung,[a,c] Hae-Weon Lee,[a] Byung-Kook Kim,[a] Jong-Ho Lee,[a] and Ji-Won Son[a,*]
[a]High-Temperature Energy Materials Research Center, Korea Institute of Science and Technology, Seoul 136-791, Korea
[b]Department of Materials Science and Engineering, Korea University, Seoul 136-701, Korea
[c]Department of Materials Science and Engineering, Yonsei University, Seoul 120-749, Korea
jwson@kist.re.kr

ABSTRACT

By introducing the cathode-electrolyte composite concept to the thin-film deposition and employing a gradient cathode structure, the adhesion of the interface between the thin-film cathode and the electrolyte could be improved and as a result, stability of high-temperature performance is increased. In this study, lanthanum strontium cobaltite (LSC) and Gd doped ceria (GDC) are used for fabricating composite cathode and this composite cathode was applied on the thin-film solid oxide fuel cells.

1. Introduction

Solid oxide fuel cells (SOFCs) have gained increasing attention in these days as promising candidates for next generation portable power sources because of high power and energy densities, system efficiencies, and fuel flexibility. [1]

For obtaining high performance of SOFCs at a lower operating temperature, cathode materials with a high mixed ionic and electronic conducting (MIEC) property such as lanthanum strontium cobaltite (LSC) were widely investigated.

In our previous study, [2] the SOFC cell consisting of Ni, yttria-stabilized zirconia (YSZ), Gd doped ceria (GDC) with 3~5 μm-thick thin-film processed nano-structure LSC cathodes demonstrated an appreciable performance compared with that of the cell with ~30 μm-thick powder processed LSC-base cathodes at 650 °C. This results showed that the thin-film process can develop the nano-structure of the cathode easily, which increase the surface area of the reaction sites of the cathode. However, single-phase LSC thin-film cathode was limited by microstructural problems. When the thin-film cathode become thicker, the performance of the cell is increased but the probability of loss of the adhesion at the electrolyte/cathode interface is also increased especially when the cathode thickness exceeds a certain thickness level.

In this study, LSC-GDC composite cathode layer was introduced for more reliable and practically applicable thin-film processed cathode. Microstructure observation of single and composite cathode thin films and reliability improvement of a thin-film SOFC by composite cathode will be presented.

2. Experimental

By using pulsed laser deposition (PLD), 1 μm-thick single LSC and LSC-GDC composite thin films were deposited on the electrolyte made by powder processing. A KrF eximer laser (COMPEX Pro 201F, Coherent) was used as an ablation source and the laser fluence was about 3 J/cm^2. Targets were fabricated by sintering a uniaxially pressed powder pellet at 1200 °C for 3 hrs. The powder used for making single LSC target was commercial $La_{0.6}Sr_{0.4}CoO_{3-\delta}$ and for LSC-GDC composite target was $La_{0.6}Sr_{0.4}CoO_{3-\delta}$ and $Ce_{0.9}Gd_{0.1}O_{2-\delta}$ powder mixture (mixing volume ratio = 1:1). Each deposition was done by PLD under various deposition conditions and their microstructures were observed by using scanning electron microscopy (SEM)

Next to the reliability test, two of TF-SOFC cells were fabricated. At first, a NiO-YSZ anode interlayer was deposited on a NiO-YSZ support made by powder process. Then, we deposited 1 μm-thick YSZ electrolyte, 200nm-thick GDC onto the anode interlayer, layer by layer. And different types of the cathode structures were finally fabricated on each cell. One of the cells has only 5 μm-thick LSC single phase cathode, and the other one has 3 layers. The first layer contacting GDC was a 1.5 μm-thick LSC-GDC composite layer deposited at T_s=700 °C and P_{amb}=26.66 Pa, the second layer was a 1.5 μm-thick LSC-GDC composite layer deposited at T_s=700 °C and P_{amb}=39.99 Pa, and the third (top) layer was a 2 μm-thick LSC single-phase layer deposited at room temperature and P_{amb}=13.33 Pa. All of depositions were done by using PLD and GDC was introduced as buffer which prohibits the reaction between YSZ and each cathode.

After an in-situ reduction of the anode in H_2, the cell performance was measured at 600℃ using humidified H_2 for a fuel and air for an oxidant until 12 hours

3. Results and Discussion

Figure 1 is the SEM graphs of the single LSC and LSC-GDC composite thin films deposited on the YSZ electrolyte with GDC buffer at 700℃. As shown in figure 1, only single LSC thin film is cracked out from the electrolyte because there is large thermal expansion coefficient (TEC) mismatch between LSC and electrolyte and the LSC cannot release the stress induced from the TEC mismatch. Relatively, TEC mismatch is decreased in the case of LSC-GDC/GDC interface, so there is no crack.

The performance and long term stability of the cell with the LSC-GDC composite cathode were compared with those of the cell with the single LSC cathode. The performance of the cell with single LSC was slightly higher but the difference was not considerable, and this indicates that the composite layer did not significantly

degrade the cell performance.

However, as shown in figure 2, the resistance of single LSC cathode cell is drastically increased during cell test for 12 hours and this performance drop originated with delamination of cathode, as mentioned. On the contrary, as shown in figure 3, the resistance of LSC-GDC composite cathode cell is not changed remarkably. This indicates that the composite cathode is more stable than single phase cathode in the viewpoint of long-term operation.

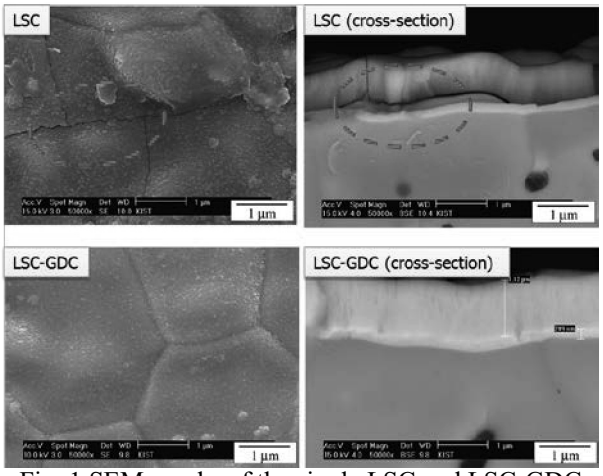

Fig. 1 SEM graphs of the single LSC and LSC-GDC composite thin films deposited on the electrolyte

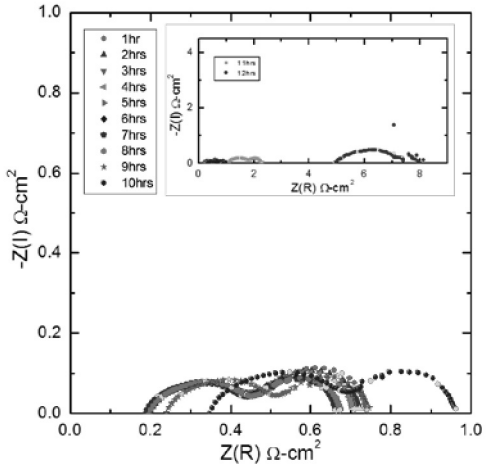

Fig. 2 Impedance spectra change of tested cells without LSC-GDC composite cathode layer

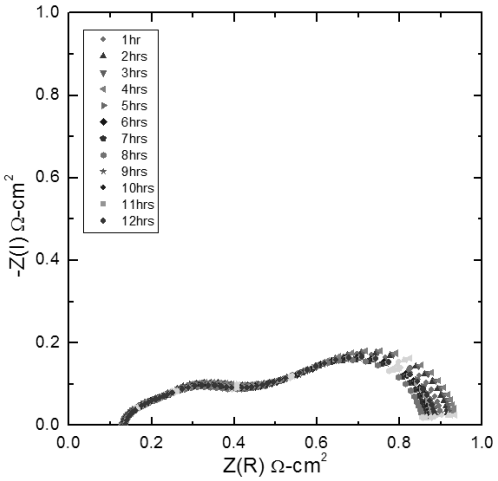

Fig. 3 Impedance spectra change of tested cells with LSC-GDC composite cathode layer

4. Concluding remarks

By introducing LSC-GDC composite thin-film cathode by PLD, the microstructural stability of the thin film could be significantly improved. The defects due to the TEC mismatch was decreased in the composite layer compared with the single-phase LSC layer when deposited at a high temperature. A single LSC cathode showed significant degradation after 8 hours of operation. However improved LSC-GDC composite cathode did not exhibit remarkable degradation after 12 hours long-term operation.

References

[1] H.-S. Noh, J.-W. Son, H. Lee, H.-I. Ji, J.-H. Lee, H.-W. Lee, J. Eur. Ceram. Soc., **30** (2010), 3415

[2] H.-S. Noh, H. Lee, H.-I. Ji, H.-W. Lee, J.-H. Lee, and J.-W. Son, J. Electrochem. Soc., **158** (2011), B1

Eighth International Conference on Flow Dynamics
November 9 - November 11, 2011

Evaluation Method of Stress Conditions in Operated SOFC by In-Situ Raman Scattering Spectroscopy

Syo Onodera, Masafumi Nagai, Fumidata Iguchi, Noriko Sata, Tatsuya Kawada, and Hiroo Yugami[*1]
Graduate School of Engineering, and [*2]Graduate School of Environmental Studies, Tohoku University,
Aoba 6-6-01, Aramaki, Aoba, Sendai, 980-8579 Japan.
s_onodera@energy.mech.tohoku.ac.jp.

ABSTRACT

We developed the new evaluation method of stress conditions in operated SOFC. It was based on the observation of lattice conditions by in-situ Raman scattering spectroscopy. Temperature and pressure dependences of the Raman spectra of 20 mol%Sm-doped ceria (20SDC), which was often used as an interlayer of the SOFC cell, were studied. Based on the results, we applied this method to the typical anode supported type cells with 20SDC interlayer. It was suggested from this in-situ evaluation that the risk of the destruction of the electrolyte is increased when the anode exposed to the redox cycle by stopping the operation.

1. Introduction

SOFC (Solid Oxide Fuel Cells) is exposed to high temperature and high oxygen potential gradient under the operating conditions. At that time, stress conditions are changed due to the thermal expansion coefficient (TEC) mismatch of the materials and the volume change by the redox of the electrode. These changes of stress conditions cause mechanical damage to the SOFC. So, measuring methods to evaluate the stress condition at operating conditions are strongly required for improve durability and reliability of the SOFC. Raman spectroscopy is the contactless and non-destructive method. It can obtain the knowledge of the crystal structure, defect structure and temperature from the scattered light in the laser irradiated to the object. This method can apply in-situ measurement for SOFC in operating conditions by using a glass chamber with an optically transparent window in which temperature and atmosphere can be controlled. So, we are studying for establish an in-situ evaluating method for SOFC by the information of the crystal structure, defect structure and temperature, these measured from in-situ Raman spectroscopy, and mechanical properties. In this study, we evaluated the stress condition of SOFC model cell in operating conditions based on the knowledge from temperature dependence and pressure dependence of Raman spectra of SOFC component.

2. Experimental

20mol% Samarium doped Ceria ($(Sm_{0.2},Ce_{0.8})O_2$), which is often used for SOFC interlayer, is used as the object. The sample powder was prepared by coprecipitation method from $Ce(NO_3)_3 \cdot 6H_2O$ and $Sm(NO_3)_3 \cdot H_2O$. Calcination condition is 5hour by 900^oC. The pellet was sintered at 1500^oC by 5 hour in air after hydrostatic press. After shaping, the pellet was annealed at 1000^oC by 3 hour for eliminate the residual stress. The powder was used for pressure dependence measurement and the pellet was used for temperature dependence measurement. Typical anode supported type cells with 20SDC interlayer (JAPAN FINE CERAMICS) were used for evaluation of stress condition during operation. Table 1 shows component materials and preparing method of purchased model cells. Raman scattering spectra were measured using RAMANOR T64000 (Horiba-Jobin Yvon) with an Ar ion laser (λ=488nm). The spectrometer was calibrated with Ne atomic emission spectra. As a result, the accuracy of the Raman peak position measurement was better than 0.1cm^{-1}. In pressure dependence measurement, Raman spectra under the hydrostatic pressure were measured using a lever type diamond anvil cell (DAC) and evaluated it. Schematic illustration of the DAC is shown in figure 1. Pressure in the DAC was measured by the ruby fluorescence method. In order to measure temperature dependence of the 20SDC pellet and stress conditions of the model cell in operating conditions, we developed a glass chamber with an optically transparent window in which temperature and atmosphere can be controlled. Schematic illustration of the glass chamber is shown in figure 2, and figure 3 shows the operating conditions.

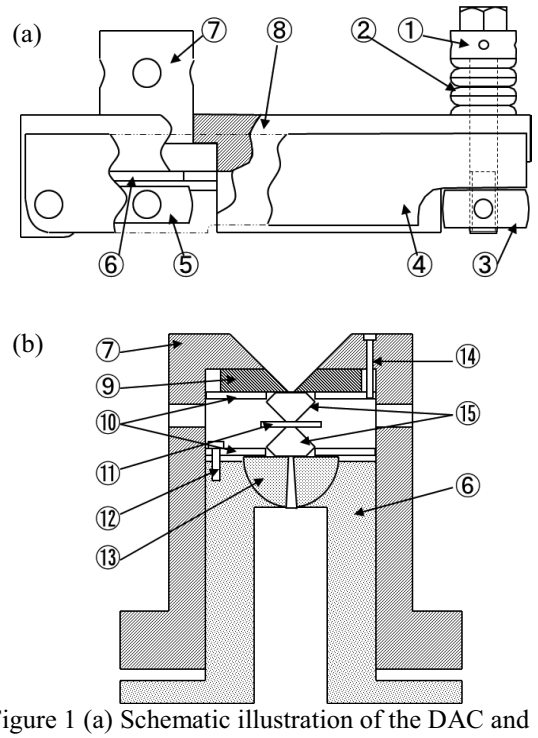

Figure 1 (a) Schematic illustration of the DAC and (b) detail of the cylinder; 1: drive screw, 2:bellville washers, 3:lever thrust block, 4:lever, 5:thrust block, 6:piston, 7:cylinder, 8:main body, 9:mounting plate, 10:flat plate, 11:gasket, 12,14:tilting screw, 13:hemisphere support, 15:diamond anvil

Table 1 Components and preparing method of model cell

	Materials	Thickness	Method	Sintering
Anode	NiO/8YSZ (60/40wt% ratio)	1mm	Tape cast	1400°C
Electrolyte	8YSZ	15μm	Screen print	
Cathode interlayer	$Ce_{0.8}Sm_{0.2}O_{2.9}$ (20SDC)	5μm		
Cathode	$La_{0.6}Sr_{0.4}Co_{0.2}Fe_{0.8}O_3$	30μm		1000°C

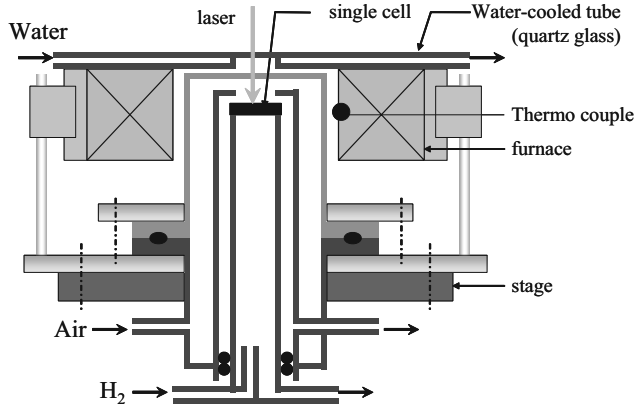

Figure 2 Schematic illustration of the experimental apparatus

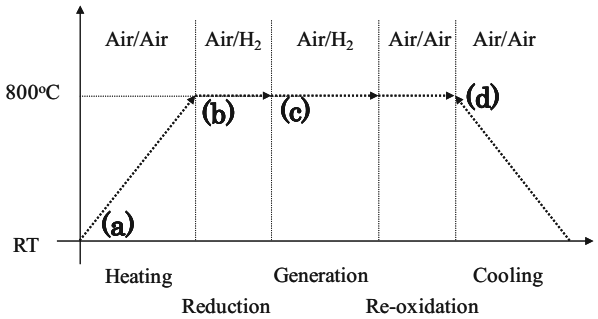

Figure 3 Operating conditions of model cell

3. Results and Discussion

3·1.Temperature dependence measurement

Figure 4 shows the temperature dependence of F_{2g} Raman peak of 20SDC. The F_{2g} Raman peak was sifted to low wavenumber side with increasing temperature. Because 20SDC pellets used in this measurement are regarded as non-stress conditions, Raman peak positions that obtained in this measurement can be used as the reference point of non-stress condition for each temperature.

3·2.Pressure dependence measurement

Figure 5 shows the pressure dependence of F_{2g} Raman peak of 20SDC. Vertical axis shows the pressure and positive direction means the tensile stress. From the linear approximation of 20SDC plot, the pressure dependence was 3.40 (cm^{-1}/GPa). Because the stress of SDC in the cell is considered to be plane stress, hydrostatic stress was converted plane stress using variation of Raman shift - volumetric strain relation,

$$\frac{dk_R}{k_R} = -\gamma_K \frac{dV}{V} \qquad (1)$$

and hydrostatic stress - volumetric strain relation,

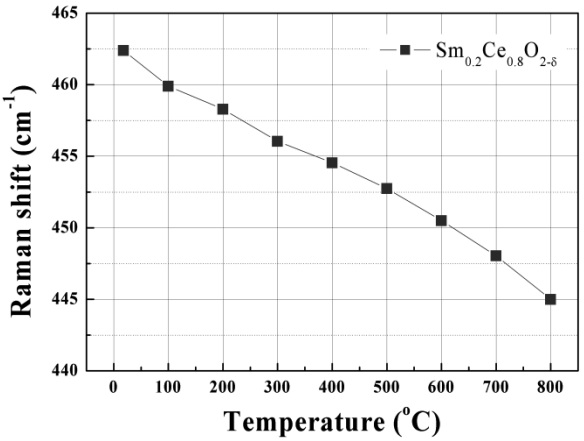

Figure 4 Temperature dependence of 20SDC Raman peak position

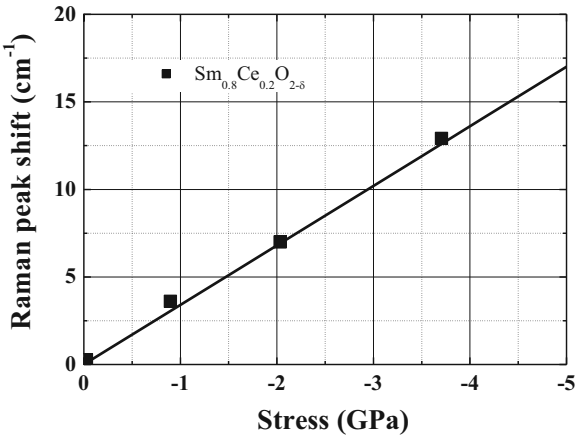

Figure 5 Hydrostatic pressure dependence of 20SDC Raman peak position at RT

Table 2 Hydrostatic and plane pressure dependence of F_{2g} Raman peak shift

Temperature [°C]	Hydrostatic stress [cm^{-1}/GPa]	Plane stress [cm^{-1}/GPa]
25	-3.40	-2.26
800	-4.61	-3.07

$$\frac{dV}{V} = \frac{3(1-2\nu)}{E}\sigma = \frac{\sigma}{K} \qquad (2)$$

and hydrostatic stress - volumetric strain relation,

$$\frac{dV}{V} = \left(1-\frac{2\nu}{E}\sigma\right)\left(1+\frac{1-\nu}{E}\sigma\right)^2 - 1 \qquad (3)$$

where k_R is Raman shift, γ_K is Grüneisen parameter, V is the volume, E is the Young's modulus, σ is the stress, ν

is the Poisson's ratio and K is bulk modulus. Young's modulus and Poisson's ratio was quoted from measured values by resonance method [1]. Result is shown in table 2. The stress measurement error is ± 22MPa at room temperature and ± 30MPa at 800°C.

3 · 3.Measurement of model cell under operating conditions

We evaluated the stress condition of the model cell in the operating conditions based on the knowledge from the 3.1 and 3.2. Figure 6 shows stress conditions of five model cells in operating conditions.(a)Before operation, the electrolyte of all cells contained the compressive tensile stress. (b)During temperature rising, the compressive stress decreased. (c)The stress conditions had changed into the tensile side by the inflow of the fuel.(d) Standard deviation had increased when the anode was oxidized. In addition, optical micrographs at 800°C are shown in figure 7. Many cracks were observed on the electrolyte after several hours from re-oxidizing. These results indicate the following. Compressive residual stress was introduced into the electrolyte during the fabrication process. It was decreased by the expansion of the components by the temperature rise. When the anode was reduced, the compressive stress of the electrolyte was relaxed by plastic deformation of the anode that caused by ductility of Ni-YSZ at high temperature [2]. The anode was re-oxidized when the operation was stopped. Since the expansion rate of Ni at that time is higher than the initial state, the tensile stress was occurred in the electrolyte by expansion from the re-oxidation of the anode. Electrolyte membrane was broken from tensile stress concentration point that exceeded the destruction strength. Destruction strength of typical doped ceria is reported to be 100 - 200MPa [3]. All of the re-oxidized cells were broken after several hours from re-oxidizing. But reduced cells did not reach the destruction nevertheless tensile stress of the 20SDC interlayer indicated 100MPa or more. One of the reasons is the effect of the temperature measurement at the measuring temperature of the furnace. If the difference of the real

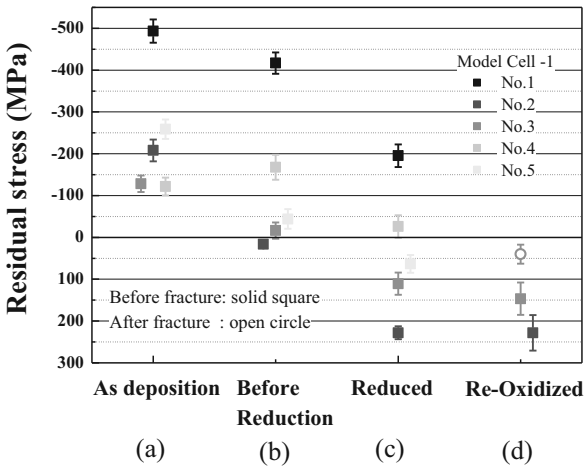

Figure 6 Variation of the stress conditions in 20SDC interlayer of model cells during operation

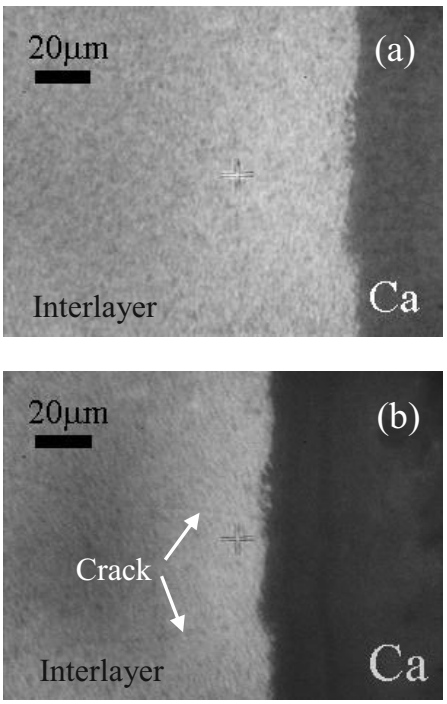

Figure 7 Optical images of cathode side of the model cell at 800°C (a) Before re-oxidized (b) After 3 hour from re-oxidized

temperature and obtained temperature becomes 10°C at the measurement at 800°C, the error of the stress becomes almost 80MPa. So, we need to establish an accurate temperature measurement method in the measurement point. Moreover, we ignore the effect of the cathode to the stress condition of the electrolyte membrane. In the future, we must analyze the mechanical properties of LSCF and the effect to the stress condition must be taken into account.

4. Concluding remarks

In this study, we developed the in-situ evaluation method for the stress conditions of SOFC based on the knowledge from temperature dependence and pressure dependence of Raman spectra of 20 SDC. For the quantification of stress, we measured temperature dependence and the pressure dependence of the F_{2g} Raman peak shift. The stress measurement error from the measuring instruments was 20 - 30 MPa. We applied this method to typical anode support cell at real operating conditions, and evaluated the effect on the state of stress of the electrolyte membrane from the temperature change and redox of the anode. During rising temperature, residual stress in the electrolyte was retained compressive stress. But the redox cycle of the anode causes residual stress of the electrolyte to the tensile stress. It was suggested from this in-situ evaluation that the risk of the destruction of the electrolyte is increased when the anode exposed to the redox cycle by stopping the operation. We were able to clarify the change of stress conditions during operation. This result indicates that Raman scattering spectroscopy is an effective *in-situ* evaluation method of stress conditions in SOFC. To increase the accuracy of the

measurement, we need to establish an accurate temperature measurement method in the measurement point. Further investigation of the effect to the electrolyte from LSCF is also needed.

5. Acknowledgement

This work was carried out as a part of the New Energy and Industrial Technology Development Organization (NEDO) project, "Development of Systems and Elemental Technology on SOFC".

References

[1] T. Kushi, K. Sato, A. Unemoto, S. Hashimoto, K. Amezawa, T. Kawada, *Journal of Power Sources*, 2011, 196 (19), 7989-7993.

[2] H. Kitahara, F. Iguchi, N. Sata, H. Yugami: *The 36th Symposium on Solid State Ionics in Japan Extended Abstracts*, 2010, 228-229

[3]T. Ishida, F. Iguchi, K. Sato, T. Hashida, H. Yugami, *Solid State Ionics*, 2005, 176, 2417-2421.

Study of Alcohol Fueled Single Chamber Solid Oxide Fuel Cells

Ryusuke Mihara, Noriko Sata, Kohei Oba, Yuu Sugawara, Yuki Nagao*, Fumitada Iguchi, Hiroo Yugami
Department of Mechanical Systems and Design, Graduate school of Engineering,
Tohoku University, Sendai 980-8579, Japan
*Department of Chemistry, Graduate School of Science, Kyoto University, Kyoto 606-8502, Kyoto Japan

E-mail: r_mihara@energy.mech.tohoku.ac.jp

ABSTRACT

In order to improve the performance of alcohol fueled Single Chamber SOFCs (SC-SOFCs), ethanol and dimetyl ether (DME) as the new fuels were tested. Thermodynamic equilibrium calculations were performed for the prediction of reactions in the furnace. Pt/ yttria-stabilized zirconia, $Ce_{0.9}Gd_{0.1}O_{1.9}$ or $SrCe_{0.95}Yb_{0.05}O_{3-\delta}$ /SSC cells using ethanol and DME generated lower cell voltages than methanol fueled cells. It was suggested that ethanol fueled SC-SOFCs was hard to handle the cell operation. Detail investigation into the potential of DME fueled SC-SOFCs through the cell test is demanded.

1. Introduction

Solid Oxide Fuel Cells (SOFCs) have high fuel flexibility and high overall efficiency because of high operating temperatures (800~900°C). However, both high operating temperature and separating anode and cathode cause problems such as thermal stress. Especially, failure of a gastight seal in a cell stack is a very serious problem, causing gas leakage and eventual destruction of the stacked cells. Operation in a fuel-air mixed atmosphere, i.e. in a separator-free single chamber, is known as one of the solutions of this problem. This type of SOFC is called Single-Chamber SOFC (SC-SOFC). SC-SOFC has several advantages. Electrolytes can be porous and the risk of carbon deposition would be lower. Separator-free design may downsize the system of SOFCs.

In recent studies, SC-SOFCs with a mixture feed of methane and air have shown as high performance as conventional SOFCs[1-3]. However, methane and other gas fuels are difficult for storage. On the other hand, alcohols such as methanol and ethanol which are liquid in ambient condition are easy to store and portable. Furthermore, liquid fuels have higher energy density than gas fuels. Considering those advantages of alcohol fuels, alcohol fueled SC-SOFCs have potential for applications to portable electronic devices.

We have studied methanol fueled SC-SOFCs as a starter of alcohol fueled SC-SOFCs. Compared with methane fueled SC-SOFCs, however, the performance was relatively low. For practical applications, development of the performance is demanded, thus we have to resolve several problems of alcohol fueled SC-SOFCs, in particular the low cell voltage and the high electrode reaction resistance. In this study, we tried new fuels for SC-SOFCs, ethanol and dimethyl ether (DME) as one of the ways to develop the performance of alcohol fueled SC-SOFCs. Ethanol and DME have same molecular composition and both fuels are harmless to human unlike methanol.

2. Method

In order to predict what reactions could occur in ethanol- and DME-air mixture gas, we simulated the reactions by thermodynamic equilibrium calculations with Thermodynamic Database MALT for Windows (Kagaku Gijutsu-Sha).

Yttria-stabilized zirconia (YSZ) and $Ce_{0.9}Gd_{0.1}O_{1.9}$ (GDC) possessing oxygen ion conductivity and $SrCe_{0.95}Yb_{0.05}O_{3-\delta}$ (SCYb) possessing proton conductivity were used as the electrolyte materials. YSZ powder was purchased from TOSOH CORPORATION. GDC powder was prepared by solid state reaction method. These powders were pressed into pellets, and sintered. SCYb pellets were purchased from TYK Corporation. These pellets were ca. 1mm thick. The surface of the pellet electrolytes was screen-printed with a slurry of $Sm_{0.5}Sr_{0.5}CoO_3$ (SSC) cathode, and calcined. SSC powder was prepared by solid state reaction method. The opposite surface of the electrolytes were sputtered Pt as anode. Electrode area was ca. $1cm^{-1}$.

Fig. 1 shows schematic illustration of the experiment system. The cell was set up in grass tube, and fuel-air mixture gas was supplied to the cell at total flow rate 60mL min^{-1}. Two thermocouples observed the furnace temperature and the temperature adjacent to the cell, respectively. As electric collector, Au meshes were on the surfaces of both electrodes. The outlet gas was analyzed on gas chromatography.

3. Results and Discussion

Ethanol and DME have two oxidation reaction, partial oxidation (eq.1) and deep oxidation (eq.2).

$$C_2H_6O + \frac{1}{2}O_2 \rightarrow 2CO + 3H_2 \quad (1)$$

$$C_2H_6O + 3O_2 \rightarrow 2CO_2 + 3H_2O \quad (2)$$

Other various reactions may occur in the ethanol- or DME-air mixture gas in the furnace.

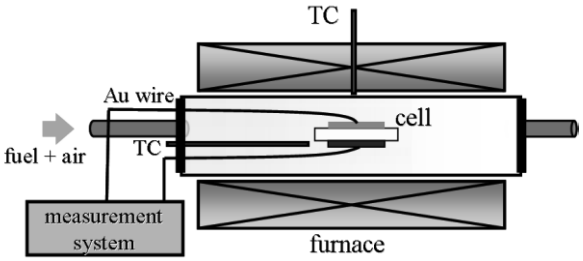

Fig. 1 Schematic illustration of the experiment system.

Fig. 2 shows the results of the thermodynamic equilibrium calculations at 300°C. Calculated molar number of the components at equilibrium in ethanol-air mixed gas corresponded exactly to the result of DME-air mixture gas because ethanol and DME have same molecular composition. At equilibrium, only CO_2 and H_2O were produced in fuel-air mixture gas whose fuel/O_2 molar ratio was less than 0.33, the stoichiometric ratio of the deep oxidation (eq.2). On the other hand, in fuel-rich gas over the stoichiometric ratio, not only H_2O and CO_2 but also H_2 were produced because of the partial oxidation. However, the amount of carbon deposition got increased with fuel/O_2 molar ratio. Thus, ethanol- or DME-air mixture gas which was closely mixed at the stoichiometric ratio of the deep oxidation was used for supply gas to the cell.

Fig. 3 shows OCVs of the Pt/GDC/SSC cell at several experimental conditions. The OCVs turned into positive across the stoichiometric ratio of the deep oxidation. The highest OCV were measured at 300°C. Using oxygen ion conductors as electrolytes of fuel cells, OCV depends on the oxygen partial pressure gradient between the two electrodes. From the results of gas chromatography without the cell, little oxygen consumption was observed at 300°C while the consumption was measurably observed at 400°C and 500°C. Consequently, at 300°C, the ethanol reforming reaction may occur just by the catalytic activity of the

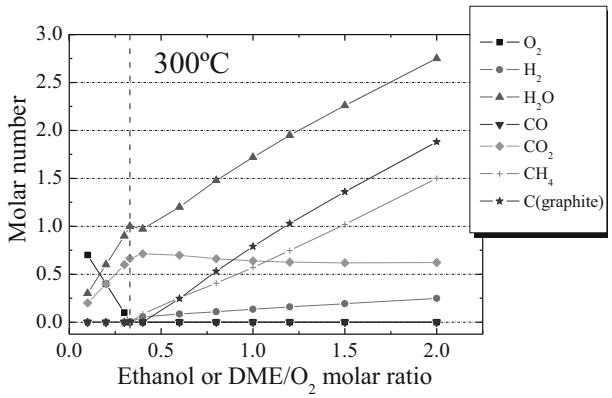

Fig. 2 Calculated molar number of the components at equilibrium in ethanol- or DME-air mixture gas at 300°C.

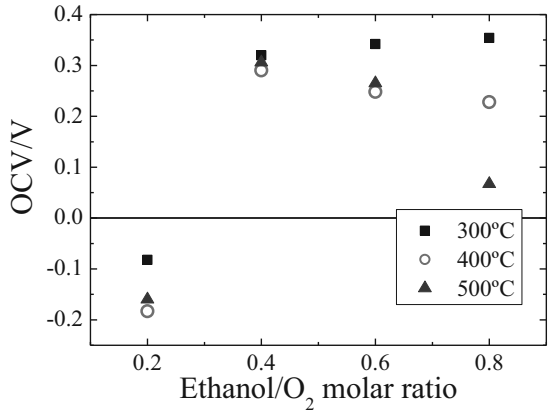

Fig. 3 OCVs of the ethanol fueled cell (Pt/GDC/SSC) as a function of ethanol-oxygen molar ratio.

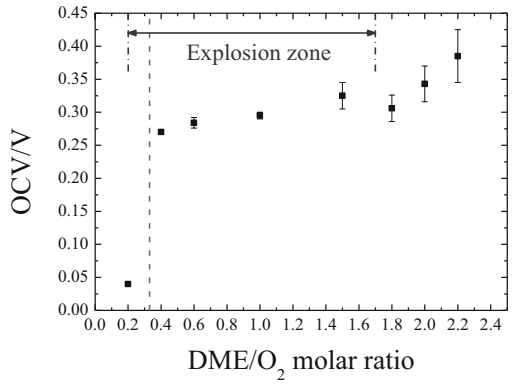

Fig. 4 OCVs of the DME fueled cell (Pt/YSZ/SSC) as a function of DME-oxygen molar ratio at 300°C.

electrodes, thus the largest oxygen partial pressure gradient between the electrodes was arisen at 300°C. However, the OCVs were lower than the OCVs using methanol (ca. 0.5V). In addition, the deteriorations of the anode such as terrible carbon deposition on the surface and detachment from the electrolyte were observed after the cell test. This means it is hard to handle the cell operation using ethanol. The deteriorations were more terrible in case of the cell using SCYb as the electrolyte, and the cell voltages were unstable.

Fig. 4 shows OCVs of the Pt/YSZ/SSC cell as a function of DME-oxygen molar ratio at 300°C. The OCVs were nearly equal the OCVs of the ethanol fueled cell. At DME-rich conditions, the cell voltages cyclically vibrated. This must result from PID controlling of the temperature controller. The unstable cell voltages made it hard to measure the electrochemical properties of the cell such as the discharge properties and the impedance spectra. Tuning of the temperature controller was demanded.

4. Concluding remarks

The thermodynamic equilibrium calculations of ethanol- and DME-air mixture gas showed that the reaction products were different across the stoichiometric ratio of the deep oxidation. Ethanol fueled SC-SOFCs generated lower cell voltages than methanol fueled SC-SOFCs, and the anodes were damaged during the generations. The OCVs of the DME fueled SC-SOFC were nearly equal the OCVs of the ethanol fueled cell. In order to detail electrochemical properties of the cell, we must stabilize the cell voltage by tuning the temperature controller.

For the future, first, we should investigate in detail the potential of DME fueled SC-SOFCs through the cell test. Then the reduction of the electrode reaction resistance is demanded by development of the electrodes.

References

[1] X. Jacques-Bedards, T.W. Napporn, R. Roberge, M. Meunier, J. Power Sources, **153** (2006) 108.
[2] T. Hibino, A. Hashimoto, M. Yano, M. Suzuki, S. Yoshida, M. Sano, J. Electrochem. Soc. **149** (2002) A133
[3] A. Tomita, S. Teraishi, M. Nagao, T. Hibino, M. Sano, J. Electrochem. Soc. **153** (2006) A956

Nonstoichiometry and Thermoelectric Efficiency of β-$Ag_{2+\delta}Te$

Wonhyo Joo
Department of Materials Science and Engineering, Seoul National University, Seoul 151-744, South Korea
templerj@snu.ac.kr

ABSTRACT

$Ag_{2+\delta}Te$ is one of the host materials of promising thermoelectric Pb-Sb-Ag-Te (LAST) compounds. Because $Ag_{2+\delta}Te$ undergoes an n-type-to-p-type transition within its single phase region, it exhibits considerable variations in electronic properties and consequently thermoelectric efficiency with nonstoichiometry (δ). In this work, we have measured the electrical conductivity and thermopower of β-$Ag_{2+\delta}Te$ as function of nonstoichiometry across its entire stability field at 373K. The behaviors of electrical properties are explained and the way to optimize the thermoelectric efficiency is proposed.

1. Introduction

Efficiency of thermoelectric energy conversion is normally formulated as figure of merit,

$$Z = \frac{\sigma\theta^2}{\kappa} \quad (1)$$

where σ, θ, and κ are electrical conductivity, thermopower and thermal conductivity, respectively. In this formula, the numerator $\sigma\theta^2$ is called power factor (PF) and it is also an important factor to evaluate the thermoelectric efficiency.

$Ag_{2+\delta}Te$ is one of the host materials of promising thermoelectric Pb-Sb-Ag-Te (LAST) compounds. Electronic properties such as σ, θ, and consequently PF are changed with nonstoichiometry δ, because the concentration of electron and hole are changed considerably. In contrast to higher temperature cubic α-$Ag_{2+\delta}Te$, lower temperature monoclinic β-$Ag_{2+\delta}Te$ has not been yet examined precisely[1, 2]. In this work, σ, θ, and PF of β-$Ag_{2+\delta}Te$ are examined at 373K. Behaviors of electrical properties are explained and the way to optimize the thermoelectric efficiency is proposed.

2. Experimental

$Ag_{2+\delta}Te$ specimen was prepared by following procedure. First, Ag_2Te granule (Kojundo, 99.9%, Japan) was ball milled and screened with 100 μm-mesh-sieve. Second, the powder was sintered at 700°C for 24 hours and the sintered sample was cut into parallelepiped. The phase purity of the sample was examined by X-ray diffraction at room temperature, and microstructure was observed by Scanning Electron Microscope (SEM). The bulk density of the sample is measured by Archimedes method.

In order to synthesize solid electrolyte $RbAg_4I_5$, 1:4 mixture of RbI (Aldrich, 99.9%, USA) and AgI (Aldrich, 99%, USA) was melted at 440°C and quenched to room temperature. Quenched powder was annealed at 150°C for 24 hours, ground and shaped into a disk, and finally sintered at 150°C for 8 hours.

Nonstoichiometry of $Ag_{2+\delta}Te$ specimen was adjusted by coulometric titration technique. Figure 1 is the schematic diagram of cell design. Titration current was flown between the sample and pure silver, a source or sink of Ag^+ ion, through solid electrolyte $RbAg_4I_5$, which has ionic conductivity as high as 0.1 $\Omega^{-1}cm^{-1}$ even at room temperature while electronic conductivity is negligibly small. Amount of injected or extracted Ag^+ ion is calculated by Faraday equation,

$$\Delta n_{Ag} = \frac{It}{z_{Ag}F} \cdot \quad (2)$$

In this equation, Δn_{Ag}, I, t, z_{Ag}, and F are the change in number of moles of silver ions, the amperage of injected current, duration of titration, valence number of Ag^+ ion, and Faraday constant respectively.

Ag nonstoichiometry of $Ag_{2+\delta}Te$ specimen is

$$\delta = \delta^* + \Delta\delta = \delta^* + \frac{\Delta n_{Ag}}{n^o_{Ag}} = \delta^* + \frac{It}{z_{Ag}F} \cdot \frac{1}{n^o_{Ag}}, \quad (3)$$

δ^* is initial nonstoichiometry of as-sintered sample, and n^o_{Ag} is mole number of the specimen.

During the experiment, Ag activity was monitored by measuring the EMF between $Ag_{2+\delta}Te$ sample and pure silver electrode as a reference, whose Ag activity is equal to unity. Electrical conductivity was measured by general 4-point-probe method with outer thermocouples as current probes and inner Pt wires as voltage probes. Thermopower was measured by raising the temperature difference between two ends of the sample with local heater placed near the sample as shown in Figure 1, and reading the thermal voltage by heat pulse method.

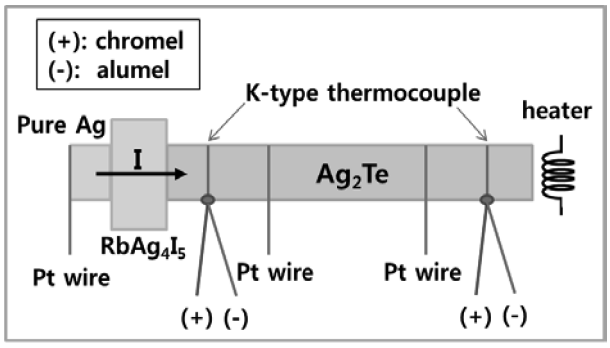

Fig. 1 Schematic diagram of the cell.

3. Results and Discussion

The X-ray diffraction pattern shows that the sample has monoclinic β-$Ag_{2+\delta}Te$ single phase. The bulk density of the sample is (71.0±1.0) % relative to the theoretical density, and porous microstructure of the sample is also observed by SEM image as shown in Figure 2.

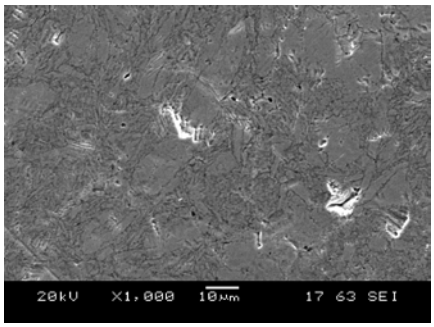

Fig. 2 SEM image of β-$Ag_{2+\delta}Te$ sample.

The relation between Ag nonstoichiometry change and Ag activity at 373K is shown in Figure 3. Because β-$Ag_{2+\delta}Te$ undergoes n-type-to-p-type transition within its single phase region, the stoichiometric point exists within the β-$Ag_{2+\delta}Te$ single phase region, and it can be determined using defect chemical analysis, in short,

$$\delta = \frac{V_m}{N_A}(n-p) = 2\frac{V_m}{N_A}K_i^{1/2}\sinh\left(\ln\left(\frac{a_{Ag}}{a^o_{Ag}}\right)\right). \quad (4)$$

In this equation, V_m is molar volume, N_A is Avogadro number, n is density of electrons, p is density of holes, K_i is equilibrium constant of n-p pair generation and a^o_{Ag} is Ag activity at stoichiometric point. Figure 3 shows best fitted line to equation (3) and δ was determined from the fitting result.

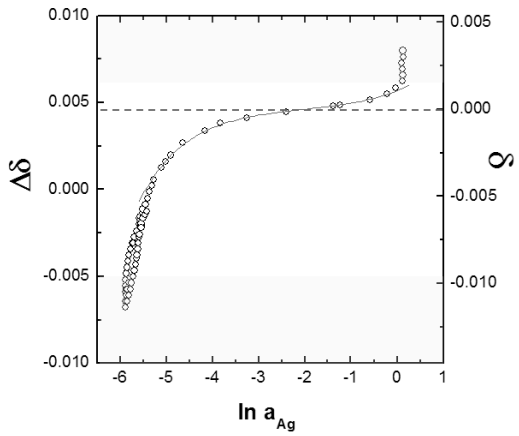

Fig. 3 The relation between Ag nonstoichiometry change and Ag activity. Solid line is best fitted to equation 4 and dashed line indicates inflexion point of the curve, which means stoichiometric condition (δ=0). Shaded regions are 2-phase regions.

Electrical conductivity, thermopower, and power factor of β-$Ag_{2+\delta}Te$ with δ at 373K is shown in Figure 4. Electrical conductivity increases with δ and it undergoes considerable change when δ=0. It indicates that the electrical conductivity of β-$Ag_{2+\delta}Te$ is higher when the sample is n-type, that is, mobility of electrons is far higher than that of holes. Thermopower has maximum value near δ=0 and it decreases with increasing |δ|. Consequently, the power factor of β-$Ag_{2+\delta}Te$ increases with δ, and it shows nearly no change when δ>0, even in Ag and β-$Ag_{2+\delta}Te$ two phase region.

Changing nonstoichiometry, thermoelectric efficiency can be improved by adjusting density of electrons and holes. This method can be adapted to other materials, especially those undergo n-type-to-p-type transition.

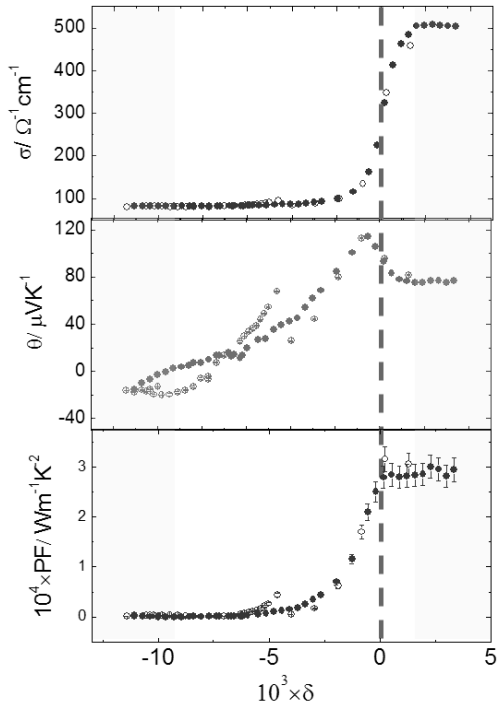

Fig. 4 Conductivity, thermopower, and power factor of β-$Ag_{2+\delta}Te$ sample. Dashed line indicates stoichiometric point (δ=0), shaded regions are 2-phase regions.

4. Conclusion

Electrical conductivity and thermopower of β-$Ag_{2+\delta}Te$ is measured at 373K with nonstoichiometry change. Because β-$Ag_{2+\delta}Te$ undergoes n-type-to-p-type transition within its single phase region, it exhibits drastic variation of electrical conductivity and thermopower. Power factor is calculated from electrical conductivity and thermopower and it increases with nonstoichiometry. When δ>0, even in Ag and β-$Ag_{2+\delta}Te$ two phase region, power factor is optimized and it shows little change. Possibility of changing nonstoichiometry to improve thermoelectric efficiency is confirmed.

References

[1] S.–Y. Miyatani, J. Phys. Soc. Jap., **13** (1958), 341
[2] A. Bürgermeister and W. Sitte, Solid State Ionics, **141-142** (2001), 331

Eighth International Conference on Flow Dynamics
November 9 - November 11, 2011

Effects of Temperature and Oxygen Partial Pressure on Mechanical Properties of $La_{0.6}Sr_{0.4}Co_{1-y}Fe_yO_{3-\delta}$

Yuta Kimura[a], Takuto Kushi[a], Shin-Ichi Hashimoto[a], Satoshi Watanabe[a], Koji Amezawa[a], Tatsuya Kawada[a], Yasuhiro Fukuda[b], Atsushi Unemoto[b], Keiji Yashiro[b], Junichiro Mizusaki[b], Kazuhisa Sato[c], and Toshiyuki Hashida[c]
[a] Graduate School of Environmental Studies, Tohoku University, Sendai, Miyagi 980-8579, Japan
[b] IMRAM, Tohoku University, Sendai, Miyagi 980-8577, Japan
[c] FRRI, Tohoku University, Sendai, Miyagi 980-8579, Japan
kimura@ee.mech.tohoku.ac.jp

ABSTRACT

Elastic modulus of $La_{0.6}Sr_{0.4}CoO_{3-\delta}$ (LSC), $La_{0.6}Sr_{0.4}Co_{0.2}Fe_{0.8}O_{3-\delta}$ (LSCF6428) and $La_{0.6}Sr_{0.4}FeO_{3-\delta}$ (LSF) was evaluated in the temperature range between 298 to 1173 K, and the oxygen partial pressure, $P(O_2)$, range between 1×10^{-1} to 1×10^{-4} bar using the resonance method. Lattice expansion and crystal structure change were considered to have large effect on elastic modulus at high temperatures.

1. Introduction

There are great expectations for the commercialization of Solid Oxide Fuel Cells (SOFCs) since SOFCs have many advantages such as high power generation efficiency, fuel flexibility and high-temperature waste heat. Hence in Japan, New Energy and Industrial Technology Development Organization (NEDO) has promoted fundamental and demonstrative research projects under cooperation with domestic companies in order to commercialize SOFCs[1]. From their researches, it was revealed that there are still problems in aspects of durability and reliability of SOFCs. One of main causes which deteriorates durability and reliability is mechanical damages in SOFC components, *e. g.* cracks and delaminations[2, 3]. In order to effectively suppress mechanical damages in SOFC components, it is necessary to understand mechanical properties of SOFC components. Materials used in SOFCs are exposed to high temperatures and a certain oxygen potential gradient, and distributions of temperature and oxygen potential vary depending on operating conditions. Thus, knowledge on mechanical properties as functions of temperature and oxygen partial pressure, $P(O_2)$, are indispensable for the precise evaluation of mechanical stresses and operational margin of SOFCs.

$La_{1-x}Sr_xCo_{1-y}Fe_yO_{3-\delta}$ (LSCF) is a widely used material as a cathode for SOFCs because of its high mixed electronic-ionic conductivity and fast oxygen surface exchange[4]. A number of studies has addressed that the oxygen nonstoichiometry, the lattice constants and crystal structures of LSCF vary with temperature and $P(O_2)$[5-16]. Such variations of oxygen nonstoichiometry, the lattice constants and crystal structures may have influence on the mechanical properties of LSCF. However, there are few studies which investigated the effect of temperature and $P(O_2)$ on the mechanical properties. Thus we evaluated mechanical properties of LSCF as functions of temperature and $P(O_2)$, and discussed in terms of the oxygen nonstoichiometry, the lattice constants and the crystal structures.

2. Experimental

2.1. Sample Preparation

Powders of $La_{0.6}Sr_{0.4}Co_{1-y}Fe_yO_{3-\delta}$ series (y = 0, *i. e.* LSC, 0.8, *i. e.* LSCF6428 and 1.0, *i. e.* LSF) were prepared by Pechini method or obtained from AGC SEIMI CHEMICAL Co., Ltd.. Powders were first hydrostatically pressed at 150 MPa and sintered at 1473 ~ 1573K for 6 hours and then slowly cooled (106K / h) to avoid cracking. The sintered specimens were cut into rectangular shape with the size of *ca.* 45×10×1.5mm and polished with a diamond paste of 3μm. Relative densities of obtained samples were over 95%.

2.2. Measurements of mechanical properties

The apparent modulus of elasticity of LSCF was measured using an elastic modulus and an internal friction meter (JE, JG, EGII - HT, Nihon technoplus Co. Ltd.). In this work, the values obtained from the flexural and the torsional oscillations were defined as Young's modulus, E, and the shear modulus, G, respectively. JE and JG perform free hold resonance measurements while EGII – HT performs cantilever resonance measurements. Since free hold resonance measurements have higher measurement accuracy than cantilever measurements[17], Values obtained by JE and JG at room temperature were used for calibrations of the values obtained by EGII - HT. Flexural and torsional oscillations were electrostatically excited and applied to samples. JE and JG detected resonance frequency for each oscillation by an acoustic wave displacement sensor while EGII - HT detected the resonance frequencies by an eddy current displacement sensor.

With the flexural resonance frequency (f_f), the torsional resonance frequency (f_t) and the sample dimension, Young's modulus (E) and the shear modulus (G) were calculated as follows,

$$E = \frac{4\pi^2 L^4}{\alpha^2} \cdot \frac{\rho S}{I} \cdot f_f^{\,2} \quad (1)$$

$$G = \frac{16L^2 \cdot \rho K^2}{\beta} \cdot f_t^{\,2} \quad (2)$$

where L, α, ρ, S, I, K, β are the length of a sample, a constant given by boundary condition, the density of a sample, the cross-sectional area of a sample, the second moment of area, the adjustment parameter, the inertia moment of the driven section, respectively.

The temperature dependences and the $P(O_2)$ dependences of elastic modulus such as Young's modulus and the shear modulus was evaluated. The measurement of temperature dependences was carried out in the temperature range between 298 and 1173 K under constant $P(O_2)$ of 1 x 10^{-1} and 1 x 10^{-4} bar. In addition, the measurement of the $P(O_2)$ dependences was carried out in the $P(O_2)$ range between 10^{-1} and 10^{-4} bar at constant temperatures, 873 K, 973 K, 1073 K and 1173 K. $P(O_2)$ in a sample chamber was controlled by flowing mixture gases of O_2 and Ar, and was monitored by an YSZ oxygen sensor. Measurements were repeated at each condition until measured values reached constant.

3. Results and Discussion

3. 1. Temperature dependences of elastic modulus of LSCF

The temperature dependences of elastic modulus such as Young's modulus and the shear modulus of LSCF series (y = 0, 0.8, 1.0) under $P(O_2)$ of 1.0 x 10^{-1} and 1.0 x 10^{-4} bar are shown in Fig. 1 and Fig. 2, respectively. Under $P(O_2)$ of 1.0 x 10^{-1} bar, elastic modulus of LSC gradually decreased from 298 to 773 K and then sharply increased in the temperature range from 823 to 923 K. Above 923 K, elastic modulus gradually decreased with increasing temperature. Elastic modulus of LSCF6428 and LSF under $P(O_2)$ of 1.0 x 10^{-1} bar showed similar trends. They gradually decreased from 298 to 823 K and then sharply increased above 873 K. As is the case under $P(O_2)$ of 1.0 x 10^{-1} bar, elastic modulus of LSCF with each composition decreased with increasing temperature at low temperatures and sharply increased at high temperatures under $P(O_2)$ of 1.0 x 10^{-4} bar. However, the temperatures at which elastic modulus sharply increased were 50 – 100 K lower than under $P(O_2)$ of 1.0 x 10^{-1} bar for each composition.

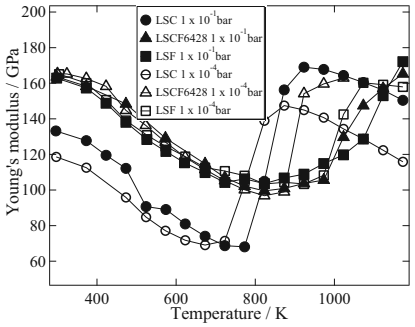

Fig. 1. Temperature dependences of Young's modulus of LSC, LSCF6428 and LSF under $P(O_2)$ of 1.0 x 10^{-1} and 1.0 x 10^{-4} bar. Closed symbols indicate values measured under $P(O_2)$ of 1.0 x 10^{-1} bar and open symbols indicate values under $P(O_2)$ of 1.0 x 10^{-4} bar. Solid lines are guides to the eye.

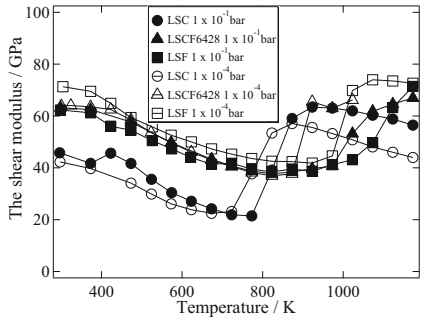

Fig. 2. Temperature dependences of the shear modulus of LSC, LSCF6428 and LSF under $P(O_2)$ of 1.0 x 10^{-1} and 1.0 x 10^{-4} bar. Closed symbols indicate values measured under $P(O_2)$ of 1.0 x 10^{-1} bar and open symbols indicate values under $P(O_2)$ of 1.0 x 10^{-4} bar. Solid lines are guides to the eye.

Such a sharp increase in elastic modulus of LSCF at high temperatures is distinguishing compared with Young's modulus of aluminum oxide which monotonically decreases with increasing temperature[18]. The temperature dependence of Young's modulus of aluminum oxide can be explained as a result of thermal lattice expansion. A lattice expansion reduces bond strength in a crystal due to the increase in atomic distances and hence is assumed to reduce Young's modulus. To take this fact into considertaiton, it is suggested that sharp increases in elastic modulus of LSCF at high temperatures were not due to thermal lattice expansion but to some other factors.

Oxygen nonstoichiometry and crystal structures of LSCF vary with temperature and $P(O_2)$[5–16]. Thus it is possible that elastic modulus of LSCF was influenced by the change in oxygen nonstoichiometry and crystal structures. Therefore, the influence of the change in oxygen nonstoichiometry was examined first. Fig. 3 shows the oxygen nonstoichiometry, 3-δ, in LSCF series as a function of temperature which were taken from literatures[5, 9, 16]. Oxygen vacancy concentrations in all LSCF composition monotonically increase with increasing temperature at high temperatures.

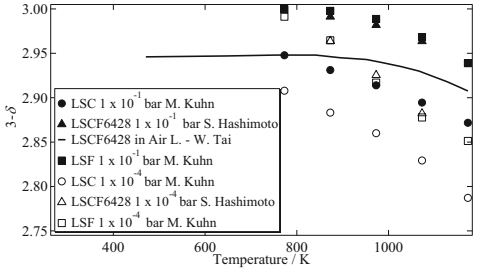

Fig. 3. Oxygen nonstoichiometry of LSC, LSCF6428 and LSF in air or under $P(O_2)$ of 1.0 x 10^{-1} and 1.0 x 10^{-4} bar. Closed symbols indicate values measured under $P(O_2)$ of 1.0 x 10^{-1} bar and open symbols indicate values under $P(O_2)$ of 1.0 x 10^{-4} bar. A solid line indicates the data taken from Tai *et al.*.

In previous study of our group, the correlation between elastic modulus and oxygen nonstoichiometry of

$(Gd_2O_3)_{0.1}(CeO_2)_{0.9}$ (GDC) was discussed[19]. It is concluded that the reductive lattice expansion caused by the increase in oxygen vacancy concentration reduced the elastic modulus of GDC. However, contrary to GDC, the elastic modulus of LSCF began to increase considerably at the temperatures at which oxygen vacancy concentration started to increase. A possible explanation for such contradicting results is the phase transition. In the case of LSCF, increase in oxygen vacancy concentration also cause phase transition from rhombohedral to cubic [12, 14, 16]. In addition, it is reported that crystal structure change has large influence on elastic moduli of ceramics [20-22].Young's modulus of LSCF6428 is shown in Fig. 4 as a function of rhombohedral angle. Rhombohedral angle of LSCF6428 was calculated from data of *in-situ* XRD. At room temperature, it was about 60.30° and the crystal structure could be regarded as rhombohedral. In contrast, if the rhombohedral angle is 60.00°, the crystal structure of LSCF6428 is regarded as cubic. As is seen in Fig. 4, rhombohedral angle of LSCF6428 did not become 60.00° but it seemed to converge on $\alpha = 60.07°$. As the rhombohedral angle approaches to 60.07° from 60.30°, Young's modulus of LSCF6428 appeared to first decrease gradually and then sharply increase when the rhombohedral angle became very close to $\alpha = 60.07°$.

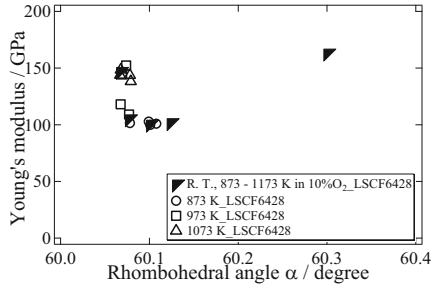

Fig. 4. Young's modulus of LSCF6428 as a function of rhombohedral angle. Closed symbols indicate the data obtained from the measurement of temperature dependence under $P(O_2)$ of 1.0 x 10^{-1} bar and open symbols indicate the data obtained from measurements of $P(O_2)$ dependence.

The change in the Young's modulus due to that in the crystal structure may be interpreted in terms of the change in the Gibbs energy curve. A similar interpretation is often given when the change in the dielectric constant of ferroelectric ceramics due to that in the crystal structure is discussed. Displacements of atoms are induced by an electrostatic force when considering dielectric properties, while by a mechanical stress when considering elastic properties. Thus, it could be reasonable to discuss the change in the elastic properties accompanied by the crystal structure change based on a similar interpretation as that for the dielectric properties. Schematic images of the Gibbs energy curves for LSCF at various temperatures were depicted in Fig. 5. The horizontal axis for each Gibbs energy curves is the interatomic distance. Since the interatomic distance in the rhombohedral phase is longer than that in the cubic phase, the Gibbs energy curve for the rhombohedral LSCF is located at longer interatomic distance side compared with the curve for the cubic LSCF. Considering the stability of the rhombohedral, the Gibbs energy curve for the rhombohedral phase should be lower than that for the cubic phase at lower temperatures. Total Gibbs energy curve is given as the sum of two Gibbs energy curves. The atoms stay to averagely keep the interatomic distance for the lowest Gibbs energy, *i. e.* the bottom of the curve, when no external forces such as mechanical and electrostatic forces are applied to the crystal. As temperature increases, the Gibbs energy curve for the cubic phase becomes lower because the cubic phase is more stable at higher temperature and comparable to that of the rhombohedral phase at the phase transition temperature. As temperature approaches to the phase transition temperature, the atoms are more likely to move between the bottoms of the two curves when external forces such as mechanical forces are applied. This means the crystal becomes more deformable. the elastic modulus decreases. At further higher temperatures, the Gibbs energy curve for the cubic phase becomes lower than that for the rhombohedral phase, meaning that the atoms are trapped in the bottom of the curve for the cubic phase. Then the crystal becomes less deformable. Based on hypothesis mentioned above, elastic modulus is considered to first decrease with increasing temperature, reach a minimum at the phase transition temperature and increase at further higher temperature. Considering above discussion, it is assumed that the temperature dependence of elastic modulus of LSCF are associated with not only thermal lattice expansion but also the change in deformability due to the phase transition.

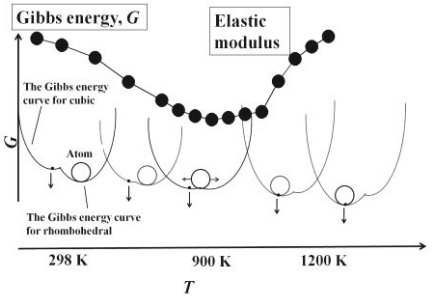

Fig. 5. A schematic image of Gibbs energy and stable sites of an atom at various temperatures.

3. 2. $P(O_2)$ dependences of Young's modulus of LSCF6428

$P(O_2)$ dependences of Young's modulus of LSCF6428 are described in Fig. 6. $P(O_2)$ dependences showed considerably different trends at each temperature. At 873 K, Young's modulus was almost independent of $P(O_2)$. On the other hand, it considerably increased with decreasing $P(O_2)$ at 973 K. At 1073 K, Young's modulus slightly increased with decreasing $P(O_2)$ down to 5 $\times 10^{-3}$ bar and then decreased in further lower $P(O_2)$. At 1173 K, it monotonically decreased with decreasing $P(O_2)$. Such complicated $P(O_2)$

dependences of Young's modulus of LSCF6428 are may be explained by both of reductive lattice expansions and the change in deformability due to the phase transition. The decrease in $P(O_2)$, more practically, the increase in oxygen vacancy concentration of LSCF6428 induces not only reductive lattice expansion but also the phase transition from rhombohedral to cubic. As mentioned above, the reductive lattice expansion is considered to decrease Young's modulus. In contrast, the change in deformability due to the phase transition is assumed to increase Young's modulus right above the phase transition temperature. At 873 K, the change in oxygen vacancy concentration with decreasing $P(O_2)$ is relatively small and hence Young's modulus is considered to be almost independent of $P(O_2)$. Meanwhile, at 973 K at which the sharp increase in Young's modulus was observed in temperature dependence measurement, it is appeared that the effect of the phase transition is much larger than the effect of the reductive lattice expansion and thus Young's modulus increased with decreasing $P(O_2)$. At 1073 K at which the increase in Young's modulus is more relaxed than 973 K, it is assumed that the phase transition is close to finish and hence effects of the phase transition and the reductive lattice expansion became comparable. As a result, both increase and decrease in Young's modulus were observed at 1073 K. At 1173 K, the phase transition is assumed to finish and therefore have no effect on Young's modulus. Consequently, Young's modulus monotonously decreased with decreasing $P(O_2)$ due to the reductive lattice expansion.

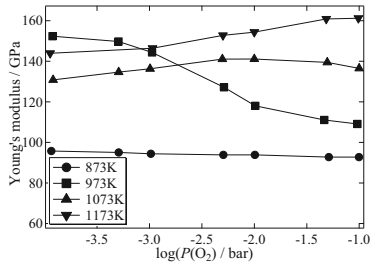

Fig. 6. $P(O_2)$ dependence of Young's modulus of LSCF6428 measured at 873, 973, 1073 and 1173 K. Solid lines are guides to the eye.

4. Conclusions

Elastic modulus of $La_{0.6}Sr_{0.4}CoO_{3-\delta}$ (LSC), $La_{0.6}Sr_{0.4}Co_{0.2}Fe_{0.8}O_{3-\delta}$ (LSCF6428) and $La_{0.6}Sr_{0.4}FeO_{3-\delta}$ (LSF) was evaluated as functions of temperature and $P(O_2)$ with the resonance method. The sharp increase in the Young's modulus was observed for each composition at high temperatures. Such considerable changes in the Young's modulus were correlated with the phase transition. The $P(O_2)$ dependences showed different trends at each temperature. Such behavior was explained as resulting from both the reductive lattice expansion and the phase transition induced by the change in oxygen vacancy concentration.

Acknowledgement

This work was made as a part of the research project on development of systems and elemental technology on SOFC, which was supported by the New Energy and Industrial Technology Development Organization (NEDO), Japan.

References

[1] K. Hosoi, M. Ito, M. Fukae, *ECS Transactions*, **35** (2011)11.
[2] J. Malzbender, R. W. Steinbrech, L. Singheiser, *Fuel Cells*, **6**(2009)785.
[3] K. Sato, H. Omura, T. Hashida, K. Yashiro, H. Yugami, T. Kawada, J. Mizusaki, *J. Testing and Evaluation*, **25**(2009)2375.
[4] M. Katsuki, S. Wang, M. Dokiya, T. Hashimoto, *Solid State Ionics*, **156**(2003)453-461.
[5] S. Hashimoto, Y. Fukuda, M. Kuhn, K. Sato, K. Yashiro, J. Mizusaki, *Solid State Ionics*, **181**(2010)1713.
[6] J. Mizusaki, Y. Mima, S. Yamauchi, K. Fueki, *J. Solid State Chemistry*, **80**(1989)102.
[7] J. Mizusaki, M. Yoshihiro, S. Yamauchi, K. Fueki, *J. Solid State Chemistry*, **58**(1985)257.
[8] Y. Fukuda, S. Hashimoto, K. Sato, K. Yashiro, J. Mizusaki, *ECS Transactions*, **25**(2009)2375.
[9] L. –W. Tai, M. M. Nasrallah, H. U. Anderson, D. M. Sparlin, S. R. Sehlin, *Solid State Ionics*, **76**(1995)273.
[10] T. Kawada, J. Suzuki, M. Sase, A. Kaimai, K. Yashiro, Y. Nigara, J. Mizusaki, K. Kawamura, H. Yugami, *J. the Electrochemical Society*, **149**(2002)E252.
[11] A. N. Petrov, O. F. Kononchuk, A. V. Andreev, V. A. Cherepanov, P. Kofstad, *Solid State Ioncis*, **80**(1995)189.
[12]A. Mineshige, M. Kobune, S. Fujii, Z. Ogumi, M. Inaba, T. Yao, K. Kikuchi, *J. the Solid State Chemistry*, **142**(1999)374.
[13] B. X. Huang, J. Malzbender, R. W. Steinbrech, L. Singheiser, *Solid State Ionics*, **180**(2009)241.
[14] S. Wang, M. Katsuki, M. Dokiya, T. Hashimoto, *Solid State Ionics*, **159**(2003)71.
[15] A. Fossdal, M. Menon, I. Waernhus, K. Wiik, M. –A. Einarsrud, T. Grande, *J. the American Ceramic Society*, **87**(2004)1952.
[16] M. Kuhn, S. Hashimoto, K. Sato, K. Yashiro, J. Mizusaki, "Oxygen Nonstoichiometry, Thermo-chemical Stability and Crystal Structure of $La_{0.6}Sr_{0.4}CoO_{3-\delta}$and $La_{0.6}Sr_{0.4}FeO_{3-\delta}$", MS & T'10, Houston, U. S. A., October, 2010.
[17] Test method for Young's modulus of metallic materials at elevated temperature, Japanese Industrial Standards, JIS Z2280, 1993.
[18] J. B. Wachtman, Jr., W. E. Tefft, D. G. Lam, Jr., C. S. Apstein, *Physical review*, **122**(1961)1754.
[19] K. Amezawa, T. Kushi, K. Sato, A. Unemoto, S. Hashimoto, T. Kawada, *Solid State Ionics*, to be published (2011).
[20] T. Kushi, K. Sato, A. Unemoto, S. Hashimoto, K. Amezawa, T. Kawada, *J. Power Sources*, to be published (2011).
[21] B. L. Cheng, M. Gabbay, M. Maglione, G. Fantozzi., *J. Electroceramics,* **10**(2003)5.
[22] M. A. Carpenter, *American Mineralogist*, **92**(2007)309.

Eighth International Conference on Flow Dynamics
November 9 - November 11, 2011

Evaluation of High Temperature Mechanical Properties of $La_{1-x}Sr_xMnO_{3+\delta}$ under Controlled Atmosphere

Yoshikazu Shirai[A], Yuta Kimura[A], Takuto Kushi[A], Shin-Ichi Hashimoto[A], Kazuhisa Sato[B],
Keiji Yashiro[C], Koji Amezawa[A], Junichiro Mizusaki[C] and Tatsuya Kawada[A]
[A]Graduate School of Environmental Studies, Tohoku University, Japan
[B]Fracture and Reliabirity Research Institute, Graduate School of Engineering, Tohoku University, Japan
[C]Institute of Multidisciplinary Research for Advanced Materials, Tohoku University, Japan
Email of corresponding Author: shirai@ee.mech.tohoku.ac.jp

Abstract

Mechanical properties, such as Young's modulus, shear modulus, Poisson's ratio and internal friction of $La_{0.6}Sr_{0.4}MnO_{3+\delta}$ (LSM641) were evaluated by using resonance method in the temperature range between room temperature and 1273 K under $P(O_2) = 10^{-1}$ bar. It was found that the elastic modulus of LSM641 first decreased with increasing temperature and drastically increased above 973 K. Such mechanical properties changes were discussed in terms of the lattice constant, oxygen nonstoichiometry, and the crystal structure change.

1. Introduction

Solid oxide fuel cells (SOFCs) are expected to be one of the next-generation power sources. It is important to improving durability and reliability for the practical use of SOFCs. However, it has not yet been fully defined how SOFCs degrade in each situation such as manufacture, start-up, operation and stoppage. For elucidating degradation mechanism, there is an urgent need to developing the degradation simulations or accelerated test. It is also necessary to evaluate mechanical properties of SOFC components under operating condition.

Previous works in our group showed that mechanical properties of SOFC components were affected by the change of the lattice constant, the crystal structure change and oxygen nonstoichiometry. Amezawa *et al*. studied the temperature and oxygen partial pressure ($P(O_2)$) dependancies of the elastic moduli of $Ce_{0.9}Gd_{0.1}O_{2-\delta}$ (GDC) and reported that the elastic moduli of GDC were changed by the change in interatomic distance due to the thermal expansion with increasing temperature and/or the chemical expantion with the variation in the oxygen nonstoichiometry and the average valence of cerium ion [1-2]. Kimura *et al*. reported that Young's modulus of $La_{0.6}Sr_{0.4}Co_{0.2}Fe_{0.8}O_{3-\delta}$ (LSCF6428) decreased with increasing temperature first, and then drastically increased above 873 K [3]. Around 873K, not only the crystal structure change from rhombohedral to cubic structure but also the change of oxygen nonstoichiometry occurs in LSCF6428 [4-6]. Such changes most likely cause the complicated change of Young's modulus in LSCF6428.

The perovskite-type oxide solid solution $La_{1-x}Sr_xMnO_{3+\delta}$ (LSM) are widely used as cathode material in the SOFCs. There are some studies which report on mechanical properties of LSM at room temperature [7-8]. However, no study has been reported on the mechanical properties of LSM under SOFC operating conditions.

It is known that LSM can have not only $\delta \geq 0$ but also $\delta < 0$ [9-10] in the oxygen nonstoichiometry, and the crystal structure change [11], which depends on temperature, $P(O_2)$, and Sr contents (x). In particular, oxygen nonstoichiometry of $La_{0.6}Sr_{0.4}MnO_{3+\delta}$ (LSM641) can show $\delta = 0$ over a wide range including SOFC operating conditions [9]. Meanwhile, Tagawa *et al.* reported that the crystal structure of LSM641 gradually changes from rhombohedral to cubic structure with increasing temperature and/or decreasing $P(O_2)$ [11]. The temperature of crystal structure change from rhombohedral to cubic structure was c.a. 873 K under $P(O_2) = 1$ bar although the indicated transition temperature is not exactly clear.

Considering these backgrounds, the mechanical properties of LSM641 can be discussed in terms of the crystal structure change without oxygen nonstoichiometry. Thus, LSM641 were evaluated as a function of temperature under controlled atmosphere by using resonance method. And the crystal phase of LSM641 was observed by a high temperature X-ray diffractometer on the same condition to confirm the crystal structure change. The objective of this work was

to investigate the effect of the cristal structure change on the mechanical properties of LSM641 under the condition that oxygen nonstoichiometry vanishingly is small to minimize the impact of oxygen nonstoichiometry.

2. Experimental

2.1 Sample preparation

LSM641 powders were prepared by a Pechini method. First, the powder of La_2O_3 (heat pretreated), $SrCO_3$, Mn_2O_3 were mixed in an appropriate ratio and dissolved in nitric acid. The solutions were mixed with citric acid monohydrate, ethylene glycol and then calcined at 1223 K for 8 hours in air. The powders were hydrostatically pressed at 150 MPa into compacts, and then sintered in air at 1623 K for 6 hours with cooling rate 100 K / hours. The sintered compacts were cut into rectangles, 45 mm × 8-10 mm × 1-2 mm, and polished. The Samples were analyzed by X-ray diffractometer (Mac Science M18X) with CuKα irradiation in air at room temperature after polishing.

2.2 High temperature XRD analysis

To confirm the phase transition, the crystal phase of $La_{0.6}Sr_{0.4}MnO_{3+\delta}$ was observed by a high temperature X-ray diffractometer (D8 Advance, Bluker AXS) using CuKα irradiation. XRD patterns of LSM641 were measured at 473 K, 673 K, 773 K, 873 K, 923 K, 973 K, 1023 K, 1073 K, 1173 K, 1273 K under $P(O_2) = 10^{-1}$ bar and isothermal holding time was 3 hours. Temperature around the sample was controlled by a Pt heater. Lattice parameter was calculated from the diffraction patterns by Whole Powder Pattern Decomposition method with TOPAS software [12].

2.3 Mechanical property measurements by resonance method

Mechanical properties of LSM641 were measured by resonance method at high temperature under controlled atmospheres. Resonance method shows a high accuracy and a good reproducibility compared to static methods such as the bending test and the small punch test. It is known that the sample, which has uniform cross-section shape, has natural frequency [13]. If vibration frequency and natural frequency are equal, the sample resonate. According to the following equation, Young's modulus (E) and shear modulus (G) are caluculated from the bending resonance frequency (f_b) and the torsional resonance frequency (f_t),

$$E = \frac{4\pi^2 L^4}{\alpha^2} \cdot \frac{\rho S}{I} \cdot f_b^{\,2} \tag{1}$$

$$G = \frac{16L^2}{K^2} \cdot \frac{\rho}{\beta} \cdot f_t^{\,2} \tag{2}$$

where L, α, ρ, S, I, K, β are the length of a sample, a constant given by boundary condition, the density of sample, the cross-sectional area of sample, the second moment of area, the adjustment parameter, the inertia moment of the driven section, respectively. Poisson's ratio (μ) was calculated as follows,

$$\mu = \frac{E}{2G} - 1 \tag{3}$$

Internal friction (Q^{-1}) was also measured in parallel with Young's modulus using dumping technique.

The measurement system consists of a chamber with an electrical furnace, an elastic modulus and internal friction meter (EG-HT, Japan Techno-Plus Co. Ltd.). To control the atmospheres, a gas mixing system is additionally connected to the commercial system. $P(O_2)$ was monitored by an oxygen sensor at the outlet gas stream from the chamber, and was controlled by O_2/Ar gas mixtures.

The measurement of temperature dependencies of mechanical properties were performed from room temperature to 1273 K in 50 K steps under $P(O_2) = 10^{-1}$ bar. The sample was stayed isothermal for 24 hours at maximum until the value of elastic modulus converged.

3. Results and discussion

3.1 Prepared Sample

Fig.1 shows the X-ray diffraction patterns of LSM641 at room temperature in air. It suggests that the prepared sample consisted of single phase and the crystal structure was the rhombohedral structure at room temperature due to all peaks can be indexed on the basis of a rhombohedral unit cell (space group, R-3c). And it is found that the lattice constant (a) is 5.4640 Å, the rhombohedral angle (α) is 60.293 degree at room temperature .

Shen *et al.* reported that lattice parameter of LSM641 at room temperature is a = 5.467 Å, α = 60.306 degree (ICSD number 51276, rhombohedral conversion)[14]. Moreover, they determined that the Mn valence of LSM641 is around 3.43±0.05 by the Mn

2*p*-edge X-ray absorption near edge structure (XANES), and also around 3.42±0.04 by chemical titration at room temperature. Then, oxygen nonstoichiometry is around δ = 0.015±0.025 which can be calculated by the result of the Mn valence. Since the lattice parameter of prepared sample in this study close in value to their result, oxygen nonstoichiometry of prepared sample vanishingly is small at room temperature.

Oxygen nonstoichiometry of LSM641 depends on temperature and $P(O_2)$, and has two different region (δ=0, δ<0) as shown in Fig.2 [9]. Fig.2 shows that LSM641 has oxygen nonstoichiometry of zero in ($P(O_2)$) range from 10^{-5} to 10^{0} bar. Thus, it is considered that the effect of oxygen nonstoichiometry on mechanical properties of LSM641 vanishingly is small in the condition of this measurement.

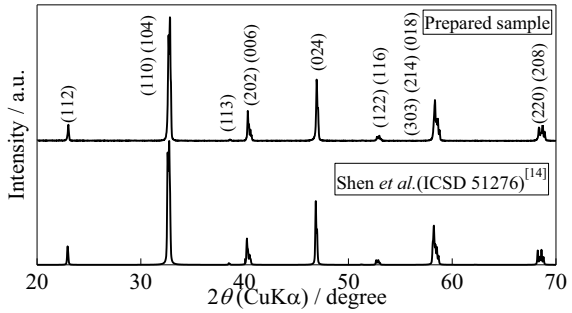

Fig.1. XRD patterns of $La_{0.6}Sr_{0.4}MnO_{3+\delta}$ at room temperature in air .

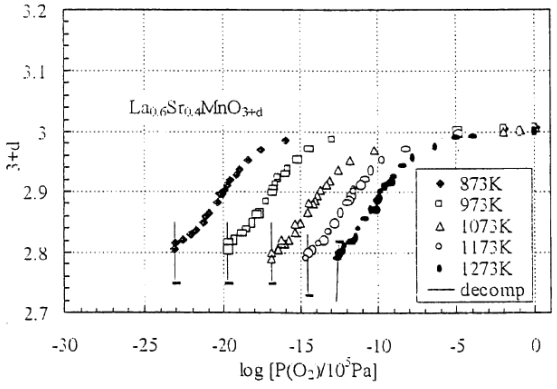

Fig.2. Oxygen partial pressure dependencies of oxygen nonstoichiometry of $La_{0.6}Sr_{0.4}MnO_{3+\delta}$ [9].

3.2 Phase transition at high temperature

The X-ray diffraction patterns of LSM641 were observed from room temperature to 1273 K under $P(O_2)$ = 10^{-1} bar and analyzed. It suggests that prepared sample consisted of single phase due to all peaks can be indexed on the basis of a rhombohedral unit cell (space group, *R*-3*c*) or cubic unit cell (space group, *Pm3m*). And the rhombohedral angle were evaluated to confirm the temperature of phase transition. In the rhombohedral structure, the magnitude of the distortion from the cubic structure can be evaluated from the rhombohedral angle. If the rhombohedral angle come at α=60°, it can be thought that the crystal structure changes from the rhombohedral structure to the cubic structure.

Fig.3 shows the lattice parameters of $La_{0.6}Sr_{0.4}MnO_{3+\delta}$ calculated with TOPAS software. The lattice constant increases with increasing temperature due to the increase of the atomic distance which is induced by thermal expansion. The rhombohedral angle gradually approach α=60° with increasing temperature, and it comes at α=60° around 973 K. It can be seen that the crystal structure of LSM641 is changed from the rhombohedral structure to the cubic structure around 973 K under $P(O_2)$ =10^{-1} bar. This result varies from the result by Tagawa *et al*. because there may be the difference in $P(O_2)$ or the heat gradient in sample during measurement or the error of calculating.

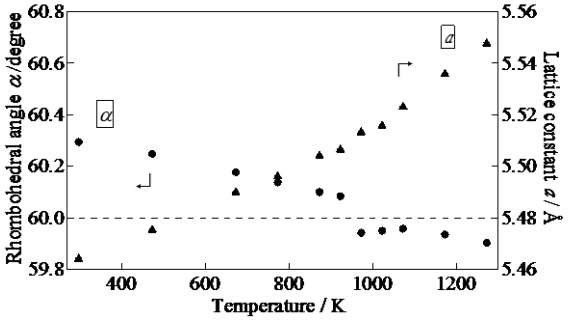

Fig.3. Rhombohedral angle (α) and lattice constant (a) of $La_{0.6}Sr_{0.4}MnO_{3+\delta}$ as a function of temperature under $P(O_2)$ = 10^{-1} bar.

3.3 The mechanical properties of $La_{0.6}Sr_{0.4}MnO_{3+\delta}$ under $P(O_2)$ = 10^{-1} bar

The mechanical properties of $La_{0.6}Sr_{0.4}MnO_{3+\delta}$ were evaluated in the temperature range between room temperature and 1273 K under $P(O_2)$ = 10^{-1} bar as shown in Fig.4. Young's modulus and shear modulus gradually decrease with increasing temperature from room temperature to 973 K and drastically increase above 973 K. Poisson's ratio is almost stable in 0.37-0.43 under 1023 K and remarkably decrease above 1073 K. Internal friction increases from temperature to 673 K, and decreases above 673 K.

The decrease of the elastic modulus may be due to the increase of the atomic distance which is induced by thermal expansion. These decreases have been reported

on the mechanical properties of Al_2O_3 as well, which is typical ceramic materials [13].

It is considered that the increase of elastic modulus over 973 K are due to the crystal structure change from the rhombohedral structure to the cubic structure because the temperature at which elastic modulus is drastically enhanced and the phase transition temperature are near each other.

Moreover, the mechanical properties of $La_{1-x}Sr_xMnO_{3+\delta}$ (x = 0.2, 0.3, 0.4, 0.5, 0.6) were evaluated in the temperature range between room temperature and 1273 K under $P(O_2) = 10^{-4}$ bar, but this result can't be showed due to limitations of space. However, no study has been reported on the crystal structure change of LSM under this condition. Thus, lattice parameter analysis of LSM (x = 0.2, 0.3, 0.4, 0.5, 0.6) will be evaluated in the temperature range between room temperature and 1273 K under $P(O_2) = 10^{-4}$ bar in future. These results will conducive to investigate the effect of the cristal structure change on the mechanical properties of LSM.

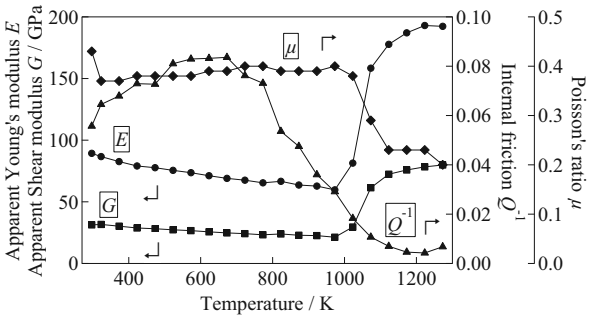

Fig.4. Young's modulus (E), shear modulus (G), internal friction (Q^{-1}) and Poisson's ratio (μ) of $La_{0.6}Sr_{0.4}MnO_{3+\delta}$ as a function of temperature under $P(O_2) = 10^{-1}$ bar.

4. Conclusions

The X-ray diffraction patterns of LSM641 were observed from room temperature to 1273 K under $P(O_2) = 10^{-1}$ bar and analyzed. As a result, it's suggested that the crystal structure of LSM641 is changed from the rhombohedral structure to the cubic structure around 973 K under $P(O_2) = 10^{-1}$ bar.

Mechanical properties, such as Young's modulus, shear modulus, Poisson's ratio and internal friction of $La_{0.6}Sr_{0.4}MnO_{3+\delta}$ were evaluated by using resonance method in the temperature range between room temperature and 1273 K under $P(O_2) = 10^{-1}$ bar. Mechanical properties of LSM641 change with increasing temperature. The elastic modulus of LSM641 decrease from room temperature to 973 K due to the increase of the atomic distance which is induced by thermal expansion. On the other hand, that of LSM641 drastically increase over 973 K may be due to the crystal structure change. Such mechanical properties changes were discussed in terms of the lattice constant and the crystal structure change.

5. Acknowledgments

This investigation was made as a part of the research project on development of systems and elemental technology on SOFC, which was supported by the New Energy and Industrial Technology Development Organization (NEDO).

References

[1] K.Amezawa *et* al., *Solid State Ionics*, in press.
[2] T.Kushi *et al*, *ECS transactions*, **25**(2) (2010) 1673-1677.
[3] Y.Kimura *et* al., *ECS Transactions*, **35** (1) (2011) 2429-2434.
[4] Y. Fukuda *et al*., *ECS Trans.*, 25(2009)2375-2380.
[5] L-W. Tai *et al*., *Solid State Ionics*,76(1995)273-283.
[6] Y. Kimura *et al*., The 219th ECS Meeting, 709, Montreal, Canada, May, 2011(Poster presentation),
[7] S.Giraud *et al*, *Journal of the European Ceramic Society*, **28** (2008) 77-83.
[8] D.L.Meixner *et al*, *Solid State Ionics*, **146** (2002) 273-284.
[9] J.Mizusaki *et al, Solid State Ionics*, **129** (2000) 163-177.
[10] K.Yasumoto *et al*, *Jounal of The Electrochemical Society*, **148** (1) (2001) A105-A111.
[11] H.Tagawa, "*Solid Oxide Fuel Cell and Gloval Environment*", *agne-shohusya*, (1998).
[12] Bruker AXS, User's Manual Bruker AXS, Karlsruhe, Germany (2008).
[13] *Japanese Industrial Standards*, JIS Z2280 (1993).
[14] Shen *et al. Journal of Solid State Chemistry,* **156** (2001) 117-121.
[15] J. B. Wachtman *et al*, *Physical review ,***122** (1961) 1754.

Electrical Conductivity of La-doped $BaTiO_3$ Thin Film via Pulsed Laser Deposition

Hannah Cho
Department of Materials Science and Engineering,
Seoul National University, Seoul 151-744, Korea
jewelofsky@snu.ac.kr

ABSTRACT

In order to understand dopant effect in $BaTiO_3$ thin films, $BaTiO_3$ thin film with different doping level were fabricated via PLD (Pulsed Laser Deposition), and its electrical conductivity investigated. The electrical conductivity of La-doped $BaTiO_3$ thin films, $(Ba_{1-x}La_x)[Ti_{1-x/4}V_{x/4}]O_{3+\delta}$(x=0.005, 0.02) (V: Vacancy), was measured by impedance spectroscopy in the range of oxygen activity from 1 to 10^{-5} at temperatures between 600℃. We found that higher doping level leads to higher electrical conductivity and the thin films shows p-type behavior in that range of oxygen activity while the bulk material shows n-type behavior in the same range.

1. Introduction

$BaTiO_3$ has been the subject of many studied as a model perovskite system due to its unique electrical characteristics. $BaTiO_3$, a ferroelectric material, shows transition from ferroelectrics to paraelectrics when donor materials are added, while this ferroelectrics can be applied to dielectric materials of high-capacity ceramic capacitors (MLCC). [1] Electrical conductivity of $BaTiO_3$ has been studied mainly in undoped or accepter-doped systems, and a few studies have been conducted in donor-doped $BaTiO_3$ systems due to their very slow kinetics. [2, 3] Furthermore, electrical conductivity of thin films remains almost an unknown area till now even though some studies have observed that the materials represent different properties when they are changed from bulk to thin-film. [4] Therefore, electrical conductivity of donor-doped $BaTiO_3$ thin film should be investigated. In this regard, electrical properties of donor-doped $BaTiO_3$ thin film was studied by former researcher in our group, and she reported that donor-doped $BaTiO_3$ has p-type behavior at $10^{-5} \leq a_{O_2} \leq 1$ and 600≤T/℃≤750, and we plan to investigate the reproducibility and the reason of the result.

In this study, we fabricate La-doped $BaTiO_3$ thin films that are few hundred nanometers with two kinds of doping condition (La=0.5 m/o and 2 m/o), and measured electrical conductivity as a function of temperature (600≤T/℃≤750) and oxygen partial pressure ($10^{-5} \leq a_{O_2} \leq 1$) to understand the electrical property of donor-doped $BaTiO_3$ thin film.

2. Experimental

La-doped $BaTiO_3$ targets with composition $(Ba_{1-x}La_x)[Ti_{1-x/4}V_{x/4}]O_{3+\delta}$(x=0.005, 0.02) (V: vacancy) was prepared by sintering at 1400℃ for 6 hours. A pulsed KrF excimer laser (LAMBDA PHYSIK COMPexPro201) operated at 5 Hz, with energy density 2.6 J/cm^2 employed to deposit La-doped $BaTiO_3$ thin films. As substrate, single crystal MgO (100) which is an insulator was used. Films were deposited at 800℃ and target-substrate distance was fixed as 50 mm, while the chamber pressure during deposition was controlled to be 70 mTorr at 800℃. X-ray diffraction measurements (Bruker D5005, Germany) were performed to find out the crystal orientation of grown films. Also scanning electron microscopy (SU70, Hitachi, Japan) was used to examine the microstructure and thicknesses of thin films.

The electrical conductivity of thin films was measured by impedance spectroscopy (SI1260+SI1296, Solatron, UK) with 2-probe measurement technique. The amplitude of input voltage and analyzed frequency range were set to 500 mV and 1 MHz to 1 Hz. Oxygen activity was controlled by mixing argon and oxygen in appropriate ratios and monitored by using a zirconia oxygen sensor.

3. Results and Discussion

XRD result of La-doped $BaTiO_3$ thin films is shown in Fig.1. Both 0.5 m/o and 2 m/o La-doped $BaTiO_3$ films seem to be grown in (100), (200), and (111) directions on MgO (100) substrate, and this growing direction means that these films are polycrystalline. Some peaks are unknown, but we found that these unknown peaks are not La_2O_3 or other second phases. In this work, we considered that these unknown peaks are some unexpected impurities which do not affect significantly and used these samples for measuring electrical properties.

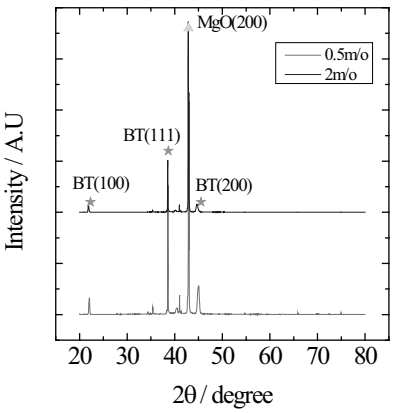

Fig. 1 XRD results (θ-2θ scan) of 0.5 m/o and 2 m/o La-doped $BaTiO_3$ films

From SEM images, Fig. 2, film thickness and

vertical structure were observed. Thicknesses of samples were 230nm and 150nm, respectively.

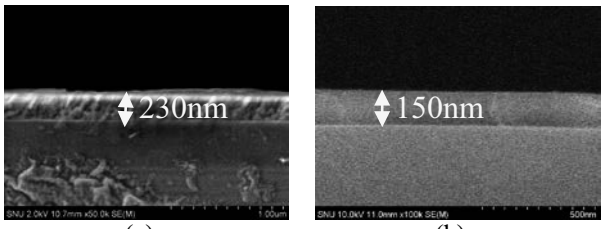

(a) (b)

Fig. 2 SEM images of as-deposited samples, cross-section images, (a) 0.5 m/o, (b) 2 m/o La-doped $BaTiO_3$ film

Electrical conductivity was measured as a function of oxygen activity, and the results are shown in Fig.3

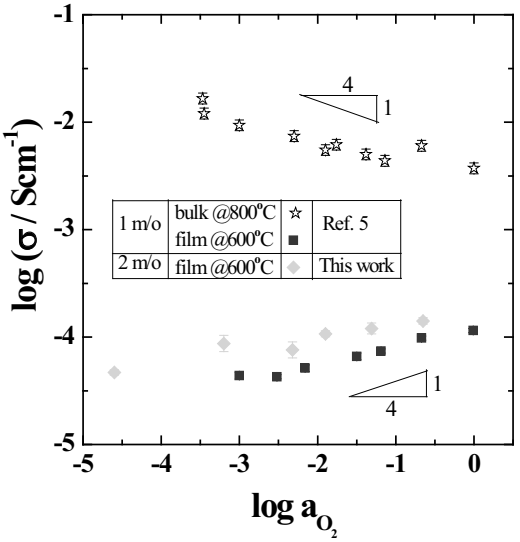

Fig. 3 Electrical conductivity of Bulk and 1m/o La-doped $BaTiO_3$ film [5] and 2m/o La-doped $BaTiO_3$ film as function of oxygen activity

Square symbol represent electrical conductivity of 1 m/o La-doped $BaTiO_3$ thin film studied by former researcher S.W. Kim [5], and this data used as a reference data in this study. As shown on Fig. 3, $BaTiO_3$ thin film represents p-type behavior, like acceptor doped case when La is added. The sample with 2 m/o La also shows p-type behavior, but its electrical conductivity slightly higher than 1 m/o La-doped $BaTiO_3$ film and the slope of the data is 1/6 for 1 m/o La doped $BaTiO_3$ and less 1/6 for 1 m/o La doped $BaTiO_3$, and both are less than 1/4 slope. As the result, we suspect that there is dopant level dependence on electrical conductivity of $BaTiO_3$ thin film, and p-type behavior at $10^{-5} \leq a_{O_2} \leq 1$ is a same property of both of 1 m/o and 2 m/o La-doped $BaTiO_3$ thin films.

This abnormal result is also different to the data from Waser *et al.* [6] which reported 2 m/o La-doped $SrTiO_3$ shows -1/4 slope at $10^{-4} \leq a_{O_2} \leq 1$, so the result of this work is very interesting and to confirm this it should be studied follow-up experiment, like same measurement with 0.5 m/o La-doped $BaTiO_3$ or other experiment to support this abnormal behavior.

4. Conclusion and Further work

It is found that 2 m/o La-doped $BaTiO_3$ thin film has higher electrical conductivity compared to 1 m/o doped $BaTiO_3$, and both represent p-type behavior in the range of oxygen activity $10^{-5} \leq a_{O_2} \leq 1$, the conductivity decreases with decreasing oxygen activity.

For investigating the dependence of doping level and temperature we will conduct additional experiment with 0.5 m/o La doped $BaTiO_3$ and temperature variation, and will deal with these all measurement data later.

Also, to find the reason of the abnormal p-type behavior of donor doped $BaTiO_3$ thin films we will additionally obtain HR-TEM (High Resolution Transmission Electron Microscope) images, and investigate which site La actually replaces between Ba site and Ti site. If, La replace Ti site, it may explain why La-doped $BaTiO_3$ shows p-type conduction behavior.

References

[1] H. I. Yoo, C. R. Song, and D. K. Lee, J. electroceram., 8, 5-36 (2002)
[2] J. Daniels and K.H. Härdtl, Philips Res. Repts., 31, 489-504 (1976)
[3] S. B. Desu and D. A. Payne, J. Am. Ceram. Soc., 73, 3407-15 (1990)
[4] P. Pasierb, S. Komornichi, and M. Rekas, J. Phys. Chem. Solids, 60, 1835-1844 (1999)
[5] S. W. Kim, M.S. Thesis, Seoul National University, Seoul, Korea (2010)
[6] C. Ohly, S. Hoffmann-Eifert, K. Szot, R. Waser, J. eur. ceram. Soc., 21, 1673-1676 (2001)

Eighth International Conference on Flow Dynamics
November 9 - November 11, 2011

Oxygen Potential Measurement in Oxygen Nonstoichiometric Oxides under the Stress

Tomohisa Masumitsu*, Satoshi Watanabe, Shin-Ichi Hashimoto, Koji Amezawa, Tatsuya Kawada
Graduate School of Environmental Studies, Tohoku University,
6-6-01 Aoba, Aramaki, Aoba-ku, Sendai, 980-8579, Japan
*Corresponding author: masumitsu@ee.mech.tohoku.ac.jp

ABSTRACT

Oxygen potential, $\mu(O_2)$, changes in $La_{0.6}Sr_{0.4}Co_{0.2}Fe_{0.8}O_{3-\delta}$ (LSCF6428) under mechanical stresses were evaluated from *emf* measurements by using a YSZ potential probe. When a compressive stress was applied to LSCF6428, *emf* first decreased suddenly, then gradually increased with time, and finally reached to constant. When the stress was released, *emf* first increased, then decayed slowly with time, and became constant. These results indicated LSCF6428 was in a reducing state by applying the stress and such a $\mu(O_2)$ change was relaxed as the oxygen nonstoichiometry in LSCF6428 under the stress was equilibrated with ambient $P(O_2)$.

1. Introduction

In recent years, anomalous ionic conduction properties were reported in thin films, nano-size particles and hetero-interfaces of ionic conductors. Although it was pointed out that the presence of space-charge layers [1], the local strain [2] and the compositional segregation were possible causes, natures of such anomalous properties have not been understood yet. In our previous study, in order to obtain a piece of information for understanding the anomalous properties, the electronic and the local structure of thin films were investigated by applying the depth-resolved x-ray absorption spectroscopy [3]. Epitaxial thin films of $Nd_2NiO_{4+\delta}$ on YSZ single-crystal substrates were chosen as a model system. Consequently it was demonstrated that the lattice distortion in the films due to the lattice misfit between the film and the substrate induced variations of oxygen nonstoichiometry in the films.

Above mentioned results indicated that mechanical stresses may cause local compositional variation, thus ionic conduction being different from one in the bulk. Based on this hypothesis, in this study, we aimed to investigate how the application of the mechanical stress affects the oxygen nonstoichiometry. For this purpose, the relationship between the mechanical stress and the oxygen potential, $\mu(O_2)$, in oxides should be clarified. In this study, we chose $La_{0.6}Sr_{0.4}Co_{0.2}Fe_{0.8}O_{3-\delta}$ as a model nonstoichiometric oxide, and employed *emf* measurements using a YSZ potential probe to evaluate $\mu(O_2)$ on the surface of the oxide under mechanical stress. Measurements of *emf* and its relaxation were performed when compressive stresses were applied onto the oxide by using a small punch testing machine.

2. Methods

2.1. Sample preparation

The sample used in this study was a polycrystalline sintered compact of $La_{0.6}Sr_{0.4}Co_{0.2}Fe_{0.8}O_{3-\delta}$ (LSCF6428). Commercial LSCF6428 powder (AGC SEIMI CHEMICAL CO., LTD.) was uniaxially pressed into a pellet, and then hydrostatically pressed at 200 MPa. The compact was sintered at 1523 K for 6 hours, and slowly cooled down to room temperature with the rate of 102 K/h to avoid cracking. The sintered compact was cut into a plate (7.1×7.1×2.3mm), and mirror polished. Relative density of the sample was over 97 %. A Pt wire with Pt paste was set on the side of the sample as a current collector. The sample was finally fired at 1273 K for 2 hours to sinter Pt paste.

2.2. Oxygen potential measurements under mechanical stresses

A uniaxial compressive load was applied to the specimen by using the small punch (SP) testing machine (5565 type, Instron). A ball of 4 mol% yttria-stabilized zirconia (4YSZ) was used as an indenter. This YSZ ball also worked as an electrolyte of an oxygen potential probe. The YSZ ball was winded by a Pt wire as a reference electrode. Figure 1 shows a schematic illustration of the oxygen potential probe used. In this setup, $\mu(O_2)$ on the LSCF6428 surface could be evaluated from measured *emf* of the probe according to following equations.

$$emf = -\frac{\Delta G}{4F} \tag{1}$$

$$\Delta G = \mu(O_2) - \mu(O_{2,\,air}) \tag{2}$$

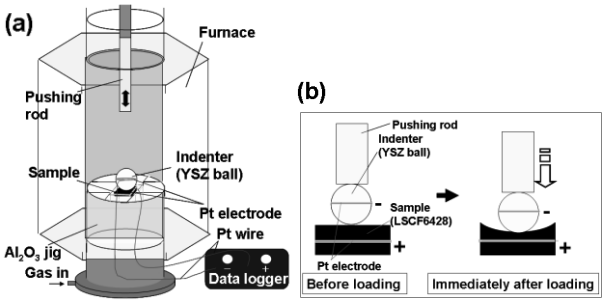

Fig. 1. Schematic illustration of (a) the experimental apparatus and (b) the oxygen potential probe for *emf* measurements.

3. Results and Discussion

Figure 2 shows *emf* change, ΔE, of $La_{0.6}Sr_{0.4}Co_{0.2}Fe_{0.8}O_{3-\delta}$ at various temperatures in air when the compressive stress was applied. ΔE in this figure presents *emf* values relative to the average *emf* before the mechanical loading. t=0 was set to the time when the stress was applied. Here one should note that the applied stress was not same at each temperature, because the mechanical stress was applied so that the

displacement became constant as 0.015 mm. As is seen, significant changes in ΔE were observed immediately after the mechanical stress was applied and released; a rapid decrease and increase for the mechanical loading and unloading, respectively. During loading, ΔE slowly increased with time and finally became zero. After unloading, ΔE gradually decreased and reached to zero.

According to Hashimoto *et al*. [4], with increasing $P(O_2)$, the oxygen nonstoichiometry, δ, in $La_{0.6}Sr_{0.4}Co_{0.2}Fe_{0.8}O_{3-\delta}$ decreased, and correspondingly the lattice constants decreased. That is, the partial oxidation of LSCF6428 induces the shrinkage of the lattice volume. These facts give us a hypothesis that the oxide is oxidized if its lattice is mechanically shrunk. However, it would take some time until the oxide under the mechanical stress equilibrates with the ambient $P(O_2)$, because such partial oxidation accompanies diffusion of oxide ions in the oxide. Thus it is considered that $\mu(O_2)$ in the oxide is under a reducing condition immediately after the compression stress is applied. This corresponds to the rapid decrease in *emf* observed at the initial stage of the mechanical loading. As time goes, the reducing situation is considered to be gradually relaxed as the oxygen nonstoichiometry under the stress was equilibrated with ambient $P(O_2)$. Accordingly it is supposed that ΔE gradually reached to zero. The relaxation time of ΔE decreased with increasing temperature. This is reasonable since the oxygen diffusion becomes faster with higher temperature.

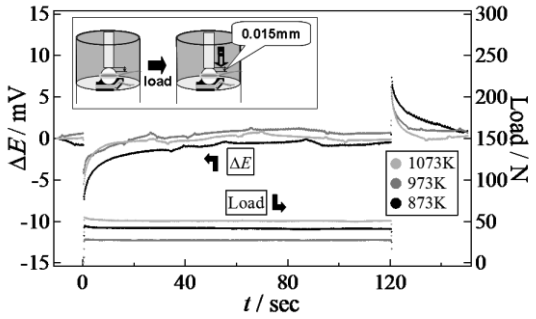

Fig. 2. *Emf* change, ΔE, when the compressive stress was applied to $La_{0.6}Sr_{0.4}Co_{0.2}Fe_{0.8}O_{3-\delta}$ at various temperatures in air. The compressive stress was applied so that the displacement became constant as 0.015 mm.

Figure 3 shows *emf* change, ΔE, of $La_{0.6}Sr_{0.4}Co_{0.2}Fe_{0.8}O_{3-\delta}$ at 973 K in air when the displacement during the loading was varied. The maximum value of the measured ΔE depended on the displacement and increased with increasing the displacement. Here larger displacement leaded to larger mechanical stress, although the resulting mechanical stress was not proportional to the displacement. Figure 4 shows the maximum value of ΔE of $La_{0.6}Sr_{0.4}Co_{0.2}Fe_{0.8}O_{3-\delta}$ as a function of the applied load at 973 K in air. This result clearly demonstrates that larger displacement, thus larger mechanical stress, leads to larger *emf* change, thus larger oxygen potential change.

In this way, *emf* behavior of LSCF6428 under mechanical stresses, shown in Figs. 2 and 3, can be qualitatively explained by assuming the hypothesis that the mechanical loading onto an oxide induces the $\mu(O_2)$ change. The results presented in this work are clear evidences showing significant influences of mechanical stresses on oxygen nonstoichiometry change.

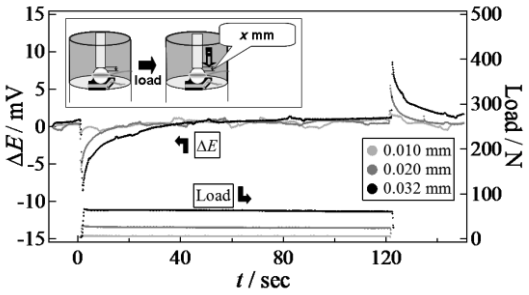

Fig. 3. *Emf* change, ΔE, of $La_{0.6}Sr_{0.4}Co_{0.2}Fe_{0.8}O_{3-\delta}$ at 973 K in air when the displacement during the loading was varied.

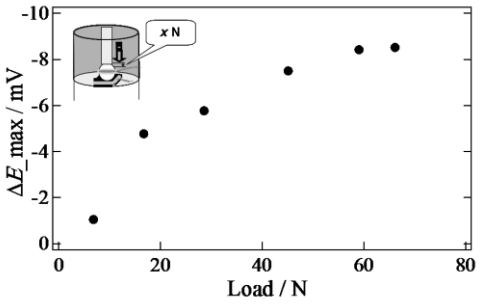

Fig. 4. Maximum value of ΔE of $La_{0.6}Sr_{0.4}Co_{0.2}Fe_{0.8}O_{3-\delta}$ as a function of the applied load at 973 K in air.

4. Concluding remarks

Influences of mechanical stresses on oxygen potential, $\mu(O_2)$, were investigated through *emf* measurements of $La_{0.6}Sr_{0.4}Co_{0.2}Fe_{0.8}O_{3-\delta}$ under stress by using a YSZ potential probe. An apparent decrease and increase of *emf* changes were observed when the mechanical stress was applied and released, respectively. As time progressed, *emf* slowly decayed and finally became constant. The relaxation time decreased with increasing temperature. The maximum value of *emf* change increased with increasing the applied load. These results were interpreted based on the idea that the application of mechanical stress causes $\mu(O_2)$ change in the oxide. In order to further understand influences of mechanical stress on $\mu(O_2)$, it is useful to do similar *emf* measurements with other oxides having different oxygen nonstoichiometry, chemical expansion coefficient, and elastic modulus and so on.

References

[1] N. Sata *et al*., *Nature.* **408** (2000) 946-949
[2] A. Yamada *et al*., *Adv.Mater.* **20** (2008) 4124-4128
[3] K. Amezawa *et al.*, 217th ECS Meeting, Session B11, #730 (2010)
[4] S. Hashimoto *et al.*, *Solid state ionics.* **186** (2011) 37-43

Insulation Resistance Degradation of $BaTiO_3$ under D.C Bias

Hyung-Soon Kwon
Solid State Ionics Research Laboratory
Department of Materials Science and Engineering
Seoul National University, Seoul 151-744, Korea
E-Mail : khs82@snu.ac.kr

ABSTRACT

To understand the mechanism of resistance degradation in $BaTiO_3$-based capacitors, the change of local resistance in $BaTiO_3$ specimen under applied D.C bias was investigated. Also, using impedance spectroscopy, each part of resistance was observed between initial and degraded states. Our experiments revealed the change of electrode resistance dominates the total resistance change. This means resistance degradation in oxide-based electroceramic devices is considered in aspect of variation at electrode/semiconductor interface.

1. Introduction

Multi-layer ceramic capacitors (MLCCs) are essential passive components in the circuitry of electronic products because of their properties of high capacitance with small size, high reliability, and excellent high-frequency characteristics [1]. The internal structure of MLCC consists of ceramic layers with alternating metallic electrode layers, which are co-fired at a high temperature followed by cooling. Barium titanate, because of its exceptionally high dielectric constant, has been used extensively as a MLCC ceramic layer material.

But fatal shortcoming, namely decreased insulation resistance degradation under high d.c. voltage stresses, has been observed. The insulation resistance degradation means that dielectric constant of ceramic layer gets smaller and smaller under simultaneous temperature and dc electric field. As the electric field in multi-layer capacitors is especially high, due to very thin ceramic layers, these devices can be seriously affected by degradation [2].

This unwanted failure must be solved to improve MLCC performance and reliability. The behaviors of resistance degradation have been intensively studied and typical degradation mechanism in perovskite materials has been established [3-5]. Under simultaneous temperature and dc field stress, the electromigration of highly mobile oxygen vacancies occurs, resulting in depletion and pile-up of oxygen vacancies and consequent generation of holes and electrons in the positive-biased and negative-biased region, respectively. This situation is similar to the forward-biased p-n junction diode, and thus leakage current is enhanced, resulting in resistance degradation.

However, other researchers have pointed out that resistance degradation in MLCC is originated from degradation of resistance between electrode and dielectric interface rather than due to highly mobile oxygen vacancy migration [6-8].

The objective of the study reported in this paper is to confirm the main factor that induce degradation phenomena in MLCC. The electrical performance during degradation will be observed for each locally divided section.

2. Experimental procedure

In this experiment, the Al(1.8 m/o) doped $BaTiO_3$ specimens were used. These were made by usual solid state reaction method. The detail procedure was described earlier [9]. The sintered samples were all found to be of single phase(by x-ray diffraction analysis) with 96% relative density. The grain size of samples were about 20μm. Electrodes for the measurement of leakage currents were prepared by Au sputtering. The behaviors of resistance degradation were measured at the temperature of 250°C by applying dc field of 200 V/cm up to 1000 V/cm. To measure the change of local resistance, microprobes were contacted to the surface of specimen. The leakage current was measured by using high voltage measure unit (model 237, Keithley, USA) and impedance spectroscopy was measured by using a Solatron 1260 and 1296 analyzer (Solatron, UK).

3. Results & discussion

Figure 1 shows degradation behavior of specimen at given condition. The degradation starts after about 4500s. Typically, the lifetime (τ) of dielectrics is defined by the point where the leakage current is increased ten-fold compared to the minimum value [10].

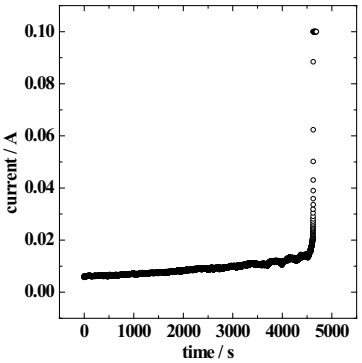

Figure 1. Degradation behavior of Al(1.8 m/o) doped $BaTiO_3$ under 400V/cm at 250°C

To find out the reason of this dramatic change of current, impedance analysis was performed between the initial state and degraded state. (Fig. 2) The resistance of grain is almost the same, whereas the resistance of electrode is considerably changed.

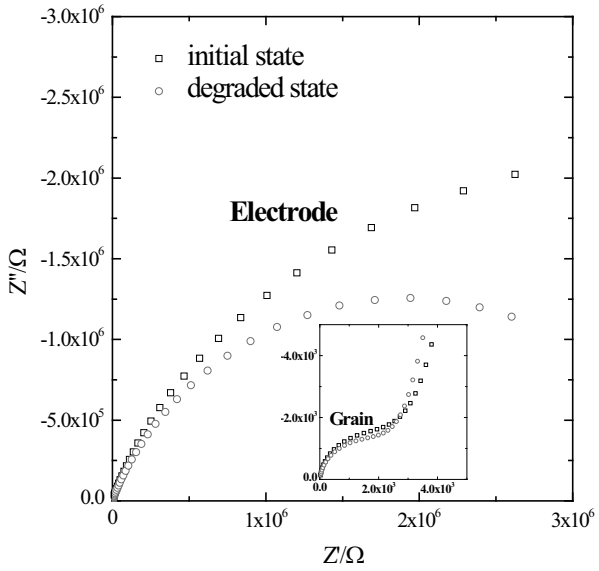

Figure 2. Impedance plot between initial and degraded state under 500V/cm at 250°C

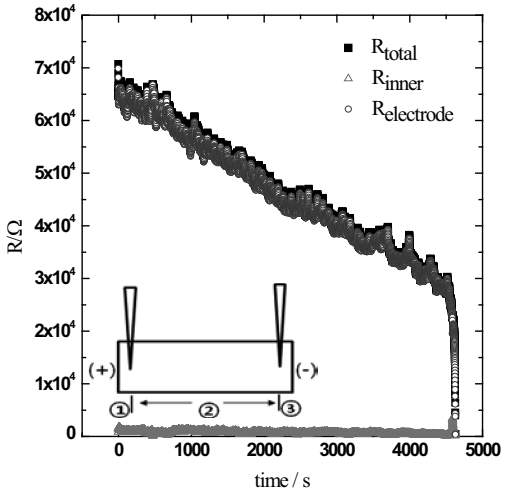

Figure 3. The measurement of resistance change by using microprobe (R_{inner}: ②, $R_{electrode}$:①+③)

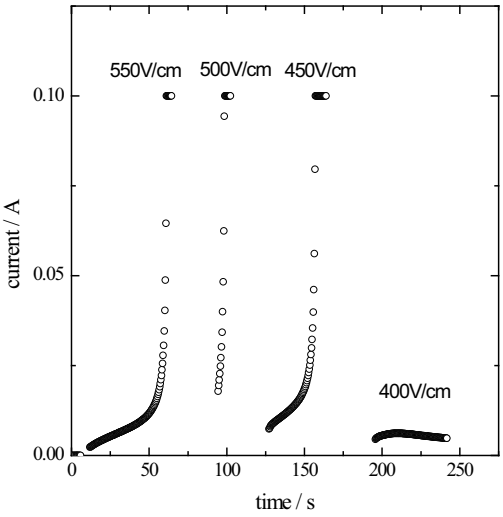

Figure 4. Leakage current variation with varying applied electric field

By using microprobes, local resistance changes that divided three parts were measured. (Fig. 3) The inner resistance between two microprobes is almost same. However, changes of other resistance parts dominate the total resistance change. This result suggests the characteristics of electrode or electrode/dielectric interface is important factor to control degradation behavior. An another evidence is that the leakage current is rapidly increased above a critical electrical bias. (Fig. 4) Above 400V/cm, the leakage current is abruptly increased, while below 400V/cm, the leakage current seems to be reaching steady state. The existence of onset voltage means that leakage current is originated from conduction through schottky barrier at the electrode/dielectric interface.

4. Conclusions

In this study, we investigated the main factor that induce resistance degradation phenomena. So far, the electromigration of highly mobile oxygen vacancy was considered as the main cause of resistance degradation in MLCC. However, our experiments revealed total resistance is dominated by resistance of electrode or electrode/dielectric interface, not the grain. This means resistance degradation in MLCC should be considered in the aspect of conduction through schottky barrier at electrode/dielectric interface. Of course, the electromigration of oxygen vacancy is also regarded as major factor of resistance degradation. To identify the mechanism of resistance degradation, more rigorous research and discussion will be needed.

References

[1] G. Arlt et al., J. Appl. Phys., **58**, 1619 (1985)
[2] J. Rodel and G. Tomandl, J. Mater. Sci., **19**, 3515 (1984)
[3] R. Waser et al., J. Am. Ceram. Soc., **73**, 1645 (1990)
[4] R. Waser et al., J. Am. Ceram. Soc., **73**, 1654 (1990)
[5] T. Baiatu et al., J. Am. Ceram. Soc., **73**, 1663 (1990)
[6] G. Y. Yang et al., J. Appl. Phys., **96**, 7492 (2004)
[7] G. Y. Yang et al., J. Appl. Phys., **96**, 7500 (2004)
[8] A. V. Polotai et al., J. Electroceram., **23**, 6 (2009)
[9] H.-I. Yoo et al., Phys. Chem. Chem. Phys., **11**, 3115 (2009)
[10] R. Waser et al., Mater. Sci. Eng. A, **109**, 171 (1989)

Eighth International Conference on Flow Dynamics
November 9 - November 11, 2011

Development of Evaluation Techniques of the Electrochemically Active Zone in a Ni-GDC Cermet Anode for SOFC

Hidetaka WATANABE[1], Shin-ichi HASHIMOTO[2], Koji AMEZAWA[1], Tatsuya KAWADA[1]
1: Graduate School of Environmental Studies, Tohoku University
6-6-01 Aoba, Aramaki, Aoba-ku, Sendai 980-8579, Japan
2: Graduate School of Engineering, Tohoku University
6-6-01 Aoba, Aramaki, Aoba-ku, Sendai 980-8579, Japan
E-mail address of corresponding author: watanabe@ee.mech.tohoku.ac.jp
TEL: +81-(0)22-795-6976 FAX: +81-(0)22-795-4067

ABSTRACT

A transmission line, TML, model was introduced as simple kinetic model which including current distribution for the fictive cermet electrode. Faradaic current distribution in the cermet anode was simulated with various values of ionic resistance Ro, electronic diffusion resistance Re and the reaction resistance Rreact. And then, the impedance spectra were calculated by using those resistnaces and the capacitance. Since the electrochemically active zone, EAZ, in the cermet electrode was evaluated. Also the EAZ of R-C parallel circuit approximation was verified by comparing the ERZ of TML model.

1. Introduction

Solid oxide fuel cell (SOFC) is an energy conversion device with high efficiency in which various kinds of hydrocarbon fuels can be utilized. In most of SOFCs, Ni-containing composites (Ni-cermet) are used as anodes. They show an excellent catalytic activity for the anodic reaction of hydrogen or reformed hydrocarbon fuels. It is well known that the electrode reaction can take place only in the vicinity of triple phase boundary, TPB.[1,2] In a cermet anode, Ni and ceramics (YSZ and GDC for instance) work as electronic and ionic paths, respectively, which improves the overall performance by extension of the electrochemically active zone, EAZ. In the case of ceria based anode, the electronic conduction in ceria may also contribute to construct the network of the electronic path.

The thickness of the EAZ is one of parameters when the electrode performance and its degradation are discussed.[3,4] Nakamura et al. proposed the thickness of the EAZ in a porous GDC single phase electrode could be estimated from its "chemical capacitance" observed in ac impedance response. [3] We applied this technique to evaluated EAZ in Ni-GDC cermet electrode.[4] In our previous work, however, a simple R-C parallel circuit was used to fit the impedance spectra and obtain the chemical capacitance. The fitting by using this equivalent circuit was very convenient as an instant analysis, but not correct in a precise sense because the faradaic current was not uniformly distributed in the cermet electrode. In this paper, we first simulate the faradaic current distribution in a fictive cermet electrode by using a transmission line model, while assuming desired values for diffusion and reaction resistances of the components of the electrode. From this simulation, the EAZ in the fictive cermet electrode can be determined. And then, the impedance spectra for the fictive cermet electrode, which are calculated from the transmission line model, is fitted by using a simple R-C parallel circuit, and the EAZ is evaluated from the obtained chemical capacitance. Throughout these simulations, the validity of the EAZ evaluated from chemical capacitance is discussed.

2. Transmission line model

In this paper, a transmission line model shown in Fig.1 was introduced as an equivalent circuit model to express a porous Ni-GDC cermet. The transmission line model was proposed by Bisquert et al. to analyze the impedance of porous film electrodes in aqueous solution.[5,6] The model in this work assumed finite length for diffusion, and diffusion paths of ions and electrons were in GDC and Ni particles, respectively. In lower oxygen partial pressure region (< *ca.* $\log P(O_2)$ = -16 bar at 1073 K for instance), GDC also has electronic conductivity caused by the increase of concentration of Ce^{3+}. Electronic path in GDC particle was neglected in this model because the conductivity is sufficiently small compared with that of Ni. In Fig. 1, Z_A, Z_B and Z_C denote the ionic diffusion resistance, the reaction impedance and electronic diffusion resistance, respectively. The reaction impedance Z_B consists of the electrode reaction resistance R_{react} at the TPB of Ni/GDC/gas and the chemical capacitance C_{chem} of a GDC particle. As seen in Fig. 1, ionic current comes from electrolyte via terminal A while a part of ionic current is converted to electronic current though the electrode reactions. Electronic current increases with increasing the distance from the electrolyte and finally is released to terminal D. The EAZ is defined as the place where certain amount of the faradaic current, *i.e.* the current in Z_B, is observed. Considering the circuit in Fig. 1, the faradaic current strongly depends on the reaction resistance and the diffusion resistances.

Figure 2 shows the faradaic current distribution calculated from the transmission line model when assuming specified values for the resistance of oxygen ionic diffusion R_O, the resistance of electronic current R_e. The reaction resistance R_{react} was fixed to 10 Ω. Three cases were demonstrated in figure 2; (a) when R_O was larger than R_{react} and R_e was negligibly small, (b) when R_e was larger than R_{react} and R_O was negligibly small and (c) R_o and R_e are comparable with each other and were larger than R_{react}. The faradaic current was consumed mainly in the vicinity of electrolyte/electrode interface in the case (a), whereas in the vicinity of the current

collector in the case (b). In the case (c), increases in the faradaic current were observed both in the vicinity of electrolyte/electrode interface and the current collector. In general, RO is much larger than Re for the Ni-GDC cermet anode. Thus, situations close to the case (a) are considered to be established in the Ni-GDC cermet anode.

Figure 3 shows the faradaic current distribution from the transmission line model when assuming specified values for the resistance of oxygen ionic diffusion R_O, the resistance of electronic current R_e. The electronic current R_e and the reaction resistance R_{react} were fixed to 0.1 and 10 Ω, respectively. Figure 4 shows the faradaic current distribution from the transmission line model when assuming specified values for the resistance of oxygen ionic diffusion R_O, the resistance of electronic current R_e. The electronic current R_e and the oxygen ionic diffusion resistance R_O were fixed to 0.1 and 10 Ω, respectively. The amount of faradaic current decreased with the distance in all cases. When the ionic diffusion resistance was small, the faradaic current remains until the top of the electrode. Then the electrochemically active zone was expanded whole electrode. On the other hand, when the ionic diffusion resistance was large, the faradic current was consumed in the electrode. Then the electrochemically active zone was expanded in a part of the electrode. Since impedance spectra were simulated by using those resistances and 0.001 F of capacitance. The simulated impedance spectra were shown in Fig. 5.

Since the simple R-C parallel circuit approximation was carried out on those impedances. Then the capacitance of R-C parallel circuit was calculated by following equation,

$$C_{\mathrm{R-C}} = \frac{1}{2\pi f R} \tag{1}$$

where f and R were peak frequency of the arc and the resistance of lower frequency region. The simulated result of the impedance spectra by using R-C parallel circuit and the capacitance of transmission line model were shown in table 1. Corresponding capacitance decreased with increasing ionic diffusion resistance.

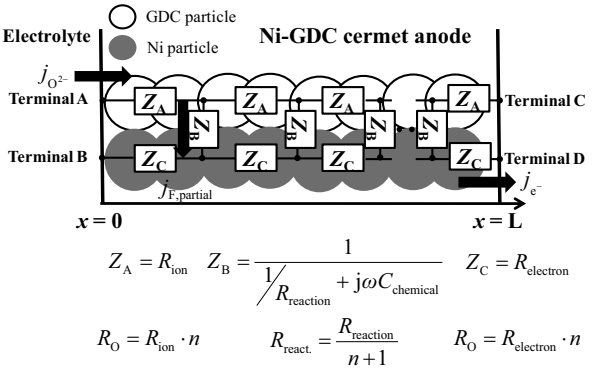

Fig. 1. Schematic illustration of a transmission line model. Z_A, Z_B and Z_C denote a part of ionic diffusion resistance, the electrode reaction impedance and electronic diffusion resistance, respectively. n is the number of partition.

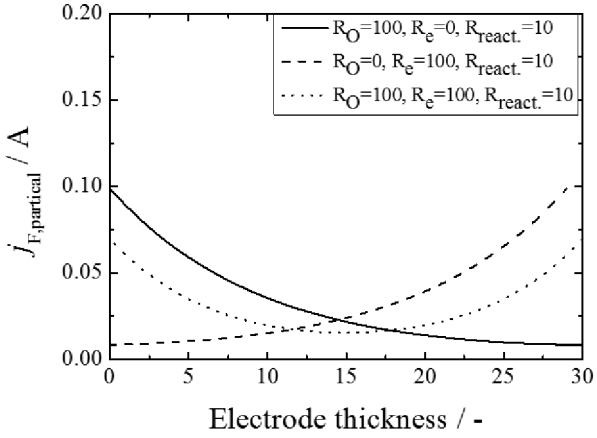

Fig. 2. Faradaic current distribution calculated from the transmission line model when assuming specified values for the resistance of oxygen ionic diffusion R_O, the resistance of electronic current R_e. The reaction resistance R_{react} was fixed to 10 Ω.

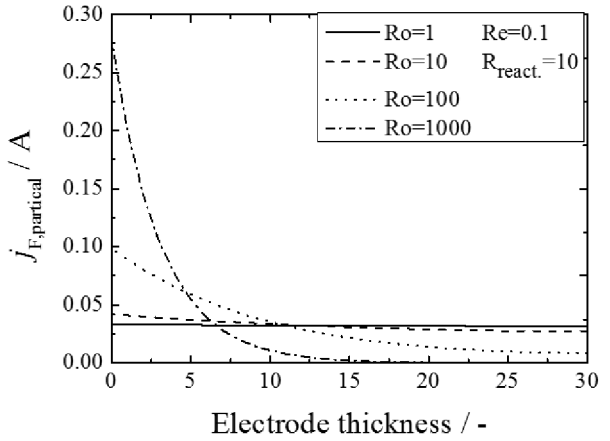

Fig. 3. Faradaic current distribution from the transmission line model when assuming specified values for the resistance of oxygen ionic diffusion R_O, the resistance of electronic current R_e. The electronic current R_e and the reaction resistance R_{react} were fixed to 0.1 and 10 Ω, respectively.

In our previous work, nonstoichiometry change was observed only in GDC particles where electrode reaction took place. Thus, the EAZ could be evaluated by comparing the observed capacitance with the chemical capacitance for the whole electrode. This observed capacitance was fitted by using simple R-C parallel circuit. Then the ERZ can be written as

$$EAZ = \frac{C_{\mathrm{observed}}}{C_{\mathrm{theoretical}}} V_{\mathrm{electrode}} \tag{2}$$

where $C_{observed}$, $C_{theoretical}$ and $V_{electrode}$ are the capacitance corresponding the electrode reaction, the chemical capacitance for GDC particles for the whole electrode and volume of the electrode. Here, $C_{theoretical}$ can be written as

$$C_{\text{theoretical}} = -\frac{8F^2}{RTV_{\text{m}}} \cdot \frac{\mathrm{d}\delta}{\mathrm{dln}[P(\mathrm{O}_2,\mathrm{eff})]} V_{\text{electrode}} \qquad (3)$$

where F, R, T, Vm, δ, and $P(O_2,\mathrm{eff})$ are the faradaic constant, the gas constant, the temperature, the molar volume of nonstoichiometric oxide, the effective oxygen partial pressure, respectively.

Table 1 show the EAZ of the calculated impedance by using the simple R-C parallel circuit approximation and the ionic diffusion resistance. The electrochemically active zone for a transmission line model can be evaluated where the partial faradaic current is equal to zero. Table 2 shows the relationship between $R_{\text{react}}/R_{\text{O}}$ and the ratio of the $EAZ_{\text{R-C}}/EAZ_{\text{TML}}$. Adaptive possibility of the simple R-C parallel circuit approximation was predicted from table 2; (A) When the $R_{\text{react}}/R_{\text{O}}$ is larger than 1, the impedance of Ni-GDC cermet anode can be fitted by using R-C parallel circuit approximation without error, (B) when the $R_{\text{react}}/R_{\text{O}}$ is *ca.* 0.1, the EAZ of R-C parallel circuit approximation corresponds to *ca.* 20 % of total consumption of faradaic current from electrode/electrolyte, (C) when the $R_{\text{react}}/R_{\text{O}}$ is smaller than *ca.* 0.01, the EAZ of R-C parallel circuit approximation corresponds to *ca.* several % of total consumption of faradaic current from electrode/electrolyte. In the case (C), R-C parallel circuit approximation was ruled unfit to fit the impedance response of a Ni-GDC cermet anode. For instance the faradaic current is distributed discretely or the electrode reaction only takes place in the vicinity of electrolyte/electrode interface.

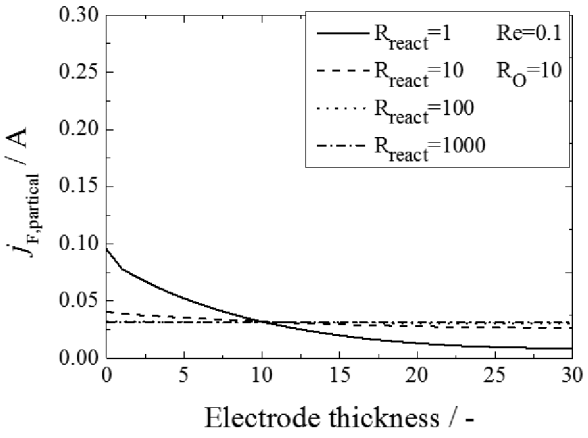

Fig. 4. Faradaic current distribution from the transmission line model when assuming specified values for the resistance of oxygen ionic diffusion R_{O}, the resistance of electronic current R_{e}. The electronic current Re and the oxygen ionic diffusion resistance R_{O} were fixed to 0.1 and 10 Ω, respectively.

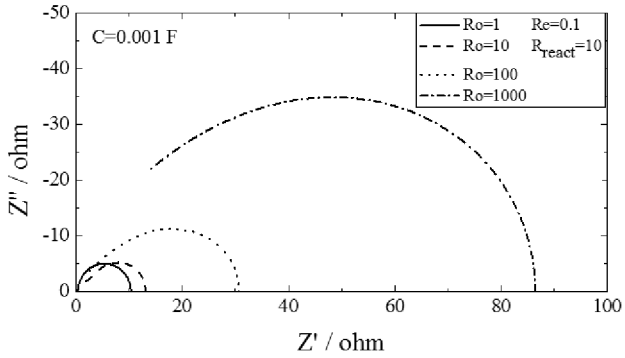

Fig. 5. Simulated impedance spectra of the fictive cermet electrode. The capacitance was fixed to 0.001 F.

Table 1. The results of simple R-C parallel circuit approximation for Fig. 3.

	R / Ω	f / Hz	C / F
———	10.39	16.55	0.0009257
–·–·–	10.43	16.55	0.0009223
·····	28.39	28.39	0.0002188
–·–·–·	79.96	28.39	0.00007012
TML			0.001

Table 2. The ratio of evaluated EAZ

	$R_{\text{react}}/R_{\text{O}}$	$EAZ_{\text{R-C}}/EAZ_{\text{TML}}$
———	10	**0.9257**
–·–·–	1	**0.9223**
·····	0.1	**0.2188**
–·–·–·	0.01	**0.07012**

5. Concluding remarks

The faradaic current distribution for the fictive cermet anode was demonstrated by using a transmission line model when assuming specified values for the resistance of oxygen ionic diffusion R_{O}, the resistance of electronic current R_{e}. Impedance spectra were calculated by using those resistances and fictive capacitance. The electrochemically active zone, EAZ was evaluated by using the R-C parallel circuit approximation and a transmission line model. Those EAZ were compared. From the results, it is indicated that the adaptive possibility of simple R-C parallel circuit approximation were distinguished three cases. (A) When the $R_{\text{react}}/R_{\text{O}}$ is larger than 1, the impedance of Ni-GDC cermet anode can be fitted by using R-C parallel circuit approximation without error, (B) when the $R_{\text{react}}/R_{\text{O}}$ is *ca.* 0.1, the EAZ of R-C parallel circuit approximation corresponds to *ca.* 20 % of total consumption of faradaic current from electrode/electrolyte, (C) when the $R_{\text{react}}/R_{\text{O}}$ is smaller than *ca.* 0.01, the EAZ of R-C parallel circuit approximation corresponds to *ca.* several % of total consumption of faradaic current from electrode/electrolyte.

6. Acknowledgement
This work was carried out as part of the NEDO project, “Development of Systems and Elemental Technology on SOFC”

References
[1] J. Mizusaki *et al.*, *Solid State Ionics*, **70-71** (1994) 52
[2] A. Bieberle *et al.*, *J. Electrochem. Soc.*, **148** (2001) A646
[3] T. Nakamura *et al.*, *J. Electrochem. Soc.*, **155**, (2008) B1244
[4] H. Watanabe *et al.*, *ECS transactions*, **25**, (2009) 1939
[5] J. Bisquert *et al.*, *Electrochem. Commun.*, **1**, (1999) 429
[6] J. Bisquert *et al.*, *J. Phys. Chem. B*, **104**, (2000) 2287

A Correct Access to Hydration Phenomenon of the Proton Conductor, Barium Zirconate, and Effects of NiO as a Sintering Aid.

Euisung Kim
Department of Materials Science and Engineering, Seoul National University, Seoul 151-744, South Korea
euisung@snu.ac.kr

ABSTRACT

One of the promising materials for solid electrolyte of fuel cells, Y-doped Barium Zirconate (BZY) is of interest because of its chemical stability and high protonic conductivity. However, its difficulty in sintering has been an obstacle to various applications. It have been sintered successfully by doping NiO as sintering aid at 1500℃. (~95% relative density) It will be discussed here about the electrical property differences between pure BZY and BZY with NiO.

1. Introduction

Since Iwahara et al.[1] found proton conduction in some oxides, proton conductor based SOFCs have been of interest due to its lower operating temperature compared to that of typical SOFCs. Additionally some proton conductors like 20 mol% Y-doped barium zirconate (BZY20) exhibit protonic conductivity exceeding the oxide ion conductivity of the best oxide ion conductors [2].

BZY has the high protonic conductivity although it has to be sintered at high temperature above ~1700℃, which is an obstacle to various applications. A lot of effort has gone into lowering the sintering temperature of barium-based materials for its diverse applications. Many researchers have used sintering aids to lower the sintering temperature of BZY. For example, Shanwen et al.[3] successfully sintered BZY at 1325℃ via addition of 1 wt% ZnO, and Yeon and Yoo [4] sintered BZY20 with 1 wt% NiO at 1500℃.

On the one hand, hydration/dehydration kinetics of acceptor doped perovskite BZY20 studied in [4] were twofold by fast H-diffusion and sluggish O-diffusion.

In this paper, hydration/dehydration behaviors of acceptor-doped perovskite oxides demonstrated in [4], two-fold nonmonotonic conductivity relaxations are reproduced by purely sintered BZY20 [5], and the extracted information from those is compared to the electrical properties of BZY20 sintered with 1 wt% NiO.

2. Method

Both the BZY20s sintered with NiO and purely sintered specimens were prepared by solid state reaction method and the relative densities of each specimens are ~95% and ~94% relatively. For more details, the readers is requested to refer to the literatures [4-5].

X-ray diffraction analysis, Fig. 1 (a), (b), indicates that there is no second phase in the both specimens. Mean grain sizes of both specimens from SEM images, Fig. 2 (a), (b), are relatively 4.7±0.8 ㎛ and 0.98±0.07 ㎛. From Fig. 2 (a), Ni seems to be enriched along the grain boundaries.

To measure the conductivity relaxation behavior, both specimens were cut into perallelepipede, 1x1x15 mm^3. Smaller dimensions th3an those of previous work [3] are due to very slow kinetics of BZY20 and are to obtain the relaxation curves which are not controlled by

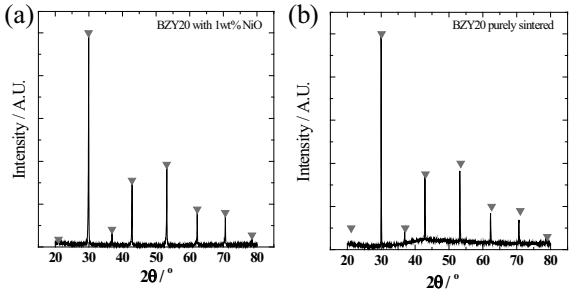

Fig. 1. XRD analysis on (a) BZY20 with 1wt% NiO, (b) BZY20 purely sintered.

diffusions. Using DC 4-probe method, conductivity relaxation measurement was done and to obtain same condition for both specimens, the specimens were put into same chamber like Fig. 3.

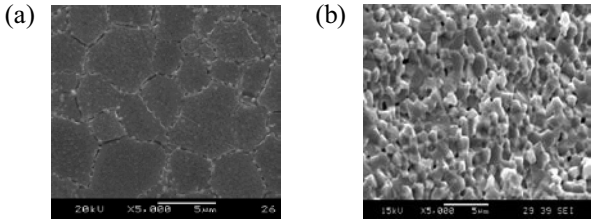

Fig. 2. SEM images of (a) BZY20 with 1 wt% NiO, (b) BZY20 purely sintered.

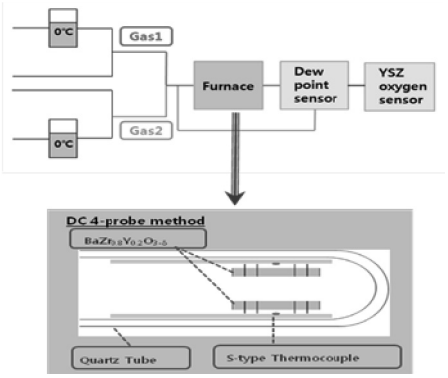

Fig. 3. Schematic diagram of experimental set.

The partial pressures of H_2O and O_2 are measured by a hygrometer (General Eastern, M4) and an YSZ oxygen sensor.

The conductivity relaxation was measured upon a sudden change of partial pressure of H_2O with no change of partial pressure of O_2 nor change of temperature at 700℃. The controlled gas mixture was taken by mixing the gas saturated of 0℃ water with dry gas.

3. Results and Discussion

When hydration occurs, as expected from a previous work [4], the conductivities of both specimens decreases quickly, and then increases slowly to saturated value.

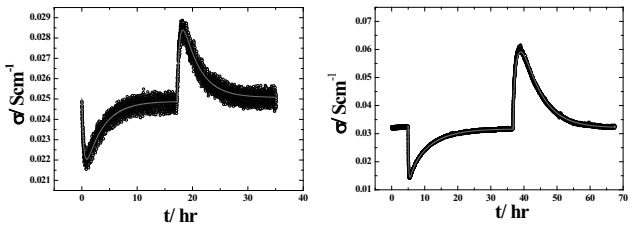

(a) (b)

Fig. 4. The conductivity relaxation curves upon hydration/dehydration. (a) BZY20 with 1 wt% NiO, (b) BZY20 purely sintered.

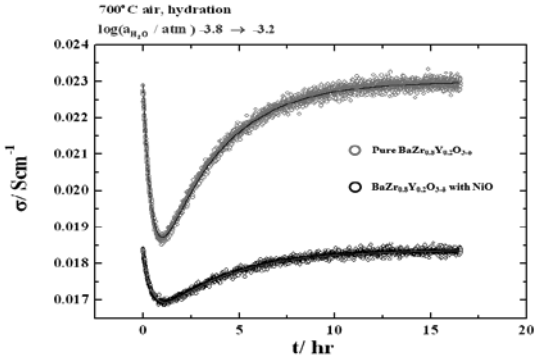

Fig. 5. The conductivity relaxation difference upon hydration between BZY20 with NiO (black symbol) and BZY20 purely sintered (red symbol).

Fig. 4 shows two fold nonmonotonic conductivity relaxation upon hydration/dehydration. From these curves, kinetic parameters can be extracted by fitting to equations (1) and (2) [6-7].

$$\Delta\sigma = \bar{\sigma}-\sigma_0 = A_v[1-f(\tau_v)]-A_i[1-f(\tau_i)] \qquad (1)$$

$$f(\tau_k) = \left(\sum_{l=1}^{\infty}\frac{2L^2\exp\left(-\frac{\beta_l^2 D_{kH}t}{a^2}\right)}{\beta_l^2(\beta_l^2+L^2+L)}\right)\times\left(\sum_{m=1}^{\infty}\frac{2M^2\exp\left(-\frac{\gamma_m^2 D_{kH}t}{b^2}\right)}{\gamma_m^2(\gamma_m^2+M^2+M)}\right)\times\left(\sum_{n=1}^{\infty}\frac{2N^2\exp\left(-\frac{\lambda_n^2 D_{kH}t}{c^2}\right)}{\lambda_n^2(\lambda_n^2+N^2+N)}\right) \qquad (2)$$

Table 1. Kinetic information from the conductivity relaxation.

	BZY with NiO		BZY purely sintered	
	Hyd	**Dehyd**	**Hyd**	**Dehyd**
A_i	(6.36±0.09) x 10^{-3}	(8.93±0.14) x 10^{-3}	(1.73±0.02) x10^{-2}	(3.36±0.03) x10^{-2}
A_v	(6.39±0.09) x 10^{-3}	(8.61±0.13) x 10^{-3}	(1.69±0.03) x10^{-2}	(3.36±0.03) x10^{-2}
D_{iH} /cm^2 s^{-1}	(1.38±0.05) x 10^{-6}	(1.17±0.03) x 10^{-6}	(1.50±0.10) x10^{-6}	(4.50±0.17) x10^{-7}
D_{vH} /cm^2 s^{-1}	(1.85±0.03) x 10^{-7}	(1.97±0.04) x 10^{-7}	(5.70±0.02) x10^{-8}	(7.14±0.02) x10^{-8}

The extracted kinetic parameters shown in Table 1. Chemical diffusivity of oxygen ion of BZY purely sintered is slower than that of the other speciemens by ~3 factors. It can be the reason why first decrease in the curve of BZY20 purely sintered is bigger than that of the other specimen. However, many factors can be the reason of that, so more investigations about partial protonic conductivity are needed.

Particularly, in the case of BZY purely sintered, chemical diffusivities of proton is different each other upon hydration/dehydration.

4. Conclusion

One of the most promising materials, pure BZY20s, were compared with BZY20 sintered with 1wt% NiO. DC 4-probe method was applied to both specimens. Chemical diffusivities of oxygen ions of both differs each other. It is expected that this is reason why both conductivity relaxation curves differ. However, we cannot be sure whether it is the main factor of that difference or not. More investigations about partial protonic conductivity are needed.

References

[1] T. Takahashi and H. Iwahara, Solid State Ion., Rev, Chim. Miner.,**17**, (1980), 243.

[2] K. D. Kreuer, Annu. Rev. Mater. Res., **33**, (2003), 333.

[3] S. Tao, J. T. S. Irvine, J. Solid State Chem., **180**, (2007), 3493.

[4] J. I. Yeon, H. -I. Yoo. Solid State Ion., **181**, (2010), 1323.

[5] Y. Yamazaki, R. Hernandez-Sanchez, S. M. Haile, Chem. Mater., **21**, (2009), 2755.

[6] C.-R.Song, H.-I. Yoo, Solid State Ion., **120**, (1999), 141.

[7] H. –I. Yoo, C. –E Lee, J. Am. Ceram. Soc., **88**, (2009), 617.

Eighth International Conference on Flow Dynamics
November 9 - November 11, 2011

Electrochemical Oxygen Reduction Process on $LaNi_{0.6}Fe_{0.4}O_3$ Electrode

Riyan Achmad Budiman, Shin-Ichi Hashimoto, Koji Amezawa, Tatsuya Kawada
Graduated School of Environmental Studies, Tohoku University
6-6-01 Aoba, Aramaki, Aoba-ku, Sendai 980-8579, Japan
Corresponding author: riyanab@ee.mech.tohoku.ac.jp

ABSTRACT

$LaNi_{0.6}Fe_{0.4}O_3$ porous and dense electrode was investigated by impedance spectroscopy as functions of temperature (923~1153K) and oxygen partial pressure (10^{-3}~1 bar). From fitting the impedance responses by using appropriate equivalent circuits, origins of electrochemical processes were separately identified. The large resistive and capacitive impedance at medium frequency was dominating the impedance response. From this work the reaction mechanism of LNF related to the absorption and dissociation of oxygen molecules in the surface reaction, although it might be the other reaction occurred.

1. Introduction

Solid oxide fuel cells (SOFCs) have attracted high attention as next generation power generators due to their efficiently convert from chemical energy to electrical energy. SOFCs combine the benefits of the environmentally friendly and fuel flexibility. SOFCs operated in high temperature at about 1273K. In high temperature operation causes material problems such as electrode (cathode)-electrolyte delamination which cause the low performance of SOFCs. The performance of the SOFC cathode is very important, since the cell efficiency affected by the electrochemical process on the cathode. To overcome this problem the material that can be used for intermediate temperature SOFC (IT-SOFCs) is needed. $LaNi_{0.6}Fe_{0.4}O_{3-\delta}$ (LNF) is one of the promising cathode materials for IT-SOFCs operated, because of its high catalytic activity, high electrical conductivity, excellent durability against chromia poisioning, and better TEC match with electrolyte [1, 2]. Numerous studies on this material so far concerned only the performance, and just few did the mechanism of the oxygen reduction process. Thus, the electrochemical kinetics on this electrode material is not clear yet. In this work, electrochemical oxygen reduction process on a LNF dense and porous film electrode was investigated by impedance spectroscopy as functions of temperature and oxygen partial pressure. The dense electrode is well defined system which was used to determine the reaction mechanism on the LNF cathode.

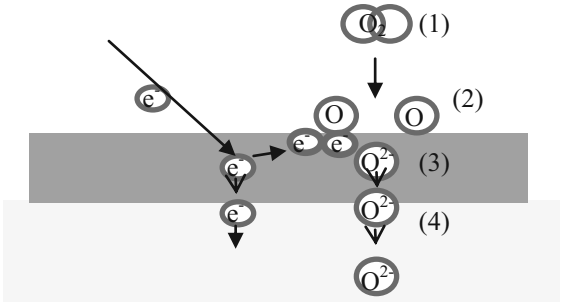

Fig. 1 Schematic view of oxygen incorporation reaction through the electrode.

A schematic diagram for reaction mechanism on the electrode dense shown in figure 1. A dense film electrode of mixed ionic and electronic conductor is formed on an oxide ion conductor. Oxygen exchange reaction on a dense mixed conductor electrode consists of (1) gas phase diffusion, (2) surface reaction (adsorption, incorporation) on the electrode, (3) O2- diffusion in the electrode layer, and (4) O2- ion transfer at the electrode/electrolyte boundary. On the other step, measurement on the porous electrode gives knowledge of reaction mechanism of real cathode system from point of view application, which has disadvantages of structure and geometry effect. The first step of analyses the impedance spectra was fitted by using tentative equivalent circuits, and the origins of electrochemical processes have been separately identified.

2. Experimental

2.1. Electrochemical Cell Preparation

Electrochemical coin cells using $Ce_{0.9}Gd_{0.1}O_{1.95}$ (GDC) electrolyte were prepared for evaluating electrochemical properties of LNF cathodes. Powders of GDC were prepared by a co-precipitation method, pressed into pellet and sintered at 1823 K for 5 hours. The GDC pellet sintered was about 10 mm in diameter and 1.7mm in thickness. The relative density was higher than 98%. The pellet surface was polished and used as a substrate for LNF.

$LaNi_{0.6}Fe_{0.4}O_{3-\delta}$ (LNF) powder which was synthesized by the pechini method was used for the porous electrode formation and target preparation aimed at the dens film formation. The LNF powers are calcined at for 24 hours. The X-ray diffraction patterns suggested that the products consisting of single phase.

The LNF powder was pressed into a disc and sintered at 1273K in air for 6 hours to prepare the target for dens film formation. LNF film was formed on the polished GDC pellet by pulsed laser deposition (PLD) using the prepared LNF target. Nd-YAG laser was used as laser source. Film was deposited in 1 Pa oxygen at 1073K. After PLD process, the sample was annealed in oxygen of 10^5 Pa for about 30 minutes. From–observation by FE-SEM (JEOL, JSM – 7001F) the thickness of film was about 1.5 μm. As is the case in the electrochemical cell for the evaluation of porous LNF cathode, the LNF porous electrode and Pt electrode were used for the counter and reference electrode, respectively.

For evaluation of porous LNF cathode, LNF paste which was consisted of LNF power, ethylcellulose powder (Wako Pure chemical industries Ltd.) and

organic solvent (Tanaka kikinzoku Co. Ltd., TMS-1), was painted onto the GDC pellet by screen printing method. LNF paste was also painted onto the opposite side surface of the GDC pellet and as the counter electrode. Pt wire as a reference electrode was attached to lateral surface of the GDC pellet via Pt paste. All of the electrodes were concurrently sintered in the air at 1273K for 6 hours.

2.2. Electrochemical Measurement

Electrochemical properties of the porous and dense LNF electrodes were investigated by the impedance spectroscopy in a single chamber cell as a function of temperature (923 – 1073 K) and oxygen partial pressure (10^{-3}-1 bar). In the dense electrode measured with and without dc bias. For the dc bias case, the oxygen potential which has been raised up by applied voltage, does not decrease through the dense electrode. Since oxygen potential drops only by the resistance of oxygen adsorption/dissociation or incorporation at gas/electrode interface, it exhibits as same potential as that at the electrode/electrolyte potential. For such a case, oxygen potential can be electrochemically provided through the whole thickness of the electrode material. At first, oxygen potential at the electrode/electrolyte interface, $\mu_{o,int}$, is defined as:

$$\mu_{o,int} = \mu_{o,g} + 2F\Delta E$$

where $\mu_{o,g}$ is the equilibrium oxygen potential in the gas phase around the reference electrode.

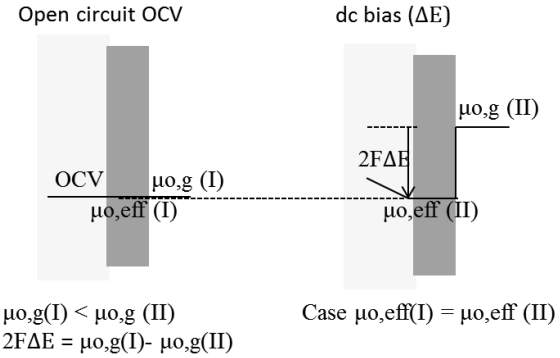

Fig. 2 Chemical Capacitance on the LNF that related with surface reaction which is has large value of capacitance

Electrochemical impedance spectra were measured by combination of potentio-galvanostat (Toho technical research Co., Ltd., Model 2000) and gain phase frequency response analyser (NF Co,Ltd., Model FRA5097) between working electrode and the reference electrode. Zview (Scribner Associates, Inc.) was used to analyses of the impedance responses. Equivalent circuits with two or three R (resistance) -CPE elements (a resistance, R, and a constant phase element, CPE, connected in parallel) were fitted to identify their physical meanings.

3. Results and Discussion

3.2 Dense film electrode

The LNF dense electrode on ceria electrolyte basically showed a single arc, which consists of parallel circuit of resistance, R_s, and a capacitance, CPE. The intercept of the arc at the high frequency side is considered to originate from the ohmic loss of the ceria electrolyte. An arc should appear at the high frequency side next to main arc if the grain boundary resistivity is large in ceria. The peak frequency of the arc for the LNF electrode impedance was very low, which was in the range of 1Hz to 0.01 Hz. Figure 3(a) shows the typical impedance spectra on the LNF dense electrode on GDC electrolyte at 1073K. The electrode impedance increased when the oxygen partial pressure decreased. It decreased when the electrode was on the anodic polarization, and increased when the electrode was on the cathodic polarization.

The impedance spectra of LNF didn't show the ideal capacitor, and the it show depressed spectra as shown on the figure 3(a). An equivalent circuit system used to identify the impedance spectra of the dense electrode as shown in figure 3(b). Since the resistance in the ionic and electronic path in the cathode bulk are smaller than the surface reaction resistance, reaction rate is controlled by the surface process. In addition, if the electronic conductivity of the electrolyte is much smaller than the ionic conductivity, then the equivalent circuit can be simplified as figure 3(b).

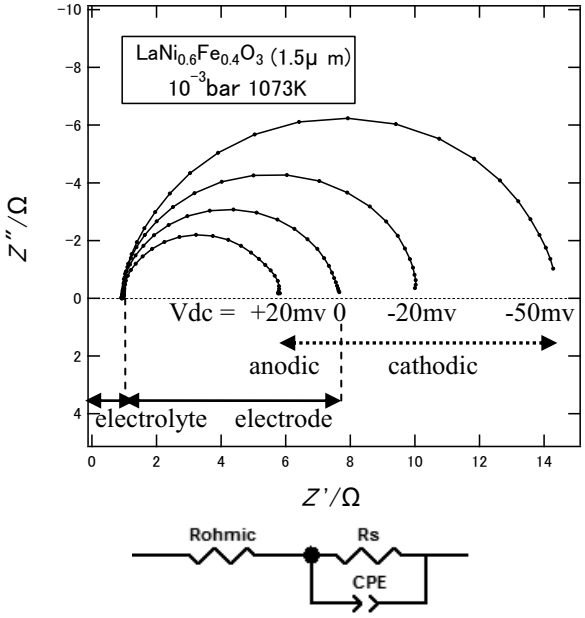

Fig. 3 (a)Typical impedance response of LNF electrode on GDC electrolyte under various dc bias. (b) A simplified equivalent circuit for dense electrode material.

Such a large capacitance, which exhibits strong dependency on the electrochemical polarization of the electrode, can be explained as a chemical capacitance. This large capacitance is associated with adsorption and dissociation of oxygen in the surface of the cathode material. The concept of the chemical capacitance has been discussed by several researchers [2,3]. The use of the chemical capacitance, in some cases, gives useful

information in the electrode reaction analysis. Oxygen vacancy concentration in the electrode material is change with an applied over potential, will cause a large chemical capacitance in the AC impedance as shown in figure 4.

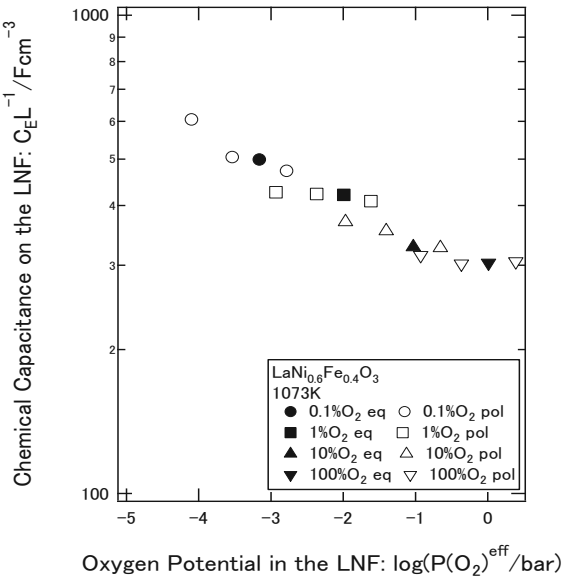

Fig. 4 Chemical Capacitance on the LNF electrode at 1073K with or without applying dc bias in various gaseous oxygen partial pressure.

Although the rate determining step (RDS) of LNF attached to the surface reaction, but the impedance spectra didn't show the ideal capacitor on the results. Several researchers show that ideal capacitor is attached to the surface reaction [3,7]. In this case the impedance spectra depressed and this is not ideal capacitor, it might be another reaction on the LNF besides surface reaction. There wasn't enough data to conclude the works in the LNF electrode, especially in the capacitance. The nonstoichiometric data needed to make the situation clear and thermodynamics properties on the LNF is also needed, and the measurement on the porous showed another insight on the LNF electrode.

3.1 Porous electrode

Figure 5 show the typical ac impedance spectra of LNF porous electrode. Electrochemical impedance response of these electrodes consisted of at least three primary elements; a small arc in a high frequency (HF) range (10 kHz~), an arc having a large resistive and capacitive impedance in the intermediate frequency (MF) range (0.5 Hz- 1 kHz), and an arc in the low frequency (LF) range (0.01-0.5 Hz). Capacitance value of arc in the HF is being independent to the p_{O2} as shown in the figure 5. Such a fast reaction happened in the HF range. In the dense electrode, the HF side was not clearly observed in the impedance spectra. The one of possibility there was a bad contacting area between electrode and electrolyte which could be happened in the HF range. The other possibility might be other reactions that very fast pass through the electrode. It might be surface diffusion happened in the electrode or small inhomogeneous internal diffusion happened in the electrode. On the other side MF arc was dominating the impedance spectra. Such a large capacitance in the MF arc, which exhibits strong dependency on the electrochemical polarization of the electrode, could be explained as a chemical capacitance. Figure 6 shows the capacitance of LNF cathode at 923K as a function of p_{O2}. The unusual capacitance in the MF arc leads to the several possibility. The capacitance increased when the p_{O2} increased. It might be related to the change valence on B-side on perovskite structure. Such a measurement on nonstoichiometric needed to prove this probability.

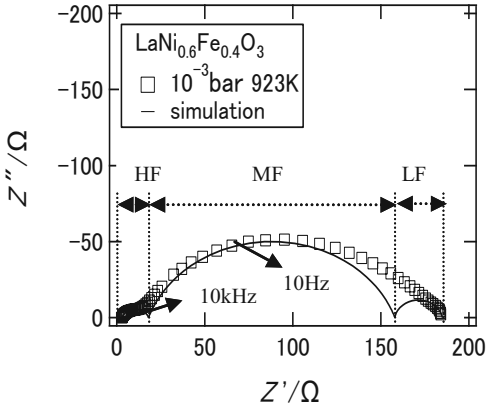

Fig. 5 Typical impedance spectra of LNF porous electrode which has three primary parts

The unusual nonstoichiometric behavior on $LaNi_{0.6}Fe_{0.4}O_3$ might be happened in the high p_{O2} and low temperature for porous electrode. In this case the capacitance values at high temperature show the same tendency as low temperature. The other possibility is the value capacitance is not from single reaction, and there are several reaction affect the capacitance. The porous electrode and the dense electrode have same large capacitance value, and this large capacitance value is related to the surface reaction on the electrode. The dense electrode has different value porous electrode, and also the different tendency. The possibility of this case, it might be related to the thermodynamics parameter of porous and dense electrode. The nonstoichiometric data needed to make the situation clear, and thermodynamics properties on the LNF is needed also.

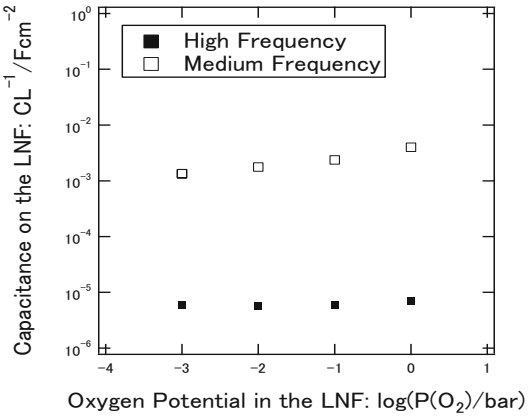

Fig. 6 capacitance as function of p_{O2} at 923K

The electrode impedance increased when the oxygen partial pressure decreased. The area specific conductivity σ_E for the medium frequency arc was proportional to $p_{O2}^{1/2}$ at 923 K or at lower temperatures, as shown in Fig. 7.

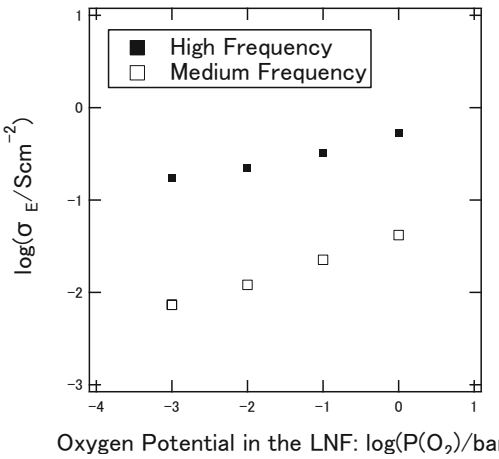

Fig. 7 σ_E as function of p_{O2} at 923K. LNF at low temperature is proportional to $p_{O2}^{1/2}$

It clearly can be seen at higher temperatures p_{O2} which had small effects on the σ_E which is shown on the figure 8. At higher temperature the σ_E values reach saturation value. These suggested that the response on the LNF might not be from a single process, although it is considered to be principally attributed to the surface reaction. The work on the nonstoichiometric measurement and isotope exchange measurement will give better understanding of LNF cathode.

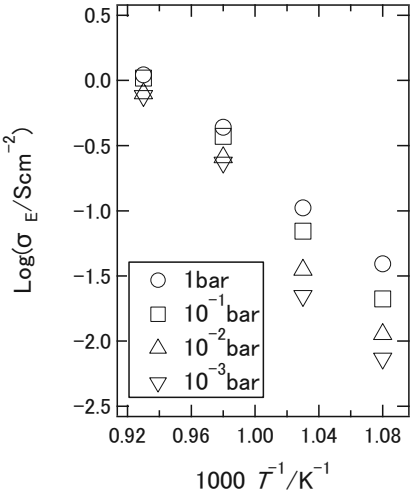

Fig. 8 Area specific conductivities σ_E of LNF as function of temperature.

4. Conclusion

The large capacitance, which exhibits strong dependency on the electrochemical polarization of the electrode, can be explained as a chemical capacitance. Oxygen vacancy concentration in the electrode material is change with an applied over potential, will cause a large chemical capacitance in the AC impedance. The reaction mechanism of LNF related to the absorption and dissociation of oxygen molecules in the surface reaction, although it might be the other reaction occurred. There wasn't enough data to conclude the works in the LNF electrode, especially in the capacitance. The nonstoichiometric data needed to determine the capacitance values and thermodynamics properties on the LNF is also needed in order to get better understanding on the reaction mechanism.

References

[1] R. Chiba *et al.*, *Solid State Ionic*, **124** (1999) 281.
[2] T.Kawada *et al.*, *Solid State Ionic*, **121** (1999) 271.
[3] J. Jamnik *et al.*, Phys. Chem. Chem. Phys., 3 (2001) 1668-1678

Eighth International Conference on Flow Dynamics
November 9 - November 11, 2011

Stress Effect for Conductivity Characteristics of Functional Ceramics

Yusuke Kawamura[1], Kazuhisa Sato[2], Keiji Yashiro[1], and Junichiro Mizusaki[1]
[1] Institute of Multidisciplinary Research for Advanced Materials, Tohoku University, Japan
[2] Fracture and Reliability Research Institute, Graduate School of Engineering, Tohoku University, Japan
E-mail: y-kawamu@mail.tagen.tohoku.ac.jp

ABSTRACT

Electrical conductivity of $La_{0.6}Sr_{0.4}CoO_{3-\delta}$ thin-film was measured under four-point bending test at room temperature. It was observed that conductivity was decreased as strain increased.

Density of states about La_2NiO_4 at compressive strain was simulated by first-principles calculations and estimated effect of strain on electrical conductivity. Band gap and band structure unchanged mostly each strain. It suggested that electronic density does not relate to conductivity changing by strain.

1. Introduction

It is reported that electrochemical properties and mechanical properties of functional ceramics are connected to crystal structure and nonstoichiometry [1,2,3,4]. It is noted that electrochemical properties, mechanical properties, and interstitial volume are transmuted by change of crystal structure and nonstoichiometry. Thus there is a possibility that electrochemical properties are transmuted by kinetic load.

Functional ceramics are used in various applications, for example, solid oxide fuel cells (SOFCs), sensors, transistors, thermistors, and so on. On devises, these materials are subject to residual stress or other kinetic load by surrounding materials. Therefore it is important for prediction and optimization of material properties to clarify effect of electrochemical properties by changing interstitial volume and crystal structure.

This effect for typical functional ceramics was investigated by this research group [5]. For example, in the case of yttria-stabilized zirconia (YSZ) and gadolinia-doped ceria (GDC) as ionic conductors, conductivity decreased as stress increased under uniaxial compressive stress. In contrast, in the case of $YBa_2Cu_3O_{7-\delta}$ (YBCO) and $La_2NiO_{4+\delta}$ (LNO) as electronic conductor, conductivity increased as stress increased under uniaxial compressive stress. In the case of YSZ, GDC and LNO, the conductivity variation is considered that it was caused by change in mobility. In the case of YBCO, the conductivity variation is considered that it was caused by changes in mobility and carrier concentration.

Causation of these phenomena is not clarified yet. This study is intended to clarify the causation of effect of strain to electrical conductivity by two methods.

In first method, effect of strain on electrical conductivity about thin-film ceramics was investigated by four-point bending test. In this study, Conductivity of $La_{0.6}Sr_{0.4}CoO_{3-\delta}$ (LSC40) thin-film on MgO substrate was investigated.

In second method, density of states (DOS) about functional ceramics was simulated by first-principles calculations and estimated effect of strain on electrical conductivity. In this study, DOS about La_2NiO_4 (LNO) was investigated.

2. Electrical conductivity of thin-film ceramics

2.1. Methods

Sample preparation

In this study, we used thin-film layered specimen. Thin-film layered specimen was made by PLD (Pulsed Laser Deposition) method using a YAG laser (λ= 266 nm). $La_{0.6}Sr_{0.4}CoO_{3-\delta}$ was used in thin-film conductor. LSC40 was prepared by a citric acid method. Single-crystal MgO was used in substrate. Dimension of substrate is 15 mm × 15mm × 0.5 mm. Miller index of substrate is (1 0 0).

Condition of PLD is shown in table 1. The substrate temperature was kept at 923 K during deposition. Oxygen pressure in the chamber was 1 Pa. After deposition, substrate temperature was kept at 923 K at oxygen pressure in 1.0×10^5 Pa O_2 for 9 h. Dimension of thin-film is 8 mm × 8 mm × 0.8μm.

After PLD, Pt-probe was made by sputtering deposition as shown in figure 1. Thickness of Pt-probes is approximately 0.2 μm. Distance of current probes is 2 mm, and distance of voltage probe is 6 mm.

Table 1 PLD condition

Target	$La_{0.6}Sr_{0.4}CoO_{3-\delta}$
PLD condition	923 K 1 Pa O_2 10 Hz for 2 h
Post annealing	923 K 1.0×10^5 Pa O_2 for 9 h
Film thickness	ca. 0.8 μm

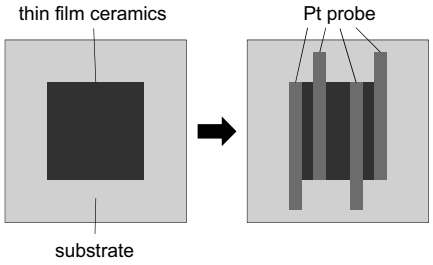

Figure 1. Diagram of thin-film layered specimen

Measurement setup

The diagram of the experimental setup is shown in figure 2. The uniaxial compressive load was applied to the specimen by the compression testing machine (Instron, 5565) and controlled by the load cell. The electrical furnace (Makuhari rikagaku glass Co.) was fixed into the testing machine.

Jigs of four-point bending are made by Al_2O_3. The specimen was placed between these jigs. In this study, thin-film ceramics ware set lower side of specimen as figure 2. The wires were connected to current source meter (KEITHLEY, 6221 AC and DC Current Source) and voltage meter (KEITHLEY, 2182A Nanovoltmeter) for the electrical conductivity measurement.

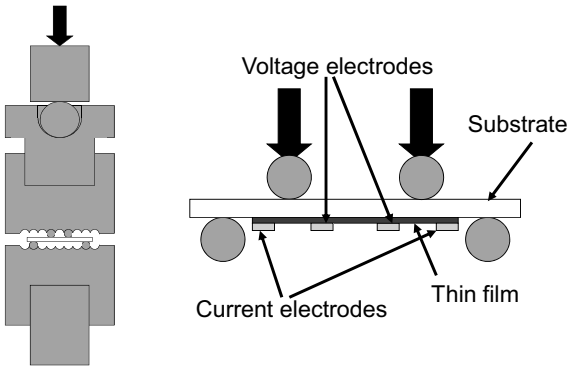

Figure 2. Setup detail around the fixed specimen

Measurement

Electrical conductivity was measured by DC four-probe method. The applied currents were 1 mA.

The measurement procedures are shown in figure 3. After temperature was stabilized, an impedance measurement was carried out under constant load and electrical conductivity was calculated. That was repeated at regular time intervals under the load. After stable conductivity was confirmed, load was raised and the measurement was carried out in a similar way. These processes were repeated until the load reached to maximum load. And then, the load reducing processes were measured in a similar way with load raising processes until load reached the minimum load. These processes were repeated a few times in order to confirm the reproducibility.

In the four-point bending test, the bending strain in the film ε_f is shown in following equation. It is able to be estimated from flexural rigidity EI, uniaxial load W, distance between the outer and inner bearing a, and distance between the inner bearings b. (show in figure 4) In this study, both of a and b is 4 mm.

$$\varepsilon_f = \frac{(2EI)^2 Wa}{\{(2EI)^2 + (Wab)^2\}^{\frac{3}{2}}} \quad (1)$$

In this study, young's modulus is referred from [6]. At 300 K, young modulus E of Single-crystal MgO substrate is 309.6 GPa.

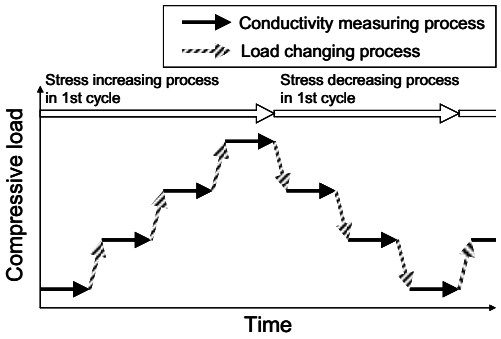

Figure 3. Procedure of experimental measurement

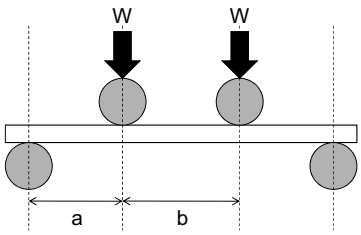

Figure 4. Schematic of dimension of four-point bending

2.2. Results and discussion

Electrical conductivity of LSC40 thin-film at room temperature in air as a function of uniaxial load is shown in figure 5, and function of strain is shown in figure 6. The strain estimated by equation (1).

Figure 5 show that conductivity changed by time. It phenomenon was caused by changing room temperature. Conductivity changed rapidly as soon as changing uniaxial load. The conductivity decreased as load increased, and increased as load decreased. Conductivity variation is 0.0015 Scm^{-1} per 10 N. In this study, thin-film ceramics ware set lower side of specimen. So the more the uniaxial load increase, the more tensile strain was subjected for thin-film. This behavior fit to behavior of balk of other electronic conductive ceramics.

Figure 6 is enlarged view of a part of figure 5. It shows that conductivity variation rate is 0.025 % per 0.01 % strain. This variation rate is lower than rate of balk of other electronic conductive ceramics.

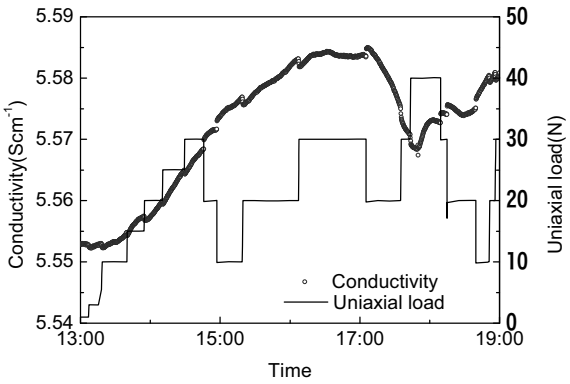

Figure 5. Conductivity and uniaxial load of LSC40 at room temperature in air

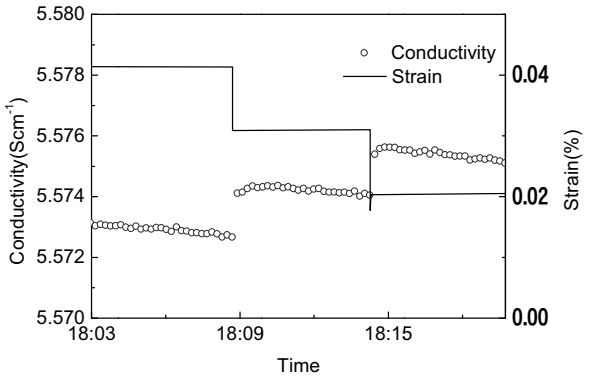

Figure 6. Conductivity and strain of LSC40 at room temperature in air

3. First-principles calculations

3.1. Methods

First principles total energy calculations were performed using VASP code [7]. The interaction between ions and valence electrons was described by the projector augmented wave (PAW) method [8]. The exchange and correlation effects were treated by the generalized gradient approximation parameterized by Perdew, Burke, and Ernzerhof (GGA-PBE) [9].

We used perfect La_2NiO_4 crystal (Space Group; I4/mmm) for calculation. (show in figure 7) The Cut-off energy of plane wave was set to 500 eV. The k-point mesh of Brillouin zone was set to 5 × 5 × 5. Cut-off energy and k-mesh decided by convergence of relative energies that become better than 1 meV/atom.

Lattice parameters and internal positions were fully optimized under the condition of residual Hellmann-Feynman forces become less than 0.02 $eVÅ^{-1}$.

After structure optimization, strain was introduced in primitive cell. In this study, strain of c-axis is 0.05 %, 0.10 %, 0.15 %, and 0.20 %. After introduction of strain, density of states (DOS) was calculated respectively.

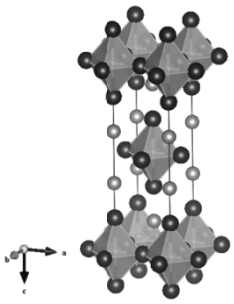

Figure 7. La_2NiO_4 crystal (Space Group; I4/mmm)

3.2. Results and discussion

3.2.1. Structure optimization

Experimental lattice parameter [10] and calculated lattice parameter are shown in table 2.

After structure optimization, lattice parameter changed less than 1.8 % from experimental lattice parameter.

Table 2 Lattice parameter of La_2NiO_4

	a / Å	c / Å
Experimental	3.9008	12.731
Calculation	3.9232	12.502

3.2.2. Introduction of strain for primitive cell

After structure optimization, strain was introduced in primitive cell. In this study, c-axis compressive strain was introduced 0.05 %, 0.10 %, 0.15 %, and 0.20 %. At each strain ratio, a-axis length was optimized by energies.

Optimization of a-axis is shown by figure 8. Lattice parameters after introduced strain are shown by table 3.

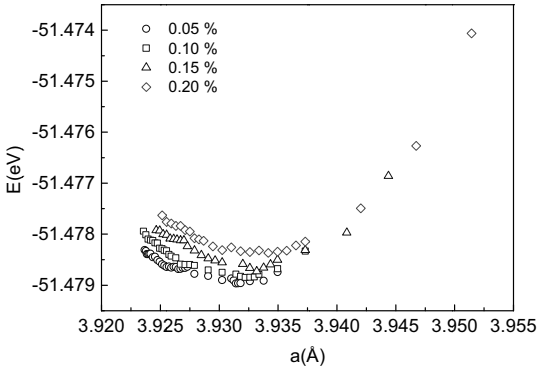

Figure 8. Energy of La_2NiO_4 as changing a-axis length

Table 3 Range of lattice parameter at each strain

strain	lattice parameter	
ε_c / %	c / Å	a / Å
0.05	12.496	3.9314
0.10	12.490	3.9322
0.15	12.483	3.9332
0.20	12.477	3.9342

3.2.3. Calculation of density of states

After introduction of strain, DOS was calculated each strain. Figure 9 shows total DOS before introduction of strain. Figure 10 shows total DOS after in introduction of strain.

Figure 9 shows that band gap of La_2NiO_4 of this structure is 0.45 eV.

Figure 9 and 10 shows that band gap and band structure unchanged mostly each strain. It is possible that electronic density does not relate to conductivity changing by strain. So if mobility relates electronic density, this result will not match prediction of previous study.

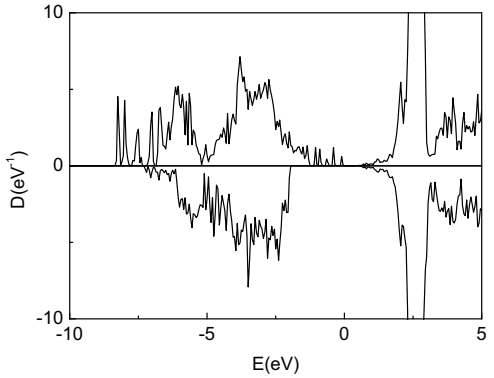

Figure 9. Total density of states of La_2NiO_4 before introduction of strain

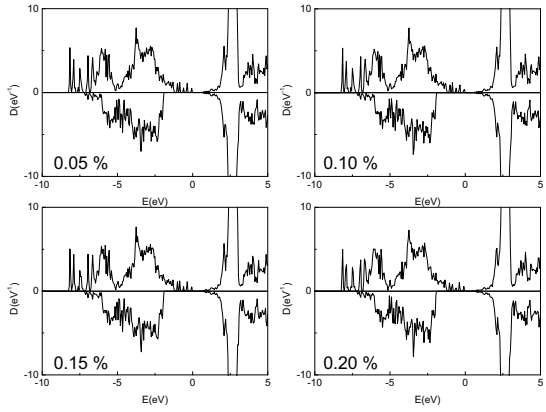

Figure 10. Total density of states of La_2NiO_4 after introduction of strain 0.05 %, 0.10 %, 0.15 %, and 0.20 %

4. Conclusion

In the second chapter, conductivity changing of LSC40 thin-film was discussed.

Conductivity changed rapidly as soon as changing uniaxial load. The conductivity decreased as tensile strain increased, and conductivity increased as tensile strain decreased. Conductivity variation rate is 0.025 % per 0.01 % strain. This behavior fit to behavior of balk of other electronic conductive ceramics. However, this variation rate is lower than balk of other electronic conductive ceramics. It is suggested that conductivity variation mechanism relate to difference of conductivity mechanism between thin-film and balk.

For the future, we measure conductivity at high temperature. In addition, effect of strain for electrical properties needs to clarify at both bulk and thin-film.

In the third chapter, DOS of La_2NiO_4 calculated by first principles calculation was discussed.

At strain of c-axis is 0.05 %, 0.10 %, 0.15 %, and 0.20 %, band gap and band structure unchanged mostly each strain. It suggested that electronic density does not relate to conductivity changing by strain. This result will not match prediction of previous study.

For the future, causation of this unmatched result need to be clarifies. In addition, we will use the supercell of $La_2NiO_{4+\delta}$ including oxygen excess. It would enable to discuss conductivity changing by strain caused by carrier concentration.

Finally we would like to clarify the causation of effect of strain to electrical conductivity.

References

[1] T. Nakamura, K. Yashiro, K. Sato and J. Mizusaki, *Phys. Chem. Chem. Phys*., 11, 3055–3062 (2009)

[2] S. Wang, M. Katsuki, M. Dokiya and T. Hashimoto, *Solid State Ionics*, 159, 71–78 (2003)

[3] S. Yamaguchi K. Terabe, A. Imai and Y. Iguchi, *Jpn. J. Appl. Phys*., 27, 220-222 (1988)

[4] J. Mizusaki, H. Tagawa, K. Hayakawa and K. Hirano, *J. Am. Ceram. Soc.*, 78, 1781-1786 (1995)

[5] T. Izumi, R. Narumi, K. Sato, K. Suzuki, K. Yashiro, T. Hashida and J. Mizusaki, *ECS Transactions*, *214th ECS Meeting*, *Solid State Ionic Devices 6 – Nanoionics*, 16(51), 125-132 (2008)

[6] Y. Sumino, Orson L. Anderson, and I. Suzuki, *Phys Chem Minerals*, 9, 38-47 (1983)

[7] G. Kresse and J. Furthmüller, *Phys. Rev. B,* 54, 11169-11186 (1996)

[8] P. E. Blöchl, *Phys. Rev. B*, 50, 17953-17979 (1994)

[9] J. P. Perdew and A. Zunger, *Phys. Rev. B*, 23, 5048-5079 (1981)

[10] S. J. Skinner, *Solid State Sciences*, 5, 419-426 (2003)

The Effect of Electric Field on Ternary Oxides – Electrotransport and Decomposition in Model System $NiTiO_3$

Jakyu Chun
Solid State Ionics Research Laboratory, Department of Materials Science and Engineering
Seoul National University, Seoul, Korea 151-744
qtkool1@snu.ac.kr

ABSTRACT

Complex oxides making up devices such as solid oxide fuel cells are exposed to various thermodynamic driving forces, i.e. electric field, chemical potential gradient, etc. These driving forces affect the devices in such a way that the performance of the devices slowly degrades over a period of time. In this work a model ternary oxide system of $NiTiO_3$ was put under DC electric field and the effects of the applied electric field was analyzed through microstructural and compositional analysis. It is shown that the electric field causes decomposition of $NiTiO_3$ into the component oxides, proposing a mechanism for performance degradation.

1. Introduction

Various modern day devices incorporate complex oxides (ternary or higher) as their components. For example, the cathodes of solid oxide fuel cells (SOFC) are made primarily of perovskite oxides with La, Sr, Co and Fe as cationic species. The cations in these oxides are virtually immobile compared to the oxygen ions due to their meager diffusivities.

The fact that the cations are virtually immobile takes a different turn when long-term stability of oxides is taken into account. These oxides are constantly under influence of driving forces such as chemical potential gradient, external electric field, thermal gradient, etc. Upon long-term application, the cations, albeit their slow mobility, migrate with different speed, creating nonuniform cationic distribution throughout the oxide. This phenomenon is termed kinetic demixing, and when the extent is demixing is severe enough the oxide decomposes into its component oxides, a phenomenon called kinetic decomposition.

Kinetic demixing and decomposition creates various secondary effects that are crucial to the lifetime of devices – lattice displacement, secondary phase formation (i.e. a highly resistive phase), cation diffusion into/from other parts in the device (due to increase in activity), etc. In other words, the devices are degraded upon cationic transport.

There have been many works by various researchers on kinetic demixing and decomposition, dating as far back as the 1979 work by Schmalzried et al. on (Co,Mg)O [1]. Works by Schmalzried and Laqua [2], M. Martin and Schmackpfeffer [3-5] discuss the effect of oxygen partial pressure gradient on demixing and decomposition, while other works [6-9] focus on the effect of electric field. An interesting thing is that while both demixing and decomposition occurred under oxygen partial pressure gradient, only demixing was observed under electric field. M. Martin recently presented preliminary results showing decomposition under electric field [10].

In this work, before putting the actual cathode material of SOFC into trial a model ternary oxide system of $NiTiO_3$ was put under DC electric field. After removal, the specimen was analyzed using SEM, EDS and EPMA (soon to be followed by micro-XRD). Specific methods and results are shown in the following sections. The most notable result is the occurrence of kinetic decomposition at the electrodes.

2. Method

The $NiTiO_3$ powders were prepared by solid state reaction of NiO (Seimi Chemical, Japan) and TiO_2 (Sigma Aldrich, USA) commercial powders. After ball milling for 12 hours the mixture was dried and calcined at 1100°C for 5 hours. The calcined powder was molded and cold isostatically pressed (CIP) at 150 MPa for 5 minutes, then sintered at 1500°C for 5 hours. The resulting slab had bulk density of 4.838±0.012 g/cm^3 (96.8% relative density) and grain size of 15±2 um. The bulk was of rhombohedral ilmenite structure. The slab was cut into specimen size of (2.12±0.04) x (2.19±0.02) x (2.537±0.005) mm^3 and Pt mesh (100 mesh, Sigma Aldrich, USA) were attached as electrodes on both ends with Pt paste (HLG6926, Engelhard, USA) in between. The cell setup is schematically shown in Fig. 1. A DC voltage of 12 V (field strength of 47 V/cm) was applied for 14870 seconds, the total current flown being ca. 5710 C (±5%). The temperature was 1330.7±0.8°C and the atmosphere was ambient air.

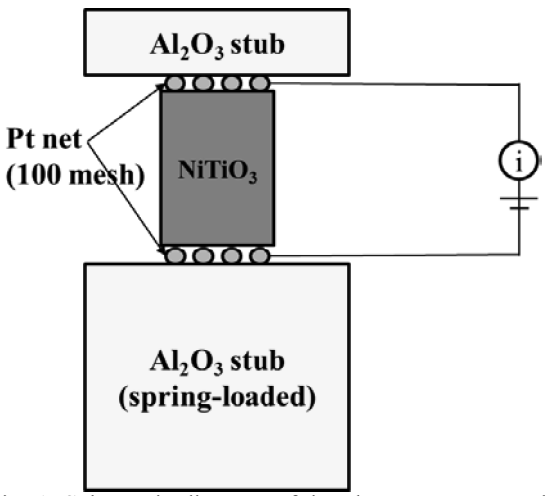

Fig. 1. Schematic diagram of the electrotransport cell

After electrotransport run, the specimen was quenched in air. It was then dissected into two halves parallel to the electric field. The dissected surfaces were polished down to 1 um. The microstructure of the specimen was observed by SEM (JSM-5600 and JSM-6360, JEOL, Japan) and optical microscope (Axiolab A, Carl Zeiss GmbH, Austria) after thermal annealing at 1400°C for 5 minutes. The chemical compositions were taken by EDS and EPMA (JXA-8900R, JEOL, Japan).

3. Results and Discussion

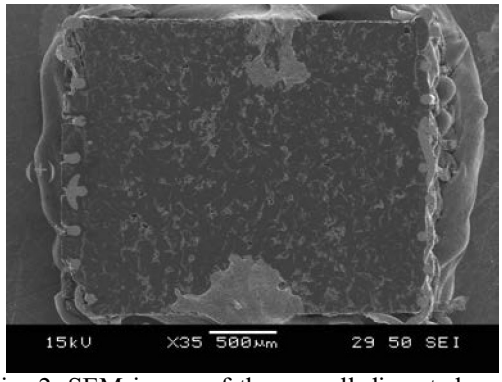

Fig. 2. SEM image of the overall dissected surface. The light gray regions at the top and bottom are Ag paste used for electrical channels during SEM image obtaining.

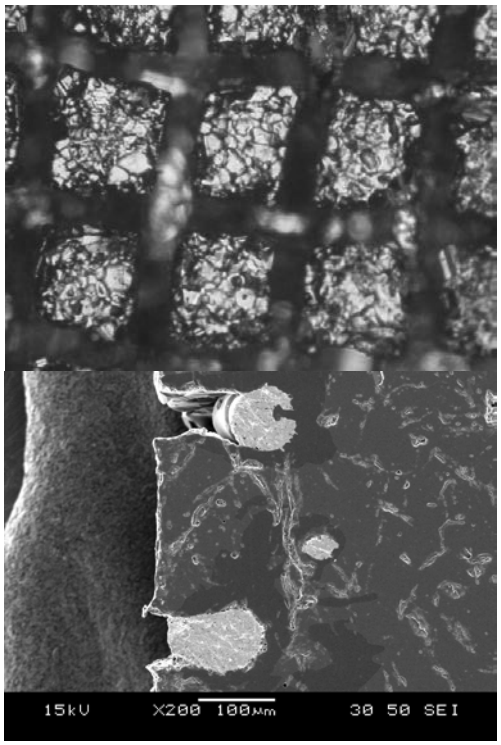

Fig 3. (a) Optical image of the anode surface (b) the SEM image of the dissected surface on the anode side.

Fig. 2 shows the overall dissected surface of the electotransport specimen after polishing down to 1 um. Fig. 3. shows the microstructure of the (+) electrode (anode). One can see that the Pt mesh penetrated into the $NiTiO_3$ lattice, indicating the annihilation of the original lattice through the reaction

$$NiTiO_3 \rightarrow Ni^{2+} + Ti^{4+} + 3/2\ O_2 + 6e^-. \qquad (1)$$

A point worth noting is clearly shown in Fig. 3 (b). The direct vicinity of Pt anode is noticeably darkened in color compared to the original matrix. This indicates that the darkened region has a different chemical composition (and probably of lower density since it is shown darker) from the original matrix. This is further discussed below. The distribution of the darkened region is quite irregular, indicating that the electrical field is not quite uniform at the interface.

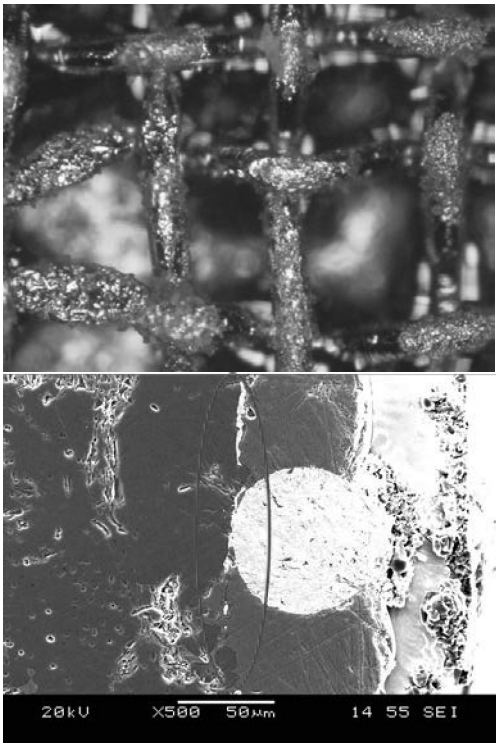

Fig. 4. (a) Optical image of the cathode surface (b) the SEM image of the dissected surface on the cathode side. One can see the inert Pt markers indicating the original surface of the oxide.

At the (-) electrode (cathode) one can observe the contrary – the lattice is newly grown at the bulk-electrode interface by the reverse reaction of (1), as shown in Fig. 4. The neutral Pt particles from the Pt paste can be found inside the oval in Fig. 4 (b). Because these particles act as inert markers, they indicate the original specimen surface.

It was shown that at the anode side there were darker patches around the electrodes. Therefore it would be reasonable to assume that a similar phenomenon would occur at the cathode side. Through both electron images and backscattered images we found that this indeed was the case. The newly grown lattice was lighter in color compared to the original lattice, meaning that this region is heavier than the original lattice. The theoretical densities of NiO, $NiTiO_3$ and TiO_2 are 6.67, 5 and 4.26

g/cm^3, respectively. Therefore we can predict that the darkened region to be TiO_2-enriched and the newly formed lattice to be mostly NiO.

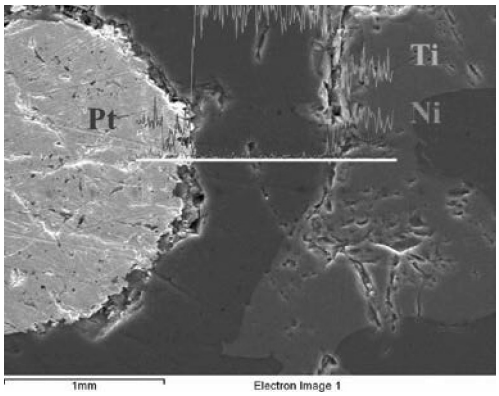

Fig. 5. The EDS profile of Ni, Ti and Pt at the anode. The red line corresponds to oxygen and is irrelevant. The yellow line is the line of profile.

To further analyze the chemical composition, EDS and EPMA were performed. Fig. 5 and 6 show the EDS results for the anode and cathode, respectively. In Fig. 5, one can immediately notice that the darkened area is Ti-rich, as stated above. On the other hand, Fig. 6 shows that the newly created lattice is relatively rich in Ni.

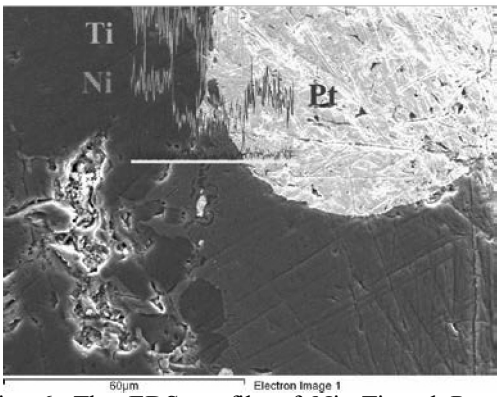

Fig. 6. The EDS profile of Ni, Ti and Pt at the cathode. The red line corresponds to oxygen and is irrelevant. The yellow line is the line of profile.

To obtain quantitative values of the compositions in various regions mentioned, EPMA was performed. Fig. 7 shows the EPMA result of the overall dissected surface. The beam spot size was 5 um. The red lines indicate the original lattice. In the central region, there is virtually no demixing and the cationic ratio Ti/Ni is nearly constant (0.96±0.03), insisting that the specimen is in overall slightly Ni-rich. However, at the anode side the Ni amount is virtually zero, suggesting that the darkened region is indeed TiO2. On the other hand, the newly formed lattice on the cathode side shows the contrary, indicating that the novel lattice is virtually NiO. In order to finalize the phase decomposition a micro-XRD analysis is required. This is soon to be done.

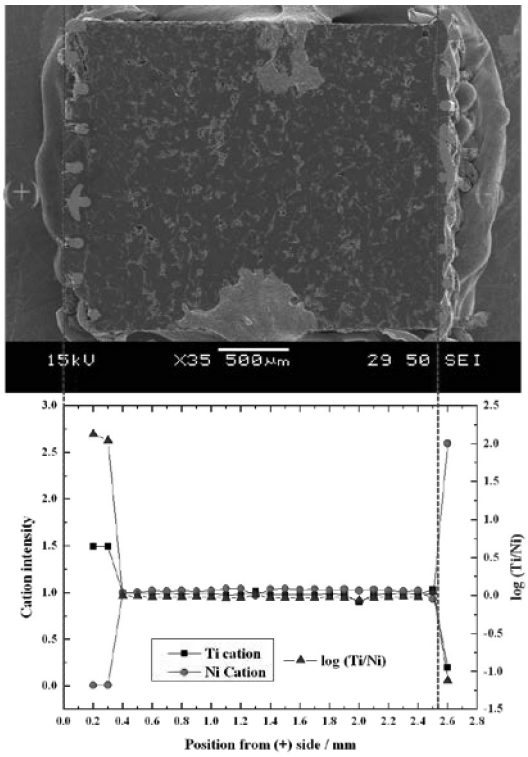

Fig. 7. The EPMA result of the overall specimen

Theoretically, in a ternary oxide, the faster of the cations migrate first to the (-) side and the slower ones are concentrated on the (+) side. In this work one can see that $D_{Ni} > D_{Ti}$ in the ilmenite $NiTiO_3$ phase. This coincides with the result by Schmalzried and Laqua [2]. In their work $NiTiO_3$ was place in an oxygen partial pressure gradient. Theoretically the faster cation migrates to the high-Po_2 side, which was the case in their work. Therefore their work and this work support one another.

Another thing that should be taken into account is the magnitude of the applied electric field. In this work an external DC voltage of 12 V was applied via Pt mesh electrodes. However, due to overpotential at the electrodes, not all the driving force is applied to the specimen. The actual driving force acting on the specimen was not measured in this work. There however is a theoretical threshold for the decomposition to occur. According to various thermodynamic measurements, the decomposition voltage of $NiTiO_3$ at 1330^{o}C is between 30 to 50 mV [11-14]. The effective applied voltage should be greater than this for decomposition to occur.

4. Concluding remarks

A model ternary oxide system of $NiTiO_3$ was put under DC electric field. Electrotransport of cations occurred due to the external electric field, along with decomposition at the electrodes. At the anode side TiO_2 was formed while the newly created lattice at the cathode side is made up primarily of NiO.

To kinetically analyze the specimen, the following works should be performed: i) micro-XRD analysis of

the newly formed phases should be made ii) EPMA of the newly formed phases should be extensively done to find the local cationic profiles iii) the effective driving force actually acting on the specimen should be obtained. The above-mentioned points are under way. Because the transport data for $NiTiO_3$ system are quite scarce, the same experiment and analysis may be applied to another model system (such as $LaCrO_3$, etc.). After obtaining refined results we can perform detailed kinetic analysis.

After the model systems are analyzed, the analysis can be finally applied to the actual oxides used in SOFC's (such as LSM, LSCF, etc.) to find the degradation mechanism.

References

[1] H. Schmalzried, W. Laqua, P. L. Lin, *Z. Naturforsch*, **34a** (1979), 192

[2] H. Schmalzried and W. Laqua, *Oxid. Met.*, **15**, (1981) 339

[3] M. Martin and R. Schmackpfeffer, *Ber. Bunsenges. Phys. Chem.*, **93** (1989), 1271

[4] M. Martin, *Ceram. Trans.* **24** (1991), 91

[5] M. Martin and R. Schmackpfeffer, *Solid State Ionics* **72** (1994), 67

[6] D. Monceau, M. Filal, T. Tebtoub, C. Petot, G. Petot-Ervas, *Solid State Ionics* **73** (1994), 221

[7] O. Teller and M. Martin, *Ber. Bunsenges. Phys. Chem.* **101** (1997), 1377

[8] O. Teller and M. Martin, *Solid State Ionics* **101-103**, 475

[9] J. –O. Hong, Ph. D Thesis, Seoul National University (1999)

[10] M. Martin, in *1st Workshop on Stability and Degradation of Functional Materials under Thermodynamic Forces*, Seoul, Korea, April 2011

[11] M. Lerch, H. Boysen, R. Neder, F. Frey, W. Laqua, *J. Phys. Chem. Solids* **53** (1992), 1153

[12] R. W. Taylor, H. Schmalzried, *J. Phys. Chem.* **68** (1964), 2444

[13] K. T. Jacob, V. S. Saji, S. N. S. Reddy, *J. Chem. Thermodynamics* **39** (2007), 230

[14] G. M. Kale, *Metallurgical and Materials Trans. B* **29** (1998), 31

Eighth International Conference on Flow Dynamics
November 9 - November 11, 2011

Conductivity variation in mixed ions electric conductor under uniaxial stress

Shusaku Nakakawaji, Kazuhisa Sato, Keiji Yashiro, Junichiro Mizusaki
Institute of Multidisciplinary Research for Advanced Materials, Tohoku University
2-2-1 Katahira, Aoba-ku, Sendai 980-8577, Japan
E-mail: s-naka@mail.tagen.tohoku.ac.

ABSTRACT

Electrical conductivity of $La_2NiO_{4+\delta}$,that is one of the mixed ions electric conductors, under uniaxial compressive stress was measured at room temperature. Electrical conductivity increases as applied compressive stress increases in the stress region above 50 MPa. Electrical conductivity decreases as applied compressive stress increases in the stress region below 50MPa.This is different from the previous study by Izumi et al[1]. This difference will be clarified with future experiments.

1. Introduction

Recently, a lot of electric devices are used in many scenes of our life. The development of these devices is due to the material development. Development of conductive ceramics is one of the main material developments. Conductive ceramic is divided into two parts; ionic conductor and mixed ions electric conductor. Ionic conductor is ion conductor rich, mixed ions electric conductor is electric conductor-rich.

These devices are required to be higher efficiency and smaller. In order to be smaller, these devices should be under stress. Thus, it is important to clarify the conductivity variation under stress.

$La_2NiO_{4+\delta}$ is one of mixed ions electric conductors. Crystal structure changes as oxygen content changes, and finally electric conductivity changes. In this study, the effect of stress on electrical conductivity was investigated. Electrical conductivity was measured under uniaxial compressive stress at room temperature condition.

2. Experimental

2.1 Sample Preparations

$La_2NiO_{4+\delta}$ were prepared by a citric acid method. $La(NO_3)_3{\cdot}6H_2O$ (99.99%, KANTO CHEMICAL) and $Ni(NO_3)_2{\cdot}6H_2O$ (99.95%, KANTO CHEMICAL) were dissolved separately into de-ionized water. The concentration of each solution was determined by a chelate titration. These solutions were mixed together in the ratios of La:Ni=2:1. Citric acid whish amount was 8 times the number of metal ions, was added to the mixed solution. A precursor was obtained by heating the solution at 573 K to remove water and nitrogen oxides. They were fired in air at 1273 K for 10 hours. After grinding with ethanol, they were sintered again at 1473 K for 10 hours [1]. They are checked whether they were single phase with XRD. They were molded into a pellet using uniaxial press and pressed under 180MPa using cold CIP. The pellet was sintered at 1773K for 10 hours in air. The sintered pellet had approximately 99.6% relative density.

This pellet was cut into rectangular parallelepipeds (2.0mm × 1.5mm × 8.0mm). Pt paste (Tanaka Precious Metals, TR-7905) was applied to these specimens as four probes as shown in figure 1 and sintered at 900°C for 3 hours. The distance between two Pt voltage probes was 4mm. Pt wires (Tanaka Precious Metals, φ 0.2 mm) were twisted around the four probes as current collectors.

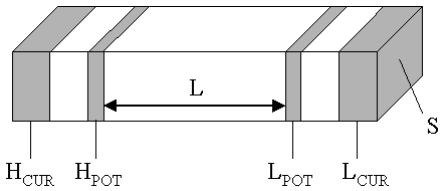

Figure 1. The diagram of experimental specimen.[1]

2.2 Measurement setup

The diagram of the experimental setup is shown in fugure 2. The uniaxial compressive load was applied to the specimen by the universal testing machine (Instron, 5565) and controlled by the load cell. The electrical furnace (Makuhari rikagaku glass Co.) was fixed into the testing machine. Two columnar Al_2O_3 cylinders were used as jigs for applying uniaxial compressive stress to specimen due to its insulation and hardness properties even at high temperature. The specimen was placed between these jigs. The two outside wires twisted around the specimen were connected to DC and AC current source (KEITHLEY, 6221) and the two inside wires were connected to Nanovoltmeter (KEITHLEY, 2182A) for the electrical conductivity measurement.

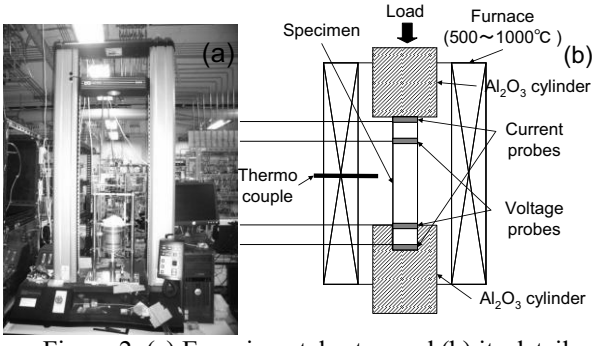

Figure 2. (a) Experimental setup and (b) its detail around a fixed specimen.[1]

2.3 Measurement

Electrical conductivity was measured by DC four-probes method at room temperature. So as not to polarize, the applied current was alternately positive and negative. Uniaxial compressive load of 0 MPa to

300MPa was applied to a specimen.

The measurement procedures are shown in figure 3. The current was applied through the measurement. Electrical conductivity was calculated by gradients of I-V line. This calculation was repeated under constant stress at a constant time intervals. After The electrical conductivity was stable, the applied stress was raised. These processes were repeated until applied stress was reached the maximum value. After that, stress decreasing processes were measured in similar ways. In order to confirm the repeatability, these processes that are stress increasing processes and stress decreasing processes were repeated several times. The data of conductivity variation in stress increasing process in first cycle was not used to exclude the effect of unexpected initial degradation.

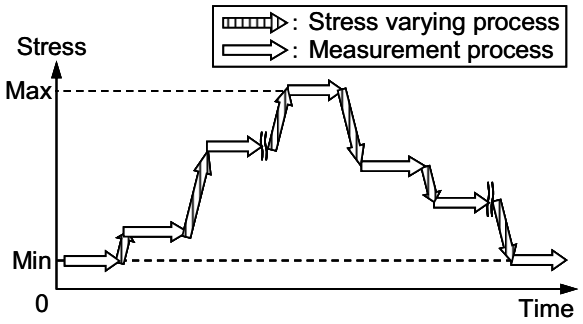

Figure 3. Measurement procedures[1].

3. Results and Discussion

Electrical conductivity and applied compressive stress at room temperature are shown in figure 4. Electrical conductivity rapidly changed as soon as applied compressive stress changed. After second cycle, electrical conductivity decreased relatively. This phenomenon is attributed to decreasing in room temperature. Next, conductivity variation rate at room temperature as a function uniaxial compressive stress is shown in figure 5. In order to compare this study to the previous study[1], the value at 50 MPa in increasing process in second cycle was decided to be a reference value (the conductivity variation rate was 0%). In the stress region above 50 MPa, conductivity variation rate increased as applied compressive stress increased. Conductivity variation rate above 50 MPa is almost same as previous study by Izumi et al. Although conductivity variation rate decreased as applied compressive stress decreased below 50 MPa in previous study, conductivity variation rate increased as applied compressive stress decreased below 50 MPa in this study.

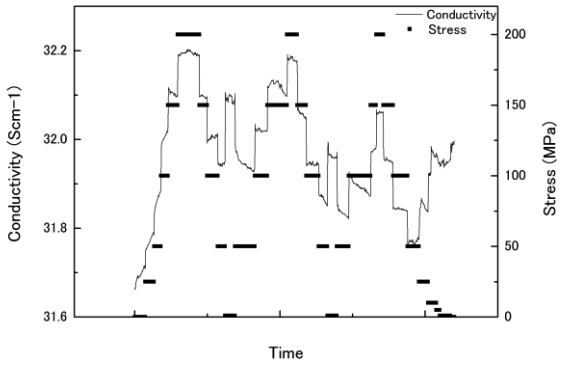

Figure 4. Electrical conductivity and applied compressive stress.

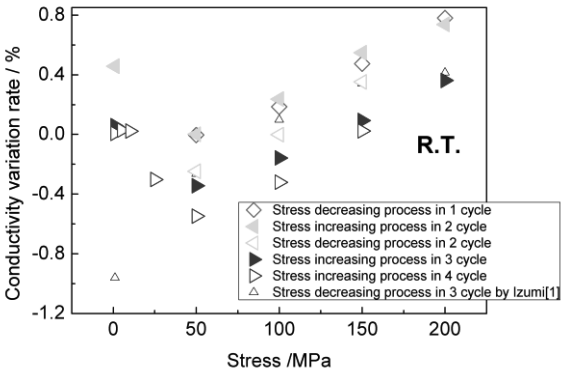

Figure 5. Conductivity variation rate as a function of uniaxial compressive stress

4. Concluding remarks

As mentioned in previous chapters, electrical conductivity increases as applied compressive stress increase in the stress region above 50 MPa. That is same as the previous study. On the other hand, electrical conductivity decreases as applied compressive stress increases in the stress region below 50MPa. That is different from the previous study. The reason why this difference happens is not clarified. But the reason will be clarified with experiments that are measurements at high temperature and keeping the sample applied compressive stress long time.

References

[1] T.Izumi, Master Thesis, Tohoku Univ., (2010)

Eighth International Conference on Flow Dynamics
November 9 - November 11, 2011

Design of Surface Periodic Microstructure on Refractory Metals for Solar Selective Absorbers

Kiyotaka Konno, Makoto Shimizu, Hiroaki Kobayashi, Fumitada Iguchi and Hiroo Yugami
Graduate School of Engineering, Tohoku University, 6-6-01 Aoba Aramaki Aoba-ku Sendai 980-8579, Japan
E-mail: k_konno@energy.mech.tohoku.ac.jp

ABSTRACT

The use of a solar selective absorber is effective technique for increasing the efficiency of concentrating solar power generation (CSP). The spectral selectivity is obtained by fabricating periodic microstructure with feature size in the light wavelength range on metal surface. The performance of spectral selectivity depends on sizes of microstructures. In this study, we tried to control the sizes of periodic microstructure by metallic heat treatment. In conclusion, the sizes of microstructure were increased with a rise in temperature of heat treatments. However, these solar selective absorbers little change in reflectivity spectra.

1. Introduction

The effective utilization of solar energy is necessary because of running out of oil, air pollution and global worming. One of the typical methods for utilization of solar energy is concentrating solar power generation (CSP).

The CSP consisting of collection mirror, absorber, heat engine and generator is expected to power plant for the next generation. At first, solar energy collected by a number of collection mirrors is transmitted to absorber. Then, the steam is generated by using heat sourced from absorber. Electrical power is produced in steam turbine connected to a power generator. But, the problem of CSP is lower efficiency than the present power plants. Heat loss due to an absorber is matter of low efficiency. The absorber needs two properties. The first one is to absorb solar radiation that range from 0.3μm to 3μm. The other one is to suppress thermal radiation loss from absorber in infrared region. For absorber having these properties, it is described as solar selective absorber. Figure 1 shows spectra of solar radiation, black-body radiation and reflectivity of ideal solar selective absorber.

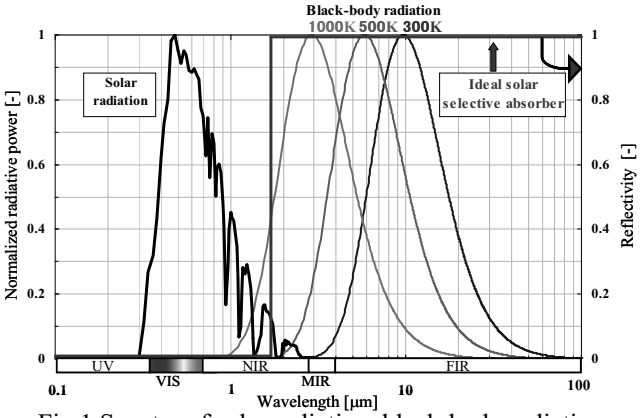

Fig.1 Spectra of solar radiation, black-body radiation and reflectivity of ideal solar selective absorber

Our group has studied for a variety of solar selective absorber. The spectral selectivity is obtained by fabricating periodic microstructure with feature size in the light wavelength range on metal surface. Until now, periodic microstructure has been fabricated by micro-electromechanical system (MEMS) process like photolithography technique. But, the fabrication by MEMS process is expensive because of multiple complex steps. Additionally, it is hard to put into practical use because of a limitation on the large area fabrication.

For solving these problems like large area fabrication and cost, our group has studied solar selective absorber using refractory metals with proper treatment. For refractory metals proper heat-treated, the metallographic structure separate two phase. The two phase structure is consisted of cube geometry structures sized nano to micro scale and grid structures that surround them. Besides, their structures are periodically fabricated and have different chemical property. Thereby, the periodic microstructure is obtained by removing only one phase by wet etching that is applicable on the large area.

The problems of this study are low absorptivity in the solar radiation region and the position of cut-off wavelength due to sizes of microstructures.

The purpose of this study is to fabricate high performance solar selective absorber withstand more than 800 degree C on the large area. In this study, for optimizing cut-off wavelength we tried to control the size of periodic microstructure by metallic heat treatment.

2. Experiments

We used refractory metal with proper treatment. The sample is 1.5mm thick disk, and its diameter is 11mm. We performed heat-treatment for the samples.

This experiment carried out two types of heat treatments. The one is to quench sample after heat treatment using infrared heating furnace. Another is to cool slowly after heat treatment by super kanthal furnace. During heat treatment, sample temperature is measured by thermocouple that is adhered on surface. Table 1 shows conditions of heat treatments.

Table 1 Condition of heat treatments

Sample No.	Temperature [^{o}C]	Holding time [hour]	Cooling condition
1	1140	6	300[^{o}C/min]
2	1135	6	50[^{o}C/hour]
3	1175	6	50[^{o}C /hour]
4	1230	6	50[^{o}C /hour]

After heat treatment, they are mechanically polished, then immersed in etchant. During etching, etchant is kept 25 degree C by thermostat bath and agitated by rotator. Etching time is 10min.

Sample after etching is observed by scanning electron microscope (SEM). Figure 2 shows comparison between the sample before and after heat treatment. The size of microstructure and distribution is calculated by SEM image analysis.

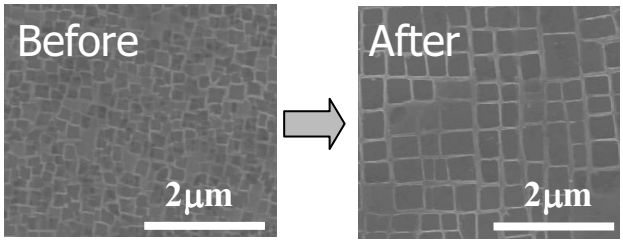

Fig.2 Comparison of SEM images before and after heat treatment

Performance of solar selective absorbers depends on optical property of the surface. In this research, reflectivity are measured and evaluated. The reflectivity spectrum is measured by Fourier transform infrared spectroscopy (FT-IR) and ultraviolet-visible spectrophotometer.

3. Results and Discussion

Figure 3 shows the SEM images of samples after heat treatments. The average sizes of microstructure and standard deviation from No.1 to No.4 sample is listed in table 2.

The SEM images show that periodic microstructures were fabricated on No.1, 2, and 3 samples by heat treatment. Besides, sizes of these microstructures were different. However, microstructures on No.4 sample are not periodic because of high temperature. From these results, it is indicated that limit temperature of fabricating periodic microstructures exist in the heat treatment.

From table 2, average sizes of microstructures grew in an order of: No.1, No.2 and No.3. For No.1 and 2 samples on equal temperature condition, sizes of their microstructures are 337nm and 350nm. It is comparable to each other. For standard deviation, No.2 sample was lower than No.1. This attributed to different cooling condition. It can be considered that the reason of low standard deviation on No.2 is a progression of homogenization of microstructure by slow cooling. For No.2 and No.3 samples, No.3 having size of microstructure of 484nm was 100nm bigger than No.2. The condition of No.3 performed high temperature compared to No.2. Therefore, it shows that microstructure sizes grew with the increasing temperature of heat treatment. But, shown in SEM image of No.4, it is considered that proper temperature needs to fabricate periodic microstructures.

Figure 4 shows spectra reflectivity of No.1, 2, 3, 4 samples and the sample before heat treatment. However, from these spectra, changing cut-off wavelength could not observe by changing size of microstructures. It is considered that the depth of microstructure is not enough.

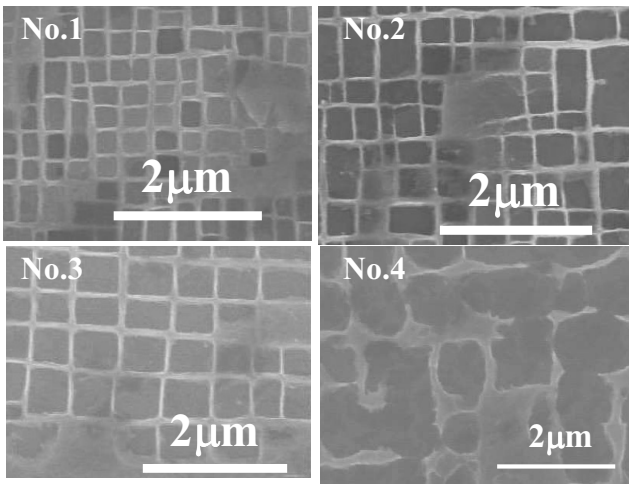

Fig.3 The SEM images of samples after heat treatments

Table 2 Microstructure size and standard deviation of samples

Sample No.	Average size [nm]	Standard deviation [nm]
1	337	103
2	350	90.3
3	484	98.3

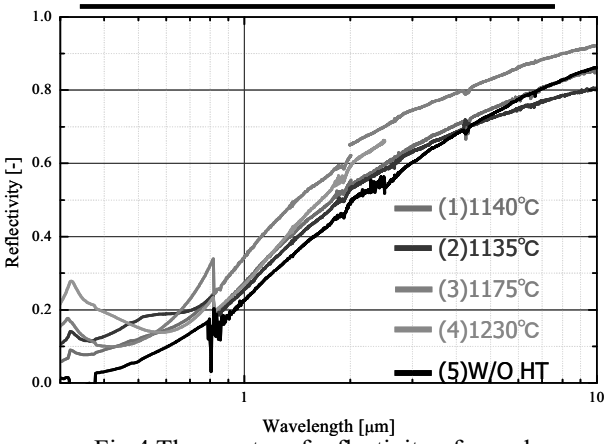

Fig.4 The spectra of reflectivity of samples after heat treatments

4. Concluding remarks

Periodic microstructures were obtained by heat treatment. The sizes of microstructure were increased with a rise in temperature of heat treatments. The periodic microstructures were broken by heat treatment at 1230 degree C. Because of shallow microstructure, there was little change in reflectivity spectra.

Outlook for the future, it need to investigate size variation for more conditions of heat treatments by changing temperature and cooling rate, and to fabricate microstructure with high-aspect ratio by using wet etching process.

Structural Characterization and CO oxidation of $Ce_{0.65}Zr_{0.25}RE_{0.1}O_2$ Nano-composite Oxides Synthesized By Glycine-nitrate-process

D.Hari Prasad, S.Y.Park, H. Ji, H.-R. Kim, J.-W. Son, B.-K.Kim, H.-W. Lee and J.-H. Lee*

High-Temperature Energy Materials Center, Future Convergence Research Division,
Korea Institute of Science and Technology, Seoul 136-791, Republic of Korea
E-mail address: jongho@kist.re.kr

ABSTRACT

In this study, $Ce_{0.65}Zr_{0.25}RE_{0.1}O_2$ (RE= Tb, Gd, Eu, Sm, Nd, Pr, La) solid-solutions were successfully prepared by glycine-nitrate-process and tested for CO oxidation activity. The Raman spectroscopy measurements suggested the presence of oxygen vacancies. From XPS, analysis it was revealed that the cerium, terbium and praseodymium are present in 3+ and 4+ oxidation states. H_2-TPR measurements showed an enhanced surface reduction at much lower temperatures for $Ce_{0.65}Zr_{0.25}Pr_{0.1}O_2$ sample than compared to others, and thus showed a significantly high CO oxidation activity.

1. Introduction

Ceria-based materials displaying high oxygen mobility and oxygen storage capacity (OSC) have been extensively investigated due to their wide application in the field of catalysis and solid oxide fuel cells.[1, 2]. Zirconia has been proved to be an excellent additive to increase the mobility of bulk oxygen and to prevent the sintering of ceria at high temperatures.

The aim of the present work is to investigate the influence of the RE (RE= Pr, Tb, Sm, Gd, La, Nd and Eu) dopants on the redox properties that effects the catalytic properties of the CZ system. The reducibility of the support material plays an important role in suppression of carbon formation during reforming reactions. We focused on CO oxidation reaction as this reaction is mostly effected by the enhanced reducibility of the oxide solid solutions. The obtained powders were characterized by using XRD, BET surface area, Raman Spectroscopy, XPS, and H_2-TPR. Furthermore, the catalytic activity towards CO oxidation has also been evaluated.

2. Method

The $Ce_{0.65}Zr_{0.25}RE_{0.1}O_2$(RE= Pr, Tb, Sm, Gd, La, Nd and Eu) powders were successfully prepared by GNP method.[3] The obtained powders were ball milled and calcined at 600°C for 2h in air atmosphere. The rate of heating and cooling were maintained at 5°Cmin^{-1}.

The catalytic activity of the samples was evaluated for oxidation of CO at normal atmospheric pressure and temperatures in the range of 25-500°C in a fixed-bed reactor at a heating ramp of 5°Cmin^{-1}. The oxidized sample was then purged with Helium and cooled to desired starting temperature. The gas flow rates were controlled by using mass flow controllers (Smart-trak: Sierra Instruments, USA) and the total flow rate was 60 ml min^{-1} with a CO/O_2 reactant feed ratio of 1. The effluent gas mixture were detected by an online Agilent 6890N gas chromatograph equipped with HP PLOT Q and molecular sieve 5Å capillary columns and a thermal conductivity detector (TCD).

3. Results and Discussion

The XRD patterns of $Ce_{0.65}Zr_{0.25}RE_{0.1}O_2$ samples calcined at 600°C are presented in Figure 1. These results reveal the formation of solid solutions with typical cubic fluorite structure.[3] From Figure 1 it can be observed that all the RE-doped samples show a slight shift of the diffraction peaks toward lower degree with respect to un-doped sample. This phenomenon could be associated with the expansion of the crystal lattice, which is induced by the larger cation radius of the dopants relative to the Zr^{4+} (0.87Å) ions.

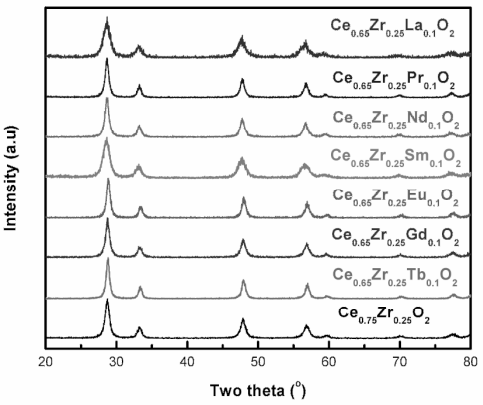

Figure 1. XRD patterns of $Ce_{0.65}Zr_{0.25}RE_{0.1}O_2$ samples calcined at 600°C for 2h

The Raman spectra of the $Ce_{0.65}Zr_{0.25}RE_{0.1}O_2$ (RE = La, Nd, Sm, Eu and Gd) samples were depicted in Figure 2(a). As shown in Figure 2(a), a slight shift in the Raman

frequency and absence of peaks related to RE oxides evidences the formation of $Ce_{0.65}Zr_{0.25}RE_{0.1}O_2$ solid solutions and thus corroborates the XRD results. Furthermore, the Raman spectra of the samples are very similar with a predominant strong band at ~470cm^{-1} and a less prominent broad band at ~600cm^{-1}. The band at 470cm^{-1} can be attributed to the F_{2g} Raman active mode of the fluorite type lattice. It can be viewed as a symmetric breathing mode of the oxygen atoms around cerium ions (O-Ce-O).According to literature, six Raman active modes (A_{1g} + $3E_g$ + $2B_{1g}$) are expected for t-ZrO2 (space group $P4_2$/nmc) while the cubic fluorite structure of ceria (space group *Fm3m*) only one mode is Raman active.[4] It can be observed for the figure that with the increase of ionic radius of RE element in $Ce_{0.65}Zr_{0.25}RE_{0.1}O_2$ solid solution, the F_{2g} band has been slightly shifted to lower values.

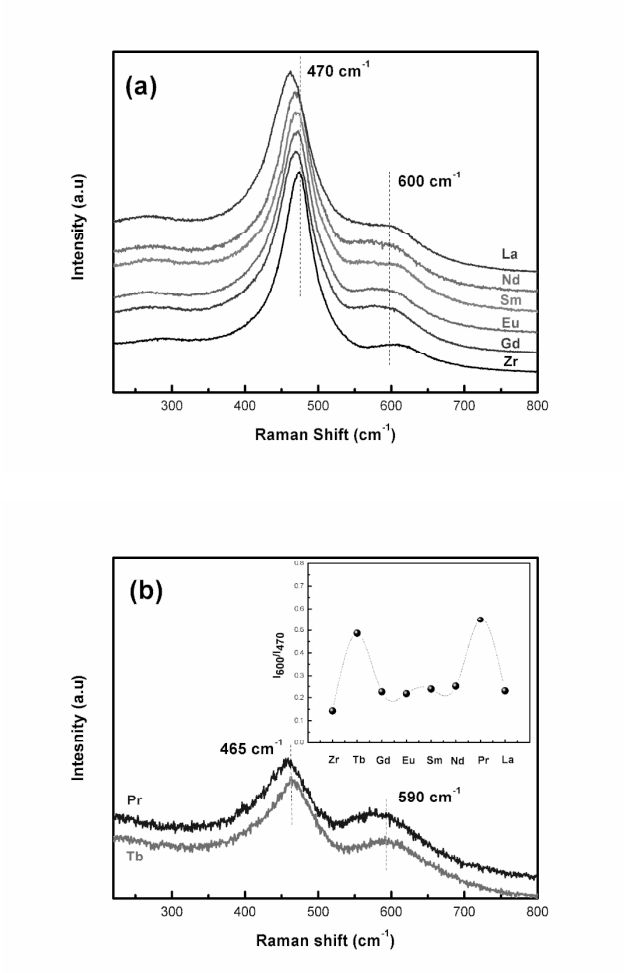

Figure 2. Raman spectra of $Ce_{0.65}Zr_{0.25}RE_{0.1}O_2$ samples (a) RE=La, Nd, Sm, Eu, Gd (b) RE= Pr, Tb. Inserted figure shows the variations in the intensity ratio of Raman bands at 600 and 465 cm^{-1}.

Figure 2(b) shows the Raman spectra of $Ce_{0.65}Zr_{0.25}RE_{0.1}O_2$ (RE=Tb, Pr) samples. The peak at 590 cm^{-1} can be attributed to lattice defects, resulting from the formation of oxygen vacancies, which will allow this mode of vibration by relaxation of the selection rules.[5] As it can be noted from Figure 2, this peak is less prominent in the case of samples studied in Figure 2(a) while it has been increased for the samples studied in Figure 2(b) suggesting the presence higher oxygen vacancies for Pr and Tb doped ceria-zirconia samples. The presence of higher oxygen vacancies in these materials could be explained by the presence of praseodymium (Pr^{+4}/Pr^{+3}) and Terbium (Tb^{+4}/Tb^{+3}) atoms whereas the other RE elements have fixed oxidation states.[6] The ratio between the intensities of 600 and 470 cm^{-1} Raman bands has been related to the concentration of oxygen vacancies in the material, and it is noted that the higher the I_{600}/I_{470} ratio, the higher the oxygen vacancies.[7] The relationship betweenI_{600}/I_{470} ratio and RE doping is presented in Figure 2(b) (inserted figure). It can be observed form this figure that the incorporation of Pr and Tb into corresponding ceria-zirconia lattice increases the vacancy concentration by about 3-4 times due to the generation of vacancies for charge compensation as a result of presence of Pr^{+4}/Pr^{+3} and Tb^{+4}/Tb^{+3} atoms.

Figure 3(a) illustrates Pr 3d core level XPS spectra of $Ce_{0.65}Zr_{0.25}Pr_{0.25}O_2$ sample. Generally, the Pr 3d spectra consist of two sets of spin-orbit multiplets at binding energies of ~933 and ~953 eV which correspond to $3d_{5/2}$ and $3d_{3/2}$, respectively.[8] The $3d_{3/2}$ sublevel presents complex features due to the multiplet effect, while the $3d_{5/2}$ sublevel consists of two features corresponding to two possible oxidation states (Pr^{3+} and Pr^{4+}).[9] Therefore, we have taken the Pr $3d_{5/2}$ region to understand the oxidation states of Pr. The spectra obtained showa pronounced shoulder at 929.7 eV and a maximum at 934.5 eV. According to the literature, we assigned the former to Pr^{3+} and the later to Pr^{4+}. This indicates that the prepared sample contains both 3+and 4+ oxidation states.

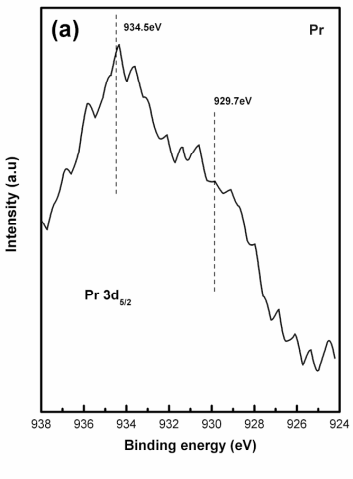

Figure 3(a) Pr 3d XPS pattern of $Ce_{0.65}Zr_{0.25}Pr_{0.1}O_2$ sample.

Figure 3(b) shows the Tb 4d core level XPS spectra of $Ce_{0.65}Zr_{0.25}Tb_{0.1}O_2$sample. In general, Tb^{3+} gives a signal below 150 eV, whereas Tb^{4+} is related to the features above 150 eV (may be around 155 eV)[10]. The spectra obtained

in this study with a pronounced shoulder below 150 eV, a peak at 151.7 eV and a maximum peak at 154.6 eV along with a small peak at 160.6 eV suggests the presence of more than one oxidation state. This indicates that the surface of sample contains Tb in both 3+ and 4+ oxidation states.

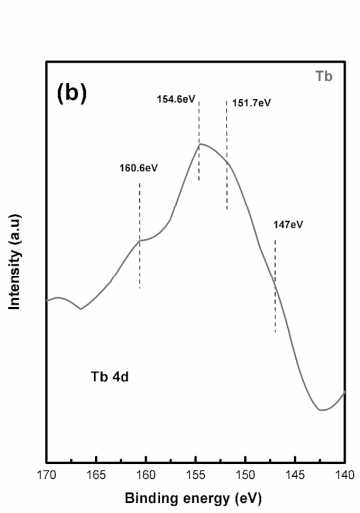

Figure 3(b) Tb 3d XPS pattern of $Ce_{0.65}Zr_{0.25}Tb_{0.1}O_2$ sample.

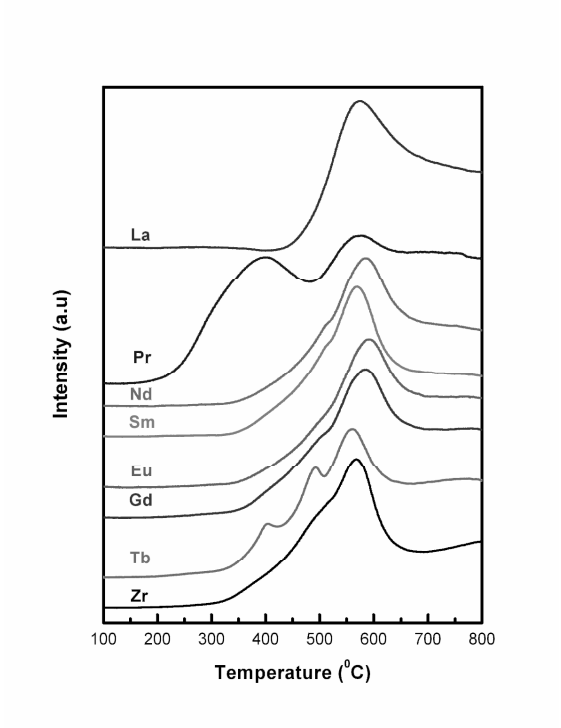

Figure 4.H_2-TPR profiles of $Ce_{0.65}Zr_{0.25}RE_{0.1}O_2$ samples calcined at 600°C.

The reducibility of $Ce_{0.65}Zr_{0.25}RE_{0.1}O_2$ samples calcined at 600°C was studied by using H_2-TPR experiments and the corresponding TPR profiles are shown in Figure 4. The $Ce_{0.75}Zr_{0.25}O_2$ sample exhibits a broad single reduction peak at 570°C and it is hard to differentiate the surface and bulk reduction peaks. It is observed that onset of H_2 consumption occurs around 320°C. According of literature, H_2-TPR profile of pure high surface area CeO_2 shows two well-resolved peaks at around 500°C and 900°C.[11] Reduction of ceria is generally accepted to occur by a step-wise mechanism; first, at lower temperatures, reduction of most outer layers of Ce^{4+} (surface reduction) then reduction of inner Ce^{4+} layers (bulk reduction) at higher temperatures.[12] Incorporation of small quantities of isovalent Zr^{4+} into CeO_2 lattice enhances its redox properties by creating structural defects with size effect and increasing the channel diameter for oxygen migration in the lattice.[12] This results in higher mobility of the lattice oxygen which leads to one major low temperature peak in the TPR profile of ceria-zirconia solid solutions in contrast to ceria with two main peaks.[13] The higher mobility of the lattice oxygen causes reduction not to be limited to surface but deeply extended into bulk of ceria-zirconia solid solution. This is in line with the shift of major reduction peak of pure ceria at 900°C to 570°C for $Ce_{0.75}Zr_{0.25}O_2$ sample.

For $Ce_{0.65}Zr_{0.25}RE_{0.1}O_2$ samples, it can be observed form Figure 4 that the bulk reduction peak was around 550-570°C. $Ce_{0.65}Zr_{0.25}Pr_{0.1}O_2$sample showed two different peaks instead of single broad reduction peak that was observed for other $Ce_{0.65}Zr_{0.25}RE_{0.1}O_2$ samples. For this sample, the onset of H_2 consumption occurred at 180°C and the surface reduction peak was located around 375°C which is much lower temperature than compared to other samples. The peak area of surface reduction is much higher than the peak area of bulk reduction indicating that reducibility of this sample is much higher and can be reduced at lower temperatures than the other samples. From the figure it can be observed that the $Ce_{0.65}Zr_{0.25}Tb_{0.1}O_2$ sample also showed two reduction peaks corresponding to surface and bulk reduction peaks. It is interesting to see that the surface reduction peak splits into multiple peaks. From literature it can be observed that the TPR profile of $TbO_{1.75}$ shows reductions bands at 303, 667, 720°C.[14] Therefore, the splitting of surface reduction peak can be presumably due to the $Tb^{4+} \rightarrow Tb^{3+}$reduction along with $Ce^{4+} \rightarrow Ce^{3+}$ reduction.[6] The reducibility of $Ce_{0.65}Zr_{0.25}RE_{0.1}O_2$ samples clearly shows that the Pr doped CZO can be easily reduced at lower temperature indicating a higher mobility of surface oxygen at lower temperatures.

We focused on the CO oxidation reaction which is most likely to be affected by the enhanced reducibility of the oxide solid solution. The catalytic activities for CO oxidation of $Ce_{0.65}Zr_{0.25}RE_{0.1}O_2$ samples calcined at 600°C are presented in Figure 5. It is evident from Figure 5 that the $Ce_{0.65}Zr_{0.25}Pr_{0.1}O_2$ sample exhibited better activity in terms of total conversion as well as light-off temperature (50% conversion). The $Ce_{0.65}Zr_{0.25}Pr_{0.1}O_2$ sample exhibited 100% conversion at 300°C and light-off temperature of 208°C, respectively.

The light-off temperatures of various catalysts followed the order: Pr>Tb>La>Nd>Sm>Gd>Eu>Zr. The oxidation

of CO on ceria occurs via Mars-van Krevelen redox type mechanism.[15] In the absence of the oxygen feed, CO gets oxidized by consuming lattice oxygen and leaving the oxygen vacancy. In the presence of oxygen feed, the lattice oxygen is replenished. Therefore, in the oxidation process lattice oxygen, conversely an oxygen vacancy is involved and acts as an active site for the dissociation of gaseous oxygen.

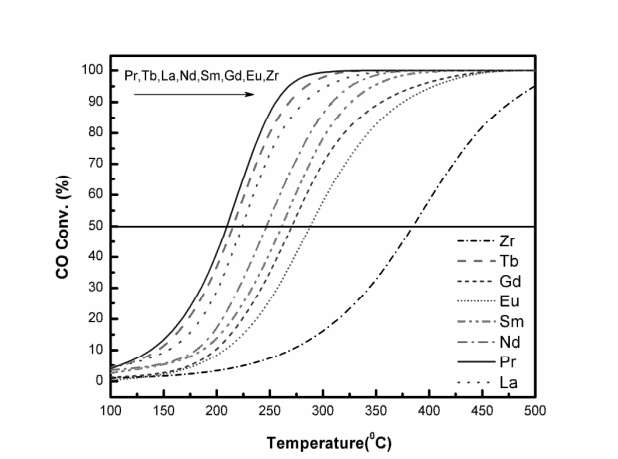

Figure 5. Conversion of CO over $Ce_{0.65}Zr_{0.25}RE_{0.1}O_2$ samples calcined at 600°C as a function of reaction temperature.

Accordingly, in the oxidation process vacancy plays an essential role. The lower reduction temperature and an increased ability to shift between Ce^{4+}/ Ce^{3+} at much lower temperature and having high oxygen vacancies is the key for the increased oxidation activity of the $Ce_{0.65}Zr_{0.25}Pr_{0.1}O_2$ sample.

4. Concluding remarks

$Ce_{0.65}Zr_{0.25}RE_{0.1}O_2$ (RE = Tb, Gd, Eu, Sm, Nd, Pr, La) solid solutions were successfully prepared by glycine-nitrate-process and the structural characteristics and CO oxidation activity of these solid solutions have been systematically investigated. The XRD results confirmed the formation of $Ce_{0.65}Zr_{0.25}RE_{0.1}O_2$ solid solutions with a cubic phase of fluorite structure. XPS results revealed the existence of cerium, terbium and praseodymium in both 3+ and 4+ chemical valance states. Raman spectroscopy results showed the remarkable increase of oxygen vacancies for $Ce_{0.65}Zr_{0.25}Pr_{0.1}O_2$ solid solution. From H_2-TPR, $Ce_{0.65}Zr_{0.25}Pr_{0.1}O_2$sampleshowed enhanced surface reduction at lower temperatures, indicating a high mobility of oxygen ions in this sample. This can be attributed to the simultaneous presence of enhanced mobile oxygen vacancies, easy surface and bulk reduction, and the cooperative redox couple (3+/4+) of Ce and Pr. The $Ce_{0.65}Zr_{0.25}Pr_{0.1}O_2$ solid solution also exhibits superior activity toward CO oxidation compared to other solid solutions. The ability to release substantial amount of oxygen at relatively low temperatures makes $Ce_{0.65}Zr_{0.25}Pr_{0.1}O_2$solid solution a potential material for oxygen storage/release and catalytic applications.

Acknowledgment. This work was supported by the Institutional Research Program of Korea Institute of Science and Technology.

References

[1] A. Trovarelli, Catalysis Reviews: Science and Engineering 38 (1996) 439 - 520.
[2] D.H. Prasad, J.W. Son, B.K. Kim, H.W. Lee, J.H. Lee, J Ceram Process Res 11 (2010) 176-183.
[3] D.H. Prasad, H.Y. Jung, H.G. Jung, B.K. Kim, H.W. Lee, J.H. Lee, Mater Lett 62 (2008) 587-590.
[4] M. Yashima, H. Arashi, M. Kakihana, M. Yoshimura, J Am Ceram Soc 77 (1994) 1067-1071.
[5] J.R. McBride, K.C. Hass, B.D. Poindexter, W.H. Weber, J Appl Phys 76 (1994) 2435.
[6] B.M. Reddy, P. Saikia, P. Bharali, Y. Yamada, T. Kobayashi, M. Muhler, W. Grünert, The Journal of Physical Chemistry C 112 (2008) 16393-16399.
[7] Z.-Y. Pu, J.-Q. Lu, M.-F. Luo, Y.-L. Xie, The Journal of Physical Chemistry C 111 (2007) 18695-18702.
[8] H. He, H.X. Dai, K.W. Wong, C.T. Au, Appl Catal A: Gen 251 (2003) 61-74.
[9] H. Borchert, Y.V. Frolova, V.V. Kaichev, I.P. Prosvirin, G.M. Alikina, A.I. Lukashevich, V.I. Zaikovskii, E.M. Moroz, S.N. Trukhan, V.P. Ivanov, E.A. Paukshtis, V.I. Bukhtiyarov, V.A. Sadykov, J Phy Chem B 109 (2005) 5728-5738.
[10] L. Liping, W. Quan, L. Hongjian, Z. Dafang, S. Wenhui, Zeitschrift für Physik B Condensed Matter 96 (1995) 451-454.
[11] J.I. Gutiérrez-Ortiz, B. de Rivas, R. López-Fonseca, J.R. González-Velasco, Appl Catal A: Gen 269 (2004) 147-155.
[12] J. Kaspar, P. Fornasiero, M. Graziani, Catal Today 50 (1999) 285-298.
[13] M. Boaro, F. Giordano, S. Recchia, V.D. Santo, M. Giona, A. Trovarelli, Appl Catal B: Envi 52 (2004) 225-237.
[14] H.X. Dai, C.F. Ng, C.T. Au, J Catal 199 (2001) 177-192.
[15] M. Boaro, C. de Leitenburg, G. Dolcetti, A. Trovarelli, J Catal 193 (2000) 338-347.

Eighth International Conference on Flow Dynamics
November 9 - November 11, 2011

The Evaluation of Solar Selective Absorbers Using Refractory Metal in Concentrated Solar Power System

Hiroaki Kobayashi, Kiyotaka Konno, Makoto Shimizu, Fumitada Iguchi, Hiroo Yugami,
School of engineering, Tohoku University, Aoba 6-6-01,
Aramaki, Aoba-ku, Sendai, 980-8579, Miyagi, Japan.
h_kobayashi@energy.mech.tohoku.ac.jp

ABSTRACT

Using solar selective absorbers is studied to advance efficiency of a solar thermal power generation. A metal surface on which fabricated microstructures shows solar selective property. Therefore, in this study, we prepared a refractory metal as a receiver which has finely-structured two phases due to a self-organization, and selectively etched the one phase to make microstructures on the metal surface and measure a reflectance of the receiver.

1. Introduction

Mainly, a solar thermal generation has three methods[1]. First method is a central tower power generation. Figure 1 shows a way of collecting the sunlight with the system. A circular array of heliostat mirrors, which are large individually tracking mirrors, used to concentrate sunlight on to a central receiver mounted at the top of a tower. Then, this central receiver surface reaches very high temperature of about 600 °C. Second method is a parabolic trough power generation. Parabolic trough-shaped mirror reflectors concentrate sunlight on to thermally efficient receiver tubes placed in the trough`s focal line. A surface temperature of absorbers tube reaches approximately 400 °C. Third method is a parabolic dish power generation. A parabolic dish-shaped reflector concentrates sunlight on to a receiver located at the focal point of the dish. The concentrated sunlight is absorbed into the receiver. A temperature of the receiver surface is approximately 500 °C.

To advance efficiency of the solar thermal power generation, to increase the temperature of the receiver by improving the properties is one of the effective methods. Figure 2 shows the mechanism of heat transfer in the receiver. There are three important points to make efficient receiver. First, high absorptance for sunlight is required because of absorbing most part of solar energy. Second, to suppress a loss of thermal radiation energy from the receiver is also necessary. As a temperature of the receiver increases, the thermal radiation loss rapidly increases because the spectral emissive power is proportional to the fourth power of temperature of the body. Third, a high thermal conductivity is needed to transfer the heat from surface of the receiver to circulated water. Then, the circulated water turns steam due to high heat of the receiver, and turbine is rotated with the steam to create electricity.

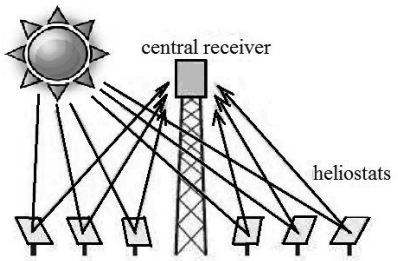

Fig.1 Central tower power plants[2]

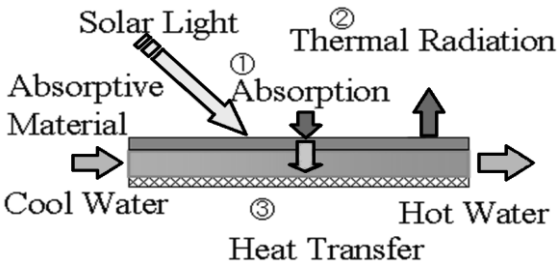

Fig.2 Mechanism of solar thermal receiver

Hence, in consideration of these three points, solar selective absorber is considered to utilize for the receiver. But, there is no solar selective absorber which can be utilized for high temperature such as 800 °C or more. Therefore, we consider controlling optical property by microstructures on a surface of the refractory metal. The size of a microstructure is close to the optical wavelengths. Accordingly the microstructure and the sunlight are interacted with each other. As a result of the interaction, optical property is changed from original property. Then, the receiver has the property of solar selective absorber. Thus, the optimization of the property is required to make efficient receiver.

Figure 3 shows the ideal absorption property for solar thermal receiver. In the Fig.3, the temperatures of 100, 400, 800 °C are the operating temperature of solar hot-water heater, parabolic trough power generation, central tower power generation, respectively. Then, the dotted line is the ideal absorption property. The property is that the receiver selectively absorbs sunlight and suppresses the loss of thermal radiation. Therefore, absorption property of the receiver is needed to come close to the dotted line in figure 3 using the microstructure.

The purpose of this study is to make the solar selective absorber as a receiver of central tower power generation, and to evaluate the property of the receiver.

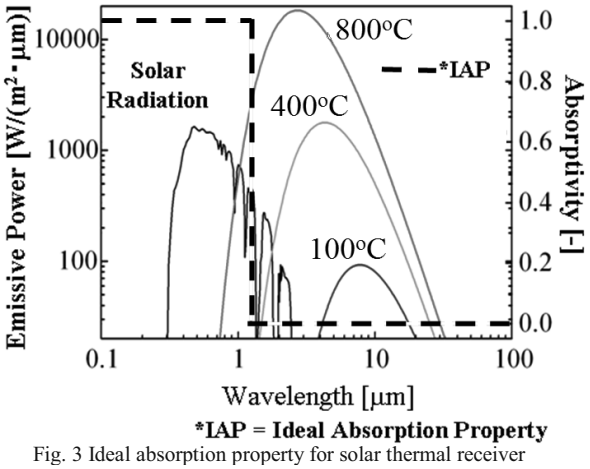

Fig. 3 Ideal absorption property for solar thermal receiver

Fig.4 Receiver before etching(mm)

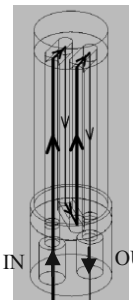

Fig.5 The image of the water circulation in the receiver

2. Sample preparation

As the receiver of the tower power generation, refractory metal are processed into cylindrical configuration. The picture of the sample as the receiver is shown in Fig.4. The size of a part which is actually exposed to sunlight is 25mm height and 9mm diameter. Four long holes of 1.8mm in diameter are digged in the receiver to circulate the water. Figure 5 shows the schematic image of the boiled-water circulation in the receiver.

The heat treatment is performed for refractory metal. Consequently, due to spinodal decomposition, the metal is separated into two phases. Size of the phase which is separated by another phase individually shows hundreds of nanometers. Therefore microstructures are made on the metal surface after etching the one phase. The detail of the etching procedure is shown below. At first, the experimental setup shown in Fig.6 is prepared and then royal water maintained at constant temperature is prepared. The etchant is continuously stirred using a stir bar. Second, the sample is soaked in the royal water for approximately 15 minutes. Consequently, microstructures are fabricated on the surface of the sample. In this study, the etching process was done two times. Though the first etched receiver was observed microstructures with a scanning electron microscope (SEM), the receiver was unevenly etched and found the scratches on its surface due to the machining processing. Therefore, receiver was polished with fine sandpaper to remove the scratches before the second etching. As a result, at the second

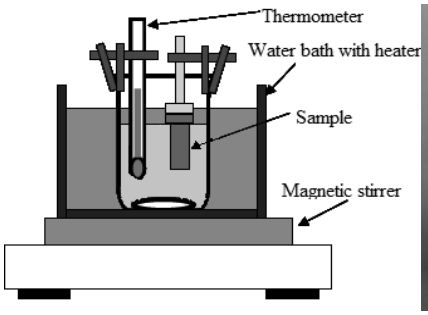

Fig.6 Experimental device

Fig.7 Receiver after the second etching

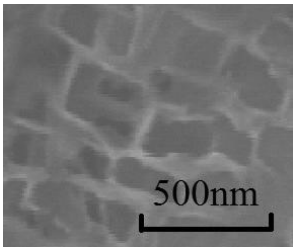

Fig.8 SEM image of microstructures

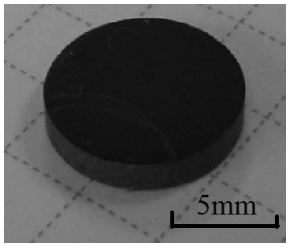

Fig.9 Comparative sample

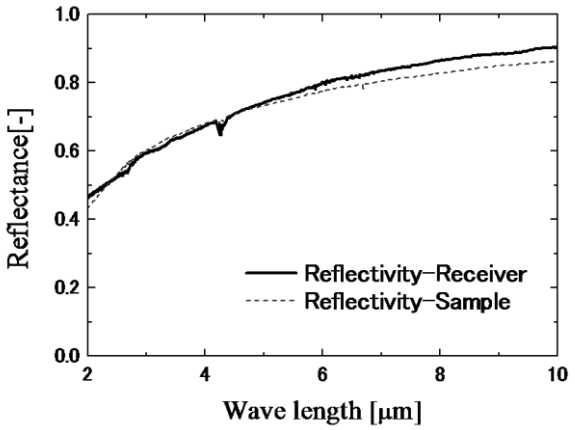

Fig.10 Reflectance of the receiver

etching the receiver was evenly etched under the condition that was for 15 minutes at 27 ^{o}C. Figure 7 shows the receiver after the second etching. In comparison with Fig.4, Figure 7 shows that the surface of the receiver is tarnished and turned to black. Figure 8 shows the SEM image of microstructures on the surface after the second etching. These microstructures were diffused on the whole surface of the receiver. Though each cavity has different in size, the cavity size is approximately 0.2 μm wide on average.

3. Results and Discussion

Reflectance at near-infrared range was measured by the Fourier transform infrared spectroscopy (FT-IR). Hence, it was difficult to measure the reflectance of the receiver due to the cylindrical configuration, a comparative sample was prepared as shown in Fig.9. Figure 10 shows the result of the measurement. The comparative sample was etched under the same condition of the receiver, so the results of the two data are approximately corresponded.

4. Concluding remarks

The microstructures were fabricated on the surface of the receiver using etching. Consequently, reflectance of the receiver gradually decreases at a range of short wavelength. Therefore the receiver shows the property of solar selective absorber after etching. However, a measurement of the reflectance at the visible wavelength is needed to confirm the reflectance successively decreases, so preparation of a sample like Fig.9 is necessary.

Next, we evaluate the etched receiver with using the solar thermal power system. Hence, we make a small central tower power generation. Specifically, we make a comparison of the solar absorption efficiency between the etched receiver and the non-etched receiver with the power generation system.

References

[1]Georg Brakmann, Rainer Aringhoff, Dr.Michael Geyer, Sven Teske. Concentrated Solar Thermal Power-Now. 2005.
[2]Concentrating Solar Power Global Outlook 09:Why Renewable Energy is Hot.

Eighth International Conference on Flow Dynamics
November 9 - November 11, 2011

Development of High Temperature Solar Selective Absorber Using Refractory Material with Surface Microstructures

Makoto Shimizu, Kiyotaka Konno, Fumitada Iguchi, Hiroo Yugami
Department of Mechanical Systems and Design, Graduate School of Engineering, Tohoku University
Aoba 6-6-01, Aramaki, Aoba-ku, 980-8579, Sendai, Japan
m_shimizu@energy.mech.tohoku.ac.jp

ABSTRACT

Spectral properties of thermal radiation can be controlled by surface microstructures. We applied this technology for solar selective absorbers of concentrated solar power generation system (CSP). We investigated spectral properties and thermal stability of two-dimensional tungsten (W) periodic surface microstructures to develop solar selective absorbers for high temperature applications. They have shown good spectral selectivity. We also investigated the mass production method of surface microcavity structures at large area using the W-Cu alloys. Then we confirm absorptivity at visible light range can be increased by using this simple method.

1. Introduction

Now, we have been faced on serious energy problems such as exhaustion of fossil fuels, increment of greenhouse gases, and etc. In recent years, we have focused on renewable energy to solve the problems. Solar energy is one of the most important renewable energy because huge amount of solar energy reaches at surface of the earth. But, we have been able to utilize only small part of the energy. Therefore, it will become alternative energy to fossil fuels, if we utilize the energy more efficiently.

There are two main way to use solar energy. One is using solar energy as light energy by photovoltaic systems, and the other is using solar energy as thermal energy. Of course the former way is the most popular way of using, but recent years, the latter way has become common as concentrate solar power generation system (CSP).

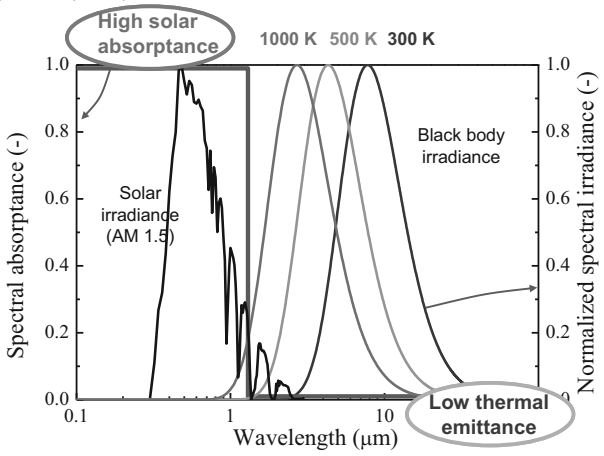

Fig.1 Comparison of the solar spectrum under the air mass of 1.5 and thermal radiation spectra described by Planck's (a)

In the CSP, one of the major problems to resolve is low energy conversion efficiency. It was approximately 13~14% at trough type or tower type CSP. The main factor of lowered energy conversion efficiency is low efficiency of solar receiver. In the CSP, the solar receiver acquires high temperature as 400°C for trough type and 800°C for tower type. Thus, the amount of radiated energy from solar receiver is too large to ignore. In this case, solar selective absorber is applied for solar receiver unit because of difference between spectrum distribution of solar radiation and thermal radiation from the receiver as shown in Fig.1.

Up to now, several groups have researched solar selective absorbers. For examples, Koltum demonstrated multilayer thin film type solar selective absorber which consists of metal and oxide materials (1). McDonald demonstrated the solar selective absorber which uses black chrome coatings (2). However, these kinds of solar selective absorbers don't have sufficient thermal stability for using at high temperature as CSP. To our knowledge, few reports have been published on practical selective coatings with good thermal stability at high temperatures over 1000K, since Peterson et al. (3) had reported on Al_2O_3-Mo-Al_2O_3 cermet selective absorber. Zhang et al. (4), Eisenhammer et al. (5), and Schön et al. (6) have reported on efficient high-temperature selective coatings, but it has not been certificated experimentally that they have sufficient thermal durability at elevated temperatures.

In this study, we research the solar selective absorbers with surface microstructures with the size of optical wavelength which is applicable for CSP.

It has been known that spectral property of thermal radiation can be controlled by periodic surface microstructures with the size of optical wavelength range. We considered applying for solar selective absorber this technology by making surface microstructures at high-melting point metals. Where the size of microstructures becomes comparable to the optical wavelength, electromagnetic waves resonate with surface microstructures and interactions occur between materials and electromagnetic waves. Some of the resonance effects such as surface plasmon polaritons and the microcavity effect are useful to control spectral property of thermal radiation. In the past, controlling of thermal radiation by periodic surface microstructures has been researched such as using one-dimensional SiC gratings (7, 8) and two dimensional metallic gratings (9, 10, 11 and 12). The spectral property is strongly dependent on material properties as well as geometrical parameters.

2. Surface structural design

2.1. Estimation of optimum optical property

The properties which demand for solar

selective absorbers are high absorptivity at solar radiation range and low absorptivity at infrared range. Thus, the cut-off wavelength which is switch over to low absorptivity from high absorptivity is important for property of solar selective absorbers. As mentioned in introduction, cut-off wavelength can be tuned by controlling of geometrical parameters of microstructures. So, we performed numerical calculations to estimate the optimum cut-off wavelength. In this estimation, we defined high absorptivity A_h as 0.95 and low absorptivity A_l as 0.05. Then, we evaluate the optimum cut-off wavelength by using parameter of solar absorptivity α_s, hemispherical total emissivity of the absorber ε_a, and spectral selectivity α_s / ε_a. The solar absorptivity α_s is usually defined by following equation [1]

$$\alpha_s = \frac{\int_0^\infty \alpha_\lambda(\lambda) E_{s\lambda}(\lambda) d\lambda}{\int_0^\infty E_{s\lambda}(\lambda) d\lambda} \qquad [1]$$

where

α_λ : spectral absorptivity of the absorbers

$E_{s\lambda}$: spectral solar irradiance

Thus, α_s represent absorptive rate in solar radiation range of the absorbers.

The hemispherical total emissivity of the absorber is defined as following equation [2]

$$\varepsilon_a(T) = \frac{\int_0^\infty \varepsilon_\lambda(\lambda) E_{b\lambda}(\lambda, T) d\lambda}{\int_0^\infty E_{b\lambda}(\lambda) d\lambda} \qquad [2]$$

where

ε_λ : spectral emissivity of the absorbers

$E_{b\lambda}$: spectral black body irradiance

Thus, ε_a represent rate of total emissive power from the absorbers and total emissive power of black body at the temperatures. For solar selective absorber, demanded parameter is that the α_s is more than 0.9 and the α_s /ε_a is more than 6.

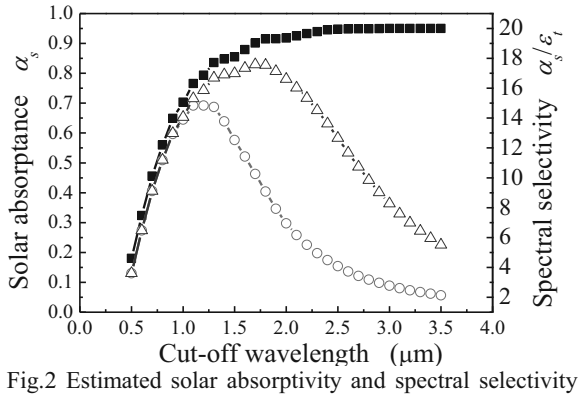

Fig.2 Estimated solar absorptivity and spectral selectivity value with changing of cut-off wavelength

Fig.2 shows the result of evaluation about optimum cut-off wavelength of the absorber. The black solid line with square symbols shows solar absorptivity. It exceeds 0.9 when cut-off wavelength is over 1.7μm. The blue solid line with triangle symbols shows solar selectivity at 400°C. It becomes over 10 in the range of 0.7μm-2.8μm. The red solid line with circle symbols shows solar selectivity at 800°C. It becomes over 6 in the range of 0.5μm-2.1μm. Hence, to meet requirements in all temperature, cut-off wavelength need to be approximately 1.7μm-2.1μm.

2.2 Numerical Calculation by using RCWA

Numerical calculation was performed by using Rigorous Coupled-Wave Analysis (RCWA) (13) for the periodic surface microstructures model as shown in Fig.3. In this calculation, a material of the model is tungsten (W) which is representative high melting point metals. The shape of microstructures is rectangular cavity which aperture size, depth size, and periodicity size are 0.9μm, 0.63μm, and 1.2μm. Microstructured W shows high absorptivity at small wavelength range although low absorptivity at infrared range as well as flat W. The inset right above Fig.3 shows electric field distribution in a microstructure. Standing wave exist in a microcavity, in other words, it can be known that modulation of thermal radiation spectrum originate from interaction between electromagnetic waves and microstructures.

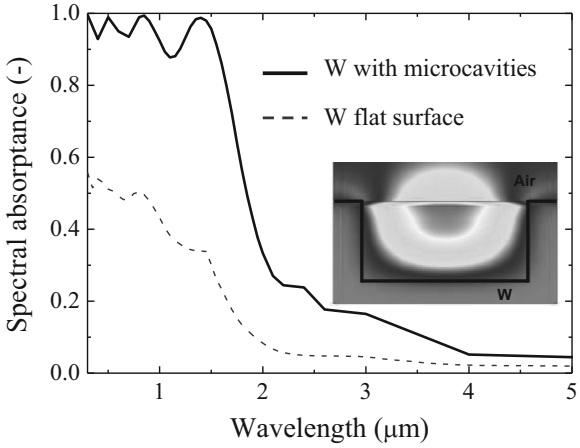

Fig.3 Comparison between the numerical calculation absorptivity spectra of W with periodic surface microstructures and flat surface W, and electric field distribution in microcavities

3. Results of fabrications

3.1. Periodical surface microstructures fabrication by MEMS process

To fabricate periodic microstructures on bulk W surface, we use MEMS (Microelectromechanical system) process. The process flow scheme is shown in Fig.4. First, a thick resist layer, an Al thin film and an EB (Electron beam) resist layer are stacked one after another on a mechanically polished W substrate. The top EB resist is exposed by an EB lithography system and a grating pattern is drawn. Fine patterns with nanometer order can be precisely drawn by EB lithography. After the development of the pattern, FAB (Fast atom beam)

etching with SF_6 gas is carried out to replicate it on the Al film. Next, FAB etching with O_2 gas is successively performed to replicate the pattern on the thick resist layer under the Al film. With this double layer method, we can obtain a deep resist mask. Finally, FAB etching with SF_6 gas is performed again and the grating pattern is transferred on the W substrate. FAB is a neutral atomic or molecular beam. It can exactly replicate the patterns drawn by EB lithography on W substrates without side etching.

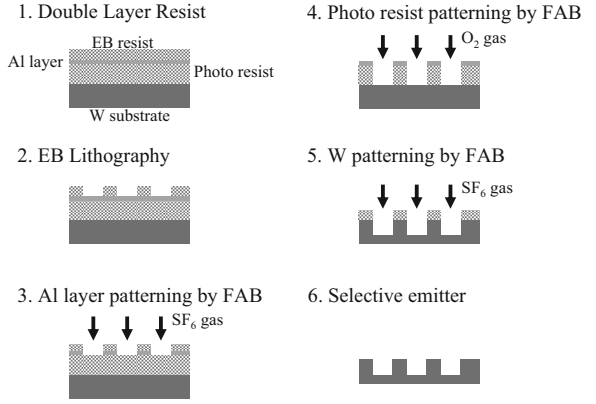

Fig.4 The fabrication process flow scheme of periodic surface microstructures on W substrate

A SEM image of the fabricated sample is shown in Fig.5. Periodic microstructures were successfully fabricated. However, the walls of each cavity are rough, but roughness is sufficiently smaller than the cavity parameters.

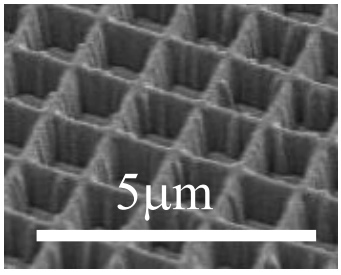

Fig.5 A SEM image of the fabricated periodic surface microstructures on W substrate

The optical properties are shown in Fig.6. We measured spectral reflectivity R on the microstructured W with the FT-IR and a UV-NIR spectrometer (Perkin Elmer; Spectrum GX, Lambda900). A diffuse reflection geometry which can collect the reflected lay with wide angle (PIKE; easidiff) was used as a substitute for an integral sphere. As predicted from the calculation results, the absorptivity shown as 1-R in Fig.6 increase drastically in $\lambda < 2.0\mu m$ keeping low absorptivity at larger λ range. The measured optical property shows good agreement with the calculation using RCWA.

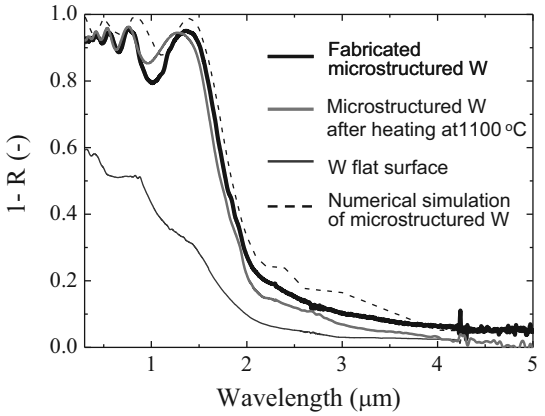

Fig.6 Comparison between the measured reflectivity and calculated spectral reflectivity obtained by numerical calculations

3.2. Large area fabrication of microstructured solar selective absorber

We can fabricate solar selective absorber applicable to CSP by MEMS process, however, the process needs high cost and too much time. To attain practical realization, the simple process which is able to fabricate microstructures in large area must be needed. Then, we focused on W-Cu alloy. This alloy is eutectic alloy and Cu grain thrust between W grains as shown in Fig. 7.

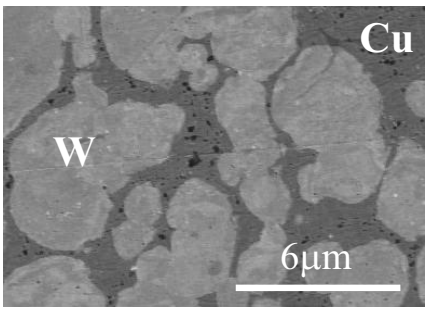

Fig. 7 Morphology of W-Cu alloy surface

Thus, we considered to obtain microstructured W surface by removing Cu grain and etching of W grain edge. The fabrication process is shown in Fig.8. This process is really simple process and easy to extend large area fabrication. First, sufficient thick of Cu grain is removed from the surface by using Cu etchant ($(NH_4)_2S_2O_8$). Then, W grain edge is etched by W etchant (mixed HF and HNO_3). The SEM picture of fabricated sample is shown in Fig.9. Almost similar sizes of W grains with the size of optical wavelength were verified at the surface. The optical property of visible light range is shown in Fig.10. In visible light range, absorptivity of the sample is increased comparing with flat W.

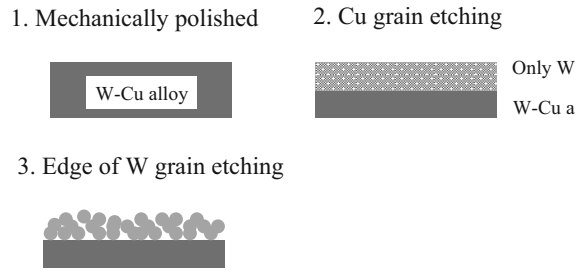

Fig.8 The fabrication process flow scheme of microstructured W based on W-Cu alloy.

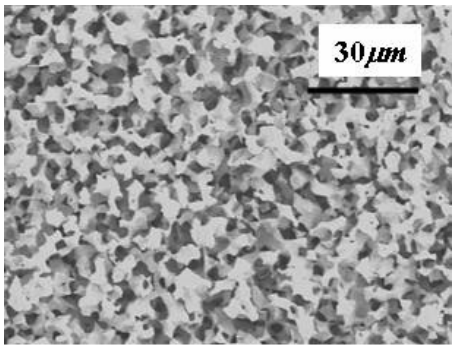

Fig. 9 A SEM image of after etching of Cu grain and edge of W grain

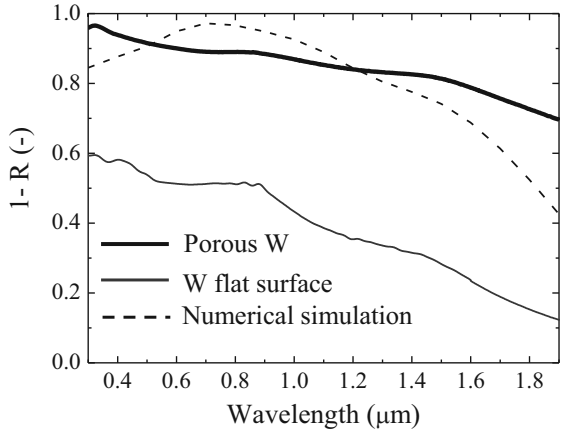

Fig.10 The absorptive property in visible light range of fabricated microstructured W

4. Conclusions

In this study, we research the solar selective absorbers with surface microstructures which applicable for CSP. From the estimation, it meets all requirements of solar selective absorbers utilized for CSP when cut-off wavelength is 1.7μm-2.1μm.

We successfully fabricated complete periodic surface microstructures on W substrate and from the measurement it is assumed to show high performance for solar selective absorber. We also consider the method which fabricates surface microstructures at large area by simple technique. We successfully to make microstructured surface using W-Cu alloy and it shows high absorptivity at visible light range.

5. References

(1) Koltum, M. M., 1972, “Selective Surfaces and Coatings in solar Radiation Engineering”, Gelioteknika, 5, pp. 70 (in Russian).
(2) McDonald, G. E., 1975, “Spectral Reflectance Properties of Black Chrome for Use as a Solar Selective Coating”, Solar Energy, 17(2), pp. 119-122.
(3) Peterson, R. E. and Ramsey, J. W., 1975, “Thin film coatings in solar-thermal power systems”, Journal of Vacuum Science & Technology, 12, pp. 174-181.
(4) Zhang, Q. C., 2000, “Recent progress in high-temperature solar selective coatings”, Solar Energy Materials & Solar Cells, 62, pp. 63-74.
(5) Eisenhammer, T., Haugender, A. and Mahr, A., 1998, “High-temperature optical properties and stability of selective absorbers based on quasicrystalline AlCuFe”, Solar Energy Materials & Solar Cells, 54, pp. 379-386.
(6) Schön, J. H. and Bucher, E., “Computer modeling of the performance of some metal/dielectric multilayers for high-temperature solar selective absorbers”, Solar Energy Materials & Solar Cells, 43, pp. 59-65.
(7) Gall, J. L., Oliver, M. and Greffet, J. J., 1997, “Experimental and theoretical study of reflection and coherent thermal emission by a SiC grating supporting a surface-phonon polariton”, Phys. Rev. B, 55(15), pp. 10105-10114.
(8) Greffet, J. J., Carminati, R. Joulain, K., Mulet, J. P., Mainguy, S. and Chen, Y., 2002, “Coherent emission of light by thermal sources”, Nature (London), 416(6876), pp. 61-64.
(9) Heinzel, A., Boerner, V., Gombert, A., Blasi, B., Wittwer, V. and Luther, J., 2000, “Radiation filters and emitters for the NIR based on periodically structured metal surfaces”, J. Mod. Opt., 47(23), pp. 2399-2419.
(10) Sai, H., Yugami, H., Akiyama, Y., Kanamori, Y. and Hane, K., 2001, “Spectral control of thermal emission by periodic microstructured surfaces in the near-infrared region”, J. Opt. Soc. Am. A, 18(7), pp. 1471-1476.
(11) Maruyama, S., Kashiwa, T., Yugami, H. and Esashi, M., 2001, “Thermal radiation from two-dimensionally confined modes in microcavities”, Appl. Phys. Lett, 79(9), pp. 1393-1395.
(12) Sai, H., Yugami, H., Kanamori, Y. and Hane, K., 2003, “Solar selective absorbers based on two-dimensional W surface gratings with submicron periods for high-temperature photothermal conversion”, Sol. Energy Mater. Sol. Cells, 79(1), pp. 35-49.
(13) Moharam, M. G., and Gaylord, T. K., 1986, “Rigorous coupled-wave analysis of metallic surface-relief grating,” J. Opt. Soc. Am. A **3**(11), pp. 1780-1787.

Eighth International Conference on Flow Dynamics
November 9 - November 11, 2011

Influence of Oxygen Nonstoichiometry Change on Thermal Properties of $La_{0.6}Sr_{0.4}Co_{1-x}Fe_xO_{3-\delta}$

Yu Cheol Shin[A,*], Atsushi Unemoto[B], Shin-ichi Hashimoto[A], Koji Amezawa[A], Tatsuya Kawada[A]
[A] Graduate School of Environmental Studies, Tohoku University, Japan
[B] IMRAM, Tohoku University, Japan
*Corresponding author: shin@ee.mech.tohoku.ac.jp

ABSTRACT

Thermal diffusivity of $La_{0.6}Sr_{0.4}Co_{1-x}Fe_xO_{3-\delta}$ (LSCF) was evaluated by laser flash method from room temperature to 1173 K in various oxygen partial pressures. It was found that the thermal diffusivity significantly depended on oxygen partial pressure. The oxygen partial pressure dependence was larger in lower oxygen partial pressure and at higher temperature. When oxygen partial pressure was changed at a constant temperature, the thermal diffusivity of LSCF6428 gradually changed as time passes. These results indicated that the thermal diffusivity of LSCF was significantly affected by the oxygen nonstoichiometry change.

1. Introduction

$La_{0.6}Sr_{0.4}Co_{1-x}Fe_xO_{3-\delta}$ (LSCF) is a potential candidate as a mixed-conducting cathode for solid oxide fuel cells, and as an oxygen separation membrane material. In order to employ these compositions either as oxide electrodes or as oxygen-permeating membranes, it is of importance to examine the oxygen deficiency and its influence on other material properties. For instance, it was reported that electrical and mechanical properties strongly depends on the oxygen nonstoichiometry [1]. However, little is known about the influe1nces of oxygen nonstoichiometry on thermal properties so far.

In this work, we report the thermal properties such as thermal diffusivity at various temperatures and oxygen partial pressures of the perovskite-type oxide $La_{0.6}Sr_{0.4}Co_{1-x}Fe_xO_{3-\delta}$. The thermal diffusivity was investigated by using the laser flash method (LFA). Dependencies of thermal diffusivities of LSCF on temperature, oxygen partial pressure were discussed in terms of the oxygen nonstoichiometry.

2. Experimental

Powders of $La_{0.6}Sr_{0.4}Co_{1-x}Fe_xO_{3-\delta}$ (LSCF) were prepared by a conventional Pechini method. Obtained powders were hydrostatically pressed at 150 MPa into compacts, and then sintered in air at 1627 K for 6h. For the thermal diffusivity measurements, the sintered compacts were cut into rectangles (*c.a.* 10 x 10 x 1 mm). The relative densities of the sintered LSCF compacts were always higher than 95%. Sintered all of pellets were single phase perovskites.

Thermal diffusivities of the sintered pellets were measured by using the laser flash method (LFA 457 Micro Flash, NETZSCH) in the oxygen partial pressure range from 10^{-4} to 0.2 bar and in the temperature range from R.T. to 1173 K. In order to control the atmospheres, a gas mixing system and an oxygen sensor are additionally attached to the laser flash method system.

The temperature dependence of the thermal diffusivities was measured with increasing temperature from R.T to 1173K while keeping atmospheres as constant. Measurements were performed with a 50 K interval. The oxygen partial pressure dependence of the thermal diffusivities was measured with decreasing oxygen partial pressure from 0.2 to 10^{-4} bar while keeping temperature at 873, 973 and 1073K. Measurements were repeated until the obtained thermal diffusivity reached to a constant value at each temperature and oxygen partial pressure.

3. Results and Discussion

Figure 1 shows the thermal diffusivities of $La_{0.6}Sr_{0.4}Co_{0.2}Fe_{0.8}O_{3-\delta}$ as a function of temperature in various oxygen partial pressures. The thermal diffusivity of LSCF first increased with increasing temperature and then decreased with increasing temperature and decreasing oxygen partial pressure at above 673K.

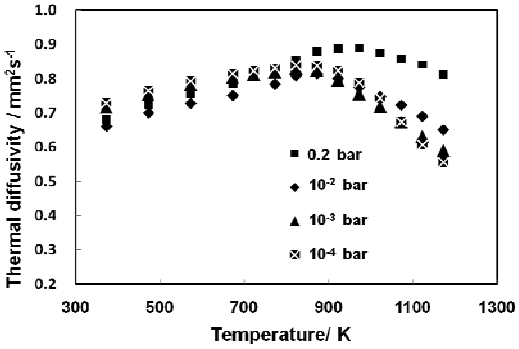

Fig. 1 Temperature dependence of thermal diffusivity for $La_{0.6}Sr_{0.4}Co_{0.2}Fe_{0.8}O_{3-\delta}$ as a function of $p(O_2)$

LSCF is known to show the oxygen nonstoichiometry changes at relatively higher temperature, although the oxygen nonstoichiometry is kept almost constant at lower temperature. According to the data by Mantzavinos *et al*. [1] and Hashimoto *et al.* [2], the oxygen deficiency δ increased with increase temperature and decreasing $p(O_2)$ in higher temperature range (above 873K). The temperature where the thermal diffusivity drastically changes seems to agree with the temperature where the oxygen nonstoichiometry changes.

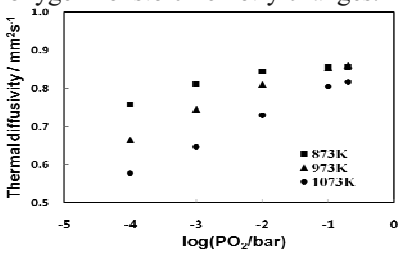

Fig. 2 Thermal diffusivity of $La_{0.6}Sr_{0.4}Co_{0.2}Fe_{0.8}O_{3-\delta}$ as a function of $p(O_2)$ at 873K, 973K and 1073K.

Therefore, it can be said that the change of the temperature dependence of the thermal diffusivities of LSCF in Fig. 1 is attributed to the oxygen nonstoichiometry changes.

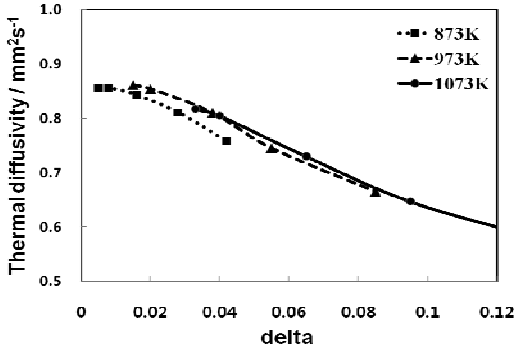

Fig. 3 Thermal diffusivity of $La_{0.6}Sr_{0.4}Co_{0.2}Fe_{0.8}O_{3-\delta}$ as a function of $\boldsymbol{\delta}$ at 873K, 973K and 1073K.

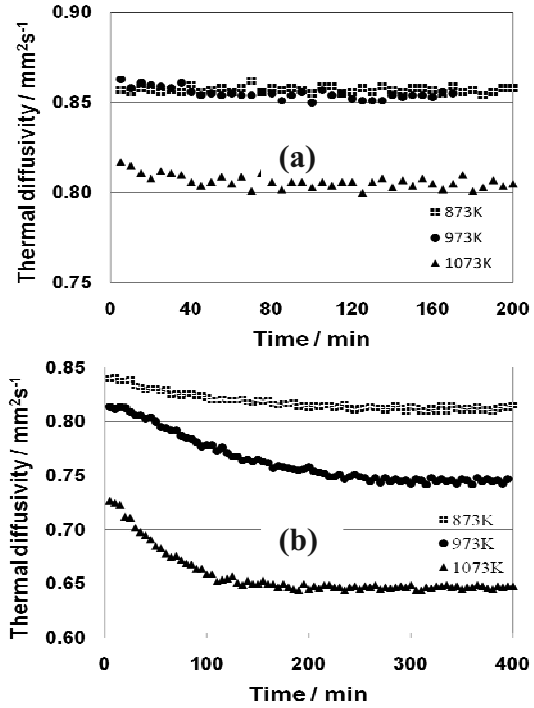

Fig. 4 Time dependence of the thermal diffusivity of $La_{0.6}Sr_{0.4}Co_{0.2}Fe_{0.8}O_{3-\delta}$ observed ~~in~~ when $p(O_2)$ was changed (a) from 0.2 to 10^{-1} bar and (b) from 10^{-2} to 10^{-3} bar at various temperatures

Figure 2 shows the thermal diffusivity of $La_{0.6}Sr_{0.4}Co_{0.2}Fe_{0.8}O_{3-\delta}$ as a function of $p(O_2)$ at 873, 973 and 1073K. Figure 2 shows similar tendency with oxygen nonstoichiometry of $La_{0.6}Sr_{0.4}Co_{0.2}Fe_{0.8}O_{3-\delta}$. Thermal diffusivity of all of temperatures decreases with decrease oxygen partial pressure.

Figure 3 shows the thermal diffusivity of $La_{0.6}Sr_{0.4}Co_{0.2}Fe_{0.8}O_{3-\delta}$ as a function of $\boldsymbol{\delta}$ at 873, 973 and1073K. Thermal diffusivity of LSCF decreased with decreasing oxygen deficiency δ. The $p(O_2)$ dependence of the thermal diffusivity decreased with increase temperature. As is known, the oxygen nonstoichiometry of $La_{0.6}Sr_{0.4}Co_{0.2}Fe_{0.8}O_{3-\delta}$ decreased with increase temperature and decrease $p(O_2)$ [3]. Such a thermal diffusivity change with $p(O_2)$ change was considered due to its oxygen nonstoichiometry change.

In order to confirm influences of the oxygen nonstoichiometry change on the thermal diffusivity, relaxation behavior of the thermal diffusivity was examined when the oxygen partial pressure was changed. Figure 4 shows the time dependence of the thermal diffusivity of $La_{0.6}Sr_{0.4}Co_{0.2}Fe_{0.8}O_{3-\delta}$ when $p(O_2)$ was changed at constant temperatures. As shown in Fig. 4(a), in higher $p(O_2)$, the thermal diffusivity showed only slight time dependence. Contrarily, in lower $p(O_2)$, time dependence of the thermal diffusivity was observed and became significant with increasing temperature.

When $p(O_2)$ was varied from 10^{-1} to 10^{-2} bar, the relaxation time was about 30 minute and the change in the thermal diffusivity was 0.02 mm^2s^{-1} at 1073K. On the other hand, When $p(O_2)$ was varied from 10^{-2} to 10^{-3} bar, the relaxation time was about 200 minute and the change in the thermal diffusivity was 0.8 mm^2s^{-1} at 1073K. The relaxation time increased with increase temperature. Because the oxygen deficiency δ increases considerably with increasing temperature (*i.e.* at $p(O_2)$ = 0.1 bar, δ increases from 0.008 at 873K to 0.04 at 1073K). For a similar reason, The relaxation time increased with decrease $p(O_2)$ (*i.e.* at 1073K, δ increases from 0.04 in 10^{-1} bar to 0.95 in 10^{-3} bar).

4. Concluding remarks

In this work, dependencies of thermal diffusivities of perovskite-type oxides $La_{0.6}Sr_{0.4}Co_{1-x}Fe_xO_{3-\delta}$ (LSCF) on temperature, and oxygen partial pressure were investigated. In 2.0 - 10^{-4} bar of $p(O_2)$ at 873 - 1073K, the thermal diffusivity of LSCF decreased with decrease $p(O_2)$. Therefore, the thermal diffusivity of LSCF was dependence. When $p(O_2)$ changed at constant temperature, the thermal diffusivity showed a little time dependence in higher $p(O_2)$, while apparent time dependence in lower $p(O_2)$. The relaxation time increased with increasing temperature. This relaxation behavior could be interpreted by the change in the oxygen nonstoichiometry, meaning that the thermal diffusivity of LSCF was significantly affected by the oxygen nonstoichiometry.

Acknowledgements

This work was supported by NEDO project "Development of System and Elemental Technology on SOFC" and Tohoku University Global COE Program "World Center of Education and Research for Trans-disciplinary Flow Dynamic".

References

[1] I. Yasuda and M. Hishinuma, *Solid State Ionics,* 80 (1995) 141-150

[2] L.-W. Tai, M.M. Nasrallah, H.U. Anderson, D.M. Sparlin and S.R. Sehilin, *Solid State Ionics*, 76 (1995) 259-271

[3] S. Hashimoto, Y. Fukuda, M. Kuhn, K. Sato, K. Yashiro, J. Mizusaki, *Solid State Ionics,* 181 (2010) 1713–1719

Partial Conductivities and Onsager Transport Coefficient Matrix of $BaCo_{0.7}Fe_{0.22}Nb_{0.08}O_{3-\delta}$

Taewon Lee
Department of Materials Science and Engineering, Seoul National University, Seoul 151-744, Korea
e-mail : rebirth2@snu.ac.kr

ABSTRACT

Despite partial electronic and ionic conductivities composing ambipolar conductivity are the key factors to determine the performance for oxygen permeable membrane materials as well as SOFC cathode materials, they are not so exhaustively characterized. In this work, we have measured the partial ionic/electronic conductivities and established the Onsager transport coefficient matrix for the system of $BaCo_{0.7}Fe_{0.3-x}Nb_xO_{3-\delta}$ (x=0.08), one of state-of-the-art materials for oxygen permeable membrane, by an electrochemical polarization technique in ion-blocking electrode condition.

1. Introduction

A variety of $BaCoO_3$-based derivatives such as $BaCo_{0.7}Fe_{0.3-x}Nb_xO_{3-\delta}$ [1] and $Ba_{0.5}Sr_{0.5}Co_{1-x}Fe_xO_{3-\delta}$ [2,3] have been attracting a wide attention as oxygen permeation membrane materials as well as SOFC cathode materials due to their superior oxygen permeability or ambipolar conductivity. Even though their partial oxygen ionic and electronic conductivities play a pivotal role on oxygen permeating phenomena and are the key properties for performance as SOFC cathode, they are not seriously characterized.

Nowadays, some researchers suggested ion/electron blocking cell techniques in order to evaluate partial ionic and electronic transport properties as well as cross effect between ionic and electronic species in MIECs (mixed ionic electronic conductors) including Pr-doped CeO_2 [4] and $LaNiO_4$ [5] system. Furthermore, since these techniques employ local ionic/electronic probes separated from ion/electron blocking electrodes, observed results are free from over-potential problem.

In this work, we recognized the benefit of blocking cell with local probes, and have measured the partial conductivities and eventually established the complete representation of all the isothermal transport properties, the Onsager transport coefficient matrix for the system of $BaCo_{0.7}Fe_{0.3-x}Nb_xO_{3-\delta}$ (x=0.08) [1], one of state-of-the-art materials for oxygen permeable membrane by an electrochemical polarization technique in ion-blocking electrode condition.

2. Theory

All the mass and charge transport properties of a mixed conductor can be completely represented by an Onsager transport coefficient matrix L such that

$$\begin{pmatrix} J_i \\ J_e \end{pmatrix} = -\begin{pmatrix} L_{ii} & L_{ie} \\ L_{ei} & L_{ee} \end{pmatrix}\begin{pmatrix} \nabla\eta_i \\ \nabla\eta_e \end{pmatrix} \quad (1)$$

where J_k and $\nabla\eta_k$ represent the flux and electrochemical potential gradient of ionic (k=i) and electronic carriers (k=e), and $L_{ie}=L_{ei}$ due to the Onsager reciprocity theorem [6].

In $BaCo_{0.7}Fe_{0.3-x}Nb_xO_{3-\delta}$ (x=0.08) system, subscript i and e were regarded as oxygen ion and hole. Since Onsager's matrix is composed of three independent transport coefficients, more than three independent electrochemical properties as a function of Onsager transport coefficients are required as follows. [7]

$$\sigma = F^2\left[2L_{ii}\left(2-\frac{L_{ie}}{L_{ii}}\right)+L_{ee}\left(1-2\frac{L_{ie}}{L_{ee}}\right)\right] \quad (2)$$

$$\sigma_e' = F^2 L_{ee}\left(1-\frac{L_{ie}^2}{L_{ii}L_{ee}}\right) \quad (3)$$

$$\alpha_i^* = \frac{L_{ie}}{L_{ii}} \quad (4)$$

Where σ, σ_e', and α_i^* refer to total conductivity, conductivity with ion transfer suppressed, and ionic charge-of-transport [8]. Equation (2)-(4) can be simply transformed into Onsager coefficients.

$$L_{ii} = \frac{\sigma-\sigma_e'}{F^2\left(\alpha_i^*-2\right)^2} \quad (5)$$

$$L_{ee} = \frac{\alpha_i^*\left(\alpha_i^*\sigma-4\sigma_e'\right)+4\sigma_e'}{F^2\left(\alpha_i^*-2\right)^2} \quad (6)$$

$$L_{ie} = \frac{\alpha_i^*\left(\sigma-\sigma_e'\right)}{F^2\left(\alpha_i^*-2\right)^2} \quad (7)$$

Moreover, partial ionic and electronic conductivities can be written as a function of three independent transport coefficients as follows. [7]

$$\sigma_i = 4F^2 L_{ii}\left(1-\frac{L_{ie}}{2L_{ii}}\right) \quad (8)$$

$$\sigma_e = F^2 L_{ee}\left(1-2\frac{L_{ie}}{2L_{ee}}\right) \quad (9)$$

3. Experimental

3.1. Electrochemical cell

$BaCo_{0.7}Fe_{0.22}Nb_{0.08}O_{3-\delta}$ specimen was synthesized by conventional solid state route. To establish local ionic and electronic probes, porous pre-sintered body was constructed. Holes for local inner probes were drilled. Porous body with 4 inner probes underwent heat treatment at 1150°C in air for 10 hours. Relative density of final body was estimated about 96%.

The schematic of the electrochemical cell was described here.

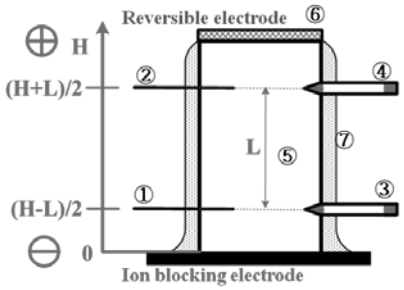

Fig. 1. The schematic of electrochemical cell with one reversible and the other ion-blocking electrode : ① ② ionic probe (8YSZ), ③④ electronic probe (Pt), ⑤ specimen, ⑥ Pt gauze, ⑦ glass sealant.

Since we recognized the significant reactivity between specimen and glass components including SiO_2, small amount of glass sealant was painted on the specimen.

3.2. Ion-blocking operation

Small amount of current flowing across the specimen from reversible electrode to ion-blocking electrode causes chemical polarization of component oxygen. Monitored electrical signals are summarized as follows.

Table 1. Signal contents

	+ (probe number)	- (probe number)	contents
u_i	④	③	$-\frac{L}{2F}\nabla\eta_i$
v_e	②	①	$\frac{L}{F}\nabla\eta_e$
u_1	②	④	$\left[\mu_{O_2}\left(x=\frac{H+L}{2}\right)-\mu_{O_2}^{Ref.}\right]/4F$
u_2	①	③	$\left[\mu_{O_2}\left(x=\frac{H-L}{2}\right)-\mu_{O_2}^{Ref.}\right]/4F$

Inter-ionic probe signal u_i and inter-electronic probe signal v_e provide the electrochemical driving forces of species i and e respectively. u_1 and u_2 include the difference between oxygen chemical potential of specimen at given position and that of surrounding atmosphere.

When the system achieves steady state polarization, the electronic conductivity under ion-blocking condition, σ_e' and the ionic charge-of-transport, α_i^* have been determined from current I, v_e and u_i.

$$\alpha_i^* = -\left(\frac{\nabla\eta_i}{\nabla\eta_e}\right)_{J_i=0} = \left(\frac{2u_i}{v_e}\right)_{J_i=0} \qquad (10)$$

$$\sigma_e' = -\frac{L}{A}\left(\frac{I}{v_e}\right)_{J_i=0} \qquad (11)$$

Where L and A stand for the distance between local probes and cross sectional area respectively.

4. Results and Discussion

4.1. Polarization behavior

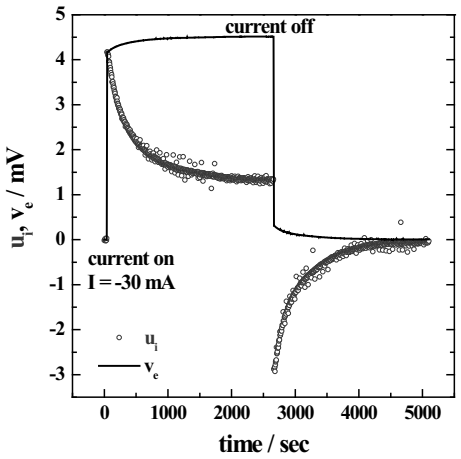

Fig. 2. Typical time dependent behavior of u_i and v_e upon switching current on and off across the specimen.

As explained before, the electronic conductivity under ion-blocking condition and the ionic charge-of-transport were acquired at steady state conditions by using cell signal and applied current. On the other hand, total conductivity (σ), the third independent electrochemical property, is calculated from voltage drop of electronic probe signal when switching current off as

$$\sigma = -\frac{L}{A}\left(\frac{\Delta I}{\Delta v_e}\right)_{t=t^{off}} \qquad (12)$$

where t^{off} is time when current is turned off.

It may be noted that non-zero value of u_i means the interference between oxygen ionic and electronic flows are not negligible.

4.2. σ and σ_e'

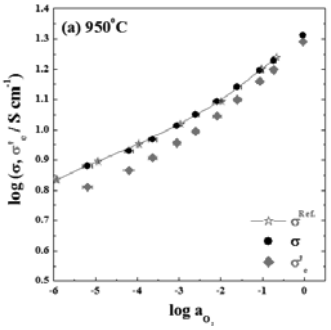

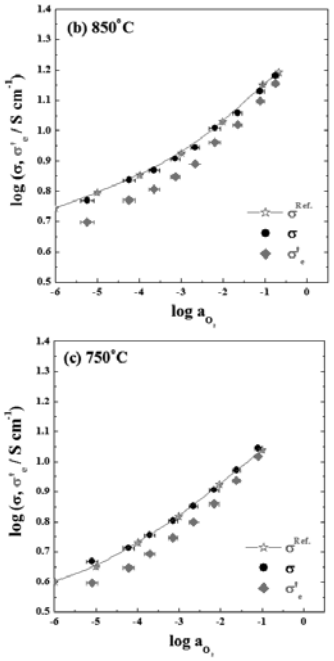

Fig. 3. σ and σ_e' as a function of oxygen activity at three different temperatures : (a) 950°C, (b) 850°C, and (c) 750°C.

In Fig. 3, circle and diamond shape closed symbols are σ and σ_e' respectively. And open symbol means $\sigma^{Ref.}$ which is independently measured total conductivity via conventional DC 4 probe method. Total conductivity acquired from ion blocking cell and one measured by means of DC 4 probe method are identical within less than 3% relative difference. Furthermore, σ_e' decreases as oxygen activity decreases, and thereby majority electronic charge carrier can be considered as hole.

4.3. α_i^*

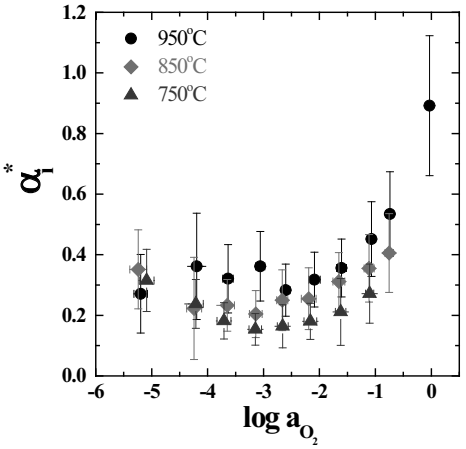

Fig. 4. α_i^* as a function of oxygen activity at three different temperatures.

On the basis of Yoo's interpretation [8], the ionic charge-of-transport can be regarded as the number of hole dragged by one moving oxygen ion. As a result, α_i^* was measured to be higher than 0.15 within entire range of experiment, and thus cross effect between oxygen ion and hole was non-negligible compared to the direct ionic transport. This means that information of ionic transport, obtained from ion-blocking experiment without any adjustment by local ionic probes, always includes at least 8% relative error compared to 'true' value.

4.4. L-matrix

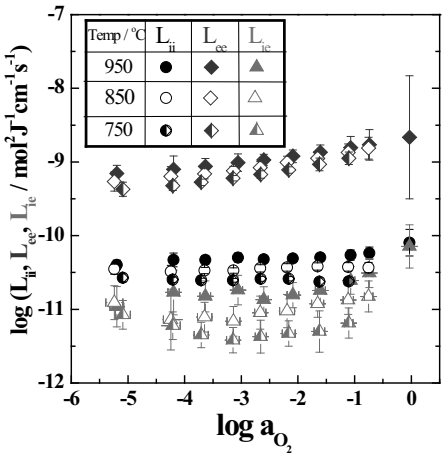

Fig. 5. Onsager matrix coefficients as a function of oxygen activity.

L-matrix was completely established by using equation (5)-(7) with three independent electrochemical properties such as σ, σ_e', and α_i^*. As is shown, cross coefficient L_{ie} is comparable to ionic transport coefficient L_{ii}. But the quantity of L_{ie} is 1~4% compared to electronic transport coefficient L_{ee}.

4.5. σ_i and σ_e

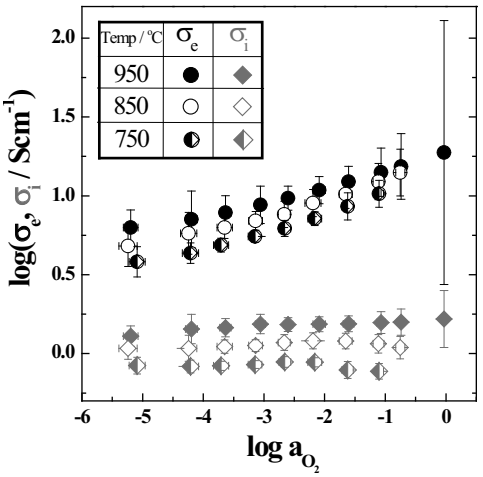

Fig. 6. Partial ionic and electronic conductivities as a function of oxygen activity.

Partial conductivities were calculated with obtained

L-matrix coefficients by using equation (8) and (9). As a result, very high ionic conductivity was observed to be higher than 1 S/cm at 850°C. With regard to dependency of partial conductivities vs. oxygen activity, ionic conductivity seems to be nearly constant within given oxygen activity domain, and logarithmic electronic conductivity linearly depends on logarithmic oxygen activity. Since expected ionic transport number are in a range from 0.04 to 0.22, $BaCo_{0.7}Fe_{0.3-x}Nb_xO_{3-\delta}$ (x=0.08) is 'real' mixed ionic electronic conductor.

5. Summary and Conclusion

In this work, we paid attention to partial ionic and electronic transport properties as key factor to determine performance as oxygen permeable membrane as well as SOFC cathode materials, and made an effort to evaluate those via electrochemical polarization technique. On basis of our observation, followings are drawn.

(i) Onsager matrix and partial ionic/electronic conductivities are established by means of ion-blocking experiment only due to non-negligible ionic transport number.
(ii) In $BaCo_{0.7}Fe_{0.3-x}Nb_xO_{3-\delta}$ (x=0.08) system, the interference between ionic and electronic charge carriers are not negligible
(iii) $BaCo_{0.7}Fe_{0.3-x}Nb_xO_{3-\delta}$ (x=0.08) is true to the name, "mixed ionic electronic conductor" due to comparable ionic conductivity to electronic one.

References

[1] Y. Cheng et al., J. Membr. Sci. **322** (2008) 484.
[2] Z. Shao and S. M. Haile, Nature **431** (2004) 170.
[3] Z. Shao et al., J. Membr. Sci. **172** (2000) 177.
[4] C. Chatzichristodoulou et al., Phys. Chem. Chem. Phys. **12** (2010) 9637.
[5] H.-S. Kim and H.-I. Yoo, Phys. Chem. Chem. Phys. **12** (2010) 12951.
[6] L. Onsager, Phys. Rev. **37** (1931) 405.
[7] K.-C. Lee and H.-I. Yoo, Solid State Ion. **86-88** (1996) 757.
[8] H.-I. Yoo et al., Z. Phys. Chem. (NF) **168** (1990) 129.

Eighth International Conference on Flow Dynamics
November 9 - November 11, 2011

Ionic Conductivity in Electrolyte Thin Films Fabricated by Pulsed Laser Deposition

Yuta Fujiwara, Yoshikazu Shibata, Fumitada Iguchi, Noriko Sata, Hiroo Yugami
Department of Mechanical Systems and Design, Graduate School of Engineering, Tohoku University,
6-6-01 Aoba, Aramaki Aoba-ku, Sendai, 980-8579, Japan
y_fujiwara@energy.mech.tohoku.ac.jp

ABSTRACT

Electrolyte thin films are fabricated by various conditions and clarifying the effect on their crystal structure and ionic conductivity. In particular, both proton and oxide ion conductor thin film are fabricated by HT-PLD and RT-PLD changing sputter rates, laser energy and oxygen partial pressure during deposition. Besides, their structural analysis and ionic conductivity is measured by XRD measurement and AC impedance measurement, respectively.

1. Introduction

Recent years, thin film fabrication techniques have been developing rapidly and more commonly utilized with the progress of nanoionics. Pulsed laser deposition (PLD) is now well known as a powerful tool to obtain epitaxial oxide thin films, especially for Perovskite-type oxides [1-2].

In a conventional PLD process, substrates are heated to crystallize the deposited particles in an epitaxial structure. When perovskite-type oxides are deposited at room temperature on a single crystal substrate, like MgO(001) by PLD with atomic oxygen irradiation (RT-PLD), it is found that the thin film can be epitaxially crystallized by post-annealing in a conventional furnace. Compared with a conventional PLD method (deposition at high temperature: HT-PLD), RT-PLD enable to obtain high-epitaxy thin films at relatively lower temperatures.

In previous studies, lattice constant of $SrZrO_3$ (SZO) thin films was compared at HT-PLD and RT-PLD (Fig.1). At HT-PLD, thin films have lattice compression in-plane lattice due to deposit at high temperature. On the other hand, at RT-PLD, thin films have lattice strains due to the large in-plane lattice of substrate MgO when the annealing temperature is lower than 670 degree C. If the annealing temperature is higher than 670 degree C, lattice strain is somewhat released and lattice parameters become closer to those of bulk crystal. These differences may be caused by the lattice mismatch between thin film and the substrate and the thermal energy.

Fig.2 shows arrhenius plot of the ionic conductivity of $SrZr_{0.95}Y_{0.05}O_3$ (SZY) thin film on MgO fabricated by HT-PLD and RT-PLD method measured in atmosphere of H_2O vapor. As a reference, Arrhenius plot of the ionic conductivity of SZY single crystal and SZO single crystal are shown. The ionic conductivity of SZY thin film fabricated by RT-PLD method is lower than that of thin film fabricated by HT-PLD method, and activation energy is higher. Conductivity mechanism of SZY thin film was proton conductivity confirmed by deuteron exchange effect, however proton conductivity mechanism of SZY thin film fabricated by HT-PLD and RT-PLD is completely deference.

As previously described, Lattice constants and ionic conductivity of thin films fabricated by HT-PLD and RT-PLD is completely deference. On the other hand, reported ionic conductivity of thin films fabricated by same HT-PLD method has been scattered. Pergolesi et al. reported that high textured, epitaxially oriented $BaZr_{0.8}Y_{0.2}O_{3-\delta}$(BZY) thin films were obtained on (100)-oriented MgO substrates, showing the largest proton conductivity ever reported for BZY samples, being $0.11Scm^{-1}$ at 500 degree C[3]. It is considered that this large proton conductivity of BZY thin films depend on the fabricating condition. However, it has not been revealed that which fabricating condition influence their crystal structure and ionic conductivity.

In this study, electrolyte thin films are fabricated by various conditions and clarifying the effect on their crystal structure and ionic conductivity. In particular, both proton and oxide ion conductor thin film are fabricated by HT-PLD and RT-PLD changing sputter rates, laser energy and oxygen partial pressure during deposition. Besides, their structural analysis and ionic conductivity is measured by XRD measurement and AC impedance measurement, respectively.

However, our experimental state has been preparation stage yet. Therefore, we shows experimental plan in this paper and present their results in Korea-Japan student's symposium.

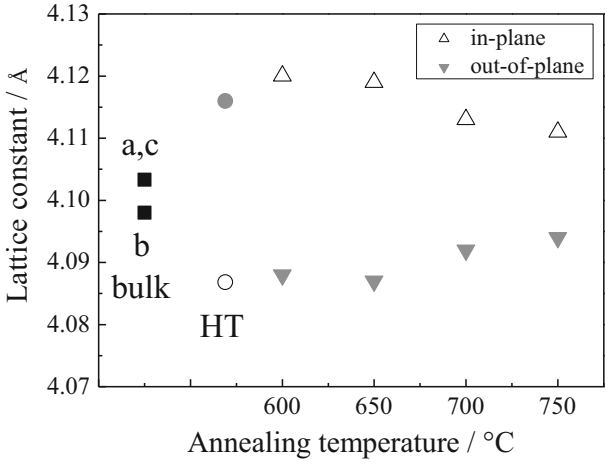

Fig.1 Lattice constants of SZO thin films on MgO (post-annealed for 10 hours) as a function of annealing temperature, and those of bulk crystals and thin films of HT-PLD process for comparison.

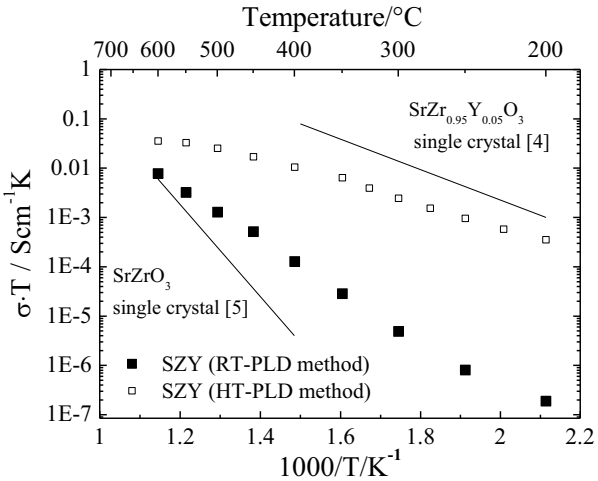

Fig.2 Arrhenius plot of the electrical conductivity of $SrZr_{0.95}Y_{0.05}O_3$ thin film on MgO fabricated by RT-PLD method measured in atmosphere of H_2O vapor.

2. Experiments

Fig.3 shows a schematic illustration of the PLD system. SZO and SZY thin films are deposited on SiO_2 or MgO substrates by HT-PLD or RT-PLD using ArF excimer laser (λ=193nm). Oxygen or atomic oxygen is fed during deposition. Sputter rates and oxygen partial pressure during deposition change various conditions. Base pressure is below 10^{-6} Pa.

The crystal structures of thin films are analysed by X-ray diffractometer (PANalytical X'Pert PRO)

Ionic conductivity of thin films is measured by AC impedance measurement. Interdigital electrodes of Pt are fabricated on the thin films like Fig.4. Fig.5 shows schematic illustration of AC impedance measurement system. Ionic conductivity was measured by AC impedance analyser (Solatron 1260 frequency response analyzer with 1296 dielectric interface).

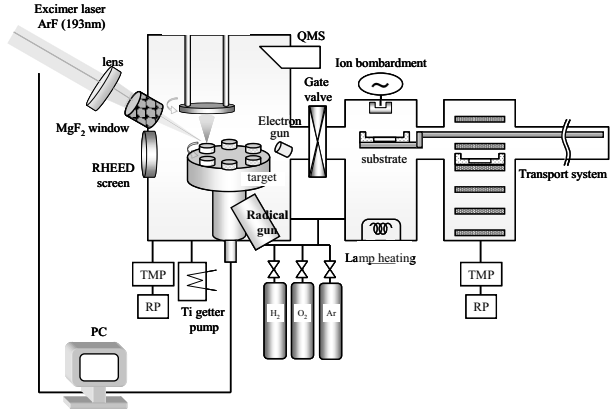

Fig.3 A schematic illustration of the pulsed laser deposition system.

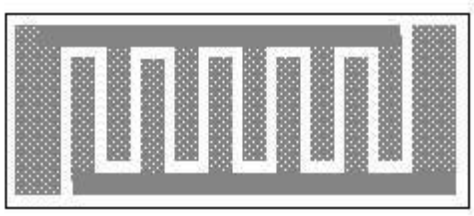

Fig.4 Pattern of Pt electrode.

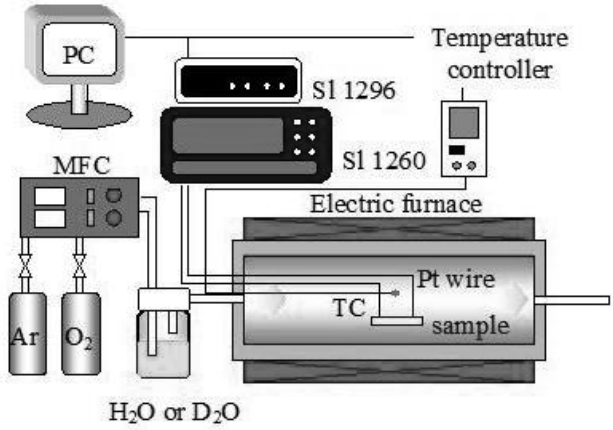

Fig.5 Schematic illustration of AC impedance measurement system.

3. Results and Discussion

SZO and SZY thin film was deposited on SiO_2 substrates by RT-PLD to calculate sputter rates and to confirm film condition. Oxygen partial pressure during deposition was about 4.5×10^{-1} Pa. Post-annealing was carried out in conventional furnace in air at 750 degree C for 10 hours. Fabricated conditions of these thin films show table 1.

The result of XRD measurement, Diffraction peak of crystallized these thin films was not confirmed. It is possible that these thin films are too thin to detect the diffraction peak.

Table 1 Fabricated conditions of SZO and SZY thin films.

Taget	Shot number / Frequency	Film thickness
SZO	30000 shots / 2Hz	50nm
SZY	30000 shots / 2Hz	61nm
	30000 shots / 4Hz	48nm

4. Future Work

SZO and SZY thin films will be fabricated by various conditions, for example, changing sputter rates, laser energy and oxygen partial pressure during deposition. Besides, we will analyze the crystal structures and measure the ionic conductivity.

Reference

[1] S. Ito et al. *Applied Surface Science* 216 (2003) 508-511.
[2] S. Ohashi et al. *Review of Scientific Instruments* 70 (1999) 178-183.
[3] Daniele Pergolesi et al. *Nature Materials* 9 (2010)
[4] T. Higuchi et al. *Jpn. J. Appl. Phys*. 40 (2001) 4162-4163
[5] T. Higuchi et al. *Jpn. J. Appl .Phys*. 41 (2002) 6440-6442

Multi-Protons Migration in Barium Zirconate Using Density Functional Theory

Dae-Hee Kim[1], Yong-Chan Jeong[1], Byung-Kook Kim[2], and Yeong-Cheol Kim[1]
[1]School of Energy, Materials & Chemical Engineering, Korea University of Technology and Education, Cheonan 330-708, Korea
[2]High Temperature Energy Materials Center, Korea Institute of Science and Technology (KIST), Seoul 136-791, Korea
E-mail of corresponding author: yckim@kut.ac.kr

ABSTRACT

Multi-protons migration as a function of the distance between them in barium zirconate was investigated using density functional theory. The energies were varied due to the attractive and repulsive interactions between protons and oxygen ions. When a proton migrated far from another proton, energy barriers were similar to that of single proton migration. A high energy barrier of 0.41 eV, however, was required for proton migration near another proton. Therefore, experimental energy barriers for proton migration in bulk yttrium-doped barium zirconate were due to the interaction between protons.

1. Introduction

Since Iwahara introduced doped $SrZrO_3$ and $SrCeO_3$ as potential proton conductors in the 1980s [1,2], many works have been devoted to perovskite-structured materials in an effort to discover commercially applicable high-temperature proton conductors (HTPCs) [3,4]. It is generally accepted that doped $BaZrO_3$ is one of the most promising potential candidates for HTPCs due to its high proton conductivity and sound chemical stability [5,6]. This high proton conductivity is mainly determined by its easy proton formation and fast proton migration.

Proton migration mechanism has been studied using density functional theory (DFT) [7,8]. Protons rotate at oxygen ion sites, and transfer between oxygen ions. Energy barriers for single proton rotation and transfer in pure bulk $BaZrO_3$ were in the range of 0.17-0.22 eV. However, many protons exist inside $BaZrO_3$. In the present study, multi-protons migration in bulk $BaZrO_3$ was investigated to understand interactions between protons and the resulting effect on their migration using DFT.

2. Calculation Method

All DFT calculations were performed using Vienna *ab initio* simulation package (VASP) code [9,10]. Electron wave functions were described using the projector augmented wave (PAW) method of Blöchl that was implemented to the code by Kresse and Joubert. The exchange correlation energy was described by Perdew, Burke, and Ernzerhof (PBE) based on the generalized gradient approximation (GGA). The cutoff energy was 500 eV, and the *k*-points mesh was 4×4×4 for 2×2×2 $BaZrO_3$ super cells using the Monkhorst-Pack grid method. The energy barriers for proton migration were calculated using the climbing nudged elastic band (CNEB) tool implemented in the VASP code, which can find a saddle point and minimum energy paths for proton migration. All ions were allowed to relax during the energy barrier calculations to find optimum transition states.

3. Results and Discussion

Fig. 1 shows energies as a function of the distance between two protons in the bulk 2×2×2 $BaZrO_3$ super cell. The energy is set to 0 eV as a reference when two protons are separated by 7.36 Å in the super cell. When the distance increased to greater than 4.4 Å in the super cell (black dotted circle in Fig. 1), there were four weak attractive interactions between protons and O ions mostly. Fig. 2(a) shows the two protons separated by 7.36 Å in the super cell. Since these weak attractive interactions were identical to the case of single proton in the pure 2×2×2 super cell, we could neglect the interaction between the two protons. When the distance was in the range of 2.65-3.96 Å (green dotted circle in Fig. 1), there were two weak and one strong attractive interactions between protons and O ions. Fig. 2(b) shows the two protons separated by 3.29 Å in the super cell. One proton (H1) was attracted to a neighboring O ion (O1) by a distance of 1.78 Å because another neighboring O ion (O2) was satisfied by another proton (H2). When the distance within 2.43 Å in the super cell (blue dotted circle in Fig. 1), there were two strong attractive and one repulsive interactions. Fig. 2(c) shows the two protons separated by 2.09 Å in the super cell. The two protons were attracted to neighboring O ions by a distance of 1.78 Å due to the repulsive interaction between the two protons. We found an unfavorable case (red dotted circle in Fig. 1, 0.28 eV energy increase), and Fig. 2(d) shows the two protons separated by 4.26 Å in the super cell.

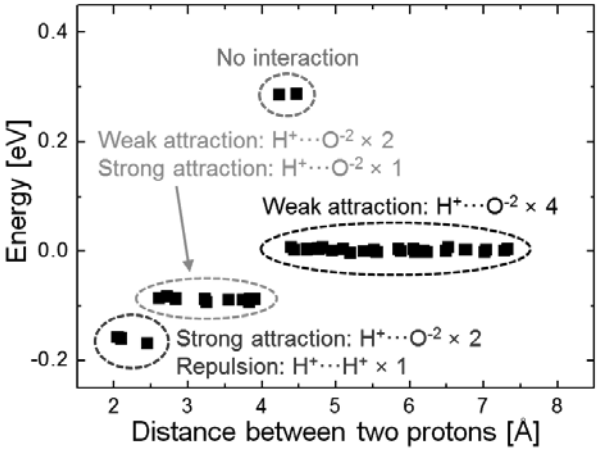

Fig. 1 Energy variation as a function of the distance between two protons in the bulk $BaZrO_3$ super cell.

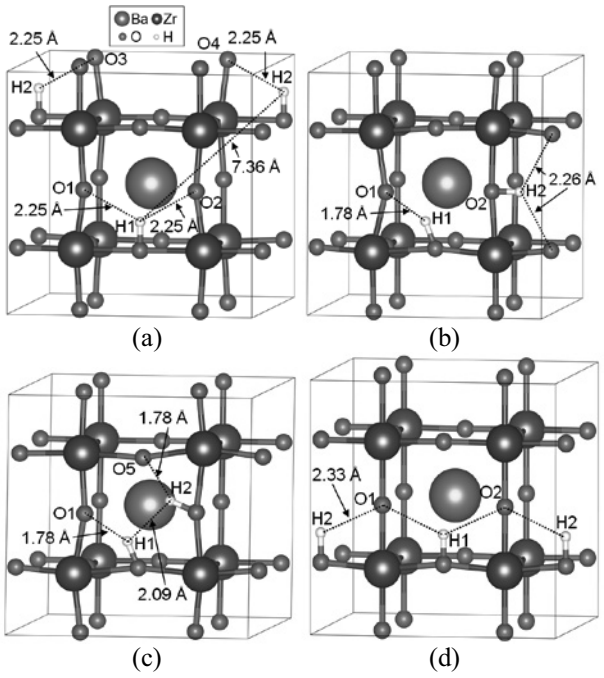

Fig. 2 Perspective views of four cases, (a) black, (b) green, (c) blue, and (d) red dotted circles in Fig. 1. The distances between the two protons of Figs. 2(a)-(d) are 7.36, 3.29, 2.09, and 4.26 Å, respectively.

Energy barriers were calculated for proton migration in the super cell. When the two protons were further separated by a distance of 7.36 Å, energy barriers for proton migration were in the range of 0.18-0.23 eV. These values were similar to that of single proton migration in the pure bulk $BaZrO_3$ super cell [7,8]. When one proton migrated near another proton, as shown in Fig. 3, a high energy barrier of 0.41 eV was required due to the repulsive interaction between the two protons.

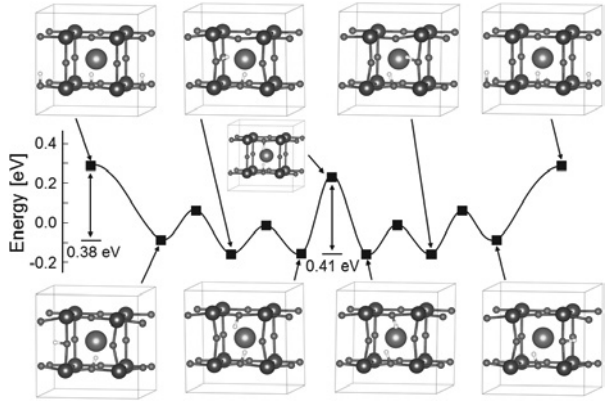

Fig. 3 Energy variation during a proton migration near another proton fixed in a position in the pure bulk $BaZrO_3$ super cell.

4. Conclusions

We studied multi-protons migration in the pure bulk $BaZrO_3$ super cell using DFT. When a proton migrated far from another proton, low energy barriers were required in the range of 0.18-0.23 eV. However, a high energy barrier of 0.41 eV was required for proton migration, when a proton migrated near another proton. Experimental energy barriers were in the range of 0.37-0.48 eV in bulk Y-doped $BaZrO_3$. Therefore, the interaction between two protons affects the energy barrier for proton migration.

Acknowledgements

This research was supported by the Fusion Research Program for Green Technologies through the National Research Foundation of Korea (NRF) funded by the Ministry of Education, Science and Technology (No.2011-0019304).

References

[1] T. Takahashi and H, Iwahara, Rev. Chim. Miner., **17** (1980), 243.

[2] H. Iwahara, T. Esaka, H. Uchida, and N. Maeda, Solid State Ionics, **3-4** (1981), 359.

[3] K. D. Kreuer, Solid State Ionics, **125** (1999), 285.

[4] H. G. Bohn and T. Schober, J. Am. Ceram. Soc., **83** (2000), 768.

[5] F. Iguchi, N. Sata, T. Tsurui, and H. Yugami, Solid State Ionics, **178** (2007), 691.

[6] P. Babilo, T. Uda, and S. M. Haile, J. Mater. Res., **22** (2007), 1322.

[7] M. A. Gomez, M. A. Griffin, S. Jindal, K. D. Rule, and V. R. Cooper, J. Chem. Phys., **123** (2005), 094703.

[8] P. G. Sundell, M. E. Björketun, and G. Wahnström, Phys. Rev. B, **76** (2007), 094301.

[9] G. Kresse and J. Hafner, Phys. Rev. B, **47** (1993), 558.

[10] G. Kresse and J. Furthmüller, Phys. Rev. B, **54** (1996), 11169.

Eighth International Conference on Flow Dynamics
November 9 - November 11, 2011

Stability of $La_{0.6}Sr_{0.4}Co_{0.2}Fe_{0.8}O_{3-\delta}$ under SOFC operating conditions

Mi-Young Oh[a], Atsushi Unemoto[b], Shin-ichi Hashimoto[a], Koji Amezawa[a], Tatsuya Kawada[a]

[a] Graduate School of Environmental Studies, Tohoku University, 6-6-01 Aoba,
Aramaki, Aoba-ku, Sendai 980-8579, Japan
[b] Institute of Multidisciplinary Research for Advanced Materials, Tohoku University, 2-2-1 Katahira,
Aoba-ku, Sendai 980-8577, Japan
myoh@ee.mech.tohoku.ac.jp

ABSTRACT

The stability of $La_{0.6}Sr_{0.4}Co_{0.2}Fe_{0.8}O_3$ (LSCF6428) was investigated by ac and dc measurement under SOFC operating conditions. The ac impedance spectra seemed to contain two semi-circles in 10^{-4} - 10^{-1} bar O_2 while one in 10^0 bar O_2. The contribution of the individual semi-circles was separately evaluated by the equivalent circuit. And the effective reaction area for the electrode reaction was evaluated by using the relation of the capacitance and the oxygen nonstoichiometry. Based on the obtained results, stabilities of LSCF6428 as an SOFC cathode were discussed.

1. Introduction

The perovskite-type $(La,Sr)(Co,Fe)O_3$ are promising cathode materials for solid oxide fuel cells (SOFCs) due to its high conductivity of both electrons and oxygen ions [1-2]. Their high electronic and oxide ionic mixed conductivities spread the reaction active area over the cathode surface [3-4]. For the practical use of $La_{1-x}Sr_xCo_{1-y}Fe_yO_{3-\delta}$ (LSCF) as an SOFC cathode, the chemical stability under the operation conditions is highly required. However, compositional and morphological instability of the electrode may occur during the long operation due to difference in mobility of the constituent cations. A possible driving force for the mass transport is the chemical potential gradient which is generated by the overpotential. Therefore, in order to ensure the durability and the reliability of SOFC using LSCF as a cathode, it is important to understand how the oxygen potential gradient is distributed in the LSCF cathode during the operation and how such a distribution affects the material stability of LSCF.

In our previous work [5], the stability of $La_{0.6}Sr_{0.4}Co_{0.2}Fe_{0.8}O_{3-\delta}$ (LSCF6428) was investigated by long-term annealing of the sintered pellets with or without applying oxygen potential gradients. The annealing at 1073 and 1273 K under uniform oxygen partial pressure of 0.21 - 10^{-4} bar for one week did not make any notable changes on the pellets. However, significant changes were observed when the pellets were placed under oxygen potential gradient. On the high oxygen partial pressure side, many particles of cobalt and strontium oxide were found along the grain boundary on the surface at 1273 K. The amount of the deposited particles increased with decreasing oxygen potential on the opposite side and/or increasing temperature. These results demonstrated that LSCF6428 may not be chemically stable enough under a certain oxygen potential gradient in the temperature range of 1073-1273 K.

It is expected that the chemical potential gradient, which is generated by the overpotential during the SOFC operation, may cause such chemical decomposition. In this work, cathodic overpotential of LSCF was measured as a function of p_{O2} in order to estimate chemical potential gradient in the porous LSCF cathode. And the effective reaction area, which is evaluated by taking the ratio of the capacitance observed in ac impedance spectra, is also estimated from the oxygen nonstoichiometry change for the whole electrode [6]. It is important that the chemical potential gradient was occurred in the effective reaction area during SOFC operation. If the effective reaction area becomes larger, the chemical potential gradient also increased. After long time operation, it affects the stability of cathode for SOFC.

From this idea, the ac impedance measurements were performed as a function of temperature and p_{O2} in order to obtain the effective reaction area. Based on the obtained results, stabilities of LSCF6428 as an SOFC cathode were discussed.

2. Experimental

2.1. Sample preparation

$La_{0.6}Sr_{0.4}Co_{0.2}Fe_{0.8}O_{3-\delta}$ (LSCF6428) powder (AGC Seimi Chemical Co., Ltd.) was used for cathode material. Powder of $Ce_{0.9}Gd_{0.1}O_{1.95}$ (GDC), which was chosen as electrolyte material, was prepared by a co-precipitation method. The GDC pellet was calcined at 1073 K for 4 hours, and then pressed and sintered at 1823 K for 5 hours to be a compact disc of about 15 mm in diameter and 1.2 mm in thickness. The platinum paste was printed onto the surface and the side of the GDC pellet as counter and reference electrodes, respectively. It was, then, sintered at 1273 K for 3 hours. Organic binder was mixed with LSCF6428 powder printed onto the other side of the pellet, and then sintered at 1173 K for 6 hours.

2.2. Evaluation of the cathode performance

AC impedance measurements were conducted in a single chamber by three-probe technique at 873 - 1173 K in oxygen partial pressure of 10^{-4} - 10^{0} bar. The amplitude of input voltage perturbation and analyzed frequency range were set to 10 mV and 500 kHz to 10 mHz, respectively. Oxygen partial pressure p_{O2} was controlled by mixing argon and oxygen in appropriate ratios and monitored by using a zirconia oxygen sensor.

2.3. Evaluation of effective reaction area

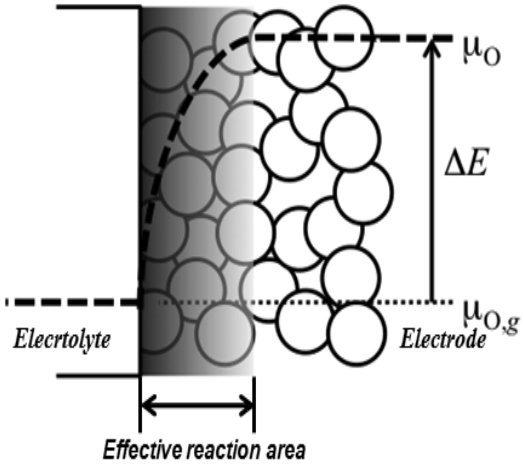

Fig. 4 A schematic illustration of oxygen chemical potential profile in mixed conducting electrode.

Figure 4 shows a schematic illustration of oxygen chemical potential profile inside the porous electrode. The overpotential, ΔE, is related to the difference of oxygen chemical potential at the interface from that in the gas phase.

$$\Delta E = \frac{1}{2F}\left(\mu_{O} - \mu_{O,g}\right) \tag{1}$$

μ_O is oxygen chemical potential standardized by 1 atm O_2. F is the Faraday constant. When the surface reaction is the rate determining step, the capacitance originated from the change of oxygen nonstoichiometry of the mixed conducting electrode with a small input voltage perturbation can be expressed by [8],

$$C = -\frac{2FLA}{V_{m}}\frac{\partial\delta}{\partial E} \tag{2}$$

L and A are the thickness and the areas of electrode. V_m and δ are the molar volume and the oxygen nonstoichiometry of electrode. The effective length for the reaction, L_{rxn}, evaluated by taking the ratio of the capacitance observed in ac impedance spectra to that estimated by the oxygen nonstoichiometry of whole electrode [6]. Combination of Eq. (1) with Eq. (2) leads,

$$C = -\frac{4F^{2}LA}{V\mathrm{m}}\frac{\partial\delta}{\partial\mu_{O}} \tag{3}$$

$$\mu_{O} = \frac{RT}{2}\ln p_{O_2} \tag{4}$$

Oxygen chemical potential, μ_O, is replaced by oxygen partial pressure, p_{O2},

$$C = -\frac{8F^{2}LA}{RTV_{m}}\frac{\partial\delta}{\partial\ln p_{O_2}} \tag{5}$$

By using this relation, the effective reaction area in a porous LSCF6428 electrode was evaluated at 873 - 1173 K under the p_{O2} of 10^{-4} - 10^{0} bar.

3. Results and discussions

3.1. Impedance analysis of LSCF cathode

Figure 1 shows the ac impedance spectra of LSCF electrode measured at 1073 K in oxygen partial pressure of 10^{-4} - 10^{0} bar. As seen in the figure, the observed spectra seem to contain at least two impedance semi-circles In order to fitting the contribution of each semi-circle, the equivalent circuit, which is shown in Fig. 2, was employed. The fitting performed in this work matches to the observed impedance spectra by using the equivalent circuit shown in Fig. 2.

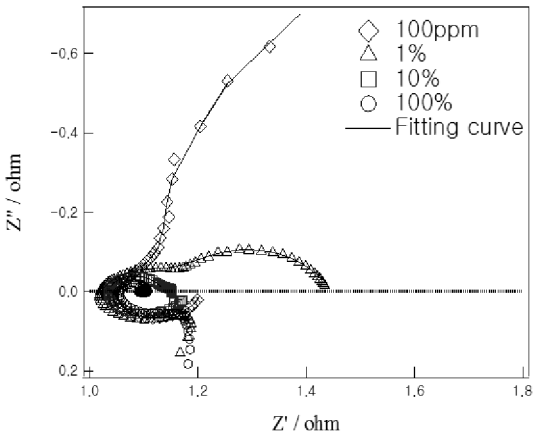

Fig. 1 AC impedance spectra of $La_{0.6}Sr_{0.4}Co_{0.2}Fe_{0.8}O_{3-\delta}$ (LSCF) cathode measured at 1073 K

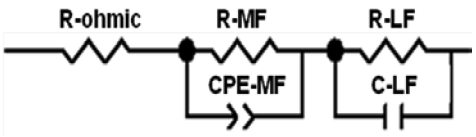

Fig. 2 Equivalent circuit for fitting of the ac impedance spectra shown in Fig. 1

Figure 3 shows the capacitance estimated from LF and MF semi-circle as a function of oxygen partial pressure. It was found that the capacitance negatively depended on p_{O2}. The impedance semi-circle of LF appeared in $p_{O2} = 10^{-4}$ - 10^{-1} seemed to disappear in $p_{O2} = 10^{0}$. When gas phase process contributes to the impedance, the capacitance contains the change of oxygen nonstoichiometry of the electrode with the input voltage perturbation [7].

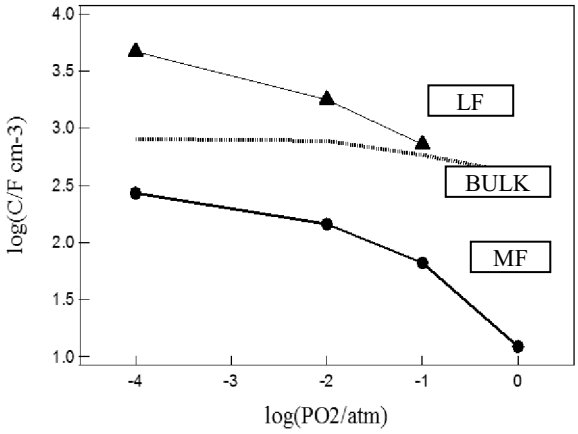

Fig. 3 The capacitance from LF and MF semi-circle as a function of oxygen partial pressure at 1073 K.

As seen in Fig. 3, the capacitance appeared in LF was comparable to that estimated from the whole electrode. As explained above, the resistance of the LF semi-circle strongly depended on p_{O2}. And the low frequency region was assigned to the gas conversion, which is not directly related to the electrode reaction, when temperature was above 1073 K [7]. These results suggest that the LF semi-circle appeared in $p_{O2} = 10^{-4}$ - 10^{-1} may be related to the gas phase transport process.

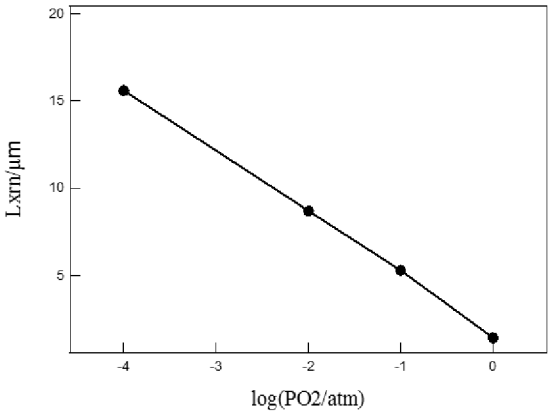

Fig. 5 Effective reaction area from MF semi-circle as a function of oxygen partial pressure at 1073 K.

Figure 5 shows effective reaction area from MF semi-circle as a function of oxygen partial pressure. The capacitance estimated by the oxygen nonstoichiometry of the bulk LSCF is also provided in Fig. 3 with broken curve. Based on the calculation explained above, effective reaction area L_{rxn} was evaluated as a function of oxygen partial pressure and displayed in Fig. 5. It was found to be 5 – 20 μm .

In this study, capacitance and effective reaction area were obtained by as impedance measurement at 1083 K as a function of p_{O2}. As a result, both capacitance and effective reaction area negatively depended on p_{O2}. Now the ac impedance measurements are in progress as a function of temperature and oxygen partial pressures.

Kawada et al. reported the change of capacitance in a thin-film $La_{0.6}Sr_{0.4}CoO_{3-\delta}$ under various applied voltages, ΔE. The capacitance slightly increased with increasing the cathodic bias [8]. According to our obtained results, the effective reaction area is may becomes larger by calculation from capacitance.

By taking the above report into consideration, the cathodic overpotential measurement of LSCF are in progress as a function of temperature and oxygen partial pressures in order to estimate chemical potential gradient in the porous LSCF cathode. Also, the long time stability of LSCF cathode test will performed by applied voltage. After that, we will analyze composition and effective reaction area in LSCF cathode. By considering the changes of the composition and effective reaction area on LSCF cathode, the degradation of LSCF cathode will discussed.

4. Summary

AC impedance measurements were performed using LSFC6428 powder as electrode in the p_{O2} of 10^{-4} - 10^{0} bar at 1073 K. The contribution of the individual semi-circles was separately evaluated by the equivalent circuit. Also, the effective length for the electrode reaction was evaluated by using the relation of the capacitance and the oxygen nonstoichiometry. The effective area was estimated as 5 - 20 μm. Both capacitance and effective reaction area negatively depended on p_{O2}.

Acknowledgements

This work was supported by Tohoku University Global COE Program and a Grant in Aid from the Japanese Ministry of Education, Culture, Sports, Science and Technology.

References

[1] J.A. Lane, S.J. Benson, D. Waller, J.A. Kilner, Solid State Ionics **121** (1999), 201-208.
[2] M. Martin, Journal of Chemical Thermodynamics **75** (2003), 889-903.
[3] J.M. Ralph, C. Rossignol, R. Kumar, J. Electrochem. Soc. **150** (2003), A1518.
[4] S.P. Simner, J.F. Bonnett, N.L. Canfield, K.D. Meinhardt, J.P. Shelton, V.L. Sprenkle, J.W. Stevenson, J. Power Sources **113** (2003), 1.

[5] M. Oh, A. Unemoto, K. Amezawa, T. Kawada, ECS Transactions, **35 (1)** (2011), 2249-2253.
[6] T. Nakamura, K. Yashiro, A. Kaimai, T. Otake, K. Sato, T. Kawada, J. Mizusaki, J. Electrochem. Soc. 155 B1244 (2008).
[7] H. Watanabe, 10th Japan-Korea student's symposium in ICFD, 392-395 (2009).
[8] T. Kawada, J. Suzuki, M. Sase, A. Kaimai, K. Yashiro, Y. Nigara, J. Mizusaki, K. Kawamura, and H. Yugamic, J. Electrochem. Soc. **149** (2002), E252.

Fabrication of Proton Conducting Ceramic Target for Physical Vapor Deposition (PVD)

Kiho Bae[a,b], Ji Won Son[b] and Joon Hyung Shim[a,*]
[a]Department of Mechanical Engineering, Korea University, Seoul, Korea
[b]Korea Institute of Science and Technology, Seoul, Korea
shimm@korea.ac.kr

ABSTRACT

This work investigated the procedure and properties in fabricating yttrium-doped barium zirconate (BZY) disks which can be used for physical vapor deposition (PVD) targets, based on solid-state reaction (SSR) method. It was found that small particles of yttria/zirconia were scattered on the surface of sintered samples due to barium loss. The crystallized $BaZr_{0.85}Y_{0.15}O_{3-\delta}$ was required high-temperature calcination (1300 ^oC) for 2h and sintering (1680^oC) for 30 h is required. X-ray diffraction (XRD) and scanning electron microscope (SEM) were used to investigate the phase composition and microstructure properties of the resulting materials.

1. Introduction

Electrolyte Proton-conducting oxides have attracted attention as electrolyte materials having better ionic conductivity than yttria stabilized zirconia (YSZ) or gadolina doped ceria (GDC), typical electrolyte materials of solid oxide fuel cells (SOFCs), in the lower operating temperature [1-3]. General formula as the proton-conducting materials is doped perovskite-type structure ABO_3; composites based on barium, such as barium cerate ($BaCeO_3$) and barium zirconate ($BaZrO_3$), are considered as noticeable materials due to their high ionic conductivity.

Thin film doped perovskites have been widely studied as electrolytes using physical vapor deposition (PVD) [2,4]. To be used for PVD targets, high density is one of the important factors. However, high sintering temperature (1600-2200 ^oC) and barium loss at high temperature (about 1200 ^oC) are barriers to come out as the targets based on the doped perovskites. P. Babilo et al was reported a reproducibly synthesis procedure to be able reproducibly to obtain high-dense yttria doped barium zirconate (BZY) using a glycine-nitrate combustion synthesis process. In this communication, we report a modified process using a solid state reaction method for obtaining synthesized BZY.

2. Experimental

The methodical process to obtain reproducible crystallized BZY was reported by P. Babilo et al using a glycine-nitrate combustion synthesis process [5]. They also referred that the both solid-state and chemical synthesis were suitable as a method to synthesize yttria doped barium zirconate. In this work, the $BaZr_{0.85}Y_{0.15}O_{3-\delta}$ (BZY15) powder was prepared by solid state reaction (SSR) method. A cost-effective $BaCO_3$ (Cerac 99.9% purity) is used as a row material with ZrO_2 (Junsei, 99% purity) and Y_2O_3 (Kojundo 99.9% purity) . Stoichiometric amounts of the materials were mixed using ball milling with stabilized zirconia media in high-purity ethanol for 24h. The resultant mixture was dried at 150 ^oC for 4 h, followed by calcination at 1300 ^oC for 2 h to yield crystallized BZY15. The ball milling was carried out again for 48h to reduce particle size of the powder with zirconia ball in ethanol same as mixing. Fine powder was obtained by passed through a 150 μm mesh-size sieve after agate mortar grinding.

The powder so prepared was mixed with a binder solution consisting of 3 g of polyvinyl butyral (PVB) and 97 g of ethanol. The ratio of the binder solution to oxide powder was approximately 1 to 5 by mass. A green pellet was obtained by uniaxial pressing under pressure of 100MPa for 5 min. The pellet was surrounded by a powder mixture of BYZ and small amount of $BaCO_3$ (about 10 wt%) in a crucible of alumina. Heating up was conducted under ambient air with several steps. In the first step, the binder was removed by a relatively slow ramp of 1 ^oC/min to 600 ^oC. Sintering was carried out by holding the pellet at 1680 ^oC (ramp of 5 ^oC/min to 1400 ^oC, followed by a ramp of 1 ^oC/min) for a period of 20 h.

The resulting materials were characterized by several techniques. The density of the sintered pellets was measured by the Archimedes method using dehydrated alcohol. The X-ray diffraction (XRD, TTK 450) patterns were collected from the synthesized BZY powder and both non-polished and polished surfaces of sintered pellets. Intensities were obtained in the 2θ range between 20^o and 80^o with an effective step size of 0.02^o. The microstructures of surface and cross-section of the sintered pellet were obtained with scanning electron microscope (SEM, FEI XL-30 FEG).

3. Results and Discussion

The relative density of the sintered pellet of BZY prepared by the careful procedures outlined was 97% (with respect to the density of yttrium doped barium zirconate, 6.022 g/cm^3) Fig. 1(a) shows surface of the pellet sintered with enclosed in excess barium. The agglomerated surface represents that the BZY pellet was fully sintered. Fig. 1(b) shows cross-section morphologies of the pellet with high density. The average grain size is approximately 0.78 μm, with a wide distribution of grain sizes (0.5-2 μm). This small grain size is consistent with rate of grain growth under typical sintering conditions [6].

Shown in Fig. 2 are X-ray diffraction patterns of the synthesized BZY powder and sintered pellet. The unpolished surface phase display the presence of an impurity phase, not appeared at the synthesized powder before sintering. P. Babilo et al studied this point of sintered $BaZr_{0.8}Y_{0.2}O_{3-\delta}$ pellets and probed to suppress dopant from the B to A site in the ABO_3 perovskite as A site become vacant due to barium loss. Such behavior

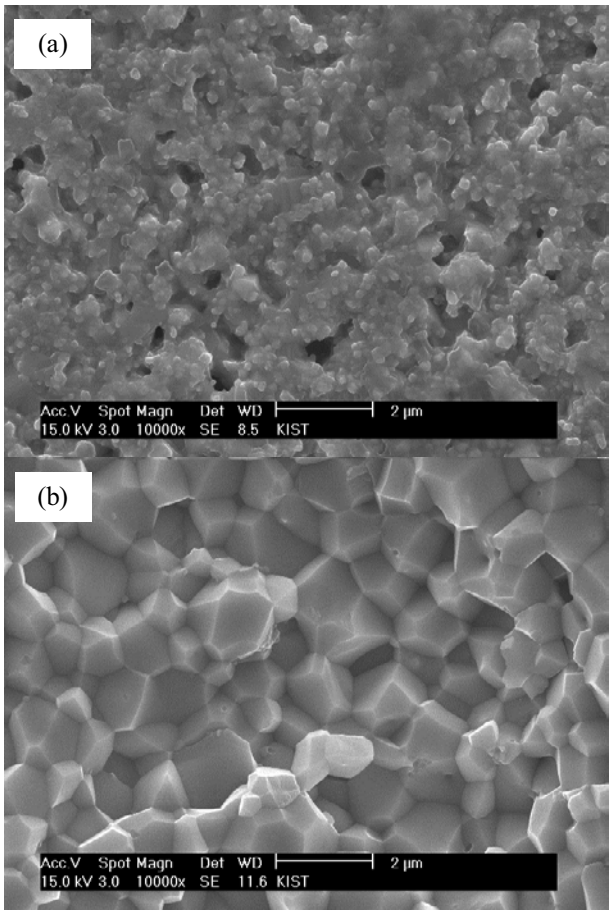

Fig. 1 Morphologies of (a) surface and (b) fracture surface of the sintered BZY pellet

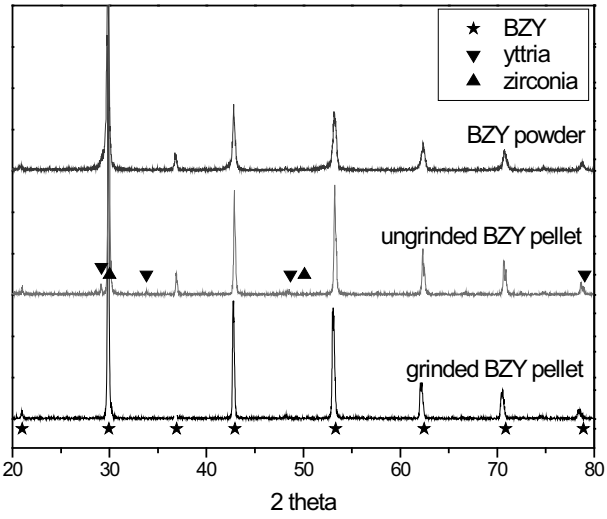

Fig. 2 X-ray diffraction patterns of the BZY powder synthesized by solid state reaction and the sintered BZY pellets with and without polishing surfaces of those.

the yttria yield by covering excess barium powder at sintering process [5]. In their study, the yttria precipitates throughout the bulk of pellets and may be that such precipitates pin grain boundaries. The decrease in cell constant on prolonged exposure to high temperatures may be attributed to the transfer of the may result from a reduction of the dopant content in the

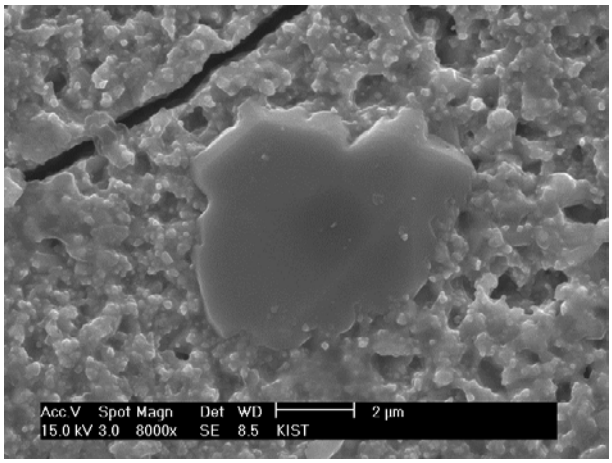

Fig. 3 Precipitation morphology on surface of the pellet

perovskite with yttria/zirconia being expelled from the structure to maintain an A-to-B stoichiometric ratio of 1 to 1. Fig. 3 shows the yttria/zirconia morphology on the surface of the sintered pellet. In the comparison of two XRD patterns in Fig. 2, unpolished pellet and polished pellet, it found that the yttria/zirconia can be removed by polishing the integrated surface layer.

Overall, the results provide clear evidence that BaZr0.85Y0.15O3-δ samples can be reproducibly obtained under typical sintering condition against decomposing to form yttria/zirconia and volatile barium oxied. The removed yttria/zirconia on the surface of the sintered pellet by polishing indicates that the volatilization of barium oxide can be kinetically suppressed with yttria/zirconia precipitates not occurred throughout overall the pellet.

4. Concluding remarks

The present study demonstrated that high-density BZY could be reproducibly obtained under solid state reaction method. It was confirmed cost-effective $BaCO_3$ could be a row material stably to supply barium to BZY. Sintering must be carried out under enclosing BZY powder contained excess barium so as to avoid barium loss. The well-synthesized composite was confirmed by X-ray diffraction, which can be used as a target for physical vapor deposition, but this point requires further studies.

References

[1] K.D. Kreuer, Annual Review of Materials Research, **33** (2003), 333.
[2] J.H. Shim, T.M. Gur, F.B. Prinz, Applied Physics Letters, **92** (2008), 253115.
[3] L. Yang, C.D. Zuo, S.Z. Wang, Z. Cheng, M.L. Liu, Advanced Materials, **20** (2008), 3280.
[4] D. Pergolesi, E. Fabbri, E. Traversa, Electrochemistry Communications, **12** (2010), 977.
[5] P. Babilo, T. Uda, S.M. Haile, Journal of Materials Research, **22** (2007), 5.
[6] P. Babilo, S.M. Haile, Journal of American Ceramic society, **88** (2005), 2362

Eighth International Conference on Flow Dynamics
November 9 - November 11, 2011

Protonic conduction and defect structures in rare earth phosphate

Hiroaki Matsuo[1,*], Hayato Takahashi[1], Akihide Kuwabara[2], Shinichi Hashimoyo[1],
Koji Amezawa[1], Tatsuya Kawada[1]
[1]Tohoku University, [2]Japan Fine Ceramics Center
6-6-01 Aramaki-Aoba, Aoba-ku, Sendai 980-8579, JAPAN[1], 2-4-1 Mutsuno, Atsuta-ku, Nagoya 456-8587, Japan[2]
*Corresponding author: matsuo@ee.mech.tohoku.ac.jp.

ABSTRACT

Defect structures in $LaPO_4$, which shows high temperature protonic conduction by doping divalent metals, were investigated by using first principle calculations. When an oxygen was deficient, condensation of two orthophosphate ions PO_4^{3-} occurred forming a pyrophosphate ion $P_2O_7^{4-}$. When an interstitial proton was introduced, a hydrogen phosphate ion HPO_4^{2-} was formed. For Sr ion substitution for La, only a slight change in the atomic configuration was observed. The oxygen deficit and the interstitial proton tended to the Sr ion at the La site.

1. Introduction

Rare earth orthphosphate ($LnPO_4$ Ln = rare earth), in which La is considered to be partially substituted with a divalent cation, is known to have protonic conductivity at high temperature under wet condition [1, 2]. This material has some advantages over proton-conducting pervoskite oxides *e.g.* $BaZrO_3$, $BaCeO_3$; excellent chemical stability and high protonic transport number. On the other hand, protonic conductivity in $LnPO_4$ is rather low compared with that in the proton-conducting oxides.

In $LaPO_4$, it is considered that protons are introduced through the equilibrium between oxygen defects and water vapor in atmosphere. In $LaPO_4$ a phosphorus has strong bonds with oxygens, and thus simple oxygen deficits like oxygen vacancies are difficult to be formed. Defect structures in $LaPO_4$ were investigated with spectroscopic methods such as MAS-NMR and FT-Raman spectrocopies. It was then suggested that a proton is introduced into the $LaPO_4$ lattice through the following defect equilibria [2].

$$1/2M_2P_2O_7 \rightarrow M'_{La} + 1/2(P_2O_7)^{\bullet\bullet}_{2PO_4} \quad (1)$$

$$1/2(P_2O_7)^{\bullet\bullet}_{2PO_4} + 1/2H_2O(g) \rightarrow (HPO_4)^{\bullet}_{PO_4} \quad (2)$$

Here, M'_{La} is a divalent cation at a La site, $(P_2O_7)^{\bullet\bullet}_{2PO_4}$ is a pyrophosphate ion condensed with two orthophosphate ion, $(HPO_4)^{\bullet}_{PO_4}$ is a hydrogen phosphate ion at an orthophosphate ion site. In this way, defect structures of $LaPO_4$ are considered to be different from those of proton-conducting perovskite oxides. But the defect structure and proton dissolution process are still in arguments.

In this work, we investigate defect structures in $LaPO_4$ by using first principle calculations. The obtained results are discussed by comparing the results of spectroscopic and electrical conductivity measurements in our previous studies.

2. Method

Total energy and electronic state were calculated by VASP code. Calculation procedures were as follows; (1) structural relaxation of the unit cell, (2) structural relaxation of the super cell having the size of 3×3×3 of the relaxed unit cell, (3) structural relaxation of the supercell with a defect, and (4) structural relaxation of the supercell with a positively and a negatively charged defect. In this study, an oxygen deficit and an interstitial proton as positively charged defects, and an Sr substituted for La as a negatively charged defect were taken into account. Calculations were performed under conditions of plane wave cut off energy = 400 eV, Hellmann-Feynman force below 0.02 eV/Å, and *k*-point mesh of 2×2×2 for the unit cell and of gamma point for the supercell. When an oxygen was deficient, an oxygen was removed from one of four equivalent oxygen sites in the supercell. When an interstitial proton is introduced, a proton was placed at an interstitial site positioned 1 Å away from one oxygen in the direction to its neighboring oxygen. When an Sr substituted La site was considered, one of La in the supercell was replaced by Sr.

3. Results and Discussion

The structural relaxation of the $LaPO_4$ unit cell was performed. The unit cell of $LaPO_4$ contains 16 atoms in total. There exist four, one, and one equivalent sites for oxygen, phosphorus, and lanthanum, respectively. A phosphorus is four-coordinated with oxygens forming a orthophosphate ion PO_4^{3-}. The calculated lattice constants were a = 6.938 Å, b = 7.144 Å, c = 6.542 Å, and β=103.67°. These were in good agreement with the experimental values within an error less than 1.6 %; a =6.825 Å, b = 7.057 Å, c = 6.482 Å, and β =103.21° reported in PDF#20-1472. Then, structure of the 3×3×3 supercell without any defects was relaxed. The relaxed structure is shown in Fig.1 (a). In following calculations, defects were introduced into this structure.

First, let us consider the structure when introducing an oxygen deficit. $LaPO_4$ has four equivalent oxygen sites as described above. Fig.1(b) presents the relaxed structure which has the lowest internal energy among the structures with an oxygen deficit at the four equivalent sites. Two PO_4 tetrahedra were condensed by sharing an oxygen forming pyrophosphate ions $P_2O_7^{4-}$. Such a formation of condensed ions was confirmed by calculation results of the differential electronic density. The defect structures of the supercells having the oxygen deficit at other three equivalent sites were similar to that shown in Fig.1(b). Differences in the internal energy among the four structures were less than

0.42eV at maximum. Oxygens in $LaPO_4$ are all bound with phosphorus forming orthophosphate ions. Thus, there is no apparent difference in the strength of each P-O bond in $LaPO_4$, even though the four oxygens of an orthophosphate ion are located at the four different equivalent sites.

Secondly, defect structures of supercells having an interstitial proton are discussed. Totally 140 initial sites for defect protons were calculated. After structural relaxation, eleven stable structures were detected. It was found that a proton was located near an oxygen. Since the distances between the proton and the oxygen, d(O-H), were in approximetry = 1 Å, the defect proton was regarded to form a hydrogen phosphate ion HPO_4^{2-}. Figure 1(c) shows the structure with a defect proton which has the lowest internal energy.

From the above results, the calculated structures having an oxygen deficit or an interstitial proton were in good agreement with those observed in FT-RAMAN and MAS-NMR measurements. That is, calculation results on defect structures supported the proton dissolution model given by eqs. (1) and (2).

In both cases of introducing an interstitial proton and an oxygen deficit, the crystal lattice was distorted. But the strain in the structure with an interstitial proton was much less than that with an oxygen deficit. It is considered that the smaller a strain is, the more difficult the defect formation is. This suggested that an interstitial proton has higher defect concentration and lower mobility than an oxygen deficit, meaning dominant protonic conduction in $LaPO_4$.

Finally, defect associations between an Sr substituted for La and an oxygen deficit or an interstitial proton are discussed. The Sr substituted for La was negatively charged, while the oxygen deficit and the interstitial proton were positively charged. Therefore, the Sr substituted for La may associate with the oxygen deficit and the interstitial proton. We considered defect associations these defects. Structural relaxation of the supercells having an Sr at the La site and an oxygen deficit or an interstitial proton were carried out. The structure of the supercell having both of a Sr and an oxygen deficit was similar to that with only an oxygen deficit. Most of the structures of the supercells with a Sr and an interstitial proton had a similar structure to that with only an interstitial proton. But some of them had different structures compared with that with an

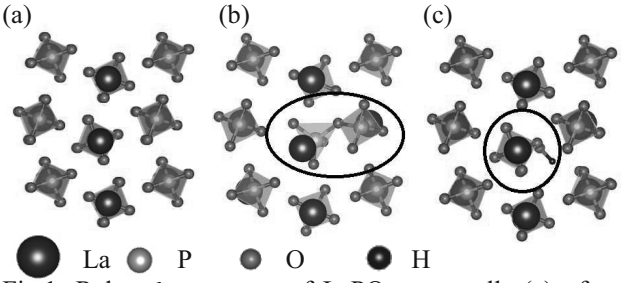

Fig.1. Relaxed structures of $LaPO_4$ supercells (a) of a perfect crystal, (b) with an oxygen deficit, and (c) with an interstitial proton.

the Sr. The internal energies of the structures having an interstitial proton. The proton moved to the vicinity of Sr and an oxygen deficit were compared with the internal energies of the structures individually having each defect according to following equations.

$$E_{bind} = \{E(\mathrm{Sr}'_{\mathrm{La}} V_{\mathrm{O}}^{\bullet\bullet})^{\bullet} + E(per)\} - \{E(\mathrm{Sr}'_{\mathrm{La}}) + E(V_{\mathrm{O}}^{\bullet\bullet})\} \quad (3)$$

$$E_{bind} = \{E(\mathrm{Sr}'_{\mathrm{La}} \mathrm{OH}^{\bullet}_{\mathrm{O}})^{\bullet} + E(per)\} - \{E(\mathrm{Sr}'_{\mathrm{La}}) + E(\mathrm{OH}^{\bullet}_{\mathrm{O}})\} \quad (4)$$

E_{bind}, and $E(per)$ and $E(\mathrm{A})$ are the association energy, the internal energy of supercell without defects, and the internal energy of supercells with defects, respectively. Figures 2 (a) and (b) gives the association energy E_{bind} as a function of the distance between the Sr and (a) the oxygen deficit and (b) an interstitial proton, respectively.

The lower E_{bind} means stronger defect association. Both results of Fig.2 (a) and (b) showed that the E_{bind} decreased with increasing the distance between the defects. This indicated that an oxygen deficit and an interstitial proton tends to associate with an Sr at the La site.

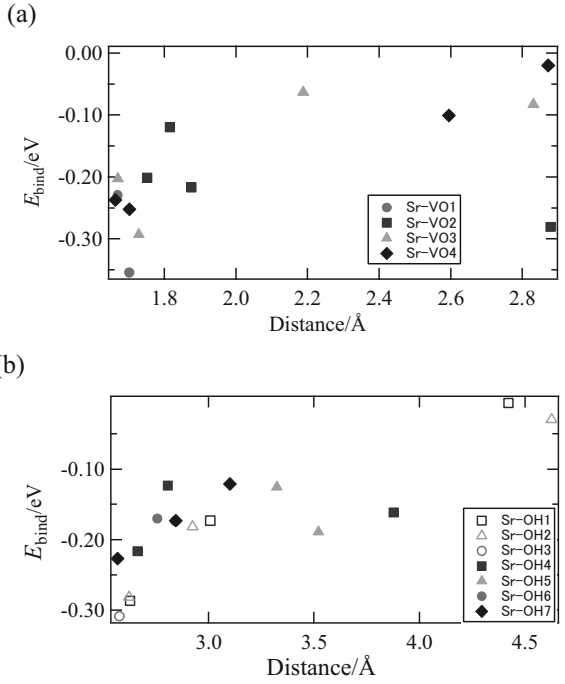

Fig.2. Association energy in $LaPO_4$ between the Sr substituted for La and (a) the oxygen deficit and (b) the interstitial proton.

4. Concluding remarks

Defect structures in Sr-doped $LaPO_4$ were investigated by first principle calculations in this study. When an oxygen deficit was introduced, condensation of two PO_4^{3-} occurred forming $P_2O_7^{4-}$. When an interstitial proton was introduced, the proton was located at an interstitial site positioned about 1 Å away from the nearest oxygen, forming HPO_4^{2-}. An oxygen deficit as well as an interstitial proton tended to associate with an Sr at the La site.

References

[1] Truls Norby,*et al, Solid State Ionics*, **125**, 1 (1999)
[2] K. Amezawa,*et al*, *Solid State Ionics*,**176**, 135 (2005)

Effects of powder synthesis process on the conductivity of doped ceria electrolytes

Ji-Hyun Kim, Jun-Young Park
HMC&INAME,Green Energy Research Institute, Faculty of Nanotechnology and Advanced Materials Engineering,
Sejong University, 98 Gunja-Dong, Gwangjin-Gu, Seoul, 143-747, Republic of Korea
silverhawk@sju.ac.kr

ABSTRACT

The ionic conductivity of doped ceria electrolytes for intermediate temperature-solid oxide fuel cells (IT-SOFCs) is investigated by various synthesis processes with the change of microstructure. $Ce_xNd_{1-x}O_{2-\delta}$ electrolytes are prepared by the solid-state, combustion, co-precipitation and hydrothermal methods. The ionic conductivity of ceria based electrolytes is measured by electrochemical impedance spectroscopy (EIS) and individual contributions of the grain and grain boundary conduction in the ionic conductivity are also analyzed to understand transport properties of oxygen ions by the microstructure change in various synthesis methods.

1. Introduction

Intermediate temperature-solid oxide fuel cells (IT-SOFCs) based on doped ceria electrolytes have been widely investigated because of their high potential for next generation energy applications. Up to now, a number of studies in IT-SOFCs are investigated in order to improve the ionic conductivity for doped ceria material through better preparation methods [1, 2]. For clarifying these efforts, however, it is necessary to investigate the difference and reason of ionic conductivity caused by different synthesis methods. In addition, micro structural effects in the ionic conductivity by various synthesis methods need to be analyzed considering a grain and grain boundary conduction. In this study, hence, neodymium which known as the optimum dopant for pure ceria are selected as a solid oxide electrolyte [3, 4, 5].

2. Method

Trivalent rare earth doped ceria powders ($Ce_xNd_{1-x}O_{2-\delta}$; x=10, 20) are prepared by a solid-state reaction, combustion, co-precipitation and hydrothermal method in order to make a difference in the microstructure. Cerium (III) oxide (CeO_2) and neodymium oxide powder are mixed by ball-milling for 24 h and then are heat-treated as shown in Table 1.

In the combustion process, cerium and neodymium nitrate hexahydrate ($Ce(NO_3)_3 \cdot 6H_2O$ + $Nd(NO_3)_3 \cdot 6H_2O$) dissolved in deionized water with the glycine as a fuel material. The solution is then heated gradually until the water is evaporated with forming a gel state [6]. On further heating, gel becomes nanopowder precursors.

The co-precipitation method is carried out using ammonium hydroxide as a precipitant [7, 8]. Dissolved nitrate solutions ($Ce(NO_3)_3 \cdot 6H_2O$ + $Nd(NO_3)_3 \cdot 6H_2O$) are stirred with precipitants and then nanopowder precipitates are formed under the basic PH state (PH=9).

In the hydrothermal process, precipitate gel obtained from the co-precipitation process synthesize to powders by the autoclave system. The autoclave system is kept under a pressure of 10 MPa and at 300 °C for 4 h. After reactions, precipitated powders are washed with distilled water and ethanol and dried in air. Each processed powders are thermally treated as specified in Table 1.

The relative densities of pellet samples are measured by the Archimedes method and the theoretical density is obtained by the XRD result. BET measurements also carry out to obtain the size and surface area of the powder.

3. Results and Discussion

Fig.1 shows the X-ray diffraction patterns of various synthesized powders. Each powders show fluorite structure as indexed by peak characteristic of powders.

Table 1. Thermal treatment conditions of each synthesized samples

	Calcination temperature	Sintering temperature
Solid state	1200℃ 4hr	1650℃ 10hr
Combustion	400℃ 2hr	1450℃ 4hr
Co-precipitation	400℃ 2hr	1450℃ 4hr
Hydrothermal	400℃ 2hr	1450℃ 4hr

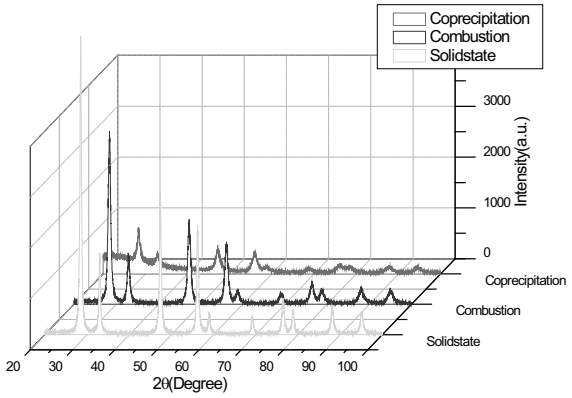

Fig. 1 XRD result of rare earth doped ceria powders synthesized through the solid state reaction, combustion, co-precipitation processes

The diffraction peaks of powders synthesized by the combustion and co-precipitation are broader than those of solid state powders. It indicates that powders by combustion and co-precipitation methods have a smaller particle size than that of solid state powders. BET

results show quite a difference in the surface area of various powders, in agreement with the results of XRD analysis. Among these, powders by combustion methods show the largest surface area. The surface areas of powders synthesized by the solid-state, combustion and co-precipitation method are 3.6143 m^2/g, 13.401 m^2/g, and 43.838 m^2/g, respectively.

Densification levels of sintered pellets using powders synthesized by various processes are attained more than 95% of the theoretical density. The powder synthesized by combustion method shows good densification at lower sintering temperature than that of solid state method due to a high surface area and smaller particle size. Furthermore, at low temperature of 650℃, the ionic conductivity of powders synthesized by the solid state, combustion and co-precipitation method is 0.0075 S/cm, 0.0391 S/cm and 0.0197 S/cm, respectively. This result may be due to the sintering temperature conditions correlated with the diffusivity of second and impurity phases like silica (SiO_2) in grain and grain boundary regions which induces higher resistivity. At high sintering temperatures, silicaceous and second phases within the grain boundary regions are likely to be formed due to the fast diffusivity and high interfacial energy of grain boundary, and thus resulting in the decreased ionic conductivity of solid-state powders.

4. Concluding remarks

The doped ceria electrolytes synthesized by various method has been investigated. The powder synthesized by combustion method shows a good densification at low sintering temperature because of its smaller powder size and higher surface area. Along with this, the ionic conductivity of combustion synthesized sample is the higher than that of samples synthesized by the solid state and co-precipitation method. This phenomenon may be due to the lower sintering temperatures correlated with the formation of highly resistive silicaceous and impurity phases in the grain boundary regions.

References

[1] S. Kuharuangrong, Journal of Power Sources, **171** (2007), 506–510
[2] D. Perez-Coll, E. Sanchez-López, G. C. Mather, Solid State Ionics **181** (2010) 1033–1042
[3] T. Karaca, T. G. Altınc¸ekic¸, M. F. O¨ ksu¨zo¨mer, Ceramics International **36** (2010) 1101–1107
[4] Ifan E.L. S, J. A. Kilner, Solid state ionics, **177** (2006) 669-676
[5] T.S. Zhang, J. Ma, H. Cheng, S.H. Chan, Materials Research Bulletin **41** (2006) 563–568
[6] R.K. Lenka, T. Mahata, P.K. Sinha, A.K. Tyagi, Journal of Alloys and Compounds **466** (2008) 326–329
[7] P. Muralidharan, S. H. Jo, D. K. Kim, J. Am. Ceram. Soc., **91** [10] (2008) 3267–3274
[8] S. B. Wen, C. H Lu, J. Am. Ceram. Soc., **91** [1] (2008) 127–131

Eighth International Conference on Flow Dynamics
November 9 - November 11, 2011

Electrochemical Properties and Thermochemical Stabilities of $Pr_{2-x}Sr_xNiO_{4+\delta}$ Cathodes

Tetsuya Hori, Keiji Yashiro and Junichiro Mizusaki.
Institute of Multidisciplinary Research for Advanced Materials, Tohoku University .
Adress:LAMR2 bldg. 2-1-1 Katahira, Aoba-ku, Sendai 980-8577, Japan
E-mail: hori@mail.tagen.tohoku.ac.jp

ABSTRACT

High temperature gravimetry and coulometric titration were performed on $Pr_{2-x}Sr_xNiO_{4+\delta}$ (x = 0, 0.2, 0.4) to measure the oxygen content. The measurements were carried out in the temperature range between 873 and 1173 K and the oxygen partial pressure range between 10^{-24} and 1 bar. In addition, it is confirmed that $Pr_{2-x}Sr_xNiO_{4+\delta}$($x$=0,0.2) were decomposed in the higher $P(O_2)$ region. It is thought this decomposition become suppressed by doping Sr. In Addition, $Pr_{1.8}Sr_{0.2}NiO_{4+\delta}$ electrode has higher interface conductivity than $La_2NiO_{4+\delta}$ electrode. This is attributed to the fact that $Pr_{2-x}Sr_xNiO_{4+\delta}$ has more interstitial oxygen.

1. Introduction

K_2NiF_4 type oxides show oxygen excess composition because interstitial oxygen can exist in the rock salt layer. Interstitial oxygen provides high oxygen diffusivity. Due to high mixed ionic and electronic conductivity and catalytic activity, K_2NiF_4 type oxides are expected to be utilized for electrochemical devices such as solid oxide fuel cells. In particular, high oxygen permeability was achieved in Pr_2NiO_4-based oxides. Therefore, high catalytic activity for oxygen reduction reaction was expected for the Pr_2NiO_4-based oxides. However, it is also repoted $Pr_2NiO_{4+\delta}$ decomposed under high $P(O_2)$ region[1].

Generally, the electrochemical properties of oxides are strongly affected by oxygen content. Then, how oxygen nonstoichiometry emerges is essential knowledge. In the present work, we measure the oxygen nonstoichiometry of the $Pr_{2-x}Sr_xNiO_{4+\delta}$ by high temperature gravimetry and coulometric titration. In addition, we investigate the thermochemical stabilities by High-Temperature X-ray Diffraction and the electrochemical properties of $Pr_{2-x}Sr_xNiO_{4+\delta}$ cathode for solid oxide fuel cells by AC impedance and steady state polarization measurements.

2. Experimental

2.1 *Sample preparations*

$Pr_{2-x}Sr_xNiO_{4+\delta}$(PSNO) ($x$=0,0.2,0.4)were synthesized by a citric acid method. Pr_6O_{11}(99.5%, DAIWA CHEMICAL) and $SrCO_3$ (99.99%, RARE METALLIC) were dissolved into regent-grade nitric acid, and $Ni(NO_3)_2{\cdot}6H_2O$ (99.95%, KANTO CHEMICAL) was dissolved separately into de-ionized water. and The concentration of each solution was determined by a chelate titration. These solutions were mixed together in a proper ratio. An excess amount of citric acid was added to the mixed solutions. A precursor was obtained by heating the solution at 573 K to remove water and nitrogen oxides. They were fired in air at 1273 K for 10 hours. After grinding with ethanol, they were sintered again at 1473 K for 10 hours.

For the electrode measurement, porous electrode of $Pr_{2-x}Sr_xNiO_{4+\delta}$ was formed on YSZ as a working electrode by screen print method. As a counter electrode, NiO-8YSZ was used. The diameters of the electrodes were 8mm. Figure 4 shows the SEM image of $Pr_{1.8}Sr_{0.2}NiO_{4+\delta}$ electrode cross-section surface and surface before measurement. The average thickness of the electrode was about 20μm.

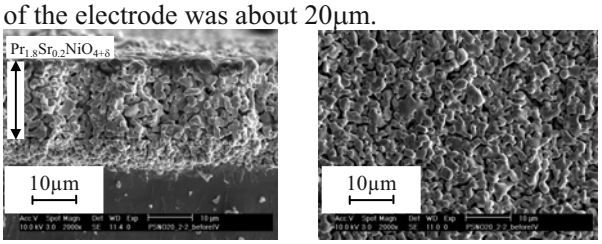

Fig.1 SEM image of $Pr_{1.8}Sr_{0.2}NiO_{4+\delta}$ electrode sintered 1473 K for 3 hours. The left side is cross-section surface image and the light side is surface image.

2.2 *High temperature gravimetry (HT-gravimetry)*

Oxygen nonstoichiometry was measured by HT-gravimetry using electronic microbalances (Sartorius M25DP and Cahn D200) in the $P(O_2)$ range from 1 to 10^{-4} bar and at the temperature range 873-1073K. Schematic of the HT-gravimetry is shown in Figure 1. The specimen was placed in a silica basket suspended by the Pt wire from the beam of the micro balance. The oxygen partial pressure was controlled by the ratio between O_2 and Ar gas into the sample chamber, where the zirconia oxygen sensor was equipped to monitor the oxygen partial pressure. It was considered that the relationship between the sample and surrounding gas phase was equilibrium when both the weight of the sample and the oxygen partial pressure became constant value. The change in oxygen content was determined from the variation of the sample weight, Δw_s,

$$\Delta\delta = \frac{M_S}{M_O}\frac{\Delta w_S}{w_S} \quad (1)$$

where $\Delta\delta$, M_s, M_O, and w_s are the variation of oxygen nonstoichiometry, the formula weight of the sample and oxygen atom and the weight of the specimen, respectively.

2.3*Coulometric titration*

In these oxides, the oxygen nonstoichiometry below 10^{-3} bar of $P(O_2)$ can be measured by the coulometric titration. Schematic of the coulometric titration is shown in Figure 2. An yttria stabilized zirconia (YSZ) tube was used as an electrolyte for a galvanic cell. The specimen was placed into the tube and mechanically pressed so that the specimen was in close contact with the tube wall. The Pt foil connected with the Pt wire was attached to the specimen as an electrode. The interior tube was evacuated down to about 10^{-1} bar and refilled with Ar gas. The pressure of Ar gas was kept at about 10^{-1} bar at room temperature. The oxygen content of the specimen was controlled by the electric charge passed through the cell. After a specified amount of electric charge was passed, the electromotive force was measured to determine the equilibrium oxygen partial pressure in the tube. The amount of oxygen nonstoichiometry was calculated by the equation

$$\Delta\delta = \frac{C}{2FM_S} \quad (2)$$

where C and F is the total amount of electric charge and Faraday constant, respectively.

2.4 *X-ray Diffraction(XRD) and High-Temperature X-ray Diffraction (HT-XRD)*

The crystal structure of $Pr_{2-x}Sr_xNiO_{4+\delta}$ was observed by XRD (MAC Science XRD-M21X) and HT-XRD (Bruker D8 Advance) using Cu Kα radiation.

HT-XRD was carried out at 873-1073K under the $P(O_2)$ range 10^{-4}- 1 bar with O_2-N_2 gas-mixtures. Each sample was put on the platinum heater directly in the chamber. O_2-N_2 gas mixtures controlled mixing ratio were let flow to the chamber. The oxygen partial pressure of the gas mixtures was monitored by the zirconia oxygen sensor placed downstream from the chamber.

2.5 *AC impedance measurement*

The complex impedance over the frequency range of 1MHz-0.01Hz was measured using a Potentiostat/ Galvanostat and frequency response analyzer (Solartron, 1287 and 1260). The measurement was carried out at the temperature range between 600°C to 800°C. The oxygen partial pressure, P_{O2}, was controlled by changing the ratio of the Ar/O_2. n addition, d.c. steady state polarization was performed under various P_{O2} and temperature condition.

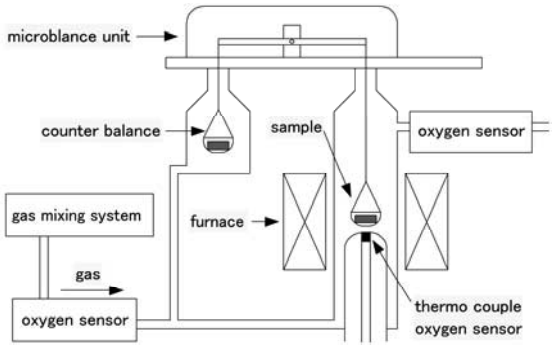

Fig.2. Schematic of the HT-gravimetry

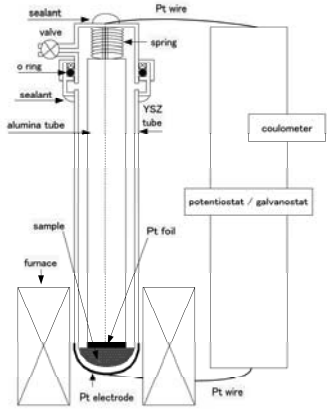

Fig.3. Schematic of the coulometric titration.

3. Results and Discussion

3.1*The oxygen nonstoichiometry of $Pr_{2-x}Sr_xNiO_{4+\delta}$*

Figures 3, 4, and 5 show measured oxygen nonstoichiometry of $Pr_{2-x}Sr_xNiO_{4+\delta}$ for x = 0, 0.2, and 0.4, respectively. In the figures, closed symbols show the data points measured by high temperature gravimetry and open symbols show those measured by the coulometric titration. $Pr_2NiO_{4+\delta}$(PNO) showed only the oxygen excess, while $Pr_{1.8}Sr_{0.2}NiO_{4+\delta}$(PSNO20) and showed both the oxygen excess in the higher $P(O_2)$ region and the oxygen deficiency in the lower $P(O_2)$ region. $Pr_{1.6}Sr_{0.4}NiO_{4+\delta}$(PSNO40) shows almost no oxygen excess composition. It shows only the oxygen deficient composition in the lower $P(O_2)$ region. As the Sr content increases, the oxygen excess region decreases and the oxygen deficient region increases. As temperature increases and $P(O_2)$ decreases, the amount of the excess oxygen decreases and the amount of the oxygen deficiency increases. ¥

3.2*Decomposition in the higher $P(O_2)$ region*

$Pr_{2-x}Sr_xNiO_{4+\delta}$ showed the weight gain after long time exposure to the higher $P(O_2)$(0.1 to 1 bar). This weight change verified that $Pr_2NiO_{4+\delta}$ is decomposed into PrNiO3 and praseodymium oxide. In PSNO20, this weight change was smaller than PNO in the high$P(O_2)$ region. It is thought K_2NiF_4 structure can be stabilized by doping Sr. To elucidate these weight change, $Pr_2NiO_{4+\delta}$ was measured by HT-XRD. HT-XRD were carried out in the temperature at 873 K, and the $P(O_2)$ ≈ 1 bar.

Figure7 shows $Pr_2NiO_{4+\delta}$ measured by HT-XRD. It shows $Pr_2NiO_{4+\delta}$ is decomposed into $PrNiO_{3-\delta}$ and $PrO_{2-\delta}$. To explain this decomposition, some researcher introduce that $Pr_2NiO_{4+\delta}$ is decomposed $Pr_4Ni_3O_{10-\delta}$ and $PrO_{2-\delta}$ [5,6].Figure 9 and 10 show Stability field for $Pr_2NiO_{4+\delta}$ and $Pr_{1.8}Sr_{0.2}NiO_{4+\delta}$. In the figures, closed symbols show the data points concluded by HT-XRD in high $P(O_2)$ region and the coulometric titration in low $P(O_2)$ region. Opened symbols show reference data[8]. It indicates that PSNO20 is more stable than PNO in the high $P(O_2)$ region. This experimental results were conformed with the HT-gravimetry's results.

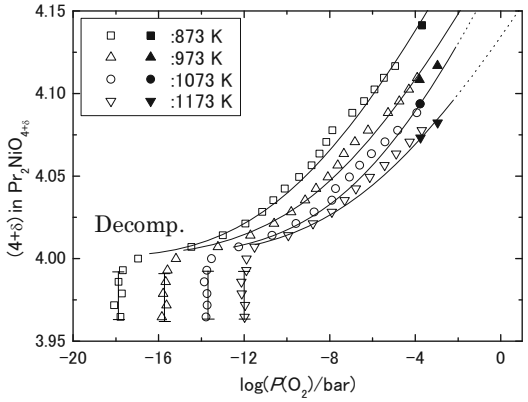

Fig.4 Oxygen nonstoichiometry and calculation results of $Pr_2NiO_{4+\delta}$. Solid lines are calculated results.

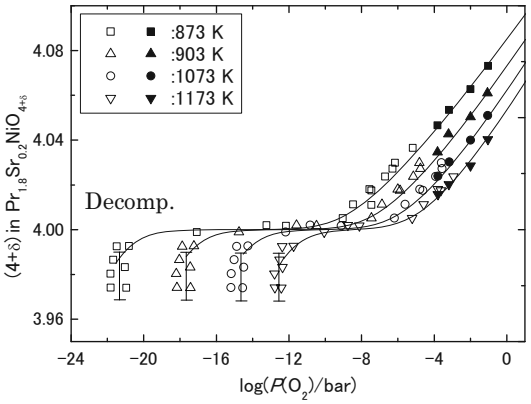

Fig.5. Oxygen nonstoichiometry and calculation results of $Pr_{1.8}Sr_{0.2}NiO_{4+\delta}$. Solid lines are calculated results.

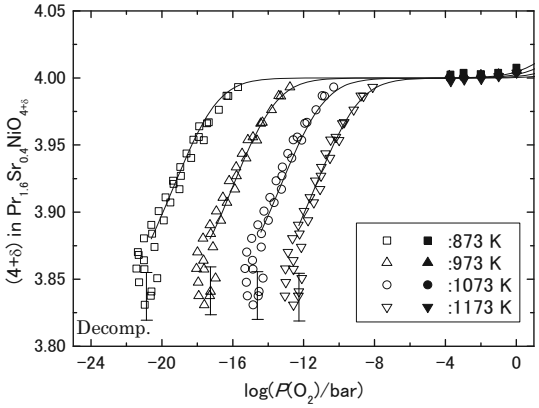

Fig.6. Oxygen nonstoichiometry and calculation results of $Pr_{1.6}Sr_{0.4}NiO_{4+\delta}$. Solid lines are calculated results.

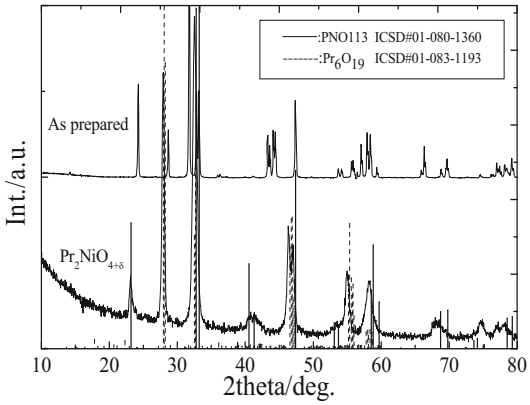

Fig.7 XRD patterns of $Pr_2NiO_{4+\delta}$ (1073 K, 1barO_2).It showed $Pr_2NiO_{4+\delta}$ was decomposed.

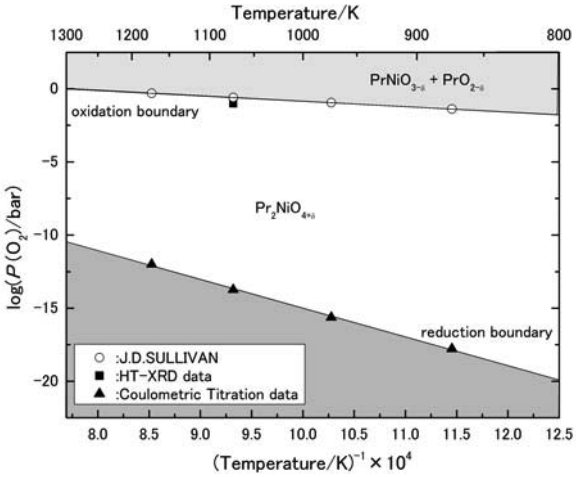

Fig.8. Stability field for $Pr_2NiO_{4+\delta}$, showing the $P(O_2)$-temperature dependence of the reduction and oxidatlon boundaries.

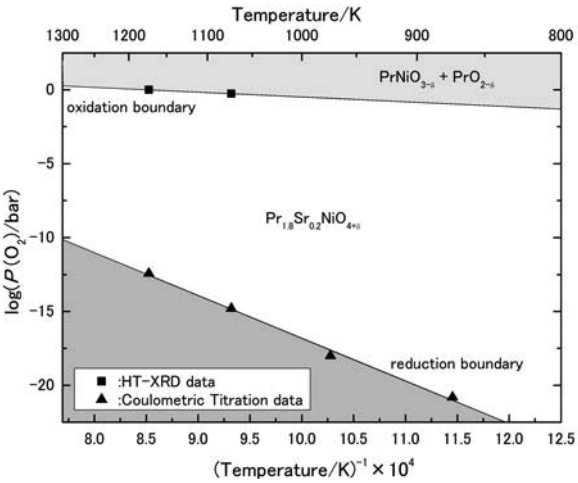

Fig.9. Stability field for $Pr_{1.8}Sr_{0.2}NiO_{4+\delta}$, showing the $P(O_2)$-temperature dependence of the reduction and oxidatlon boundaries.

3.3 *Electrode impedance*

Figure 8 shows typical complex impedance plots at 973 K. The obtained impedance plots are basically composed of two semicircles about high frequency and low frequency. From the complex impedance plot, we find three impedance components with the real part resistance R_{ohm}, R_i and R_E, as indicated figure. R_{ohm} is the bulk resistance of electrolyte. R_i is the contact resistance between the electrode/ electrolyte interface.

The electrode interfacial conductivity, σ_E, was described by the equations,

$$\sigma_E = \frac{1}{AR_E} \qquad (1)$$

where A and R_E are the apparent electrode area and the electrode resistance, respectively.

Figure 9 shows the calculated σ_E of a $Pr_{1.8}Sr_{0.2}NiO_{4+\delta}$ (PSNO20) electrode compared with $La_2NiO_{4+\delta}$(LN214) and $La_{0.6}Sr_{0.4}O_{3-\delta}$(LSC113)[5] from 873 K to 1073 K as a function of P_{O2}. PSNO20 electrode has higher interface conductivity than LN214 electrode. This is attributed to the fact that PSNO has more interstitial oxygen. Interstitial oxygen of $Pr_2NiO_{4+\delta}$(PNO) is more than PSNO20, so it indicates that $Pr_{2-x}Sr_xNiO_{4+\delta}$(PSNO) electrode(less Sr content than PSNO20) has potentiality for the comparable performance to the other high performance electrodes. It is important to clarify the right amount of Sr where PSNO shows high electrochemical performance and K_2NiF_4 structure can be stabilized.

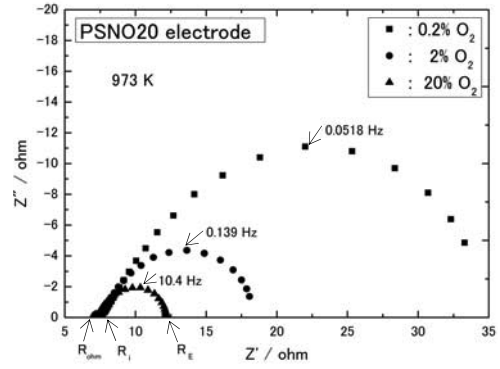

Fig.10. complex impedance plots for PSNO20 electrode at 973 K for different P_{O2}.

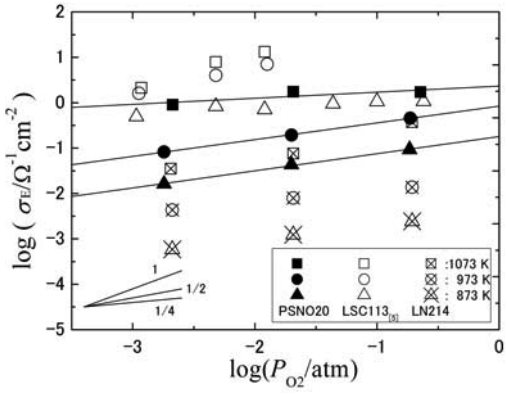

Fig.11. P_{O2} dependence of σ_E for O_2(g). Closed symbols show the data for PSNO20.

4. Concluding remarks

1. Oxygen nonstoichiometry of $Pr_{2-x}Sr_xNiO_{4+\delta}$ was measured. $Pr_{2-x}Sr_xNiO_{4+\delta}$ shows oxygen excess and oxygen deficiency depending on the Sr content, temperature and $P(O_2)$.

2. In the higher $P(O_2)$ region, $Pr_{2-x}Sr_xNiO_{4+\delta}$ (x=0,0.2) are decomposed $PrNiO_{3-\delta}$ and $PrO_{2-\delta}$. $Pr_{1.8}Sr_{0.2}NiO_{4+\delta}$ is more stable than $Pr_2NiO_{4+\delta}$ in the high $P(O_2)$ region. It is necessary to elucidate more accurate rigion considered Sr content, $P(O_2)$ and temperature.

3. PSNO20 electrode has higher interface conductivity than LN214 electrode. This is attributed to the fact that PSNO has more interstitial oxygen. It is important to clarify the right amount of Sr where PSNO shows high electrochemical performance and K_2NiF_4 structure can be stabilized.

References

[1] E. N. Naumovich, M. V. Patrakeev, V. V. Kharton, A. A. Yaremchenko, D. I. Longvinovich, F. M. B. Marques, *Solid State Sciences,* **7**, (2005) 1353-1362.

[2] V. V. Kharton, A. V. Kovalevsky, M. Avdeev, E. V. Tsipis, M. V. Patrakeev, A. A. Yaremchenko, E. N. Naumovich, J. R. Frade, *Chem. Mater,* **19**, (2007) 2027-2033.

[3] V. V. Vashook, I. I. Yushkevich, L. V. Kokhonovsky, L. V. Makhanovsky, L. V. Makhnach, S. P. Tolochko, I. F. Kononyuk, H. Ullmann, H. Altenburg, *Solid State Ionics* **119**, (1999) 23-30.

[4]M.Yashima, Makiko Enoki, Takahiro Wskita, Roushown Ali, Yoshitaka Matsushita, Fujio Izumi, and Tatsumi Ishihara, *J.Am.Chem.Soc.*, **130**,(2008)2762-2763

[5] P. Odier, Ch. Allanion, and J. M. Bassat, *J. Solid State Chem.,* **153**, (2000) 381-385

[6]A.V. Kovalevsky, V.V. Kharton, A.A. Yaremchenko, Y.V. Pivak, E.N. Naumovich, J.R. Frade, *J.Europ. Ceramic Soc.,* **27** (2007) 4269–4272

[7]T.Nakamura, Keiji Yashiro, Kasuhisa Sato, Junichiro Mizusaki, *Solid State Ionics*, **180**, (2009) 368-376

[8]J.D.Sullivan and D.J.Buttrey, *J. Solid State Chem.*, **94**, (1991) 3337-351

[9]T.Nakamura, Keiji Yashiro, Kasuhisa Sato, Junichiro Mizusaki, *J. Solid State Chem*., **182**, (2009) 1533-1537

[10]Tatsumi Ishihara, Kenichi Nakashima, Sachio Okada, Makiko Enoki, Hishige Matsumoto, *Solid State Ionics*, **179**,(2008)1367-1371

[11]C.Wagnar, *Prog. Solid State Chem*., **131** (1997) 150-159

[12]Vladimir Vashook, Jens Zosel, Ting-Lian Wen, Ulrich Guth, *Solid State Ionics*, **177**,(2006)1163-1171

[13]Kazuhiro Endo, Shigeru Yamaguchi, Kazuo Fueki and Takashi Mukaibo, *Bull. Chem. Soc. Jpn.*, **49**, (1976) 2379-2383

[2]K. Masuda, A. Kaimai, K. Kawamura, Y. Nigara, T. Kawada, J. Mizusaki, H.Yugami, and H. Arashi, in *Solid Oxide Fuel Cells V*, U. Stimming, S. C. Singhal,H. Tagawa, and W. Lehnert, Editors, PV 97-40, p. 473, The *Electrochemical Society Proceedings Series*, Pennington, NJ (1997)

Highly Laminated Electrospun ZnO Nanofibrous Film on Transparent Conducting Oxide for Photovoltaic Device

Jinsoo Kim[1], Sanghoon Yoon[2], Jung-Keun Yoo[2], Jongsoon Kim[1], Haegyeom Kim[1], Kisuk Kang[1,*]
[1]Department of Materials Science and Engineering, Seoul National University, Seoul 151-742, Republic of Korea
[2]Department of Materials Science and Engineering, KAIST, Daejeon 305-701, Republic of Korea
[*]e-mail: K. Kang, matlgen1@snu.ac.kr

ABSTRACT

Electrospinning technique is a template-catalyst-free method that can generate 1D nanostructure with the tunability and the potential for the mass production. This approach has been highlighted by the giving a direct pathways for electrical current, but the delamination of the electrospun film of inorganic has restrained the utilization, due to the thermal deformation during the calcination. In this study, we propose an electrical grounding method for the TCO and the electrospun nanowires to enhance the adhesion after the calcination, so we found the potential of the technique on the ZnO based DSSC.

1. Introduction

Dimensions of various nanomaterials have being tailored to modify the functionalities from zero-dimension to three-dimension [1-3]. Matrices with nanoparticles or nanosheets provide a great surface area, which is relative to the volume in macroscale, so the system is favorable for the high reaction rate. However, the structure consisted with the nanoparticles have numerous grain boundaries, which scatter the charge carriers, so the electrical performance can be reduced in this fashion. Otherwise, the one dimensional nanowire based matrix, for example as a carbon nanotube, induces the directional migration of the charge carriers, thus it is suitable as an electrode for many electrical applications that need a noble property.

To fabricate the one dimensional materials, some methodologies have been developed, such as a VLS technique [4], templating [5], and self-assembly [7], which are complicate and inefficient in the manner of productivity. Compared to the other method, an electrospinning technique is a powerful approach with a template-catalyst free strategy that can fabricate highly continuous 1D nanostructures with delicately tunable morphology, and it can be easily scaled up for mass productions [7-8]. In addition, many materials can be utilized through this technique not only the inorganic, but also the organic materials [9], even for the nanotube [10] and core-shell structure [11]. The gel solutions that contain the sources for the nanowires are injected from the charged orifice to the oppositely charged target with the parameters of potential difference and injection rate.

In case of general, the inorganic materials have better properties than the organic materials for the electrical applications, and it involves firing process to remove the solvent which is for the viscosity of the gel solutions. However, the as-spun nanowires have been shrunk and cracked with the calcination on the glass substrate due to the thermal deformation of the nanowires, so the films have been delaminated which cause the serious decreasing of the electrical property. Thus, a great deal of research has been carried out to obtain the electrospun films of inorganic without shrinkage after the heat treatment. Hot-pressing, sublayer applying [13], thickness controlling, and recollecting to the nanorod [14] have been reported about this issue, but these works were difficult to precisely control and not reproducible.

Therefore, we report the unique method to fabricate the highly laminated films without fractures on the transparent conducting oxide (TCO) with the electrospinning technique by grounding electrically. As the injection is progressed, the gel solution is electrostatically charged by the orifice, so the adhesion to the TCO which is oppositely charged can be improved. In this report, we applied the idea to the ZnO based dye-sensitized solar cell (DSSC) to confirm the potential. This straightforward approach is very simple and easy to set up for mass production comparing to the previously reported researches, and it can facilitate the various applications for the electrospinning technique based process.

2. Method

The gel solution for the electrospinning was prepared by vigorously mixing 0.6 g of zinc acetate for the source of the ZnO nanowire, 0.5 g of polyvinylpyrrolidone (PVP) for the viscous solution, 2 g of deionized water, and 1.45 g of ethanol for the solvent.

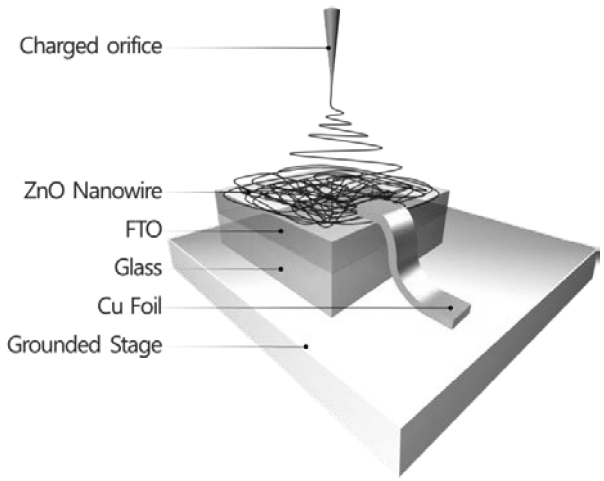

Fig. 1. Schematic Diagram represented the electrical grounding technique for the electrospinnig method.

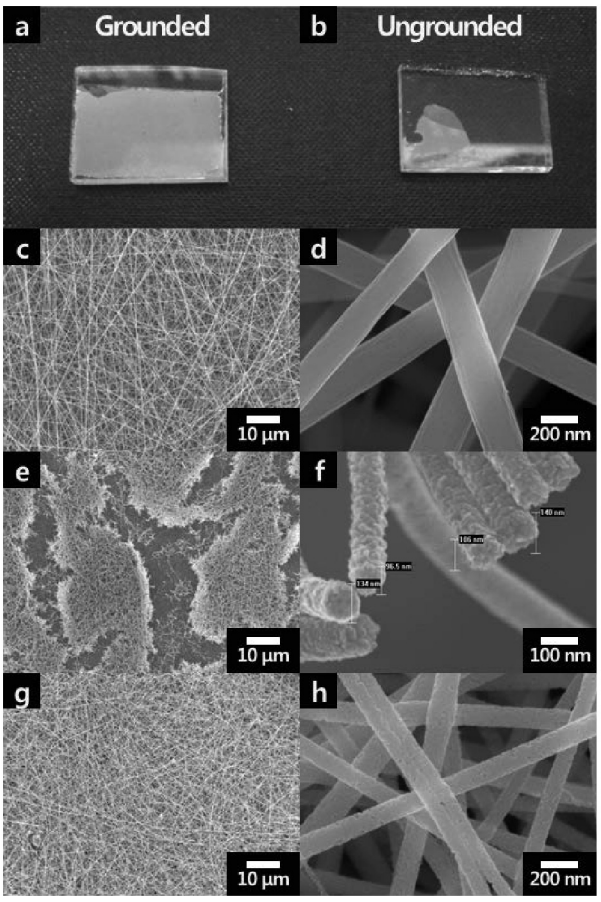

Fig. 2. Photographs showed the differences of the electrical grounded film (a) and the ungrounded film (b) for ZnO electrospinning on the FTO glass. In SEM images, the as-spun nanowires (c, d) showed smooth surface. The ungrounded nanowires (e, f) were fractured and delaminated into fragments, however the grounded nanowires (g, h) were highly laminated without defects.

0.5 ml of the solution was loaded to the syringe and injected as the conditions, which are 20 cm of distance to the target substrate, 15 V of operating voltage, and 1 μl/min of the injection rate in room temperature. Fluorine doped tin oxide (FTO) coated glass for the TCO substrate of DSSC was placed on the stage of the electrospinner, and the Cu foil was connected between the FTO glass and the stage for the electrical grounding as shown in Figure 1. The as-spun film on the FTO glass was heated to 500 °C for 30 minutes. After the heating step, the electrospun ZnO electrode was trimmed to 0.27 mm^2 and immersed into the ethanol solution which contains a 0.5 mM of N719 dye for 20 minutes to adsorb the sensitizer. The sample was rinsed with anhydrous ethanol to wash away the residual materials, and be sealed using the sealant which has a width of 1.5 mm, with the drilled counter electrode that was coated with a drop of diluted H_2PtCl_6 solution (2 mg in 1 ml ethanol) and cured for 30 minutes in 400 °C. The sealed cell was injected with a drop of electrolyte to the drilled hole, and be sealed immediately by soldering a piece of slide glass/sealant. Finally, the contact area for the connection

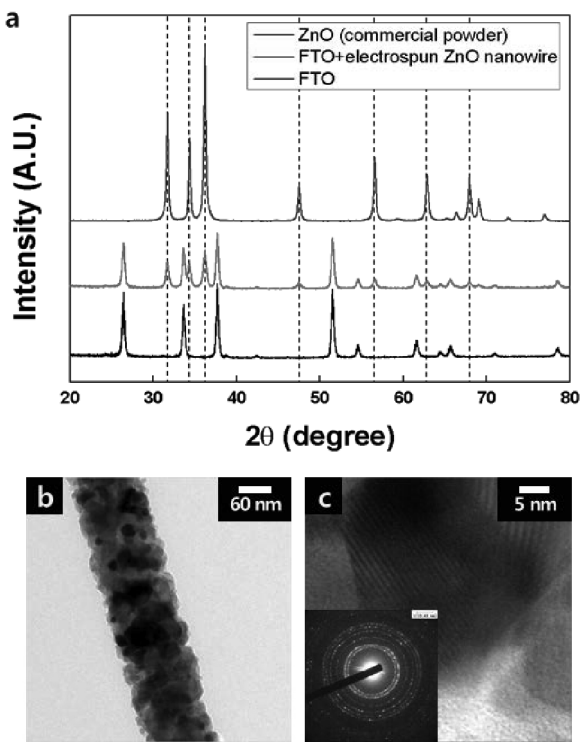

Fig. 3. XRD spectra (a) showed the electrospun ZnO nanowires after the calcination had a common phase of wurtzite on the dashed line. The electrospun nanowire had a polycrystalline with multi grains in a single wire (b, c).

to the photovoltaic source meter was painted with a silver paste. The photovoltaic measurement was carried out for AM 1.5 condition.

3. Results and Discussion

The photograph of Figure 2 (a, b) represent the electrically grounded sample and the ungrounded sample after the calcination, and the obtained films were quite different in terms of the adhesion on the FTO substrate. The film of the grounded sample was attached well on the substrate, unlike the ungrounded sample which was almost delaminated. The uniform distribution of diameter and the morphology of as-spun nanowires are shown in Figure 2 (c, d) without spherical beads which can be found in some rough conditions. Because the as-spun wires contained the polymeric binder, not only the ZnO source, so it showed smooth surfaces. However, the removal of the binder by heat treatment was essential to obtain the appropriate electrical property, so the shrinkage was occurred due to the difference of the thermal expansion/contraction between the electrospun nanowires and the FTO substrate, as Figure 2 (e) represented the topology after calcinations without electrically grounding. In Figure 2 (f), the cross-sections of fractured nanowires were observed which was seriously torn and delaminated from the substrate that could induce a drop of electrical current. After the calcination, the surfaces of the electrospun nanowires became rough slightly, which indicate the local

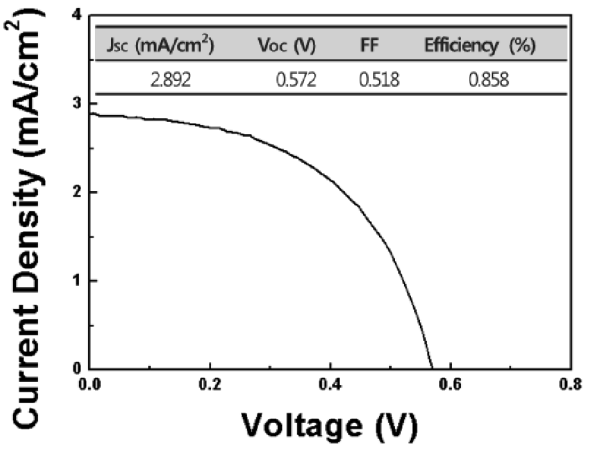

Fig. 4. The photovoltaic characteristics and the J-V curve of the DSSC using the electrospun ZnO nanowire film as an electrode.

crystallization from the as-spun precursor. The diameter of the calcinated nanowires were decreased about below 200 nm with the decomposition of polymeric binder, which lead to the peeling off of the film with the volumetric contraction. Figure 2 (g, h) shows the highly laminated morphology of the film with the electrical grounding, and any cracks or peeled fragments were not observed from the grounded sample. The diameters of this case were maintained almost same as the Figure 2 (e, f), and it is obvious that the adhesion between the electrically charged as-spun nanowires and the FTO substrate was dramatically improved by the grounding technique. In this way, it can be also applied to the organic materials for only the delaminating issue, not the fracture.

The measurement of X-ray diffraction is shown in Figure 3 (a), and it was investigated that the obtained film after the heat treatment had typical wurtzite phase of ZnO as the other literatures [15-16]. The peak intensity of ZnO was lower than that of FTO, so it can be explained as the film had a great portion of pores relative to the total film thickness. In Figure 3 (c, d) of transmission electron microscopic (TEM) image, the crystallinity of the electrospun ZnO nanowire can be identified, and it was represented for the polycrystalline phase from the images and the diffraction pattern as some grains were existed in the single nanowire. Thus, we can speculate the grounding method was effective for the combination of ZnO/FTO about the electrospinning based laminating issues, even the calcination was enough to obtain the preferential phase.

The photovoltaic measurement is shown in Figure 4. Despite of the solution for the peeling-off problem, the characteristic was not impressive, because the short circuit current density (J_{SC}) and the open circuit voltage (V_{OC}) were poor with the limitations of the dye loading and the surface area for the ZnO based 1D nanostructure [17-18]. Further works can be available for the optimization of the photovoltaic characteristics [19], and this work might be meaningful with the utilization of the electrical grounding technique, so we can suggest the other applications which are suitable with this method.

4. Concluding remarks

In conclusion, the ZnO electrospun nanowires after the calcination could be highly laminated without fractures and peeling off by the enhanced adhesion between the nanowire and the substrate through the electrical grounding technique. This work was very effective than the other related researches for the productivity. Many themes about the electrospinning technique for the inorganic/organic materials can be applied through these approaches, even the ZnO nanowire based DSSC was not fully optimized.

References

[1] Shipway, A.N., E. Katz, and I. Willner, *Nanoparticle arrays on surfaces for electronic, optical, and sensor applications.* ChemPhysChem, 2000. **1**(1): p. 18-52.
[2] Cui, Y., et al., *Nanowire nanosensors for highly sensitive and selective detection of biological and chemical species.* Science, 2001. **293**(5533): p. 1289-1292.
[3] Liu, Z., et al., *Synthesis, anion exchange, and delamination of Co-Al layered double hydroxide: Assembly of the exfoliated nanosheet/polyanion composite films and magneto-optical studies.* Journal of the American Chemical Society, 2006. **128**(14): p. 4872-4880.
[4] Yang, P., et al., *Controlled growth of ZnO nanowires and their optical properties.* Advanced Functional Materials, 2002. **12**(5): p. 323-331.
[5] Ding, J.X., et al., *Lasing in ZnS nanowires grown on anodic aluminum oxide templates.* Applied Physics Letters, 2004. **85**(12): p. 2361-2363.
[6] Thurn-Albrecht, T., et al., *Ultrahigh-density nanowire arrays grown in self-assembled diblock copolymer templates.* Science, 2000. **290**(5499): p. 2126-2129.
[7] Li, D. and Y. Xia, *Electrospinning of nanofibers: Reinventing the wheel?* Advanced Materials, 2004. **16**(14): p. 1151-1170.
[8] Greiner, A. and J.H. Wendorff, *Electrospinning: A fascinating method for the preparation of ultrathin fibers.* Angewandte Chemie - International Edition, 2007. **46**(30): p. 5670-5703.
[9] Lee, S.W., et al., *Periodic array of polyelectrolyte-gated organic transistors from electrospun poly(3-hexylthiophene) nanofibers.* Nano Letters, 2010. **10**(1): p. 347-351.
[10] Li, D. and Y. Xia, *Direct fabrication of composite and ceramic hollow nanofibers by electrospinning.* Nano Letters, 2004. **4**(5): p. 933-938.
[11] Sun, Z., et al., *Compound Core-Shell Polymer Nanofibers by Co-Electrospinning.* Advanced Materials, 2003. **15**(22): p. 1929-1932.
[12] Kim, I.D., et al., *Dye-sensitized solar cells using network structure of electrospun ZnO nanofiber mats.* Applied Physics Letters, 2007. **91**(16).
[13] Zhu, R., et al., *Improved adhesion of interconnected TiO_2 nanofiber network on conductive substrate and its*

application in polymer photovoltaic devices. Applied Physics Letters, 2008. **93**(1).
[14] Fujihara, K., et al., *Spray deposition of electrospun TiO_2 nanorods for dye-sensitized solar cell.* Nanotechnology, 2007. **18**(36).
[15] Zhang, W., et al., *Facile construction of nanofibrous ZnO photoelectrode for dye-sensitized solar cell applications.* Applied Physics Letters, 2009. **95**(4).
[16] Lotus, A.F., et al., *Effect of aluminum oxide doping on the structural, electrical, and optical properties of zinc oxide (AOZO) nanofibers synthesized by electrospinning.* Materials Science and Engineering B: Solid-State Materials for Advanced Technology, 2009. **166**(1): p. 61-66.
[17] Guillén, E., et al., *Photovoltaic performance of nanostructured zinc oxide sensitised with xanthene dyes.* Journal of Photochemistry and Photobiology A: Chemistry, 2008. **200**(2-3): p. 364-370.
[18] Chou, T.P., et al., *Hierarchically structured ZnO film for dye-sensitized solar cells with enhanced energy conversion efficiency.* Advanced Materials, 2007. **19**(18): p. 2588-2592.
[19] Zhang, Q., et al., *ZnO nanostructures for dye-sensitized solar cells.* Advanced Materials, 2009. **21**(41): p. 4087-4108.